Volume 1

Asphalt Pavements

Editor: Richard Y. Kim

CRC Press
Taylor & Francis Group
A BALKEMA BOOK

ASPHALT PAVEMENTS

This page intentionally left blank

PROCEEDINGS OF THE INTERNATIONAL CONFERENCE ON ASPHALT PAVEMENTS
RALEIGH, NORTH CAROLINA, USA, 1–5 JUNE 2014

Asphalt Pavements

Editor

Y. Richard Kim

Distinguished University Professor
Department of Civil, Construction, and Environmental Engineering
North Carolina State University, Raleigh, NC, USA

VOLUME 1

CRC Press
Taylor & Francis Group
Boca Raton London New York Leiden

CRC Press is an imprint of the
Taylor & Francis Group, an **informa** business

A BALKEMA BOOK

CRC Press/Balkema is an imprint of the Taylor & Francis Group, an informa business

Typeset by V Publishing Solutions Pvt Ltd., Chennai, India
Printed and bound in the USA by Edwards Brothers Malloy, Lillington, NC

Published by: CRC Press/Balkema
P.O. Box 11320, 2301 EH Leiden, The Netherlands
e-mail: Pub.NL@taylorandfrancis.com
www.crcpress.com – www.taylorandfrancis.com

ISBN: 978-1-138-02693-3 (Set of two volumes Hbk)
ISBN: 978-1-138-02712-1 (Vol 1)
ISBN: 978-1-138-02713-8 (Vol 2)
ISBN: 978-1-315-73675-4 (eBook PDF)

Asphalt Pavements – Kim (Ed)
© 2014 Taylor & Francis Group, London, ISBN 978-1-138-02693-3

Table of contents

VOLUME 2

This page intentionally left blank

Asphalt Pavements – Kim (Ed)
© 2014 Taylor & Francis Group, London, ISBN 978-1-138-02693-3

Welcoming remarks

It is my great pleasure and honor to welcome you to the 12th ISAP Conference on Asphalt Pavements in Raleigh, North Carolina, USA. ISAP conferences have been the premier forum for asphalt engineers around the world to exchange their research and practice on asphalt materials and pavements. We received over 250 papers from 35 countries that resulted in 181 podium presentations, 29 poster presentations, and 19 student poster presentations. Four main themes of the 12th ISAP conference are design, materials, construction, and preservation, and I am pleased to introduce you to the four excellent plenary speakers to cover these topics.

This program book contains the daily program, abstracts, general information on the conference, maps, and other information that will help you enjoy the conference and surrounding areas. One of the approaches we have taken in this conference is to publish the conference proceedings in an online e-book by Talyor and Francis. You will be receiving instructions on how to access the e-book after the conference.

In addition to the technical depth and breadth this conference will provide, we have inserted a few fun events in the program. You will enjoy the welcoming reception and visit to the Hunt Library in the Centennial Campus of North Carolina State University. We hope that you enjoy North Carolina style barbeque on Monday evening at the Troxler Electronic Laboratory in Research Triangle Park. Tuesday evening's time with the North Carolina Symphony at the magnificent Meymandi Hall will give you some relaxation from the busy conference schedule. Finally the Wednesday evening banquet and special performance will leave you with a memory to cherish for years to come.

North Carolina is one of the most popular tourist destinations in the United States during summer time due to its beautiful beaches, mountains, and historic attractions. Raleigh, along with Durham and Chapel Hill, is one of the three vertices of the Research Triangle Park, which is one of the largest research parks in the world. This area has been consistently considered one of the best cities to live and one of the highest PhD per capita areas in the USA. We hope you will enjoy the LEED Silver-certified Raleigh Convention Center with stimulating design and enjoy our Southern style hospitality.

I would like to acknowledge and thank all of our sponsors, ISAP board members, conference committee members, and volunteers from North Carolina Department of Transportation and North Carolina State University. I look forward to a very successful ISAP conference in Raleigh, North Carolina!

Best Regards,
Y. Richard Kim, Ph.D., P.E., F.ASCE
Distinguished University Professor, NC State University
Chair of the 12th ISAP Conference

This page intentionally left blank

Asphalt Pavements – Kim (Ed)
© 2014 Taylor & Francis Group, London, ISBN 978-1-138-02693-3

ISAP 2014 committees

EXECUTIVE COMMITTEE

Y. Richard Kim	*North Carolina State University, USA*
Michael Holder	*North Carolina Department of Transportation, USA*
Ellis Powell	*Carolina Asphalt Pavement Association, USA*

INTERNATIONAL ADVISORY COMMITTEE

Hervé di Benedetto	*ENTPE, University of Lyon, France*
Audrey Copeland	*National Asphalt Pavement Association, USA*
John A. D'Angelo	*D'Angelo Consulting LLC., USA*
Frank Fee	*Frank Fee LLC., USA*
John Harvey	*University of California-Davis, USA*
Shin-Che Huang	*Western Research Institute, USA*
Gerald Huber	*Heritage Research Group, USA*
Y. Richard Kim	*North Carolina State University, USA*
Manfred N. Partl	*Swiss Federal Laboratories for Material Science and Technology, Switzerland*
Jean-Pascal Planche	*Western Research Institute, USA*
A. Tom Scarpas	*Delft University of Technology, The Netherlands*
Shigeru Shimeno	*Nippon Expressway Research Institute Co. Ltd., Japan*
Saied Solomons	*SABITA, South Africa*
Gabriele Tebaldi	*University of Parma, Italy*
Koji Yokota	*Japan Road Contractors Association, Japan*

PROGRAMS COMMITTEE

John A. D'Angelo	*D'Angelo Consulting LLC., USA*
Y. Richard Kim	*North Carolina State University, USA*
David E. Newcomb	*Texas Transportation Institute, USA*
Reynaldo Roque	*University of Florida, USA*

SCIENTIFIC COMMITTEE

Jo Sias Daniel	*University of New Hampshire, USA*
Amy Epps Martin	*Texas A&M University, USA*
Gordon D. Airey	*University of Nottingham, United Kingdom*
Amit Bhasin	*The University of Texas at Austin, USA*
Eshan V. Dave	*University of Minnesota-Duluth, USA*
Elham H. Fini	*North Carolina A&T University, USA*
Daba S. Gedafa	*University of North Dakota, USA*
Nelson Gibson	*Federal Highway Administration, USA*
Cassie Hintz	*North Carolina State University, USA*
Nicole Kringos	*KTH Royal Institute of Technology, Sweden*
M. Emin Kutay	*Michigan State University, USA*
Eyal Levenberg	*Technion-Israel Institute of Technology, Israel*
Maryam S. Sakhaeifar	*Texas A&M University, USA*
B. Shane Underwood	*Arizona State University, USA*
Zhanping You	*Michigan Technological University, USA*
Adam Zofka	*Road and Bridge Research Institute, Poland*

LOCAL ARRANGEMENT COMMITTEE

Jennifer Bradenburg	*North Carolina Department of Transportation, USA*
Tammy Jeffries	*Greater Raleigh Convention and Visitor's Bureau, USA*
Rhonda Johnson	*North Carolina Department of Transportation, USA*
Ali Regimand	*InstroTek Inc., USA*
Erin Tart	*Raleigh Convention Center, USA*
Akhtarhusein A. Tayebali	*North Carolina State University, USA*
Billy Troxler	*Troxler Electronic Laboratories Inc., USA*

Asphalt Pavements – Kim (Ed)
© 2014 Taylor & Francis Group, London, ISBN 978-1-138-02693-3

Sponsors

Diamond sponsors

Gold sponsors

Silver sponsors

Bronze sponsors

Copper sponsors

Other sponsors

This page intentionally left blank

Plenary papers

Plenary session on design

This page intentionally left blank

Asphalt Pavements – Kim (Ed)
© 2014 Taylor & Francis Group, London, ISBN 978-1-138-02693-3

M-E flexible pavement design: Issues and challenges

Marshall R. Thompson
Civil Engineering, University of Illinois at Urbana-Champaign, Urbana, IL, USA

ABSTRACT: M-E flexible pavement design procedures have evolved since the late 50's and early 60's. In the analyses of the AASHO Road Test data it was demonstrated that pavement response (surface deflection) was a good indicator of pavement performance (equally as good as the Structural Number)!! Significant advances have been achieved in the last 50+ years. Current procedures and developments for materials characterization, structural modeling, distress transfer functions, and other issues are considered in the presentation. Emphases are placed on those concepts/approaches that support the development of readily useable/implementable flexible pavement design procedures.

Keywords: Mechanistic-empirical design, flexible pavements

1 INTRODUCTION

The SHELL Pavement Design Manual was presented at the 4th International Conference on Structural Design of Asphalt Pavements [1] and was published by Shell in 1978 [2]. USA interest (AASHTO) in M-E design initiated in the md-1980s. Other agencies and groups have also been engaged in developing M-E pavement design procedures. The development/evolution of the current AASHTO procedure [3] is presented in the following sections.

"Mechanistic-Empirical Design Procedures" is the title of Part IV of the 1986 AASHTO Guide [4]. The Introduction (Section 1.1) of Part IV, states:

> For purposes of this Guide, the use of analytical methods refers to the numerical capability to calculate the stress, strain, or deflection in a multi-layered system, such as a pavement, when subjected to external loads, or the effects of temperature or moisture. Mechanistic methods or procedures will refer to the ability to translate the analytical calculations of pavement response to performance. Performance, for the majority of procedures used, refers to physical distress such as cracking or rutting.
>
> However, researchers recognize that pavement performance will likely be influenced by a number of factors which will not be precisely modeled by mechanistic methods. It is, therefore, necessary to calibrate the models with the observations of performance, i.e. empirical correlations. Thus, the procedure is referred to in the Guide as a mechanistic-empirical design procedure.

Activities associated with the development of the revised "AASHTO Guide for the Design of Pavement Structures" [4] prompted the AASHTO Joint Task Force on Pavements (JTFOP) to recommend that research should be initiated immediately with the objective of developing mechanistic pavement analysis and design procedures suitable for use in future versions of the AASHTO Guide. NCHRP Project 1-26 (Calibrated Mechanistic Structural Analysis Procedures for Pavements/J. L. Brown—Texas DOT—Panel Chairman)) was the first NCHRP Project to be sponsored. The M-E principles and concepts stated in the 86 AASHTO Guide were included in the NCHRP Project 1-26 Project Statement.

The University of Illinois cooperated with the Asphalt Institute and the Concrete Technology Laboratories in the conduct of NCHRP 1-26. It was not the purpose of NCHRP Project 1-26

to devote significant effort to develop new technology, but rather to assess, evaluate, and apply available M-E technology. Thus, the proposed processes/procedures were based on the Best Demonstrated Available Technology (BDAT). NCHRP Project 1-26 was completed in December, 1992 and comprehensive reports [5,6,7] were prepared summarizing the study.

2 M-E DESIGN CONCEPTS

Figure 1 illustrates the general concepts of a M-E model as presented in NCHRP 1-26 [7]. The pavement design process is complex. The major components of the M-E procedure are: INPUTS, STRUCTURAL MODELS, TRANSFER FUNCTIONS, and RELIABILITY. These components were comprehensively discussed in the NCHRP 1-26 reports. Three of the most significant components are MATERIAL CHARACTERIZATION, STRUCTURAL MODELS and TRANSFER FUNCTIONS.

Calculated pavement structural responses are for "given time," "given climate," "given pavement structure," "given material properties," and "given loading" inputs. Pavement responses change as these inputs vary throughout the pavement service life. Pavement performance is a long term consideration and mechanistic analysis and design procedures must account for the effect of the varying time-related inputs to the STRUCTURAL MODEL.

3 STRUCTURAL MODELS

A major task in Phase 1 of NCHRP 1-26 [5,6] was the review/evaluation of available mechanistic analysis procedures. It was concluded that the available flexible pavement structural models and computer codes for mechanistic analysis are adequate for supporting the development and initiating implementation of M-E thickness design procedures. Stress dependent finite element programs (like ILLI-PAVE, MICH-PAVE, and Texas ILLI-PAVE) and elastic layer computer programs (like BISAR, WESLEA, JULEA, CHEVRON, ELSYM 5, CIRCLY) were recommended for flexible pavements. The finite element programs are more versatile and can accommodate stress dependent moduli properties (stress-hardening for

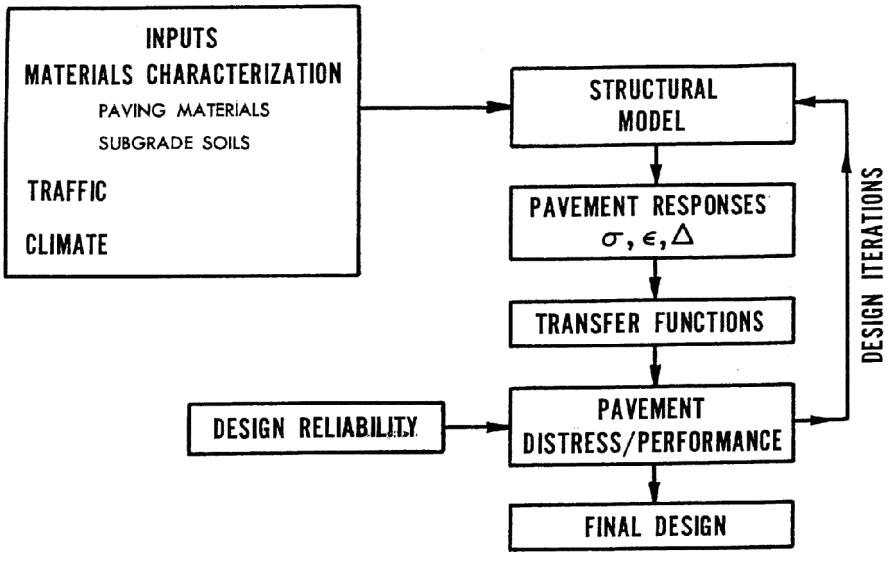

Figure 1. M-E flow chart.

granular materials; stress-softening for fine-grained soils) and also can incorporate failure criteria (such as the Mohr-Coulomb model in ILLI-PAVE).

4 TRANSFER FUNCTIONS

Transfer functions (distress models) relate the pavement responses determined from mechanistic models to pavement performance as measured by the type and severity of distress (rutting—cracking—roughness—etc.). Transfer functions were extensively reviewed in NCHRP 1-26. Modes of distress such as the fatigue and permanent deformation of paving materials and subgrade soils can be characterized from extensive testing of specimens under controlled laboratory conditions. The effects of such factors as stress level, frequency of load repetitions, rest periods, mixture variables, moisture content/density factors, etc. can be readily considered in laboratory-based studies.

The most common flexible pavement TRANSFER FUNCTIONS are a) Asphalt Concrete (AC) flexural strain—fatigue life algorithms, b) subgrade vertical strain—pavement life relations (for a given level of pavement rutting), c) permissible subgrade stress ratios [subgrade stress/subgrade strength] for various ESAL levels, and d) surface deflection—pavement life relations (surface deflection is a reliable indicator of AC flexural strain, subgrade vertical strain, and subgrade stress ratio).

Other flexible pavement distress phenomenon like AC block cracking and AC thermal cracking are more complex and are generally studied/evaluated from actual field performance data. In the field, the significant influencing factors can not be readily controlled/measured as for laboratory-based conditions. Thus, it is more difficult to develop accurate/refined TRANSFER FUNCTIONS for these distress modes.

The NCHRP 1-26 study concluded transfer functions are **weak links** in the M-E design approach. Extensive field calibration and verification are required to establish reliable distress prediction models. The NCHRP 1-26 study indicated:

- Useable flexible pavement transfer functions (distress models) are available for AC fatigue and subgrade rutting.
- The transfer functions for AC and granular material rutting are marginal.
- AC rutting is best considered by material selection and mixture design procedures and practices. (NOTE: The SUPERPAVE Level I Mixture Design procedure is a good example of this approach).
- Granular material rutting considerations can be accommodated by establishing "minimum" AC surface thickness requirements for given classes (based on shear strength and moisture sensitivity) of granular base/subbase materials.

5 NCHRP-1-26/PAVEMENT DESIGN

In NCHRP 1-26 working versions of M-E design processes and procedures were proposed for flexible pavements (Conventional Flexible Pavements, FULL-DEPTH AC pavements, High Strength-Stabilized-Base Pavements). The proposed procedures relate pavement responses (stresses, strains, and deflections) to the development of specific pavement distresses. As opposed to running a PC program, the responses can be predicted from pavement response prediction algorithms [9,10,11] to accomplish routine pavement designs. The pavement response algorithms were developed from comprehensive ILLI-PAVE data bases.

NCHRP 1-26 calibration activities were minimal due to the lack of adequate data. As an alternative, the concept of "Design Confirmation" was suggested. In this approach, the M-E procedure is utilized to explain pavement performance "SUCCESSES" and "FAILURES." (NOTE: Care should be taken to ensure that undue weighting is not given to "long term survivor" sections and inadequate attention provided to "early life" failures.) Modifications and adjustments are made in the M-E procedure to reconcile identified discrepancies.

Confidence and improved accuracy/reliability are thus developed in the M-E procedure. The design confirmation approach can be employed as a "check procedure" for the SHA's current pavement design procedure. In most cases, additional information and data (beyond that required for the current SHA procedure) will be required. Frequently, the pavement FAILURES associated with a section designed by the routine SHA procedure can be explained by M-E analysis and design concepts/procedures.

NCHRP 1-26 emphasized that M-E pavement design is very important, but it is only a segment of a larger scenario. A M-E design process can not realistically adequately address all pertinent factors and issues associated with or related to load responses, distress development, and ultimate pavement system performance. Thickness related factors are most readily addressed by M-E pavement design and that was the emphasis of NCHRP 1-26. AC fatigue and pavement rutting were the distresses that were considered. Some other significant and important factors are material selection practices and material specifications, construction policies and specifications, quality control/quality assurance procedures, maintenance and rehabilitation practices.

6 NCHRP 1-37A

A follow-up project (NCHRP 1-37A—Development of the 2002 Guide for the Design of New and Rehabilitated Pavement Structures: Phase II) was initiated in February, 1998 with ARA, Inc.—Eres Consultants Division. The Flexible Pavement Team was led by Dr. Matt Witczak (University of Maryland/Arizona State University). The following excerpts from "The Manual of Practice ([12] present the evolution and development of the MEPDG (Mechanistic-Empirical Pavement Design Guide).

> From the early 1960s through 1993, all versions of the American Association for State Highway and Transportation Officials (AASHTO) Guide for Design of Pavement Structures were based on limited empirical performance equations developed at the AASHO Road Test in the late 1950s. The need for and benefits of a mechanistically based pavement design procedure were recognized when the 1986 AASHTO Guide for Design of Pavement Structures was adopted. To meet that need, the AASHTO Joint Task Force on Pavements, in cooperation with the National Cooperative Highway Research Program (NCHRP) and the Federal Highway Administration (FHWA), sponsored the development of an M-E pavement design procedure under NCHRP Project 1-37A.
>
> A key goal of NCHRP Project 1-37 A—Development of the 2002 Guide for Design of New and Rehabilitated Pavement Structures: Phase II—was the development of a design guide that utilized existing mechanistic-based models and data reflecting the current state-of-the-art in pavement design. This guide was to address all new (including lane reconstruction) and rehabilitation design issues, and provide an equitable design basis for all pavement types.
>
> The Mechanistic-Empirical Pavement Design Guide (MEPDG), as it has now become known, was completed in 2004 and released to the public for review and evaluation. A formal review of the products from NCHRP Project 1-37 A was conducted by the NCHRP under Project 1-40A. 'This review has resulted in a number of improvements, many of which have been incorporated into the MEPDG under NCHRP Project 1-40D. Project 1-40D has resulted in Version 1.0 of the MEPDG software and an updated design guide document.
>
> Version 1.0 of the software was submitted in April 2007 to the NCHRP, FHWA, and AASHTO for further consideration as an AASHTO provisional standard and currently efforts are underway on Version 2.0 of the software. Simultaneously, a group of state agencies, termed lead states, was formed to share knowledge regarding the MEPDG and to expedite its implementation. The lead states and other interested agencies have already begun implementation activities in terms of staff

training, collection of input data (materials library, traffic library, etc.), acquiring of test equipment, and setting up field sections for local calibration.

The NCHRP 1-37A project was much more comprehensive and broad-based than NCHRP 1-26 and considered the development of the following distresses: HMA alligator cracking, HMA longitudinal cracking, HMA transverse cracking, and pavement rutting. A considerable emphasis was placed on predicting pavement IRI (International Roughness Index). An important feature of the MEPDG is that reliability estimates are provided for the distress models and IRI.

The elastic layer program (JULEA—Jacob Uzan Linear Elastic Analysis) is the flexible pavement structural model in the current version of the MEPDG. In the initial versions of the MEPDG, a 2-D finite element program was included. However, the program was not used in the calibration studies and it is not available for use in the current software. AASHTO initially issued the MEPDG as "DARWIN-ME." The most recent version of the MEPDG [3] was issued as "AASHTOWare Pavement ME Design" in 2013. The software is periodically modified as it is utilized.

Comprehensive reports on many topics/issues were prepared by the Flexible Pavements Team during the conduct of NCHRP 1-37A. The major findings and recommendations were presented in the March 2004—NCHRP 1-37A Final Report (Part 1. Introduction/Part 2. Design Inputs/Part 3. Design Analysis/Part 4. Low Volume Roads).

7 NCHRP 1-37A CALIBRATION

GLOBAL CALIBRATIONS for pavement distress were developed in the NCHRP 1-37A project. The calibration results [as presented in Ref.12] for fatigue, rutting, and IRI are shown in Figures 2–4. The statistical summary data shown in the figures (R^2, Se, Sy, Se/Sy) indicate the difficulty in establishing accurate/precise transfer functions on a large scale.

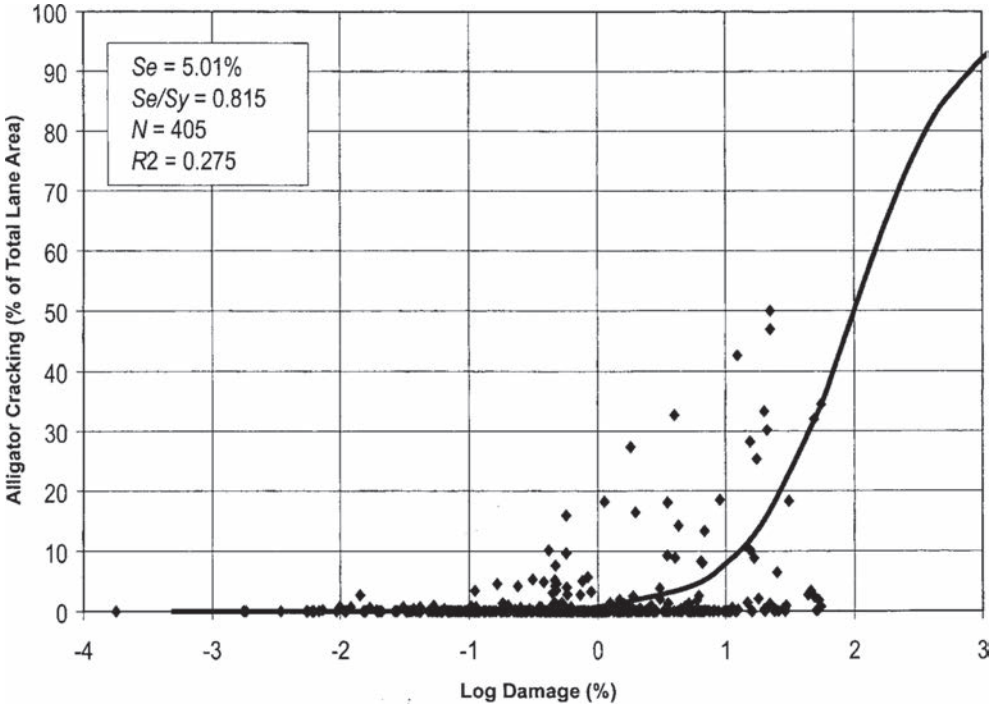

Figure 2. Alligator cracking calibration.

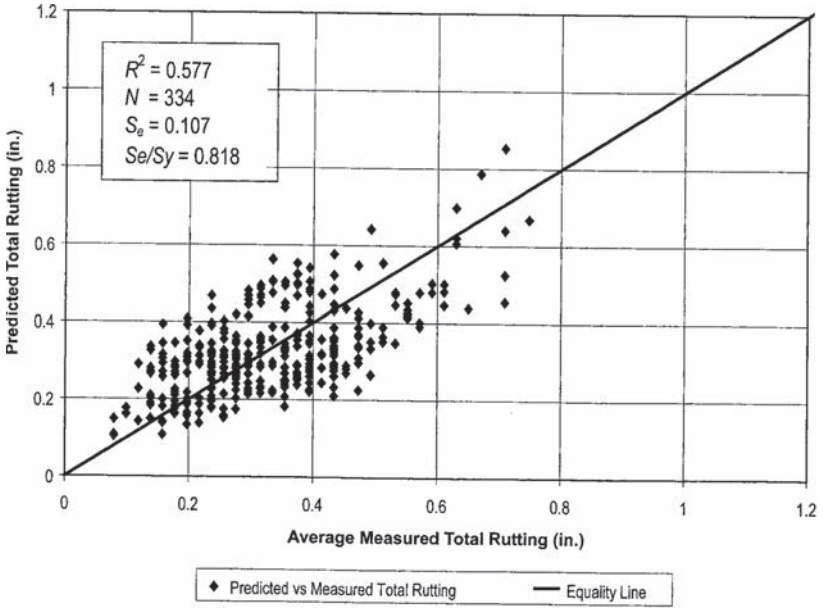

Figure 3. Rutting calibration.

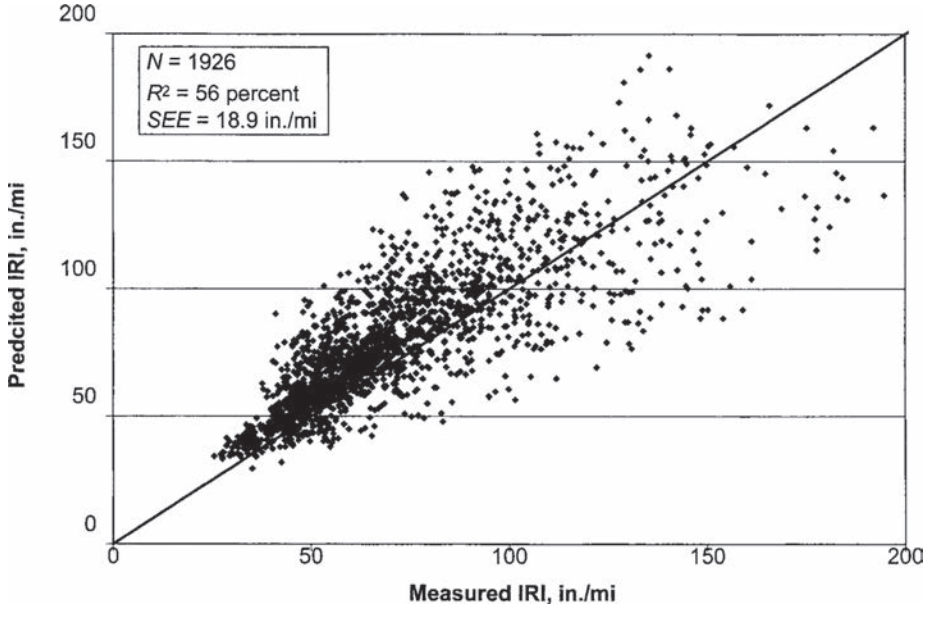

Figure 4. IRI calibration.

AASHTOWare [3] has indicated:

> "AASHTO encourages each licensing agency to calibrate and validate using local materials."

Many agencies have conducted calibration studies and established "typical" input values for routine pavement design. The distress prediction models are "tweeked" by adjusting the model β factors to achieve better model statistics.

8 EXISTING TECHNOLOGY

It is important to note that both NCHRP 1-26 and NCHRP 1-37A were to utilize "currently available technology."

- It was not the purpose of NCHRP Project 1-26 to devote significant effort to develop new technology, but rather to assess, evaluate, and apply available M-E technology.
- A key goal of NCHRP Project 1-37A was the development of a design guide that utilized existing mechanistic-based models and data reflecting the current state-of-the-art in pavement design.

As implementation issues emerge and new technology is developed, there are ongoing efforts to incorporate the developments into AASHTOWare Pavement ME Design.

9 ISSUE AND CHALLENGES

M-E flexible pavement design has made significant progress since the late 50's and early 60's. There are many examples of successful utilization of M-E procedures by various US and international entities. However, as noted in previous sections of this paper, there are still issues and challenges to be addressed that are common to many of the procedures.

Several important (per the author's opinion) issues and challenges are noted below.

- Stress dependent moduli characterization of soils and granular materials.
- Stress dependent finite element models that can accommodate stress dependent soil/material moduli and failure criteria should be further considered for implementation.
- Transfer functions (HMA fatigue/HMA fatigue endurance limit, HMA rutting, granular material and subgrade soil rutting).

Progress continues in addressing these issues and challenges. The resources/ability to develop/provide good inputs, ease of use/complexity, implementation potential, ability to accommodate new technology/developments (particularly new materials and pavement loading conditions) are some key factors that should be considered as M-E flexible pavement design procedures continue to evolve and improve.

REFERENCES

[1] A.I.M. Claessen, J.M. Edwards, J.M. Sommer and P. Uge. Asphalt Pavement Design—The Shell Method, Proceedings 4th International Conference on Structural design of Asphalt Pavements. University of Michigan, Vol. 1, 1977.

[2] Shell Pavement Design Manual: Shell International Petroleum Company Limited, London 1978.

[3] AASHTOWare Pavement ME Design, American Association of State Highway and Transportation Officials, Washington, DC, 2013.

[4] Guide for the Design of Pavement Structures, American Association of State Highway And Transportation Officials (First version, 1986; Second version, 1993).

[5] Calibrated Mechanistic Structural Analysis Procedure for Pavement, Volume I—Final Report, Phase 1—NCHRP Project 1-26, University of Illinois @ Urbana-Champaign/Construction Technology Laboratories/Asphalt Institute, National Cooperative Highway Research Program, Transportation Research Board, March, 1990.

[6] Calibrated Mechanistic Structural Analysis Procedures for Pavements, Vol. II—APPENDICES, Phase 1—NCHRP Project 1-26, University of Illinois @ Urbana-Champaign/Construction Technology Laboratories (A Division of the Portland Cement Association)/Asphalt Institute, National Cooperative Highway Research Program, Transportation Research Board, March, 1990.

[7] Calibrated Mechanistic Structural Analysis Procedure for Pavements, Volume I—Final Report, Phase 2—NCHRP Project 1-26, University of Illinois @ Urbana-Champaign/Construction Technology Laboratories (A Division of the Portland Cement Association)/Asphalt Institute, National Cooperative Highway Research Program, Transportation Research Board, December, 1992.

[8] Calibrated Mechanistic Structural Analysis Procedures for Pavements, Vol. II—APPENDICES, Phase 2—NCHRP Project 1-26, University of Illinois @ Urbana-Champaign/Construction Technology Laboratories (A Division of the Portland Cement Association)/ Asphalt Institute, National Cooperative Highway Research Program, Transportation Research Board, December, 1992.
[9] Mechanistic Pavement Design—Supplement to Section 7 of the Illinois Department of Transportation Design Manual, Illinois DOT, Springfield, IL, August, 1989.
[10] Conventional Flexible Pavement Design for Local Agencies, Bureau of Local Roads and Streets, Illinois Department of Transportation, Springfield, IL, August, 1995.
[11] Full-Depth Bituminous Concrete Pavement Design for Local Agencies, Bureau of Local Roads and Streets, Illinois Department of Transportation, Springfield, IL, August, 1995.
[12] Mechanistic-Empirical Pavement Design Guide—A Manual of Practice, American Association of State Highway and Transportation Officials, July, 2008.

Plenary session on materials

This page intentionally left blank

Asphalt Pavements – Kim (Ed)

Insights into binder chemistry, microstructure, properties relationships—usage in the real world

Jean-Pascal Planche
Western Research Institute, Laramie, WY, USA

ABSTRACT: Asphalts/bitumens have been extensively used for years in road paving, making them perceived as commodity materials by most road stakeholders. However, bitumen production has changed significantly over the past two decades, following the impact of oil recovery from bituminous/tar sand and oil shales. Refining processes have adapted to this new context as well as to changes in fuel demand. This evolving context not only has made asphalt/bitumen a specialty product for oil companies but an even more complex material with chemical composition and properties more dependent on the crude oil source and process. Simultaneously, worldwide economic crises and environmental awareness have shown the need for more durable pavements and increased recycling of old pavements, promoting the use of modified binders, long lasting roads concepts, Warm Mix Asphalts, Reclaimed Asphalt Pavement recycling and their combinations. Consequently needs have been created for R&D efforts and more engineered bituminous binders meeting Life Cycle Cost Assessment constraints. New sophisticated analytical tools, rheological measurements and concepts are emerging that will certainly impact binder selection and modification.

This paper gives examples and trends to help understanding the relationships between binder chemical composition, microstructure and properties and using this understanding in the binder selection or formulation. This challenge has stakes of the utmost importance in the new economic and environmental context.

Keywords: Asphalt, composition, microstructure, properties, relationships

1 INTRODUCTION

Asphalts/bitumens (terms used interchangeably in this paper) have been extensively used for years in road paving, so much that they are part of the scenery and are perceived as standard engineering materials by the road users and even by most of the stakeholders. But are they?

Bitumen production has changed significantly over the past two decades. Crude oil availability has gone towards heavier, higher sulfur crudes, ultimately to residues from bitumen/tar sands. Meanwhile, economics and demand for lighter petroleum products have driven the refining industry to modify refinery processes and install cokers, notably in North America, which can quasi-eliminate bitumen production. This complex evolving context has made bitumen a specialty product as opposed to a commodity product from an oil company marketing and strategy standpoint. From a technical standpoint the impact is also significant, since asphalt is a very complex material with chemical composition and properties highly dependent on the crude oil origin and refinery process.

Simultaneously, worldwide economic crises and environmental awareness have shown the need for more durable pavements and recycling of old pavements. This evolving context has impacted regulations and asphalt materials application techniques tremendously. Although materials specifications differ a lot from one country to another, there is a common trend in developed countries to move towards Performance Related Specifications (PRS). This move is more or less advanced whether in the US or in Europe, for example, but it exists for both

binders and mixes. Implementation of durable pavements has promoted the use of modified binders [1, 2] and new concepts for long lasting roads, whereas the search for more sustainable and economic application techniques has favored the use of Warm Mix Asphalt (WMA) technologies, Reclaimed Asphalt Pavement (RAP) recycling and combinations of all.

As a result of these context changes, needs have been created for research and development efforts to develop more relevant characterization methods and more engineered bituminous binders to meet life cycle cost assessment constraints.

For the most part, binder engineering has been trial and error, but new sophisticated analytical tools will certainly have an impact on binder selection and modification. This paper gives some examples of those evolutions in binder characterization and the main insights to take away from them in the understanding of binder behavior, particularly the relationships between asphalt composition/microstructure/physical properties.

2 ISSUES WITH ASPHALT CHARACTERIZATION

Regardless of the precision of a standard and application of best practices, difficulties inherent to asphalt binders tend to pop up when trying to characterize them.

The bitumen composition and structure are generally assumed to follow the model of a colloidal suspension of asphaltenes in a maltene matrix [3]. Although widely used, this model contains a few inherent issues: it describes a generic bitumen composition based on solubility properties which do not consider molecular weight of species and their possible interactions and/or associations.

Works by LCPC now IFFSTAR, the Highway Central Laboratory of the France Road Administration, on high concentration and fast Gel Permeation Chromatography showed in the late 80's how important these interactions were, and how they could increase with aging [4]. Works by others showed that asphaltenes were not such high molecular weight molecules but were susceptible to self association in clusters behaving as higher molecular weight materials [5].

Oxidative aging is another important parameter affecting all bitumen chemical and mechanical characteristics. It occurs during mixing with aggregates in the plant, continues during the asphalt pavement service life, and varies with pavement porosity and depth. Although studied for a long time [6], both reaction mechanisms and kinetics are still largely unknown and have prevented finding effective solutions to increase pavement service life.

Another issue with binder structure is its temperature dependency resulting from the chemical types present and from the strengths of the intermolecular interactions in the bitumen. The interactions can be Van der Waals forces, aromatic pi stacking, hydrogen and ionic bonds. Major contributors to the temperature dependency are paraffinic waxes which are naturally present in some bitumen. They have an impact on bitumen morphology or microstructure as well as on mechanical properties.

Temperature dependency makes bitumen morphology tricky to observe and to interpret.

Key questions are: at which temperature is the sample examined correlatively to the temperature at which it is tested, is the observed area an average or is it local? Risks of artifacts are enormous: many asphaltene observations in the past were in fact waxes!

Obviously, binder mechanical properties are temperature dependant. Bitumen may be the most temperature susceptible engineering construction material as it changes from a glassy solid brittle material to a true flowing liquid in less than 80 ºC. Whereas, for decades practitioners have used empirical testing to evaluate and grade bitumen, like penetration and ring and ball, the advance of bitumen modification and changes in refining practices have led to looking more and more into more rational binder rheology.

Dynamic oscillatory Shear Rheology (DSR) was largely developed during the Strategic Highway Research Program (SHRP) and was a huge move towards PRS. Based on measurement of modulus and phase angle in the linear viscoelastic domain, it captures the time and temperature related responses of straight-run bitumens. However it misses some features of modified binder, particularly their response to non linear solicitation under repeated heavy load.

Current test methods tend to underestimate the effect of thermal history on the material response as well, although the real impact on asphalt performance has not been fully established yet. Binder thermal properties play an important role in steric and physical hardening which occur during storage of a bitumen sample at temperatures near the bitumen glass transition. This time-dependent hardening is an intrinsic property of materials. It is widely observed and accounted for in the polymer field, but vastly ignored in the bitumen field, although it does play a role in the low temperature fragility of bitumen and pavement thermal cracking.

3 ADVANCES IN BINDER CHARACTERIZATION AND STRUCTURE KNOWLEDGE

This brief panorama of the main issues affecting binder characterization may sound pessimistic; however, researchers from various institutions have made tremendous progress in recent years opening doors to a better understanding of bitumen composition and behavior. Here are some examples, not meant to be exhaustive.

3.1 *Composition*

- Bitumens can be separated into five chromatographic fractions and three asphaltene solubility subfractions with the automated SAR-AD (saturates, aromatics, resins-Asphaltene Determinator) separation. The fractions obtained provide correlations with stability, phase separation propensity, and degree of aging [7, 8].
- Crystallized fractions measured by Differential Scanning Calorimetry (DSC) can compete with asphaltenes and lead to phase separation, affecting bitumen mechanical properties [9, 10]. See Figure 1.

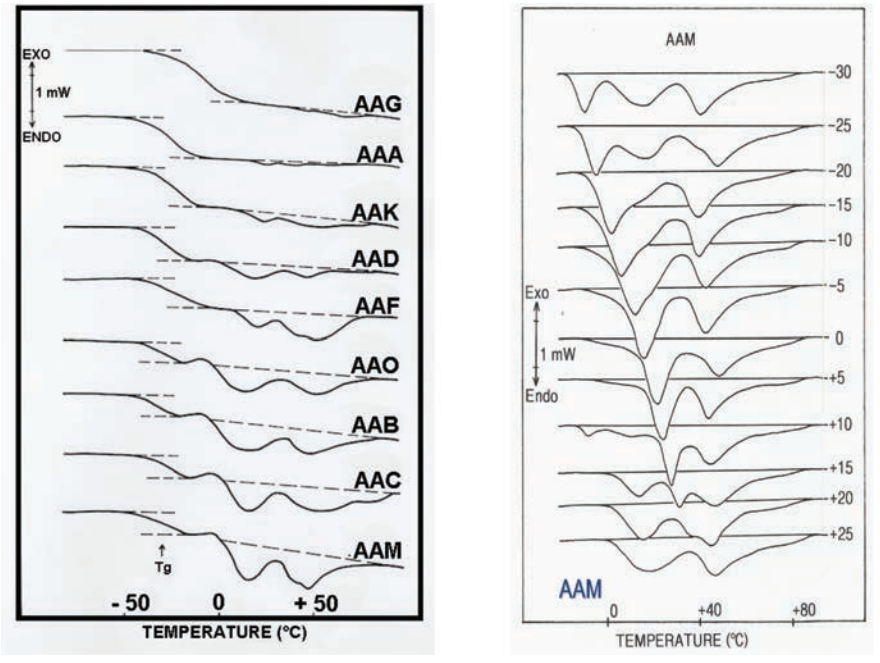

Figure 1. DSC measurement of the glass transition temperature and crystallized fraction for 9 SHRP core asphalts (left) and effect of 1 day isothermal conditioning (from −30 to +25C) on Waxy bitumen AAM thermal properties (right)—*Credit to Thermochimica Acta 324 (1998) 223−227.*

- 3D solubility parameter accounts for various interactions between the various bitumen molecules and helps to embrace solubility issues as a whole [11]. See Figure 2.

3.2 *Thermal properties*

- Bitumen thermal properties and history dependency as a function of conditioning temperature time can be assessed by Differential Scanning Calorimetry (DSC). This technique allows understanding the role of the crystallized fraction and the glass transition temperature in the binder mechanical properties [10].

3.3 *Morphology and microstructure*

- Crystallized fraction can be observed through optical microscopy techniques in phase contrast or dark field modes, upon cooling or heating [10]. See Figure 3. They stand out at the interface air-asphalt as a bee-like structure due to surface freezing as seen under Atomic Force Microscopy. See Figure 4 [12].

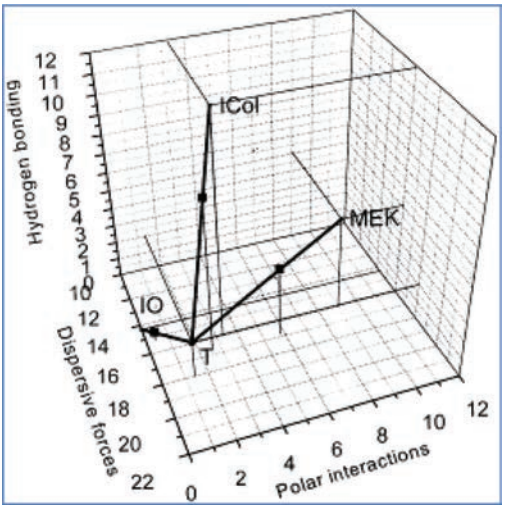

Figure 2. 3D Diagram of titration of venezuelan bitumen—black squares indicating precipitation points—*Credit To Fuel 79 (2000) 27–35.*

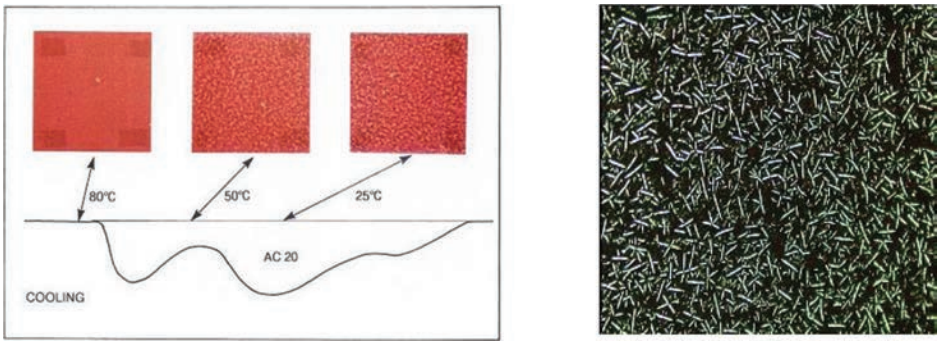

Figure 3. Observation of crystallized fraction precipitation upon cooling by DSC and phase contrast microscopic observation (left—*Credit to Thermochimica Acta 324 (1998) 223–227)*, and by dark field microscopy (right).

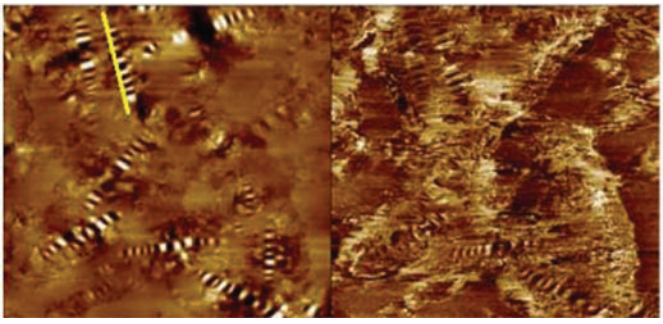

Figure 4. Observation of bee structures in asphalt by AFM—credit to T. Pauli, WRI.

- Polymer modified Binders (PmB) have very complex morphology depending on the polymer compatibility with the bitumen matrix. Polymer molecules usually swell with oily aromatic maltene molecules—this local phase separation can be quantified by FTIR microscopy [13]. How well-dispersed the polymer is affects its "reptation ability" which is highly responsible for some PmB mechanical properties—a phenomenon earlier described by Nobel prize De Gennes [14].

3.4 *Links with mechanical properties*

- Thermal susceptibility of binders impacts their rheology. Black space diagram plotting with no shift phase angle as a function of the stiffness modulus from DSR measurement shows a single smooth curve for rheologically simple binders, but not for complex binders. The shape of the black curve can be related to asphalt composition, particularly the asphaltenes and crystallized fractions contents [15] which undergo time dependent phase transition. See Figure 5.
- Isothermal physical hardening at low temperature has an effect on bitumen low temperature mechanical properties. This was shown during the SHRP program measuring bitumen stiffness and relaxation after various conditioning times. This was later related to some extent to the bitumen crystallized fraction and quantified relative to its glass transition temperature See Figure 6 [10]. These composition parameters also show up in steric hardening, affecting fatigue measurement.
- In real life, binders can be subjected to stresses outside the linear domain. The Multiple Stress and Recovery (MSCR) test allows measuring unrecovered strain which is related to permanent deformation and to the binder impact in mix rutting. Evaluating binders under conditions closer to field conditions is even more relevant for highly structured or modified binders which respond differently [16]. It shows reasonable relationships with mixture rutting performance evaluated in the lab, as shown in Figure 7.
- Other DSR tests are under development to capture binder fatigue properties, like the linear amplitude sweep or the time sweep. Fracture mechanics based tests run on notched specimens are getting attention for characterizing thermal cracking both in Europe and North America. These tests are pushing the limits of classical rheology theories.

3.5 *Aging*

- Bitumen oxidative aging has long been studied [6]. Work at Western Research Institute under the US Federal Highway Administration (FHWA) contracts has shown lately that formation of carbonyls and sulfoxides under reaction with oxygen, measured through Fourier Transform Infrared (FTIR) spectroscopy, accounts for changes in unmodified asphalt rheological properties as a function of oxidation time. These researchers also confirmed by modulated DSC that a change of molecular interaction under oxidative aging expands the bitumen glass transition temperature range.

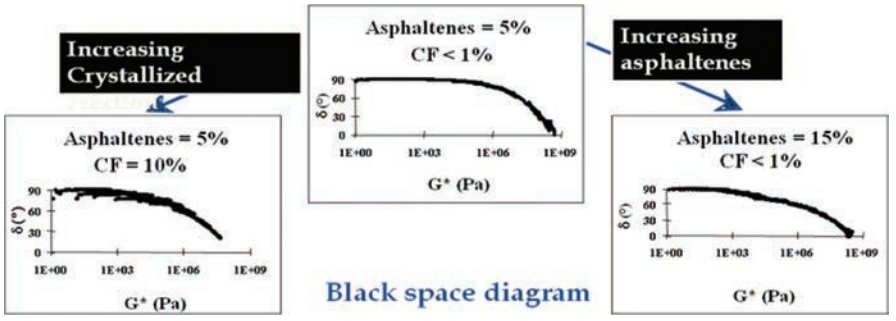

Figure 5. Effect of composition on black space diagram—from [15].

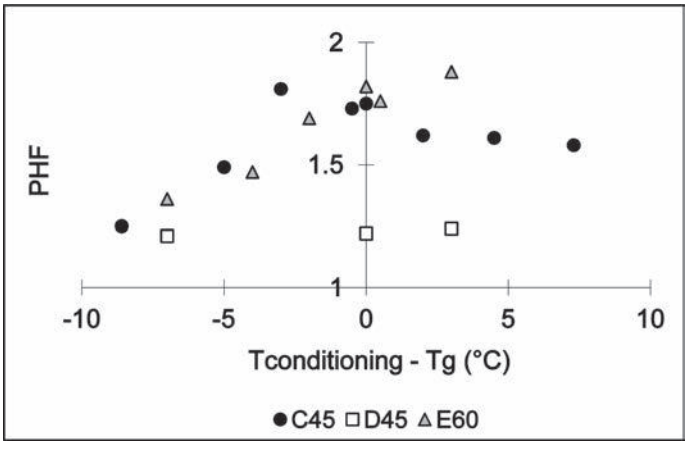

Figure 6. Effect of the glass transition temperature (Tg) and Crystallized Fraction (CF) on bitumen physical hardening—C45, D45, E60 having respectively 3.6, 0.5, 4.3% CF—*Credit to Thermochimica Acta 324 (1998) 223–227.*

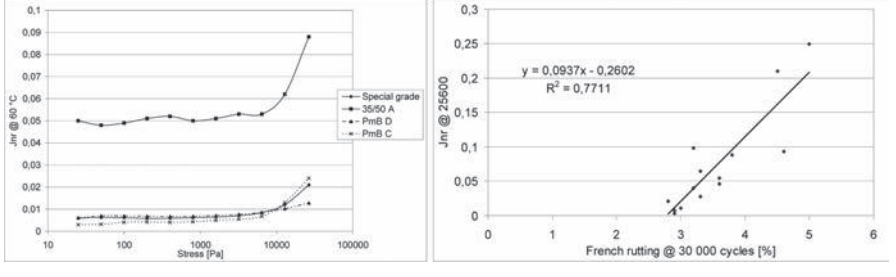

Figure 7. a) Non-recovered strain values at several stress levels for binders of same Pen. Range. b) Correlation between Jnr at 26500 Pa and rutting—*Credit to 7th Int'l RILEM, Symposium on Advanced Testing and Characterization of Bituminous Materials, Rhodes, Greece, Vol. 2, 2009, pp. 971–980.*

- Polymer modified bitumen aging gets very complex: FTIR microscopy studies using an oxidation cell have shown that the respective oxidation of the bitumen and the polymer molecules change the system compatibility [13]. Homogeneous Polymer modified Binders (PmB's) tend to evolve less than heterogeneous materials from both a morphology and rheology standpoints. Polymer chain scission, although related to polymer degradation,

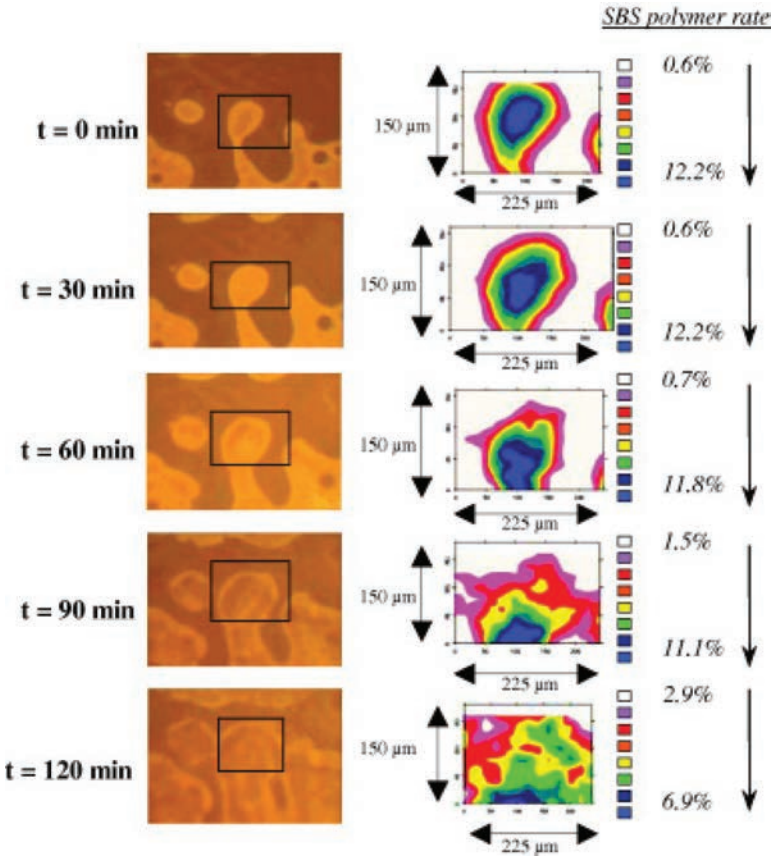

Figure 8. Kinetic evolution of the polymer network of a 6% SBS PmB by infrared mapping (130 °C under air during 2 h) (based on the ratio of SBS infrared absorption band at 965 cm^{-1} to the specific bitumen band at 1376 cm^{-1})—*Credit to Fuel 87 (2008) 1270–1280.*

can actually improve polymer dispersion, whereas stable macromolecules can become less compatible and phase separate. See Figure 8.

4 CONCLUSIONS AND PERSPECTIVES

Bituminous materials feature unique chemical and physical properties that make them difficult to analyze and characterize. Traps are numerous, but advances in this field are likely to improve binder understanding and create applications more relevant to the stakeholders, from researchers to producers, road users, all the way to tax payers.

Among those significant improvements, one must cite the assessment and understanding of molecular associations and interactions, phase separations, their impact on thermal history to compare binders in the same physical state. This will allow to measure intrinsic properties that ultimately influence pavement performance.

Powerful tools and research teams are becoming available to look at the fundamentals, from the nano molecular level all the way to the pavement performance. The FHWA Asphalt Research Consortium, for instance, looks at the mechanics of bitumen at nano-level using atomic force microscopy to attempt to predict field cracking behavior, with the support of TU Delft.

These advances will have an impact on binder production. Smart engineering will be able to replace classical refined asphalt “goodies” and make durable and performing binders.

There will be more cost effective additives that will be more widely used. They will include new polymer types, bio-additives and nanotechnology modifiers … Developing relevant analytical techniques for asphalt binders will foster innovation from industrial partners that are not currently present in the field.

Furthermore, governmental agencies have officially initiated the move towards greener/durable and LCA efficient pavements through projects like European "Forever open road" or "Every Day Counts Innovation Initiative" from the FHWA [16, 17]. Lately the Infravation Transnational Project was launched to boost innovation in infrastructure [18].

ACKNOWLEDGEMENTS

The author would like to acknowledge FHWA, WRI and Total Bitumen research teams and a number of experts whose stimulating input over the years has contributed in improving bitumen binder knowledge, particularly David A. Anderson, Pierre Claudy, John D'Angelo, Gayle N. King, Didier Lesueur, Claine Petersen, Per Redelius, Francis Rondelez, Christian Such and Jack Youtcheff.

REFERENCES

[1] PIARC International Workshop, Use of modified bitumonous binders, special bitumens and bitumens with additives in pavement applications, Rome. 1998.
[2] Transportation Research circular E-C160: PolyPhosphoric Acid Modification of Asphalt Binders. 2012.
[3] D. Lesueur. The colloidal structure of bitumen: Consequences on the rheology and on the mechanisms of bitumen modification, *Advances in Colloid and Interface Science*, 145, pp. 42–82. 2009.
[4] I. Ishai, B. Brule, J.C. Vaniscote, and G. Ramond. Some Rheological and Physico-Chemical Aspects of Long-Term Asphalt Durability, Journal of AAPT, 57–88, p. 65, 1988.
[5] J.F. Schabron, A.T. Pauli, and J.F. Rovani Jr. Molecular weight polarity map for residua pyrolysis, *Fuel*, 80, pp. 529–537. 2001.
[6] J.C. Petersen. A Review of the Fundamentals of Asphalt Oxidation Chemical, Physicochemical, Physical Property, and Durability Relationships, *Transportation Research Circular* E-C140. 2009.
[7] J.F. Schabron et al. Asphaltene Determinator for Automated on-column precipitation and redissolution of pericondensed aromatic asphaltene components, *Energy Fuels*, 24, pp. 5984–5996. 2010.
[8] R.B. Boysen and J.F. Schabron. The Automated Asphaltene Determinator Coupled with Saturates, Aromatics, and Resins Separation for Petroleum Residua Characterization, *Energy Fuels*, 27, pp. 4654–4661. 2013.
[9] H.U. Bahia and D.A. Anderson. Glass Transition Behavior and Physical Hardening of Asphalt Binders. Proc., Association of Asphalt Paving Technologists, Vol. 62, 1993, pp. 93–129.
[10] J.P. Planche et al. Using thermal analysis methods to better understand asphalt rheology, *Thermochimica Acta*, 324, pp. 223–227. 1998.
[11] P.G. Redelius. Solubility parameters and bitumen, *Fuel*, 79, pp. 27–35. 2000.
[12] A.T. Pauli, R.W. Grimes, A.G. Beemer, T.F. Turner, and J.F. Branthaver. Morphology of asphalts, asphalt fractions and model wax-doped asphalts studied by atomic force microscopy, *International Journal of Pavement Engineering*, 12, pp. 291–309. 2011.
[13] V. Mouillet et al. Infrared microscopy investigation of oxidation and phase evolution in bitumen modified with polymers, *Fuel*, 87, pp. 1270–1280. 2008.
[14] F. Rondelez. When basic research spawns industrial innovation, *Liaisonsbitume* N° 7. 2008.
[15] L. Champion, J.F. Gérard, J.P. Planche, D. Martin, and D.A. Anderson, Asphaltenic—waxy bitumens: limitations to the time—temperature superimposition principle, paper 48, Eurobitume workshop. 1999.
[16] http://www.foreveropenroad.eu/.
[17] www.fhwa.dot.gov/everydaycounts.
[18] http://www.fhwa.dot.gov/research/resources/infravation.cfm.

Plenary session on preservation

This page intentionally left blank

Asphalt Pavements – Kim (Ed)
© 2014 Taylor & Francis Group, London, ISBN 978-1-138-02693-3

Why preservation-definitions, treatment types, benefits, and challenges

R. Gary Hicks & Dingxin Cheng
CP2 Center, CSU Chico, Chico, CA, USA

ABSTRACT: Pavement preservation has been an important topic for flexible pavements for many years. It was not until the Foundation for Pavement Preservation (FP2) was established in 1992 that it became an important aspect in the area of system maintenance and preservation. There are several types of treatments included in the pavement preservation tool box including thin HMA overlay, chip seals, slurry surfacings, and cape seals. This paper addresses the definitions, types of treatments currently included in the tool box, the reported benefits of the treatments (including, cost, energy and environmental), and the challenges still facing agencies in documenting the benefits and increasing the use of these types of treatments. Recent developments with funding pavement preservation and rehabilitation and the implications of the new Technical Advisory for the ADA act are also discussed.

Keywords: Pavement preservation definitions, challenges, benefits, pavement management systems

1 INTRODUCTION

Americans are accustomed to easy mobility on safe, smooth, and well maintained roads. These same roads play a critical role in the nation's economy providing opportunities for agriculture, industry, commerce and recreation. Unfortunately, many of our road networks are deteriorating in quality requiring better management of our assets. This paper discusses the importance of preservation and many of its benefits and challenges. We have come a long way, but still have much to do.

2 BACKGROUND

Pavement preservation is similar in concept to conducting regular maintenance on an automobile or a house to keep them in good condition. For example, a low-cost maintenance activity such as routinely changing the motor oil in an automobile can improve the likelihood that the engine will not require a major overhaul prematurely and extend the lifespan of the engine. Similarly, paying for minor work now to prevent major work earlier in the future is an important concept of pavement preservation.

For example, the California Department of Transportation (Caltrans) has been describing the benefit of pavement preservation to that of pavement rehabilitation using a 6 to 1 ratio, meaning that the costs of pavement preservation treatments are about 1/6 of that for pavement rehabilitation [1]. Figure 1 illustrates this concept, where $1 invested in preventative measures while the pavement is in good condition can delay or avoid spending $6 for more substantive work. It is important to note that these figures are based on first costs only and do not consider the lives of the treatments, the life extension of the existing pavement associated with the treatments, and other costs such as user and safety costs; including these other factors and costs would result in even greater savings.

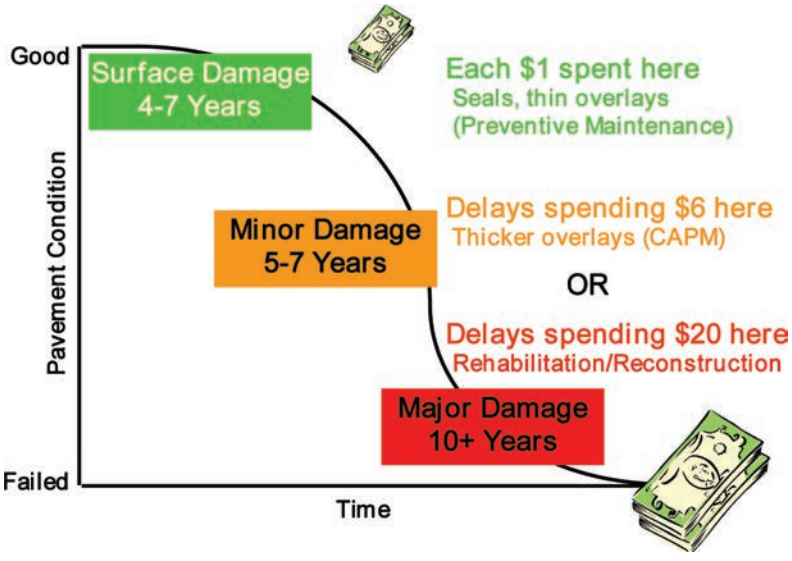

Figure 1. Pavement preservation concept used by Caltrans and other agencies.

3 DEFINITIONS

A clear presentation of pavement preservation in the United States requires the development and adoption of standard definitions. The following presents the current definitions related to pavement preservation used by the Federal Highway Administration (FHWA) and the American Association of State Highway and Transportation Officials (AASHTO).

3.1 *Asset management*

FHWA and AASHTO define asset management as a systematic process of maintaining, upgrading, and operating physical assets cost-effectively [2]. Asset management combines engineering principles with sound business practices and economic theory and provides tools to facilitate an organized, logical approach to decision-making. Asset management provides a framework for both short- and long-range planning. Asset management is important to state and local governments because of the Governmental Accounting Standards Board's (GASB) Policy Statement 34, "Basic Financial Statements for State and Local Governments," issued in June 1999. GASB 34 encourages government agencies to promote asset management practices and to report the value of capital assets such as utilities, roadways, and other infrastructure [3]. The value and maintenance of these assets eventually affects the bond ratings of government agencies, which in turn affect the government's ability to borrow the money to repair and replace the investments. The objective of an asset management program, therefore, is to:

- Consider various investment strategies,
- Provide a more rational decision process, and
- Improve the overall condition of the highway system at a lower cost.

3.2 *Preventive maintenance*

According to AASHTO, preventive maintenance is a planned strategy of cost-effective treatments that preserves, maintains, or improves a roadway system and its appurtenances and retards deterioration, but without substantially increasing structural capacity [4]. Preventive maintenance is a tool for pavement preservation where non-structural treatments are applied early in the life of a pavement to prevent deterioration and extend the life of pavement.

3.3 *Pavement preservation*

Pavement preservation is the sum of all the activities to provide and maintain serviceable roadways, including corrective and preventive maintenance, as well as activities such as pothole patching, rut filling, or unplugging drainage facilities. Reactive maintenance, therefore, is unscheduled; sometimes immediate response is necessary, to avoid serious consequences.

3.4 *Emergency maintenance*

Extreme conditions, when life and property are at risk, require emergency maintenance. Examples include washouts, rigid pavement blow-ups (the shattering or upward buckling of concrete slabs along a joint), and rockslides or earth slides.

4 TREATMENTS

In the past, many maintenance practices have not been effective, because they were applied reactively to roads in poor condition instead of proactively to roads still in good condition. Succinctly stated, the correct approach to preventive maintenance is to "place the right treatment on the right road at the right time." They also need to be placed in the right way.

Preservation became a topic in the early 1990s, when highway agencies examined effective maintenance practices. The preservation concept, whether for pavements or for bridges, is a departure from traditional approaches, which wait until deficiencies are evident and until reconstruction or major rehabilitation are the only means to correct the problem.

Preservation, however, addresses minor deficiencies early, before the defects become major problems, and extends the life of the asset at a relatively low cost. A strong preservation program is essential to asset management. Because preservation activities include so many kinds of treatments, agencies should build their own preservation toolboxes to serve their particular needs. Just as a mechanic's toolbox contains many different tools, each designed for a specific job, a preservation toolbox should include a host of treatments to address specific conditions.

No treatment will be suitable for every location. For example, a chip seal may be a long-lasting, cost-effective surface treatment in a rural area, but not in a large urban area. Conversely, concrete ultrathin white-topping may be cost-effective in a large urban area, but not in a rural area. Similarly, performance and cost-effectiveness should be evaluated in the context of the areas in which the preservation treatments are applied. Typical treatments used for flexible and rigid pavements in California are given in Table 1 [1].

Table 1. Caltrans maintenance technical advisory guide-volumes and chapters.

Flexible pavements	Rigid pavements
1. Introduction	1. Introduction
2. Materials	2. Surface characteristics
3. Treatment selection	3. Treatment selection
4. Crack sealing	4. Joint resealing & crack sealing
5. Patching & edge repair	5. Diamond grinding & grooving
6. Fog and rejuvenating seals	6. Dowel bar retrofit
7. Chip seals	7. Isolated partial depth concrete repair
8. Slurry seals	8. Full depth concrete repair
9. Microsurfacing	
10. Thin maintenance overlays	
11. Bonded wearing course	
12. Interlayers	
13. In-place recycling	

The preservation community has identified several potential benefits associated with implementing a pavement preservation program. The most significant benefits include the following:

- Life extension of the existing pavements. Pavement preservation treatments can extend the life of a pavement thereby delaying the need for pavement rehabilitation [5]. Figure 2 illustrates this conceptually. That is, timely, low-cost treatments that defer pavement rehabilitation or reconstruction preserve current funds for use on other more urgent or needed activities.
- Lower treatment costs. Pavement preservation treatments typically cost from $1–6 per square yard, while the cost to rehabilitate roads can be 6 to 10 times more expensive, and the cost to reconstruct roads can be 15 to 30 times more expensive [6].
- Reduced user costs. Driving on rough roads increases vehicle operating costs through accelerated vehicle depreciation, reduction in fuel efficiency, and damage to tires and suspensions. TRIP estimates an added cost of $335 annually for the average driver to as high as $746 annually for drivers in urban areas with high concentrations of rough roads [7].
- Improved safety (to the public and the workforce). As compared with rehabilitation work, pavement preservation treatments usually take less time to complete; that is, the contractor can get in and get out faster minimizing the chances for work-zone crashes during long work periods. Better roads surfaces also provide for good drainage and skid resistance thereby improving safety to road users [8].
- Improved overall network health. Some agencies have shown an improvement in overall network health by keeping good roads in good condition.
- Pavement preservation is "green." Use of preventative maintenance treatments such as chip seals and micro-surfacing consume 12 to 34% of the annualized energy and emit 10 to 27% of annualized greenhouse gases in comparison with major rehabilitation work involving a 4-inch hot mix asphalt overlay [9]. The comparisons include the energy required for and emissions produced in obtaining the raw materials from the earth and all the operational steps (i.e., transport, refining, manufacturing, mixing, and placement) required to produce a finished product. The comparison also accounted for differences in life extension of a pavement provided by the different treatments. According to the authors, energy savings are slightly lower and greenhouse gas emissions are about the same when compared to major rehabilitation work involving a 4-inch warm mix asphalt overlay. In addition, use of preventative maintenance treatments such as fog seals and cracking sealing resulted in substantially lower consumption of energy and emission of greenhouse gases.

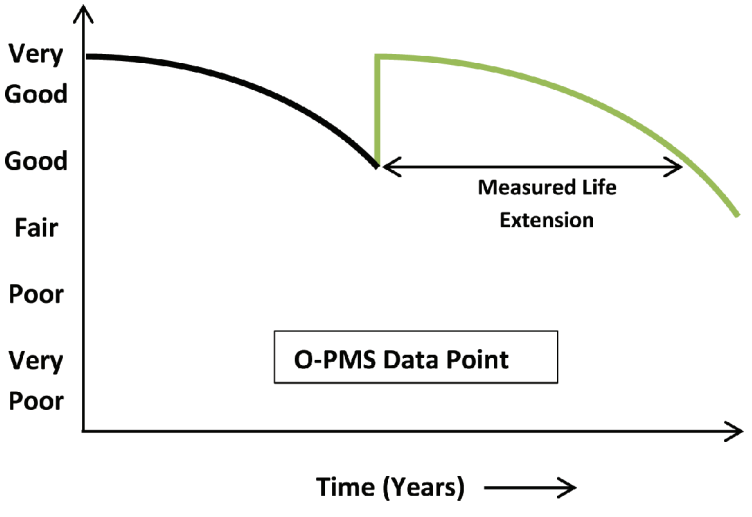

Figure 2. Life extension due to preventative maintenance.

To realize the above benefits, agencies and industry need better information to convince the transportation commission and the legislature (or the other decisions makers) to provide more dedicated funding for pavement preservation while at the same time finding additional funds to repair pavements beyond the preservation stage. Work has been accomplished at the California Pavement Preservation Center (CP2 Center) to provide better information on the economic benefits of pavement preservation [10].

5 CHALLENGES

Several issues and barriers can be identified for implementing pavement preservation. Some of these are discussed below.

5.1 *Agency issues*

The first and most important is dealing with the paradigm shift from fixing worst pavements first to fixing good pavements first. One of the biggest obstacles to overcome is to convince agency personnel to move from the conventional worst-first practice of fixing pavement problems to fixing good pavements first while letting the bad ones continue to deteriorate. People simply have a hard time making this adjustment without documented evidence of the cost savings associated with pavement preservation.

Next there is a need for top management commitment. Pavement preservation programs will not succeed without top management commitment. This includes getting a commitment for dedicated funding and for resources needed to collect information on the effectiveness of preventive maintenance treatments. Caltrans has done much in this area without the best of data due to an inadequate pavement management system. This is now being dealt with as Caltrans moves forward with the development of a new and improved pavement management system.

There is also a need to identify a champion for the program within the agency. Pavement preservation programs need a champion for them to be effective. As with any new effort or program within an agency, someone must be constantly promoting the importance and benefits of the effort. Without a champion, the new effort will simply not succeed. For example, Caltrans has champions for pavement preservation and they are promoting the benefits of the program to the legislature [11, 12].

It is necessary to show the early benefits of the pavement preservation program using pavement management system that is able to show treatment lives, life extensions, and/or reduced life cycle costs. In the absence of good data from Pavement Management Systems, alternative methods for estimating treatment lives and life extension may have to be employed.

Preventive maintenance treatments can be ineffective if the correct treatments are not used at the right time. One failure is equivalent to hundreds of successes in a new program such as one like pavement preservation. It is important that the right treatment be used on the pavement and that it is applied in a timely manner. In a recent study for FHWA, it was determined that the loss of life and increased costs of not placing treatments right can be significant as shown in Figure 3.

5.2 *Industry issues*

The issues and barriers for industry groups mostly involve reluctance to disturb the status-quo and include the following:

- Competition between the suppliers of maintenance and rehabilitation treatments. With the shift from the traditional rehabilitation programs of HMA overlays applied every 10 to 20 years to pavement preservation programs using new or different treatments, some resistance has occurred from the suppliers of traditional rehabilitation materials. For example, hot-mix suppliers might\resist new cold treatments because of the likely loss in market share.
- Competition between various suppliers of maintenance treatments. When markets have been established for certain types of treatments and a new treatment type is being

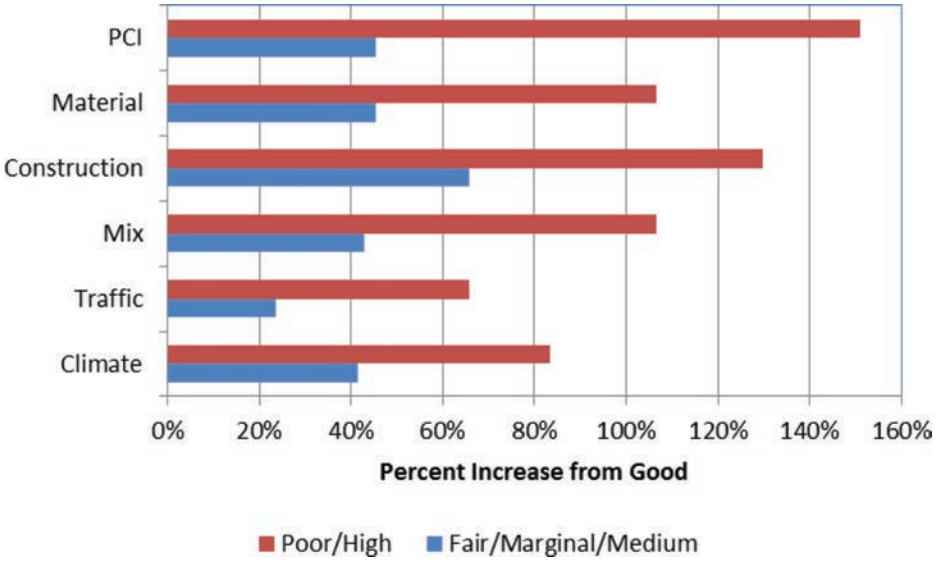

Figure 3. Cost impact if thin HMA treatments are not placed on the right road using good practice for climate, traffic materials and construction factors [13].

introduced, industry often works to block the new products, whether for technical reasons or for business reasons, again to avoid loss of market share.

- Political lobbying to prevent use of new maintenance treatments. In some cases, industry will resort to political lobbying to prevent new technologies from entering the market. Again the reasons may be technical but more than likely are related to the effect on the market if an agency adopts the new technology.
- Establishing the benefits of new technologies or treatments. Suppliers often introduce new technologies without adequate evidence of the benefits. The supplier must provide the agency with detailed documentation of the product's benefits and performance.

5.3 *Convincing the public*

The introduction of preservation programs also affects the traveling public, the ultimate customer, raising a different set of issues and barriers as follows:

- Understanding the shift from repairing the worst pavements first to the best pavements first. The public does not understand why agencies would be working on good roads but letting the bad roads deteriorate. Most of the public understands the importance of maintaining a car or a house to prevent major repairs. Pavement preservation engineers should be able to explain the value of preventive maintenance treatments now compared with the cost of major repairs later.
- Understanding the effects of the various maintenance and rehabilitation strategies on delays and vehicle costs. Primary benefits of pavement preservation include the potential for reducing traffic delays by using faster repair techniques and for reducing user costs by maintaining pavement net-works in better condition. Although widely acclaimed, these benefits still lack the documentation of national studies.
- Understanding safety issues. Increased safety for the traveling public and for workers in the work zone are other potential benefits from keeping roads in good condition through pavement preservation treatments; these benefits also need to be documented and communicated.
- Another challenge is to convince public that frequent short-term interruptions to their travel plans are better than less frequent long-term interruptions, especially in business districts.

5.4 *Regulatory*

A recent issue emerged in 2013 when the US Department of Justice and the USDOT jointly issued a technical advisory that redefines what maintenance and alteration is in terms of requiring curb ramps according to the Americans with Disabilities Act of 1990 (ADA) requirements. In the new technical advisory, slurry seals are defined as maintenance and microsurfacing is defined as alterations which requires construction of missing or upgrading of noncompliant curb ramps. Cape seals and thin bonded overlays are now alternations as well. It is expected that this issue will impact the treatments that will be used by agencies as well as the cost of providing well maintained roads and streets in urban areas [14].

6 SUMMARY AND RECOMMENDATIONS

Many agencies have been very successful in implementing a pavement preservation program, but there is still more to do. This section summarizes the major accomplishments during the past two decades:

- In the United States, formation of the FP2 Inc. and Preservation Centers at Michigan State, University of Texas, and CSU, Chico. Also, pavement preservation partnerships were developed for the various regions of the United States. These have aided in promoting the concept of pavement preservation and provide for opportunities to exchange ideas on treatments and specifications.
- Many agencies have developed and implemented a pavement preservation program with top management support. This includes permanent funds for pavement preservation. For example, Caltrans is currently funded at nearly $300 million per year for preservation. This should be increased to $800 million per year in order to treat 7,000 lane-miles per year. By doing this, they can save 50% or more of the rehabilitation budget each year, allowing the savings to help reconstruct the more distressed roads.
- Agencies have developed guidelines for preservation for flexible and rigid pavements. These have assisted the states as well as local agencies to become more aware of the available techniques and how and when to apply them.
- Agencies have developed innovative programs to place new preservation techniques. In California, these new technologies are monitored by the CP2 Center using a pavement preservation database that can be accessed by agencies or industry to help with this effort. This has been used by industry to show the performance of their new innovations.
- Caltrans developed a computerized strategy selection program which considers cost effectiveness of the various treatments. This is available on the CP2 Center website for use by state or local agencies. It continuously undergoes upgrades as new treatments or technologies are deployed.

Recommendations for the next several years included the following:

- Developing new and improved tests for mix designs and quality control and acceptance testing for pavement preservation treatments. The industry still has much to do in this regard.
- Upgrading performance based specifications for many of the treatments to minimize the chances for early failure.
- Providing continuous education on how to place successful pavement preservation treatments.
- Documenting the long term performance of the various treatments using improved databases

REFERENCES

[1] California Department of Transportation (Caltrans), "Maintenance Technical Advisory Guide, Volume I—Flexible Pavement Preservation", Second edition, Website: http://www.dot.ca.gov/hq/maint/MTA_GuideVolume1Flexible.html.

[2] Asset Management Primer. FHWA-IF-00-010, Office of Asset Management, Federal Highway Administration, U.S. Department of Transportation, December 1999.
[3] Primer: GASB 34. FHWA-IF-00-010, Office of Asset Management, Federal Highway Administration, U.S. Department of Transportation, November 2000.
[4] FHWA, Pavement Preservation Definitions, Memorandum, September 2005. http://www.fhwa.dot.gov/pavement/preservation/091205.cfm.
[5] Principles of Pavement Preservation, Definitions, Benefits, Issues, and Barriers. TR News, Issue Number: 228. Transportation Research Board, Sept 2006. Galehouse, L. J.S. Moulthrop, and R.G. Hicks.
[6] AASHTO. *Rough Roads Ahead, Fix Them Now or Pay for It Later*. American Association of State Highway and Transportation Officials, Washington DC, 2009.
[7] TRIP, Key Facts about America's Surface Transportation System and Federal Funding, Washington DC, accessed 2014.
[8] Foundation for Pavement Preservation, "Pavement Preventive Maintenance Guidelines." Foundation for Pavement Preservation, Falls Church, VA, 2001.
[9] Chehovits, J. and Galehouse, L., Energy Usage and Greenhouse Gas Emissions of Pavement Preservation: Processes for Asphalt Concrete Pavements. Proceedings, 1st International Conference on Pavement Preservation, Newport Beach, CA, 2010.
[10] Cheng, D, Hicks, R.G., and Scholz, T., Pavement Preservation—Protecting Our Investment on the Road, presented at TRB, 2012.
[11] Caltrans: State of the Pavement Report, Department of Transportation, CA, 2013. http://www.dot.ca.gov/hq/maint/Pavement/Pavement_Program/PDF/2013_SOP_FINAL-Dec_2013-1-24-13.pdf.
[12] Caltrans: Five Year Maintenance Plan. Department of Transportation, CA, 2011. http://www.dot.ca.gov/docs/reports/5-Year_Mtce_Plan_Report.pdf.
[13] Hicks, R.G., Visintine, B., Cheng, D., Elkins, G., and Groeger, J., Factors Affecting the Performance of Pavement Preservation Treatments: Final Report. DTFH61-07-D-00030-T-12001. FHWA, Washington DC, March 2014.
[14] U.S. Department of Justice, Joint Technical Advisory on the ADA Requirements to Provide Curb Ramps when Streets, Roads, or Highways are Altered through Resurfacing, Washington DC, 2013. http://www.fhwa.dot.gov/civilrights/programs/doj_fhwa_ta.cfm.

Podium papers

Environmental protection and socio-economic impacts

This page intentionally left blank

Asphalt Pavements – Kim (Ed)
© 2014 Taylor & Francis Group, London, ISBN 978-1-138-02693-3

Urban heat island effect: Comparing thermal and radiation effects of asphalt and concrete pavements on adjacent buildings using CFD methods

Malcolm Swanson & Andrew Hobbs
Astec Inc., Chattanooga, TN, USA

ABSTRACT: There is a the perception among some that asphalt pavements, particularly as surfaces for parking lots for facilities such as shopping centers, apartment buildings, and office buildings, are contributing to global warming through the so called urban heat island effect. The contention is that Portland Cement Concrete (PCC) is a less significant contributor to global warming via this mechanism and is, therefore, the preferred paving material. This rationale with some supporting science has succeeded sufficiently to result in PCC being given an advantage in building codes toward obtaining building LEED certification. The basis for this thought is that, since asphalt pavements are black and concrete pavements are white, the asphalt will absorb more solar radiation and become hotter during the course of daylight hours. Because empirical data in urban environments is difficult to obtain and clouded by a myriad of other effects Computational Fluid Dynamics (CFD) was chosen to compare an idealized configuration of an office building and parking lot. Only the reflectivity (albedo) of the parking lot was altered to simulate both asphalt and concrete. The results showed that the building surface temperature was actually higher for the concrete parking lot than the asphalt lot indicating a higher cooling load would be required. These results run counter to commonly held beliefs about the superiority of concrete pavements in urban environments and suggest the need to re-examine the suitability of asphalt pavement in urban settings.

Keywords: Asphalt pavement, urban thermal loading, urban heat island effect, CFD, environmental radiation

1 INTRODUCTION

Urban areas with a high percentage of paved surfaces are often several degrees warmer than rural areas with less paved surfaces. Because most paved and roof surfaces are dark they absorb more solar radiation resulting in higher local temperatures. This is commonly known as the Urban Heat Island effect (UHI). Higher localized air temperatures increase the energy required for cooling and as a result contribute to global warming [1]. Some studies suggest that the mitigation of UHI can result in peak utility savings of 5 to 10% [2].

In an effort to mitigate UHI green infrastructure often requires the use of cool pavements—pavements which reflect more solar radiation. Cool pavements are in integral part of a strategy to minimize the effects of UHI put forward by the U.S. EPA [3]. Because PCC has greater reflectivity than traditional asphalt pavements it is often preferred [4]. However recent work has called into question the use of materials with higher reflectivity siting many potential negative effects [5].

Because uncluttered thermal data is difficult to collect in urban setting a computer simulation whereby all the environmental inputs are controlled is a good method to test the effects of pavement reflectivity on adjacent buildings, specifically the difference between two common paving materials: asphalt and PCC.

2 SIMULATION METHODS

Computational Fluid Dynamics (CFD) has been well established as a tool for simulating fluid phenomena in a wide range of industrial applications [6–8]. Because CFD methods are well documented only an overview of the models used in this study are mentioned. The governing equations are time averaged using the Reynolds Average Navier-Stokes (RANS) method. The equations are discretized over a computational grid and solved iteratively. The k-epsilon turbulence model was used and incompressible ideal gas which provides temperature dependent density was used for air. The Discrete Ordinates (DO) radiation model was used to calculate the radiation heat transfer. The DO model solves the Radiation Transport Equations (RTE) shown in Eq.(1) for emitting, absorption, and scattering within the fluid domain.

$$\frac{dI(\vec{r},\vec{s})}{ds} + (a+\sigma_s)I(\vec{r},\vec{s}) = an^2\frac{\sigma T^4}{\pi} + \frac{\sigma_s}{4\pi}\int_0^{4\pi} I(\vec{r},\vec{s}^{\,t})\Phi(\vec{s}\cdot\vec{s}^{\,t})d\Omega^t \tag{1}$$

where $\vec{r}$ = position vector
$\vec{s}$ = direction vector
$\vec{s}^{\,t}$ = scattering direction vector
s = path length
a = absorption coefficient
n = refractive index
σ_s = scattering coefficient
σ = Stefan-Boltzmann constant (5.672×10^{-8} W/m^2 – K^4)
I = radiation intensity, which depends on position $\vec{r}$ and direction $\vec{s}$
T = local temperature
Φ = phase function
Ω = solid angle

The RTE are solved for a finite number of discrete solid angles in the global Cartesian system each with a direction vector $\vec{s}$ as shown in the field equation for the RTE, Eq. (2). The DO model solves as many transport equations as there are directions defined by $\vec{s}$ with the angular discretization of $\vec{s}$ as a user input [9].

$$\nabla\cdot(I(\vec{r},\vec{s})\vec{s}) + (a+\sigma_s)I(\vec{r},\vec{s}) = an^2\frac{\sigma T^4}{\pi} + \frac{\sigma_s}{4\pi}\int_0^{4\pi} I(\vec{r},\vec{s}^{\,t})\Phi(\vec{s}\cdot\vec{s}^{\,t})d\Omega^t \tag{2}$$

The appropriate solar loading for the specified geographic location, time, and date was calculated using Fluent's Solar Calculator and applied as radiation emitter from the sky boundary. The solar load was applied using direction and intensity calculated according the solar conditions listed in Table 1. The Solar Calculator uses the ASHRAE Fair Weather Conditions method to solve for the direct normal solar irradiation given by Eq. (3) where A is apparent solar irradiation at air mass m = 0, B is the extinction coefficient, and β is the solar altitude in degrees above the horizontal.

$$Edn = \frac{A}{e^{\frac{B}{\sin(\beta)}}} \tag{3}$$

To pursue this analysis, it was arbitrarily decided that a 10 story office building with a large parking lot would represent an idealized test case. A 3D CAD model of the building, parking lot, and surrounding ground and air was created and a computational mesh generated comprising of 9.6 million cells with prism boundary layers on the building, ground, and parking lot. Dimensions of the building and parking lot along with boundary conditions are shown in Table 2.

Table 1. Inputs and outputs of solar calculator.

Inputs	
Date, time	July 4th, 1 PM
Position	Chattanooga, TN
Orientation	South facing parking lot
Outputs	
Sun direction vector	(–0.21, 0.975, –0.057)
Direct normal solar irradiation	880.02 W/m^2
Diffuse solar irradiation—vertical surface	78.372 W/m^2
Diffuse solar irradiation—horizontal surface	118.685 W/m^2
Ground reflected solar irradiation—vertical surface	97.74 W/m^2

Table 2. Building and parking lot dimensions and boundary conditions.

Parking lot	$228.6 \times 76.2 \times 0.61$ m
Building	$60.96 \times 30.48 \times 60.96$ m
Ambient temp	300 K
Wind	2.23 m/s West to East
Gravity	(0, –9.81 m/s, 0)

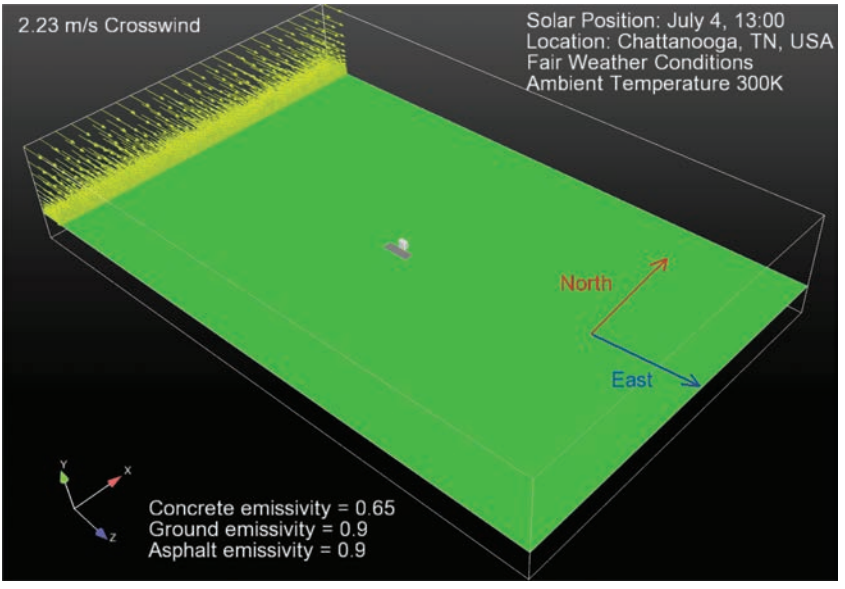

Figure 1. CFD boundary conditions with solar load inputs.

Table 3. Material properties.

	Asphalt	Concrete	Ground
Density (kg/m^3)	2240	2240	1600
Specific heat (J/kg-K)	750	750	800
Thermal conductivity (W/m-K)	1	1	0.5
Reflectivity	0.1	0.35	0.1
Emissivity	0.9	0.65	0.9

The CFD simulations were performed using the commercial CFD code ANSYS Fluent. The fluid domain and boundary conditions along with the dimensions of the building and parking lot are shown in Figure 1. A 2.23 m/s cross wind was set using a velocity inlet condition on the west wall with a pressure outlet on the east wall. The wall and sky boundaries were positioned far enough away to have minimal effect on the area of interest. The parking lot was modeled with a depth of 0.61 m while the ground layer surrounding the parking lot had a depth of 243.84 m. The building itself was modeled as a solid volume of concrete.

The Fluent radiation model assumes grey band radiation which implies that reflectivity or albedo of an opaque wall is defined as 1—emissivity. With the exception of reflectivity and emissivity identical physical properties were used for both asphalt and concrete. The material properties with surface emissivities and reflectivities are shown in Table 3.

3 RESULTS

The CFD results can be visualized by coloring the surfaces by the element value of the variable in question. Temperature contour plots show that the asphalt parking lot becomes hotter than the concrete parking lot (Fig. 2). Plotting reflected radiation on the same surfaces (Fig. 3) shows that indeed more radiation is reflected from the concrete parking lot and more is absorbed by the asphalt parking. However, closer examination of the building surface temperature reveals that higher temperatures are seen with the concrete parking lot (Fig. 4).

Temperature data was taken on a vertical line at the peak temperature on the southern face of the building to compare values. The data plotted in Figure 4 shows higher surface temperatures for the concrete parking lot.

The explanation for these higher temperatures is that lower absorptivity of the concrete parking lot reflects more radiation (Fig. 5) than the higher absorptivity of the asphalt.

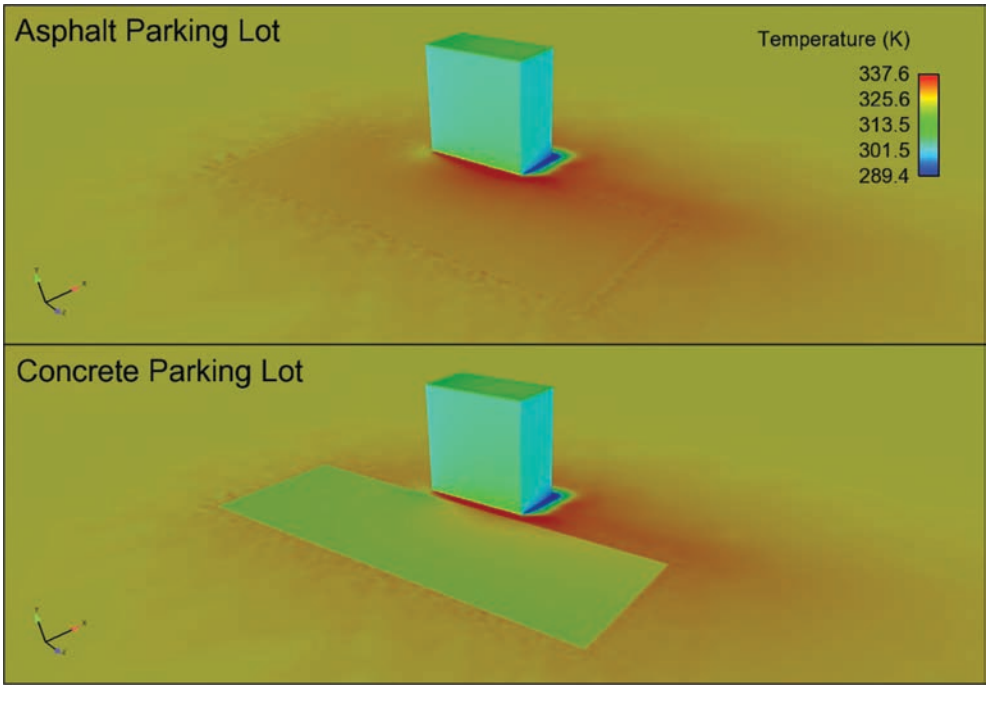

Figure 2. Surface temperature on ground, building, and parking lot.

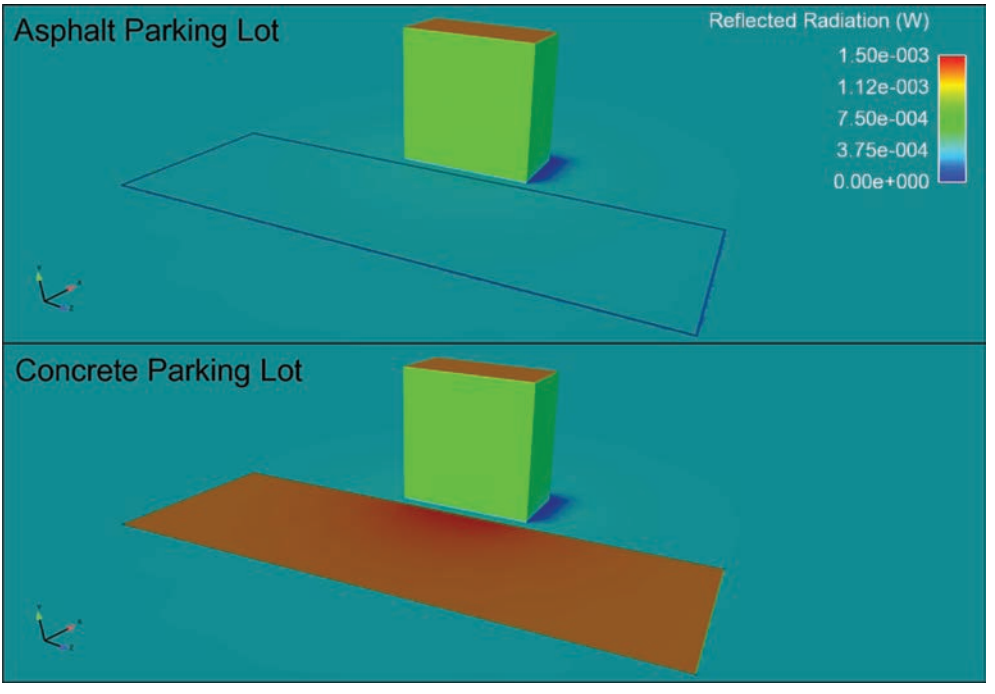

Figure 3. Reflected radiation heat flux on building, ground, and parking lot.

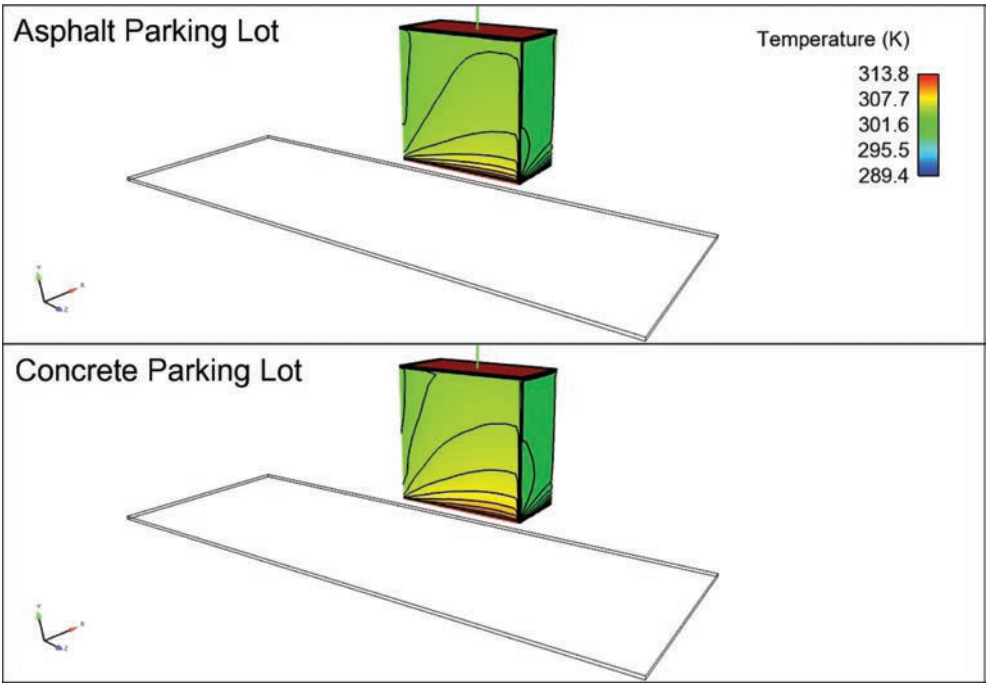

Figure 4. Contours of temperature on building surface.

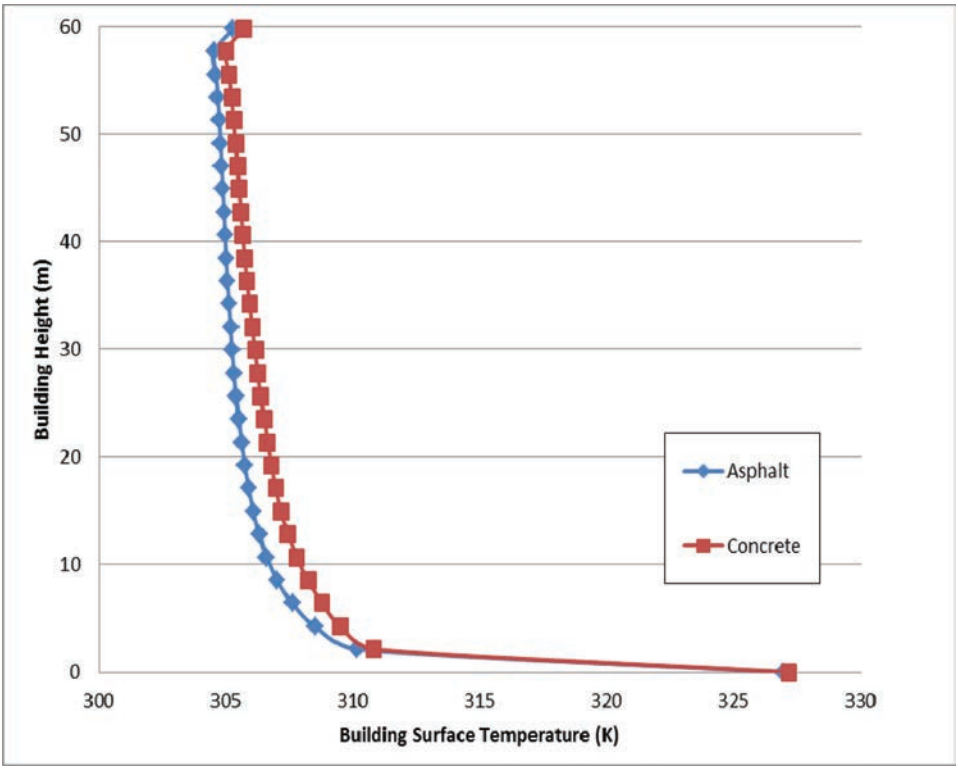

Figure 5. Building surface temperature on southern face.

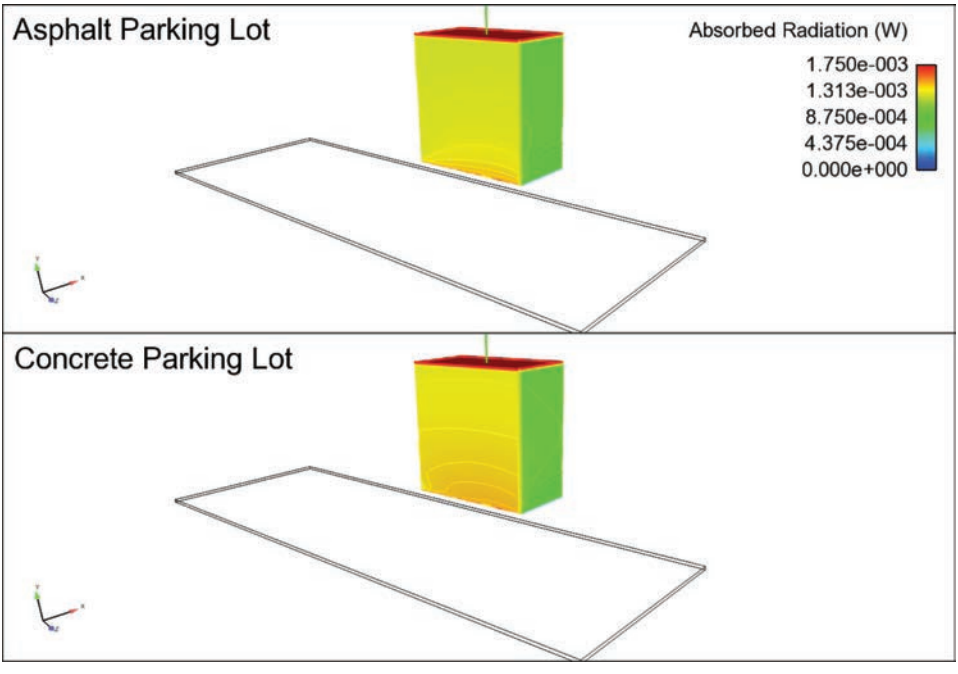

Figure 6. Absorbed radiation flux on the building.

Table 4. Summary of results.

	Asphalt	Concrete
Building average temperature (K)	327.01	326.99
Parking lot average temperature (K)	328.71	323.26
Parking lot reflected radiation (W)	1.898E+06	6.646E+06
Building incident radiation (W)	7.777E+06	7.882E+06
Building absorbed radiation (W)	5.055E+06	5.123E+06

As a consequence more incident radiation is received on the building surfaces for the concrete lot and more of this radiation is absorbed (Fig. 6) resulting in higher surface temperatures. Table 4 shows a summary of the results.

4 CONCLUSIONS

The results of the CFD study show that for this particular idealized case the pavement with lower absorptivity and highest reflectivity (PCC) actually created moderately higher building surface temperatures. This is clearly related to the increased amount of incident radiation on the building from radiation reflected by the PCC parking lot (Table 4). This runs counter to published advice [3] on mitigating UHI, and calls into question the use of so called cool pavements for all applications. This study demonstrates that for certain scenarios it is better for pavements to absorb rather than reflect solar radiation. The assumption that PCC is superior to asphalt for mitigating UHI is not supported by the results of this study. Certainly reducing energy consumption via mitigating UHI is a worthwhile endeavor, but a balanced approach that considers all modes of heat transfer including reflected radiation as well as the local urban infrastructure is needed.

REFERENCES

[1] Akbari H., Menon S., Rosenfeld A. Global cooling: increasing world-wide urban albedos to offset CO2. Climatic Change, 94 (3–4), pp. 275–286 2009.

[2] Taha, Haider, Alan K. Meier, Weijun Gao, and Toshio Ojima. "Mitigation of urban heat islands: meteorology, energy, and air quality impacts." Journal of Architecture, Planning and Environmental Engineering 529, pp. 69–76 2000.

[3] U.S. EPA Heat Islands Compendium of Strategies: Cool Pavements, 2008.

[4] Santamouris M., Synnefa A., Karlessi T., Using advanced cool materials in the urban built environment to mitigate heat islands and improve thermal comfort conditions, Solar Energy 85 (12), pp. 3085–3102.

[5] Yang, J., Z.H. Wang, and K.E. Kaloush, Unintended consequences: A research synthesis examining the use of reflective pavements to mitigate the urban heat island effect, The National Center of Excellence for SMART Innovations, Arizona State University, 2013.

[6] Hobbs A. Cutting development time, *Asphalt Contractor*, 12, pp. 26–30, 2004.

[7] Gouesbet G., Berlemont A., Eulerian and Lagrangian approaches for predicting the behaviour of discrete particles in turbulent flows. Progr. Energy Combust. Sci. 25, pp. 133–159, 1999.

[8] Griffith W.D. and Boysan F. Computational fluid dynamics (CFD) and empirical modeling of the performance of a number of cyclone samplers. *J. Aerosol Sci.* 27, pp. 281–304. 1996.

[9] FLUENT ANSYS, *Fluent User's Manual*, Lebanon, NH: Software Release 14.0. 2012.

This page intentionally left blank

Asphalt Pavements – Kim (Ed)
© 2014 Taylor & Francis Group, London, ISBN 978-1-138-02693-3

Worker exposure to ultrafine particles in asphalt laboratory

Somayeh Asadi
Department of Civil and Architectural Engineering, Texas A&M University, Kingsville, TX, USA

Marwa M. Hassan
Department of Construction Management, Louisiana State University, LA, USA

ABSTRACT: Air pollution is a public health issue that may cause health problems for workers in the construction industry including workers involved in asphalt paving operations. Epidemiological studies have reported an increase loss of lung function among asphalt workers over the asphalt paving season. Therefore, the goal of this study is to quantify and characterize nanoparticle and ultrafine particle exposure to workers during asphalt mixture preparation activities in an asphalt laboratory. Scanning Mobility Particle Sizer (SMPS) was used to measure the size distribution, surface area, mass, and particle concentrations during pouring, mixing, and compaction activities. Particles were also characterized using Transmission Electron Microscopy (TEM) and Scanning Electron Microscopy (SEM) to get a better understanding of their particle size and morphology. Based on the results of the study, the highest number of particles was observed during the pouring process. Laboratory measurement showed that more than 70% of particles in asphalt preparation activities were ultrafine particles, which have diameter smaller than 0.1 micrometer. In addition, the size of the particles obtained by SMPS was compared to the particle size based on the TEM analysis. The estimated sizes obtained by TEM analysis in the asphalt workplace study were in agreement with the estimate size obtained by calculations using SMPS.

Keywords: Hot-Mixed Asphalt, ultrafine particles, worker exposure, construction safety

1 INTRODUCTION

The growth of using nanomaterials in different products increases the concern for their potential impacts on the environment and on the biological systems. Inhalation of nanoparticles has been associated with adverse health effects that range from myocardial infarction to decrements of lung function among asthmatics. Epidemiological studies have showed the relationship between ambient ultrafine particle concentrations and mortality or morbidity of urban populations. These studies indicated that exposure to ultrafine particles may cause pulmonary diseases, cardiovascular health effects and impairment of the immune system. The toxicological mechanisms behind these effects are not clear [1, 2]. Animal nanoparticles exposure studies also showed that ultrafine particles cause a stronger airway inflammation than similar mass concentrations of larger particles [3]. Epidemiological data indicated that exposure to ambient ultrafine particles worsens respiratory diseases [4].

Nanoparticle exposure can be from natural, incidental or engineered nanoparticles making risk assessments even more problematic. Naturally occurring nanomaterials such as volcanic ash, ocean spray, magnetotactic bacteria, mineral composites and others exist in our environment. Incidental nanoparticles, sometimes called ultrafine particles, are particles unintentionally produced during an intentional operation. Combustion, welding, metal processing, and emissions from diesel engines are examples of major sources of incidental nanoparticles. Engineered nanoparticles are particles designed and produced intentionally to have a certain structure and size, usually less than 100 nm. Both natural and incidental nanoparticles may have

irregular or regular shapes. Engineered nanoparticles most often have regular shapes, such as tubes, spheres, ring, etc. [5, 6]. However, the difficulties in distinguishing between engineered and incidental occurring nanoparticles complicate the assessment of exposure to humans and the environment. In order to understand the potential effect of the nanoparticles on the environment, the levels of the natural, incidental, and engineered nanoparticles should be quantified.

Safety in nanotechnology is determined through comprehensive studies that include exposure assessment, determination of metrics, toxicological and epidemiological studies, and life cycle analysis [7]. Studies show that a major route of exposure to ultrafine particles is through the respiratory system [8]. Several factors including size, shape and particulate matter density influence the impact of these particles on different parts of the respiratory system and the amount of time that it takes for them to settle [8]. Thus, exposure measurements that use an appropriate dose metrics such as number, mass and surface area concentration of particles should be considered. Several studies have investigated the toxicity and risk management of nanoparticles based on the different exposure scenarios that may occur during the production and use; however, little is known about nanoparticle exposure from construction activities [2, 6, 7, 9–13].

One reason for this trend is that there are currently no national or international standards on measurement techniques for nanomaterials in the workplace. The National Institute for Occupational Safety and Health (NIOSH) established a nanotechnology field research team that identified numerous techniques to measure airborne nanomaterials with respect to particle size, mass, surface area, number concentration, and composition. One of these measurement techniques is the Nanoparticle Emission Assessment Technique (NEAT) that uses a combination of measurement techniques and instruments to assess potential inhalation exposures in facilities that handle or produce nanomaterials [14]. The following instrumentations are recommended to be used by NEAT for measuring ultrafine particles in workplaces: the Condensation Particle Counter (CPC), Optical Particle Counter (OPC), Scanning Mobility Particle Sizer (SMPS), Fast Mobility Particle Sizer (FMPS), and Electrical Low-Pressure Impactor (ELPI). These technologies measure the number, surface area or mass metric directly or indirectly. In order to characterize morphology of the particles and verify the primary size distribution, Scanning Electron Microscopy (SEM) and Transmission Electron Microscopy (TEM) can be used [1].

The objective of this study is to assess the exposure to nanoparticles associated with different asphalt laboratory activities. To achieve this objective, the number concentration, size distribution, surface area concentration, and mass concentration were measured for different activities including dry mixing, wet mixing, pouring, and compaction in an asphalt laboratory using a SMPS. SEM and TEM were also used to characterize morphology, geometry, and to verify the primary size distribution of the particles.

2 METHODOLOGY

2.1 *Sampling site*

An AMRL accredited asphalt laboratory with an area of 23 m^2 was used as the test environment in this study. The total particle concentrations and size distributions were measured for asphalt mixture preparation activities in a laboratory environment under different preparation tasks including pouring, mixing, and compaction, see Figures 1 and 2. Background levels were measured every day prior to the start of any work and between tasks. The results of the nanoparticles released during each task were compared to background nanoparticles counts of the laboratory indicating that nanoparticles were released. The measuring instruments were located as close as possible to the job activities without disturbing the ongoing work. The experimental plan and testing conditions are summarized in Table 1.

2.2 *Sampling strategy*

Since nanoparticles naturally exist in the environment and to accurately assess occupational exposure risk, it is important to characterize background nanoparticles before quan-

Figure 1. Mixing aggregates with asphalt binder.

Figure 2. Asphalt compaction.

Table 1. Experimental plan and test condition.

Material type	Task	Task description
Asphalt	Pouring	Pouring binder into the aggregates
	Mixing	Mixing binder and aggregates
	Compaction	Compacting the ready mix by using gyratory compactor

tifying the nanoparticles resulting from the different laboratory activities. This includes particles that penetrate from outdoors to indoors and particles that are suspended by background activities in the facility. Thus, a preliminary measurement was conducted to quantify additional sources of ultrafine particles in order to distinguish those emitted from asphalt laboratory activities. The first step is to identify the sources of ultrafine emissions in the workplace atmosphere by measuring particle number, particles concentration, and size distribution. Thus, to determine the nanoparticle concentration level in the laboratory under normal conditions, background data were collected before the start of laboratory activities. Background measurements were collected before the beginning of each task.

2.3 *Particles measurements and characterization*

Characteristics of nanoparticles were measured in the workplace using a CPC and SMPS. Size distributions were measured by a SMPS system, which consists of an electrostatic

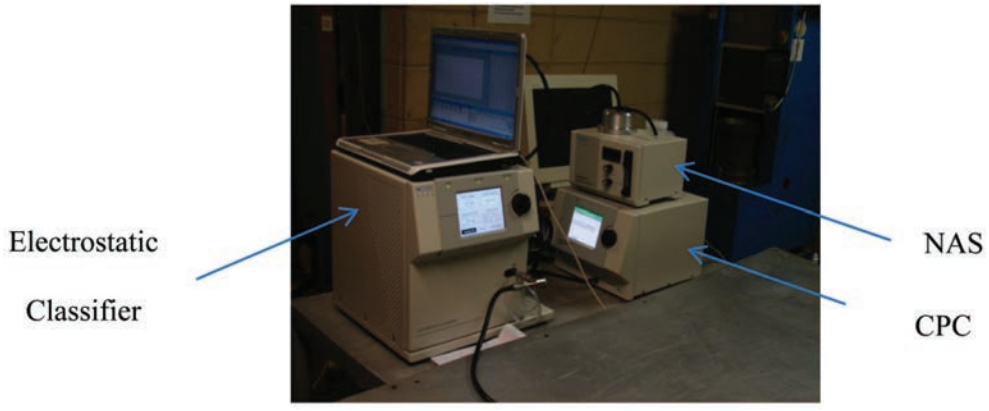

Figure 3. Scanning Mobility Particle Sizer (SMPS).

classifier (TSI Model 3080) and a Differential Mobility Analyzer (DMA, TSI 3081) coupled with CPC (TSI model 3776) (see Fig. 3). Scanning mobility particle sizer brings aerosol to electrostatic equilibrium ensuring that the aerosol has known charge distribution. The system was operated at 1.5 lpm of sheath flow rate and 1.5 lpm of aerosol inlet flow rate. The aerosol instrument manager software is capable of collecting data weighted by number concentration, diameter, surface area, volume, and mass, recorded the SMPS spectrometer data. Particles were collected on silicon nitride grids with 100 nm square membrane using a vacuum pump sample collector set to 7000 V. The collected particles were analyzed by SEM (Model Quanta 3D FEG, FEI Company, USA) and TEM (Model JEOL 100CX) for size and shape characterization.

3 RESULTS AND DISCUSSION

3.1 *Asphalt laboratory activities*

Figure 4 shows the particle number concentration as measured in the background before any activity, and after pouring, mixing, and compaction. Background level as measured prior to process was 9,436 particles per cm^3, background level after mixing was 11,851 particles per cm^3 and background level after compaction was 12,057 particles per cm^3. Peak concentration was 85,500 particles cm^3, which was during pouring process. As shown in Figure 4, the pouring process had the highest concentration. Furthermore, subtracting the total number of background particle concentration from the total number concentration of each activity shows that 1,179,000, 459,000, and 155,600 particles per cm^3 are emitted during pouring, mixing, and compaction, respectively.

Table 2 shows the total concentration, mean size, and ultrafine particle percentage for each task separately. As shown in this table, the mean size of pouring and mixing activities is almost the same while compaction has a higher mean size (160 nm). Based on these results, it was determined that the total concentration of pouring and mixing is higher than the total concentration for compaction.

Figure 5 shows the particle number size distribution of ultrafine particles during background, pouring, mixing, and asphalt compaction. The total number concentration of the particles during pouring, mixing, and compaction was 2×10^6, 1.28×10^6, 9.77×10^5 particles per cm^3, respectively. Ultrafine particles originated mainly from pouring and mixing. It is also noted that the background after mixing and compaction activities is slightly higher than the background before any activity began. This suggests that some of the ultrafine particles emitted remain in the air after completion of the activities.

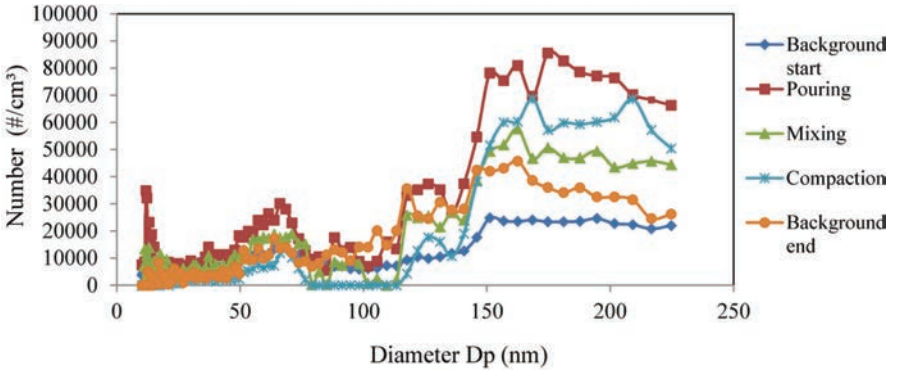

Figure 4. Particle number size distribution.

Table 2. Exposure measurement to nanoparticles during asphalt preparation activities.

Task (1)	Particle size measured		Total concentration (#/cm³) (4)	Mean particle diameter (nm) (5)	Mean mass (μg/m³) (6)	Ultrafine particle percentage (7)
	Min (nm) (2)	Max (nm) (3)				
Pouring	10.2	224.7	$2.00 \times 10^{\wedge 6}$	121	172	40%
Mixing	10.2	224.7	$1.28 \times 10^{\wedge 6}$	122	171.6	40%
Compaction	10.2	224.7	$9.77 \times 10^{\wedge 5}$	160	17.8	14%

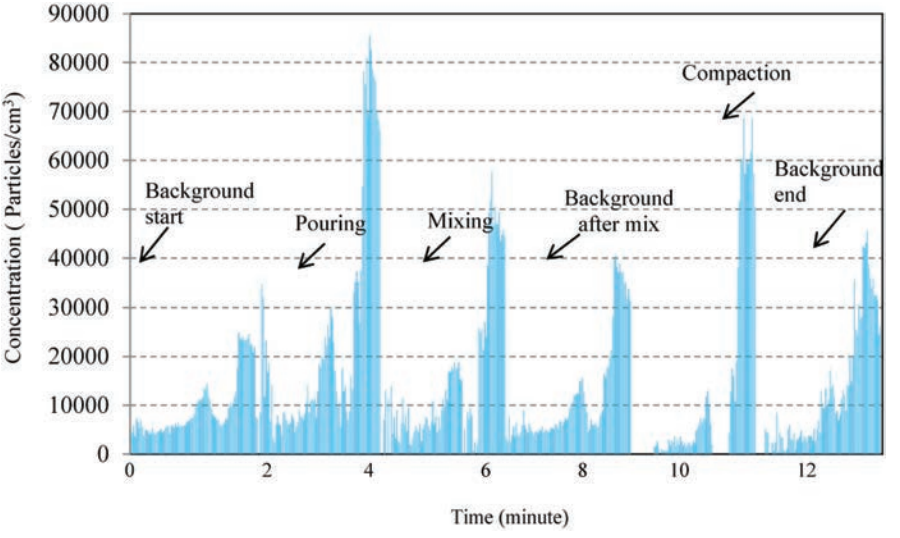

Figure 5. Particle number concentration.

The measurements carried during background, pouring, and mixing are presented in a box plot in Figure 6. The plot shows the minimum, the 25% percentile, the median value, the 75% percentile and the maximum nanoparticles concentrations. Pouring released more nanoparticles compared to the nanoparticles released during background, mixing, and compaction. As shown in Figure 6, the nanoparticle concentration is widely spread during pouring, mixing, and compaction activities.

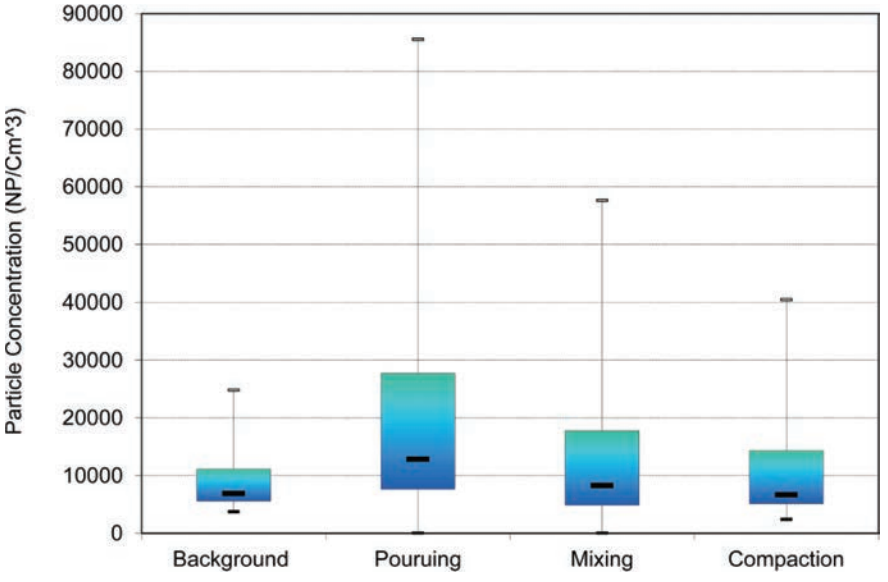

Figure 6. Concentration of nanoparticles released during the various asphalt construction activities.

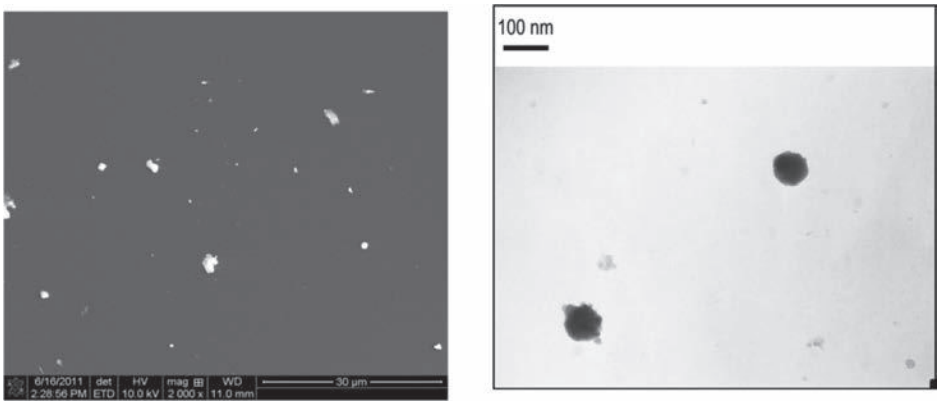

Figure 7. (a) SEM images of particles collected on electron microscope grids. (b) TEM images of particles collected on electron microscope grids.

3.2 *TEM and SEM characterization results*

The morphology, geometry, shape, surface, composition, and size of the nanoparticles released during asphalt preparation were characterized. To identify these properties, electron microscope analysis was used. Typical images obtained from SEM and TEM are presented in Figures 7(a and b). Figure 7 shows the size, shape, and morphology of the particles collected during asphalt preparation. SEM images show that the particles are spherical in shape with primary particle size less than 400 nm. To get a higher resolution image of the smaller particles, TEM was used. Figure 7(b) shows the size, shape, and morphology of the particles collected during asphalt mixture preparation. As shown in this figure, TEM images show spherical particles with primary particle size less than 100 nm. It is noted that several smaller particles were unstable and were destroyed by the electron beam, thus they were not detected in Figure 7(b). The estimated sizes that were obtained by TEM analysis are very similar to the sizes obtained by calculations using SMPS in the experimental study.

4 CONCLUSIONS AND RECOMMENDATIONS

Ultrafine particles are increasingly being recognized as a potential threat to human health. Aerosols in workplace environments may come from a wide variety of sources, depending on the type of activity and processes taking place. Measurements from a laboratory in this study showed that more than 70% of the particles in the asphalt preparation activities were ultrafine particles. However, the best choice of ultrafine particle metric in relation to health effects in workplaces is not yet fully understood. Therefore, it is important to measure several particle metrics in an attempt to find suitable particle characteristics to use in relation to health effects. The particle number is generally a good metric in the measurement of nano-sized particles since a high particle concentration is often connected to the presence of ultrafine particles. The estimated sizes obtained by TEM analysis in the asphalt workplace study were in agreement with the sizes obtained by calculations using SMPS in the experimental study. Based on the results of this study, further research is needed to characterize the hazardous nature and possible health effects of the emitted particles.

ACKNOWLEDGMENTS

The authors would like to acknowledge the assistance of TSI INC. & UTC (Gulf Center) for providing the required equipment for this study and the Louisiana Transportation Research Center.

REFERENCES

[1] Brouwer, D.H., Gijsbers, J.H.J., and Lurvink, M.W.M., *Personal exposure to ultrafine particles in the workplace: Exploring sampling techniques and strategies.* Ann Occup Hyg, 2004. 48(8): p. 439–453.

[2] Limbach, L.K., Wick, P., Manser, P., Grass, R.N., Bruinink, A., and Stark, W.J., *Exposure of engineered nanoparticles to human lung epithelial cells: Influence of chemical composition and catalytic activity on oxidative stress.* Environ Sci Technol, 2007. 41(11): p. 4158–4163.

[3] Oberdoester, G., Gelein, R.M., Ferin, J., and Weiss, B., *Association of particulate air pollution and acute morality: Involvement of ultrafine particles.* Inhalation Toxicology, 1995. 7: p. 111–124.

[4] Peters, A., Wichmann, H.E., Tuch, T., Heinrich, J., and Heyder, J., *Respiratory effects are associated with the number of ultrafine particles.* Am J Resp Crit Care, 1997. 155(4): p. 1376–1383.

[5] Kreyling, W.G., Semmler-Behnke, M., and Moller, W., *Health implications of nanoparticles.* J Nanopart Res, 2006. 8(5): p. 543–562.

[6] Oberdorster, G., Oberdorster, E., and Oberdorster, J., *Nanotoxicology: An emerging discipline evolving from studies of ultrafine particles.* Environ Health Persp, 2005. 113(7): p. 823–839.

[7] Sahu, M., and Biswas, P., *Size distributions of aerosols in an indoor environment with engineered nanoparticle synthesis reactors operating under different scenarios.* J Nanopart Res, 2010. 12(3): p. 1055–1064.

[8] Politis, M., Pilinis, C., and Lekkas, T.D., *Ultrafine Particles (Ufp) and Health Effects. Review and Analysis* Global Nest J, 2008. 10(3): p. 439–452.

[9] Nel, A., Xia, T., Madler, L., and Li, N., *Toxic potential of materials at the nanolevel.* Science, 2006. 311(5761): p. 622–627.

[10] Sayes, C.M., Reed, K.L., and Warheit, D.B., *Assessing toxicity of fine and nanoparticles: Comparing in vitro measurements to in vivo pulmonary toxicity profiles.* Toxicol Sci, 2007. 97(1): p. 163–180.

[11] Jiang, J., Oberdorster, G., Elder, A., Gelein, R., Mercer, P., and Biswas, P., *Does nanoparticle activity depend upon size and crystal phase.* Nanotoxicology, 2008. 2(1): p. 33–42.

[12] Schulte, P., Geraci, C., Zumwalde, R., Hoover, M., and Kuempel, E., *Occupational risk management of engineered nanoparticles.* J Occup Environ Hyg, 2008. 5(4): p. 239–249.

[13] Brouwer, D., *Exposure to manufactured nanoparticles in different workplaces.* Toxicology, 2010. 269(2–3): p. 120–127.

[14] Methner M.H.L., Geraci, C., *Nanoparticle emission assessment technique (NEAT) for the identification and measurement of potential inhalation exposure to engineered nanomaterials—Part A*. J Occup Environ Hyg, 2010a. 7: p. 127–132.

This page intentionally left blank

Asphalt Pavements – Kim (Ed)
© 2014 Taylor & Francis Group, London, ISBN 978-1-138-02693-3

Method for calculating warm mix energy saving based on stack gas measurements

Bob Frank
Compliance Monitoring, LLC, Linwood, NJ, USA

Brian Prowell
Advanced Materials Services, LLC, Auburn, AL, USA

ABSTRACT: In the 1950's the Barber Greene Company studied aggregate dryers in an effort to understand thermodynamics involved with producing Hot-Mix Asphalt (HMA). To reduce variables, they recirculated aggregate feed and metered water onto completely dry material. Efforts today to measure energy savings at asphalt plants are similarly challenged to accurately measure properties that can easily vary over the period of investigation: aggregate moisture, exit temperatures, process rates, and etc.

Fortunately, United States Environmental Protection Agency (USEPA) developed stack test procedures that measure surrogate properties continuously to arrive at true average values. Consequently, stack test data can be used in conjunction with plant process data to calculate reasonably accurate energy balance at asphalt plants. Results still depend on accurate data collection, but produce a very detailed picture of plant efficiency and energy losses. It is possible to calculate energy used to heat and dry aggregate, energy in stack gases, and energy lost through uninsulated exposed steel surfaces.

A recent evaluation of stack test data for NCHRP 9-47 A found one-half of Warm Mix energy savings are due to reducing plant casing loss. This paper present the thermodynamics used to conduct an energy balance using stack test data. It also presents sensitivity analysis of process variables to demonstrate importance of accurate data collection.

Keywords: Warm Mix Asphalt (WMA), energy savings, stack testing, asphalt plant casing loss

1 BACKGROUND

1.1 *Energy to produce HMA/WMA*

Asphalt mixtures are produced by drying aggregate particles and mixing the dry aggregate with asphalt binder at a temperature sufficient to (1) coat the aggregates, and (2) allow the mixture to be properly compacted after storage (silo), haul, and placement. Aggregates start at ambient temperature with moisture contents that vary depending on how they are produced, stored, and local weather conditions. Aggregate is heated in the dryer drum for a batch plant or beginning portion of the drum for a drum plant. Fine aggregate tends to be heated by convection while showering through the hot exhaust gases due to its high surface area. Coarse aggregate is primarily heated by conduction from the fine aggregate while lying in the bottom of the dryer due to its large mass. This is why large stone mixes are so difficult to heat when all fines are provided by Reclaimed Asphalt Pavement (RAP). A significant amount of energy is required to turn water into steam or otherwise dry the aggregate. Theoretically, the temperature of the aggregate cannot increase above 100°C until surface moisture has evaporated. Once the aggregate is dry, continued heating will bring the aggregate to the mixing temperature. Energy to dry then heat aggregate is illustrated in Figure 1.

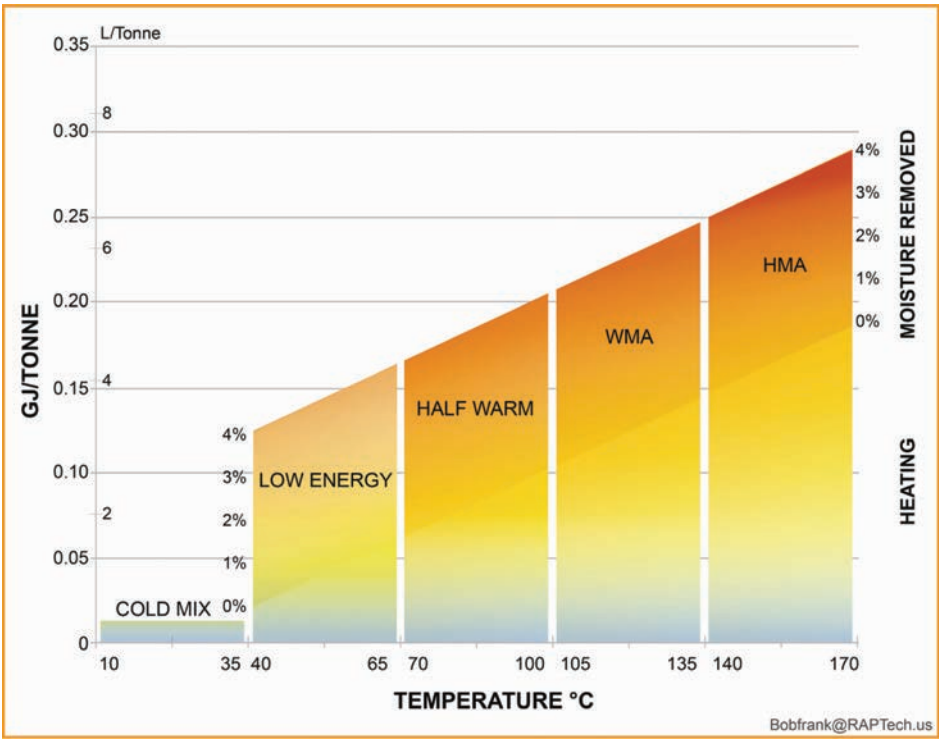

Figure 1. Energy use as a function of aggregate heating.

Figure 2 shows a frequency distribution of fuel usage based on data collected in the Mid-Atlantic region of the United States. The data includes both batch and drum plants. Fuel types include: natural gas, No. 2 fuel oil, and reclaimed oil. Two distributions are shown, one for data collected during stack emissions tests at 35 plants and another based on average use over a two-year period at the same plants. Typically, plants were operating at maximum design capacity for the full three hours of stack emission tests. The two-year average values, however, include fuel used during plant warm-up, plant waste, and unsold mix. Stack test data indicates drying/heating fuel usage for HMA average 0.271 GJ/tonne. By comparison, fuel usage based on year-end production totals averages 0.290 GJ/tonne, indicating 6.9 percent waste compared to steady-state production. This inherent difference between energy use during steady state operation and historical averages demonstrates comparisons between HMA and WMA must be based on identical time intervals to be meaningful.

1.2 *Reported energy savings from WMA*

WMA technologies allow the complete coating of aggregates, placement, and compaction of asphalt mixtures at lower temperatures than conventional hot-mix asphalt. Although the reduction in temperature varies by technology, WMA is generally produced at temperatures ranging from 20°C lower than hot-mix asphalt (HMA) to the approximate boiling point of water (100°C). Simply put, these technologies are workability and compaction aids.

A reported benefit of WMA technologies is reduced fuel usage. Reduced fuel consumption saves natural resources and cost. One objective of NCHRP 9-47 A, "Properties and Performance of Warm Mix Asphalt Technologies," was to document the relative energy usage between WMA and HMA. Theoretical calculations indicate that a temperature reduction of 28°C should result in a fuel savings of 11 percent [1]. Fuel savings reported from

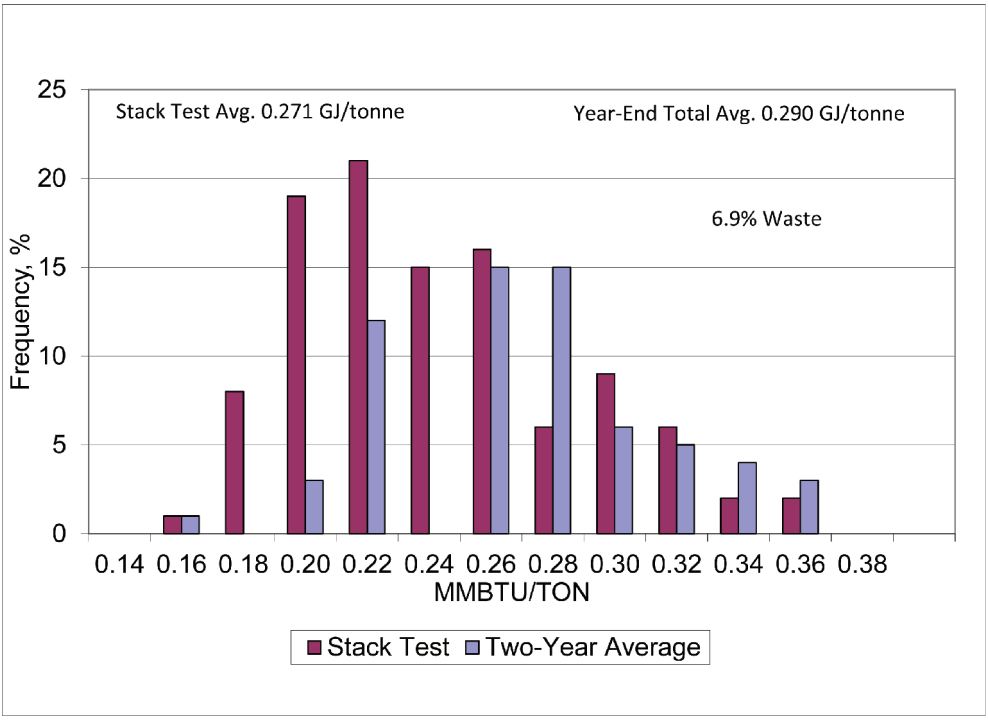

Figure 2. Typical HMA drying and heating fuel usage in MMBTU/ton (1 MMBTU/ton = 1.164 GJ/tonne).

early European WMA projects ranged from 24 to 55 percent [2–4] with typical values being between 20 and 35 percent [5]. Reported fuel savings from fifteen North American WMA projects, representing six technologies, ranged from a 15.4 percent increase to a 77 percent reduction [6–15]. The average fuel savings was 23 percent.

Larger fuel savings typically occurred with technologies like Low Emission Asphalt (LEA), WAM-Foam (Warm Asphalt Mix), and in some cases Evotherm™ ET (Emulsion Technology), which tend to have the lowest production temperatures. LEA and WAM-Foam production temperatures are usually close to 100°C. Casing losses and other inefficiencies are believed to account for some of the difference between theoretical and observed fuel savings [16] but these contributions were never quantified.

2 RESEARCH APPROACH

Data were collected from eight field projects as part of NCHRP 9-47 A. Fuel usage data was collected from six of the projects and stack emissions were measured for three, multi-technology projects. All projects included an HMA control section. The projects included in this study are shown in Table 1.

2.1 *Direct fuel usage measurements*

Fuel usage depends on a number of factors including, but not limited to: aggregate (and recycled materials, if used) moisture content, production rate, mix and stack temperatures, and excess air (leakage, baghouse pulse air, burner air). For this study, data collection forms were developed to collect information on plant energy usage, including many of the above factors, during production.

Table 1. Summary of information for projects used in the study.

Date	Project location	Plant site and description	Mixes
Jul. 19–21, 2010	County Road 315, Rapid River, MI	Escanaba, MI, uninsulated parallel flow drum	HMA, Advera, Evotherm 3G
Sep. 14–15, 2010	Calumet Ave., Munster, IN	Griffith, IN, insulated, counter flow dryer	HMA, Gencor foam, Evotherm 3G, Heritage Wax
Oct. 19–22, 2010	Little Neck Pkwy., Queens, NY	New York City, NY, batch plant with mini drum uninsulated dryer	HMA, Cecabase RT, SonneWarmix, BituTech PER
Apr. 19–20, 2010	US 12 near Walla Walla, WA	Walla Walla, WA, portable plant, uninsulated, parallel flow drum	HMA, Maxam foam
Jun. 21–22, 2010	I-66 eastbound, near Centreville, VA	Centreville, VA, Double Barrel counter flow	HMA, Astec foam
Aug. 11–12, 2010	MT route 322, south of Baker, MT	Baker, MT, Partially insulated parallel flow drum	HMA, Evotherm DAT

The participating contractors were requested to tune their plant's burner prior to producing for NCHRP 9–47 A. For the three projects where stack emissions tests were performed, at Rapid River, MI; Griffith, IN; and New York, NY, burner tuning was conducted by Bob Frank. Asphalt plant burners have actuator motors that drive dampers and fuel modulating valves. As the burner percentage is increased, dampers and fuel valves open to increase air and fuel proportionately. If plant operators increase fuel pressure to increase production rate, incomplete combustion is likely to occur, wasting fuel. One plant showed a 24.8 percent reduction in fuel usage for HMA after burner tuning. This was an important variable to correct prior to quantifying energy savings from lower mix temperatures.

There are a number of ways fuel usage has been reported in prior studies. As shown in Figure 2, fuel usage collected over the long-term includes fuel used during plant warm-up, plant waste, and for unsold mix, resulting in 6.9 percent increase when compared to steady-state runs. Typically, each mix evaluated in NCHRP 9-47 A represented one-day's production. Fuel usage was monitored with a number of techniques depending on the fuel used:

- Natural Gas—gas meter readings,
- Liquid Fuel Oils—fuel meters or tank sticks, and
- Liquid propane—percent of tank volume.

Cumulative production tonnage was collected at approximately the same time that the meter readings were taken. After the data were collected, it was found that commercial gas meters only update periodically (up to 15 minute intervals) and therefore could give inaccurate measurements of fuel usage over short-time intervals. Additional discussion will be provided in the results and analyses.

The Rapid River, MI project used reclaimed motor oil as fuel. Since the Rapid River plant did not have a fuel meter, fuel consumption was calculated using tank charts and tanks sticks at the beginning and end of each day's production. The Baker, MT project used Liquid Propane (LP). Fuel usage for the LP was based on percent tank volume. The Griffith, IN and New York, NY, projects used natural gas with gas meter readings taken hourly at beginning and end of each stack test run. Gas meter readings were taken at the beginning and end of each day's production for Centreville, VA and Walla Walla, WA.

2.2 *Stoichiometric fuel measurements*

Unfortunately, precision of direct fuel measurements was questionable for a number of reasons and an alternative method to determine average heat input was investigated. Stack

emission tests were conducted at Rapid River, MI; Griffith, IN; and New York, NY sites with flow rate and composition of the exhaust gases measured continuously for two, one-hour runs on each WMA technology and HMA control. These stack gas data enabled back calculating average heat input using US EPA's Method 19 f-Factor. EPA developed f-Factors for commercially available fuels to calculate the stoichiometric volume of exhaust gases generated by burning one MMBTU (1.06 GJ) of fuel. For example, burning 27.2 cubic meters of natural gas (1.06 GJ) results in 246.6 dry standard cubic meters of (exhaust) gas at zero percent oxygen. Zero percent oxygen is what makes it a stoichiometric volume.

Stack gas velocity was measured according to US EPA Method 2 based on velocity pressures. Molecular weight and percent water vapor of the gas stream were measured using US EPA Method's 3 and 4, respectively. Carbon dioxide (CO_2) and oxygen (O_2) concentrations were also determined using US EPA Method 3. Stack gas velocity was converted to dry volumetric flow rate at a standard temperature and pressure based on stack area and percent water vapor in exhaust gases. These calculations are typically provided in any stack test reports and are too complex to cover here.

Fuel firing rate can be calculated from the average exhaust flow rate and oxygen concentration using Equation 1:

$$\text{Fuel usage} = \frac{60 \times Q \times \left(\frac{20.9 - O_2\%}{20.9} \right)}{F}$$

where,
Fuel usage = MMBTU/hr, (1.0 MMBTU/hr = 1.06 GJ/hour)
60 = minutes/hr., converts flow per minute to flow per hour
Q = average stack gas dry volumetric flow rate (dscfm) at standard temperature and pressure,
20.9 = standard O_2% of air,
O_2% = percent stack O_2 by volume, dry basis, units are percent and not decimal.
$(20.9 - O_2\%/20.9)$ = correction factor to remove excess air and calculate resulting stoichiometric volume
F = volume of combustion products per unit of heat content dscf/MMBTU: 8,710 dscf/MMBTU for natural gas and propane and 9,190 for oil (US EPA Method 19).

3 RESULTS AND DISCUSSION

3.1 *Direct fuel usage measurements*

Table 2 summarizes fuel usage based on direct measurement and back calculated fuel consumption and the corresponding cumulative production. An error was made reading the gas meter for the Virginia HMA; therefore fuel usage for that mix is not reported.

The potential error in determining fuel usage over a short time period based on tank sticks is illustrated in Table 2. The Michigan Advera and Evotherm 3G mixes were produced at the same average temperature. The production rates are almost identical. The aggregate moisture content was 0.2 percent higher for the Evotherm 3G, which would tend to increase fuel usage. However, the fuel usage based on tank measurements for the Evotherm 3G production is 0.044 GJ/tonne (17 percent) less than that calculated for the Advera WMA. By comparison the fuel usage based on stoichiometric calculations, corrected for a slight difference in aggregate moisture, are identical.

Similar inconsistencies between measured mix temperature and fuel usage were noted for the Indiana mixes. The local Indiana stack emissions contractor did not take stack velocity readings during the HMA and Heritage Wax stack emissions runs. Readings were taken only at the end of the run. Therefore, the stoichiometric calculations of fuel usage for those two mixes are suspect. The Indiana fuel usage in Table 2 based on gas meter readings are

Table 2. Fuel usage.

Site	Plant[1]	Mix	Avg. stockpile moist., %	Avg. prod. rate, metric TPH	Avg. mix temp., °C	Avg. stack temp. °C	Fuel use, GJ/tonne	Stoichiometric fuel use GJ/tonne	Agg. moisture correction GJ/tonne	GJ/tonne corrected for agg moisture	Delta GJ/ tonne	Delta GJ/°C
WA	Uninsulated PF drum	HMA	2.6%	287	163	171	0.324	NA	NA	0.324		
		Maxam foam	3.0%	281	141	146	0.254	NA	0.01	0.243	0.080	0.0036
VA	Double Barrel	HMA	2.3%	245	159	103	NA	NA	NA	NA		
		Astec foam	2.1%	200	142	88	0.236	NA	–0.006	0.242		
MI	Uninsulated PF drum	HMA	3.6%	281	149	166	0.315	**0.332[2]**	NA	0.332		
		Advera	3.9%	293	132	144	0.262	**0.276**	0.008	0.268	0.064	0.0037
		Evotherm 3G	4.1%	290	132	147	0.218	**0.281**	0.013	0.268	0.064	0.0037
MT	Partially insulated PF drum	HMA	1.3%	336	148	121	0.183	NA	NA	0.183		
		Evotherm DAT	1.5%	343	122	114	0.159	NA	0.006	0.154	0.029	0.0011
IN	Insulated CF Dryer	HMA	3.2%	265	149	117	**0.263[2]**	0.234[3]	NA	0.263		
		Gencor foam	3.5%	272	136	111	**0.243**	0.260	0.008	0.235	0.028	0.0022
		Evotherm 3G	3.8%	272	124	105	**0.247**	0.241[3]	0.016	0.230	0.033	0.0014
		Heritage wax	3.8%	253	131	108	**0.234**	0.185	0.016	0.218	0.045	0.0025
NY	Batch-mini drum uninsulated dryer	HMA	3.1%	246	167	140	0.303	**0.348[2]**	NA	0.348		
		Cecabase RT	3.4%	221	116	101	0.275	**0.274**	0.008	0.265	0.083	0.0016
		SonneWarmix	2.4%	242	122	91	0.251	**0.230**	-0.019	0.249	0.099	0.0022
		BituTech PER	3.6%	243	123	94	0.294	**0.246**	0.013	0.233	0.115	0.0026

[1]PF = parallel flow, CF = counter flow. [2]Highlighted values used where two measures of fuel usage available. [3]Stack velocity measurements only taken at end of each stack emissions run, stoichiometric fuel usage believed to be erroneous.

overall daily averages. Increased fuel usage of 0.261 GJ/tonne for the Gencor foam WMA was observed over the course of the day, including start up, pre-heat, plant waste, and shut down (values in Table 2 correspond to hourly readings taken during stack emissions tests). The production temperature of the Gencor foam mix was increased to HMA temperatures after stack emissions tests were completed.

3.2 *Fuel savings*

The average fuel usage for the HMA production based on five projects was 0.290 GJ/tonne. This compares well with the 0.271 GJ/tonne calculated based on the data from the Mid-Atlantic region reported in Figure 2. To make meaningful comparisons between the WMA and HMA, the WMA fuel usage were corrected for the difference between the HMA and WMA aggregate moisture content at each site. By definition, it takes 1 British Thermal Unit (BTU) (1055.1 J) to raise the temperature of 1 lb (0.454 kg) of water by 1 °F (0.556 °C). Similarly, it takes 4.184 J (one calorie) to raise the temperature of 1 g of water 1 °C. Therefore, it takes 142 BTUs to raise the temperature of water from an ambient temperature of approximately 70 °F to 212 °F and 1,000 BTU to vaporize 1 lb. of 212°F water. Similarly, it takes 330,118 J to heat 1 kg of water from 21.1 to 100 °C and 2,260,000 J to vaporize 1 kg of water. The fuel usage was corrected based on 2,590,118 J/kg (1,142 BTU/lb) of moisture difference. The fuel usage for the normalized WMA data indicated an average savings of 0.064 GJ/tonne, or approximately 22.1% for an average temperature reduction of 27 °C (48 °F). This compares well to the average 23 percent savings reported in the literature. Since final mix temperatures for all mixes were greater than 100 °C, the theoretical fuel savings should be equal to differences between WMA and HMA mix temperatures multiplied by the specific heat of the aggregate. Assuming a specific heat of 1004.8 J/kg/°C (0.24 BTU/lb/°F) for a bituminous mixture, a 27 °C reduction in temperature should result in 0.0268 GJ/tonne savings, or 9.3 percent. The question then becomes how to account for the additional 13 percent in fuel savings from WMA technologies over and above the theoretical 9.3 percent savings due to lower mix temperatures?

3.3 *Distribution of fuel savings*

Additional calculations were performed to allocate fuel savings for the multi-technology sites where stack emissions tests were performed. Thermal energy generated to produce hot or warm mix is consumed by drying aggregate moisture, heating aggregate, heating stack gases, and casing losses. Casing losses are thermal energy used to heat plant iron and then radiated to the atmosphere, rather than being used to heat the aggregate. Components that account for the majority of casing loss include aggregate dryer, duct work, baghouse and batch tower/mixing chamber (if applicable). The differences in fuel usage reported in Table 2 were allocated based on thermodynamic properties to three sources: 1) differences in mix temperature, 2) differences in stack exhaust mass, moisture, and temperature, and 3) the remainder, believed to be attributed to casing losses.

Table 3 shows the results of calculations to appropriately allocate energy savings. Differences in thermal energy based on mix temperature were calculated using a specific heat of 1005 J/kg/°C for the asphalt mixture. The difference in the average HMA and WMA mix temperature at a site were multiplied by 1004.8 J/kg/°C, converted to GJ, and expressed as a percentage of the difference (delta) in GJ/tonne, corrected for aggregate moisture. Differences in mix temperature (% Mix Temp.) explained 27 to 76 percent of the fuel savings, with an average of 45 percent. Actual stack exhaust flow rates in cubic feet per minute (ACFM) were converted to standard conditions at 21.1°C (SCFM). The energy required to heat the air and moisture in the exhaust gas between the minimum observed stack gas temperature of 90.6 °C and the average stack exhaust temperatures was calculated for each mix (GJ/tonne up stack). The average stack gas temperature for NY SonneWarmix was 90.6 °C, therefore its GJ/tonne up the stack = 0.000. The calculation used a specific heat of 1842 J/kg/°C for water vapor and 1005 J/kg/°C for dry air. Air at standard conditions has a mass of 1.227 kg/m^3. The difference between the HMA and WMA GJ/tonne up stack at a given site (relative to 90.6°C) was expressed as a percentage

Table 3. Breakdown of fuel savings.

Site	Plant	Mix	Avg. prod. rate, metric TPH	Avg. mix temp °C	Avg. stack temp °C	Fuel usage, GJ /tonne corrected for Agg. moisture	Delta (HMA-WMA) GJ/tonne	ACFM	SCFM	% Moisture	GJ/tonne up stack (above 90.6C)	% Stack temp.	% Mix Temp.	% Casing Loss
MI	Uninsulated PF drum	HMA	281	149	166	0.332		53,656	35,997	33.0%	0.0256			
		Advera	293	132	144	0.268	0.064	50,870	35,853	33.0%	0.0176	13%	27%	60%
		Evo. 3G	290	132	147	0.268	0.064	50,704	35,546	33.0%	0.0184	11%	27%	62%
IN	Insulated CF dryer	HMA	265	149	117	0.263		48,380	36,526	29.0%	0.0094			
		Gencor foam	272	136	111	0.235	0.028	46,844	35,878	28.0%	0.0070	9%	46%	45%
		Evo. DAT	272	124	105	0.230	0.033	49,494	38,520	33.0%	0.0055	12%	76%	12%
		Heritage wax	253	131	108	0.218	0.045	44,944	34,673	33.0%	0.0065	6%	40%	54%
NY	Batch-mini drum uninsulated dryer	HMA	246	167	140	0.348		67,820	48,313	21.0%	0.0240			
		Cecabase RT	221	116	101	0.265	0.083	54,566	42,972	21.0%	0.0048	23%	62%	14%
		SonneWarmix	242	122	91	0.249	0.099	54,088	43,766	16.0%	0.0000	24%	45%	31%
		BituTech PER	243	123	94	0.233	0.115	53,267	42,646	14.5%	0.0016	19%	38%	43%
						Average	0.0664					15%	45%	40%

Note: 1.0 CFM = 0.0283 cubic meters per minute.

of the total delta in energy usage per ton (% Stack Temp.). The remaining unexplained differences in the measured energy use are attributed to casing losses (% Casing Loss). These losses are heat lost through, for example, the shell of the drum and ductwork.

3.4 *Influence of aggregate moisture content*

A recommended best practice for both HMA and WMA is to minimize aggregate moisture content. Average aggregate moisture content for the Montana project was 1.4 percent; less than half the average moisture content from the other sites. Measured fuel usage for the Montana HMA was 0.183 GJ/tonne, compared to an average of 0.317 GJ/tonne for all other HMA and 0.299 for the Michigan and Indiana HMA, which were produced at the same average temperature. This indicates a savings of 0.061 GJ/tonne per percent of moisture reduction. Thus, a one percent reduction in stockpile moisture content can produce savings similar to the average savings between HMA and WMA, 0.064 GJ/tonne.

4 CONCLUSIONS

- To make meaningful comparisons, fuel usage between HMA and WMA should be compared over short, steady-state runs at similar production rates and aggregate moisture.
- WMA mixes were produced an average of 27 °C cooler than the corresponding HMA mixes, resulting, on average, in 22.1 percent fuel savings.
- The measured fuel savings were higher than predicted by calculations of energy required to dry then heat mix and exhaust gases.
- The additional fuel savings are attributed to casing losses—heat radiated through the drum, ductwork and baghouse or otherwise lost. Insulated plants will have lower fuel savings from WMA technologies than uninsulated plants.
- Best practices, such as burner tuning and reduced stockpile moisture, produced reductions of similar magnitude to the use of WMA.
- There is a high potential for error when calculating fuel usage over short intervals from tank fuel depth measurements (tank sticks), or natural gas meter readings. A difference of two minutes between fuel and tonnage produced measurements can result in a 3.3 percent error in hourly fuel usage calculations. A 2.5 mm (1/10 inch) error in a tank depth of a 75,708 liter (20,000 gallon) horizontal tank at the 37,854 liter (10,000 gallon) mark results in a 129 liter (34 gallon) (5.489 GJ (4.715 MMBTU)) error in measured fuel usage.

5 RECOMMENDATIONS

- Fuel *savings* should be based on comparison of steady state conditions and be of the longest duration possible. Historic average fuel use may be informative but a poor basis to quantify savings.
- Stoichiometric fuel calculations, in accordance with EPA Method 19, should be made in conjunction with direct measurements of fuel consumption when stack tests are part of demonstration or study.
- Take fuel meter and cumulative tonnage readings at the same time and over as long of an interval as possible to minimize errors due to measurement accuracy.

ACKNOWLEDGEMENT

This work was sponsored by the National Cooperative Highway Research Program, Project 9-47 A. The authors worked under subcontract to the National Center for Asphalt Technology.

REFERENCES

[1] Cervarich, M., "Foaming the Asphalt: New Warm-Mix Technique Challenges Conventional Wisdom." Hot Mix Asphalt Technology, Volume 12, Number 4, National Asphalt Pavement Association, Lanham, MD, pp 23–24, 42, July/August 2007.

[2] Koenders, B., D. Stoker, C. Bowen, P. de Groot, O. Larsen, D. Hardy, K. Wilms, "Innovative Process in Asphalt Production and Placement to Obtain Lower Operating Temperatures," 2nd Eurasphalt & Eurobitume Congress. Barcelona, Spain, 2000.

[3] von Devivere, M., W. Barthel and J-P. Marchand. *Warm Asphalt Mixes by Adding Aspha-min, a Synthetic Zeolite*. XXIInd PIARC World Road Congress. Durban, South Africa, 2003.

[4] Ventura, A., P. Moneron, A. Jullien, P. Tamagny, F. Olard, and D. Zavan, "Environmental Comparison at Industrial Scale of Hot and Half-Warm Mix Asphalt Manufacturing Processes." Transportation Research Board, 2009 Annual Meeting DVD.

[5] D'Angelo, J., E. Harm, J. Bartoszek, G. Baumgardner, M. Corrigan, J. Cowsert, T. Harman, M. Jamshidi, W. Jones, D. Newcomb, B.D. Prowell (Report Facilitator), R. Sines, and B. Yeaton, *Warm-Mix Asphalt: European Practice*. International Technology Scanning Program, Federal Highway Administration, December 2007.

[6] Harder, G.A., "LEA Half-Warm Mix Paving Report, 2007 Projects for NYSDOT." McConnaughay Technologies, Cortland, NY, 2008.

[7] Davidson, J.K., "Evotherm Trial in Aurora, Ontario on August 8, 2005." McAsphalt Engineering Services, Toronto, Ontario. 2005.

[8] Davidson, J.K., "Evotherm Trial Ramara Township Road 46." McAsphalt Engineering Services, Toronto, Ontario, December 2005.

[9] Lecomte, M., F. Deygout, A. Menetti. Emission and Occupational Exposure at Lower Asphalt Production and Laying Temperatures. WAM Environmental Benefits of Reducing Asphalt Production and Laying Temperature, Shell Bitumen, Accessed from *www-static.shell.com/static/bitumen/downloads/wam_field_test_results_italy.pdf*., 2007, accessed April 14, 2011.

[10] Chief Environmental Group, LTD. "Emission Test Results for: Warm Mix Asphalt Trial Project Mar-Zane Materials, Inc. Asphalt Plant #13 Byesville, Ohio." No Date.

[11] ETE, "Warm Mix Stack Emission Test." Environmental Technology & Engineering Corporation, Elm Grove, WI, June, 20, 2006.

[12] Powers, D., "Warm Mix Asphalt 2008 ODOT Field Trials." Presentation at 2009 ODOT Asphalt Paving Conference.

[13] Ventura, A., P. Moneron, A. Jullien, P. Tamagny, F. Olard, and D. Zavan, "Environmental Comparison at Industrial Scale of Hot and Half-Warm Mix Asphalt Manufacturing Processes." Transportation Research Board, 2009 Annual Meeting DVD.

[14] Davidson, K.J., and R. Pedlow, "Reducing Paving Emissions Using Warm Mix Technology." Proceedings of the 52nd Annual Conference of the Canadian Technical Asphalt Association, pp 39–59, 2007.

[15] Middleton, B., and R.W. Forfylow, "An Evaluation of Warm Mix Asphalt Produced with The Double Barrel Green Process." Transportation Research Board, 2009 Annual Meeting DVD.

[16] Harder, G., Y. LeGoff, A. Loustau, Y. Martineau, B. Heritier, and A. Romier. "Energy and Environmental Gains of Warm and Half-Warm Asphalt Mix: Quantitative Approach." Transportation Research Board, 2008 Annual Meeting DVD.

Additives and modifiers for asphalt concrete—I

This page intentionally left blank

Asphalt Pavements – Kim (Ed)
© 2014 Taylor & Francis Group, London, ISBN 978-1-138-02693-3

Surface energy measurements and wettability investigation of different minerals and bitumen for cold asphalts

Abdullah Khan
Highway and Railway Engineering, KTH Royal Institute of Technology, Stockholm, Sweden

Per Redelius
NYNAS Bitumen AB, Nynäshamn, Sweden

Nicole Kringos
Highway and Railway Engineering, KTH Royal Institute of Technology, Stockholm, Sweden

ABSTRACT: For environmental reasons, low installation cost and initial investment; low energy infrastructure materials are becoming of high interest. A potential option to replace current hot mix asphalts is emulsifications, where bitumen binder is dispersed in a water phase aided by emulsifier and shear forces, and mixed at ambient temperature with unheated stones. Long term performance must, however, be guaranteed, otherwise the application benefits will be significantly diminished. In this paper, the main issues of cold mix (emulsion based) asphalt, like wetting in the presence of moisture and dust, and coalescence issues are discussed. Since both bitumen droplets and mineral surfaces were upscaled, pure mineral surfaces were investigated as stone material consists of different minerals. As a measure of the interfacial bond strength, surface free energies of different mineral aggregates and bitumen have been investigated in this paper as a stepping stone for further analyses of emulsions. From the analyses it was found that bitumen has only dispersive forces whereas most of the minerals surfaces have polar nature. According to Fowke's additive nature of the forces, bitumen and water are roughly equally strongly adsorbed to plagioclase and calcite, whereas water will displace bitumen from quartz, gypsum, potassium feldspar and mica surface.

Keywords: Low energy infrastructure materials, cold mix asphalts, bitumen emulsions, wettability, minerals Surface energy

1 INTRODUCTION

Bitumen is a highly viscous semi-solid at room temperature and there are many ways to reduce its viscosity and thus make it as an effective binder such as heating, dissolving in solvents (cut-back bitumen), foaming the bitumen, or making oil/water type bitumen emulsions. In the pavement industry, hot mix and, more and more, warm mix asphalts are rather common practices. Cold mixture is however much less used and its applications have been mainly limited to recycling of low traffic roads. There are several options in cold mix technology like foaming the bitumen, cutback bitumen and bitumen emulsions. In bitumen emulsification, the bitumen phase is heated and dispersed in water in the presence of emulsifier by the application of shear forces. The process of manufacturing bitumen emulsions must be highly controlled to ensure the storability, workability and adhesion, making it thus an effective binder for road products. In cold asphalt mixtures, the aggregates are not heated and, as a result, a lot of energy can be saved. In addition to this, initial investment cost in terms of cold mix setup and transportation of raw material is low as compared to hot mix technology [1–2].

All types of emulsions (except for micro emulsions) are thermodynamically unstable and generally separate into two phases over a certain period of time [3]. Bitumen emulsions are classified in grades according to their reactivity, particle charge and physical properties. These are basically o/w type emulsions and contain 60–80 wt% bitumen, around 0.15–2 wt% emulsifier [4] and 20–40 wt% water plus minor additives like salts. The particle size of bitumen in bitumen emulsions is generally in the range of few μm (0.5–10 μm) and size distribution is strongly influenced by the emulsion recipe, temperature of the bitumen and water phase, mechanics and the operating conditions of the emulsion manufacturing mill [5]. Furthermore, the size of the droplets and the nature of the bitumen are two major variables that affect the breaking and coagulation of bitumen emulsions. But how they affect the breaking rate and curing process is not yet clear [6].

The emulsions are formulated to have a sufficient level of repulsive force between the particles that prevents any premature coagulation. The coalescence will occur if changes occur in the hydrophilic/lipophilic balance of the emulsifier, a variation in the pH, an increase in the ionic force of the medium or desorption of surfactant at bitumen-water interface. The interaction between the emulsion and the aggregates is the main cause for one of more of these changes [6]. The main purpose and an effective use of emulsification are to transport bitumen to the right location between the aggregates. The phase separation must thus take place at the right place followed by wetting of the stone surfaces and gluing the aggregates together. Along with water separation from the bitumen; a good adhesion to the stone surface is also required. Generally due to the hydrophilic nature of the stone surface, affinity for the water at aggregate surface is higher as compared to the bitumen that can be modified with emulsifiers which displace water from the stone surface and improve adhesion between the binder and the aggregates. This desired breaking process varies according to the required applications e.g. fast, medium and slow breaking as well as some other applications like dry, wet, clean or dusty stone surface. The exact nature of breaking mechanism of bitumen emulsion is not completely known. The bitumen emulsions are destabilized due to the adsorption of emulsifiers on the aggregate surface and agglomeration of bitumen particles forming a cheesy state that further more leads to coalescence of the bitumen droplets. A complete adhesion between binder and aggregate surface is achieved after complete evaporation of water and the strength of the asphalt is improved with time [7].

Bitumen emulsions are designed to start breaking or rupturing when mixed with aggregates, and a phase separation by flocculation and coalescence should quickly occur that leads to partial loss of water in emulsion as shown in Figure 1. A continuous film of bituminous

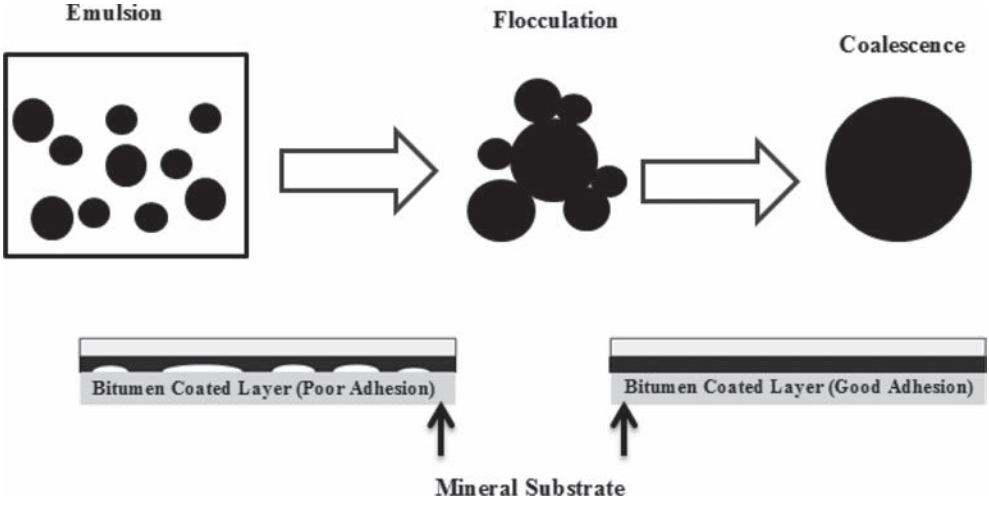

Figure 1. Coalescence process in bitumen emulsion and bitumen interactions with aggregates.

binder is developed that, if all is well, covers the aggregates completely followed by curing or setting of the binder which eventually gives the mechanical strength. Considering the relative complexity of emulsion technology compared with hot mix technology, there are several components in emulsion technology that need to be investigated more closely to ensure the long term performance of cold mix asphalt and reduce the sensitivity of their application. With regard to asphalt pavements, it is common knowledge that adhesion between bitumen and stones can be reduced in the presence of moisture (stripping) and that dust particles on the surface of the aggregates can lead to poor adhesion. In the case of bituminous emulsion, this risk is amply present, since moisture is available from the emulsions as well as the wet aggregates and dust can be present on the (unheated) stones, Figure 1. But on the other hand a well-chosen emulsifier could improve the bitumen wetting of the stones.

The coalescence process plays an important role in the water separation and evaporation process. It is possible that during this process, some of the water after separation from the emulsion, cannot evaporate and gets trapped inside the mixture. The presence of trapped water in the wrong locations can seriously affect the durability and performance of the pavement. This is one of many factors that must be considered carefully when designing the emulsion. Thus an in depth understanding of the forces that come into play during the breaking and curing of bitumen emulsion binders is fundamental in order to control their behavior and to produce high quality pavements.

To investigate the thermo-dynamical interface properties of bitumen-stone combinations, the surface energy properties of both binder and aggregates need to be determined. Sessile drop is one method utilized for such investigations. In this paper, pure mineral and bitumen surfaces were examined using surface chemistry principles by measuring static contact angles of different probe liquids. Both dispersive and non-dispersive surface free energy components for the binder and aggregates were calculated using the Fowkes theory, as it is more applicable to the situations where adhesion occurs in the stone-bitumen system.

1.1 *Theoretical background*

The theories of adhesive and cohesive bonding are well established in the fields of surface chemistry and physics. All materials, including bitumen and aggregate, have surface energies that can be measured independently from each other. From this information, one can predict how well asphalt mixture component will wet each other and thus their bonding potential. Investigations of surface free energies of bitumen and aggregates have been performed over the last years by many researchers. [e.g. 8–9] whereby the focus mainly lied on hot mix asphalt applications.

Surface energy 'γ' is the amount of work required to create a unit area of a given materials in a vacuum. This surface energy is known to have dispersive (non-polar) and non-dispersive (polar and hydrogen bonding) components. The direct measurement of surface energy of a solid is for practical reasons not a very common practice and usually indirect methods are used to measure surface energies of solids. Therefore, some methods [10] have been developed to study the interactions between liquid, solid and gas surfaces that among others include contact angle measurements, gas adsorption, inverse gas chromatography and micro calorimetry. Among all, contact angle measurement is the most economical, easy to operate and less time consuming. Surface tension and contact angles are outcomes of short-range intermolecular forces. Methods for measuring interfacial tension include Wilhelmy Plate, Du Nouy Ring, Pendant Drop and Sessile Drop. Each method describes the surface energy parameters and Wilhelmy plate and Sessile drop are today the most commonly used for liquid-solid substrates. The Wilhelmy plate method is used for dynamic contact angle measurement while sessile drop measure static contact angle. The Du Nouy Ring method is developed for liquid-air interface and Pendent drop method is opted for liquid-liquid interface. An in depth understanding of the surface forces action is very important to explain the wetting and spreading processes.

Young-Laplace developed a relation between contact angle and surface energy as below;

$$\gamma_S = \gamma_{SL} + \gamma_L * \cos\theta \quad (1)$$

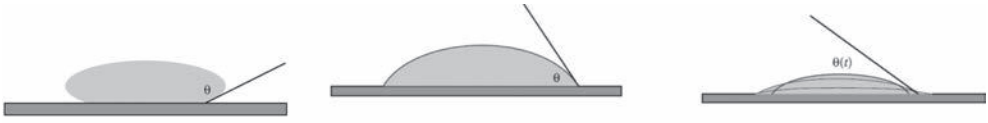

No Wetting (θ is bigger than 90^0) | Partial Wetting (θ is between 0 and 90^0) | Complete Wetting (θ become Zero with time)

Figure 2. Wettability as a function of contact angle [11].

γ_S is solid surface energy, γ_L is liquid surface energy, γ_{SL} is solid-liquid interface energy and θ is contact angle as shown in Figure 2.

Fowkes developed a theory to calculate the component of surface energy from the known surface tension as shown below; (D represents the dispersive component of surface energy)

$$\gamma_{SL} = \gamma_S + \gamma_L - 2\sqrt{(\gamma_S^D * \gamma_L^D)} \quad (2)$$

Later on, Fowkes uses the above relationship in Equation 2 combined with Young's equation, Equation 1, to create an equation 3 based upon the contact angle.

$$\cos\theta = 2\sqrt{(\gamma_S^D)} * [1/\sqrt{\gamma_L^D}] - 1 \quad (3)$$

By plotting the contact angle versus the known dispersive surface energy of the liquid, this equation can be used to find the dispersive surface energy of the solid, which is the slope of the line. The polar component is also found using a linear regression relationship. Fowkes extended equation 2 to include the polar components of surface energy by the following equation.

$$\gamma_{SL} = \gamma_S + \gamma_L - 2[\sqrt{(\gamma_S^D * \gamma_L^D)} + \sqrt{(\gamma_S^P * \gamma_L^P)}] \quad (4)$$

In the Sessile method, dispersive and polar components required a minimum of two probe liquids with known surface tensions.

2 MATERIALS AND EXPERIMENTAL METHODS

A bottom-up approach was considered to investigate surface free energy of aggregate material. Stone materials that are mostly being used for the roads constructions consist of many minerals like quartz, mica, potassium feldspar, gypsum, biotite, calcite, plagioclase and others. For example Skärlunda granite in Sweden contains 40 vol.% quartz, 35.5 vol.% k-feldspar, 14 vol.% plagioclase, 4 vol.% mica, 3 vol.% biotite, 2.5 vol.% chlorite and 1 vol.% other materials. Since in this research, emulsions are the main focus point, bitumen droplets are being up-scaled to (later on) represent the microscale droplets present in emulsions. Similarly, mineral surfaces are up-scaled by studying each mineral individually. Hereby the future assumption is made that the different types of aggregated stone material can be described as the sum of its component minerals, as well as to develop fundamental understanding of the effect of the individual minerals themselves.

The samples have been cut using power hexa machine and surfaces of these minerals were polished using different mesh size Silicon Carbide papers starting from coarse to a fine mesh. No polishing aids have been used since they may affect surface tension. The surface smoothness of the minerals was given much more importance, since the investigation is focused on the surface interaction of between the liquid and mineral. The level of smoothness or texture was compared under optical microscope. Later on, these polished samples were mounted on

glass slides to achieve plane symmetry condition for getting precise measurement of contact angles. KRÜSS DSA100—Drop Shape Analysis System was used to measure contact angles of known probe liquids drops on the analyzing substrate surface. KRÜSS uses optical method for contact angle measurement and DSA100 setup can be used for sessile drop as well as pendent drop methods. It contains four automatic dosing units on its left arm that are connected through four channels for different probe liquids and one manual dosing unit. Contact angle is measured when drop is static and gravitational forces are balanced with inter facial tension. In this study, drop size was 7 µl for all probe liquids and deposition height was optimized to avoid splashes. Bitumen 160/220 samples were heated around 90 °C and coated on glass slides and cooled down till room temperature under covered glass hood to prevent any dust on the surface of the bitumen coating. An emulsion grade unaged and unmodified straight run bitumen 160/220 was investigated in this study and provided by Nynas AB, Sweden. The chemical constituents according to latroscan or SARA fractions for bitumen 160/220 are 9% Saturates, 54.3% Aromatics, 22.2% Resin and 14.5% Asphaltenes.

3 RESULTS AND DISCUSSIONS

From the Sessile drop contact angle measurement, the drop shape [12] was analyzed using three different approaches known as height-width, Young-Laplace and circle fitting methods. Each method has advantages and limitations. For example, all methods are applicable for static drops and not valid for dynamic drops. The reason behind this comparison was to achieve precision and accuracy in results. In height-width method, the drop contour line is enclosed within a rectangle. In this method, the drops are regarded as being symmetrical that means contact angle at left side is equal to the contact angle at right. This is the main limitation of the height-width method. In the circle method, the drop contour is fitted to a segment of a circle and it follows the same assumption of drop being symmetrical as in height-width method. In the case of Laplace-Young method, a complete drop contour is evaluated that is why it is the most complicated. It includes both interfacial and gravitation effects in the calculations. The slope of the contour line at three phase contact point is represented in terms of mathematical equation that is very well known and often called Laplace-Young equation (1).

The liquid used, called the probe liquid, must be a non-reactive, homogeneous liquid, for which the surface energy components (Dispersive, Polar, H-H, acid, base, etc.) are known. Generally, there are five liquids recommended for use with this method, water, ethylene glycol, methylene iodide, glycerol, and formamide. Commonly, two to four probe liquids are used to find the surface energy of the solid substrate [13]. For investigation of surface free energy and contribution of surface interactions has been studied by using following three probe liquids as shown below in Table 1a.

The liquids, used for contact angle measurement and in surface energy calculations, are very well known from a chemistry point of view and many references can be found in the literature [14–28] where surface tensions and surface energy components are reported for such liquids. Many researchers proposed different surface tensions of the liquids used in this study as presented in Table 1b. Thus, selected values of surface tensions in Table 1a are the most commonly agreed ones in surface chemistry society.

Table 1a. Probe liquids used and their surface tensions [14–15].

Probe liquids	Total liquid IFT (l) [mN/m]	Dispersive part (d) [mN/m]	Polar part (p) [mN/m]
Diiodo-methane	50.80	48.50	2.30
Formamide	58.20	39.50	18.70
Water	72.80	21.80	51.00

Table 1b. Referred surface tensions of probe liquids in literature.

Substance	Total IFT [mN/m]	Dispersive [mN/m]	Non-dispersive (polar) [mN/m]
Water	72.10[16]	19.90	52.20
	72.30[17]	18.70	53.60
	72.75[18]	22.10	50.65
	72.80[19]	26.00	46.80
	72.80[14–15,20–23]	21.80	51.00
Diiodo-methane	50.00[16]	47.40	2.60
	50.80[14]	48.50	2.30
	50.80[15,20–21,23]	50.80	0.00
	50.80[24]	49.50	1.30
Formamide	56.90[16]	23.50	33.40
	58.00[21,23]	39.00	19.00
	58.20[14,22]	39.50	18.70
	58.30[22]	37.90	20.40

Table 2. Mean contact angles of probe liquids on minerals surface using LY-method.

Minerals	Quartz	Mica	K-Feldspar	Gypsum	Biotite	Calcite	Plagioclase	Probe liquids
Mean contact angle [deg.]	31.5	46.8	31.4	33.6	63.2	57.1	37.1	Diiodo-methane
(Laplace-Young	13.7	24.1	14.5	5.2	52.9	39.1	42.1	Formamide
method)	10.3	26.7	24.3	13.9	59.9	82.0	74.0	Water

Table 3. Surface energy contributions of different minerals based on LY-method.

Mineral	Total IFT [mN/m]	Dispersive [mN/m]	Non-dispersive (Polar and H-H) [mN/m]
Gypsum	68.1 ± 0.32	26.5 ± 0.09	41.7 ± 0.22
Quartz	68.0 ± 0.49	26.8 ± 0.25	41.2 ± 0.24
Potassium-feldspar	64.6 ± 1.28	28.1 ± 0.49	36.5 ± 0.78
Mica	63.3 ± 3.14	21.6 ± 1.0	41.7 ± 2.14
Plagioclase	43.7 ± 1.84	36.6 ± 1.12	7.1 ± 0.71
Biotite	41.0 ± 4.4	17.6 ± 1.64	23.4 ± 2.75
Calcite	37.0 ± 2.76	28.6 ± 2.0	8.4 ± 0.76

Table 4. Mean contact angles of probe liquids on minerals surface using HW-method.

Minerals	Quartz	Mica	K-Feldspar	Gypsum	Biotite	Calcite	Plagioclase	Probe liquids
Mean contact angle [deg.]	29.5	42.4	24.3	34.2	50.3	50.9	36.8	Diiodo-methane
(height-width	13.5	24.6	21.5	12.0	50.5	34.3	35.0	Formamide
method)	10.8	25.3	23.0	11.8	54.2	78.6	59.3	Water

The contact angles were evaluated with three different methods which have resulted in different surface energy calculations. These methods are Laplace-Young (LY), Height-Width (HW) and Circle (CIR) methods, which are based on different approaches to analyze drop shapes. Tables 2, 4 and 6 present the mean contact angles of different probe liquids evaluated on the surface of different minerals by LY, HW and CIR methods respectively.

Table 5. Surface energy contributions of different minerals based on HW-method.

Mineral	Total IFT [mN/m]	Dispersive [mN/m]	Non-dispersive (polar and H-H) [mN/m]
Gypsum	68.1 ± 0.22	25.9 ± 0.07	42.2 ± 0.15
Quartz	67.9 ± 1.09	27.5 ± 0.47	40.4 ± 0.62
Potassium-feldspar	64.1 ± 1.13	30.0 ± 0.44	34.1 ± 0.69
Mica	63.3 ± 2.93	23.8 ± 0.82	39.5 ± 2.11
Plagioclase	48.2 ± 2.23	32.5 ± 0.57	15.7 ± 1.66
Biotite	44.7 ± 3.88	23.0 ± 1.82	21.7 ± 2.06
Calcite	40.4 ± 1.62	31.6 ± 0.71	8.8 ± 0.9

Table 6. Mean contact angles of probe liquids on minerals surface using CIR-method.

Minerals	Quartz	Mica	K-Feldspar	Gypsum	Biotite	Calcite	Plagioclase	Probe liquids
Mean contact angle [deg.]	29.6	43.5	24.7	37.6	50.9	49.8	36.2	Diiodo-methane
(circle	13.1	24.1	17.6	11.5	50.4	35.1	37.8	Formamide
method)	10.1	25.6	23.0	11.6	56.3	78.9	56.9	Water

Table 7. Surface energy contributions of different minerals based on CIR-method.

Mineral	Total IFT [mN/m]	Dispersive [mN/m]	Non-dispersive (polar and H-H) [mN/m]
Gypsum	68.4 ± 0.52	24.6 ± 0.2	43.8 ± 0.32
Quartz	68.0 ± 0.99	27.5 ± 0.46	40.6 ± 0.52
Potassium-feldspar	64.7 ± 1.23	30.1 ± 0.4	34.5 ± 0.82
Mica	63.4 ± 1.71	22.9 ± 0.43	40.5 ± 1.28
Plagioclase	48.5 ± 2.9	31.8 ± 1.37	16.7 ± 1.53
Biotite	43.8 ± 5.36	23.2 ± 1.78	20.6 ± 3.58
Calcite	40.5 ± 2.04	32.3 ± 1.48	8.2 ± 0.56

Fowke's theory was used to calculate the surface free energy of different minerals. Tables 3, 5 and 7 show the calculations based on contact angles measured by LY, HW and CIR methods respectively. All these methods are well explained in many literatures [29–30].

Based on the measured sessile drops contact angles using LY, HW and CIR methods, it can be observed that results of HW and CIR methods are very much overlapping quantitatively as compared to LY method. Similar observation can be made in surface energy calculations where the HW and CIR methods seem to agree very well, whereas the LY-method seems to deviate from the other two on the lower IFTs. These small deviations depend upon different factors for example physics behind shape analysis, optical resolution of the image and base line position. The results obtained with HW and CIR methods are more accurate as compared to LY method.

The results in Table 3 indicate that gypsum, quartz, potassium feldspar and mica have very high total Interfacial Tensions (IFTs) due to high wettability. Furthermore, non-dispersive (Polar and H-H) interactions for these minerals are very dominant as compared to the dispersive part. The high polarity of these mineral surfaces will make them more hydrophilic than hydrophobic. On the other hand, plagioclase and calcite surfaces appeared in the range with major dispersive interaction with low total IFTs. Biotite mineral has a low total IFT similar to plagioclase and calcite, but its surface is more polar. Plagioclase and calcite have similar polarity but plagioclase is more dispersive than calcite as shown in Table 3.

The contact angles that are presented in Tables 2, 4 and 6 are mean contact angles based on at least five repeated measurement.

Surface free energy contributions of same minerals were calculated using Fowkes approach in Table 5 as well. The quantitative results were slightly different from this method as presented in Table 3 but qualitatively they followed similar paths. Biotite surface that seems to be more polar than dispersive with LY method, turned out more dispersive with the HW method. Whereas plagioclase showed almost double polarity as compared to calcite in HW calculations.

So we can conclude from these results that though most minerals have dominance of polar interactions, they do have some subtle differences which can become important especially in sensitive systems such as emulsified bitumen. Results of all these methods are comparable with each other and Table 7 shows that major contribution in the total interfacial tension is due to polar interactions for gypsum, quartz, potassium feldspar and mica. The results obtained in HW and CIR methods are very much similar and according to the calculations calcite has the lowest total IFT with high dispersive surface energy contribution. An important observation could be the surface energy and almost hydrophobic surface nature of the calcite mineral.

In the methodology section it was earlier described how the bitumen samples were prepared for the surface energy studies. Table 8 shows the mean contact angles of same probe liquids described in Table 1a on bitumen surface.

Table 8. Mean contact angles of probe liquids on the surface of emulsion grade binder.

Bitumen substrate	Mean contact angle [deg.] (Laplace-Young method)	Mean contact angle [deg.] (circle method)	Mean contact angle [deg.] (height-width method)	Probe liquids
160/220	37.4	32.8	33.0	Diiodo-methane
	91.9	86.5	87.2	Formamide
	97.7	93.4	93.7	Water

Table 9. Image views of contact angles measurements on binder surface.

Bitumen substrate	Mean contact angle [deg.] (Laplace-Young method)	Mean contact angle [deg.] (circle method)	Mean contact angle [deg.] (height-width method)	Probe liquids
160/220	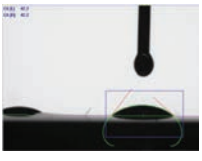	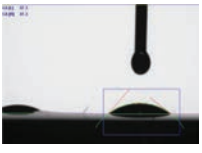	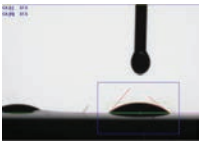	Diiodo-methane
	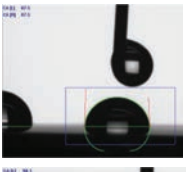	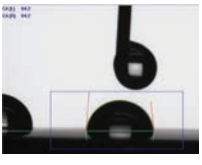	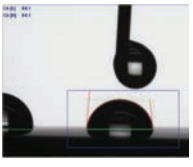	Formamide
	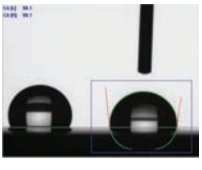	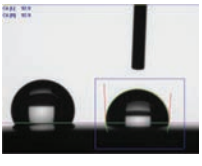	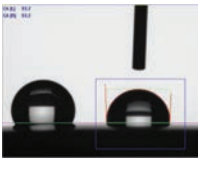	Water

Table 10. Surface energy contributions of emulsion grade binder.

Bitumen (160/220)	Total IFT [mN/m]	Dispersive [mN/m]	Non-dispersive (polar and H-H) [mN/m]
Laplace-Young method	37.7 ± 1.46	37.5 ± 1.41	0.2 ± 0.05
Circle method	39.0 ± 1.36	39.0 ± 1.24	0.0 ± 0.12
Height-width method	38.9 ± 1.43	38.8 ± 1.32	0.0 ± 0.11

In Table 8, it can be seen that Circle and Height-Width methods results for bitumen surface are also very close as compared to Laplace-Young method. Height-Width method is less robust than Circle fit whereas Laplace-Young fit is reliable for angles above 30°. As wetting angle of the water on bitumen surface is greater than 90°, thus it is truly hydrophobic. These variations in contact angles and profiles can be visually observed in Table 9 that shows image views of these measurements. Accuracy of the results can be compared only when such comparison are made. Accurate baseline detection, smooth and clean surface, optical clearance and gray levels; these all parameters contribute to high quality results.

Surface free energy calculations of bitumen are presented in Table 10 and here the major contributions are due to dispersive interactions. From the results, it can be expected with regards to Fowke's hypothesis that the two categories of forces are additive! Bitumen has only dispersive forces i.e. it can develop bonds to minerals which are equal to the smaller of the mineral and bitumen. For water it is the sum of the smallest dispersive force acting between the mineral and bitumen and the smallest non-dispersive forces acting between water and the mineral. Furthermore, bitumen and water are roughly equally strongly adsorbed to plagioclase and calcite, whereas water will displace bitumen from the other minerals.

As bitumen emulsions contain water, it is of paramount importance that water is either pushed out completely from the mineral-bitumen interface, giving it the opportunity to evaporate or drain off. Furthermore, the above measurements will be important when introducing the emulsifier itself to the system and will largely determine where it will go after the breaking of the system or in other words phase separation.

4 CONCLUSIONS

It can be concluded from the above research work that bitumen has only dispersive forces whereas most of the minerals surfaces have polar nature. According to Fowke's additive nature of the forces, bitumen and water are roughly equally strongly adsorbed to plagioclase and calcite, whereas water will displace bitumen from quartz, gypsum, potassium feldspar and mica surface. Height-Width method is less robust than Circle fit whereas Laplace-Young fit is reliable for angles above 30°. Future research will focus on the introduction of emulsions into the bitumen mineral system and the effect of adding mineral fillers to the bitumen and the characterization of long term performance of emulsion based asphalts, taking into consideration the fundamental properties, such as Surface Free Energy (SFE).

ACKNOWLEDGEMENTS

This research work was sponsored by NYNÄS AB and KTH Royal Institute of Technology, Sweden. The authors acknowledge Måns Collin and Björn Birgisson for many valuable discussions.

REFERENCES

[1] J. Read, et al., The Shell Bitumen Handbook, 5th ed., Thomas Telford Publishers, London 2003.
[2] A.J. Hoiberg, Bituminous Materials: Asphalts, Tars, and Pitches, Interscience Publishers, New York 1965.
[3] R.P. Borwankar, et al., J. Colloids and Surfaces, 69, pp.I35–146, 1992.
[4] P. Becher, Emulsions: Theory and Practice, 2nd ed., Robert E. Krieger Publishing Company Inc., Florida 1966.
[5] G. Jean-Philippe, et al., Chemical Eng. and Process., 44, pp-979–986, 2005.
[6] R. Jean-Claude, Routes de France, Section SFERB: Bitumen Emulsions, Paris 2008.
[7] P. Redelius, et al., Chap.11-Bitumen Emulsions; Emulsions and Emulsions Stability, CRC Press 2005.
[8] R.L., Lytton, et al., Texas Transportation Institute; *Rep. No.* 0-4524-2, 2005.
[9] D.N. Little, et al., Self-Healing Materials. An Alternative Approach to 20 Centuries of Materials Science, S. van der Zwaag (ed)., pp. 205–218, 2007.
[10] Żenkiewicz, J. Achievements in Materials and Manufacturing Engineering, 24(1), pp. 137–145, 2007.
[11] G. Bracco, Surface Science Techniques, B. Holst (eds.), Springer-Verlag Berlin Heidelberg 2013.
[12] B.G.M.O. Stephen, et al., J. Chem. Soc., Faraday Trans., 87, pp.1579–1583, 1991.
[13] Hans-Juergen B., et al., Physics and Chemistry of Interfaces, Wiley-VCH, Verlag GmbH & Co. KGaA, Weinheim, Germany 2003.
[14] F.M. Fowkes, J. Ind. and Eng. Chem., 56 (12), pp. 40–52, 1964.
[15] G. Ström et al., J. Colloid Interf. Sci., 119 (2), pp. 352–361, 1987.
[16] H.J. Busscher et al., J. Coll. and Surf., 9, pp. 319–331, 1984.
[17] W. Rabel, Farbe U. Lack, 77, pp. 997–1006, 1971.
[18] P.J. Sell et al., J. Angewandte Chemie, 83 (22), p. 932, 1971.
[19] K.F. Gebhardt, FHG IGB Stuttgart, 1982.
[20] C.D. Volpe et al., J. Colloid Interf. Sci.,195 (1), pp. 121–136, 1997.
[21] M.L. Gonzalez-Martin et al., J. Langmuir, p. 5991, 1997.
[22] G. Koerner et al., J. Goldschmidt-Hauszeitschrift, 2, H.29, S.2/41, 1974.
[23] M.N. Bellon-Fontaine et al., J. Cell Biophys., 17 (1), pp. 93–106, 1990.
[24] D.K. Owens et al., J. Appl. Polym. Sci., 13, p. 1741, 1969.
[25] V.J. Oss, J. Colloid Interface Sci., 128, pp. 313–317, 1989.
[26] C. Jie-Rong., J. Appl. Polym.Sci., 63, pp. 1733–1739, 1997.
[27] B. Janczuk, J. Colloid Interf. Sci., 127 (1), P. 189, 1989.
[28] I.G. Reilly, J. Chem. Engg., 72 (1), pp. 3–12, 1994.
[29] K.L. Mittal, Contact Angle, Wettability and Adhesion, VSP BV Netherlands, 1993.
[30] A.W. Adamson, et al., Physical Chemistry of Surfaces, Wiley, New York, 1997.

Asphalt Pavements – Kim (Ed)
© 2014 Taylor & Francis Group, London, ISBN 978-1-138-02693-3

Damage in asphalt concrete during the dynamic complex modulus and flow number tests

Mostafa A. Elseifi
Department of Civil and Environmental Engineering, Louisiana State University, Baton Rouge, LA, USA

Louay N. Mohammad
Louisiana Transportation Research Center, Department of Civil and Environmental Engineering, Louisiana State University, Baton Rouge, LA, USA

Emad Kassem
Texas Transportation Institute, Texas A&M University, College Station, TX, USA

Hao Ying
Department of Civil and Environmental Engineering, Louisiana State University, Baton Rouge, LA, USA

Eyad Masad
Texas A&M University at Qatar, Doha, Qatar

ABSTRACT: The dynamic complex modulus test for asphalt mixtures is conducted in the linear viscoelastic region and measurements assume that no damage is induced during the testing process. In contrast, the level of damage taking place in the flow number test is expected to be significant but it has not been quantified. The objectives of this study are to quantify the levels of damage in the dynamic complex modulus and flow number tests using x-ray Computed Tomography (CT) and to characterize the heterogeneous properties of asphalt mixtures under loading. Four asphalt mixtures, one conventional Hot-Mix Asphalt (HMA) and three Warm-Mix Asphalt (WMA) mixes, were evaluated. Two WMA processes (i.e., water foaming and Rediset™ additive) were used in the preparation of the WMA mixes. Results of the experimental program indicated that the damage taking place in the dynamic modulus test is minimal and homogeneous while the damage taking place in the flow number test is significant and heterogeneous. In addition, preparation procedure may significantly influence the three-dimensional air voids distribution in laboratory-compacted specimens.

Keywords: Asphalt pavements, x-ray computed tomography, dynamic modulus test, damage, warm mix asphalt

1 INTRODUCTION

The Mechanistic-Empirical Pavement Design Guide (MEPDG) introduced new concepts and methodologies that address limitations in previously employed semi-empirical design models such as the 1993 AASHTO design guide [1]. A major milestone of the MEPDG is that Hot-Mix Asphalt (HMA) is no longer described as a purely linear elastic material. Instead, both the effects of temperature and rate of loading on the behavior of HMA are considered through the complex modulus |E*| [2]. The dynamic modulus test was introduced in NCHRP 9-19 as a Simple Performance Test (SPT) that can be used to predict field performance of asphalt mixes [3]. Research activities in NCHRP 9-19 also recommended the use of the Flow Number (Fn), from the triaxial repeated load test, as a performance indicator of mix resistance to permanent deformation.

The standard test method for determining the dynamic modulus of asphalt mixes, AASHTO T342 "Standard Method of Test for Determining Dynamic Modulus of Hot-Mix Asphalt Concrete Mixtures," assumes that measurements are conducted within the linear viscoelastic region, in which the dynamic modulus is independent of the stress or strain amplitude. To ensure that the relationship between stress and strain is linear, the axial strains in the specimen should range between 50 and 150 microstrains. Calculation of the dynamic modulus also assumes proportionality of the induced strain to the applied stress on the specimen. Therefore, no damage should be induced in the specimen in order to ensure validity of the measurements and the calculations. In contrast, the flow number test is continued until 10,000 cycles or until the specimen fails through excessive tertiary permanent deformation. Therefore, substantial damage is expected to occur during the test process.

Although the assumptions made in the dynamic modulus test and the flow number test are well-defined, the levels of damage taking place during testing have not been quantified. The objectives of this study are to quantify the levels of damage in the dynamic complex modulus and flow number tests using x-ray Computed Tomography (CT) and to characterize the heterogeneous properties of asphalt mixtures under loading. Results of this experimental program were used to provide insight into damage and Three-Dimensional (3D) air voids distribution in asphalt mixes prior to and after loading. While this approach neglects the area of micro-cracks in the CT image, it provides a valid indication of damage in the material.

2 BACKGROUND

Digital image analysis allows one to enhance desired features in acquired digital images and to analyze the images based on the differences in grayscale intensities of the features. Enhanced digital images can also be converted into a numerical FE mesh. In the 1990s, digital image analysis techniques were utilized to analyze the surface characteristics of HMA [4]. This methodology was utilized to investigate the influence of compaction levels on the internal structure of HMA in the field and in the laboratory [5]. Elseifi and co-workers (2008) employed a high resolution digital camera to investigate the concept of asphalt binder film thickness in asphalt mixtures [6]. Adhikari and You (2007) used x-ray CT imaging technology to characterize aggregate orientation, aggregate gradation, mastic distribution, and air void distribution in HMA [7]. The locations of aggregates, air voids, and mastic were defined based on the grayscale intensities of x-ray CT images. Kassem et al. (2009) successfully employed 3D x-ray CT to evaluate the quality of the compaction of asphalt layers within full-depth pavements [8]. Image analysis technique was used to determine the average percent of air voids through the depth of the HMA layer. In general, it is widely recognized that x-ray CT is an effective method to evaluate the internal structure of asphalt mixtures.

3 EXPERIMENTAL PROGRAM

3.1 *Test materials*

Four dense-graded asphalt mixtures including one conventional HMA and three Warm-Mix Asphalt (WMA) mixes were evaluated. Two processes (i.e., water foaming and Rediset™ additive) were used in the preparation of the WMA mixes. In addition, Reclaimed Asphalt Pavement (RAP) was used in the preparation of the mixes at a content ranging from 15 to 30%. Table 1 provides a description of the eight test specimens. For the dynamic modulus specimens, loose mixtures were sampled from plant-produced materials for a project in Louisiana, located on US 171, and were compacted in an on-site mobile laboratory using a Superpave pneumatic gyratory compactor with no reheating to a target air voids content of 7.0%. Dynamic complex modulus specimens were compacted to a 165-mm height and a 150-mm diameter. Test specimens were then cored and cut from the center of the gyratory specimens to result in 100-mm diameter by 150-mm high specimens. For the flow number specimens,

Table 1. Descriptions of the test specimens.

Mix type	Specimen ID	Test	VTM[1] (%)	
			Before testing	After testing
WMA 15% RAP foamed	1	Dynamic modulus	7.3	7.4
	2	Flow number	6.3	9.5
WMA 30% RAP foamed	3	Flow number	5.5	9.2
	4	Dynamic modulus	5.8	5.8
Conventional 15% RAP	5	Flow number	7.1	9.9
	6	Dynamic modulus	7.0	7.5
WMA 15% RAP rediset™	7	Dynamic modulus	7.8	8.2
	8	Flow number	7.4	10.2

[1] VTM: Voids in the total mix.

loose asphalt mixtures sampled from the same project were transported to the Louisiana Transportation Research Center (LTRC) laboratory, reheated, and were compacted using a pneumatic Superpave gyratory compactor to a target air voids content of 7.0%. Flow number specimens were compacted to a 165-mm height and a 100-mm diameter. Test specimens were cut to result in 100-mm diameter by 150-mm high specimens.

3.2 *The dynamic modulus test*

The dynamic modulus test was conducted in accordance with AASHTO T342. The test was conducted by applying a uniaxial sinusoidal (i.e., haversine) compressive stress to an unconfined HMA cylindrical test specimen. The haversine compressive stress was applied on each specimen to achieve a target vertical strain level of 100 micro-strains in an unconfined test mode. The dynamic modulus test was conducted at four temperatures (4.4, 20.0, 37.8, and 54.4 °C) and at six loading frequencies of 0.1, 0.5, 1.0, 5.0, 10.0, and 25.0 Hz at each temperature.

3.3 *The flow number test*

The flow number test was used to assess the permanent deformation characteristics of paving materials by applying a repeated dynamic load for several thousand repetitions on a cylindrical asphalt specimen [9]. The "Flow Number" is defined as the starting point, or cycle number, at which tertiary flow occurs on a cumulative permanent strain curve obtained during the test. A loading cycle of 1.0 second in duration was used and consisted of applying 0.1-second haversine load followed by 0.9-second rest period. Permanent axial strains are recorded throughout the test. The test was conducted at an effective temperature (T_{eff}) of 54 °C and at a stress level of 207 kPa.

3.4 *X-ray computed tomography*

The x-ray CT system in the Advanced Characterization of Infrastructure Materials (ACIM) laboratory at Texas A&M University was used to scan the test specimens. The x-ray system had a 350 kV x-ray source and a linear detector with a resolution of 0.17 mm/pixel. The following imaging parameters were used; x-ray tube current = 1.6 mA, voltage = 345 kV, and copper filter = 3.2 mm thick. The test specimen was placed on a sample stage in between the x-ray source and the detector. The specimen stage rotates a full rotation with a constant speed during the scanning, and moves down at a specific distance. In this study, the interval between two subsequent x-ray CT images was 1 mm and scanning time of each x-ray CT images was 2 minutes. The intensity of the x-rays changes after going through the test specimen. The change in the intensity of the x-rays is related to the linear attenuations of different constituents within the test specimen, where the linear attenuation of a substance is related to

its density among other things. In an x-ray CT image, the low density material is represented with a darker color, while the high density material is represented by a brighter color (on a 256 gray level scale). Figure 1(a) shows an x-ray CT image for one of the asphalt mixture specimens.

In this study, the main focus was to determine the internal air voids distribution along the height of the test specimen. Macros that were developed in the Image-Pro® software were used to conduct the analysis [10]. By choosing the proper gray level, the air voids phase was thresholded from the other constituents (mastic and aggregates). This method relies on matching the calculated percent air voids using Equation (1) with the measured laboratory percent air voids. The total percent of air voids ($\%AV_t$) in a test specimen was calculated using Equation (1), while the average percent air voids in an image ($\%AV_i$) and the average radius of air voids (R) were calculated based on Equations (2), and (3), respectively:

$$\%AV_t = \frac{1}{N}\sum_1^N \%AV_i \tag{1}$$

$$\%AV_i = \frac{A_{tv}}{A_t} \tag{2}$$

$$R = \sqrt{\frac{A_{tv}}{\pi n}} \tag{3}$$

where N *is* the number of images, A_{tv} is the total area of the air voids an image, A_t is the total cross-sectional area of an image, and n is the number of the air voids in an image.

A scalar variable ξ was defined to quantify the levels of irreversible damage in HMA [11, 12]:

$$\xi = 1 - \frac{\overline{A}}{A_o} \tag{4}$$

where A_o is the initial area of the undamaged section and $\overline{A}$ is the effective cross-sectional area in the current damaged state. The variable ξ describes a positively monotonically increasing function. For the undamaged material, ξ is equal to 0, while for the totally damaged material, ξ is equal to 1. The effective cross-sectional area of the specimen was

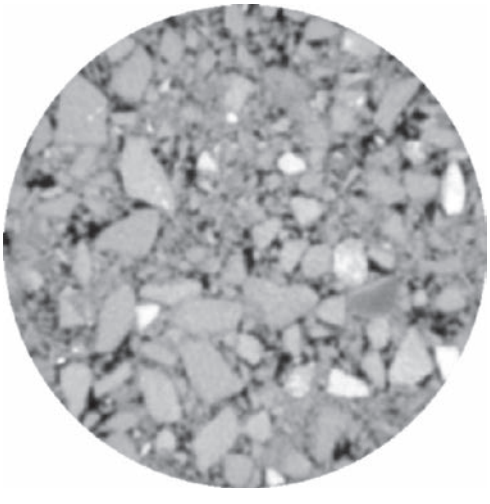

Figure 1. Two-dimensional X-ray image of an asphalt mixture.

determined by calculating the total area of air voids in a CT image using image analysis and then subtracting the areas of air voids from the total cross-sectional area of the CT image.

4 RESULTS AND ANALYSIS

4.1 *Air voids distribution*

Figure 2 presents the air voids distribution along the depth of two of the eight specimens before and after testing. While Specimen 1 is a dynamic modulus sample, Specimen 2 is a flow number sample. Similar air voids distributions were measured for the other test specimens. As shown in Figure 2, air voids distributions were distinctively different for the dynamic modulus and flow number specimens. For the dynamic modulus specimens, a relatively homogeneous air voids distribution was observed along the specimen height with higher air voids content in the top or bottom parts of the specimen. While past research has reported a "C" shape for the air voids distribution [4], the reason that only a partial C-shape was observed in this study is possibly due to the uneven cutting of the top and bottom parts of the specimen. To ensure uniformity of air voids, an equal length should be cut from both edges of the specimen. In contrast, the flow number specimens were highly heterogeneous with low air voids concentration in the bottom and the top thirds and a significant greater air voids concentration in the middle third of the specimen.

The discrepancy in air voids distribution is due to the different specimen sizes used in the compaction of the dynamic modulus and the flow number specimens and the reheating of the mixtures used in the preparation of the flow number specimens. Although both sets of specimens were compacted to a target air voids content of 7.0%, dynamic modulus specimens were compacted to a 150-mm diameter and flow number specimens were compacted to a 100-mm diameter. As shown in Figure 2, the gyratory compaction process results in a

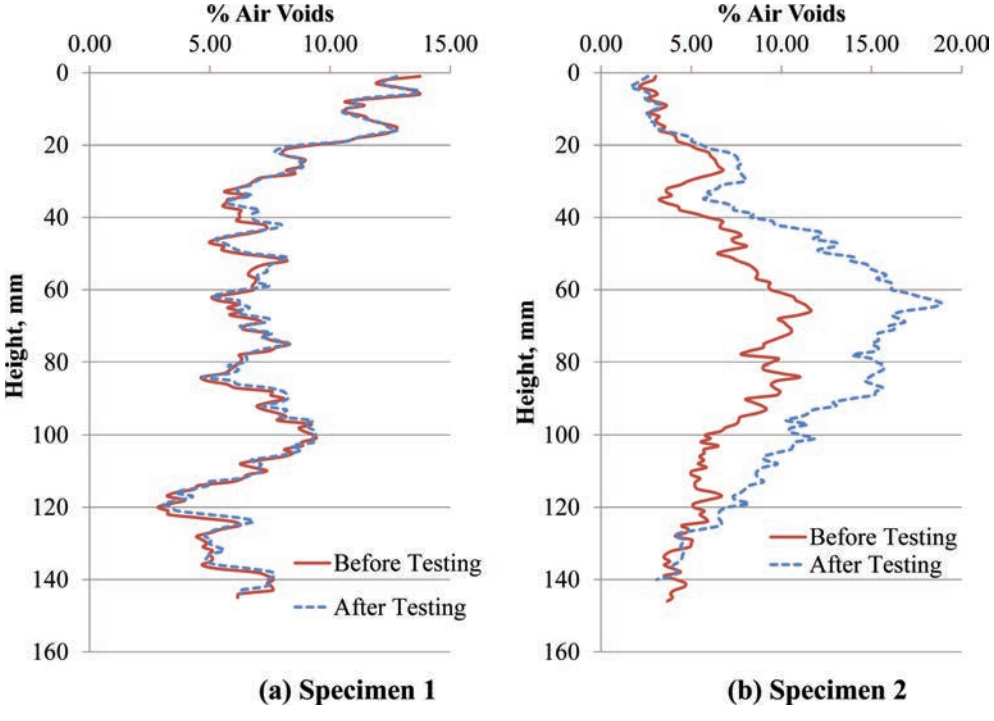

Figure 2. Air voids distribution along the depth for Specimens 1 and 2.

more uniform air voids distribution in the center of the specimen than around its circumference, which may explain the relatively more uniform air voids distribution observed in the dynamic modulus specimens. The effect of the foaming agent and WMA additive in facilitating the compaction process may have also been reduced upon reheating of the asphalt mixtures.

The concentration of air voids in the top, middle, and bottom thirds of Specimens 1 and 2 is quantified in Figure 3 before and after testing. The values presented in this figure confirm the homogeneous air voids distribution in the dynamic modulus specimen and the heterogeneous air voids distribution in the flow number specimen. It also indicates that the air voids contents in the dynamic modulus specimen remained relatively unchanged after testing while a significant increase in air voids occurred in the flow number specimen after testing.

4.2 *Damage analysis*

Figure 4 presents the x-ray visualization of the dynamic modulus and flow number specimens prior to and after testing (Specimens 1 and 2). As shown in Figure 4(a), the general visualization of the dynamic modulus specimen before and after testing appears to be similar indicating that little or no damage occurred during testing. In contrast, the specimen used in the flow number test experienced significant volume change especially in the middle third indicative of damage taking place during testing in a localized area of the specimen.

The level of damage taking place during testing was quantified through the damage parameter, ξ, previously defined in Equation (4). Figure 5 illustrates the calculated damage parameters for the dynamic modulus and flow number specimens after testing. As shown in Figure 5, little damage occurred during the dynamic modulus testing. In addition, the damage parameter was practically uniform throughout the height of the test specimens. In contrast, the damage experienced in the flow number test was not uniform with respect to the specimen height with little to no damage occurring in the top and bottom thirds of the specimens and most of the damage taking place in the middle third of the specimens. These results confirm that the assumption of no damage taking place in the dynamic modulus test is valid. In contrast, the damage taking place in the flow number test is heterogeneous with most of the damage occurring in the middle third of the specimen. These findings agree with Tashman et al. [11], who reported that damage in HMA is a localized phenomenon occurring in a critical location in the specimen due to the heterogeneity of the mix.

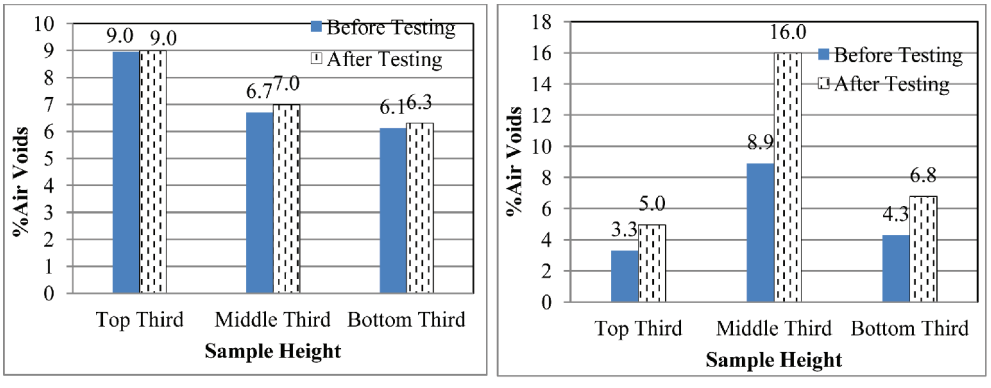

Figure 3. Air voids content along specimen height for (a) Specimen 1 (dynamic modulus) and (b) Specimen 2 (flow number).

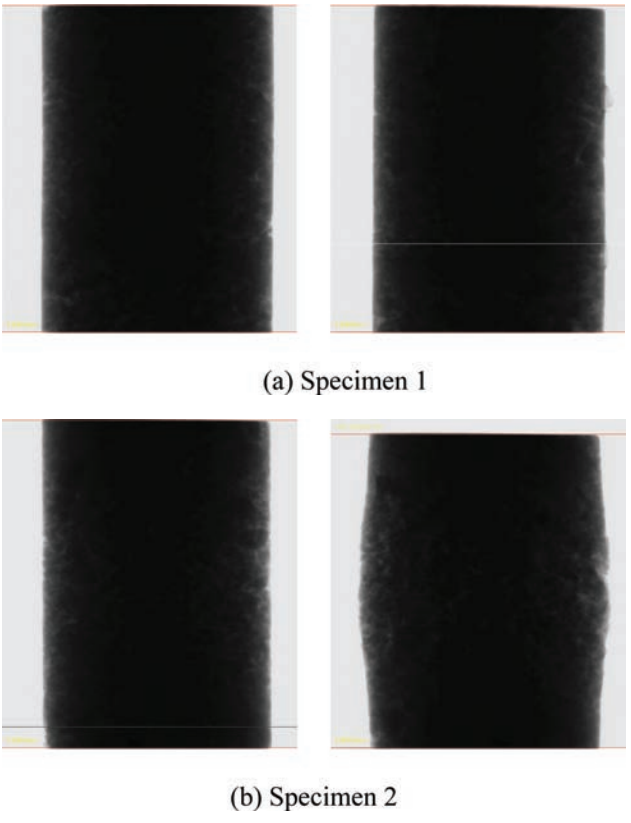

Figure 4. Visualization of specimens prior to and after testing for (a) Specimen 1 (dynamic modulus) and (b) Specimen 2 (flow number).

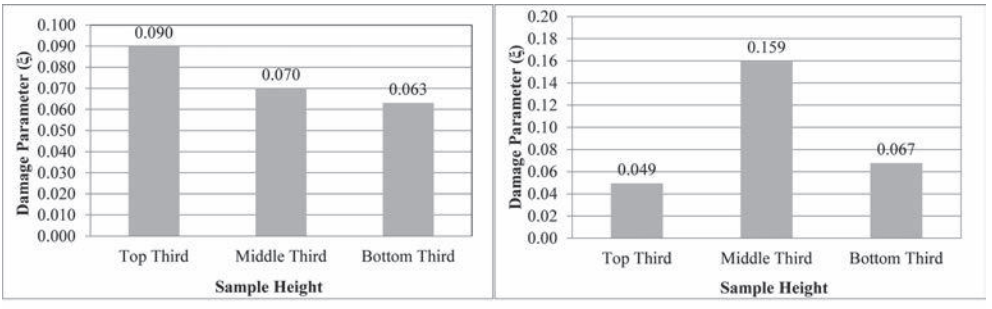

(a) Specimen 1 **(b) Specimen 2**

Figure 5. Levels of damage for (a) Specimen 1 (dynamic modulus) and (b) Specimen 2 (flow number).

5 CONCLUSIONS

The objectives of this study were to quantify the level of damage taking place in the dynamic complex modulus and flow number tests using x-ray CT and to characterize the heterogeneous characteristics of asphalt mixtures under loading. Based on the results of the experimental program, it was determined that the damage taking place in the dynamic modulus

test is minimal and homogeneous while the damage taking place in the flow number test is significant and heterogeneous. These results confirm that the assumption of no damage taking place in the dynamic modulus test is valid. In addition, specimen preparation may significantly influence the air voids distribution in HMA. To achieve relatively homogeneous air voids distribution, 150-mm in diameter by 165-mm in height specimens should be prepared, cored, and evenly cut from both sides of the specimen.

ACKNOWLEDGMENTS

This research was funded by the Louisiana Board of Regents—Research Competitiveness Subprogram (RCS). The assistance of the Louisiana Transportation Research Center (LTRC) and B. Vallabhu in preparing the asphalt concrete specimens is greatly appreciated.

REFERENCES

1. ARA, Inc., and ERES Consultants Division. (2004). *Guide for Mechanistic-Empirical Design of New and Rehabilitated Pavement Structures,* Final report, NCHRP Project 1–37A. Transportation Research Board of the National Academies, Washington, D.C., www.trb.org/mepdg/guide.htm.
2. Al-Qadi, I.L, Elseifi, M.A., Yoo, P.J., Dessouky, S.H., Gibson, N., Harman, T., D' Angelo, J., and Petros, K. (2008). Accuracy of Current Complex Modulus Selection Procedure from Vehicular Load Pulse in NCHRP 1–37A Mechanistic-Empirical Pavement Design Guide. Transportation Research Record: Journal of the Transportation Research Board, No. 2087, Washington, D.C., 81–90.
3. Witczak, M.W., Kaloush, K., Pellinen, T., El-Basyouny, M., and Von Quintus, H. (2002). Simple Performance Test for Superpave Mix Design, NCHRP Report 465, TRB, Washington, D.C.
4. Eriksen, K., and Wegan, V. (1993). Optical Methods for the Evaluation of Asphalt Concrete and Polymer-Modified Bituminous Binders. Note 244, Danish Road Institute.
5. Masad, E., Jandhyala, V.K., Dasgupta, N., Somadevan, N., and Shashidhar, N. (2002). Characterization of Air Void Distribution in Asphalt Mixes Using X-ray Computed Tomography. *Journal of Materials in Civil Engineering*, ASCE, Vol. 14, No. 2, 122–129.
6. Elseifi, M.A., Al-Qadi, I.L., Yang, S-H., and Carpenter, S. (2008). "Validity of Asphalt Binder Film Thickness Concept in Hot-Mix Asphalt," Journal of the Transportation Research Board, National Research Council, Washington, D.C.
7. Adhikari, S., and You, Z., (2007). Distinct Element Modeling of the Asphalt Mixtures: from Two-dimensional to Three-dimensional Models, Transportation Research Board, National Research Council, Washington, D.C.
8. Kassem, E., Masad, E., Bulut, R., Lytton, R. (2009). Measurements of the Moisture Diffusion Coefficient of Asphalt Mixtures and its Relationship to Mixture Composition. International Journal of Pavement Engineering, Vol. 10, No. 6, pp. 389–399.
9. Bonaquist, R.F., Christensen, D.W., and Stump, W. (2003). Simple Performance Tester for Superpave Mix Design: First-Article Development and Evaluation. National Cooperative Highway Research Program (NCHRP) Report 513, Transportation Research Board, National Research Council, Washington, D.C.
10. Image-Pro Plus, Media Cybernetics, L.P. Version 4.1, Georgia, MD. (1999).
11. Tashman, L., Masad, E., Little, D., and Zbib, H. (2005). A Microstructure-based Viscoplastic Model for Asphalt Concrete. *International Journal of Plasticity*, No. 21, 1659–1685.
12. Kachanov, L.M. (1986). *Introduction to Continuum Damage Mechanics*, Martinus Nijhoff Publishers, Dordrecht, the Netherlands.

Asphalt Pavements – Kim (Ed)
© 2014 Taylor & Francis Group, London, ISBN 978-1-138-02693-3

The Universal Simple Aging Test (USAT): Simulating short- and long term hot and warm mix oxidative aging in the laboratory

Michael J. Farrar, Jean-Pascal Planche, R. William Grimes & Qian Qin
Western Research Institute, Laramie, WY, USA

ABSTRACT: In a recent article Farrar et al. [Eurasphalt & Eurobitume Congress, Istanbul, Turkey, June 13–15, 2012] report development of a thin film (300 μm) short- and long-term aging test as an alternative to the standard Rolling Thin Film Oven (RTFO) and Pressure Aging Vessel (PAV) tests. This new thin film oven test is referred to as the Universal Simple Aging Test (USAT). The RTFO is not suitable for simulating the oxidative aging that occurs during "warm" mix production and is problematic for aging highly modified binders. The USAT resolves both of these problems. The focus of the previous paper was applying the USAT for unmodified asphalt. This one examines and proposes application of the USAT for modified asphalt binders. In addition, we propose application of the USAT for simulating warm mix asphalt production in the laboratory. The technology that makes the USAT feasible is a Dynamic Shear Rheometer (DSR) technique recently developed at Western Research Institute as an alternative to the Bending Beam Rheometer (BBR). The new DSR method is commonly referred to as 4-mm DSR. This new DSR technique allows testing to very low temperature (−40°C), requires only 25 mg of binder, and can estimate BBR m-value and creep stiffness.

Keywords: Asphalt, aging, oxidation, RTFOT, durability

1 INTRODUCTION

The Universal Simple Aging Test (USAT) is a new thin film (300 μm) short- and long-term aging test developed at Western Research Institute (WRI) and proposed as an alternative to the standard Rolling Thin Film Oven (RTFO) and Pressure Aging Vessel (PAV) tests. The new test can be applied to neat and modified asphalt binders for Hot Mix Asphalt (HMA) and warm mix asphalt (WMA). Also, the USAT can be applied to emulsion residue recovery and oxidative aging of the residue [1].

The USAT, and its use in conjunction with 4-mm DSR was first described in 2012 by Farrar et al. [2] and was developed by adapting and extending previous research on thin film aging, particularly the work performed by Glover et al. [3,4] and Petersen [5].

Before the Strategic Highway Research Program, there was considerable interest in static thin film aging. However, the RTFO test, which at the time was already in common use, was adopted for short term aging because of the large amount of aged asphalt needed for the Bending Beam Rheometer (BBR) test. Since the adoption of the RTFO, it has been found problematic for aging highly modified binders. In the case of warm mix binders, RTFO testing at lower temperature to simulate a "warm" plant limits the rolling needed to uniformly age the material. The USAT eliminates the "rolling" issue for more viscous polymer modified and warm mix asphalts.

A new Dynamic Shear Rheometer (DSR) technique, recently developed at WRI allows DSR testing from intermediate to very low temperature (–40°C) and requires only 25 mg of binder [6,7]. The technique which uses 4 mm diameter plates is commonly referred to as 4-mm DSR. By combining 4-mm DSR with the USAT, the low and intermediate temperature

rheology of short and long-term aged asphalt binders can be determined, including estimating BBR m-value and creep stiffness, as well as the thermal stress build-up in the binder and mix from a cooling event [2,8,9]. In addition to low and intermediate temperature DSR, the USAT generates sufficient aged material to perform high temperature DSR using 25 mm diameter plates.

The first USAT report in 2012 considered only unmodified asphalts and proposed USAT aging protocols to simulate RTFO and standard PAV. In this report USAT aging of two polymer modified asphalt binders has been analyzed to support and supplement the 2012 Farrar et al. study [2], and a USAT short-term aging protocol to simulate the aging that occurs in a "warm" plant is proposed. The approach taken to establish a USAT short-term aging protocol for WMA was simply to compare differences in rheological properties between HMA and WMA recovered binders and find a USAT WMA short term aging time and temperature that results in similar differences between USAT HMA and WMA short term aging.

2 EXPERIMENTAL AND MATERIALS

2.1 *Dynamic shear rheometry using 4 mm diameter parallel platens*

Rheology was performed on a Malvern Kinexus stress control Dynamic Shear Rheometer (DSR), and in a few cases on a TA Instruments ARES strain control rheometer. Results from both instruments were very comparable. The low and intermediate temperature rheological properties of the recovered binders were measured with 4 mm diameter parallel plate geometry (4-mm DSR). High temperature rheological properties were measured using 25 mm diameter parallel plate geometry.

The 4-mm DSR test method is described elsewhere by Sui et al. [6] and Farrar et al. [7]. Low and intermediate temperature frequency sweeps were typically performed at 15 or 20°C intervals over a temperature range of –30 to 30°C and an angular frequency range of 0.1 to 50 rad/sec. High temperature frequency sweeps using 25 mm diameter plates were typically performed at 50 and 70°C.

2.2 *Materials*

Table 1 describes the four asphalt binders used in this study. They are tank asphalts collected during construction. Two of the four asphalts were modified at the refinery with Styrene Butadiene Styrene (SBS) copolymer.

2.3 *Development of the USAT for simulating RTFO and RTFO/PAV*

Using a thin film aging procedure is not a completely new idea. Asphalt thin-film oxidative aging has been extensively studied over the last 70 years; a good summary of the literature has been performed by Airey [10].

Behera et al. [11] recently reported a study on thin film aging as an alternative to standard RTFO and PAV aging and some aspects and conclusions of the Behera et al. study are similar to this study and the Farrar et al. study [2]. Behera et al. concluded that a binder of 650 μm

Table 1. Description: asphalt binders used in the USAT study.

Project location	Date constructed	Asphalt binder label	PG	Description
Yellowstone National Park	2007	YNP	58-34	SBS modified binder
College Drive, Cheyenne, WY	2011	WCD	70-28	SBS modified binder
Olmsted County, MN, CR 113	2006	MN1-3	58-28	Unmodified binder
S Manitoba Hwy 14	2010	MB	58-28	Unmodified binder

film thickness aged in a non-forced draft oven at 163°C can produce a similar effect as RTFO aging. The time at 163°C varied from 3 to 4.5 hours depending on the type of asphalt. Also, Behera et al. concluded that 3 to 4 days of oven aging at 85°C for normal binders and 4 to 5 days for modified binders produced long-term aging similar to PAV aging.

The USAT aging protocols developed in the Farrar et al study [2] and validated in this study for polymer modified asphalt are summarized in Table 2. The option of using a forced draft oven for the long term aging rather than a PAV was included in the Farrar et al. study [2].

One of the principal goals during development of the USAT was to make the asphalt film as thin as possible to reduce oxygen diffusion effects. The USAT film thickness of 300 μm was arrived at as a compromise in trying to prepare a uniform thin film without solvent casting and yet obtain the amount of sample required for rheological and chemical testing.

Figure 1A shows the latest USAT prototype for short and long-term thin film aging. There are three slots on the plate to allow aging of three separate films. Each slot requires 1.00 g of asphalt binder, which produces a film thickness of about 300 μm. The film thickness is a function of the specific gravity of the particular binder and temperature. The film thickness variation is estimated to be ±10 μm.

Preparing USAT asphalt thin films for oxidative aging involves bringing a hot plate to approximately 120°C in a nitrogen saturated glove box or tent and then placing the USAT plate (with asphalt) onto the hot plate. The nitrogen atmosphere is used to prevent undesirable oxidation. As the asphalt temperature approaches 120°C it spreads out to roughly two-thirds of the slot surface. A small spatula is used to spread the asphalt to the remaining unwetted surface as shown in Figure 1B. After spreading, the asphalt is allowed to remain at temperature for several minutes to level and evenly spread out. The USAT plate is then removed from the hot plate and allowed to return to room temperature under nitrogen.

The USAT short and long-term aging scheme is illustrated in Figure 2. The USAT plate is placed on a preheated block of aluminium to rapidly bring the USAT plate to temperature. The plate dimensions were selected so the plate can be inserted into a standard pressure aging vessel tray.

Table 2. USAT HMA binder protocol descriptions.

USAT protocol	Description	Equivalent AASHTO aging test
ST USAT HMA	Short term universal simple aging test 50 min. at 150°C in a forced draft oven	RTFO (ASTM D2872, AASHTO T240)
LT USAT PAV[a]	Long term universal simple aging test in a pressure aging vessel for 8 hours at 100°C	RTFO/PAV (ASTM D6521, AASHTO R28)
LT USAT FDO[a]	Long term universal simple aging test in a forced draft oven for 40 hours at 100°C	~ RTFO/PAV (ASTM D6521, AASHTO R28)

[a] LT USAT PAV or LT USAT FDO samples are initially aged using either the ST USAT HMA or WMA protocols.

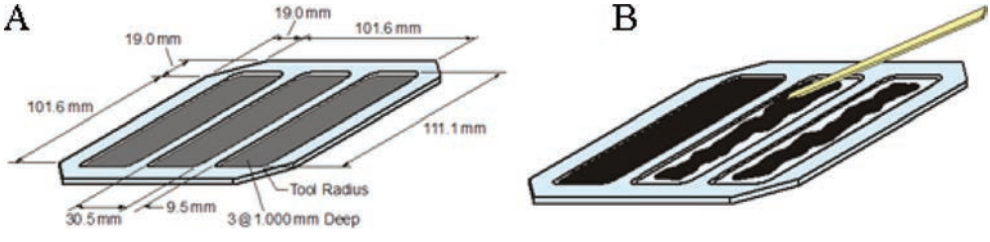

Figure 1. USAT plate dimensions (A) and spreading asphalt to unwetted surfaces using a small spatula (B).

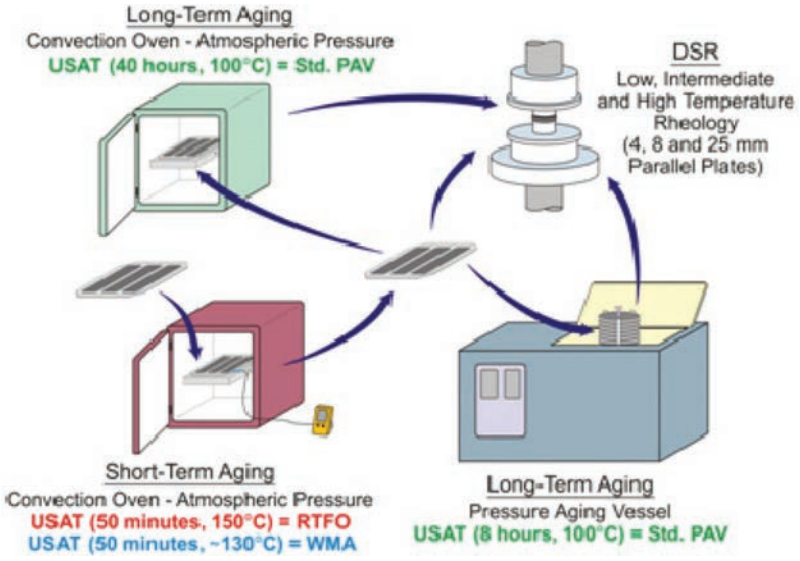

Figure 2. USAT short and long term aging scheme.

3 CONTINUOUS GRADE AND RHEOLOGICAL COMPARISON (USAT VS. RTFO AND RTFO/PAV) FOR MODIFIED ASPHALTS

3.1 *Linear viscoelastic region*

The continuous grade of the RTFO, RTFO/PAV, and USAT aged binders are presented in Table 3 for the YNP and WCD binders. For both the short and long-term aging, good agreement was found between USAT aging (Table 2 aging protocols) and RTFO and RTFO/PAV aging.

Comparisons of the low (m-value) and creep stiffness S(t), intermediate (G* sin δ), and high temperature (G*/sin δ) grading criteria for the USAT, RTFO and RTFO/PAV are shown in Figure 3. All of the asphalt binders either fall within or are close to falling within the single operator precision limits (d2 s%), indicating the USAT and RTFO and RTFO/PAV rheological measurements are comparable.

3.2 *Nonlinear viscoelastic region*

Table 4 compares the MSCR non-recoverable creep compliance (J_{nr}) at 64°C and 58°C and 0.1 and 3.2 kPa stress levels for the YNP and WCD aged using the USAT short term HMA aging protocol and RTFO aging. The J_{nr} results are surprisingly close.

4 DEVELOPMENT OF THE USAT FOR SIMULATING THE SHORT-TERM AGING THAT OCCURS IN A "WARM" PLANT

Table 5 describes the short term USAT aging protocol considered for WMA in this study.

4.1 *Rheological differences in recovered asphalt binder: HMA versus WMA*

4.1.1 *Linear viscoelastic region*

In a recent study, Bonaquist [12] evaluated the low, intermediate and high continuous grades of recovered binders from a number of HMA/WMA projects. Bonaquist found that for

Table 3. Linear viscoelastic region: comparison USAT versus RTFO and RTFO/PAV.

Asphalt binder	Aging method	Continuous grade temperature (°C)		
		Low	Intermediate	High
YNP	RTFO			60.3
	ST USAT HMA			59.4
	RTFO/PAV	–37.0	14.2	
	ST USAT HMA LT PAV	–37.0	14.0	
WCD	RTFO			70.5
	ST USAT HMA			70.6
	RTFO/PAV	–31.0	14.6	
	ST USAT HMA LT PAV	–32.0	17.2	

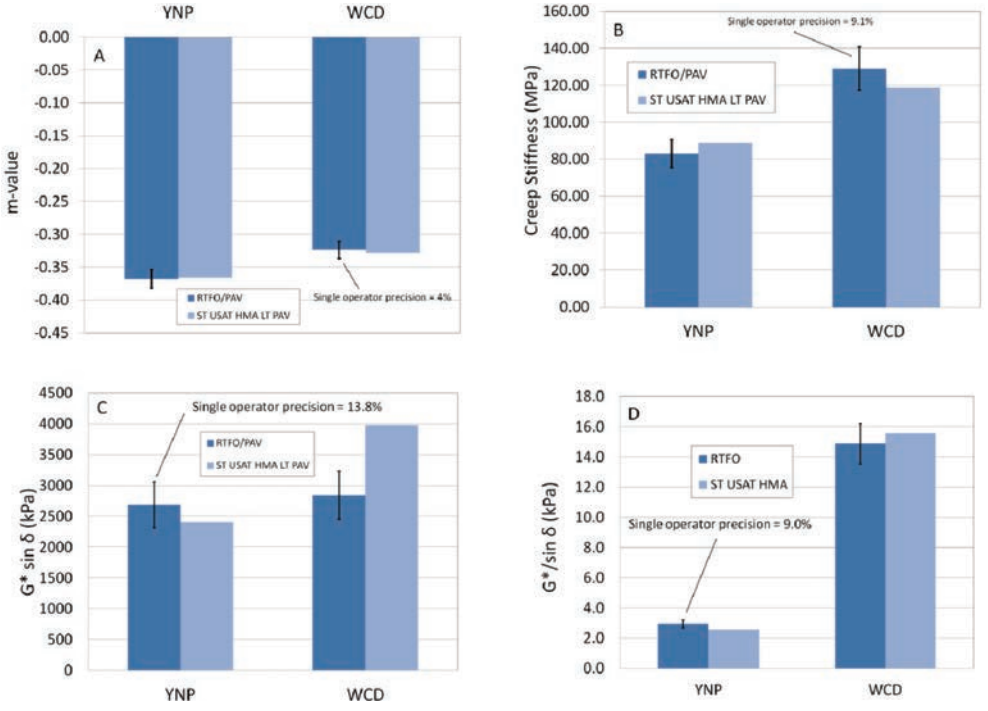

Figure 3. Comparison grading criteria: A—low temperature (m-value) (–28°C); B—low temperature grading criteria (creep stiffness) (–28°C); C—intermediate grading criteria (G* sin δ) (19°C); D—high temperature grading criteria (G*/sin δ) (58°C).

Table 4. Nonlinear viscoelastic region: comparison USAT versus RTFO.

Project asphalt	USAT protocol	J_{nr} 58°C (kPa^{-1})		J_{nr} 64°C (kPa^{-1})	
		0.1 kPa	3.2 kPa	0.1 kPa	3.2 kPa
YNP	ST USAT HMA 150°C	2.33	3.42	5.09	7.89
	RTFO	2.17	3.00	4.69	6.81
WCD	ST USAT HMA 150°C	0.16	0.15	0.26	0.36
	RTFO	0.17	0.17	0.31	0.44

Table 5. USAT WMA binder protocol description.

USAT protocol	Description	Equivalent AASHTO aging test
ST USAT WMA 130°C[a]	Short term universal simple aging test 50 min. at 130°C in a forced draft oven	None

[a] LT USAT PAV or LT USAT FDO samples are initially aged using either the ST USAT HMA or WMA protocols.

Table 6. Summary: continuous grading of recovered modified asphalt binders.

Project asphalt	Process	Production temperature (°C)	Continuous grade temperature (°C)		
			Low	Intermediate	High
YNP	Specified	N/A	–28.0	–	58.0
	HMA	163	–39.2	12.1	59.2
	Advera	135	–41.0	8.6	61.1
	Difference	–28	–1.8	–3.5	1.9
WCD	Specified	N/A	–28.0	–	70.0
	HMA	166	–36.0	14.4	71.0
	Foam	132	–39.0	12.6	71.6
	Difference	–34	–3.0	–1.8	0.6
Average difference		–31	–2.4	–2.7	1.3

Table 7. J_{nr} recovered asphalt binders.

Project asphalt	Process	Production temperature (°F)	J_{nr} 58°C (kPa^{-1})		J_{nr} 64°C (kPa^{-1})	
			0.1 kPa	3.2 kPa	0.1 kPa	3.2 kPa
YNP	Specified	N/A	N/A	N/A	N/A	N/A
	HMA	163	0.88	1.22	2.01	3.09
	Advera	135	0.94	1.31	2.16	3.27
	Diffrence	–28	0.06	0.09	0.15	0.18
WCD	Specified	N/A	N/A	N/A	N/A	N/A
	HMA	166	0.10	0.10	0.16	0.23
	Foam	132	0.07	0.06	0.03	0.12
	Diffrence	–34	–0.03	–0.04	–0.13	–0.11
	Average difference	–31	0.02	0.03	0.01	0.04

the high-temperature grade of the binder an approximately 28°C reduction in production temperature resulted in less than a 1°C decrease in high-temperature grade. Bonaquist also reported that an approximate 28°C reduction in production temperature resulted in an average improvement in the low temperature grade of the binder of 1.5°C.

To supplement Bonaquist's findings the continuous grades for the recovered binders from the YNP and WCD HMA/WMA projects were determined and are shown in Table 6. The results indicate that for an SBS modified binder and an approximate 31°C reduction in the production temperature results in about a 1.3°C improvement in continuous high temperature grade and a 2.4°C improvement in the low temperature grade.

These results tend to support Bonaquist's [12] contention that binder grade changes are not necessary for WMA since the average differences in continuous grade are only one to two degrees. However, it is particularly interesting to note the WMA process resulted in an

improvement not only in the low temperature continuous grade, which was expected, but also in the high temperature continuous grade, which was not totally expected. However such an improvement has already been reported by Fort et al [13] in the case of polymer modified asphalt used in WMA. Fort et al attributed this effect to a lower aging of the polymer network, maintaining a stronger integrity under warm mixing conditions as opposed to chain scissions occurring during high temperature HMA mixing.

4.1.2 *Nonlinear viscoelastic region*

To help evaluate the results presented in Table 6, the Multiple Stress Creep Recovery (MSCR) test was performed on YNP and WCD recovered binders. Table 7 presents the MSCR non-recoverable creep compliance (J_{nr}) at 64°C and 58°C and 0.1 and 3.2 kPa stress levels for the YNP and WCD recovered binders. In the case of the YNP binder there is a slight increase in J_{nr} at both temperatures and stress levels in terms of the effect of a lower production temperature; and in the case of the WCD binder there is a slight decrease in the J_{nr} at both temperatures and stress levels in terms of the effect of a lower production temperature. Overall, an average reduction of 31°C in the production temperature results in essentially no change in J_{nr}.

5 ESTABLISHING THE USAT TIME AND TEMPERATURE NECESSARY TO SIMULATE THE OXIDATIVE AGING THAT OCCURS IN THE "WARM" PLANT DURING THE PRODUCTION OF WMA

The approach taken here to establish the USAT short-term aging protocol for WMA is simply to compare the differences in rheological properties between HMA and WMA recovered binders and find a USAT time and temperature for WMA binders that results in similar differences in rheological properties between USAT HMA and WMA aging.

5.1 *USAT linear viscoelastic region*

Table 8 summarizes the continuous grade temperatures using the proposed ST USAT WMA protocol (Table 5) and the established ST USAT HMA protocol (Table 2) for both SBS

Table 8. Continuous grading: HMA and WMA ST USAT aged asphalt binders.

		Continuous grade temperature (°C)		
Project asphalt	USAT protocol	Low	Intermediate	High
MB	ST USAT HMA 150°C	–37.9	11.3	58.9
	ST USAT WMA 130°C	–40.4	9.8	57.1
	Difference	–2.5	–1.5	–1.8
MN1-3	ST USAT HMA 150°C	–36.6	14.5	61.8
	ST USAT WMA 130°C	–36.8	12.9	58.5
	Difference	–0.2	–1.6	–3.3
Average difference unmodified binders		–1.4	–1.6	–2.6
Average difference (Bonaquist, ref [12])		–1.5		–1.0
YNP	ST USAT HMA 150°C	–41.7	9.1	59.4
	ST USAT WMA 130°C	–41.2	9.7	60.5
	Difference	0.5	0.6	1.1
WCD	ST USAT HMA 150°C	–39	11.9	70.6
	ST USAT WMA 130°C	–39.1	11.2	71.6
	Difference	–0.1	–0.7	1.0
Average difference modified binders		0.2	–0.1	1.1
Average difference modified recovered binders (Table 6)		–2.4	–2.7	1.3

Table 9. J_{nr} HMA WMA ST USAT aged asphalt binders.

		J_{nr} 58°C (kPa^{-1})		J_{nr} 64°C (kPa^{-1})	
Project asphalt	USAT protocol	0.1 kPa	3.2 kPa	0.1 kPa	3.2 kPa
YNP	ST USAT HMA 150°C	2.33	3.42	5.09	7.89
	ST USAT WMA 130°C	1.79	2.55	3.96	6.06
	Difference	–0.54	–0.87	–1.13	–1.83
WCD	ST USAT HMA 150°C	0.16	0.15	0.26	0.36
	ST USAT WMA 130°C	0.17	0.16	0.28	0.42
	Difference	0.01	0.01	0.02	0.06
Average difference		–0.27	–0.43	–0.56	–0.89
Average difference recovered binders (Table 7)		0.02	0.03	0.01	0.04

modified binders (YNP and WCD) as well as two unmodified binders (MN1-3 and MB). For the unmodified asphalts, the average differences between the USAT HMA and WMA short term aging protocol results are compared to the differences reported by Bonaquist [12]. For the modified asphalts, the differences between the USAT HMA and WMA short term aging protocol results are compared to the differences of the recovered binders (Table 6). Overall, the average differences compare reasonably well.

5.2 *USAT nonlinear viscoelastic region*

Table 9 presents the MSCR J_{nr} results at 64°C and 58°C and 0.1 and 3.2 kPa stress levels for the YNP and WCD binders aged using the ST USAT WMA and HMA protocols. The average differences between the USAT and recovered binders are compared. As with the continuous grade temperature, the differences compare favourably although the J_{nr} of the recovered binders tends somewhat lower than the USAT aged binders.

6 CONCLUSION

The USAT short and long term aging protocols for HMA when applied to polymer modified asphalt compare favourably to RTFO and RTFO/PAV aging of the same asphalts. This conclusion is based on evaluation of the rheology in both the linear and nonlinear viscoelastic regions.

In terms of applying the USAT for WMA, the differences in linear and nonlinear viscoelastic properties between the short term USAT WMA and HMA aging and the differences in recovered binder for the same asphalts are similar, which indicates the USAT short term aging protocol for WMA is a relatively robust and promising method. To the authors' knowledge, this is the only method currently available for WMA short term aging in the laboratory.

ACKNOWLEDGMENTS

The authors gratefully acknowledge the Federal Highway Administration, U.S. Department of Transportation, for financial support of this project under contract no. DTFH61-07D-00005. The RHEA™ software package, developed by Abatech Consulting Engineers, was used extensively during the data analysis phase of this study.

DISCLAIMER

This document is disseminated under the sponsorship of the Department of Transportation in the interest of information exchange. The United States Government assumes no

liability for its contents or use thereof. The contents of this report reflect the views of Western Research Institute which is responsible for the facts and the accuracy of the data presented herein. The contents do not necessarily reflect the official views of the policy of the Department of Transportation.

REFERENCES

[1] Farrar, M.J., S.L. Salmans, and J-P. Planche. Recovery and Laboratory Testing of Asphalt Emulsion Residue: Application of Simple Aging Test (SAT) and 4-mm Dynamic Shear Rheometry, *Transportation Research Record*, accepted for publication, February 2013.

[2] Farrar, M.J., R.W. Grimes, C. Sui, J-P. Planche, S-C. Huang, T.F. Turner, and R. Glaser. Thin Film Oxidative Aging and Low Temperature Performance Grading Using Small Plate Dynamic Shear Rheometry: An Alternative to Standard RTFO, PAV, and BBR, *Proc.*, 5th Eurasphalt & Eurobitume Congress, Istanbul, June 13–15, 2012.

[3] Glover, C.J., R.R. Davison, N. Vassiliev, T. Hausman, and S.A. Williamson. Development of Stirred Air-Flow Test (SAFT) for Improved HMAC Plant Binder Aging Simulation and Studies of Asphalt Air Blowing, Texas Transportation Institute, Report No. FHWA/TX-02/1742-2. 2001.

[4] Glover, C.J., R.R. Davison, C.H. Domke, Y. Ruan, P. Juristyarini, D.B. Knorr, and S.H. Jung. Development of a New Method for Assessing Asphalt Binder Durability with Field Validation, Texas Transportation Institute, Report No. FHWA /TX-05/1872-2. 2005.

[5] Petersen, J.C. A Thin Film Accelerated Aging Test for Evaluating Asphalt Oxidative Aging, *Proc.*, Assoc. Asphalt Paving Technol., 58, pp. 220–237. 1989.

[6] Sui, C., M.J. Farrar, W.H. Tuminello, and T.F. Turner. New Technique for Measuring Low-Temperature Properties of Asphalt Binders with Small Amounts of Material, *Transportation Research Record 2179*, pp. 23–28. 2010.

[7] Farrar, M.J., C. Sui, S. Salmans, and Q. Qin. Determining the Low Temperature Rheological Properties of Asphalt Binder Using a Dynamic Shear Rheometer (DSR). Product: FP 08, Fundamental Properties of Asphalts and Modified Asphalts, III, Prepared for Federal Highway Administration Contract No. DTFH61-07-D-00005 by the Western Research Institute, October 2013.

[8] Sui, C., M.J. Farrar, P.M. Harnsberger, W.H. Tuminello, and T.F. Turner. A New Low-temperature Performance Grading Method Using 4 mm Parallel Plates on a DSR, *Transportation Research Record 2207*, pp. 43–48. 2011.

[9] Farrar, M.J., E.Y. Hajj, J-P. Planche, M.Z. Alavi. A method to estimate the thermal stress build-up in an asphalt mixture from a single cooling event, *Road Materials and Pavement, Design*, 14:sup1, pp. 201–211. 2013.

[10] Airey, G.D. State of the Art Report on Ageing Test Methods for Bituminous Pavement Materials, *International Journal of Pavement Engineering*, 4(3), pp. 165–176. 2003.

[11] Behera, P.K., A.K. Singh, and M. Amaranatha Reddy. An alternative method for short- and long-term ageing for asphalt binders, *Road Materials and Pavement Design*, OI:10.1080/14680629.2013.799086. 2013.

[12] Bonaquist, R. Mix Design Practices for Warm Mix Asphalt, NCHRP Report 691, Transportation Research Board, Washington, D.C. 2011.

[13] Fort, Jean-Paul. Laboratory and Field Performance of Foam WMA, P3 Symposium, Laramie, Wyoming, July 2012.

This page intentionally left blank

Maintenance and rehabilitation—I

This page intentionally left blank

Asphalt Pavements – Kim (Ed)
© 2014 Taylor & Francis Group, London, ISBN 978-1-138-02693-3

Performance study of fog or rejuvenating seals on gap and open graded surfaces for Caltrans

Dingxin Cheng & Lerose Lane
California Pavement Preservation Center, Chico, CA, USA

Peter Vacura
Caltrans, Sacramento, CA, USA

ABSTRACT: Based on Caltrans Maintenance Technical Advisory Guide (MTAG), there are many advantages of using fog or rejuvenating seals. Fog seals improve sealing or waterproofing of existing pavement, reduce aging of binder or prevent further stone loss by holding aggregate in place, or by simply improving the surface appearance. Rejuvenating seals are a combination of various rejuvenating oils, and/or a mixture of asphalt emulsion and recycling oils applied to the asphalt pavement surface. Rejuvenating emulsions restore the maltenes or light components that have oxidized and soften the existing binder, thus reducing the viscosity and improving the flexibility of the binder. Caltrans has been using fog or rejuvenating seals on shoulders and highways through maintenance activities. In order to safely utilizemore fog or rejuvenating seals on the mainline of its highways, Caltrans placed a series of pilot projects during the past five years.

This paper documents the findings from the fog or rejuvenating seal pilot studies on gap graded and open graded surfaces. Caltrans built test sections from 2007 to 2009 with six different fog or rejuvenating seal products on gap- and open- graded surfaces. Through field and laboratory studies on these products, Caltrans quantified the benefits and performance of the fog or rejuvenating seal products commonly used in California. After reviewing the positive results from these test sections, Caltrans placed another 12 pilot projects in 2012 and 9 pilot projects in 2013 under various surface types, locations, climates, and traffic levels. Project reports were generated by the California Pavement Preservation Center (CP2 Center) to document the surface texture, application rates, performance, and skid resistance for these pilot projects. These results were used to support Caltrans with its new specification development for fog or rejuvenating seal applications.

Keywords: fog seals, rejuvenating seals, surface texture, skid resistance, open grade, gap grade

1 INTRODUCTION

1.1 *Background*

Asphalt binders harden as they age because they gradually loss lighter molecular weight part of oils and become oxidized. Asphalt hardening takes place at different rates depending on environmental conditions and the exposure to air. Permeable pavements or pavements with high void contents such as open graded mixes can therefore age faster. Water ingress can also carry dissolved oxygen and trace elements that may promote aging. This means that pavements with open surfaces tend to age faster than those with closed surfaces. Aging of binder can cause cracking under traffic and loss binding ability and raveling (MTAG, 2008).

Based on the Asphalt Emulsion Manufactures Association (AEMA), the fog seal is defined as a light spray application of dilute asphalt emulsion used primarily to seal an existing

asphalt surface to reduce raveling and enrich dry and weathered surfaces (MTAG, 2008). The rejuvenating seal is a combination of various rejuvenating oils or a mixture of asphalt emulsion and recycling oils applied to the asphalt pavement surface. Rejuvenating emulsions restore the light components that have oxidized and soften the existing binder, thus reducing the viscosity and improving the flexibility of the binder (MTAG, 2008).

Fog or rejuvenating seals are used to seal the existing surface, prevent raveling, and/or restoring properties of aged or oxidized binders, and such extending the pavement service life. In California, fog seals are also used right after the chip seals to improve rock retention and prevent windshield damage.

On shoulders, gores, or dikes, surface texture with the application of fog seals is not as critical. Fog seals will protect the surface from weathering and aging. On travel ways, fog seals should only be used on surfaces with adequate surface texture. Fog seals applied on tight surface without addings and will create a slippery surface with safety concerns.

1.2 *Objective*

The objectives of this paper are to

- Evaluate the performance of various fog or rejuvenating seal products commonly used in California, and
- Study the texture requirements for fog seal applications on travel way of Caltrans roadway network and relate it to skid resistance.

2 PERFORMANCE STUDIES ON 2009 PROJECTS (ROSE TO REVIEW)

After a test site was built in 2007 on SR58 near Mojave, three additional sites were constructed in 2009 to evaluate different fog or rejuvenating seal products and their performances. At each site, Caltrans placed a total of six different products including CQS-1h, CRF, PASS-QB, Reclamite, TOPEIN C, and Styraflex (Stroup-Gardiner et. al., 2011).

The SR 128 in Boonville test sections were the first to be placed on June 7 and 8, 2009. This rural roadway is a located in slightly rolling terrain, and has two lanes with no shoulders and has an AADT level below 3,500. The existing surface was open-graded hot mix asphalt. Boonville is located in a cool coastal California climate in Caltrans, District 1. The US 395 sections in Alturas were placed on June 16, 2009. Alturas is located in the upper northeast portion of California near both the Oregon and Nevada state lines in Caltrans, District 2. This area is located in the high desert plains and has severe winters. The existing surface was ½ inch rubberized gap graded hot mix asphalt with high void content (greater than 10%) and a low binder content (about 7%) by weight of the mix. The highway is two lanes without shoulders.

The third project was located on US 395 in Inyo County in Caltrans District 9. The existing surface was dense-graded hot mix asphalt which was constructed in 2009.

The following are discussions of the performance of open-graded surface on State Highway 128 in Boonville and gap-graded rubberized asphalt surface on US 395 in Alturas. The dense graded projects were not the focus of this study.

A number of tests were performed on these sections including texture and skid tests, tests on the recovered binder, and Hamburg tests. Only a portion of the test results is included in this paper.

2.1 *Fog or rejuvenating seals on open graded mix on SR 128 in Boonville*

2.1.1 *Field performance study*

Before construction, there was some pumping of base fines up through existing cracks. The open-graded HMA surface was raveled in places, particularly in the wheel paths. There were occasional small depressions or potholes. Figure 1 shows typical distresses of the existing pavement. CP2 Center revisited the project site in 2011, two years after the seal coats.

Figure 1. Existing pavement showing cracking and raveling.

Table 1. SR 128 test section two year pavement condition survey summary.

Section	Transverse cracking	Longitudinal cracking	Potholes	Ravelling	Overall condition
Control	Throughout the section	Isolated	None	Extensive	Poor
Product A	Similar to the control, but less	None	None	Some	Fair
Product B	Similar to the control but less	None	Some	Some	Not as good as the Product A
Product C	Similar to control but less	Isolated	Some	Some	Fair to good
Product D	Similar to control but less	Isolated	Some	Some	Fair to good
Product E	Similar to control but less	Isolated	Some	Some	Fair to good
Product F	Similar to control but less	Isolated	Some	Some	Fair to good

Table 1 summarizes the condition of the various test sections. The major distresses were raveling, transverse cracking, and some potholes. All products performed better than the control section, and especially had less ravelling distress.

2.1.2 *Laboratory performance study*

To evaluate the performance of the seal coat at the SR128 test site, a set of 6 inch cores were taken at the control section as well as six different products test sections. Several tests were performed using the cores including penetration and viscosity tests on recovered binders, stiffness test using Bending Beam Rheometer, and Hamburg Wheel Tests on control and treated cores. The Hamburg Wheel test has the advantage over the BBR test because it utilizes larger samples. CP2 Center conducted Hamburg Wheel Tests on the core samples. The tests were performed under water with temperature of 50°C. The fog or rejuvenating seal products had better resistance to rutting and moisture damage based on the graph shown in Figure 2. The results of the other tests are included in the full report (Stroup-Gardiner et. al., 2011).

2.2 *Fog or rejuvenating seals on gap graded mix on US 395 in Alturas*

2.2.1 *Field performance study*

The CP2 Center reviewed the performance of this project two years after construction in 2011. The results indicated that the seals were effective in controlling ravelling compared to

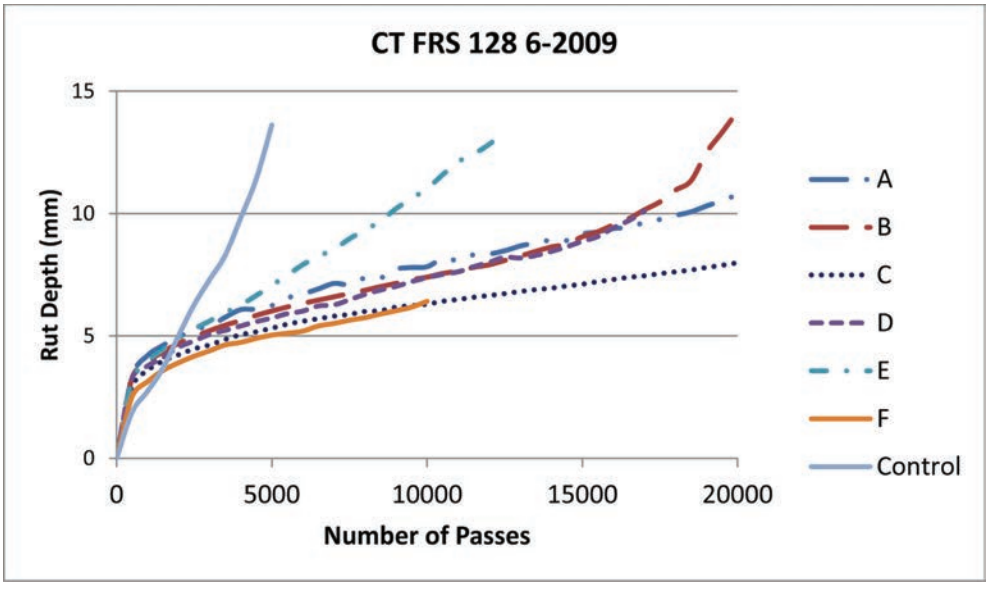

Figure 2. Hamburg test results for core samples from SR 128 in Boonville.

Figure 3. Visual comparison of sealed with non-sealed section at the US 395 test site.

the control section. Figure 3 illustrates that a fog sealed section seals the surface and lessens ravelling when compared with the non-sealed control section.

Table 2 summarizes the condition of the pavement in 2011. The predominant distress was thermal cracking with some minor longitudinal cracking.

2.2.2 *Laboratory performance study*

To evaluate the performance of the seal coat at the US 395 test site, a set of 6 inch cores were taken at the six different products test sections before and after fog or rejuvenating seal applications. CP2 Center conducted Hamburg Wheel Tests on the core samples. The tests were performed under water with temperature of 50°C. Figures 4 and 5 show the Hamburg Wheel

Table 2. US 395 testing section two year pavement condition survey summary.

Section	Transverse cracking	Longitudinal cracking	Potholes	Raveling	Overall condition
Control-in between test sections pavement	Throughout the section	Isolated	None	Some	Fair
Product A	Similar to the control	None	None	Little to some	Fair
Product B	Similar to the control	None	None	Little	Fair to good
Product C	Similar to control	Isolated	None	Little	Fair to good
Product D	Similar to control	Isolated	None	Little	Fair to good
Product E	Similar to control	Isolated	None	Little	Fair to good
Product F	Similar to control	Isolated	None	Little	Fair to good

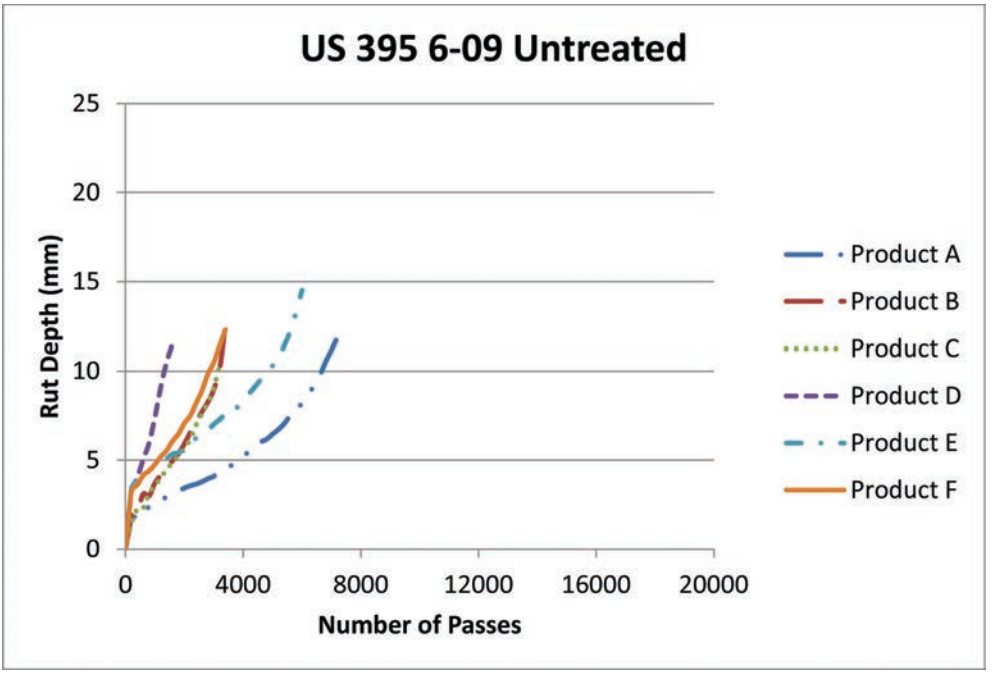

Figure 4. Hamburg tests on samples before fog seal treatment from US 395 test site.

Testing results for the six products sites before and after treatments. The fog or rejuvenating seal products had better resistance to rutting and moisture damage as the number of passes to reach 10 mm rut depth were much higher for treated than untreated surfaces.

2.3 *Summary of 2009 performance studies*

Based on the field evaluation and laboratory study on the performance of the 2009 pilot projects, the following conclusions can be drawn:

- The field evaluation clearly showed that fog or rejuvenating seal treatment sections performed better than the untreated or control sections. The treatment reduced the rock loss and preserved the surface with slower rate of deterioration.
- Six different fog or rejuvenating seal products were evaluated in the fields. Although they all performed better than the control section, they performed differently.

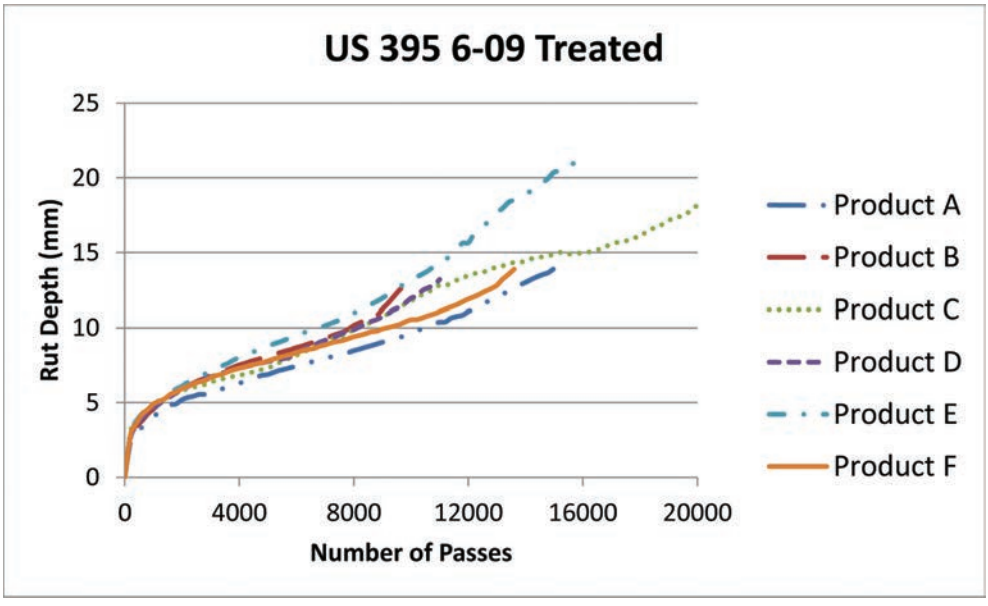

Figure 5. Hamburg tests on samples after fog seal treatment from US 395 test site.

- Performance based laboratory testing was conducted using the cores extracted at various locations of the 2009 pilot projects. The Hamburg Wheel Track tests showed that fog or rejuvenating seal treated cores had better rutting resistance and less moisture damage than the control cores, but different products performed differently.

3 TEXTURE AND SKID STUDY ON GAP AND OPEN GRADED SURFACES IN 2012 AND 2013

After the positive results of the 2007 and 2009 test sections, Caltrans continued the pilot projects in 2012 to further study the surface texture, skid resistance, and proper application rates for fog and rejuvenating seals. The following tests were conducted at the 2012 pilot sites.

3.1 *Field performance testing*

Several tests were performed on the various projects to evaluate the effectiveness and safety of the fog seals. Tests included Circular Track Meter (CTM) ASTM E2157, Dynamic Friction Test (DFT) ASTM E1911, Ring Test, Sand Patch Test ASTM E965, British pendulum test (BPT) ASTM E303, and the ASTM skid trailer ASTM E274.

3.2 *2012 pilot projects*

In an effort to return to the use of fog seals as a strategy to extend the life of mainline pavements in California, Caltrans conducted a series of fog or rejuvenating seal pilot projects in 2012. The goals of these projects were to measure surface textures before and after fog seals; to determine optimum applications rates for the fog seal, and the friction coefficient of the pavement. Application rates were studied using the ring test, the surface texture information such as mean texture profile and Mean Texture Depth (MTD) were explored using a Circular Track Meter (CTM) and sand patch test, respectively. Pavement skid resistance was studied using a Dynamic Friction Tester (DFT), British Pendulum Tester (BPT), and the ASTM E274 skid trailer (Winter, et. al., 2012).

Table 3. Caltrans 2012 fog or rejuvenating seal pilot projects information.

District	County	Highway	Construction date (2012)	PM starts	PM ends	Num of lanes	One/two way	Existing pavement type	Application rates, gal/sqyd	Sanding yes/no
2	Modoc	SR-395	7/31-8/1	45	61.5	2	Two	GG	0.12	Yes
2	Shasta	SR-299	8/18-8/19	24	30.3	4/2	Two	GG	0.12	Yes
2	Shasta	I-5	8/21-8/22	7.2	10.8	4	Two	OG	0.14	Yes
2	Siskiyou	SR-96	8/13-8/15	23.23	50	2	Two	Chip seal	0.10	Yes
3	Placer	SR-193	9/10-9/11	1.8	3.3	2	Two	OG	0.11	Yes
3	Placer	SR-193	9/12	4	5.7	2	Two	DG	0.08	Yes
3	Sutter	SR-99	10/10-10/11	14.3	16.6	4	Two	OG	0.10	Yes
3	Sutter	SR-20	10/9	2.5	4.22	2	Two	OG	0.10	Yes
10	San Joaquin	SR-12	10/10-10/11	23.4	27.4	2	Two	Chip seal/DG	0.10/0.07	No
10	Stanislaus	SR-132	8/26-8/27	41	51	2	Two	Chip seal	0.12	No
10	Tuolumne	SR-120	10/1-10/2	7.4	11.3	2	Two	GG	0.11	Yes
10	Calaveras	SR-12	10/3-10/4	10.5	18.2	2	Two	GG	0.11	Yes

Table 4. Caltrans 2013 fog or rejuvenating seal pilot projects information.

District	County	Highway	Construction date (2013)	PM starts	PM ends	Num of lanes	One/two way	Existing pavement type	Application rates, gal/sqyd	Sanding yes/no
2	Tehama	I-5	7/8-7/9	0.0	5.6	4	Two	HMA-O	0.14	Yes
2	Tehama	I-5	6/19-6/20	5.6	11.34	4	Two	HMA-O	0.14	Yes
2	Tehama	I-5	7/10-7/11	11.34	17.34	4	Two	HMA-O	0.14	Yes
2	Tehama	I-5	6/17-6/18	17.34	22.14	4	Two	HMA-O	0.14	Yes
3	Colusa	20	6/5-6/6	23.7	28.2	2	Two	RHMA-O	0.10	Yes
3	Glenn	45	6/4	17.2	20.7	2	Two	HMA-O	0.10	Yes
10	Tuolumne	120	8/7	32.8	35.8	2	Two	HMA-Dense	0.07	No
10	Tuolumne	120	8/6	46.8	51.65	2	Two	RHMA-G	0.09	No
10	Amador	104	8/16	0.0	5.0	2	Two	RHMA-G	0.11	Yes

A total of 12 pilot projects were visited in Caltrans Districts 2, 3, and 10 with a variety of pavement types including open-graded, gap-graded, dense-graded, and chip sealed surfaces. Table 3 shows the locations, application rates, and surface type information of these pilot projects.

3.3 *2013 pilot projects*

To further study the performance and safety of fog or rejuvenating seals, Caltrans conducted 9 additional pilot projects in 2013. The goals of these projects are the same as the earlier pilot projects. These pilot projects were placed in Caltrans Districts 2, 3, and 10 with a variety of pavement types including open-graded, gap-graded, and dense-graded. Because of the rough texture and high skid resistance of chip seals, no chip seal surface was selected for the 2013 study. Table 4 shows the locations, application rates, and surface type information of the 2013 pilot projects.

3.4 *Summary of the 2012 and 2013 pilot projects*

From the testing conducted in this study, the following conclusions were made:

- Generally, with all pavement types the MTD decreased when the fog seal application was applied. This was verified by both the sand patch test and the CTM. In addition, a direct correlation was demonstrated between the CTM and sand patch test results.
- The emulsion breaking times of the ring tests using fog or rejuvenating seals were highly dependent on the temperature, climate, type of fog seal material, application rate, and pavement type.
- Generally, skid resistance of the pavement surfaces decreased after the fog seal was applied but then increased on the projects that included sanding or texture sealing as a precaution. The ASTM skid trailer and the DFT, which both provided data for high speed skid resistance, supported this trend. The BPT was used to determine the low speed skid resistance and how it changed with applications. The data gathered from the BPT tests also supported the same findings mentioned above.
- With increased application rates on both the open-graded and chip sealed surface, the MTD decreased. The effects of increased application rates on the gap-graded pavement were inconclusive and increased application rates on dense-graded pavements did not significantly change the MTD.
- Depending on materials, project sizes, and locations, the costs of fog seals are between $0.40/sqyd and $0.6/sqyd for these projects.

4 TEXTURE AND SKID STUDY ON GAP AND OPEN GRADED SURFACES

One purpose of this study was to measure the surface friction and texture of an asphalt pavement after applying a fog or rejuvenating seal. When applied, the surface of asphalt pavement will experience a short term reduction of friction and loss of texture. Friction is affected by a combination of microtexture and macrotexture of pavement surface, and fog seal application rates. Sand Patch, CTM are simply measures of the macrotexture. This study measured those characteristics to assess whether the reduced skid resistance levels were still acceptable for placing traffic on the roadway. Table 5 is a summary of skid and macrotexture measurement results for the gap-and open-graded flexible pavement surfaces of the 2012 and 2013 pilot projects. Friction was measured with a ASTM skid trailer (ASTM E274). Texture was measure using the Sand Patch (SP) (ASTM E965). Tests were performed before and after applying the fog or rejuvenation seals.

4.1 *Macrotexture summary*

The pavement experienced a slight reduction in the macrotexture measurements after treatment based on Table 5. The reduction can be attributed to both the fog seal and application

Table 5. Summary of skid and macrotexture measurements for 2012 and 2013 pilot projects.

Location	Road surface type	Direction/ lane #	Construction date	Texture (SP) (before), mm	Texture (SP) (after), mm	Skid number (before)	Skid number (after)
Sha-5-7.2/10.8	HMA-O	NB/#2	8/21/2012	2.23	1.90	54	41
Teh-5-0.0/5.6	HMA-O	NB/#1	7/8/2013	1.82	1.27	52	41
Teh-5-0.0/5.6	HMA-O	NB/#2	7/8/2013	1.15	1.10	47	32
Teh-5-17.3/22.1	HMA-O	NB/#1	6/17/2013	1.36	1.01		42
Teh-5-5.6/17.3	HMA-O	SB/#1	6/19/2013	1.47	1.01	52	39
Teh-5-5.6/17.3	HMA-O	SB/#2	6/19/2013	1.55	1.10	47	30
Teh-5-17.3/22.1	HMA-O	SB/#1	6/17/2013	2.03	1.13		39
Teh-5-17.3/22.1	HMA-O	SB/#2	6/17/2013		0.87	50	29
Col-20-23.7/28.2	HMA-O	WB/#1	6/5/2013	1.63	1.47	42	30
Gle-45-17.2/20.7	RHMA-O	SB/#1	6/4/2013	1.32	0.94	42	32
Cal-12-10.5/18.2	RHMA-G	WB/#1	10/4/2012	1.21	1.05	47	33
Ama-104-0.0/5.0	RHMA-G	EB/#1	8/16/2013	1.37	0.92	47	40
Ama-104-0.0/5.0	RHMA-G	WB/#1	8/16/2013	0.95	0.66	47	36
Tuo-120-46.8/56.5	RHMA-G	EB/#1	8/6/2013	1.06	0.94	51	35
Tuo-120-46.8/56.5	RHMA-G	WB/#1	8/6/2013	0.75	0.66	51	30
Tuo-120-7.4/11.3	RHMA-G	WB/#1	9/30/2012	1.38	1.25	50	42

Note: The empty cell in the table means that no test was performed due to construction schedule conflict.

of sand filing up valley of the surface texture. The purpose of the sanding was to enhance the friction of the surface immediately after fog seal applications. The skid number usually increased after sanding applications.

The texture test results show that texture levels for open-graded asphalt were between 1.15 to over 2.00 mm before fog seal applications and were reduced between 0.87 and 1.90 mm after fog seal applications. For gap-graded asphalt surfaces, the macrotexture levels were between 0.75 and 1.38 mm before fog seal applications and between 0.66 and 1.05 mm after fog seal applications. These are typical values for the surfaces measured for RHMA-G and HMA-O, which are greater than typical macrotexture on HMA surfaces (0.50 and 0.75 mm).

4.2 *Skid testing summary*

In all cases, the average friction measurement exceeded the 30 minimum threshold recommended by Caltrans on all pavement surfaces except at one location on Tehama County I-5 between post mile 17.3 and 22.1. The skid number on the first day after fog seal application at this location dropped to 29, and then the skid number came back to 34 a month later. Generally, the skid numbers dropped right after the fog seal application and returned to higher values within a few days. The application of sand increases the short term skid numbers.

4.3 *Texture and skid correlations*

Both microtexture and macrotexture contribute to the friction between tire and pavement. The microtexture dominates the friction at low speed while the macrotexture is an important high speed component for overall friction. The macrotexture provides both the escape for the surface water and subsequently good contact between the tire and pavement when a vehicle travels at high speed. The friction component due to macrotexture increases with speed significantly, and at speeds above 65 mph (105 km/hr) accounts for over 95 percent of the friction (PIARC, 1987).

4.4 *International friction index*

The International Friction Index (IFI) was developed by Permanent International Association of Road Congress (PIARC) to harmonize different friction and texture measurement methods. The IFI is composed of two numbers, F(60) and SP, while F(60) is the international friction number and *Sp* is the speed constant (gradient). Both F(60) and Sp are closely related to the macrotexture of pavement surface.

4.4.1 *Speed constant*

The friction changes with different sliding speed. The speed constant is related to the gradient of the friction—sliding speed curve. Based on ASTM E1960, S_p can be calculated using the following equation:

$$S_P = a + b \times TX \tag{1}$$

where TX = Macrotexture, mm, and
a, b = Calibration constants dependent on the method used to measure macrotexture. For the CTM, measuring *MPD* (ASTM E1845) (Liu and Steven, 2006),

$$S_P = -3.75 + 107.6\ MPD_{CTM} \tag{2}$$

The MPD can be calculated using Sand Patch, MTD value as following:

$$MPD = 1.056 \times MTD - 0.073 \tag{3}$$

4.4.2 *International friction number*

The international friction number can be calculated using the following equation:

$$F(60) = A + B \times FR(60) + C \times TX \tag{4}$$

where A, B = Calibration constants dependent on friction measuring device,
C = Calibration constant required for measurements using ribbed tire, and $FR(60)$ = Adjusted value of friction measurement $FR(S)$ at a slip speed of S to a slip speed of 60 km/hr.

Based on a study by UCPRC (Liu and Steven, 2006), the constant A, B, and C for ASTM skid trailer are—0.023, 0.607, and 0.098, respectively. The $FR(60)$ can be calculated using the following equation:

$$FR(60) = FR(S) \times e^{\left(\frac{S-60}{S_p}\right)} \tag{5}$$

where $FR(S)$ = Friction value at selected slip speed S.
S = Selected slip speed, km/hr.

Vice versa, one can calculate the friction at any speed $FR(S)$ if the friction value are given for the standard speed, $FR(60)$ by following equation:

$$FR(S) = FR(60) \times e^{-\left(\frac{S-60}{S_p}\right)} \tag{6}$$

4.5 *Recommended minimum macrotexture*

Based on the previous section, both S_p and F(60) are directly related to the macrotexture of the pavement surface. From Equation 1, the higher the macrotexture, the higher the speed constant, S_p. From Equation 4, the higher the macrotexture, the higher the international friction number, F(60).

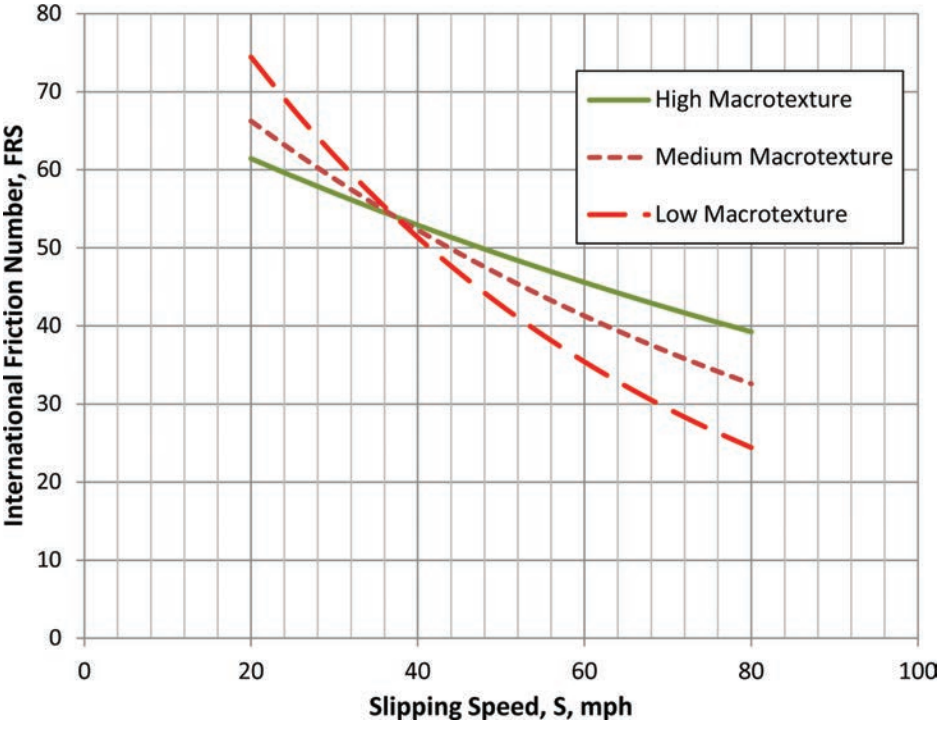

Figure 6. IFI friction model for different macrotexture depths.

To further illustrate the importance of macrotexture, especially at high speed, the friction speed curve shown in Figure 6 was developed using the constants developed by UCPRC in Equation 4. Figure 6 shows that the higher the macrotexture, the flatter the friction-speed curve and higher the friction at high speed. For low macrotexture surfaces, the friction drop significantly at high speed. Therefore, minimum macrotexture level should be provided to ensure the safety of vehicles under high speed and wet pavement conditions.

Based on the testing results of the 2012 and 2013 skid and texture measurement, the recommended minimum macrotexture for open-and Gap Graded RHMA are 1.15 and 0.75 mm, respectively. These two macrotexture values are corresponding to skid numbers that are greater or equal to 30 for ASTM skid trailer test.

Calculated using the UCPRC developed constants, the IFI corresponding to the minimum macrotexture for the HMA open-graded are $F(60) = 19$, and $S_p = 74$ mph, while the IFI corresponding to the minimum macrotexture for the RHMA-Gap Graded are $F(60) = 19$, and $S_p = 46$ mph.

5 CONCLUSIONS AND RECOMMENDATIONS

Based on the fog or rejuvenating seal studies in 2007 and 2009, and the pilot project placed by Caltrans in 2012 and 2013, the conclusions and recommendations are as follows:

5.1 *Conclusions*

The following are the major conclusions of the fog or rejuvenating studies of Caltrans:

- The field evaluation showed that fog or rejuvenating seal treatment sections performed better than the untreated or control sections. The treatment reduced the raveling and had fewer distresses. However, different products performed differently.

- Performance based laboratory testing were conducted on field cores. The Hamburg Wheel Track test results showed that fog or rejuvenating seal treated cores had better rutting resistance and less moisture damage than the control cores. Again different products performed differently.
- Generally, the macrotexture decreased when the fog seal application was applied. This was verified by both sand patch test and the CTM.
- The emulsion breaking times of the ring tests using fog or rejuvenating seals were highly dependent on the temperature, climate, type of fog seal material, application rate, and pavement type. Based on the pilot projects, a 15–20 minutes emulsion breaking time can help to determine the proper fog or rejuvenating seal application rates. Longer breaking time indicates that application rates is too heavy and may cause skid loss.
- Generally, skid resistance of the pavement surfaces decreased after the fog seal was applied but then increased on the projects that included sanding or texture sealing.
- High macrotexture surface generally has higher high speed friction than low macrotexture surface for the same type of pavement. Macrotexture is a very important parameter for increasing speed constant and friction number of the international friction index.
- For the 2012 and 2013 pilot projects, the range of texture levels for open-graded asphalt were from 1.15 to over 2 mm. Generally, the skid numbers of these open-graded pilot projects were higher than Caltrans recommended minimum skid number.
- For the 2012 and 2013 pilot projects, the range of texture levels for gap-graded asphalt were from 0.75 to 1.38. The skid numbers of these gap-graded pilot projects were higher than Caltrans recommended minimum skid number.

5.2 *Recommendations*

The following are the recommendations from this Caltrans fog seal study:

- To account for these varying textures and pavement types, a ring test (similar to CT 345) should be run to determine the appropriate application rate of the fog seal. This test determines the rate that provides adequate coverage and also has break time approximately 15–20 minutes. This is an important feature when considering opening to traffic. The finished surface will typically be dry and slightly tacky.
- Good results can be attained when the fog seal is placed at the pavement temperature above 50°F, ambient temperatures above 60°F, no anticipated precipitation for 3–5 days.
- The higher the macrotexture levels, the less the risk for safety issue due to high speed skid loss. Based on the 2012 and 2013 Caltrans pilot studies, the recommended minimum macrotexture for open-graded mixes is 1.15 mm, and the recommended minimum macrotexture level for rubberized gap-graded mixes is 0.75 mm.
- Different fog or rejuvenating seal products perform differently. Some would have less friction than others. Sanding should be applied to ensure the initial friction right after these fog seal applications on highways.

ACKNOWLEDGEMENT

We would like to extend our gratitude to Caltrans Engineers in Headquarters, Districts 2, 3, 9, and 10, who provided continuous support to this project. The authors also appreciate the support from Dr. R. Gary Hicks who provided detailed review to this paper. CP2 Center Student assistants Brian Winter, Brandon Fraser, Katie Fitzgerald, Brennen Urbanek provided support and performed testing for this project.

REFERENCES

1. Caltrans. Maintenance Technical Advisory Guide, Volume I—Flexible Pavement Preservation, Second Edition. Chapter 6, Fog and Rejuvenating Seals. Division of Maintenance, California Department of Transportation, Sacramento, CA. March 2008.

2. Hall, J.W., K.L. Smith, L. Titus-Glover, J.C. Wambold, T.J. Yager, and Z. Rado. NCHRP 108 Guide for Pavement Friction, Final Report for NCHRP Project 01-43, February 2009.
3. Lu, Q. and B. Steven. Friction Testing of Pavement Preservation Treatments: Literature Review. Technical Memorandum: UCPRC-TM-2006-10, University of California Pavement Research Center, December 2006.
4. Stroup-Gardiner, M., D. Cheng, and R.G. Hicks, Fog and Rejuvenator Seal Test Sections on State Highway 58, Kern County. Report Number: CP2C-2008-102, California Pavement Preservation Center, May 2009, revised September 2011.
5. Stroup-Gardiner, M., R.G. Hicks, and D. Cheng. Fog and Rejuvenating Seal Coats in California 2009. Report Number: CP2C-2009-101, California Pavement Preservation Center, October 2009, revised October 2011.
6. Winter, B., D. Cheng, B. Fraser, and L. Lane. 2012 Caltrans Fog Rejuvenating Seal Pilot Projects in Northern California. Report Number: CP2C-2012-112, California Pavement Preservation Center, December 2012.

This page intentionally left blank

Asphalt Pavements – Kim (Ed)
© 2014 Taylor & Francis Group, London, ISBN 978-1-138-02693-3

Evaluation of early aggregate retention performance of chip seals with Polymer-Modified Emulsions

Jeong Hyuk Im & Y. Richard Kim
Department of Civil, Construction and Environmental Engineering, North Carolina State University, Raleigh, NC, USA

ABSTRACT: One of the most cost-effective pavement preservation treatments is the chip seal. Roads with newly constructed chip seals normally are opened to traffic three to four hours after construction, so it is important that the chip seals reach a sufficient performance level within three to four hours. In order to evaluate this early performance of chip seals, this study compares PMEs to an unmodified emulsion for their usage in chip seals in terms of curing and aggregate retention. The curing and adhesive behavior study of the two types of emulsion was performed using the evaporation test, Bitumen Bond Strength (BBS) test, and Vialit test. The third-scale Model Mobile Load Simulator (MMLS3) was employed for aggregate retention testing.

Based on the test results, the main findings presented in this paper are: (1) the use of PMEs improves chip seal performance and (2) four hours is not long enough for the CRS-2 (unmodified) emulsion to exhibit sufficient aggregate retention performance, but within four hours (at least three hours) is enough time for the PMEs to exhibit sufficient aggregate retention performance.

Keywords: Chip seal, early performance, aggregate retention, curing and adhesive behavior, Polymer-Modified Emulsion

1 INTRODUCTION

Chip seals are one of the most efficient and cost-effective methods of pavement preservation and offer significant advantages in terms of skid resistance and fast construction. Chip seals have proved to be cost-effective due to their low initial costs in comparison with thin asphalt overlays and due to other factors that affect treatment selection decisions where the structural capacity of the existing pavement is sufficient to sustain its existing loads [1].

Due to the low-cost maintenance benefits of chip seals, state highway agencies would like to extend their use to include roadways with traffic volumes that are higher than those typically used. For high-volume roads, Polymer-Modified Emulsions (PMEs) can be used in the chip seal design because the polymer modification decreases the pavement's susceptibility to changes in temperature, increases adhesion to reduce aggregate loss, and allows the road to be opened to traffic earlier than would otherwise be the case. Together, these benefits have led to the increased use of PMEs by the chip seal industry.

The use of emulsions is very common in pavement preservation because emulsions do not require a hot mix set-up, they have a low sensitivity to temperature changes, and they are not likely to be hazardous to the construction crew. In addition to these benefits, most sources agree that the use of PMEs also provides benefits to the binder after modification. Most scientific sources are also in agreement that the best and most effective concentration of polymers is one that allows for the formation of a continuous polymer, and 3% to 5% is a typical advisable application rate for polymers [2, 3].

The adhesion of the emulsion to the aggregate in a chip seal system is strongly associated with the performance and service life of the chip seal. Wood et al. [4] explain that the addition of polymer can enhance certain properties of an asphalt emulsion. Generally, four types of polymers can be used in PMEs: natural latex, synthetic latex, Styrene Butadiene Rubber (SBR), and Styrene Butadiene Styrene (SBS). Typically, approximately 2.5% to 3% polymer, by weight, is added to the emulsion. When polymer is added to the emulsion, several benefits emerge; e.g., early aggregate retention raises the softening point of the base asphalt, the chip seal is better protected, and fewer materials are wasted.

One of the most prevalent failures of chip seals is the aggregate loss that occurs from traffic loading. One of the benefits of using PMEs for chip seals is that PMEs mitigate such aggregate loss. Takamura [5] compared the aggregate retention performance of unmodified emulsion and PME (3% cationic SBR latex). The brush test, which was developed to reduce problems associated with loose aggregate in chip seal operations, was used. The brush test was conducted using eight different aggregate types after five hours of curing at 35°C (95°F). A comparison of the unmodified emulsion and the emulsion modified with SBR latex showed that the SBR latex-modified asphalt emulsion provided faster strength development, with above 80% aggregate retention, than the unmodified emulsion.

Kim and Lee [6] compared the aggregate retention performance of an unmodified emulsion (CRS-2) and two PMEs (CRS-2L and CRS-2P). They performed the third-scale Model Mobile Load Simulator (MMLS3) test, flip-over test, Vialit test, bleeding test, and rutting test on both laboratory and field-fabricated samples under different temperature conditions. The benefits of using PMEs in chip seal construction are supported by this study. The CRS-2L emulsion manifested a reduction in the amount of aggregate loss during early curing times, less curing time needed to obtain the desired adhesion, and the ability to allow traffic on the newly constructed road safely and relatively soon. Also, the CRS-2L emulsion improved the aggregate retention performance at low temperatures. The CRS-2L emulsion tested by the Vialit test met the Alaska Department of Transportation specifications criterion of 10% maximum allowable aggregate loss at –20°C and 5°C.

Building on the work of these previous studies, this study investigates the curing and adhesive behavior and the aggregate retention performance properties of chip seal samples fabricated in the laboratory using an unmodified emulsion and five PMEs to evaluate the early performance of chip seals.

2 OBJECTIVE

The objective of this paper is to evaluate the early aggregate retention performance of chip seals made with PMEs in the laboratory based on a comparative study. Because public traffic typically is allowed on roads with newly constructed chip seals three to four hours after construction is completed, the early aggregate retention performance plays a vital role in the success of chip seals.

3 MATERIALS

One unmodified emulsion (CRS-2) and five PMEs (PME-A, PME-B, PME-C, PME-D, and PME-E) are used in this study. The CRS-2 and PME-A (SBR latex-modified) emulsions were selected because they are used widely in North Carolina and best match the surface charge of the granite aggregate that is commonly used in North Carolina. In order to compare the emulsion properties of the PMEs, PME-B and PME-C were selected as SBS PMEs. In addition, PME-D and PME-E are employed in this study because they are produced especially for high performance chip seals. Based on the most common usage for chip seal construction in North Carolina, a 78 M graded granite aggregate was used to fabricate the laboratory samples. Figure 1 shows the gradations of the granite aggregate plotted on the 0.45 power chart.

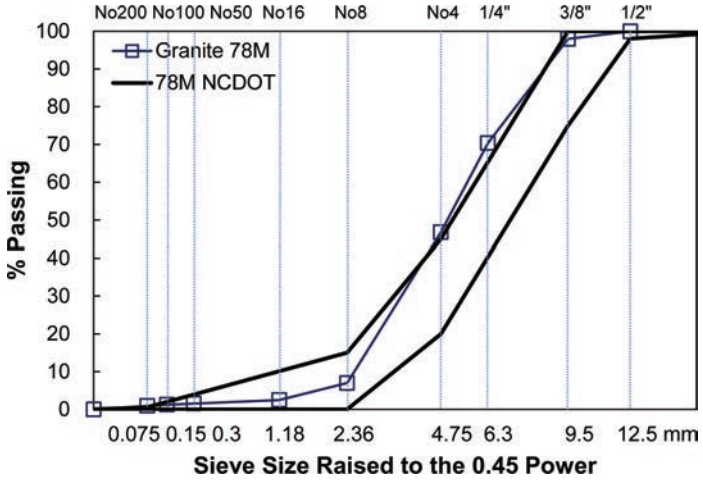

Figure 1. Aggregate gradations for granite aggregate.

For the aggregate loss tests (the Vialit test and MMLS3 test), single-seal specimens were fabricated using the granite 78 M aggregate. The optimal Aggregate Application Rates (AARs) and Emulsion Application Rates (EARs) were determined for these single seals based on an earlier chip seal mix design study [7]. All the specimens were fabricated with AARs of 8.7 kg/m^2 (16 lb/yd^2). For all the specimens, an EAR of 1.13 L/m^2 (0.25 gal/yd^2) was applied for all the emulsion types.

4 EXPERIMENTAL PROGRAMS

In order to evaluate the curing and adhesive behavior of the chip seals, evaporation testing was used for a direct comparison of the curing characteristics of the test emulsions. The BBS test and the Vialit test were conducted at four curing times (30, 60, 120, and 240 minutes) and at three curing temperatures (15°C, 25°C, and 35°C) to investigate the performance within the early curing times. The aggregate retention performance, which reflects one of the main failure characteristics of chip seals, i.e., aggregate loss, was evaluated using the Vialit test and MMLS3 test.

Figure 2 (a–c) show the apparatus used for the evaporation test, BBS test, and Vialit test, respectively.

4.1 *Evaporation test*

It is important to determine the curing times that are required for the respective emulsions to reach their asymptotic percentage of water loss, that is, the point at which no more water loss occurs. This determination requires a direct comparison of the curing characteristics of the test emulsions. For these evaporation tests, emulsions were heated to the application temperature, 60°C, and placed in small cans 90 mm diameter each. All emulsion samples were exposed to the same curing condition; i.e., each was subjected to the same curing temperature, 35°C, and EAR of 0.25 1.13 L/m^2 (gal/yd^2) in the environmental chamber.

4.2 *Bitumen Bond Strength (BBS) test*

In the pavement field, the Pneumatic Adhesion Tension Testing Instrument (PATTI) test can be used to measure the bond strength between the hot asphalt binder and aggregate surface or between the emulsion and aggregate surface by providing the maximum pull-off tensile

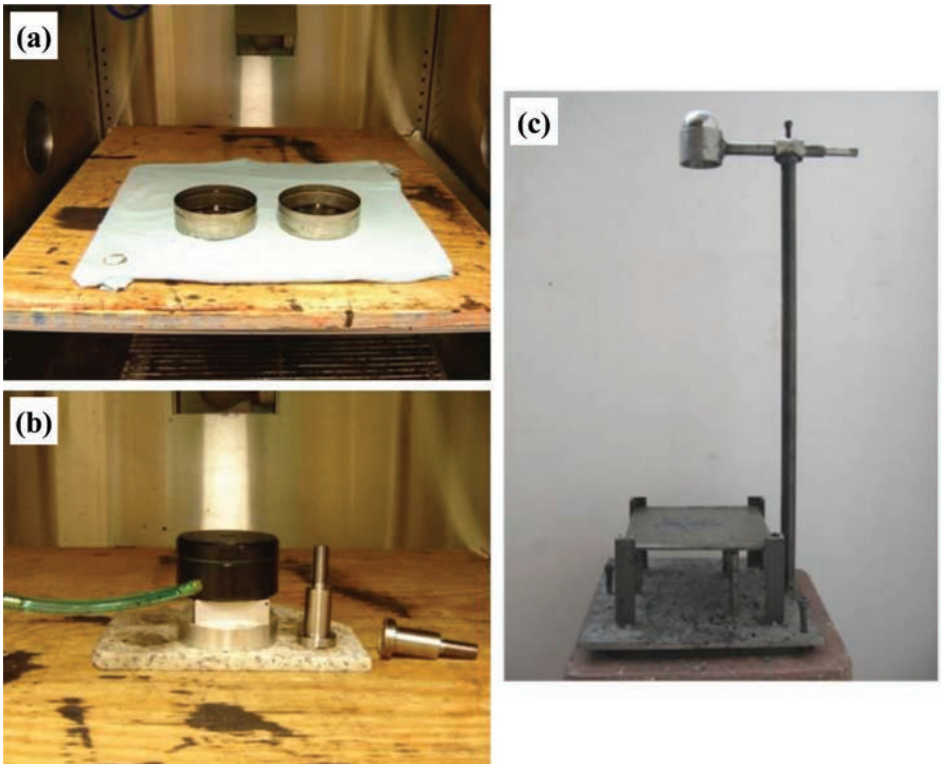

Figure 2. Apparatus used for: (a) Evaporation test, (b) BBS test, and (c) Vialit test.

strength that is converted from air pressure. AASHTO TP-91 was developed for asphalt binders and emulsions and provides the specifications for the BBS test [8].

In this study, the BBS test is used to compare the adhesive behavior of each emulsion as a function of different curing times and temperatures. Therefore, the BBS test results are used to determine not the bond strength itself, but the change in bond strength as a function of curing time. In previous fog seal research [9], the BBS procedure was modified so that it can be applied to fog seal emulsions. From the fog seal BBS test results, it was found that the modified BBS procedure works well. The only difference between the BBS procedure and the modified BBS procedure is the testing time. In the BBS procedure [8], once the pull-stubs are affixed, one hour is required to allow the samples to acclimate to the test conditions. Therefore, when the BBS test is conducted for two hours of curing, the actual test is performed at three hours of curing. This additional one hour not only can affect the bond strength but it also can be a major variable in determining the emulsion curing rates, because any significant change in the curing rate of the emulsion normally occurs during the early part of the test. Therefore, in this study, the modified BBS test procedure, whereby the actual test is performed at an exact curing time in an environmental chamber, is used for analysis of the adhesive behavior of each emulsion.

The BBS tests were conducted for all the test emulsions with granite aggregate under the same conditions. In order to capture the early bond strength, the BBS tests were performed at four curing times (30, 60, 120, and 240 minutes) and at three curing temperatures (15°C, 25°C, and 35°C).

4.3 *Vialit test*

The Vialit test was developed by the French Public Works Research Group and is standardized in BS EN 12272-3 [10]. This test method can be used as an indicator of aggregate

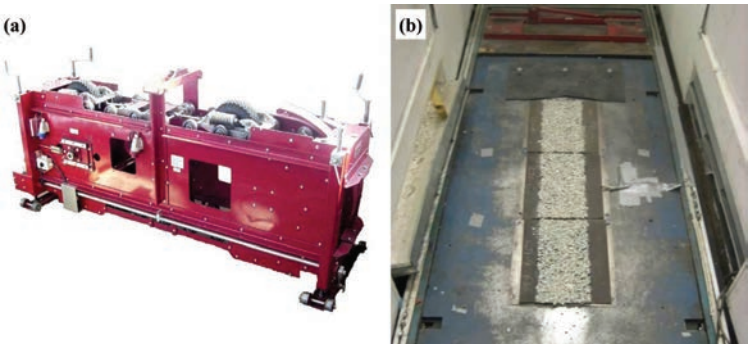

Figure 3. (a) MMLS3 and (b) Samples in MMLS3 chamber.

retention for chip seal specimens. A stainless steel ball is dropped three times from a height of 50 cm (19.7 inches) onto an inverted chip seal specimen. The averaged percentage of aggregate loss after three ball drops is used to evaluate the aggregate retention of the specimen.

In this study, the Vialit test was performed for granite aggregate to determine the adhesive behavior of the chip seal specimens and to evaluate their aggregate retention performance at different curing times (30, 60, 120, and 240 minutes) and at different curing temperatures (15°C, 25°C, and 35°C). Four replicates were fabricated for each condition to ensure confidence in the resultant data.

4.4 *Third-scale Model Mobile Load Simulator (MMLS3) test*

Figure 3 (a) and (b) present the MMLS3 and chip seal samples in the environmental chamber, respectively. The MMLS3 uses a continuous loop for trafficking. It is comprised of four bogies each with one wheel, which is a pneumatic tire that is 30 cm (11.8 inches) in diameter, one-third the diameter of a standard truck tire approximately, per bogie. The MMLS3 provides repeated wheel loads onto the pavement surface at a consistent rate (990 wheel loads applied every 10 minutes) and accelerates wear on the pavement. The MMLS3 allows researchers to simulate years of damage in mere days. Also, the MMLS3 can simulate the actual wandering of vehicles across the wheel path by wandering across the entire width, 17.8 cm (7 inches), of chip seal specimens. In order to control the test temperatures, the MMLS3 is placed inside a temperature chamber during testing.

Specimens for MMLS3 testing can be fabricated in the field or in the laboratory. For the laboratory-fabricated specimens, asphalt felt disks are cut to 30.5 cm by 35.6 cm (12 inches by 14 inches), and emulsion is applied on the felt paper in dimensions of 17.8 cm (7 inches) wide and 30.5 cm (12 inches) long, which covers the MMLS3 wheel path (Kim and Lee 2005). The MMLS3 test procedure involves the following steps [6, 7, 11]:

1. Cure the specimens in the temperature chamber at 35°C (95°F) for 12 hours and 35 ± 3% relative humidity, as specified by ASTM D7000 [12].
2. Weigh the initial specimen.
3. Condition the specimens to 25°C (77°F) for 3 hours.
4. Apply MMLS3 loading for 10 minutes, which is the time required for the MMLS3 to complete one wandering cycle, and then weigh the specimen.
5. Apply MMLS3 loading for 120 minutes, and weigh the specimen periodically.

5 PERFORMANCE EVALUATION BY LABORATORY TESTING

5.1 *Curing and adhesive behavior*

Figure 4 (a) shows the evaporation test results and (b), (c), and (d) show the BBS test results for curing at 15°C, 25°C, and 35°C, respectively.

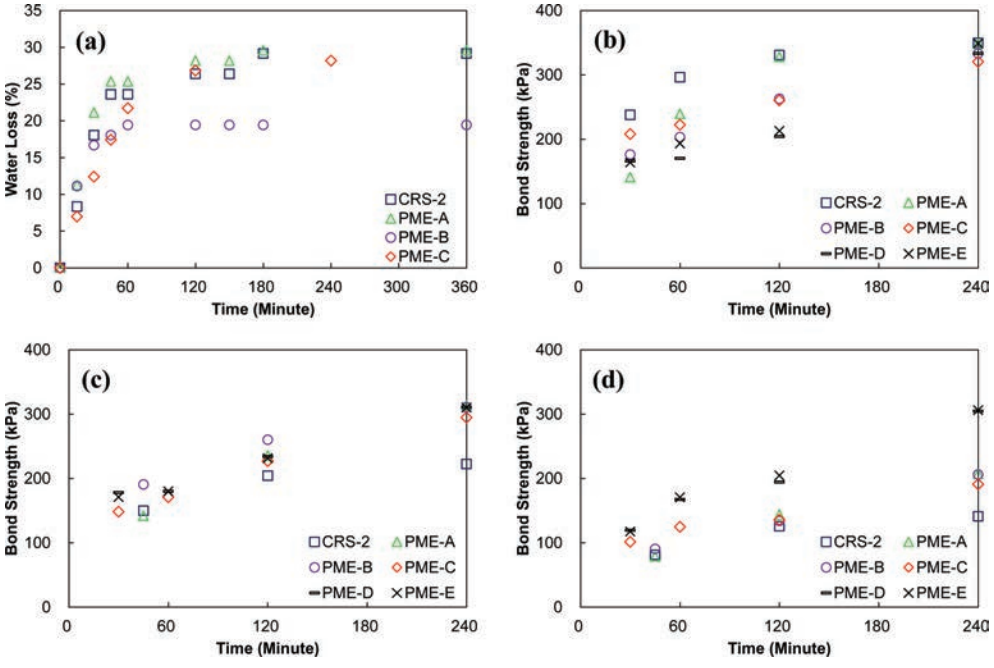

Figure 4. Curing and adhesive behavior test results: (a) Evaporation test; and BBS test at (b) 15°C, (c) 25°C, and (d) 35°C.

5.1.1 *Evaporation test*

Figure 4 (a) presents the evaporation test results that indicate that the PME-B emulsion reaches its asymptotic final percentage of water loss (curing) the fastest of all the emulsion types. It reaches its asymptotic curing value in approximately one hour, and the PME-C emulsion reaches its asymptotic curing value in two hours. Both the CRS-2 and PME-A emulsions reach their asymptotic curing values at around three hours. Thus, in this test, the PME-B emulsion cures about two times faster than the PME-C emulsion and about three times faster than the CRS-2 and PME-A emulsions.

5.1.2 *Bitumen Bond Strength (BBS) test*

The BBS test results (see Fig. 4 (b–d)) indicate that the PMEs show better bond strength than the CRS-2 unmodified emulsion at 35°C and 25°C not only during curing, but also after curing. However, at 15°C, the PMEs show lower bond strength values than the CRS-2 emulsion in the early curing times (before four hours). The bond strength values of the PMEs after four hours of curing are similar to that of the CRS-2 unmodified emulsion. This unexpected behavior at 15°C seems to be related to the contact area between the pull-off stubs and aggregate substrate and seems also to be dependent on the test temperature. The test temperature may affect the viscosity of the emulsion, and the viscosity will then affect the penetration of the emulsion into the voids in the aggregate substrate. For BBS testing, it is important to maintain the same contact areas in order to compare the bond strength values directly, because a smaller contact area causes less bond strength when the same load is applied to the specimen. The porosity of the aggregate substrate also can affect the bond strength because air can be trapped in the surface voids when the emulsion is poured [13].

5.1.3 *Vialit test*

Figure 5 (a–c) show the Vialit test results as percentages of aggregate loss at the different curing times for all six emulsion types with granite aggregate at 15°C, 25°C, and 35°C, respectively. Figure 5 shows that low curing temperatures lead to more aggregate loss than

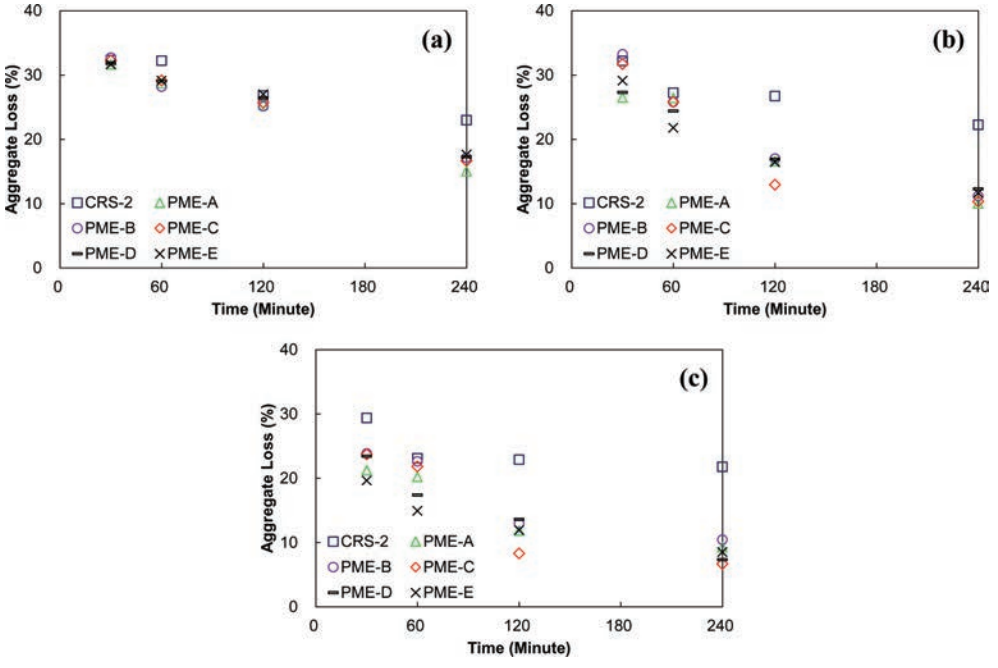

Figure 5. Vialit test results at: (a) 15°C (b) 25°C (c) 35°C for granite aggregate.

high curing temperatures. The reason for this outcome is that emulsion is more fluid at higher temperatures, and this emulsion state allows the aggregate particles to be reoriented in a manner that maximizes the embedment depth in the compaction state and improves aggregate retention. As expected, a direct relationship is found between the curing temperature and aggregate loss results, regardless of emulsion type.

At four hours of curing, the CRS-2 specimens show more aggregate loss than the PME specimens regardless of the PME type and test temperature. The difference in aggregate retention performance between the unmodified emulsion and the PMEs becomes greater as the temperature increases. Recognizing that the chip seals are constructed more frequently at temperatures closer to 25°C and 35°C, the improved aggregate retention benefits of the PMEs would be an important factor in the early aggregate retention performance of chip seals.

5.2 *Aggregate retention performance*

Figure 6 (a) and (b) present the cumulative aggregate loss results obtained by the MMLS3 tests and the aggregate loss comparison between the MMLS3 and Vialit test results, respectively. Figure 6 (a) presents aggregate retention test results that show that the CRS-2 chip seal performs the worst of all the emulsion types; in particular, the CRS-2 samples show approximately 12% aggregate loss after MMLS3 loading. This result can be considered to be a failure of chip seal performance according to the maximum allowable aggregate loss (10%) criterion established by the Alaska Department of Transportation. The PMEs meet the criterion.

Figure 6 (b) shows that the Vialit test leads to more aggregate loss than the MMLS3 test for all emulsion types. In particular, the difference in aggregate loss between the Vialit and MMLS3 test results is the greatest for the CRS-2 emulsion. The benefit of improved aggregate retention in the PMEs over the CRS-2 emulsion is more dramatically captured by the Vialit test than by the MMLS3 test. This difference is probably due to different loading mechanisms employed by the two test methods to cause aggregate loss in chip seal samples, i.e., the third scale of tire loading in the MMLS3 test and the impact loading by steel ball drop in the Vialit test.

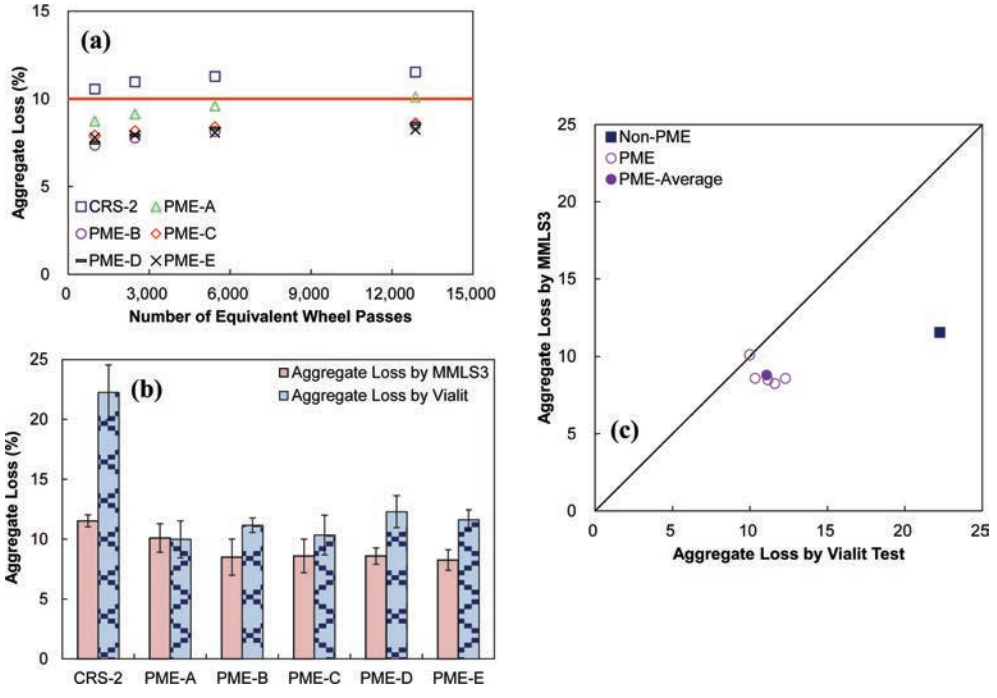

Figure 6. (a) Cumulative aggregate loss from MMLS3 test, (b) Aggregate loss comparison between MMLS3 and vialit test results, and (c) Correlation between aggregate loss by vialit test and by MMLS3 test.

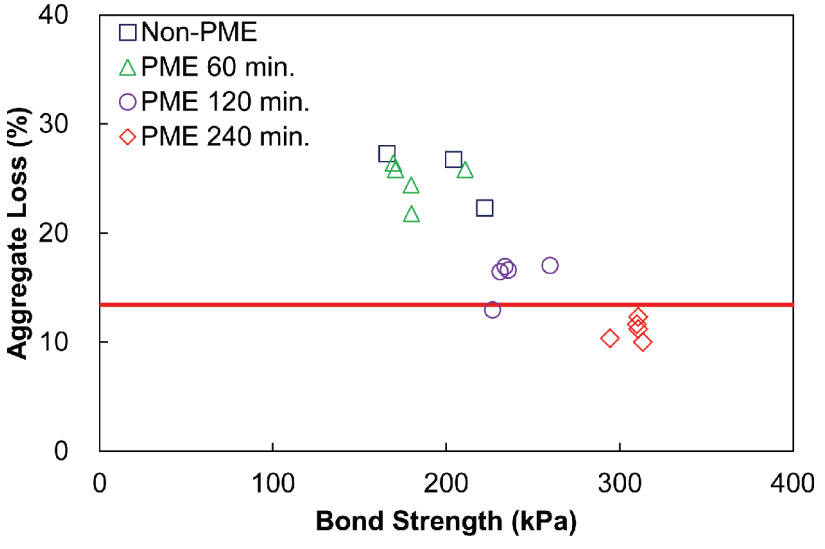

Figure 7. Correlation between vialit and BBS test results.

The relationship between the aggregate loss measured by the Vialit test and by the MMLS3 test is depicted in Figure 6 (c). It is noted that the aggregate loss under real traffic is better represented by the moving load imparted by the MMLS3. However, the Vialit test is much simpler and more practical to be used in specifications and routine evaluation of chip seals by state highway agencies. Therefore, there is a need to convert the maximum allowable

aggregate loss (10%) criterion established by the Alaska Department of Transportation into the aggregate loss by the Vialit test. According to the relationship shown in Figure 6 (c), the 10% aggregate loss in the MMLS3 test is approximately 13% aggregate loss in the Vialit test.

5.3 *Correlation between BBS and aggregate loss by vialit test*

Figure 7 presents the correlations between the Vialit test results and the BBS test results in terms of aggregate loss. The inverse relationship between the aggregate loss and the bond strength is clearly shown in Figure 7. The maximum allowable aggregate loss of 13% from the Vialit test results in the minimum bond strength of approximately 270 kPa. According to the data shown in Figure 7, all the emulsions at 2 hour curing time do not meet this criterion. Also the CRS-2 emulsion does not meet the criterion even after 4 hours of curing time. This approach can be used to develop the emulsion specification criteria for chip seals.

6 CONCLUSIONS

This paper presents an evaluation of the early aggregate retention performance of polymer-modified chip seals. For the evaluation, the curing and adhesive behavior of different emulsions was investigated, and chip seal aggregate retention performance testing was conducted in the laboratory. Based on the test data and findings, the following conclusions are drawn:

- PMEs show better performance in curing and adhesive behavior and aggregate retention than the unmodified emulsion (CRS-2 in this study).
- The curing temperature of 15°C is too low for the Vialit specimens made of granite aggregate and for PMEs to be cured completely within four hours.
- Maximum allowable aggregate loss criteria of 10% in the MMLS3 test is equivalent to about 13% of aggregate loss in the Vialit test.
- There exists a strong inverse relationship between the aggregate loss in the Vialit test and the bond strength in the BBS test. The maximum allowable aggregate loss of 13% in the Vialit test translates to about 270 kPa of bond strength.
- The CRS-2 unmodified emulsion does not exhibit sufficient aggregate retention within four hours, but PMEs do exhibit sufficient aggregate retention within four hours.

REFERENCES

[1] Gransberg, D.D. Correlating Chip Seal Performance and Construction Methods. *Transportation Research Record: Journal of the Transportation Research Board*, No. 1958, pp. 54–58. 2006.

[2] Voth, M. Federal Lands Highway-Pavement Preservation Team. Report on Status of Study: Using Modified Asphalt Emulsions in Surface Treatments. 2006.

[3] Stroup-Gardiner, M. and D. Newcomb. An Evaluation of Rheological Measurements for Unmodified and Modified Asphalt Cements. *Transportation Research Record*, No. 1488. 1995.

[4] Wood, T.J., D.W. Janisch, and F.S. Gaillard. *Minnesota Seal Coat Handbook 2006*. Minnesota Local Road Research Board (LRRB). http://www.lrrb.org/PDF/200634.pdf. 2006.

[5] Takamura, K. *Improved Fatigue Resistance of Asphalt Emulsion Residue Modified with SBR Latex*. Presented at the AEMA Annual Meeting in Nashville, TN. 2003.

[6] Kim, Y.R. and J. Lee. *Performance Based Analysis of Polymer Modified Emulsions in Asphalt Surface Treatments*. Final Report, Report No. FHWA/NC/2007-06 (HWY-2007-06), North Carolina Department of Transportation, Raleigh, NC. 2009.

[7] Kim, Y.R. and J. Adams. *Development of a New Chip Seal Mix Design Method*. Final Report, Report No. HWY-2008-04, North Carolina Department of Transportation, Raleigh, NC. 2011.

[8] American Association of State and Highway Transportation Officials (AASHTO). *AASHTO TP: 91. Standard Test Method of Test for Determining Asphalt Binder Strength by Means of the Asphalt Bond Strength (ABS) Test*. 2011.

[9] Im, J.H. and Y.R. Kim. Methods for Fog Seal Field Test with Polymer-Modified Emulsions: Development and Performance Evaluation. *Journal of the Transportation Research Board*, No. 2361, pp. 88–97. 2013.

[10] British Standards (BS). EN 12272-3: *Surface Dressing. Test Methods. Determination of Binder Aggregate Adhesivity by the Vialit Plate Shock Test Method*.
[11] Kim, Y.R. and J. Lee. *Optimizing Gradations for Surface Treatments*. Final Report No. FHWA/NC/2005-15, North Carolina Department of Transportation, Raleigh, NC. 2005.
[12] ASTM. D: 7000-08: *Standard Test Method for Sweep Test of Bituminous Emulsion Surface Treatment Samples.*
[13] Moraes, R., R. Velasquez, and H.U. Bahia. Measuring the Effect of Moisture on Asphalt-Aggregate Bond with the Bitumen Bond Strength Test. *Transportation Research Record: Journal of the Transportation Research Board*, No. 2209. 2011, pp. 70–81.

Asphalt Pavements – Kim (Ed)
© 2014 Taylor & Francis Group, London, ISBN 978-1-138-02693-3

Pavement and Materials Technology Review for municipalities—including a case study

Ludomir Uzarowski & Vimy Henderson
Golder Associates Ltd., Mississauga, Ontario, Canada

ABSTRACT: Pavement and Materials Technology Review (PMTR) is a method that can provide guidance in assessing improvements and advancements that are applicable to a specific municipality. A PMTR first involves an evaluation of typical pavement condition in the area and determining the current state-of-the-practice. This includes thorough assessment of the current specifications, submittals from contractors, construction testing results, laboratory testing results that cover the span of multiple recent years, acceptance and follow ups. With this information it is possible to identify practices that are working well and producing quality results and also highlight areas where improvements or changes are required.

Findings of a PMTR and action recommendations are specific to a particular area and may include any or all of the following: appropriate technology; modification to specifications; acceptance; enforcement of specifications; follow ups; staff training and education/workshops within the area including owners, contractors and consultants; and implementation of new technologies. The conclusion of a PMTR is intended to be the development of a clear system that can be routinely applied to projects within the municipality.

The PMTR completed for the City of Moncton in 2010 is used as a case study in this paper.

Keywords: technology review, state-of-the-practice, pavement performance, specifications, training

1 INTRODUCTION

Advancements and improvements in technologies are continual in the pavement industry. Some of the current areas of advancement and growth include: materials including asphalt cements; mix designs; recycling; rehabilitation methods; pavement preservation; and pavement design methodologies. Various reasons lead to the advancement of pavement technology. Economics are generally a substantial contributor when there is a need to change the current method or materials. Other contributing factors include performance improvements and sustainability. Evaluating and understanding which of these is applicable for a particular municipality can be challenging. In order to effectively determine when and which method or technologies should be integrated it is necessary to understand the current state of the practice in the municipality. By understanding the current state of the practice it is possible to select new methods and technologies that will at least maintain the current quality of pavement or possibly lead to improvements in quality of pavements.

It is necessary to understand the current practices before new technologies and methods can be implemented. A Pavement and Materials Technology Review (PMTR) carried out by an experienced pavement engineer can provide guidance in assessing improvements and advancements that are applicable to a specific municipality. A PMTR involves pavement condition inspection and identifying typical pavement distresses in new, relatively new and older pavements and an evaluation of the current state-of-the-practice in a municipality. This includes a thorough assessment of the current specifications, submittals from contractors,

construction testing results, laboratory testing results that covers the span of multiple recent years, acceptance, and follow ups. With this information it is possible to identify practices that are working well and producing quality results and also highlight areas where improvements or changes are required. A successful PMTR is a combined effort between the municipality technical staff members and the reviewing engineer, with the goal of both parties aiming to continually improve the quality of pavements in a municipality.

Many municipalities find premature distresses developing on pavements and the causes are often unclear. Probably the most common premature distresses noticed by Canadian municipalities are: poor longitudinal joint performance; early ravelling; and premature cracking. The purpose of a PMTR is to work with the municipality and identify areas in the current practice that could be improved and determine what improvements would be most effective, suitable and feasible.

2 OBJECTIVE

The intent and objective of a PMTR is described in the following section. The objective of this paper is to describe the basics of PMTR and describe a case study. A PMTR was completed for the City of Moncton (City) in 2009 and will be presented in this paper to demonstrate the various aspects of the PMTR. The objective of carrying out the PMTR in the City was to identify problems with pavement performance and to evaluate the current state of the practice of the pavement industry in the City. After identifying and understanding the current state of the practice the intent was to build on the successful aspects and identify those that could be improved or changed.

3 PAVEMENT AND MATERIALS TECHNOLOGY

A PMTR is an objective method of evaluating the current state of the practice of the pavement industry in a particular municipality. It is a tool that can assist a municipality in effectively managing its pavement assets. A PMTR can be carried out in municipalities of various sizes and is highly dependent on the involvement of municipal staff members. A PMTR includes the following steps, each of which will be discussed in the following sections:

- Document and results review from current and previous years;
- Field visits and condition evaluation of new, relatively new and older pavements;
- Specification review;
- Evaluation of current state of the practice;
- Identification of effective aspects;
- Identification of possible areas of improvement;
- Implementation, including staff training;
- Monitoring; and
- Updating.

Figure 1 presents a flowchart describing a PMTR.

Figure 1 shows the connections between various aspects of a PMTR. The terms referenced in Figure 1 generally represent aspects of a PMTR and change slightly depending on the specific municipality. The ability to link these various aspects within a municipality is one of the key reasons that PMTR are successful. Municipalities vary in size and many have multiple departments that all contribute to work with the paving industry, such as tenders and contracts, design, field inspection and maintenance. It can be challenging to connect the work from various departments together and objectively assess the effectiveness of the final outcome: short and long term quality of pavement. In a PMTR an objective review is undertaken with the assistance and involvement of the municipal staff. The outcome is an understanding of the current state of the practice in a municipality, that bridges across all involved groups.

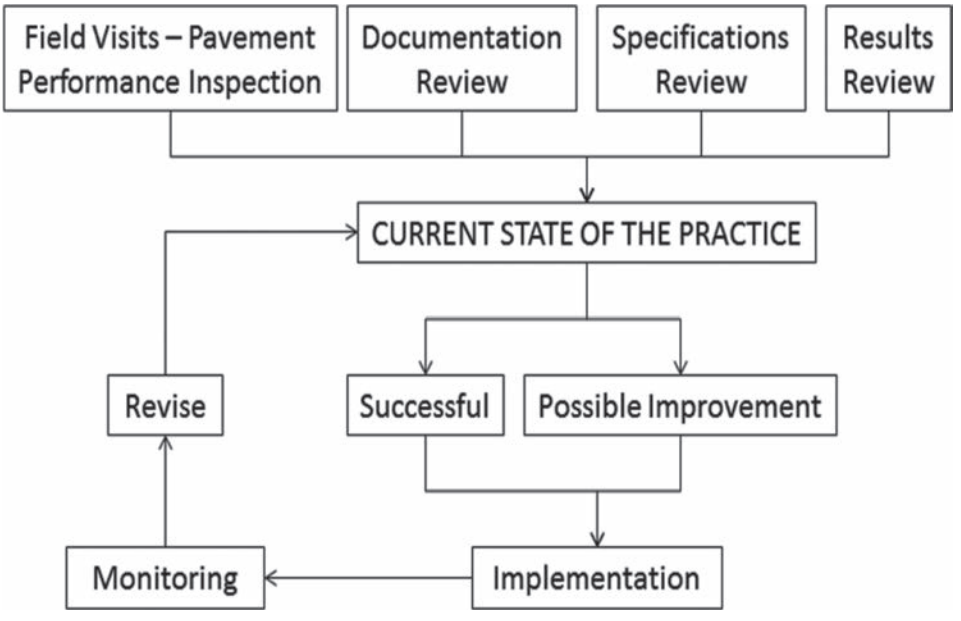

Figure 1. Flowchart describing PMTR.

3.1 *Field visits—pavement performance inspection*

Site visits typically start with a meeting with municipal technical staff to discuss their concerns and observations about pavement performance, pavement design methodology, types of materials used including granular materials and asphalt and concrete mixes and their quality, concern about specifications and quality of construction, effectiveness of Quality Control (QC) and Quality Assurance (QA), capability of local contractor in delivering quality products, suggestions about technology improvements including rehabilitation methods, pavement preservation and maintenance. The technical people have often years of experience and deep knowledge of local sources of material and potential problems with technology currently being used. Their input is particularly important to achieving better quality, longer lasting pavements.

During the PMTR it is important to complete field visits on a variety of roads throughout the municipality. At minimum this should include those currently under construction or just completed (less than one year old), roads two to five years old and roads more than five years old. Visits should also be made to construction sites to evaluate the construction practice. Also, if there are issues with the quality of aggregates and granular materials, a visit to aggregate quaries or pits can be arranged, if feasible. Staff members are typically directly involved in the projects since they are very familiar with the roads in the municipality. These individuals will be able to highlight pavements that are performing well and any that are deemed to be under performing. Comments and experiences shared by the municipal staff is critical in fully assessing the current state of the practice in a municipality.

The quality of the construction of a pavement will be one of the ultimate factors in the long term performance. The combination of pavement design, materials, construction and maintenance will determine the long term performance. However, if one of the three initial items is insufficient then maintenance will typically not be able to correct it. Observations made during construction field visits can be very useful to municipal staff members as well. Findings should be shared with staff members, especially during the implementation stage and with management. It is unfair to expect staff members to be able to adequately inspect construction practices if they have not had the opportunity to learn about the methods themselves.

Properly carried out pavement condition inspections by an experienced pavement engineer will not only identify the types, severity and density of the distresses but will also help in identifying their causes, such as deficient pavement design, poor materials, poor construction practice or environmental impact. The most commonly observed pavement distresses can be grouped as follows:

- Structural—including alligator cracking on rutting in the wheel path. They occur mainly due to insufficient pavement structure to support the traffic loading. They should be addressed by proper design including necessary geotechnical/soil information, anticipated traffic loading calculation and using proper design methodology;
- Materials—including polished aggregate, shoving and swelling. These distresses occur due to the characteristics of the materials throughout the pavement structure. The maintenance or repair to address these distresses varies dependent on the distress. Proper selection of the materials and laboratory testing should eliminate these distresses.
- Construction—including ravelling, bleeding, bumps, sags, depressions, edge cracking, longitudinal cracking, joint opening and slippage cracking. These distresses develop due to the practices that were used during construction. Depending on the severity of the distress is maybe possible to apply maintenance such as crack sealing. Otherwise the material that was poorly constructed would need to be replaced. The major objective here is to make sure that proper construction practice is followed so that premature distresses can be avoided.
- Environmental—including transverse cracking, frost heaves and block cracking. These distresses develop due to an inability for the pavement structure to perform under changing climatic conditions, particularly freeze-thaw cycling.

Although it is impossible to eliminate the impact of the environment on the pavement, the potential for environmental distresses can be reduced or minimized by using proper design, particularly rehabilitation of existing pavements, and good quality materials.

3.2 *Document review*

Available documentation is provided to the pavement engineer carrying out the review. The documentation would typically include annual paving plans, pavement designs, contract documents, specification requirements, QC/QA, reports, municipality inspection reports and maintenance plans.

Additionally, information about the current pavement design practices in the municipality would be provided for review. Municipalities are often responsible for a wide range of roadways and it is understood that having simple templates or a design matrix is often considered to be a feasible solution. The templates or matrices should consider relevant design inputs, such as, soil and water conditions, traffic and pavement materials characteristics. It is also important to ensure that adequate design information is used for the new construction, reconstruction or rehabilitation design for at least major roads in the municipality. Pavements will begin to deteriorate immediately following construction but sufficient pavement structure, materials and construction will decrease the rate of deterioration. Suitable maintenance throughout the life of the pavement is necessary as well to achieve the optimum performance.

The documentation should also include all documents associated with submitted mix designs. The submitted documents for each mix would be compiled and reviewed to evaluate if all required information was being submitted to the municipality prior to the initiation of construction of a project. These submittals should be complete for each project.

3.3 *Specification review*

Specifications are very important to a municipality as they are one of the steps in ensuring that the pavement that is constructed is as intended. As with many of the aspects of a PMTR, the specifications do not alone ensure that a quality pavement will be constructed, they need to be updated periodically and need to be understood between various areas

in the municipality. A PMTR goes through the existing specifications in detail and provides an objective interpretation of them. Some of the key considerations when reading a municipality's specifications include:

- Clarity;
- Do they reflect current practices being used in the municipality and by the industry;
- Are requirements for acceptance payment outlined; and
- Are consequences of failure to meet requirements described.

Although municipality's specifications are a critical tool in achieving quality pavement, they are often large documents and can be intimidating and challenging to work with. An objective review can be helpful as it will assist in the interpretation of the existing specifications and identify if areas exist that should be improved or changed to reflect the municipality's goals and affordable budgets. The state of the specifications will be reflected in the quality of pavement that is produced in a municipality.

3.4 *Results review*

All results from years in consideration should be provided to the pavement engineer carrying out the review for compilation and analysis. Results will be analyzed in consideration of a variety of aspects, such as type, year, specific mix design, construction, QC/QA and acceptance. Analysis of the available results, generally construction QA can identify aspects of the current practices that are effective; and lead to success as well as those that are not meeting the acceptance criteria. The analysis of the results combined with the field visits can help to identify which particular distress or scenario is occurring. Figure 2 shows an example of the analysis of asphalt cement content variance in QA sample results for a municipality.

Figure 2 shows the asphalt cement content variance from the JMF results from all projects in a municipality in 2011. Figure 2 presents a clear picture of the asphalt cement content variance

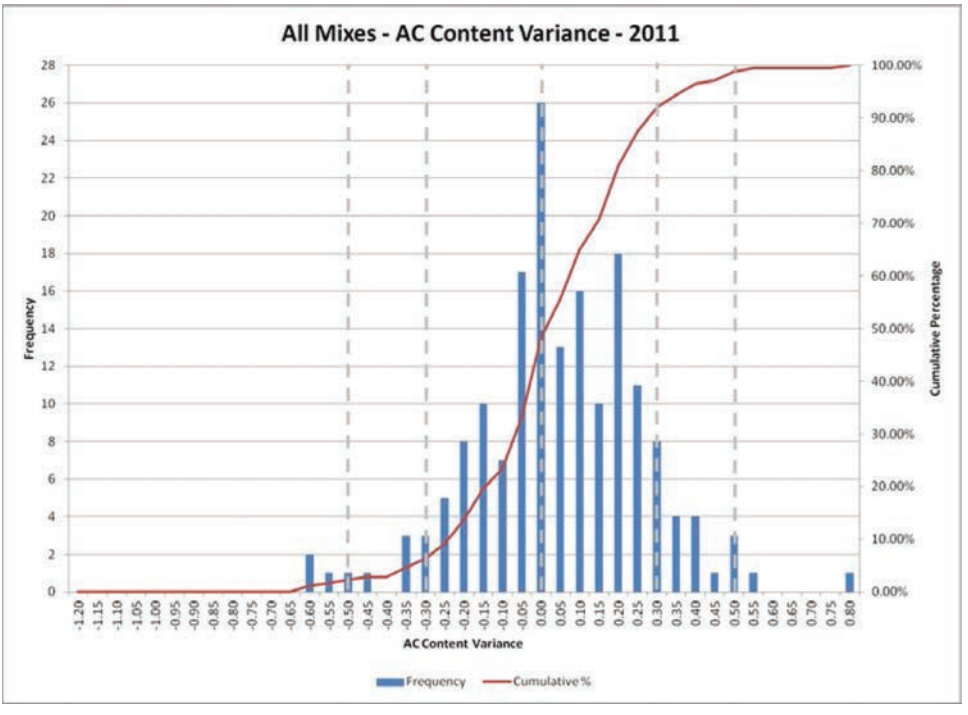

Figure 2. Asphalt cement content variance results compiled for a municipality.

results that are experienced in this municipality and it would be challenging to appreciate this data without it being compiled in this manner. The dashed vertical lines represent the acceptable, borderline and rejectable result limits. Figure 2 shows that although the majority of the results are in the acceptable zone of the designed asphalt cement content (+/–0.3% tolerance), there are a number of results within the borderline zone (+/–0.3% to +/–0.5%) and a few results in the rejectable zone (>+/–0.5%). Comparing asphalt cement content variance in a few subsequent years will show what the trend is. In some cases tightening the specification tolerance limits may be effective in getting much closer to the designed value.

3.5 *Evaluation of current state of the practice*

By compiling the four previously discussed areas: field visits; documentation review; specification review; and results review then the current state of the practice in the municipality can be evaluated. This is one of the largest aspects of the PMTR. During this evaluation, the intent is to draw links between the four noted areas. In general, identify a pavement that showed good and poor performance in the field visit and then examine the specifications that were used as well as the associated documentation. By compiling all of this information for both good and poor performing pavements it will be possible to identify trends within the municipality.

In addition to looking at specific projects, all data is also analysed. The available data is typically examined based on year and type. As an example, the asphalt cement content results from 2011, would be compiled and plotted to evaluate if trends existed, such as routinely lower asphalt cement content within borderline or rejectable limits for one particular mix type. Analysis of the data in this manner allows for repeat occurrences to be highlighted that may not have been evident in the evaluation of specific projects.

Evaluation of the current state of the practice is a relatively cumbersome process; however, is one of the most effective aspects of a PMTR. The conclusions drawn from this evaluation are applied in the following steps.

3.6 *Identification of effective aspects*

Using the conclusions and findings from the evaluation of the current state of the practice it is possible to identify aspects that are effective. Effective aspects would be those that lead to quality pavement performance. These include effective specifications, suitable materials and quality construction practices.

3.7 *Identification of possible areas of improvement*

Through analysis of all results and field visits, areas that are inadequate will be identified. The analysis of all results can clearly highlight aspects that are being missed or not performed sufficiently, such as mix design verification or implementing consequences if there are unacceptable results in quality assurance testing. Observations during field site visits will trigger areas that may require improvement. Distresses observed in the field that are typically caused by unsuitable mix designs can reinforce the need to evaluate the mix designs and acceptance method. Observations in the field and in analysis of all results may also identify a weakness in the specifications that needs to be revised. Practical experience with pavement and material technology reviews shows that poor specifications and lack of specification enforcement are the major reasons for poor quality pavement.

3.8 *Implementation*

After evaluating the current state of the practice in the municipality and identifying both effective and not effective aspects it is important to discuss what, if any changes, should be made for future projects. Results of the PMTR to this point and possible revisions to current practices would initially be discussed with management at the municipality. Following discussions, agreed upon revisions would be carried out where necessary. These revisions would

typically be covered in two aspects, modifications to current specifications and supplementary education for staff members.

If modifications to existing specifications are needed they would be carried out with the intent of updating any out of date specifications and providing clarity where current requirements may lead to confusion. One method of revising specifications that can be effective for both material suppliers, contractors and owners (the municipality) is to develop special provisions to the currently existing provincial specifications. An example of this would be for a city in the province of Ontario. An outcome of the PMTR would be a set of Special Provisions for the city, to the Ontario Provincial Standard Specifications (OPSS) [1].

After agreed upon revisions have been completed it is critical to share the findings of the PMTR with the current staff of the municipality. If the staff members are not included in the findings then it will not be possible to implement changes in the current practices effectively as these individuals who are involved in the day to day activities. The results of the PMTR should be made available to staff members and clearly explained, which can be effectively carried out through a training and open question and answer session. If new technologies or methods have been implemented in the municipality given the findings of the PMTR then it is critical to educate associated staff members on these new areas.

3.9 *Monitoring*

Following the implementation of the proposed revisions from the PMTR results it is important to monitor if the improvement or changes are effective. Initially some challenges may exist if transitions in technologies or methods are being carried out, such as for example moving from Marshall mix design to Superpave mix design. Challenges during transitions are common and expected. Part of the PMTR is the involvement of the review engineer in finding solutions to these challenges, should they arise. In many cases the solution is to provide explanation and education to not only municipality staff members but also common suppliers and contractors. Explanation of changes to prior specifications can be extremely beneficial to everyone involved as this can reduce unneeded expenses and delays in the future and lead to improved performance of the pavements in some areas.

Changes may also be incremental in a municipality, such as trialing a new method on lower volume roads before implementing it on all projects. Monitoring these types of initiatives is important to achieving success on projects in the future.

3.10 *Updating*

The final step of a PMTR is updating the findings of the initial evaluation of the current state of the practice. Through monitoring the implementation of new methods and technologies and revisions to the specifications, areas maybe identified that should still be updated. Additionally, results from subsequent years after the initial PMTR should be compiled and analyzed as was done previously, to evaluate the effects of the implemented changes. It is anticipated that deficiencies in the initial PMTR will have been addressed; however, if they remain then further investigation will be required to determine the continuing cause of these challenges.

4 CITY OF MONCTON CASE STUDY

The City of Moncton (the City) in New Brunswick worked with Golder Associates Ltd. (Golder) to carry out a PMTR in 2008. The City retained Golder to carry out a PMTR in order to improve the state of pavement technology in the City. The PMTR involved the following tasks:

- Meeting with the City's technical staff to get an understanding of the current state of the practice;
- Review of the current City and New Brunswick Department of Transportation (NBDOT) specifications and pavement design methodologies;

- Pavement visual condition inspection of selected roads and streets;
- Site visits to suppliers of aggregates typically used in the City;
- Review of laboratory and field testing results from consultants and contractors/suppliers;
- Site visits to construction sites to review the current construction practice and QC/QA procedures;
- Review of the City's current subdrain installation practice;
- Recommendations for improvements in pavement and materials technology; and
- Training of City's technical staff.

The following sections describe the findings of each of above noted tasks in the project.

4.1 *Meeting with city's technical staff*

Two meetings were arranged with key staff from the City of Moncton to gain an appreciation for the current practices in the City. The discussion included:

- Pavement design methodologies—the City was concerned that the pavement designs used in Moncton were outdated and did not take into account all necessary aspects;
- The type of asphalt cements used such as Penetration Grade or Viscosity Grade;
- The quality of granular materials and aggregates—some of the quarries were known to supply materials that generally did not meet the specified requirements (mainly freeze-thaw); how, if at all, could the substandard quality be compensated in the pavement designs and construction;
- The type and range of asphalt mixes—what kind of improvement would be necessary;
- The quality of construction with particular emphases on the effectiveness of the QA system used by the City;
- The capability of the local contractors in terms of constructing quality pavements, techniques used to rehabilitate existing pavements; and
- Construction specifications including the clarity of the QA system used.

These factors were discussed as particularly important to achieving better quality, longer lasting flexible pavements. The subjects discussed at the meetings formed the basis for the pavement and materials technology review.

4.2 *Review of city specifications and pavement design procedures*

The City's specifications related to pavement and materials were reviewed and the following is a summary of the findings:

- Requirements for QC/QA testing were generally not specified;
- Mix design details in terms of type and required documentation were unclear; and
- Work acceptance criteria and corrective action for inadequate results were not determined.

From the earlier meeting with the City's technical staff it was apparent that there was interest throughout to update the specifications to achieve quality, better performing pavements.

The existing pavement design procedure used in the City was reviewed by Golder. The procedure was found to be overly generalized and over simplified and did not consider traffic volumes.

4.3 *Review of laboratory and field results*

The City provided Golder with available laboratory and field testing results for analysis purposes. Golder reviewed the results and found that often the results were outside the acceptable criteria but no corrective action was recorded as having been carried out. This was found in the results of aggregate and granular materials and during construction. A limited number of mix designs had been provided to the City. In general only a part of the supplied

information for each mix met the requirements in the City's specifications. However, only a small amount of the required documentation was provided to the City for each mix.

4.4 *Construction and existing pavement site visits*

Representatives of Golder visited construction sites and existing pavements in the City. During the construction visits, Golder was able to observe the techniques commonly used in the City. Having observed the current techniques, appropriate recommendations were made for specification revisions and inspector training.

Pavements of varying ages were visited (from newly constructed to more than five years since construction). The most commonly observed distresses were fatigue cracking, rutting, premature longitudinal and transverse cracking, joint failure and material segregation. The premature distresses were likely due to a combination of factors: inadequate pavement design; poor quality granular materials; poor quality mixes and mix ingredients; poor construction practices; poor QC/QA system; insufficient inspection; lack of specification enforcement and follow ups and unclear specifications. Figures 2 and 3 show examples on the pavement observed during the field site visits.

4.5 *Recommendations*

The conclusions of the PMTR were the following recommendations to advance the state of the practice in the City:

- Revise current specifications to meet NBDOT requirements where feasible;
- Include requirements for asphalt mix designs, aggregate materials and granular materials in revised specifications;
- Revised specifications should include acceptance criteria and corrective actions that will be required in criteria is not met and clear methods of enforcing them;
- Updating of pavement design matrix for future projects to include traffic loading and soil type;
- Avoidance of cold joint construction by using infrared joint heaters or paving in echelon, using good quality construction methods if it is necessary to construct cold joints [2];
- Adequate inspection during construction;
- Development and implementation of effective QC/QA program;
- Training of the City's technical staff;
- Implementing new feasible methods of pavement rehabilitation; and
- Implementing pavement preservation [3].

Prior to the initiation of the PMTR with the City, their current state of the practice was not reflecting currently available methods and technologies. The PMTR was a combined effort by the City and Golder. The conclusion was a thorough evaluation of the current practices and the development of simple guidelines for updating the current practices in the City. Golder provided an objective review of the practices in the City and worked closely with staff members to identify potential areas of improvement that would ultimately increase the quality of pavement in the City.

5 CONCLUSIONS

Pavement materials and technology reviews are an objective method of evaluating the current state of the practice in a municipality. An experienced pavement and materials engineer meets with the municipality technical staff to discuss their concerns and observations about pavement performance, pavement design methodology, types of materials used including granular materials and asphalt and concrete mixes and their quality, concern about specifications and quality of construction, effectiveness of Quality Control and Quality Assurance, capability of local contractor in delivering quality products, suggestions about technology

improvements including rehabilitation methods, pavement preservation and maintenance. Field visits are then completed to assess the typical condition of pavements of various ages. A thorough review of documentation, specifications and results is completed to determine the reasons for the performance observed in the field visits. All of these aspects are compiled to evaluate the current practices in a municipality and determine where areas exist that could be improved or changed. Following this the pavement engineer works closely with the municipality to implement recommended changes, such as modifications to current specifications, training for technical staff members and integration of new methods and technologies. This is later followed by monitoring if the improvements or changes were effective and making any updates, if necessary.

The City of Moncton retained Golder to carry out a pavement materials and technology review in 2008. The current practices in the City were evaluated and it was identified that improvements could be made in aspects of the pavement designs, specifications, required documentation, quality assurance testing, specification enforcement and construction practices. Recommendations were provided to the City for these various improvements and training was provided to technical staff members. The completion of the pavement materials and technology review enabled the City to understand the current practices being carried out and direct efforts to the most important aspects, with the intent of improving the quality of their pavements.

REFERENCES

1. **Ontario Ministry of Transportation.** Ontario Provincial Standards for Roads and Public Works. *Ontario Provincial Standards.* [Online] December 2008. http://www.raqsb.mto.gov.on.ca/techpubs/ops.nsf/OPSHomepage.
2. **Uzarowksi, Ludomir, et al.** *Innovative Infrared Crack Repair Method.* Edmonton, Alberta: TAC, 2011. Transportation Association of Canada.
3. **Uzarowski, Ludomir, Farrington, Gary and Chung, Wilson.** *Pavement Preservation—Effective Way of Dealing with Scarce Maintenance Budget.* Vancouver, BC: TAC, 2009. Transportation Association of Canada.

Experimental characterization of asphaltic materials—I

This page intentionally left blank

Asphalt Pavements – Kim (Ed)
© 2014 Taylor & Francis Group, London, ISBN 978-1-138-02693-3

Field applications of portable infrared spectroscopy to asphalt products

Iliya Yut
University of Connecticut, Storrs, CT, USA

Alexander Bernier
Stantec Inc., Manhattan, NY, USA

Adam Zofka
Road and Bridge Research Institute, Warsaw, Poland

ABSTRACT: The scope of the SHRP2 Renewal Project R 06(B) involved evaluating applications of field spectroscopy devices to fingerprint a variety of asphalt materials commonly used in pavement construction. In particular, portable infrared spectrometers in reflection sampling mode were found successful in identifying additives in asphalt binders and emulsions without special sample preparation. An ongoing study targets pavement aging-related changes in chemical composition of asphalt recycled and warm-mix asphalt products over the service life. Powdered samples are collected from road and airport asphalt surfaces in New England and scanned by Attenuated and Diffused Reflectance spectrometers. The absorbance spectra of asphalt samples are processed to quantify aging rate of pavements constructed with non-modified and polymer-, RAP- modified hot and warm mix asphalts. Preliminary results indicate that in-situ oxidation measurements by portable infrared devices can be incorporated in pavement management systems to determine optimal timing of pavement preservation treatments.

Keywords: Infrared spectroscopy, asphalt, field aging, oxidation, Recycled Asphalt Pavement, Warm-Mix Asphalt

1 INTRODUCTION

It is apparent that the aging highway system in the U.S. has increasingly become the focus of the transportation agencies, industry, and research community. The adequate design and Quality Control/Quality Assurance (QC/QA) of construction process remains crucial to ensure durability and satisfactory performance of asphalt pavements that comprise the majority of roads in the U.S. In order to explore innovative field testing methods, the second Strategic Highway Research Program (SHRP 2) Renewal project R-06(B) targeted evaluation of handheld spectroscopic equipment for in situ analysis of commonly used construction materials [1]. The most significant portion of this study concerned asphalt products (binders, emulsion, and mixes) and their additives, i.e. polymers, and anti-stripping agents. Recycled asphalt binders and mixes were included in the project as well.

The major outcome of the SHRP2 R06(B) project was the identification of portable Fourier Transform Infrared (FT-IR) spectrometer with Attenuated Total Reflectance (ATR) accessory as the most successful device for the analysis of polymer-modified asphalt binders and emulsions at the plant and in the field [1, 2]. The follow-up studies report significant progress in using portable FT-IR spectrometers in Diffused Reflection (DR) mode for direct measurements of oxidation levels in Hot Mix Asphalts (HMA) and Recycled Asphalt

Pavements (RAP) [3, 4]. This manuscript presents the historical background and the current status of FT-IR applications to asphalt products.

2 BACKGROUND

2.1 *Infrared spectroscopy techniques*

Infrared spectroscopy relies on measuring energy of the infrared electromagnetic waves (0.78 to 1000 μm wavelengths) transmitted, absorbed, or reflected by a material [5]. FT-IR spectrometers record the absorption of electromagnetic energy by the specific groups of atoms in molecules. Specific peaks are easily identified on a spectrogram and can be used to fingerprint a compound in a mixture once its IR peaks are known from the analysis in a pure state.

Most IR spectrometers operate in transmission sampling mode (Fig. 1 left), which is very accurate in determining the concentration of a specific chemical moiety [6]. The transmission IR testing of asphalts requires elaborate sample preparation including the use of solvents and potassium bromide (KBr) pellets, which only make it suitable for testing extracted binders [7]. Attenuated Total Reflection (ATR) sampling method (Fig. 1 center) allows for direct testing both viscous and liquid samples (Harrick1967). In case of asphalt binder, the ATR method does not require any special sample preparation. One disadvantage of using ATR technique for evaluating the HMA samples is that it interrogates only 1 to 2 μm of sample thickness and a very small area. In the case of HMA, aggregate particle size and uniformity may influence the variability in ATR measurements [1].

The Diffused Reflection (DR) sampling method (Fig. 1 right) is best suited for measurements on the rough solid surfaces of powdered samples (Fuller1978). Conversion of the DR measurement units to log (1/Reflectance) not only increases intensity, hence readability of DR spectrum but also facilitate their direct comparison with traditional absorbance and transmittance equivalents [8]. The main advantage of the DR over ATR is that it captures entire sample depth. Control over of the particle size is necessary to achieve a good signal-to-noise ratio.

2.2 *Historical studies of asphalts by FT-IR*

Asphalt researchers have successfully used FT-IR spectroscopy since as early as 1960s. The most remarkable progress was made under SHRP asphalt binder study in studying chemical structure of asphalt binders and its evolution during short- and long-term aging [9–11]. Using transmission IR mode, the researchers polar chemical Functional Groups (FG) naturally occurring in asphalts, such as 2-Quinolone, phenolics, and pyrrolics. They also studied FG that formed during oxidative aging, i.e. ketones, dicarboxilic anhydrides, carboxylic acids, and sulfoxides [9–11]. Later studies concentrated on relating carbonyl content to the changes in asphalt viscosity [12, 13].

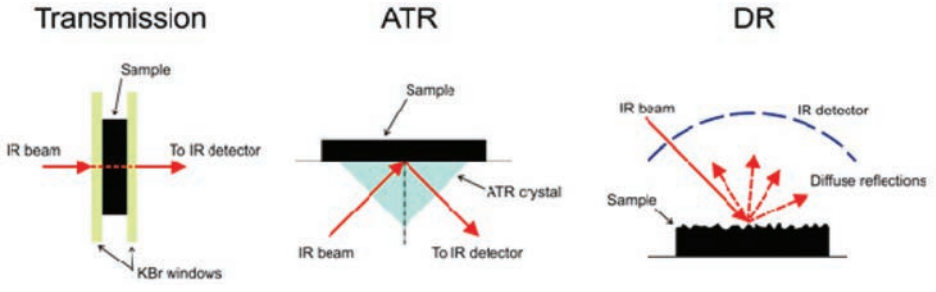

Figure 1. Infrared spectroscopy sampling modes: transmission (left), attenuated total reflectance (center), and diffused reflectance (right).

With the advance in asphalt technology and introduction of polymers, antioxidants, and antistripping agents, the FT-IR technique have been successfully used for identification and quantification of these additives in asphalt binders. Numerous studies investigated effect of Styrene-Butadiene–based polymers (e.g., SBS and SBR) as well as n-polyethylene-based polymers (e.g., Elvaloy, EVA) on chemical and physical properties of asphalt [14–16]. Only a few studies used FT-IR to explore changes in cured emulsions [17, 18]. Lastly, FT-IR was used to study the effect of highly reactive deicers on degradation of flexible airport pavements [19].

The vast majority of asphalt studies by FT-IR spectroscopy have been performed on solutions of virgin or extracted asphalt binders in transmission mode. However, a few attempts to fingerprint asphalt mix samples and evaluate level of oxidation in asphalt mixes span early 1970s and late 2000s [20, 21]. Obviously, until recently, the limitations of the commercially available FT-IR instruments prevented asphalt researchers and engineers from using this technology outside the laboratories and research facilities.

3 SHRP-2 ADVANCES IN FIELD FT-IR STUDIES OF ASPHALT PRODUCTS

3.1 *Field testing protocol*

One of the major goals of the SHRP2 R06(B) project was to evaluate feasibility of using portable ATR FT-IR spectrometer in the field environment for direct measurements on various asphalt products. To achieve this goal, first, the typical IR absorbance spectra of asphalt binder, mix, and emulsion samples were obtained in the laboratory. Next, a series of field tests were undertaken where the FT-IR instrument was set up in the back of a van in the proximity of the paving project. The field spectra of a targeted material were compared with those obtained in the lab to evaluate repeatability and reproducibility of the test. Table 1 summarizes project locations, materials and description of samples evaluated in the field phase of the project. Figure 2 illustrates the field process of the testing a polymer-modified emulsion.

To obtain spectra for the material in Table 1, several drops of a liquid or approximately 0.5 g of a solid were placed on the ATR sampling plate and 24 co-averaged scans were collected at a resolution of 4 cm^{-1}. In the case of thin films and powders, pressure was applied to the sample to ensure full contact with the ATR prism surface. The main issue with ATR testing of HMA was relatively high (up to 30%) standard deviation from the mean of 5 replicates, mostly due to variability in particle size and material composition. The pulverized HMA samples, however, did not yield variation higher than 15% of the mean.

During field experiments, it was helpful to analyze the binder component of the HMA mixes using dichloromethane (DCM) extraction. The DCM was found to be a more reactive, faster evaporating, and less toxic alternative to the AASHTO-standardized TCE solvent. The DCM extraction procedure included shaking 1HMA:3DCM solution for 1–2 min and filtering the solution through the regular 2-layer tissue paper. To collect ATR spectra, several drops of the solution were placed on the ATR prism and left for 2 min to allow the DCM to evaporate completely. Next, the ATR absorbance spectrum was collected in the same fashion as the rest of liquid materials.

Table 1. Summary of field tests by portable ATR FT-IR.

Project type	Material category	Sample type
HMA paving	Polymer modified asphalt binders and mixtures	Fresh mix from the truck Extracted binder solution
Nova chip seal paving	Polymer-modified asphalt emulsions	Emulsion from the road surface (before breaking) Coated seal aggregate from the road surface
Rubberized chip seal paving	Polymer-modified asphalt binders	Binder from the truck Coated aggregate from the truck Binder from the road

3.2 *Polymers in binders, emulsions, and HMA*

The analysis of the IR spectra of the field samples aimed at (1) verification of the presence of an additive (polymer, anti-strip agent etc.) in a binder or mix, and (2) quantification of an additive within a compound. The elastomer styrene-butadiene-based polymers were easily identified in the liquid samples of polymer-modified emulsions (Fig. 3) and solid samples of

Figure 2. Sampling emulsion (top left), Novachip application (top right), ATR testing setup (bottom left), sample placement (bottom right).

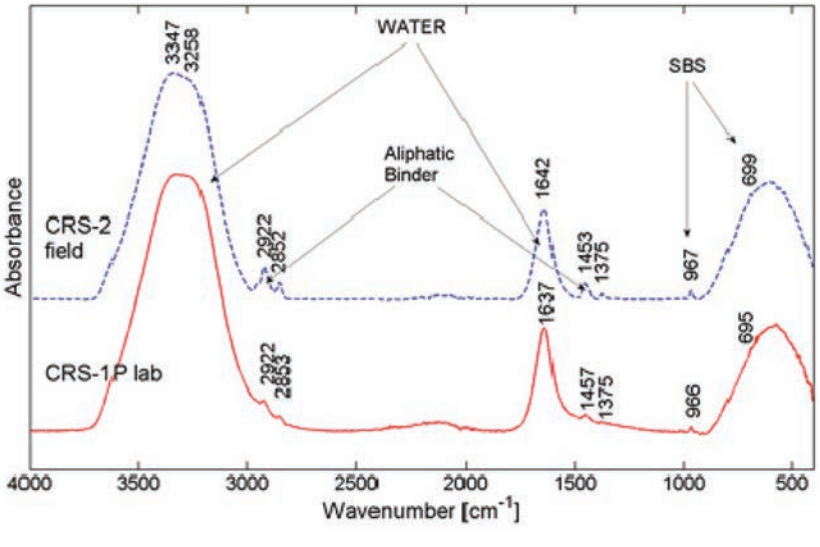

Figure 3. ATR spectra of polymer-modified emulsions.

polymer-modified binders. While identification of polymer in the field HMA mix and coated seal aggregates presented a challenge, the fast binder extraction procedure in the field with using DCM solvent appeared to be a feasible alternative to direct evaluation of binder- and emulsion-coated aggregates (Fig. 4).

The quantitative method of spectral analysis involved normalization of Polybutadiene (PB) or Polystyrene (PS) absorption peak intensity at ~965 and ~700 cm^{-1} wavenumbers, correspondingly, to that associated with aliphatic CH stretching or bending vibrations at ~2920 cm^{-1} that did not change with increase in polymer concentration (e.g., A966/A2920 and A700/A2920). Typical spectrum of an SBS-modified binder is shown in Figure 5. It was recommended to use A966/A2920 ratio for calibration curves. Note that increase in variation in measured absorption peaks with an increase in polymer concentration can be attributed to non-uniform distribution of polymer phase within asphalt binder matrix [1]. Quantifying an additive in a compound may be dependent on the coefficient of absorptivity (or extinction) of the additive within a given moiety. Therefore, the same SBS polymer was added to the binders from at least three different sources across the continent to compare the slopes of calibration curves, i.e. coefficients of absorptivity. Remarkably, the SHRP2 R-06(B) study found no significant difference in coefficient of extinctions between three sources [1].

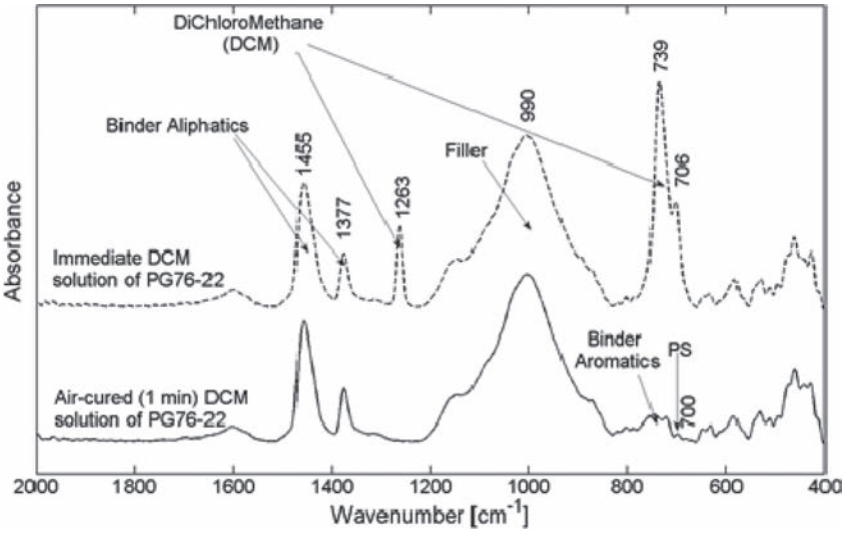

Figure 4. Identification of SBS polymer in asphalt binder PG76-22 extracted from HMA.

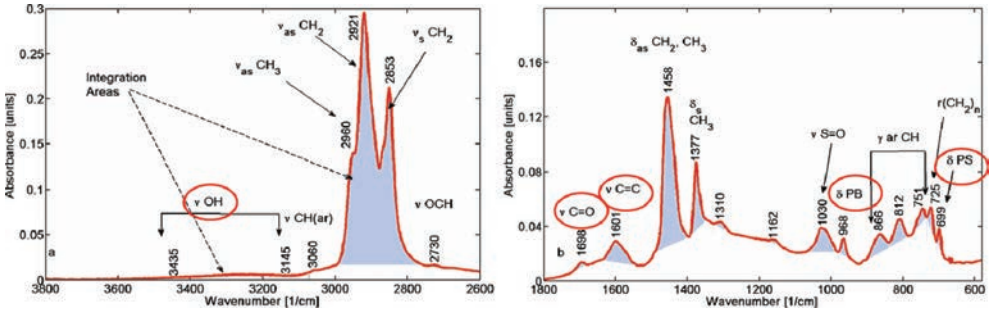

Figure 5. Typical ATR spectrum of an SBS-modified asphalt binder.

3.3 *Oxidation in recycled asphalt pavements*

The ATR FT-IR experiments on Recycled Asphalt Pavements (RAP) targeted the feasibility of the identification of elevated oxidation level in the RAP-modified binder blends and HMA mixes. Of the particular interest was a possibility of the determination of RAP content in binder blend/ HMA mix based on the concentration of the oxidized chemical functionalities. The SHRP2 study explored two types of samples were prepared in the laboratory: (1) binder blends containing 15 to 40 percent weight RAP-binder and (2) loose HMA samples modified by up to 80 percent weight RAP.

To track the changes in chemical composition of the RAP-modified samples due to an increase in RAP content, the ATR FT-IR spectrum of each sample was analyzed both qualitatively and quantitatively. The qualitative analysis involved identifying characteristic IR absorption bands for the binder and aggregates to separate them from, the oxidation products such as hydroxyls (OH), carbonyls (C = O), and sulfoxides (S = O) as shown in Figure 6. To quantify spectral changes due to RAP presence in binder blends, bands area for OH, C = O, and S = O functionalities were valley-to-valley integrated within the limits shown in Figure 7 and normalized to the sum of all band areas to calculate individual oxidation indices

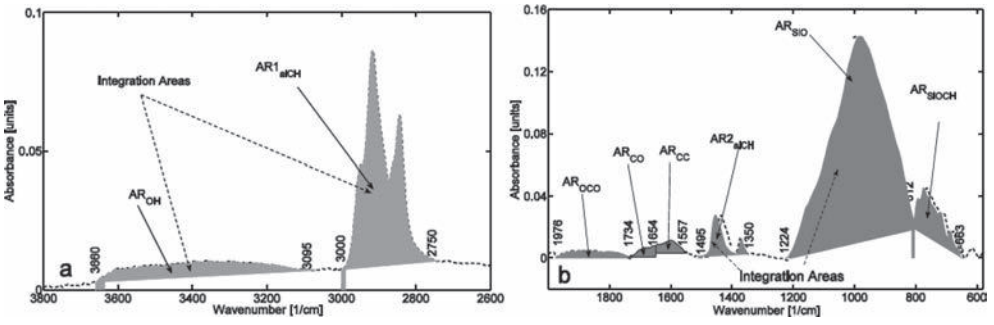

Figure 6. Typical ATR FT-IR spectra of 80-wt% RAP-modified HMA mix (Yut_Rap2012).

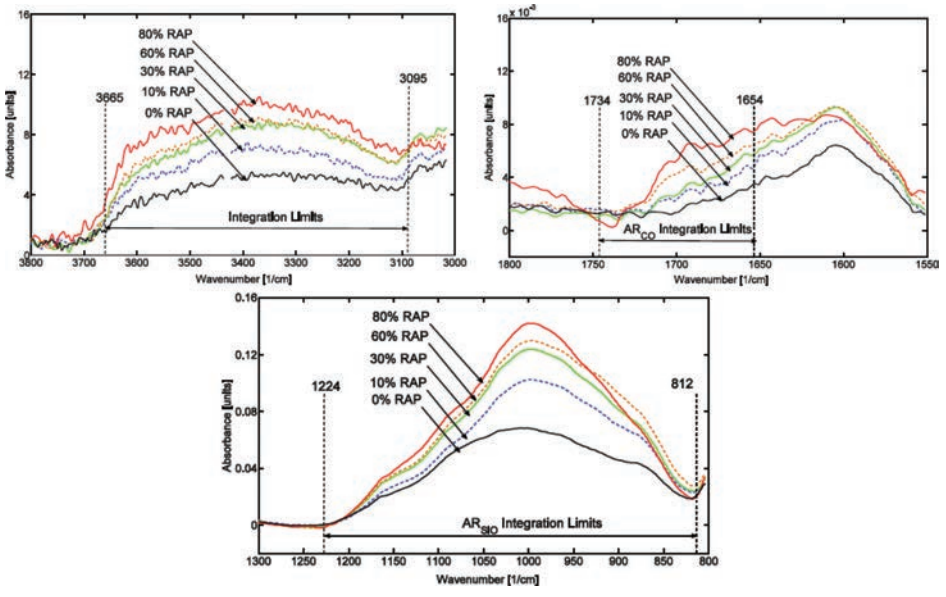

Figure 7. Integration limits for hydroxyl (AR_{OH}) (top left), carbonyl (AR_{CO}) (top right), and silicate/ sulfoxide (AR_{SiO}) (bottom) absorption bands (Yut_RAP2012).

I_{OH}, I_{CO}, *and* I_{SO} (). A similar approach was applied to the RAP-modified HMAs. The only difference was associated with using SiO absorption band instead of S = O band because of their large overlap.

Based on the multiple correlation analysis of the oxidation indices against RAP content (C_RAP), the best-fit linear models were developed for predicting the RAP content in binder blends and RAP-containing mixes. A sum $I_{OH} + I_{CO} + I_{SO}$ appeared to yield best prediction for binder blends with R-squared of 0.97 and standard error of 7 percent. The best-fit model for the RAP mixes, on the other hand, utilized I_{CO} and I_{SiO} as independent predictors with significantly lower R-squared of 0.86 and standard error of 11 percent. Two reasons would explain a lower agreement in prediction models in HMA. First, a much higher standard error for HMA data as compared with binders' data is mostly governed by non-uniformity of replicate samples due to variation in particle size. Second reason for lower linear agreement can be a lack of interaction between binder adsorbed to RAP particles and the virgin binder (no blending).

4 FURTHER APPLICATIONS OF PORTABLE FT-IR TO AGED ASPHALTS

4.1 *Accelerated aging of asphalt binders*

Based on the success in fingerprinting asphalt binders during SHRP2 study (Zofka_SHRP2) and previous progress in use of transmission IR mode for evaluating oxidation levels in dissolved binders (Lamontagne2001), the research team has developed a prototype of an accelerated aging apparatus based on a portable ATR FT-IR spectrometer [3]. The apparatus employs a compact Attenuated Total Reflection spectrometer and airflow Aging Cell (ATRAC) equipped with a temperature controller (Fig. 8). In ATRAC, a small sample of asphalt binder is subjected to heated airflow at 135 ºC for 45 minutes. Concurrently, the absorbance spectra are collected every 5 minutes. The carbonyl content is computed for each spectrum, and the aging rate of a binder sample, $\mathbf{r_{CA}}$, is evaluated as a slope of Carbonyl Area (CA) versus time (Fig. 9).

The ATRAC device demonstrated high sensitivity to temperature susceptibility of asphalts. For instance, the aging slopes of the three SHRP core asphalts depicted in Figure 9, clearly show that softer asphalt AAC oxidizes much faster than harder asphalt AAA. The slope of increase in CA for AAK, which has the highest viscosity of the three, can be neglected. When compared with Superpave™ aging procedures, the ATRAC system demonstrated higher sensitivity to the presence of polymers in the binder than the standard Pressurized Aging Vessel

Figure 8. Image of ATRAC prototype.

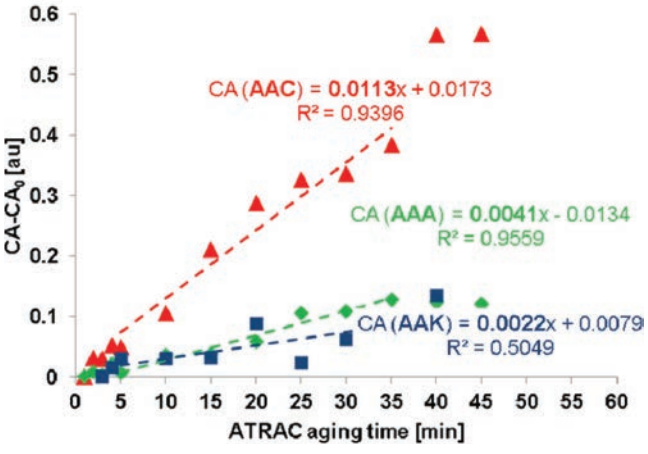

Figure 9. Comparison of ATRAC oxidation rates for SHRP core asphalts.

Table 2. Summary of origin, PG and ATRAC parameters for binder ranking.

Binder ID	Source	True PG, RTFO	r_{CA} in ATRAC ($*10^{-5}$)
Conn 64-22	Venezuela	74.7	0.9
AAK	Venezuela	73.2	1.4
AAM	W Texas	70.8	2.6
AAG	Ca. Valley	66.6	3.3
Conn 58-28	Venezuela	61.6	3.7
AAB	Wyoming	61.5	3.9
AAC	Redwater	58.4	4.1
AAD	Ca. Valley	63.4	4.2

(PAV) procedure. Furthermore, the proposed setup was found capable of inducing similar oxidation rates to the PAV in minutes rather than hours [3].

4.2 *High-temperature performance ranking of asphalt binders*

The optimistic results of ATRAC and well-documented aging history of the SHRP core asphalts [22] motivated the attempt at ranking asphalts by ATRAC oxidation rate ($\mathbf{r_{CA}}$) and superimposing it with reported Performance Grade (PG) values. In addition, two binders from Connecticut, U.S.A. (source unknown) were included in the dataset. While examining the values of listed in Table 2, one can note that only binder AAD does not follow the inverse trend between the oxidation rate and true PG of binders aged by the Rolling Thin Film Oven (RTFO) procedure.

4.3 *In-situ aging diagnostics of asphalt pavements*

As mentioned earlier, the DR sampling method was found best suited for powdered HMA samples. The first field feasibility study of portable DR spectrometer on asphalt pavement has showed that powdered asphalt mix samples with nominal maximum aggregate size of 150 μm produced very smooth spectra with minimum noise [3]. The most recent studies at the University of Connecticut proved direct correlation between DR and ATR spectra of the same asphalt binder/mix sample [3, 23]. A study on Connecticut and Rhode Island

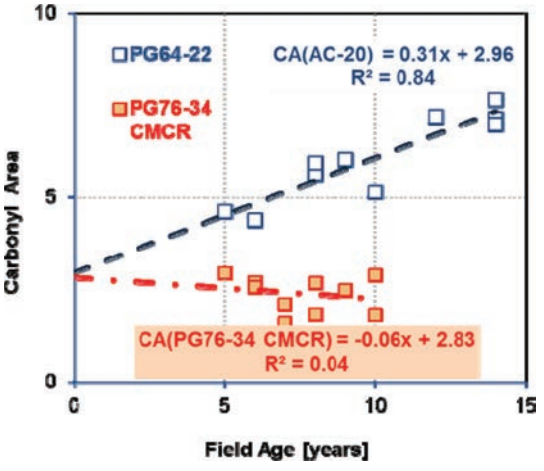

Figure 10. In-situ oxidation trends for PG64-22 and PG76-34.

pavements of similar age, structure located a similar climate yet paved with different binders demonstrated ability of portable DR spectrometer to differentiate aging rate of in-situ asphalt surfaces [3]. The field samples were obtained by hammer-drilling 1-in deep at 1-in diameter holes in pavement surface and collecting the resultant powdered residue. Figure 10 contrasts the aging rates of the pavement surfaces in Connecticut and Rhode Island. The approximated linear trends in Figure 10 clearly distinguish between increase in carbonyl content, i.e. oxidation, in HMA pavement where non-modified PG64-22 binder was used and virtually no change in CA for HMA produced with crumb rubber-modified PG76-34-CMCR binder.

5 SUMMARY OF FINDINGS

This manuscript presents the recent development in the use of portable FT-IR spectrometers for fingerprinting asphalt products and applications of the FT-IR technique to evaluating aging of asphalt pavements.

The SHRP 2 R-06(B) project has identified portable FT-IR spectrometer with ATR accessory as a potentially useful tool for verification of presence of additives and contaminants in asphalt as long as the concentration of additive/contaminant is higher than 0.5 percent weight. In particular, the ATR spectrometer allowed for determining chemical composition of polymer-modified binders, emulsion, and HMA mixes. In addition, the ATR measurements on RAP-containing binder blends and mixes allowed evaluating the effect of RAP content on the extent of oxidation in binders and mixes.

Based on the success in ATR measurements on aged asphalt binders, an original accelerated aging apparatus with use of ATR and miniature aging cell (ATRAC) was developed. The ATRAC apparatus appeared to be sensitive to temperature susceptibility of asphalt binders. Furthermore, the oxidation rates measured by ATRAC seem to be highly correlated with the high-temperature performance grade of binder, which make ATRAC suitable candidate to replace RTFO procedure in predicting short-term aging trends.

Most recently, a portable DR spectrometer has been used to evaluate aging of pavement surfaces by direct measurements of carbonyl content on powdered asphalt mix residues. The DR technique appears to be successful in in-situ ranking of in-service asphalt pavement. It is believed that in-situ DR measurements of oxidation can be incorporated into a pavement management program as a quantitative QC/QA process to determine thresholds for pavement preservation treatments.

ACKNOWLEDGEMENTS

The SHRP2 R06 (B) project was sponsored by Federal Highway Administration in cooperation with the American Association of State Highway and Transportation Officials, and was conducted in the Strategic Highway Research Program, which is administered by the Transportation Research Board of the National Academies. The opinions and conclusions expressed or implied in the report are those of the research agency. They are not necessarily those of the Transportation Research Board, the National Academies, or the program sponsors.

REFERENCES

[1] Zofka, A., M. Chrysochoou, I. Yut, et al. Evaluating Applications Of Field Spectroscopy Devices To Fingerprint Commonly Used Construction Materials, SHRP2-R06 (B)-RR1 Final Report, Transportation Research Board, Washington, D.C., 2012.

[2] Yut I., Zofka A., Attenuated Total Reflection Fourier Transform Infrared Spectroscopy of Oxidized Polymer-Modified Bitumens. Applied Spectroscopy, Vol. 65 (7), 765–770, 2011.

[3] Yut I., Bernier A., Zofka A., Development of a Compact Laboratory Aging Procedure for Asphalt Binders, Journal of the Association of Asphalt Paving Technologists, Vol. 81, 630–651, 2012.

[4] Yut I., Zofka A., Spectroscopic Evaluation of Recycled Asphalt Pavement Materials, TRB Pape#12-1259, 91th Annual TRB Meeting Compendium of Papers, Transportation Research Board, Washington, DC, 2012.

[5] Silverstein R.M., Webster F.X., Spectrometric Identification of Organic Compounds, 6th ed., John Wiley and Son, Inc., New York, 1998.

[6] Coates, J. "Interpretation of Infrared Spectra, A Practical Approach," In Encyclopedia of Analytical Chemistry, John Wiley & Sons Ltd., Chichester, 2000.

[7] Jemison, H.B. et al., Application and Use of the ATR FTIR Method to Asphalt Aging Studies, Fuel Science Technology International, Vol. 10, pp. 795–808, 1992.

[8] Olinger, J., and P. Griffiths, Quantitative Effects of an Absorbing Matrix on Near-Infrared Diffuse Reflectance Spectra, Journal of American Chemical Society 60(21) pp. 2427–2435, 1988.

[9] Petersen J.C. Quantitative Functional Group Analysis of Asphalts Using Differential Infrared Spectrometry and Selective Chemical Reactions-Theory and Application, Transportation Research Record 1096, pp. 1–11, 1986.

[10] Branthaver J.F. et al., Binder Characterization and Evaluation. Volume 2: Chemistry. Report SHRP-A-368, SHRP, NRC, Washington, DC, 1993.

[11] Petersen, J.C., et al., Binder Characterization and Evaluation. Volume 4: Test Methods. Report SHRP-A-370, Strategic Highway Research Program (SHRP), National Research Council (NRC), Washington, D.C., 1994.

[12] Martin, K.L., R.R. Davison, C.J. Glover, J.A. Bullin, Asphalt Aging in Texas Roads and Test Sections, Transportation Research Record, Journal of National Research Council, Vol. 1269, 9–19. 1990.

[13] Ruan, Y., R.R. Davison, and C.J. Glover. An Investigation of Asphalt Durability: Relationships between Ductility and Rheological Properties for Unmodified Asphalts. Petroleum. Science and Technology, Vol. 211, No. 2, pp. 231–254, 2003.

[14] Lu, X. & Isacsson, U., Chemical And Rheological Evaluation Of Ageing Properties Of SBS Polymer Modified Bitumens. Fuel, 77, 961–972. 1998.

[15] Masson, J-F.; Pelletier, L.; Collins, P. Rapid FTIR method for quantification of styrene-butadiene type copolymers in bitumen, Journal of Applied Polymer Science, 79 (5), pp. 1034–1056, 2001.

[16] Woo, W.J., J.M. Hilbrich, and C.J. Glover, Polymer-Modified Binder Durability Loss with Oxidative Aging: Base Binder Stiffening Versus Polymer Degradation Transportation Research Record 1998, pp. 38–46, 2007.

[17] Gueit, C., M. Robert, and G. Durand. Transportation Research Circular E-C122: Characterization of the Different Phases in the Life Cycle of the Binder in a Bitumen Emulsion: Recovery Methods. Transportation Research Board, Washington, D.C., pp. 1–10. 2007.

[18] Hazlett, D. Transportation Research Circular E-C122: Emulsion Residue Recovery Techniques: How Do We Get Emulsion Residue Representative of In-Service Binder? Transportation Research Board of the National Academies, Washington, D.C., pp. 15–23. 2007.

[19] Pan, T., He, X., and Shi, X., Laboratory Investigation of Acetate-Based Deicing/Anti-Icing Agents Deteriorating Airfield Asphalt, Journal of AAPT, Vol. 77, pp773–794. 2008.
[20] Lee, D.Y., and R.J. Huang. Weathering of Asphalts as Characterized by Infrared Multiple Internal Reflection Spectra. Applied Spectroscopy, Vol. 27, pp. 435–440, 1973.
[21] Farrar, M., Subtask 2-2.3 Age Hardening—Field Validation Sites Fundamental Properties and Advanced Modeling of bituminous Materials. Expert Task Group Meeting in Denver Colorado, July 24, 2007, http://www.asphaltmodelsetg.org/Farrar_ETG_7_24%20v3.pdf, Accessed on May 10, 2011.
[22] Mortazavi M., Moulthrop J.C., The SHRP Materials Reference Library, Report SHRP-A-646, Strategic Highway Research Program, National Research Council of Academies, Washington, DC, 1993.
[23] Yut I., Spectrometric Investigation of Aged Polymer-Modified Asphalts, Ph.D. Dissertation, University of Connecticut, Storrs, CT, 2012.

This page intentionally left blank

Asphalt Pavements – Kim (Ed)
© 2014 Taylor & Francis Group, London, ISBN 978-1-138-02693-3

Experimental investigation of frost/thaw effects on bituminous mixes under wet conditions

Caroline Mauduit, Éric Crégut, Sylvain Joly & Sébastien Liandrat
CEREMA/Laboratoire des Ponts et Chaussées de Clermont-Ferrand, France

Olivier Chupin, Ferhat Hammoum & Jean-Michel Piau
IFSTTAR, France

ABSTRACT: Subsequently to serious pavement disorders appearing suddenly during winters and characterized by series of potholes, CEREMA and IFSTTAR launched an experimental program to understand the mechanisms at play and possibly provide technical recommendations for the future. Based on *in-situ* observations showing the concomitance of frost/thaw cycles and wet conditions during these events, the study focused on the impact of frost propagation on the behavior of asphalt mixes partially saturated with water. Cyclic thermal tests performed free of external loading (except the own weight of the samples) show significant swelling and contraction of the samples because of the phase changes of pore water from liquid to solid and *vice versa*. Additional tests intended to the measurement of the complex modulus of bituminous mixes also show evidence of a frost effect on wet samples, characterized by the stiffening of the material. These effects could be at the origin of the disorders under consideration. Further work should help validate this hypothesis and find remedies to the problem.

Keywords: Pavement, winter disorders, potholes, frost/thaw, bituminous mix, porous material, water saturation, swelling, complex modulus

1 INTRODUCTION

During their lifetime, pavements are exposed to important thermal and mechanical constraints because of traffic and climatic conditions. In particular, pavements undergo important temperature variations and are subjected to frost/thaw phenomena. Nowadays, the mechanisms affecting soil frost are understood and are integrated into pavement design to avoid structural disorders. However, in recent winters, sudden deteriorations at the surface of pavements were observed in the North and East of France and also in parts of the borderlands. These events occur in a few hours and lead to series of potholes over tens or hundreds of kilometers. Investigations done on the French network show that the sudden degradations occur during wet periods of alternating frost and thaw cycles, and temperatures reaching around –10 °C. These deteriorations often affect bituminous pavements which have been through maintenance works, consisting in placing a new layer either on the old wearing course or after milling. Cores drilled close to potholes show that generally damages are localized within the old layers. Note also that the same problem but with origin found deeper in the structure was observed on old rigid pavements reinforced with a bituminous base course after slab breaking. However in all cases the investigations revealed an important quantity of water stored in the layer of bituminous mix from which the raveling was initiated [1], [2].

In order to understand the mechanisms of the disorders and to answer the questions of road owners (how to repair, to detect road sections at risk and to avoid the problem in the future?) CEREMA and IFSTTAR launched an experimental program. Based on the

field observations, it focused on the evaluation of the effect of frost/thaw phenomena on bituminous mixes under wet conditions. Cyclic thermal tests (without external stress) were first performed on homogeneous and then on two-layer samples using the experimental device dedicated until now to study soil frost. Complex modulus tests were also conducted to analyze the impact of frost on the stiffness of wet bituminous concrete.

2 EXPERIMENTAL SET-UP AND MATERIAL TESTED

This section presents the test device used to apply freeze/thaws cycles to bituminous mixes, the properties of the materials tested and the instrumentation that allows to record temperature as well as strain during a test.

2.1 *Test device*

The tests on bituminous mixes are performed using an experimental device adapted from that used to study frost heaving of soils. This device makes frost propagate in the vertical direction (one-dimensional condition). It is composed of 6 cells in which different samples can be tested simultaneously. A vertical cross-section showing one cell is displayed in Figure 1. The device consists of a tank filled up with a liquid maintained at a temperature slightly above 0 °C in which the cells are located. A refrigerated metal piston is used to apply freeze/thaw cycles at the top surface of the samples placed in the cells. Although not used in the experiments presented in this paper, a temperature-controlled water bath at 1 or 2 °C can be added at the bottom of the specimens to better control the boundary condition at this location.

2.2 *Properties of materials tested and built-up of the specimens*

The materials tested are hot bituminous mixes as those commonly used for wearing courses in France. They are formulated in the laboratory from crushed Rhyolite aggregates of

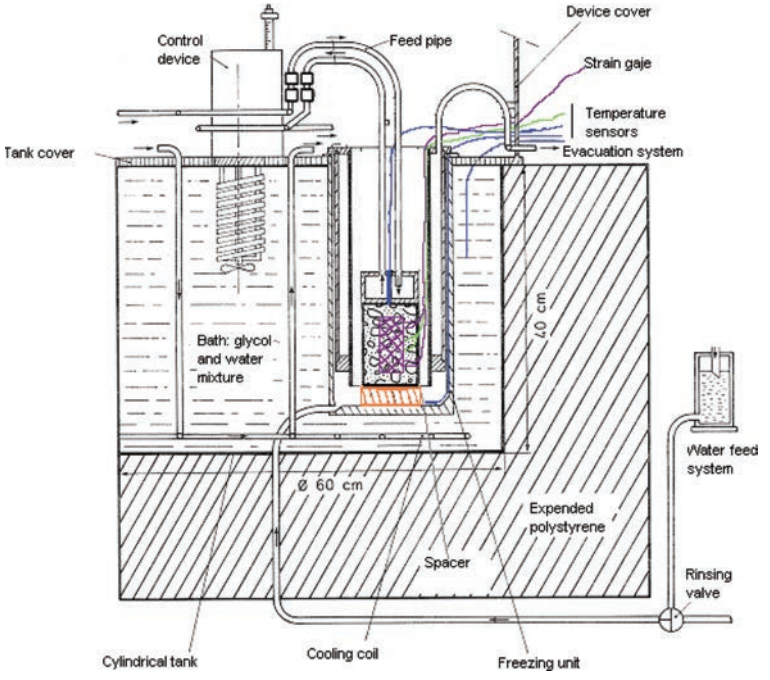

Figure 1. Cross section of the experimental testing apparatus.

which the distribution of the grain size is shown in Table 1. The binder utilized is bitumen of type 35/50.

Cylindrical samples of height 90 mm and diameter 80 mm are molded by compaction following the standard EN 12697-12, method B for homogeneous samples. For two-layer samples, the compaction is performed in several phases: compaction of the lower layer, application of a bitumen emulsion until its break and compaction of the upper layer. Homogeneous sample present 11% of voids content. Two-layer samples, composed of the same bituminous mix but compacted at different levels, present a void content of 11% in the upper layer and 6% in the lower layer.

The samples are partially saturated by first applying a negative pressure to the dry sample and then by immersing the sample maintaining the depression. The degree of saturation (S_w) obtained for a negative pressure of 98 kPa is equal to 65% and 78% for the upper and the lower layers respectively. The corresponding volumetric water content (ϕS_w) are 7.1% and 4.7%.

2.3 *Instrumentation*

2.3.1 *Temperature measurement*

Preliminary tests are performed to evaluate the temperature to be applied at the surface of the samples and the duration of frost/thaw cycles. Cycles of 24 hours varying between +10 °C and −10 °C allowed to obtain sufficient negative temperatures within the sample and avoid supercooling phenomena. Figure 2 shows the temperature variation recorded by sensors located at different heights of the two-layer sample during these cycles. The extreme values of temperature go from +8 °C to −5.5 °C in the upper part of the sample, from +7.5 °C to −4.0 °C

Table 1. Hot bituminous mix sample.

Granular fraction	Nature	Mass percentage
0/4	Rhyolite	43
4/6	Rhyolite	12
6/10	Rhyolite	41
Filler	Limestone	4
Bitumen	35/50	5.8

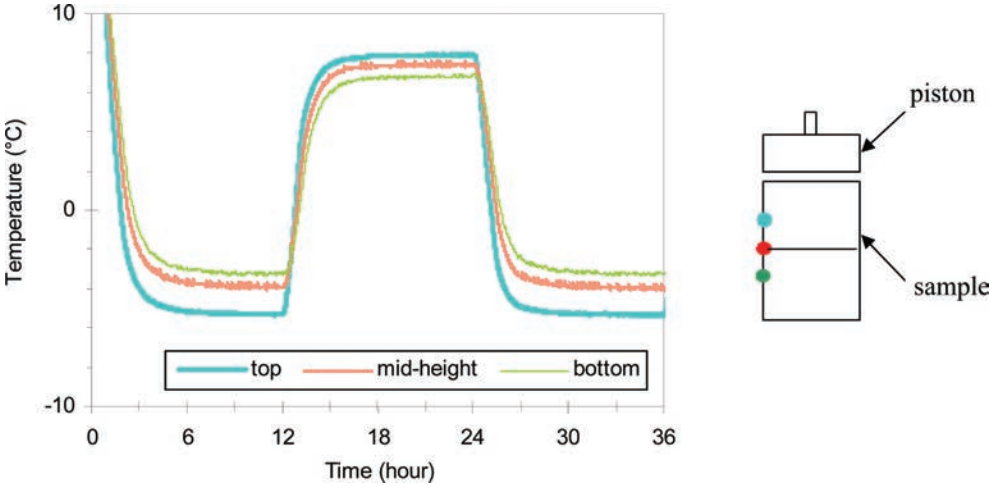

Figure 2. Left evolution of temperature with time recorded during a test by sensors positioned at different heights of a specimen. Right location of temperature gauges.

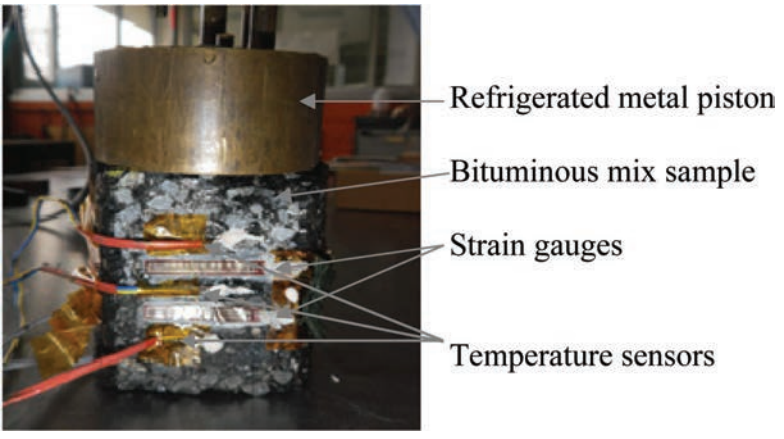

Figure 3. Temperature sensors and gauges mounted on a bituminous mix sample with a cut face.

at mid-height and from +5 °C to –3.5 °C in the lower part. The range of variation in the lower part is smaller because of the influence of the boundary condition at the bottom. Preliminary measurements performed at the edge and at heart of the specimen showing non significant differences, temperature at the edge of the sample was taken as reference, as shown in Figure 2.

2.3.2 *Radial strain measurement*

Strain measurements are made using gauges of length 30 mm and a self-temperature compensated method. A strain gauge in a half bridge circuit configuration is indeed utilized to evaluate deformation of the specimen. The temperature compensation is done using a similar sensor mounted on a rod of silicate of titanium, whose deformation can be considered as independent from temperature variations.

The sample is cut as shown in Figure 3, to provide a plane surface to paste easily sensors and avoid border effects of the confection mould. The gauges are placed horizontally to measure radial strain. Gauges placed horizontally are better suited to capture sharp events occurring at the freezing front than those placed in the vertical direction (i.e. the propagation direction of the front) which average over their height the phenomena observed (as it was made in [3]). As shown in Figure 3 the temperature sensors are placed as close as possible of the strain gauges to accurately perform the temperature compensation. In the case of a two-layer sample, two strain gauges are mounted near the interface on both sides of it to highlight a possible differential behavior.

The validation of experimental measurements was carried out using a steel alloy sample of known thermal coefficient. It showed a good correlation between theoretical calculations of contraction/expansion and measured thermally compensated strain subjected to temperature cycles.

3 RESULTS OF THE FROST/THAW TESTS

3.1 *Homogeneous samples*

Figure 4 shows the response in terms of strain of the dry and partially saturated homogeneous samples when subjected to frost/thaw cycles. The temperature at the location of the strain gauge (mi-height of the sample) is also plotted in this figure.

During a cycle, the deformation of the dry asphalt concrete varies almost proportionally with its temperature showing that the asphalt concrete mostly verifies the usual law of thermal deformation. Figure 5 shows also that under the test conditions of free deformation (except for the weight of the piston and the sample) a remaining creep component in extension after

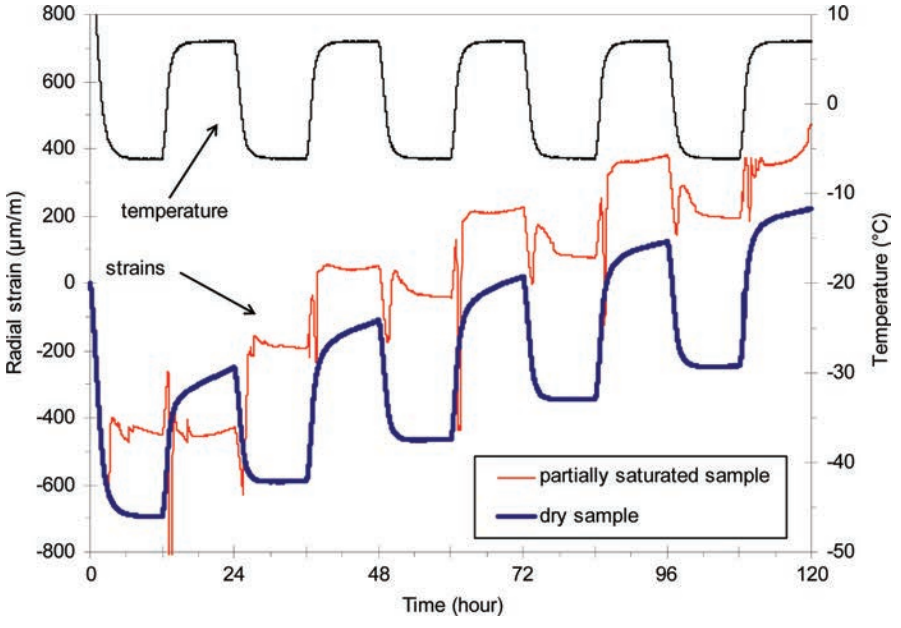

Figure 4. Radial strain measured during frost/thaw cycles applied to a dry and a partially saturated homogeneous sample of asphalt concrete (Convention: extension is in the upward direction on the graph).

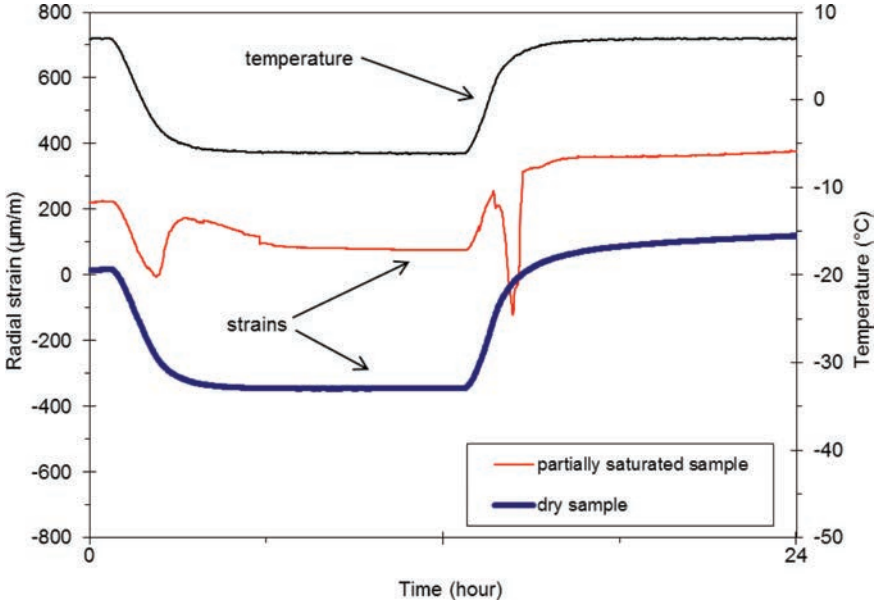

Figure 5. Close up view of radial strain measured during frost/thaw cycles applied to a dry and a partially saturated homogeneous sample of asphalt concrete.

each cycle, which in turn leads to a progressive swelling of the sample by cumulative effect. However this phenomenon is considered of secondary importance for our purpose and its explanation is not addressed here. The computation of the average thermal coefficient, $\alpha = \Delta\varepsilon_r / \Delta T$, between the two plateau temperatures of a same cycle yields a value of the order of 30.10–6/°C which is in accordance with values found in literature [4], [5], [6].

Concerning the partially saturated specimen, the response of the material is way more complex. In particular, we notice peaks of deformation (either in the upward or downward directions) each time the measure of temperature goes through zero at the location of the radial gauge. At this time, if the temperature is decreasing then the material undergoes a sharp extension which can be undoubtedly attributed to the dilatation of water within the porosity of the asphalt concrete during the phase change from liquid to solid (for recall the volume expansion of liquid water to ice is 9%).

If the temperature is increasing the material undergoes a large phase of contraction followed shortly after by a phase of expansion of similar amplitude probably due to the inverse transformation of water from solid to liquid and its decrease of volume. These successive contraction and expansion phases occurring in a short time may result from a negative pressure effect (as compared to the atmospheric pressure) of the newly melt water, followed by a readjustment of the air/liquid water pressures to the atmospheric pressure. More details about the response of partially saturated homogeneous specimens to frost/thaw cycles are given in Mauduit et al. (2014) [7]. Part of the tests not related here also shows that as expected the frost/thaw effect increases with the degree of saturation or still with the water content.

3.2 *Two-layer samples*

The two-layer sample tests are performed in order to approach the case of a multilayer bituminous pavement composed of mixes of different porosity separated by a coat layer. In dry conditions, results obtained but not shown here, are qualitatively similar to those obtained for homogeneous samples. However, the situation is quite different for the partially saturated two-layer samples as shown in Figure 6.

The upper part of the sample (ϕ = 11%) exhibits a behavior similar to that of the homogeneous wet sample of same porosity already shown in section 3.1, with even greater positive (swelling) and negative jumps induced by frost/thaw effects. Besides, the lower part of the sample shows a behavior close to that of a dry material probably due to the relatively small water content. Nonetheless a small frost/thaw effect is still present. Thus, the two-layer samples under wet conditions exhibit a complex response characterized by significant opposite strain evolutions at some times. These differential strains

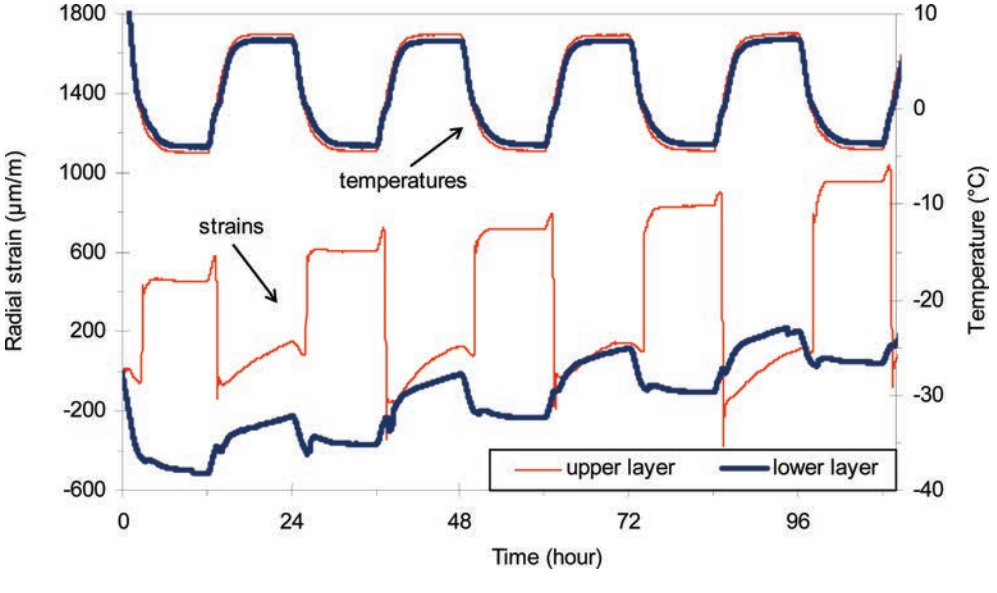

Figure 6. Graph of radial deformations of partially saturated two-layer sample.

probably induce high stress levels in the sample which however cannot be evaluated from these tests.

4 COMPLEX MODULUS TESTS

The previous tests have shown the significant effect of frost/thaw on strain. Additional tests are presented in this section to illustrate the effect of frost on the stiffness of asphalt concrete. Here the specimen are frozen prior to the beginning of the tests and then temperature is increased step-by-step (see Table 2). The impact of multiple freeze-thaw cycles on the possible damage of the samples is not addressed here.

Complex modulus tests (NF EN 12697-26 A1) are performed on asphalt concrete trapezoidal samples under dry and then partially saturated (~70%) conditions. The void content of the specimens tested is between 7 and 8%. The tests are run for the cross-conditions of temperature and loading frequency of Table 2.

The typical results obtained are presented in the Cole-Cole diagram which plots the imaginary part of the complex modulus as a function of the real part. Figure 7 shows this diagram obtained for a given sample under dry and then wet conditions. With regards to the dry condition, the curve clearly shows continuity at the junction between the isotherms, as usually observed for bituminous materials. This feature is classically reflected through the equivalence principle between time (or frequency) and temperature.

For the wet sample, the curve is superimposed with that of the dry condition in the domain of the positive or nil test temperatures. In the absence of stripping, this shows that

Table 2. Temperature and frequency conditions for complex modulus tests.

Temperature (°C)	–20	–10	–5	0	10	15	20	30		
Frequency (Hz)	1	2	3	5	10	15	20	25	30	40

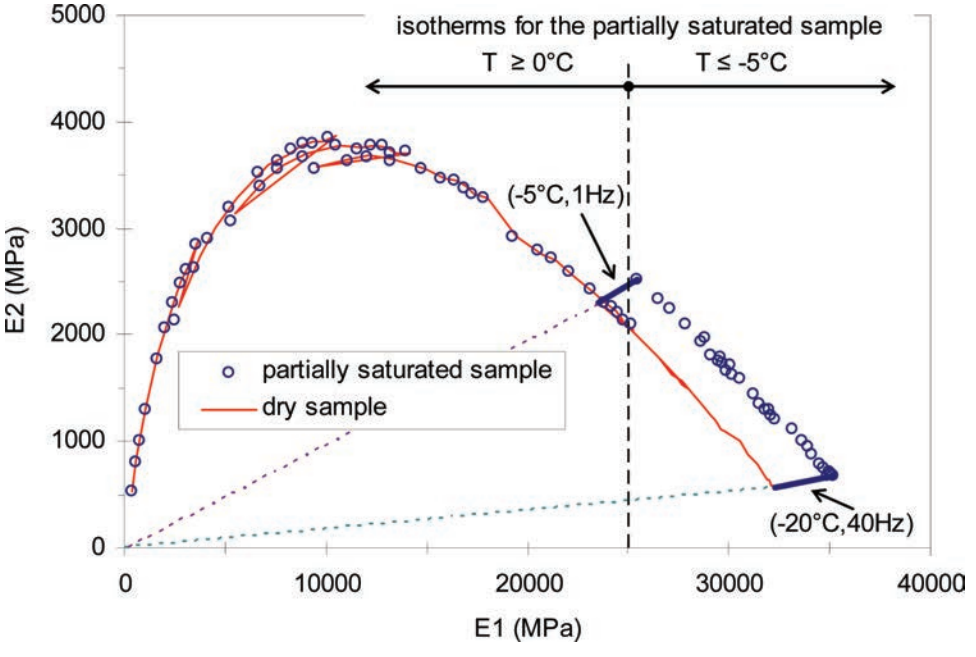

Figure 7. Cole-Cole diagram for the dry and partially saturated (70%) samples. Thick segments link points obtained for dry and wet conditions at the same temperature and frequency.

the viscoelastic behavior of the material is not affected by the present partial saturation in liquid water. Besides, the isotherms at temperature equal to or lower than −5 °C also show continuity at their junction but clearly exhibit another trend as if we were in the presence of a stiffer material. As shown by the thick segments in Figure 7, the complex modulus curve for wet condition looks homothetic to that for dry condition with a coefficient around 110%. This shows another effect of the change of pore water to ice, which is akin to an increase of the "granular" part (solid phase) of the mix.

5 CONCLUSION

The sudden disorders observed on pavements during some last winters made us investigate the freeze/thaw effect on bituminous mixes under wet conditions. Freeze/thaw tests (without external loading), performed on partially saturated bituminous samples, have shown significant swelling and contraction effects at the frost/thaw front. These effects appear to be function of the volumetric water content (ϕS_w). Besides, complex modulus test have shown a stiffening effect due the change of the pore water into ice.

Now it is believed that such effects can be at the origin of the sudden *in-situ* disorders observed on pavements, probably due to strong differential strains and self-stress developing in the asphalt layers at the frost front.

To deepen the understanding of the phenomenon and to be able to make practical recommendations to avoid these disorders, we plan further work to answer the following questions among others:

- Can the aforementioned effects be responsible of high stress levels in pavements able to break materials or interfaces?
- Is there a threshold of porosity under which the frost/thaw effect becomes negligible for wet conditions?
- Can cryosuction contribute to saturation of bituminous concrete as observed in some soils?
- Aside from the sudden occurrence of the aforementioned disorders, how do multiple freeze-thaw events damage asphalt materials and pavement structures?

REFERENCES

[1] Mauduit V., Mauduit C., Vulcano-Greullet N., Coulon N. (2007). Dégradations précoces de couches de roulement à la sortie des hivers, Revue Générale des Routes et Aérodromes, N° 858, pp 67–72.

[2] Vulcano-Greullet N, Kerzreho J.P., Chabot A., Mauduit V. (2010). Stripping phenomenon of top layers of thick pavements. Congrès ISAP2010, Nagoya, Japan.

[3] Mauduit C., Hammoum F., Piau J-M., Mauduit V., Ludwig S. Quantifying expansion effects induced by Freeze-Thaw cycles in partially water saturated bituminous mix: Laboratory Experiments. EATA, Congress and Road Materials and Pavement Design—Special Issue, 2010.

[4] Di Benedetto H., Neifar M. (1997). Coefficients de dilatation et de contraction thermiques d'un enrobé bitumineux avec et sans chargement mécanique, Mechanical Tests for Bituminous Materials, Di Benedetto & Francken Editors.

[5] Neifar Mondher. Comportement thermomécanique des enrobés bitumineux: expérimentation et modélisation, Thèse de doctorat, ENTPE-INSA, Lyon, 1997, 207p.

[6] Stoffels S.M., « Determination of the coefficient of thermal contraction of asphalt concrete using the resistance strain gage technique », Annual Meeting of the Association of Asphalt Paving Technologists, Baltimore, 18–20 mars 1996.

[7] Mauduit C., Liandrat S., Crégut E., Bertuit G., Chupin O., Hammoum F., Piau. J-M. Sudden pavement winter disorders and behaviour of bituminous materials under frost/thaw conditions. 14th International Winter Road Congress, Andorre 2014.

Asphalt Pavements – Kim (Ed)
© 2014 Taylor & Francis Group, London, ISBN 978-1-138-02693-3

Determination of discrete retardation spectra of asphalt binders using Modified Windowing Method

Yiren Sun, Jingyun Chen, Jiayin Liu & Hui Xu
School of Transportation and Logistics, Dalian University of Technology, Dalian, China

ABSTRACT: This paper describes a recursive algorithm termed the Modified Windowing Method (MWM) to fit Prony series models to creep data. The proposed method can generate discrete retardation spectra from test data without producing negative spectrum lines. The original Windowing Method (WM) assumes the equilibrium compliance of the Prony series representation to be equal to the largest data point. In that case, some errors may be introduced in calculation of spectrum lines from the data that do not cover the equilibrium region. In contrast to the WM, the MWM provides a more appropriate estimated value for the equilibrium compliance by fitting a straight line to the data in the last modelling window on the logarithmic time scale, thus resulting in a better fit. The effectiveness of the MWM was demonstrated through a numerical example in which the two algorithms were both applied to data read from a mathematical model for creep compliance. Finally, the MWM was applied to the Bending Beam Rheometer (BBR) data for determining the discrete retardation spectra of three asphalt binders.

Keywords: Asphalt binder, viscoelasticity, creep test, Prony series, retardation spectra

1 INTRODUCTION

Asphalt provides viscoelastic properties for asphalt mixtures used in pavement structures. Therefore, it is useful to investigate Linear Viscoelastic (LVE) responses of asphalt binders under different loads for performance prediction of asphalt pavements. In linear viscoelasticity, a discrete retardation spectrum which contains complete information on linear viscoelasticity is usually used to describe retardation behavior of viscoelastic materials, since the related retardation functions such as creep compliance, storage compliance and loss compliance can be easily calculated from it. Determination of a discrete retardation spectrum is essentially a procedure of fitting generalized Voigt model response to retardation data. The generalized Voigt model response can be mathematically described by a Prony series. The Prony series coefficients that a fit produces must be positive because spring stiffnesses should be positive ones. Many authors presented their fitting procedures of determining discrete retardation spectra using the Prony series [1–5]. Among these methods, the Windowing Method (WM) described by Emri and Tschoegl is a good approach that does not generate negative spectrum lines.

The WM is pretty effective for the data that cover all the three regions: the glassy region, the transition region and the equilibrium (or rubbery) region. However, due to the laboratory instrument limits or the material nature, one frequently cannot obtain such data. For example, the Bending Beam Rheometer (BBR) data obtained at low temperatures do not cover the equilibrium region. In that case, the WM may introduce some errors in calculation of the spectrum lines, since the method assumes the equilibrium compliance of the Prony series representation to be equal to the largest data point. To overcome this shortcoming, this paper presents a Modified Windowing Method (MWM), which provides a more appropriate value for equilibrium compliance in terms of the characteristic properties of the exponential

kernel functions. The effectiveness of this method was demonstrated through data read from a mathematical model. Finally, the MWM was applied to the BBR test data for determining the discrete retardation spectra of three asphalt binders.

2 BBR TEST DATA

Three asphalt binders were chosen for the purpose of this study. Two of these binders are unmodified, AH-90 and AH-70 (penetration grade). Another one is a Rubber Modified Asphalt (RMA) mixed with the AH-70 and Crumb Rubber Modifier (CRM). The CRM particle size is 80-mesh and the CRM content is 20% by weight of the basic binder. The specification parameters of penetration (at 25°C, 100 g, 5 s) and softening point for the three binders are presented in Table 1. The BBR was used to access creep data. For the AH-90, the tests were conducted at four different temperature levels: –6, –12, –18 and –24°C, while for the AH-70 and RMA, at –12, –18, –24 and –30°C. From the BBR test, the deflection at the midspan of the asphalt beam, $\delta(t)$, can be obtained. The creep stiffness, $S(t)$, and the creep compliance, $D(t)$, can be calculated as follows

$$S(t) = \frac{1}{D(t)} = \frac{Pl^3}{4bh^3\delta(t)} \tag{1}$$

where P is the applied constant load, 980 mN, b is the width of the asphalt beam, 12.7 mm, h is the thickness of the asphalt beam, 6.35 mm and l is the span length, 101.6 mm. Figure 1 presents the creep compliance data for the AH-90 at different temperatures.

Asphalt binder in LVE range is known to be thermorheologically simple and, as such, the Time-Temperature Superposition Principle (TTSP) can be employed to construct the master curve of the creep compliance. For asphalt binder in LVE range, the effects of temperature, T, and loading duration, t, can be combined into the reduced time, t_r, according to the TTSP. The reduced time is defined as follows

$$t_r = \frac{t}{\alpha_T} \tag{2}$$

Table 1. Asphalt binder properties.

Asphalt	Penetration (dmm)	Softening point (°C)
AH-90	87	46
AH-70	71	48
RMA	43	63

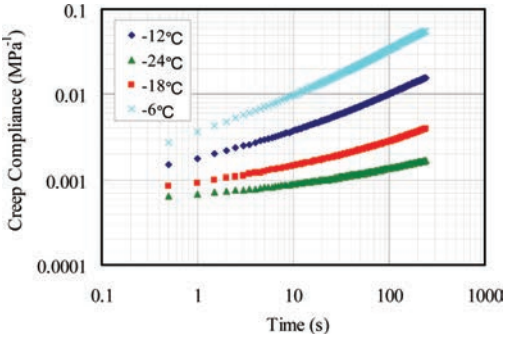

Figure 1. Creep compliance data for the AH-90 at different temperatures.

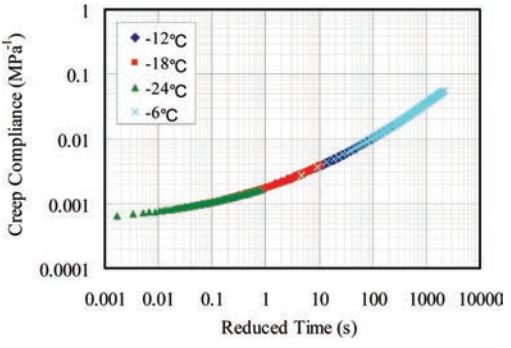

Figure 2. Master curve of creep compliance for the AH-90 at –12°C.

where α_T is the time-temperature shift factor. α_T can be employed to horizontally shift the test results measured at different temperatures to a preselected reference temperature, T_0, to form a smooth master curve. The relationship between creep compliance at reference temperature and that at test temperature is given by

$$D(T,t) = D(T_0,t_r) \tag{3}$$

Figure 2 presents the master curve of creep compliance for the AH-90 at the reference temperature of –12°C.

3 MECHANICAL MODEL

The generalized Voigt model is usually used to describe the creep behavior of LVE materials. The Prony series derived from the generalized Voigt model has the following form

$$D(t) = D_g + \sum_{i=1}^{N} D_i\left(1 - e^{-t/\tau_i}\right) + \frac{t}{\eta_0} = D_e - \sum_{i=1}^{N} D_i e^{-t/\tau_i} + \frac{t}{\eta_0} \tag{4a}$$

$$D_e = D_g + \sum_{i=1}^{N} D_i \tag{4b}$$

where η_0 is the zero-shear viscosity, D_g is the instantaneous (or glassy) compliance, D_e is the equilibrium (or rubbery) compliance, D_i are the retardation strengths, τ_i are the retardation times and (D_i, τ_i) is the discrete retardation spectrum. In this paper, the asphalt binders at low temperatures are assumed to behave as a LVE solid, and thus η_0 is set to ∞.

4 FITTING PROCEDURE

4.1 *Windowing Method*

To eliminate the negative spectrum lines and the oscillations that a fit produces, Emri and Tschoegl proposed a recursive computer algorithm referred as to the Windowing Method (WM) by using the characteristic properties of the exponential kernel functions. The method is based on the fact that a single Prony term exp(-t/τ) is only significantly time-dependent in the interval of one decade that contains the time constant, τ, whereas, outside the interval, it behaves like a unit step function. This interval of one decade is defined as the modelling window. By means of the exactly defined test data within each modelling window, the corresponding spectrum line can be determined. A set of equally

spaced retardation times needs to be preselected. Several key equations of the WM are summarized as follows:

At first, the creep data and the spectrum strengths are normalized, respectively

$$\hat{d}(t_j) = \frac{d(t_j)}{\max d(t_j) - \min d(t_j)} \tag{5}$$

$$\hat{d}_k = D_k \Big/ \sum_{i=1}^{N} D_i \tag{6}$$

The normalized creep compliance can be expressed as

$$\hat{d}(t_j) = \max \hat{d}(t_j) - \sum_{i=1}^{N} \hat{d}_i e^{-t_j/\tau_i} \tag{7}$$

Then, the absolute errors, Δ_j, between the data points and the normalized creep compliance are introduced and the sum of squares of Δ_j is formed with M function values in the modelling window

$$f_k = \sum_{j=1}^{M} \Delta_j^2 = \sum_{j=1}^{M} \left[\hat{d}(t_j) - \max \hat{d}(t_j) + \sum_{i=1}^{k-1} \hat{d}_i e^{-t_j/\tau_i} + \hat{d}_k e^{-t_j/\tau_k} + \sum_{i=k+1}^{N} \hat{d}_i e^{-t_j/\tau_i} \right]^2 \tag{8}$$

Minimizing the above error function according to $\partial f_k / \partial \hat{d}_k = 0$ leads to

$$\hat{d}_k = -\frac{\sum_{j=1}^{M} \left[\hat{d}(t_j) - \max \hat{d}(t_j) + \sum_{i=1}^{k-1} \hat{d}_i e^{-t_j/\tau_i} + \sum_{i=k+1}^{N} \hat{d}_i e^{-t_j/\tau_i} \right] e^{-t_j/\tau_k}}{\sum_{j=1}^{M} e^{-2t_j/\tau_k}} \tag{9}$$

The computation begins with the Nth spectrum line, that is, the one related to the largest retardation time, τ_N. In the first sweep, all the spectrum strengths are set to zero. In the succeeding sweeps, all positive strength values are saved and negative ones are set again to zero. The iteration is terminated when the difference between the previously found and the newly computed spectrum lines is smaller than a preset criterion. Finally, the unknown spectrum strengths, D_i can be calculated from the normalized ones.

4.2 *Modified Windowing Method*

For the data that do not cover the equilibrium region, such as the BBR data, the WM may introduce some errors in calculation of the spectrum lines. This is because the method is based

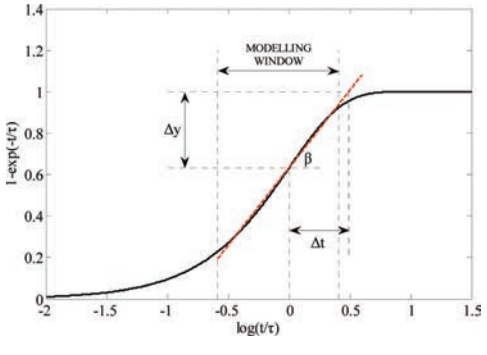

Figure 3. Graph of (1-exp(-t/τ)).

on the assumption that the equilibrium compliance of the Prony series representation is equal to the largest data point that, however, is not at the equilibrium stage. In order to overcome this shortcoming, a Modified Windowing Method (MWM) is proposed in this paper.

The MWM is still based on the characteristic properties of the exponential kernel functions. For creep compliance, the graph of (1-exp(-t/τ)) on the logarithmic time scale can make it easier to comprehend the method, represented in Figure 3. It is readily seen that (1-exp(-t/τ)) behaves like a straight line in the modelling window and a unit step function outside the window. Thus, the function value of (1-exp(-t/τ)) at the equilibrium stage can be estimated by adding $\Delta y = \beta\Delta t$ to the function value at $t = \tau$, where Δt is about 0.5. According to these properties of (1-exp(-t/τ)), the MWM sets the time associated with the last data point to the last retardation time, τ_N. The other retardation times are equally spaced before τ_N on the logarithmic time scale. The slope, β, is calculated by fitting a straight line to the data in the last modelling window. In the MWM, the equilibrium compliance is modified by replacing $\max \hat{d}(t_j)$ (see Eq. (7)) with $(\max \hat{d}(t_j)\ \beta\Delta t)$, which leads to a better fit to the creep data. It is worth noting that the MWM can also be used to identify discrete relaxation spectra from relaxation data.

5 RESULTS AND DISCUSSION

Since any true spectrum of test data is unknown, only the approximation to the true spectrum can be obtained. The success of a spectral identification is evaluated by comparing the original test data with those reconstructed from the identification [1]. To demonstrate the effectiveness of the MWM, both the WM and the MWM were applied to the identification of data read from a mathematical model for creep compliance because the spectrum of the model is known. The mathematical model is randomly given by

$$D(t) = 2 - 0.22e^{-t/1} - 0.46e^{-t/10} - 0.32e^{-t/100} \tag{10}$$

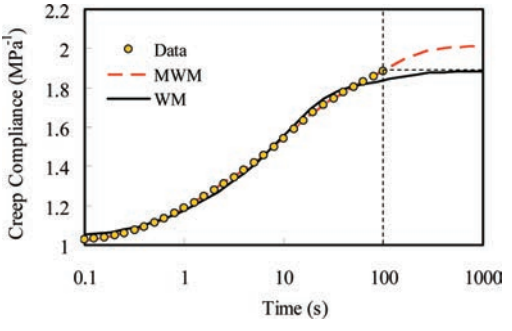

Figure 4. Fitting curves for two different methods.

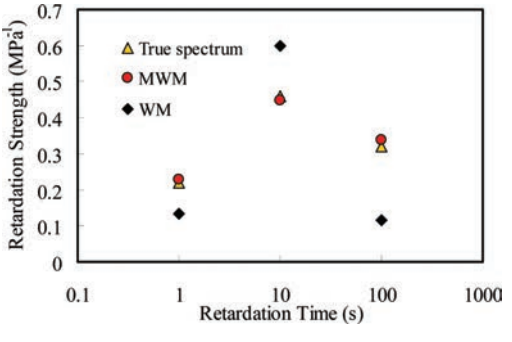

Figure 5. Discrete retardation spectra for two different methods.

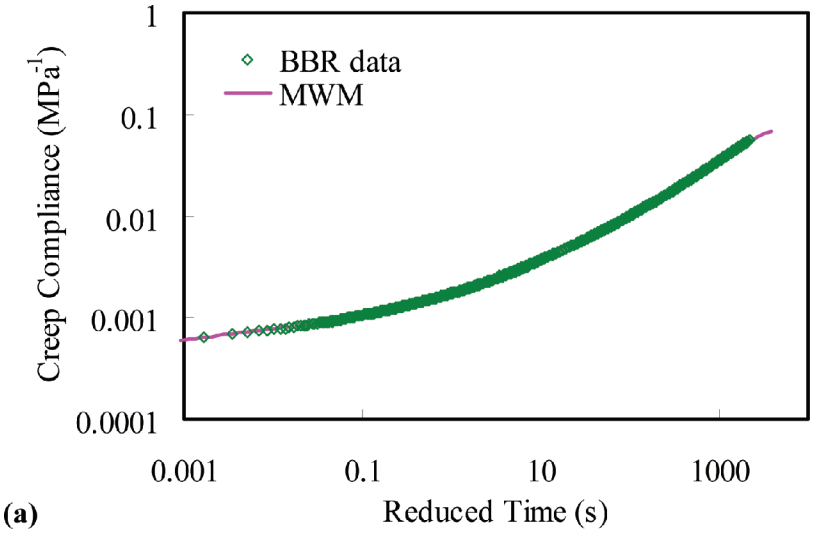

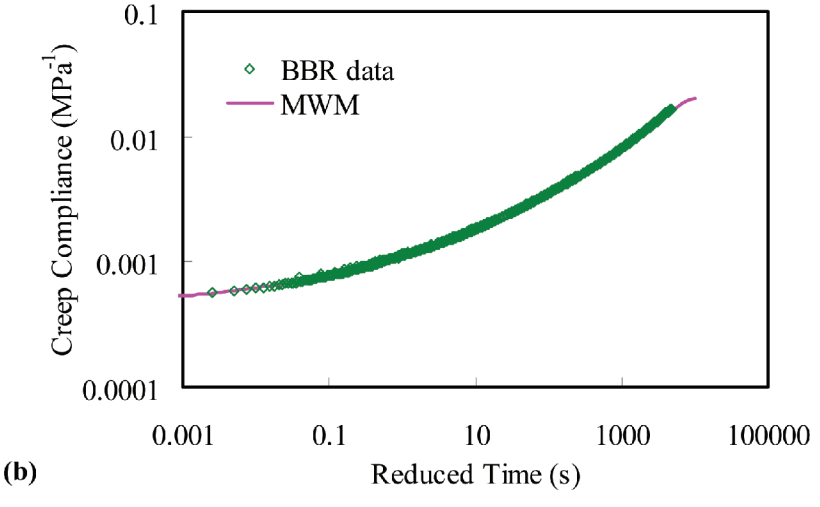

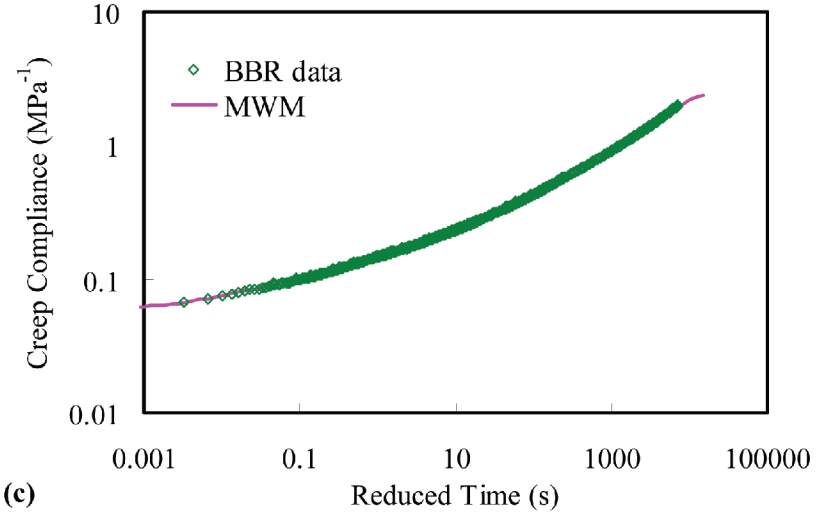

Figure 6. Fitting curve for BBR data by the MWM: (a) AH-90; (b) AH-70; (c) RMA.

Table 2. Discrete retardation spectra.

AH-90		AH-70		RMA	
τ_i (s)	D_i (MPa^{-1})	τ_i (s)	D_i (MPa^{-1})	τ_i (s)	D_i (MPa^{-1})
2.22e-3	2.02e-4	4.80e-3	9.25e-5	7.20e-3	1.57e-2
2.22e-2	8.74e-5	4.80e-2	9.93e-5	7.20e-2	2.20e-2
2.22e-1	5.05e-4	4.80e-1	3.43e-4	7.20e-1	5.06e-2
2.22e+0	5.98e-4	4.80e+0	4.65e-4	7.20e+0	6.94e-2
2.22e+1	3.46e-3	4.80e+1	1.47e-3	7.20e+1	1.92e-1
2.22e+2	4.57e-3	4.80e+2	2.37e-3	7.20e+2	3.66e-1
2.22e+3	7.05e-2	4.80e+3	1.71e-2	7.20e+3	1.85e+0

Ten data points per time decade were produced from Eq. (10), equally spaced between $-1 \le \log t \le 2$, and not covering the equilibrium region. According to the true spectrum of the mathematic model, the retardation times were preselected as 1, 10 and 100 s. Figures 4 and 5 show the fitting curves and the discrete retardation spectra for the two different methods, respectively.

It can be clearly seen from Figure 4 that the MWM yielded a better fit than the WM did. The WM forced the equilibrium compliance to equal the largest data point and this made the fitting curve have to reach equilibrium value that was equal to the largest data, thus leading to the deviation from the data. Unlike the WM, the MWM provided a modified creep compliance value in accordance with the developing trend of the data by fitting a straight line to the data in the last modelling window. Hence, the curve from the MWM fitted the data better. Figure 5 shows that the spectrum from the WM oscillates around the true spectrum while the spectrum from the MWM is very close to the true spectrum. This is also due to the inappropriate assumption that the equilibrium compliance is equal to the largest data point.

Based on the above theory, the MWM can be applied to the BBR data for determining the discrete retardation spectra. The reference temperatures for the AH-90, AH-70 and RMA are –12, –18 and –18°C, respectively. The fitting curves are shown in Figure 6, and the discrete retardation spectra are tabulated in Table 2. The results show that the MWM can well identify the discrete retardation spectra of the asphalt binders at low temperatures. Once the discrete retardation spectrum is determined, the related retardation functions, such as creep compliance, storage compliance and loss compliance are automatically established. In addition, the discrete relaxation spectrum which is usually used to describe the relaxation behavior of viscoelastic material can be obtained through various interconversion methods, which are well documented in the literature [6, 7]. These discrete retardation or relaxation spectra can be effectively and efficiently used for numerical analysis with techniques such as the finite element method.

6 CONCLUSIONS

A recursive algorithm termed the MWM was presented to determine the discrete retardation spectra of the creep data that do not cover the equilibrium region. The original WM assumes the equilibrium compliance of the Prony series representation to be equal to the largest data point, which may introduce some errors in calculation of the spectrum lines from such data. The MWM provides a more appropriate estimated value of the equilibrium compliance to overcome this shortcoming by fitting a straight line to the data within the last modelling window on the logarithmic time scale. The modified value of the equilibrium compliance results in close agreement with the test data and enhances the fitting accuracy. The effectiveness of the method was demonstrated through the data read from a mathematical model. The discrete retardation spectra of three asphalt binders were successfully determined by applying the MWM to the BBR test data.

REFERENCES

[1] Emri, I. and Tschoegl, N.W. Generating Line Spectra from Experimental Responses. Part I: Relaxation Modulus and Creep Compliance, *Rheologica Acta*, 32, pp. 311–321. 1993.

[2] Gerlach, S. and Matzenmiller, A. Comparison of Numerical Methods for Identification of Viscoelastic Line Spectra from Static Test Data, *International Journal for Numerical Methods in Engineering*, 63, pp. 428–454. 2005.

[3] Park, S.W. and Kim, Y.R. Fitting Prony-series Viscoelastic Models with Power-law Presmoothing, *Journal of Materials in Civil Engineering*, 13(1), pp. 26–32. 2001.

[4] Schapery, R.A. A Simple Collocation Method for Fitting Viscoelastic Models to Experimental Data, *Rep. GALCIT SM 61-23A*, California Institute of Technology, Pasadena, California. 1961.

[5] Cost, T.L. and Becker, E.B. A Multidata Method of Approximate Laplace Transform Inversion, *International Journal for Numerical Methods in Engineering*, 2, pp. 207–219. 1970.

[6] Tschoegl, N.W. and Emri, I. Generating Line Spectra from Experimental Responses. Part III: Interconversion between Relaxation and Retardation Behavior, *International Journal of Polymeric Materials*, 18, pp. 117–127. 1992.

[7] Park, S.W. and Schapery, R.A. Methods of Interconversion between Linear Viscoelastic Material Functions. Part I: a Numerical Method Based on Prony Series, *International Journal of Solids and Structures*, 36, pp. 1653–1675. 1999.

Life cycle cost analysis/modeling of compaction in the laboratory and in the field

This page intentionally left blank

Asphalt Pavements – Kim (Ed)
© 2014 Taylor & Francis Group, London, ISBN 978-1-138-02693-3

DAsphalt—Innovative asphalt mix for PPP projects with increased lifetime

Sivapatham Pahirangan & Norbert Simmleit
TPA GmbH, Competence Centre of Strabag S.E. for Construction Material, Cologne, Germany

ABSTRACT: In the scope of the Private Public Partnership projects or build and maintenance project, the construction company can apply their knowledge, experience and competence in the form of the technical innovation to reduce the construction and maintenance costs. Hence, in this study asphalt material with long lifetime and low maintenance cost shall be developed. Therefore, several asphalt materials for base course, binder course and wearing course with different grading and binder types have been produced and tested in the laboratory of TPA, Cologne, Germany. The gained test results show, that the mechanical property and performance behaviour of asphalt mix can be improved significantly through optimization of mix composition. Hence, in this study the newly developed asphalt material DAsphalt (Deutsche Asphalt) has been selected for a highway construction with a contract: build and maintenance for a concession period of 23 years or design load of 50 Mio. 10-t ESAL by the international construction company STRABAG. The test result of analytical pavement design method show that the layer thickness of asphalt pavement with newly developed innovative asphalt DAsphalt can be reduced up to 10 cm compared to the conventional asphalt construction (thickness of 28 cm) according to German empirical design guide.

Keywords: Polymer modified asphalt, long lifetime, PPP project, DAsphalt

1 INTRODUCTION

The current economic crisis encourage the public authorities to establish joint ventures with private partners, because the budget of public authorities resources for infrastructure projects runs short and the budget has to be adjusted. This form of relationship is called Public Private Partnership (PPP). Additionally the number of projects: Building and Maintenance construction (B&M project) are also increasing. However, the PPP and B&M projects approaches are not new and have been successfully implemented for a number of years worldwide.

Moreover, the rising long-distance heavy traffic volumes stress pavement constructions enormously. To face this challenge only new technologies and product innovations can offer the solution. In the scope of PPP and B&M projects, the construction company can apply their knowledge, experience and competence to provide smoothen infrastructure with long lifetime and low maintenance cost. In comparison to traditional type of projects, in the scope of the PPP and B&M projects, the Private companies mostly bring private investment, build and maintain the infrastructure within tendered budget and period agreed with the public authorities. Due to, the private company has to take the full responsibility and risks involved through the lifetime for a given project. Furthermore the construction company will also form a crucial element of lifecycle analysis, by enabling the comparison of costs and benefits of different pavement construction and rehabilitation strategies. Therefore, PPP and B&M projects will provide new opportunities to reach high efficiency through speedy completion, cost-effectiveness and innovation at the infrastructure projects.

In common the construction and maintenance cost of infrastructure project can average up to 45% of the total project amount. Thus, the reduction of construction and maintenance costs can contribute significantly for cost effectiveness. Hence, in the scope of this study asphalt pavement with low construction and low maintenance cost for defined lifetime shall be developed. As a result, asphalt pavement with lower asphalt layer thickness in combination with long lifetime compare to reference asphalt according to German Standard has to be designed. These greater demands on asphalt pavements with long lifetime and low life cycle costs leads properly to the development of innovative asphalt mixes.

According to the tender document of building and maintenance project (B&M project) of motorway A 31, Section Gescher, the asphalt pavement construction can be calculated by means of analytical pavement design guide RDO Asphalt 09 [1]. Thereby the selected pavement shall be able to bear a load cycle of 50 Mio. 10 t-ESAL during the lifetime of 23 years. As result, the international construction company STRABAG decided to apply innovative asphalt mixes with high lifetime and low construction costs as well as low maintenance expense [2]. Due to, in this study adequate asphalt pavement base course mix, asphalt binder course mix and asphalt wearing course mix shall be developed. The efficiency of optimized asphalt mixes have been determined by means of analytical pavement design method with respect to the determined performance properties of newly developed asphalt mixes in comparison to reference asphalt pavement construction corresponding to German Standard [3, 4].

Finally, an economic feasibility study has been undertaken to calculate the life cycle cost of newly developed asphalt pavement construction in comparison to the reference asphalt pavement construction corresponding to German Standard.

2 ANALYTICAL ASPHALT PAVEMENT DESIGN

2.1 *Analytical pavement design*

Worldwide several pavement design methods are available to calculate the thickness of asphalt pavement construction and maintenance treatments. But the design methods differ from country to country according to their own requirements and Standards. Generally the methods are mostly based on linear elastic theory and can be used to calculate stresses, strains and deformations at critical locations of flexible pavement structures. In this study, an analytical pavement design method (Pavement Design Tool: PaDesTo) with respect to German analytical pavement design guide RDO Asphalt 09 [1] based on Multi-Layer Theory has been used.

2.2 *Pavement design criteria*

The crucial asphalt properties are the resistance against permanent deformation, low temperature performance, resistance against fatigue, ageing and adhesion between binder and aggregate. The criterion of pavement design has to be selected in relation to expected deterioration mechanisms according to climatic effect and traffic volume, so that low life cycle costs occur. Because of the complexity of deterioration mechanism caused by several loading, it is not very easy to take into account all the asphalt properties. The classical pavement design criteria are the fatigue at the bottom of the asphalt base layer, and the structural rutting originating in the granular layer and/or subgrade. But most important for flexible pavements are permanent deformation and cracking initiating at the surface [5]. For this paper following deterioration mechanisms were taken into account as design criteria:

- resistance rutting (asphalt surface layer and asphalt binder layer),
- resistance against fatigue (at the bottom of asphalt base layer) and
- resistance against deformation (granular layer and subgrade).

2.3 *Mechanical and performance characteristics of material*

As well known, asphalt is an elasto-viscous material and its behaviour changes with temperature. Due to, the mechanical properties of the asphalt layer varies regarding the temperature of the asphalt. As consequence, the asphalt tends at higher temperature (>35 °C) to deform and at medium as well as at lower temperature range (below 0 °C) to crack. Thus, the temperature of asphalt during the service time has to be considered as exactly as possible.

The stiffness modulus characterizes the stiffness of asphalt mixtures and indirectly also performance properties. The bearing capacity of asphalt layers increase with increasing stiffness. Consequently the thicknesses of pavement constructions with high stiffness asphalt can be reduced compared to pavement constructions with lower stiffness asphalt. The resulting strain and stress at the position of interest for relevant temperature can be calculated with respect to the mechanical properties of asphalt. In addition, the resistance against rutting at high temperatures can be estimated by means of temperature dependent stiffness: the higher the stiffness at high temperatures the higher the resistance against permanent deformation.

Furthermore, the performance characteristics of asphalt mixture used: permanent deformation (rutting) and fatigue line were considered by means of behaviour models derived from the laboratory test results of the wheel tracking test and dynamic indirect tensile test (fatigue line). The characteristics for unbounded granular layer and subgrade will be considered by means of bearing capacity and layer thickness. In addition the adequate Poisson ratios for asphalt and unbounded material have been selected.

3 ASPHALT MIX DESIGN

Several asphalt materials for asphalt base course, binder course and wearing course with the target to improve the mechanical properties and performance behaviour have been produced and tested. Thereby the composition and binder used for respective asphalt variants have been systematically selected.

For asphalt base course several grading in combination with high/low amount of mastix with hard and soft pen bitumen to improve the bearing capacity and fatigue resistance has been systematically selected compared to the conventional base layer mix according to German Standard. It is well known, that the rutting occurs because of high lateral shear in the depth of the 4 cm and 10 cm. Due to, in this range an asphalt layer with high stiffness at high temperature and high resistance against rutting shall be placed. As consequence the mix design for asphalt binder layer has to be optimised to improve the stiffness and rutting resistance compared to the conventional binder layer mix for highways used in Germany. Asphalt wearing course shall bring resistance against rutting and cracking initiating at the surface as well as grip. With respect to these requirements Stone Mastic Asphalt (SMA) with a polymer modified binder PmB 25/55-55A for asphalt wearing course has been selected. The bitumen for SMA has been selected with respect to the asphalt behaviour at higher and lower temperatures.

Three different asphalt mix-types with several optimizations were produced after European Standard EN 12108-1. As bitumen pen graded conventional bitumen and polymer modified bitumen in combination with additives were used.

4 LABORATORY TESTS

Several asphalt material have been tested in this study, but in this paper only the variant of the selected asphalt mixes for respective layer with a long lifetime has been compared to the conventional variant. The test results of following asphalt types will be discussed for respective layers.

- stone mastic asphalt, surface course with polymer modified bitumen [SMA 8S],
- asphalt concrete, binder course with PmB 25/55-55A (conventional variant) and PmB 10/40-65A + Additive (optimised variant with special bitumen) [AC 16 BS] and

- Asphalt concrete, conventional asphalt base layer [AC 22 TS + 50% RA] and modified asphalt base course mix: **DA**sphalt 22 TS + 40% RA with special bitumen.

The design of stone mastix asphalt has been not change compared to the German Standard. To characterize the binders, conventional and performance oriented binder test were conducted according to respective European Standard. The results are listed in Table 1. The test results of polymer modified bitumen PmB 25/55-55A and 10/40-65A + Additive indicate on hard bitumen with a high viscosity compared to the other binders. As consequence the asphalts with this bitumen will show high stiffness modulus and resistance against deformation.

The determined stiffness after EN 12697-26 (indirect tensile test) show that the asphalt base course mix DAsphalt 22 TS and asphalt binder course mix AC 16 BS + PmB 10/40–65A have significantly high stiffness compared to conventional variant at lower and higher temperatures, see Figures 1 and 2. This high stiffness increases the bearing capacity of asphalt construction and will result in lower strain at the bottom of the asphalt layer compared to the conventional variant. The briefing of the stiffness can be taken from the Table 2.

4.1 *Fatigue test*

The fatigue tests for asphalt base course material have been carried out after EN 12697-24 by means of the dynamic indirect tensile fatigue test. Different specimens are loaded with different stress levels. The number of load cycles to failure N_f have been plotted versus the corresponding initial strain on a log-log scale. Fatigue line can be generated for each asphalt

Table 1. Result of binder properties.

	50/70	PmB 25/55-55 A	PmB 10/40-65 A + Additive	Special bitumen
Penetration (1/10 mm) at 20 °C				
Virgin	67.6	41.9	26.7	36.8
RTFOT	31.4	31.4	16.3	22.9
PAV	14.6	15.1	14.8	16.3
Extracted	19.0	29.8	12.2	40.6
SP R&B (°C)				
Virgin	50.9	62.6	93.2	57.1
RTFOT	58.4	66.1	94.2	63.4
PAV	70.4	74.8	101.6	76.0
Extracted	67.6	–	80.6	[–]
BP Fraaß (°C)				
Virgin	–7.6	–12.6	–8.3	–8.3
RTFOT	–3.0	–7.7	–6.6	–5.0
PAV	–0.9	–4.6	–1.4	–0.3
Extracted	–6.2	[–]	–4.45	[–]
Elastic recovery (mm) at 25 °C				
Virgin	[–]	90	80	[–]
Extracted	[–]	70	70	[–]
DSR at 60 °C [G/φ]*				
Virgin	1620	6190	34100	4960
RTFOT	6600	13700	113000	14800
PAV	37900	58100	340000	53800
Extracted	21800	18271	94800	12639
BBR				
Virgin	278.1	223.9	294.1	261.1
Extracted	298.9	243.1	265.4	217.0

[–] no requirement/not determined.

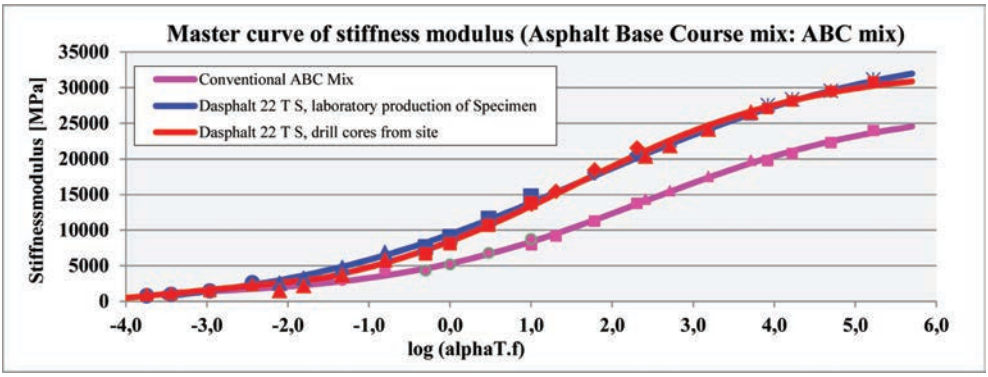

Figure 1. Master curve of stiffness modulus for asphalt base course mix.

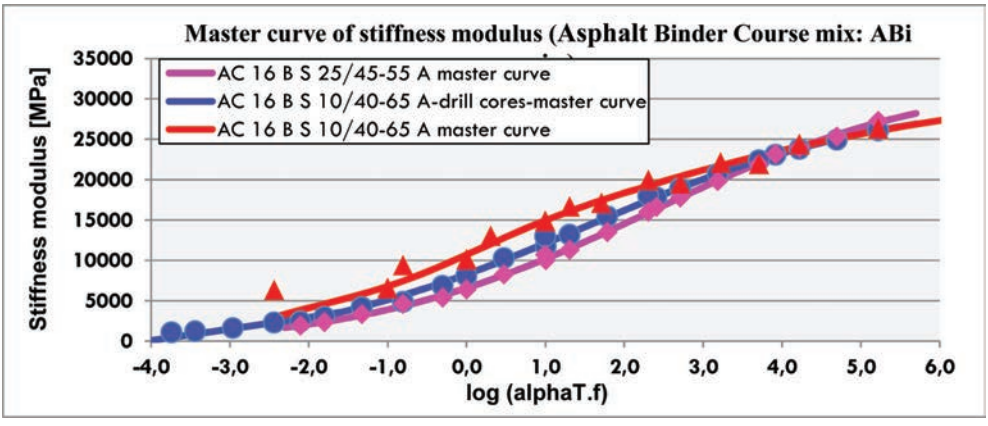

Figure 2. Master curve of stiffness modulus for asphalt binder course mix.

base course variant. In Figure 3 the fatigue line of conventional (AC 22 TS) and modified (DAsphalt 22 TS) asphalt base course mixes are displayed. The coefficient of fatigue line equation will be considered as material parameter for the analytical pavement design method, Table 3. The modified asphalt base course mix (DAsphalt 22 TS) show significant improvement of fatigue behaviour compared to the conventional variant.

4.2 *Permanent deformation (rutting)*

Worldwide numerous test methods and mixture response parameters to characterize rutting are exiting. In this work the resistance against rutting was determined by means of the wheel-tracking test according to the European Standards EN 12697-22. This method has been widely adopted as a straightforward method to evaluate rutting. The stone mastix asphalt mixture-slabs and asphalt binder mixture-slabs were tested in a tempered device at 60 °C using a rubber wheel. The slabs are loaded for 20 000 passes and the rut depth is the result of two simultaneously tested slabs. The determined test results of asphalt binder layer mixes are displayed in Figure 4. The test result of stone mastix asphalt is not displayed, because only one variant has been considered in this study.

The progression of rut depth clearly show the influence of the binder used. The variant with PmB 25/55-55A has higher rut depth compared to the variant with PmB 10/40-65A + Additive. The test result of variant with PmB 25/55-55A show also high resistance against

Table 2. Material characteristics/input data for the pavement calculation method [RDO Asphalt 09].

Asphalt mischgut	Bulk density (g/cm³)	Maximum density (g/cm³)	Needle penetration (1/10 mm)	Softening point ring and balls (°C)	Bitumen content (M.-%)	Stiffness modulus at 10 Hz [MPa]							
							–20 °C	–10 °C	0 °C	10 °C	15 °C	20 °C	35 °C	50 °C
Asphalt wearing course Stone mastix asphalt SMA 8S	2.402	2.469	38	59	7.0	Test value	[–]	23912	20151	15570	[–]	8502	3906	[–]
						Calculated value	25697	23731	20175	15086	12276	9538	3057	897
Conventional Asphalt binder mix AC 16 BS + PmB 25/55-55A + 30% RA	2,348	2.486	32	65	4.5	Test value	[–]	27331	21803	16000	[–]	10296	5748	[–]
						Calculated value	30546	27175	21850	15558	12603	10007	4759	2367
Modified asphalt binder mix AC 16 BS, PmB 10/40-65A + Additive specimen produced in laboratory	2.353	2.500	28	74.9	4.6	Test value	[–]	26319	21965	19979	[–]	14873	9407	6356
						Calculated value	28564	26048	22952	19253	17176	14952	7458	2975
Modified asphalt binder mix AC 16 BS PmB 10/40-65A + Additive drill cores from site	2.353	2.492	25	86.2	4.7	Test value	[–]	27547	22625	18123	[–]	12688	5248	1993
						Calculated value	30092	27540	23220	17493	14505	11687	5306	1996
Conventional asphalt base course mix AC 22 TS with bitumen 50/70 specimen produced in laboratory	2.421	2.545	23	61	4.0	Test value	[–]	27547	22626	18124	[–]	11312	4402	1993
						Calculated value	29499	27391	23328	17418	14234	11239	4760	1775
Modified asphalt base course mix AC 22 TS with special bitumen, specimen produced in laboratory	2.451	2.580	26	59.4	4.5	Test value	[–]	31128	25627	20623	[–]	14756	6845	2613
						Calculated value	33785	30945	26296	20178	16942	13835	6461	2322
Modified asphalt base course mix AC 22 TS with special bitumen, drill cores from site	2.460	2.538	24	62	4.5	Test value	[–]	30819	26556	21539	[–]	13821	5818	2334
						Calculated value	31850	30252	26670	20584	16965	13395	5404	1838

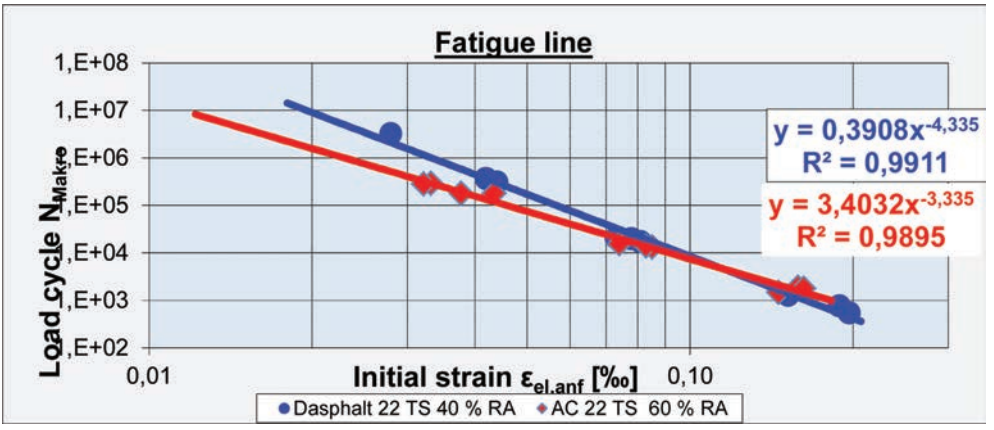

Figure 3. Result of dynamic indirect tensile fatigue test [EN 12697-24].

Table 3. Material parameter of fatigue test [RDO Asphalt 09].

	Conventional asphalt base course mix AC 22 TS with bitumen 50/70 specimen produced in laboratory	Modified asphalt base course mix AC 22 TS with special bitumen, specimen produced in laboratory	Modified asphalt base course mix AC 22 TS with special bitumen, drill cores from site
Fatigue line	$y = 3.403x^{-3.335}$	$y = 0.3908x^{-4.335}$	$y = 1.634x^{-3.704}$

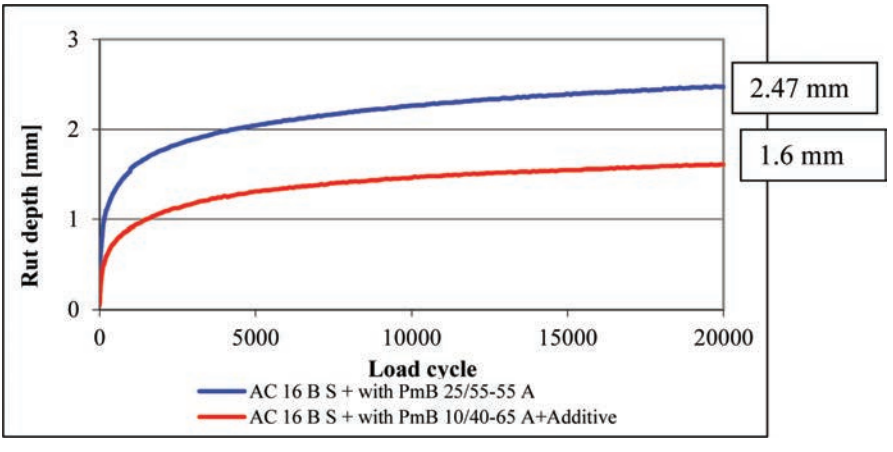

Figure 4. Result of wheel tracking test.

rutting. But, by means of improvement of rutting resistance of optimised asphalt binder mix compared to the conventional binder with PmB 25/55-55A the lifetime of asphalt binder layer shall be increased. Thus, the asphalt binder mix has been optimised with a high viscosity binder PmB 10/40-65A in combination with additives to improve the workability. The gained rut depth shows an improvement of rutting resistance. Due to, the lifetime of asphalt binder will increase. As consequence the maintenance can be reduced.

5 DAsphalt FOR BUILDING AND MAINTENANCE PROJECT OF MOTORWAY A 31

According to tender document of project motorway A 31, Section Gescher with building and maintenance construction contract, the selected asphalt pavement construction shall be able to bear a load cycle of 50 Mio. 10 t-ESAL during the lifetime of 23 years. As result, the international construction company STRABAG decided to apply asphalt mixes with high mechanical and performance properties with the target of increase of lifetime and reduce of the construction as well as maintenance costs. Due to, in this study developed innovative asphalt base course mix DAsphalt 22 TS and asphalt binder course mix AC 16 BS + PmB 10/40-65A with additives have been selected. The suitability of the selected asphalt pavement thickness shall be proofed by analytical pavement design guide RDO Asphalt 09 with respect to the selected traffic and climatic loading.

5.1 *Traffic loading*

The design method (RDO Asphalt 09 [1]) consider up to 11 different axle-load categories in combination with the frequency of the specified different axle-load categories. For the each category of the axle load the resulting stresses and strain at the affected location can be calculated according to RDO Asphalt 09. Only, by this way the effect of each single load on fatigue can be exactly considered. In this B&M project axle-load categories in combination with selected frequency of a high way has been considered, see Figure 5.

5.2 *Climatic condition*

According to RDO Asphalt 09 [1] 13 surface temperature in combination with the frequency of the specified value subject to the project location can be considered. For this B&M project the surface temperature, displayed in Figure 6 has been considered. For each position of interest the asphalt temperature can be determined based on considered surface temperature. Finally, for each combination of temperature frequency (13*) and axle load category (11*), the resulting strain and stress at interested position can be calculated.

5.3 *Asphalt thickness calculation*

The necessary layer thickness of asphalt pavement on the basis of prognosticated traffic loading, climatic conditions, material parameter and layer positioning has been calculated. The considered material parameters for analytical pavement design are displayed in chapter 4. The frequency of axle-load category and surface temperature considered can be taken from the Figure 5 and 6. The analytical pavement calculation show, that an asphalt pavement with

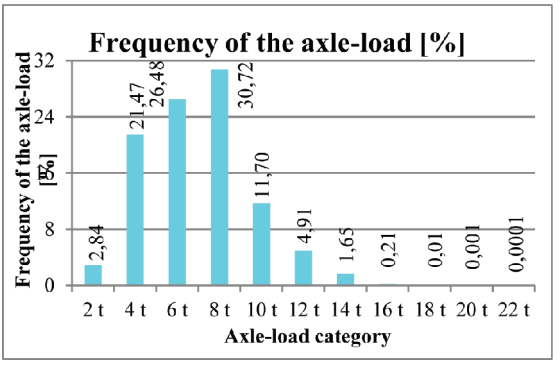

Figure 5. Frequency of the axle-load category.

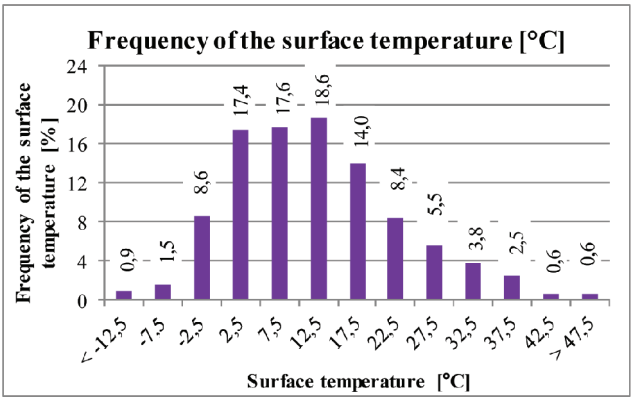

Figure 6. Frequency of surface temperature.

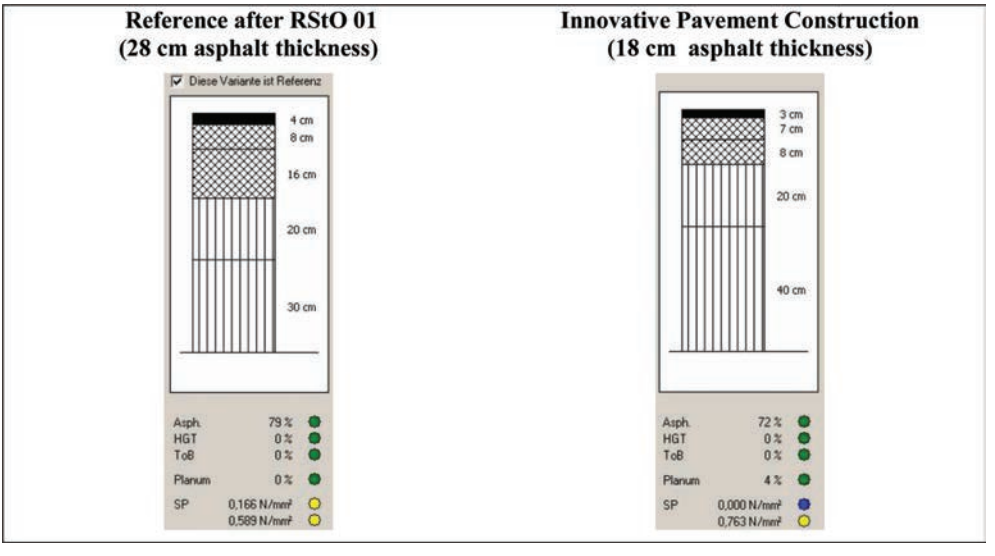

Figure 7. Comparison of conventional and innovative asphalt pavement.

layer thicknesses of 18 cm (DAsphalt 22 TS: 8 cm, AC 16 BS with 10/40-65A with additive: 7 cm and stone mastix asphalt SMA 8S: 3 cm) can be applied for the prognosticated load cycle of 50 Mio. 10-t ESAL.

According to Germany design guide [RStO 01] asphalt pavement thickness of 28 cm with conventional asphalt mixes (AC 22 TS: 16 cm, AC 16 BS: 8 cm and SMA 8S: 4 cm) has to be placed for prognosticated design load. The gained result of this study show, that the thickness of asphalt pavement can be significantly reduced in the case of use of newly developed innovative asphalt.

In addition, a rehabilitation of binder layer for an estimated traffic volume of 50 Mio. 10-t-ESAL within a lifetime of 25 years will not be necessary. According to the experience of selected stone mastix asphalt in Germany, the asphalt wearing course SMA 8S has to be completely changed one time during the concession period of 23 years. The economic feasibility study show that developed innovative asphalt pavement has a better cost effectiveness compared to the conventional asphalt pavement of German empirical design guide RStO 01 [2]. Based on this innovative knowledge the construction company STRABAG

selected this asphalt pavement concept to place at above mentioned B&M project with a thickness of 19 cm.

For validation the material parameter determined in the laboratory during this study, drill cores on systematically selected construction area, built on several days of a year has been taken and tested in the laboratory. The gained test results of analytical pavement design by means of material parameter determined on drill cores confirm that the calculated asphalt thicknesses of 18 cm is adequate to bear the prognosticated design loads of 50 Mio. ESAL.

6 SUMMARY

The calculated results show that the thickness of newly developed asphalt pavement can be reduced up to 10 cm compared to the asphalt pavement according to German empirical design guide for a design load of 50 Mio. 10-t ESAL. In addition, maintenance effort compared to the reference variant can be significantly reduced and the rehabilitation of binder layer will not be necessary. The international construction company STRABAG selected this innovative asphalt pavement for a construction of build and maintenance project of a highway in Germany for a concession period of 23 years. In addition, the validation of test result determined on the laboratory produced Specimen has been carried out by means of determination of material parameter on drill cores, sampled at several position of construction paved on different days. The gained test result of analytical pavement design method confirm with low deviances the test results determined at the Specimen produced in the laboratory. In addition, it shows that the selected asphalt pavement thickness of 18 cm is adequate to bear the prognosticated design load without to rehabilitation of asphalt base and binder course.

REFERENCES

[1] RDO Asphalt 09: Analytical Pavement design guide (original in German language), FGSV Press, Cologne 2009, Germany.

[2] H. J. Beckedahl, P. Sivapatham 2, L. Neutag: Performance of asphalt pavements with high Polymer modified bitumen—A Life-Cycle Study-, Euroasphalt and Eurobitumen conference, 2008 in Copenhagen, Denmark.

[3] RStO 01, Standardization of German pavement design guide (original in German language), FGSV Press, Cologne 2001, Germany.

[4] ZTV Asphalt-StB 01: Zusätzliche Technische Vertragsbedingungen und Richtlinien für den Bau von Fahrbahndecken aus Asphalt (original in German language), FGSV Press, Köln, 2001.

[5] COST 333: Development of New Bituminous Pavement Design Method, Final Report of the Action, European Commission Directorate General Transport, Luxembourg 1999.

Asphalt Pavements – Kim (Ed)
© 2014 Taylor & Francis Group, London, ISBN 978-1-138-02693-3

Superpave Gyratory Compactor as a compaction predictor tool for unbound material

Craig Kumpel, Adam Bagriacik, Robert Cohen, Stephen Rossi,
Colin Yurick & Wing Ho Ma
Civil Engineering, Rowan University, Glassboro, NJ, USA

Ali Daouadji
Laboratoire d'Etude des Microstructures et de Mécanique des Matériaux (LEM3), UMR CNRS 7239, Université de Lorraine—Metz, Metz, France

M. Beena Sukumaran
Civil Engineering, Rowan University, Glassboro, NJ, USA

ABSTRACT: This study presents data which supports that the Superpave Gyratory Compactor (SGC) can be used as a suitable means of compacting unbound material. The SGC was utilized to test unbound material used by the Federal Aviation Administration (FAA) for the base and subbase layer for airport pavements at the National Airport Pavement Test Facility (NAPTF). Three different materials were tested using the SGC, namely the P-154, P-209 and DGA. This paper focuses solely on P-154 and P-209. The P-154 and DGA have been used as subbase layers and P-209 for the base layer at the NAPTF for various construction cycles. The results from the SGC have been compared to field compaction and trafficking data obtained from the NAPTF. It is evident that the SGC can be used as a suitable predictor of field performance due to construction compaction and possibly trafficking. The SGC better simulates field compaction due to the contribution of both shear and vertical work. Energy measurements have also been used to determine the dependence of material type on the compactive effort required. The micro-mechanics behind compaction has been examined and has been found to be due to attrition and abrasion of the aggregate.

Keywords: compaction; superpave gyratory compactor; airport pavements

1 INTRODUCTION

With the introduction of larger planes, such as the Airbus A380, which weighs approximately 1.3 million pounds (0.6 million kg), the FAA is testing airport pavements under heavy aircraft loading at the National Airport Pavement Test Facility (NAPTF) in Atlantic City, NJ, USA. The NAPTF located at the FAA William J. Hughes Technical Center, Atlantic City International Airport, New Jersey, USA opened for testing on April 12, 1999 as a joint venture between the FAA and the Boeing Company. The test facility consists of an indoor simulated runway 274 m (900 ft) long by 18.3 m (60 ft) wide. The test strips are constructed using techniques typical for runway construction. Instrumentation is installed in the test strip to monitor responses in the subbase and subgrade due to repeated trafficking. A test vehicle is used to simulate the field trafficking of aircraft weighing up to 1.3 million pounds. As a result of the heavy aircraft loading, the FAA found that the subbase layer compacted past the maximum Modified Proctor Density [1] during the simulated trafficking with very little crushing of the material.

The NAPTF Construction Cycle 5 (CC5) is the most recent construction cycle of interest. The test pavement of CC5 is comprised of 4 flexible pavement test items, namely LFC1, LFC2, LFC3 and LFC4, constructed over a low strength subgrade known as DuPont Clay. CC5 is utilized to study the effects of various gear configurations as well as subbase material depth and quality on the flexible pavement's performance. Test items LFC-1 and LFC-4 were constructed with 34 inches of subbase material. On the other hand, LFC-2 and LFC-3 have 38 inches of subbase material. The granular subbase material is comprised of two different materials including crushed quarry screenings, P-154, and Densely Graded Aggregate (DGA). Additionally, 8 inches of P-209 crushed stone base was placed on the subbase and topped off with a 5-inch thick asphaltic concrete surface layer [2].

1.1 *Superpave gyratory compactor*

In order to understand the compaction and shear flow characteristics of the subbase layer during construction and trafficking, the subbase material was compacted in the Superpave Gyratory Compactor (SGC) at various stress levels and moisture contents. To operate the SGC, a sample is placed in the mold, which is inserted in the machine. Compaction occurs due to the pressure from the ram and the kneading action provided by the revolving angle. The SGC records the height of the ram head at each gyration during the compaction process [3]. By transferring the height data from the SGC to a computer and combining the height of the sample at a given gyration with the known diameter of the mold, the volume of the sample at a given time in the compaction process can be determined. Because the weight and volume of the sample are known, the density of the sample can be determined at any gyration level during the compaction process.

1.2 *Pressure distribution analyzer*

To find the energy input in the SGC during compaction, a Pressure Distribution Analyzer (PDA) was placed in the SGC mold. The PDA has three load cells that are placed 120 degrees from each other at equal radial distances. The PDA is started on a delayed cycle, so that it can be unplugged from the computer, and placed in the mold before the test starts. It then collects the load data and stores it until the user transfers the data to the computer after the test.

The SGC inputs both a vertical component and a shear component of work due to the gyration of the mold. Vertical work, w_v is computed from:

$$w_v = PA\Delta h \tag{1}$$

where P is the pressure of the hydraulic ram, A is the cross-sectional area of the sample (28.27 in^2) and h is the height of the sample. The second component of the energy is the shear work, w_s, which is:

$$W_S = \frac{4Pe\theta}{Ah} \tag{2}$$

where e is the eccentricity and θ is the tilt angle (1.25 degrees). All other variables are the same as in Eq. (1).

2 PREVIOUS INVESTIGATIONS

There have been investigations into the possibility of using a SGC to simulate the compaction and lifecycle of unbound soils commonly used for roads and airport runways/taxiways. Many studies have started their testing based on the standards set for testing asphalt, due to the SGC's origin as a device for testing the compaction and life of asphalt mixes [4]. One such study performed at Montana State University [5] focused on varying only the pressure

and moisture content of the soils. Four different soil types were investigated with AASHTO Classifications of A-1-a (gravel), A-3 (sand), A-4 (silt), and A-7-6 (clay). The pressure was varied from 200 kPa to 600 kPa in 100 kPa increments and the moisture content was varied from dry to saturated for each soil. Comparison of the testing data showed that dry density vs. moisture content curves were found to be very similar to Standard and Modified Proctor tests, despite the differences between the compaction mechanism used by the SGC and the Proctor tests. Two observations were evident from these series of tests. Granular soils were more affected by the SGC because the gyrations create shear work that overcome interlock. The variables that have the most significant impact on the final dry density of granular soils were found to be the moisture content and the number of gyrations [5].

3 SGC TESTING PARAMETERS

The SGC allows several parameters to be changed prior to testing: confining pressure, gyration angle, rate of gyration, and number of gyrations per test. Initial testing parameters were adopted from standards for testing asphalt. Using AASHTO design standard T 312-04 [6] as a baseline, the following testing parameters were established. Confining pressure was set at 600 kPa, 800 kPa, or 1000 kPa due to the high pressure environment expected under heavy aircraft loads. The angle of gyration and gyration rate were held constant at 1.25 degrees and 30 gyrations per minute, respectively. The number of gyrations per test was most commonly 800 gyrations; however 1600 and 3200 gyration tests were also conducted.

4 RESULTS

4.1 *SGC compaction results*

A database was compiled for analysis by conducting tests on P-154, P-209, and DGA; the subbase and base materials used for construction at the NAPTF. Due to length constraints this article will focus on P-154 and P-209; however, P-209 and DGA yielded similar compaction characteristics.

To get a baseline of comparison for the SGC compaction tests, Modified Proctor tests, ASTM D1557-07 [1], at different moisture contents were performed. Different sample sizes were used to simulate the different lift heights in the field. 3000 g and 5000 g translate to 4 inch and 6 inch lift height respectively. At approximately the same water content, the 3000 g sample after 800 gyrations reached a higher density than the 5000 g sample at 800 gyrations. It was determined from the data that the compacted height of the 3000 g sample was approximately 8 cm as opposed to the 13 cm height obtained with 5000 g sample. Therefore, during construction, smaller lift heights would create a more compacted soil resulting in a runway/taxiway less prone to failure. Figure 1 show the results of the SGC tests relative to the Modified Proctor density curve. Compaction in the SGC resulted in final dry densities much higher than the Modified Proctor Density at lower moisture contents.

The testing procedures used above on the P-154 were repeated for P-209. Once again, before any SGC tests were run on the P-209 material, Modified Proctor tests [1] were performed on the P-209 to obtain the optimum moisture content and maximum Modified Proctor density. However, 56 blows per layer and a larger mold, 0.075 cubic feet of volume, were used due to the larger aggregate size.

As testing data was compiled, it was apparent that the tests displayed repeatability. Results showed that displacement and density for all tests at respective moisture contents and pressures had a tolerance of approximately 1–2 percent. The P-209 showed a significant increase in displacement and density with increases in moisture content, as illustrated in Figure 2. The increase in confining pressure did not significantly change compaction density. Similar to the P-154 results, the densities achieved by the compaction of P-209 in the SGC were greater than those achieved by the Modified Proctor at a moisture content dry of optimum.

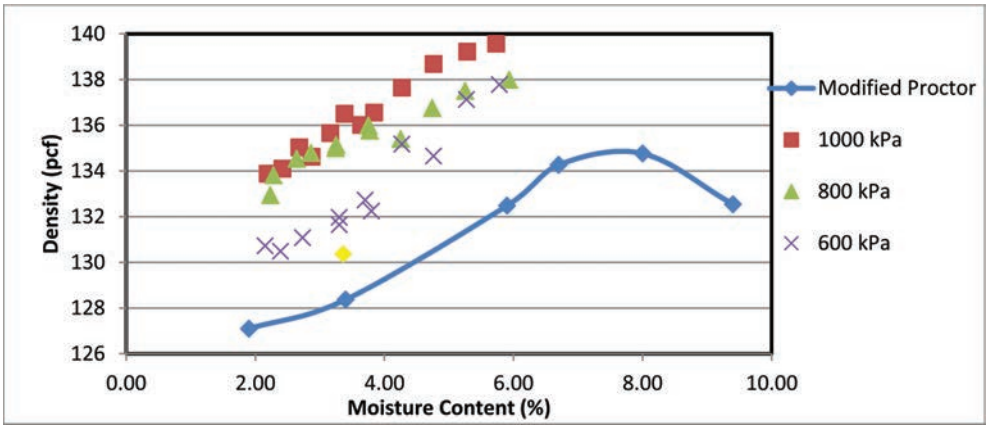

Figure 1. Evaluation of P-154 results below OMC.

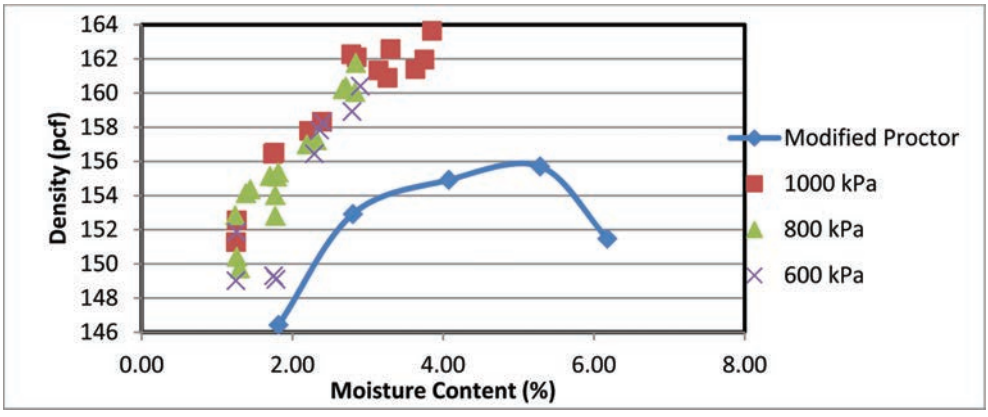

Figure 2. Evaluation of P-209 SGC results below OMC.

4.2 *Field compaction data compared to SGC compaction data*

Throughout the construction of CC5 at the NAPTF, dry density along with the number of roller passes required to reach that density was recorded. The primary compactor used for the preparation of the subbase material is a pneumatic tire roller, which was configured to weigh 205.5 kN giving it a ground contact pressure per wheel ranging from 345 kPa to 965 kPa depending on the tire pressure [7]. A drum roller was also used on the subbase during construction, which used a 2.13-m wide single-drum vibratory compactor with an operating weight of 117.5 kN and centrifugal force of 256 kN. Each roller makes passes until the maximum achievable density has been reached. As with the gyratory compactor, the material will eventually reach a point where additional passes will no longer increase the density. The density obtained in the field was obtained using either a nuclear density gauge or a sand cone, described in ASTM D6938 and ASTM D1556 [8,9]. These densities were then compared to densities achieved in the SGC by converting them into percentages of the Maximum Modified Proctor Density. These comparisons can be seen for P-154 and P-209 in Figures 3 and 4 respectively.

The results show that SGC is capable of achieving densities that the rollers achieve during field compaction. The ratio of passes of roller:SGC gyrations to achieve similar densities are approximately 1:2 and 1:10 for P-154 and P-209 respectively. Increase in ratio is most likely the result of P-209 having a denser gradation than P-154 which requires more gyrations to rearrange the material into a denser formation.

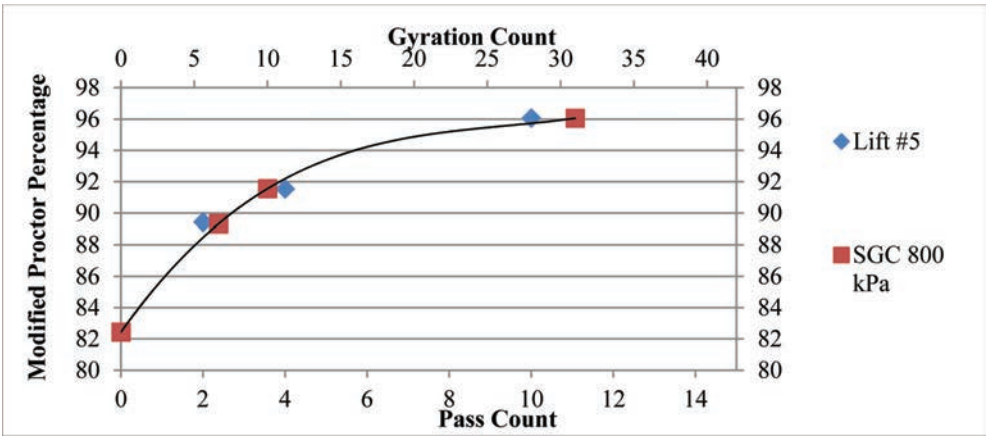

Figure 3. P-154 density to construction correlation.

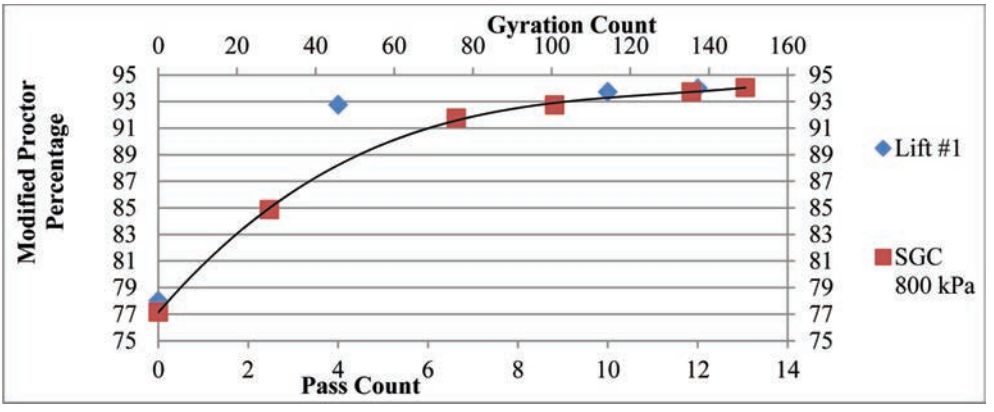

Figure 4. P-209 density to construction correlation.

4.3 *Energy measurements*

Since the SGC output includes height vs. gyration, the energy per gyration and the total energy were calculated using the data from the PDA. All energy measurements were completed at 600 kPa due to the PDA's limited load capacity. A constant 800 gyrations was also used. For the first 10 gyrations of each test the shear work was zeroed. The shear work was zeroed in order to eliminate discrepancies in the data and allow for a standard at which the PDA was leveled and not jammed against the mold. They were also zeroed because the first 10 gyrations were mostly vertical work.

Figure 5 shows the total work for P-154. As can be seen in Figure 5, as moisture content increases the sum of the total work (Fig. 5) at 800 gyrations decreases. The major component of the total work is shear work and is not shown here separately. These results are as expected because as more water is added, it is easier to compact the sample due to better lubrication of aggregate particles reducing inteparticle friction.

Similar tests were performed on P-209 and the energy results are displayed in Figure 6. The energy measurements for P-209 do not display a clear trend as was the case for P-154. This may be a result of the larger gradation of P-209. Though there is no clear trend for P-209, it appears that there is more energy input into the P-209 sample than the P-154. This is likely a result of the more uniform gradation of P-209 requiring more energy to compact because of the better aggregate interlock. The SGC mold may not be large enough to produce a

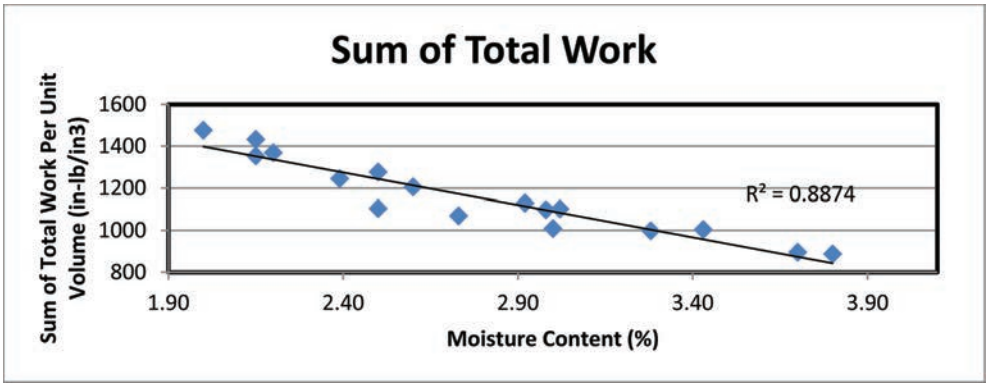

Figure 5. P-154 energy measurements.

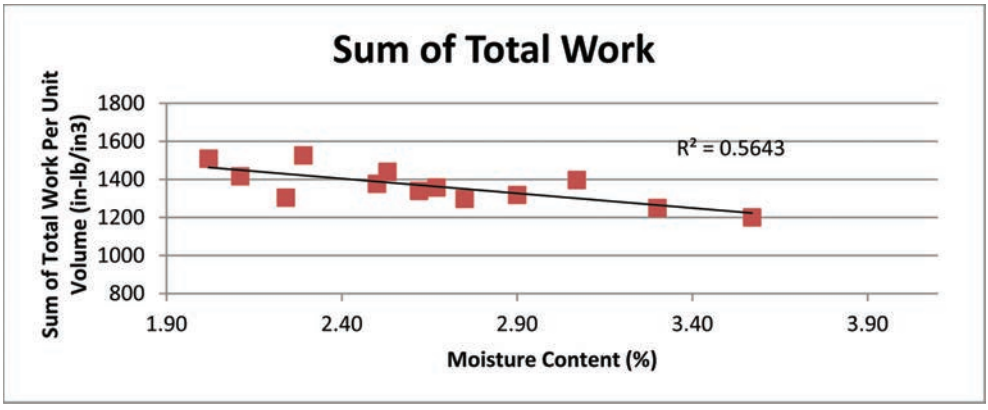

Figure 6. P-209 energy measurements.

representative sample. More tests are planned to confirm the energy measurements for P-209. P-209 does show a trend similar to P-154 in that the major component of the work done is a result of shear work and that the total work at 800 gyrations decreases as the moisture content is increased.

A comparison of the cumulative energy measurements in the SGC was also completed. The vertical work on each material at similar moisture content was developed. Only one plot is displayed below in Figure 7 because the trend is very similar for each moisture content. The vertical work is very high for the first 50 gyrations and eventually becomes almost negligible. This shows that most of the work completed in the first 50 gyrations is vertical work.

A similar comparison was made comparing the cumulative shear work for each gyration. Comparisons were made at 2.50, and 3.00 percent moisture content. The results of this analysis are displayed below in Figures 7 and 8 for 2.5% and 3% moisture content respectively. It can be seen that there is usually a significant difference in the shear energy between P-154 and P-209. Typically P-154 has much lower shear energy per gyration result than P-209. This is likely because P-154's poorer gradation makes it easier to compact than P-209. The difference in energy is greater at higher moisture contents.

Table 1 shows the average number of gyrations needed to reach a specific density range. This table is a summary of all the data that has been accrued throughout the project. It also shows that dry density values higher than the Maximum Modified Proctor Density are possible at relatively low moisture contents with increased compactive effort.

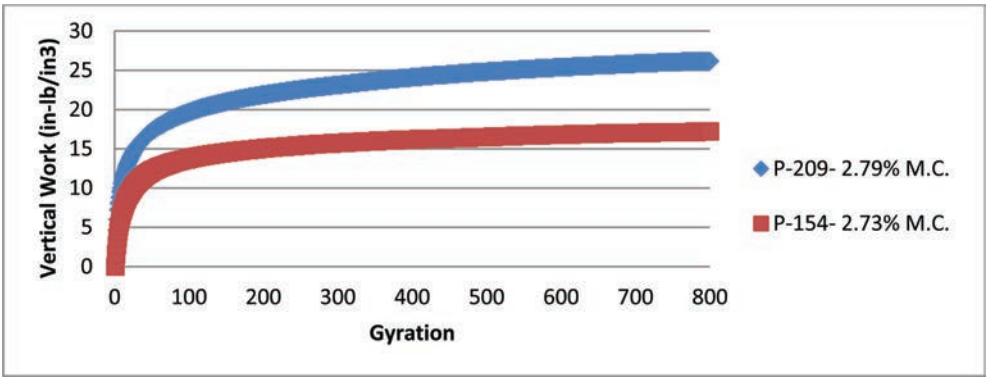

Figure 7. Cumulative vertical work per gyration at 2.75% M.C. for P-154 and P-209.

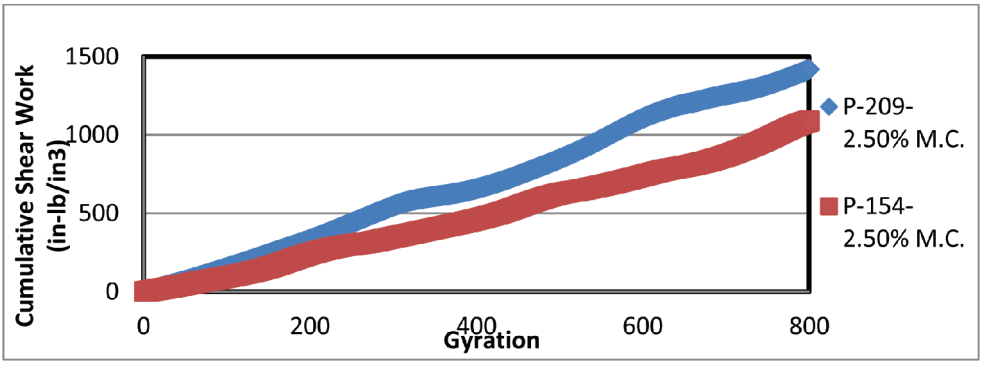

Figure 8. Shear work per gyration of P-154 and P-209 at 2.50% MC.

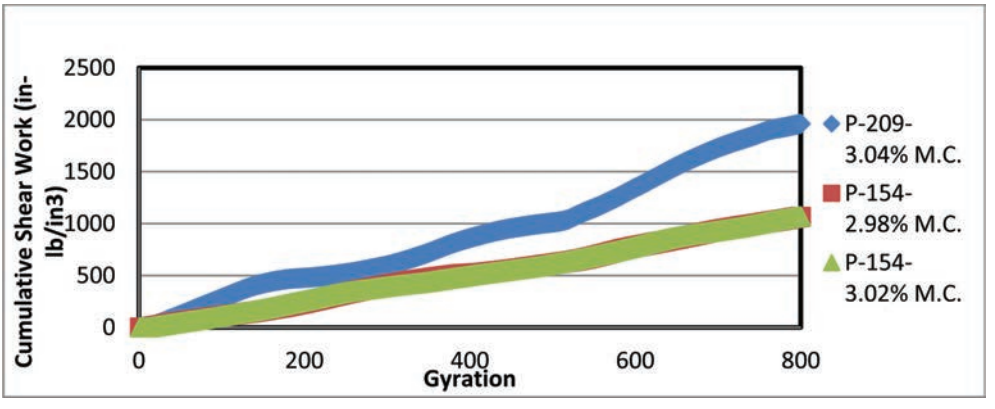

Figure 9. Cumulative shear work per gyration of P-154 and P-209 at 3.00% MC.

Table 1 also shows that as the applied pressure decreases, the number of gyrations to reach the target density is largely a function of the moisture content and it shows a more rapid increase in the number of gyrations required when pressure is decreased from 800 kPa to 600 kPa rather than from 1000 kPa to 800 kPa. This would seem to imply that increase in pressure beyond a certain threshold is not really beneficial for field compaction.

Table 1. Effect of pressure and moisture content on number of gyrations required to achieve target density for P-154.

Pressure (kPa)	1000	800	600	1000	800	600	1000	800	600	1000	800	600
Average moisture (%)	2–2.5	2–2.5	2–2.5	2.5–3	2.5–3	2.5–3	3–3.5	3–3.5	3–3.5	3.5–4	3.5–4	3.5–4
No. of tests	2	2	2	2	2	2	2	2	2	2	2	2
% max mod. Proctor	*Average number of gyrations*											
80–85%	2	2	4	2	3	4	2	4	6	3	4	6
85–90%	8	7	17	8	11	19	8	11	19	9	10	18
90–95%	39	43	131	32	44	123	30	42	107	33	37	93
95–100%	433	438	517	397	436	508	249	396	493	242	283	480
>100%	–	–	–	771	–	–	626	762	–	616	654	–

Table 2. Effect of pressure and moisture content on number of gyrations required to achieve target density for P-209.

Pressure (kPa)	1000	1000	800	800	600	600
Moisture (%)	2.0–2.5	2.5–3.0	2.0–2.5	2.5–3.0	2.0–2.5	2.5–3.0
No. of tests	2	2	3	3	3	3
% maximum mod. proctor	*Average number of gyrations*					
80–85%	29	11	20	15	19	17
85–90%	84	34	72	52	70	59
90–95%	273.5	124	299	196	308	237
95–100%	612	499	643	556	653	591
100–105%	–	–	–	–	–	–

Table 2 shows the results for P-209 and as can be seen, the number of gyrations required to achieve 100% Maximum Modified Proctor Density is larger than that for P-154. It is also to be noted that the effect of pressure is not as pronounced on the P-209 as the P-154.

In order to determine the mechanism contributing to compaction as well as assess crushing during compaction, gradation analyses were performed on virgin P-154 and P-209 as well as compacted P-154 and P-209. A wash-sieve was completed for each test to acquire an accurate representation of the fine material. The gradation analysis is not shown here but there was a movement of the grain size distribution of the materials to a finer gradation at all sieves sizes indicating that the mechanism of compaction was a combination of attrition, abrasion and fracture.

There are other means of analyzing breakage of material during compaction. For instance, the P-209 material had a much larger gradation than the P-154 material; consequently, it lent itself well to a flat and elongated particle test, described in ASTM D4791. This testing was useful in determining the change in particle morphology characteristics due to compaction. The analyses showed a decrease in flat and elongated particles for the compacted material. This backs the theory that fracture was also a method of compaction during compaction. Additionally, the fracture produced sharp edges that were easily broken by attrition or rounded by abrasion.

5 CONCLUSIONS

The SGC is capable of achieving densities greater than the maximum dry densities determined by modified proctor tests. These higher densities more closely resemble the densities

achieved in the field during construction and aircraft trafficking. Energy analysis has also shown that shear work is the main contributor to the advanced densification achieved in the SGC and is most likely why field results show densification due to trafficking much higher than the theoretical maximum dry densities. The SGC has proven to be a better option for predicting material behavior in the field than the modified proctor. The SGC could even replace expensive full scale testing once a reliable method for recording energy during field compaction is determined.

REFERENCES

[1] ASTM Standard Method of Test, *Standard test methods for laboratory compaction characteristics of soil using modified effort*, ASTM Designation: D1557-09. ASTM International, West Conshohocken, PA, 2009.

[2] National Airport Pavement Test Facility website, http://www.airporttech.tc.faa.gov/naptf/, Accessed July 8, 2013.

[3] United States Department of Transportation website, *Asphalt Pavement Technology*. http://www.fhwa.dot.gov/pavement/asphalt/labs/mixtures/sgc.cfm. Accessed June 25, 2013.

[4] Harmon, T., J.R. Bukowski, F. Moutier, G. Huber, and R. McGennis. The History and Future Challenges of Gyratory Compaction: 1939 to 2001. In *Transportation Research Record: Journal of the Transportation Research Board*, *No. 1789*, Transportation Research Board of the National Academies, Washington, D.C., 2001, pp. 200–207.

[5] Mokwa, R.L., E. Cuelho, and M. Browne. Laboratory testing of soil using the Superpave gyratory compactor. Proceedings of the *88th Transportation Research Board Annual Conference*, TRB, Committee AFS10 (Transportation Earthworks), Washington D.C., 2008.

[6] AASHTO Standard Method of Test, *Determining the density of hot mix asphalt (HMA) specimens by means of the superpave gyratory compactor,* AASHTO Designation: T312-0. AASHTO, Washington, DC, 2004.

[7] Lambert, N., K. Denny, B. Sukumaran, and Y. Mehta. Investigation of the performance of flexible airport pavements under moving aircraft wheel loads with wander using finite element analysis. *ASCE Geotechnical Special Publication on Challenges and Recent Advances in Pavement Technologies and Transportation Geotechnics*, 2009.

[8] ASTM Standard Method of Test, *Standard test method for in-place density and water content of soil and soil-aggregate by nuclear methods*, ASTM Designation: D6938-10. ASTM International, West Conshohocken, PA, 2010.

[9] ASTM Standard Method of Test, *Standard test method for density and unit weight of soil in place by the sand cone method*, ASTM Designation: D1556-07. ASTM International, West Conshohocken, PA, 2007b.

This page intentionally left blank

Asphalt Pavements – Kim (Ed)
© 2014 Taylor & Francis Group, London, ISBN 978-1-138-02693-3

Including asphalt cooling and rolling regimes in laboratory compaction procedures

Frank R. Bijleveld & André G. Dorée
Department of Construction Management and Engineering, University of Twente, Enschede, The Netherlands

ABSTRACT: Given the various changes occurring in the asphalt construction industry, improved process and quality control is becoming essential. The significance of appropriate rolling and compaction for the quality of asphalt is widely acknowledged and vital for improved process control. But what constitutes appropriate rolling and what are appropriate instructions for operators? Existing laboratory procedures generate a single compaction temperature based on binder viscosity. However, in practice, roller operators choose various windows in terms of both time and temperature for compaction activities. This makes it difficult to design the compaction process and give proper instructions to operators.

This research project has aimed to (1) develop laboratory compaction procedures that take account of asphalt cooling during compaction and (2) determine the effects of different compaction strategies on the asphalt quality. Field compaction processes for two mixtures, an AC 16 base/bind and SMA 11 surf, were simulated in the laboratory using different temperature windows and applying different rolling regimes using a slab compactor and a 2.5 ton roller to produce 500 mm square slabs. The resultant densities and Indirect Tensile Strengths (dry and retained) were assessed based on 16 cores drilled from each slab.

The experimental results show that it can be important to design rolling strategies within clearly defined temperature windows. If an SMA 11 surf is compacted outside the optimal temperature window, or using a sub-optimal rolling strategy, the density may drop by 30 kg/m^3 and the Indirect Tensile Strength fall by up to 10%. Such experimental results are vital if one is to design appropriate rolling regimes and give appropriate instructions to roller operators. Also, the results can help to close the gap between field processes and laboratory compaction techniques. Overall, the results reflect a valuable step in the quest toward improved process and quality control.

Keywords: Asphalt temperature, cooling, compaction, density, Indirect Tensile Strength

1 INTRODUCTION

The final stage of the asphalt road construction process remains a grey area when it comes to quality control. Although substantial research effort is put into creating a mix with the desired characteristics, the actual compaction sequence, once this is delivered to a site, primarily depends on the experience and gut feelings of the roller operators. This unknown element in quality control is of increasing concern to contractors. The search is on for properly validated compaction procedures because significant changes are occurring in the asphalt construction industry that result in new roles for agencies (clients) and contractors. In particular, agencies are shifting toward service-level agreements with lengthy guarantee periods. With these new roles and contracts, contractors are directly confronted with any quality shortcomings that appear during the guarantee period. As such, it is important for contractors to professionalize their operations and improve process and quality control during construction. The current asphalt construction process is mainly based on experience and craftsmanship, and

is still mostly carried out without the use of high-tech instruments to monitor key process parameters, and little research effort has been put into the systematic mapping and analysis of construction processes [1]. Therefore, contractors have little knowledge of what actually transpired during construction and how the operations were carried out. It is therefore near impossible to relate the operations to quality parameters, to identify poor and good practices, and thus also to improve process control.

In the current technological age, various technologies are being developed to make construction processes explicit in real-time by both geodetic companies (Trimble, Topcon) and machine manufacturers (Bomag, Wirtgen, Ammann, Dynapac, Caterpiller). Using modern technologies, it becomes possible to make the construction processes explicit and systematically monitor, map, and analyze on-site processes. Several studies have demonstrated, using these technologies, that there is significant variability in both construction processes and key parameters [1–4]. To reduce this variability, it is essential to change from the current experience-based working methods toward a more method-based working. To enhance this change, it is vital to design and specify the optimum construction process before actual construction. However, it is difficult to relate the various construction processes to quality parameters in field projects given the many changing variables. Ideally, one would like to design the construction process in advance within the laboratory. However, procedures to design on-site construction processes within the laboratory are lacking and thus there remains a lack of appropriate instructions for operators. If the process could be designed in advance in the laboratory, better instructions could be provided for on-site operators.

This paper focuses on the compaction process in the laboratory (a process which on-site uses rollers). The existing laboratory compaction procedures mainly generate a single optimum compaction temperature based on binder viscosity. However, in practice, roller operators use a range of time and temperature windows for compaction (observed using GPS tracking and on-site measurements). This paper proposes a procedure to accommodate asphalt cooling and compaction rolling regimes in laboratory compaction procedures. The paper starts with a literature review of research addressing asphalt compaction, followed by the objectives and approach followed in this research. Next, the compaction procedures and materials used will be described, followed by the experimental results. The paper concludes by addressing the implications of the findings for the asphalt industry and considering opportunities for future research.

2 LITERATURE ASPHALT COMPACTION

2.1 *Asphalt compaction*

An extensive literature review by Miller [1] concludes that the majority of the literature deals with the characteristics of asphalt from the perspective of a construction material and that only about 5% of the asphalt-related journals deal with asphalt laying and compaction operations. Further, in this small research area, the studies have been conducted in separate niche areas such as ‘temperature variability’, ‘temperature segregation’, and ‘compaction problems’. Nevertheless, this literature [1,5,6] has identified two important facets within the construction process that are important for the final quality of the asphalt pavement: (1) compaction operations; and (2) the asphalt temperature during these compaction operations.

First, there are the compaction operations: inadequate compaction in vital areas of the road section can lead to premature failure. Roller operators have a limited window of opportunity to carry out their operations if they are to reach a certain quality level [7–12]. They have to take into account a number of factors including the temperature of the existing surface, the initial material temperature, the thickness of the layer, and the weather conditions. Further, the operators have to perform their tasks under frequently changing site conditions involving wind, rain, and layer thickness [1,7,8]. This all contributes to compaction being a complex task.

The second facet is the temperature of the asphalt mixture during the paving and compaction phase. In the asphalt paving industry, both researchers and practitioners recognize that the temperature of the asphalt mixture during compaction is an important determinant of the final quality of the pavement [1,7,12–17]. Some authors suggest that compaction should be completed in a specific temperature range such as between 90 °C and 100 °C [13] or have specified either maximum temperatures of about 130 °C [18] or minimum temperatures between 70 and 80 °C [19, 20]. If the material temperature is too low during compaction, the bitumen can no longer lubricate the mixture resulting in an open surface. If the temperature is too high, the binder is too fluid and the resulting aggregate structure is weak as the roller loads will simply displace or "shove" the material rather than compact it, cracks may originate behind the rollers, and the rollers sink into the mixture. Kari [10] describes these minimum and maximum temperatures as understressed and overstressed situations.

Traditionally, the optimal compaction temperature has been determined by plotting log-viscosity vs. log-temperature, and the ideal compaction temperature coincided with a bitumen viscosity of 1.7 poise [21]. Subsequently, Jordan and Thomas [22] and Luoma et al. [23] developed tools to predict a temperature window, and the starting and ending temperatures at which to compact. Later, Chadbourn et al. [7] and Timm et al. [12] developed Windows-based computer programs (PaveCool, Calcool, and Multicool) that produced solutions that predicted the pavement cooling phenomenon and suggested starting and stopping times for compaction. The main problem with these methods is that they are based on viscosity and density rather than final quality characteristics such as resistance against fatigue, rutting, and cracking. Decker [24] argues that determining the compaction temperature through viscosity-temperature plots is no longer appropriate with more viscous bitumens since these can have a higher compaction temperature leaving insufficient time to compact the mixture. Similarly, Bahia et al. [25] showed that these traditional approaches indicated unreasonably high temperatures for modified asphalts.

In conclusion, the compaction process and the temperature during this process are key determinants of the final quality of the pavement. However, how the density and mechanical properties of the pavement are influenced by the various operational compaction strategies remains unclear.

2.2 *Simulation of field compaction in the laboratory*

Several studies have shown that conventional laboratory compactors, such as Marshall compactors, vibratory compactors, and gyratory (kneading) compactors, do not truly simulate the compaction in the field. In the last decade, a new type of compactor has entered the laboratory asphalt compaction market—the rolling compactor (EN 12697-33)—that produces relatively large slabs. The principle of these compactors is a segmented roller that moves back and forth across the mixture in a mold to produce relatively large slabs, often 500 mm by 500 mm.

From various studies, it has become clear that rolling compaction is closest to field compaction [26–30]. Also, the instrument can be pre-heated and can produce several test samples at the same time, and this diminishes variability between subsequent tests. The University of Wuppertal has conducted research so as to be better able to simulate, in the laboratory, field compaction and more accurately simulate pre-compaction [28]. These new laboratory compactors are available on the international market. Companies in Europe, including BPS Wennigsen and Infratest Testing Systems in Germany (who have sold 66 machines worldwide since 2006) have developed several compactors as has IPC Global based in Australia. However, less research effort has been put into determining relationships from an operational (process) perspective related to the final mechanical properties of the asphalt mixture. As a result of these studies and developments, we believe that rolling compaction has now reached a stage where it can play an important role in simulating the field compaction process, and with that in the design of improved compaction procedures. The next section discusses the objectives of this research and the approach followed.

3 OBJECTIVES AND APPROACH

The objectives of this research were: (1) to develop laboratory-scale compaction procedures that include asphalt cooling; (2) to develop laboratory procedures to imitate actual rolling regimes with various rollers; and (3) to compare the compaction procedures used in various laboratories using different compaction methods. Overall, the aim was to improve understanding of operational strategies and narrow the gap between field compaction and compaction in the laboratory. The objective of this paper is to demonstrate the merits of the developed compaction procedures and the range of experimental results when the compaction procedures were varied.

To achieve the objectives, three experiments were designed and conducted. In these experiments, some elements of the compaction process were varied and quality parameters were determined. More specifically, the temperature window and the roller types used for compaction were varied (the independent variables) and the quality of the finished product was determined in terms of density and Indirect Tensile Strength (ITS) (the dependent variables).

The 'temperature window' variable warrants further explanation. From the literature review, it is clear that the traditional approach to specifying the compaction temperature from laboratory tests results in a single compaction temperature based on viscosity whereas, during field compaction, subsequent roller passes are made while the asphalt mixture cools, resulting in a temperature window. Timm et al. [12] put forward the idea that there is an ideal window of temperatures in which to compact the asphalt mixture and, if this is met, then it is highly likely that the desired mechanical characteristics will be achieved. Depending on the cooling rate of the asphalt mixture, this also means that there is an optimal time window in which to compact. If the asphalt mixture is compacted outside these windows, the asphalt mixture will be understressed (if the mixture is compacted at too low temperatures) or overstressed (if the temperatures are too high). Figure 1, which shows schematically the temperature of the mixture as a function of time, illustrates these conditions.

4 MATERIALS AND COMPACTION PROCEDURES

The experiments were conducted using two asphalt mixtures, namely an AC16 base/bind and an SMA 11 surf. These mixtures were chosen since the AC 16 base/bind is a frequently used asphalt mixture under less than ideal circumstances in the Netherlands and the SMA 11 surf is known to be a critical mixture in terms of compaction. Both mixtures were made without incorporating Recycled Asphalt (RAP) in order to increase the homogeneity of the mixtures. All the materials were ordered as a single batch to decrease the risk of excessive variability in the raw materials. The compositions of the two asphalt mixtures are shown in Table 1. These mixtures were then compacted using two different compaction methods, namely a Slab Compactor (SC) and small 2.5 ton Roller Compactor (RC) to create 500 mm squared slabs—shown in Figure 2.

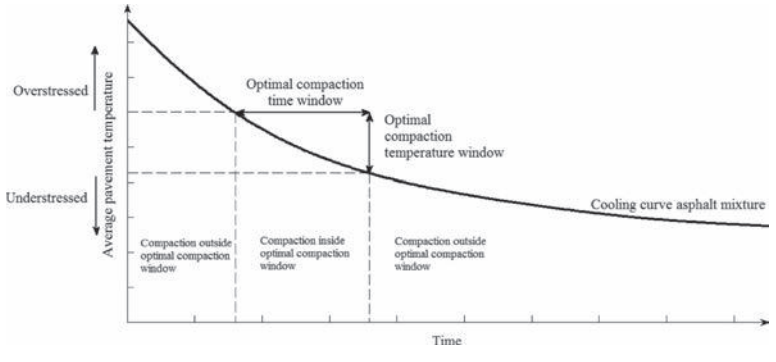

Figure 1. Compaction window (based on Timm et al. [12]).

Table 1. Composition asphalt mixtures.

Material	AC 16 base/bind	SMA 11 surf
Bestone 4/8	–	30.9%
Bestone 8/11	–	47.3%
Granite 2/8	22.7%	–
Granite 8/16	35.0%	–
Sand	35.8%	12.0%
Wigras 40 K (filler)	6.5%	9.8%
Bitumen 40/60	4.5%	–
Bitumen 70/100	–	7.0%

Figure 2. Slab compactor (left) and 2.5 ton roller (right).

Three experiments were designed and conducted: (1) varying the temperature window for the AC 16 base/bind mixture using both compaction methods, (2) varying the temperature window for the SMA 11 surf mixture using both compaction methods, and (3) varying the rolling regime for the SMA 11 surf mixture using only the slab compactor. The specified compaction procedures are shown in Table 2. In total, 47 slabs were produced in four laboratories from which 752 cores were extracted and analyzed.

The steps (i.e. the procedure) conducted in the experiments were as follows:

1. Mixing the raw materials. This involved heating the bitumen and aggregate to 170 °C. First, the aggregate, sand and filler were put in the mixer, these were mixed for 15 seconds, then the bitumen was added and mixed for 3 minutes.
2. Compacting the asphalt mixture using the slab compactor or the 2.5 ton roller. First, the asphalt mixture was pre-compacted to 90% of the target density (simulating screed compaction). Then the 4–5 rolling phases shown in Table 2 were simulated (also based on procedures from Mollenhauer [31]).
   a. To ensure the roller passes were carried out at the intended temperatures, thermocouples were placed in the asphalt mixture at the bottom and middle of the height through the slab. In practice, there was little difference between these two temperatures so the slabs can be considered homogenous in terms of temperature.
   b. The loads applied by the slab compactor were calculated based on the Dutch roller factor, which is calculated by the load of the roller divided by the product of the width and the square of the diameter of the roller. A force of 14 kN was used to simulate a tandem roller, and a force of 25 kN to simulate a three-drum roller.
3. Drilling and removing cores from the slab. Sixteen cores with a diameter 100 mm were extracted from each slab according to a standard drilling scheme.
4. Determining the dimensions and densities of the drilled cores. The dimensions of the cores was measured four times using a digital rod and the density was determined by a procedure based on Archimedes' Law.

Table 2. Design of the compaction procedures.

Experiment 1: AC 16 base/bind		
Procedure 1: 10 slabs	Procedure 2: 3 slabs	Procedure 3: 2 slabs
5 tandem passes at 150 °C	5 tandem passes at 120 °C	5 tandem passes at 120 °C
5 tandem passes at 115 °C	5 tandem passes at 100 °C	5 tandem passes at 80 °C
5 tandem passes at 90 °C	5 tandem passes at 80 °C	5 tandem passes at 60 °C
5 tandem passes at 70 °C	5 tandem passes at 60 °C	5 tandem passes at 40 °C
Experiment 2: SMA 11 surf		
Procedure 1: 12 slabs	Procedure 2: 12 slabs	
5 tandem passes at 150 °C	5 tandem passes at 120 °C	
5 tandem passes at 115 °C	5 tandem passes at 100 °C	
5 tandem passes at 90 °C	5 tandem passes at 80 °C	
5 tandem passes at 70 °C	5 tandem passes at 60 °C	
5 tandem passes at 50 °C	5 tandem passes at 40 °C	
Experiment 3: SMA 11 surf		
Procedure 1: 3 slabs	Procedure 2: 3 slabs	Procedure 3: 2 slabs
5 three-drum passes at 150 °C	5 tandem passes at 150 °C	5 tandem passes at 150 °C
5 three-drum passes at 115 °C	5 tandem passes at 115 °C	5 tandem passes at 115 °C
5 three-drum passes at 90 °C	5 tandem passes at 90 °C	5 tandem passes at 90 °C
5 tandem passes at 70 °C	5 three-drum passes at 70 °C	5 tandem passes at 70 °C
5 tandem passes at 50 °C	5 three-drum passes at 50 °C	5 tandem passes at 50 °C

5. Polishing the cores: The AC16 base/bind slabs were compacted to a thickness of 80 mm and polished to a depth of 60 mm for testing. The SMA 11 surf slabs were compacted to 60 mm and polished to 50 mm for testing.
6. Determining the dimensions and densities of the polished cores. As in Step 4, the dimensions were measured four times using a digital rod and the density was determined using Archimedes' Law.
7. Conditioning of the polished cores: Eight cores were conditioned in air at 15 °C for 72 hours (further called dry cores) and eight cores were conditioned in a water bath at 5 °C for 72 hours (further called retained cores).
8. Conducting ITS tests: ITS tests were conducted according to EN-12697–23. The ITS tests determine the peak load (P_{max}), the Indirect Tensile Strength (ITS), the work of fracture (W_f), and the fracture energy (G_f). The fracture energy was calculated according to the RILEM TC 50-FMC specification (1985). The work of fracture (W_f) was computed as the area under the load(P)—displacement(u) curve, and the fracture energy (G_f) was calculated by dividing the work of fracture by the ligament area (the product of the diameter (D) and the height (H) of the specimen).

5 EXPERIMENTAL RESULTS

Three experiments were conducted in four different laboratories. These laboratories are here numbered 1 to 4, and in 1 and 2 the mixtures were compacted using a Slab Compactor (SC) and in 3 and 4 the mixtures were compacted using a 2.5 ton Roller Compactor (RC). From each compacted slab, 16 cores were extracted and analyzed. The following aspects were assessed in detail: (1) layer thickness progression during compaction; (2) density before and after polishing; and (3) indirect tensile strength.

5.1 *Experiment 1: Varying temperature window—AC 16 base/bind*

The progression in the layer thickness during compaction is automatically determined when using a slab compactor and determined using a theodolite in the laboratories using a 2.5 ton roller. The progression in layer thickness using the slab compactors (laboratories 1 and 2) showed a consistent trend as shown in Figure 3: During pre-compaction, the layer thickness decreased by around 3–4 mm. In the first three roller phases, the layer thickness decreased by 0.1–0.6 mm in each phase. Following this, in the final phase, the layer thickness increased slightly (0.2–0.3 mm). These results are similar to the results of Faheem et al. [32] who also found that density does not always increase as the temperature falls, as we saw in the last compaction phase in our testing. In contrast, the changes in the layer thickness using the 2.5 ton roller (laboratories 3 and 4) were much more variable and no trend could be discerned.

Next, the densities of the extracted asphalt cores were determined. With this mixture, no significant differences in density were observed for a given procedure undertaken in different temperature windows. However, differences in density were observed between the two compaction methods and between the laboratories. The average slab density compacted with the slab compactors was 2296 kg/m^3, whereas the average density of slabs compacted with the 2.5 ton roller was 2339 kg/m^3. Also, the average density of slabs compacted with the same roller procedure was 2301 kg/m^3 in one laboratory and 2371 kg/m^3 in the other. The density variability within a slab was also analyzed and the variation within a slab was of a similar order. The average difference between the minimum and maximum densities within a slab was 53 kg/m^3.

Finally, the results of the ITS tests, presented as fracture energy (G_f) values in Figure 4, were considered. We concluded that there were large differences between ITS results for slabs compacted using the same procedure—both from slab to slab and from lab to lab. For the

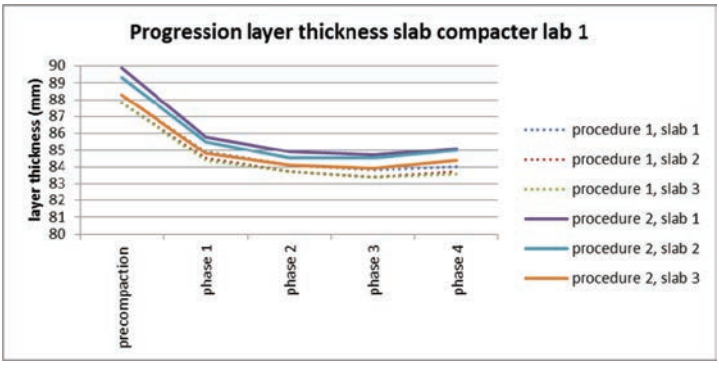

Figure 3. Progress in the layer thickness using the slab compactor.

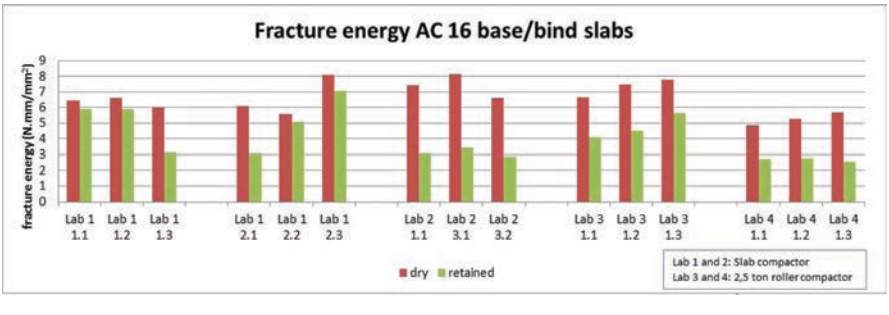

Figure 4. Average fracture energy values AC 16 base/bind slabs.
*The coding indicates the procedure (1st number) and the slab number (2nd number).

dry samples, G_f values ranged from 4.9 to 8.2 Nmm/mm^2. Given this high variability from one slab to another, it was not possible to determine a relationship between the different compaction procedures. Further, it is apparent that the retained ITS values of the slabs compacted in laboratories 2 (SC) and 4 (RC) are relatively low compared to those in the other two laboratories (by 1.97 Nmm/mm^2 on average). As a consequence, the ratio between the dry and retained values (ITSR) are relatively low in laboratories 1 (SC) and 3 (RC), and overall show a wide range (41–91%).

5.2 *Experiment 2: Varying temperature window SMA 11*

SMA 11 surf slabs were compacted in two different temperature windows, namely at 150-115-90-70-50 °C (Procedure 1), and at 120-100-80-60-40 °C (Procedure 2). Five roller passes with a tandem roller (Hamm DV70) were carried out in each of the five rolling phases.

Again, the progression in layer thickness during compaction was more consistent using the slab compactor than the 2.5 ton roller. Using the slab compactor it was possible to compact slabs with a maximum difference in layer thickness of 2.5 mm (59,7–62,2 mm). Using the 2.5 ton roller, the differences in thickness were much more variable (58,9–65,3 mm).

From an analysis of the progression in layer thickness, it seems that Procedure 2 was less successful in achieving the desired layer thickness than Procedure 1. This is also reflected in the final densities of the extracted cores. Although all the cores show a compaction degree of 100 to 102%, the densities of the cores compacted using Procedure 2 are approximately 30 kg/m^3 lower than those produced using Procedure 1. As with the AC16 base/bind mixture, the variability in density within a slab was high. Differences between the minimum and maximum densities in a slab were as high as 80 kg/m^3. However, the cores extracted from the central area of the slabs were much more consistent with the maximum difference between the minimum and maximum densities within a slab being 25 kg/m^3.

ITS tests were performed on the extracted and polished cores. Even when the largest differences in density were discounted (by selecting the middle cores of the slabs), there still seems to be a difference in ITS values between the cores compacted using the two procedures. The ITS values from the cores compacted according to Procedure 1 vary from 0.91–1.09 MPa, and using Procedure 2 from 1.01–1.20 MPa. The average ITS of the cores compacted using Procedure 2 was 0.11 MPa (≈10%) higher than the ITS of those compacted using Procedure 1. We then looked for a relationship between the density and the ITS of the cores. No relationship was found between the ITS and the density, for the obtained density range (2330 to 2370 kg/m^3).

5.3 *Experiment 3: Varying roller regime SMA 11*

In Experiment 3, SMA 11 surf slabs were compacted following three different roller regimes, namely using a three-drum roller and then a tandem roller (further called D-T), using a tandem roller and then a three-drum roller (further called T-D), and using a tandem roller, followed by a second tandem roller (further called T-T). In all cases, compaction took place in five phases at temperatures of 150–115–90–70–50 °C with five roller passes in each phase.

The successive changes in layer thickness show that the D-T rolling regime results in a much faster reduction in slab thickness than in the slabs compacted using the T-D and the T-T rolling regimes.

Following the procedure, next cores were extracted and analyzed. All the slabs achieved the target density or higher densities. However, the cores compacted using the D-T rolling regime were denser than both the target density and the ones produced using the other rolling regimes. The average density of the cores compacted using the D-T rolling regime were about 30 kg/m^3 higher than those produced in the other regimes (see Fig. 5). Again, the variability within a slab was high, although the densities in the middle part of a slab were rather constant with the difference between the minimum and maximum densities no more than 25 kg/m^3.

ITS tests were then performed to complete the experiment. With the largest differences in density being discounted by selecting only the middle cores of the slabs, there seems to be a

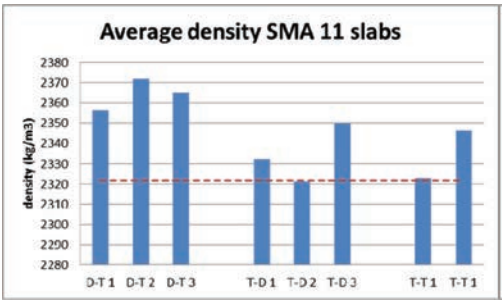

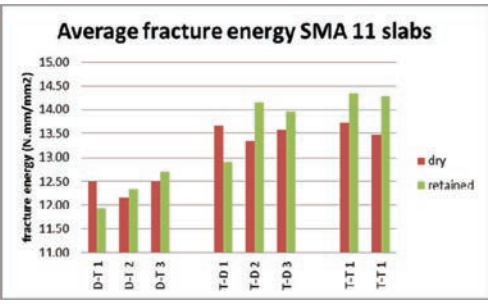

Figures 5 and 6. Average density. Average fracture energy.
*D and T indicate the roller type (three-drum (D) and tandem (T)) and the numbers correspond to the slab number.

relationship between ITS and the rolling regime. The ITS of the cores compacted using the D-T rolling regime were about 10% lower than the cores compacted using the other rolling regimes (see Fig. 6). A possible explanation is that the three-drum roller is too heavy and so creates micro-cracks at the high temperature of 150 °C. However, this hypothesis needs to be confirmed or rejected in other laboratories.

6 DISCUSSION AND FUTURE RESEARCH

Although we have succeeded in simulating the asphalt cooling process in laboratory compaction procedures, there are still various points to address. First, we have seen that there is still significant variability in both density and Indirect Tensile Strength (ITS) within the asphalt slabs. As such, the procedures need to be improved to reduce the variability in density. Possibly, this could be achieved by automating the filling of the mold with the asphalt mixture related to the pre-compaction of the paver. Further, the variability in ITS values has a strong influence on the ratio between the dry and retained values (ITSR), and this makes the ITSR an even more unreliable parameter for use in analysis and comparison. A final concern is that the ITS test may not be sufficient to observe differences between slabs that were compacted within different temperature windows. In future research it may therefore be valuable to test cores using other mechanical tests such as the triaxial test or the four-point bending test. Also, additional research could usefully be devoted to further experimenting with different roller regimes, and specifically with more critical mixtures when it comes to compaction, such as thin surfaces. In case of using asphalt mixtures with multiple aggregate sources, it may be better to evaluate the air voids rather than the density. Further, more extreme loads could be tried to determine when micro-cracks due to roller loads may arise. We also plan to explore other variables in the compaction process, such as the timing of the first roller pass and the effect of roller speed, and to determine the effects of additional roller passes once the target density is achieved.

Finally, it is important to validate the experimental results obtained in the laboratory with field experiments. Therefore, further research effort is planned that involves designing a field experiment in which a rolling strategy will be given to roller operators and its implementation monitored using GPS equipment. Following this, the rolling process will be closely simulated in the laboratory and the resulting mechanical properties compared.

7 CONCLUSIONS

The significance of appropriate rolling and compaction for road quality is widely acknowledged and improved process and quality control are vital. However, procedures to design

or specify compaction processes are lacking and thus also methods to provide appropriate instructions for roller operators. Existing laboratory procedures generate a single 'ideal' compaction temperature based on the binder viscosity, while in practice roller operators have to select and work within windows based on time and temperature. This paper has described initial work to include asphalt cooling and rolling regimes in laboratory compaction procedures. Typical field compaction processes for an AC 16 base/bind and for an SMA 11 surf were simulated in the laboratory within different temperature windows by applying specified rolling regimes using a slab compactor and a 2.5 ton roller. In this initial stage, we succeeded in imitating, in the laboratory, field compaction processes in terms of temperature windows and rolling regimes. By following a standard procedure, it was possible to conduct roller passes at various temperatures and so compact the asphalt within a specified temperature window.

Using the AC16 base/bind, three temperature compaction windows were experimented with: from 140 down to 70 °C, 120–60 °C, and 120–40 °C. None of these tests suggested a significant and consistent relationship between temperature window and final density and Indirect Tensile Strength. Similarly, two temperature windows were used with the SMA 11 surf mixture, from 150 °C down to 50 °C and 120–40 °C. With this mixture, the slabs compacted in the cooler temperature window were less dense, typically by 30 kg/m^3. When the differences in density were discounted, the slabs compacted in the lower temperature window have Indirect Tensile Strengths (ITS) that are about 10% higher. In a final set of experiments, the rolling regime for the SMA 11 surf was varied. Three regimes were tested: (1) first a three-drum roller and then a tandem roller, (2) first a tandem roller and then a three-drum roller, and finally (3) two successive tandem rollers after each other. The slabs compacted using the first roller regime with a three-drum roller followed by a tandem roller were about 30 kg/m^3 higher in density. However, the ITS of the slabs compacted using this roller regime were about 10% lower.

The results demonstrate that it is certainly important to specify rolling strategies based on temperature windows that depend on the asphalt mixture. If an SMA 11 surf is compacted outside the optimal temperature window, or using a sub-optimal rolling strategy, the density may drop by 30 kg/m^3 and the Indirect Tensile Strength by up to 10%. These experimental results could help in designing appropriate rolling regimes and providing better instructions to roller operators. The results reflect a step forward in diminishing the gap between field and laboratory compaction outcomes. Further research effort will be put into verifying the results under in-situ conditions. Overall, the results are a valuable step in the quest for improved process and quality control.

ACKNOWLEDGEMENTS

This research would not have been possible without the cooperation provided within the ASPARi network. We would especially like to acknowledge the eleven contractors for the opportunity to conduct research at their construction sites and in their laboratories.

REFERENCES

[1] Miller, S.R. Hot mix asphalt construction, towards a more professional approach. Construction management and engineering, Enschede, The Netherlands, University of Twente. PhD Thesis, 2010.

[2] Bouvet, D., Froumentin, M., Garcia, G. "A real-time localization system for compactors." Automation in construction 10 (2001) 417–428.

[3] Gallivan, V.L. Chang, G.K. Horan, R.D. "Practical implementation of intelligent compaction technology in hot mix asphalt pavements." Proceedings of the Association of asphalt paving technologists 2011. March 27–30, 2011, Tampa, Florida.

[4] Krishnamurthy, B.K., Tserng, H., Schmitt, R.L., Russel, J.S., Bahia, H.U., Hanna, A.S. "AutoPave: towards an automated paving system for asphalt pavement compaction operations." Automation in construction 8 (1998) 165–180.

[5] Asphalt-Institute. MS 4—The Asphalt Handbook. Lexington, USA, The Asphalt Institute, 2007.
[6] Elhalim, A., Phang, W., Haas, R. "Unwanted Legacy of Asphalt Pavement Compaction." Journal of Transportation Engineering-Asce 119(6): 914–932, 1993.
[7] Chadbourn, B.A., Newcomb, D.E., Voller, V.R., Desombre, R.A., Luoma, J.A., en Timm, D.H. "An asphalt paving tool for adverse conditions." Minnesota Dept. of Transportation Final Report MN/RC-1998, 18.
[8] Daines, M.E. Cooling time of bituminous layers and time available for their compaction. Transport and road research laboratory report, 4, 1985.
[9] Delgadillo, R. and Bahia, H. "Effects of temperature and pressure on Hot Mix Asphalt Compaction: Field and laboratory Study." Journal of materials in civil engineering, Society of civil engineers, vol. 20, no. 6, pp. 440–448, 2008.
[10] Kari. W.J. "Mix properties as they affect compaction. Asphalt paving technology", Proceedings: Association of Asphalt Paving Technologists Technical Sessions 36. 295–309, 1967.
[11] Kassem, E., Masad, E., Chowdhury, A., Claros, G. "Influence of Field Compaction Pattern on Asphalt Pavement Uniformity." Proceedings of the Association of asphalt paving technologists 2008. April 27–30, 2008, Philadelphia, Pennsylvania.
[12] Timm, D.H., Voller, V.R., Lee, E., en Harvey, J. "Calcool: A multi-layer Asphalt Pavement Cooling Tool for Temperature Prediction During Construction." International Journal of Pavement Engineering 23: 169–185, 2010.
[13] Floss, R. Compaction Technology in Earthwork and Highway and Transportation Engineering. Specialist book published by BOMAG GmbH & Co. OHG, Germany, 1st edition 2001.
[14] Schmitt, R.L., Johnson, C.M., Bahia, H.U., Hanz, A. "Effects of temperature and compaction effort on field and lab densification of HMA." Proceedings of the Association of asphalt paving technologists 2009. March 15–18, 2009, Minneapolis, Minnesota.
[15] Stroup-Gardiner, M., Law, M., Nesmith, C. "Using infrared thermography to detect and measure segregation in hot mix asphalt pavements." International journal of pavement engineering, 2000, Vol. 1(4), pp. 265–284.
[16] ter Huerne, H.L., Compaction of asphalt road pavements using finite elements and critical state theory. Construction Management and Engineering. Enschede, University of Twente. PhD Thesis, 2004.
[17] Willoughby, K.A. "Construction-related variability in pavement mat density due to temperature differentials." Transportation Research Record No. 1849, pages 166–173, 2003.
[18] Commuri, S. and M. Zaman. "A novel neural Network-based asphalt compaction analyzer." The International Journal of Pavement Engineering 9(3): 177–188, 2008.
[19] Alexander, M.L. and C.S. Hughes. "Compaction of asphalt pavement." Transportation Research Board National Research Council. Washington, D.C., 1989.
[20] van Dee, R. Modelling of the compaction of asphalt layers: A survey into the influence of various factors on the compaction of asphalt layers in practice. Delft University of technology, MSc thesis, Delft 1999.
[21] Corlew, J.S. and P.S. Dickson. "Methods for calculating temperature profiles of hot-mix asphalt concrete as related to the construction of asphalt pavements." Proceedings: Association of Asphalt Paving Technologists. Technical session 37: 101–140, 1968.
[22] Jordan, P.G. & Thomas, M.E. Prediction of cooling curves for hot-mix paving materials by a computer program. Transport and road research laboratory report, 1976.
[23] Luoma, J.A., Allen, B., Voller, V.R., Newcomb, D.E. "Modeling of heat transfer during asphalt paving." Numerical methods in thermal problems, 6 2, 1125–1135, 1995.
[24] Decker, D.S. "State-of-the-Practice for Cold-Weather Compaction of Hot-Mix Asphalt Pavements." Transportation Research E-Circular, E-C105, Washington, D.C., pages 27–33, 2006.
[25] Bahia, H.U., Fahim, A., Nam, K. "Prediction of compaction temperatures using binder rheology." Transportation Research E-Circular, E-C105, Washington, D.C., 2006, pages 3–17.
[26] Bijleveld, F.R. Temperatuur- en tijdsvensters verdichten asfaltmengsels op basis van mechanische eigenschappen—Temperature and time windows for the compaction of asphalt mixtures based on mechanical properties. Construction Management and Engineering. Enschede, The Netherlands, University of Twente. M.Sc. thesis, 2010.
[27] Muniandy, R., Jakarni, F.M., Hassim, S., Mahmud, A.R. "Development of criteria for slab compaction of laboratory roller compactor Turamesin." American Journal of applied sciences 4 11: 908–911, 2007.
[28] Paffrath, T.D., Beckedahl, H.J., Nussbaum, J.M., Martus, M. "Laboratory Production of Large-Sized Asphalt Specimens." Proceedings of the Eurasphalt & Eurobitume congress 2012, Instanbul, Turkey.

[29] Renken, P. Verdichtung von walzasphalt im laboratorium und im Felde—Compaction of asphalt in the laboratory and in practice. TU Braunschweig, Institüt für Strassenwesen, PhD thesis, Braunschweig, 2002.
[30] Visscher J. de, Maeck, J, Vanelstraete, A. "The permanent deformation law of asphalt mixtures: investigation of the effect of mix composition and material properties" Proceedings of the International Society in Asphalt Pavements conference. Quebec, 2006.
[31] Mollenhauer, K. "Standard compaction procedure." Workshop RILEM, Rhodos, 2009.
[32] Faheem, A.F., Kamle, N., and Bahia, H.U. "Compaction and tenderness of HMA Mixtures: A laboratory study", Proceedings of the transportation research board 86th Annual Meeting, Washington, D.C., 2007.

Perpetual pavements

This page intentionally left blank

Asphalt Pavements – Kim (Ed)
© 2014 Taylor & Francis Group, London, ISBN 978-1-138-02693-3

Oxidative aging of long-life asphalt pavements in Hong Kong

Yuhong Wang, Yong Wen & Kecheng Zhao
Department of Civil and Environmental Engineering, HK Polytechnic University, Hung Hom, Hong Kong

Jianming Wei
State Key Laboratory of Heavy Oil Processing, China University of Petroleum (East China), Qingdao, Shandong, China

Hainian Wang
Highway Engineering Department, Chang'an University, Xi'an, Shanxi, China

Alvin S.T. Wong
Research and Design Division, Highways Department, Hong Kong SAR

ABSTRACT: Hong Kong (HK) is currently developing a new flexible pavement design standard with the goal of building long-life pavement in the future. Long-life pavement is expected to last for at least 40 years without major structural damage. The design of long-life flexible pavement has been traditionally focused on structural design, in particular the control of tensile strain at the bottom of Asphalt Concrete (AC) layer and compressive strain at the top of subgrade. Changes of fundamental asphalt binder properties and performance due to its oxidative aging throughout the pavement structure often receive little attention. However, understanding the evolution of asphalt binder properties is critically important for long-life pavement design. It not only affects the load-induced mechanistic responses of the flexible pavement system, but also the fracture and cracking potentials of the binder *per se*. In this study, AC samples were taken from a heavily trafficked road in HK that has been in service for 36 years with only being periodically resurfaced. The cores were cut into six slices and asphalt binders were extracted and recovered for the analysis of their aging characteristics by using Gel Permeation Chromatography (GPC), Fourier Transform Infrared spectroscopy (FTIR), and Dynamic Shear Rheometer (DSR). The analysis results indicate that oxidative aging penetrates deep into the asphalt pavement layers, but there are variations in the extent of aging. In general, asphalt binder is severely aged at different depths, but at certain locations it exhibits less aging. The causes of the aging variations need to be further researched.

Keywords: long-life pavement, oxidative aging, Gel Permeation Chromatography, Fourier Transform Infrared spectroscopy, Dynamic Shear Rheometer

1 INTRODUCTION

From highway agencies' perspectives, the goal of road planning, construction, and maintenance is to maximize the value of road investment. This is often equivalent to minimizing the total amount of the agencies' construction and maintenance costs and road travelers' usage costs in the life-cycle of the planned road. For heavily trafficked roads, the social costs of road closure for reconstruction are so high that a long-life pavement is often desired. For instance, in the United Kingdom (UK), 40 years of pavement design life are believed to be the most economical for truck roads including motorways [1]. These pavements, referred to as long-life pavements, are constructed with thick bound layers built upon good foundations

and are expected to maintain their structural integrity in 40 years if the surface distress can be timely treated [1]. In the United States (US), a similar concept is placed under the name of "perpetual pavement" [2], which is expected to last longer than 50 years without structural rehabilitation or reconstruction. Hong Kong (HK) is not only the most densely populated city in the world, but also heavily relies on logistics and transportation as one of its key industries. Road closure for reconstruction always incurs significant economic, social and environmental impacts. Therefore, the highway agency in HK is pursuing a long-life pavement design strategy for new road construction and upgrading its existing major roads to long-life capacity when opportunities for rehabilitation or reconstruction arise.

The development of long-life pavement has been traditionally focused on structural design, particularly on controlling tensile strain at the bottom of Asphalt Concrete (AC) layer and compressive strain at the top of subgrade [3,4]. It is believed that if the two strains are small enough, cumulative fatigue and permanent deformation damage will not likely occur at the bottom of AC layer and at the top of subgrade layer, respectively. Monismith and Long [4] further suggest that tensile strain at the bottom of AC layer be no greater than 60 με and the vertical strain at the top of subgrade be limited to 200 με. A survey conducted by New Mexico Department of Transportation (DOT) in the US suggest that 70 με limiting tensile strain is the most commonly used value among the state DOTs for perpetual pavement design [5]. If the magnitudes and configurations of traffic loads, climate conditions, and material properties are provided, a proper combination of thickness and mixture types can be designed to meet the limiting tensile or compressive strain requirements based on well-established mechanistic analysis procedures. For instance, the design can be conveniently carried out by following the procedure in the Mechanistic-Empirical Pavement Design Guide (ME-PDG) [6].

However, as an organic material, bitumen in AC will likely undergo significant changes during its long service life. The most noticeable change is oxidative aging. As bitumen ages, its stiffness will increase and its ductility will decrease, making it susceptible to embrittlement and cracking. Although such changes are closely related to the mechanistic behaviors and performance of bituminous mixture, they often receive little attention in long-life pavement design. Particularly missing appear to be the following aspects:

- To what extent will the asphalt binder be oxidatively aged throughout the AC layers?
- How will the oxidative aging change the properties and performance of asphalt binder?
- How will the property changes of the binder affect the mechanistic property change of the mixture?

Oxidative aging causes asphalt hardening and concurrently increases the stiffness of AC. Although this may be beneficial to control permanent deformation, age hardening will cause pavement embrittlement, which leads to the development of distresses including cracking, fracture, or raveling. Early studies suggest that asphalt pavement aging primarily occurs at pavement surface (about one or one-half inches), below which there is little change in oxidative aging [7]. Using 134 data points from three roads of 43 test sections, Mirza and Witczak [8] demonstrated a clear decay of aging with AC pavement depth. For instance, the changes in relative viscosity (ratio of viscosity of the hardened asphalt to the original asphalt viscosity) at 25 °C decreases from 14.39 at the surface to 5.54 at the lowest layer (38–44 mm), and the changes in relative viscosity at 135 °C decrease from 2.25 at the surface to 1.56 at a lower layer (19–25.4 mm). These findings are widely cited and have significant impacts on academic research and engineering practices. They are also adopted in the global aging model of the Mechanistic-Empirical Pavement Design Guide (ME-PDG). However, a recent study argues that asphalt aging may not be only limited to pavement surface [9]. Using asphalt pavement cores from Texas and Minnesota, Al-Azri et al [9] found that oxidative aging "relentless" penetrates into deeper asphalt layers. However, some of the cores used in the study were obtained from the Long-Term Pavement Performance (LTPP) material reference library in Texas. The cores were stored in warehouse without air conditioning for more than 10 years. "Further aging" of the extracted cores may likely occur. In a more recent Ph.D. study, Han [10], supervised by Glover, reported aging of asphalt extracted from seven sites. The study developed an oxidation rate model and compared the predicted oxidation rate with measured bulk

oxidation rate from the sample cores. However, the variation of oxidation rate with pavement depth is not reported, and the study recommended that additional data to be included for model calibration and validation.

The change of asphalt binder aging with time and pavement depth has great implications on long-life pavements. If asphalt binder indeed ages very little at greater depth, i.e., beyond 40 mm, highway agencies can always periodically mill and resurface the wearing course of the long-life pavement and preserve the load-carrying base layers. Thus, the goal of "long life" or "perpetual" can be achieved. However, the application of the findings from the existing aging studies to long-life asphalt pavement suffers three major drawbacks. First, the reported asphalt pavements in the existing studies were typically not "old" enough to be even close to the "long-life" pavement standard. The pavements included in the study by Coons and Wrights [7] ranged from 1 to 13 years, and the oldest pavement cited in their paper was 19 years. Second, asphalt pavements in the existing studies were not as thick as that typically designed for long-life pavements. In the Mirza and Witczak [8] study, the maximum pavement depth examined was up to 44 mm. It is not uncommon that the total AC depth of a long-life pavement exceeds 250 mm. In the study reported by Han [10], only one thick pavement was used, but the cores taken from the project were only 1–2 years old. Third, the cores used in the existing studies were limited to a few locations primarily from Texas, with a few from Minnesota. As a result, the effects of intense precipitation and high humidity combined with long period of high temperature are not included. Therefore, the findings may not well represent long-life pavement behaviors in a subtropical climate such as HK.

2 RESEARCH BACKGROUND AND METHODOLOGY

2.1 *Research background*

This paper is based on a study to analyze sample cores taken from Tuen Mun Road in HK. Tuen Mun Road, with a total of six lanes, is one of the most heavily trafficked expressways in HK. The first phase (3 lanes in eastbound) of the road was open to traffic in 1977, while the second phase was open a few years later. The AC layers of the road consist of 40 mm Wearing Course (WC), 60 mm Base Course (BC), and 150 mm roadbase (RB). Since the completion of the road, several resurfacings have been performed in various locations and the most recent resurfacing on the tested section was conducted in November, 2006, but the BC and RB have never been replaced. Therefore, the asphalt materials in BC and RB are 36 years old. The general conditions of the road at a distressed section and a non-distressed section are shown in Figure 1. As can be seen, except for some fatigue cracks of low to medium severity in the wheelpath of the first section, the overall conditions of the road are reasonably good. It is confident that the road can last for another 4 years to literally meet the "long-life" pavement definition [11]. Therefore, this road was selected to study the characteristics of binder aging. It is expected that the findings will help improve future long-life pavement design, construction, and maintenance practices.

Figure 1. General conditions of Tuen Mun Rd (left: distressed section, right: non-distressed section).

A total of 36 sample cores were initially taken from this road. The majority of the cores were in intact conditions, as shown in Figure 2a and b. These cores were stored in an indoor environment for about one year before being tested for Indirect Tensile Stiffness Modulus (ITSM), Indirect Tensile Fatigue (IDF), binder extraction and size extraction chromatograph (SEC, or Gel Permeation Chromatography, GPC), and dynamic modulus test using Simple Performance Tester (SPT). In performing the tests, we found that the cores exhibit much greater stiffness than todays' asphalt mixtures that use the same mix design. In addition, we found that the proportion of large molecules in RB is greater than that in BC or WC. It appears that age hardening has a great impact on the conditions of the 36 year old samples. To avoid the possible impact of further aging in air on the bottom of the cores, which might have been always exposed in a low oxygen environment in the field, a second batch of six cores were taken from the road (Fig. 2c). Meticulous efforts were taken to reduce the chance of the samples to further contact air during sample preparation and binder extraction. The analysis below is primarily based on four samples from the second batch of cores.

2.2 *Bitumen sample preparation*

Immediately after the 250 mm cores were taken from the road, they were placed in glass jars that were subsequently filled with nitrogen gas and sealed to preclude further contact with air (Fig. 3c). These cores were then cut into six slices, including the OGFC layer, WC, BC, and

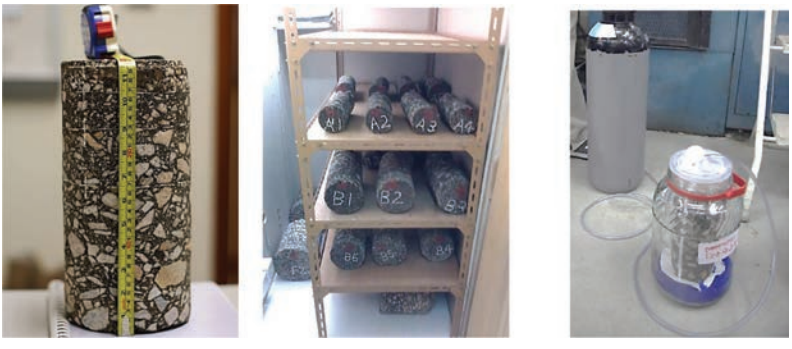

Figure 2. Photos of samples cores used in this study. 2a. Conditions of cores. 2b. Cores stored in the lab. 2c. Core stored in a glass jar filled with nitrogen.

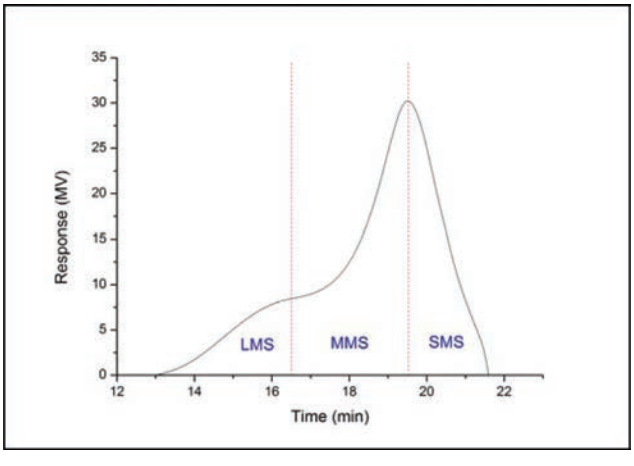

Figure 3. Typical GPC chromatogram.

three slices of RB. The OGFC slice was not used for further analysis. The separated cores were placed back into the glass jars with silica gel to absorb residual water used in the cutting process, refilled with nitrogen, tightly sealed, and stored in an air-conditioned environment.

After the majority of water from the sliced cores was removed (by observing the color change of silicon gels), they were taken out from the glass jars and broken into small pieces by hammer. Bitumen from these small pieces of samples was extracted by using an extraction unit bowl according to the ASTM standard D2171/D2172M-11. The solvent used for extraction was dichloromethane. To ensure that the fine particles were thoroughly removed, the extracted bitumen solution was further clarified in a sample tube centrifuge machine according to the European Standard EN 12697-3:2005. During the centrifuging process, a small amount of silica gel passing a 0.063 mm sieve was added to the solution to further remove the residual water. Asphalt binder was recovered from the clarified solution by using a rotary evaporator by following the European Standard EN 12697-3:2005. To ensure that the solvent was thoroughly removed during the rotary evaporation, the extracted bitumen was examined by Fourier Transform Infrared Spectroscopy (FTIR). A lack of peak at the infrared band of 1265 cm^{-1} in the FTIR spectrum indicates the total evaporation of the solvent. After the bitumen was recovered from the rotary evaporation, it was stored in a jar, refilled with nitrogen, and placed in refrigerator for further analysis.

2.3 *Test methods*

The focus of this study was to test and evaluate the extent of aging of asphalt binder extracted at different depth of the asphalt pavement. The chemical components of these specimens were analyzed by using the Attenuated Total Refraction (ATR) mode of FTIR and GPC. The rheological properties of the specimens were tested by using a Dynamic Shear Rheometer (DSR). FTIR and GPC testes were tested on four groups, each including three slices of RB, BC and WC, whereas DSR tests were performed on one group of the specimens.

In measuring FTIR spectra, scanning was performed in the middle infrared region (MIR, 400–4000 cm^{-1}). Duplicate measurements were conducted on each binder specimen to ensure the consistency of the measurements. However, only one spectrum was chosen from each specimen for further analysis because the duplicate measurements match each other very well.

Waters GPC equipment with 1515 isocratic HPLC pump and 2414 refractometer detector was used in the study for chromatographic analysis. A series of two columns (Styragel Column, HR3, 5 μm, 7.8 mm × 300 mm; Styragel Column, HR4, 5 μm, 7.8 mm × 300 mm) were used for detecting the molecular weight of 1000 to 500000. The mobile phase was tetrahydrofuran (THF) and the flow rate was maintained at 1 ml/min. About 100 mg samples was dissolved into 10 ml THF at room temperature and filtered through a 0.22 m membrane prior to injection. Each sample of 25 μl was injected into the system. The test took twenty-five minutes to complete and each test was repeated twice.

DSR tests were conducted under the controlled stress model and the strain levels were chosen to be in the linear viscoelastic range (0.05% at 40 °C or lower and 0.1% at 46 °C or higher). Both 8 mm plate with 2 mm gap, 25 mm plate with 1 mm gap, and 25 mm plate with 0.5 mm gap were attempted. The data used for constructing master curves was obtained by using the 8 mm plate with 2 mm gap. The temperature of the tests ranges from 10 °C to 70 °C with an equal increase of 12 °C, and frequency ranges from 0.1 Hz to 30 Hz. Due to the size limit of the paper, the master curves are not presented.

3 RESULTS AND DISCUSSION

3.1 *GPC test results*

A typical chromatogram of the extracted asphalt binder is illustrated in Figure 3. The chromatograms are equally divided into 13 slices according to the retention time [12]. The slices from 1 to 5 correspond to asphalt constituents of Large Molecular Size (LMS), the slices

from 6 to 9 correspond to Medium Molecular Size (MMS), and slices from 10 to 13 correspond to small molecular size [12]. It was concluded by several studies that the proportions of LMS correlate with the extent of aging of the binders [13–15].

The percent areas of the chromatograms corresponding to the LMS, MMS, and SMS of the different samples are calculated and shown in Table 1. The percentages reveal the relative proportions of molecules of different sizes.

The paired t-test was used to compare the average difference between the asphalt binder extracted from RB3 and that from BC and RB1. Pairwise comparisons were made for binders extracted from the same core. The test results are shown in Table 2. The results show that, on average, that the bottom lifts have a higher percentage of large molecules. However, the test results are not statistically significant. There is no strong evidence that asphalts in BC or RB1 were aged less than that in RB3.

3.2 *Analysis of FTIR spectra*

Infrared spectrometry has been widely used to study asphalt oxidation [e.g., 16–19]. The carbonyl functional group (C = O) is shown to be the major product of asphalt oxidation [16–19]. For the same asphalt, carbonyl content grows linearly with oxygen uptake, although the growth rate may vary between different asphalt [20]. A commonly used indicator of oxidative

Table 1. Percentage of LMS, MMS, and SMS of asphalt binder from various layers of different samples (*removed data due to abnormal results).

Sample no.	Sample location	Percentage (%)		
		LMS	MMS	SMS
C1	WC	10.9	49.7	39.3
C1	BC	15.6	49.2	35.2
C1	RB1	15.9	51.2	32.9
C1	RB2	17.4	49.9	32.8
C1	RB3	17.2	49.6	33.1
C2	WC	10.2	48.0	41.8
C2	BC	15.8	48.6	35.6
C2	RB1	–*	–	–
C2	RB2	14.9	49.5	35.6
C2	RB3	15.0	49.6	35.4
C5	WC	11.8	48.5	39.7
C5	BC	15.0	45.9	39.2
C5	RB1	16.4	49.6	35.9
C5	RB2	16.2	48.7	35.0
C5	RB3	18.7	49.1	32.2
C6	WC	12.4	48.1	39.5
C6	BC	15.1	46.7	38.3
C6	RB1	17.1	48.4	34.5
C6	RB2	18.4	48.7	32.9
C6	RB3	16.4	51.6	31.9

Table 2. The results of paired-t test between RB3 and the other two middle layers.

Difference	Average difference	Std. dev.	t-value	p-value (tail)
RB3-BC	1.45	1.841195	1.5751	>0.05
RB3-RB1	0.967	1.5275	1.0961	>0.05

aging is the "carbonyl area," which is the integrated area under the absorbance peaks of IR spectrum from 1650 cm^{-1} to1820 cm^{-1}. Two indexes were used in this study to characterize the extent of oxidative aging based on FTIR results: the ratio between the absorbance peak height at about 1695 cm^{-1} (C = O band) to that at about 1455 cm^{-1} (saturated C-C band) [21] and the ratio between absorbance peak areas at these two peaks, as illustrated in Figure 4.

The ratios between the absorbance peak height at about 1695 cm^{-1} and that at about 1455 cm^{-1} and the ratios between absorbance peak areas at these two peaks were calculated and shown in Figure 5 and Figure 6, respectively.

Several observations can be made from Figures 5 and 6: 1) the oxidative aging of the asphalt in WC is the least severe, 2) the oxidative aging of asphalt in BC appears to be less severe than those in RB lifts, 3) the absorbance peak height ratios and peak area ratios are generally consistent. The paired-t tests of the absorbance peak area ratios are shown in Table 3.

Table 3 shows that there are no statistically significant differences in FTIR absorbance peak area ratios between the bottom lift and the BC layer, but the difference between the

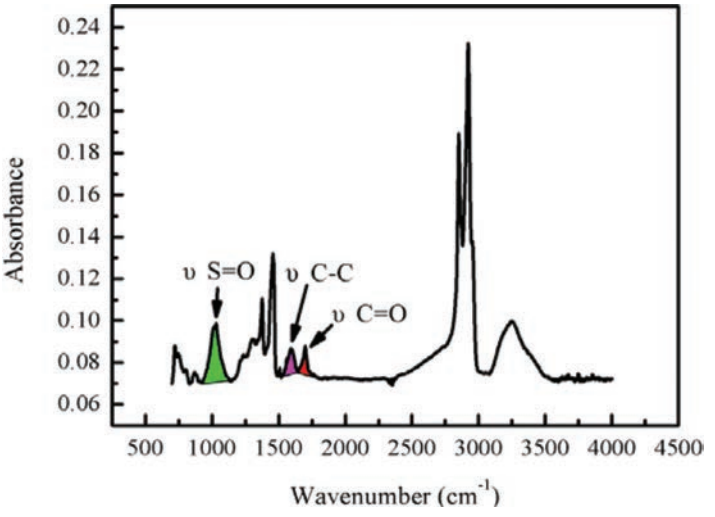

Figure 4. Illustration of S=O, C–C, and C=O bands from one of the specimens.

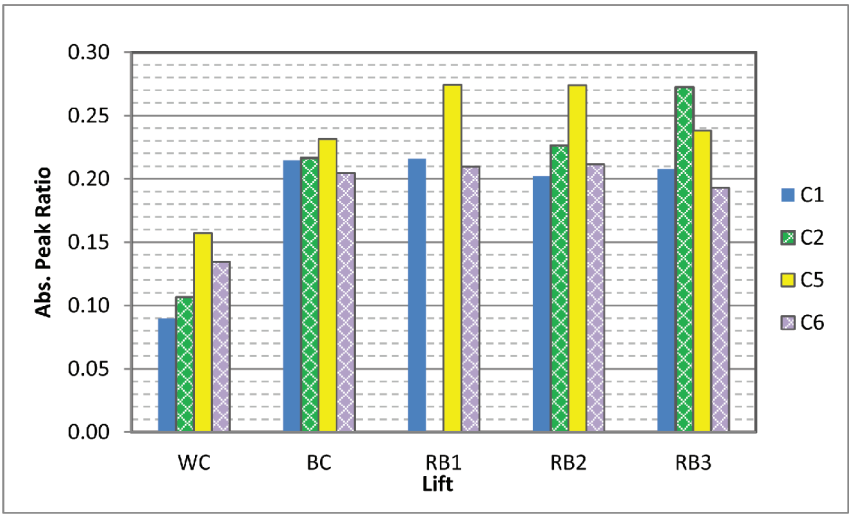

Figure 5. Abs. peak height ratios of the different lifts of the four samples.

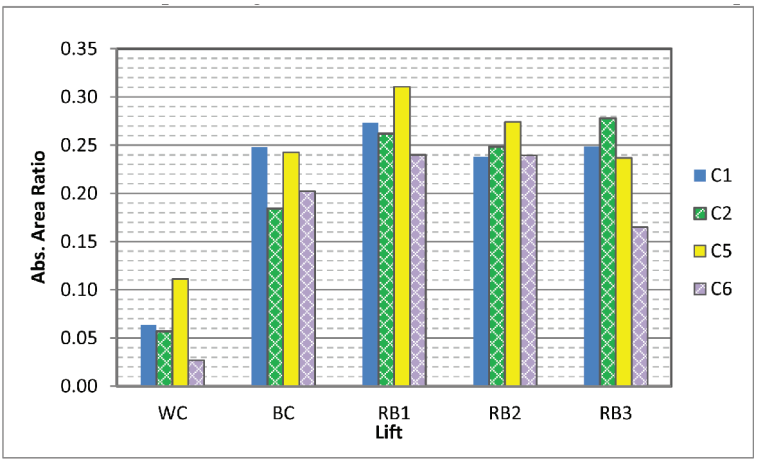

Figure 6. Abs. peak area ratios of the different lifts of the four samples.

Table 3. Pairwise comparisons of the absorbance peak area ratios of the bottom lift (RB3) and two middle lifts (BC and RB1).

Pairwise comparison	Absorbance peak area ratios			
	Avg. Dif.	Std. Dev.	t-value	p-value (tail)
RB3-BC	0.0128	0.0563	0.5551	>0.05
RB3-RB1	–0.0579	0.0287	–3.4975	<0.05

Table 4. DSR parameters used to calculate DSR function and ductility.

Lift	δ	G* (MPa)	G′ (MPa)	η′ (MPa)	DSR func. (MPa)	Derived duc. (cm)
WC	59.66	693600	350378	59860	0.00102544	4.75
BC	44.63	1009747	718639	70933	0.00364036	2.72
RB1	36.43	2833500	2279879	168252	0.01544660	1.44
RB2	38.69	1829833	1428275	114382	0.00891736	1.83
RB3	38.86	1601588	1247127	100487	0.00773897	1.95

bottom lift (RB3) and top lift (RB1) of the same RB layer is significant. It appears that the asphalt at the top of the RB layer aged more.

3.3 *Reological properties of recovered binder*

The recovered binders from one of the samples (sample no. C5) were tested for reological properties by a DSR. It has been long recognized that the durability of asphalt binder is well related to its ductility, particular ductility at the temperature level of about 15 °C and with an elongation rate of 1 cm/min [22–24]. Ruan et al. [25] found that if an asphalt binder's ductility is less than 10 cm, the ductility tested at the above temperature and loading condition correlates well to a rheological parameter G′/(η′/G′), namely DSR function. The η′ and G′ are measured at 44.7 °C and 10 rad/s using a DSR and are converted to those at 15 °C and 0.005 rad/s. It is further recommended the use of ductility of about 3 cm at 15 °C, 1 cm/min (with DSR function value > 0.003 MPa/s) as the threshold for binder failure and ductility of 5 cm under the same condition (DSR function value > 0.0009 MPa/s) as the threshold for pavement cracking [25]. The DSR function values, estimated ductility, and

other relevant parameters for sample C5 are calculated and shown in Table 4. The data show that the derived ductility values at 15 °C and 1 cm/min of all the RB binders have reached "failure" status, whereas the ductility of the WC binder researches to a "critical" condition. The data indicates that binders in the three lifts of the RB are all severely aged, and extent of aging is slightly higher than that in BC.

4 SUMMARY AND CONCLUSION

Four sample cores were taken from wheelpath and non-wheelpath of one of the most heavily trafficked roads in HK that have served for 36 years without reconstruction or rehabilitation. Each sample was cut into different slices to study the variation of binder aging along the pavement depth. Meticulous efforts were taken to prevent further aging of asphalt binder during coring, storage, and binder extraction. The extracted binders were tested by GPC, FTIR, and DSR. The GPC test results show that the percentage of large molecules of the asphalts in the bottom of RB layer and in the BC layer is not significantly different. The absorbance peak height ratios between the C = O and C–C band, however, show that the asphalt in the bottom lift of the RB layer aged more than that in the top lift of the RB layer. DSR tests on one of the samples show that the derived ductility values of the three binders from RB are lower than that from BC, which is lower than that from WC. This implies that the extent of aging does not necessarily decrease with pavement depth. These results indicate that oxidative aging penetrates deep into the long-life AC layers. More samples are needed in the future to make a more decisive conclusion. In addition, a further investigation of the factors affecting the aging variations may assist the improvement of design, construction, and maintenance practices to prevent the detrimental effects of oxidative aging shortening the longevity of the long-life asphalt pavement.

REFERENCES

[1] UK Highways Agency, Department for Transport, 2013. Design Manual for Roads and Bridges (DMRB) (Vol. 7: Pavement Design and Maintenance).

[2] APA (Asphalt Pavement Alliance). "Perpetual Pavements: A Synthesis" Asphalt Pavement Alliance. 2002.

[3] Charles J. Glover, Richard R. Davison, Chris H. Domke, Yonghong Ruan, Pramitha Juristyarini, Daniel B. Knorr, Sung H. Jung. Development of a new method for assessing asphalt binder durability with field validation. FHWA/TX-05/1872-2. 2005.

[4] Monismith C.L., and F Long. Overlay Design for Cracked and Seated Portland Cement Concrete (PCC) Pavement—Interstate Route 710, Technical Memorandum TM UCB PRC 99-3, Pavement Research Center, Institute for Transportation Studies, University of California, Berkeley. 1999.

[5] Tarefder R.A. and D. Bateman. Future Design of Perpetual Pavements for New Mexico. Research Report No. NM08MSC-01, University of New Mexico, Albuquerque, NM. 2009.

[6] ARA. Guide for Mechanistic-Empirical Design of New and Rehabilitated Pavement Structures. ARA, Inc., Champaign, Illinois. 2004.

[7] Coons R.F. and Wright P.H. An investigation of the hardening of asphalt recovered from pavement of various ages. Proceedings, The Association of Asphalt Paving Technologists, Vol. 37, pp. 510–522. 1968.

[8] Mirza M.W. and Witczak M.W. Development of a global aging system for short and long term aging of asphalt cements. Journal of the Association of Asphalt Paving Technologists, Vol. 64, pp. 393–430. 1995.

[9] Al-Azri, N.A., S.H. Jung, K.M. Lunsford, A. Ferry, J.A. Bullin, R.R. Davison, and C.J. Glover. Binder Oxidative Aging in Texas Pavements: Hardening Rates, Hardening Susceptibilities, and the Impact of Pavement Depth. *Trans. Res. Rec*. 2006.

[10] Han R. Improvement to a transport model of asphalt binder oxidation in pavements: pavement temperature modeling, oxygen diffusivity in asphalt binders and mastics, and pavement air void characterization, Ph.D. Dissertation, Texas A&M University, Texas. 2011.

[11] Harvey, J., Monismith, C., Horonjeff, R., Bejarano, M., Tsai, B.W. and V. Kannekanti. Long-Life AC Pavements: A Discussion of Design and Construction Criteria Based on California Experience, International Symposium on Design and Construction of Long Lasting Asphalt Pavements: Proceedings, National Center for Asphalt Technology, pp. 285–333. 2004.
[12] Kim, H., Lee, S., Amirkhanian, S., and Jeong, K. Quantification of Oxidative Aging of Polymer-Modified Asphalt Mixes Made with Warm Mix Technologies. *J. Mater. Civ. Eng.,* 25(1), pp. 1–8. 2012.
[13] Al-Abdul Wahhab, H.I., Asi, I.M., Ali, F.M., and Al-Dubabi, I.A. Prediction of asphalt rheological properties using HP-GPC, *J. Mater.Civ. Eng.,* 11(1), pp. 6–14. 1999.
[14] Jennings, P.W. High pressure liquid chromatography as a method of measuring asphalt composition, FHWA-MT-7930, U.S.Dept. of Transportation, Washington, DC. 1980.
[15] Kim, K.W., Kim, K.A., Doh, Y.S., and Amirkhanian, S. Estimation of RAP's binder viscosity using GPC without binder recovery, *J. Mater. Civ. Eng.,* 18(4), pp. 561–567. 2006b.
[16] Lee, D.Y., and R.J. Huang. (1973) Weathering of Asphalts as Characterized by Infrared Multiple Internal Reflection Spectra. *Anal. Chem.*, Vol. 46, p. 2242.
[17] Martin, K.L., R.R. Davison, C.J. Glover, and J.A. Bullin. (1990) Asphalt Aging in Texas Roads and Test Sections. Transp. Res. Rec., Vol. 1269, pp. 9–19.
[18] Lau, C.K., K.M. Lunsford, C.J. Glover, R.R. Davison, and J.A. Bullin. (1992) Reaction Rates and Hardening Susceptibilities as Determined from POV Aging of Asphalts. Transp. Res. Rec., Vol. 1342, pp. 50–57.
[19] Petersen, J.C., J.F. Branthaver, R.E. Robertson, P.M. Harnsberger, J.J. Duvall, and E.K. Ensley. (1993) Effects of Physicochemical Factors on Asphalt Oxidation Kinetics. Transp. Res. Rec., Vol. 1391, p. 1.
[20] Liu, M. (1996) The Effects of Asphalt Fractional Composition on Properties. Ph.D. Dissertation, Texas A&M University, College Station, TX.
[21] Ioan Negulescu, Louay Mohamm, William Daly, Chris Abadie, Rafael Cueto, Codrin Daranga and Ionela Glover, Chemical and Rheological Characterization of Wet and Dry Aging of SBS Copolymer Modified Asphalt Cements: Laboratory and Field Evaluation, UK Highways Agency, Department for Transport. 2013.
[22] Kandhal, P.S. Low-Temperature Ductility in Relation to Pavement Performance. In ASTM STP 628: Low-Temperature Properties of Bituminous Materials and Compacted Bituminous Paving Mixtures, C.R. Marek (Ed.), American Society for Testing and Materials, Philadelphia, PA, pp. 95–106. 1977.
[23] Kandhal, P.S., and W.C. Koehler. Significant Studies on Asphalt Durability: Pennsylvania Experience. Transp. Res. Rec., Vol. 999, pp. 41–50. 1984.
[24] Vallerga, B.A., and W.J. Halstead. The Effect of Field Aging on Fundamental Properties of Paving Asphalts. *Highway Research Record*, Vol. 361, pp. 71–92. 1971.
[25] Ruan, Y., Davison, R.R., and Glover, C.J. An Investigation of Asphalt Durability: Relationships between Ductility and Rheological Properties for Unmodified Asphalts, Petroleum Science and Technology, 21(1&2), pp. 231–254. 2003.

Asphalt Pavements – Kim (Ed)
© 2014 Taylor & Francis Group, London, ISBN 978-1-138-02693-3

Mechanistic responses in perpetual pavement

Daba Gedafa
University of North Dakota, Grand Forks, ND, USA

Mustaque Hossain
Kansas State University, Manhattan, KS, USA

Stefan Romanoschi
University of Texas-Arlington, Arlington, TX, USA

ABSTRACT: The Kansas Department of Transportation (KDOT) instrumented four perpetual pavement sections with stress and strain gauges to investigate the suitability of perpetual pavement concept. Pavement response measurements under known vehicle load at three different speeds were performed on seven occasions. Falling-Weight Deflectometer (FWD) first-sensor (center) deflections were normalized and corrected to 20 °C temperature based on measured mid-depth pavement temperature. FWD deflection data were also used to back-calculate layer moduli. Dynamic modulus tests were done in the laboratory. The results show no clear trend of an increase or a decrease in stress, strain, center deflection, and back-calculated AC layer modulus with time at the early age. There is a decrease in stress and strain with an increase in traffic speed. A change in speed from 64 km/h to 32 km/h has a higher impact on the stress and strain than a change in speed from 96 km/h to 64 km/h for thicker sections and vice versa for thinner section. The assumed endurance limit of 70 microstrain was exceeded in the thinnest section. The effect of high temperature on stress and strain is more pronounced at the lower traffic speed and on the thinner section. Laboratory dynamic modulus is higher than the back-calculated modulus.

Keywords: mechanistic responses; perpetual pavement; FWD deflection; back-calculated modulus; dynamic modulus; endurance limit

1 INTRODUCTION

Increasing traffic volumes and heavy vehicle loads have led to the accelerated wear of pavement structures resulting in increased maintenance and rehabilitation expenditures. These trends, along with the desire for a longer lasting transportation infrastructure, have resulted in the need for extending asphalt pavement life from 20 to 50 years or more. The asphalt paving industry responded to this need by introducing the concept of perpetual pavements, which has been gaining momentum nationally and internationally (1). Perpetual pavement concept leads to pavement structures that crack only at the surface, and would need repair only at the surface. This failure mode leads to a significant monetary savings for the repair, rehabilitation, and reconstruction of these pavements (2).

Structural capacities of flexible pavements are determined from surface deflection measurements. Measured deflections by Falling-Weight Deflectometer (FWD) must be corrected to a standard load and to a predefined environmental condition. The most critical environmental factor affecting deflections in flexible pavements is the temperature of the Asphalt Concrete (AC) layer (3–5). Thus pavement deflection data must be adjusted to a reference temperature (6).

The main objective of the study was to investigate the mechanistic responses i.e. stresses, strains, and surface deflections of the perpetual pavement sections in Kansas.

2 TEST SECTIONS

The Kansas Department of Transportation (KDOT) developed a field trial to investigate the suitability of perpetual pavement concept for Kansas highway pavements. The experiment involved design and construction of four thick pavement structures on a new alignment of US-75 near Sabetha, Kansas. The design layer thicknesses were close to those recommended by the KDOT's structural design method for flexible pavements based on the 1993 American Association of State Highway and Transportation Officials (AASHTO) Pavement Design Guide (7). The Kansas Asphalt Pavement Association (KAPA) provided the thickness designs for Sections 1, 2, and 3. Section 4 was designed by KDOT. Sections 1 and 3 have the same thickness, but a softer binder was used in the base asphalt mix (PG 64-22 instead of PG 70-22), and a richer and more ductile Superpave Mix (SM) was used in the bottom lift of the base layer for Section 3. Section 2 is the thinnest section (total HMA thickness of 288 mm). Table 1 shows the pavement structures (2).

The test sections were constructed on a fill and each is approximately 390 m long with approximately 150 m transition zones in between them. The embankment on all four pavement sections was brought to grade and the top 150 mm of the soil were stabilized with 6% hydrated lime (by weight). The project was completed and the sections were opened to traffic at the beginning of November 2005 (8). The sections carried about 850,000 Equivalent Single Axle Load (ESAL) until summer 2013.

To verify the approach of designing perpetual pavements based on an endurance strain limit, all four pavements were instrumented with gauges for measuring tensile strains at the bottom of the asphalt base layers. A Geokon stress cell was also placed at the center of the outside wheel path to measure the stress at the top of the lime-treated subgrade (8).

3 DATA COLLECTION

3.1 *Stress and strain*

Pavement response measurements under known vehicle load were performed on seven occasions between July 2005 and October 2007, before and after the pavement sections were opened to traffic. In each occasion, the same single-axle dump truck owned by KDOT was used as the loading vehicle. According to the Federal Highway Administration (FHWA) vehicle classification system, this truck is a class 5 vehicle. On each section, three sets of five

Table 1. Configuration of experimental sections (2).

Section	1	2	3	4
Acronym	KAPA (standard)	High reliability	KAPA 2 (modified)	KDOT
Surface course	40 mm, SM 9.5 A (PG70-28)			
Binder course	60 mm, SM 19 A (PG70-28)			
Base course	225 mm, SM 19 A (PG70-22)	188 mm, SM 19 A (PG64-22)	225 mm, SM 19 A (PG64-22)*	300 mm, SM 19 A (PG64-22)
Stabilized subgrade	150 mm, 6% hydrated lime mixed with the natural soil			
Natural subgrade	High plasticity clay (A-7-6)			

* Bottom 75 mm was designed at 3% air voids for a binder-rich layer (P_b = *6.0%, Design Air Voids = 3% ± 2%; VFA = 77%*).

Table 2. Weighted average of measured mid-depth pavement temperature.

Test date	Section 1	Section 2	Section 3	Section 4
9/29/2005	18.2	19.8	21.8	23.7
4/13/2006	19.1	24.4	39.6	31.5
8/1/2006	36.3	39.6	–	40.4
10/13/2006	9.4	9.3	11.6	12.5
5/1/2007	21.9	21.7	22.3	21.8

Note: Measurements were not performed on Section 3 on 8/1/2006.

passes of the loading vehicle were performed. Five passes each were performed with the truck passing at about 32 km/h (20 mph), 64 km/h (40 mph) and 96 km/h (60 mph), in order to determine the effect of vehicle speed on the pavement responses (8).

3.2 *Pavement temperature and deflection*

The thermocouple of a temperature gauge was lowered in the holes drilled in the Hot-Mix Asphalt (HMA) layers and filled with oil to measure the temperature at the mid-depth of each HMA layer. Oil was used as the heat transfer fluid to prevent evaporative cooling and freezing. Table 2 shows weighted average of measured mid-depth pavement temperature for each section. For all sessions, the temperature in the surface layers was the lowest in Section 1 and highest in Section 4. This happened since the response measurements were done on Sections 1 and 2 in the morning, on Section 3 around noon, and on Section 4 in the early afternoon (2).

FWD deflection data were collected at 15 m (50 ft) intervals. Measured mid-depth temperature was used to correct normalized FWD first-sensor (center) deflection data and back-calculated moduli to a standard temperature of 20°C (68°F).

4 DATA ANALYSIS

4.1 *Center deflection temperature correction*

Chen *et al.* (6) developed a universal temperature-correction equation for deflection of flexible pavements in Texas using an optimization technique based on the concept of minimum least-square difference between the target values and the predicted results. Eq. (1) has been used to correct normalized center deflection to 20°C temperature in this study.

$$W^1_{T_w} = W^1_{T_c}\left(\frac{1.0823^{-0.0098\times t}}{0.8631}\right) \times T_w^{0.8316} \times T_d^{-0.8419} \quad (1)$$

where $W^1_{T_w}$ = deflection adjusted to temperature T_w (mm); $W^1_{T_c}$ = deflection measured in the field (mm); t = thickness of the pavement (mm); T_d = mid-depth pavement temperature at time of FWD data collection (°C); and T_w = temperature to which deflection is adjusted (°C).

4.2 *Back-calculated modulus temperature correction*

Back-calculation was done using multilayered linear-elastic theory. The moduli of thin surface layers or layers "sandwiched" between the layers are usually difficult to obtain since surface deflections are often insensitive to changes in these layer moduli (9). In this study, all pavement sections were modeled as three-layer systems by combining all HMA layers into

one layer. EVERCALC was used to back-calculate layer moduli (10). It uses an iterative approach to find a set of moduli that would provide a calculated deflection basin closest to the measured deflection basin as characterized by the Root-Mean-Square (RMS) error (11).

Chen *et al.* (6) has developed Eq. (2) based on deflections from intact locations. Eq. (2) has been used to correct back-calculated modulus to 20 °C based on measured mid-depth pavement temperature.

$$E_{T_W} = \frac{E_{T_C}}{\left[\left(1.8T_W + 32\right)^{2.4462} \times \left(1.8T_C + 32\right)^{-2.4462}\right]} \quad (2)$$

where E_{T_W} = adjusted modulus of elasticity at T_W (MPa); E_{T_C} = measured modulus of elasticity at T_C (MPa); T_W = temperature to which the modulus of elasticity is adjusted (°C); and T_C = mid-depth temperature at the time of FWD data collection (°C).

4.3 *Laboratory dynamic modulus test*

Dynamic modulus samples were prepared from the mixtures mixed in the laboratory and compacted by the Superpave Gyratory Compactor (SGC). The 150-mm-diameter SGC-compacted samples were then cored in the laboratory to get 100-mm-diameter dynamic modulus test samples. Dynamic modulus tests were conducted using a Universal Testing Machine (UTM-25). Details have been published somewhere else (12).

5 RESULTS AND DISCUSSIONS

Because of installation issues, the strain results showed some inconsistency in Section 3. Thus, data from Section 3 were not used in this study.

5.1 *Stress and strains*

Stress and strain data from all seven measurement sessions have been analyzed in this study. The first two measurements were made before the sections were opened to traffic. All stress and strain data were corrected to 20 °C based on measured mid-depth pavement temperature. The result showed a decrease in stress and strain with an increase in traffic speed. The result also showed no clear trend as to whether there is an increase or a decrease in stress and strain with time. This may be due to the short time span over which data were collected.

Percent decrease in average stress on the top of subgrade, average longitudinal and transverse strain at the bottom of HMA due to an increase in speed from 32 km/h to 64 km/h and 64 km/h to 96 km/h, respectively, has been calculated. The results showed that a change in speed from 64 km/h to 32 km/h has a higher impact on the stress and strain than a change in speed from 96 km/h to 64 km/h for thicker sections (Sections 1 and 4) and vice versa for thinner section (Section 2). The results were not included for brevity.

The effect of traffic speed, offset (lateral wander), and age on stress and strain has been investigated in greater detail by using scatter plots. Results from Section 1 were not included for brevity.

5.1.1 *Stress on the top of subgrade*

Figure 1 shows stress on the top of lime-treated subgrade for Section 2. Sessions 3 and 5 data show consistency whereas session 6 shows more variation at all speeds. Offset (lateral wander) does not have significant effect on the magnitude of the stress. It is not clear whether there is an increase or a decrease in stress on the top of subgrade with time.

Figure 2 shows the stresses at the top of lime-treated subgrade for Section 4. Data from Sessions 3 and 5 are consistent and they are the smallest in magnitude. In general, data from Sessions 1 and 2 show more variation and higher in magnitude. It should be noted that

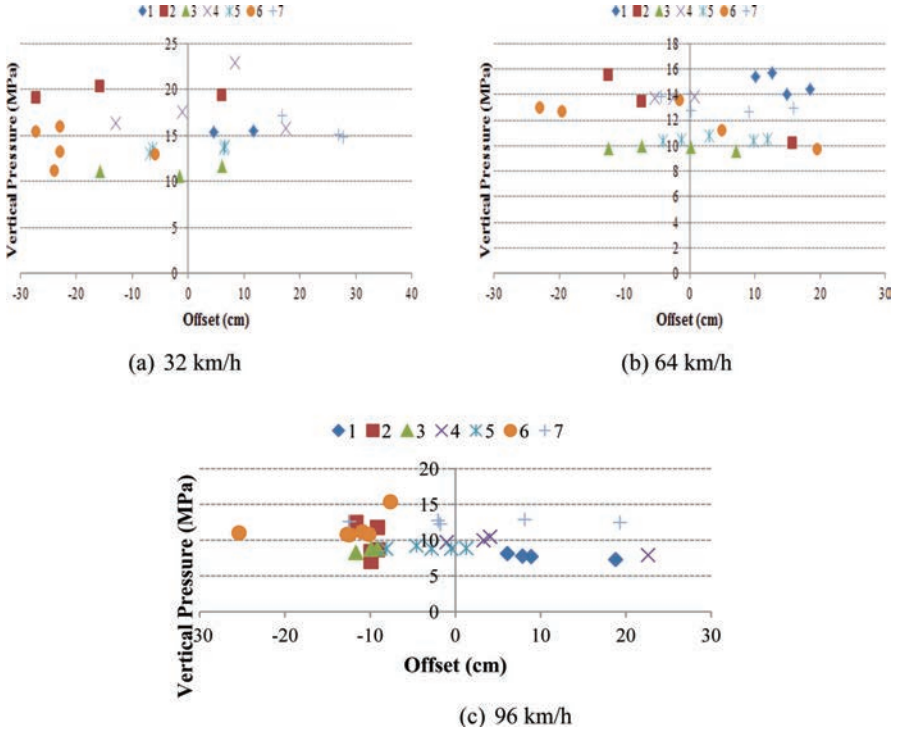

Figure 1. Vertical stresses on the top of subgrade during different sessions in section 2.
Note: 1 = 7/14/05; 2 = 9/29/05; 3 = 4/13/06; 4 = 8/1/06; 5 = 10/13/06; 6 = 5/1/07; and 7 = 10/5/07.

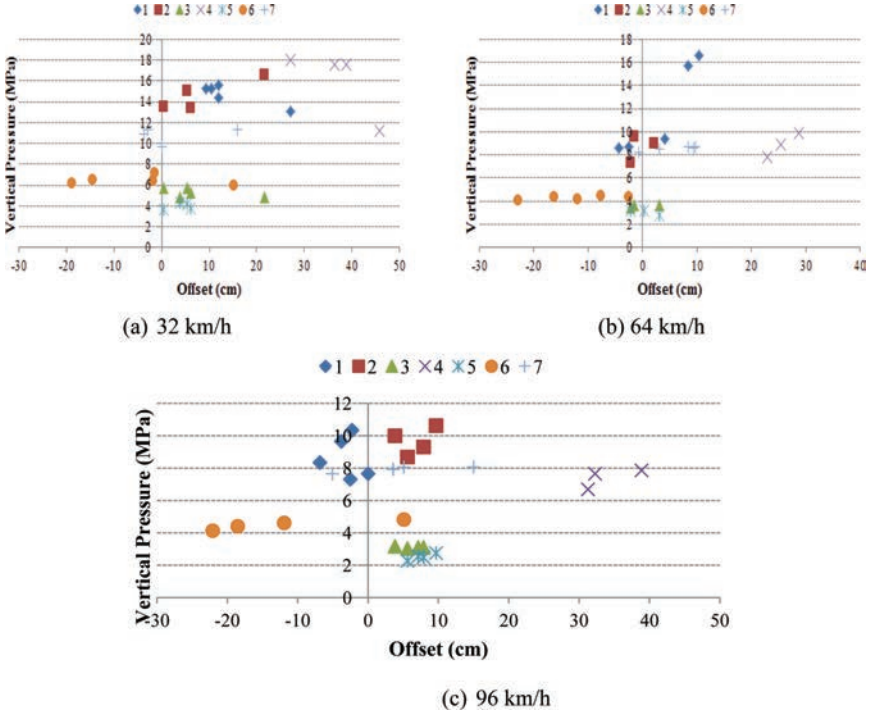

Figure 2. Vertical stresses at the top of subgrade during different sessions in section 4.

Sessions 1 and 2 were conducted before the section was open to traffic. Offset (lateral wander) does not have significant effect on stress magnitude. It is not clear whether there is an increase or a decrease in stress at the top of lime-treated subgrade with time.

5.1.2 *Longitudinal strain*

Figure 3 shows longitudinal strain at the bottom of HMA for Section 2. Longitudinal strain data were not collected at 32 km/h during session 2. Most data were collected at negative offset (lateral wander). Session 1 data show the highest variation at 64 km/h and 96 km/h speeds whereas session 4 data show the highest variation at 32 km/h speed. Session 4 data show the highest longitudinal strain at 32 km/h and two of the readings are greater than the endurance limit of 70 microstrain. This may be due to high pavement temperature during this session and the thinness of the section. Temperature effect may be more pronounced at lower traffic speed. Data from all sessions are consistent at 64 km/h and 96 km/h except Session 1 data. Offset (lateral wander) does not have significant effect on the magnitude of the strain. It is not clear whether there is an increase or a decrease in longitudinal strain at the bottom of HMA with time.

Figure 4 shows longitudinal strain at the bottom of HMA for Section 4. Most of the data were collected at negative offset (lateral wander). Session 1 data show the highest variation at 64 km/h. Session 4 data are on the higher side at 32 km/h and on the lower side at 64 km/h and 96 km/h. High temperature effect may be more pronounced at lower traffic speed. There is

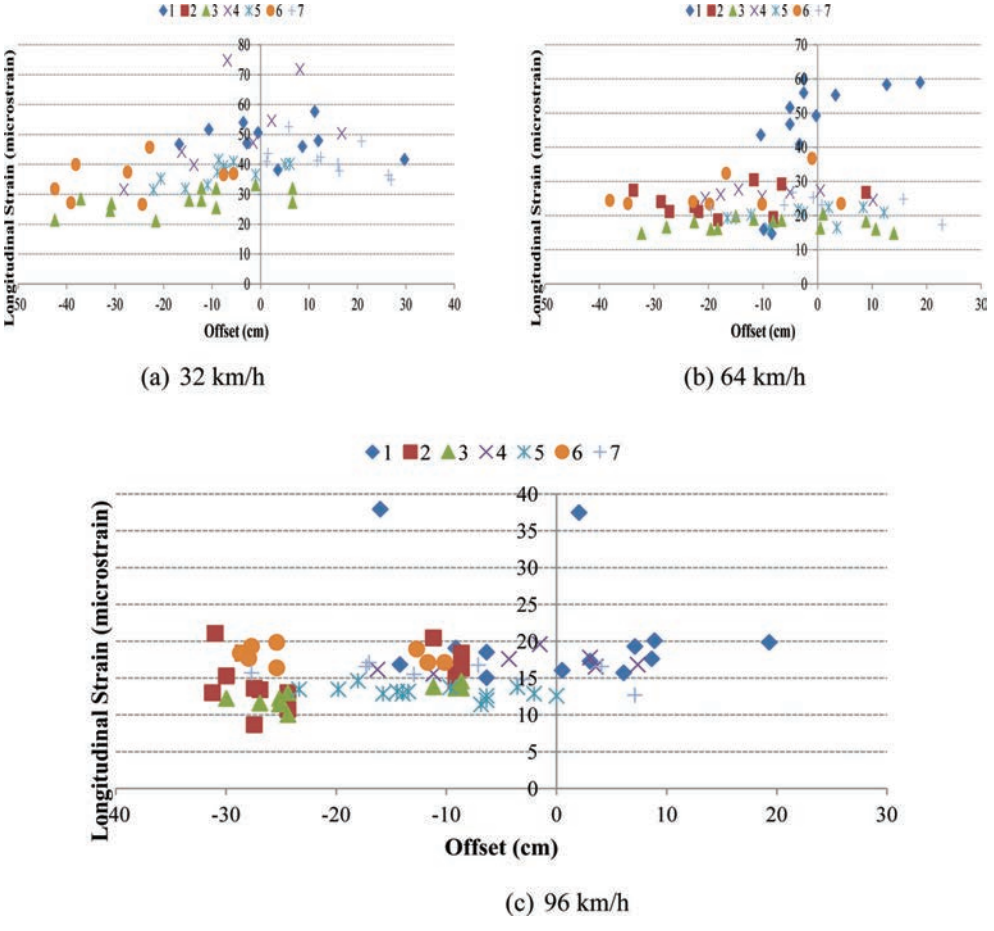

Figure 3. Longitudinal strains at the bottom of HMA during different sessions in section 2.

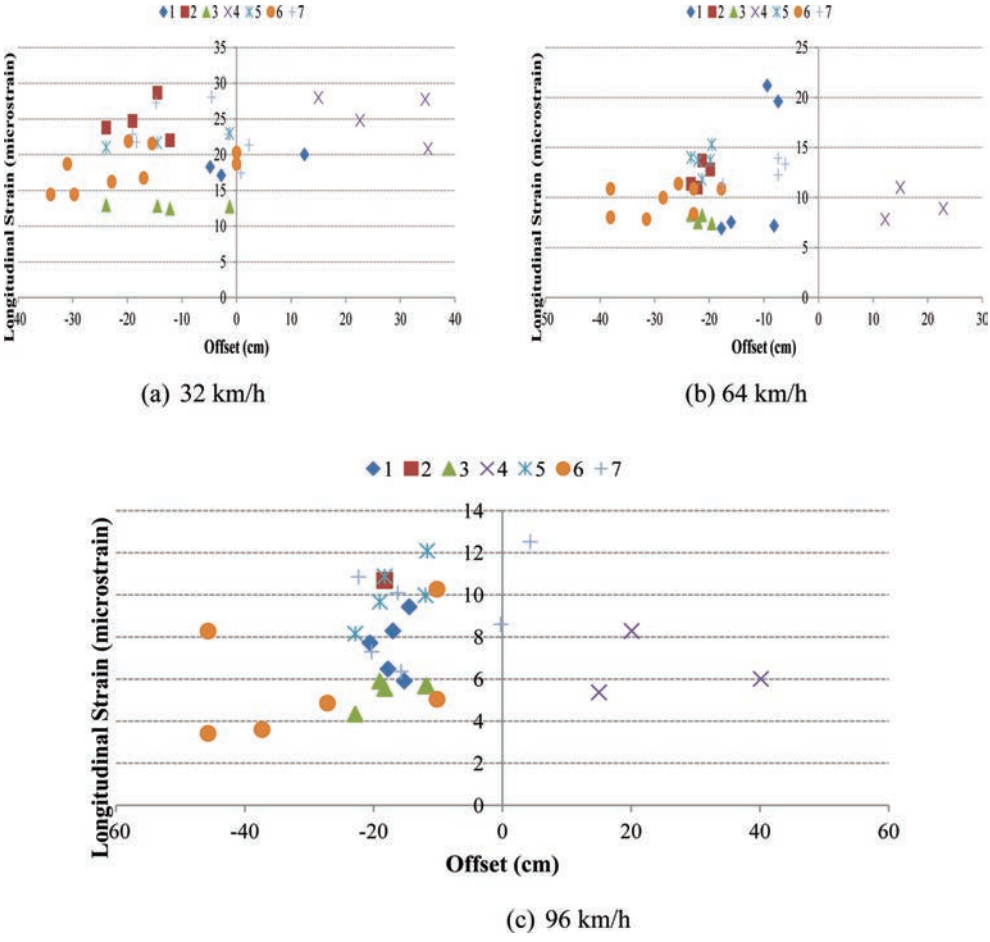

Figure 4. Longitudinal strains at the bottom of HMA during different sessions in section 4.

more variation in Section 4 at 64 km/h and 96 km/h as compared to other sections. This may be due to high pavement temperature in Section 4 during all sessions. Offset (lateral wander) does not have significant effect on the magnitude of the strain. It is not clear whether there is an increase or a decrease in longitudinal strain at the bottom of HMA with time.

5.1.3 *Transverse strain*

Figure 5 shows transverse strain at the bottom of HMA for Section 2. Transverse strain data were not collected at 32 km/h during session 2. A significant number of transverse strain readings show values greater than an endurance limit of 70 microstrain. This may be due to the thickness of the section, which is the thinnest. Transverse strain during session 4 is on the higher side at 32 km/h and on the lower side at 96 km/h. High temperature effect may be more pronounced at lower traffic speed. There is an increase in transverse strain due to temperature and age in general. Offset (lateral wander) does not have significant effect on the magnitude of the strain.

Figure 6 shows transverse strain at the bottom of HMA for Section 4. All readings are less than the endurance limit even though Section 4 was tested at higher temperature than Section 2 during all sessions. This clearly shows the effect of pavement thickness on strain. Transverse strain during session 4 is not the highest though the data were taken at the highest temperature. This shows pavement temperature has more pronounced effect on strains for thinner sections. Transverse strains before the section was opened to traffic are higher at all temperatures.

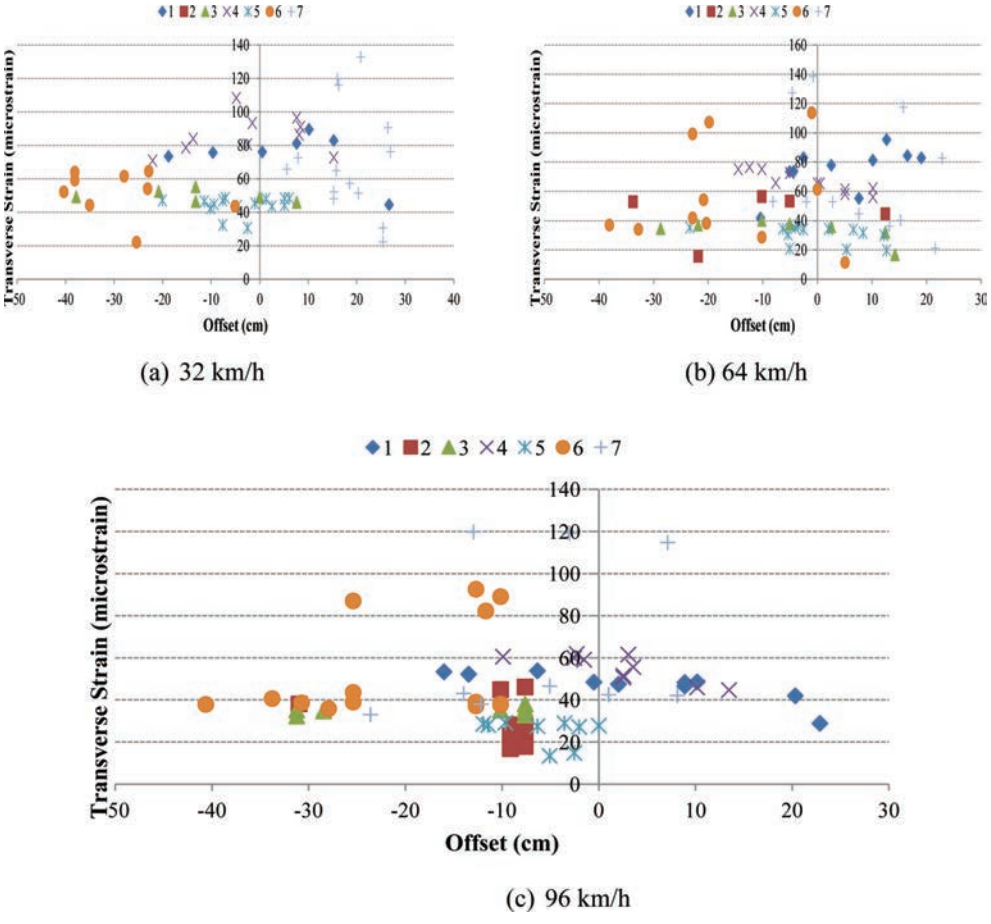

Figure 5. Transverse strains at the bottom of HMA during different sessions in section 2.

5.2 *Center deflection and back-calculated asphalt modulus*

FWD deflection data were not collected during session 1. FWD deflection data were collected on different dates than stress, strain, and pavement temperature data during session 6. As a result, FWD deflection data from only five sessions were analyzed. Center deflection data from Station 1 of Section 1 were normalized to a 40-kN load and then corrected to 20 °C using Eq. (1) based on measured mid-depth pavement temperature in Table 2. Table 3(a) shows the center deflection and biases. As shown in Table 2, mid-depth pavement temperature was the lowest and highest in October 2006 and August 2006, respectively. Center deflections from the two sessions are the first and second highest. This shows that both very low and very high temperature have significant impact on center deflection of the pavement. Biases were calculated using the first center deflection as a reference. The bias varies from –25.6 to 26.0 micron and –21.3% to 21.7%. There is no clear trend whether there is an increase or a decrease in center deflection with time.

EVERCALC was used to back-calculate layer moduli. Eq. (2) was used to correct back-calculated asphalt modulus to 0 °C based on the measured mid-depth pavement temperature in Table 2. Table 3(b) shows the biases calculated using laboratory dynamic modulus at 20 °C and 25 Hz as a reference. Frequency of 25 Hz was selected as a reference since it is the closest to the frequency of FWD deflection measurement and it is reasonable to compare measured and back-calculated moduli at this frequency. Bias varies from –50.6%

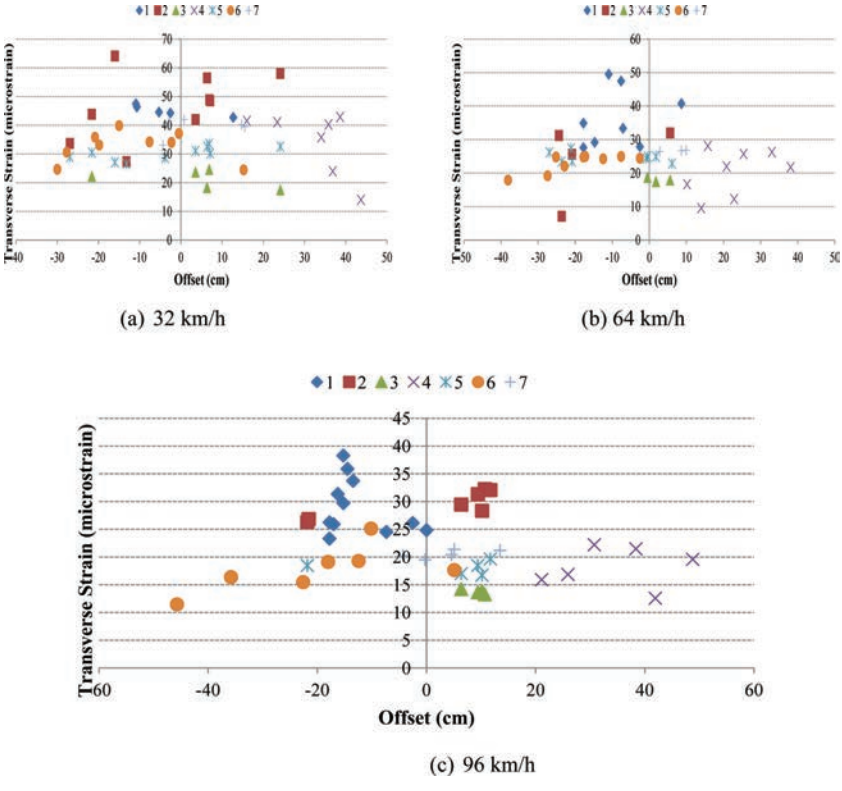

Figure 6. Transverse strains at the bottom of HMA during different sessions in section 4.

Table 3. Effect of aging on center deflection and back-calculated modulus.

Variable	FWD deflection data collection date				
	9/29/2005	4/13/2006	8/1/2006	10/13/2006	10/5/2007
(a) Center deflection					
d_0 (μm)	120.1	107.0	126.8	146.1	94.5
Bias (μm)	–	–13.1	6.7	26.0	–25.6
Bias (%)	–	–10.9	5.6	21.7	–21.3
(b) Back-calculated modulus relative to measured dynamic modulus of 9513.5 MPa					
Modulus (MPa)	6547.9	5990.3	4843.8	4703.8	7618.7
Bias (MPa)	–2965.3	–3523.0	–4669.4	–4809.4	–1894.6
Bias (%)	–31.2	–37.0	–49.1	–50.6	–19.9
(c) Back-calculated modulus relative to session 1 modulus of 6547.9 MPa					
Modulus (MPa)	6547.9	5990.3	4843.8	4703.8	7618.7
Bias (MPa)	–	–557.6	–1704.1	–1844.1	1070.7
Bias (%)	–	–8.5	–26.0	–28.2	16.4

to –19.9%. This shows that the laboratory dynamic modulus is higher than the back-calculated moduli.

Table 3(c) shows biases calculated relative to the first back-calculated modulus. The percent bias varies from –28.2 to 16.4. Back-calculated modulus is the largest for the last data collection session. This can be due to asphalt concrete hardening due to aging and/or other factors such as test temperature.

6 CONCLUSIONS

Based on this study, the following conclusions can be made:

- There is no clear trend whether there is an increase or a decrease in stress, strain, surface deflection, and back-calculated modulus with age for Kansas perpetual pavement test sections. This may be due to the short time span of data collection (two years) from the first to the last session.
- There is a decrease in stress and strain with an increase in traffic speed.
- A change in speed from 64 km/h to 32 km/h has a higher impact on the stress and strain than a change in speed from 96 km/h to 64 km/h for thicker sections and vice versa for thinner section.
- Endurance limit of 70 microstrain was exceeded in the thinnest section (288 mm total HMA thickness), which carried about 850,000 ESALs so far.
- The effect of high temperature on stress and strain is more pronounced at lower traffic speed and on the thinner section.
- Both very low and very high temperatures have significant impact on the center deflection.
- Laboratory dynamic modulus is higher than the back-calculated modulus.

REFERENCES

1. TRB. *Transportation Research Circular 503: Perpetual Bituminous Pavements.* Transportation Research Board of the National Academies, Washington, D.C., 2001.
2. Romanoschi, S.A., A.J. Gisi, M. Portillo, and C. Dumitru. First Findings from the Kansas Perpetual Pavements Experiment. *Transportation Research Record: Journal of the Transportation Research Board,* 2068, pp. 41–48, 2008.
3. Kim, Y.R. and Y.-C. Lee. Interrelationships among Stiffnesses of Asphalt-Aggregate Mixtures. *Journal of the Association of Asphalt Paving Technologists,* 64, pp. 575–609, 1995.
4. Park, H.M., Y.R. Kim, and S. Park. Temperature Correction of Multiload-Level, Falling-Weight Deflectometer Deflections. *Transportation Research Record: Journal of the Transportation Research Board,* 1806, pp.3–8, 2002.
5. Shao, L., S.W. Park, and Y.R. Kim. Simplified Procedure for Prediction of Asphalt Pavement Subsurface Temperatures Based on Heat Transfer Theories. *Transportation Research Record: Journal of the Transportation Research Board,* 1568, pp.114–123, 1997.
6. Chen, D.H., J. Bilyeu, H.H. Lin, and M. Murphy. Temperature Correction on Falling-Weight Deflectometer Measurements. *Transportation Research Record: Journal of the Transportation Research Board,* 1716, pp.30–39, 2000.
7. American Association of State Highway and Transportation Officials (AASHTO). *Guide for Design of Pavement Structures*. AASHTO, Washington, D.C., 1993.
8. Portillo, M.M. *Measured and Theoretical Response of Perpetual Pavement Structures*. M.S. Thesis, the University of Texas at Arlington, December 2008.
9. Chou, Y.J., and R.L. Lytton. Accuracy and Consistency of Back-calculated Pavement Layer Moduli. *Transportation Research Record: Journal of the Transportation Research Board,* 1293, pp.72–85, 1991.
10. Chen, J., M. Hossain, and T.M. Latorella. Use of Falling Weight Deflectometer and Dynamic Cone Penetrometer in Pavement Evaluation. *Transportation Research Record: Journal of the Transportation Research Board,* 1655, pp.145–151, 1999.
11. Zhou, H., G.R. Rada, and G.E. Elkins. Investigation of Back-calculated Moduli Using Deflections Obtained at Various Locations in a Pavement Structure. *Transportation Research Record: Journal of the Transportation Research Board,* 1570, pp.96–107, 1997.
12. Gedafa, D.S., M. Hossain, S. Romanoschi, and A.J. Gisi. Field Verification of Superpave Dynamic Modulus. *Journal of Materials in Civil Engineering,* 22 (5), pp. 485–494, 2010.

Asphalt Pavements – Kim (Ed)
© 2014 Taylor & Francis Group, London, ISBN 978-1-138-02693-3

Long life surfaces for busy roads

Richard Elliott
URS, Chetwynd Business Park, Chilwell, Nottingham, UK

Carl Fergusson & John Richardson
Colas, Crawley, West Sussex, UK

Andy Stevenson
Cornwall Council, Central Group Centre, Bodmin, UK

Donna James
Highways Agency, Dorking, UK

ABSTRACT: Research carried out between 2001 and 2007 identified that: (i) there were likely to be economic benefits from development of road surfacing materials with a service life in excess of 30 years (Long Life Surfacing), and; (ii) laboratory and accelerated load testing of two materials (Epoxy Asphalt and High Performance Cementitious Materials) with the potential to fulfil these requirements could be successfully laid in pilot scale trials and performance verification tests satisfied the target (high) performance for the design mixtures.

This paper describes the planning, executing and monitoring of a full scale trial of Epoxy Asphalt in the UK, to demonstrate that the performance envisaged from the laboratory and accelerated testing would hold true within the period of the trial under real traffic and environmental conditions. Additional aims included to develop construction methods, optimise mixtures and increase contractor experience levels.

The trial was successfully completed and has now been monitored for one year. The target service life is at least twice as long as that typically expected from surfacings generally used in road pavements and involves higher initial expense, but aims to avoid major maintenance costs over the lifetime of the pavement, generate overall savings and be environmentally more sustainable.

Keywords: asphalt modifiers; field performance; innovation; perpetual pavements; sustainability

1 INTRODUCTION

In recent years, road pavements in developed countries have been subject to massively increased traffic loading, to a level that may compromise the longevity and serviceability of the pavement. In addition, other issues such as traffic congestion, road user charging, whole life cost and sustainable construction have placed greater pressure on road administrators to provide users with more robust road networks, with a reduced maintenance frequency and less interruption to traffic. In this context, 'Long Life Pavements', with a prolonged service life, are seen as particularly desirable for heavily trafficked roads and have been shown to be achievable for the subsurface layers. However, the surface layer or wearing course, which is critical for safe and comfortable driving, remains the Achilles' heel of the concept.

Against this background, since 2001, the UK has been involved in a joint research project on Economic Evaluation of Long Life Pavements, in collaboration with a number of national institutions under the umbrella of the Organisation for Economic Co-operation and

Development/European Conference of Ministers of Transport (OECD/ECMT). Phase I of this project, carried out between 2001–2003, identified that there were likely to be economic benefits from development of road surfacing materials with a service life in excess of 30 years (Long Life Surfacing), [1]. Phase II of the project (now called Long Life Surfaces for Busy Roads and prepared under the aegis of the Joint OECD/ITF (International Transport Forum) Transport Research Centre), carried out between 2004 and 2007, comprised laboratory and accelerated load testing of two materials (Epoxy Asphalt and High Performance Cementitious Materials) identified as having the potential to fulfil the requirement of Phase I [2]. The present paper summarises the work done in the United Kingdom in Phase III of the project; to plan, execute and monitor full scale trials of the optimum epoxy asphalt mixture design formulation that had been developed in earlier stages of the project. Specifically, monitoring results up to 12 months are provided from a field trial completed on the A390 Trunk Road in the South West of England.

2 EPOXY ASHPALT

Epoxy asphalt surfacing systems are not new; they have been used on a number of major bridges around the world. Excellent performance has been recorded, most notably on the San Mateo-Hayward Bridge, where epoxy asphalt surfacing has been in service for more than 45 years without failure [3]. Due to its superior resistance to aircaft fuel and jet-blast, the material has also been used on a number of military airfields in the USA [4]. Prior to the current project, the main use of epoxy asphalt in the UK in recent times had been on a limited number of steel bridge decks (Erskine and Humber), where the design was based on Hot Rolled Asphalt. To the authors' knowledge, epoxy asphalt surface course has not been used to any significant degree for highway surfacing. However, as part of the current project, successful trials of epoxy modified Open Graded Porous Asphalt were carried out on State Highway 1 in Christchurch, New Zealand in 2007 [5].

Due in large part to its thermosetting nature, past experience suggests that epoxy asphalt production has to be carefully controlled in order to optimise the curing profile for the local conditions, and to ensure satisfactory production, transport, laying and compaction. Furthermore, this material also requires a sound (stiff) substrate and good weather during construction.

The mixture design developed for this project was based on a generic surface course system that is widely used for the surfacing of major road networks around the world, namely Stone Mastic Asphalt (SMA). Essentially, the design of the epoxy asphalt SMA material was similar to that of conventional SMA, with the subsititution of a slightly increased quantity of the epoxy binder components, in place of the standard binder. Full details have been reported elsewhere [2, 6, 7].

3 OBJECTIVES AND SCOPE OF PHASE III TRIALS

The overall objective of the field trials was to demonstrate that the performance envisaged from the laboratory and accelerated testing would hold true within the period of the trial under real traffic and environmental conditions. Additional aims were to develop construction methods, optimise mixtures, and increase contractor experience levels.

In the UK, the Highways Agency (HA), an executive agency of the Department of Transport with responsibility for operating, maintaining and improving the Strategic Road Network in England, provided support to Scott Wilson (now URS) to assist in the organisation of the full scale epoxy asphalt trial. The scope of the support also encompassed monitoring performance over time, and relevant in situ and laboratory tests, the latter on cores extracted from the trial section.

It was intended that the epoxy asphalt would be laid as a 30 mm or 40 mm thick SMA surface course as a like-for-like and cost neutral replacement for the originally specified material;

the benefit to the road owner permitting the trial was that its life would be expected to be at least as long as that of the traditional material. The Phase I study identified an expected life for conventional SMA surface course ranging from 5 to 15 years, depending particularly on incidence of studded tyre use and level of traffic. 10 years was selected as the average expected life to be used for the economic evaluation [1], although it should be noted that EAPA quotes lives ranging from 16 to 25 years where SMA is used on secondary roads [8].

Mixture designs had been trialled in Phase II for 0/14 mm and 0/10 mm SMA for use in 40 or 30 mm lifts, respectively. From a practical perspective, the aggregate grading and binder content are effectively identical to those for conventional material, and the manufacture, transport, laying, rolling and aftercare for the epoxy asphalt SMA is carried out in a similar manner to that for conventional material. However, the thermosetting nature of the product necessitates special consideration in the plant, and for this reason, Colas, who have many years experience in manufacturing and laying epoxy asphalt, were involved at an early stage. The material requires a good quality substrate, and in practice could be laid over a new high performance base/binder course material such as EME, or a good quality residual material, where, for example, the old surfacing has been planed out because of surface (non-structural) deterioration.

4 TRIAL INSTALLATION

The UK Trial Site is located in Threemilestone, on Lane 1 (L1) of the A390 inbound carriageway towards Truro, in the South West of England. The trial encompasses an area approximately 110 metres long by 3.65 metres wide where approximately 40 tonnes of 10 mm nominal size epoxy asphalt SMA trial material was laid 30 mm thick; a comparable length and volume of control material was laid immediately afterwards.

The traffic data for this section of the A390, factored up to January 2012 from a 2006 traffic count, indicate an AADT of 29100 vehicles, with 830 (3%) Heavy Class Vehicles (HCV) of gross weight > 7500 kg and 1100 (4%) Medium Class Vehicles (MCV) of gross weight 3500–7500 kg. The pavement construction is flexible with a full depth asphalt construction ranging in thickness from 312 to 390 mm. The surfacing was due for replacement in 2012 due to surface deterioration (predominantly crazing and fretting, with poor profile due to patch reinstatement) but the substrate was considered to be sound. The logistical, practical and procurement issues were resolved in two meetings involving URS, Colas and the local authority (Cornwall County Council, CCC) held on 11 January and 30 March, and the material sourcing, production and laying of the road trial was successfully completed on Saturday 28 April 2012.

As the specific requirements of the site necessitated a 30 mm thick surfacing layer, it was decided that 10 mm nominal maximum aggregate size was more appropriate, rather than 14 mm as used in the Phase II work. After planing out the original surfacing and before laying the trial and control material, Colbond 50 polymer modified bond coat was applied to the planed surface at a nominal spread rate of 0.7 litres/m^2 (equivalent to 0.35 kg residual binder/m^2) and left until clearly 'broken' before laying the new surfacing. The trial proceeded without incident, apart from minor difficulty related to the paving of the 4th load, which was delayed in traffic between the quarry and the site, leading to a minor surface blemish where the paver stopped moving forward. Full details of the mixture design, plant trials, modification to the bitumen delivery system for the two part epoxy asphalt binder, and the particular trial specification criteria for materials, transport, laying and compaction of the epoxy asphalt, have been provided elsewhere [7].

The early life traffickability of epoxy modified SMA is the subject of ongoing research, but, for the trial, L1 was closed to traffic until Monday night (30 April 2012), when the Traffic Management was lifted. In order to monitor the quality control and 'strength' development of the manufactured product, and so that they could advise when it was appropriate to open to traffic, Colas produced specimens for Marshall testing, to BS EN 12697-34 [9]. The requirements were a minimum stability and maximum flow of 5 kN and 4 mm, respectively, after

24 hours curing at ambient temperature, and 30 kN and 7 mm, respectively, after 20 hours curing at 120°C.

5 MONITORING

5.1 *Scope*

The requirements for assessment, testing and monitoring of the epoxy asphalt field trials, established by the OECD/ITF steering group in July 2009, involved monitoring before, during and after the trial, the latter including monitoring at early age and after 1 year in service. Accordingly, two visits were made to the site: (i) an initial monitoring visit on the night of 09 May 2012, 11 days after the material was laid and 9 days after the trial section was re-opened to traffic, and; (ii) a final, 12 month, visit on 30 April 2013.

On both occasions, the monitoring work was done under a partial lane closure from 19.00 onwards, with L1 closed to traffic over the trial and control sections, and all inbound Truro traffic using L2. The work carried out comprised the following:

- Photographic record of visual condition
- Longitudinal profile, in accordance with Volume 1 of the Manual of Contract Documents for Highways Works (MCHW1) Clause 702, Table 7/2 [10]
- Surface macro-texture by volumetric patch method as described in BS EN 13036-1 [11] and BS 594987, Clause 8.2, [12], (with additional tests across full width of lane)
- Falling Weight Deflectometer (FWD) testing, broadly to the requirements of HD 29/08 (Volume 7 of the UK Design Manual of Roads and Bridges (DMRB7) [13])
- Coring, to establish depth of bound material and to recover samples for materials testing.

In the event, the weather during the initial visit was very poor (heavy rain), and the initial surface macro-texture could not be determined. A noise assessment was also planned but local topography and proximity of dwellings made this impractical.

5.2 *Visual and surface characteristics*

Visually, the surface appearance of the epoxy asphalt test section was indistinguishable from that of the control section (although see below) and from conventional SMA. Also, there had been no discernible change in appearance between the initial and 12 month visits. The longitudinal profile complied with the requirements of MCHW1 Clause 702, Table 7/2 [10], and the results from the two visits were essentially similar, indicating no change with time; two 7 mm irregularities found in the epoxy asphalt test section were on the joints at the beginning (0 m) and end (110 m) of the section respectively, and are a reflection of the site situation rather than a failure to achieve a consistent profile. These surface irregularities at the beginning and end of the test section can be detected when travelling over the test section by car, as can the location (around Chainage 80) where the surface profile was influenced by the paver coming to a halt between the 3rd and 4th loads of epoxy asphalt material. However, in the latter case, any impact on ride quality was not reflected in the surface regularity assessment.

The surface macro-texture data at 12 months show that the mean texture depth for the trial and control sections (set of 10 measurements) were both 1.1 mm. These values comply with the current UK requirements [10] for thin surface course systems for lower speed roads ($\geq$ 1.0 mm (average per 1000 m section); $\geq$ 0.9 mm (average per set of 10 measurements)).

5.3 *FWD testing*

The FWD testing was done at 2 m centres in two lines running longitudinally from Chainage 0 to 220 m, in the NearSide Wheel Track (NSWT) and Lane Centre (LC), at contact pressures of 700, 850 and 1000 kPa. The NSWT tests were offset by 1 m from the LC tests, and similarly offset from the cores (see below) where applicable.

The primary purpose of the FWD testing was to establish that the pavement was structurally competent in both the trial and control areas, and that the trial and control pavements were essentially similar. A detailed summary of the testing is beyond the scope of this paper. However, in overview, the analysed FWD data show that the asphalt stiffnesses were generally low throughout (it is possible that this may in part be a reflection of variable bond between asphalt layers influencing the back analysis) and the foundation stiffnesses were indicative of good performance throughout. Although there was some individual variation, overall the structural assessment of the site carried out using the FWD confirmed broadly similar performance in the trial and control areas.

5.4 *Coring and laboratory testing*

For both visits, twenty number 100 mm diameter cores were taken, evenly spaced along the centre of L1, ten in the epoxy asphalt test material and ten in the control material. Selected cores were drilled to full depth, revealing an asphalt construction comprising 6 to 8 discernible layers, typically:

- new SMA surface course, overlying;
- 2–3 layers of asphalt concrete, overlying;
- 1–2 layers of hot rolled asphalt, overlying;
- 1–2 layers of asphalt concrete.

The full depth of asphalt ranged from 312 mm to 390 mm, and was generally found to be slightly thicker in the test section (370–390 mm) than in the control section (312–350 mm). The full depth cores showed some lack of bond in their lower layers; the depth to the first layer showing lack of bond ranged from 111 to 240 mm, measured from the top of the pavement. Generally, the cores revealed a relatively thick asphalt construction encompassing several different material types, typical of a structure that has developed over time as new material has been laid over existing.

In order to provide baseline data on the mechanical and volumetric properties of the trial and control material, and to assess any change in mechanical properties occurring over time, a selection of the extracted cores from each section and from each visit was subjected to a bespoke programme of storage and testing. Thus the cores from the Final Visit, after 12 months curing in situ, were tested as soon as possible after extraction, while the cores extracted from the Initial Visit were stored at laboratory ambient temperature (20°C), after extraction from the road, until required for testing.

The testing carried out comprised bulk and maximum density, and calculated air voids, to BS EN 12697 Parts 5, 6 and 8 [14, 15, 16], Indirect Tensile Stiffness Modulus (ITSM) to BS EN 12697 Part 26 [17] and Indirect Tensile Splitting Strength (ITST) to BS EN 12697 Part 23 [18]. The indirect tensile stiffness and strength data are important parameters to assess likely pavement material performance over time, and are particularly useful here to illustrate the special properties of epoxy asphalt. A summary of the key mechanical property data from these two tests is presented below.

Figure 1 shows the mean stiffness data at 0, 20 and 30ºC, for in situ cured cores tested after 13 months (similar results were obtained with laboratory cured cores, tested one month after production). Figure 1 shows that the stiffness of epoxy asphalt is higher than that of the control mixture, regardless of the test temperature. At 20°C and 30°C, the stiffness of the epoxy asphalt is significantly higher than that of the control, which is likely to be beneficial with respect to the rutting potential of asphalt mixtures. Indeed, the dramatically improved deformation resistance of epoxy modified mixtures, compared with that of standard material, has been demonstrated in earlier work [6]. In addition, the result indicated that there is a strong exponential relationship between the stiffness and temperature for both mixtures.

The changes in stiffness (ITSM) over time for the epoxy modified and control mixtures are shown in Figure 2, for laboratory cured cores tested at 20ºC. It can be seen that the stiffness of the epoxy asphalt mixture is significantly greater than the control mixture at all ages. Furthermore, the stiffness of the latter remains at a constant (and relatively low) level

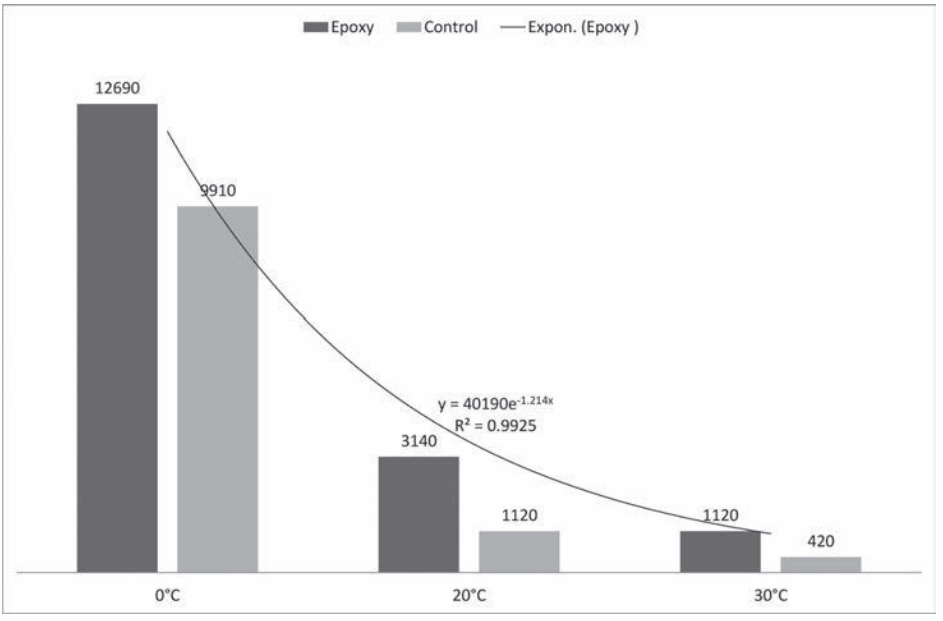

Figure 1. Mean stiffness (ITSM) data at three temperatures, performed on in situ cured cores, 13 months after production.

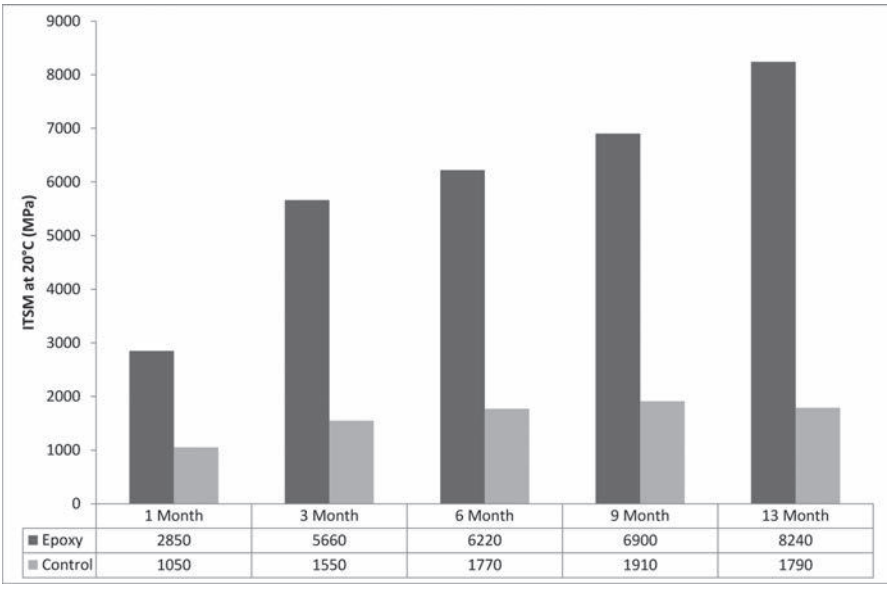

	1 Month	3 Month	6 Month	9 Month	13 Month
Epoxy	2850	5660	6220	6900	8240
Control	1050	1550	1770	1910	1790

Figure 2. Mean stiffness (ITSM) data at 20°C, performed on laboratory cured cores, at various ages after production.

between 6 and 13 months, whereas the stiffness of the epoxy modified mixture continues to rise throughout the period of monitoring.

Finally, Table 1 summarises the results of tensile strength (ITST) tests performed on laboratory and in situ cured cores. A direct comparison of the results of laboratory cured cores shows that the strength of the epoxy asphalt mixture increased by 50% between one and

Table 1. Mean tensile strength (ITST) data at 20°C at various ages after production.

	Mean ITST (MPa) at 20°C		
	Laboratory cured cores		In situ cured cores
Material	1 month	13 month	13 month
Epoxy	1.6	2.4	2.0
Control	0.6	0.6	0.8

Figure 3. Epoxy asphalt trial section after 12 months trafficking (2013).

13 months, while the strength of the control mixture did not experience any change. The in situ results also indicate that the strength of the epoxy modified mixture is substantially higher than that of the control.

In comparison with earlier results generated during Phase II of this project [2, 6], it is noteworthy that the laboratory cured stiffness at 20ºC of the field cores is substantially lower (8240 MPa after 13 months compared with 13400 MPa after 60 days). The reason for this difference is unexplained, but the slightly reduced stiffness of the field cores may be beneficial in the long term, as discussed further below.

6 CURRENT CONDITION OF THE ROAD

Figure 3 shows the condition of the epoxy asphalt trial section (Lane 1 in the photograph below) after 12 months trafficking.

Feedback received from CCC reveals the following:

1. Data from: routine SCANNER measurements (traffic-speed surveys of the network, using the Surface Condition Assessment of the National NEtwork of Roads (SCANNER) system, to determine rut depth, texture, profile and cracking, carried out according to the

User Guide and Specifications published by the UK Roads Board (2011), [19]), completed on 31 May 2012, and; SCRIM measurements (in-service skid resistance using a Sideway-force Coefficient Routine Investigation Machine (SCRIM), carried out according to HD 28/04 of DMRB7, [20]), completed on 06 July 2012; reveal that the surface has so far not shown any indication of change since it was opened to traffic.

2. Personal feedback from CCC staff who drive this section of road frequently is that nothing registers apart from the section where the paver stood for a period (see section 4 above), and even here there has been no sign of change since the road was opened to traffic.

7 CONCLUDING DISCUSSION

In earlier phases of this OECD/ITF research project, Long Life Surfaces for Busy Roads, an economic appraisal had demonstrated the likely benefits from development of road surfacing materials with a service life in excess of 30 years, which were subsequently characterised in laboratory and accelerated load testing of two candidate materials (Epoxy Asphalt and High Performance Cementitious Materials). The present report summarises the work done in the United Kingdom in Phase III of the research project; specifically, to plan, execute and monitor full scale trials of the optimum epoxy asphalt mixture design formulation that had been developed in the earlier stages of this project.

The site in question was located on a heavily trafficked section of the A390 inbound carriageway toward Truro, where the surfacing required replacement due to surface deterioration but the substrate was considered to be sound. The epoxy asphalt mixture design was a 10 mm nominal size SMA material, incorporating epoxy binder, which was laid 30 mm thick over 110 m of Lane 1 of the carriageway. A comparable 10 mm nominal size SMA control material, incorporating 50 penetration grade binder, was laid over the succeeding 110 m. Both the epoxy asphalt and control material were manufactured, transported and laid using conventional plant, generally without incident. Full details of the field trial installation have been published elsewhere [7].

Data from two monitoring visits over the first year of service and feedback from CCC indicates good performance to date, with comparable surface characteristics (regularity and texture) on the trial and control sections and no indication of change since the trial site was opened to traffic. In one location in the final quarter of the epoxy asphalt section, there are some surface blemishes which occurred as a result of an unforeseen break in the paving operation (delivery lorry delayed in traffic). However, although this is visible to the naked eye and detectable when driving over the site in a vehicle, the surface regularity complies with the current UK requirements. A structural assessment of the site carried out using the FWD has confirmed broadly similar performance in the trial and control areas. Testing of cores extracted from the site and subsequently stored in the laboratory, indicate that the epoxy asphalt material has substantially greater stiffness and tensile strength than the control material. The mean stiffness at 20°C of the epoxy asphalt has increased from 2850 MPa at 1 month to 8240 MPa at 13 months, compared with a comparable change for the control material from 1050 MPa to 1790 MPa. In addition, the mean tensile strength of epoxy asphalt has increased from 1.6 MPa at 1 month to 2.4 MPa at 13 months, whereas the control mixture has shown no change in strength over time and a much lower absolute value (0.6 MPa).

The primary objective of the field trials was to demonstrate that the performance envisaged from the laboratory and accelerated testing would hold true within the period of the trial under real traffic and environmental conditions. To date, this objective has been comfortably met, although, as noted in section 5, the stiffness of the epoxy modified mixtures are generally lower than previously determined in the laboratory [2, 6]. However, the stiffness is still comfortably in excess of that of standard surfacing mixtures, with consequent benefits for predicted life, and a slightly lower stiffness may be no bad thing to help mitigate any potential for cracking. Secondary objectives were to develop construction methods, optimise mixtures and increase contractor experience levels. It is certainly the case that the field trial has successfully demonstrated that the full-scale manufacture and construction of an

epoxy modified SMA surfacing can be accomplished with standard plant and equipment, and with only very minor changes to practice. In terms of increasing contractor experience levels and optimising mixtures, it is likely that this will only come with increased uptake of the concept. From the present research, obvious targets for mixture optimisation would include extending the workability window, improved knowledge of how curing temperature influences early traffickability and ultimate mechanical properties, and making best use of the potential to manufacture and lay epoxy modified mixtures at lower temperature than conventional material.

The economic case for long life surfacing of the type described in this paper depends on achieving a service life at least twice as long as that typically expected from asphalt surfacing currently used in road pavements. As an example, the expected life of 'conventional' Stone Mastic Asphalt (SMA) surface courses popularly used in Europe and North America were reported to range between 5 and 15 years [1]. Clearly, the current trial has a long way to go before a life of 30 years can be demonstrated, but early signs are encouraging. Although the envisaged monitoring of the field trial has now been completed, CCC has kindly agreed to supply future routine SCANNER and SCRIM data as they become available; this will be recorded for potential future use.

A long life surfacing is an essential requirement for the advanced and affordable transport infrastructure envisaged by the Forever Open Road (FOR) concept, which aims to bring together the best of what we have today with the best of what's to come. Long lasting overlays as part of durable and integrated pavements are one of the key research and innovation themes of FOR, to produce an affordable road for a society that cannot afford the closure of roads [21].

It is of course recognised that the additional cost and marginally increased construction complications will mitigate against the use of such material for many conventional applications. However, as traffic levels continue to rise, and in certain network 'hot spots' where any loss of serviceability is unacceptable, the justification for longer life surfacing materials can only increase.

REFERENCES

[1] OECD, *Economic Evaluation of Long-Life Pavements*. Paris: OECD Transport Research Centre, 2005. ISBN 92-64-00856-X.

[2] OECD, *Long-life surfaces for Busy Roads*. Paris: OECD International Transport Forum, 2008. ISBN 978-92-821-0158-2.

[3] Lu, Q., Gaul, R.W., and J. Bors, *Alternate Uses of Epoxy Asphalt on Bridge Decks and Roadways,* Proceedings of the 5th Eurasphalt & Eurobitume Congress, 2012, Istanbul.

[4] Simpson, W.C., Sommer, H.J., Griffin, R.L., and T.K. Miles, *Epoxy asphalt concrete for airfield pavements*, ASCE Journal of the Airport Division, Vol 86, No 1, 1960, pp 55–71.

[5] Herrington, P.R., *Epoxy-modified porous asphalt*. NZ Transport Agency research report 410, 2010.

[6] Elliott, R.C., Widyatmoko, I., Chandler, J., Badr, A. and W.G. Lloyd, *Laboratory and pilot scale assessment of long life surfacing for high-traffic roads*. Paper 300-005 in Proceedings of the 4th Eurasphalt & Eurobitume Congress, 21–23 May 2008, Copenhagen.

[7] Elliott, R.C., Fergusson, C., Richardson, J., Stevenson, A. and D. James, *Field Trials of a Long Life Surfacing Material*, Asphalt Professional, Issue 57, in preparation, September 2013.

[8] EAPA, *Long-Life Asphalt Pavements*, June 2007.

[9] BS EN 12697-34, *Bituminous mixtures—Test methods for hot mix asphalt—Part 34: Marshall test*.

[10] Department of Transport, *Specification for Highway Works*, Manual of Contract Documents for Highway Works, The Stationery Office, London, Vol. 1.

[11] BS EN 13036-1, *Road and airfield surface characteristics. Test methods. Measurement of pavement surface macrotexture depth using a volumetric patch technique*.

[12] BS 594987, Asphalt for roads and other paved areas. Specification for transport, laying, compaction and type testing protocols.

[13] Department for Transport, *Pavement design*, HD29/08, Design Manual for Roads and Bridges Volume 7 Section 3, 2008.

[14] BS EN 12697-5, *Bituminous mixtures. Test methods for hot mix asphalt. Determination of the maximum density*.
[15] BS EN 12697-6, *Bituminous mixtures. Test methods for hot mix asphalt. Determination of bulk density of bituminous specimens*.
[16] BS EN 12697-8, *Bituminous mixtures. Test methods for hot mix asphalt. Determination of void characteristics of bituminous specimens*.
[17] BS EN 12697-26, *Bituminous mixtures. Test methods for hot mix asphalt. Stiffness*.
[18] BS EN 12697-23, *Bituminous mixtures. Test methods for hot mix asphalt. Determination of the indirect tensile strength of bituminous specimens*.
[19] Department of Transport, *SCANNER Surveys for Local Roads, User Guide and Specification, Volume 3, Advice to Local Authorities: Using SCANNER survey results*, Version 1.0, 2011 Edition: http://www.pcis.org.uk/iimni/UserFiles/Applications/Documents/Downloads/SCANNER%20and%20TTS/SCANNER%20Specification/SCANNER_Spec_2011_Volume_3.pdf (last accessed 28 August 2013).
[20] Department for Transport, Skid resistance, HD28/04, Design Manual for Roads and Bridges Volume 7 Section 3, 2004.
[21] http://www.foreveropenroad.eu (last accessed, 28 August 2013).

Asphalt Pavements – Kim (Ed)
© 2014 Taylor & Francis Group, London, ISBN 978-1-138-02693-3

Optimising long life low noise porous asphalt

David Alabaster
NZ Transport Agency, Christchurch, New Zealand

Philip Herrington
Opus Research, Wellington, New Zealand

Jeff Waters
Fulton Hogan, Christchurch, New Zealand

ABSTRACT: The NZ Transport Agency's (NZTA) has been developing an epoxy-modified Open-Graded Porous Asphalt (OGPA) with the aim of creating a low-maintenance long-life (>30 years) low noise surfacing material.

The New Zealand laboratory studies and field trials form part of a larger collaborative research programme conducted under the auspices of the OECD/ECMT (European Conference of Ministers of Transport) Joint Transport Research Centre, focused on the economic evaluation of long-life pavements.

Investigations into the cohesive properties and oxidation resistance of an acid-cured, epoxy-modified OGPA were undertaken in the laboratory. The initial trials at the NZTA's Canterbury Accelerated Pavement Testing Indoor Facility (CAPTIF) demonstrated the practicality of the project.

A field trial constructed on State Highway 1 in Christchurch in December 2007 demonstrated that full-scale manufacture and construction using the epoxy OGPA, could be undertaken without any significant modification to plant or operating procedures in a normal surfacing operation. The trial has been in place for 6 years and is performing well.

The original 2007 work has been optimised for cost, manufacture and construction. Test sections were placed on the Christchurch Southern Motorway in 2012 and this paper reports the optimisation and findings on manufacture and construction of the 2012 test sections.

Keywords: CAPTIF, long life surfaces, epoxy-modified open graded porous asphalt

1 INTRODUCTION

This paper discusses laboratory investigations and a trial of Epoxy Modified bitumen OGPA (EMOGPA) on the Christchurch Southern Motorway in November 2012. Concentrations of EMOGPA from 25% to 100% were studied and the results compared with conventional OGPA [1].

Economic analysis shows that 25% EMOGPA is a sound investment and has the potential to significantly reduce the NZTA's surfacing budget. Adopting 25% EMOPGA would in the long term reduce the NZTA resurfacing budget to 1/6 of its current level, or alternatively provide the ability to apply a far greater volume of noise reducing surfaces within the current OGPA budget level. These figures are based on a 40 year life for EMOGPA which is considered conservative (e.g. the epoxy asphalt on the San Francisco Bay Bridge, with 25,000 vehicles per lane per day is 40 years old and still performing satisfactorily). Laboratory studies predict much longer lives [2].

The epoxy modified bitumen concept was originally developed by Shell Oil in the 1960's. Commercially available epoxy bitumen is a two part system consisting of specially formulated

epoxy resin and a hardener-bitumen blend. As with standard epoxy materials the two components are mixed just prior to use and curing takes place over time. Epoxy modified bitumen is significantly different from common, rapid curing epoxy materials such as those used in adhesives or in high-grip surfacing formulations.

Epoxy modified bitumen uses a slow acid-curing chemistry so that it can be handled and applied at high temperatures (100–150°C) without excessive curing. Like other epoxy materials, epoxy modified bitumen is thermosetting (i.e. it will not melt once cured) but differs significantly from many other epoxies in that it cures to a flexible rubbery consistency at room temperature rather than a brittle 'glass'. Chemical changes on curing and oxidation of epoxy bitumen have been studied as part of the overall research programme [3].

The formulation of commercially available epoxy bitumens is proprietary but the product typically consists of about 20% wt epoxy resin and hardener and 80% of, an approximately, 80 pen bitumen.

Epoxy modified bitumen technology has been improved significantly since its first introduction and has found a niche application in providing very long life asphalt surfacings for high deflection bridge decks ([4],[5],[6]). The Bay Bridge in San Francisco for example was surfaced with epoxy asphalt in 1976–77 which is still in service today (35 years later) carrying 27,000 vehicles per lane per day [7]. Epoxy asphalts are characterised by a high modulus, fatigue resistance, resistance to permanent deformation (rutting) and damage from fuels and oil ([8],[9],[10]).

Recently the potential benefits of the application of epoxy modified bitumen in asphalts for general road surfacing applications have been demonstrated through an OECD project involving research agencies in New Zealand, Europe and the USA ([11],[12]). Research funded by the NZTA formed part of the OECD project and focused on Epoxy Modified bitumen Open Graded Porous Asphalts (EMOGPA). EMOGPA was found to offer the potential for open-graded porous asphalt with lifetimes in the field well in excess of 30 years compared with an average life of 7.5 years the NZTA achieves for standard OGPA. The work resulted in successful full scale trials being constructed on CAPTIF ([3],[13]) and on the State Highway 1, the Main North Road in Christchurch in 2007 ([2],[14]). Several related research projects have been completed since that time, further demonstrating the potential benefits of epoxy OGPA performance and in particular the potential for reducing costs by diluting commercially available epoxy binder with standard bitumen [2].

In general epoxy modified asphalts have been found to have very high strength, fatigue resistance and resistance to oxidative degradation. The only drawback with the material from an engineering perspective is the fact that curing limits the handling time available for manufacture and construction (about 60–90 minutes). Manufacture of epoxy asphalt is straightforward with only minor modifications needed to the asphalt plant to allow in line blending of the epoxy components (before entering the drum). No changes to plant or procedures are needed to lay the mix.

This paper deals with an additional EMOGPA trial constructed on the Christchurch Southern Motorway in November 2012 carried out in collaboration with Fulton Hogan Ltd. Laboratory investigations on durability and curing rate of the trial mixes are also reported together with suggested changes to the New Zealand Transport Agency (NZTA) P/11 specification needed to accommodate EMOGPA.

2 PROJECT DESIGN

2.1 *Object and research outline*

The object of the project was to gain further experience with large scale manufacture and construction with EMOGPA and to provide a further site for evaluation of performance over time for mixes that had been optimised for cost and performance. Sections of various EMOGPA materials were laid on the Christchurch southern motorway, sample of the mixes were tested in the laboratory for durability and curing rate. A brief cost analysis of EMOPA was also conducted.

2.2 *Trial sections*

Four different OGPA materials with the same mix design and binder content, but different binders, were laid:

- 100% EMOGPA (using the epoxy bitumen as specified by the supplier)
- 50% EMOGPA (50/50 blend of epoxy bitumen diluted with standard 80–100 penetration grade)
- 25% EMOGPA (25/75 blend of epoxy bitumen diluted with standard 80–100 penetration grade)
- Control (using 80–100 penetration grade bitumen).

2.3 *Materials test methods*

2.3.1 *Trial materials and test specimens*

The epoxy bitumen (supplied by ChemCo Systems Ltd, California) is a two-part product that is blended just before use. Part A (used at 14.6% by weight) consists of an epoxy resin formed from epichlorhydrin and bisphenol-A. Part B type V (85.4%) consists of a fatty acid curing agent in approximately 80 penetration grade bitumen. The product is free from solvents.

The bitumen used for all control mixtures was 80–100 penetration grade bitumen, manufactured from Middle Eastern crudes, comprising both air-blown and butane-precipitated material, and conforming to the NZTA M/1:2007 specification.

The same, nominal 20% air void OGPA mix design conforming to the NZTA P/11 OGPA specification [15] was used for all trial sections (see Table 1).

For all mixes, 100 mm diameter specimens were prepared in the Fulton Hogan Laboratory on the day of the trial by compaction (50 blows per side) in a Marshall Hammer, according to ASTM D6926 [16]. The average air voids of the specimens used, measured according to ASTM D3203-05 [17] are given in Table 1. These specimens were used in laboratory studies of durability and low temperature curing at Opus Research.

2.3.2 *Laboratory prepared specimens for specification development*

For the work reported in section 4.3 (specification development) additional specimens were prepared using the same mix design, aggregates and binders as used in the field trial work. The control mixtures using 80–100 bitumen were manufactured at a temperature of 125°C. The epoxy bitumen mixtures were made with parts A and B heated to 90°C and 125°C respectively, and blended just before addition to the aggregate, held at 125°C. The epoxy bitumen mixtures were held at 125°C for 45 minutes before compaction in the Marshall hammer (50 blows per side).

Further specimens were made using another mix design with different aggregates (Winstones Quarry, Wellington) but the same binders. The grading for these specimens is given in Table 2.

Specimens were subjected to the durability test procedure specified in NZTA P/11 (NZTA T/13). This involves oxidation at 80°C for 72 hours under an air pressure of 2069 kPa (300 psi).

2.3.3 *Durability studies*

Compacted mix specimens were oxidised by heating in a forced draft oven at 85 ± 1°C. The sides of specimens were wrapped in a silicone release paper to prevent slumping and were

Table 1. EMOGPA grading for field trial (typical).

Passing (%) sieve size (mm)					Bitumen content (%)	Air voids % (±95% CL)
13.2	9.5	4.75	2.36	0.075		
95	38	16	11.4	3.6	4.5	20.7 ± 0.4

Table 2. Additional EMOGPA grading for specification development work (typical).

Passing (%) sieve size (mm)					Bitumen content (%)	Air voids % (±95% CL)
13.2	9.5	4.75	2.36	0.075		
99.8	95	22.6	16.8	3.2	5.5	22.2 ± 1.1

supported on solid steel trays. The position of the specimens in the oven was interchanged periodically to minimise effects due to temperature variations in the oven. The specimens were inverted approximately weekly to minimise bitumen drainage, although some minor drainage was observed.

The specimens were aged for 40 days which corresponds to approximately 7–8 years in the field [2].

2.3.4 *Cantabro test procedure*

Mixture abrasion resistance and cohesion was measured using the Cantabro Test. The test procedure and detailed specifications for the equipment are given in APRG 18 [18], which is in turn based on the Los Angeles abrasion test described in AS 1141.234 [19]. In this test, cylinders of compacted mix (100 mm diameter and 50–70 mm high) are brought to a temperature of 25 ± 0.5°C in an incubator and then tumbled in a steel drum (maintained at 25 ± 3°C) for 300 revolutions at 30rpm. The mass of aggregate lost from the specimen through abrasion is recorded as a percentage of the original mass. Specimens tested as part of the durability study were tested at 10 ± 2°C to provide more stringent conditions and for comparison with earlier work [2].

Measurements of 'zero' time specimens (i.e. uncured or unoxidised) were made within 24–48 hours of manufacture. At least four hours (usually overnight) were allowed for specimens to stabilise at the test temperature. The test machine was enclosed in a large cabinet through which temperature-controlled air from a refrigeration/heating unit was circulated.

The Cantabro Test results presented are the mean percentage losses of 4–8 replicates. The error in the mean test results reported was 14% (mean 95% confidence limit).

2.3.5 *Indirect Tensile Modulus (ITM)*

ITM measurements were conducted on a 5 kN test frame (Model UTM-5, IPC Australia Ltd) at 25°C, according to AS 2891.13.1 [20]. This procedure employs a recovered horizontal strain of 50 micro strain (με), a rise time (90%) of 0.04 seconds and a pulse repetition of 3.0 seconds. A Poisson's ratio of 0.35 was assumed. The moduli of 'zero' time specimens (i.e. uncured or unoxidised) were measured within 24–48 hours after manufacture. At least four hours were allowed for specimens to stabilise at the test temperature. The ITM results presented were the mean of 4 replicates. Based on a large number of previous tests the precision of the test results was ±17% (95% confidence limits).

2.3.6 *Curing at 'ambient' temperatures*

Specimens of mix from the road trial were kept in a constant temperature chamber at 23°C and 43% humidity. The sides of the specimens were wrapped with silicone release paper (baking paper) to prevent slumping. The IDT of the specimens was measured periodically at 25°C as described above (section 2.3.5).

3 ROAD TRIAL CONSTRUCTION

3.1 *EMOGPA manufacture*

The EMOGPA mixes were manufactured at the Fulton Hogan asphalt plant in Miners Road Christchurch which is a continuous drum plant with a mixing box. Aggregate is heated to the

desired temperature in a rotating drum before entering a "mixing box" into which bitumen is feed at the desired rate. Mixing is achieved by two rotating mixing arms in the box. The box is not separately heated.

Part A (the less viscous component) was heated to 85°C in a small tank, whilst Part B was decanted from the 200 L drums in which it was supplied into a bitumen distributor truck and maintained at 125°C. Part A was pumped into the main bitumen line (through which Part B travelled). Part A and B proportions were controlled by previously calibrated mass flow meters.

For the 25% and 50% EMOGPA mixes the epoxy bitumen Part B was diluted with the appropriate amount of 80/100 bitumen in a load cell controlled blend tank at Lyttelton and loaded into a small trailer tanker and towed to site.

3.2 *Trial construction*

The trial was constructed on the Christchurch southern motorway duplication in November 2012. Each EMOGPA trial section was about 210 m (100 tonnes) it was laid 40 mm deep and constructed in the west bound left hand lane. The 100% EMOGPA was laid first (starting at the eastern end of the Lincoln road overpass) followed by a control section then the 50% EMOGPA. The 25% section was laid on the westbound lane on 5 November 2012.

All sections were constructed over 125 mm of dense asphalt mix (NZTA AC14) on top of 200 mm of 3.5% cement stabilised basecourse (see Fig. 1). The dense asphalt was laid approximately 2 weeks before the trial; a tack coat of 70% CRS 80/100 emulsion was applied.

The EMOGPA was laid using standard operating procedures and paving equipment. The travel time to the site was approximately 45–60 minutes and trucks typically waited for no more than 15 minutes before unloading into the paver. Air temperatures during construction were about 20°C and the surface temperatures before laying were around 30°C.

The target manufacturing temperature for the control OGPA was 135°C and 120°C for the EMOGPA, however this was exceeded in the case of the 50% material. The mix temperature leaving the paver was 107–110°C for the 100% and 25% EMOGPA but about 10–12°C higher for the 50% material. This error resulted from the plant still being hot from the previous run manufacturing the control mix so that when switching to the short run of 50% EMOGPA the initial manufacturing temperature was too high. The higher mix temperature resulted in some 'dull' discoloured areas (but without segregation) of the 50% EMOGPA section.

Figure 1. Trial pavement structure. Upper most layer is the final OGPA surfacing.

Rolling with steel drum vibrating rollers began generally within a few minutes of paving which resulted in some pick up of mix on the roller especially in the case of the 50% section which had been manufactured at a higher temperature than the other EMOGPA's. Pick-up was avoided simply by letting the mix cool before further rolling or in the case of the 50% EMOGPA site cooling with a water cart. The viscosity of the epoxy bitumen is substantially lower than that of 80–100 bitumen when first mixed and takes time to build. Pick-up observed when rolling was attempted at temperatures above about 70°C; below 50°C no pick-up was observed but rolling of ridges etc. was still easily achieved even at 45°C. The 25% EMOGPA was the easiest to lay and was similar in handling to the conventional OGPA.

3.3 *Initial trial site monitoring*

Water permeability, rutting and friction were measured on the shoulder and outer wheel path of each site about 3 months after construction. Water permeability was measured according to the method given in NZTA P23 notes: 2005 appendix A. method, friction using a British Pendulum tester [21] and rut depth using a straight edge and wedge (Fulton Hogan internal method 2013).

The results show permeabilities to be similar for all sections with the exception of the shoulder on the control site which shows a very wide range of values, the reason for which is not clear.

Friction values were higher on the shoulders than the wheel path in all cases but all four sections gave similar results. In the wheel path the 100% EMOGPA site was slightly higher than the other sections but the difference was not statistically significant.

None of the sections showed any indications of rutting. A visual assessment found all of the sections to be in good condition. The discolouration on the 50% site was still apparent but less pronounced.

4 LABORATORY STUDIES

4.1 *Durability*

Earlier work predicts that EMOGPA should have very long lifetimes in the field [2]. To provide further evidence of the improved durability of EMOGPA compared to standard OGPA mix specimens were oven aged as described in section 2.3.3 and 2.3.4. Results are shown in Figure 2. As the specimens had to be packed and shipped to the testing laboratory the initial ('t = 0') results presented were obtained on specimens that had been at ambient temperature (15–20°C) for 10 days.

The results show that mass loss increases as the epoxy bitumen content decreases, this is consistent with earlier work [2]. The absolute value of the mass losses of the control specimens was higher than observed in earlier work and probably relates to differences in mix design. Even when tested at 25°C control mix specimens lost substantially more mass than is typical for most OGPAs.

The difference between the mean mass loss of the 25% epoxy bitumen EMOGPA specimens (64%) and the controls (84%) was statistically significant at the 95% confidence level.

The 100% specimens showed a decrease in mass loss after oxidation which has been noted previously and can be ascribed to the increased strength due to the curing (crosslinking) process outweighing any effects due to oxidation.

4.2 *Curing at ambient temperature*

Specimens were maintained at 23°C to study the rate of 'strength' (modulus) increase at near ambient temperatures. In previous work on ambient cure specimens were exposed outdoors near the trial site but this procedure was not practical in the current case. Results are shown in Figure 3.

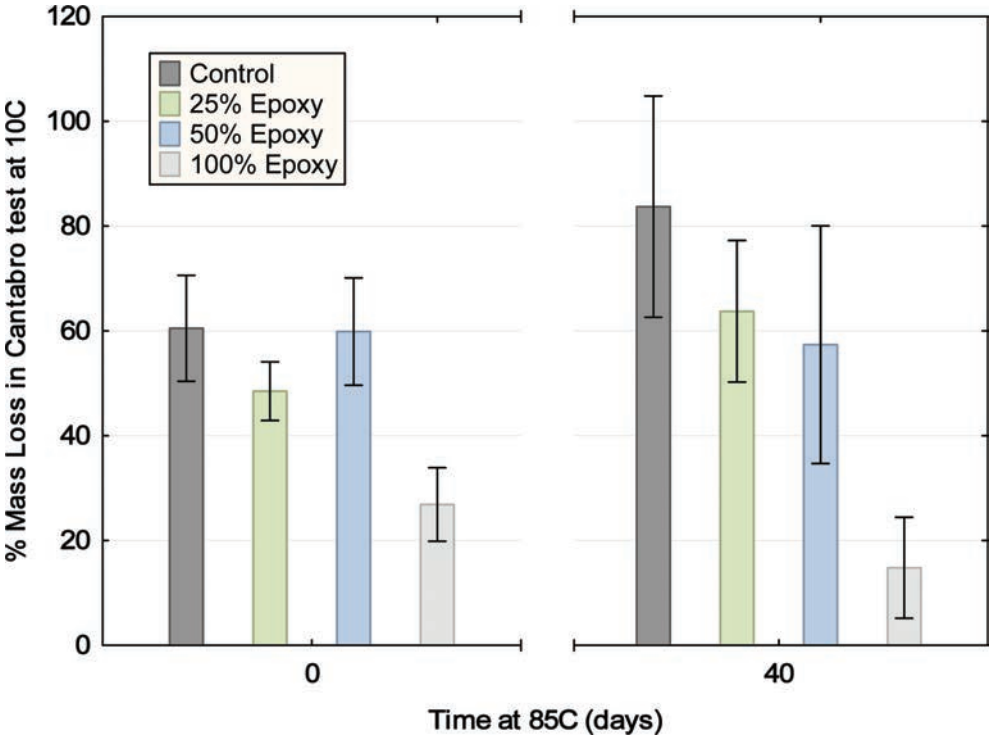

Figure 2. Cantabro test mass losses at 10°C before and after oxidation at 85°C for 40 days.

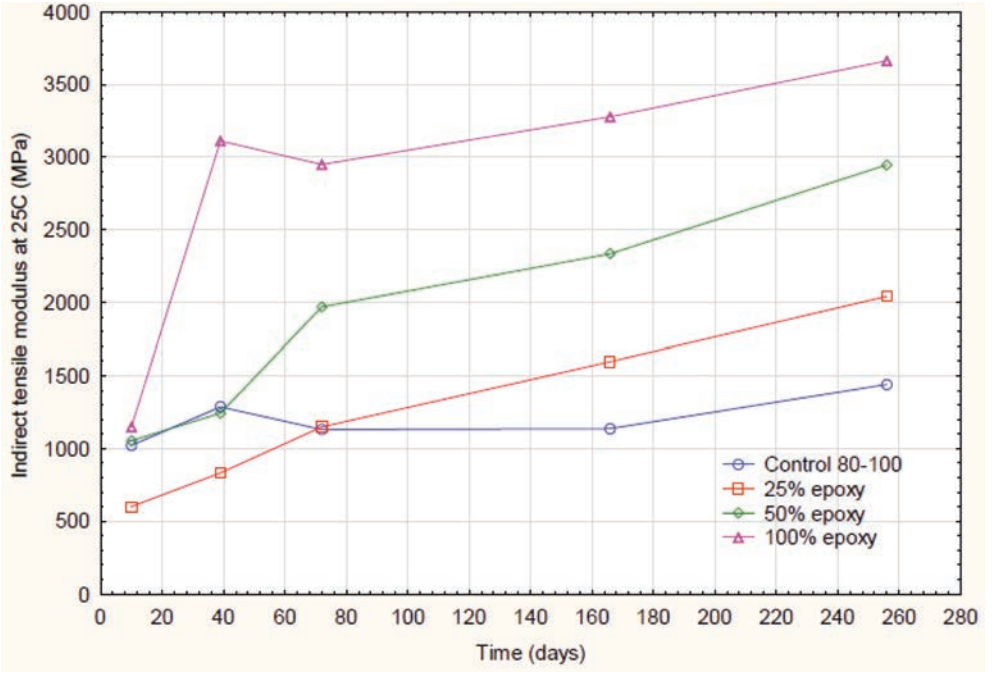

Figure 3. Change in IDT (measured at 25°C) after curing at 23°C.

The control specimens show effectively no net increase in modulus after 160 days. The 25% and 50% EMOGPA specimens show a similar rate of increase in modulus although the initial value of the 50% material is higher perhaps as a result of the (accidentally) higher manufacturing temperature and faster curing. The viscosity of the epoxy bitumen is lower than that of the control 80/100 on first mixing so that both 25% and 50% specimens would be expected to have lower initial moduli than the control. The viscosity of the 100% material should also be lower than that of the other three binders but the higher initial modulus probably is as a result of the faster curing rate of that binder. As noted above the specimens had been transported and stored at ambient temperature for 10 days before the initial measurements were made.

The 100% EMOGPA shows a rapid increase after 40 days but little change thereafter.

4.3 *Specification development*

The NZTA P/11 specification was not written with products such as EMOGPA in mind. In order for epoxy modified products to be specified some criterion that relates either to the chemical composition, enhanced durability of the material or the strength gain through curing needs to be developed. Chemical analysis requires specialist techniques that are generally not readily available in the industry so a physical property measurement is desirable.

For specification purposes a simple measurement of curing rate, in terms of the increase in indirect tensile modulus, at near ambient temperature would be sufficient to confirm the presence of epoxy modified bitumen (see Fig. 3). The drawback of low temperature curing is that the time required to obtain unambiguous results is quite long, 30–40 days. However low temperature ageing does highlight the difference between epoxy materials and standard OGPA more clearly than ageing at higher temperatures, where bitumen oxidation, resulting in hardening of standard mixes, becomes more significant.

5 COST-BENEFITS OF EMOGPA

A long term economic analysis looking at just Agency costs was undertaken on the 25% EMOPGA to determine if it was economically viable to use it. To calculate a mix cost per square meter in place, it was assumed that the binder content of the mix was 5.0%, the compacted mix was laid 40 mm thick and had an air void content of 20% giving a bulk density of 2.015 t m^{-3}. This resulted in an estimated increase in initial cost of \$NZ 6/m^2 for the 25% EMOPGA, this being the cost of more expensive binder. The rates for the conventional OGPA were very low due to the size of the Christchurch Southern Motorway contract and peer review suggests that they were likely a result of front loading the contract rates to improve the contractor's cash flow. Despite this the economic analysis proved very attractive.

Economic analysis using a 6% discount rate over a 40 year analysis period shows the OGPA with an 8 year life has a Present Worth of Costs 2.4 times higher than the 25% EMOGPA with a 40 year life.

There is a financial risk if the material does not perform as well as expected—however this is minor as a 40 year economic analysis at a 6% discount rate shows the 25% EMOGPA only needs an 11 years life to have the same Present Worth of Costs as an OGPA with an 8 year life. The Economic Indicator (EI) for the project was reviewed. The EI being the change in Present Worth of Costs over the change in Initial Cost, it was very favourable at 4.7 and only requires a 14 year life for the 25% EMOGPA to reach an EI of 1.

6 CONCLUSIONS

The trial confirmed earlier trials in that it successfully demonstrated that epoxy modified OGPA can be manufactured and placed without any significant changes to practice. The

25% EMOGPA was the easiest to lay of the EMOPGA materials with similar handling to standard OGPA. Its conventional strength eliminates the risk to plant and pavers of material setting hard if equipment breakdowns occur. The superior oxidation resistance will result in extremely long life when placed in mainline applications where skid resistance issues do not dominate life.

Durability studies using oven ageing at 85°C confirmed earlier work that showed EMOGPA should have a much greater resistance to oxidation than standard OGPA. The effectiveness of the epoxy bitumen modification both in durability and rate of curing reduces as the percentage level is decreased. As in previous work there appears only a small difference between the 25% and 50% modified materials.

A simple procedure based on the rate of curing at near ambient temperatures could be used in a specification to check for the presence of epoxy modified bitumen and potentially as a measure of the concentration present.

With an Economic Indicator of 4.7 the economic case for using 25% EMOGPA is compelling purely on Agency costs alone. These calculations assume a lifetime of at least 40 years for the EMOGPA. Evidence from laboratory studies and practical application of dense epoxy asphalt mixes overseas demonstrates that lives in excess of 40 years lives are easily obtainable. EMOGPA thus has the potential in the long term to reduce the NZTA's current OPGA surfacing budget to 1/6 of its current value, or alternatively provide the ability to far greater volume of noise reducing surfaces at the current OGPA budget level.

REFERENCES

[1] Herrington, P (2013). Epoxy Modified OGPA—Christchurch Southern Motorway 2012 Contract No. 12-838. *Opus Research Report. Wellington.* 27pp.

[2] Herrington, P (2010). Epoxy-modified porous asphalt. *NZ Transport Agency research report 410*. 36pp.

[3] Herrington, P., and Alabaster, D (2008). Epoxy modified open-graded porous asphalt. *Road Materials and Pavement Design 9*, no.3: 481–497.

[4] Balala, B (1969). Studies Leading to Choice of Epoxy Asphalt for Pavement on Steel Orthotropic Bridge Deck of San Mateo-Hayward Bridge. Highway Research Record 287, p. 12–18.

[5] Rebbechi, J.J. (1980). Epoxy Asphalt Surfacing of West Gate Bridge. Proceedings of the 10th Australian Road Research Board Conference, Sydney, Australia, Vol. 10, Part 3, p. 136–146.

[6] Gaul, R. (1996). Epoxy asphalt concrete—a polymer concrete with 25 years experience. *Properties and uses of polymers in concrete*. J. Fontana, A. Kaeding and P. Krauss (Eds). *American Concrete Institute Publication SP:166,* no.13: 233–251.

[7] Lu, Q., Gaul, R., Bors, J. (2012). Alternative Uses of Epoxy asphalts on Bridge Decks and Roadways. ISAP 2012 International Symposium on Heavy Duty Pavements and Bridge Deck Pavements, Nanjing, China, 23–25 May.

[8] Burns, C.D. (1964). Laboratory and Field Study of Epoxy-Asphalt Concrete. Technical Report 3–368, 48pp., US Army Engineer Waterways Experiment Station, US Corps of Engineers.

[9] Dinnen, A. (1981). Epoxy Bitumen for Critical Road Conditions. Proceedings of the 2nd Eurobitume Symposium, Cannes, France, Vol. 2, p. 294–296.

[10] Mayama, M. (1997). The Evaluation of Heavy Duty Binders in Bituminous Road Materials. Proceedings of the Institution of Civil Engineers, Transport, Vol. 123, p.39–52.

[11] Widyatmoko, I., Zhao, B., Elliot, R.C., Lloyd, W.G. (2006). Curing Characteristics and the Performance and Durability of Epoxy Asphalts. Proceedings of the 10th Conference on Asphalt Pavements, Quebec, Canada, 12–17 August 6.

[12] OECD (2008). Long-life surfaces for busy roads. Paris: OECD Transport Research Centre. 185pp.

[13] Herrington, P., Alabaster, D., Arnold, G., Cook, S., Fussell, A., and Reilly, S., (2007). Epoxy modified open-graded porous asphalt. *Land Transport New Zealand research report 321*. 27pp.

[14] Alabaster, D., Herrington, P.R., Waters, J. (2012). Ultra-Long Life Low Noise Road Surfacings. Acoustics 2012 Conference, Hong Kong, 13–18 May, 2012.

[15] NZTA (2007). Specification for open-graded porous asphalt (OGPA). *NZTA P/11:2007*.

[16] ASTM (American Society for Testing and Materials) (2004). Standard practice for preparation of bituminous specimens using Marshall apparatus. *ASTM D6926-04*.

[17] ASTM (American Society for Testing and Materials) (2005). Standard test method for percent air voids in compacted dense and open bituminous paving mixtures. *ASTM D3203-05*.
[18] APRG (Austroads Pavement Reference Group) (1999). Selection and design of asphalt mixes: Australian provisional guide. *APRG report 18*. Sydney: Austroads.
[19] Standards Australia (1995). Methods for sampling and testing aggregates—Los Angeles value. *AS 1141.23:1995*.
[20] Standards Australia (1995). Methods of sampling and testing asphalt—determination of the resilient modulus of asphalt—indirect tensile method. *AS 2891.13.1:1995*.
[21] NZTA (2000). Standard test procedure for measurement of skid resistance using the British Pendulum Tester. Draft NZTA T/2:2000.

Pavement management systems

This page intentionally left blank

Asphalt Pavements – Kim (Ed)
© 2014 Taylor & Francis Group, London, ISBN 978-1-138-02693-3

A performance-based Pavement Management System for the road network of Montreal city—a conceptual framework

Md Shohel Reza Amin & Luis E. Amador-Jiménez
Department of Building, Civil and Environmental Engineering, Concordia University, Montreal, Canada

ABSTRACT: Arterial roads of Montreal city, mostly constructed in 1950's, are at an advanced state of deterioration and need major rehabilitation, upgrading, or even reconstruction. City of Montreal has allocated over $1.6 billion for road infrastructure in its 2012–2014 Three-year Capital Work Program. This investment can be wasted without proper infrastructure asset management system. The current practice of mill and asphalt overlay method by City of Montreal to rehabilitate the pavement is inadequate to repair potholes, fatigue and cracking. A performance-based pavement management system can predict the response and performance of pavement under actual dynamic traffic loads. As of today, implementations of Pavement Management Systems (PMS) are dedicated to achieve optimal levels of condition under budget restrictions. Other important objectives (e.g. mobility, safety, accessibility and social cost), along with investments to upgrade and expand the network, are normally left outside the modelling. This paper presents a conceptual framework of a dynamic PMS for the road network of Montreal City. This dynamic PMS will manage continuous aggregate behaviour of transportation system and can solve optimization problems of pavement management at any time interval.

Keywords: Pavement Management System, dynamic, performance modelling, optimization

1 INTRODUCTION

The pavement management systems is an approach that incorporates the economic assessment of trade-offs between competing alternatives [1, 2, 3]. Historically, pavement management tools such as PAVER and HDM3 [4] were based on cost-benefit analysis incapable of trading-off decisions across asset types and modes of transportation [5]. The adaptation of linear programming and other heuristic optimization techniques for asset management came to address most of these issues [6, 7]. These techniques are capable of finding the optimal path to take full advantage of cost-effectiveness of individual treatments, associated with individual asset elements, and the benefits of advancing or deferring a certain treatment [1, 8]. However, the economic impact of multiple strategies (i.e., rehabilitation versus capital investments) has not yet been addressed for safety, pavement condition, congestion, pollution and social cost. The perception of congestion combined with pavement condition, highway capacity, accessibility, financial incentives, personal safety, and to a lesser degree environmental responsibility impacts personal choices of modes, routes and links [9]. Periodic incorporation of choice models into the Pavement Management System (PMS) will not only render it more tractable mathematically and more consistent with most growth-theory frameworks and distribution models, but also provide a better way of depicting on-going aggregate behaviour and a more satisfactory PMS [9].

The objective of this paper is to outline a conceptual framework of a pavement management system for the road network of Montreal City incorporating dynamic states of land use, traffic volumes, design capacities, and pavement conditions of arterial roads. Most of the arterial roads of Montreal city are constructed in 1950's and are at an advanced state of dete-

rioration. The commonly cited factors of this advanced state of deterioration are improper maintenance, low priority on infrastructure maintenance, inadequate funding, and the use of poor materials in the original construction. The City council seems to focus more on improving patching technology and execution, which don't appear to survive beyond two to five years. Moreover, the investments of City of Montreal on road system have increased more than 560% since 2001. The Three-year Capital Works Program (TCWP) 2012–2014 allocated over $130 million for maintaining and upgrading the city's roads, including $2.5 million that will be used solely for minor bridge and tunnel repairs [10]. A performance-based PMS can predict the response and performance of pavement under actual dynamic traffic loads, and can ensure cost effective scheduling of maintenance and rehabilitation operations.

2 MEASUREMENT OF THE ROAD INFRASTRUCTURE PRODUCTIVITY

The pavement investment policies face important policy questions regarding the uses of pavement maintenance and rehabilitation (M&R) funds such as: What is the optimal level of pavement M&R funding? How can the need for this level of M&R funding be validated persuasively? What choices of M&R sections in the current budget period would most effectively move pavement conditions toward an optimal level in the long-term? [11] There is a wide range of options to achieve a appropriate investment policy. They are: construction with a low initial cost followed by frequent low cost strengthening by overlays, construction of high quality pavements with higher initial costs but lower future maintenances costs, and construction of higher strength initial pavement followed by frequent thin overlays [12, 13, 14]. The first option is applicable when initial capital is limited but a steady flow of maintenance funds are available, however, the second and third options are supported by optimization and design studies.

The productivity of a road infrastructure needs to be understood before developing the optimization and design studies for pavement investment strategies. There is no universally accepted methodology to measure the productivity of a road infrastructure probably because of the lack of methodological consensus and the complexity of the hierarchical characteristics of many sub-systems within the road infrastructure system [15]. The development of cost efficiency analysis methods and methods for analysing deterioration, maintenance and renewal under a budget constraint is necessary [15]. An economic optimization model, with given budget constraints, can differentiate different maintenance scenarios while identifying optimal actions and scheduling schemes [15].

The economic optimization model for PMS consists of pavement deterioration model; user cost model; and construction, maintenance and rehabilitation cost model under possible budgets constraints [11]. Life-Cycle Cost Analysis (LCCA), which is associated with the evaluation of an asset with a definite life expectancy, is an appropriate economic optimization model to examine the subsequent maintenance works on the pavement [12].

3 STUDIES ON LIFE-CYCLE COST ANALYSIS (LCCA)

LCCA is a tool to assess total cost of M&R operations, to distinguish between alternatives, and to provide a basis for identifying trade-offs related to alternatives [16]. LCCA for PMS have been applied in a number of studies [4, 17]. Uddin et al. [17] describe a LCCA program developed for the Pennsylvania Department of Transportation (DOT). The program economically evaluates a range of strategies for design and rehabilitation of road pavements. However, the pavement deterioration algorithm is somehow simplistic [17].

Haas and Hudson [2] suggest a pavement management working system, including pavement deterioration prediction, decision optimization and feedback, and minimum serviceability index. The minimum serviceability index can be computed by Markov Decision Process (MDP) which may also minimize the long-term maintenance costs [18]. Kher and Cook [19] describe the Program Analysis of Rehabilitation System (PARS) model developed by the

Ontario Ministry of Transportation and Communication. The application of maintenance treatments and action timings can also be optimized by MDP [18].

The Texas Transportation Institute has developed optimization models to allocating M&R funds and other resources among highway districts. Under the budget constraints, the models attempt to maintain the quality of the road segments to some pre-specified level [18]. The use of a MDP would take a different approach to optimization since the specified quality of road segments would be calculated in determining the optimal (minimum cost) maintenance policy; an optimum (minimum) budget would then be computed [18]. Scullion and Stein [20] use the pavement deterioration matrices in planning M&R needs, however, the threshold levels of pavement deterioration for taking certain maintenance actions are determined exogenously [18].

Artman and Liebman [21] develop a dynamic optimization programming to schedule the rehabilitation projects of the airfield pavement. The rehabilitation projects are scheduled by maximizing the area under a utility-weighted Pavement Condition (PCR) versus time curve. The optimization programming is somehow similar to MDP; however, it uses the maximization of utility function of pavement condition rather than minimization of cost measures. Another drawback of this method is that the PCR prediction is based on the regression analysis, which does not include current or recent pavement condition data [18].

The discussion of the above-mentioned studies explains that the optimization of PMS can better be addressed by MDP, as it results in optimal solution of preventive maintenance strategies depending on the pavement conditions. The conventional MDP applies an infinite horizon probabilistic Dynamic Programming (DP) to solve the optimization problems in which LCCA is performed on the basis of long-term behaviour of the pavement structure [22].

The applications of MDP for optimization problems of PMS are justifies by various studies. Golabi et al. [23] determine the implications of implementing MDP for the Arizona DOT. Golabi et al. [23] identify that a total of $40 million was saved from the road preservation budget because of applying MDP optimization method. The Arizona MDP model applies two-steps linear programming to get a steady-state solution. A set of steady state maintenance actions was calculated to minimize the expected long-term average costs. If a road was found to be in a particular state, there was a specified probability that a particular maintenance action would be taken. Golabi et al. [23] argue that the PMS has provided a 'defensible procedure for preparing one-year and five-year budgets' and has helped to 'justify the revenue requests before oversight legislative committees.' However, the maintenance policy was found to be stationary, and random and long-term performance standards were not included [18].

Carnahan et al. [24] develop MDP model for optimal decision-making capability of PAVER, which is a PMS developed by the U.S. Army Corps of Engineers Construction Engineering Research Laboratory (CERL). Unlike Arizona MDP model, this model incorporates pavement data as a Pavement Condition Rating (PCR) based inventory at a single point in time. A transition matrix is developed to identify a Markov chain for each pavement type [18]. Feighan et al. [25] also employed dynamic programming in conjunction with a Markov chain probability-based prediction model to obtain minimum cost maintenance strategies over a given LCCA period.

4 PAVEMENT PERFORMANCE MODELLING

The appropriate and effective pavement performance models are the foundation for the long-term analysis of PMS. The performance models calculate the future condition of the pavement based on which PMS optimizes several maintenance treatments in the long-term maintenance process. The performance models have significant features in the PMS such as (1) the performance prediction models are used when the prioritization of maintenance treatments is required for each segments of road network [26], (2) the models enable the transportation agencies to estimate long-range investment requirement during the life-span of the pavement [26], (3) the models also estimate the consequences of budget allocation for maintenance treatments of a particular road segment on the future pavement condition

of that road segment [26], (4) the models can be applied for life-cycle economic evaluation of the pavement as they relate the pavement exposure variables to pavement deteriorations in the performance indicators [26], (5) many components of PMS such as pavement structural design, maintenance treatment strategies, and priority programming are directly related to the output of the Pavement Performance Prediction (PPP) models [27].

The PPP models should be selected carefully; otherwise they may make the highway system costly and may cause optimal pavement design and selection of optimal rehabilitation strategies and timing of projects impossible [28, 29]. Early PMS did not have PPP models rather they evaluated only the current pavement conditions. Later, simplified PPP models, usually based on the engineering opinions on the expected design life of different M&R actions, were introduced by considering age of the pavement as the only predictive variable [30]. The PPP modelling is explicitly complicated as it is very difficult to estimate incorporating a large number of parameters of pavement performance. A variety of approaches can be used to predict pavement performance such as regression [31, 32], survivor curves [33], latent variable models [34], mechanistic models [35] and Markov chain probabilistic models [36].

Probabilistic models recently have received considerable attention from pavement engineers and researchers. Typically, a probabilistic model is represented by the Markov transition process, which is a knowledge-based expert decision model for the prediction of pavement deterioration [27]. Knowing the 'before' condition' or state of pavement in probabilistic form, one can employ the Markov process to predict the 'after' state, again in probabilistic forms, for as many time steps as are desired [26]. The major challenge, facing the existing stochastic pavement performance models, includes difficulties in establishing Transition Probability Matrices (TPMs).

TPMs are estimated using a non-linear programming approach. The objective function of TPMs is to maximize the absolute distance between the actual PCR versus age data points and the predicted PCR for the corresponding age generated by the Markov chain [25]. The assumption is that the pavement condition will not drop by more than one state in a single year. Thus, the pavement will either stay in its current state or transit to the next lowest state in one year. The probability transition matrix has a diagonal structure. The pavement condition cannot transit from this state unless repair action is performed [25].

Several studies [26, 37] applies empirical-mechanistic pavement performance model to calculate PCR. George, et al. [26] executes various regression analyses to develop empirical-mechanistic performance model for the highways in Mississippi based on the pavement condition data during the period of 1986–1988. Several different models were constructed and evaluated. The evaluation was based on rational formulation and behaviour of the model and on its statistical parameters. Exponential and power functions of both concave and convex shapes are identified as statistically significant. The best-fit models for the performance prediction (PCR_t) of flexible pavement with no overlay (Equation 1), flexible pavement with overlay (Equation 2) and composite pavement (Equation 3) are given below [26]:

$$PCR_t = 90 - a[\exp(t^b) - 1]\log\left[\frac{ESAL}{SN^c}\right] \forall a = 0.6349;\ b = 0.4203;\ C = 2.7062 \tag{1}$$

$$PCR_t = 90 - a[\exp(t^b) - 1]\log\left[\frac{ESAL}{SN^c \times T}\right] \forall a = 0.8122;\ b = 0.3390;\ C = 0.8082 \tag{2}$$

$$PCR_t = 90 - a[\exp\left(\left(\frac{t}{T}\right)^b\right) - 1]\log[ESAL] \forall a = 1.7661;\ b = 0.2826 \tag{3}$$

The prediction models recognize the yearly *ESAL* and Structural Number (*SN*) are of only minor importance, while age (t) being the most important factor of pavement performance modelling. George, et al. [26] argue that *ESAL* would be the weakest link in the cumulative traffic computation because several questionable input parameters (e.g. traffic count, the growth factor, the truck factor) are associated with the *ESAL* estimation. George, et al. [26] apply the same argument for the exclusion of the environmental loads which include thermal effects, subgrade movements in expansive clays if applicable, freeze-thaw effects, and bitumen

aging. George, et al. [26] find out that computational accuracy along with the direct influence of *SN* and asphalt concrete thickness (*T*) on the mechanistic parameters (e.g. stress, strain and deflection) is the reason for its significance in the performance model [26].

Lee, et al. [52] develops the Present Serviceability Rating (PSR) of flexible pavements as a function of structural number, age, and cumulative equivalent single-axle loads (Equation 4).

$$\log_{10}(4.5 - PSR) = 1.1550 - 1.8720 \times \log_{10} SN + 0.3499 \times \log_{10} t + 0.3385 \times \log_{10} ESAL \quad (4)$$

Smadi and Maze [37] determine the Pavement Condition (PCR) for the Iowa Interstate 80 based on the 10 years traffic data. The performance curve of PCR is assumed to be a function of only the total number of 18 kip Equivalent Single-Axle Loads (*ESAL*s) that the pavement has experienced (Equation 5) [37]:

$$PCR = 100 - a(ESAL), \text{ a is constant depends on surface type} \quad (5)$$

Traffic volumes, which are transferred into *ESAL*s, can be calculated for each road link by applying four-step transportation modelling—trip production, trip distribution, modal split and choice analysis, and traffic assignment. Trip production is performed by relating the number or frequency of trips to the characteristics of the individuals, of the zone, and of the transportation network. Discrete choice models use disaggregate household or individual level data (personal, household, zonal and transportation network characteristics) to estimate the probability with which any household or individual will make trips. The outcome can then be aggregated to predict the number of trips produced.

Trip distribution models (e.g. growth factor models and gravity models) are used to predict spatial pattern of trips or other flows between origins and destinations. Modal choice model estimation and application is done to predict the zonal shares of trips by mode. The Multinomial Logit (MNL) model relates the probability that a decision unit chooses a given alternative from a set of alternatives to the utility of these alternatives.

The traffic assignment models (All-or-Nothing, STOCH, Incremental, Capacity Restraint, User Equilibrium, Stochastic User Equilibrium, and System Optimum) predict the network flows that are associated with future planning scenarios, and generates estimates of the link travel times and related attributes that are basis for benefits estimation and air quality impacts. The traffic assignment model is also used to generate the estimates of network performance that are used in the mode choice and trip distribution stages of many models.

5 DYNAMIC PROGRAMMING PROCESS OF PMS

The dynamic programming process starts with the calculation of the routine maintenance cost for each state condition in every family (categorized based on the pavement characteristics e.g. type, structure, construction history, condition, use, and rank) in a particular year. Routine maintenance is not feasible if $R_{ijk} = 0$ or state condition $S_j \geq i$ for family *j*. For all feasible states, the cost of routine maintenance is obtained from $C_{ijk,N} = C_{ijk}$, where *k* is the maintenance alternatives [25]. The cost of all feasible maintenance alternatives for year *N–n* is given by Equation 6 [25].

$$C^*_{ijk,N-n} = C_{ijk} + \left[P^1_{ij} * C^1_{ij^1,N-n+1} + \left(1 - P_{ij^1 1}\right) * C^1_{2j^1,N-n+1} \right] * \frac{1}{(1+i^*)} \quad (6)$$

where P_{ij} is the Markov Transition probabilities for state *i* (1 … 10 states) of matrix *j* (1 … *m* families). C_{ijk} is the cost of applying treatment *k* (1 … *n* maintenance alternatives) to family *j* in state *i*. R_{ijk} is the feasibility indicator for alternative *k* when in state *i* of family *j*. $R_{ijk} = 1$ if maintenance alternative is feasible and 0 for infeasible alternative [25].

The first part (C_{ijk}), of the right side of Equation 6, is the immediate cost of routine maintenance in year *n*. The second part ($[P^1_{ij} * C^*_{ij^1,N-n+1} + (1 - P_{ij^1 1}) * C^*_{2j^1,N-n+1}] * 1/(1+i^*)$) is the

total expected cost to be incurred in the remaining years as a consequence of applying routine maintenance operations. This expected cost is obtained by identifying the probability of remaining in a given state and multiplying this probability by the expected cost of that state and then finding the associated probability of dropping a state if routine maintenance is applied and multiplying this by the expected cost of the lower state. This sum is then discounted by the effective interest rate, i^*, to calculate the present net value in the year $N–n$ [25].

The optimum maintenance strategy is then given by Equation 7 [25].

$$C^*_{ijk,N-n} = Min[C_{ij1,N-n}, Ci_{jk,N-n}] \text{ for all } k. \tag{7}$$

With the related optimal maintenance alternative to be performed for this (i,j) family or state combination in year $N–n$ being the choice of k that minimizes the cost in Equation 6. This backward recursion is performed for every successive year of the analysis period until the analysis for year 0, or stage N, is reached. [25].

5.1 *Road user costs of pavement management system*

The objective function of life-cycle cost optimization is not only to reduce the maintenance costs but also to reduce the user costs. The road user costs are defined as the consequences of the periodic M&R strategies of pavement section. Moreover, the vehicle, accident and time costs are directly associated with pavement condition deterioration. Vehicles costs for fuel, lubricants, tires, repairs and depreciation are proportionately related to the pavement surface condition. For example, fuel consumption is a function of vehicle's speed and the road geometry (mainly vertical upgrade and downgrade) [38]. Although an increase of *IRI* has very insignificant impact on fuel consumption and lubricant costs, the impact of rutting is high during the wet season. In rain, when the ruts are full of water, the rolling resistance increases as a function of water depth. The average water depth is a result of cross-fall, rut depth, precipitation levels and intensity, traffic volume, and the driver's behavior. The increase in rolling resistance gives an increase in fuel consumption when driving on wet surfaces [38]. However, repair costs of vehicles are related to *IRI* rather than rutting. For example, the roughness can affect 50% of repair costs for passenger cars and 25% for heavy goods vehicles in Norway road network [38].

The cost of travel time is a product of value of time and the time to travel a certain distance. Traveling time is a result of traveling speed, which is the function of speed limit, road width, and curvature. Speed limit, road width, and curvature generate a speed of 70 km/hr at an average roughness of 2.7 (*IRI*) [38].

The number of accidents within a road section is a product of various casual factors. The Transportation Association of Canada has categorized causal factors into three main groups: road geometry elements, environmental factors and human characteristics [39, 40]. De Leur and Sayed [41] categorized the causal factors into three generic groups such as exposure, consequences and probability. Exposure has been defined as the extent of exposure to road accidents by road users [39, 40]. Consequences can be expressed by the severity of road accidents and the probability was explained as the likelihood of accidents occurrence [39, 40]. Sayyadi et al. [40] identify several road geometrics, traffic and environmental characteristics as the causal factors of road accidents. These are: individual car accident percentage, vehicle's speed, intersections per kilometer, severity of horizontal and vertical alignment, length of the road section, Annual Average Daily Traffic (AADT), light condition, weather-surface condition, road cross-section characteristics, and shoulder and land width.

The objective function (Equation 8) is also to minimize societal cost under budget constraints (Equation 9) [11].

$$Min \sum_i \sum_j \sum_k w_{ik} (C^*_{ik,N-n} + U_{ik}) \forall \sum_i \sum_j \sum_k w_{ik} = 1 \tag{8}$$

$\sum_k w_{ik} \le \varepsilon_i (1+\phi)$ for all unacceptable i and $\sum_k w_{ik} \ge \varepsilon_i (1+\phi)$ for all acceptable i.

$$B(1-\Omega) \leq \sum_i \sum_j \sum_k w_{ik}(C^*_{ijk,N-n}) - \beta \leq B(1+\Omega) \quad (9)$$

where w_{ik} is the fraction of area of pavement in state i with action k applied, B is the budget constraint per year, β is the parametric analysis adjustment on budget constraint, Ω is the tolerance on budget constraint, ε_i is the condition constraint for state i, ϕ is the tolerance on condition constraints [11].

5.2 *Drawbacks of Markov Decision Process (MDP)*

The main drawback of MDP approach is that it does not accommodate budget constraints [42]. Another important drawback of this approach is that pavement sections have to be grouped into a large number of roughly homogeneous families based on pavement characteristics [43]. A large number of families mean fewer sample of pavement sections in each family, which compromises the reliability and validity of the Transition Probability Matrix (TPM) generated for each family [43]. There are equally large numbers of M&R treatments for each family of pavement sections. It is suggested that all pavement sections should be categorized into small numbers of families. As the MDP addresses the performance evaluation of the pavement section as a group, it is not possible to address the performance condition of individual pavement section. Similarly, the optimization programming of M&R strategies are determined for a group of pavement sections rather than an individual section under a given budget. Moreover, the optimization programming of M&R strategies are calculated from the steady-state probabilities. However, in reality, the pavements under a given maintenance policy usually takes many years to reach the steady state and the proportion of the pavements are changing year by year. Therefore, the use of steady-state probabilities in the optimization objective function does not fully reflect reality, especially when this transition period is very long [43].

5.3 *Project-based PMS—an alternative modelling approach*

The project-based modelling approach is based on the analysis of historical performance data stored in the database to develop model coefficients for individual pavement sections. For each individual section, the available historical performance data since the last rehabilitation or construction is analysed to determine the model that matches the observed performance of the section and thus predict the future performance. The cost effectiveness, later on, derived from the prediction performance curve. The pioneer of project-based optimization method for pavement M&R strategies and projects is Arizona DOT [43].

Thompson et al. [11] divide the Finnish highway network into six regional class sub-networks and propose individual optimization model for each of the sub-network group rather than for an individual road segment. Each model is classifed among four dimensions—bearing capacity, pavement defects, rutting, and pavement roughness.

The proposed models by Arizon DOT and Thompson et al. [11] solve the opitmization problem at an individual or group of pavement section, however, the deterioration uncertainty has not yet been resolved. The required budget should treat the uncertainty of deterioration carefully by incorporating stochastic characteristics of road data.

Butt et al. [44] introduce different duty cycles to allow the changes in traffic loads and maintenance polices over the pavement life. This nonhomogeneous Markov model divides the life of the pavement into different zones assuming a constant rate of deterioration for each of these zones. A homogeneous Markov chain and a separate TPM are developed for each zone. On the other hand, a nonhomogeneous Markov chain has been used for transition from one zone to another [44].

A research project titled 'Maintenance Cost Prediction for Road' under the Cooperative Research Centre (CRC) for Construction Innovation has also developed a method that takes into account the variability and uncertainties of road data in investment analysis [45].

Piyatrapoomi et al. [45] identify the variability parameters of the predicted budget, which includes rut depth, AADT, initial roughness and pavement strength [45]. The variability of these parameters was quantified by probability distributions, means and standard deviation for each category. The best fitted probability distribution functions (pdf) for International Roughness Index (IRI), rut depth, and AADT of the Queensland road network are Beta General, log normal and exponential distributions, respectively [45]. Piyatrapoomi et al. [45] apply Latin-hypercube sampling technique to simulate the variability of above-mentioned parameters.

The major drawback to practice project-based optimization is that the complexity of pavement management problems increases exponentially with the size of the problem. For example, the number of possible solutions for project-based optimization problems is M^T, where M is the number of maintenance actions to be considered and T is the number of years (or periods) in the analysis period. If the solution space size for a single section given a certain analysis period and number of available maintenance actions (project level) is C, the solution space size of the network problem, assuming S similar sections, is $\boldsymbol{C}^{\boldsymbol{S}}$. With the general project-level complexity, therefore, this equates to $(A^T)^{CS}$ [46].

Pilson et al. [46] propose a Genetic Algorithm (GA) optimization model to overcome this complexity. The GA optimization model considers each analysis period as a 'gene' and maintenance actions as 'allele' values. A chromosome represents a maintenance strategy for a particular period. The second step of GA optimization model is to measure the 'fitness' of the chromosomes [46]. However, the major drawback of GA optimization model for PMS is that the chromosome has one gene for each pavement section and each gene can take on any value from that section's efficient set. This decomposition of the network problem relies on the independence of the project-level problems, which is not theoretically acceptable for annual budgets [46].

The project-based PMS is still struggling with the large size of problems and solutions. Although we can solve this problem by GA optimization model, there is a decomposition problem of the independence of the project-based PMS. This is not suitable under an annual budget for the whole road network. Moreover, the above-mentioned models optimize the PMS by minimizing the cost, ignoring the maximization of pavement condition.

5.4 *Multicriteria pavement management system*

PMS should include the effect of M&R strategies on other road users such as residents in close proximity from the road, industrial settlements, trade centres, etc. [47]. The Action de Préparation, d'Accompagnement, et de Suivi (APAS) transport research project, funded by the European Commission, develop some indicators for the choice of transport projects using decision criteria optimization [48]. The indicators are developed through simplified Multicriteria Analysis (MCA) techniques such as Elimination et Choix Traduisant la Realité (ELECTRE III) [49, 50] and the Analytical Hierarchy Process (AHP) [51]. Highway Development and Management Tool (HDM-4) applies AHP method to integrate multicriteria factors with the PMS [47].

Cafiso et al. [47] identify ride comfort and environmental factors as the criteria of PMS along with agency costs and user costs. The ride comfort is defined as Ride Number (*RN*) values by National Cooperative Highway Research Program (NCHRP). Ride Number (*RN*) values for alternative k of the section j are obtained from *IRI* (m/km) through Equation 10. IRI_{jkn} equals to *IRI* for the alternative k of the section j at year N [47].

$$RN_{jk} = \frac{\sum_{n=1}^{N}\left(5 - 2.63 \times \log\frac{IRI_{jkn}}{0.343}\right)}{N} \tag{10}$$

The environment parameter for a road segment can be calculated by deriving Air Quality Index (AQI). AQI can be calculated by applying Equation 11 [47].

$$AQI_{jk} = \sum_n \frac{\sum_p E_{pjkn} \frac{1}{S_p}}{\sum_p \frac{1}{S_p}} \times AADT_{jn} \times \frac{L_j}{1000} \tag{11}$$

where AQI_{jk} = AQI for the alternative k of the section j; E_{pjkn} = emission value of the substance p for the alternative k of the section j at year n; $AADT_{jn}$ = average annual daily traffic for the section j at year n; L_j = length of the section j; S_p = concentration limits of a single substance p [47].

Socio-economic development parameter can have significant relation with the PMS. The residents, in close proximity to the invested road infrastructure, may achieve significant socio-economic benefits from the PMS strategies. The characteristics of development parameters of urban area can be demographic characteristics, economic characteristics, social and community characteristics, transportation facilities, urban services and facilities, and environmental characteristics.

Instead of project-based PMS, this paper proposes a PMS for different categories of road groups with different pavement performance curves for each group.

The objective functions of multicriteria PMS are given by Equation 12 and 13.

$$Min \sum_i \sum_j \sum_k w_{ik} (C^*_{ijk,N-n} + U_{ik}) \; \forall \sum_i \sum_k w_{ik} = 1 \tag{8}$$

$\sum_k w_{ik} \le \varepsilon_i (1+\phi)$ for all unacceptable i and $\sum_k w_{ik} \ge \varepsilon_i (1+\phi)$ for all acceptable i.

$$\text{Subject to: } \sum_{n=1}^{N} \sum_{i=1}^{I} L_i Q_{n,i} \ge (LOS) \sum_{i=1}^{I} L_i \tag{12}$$

$$Max \quad \sum_{n=1}^{N} \sum_{i=1}^{I} (W_i * L_i Q_{n,i} + W_2 * MCI_i) \tag{13}$$

$MCI_i = f$(comfort, environment, socio– economic development criteria)

$$\text{Subject to: } B(1-\Omega) \le \sum_i \sum_j \sum_k w_{ik} (C^*_{ijk,N-n}) - \beta \le B(1+\Omega) \tag{9}$$

where $Q_{n,i}$ = Condition Index for asset i on year n; MCI_i = multicriteria index for asset i, and W_1 and W_2 are the weights of the condition index and multicriteria index.

6 CONCLUSION

The pavement management systems incorporate the economic assessment of trade-offs between competing maintenance and rehabilitation alternatives. The conventional techniques are capable of finding the optimal path to take full advantage of cost-effectiveness of individual treatments, however, incapable of addressing safety, condition, congestion, pollution and social cost. The objective of this paper is to outline a conceptual framework of a Pavement Management System (PMS) for the road network of Montreal City.

This paper initially describes the life-cycle cost analysis as the economic optimization model for PMS. The methods of appropriate and effective pavement performance modelling are discussed as the pavement deterioration modelling is the foundation for the long-term analysis of PMS. The framework of Integrated Land Use and Transportation (ILUT) modelling, applying four-step transportation modelling, is explained to predict the future traffic volume during the life-cycle of pavement. ILUT modelling is discussed because the predicted traffic volumes of each segment of road network are transferred to Equivalent Single Axle Loads (*ESAL*s).

The proposed dynamic programming process of PMS points out the drawbacks of the Markov decision process of network-based PMS and is brokering the project-based PMS. The project-based PMS is still struggling with exponentially increasing size of problems and M&R solutions. This study proposes a PMS for different categories of road groups with different pavement performance curves for each group. This paper also proposes the incorporation of road user costs and socio-economic development of the residents (in close proximity to road infrastructure) along with agent costs in the PMS. This dynamic PMS will manage continuous aggregate behaviour of transportation system and can solve optimization problems of pavement management at any time interval.

REFERENCES

1. Hudson, W.R., R. Haas, and W. Uddin. *Infrastructure Management.* New York: McGraw Hill, 1997.
2. Haas, R., and W.R. Hudson. *Pavement management systems.* New York, N.Y.: McGraw-Hill, 1978.
3. Ouertani, M.Z., A.K. Parlikad, and D. Mcfarlane. "Towards an approach to select an asset information management strategy." *International Journal of Computer Science and Applications* 5, no. 3b (2008): 25–44.
4. Watanatada, T., Harral C.G., Paterson W.D.O., Dhareshwar A. .M., Bhandari A., and K. Tsunokawa. *The Highway Design and Maintenance Standard Model.* Washington D.C.: The John Hopkins University Press, 1987.
5. NCHRP. *Analytical tools for Asset Management.* Report 545, Washington D.C.: Transportation Research Board, National Cooperative Research Program, 2005.
6. Robelin, C.A., and S.M. Madanat. "History-dependent bridge deck maintenance and replacement optimization with Markov decision processes." *Journal of Infrastructure Systems* 13, no. 3 (2007): 195–201.
7. Chootinan, P., A. Chen, M.R. Horrocks, and D. Bolling. "A multi-year pavement maintenance program using a stochastic simulation-based genetic algorithm approach." *Transportation Research Part A* 40, no. 9 (2006): 725–743.
8. NAMS. *International Infrastructure Management Manual.* New Zealand: National Asset Management Steering Group, 2006.
9. Donaghy, K.P., and L.A. Schintler. *A Prototype Dynamic Transportation Network Management Model.* Final report, Delaware: Delaware Department of Transportation, 1993.
10. City of Montreal, C. *2012 Operating Budget at a Glance.* Montreal: City of Montreal, 2012.
11. Thompson, P.D., L.A. Neumann, M. Niettinen, and A. Talvitie. "A Micro-Computer Markov Dynamic Programming System for Pavement Management in Finland." *Pavement Management.* 1987. http://www.pavementmanagement.org/ICMPfiles/1987042.pdf (accessed June 28, 2013).
12. Ockwell, Anthony. *Pavement Management: Development of a Life Cycle Costing Technique.* Occasional Paper 100, Bureau of Transport and Communications Economics, Department of Transport and Communications, Canberra: Australian Government Publishing Service, 1990.
13. Potter, D.W., and W.R. Hudson. "Optimisation of Highway Maintenance Using Highway Design Model." Australian Road Research 11, no. 1 (1981).
14. Powell, D.W., J.F. Potter, H.C. Mayhew, and M.E. Nunn. The Structural Design of Bitumen Roads. Laboratory Report 1132, Crowthorne, England: Transport and Road Research Laboratory, 1984. Ramaswamy, R. *Estimation of Latent Performance from Damage Measurements.* Ph.D thesis, Cambridge, Massachusetts: Massachusetts Institute of Technology, 1989.
15. Karlsson, Charlie, Borje Johansson, William P. Anderson, and Kiyoshi Kobayashi. "Infrastructure Meansurement and Management: An Introduction." In *The Management and Measurement of Infrastructure: Performance, Efficiency and Innovation*, edited by Charlie Karlsson, William P. Anderson, Borje Johansson and Kiyoshi Kobayashi, 1–24. Massachusetts, USA: Edward Elgar Publishing Inc., 2007.
16. Christensen, P.N., G.A. Sparks, and K.J. Kostuk. "A Method-based Survey of Life Cycle Costing Literature Pertinent to Infrastructure Design and Renewal." *Canadian Journal of Civil Engineering* 32 (2005): 250–259.
17. Uddin, W., R.F. Carmichael, and W.R. Hudson. Life Cycle Analysis of Pavement Management Decision Making. Final Report, Washington D.C.: Department of Transportation, 1986. Voogd, H. *Multicriteria Evaluation for Urban and Regional Planning.* London: Pion Limited, 1983.

18. Carnahan, J.V. “Analytical Framework for Optimizing Pavement Maintenance.” *Journal of Transportation Engineering* 114, no. 3 (1988): 307–322.
19. Kher, R., and W. Cook. “PARS-the MTC Model for Program and Financial Planning in Pavement Rehabilitation.” *North American Pavement Management Conference.* Washington D.C.: Ontario Ministry of Transportation and Communication, U.S. Federal Highway Administration, 1985. 6.24–6.40.
20. Scullion, T., and A. Stein. “Predicting Maintenance and Rehabilitation Needs for the State of Texas.” *North American Pavement Management Conference.* Washington D.C.: Ontario Ministry of Transportation and Communication, U.S. Federal Highway Administration, 1985. 5.54–5.64.
21. Artman, D., and J. Liebman. “Optimization of Long-range Major Rehabilitation of Airfield Pavements.” *Transportation Research Record* 938, no. January (1983): 1–11.
22. Winston, W. *Operations Research: Applications and Algorithms.* 4th. Belmont, California: homson-Brooks/Cole, 2004.
23. Golabi, K., Kulkarni.R., and G. Way. “A statewide pavement management system.” *Interfaces* 12, no. 6 (1982): 5–21.
24. Carnahan, J., W. Davis, M. Shahin, P. Keane, and M. Wu. “Optimal Maintenance Decisions for Pavement Management.” *Journal of Transportation Engineering* 113, no. 5 (1987): 554–572.
25. Feighan, K.J., M.Y. Shahin, and K.C. Sinha. “Dynamic Programming Approach to Optimization for Pavement Management Systems.” *Transportation Research Board (TRB) Committee AFD10 on Pavement Management Systems.* 1987. http://www.pavementmanagement.org/ICMPfiles/1987039.pdf (accessed June 28, 2013).
26. George, K.P., A.S. Rajagopal, and L.K. Lim. “Models for Predicting Pavement Deterioration.” *Transportation Research Record: Journal of the Transportation Research Board* (Transportation Research Board of the National Academies) 1215 (1989): 1–7.
27. Li, N., R. Haas, and W-C. Xie. “Investigation of Relationship Between Deterministic and Probabilistic Prediction Models in Pavement Management.” Transportation Research Record 1592 (1997): 70–79.
28. Johnson, K.D., and K.A. Cation. “Performance Prediction Development Using Three Indexes for North Dakota Pavement Management System.” Transportation Research Record (Transportation Research Board, National Research Council, Washington, D.C.) 1344 (1992): 22–30.
29. Attoh-Okine, N.O. “Analysis of Learning Rate and Momentum Term in Backpropagation Neural network Algorithm Trained to Predict Pavement Performance.” Advances in Engineering Software 30 (1999): 291–302.
30. Kulkarni, R.B., and R.W. Miller. “Pavement Management Systems Past, Present, and Future.” Transportation Research Record 1853 (2002): 65–71.
31. Humplick, F. *Predicting Pavement Expenditures in Highway Life Cycle Costing.* MSc thesis, Cambridge, Massachusetts: Massachusetts Institute of Technology, 1986.
32. Butler, B.C., R.F. III Carmichael, and P.R. Flanagan. *Impact of Pavement Maintenance on Damage Rate.* Final Report, Vol. 2, Austin, Texas: ARE Inc., n.d.
33. McNeil, S., M. Markow, L. Neumann, J. Ordway, and D. Uzarski. “Emerging Issues in Transportation Facilities Management.” *Journal of Transportation Engineering* 118 (1992): 477–495.
34. Ramaswamy, R. Estimation of Latent Performance from Damage Measurements. Ph.D thesis, Cambridge, Massachusetts: Massachusetts Institute of Technology, 1989.
35. Paterson, W.D.O. *Road Deterioration and Maintenance Effects: Models for Planning and Management.* World Bank Highway Design and Maintenance Standards Series, Baltimore, Maryland: Johns Hopkins University, 1988.
36. Wang, K.C.P., J. Zaniewski, and G. Way. “Probabilistic Behavior of Pavements.” ASCE Journal of Transportation Engineering 120, no. 3 (1994): 358–375.
37. Smadi, O.G., and T.H. Maze. “Network Pavement Management System Using Dynamic Programming: Application to Iowa State Interstate Network.” San, Nation. *Third International Conference on Managing Pavements.* Antonio, Texas: Transportation Research Board, National Research Council, 1994.
38. Haugodegard, T., J.M. Johansen, D. Bertelsen, and K. Gabestad. “Norwegian Public Roads Administration: A Complete Pavement Management System in Operation.” *3rd International Conference on Managing Pavements.* San Antonio, Texas: National Research Council, Transportation Research Board, 1994.
39. Afghari, A.P. *Incorporation of Road Safety into Road Management Systems.* MSc Thesis, Montreal: Department of Building, Civil and Environmental Engineering, Concordia University, 2012.
40. Sayyadi, G., L.E. Amador, and M.S.R. Amin. “A Multivariate Analysis of Road Severity Accident Index.” *23rd Canadian Multidisciplinary Road Safety Conference.* Montréal, Québec: The Canadian Association of Road Safety Professionals, May 26–29 2013.

41. De Leur, P., and T. Sayed. "Development of a Road Safety Risk Index." *Transportation Research Record: Journal of the Transportation Research Board* (Transportation Research Board of the National Academies) 1784 (2002): 33–42.
42. Liebman, J. "Optimization Tools for Pavement Management." *North American Pavement Management Conference.* Washington D.C.: Ontario Ministry of Transportation and Communication, U.S. Federal Highway Administration, 1985. 6.6–6.15.
43. Li, Y., A. Cheetham, S. Zaghloul, K. Helali, and W. Bekheet. "Enhancement of Arizona Pavement Management System for Construction and Maintenance Activities." *Transportation Research Record: Journal of the Transportation Research Board* 1974 (2006): 26–36.
44. Butt, A.A., M.Y. Shahin, S.H. Carpenter, and J.V. Carnahan. "Application of Markov Process to Pavement Management Systems at Network Level." *3rd International Conference on Managing Pavements.* San Antonio, Texas: Transportation Research Board, National Research Council, 1994. 159–172.
45. Piyatrapoomi, N., A. Kumar, N. Robertson, and J. Weligamage. "A Framework for Risk-based Analysis of Investment in Maintenance and Rehabilitation of Large Road Networks." *Joint International Conference on Computing and Decision Making in Civil and Building Engineering, June 14–16.* Montreal, 2006.
46. Pilson, C., R. Hudson, and V. Anderson. "Multiobjective Optimization in Pavement Management by Using Genetic Algorithms and Efficient Surfaces." *Transportation Research Record* 1655 (1999): 42–48.
47. Cafiso, S., A. Di Graziano, H.R. Kerali, and J.B. Odoki. "Multicriteria Analysis Method for Pavement Maintenance Management." *Transportation Research Record* 1816 (2002): 73–84.
48. European Commission, E. *Evaluation Methods: APAS Road Transport Research Project.* Luxembourg: European Commission, 1996.
49. Roy, B. "The Outranking Approach and the Foundations of ELECTRE Methods." *Theory and Decision* 31, no. 1 (1991): 49–73.
50. Hokkanen, J., and P. Salminen. "ELECTRE III and IV Decision Aids in an Environmental Problem." *Journal of Multi-Criteria Decision Analysis* 6, no. 4 (1997): 215–226.
51. Saaty, T.L. *The Analytic Hierarchy Process: Planning, Priority Setting, Resource Allocation*. Pittsburgh, Pennsylvania: RWS Publications, 1990.
52. Lee, Y-H., A. Mohseni, and M.I. Darter. Simplified Pavement Performance Models. In *Transportation Research Record: Journal of the Transportation Research Board*, No. 1397, Transportation Research Board, National Research Council, Washington, D.C., 1993, pp. 7–14.

Asphalt Pavements – Kim (Ed)
© 2014 Taylor & Francis Group, London, ISBN 978-1-138-02693-3

Noise related to pavement preservation surfaces in NJ

John Hencken, Ed Haas, Mike Tulanowski & Thomas Bennert
Center for Advanced Infrastructure and Transportation (CAIT), NJ, USA

ABSTRACT: NJDOT is evaluating the benefits of pavement preservation surfaces and techniques for interstate rehabilitation as a method to increase pavement life while reducing overall cost. A preliminary noise evaluation was conducted at the tire/pavement interface to compare the alternative surfaces to existing in-service pavements as part of a trial study being conducted by the NJDOT. Pavement preservation surfaces provide a benefit in relation to the speed of construction, which reduces the time required for lane closures, increasing public acceptance. Micro-surfacing and chip-sealing were specifically identified as having the highest potential to be applicable at the interstate level. The outcome for the project is to determine an appropriate treatment to reduce oxidization and extend pavement life quickly for a relatively low cost, when a 2% distress level is identified.

Although the design, implementation, and overall properties are different for these pavements, each yielded high noise levels when they were initially paved. It was considered important to conduct measurements at various speeds because these surfaces are frequently used within residential areas. This paper examines the pavement preservation techniques and the related pavement noise measured using the On-Board Sound Intensity Method compared to more commonly used pavements for reference.

Keywords: Pavement preservation, asphalt, noise, OBSI

1 BACKGROUND

The New Jersey Pavement Management System (PMS) has proven to be a critical system to enable the NJDOT to maintain the statewide roadway network effectively. Pavement management systems maximize the return on investment for maintenance and rehabilitation of the statewide network. Pavement management also provides valuable data to legislators and the public to explain the status of the road network [1]. The PMS is also useful to identify areas that need maintenance and to establish minimum condition requirements [1]. The NJDOT is determined to rehabilitate the overall state network to 80% acceptable levels of PCI by 2021. To accomplish this goal they have concluded that pavement preservation and preventative maintenance needs to be conducted earlier in a pavement's lifespan to ensure that the currently acceptable sections remain that way. Micro-surfacing has been suggested as a cost effective method to reduce oxidative aging of an underlying pavement and return PCI to 100% [2]. As such, the state is conducting in-service test applications on various state-maintained roadways to determine how well the technique works. One concern that arises with the increase in use of micro-surface and other pavement preservation techniques is whether or not the new surfaces will provide similar noise properties to current in-service surfaces.

1.1 *Micro-surface*

A micro-surface is a pavement preservation technique that provides a new high friction surface and returns a pavement to 100% Pavement Condition Index (PCI) by applying a thin slurry seal directly on the existing pavement surface. It is utilized in areas that have high crash potential,

to cap pavements that are beginning to exhibit wear, and to increase ride quality on rutted surfaces [2]. It should resist compaction after the initial curing period, and exhibit a skid resistant texture throughout its service life [2]. Micro-surfacing has been utilized in New Jersey previous to this study on at least two roadway sections in 2002 on US-202 S and NJ-29 [3]. This previous micro-surface application was designated as a type III micro-surface which is recommended for use to obtain maximum skid resistance on heavily traveled pavements, to level the existing surface eliminating rutting, or simply to implement a new highly textured surface [2, 3]. The micro-surfaces evaluated in this project are type II, which are used primarily to fill surface voids such as cracks and to provide a durable wearing surface [2]. Micro surfacing can be considerably cheaper than milling and paving by utilizing it as a capping surface when the pavement begins to show distress providing an expected performance of 3–5 years on a high-volume facility [4].

1.2 *Asphalt rubber chip seal*

Chip sealing is an asphalt surface treatment in which an emulsified asphalt binder is applied to the asphalt pavement surface followed by the immediate application of aggregate chips that are rolled to maximize aggregate embedment [4]. By introducing rubber into the emulsification, the chip seal is expected to last longer than a conventional polymer modified mix. Chip seals are used as a wearing course on low volume roads to enhance friction performance, correct minor cracking, roughness, bleeding, and other minor surface distresses [4]. Since the material is cheap to produce, quick to install, and has worked for a variety of road surfaces in NJ, the DOT was interested to learn about the noise levels associated with the surface to determine if it would be a potential application for some of the larger state-maintained roadways. This will be especially important if the longevity of the chip seal is extended due to the use of modified binder and the introduction of rubber.

1.3 *Other pavement preservation surfaces*

This study focused on the implementation of the micro-surface test sections put in place by the NJDOT in November 2012 and the AR chip seal sections laid in October 2012, but it was considered important to include data collected on the other thin-lift surfaces in service throughout the state. There is a significantly comprehensive review of the most current preservation techniques in the Strategic Highway Research Program (SHRP2) renewal research papers, "Preservation Approaches for High-Traffic-Volume Roadways," [5], and the "Guidelines for the Preservation of High-Traffic-Volume Roadways," [4]. The SHRP2 study evaluated a variety of twelve different preservation treatments related to Hot Mix Asphalt (HMA) surfaced pavements that are already in use on high-traffic-volume roadways [5]. An Open-Graded Friction Course (OGFC) is a functional asphalt overlay designed with a uniformly graded aggregate [5]. Stone Mastic Asphalt (SMA) is hot-mix asphalt in which mineral filler is introduced to the bituminous asphalt binder creating a mastic binder mixed with highly angular, uniformly graded aggregate [5]. High Performance Thin Lift overlays are plant mixed HMAs that are placed at roughly 0.75″ to 1.5″ (19–38 mm) with polymer modified binders [5]. An ultrathin bonded wearing course is a thin layer of high quality aggregate which has a gap graded design placed between 0.375″ (9.5 mm) to 0.75″ (19 mm) thick over a polymer modified emulsified membrane; this application is referred to as Novachip. NJ has examples of each of these pavements that are in service and have been tested using OBSI previously. Any functional overlay that could be utilized as a thin-lift laid up to 1″ (25.4 mm) could be considered a pavement preservation technique even though it may undergo performance testing and standardization typical to a HMA mix.

2 NOISE TESTING

2.1 *Testing procedure*

The method utilized to measure the tire/pavement noise for this study was the OBSI method, which provides sound intensity levels measured in dBA [6]. The testing was conducted in

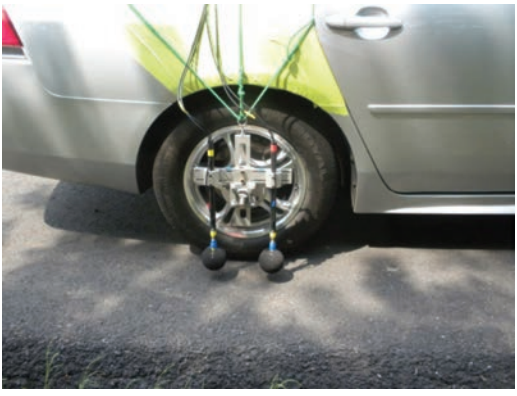

Figure 1. OBSI testing rig.

the right lane of each section to ensure equal comparisons for each section. The equipment utilized to measure the tire/pavement noise on the outside of the vehicle, shown in Figure 1, included four G.R.A.S. phase-matched free-field microphones and preamplifiers for the two probe systems.

The measurements were recorded over a 5.0 second measurement period at 60 mph (96.6 km/h). A minimum of three runs were completed to exceed the coherence, PI index, and run-to-run criteria outlined in AASHTO TP 76-12 [6].

2.2 *Analysis procedure*

The analysis of the measurements taken was completed in several separate processes using the following methods. Each test site was averaged together to get a representation for each material. A table and coinciding bar graph of overall material averages were compiled for each pavement to show the range of differences between each of the pavements tested. Secondly, one-third octave band frequency spectrum graphs were created for each site and averaged to represent each pavement section. The frequency graphs show the measured sound intensity levels along the one-third octave band spectrum, which is the typical frequency band used to show sound measurements for OBSI. Then comparisons were made between different materials. Typically, people are more sensitive to the higher frequencies between 2,000 and 4,000, and the less sensitive to lower frequencies [7].

3 RESULTS AND ANALYSIS

3.1 *Environmental conditions*

The environmental conditions throughout testing were similar for each of the sections, with the exception of the NJ Rt. 24 tested on November 12th, which had an almost 30°F warmer ambient temperature and 21.5°F warmer pavement temperature than the coldest test day, which was experienced on November 15th, at the I-287 test section. Table 1 below shows the ambient, tire, and pavement temperature recorded each test day. The ambient temperature was measured with a handheld Kestral© portable weather station, the pavement and tire temperatures were measured with infrared probes mounted on the OBSI rig.

3.2 *Mix designs*

The mix designs for the micro-surface were completed by Road Science™ and they fell within the specification for type II micro-surfaces outlined in the Recommended Performance Guideline for Micro-Surfacing [2]. Figure 2 shows the gradation chart for the mix, which

Table 1. Environmental and site conditions.

Road	Date tested	AADT	Ambient temp	Tire temp	Pavement temp	Elevation	Number of sites
I-287	11/15/2012	92,020	49.2	61.7	45.7	308	20
I-287	5/16/2013	92,020	68.8	80.2	63.6	308	20
NJ Rt. 24	11/12/2012	109,963	71.2	89	67.2	196	18
NJ Rt. 24	4/8/2013	109,963	78.7	109.1	98.4	145	18
NJ Rt. 133	11/30/2012	16,276	48.1	71.4	45.9	97	26
NJ Rt. 133	5/2/2013	16,276	68.6	98.4	106.9	101	26
NJ Rt. 206	12/6/2012	24,178	54.3	60.7	47.3	583	8
NJ Rt. 23	11/29/2012	2,064	41.4	62.6	47.4	836	8
River	10/8/2012	400	60.5	67.8	59	53	2

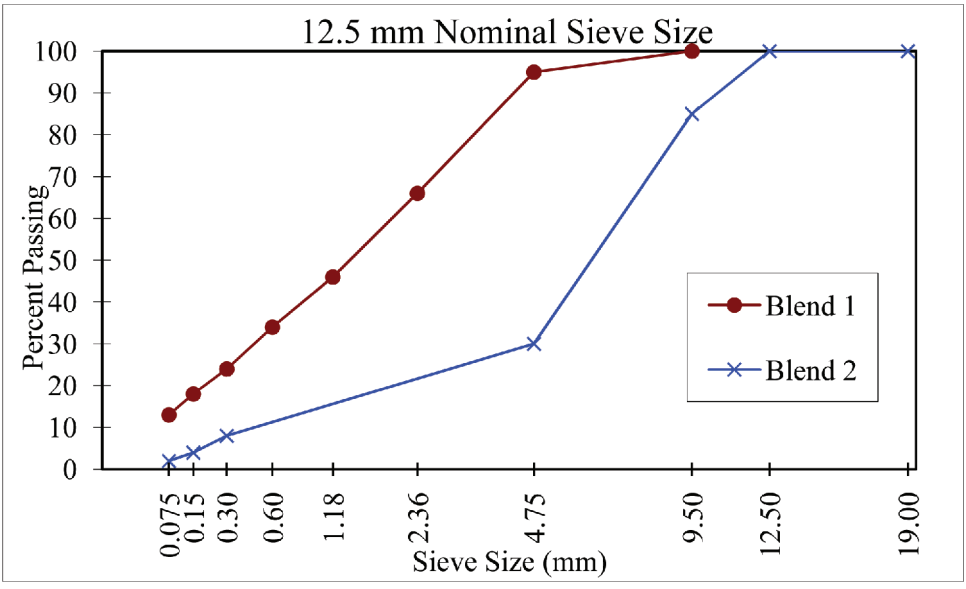

Figure 2. Type II micro-surface and AR chip seal mix gradation.

is labeled Blend 1. The aggregate source was Tilcon Inc. from Oxford, NJ which provided granite type II. The filler used was type I Portland Cement and the asphalt was CSS-1H latex modified MicroTekk™ provided by Road Science™ in Hammonton, NJ.

The AR Chip Seal utilized for this study was paved by the Branchburg Township municipal department, the aggregates were pre coated with PG64-22 by Stavola Inc. and stockpiled at the township complex. The AR binder PG58-28 was applied at a rate of 0.60 gal/yd^2 (0.003 L/m^2). The gradation for the AR Chip seal is shown in Figure 2, labeled Blend 2. An additional specification to screen off undersized material during the pre-coat was specified to allow the high binder content to permeate the mix.

3.3 *Noise levels*

The preliminary and secondary measured values for the micro surface sections on I-287 and NJ Rt. 133 are shown in Figure 3. It also shows the single measured value for AR chip seal tested on River Road in Branchburg Township for both the overall values and the one-third octave band spectrum. Unfortunately, a second test at 60 mph on the AR chip seal was not collected due to safety concerns.

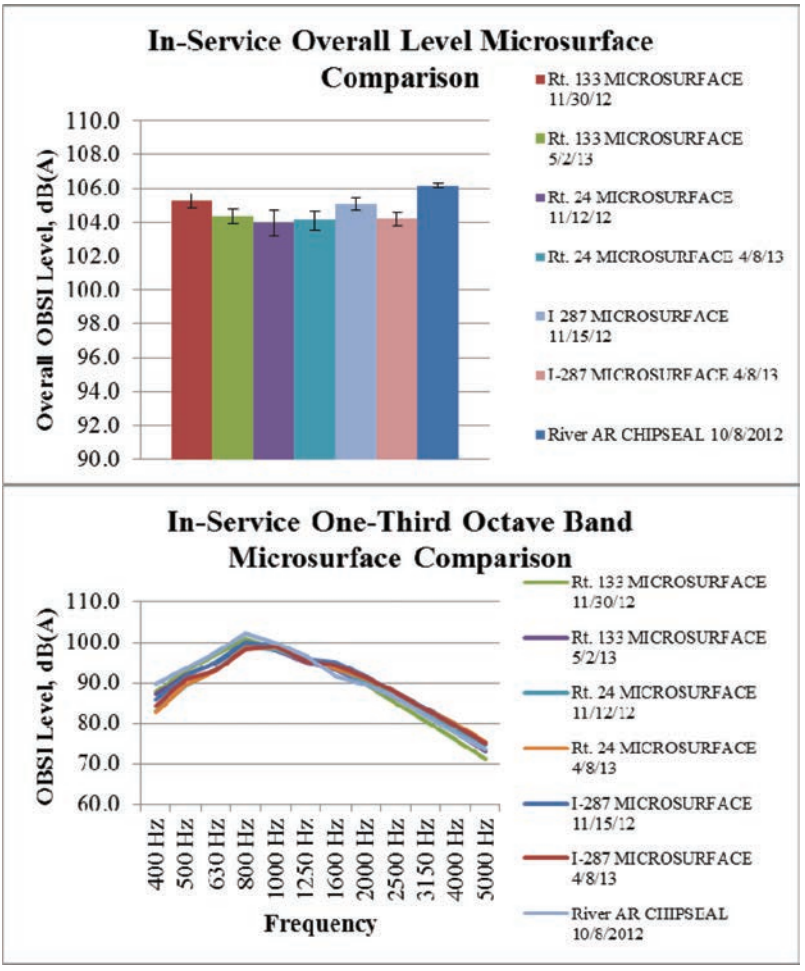

Figure 3. 60 mph (96.6 km/h) micro surface noise levels.

It is easy to see that the AR Chip seal is a loud surface at 60 mph (96.6 km/h). Since AR Chip seal would only be paved on low volume roads and would likely never see legal vehicle speeds as high as 60 mph (96.6 km/h). Initially the I-287 micro-surface had an overall level of 105.1 dBA with a standard deviation of 0.3 dBA. After half a year, the second measurement had an overall average of 104.2 dBA with a standard deviation of 0.4 dBA. The Rt. 24 micro-surface showed a maximum overall level measured at 104.7 dBA and a minimum recorded level at 102.6 dBA, which was a 2.1 dBA difference. The second round of testing measured an overall average of 104.1 dBA with a standard deviation of 0.6 which was similar to the original measured value. NJ Rt. 133 initially measured an average of 105.3 dBA with a standard deviation of 0.4 dBA. The second measurement date on that surface had an average of 104.4 dBA with a standard deviation of 0.4 dBA.

3.4 *Compiled results and external comparisons at 60 mph (96.6 km/h)*

Figure 5 shows the comparison of other in-service pavements throughout the state of NJ to compare noise levels experienced on different pavement surfaces and how those levels relate to the two pavement preservation surfaces measured here. The Novachip and HPTO surfaces would be directly considered pavement preservation surfaces, but AROGFC is shown as well. AROGFC is typically referred to as a quiet pavement, but as a functional

HMA overlay. In addition, a separate graph will relate overall values of other HMA surfaces typically found in NJ.

Figure 4 shows the overall and one-third octave band comparison of pavement preservation materials tested in NJ. The AROGFC measured the lowest on average around 100.0 dBA while the highest was the AR chip seal, which was an average of 106.2 dBA. From the spectral frequencies, the micro surface section was loud in the lower frequencies, which leads us to believe that because the micro-surface is not rolled it has a positive texture that increased the tread impact vibration. The chip seal was also loud in the low frequencies, which is due to the high texture related to that mix. The HPTO noise was also related to the properties of the mix gradation. The well graded small aggregate size mix with low air voids provided a smooth surface with decreased low frequency tread impact noise and louder high frequency noise due to more stick-slip interaction.

Figure 5 shows the comparison of micro-surface to typical HMA surfaces that are in service in NJ in addition to one Portland Cement Concrete (PCC). The micro surface was loud in overall decibel level and was only slightly quieter than the average PCC. It only differed from the PCC in the high end frequency range. The HPTO aligned well with the SMA and DGA, while the SMA was quieter in the low to mid frequencies. AROGFC remains the quietest in-service pavement in NJ, due to the attenuation of sound in the high air void mix.

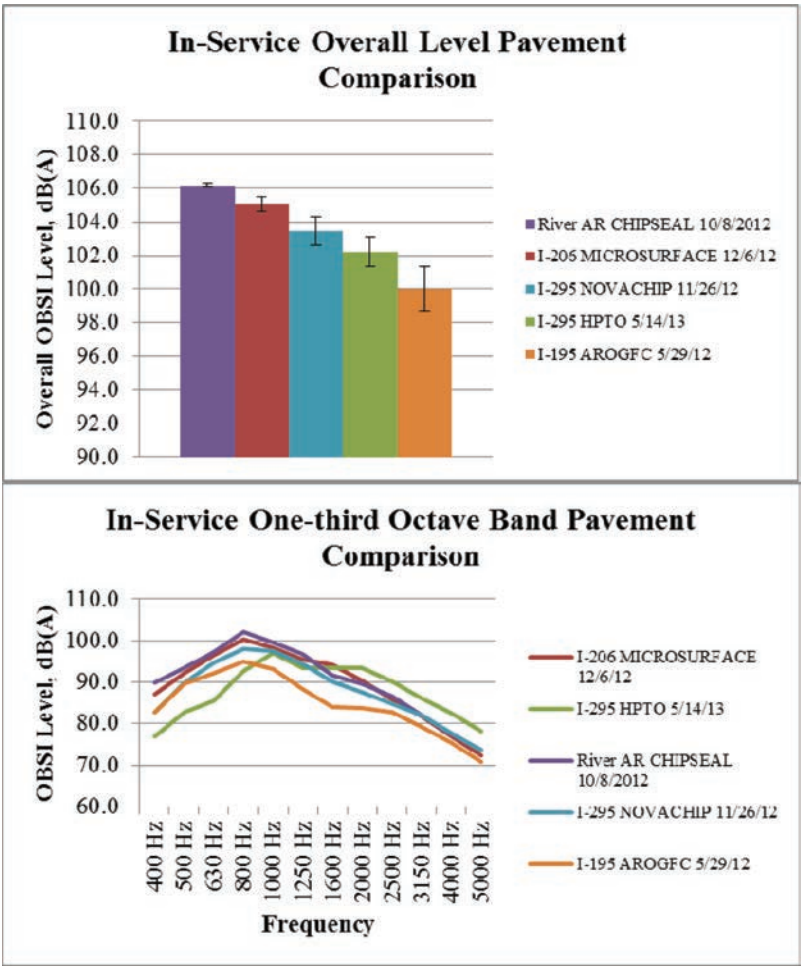

Figure 4. OBSI comparison of pavement preservation alternatives at 60 mph (96.6 km/h).

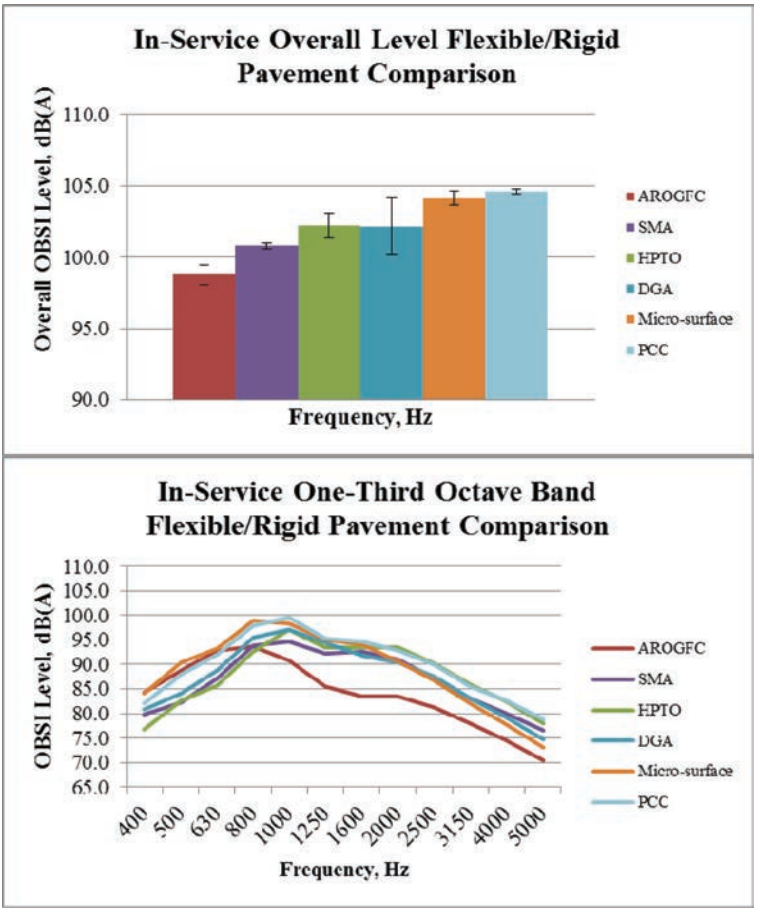

Figure 5. OBSI comparison of microsurface to convetional pavement at 60 mph (96.6 km/h).

4 CONCLUSIONS

4.1 *Noise analysis*

The NJDOT is interested to determine the noise levels for pavement preservation surfaces as they grow in popularity with the state PMS. The focus of the state is shifting to start using micro-surface as a pavement cap for pavements showing as little as 2% distress as measured by PCI. As the PMS switches from rehabilitative to preventative maintenance, the use of preservation techniques as a whole will continue to grow. Since the noise generated at the tire/pavement interface is closely related to the amount of overall traffic noise [8] it is important to understand how the state will be altering the environment for local constituents, especially when evaluating state-maintained arterial system.

Five micro surface sections and three AR chip seal sections were laid because of their low cost, speed of construction, and ease of application. Then these surfaces were noise tested and compared side by side to other pavement preservation techniques utilized throughout the state, namely HPTO, Novachip, and AROGFC. Finally, the micro-surface and AR chip seal were compared to other standard HMA mixes also in-service throughout the state including DGA, SMA, and PCC.

The micro-surface sections were tested initially in November 2012 purportedly a short time after they had been laid. All of the micro-surfaces measured similar values and provided similar one-third octave band spectrum results. The major trend was that the micro-surface seemed

to undergo some smoothing, that lowered the overall value by 1 dBA after a 6 month period except for one pavement measured on NJ Rt. 24, which is thought to have been paved at least 6 months prior to this study. Since the micro-surface on NJ Rt. 24 did not change between the two different tests and because both times it was measured at the lower value, it can also be presumed that after the initial 6 month break in period, the noise level would stabilize. Monitoring of these sections will continue in the future to determine how the acoustic longevity would perform, since there is still potential for more smoothing to occur, which may continue to decrease the overall level. They were a loud pavement option compared to the average DGA measured around 102 dBA, the SMA measured around 100 dBA, and the AROGFC measured around 99 dBA. As shown in Figure 5, it is notable that the micro-surface noise is more prevalent in the lower frequencies, so although the overall level is approaching that of a PCC, the micro-surface would not exhibit the high-frequency whine associated with concrete.

The AR chip seal pavement was tested at a variety of speeds which was useful for comparison purposes. It was tested one time at 60 mph (96.6 km/h) which was helpful for comparison to other pavements within the NJ noise database. Even though the measured value of 106.2 dBA at 60 mph (96.6 km/h) is very loud, the AR chip seal is not a very likely candidate for roads that allow high speeds.

The HPTO, due to its specific uniformly graded attribute of small aggregate, has an average overall noise level of 102.2 dBA, with prevalently loud high frequency noise. Similarly the Ultra-thin Bonded wearing course, or Novachip, has consistently measured an average of 103.5 dBA, which is louder than the HPTO. Since the HPTO, like Novachip, has specific structural uses and is required to undergo HMA performance testing similar to any other HMA, their use is still suggested when necessary.

There are factors other than noise to consider when choosing a pavement preservation surface including the safety associated with that surface, such as skid resistance and the reduction of splash and spray during wet weather. Cost and return on investment are also significant factors in pavement preservation technique selection. The general consensus in NJ is that as long as the new surface is not much more than 3 dBA louder than the original surface, which would be below the normal human perception threshold, it would still be considered acceptable. When there is a desire to specifically reduce noise, the data within this paper suggests that utilizing a thin AROGFC overlay may be the most beneficial option followed by an SMA. At this time in NJ, the SMA surfaces and AROGFC have shown similar longevity of life, but it would also be important to consider that future maintenance such as placing a micro-surface to reduce oxidation, would be applicable on an SMA surface, but not on an AROGFC.

REFERENCES

[1] Shahin, Mo Y. *Pavement management for airports, roads, and parking lots*. Springer, 2005.

[2] International Slurry Surfacing Association. *A143—Recommended Performance Guideline for Micro Surfacing.* Annapolis, MD. 2010.

[3] Bennert, Thomas, et al. "Comparison of Thin-Lift Hot-Mix Asphalt Surface Course Mixes in New Jersey." Transportation Research Record: Journal of the Transportation research Board. No.1929. Transportation Research Board of the National Academies, Washington, D.C., 2005. pp. 59–68.

[4] Peshkin, D., et al. "SHRP2-S2-R26-RR-2—Guidelines for the Preservation of High-Traffic-Volume Roadways." Transportation Research Board of the National Academies, Washington D.C., 2011.

[5] Bennert, Thomas, et al. "Influence of pavement surface type on tire/pavement generated noise." *Journal of Testing and Evaluation.* 33.2 (2005): 94–100.

[6] AASHTO TP076-12. "Provisional Standard Test Method for Measurement of Tire/Pavement Noise Using the On-Board Sound Intensity (OBSI) Method." AASHTO, Washington D.C. 2012.

[7] Bernhard, Robert J., and Rebecca S. McDaniel. "Basics of noise generation for pavement engineers." *Transportation Research Record: Journal of the Transportation Research Board* 1941.-1 (2005): 161–166.

[8] FHWA., the. "Procedures for Abatement of Highway Traffic Noise and Construction Noise." *U.S. Government Printing Office Home Page*. Version Volume 75 Issue 133. Federal Register, 13 July 2010. Web. 30 July 2013. <http://www.gpo.gov/fdsys/pkg/FR-2010-07-13/html/2010-15848.htm>.

Asphalt Pavements – Kim (Ed)
© 2014 Taylor & Francis Group, London, ISBN 978-1-138-02693-3

Significance of non-load related distresses on airfield asphalt pavements: Review of 25 years of pavement management data

John F. Rushing, Jesse D. Doyle & Andrew Harrison
U.S. Army Engineer Research and Development Center, Vicksburg, MS, USA

ABSTRACT: Non-load related distresses are a major factor contributing to the need for maintenance and rehabilitation of Hot-Mix Asphalt (HMA) airfield pavements. By using pavement management system data, the quantity of these non-load related distresses can be determined. This paper summarizes data gleaned from the analysis of over 8 million square meters of HMA airfield pavement to identify the most significant types of surface distresses according to the Pavement Condition Index (PCI). These data represent 25 years of using the pavement management system, Micro PAVER, to determine the condition of U.S. Army airfield pavements. The quantity of longitudinal and transverse cracking, raveling and weathering, and block cracking was extracted from the database for various ages of pavements. In addition, the total percentage of non-load related distresses was identified for various ages of pavements. Findings from this analysis of existing data highlight the need for improved maintenance procedures to combat the need for maintenance and rehabilitation related to non-load distresses in HMA. The benefits of preventive maintenance are discussed, along with the need to monitor the application of various approaches using techniques employed by pavement management systems.

Keywords: pavement management, preventive maintenance, asphalt pavement, pavement distress, environmental damage

1 INTRODUCTION

Both airfield and highway pavements are designed to withstand the stresses exerted by wheel loads for a projected analysis period and traffic volume. The major difference in designing the two types of pavements is in the wheel load magnitudes and in the number of load repetitions anticipated during the design life. Highway pavements typically experience much higher traffic volumes during their service lifetimes than do airfield pavements. As such, highway pavement design requires a detailed analysis of the expected tensile strains at the bottom of the Hot Mix Asphalt (HMA) layer for fatigue consideration. On the other hand, airfield pavements are frequently designed with very thick base course layers compared to highway pavements to reduce stress on the subgrade under aircraft loadings. Traditional conservative design approaches for airfield pavements use a minimal thickness of HMA and often underestimate its structural capacity. In many cases, the HMA layer is in compression during loading, resulting in few occurrences of fatigue damage on airfield pavements. This conservatism generally results in few overall structural failures as long as traffic is limited to the design aircraft.

Most pavement distresses are caused by the interaction of traffic and environment effects, however they can be broadly categorized as primarily load (traffic) related or primarily non-load (environment, materials, construction) related. Many areas of typical airfields will experience limited or no direct aircraft wheel load applications and only occasional light vehicle traffic during their service life. As a consequence, non-load related distresses are the most frequent causes of airfield asphalt pavement damage. Climate, asphalt cement crude source, mixture variables,

and construction variables all contribute to the development of non-load related distresses [1]. Climate is a major contributor to distress formation in HMA. As the binder in the HMA ages, it becomes harder and more brittle, resulting in a less durable pavement. This change in the binder characteristics makes the pavement surface more likely to experience a loss of aggregate (weathering or raveling) or non-load associated cracking. Improper volumetric mixture proportions or poor construction techniques can exacerbate this mixture durability loss.

The U.S. Army Engineer Research and Development Center (ERDC) maintains a database containing information from Pavement Condition Index (PCI) surveys on U.S. Army airfields from 1986 to 2011. In 2011, the database contained information on over 8 million square meters of asphalt-surfaced airfield pavement. These pavement areas included runways, taxiways, and parking aprons. The database contains the most recent inspection data and includes a list of all distresses observed on the pavement surface. Data for asphalt concrete surfaces contained in this database were analyzed to determine the type, quantity, and magnitude of surface distresses. This paper presents findings from this analysis as well as implications for proactive pavement preservation and selection of durable asphalt paving materials.

2 PAVEMENT MANAGEMENT SYSTEM DATA ANALYSIS

The U.S. Army airfield pavement management database contains pavement surface distress data separated into three categories by the pavement management software Micro PAVER. These categories define distresses as primarily load-related, climate-related, or other-related. Primarily load-related distresses include alligator cracking and rutting. Primarily climate-related distresses include weathering/raveling, longitudinal and transverse cracking, and block cracking. Other-related distresses are relatively uncommon distresses such as bleeding, jet blast, and swelling. The analysis of this database is described in the following sections.

2.1 *Distribution of pavement age*

The pavements were first categorized according to their age before further analysis was conducted. Figure 1 shows the total area of asphalt-surfaced pavements in each age group. Figure 1 illustrates the unbalanced proportion of older asphalt-surfaced pavements in the database. The higher proportion of older pavements is likely attributed to two major factors.

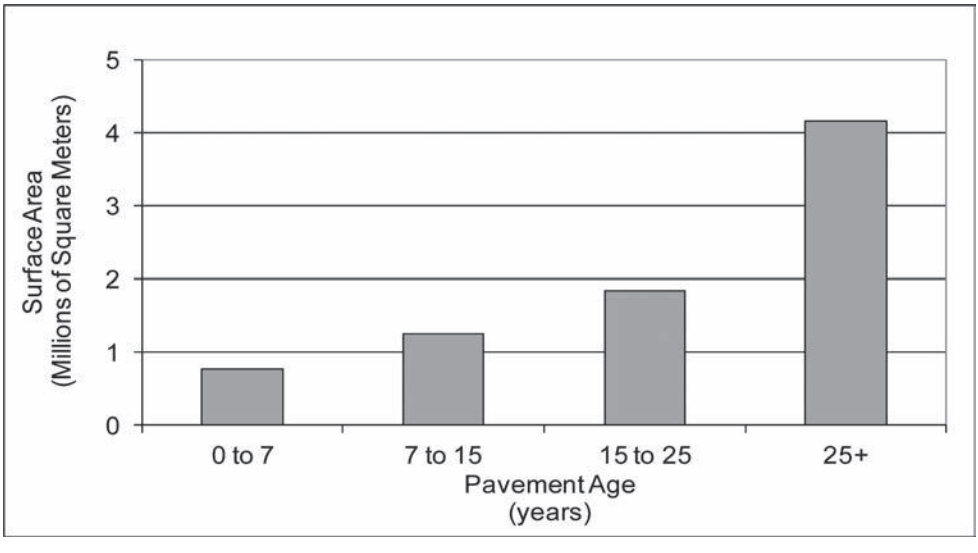

Figure 1. Distribution of pavement in database by age.

First, consolidation of forces and changes in mission requirements has reduced the need for pavement features at some installations. Therefore, the existing pavements have been allowed to age and deteriorate without maintenance and/or rehabilitation. Second, funding constraints have led to prioritization of maintenance projects, and non-essential pavement areas are often neglected. Maintenance funding problems have been realized by many transportation agencies, resulting in an enhanced awareness of the need to improve pavement management practices.

2.2 *Distribution of overall pavement condition*

The condition of the pavements in the database was denoted by the PCI. The PCI is an index from 0 to 100 used to describe the pavement condition through visual inspection [2]. This index only considers surface distresses. The PCI is determined by a cumulative reduction in points from 100 (no distresses) according to distress type and severity. Many transportation agencies use PCI to dictate threshold serviceability levels. The U.S. Army requir es runways, taxiways, and aprons to have minimum PCI values of 70, 60, and 55, respectively [3]. The PCI values reported in the database were computed by the Micro PAVER computer software [4]. Figure 2 shows the average PCI of the pavements in the database according to their age group.

The relative condition of the pavements follows a generally accepted trend. The initial condition of the pavement is expected to be 100 immediately after construction. The early years in the life of a pavement tend to reveal mix or construction deficiencies that result in small deductions in the PCI. Additional years of aging results in rapidly increasing deterioration, as evidenced by the reduction in the average PCI of those pavements greater than 15 years old (Fig. 2). The reduction in PCI is often enhanced because surface distresses allow rapid intrusion of moisture into the pavement system, often leading to additional distress formation. Moreover, the PCI rating system deducts more points as the distresses continue to become more severe. The deterioration of pavements with time is an expected phenomenon. Nearly all infrastructure systems require maintenance and rehabilitation to continue to perform at acceptable levels. The intention of this analysis is to enhance awareness of the nature of the deterioration in order to provide potential solutions for mitigation.

2.3 *Distribution of pavement distresses by type*

Figure 3 shows the relative percentage of each type of distress according to the pavement age. Pavements less than 7 years old have nearly equal proportions of load-related and non-load

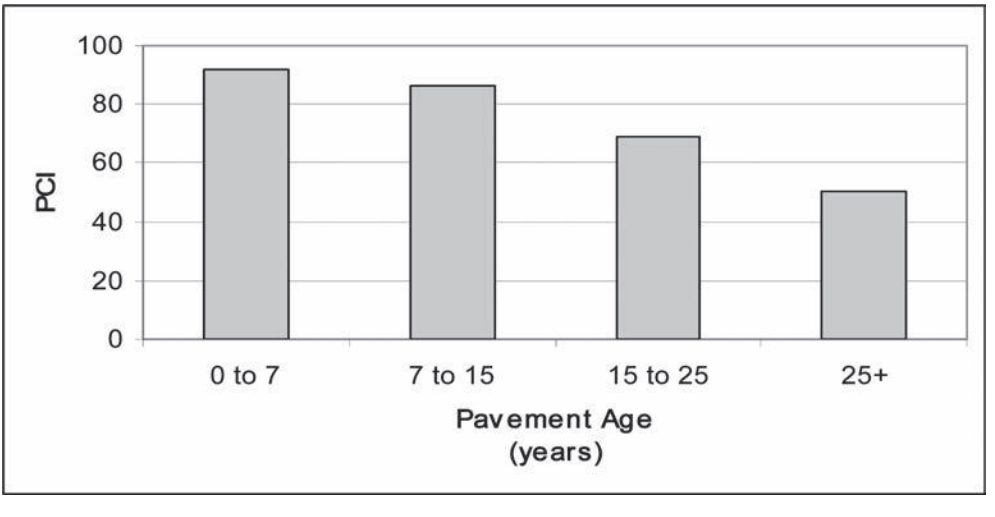

Figure 2. Average PCI of various pavement age groups in database.

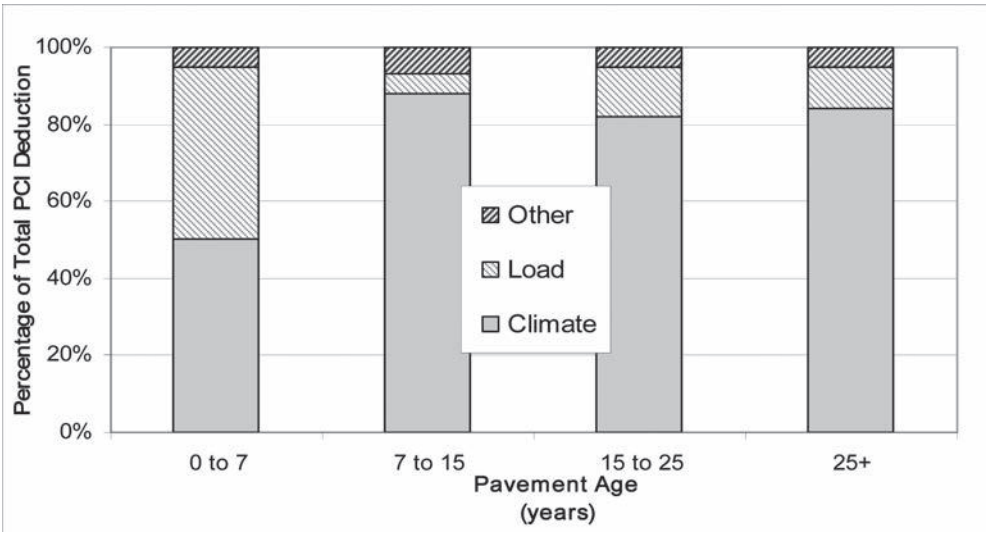

Figure 3. Distribution of PCI deduction factors for various pavement ages.

related distresses. The magnitude of both types of distresses is very low, as evidenced by the average PCI of 92 for these pavements shown in Figure 2. The distresses that do occur can likely be attributed to mixture or construction deficiencies or by external influences such as fuel or oil spillage. These early distresses tend to be minor in nature when adequate quality mixtures are properly placed.

Pavements from 7 to 15 years old had only 5 percent load-related PCI deductions. This range of age is when many of the pavements began to experience longitudinal and transverse cracking and raveling/weathering, and the reduction in PCI is mostly attributed to environmental factors. Pavements greater than 15 years old experience approximately 10 to 15 percent load-related distresses. The increased percentage of load-related distresses is likely caused by softening of the underlying pavement layers from increased moisture intrusion and from the reduction in load-distributing ability of the disintegrated HMA surface layer.

Overall, the data indicates the vast majority of distresses on airfield asphalt pavements are not load-related. Therefore, most of the maintenance and rehabilitation requirements are not caused by traffic volume and will be necessary even if the pavement is not used. Mitigating these types of distresses could result in substantial monetary savings when maintaining HMA pavements. Any maintenance procedure, whether preventive or corrective, must be performed in a timely manner to be effective. Pavement distresses left untreated tend to lead to accelerated deterioration and more expensive repair requirements. Implementing timely, practical maintenance programs is a necessity of a good pavement management system.

2.4 *Detailed analysis of climate-related distresses*

In order to further examine the formation and propagation of non-load related distresses in airfield asphalt pavements, the database was used to extract quantities of each distress type described as climate-related by Micro PAVER. These distresses included weathering/raveling, longitudinal and transverse cracking, and block cracking. The quantity and magnitude of each occurrence was tabulated to determine the overall percentage of the pavements with each distress and severity. Total distress quantities are extrapolated by Micro PAVER from the sample units surveyed during the pavement inspection.

Figure 4 shows the percent of the pavement area with low, medium, and high severity weathering/raveling. This type of distress existed on 0.4 and 7.4 percent of the pavement area from 0 to 7 and 7 to 15 years old, respectively. From 15 to 25 years, the pavements

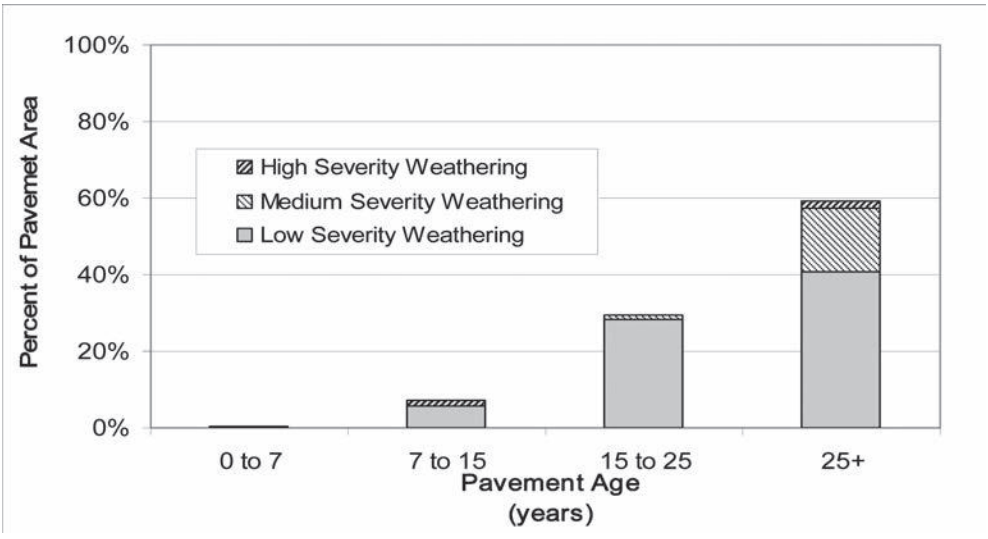

Figure 4. Percentage of pavements with weathering for various pavement ages.

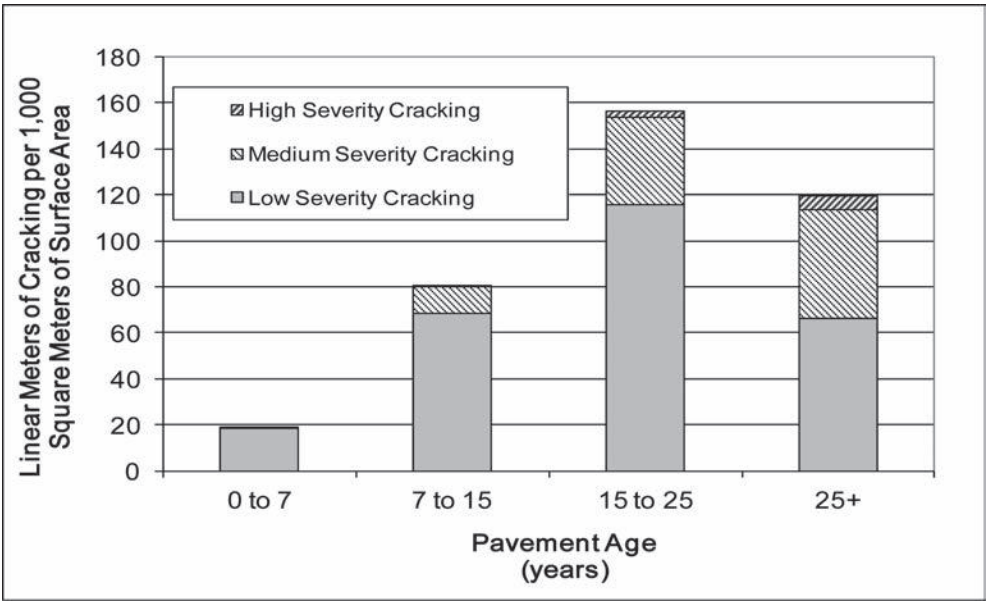

Figure 5. Quantity of longitudinal and transverse cracking for various pavement ages.

experienced weathering on nearly 30 percent of the surface area, and most of the weathering was low severity. After 25 years, a majority of the pavement surfaces was weathered, with an increasing percentage of medium and high severity conditions.

Figure 5 shows the quantity of low, medium, and high severity longitudinal and transverse cracking in the pavement. The quantity of cracking is shown as the number of linear meters of cracking per 1,000 square meters of pavement area. Pavements less than 7 years old experienced approximately 18 meters of linear cracking per 1,000 square meters of pavement area. This proportion would typically represent only a few minor cracks along the longitudinal construction joint or occasional small transverse cracks. Pavements between 7 and 15 years

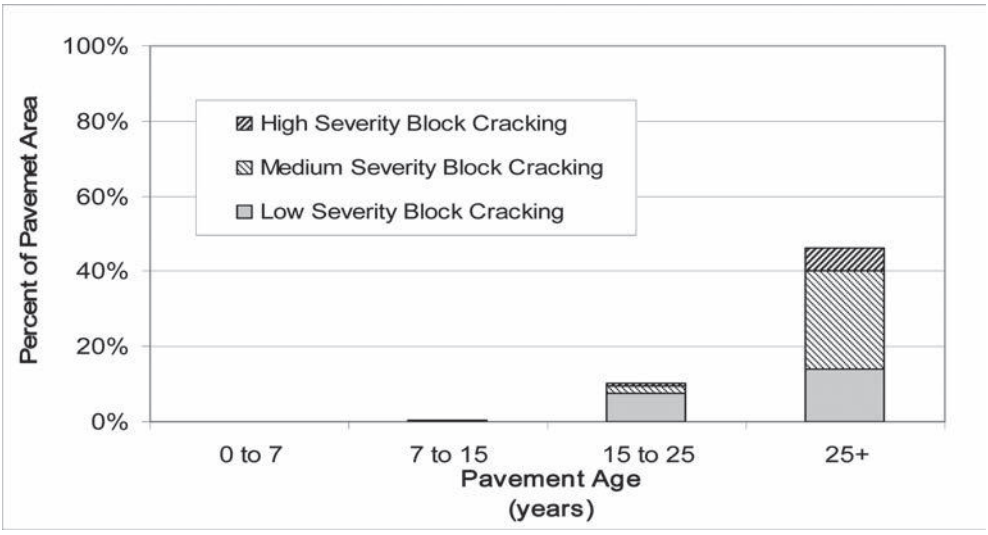

Figure 6. Percentage of pavements with block cracking for various pavement ages.

old experienced approximately 80 linear meters of cracking per 1,000 square meters of pavement area. A small percentage of the cracks were medium severity. This age range is when most pavements began to show visible evidence of cracking. The quantity of cracks likely represents short areas (1 to 5 meters) of cracking along the longitudinal construction joints and some uniformly-spaced transverse cracks. Pavements between 15 and 25 years contained approximately 155 linear meters of cracking per 1,000 square meters of pavement area. This age range is when the pavements begin to rapidly deteriorate. Both the quantity and severity of longitudinal and transverse cracks increases during this time. This increase is likely more significant than the data indicates, because much of the pavement area can be assumed to have received maintenance to fill medium-severity cracks. Additionally, some of the existing cracks begin to interconnect and create areas identified as block cracking. Pavements older than 25 years contained a higher number of medium- and high-severity cracks, indicating a failed asphalt concrete surface.

Figure 6 shows the percent of the pavement area with low, medium, and high severity block cracking. These percentages follow the same trends as the figure above displays. The percentage of the area containing block cracking exponentially increases with age. This correlation is expected because block cracking is the result of interconnecting longitudinal and transverse cracks. Very little block cracking exists in pavements less than 15 years old. Once block cracking is observed, the pavement appears to rapidly deteriorate. The rapid deterioration is likely caused by significant infiltration of water into the pavement system.

3 DATA IMPLICATIONS

3.1 *Pavement preservation*

An implication of the analysis of airfield pavement management data presented in this paper is the value of pavement preservation as a maintenance strategy. Pavement preservation is a concept that targets maintenance of pavement distresses early in the service life so that major rehabilitation is not required. This type of maintenance is often described as preventive maintenance. The rationale for preventive maintenance is that repetitive, low-cost treatments can improve a pavement's condition and reduce the life cycle cost compared to traditional rehabilitation methods that are usually delayed until the pavement is no longer serviceable. Preventive maintenance is particularly attractive for combating non-load related distresses,

because structural improvements to the pavement system are not required. The expectation with preventive maintenance is that pavement condition is maintained above the threshold where rapid deterioration begins to take place.

Transportation agencies are continually challenged with maintaining transportation assets and meeting growing traffic demands, often with reduced budgets. This realization has led to significant growth in the market for pavement preservation products during the past several years. A wide range of materials is currently available. Although the components of these materials vary drastically, the primary component is typically an organic compound that is compatible with asphalt cement. Many products are actually asphalt-cement based. The mechanism by which effective maintenance is achieved by these products is typically the same.

A frequent cause of non-load related distresses is aging of the binder in the asphalt concrete pavement. Binder aging processes include volatilization and oxidation which cause the binder to become stiffer, more brittle and less durable. The ability of the binder to hold aggregate in place is reduced, and the propensity of the asphalt concrete layer to crack in response to internal tensile stresses is increased. The visible effect of these changes is weathering or raveling of the pavement surface and the appearance of longitudinal and transverse cracking.

Preventive maintenance products target these distresses by one of two major methods. The first is that some products contain light oils and soft organic compounds that integrate with the binder in the pavement. The addition of these materials softens the aged binder and enhances flexibility and ductility. Although oxidation of the binder cannot be reversed, the addition of the new material reduces the detrimental effects and returns the mechanical properties of the binder to a condition more similar to its original placement.

The second major method of preventive maintenance is the addition of a sacrificial layer on the pavement surface. This layer can be a very thin spray-applied material or a thicker layer of aggregate and binder placed as slurry. Sacrificial layers seal the pavement, reducing the rate of oxygen and moisture intrusion. The layer itself is allowed to oxidize and deteriorate, protecting the underlying asphalt concrete. Reapplication or replacement of the sacrificial layer must be less expensive than milling and overlaying the existing asphalt concrete for this pavement preservation approach to be effective.

Pavement preservation requires more frequent maintenance than traditional rehabilitation approaches. The cost of these treatments is much lower, however. For example, traditional pavement management establishes a minimum condition index threshold value that a pavement must exceed to be considered serviceable. PCI is one example of a numerical pavement serviceability index scale [2]. Many transportation agencies use PCI to establish threshold serviceability values. Pavements with assessments that show the current condition above the threshold are not scheduled for maintenance. Action only takes place when the pavement condition falls below the threshold value. This type of pavement management is reactive in nature and requires significant funding to replace deteriorated pavements.

A preventive maintenance approach to pavement management includes routine recurring funding to maintain pavements in good condition. By doing this, the pavement condition index is sustained at a high level for many years without requiring major rehabilitation. Figure 7 illustrates the difference between preventive maintenance and traditional reactive rehabilitation.

The example of a pavement preservation approach illustrated in Figure 7 could be the use of a slurry seal on a pavement. The initial slurry seal should be placed early in the pavement life, while it is in good condition. This initial investment would maintain the pavement in good condition for several years until another slurry seal is required. If the cost of the slurry seal is approximately $2 per square meter, the total cost (not adjusted for inflation) of maintaining the pavement would be $4 per square meter over the analysis period. Assuming the alternative is a 2-inch mill and overlay, the cost of allowing deterioration to the threshold value is approximately $7 per square meter. The final pavement condition is similar, resulting in a net savings of $3 per square meter by using the preventive maintenance approach.

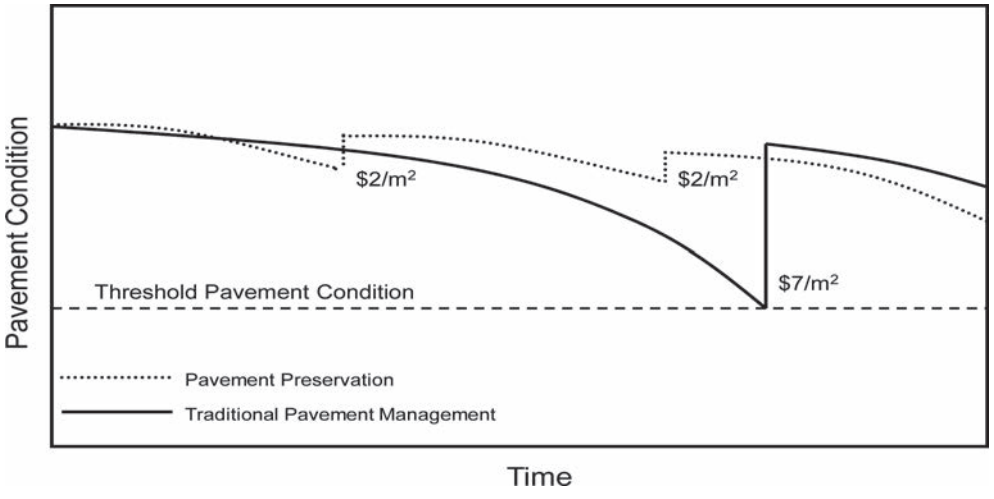

Figure 7. Typical pavement condition with time.

This type of cost analysis has been used to promote pavement preservation to many transportation agencies. The problems with the analysis are the number of variables affecting the true cost and the accuracy of the maintenance requirements. A true gage of the effectiveness of preventive maintenance is needed if there is to be a fundamental shift in the way pavements are maintained. The data presented in this paper provide a confident assessment of the condition of airfield asphalt pavements managed using a traditional rehabilitation approach. It is recognized that funding availability has a significant influence on the timing of maintenance and rehabilitation. However, the major trigger for initiating maintenance and rehabilitation has been a reaction to pavement degradation beyond the threshold values set by operational policy.

3.2 *Mixture materials selection*

An additional implication of the pavement management data analyzed in this paper is the value of selecting combinations of raw materials that result in the most durable possible pavements. Some mixtures are more prone to durability problems related to mixture aging that manifest themselves over time as climate-related distresses such as weathering/raveling and non-load associated cracking. Research has suggested that different aggregate types, binder grades, and volumetric properties have an effect on the durability potential of asphalt mixtures [5]. Furthermore, the compatibility of certain combinations of aggregate and asphalt binder can affect asphalt mixture durability over time [6]. For airfield pavements in particular, the ability to assess the long term durability potential of different asphalt mixtures during mixture design and construction is needed. Ideally, a mixture durability test method and associated conditioning protocol to simulate the effects of long term aging will be simple to perform and able to be used during mixture design and for quality control/quality assurance activities during construction. By selecting material combinations and mixtures with the best durability potential, pavement service life can be maximized. In combination with properly timed application of appropriate preventative maintenance techniques, airfield pavement life can be noticeably improved.

4 SUMMARY AND RECOMMENDATIONS

Data presented in Figure 2 shows that asphalt concrete pavements have an increasing rate of deterioration with time as indicated by PCI. This model of deterioration has been well

documented in literature. Figure 3 indicates that this deterioration is heavily influenced by non-load related factors, as indicated by the small percentage of load-related distresses throughout the life of the pavement. Figures 4–6 solidify the argument that rapid deterioration is attributed to non-load related distresses by showing the rapid increase in quantity and severity of these distresses over time.

A focused research effort is needed to strategically apply preventive maintenance techniques on airfield asphalt pavements in order to quantify the benefits of this pavement management approach. The research should evaluate several prevalent methods of pavement preservation. The cost associated with various treatment methods, as well as the changes in pavement condition with time, must be well documented. A standard condition index such as PCI is a reasonable method of quantifying the appearance of pavement distresses. An analysis period equal to the expected life of an unmaintained pavement will be required to develop the necessary confidence in the results. The documented pavement condition with age can be compared to the data presented in this paper to develop a relationship between the preventive maintenance technique and improvement in pavement condition over time. The costs of the preventive maintenance can be compared to the cost of rehabilitation to show if any financial savings can be achieved by using preventive maintenance. Without this type of data, pavement management personnel will continue to be bombarded by multiple product claims of enhanced performance shrouded in trappings of fiscal responsibility without any tangible evidence that the methods are valid. However, it is reasonable to expect that one or more types of products will prove to have the ability to reduce the rate of appearance of non-load associated distresses in asphalt pavements. Continued research on binder aging mechanisms will provide additional information leading to more successful mitigation techniques. Identifying these techniques and implementing timely preventive maintenance to mitigate the significance of non-load associated distresses as presented in this paper can lead to an enormous improvement in the overall condition of airfield asphalt pavements and reduction in the annual funding required to maintain pavements.

ACKNOWLEDGEMENT

Permission to publish this information was granted by the Director, Geotechnical and Structures Laboratory, U.S. Army Engineer Research and Development Center.

REFERENCES

[1] Hanson, D.I., G. King, M. Buncher, J. Duval, P. Blankenship, and Anderson, M. "Techniques for Prevention and Remediation of Non-Load Related Distresses on HMA Airport Pavements," AAPTP 05-07, Auburn, AL, 2009.

[2] American Society of Testing and Materials. "Standard Test Method for Airport Pavement Condition Index Surveys," Designation: D 5340-10. West Conshohocken, PA. 2004.

[3] Army Regulation (AR) 420-1, Headquarters, Department of the Army 2007.

[4] Shahin, M.Y., Micro PAVER Version 5.3 User Manual, U.S. Army Corps of Engineers, ERDC-CERL. http://www.cecer.amry.mil/paver.

[5] Doyle, J.D., and Howard, I.L. "Characterizing Dense-Graded Asphalt Concrete with the Cantabro Test," Transportation Research Board 93rd Annual Meeting, TRB, Jan. 12–16, 2014, Washington, D.C., Paper No. 14-4013, 2014.

[6] Howard, I.L., and Doyle, J.D. "Interaction of Construction Parameters, Environmental Conditions, and Dense-Graded Asphalt Concrete Measured by Cantabro Test," Submitted to Construction and Building Materials.

This page intentionally left blank

Asphalt Pavements – Kim (Ed)

Analysis of rolling resistance models to analyse vehicle fuel consumption as a function of pavement properties

James Bryce
Virginia Tech Transportation Institute, Blacksburg, VA, USA

Joao Santos
University of Coimbra, Coimbra, Portugal
Virginia Tech Transportation Institute, Blacksburg, VA, USA

Gerardo Flintsch
Center for Sustainable Transportation Infrastructure, Virginia Tech Transportation Institute, Blacksburg, VA, USA
The Charles Via, Jr. Department of Civil and Environmental Engineering, Blacksburg, VA, USA

Samer Katicha
Virginia Tech Transportation Institute, Blacksburg, VA, USA

Kevin McGhee
Virginia Center for Transportation Innovation and Research, Charlottesville, VA, USA

Adelino Ferreira
Road Pavements Laboratory, Department of Civil Engineering, University of Coimbra, Coimbra, Portugal

ABSTRACT: This paper presents an analysis of two recently developed models that relate pavement properties to vehicle rolling resistance and fuel consumption, as well as the sensitivity of each model to roughness, texture and future traffic predictions. The two models are the Vehicle Operating Cost model developed as part of the National Cooperative Highway Research Program (NCHRP) project 1–45 outlined in NCHRP report 720, and the model developed as part of an international collaboration, Models for rolling resistance In Road Infrastructure Asset Management systems (MIRIAM). Furthermore, several pavement related factors that contribute to vehicle rolling are discussed in this paper. It was found that the fuel consumption was highly sensitive to future traffic growth projections. Also, the pavement macrotexture can have a significant impact on excess fuel consumption of vehicles, particularly in the case that the MIRIAM model is used to calculate fuel consumption.

Keywords: Pavements; energy Consumption; rolling resistance; lifecycle assessment

1 INTRODUCTION

According to the Texas Transportation Institute (TTI), in 2011, congestion in the top U.S. urban areas resulted in an average of 19 gallons of excess fuel consumption per auto commuter per year [1]. Although it is expected to be significant, there is no similar figure assessing the wasted fuel due to the trillions of Vehicle Miles Travelled (VMT) over rough pavement sections that contribute to relatively high rolling resistance values. Rolling resistance is the mechanical energy loss by a tire moving a unit distance along the roadway, and is effected by both properties of the tire and of the pavement [2]. The energy that is lost comes directly from the power that is used to propel the vehicle, and as a consequence, more fuel must be

consumed to propel a vehicle over a pavement with higher rolling resistance. Evans et al. [2] reported that as much as 1/3 of the total energy that is available to the wheels can be expended to overcome the rolling resistance. Other factors that consume the energy used to propel the vehicle (the energy that makes it through to the driveline) are aerodynamic resistance and braking [3].

Evans et al. [2] measured the rolling resistance of several different tire types and reported that 0a 10 percent reduction in rolling resistance can lead to a 1 to 2 percent reduction in fuel consumption, with an average reduction of 1.1 percent. Schuring and Futamura [4] have shown that this relationship can be taken as linear. TIAX [5] reported that during highway driving, the 2 percent reduction in fuel consumption per 10 percent reduction in rolling resistance is expected, and the figure is closer to a 1 percent reduction during urban driving. Some estimations have shown that a 10 percent reduction in rolling resistance could save between 1 and 2 billion gallons of fuel annually (of 130 billion gallons currently consumed) among the passenger car fleet, assuming the driving habits used in the 2006 study [3]. Thus, it can be conclusively said that if the rolling resistance of a pavement were reduced, the vehicle fuel consumption along that pavement would also be reduced.

2 OBJECTIVE

The objective of this paper is to discuss the impact of pavement properties on vehicle rolling resistance, as well as present an analysis and comparison of current rolling resistance models. Two commonly used models to assess the additional vehicle fuel consumption due to rolling resistance will be compared, one model from the United States and one from Europe.

3 BACKGROUND

Many factors contribute to the fuel consumption of a vehicle, not the least of which is the interaction of the vehicle tire with the pavement surface. One of the earliest studies on the effects of road roughness on fuel consumption was performed in 1983 in Sweden at VTI (the Swedish National Road and Transportation Research Institute) [6]. The study evaluated 20 different roadway characteristics representing the full range of Swedish roads at speeds of 50, 60 and 70 km/h (30, 37 and 45 mph). Vehicle fuel consumption was found to be correlated best with short wave unevenness ($r = 0.91$), mega-texture ($r = 0.83$) and macro-texture ($r = 0.60$).

Mega-texture is generally defined as a pavement surface texture due to surface irregularities having a relative wavelength between 5 cm and 0.5 meters (2 in and 20 in) [7]. Pavement macro-texture is generally defined as a pavement surface texture having a relative wavelength between 0.5 mm and 50 mm (20 mils to 2 inches), and is a result of large aggregate particles in the mixture [7]. It is important to note that macro-texture plays an important role in pavement friction. The short wave unevenness range is close to the wavelength sensitivity range of the IRI which is between 1.2 to 30 m (4 to 100 ft) [8]. The following are pavement related factors that have been identified in past research as pertinent to consider during an analysis of the rolling resistance of the pavement [9, 10, 11]: macro-texture, pavement stiffness, roughness, rutting and the transversal slope of the pavement.

3.1 *Macro-texture*

Chatti and Zaabar [11] evaluated the effect of pavement macro-texture on fuel consumption, and determined that an increase in fuel consumption with increasing mean profile depth of the pavement was statistically significant at the 95 percent confidence level for lower speeds. Laganier and Lucas [12] found that macro-texture could lead to overconsumption of up to 5 percent from a base consumption of 0.7 l/km (0.3 gallons/mile). At high speeds, it is expected that aerodynamic resistances dominate the resistance forces, thus causing the

effect of macro-texture to be overshadowed. Conversely, Sandberg [6] found that the effect of macro-texture on fuel consumption was more defined at higher speed; though the author pointed to a possible cause of low speed driving having a lower correlation as poorly selected driving conditions.

The increase in fuel consumption as a function of the pavement macro-texture is dependent on the vehicle type, and is expected to be higher for heavy vehicles. According to Sandberg [13], the lower limit for expected effect of macro-texture on rolling resistance is a 2.5 percent increase in rolling resistance per unit increase of mean profile depth (in mm). Zaabar [14] reported that for trucks, an increase in mean profile depth from 0.5 mm (0.02 in) to 3 mm (0.12 in) is expected to result in an increase in fuel consumption between 1 and 1.6 percent. Hammarström et al. [15] used coast-down methods, or measurements of a vehicles velocity or acceleration while it is allowed to roll freely across a section of pavement, to measure the impact of pavement roughness, travel velocity and macro-texture on rolling resistance. The research proposed a set of equations to relate rolling resistance to macro-texture and roughness by comparing measurements taken during the research and theoretical models used to quantify the impact of each factor. The tests were conducted using a car, light truck and heavy truck. Some generalized results presented by Hammarström et al. [15] are that an increase in rolling resistance of 17 percent per unit of mean profile depth is expected for a starting speed of 50 km/h (30 mph) for the car, and an increase of 30 percent per unit of mean profile depth is expected for a starting speed of 90 km/h (55 mph) for the car. The results showed that if the total driving resistance is considered, an increase in mean profile depth from 0 to 1 mm (0.04 inches) at 50 km/h (30 mph) is expected to lead to an increase of driving resistance of 10.5 percent for the car. The researchers noted that more measurements would be required to obtain results for the trucks.

3.2 *Pavement stiffness*

Much of the research pertaining to the impact of pavement stiffness on rolling resistance has been derived from studies comparing asphalt concrete pavements to Portland cement concrete pavements. Taylor and Patten [16] conducted field tests using both cars and heavy trucks driven over asphalt concrete pavements and Portland cement concrete pavements in order to evaluate differences in fuel consumption for each case. The research also tested over multiple seasons and the trucks were subjected to multiple loading conditions. In most cases, the results of the research showed anywhere from a 1 percent to a 5 percent savings in fuel consumption when driving on concrete pavements. However, during many of the tests during summer days, the research indicated a fuel saving for composite pavements when compared to concrete pavements [16]. Although the test results indicated differences in fuel consumption with varying pavement stiffness, the developed models did not include surface wear and anomalies (e.g. potholes). Furthermore, other surface properties, such as tining of the concrete surface or texture of the pavement, were not accounted for in the study. Thus, the results of the study are not considered ideal for inclusion in an LCA of the use phase of the pavement.

Santero et al. [9] evaluated the impact that the pavement stiffness has on the fuel consumption of a vehicle travelling along the pavement by developing a mechanistic model. The researchers proposed a beam on elastic foundation as the model to describe the behaviour of the pavement subjected to a wheel load, and calibrated their model using data from the Long Term Pavement Performance (LTPP) database. The model indicated less fuel consumption over more stiff pavements, especially in the case of truck traffic. However, it is important to note that the model was developed in order to better understand the mechanisms that contribute to increasing rolling resistance with increased deflections, and field studies were not conducted to calibrate the model.

A follow up to the study by Santero et al. [9] was conducted that calibrated the model that was developed to describe pavement deflections, and scaling factors were developed for each of the inputs [17]. The calibration was conducted using additional sites from the LTPP database, and an example application of implementing the model into an LCA was conducted

using data from the Athena Institute. The results of the study indicated that for high volume roads, the Greenhouse Gas (GHG) emissions from the pavement-vehicle interaction can be greater than the GHG emissions from the materials and construction phases [17].

Whereas much research has been conducted on the differences in pavement type on rolling resistance, Wang et al. [18] pointed out that sufficiently validated models have yet to be developed to calculate the impact of pavement stiffness on fuel consumption and emissions. This is mainly a consequence of the experimental designs of the studies that compare asphalt pavements to concrete pavements. Although models were developed by Akbarian and Ulm [17] as well as Santero et al. [9] to quantify the impact of stiffness on fuel consumption, these models are generally considered first order attempts at understanding the mechanism of the pavement vehicle interaction, and are not yet sufficiently corroborated with field measurements to be used in a pavement LCA.

However, even in the absence of calibrated models, there is strong research demonstrating the differences in fuel consumption between asphalt and concrete pavements over certain conditions. Zaabar [14] showed that at 56 km/hr (35 mph) during summer conditions, there is a statistically significant difference between vehicle fuel consumption along apshalt and concrete pavements for trucks. The development of more accurate models in the future will facilitate the inclusion of pavement type, or pavement stiffness, into a pavement use phase LCA.

3.3 *Pavement roughness*

An early study on the impact of the pavement roughness on fuel consumption was conducted in 1983 in Sweden at VTI [6]. The difference in fuel consumption between smooth and rough pavement was around 4.5 percent [19]. Laganier and Lucas [12] found that pavement unevenness could lead to overconsumption of fuel of up to 6 percent from a base consumption of 0.7 l/km (0.3 gallons/mile). Laganier and Lucas [12] also calculated the power lost in the shock absorbers as a function of roughness level and found most loss occurs at wavelength between 1 m (3.3 feet) and 3.3 m (10.8 feet) which corresponds to the unevenness range as well as the most sensitive IRI range. According to Sandberg [13], the lower limit for expected effect of roughness on rolling resistance is a 0.8 percent increase in rolling resistance per unit increase of IRI (in m/km).

In the United States, WesTrack test results showed that rougher pavements result in increased fuel consumption of trucks [20]. Zhang et al. [21] used the WesTrack models in the LCA of an overlay system. One downfall of the WesTrack model was that it was developed for heavy trucks over a small variation of conditions. Zaabar [14] evaluated the impact of pavement roughness (in terms of IRI) on the change in fuel consumption, and used the data to calibrate HDM 4 prediction models.

Hammarström et al. [15] also measured the impact of pavement roughness on rolling resistance using coast-down measurements. The research found that for the car, an increase in rolling resistance of 1.8 percent per unit of IRI is expected for a starting speed of 50 km/h, and an increase of 6 percent per unit of IRI is expected for a starting speed of 90 km/h. The results for the car showed that if the total driving resistance is considered, an increase in mean profile depth from 0 to 1 at 50 km/h is expected to lead to an increase of driving resistance of 1.2 percent. The researchers noted that more measurements are required to obtain results for trucks.

Chatti and Zaabar [11] reported the results of calibrating the HDM 4 models for vehicle operating costs in the National Cooperative Highway Research Program (NCHRP) report 720. During this research, fuel consumption models as a function of pavement roughness for several vehicles and several speeds were calibrated. A vehicle operating cost modelling program was developed in the form of a spreadsheet tool by Chatti and Zaabar [11] as a part of the NCHRP project. Part of the spreadsheet output is the estimation of the additional fuel consumption as a function of the following variables; pavement roughness, mean texture depth, roadway grade, super-elevation, pavement type (i.e. asphalt vs. concrete), vehicle speed and air temperature.

3.4 *Rutting*

Rutting was one of the variables analysed in a VTI report aimed at using coast down measurements to determine the effect of the road surface conditions on rolling resistance [15]. However, rutting was not found to be significant on its own, and the researchers noted that the high correlation between rutting and the measured IRI may be good reason to leave rutting out of a generalized driving resistance model. The relationship between rutting and roughness has been demonstrated elsewhere [22], thus a separate factor relating rutting to rolling resistance would require rutting to be decoupled from the IRI effect if it was developed.

3.5 *Transverse slope*

The transverse slope of the pavement, sometimes known as the crossfall or crossslope of the pavement, has an impact on the side forces of the vehicle, which in turn affects the rolling resistance along the pavement [23]. Although this feature of the pavement is recognized to impact rolling resistance, similar to superelevation, no significant amount of research exists to quantify its effects. However, Chatti and Zaabar [11] included superelevation as a variable in the spreadsheet resulting from the NCHRP report 720, and it can be expected that the mechanism relating crossfall to rolling resistance behaves similar to the mechanism relating superelevation to rolling resistance.

4 ROLLING RESISTANCE MODELS

Two commonly used models relating pavement properties to rolling resistance and fuel consumption have been developed in recent years. One model was developed by Chatti and Zaabar [11] by calibrating the HDM 4 models for vehicle operating costs. The fuel consumption model was calibrated over several pavements in the state of Michigan using six different vehicles: a medium car, sport utility vehicle, van, light truck, and an articulated truck. The details of the model can be found in the NCHRP report 720 [11], along with a Microsoft Excel™ tool developed as part of the NCHRP project that can be used to estimate vehicle operating costs (as well as vehicle fuel consumption) given several conditions.

The second model was developed as part of an international collaboration, Models for rolling resistance In Road Infrastructure Asset Management systems (MIRIAM), and is described in detail in Hammarstom et al. [24]. The model was developed based on empirical results from coast down measurements in Sweden, and includes impacts of: pavement roughness, macrotexture, temperature, speed, horizontal curvature and the road grade. The model was developed for three vehicle types, a car, a heavy truck and a heavy truck with a trailer.

4.1 *Impact of pavement roughness on vehicle speed*

An important variable that must be considered when evaluating fuel consumption as a function of pavement properties is the impact of the pavement roughness on the average vehicle speed. Hammarstom et al. [24] investigated the impact of roughness on speed for European conditions. It is noted in Hammarstom et al. [24] that reducing roughness may have the effect of increasing vehicle fuel consumption due to a corresponding increase in average vehicle travel speed. Yu and Lu [25] investigated the relationship between roughness and speed and found that the average speed of a vehicle decreases 0.84 km/h for every increase in roughness of 1 m/km (0.0083 mph per every 1 in/mile). The data used in developing the relationship were taken from vehicles travelling along several pavement sections in California (both rigid and flexible pavements), and was limited to vehicles travelling between 80 and 145 km/hr (50 to 80 mph) to exclude times of congestion and vehicles that are potentially exceeding the speed limit by a significant amount.

5 ANALYSIS

In order to analyze and compare the two rolling resistance models, a baseline case of traffic was evaluated with the parameters shown in Table 1. The change in fuel consumption based on four variables will be evaluated: (1) the change in fuel consumption based on varying the roughness as a function of time, (2) the impact of the relationship between the reduction in average speed as a function of pavement roughness, (3) sensitivity to traffic growth, and (4) sensitivity to macrotexture. The relationship between roughness and average speed given by Yu and Lu [25] was included in the baseline calculations.

A second order polynomial was assumed for the roughness growth model which (with IRI given in units of in/mile) as $a*(x)^2 + b*(x) + c = IRI(x)$, where $IRI(x)$ is the value of the IRI in year x, c was set at 0.87 m/km (55 in/mile), b was set as 0.02 m/km/yr (1.23 in/mi/yr) and a was changed from the following values [0, 0.15, 0.3, 0.45, 0.6], with a value of a=0 chosen as the baseline case for roughness. This value is taken from McGhee and Gillespie [26] which reported a near constant growth in IRI of 0.02 m/km/yr (1.23 in/mi/yr) for a seven year time period for asphalt pavements in Virginia. The roughness growth over a ten year time frame can be seen in Figure 1 for each value of a. A ten year analysis period was evaluated, and the additional fuel consumption (i.e. the fuel consumption above the baseline case) was calculated per 1 km (0.62 miles) of pavement using the MIRIAM model [24] as well as the software that accompanied the NCHRP report 720 [11]. The results are shown in Figure 2.

It can be seen in Figure 2 that the NCHRP model is much more sensitive to the speed reduction due to an increase in IRI than the MIRIAM model. Although the models produce similar results, the highest amount of fuel consumption occurs when no speed reduction is taken into account and the NCHRP model is used. Conversely, the lowest amount of fuel

Table 1. Baseline case for evaluating the models.

Variable	Baseline value	Variable	Baseline value
Initial roughness	0.87 m/km (55 in/mile)	Traffic (AADT)	30,000
Temperature	20°C (68°F)	Traffic growth rate	3%
Horizontal curvature	0	Medium trucks	10%
Grade	0%	Articulated trucks	15%
Crossfall	0%	Speed	105 km/h (65 mph)
Macrotexture	0.5 mm (0.02 inches)	Pavement type	Flexible

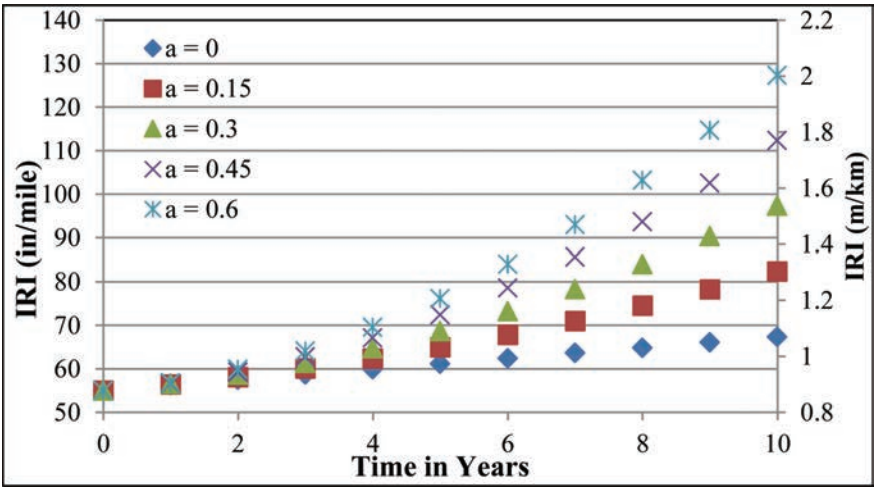

Figure 1. Roughness growth models.

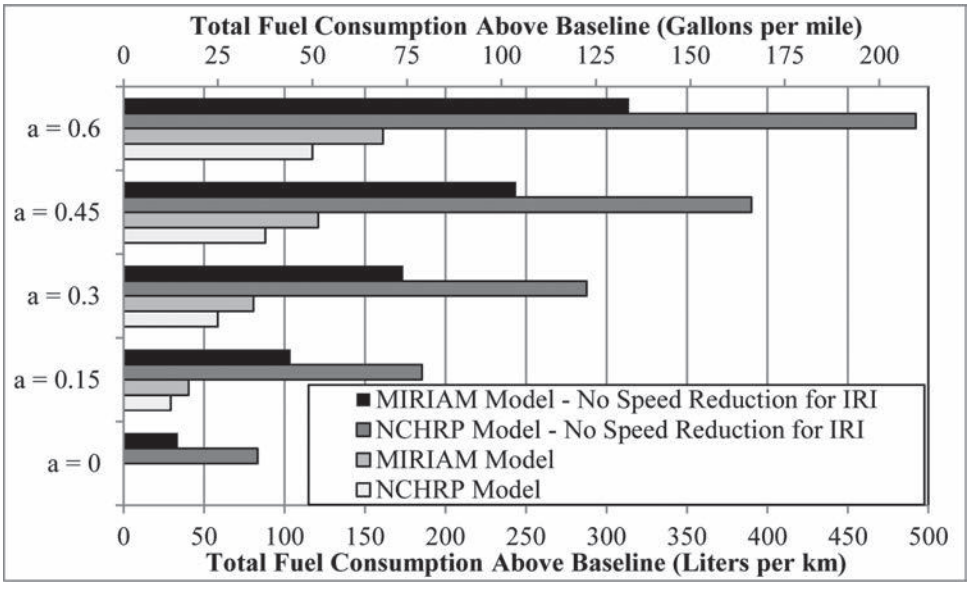

Figure 2. Fuel consumption above baseline case as a function of roughness.

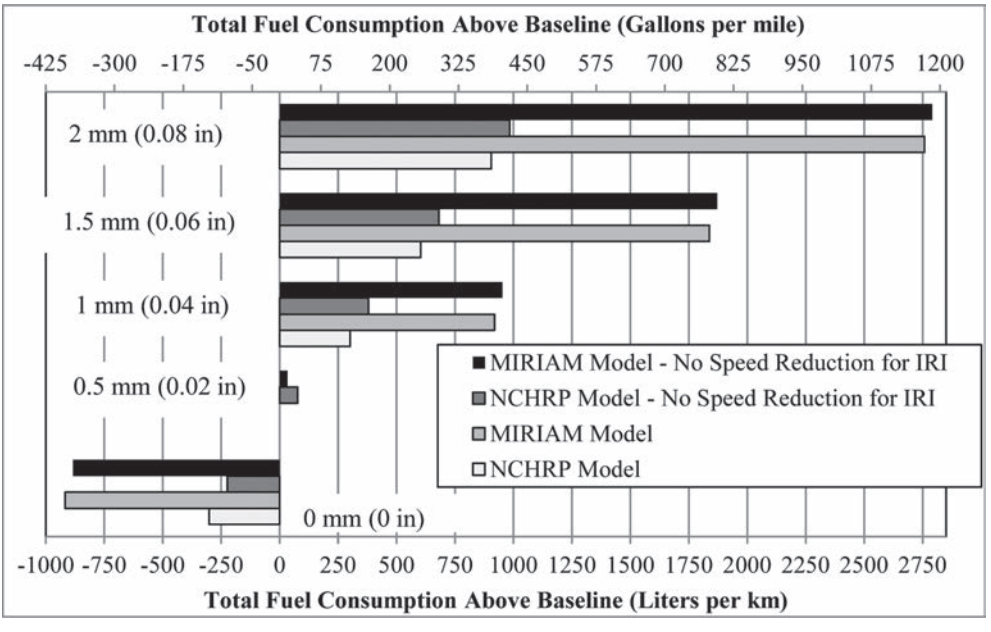

Figure 3. Fuel consumption above baseline case as a function of macrotexture.

consumption occurs with the NCHRP model when the speed reduction is taken into account. Next, the influence of macrotexture on the excess fuel consumption was calculated, assuming the baseline case of 0.5 mm (0.02 in), and a constant growth in roughness of 0.02 m/km/yr (1.23 in/mile/yr) per McGhee and Gillespie [26]. The results can be seen in Figure 3.

It can be seen in Figure 3 that the MIRIAM model is much more sensitive to changes in macrotexture than the NCHRP model. Also, the difference between the case where the speed reduces as a function of IRI and the case where no speed reduction is considered is nearly

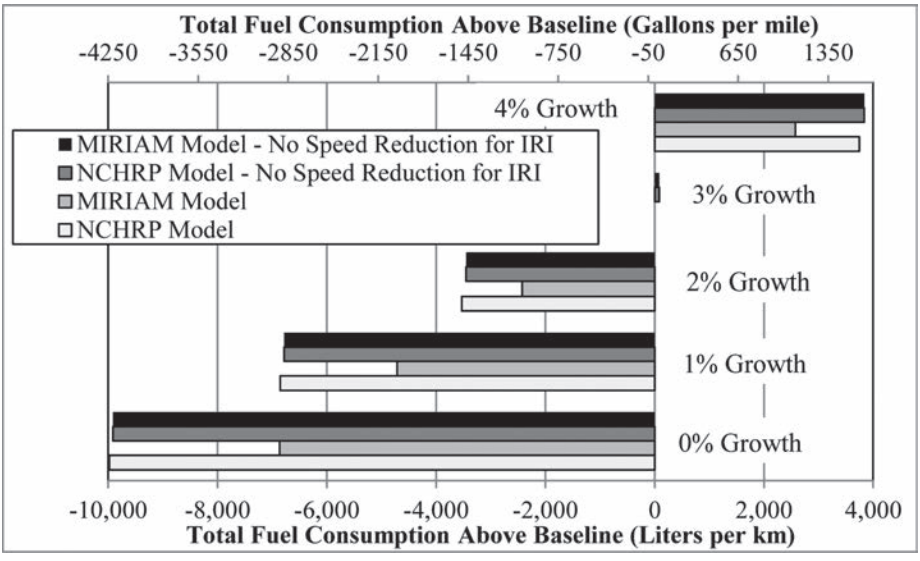

Figure 4. Fuel consumption above baseline case as a function of traffic growth.

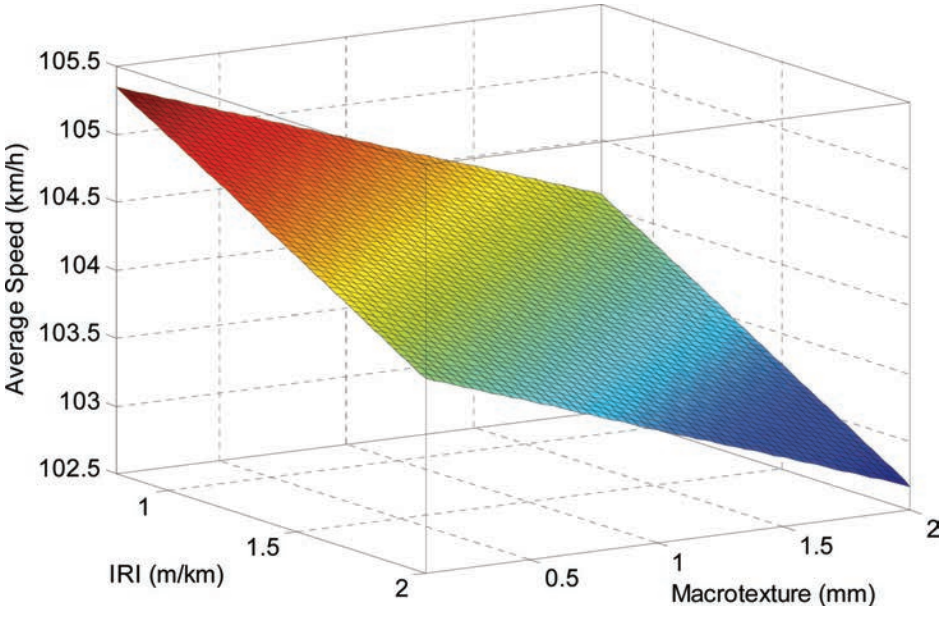

Figure 5. Surface for constant fuel consumption using the NCHRP model.

insignificant when compared to changes in the values for macrotexture. Finally, the influence of the traffic growth rate on the excess fuel consumption above the baseline case was evaluated, and the results can be seen in Figure 4.

Of the four variables analysed (IRI growth, macrotexture, speed reduction as a function of IRI, and traffic growth rate), it can be seen that the traffic growth rate most significantly impacts the excess fuel consumption. This seems to indicate that if a transportation agency has the goal of reducing fuel consumption within a pavement network, the most influential factor of the factors that were analysed is to reduce the number of vehicles travelling

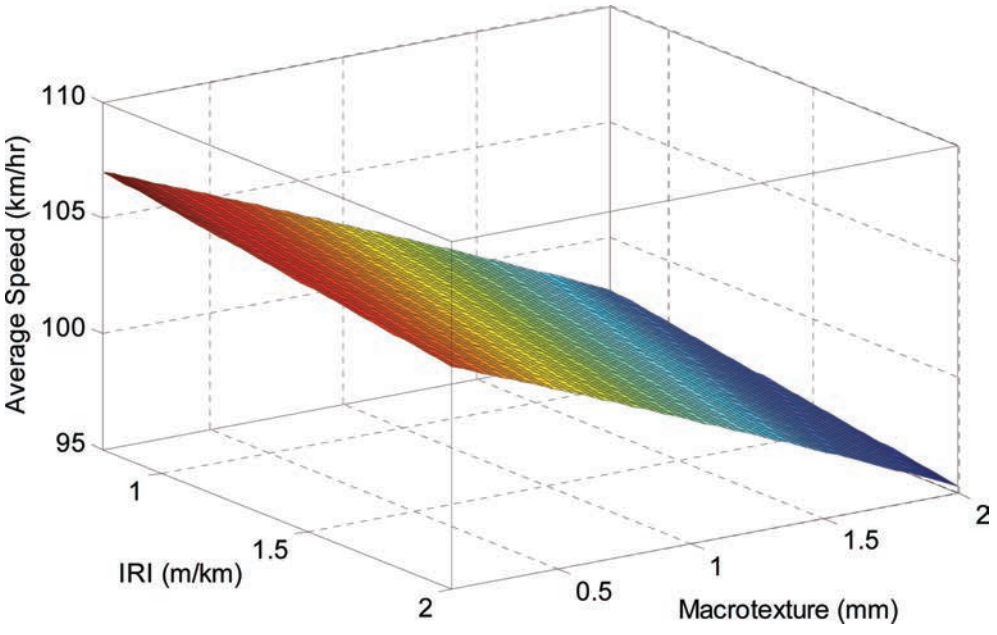

Figure 6. Surface for constant fuel consumption using the MIRIAM model.

in the network in future years. Second to the traffic growth rate is the macrotexture of the pavement. However, it is important to note that macro-texture plays an important role in pavement friction [7], as well as an important role in controlling pavement noise.

In order to better represent the sensitivity of the fuel consumption on the macrotexture, roughness and speed for each model, the three variables were plotted on the same figure for values that yield the same fuel consumption (Figs. 5 and 6). The value for fuel consumption chosen as the iso-plane was taken as the baseline case (defined in Table 1). One notable result is that the NCHRP model is more sensitive to changes in the average vehicle speed than the MIRIAM model (as seen by the smaller variation in speed in Fig. 5). Secondly, both models produce flat planar surfaces, as opposed to having curvature.

6 DISCUSSION AND CONCLUSIONS

Models that relate vehicle rolling resistance to pavement properties can prove to be a valuable resource for transportation agencies, particular when they are concerned with analysing such factors as the impact of excessive roughness on fuel consumption or the potential value of smoothness to road users. This paper presented two recently developed models, as well as an evaluation of their sensitivity to variables pavement roughness, pavement macrotexture and average vehicle speed. It is clearly shown that small variations in average speed can have a much more significant impact on the vehicle fuel consumption than the typical range of pavement roughness or macrotexture. Also, it was found that the total excess fuel consumption was highly sensitive to future traffic growth projections. Furthermore, the pavement macrotexture has a significantly higher impact on excess fuel consumption of vehicles than pavement roughness for both models analysed.

ACKNOWLEDGEMENTS

This paper was produced under the sponsorship of the Transportation Pooled Fund TPF-5(268) National Sustainable Pavement Consortium. The authors would like to thank the

Mississippi, Pennsylvania, Virginia, and Wisconsin Departments of Transportation, as well as the Federal Highway Administration for their support and guidance. Support was also provided by the Portuguese Foundation for Science and Technology under the Grant [SFRH/BD/79982/2011]; European Regional Developing Funding [CENTRO-07-0224-FEDER-002004].

REFERENCES

[1] Schrank, D., Eisele, B., & Lomax, T. TTI's 2012 Urban Mobility Report. College Station, TX: Texas A&M Transportation Institute. 2012.

[2] Evans, L.R., Jr., J.D., Harris, J.R., Yates, K., Dudek, W., Holmes, J., et al. NHTSA Tire Fuel Efficiency Consumer Information Program Development: Phase 2—Effects of Tire Rolling Resistance Levels on Traction, Treadwear, and Vehicle Fuel Economy. East Liberty, OH: National Highway Traffic Safety Administration. 2009.

[3] Transportation Research Board: Committee for the National Tire Efficiency Study. Tires and Passenger Vehicle Fuel Economy: Informing Consumers, Improving Performance. *TRB Special Report 286*. Washington, D.C.: Transportation Research Board. 2006.

[4] Schuring, D.J. and S. Futamura. Rolling Loss of Pneumatic Highway Tires in the Eighties. Rubber Chemistry and Technology: Vol. 63, No. 3, pp. 315–367. 1990.

[5] TIAX, LLC. *California State Fuel-Efficient Tire Report: Volume 2*. Cupertino, CA: California Energy Commission. 2003.

[6] Sandberg, U. Road Macro and Mega Texture Influence on Fuel Consumption. In W.E. Meyer, & J. Reichert, *Surface Characteristics of Roadways* (pp. 460–479). Baltimore, MD: American Society for Testing and Materials. 1990.

[7] Flintsch, G.W., León, E.d., McGhee, K.K., & Al-Qadi, I.L. Pavement Surface Macrotexture Measurement and Applications. *Transportation Research Record 1860*, pp. 168–177. 2003.

[8] Sayers, M., & Karamihas, S. The Little Book of Profiling. Ann Arbor, MI: The University of Michigan. 1998.

[9] Santero, N., Loijos, A., Akbarian, M., & Ochsendorf, J. Methods, Impacts and Opportunities in the Concrete Pavement Life Cycle. Cambridge MA: Massachusetts Institute of Technology. 2011.

[10] Sandberg, U. Rolling Resistance—Basic Information and State of the Art on Measurement Methods. Linköping, Sweden: Swedish Road and Transport Research Institute. 2011.

[11] Chatti, K., & Zaabar, I. Estimating the Effects of Pavement Condition on Vehicle Operating Costs. National Cooperative Highway Research Program, Report 720. Washington, DC. 2012.

[12] Laganier, R. and Lucas, J. The Influence of Pavement Eveness and Macrotexture on Fuel Consumption. Surface Characteristics of Roadways: International Research and Technologies. ASTM STP 1031, ASTM International, Philadelphia. 1990. pp. 454–459.

[13] Sandberg, U. Influence of Road Surface Texture on Traffic Characteristics Related To Environment, Economy and Safety. VTI notat 53A-1997. Statens väg- och transportforskningsinstitut. Linköping. 1997.

[14] Zaabar, I. Effect of Pavement Conditions on Vehicle Operating Costs Including Fuel Consumption, Vehicle Durability and Damage to Transported Goods. East Lansing, MI: Michigan State University. 2010.

[15] Hammarström, U., Karlsson, R., & Sörensen, H. Road surface effects on rolling resistance—coastdown measurements with uncertainty analysis in focus. Linköping: Swedish National Road and Transport Research Institute. 2008.

[16] Taylor, G., & Patten, J. Effects of Pavement Structure on Vehicle Fuel Consumption—Phase III. Ottawa, Ontario: Centre for Surface Transportation Technology—National Research Council of Canada. 2006.

[17] Akbarian, M., & Ulm, F.-J. Model Based Pavement-Vehicle Interaction Simulation for Life Cycle Assessment of Pavements. Cambridge, MA: Massachusetts Institute of Technology—Concrete Sustainability Hub. 2012.

[18] Wang, T., Lee, I.-S., Kendall, A., Harvey, J., Lee, E.-B., & Kim, C. Life cycle energy consumption and GHG emission from pavement rehabilitation with different rolling resistance. Journal of Cleaner Production, pp. 86–96. 2012.

[19] EAPA/EuroBitume. Environmental Impacts and Fuel Efficiency of Road Pavements—Industry Report. Brussels, Belgium: Joint EAPA/EuroBitume Task Group on Fuel Efficiency. 2004.

[20] Epps, J.A., Leahy, R.B., Mitchell, T., Ashmore, C., Seeds, S., Alavi, S., et al. WESTrack—The Road to Performance Related Specifications. International Conference on Accelerated Pavement Testing;. Reno, NV: University of Nevada, Reno. 1999.
[21] Zhang, H., Lepech, M., Keoleian, G., Qian, S., & Li, V. Dynamic Life-Cycle Modeling of Pavement Overlay Systems: Capturing the Impacts of Users, Construction, and Roadway Deterioration. ASCE Journal of Infrastructure Systems, pp. 299–309. 2010.
[22] Mactutis, J., Alavi, S., & Ott, W. Investigation of relationship between roughness and pavement surface distress based on WesTrack project. Transportation Research Record No. 1699, Washington, DC. pp. 107–113. 2000.
[23] Sandberg, U. Rolling Resistance—Basic Information and State of the Art on Measurement Methods. Linköping, Sweden: Swedish Road and Transport Research Institute. 2011.
[24] Hammarström, U., Eriksson, J., Karlsson, R., and Yahya, M. Rolling Resistance Model, Fuel Consumption Model and the Traffic Energy Saving Potential fom Changed Road Surface Considtions. Linköping: Swedish National Road and Transport Research Institute. 2011.
[25] Bin Yu & Qing Lu. Empirical model of roughness effect on vehicle speed, International Journal of Pavement Engineering, DOI:10.1080/10298436.2013.792931. 2013.
[26] McGhee, K.K., & Gillespie, J.S. Impact of a Smoothness Incentive/Disincentive on Hot-Mix Asphalt Maintenance Resurfacing Costs. Charlottesville, VA: Virginia Transportation Research Council. 2006.

This page intentionally left blank

Additives and modifiers for asphalt concrete—II

This page intentionally left blank

Asphalt Pavements – Kim (Ed)
© 2014 Taylor & Francis Group, London, ISBN 978-1-138-02693-3

Physicochemical characteristics of RAP binder blends

Shin-Che Huang & Adam T. Pauli
Western Research Institute, Laramie, WY, USA

Qian Qin
GAF Materials, Ennis, TX, USA

ABSTRACT: Two chemically and physically different SHRP asphalts (AAA-1 and AAC-1) were mixed with 15 and 50 percent of extracted RAP binders, designated Manitoba and South Carolina. Several analytical techniques including dynamic shear rheometry, Automated Flocculation Titrimetry (AFT), and Differential Scanning Calorimetry (DSC) were used to characterize physical properties of the starting materials and RAP binder mixtures. Results indicate that different virgin binders interact differently with different RAP binders suggesting that PG grade adjustment is both asphalt and RAP binder dependent where certain virgin binders require higher PG grade adjustment compared to other blends. This finding is somewhat contradictory to what current literature recommends. Results obtained in the present study seem to suggest that knowledge of the stiffness of starting materials alone does not adequately explain observed differences in PG grade change. Rather, information of the composition, specifically asphaltene content, lends additional insight into observed differences in PG grades of virgin with RAP binder mixtures.

Keywords: RAP, physicochemical characteristic, rheology, compatibility, AFT

1 INTRODUCTION

The use of Recycled Asphalt Pavement (RAP) has become relatively common practice in most states as it is both an environmentally and economically attractive proposition. However, most highway agencies currently allow only low percentages of RAP-less than 25 percent by weight of aggregate even though specifications allow up to 30 percent. The reason is that recycled binders are less strain-tolerant and may be more susceptible to cracking under certain application. State agencies are concerned that the use of high RAP mixtures may adversely affect performance of asphalt pavements, ultimately resulting in higher maintenance and rehabilitation costs [1].

Some states have used RAP in Marshall mix designs with success [2–6]. Others have tried to use RAP in Superpave® mixture design [7–9]. Some highway agencies, when using low percentages of RAP, do not consider the aged asphalt in RAP in the total asphalt content and properties, and therefore, consider RAP as a "black rock". The question of whether RAP, at any percentage, should be considered as "black rock" has not been answered conclusively even after more than 30 years of application. The current Superpave® system does not provide any guidelines for characterizing asphalt binders extracted from RAP, nor are there any test procedures available for recycled hot-mix asphalts. Furthermore, the interaction between new and old asphalt binders in the mixtures containing RAP has not been studied extensively and the physico-chemical interaction is still not well understood.

It is essential to understand the fundamental properties of recycled asphalt binder as well as the interaction between the old binder in the recycled asphalt and the fresh binder in the new mix. The objective of this study is to investigate the interaction between fresh binders and RAP binders and how RAP binders influence physical properties of fresh binders.

2 EXPERIMENT DESIGN

Two RAP sources from Manitoba (Man) and South Carolina (SC) were used in this study. RAP binders were extracted from these two RAP sources by using 85% toluene/15% ethanol. The SHRP asphalts AAC-1 and AAA-1 were mixed with the extracted RAP binders at 15 and 50 percent for the aging study.

The rheological properties of unaged neat asphalts and laboratory aged asphalts and blends were measured using either a Rheometrics RDAII or an ARES rheometer. Data were obtained in the region of linear strain at frequencies of 0.1 to 100 radians per second and temperatures of –20, 0, 20, 40, 60, and 80°C using 25-mm, 8-mm, or 4-mm parallel plates with 1 mm, 2 mm or 1.75 mm sample gap. Master curves were constructed by using time-temperature superposition. The Christensen-Anderson model [10] was used to shift all temperatures to a reference temperature of 20°C. DSR measurements were used to calculate the PG grade of each binder including low temperature grades. The four binders AAA-1, AAC-1, Manitoba RAP binder, South Carolina RAP binder are graded as PG61-33, 69-33, 91-28, and 95-18. Note that Manitoba RAP represents "young" RAP and South Carolina RAP represents "old" RAP in this study.

The glass transition of RAP binder blends was measured on a TA instruments Q2000 differential scanning calorimeter. Temperature Modulated Differential Scanning Calorimetry (TMDSC) was used for this study in order to effectively separate the glass transition from other complex overlapped effects such as cold crystallization and enthalpy recovery. The limiting fictive temperature T_f' was determined from the reversing heat flow curve during the second heating scan at the average scanning rate of 2°C/min with modulation amplitude of 0.5°C every 80 seconds. T_f' was used as the glass transition temperature, T_g, since it has been widely accepted that T_f' is approximately equal to the glass transition temperature T_g obtained from the cooling scan at the same scan rate [11,12].

3 RESULTS AND DISCUSSIONS

The fresh binders were investigated to observe how their rheological properties change when they are mixed with RAP binders at different concentrations. Figure 1 shows typical complex modulus versus phase angle plot with respect to different RAP concentrations at reference temperature of 20°C. The important role of phase angle on the flow properties of asphalt materials has been extensively applied by several researchers [13–15]. The phase angle indicates the level of viscoelasticity in the asphalt. It is desirable to have a certain level of viscous flow behavior in an aged asphalt to provide the relaxation of stress. An asphalt exhibiting a higher strain to failure at the same stiffness is more resistant to thermal or fatigue cracking than an asphalt binder with a lower strain to failure at the same stiffness. In other words, it is reasonable to assume that the lower the phase angle at the same stiffness, the more susceptible asphalt becomes to fatigue cracking. The logarithm of the complex modulus and the phase angle are plotted for RAP blends at different contents, as shown in Figure 1. Surprisingly, a linear (R-Squared = 0.954) relationship between complex modulus and phase angle for all the RTFO-aged AAA-1, AAC-1, and their RAP blends is observed. This indicates that the changes in log stiffness are proportional to phase angle for RAP blends at all RAP concentrations. The results from the log G* versus phase angle plot suggest that this plot may be used as an alternative approach to characterize material's flow property or blending chart.

To evaluate how addition of RAP binders influence the PG grade system of fresh asphalts, the measurements obtained from dynamic shear rheometer including 4 mm plate were used to calculate both high and low temperature grades [16]. Figure 2 shows high and low temperature grades for RTFO-aged asphalt AAA-1 and its RAP blends with Manitoba RAP binder at different concentrations. As seen from Figure 2, the high temperature PG grade of RTFO-aged AAA-1 was increased from 61°C to 70°C with 15% Manitoba RAP binder and 78°C with 50% Manitoba RAP binder and up to 91°C with 100% Manitoba RAP binder. A linear regression on high temperature grades for RTFO-aged AAA-1 and its RAP blends

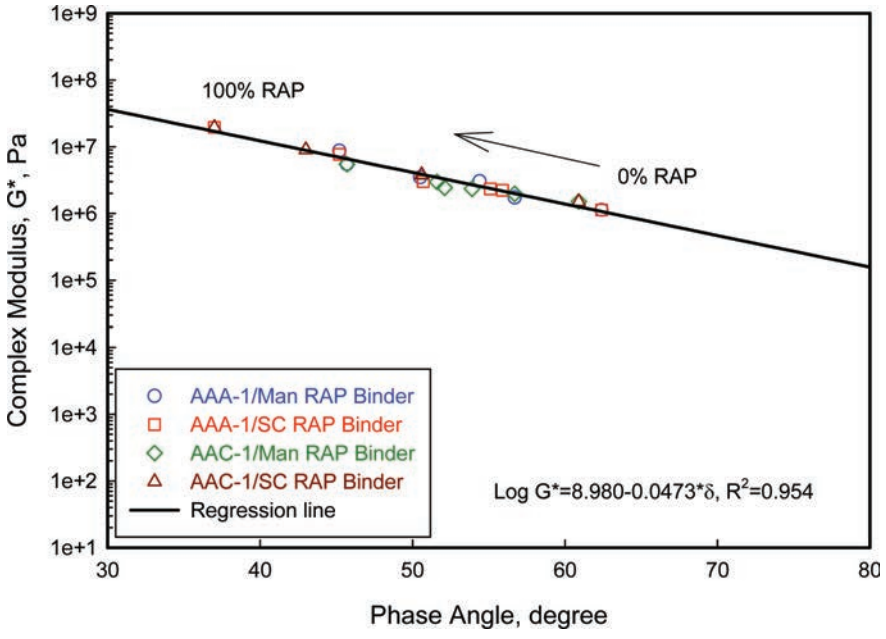

Figure 1. Complex modulus versus phase angle for aspahlts AAA-1, AAC-1 and their different concentrations of RAP binders.

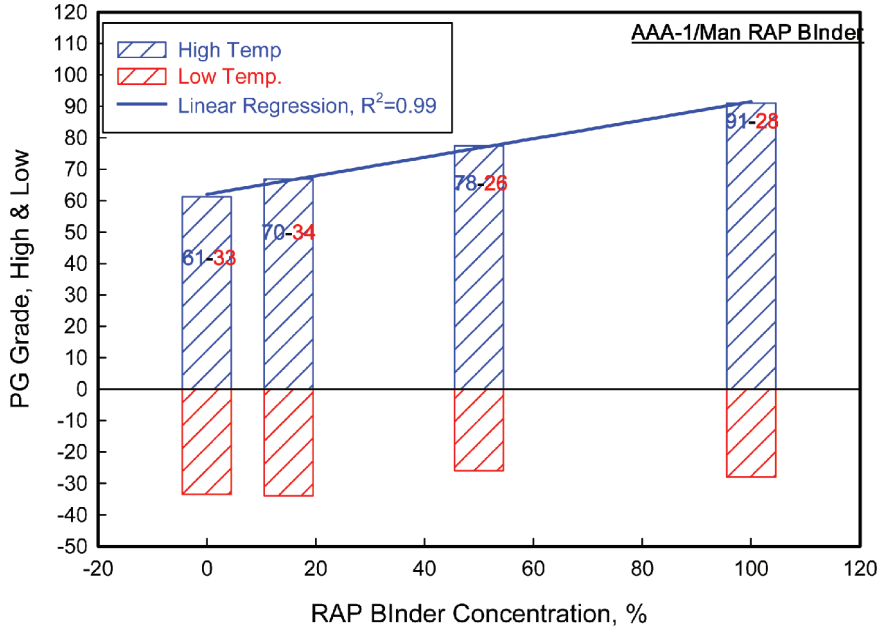

Figure 2. PG grades for RTFO-aged AAA-1 and its Manitoba RAP blend binders.

at different concentrations (0, 15, 50 and 100%) shows a linear relationship, R-squared of 0.99, between PG high temperature grade and RAP content. Further conversion indicates that the approximate changes of PG grade will be 3 PG grades when addition of 50 percent of Manitoba RAP binder is mixed into this particular asphalt (Fig. 2). A similar regression was also obtained for another RTFO-aged AAC-1 mixed with the same Manitoba RAP

binder at different concentrations and not shown in the paper. However, the result shows that the PG grade is changed to only one grade when 50 percent of RAP binder is mixed to this asphalt, RTFO-aged AAC-1. The same linear relationships are also observed on the other two blends of RTFO-aged AAA-1 and AAC-1 with South Carolina RAP binder and are not shown in the paper. The R-squared of these two blends are 0.91 and 0.91, respectively. Further conversion indicates that the PG grade needs to be adjusted up to 4 PG grades when 50 percent of South Carolina RAP binder is going to be mixed into the asphalts. The low temperature grade shows some scattering, however, the general trend still can be seen from Figure 2: addition of RAP binder into fresh asphalt increases its low temperature grade from –33 for RTFO-aged AAA-1 to –28 for the Manitoba RAP binder. Note that the Manitoba RAP binder was graded as PG91-28, and the South Carolina RAP binder was graded as PG95-18. These results indicate that different virgin binders interact differently with different RAP binders.

Asphalts, viewed by a majority of investigators as colloidal in nature, are derived from different crude sources. They are often classified as either gel-type (less compatible) or sol-type (more compatible) [17,18]. With "more" compatible asphalts, asphaltenes are usually lower in natural abundance and well dispersed or peptized by the maltene solvent phase. Compatible asphalts also exhibit "more" Newtonian-like flow properties, are more sensitive to temperature change, and generally are more ductile than less compatible asphalts. Conversely, "less" compatible asphalts, relatively speaking, will exhibit more of an elastic property, and hence, are less ductile than compatible asphalts. Based on this description of asphalt compatibility, asphaltene content is one type of measure of compatibility.

A convenient approach to characterize asphalt compatibility is by defining a state of dispersion of asphaltenes suspended in the maltene phase. Pauli [19, 20] considered Heithaus compatibility parameters utilizing an automated flocculation titrimetry test. This approach is thought to characterize the suspension-like colloidal stability of asphalt in the bulk phase [21–23]. Heithaus compatibility parameters have long been applied to quantify asphalt "molecular" compatibility, defined as the measure of mutual miscibility among molecular species present in an asphalt system. This is achieved by defining an equilibrium or steady state of a colloidal suspension, also referred to as the state of peptization [23]. Asphalts observed to be higher in values of compatibility parameters are generally designated sol-type asphalts while asphalts lower in these values are designated as gel-type. As a simple rule of thumb, in Figure 3 the asphaltene peptizability parameter p_a is shown to be proportional to the asphaltene content as $\chi_a \propto \phi = 1 - p_a$. Assuming that asphaltene content increases with addition of RAP, Figure 4 shows a logical trend in $\chi_a = f(\phi) = f(1 - p_a)$ and RAP content.

The limiting fictive temperature T_f', which is equivalent to the glass transition temperature T_g, is plotted against RAP concentration in Figures 5 and 6. The empirical Fox equation, as expressed in Equation (1), is used to fit the above mentioned experimental data.

$$Fox: \frac{1}{T_g} = \frac{w_1}{T_{g1}} + \frac{w_2}{T_{g2}} \tag{1}$$

where component 1 refers to the virgin binder and component 2 is the RAP binder; w is the weight fraction of the component.

As seen from Figure 5, the Fox equation can't satisfactorily describe T_g change of RTFO aged AAA-1 blends with either Manitoba RAP or South Carolina RAP (inset plot).

A similar trend is also found for RTFO aged AAC-1 blends with Manitoba or South Carolina RAP binders in Figure 6. The deviation of blends' T_g from the Fox equation is presumably due to the relative closeness in T_g for RTFO aged binder and RAP binder. Further, the possible inhomogeneity caused by the blending process in combination with small amount (~5 mg) of sample for DSC tests, might also contribute to the break-down of the Fox equation.

Results shown in Figures 5 and 6 indicate that T_g difference between fresh binders and RAP binders is relatively small with the largest difference of less than 10°C. Due to the lack of significant difference in T_g and the similarity in chemical structure of constituent components,

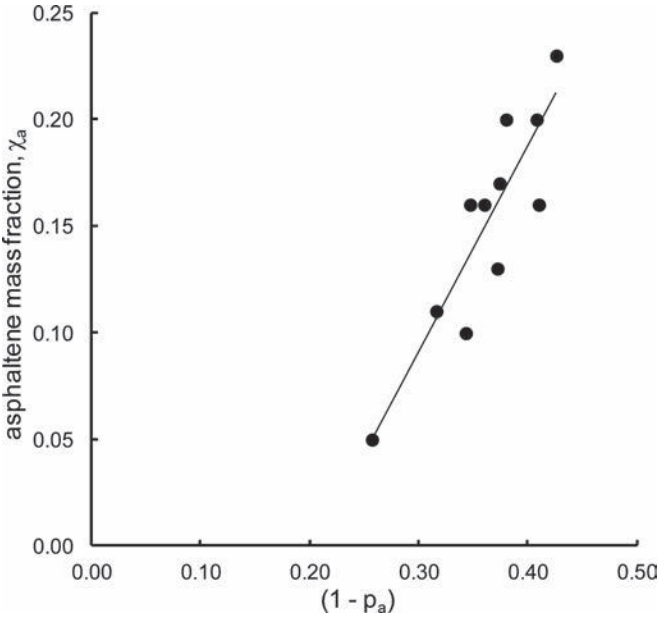

Figure 3. Correlation plot of asphaltene content to compatibility parameter p_a (data from Robertson et al. [24]).

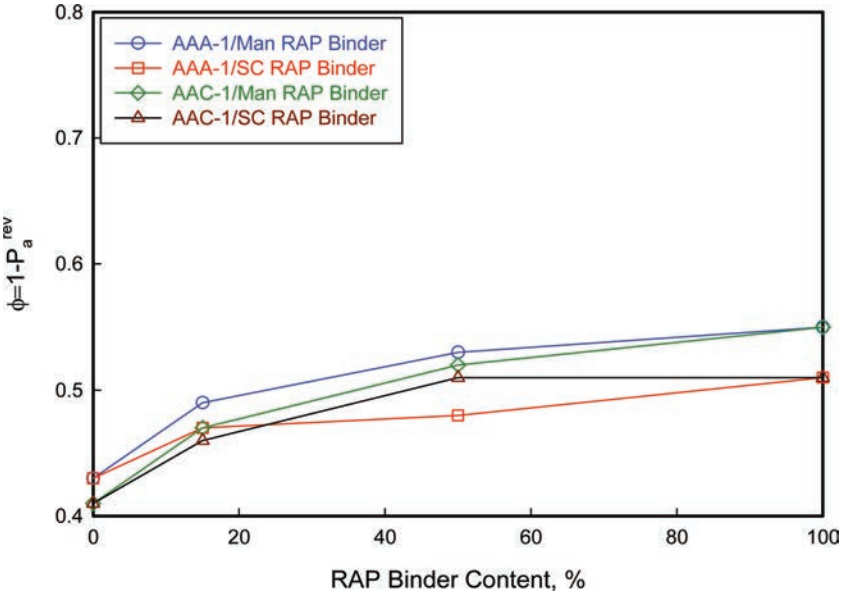

Figure 4. Asphaltene parameter $\phi = 1 - p_a$ plotted as a function of RAP content.

the severe incompatibility of those blends is not expected. As shown in Figure 7, the broadness of glass transition, as characterized by the temperature derivative of reversing heating capacity, remains unchanged for RTFO aged AAA-1/ Manitoba RAP blends. Similarly, no significant glass transition broadening is found for RTFO aged AAA-1/ South Carolina RAP blends, as shown in the inset of Figure 7.

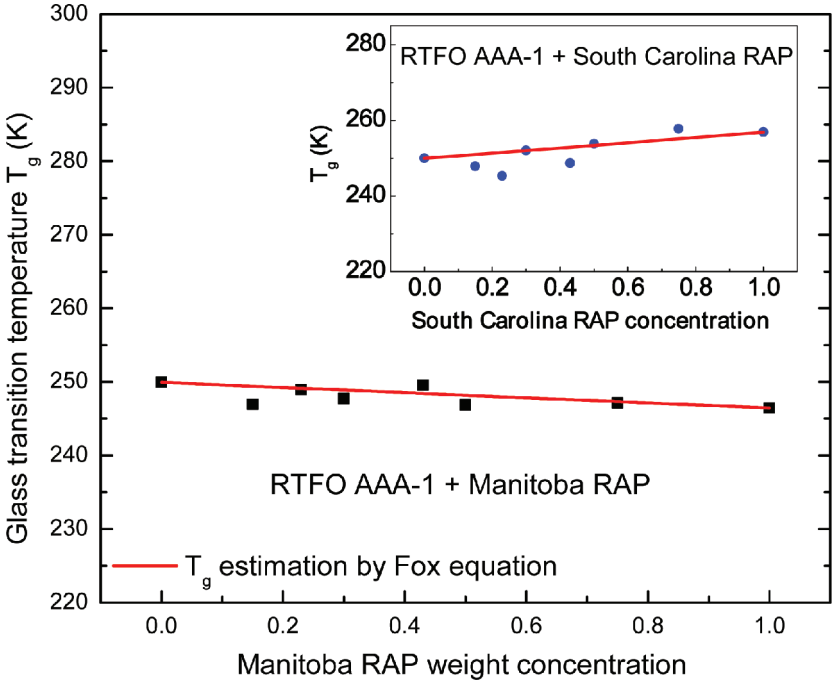

Figure 5. Glass transition temperatures of RTFO AAA-1/Manitoba RAP blends as a function of RAP concentration; the inset is for AAA-1/South Carolina RAP blends.

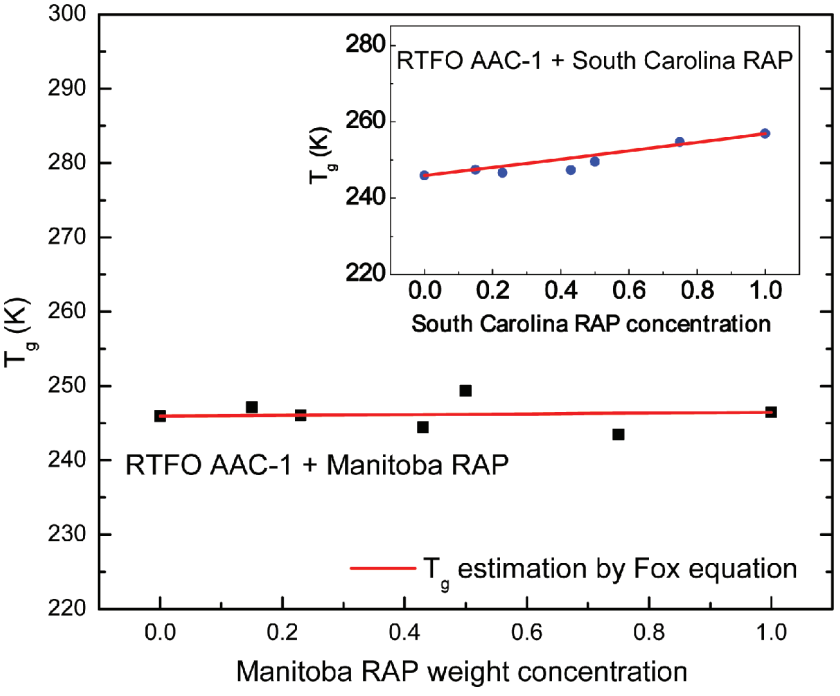

Figure 6. Composition dependence of glass transition temperatures for RTFO AAC-1/Manitoba RAP blends; the inset is for AAC-1/South Carolina RAP blends.

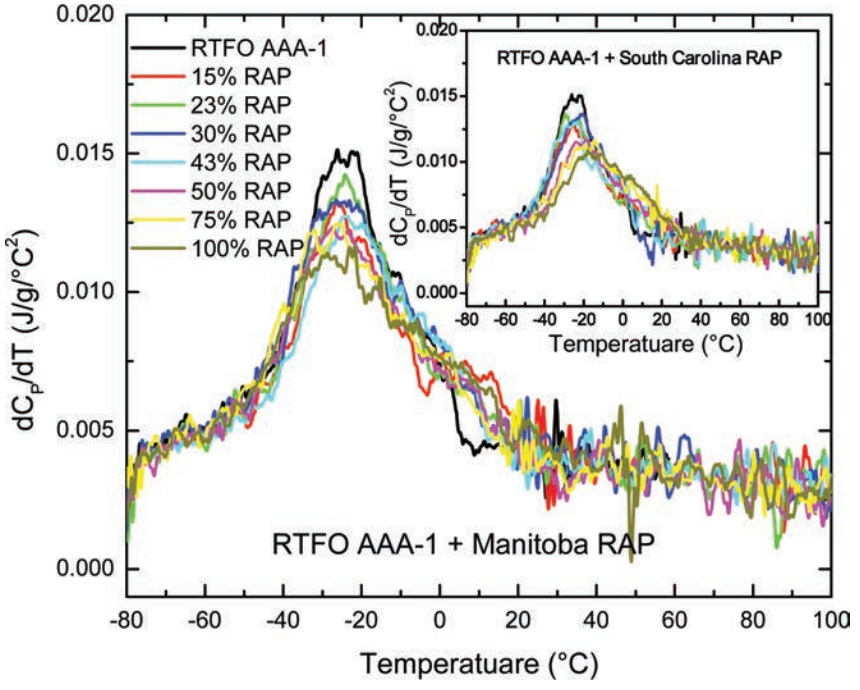

Figure 7. Glass transition broadness of RTFO AAA-1/Manitoba RAP blends; the inset is the same plot for AAA-1/ South Carolina RAP blends.

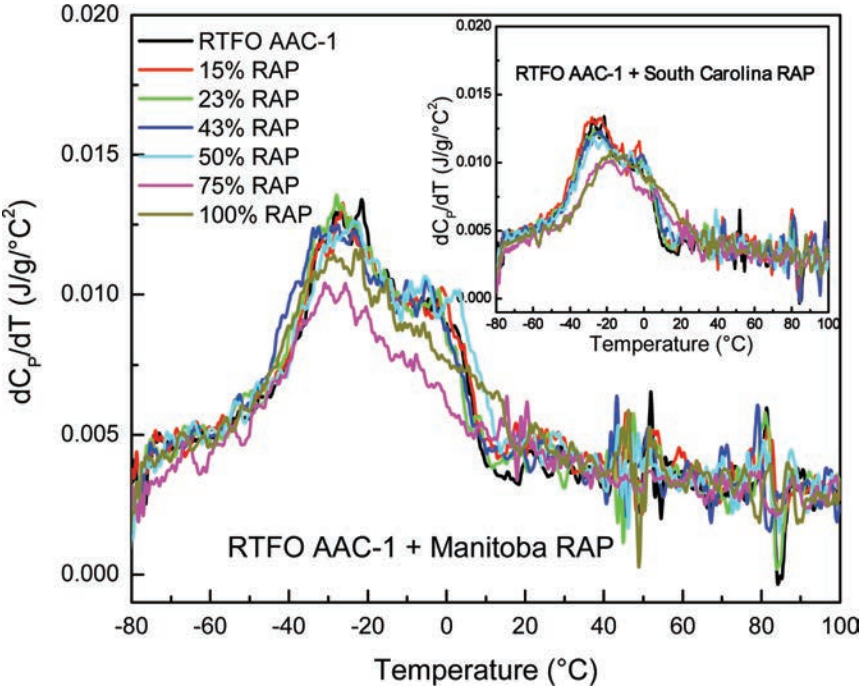

Figure 8. Glass transition broadness of RTFO AAC-1/Manitoba RAP blends; the inset is the same plot for AAC-1/ South Carolina RAP blends.

Figure 8 is the temperature derivative of reversing heat capacity of RTFO aged AAC-1/RAP blends. At RAP concentration of up to 50 percent, especially for South Carolina RAP, both the glass transition temperature and broadness is very close to RTFO aged AAC-1 binder. On the other hand, at 75 percent of RAP, the glass transition temperature and broadness is similar to that of RAP binders. These facts imply that the compatibility of RTFO aged AAC-1 with South Carolina RAP is not as good as RAP blends with RTFO aged AAA-1.

4 CONCLUSIONS

Two chemically and physically different asphalts were mixed with addition of 15 and 50 percent of extracted RAP binders, Manitoba and South Carolina. Several analytical techniques including dynamic shear rheometry, Automated Flocculation Titrimetry (AFT), and Differential Scanning Calorimetry (DSC) were used to measure physical properties of RAP binder blends.

The results indicate that different virgin binders interact with different RAP binders differently and the PG grade adjustment is asphalt and RAP binder dependent. Some asphalts require higher PG grade adjustments than the others. This finding is different from what the literature recommends [7]. The interaction between virgin binders and RAP binders contributes to different stiffening effects.

Temperature modulated DSC was used to investigate the thermal behavior of RAP binder blends. Due to the lack of sufficient difference in T_g and similarity in chemical structure of the binary components, the empirical blending equation can't reasonably describe the plasticization effect. No apparent broadening of glass transition is observed for all blends investigated. In comparison to RTFO aged AAC-1/RAP blends, RTFO aged AAA-1/RAP blends exhibit relative better compatibility.

ACKNOWLEDGEMENTS

The authors gratefully acknowledge the Federal Highway Administration, U.S. Department of Transportation, for financial support of this project under contract no. DTFH61-07-D-00005. Thanks are also expressed to Ms Pamela Coles and Mr. Gerald Forney for the sample preparation and data measurement. Thanks are also expressed to Ms. Jackie Greaser for preparation of the manuscript.

DISCLAIMER

This document is disseminated under the sponsorship of the Department of Transportation in the interest of information exchange. The United States Government assumes no liability for its contents or use thereof. The contents of this report reflect the views of Western Research Institute which is responsible for the facts and the accuracy of the data presented herein. The contents do not necessarily reflect the official views of the policy of the United States Department of Transportation. Mention of specific brand names of equipment does not imply endorsement by the United States Department of Transportation or Western Research Institute.

REFERENCES

[1] Copeland, Audrey. Sustaining our Highways: A National Perspective on RAP Usage & Best Practices for Recycled Asphalt Pavements, presented at the Pavement Performance Prediction Symposium, Laramie, Wyoming, July 16, 2008.

[2] Decker, D. Hot Mix Recycling: State of the Practice, *Journal of the Association of Asphalt Paving Technologists*, 66, pp. 704–722. 1997.
[3] Kandhal, P. Recycling of Asphalt Pavements-An Overview, *Proceedings of the Association of Asphalt Paving Technologists*, 66, pp. 686–703. 1997.
[4] Terrel, R., J. Epps, and J. Sorenson. Hot in-Place Recycling: State of the Practice, *Journal of the Association of Asphalt Paving Technologists*, 66, pp. 723–745. 1997.
[5] Huffman, J. Full-Depth Pavement Reclamation: State of the Practice. *Journal of the Association of Asphalt Paving Technologists*, 66, pp. 746–759. 1997.
[6] Kearney, E. Cold Mix Recycling: State of the Practice, *Journal of the Association of Asphalt Paving Technologists*, 66, pp. 760–802. 1997.
[7] McDaniel, R.S., and A. Shah. Use of Reclaimed Asphalt Pavement (RAP) Under Superpave Specifications, *Journal of the Association of Asphalt Paving Technologists*, 72, pp. 226–252. 2003.
[8] Mohammad, L., Z. Wu, C. Abadi, W. Daly, and C. Daranga. Investigation of the Use of Recycled Polymer Modified Asphalt Binder in Asphalt Concrete Pavement, *Journal of the Association of Asphalt Paving Technologists*, 72, pp. 551–594. 2003.
[9] Daniel, J.S., G.R. Chehab, and D. Ayyala. Sensitivity of RAP Binder Grade on Performance Predictions in the MEPDG, *Journal of the Asphalt Paving Technologists*, 78, pp. 352–376. 2009.
[10] Christensen, D.W., and D.A. Anderson. Interpretation of Dynamic Mechanical Test Data for Paving Grade Asphalt, *Journal of the Association of Asphalt Paving Technologists*, 61, pp. 67–116. 1992.
[11] McKenna G.B., and S.L. Simon. *Handbook of Thermal Analysis and Calorimetry*, S.Z.D. Cheng, Ed., Chapter 2, Elsevier, New York. 2002.
[12] Badrinarayanan, P.W. Zheng, Q. Li, and S. L. Simon. The glass transition temperature versus the fictive temperature, *J Non-Cryst Solids*, 353, pp. 2603–2612. 2007.
[13] Huang, Shin-Che, and Will Grimes. Influence of Aging Temperature on Rheological and Chemical Properties of Asphalt Binders, *Transportation Research Record: Journal of the Transportation Research Board*, No. 2179, Transportation Research Board of the National Academies, Washington, D.C., pp. 39–48. 2010.
[14] Huang, Shin-Che, F. Miknis, W. Schuster, S. Salmans, M. Farrar, and R. Boysen. Rheological and Chemical Properties of Hydrated Lime and Polyphosphoric Acid Modified Asphalts with Long term Aging, *Journal of Materials in Civil Engineering*, 23(5), pp. 628–637. 2011.
[15] King, G.N., M. Anderson, D. Hanson, and P. Blankenship. Using Black Space Diagrams to Predict Age-Induced Cracking, Rilem Fatigue Cracking Conference, Delft, NL, June 20–22, 2012.
[16] Sui, C., M.J. Farrar, W.H. Tuminello, and T.F. Turner. New Technique for Measuring Low-Temperature Properties of Asphalt Binders with Small Amounts of Material, *Transportation Research Record: Journal of the Transportation Research Board*, No. 2079, Transportation Research Board of the National Academies, Washington, D.C., pp. 23–28. 2010.
[17] Barth, E.J. *Asphalt Science and Technology*, Gordon and Breach Science Publishers, New York. 1962.
[18] Pfeiffer, J.P., and R.N.J. Saal. Asphalt Bitumen as Colloidal System, *Phys. Chem.*, 44, pp. 139–149. 1940.
[19] Pauli, A.T., J.F. Branthaver, and R.E. Robertson. Modification of the Automated Flocculation Titrimetry (AFT) Procedure Applied to SHRP Asphalts. *American Chemical Society Division of Fuel Chemistry Preprints*, 47(1), pp. 22–25. 2002.
[20] Pauli, A.T. Asphalt Compatibility Testing Using the Automated Heithaus Titration Test. *American Chemical Society Division of Fuel Chemistry Preprints*, 41(4), pp. 1276–1281. 1996.
[21] Pauli, A.T., and J.F. Branthaver. Relationship between Asphaltenes, Heithaus Compatibility Parameters, and Asphalt Viscosity, *Petroleum Science and Technology*, 16(9&10), pp. 1125–1147. 1998.
[22] Pauli, A.T., and J.F. Branthaver. Rheological and Compositional Definitions of Compatibility as They Relate to the Colloidal Model of Asphalt and Residua, *American Chemical Society Division of Petroleum Chemistry Preprints*, 44, pp. 190–193. 1999.
[23] Heithaus, J.J. Measurement and Significance of Asphaltene Peptization. *Journal of the Institute of Petroleum*, 48, pp. 45–53. 1962.
[24] Robertson, R.E., J.F. Branthaver, P.M. Harnsberger, J.C. Petersen, S.M. Dorrence, J.F. McKay, T.F. Turner, A.T. Pauli, S.-C. Huang, J.-D. Huh, J.E. Tauer, K.P. Thomas, D.A. Netzel, F.P. Miknis, T. Williams, J.J. Duvall, F.A. Barbour, and C. Wright. *Fundamental Properties of Asphalts and Modified Asphalts, Volume I: Interpretive Report*, FHWA-RD-99-212. Federal Highway Administration, U.S. Department of Transportation, McLean, VA. 2001.

This page intentionally left blank

Asphalt Pavements – Kim (Ed)
© 2014 Taylor & Francis Group, London, ISBN 978-1-138-02693-3

Evaluation of test sections with Polymer Modified Bitumens

Xiaohu Lu
Nynas AB, Nynäshamn, Sweden

Safwat Said & Håkan Carlsson
VTI, Linköping, Sweden

Hilde Soenen & Serge Heyrman
Nynas NV, Antwerp, Belgium

Per Redelius
Nynas AB, Nynäshamn, Sweden

ABSTRACT: It has been recognized that Polymer Modified Bitumens (PMB) have more potential for use in asphalt paving and can clearly demonstrate the value of their initial higher cost. To further assess sustainable benefits on heavy trafficked roads, test sections using various PMBs were built on highway E6 in Sweden during 2003–2006. The main objective of this paper is to study the aging and rheological properties of the binders used. A large number of cores were drilled and characterized with respect to stiffness, fatigue and permanent deformation. The binders (original, lab aged and recovered) were investigated extensively with rheological and chemical methods. It was found that PMBs, particularly SBS modified, demonstrate better rheological properties as compared to unmodified bitumens, even after several years in the field. These include higher strain recovery and lower non-recoverable compliance at high temperatures, and lower stiffness at low temperatures. For the SBS modified binders, good aging resistance was observed. The high resistance to aging for the SBS modified binders was also evident in the stiffness measurement made on asphalt field cores. Although significant differences have not yet been seen between the test sections (all the sections are in good condition after six years of traffic), the observed improvements for the modified binders are expected to be confirmed by a longer follow-up of the test road.

Keywords: test road; polymer modified bitumen; sustainability; aging; durability

1 INTRODUCTION

Over the years increased traffic volume and traffic loading along with a pressure of reducing material costs has created high performance requirement for asphalt pavements. In order to ensure pavement long-term durability, thus minimizing maintenance cost and conserving resources, proper selection of paving materials together with optimal mix and pavement design are of great importance. Numerous laboratory studies have shown beneficial effects of adding polymers to bitumen and using Polymer Modified Binders (PMB) in asphalt mixtures [1, 2]. Performance improvements are normally found with respect to permanent deformation (rutting), fatigue resistance and low temperature cracking, particularly for the modified binders with Styrene-Butadiene-Styrene copolymer (SBS). These improvements are also confirmed in full-scale tests using for example Heavy Vehicle Simulator (HVS) [3], and field trials, such as test sections in the Long Term Pavement Performance (LTPP) program in North America [4] and airfield runways [5]. The American LTPP study indicated that test sections with PMB mixtures had less fatigue cracking, thermal cracking and rutting compared to

conventional companion sections. Thus, the use of PMBs extends the service life of flexible pavements and HMA overlays [4].

In spite of recognized good performance, the application of PMB to asphalt paving has been quite limited in many countries probably because of higher initial cost. To determine whether it is cost-effective to use PMB and to assess its sustainable benefits on heavy trafficked roads under the Nordic conditions (long and cold winter time, use of studded tyres, etc.), a test road was built in Sweden during 2003–2006. The objective of constructing such a test road is also to validate if binder tests can quantity the functional properties of asphalt pavements. The test road is located in Geddeknippel—Kalsås, and was built as part of highway E6 north of Uddevalla where the Average Daily Traffic (ADT) was around ten thousand vehicles per day. The whole field trial consisted of five northbound and ten southbound sections. The northbound sections were only tested in the wearing course, whereas in the southbound sections various PMBs were tested in all asphalt layers, i.e. the wearing course, binder course and base course. The test road has been monitored continuously and a follow-up research was carried out. The research project includes field performance measurements, testing of asphalt cores, binder tests and evaluation, deterioration modeling, as well as Life Cycle Cost Analysis (LCCA). The present paper focuses on binder characterization with respect to aging and rheology. The binders used in the southbound test sections were studied.

2 MATERIALS, TEST SECTIONS AND FIELD SAMPLING

Table 1 shows the conventional properties of the binders selected for the test sections. The modified binders were produced using different polymers and different polymer concentrations. The 50/70-53 SBS, 50/100-75 SBS and 100/150-75 SBS contains 3, 4 and 6% SBS (by weight), respectively. In 50/70-53 EVA (ethylene vinyl acetate), the polymer content is 6%. All the modified binders are storage-stable according to the European standards EN 13399. Selection of the binders was based on intensive laboratory investigations on binder properties, and on asphalt mixture performance tests, including fatigue, permanent deformation (rutting), water sensitivity, and wear resistance, etc. [6, 7].

In the test road (southbound), two reference sections and eight sections with different binder combinations were built (Table 2). These sections were constructed in 2003/2004 by laying 100 mm base course (50 mm over-layer and 50 mm under-layer, both with hot-mix AG22) on a 80 mm unbound sub-base, and followed by 50 mm binder course of asphalt concrete ABb22. After about two years of traffic, 40 mm wearing course of stone mastic asphalt (ABS16) was applied to the binder course in September 2006. Detailed technical requirements for the used asphalt mixture types can be found in [8].

Field sampling was made in September 2010 when asphalt cores were drilled from two different positions—the wheel path (or under track) and between the tracks, denoted as UT and

Table 1. Binders used in the test road and their conventional properties.

Asphalt layers	Binder types*	Polymer % wt	Penetration, 1/mm	Softening point, °C
Wearing course	70/100	0	77	46
	50/100-75 SBS	4	58	98
Binder course	50/70	0	55	50
	50/70-53 SBS	3	58	58
	50/70-53 EVA	6	52	66
Base course	100/150	0	127	43
	160/220	0	190	38
	100/150-75 SBS	6	123	90

* Currently, 50/70-53 = 45/80-55; 50/100-75 = 40/100-75; 100/150-75 = 90/150-75.

Table 2. Test sections with various combinations of binders.*

Test sections	Ref 1	1a	1b	2a	2b	3a	3b	4a	4b	Ref 2
Wearing course	70/100	70/100	50/100-75 SBS			70/100				70/100
Binder course	50/70	50/70	50/70-53 EVA					50/70-53 SBS		50/70
Base course—over	100/150	100/150-75 SBS		100/150						100/150
Base course—under	100/150	100/150-75 SBS		100/150	160/220	160/220	100/150	160/220	100/150	100/150

* Currently, 50/70-53 = 45/80-55; 50/100-75 = 40/100-75; 100/150-75 = 90/150-75.

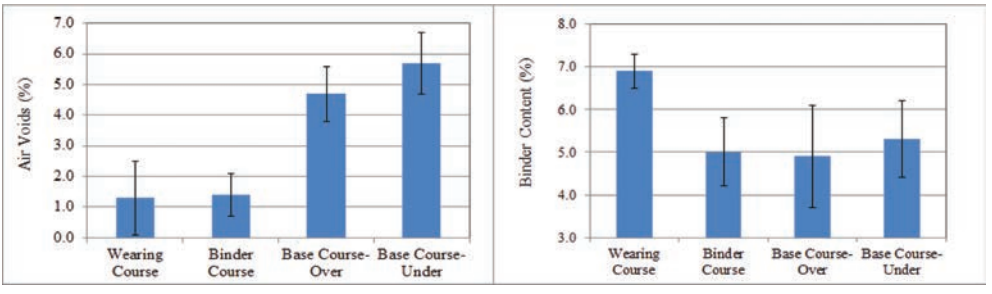

Figure 1. Binder contents and air void contents averaged for different asphalt layers.

BT, respectively. General analyses were conducted on the field cores with respect to binder contents and air void contents. The data averaged for different asphalt layers are compared in Figure 1.

3 CHARACTERIZATION OF BINDERS

Comprehensive tests were carried out on original binders, lab aged samples according to the Rolling Thin Film Oven Test (RTFOT, EN 12607-1) and the Pressure Aging Vessel (PAV, EN 14769), and recovered binders from the test sections. For binder extraction and recovery, the European standards EN 12697-1 and EN 12697-3 were followed. The solvent used was dichloromethane. Binder tests include penetration, fluorescence microscope (morphology), Gel Permeation Chromatography (GPC), Fourier Transform Infrared spectroscopy with Attenuated Total Reflectance (FTIR-ATR), and rheology with a Dynamic Shear Rheometer (DSR).

In the microscopic test, specimens were prepared by taking a drop of sample at 180°C on a glass plate, and morphologies measured at room temperature. The microscope used was Carl Zeiss Axioskop 40F1 equipped with a digital camera DP200.

GPC is a technique to determine molecular weights and molecular weight distribution. In this study, an Alliance 2690 Separation Module (Waters) with UV or refractive index detector was employed. Sample solutions of 0.4% were prepared using Tetrahydrofuran (THF). This solvent was also used as mobile phase.

In FTIR-ATR, a very small amount of bitumen sample was directly placed on an ATR crystal and IR reflection from the sample was detected. Spectra were recorded at wavelengths ranging from 500 to 4000 cm^{-1}. The compositional information was measured for polymers,

e.g. SBS at 966 cm^{-1} (butadiene) and 699 cm^{-1} (styrene), and for bitumen functional groups, such as carbonyl compounds at around 1700 cm^{-1} and aromaticity at about 1600 cm^{-1}.

With DSR, frequency sweeps (0.01 to 10 Hz) were performed at different temperatures ranging from 0 to 90°C, and Multiple Stress Creep and Recovery test (MSCR) according to ASTM D7405. Depending on test temperature, parallel plates of 25 mm in diameter and 1 mm in gap or 8 mm in diameter and 2 mm in gap were used.

3.1 *Morphology*

The morphologies of the modified binders measured at room temperature are presented in Figure 2. As expected, at a low concentration (3 or 4% by weight), the polymer exhibits dispersed phase in the binder. At a sufficiently high concentration of 6%, a continuous polymer phase is formed. The morphologies are also affected by aging. Apparently, in the studied binders of dispersed polymers, finer structures can be seen after the RTFOT-PAV. The polymer morphology may significantly influence the rheological properties of the binder [9, 10]. But for mixture performance, it is probably more important to know polymer structures in the mixture or mastics and to determine its structural impact. Further research on this aspect is needed.

3.2 *Retained penetration*

In assessing the age-hardening of bitumen or PMB over the time, an empirical parameter is retained penetration. It was found that after several years in the field, the modified binders used in the wearing course and base course generally showed higher retained penetration (i.e. less age-hardening) than the unmodified. The results are exemplified in Figure 3 for the binders extracted from the base course (AG22) which has been in the field for six years. On average, the degree of the age-hardening of 100/150-75 (SBS) is about half of that of bitumen 100/150 pen. This is probably due to polymer modification starting with soft bitumen and/or aged SBS acting as a softener in the bitumen. In the binder course, this effect was not seen for the binders modified by EVA or with a low concentration of SBS (3% by weight).

3.3 *Rheological properties*

From DSR frequency sweeps at different temperatures, complex moduli are plotted against phase angles. The so called black diagrams provide a method to check for the Time Temperature Superposition (TTS) principle and give information about chemical or structural changes during the rheological measurements. As exemplified in Figure 4, for the unmodified bitumens, no matter if aged or unaged, these curves are quite smooth, suggesting no structural changes during the rheological tests. On the other hand, it was not possible for the EVA

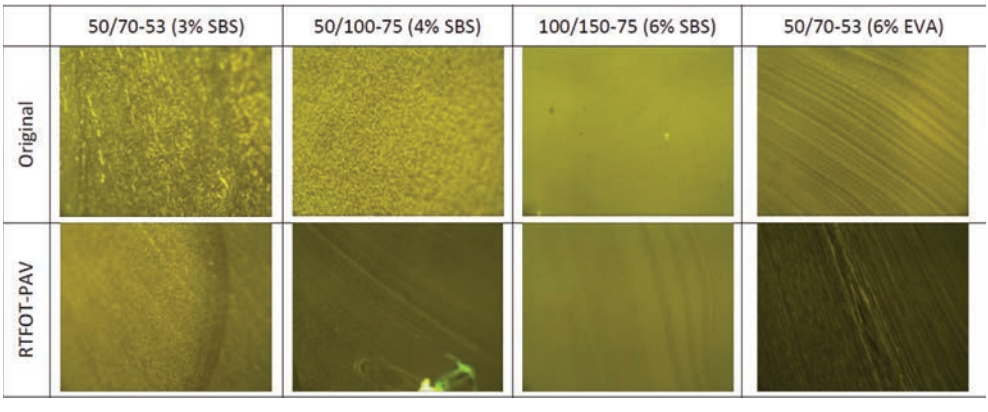

Figure 2. Morphologies of polymer modified binders (magnification 200×).

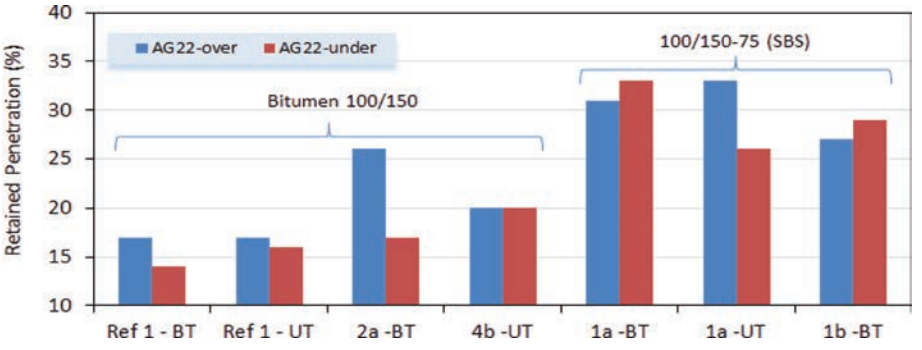

Figure 3. Retained penetration for the binders used in the base course (AG22).

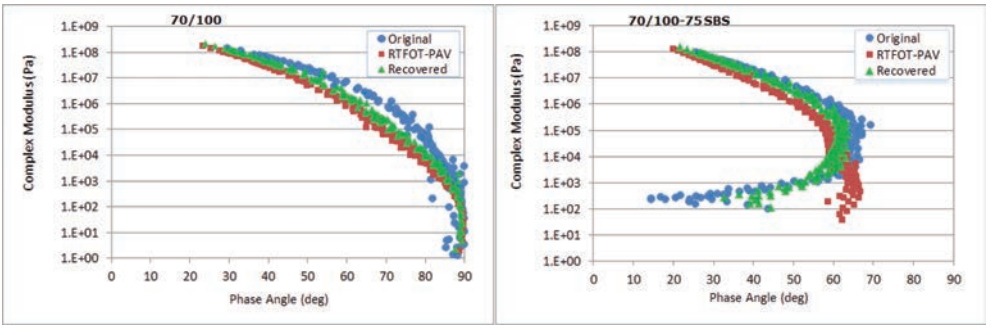

Figure 4. Complex modulus *vs* phase angle for different binders before and after aging.

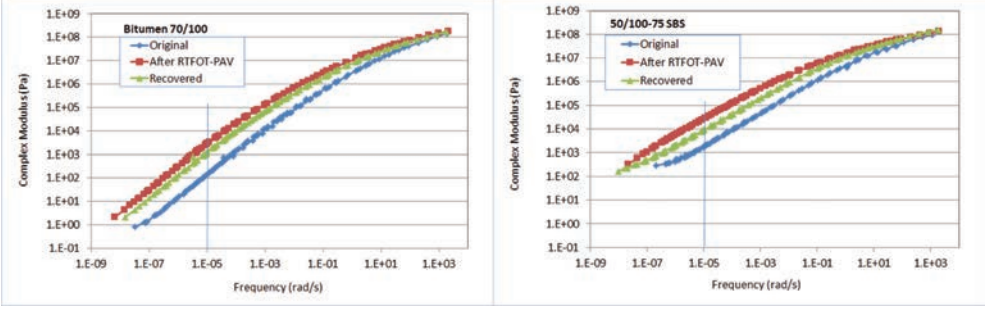

Figure 5. Complex modulus master curves at reference temperature 10°C.

modified binder to get a single smooth plot (figures are not shown). This is attributed to a phase change induced by the melting of the polymer. In the case of SBS modification, higher elasticity (lower phase angle) is very evident even at low complex moduli (at high temperatures and/or low frequencies), as well as after laboratory aging or several years in the field. This is beneficial when the resistance to permanent deformation is considered.

The DSR frequency—temperature sweeps are also used to construct master curves by applying the TTS principle [11]. Using master curves, bitumen rheological behavior and the effect of aging may be characterized over wider ranges of time or frequency at a specified temperature. Examples of the master curves of complex modulus are shown in Figure 5 for the binders used in the wearing course. For both the modified and unmodified binders, the transition to the glassy state can be seen at high frequency. The differences between the

binders, as well as the effect of aging, are more evident at low frequency range; the SBS modified binder exhibits significantly higher modulus than the pen bitumen, which is beneficial with respect to deformation resistance. For example, at a frequency of 1E-5 rad/s, the complex moduli of the modified binder are about 10 to 20 times higher than the unmodified bitumen, depending on if they are aged or not. In addition, the master curves of the recovered binders from the wearing course (4 years on the test road) lie between the original and RTFOT-PAV aged samples, implying the laboratory aging test predicts field aging quite well in this case.

To quantify the aging sensitivity of the different binders in the test road, it was intended to use aging index based on Zero Shear Viscosity (ZSV) measurements. Unfortunately it was not possible to precisely define ZSV for most of the modified binders. Instead, the complex viscosities measured at a low frequency of 0.001 Hz and at 60°C (LSV) are used to calculate the aging index (LSV of the extracted binders divided by that of the virgin samples). The averaged aging indices are: 6.77 for bitumen 70/100, 4.29 for bitumen 50/70, 5.05 for 50/70-53 EVA, 1.02 for 50/70-53 SBS, and 0.90 for 50/100-75 SBS. These data indicate that, of the binders used in the test sections, the SBS modified binders are the most resistant to aging. The high resistance to aging of the SBS modified binders is also confirmed by stiffness measurements on asphalt field cores; this will be shown later.

In the literature, several rheological parameters are used to assess binder rutting resistance. One test which can distinguish differences in the rutting potential is Multiple Stress Creep and Recovery test (MSCR) [12]. The measured parameters include strain recovery and non-recoverable compliance (Jnr). Typical examples of binder response to repeated loading are shown in Figure 6. Differences in strain recovery at 3.2 kPa and 60°C between the binders and the effect of aging are compared in Table 3. Obviously, the SBS modified binders show much higher strain recovery compared to others. Considering the effect of aging, the unmodified and EVA modified binders follow the same trend; the increased strain recovery for the aged and recovered samples is due to bitumen oxidation that makes the binders more elastic. In the case of SBS modification, aging may reduce binder strain recovery probably due to oxidation of the polymer. However, even after laboratory or field aging, the SBS modified binders still retain a higher level of strain recovery as compared to other binders.

Differences between the binders, as well as the effect of aging, are also evident when the non-recoverable compliances, Jnr 3200, are compared (see Table 3). Regardless of sample state (original, laboratory aged, or extracted from the test road), the polymer modified binders always show lower values of Jnr 3200 than the reference, suggesting higher rutting resistance for the modified binders.

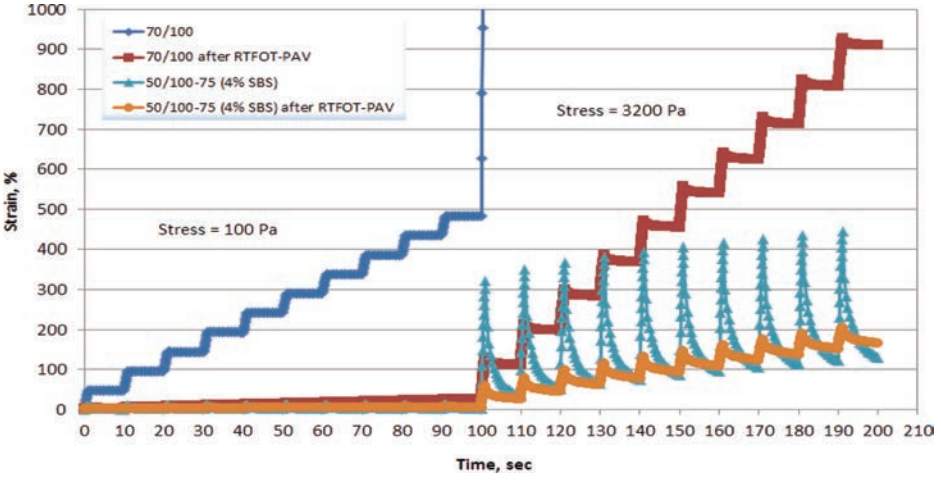

Figure 6. Strain response to repeated loading at 60°C for unmodified and SBS binders.

Table 3. Strain recovery and non-recoverable compliances (Jnr) measured at 60°C.

Asphalt layers	Binder types	Strain recovery, %			Jnr 3200, kPa^{-1}		
		Original	RTFOT-PAV	Recovered	Original	RTFOT-PAV	Recovered
Wearing course	70/100	0	16	5	5.16	0.28	0.69
	50/100-75 SBS	96	70	87	0.04	0.05	0.04
Binder course	50/70	0	13	6	3.55	0.41	0.84
	50/70-53 EVA	6	54	34	1.76	0.04	0.15
	50/70-53 SBS	47	51	32	1.00	0.09	0.34
Base course	100/150-75 SBS	99	90	78	0.01	0.08	0.34

MSCR tests were also carried out at 40°C for some test sections. Not surprisingly, differences between the binders became smaller as compared to the measurements at 60°C. For the unmodified and EVA modified binders, the strain recoveries increased to about 40 and 60%, respectively, while for the SBS modified binders, strain recoveries were more than 70%. In all cases, low values of Jnr were seen at 40°C (<0.03 kPa^{-1} at stress level of 3.2 kPa).

So far the above observation on binder rutting properties has not been validated by field measurement. All the test sections are in good conditions and very little rutting was observed.

Another aspect of particular importance to the Nordic countries is low temperature cracking. For the binders used in the surface layer, low temperature tests were performed according to Performance Grading (PG). It was found that 70/100 bitumen and 50/100-75 SBS were in a similar low temperature range of –22°C to –28°C. In addition, the critical cracking temperatures were determined in accordance with AASHTO PP42, and 70/100 bitumen and 50/100-75 SBS had –28.6°C and –29.1°C, respectively. The critical cracking temperatures are far below the lowest pavement temperature which is about –10°C.

For the binders recovered from the test sections, BBR tests were not performed due to limited amounts of samples. Instead, DSR with 8 mm parallel plate geometry was applied to measure binder stiffness (complex modulus) at –25°C. It was observed that at this low temperature and at 10 rad/s, the stiffness of the SBS modified binder was about 25% lower than that of the unmodified bitumen.

3.4 *Chemical analyses*

Using FTIR-ATR, the compositional information can be obtained directly on the binders without preparing a sample solution. Examples of the IR spectra are shown in Figure 7. To evaluate bitumen oxidation, IR absorbances are measured for oxygen-containing functional groups—carbonyl compounds at 1700 cm^{-1}, as well as aromaticity at 1600 cm^{-1}. As expected, the amount of the carbonyl compounds and aromaticity increase after laboratory aging (Fig. 8). However, for some test sections, the aromaticity and the carbonyl compounds measured for the recovered binders are lower compared to the original and lab aged samples. This could suggest that the functional groups are probably not completely extracted from asphalts, or there might be strong interactions between the bitumen and aggregates or fillers.

FTIR also showed that aging did not change EVA as reflected by more or less unchanged absorbance at 1241 cm^{-1} for the polymer. For the SBS modified binders, the butadiene signal at 966 cm^{-1} decreased slightly while the styrene at 699 cm^{-1} remained unchanged after aging (Fig. 7). Although the SBS polymers take part in chemical reactions and degradation of the polymers may occur during aging, the fragments formed are still kinds of polymer which are large enough to affect the binders in a beneficial way. It was shown by GPC that there were no significant changes in the contents of SBS polymer (and its fragments) after the laboratory aging or field aging.

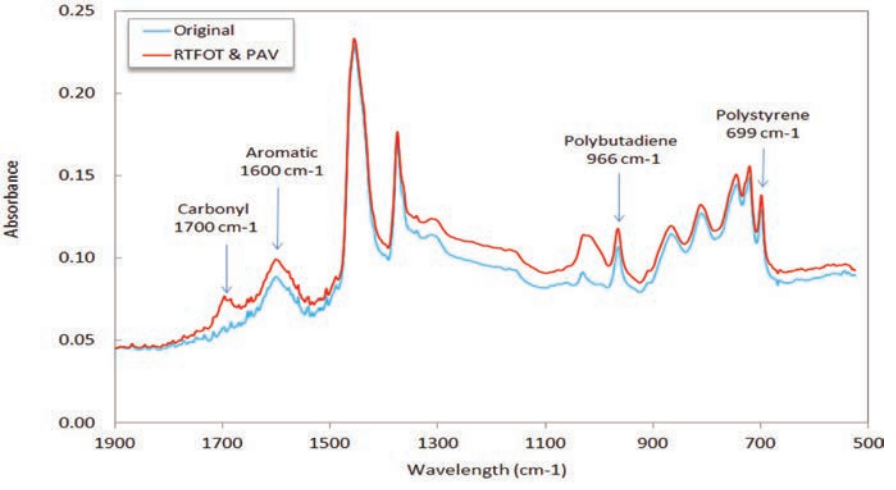

Figure 7. FTIR spectra of 50/100-75 SBS before and after aging.

Figure 8. Carbonyl compounds and aromaticity measured by FTIR-ATR.

4 MECHANICAL TESTS ON ASPHALT FIELD CORES

Several types of tests were performed on asphalt field cores, including stiffness measurement and repeated creep test. Based on stiffness results at 10°C, aging indices of the asphalt mixtures, defined as relative increase in stiffness modulus per year in percentage, are calculated. As shown in Figure 9, in both wearing course and binder course, the asphalt concretes made of the SBS-binders are less aged than those with other binders. This is in agreement with binder test results. Unexpectedly, in the base course, the mix with the SBS modified binder display a slightly higher aging index than the unmodified one. However, in spite of that, the SBS modified base course has shown better fatigue

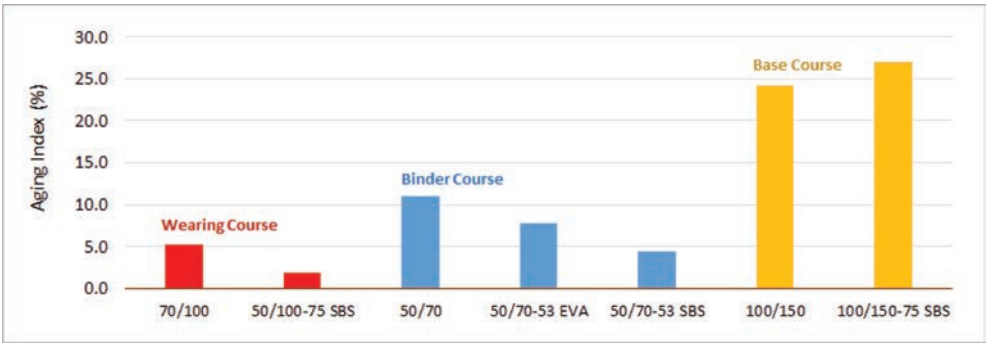

Figure 9. Aging indices of asphalt mixes at 10°C.

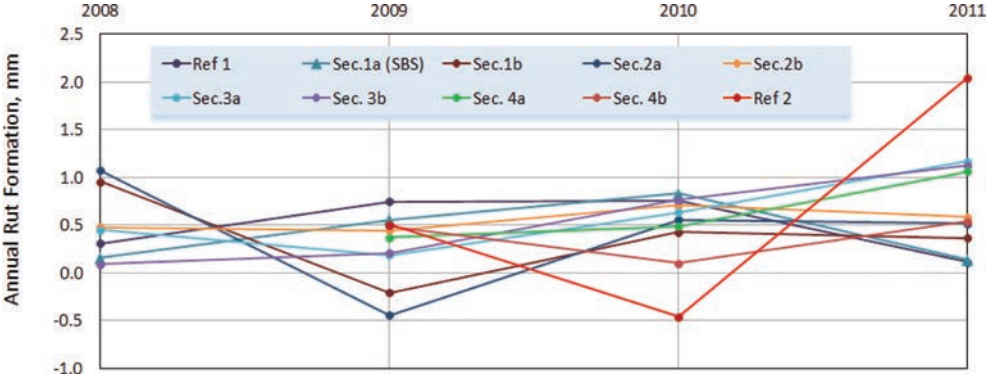

Figure 10. Annual rut formation of different test sections.

resistance than the conventional mix based on laboratory fatigue testing on field cores (data not shown).

Figure 9 also reveals that the aging of the base course mix is much higher than the wearing course and binder course mixes. Notice that in addition to the low binder content in the base course mix, the air voids content of the mix is about 5%; however in the wearing course and binder course, the air voids content is less than 2% (Fig. 1). An easier access to oxygen due to higher air voids combined with thinner binder layer (lower binder content) has caused a higher degree of aging for the base course mix.

5 FIELD PERFORMANCE OF THE TEST ROAD

The performance of the test road has been monitored since its opening to traffic. Annual field measurements and inspection show that all the sections are in good conditions. After 6 years traffic (2012), the rut depth measured on the wearing course was less than 7 mm, and rather small differences (about 2 mm) were found between the different sections. In Figure 10, the annual rutting in asphalt concrete layers estimated with Road Surface Tester (RST) between 2008 and 2011 is compared for different sections. In the estimation, wear rutting caused by studded tires is excluded. In addition to rutting, other deteriorations, such as stripping and low temperature cracking, have not been seen on the test road. To make definite comparisons on performance, a longer time of follow-up of the test road is obviously needed.

6 CONCLUSIONS

The polymer modified binders studied in this paper demonstrate better rheological properties than the unmodified bitumens, even after several years in the test road. These include higher strain recovery and lower non-recoverable compliance (Jnr) at high temperatures, and lower stiffness at low temperatures. For the SBS modified binders, good aging resistance is found. The high resistance to aging for the SBS modified binders is confirmed by stiffness measurements on asphalt field cores. The variation on binder rutting parameters (MSCR) has not yet been validated by the field performance of the test sections. So far, all the test sections are in good conditions and differences in rut depth are small. It is, however, believed that the improved binder properties should be beneficial to pavement performance. This is expected to be confirmed by a longer time of follow-up of the test road.

ACKNOWLEDGEMENTS

The authors gratefully acknowledge Carl-Gösta Enocksson, The Swedish Transport Administration, for supporting this research. They would also like to thank their technical staffs, Orjan Otterstrom and Petri Uhlback (Nynas), and Hassan Hakim and Andreas Waldemarson (VTI), for laboratory assistance.

REFERENCES

[1] Woo W.J., Ofori-Abebresse E., Chowdhury A., Hilbrich J., Kraus Z., Martin A. E. and Glover C.J., Polymer Modified Asphalt Durability in Pavements, FHWA/TX-07/0-4688-1, July 2007.
[2] Isacsson U. and Lu X., Testing and Appraisal of Polymer Modified Road Bitumens—State of the Art, Materials and Structures, Vol. 28, pp. 139–159, 1995.
[3] Roque R., Birgisson B., Drakos C. and Sholar G., Guidelines for Use of Modified Binders, Final Report 4910-4504-964-12, University of Florida, 2005.
[4] Von Quintus H.L., Mallela J. and Buncher M., Quantification of Effect of Polymer-Modified Asphalt on Flexible Pavement Performance, Transport Research Record, No. 2001, pp. 141–154, 2007.
[5] Aurstad J., Lange G. and Sturm D., Long Term Pavement Performance on Norwegian Asphalt Runways—A Field and Laboratory Study, The 10th ISAP Conference on Asphalt Pavements, Quebec, Canada, August 12–17, 2006.
[6] Nordgren T., PMB identifiering av egenskaper i bitumen som ger rätt egenskaper i beläggning, SBUF Rapport (projekt 11138, 11400), 2004.
[7] Stenberg N., PMB—Inverkan på asfaltbeläggningens funktionella egenskaper, SBUF Projekt 11692, 2007.
[8] The Swedish Transport Administration, 2011, TRVKB 10 Bitumenbundna lager, TRV 2011:082.
[9] Soenen H., Lu X. and Redelius P., The Morphology of Bitumen-SBS Blends by UV Microscopy—An Evaluation of Preparation Methods, Road Materials and Pavement Design, Vol. 9, pp. 97–110, 2008.
[10] Lu X., Soenen H. and Redelius P., SBS Modified Bitumens: Does Their Morphology and Storage Stability Influence Asphalt Mix Performance, The 11th ISAP Conference on Asphalt Pavements, Nagoya, Japan, August 1–6, 2010.
[11] Christensen Jr D.W. and Anderson D.A., Interpretation of Dynamic Mechanical Test Data for Paving Grade Asphalt Cements, Proc. of AAPT, Vol. 61, pp. 67–115, 1992.
[12] D'Angelo J., New High-Temperature Binder Specification Using Multistress Creep and Recovery, Transportation Research Circular E-C147, pp. 1–13. December 2010.

Asphalt Pavements – Kim (Ed)
© 2014 Taylor & Francis Group, London, ISBN 978-1-138-02693-3

The low temperature characterization of bio-modified shingles

Daniel Oldham, Elham H. Fini & Albert Onochie
North Carolina A&T State University, Greensboro, NC, USA

ABSTRACT: With depleting natural resources and increasing material costs, the reusing of defective Roofing Shingles (RAS) has gained increasing attention. However, it has been noted that the use of aged asphalt materials can adversely affect low temperature performance shown both in the field through decreased pavement life and in the laboratory through the induction of micro-cracking. Another development in sustainable infrastructure is that of Bio-Modified Binder (BMB) particularly that derived from swine manure. The use of BMB in HMA has shown trends of increasing low temperature performance specifically in samples containing aged materials. In this paper, samples were subjected to dry air conditioning times of 0, 24, 48, and 72 hours to simulate low temperature field conditions. Through Bending Beam Rheometer (BBR) testing, stiffness showed a trend of being lower and m-values were higher in samples containing BMB in conditioned samples. Direct Tension Tester (DTT) results revealed congruent results; however, a drop in failure stress, strain, peak load, fracture energy, and ductility at 24 hour conditioning was observed to indicate micro-cracking as a discontinuity in results was observed.

Keywords: roofing shingles; swine manure; bio-binder; physical hardening; micro-cracking

1 INTRODUCTION

According to the American Society of Civil Engineer's 2013 Report Card for America's Infrastructure, America's highways received a grade performance of D with 32% of America's major roads in poor or mediocre condition. This in turn, cost US motorists, who are traveling on deficient pavement, approximately $67 billion a year in repairs to their vehicles [1]. One reason for the increase in deficient pavement, is that over the past 9 years, asphalt binder prices has risen 255% as a result of increasing crude petroleum prices and refining modifications that have resulted in a reduction of asphalt binders supply in the market. As a result, the maintenance of our nation's highways has become more costly and harder to manage [2–3]; therefore, it is essential for America's economic vitality to adopt more sustainable practices in the asphalt paving industry that would reduce material costs while improving pavement performance.

The use of recycled materials in asphalt pavement particularly that of Recycled Asphalt Shingles (RAS) has been well documented; RAS has been used in HMA for over 25 years as a means of economic value as well as landfill diversion. It is estimated that approximately 11 million tons of asphalt roofing shingles is discarded into landfills each year with 10 million tons being that of Post-Consumer Tear-Off Scrap Shingles (TOSS) and the remaining one million being Manufactured Waste Scrap Shingles (MWSS). This is equivalent to disposing approximately 5.8 million tons of useable mineral aggregates and nearly 3.1 million tons of reusable asphalt binder annually [4–5]; however, despite the potential benefits of utilizing such a vast resource, only approximately 10% of disposed roofing shingles are recycled for new pavement construction [6]. One of the reasons for strict limitation on RAS usage is the potential for adverse negative low temperature effects of the asphalt mixture. It has been shown that the low temperature grade of the base

binder increases approximately 1.9°C for every one percent increase in RAS usage in neat asphalt [4].

Previous research has indicated that low temperature performance of asphalt pavement is a key contributor to the overall performance of the asphalt pavement, particularly in cold regions. Nationally, this phenomenon cost various agencies approximately $45 billion dollars in expenditures in 2006 [3]. The main contributor to adverse low temperature properties has been that of high thermal stresses formed within the asphalt binder when the temperature drops suddenly. For this reason, the use of recycled materials in new pavement construction has been limited despite initial cost savings, better waste management practices and more sustainable development [4–7]. It has been well documented that the increase in high thermal stresses is due to the stiffer oxidized/aged binder added to the base binder upon introduction of recycled asphalt [8–12].

The use of recycled materials particularly the use of oxidized/aged binder such as Recycled Asphalt Pavement (RAP) and Recycled Asphalt Shingles (RAS) adversely affects low temperature performance of asphalt due to low-level interactions between the asphalt binder and the oxidized recycled binder; therefore, it is well documented that the use of wet processing can lead to significant improvements in overall pavement performance as well as consistency compared to dry processing [13–18]. In order to accommodate increased RAS percentages, wet processing of RAS was utilized for this paper [19]. However, the specimens are categorized as mastics rather than binders due to the addition of 85.5 μm size particles as well as the relatively high percentage of RAS introduced by weight of the shingles and base asphalt.

The presence of particles, in asphalt binder to form mastics, has been found to have a direct correlation and could be the sole contributor to premature failure of the overall asphalt mixture due to the particle's high surface area in the mix [20–24]. Other effects on the overall mixture from mastics can vary from air voids content, moisture sensitivity leading to stripping, as well as mixture stiffness resulting in increased brittleness [22–26]. Therefore, in order to increase sustainability, the use of bio based binder derived from swine manure was studied to determine if it's presence could alleviate the adverse effects from the RAS [27–29].

Swine manure based bio-binder is a newly developed technology with the potential of replacing petroleum based asphalt binder. Having been produced from swine manure, it offers considerable benefits both environmentally through being a best practice management solution and economically through a 70% reduction in production cost to that of petroleum based as well as improved profits for hog farmers [30–32].

This paper studies the low temperature properties of bio-binder in the presence of high percentages of recycled asphalt shingles (mixed by wet processing). In order to simulate actual low temperature field conditions, samples were conditioned in a freezer for 24 hours, 48 hours, and 72 hours at −18°C. Specimens were then tested using the Bending Beam Rheometer (BBR) and the Direct Tension Tester (DTT). The BBR was used to determine the m-value and stiffness for each of the blended samples while the DTT results were used to look at the blend's fracture energy, ductility, failure stress, failure stain, and peak load which are all indicators for thermal cracking resistance.

2 MATERIAL AND METHODS

2.1 *Asphalt roofing shingles*

For this project, Tear-Off Scrap Shingles (TOSS) were chosen and donated by S.T. Wooten's Quality Control lab located in Sanford, NC. Some states that allow RAS in new construction limit the selection to only that of Manufacture Waste Scrap Shingles (MWSS) due to it's consistency, separation from other Construction and Demolition (C&D) waste, and that it is considerably less aged than TOSS (7); therefore, this study investigates the feasibility of the application of high percentages of TOSS as the most severe scenario. The gradation of the shingles is given in Table 1.

Table 1. Recycled asphalt shingle gradation.

Mesh	Size (mm)	Weight retained (g)	Cumulative weight retained (g)	Cumulative % weight retained	Cumulative % passing
3/8 in.	9.51	0.00	0.00	0.00	100.00
No. 4	4.75	219.95	219.95	4.61	95.39
No. 8	2.36	370.32	590.27	12.36	95.39
No. 16	1.00	865.82	1456.09	30.49	69.51
No. 30	0.60	1044.38	2500.47	52.36	47.64
No. 50	0.30	735.84	3236.31	67.77	32.23
No. 100	0.15	629.47	3865.78	80.95	19.05
No. 200	0.075	613.91	3379.69	93.81	6.19
Pan		295.70	4775.39	100.00	0.00

2.2 *Recycled Asphalt Shingle (RAS) modified mastic*

The base binder for the study was Superpave 64-22, which is commonly used across the United States. The 40% RAS particles with an average size of 85.5 μm by total binder mass was blended with the neat binder by means of a mechanical shear mixer rotating at approximately 450 rpm for 1 hour. There wasn't any extraction preformed on RAS particles since particles were added as is. Therefore, due to the large percentage of particles and to avoid segregation, the mastic was re-blended at 135°C for 5 minutes at 750 rpm prior to preparing each test specimen.

2.3 *Bio-binder production*

The bio-binder was produced by means of a thermochemical conversion of swine manure at the Swine Farm Unit at NC A&T. The processing begins with subjecting the manure to anaerobic atmosphere by purging the air 3 times by use of nitrogen gas. Once completed, the manure is heated to 300°C at which the temperature and pressure is maintained for a specified amount of time. After heating, the manure is cooled down to room temperature at which it is then removed from the reactor, separated by means of filtration, then finally undergoing a vacuum distillation.

2.4 *Bio-Modified Shingles (BMS) mastic*

The Bio-Modified Shingles (BMS) were the resultant of blending the 40% RAS mastic binder with 10% Bio-binder by mass. The mixing was conducted by means of a mechanical shear mixer rotating at 750 rpm for 30 minutes. Due to bio-binder specifications, the mixture temperature was reduced to 135°C due to the additive's ability to improve workability at lower temperatures, which also reduces excess aging.

2.5 *Sample conditioning*

For this paper, both DTT and BBR specimens were subjected to dry isothermal conditioning of −18°C to simulate the low temperature conditions in the field. Conditioning times were 0, 24, 48, and 72 hours to determine if a trend would be shown with increased conditioning time. Specimens were demolded in order to eliminate the influence of the molds as shown in Figure 1. All test specimens were still conditioned for 1 hour in the alcohol bath as stated by the respected ASTM standards; however, it is not considered in the conditioning time since it was not dry isothermal conditioning.

2.6 *Bending Beam Rheometer (BBR)*

In order to establish the low temperature performance of the modified binder, the BBR was used to determine flexural-creep stiffness and m-value parameters following AASHTO T 313.

Figure 1. DTT specimen preparation and testing.

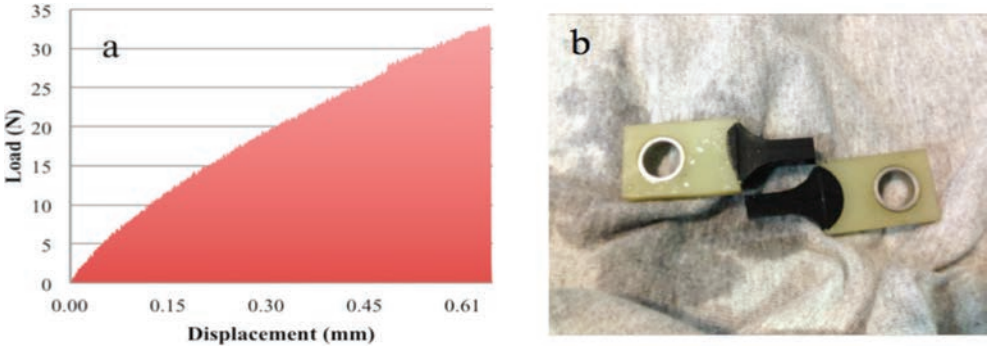

Figure 2. Load-displacement curve; (b) Fractured DTT specimen.

According to the Superpave™ specification, this test evaluates the binder's possible abilities of stress relaxation and thermal cracking. In this study, the testing temperature was –18°C with the stiffness and m-values recorded. Using Equation (1), the stiffness of the asphalt binder was calculated.

$$S(t) = \frac{PL^3}{4bh^3\delta(t)} \tag{1}$$

where:

P = applied constant load (100 g or 0.98 N)
L = distance between beam supports (102 mm)
b = beam width (12.7 mm)
h = beam thickness (6.25 mm)
$S(t)$ = asphalt binder stiffness at a specific time
$\delta(t)$ = deflection at a specific time

2.7 *Direct Tension Tester (DTT)*

The Direct Tension Test is typically used to determine the failure strain and failure stress of asphalt binders by means of direct tensile force using the Direct Tension Tester (DTT) apparatus developed by Interlaken Inc. Test specimens are prepared by pouring hot asphalt binder into a respected dog-bone shaped mold with two plastic end pieces. The two end pieces are also used to transfer the tensile load from the test machine to the asphalt binder. According to ASTM 6723-12, the rate at which the tensile is applied was approximately 1.00 mm/min. In this study, percent strain, stress, and load readings were recorded until the fracture failure was reached. The test must be conducted at temperatures where the specimens exhibit brittle behavior in order to capture fracture rather than ductile failure. For this paper, the testing temperature was –18°C which is 4 degrees above the low temperature grade of the PG 64-22 base binder.

Using load and displacement data collected during the DTT test, fracture energy was calculated using Equation (2) [27]. An example of the $A_{L\text{-}D\ Curve}$ and an image of DTT sample after fracture are shown in Figure 2.

$$\text{Fracture Energy} = \frac{\sum \text{Area}_{L-D.Curve}}{\text{Area}_{C.S.A}} \quad (2)$$

where:

$\text{Area}_{L\text{-}D.Curve}$: The area under the load—displacement curve (N*m)

$\text{Area}_{C.S.A}$: The cross section area at fracture (m^2)

3 DISCUSSION AND ANALYSIS

3.1 *BBR results*

It is evident from the trend discerned in Figure 3, that the longer the conditioning period in –18°C the stiffer the RAS samples. It was further observed that by conditioning the RAS samples for 24, 48 and 72 hours the creep stiffness increased by an average of 25%, 50% and 69% respectively from 0 hours conditioning.

As shown in Figure 3, the conditioning of BMS for 24, 48 and 72 hours increased stiffness by an average of 32% and 42% respectively. By observing the steady increase in creep stiffness with respect to the conditioning time and the constant temperature of –18°C, a phenomenon known as physical hardening was observed [33]. This phenomenon causes time dependent isothermal changes in specific volume and consequently changes in mechanical properties, though it has been noted that the effect of physical hardening is completely removed when the material is heated up to room temperatures [34]. This phenomenon occurs as a consequence of isothermal reduction of free volume at temperatures close to the glass transition temperature [35]. The effect of physical hardening is typically reflected in an increase in the stiffness values and a reduction of the stress relaxation capacity of the asphalt binder.

Figure 3 also indicates that the addition of 10% bio-binder reduced the RAS stiffness and a clear trend was observed as increased conditioning time lead to improved BMS sample performance over RAS. At 0 hours conditioning, the BMS reduced the stiffness by an average of

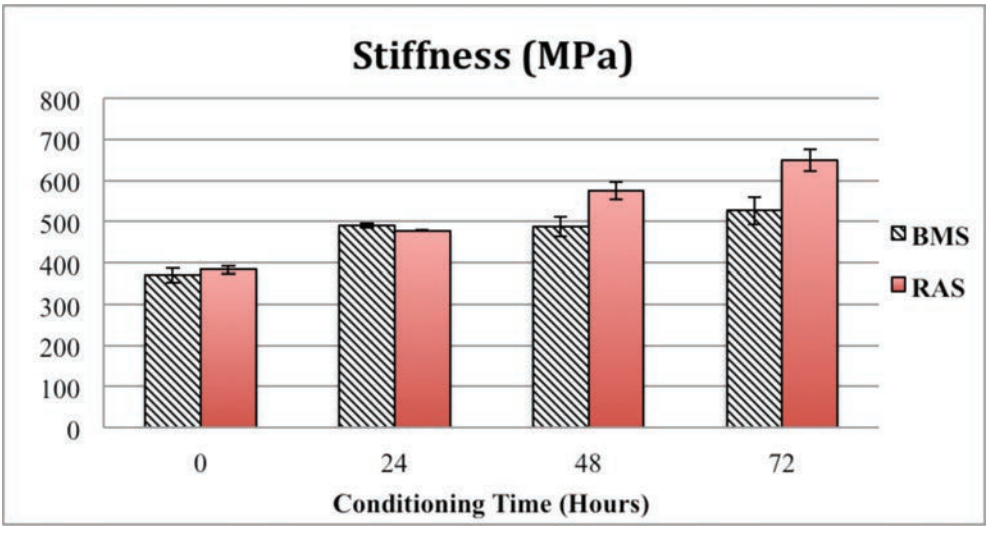

Figure 3. Time-dependent creep stiffness curves for 40% RAS.

4% at time 60 seconds and at 24 hours conditioning no reduction is clearly seen. Accounting for the little to no reduction in these two times would be the increased susceptibility of oxidative and thermal aging in BMS compared to the RAS samples. It can be seen that at 48 hours and 72 hours stiffness is reduced by an average of 18% and 23% respectively at time 60 seconds.

However, Figure 4 further demonstrates a clear trend of BMS performing better than RAS as the conditioning time was increased in that the m-values are constantly higher than the RAS specimens. At 0, 24, 48 and 72 hour conditioning, BMS saw an average increase in m-value of 4%, 5%, 15% and 16% respectively.

3.2 *DTT results*

The strain values were conducted using the DTT at a testing temperature of –18°C. As shown in Figure 5, as conditioning time increases, the failure strain decreases both in RAS

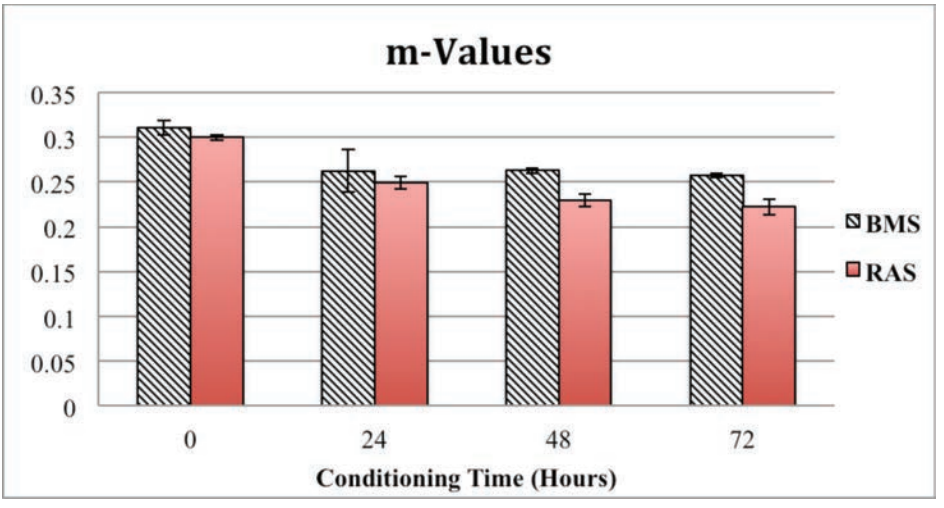

Figure 4. m-value results for BMS and RAS.

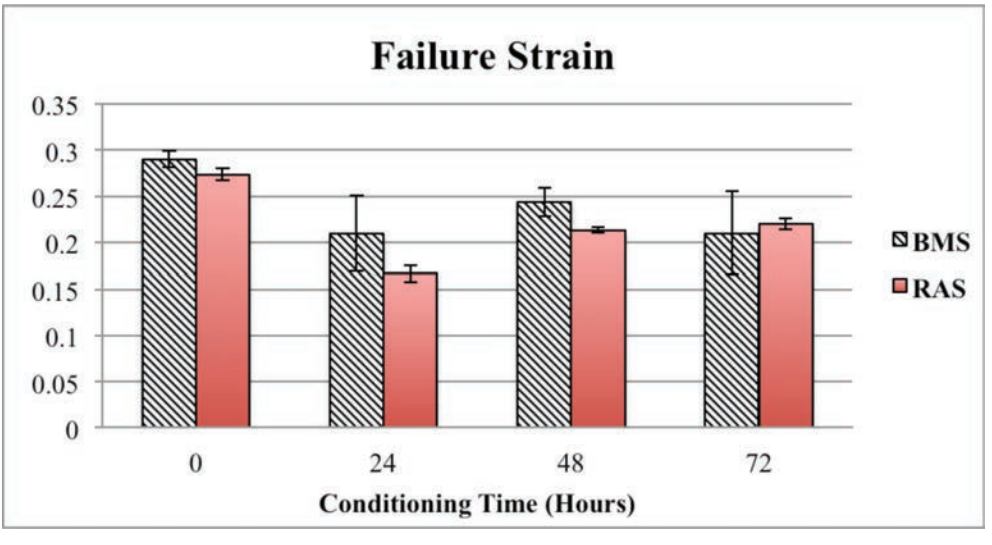

Figure 5. Failure strain for BMS and RAS samples.

and BMS samples. The strain findings as well as the stress findings in Figure 6 are both consistent with what was found in a prior mastic study which showed failure stain and stress to increase with increasing percentage of particles [36]. However, it is interesting to note that the strain value for both BMS and RAS dropped at 24 hour conditioning then proceeded to increase before declining again. When comparing the RAS and BMS, BMS had consistently higher Failure Strain values until 72 hour conditioning in which they were both relatively the same. This same trend was found for failure stress values as well in Figure 6 except that failure stress was consistently higher for all RAS samples compared to BMS, except for the 24 hour specimens, which indicates the material is stiffer due to the increase in stress.

The peak load is the maximum load placed on the specimen before fracture. As indicated from the failure stress and strain, the peak loads show a similar trend in Figure 7. Higher peak

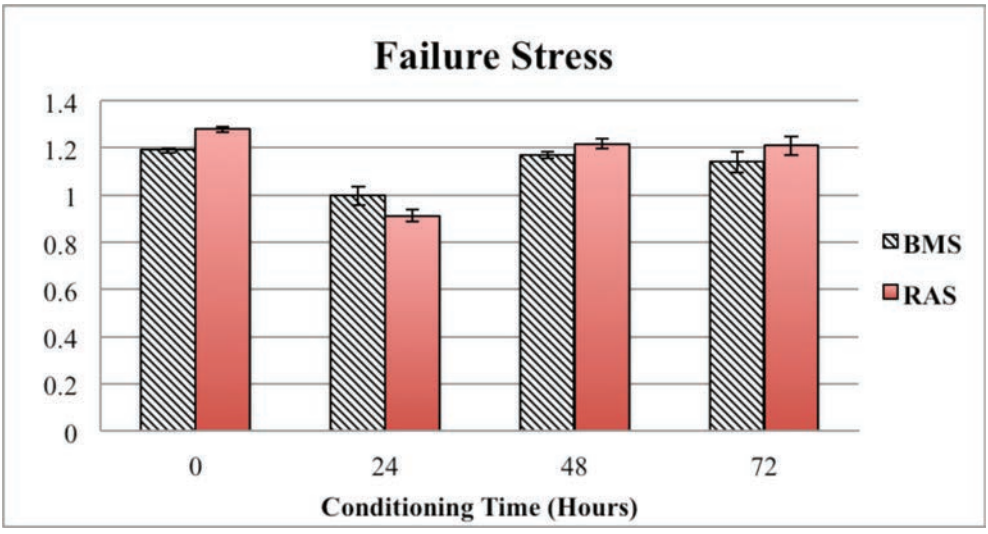

Figure 6. Failure stress of BMS and RAS samples.

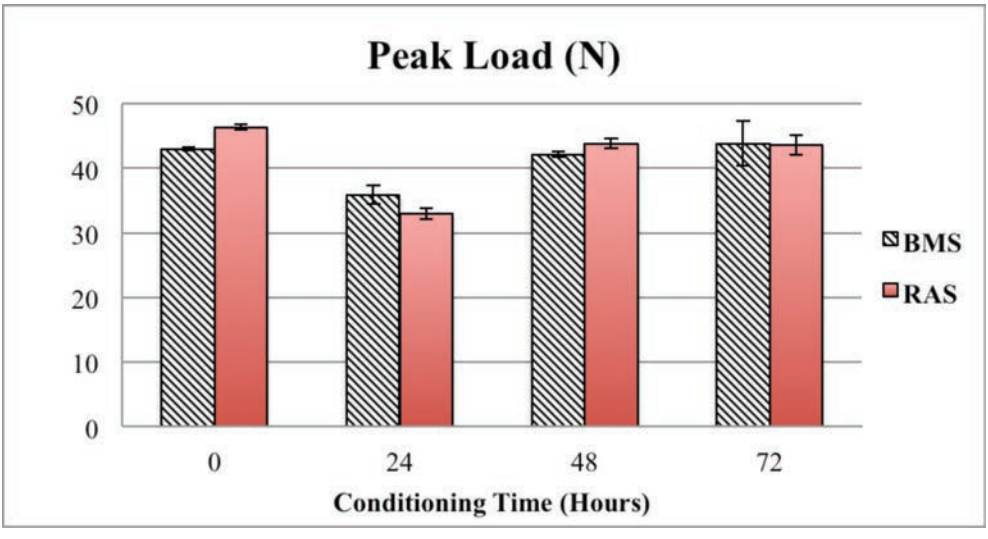

Figure 7. Peak loads of BMS and RAS samples.

loads have been related to more brittle materials. The peak loads for 0 and 48 hour RAS samples appear to be slightly higher, the 72 hour results being relatively the same, and the 24 hour samples indicate BMS as a higher peak load.

The fracture energy as calculated from Equation (2), is shown in Figure 8. From the results, it is shown that the BMS has higher fracture energy values compared to RAS except for 0 hours conditioning. It has been observed that materials with higher fracture energy values tend to have improved low temperature performance [27]. In Figure 9, ductility results show BMS with consistently higher values than RAS samples which also indicates RAS samples show more brittle behavior at low temperatures. The drop in performance could be attributed to the presence of micro cracking which has been indicated previously in sudden decreases in pavement performance during prolonged conditioning [37–38].

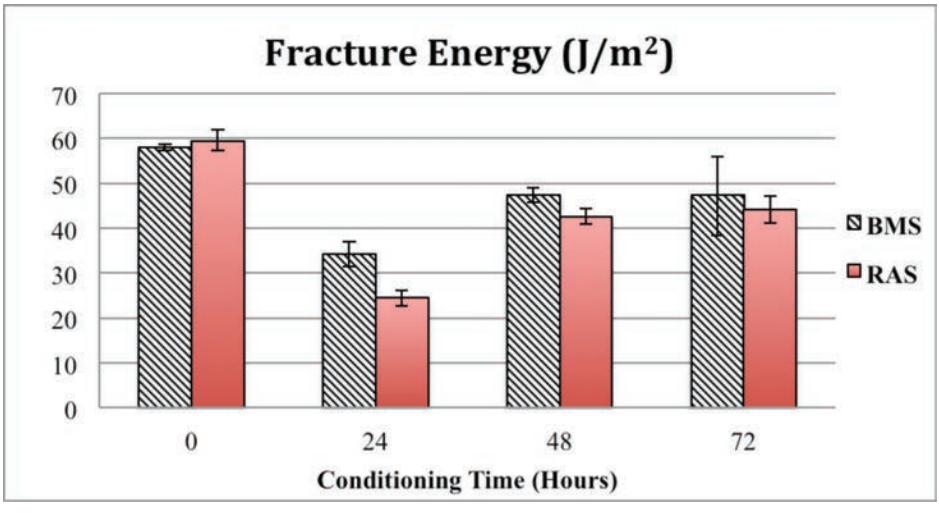

Figure 8. Fracture energy for BMS and RAS samples.

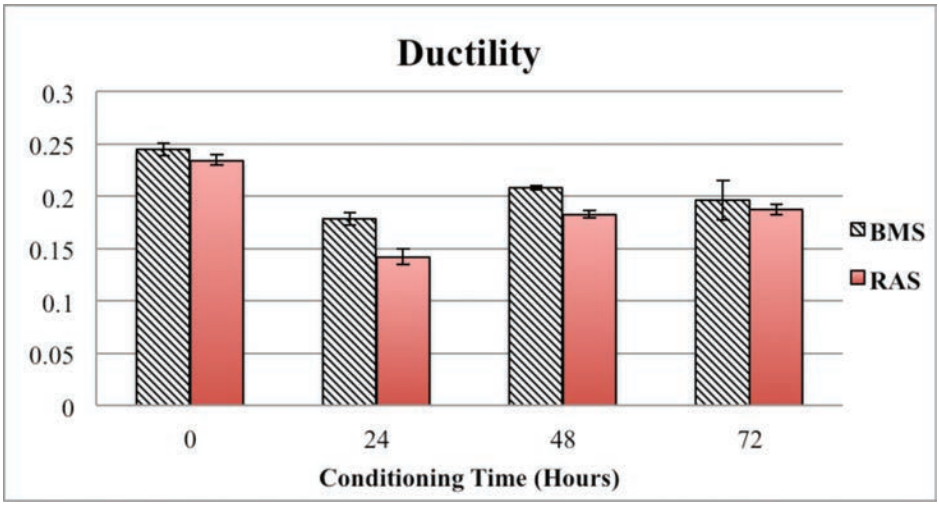

Figure 9. Ductility for BMS and RAS samples.

4 CONCLUSIONS

From these results, the follow conclusions were made:

- The performance of RAS based mastic samples was observed to have adverse low temperature effects compared to the neat binder.
- The performance of RAS samples was observed to have generally adverse low temperature performance as conditioning time increased.
- The performance of BMS samples was observed to have deteriorating low temperature performance similar to RAS samples; however, the presence of bio-binder showed trends of adverse low temperature performance mitigation.
- The RAS and BMS sample subjected to increasing increments of low temperature conditioning showed trends to physical hardening.
- The drop in performance observed in both BMS and RAS DTT samples subjected to 24 hour conditioning shows similar characteristics to the phenomena known as micro-cracking.

ACKNOWLEDGMENTS

This research is sponsored by the National Science Foundation (Award No: 1150695) and NCHRP IDEA Project 171. The authors would like to acknowledge the invaluable assistance provided by Farrokh Mirzaefard of North Carolina A&T State University. The contents of this paper reflect the view of the authors, who are responsible for the facts and the accuracy of the data presented. This paper does not constitute a standard, specification, or regulation.

REFERENCES

[1] American Society of Civil Engineers (ASCE). 2013 Report Card for America's Infrastructure. ASCE. March, 2013.
[2] Monthly Terminal Asphalt Binder & Fuel FOB Prices. North Carolina Department of Transportation Business Partner Resources. 2013. Last accessed: September 15, 2013.
[3] Marasteanu, M., Zofka, A., Turos, M., Xinjun, L., Velasquez, R., Li, X., Buttlar, W., Paulino, G., Braham, A., Dave, E., Ojo, J., Hussain Bahia, Williams, C., Bausano, J., Gallistel, A., and McGraw, J. Investigation of Low Temperature Cracking in Asphalt Pavements: National Pooled Fund Study 776. Minnesota Department of Transportation Final Report No. MN/RC 2-7-43. 2007.
[4] Williams, R.C., Cascione, A., Yu, J., Haugen, D., Marasteanu, M., and McGraw, J. Performance of Recycled Asphalt Shingles in Hot Mix Asphalt Final Report, Institute for Transportation Iowa State University, TPF-5(213). 2013.
[5] Maupin, G.W. Investigation of the Use of Tear-Off Shingles in Asphalt Concrete. Virginia Transportation Research Council. Final Report: FHWA/VTRC 10-R23. 2010.
[6] Hansen, R., and Newcomb, D. (2011). Asphalt Pavement Mix Production Survey on Reclaimed Asphalt Pavement, Reclaimed Asphalt Shingles, and Warm-Mix Asphalt Useage: 2009–2010. National Asphalt Pavement Association. Final Report 2009–2010.
[7] Zhou, F., Hu, S., and Scullion, Tom. Balanced RAP/RAS Mix Design and Performance Evaluation System for Project-Specific Service Conditions. Federal Highway Administration Final Report No. FHWA/TX-13/0-6092-3. 2013.
[8] Soleimanbeigi, A., Edil, T.B., and Tinjum, J.M. Effect of Temperature on Shear Strength of Recycled Asphalt Shingles. TRB 92nd Annual Meeting Compendium of Papers. Transportation Research Board of the National Academies. Washington, D.C., 2013, Paper #13–3109. 2013.
[9] Maupin, G.W. Investigation of the Use of Tear-Off Shingles in Asphalt Concrete. Virginia Transportation Research Council. Final Report: FHWA/VTRC 10-R23. 2010.
[10] Goh, S. and You, Z. Evaluation of Recycled Asphalt Shingles in Hot Mix Asphalt. *Transportation and Development Institute Congress*: pp. 638–645. 2011.
[11] Lippert, D. and Brownlee, M. Use of Reclaimed Asphalt Shingles in Illinois. Illinois Department of Transportation: Physical Research Report No. 162. 2012.

[12] Ozer, H., Al-Qadi, I., Kanaan, A., and Lippert, D. Performance Characterization of High Asphalt Binder Replacement with Recycled Asphalt Shingles (RAS) for Low N-design Mixture. Transportation Research Board of the National Academies. Washington, D.C., 2011. Paper #13–4500. 2013.
[13] Caltrans. Use of Scrap Tire Rubber: State of the Technology and Best Practices. State of California Department of Transportation Materials Engineering and Testing Services. Sacramento, CA. Final Report. 2005.
[14] Amirkhanian, S.N. Utilization of Scrap Tires in Flexible Pavements—Review of Existing Technology. *Use of Waste Materials in Hot-Mix Asphalt*. American Society for Testing and Materials. STP 1193. pp 233–250. 1993.
[15] Eaton, R.A., Roberts, R., and Blackburn, R. Use of Scrap Rubber in Asphalt Pavement Surface. U.S. Army Cold Regions Research and Engineering Laboratory, Hanover, NH. Special Report 91–127. 1991.
[16] Hansen, K., and Anderton, G. A Laboratory Evaluation of Recycled Tire Rubber in Hot-Mix Asphalt Paving Systems. *Use of Waste Materials in Hot-Mix Asphalt.* American Society for Testing and Materials. STP 1193. pp 69–83. 1993.
[17] Kandhal, P. Waste Materials In Hot Mix Asphalt—An Overview. *Use of Waste Materials in Hot-Mix Asphalt*. American Society for Testing and Materials, STP 1193. pp 3–16. 1993.
[18] Lundy, J., Hicks, R., and Zhou, H. Ground Rubber Tires in Asphalt-Concrete Mixes—Three Case Histories. *Use of Waste Materials in Hot-Mix Asphalt*. American Soceity for Testing and Materials, STP 1193. pp 262–275. 1993.
[19] Elseifi, M., Saman, S., Mohammad, L., Hassan, M., Daly, W., and Dessouky, S. New Approach to Recycling Asphalt Shingles in Hot-Mix Asphalt. *Journal of Materials in Civil Engineering,* 24(11). pp 1403–1411. 2012.
[20] Soenen, H., and Teugels, W. Rheological Investigation on Binder-Filler Interactions, Eurobitume Workshop 99—Performance Related Properties for Bituminous Binders, European Bitumen Association, Luxembourg, Paper No. 102. 1999.
[21] Kavussi, A., and Hicks, R.G. Properties of Bituminous Mixtures Containing Different Fillers. *Journal of the Association of Asphalt Paving Technologists,* 66, 153–186. 1997.
[22] Muniandy, M., and Aburkaba, E. Effect of 20 Micron Filler Particle Size and Filler Type on Rheological and Performance Properties of Stone Mastic Asphalt-filler Mastics. *Austrailian Journal of Basic and Applied Sciences*. 7(1): 105–116. 2013.
[23] Soenen, H., De La Roche, C., and Redelius, P. Predict Mix Fatigue Tests from Binder Fatigue Properties, Measured with a DSR. Proceedings from 3rd Eurasphalt and Eurobitume Congress, Foundation Eurasphalt, Breukelen, Netherlands. 2004.
[24] Hartman, A.M., and Gilchrist, M.D. Evalutaion Four-Point Bend Fatigue of Asphalt Mix Using Imagining Analysis. *Journal of Materials in Civil Engineering,* 16(1), 60–68. 2004.
[25] Liao, M. and Chen, J. Zero Shear Viscosity of Bitumen-Filler Mastics, *Journal of Materials in Civil Engineering,* 23(12), 1672–1680. 2011.
[26] Liao, M., Chen, J., and Tsou, K. Fatigue Characteristics of Bitumen-Filler Mastics and Asphalt Mixtures. *Journal of Materials in Civil Engineering,* 24(7), 916–923. 2012.
[27] Hill, H., Oldham, D., Behzad, B., Fini, E., Buttlar, W., and Henrique, R. Low-Temperature Performance Characterization of Bio-Modified Asphalt Mixtures Containing Reclaimed Asphalt Pavement. TRB 92nd Annual Meeting Compendium of Papers. Transportation Research Board of the National Academies, Washington, D.C., 2013, Paper #13–3773. 2013.
[28] Fini, E., Oldham, D., and Abu-Lebdeh, T. Synthesis and Characterization of Bio-Modified (BMR) Asphalt: A Sustainable Waste Management Solution for Scrap Tire and Swine Manure. *Journal of Environmental Engineering.* 10,1061/(ASCE)EE. 1943–7870. 2013.
[29] Mogawer, W.S., Fini, E.H., Austerman, A.J., Booshehrian, A., and Zada, B. Performance Characteristics of High RAP Bio-Modified Asphalt Mixtures. TRB 91st Annual Meeting Compendium of Papers DVD. Transportation Research Board of the National Academies, Washington, D.C., 2013, Paper #12–2411. 2012.
[30] Karmakar, S., NKetia, M., Laguë, C., & Agnew, J. Development of expert system modeling based decision support system for swine manure management, *Computers & Electronics In Agriculture*, 71(1): 88–95. 2010.
[31] Fini, E.H., Kalberer, E.W., Shahbazi, A., Basti, M., You, Z., Ozer, H., & Aurangzeb, Q. Chemical Characterization of Biobinder from Swine Manure: Sustainable Modifier for Asphalt Binder. *Journal Of Materials In Civil Engineering,* 23(11), 1506–1513. 2011.
[32] Xiu, S.N., H.K. Rojanala, A. Shahbazi, E.H. Fini and L. Wang. 2011. Pyrolysis and Combustion Characteristics of Bio-Oil from Swine Manure. *Journal of Thermal Analysis and Calorimetry*, 107(2): 823–829.

[33] Tabatabaee, H., Mangiafico, S., Velasquez, R., and Bahia, H. Investigation of Low Temperature Cracking in Asphalt Pavements. *National Pooled Fund Study-Phase II.* 2010.
[34] Hesp, S., and Subramani, S. Another Look at the Bending Beam Rheometer for Specification Grading of Asphalt Cements. Proceedings of 6th MAIREPAV Conference, Torino, Italy. 2009.
[35] Romero, P., Youtcheff, J., Stuart, K., Low-Temperature Physical Hardening of Hot-Mix Asphalt. Transportation Research Record: Journal of Transportation Research Board 1661 pp. 22–26. 1999.
[36] Wang, D., Wang, L., Gu, X., and Zhou, G. Effect of Basalt Fiber on the Asphalt Binder and Mastic at Low Temperature. *Journal of Materials in Civil Engineering*. 25(3): 355–364. 2013.
[37] Baumgardner, G., Rowe, G., and Reinke, Gerald. Bending Beam Rheological Evaluation of Wax Modified Asphalt Binders. 7th Rilem International Conference on Cracking in Pavements. pp. 901–910. 2012.
[38] King, G., Anderson, M., Hanson, D., and Blankenship, P. Using Black Space Diagrams to Predict Age-Induced Cracking. 7th Rilem International Conference on Cracking in Pavements. pp. 453–463. 2012.

This page intentionally left blank

Asphalt Pavements – Kim (Ed)
© 2014 Taylor & Francis Group, London, ISBN 978-1-138-02693-3

Optical fiber sensors with flexible encapsulation for pavement behavior monitoring

Wanqiu Liu
Department of Transportation and Logistics, Dalian University of Technology, Ganjingzi District, Dalian, Liaoning, China

Xiaoying Xing
School of Civil Engineering, Dalian University of Technology, Ganjingzi District, Dalian, Liaoning, China

Yanqing Zhao & Zheren Wang
Department of Transportation and Logistics, Dalian University of Technology, Ganjingzi District, Dalian, Liaoning, China

Ling Kang
Department of Computer Science, Dalian Neusoft University of Information, Dalian, Liaoning, China

ABSTRACT: Due to the increasing needs for robust highway pavement structural monitoring tools with high accuracy and functionality, this paper introduces some preliminary outcomes from our research on developing an optical fiber based pavement behavior monitoring sensing system. The major content of this paper discusses the sensing system design concept and a novel optical fiber flexible encapsulation technique. The proposed sensing system integrates Fiber Bragg Grating (FBG) and Brillouin Optical Time Domain Analysis/ Reflectometry (BOTDA/R) techniques to ensure the large coverage and local high accurate monitoring. A new flexible encapsulation technique for optical fiber has been proposed to overcome the difficulties in withstanding the harsh working environment in pavement structures. Lab and field tests have also been carried out to study the effectiveness of the proposed flexible encapsulation method. It has been found that the proposed sensors has high survival rate (>75%) and are efficient for long term pavement structural behavior monitoring.

Keywords: Optical fiber, pavement structure, structural monitoring sensing system, encapsulation

1 INTRODUCTION

Roads, especially highways, are one of the most important parts of the nation's transportation infrastructure system. Their construction and service condition also influence traffic safety. Currently, China is entering a new era of rapidly building roads and expanding the highway system. The "national expressway network" of China [1] has planned to spend 300 billion dollars to finish the construction of the 7918 highway system within 30 years. However, the state of art in designing road structures still cannot fulfill the increasing requirements for long life and bearing heavy traffic. Research is needed to better understand the performance of road structures under different service conditions.

One of the key ways to assess the condition of road structures is through effective inspection, and therefore high accurate testing facilities are especially critical. According to the differences of testing location, road structure inspection technologies can be classified into two categories: lab test and field inspection. Comparing to field inspection, there are less restric-

tions (size, portability, etc.) to the test equipments for lab test and therefore high accurate data can be obtained. However, testing small road material samples in lab often cannot reflect their real working status. Due to technology limitation, road structure three dimensional stress fields are very hard to be simulated or measured. Zhou, et al. [2, 3] have designed an optical fiber based sensor trying to measure three dimensional strain field of road structures.

With the development of Non-Destructive Testing (NDT) technologies, more and more researches have been focused on using NDT instruments for pavement structure in-situ inspection. Falling weight deflectometers have been used to predict pavement structure elastic modulus [4]. Grote et al. [5] have used ground penetrating radar to detect damage and evaluate infiltration in layered pavement structures. Capacitance sounding technologies have also been adopted to measure the thickness of pavement structures. Although NDT instruments won't damage pavement structures during/after inspection, structural health information are obtained indirectly. Usually, complex inverse problems are needed to be solved in order to link the data with structural parameters, and therefore, the inspection accuracy is low. Besides, the inspection cost and small coverage are also the restrictions for large scale applications of NDT in pavement inspection.

Embedded sensors in pavement structures can provide real time pavement performance data with relatively high accuracy [6]. The harsh working environment and unique characteristics of pavement structures require the sensors to endure high temperature (up to 200°C), moisture, large compaction force, repeated heavy loading, etc., and have large coverage. Most of the traditional sensors for civil structures are not suitable for pavement structures [7]. The advantages of optical fiber sensors, such as small size, high accuracy, low cost, distributed large coverage, reliable durability, etc., make them the attractive choice for long term pavement health monitoring [8, 9]. However, bare optical fibers are vulnerable to shear stress, and therefore, encapsulation is needed before application. Due to the differences of material mechanical properties, the packaging material will increase the complexity of analyzing strain transfer from host material to the sensor core [10, 11]. For pavement materials with lower elastic modulus than optical fiber, this problem is more severe. Besides, the sensing system should be well designed in order to capture information of major damage modes (rutting, cracking, etc.) that distributed uncertainly [12–14].

The objective of our research is trying to develop a robust sensing system that can provide life cycle performance monitoring to in service pavement structures. The real time monitoring data then can be used for pavement structural health condition assessment and damage evolution pattern development. Currently, few references have been found related to using optical fiber sensors for pavement structural health monitoring except the works from our research group.

This paper will introduce some results from the preliminary study on optical fiber sensors for asphalt pavement performance monitoring. The sensing system design will firstly be discussed. A flexible encapsulation method for optical fiber will then be introduced. Lab and field tests have been carried out to evaluate the performance of the proposed sensors. A Fiber Bragg Grating (FBG) based curvature measurement sensor design as an alternative sensing method without encapsulation has also been introduced in the last part of the paper. The feasibility of the proposed design is discussed based on lab test results.

2 OPTICAL FIBER BASED SENSING SYSTEM DESIGN

2.1 *Introduction to optical fiber sensors*

As the most popular sensors with big application potential at the end of the 20th century, optical fiber sensors have many different types and their functions also differ a lot. FBG and Brillouin Optical Time Domain Analysis/Reflectometry (BOTDA/R) are the most typical optical fiber based sensing techniques [15]. Optical fiber gratings on a single-mode fiber are made by laterally exposing its core to a periodic pattern of intense ultraviolet light. FBG can measure strain of the optical fiber by detecting the change of Bragg wavelength transmitting in the fiber [16]. The low cost and almost absolute measurement are the distinguishing properties of FBG sensors. BOTDA/R is based on the fact that temperature or strain information received by an

optical fiber can be detected by the shift of Brillouin back scattering frequency. It can measure strain continuously in an optical fiber and therefore can measure the distribution of physical parameters over long distance [17]. Comparing to FBG sensing technique, the precision of BOTDA/R is lower, but BOTDA/R uses normal optical fiber as the strain sensor and therefore the sensor cost is much lower [18]. The BOTDA/R analyzer can detect strain along more than 30 km distance at one time to provide distributing measurement. The sensing system that will be introduced in this paper is also based on these two types of sensing techniques.

For FBG based sensors, it is investigated that the central wavelength of the reflected component satisfies the Bragg condition [19]:

$$\lambda = 2n\Lambda \tag{1}$$

where n is the effective index of refraction and Λ is the grating periodicity of the FBG.

Due to temperature and strain dependence of the parameters n and Λ, the wavelength of the reflected component will change as function of temperature and strain. The general expression for the strain of the sensor can be expressed as:

$$\varepsilon = \frac{1}{(1-P_e)}\left(\frac{\Delta\lambda_1}{\lambda_1} - \frac{\Delta\lambda_2}{\lambda_2}\right) \tag{2}$$

in which P_e is the optical elasticity coefficient. λ_1 is the Bragg wavelength of the grating experiencing both strain and temperature changes and λ_2 is the Bragg wavelength of the grating experiencing temperature changes only.

2.2 *Proposed sensing system design*

The proposed sensing system is designed to have multiple functions to fulfill the special requirements for pavement structural performance monitoring (Fig. 1). The sensor layout

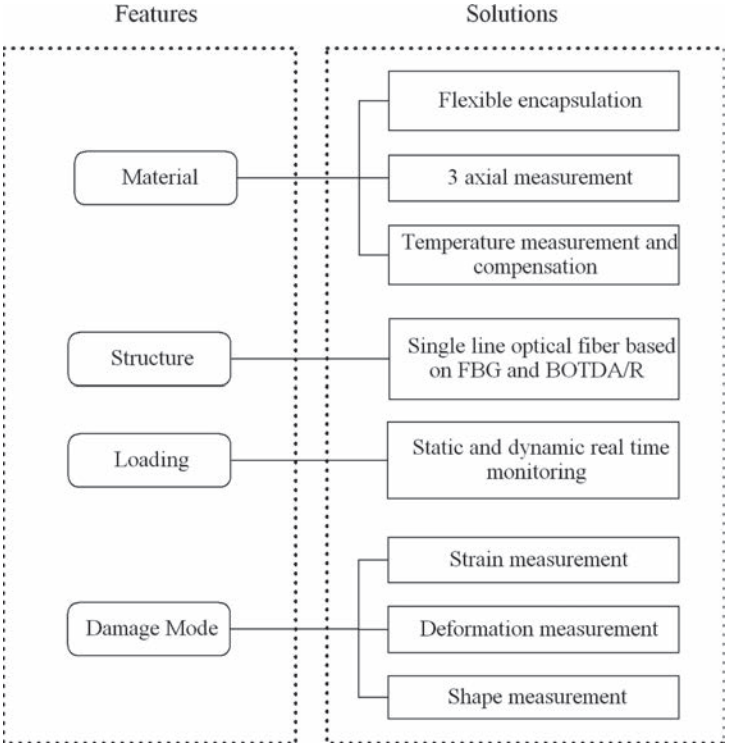

Figure 1. Major functions of the proposed sensing system.

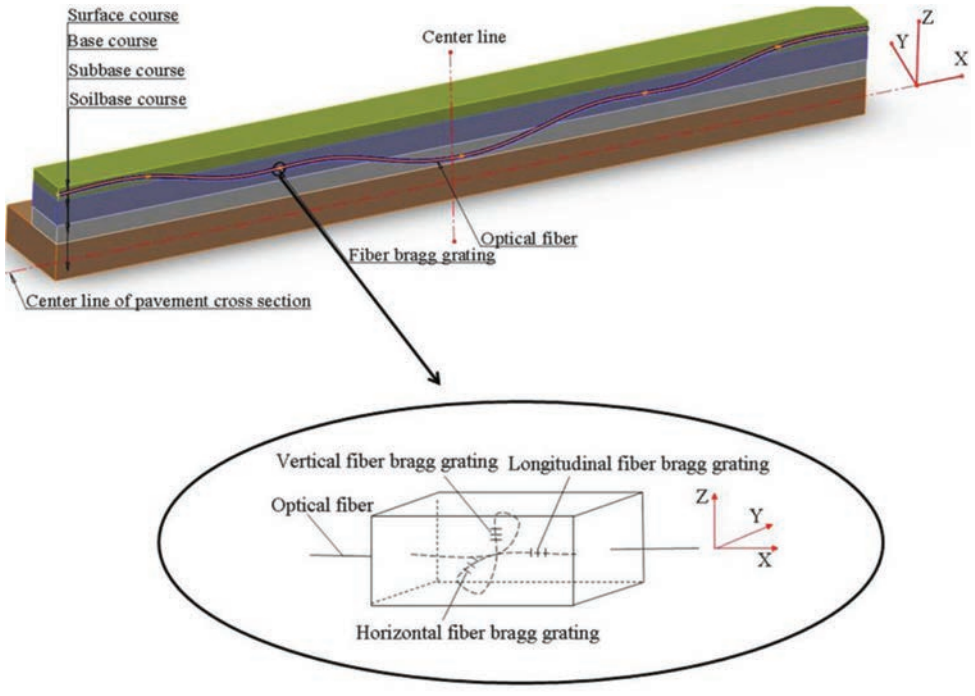

Figure 2. Proposed optical fiber based sensing system for multi-layered pavement structure.

diagram of the sensing system is shown as Figure 2. Firstly, the optical fiber sensors adopted by the system are packaged with flexible encapsulation. The bonding between the sensor core and pavement host materials is then enhanced and the strain transfer error will be reduced to some extent. Detailed encapsulating technique will be discussed in the latter section of this paper. Secondly, the FBG based sensors and BOTDA/R based sensors will both be used and sharing single line to ensure the local high accurate strain monitoring and long distance coverage. At particular interest point, the sensing line can be convoluted to provide three axial monitoring (Fig. 2). The entire sensing optical fiber line can be bent vertically at certain distance to cover all the layers of a pavement structure.

Thirdly, at each precise monitoring point, FBG temperature compensation sensor will be embedded simultaneously to measure the circumstance temperature and compensate temperature change introduced strain of the FBG based strain sensor. Since FBG sensors can provide low frequency dynamic measurement, both pavement structure static and dynamic real time performance data can be obtained under given loading condition. Besides, optical fiber shape measurement concept [20] can be adopted by this sensing system to measure bend and twist (curvature) of the sensor and therefore predict the deformation inside the pavement structure. Then the road subgrade settlement and its influence to pavement structure can be monitored. Pavement rutting information can also be obtained if the shape measurement happens at the surface layers of a pavement structure.

3 FLEXIBLE ENCAPSULATION DESIGN FOR OPTICAL FIBER SENSOR

Encapsulation of optical fiber is very important to protect the sensing element and ensure the strain transfer from host pavement material to the sensor core. Although cement concrete often has larger elastic modulus than asphalt concrete, the generated forces to the embedded sensor during the forming procedure are much less than that of asphalt concrete. The forming of cement concrete is a solidification process while the forming of asphalt concrete

pavement structure is a roller compaction process. During the compaction process, the movement of aggregates can generate large stress at the tips. Therefore the encapsulation must be strong enough to isolate the optical fiber sensor core from these destructive forces. However, the notable structural flexibility of the asphalt pavement (especially at high temperature) will make the rigid encapsulated sensor fail to obtain strain as the host pavement material deforming. Therefore, the encapsulation of the optical fiber sensor for asphalt pavement structure needs to be well designed to overcome these conflicts.

In this section, a flexible encapsulation technique for optical fiber will be introduced. Rough sensors based on the proposed encapsulation technique have been produced in lab.

3.1 *Design principle*

Armor for cables has been selected as the encapsulation material for the sensing element of the proposed sensor in this paper. It can bear strong compaction force, but bend freely. The structure of the sensor is shown in Figure 3. Two annuls made with epoxy resin are fixed at both sides of the FBG sensing element with design distance to increase the tension/compression strain transfer efficiency between the sensing element and the host material. The cable armors are also embedded into the annuluses but covered with a short rubber connection. Therefore, the modulus of the sensor in the axial direction will be increased within a limit.

To sustain the compaction induced large deformation and add damage information capturing capability, a precision spring has been attached beside the FBG sensing element. The transmission part of the optical fiber is also protected by the cable armor. The scale of the sensor can be adjusted by the distance between two annuluses. For BOTDA/R based sensor, the encapsulation of the optical fiber can use the same method, but much larger in length.

3.2 *Sensor calibration test*

All the sensors used in this paper were fabricated in lab. The axial elastic modulus of the proposed sensor was evaluated using a material testing machine and was found to be around 48 MPa. This value was much lower than the modulus of asphalt mixtures even at high temperature. Hence, the influence of the proposed sensor to the stress field of the host material can be ignored.

The precision of FBG sensors for strain measurement is high and can often be treated as absolute measurement. The influence of the precision spring to whole accuracy of the sensor has been tested in lab. Figure 4 show the tension test data of a FBG connected with a precision spring. The result show good linearity of the proposed sensor assembly. The total displacement of the sensor assembly has also been measured. The FBG received half the strain value of the total sensor, which fit well with the calculation based on the modulus of the precision spring and that of the optical fiber. The FBG can bear more than 10000 με before break.

3.3 *Sensor assembly field tests*

A mini test track has been constructed on a vacant lot to evaluate the performance of the proposed sensors. The length of the pavement structure is about 10 m and its width is around

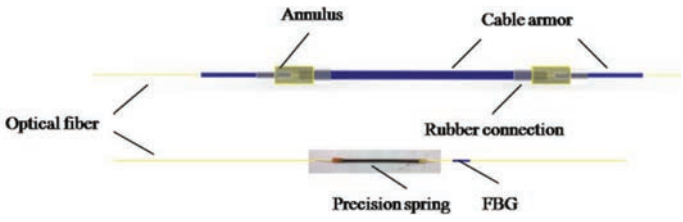

Figure 3. Proposed optical fiber assembly diagram.

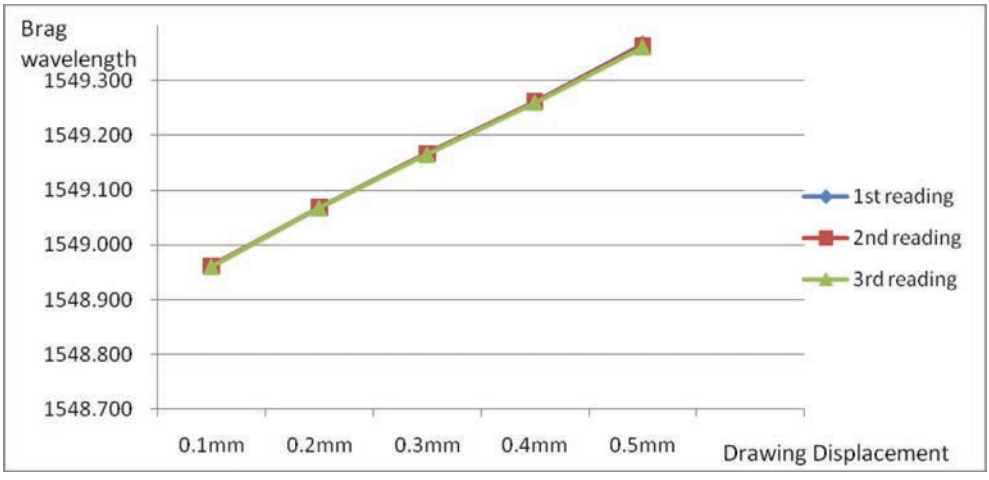

Figure 4. Tension test data of a FBG connected with a precision spring.

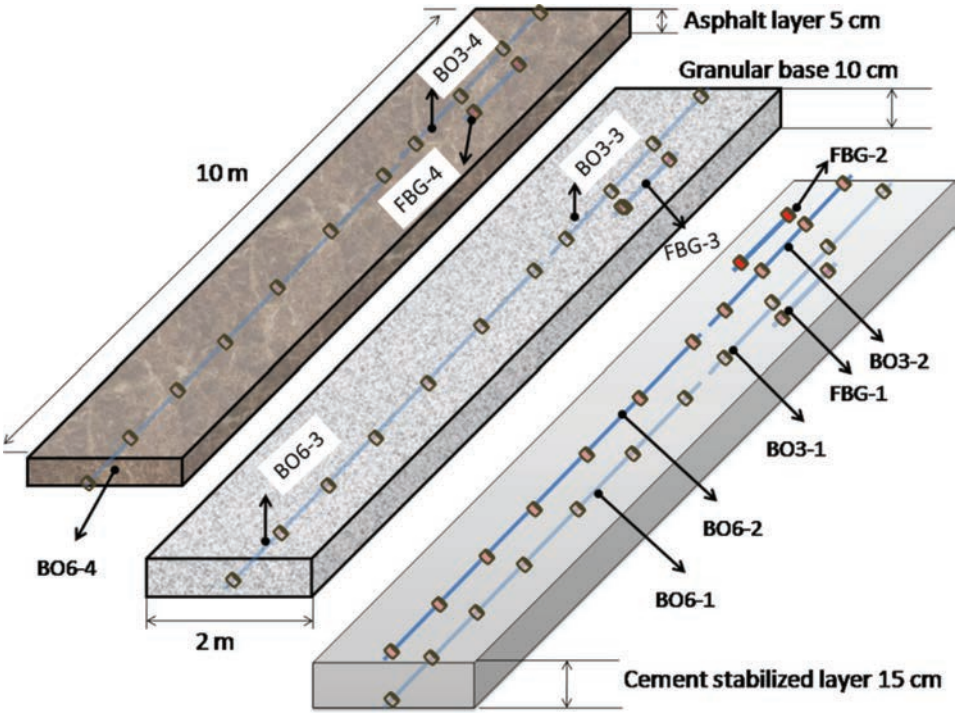

Figure 5. Sensor arrangement in pavement structure.

2 m. The pavement structure is simply composed of three layers. They are the asphalt layer, granular base and cement stabilized layer from top down and the ground is made up of hard rock. Their layer arrangement is shown in Figure 5. To make the structure stable, the width of each layer is increasing with depth.

Both FBG and BOTDA/R based sensors have been embedded into the pavement structure during construction directly. The gauge length of the FBG based sensor is 0.25 m and that of the BOTDA/R based sensor is 1 m. The optical fiber length of the FBG based sensor is shorter than the sensor used in lab calibration. Based on the length difference, it can be calcu-

lated that the actual strain of the whole FBG based sensor is around 1.2 times larger than the reading of the FBG. The sensor arrangement can be seen in Figure 5. Another FBG based temperature compensation sensor has also been embedded in the surface asphalt pavement layer. The sensing element in the temperature compensation sensor is in its free state and also protected by the armor for cables. Therefore the data of other strain sensors minus the strain data from the temperature compensation are the stain data caused only by external forces.

Since paver was not used in the pavement construction and there were no lateral restrictions to the structure during construction, the pavement construction materials have been flattened only by a road roller. The pavement construction material moved more than that during the real highway construction, and therefore the compaction forces to the sensors were also larger. Nonetheless, 75% of the sensors were in good condition.

3.4 *Data collection and analysis*

The strain data of all the intact sensors during eight whole days have been collected. Due to the large compaction displacement, most of the BOTDA/R based sensors were wrinkled. It made the data from BOTDA/R based sensors unreliable. The embedding technology for BOTDA/R based sensor should be improved in the future. Therefore this paper will only discuss the data from FBG based sensors.

The FBG based sensor FBG-1 in the cement stabilized layer was damaged. The data from other FBG based sensors are shown in Figures 6–9. It has been raining in Aug. 21 and Aug. 28, and it was cloudy in Aug. 26. From Figure 6 it can be seen that the temperature induced strain reading can be up to 250 με during a day. The temperature induced strain reading is not the actual strain, and therefore will not be influenced by the spring. For the deformation induced strain, the spring will make it smaller in reading. The data from FBG-2, FBG-3 and FBG-4 show that the temperature changing patterns are different in these three layers. The highest temperature appeared around 13:30–14:20 in the asphalt layer. The highest temperature in the granular base was after 15:00 and the temperature varying range was much lower than that of the asphalt layer and the cement stabilized layer. The highest temperature of the cement stabilized layer appeared after 16:00 and dropped gradually after 18:00.

Figure 6 shows that the temperature differences among Aug. 23, Aug. 27 and Aug. 29 are not obvious. However, the strain reading in Aug. 23 is obviously higher than that in Aug. 27 and Aug. 29 in the cement stabilized layer (Fig. 7). The lower strain reading in Aug. 29 was due to the rain in Aug. 28. There was no rainy day between Aug. 22 and Aug. 27. The strain difference between Aug. 23 and Aug. 27 is caused by the air shrinkage effect. Considering the function of the precision spring, the air shrinkage should be between 32–76 με. The cor-

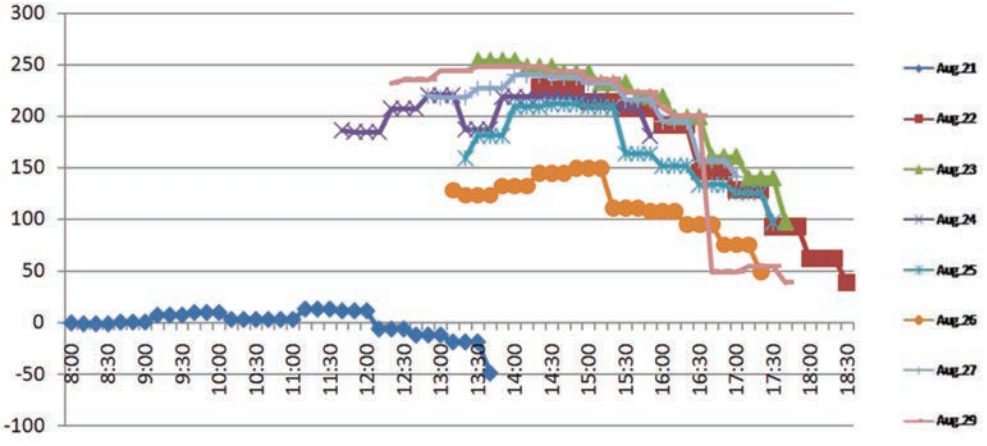

Figure 6. Strain reading from temperature compensation sensor.

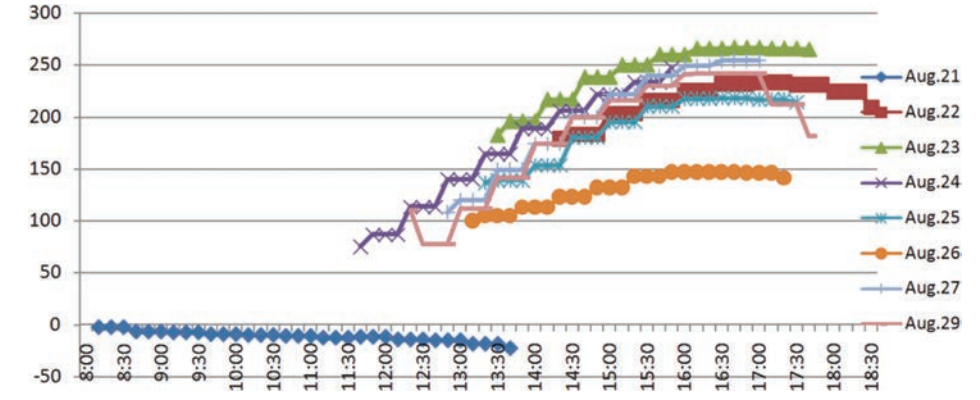

Figure 7. Strain reading from FBG-2.

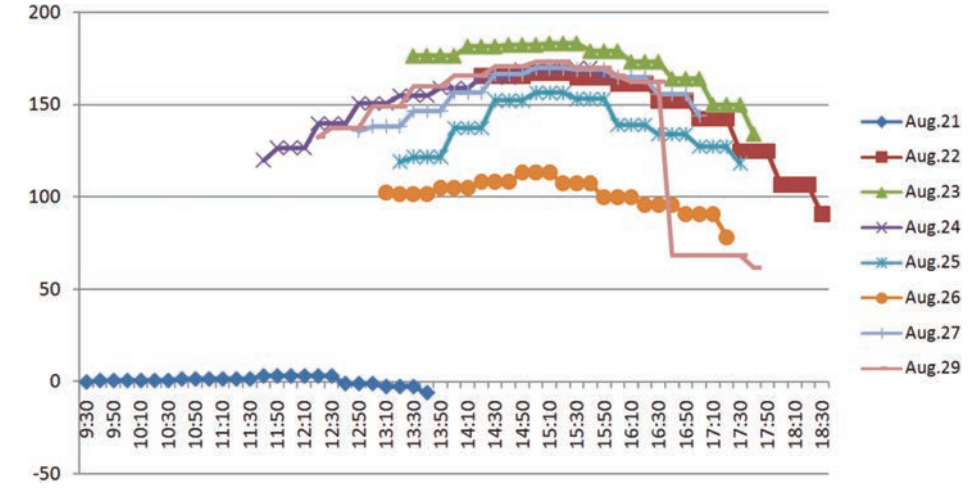

Figure 8. Strain reading from FBG-3.

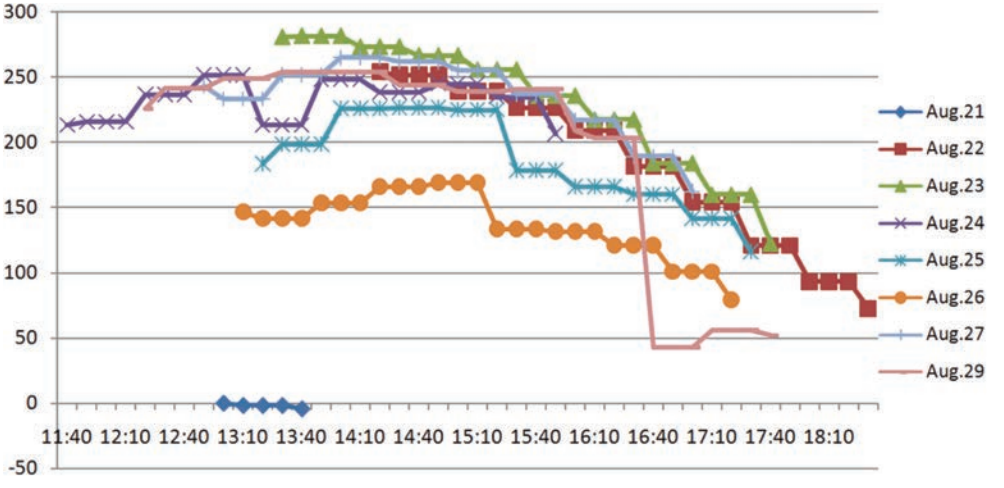

Figure 9. Strain reading from FBG 4.

responding lab test gave the shrinkage of about 68 με between the third day and the seventh day, which is close to the data from the FBG based sensors.

One of the shortages of this field test is that temperature compensation sensors have not been embedded into all the layers of the pavement structure. This makes the analysis of the material shrinkage strain of the lower layers difficult. Therefore only the data of the asphalt layer with temperature compensation will be discussed more in depth in this paper.

Figures 10–12 shows the strain readings from the FBG-4 and temperature compensation sensor minus the strain reading picked at 14:20 in Aug. 22 of each corresponding sensor.

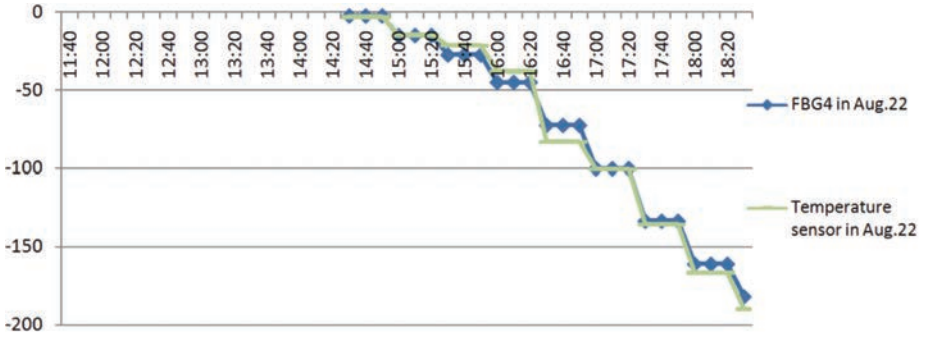

Figure 10. Comparison of data from sensors in asphalt layer.

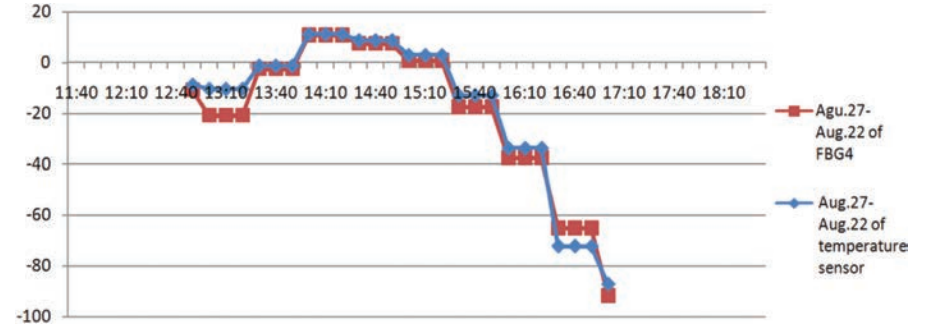

Figure 11. Comparison of data from sensors in asphalt layer of Aug. 27.

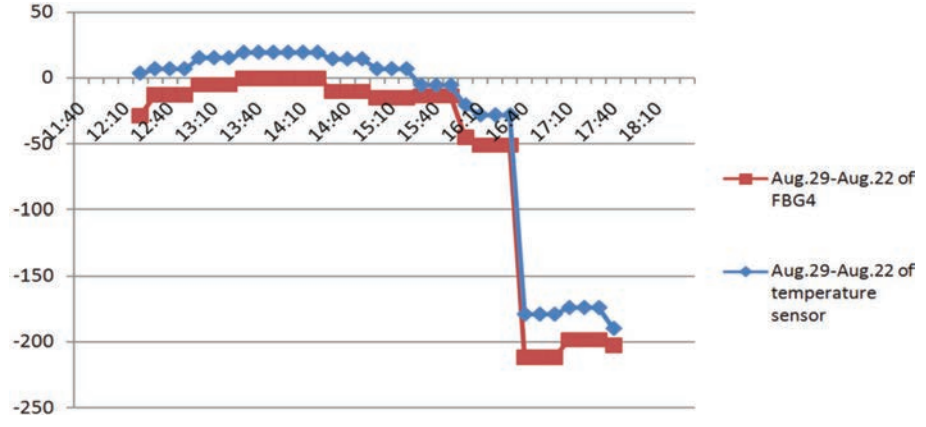

Figure 12. Comparison of data from sensors in asphalt layer of Aug. 29.

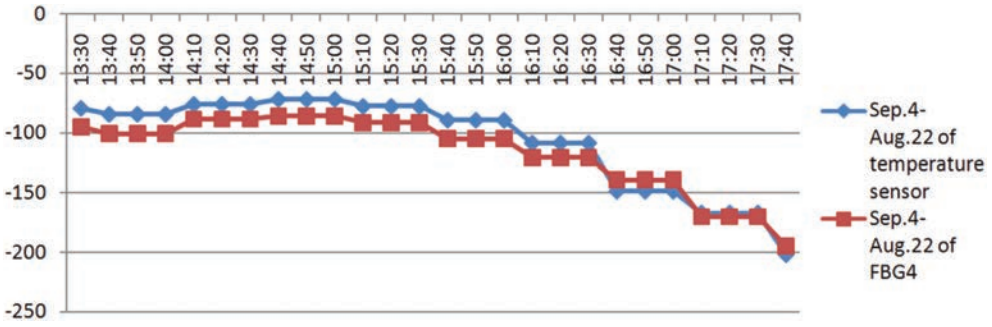

Figure 13. Comparison of data from sensors in asphalt layer of Sep. 4.

It can be notice that even after 5 days, the strain data of Aug. 27 of the two sensors are all most the same (Fig. 11). However, after a rainy day of Aug. 28, obvious strain difference can be noticed in Aug. 29 (Fig. 12). One of the conclusions can be deduced is that the asphalt layer has not shrinked during a short time in sunny days, but after a rainy day, the asphalt layer deformed for about 120 με. Another set of data have been collected in Sep. 4 and the comparison data in Figure 13 also show the same deformation strain. This permanent strain may be caused by the rain induced granular base material movement.

The field test has proved the high survival rate of the proposed encapsulation method. The collected data show the sensitivity of the FBG based sensors in strain monitoring. The sensors are efficient in pavement material shrinkage monitoring. The survival from the large compaction displacements and strain sensitiveness also prove the feasibility of the proposed sensors in pavement life cycle performance and damage monitoring.

4 CONCLUSIONS AND DISCUSSIONS

This paper introduces an optical fiber based pavement monitoring sensing system design. Special features of pavement structures are first summarized. Due to the complexity of pavement structural monitoring and few available references, the system should be well designed and should take into the consideration of these special features.

A new flexible encapsulation method for both FBG and BOTDA/R based sensors has been introduced. Lab and field tests have been carried out to study the feasibility of the proposed sensors. The sensors with flexible encapsulation show high "survival rate" after installation. The field test data also proves the potential of using optical fiber based sensors for pavement structure shrinkage monitoring and life cycle performance monitoring in a wide range.

Since the works present in this paper are only the preliminary results from the relative researches, many design concepts and operation procedures could be improved. The strain transfer error between the sensor core and pavement host materials will be studied in the future. However, the current results already show the feasibility and prospect of the proposed sensing system.

ACKNOWLEDGEMENTS

This paper was supported by National Natural Science Foundation of China (Grant No. 51108061) and Supported by Doctoral Program Foundation of Institutions of Higher Education of China new teacher category (Grant No. 20110041120008).

REFERENCES

[1] Transport Planning Research Institute. National Expressway Network Planning, Transport Planning Research Institute, Beijing. 2004.

[2] Zhou, Z., Wang, H., Hu, Q., Li, H., and Ou, J.P. Highway Road Monitoring using High-durable Packaged 3-dimension FBG Sensors. OFS18, Mexico. 2006.
[3] Zhou, Z., Liu, W.Q., Huang. Y., Wang, H.P., He, J.P., Huang, M.H., and Ou, J.P. Optical Fiber Bragg Grating Sensor Assembly for 3D Strain Monitoring and Its Case Study in Highway Pavement. Mechanical Systems and Signal Processing, 28, pp. 36–49. 2012.
[4] Seo, J.W., Kim, S., Choi, J.S., and Park, D.W. Evaluation of Layer Properties of Flexible Pavement using a Pseudo-static Analysis Procedure of Falling Weight Deflectometer. Construction and Building Materials, 23(10), pp. 3206–3213. 2009.
[5] Grote, K., Hubbard, S., Harvey, J., and Rubin Y. Evaluation of Infiltration in Layered Pavements using Surface GPR Reflection Techniques. Journal of Applied Geophysics, 57, pp. 129–153. 2005.
[6] Sargand, S. Continued Monitoring of Pavement in Ohio. FHWA/OH-2002/035. 2002.
[7] Zhang, W., Wang, Q., Ma, S., and Li, X. Field Experimental Study on Measurement and Analysis Strain on the Rigid Pavement Slab Subjected to Moving Vehicle Loads. ASCE Int. Conf. on Transp. Eng, pp. 2741–2746. 2007.
[8] Hu, Q.L., Zhou, Z., Li, H., and Ou, J.P. Health Monitoring on Asphalt Pavement of Highway based on FBG Technique. Proc. of SPIE, 6595, pp. 659535:1–6. 2007.
[9] Hu, Q.L., Wang, C., and Ou, J.P. Development and Performance Research of FBG Strain Sensor for Monitoring on Asphalt Concrete Pavement. Proc. of SPIE, 7647, pp. 76474M:1–10. 2010.
[10] Zhou, Z., Graver, T., and Ou, J.P. Techniques of advanced FBG sensors: manufacturing, demodulation, encapsulation and their application in the structural health monitoring of bridges. Pacific Science Review, 5(1), pp. 116–121. 2003.
[11] Li, H.N., Zhou, G.D., Ren, L., and Li, D.S. Strain Transfer Analysis of Embedded Fiber Bragg Grating Sensor under Nonaxial Stress. Optical Engineering, 46(5), pp. 054402-1-8. 2007.
[12] Ishikawa, Y., Miyazaki, S., Uehara, H., and Inoue, U. Design of integrated heterogeneous sensor systems for disaster and environmental monitoring. Proc. of INSS. 2004.
[13] Timm, D.H., Guzina, B.B., and Voller, V.R. Prediction of Thermal Crack Spacing. Int. J. Solids Struct., 40, pp. 125–152. 2003.
[14] Kim, K.S., Baek, Y., and Yoo, I.K. Pavement Roughness Monitoring Method using Fiber Optic Vibration Sensors. Proc. of SPIE, 7647, pp. 76472G-1-8. 2010.
[15] Zhou, Z., Huang, M.H., He, J.P., Chen, G.D., and Ou, J.P. Ice Structure Monitoring with an Optical Fiber Sensing System. Cold Regions Science and Technology, 61(1), pp. 1–5. 2010.
[16] Rao, Y.J. Recent Progress in Applications of in-fiber Bragg Grating Sensors. Optics and Lasers in Engineering, 31, pp. 297–324. 1999.
[17] Ohno, H., Naruse, H., Yasue, N., Miyajima, Y., Uchiyama, H., Sakairi, Y., and Li, Z.X. Development of Highly Stable BOTDR Strain Sensor Employing Microwave Heterodyne Detection and Tunable Electric Oscillator. Proc. of SPIE, 4596, pp. 74–85. 2001.
[18] Zhao, X.F., and Ou, J.P. Research on BOTDR Sensing Technique in Structural Health Monitoring. Earth and Space 2010: Engineering, Science, Construction, and Operations in Challenging Environments, pp. 2487–2493. 2010.
[19] Yuan, H.Q., Yuan, J., Du, J. The Sensing Principle of FBG and Its Experimental Application in Structure Strengthening Detection. Journal of Wuhan University of Technology (Material Science Edition), 18(3), pp. 94–96. 2003.
[20] Danisch, L., Englehart, K., and Trivett A. Spatially Continuous Six Degree of Freedom Position and Orientation Sensor. Sensor Review, 19(2), pp. 106–112. 1999.

This page intentionally left blank

Sustainable asphalt technologies—I

This page intentionally left blank

Asphalt Pavements – Kim (Ed)
© 2014 Taylor & Francis Group, London, ISBN 978-1-138-02693-3

New surface layers with low rolling resistance tested in Denmark

Matteo Pettinari
Department of Civil Engineering, Technical University of Denmark, Lyngby, Denmark

Bjarne Schmidt
Danish Road Directorate, Hedehusene, Denmark

Bjarne Bo Jensen
NCC Roads A/S, Vejen, Denmark

Ole Hededal
Department of Civil Engineering, Technical University of Denmark, Lyngby, Denmark

ABSTRACT: The project 'CO_2 emission reduction by exploitation of rolling resistance modeling of pavements' (COOEE) was started in 2011 to establish a scientific background for development of novel pavement types and asset management solutions that minimize the rolling resistance for cars and trucks, the purpose being to reduce CO_2 emission from the transport sector.

In summer 2012, three different test sections were constructed on a highway located near Vordingborg, Denmark, in order to verify the respective Rolling Resistances; the main purpose was to develop and design new surface layers with reduced Rolling Resistance coefficient that could improve energy efficiency of the roads. In particular, two new types of Split Mastic Asphalt (SMA) were developed and compared to a reference one; both mixtures have a relatively small maximum grain-size, 6 mm and 8 mm, respectively. Surface measurements such as Skid Resistance and Mean Depth Profile were appropriately verified in order to fulfill these essential texture values. Samples were taken and studied in the laboratory to analyze the volumetric characteristics. Rolling resistance measurements have shown that both new SMAs have a reduced Rolling Resistance compared to the traditional one.

Keywords: pavement maintenance; asphalt mixture; aggregates gradation; Rolling Resistance; texture

1 INTRODUCTION

In recent years, the stabilization of greenhouse emission is one of most important instruments in order to avoid global climate change. Carbon dioxide (CO_2), generated from various sectors, is identified as one of key greenhouse gases to control. In 2004 in the United States, transportation as a whole accounted for approximately 33% of CO_2 emissions, of which 80% came from cars and trucks traveling on the roadway system [1]. In Denmark, these percentages were confirmed; in fact in 2006 the carbon dioxide emission was 52.5 million tons, of which the transport sector contributed with 16 million ton. In order to reduce these emissions, policy makers are primarily pushing for more efficient vehicles and the development of alternative fuels [2]. The European Union adopted in 2009 sets of mandatory emission reduction targets for new cars.

The Cooee project, aiming to design an overall more environmentally friendly road infrastructure, approaches the goal of reducing vehicle CO_2 emission by centering the attention to the road pavement characteristics. It focuses on establishing a scientific background for

development of novel pavements types and asset management solutions that minimize the rolling resistance for cars and trucks, thus improving the pavement energy efficiency.

Rolling resistance, together with wind drag and transmission losses, influences the need for motor power and resulting emissions. The influence of road surface properties, such as macrotexture and unevenness, on rolling resistance and fuel consumption is an important factor to consider when determining the coating of a road surface [3]. Surface texture and unevenness create vibrations in the tires and suspension. These vibrations reduce energy efficiency of motion because the shock absorbers and the tires are absorbing this energy, thus improving passenger comfort and reducing vehicle vibrations. Therefore, surface texture influences fuel consumption by inducing these vibrations. Microtexture affects the energy lost due to wear and small scale contact on the tires.

2 BACKGROUND

Over the years, many different studies have been conducted on the influence of road surface texture on the tire rolling resistance. Deraad [4] was—in 1978—among the first to show that road surface texture can significantly influence the rolling resistance losses. Data collected from laboratory tire dynamometer tests and outdoor tests, conducted on various types of paved public road, indicated that tire rolling resistance losses increase as road surface texture increases. Moreover, he focused on the point of the test surface adopted and how this can affect the results.

In 1980, the Wisconsin Department of Transportation conducted a local field study that sought to define the relation between automobile fuel consumption and pavement roughness. Five pavement sections, representing a wide range of roughness, were travelled by three different automobiles. For these pavements, roughness was expressed in terms of serviceability index, as measured by Wisconsin's electronic road meter. The collected data showed a very modest increase in fuel consumption as pavement roughness increased [5].

X.P. Lu [6], following a theoretical approach, introduces a linear model for evaluating the influence of pavement surface roughness on rolling resistance. Du Plessis et al. [7] show that rolling resistance losses, related with the road surface characteristics, are dependent from the mass of the vehicle. Surface texture was found not to be significant in determining rolling resistance for trucks with high pressures and hard rubber types associated with commercial vehicle tires. Sandberg [8], in order to improve the study of the tire-road interaction, introduced a more complete characterization of the pavement surfaces. In particular he defined macrotexture, microtexture, megatexture and unevenness characteristics, successively adopted by ISO 13473-1, and measured the respective induced fuel consumptions.

Delanne [9] compared the influence of different surface dressing on light vehicle fuel consumption on paved roads. The collected data have shown that unevenness and macrotexture can influence fuel consumption respectively up to 6% and 5%.

In 2004, Beuving [10] compared the impact of pavement surface characteristics on fuel consumption. The obtained results confirmed that different textures of road surfaces influence fuel consumption for passenger cars by up to 10%. No differences in fuel consumption were recorded between asphalt and concrete road surfaces for passenger cars. However, an important influence of the pavement surface roughness on the fuel consumption has been proven. Rolling resistance of a tire on concrete or asphalt pavements with the same profile or texture should be practically identical [11].

In 2009, the MIRIAM project was started with the intention to provide the road asset management systems of an integrated methodology for improved control of road transport CO_2 emissions related to road pavement conditions [12]. At the moment, a wide scatter of results are found and there is still much confusion and uncertainty about how large the influence actually is [3]. Moreover, the precision of the measurement systems are often in the same order of magnitude as the measured values, hence data may be highly affected by measurement noise. In any case, further research is needed to optimize pavement texture for rolling resistance without sacrificing friction and safety.

3 OBJECTIVE

The Danish Cooee project is based on the idea of providing a sustainable and environmentally friendly road infrastructure maintenance and design. The purpose is to develop new material types, creating a basic insight in wear and aging of asphalt pavement and fundamental research on the interface between the vehicle tire and the pavement surface.

The main objective of the present paper is to evaluate how different types of surface layer of a road pavement can condition the energy efficiency of the pavement itself. In particular, the Rolling Resistance of a pavement structure with different Split Mastic Asphalts (SMA) was studied. Rolling resistance is a fundamental property of the asphalt mix, traditionally neglected during mix and pavement design, which could represent the key a sensible reduction of the traffic CO_2 emission.

4 EXPERIMENTAL PROGRAM DESCRIPTION

The experimental program can be divided in four different phases.

- Laboratory mix design;
- Field sections construction (Fig. 1);
- Description of the volumetric and surface properties of field mixes;
- Analysis of the rolling resistance.

The asphalt mixtures were designed by NCC Roads A/S. Volumetric characterization was completed in order to optimize the laying and compaction of three different wearing courses. In particular, two new SMAs, with maximum grain-size respectively of 8 and 6 mm (SMA 8, SMA 6), were compared to a traditional SMA 0–8 mm (Reference).

The pavement section, selected for the rolling resistance analysis, was the Main Road 619 near Vordingborg, Denmark. The entire pavement section is 1.5 km which were paved with 500 m of each asphalt mixture type. A constant thickness was compacted over the same pavement structure with all the studied SMAs as part of a traditional maintenance replacement of the wearing course. Cores from each section were analyzed in order to verify the volumetric characteristics such as layer thickness and voids content. The binder content measurements were collected from the production plant and verified on samples taken from the paver machine. The surface texture of the three different pavement sections was characterized measuring the Mean Profile Depth (MPD) and the Skid Resistance. After material and field characterization, the study of the Rolling Resistance of the mixtures was carried out using the TUG trailer with three different reference tires.

Figure 1. Field section activities (a), SMA 8 (b), SMA 6 (c).

5 MATERIALS AND TEST DEVICE DESCRIPTION

5.1 *Mix design*

The new SMAs were studied in order to obtain dense and durable surface structure. To achieve these characteristics and reducing relative movement between the stone aggregates of the mixes, the mastic component of SMA 8 and 6 were appropriately optimized. Different aggregates and filler types were examined together with the desired Polymer Modified Binder. The aggregate types were: Hyperit and Jelsa from Norway and Ronne from Denmark. Abrasion and Adhesion Resistance of the aggregates were verified with standard procedures (EN 1097-2, EN 12697-11). The fillers, once combined as represented in Table 1, were mixed with the three different aggregates and the adopted asphalt binder and tested by using Tumbler Abrasion test (EN 12274-7).

The results showed that F3 has a rather bad strength compared to those obtained with the two different limestone fillers (F1, F2), independently of the adopted aggregates source. F1 and F2 fillers gave comparable results. Based on the location of the desired real test section, F1 filler was chosen and blended with Danish aggregates, Ronne.

The binder content was chosen to achieve approximately 4% of average voids. Based on the adopted mix designs, target voids and trial productions on the asphalt plant, the bitumen content for both SMA 8 and 6 was 7.5%. The binder content of the reference mixture was 6.9%.

5.2 *Volumetric and surface characteristics of the mixtures in the field*

Before studying the Rolling Resistance of the three designed mixtures, they were characterized verifying their volumetric and surface properties in the field. Surface properties in particular are directly related with the texture of the mixture and consequently with the rolling resistance itself [13].

With regard to the volumetric properties, a total of 6 specimens for each mixture were cored from the pavement section. For each specimen, the layer thickness and the voids content were verified according to EN 12697-8, see Table 2.

The field surface characteristics were measured as MPD and Skid Resistance respectively following the ISO 13473-1 and the CEN/TS 15901-5, see Table 2.

Table 1. Asphalt mixtures properties.

Fillers type	Portland cement [%][1]	Limestone filler A [%][1]	Limestone filler F [%][1]	Aggregates filler [%][1]
F1	20	45	0	35
F2	20	0	45	35
F3	0	0	0	100

[1]By mass of total filler.

Table 2. Asphalt mixtures properties.

	Volumetric characteristics				Wearing characteristics			
	Layer thickness		Voids content		MPD		Skid resistance	
Materials	Average [cm]	St. Deviation [cm]	Average [%]	St. Deviation [%]	Average [mm]	St. Deviation [mm]	Average [–]	St. Deviation [–]
Reference	2.9	0.2	5,1	1,4	0.77	0.06	0.65	0.05
SMA 8	2.4	0.4	4.4	2.2	0.75	0.07	0.64	0.06
SMA 6	2.0	0.3	8.2	0.7	0.72	0.06	0.70	0.05

No significant variations in surface characteristics were measured. In terms of percentage of voids, the SMA 6 reaches a lower degree of compaction compared to the Reference and SMA 8.

5.3 *Rolling resistance device description*

The Trailer (TR) method was adopted to describe the Rolling Resistance. It was chosen to use the TUG trailer (Fig. 2), developed by the Technical University of Gdansk (TUG) due its repeatability of results and correlation with MPD. At the moment no standard or common practice has been published for measurement of rolling resistance properties of pavements [13].

Figure 3 represents the measurment principle. The horizonal arm (1) connect the front and rear suspension. The load (6) is provided by arm (2) that has a common rotation axis with arm (1). The arm (4) connects the rear end of the arm (1) to the test wheel hub. Foucault currents electromagnetic brake suppresses the undesirable vibrations of the vertical arm (4) that may be induced during tests. Inflation pressure in the test wheel is maintained by remote controlled release valve and pressure sensor. During tests, the vertical arm (4) is pulled from the test wheel where the rolling resistance force acts. A laser sensor, installed on arm (1) and sending the laser beam towards arm (4), measures the deflection rate. Rolling Resistance Coefficient (RR), expressed by Eq. (1), is defined as a ratio of rolling resistance force P_f and vertical load F_z measured by the respective load cells.

$$\mathrm{RR} = \frac{P_f}{F_z} \tag{1}$$

Figure 2. The tire/road Rolling Resistance measurement TUG trailer.

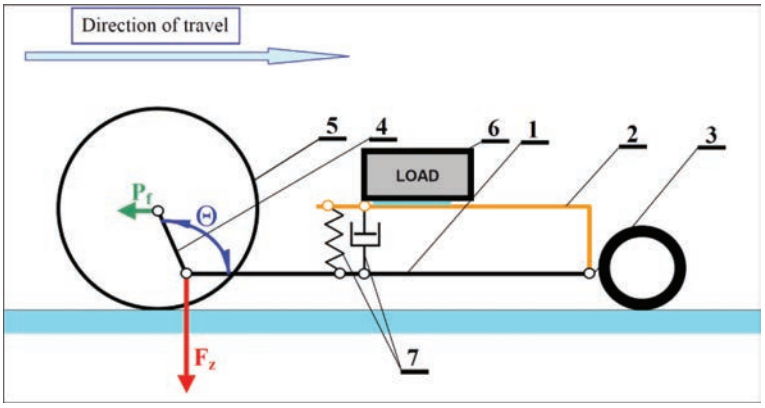

Figure 3. The TUG trailer measurement principle.

Figure 4. Types of tire used for Rolling Resistance measurement.

Table 3. Tires characteristics.

Tire	SRTT	AAV4	MCEN
Size	225/60R16	195R14C	225/60R16
Construction	Tread: 1 polyester + 2 steel Sidewalls: 1 polyester	Tread: 1 nylon + 2 steel + 2 polyester Sidewalls: 2 polyester	Tread: 1 polyester + 2 steel + 1 polyamid Sidewall: 1 polyester
Max load [kG]	730	950/900	750
Max inflation [kPa]	240	450	350
Hardness [Sh]	65	62	63

The position of arm (1) in relation to the road surface is monitored by two laser sensors.

The trailer is equipped with a device that eliminates influence of factors such as road inclination and longitudinal acceleration.

Three tires were adopted and compared for the measurement of the RR values (Fig. 4 and Table 3). The SRTT ("Standard Reference Test Tire") is specified in ASTM F2393 as a reference tire for various purposes. The AAV4, light truck tire, is a tire tested and found to classify pavements (for noise) in roughly the same way as a selection of regular heavy truck tires do. The smallest dimension for this series of tires, SRTT, fits on large passenger cars. The MCEN tire was used by TUG from the time when they started to make RR measurements, and has been kept for the purpose of providing a link to old measurements [12].

Before testing, the test tires were warmed-up long enough to stabilize the inflation pressure.

6 RESULTS ANALYSIS

For each pavement section and type of tire, three passes were completed. Air and pavement surface temperatures were respectively of 12°C and 16°C. Table 4 summarizes the average adopted speed for each test section and tire type. The differences between those, being relatively small, do not affect the Rolling Resistance measurement [13].

Figures 5–7 summarize all results.

The Standard Deviation between the three RR measurements obtained at the same longitudinal coordinate of the same test section was calculated for all the studied cases. The averages of these, expressed in percentage (referred to the mean of the corresponding of RR coefficients), are summarized in Table 5. No significant variations were detected within the three passes on the same longitudinal coordinate. The percentage of the standard deviation between the three passes of the TUG trailer with same tire type does not exceed 1.7%. These confirm the reliability of the data collected from all the test sections.

Table 4. Average speed during Rolling Resistance measurement.

	Av. Speed [km/h]		
Materials	SSRT	AAV4	MCEN
Reference	78.50	78.76	79.48
SMA 8	78.93	79.52	79.92
SMA 6	77.75	78.38	78.73

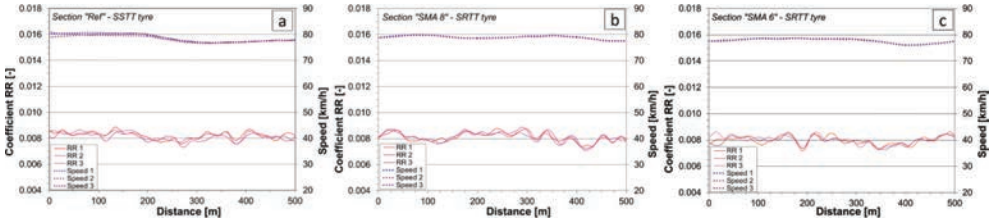

Figure 5. Coefficient of Rolling Resistance vs distance with SRTT tire.

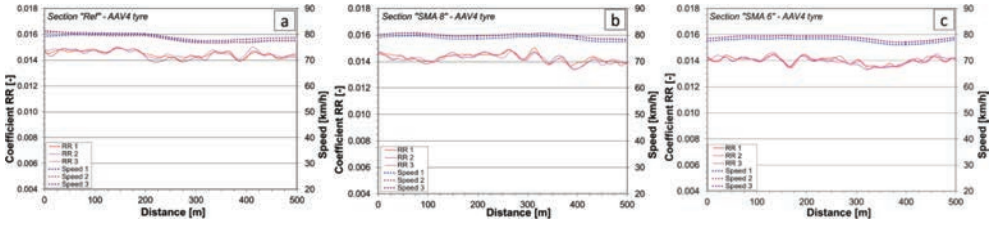

Figure 6. Coefficient of Rolling Resistance vs distance with AAV4 tire.

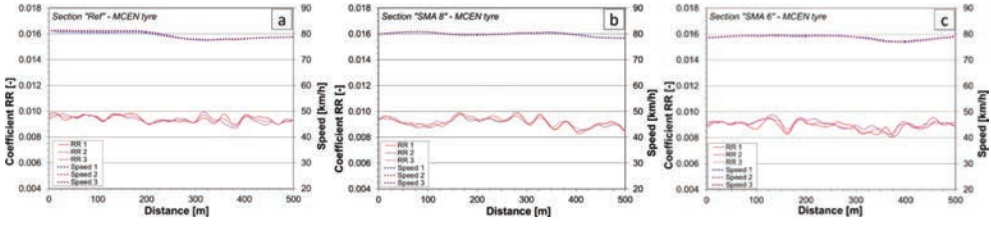

Figure 7. Coefficient of Rolling Resistance vs distance with MCEN tire.

With regard to the average Rolling Resistance Coefficients (Ave. RR) measured with the three different types of tire on each entire section, the collected results confirm the presence of dependence from the aggregates gradation (Table 6 and Fig. 5). The highest average RR Coefficient was measured with the Reference mixture while the lowest with SMA 6.

The differences between the average Coefficient RR are shown in Table 7. The Standard Deviations of the RR coefficients of two different wearing courses (Table 6) are generally higher than the respective difference between the average RR coefficients (Table 7). The two exceptions are the differences between the Reference and SMA 6 mixture with AAV4 and MCEN tires.

Even if differences between the RR measurements of the three test sections are not statistically significant in all the studied cases; it is possible to show a trend between the three

Table 5. Average of standard deviations between the three passes.

	SSRT	AAV4	MCEN
Materials	Ave. ST.D. RR.[1] [%]	Ave. ST.D. RR.[1] [%]	Ave. ST.D. RR.[1] [%]
Reference	1.70	0.76	0.91
SMA 8	1.47	0.81	1.11
SMA 6	1.63	0.68	1.62

[1]Average of the % of standard deviations for the three different RR measurements at the same position of each test section.

Table 6. Summary of Rolling Resistance results.

	SSRT			AAV4			MCEN		
Materials	Ave. RR[1] [–]	ST.D. RR [–]	ST.D. RR [%][2]	Ave. RR[1] [–]	ST.D. RR [–]	ST.D. RR [%][2]	Ave. RR[1] [–]	ST.D. RR [–]	ST.D. RR [%][2]
Reference	8.17E-03	2.76E-04	3.38	1.45E-02	2.72E-04	1.88	9.39E-03	2.51E-04	2.67
SMA 8	8.12E-03	3.62E-04	4.45	1.42E-02	3.12E-04	2.19	9.17E-03	3.40E-04	3.71
SMA 6	7.97E-03	3.17E-04	3.98	1.40E-02	2.78E-04	1.99	8.98E-03	3.21E-04	3.57

[1]Average Coefficient RR of each full pavement section. [2]Percentage referred to the corresponding Ave. RR.

Table 7. Differences between Rolling Resistance coefficients.

	SSRT		AAV4		MCEN	
	Diff. Ave. RR		Diff. Ave. RR		Diff. Ave. RR	
Materials	[–]	[%][1]	[–]	[%][1]	[–]	[%][1]
Ref-SMA 8	4.74E-05	0.58	2.42E-04	1.67	2.14E-04	2.28
Ref-SMA 6	1.99E-04	2.43	4.91E-04	3.39	4.11E-04	4.38
SMA 8-SMA 6	1.51E-04	1.86	2.49E-04	1.74	1.98E-04	2.15

[1]Percentage referred to the maximum Ave. RR coefficient of the difference.

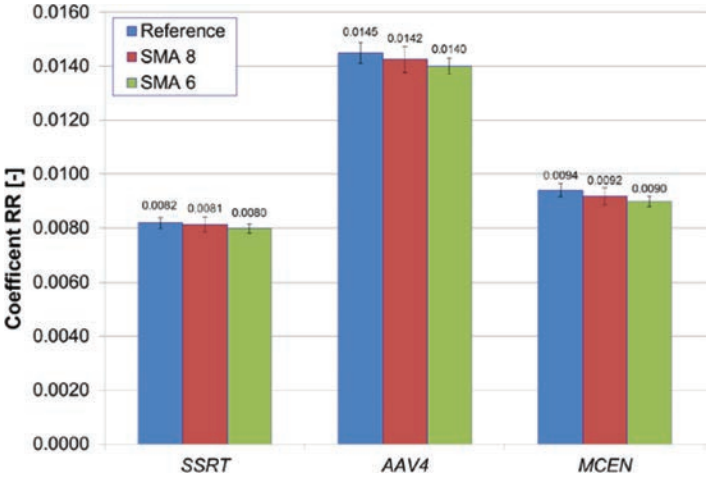

Figure 8. Summary of the Av. RR Coefficients.

studied mixes, confirmed with all the adopted tires. The SMAs developed for this research exhibit reduced Rolling resistance compared to the Reference mix. In particular, SMA 6 appears to satisfy the goal of the research project. All the adopted tires were capable to detect the differences between the pavement sections even if the MCEN tire seems more susceptible, compared to the other, to register it (Table 5).

7 CONCLUSIONS

Road maintenance is a fundamental aspect to consider in pavement management, not only for the safety and comfort of the driver and for preserving the pavement structure, but even in perspective of optimizing the energy efficiency of the pavement itself during its service life. CO_2 emissions, related to the Rolling Resistance, are dependent on vehicle's weight and tire, but also on pavement surface properties and conditions. The Cooee project is based on the idea of optimizing pavement surface characteristics and developing new material types. Creating a basic insight in wear and aging properties of asphalt pavement and fundamental research on the interaction between vehicle tire and pavement surface, it is the hypothesis that it is possible to reduce the Rolling Resistance of the pavement itself, thus improving its energy efficiency.

The present paper highlights the importance to characterize the Rolling Resistance of the asphalt mixtures. In particular, this property was analysed for three different SMAs; two of these were appropriately developed with maximum gradation size respectively of 8 mm (SMA 8) and 6 mm (SMA 6). The reference mixture was a 0–8 mm SMA (Reference). Three different test sections were studied and the TUG trailer was used for the RR measurements.

The preliminary conclusions drawn from this investigation are:

- The mix design of a Split Mastic Asphalt can be optimized to reduce Rolling Resistance of the mixture itself. This is not only related to the maximum dimension of the adopted aggregates, but is even dependent of the mastic properties. A reduction in the maximum dimension of the aggregates amplifies the positive contribution in terms Rolling Resistance;
- Volumetric characteristics of the wearing course, like layer thickness and voids content, do not seem to influence the Rolling Resistance response of the pavement. However, a deeper analysis focused on these aspects is suggested;
- Rolling resistance coefficient may be correlated with texture characteristics of the surface layer such as MPD ad Skid Resistance;
- The Rolling Resistance measurement depends on the type of adopted tire; MCEN seems more sensitive to measure the differences between the studied mixtures.

Rolling resistance should be considered during mix design of surface layers, combined with traditional procedures, in order to achieve mechanical resistance, safety standards and high-energy efficiency.

REFERENCES

[1] Barth M. and Boriboonsomsin K., Real-World Carbon Dioxide Impacts of Traffic Congestion, Journal Transportation Research Record: Journal of the Transportation Research Board Publisher, Transportation Research Board of the National Academies, Vol. 2058/2008, pp. 163–171, 2008.

[2] Fong D., Mizutani C., Shapiro R. and Matthews S.W., Options to Reduce Petroleum Fuel Use, Second Edition, California Energy Commission Staff report, CEC-600-2005-024-ED2, July, 2005.

[3] Karlsson R., Hammarström U., Sörensen H. and Eriksson O., Road Surface Influence on Rolling Resistance Coastdown Measurements for a Car and an HGV, Report VTI 24 A-2011, 2011.

[4] Deraad L.W., The Influence of Road Surface Texture on Tire Rolling Resistance, Society of Automotive Engineers, Technical Paper Series, pp. 143–149, 1978.

[5] Ross F.R., Effects of Pavement Roughness on Vehicle Fuel Consumption, Transportation Research Record No. 846, Transportation Research Board, National Research Council, Washington, DC, pp. 1–6, 1982.

[6] Lu X.P., Effect of Road Roughness on Vehicular Rolling Resistance, in Measuring Road Roughness and Its Effects on User Cost and Comfort, ASTM STP 884, pp. 143–161, T.D. Gillespie and M. Sayers, Philadelphia, 1985.
[7] Du Plessis H.W., Visser A.T. and Curtayne P.C., Fuel Consumption of Vehicles as Affected by Road-Surface Characteristics, in Surface Characteristics of Roadways: International Research and Technologies, ASTM STP 1031, pp. 480–496, W.E. Meyer and J. Reichert, Philadelphia, 1990.
[8] Sandberg Ulf S.I., Road Macro- and Megatexture Influence on Fuel Consumption, in Surface Characteristics of Roadways: International Research and Technologies, ASTM STP 1031, pp. 460–479, W.E. Meyer and J. Reichert, Philadelphia, 1990.
[9] Delanne, Y., The Influence of Pavement Unevenness and Macrotexture on Fuel Consumption, in Vehicle-Road Interaction, ASTM STP 1225, pp. 240–247, Bohdan T. Kulakowski, 1994.
[10] Beuving E., De Jonghe T., Goos D., Lindahl T. and Stawiarski A., Environmental Impacts and Fuel Efficiency of Road Pavements, Fuel Efficiency report, Eurasphalt @ Eurobitume, Vienna, Austria, 2004.
[11] Jackson R.L., Willis J.R., Arnold M. and Palmer C., Synthesis of the Effects of Pavement Properties on Tire Rolling Resistance, NCAT Report 11-05, 2011.
[12] Sandberg Ulf S.I., Rolling Resistance—Basic Information and State of the Art on Measurement methods, Models for rolling resistance In Road Infrastructure Asset Management systems, MIRIAM report, 2011.
[13] Bergiers A., Goubert L., Anfosso-Lédée F., Dujardin N., Ejsmont J.A. and Zöller U.S.M., Comparison of Rolling Resistance Measuring Equipment—Pilot Study, Models for rolling resistance In Road Infrastructure Asset Management systems, MIRIAM Report, 2011.

Asphalt Pavements – Kim (Ed)
© 2014 Taylor & Francis Group, London, ISBN 978-1-138-02693-3

Design alternative comparison system for pavements

Dragos Andrei
Civil Engineering Department, California State Polytechnic University, Pomona, CA, USA

ABSTRACT: While there are several sustainability rating systems available for pavements, their immediate use in the design phase of a project is somewhat difficult. These rating systems are fairly complex and some of them require the services of a third party, for a fee, or the expertise of certified individuals to evaluate and certify projects. Designers looking for sustainable pavement rehabilitation solutions on smaller projects and with limited budgets may not have the time and resources to use these existing rating systems. This paper describes the development of a simple, fast and convenient system that can be used to compare different design and rehabilitation alternatives based on their sustainability features. Four components are included in the analysis: materials, construction methods, surface properties and cost effectiveness. Colors are used to emphasize the sustainable aspects of a given alternative.

Keywords: sustainability; rating system; pavement design; pavement rehabilitation

1 INTRODUCTION

In recent years, the civil engineering community has become more receptive to sustainability and sustainable design. Many rating systems have been developed to encourage and reward the use of sustainable practices in civil engineering design [1]. Some of the most known "green" rating systems are the ones used by the Leadership in Energy and Environmental Design or LEED program [2]. In the LEED rating systems, sustainable practices are rewarded with credits and more credits will earn a higher LEED certification. Different rating systems have been developed to evaluate: buildings, retail developments, schools, home and neighborhoods.

Specific to pavements, LEED includes a range of applicable credits falling in the following major categories:

- Storm water management—and the recommended use of porous pavements
- Heat island effect reduction—and the recommended use of pavement surfaces with high Surface Reflective Index (SRI)
- Recycled content in infrastructure—and the recommended use of recyclable materials
- Construction waste management—and the recommendation to divert recyclable materials from disposal

Many other credits are included in LEED, for example for providing bike lanes, carpool lanes, building "walkable" streets, etc. However, pavement engineers are mostly concerned with the technologies and materials used to construct, maintain or rehabilitate a pavement structure and many times have little say in the geometric aspects of the design or rehabilitation.

Another very successful rating system used in the United States is Greenroads [3]. This rating system was developed specifically for roadways and transportation infrastructure. Projects have to meet eleven requirements to be eligible for certification:

- Environmental review process
- Lifecycle cost analysis

- Lifecycle inventory
- Quality control plan
- Noise mitigation plan
- Waste management plan
- Pollution prevention plan
- Low impact development
- Pavement management system
- Site maintenance plan
- Educational outreach

In addition, projects receive points for using sustainable practices. More points will result in a higher level of certification.

Both rating systems described above require registration and documentation of a project before it can be certified. Also, the systems are fairly complex because they take into account not only the environmental implications of a project but also the social and economic aspects of the proposed design.

In the United States, pavement engineers are most often confronted with the rehabilitation of existing pavements rather than new construction. In California for example, 81% of roads are managed by cities and counties. According to a recent study, the overall condition of these roads is "at risk" and continues to deteriorate [4]. In other words, these pavements are in need of maintenance and rehabilitation. The same study found that the funding available for maintenance and rehabilitation is only about a third of what is needed to prevent further deterioration. As a result, rehabilitation projects are often limited to restoring the structural and functional properties of the pavement and do not include any improvements such as widening or landscaping that could add more sustainable features to a project.

On such projects it may be impractical to use some of the existing rating systems which seem to be more appropriate for projects with larger budgets and greater publicity. "Green Up" is a comparison system that can be used to compare possible rehabilitation alternatives in terms of sustainability. Although the proposed system cannot be used to certify or rate projects, its purpose is to offer the designer a quick look at the sustainable aspects of different design alternatives and the choice to learn more about sustainable pavement rehabilitation options.

2 "GREEN UP" COMPARISON SYSTEM

2.1 *Methodology*

In developing the methodology, the intent was to provide pavement engineers with a tool that is easy to use and quick to provide results. To keep things simple, "Green Up" includes only design variables specific to structural pavement design:

- The choice of materials and thickness
- The choice of maintenance and rehabilitation strategies
- Surface properties such as permeability, surface reflectivity, and noise;
- Cost effectiveness

The number of inputs was minimized to ensure that users can enter the information for one design alternative in a matter of minutes. Once the information is entered, a software application is used to produce a graphic made of colored areas to convey a quick summary of the sustainability features of a project, as illustrated in Figure 1.

The image produced by the software resembles the three sides of a cube. The left side of the cube is reserved for materials. The colored areas indicate different categories of materials and their thickness. The right side of the cube is reserved for technologies. Colors are used differentiate between different technologies based on their carbon footprint and energy consumption. The areas reflect the volume of work specific to each category

Figure 1. Color coded image generated with the green up system.

of technologies. Finally, the surface or top face of the cube is divided into four diamonds which indicate:

- Surface permeability (the water drop symbol)
- Surface reflectivity (the sun symbol)
- Tire-pavement noise (the speaker symbol)
- Life cycle cost (the heart symbol)

The four diamonds will change colors depending on how these four aspects of sustainability are being addressed.

Note that there is no overall rating or numerical index associated to one design alternative. The purpose of the proposed system is not to rank alternatives but to allow engineers to identify and compare key sustainability features of different pavement rehabilitation alternatives.

Comparing different design alternatives is easily achieved by producing similar graphical representations for two or more alternatives and then comparing them visually. More green indicates more sustainable design, materials and construction. More red is an indication of the opposite. Colors like Green-Yellow, Yellow and Orange are used to represent materials and technologies in between the two extremes:

- Green = Sustainable
- Red = Not Sustainable

2.2 *Material categories*

"Green Up" divides materials into 5 major categories which are described in Table 1.

The ranking and categories described in Table 1 are based on engineering judgment. At the top of the sustainability scale are pavement materials recycled in place. Recycling makes perfect sense from a sustainability point of view. When recycling can be performed in place, the need to transport materials to and from the job site is minimized or eliminated. In addition, the owner agency will spend less on new materials by making use of the materials they already paid for in the past, when the pavement was originally built.

Table 1. Material categories.

Category	Color code	Description	Examples
Recycled in-place	Green Color	This category ranks highest on the sustainability scale. It includes materials recycled or reused in place, i.e. transportation to/from the job site is not required.	Asphalt concrete recycled in place, soil stabilization, Rubblized Concrete Pavement (RCP)
Recycled import (alternative materials)	Light Green Color	This category ranks second on the sustainability scale. It includes materials stockpiled offsite that will be incorporated into the pavement. It also includes materials that are byproducts of other industrial processes.	Reclaimed Asphalt Pavement (RAP), Recycled Asphalt Shingles (RAS), crumb tire rubber, Recycled Concrete Aggregate (RCA), blast furnace slag, fly ash, etc.
Recyclable export	Yellow Color	This category ranks third on the sustainability scale. It includes materials that will be removed from the road but can be stockpiled for future use in pavement projects or other civil engineering applications.	RAP, RCA, RCP, reinforcing steel
Virgin import	Orange Color	This category ranks fourth on the sustainability scale. It includes virgin materials.	Asphalt cement, asphalt emulsion, portland cement, lime, virgin aggregate, interlayers, and other materials or additives that are not recycled/reused products
Non-recyclable export (waste)	Red Color	The fifth and last category is reserved for materials that will be transported to a landfill with very little chances of reusing/ recycling.	RAP contaminated with fines or other deleterious materials, damaged concrete pavement, etc.

Transporting construction materials requires the use of fossil fuels and results in the production of green house gases. Heavy truck traffic also contributes to the accumulation of damage on the pavements that carry these trucks from aggregate quarries to asphalt and concrete plants, to job sites, to storage areas or landfills. The larger the amount of materials imported or exported from a project, the larger the amount of fossil fuel used, greenhouse gas emissions produced and damage caused to existing pavements.

To produce the left side of the Green Up cube, the volume of material(s) falling into each of the five categories is first determined. Then, parallelograms that correspond in thickness to the volume of material(s) in a certain category are drawn. The obtained image is a rough representation of the thickness of material in each category.

2.3 *Technology categories*

A similar approach is used to generate the right face of the Green Up cube. This time, technologies are ranked in terms of energy consumption and Greenhouse Gas (GHG) emissions. Starting from the findings of a 2003 Colas report [5], the Green Up systems uses four categories to differentiate between technologies in terms of energy consumption and greenhouse gas emissions. These categories are described in Table 2.

Table 2. Technology categories.

Category	Color code	Description	Examples
Cold	Green Color	Manufacturing and construction processes that make use of very little heat/energy and therefore generate very little emissions compared to other processes.	CIR, CCPR, FDR
Warm	Yellow Color	Manufacturing and construction processes derived from hot processes but where the mixing and compaction temperatures can be lowered with the addition of warm mix additive.	WMA
Hot	Orange Color	Manufacturing and construction processes that require considerable heating of materials	HMA, HIR
Big foot	Red Color	The manufacturing of portland cement and steel has a significantly higher carbon footprint than other binders used in construction. For this reason, concrete pavement falls in this fourth category.	Plain PCC, reinforced PCC

2.4 *Surface properties*

Besides materials and technologies, there are several key aspects specific to the surface of the pavement that can be related to sustainability.

2.4.1 *Porosity*

Porosity or the ability of the pavement surface to allow rain water to drain through the pavement surface and infiltrate into soil. Three categories are proposed:

- Porous (Green Color)
- Impervious (Red Color)
- Not Applicable (Gray Color)

Several types of pavement surfaces can be porous: pervious concrete, porous asphalt concrete and some types of interlocking concrete pavers.

2.4.2 *Surface reflectivity*

Surface reflectivity will influence the rate of cooling of the pavement after being exposed to sunlight during the day. In urban areas, pavements that take longer to cool down contribute to the so called "heat island" effect which contributes to increased energy costs and greenhouse gas emissions. To take into account surface reflectivity, pavement surfaces are divided into the following broad categories:

- Cool (Green Color): for pavements with high surface reflectivity
- Hot (Red Color): for pavements with low surface reflectivity
- Not Applicable (Gray Color): for pavements in rural areas or other scenarios where the heat island effect is not of interest.

2.4.3 *Noise*

Noise generated at the tire-pavement interface is a known source of noise pollution, especially in urban areas. The use of certain surface materials can minimize noise and thus improve the overall sustainability of the design. The following categories are defined as far as noise:

- Quiet (Green Color): where surface materials or treatments are planned to reduce noise
- Noisy (Red Color): where the materials/technologies used do not reduce noise
- Not Applicable (Gray Color): for pavements where tire-pavement noise is not a nuisance.

Noise can be reduced by using an open-graded friction course, rubberized asphalt concrete or by diamond grinding portland cement concrete.

Table 3. Cost efficiency categories.

Life	Temporary	Normal	Long-Life	Perpetual
High Cost	Very Poor	Poor	Fair	Saver
Moderate Cost	Poor	Fair	Saver	Super Saver
Low Cost	Fair	Saver	Super Saver	Excellent

2.5 *Life and cost analysis*

The last element included in the Green Up comparison system is the cost of the strategy over the life of the pavement. Life and cost considerations are included to encourage designers to think long term and to plan and include in the cost of the proposed solution both the initial construction cost and the cost of future maintenance and rehabilitation activities.

Based on the expected service life of a pavement the following categories are identified:

- Perpetual: where the design recommendations together with future maintenance and rehabilitation recommendations ensure that the pavement could be maintained in service indefinitely. For practical purposes, perpetual pavements should last more than three generations or 75 years.
- Long Life: these are pavements that are designed to last more than two generations or 50 years.
- Normal: traditionally, flexible pavements are designed for 20 years life; rigid pavements for 40 years. These pavements will fall under the Normal category.
- Temporary: these are design alternatives that will extend the life of the pavement for less than 20 years.

To compare design alternatives in terms of cost, the total cost that will likely be incurred over the life of the pavement is divided by the number of years the pavement will be in service. The total cost includes the following basic elements:

- The cost of initial construction and the resulting life extension in years
- The estimated cost of preventive maintenance and the frequency
- The estimated cost of reactive maintenance and the frequency
- The estimated cost of subsequent rehabilitation and the resulting life extension

Based on the calculated yearly life cycle cost, a proposed rehabilitation scenario may fall into one of the following cost categories:

- High Cost
- Moderate Cost
- Low Cost

Based on the categories defined for pavement life and cost, Table 3 is used to determine the Cost Efficiency category of a given design alternative.

The lower-central diamond on the surface of the Green Up cube will take the color shown in Table 3 to indicate the sustainability of the solution based on life and cost considerations.

2.6 *Green up software*

It would be impractical and time consuming to generate the color-coded images specific to each design alternative manually. A software application has been developed for Windows PC's and it will be made available for download online.

3 "GREEN UP" EXAMPLE

In California's urban areas, many cities use the "mill and fill" approach to rehabilitate their pavements. Typically, 50 to 75 mm (2 to 3 inches) of the existing asphalt concrete is removed

and replaced with new hot mix asphalt overlay. Milling is required because the final elevations of the pavement surface have to align with the existing concrete curb and gutter structures. This solution is also traditionally included in pavement management programs and the multi-year plans produced by pavement management software. However, it should be noted that the mill and fill method only removes distress at the surface of the pavement thus leaving the pavement susceptible to reflective cracking after only a few years of service.

A different approach is to recycle the existing asphalt Concrete in Place (CIR) and cap it with a thinner hot mix overlay. In order to maintain the same surface elevations, milling will also be required to make room for the hot mix overlay. The CIR layer will provide support for the HMA overlay and possibly delay or prevent the propagation of cracks from the original asphalt concrete to the surface. This strategy will likely result in a longer life extension. Also, this alternative makes better use of the materials already available at the site. How do the two alternatives compare in terms of sustainability? The Green Up system and software was used to compare the following two possible design alternatives:

1. Mill and Fill scenario:
   a. Mill 75 mm (3 inches)
   b. HMA Overlay 75 mm (3 inches)
2. Mill, CIR and Fill scenario:
   a. Mill 38 mm (1.5 inches)
   b. CIR 75 mm (3 inches)
   c. HMA Overlay 38 mm (1.5 inches)

Table 4. Green up inputs.

Input	Scenario 1: Mill and Fill	Scenario 2: Mill, CIR, Fill
Milling thickness	75 mm (3 inches)	38 mm (1.5 inches)
How much of the removed material will be reused on the project	0%	0%
How much of the removed material will be recyclable export (such as RAP)	90%	90%
How much of the removed material will be taken to a land fill (waste)	10%	10%
CIR thickness	–	75 mm (3 inches)
Percent recycling agent	–	3.5%
Percent recycling additive	–	0.5%
Percent water	–	3%
HMA thickness	75 mm (3 inches)	38 mm (1.5 inches)
Asphalt content	5%	5%
RAP	25%	25%
Crumb rubber	0%	0%
Surface drainage	Impervious	Impervious
Surface reflectivity	Low	Low
Noise	Noisy	Noisy
Initial rehabilitation		
Cost per unit area	$20/m^2 ($20/SY)	$20/m^2 ($20/SY)
Life extension	10 years	15 years
Preventive maintenance		
Cost per unit area	$2/m^2 ($2/SY)	$2/m^2 ($2/SY)
Frequency	Every 4 years	Every 4 years
Reactive maintenance		
Cost per unit area	$3/m^2 ($3/SY)	$3/m^2 ($3/SY)
Frequency	Every 6 years	Every 6 years
Subsequent rehabilitation		
Cost per unit area	$20/m^2 ($20/SY)	$20/m^2 ($20/SY)
Life extension	10 years	15 years
Cost level	Moderate	Moderate

The inputs required to use the software for this specific analysis are summarized in Table 4. The values used are typical for Southern California urban areas. The calculated values used to draw the Green Up cube images are summarized in Table 5. Figure 2 shows the two images side by side.

As shown in Figure 2, the two scenarios are similar in terms of surface properties: impervious, low reflectivity and noisy. Hence the red color for the top three diamonds. In terms of life and cost, both scenarios fall in the "Fair" category which corresponds to Moderate cost and 20 to 50 years design life (see Table 3).

The left side of the Green Up cube however tells a different story. The Mill and Fill scenario shows an almost 50/50 distribution of virgin material and recyclable export material. Also visible are lower proportions of recyclable import and waste. In comparison, the Mill, CIR and Fill scenario shows that almost half of the materials are recycled in place. The remaining materials consist of virgin material and recyclable export plus very little recyclable import and waste.

The right side of the cube shows that half of the materials in the Mill and Fill scenario are processed with a Cold technology while the other half uses a Hot technology. In comparison,

Table 5. Green up calculated paramteres.

Output	Scenario 1: Mill and Fill	Scenario 2: Mill, CIR, Fill
Thickness of materials		
Recycled in place	–	73 mm (2.88")
Recycled import	19 mm (0.75")	9.5 mm (0.375")
Recyclable export	68.5 mm (2.7")	34 mm (1.35")
Virgin import	57 mm (2.25")	31.5 mm (1.245")
Waste	8 mm (0.3")	4 mm (0.15")
Thickness of materials processed by		
Cold technology	75 mm (3")	114 mm (4.5")
Warm technology	–	
Hot technology	75 mm (3")	38 mm (1.5")
Big foot technology	–	
Service life	20 years	30 years
Yearly cost	$3/m^2/Year	$2.34/m^2/Year

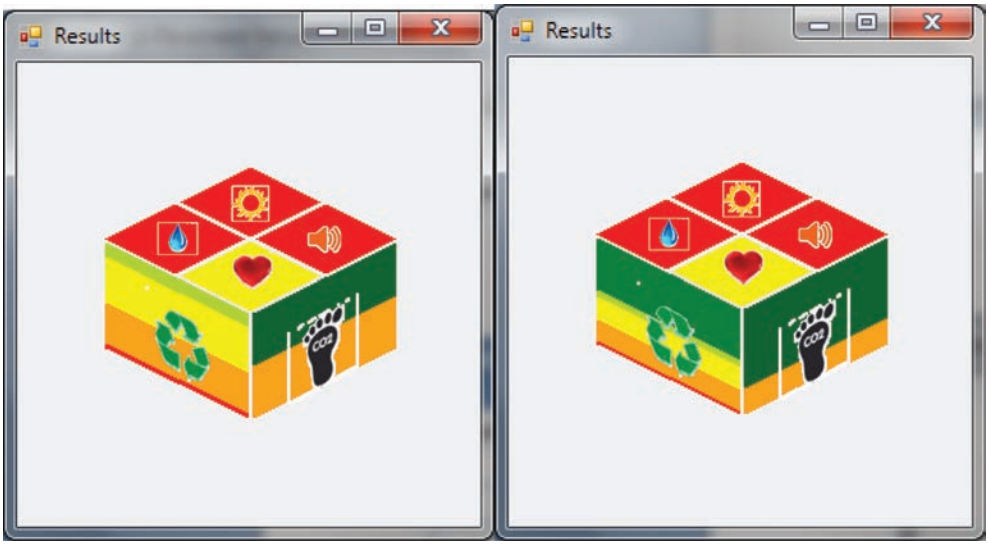

Figure 2. Green up cube for Mill and Fill Scenario 1 (left) and for Mill, CIR, Fill Scenario 2 (right).

75% of materials are processed with a Cold technology in the Mill, CIR and Fill scenario and only 25% with the Hot technology.

Is one approach more sustainable than the other? Could we get even more "green" in the picture? As mentioned before, a computer program was developed to facilitate the use of the system. To encourage users to learn more about sustainable pavement practices, many of windows that make the user interface are provided with a button labeled "Green Up." The Green Up button is a gateway to more information about sustainable pavement rehabilitation practices. Clicking on the button users can access websites and links with more information about a specific subject, such as pervious pavements for example.

4 CONCLUSIONS

The Green Up system provides design professionals with a method of comparing pavement rehabilitation alternatives in terms of four key sustainability features:

- Materials: based on the concept that material reusing and recycling is a sustainable practice;
- Technologies: based on the concept that reducing green house gas emissions and energy consumption is a sustainable practice;
- Surface properties such as:
  - Permeability: the ability to reduce the amount of storm water runoff;
  - Surface reflectivity: the ability to minimize the heat island effect;
  - Noise: and the ability to reduce noise pollution;
- Life and cost: based on the assumption that pavement rehabilitation solutions that cost less and result in a longer life extension are more sustainable.

Before using the Green Up system, designers should use the standards and methods appropriate to their project and jurisdiction to design pavements that are safe, smooth, and economically viable. After producing several design alternatives, the Green Up system can be used to compare and improve the proposed design in terms of sustainability.

The Green Up system was designed to be fast and simple. It limits the amount of information that needs to be provided by the user in an effort to minimize the amount of time needed to use the system. When time and resources are available, designers are encouraged to also use one of the more comprehensive sustainability rating systems such as Greenroads.

REFERENCES

[1] Eisenman, A.A., Sustainable Streets and Highways: an Analysis of Green Roads Rating Systems, Master Thesis, Georgia Institute of Technology, Atlanta, Georgia. 2012.

[2] US Green Buidling Council, "LEED," 4 June 2013. [Online]. Available: http://www.usgbc.org/LEED/.

[3] S. Muench, J. Anderson, J. Hatfield, J. Koester and M. e. a. Söderlund, "Greenroads Manual v1.5.," University of Washington, Seattle, 2011.

[4] M. Yapp, "California Statewide Needs Assessment Local Road System 2012 Update," Ontario, California, 2013.

[5] M. Chappat and J. Bilal, "Sustainable Development. The Environmental Road to the Future. Life Cycle Analysis. Energy Consumption and Greenhouse Gas Emissions," Colas, Boulogne-Billancourt, 2003.

This page intentionally left blank

Asphalt Pavements – Kim (Ed)
© 2014 Taylor & Francis Group, London, ISBN 978-1-138-02693-3

Development of water-based curing reactive cold asphalt repair material

Hirochika Moriyasu, Hiroshi Taniguchi & Kentaro Koshi
Technical Department, Maeda Road Construction Co., Ltd., Oosaki, Shinagawa, Tokyo, Japan

Keigo Hatakeyama
Technical Research Institute, Maeda Road Construction Co., Ltd., Oobatake, Tsuchiura, Ibaraki, Japan

ABSTRACT: In Japan, bagged cold asphalt repair materials are usually used for repairing pavements. They are not as strong as hot asphalt mixtures and are therefore mainly used for the temporary rehabilitation of lightly trafficked roads. In recent years, various highly durable cold mixtures have also been developed, but none match up to the quality of hot asphalt mixtures. Representative problems caused by cold mixtures include rutting and aggregate scattering, particularly immediately after traffic release and during the summer, as well as the limited use in rain or on wet areas.

To solve these problems, we developed a curing, reactive, highly durable, cold asphalt repair material used with a water activating system, which boasts quality equivalent to or higher than hot asphalt mixtures. Presently, the product is used widely throughout Japan, with more than 300,000 bags shipped annually. This paper discusses details of the background of the development and efforts made to put it to practical application.

Keywords: cold asphalt mixture, high durability, the bag, all weather, long preservation

1 INTRODUCTION

Bagged cold asphalt repair materials (cold asphalt mixtures) are used for different purposes such as repair of potholes and bumps in pavements making paving work easy and storage stability high. However, because their strength development is slow compared to hot asphalt mixtures (hot mix asphalt concrete) and durability is also poorer, cold asphalt mixtures are mainly used for the temporary rehabilitation of lightly trafficked roads. Meanwhile, the recent years have seen efforts being made to improve the durability of cold asphalt mixtures in the aim to apply them for the repair of roads with relatively heavy traffic, as well as for mid- and long-term temporary and permanent rehabilitation works. This has led to the development of various highly durable products. Unfortunately, the strength, development time, and durability of cold asphalt mixtures have yet to reach the level of hot mix asphalt concrete, and frequently cause damages such as rutting and aggregate scattering immediately after paving work and during summer. There are also limits to the use of cold asphalt mixtures in paving work during rain or when the repaired area becomes wet.

To solve these problems, we developed an all-weather highly durable cold asphalt mixture [1] which can be used for paving work even in rain and at wet areas while demonstrating the same strength as hot mix asphalt concrete, and put the innovative product to commercial application.

This paper discusses the properties of the mixture, scope of application, and some examples of paving work.

2 CONVENTIONAL COLD ASPHALT MIXTURES

Lubricating oil is combined to produce cut-back asphalt to ensure workability of the conventional cold asphalt mixture at cold temperatures (in the range of temperatures at which the mixture asphalt is used). After paving, the lubricating oil volatilizes, and the mixture is able to undergo strength development. However, as volatilization takes time (from several days to several months), some repaired areas may be damaged soon after the paving work, or even several months after the repair, particularly during summer, because the lubricating oil near the paved surface volatilizes but that inside remains. In addition, when paving work is carried out in the rain or in water puddles, the water causes the durability of the mixture to be reduced as well as the lubricating oil to leach out, resulting in many cases of paving problems, and creating environmental issues.

3 OUTLINE OF MIXTURE

3.1 *Mechanism of strength development*

Figure 1 shows the mechanism of strength development of the cold asphalt mixture. By coating the asphalt surface with special non-petroleum lubricating oil, workability in normal temperature can be ensured. In addition, by spraying water after laying down asphalt (before rolling), the special lubricating oil, reaction assisting material, and water chemically react and harden, and the mixture undergoes strength development.

As the special lubricating oil and asphalt have very good compatibility and products made of the special lubricating oil have the same or more strength than asphalt at service temperatures, the mixture can acquire high durability equivalent to or above hot mix asphalt concrete. Furthermore, as the speed of the chemical reaction is faster than the volatilization of the lubricating oil, the strength development of the mixture is also fast, promising early traffic release after the paving work.

3.2 *Manufacturing method of mixture*

This mixture can be manufactured using the same method as normal hot mix asphalt concrete. However, it should be noted that the mixing temperature of the mixture must be above 110°C because the chemical reaction of the lubricating oil initiates with the slightest amount of water, which may cause the mixture to harden due to the residual moisture in the aggregate.

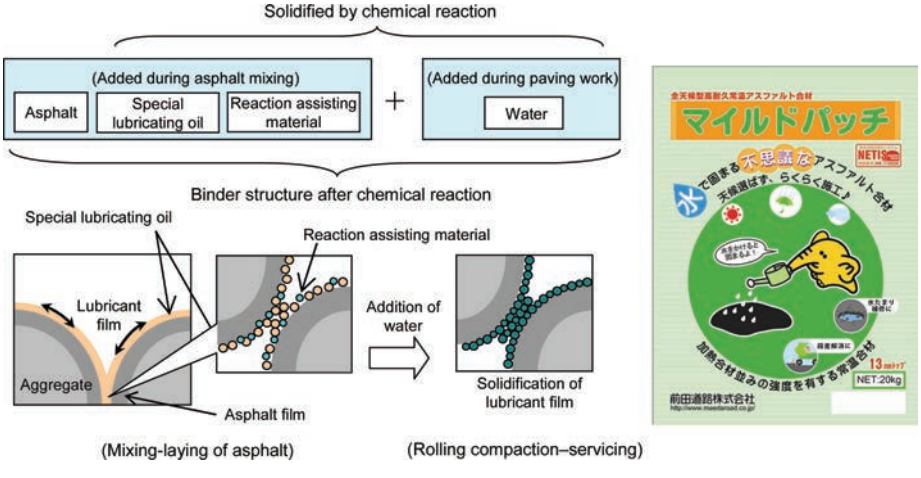

Figure 1. Hardening mechanism.

3.3 *Mixture types*

In fact the aggregate particle size is not specified and various particle sizes are used. Although the dense grade with maximum aggregate particle size of 13 mm is the major type. The product series provides a range of particle sizes to meet different needs. However, the porous type has lower strength compared to the continuous grading type because the binder serves as spot glue, and is thus difficult to use for places where rest steering and torsional effects of tires are frequent. We are therefore currently investigating the application of the mixture as repair material for porous asphalt pavements (drainage pavement).

3.4 *Deciding the binder content*

To determine the binder amount (total of asphalt and special lubricating oil) of the mixture, the tentative binder amount is calculated using the heat mixing method equation (1) described in the Manual for Asphalt Pavement [2] issued by the Japan Road Association, then test mixing is carried out at the calculated binder amount to evaluate the state of the mixture, based on which the binder amount is adjusted and decided. For better adhesiveness to the existing pavement, slightly more binder is included compared to hot mix asphalt concrete.

$$\text{Binder content (\%)} = 0.023a + 0.065b + 0.130c + 0.11d + 1.13 \quad (1)$$

where
a: weight percentage (%) of residue in a 2.36 mm sieve from the aggregate used
b: weight percentage (%) of residue in a 0.3 mm sieve after passing through a 2.36 mm filter
c: weight percentage (%) of residue in a 0.075 mm sieve after passing through a 0.3 mm filter
d: weight percentage (%) of portion passing through a 0.075 mm sieve.

4 INDOOR EVALUATION TEST

4.1 *Properties of mixture*

As there is no prescribed evaluation method for bagged cold asphalt mixtures, Marshall stability and Wheel Tracking (WT), general evaluation methods for asphalt mixtures, were used for the process. The test temperatures were 20°C (in comparison with other cold asphalt mixtures) and 60°C (in comparison with hot mix asphalt concrete).

1. Comparison with other cold asphalt mixtures
   To evaluate the mixture strength immediately after paving and after placing the road in service, Marshall stability test was conducted at normal temperature one hour after preparing the test samples. Given that the cold asphalt mixtures for comparison were of the lubricating oil volatilization type, test samples were cured at 60°C for seven days to completely volatilize the lubricating oil, after which normal temperature Marshall stability and normal temperature WT test were carried out. General type and highly durable type were used as the cold asphalt mixtures for comparison.

   Figures 2 and 3 show the results. This mixture was found to have stability of more than ten-fold that of the general type in the initial stage and three- to seven-fold that of the highly durable type. It was also confirmed that even when the road was placed in service, the mixture had very high strength compared to the other two cold asphalt mixtures for both Marshall stability and dynamic stability.
2. Comparison with hot mix asphalt concrete
   To compare properties of this mixture with those of hot-mix mixtures, normal temperature (60°C), Marshall and WT test were conducted. Taking the particle size of the hot mix asphalt concrete to be the same as that of this mixture, straight asphalt 60/80 binder was used.

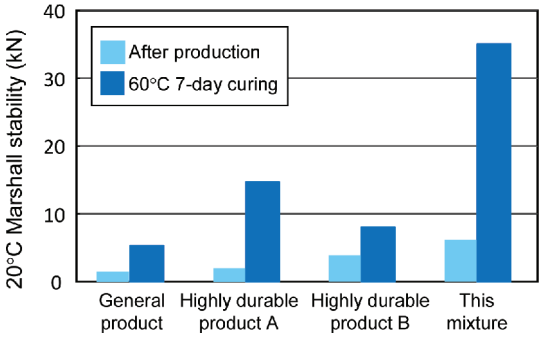

Figure 2. Marshall test results (20°C).

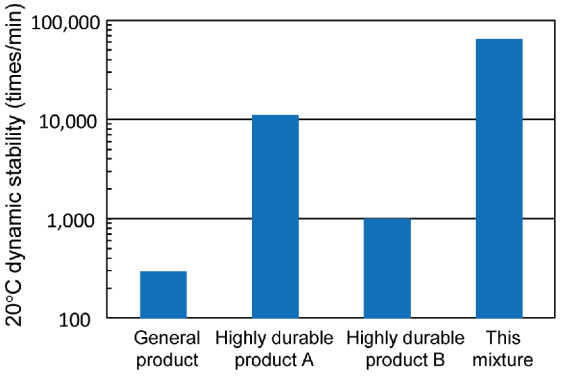

Figure 3. WT test results (20°C).

Table 1 shows the results. This mixture indicated values equivalent or above the hot-mix mixture, confirming that this mixture has the same strength as hot-mix mixtures even though it is a bagged cold asphalt mixture.

4.2 *Strength development*

This material develops strength not by the volatilization of the lubricating oil but by chemical reaction. As its chemical reaction time is faster than volatilization time, strength development of this mixture is faster than that of normal cold asphalt mixtures, suggesting that quick traffic release can be expected.

1. Initial strength of mixtures
   The speed of strength development of this mixture was verified by normal temperature Marshall test. Figure 4 shows the test result. The strength of the mixture increases with time, confirming that the strength of the mixture was higher than the general type (20°C, 7-day curing) 30 minutes after sample preparation, and higher than highly durable products (20°C, 7-day curing) one hour after.
2. Durability immediately after paving work
   To verify the strength of this mixture immediately after paving work, a car was driven over the road immediately after pothole repair (Photo 1), and the road surface profile before and after the tires had run over the road were measured (Photo 2). Tables 2 and 3 show the test conditions and results. Rutting is less compared to the general type and highly durable type, indicating that the mixture has superior initial durability. In addition, there were no cracks caused by aggregate scattering or displacement.

Table 1. Properties of mixture.

Item	Test value		Specification*
	This mixture	Hot mix asphalt concrete	
Marshall stability (kN)	9.2	9.8	≥ 4.9 kN
Dynamic stability (times/mm)	6,000	500	–

*Guideline for pavement design and construction [3].

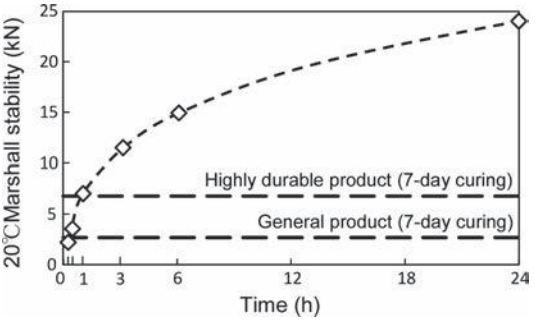

Figure 4. Results of verifying strength development.

Photo 1. Road condition.

Photo 2. Measurement road surface profile condition.

Table 2. Measuring conditions.

Item	Details
Paving work	
Paving scale	Approx. 0.15 m^2 (t = 50 mm)
Rolling compaction method	Harden by stepping with foot
Running vehicle	
Vehicle used	Passenger car (Tire ground contact pressure: 0.37 N/mm^2)
No. of runs (running time)	10 times (within 3 minutes from completion of paving work)
Road surface profile measuring device	MRP (multi-load profiler)

Table 3. Rut depth.

Type	Rut depth (mm)
This mixture	2.7
General product	5.1
Highly-durable product	4.0

Table 4. Paving method and mixture properties in low temperatures.

Compaction temperature (°C)	Density (g/cm^3)	Compaction degree compared with 20°C (%)	Workability (handling)	Marshall stability at 20°C (kN)	
				3-hour curing	7-day curing
20	2.342	100	Good	10.5	≥30
0	2.314	98.8	Good	9.7	≥30
–10	2.300	98.2	Good	9.5	≥30

Table 5. Storage stability verification results.

Type of bag	Sealing method	Hardening rate of mixture in bag (%)			
		1 month	2 months	3 months	6 months
Conventional type	Stitching by sewing	0	20	70	100
Dedicated type		0	0	50	80

4.3 *Workability in low temperatures*

Table 4 shows the results of verifying workability of this mixture in low temperatures. Evaluation was carried out by normal temperature Marshall test and handling during work.

In this study, the mixture temperature was decreased to the paving temperature (0, –10°C), so the compaction density was slightly lower than when paving was carried out at 20°C. However, there was essentially no drop in workability and mixture strength, confirming that there is no sharp decrease in durability even in paving at low temperatures.

As the freezing of the sprayed water during paving can cause inadequate compaction, there is a need to carry out compaction quickly. Compaction density can also be improved by placing the mixture inside before use to adjust its temperature to around 20°C.

4.4 *Storage stability*

As this mixture develops strength by adding water and it can start reacting gradually even with the slightest amount of water such as moisture in the air, etc., ideally the mixture should be stored in such a way that all entry of humidity, etc. is shut off. Table 5 shows the results of verifying storage stability. When bags used for storing general cold asphalt mixtures are sealed by stitching with a sewing machine, hardening started one to two months after storage. However, with storage bags with better humidity prevention and waterproofing performance are used, it was confirmed that sealing the bags by thermal compression to increase airtightness enabled storage for six months. In addition, workability and properties of a mixture which had been stored for six months were checked, and it was found that conditions were good and not different from mixtures just manufactured.

5 PAVING PROCESS

The paving process with this mixture is the same as normal cold asphalt mixtures other than the spraying of water before compaction. The following describes the paving process using pothole repair as an example.

5.1 *Pouring and spreading the mixture*

The required amount is poured over the area to be paved. The shrinkage allowance is about 30%.The paved area can be wet. Although scattering of emulsion is not required, it is still performed as necessary because it improves durability. The mixture is then spread as done with normal cold asphalt mixtures, however, efforts must be made to prevent the coarse aggregate from concentrating in one place as this causes aggregate scattering.

5.2 *Water spraying*

Water must always be sprayed before rolling. As shown in Photo 3, water is sprayed using a plastic bottle, watering can, etc. over the whole surface evenly. The amount of water to be sprayed is 1 per bag of mixture (20 kg), and can be slightly more or less than this. However, more will not cause any problems, but inadequate spraying can delay strength development.

5.3 *Rolling*

Rolling was carried out promptly after water spraying. As shown in Photo 4, compaction by stepping with the foot is adequate. Durability is better when rolling machines such as plate, etc. are used. If rolling is delayed, reaction with the mixture progresses, resulting in paving problems. For this reason, rolling need to be carried out promptly.

Photo 3. Water spraying.

Photo 4. Rolling compaction.

5.4 *Traffic release*

In small-scale paving work such as repair of potholes, etc., traffic release may be possible after completion of the paving work. However, curing may need to be carried out for about one to two hours when large cars are scheduled to frequently run over the areas where torsional effects of tires occur or at large areas of paving work.

6 EXAMPLES OF APPLICATION

6.1 *Restoration work after earthquake*

This mixture was used for repairing potholes (Photo 5) that had formed on roads in Miyagi Prefecture during the Great East Japan Earthquake. Conditions remain good even after two years from paving.

6.2 *Restoration work after north Kyushu heavy rain disaster*

As shown in Photo 6, a torrential downpour which occurred in the northern part of Kyushu in July 2012 severely damaged roads in Fukuoka Prefecture. This mixture was used in restoration work to repair the roads (Photo 7). More than 100 bags (containing 20 kg) were used.

6.3 *Application to sites with torsional effect (exit/entrance of distribution center)*

Photo 8 shows the repair situation at the entrance/exit of a distribution center. There is an area showing torsional effect of large-vehicles. Repairs had been carried out several times but

Photo 5. Restoration after earthquake.

Photo 6. Damage situation.

Photo 7. Urgent repair situation.

Photo 8. Repaired state at entrance/exit of distribution.

the area quickly became damaged again after each repair. When it was repaired using this mixture which has high durability, good serviceability was confirmed.

7 SUMMARY OF RESULTS

This mixture has the following features:

- Although it is a bagged cold asphalt mixture, it has the same durability as hot mix asphalt concrete.
- Strength development is via chemical reaction and is thus faster than volatile cold asphalt mixtures, enabling early traffic release.
- Paving is possible even in rain and subzero temperatures.
- Applicable to all particle sizes. (However, the porous type is limited to sidewalks.)
- Can be stored for a long time (about 6 months).
- Paving method is the same as conventional cold asphalt mixtures except for water spraying. No special paving machine is required.

8 NEW ENDEAVORS

This mixture can be applied for various purposes using techniques developed for it. Some new methods of use are introduced below.

8.1 *Use as normal hot mix asphalt concrete*

As this mixture does not need to be bagged and sealed immediately and can be used as long as it is on the day it was made (about 12 hours from production), it can be used as normal hot mix asphalt concrete. In addition, the workable temperature can be set freely by changing the amount of special lubricating oil added, thereby allowing use for the following purposes.

1. Use for small-scale repairs and several locations in one day
   By setting the workable temperature low (about 50–90°C), the mixture can be used cold. This means that when small-scale repairs are required at several locations in one day, mixtures delivered in the morning can be used even in the evening. Thus no mixtures are wasted and there is no need to go all the way to the manufacturing plant to obtain more stock when it runs out.
2. Application to warm-mix asphalt and improved workability asphalt mixtures
   As the manufacturing temperature of the mixture can be decreased to 110°C (temperature at which the residual water in the aggregate becomes more or less zero), it can be reduced by about 50°C for normal mixtures and by about 70°C for modified mixtures. This enables CO_2 emissions to be cut, work environment of employees to be improved (prevent heat stroke), and traffic to be released early due to the fast chemical reaction of the special lubricating oil. By setting the shipment temperature the same as normal temperature, the mixture can also be used as an improved workability mixture in paving work where temperature drops of the mixture are anticipated such as winter.
3. Transportable over long distances
   Normally, hot mix asphalt concrete should be used within two hours from shipment due to decrease in temperature. This is difficult in areas without asphalt mixing plants in the vicinity. In such cases, paving problems tend to occur easily, and this may cause early damage of pavements. This mixture is also useful for resolving this problem and is suitable for long distance transportation.

8.2 *Stockpile mixture bagged in flexible container*

This mixture needs to be sealed in an airtight bag for long term storage as it starts to react even with the moisture in the atmosphere. Small amounts such as 20 kg can be sealed in

airtight bags but large amounts like 1t are difficult and cannot be stored over long periods of time. Since mixtures harden as a result of the mixture and chemical reaction of the special lubricating oil, reaction assisting material, and water, as long as one of these is not present, the mixture can be stored semi-permanently. Consequently, by manufacturing the mixture without adding the reaction assisting material, then transporting the mixture to the site of use and mixing in the reaction assisting material just before paving work as shown in Photo 9, large amounts can be stored in flexible container bags, etc. This method not only enables asphalt paving in regions that do not have mixing plants such as remote islands, but also allows the mixture to be brought to disaster sites from afar and to be stored there. This is considered a technique useful for the restoration work after earthquake disasters.

Currently, kneading and paving tests are being conducted to verify the serviceability of this technique. A simple device for mixing reaction assisting material on site is also being developed in the aim to put it to practical application.

8.3 *Decolorizing*

This mixture can also be applied to decolorizing binders, as well as fieldstone and bagged colored cold asphalt mixtures (Photo 10, 11). Presently, durability and weather resistance are being verified. Applications such as repair material for fieldstone and colored pavements, small-scale pavements such as parks, and normal households are being considered.

Photo 9. Stockpile materials bagged in flexible container.

Photo 10. Application to natural stone pavement.

Photo 11. Application to colored pavement.

9 CONCLUSION

This mixture is a new type of cold asphalt mixture with sharply improved strength development and durability during the winter and summer, which has been the challenge of conventional cold asphalt mixtures.

In the future, efforts will be made to further increase the scope of application such as use as decolorizing agent of natural color pavements and color pavement, and application as repair material of porous asphalt pavements, etc.

REFERENCES

[1] All-weather highly durable cold asphalt mixture "MILDPATCH": http://www.maedaroad.co.jp/products/mildpatch/mildpatch_hm.htm.
[2] Japan Road Association: Manual for low cost pavement (1977 edition).
[3] Japan Road Association: Guideline for pavement design and construction (2006 edition).

This page intentionally left blank

Asphalt Pavements – Kim (Ed)

Effect of moisture on asphalt mastic tensile properties at ambient temperature

Alex K. Apeagyei, James R.A. Grenfell & Gordon Airey
Nottingham Transportation Engineering Centre, Department of Civil Engineering, University of Nottingham, University Park, Nottingham, UK

ABSTRACT: The purpose of this study was to investigate moisture absorption characteristics and their impact on tensile properties of asphalt mastics subjected to long-term soaking under ambient conditions (20°C and 50% relative humidity). The objective was to better understand the moisture damage phenomenon by providing suitable material inputs that can be used for numerical simulation. Understanding the effect of moisture on the mechanical properties of the asphalt mastics investigated is of utmost importance because they are commonly used in the construction of open-graded asphalt mixtures. The experimental approach adopted for studying the effect of moisture on mechanical properties of asphalt mastics consisted of exposing initially dry samples to moisture under controlled temperature and relative humidity, recording the moisture uptake until equilibrium using an ultra-sensitive balance, and then drying back and performing mechanical testing at multiple levels of saturation (moisture contents). The mechanical tests were all conducted at 20°C using a loading rate of 20 mm/min on dog-bone shaped samples. Using this approach, it was possible to identify the reversible and irreversible moisture absorption and its effects on mechanical properties. Moisture absorption of up to 0.4 wt% was observed and was largely recoverable upon drying for most of the mastics tested. The results suggest that the degradation of mastic tensile properties associated with moisture absorption is partially recovered upon drying. The effect of moisture conditioning on mastics appears to be aggregate type dependent as higher degradation in stiffness response was observed in the granite mastics than in the limestone mastics. Tensile strength in moisture saturated mastics was generally lower than in drier samples and was largely recoverable upon specimen drying. The failure mode in all the mastics considered were ductile which suggests that at the temperature and loading rate employed, the effect of moisture on failure mode is minimal. Aggregate type can accentuate the influence of moisture on tensile properties of asphalt mastics.

Keywords: asphalt mastic; moisture absorption; stress-strain relationship; tensile strength; moisture damage

1 INTRODUCTION

From a micro-mechanical point of view, asphalt mastic comprising of bitumen, fine aggregate and mineral filler can be considered as one of the two key components of conventional asphalt mixtures. The second component is mineral aggregate. In this case, the mastic, not the bitumen, may be considered as the adhesive that binds the aggregates together. The adhesive bond at the asphalt mastic-aggregate interface and/or the cohesion within the bulk mastic controls the mechanical properties of asphalt mixtures. However, both adhesive and cohesive properties of asphalt mastic can be susceptible to the detrimental effects of moisture in a phenomenon known as moisture induced damage [1]. Moisture damage can lead to significant degradation of mechanical properties and is generally recognized as one of the most important factors that influence long-term durability of asphalt pavements [1–10].

Most damage in asphalt mixtures involves extremely complex mechanisms that are not completely understood yet. Recent attempts aimed at better understanding the mechanisms of moisture damage have involved two main approaches: the application surface energy methods based on physico-chemical properties and the application of finite element techniques for simulating the moisture damage [3–9]. In both approaches, fundamental physical and material properties are required as inputs that are currently not routinely available. Critical input parameters for the FE approach, which is the focus of this study, include the bulk mastic tensile properties of asphalt mastics and the effect of moisture on the same. The second important FE input material property is related to the influence of moisture on interfacial bonds is beyond the scope of this paper.

Asphalt mastic show sensitivity to moisture due to physico-chemical interactions between water molecules and some polar groups found in bitumen and mineral aggregates (aggregates and fillers). This sensitivity is also a function of the mineralogical composition of aggregates and mineral fillers. The latter controls both moisture uptake and diffusion properties that are fundamental input parameters many numerical simulation models for moisture damage. Through the application of Fick's laws of diffusion [11] the amount of moisture transport through asphalt mastic can be modelled as a function of time and the results used to relate moisture content to damage. A simple but useful approach for studying the effect of moisture on mechanical properties of asphalt mastics consists of exposing an initially dry sample to moisture under controlled temperature and Relative Humidity (RH), recording the moisture uptake until equilibrium using an ultra-sensitive balance, and then drying back and performing mechanical testing at multiple degrees of saturation (moisture contents). Using this approach, it is possible to identify the reversible and irreversible moisture absorption and its effects on mechanical properties. Almost all currently available testing protocols for evaluating moisture damage assumes moisture induced damage in asphalt mixtures is irreversible or fail to consider the possibility reversible moisture induced-damage. On the basis of this assumption, if asphalt mastic is exposed to moisture for long period of time, permanent damage should be expected. As this paper will demonstrate, this supposition may not be the case for certain asphalt mixtures.

This study reports on an investigation of the effects of moisture on tensile properties of asphalt mastics under accelerated moisture conditioning regimes in the laboratory. Tensile properties are evaluated from controlled strain loading at ambient temperatures. The observed tensile response of asphalt mastic to moisture exposure is rationalized based on physico-chemical analysis in conjunction petrographic data from a Mineral Liberation Analyser (MLA).

2 MATERIALS AND METHODS

2.1 *Aggregates properties*

Four asphalt mastics (LALF, LAGF, GALF and GAGF) containing different fine aggregate and mineral filler types were used. Combination of the two fine aggregates and two fillers types yielded the four different mastics. Materials passing the 1.00 mm sieve but retained on 0.125 mm sieve were considered as fine aggregates while the mineral filler was defined as material passing the 0.063 mm sieve. The aggregates and mineral fillers differed in terms of their petrological type (granite or limestone), mineralogical compositions, surface characteristics and specific gravities. The mineralogical compositions of the aggregates were characterized using a Mineral Liberation Analyzer (FEI Quanta 600 SEM). The device combines an automated Scanning Electron Microscope and multiple Energy Dispersive X-ray detectors with state-of-the-art analysis software to produce quantitative mineralogy measurements. The results were used to identify key mineral phases and their possible influence on the moisture-induced asphalt mastic tensile property degradation. Figure 1 shows the mineralogical composition of the aggregates obtained from the Mineral Liberation Analyzer. The results show that the mineral compositions of the granite and limestone aggregates are significantly different in

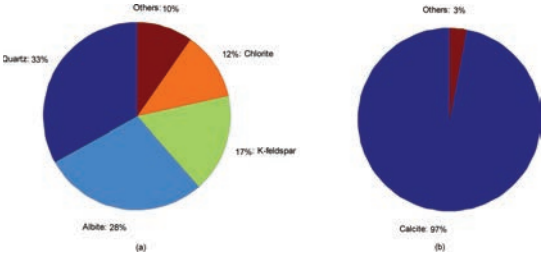

Figure 1. Petrographic type and mineral composition of aggregates and fillers. K-feldspar = potassium-dominant feldspar. a) Granite. b) Limestone.

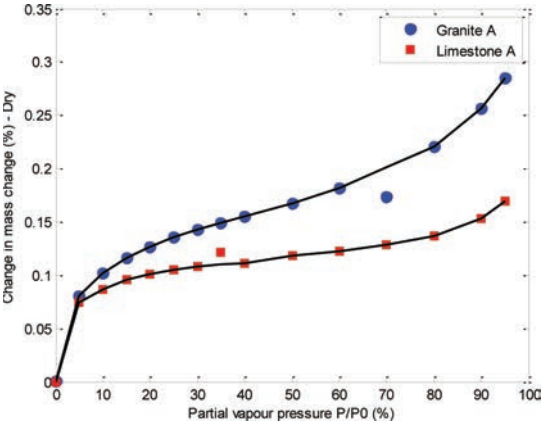

Figure 2. Octane sorption isotherms for aggregates (1.18 mm size fraction) used for fabricating mastics. The higher the absorption the more porous is the aggregate.

terms of the number and amount of mineral phases present. While the granites were made up of a large number of different dominant mineral phases (quartz, albite, potassium-dominant feldspar, and chlorite), the limestone consisted of predominantly (about 97%) calcite.

The aggregates for the mastics were mechanically sieved in the laboratory to obtain only materials passing the 1-mm sieve and retained on 0.125-mm sieve (fine aggregate). In addition to the fine aggregates, limestone and granite mineral fillers satisfying BS EN 1097-7-2008 were used. Again, the choice of the mineral fillers was made to quantify the effect, if any, of different types of fillers used in asphalt mixtures.

Surface characteristics such as porosity, specific surface area, and surface free energy, are key physico-chemical properties of aggregates that influence the adhesion between materials. The physico-chemical properties of samples of the aggregates were characterized using a Dynamic Sorption Device (DVS Advantage), with octane as a probe, to generate a series of sorption isotherms (Fig. 2). The absorption of octane was higher in the granite than in the limestone suggesting the former is more porous than the latter. Also, as can be seen in Figure 2, the isotherms are similar to type II isotherms. Therefore, the BET specific surface area for the 1.18 mm aggregate was calculated giving a value of 3.49 m^2/g and 2.57 m^2/g, respectively, for the granite and the limestone. Additional detailed characterization of the physico-chemical properties of the aggregates are provided elsewhere [5, 6]. From this study, the total SFE of the granite and limestone was reported as 353 and 223 mJ/m^2, respectively.

The specific gravities of the aggregates and mineral fillers were not significantly different. They were 2.663, 2.720, 2.626 and 2.680, respectively, for the Limestone Aggregate (LA), Limestone Filler (LF), Granite Aggregate (GA) and Granite Filler (GF).

2.2 *Asphalt mastics*

The same 40/60 penetration grade bitumen (40/60 pen) was used in the manufacture of all the four asphalt mastics examined. The bitumen is typical of those that are commonly used for asphalt mixture production in the UK with a reported total surface free energy of about 31 mJ/m^2 [5–6]. The proportion of the constituent components (fine aggregate, mineral filler, bitumen) of the mastics used was 50:25:25 by weight of mixture or about 36:18:46 by volume. These proportions were chosen to mimic mastic mix design typically used in open-graded friction course asphalt mixtures in The Netherlands [8]. The mastics were produced by combining the dried aggregates and molten bitumen using a Hobart mechanical mixer at a mixing temperature of 185°C. The mastics were then put in quart tins and stored in temperature controlled (20°C, 50% RH) conditions until testing. The bulk specific gravity of the mastics was estimated to be approximately 1.917.

2.3 *Specimen fabrication*

Mastic specimens shaped in the form of a dog-bone with dimensions of 17.75 mm at the middle, 21 mm at the top, and 62 mm tall (Fig. 3), was used to determine the cohesive tensile properties of the mastics. The dog-bone shaped nature of the mastic specimens required custom-made stainless stress moulds to be procured. In addition stainless steel rings measuring 21 mm diameter by 5 mm high were used for gripping the specimens. The average dry weight of each mastic specimens (excluding the two steel rings) was about 30 g. Similar specimen configurations have been used to measure tensile strength of mastic in the past [8]. The dog-bone shaped specimens were fabricated by pouring molten mastic (135°C–140°C) in the steel mold with any form of compactive effort applied.

2.4 *Moisture conditioning*

Schematic of the moisture conditioning test set-up is shown in Figure 4. Special mats were made to cradle the fragile dog-bone shaped specimens to ensure that damage to the specimen were kept to a minimum during the rather long conditioning time (over 200 days of absorption and desorption) required. Moisture uptake during soaking (absorption) and during drying (desorption) was captured at regular intervals using an ultra-sensitive microbalance with a 0.1 μg resolution. It should be noted that while the specimens were fully submerged (and therefore diffusion of moisture into the mastic occurred through all exposed surfaces) during the absorption stage, moisture flow during the drying (desorption) stage was restrained to occur only at the ends of the mastics by covering the middle portion of the specimens with

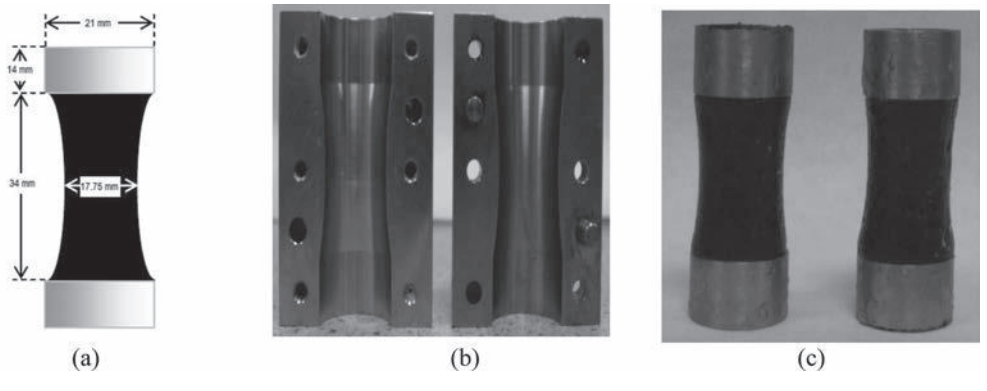

Figure 3. Specimen fabrication details for cohesive tensile strength testing. a) Specimen dimensions. b) Bespoke, reusable steel mould for fabricating dog-bone shaped specimens. c) Sample fabricated mastic specimens.

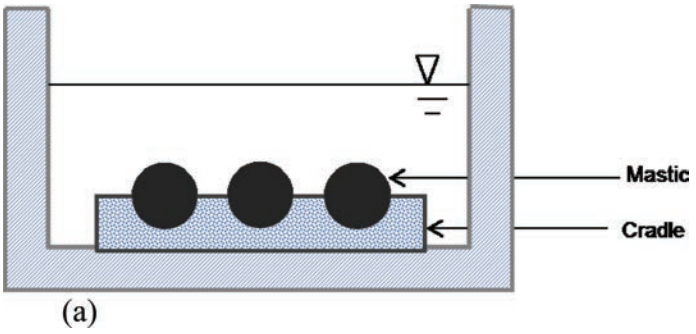

Figure 4. Schematic diagram of moisture conditioning test set-up for dog-bone shaped asphalt mastic specimens. All conditioning were conducted at 20°C and 50% RH.

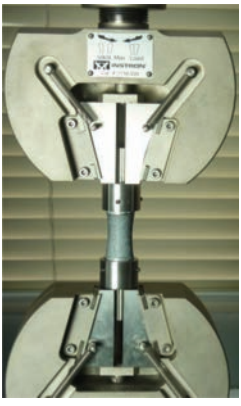

Figure 5. Details of tensile strength test set-up with mastics specimens connected to the Instron through wedge-action grips.

plastic sheeting. This was to ensure that moisture was always present at the most critical location (middle of the specimen) during mechanical testing at all saturation levels. Similar approach was used by Kringos et al., 2011 [8]. Moisture uptake was computed as the ratio of moisture uptake at given conditioning time to the weight of the dry mastic.

2.5 *Tensile testing*

Figure 5 shows the details of the test set-up developed for examining the effect of moisture on tensile properties of asphalt mastics. The same Instron machine with a load cell of 5 kN were used for both set-ups. In both cases, the test specimens were attached to the Intron machine through mechanical wedge-action grips via two custom-made steel loading rings. The applied loading rate of 20 mm/min was also the same for the cohesive and adhesive strength test sets. A single testing temperature of 20°C was used. An additional feature for cohesive strength test was the use of a video gauge capable monitoring both the transverse and longitudinal strains using virtual targets (speckle patterns) that enable accurate stress-strain characteristics of the mastic to be made in a non-obstructive manner.

2.5.1 *Mastic cohesive tensile properties*

The samples were mechanically tested after four different moisture conditioning regimes: 1) dry samples stored under ambient conditions (20°C and 50% RH) for about 112 days, 2) after 112 days of soaking, 3) 112 days of soaking followed by about 30 days of partial

drying and 4) 112 days of soaking followed by 112 days of partial drying. To obtain the partially dried samples, samples of the 112 moisture conditioned specimens were covered with plastic on all sides except the two ends so that water can evaporate from the ends only. The applied load and the resulting cross-head displacement were monitored continuously by software connected to the Instron machine. The results were used to determine both stiffness and tensile strength of the mastics as a function of moisture conditioning and moisture absorption.

3 RESULTS AND DISCUSSION

3.1 *Mastic cohesive tensile properties*

A key objective for conducting the cohesive tensile testing on the mastics was to examine the effect of absorbed moisture on the bulk mastic properties. Bulk asphalt mastic properties of interest included stress-strain behaviour (load versus cross-head displacement), ultimate tensile strength (cohesive strength) and strain at ultimate strength. It was anticipated that the relationship between mastic properties and moisture absorption profiles could be used as inputs into a finite element model for simulating moisture damage in asphalt mixtures.

3.1.1 *Mastic moisture absorption profiles*

For each of the four mastic types considered, at least 6 replicate specimens were tested to determine their moisture absorption and desorption characteristics. The results are depicted in Figure 6 where differences in the rate and amount of moisture absorbed or desorbed could be seen depending on aggregate type. The amount and rate of moisture absorbed was higher in mastics containing limestone aggregates than that in granite aggregate mastics for the conditioning period of up to 112 days considered in this study. More than 80% of moisture uptake occurred during the first 50 days of the 112-day conditioning period for the limestone mastics compared with just over 20% for the granite mastics over the same period. This suggests moisture absorption in the limestone mastics appear to be approaching 'equilibrium' after 112 days of soaking. On the contrary, for the mastics containing granite aggregates, it appears that equilibrium could not be reached after 112 days of soaking in 20°C water. However, the lack of a plateau in the moisture uptake profiles suggests none of the mastics

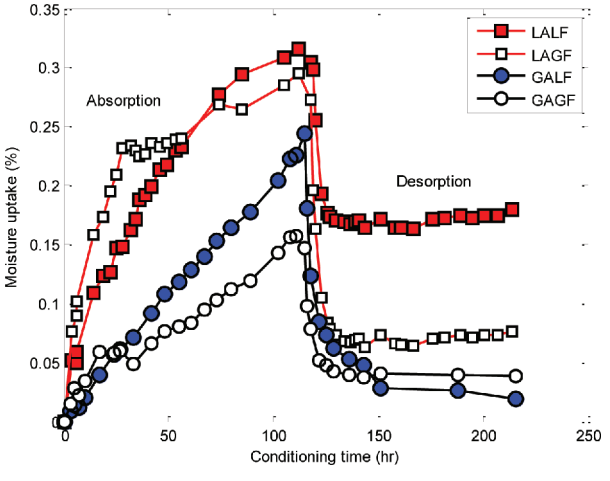

Figure 6. Moisture absorption and desorption profiles for asphalt mastics. Moisture uptake profile during absorption was obtained by soaking in water at 20°C. Desorption profile was obtained by drying partially covered specimens at 20C and 50% relative humidity. LA = limestone aggregate; LF = limestone filler; GA = granite aggregate; GF = granite filler.

achieved true equilibrium moisture after 112 days of moisture conditioning at 20°C. The four mastics tested were nominally similar except the type of aggregates and mineral fillers used. Therefore, any differences in moisture absorption could be attributed to physico-chemical properties of the aggregates and fillers.

Even though the absorption and desorption profiles shown in Figure 6 cannot be compared directly because desorption was constrained to occur only in one direction while absorption occurred in all directions, a key feature of the desorption profile was that it occurred at a relatively faster rate than absorption. For 3 out of the 4 mastics considered, it took less than 20 days to reach the residual moisture content of 0.025 to 0.05% (about 20% of peak uptake value) while it took over 110 days for each mastic to reach the pseudo-peak value.

3.1.2 *Effect of moisture conditioning on mastic stress-strain relationship*

Like many polymeric materials, asphalt mixtures can absorb moisture with time during moisture conditioning. A key effect of the presence of moisture on asphalt mixtures is the degradation of mechanical properties associated with moisture conditioning time. For dense-graded asphalt mixtures, stiffness degradation of up to 80% of unconditioned sample stiffness is possible. It was therefore anticipated that conditioning asphalt mastic in water at 20°C for up 110 days would induce significant measurable degradation in tensile properties. To test the hypothesis, mastic samples were soaked in water for about 112 days and then dried. Tensile strength tests were conducted after specified periods of drying including 0 days, 33 days and 112 days. The effect of absorbed water on the stress-strain behaviour of mastics dog-bone specimens as a function of conditioning regime (drying time) is depicted in Figure 7. In majority of the mastics, the longer drying times the higher the load-displacement (stiffness) curve plots; peak load for mastics conditioned dried for 112 days were always higher than those dried for 0 days. The results suggest that the degradation of mastic stiffness associated with moisture absorption is partially recovered upon drying. The effect of moisture conditioning on mastics appears to be aggregate type

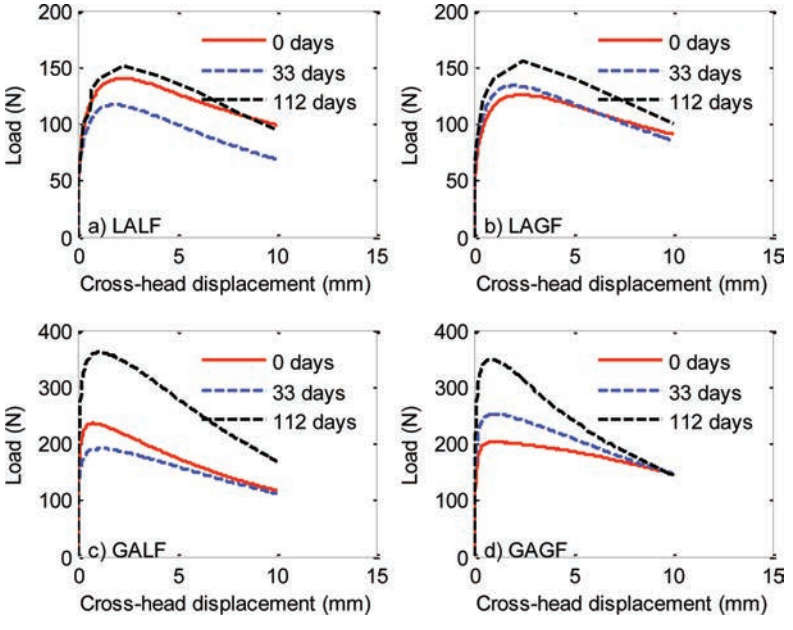

Figure 7. Effect of wetting and drying on asphalt mastics stress-strain response at 20C and 20 mm/min loading rate. All specimens were conditioned in water at 20°C for about 112 days before been dried for 0, 33 or 112 days for testing. Mixtures dried for 112 days contained the least amount of moisture while mixtures labelled 0 days were the wettest.

dependent as higher degradation in stiffness response was observed in the granite mastics than in the limestone mastics.

3.1.3 *Effect of moisture on mastic ultimate strength*

From the load versus longitudinal displacement plots (similar to those depicted in Fig. 7) for each mastic type, ultimate tensile strength values were computed as the ratio of the peak load to cross-sectional area of the neck of the dog-bone specimen. The results are summarized in

Table 1. Effect of moisture on tensile properties of asphalt mastics.

Exposure conditions	Moisture uptake (%)	Tensile strength (MPa)	Strain at ultimate strength (%)	Failure mode
LALF				
112 days in water at 20°C	0.315	0.62 ± 0.17	3.90 ± 0.45	Ductile
Then dry at 20°C 50% RH for 33 days	0.165	0.52 ± 0.04	4.14 ± 0.96	Ductile
Then dry at 20°C 50% RH for 112 days	0.180	0.59 ± 0.11	3.70 ± 0.30	Ductile
LAGF				
112 days in water at 20°C	0.295	0.70 ± 0.220	4.04 ± 0.40	Ductile
Then dry at 20°C 50% RH for 33 days	0.063	0.53 ± 0.10	3.54 ± 0.08	Ductile
Then dry at 20°C 50% RH for 112 days	0.077	0.65 ± 0.03	4.14 ± 1.04	Ductile
GALF				
112 days in water at 20°C	0.244	0.83 ± 0.12	1.76 ± 0.39	Ductile
Then dry at 20°C 50% RH for 33 days	0.029	0.66 ± 0.11	1.75 ± 0.16	Ductile
Then dry at 20°C 50% RH for 112 days	0.019	1.14 ± 0.02	1.90 ± 0.08	Ductile
GAGF				
112 days in water at 20°C	0.157	0.76 ± 0.12	1.85 ± 0.17	Ductile
Then dry at 20°C 50% RH for 33 days	0.041	0.86 ± 0.05	1.72 ± 0.31	Ductile
Then dry at 20°C 50% RH for 112 days	0.039	1.16 ± 0.10	1.71 ± 0.23	Ductile

RH = relative humidity.

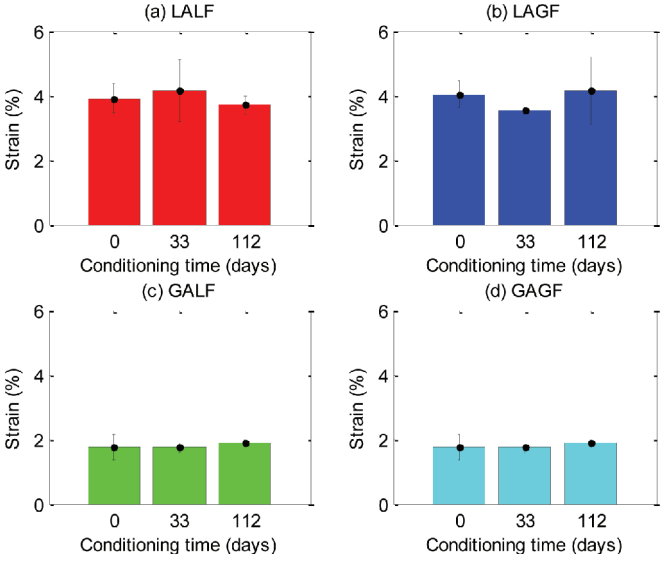

Figure 8. Strain at peak stress. Conditioning time is the number of drying days after specimens have been moisture conditioned for about 112 days in water at 20°C.

Table 1. They show that tensile strength in saturated (wetter) mastics is generally lower than in drier samples. The results also show that tensile strength in moisture saturated mastics largely recover upon drying. The failure mode in all the mastics considered were ductile which suggests at the temperature and loading rate employed, the effect on moisture on failure mode is minimal. It can be seen in Table 1 that aggregate type can accentuate the influence of moisture on tensile properties of asphalt mastics. Recovered tensile strength was generally higher in granite mastics than in limestone mastics. Also the strain at peak strength was significantly higher in limestone mastics compared with granite mastics under similar testing conditions (Fig. 8).

4 CONCLUSIONS

The objective of this paper was to investigate the effect of moisture on the tensile properties of asphalt mastics. The following conclusions were reached based on the data presented in the paper:

- Differences in the rate and amount of moisture absorption in mastics could be attributed in part to physico-chemical properties of the constituent aggregates and fillers.
- The rate of moisture absorption in asphalt mastics is significantly lower than the rate of moisture desorption. For most of the mastic studied, moisture absorption was about 80% recoverable.
- For moisture-conditioned asphalt mastics, the longer drying times the higher the stiffness. The results suggest that the degradation of mastic tensile properties associated with moisture absorption is partially recovered upon drying.
- The effect of moisture conditioning on mastics appears to be aggregate type dependent as higher degradation in stiffness response was observed in the granite mastics than in the limestone mastics.
- Tensile strength in moisture saturated mastics is generally lower than in drier samples and is largely recoverable upon specimen drying.
- The failure mode in all the mastics considered were ductile which suggests at the temperature and loading rate employed, the effect of moisture on failure mode is minimal.
- Aggregate type can accentuate the influence of moisture on tensile properties of asphalt mastics.
- Recovered tensile strength was higher and strain at peak strength significantly lower in granite mastics compared to limestone mastics under the conditions investigated in this study.

This study offers insight into the practical and measurable consequences to asphalt concrete caused by moisture damage and the often overlooked recoverable tensile properties associated with the phenomenon. The concept of recoverable tensile strength after a drying period maybe analogous to the micro-damage healing effect often associated with fatigue cracking models. Proper implementation of these concepts could offer important improvements to moisture damage models. Further studies aimed at understanding what factors influence reversible moisture-induced damage in asphalt mixtures is recommended.

ACKNOWLEDGEMENTS

The funding for this project was provided in part by the UK Engineering and Physical Sciences Research Council (EPSRC).

REFERENCES

[1] Airey, G.D. and Choi, Y.K. State of the Art Report on moisture sensitivity test methods for bituminous pavement materials. Road Materials and Pavement Design, Vol. 3, Issue 4, 2002, pp. 355–372.

[2] Arambula, E., Caro, S., and Masad, E. (2010). Experimental measurement and numerical simulation of water vapor diffusion through asphalt pavement materials. J. Mater. Civ. Eng., 22 (6), 588–598.
[3] Bhasin, A., Masad, E., Little, D., and Lytton, R. (2006). Limits on adhesive bond energy for improved resistance of hot-mix asphalt to moisture damage. Transportation research record: Journal of the Transportation Research Board TRR 1970: 3–13.
[4] Caro, S. et al., 2008. Moisture susceptibility of asphalt mixtures, part 1: mechanisms. International Journal of Pavement Engineering, 9 (2), 81–98.
[5] Grenfell, J.R.A., Ahmad, N., Liu, Y. Apeagyei, A.K., Airey, G.D., and Large, D. Application of surface free energy techniques to evaluate bitumen aggregate bonding strength and asphalt mixture moisture sensitivity. ICE Construction, 2013. In Press.
[6] Grenfell, J.R.A., Ahmad, N., Liu, Y. Apeagyei, A.K., Airey, G.D., and Large, D. Assessing asphalt mixture moisture susceptibility through intrinsic adhesion, bitumen stripping and mechanical damage. RMPD, 2013. In Press.
[7] Kringos, N., Scarpas, A., and Kasbergen, C. Three Dimensional Elasto-Visco-Plastic Finite Element Model for Combined Physical-Mechanical Moisture Induced Damage in Asphaltic Mixes. Journal of the Association of Asphalt Paving Technology, Vol. 76, 2007. pp. 495–524.
[8] Kringos, N., Scarpas, A., and deBondt, A. (2008a). Determination of moisture susceptibility of mastic-stone bond strength and comparison to thermodynamical properties. Journal of the Association of asphalt Paving Technology, Vol. 77. pp. 435–478.
[9] Kringos, N., Scarpas, A., Kasbergen, C., and Selvadurai, A.P.S. (2008b). Modelling of combined physical-mechanical moisture induced damage in asphalt mixes—Part 1: governing processes and formulations. International Journal of Pavement Engineering, 9 (2), 115–128.
[10] Vasconcelos, K.L., Bhasin, A., Little, D.N., and Lytton, R.L. (2011). Experimental measurement of water diffusion through fine aggregate mixtures. Journal of Materials in Civil Engineering Vol. 23 Issue 4, pp. 445–452.
[11] Crank, J. The mathematics of diffusion, 2nd ed.; Oxford University Press: New York, 1975; pp. 414.

Experimental characterization of asphaltic materials—II

This page intentionally left blank

Asphalt Pavements – Kim (Ed)
© 2014 Taylor & Francis Group, London, ISBN 978-1-138-02693-3

Triaxial Cyclic Compression Testing of hot mix asphalt with cyclic confining pressure

Bernhard Hofko, Markus Hospodka & Ronald Blab
Research Center of Road Engineering, Institute of Transportation, Vienna University of Technology, Vienna, Austria

ABSTRACT: Permanent deformation in terms of rutting is a major deterioration mode of bituminous bound pavements. The Triaxial Cyclic Compression Test (TCCT) is a scientifically accepted and standardized test method to assess the resistance to permanent deformation. In most cases, TCCT is carried out with cyclic axial loading and constant confining pressure. In road pavements dynamic traffic loading due to passing tires leads to dynamic confining pressures. Thus, to bring the TCCT closer to reality, within the study presented in this paper, the radial response and its phase lag to axial loading in standard TCCTs is measured and an enhanced TCCT with cyclic confining pressure which takes into account the viscoelastic material response in terms of radial phase lag to axial loading is introduced. In a subsequent test program TCCTs with various confining pressure amplitudes are run on an AC 11 70/100 and results from standard and enhanced TCCTs are analyzed and compared in terms of resistance to permanent deformation. It is shown that the resistance to permanent deformation increases significantly when the viscoelastic material response is taken into account in the TCCTs with cyclic confining pressure.

Keywords: triaxial testing; permanent deformation; viscoelasticity; hot mix asphalt; cyclic confining pressure

1 INTRODUCTION

Besides low-temperature and fatigue cracking, permanent deformation at elevated temperature is a third major distress mode of bituminous bound pavements. Permanent deformation or rutting occurs especially as transverse profile deformations within the wheel paths but can also be seen as longitudinal profile irregularities [1]. Rutting is an important deterioration mode since it affects the comfort and safety of road users. Thus, various test methods have been developed to address the permanent deformation behavior of Hot Mix Asphalt (HMA). A commonly used test method to assess the permanent deformation behavior of HMA is the Triaxial Cyclic Compression Test (TCCT) with a well-defined external stress state. Research in this field in the 1970s and 1980s [2–5] was a major source for developing a European standard for TCCTs EN 12697-25 [6]. Recent studies show the importance of taking into account triaxial behavior with confining pressure [7–12]. In the standard TCCT according to EN 12697-25 cylindrical specimens are stressed by a cyclic axial loading in the compressive domain to simulate traffic loading by passing tires. The axial loading can either be shaped as a sinusoidal function or a block-impulse. The confining pressure can either be held constant or cyclic without giving more specific information in the standard. However, most laboratories that have integrated the TCCT on HMA into their test procedures use constant confining pressure, especially since the test control gets even more complex with two independent cyclic loadings.

Research on TCCT with cyclic confining pressure was mainly carried out in the area of unbound granular materials [13–26]. While earlier studies [e.g. 14] did not find significant

differences in the deformation behavior of unbound material for tests with constant and cyclic confining pressure, more recent studies [e.g. 17] showed that differences in permanent deformation occur depending on the ratio of the axial and radial stress amplitude.

The main difference between testing of unbound granular materials and bituminous bound materials (e.g. HMA) is that due to the viscoelastic nature of bituminous bound materials the phase lag between axial loading and radial response ($\phi_{ax,rad}$) must be analyzed and used for cyclic confining pressure to address the viscoelastic material response correctly [18] showed by finite element simulation of a pavement under a passing tire that cyclic axial loading leads to cyclic radial confining pressure within the pavement structure. Thus, the present practice of testing HMA specimens with constant confining pressure is a simplification. Only a small number of studies that work with the TCCT on HMA [19,20] have been carried out with cyclic confining pressure. The mentioned studies set a constant phase lag between axial loading and radial response of 36° for all tested materials at all temperatures and frequencies. Knowing that HMA shows a temperature and frequency dependent viscoelastic behavior, it is questionable whether this constant radial phase lag is correct for all materials, temperatures and frequencies.

2 OBJECTIVES AND APPROACH

Since the standard TCCT with constant confining pressure does not represent the state of stress in a pavement structure and the phase lag between axial loading and radial response for TCCTs given in literature do not match the common understanding of the theory of viscoelasticity [21] that viscoelastic material properties change with temperature and frequency, the main objectives of this study are to measure the radial phase lag $\phi_{ax,rad}$ between axial loading and radial response accurately and to incorporate cyclic confining pressure with a well-defined phase lag $\phi_{ax,rad}$ to have a more realistic simulation in the TCCT. Results from TCCTs with constant and cyclic confining pressure shall be compared exemplarily for an AC 11 70/100. To reach the objectives, the following approach is taken:

- Carry out standard TCCTs with constant confining pressure, record and analyze the phase lag between axial loading and radial response $\phi_{ax,rad}$ with high precision.
- Use the obtained data for the radial phase lag in the further course to incorporate it in an enhanced TCCT with cyclic confining pressure that thus takes into account the viscoelastic material response.
- Carry out a test series with the enhanced TCCT with a variation of the amplitude of the cyclic confining pressure to study the impact of the stress deviator on the permanent deformation behavior.
- Analyze, compare and interpret results of standard and enhanced TCCTs exemplarily run on an AC 11 70/100.

Thus, the main goal of this study is to lay the basis for an improved test procedure to address the permanent deformation behavior of HMA. Different from former studies the test will incorporate the actual (measured) radial phase lag of the material to take into account the viscoelastic behavior of HMA. The test can be employed in the future for a more efficient and realistic mix design optimization.

3 TEST EQUIPMENT

The equipment employed for this study consists of:

- a test machine with two circuits, one hydraulic circuit for axial loading including a load cell and a pneumatically driven device for application of static and cyclic confining pressure including a pressure cell,
- a temperature chamber to control the test temperature,

- a triaxial cell, and
- displacement sensors to record axial and radial deformation.

To realize cyclic confining pressures at high frequencies (3 Hz), a new device (see Fig. 1) has been developed that based on pneumatics where compressed air is used to activate a stiff membrane. The membrane can be described as a high-end shock absorber also used in Heavy Goods Vehicles (HGVs). It works as a pressure transmitter since it is filled with water and connected to the triaxial cell. The actual control mechanism is a valve that controls the air pressure on the membrane. The more compressed air is put onto the membrane the more water is pressed into the cell. Since the cell is filled with water and the system is water-tight, the pressure within the cell is changed by the volume of water pressed into the cell from the membrane. The triaxial cell is equipped with a pressure gauge. The gauge not only records the pressure, it is also connected to the control unit of the test machine. The control unit drives the valve in the pneumatic device according to the signal of the gauge to reach the target pressure given by the user. An additional Linear Variable Differential Transducer (LVDT) below the membrane records the position of the membrane and is a safety device to keep the membrane within safe operation limits.

For the measurement of radial strain, strain gauges are attached directly to the surface of the specimens (see Fig. 2). One 150 mm strain gauge is laid tightly around the circumference at half height and glued at both of its ends to the specimen. Usually strain gauges are attached to an object over its complete length in order to transfer strain from the object in tension and compression. Since the stiffness of HMA specimens especially at elevated temperatures (in this case 50°C) is significantly lower than the stiffness of the adhesive, gluing the strain gauges over the complete length would prevent any deformation within this area. The method used in this study to attach only the end parts of the strain gauge to the

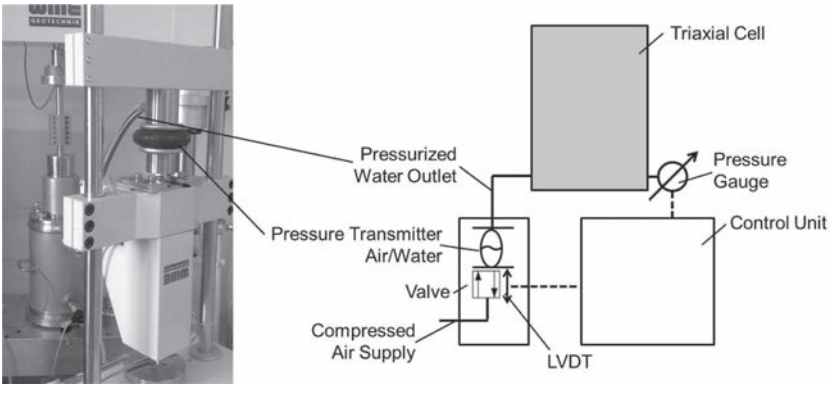

Figure 1. Principle of the pneumatic device to apply cyclic confining pressure.

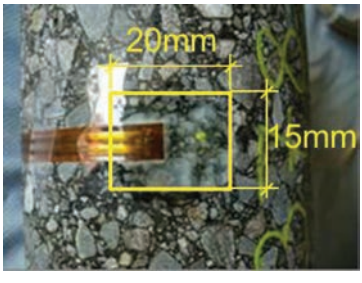

Figure 2. End of a strain gauge glued to an HMA specimen.

specimen is sufficient since radial deformation will only be positive in a purely compressive test. A study in [22] compares readings from strain gauges attached only at their end parts to readings from LVDTs and confirms correct measurements of strain gauges in the tensile domain. Figure 2 shows a detail of a strain gauge attached to an HMA specimen. The figure also contains information on the exact size (15 × 20 mm) of the glued area. To ensure that the glued area was the same for every specimen, the area was defined by marking its edges with adhesive tape prior to gluing the strain gauge.

4 MATERIALS AND TEST PROGRAM

4.1 *Materials*

For the present study an asphalt concrete with a maximum nominal aggregate size of 11 mm (AC 11) was used. The coarse aggregate used for the mixes is a porphyrite (specific gravity: 2830 kg/m³), the filler is powdered limestone (specific gravity: 2700 kg/m³). The binder is an unmodified bitumen 70/100 pen. The main characteristics of the binder are presented in the table in Figure 3. The optimum binder content according to Marshall is 5.3% by mass which was used for the mix. The target void content was set to 3.0% by volume. The grading curve is shown in Figure 3. The diagram also contains upper and lower limits for AC 11 mixes according to the national standard ON B 3580-1 [22]. The maximum density of the mix was determined to be 2564.0 kg/m³.

4.2 *Specimen preparation*

The complete process of specimen preparation from mixing and compaction to coring and cutting was carried out in accordance to the respective European Standards (EN). The mix was produced in a reverse-rotation compulsory mixer according to EN 12697-35 [24]. The mix drum as well as the mixing device are heated to ensure correct mix and compaction temperatures. Subsequent to the mixing process the material is compacted in a segment roller compactor according to EN 12697-33 [25]. Slabs compacted by the device have a base area of 50 × 26 cm and a variable height of up to 22 cm. The radius of the segment of 55 cm corresponds to the size of standard roller compactors used in the field.

The slabs were compacted to a target height of 13.0 cm in a displacement-controlled way. The complete slab was compacted in two layers hot on hot. Single-layered compaction leads to a large scatter of the density between upper and lower parts of the slab [26]. Since the maximum density is known as well as the target content of air voids, the target unit weight can be derived. The target unit weight and the target volume of the slab define the necessary mass of the material for compaction.

Parameter	70/100
Penetration [1/10 mm]	84
Ring and Ball [°C]	46.8
Fraass Braking Point [°C]	-17
SHRP PG [°C]	58-22
Mixing Temperature [°C]	160
Compaction Temperature [°C]	135 - 160

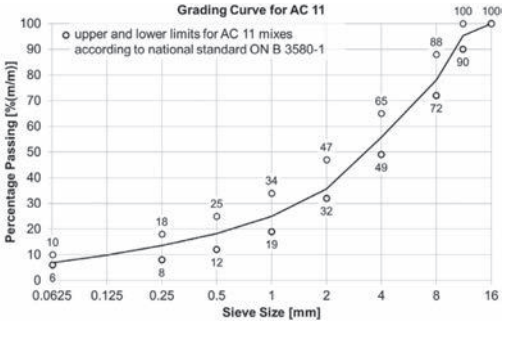

Figure 3. Main characteristics of the binder (left) and grading curve of AC 11 (right).

Table 1. Test program.

	Test conditions	$\sigma_{ax,l}$ [kPa]	$\sigma_{ax,u}$ [kPa]	$\sigma_{rad,l}$ [kPa]	$\sigma_{rad,u}$ [kPa]
Standard	50°C, 3 Hz, 25,000 load	150	750	150	150
Enhanced	cycles	150	750	150	250
		150	750	150	300
		150	750	150	350

From each slab, four specimens were cored out with a diameter of 100 mm. The obtained specimens were then cut to a height of 200 mm. Before the specimens were finally tested they were stored at the test temperature for at least 4 h but no longer than 7 h.

4.3 *Test program*

The test temperature was set to 50°C, the sinusoidal test frequency was set to 3 Hz. All tests were run for 25,000 load cycles. To introduce an enhanced TCCT with cyclic confining pressure, the radial phase lag $\phi_{ax,rad}$ between axial loading and radial deformation was determined in standard TCCTs. To study the impact of the amplitude of the confining pressure, enhanced TCCTs were carried out at three different amplitudes on three specimens for each amplitude. Table 1 shows the layout of the test program. The table presents the lower and upper value of the axial stress ($\sigma_{ax,l}$ and $\sigma_{ax,u}$) and the radial confining stress ($\sigma_{rad,l}$ and $\sigma_{rad,u}$). The lowest radial stress amplitude (i.e. the difference between upper and lower stress value) is 50 kPa, the other two are set to be 75 kPa and 100 kPa.

5 DATA EVALUATION

For the analysis of the periodic (sinusoidal) component of the test data a regression analysis was employed with the following function:

$$f(t) = a_1 + a_2 \cdot \sin(2\pi \cdot f \cdot t + a_3) + a_4 \cdot t \tag{1}$$

$f(t)$ Regression function of the periodic component of test data
a_1 Vertical offset of the regression function
a_2 Amplitude of the regression function
a_3 Phase lag of the regression function
a_4 Gradient of the linear term of the regression function
f Frequency [Hz]
t Time [s]

For the regression analysis the test data is split into individual sets of three oscillations. For each of these sets a regression analysis with the function shown above is carried out. The reason to take three oscillations for each analysis is to achieve a more robust and stable evaluation routine. The sum of square errors between test data and approximation function is aimed to become a minimum by systematically varying the parameters of the function. The quality of the approximation is described by the coefficient of determination R^2. If R^2 is below 0.95, the oscillation set is omitted from the subsequent data analysis since the deviation between approximation function and test data is considered too large. This regression is carried out for data from the axial load cell, the mean value of the two axial LDVTs, the data from the radial strain gauge and from the pressure cell recording confining pressure. The analytical functions of the periodic component are then used to calculate extreme values and from that the time lag between different sensor data to obtain phase lags between axial loading and radial deformation for all applied load cycles.

The non-periodic, axial deformation component for data from tests in the compressive domain can be described by a creep curve to assess the permanent deformation behavior.

To determine the permanent axial strain from the test data, the minimum axial strain value from the analysis of the periodic component of each load cycle is used to create the creep curve. Creep curves obtained from TCCTs according to EN 12697-25 can be divided into three different phases (Fig. 4):

- The primary phase (1): Within the first phase of a TCCT a certain amount of recompaction leads to decreasing slope of the curve with increasing number of load cycles.
- The secondary phase (2): The main phase of the TCCT is characterized by a quasi-constant slope of the curve.
- The third phase (3): Usually the standard TCCT does not reach this state where the deterioration of the specimen leads to an increase of the slope of the curve with increasing number of load cycles.

The axial strain is determined for the complete test and presented in a load-cycle-strain-diagram with linear scale for both axes. The secondary creep phase with a quasi-constant incline of the creep curve is approximated by the following linear function by using the method of least squares:

$$\varepsilon_{ax}(n) = A_1 + B_1 \cdot n \tag{2}$$

$\varepsilon_{ax}(n)$ Approximated function for permanent axial strain at the load cycle n [%]
A_1 Regression parameter describing the intersection of the approximation function with the y-axis (offset) [%]
B_1 Regression parameter describing the incline of the approximation function [%/load cycle]
n Load cycle

To define the secondary quasi-linear phase, the linear regression is used to approximate the creep curve starting between load cycles 1,000 and 20,000. If the coefficient of determination R^2 is below 0.98 for this range of load cycles, the lower load cycle limit for linear regression is increased in steps of 500 until R^2 is above 0.98. For all tests carried out in this study the load cycle range for the secondary phase was from load cycle 5,000 to 20,000.

The creep rate f_c is determined as the incline B_1 [%/load cycle] of the linear function in micrometers per meter (i.e. µstrain) per load cycle:

$$f_c = B_1 \cdot 10^4 \tag{3}$$

f_c is used to determine the resistance of a specimen to permanent deformation. The smaller its absolute value, the smaller is the increase of permanent deformation vs. load cycles.

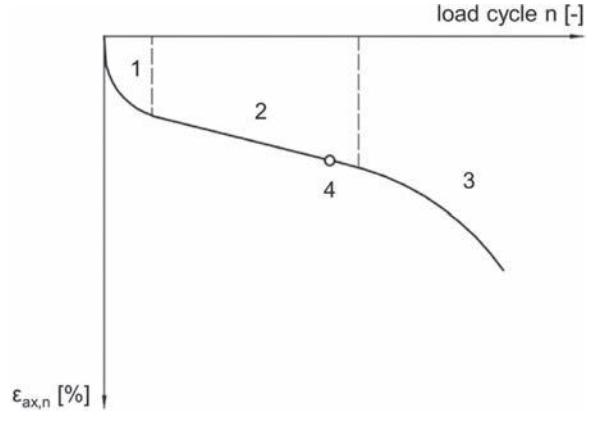

Figure 4. Example of a creep curve.

Thus, a smaller absolute value of f_c means that the resistance to permanent deformation is higher.

In addition the permanent deformation is also described by the total axial strain $\varepsilon_{ax,tot}$ after 10,000 load cycles. Since both, the axial and radial deformation is recorded for all tests, two strain components of the total axial strain, the volumetric and deviatoric strain component can be determined as follows: A cylindrical specimen shall have an initial height h_0, an initial diameter of d_0 and thus an initial volume of

$$V_0 = \frac{{d_0}^2 \pi}{4} \cdot h_0 \tag{4}$$

The change in height Δh_n and in diameter Δd_n with each load cycle n results in the volume

$$V(n) = \frac{\left(d_0 + \Delta d_n\right)^2 \pi}{4} \cdot \left(h_0 - \Delta h_n\right) \tag{5}$$

If the pure deviatoric part of the deformation (without any change in volume) shall be derived, $V(n)$ in the formula above has to be substituted by V_0 and solved for Δh_n which then becomes $\Delta h_{n,dev}$:

$$\Delta h_{n,dev}(n) = h_0 - \frac{V_0 \cdot 4}{\left(d_0 + \Delta d_n\right)^2 \cdot \pi} \tag{6}$$

This change in height can be converted to an axial strain component by dividing it by the initial height h_0. If the total axial strain is referred to as $\varepsilon_{ax,tot}$ then the deviatoric and volumetric strain component can be defined as follows:

$$\begin{aligned} \varepsilon_{ax,dev}(n) &= \frac{\Delta h_{n,dev}(n)}{h_0} \\ \varepsilon_{ax,vol}(n) &= \varepsilon_{ax,tot}(n) - \varepsilon_{ax,dev}(n) \end{aligned} \tag{7}$$

$\varepsilon_{ax,vol}$ volumetric part of the axial strain
$\varepsilon_{ax,dev}$ deviatoric part of the axial strain

6 RESULTS AND INTERPRETATION

6.1 *Analysis of phase lag $\phi_{ax,rad}$*

As a first step standard TCCTs with constant confining pressure were carried out on three specimens for the two mixes. Test data was evaluated in terms of phase lag $\phi_{ax,rad}$ between axial loading and radial deformation. Figure 8 presents an example of the evolution of $\phi_{ax,rad}$ vs. the number of load cycles for one specimen. For the evaluation of the phase lag, data from load cycle 500 on were considered since there is a strong change in the phase lag within the first 500 load cycles due to recompaction in the first phase of a TCCT. The grey lines show the actual test data, the black line the mean value of all data and the dashed black lines the 95% confidence interval. The confidence interval shows a scattering of around 6°.

For the further evaluation of $\phi_{ax,rad}$, data from the three single standard TCCTs were merged and statistically analyzed. Table 3 shows mean values of of $\phi_{ax,rad}$ as well as the 2.5% and 97.5% quantiles. The scattering of $\phi_{ax,rad}$ in terms of the 95% confidence interval is 12.8° for the tested mix AC 11 70/10. The mean value of $\phi_{ax,rad}$ serve as input values for the enhanced TCCTs to set the phase lag between axial loading and radial confining pressure and thus take into account the viscoelastic material response in the enhanced TCCT.

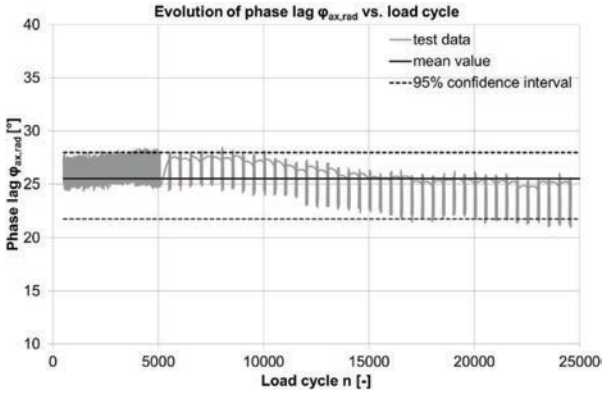

Figure 5. Evolution of phase lag between axial loading and radial deformation $\phi_{ax,rad}$ vs. number of load cycles for one specimen in standard TCCT (T_{test} = 50°C, f = 3 Hz, $\sigma_{ax,l}$ = 150 kPa, $\sigma_{ax,u}$ = 750 kPa, $\sigma_{rad,l} = \sigma_{rad,u}$ = 150 kPa).

Table 2. Phase lag $\phi_{ax,rad}$ derived from standard TCCTs (T_{test} = 50°C, f = 3 Hz, $\sigma_{ax,l}$ = 150 kPa, $\sigma_{ax,u}$ = 750 kPa, $\sigma_{rad,l} = \sigma_{rad,u}$ = 150 kPa).

	AC 11 70/100
2.5% quantile	14.8°
Mean value of 3 samples	21.2°
97.5% quantile	27.6°

6.2 *Analysis of TCCTs with cyclic confining pressure*

Figure 9 gives an example of the recorded test data from an enhanced TCCT. It shows 3 oscillations of the axial stress on the top, the confining pressure in the middle and the resulting radial deformation on the bottom. The solid vertical line indicates a minimum of the axial loading, and the dashed line a minimum of the confining pressure. This demonstrates that the test machine is working correctly and the confining pressure actually lags behind the axial loading as set by the user. The extreme values of the confining pressure also coincide with the extreme values of the radial deformation. This shows that the chosen phase lag for the confining pressure taken from standard TCCTs is correct and accounts for the viscoelastic material response.

For the employed mix, three specimens were tested at each test condition. The air void content of the successfully tested specimens is listed in Table 3.

All tests were run at 50°C and 3 Hz for 25,000 load cycles and an axial stress amplitude of 150 kPa to 750 kPa. Different from the standard TCCT according to EN 12697-25 the radial stress amplitude is varied in three ranges. The test procedure starts from a hydrostatic state of stress on the low level where both the radial and axial stress are at the same level at 150 kPa. This pre-loading phase is held constant for 120 s. Then, the axial sinusoidal loading starts and with a well-defined time lag (i.e. the phase lag $\phi_{ax,rad}$) the confining pressure starts to oscillate sinusoidally as well. The stress applied to the specimen for each point in time t can be given as:

$$\sigma_{dev}(t) = \sigma_{ax,m} + \sigma_{ax,a} \cdot \sin(2\pi t) - [\sigma_{rad,m} + \sigma_{rad,a} \cdot \sin(2\pi t - \varphi_{ax,rad})] \quad (8)$$

σ_{dev} Stress deviator
$\sigma_{ax,m}$ Mean axial stress

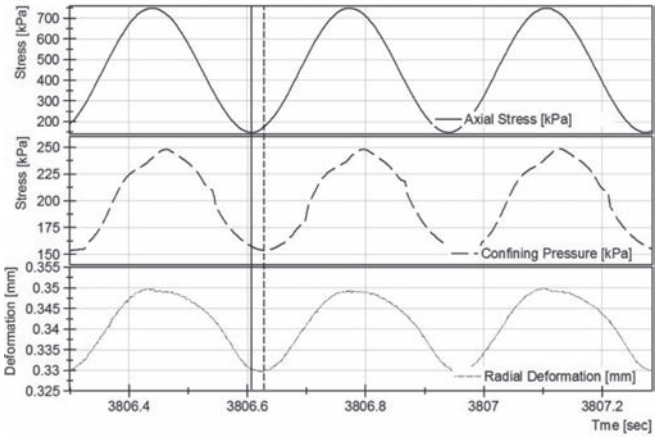

Figure 6. Example of recorded test data from enhanced TCCT for one specimen with cyclic confining pressure (T_{test} = 50°C, f = 3 Hz, $\sigma_{ax,l}$ = 150 kPa, $\sigma_{ax,u}$ = 750 kPa, $\sigma_{rad,l}$ = 150 kPa, $\sigma_{rad,u}$ = 250 kPa).

Table 3. Air void content [% by volume] of all successfully tested specimens.

	Radial stress levels ($\sigma_{rad,l} - \sigma_{rad,u}$) [kPa]			
AC 11 70/100	150–150	150–250	150–300	150–350
Specimen #1	3.2	3.3	2.7	3.5
Specimen #2	2.8	2.7	–	3.0
Specimen #3	2.7	2.9	–	–
Mean value	2.9	3.0	2.7	3.3
Standard deviation	0.3	0.3	–	0.4

$\sigma_{ax,a}$ Axial stress amplitude
$\sigma_{rad,m}$ Mean radial stress
$\sigma_{rad,a}$ Radial stress amplitude

The expression above is also valid for standard TCCTs where the mean radial stress is set to 150 kPa and the radial stress amplitude is set to 0. One objective of the following investigation is to compare results from standard and enhanced TCCTs. To carry out this investigation, the stress applied on the specimen within one load cycle must be calculated to be able to compare different test conditions. Thus, equation (8) can be integrated over one oscillation period $T_p = 2\pi/f$, or since all tests were run at the same frequency over 2π. This number is equal to an impetus and is independent of the radial phase lag $\phi_{ax,rad}$. For the lowest radial stress amplitude from 150 kPa to 250 kPa a value of 500π results from the integration, for the medium amplitude of 450π and for the highest amplitude of 400π. The value for the standard TCCT with constant confining pressure is 600π.

For the enhanced TCCTs the phase lag between axial loading and radial confining pressure was set according to the results from standard TCCTs listed in Table 2. To check how well the given phase lag was controlled by the test machine throughout the test, the actual phase lag between axial loading and confining pressure was analyzed with regard to the time shift between both signals for each test and load cycle. Figure 7 shows these results for the three different test conditions. The diagrams show the mean value as well as the 95% confidence interval (light grey bar 2.5% quantile to MV, dark grey bar MV to 97.5% quantile) of the deviations between given and actual phase lag. At the lowest radial stress amplitude (Fig. 7 a)) all specimens were tested successfully. The worst deviation between given and actual phase lag is 9.6° or 5.3% (the basis is 180°). 97.5% of the test data show a lower deviation. At the

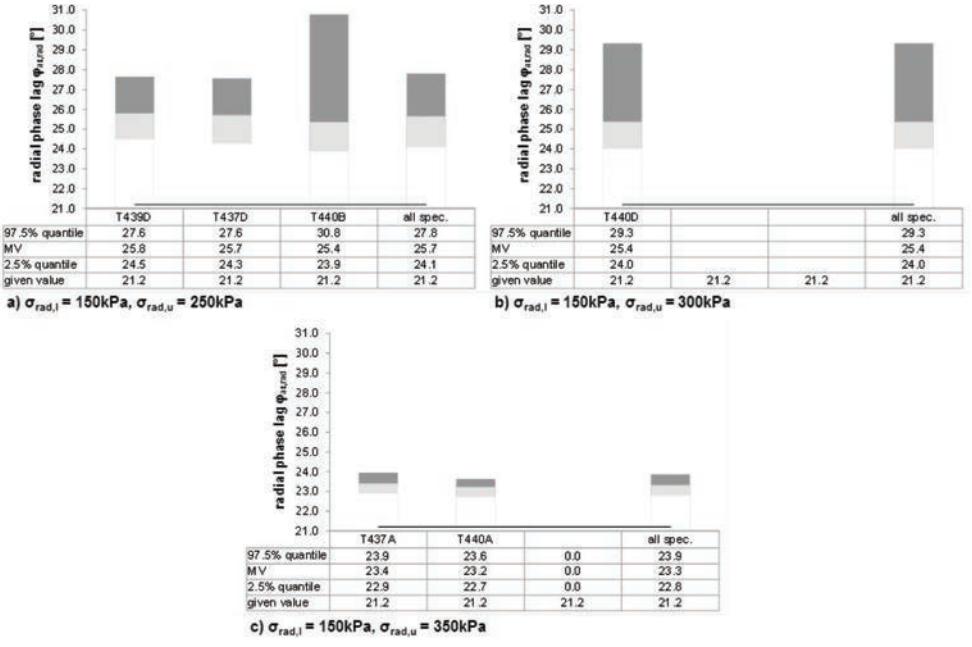

	T439D	T437D	T440B	all spec.
97.5% quantile	27.6	27.6	30.8	27.8
MV	25.8	25.7	25.4	25.7
2.5% quantile	24.5	24.3	23.9	24.1
given value	21.2	21.2	21.2	21.2

a) $\sigma_{rad,l}$ = 150kPa, $\sigma_{rad,u}$ = 250kPa

	T440D			all spec.
97.5% quantile	29.3			29.3
MV	25.4			25.4
2.5% quantile	24.0			24.0
given value	21.2	21.2	21.2	21.2

b) $\sigma_{rad,l}$ = 150kPa, $\sigma_{rad,u}$ = 300kPa

	T437A	T440A		all spec.
97.5% quantile	23.9	23.6	0.0	23.9
MV	23.4	23.2	0.0	23.3
2.5% quantile	22.9	22.7	0.0	22.8
given value	21.2	21.2	21.2	21.2

c) $\sigma_{rad,l}$ = 150kPa, $\sigma_{rad,u}$ = 350kPa

Figure 7. Phase lag between axial loading and radial confining pressure induced by the test machine vs. given value from the standard TCCTs with a confining pressure of 150 to 250 kPa (a), 150 to 300 kPa (b) and 150 to 350 kPa (c), (T_{test} = 50°C, f = 3 Hz, $\sigma_{ax,l}$ = 150 kPa, $\sigma_{ax,u}$ = 750 kPa).

second amplitude (150 kPa to 300 kPa, Fig. 7 b)) only one out of three tests ran successfully. The maximum deviation is similar to the tests with the lowest amplitude. Since the deviations were higher than expected, the test machine was optimized once more by adapting the PID (Proportional-Integral-Derivative) control of the pneumatic device responsible for the confining pressure. After this optimization the test series was continued. For the largest radial amplitude (150 kPa to 350 kPa, Fig. 7 c)) two specimens were tested successfully. The error of the actual to the given radial phase lag is below 2.7° or 1.5% in 97.5 out of 100 cases.

For the further analysis, it is of great interest, how the different radial amplitudes affect the results of TCCTs in terms of resistance to permanent deformation and if there are any differences between standard and enhanced TCCTs. For this reason, a number of diagrams compare the stress deviator to various parameters which describe the deformation behavior. The stress deviator multiplied by π is congruent to the impetus put into the specimen at each load cycle and thus a proper parameter to compare different test conditions. Each diagram in Figures 8 and 9 contains data from each single enhanced TCCT, highlighted in grey together with a linear regression. In addition, a 95% confidence interval was place around the linear regression. The confidence interval was derived by computing the relative error RE between each data point and the linear regression. In the following, the 2.5% and 97.5% quantiles were obtained for this relative error. These quantile values were then used to create the two confidence interval lines from the linear regression as follows:

$$f(x) = (a \cdot x + b) \cdot (1 + RE_{2.5\%})$$
$$f(x) = (a \cdot x + b) \cdot (1 + RE_{97.5\%}) \quad (9)$$

a slope of the linear regression
b Y-intercept of the linear regression
$RE_{2.5\%}$ 2.5% quantile of the relative error
$RE_{97.5\%}$ 97.5% quantile of the relative error

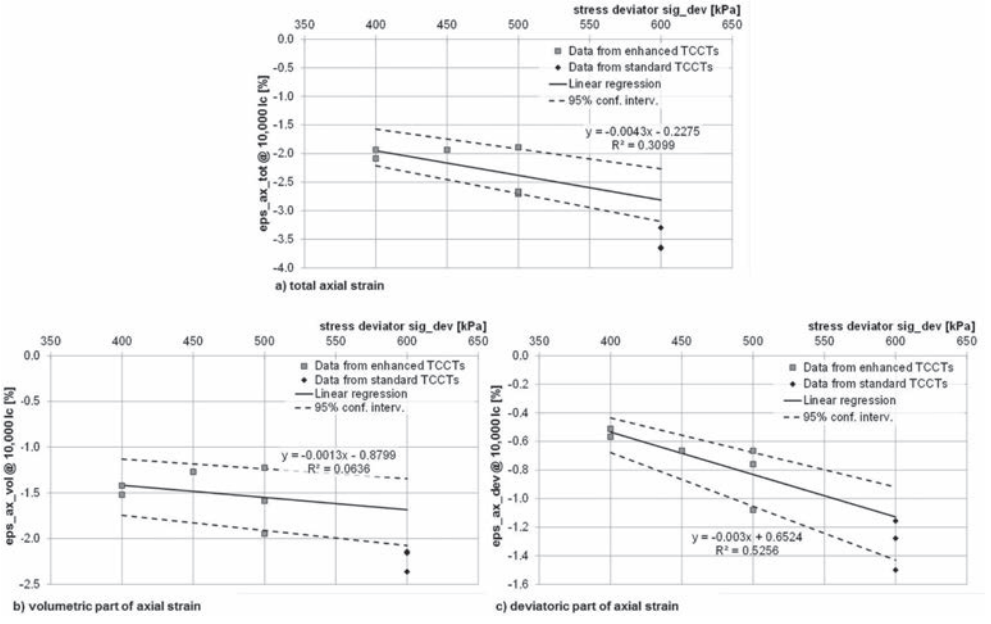

Figure 8. Total axial strain (a), volumetric axial strain (b) and deviatoric axial strain (c) at load cycle 10,000 in % at different stress deviators from standard and enhanced TCCTs (T_{test} = 50°C, f = 3 Hz).

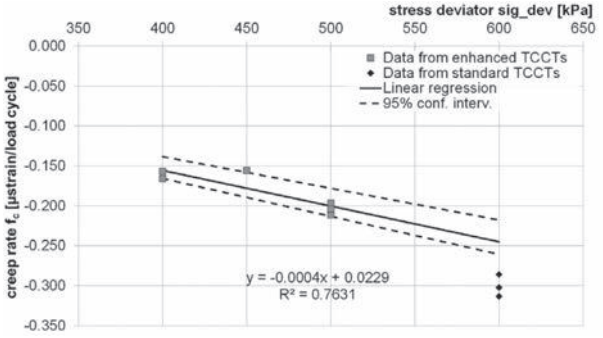

Figure 9. Creep rate f_c in µstrain/load cycle at different stress deviators from standard and enhanced TCCTs (T_{test} = 50°C, f = 3 Hz).

Data from standard TCCTs are also shown in the diagrams marked in black to compare enhanced TCCT to standard TCCT results.

Figure 8 shows a compilation of all test results from enhanced TCCTs in terms of axial strain at load cycle 10,000 vs. the stress deviator. Figure 8 a) shows the total axial strain. There is a decreasing trend with increasing stress deviator showing that a higher stress level leads to more deformation. Although the 95% confidence interval is quite large, the standard TCCT results in significantly more total axial strain (–3.5% vs. –2.8% from enhanced TCCTs) at comparable stress levels. Thus, specimens tested in the standard TCCT setup suffer 25% more axial strain than those tested under enhanced conditions at comparable stresses. This benefit of the enhanced TCCT can be explained by the fact that the viscoelastic material response of the material is taken into account by the radial phase lag. When the volumetric and deviatoric part of the axial strain are taken into consideration, it can be analyzed which strain component is affected by taking into consideration the viscoelastic material response.

Figure 8 b) and c) present the situation for the volumetric and deviatoric part of the axial strain. The scatter of results is quite large. It seems that the axial volumetric strain hardly depends on the stress level. This may be due to the high degree of compaction (3.0% by volume voids). The standard TCCTs (MV of $\varepsilon_{ax,vol}$ –2.2%) results in 32% more volumetric deformation than the prediction from enhanced TCCTs (–1.7%). From Figure 8 c) it is clear that the impact of the stress deviator on the deviatoric strain component is more significant. The standard TCCT results in a MV of $\varepsilon_{ax,dev}$ of –1.7% compared to a value of –1.3% from enhanced TCCT at the same stress level. The material exhibits 21% less deviatoric strain when tested with the enhanced test setup. It can therefore be stated that this mix reacts in a positive way (i.e. shows a better resistance to permanent deformation) when the viscoelastic material response is taken into account.

The same analysis is also provided for the creep rate f_c in Figure 9. The situation here is more significant since the scatter of results is less severe. The creep rate decreases with increasing stress deviator, showing—analogue to the total axial strain—that the material exhibits more permanent deformation when the stress level is increased. Again, it is obvious that the material contains a potential of better resistance to permanent deformation when the viscoelastic material response is considered in the TCCT. For the creep rate, standard TCCTs result in a MV of –0.301 µstrain/load cycle, enhanced TCCTs at the same stress level in a MV of –0.245 µstrain/load cycle (–19%).

7 SUMMARY AND OUTLOOK

Within the study presented in this paper cyclic confining pressure was introduced into the TCCT to simulate the state of stress that occurs in the field in a more realistic way. The results of standard and enhanced TCCTs are compared and interpreted. The main findings are summarized below:

- The pneumatic device developed for TCCTs with cyclic confining pressure was successfully employed in the study for the first time. After preliminary problems with the control of the target phase lag between axial loading and confining pressure (deviations of up to 9.6° between given and actual phase lag), a second optimization of the device was carried out. After that the error of the actual to given phase lag was around or below 4°. This is satisfactory when it is kept in mind that a scattering of $\phi_{ax,rad}$ of around 6° occurs when measured on specimens in standard TCCTs.
- An AC 11 70/100 was tested to show the impact of cyclic confining pressure with radial phase lag exemplarily. The total axial strain $\varepsilon_{ax,tot}$ after 10,000 load cycles decreases when the enhanced TCCT is compared to the standard TCCT with constant confining pressure at comparable stress levels. The tested mix suffers from 25% more axial strain in the standard TCCT.
- The volumetric strain component $\varepsilon_{ax,vol}$ is 32% higher in the standard TCCT and the deviatoric strain component $\varepsilon_{ax,dev}$ 21% higher in the standard TCCT. These findings can be explained by the fact that the viscoelastic material response is taken into consideration in the enhanced TCCT. This means that the maximum confining pressure is activated at the point of maximum radial deformation. Thus, the deviatoric strain component, which is the component responsible for changes in the shape of a specimen, decreases.
- The creep rate f_c is the benchmark parameter for the assessment of the resistance to permanent deformation in the European standard for production classification of HMA. The quality of a mix is defined by classes of the creep rate ($0.0 \le f_c < 0.2$, $0.2 \le f_c < 0.4$, $0.4 \le f_c < 0.6$, …). f_c decreased when specimens were tested in the enhanced TCCT. The tested mix shows a 19% lower creep rate compared to standard TCCT results.

Since only one mix was tested so far for this study, the significance of the findings is limited. Still, the potential of enhancing the TCCT not only by introducing cyclic confining pressure but especially by taking into consideration the viscoelastic material response with the radial phase lag $\phi_{ax,rad}$ for the cyclic confining pressure could be shown by the investigation.

Specimens tested in the enhanced TCCTs show a significantly higher resistance to permanent deformation. To create more findings and put the presented conclusions on a stronger basis, a future test program will take into account a variation of void content, gradation type and binder type and content of mixes. By expanding the test program, a sensitivity analysis will be carried out to quantify the impact of different mix design parameters on the ratio of results from standard vs. enhanced TCCT. Since the enhanced TCCT takes into account the viscoelastic material response and thus can be expected to simulate the field performance in a more realistic way, the larger test program will provide information on which mix design parameters have the largest impact on the performance and need to be taken into consideration for efficient mix design optimization.

REFERENCES

[1] Verstraeten, J. Bituminous material with a high resistance to flow rutting, Proceedings of PIARC (Permanent International Association of Road Congresses), Technical committee on Flexible Roads, Belgium, 1995.

[2] Francken, L. Permanent deformation law of bituminous road mixtures in repeated triaxial compression, Proceedings of the 4th International Conference on Asphalt Pavements, Ann Arbor, 1977.

[3] Jaeger, W. Mechanisches Verhalten von Asphaltprobekoerpern (in German), Publication of the Institute for Road And Railway Engineering, University of Karlsruhe, Germany, 1980.

[4] Krass, K. Kriechverhalten an zylindrischen Asphaltprobekoerpern (in German), Publication of the Institute for Road And Railway Engineering, University of Karlsruhe, Germany, 1971.

[5] Weiland, N. Verformungsverhalten von Asphaltprobekörpern unter dynamischer Belastung (in German), Publication of the Institute for Road And Railway Engineering, University of Karlsruhe, Germany, 1986.

[6] EN 12697-25. Bituminous mixtures—Test methods for hot mix asphalt—Part 25: Cyclic compression test, European Standardization Committee, 2005.

[7] Clec'h, P., Sauzeat, C., and Di Benedetto, H. Multidirectional behavior of bituminous mixture, Proceedings of Bearing Capacity of Roads, Railways and Airfields, Chicago, IL, 2009.

[8] De Visscher, J., Maeck, J., and Vanelstraete, A. The permanent deformation law of asphalt mixtures: Investigation of the effect of mix composition and material properties. Proceedings of the 10th International Conference on Asphalt Pavements, Quebec, Canada, 2006.

[9] Ebels, L., and Jenkings, K. Determination of material properties of bitumen stabilized materials using tri-axial testing, Proceedings of the 10th International Conference on Structural Design of Asphalt Pavements, Quebec, Canada, 2006.

[10] Hofko, B., and Blab, R. Assessment of Permanent Deformation Behavior of Asphalt Concrete by Improved Triaxial Cyclic Compression Testing, Proceedings of the 11th International Conference on Asphalt Pavements, Nagoya, Japan, 2010.

[11] Taherkhani, H., and Collop, A. Compressive axial and triaxial testing of asphaltic mixtures, Proceedings of the 10th International Conference on Asphalt Pavements, Quebec, Canada, 2006.

[12] Song, J. and Pellinen, T. Dilatation Behavior of Hot Mix Asphalt under Triaxial Loading, International Journal of Road Materials and Pavement Design, Vol. 8, No. 1/2007.

[13] Allen, J.J., and Thompson, M.R. Resilient Response of Granual Materials Subjected to Time-Dependent Lateral Stresses, Transport Research Record, 510:1–13, 1974.

[14] Brown, S.F., and Hyde, A.F.L. Significance of Cyclic Confining Stress in Repeated-load Triaixal Testing of Granual Material, Transport Research Record, 537:49–58, 1975.

[15] Nataatmadia, A., and Parkin, A.K. Characterization of Granual Materials for Pavements, Canadian Geotechnical Journal, 26:725–730, 1989.

[16] Zaman, D., Chen and Laguros, J. Resilient Moduli of Granular Materials, Journal of Transportation Engineering, 120(6):967–988, 1994.

[17] Rondón, H.A., Wichtmann, T., Triantafyllidis, T., and Lizcano, A. Comparison of cyclic triaxial behavior of unbound granular material under constant and variable confining pressure, Journal of Transport Engineering, 135(7):467–478, 2009.

[18] Kappl, K. Development of New Test Methods by Modeling Traffic Load with FEM, Presentation at the Evaluation of the Christian Doppler Laboratory for Performance Based Optimization of Hot Mix Asphalt, Vienna, Austria, 2004.

[19] von der Decken, S. Triaxialversuch mit schwellendem Axial- und Radialdruck zur Untersuchung des Verformungswiderstands von Asphalten (in German). Publication of the Institute for Road Engineering, University of Brunswick, Germany, 1997.
[20] Weise, C., and Wellner, F. Determination of the Fatigue Behavior of Asphalt Mixes with the Triaxial Test, Proceedings of the 4th Euroasphalt and Eurobitume Congress, Copenhagen, Denmark, 2008.
[21] Findley, W.N., Lai, J.S.Y., and Onaran, K. Creep and Relaxation of Nonlinear Viscoelastic Materials, Mineola, US: Dover Publications Inc., 1989.
[22] Hofko, B. Hot Mix Asphalt under Cyclic Compressive Loading, Südwestdeutscher Verlag für Hochschulschriften, Saarbrücken, Germany, ISBN: 978-3-8381-3298-3, 2012.
[23] ON B 3580-1. Bituminous mixtures—Material specifications—Part 1: Asphalt Concrete—Rules for the implementation of ONORM EN 13108-1, Austrian Institute of Standardization, Vienna, Austria, 2009.
[24] EN 12697-35. Bituminous mixtures—Test methods for hot mix asphalt—Part 35: Laboratory mixing, European Standardization Committee, 2007.
[25] EN 12697-33. Bituminous mixtures—Test methods for hot mix asphalt—Part 33: Specimen prepared by roller compactor, European Standardization Committee, 2007.
[26] Hoeflinger, G. Untersuchungen zur Probekoerperherstellung von Walzasphalten mit dem Walzsegmentverdichter (in German), Master Thesis, Vienna University of Technology, Vienna, 2006.

Asphalt Pavements – Kim (Ed)
© 2014 Taylor & Francis Group, London, ISBN 978-1-138-02693-3

Impact of field ageing on low-temperature performance of binder and hot mix asphalt

Bernhard Hofko, Markus Hospodka, Ronald Blab & Lukas Eberhardsteiner
Research Center of Road Engineering, Institute of Transportation, Vienna University of Technology, Vienna, Austria

Josef Füssl
Institute for Mechanics of Materials and Structures, Vienna University of Technology, Vienna, Austria

Hinrich Grothe & Florian Handle
Institute of Material Chemistry, Vienna University of Technology, Vienna, Austria

ABSTRACT: To monitor field ageing of bitumen and hot mix asphalt closely, a test field has been constructed in September 2012. The test field consists of two mixes, an asphalt concrete with 11 mm maximum nominal aggregate size (AC 11) with an unmodified 70/100 pen and an SBS-modified PmB 45/80-65. Pavement temperature and weather conditions are recorded continuously. First HMA samples were taken from the test field after 6 and 12 months. The low-temperature performance by cooling (TSRST) and Tensile Strength Testing (UTST), as well as the viscoelastic behavior (dynamic modulus |E*| and phase lag φ) with temperature and frequency sweep are obtained. Results from unaged and field-aged specimens are compared. In addition, bitumen was extracted and recovered from HMA slabs to investigate field ageing. Penetration, Softening Point Ring & Ball, DSR tests with temperature and frequency sweep and BBR tests were run on fresh binder, lab-aged and field-aged samples.

This paper analyzes first data on the low-temperature behavior of binder and mixes. Significant differences start to occur after 12 months of field ageing on mix and binder level. A slight but non-significant adverse impact of double heating of the mix was found on the low-temperature behavior. Direct comparison of unmodified and SBS-modified mixes shows a 90% higher resistance to thermal cracking for the modified mix.

Keywords: field ageing; hot mix asphalt; performance based testing; low-temperature performance; master curve

1 INTRODUCTION

Bitumen as an organic material is subject to ageing due to thermal and atmospheric influences. When bitumen is used as a binder for hot mix asphalt as a paving material, its ageing can be divided into (a) short-term ageing during the mixing, transportation and compaction at the construction site and (b) long-term ageing in the field [1]. While short-term ageing is mostly affected by high temperatures during mix production within several minutes to hours, long-term ageing is a slow process taking several years. Ageing of bitumen leads to increased stiffness and brittleness of the material and has a major impact on the durability of pavement structures [2, 3]. Especially the low-temperature resistance to thermal cracking is reduced by bitumen ageing [4, 5].

While the process of short-term ageing of bitumen is well explained in literature by loss of volatiles and oxidation due to high temperatures and a large specific surface of the material while mixing [6], the mechanisms of long-term ageing are still subject to scientific

discussion [7–10]. The chemical mechanisms are not thoroughly understood yet and the influence of different possible ageing agents available in the atmosphere (e.g. oxygen, UV radiation, ozone, aqueous solutions) are not clear [11, 12].

Analogue uncertainties can be stated for lab methods to simulate ageing of bitumen and mixes. While the Rolling Thin Film Oven Test (RTFOT) is commonly used and seen as a capable tool to realistically simulate short-term ageing of bitumen, the Pressure Ageing Vessel (PAV) is also commonly used, but the question whether it simulates 1 year, 3 years or 5 to 10 years of field ageing has not been answered clearly [13–16]. Or rather, it depends strongly on bitumen, mix and location of the field ageing whether the PAV represents several months or several years of field aging. When it comes to methods to simulate ageing of HMA in the lab, various methods have been developed [17–20]. In all of them HMA specimens are stored at significantly higher temperatures than in the field to accelerate ageing. It is questionable from a chemical point of view whether the processes activated at elevated temperatures are the same as the processes occurring in field ageing.

Thus, a detailed investigation and long-term study of field ageing of HMA and bitumen is necessary to increase knowledge on the chemical processes and mechanical changes in binder and mix during field ageing, understand ageing mechanisms and improve existing methods to simulate long-term ageing of binder and mixes.

2 OBJECTIVES AND APPROACH

Since there is only a minor number of studies monitoring field ageing of bitumen and asphalt mixes over an extended period of time with short intervals between testing, the following objectives are aimed for in the on-going study of a test field laid in September 2012:

- Investigate the change in performance of binders and asphalt mixes due to field ageing versus time and depth (distance to the pavement surface)
- Link changes in the performance of bitumen due to ageing to changes in the performance of asphalt mixes
- Analyze the differences in ageing of unmodified and polymer-modified (styrene-butadiene-styrene SBS) binders
- Understand ageing mechanisms better by combining mechanical and chemical testing as well as multi-scale modeling
- Analyze the effect of winter maintenance (de-icing by applying NaCl) on ageing
- Employ results of the comprehensive investigations to optimize methods to simulate short- and long-term field ageing of binder and asphalt mixes in the lab.

To achieve these goals, the following approach is taken:

- Build a test field consisting of HMA slabs made from unmodified and SBS-modified binder.
- Install a weather station to monitor the most important meteorological data and thermal couples in various depths within the HMA slabs to monitor pavement temperature.
- Take slabs from the test field at predefined dates after construction. Cut and core HMA specimens from the slab to investigate mix performance. Extract binder from the mix to investigate binder performance by means of mechanical and chemical analysis.

This paper discusses first analyses on the effect of field ageing on the low-temperature performance of HMA with unmodified and SBS-modified binder, as well as the extracted binders themselves after 6 and 12 months of field ageing.

3 MATERIALS AND TEST PROGRAM

3.1 *Materials*

For the test field, two binders were used: An unmodified 70/100 pen (PG 58-22) and an SBS-modified PmB 45/80-65 (PG 76-22). To ensure comparability of the binders, the 70/100 pen

was the source for producing the PmB. The main characteristics of both binders are listed in Table 1.

An asphalt concrete with a maximum nominal aggregate size of 11 mm (AC 11) was used for the test field. The coarse aggregate used for the mix is a porphyrite, the filler is powdered limestone. The binder content was set to 5.4% by mass with a target void content of 7.0% by volume. The maximum density of the AC 11 70/100 was determined to be 2.594 kg/m³ and 2.566 kg/m³ for the AC 11 PmB 45/80-65. The grading curve is shown in Figure 1.

The mix for the test field was prepared in a commercial mixing plant with mixing temperatures of 160°C for the unmodified mix and 185°C for the modified mix, filled into bags of 25 kg and stored in the lab. In addition, samples of the fresh binders and the aggregates used for the mix were also taken and stored in the lab.

3.2 *Preparation of HMA slabs for the test field*

The test field consists of 72 single HMA slabs compacted in the lab. The reason for using lab compacted slabs instead of one uniformly compacted pavement prepared by a commercial compactor is mainly because a substantial amount (30 to 130 kg) of asphalt mix is taken every 3 to 6 months from the test field to monitor field ageing closely. Removing slabs from the test field is more efficient than taking up to 32 cores every 3 months.

For the preparation of the slabs, the plant-produced mix was pre-heated for 5 hours and compacted in a roller compactor according to EN 12697-33 [21] to slabs with dimensions $50 \times 26 \times 10$ cm. The radius of the roller segment of 55 cm corresponds to the size of standard roller compactors used in the field. The slabs were compacted with one lift.

3.3 *Test field*

The test field is located in Vienna, Austria (coordinates: 48.189866, 16.394048). The field can be divided into four parts: one section consists of AC 11 70/100, the other section of AC 11 PmB 45/80-65. In each of these sections, winter maintenance is simulated on one subsection by removing snow and spraying a 20% by mass NaCl brine on as needed. The other subsection is only taken care of in winter by removing any snow from the surface.

Table 1. Main characteristics (mean values) of binders.

Parameter	70/100 pen
Penetration [1/10 mm]	90.9
Softening point ring & ball [°C]	46.7
SHRP PG [°C]	58-22

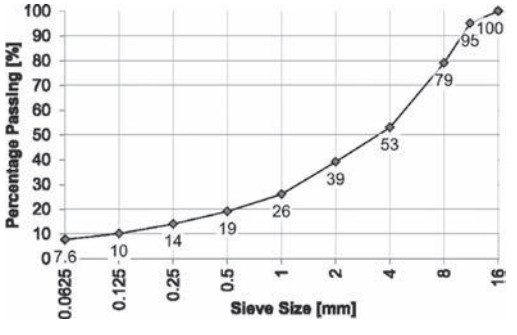

Figure 1. Grading curve of AC 11.

An aerial view of the test field is depicted in Figure 2a. Figure 2b shows a cross section of the test field. The slabs were laid on a drainage with a slope of 3%. The 1.0 cm joints between the slabs were filled with fine aggregates 0/2 mm and the joints were sealed by using hard bitumen 90/10 (5–15 1/10 mm penetration; 85°C–95°C softening point). Two slabs were instrumented with thermo couples in various pavement depths to monitor surface and pavement temperatures. One slab is situated in the section with winter maintenance, the other one in the section without winter maintenance. Figure 2c shows a profile of a slab with the position of the five thermo couples: One was situated in a groove on top of the slab and sealed with bitumen, the other four were put in depths of 1.25 cm, 3.75 cm, 6.25 cm and 8.75 cm. In addition a weather station in the vicinity of the test field records air temperature, humidity, precipitation, wind speed and direction and global solar radiation. All instruments record data with a rate of 6 values per hour (every 10 min).

As it can be seen from Figure 3 the test field is located on a non-trafficked part of the laboratory side. This means that the HMA is only exposed to loading due to weather and climate

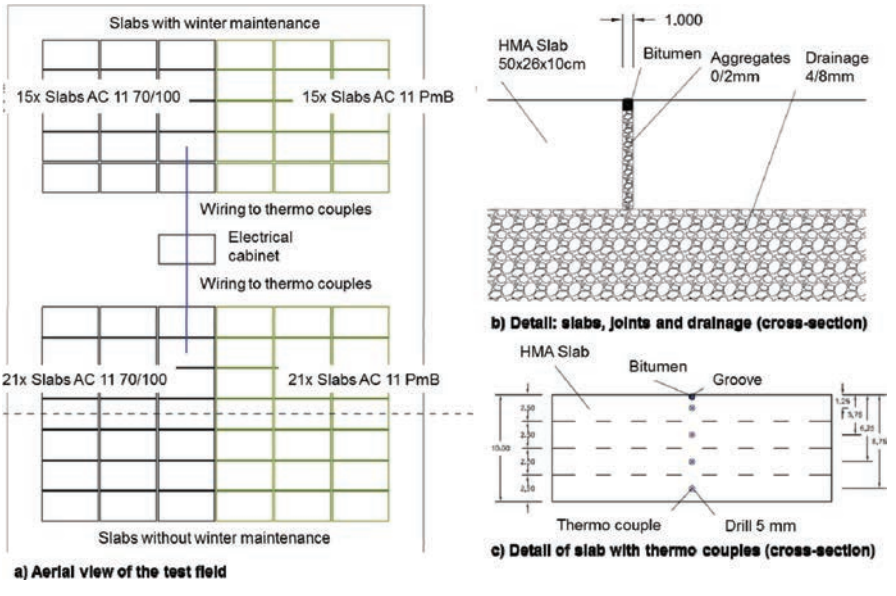

Figure 2. Details of the test field: a) aerial view, b) detail of slabs, joints and drainage, c) detail of instrumentation.

Figure 3. Photo of the test field with winter maintenance section (left), electric cabinet (center) and section without winter maintenance (right).

and no traffic loading or emissions from traffic are considered. Since the common understanding [6, 22] is that mainly climatic conditions (temperature, humidity, UV radiation) are responsible for bitumen ageing in the field, the lack of traffic on the test field is a minor setback. All slabs for the test field were produced in the lab in August and early September 2012 and the test field was laid on September 18th 2012. By June 2014 the test field will have been aged for 21 months.

Since no significant difference between slabs with and without winter maintenance can be found at this time, only data from slabs without simulated winter maintenance are taken into consideration.

3.4 *Specimen preparation for testing*

HMA specimens and bitumen samples are extracted from the test field at predefined dates after construction to monitor field ageing closely. For testing of the mix characteristics, the slabs with a height of 10 cm are cut into two halves to obtain HMA specimens from the upper and lower layer. Specimens are then obtained by coring and cutting, the dimension of the specimens as well as the bulk density is determined according to EN 12697-6 [23] and the void content according to EN 12697-8 [24].

For bitumen testing the slabs taken from the test field are cut into four layers with 2.5 cm each. For each layer, bitumen is extracted according to EN 12697-3 [32] with tetrachloroethylene (C_2Cl_4) as a solvent. The solvent-bitumen solution is distilled according to EN 12697-3 to recover the bitumen. The residual solvent in the recovered bitumen is determined by gravimetric analysis. Samples with a residual solvent content of larger than 0.5% by mass are discarded. By extracting one bitumen sample for each layer, ageing can not only be monitored versus time but also versus depth, i.e. distance to the surface.

3.5 *Test program*

Testing of HMA specimens consists of the following test methods:

- Thermal Stress Restrained Specimen Tests (TSRST) according to EN 12697-46 [25]. TSRST are carried out from an initial temperature of +10°C with a cooling rate of 10°C/h on prismatic specimens (50 × 50 × 200 mm). Results of TSRST are the cryogenic stress versus temperature $\sigma_{crack}(\tau)$ and the cracking temperature T_{crack} by triple determination.
- Uniaxial Tensile Stress Tests (UTST) according to EN 12697-46. UTST are run at temperatures of +5°C, –10°C and –25°C with a strain rate of 112.5 µstrain/sec. The tensile strength against temperature $\beta_t(\tau)$ is obtained from the test.
- The difference between cryogenic stress from TSRST and tensile strength from UTST gives the tensile strength reserve $\Delta\beta_t(\tau)$. It correlates to the stress that can be applied on a pavement by traffic loading in addition to the thermal stress at a certain temperature τ before failure [26].
- Direct Tension/Compression tests (DTC) are run at temperatures of –20°C, 0°C and +20°C and frequencies ranging from 0.1 Hz to 20 Hz according to EN 12697-26 [27]. From test data the norm of the complex modulus or dynamic modulus $|E^*|$ and the phase angle φ against temperature and frequency can be determined [28].

Table 2 gives an overview of the test program on HMA specimens. Since slabs for the test field were compacted in the lab from plant-produced mix (C_L000), the mix was heated twice for compaction. To compare the impact of double heating on short-term ageing, slabs were also produced from a lab-produced mix where fresh binder and aggregates were only heated once for compaction (C_F000). For slabs from the test field two series of specimens were obtained: one series from the upper 5 cm (upper layer UL) and one series from the lower 5 cm (lower layer LL). Up to now specimens from the lab-mixed slab, the plant-mixed slab and from the test field after 6 and 12 months have been tested. The paper contains results from low-temperature tests (TSRST, UTST).

Table 2. Test program for HMA specimens (x = test completed, (x) = test planned).

Source	Code	TSRST	UTST	DTC
Slab from lab-mix slab	C_L000	x	x	x
Slab from plant-mix slab	C_F000	x	x	x
Slab from test field after 6 months	C_F006	x		x
After 12 months	C_F012	x	x	x
After 18 months	C_F018	(x)		(x)
After 24 months	C_F024	(x)		(x)
After 36 months	C_F036	(x)	(x)	(x)
After 60 months	C_F060	(x)	(x)	(x)

Table 3. Test program for binder samples (x = test completed, (x) = test planned).

Source	Code	Pen	R&B	DSR	BBR
Fresh Binder	A	x	x	x	x
RTFOT-aged	B_LRTF	x	x	x	x
RTFOT + PAV-aged	C_LPAV	x	x	x	x
From lab-mix slab	C_L000	x	x	x	x
From plant-mix	B_F000	x	x	x	x
From plant-mix slab	C_F000	x	x	x	x
From test field 6 m	C_F006	x	x	x	x
From test field 12 m	C_F012	x	x	x	x
From test field 18 m	C_F018	(x)	(x)	(x)	(x)
From test field 24 m	C_F024		(x)	(x)	
From test field 36 m	C_F036	(x)	(x)	(x)	(x)
From test field 60 m	C_F060	(x)	(x)	(x)	(x)

Bitumen samples recovered from HMA will be subjected to various physico-chemical analytical techniques to supplement mechanical testing with a solid physico-chemical background. This holistic approach will provide the basis for the formulation of a new and enhanced ageing theory for bitumen. For mechanical testing the following methods are employed:

- Needle Penetration at 25°C according to EN 1426 [33]
- Softening Point Ring & Ball according to EN 1427 [34]
- Dynamic Shear Rheometer (DSR) tests with a temperature and frequency sweep according to EN 14770 [35]. At temperatures from −10°C to +30°C tests with the small plate (diameter: 8 mm) and a 2 mm gap are run, from +30°C to +80°C with the large plate (diameter: 25 mm) and a 1 mm gap. A frequency sweep between 0.1 Hz and 10 Hz is employed.
- Bending Beam Rheometer (BBR) tests according to EN 14771 [36] to assess the low-temperature behavior at −12°C, −18°C and −24°C.

Table 3 shows the test program for the binder samples. In addition to samples extracted from the test field, samples of the fresh binder (A), RTFOT-aged (B_LRTF) (according to EN 12607-1 [37]) and RTFOT + PAV-aged (C_LPAV) (according to EN 14769 [38]) binder are taken into account to compare lab to field ageing. Also, extracted samples from a lab-mix slab (C_L000), the plant-mix (B_F000) and the plant-mix slab (C_F000) are tested to investigate effects of double heating and compare lab to plant mixing. At this time all samples up to 12 months have been tested. This paper contains results from low-temperature testing (BBR) of the samples.

4 RESULTS AND DISCUSSION

4.1 *Weather data and pavement temperatures*

Since field ageing is crucially dependent on the climatic conditions of the test site, Figures 4 and 5 give details about the weather conditions from January 2013 to February 2014. The test field was constructed in September 2012, which is also the starting point for monitoring weather and pavement temperature. Due to malfunction of the data logger for the instrumentation, data is only available from the beginning of January 2013 on. Figure 4 shows a diagram with the temperature distribution of air, surface and pavement temperatures in various depths. On the right side in Figure 4, a table shows quantiles for the temperature distribution, as well as the absolute maximum and minimum of temperatures and the frequency by which certain temperatures were exceeded and undercut. The air temperature was below 0°C at around 12% of the time, and around 10% at the surface and in layer 1. Due to the thermal capacity of the material and the constant thermal flow from the subgrade, the frequency of lower temperatures decreases with lower layers to around 8% in layer 4. Although the air temperature did not exceed 40°C, the surface temperature of the test field was higher than 40°C in 9% of the time, and even exceeded 50°C (3%) and 60°C (0.4%). Even in layer 4, around 9 cm from the surface, the maximum temperature was 56.8°C.

Figure 5 shows the distribution of humidity (a) and precipitation [mm/24 h] (b) at the test site. In around 50% of the time the humidity is between 60% and 80%. No precipitation was recorded in 77% of the days, and a sum of 234 mm of rain was recorded between January 2013 and February 2014.

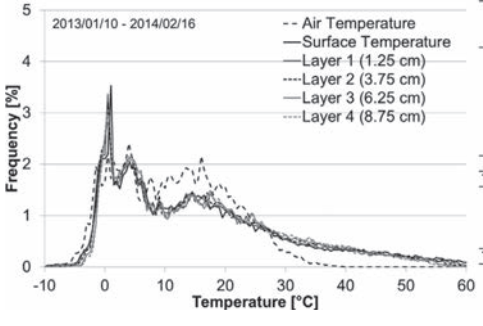

	Temperature [°C]					
Quantile [%]	Air Temperature	Surface Temperature	Layer 1 (1.25 cm)	Layer 2 (3.75 cm)	Layer 3 (6.25 cm)	Layer 4 (8.75 cm)
min	-9.6	-10.0	-9.8	-9.3	-8.7	-8.4
1	-4.6	-3.5	-3.4	-3.0	-2.5	-2.2
5	-2.0	-1.2	-1.3	-1.1	-0.8	-0.6
50	10.9	13.0	13.0	13.1	13.3	13.3
95	26.6	46.7	45.0	43.4	42.6	41.9
99	32.0	57.2	55.0	53.1	51.8	50.9
max	39.0	64.1	61.7	59.5	58.0	56.8

Temperature [°C]	Frequency above given temperature [%]					
60	0.0	0.4	0.1	0.0	0.0	0.0
50	0.0	3.4	2.7	2.0	1.5	1.2
40	0.0	8.9	8.1	7.3	6.7	6.1
30	1.9	16.7	16.3	16.0	16.0	15.8
Temperature [°C]	Frequency below given temperature [%]					
0	11.8	9.8	10.4	9.9	8.5	8.0
-5	0.8	0.4	0.3	0.3	0.3	0.2
-10	0.0	0.0	0.0	0.0	0.0	0.0

Figure 4. Temperature distribution for air, surface and pavement temperatures on the test field from 2013/01/10 to 2014/02/16.

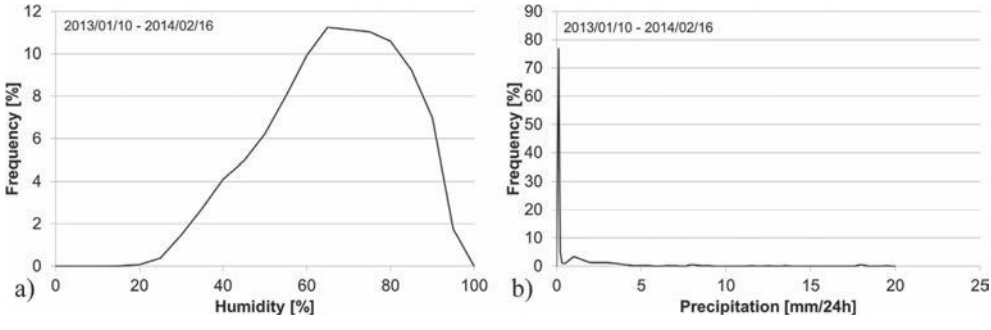

Figure 5. Humidity (a) and precipitation (b) distribution at the test field from 2013/01/10 to 2014/02/16.

4.2 *Tests on HMA specimens*

4.2.1 *Cooling Tests (TSRST)*

According to the test program for HMA (Table 2), specimens were tested in TSRST before ageing (C_F000), after 6 months of ageing (C_F006) (after the first winter) and after the first year of ageing (C_F012). Since all slabs for field ageing were heated twice for mixing in the plant and then for compaction in the lab, additional slabs with identical mix design were produced completely in the lab by mixing fresh binder and aggregates in the lab and compacting it subsequently in the roller compacter. Thus, the binder was only heated once for the lab-mixed slab (C_L000). Differences between non-field aged plant-mixed slabs (C_F000) and non-field aged lab-mixed slabs (C_L000) show the impact of double heating on the performance of the HMA.

Figure 6a shows the air void distribution of AC 11 70/100 specimens tested in TSRST. The value given in the diagram is the mean value (MV), the bars show the 95% confidence interval based on the Standard Deviation (SD). Figure 6b shows the results of the statistical analysis of air void distribution. The numbers in the table give the significance according to the t-test [29]. The significance level was set to 5%. For values below 5% it is considered that the air void content differs significantly for the compared set of specimens. As it can be seen from Figure 6b, the specimens after 6 months of field ageing from the lower layer (C_F006_LL) are significantly different from all other specimens. This is in accordance with the data shown in Figure 6a. Thus, any differences in results from C_F006_LL may be due to differences in the volumetric composition of the specimens and will not be taken into consideration.

Figure 7 gives the results of TSRST for AC 11 70/100 specimens. The diagram shows the temperature at which the specimens fail due to cryogenic stress (T_{crack}) and the stress at cracking (σ_{crack}). Again, the given values represent the MV and the bars indicate the 95% confidence interval. As expected, the lab-mix (C_L000) produced better low-temperature behaviour than the plant-mix (C_F000) in terms of a 1.3°C lower T_{crack}. The results from 6-month field-aged specimens do not show large differences to the non-aged specimens. After 12 months of field ageing, the upper layer (C_F012_UL) seems to be affected stronger by ageing than the lower layer (C_F012_LL). The crack temperature on the UL is 2.6°C higher than on the LL. Interestingly enough, most of the field-aged specimens produce better low-temperature behaviour than the non-aged specimens from the plant-mix.

Table 4 presents results for the statistical analysis of TSRST results of AC 11 70/100. Again a significance level for the t-test of 5% is taken into consideration. Table 4a gives data for T_{crack}, Table 4b for σ_{crack}. The only significant difference can be found for T_{crack} between 12-month field aged specimens at the lower layer (C_F012_LL) and non-aged specimens (C_F000), as well as at the upper layer (C_F012_UL). It can be concluded from these results,

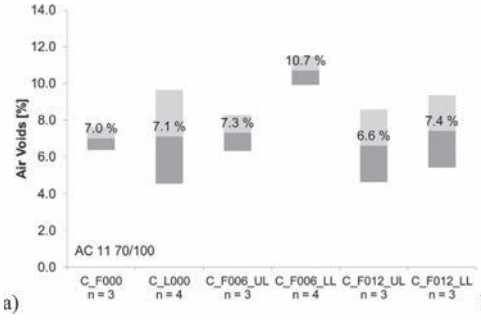

b)

AC 11 70/100 - Results of T-Test for air voids

	C_F000	C_L000	C_F006_UL	C_F006_LL	C_F012_UL	C_F012_LL
C_F000		90.4	43.1	*0.0*	54.6	54.6
C_L000			59.1	*0.0*	45.6	64.7
C_F006_UL				*0.2*	47.6	91.7
C_F006_LL					*0.1*	*0.2*
C_F012_UL						38.3
C_F012_LL						

Figure 6. Air void distribution of AC 11 70/100 Specimens for TSRST testing (a) and statistical analysis of significant differences in air voids (b).

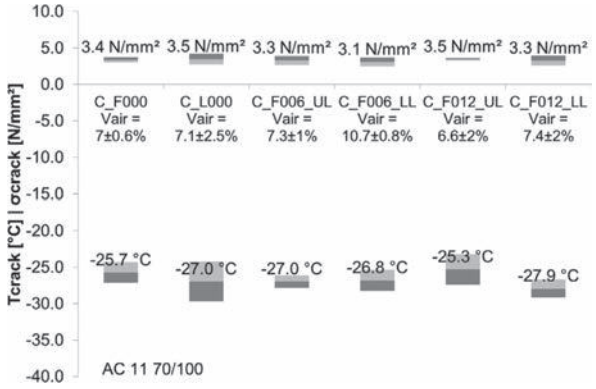

Figure 7. Results of TSRST of AC 11 70/100 for non-field aged slabs from plant mix (C_F000) and from lab mix (C_L000) and after 6 and 12 months of field ageing for upper layer (C_F006_UL, C_F012_UL) and lower layer (C_F006_LL, C_F012_LL).

Table 4. Statistical analysis of results of TSRST of AC 11 70/100 for T_{crack} (a) and σ_{crack} (b)—statistically significant differences marked in grey (significance level: 5%).

a)

AC 11 70/100 - Results of T-Test for T_crack

	C_F000	C_L000	C_F006_UL	C_F006_LL	C_F012_UL	C_F012_LL
C_F000		22.4	6.4	11.4	59.1	1.7
C_L000			99.8	82.3	14.5	32.3
C_F006_UL				72.0	6.7	9.5
C_F006_LL					7.7	8.1
C_F012_UL						2.1
C_F012_LL						

b)

AC 11 70/100 - Results of T-Test for sig_crack

	C_F000	C_L000	C_F006_UL	C_F006_LL	C_F012_UL	C_F012_LL
C_F000		68.1	73.8	18.2	49.8	64.3
C_L000			53.7	14.2	92.7	47.2
C_F006_UL				35.9	43.2	88.3
C_F006_LL					8.3	47.8
C_F012_UL						39.6
C_F012_LL						

that ageing starts to affect the low-temperature behavior significantly after a year of ageing. At this time, significant differences in terms of ageing time and distance of the material to the surface can be found. No significant differences were detected for σ_{crack}.

The same analysis as for the unmodified mix AC 11 70/100 is shown in the following for AC 11 PmB 45/80-65. Figure 8 shows data for the air void distribution of specimens for TSRST testing. As it can be seen from Figure 8b, the specimens after 12 months of field ageing from the upper layer (C_F012_UL) show significantly different air void distribution compared to all other specimens. Any differences found for these specimens will not be considered as significant since an influence of the air void content is possible.

Figure 9 shows results for the TSRST at specimens from the modified mix AC 11 PmB 45/80-65. Again, a small difference between lab- and plant-mix can be detected in terms of T_{crack}. The lab mix results in a 0.3°C lower crack temperature. All field-aged specimens show similar low-temperature behaviour compared to the non-aged specimens from the plant mix.

When the results for the polymer-modified mix (Fig. 9) are compared to the results of the non-modified mix (Fig. 7), the positive effect of the SBS modification on the low temperature behaviour becomes obvious. Since the SBS-modified binder can bear higher tensile stresses, the cracking temperature of the modified mix is about 8°C lower than of the non-modified mix.

Table 5 provides information on the significance of differences between the mixes for T_{crack} (a) and σ_{crack} (b). The statistically significant differences for 12-months field-aged specimens from the upper layer (C_F012_UL) cannot be taken into account since they also differ in their air-void content significantly from all other mixes. Specimens from the lower layer after 6 months of ageing (C_F006_LL) show a significantly better low-temperature performance than the non-field aged mix. Material that is further away from the surface is therefore not affected from ageing as much as material closer to the surface. The same can be said about the lower layer after 12 months of ageing (C_F012_LL).

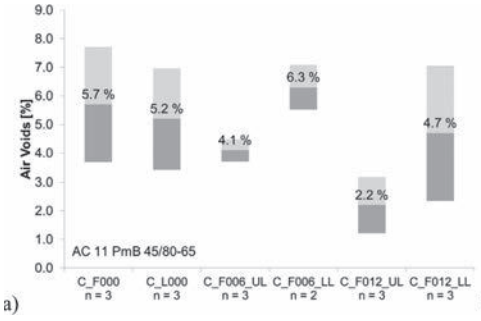

a)

b)

AC 11 PmB 45/80-65 - Results of T-Test for air voids

	C_F000	C_L000	C_F006_UL	C_F006_LL	C_F012_UL	C_F012_LL
C_F000		56.0	5.7	50.5	*0.6*	33.4
C_L000			14.3	26.0	*1.0*	61.3
C_F006_UL				5.2	*3.3*	52.7
C_F006_LL					*0.2*	18.0
C_F012_UL						*2.9*
C_F012_LL						

Figure 8. Air void distribution of AC 11 PmB 45/80-65 specimens for TSRST testing (a) and statistical analysis of significant differences in air voids (b).

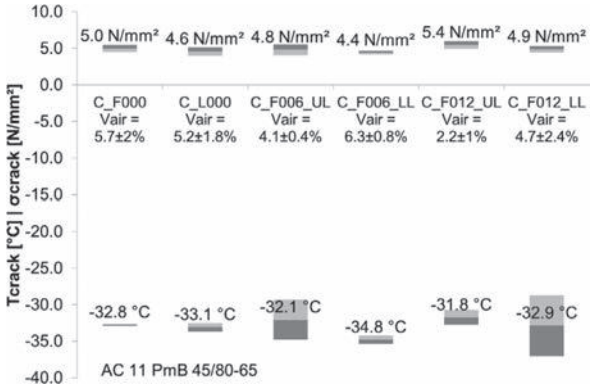

Figure 9. Results of TSRST of AC 11 PmB 45/80-65 for non-field aged slabs from plant mix (C_F000) and from lab mix (C_L000) and after 6 and 12 months of field ageing for upper layer (C_F006_UL, C_F012_UL) and lower layer (C_F006_LL, C_F012_LL).

Table 5. Statistical analysis of results of TSRST of AC 11 PmB 45/80-65 for T_{crack} (a) and σ_{crack} (b)—statistically significant differences marked in grey (significance level: 5%).

a)

AC 11 PmB 45/80-65 - Results of T-Test for T_crack

	C_F000	C_L000	C_F006_UL	C_F006_LL	C_F012_UL	C_F012_LL
C_F000		14.1	43.8	*0.1*	*2.6*	94.3
C_L000			28.8	*0.7*	*1.7*	86.6
C_F006_UL				8.2	73.6	61.8
C_F006_LL					*0.5*	30.9
C_F012_UL						42.9
C_F012_LL						

b)

AC 11 PmB 45/80-65 - Results of T-Test for sig_crack

	C_F000	C_L000	C_F006_UL	C_F006_LL	C_F012_UL	C_F012_LL
C_F000		13.4	55.1	6.1	8.9	65.1
C_L000			42.9	49.6	*1.7*	19.9
C_F006_UL				25.1	7.3	77.6
C_F006_LL					*1.5*	6.8
C_F012_UL						*4.6*
C_F012_LL						

4.2.2 *Combined analysis of cooling tests (TSRST) and Uniaxial Tensile Strength Tests (UTST)*

To explain the concept of combined analysis of TSRST and UTST, Figure 10 shows results of both tests for the plant-mixed (C_F000) AC 11 70/100 (a) and AC 11 PmB 45/80–65 (b). The diagrams contain data of the three single TSRST (light grey) and the MV of the TSRST (long dashed black line). The TSRST results give the thermally induced (cryogenic) stress versus temperature. In addition the single results (tensile strength) from UTST at different temperatures are shown by diamonds. The UTST results versus temperature are approximated by a quadratic function. The difference between UTST (tensile strength) and TSRST (cryogenic stress) is the tensile strength reserve ($\Delta\beta_t$), which is given by the small dashed black line. The higher the reserve is, the more stress additional to thermal stress can be applied to

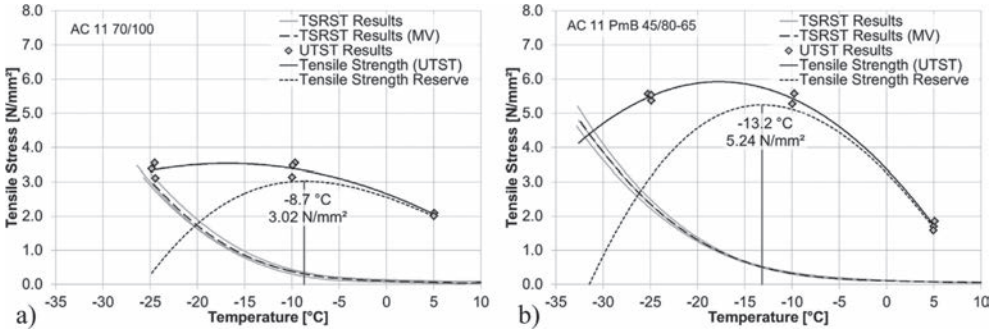

Figure 10. Combined results of TSRST and UTST for non-field aged (C_F000) AC 11 70/100 (a) and AC 11 PmB 45/80-65 (b).

the pavement (e.g. by traffic) before it fails due to cracking. The maximum strength reserve for the AC 11 70/100 occurs at –8.7°C and 3.0 N/mm² and at -13.2°C and 5.2 N/mm² for the AC 11 PmB 45/80-65 respectively. Thus, the modified mix shows a more than 70% higher maximum strength reserve. As another parameter to assess the resistance to thermal cracking the area between the x-axis and the tensile strength reserve curve from 0°C to the interception of the tensile strength reserve curve with the x-axis is introduced. This sums up the tensile strength reserve for the critical temperature range (< 0°C) to one single value. This Cumulative Tensile Strength Reserve (CTSR) is defined as follows:

$$\mathrm{CTSR} = \int_{\tau=I_{\Delta\beta t|x}}^{0°C} \Delta\beta_t \, d\tau = \int_{\tau=I_{\Delta\beta t|x}}^{0°C} \left(\beta_t(\tau) - \sigma_{cry}(\tau)\right) d\tau \qquad (1)$$

where

$I_{\Delta\beta t|x}$ left interception of $\Delta\beta_t$ with the x-axis ($\Delta\beta_t = 0$) in °C

$\beta_t(\tau)$ tensile strength from UTST as a function of temperature τ in N/mm²

$\sigma_{cry}(\tau)$ cryogenic stress from TSRST as a function of temperature τ in N/mm².

For the unmodified mix, CTSR comes to 59.8 N/mm²*°C and to 113.7 N/mm²*°C for the modified mix, which means a 90% higher resistance to thermal cracking for the modified mix. Since the mix design of both materials is the same, the higher resistance is due to the SBS-modification of the bitumen.

UTST were also carried out on specimens from the lab-mix (C_L000) to see differences between lab- and plant-mix (C_F000). In addition, UTST were run on specimens from slabs after 12 months of field ageing for upper and lower layers. Figure 11 presents results for the unmodified AC 11 70/100. Maximum tensile strength reserve and the temperature at which this maximum strength occurs are given in Figure 11a. The lab-mix indicates a 27% higher strength reserve at a 2.2°C lower temperature than the unaged plant-mix. Both values show that the low-temperature behavior is more favorable for the lab-mix. The results after 12 months of field ageing show only slight changes, the maximum strength reserve is around 10% higher for upper and lower layers compared to the unaged plant-mix.

Figure 11b compares the CTSR. Results are analogue to the maximum strength reserve. The lab-mix shows 31% better results than the plant mix. The 12-month field-aged specimens have a 10% higher CTSR.

Figure 12 shows the combined results of TSRST and UTST for the SBS-modified AC 11 PmB 45/80-65. The lab-mix shows a slightly better (+13%) performance in terms of maximum strength reserve (Fig. 12a) than the plant-mix. The 12-month field aged samples show a similar or slightly better performance than the non-aged mix as well. In terms of the CTSR (Fig. 12b), again, lab-mix and field-aged plant-mix show better results than the non-aged plant mix.

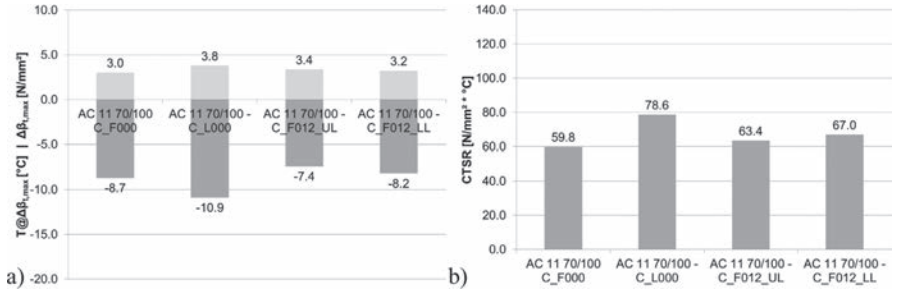

Figure 11. Combined results of TSRST and UTST of AC 11 70/100 for non-field aged slabs from plant mix (C_F000) and lab mix (C_L000) and after 12 months of field ageing for upper layer (C_F012_UL) and lower layer (C_F012_LL).

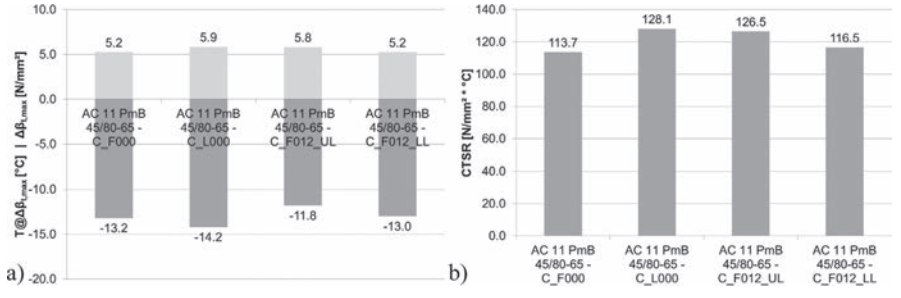

Figure 12. Combined results of TSRST and UTST of AC 11 PmB 45/80-65 for non-field aged slabs from plant mix (C_F000) and lab mix (C_L000) and after 12 months of field ageing for upper layer (C_F012_UL) and lower layer (C_F012_LL).

4.3 *Tests on binder samples*

To compare performance of the mixes to the performance of the binders, exact lower PGs were derived from Bending Beam Rheometer (BBR) testing according to the SHRP procedure. Therefore, the stiffness and the m-value of the binder were investigated after 60 s of testing versus test temperature. The temperature where the stiffness exceeds 300 MPa and the m-value falls below 0.3 was determined. The higher of both temperature values is taken to derive the lower PG by subtracting 10°C from the determined temperature value. The results are given in Figure 13a for the non-modified 70/100 and in Figure 13b for the SBS-modified PmB 45/80–65. The left three bars show the lower PG for the fresh, the RTFOT and the RTFOT+PAV aged binder, the middle four bars for the 6- and 12-month field-aged binders and the right three bars for binder samples extracted from different mix sources to compare lab- versus plant-mix. The results for the fresh and lab-aged samples are given as a reference.

When the non-aged binder from the plant mix (C_F000) is compared to the field-aged samples, it can be seen from both binder types, that the field-aged sample show only slightly worse lower PGs. In any case they cannot be seen as significant showing, that the first year of field ageing does not seem to have a crucial impact on the binder performance. Also, the differences between upper and lower layers of field aged samples do not differ strongly.

Different from the mix performance, where the benefit from SBS modification reflected in better low-temperature behavior, this cannot be stated for the binder performance to the same extent. In terms of lower PG, the SBS-modified binder results in only around 5% better values than the non-modified binder.

A better low-temperature binder performance can be found for the binder extracted from the once heated lab mix compared to binder extracted from the double heated plant mix for

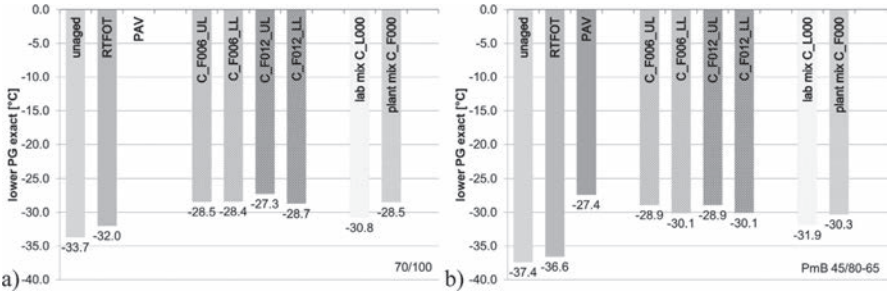

Figure 13. Exact lower PGs derived from BBR testing of binder samples from non-modified mix (AC 11 70/100) (a) and SBS-modified mix (AC 11 PmB 45/80-65) (b).

the non-modified 70/100 (Fig. 13a) where the lower PG is 2.3°C lower, as well as for the SBS-modified PmB 45/80-65 with a 1.6°C lower lower PG.

5 SUMMARY AND OUTLOOK

This paper contains first investigations on a test field to monitor field ageing of bitumen and HMA. The test field consists of 72 slabs ($50 \times 26 \times 10$ cm) from plant-mixed, lab-compacted HMA. Thermo couples and a weather station monitor pavement temperatures in various depths and most important climatic parameters. Two mixes (AC 11) are investigated: One mix is made from unmodified bitumen 70/100 pen, the other mix from PmB 45/80-65. The test field was constructed in September 2012. Thus, the material will have been aged for 21 months in June 2014. The focus of this paper is the low-temperature performance of field-aged mix and extracted binder after the first 12 months of field ageing in terms of cooling tests (TSRST) and tensile strength tests (UTST) for the mix and BBR tests for the binders.

All slabs for the test field were heated twice: once in the plant for mixing and another time in the lab for compacting (C_F000). To analyze the impact of double heating on ageing, slabs with lab-mixing and—compaction were produced for which the mix was only heated once (C_L000):

- Double-heated mixes (C_F000) resulted in a slightly worse low-temperature performance than lab-produced mixes made in the lab (C_L000). The non-modified mix showed a 1.3°C higher cracking temperature, the SBS-modified mix in a 0.3°C higher T_{crack}. These differences were not found to be significant.
- Combined analysis of TSRST and UTST in terms of maximum tensile strength reserve ($\Delta\beta_{t,max}$) and Cumulative Tensile Strength Reserve (CTSR) showed that the non-modified mix performed around 30% and the SBS-modified mix around 13% better when heated only once compared to double heating.
- The lower PG determined from BBR testing on the extracted binder from lab- and plant-mix confirmed the trends seen for the mix. Both binders show a better low-temperature performance, for the non-modified 70/100 the lower PG is 2.3°C lower when lab-mix is compared to plant-mix, for the SBS-modified PmB 45/80-65 it is 1.6°C lower.
- All analyzed data show that the effect of double heating is harsher on the non-modified binder with smaller impact on the SBS-modified binder.

The impact of field-ageing on the mix- and binder-performance was tested after 6 and 12 months of ageing:

- Regarding the cooling tests and resulting cracking temperatures, no significant difference were found after 6 months of field-ageing compared to non-aged samples for both mixes. Also, no difference between upper and lower layer was found after this period of ageing.

- After 12 months of field ageing, the difference in cracking temperature between upper and lower level is significantly different for the non-modified mix, the lower layer showing a 2.6°C lower (i.e. better) T_{crack}. Also, the difference between non-aged and 12-month field-aged lower layer results is significant for the non-modified mix. Interestingly enough, the lower layer after a year of ageing shows a better performance than the non-aged sample.
- Regarding the tensile strength reserve derived from combined analysis of TSRST and UTST only slight changes can be observed between non-aged and field-aged mixes with both binders. Interestingly enough, the low-temperature performance is 6% to 12% better for field-aged mixes. This is contradictory to the common understanding that the low-temperature performance decreases with increasing field ageing. Since the differences are rather small, no certain conclusions can be drawn from the results at this time. A better performance after one year of ageing could be linked to a stress relaxation phenomenon that occurs if the HMA slabs have time to rest after compaction. This is not the case for non-aged samples since they were tested around 5 days after production. Further investigation into this field have to be carried out to analysis this phenomenon in more details.

A direct comparison between non-modified and SBS-modified mix is sensible in this case since the mix design is the same for both mixes and the SBS-modified binder was produced from the same crude oil source as the non-modified binder. The benefit of SBS modification is obvious. The cracking temperature in TSRST is 8°C lower for the SBS-modified mix, the tensile strength reserve is 70% (maximum strength reserve) to 90% (cumulative strength reserve) higher. Interestingly enough, no significant differences can be seen in binder performance when comparing the lower PG derived from BBR testing.

Further results from Direct-Tension and Compression testing (DTC) on the mix and from traditional testing as well as DSR testing on the binder are still being analyzed. In addition, testing of specimens after 24, 36 and 60 months of field ageing is planned. Together with an in-depth analysis of bitumen samples extracted from the field-aged slabs, which will be analyzed by chemical methods, a better understanding of field aging is expected. Since winter maintenance is simulated on parts of the test field, the influence of de-icing by thawing salt will be investigated more closely in the further course of the study. The outcomes of this long-term study will help to optimize existing lab ageing methods for binder and mixes to simulate short- and long-term ageing in a more realistic way.

REFERENCES

[1] Nicholls C. (editor). Analysis of Available Data for Validation of Bitumen Tests, Report on Phase 1 on of the BitVal Projekt, 2005.

[2] Corbett, L.W., and R.E. Merz. Asphalt Binder Hardening in the Michigan Test Road After 18 Years of Service, Transportation Research Record 544, Washington DC, 1975.

[3] Martin, K.L., R.R. Davidson, C.J. Glover, and J.A. Bullin. Asphalt Aging in Texas Roads and Test Section, Transportation Research Record 1269, Washington DC, 1990.

[4] Kliewer, J., Zeng, H., and Vinson, T. Aging and Low-Temperature Cracking of Asphalt Concrete Mixture, Journal of Cold Regions Engineering, 10(3), 134–148, 1996.

[5] Teshale E.Z., Moon K.-H., Turos M., and Marasteanu M. Pressure Aging Vessel and Low-Temperature Properties of Asphalt Binders; Transport Research Record, Washington DC, 2011.

[6] Petersen J.C. A Review of the Fundamentals of Asphalt Oxidation—chemical, Physicochemical, Phycial Property, and Durability Relationships, Transport Research Circulare E-C140, Washington DC, 2009.

[7] Herrington, P.R., J.E. Patrick, and G.F.A. Ball. Oxidation of Roading Asphalts, Industrial and Engineering Chemistry Research, Vol. 33, 1994.

[8] Mirza, M.W., and M.W. Witczak. Development of a Global Aging System for Short- and Long-Term Aging of Asphalt Cements, Journal of the Association of Asphalt Paving Technologists, Vol. 64, 1995.

[9] Dickinson, E.J. Prediction of the Hardening of the Bitumen in Pavement Surfacing by Reaction with Atmospheric Oxygen, Road Materials and Pavement Design, Vol. 1, No. 3, 2000.

[10] Ruan Y., Davison R.R., and Glover C.J. The Effect of Long-Term Oxidation on the Rheological Properties of Polymer Modified Asphalts, Fuel, 82, 1763–1773, 2003.

[11] Petersen J.C. Asphalt Oxidation—an overview including a new model for oxidation proposing that physicochemical factors dominate the oxidation kinetics, Fuel, 11, 1993.
[12] Lesueur D. The colloidal structure of bitumen: Consequences on the rheology and on the mechanisms of bitumen modification, Advances in Colloid and Interface Science, 145, 2009.
[13] Durrieu F., Farca F., and Mouillet V. The Influence of UV Aging of an SBS Modified Bitumen: Comparison between Laboratory and on Site Aging, Fuel, 86, 1446–1451, 2007.
[14] Woo W.J., Chowdhury A. and Glover C.J. Field Aging of Unmodified Asphalt Binder in Three Long-Term Performance Pavements, Transport Research Record, Washington DC, 2008.
[15] Xiang L., Tu J., Cheng J., and Que G. Outdoor Aging of Road Asphalt and SBS modified Asphalt, Frontiers of Chemical Science Engineering, 5, 35–42, 2011.
[16] Huang S.C., Tia M., and Ruth B.E. Laboratory Aging Methods for Simulation of Field Aging of Asphalts, Materials in Civil Engineering, 1996.
[17] Kandhal P.S., and Sanjoy C. Effect of Asphalt Film Thickness on Short and Long Term Ageing of Asphalt Paving Mixtures, Transport Research Record 1535, Washington DC, 1996.
[18] Pierard N., and Vanelstraete A. Developing a Test Method for Accelerated Ageing of Bituminous Mixtures in the Laboratory, Advanced Testing and Characterization of Bituminous Materials, 2009.
[19] Mollenhauer K., Pierard N., Tusar M., Moulliet V., Gabet T.: Development and Validation of a Laboratory Ageing Method for the Accelerated Simulation of Reclaimed Asphalt, Journal of Wuhan University of Technology, 2010.
[20] van de Ven M.F.C., Voskuilen J.L.M. and Jacobs M.M.J. Practical Laboratory Ageing Method for Porous Asphalt, Proceedings of the 5th E&E Congress, Istanbul, Turkey, 2012.
[21] EN 12697-33. Bituminous mixtures—Test methods for hot mix asphalt—Part 33: Specimen prepared by roller compactor, European Standardization Committee, 2007.
[22] Moulliet V., Farcas F., and Besson S. Ageing by UV-Radiation of an Elastomer Modified Bitumen, Fuel, 87, 2408–2419, 2008.
[23] EN 12697-6. Bituminous mixtures—Test methods for hot mix asphalt—Part 6: Determination of bulk density of bituminous specimens, European Standardization Committee, 2012.
[24] EN 12697-8. Bituminous mixtures—Test methods for hot mix asphalt—Part 8: Determination of void characteristics of bituminous specimens, European Standardization Committee, 2003.
[25] EN 12697-46. Bituminous mixtures—Test methods for hot mix asphalt—Part 46: Low-temperature cracking and properties by uniaxial tension tests, European Standardization Committee, 2012.
[26] Arand W., Steinhoff G., Eulitz J., and Milbradt H.: Verhalten von Asphalten bei tiefen Temperaturen; Entwicklung und Erprobung eines Prüfverfahrens (in German). Forschung Straßenbau und Straßenverkehrstechnik des Bundesministers für Verkehr, Abteilung Straßenbau, Heft 407, 1984.
[27] EN 12697-26: Bituminous mixtures—Test methods for hot mix asphalt—Part 26: Stiffness, European Standardization Committee, 2012.
[28] DiBenedetto H., Partl M.N., Francken L., and De La Roche C. Stiffness testing for bituminous mixtures, Materials and Structures, 34, 2001.
[29] Bamberg G., Baur F., and Krapp M. Statistik (in German), Oldenburger Wissenschaftsverlag, 2011.
[30] Findley, W.N., Lai, J.S.Y., and Onaran, K. Creep and Relaxation of Nonlinear Viscoelastic Materials, Mineola, US: Dover Publications Inc., 1989.
[31] Hofko B., Blab R., and Mader M. Impact of Air Void Content on the Viscoelastic Behavior of Hot Mix Asphalt, Four-Point Bending, Taylor & Francis Group, London, ISBN 978-0-415-64331-3, 2012.
[32] EN 12697-3. Bituminous mixtures—Test methods for hot mix asphalt—Part 3: Bitumen recovery: Rotary evaporator, European Standardization Committee, 2013.
[33] EN 1426. Bitumen and bituminous binders. Determination of needle penetration, European Standardization Committee, 2007.
[34] EN 1427. Bitumen and bituminous binders—Determination of the softening point—Ring and Ball method, European Standardization Committee, 2007.
[35] EN 14770. Bitumen and bituminous binders. Determination of complex shear modulus and phase angle. Dynamic Shear Rheometer (DSR), European Standardization Committee, 2012.
[36] EN 14771. Bitumen and bituminous binders—Determination of the flexural creep stiffness—Bending Beam Rheometer (BBR), European Standardization Committee, 2012.
[37] EN 12607-1. Bitumen and bituminous binders. Determination of the resistance to hardening under influence of heat and air. Part 1. RTFOT method, European Standardization Committee, 2013.
[38] EN 14796. Bitumen and bituminous binders. Accelerated long-term ageing. Pressure Ageing Vessel (PAV), European Standardization Committee, 2012.

This page intentionally left blank

Asphalt Pavements – Kim (Ed)
© 2014 Taylor & Francis Group, London, ISBN 978-1-138-02693-3

Advanced Shear Tester for solid and layered samples

Adam Zofka
Road and Bridge Research Institute, Warsaw, Poland

Alexander Bernier
Stantec Consulting, New York, NY, USA

Ramandeep Josen
Fay, Spofford & Thorndike Inc., Burlington, MA, USA

Maciej Maliszewski
Road and Bridge Research Institute, Warsaw, Poland

ABSTRACT: This paper presents the Advanced Shear Tester (AST) device capable of testing of 150 mm in diameter cylindrical samples in the shear mode. Samples can be either typical bi-layer pavement cores or solid gyratory compacted specimens. Validation of the AST design was performed on the Hot-Mix Asphalt (HMA) specimens prepared in laboratory conditions as well as cored from the asphalt pavement. For the comparison, the abbreviated triaxial test was conducted in order to determine the Mohr-Coulomb failure criterion of the HMA samples. The results demonstrated that monotonic strength tests in the AST device can be used to determine the Mohr-Coulomb failure envelope for solid HMA samples. Additionally, the AST can differentiate between different application rates of the interlayer bonding agent during the shear strength and shear fatigue tests. It was observed that the dissipated energy parameter from the fatigue testing is the most indicative of the application rate of the interlayer material.

Keywords: Asphalt pavements, shear properties, interlayer bond

1 INTRODUCTION

Proper bonding between different layers in the pavement structure provides an adequate bearing capacity of the entire structure and greatly influences its long term performance. Since the interlayer bonding is very important there has been numerous experimental procedures to examine the interface conditions. The first credited source for the HMA shear testing was Leutner [1]. Various modifications of this test have become standards in European countries and are used as interlayer performance measures [2]. The original procedure calls for a monotonic test on an unconfined asphalt specimen along its interlayer interface at a rate of 50 mm/min. Similar work reported by [3] emphasized the importance of the interface horizontal reaction modulus (K) and its relationship to shear stress and strain. Numerous studies since Leutner have developed new devices to look at the shear strength as means of optimizing interlayer bonding material (tack coat) in composite samples [4]–[10]. Further studies have explored unconfined shear tests as a means of differentiating or characterizing shear properties of the HMA [11]–[14]. Although, there is a large number of devices available, there is still a need to develop new protocols due to several important reasons discussed in details by [14]. Considering these issues, the Advanced Shear Tester (AST) was designed and manufactured. This paper presents only

selected aspects of the development effort so the specific emphasis was made on the following items:

– To present the design and main features of the AST,
– To report the validation process of the AST on the HMA samples.

2 ADVANCED SHEAR TESTER

The AST is an unique sample fixture that allows for the confined shear testing in the uniaxial load frame. The confinement load is applied via a system of sandwich plates connected by the specially selected four die springs (see Fig. 1). The initial confinement is set and then monitored by the in-line load cell. In terms of the shearing load, its history can be arbitrarily programmed by the closed-loop load frame system. It should be mentioned the AST allows for the bi-directional shear loading, i.e. a monotonic shear testing as well as bi-directional cyclic testing can be conducted. The AST was design with a relatively small foot-print and it can be placed in the 40 by 40 cm environmental chamber. However, all tests discussed in this paper were conducted at the room temperature (approx. 25°C) except for the cyclic tests that were performed at 35°C.

3 VALIDATION PROCESS

As the part of the development process, validation of the AST was performed on various HMA samples prepared both in the laboratory conditions as well as cored from the freshly

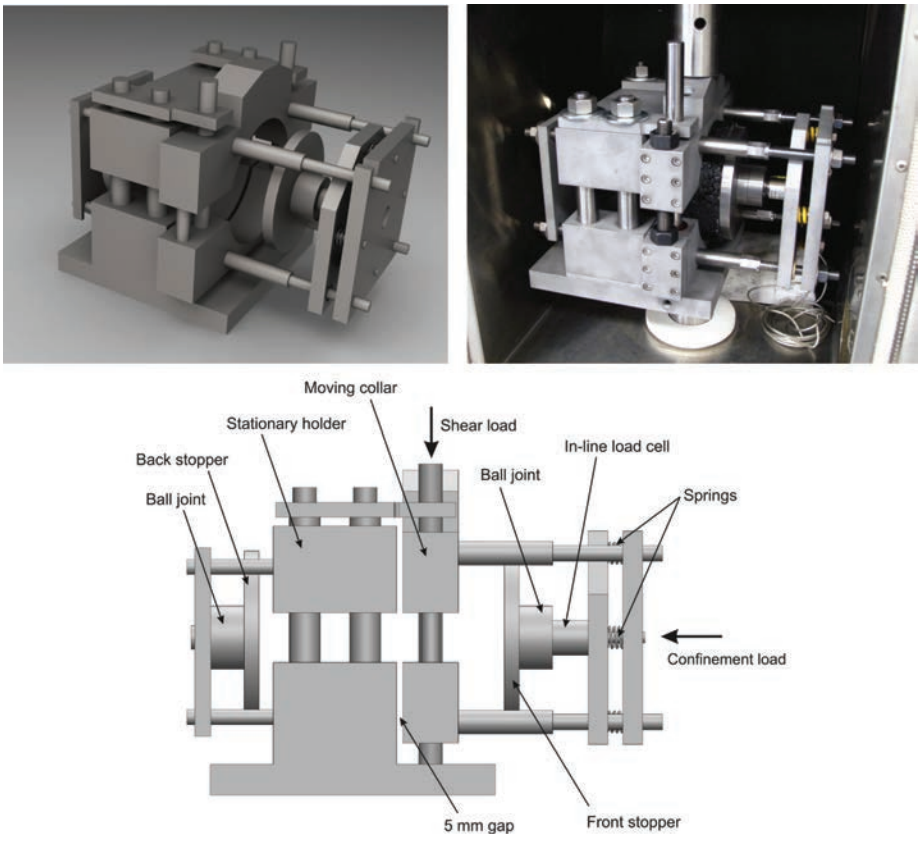

Figure 1. 3D model, image and schematics of the AST device.

constructed pavement section. The following paragraphs present the details on the materials/samples and experimental protocols.

3.1 *Experimental design—materials*

Validation effort comprised both laboratory- and field-prepared samples. In the laboratory, samples were prepared using gyratory compactor and two types of samples were used:

– Two (2) types of uniform samples that differed NMAS (9.5 mm and 12.5 mm).
– Four (4) types of bi-layer (composite) samples.

The laboratory composite specimens were fabricated in two steps. For 2 of the 4 treatments, the first 75 mm of compacted sample was left in the gyratory mold overnight to cure before an additional 75 mm layer was compacted on the top ("hot on cold"). The additional factor was the presences of a polymer-modified asphalt tack coat placed in between each level of the specimen as 50 g disk. For the other 2 treatments, the second layer was compacted immediately after the first layers were prepared ("hot on hot"). This difference was to simulate hot versus cold interfaces where either of those factors had tack coat present or absent.

The three field test sections had identical base and surface layers, both having 9.5 mm NMAS with varied amounts of tack coat at the interface. The control section was constructed without a tack coat, second treatment had a 'standard' tack coat application rate, 0.4 L/m^2 (0.1 gal/yd^2), and a third with a "heavy tack coat" application rate, 0.8 L/m^2 (0.2 gal/yd^2). The field effort amounted to 12 cores, 4 from each section (see Table 1) extracted using a 150 mm diameter diamond-impregnated coring bit. Tack coat application rates were verified by placing corrugated cardboard strips within the test sections and the weights were evaluated after a prolonged curing period.

3.2 *Experimental design—testing*

Uniform laboratory-prepared samples were examined in 3 experimental setups. Unconfined Compressive Strength (UCS) and Indirect Tensile strength (IDT) were used in order to construct Mohr-Coulomb (M-C) failure envelopes according to the abbreviated protocol for triaxial testing proposed by [15]. Uniform samples as well as composite samples were also tested in the AST in the simple shear mode (constant crosshead rate) (see Table 1 for experimental details). Additionally, composite field-prepared samples were examined in the AST under cyclic haversine loading (load-controlled). The loading amplitudes were set to 60% of the simple shear bond strength.

Table 1. Summary of validation effort.

Type	Treatment	# of replicates	Test performed
Uniform	9.5 mm NMAS	6	UCS[1], IDT[2],
	12.5 NMAS	5	AST (mono)[3]
Composite prepared in the laboratory	Hot on cold, w/o tack	6	AST (mono)[3]
	Hot on cold, w/tack	7	
	Hot on hot, w/o tack	7	
	Hot on hot, w/tack	7	
Composite cut from the field pavement section	No tack	4	AST (mono)[3]
	Normal tack	4	AST (cyclic)[4]
	Double tack	4	
Total HMA samples		50	

[1]UCS (unconfined compressive strength); 7.5 mm/min @25C.
[2]IDT (indirect tensile strength); 3.75 mm/min @25C.
[3]AST (mono) simple shear test in AST; 1 mm/min @25C; 1.5, 3 and 6 kN confining load.
[4]AST (cyclic) cyclic shear test in AST; 1 Hz w/0.7 s rest; @35C; 0.5 kN confining load; 14,400 cycles.

Table 1 presents a summary of all samples and corresponding treatments used in the HMA validation phase.

The results from the simple shear AST testing are reported on the M-C plane using shear stress at failure and corresponding normal stress. Additionally, as the alternative to the simple "shear strength" (i.e. shear load at failure over sample area), the mean peak (failure) stress parameter was determined using the following formula:

$$\sigma_m = \frac{\left(\tau_{peak} + \sigma_{peak}\right)}{2} \tag{1}$$

σ_m mean peak (failure) stress,
τ_{peak} shear stress at peak (failure),
σ_{peak} corresponding normal stress.

The results from the cyclic testing were reported in terms of two parameters:

1. Apparent secant modulus E_i and corresponding damage D_i.
2. Dissipated energy W_i.

Secant modulus E_i was defined as the ratio of the incremental increase in force and corresponding change in displacement during a loading part of a given fatigue cycle. Secant modulus E_i is a measure of material damage and it is typically used to plot damage D_i in the ith cycle as the fractional loss in the secant modulus from its initial value. The other parameter, dissipated energy W_i was calculated in each cycle as the area encompassed by the loop of experimental points in force-displacement space. After taking into consideration specimen geometry, the energy is expressed in J/m^2 and presented as a function of cycle number, similar to the dimensionless damage parameter D_i.

4 VALIDATION RESULTS

Figure 2 shows an example of two direct shear tests performed on 9.5 NMAS and 12.5 NMAS uniform GCS with 3 kN initial confinement load. The larger aggregate mix had a higher peak shear load and a higher residual shear load than the finer mix. Likewise, the confinement load monitored during the test increased significantly for the larger size mix. This was expected due to dilation of the larger aggregate particles on the shear interface that are forcing the sheared part to move further than the aggregate in the finer mix.

The results in Figure 3 display the average mean peak stress for each treatment of laboratory prepared specimens. It can be seen that the uniform specimens and cold specimens

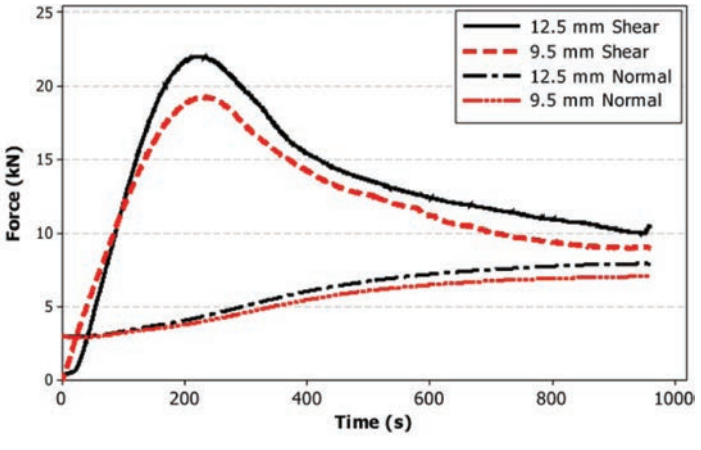

Figure 2. Typical force data measured in the AST.

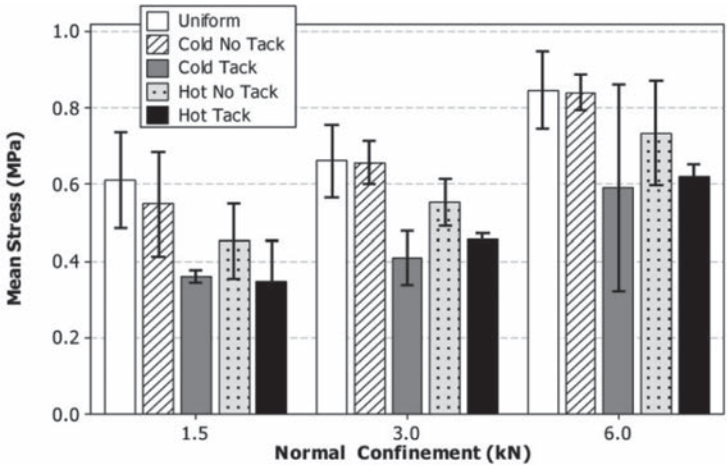

Figure 3. Mean peak stress for lab prepared samples (mean value and its 95% confidence interval).

Table 2. Summary of friction angle and cohesion for lab composite samples determined from AST.

Interface type	Friction angle (deg)	Cohesion (MPa)
Hot on cold, w/o tack	48.04	0.8827
Hot on cold, w/tack	40.81	0.4865
Hot on hot, w/o tack	50.47	0.6554
Hot on cold, w/tack	43.91	0.4708

Table 3. Summary of friction angle and cohesion for lab uniform samples determined from abbreviated 3-axial and AST.

	Friction angle (deg)	Cohesion (MPa)
Abbreviated 3-axial (UCS/IDT) (mean)	40.7	1.08
AST (mean and 95% confidence interval)	42.3 (13.8 to 57.5)	0.93 (0.76 to 1.11)

without tack produced similar results. Both treatments with the 50 g tack coat interface decreased the mean stress significantly which indicates the shear fixture is capable of differentiating between various interfaces. Table 2 provides a summary of friction angles and cohesion values for each interface type. It can be seen from the Table 2 that all four friction angles fall between 40 and 51 degrees. The cohesion followed no apparent pattern but, as suggested, was the most sensitive parameter. Analysis of Variance (ANOVA) for the means of each treatment was performed using Fisher Least Significance Difference (LSD). The LSD results support the expected outcome of the different treatments, i.e. hot and cold interfaces with tack coat had statistically equal mean peak stress values which would suggest the large amount of tack coat applied during fabrication would mask the effects of other parameters. The control specimens and the cold interface without tack coat were always statistically the same. The hot interface without tack was statistically different of the other treatments.

Table 3 shows the comparison of the M-C parameters (friction angle and cohesion) for the uniform GCS tested in the abbreviated 3-axial and the AST. It can be noticed that both protocols produced similar average values and observed variability in the AST should be further investigated in the larger experimental effort with various treatments.

Figure 4 indicates the mean stress at peak for the field-prepared samples. Statistical analysis showed that only the double tack coat group is different than the other two groups. Additionally, the values for the mean peak stress (and shear bond strength) obtained for the field samples were lower than corresponding values determined for the laboratory-prepared samples (shown in Fig. 3). Since the results from the simple shear testing were not sufficiently indicative of the tack coat application rate, the field samples were subjected to the cyclic loading in the AST fixture. It is believed that conceptually results from cyclic testing should translate the best to the actual field performance, especially under significant shear loads.

The evolution of the damage parameter as a function of cycle number for all three different interface treatments is presented in Figure 5. The results show similar trends in damage for all three types of interfaces. It seems that damage progresses at fairly constant rate for the "zero" interface whereas in case of the double tack coat" interface it accumulates quickly at the beginning of the fatigue testing and then levels out. The terminal values of the D_i parameters are similar and they are oscillating around 0.30 at 14,400 cycles.

Figure 6 shows the total accumulated dissipated energy from the cyclic testing in the AST. It can be easily observed that this parameter provides a clear distinction between different

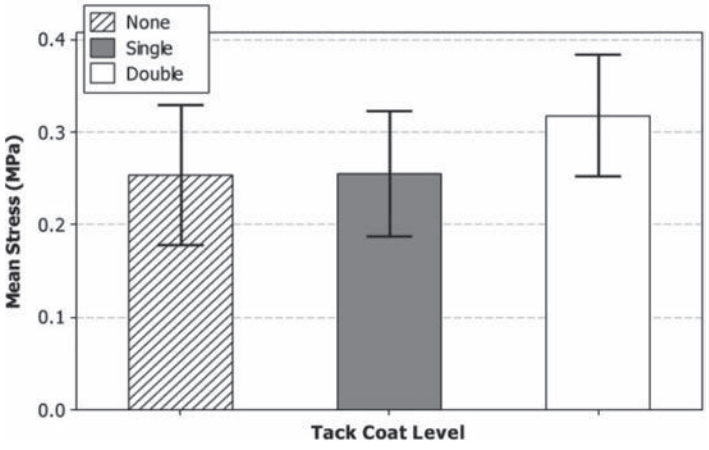

Figure 4. Mean peak stress for field composite samples (mean value and its 95% confidence interval).

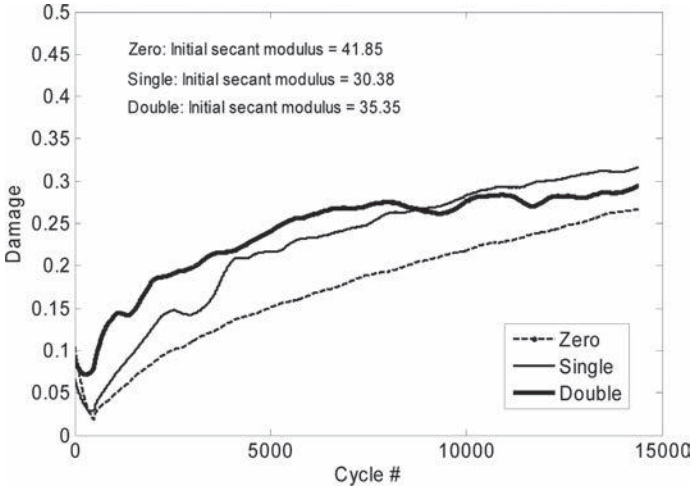

Figure 5. Evolution of damage parameter D_i for field composite samples.

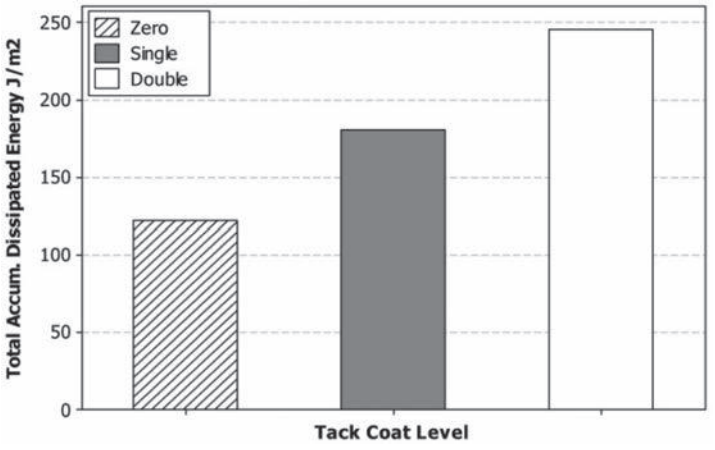

Figure 6. Total dissipated energy at 14,400 cycles for field composite samples (single samples).

interfaces. Since the fatigue results were obtained on single replicates, it needs further statistical verification but the large differences between total dissipated energies are very encouraging and are difficult to neglect. More research is planned to further examine these observations.

5 SUMMARY

The validation results reported in this paper show that the AST fixture can differentiate between various interlayer treatments as well as it can be used to examine shear properties of the solid samples. In particular, the results demonstrated that monotonic strength tests in the AST device can be used to determine the Mohr-Coulomb failure envelope for solid HMA samples. Additionally, the AST can differentiate between different application rates of the interlayer bonding agent during the shear strength and shear fatigue tests. It was observed that the dissipated energy parameter from the fatigue testing is the most indicative of the application rate of the interlayer material.

Although results presented in this paper were obtained on the limited number of samples, they are still encouraging and proved that the AST can be a valuable addition to the existing suite of the shear devices in the asphalt industry. More research is planned in order to further excel the capabilities of the AST and to employ it on larger experimental effort with diverse treatments.

ACKNOWLEDGEMENTS

The authors would like to thank University of Connecticut, Connecticut Department of Transportation and Tilcon CT, Inc. for supporting this study. The opinions and conclusions presented in this publication are not necessary of those entities and are only of its authors. The authors would like also to express a special appreciation to Prof. Andrew Drescher from the University of Minnesota for the valuable discussion and comments.

REFERENCES

[1] Leutner R. "Untersuchung des schichtenverbundes beim bituminosen oberbau." Hamburg, Germany: Bitumen, Heft 3, ARBIT; 1979.

[2] C. Raab, and M.N. Partl. "Effect of Tack Coats on Interlayer Shear Bond of Pavements." Proceedings of the 8th Conference on Asphalt Pavements for Southern Africa. Sun City, 2004.

[3] J. Uzan, M. Livneh, and Y. Eshed. "Investigation of Adhesion Properties between Asphaltic-Concrete Layers" AAPT Vol. 47 p. 495, 1978.
[4] S. Romanoschi. "Characterization of Pavement Layer Interfaces." PhD Dissertation, Louisiana State University, 1999.
[5] F. Canestrari, G. Ferrotti, M.N. Partl, E. Santagata. "Advanced Testing and Characterization of Interlayer Shear Resistance" TRR, No. 1929, p. 69–78, 2005.
[6] Diakhate, M.; Phelipot, A.; Millien, A.; Petit, C. 2006. Shear Fatigue Behaviour of Tack Coats in Pavements, Road Materials and Pavement Design 7(2): 201–222.
[7] R.C. West, J. Zhang, J. Moore. "Evaluation of Bond Strength between Pavement Layers." National Center for Asphalt Testing, 2005.
[8] I.L. Al-Qadi, S.H. Carpenter, Z. Leng, H. Ozer and J.S. Trepanier. "Tack Coat Optimization for HMA Overlays: Laboratory Testing." Federal Highway Administration, Report No. FHWA-ICT-08-02, 2008.
[9] L.N. Mohammad, A. Bae, M.A. Elseifi, J. Button, and N. Patel. "Effects of Pavement Surface Type and Sample Preparation Method on Tack Coat Interface Shear Strength" Journal of the Transportation Research Board, No. 2180. Washington, D.C., 2010 pp. 93–101.
[10] M. Diakhaté, A. Millien, Ch. Petit, A. Phelipot-Mardelé, B. Pouteau. "Experimental investigation of tack coat fatigue performance: Towards an improved lifetime assessment of pavement structure interfaces", Construction and Building Materials, Volume 25, Issue 2, 2011, Pages 1123–1133.
[11] A.C. Collop, M.H. Sutanto, G.D. Airey, R.C. Elliott. "Shear bond strength between asphalt layers for laboratory prepared samples and field cores." Construction and Building Materials, 2008.
[12] A.C. Collop, M.H. Sutanto, G.D. Airey, R.C. Elliott. "Development of an automatic torque test to measure shear bond strength between asphalt." Construction and Building Materials, 2010.
[13] Raab, C.; Partl, M.N. 2008. Investigation on Long-Term Interlayer Bonding of Asphalt Pavements, The Baltic Journal of Road and Bridge Engineering 3(2): 65–70.
[14] Raab, C., Partl, M.N. Abd El Halim A.O.: Evaluation of Interlayer Shear Bond Devices for Asphalt Pavements. Baltic Journal of Road and Bridge Engineering. Vol. 4 No. 4, pp. 176…195, (2009).
[15] D.W. Christensen, R. Bonaquist, and D.P. Jack. "Evaluation of Triaxial Strength as a Simple Test for Asphalt Concrete Rut Resistance." Pennsylvania Dept. of Transportation, Report No. FHWA-PA-2000-010+97-04.

Asphalt Pavements – Kim (Ed)
© 2014 Taylor & Francis Group, London, ISBN 978-1-138-02693-3

Effect of cooling rate on the thermo-volumetric, thermo-viscoelastic, and fracture properties of asphalt mixtures

Mohammad Zia Alavi & Elie Y. Hajj
University of Nevada, Reno, NV, USA

ABSTRACT: Thermal cracking of asphalt pavements has been known to be highly influenced by both the climatic conditions at the project location and the asphalt mixture properties. Hence, characterization of asphalt mixtures under thermal regimes is essential for appropriate selection of thermal crack resistant material. In this study thermo-volumetric, thermo-viscoelastic, and fracture properties of asphalt mixtures were evaluated by measurements of thermally induced stresses and strains under various cooling rates (2.5, 5, 10, and 17.5°C/hr). Dense-graded asphalt mixtures with two types of asphalt binders (unmodified and polymer-modified) were examined. Thermo-volumetric (i.e., coefficient of thermal contraction) and fracture properties were obtained directly from the thermal strain and thermal stress measurements, respectively. The thermo-viscoelastic properties at the viscous softening stage, viscous-glassy transition stage, glassy hardening stage, and crack initiation stage of the evaluated asphalt mixtures were determined from the evolution of the stiffness, i.e., modulus, as a function of temperature. The modulus was determined using the Boltzmann's superposition principle with the concurrent measurements of thermally induced stress and strain. The results showed that the fracture stress, fracture temperature, and thermo-viscoelastic properties of the evaluated mixtures were influenced by the applied cooling rate and the impact of cooling rate depended on the type of asphalt binder. The coefficient of thermal contraction was not significantly affected by the rate of cooling.

Keywords: Asphalt mixture, thermo-volumetric, thermo-viscoelastic, fracture, thermal stress, thermal strain, cooling rate

1 INTRODUCTION

The resistance of asphalt pavements to thermal cracking are generally influenced by asphalt mixture properties (e.g., thermal volumetric, viscoelastic, and fracture properties), environmental conditions (e.g., temperature, rate of cooling, pavement age), and pavement structure (e.g., interlayer characteristics) [1]. Therefore, an accurate characterization of asphalt mixtures is essential to appropriately model thermal cracking in asphalt pavements and/or in the selection of thermal cracking resistant mixtures. In the mechanistic-empirical design of flexible pavements, the frequency and amount of thermal cracking are estimated using the coefficient of thermal contraction, the relaxation modulus, and the tensile strength properties of the asphalt mixture.

The coefficient of thermal contraction of an asphalt mixture has been traditionally considered constant as a function of temperature within a reasonable range. It has been typically predicted for a given mixture from the volumetric coefficient of thermal contraction of the asphalt binder and aggregate [2]. However the dependency of the thermal coefficient of asphalt mixtures to temperature has been revealed by several researchers [3–7].

Although the direct approach for measuring relaxation modulus is theoretically sound, it is typically difficult to consistently run the test in the laboratory because of equipment control limitations. Therefore, the relaxation modulus is usually obtained by inter-conversion

from other viscoelastic functions, such as creep compliance or complex modulus, considering the materials must behave in the linear viscoelastic range [8–10].

In the case of the fracture properties of asphalt mixtures, several tests have been developed and used throughout the years such as single notch beam, SE(B) [11]; indirect tension, IDT [12]; semi-circular bend, SCB [13]; and the disc-shape compacted tension, DC(T) [14] tests. These tests provide the essential fracture mechanics properties, i.e., tensile strength and fracture energy, in order to characterize crack propagations in asphalt mixtures.

Overall, the aforementioned test methods utilize mechanical loading instead of thermally induced loading to determine the viscoelastic and fracture properties of asphalt mixtures at low temperatures. More precise designs of thermal crack resistant mixtures could be considered if the mixture properties were obtained by suitable thermally-induced loading conditions. Additionally, assuming the thermal coefficient of contraction constant at any temperature results in a thermally-induced strain that is linear at a constant cooling rate, which is contradictory to the basic properties of a viscoelastic material.

The Thermal Stress Restrained Specimen Test (TSRST), historically, was one of the few test methods which could describe the fundamental behavior of asphalt mixture under thermal loading. Relationships between the field cracking temperature and frequency have been observed with the results of the TSRST [15]. The original TSRST method is not in the current AASHTO standard methods. However, a European standard, EN 12697-46, for TSRST has been developed and is currently available [16].

In the earliest work done by Monismith et al. [17], an asphalt mixture beam was subjected to cooling at a rate of 4°C/hr. It was found that no thermal stress were developed in the specimen at the temperatures above 10°C and the measured stress was relatively small down to 0°C. Febb [18] used the TSRST to evaluate gap-graded asphalt mixtures with three cooling rates (5, 10, and 27°C/hr). It was observed that the fracture temperatures were independent of the cooling rate. Sugawara et al. [19] confirmed this finding by conducting the tests on beam specimens under different cooling rates (3, 6, 12, 18, 24, and 30°C/hr) and concluded that cooling rate does not significantly affect the fracture stress or temperature, if the rates were faster than 5°C/hr.

As a part of the Strategic Highway Research Program (SHRP), Jung and Vinson [1] were conducted extensive research on the effects of binder type, aggregate type, mixture air voids, aging levels, cooling rates, and specimen size on the low-temperature characteristics of asphalt mixture beams in the TSRST. All these factors were found to be significant. Correlations between cooling rate and TSRST results (i.e., fracture stress and temperature) were found to depend upon the asphalt binder type. Specimens with a stiffer binder exhibited no significant difference in fracture strength regardless of the applied cooling rate. For specimens containing softer binder, the fracture strengths were greater for faster cooling rates. For evaluated asphalt binder types, both the fracture and transition temperatures were warmer for higher cooling rates.

As part of the National Pooled Fund Study 776 [7], preliminary tests were conducted to evaluate the effect of cooling rate at 2 and 10°C/hr along with specimen shape, beam versus cylinder, on the TSRST. The study revealed that specimens subjected to the faster cooling rate had warmer fracture temperatures. However, the fracture stress did not follow the expected behavior, as it increased slightly with the decrease in the cooling rate. The specimen shape analysis observed that the cylindrical specimens had slightly lower fracture temperatures and higher fracture stresses when compared to beam specimens. Ultimately, the authors recommended additional studies to examine the effects of cooling rate and specimen geometry.

Tabatabaee et al. [20] evaluated the effect of cooling rate and physical hardening on the thermal build up stress and strain in asphalt mixtures. The stress and strain were measured continuously while conducting the test at various cooling rates and isothermal contraction periods (i.e., physical hardening). A slower increase in thermal stress was observed at lower cooling rates.

2 MOTIVATION AND OBJECTIVE

A new test method and associated analysis procedure has been recently introduced and used by the research group at the University of Nevada, Reno, in order to characterize

thermo-volumetric, thermo-viscoelastic, and fracture properties of asphalt mixtures [21, 22]. The calculation of these properties requires direct measurement, with good repeatability, of the thermally induced stress and strain. Therefore, improvements were applied to the conventional TSRST set up to increase the repeatability and to measure the thermal strain of asphalt mixtures from an unrestrained specimen. The enhanced set up is termed the Uniaxial Thermal Stress and Strain Test (UTSST). Details of the UTSST set up can be found in the literature [21, 22].

It is noted that the Asphalt Thermal Crack Analyser (ATCA) set-up has been simultaneously developed at University of Wisconsin, Madison which can also measure the thermal stress and strain while undergoing selected thermal history [23]. The results of the ATCA can also be analyzed in a similar fashion to the results of the UTSST. Ongoing collaborative research is being undertaken to standardize these test methods to analyze the low temperature cracking properties of asphalt mixtures as currently specified in a draft AASHTO standard procedure [24].

With the established test method and respective evaluation procedure, the effect of cooling rates on thermo-volumetric, thermo-viscoelastic, and fracture properties of asphalt mixtures will be evaluated in this study in an attempt to extend the previous knowledge which has been based solely on the fracture stress and temperature.

3 EXPERIMENTAL PLAN

Two types of dense graded asphalt mixture with nominal maximum aggregate size of 12.5-mm were evaluated in this study. The mixtures were fabricated using graded aggregate from the same local aggregate source, and two grades of asphalt binders: an unmodified PG64-22, and a Styrene-Butadiene-Styrene (SBS) modified PG64-28. The asphalt mixtures were designed following the Superpave volumetric mix design method, AASHTO M323, for a medium traffic level equivalent to 3–10 million ESALs. The binder content of mixtures with PG64-22 and PG64-28 were determined to be 5.8 and 5.5 percent by weight of total mix, respectively. After mixing, loose mixtures were subjected to short-term oven aging for 4 hours at 135 ± 3°C. The mixtures were then compacted using a Superpave gyratory compactor to a target air void of 8.0 ± 0.5%. Compacted samples were subjected to long-term oven aging for 5 days at 85°C in accordance with AASHTO R30. Specimens were long-term aged because thermal cracking is a long-term distress mode. Ultimately, two cylindrical specimens were cored from each Superpave compacted specimen perpendicular to the compaction direction (i.e., sideways), with a diameter of 57 mm and height of 135 ± 5 mm. This specimen geometry was found to improve the repeatability of thermal build up stress measurements significantly when compared to other geometries including traditional prismatic specimens, i.e., beams [25].

The mixtures were evaluated in the UTSST using four cooling rates of 2.5, 5, 10, and 17.5°C/hr and an initial equilibrium temperature of 20°C. The cooling rate of 2.5°C/hr is in the range of typically observed daily cooling rates in asphalt pavements [26]. The 10°C/hr is the commonly used cooling rate in the TSRST and the 17.5°C/hr was the fastest cooling rate that can be implemented in the laboratory. The 5°C/hr, according to the literature, was the cooling rate beyond which the fracture temperature and stress were not sensitive to the applied cooling rate [19].

It is noted that the TSRST is traditionally conducted by cooling from an initial temperature of 5°C, although the current European standard recommends 20°C as the initial equilibrium temperature. Asphalt mixture specimens must be conditioned at the initial temperature to reach thermal equilibrium before the start of the test. It should be noted that considerable physical hardening may happen to the asphalt mixture specimen if conditioned at 5°C. Moreover, the initial temperature of 20°C will provide the necessary data needed to examine the evolution of the asphalt mixture properties with temperature.

A total of two replicates for the restrained specimen were tested for each of the evaluated mixtures. In the case of thermal strain, the same unrestrained specimen was tested twice, once for each of the corresponding retrained specimen replicate tests.

4 METHODOLOGY

4.1 *Determination of thermo-volumetric properties*

The thermal contraction strain of the unrestrained specimen caused by the constant cooling rate is plotted against temperature; Figure 1. Then, the model proposed by Bahia et al. [27] and shown in Eq. (1) is fitted to the data.

$$\varepsilon_{th} = \frac{\Delta l}{l_0} = C + \alpha_g (T - T_g) + \ln\left\{\left[1 + e^{\frac{(T-T_g)}{R}}\right]^{R(\alpha_l - \alpha_g)}\right\} \quad (1)$$

where, $\Delta l/l_0$ is the relative change of length or thermal strain; C is intercept with no physical meaning; α_l and α_g are, respectively, the liquid and glassy coefficients of thermal contraction; T_g is glass transition temperature; and, R is the parameter representing the curvature between the two linear asymptotes. The glass transition temperature is determined at the intersection of the two linear portions of the curve in respect to the liquid and glassy coefficients of thermal contraction.

4.2 *Determination of thermo-viscoelastic and fracture properties*

The measured thermal build up stress can be related to the corresponding measured thermal build up strain using the uniaxial constitutive equation for linear viscoelastic materials, i.e., Boltzmann equation [9] as follows.

$$\sigma(t) = \int_0^t E_r(t - t') \frac{\partial \varepsilon(t')}{\partial t'} dt' \quad (2)$$

where, $E_r(t)$ is the relaxation modulus; $\sigma(t)$ is the thermal stress; $\varepsilon(t)$ is the thermal strain; and, t' is the variable of integration. In discrete form, the same Boltzmann equation can be written as:

$$\sigma(t_n) = \sum_{i=1}^{n} E(t_n - t_i) \times (\varepsilon(t_i) - \varepsilon(t_i - 1)) \quad (3)$$

where, n is the time index, and $\sigma(t_0)$ and $\varepsilon(t_0)$ are set to zero corresponding to initial test conditions. By considering the synchronized thermal stress and thermal strain, the modulus at each temperature can be derived from the discrete form of the Boltzmann constitutive equation as follows.

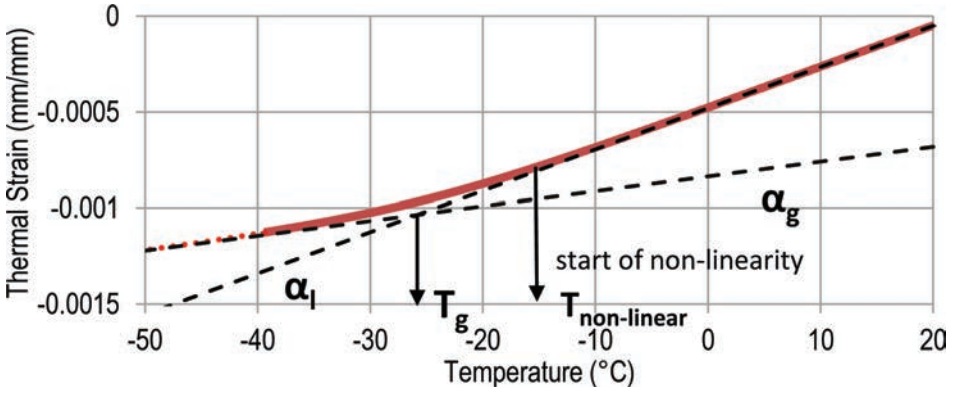

Figure 1. Determination of thermo-volumetric properties from thermal strain measurements.

$$E(T(t_n)) = \frac{(\sigma(t_{n+1}) - \sum_{i=2}^{n+1} E(t_{n+1} - t_i)(\varepsilon(t_i) - \varepsilon(t_{i-1})))}{\varepsilon(t_1)} \quad (4)$$

Figure 2a shows an example of the thermal stress and strain measurements for a typical asphalt mixture. Figure 2b illustrates the modulus curve determined from the thermal stress and strain measurements following Eq. (4).

Five characteristic stages describe the thermal behavior of the asphalt mixture as observed by changes in the stiffness, i.e., modulus, with temperature. These stages, briefly described as follows, can be identified mathematically by the second derivative of the relaxation modulus with respect to temperature [21, 22].

– **Viscous softening.** From this stage the relaxation modulus of the asphalt mixture increases rapidly, mostly in a linear fashion, with decreasing temperature (Fig. 2b). A considerable build up in thermal stresses is observed for temperatures colder than the viscous softening temperature.
– **Viscous-glassy transition.** At this stage the glassy properties of the material overcome the viscous properties (Fig. 2b).
– **Glassy hardening.** At this stage the relaxation property of the asphalt mixture mostly disappears and the material behavior becomes mainly glassy (Fig. 2b).

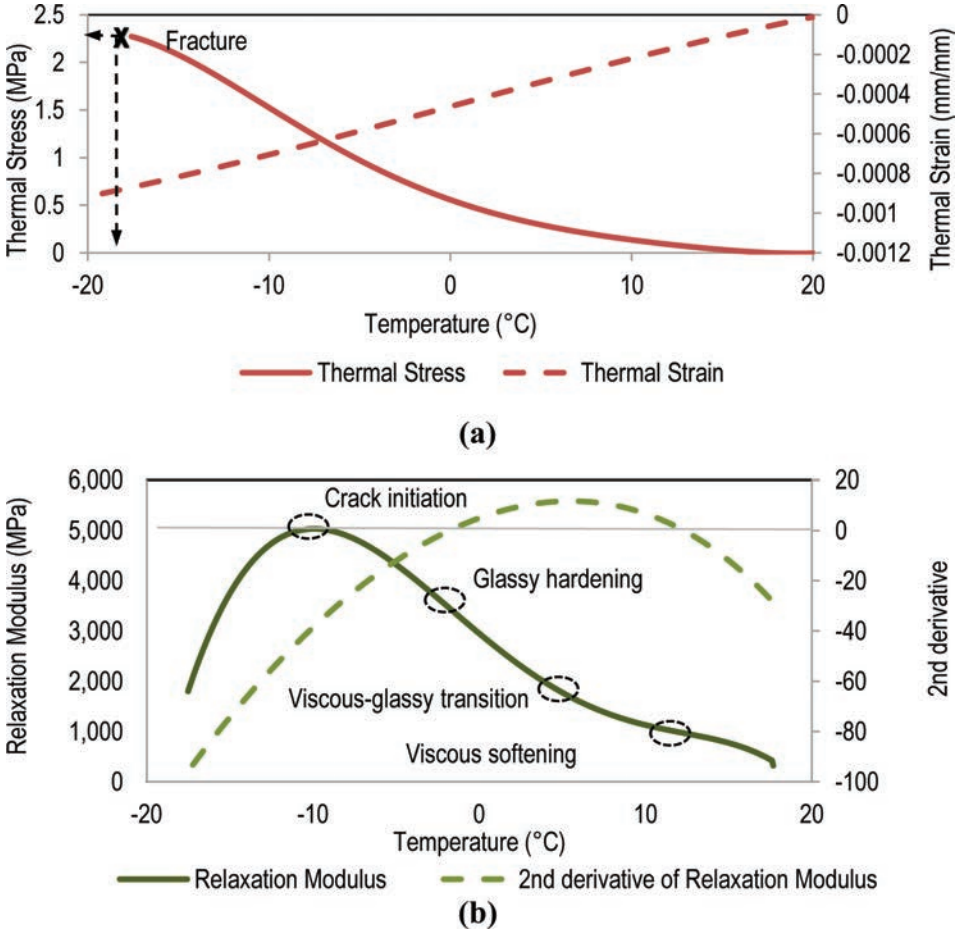

Figure 2. (a) measured thermal stress and strain; (b) calculated relaxation modulus and associated characteristic stages.

– **Crack initiation.** At this stage micro-cracks occur in the specimen due to the induced thermal stresses when the material behavior is glassy (Fig. 2b). Significant instantaneous decrease in the stiffness after this point can be related to the loss of specimen uniformity due to the initiation of micro-cracks.
– **Fracture.** At this stage a global failure occurs in the asphalt mixture specimen mainly due to the propagation of micro-cracks by the induced thermal stresses (Fig. 2a).

5 TEST RESULT AND DISCUSSION

Figure 3 shows the average thermal stress, percentage change in thermal stress, thermal strain, and modulus curves for the evaluated mixtures at the various cooling rates. Examining the data in Figure 3, the following general observations can be made:

– Thermal build up stresses were generally slightly higher for the faster cooling rates as observed for both PG64-22 and PG64-28 mixtures. The percent change in thermal stress for 5, 10, and 17.5°C/hr cooling rates compared to the thermal stress at 2.5°C/hr, are shown for both asphalt mixtures.
– The thermal stress was higher and started to build up at warmer temperatures for the PG64-22 mixture when compared to the PG64-28 mixture, regardless of the cooling rates. The polymer-modified PG64-28 mixture had higher potential for relaxation under cooling events which resulted in lower stress build up and reaching fracture at considerably colder temperatures.
– The change of thermal strain with temperature does not seem to be strongly affected by the cooling rates regardless of the binder type. Overall, the average percent differences in thermal strains at cooling rates of 5, 10, and 17.5°C/hr compared to the 2.5°C/hr were not less than 10% for both mixtures.
– The thermal strains for the PG64-22 and PG64-28 mixtures were generally similar in magnitude.
– The modulus at a given temperature was found to be higher for faster cooling rates, i.e., 10 and 17.5°C/hr. The lowest values for the modulus were observed at the cooling rate of 5°C/hr for both mixtures. The difference in modulus was more noticeable in the case of the PG64-22 mixture.
– The modulus of the PG64-22 mixture was higher than the PG64-28 mixture at temperatures between 20 to –15°C. However, the maximum observed modulus for the PG64-22 mixture was lower than that of the PG64-28 mixture. It should also be noted that, for the various cooling rates, the maximum modulus occurred at considerably colder temperatures in the case of the PG64-28 mixture as compared to the PG64-22 mixture. The substantial relaxation potential of the polymer-modified PG64-28 mixture provided the mixtures with the ability to tolerate colder temperatures before fracture.

5.1 *Effect of cooling rate on thermo-volumetric properties*

The thermo-volumetric properties of asphalt mixtures including liquid and glassy coefficient of thermal contraction, and glass transition temperature, where determined from fitting Eq. (1) to the thermal strain versus temperature data. In addition to these parameters, the temperatures at which the evolution of thermal strain with temperature deviates from linearity were determined and named, $T_{non\text{-}linear}$. This temperature may describe the initiation of glassy properties. The average values of these thermo-volumetric properties for various cooling rates are shown in Table 1. The following observations can be made:

– The glassy coefficients of thermal contraction, α_g, were at least 1.5 times smaller than the corresponding liquid coefficients of thermal contraction, α_l. This observation reveals that considering constant value for coefficient of thermal contraction, irrespective of temperature, may cause significant errors in the prediction of thermal build up stresses.

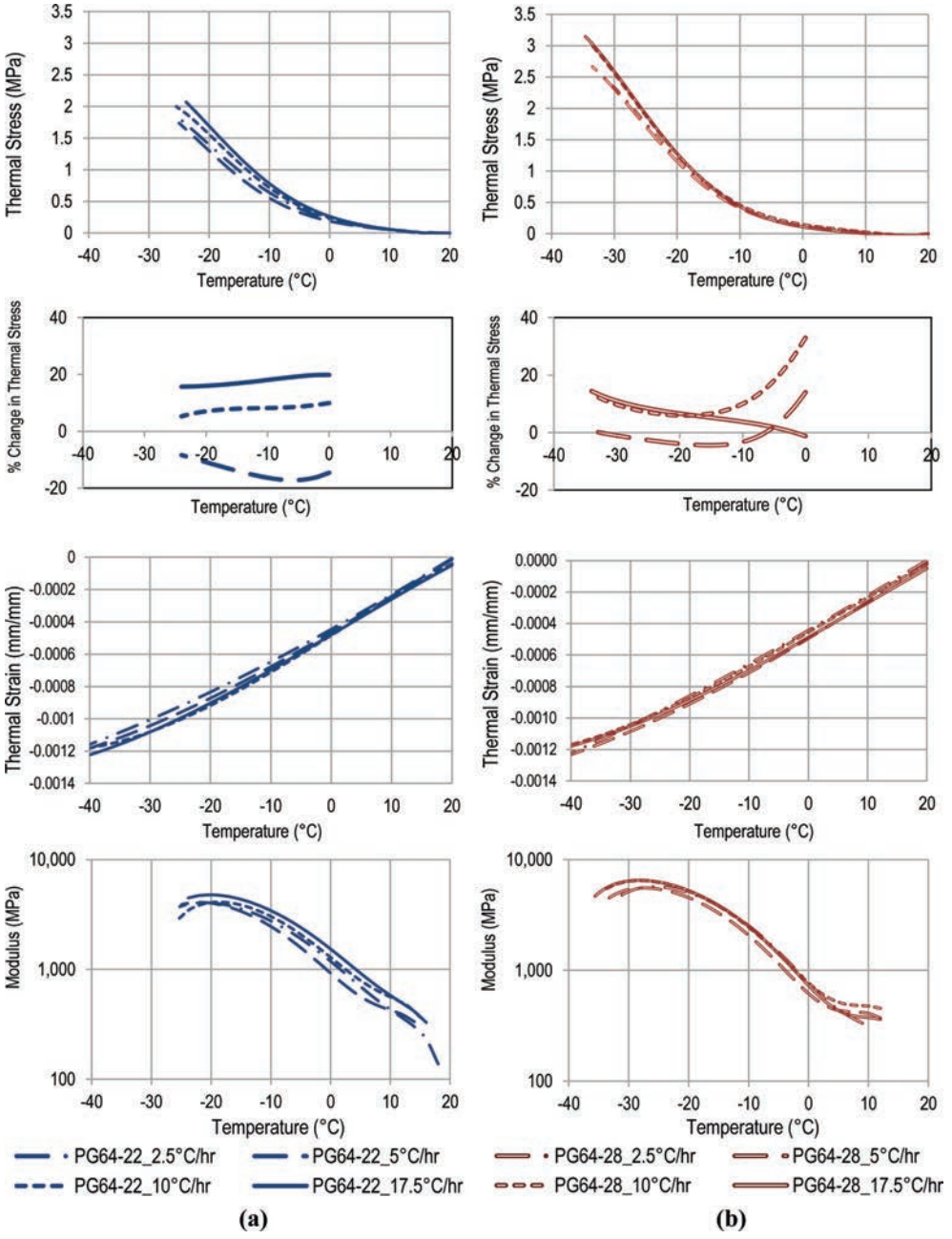

Figure 3. Thermal stress, percentage change in thermal stress, thermal strain, and modulus under various cooling rates for (a) PG64-22 Mixture; (b) PG64-28 Mixture.

- The liquid coefficients of thermal contraction, α_l, were not found to be affected by the evaluated cooling rates.
- The glassy coefficient of thermal contraction, α_g, slightly decreased with the increasing cooling rate except for the PG64-22 mixture at 17.5°C/hr.
- The glass transition temperatures, T_g, for both asphalt mixtures were found to be around –26 ± 1°C for various cooling rates.

Table 1. Thermo-volumetric properties of asphalt mixtures under various cooling rates.

Cooling rate (°C/hr)	α_l (1/°C)		α_g (1/°C)		T_g (°C)		$T_{non\text{-}linear}$ (°C)	
	PG64-22	PG64-28	PG64-22	PG64-28	PG64-22	PG64-28	PG64-22	PG64-28
2.5	2.26E-05	2.22E-05	1.06E-05	1.33E-05	–25	–25	–9	–14
5	2.35E-05	2.23E-05	1.02E-05	1.25E-05	–27	–24	–10	–14
10	2.37E-05	2.23E-05	6.48E-06	1.00E-05	–27	–27	–11	–15
17.5	2.15E-05	2.20E-05	7.55E-06	9.52E-06	–26	–27	–10	–15

– The deviation from the linear portion of thermal strain (i.e., $T_{non\text{-}linear}$) occurred at colder temperatures for the PG64-28 mixture (around 4°C colder on average). This temperature, $T_{non\text{-}linear}$, was not considerably affected by the cooling rate. The colder $T_{non\text{-}linear}$ for the polymer-modified PG64-28 mixture indicates a higher relaxation potential under thermal loadings.

5.2 *Effect of cooling rate on thermo-viscoelastic and fracture properties*

Table 2 summarizes the thermo-viscoelastic and fracture properties calculated for the individual replicates of the various evaluated mixtures and cooling rates.

5.2.1 *Thermo-viscoelastic properties*

Figure 4 shows the change in the average thermo-viscoelastic properties of the evaluated asphalt mixtures as a function of cooling rate. The following observations can be made:

– Based on Figure 4a, the viscous softening modulus of the PG64-22 and PG64-28 mixtures increased with the increase in cooling rate to reach a maximum value at 10°C/hr beyond which a decrease in the viscous softening modulus was observed. No considerable change in the viscous-glassy transition modulus as a function of the cooling rate was observed for both mixtures. The PG64-22 and PG64-28 mixtures exhibited different trends for the change in moduli at the glassy hardening and crack initiation stages as a function of cooling rates. The glassy hardening and crack initiation moduli of the PG64-22 mixture decreased with the increase in cooling rate up to the 10°C/hr, after which the moduli increased with the faster cooling rate. On the contrary, the glassy hardening and crack initiation moduli of the PG64-28 mixture increased with the increase in cooling rate up to 10°C/hr, after which a decrease in the moduli values was observed with the faster cooling rate.
– Based on Figure 4b, the viscous softening temperatures of both asphalt mixtures were not considerably affected by the change in the cooling rate. The effect of cooling rate appeared on the other thermo-viscoelastic stages. It was attractive to observed that the effect of cooling rate on these thermo-viscoelastic properties were different in respect to the mixture type. The PG64-22 mixture reached the viscous-glassy transition, glassy hardening, and crack initiation stages at warmer temperatures with the increase in cooling rate. On the other hand, the PG64-28 mixture exhibited colder temperatures for the various stages with the increase in cooling rate. Furthermore, it was observed that the glassy hardening temperatures which were obtained from the curvature of the relaxation modulus and the temperatures at which non-linearity occurs in the thermal strain measurements, $T_{non\text{-}linear}$, were relatively similar (Fig. 4c).

5.2.2 *Micro-crack and fracture properties*

Figure 5 shows the relationship between the cooling rate and average fracture properties of the asphalt mixtures. The following observations can be made.

– The effect of cooling rate on the fracture and crack-initiation stresses was mixture dependent. For the PG64-22 mixture, these stresses decreased with the increase in the cooling rate

Table 2. Thermo-viscoelastic and fracture properties of asphalt mixtures under various cooling rates.

Stage of behavior			Fracture		Crack initiation			Glassy hardening		Viscous-glassy transition		Viscous softening	
Cooling rate (°C/hr)	Mixture		T.* (°C)	St.** (MP)	T. (°C)	St. (MP)	Mod.+ (MPa)	T. (°C)	Mod. (MPa)	T. (°C)	Mod. (MPa)	T. (°C)	Mod. (MPa)
2.5	PG64-22	a	–25.8	1.9	–21.1	1.5	4,053	–9.1	2,607	1.9	976	13	329
		b	–24.6	1.9	–20.1	1.5	4,226	–8.7	2,728	1.6	1,046	12	371
	PG64-28	a	–34.5	2.4	–25.3	1.7	5,058	–14.7	3,211	–4.1	1,034	7	432
		b	–30.2	2.5	–26.5	2	6,331	–13.2	3,805	0	887	11.9	250
5	PG64-22	a	–25.1	1.7	–22.11	1.4	4,087	–11.25	2,647	–0.9	993	9.2	480
		b	–24.8	1.8	–21.8	1.5	4,064	–10.5	2,596	0.5	8,89	11.8	360
	PG64-28	a	–33.3	2.6	–26.2	1.9	5,273	–14.8	3,318	–3.4	1,016	8.2	414
		b	–33.6	2.7	–28.8	2.1	5,916	–16.8	3,676	–4.7	1,011	7.6	416
10	PG64-22	a	–25.4	2.2	–18.7	1.6	4,374	–7.7	2,867	2.2	1,206	11.7	555
		b	–25.5	1.8	–18.7	1.3	3,824	–8.5	2,485	1.2	947	10.5	490
	PG64-28	a	–33.8	3.1	–26.9	2.3	6,698	–14.6	4,160	–2.5	1,200	9.2	484
		b	–33.8	2.9	–29.9	2.4	6,316	–17.3	3,919	–4.6	1,107	7.7	475
17.5	PG64-22	a	–22.2	1.9	–22.1	1.9	5,109	–9.5	3,271	2.1	1,230	13.3	428
		b	–25.4	2.2	–18.7	1.6	4,562	–7.4	2,946	2.8	1,145	12.6	489
	PG64-28	a	–33.6	2.6	–29.2	2.1	6,404	–17.2	3,876	–4.6	843	8.1	402
		b	–35.6	3.2	–28.3	2.3	6,507	–15.6	4,014	–3	1,084	9.3	376

*T. = Temperature, **St. = Stress, and + Mod. = Modulus

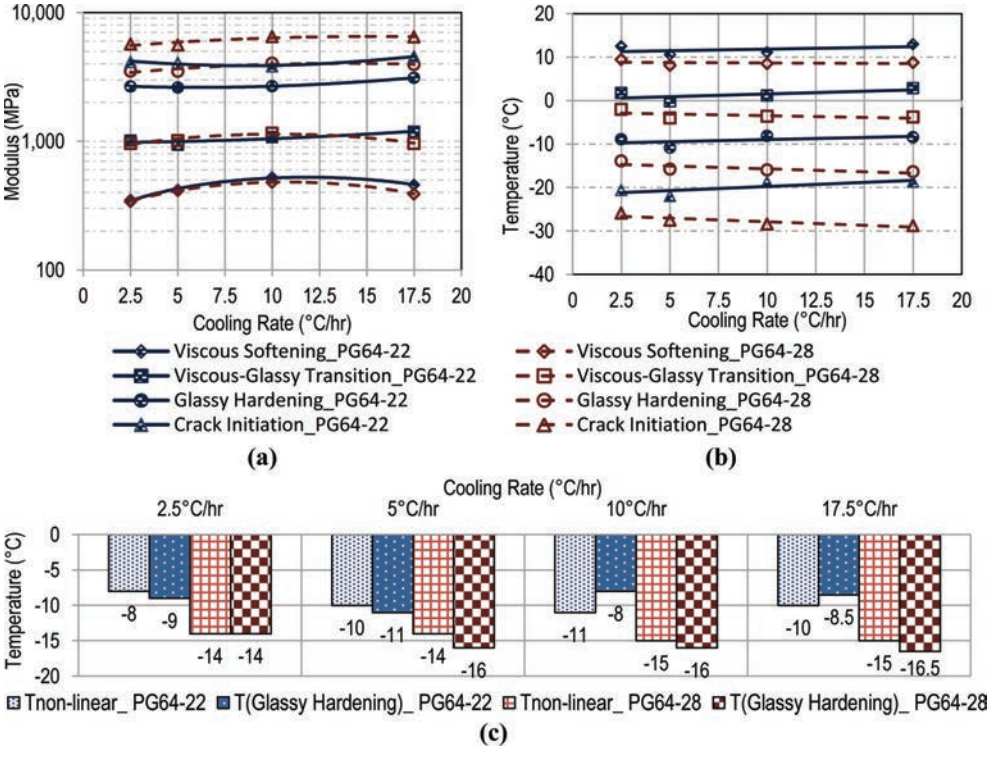

Figure 4. Thermo-viscoelastic properties of asphalt mixtures.

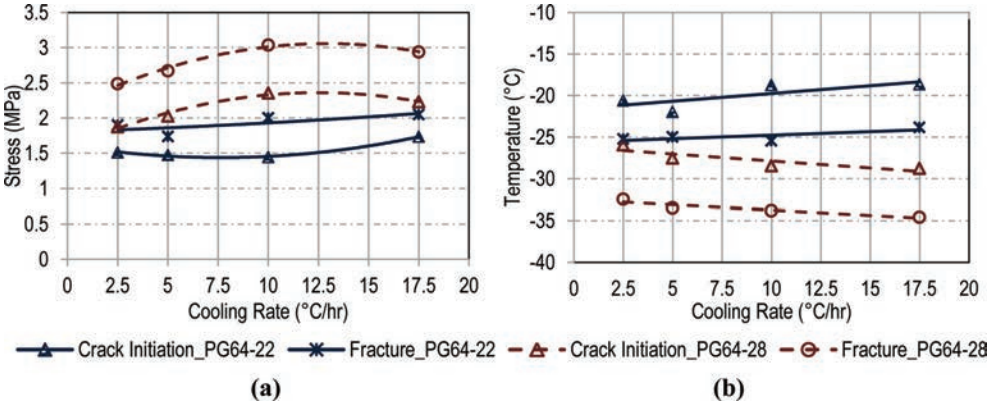

Figure 5. Fracture properties of asphalt mixtures.

up to 10°C/hr beyond which an increase in the stresses was observed for the 17.5°C/hr. Conversely, an increase in the fracture and crack initiation stresses was observed for the PG64-28 mixture with the increase in cooling rate up to 10°C/hr, beyond which the stress values decreased with the 17.5°C/hr.

– In the case of PG64-22 mixture, the fracture and crack initiation temperatures increased (i.e., warmer) with the increase in cooling rate. The opposite behavior was observed for the PG64-28 mixture.

– It is worth to note that in the case of both mixtures, the micro-crack temperatures obtained from the analysis of the modulus at various cooling rates were in the volumetric transition zone of the thermal strain between the liquid and glassy contraction.

Generally, the effect of cooling rate on the thermo-viscoelastic, crack initiation and fracture properties of asphalt mixture depended on the asphalt binder type, i.e., unmodified versus polymer-modified. A study covering additional asphalt binders would assist clarifying the impact of polymer-modification on the thermal behavior of asphalt mixtures.

6 SUMMARY AND RECOMMENDATIONS

In summary this paper evaluated the effect of cooling rate on the thermo-volumetric, thermo-viscoelastic, and fracture properties of two asphalt mixtures using a recently developed test method and analysis procedure at the University of Nevada, Reno. To measure such properties the thermal stress and strain of an asphalt mixture were measured from, respectively, restrained and unrestrained specimens using the Uniaxial Thermal Stress and Strain Test (UTSST), developed at the University of Nevada, Reno. The concurrent measurements of thermal stress and strain were obtained by cooling the specimen from an initial temperature of 20°C at a rate of 2.5, 5, 10, and 17.5°C/hr. In general, it was found that the cooling rate influenced the thermo-viscoelastic and, to a higher level, the fracture and crack-initiation properties of the mixtures. The effect of cooling rate on thermo-viscoelastic and fracture properties were found to depend on the asphalt binder property, i.e., unmodified versus polymer-modified. The effect of cooling rate on the thermo-volumetric property (i.e., coefficient of thermal contraction) was not found to be significant for the evaluated mixtures.

In summary the UTSST showed lower thermal stress build up, lower stiffness, and colder glassy hardening, crack initiation, and fracture temperatures for the PG64-28 asphalt mixtures. These observations can be related to the potential field performance of the asphalt mixture especially that the polymer-modified PG64-28 has historically been outperforming the performance of the unmodified PG64-22 asphalt binder in terms of thermal cracking in the state of Nevada.

The understanding of the characteristics of the asphalt mixture in terms of its thermo-volumetric, thermo-viscoelastic, and fracture properties is an important step toward improved mix designs of thermal crack resistant mixtures. It is recommended that the study be repeated to include asphalt mixtures with different binder sources, binder modifications, aggregate types, and recycled material, possibly with field performance history of the mixtures, to better understand their effect on the mixture resistance to thermal cracking.

REFERENCES

[1] Jung, D.H., and T.S. Vinson. Low-Temperature Cracking: Test Selection, Strategic Highway Research Program. SHRP A-400, Washington DC, 1994.

[2] Lytton, R.L., J. Uzan, E.G. Fernando, R. Roque, D. Hiltunen, and S.M. Stoffels. Development and Validation of Performancee Prediction Models and Specifications for Asphalt Binders and Paving Mixtures, SHRP-A-357, Strategic Highway Research Program, National Research Council, Washington, D.C., 1993.

[3] Littlefield, G. Thermal Expansion and Contraction Characteristics of Utah Asphaltic Concretes, Proceedings of the Association of Asphalt Paving Technologists, Vol. 36, pp. 673–702, 1967.

[4] Stoffels, S.M., and F.D. Kwanda. Determination of the Coefficient of thermal contraction of asphalt concrete using the resistance strain gage technique, Proceeding of the association of asphalt paving technologists, Vol. 65, pp. 73–98, 1996.

[5] Zeng, M., and D.H. Shields. Nonlinear Thermal Expansion and Contraction of Asphalt Concrete, Canadian Journal of Civil Engineering, Vol. 26, pp. 26–34, 1999.

[6] Mamlouk, M.S., M.W. Witczak, K.E. Kaloush, and N. Hasan. Determination of Thermal Properties of Asphalt Mixtures, Journal of Testing and Evaluation, Vol. 33, No. 2, pp. 1–9, 2005.

[7] Marasteanu, M., A. Zofka, M. Turos, X. Li, R. Velasquez, W. Buttler, G. Paulino, A. Braham, E. Dave, J. Ojo, H.U. Bahia, C. Williams, J. Bausano, A. Gallistel, and J. McGraw. Investigation of Low Temperature Cracking in Asphalt: Pavements National pooled Fund Study 776, Minnesota Department of Transportation, MN/RC 2007-43, 2007.
[8] Kim, Y.R. Modeling of Asphalt Concrete, ASCE Press, American Society of Civil Engineers, 2009.
[9] Christensen, R. Theory of Viscoelasticity, Dover Publication incorporation, New York, 2003.
[10] Hao, Y.,G.R. Chehab, S.M. Stoffels, T. Kumar, and L. Premkumar. Use of Creep Compliance Interconverted from Complex Modulus for Thermal Cracking Prediction Using the M-E Pavement Design Guide, International Journal of Pavement Engineering, Vol. 11, Issue 2, pp. 95–105, 2010.
[11] Wagoner, M.P., W.G. Buttlar, and G.H. Paulino. Development of a Single-Edge Notched Beam Test for Asphalt Concrete Mixtures, Journal of Testing and Evaluation, Vol. 33, No. 6, pp. 452–460, 2005a.
[12] Roque, R., Z. Zhang, and B. Sankar. Determination of Crack Growth Rate Parameters of Asphalt Mixtures Using the Superpave IDT, Journal of the Association of Asphalt Paving Technologists, Vol. 68, pp. 404–433, 1999.
[13] Chong, K.P., and M.D. Kuruppu. New Specimens for Mixed Mode Fracture Investigations of Geomaterials, Engineering Fracture Mechanics, Vol. 30, No. 5, pp. 701–712, 1988.
[14] Wagoner, M.P., W.G. Buttlar, G.H. Paulino. Disk-Shaped Compact Tension Test for Asphalt Concrete Fracture, Society for Experimental Mechanics, Vol. 45, No. 3, pp. 270–277, 2005b.
[15] Kanerva, H., T.S. Vinson, and H. Zeng. Low-Temperature Cracking: Field Validation of Thermal Stress Restrained Specimen Test. SHRP A-401, Strategic Highway Research Program, National Research Council, Washington D.C., 1994.
[16] Low Temperature Cracking and Properties by Uniaxial Tension Tests. Part 46, European Standard, Test method for Hot Mix Asphalt, EN 12697-46, 2012.
[17] Monismith, C.L., G.A. Secor, and K.E. Secor. Temperature Induced Stresses and Deformations in Asphalt Concrete, Journal of the Association of Asphalt Pavement Technologists, Vol. 34, pp. 245–285, 1965.
[18] Fabb, T.R.J.. The Influence of Mix Composition, Binder Properties and Cooling Rate on Asphalt Cracking at Low Temperatures, Journal of the Association of Asphalt Paving Technologists, Vol. 43, pp. 285–331, 1974.
[19] Sugawara, T., H. Kubo, and A. Moriyoshi. Low Temperature Cracking of Asphalt Pavements, Proceedings, Workshop in Paving in Cold Areas, Vancouver, B.C., Vol. 1, pp. 1–42, 1982.
[20] Tabatabaee, H.A., R. Velasquez, and H.U. Bahia. Modeling Thermal Stress in Asphalt Mixtures Undergoing Glass Transition and Physical Hardening, Journal of Transportation Research Board, Vol. 2296, Washington. D.C., pp. 106–114, 2012.
[21] Alavi, M.Z., E.Y. Hajj, N.E. Morian, and P.E. Sebaaly. Low Temperature Characterization of Asphalt Mixtures by Measuring Visco-Elastic Properties under Thermal Loading. ISCORD 2013: Proceeding of International Symposium on Cold Regions Development, American Society of Civil Engineering, pp. 404–415, 2013.
[22] Hajj, E.Y., M.Z. Alavi, N.E. Morian, and P.E. Sebaaly. Effect of Select Warm-Mix Additives on Thermo-Viscoelastic Properties of Asphalt Mixtures. Journal of Road Material and Pavement Design, Vol. 14, Special Issue: EATA2013, pp. 175–186, 2013.
[23] Bahia, H.U., H. Tabatabaee, and R. Velasquez. Asphalt Thermal Cracking Analyser (ATCA), Proceeding of 7th RILEM International Conference on Cracking in Pavements. RILEM Bookseries Vol. 4, pp. 147–156, 2012.
[24] Hajj, E.Y., M.Z. Alavi, N.E. Morian, and P.E. Sebaaly. Draft AASHTO Standard Method of test: Determination of Thermal Visco-elastic Properties of Asphalt Mixtures Using Uniaxial Thermal Stress and Strain Test (UTSST), Presented to the FHWA Mixture Expert Task Group, Charlotte, NC, April 29–May 3, 2013.
[25] Cortez, E., E.Y. Hajj, P.E. Sebaaly, and M.Z. Alavi. Investigating Low-Temperature Properties of Cylindrical Superpave Gyratory-Compacted Asphalt Concrete Specimens using the Thermal Stress-Restrained Specimen Test (TSRST), Presented at 90th Annual Meeting of the Transportation Research Board, Washington, D.C., Jan. 2011.
[26] Hajj, E.Y., E. Cortez, P.E. Sebaaly, N.E. Morian, and M.I. Souliman. Study of Pavement Temperature Rates in Hot Mix Asphalt Layers. Final Reports, FHWA-RD-XX-XXX, Federal Highway Administration, September 2013. (*Under Technical Review*).
[27] Bahia, H.U.. Low-Temperature Isothermal Physical Hardening of Asphalt Cements. Ph.D. Dissertation, Pennsylvania State University, University Park, Pa, 1991.

Nondestructive testing of asphalt pavement

This page intentionally left blank

Asphalt Pavements – Kim (Ed)
© 2014 Taylor & Francis Group, London, ISBN 978-1-138-02693-3

Study of the cavity problem under the pavement caused by the earthquake in 2011

Futoshi Kawana
Tokyo University of Agriculture, Setagaya, Tokyo, Japan

Kazuyuki Kubo & Nobuhito Ueda
Public Works Research Institute, Tukuba, Ibaraki, Japan

Yasushi Takeuchi
Tokyo University of Agriculture, Setagaya, Tokyo, Japan

Kunihito Matsui
Tokyo Denki University, Ishizaka, Hatoyama, Hiki, Japan

ABSTRACT: The cavities under the asphalt pavement cause unexpected collapse accidents due to repeated traffic load or the influence of temperature. So, the early detection and rapidly repair of cavities under the pavement are essentially to ensure the safety of user. In the usual case, the cavity is often found around the underground structure. The mechanism of cavities under the pavement has been investigated from site to site based on ground conditions and influence of the underground structure. But the detail mechanism is not well known.

In this study, the tendency of cavities under the pavement caused by "The 2011 Great East Japan Earthquake" was investigated comprehensively. According to the damage pattern after the earthquake, it is often the case that the cavities caused by sand boils due to liquefaction, soil loss at the damaged underground pipe and compacting the loose ground. And the location of cavities is similar to the usual case. Moreover, non-distractive evaluation method of the specification of cavities under the pavement was examined. As the result, the validity of the survey method by use of both FWD and GPR to detect the particular cavity which is possible to reduce the safety of user was demonstrated.

Keywords: The 2011 Great East Japan Earthquake, cavities under the pavement, collapse, FWD, GPR

1 INTRODUCTION

The 2011 Great East Japan Earthquake Disaster claimed many lives and property, as well as causing enormous damage to infrastructure. Many cases of road damage were reported after the earthquake, including collapse, faulting, and impaired traffic function due to sand boils caused by liquefaction. Takeuchi [1] investigated the relationship between liquefaction and damage of pavement in the Tohoku region and pointed out that cavities may have formed under the pavement over a wide area. Cavities under the asphalt pavement can cause unexpected collapse accidents due to repeated traffic load, fluctuations in temperature, or other relevant influences. Therefore, it is essential to detect and repair cavities early to ensure the safety of user. However, as it is difficult to investigate entire disaster area in a short period of time after an earthquake, it is reasonable to prioritize investigation and repair area according to site condition, importance of route, risk for collapse accident due to cavities, and other relevant factors, similar to the medical concept of triage. In order to introduce this concept, the mechanism for forming cavities under the pavement should be clarified, and a simple

investigation method to immediately evaluate the possibility of existence of cavity under the pavement and the risk for collapse accident due to cavities should be developed.

Ordinarily, cavities under the pavement are usually investigated by visual inspection (patrol) or GPR (Ground Penetrating Radar). GPR is a non-destructive exploration technology used to detect a buried object or underground cavity based on the reflected travel time of an electromagnetic wave radiated into the ground. This investigation method allows planar or spatial detection of abnormal areas and also can estimate the specification and location of cavity roughly based on the characteristics of the reflected wave [2], [3]. However, as interpretation of the measurement data can be difficult in certain cases, it requires skill and experience to accurately detect the cavity under the pavement. On the other hand, in cases of an earthquake or other disaster where many cavities can be formed, quantitative evaluation of the risk for collapse accident due to the cavity, as well as the determination of existence of cavities, can be useful for planning investigation and repair strategy. When evaluating the risk for collapse accidents due to cavities, it is necessary to examine the influence of the cavity on the deformation of pavement using dynamical methods.

RWD (Rolling Wheel Deflectometer), TSD (Traffic Speed Deflectometer) and other mobile deflection measurement devices have been developed as dynamical non-destructive investigation methods to identify the continuous status of pavement [4–6]. However, as these testing methods cover a wide investigation area, application to a local abnormality (such as a cavity) has not yet been examined. Therefore, it is considered that the most practical investigation at present combines planar investigation, such as GPR investigation, with dynamical investigation at a fixed point, such as FWD (Falling Weight Deflectometer) test.

In this study, a questionnaire survey of local municipalities in the disaster area was conducted to identify the tendency of cavity under the pavement. Moreover reasonable investigating method for cavities after earthquakes using both GPR survey and FWD test is demonstrated.

2 OVERVIEW OF THE GREAT EAST JAPAN EARTHQUAKE DISASTER

The 2011 off the Pacific coast of Tohoku Earthquake occurred at 14:46 JST on March 11, with a magnitude of 9.0 (Mw)—the greatest observed in the history of Japan. As shown in Figure 1, strong earthquake motions were observed in a wide area extending from the

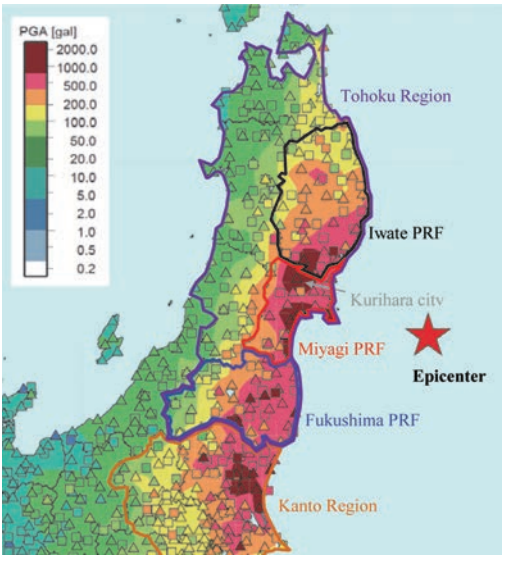

Figure 1. Epicenter and maximum acceleration distribution of the Tohoku earthquake (adapted from Fig. 1, p. 64, in reference [7]).

Tohoku to Kanto regions. According to strong motion seismogram published by the National Research Institute for Earth Science and Disaster Prevention [7], the maximum acceleration in this earthquake reached 2933 gal (in Kurihara City, Miyagi Prefecture) in terms of the three-component composition value, and acceleration exceeding 1G (980 gal) was recorded in some observation points along the Pacific coast. Although it is difficult to identify pavement damage directly caused by earthquake motions, the earthquake caused the road flooding associated with sedimentation (land subsidence) in some parts of coastal area.

Furthermore, the massive tsunami and liquefaction associated with the earthquake led to heavy loss of lives, property, and infrastructure. An investigation of trace of tsunami height reported that tsunami heights exceeded 10 m or higher, causing devastating damage to the coast of the Iwate, Miyagi, and Fukushima prefectures [8]. Reported road damage include stripping surface layer and washing away of blocks due to soil scour around and under pavement. In the Kanto region, liquefaction and sedimentation, sand boils, manholes floating occur in a wide area of reclaimed lands, rivers, and lakes [9], [10].

3 INVESTIGATION OF CAVITY FORMATION TENDENCIES

A questionnaire survey was conducted in the local municipalities affected by The 2011 Great East Japan Earthquake Disaster in order to investigate the occurrence tendency of cavities under the pavement after earthquakes. The questionnaire, which was implemented in November 2012, collected 62 responses from urban areas in the Kanto and Tohoku regions, which experienced particularly strong earthquake motions (as shown in Fig. 1). Questions in the survey concerned with the status of road damage, liquefaction around the affected loads, installation status of underground infrastructure (e.g. sewage pipes, subway systems, catchment basins, etc.), status of cavity investigation implementation, and so on. Figure 2 outlines the results of the survey.

According to the results of questionnaire, pavement damage caused by the Great East Japan Earthquake Disaster included collapse, faulting, manhole floating, and other forms of destruction, such as cracking and undulation. Many of the collapse occurred near sewage pipe, cross drainpipes, catchment basins, manholes, subway systems. Collapses occurred particularly frequently at open-cut construction sites, which indicate the difficulties of selection of backfilling material and compaction around the underground structure. There were 29 sites where sand boils and other traces of liquefaction were confirmed near the affected road, which indicates a strong cause-and-effect relationship between liquefaction and pavement damage. Within the scope of this survey, approximately 80% or more of the affected roads are influenced by underground infrastructure and nearby backfilling areas.

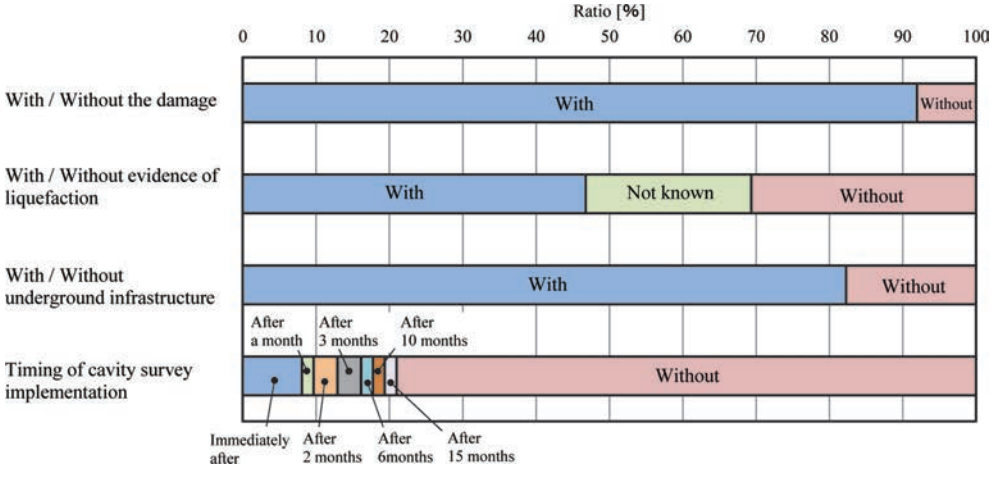

Figure 2. Results of the questionnaire survey.

Table 1. Cavity formation locations.

Categories	Sub-categories
Location where settlement occurred	/Site where the amount of settlement is great
	/Site where differential settlement occurred
	/Site where settlement continues
	/Site where looseness on the ground has been confirmed
Near underground infrastructure	/Around buried pipes (water and sewage pipes)
	/Around manholes
	/Around box culverts
	/Around subways (open-cut areas)

Timing of cavity survey implementation, as shown in Figure 2, refers to the timing of the implementation of underground radar exploration or other non-destructive investigations, and excludes visual inspection (patrol). Although approximately 20% of the municipalities had implemented cavity surveys by the time the questionnaire was conducted, respondents pointed out several implementation issues, including unclear the survey method and priority determining method for investigation routes, shortage of manpower, and economic matters (such as survey cost). Table 1 summarizes the locations of detected cavities. These patterns did not appear to differ significantly from ordinary occurrence tendencies of cavities.

4 CAVITY EVALUATION METHOD

For a common investigation of cavities under the pavement, a simplified survey is performed, consisting of visual inspection (patrol) and underground radar exploration. If the possibility of existence of the cavity under the pavement is suggested, a detailed survey such as a scope, drilling, open-cut, simplified dynamic cone penetration test, etc., is performed to confirm the presence of a cavity. When cavities exist under the pavement, possible appropriate approach (such as repair or progress observation) are determined based on the scale of the cavity, situation of the site, and other necessary factors. These procedures are highly effective at ensuring accurate identification of cavities and prevention of serious accidents. However, in a situation where many cavities may form under the pavement, such as during an earthquake or similar emergency, the possibility of collapse accident caused by cavities should be identified immediately. This requires supplementing conventional methods with a dynamical evaluation. Therefore, this study examines the applicability of a combined planar-dynamic method for detecting cavities, which uses GPR survey and FWD test.

GPR survey and FWD test were conducted at the pavement test field of the Public Works Research Institute shown in Photograph 1. Figure 3 shows the pavement composition and location of Styrofoam simulated cavities, which were buried in the granular base (M-30, layer thickness = 20 cm) and cement treated soil (CBR4%, layer thickness = 30 cm). The specifications of the simulated cavities, made of commercially available Styrofoam, are described in Table 2.

The GPR survey used a chirp radar exploration device (GROUNDSEER GN-01, manufactured by The Nippon Signal, Co., Ltd, with the frequency of 800 MHz) shown in Photograph 2. Measurements taken along the survey line (shown in Fig. 3) are displayed in Figure 4. The survey detected abnormal signals at the points where simulated cavities were buried. Although permittivity varies depending on materials, density, moisture content, etc., this study assumes the value of common asphalt permittivity. This assumption may have generated errors in depth measurement. But it is obvious that the relative position and size of cavities can be confirmed by the GPR survey results. This shows the GPR survey results are available for the determination of measurement points of FWD test.

FWD test was conducted by setting measurement points at 0.5 m intervals along the same survey line as the GPR survey. These intervals differ from actual survey intervals, as they are set to identify the relationship between cavity location and surface deflection. The magnitude of

Photograph 1. Pavement test field.

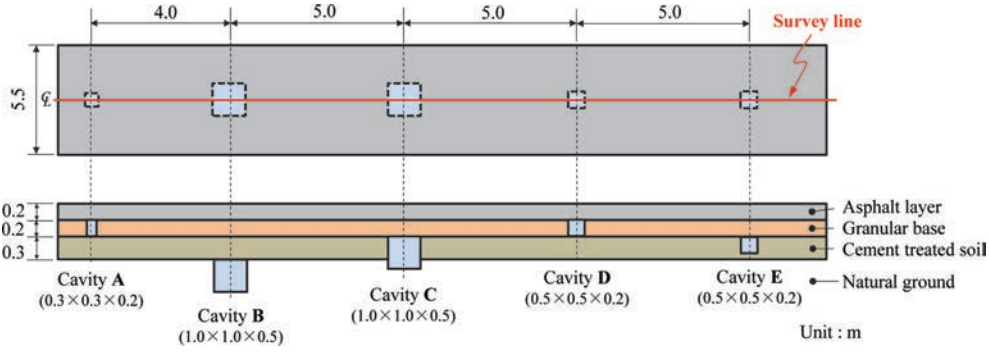

Figure 3. Pavement composition and cavity installation.

Table 2. Specifications and location of simulated cavities.

Cavity	Dimension [m]	Depth [m]		Remarks
		Upper	Lower	
A	0.3 × 0.3 × 0.2	0.2	0.4	Installed in granular base
B	1.0 × 1.0 × 0.5	0.7	1.2	Installed under cement treated soil
C	1.0 × 1.0 × 0.5	0.4	0.9	Installed in cement treated soil
D	0.5 × 0.5 × 0.2	0.2	0.4	Installed in granular base
E	0.5 × 0.5 × 0.2	0.4	0.6	Installed in cement treated soil

load was 49 kN. Figure 5 shows the deflection immediately below the loading plate (hereafter referred to as D_0 deflection) for each measurement point. By comparing D_0 deflection between Cavity A and D, and between Cavity C and E, it was observed that the surface deflection is large and the area where surface deflection affected by cavity is wide, as the cavity scale is large. Additionally, the comparison of D_0 deflection between Cavity B and C and between Cavity D and E showed that deflection is small and the area where surface deflection affected by cavity is wide, as the cavity location is deep. This suggests that dynamical surveys such as FWD test can discern the cavities which affect running of the vehicle or have a high risk of

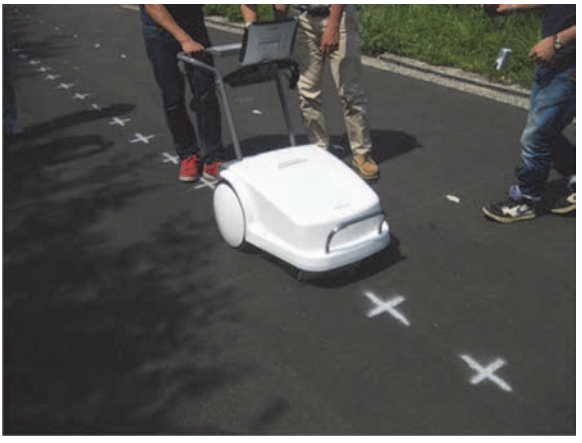

Photograph 2. GPR survey apparatus.

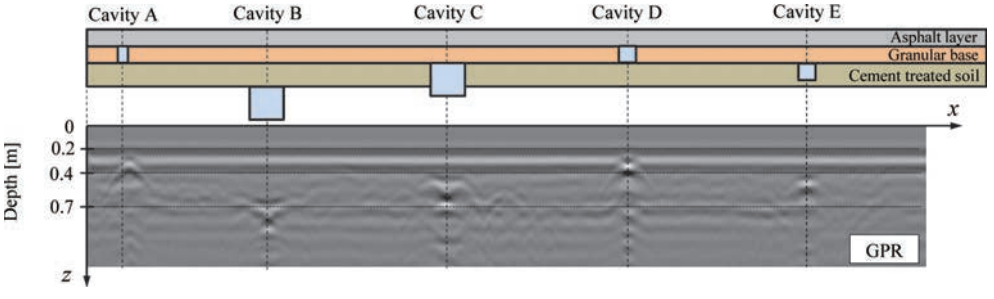

Figure 4. Results of the GPR survey.

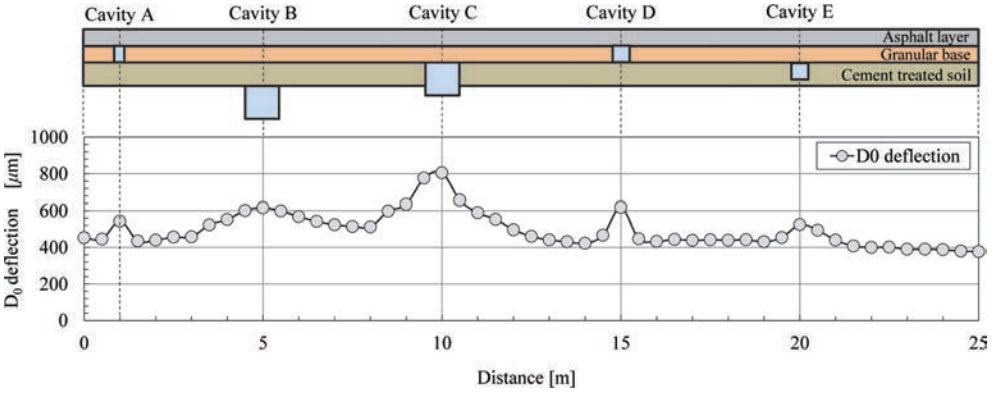

Figure 5. Results of FWD test.

collapse accident. As mentioned above, it is shown that the cavities under the pavement can be efficiently detected by combining the GPR survey with FWD test.

Finally, the evaluating method of the cavity under the pavement using the FWD test results was examined. As shown in Figure 5, when the load applied at the surface of pavement near the cavity, D_0 deflection increased. It indicated that the comparison between D_0 deflection for the sound part of same cross-section and the measurement value enable to detect cavities

under the pavement. However, D_0 deflection obtained from FWD test vary even the same cross-section due to the stiffness heterogeneity of each pavement layer, uneven layer thickness, loading conditions, etc. Therefore, it is reasonable to set the upper limit for confidence interval as the threshold of D_0 deflection using interval estimation of population mean value for samples of D_0 deflection in the sound section. The threshold of D_0 deflection is defined by the following equation.

$$D_{lim} = D_{0ave} + t_x \, SE \tag{1}$$

where,
D_{lim} : Threshold of the D_0 deflection
D_{0ave} : Average of the D_0 deflection for the sound section
SE : Standard error of sample
t_x : Factor corresponding to the reliability x% based on the distribution of t

An example of the cavity evaluation is shown below. First, FWD test was conducted at 12 points on sound parts with the same cross-section shown in Figure 3. The average value of D_0 deflection at the 12 points was 384 μm, with a variation coefficient of 5.6%. Next, the confidence intervals were calculated respectively for 3, 4, 6, 8, and 12 samples extracted from the D_0 deflection at the 12 points. As an example of these calculations, the upper limit for 99, 95 and 90% confidence interval are given in Table 3. Figure 6 compares D_0 deflection on the simulated cavities (Fig. 5), with the upper limit for 99% confidence interval with 12 samples, and the upper limit for 95% confidence interval with 3 samples. For example, when setting the upper limit for 95% confidence interval as the threshold (with 3 samples, shown with a green dashed line in the figure), the D_0 deflection of Cavities B and C exceed the threshold in a wide area. In comparison, setting the upper limit 99% confidence interval as the threshold (with 12 samples, shown with a red dashed line in the figure), all cavities exceed the threshold. Also, as this examination uses results for the test filed where pavement layer thickness and

Table 3. Upper limit of the confidence interval [μm].

Average [μm]	Standard deviation [μm]	Sample number	Reliability index [%]		
			99	95	90
384	22	12	403	398	395
380	26	8	412	402	397
381	30	6	431	413	406
380	39	4	493	442	426
373	44	3	626	483	448

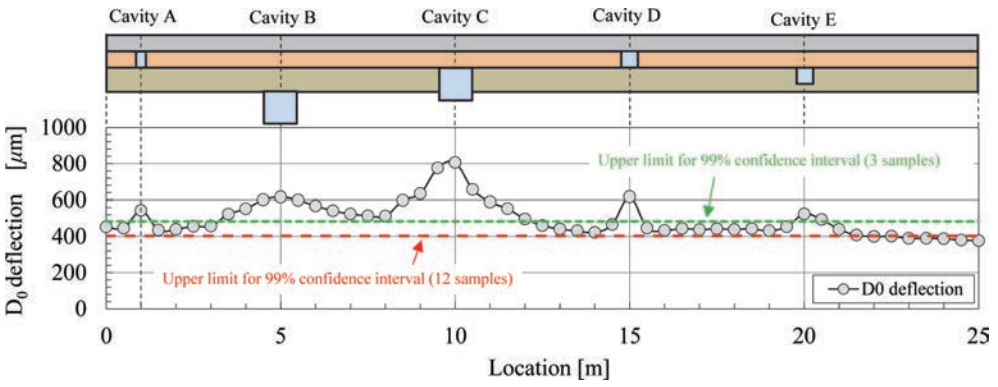

Figure 6. Results of the FWD test.

compaction level were strictly controlled, the number of samples necessary for the evaluation and the method for setting the reliability are not to be discussed.

5 SUMMARY

In this study, a survey on pavement damage caused by the Great East Japan Earthquake Disaster was conducted in order to understand the occurrence tendency of cavity under the pavement after an earthquake. Additionally, non-distractive investigation method of cavities under the pavement using GPR and FWD test was examined. The major findings of this study are as described below.

1. Cavity formation patterns during earthquakes are similar to those under ordinary case.
2. The relative location and size of cavities can be confirmed by the GPR survey. This shows the GPR survey results are available for the determination of measurement points of FWD test.
3. From the results of FWD test for simulated cavities, it is confirmed that the D_0 deflection varies significantly by the location and size of cavities. This suggests that the risk for collapse accident due to cavities under the pavement can be estimated by dynamical method such as FWD test.
4. As mentioned above, it is shown that the cavities under the pavement can be efficiently detected by combining the GPR survey with FWD test.

In future research, we will evaluate the relationship between pavement composition, FWD deflection, and the risk of cavities based on collapse accident reports.

ACKNOWLEDGMENT

We would like to express our deepest gratitude to local municipal authorities for their extensive cooperation in the questionnaire survey, despite their busy disaster recovery schedule.

REFERENCES

[1] Y. Takeuchi. Inspection of the Pavement in the Tohoku District Stricken Area, ASPHALT, Vol. 54, No. 227, pp. 11–17, 2012.
[2] H. Tomita, H. Tada, K. Chou, T. Nakamura and T. McGregor. Nature and Detection of Void-Induced Pavement Failures, Transportation Research Record 1505, pp. 9–16, 1995.
[3] H. Nakamura and H. Suzuki. Understanding the Circumstances of the Occurrence of Cavities in Road Beds Caused by the Tohoku Earthquake Using Skeleka Technology, 22th Trechless Technology Workshop, pp. 11–16, 2011.
[4] Brian K. Diefenderfer. Investigation of the Rolling Wheel Deflectometer, Virginia Transportation Research Council, Final Report VTRC 10-R5, 2010.
[5] Mostafa A. Elseifi: Evaluation of Continuous Deflrction Testing Using the Rolling Wheel Deflectometer in Louisiana, Journal of Transportation Engineering, pp. 414–422, ASCE, April, 2012.
[6] B. Ferne, P. Langdale and N. Round: Development of the UK highways agency traffic speed deflectometer, Bearing Capacity of Roads, Railways and Airfields, pp. 409–418, 2009.
[7] Y. Okada et al. Research Report on the 2011 Great East Japan Earthquake Disaster, Natural Disaster Research Report of the National Research Institute for Earth Science and Disaster Prevention, Vol. 48, March 2012.
[8] S. Takahashi et al. Urgent Survey for 2011 Greate East Japan Earthquake and Tsunami Disaster in port and Coasts, technical note of the port and airport research institute, No. 1231, April, 2011.
[9] H. Kyokawa, T. Kiyota, Y. Kondo and K. Konagai. Survey report on Liquefaction-induced damage in Urayasu city caused by The 2011 of the Pacific coast of Tohoku Earthquake, Japanese Geotechnical Journal, Vol. 7, No. 4, pp. 265–273, 2012.
[10] S. Yasuda, K. Harada and K. Ishikawa. Damage to structures in Chiba Prefecture during the 2011 Tohoku-Pacific Ocean Earthquake, Japanese Geotechnical Journal, Vol. 7, No. 1, pp. 103–115, 2012.

Asphalt Pavements – Kim (Ed)
© 2014 Taylor & Francis Group, London, ISBN 978-1-138-02693-3

Performance of Permeable Friction Course (PFC) pavements over time

Edith Arambula, Cindy K. Estakhri & Amy Epps Martin
Texas A&M Transportation Institute, College Station, TX, USA

Manuel Trevino, Andre Smit & Jorge Prozzi
Center for Transportation Research, Austin, TX, USA

ABSTRACT: Performance of Permeable Friction Courses (PFCs) was evaluated over time and compared against other mixture types. Several pavement sections including Asphalt Rubber (AR) PFCs, Performance Graded (PG) PFCs, and dense-graded Hot Mix Asphalt (HMA) were monitored over a four-year period. On-site measurements included noise, drainability, texture, friction, and skid. The change of these variables with time as well as the influence of traffic, binder/mixture type, aggregate classification, and climatic region was evaluated. Accident data was also gathered and analysed on a more comprehensive number of pavement sections across the state of Texas.

Performance of PFCs over time was adequate. PFCs had lower overall noise levels when compared to HMA, and AR-PFCs were quieter than PG-PFCs. With regard to drainability, the water flow values had a tendency to increase early in the life of the pavement and remain relatively constant afterwards. PG-PFCs showed better drainability as compared to AR-PFCs. Texture for PFCs remained practically unchanged over time. Both AR- and PG-PFCs had superior texture and skid vs. HMA pavements. With regard to friction and skid, sections with lower quality aggregates had inferior values. The accident data indicated that PFCs reduce the number of accidents, injuries, and fatalities on roads in Texas.

Keywords: Permeable Friction Course, porous asphalt, field performance, non-destructive testing

1 INTRODUCTION

Permeable Friction Course pavements (PFCs) are being used as a pavement surface layer for reasons of safety, amenity, and environmental benefits. PFCs consist of a compacted permeable mixture of aggregate, asphalt binder, and additives mixed hot in a mixing plant. These pavements are designed to achieve good drainability and reduce the generation and propagation of traffic noise. PFCs also offer better ride quality, better vehicle handling, and the flexibility of application as a wearing surface over Portland Cement Concrete (PCC) or Hot Mix Asphalt (HMA). The usual percent Air Voids (AV) in PFCs is at least 18 percent. With such a high fraction of AV, PFCs are a superior pavement in wet weather due to reduced splash and spray and hydroplaning potential [1–5].

There are also some potential disadvantages associated with the use of PFCs related to the high fraction of AV that provides its benefits. Besides the decreased expected service life for PFCs (typically 6–10 years for PFCs vs. 12–15 years for HMA), loss of safety and functionality are important factors to consider. Functionality is defined as the ability of the pavement to maintain its beneficial characteristics with regard to increased drainabil-

ity and reduced tire/pavement noise. PFC functionality diminishes when dust and debris accumulate and clog the AV structure or when the pavement densifies under the effect of traffic loads. State agencies usually schedule preventive maintenance focused on cleaning the PFC pore structure and prolonging the advantages of the pavement surface. In the absence of cleaning activities, the initial permeability and noise reduction capacity are expected to decrease such that, at the end of the functional life at approximately 6–10 years (when the functional characteristics are lost), PFC behaves more like a conventional dense-graded HMA. In addition, the durability of PFCs is usually impacted by the onset and rapid progression of raveling [6].

Recent studies have explored the mix design, construction, maintenance, noise abatement, and winter maintenance issues of PFCs [7–9]. In this study, the performance of PFCs and other types of pavement surfaces was tracked over time to quantify changes in functionality and safety. Functionality included drainability and noise reduction effectiveness. Safety was measured in terms of texture, friction, skid resistance, and accident data. Additional information about this study can be found elsewhere [10].

2 EXPERIMENTAL DESIGN

In order to track the performance of PFCs over time and compare it against other types of mixtures, 28 pavement sections across different climatic zones in Texas were selected. The first 20 sections listed in Table 1 were tracked over a 4-year period (i.e., 2009–2012) and include four conventional dense-graded HMA pavement sections that served as reference, one Thin-Bonded PFC (TBPFC), and one Ultra-Thin-Bonded HMA (UTBHMA). Two types of asphalt binders were used in the PFC sections, Performance Graded (PG) and Asphalt Rubber (AR). TxDOT specifies a finer gradation and higher binder content for the AR-PFCs as compared to PG-PFCs [11]. The rest of the pavement sections (i.e., 21–28) were used as case studies. Details of all sections are listed in Table 1.

The non-destructive on-site field tests that were performed to monitor functionality and safety are listed in Table 2. Skid values were extracted from the Texas Department of Transportation (TxDOT) Pavement Management Information System (PMIS). An evaluation of the change in each variable with time was completed first, followed by an evaluation of the effect of traffic (except for noise), binder/mixture type, aggregate classification, and climate. In addition, accident data for each pavement section was obtained from the TxDOT Crash Records Information System (CRIS).

In order to quantify the effect of traffic, on-site tests were performed both On the Wheel Path (OWP) and Between the Wheel Paths (BWP). All testing was done on the right wheel path when facing the direction of travel. Testing BWP was done by placing the equipment near the estimated centerline of the wheel paths. On-site Water Flow Value (WFV), texture, and friction measurements were performed on three equally spaced subsections approximately 150 m apart. Testing OWP and BWP was done in all three subsections and the average of the measurements reported as the OWP or BWP result for that pavement section. One WFV measurement was performed OWP and BWP in each subsection unless there was a reason to believe the result was inaccurate due to localized bleeding or clogging. In the case of the Circular Track Meter (CTM), two replicate tests about 2 inches apart from each other were performed in each subsection. The average of the six replicate measurements was reported as the OWP or BWP texture for that pavement section. Friction was measured once in each subsection by placing the Dynamic Friction Tester (DFT) in the same spot where the first texture measurement was acquired.

For the noise measurements, two valid test runs were performed per sound intensity probe position (i.e., leading edge and trailing edge), and three replicate measurements were collected at each probe location and then averaged to obtain the overall noise level. Each measurement was averaged over a 5-second period, yielding test sections that, given the testing traveling speed of 97 kph, were approximately 130 m long.

Table 1. Pavement sections included in the experimental design.

ID	CSJ	District	County	Route	Dir	Mixture type	Binder	Aggregate	SAC type[a]	Bond type	Const M/Y	Climate[b]
1	0089-06-076	Yoakum	Wharton	US 59	SB	PFC	PG 76-22S	Limestone	B	Seal	June 2007	WW
2	0598-02-043	Houston	Brazoria	SH 288	SB	PFC	AR	Granite/ limestone	A/B	Seal	Oct 2006	WW
3	0114-06-031	Austin	Bastrop	US 290	EB	PFC	AR	Sandstone	A	Seal	April 2007	M
4	0010-02-079	Paris	Hopkins	IH 30	WB	TBPFC	PG 76-22	Sandstone	A	Membrane	May 2006	WC
5	0049-06-061	Bryan	Robertson	SH 6	NB	PFC	PG 76-22	Sandstone/ limestone	A/B	–	May 2009	WW
6	0006-05-Xxx	Abilene	Taylor	IH 20	WB	PFC	PG 76-22 TR	Limestone	B	–	June 2005	DC
7	0033-06-097	Abilene	Taylor	US 83	NB	PFC	PG 76-22S	Limestone	B	Seal	Sept 2005	DC
8	0156-03-044	Wichita falls	Wichita	SH 240	NB	UTBHMA	PG 76-22	Siliceous/ limestone	A/B	Membrane	May 2008	DC
9	0049-01-085	Waco	McLennan	SH 6	WB	PFC	PG 76-22S	Limestone	B	Seal	August 2005	M
10	0265-01-103	Austin	Travis	SH 71	WB	REF	PG 76-22	Limestone/ field sand	B	–	April 2008	M
11	0521-04-223	San Antonio	Bexar	US 281	SB	PFC	AR	Traprock	A	Seal	May 2005	DW
12	0050-04-025	Houston	Waller	SH 6	NB	PFC	PG 76-22 TR	–	A	Seal	July 2005	WW
13	0089-08-086	Yoakum	Wharton	US 59	NB	REF	PG 70-22S	–	B	–	Sept 2004	WW
14	0074-05-089	Corpus christi	San Patricio	IH 37	NB	PFC	PG 76-22	Limestone/ gravel	B/A	–	May 2004	DW
15	0074-06-197	Corpus christi	Nueces	IH 37	NB	PFC	AR	Limestone	B	Seal	April 2004	DW
16	0372-01-092	Corpus christi	San Patricio	US 77	NB	REF	PG 64-22	–	B	–	July 2009	DW
17	0015-01-164	Waco	McLennan	IH 35	NB	PFC	PG 76-22 TR	Rhyolite	A	–	May 2003	M
18	0401-01-019	Paris	Hopkins	SH 154	NB	REF	PG 64-22	Sandstone	A	–	May 2003	WC
19	0495-02-057	Tyler	Van Zandt	IH 20	EB	PFC	PG 76-22 TR	–	A	Seal	June 2008	WC
20	0910-00-085	Tyler	Smith	IH 20	EB	PFC	PG 76-22 TR	Sandstone	A	Tack	August 2009	WC
21	0073-08-150	San antonio	Bexar	US 281	SB	PFC	AR	Sandstone/ limestone	A/B	Seal	Sept 2006	DW
22	1685-06-027	Houston	Fort Bend	SH 6	SB	TBPFC	PG 76-22S	Quartzite	A	Membrane	April 2005	WW
23	0224-01-054	Wichita falls	Clay	US 287	NB	UTBHMA	PG 76-22	Granite/ dolomite	A/B	Membrane	August 2005	DC

(*Continued*)

Table 1. *Continued*

ID	CSJ	District	County	Route	Dir	Mixture type	Binder	Aggregate	SAC type[a]	Bond type	Const M/Y	Climate[b]
24	0044-02-072	Wichita falls	Clay	US 82	NB	UTBHMA	PG 76-22	Granite/ dolomite	A/B	Membrane	August 2005	DC
25	0249-11-009	Wichita falls	Wichita	SL 473	SB	UTBHMA	PG 76-22	Granite/ dolomite	A/B	Membrane	May 2008	DC
26	0255-08-091	Pharr	Hidalgo	US 281	SB	PFC	AR	Gravel	A	–	May 2004	DW
27	0271-09-017	Houston	Waller	US 90	WB	PFC	AR	Sandstone	A	Seal	March 2004	WW
28	0783-01-093	Lubbock	Lubbock	SL 289	WB	PFC	AR	Gravel/ limestone	A/B	Seal	Oct 2010	DC

[a]SAC = Surface Aggregate Classification.
[b]Climate: DC = Dry Cold; DW = Dry Warm; M = Moderate; WC = Wet Cold; WW = Wet Warm.

Table 2. On-site field measurements.

Field test	Parameter	Measurement unit	Test standard	Equipment
Drainability	Water Flow Value (WFV)	Seconds	Tex 246 F	Permeameter
Noise	Overall Noise Level	A-weighted sound intensity or dBA	AASHTO TP 76	On-board Sound Intensity (OBSI) system
Texture	Mean Profile Depth (MPD)	mm	ASTM E 2157	Circular Track Meter (CTM)
Friction	Friction Number (FN) @ 60 kph	–	ASTM E 1911	Dynamic Friction Tester (DFT)
Skid	Skid Number (SN)	–	ASTM E 274 and ASTM E 524	Skid trailer

3 PAVEMENT PERFORMANCE

The effect of time, traffic, binder/mixture type, aggregate classification, and climate was explored for the on-site field measurements. The climatic regions were defined based on annual precipitation, annual freezing index, and the number of wet days and freeze/thaw days to assign the TxDOT districts into five zones [12]. To assess the differences caused by time, traffic, and aggregate classification, a two-sample t-test was performed assuming equal variances, a two-tailed distribution, and a significance level of $\alpha = 0.05$. In the case of binder/mixture type and climate, an Analysis of Variance (ANOVA) and Tukey's Honest Significant Differences (HSD) test was performed to compare the effect of these factors on the on-site measurements. A summary of observed trends is presented in Table 3.

3.1 *Noise*

Even though an increase in noise levels was expected in PFCs since their acoustic benefit is thought to diminish due to AV clogging and mixture consolidation under traffic, the results of this study did not show a clear pattern of noise level increase with time; some PFC sections even showed lower noise levels with time. A possible explanation for the reduction in noise levels is the fact that two tire types with different aging conditions were used to perform the noise measurements. A correlation model was used to enable the comparison between different tire types but no adjustment was made to account for tire age [10]. The effect of other factors on noise is summarized in Table 3.

3.2 *Drainability*

WFVs were acquired only on PFC pavement sections since UTBHMA and dense-graded HMA pavement sections are essentially impervious. To identify the effect of traffic on drainability, researchers compared OWP vs. BWP measurements. The data for both measurements showed good correlation with the OWP WFVs being somewhat higher than the BWP WFVs (as expected). In addition, after a WFV of about 90 seconds, the correlation of BWP vs. OWP became weaker. Therefore, 90 seconds was established as the threshold to define draining PFCs vs. impervious ones. The effect of time on drainability is illustrated in Figure 1 for AR-PFCs and PG-PFCs after applying the 90-second impervious threshold criteria to the subsection measurements. Only OWP measurements are presented due to the strong

Table 3. Effects of various factors on the on-site field measurements.

	Factors				
Field test	Time	Traffic	Mix/binder type	Aggregate classification	Climate
Drainability, WFV	Initial increase, constant afterwards	No effect	AR-PFC higher than PG-PFC	No effect	WW: lowest DW: largest
Noise, dBA	No effect	–	AR-PFCs ~2 dBA quieter than PG-PFCs	–	M: most quiet WC: loudest
Texture, MPD	No effect except for sections with raveling or fog seal	OWP > BWP	AR-PFC = PG-PFC PFC > HMA	No effect	DC & DW: lowest WW: largest
Friction, FN	Increasing trend on AR-PFCs sections	BWP > OWP	No effect	SAC-B lowest FN	DC & DW: lowest WC: highest
Skid, SN	Effect on many sections	–	PFC > HMA	SAC-B lowest SN	DW: lowest WC: highest

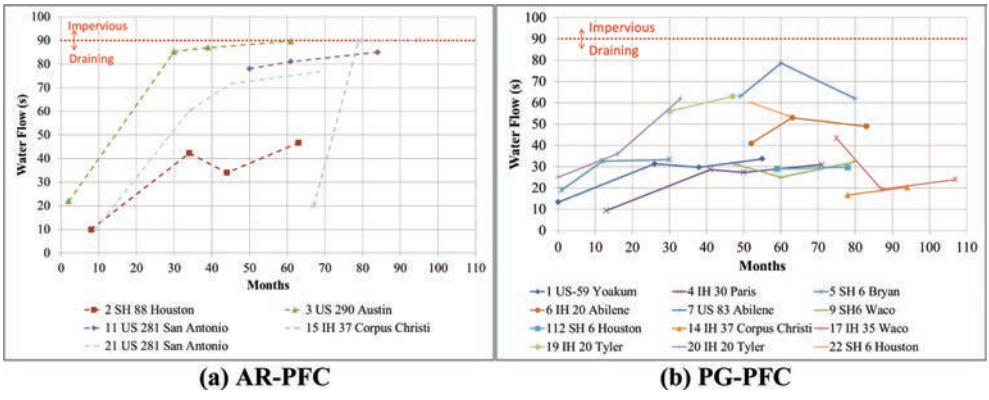

Figure 1. OWP drainability measurements with pavement life.

correlation between BWP and OWP values. In Figure 1, WFVs from five field sections (i.e., 1, 2, 3, 4, and 21) that were collected in 2007 soon after construction as part of a previous study are also included. All 2007 values were below 20 seconds.

Trends showed that WFVs tend to increase when the pavement is new and then remain relatively constant throughout the life of the pavement. For the PG-PFCs, after the initial increase in WFV, the drainability of more than one-third of the pavement sections remained constant at around 30 seconds (Fig. 1b). Conversely, the WFVs for three out of the five AR-PFC sections were close to or beyond the impervious threshold of 90 seconds. Therefore, it is likely that the AV structure of the AR-PFCs is more prone to clogging.

The effect of aggregate classification on drainability was also assessed. Some mixtures employed aggregates classified per TxDOT's Surface Aggregate Classification (SAC) system as SAC-A or SAC-B. More importantly, a few pavement sections used a combination of SAC-A and SAC-B aggregates. Aggregates classified as SAC-A consist of high-quality materials that are resistant to polishing and have higher soundness values as compared to aggregates classified as SAC-B. Some TxDOT districts have demonstrated concerns about combining SAC-A and SAC-B aggregates because they have observed crushing of the SAC-B aggregate under loading. For PFCs, this could translate into a loss in functionality (i.e., permeability and noise reduction). However, a statistical comparison of the WFVs obtained for the pavement sections with SAC-A, SAC-B, and combination of SAC-A/B aggregates showed no significant differences. The effect of the other factors on friction is summarized in Table 3.

3.3 *Texture*

Texture measurements were performed on all pavement sections in 2009, 2010, and 2012. The effect of traffic on texture was assessed by comparing OWP vs. BWP Mean Profile Depth (MPD) values. There was a strong correlation between the MPD values acquired OWP and BWP for both PFC and non-PFCs. For PFCs, the MPD values acquired BWP were slightly higher than the ones acquired OWP, which implies that texture BWP was somewhat larger than texture OWP. The change of texture with time is illustrated in Figure 2. All pavement sections with the exception of sections 14 and 15 in Corpus Christi show relatively flat texture trends. In the case of section 15, a fog seal was applied between the measurements performed in 2009 and 2010, causing the significant decrease in texture. For Section 14, the raveling experienced by the pavement towards the end of its service life more likely has caused the increase in texture. Sections 14 and 15 were considered extreme cases and excluded from the subsequent texture analysis. The effect of the other factors on texture is summarized in Table 3.

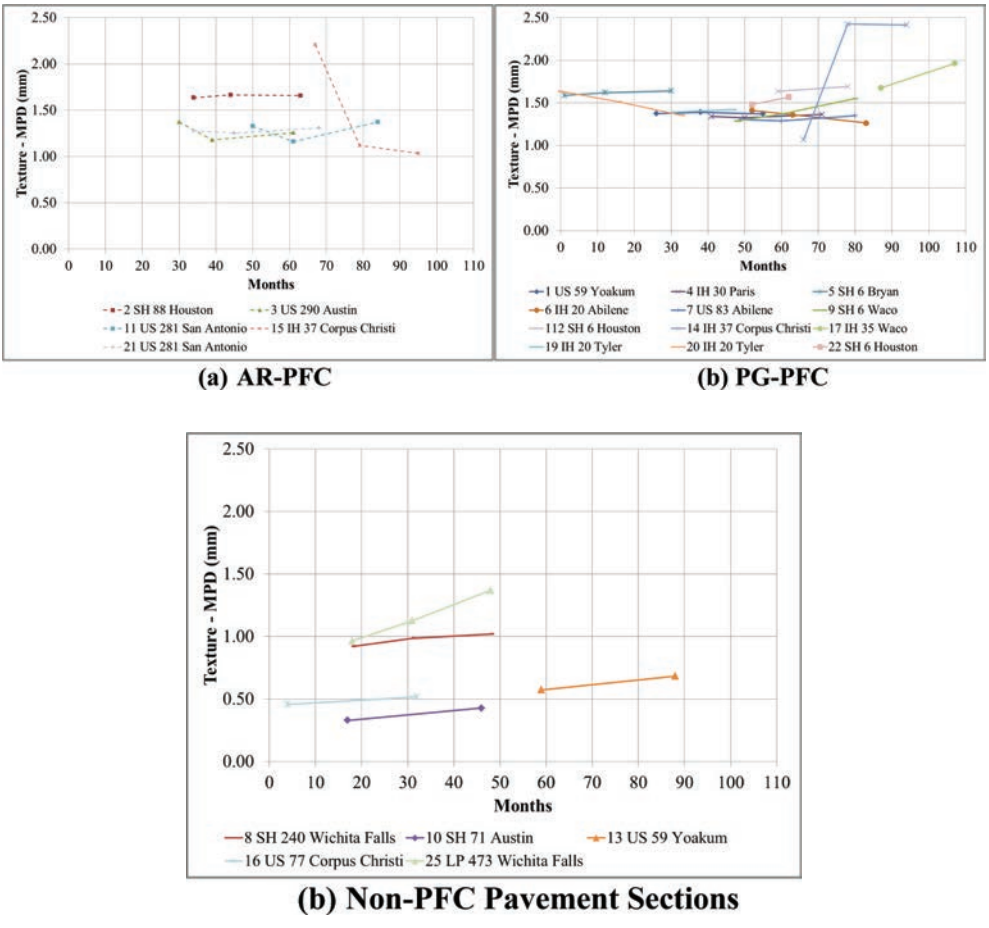

Figure 2. OWP texture measurements with pavement life.

3.4 *Friction*

The effect of traffic on friction was evaluated using OWP and BWP DFT measurements acquired at 60 kph. There was a strong correlation between the OWP and BWP values. The friction values were slightly higher BWP than OWP, especially for non-PFCs. The change in friction with time is illustrated in Figure 3. As previously mentioned, Section 14 experienced raveling, which could explain the significant increase in measured texture. Section 15, which was treated with a fog seal between 2009 and 2010, showed a decrease in friction, although not statistically significant. The significant increase in friction observed in pavement Section 20 is likely due to the fact that this pavement section was constructed just before the first measurement was acquired, and thus traffic likely wore down the asphalt binder at the surface of the pavement and the friction value increased. The effect of the other factors on friction is summarized in Table 3.

3.5 *Skid*

Skid Numbers (SNs) for the pavement sections were extracted from TxDOT's PMIS database. Not all values were available for all sections and/or all years. As compared to the other on-site field measurements, the SNs had more variability and did not follow a consistent trend. For some sections, the values increased; for others, the values decreased; and some others stayed

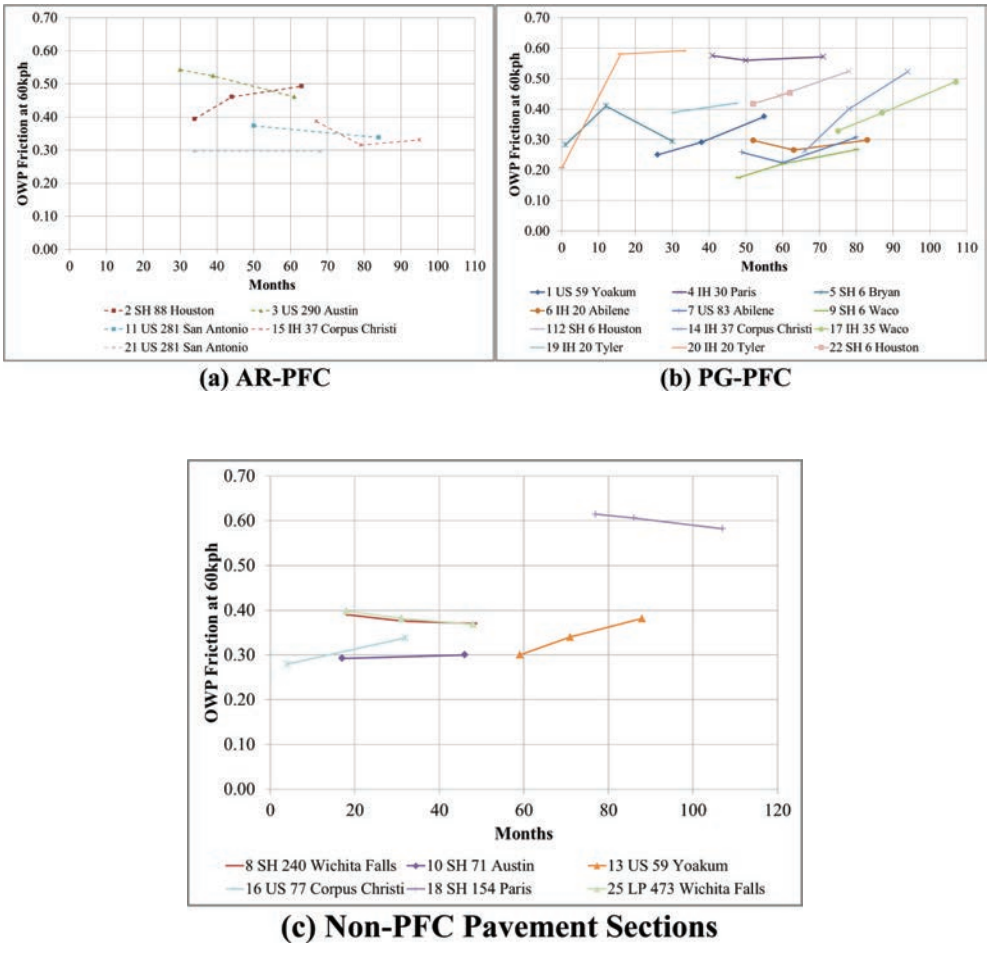

Figure 3. OWP friction measurements with pavement life.

constant. Several PFC pavement sections had statistically significant differences in their SNs with time.

The effect of binder/mixture type on SN was also evaluated. From the statistical results, it was apparent that AR-PFCs and PG-PFCs had higher SN values compared to both UTB-HMA and dense-graded HMA, with AR-PFCs having the largest SN values. When only PFCs and dense-graded HMA were included in the analysis, PFCs clustered together and were statistically different from HMA.

The effect of aggregate classification on SN was quantified as well. ANOVA and Tukey's HSD resulted in statistical significant differences between all aggregate classes (except in 2011 where SAC-A and SAC-A/B were statistically equivalent). Sections employing SAC-A aggregates had the highest SNs, while sections in which mixtures were comprised of only SAC-B aggregates had the lowest SNs. This confirms the friction observations that also showed that the sections with SAC-B aggregates had the lowest friction values as compared to the sections with SAC-A aggregates, which resulted in the largest friction values.

Finally, the effect of climate on SN showed significantly lower values in the Dry Warm (DW) climatic region, while the Wet Cold (WC) region had the highest SNs. The other climatic regions had values in between these two extremes.

3.6 *Accidents*

To investigate the wet weather safety of PFCs in Texas, accident rates under dry and wet conditions and the initial safety of PFC following construction were studied. At the onset, only the pavement sections included in this study were evaluated. However, since no significant trends were found, researchers decided to expand the dataset to include a larger sample of PFC constructed in Texas between 2003 and 2011. A total of 161 PFC projects constructed from 2003 were identified, providing a better platform to evaluate wet weather safety of PFC across Texas.

CRIS reports the weather condition at the time of the accident. Of the accidents reported, 84 percent occurred under clear or cloudy conditions and 14 percent occurred in rainy conditions with the balance occurring under windy, snowy, sleet, hail, or unknown conditions. CRIS also reports the road condition at the time of the accident, i.e., whether wet or dry. Of all the accidents, 78 percent occurred when the road was reportedly dry and 19 percent when wet. A breakdown of the accidents on the pavement sections by weather (i.e., clear/cloudy and rain) and road condition (i.e., dry surface and wet surface) with the relative proportion of the accidents that occurred under these conditions when the surface was a PFC as compared to dense-graded HMA provided a general indication that accidents on PFC were comparatively lower under rain and wet conditions.

To investigate the reported higher accidents on PFC immediately following pavement construction, an analysis of the accidents per lane mile on the PFC sections was made. Some research studies have reported similar observations claiming that apparently drivers take advantage of the reduced splash and spray on PFCs during rain events, driving faster at shorter following distances and causing more accidents [11, 13]. Results of this study showed a definite increase in the number of accidents that continued for three months following construction of the PFC pavement section. The increase in accidents was slight, however, in the order of about 0.0005 accidents per lane mile. Nonetheless, measures to improve safety right after construction should be considered.

4 CONCLUSIONS

The objective of this study was to evaluate the performance of Porous Friction Course pavements (PFCs) over time and compare them to other wearing surface pavement types. Field performance of several pavement sections including Asphalt Rubber (AR) PFCs, Performance Graded (PG) PFCs, Thin-Bonded PFCs (TBPFC), Ultra-Thin-Bonded Hot Mix Asphalt (UTBHMA), and dense-graded Hot Mix Asphalt (HMA) were monitored over a four-year period. Non-destructive on-site tests included noise measurements using On Board Sound Intensity (OBSI) measurement equipment, drainability following the Tex 246 F field water flow test procedure, Mean Profile Depth (MPD) using a Circular Track Meter (CTM), friction at 60 kph using a Dynamic Friction Tester (DFT), and skid that TxDOT collected using a skid trailer. The change of these performance variables with time as well as the influence of traffic, binder/mixture type, aggregate classification, and climatic region was evaluated. Accident data on a comprehensive number of PFC sections in the state was also gathered and analyzed.

Performance evaluation of PFCs over time demonstrated adequate performance. For drainability, PG-PFCs showed better performance as compared to AR-PFCs. In general, measurements in AR-PFCs were more variable than PG-PFCs. For PG-PFCs, the Water Flow Values (WFVs) had a tendency to increase early in the life of the pavement and remain relatively constant afterwards. A 90-second threshold was established to define pervious vs. impervious pavement sections after comparing the WFVs acquired On Wheel Path (OWP) vs. Between Wheel Path (BWP). All PG-PFCs were below the set threshold, while most of the AR PFCs were close to or above the 90-second limit. The classification of the aggregates per the Surface Aggregate Classification (SAC) system did not play a role with respect to WFVs, but climate had a significant effect. Apparently, the amount of

rainfall in a particular climatic region helped assure the continued drainability of PFCs, especially in warm climates.

There was a slight increase in OBSI noise levels with time, but the correlation was weak. The trend was observed only when all measurements were combined. When each pavement section was individually analyzed, no particular trend was observed, except for sections 9 and 14 where a substantial increase in noise levels was noted due to raveling. The binder/mixture type had a significant effect on noise levels with the statistical analysis showing a significant difference between the AR-PFCs (quieter) vs. the PG-PFCs. In addition, PFCs had lower overall noise levels when compared to dense-graded HMA reference sections, although not statistically significant. The climatic region proved to be a statistical significant factor as well.

With regard to the texture measurements, there was a strong correlation between the MPD values acquired OWP and BWP, with texture measured BWP being slightly larger than texture measured OWP. With time, the texture values remained practically unchanged. The two exceptions, where texture changed significantly, corresponded to a pavement section that was fog sealed and another one that exhibited significant amounts of raveling. Both AR- and PG-PFCs had statistical equivalent texture yet better texture than the dense-graded HMA pavement sections used as reference. Neither the aggregate classification nor the climatic region where the pavement sections were placed had a significant impact on texture. Pavement texture achieved soon after construction seemed to be more critical to performance over time.

Friction measurements acquired OWP vs. BWP also showed a strong correlation, with BWP friction values being slightly higher than OWP, especially for non-PFCs. With time, PG-PFCs demonstrated an upward trend in friction values, while AR-PFCs and non-PFCs show a flat or downward friction trend. Differences in binder/mixture type did not have an influence on friction. Aggregate classification, however, did play an important role. Pavement sections with SAC-B aggregates had statistically significantly lower friction values as compared to those pavement sections employing either SAC-A or SAC-A/B aggregates. The effect of climatic region on friction demonstrated that pavement sections in dry climates had lower friction values while pavement sections located in the WC climatic region had the highest friction.

With respect to Skid Number (SN) measurements, these seemed more variable and did not follow a consistent upward or downward trend with time. Similar to the texture observations, AR-PFCs and PG-PFCs had higher SN values compared to dense-graded HMA. Moreover, in line with the friction results, sections employing SAC-A aggregates had the highest SNs, while sections where mixtures were comprised of only SAC-B aggregates had the lowest SNs. Pavement sections in the DW climatic region had the lowest SNs, while pavement sections located in the WC regions had the highest SNs.

The analysis to investigate the safety of PFC under wet conditions included 161 PFC sections from across Texas constructed between 2003 and 2011. Accident rates on these sections were compared before and after construction of the PFC surface. To investigate the safety of PFC under wet conditions, the weather and surface conditions at the time of an accident as reported in CRIS was used. The data indicate that PFC indeed reduces the number of accidents, injuries, and fatalities on roads in Texas. Using the accident data as reported in CRIS, a slight but consistent increase in accidents on PFCs was observed immediately following construction of these surfaces. Therefore, it is recommended that the initial safety of PFC be addressed before opening the road to traffic.

REFERENCES

[1] Brown, J.R. Pervious Bitumen–Macadam Surfacings Laid to Reduce Splash and Spray at Stonebridge, Warwickshire, Report No. LR 563, Transportation Road Research Laboratory, England, 1973.

[2] Button, J.W., E.G. Fernando, and D.R. Middleton. Synthesis of Pavement Issues Related to High-Speed Corridors, Report No. 0-4756-1, Texas Transportation Institute, Texas A&M University, College Station, Texas, 2004.

[3] Kearfott, P., M. Barrett, and J.F. Malina, Jr. Stormwater Quality Documentation of Roadside Shoulders Borrow Ditches, CRWR Online Report 05-02, Center for Research in Water Resources, The University of Texas at Austin, Austin, Texas, 2005.
[4] Khalid, H. and F. Perez. Performance and Durability of Bituminous Materials. Performance Assessment of Spanish and British Porous Asphalts, E & FN Spon, London, pp. 137–157, 1996.
[5] Ruiz, A., R. Alberola, F. Perez, and B. Sanchez. Porous Asphalt Mixtures in Spain, Transportation Research Record 1265, pp. 87–94, 1990.
[6] Cooley Jr., L.A., R.B. Mallick, W.S. Mogawer, M. Partl, L. Poulikakos, and G. Hicks. Construction and Maintenance Practices for Permeable Friction Courses, NCHRP Report 640, National Cooperative Highway Research Program, Transportation Research Board, Washington, DC, 2009.
[7] Alvarez, A.E., A. Epps Martin, C. Estakhri, J.W. Button, C. Glover, and S.H. Jung. Synthesis of Current Practice on the Design, Construction, and Maintenance of Porous Friction Courses, Report No. FHWA/TX-06/0-5262-1, Texas Transportation Institute, College Station, TX, 2006.
[8] Trevino, M., and T. Dossey. Noise Measurements of Highway Pavements in Texas, Research Report 0-5185-3, Center for Transportation Research, The University of Texas at Austin, October 2009.
[9] Yildirim, Y., T. Dossey, K. Fults, M. Tahmoressi, and M. Trevino. Winter Maintenance Issues Associated with New Generation of Open-Graded Friction Courses, Report No. FHWA/TX-08-0-4834-2, Center for Transportation Research, Austin, TX, February 2007.
[10] Arambula, E., C.K. Estakhri, A. Epps Martin, M. Trevino, A. de Fortier Smit, J. Prozzi. Performance and Cost Effectiveness of Permeable Friction Course (PFC) Pavements, Report No. FHWA/TX-12/0-5836-2, Texas Transportation Institute, College Station, TX, October 2012.
[11] Texas Department of Transportation (TxDOT). Standard Specifications for Construction and Maintenance of Highways, Streets, and Bridges Adopted by the Texas Department of Transportation, Austin, Texas, 2004.
[12] Van Der Zwan. Developing Porous Asphalt for Freeways in The Netherlands: Reducing Noise, Improving Safety, Increasing Service Life, TR News 272, Transportation Research Board, January–February 2011.
[12] Freeman, T. Texas Flexible Pavement Database for FPS-19, Report No. FHWA/TX-06/0-0187-06-1, Texas Transportation Institute, College Station, TX, August 2006.
[13] Elvik, R, and G. Poul. Safety Aspects Related to Low Noise Road Surfaces, TOI Report No. 680/2003, Institute of Transport Economics, Oslo, November 2003.

This page intentionally left blank

Asphalt Pavements – Kim (Ed)
© 2014 Taylor & Francis Group, London, ISBN 978-1-138-02693-3

Implementation of algorithms for asphalt moduli temperature correction

Christina Plati, Vasilis Papavasiliou, Andreas Loizos & Christina Tsaimou
Laboratory of Pavement Engineering, National Technical University of Athens (NTUA), Zografou, Athens, Greece

ABSTRACT: Determination of Asphalt Concrete (AC) moduli is a critical issue in terms of pavement evaluation. AC moduli are strongly influenced by temperature variations and thus, determination of AC moduli to a common reference temperature is a complex task. Temperature correction of AC moduli has occupied many researchers over the years yielding the development of multiple algorithms. The main focus of the current research is to evaluate and compare correction results from multiple algorithms and to highlight potential differentiations that occur from their implementation. For this purpose, a road experiment was conducted based on Non Destructive Testing (NDT) techniques, including the Falling Weight Deflectometer (FWD) and the Ground Penetrating Radar (GPR). AC moduli were determined from in situ measurements and corrected to 20 °C. The aim of the experiment was to examine variations between the corrected moduli and the reference values for a untrafficked pavement. AC corrected moduli were examined and analyzed by plotting charts and through statistical processes. Statistical and further analysis of the AC moduli showed that there were large discrepancies between corrected values and real values.

Keywords: temperature correction of moduli, algorithms, NDT techniques

1 INTRODUCTION

Determination of Asphalt Concrete (AC) moduli is critical for monitoring pavement performance and furthermore for gathering information for rehabilitation and maintenance strategies. AC moduli can be determined through laboratory tests or in-situ measurements. The latter can be determined through Non Destructive Testing (NDT) with the Falling Weight Deflectometer (FWD), which is a commonly utilized tool to quantify the response of a pavement structure to known loads.

The modulus of asphalt layers is strongly influenced by temperature conditions and this correlation explains the fact that AC moduli for the same pavement vary in accordance with the temperature within the body of the asphalt layers. Thus, a temperature correction of AC moduli to a reference temperature is required.

Temperature correction for AC backcalculated moduli has been intensively studied by researchers over the years resulting in the development of multiple unique algorithms. Ideally FWD testing should be performed at various temperatures, in order to develop an algorithm for the temperature sensitivity of AC moduli for the site under investigation. However, this is not feasible in most cases due to the fact that there is no control on temperature variations during the survey and there are strict time limitations imposed because of road closures [1]. For this reason, existing algorithms are commonly used for temperature correction of backcalculated AC moduli.

The objective of the current research is to investigate the problems that may potentially occur from the use of existing algorithms for the correction of AC backcalulated moduli. To achieve this goal, a road experiment was conducted that included the utilization of FWD and

Ground Penetrating Radar (GPR) measurements. Deflections from the FWD were measured at three different temperatures. For each measurement AC moduli were determined through a backcalculation approach. Backcalculated moduli were then corrected to the reference temperature utilizing multiple internationally known algorithms. The analysis concerns only backcalulated moduli determined from NDT data and not laboratory determined values.

2 STATE OF THE ART

Temperature correction of moduli has been addressed in multiple studies over the years and several algorithms have been developed. For some of these algorithms there is a limitation on the reference temperature, while others permit the use of any user-specified reference temperature. The most commonly used reference temperatures are those of 20 and 25 °C. In this research, AC backcalculated moduli are corrected to 20 °C by using algorithms based only on a reference temperature 20 °C or on any user-specified reference temperature. Moreover, backcalculated moduli were corrected based on the algorithms that require only temperature data. Potentially, algorithms that need laboratory data may be more accurate, however this requires laboratory test results, which is both time consuming and in some cases difficult to perform. Table 1 indicates the temperature correction algorithms used in this research in chronological order.

Indicatively, bellow are some comments and conclusions from the relative investigations performed for the development of the algorithms. The development of Baltzer and Jansen algorithms is based on FWD measurements. Moreover the use of equation 4(b) with T_{ref} = 20 °C should be limited to a narrow temperature-interval, while equation 4(c) can be used for a wider temperature-interval [5]. Ali and Lopez [7] developed a temperature correction algorithm for backcalculated AC moduli based on in-situ measurements. FWD measurements were also used for Chen et al. [9] algorithm. They conducted a comparison of AC corrected moduli from their algorithm with the relative ones from other algorithms and there was no close agreement. Lukanen et al. [10] used temperature and deflection data from Long Term Pavement Performance (LTPP) program's Seasonal Monitoring Program (SMP). They noted that the slope does have a correlation with the latitude of the site, which is expected to relate to the grading of the asphaltic cement used. In the English Highways Agency [13] report it is noted that where a layer is known to be severely cracked throughout its depth, temperature correction should not normally be applied.

Comparison of temperature correction results from different algorithms has occupied several researchers including Park and Kim [14] which concluded that no single model can cover a broad range of mixtures with different thermoviscoelastic properties. According to Chen et al. [9], comparisons with other reported temperature correction equations showed close agreement for deflection, but not for moduli. Similar results were also derived from the research done by Chang et al. [15] who concluded that the differences among studies were higher for modulus than those for deflection correction. The results of research done by Fernando et al. [16] indicate the importance of collecting data to evaluate the temperature dependency of a given mix. This may be accomplished by laboratory testing of cores or by collecting FWD data at different pavement temperatures.

It should be noted that at reference temperature of approximately 21 °C (Eq. (3, 6)) was assumed to be equal to the 20 °C, as the 1 °C variations will have limited impact on the results. Furthermore for the purposes of this research, in spite of the fact that implementation of some algorithms may require only laboratory estimated AC moduli, it was assumed that all algorithms can be used for correction of moduli from field measurements.

3 ROAD EXPERIMENT AND ANALYSIS OF RESULTS

For the evaluation of temperature correction algorithms a road experiment was conducted using NDT techniques. The experiment consisted of three FWD measurement sets over two

Table 1. Temperature correction algorithms.

1. Ullidtz [2]

$$\frac{E_{T_0}}{E_T} = \frac{1}{3.177 - 1.673(\log T)} \quad (1)$$

where: E_{T_0}, E_T are the asphalt moduli at temperatures of T_0 and T (°C) for $T > 1$ °C.

2. Jung [3]

$$ES = EAe^{kx(TA-TS)} \quad (2)$$

where: ES is the modulus of AC layer (MPa) at the standard temperature, EA is the modulus of AC layer (MPa) corresponding to the test temperature, TA is the mean pavement temperature (°C), TS is the standard temperature (°C) and k is the equation coefficient.

3. Johnson and Baus [4]

$$\frac{E_{std}}{E_{field}} = 10^{-0.0002175}(70^{1.886} - T^{1.886}) \quad (3)$$

where: E_{std} is the AC modulus at standard (reference) temperature, E_{field} is the AC modulus field temperature and, T is the measured temperature in °F. Reference temperature = 70 °F (21.1 °C).

4. Baltzer and Jansen [5]

$$E_{ref} = \frac{E_{ac}}{1 - 2\log\left(\frac{T_{ac}}{T_{ref}}\right)} \quad (4(a))$$

where: T_{ref} is the reference temperature (°C), E_{ref} is the reference AC modulus (MPa), T_{ac} is the AC temperature measured during the FWD test at a depth of 40 mm below the surface and, E_{ac} is the AC modulus from the backcalculation, Pa.

$$\frac{E_{ref}}{E_{AC}} = \frac{1}{1 - 2.2\log\left(\frac{T_{AC}}{T_{ref}}\right)} \quad (4(b))$$

where: E_{ref} is the reference Asphalt modulus, E_{AC} is the backcalculated asphalt modulus, T_{ref} is the reference temperature (°C) and, T_{AC} is the temperature at 1/3 of pavement thickness (°C)
10°C–30°C for $T_{ref} = 25$°C.

$$\lambda_E = 10^{m(T-20)} \quad (4(c))$$

where: T is the effective AC temperature at a depth of one-third of the AC layer in °C.
5°C–30°C

5. Kim et al. [6]

$$\frac{E_{68}}{E_T} = 10^{-0.0153(68-T)} \quad (5)$$

where: E_{68} is the asphalt modulus at temperature 68 °F (20 °C), E_T is the backcalculated asphalt modulus at temperature T and, T is the temperature at mid-depth of asphalt pavement (°F)
Reference temperature = 68 °F (20 °C).

6. Ali and Lopez [7]

$$C = e^{(0.03608145*T-0.75771)} \quad (6)$$

where: T is the pavement temperature at a point 25 mm below pavement surface
$T_{ref} = 21$°C.

7. Braun Intertec [8]

$$\frac{E_1}{E_2} = 10^{0.01*(T_2-T_1)} \quad (7)$$

where: E_1 is the modulus at temperature T_1 °F and, E_2 is the modulus at temperature T_2 °F.

(*Continued*)

Table 1. (*Continued*)

8. Chen et al. [9]	$E_{Tr} = \frac{E_T}{(1.8T_r + 32)^{2.4462} \times (1.8T + 32)^{-2.4462}}$ (8) where: E_{Tr} is the modulus corrected to a reference temperature of T_r (°C) and, E_T is the modulus determined from testing at a temperature of T (°C) For any user-specified reference temperature.
9. Lukanen et al. [10]	$ATAF = 10^{slope(T_r - T_m)}$ (9) where: ATAF is the Asphalt Temperature Adjustment Factor Slope is the slope of the Log Modulus versus Temperature curve, recommended as –0.0195 for the wheel path and –0.021 for mid-lane, T_r is the reference temperature (°C) and, T_m is the pavement temperature at mid-depth (°C).
10. Noureldin et al. [11]	Temperature corrected $E = E_{back}$ / Correction Factor (10) Correction Factor $= 1.0000008^{314432 - T^3}$ (10(a)) where: T is the mean temperature of asphalt concrete layer (°F) measured at the mid-depth of that layer or calculated using air and surface data.
11. English Highways Agency [12]	$E_{20} = E_T * 10^{(0.0003*(20-T)^2 - 0.022*(20-T))}$ (11) where: E_{20} is the stiffness at 20 °C, E_T is the stiffness at temperature T and, T is the temperature of the asphalt at the time of testing (measured at 100 mm depth), from 15 to 25 °C.
12. ELMOD [13]	$E = \exp(-0.04663 * (t - t_{ref})) * E_{ref}$ (12) where: E is the bituminous stiffness at temperature t and, E_{ref} is the bituminous stiffness at reference temperature t_{ref}.

periods along the same pavement section. The first period corresponds to FWD measurements conducted in November 2012 and the second to March 2013. Temperature measurements were conducted within the body of AC layers, at different depths, according to the needs for the application of the algorithms. The most common temperature required from the algorithms is the mid-depth temperature. Table 2 shows the recorded temperatures at mid-depth of AC layers during these three measurement sets. It should be noticed, that the test refers to mild conditions (Mediterranean climate).

The test pavement is 782 m in length and consists of 2 lanes per direction. This pavement was un-trafficked (traffic only during construction). Along the pavement 10 measurement sites were chosen. GPR measurements [13] and extracted cores were utilized in order to determine pavement layer thicknesses. From further analysis it was determined that the AC thickness is equal to 14 cm. Figure 1 shows the cross section of the test pavement (typical flexible pavement). AC moduli were backcalculated from in-situ data using ELMOD software, and temperature correction was applied to AC backcalculated moduli at reference temperature of 20 °C.

AC backcalculated moduli for measurement (c) are assumed to be approximately equal to the reference moduli for reference temperature 20 °C, as measured temperature differs little from reference temperature. Thus only the AC backcalculated moduli of measurements (a) and (b) are corrected.

The test was conducted in order to examine variations between corrected moduli and the reference values. The evaluation includes two basic steps: first is the comparison of corrected moduli of measurements (a) and (b) to the reference temperature of 20 °C with the relative backcalculated values of measurement (c), and secondly the comparison of corrected moduli between measurements (a) and (b).

Table 2. Measured temperatures at mid-depth of AC layers.

Measurements	Minimum temperature	Maximum temperature
(a)	13.1	13.8
(b)	28.5	29.2
(c)	21.3	22.1

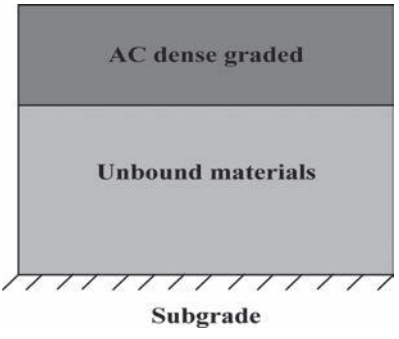

Figure 1. Cross section of the test pavement.

Figures 2 and 3 show indicatively the corrected moduli at 20 °C for each test site along the pavement for measurements (a) and (b), respectively. The bold black line illustrates the backcalculated moduli of measurement (c), i.e. the assumed reference moduli. AC corrected moduli at some sites in measurement (b) seem to be quite high, so for the purposes of this research the scale on the charts stops at 16,000 MPa. Furthermore the numeration in both charts is performed according to the algorithms numeration in Table 1.

Correction of the AC backcalculated moduli for measurement (a) was performed from a lower to a higher temperature, while correction for measurement (b) was performed from a higher temperature to a lower temperature. For measurement (a) corrected moduli seem to be underestimated in comparison with the reference values, while corrected moduli from measurement (b) are overestimated. Figures 2 and 3 also indicate that there is a large dispersion of values. In fact the deviation of some algorithms corrected moduli from the reference values is rather high.

In order to investigate the significance of the moduli values differences, the paired t-test was applied [17]. In particular, the paired t-test determined whether the corrected and the reference modulus differ from each other in a significant way. The paired t-test was applied for every two measurements. Application of the t-test between measurements (a)-(c) and (b)-(c) aims at the comparison of corrected moduli of each measurement with the reference values. T-test between measurements (a)-(b) was performed in order to examine the capability of each algorithm to result in the same or approximately the same corrected moduli regardless of the measured temperature each time. Table 3 illustrates the results of the t-test, where the symbols '√' and '–' mean that the null hypothesis is accepted or rejected, respectively.

Root Mean Square Percentage Error (RMSPE) values were calculated for corrected and reference moduli at T_{ref} = 20 °C. RMSPE is used on order to determine the percentage difference between calculated and measured values. In this case calculated values are corrected moduli and measured values are reference moduli. Table 4 summarizes RMSPE values.

Table 3 shows that the null hypothesis is rejected for almost all the algorithms. This indicates that the difference between corrected and reference moduli is significant. Thus, in general, significant variations appear to occur between corrected and reference moduli.

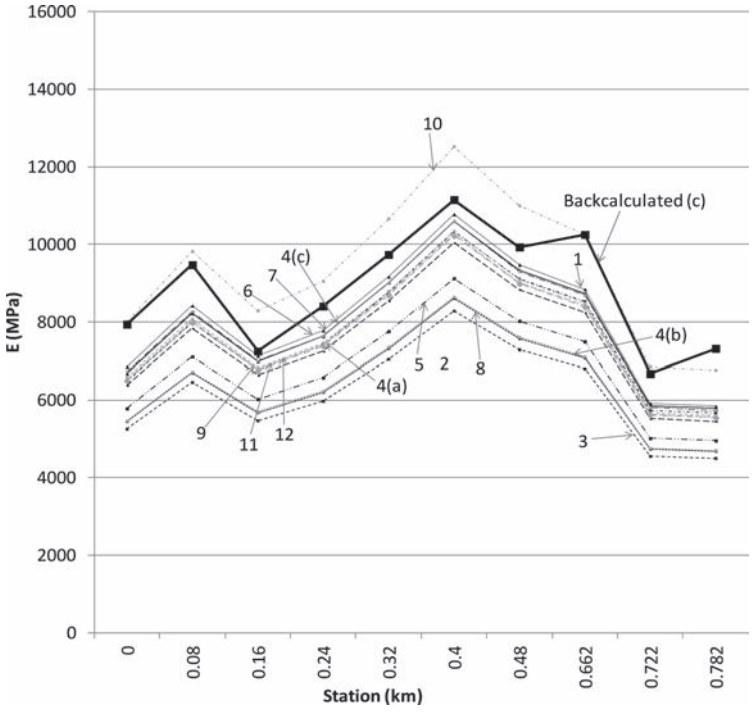

Figure 2. Backcalculated moduli for measurements (a), corrected to 20 °C.

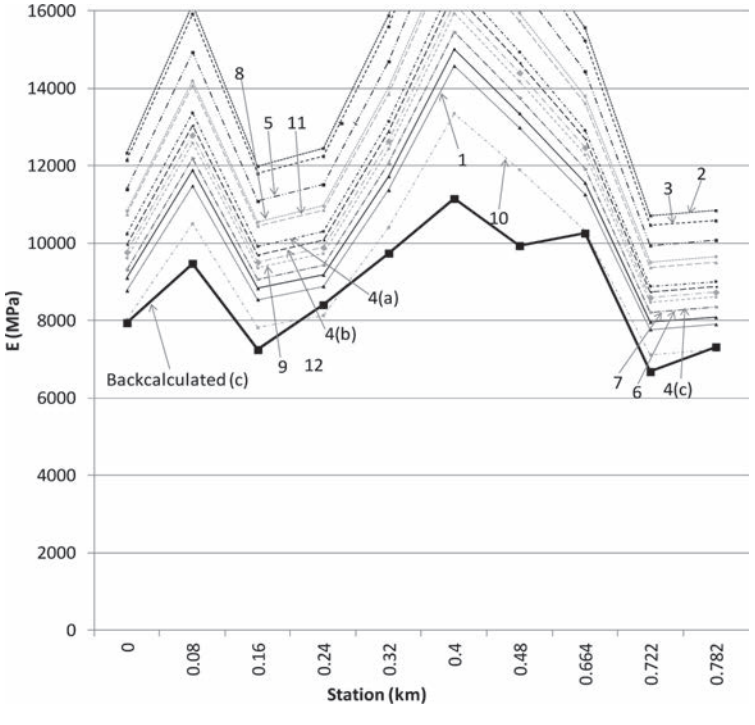

Figure 3. Backcalculated moduli for measurements (b), corrected to 20 °C.

Table 3. T-test for backcalculated and corrected moduli.

Algorithms	T-test (a)-(c)	(b)-(c)	(a)-(b)
1. Ullidtz [2]	–	–	–
2. Jung [3]	–	–	–
3. Jonshon and Baus [4]	–	–	–
4. (a) Baltzer and Jansen [5]	–	–	–
4. (b) Baltzer and Jansen [5]	–	–	–
4. (c) Baltzer and Jansen [5]	–	–	–
5. Kim et al. [6]	–	–	–
6. Ali and Lopez [7]	–	–	–
7. Braun Intertec [8]	–	–	–
8. Chen et al. [9]	–	–	–
9. Lukanen et al. [10]	–	–	–
10. Noureldin et al. [11]	–	√	√
11. English Highways Agency [12]	–	–	–
12. ELMOD [13]	–	–	–

Table 4. RMSPE for corrected and reference moduli at $T_{ref} = 20$ °C.

Algorithms	RMSPE (%) (a)-(c)	(b)-(c)
1. Ullidtz [2]	10.8	18.7
2. Jung [3]	27.9	63.7
3. Jonshon and Baus[4]	30.6	60.7
4. (a) Baltzer and Jansen [5]	14.1	36.1
4. (b) Baltzer and Jansen [5]	16.3	33.4
4. (c) Baltzer and Jansen [5]	12.2	25.4
5. Kim et al. [6]	23.7	51.7
6. Ali and Lopez [7]	12.0	22.1
7. Braun Intertec [8]	12.2	25.4
8. Chen et al. [9]	27.6	44.8
9. Lukanen et al. [10]	14.0	29.1
10. Noureldin et al. [11]	8.4	10.3
11. English Highways Agency [12]	14.6	43.2
12. ELMOD [13]	14.9	31.1

RMSPE values for measurement (a) (lower measured temperature than the reference value) seem to be lower that the respective ones for measurement (b) (higher measured temperature than the reference value). This may lead to the conclusion that algorithms have more sensitivity at higher temperatures.

In general, it could be stated that there is no close agreement between corrected and reference moduli, as well as between algorithms.

4 CONCLUSIONS

In this research temperature correction was performed on AC backcalculated moduli of a test pavement, where measurements at three different temperatures within the body of the

asphalt layer were conducted. Among the existing algorithms for temperature correction, algorithms that require only temperature data and can perform correction at 20 °C were implemented in order to correct backcalculated moduli to the reference temperature.

Statistical and further analysis of the results led to the conclusion that correction results are different from one algorithm to another. Furthermore, it is concluded that there are deviations between results of each algorithm for different temperatures, while all the algorithms show greater temperature sensitivity when the measured temperature is higher than the reference value.

Deviations of corrected moduli from reference values are larger for correction from a higher to a lower temperature than from a lower to a higher temperature in spite the fact that difference of measured and reference temperatures was approximately equal for both cases.

Based on the findings of the research it is believed that although algorithms with relative small deviation can be used for temperature correction, analysis results should be evaluated and utilized with caution. So, it is essential to expand the experiment and perform more tests examining other pavements, such as old pavements already trafficked, in order to result in final conclusions. Further research is needed.

REFERENCES

[1] Hakim, B.A., Brown, S.F. and Armitage, R.J. Pavement evaluation and strengthening design: Sixteen years experience, Ninth International Conference on Asphalt Pavements, Copenhagen, Denmark, vol. 2, Paper 3.1.1. 2002.

[2] Ullidtz, P. Pavement Analysis, Elsevier, Amsterdam, The Netherlands. 1987.

[3] Jung, F.W. Interpretation of Deflection Basin for Real-World Materials in Flexible Pavements, Research Report RR-242, Ontario Ministry of Transportation, Research and Development Branch, Ontario, Canada. 1990.

[4] Johnson, A.M. and Baus, R.L. Alternative Method for Temperature Correction of Backcalculated Equivalent Pavement Moduli, Transportation Research Record 1355, National Research Council, Washington, D.C., pp. 75–81. 1992.

[5] Baltzer, S. and Jansen, J.M. Temperature Correction of Asphalt-Moduli for FWD Measurements, Fourth International Conference on the Bearing Capacity of Roads and Airfields, Minneapolis, MN, pp. 753–768. 1994.

[6] Kim, Y.R., Hibbs, B.O. and Lee, Y.C. Temperature Correction of Deflections and Backcalculated Moduli, Transportation Research Record 1473, National Research Council, Washington, D.C., pp. 55–62. 1995.

[7] Ali, H.A. and Lopez, A. Statistical Analyses of Temperature and Moisture Effects on Pavement Structural Properties Based on Seasonal Monitoring Data, Transportation Research Board 1540, National Research Council, Washington, D.C., pp. 48–55. 1996.

[8] Lukanen, E. Temperature Adjustment for Backcalculated Asphalt Moduli, Facsimile Memorandum received from Braun Intertec Corporation, 1996.

[9] Chen, D., Bilyeu, J. Lin H.H. and Murphy M. Temperature Correction on Falling Weight Deflectometer Measurements, Transportation Research Record 1716, Transportation Research Board, Washington, D.C., pp. 30–39. 2000.

[10] Lukanen, E.O., Stubstad, R.N. and Briggs, R. Temperature Predictions and Adjustment Factors for Asphalt Pavement, Publication No. FHWA-RD-98 085, US Department of Transportation, Federal Highway Administration, USA. 2000.

[11] Noureldin, S., Zhu, K., Harris, D.A. and Li, S. Non-Destructive Estimation of Pavement Thickness, Structural Number and Subgrade Resilience along INDOT Highways. Publication FHWA/IN/JTRP-2004/35, Joint Transportation Research Program, Indiana Department of Transportation and Purdue University, West Lafayette, Indiana.2005.

[12] English Highways Agency. Design Manual for Roads and Bridges, No HD 29/08, The Stationery Office, Volume 7, Section 3, Part 2. 2008.

[13] ELMOD4. Training Course Manual.

[14] Park, S. and Kim, Y.R. Temperature Correction of Backcalculated Moduli and Deflections Using Linear Viscoelasticity and Time-Temperature Superposition, Transportation Research Record, No. 1570, Transportation Research Board, National Research Council, Washington, D.C., pp. 108–117. 1997.

[15] Chang, J.R., Lin, J.D., Chung, W.C. and Chen, D.H. Evaluating the Structural Strength of Flexible Pavements in Taiwan Using the Falling Weight Deflectometer, International Journal of Pavement Engineering, 3(3), pp. 131–141. 2002.
[16] Fernado, E.G., Liu, W. and Ryu, D. Development of a Procedure for Temperature Correction of Backcalculated AC Modulus, Federal Highway Administration/Texas Transportation Institute Report 1863-1, Texas Transportation Institute, Texas. 2001.
[17] Washington, S.P., Karlaftis, M.G. and Mannering, F. L. Statistical and Econometric Methods for Transportation Data Analysis, Charpman & Hall/CRC. 2003.

This page intentionally left blank

Asphalt Pavements – Kim (Ed)
© 2014 Taylor & Francis Group, London, ISBN 978-1-138-02693-3

Use of distributed fiber optic sensors to detect damage in a pavement

Xavier Chapeleau
Components and Systems (COSYS) Department, The French Institute of Science and Technology for Transport, Development and Networks (IFSTTAR), Bouguenais, France

Juliette Blanc & Pierre Hornych
Materials and Structures (MAST) Department, IFSTTAR, Bouguenais, France

Jean-Luc Gautier & Jean Carroget
COLAS, Campus Scientifique et Technique, Magny-les-Hameaux, France

ABSTRACT: This paper presents the feasibility of damage detection in the asphalt pavements by embedded fiber optics as a new non-destructive inspection technique. The distributed fiber optic sensing technology called "Rayleigh technique" was used in this study. The main advantage of this technique is that it allows to measure strains over long length of fiber optic with a high spatial resolution, less than 1 cm. By comparing strain profiles measured at different time, we tried to link strain changes with the appearance of damage (cracking) in the pavement. This non destructive method was evaluated on the IFSTTAR accelerated pavement testing facility, in a bituminous pavement. In our experimentation, the optical fibers were placed at 7 cm depth, near the bottom of the asphalt layer. To accelerate damage, artificial cracks were initiated in the pavement and 500 000 loads were performed during the test. Optical fiber measurements were made at regular intervals and surface cracking of the pavement was surveyed. After some traffic, a significant increase of strains was detected by the optical fibers at different points in the pavement structure, before any cracking was visible at the surface. Later, cracks appeared in the zones where the strain profiles were modified, thus indicating a clear relationship between the increased strains and crack initiation. This first test confirms thus the possibility of using a distributed fiber optic sensor to detect crack initiation in a pavement.

Keywords: Distributed fiber optic sensor, asphalt concrete pavement, cracking, non-destructive inspection

1 TECHNOLOGY OF FIBER OPTIC SENSORS

The common definition of a fiber optic sensor, as found in Wikipedia *"is a sensor that uses optical fiber either as the sensing element ("intrinsic sensors"), or as a means of relaying signals from a remote sensor to the electronics that process the signals ("extrinsic sensors")"*. Today, the technologies of intrinsic fiber optic sensors offer interesting benefits when compared with traditional sensors. The main advantages are small size, electrically passive operation, electromagnetic immunity, flexibility, corrosion resistance, etc. Fiber optic sensors can be used to perform local or distributed measurements with precision in a wide range of strain and temperature. Moreover, the technologies of fiber optic sensors become more and more efficient and reliable. All these elements contribute to a growing interest in fiber optic sensors. Several fiber optic sensor technologies have already been used for structural health monitoring and surveillance with positive results. The most promising technology is the distributed sensing technique because in one acquisition, a lot of measurement points can be obtained along a long length of fiber optic (up to 2 km).

The "Rayleigh sensing technique" is one of the distributed fiber optic sensing techniques having the highest spatial resolution (less than 1 cm). It is sensitive to both strain and temperature. This distributed sensing technique is based on the measurement of the back-scattering of light by random fluctuations of the refractive index profile along the length of the optical fiber. A strain (or temperature) profile can be obtained from two successive measurements of the Rayleigh signal, one acquired at an initial state and the second one measured at time t. The typical accuracy of the Rayleigh sensing technique is better than ±1°C in temperature and ±1 μm in strain with a centimeter spatial resolution. This high spatial resolution of the strain profile measurements is one of the main advantages of the Rayleigh sensing technique. The idea, in this study, is to use the strain profile to detect cracks in pavements. If a crack occurs transversely to the fiber optic sensor, the strain transfer from the host material to the fiber optic will be modified locally. By comparing strain profiles measured at different times to detect strain changes along the fiber optic, internal damage (cracks) in the pavement should be detectable. This non destructive method was evaluated on the IFSTTAR accelerated pavement testing facility described below.

2 DESCRIPTION OF THE EXPERIMENTATION

2.1 *Accelerated pavement testing facility*

The pavement fatigue carrousel of IFSTTAR (Fig. 1) is a large scale circular outdoor facility, unique in Europe by its size (120 m length, 6 m width) and loading capabilities [1]:

- maximum loading speed 100 km/h,
- loading rate 1 million cycles per month,
- 4 arms equipped possibly with different wheel configurations,
- lateral wandering of the loads to reproduce real traffic.

Figure 1. Accelerated pavement testing facility of IFSTTAR.

Figure 2. Fiber optic cable used as distributed sensor and measurement system.

2.2 *Fiber optic sensors and measurement system*

Common fiber optic cables (containing one or more single mode optical fibers) of telecommunication systems can be used with the Rayleigh sensing technique. However, special fiber optic cables designed for sensing measurement must be used. Indeed, they must have high enough mechanical resistance (in tension, compression, shear, against crushing etc.) for safe handling and to withstand the stresses experienced during the pavement construction process. In our experimentation, we choose to use an optical fiber cable (Fig. 2) containing 6 fibers (only one fiber optic was used) protected by an epoxy overcoat and an hytrel jacket. This cable is robust enough to be embedded in asphalt layers and its small diameter of 2 mm minimizes its intrusivity in the pavement.

Concerning the measurement system, we used a commercial device called "Optical Backscatter Reflectometer" (Luna's OBR). Strain or temperature profiles can be obtained from two measurements of Rayleigh signal. The measurement range is approximately 70 m with a measurement time less than 10 s. So, this new technology is limited to static tests up to now. However, this sensing technique has already been tested successfully for damage detection in composites laminates [2], for crack detection in concrete [3 and 4] and for structural tests of wind turbine blade [5].

3 CONSTRUCTION OF THE PAVEMENT WITH THE FIBER OPTIC SENSOR

3.1 *Pavement structure and implementation of defects*

The tested pavement structure is a typical French low traffic pavement [6] consisting of 80 mm of high modulus asphalt, over a granular subbase (300 mm thick, 300 MPa of modulus), and a sandy subgrade soil with a bearing capacity of about 95 MPa.

To accelerate damage, artificial cracks were initiated in the pavement by the implementation of steel bars with different shapes (triangle, T shaped and flat) in the layer of asphalt. These bars were placed at the bottom of the asphalt layer, to initiate bottom-up cracking. (Figs. 3 and 4). All the steel bars were placed transversely to the wheel path axis as shown

Figure 3. Triangle steel bars and T shaped steel bars fixed in the UGM.

Figure 4. Implementation of a flat steel bar in the asphalt.

on Figure 5. The distance between two identical shape steel bars is approximately 40 cm. It was expected that a crack would initiate at an early stage and propagate transversely to the wheel path axis between the two steel bars of the same shape placed 40 cm apart.

3.2 *Implementation of the distributed fiber optic sensor*

The optical cable used as distributed fiber optic sensor was placed in wheel path axis of the pavement over a length of 8 m. In this configuration, we expected that cracks initiated by

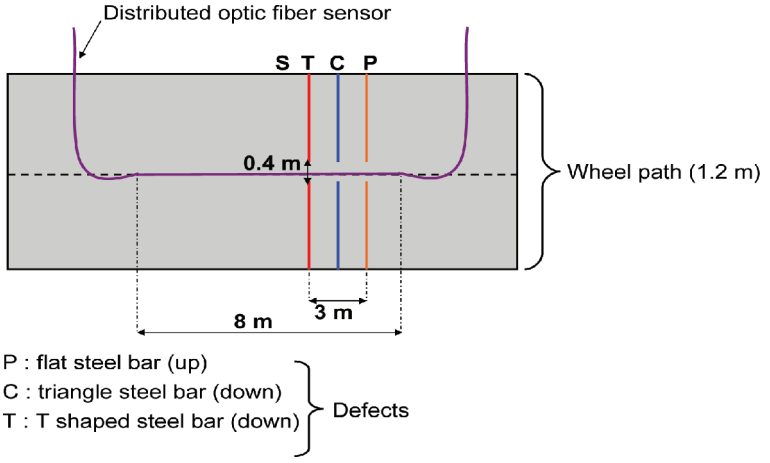

Figure 5. Plan of implementation of the steel bars and of the fiber optic cable.

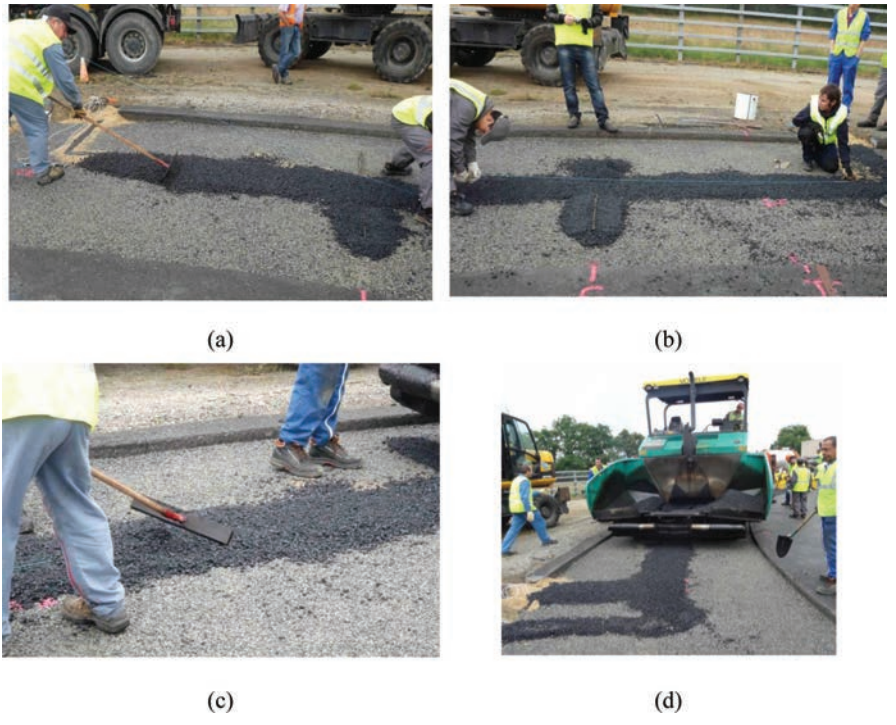

Figure 6. Steps of the process of integration of distributed fiber optic sensing in the asphalt layer.

the implementation of the steel bars would intersect the optical cable perpendicularly. The integration of the optical cable in the asphalt layer was performed in three steps. First, a thin layer of asphalt (about 10 mm thick) was placed manually on the UGM foundation and compacted (Fig. 6-a). Afterwards, the optical cable was put on this layer of asphalt in the wheel path axis (Fig. 6-b) and it was covered manually by a thin layer of asphalt (Fig. 6-c) to maintain it in place. Finally, a paver and compactor were used to place an asphalt layer of 80 mm (Fig. 6-d). By this process, the optical cable was integrated in the pavement at 70 mm depth, near the bottom of the asphalt layer.

It is worth to note that none of the optical cables put on the asphalt layer were damaged during the construction of the pavement. The optical cable chosen for this experimentation proved to be resistant enough to the high temperature of the asphalt mix (about 170°C) and to the compaction of the pavement layer by the paver and the compactor.

4 EXPERIMENTAL PROTOCOL

4.1 *Configuration of the pavement fatigue carrousel*

In our experimentation, the four arms of the pavement fatigue carrousel have been equipped with standard dual wheels, loaded at 65 kN (standard French equivalent axle load). The tires used are Dunlop 1200 R20 SP321, inflated at 850 kPa (Fig. 7). The loading speed was 6 rounds/minute (43 km/h). The lateral wandering was ±52.5 cm.

Two phases of loading were applied during the test. For the first 308 000 load cycles (from 9th August to 4th December 2013) the four arms of the fatigue carrousel have been equipped with standard dual wheels, loaded at 65 kN. For the next 221 00 load cycles (from 5th to 18th December 2013) the dual wheel loads were increased to 75 kN. At the end, 529 00 load cycles were applied on the structure.

4.2 *Fiber optic measurements*

It is important to note that two measurements of the Rayleigh signal are necessary to obtain a strain (or temperature) profile. It is similar as taking two pictures at different times and comparing them to find differences due to strain or temperature modifications along the fiber optic. Strain profiles are then relative measurements. All the strain profiles presented in this article were obtained from two successive measurements of the Rayleigh signal which were performed on the structure first with no load and then under the application of a static 65 kN load (one of the dual wheel axles of the carrousel) at different positions above the fiber optic sensor. Typically, a first measurement was made with the tires of the dual wheels of the carrousel placed outside the instrumented pavement section. Then, the tires were placed above the fiber optic at positions “P”, “C”, “T” and “S” successively (Fig. 5) and a new measurement was made at each position. This sequence of measurements was performed every 50 000 load cycles and surface cracking of the pavement was surveyed at the same time.

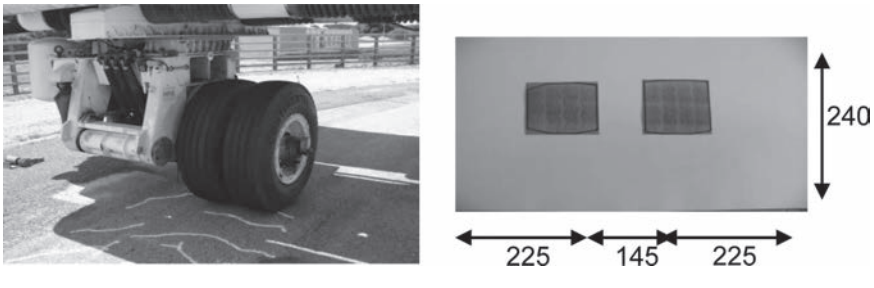

Figure 7. Dual wheel load and its dimensions in mm.

To summarize, a strain profile was obtained (for a given number of loads) from the comparison of the Rayleigh signals measured with a static load applied at each position i (i = "P", "C", "T", "S") of the test section, with the "reference signal" obtained without any load.

Moreover, it was necessary to take into account in the measurement procedure the viscoelastic behavior of the asphalt pavement. Due to viscoelasticity, when a static load was applied at a position i, the measured strain increased with time (creep phase). To reduce the dispersion of the strain profile measurements due to this effect, the same time interval was always kept between the application of the load and the Rayleigh signal measurement (one minute).

It is worth to note that the time between the optical measurements at the different positions was less than 20 minutes; so we can consider reasonably that the temperature did not change and neglect the influence of temperature in the analysis of the fiber optic measurements.

5 RESULTS AND DISCUSSION

Figures 8-a and 8-b show strain profiles measured at different numbers of load cycles, with a static load applied at the position "P" for the Rayleigh signal measurement. Until 300 000

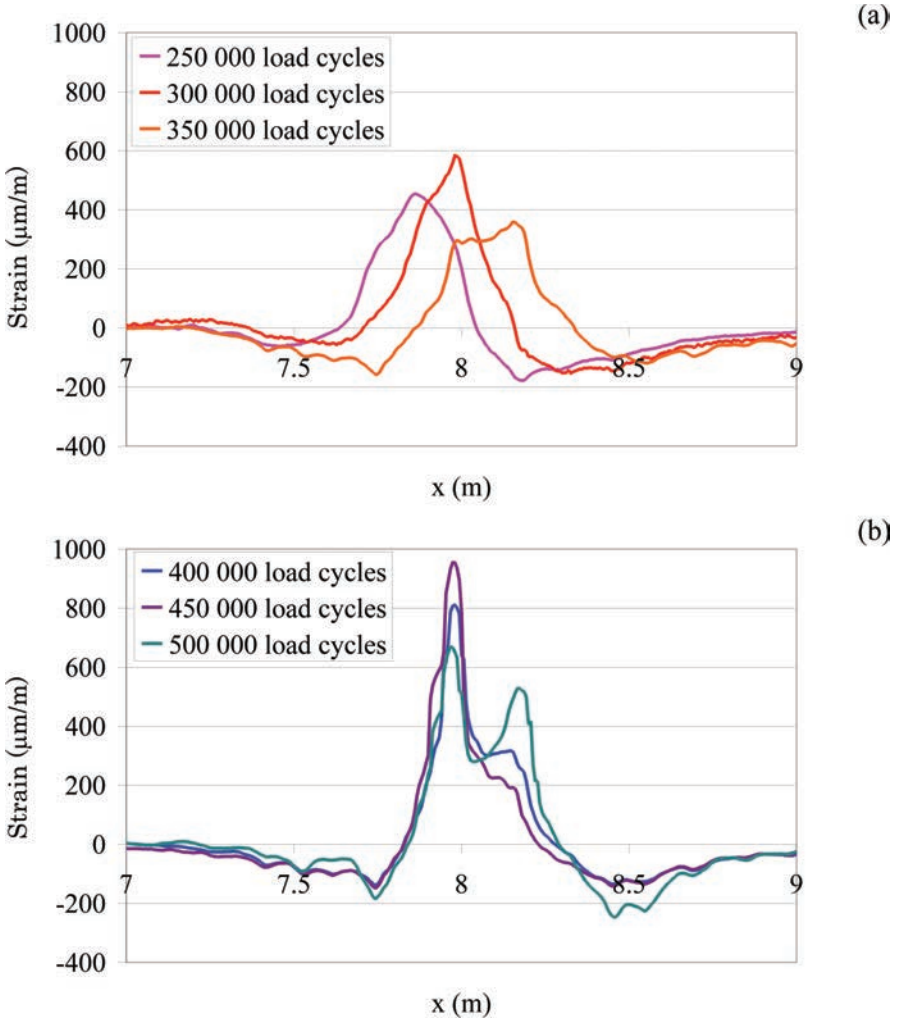

Figure 8. Strains measured at position "P" at different numbers of load cycles.

load cycles, the measured strain profiles are similar. They have the same shape, as shown in Figure 8-a. No significant change of width and maximum of the peak can be observed. The only difference is that the abscissa of the peaks are slightly shifted. It is due to the fact that the tire (the load) was not placed exactly at the same position for the different measurements. Moreover, no crack was detected on the pavement until 300 000 load cycles (see Figs. 9-a and 8-b). So, it seems logical enough to detect no change in the strain profile measurements.

The first cracks were detected on the surface of the pavement after 350 000 load cycles. They appeared at the ends of the steel bars placed in the pavement to initiate early cracks (Figs. 9-c and 9-d). The propagation of these cracks under further load cycles was surveyed. At the end of the test (500 000 load cycles), the cracks extended over the whole width of the pavement section and split (Fig. 9-e).

These observations were compared to the strain profile measurements obtained by the distributed fiber optic sensor embedded in the asphalt layer of the pavement. At 350 000 load cycles, just before the first crack appeared, the width of the peak of strain increased significantly in comparison with the previous measurements. At 400 000 and 450 000 loads cycles, the maximum of the peak continued to increase and finally the peak split into two new distinct peaks. This last measurement (at 500 000 load cycles) is particularly interesting because the two peaks of the strain profile could be unequivocally attributed to the two cracks observed at the surface of the pavement.

Similar results were obtained at the positions "C" and "T". The evolution of strain profiles at these positions was almost the same as obtained at position "P". These measurements were again consistent with observations of cracks at the surface of the pavement. In comparison, at position "S", where no crack was observed on the surface of the pavement, the shape and amplitude of the strain profiles remained almost identical until the end of the experiment (Figs. 10-a and 10-b).

All these results clearly demonstrate that distributed fiber optic sensor based on Rayleigh sensing technique could detect crack initiation and propagation by monitoring the shape of the strain profiles measured near the bottom of the pavement layer (in the longitudinal or transversal direction), at different times.

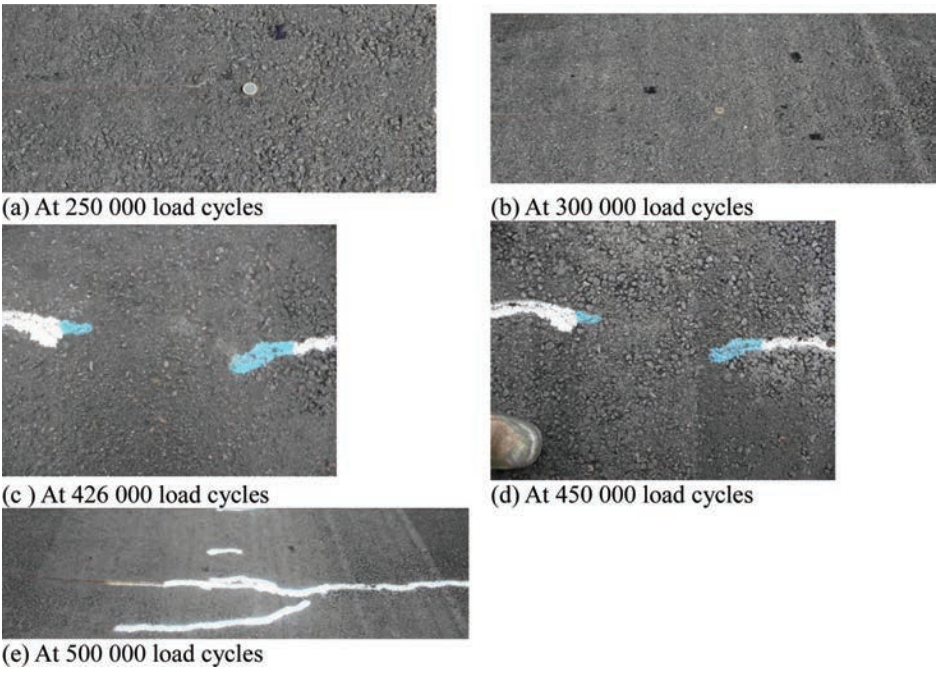

Figure 9. Evolution of cracking of the pavement structure at position "P".

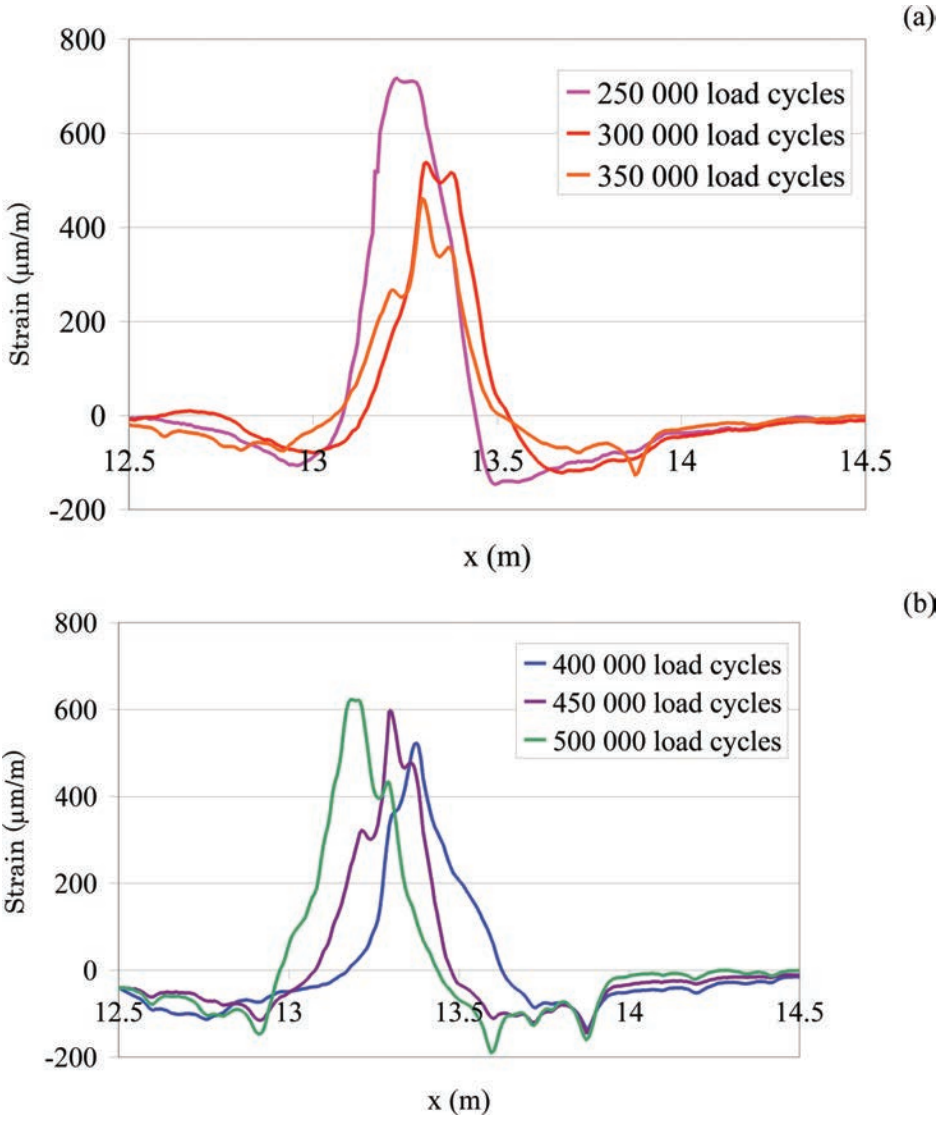

Figure 10. Strains measured at the position "S" at different load cycles.

Moreover, the experiment demonstrated the good resistance of the fiber optic sensor during construction and during traffic loading. In particular, it is worth to note that the transducer continued to respond well despite the cracking of the pavement structure.

6 CONCLUSION

A new non-destructive technique for the detection of cracking in asphalt pavements was tested at real scale on the pavement fatigue carrousel of IFSTTAR. The proposed method requires the embedment of a fiber optic cable in the pavement layer. This cable is used as a distributed sensor to obtain strain profiles by the Rayleigh sensing technique. The method is based on the comparison of the strain profiles measured at different time, after different levels of traffic.

In our study, we showed that significant changes of shape of the strain profiles could be directly linked to crack initiation and propagation. It is a promising result that confirms the possibility of using distributed fiber optic sensor to detect crack initiation in a pavement. The main originality and interest of this technique is the possibility to make continuous measurements, over relatively long distances (70 m with the equipment used in this study, but more with other techniques), with a high spatial resolution.

It is planned to continue to evaluate the efficiency of this technique. Indeed, the first results need to be confirmed for other pavement structures. Some additional tests will be performed on our pavement fatigue carrousel in the next months. A laboratory study is also planned, to carry out bending tests on pre-cracked asphalt plates, equipped with a continuous optical fiber. These tests, carried out in controlled conditions, should allow a better assessment of the sensitivity of the fiber to the presence of a crack in the asphalt, and of the influence of various parameters (loading time, temperature) on the results.

In perspective, we also study the feasibility of using distributed fiber optic sensor to detect cracks without the requirement of applying a load on the pavement. This solution would be a more efficient to monitor long lengths of pavements.

REFERENCES

[1] Autret, P., de Boissoudy, A.B., Gramsammer, J.C. *The circular test track of the laboratoire central des ponts et chaussées (LCPC) Nantes—First Results*, Proceedings of the 6th International Conference on Asphalt Pavements, vol. 1, pp. 550–561. 1987.

[2] Güemes, A., Fernández-López, A., Soller, B. Optical Fiber Distributed Sensing—Physical Principles and Applications, Structural Health Monitoring, 9, pp. 233–245. 2010.

[3] Chapeleau, X., Sedran, T., Cottineau, L.M., Cailliau, J., Taillade, F., Gueguen, I., Henault, J.M. Study of ballastless track structure monitoring by distributed optical fiber sensors on a real-scale mockup in laboratory, Engineering Structures. 2013.

[4] Henault, J-M., Salin, J., Moreau, G., Delepine-Lesoille, S., Bertand, J., Taillade, F. Qualification of a truly distributed fiber optic technique for strain and temperature measurements in concrete structures, International workshop on ageing management of nuclear power plants and waste disposal structures, vol. 12. 2011.

[5] Kaplan, A., Klutte, S., Gifford, D., Heaney, A. Distributed optical fiber sensing for wind blade strain monitoring and defect detection, 8th International Workshop on Structural Health Monitoring, Stanford (CA, USA). 2011.

[6] Corte, J.F., Goux, M.T. Design of pavement structures: the French technical guide, Transportation Research Record, vol. 1539, p.116–124. 1996.

This page intentionally left blank

Pavement condition survey/pavement smoothness/
quality control/quality assurance

This page intentionally left blank

Asphalt Pavements – Kim (Ed)
© 2014 Taylor & Francis Group, London, ISBN 978-1-138-02693-3

Evaluation of fatigue damage in asphalt pavement using FWD dissipated work

Kimio Maruyama & Masayuki Kumagai
Civil Engineering Research Institute for Cold Region, Toyohira-ku, Sapporo, Japan

ABSTRACT: The purpose of this study was to verify the relation between the secular changes in FWD dissipated work and fatigue damage, including the timing of fatigue cracking.

The FWD measurement data used in this study were acquired in research conducted from 1993 to 2007 at a national highway site. FWD dissipated work were calculated from the FWD load-deflection hysteresis loop. Investigation was made to determine whether there was correlation between fatigue cracking and FWD dissipated work. This study found the followings,

1. It was confirmed that dissipated work decreases with increases in the thickness of the asphalt mixture layer.
2. FWD dissipated work was found to show a tendency to increase with the occurrence of fatigue cracks.
3. A linear relationship on the double-logarithmic graph was found between FWD dissipated work and the number of wheel load passes.
4. FWD dissipated work is able to serve as a useful indicator in predicting the timing of fatigue failure.

Keywords: FWD, dissipated work, fatigue damage, fatigue failure, hysteresis loop

1 INTRODUCTION

In analyzing research data obtained by Falling-Weight Deflectometer (FWD), analysis based on the deflection amount or back-calculation of the elastic modulus have been commonly used; however, dissipated work has been proposed as an evaluation indicator. Dissipated work measured by FWD (hereinafter: FWD dissipated work), according to the literature, relates closely to pavement damage and pavement fatigue failure [1–3]; therefore, it is logical to expect dissipated work to relate closely to cumulative fatigue damage; however, the tendency for FWD dissipated work to change with time and the relation between FWD dissipated work and fatigue failure phenomena have not been fully verified on roads in service.

From 1993 to 2007, the authors continuously performed FWD measurements of deflection at the inner wheel path parts and between the wheel path parts on a specific site of a national highway, where asphalt pavements with eight different types of layer structures were constructed in the same lane. During the continuous investigation, fatigue cracks were detected in five of the eight layer structures. Therefore, this study was conducted with the aim of understanding secular changes in FWD dissipated work and of verifying how the secular changes relate to fatigue damage, including the timing of fatigue cracking.

2 RESEARCH METHOD

2.1 *FWD test method used at Bibi New Test Road*

The FWD measurement data used in this study were acquired in research conducted from 1993 to 2007 at a national highway site named Bibi New Test Road. The road has been in service since July 1990, when it was constructed. Since then, FWD measurements have been taken continuously at the Inner Wheel Paths (IWP) and Between the Wheel Paths (BWP) of the eight types of layer structures described in Figure 1. Table 1 shows the year and month of FWD measurement. The measurement was basically conducted in spring and autumn; however, in addition to then, it was conducted at various times of year with temperature differentials in the pavement. Additionally, 24-hour wheel load investigation has been conducted

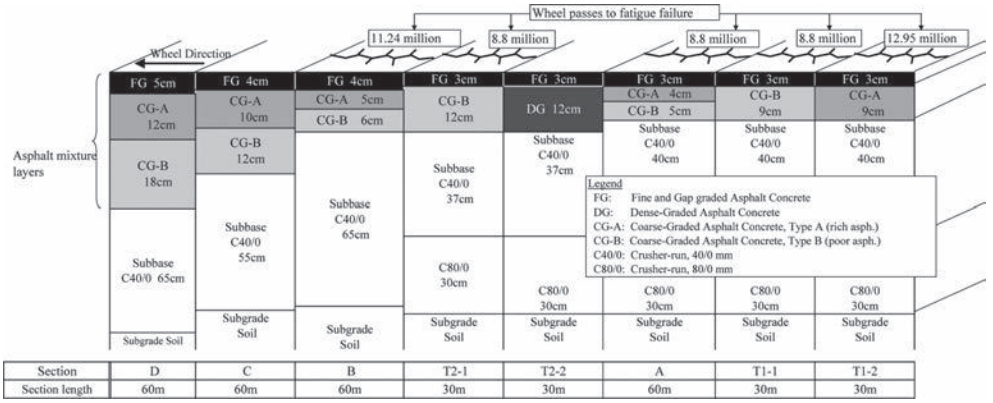

Figure 1. Pavement layer structures at Bibi New Test Road and fatigue failure conditions.

Table 1. Year and month of FWD measurement and wheel load.

Year and month of measurement		Cumulative 49 kN equivalent wheel load (million)	Year and month of measurement		Cumulative 49 kN equivalent wheel load (million)
1993	Aug.	4.0	1998	Jul.	7.4
	Sep.	4.1		Oct.	7.6
	Sep.	4.2	1999	May	7.9
	Nov.	4.6		Oct.	8.1
	Dec.	4.7	2000	May	8.5
1994	Feb.	5.1		Oct.	8.7
	Jul.	5.5	2001	Jun.	8.8
	Aug.	5.5		Oct.	9.5
	Sep.	5.5	2002	May	10.0
	Nov.	5.6		Nov.	10.4
	Nov.	5.6	2003	Jul.	10.9
1995	Feb.	5.7		Dec.	11.2
	May	5.8	2004	Jun.	11.6
	Jul.	5.9		Oct.	11.9
	Sep.	6.1	2005	Jun.	12.3
	Oct.	6.1		Oct.	12.5
1996	Jun.	6.5	2006	Jun.	12.9
	Oct.	6.7		Oct.	13.2
1997	May	7.0			
	Oct.	7.1			

on weekdays in autumn almost every year. The measurement has been conducted according to "the method of using a portable vehicle weight scale," described in the Pavement Research and Test Methods Handbook [4]. Table 1 also shows the cumulative number of 49 kN-equivalent wheel load that had been recorded until the time when the FWD measurements began.

During the continuous research, 5 of the 8 sections at the Bibi New Test Road were found to have fatigue cracks. In Section T1-1, Section A and Section T2-1, fatigue cracks occurred after 8.8 million wheel passes. In Section B, fatigue cracks occurred after 11,24 million wheel passes, and in Section T1-2, fatigue cracks occurred after 12,95 million wheel passes. Section T1-1 and Section A each had a 12-cm-thick asphalt mixture layer, and Section T2-1 and Section B each had a 15-cm-thick asphalt mixture layer. In addition, these sections had a course graded asphalt mixture type-B (poor content of asphalt type) at the bottom layer. Also, the Section T1-2 had a 12-cm-thick mixture layer and had a course graded asphalt mixture type-A (rich content of asphalt type) at the bottom layer. Fatigue cracks occurred in more than one of the layer structures; however, fatigue cracks were not detected in Section C, which had a 26-cm-thick asphalt layer, in Section D, which had a 35-cm-thick asphalt layer, or in Section T2-2, which had a dense-graded asphalt mixture layer at the bottom. It is assumed that differences in the thickness of the mixture layers and in fatigue resistance of the mixture at the bottom layers relate to the occurrence of fatigue cracks [5]. Investigation was made to determine whether there was correlation between fatigue cracking and FWD dissipated work.

2.2 *Definition of FWD dissipated work*

FWD dissipated work is defined as the area that is surrounded by the hysteresis loop on a time-series graph that plots measured load on the vertical axis and deflection on the horizontal axis, as shown in Figure 2. The work is considered to have dissipated into the asphalt layers, the subbase layers or the subgrade layers; furthermore, it is also considered to have dissipated into the rubber material or the rubber buffer under the FWD loading plate or as mechanical friction in the measuring device. Therefore, the FWD dissipated work is regarded as involving all the work that dissipated in all these portions. Accordingly, in light of accurately evaluating fatigue damage in asphalt pavement in line with the purpose of the present paper, it is ideal to start by quantitatively and separately grasping the work that has dissipated from each portion, then detect the amount of work that has dissipated into the asphalt layers, the subbase layers or the subgrade layers, and finally evaluate how the amount of work that dissipated relates to fatigue damage.

However, in light of the four viewpoints listed below, this study was conducted with the aim of specifically determining whether FWD dissipated work relates to fatigue crack phenomena in asphalt mixture layers.

1. No technique exists for determining how much of the FWD dissipated work has dissipated into each portion (e.g., the asphalt layer, the subbase layer, the subgrade layer, the rubber material, the rubber buffer under a FWD loading plate) or as mechanical friction in the measuring device.

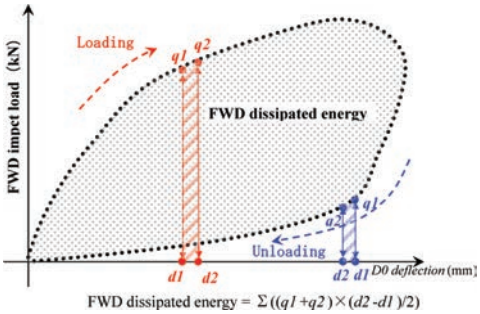

Figure 2. Calculating method of dissipated work.

2. The FWD data used in this study were obtained in the measurement test conducted with the same FWD testing machine on the same test day. Given that the testing machine produces the same discrepancies (e.g., from the rubber material and the rubber buffer under the FWD loading plate) for all the data, it was considered possible to attribute most of the differences in FWD dissipated work to the asphalt mixture layers, the subbase layers or the subgrade layers.
3. It is recognized that FWD dissipated work is always affected by the presence of an asphalt layer, since FWD dissipated work varies according to temperature and it changes depending on the asphalt layer structures such as thickness. In addition, it is thought that the degree of influence given by the subbase layers or the subgrade layers does not change much with temperature.
4. It is already known that there is a linear relationship on a double-logarithmic graph of the dissipated energy obtained by bending fatigue tests conducted in a laboratory versus the load applications to fatigue failures [6,7]. It was considered to be remarkably meaningful to verify whether there is a similar relation between FWD dissipated work and fatigue failure phenomenon in the mixture layers.

2.3 *Calculation method of FWD dissipated work*

Figure 2 and the following paragraph show the procedure for calculating FWD dissipated work from FWD time-series data.

The time-series data on loaded weight and deflection just below loading point was sampled at intervals of 0.002 seconds. FWD dissipated work, which is equivalent to the area surrounded by the hysteresis loop, was obtained by integrating the product of increase in deflection and change in load at every sampling, during the loading process and by sequentially subtracting the product of decrease in deflection and change in load during the unloading process at every sampling.

2.4 *Method of sorting temperature of asphalt mixture*

Since the properties of asphalt are known to be affected by the temperature, FWD dissipated work was also expected to be affected by pavement temperature; therefore, the values of the FWD dissipated work were sorted according to the temperature of asphalt mixture at the time of measurement. Temperature of pavement layer structure was measured by means of thermocouples buried in the four types of pavements of Section A, Section B, Section C and Section D, at the depth shown in Table 2. The temperature measurements for the asphalt layer, which correspond to the shaded parts in Table 2, were used to calculate the average temperature of the asphalt mixture layers by Formula (1).

$$t_{as} = \left((t_0 + t_1)h_1/2 + (t_1 + t_2)(h_2 - h_1)/2 + \cdots\cdots + (t_{n-1} - t_n)(h_n - h_{n-1})/2\right)h_n \quad (1)$$

Table 2. Depth of temperature measurement in each pavement layer structure (Sections A, B, C and D).

Section A	Section B	Section C	Section D
3	4	4	5
7	9	9	17
12	15	14	26
32	20	20	35
52	40	26	40
72	60	41	60
82	80	61	80
		81	100
			(cm)

Here, t_{as}: Average temperature of asphalt mixture (°C)
t_0: Road surface temperature (°C)
t_1: Asphalt temperature at depth h_1 from the road surface (°C)
h_1: Depth of the uppermost thermocouple (cm)
t_n: Asphalt temperature at depth h_n from the road surface (°C)
h_n: Depth of the thermocouple buried at the $n_{\text{-th}}$ position from the road surface (cm)

3 RESULTS AND DISCUSSION

3.1 *Relation between pavement temperature and FWD dissipated work*

The relation between temperature of asphalt mixture layer and FWD dissipated work is plotted in Figures 3 and 4, according to the type of pavement layer structure. Figure 3 plots the results from a group of layer structures, namely Sections A, B, C and D, which have the asphalt layer designed according to a TA method in a Japanese standard way; however, each of these asphalt layers has a different thickness. Figure 4-a) plots the results from the a group of layer structures that have a 12-cm-thick asphalt mixture layer, but each of these bottom layers has a different type of mixture, and Figure 4-b) plots the results from a group of layer structures that have a 15-cm-thick mixture layer, but each of these bottom layers has a different type of mixture.

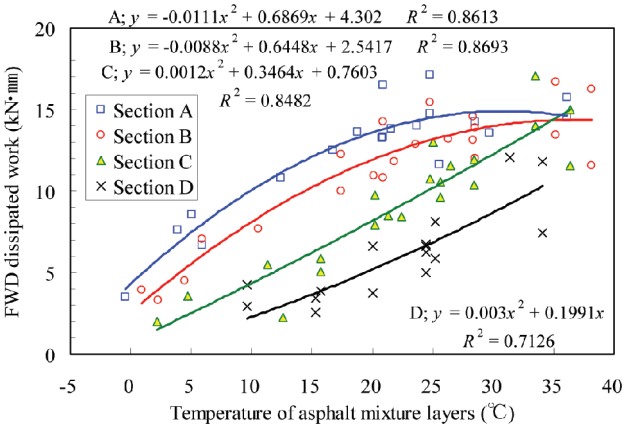

Figure 3. Relation between pavement temperature and FWD dissipated work (Sections A, B, C and D).

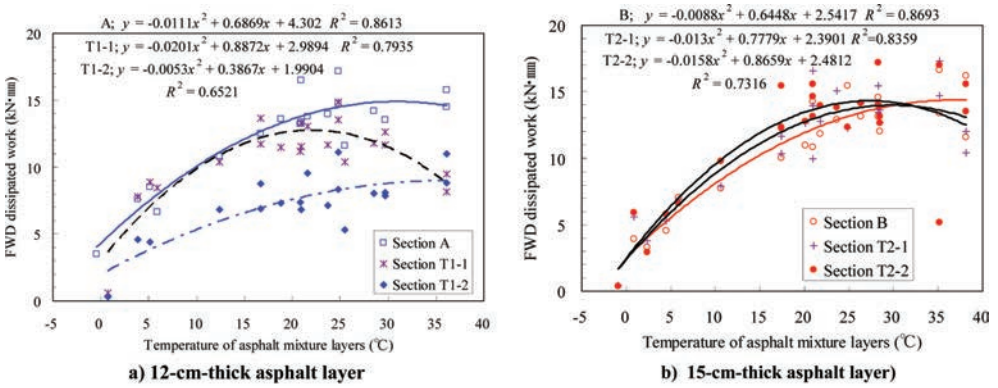

Figure 4. Relation between pavement temperature and FWD dissipated work.

First, Figure 3, Figure 4-a) and Figure 4-b) show that the FWD dissipated work increases with increase in temperature of asphalt mixture, when the pavement temperature was 25°C or lower, but the FWD dissipated work had a tendency to remain at the same level or lower when the pavement temperature was 25°C or higher. Further, Figure 3 shows that when the asphalt layers designed in a standard way according to the TA method differ in thickness from each other, the FWD dissipated work also differs. Figure 4-a) shows that the FWD dissipated work is smaller in Section T1-2, even though all the asphalt mixture layers have the same 12-cm thickness. In contrast, in Figure 4-b), differences in FWD dissipated work are not found among the pavement layer structures.

3.2 *Relation between the pavement layer structure and the FWD dissipated work*

3.2.1 *Relation between the thickness of asphalt layers and dissipated work*

The relation between the thickness of asphalt mixture layers and the FWD dissipated work is shown in Figure 5. In Figure 5, the values of FWD dissipated work calculated when the pavement temperature was 10°C, found from the regression equation for each pavement layer structure in Figure 3, Figure 4-a) and Figure 4-b), are plotted. Here, 10°C is used as a representative pavement temperature, since the average yearly pavement temperature of the Bibi New Test Road is approximately 10°C. A tendency for the dissipated work to decrease with increases in the asphalt mixture layer thickness is found here.

3.2.2 *Relation between asphalt mixture type of bottom layer and dissipated work*

Figure 6 show the relation between the asphalt mixture type of bottom layer and the dissipated work observed for Sections A, T1-1 and T1-2, and for Sections B, T2-1 and T2-2, in both of which the asphalt mixture layers have the same thickness but are made with different asphalt mixtures. In addition, the values in Figure 6 correspond to the values obtained when the pavement temperature was 10°C in the regression equation for each pavement layer structure shown Figures 3 and 4. The dissipated work in Section T1-2, whose bottom layers consisted of course graded asphalt mixture type-A (rich content of asphalt type), seems to be smaller when compared with the dissipated work in Section A and Section T1-1, whose bottom layers consisted of course graded asphalt mixture type-B (poor content of asphalt type). In contrast, the dissipated work in Section T2-2 is approximately the same as that of Section B or Section T2-1, whose bottom layers consisted of course graded asphalt mixture type-B (poor content of asphalt type). It is speculated that dissipated work would differ according to mixture type even if asphalt layers were of equal thickness; however, no specific tendency was identified.

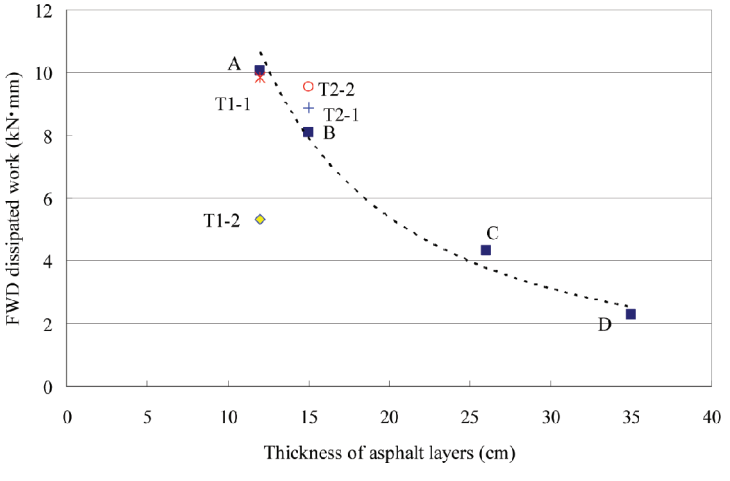

Figure 5. Thickness of asphalt layers and dissipated work (10°C).

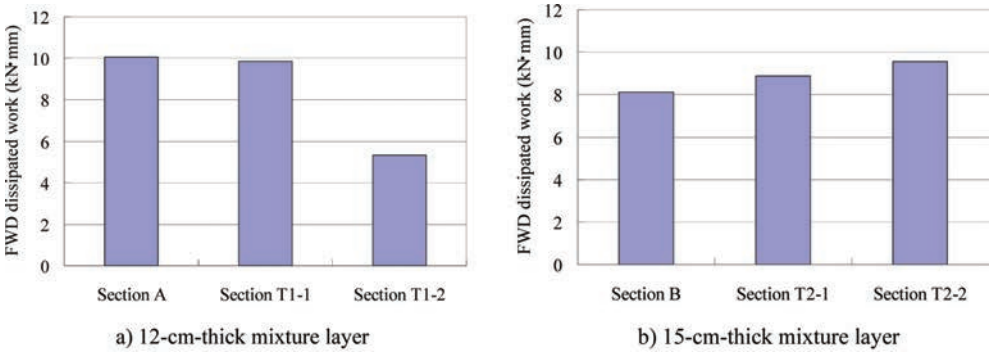

Figure 6. FWD dissipated work in layer structures (10°C).

3.2.3 *Change in dissipated work after the occurrence of cracks*

In Figure 7, the data group obtained from 1993 to 1995, when the pavement was still undamaged, the data group obtained around the time when fatigue cracks began to occur (October 2000 to October 2001) and the data group obtained around the time when reflection cracks began to occur after milling & overlay (July 2003 to June 2006) are plotted to clearly visualize the relationship between dissipated work and fatigue damage.

In Section A, the dissipated work at the IWP, which is directly affected by wheel load, has a tendency to deviate from the relation between asphalt temperature and dissipated work that was found before the layer structure was damaged, as the damage in the pavement increased. Also, in Section B, the dissipated work at the IWP, which is directly affected by load, has a tendency to deviate from the relation between mixture temperature and dissipated work that was found before the layer structure was damaged, as the damage in the pavement increased.

In contrast, in Section C and Section D, fatigue cracks did not occur during the investigation, and also during that time, secular change was not found in the relation between dissipated work and temperature.

From the above, it is speculated that the values of dissipated work show a tendency to be greater in damaged condition, where the accumulation of fatigue damage and the occurrence of fatigue cracks were found, than in sound condition.

3.2.4 *FWD dissipated work and the cumulative number of 49 kN-equivalent wheel load at the time of fatigue failure*

The relation between FWD dissipated work and the cumulative number of 49 kN-equivalent wheel load up to the occurrence of fatigue cracks, and the relation between the sum of FWD dissipated work and the cumulative number of 49 kN-equivalent wheel load up to the occurrence of fatigue cracks, were examined in the five pavement sections where fatigue cracks occurred (Sections A, T1-1, T1-2, B and T2-1). The results are shown in Figures 8 and 9. The dissipated work per FWD impact load in Figure 8 is defined as dissipated work from one-time FWD loading measurement at the pavement temperature of 10°C, which was obtained using the regression equations shown in Figures 3 and 4. The values of FWD dissipated work when the pavement temperature was 10°C were used as representative values, because the yearly average pavement temperature at the Bibi New Test Road is approximately 10°C. In addition, the total FWD dissipated work in Figure 9 is defined as the sum of dissipated work up to the time of fatigue crack occurrence, which is equivalent to the value obtained by multiplying the cumulative number of 49 kN-equivalent wheel load passes up to the occurrence of fatigue cracks, by the dissipated work per FWD impact load, on the assumption that "the dissipated work per FWD impact load ≒ dissipated work per 49 kN wheel load pass."

Moreover, fatigue crack generation was not found in Section C, Section D and Section T2-2 up to the present time; therefore, the expected cumulative number of 49 kN-equivalent wheel load up to the occurrence of fatigue cracks was calculated instead, using research

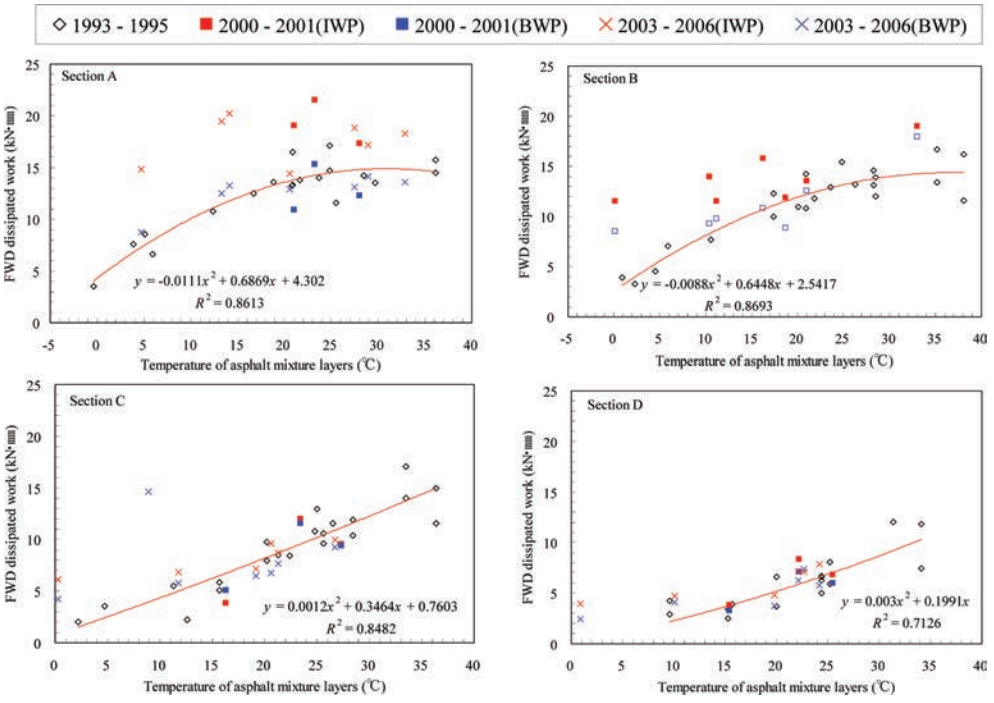

Figure 7. Change in FWD dissipated work after the occurrence of fatigue cracks.

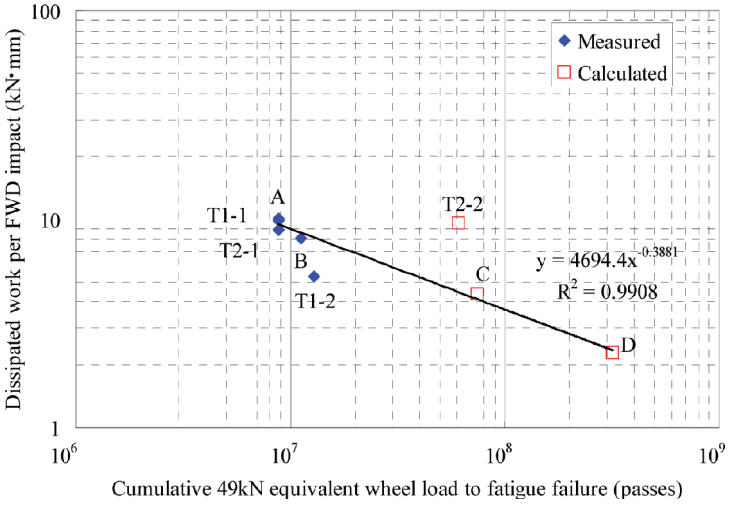

Figure 8. Relation between FWD dissipated work (10°C) and fatigue failure wheel load.

results [8] obtained by the authors, in order to predict how long it would take for fatigue failure to occur. The calculated values are plotted in Figures 8 and 9 as open square. In addition, regression lines for the data group taken from the layer structures (Sections A, B, C, D, T1-1 and T2-1), whose bottom layers consisted of course graded asphalt mixture type-B (poor content of asphalt type), are also plotted.

As shown in Figure 8, it is still difficult to identify a specific tendency only from the measured data on the pavement layer structures in which fatigue cracks were detected; however,

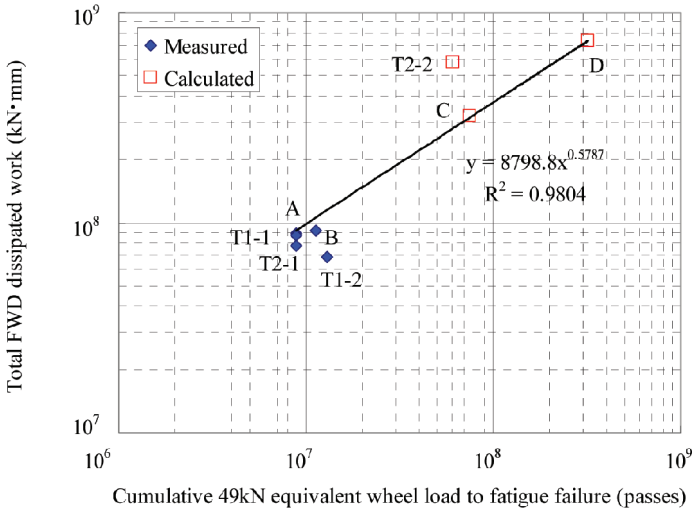

Figure 9. Relation between total dissipated work and fatigue failure wheel load.

when taking calculated values into consideration, it becomes obvious that there is a linear relationship between the dissipated work and the cumulative number of 49 kN-equivalent wheel load at the point of fatigue crack generation, in the double-logarithmic graph. Also, in Figure 9, a linear relationship in the double-logarithmic graph is found even between the total FWD dissipated work and the cumulative number of 49 kN-equivalent wheel load.

Himeno and Van Dijik have reported that there is a linear relationship on the double-logarithmic graph, between the number of fatigue failures and the values of dissipated energy obtained in laboratory bending fatigue tests [6,7]. From the obtained results, it is assumed that there is an analogous relation between FWD dissipated work and the timing of fatigue failures, and it is also assumed that FWD dissipated work is able to serve as a useful indicator in evaluating the fatigue damage of pavement.

However, as shown in Figures 8 and 9, the values for Section T1-2, whose bottom layers consisted of course graded asphalt mixture type-A (rich content of asphalt type), and the values for Section T2-2, whose bottom layers consisted of dense graded asphalt mixture, are plotted at a distance from the regression lines obtained from the values of the layer structures that have course graded asphalt mixture type-B (poor content of asphalt type) at the bottom layer; therefore, it is considered that the obtained data, including the data shown in Figures 8 and 9, do not yet allow a consistent conclusion to be drawn. As mentioned above, FWD dissipated work is able to serve as a useful indicator in predicting the timing of fatigue failure; however, it is considered that FWD dissipated work has to be further examined through data accumulated from various sites in the future.

4 CONCLUSIONS

The results of this study can be summarized as follows.

1. It was confirmed that dissipated work decreases with increases in the thickness of the asphalt mixture layer. In contrast, it was speculated that FWD dissipated work would differ by the type of asphalt mixture at the bottom layer. Expected results were obtained for the layer structure of Section T1-2; however, no significant difference was found in the results obtained from Section T2-2. Therefore, we recognize that we have not yet reached a satisfying conclusion through this verification.
2. FWD dissipated work was found to show a tendency to increase with the occurrence of fatigue cracks, compared with when it was in sound condition. It is assumed that fatigue

damage in pavement will be able to be evaluated by understanding the relation between the temperature of the mixture layer and FWD dissipated work at the time when pavement is in sound condition.

3. A linear relationship on the double-logarithmic graph was found between FWD dissipated work measured shortly after pavement construction and the number of 49 kN-equivalent wheel load passes on the pavement up to the point that the pavement suffered fatigue failure. A similar relation was also found to be associated with the total of the FWD dissipated work.
4. FWD dissipated work is able to serve as a useful indicator in predicting the timing of fatigue failure; however, it is considered that FWD dissipated work has to be further examined through data accumulated from various sites in the future.

REFERENCES

[1] Harold Von Quintus and Brian Killingsworth. Analysis Relating To Pavement Material Characterization And Their Effects On Pavement Performance, FHWA-RD-97-085, US. Department of Transportation Federal Highway Administration, 1998.1.

[2] Sigeo Higashi, Toshihiro Kanai, Toshiyuki Okabe, Shinya Hayashi and Kunihito Matsui. Application of time historical data to structural evaluation of asphalt pavements, Journal of pavement engineering, vol.3, pp.31–38, JSCE, 1998.2.

[3] Nagato Abe and Mikio Sekiguchi. Proceedings of Annual Conference of The Japan Society of Civil Engineers, Vol.59, pp.5–620, Japan society of Civil Engineers, 2004.

[4] Japan Road Association. Pavement Research and Test Methods Handbook, 2007.6.

[5] Kimio Maruyama, Jun Tako and Atsushi Kasahara. Long-term Performance of Asphalt Pavements at Bibi New Test Road, Journal of Japan society of Civil Engineering Ser.E, Vol.E-62-3, pp.519–530, Japan society of Civil Engineers, 2006.

[6] Kenji Himeno, Takashi Watanabe and Teruhiko Maruyama. Fatigue Failure Characteristics of Asphalt Mixed at Low Stiffness Modulus, Journal of Materials, Concrete Structures and Pavements, V-4-366, pp.143–151, Japan society of Civil Engineers, 1986.

[7] Van Dijk, W. Practical Fatigue Characteristics of Bituminous Mixes, Proc. of AAPT, Vol.44, pp.38–74, 1975.

[8] Kimio Maruyama, Jun Tako and Atsushi Kasahara. Fatigue Failure Life Prediction Method of asphalt pavement, Journal of Japan society of Civil Engineering Ser.E, Vol.64-3, pp.416–426, Japan society of Civil Engineers, 2008.

Asphalt Pavements – Kim (Ed)
© 2014 Taylor & Francis Group, London, ISBN 978-1-138-02693-3

Estimation of a longitudinal true profile for expressway pavements by a mobile profiling system

Kazuya Tomiyama & Akira Kawamura
Kitami Institute of Technology, Koen-Cho, Kitami, Japan

Tomonori Ohiro & Shin Tozuka
Nexco-Engineering Hokkaido Co., Ltd., Higashi Sapporo, Sapporo, Japan

ABSTRACT: In recent years, expressway authorities in Japan require an effective method for monitoring and measuring surface characteristics of their pavements. Against this background, we have introduced a mobile profiling system enabling real-time roughness data collection. The system uses two accelerometers fixed to a suspension system of any passenger and commercial vehicles to measure the International Roughness Index (IRI) based on a back-calculated profile. One of the advantages of this system is to capture the information of longitudinal profile features. However, since the measurement algorithm is optimized to compute the IRI in real-time, the back-calculated profile is distorted by the natural frequencies of suspension components. This study examines an estimation technique of a longitudinal true profile using the mobile profiling system by developing a reconstruction filter to attenuate the distortion in the spatial frequency domain by the Fast Fourier Transform (FFT) method. As the result of a validation experiment, the mobile profiling system using the reconstruction filter satisfies practical requirements as a profiler compared with a Class 1 measures. The result also indicates that the system basically has a capacity to measure the IRI in real-time, and the back-calculated profile is appropriate for the purpose.

Keywords: mobile profiling system, true profile, accelerometer, signal processing, International Roughness Index

1 INTRODUCTION

In recent years, expressway authorities in Japan require an effective method for monitoring and measuring surface characteristics of their pavements. Against this background, we have introduced a mobile profiling system enabling real-time roughness data collection. The system uses two accelerometers fixed to a suspension system of any passenger and commercial vehicles to measure the International Roughness Index (IRI) based on a back-calculated profile. One of the advantages of our system is the capability to capture the information of how the roughness deteriorates by means of longitudinal profile features. This study describes the real-time IRI measurement algorithm for the mobile profiling system. However, since the measurement algorithm is optimized to compute the IRI in real-time, the back-calculated profile is distorted by the natural frequencies of suspension components. This study examines an estimation technique of a longitudinal true profile using the mobile profiling system by developing a reconstruction filter to attenuate the distortion in the spatial frequency domain by the Fast Fourier Transform (FFT) method. Against the traditional pavement monitoring approaches based either on visual inspections or on laser profilers, the proposed system contributes to valid, quantitative, and economical monitoring activities for expressway pavements.

2 MEASUREMENT ALGORITHM OF THE MOBILE PROFILING SYSTEM

Since modern technologies for road surface condition survey with better sensors have been improved, a lot of profilers have been developed in various countries. Principle of our profiling system is based on the conventional Quarter-Car (QC) model used for calculating IRI. Therefore, two accelerometers are mounted at the sprung and unsprung mass of a vehicle. This chapter describes system configuration and measurement algorithm of the mobile profiling system.

2.1 *Overview of the Quarter-Car model*

The IRI is a mathematical model applied to a measured longitudinal road profile. The model simulates a QC model shown in Figure 1 that predicts the spatial derivative of suspension stroke in response to a profile using standard settings for speed and the vehicle properties depicted in the figure [1].

In Figure 1, V, m_u, m_s, k_t, k_s, and c_s denote vehicle forward speed, unsprung mass, sprung mass, tire spring rate, suspension spring rate, and suspension damping rate, respectively. The values called the Golden Car parameters are: = 80 (km/h), = 0.15, = 653 (1/s2), = 63.3 (1/s2), and = 6 (1/s2). The moving average baselength (B) is set to 250 mm as a standard aspect of the IRI calculation.

2.2 *Conception of the system development*

Nowadays, many approaches for measuring surface roughness have been developed. According to Sayers [2], the approaches can be grouped into the following four classifications on the basis of how directly their measures pertain to the IRI.

- Class 4—a roughness measure is not reproducible or stable with time, and can only be compared to IRI by subjective estimation,
- Class 3—a measure obtained from an RTRRMS is calibrated to the IRI scale by correlation with reference measures from a Class 1 or 2 system,
- Class 2—a profile-based method is used that is reproducible and stable with time, and that is calibrated independently of other roughness measuring instruments, and
- Class 1—a profile-based method similar to Class 2 is used. A profile-based measurement qualifies as a Class 1 measure if it is so accurate that further improvements in accuracy would not be apparent.

These classifications are attended with a conflict between accuracy and convenience on the roughness measurement. The more accurate the measurement, the convenience is sacrificed.

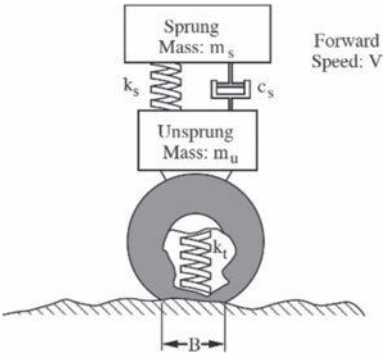

Figure 1. A schematic depiction of a Quarter-Car model.

The more convenient the measurement, on the contrary, the accuracy is impaired. The developed profiling system is intended to combine the accuracy of Class 2 and the convenience of Class 3. In other words, it can directly measure surface profiles using vehicle dynamic responses.

2.3 *System configuration and measurement algorithm*

The new profiling system can be mounted in any passenger and commercial vehicles. The system of the profiling system consists of two small accelerometers, a GPS (Global Positioning System) sensor, an amplifier, and an onboard laptop computer. A small GPS sensor is put on near the front window of the vehicle for measuring the vehicle traveling speed and location. An amplifier converts the strain of accelerometers into the electrical signal. An onboard computer records and displays the measurement results in real time.

The main feature in designing the mobile profiling system is measuring surface profiles using accelerometers. Using accelerometers contribute to save the installation costs over the use of laser sensors. Two small accelerometers are attached to the sprung and unsprung mass at a suspension system of a four-wheel vehicle. This instrumentation mechanically implements the quarter-car model used for the IRI simulation on a real car. Figure 2 shows the overview of roughness measurement algorithm of the mobile profiling system. The following sections describe the details of the algorithm.

2.3.1 *Acceleration measurement*

First, vertical accelerations of the sprung and unsprung masse (denoted by $\ddot{X}_s$ and $\ddot{X}_u$) are measured by using two accelerometers. The measurements are mathematically converted to the velocities and displacements of each mass by subsequent steps. Note that the two dots over a variable indicate a double derivative of the variable with respect to time.

2.3.2 *Pre-processing*

Second, as a pre-processing, the noise, trend, direct current excitation, and velocity dependence factors of vehicle vibrations are removed from $\ddot{X}_s$ and $\ddot{X}_u$ by use of digital filters. As the first step of this process, a Kalman filter is applied to detrend the measured acceleration. Then, as the second step, a narrow-bandpass filter removes the velocity dependence factors. As the final step, high frequency components over 30 Hz are removed by using a low-pass filter.

2.3.3 *Integration of acceleration data*

Third, $\ddot{X}_s$ and $\ddot{X}_u$ are integrated over time to calculate the velocities (denoted by $\dot{X}_s$ and $\dot{X}_u$ respectively) and the displacements (denoted by X_s and X_u respectively). Here, the dot over a variable indicates a time derivative of the variable.

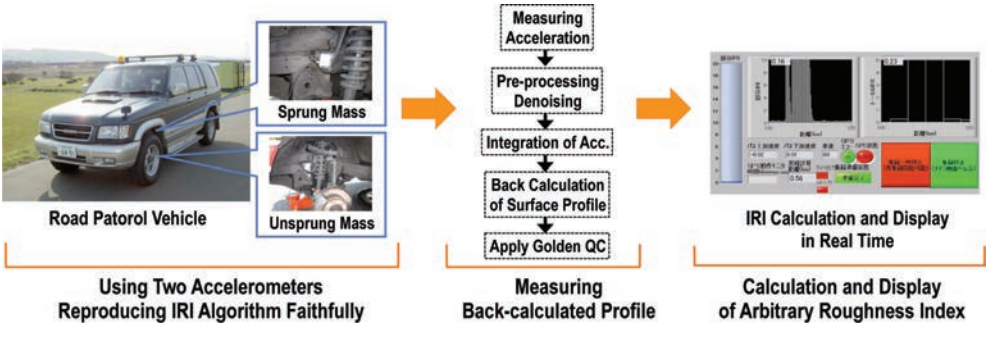

Figure 2. Overview of the measurement algorithm of the mobile profiling system.

2.3.4 *Back calculation of a surface profile*

Fourth, a longitudinal elevation profile denoted by X_p is calculated based on the back calculation of the equations related to motions of the mechanical suspension system which reproduces the quarter-car model. The equations of motions for the suspension system are described as follows:

$$m'_s\ddot{X}_s + c'_s(\dot{X}_s - \dot{X}_u) + k'_s(X_s - X_u) = 0 \tag{1}$$

$$m'_u\ddot{X}_u + c'_s(\dot{X}_u - \dot{X}_s) + k'_s(X_u - X_s) + k'_t X_u = k'_t X_p \tag{2}$$

Here, in the equations, a single prime for each coefficient indicates the value obtained from the survey vehicle.

2.3.5 *Golden Car simulation*

Fifth, the response of the Golden Car model to the measured profile X_p is simulated by use of the following equations.

$$m_s\ddot{x}_s + c_s(\dot{x}_s - \dot{x}_u) + k_s(x_s - x_u) = 0 \tag{3}$$

$$m_u\ddot{x}_u + c_s(\dot{x}_u - \dot{x}_s) + k_s(x_u - x_s) + k_t x_u = k_t X_p \tag{4}$$

Here, for the variables, a small letter "x" is used instead of the capital letter "X".

2.3.6 *IRI calculation*

Finally, IRI values for an arbitrary interval are computed by using the result of the Golden Car simulation regarding the slope profile. The IRI is an accumulation of the suspension stroke of the Golden Car in response to a slope profile, normalized by the travelled distance. Thus, the IRI represents average rectified slope, with units such as mm/m or m/km. The IRI over a number of profile samples (n) is as follows:

$$\mathrm{IRI} = \frac{1}{n}\sum_{i=1}^{n}\left|S_{s,i} - S_{u,i}\right| \tag{5}$$

Here, the motion variables x_s and x_u are redefined in terms of slope valuables S_s and S_u. Note that the feature of the developed profiling system is its ability to directly obtain surface profiles. Consequently this profiling system can calculate any other profile-based indices instead of the IRI.

3 METHOD OF LONGITUDINAL TRUE PROFILE ESTIMATION

3.1 *Overview of the true profile estimation*

The mobile profiling system calculates IRI based on back-calculated surface profile data by use of accelerometers. The measurement algorithm optimizes the back-calculated profile to compute IRI in real-time by the pre-processing (see Section 2.3.2). Figure 3 shows an example of profile measurements and Power Spectral Density (PSD) functions of surface elevation measured by Rod & Level of a Class 1 profiler and the mobile profiling system operated at 80 km/h. As shown in the figure, the mobile profiling system underestimates the PSD amplitudes with wavelengths of 14 and 1.5 m (Wave Number of 0.07 and 0.7 m^{-1}) corresponding to the natural frequencies of sprung and unsprung mass of a vehicle than Rod & Level. The other difference appears in a wavelength of 0.7 m (Wave Number of 1.5 m^{-1}) caused by the natural frequency of tire characteristics. Here, the precision of IRI measurements of the mobile profiling system is within 10% of the Rod & Level as shown in Figure 3. In the following part of this paper, we develop an estimation method of longitudinal true profiles that are compatible with Class 1 measurements by use of the mobile profiling system.

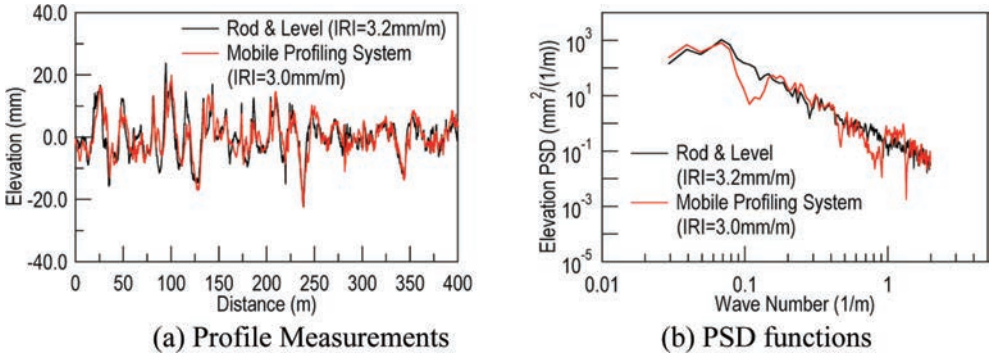

Figure 3. An example of profile measurements and PSD functions of surface elevation measured by Rod & Level and the mobile profiling system.

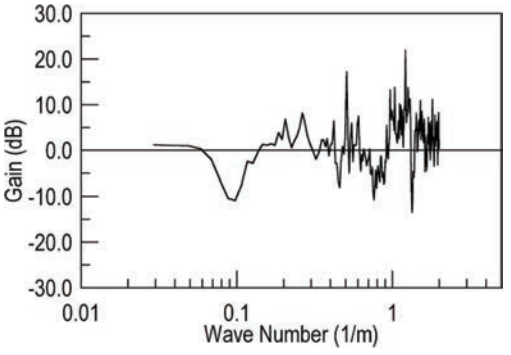

Figure 4. A wave number response of the mobile profiling system.

This chapter describes a reconstruction filter and its application to compensation of the underestimations.

3.2 *Development of a reconstruction filter*

The mobile profiling system functions as mechanical filters that have a wave number response optimized to the real-time IRI calculation. Figure 4 illustrates an example of the filter gain for profile elevation measured by Rod & Level. For the purpose of the true profile estimation, a reconstruction filter that has the inverse wave number response of Figure 4 is required. A reconstruction filter can be designed by computing a wave number response of the mobile profiling system to Rod & Level measurements. In this study, we develop a reconstruction filter on the basis of a Fast Fourier Transform (FFT) method that is performed in the spatial frequency domain. By using the FFT, convolution via the frequency domain can be faster than directly convolving the time domain signals. The final result is the same; only a more efficient algorithm has changed the number of calculations. For this reason, we use FFT convolution for the true profile estimation. Following are the detailed procedures for designing a reconstruction filter.

3.2.1 *Pre-filtering*

To remove the slope and very long undulations of road surfaces, measured profile data are filtered to limit the wavelengths to the range between 0.5 and 50-m which define the profile wavy characteristics in terms of pavement roughness by a 6th order Butterworth band-pass filter [3]. Profiles are resampled at an interval of 0.1 m for different sampling intervals in this process.

3.2.2 *Segmentation of measured profile data*

A related confusion of the FFT is the trade-off that must be made between wave number and distance resolution. The more accurately we want to measure the wave number content of a profile, the more samples we have to analyze in each frame of the FFT. Yet there is a cost to expanding the frame size—the larger the frame, the less we know about the temporal events that take place within that frame. A potential idea of applying the FFT to a very long profile is to split the profile sequence into several segments and then to average the segments at a certain overlap. By considering the trade-off between wave number and distance resolution for profile analyses, this process splits the profile data series into analytical segments of 1024 (= 2^{10}) with 50% overlap.

3.2.3 *Windowing*

The FFT algorithm assumes that the input profile data is an infinitely repeating periodic signal with the endpoints wrapping around. Thus, to the extent that the amplitude of the first point differs from the last point, the resulting frequency spectrum is likely to be distorted as result of this start point to endpoint discontinuity, which is so-called "edge effect". This can be overcome by "windowing" the data during the transformation. In this study, the hamming window function is used to attenuate the edge effects.

3.2.4 *Computation of a wave number response*

For this purpose, first, the profile data series of each segment are transformed into the spatial frequency domain by the FFT. Then, this process computes the PSD function of the transformed data series because the FFT produces a spectrum in complex form. Where the PSD functions of the profiles measured by Rod & Level and the mobile profiling system as $P_x(f)$ and $P_y(f)$, a wave number response $H(f)$ can be calculated by the following equation:

$$|H(f)| = \sqrt{P_y(f)/P_x(f)} \tag{6}$$

The gain can be expressed in a decibel unit as following:

$$|H(f)| = 10\log_{10}\left(P_y(f)/P_x(f)\right) \quad (dB) \tag{7}$$

Finally, a wave number response of the mobile profiling system can be obtained by averaging the responses for each analytical segment as shown in Figure 4.

3.2.5 *Design of a reconstruction filter*

A reconstruction filter is simply composed by the inverse factor of the wave number response shown in Figure 4 in the spatial frequency domain. Note that a reconstruction filter depends on the operated speed of the mobile profiling system.

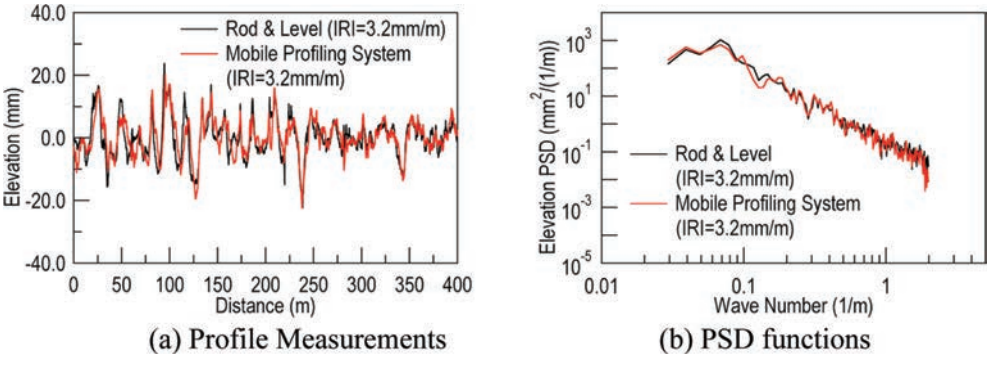

Figure 5. An example of true profile estimation result by use of the mobile profiling system.

3.3 *Estimation of a longitudinal true profile*

The basic idea of developing a reconstruction filter uses the principle of FFT-based digital filters that multiplication in the spatial frequency domain corresponds to convolution in the spatial domain. To estimate a true profile by use of the mobile profiling system, first, the measured profile data is transformed into the spatial frequency domain using the FFT, and then multiplied by the reconstruction filter developed by the previous section. Finally, the filtered data is transformed back into the spatial domain using the Inverse FFT (IFFT). Figure 5 shows an example of the estimation result of the true profile.

As shown in Figure 5, the reconstruction filtering process dramatically improves the profile measurement of the mobile profiling system compared with Rod & Level of a Class 1 measure. In the next chapter, we demonstrate the applicability of the true profile estimation regarding vehicle characteristics and operating speeds of the mobile profiling system.

4 VALIDATION EXPERIMENT OF THE TRUE PROFILE ESTIMATION

In this study, we performed a validation experiment of true profile estimation using the mobile profiling system. The experiment was carried out on an in-service expressway in Hokkaido, Japan.

4.1 *Measurement of surface profile data*

For the purpose of the validation experiment, a reference profile was manually measured by Rod & Level survey. At the same time, three different vehicles such as Sedan, SUV, and Van with the mobile profiling system recorded the relative profiles at three different speeds of 60, 80, and 100 km/h. The experimental section was 400 m long, and the profiles were sampled at an interval of 100 mm for the present study. Figure 6 shows an overview of the experimental site and the Rod & Level survey.

4.2 *Comparison of profile measurements*

This section verifies the accuracy of back-calculated profiles and true profile estimations using the mobile profiling system by comparing with the Rod & Level survey. For this purpose, average percentage errors of the PSD functions per octave-band are calculated for each measurement condition so as to quantify the discrepancy between two instruments. Table 1 summarizes the error of each back-calculated profile and true profile estimate. As shown in the table, the percentage errors are substantially decreased in the true profile estimations. Here, note that the acceptable error for longitudinal profile measurements in Japan is within 30% compared with Class 1 measures. Thus, the performance of the mobile profiling system

Figure 6. Overview of the experimental site and the Rod & Level survey.

Table 1. Profile measurement accuracy of the mobile profiling system.

Vehicle type	Operation speed (km/h)	Percentage error (%)	
		Back-calculation	True profile estimation
Sedan	60	47.6	7.9
	80	41.6	14.5
	100	37.2	11.3
SUV	60	46.9	7.4
	80	44.4	13.0
	100	38.5	10.6
Van	60	42.8	10.1
	80	54.1	17.8
	100	71.1	25.3

Table 2. IRI measurement accuracy of the mobile profiling system.

Vehicle type	Operation speed (km/h)	Percentage error (%)	
		Back-calculation	True profile estimation
Sedan	60	6.4	1.2
	80	14.0	0.1
	100	20.4	2.9
SUV	60	6.1	2.2
	80	7.0	0.6
	100	5.3	0.4
Van	60	8.7	4.0
	80	3.7	2.8
	100	4.9	5.8

satisfies the practical requirements as a profiler. This result indicates that the reconstruction filter is effective in estimating true profiles using the mobile profiling system.

4.3 *Effect on IRI measurements*

The mobile profiling system can originally reproduce IRI values within 10% error on average in real-tine. Table 2 shows the effect of the reconstruction filter on the IRI calculation. As shown in the table, the accuracy of the IRI measurement is slightly improved, but the change is not drastic. Therefore, the mobile profiling system basically has a capacity for measuring the IRI in real-time, and the back-calculated profile is appropriate regarding real-time IRI computation.

5 CONCLUSIONS

Today, expressway agencies in Japan require a proper method of monitoring the pavement roughness. This paper introduced a mobile profiling system for real-time monitoring of the IRI of expressways. The system uses two accelerometers fixed to a suspension system of any passenger and commercial vehicles to measure the IRI based on the back-calculated profile. The measurement algorithm of this system achieves both of the accuracy of Class 2 measures and the convenience of Class 3 measures. However, since the measurement algorithm is optimized to compute the IRI in real-time, the back-calculated profile is distorted by the natural frequencies of suspension components. This study also examined an estimation technique of a longitudinal true profile using the mobile profiling system based on the theory of

digital signal processing. For this purpose, we develop a reconstruction filter to attenuate the distortion in the spatial frequency domain by the FFT method. As the result of the validation experiment, the mobile profiling system using the reconstruction filter satisfies the practical requirements as a profiler of which percentage error is within 30% compared with a Class 1 measures. The result also indicated that the mobile profiling system basically has a capacity for measuring the IRI in real-time, and the back-calculated profile is appropriate for the purpose.

REFERENCES

[1] Sayers, M.W. Two Quarter-Car Models for Defining Road Roughness: IRI and HRI. Transportation Research Record, No. 1215, pp. 165–172, 1989.

[2] Sayers, M.W. Profiles of Roughness. Transportation Research Record, No. 1260, pp. 06–111, 1990.

[3] Sundberg, U., and Ejsmont, J.A. Tyre/Road Noise Reference Book, Infomex, Kisa, Sweden, 2002.

This page intentionally left blank

Asphalt Pavements – Kim (Ed)
© 2014 Taylor & Francis Group, London, ISBN 978-1-138-02693-3

A study on profile improvement in pavement repair

Keizo Kamiya & Kiyohito Yamaguchi
NEXCO Research Institute Japan, Machida, Tokyo, Japan

Akira Kawamura & Kazuya Tomiyama
Kitami Institute of Technology, Kitami, Hokkaido, Japan

ABSTRACT: Although it is generally believed that road profile will improve after a repair paving project, it was revealed that this is not always true, judging from comparing IRI levels before and after repairing on 500 sections of the Japanese toll expressways. Some 30 percent having had IRI 2.0 m/km or lower showed higher IRIs after conventional milling and overlaying methods. To find out how to steadily obtain smoother road surface, octave band analysis was conducted to compare profile data before and after the repair between improved and unimproved sections.

As a result, it is recommended that rod-and-level survey is used, when road undulation or long wavelength profile needs to be corrected. It was also found that there was quite difference in post-repair riding quality on the sections that had been controlled by a veteran asphalt finishing operator and an inexperienced person, in spite of no visual differences in the repaired field. Thus it is concluded that octave band analysis can an excellent method of controlling road profile as it can effectively differentiate unseen quality on the roadway.

Keywords: IRI, repair paving project, octave band analysis, profile, survey

1 INTRODUCTION

Roughness quality in a repair paving project is inspected using a 3-meter-profilometer with its standard deviation value whose threshold is 1.3 mm. In a repair planning stage, International Roughness Index that relates riding quality [1] has been used on the nationwide toll expressways operated by three authorized companies, namely East, Central and West NEXCO in Japan.

Recently there has been an increasing claim that IRI is not improved after repair paving projects for the purpose of a better riding quality at NEXCO. Figures 1 and 2 report the situation at a local bureau, comparing IRI values before and after the repair. The five hundred 200 m-unit IRI data were collected on a left-sided truck lane in fiscal 2011 and 2012, covering several paving contractors. According to Figure 1, IRI was slightly reduced by the repair in average and standard deviation, while the peak values were not much changed. However, Figure 2 tells that some 30% of unit-sections are higher after the repair at the sites where pre-IRI is 2.0 or lower. Needless to say, all the projects sufficiently passed the current contract criteria of the 3-meter-profilometer's standard deviation.

It is unrealistic to prescribe a recoverable level for roughness, as it varies with various field conditions. However, a newly constructed level should be a bench mark. Figure 3 compares the above post-repair IRIs with those on four newly constructed roadways just before opening to traffic in fiscal 2004 through 2010. The shape of the new data group resembles that of the repair data group. This may suggest that profile improvement in the IRI ranges less than 2.0 is difficult with a common repair method.

This paper presents several findings in the course of studying an effective repair paving method that can practically improve road roughness. From the past studies, it was indicated

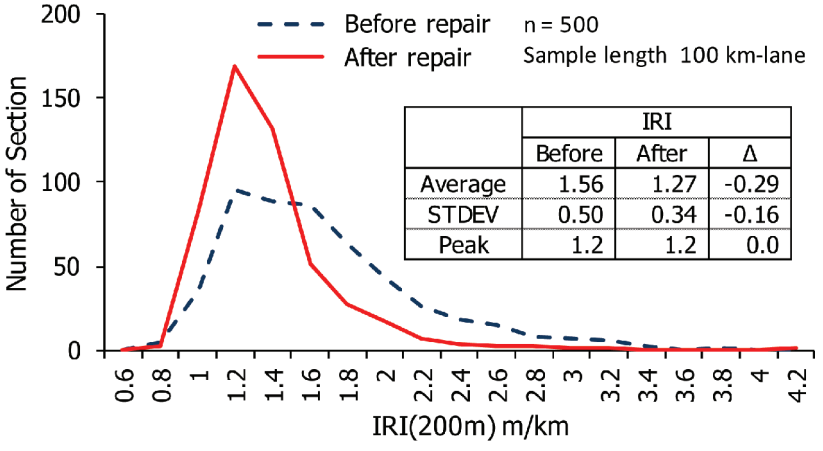

Figure 1. IRI histograms before and after repair at a local bureau.

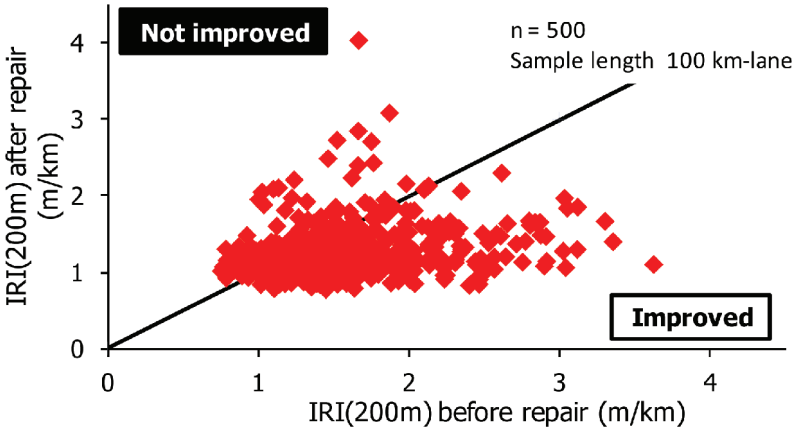

Figure 2. IRI distribution before and after repair at a local bureau.

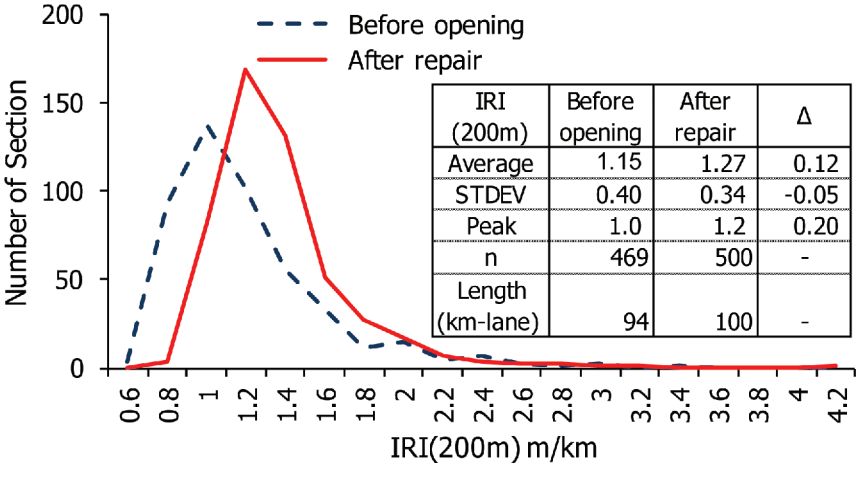

Figure 3. IRI histograms before opening and after repair at a local bureau.

that IRI is not suited for detecting irregular forms of road roughness. For understanding of localized defects, power spectral density [2], discrete Fourier transform [3], and wavelet transform [4,5] were introduced. However, these methods are too much academic to apply in the current contract procedures in Japan. In the study, octave band analysis which seems a much easier method was applied and comparison of profile data before and after several repair projects was conducted.

2 PAVEMENT REPAIR PROJECT

As a given condition in a pavement repair project, a road administrator is required to follow a traffic regulation issued by local police agency that is in charge of traffic safety in the community. The regulations are strict nationwide, due to a lack of road network system in Japan. Thus Japanese road operators and contractors are always struggling to secure safety in the field. For example, during milling and overlaying repair projects in many urban areas, only one lane closure is permitted and the closing hour for the lane is about 8 hours.

Table 1 lists typical repair projects for porous asphalt with measurements of longitudinal profile before and after rehabilitation. Project A adopts milling and overlaying two layers during a daytime 7 hours lane closure for damaged porous asphalt on an expressway nearby Tokyo. Project B repairs two layers by extending lane closure hours to 24 hours on a local route. Project C on another rural expressway strengthens the pavement structure by paving 14 cm thickness after milling 4 cm during an 8 hours daytime. Project A handles only one lane, while Project B and C repair two lanes by switching to the adjacent lane after the first.

Every 100 meter section's IRI data before and after repair among the three projects were plotted in Figure 4. Four sections out of 16 showed slightly higher IRI values after the repair.

Table 1. Typical repair Projects for porous asphalt on expressways.

	Project A	Project B	Project C
Repair method	Mill and overlay	Mill and overlay	Mill and overlay
Milling depth (cm)	4 + 6	4 + 6	4
Overlaying thickness (cm)	4 + 6	4 + 6	4 + 10
Repair month	September	October	November
Traffic regulation	6 hrs, one lane	24 hrs, one lane	8 hrs, one lane
Repair layers/day	2	1	1
Number of repair lanes	1	2	2

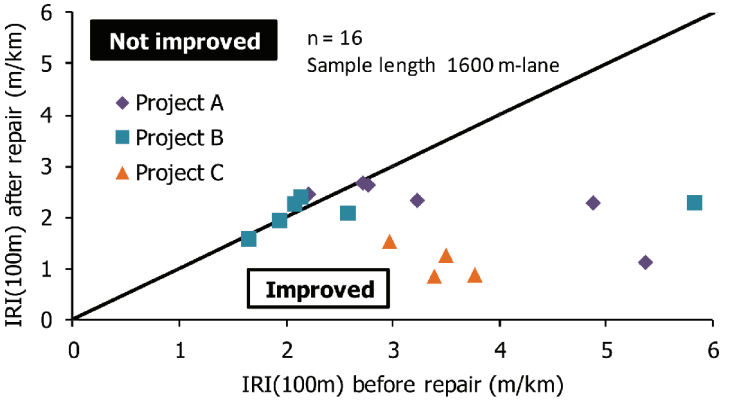

Figure 4. IRI distribution before and after repair at three projects.

The problematic sites were again observed at around 2.0. As naturally, Project C substantially improved the roughness, as it can best adjust the road profile by controlling the thicker thickness and on the neighbouring lane. Project A must be the toughest repair, since its allowable paving time was the shortest and only one lane is repaired. Although Project B had to deal with IRI levels around 2.0 in advance of repair, it covered two adjacent lanes, which is close to repair condition of Project C. A question arises here; "Was it really impossible in Project B to reduce the IRI values like in Project C?"

3 OCTAVE BAND ANALYSIS

Among six sections in Project B, three showed improvement in roughness after repair while the other three remained or increased IRI values. The most remarkable reduction in IRI was observed at its initial IRI level of 5.83. Because this worst site had suffered a slightly undulated roadway, rod-and-level survey was used as a pre-survey to correct the longitudinal profile. The other five adopted 10-meter-long-strings method to adjust milling depth.

3.1 *Band selection*

In order to find out how to steadily obtain smoother road surface, octave band analysis was conducted to compare profile data before and after the repair between 10-meter-long-strings and rod-and-level sections. In doing the octave band analysis, longitudinal profile of the selected sections was divided into nine bands, based on the known wave number response of the IRI quarter-car filter [6], as shown in Figure 5. Because IRI is mostly affected by octave band ranges No. 2 with wavelength of 51.2 m–25.6 m through No. 7 with 1.6 m-0.8 m, these 6 ranges will be focussed on hereafter.

3.2 *Pre-survey of profile*

Table 2 summarizes the comparison of a 100 meter's 10-meter-long-strings section and another 100 meter's rod-and-level survey section for each entailing octave band profile before and after the repair. Some surface distress types were also put down in the table.

All the post-repair octave band profiles in the latter section decreased more remarkably than in the former. This is quite understandable because the initial IRI value of 5.83 for the rod-and-level section diminished greatly to the post value of 2.29. However, it is noted

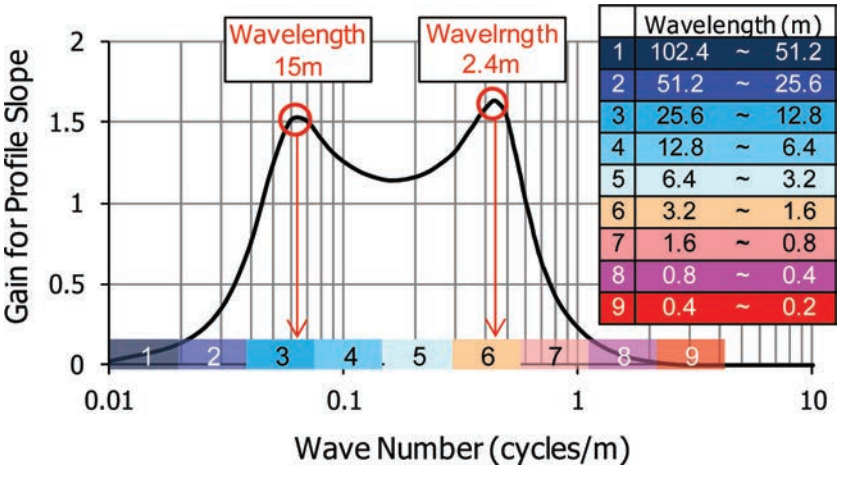

Figure 5. Wave number response of IRI quarter car filter [6].

Table 2. Octave band profiles between pre-survey methods (Project B).

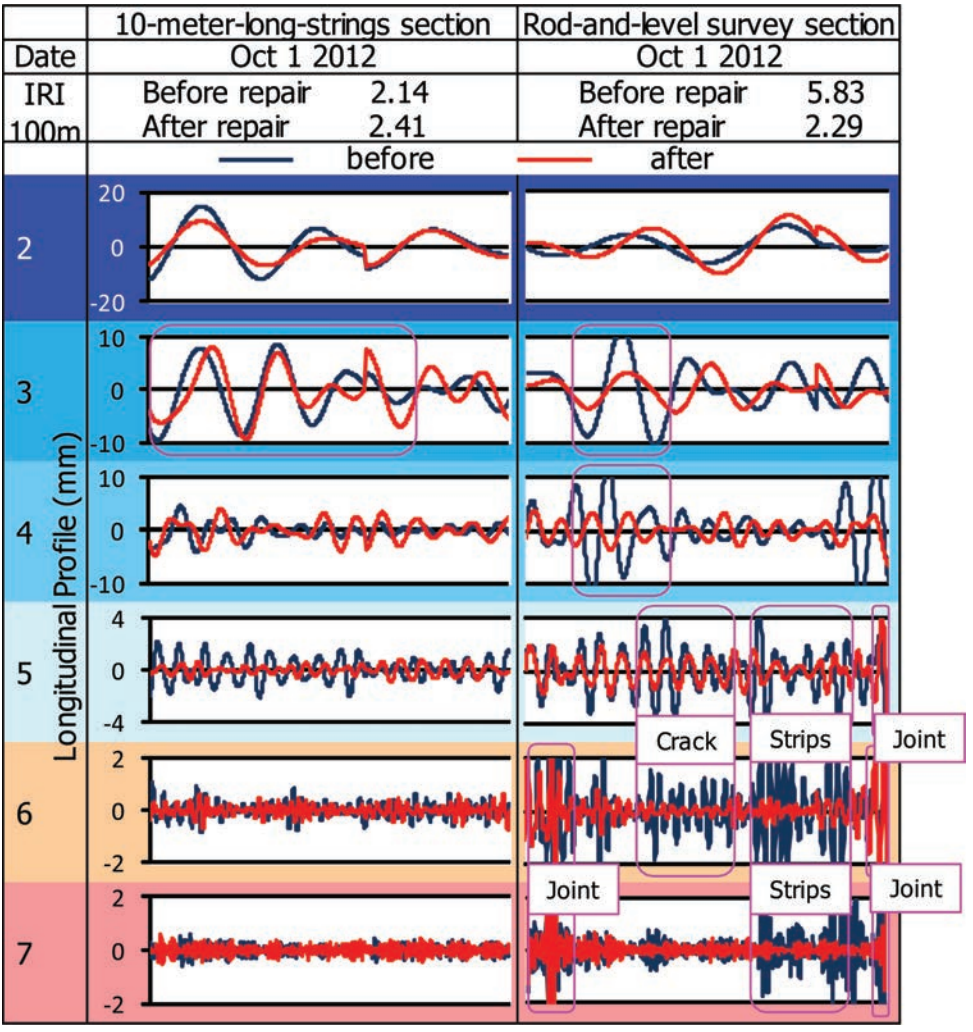

that portions of profiles on octave bands No. 3 and No. 4 were successfully improved in the rod-and-level, while those not well in the 10-meter-long-strings method. This probably indicates the limitation of the 10-meter intervals survey that cannot control road profile with its wavelength exceeding 10 meters. If rod-and-level survey had been adopted in the 10-meter-long-strings section, the post-repair IRI value would have been much lower than the initial value of 2.14.

It is also revealed that distress segments of cracking and stripping of aggregates that had emerged on octave bands No. 5 through No. 7 in the rod-and-level section were improved by the repair. This is quite reasonable, because the existing materials are replaced with new materials. At a site in Project A, however, it was confirmed that profiles on these octave bands will also be affected by the manipulation of asphalt finisher's screed during paving, which will be mentioned later. On the other hand, high profiles on adjacent bridge joints were unfortunately remained as there had been. This is because the joints were so damaged that the only new materials could not compensate for the adjacent profile.

From above findings, it was confirmed that octave bands No. 2 through No. 4 will capture undulation of road profile, while road surface distress can be explained by octave bands No. 5 through No. 7. Moreover, it is recommended that rod-and-level survey is used, when

undulation or long wavelength profile that belongs to the former octave bands needs to be adjusted.

3.3 *Finishing operator*

There was a very interesting finding at Project A where the most difficult paving procedure was required. It was proved evident that roughness quality differs on sections paved by a well experienced finishing operator and a less experienced person. Table 3 supports the evidence.

As shown in the right side of Table 3, a drastic reduction in longitudinal profiles on octave bands No. 3 through No. 7 was observed on the section paved by a veteran operator. As a result, IRI was greatly improved from 5.37 to an initial opening level of 1.13. The two days later, when an inexperienced staff took replaced him on the continuing roadway section, there was not a clear improvement in profiles after the repairing. Judging from comparing the pre-profiles between the two sites, the veteran's part was more difficult to control the finishing machine, as the profiles acted up more in the entire octave bands. Moreover to be surprise, these sections were repaired without using rod-and-level survey or 10-meter-long-

Table 3. Octave band profiles between finishing operators (Project A).

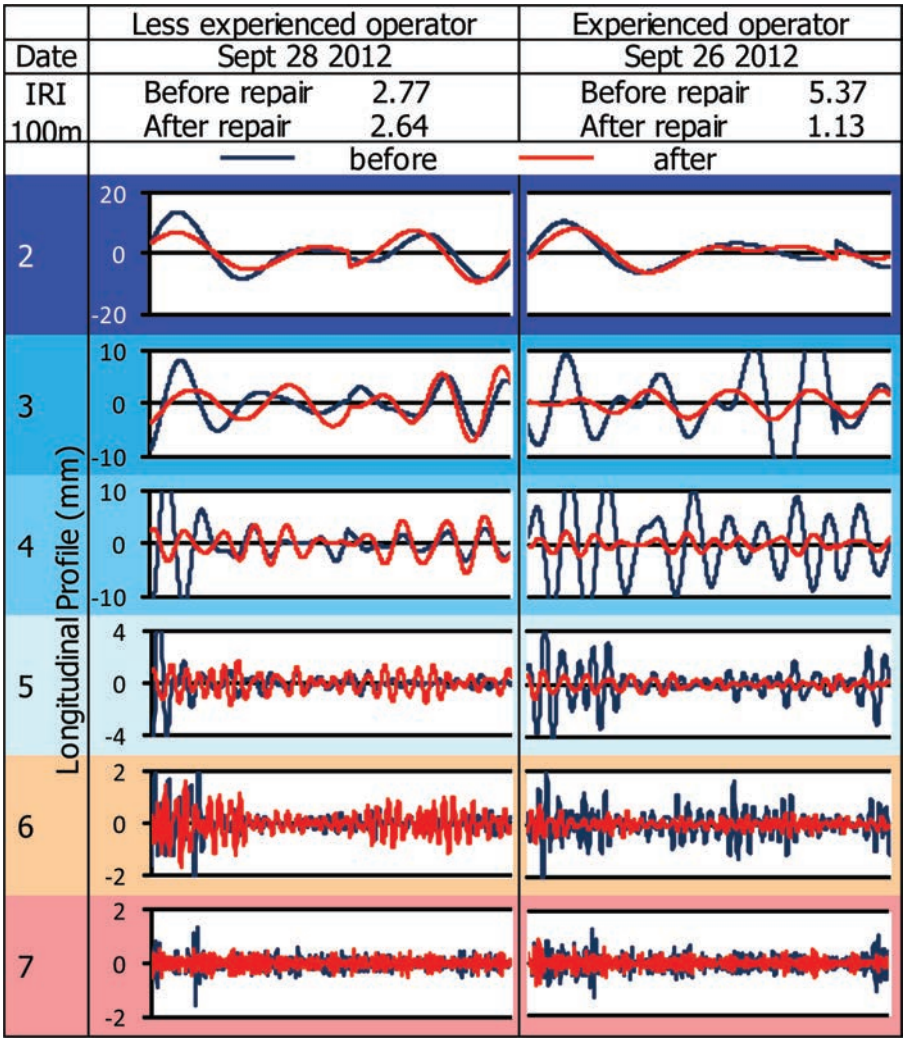

strings methods, since there was not such visual abnormality in the roadway that nobody thought of the necessity of the pre-survey. As IRI indicates the post-IRI values, there is quite difference in riding quality on the two continuing sections, although there is no visual difference. This indicates the importance of so-called an artisan's technique, which is said to be impossible to write down in words for handing down to younger generations.

Although it is not yet revealed how the veteran achieved the profile improvement, it is at least confirmed that octave band analysis can clearly differentiate unseen quality on the roadway. The next challenge is to elucidate the veteran's technique that does not require a pre-survey. If this is well done on the analysis, road profile can be improved by controlling the existing octave band profiles to newly planned ones.

4 CONCLUSION

In the wake of an increasing claim that IRI is not improved after repair paving projects at NEXCO, investigation with five hundred 200 m-unit IRI data revealed that some 30% are higher after the repair at the sites where IRI before the repair is 2.0 or lower. In the course of pursuing a consistent repair method, octave band analysis was conducted to compare profile data between specific repair paving projects. Consequently, the followings were found.

1. Octave band ranges No. 2 through No. 4 with wavelength of 51.2 m to 6.4 m will capture undulation of road profile, while road surface distress can be explained by octave bands No. 5 through No. 7 with wavelength of 6.4 m to 0.8 m.
2. It is recommended that rod-and-level survey is used, when road undulation or long wavelength profile that belongs to the octave band ranges No. 2 through No. 4 needs to be corrected.
3. There was quite difference in post-repair riding quality on the sections that had been controlled by a veteran asphalt finishing operator and an inexperienced person, in spite of no visual differences in the repaired field.
4. It is concluded that octave band analysis can an excellent method of controlling road profile as it can effectively differentiate unseen quality on the roadway.
5. If a veteran's technique can be further grasped on the analysis, road profile can be steadily improved by controlling each existing octave band profile to a newly planned one.

REFERENCES

[1] Sato, M. et al. Development of Riding Quality Evaluation in the Japanese Expressways, 7th China-Japan Workshop on Pavement Technologies, Harbin, China, pp. 1–10. 2013.

[2] O, Kropáč. and P. Múčka. Be careful when using the International Roughness Index as an indicator of road unevenness, Journal of Sound and Vibration, pp. 889–1003. ELSEVIER. 2005.

[3] Rawool, S. and Fernando, E. Methodology for Detection of Defect Locations in Pavement Profile. Transportation Research Record 1905. pp. 141–147. Transportation Research Board. 2007.

[4] Parisa Shokouhi, P. et al. Wavelet-Based Multiresolution Analysis of Pavement Profiles as a Diagnostic Tool. Transportation Research Record 1940. pp. 79–88. Transportation Research Board. 2008.

[5] Wei, L. and Fwa, T. Characterizing Road Roughness by Wavelet Transform. Transportation Research Record 1869. pp. 152–158. Transportation Research Board. 2009.

[6] Sayers, M. and Karamihas, S. The little Book of Profiling, pp. 50–51. The Regent of the University of Michigan. 1998.

This page intentionally left blank

Asphalt Pavements – Kim (Ed)
© 2014 Taylor & Francis Group, London, ISBN 978-1-138-02693-3

Assess asphalt in-place density with Intelligent Compaction measurements

George K. Chang
The Transtec Group Inc., Austin, TX, USA

Victor Lee Gallivan
US FHWA, Indianapolis, IN, USA

Qinwu Xu
The Transtec Group Inc., Austin, TX, USA

ABSTRACT: Intelligent Compaction (IC) is defined as vibratory rollers with accelerometers mounted on the axle of drums, Real-Time Kinematic (RTK) or Virtual Reference System (VRS) Global Positioning System (GPS), and on-board computers that can display various roller operating settings on color-coded maps in real time. IC measurements include roller positions, number of passes, surface temperatures, and stiffness of the compacted materials. Asphalt in-place density, a common measurement for mix durability and performance, is influenced by many factors including material properties, environment, paving, and compaction. Based on the compaction history captured by IC, a stochastic method was developed to correlate the IC measurements to asphalt in-place density, either measured with nuclear density gauges or from cores. Between 2011 and 2014, the US Federal Highway Administration (FHWA) IC Phase II research team has planned nine (9) field projects around the US to validate and enhance the statistical correlation between IC measurements and asphalt in-place density. The validation data from the first three (3) sites show that the critical period of initial breakdown compaction is the most dominating factor to achieve desired density for a given support condition. A nonlinear stochastic model was developed to correlate the in-place density with IC measurements, including the stiffness of asphalt material and underneath layers, asphalt mat temperature, and roller vibration frequency/amplitude. Once the model is fully validated with data from all remaining sites, any IC system may utilize this stochastic method developed under this research to estimate asphalt in-place density in real time and use IC as a quality control tool to optimize asphalt density. Leveraging the IC geospatial data that cover one hundred percent of compacted area, IC can also be a truth metric for compaction uniformity. The ultimate goal of this research is to achieve compaction uniformity for long lasting pavement.

Keywords: asphalt, in-place density, paving, compaction, intelligent compaction, uniformity, performance

1 INTRODUCTION

Intelligent Compaction (IC) is defined as vibratory rollers with accelerometers mounted on the axle of drums, Real-Time Kinematic (RTK) or Virtual Reference System (VRS) Global Positioning System (GPS), infrared sensors, and on-board computers that can display various roller operating settings on color-coded maps in real time as displayed in Figure 1. IC measurements include roller positions, number of passes, mat surface temperatures, and stiffness of the compacted materials.

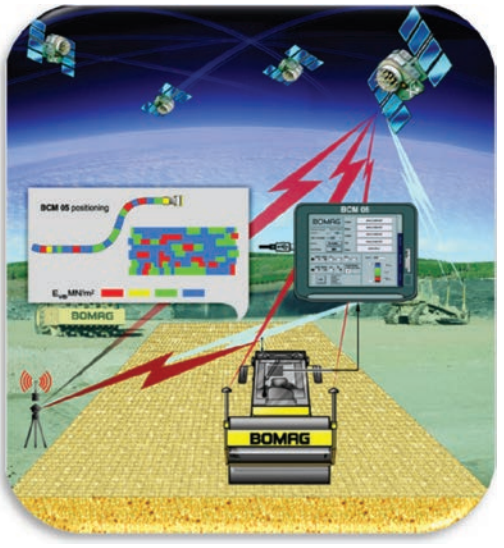

Figure 1. An illustration of intelligent compaction technology.

Asphalt in-place density, a common measurement for mix durability and performance, is influenced by many factors including material properties, environment, paving, and compaction. Based the compaction history captured by IC, a stochastic method was developed to correlate the IC measurements to asphalt in-place density, either measured with nuclear density gauges or from cores.

The Federal Highway Administration (FHWA) has been leading a national effort to advance the IC technology through a Transportation Pooled Funded (TPF) IC project (TPF-5(128)) with twelve (12) States participating and other subsequent projects. The scope of the FHWA/TPF IC project (FHWA-IC) was principally to conduct field demonstrations of the technologies in the twelve participating states on various material types including non-cohesive soils, cohesive soils, granular subbase, stabilized base, and asphalt materials and establish a knowledge base for further advancement and implementation of IC. Between 2007 and 2011, the FHWA IC research team has conducted fifteen field projects around the US to validate and enhance the statistical correlation between IC measurements and asphalt in-place density. The validation data show that the critical period of initial breakdown compaction is the most dominating factor to achieve a desired density.

The current IC technology outputs roller IC Measurement Values (ICMV) that relate to the stiffness of the underlying materials. On the other hand, density measurement is still commonly used for quality acceptance for most agencies and contractors as in-place densities often relate to long-term performance of asphalt or hot mix asphalt pavements. To accelerate the implementation of IC technology, it is essential to study the correlation between ICMV and asphalt core densities. In spite of the accomplishment of the FHWA/TPF IC projects, unsatisfactory correlation between ICMV and asphalt core density was observed from the initial IC field demonstration projects. This is due to many factors such as the differences in nature of measurements between ICMV and in-place densities, limited cores for being statistically significant, etc.

As a continuing effort under Phase II of the FHWA IC project, an extensive study is being conducted to assess the correlation between the IC measurements and asphalt core densities between 2011 and 2014. This work investigates the relationship between ICMV and core densities via extensive coring in order to establish a procedure to use IC as an acceptance tool for in-place asphalt densities.

In this paper, the preliminary results from the second phase of the FHWA IC study was reported based on the data collected from the first three of the nine field validation

sites (Utah, Florida, and Ohio). Nonlinear stochastic models were developed to correlate the in-place density with IC measurements, including the stiffness of asphalt material and underneath layers, asphalt mat temperature, and roller vibration frequency/amplitude. These stochastic models were screened and the optimal candidate model was selected. The selected stochastic model was firstly calibrated with a subset of the field data, and validated with the remaining data. Though still under development, the ultimate goal of this study is to evaluate whether IC technologies can be a reliable acceptance tool in addition to being a quality control tool. If it is a success, IC systems can incorporate the stochastic method developed under this research to estimate asphalt in-place density in real time and use IC as a quality assurance tool to optimize asphalt density during construction.

2 LITERATURE REVIEW

There are various efforts devoted to, though some partially, evaluate the potential benefits of intelligent compaction and relate ICMVs and other measurements to in-place field density. Past researches have shown poor or inconsistent correlations between ICMVs and asphalt core density, which could be due to factors such as the influences of the IC systems (e.g., vibration frequency and amplitudes) and pavement conditions (e.g., underlying layer stiffness). In summary, these factors include the following:

- Stiffness indexes derived from ICMVs of existing IC rollers represent an integral pavement structure with influence depths normally deeper than those by point test devices such as the nuclear density gauge. Therefore, these ICMVs are currently not yet decoupled to characterize individual layer stiffness.
- The current ICMVs for asphalt are tied to temperatures at test conditions instead of being normalized to a reference temperature. On the other hand, core density is independent of in-situ temperatures. Therefore, it would result in unsatisfactory correlation between ICMVs and core densities.
- Asphalt cores are normally taken after finishing rolling, while ICMVs are normally measured at breakdown or intermediate compaction. Therefore, there would be a gap of correlation created by the effects of intermediate and finishing rolling.

FHWA/TPF IC Study (2007 to 2011): The FHWA/TPF IC study was conducted between 2007 and 2011. Field demonstration projects are the major work under the FHWA-IC study. Key elements of the field demonstration include on-site training of TPF DOT and contractor personnel, comparison of IC roller technologies to traditional compaction equipment and practices, correlating IC roller measurements to in-situ spot test measurements, mapping the existing support to understand the influence of underlying layer support, selecting the appropriate machine operation parameters (e.g., speed, amplitude, frequency, etc.), and managing and analysing the IC and in-situ test data. Sixteen (16) IC field demonstration projects were performed for non-cohesive soils, cohesive soils, granular subbase, stabilized base, and asphalt materials. There were twelve (12) asphalt IC projects on various types of bases, overlay, and new construction under this study. HMA IC rollers from Bomag America, Inc. and Sakai America, Inc. were used during the above field demonstration.

The analysis results from FHWA-IC study have shown inconsistent correlations between ICMVs and nuclear density gauge (NG) densities. From the FHWA-IC study, ICMV generally increases with increasing density measurements by NG indicating that a higher stiffness corresponds with a greater material density. However, the correlation is often where the R^2 values ranges from 0.04 to 0.97. For the cases with more satisfactory correlation, it is often associated with larger number of in-place measurements on denser asphalt mixtures. On the other hand, cases associated with coarser mixtures such as the Stone Matrix Asphalt (SMA) in the Maryland demonstration often result in poor correlation. Therefore, consistent and repeatable NG measurements are the keys for improved correlation with ICMV. The analysis results from FHWA-IC study have also shown inconsistent correlations between ICMVs and asphalt core densities. The correlation reverses for some cases

such as the SMA overlay project in Maryland and new asphalt paving on the saturated base in Georgia.

As ICMV is potentially influenced by a number of factors, a multivariate analysis was conducted to include those factors as an attempt to improve the correlation under the FHWA-IC project (Xu et al. 2010; Chang et al. 2011). The factors included: ICMV from mapping the baseline structure, ICMVs during compaction of asphalt base courses, roller vibration frequencies, and asphalt surface temperatures during different stages of mapping and construction. The coefficients of determination, R^2, were improved for the multivariate linear regression compared to those from simple linear regression. For the Minnesota asphalt IC demonstration project, ICMVs from mapping the subbase as well as asphalt surface temperatures have shown significant effects on ICMVs during asphalt base course compaction. For the Wisconsin asphalt IC demonstration project, the most significant factors to the ICMVs during HMA compaction are: FWD deflections on the baseline structure, asphalt surface temperatures, and ICMVs from mapping the rubblized Portland Cement Concrete (PCC) subbase (Chang et al. 2011). Nonetheless, IC has been proven as practical tool for improving the quality control process through harmonization and standardization efforts in the US (Gallivan et al., 2011; Gallivan and Chang, 2012).

Highways for LIFE IACA Project (2008 to 2010): The Intelligent Asphalt Compaction Analyzer (IACA) is a device based on neural network technology to report the density of an asphalt pavement continuously in real time during its construction. The IACA uses a neural network to compare the vibrations of the vibratory compactor with known patterns of the vibrations and estimate the density/stiffness of the pavement. The IACA technology was developed and adapted for field study under the Highways for LIFE Technology Partnerships Program and Volvo Construction Engineering (Commuri 2009 and 2010). From this research, relatively high correlation was observed between IACA estimated density and NNG measurements. Also, similar observation was found between IACA estimated density and core and concluded that the IACA was a good tool for contractors' quality control operations. However, the IACA system is not ready for commercial production, and further independent verification study for acceptance is recommended.

Iowa DOT IC Study (2010): The Iowa Department of Transportation (Iowa DOT) Intelligent Compaction Research and Implementation was initiated in summer 2009. There was one asphalt IC field demonstration project conducted at the IA 218 asphalt overlay project under the Iowa Phase I IC research to evaluate Continuous Compaction Value (CCV) technology on the Sakai SW880 dual drum vibratory asphalt roller (White et al. 2010). The asphalt demonstration project under this study was performed to demonstrate mainly IC tracking capability for the asphalt surface temperatures and roller passes. Only qualitative analysis was performed to investigate the correlation between ICMV and core density by using approximate Geospatial references of test locations. Correlation between ICMV and core density showed a moderate correlation with linear regression R^2 equalling 0.4.

Wisconsin DOT HMA IC Study (2010): The Wisconsin Department of Transportation (WisDOT) conducted an asphalt overlay IC demonstration on US 45, during 2008–2009 (Quintus et al. 2010). The goals of this project were to help WisDOT evaluate the advantages and limitations of IC for achieving density, and to determine the material types and conditions that might cause inaccuracies in IC roller output concerning layer stiffness and other properties. Caterpillar, Bomag, and Sakai IC rollers were used for this study. However, the Caterpillar IC roller was not equipped with an accelerometer-based measurement system and the Bomag IC roller was not equipped with a GPS. The main findings identified the IC benefits including: 1) the IC roller's on-board display unit shows color-coded image to ensure adequate number of pass; 2) mapping stiffness of the underlying layer; and 3) IC response corresponds to laboratory measured resilient modulus, etc. For the asphalt IC, this research pointed out some issues including: 1) IC cannot prevent the intermediate or finish rollers from being operated in the temperature sensitive zone and reducing the density; 2) ICMV is heavily influenced by supporting layers; and 3) IC could not detect cold spots by stiffness measurements, etc. The major issue for this research is that only printed strip charts from the Bomag machines were used and no geospatial referenced data (i.e., GPS) were available for

a more precise geostatistical analysis. Therefore, results and conclusions from this study may not be supported with sufficient evidence.

Minnesota DOT HMA IC Studies (2001 to 2011): In 2001, a Minnesota Department of Transportation (MnDOT) study has shown that the thermal segregation affects the density. For example, profiles with the temperature difference below 25 °F (–3.8 °C) had 93% passing the density target, while those with the temperature difference higher than 25 °F (–3.8 °C) only had 50% passing the density target. In 2010, IC projects were conducted on TH 169 and TH 13. Results confirmed immediate IC benefits including: 1) map existing layers; 2) improve roller patterns; 3) improve roller operators' accountability; 4) improve density; 5) improve efficiency; and 6) increase information for QC/QA, etc. It pointed out that the influence depth varies dependent on the technology and site conditions. This study encouraged IC's use as a construction aid to reduce thermal segregation, and suggested to install retrofit systems on an entire roller train (Johnson 2010). In 2011, MnDOT conducted an asphalt IC study on an I-35 project with several IC retrofit systems on a break-down roller, an intermediate roller, and a finishing roller. The main goal was to track temperatures and roller passes, but there is no attempt to correlate ICMVs with in-place asphalt density.

NCHRP IDEA Project 145 (2013): An improved ICMV model was developed to decouple stiffness for each pavement layer to improve the correlation of ICMV and in-situ spot measurements under the National Cooperative Highway Research Program (NCHRP) Innovations Deserving Exploratory Analysis (IDEA) project 145 "Extraction of Layer Properties from Intelligent Compaction Data". This study used numerical Finite Element Method and Boundary Element Method (FEM/BEM) as a forward model for the roller-soils systems and trained a neural network based on the FEM/BEM results to produce a stochastic method for real-time back calculation to decouple the layer properties. The back calculation model was demonstrated for a two-layer soils system but not asphalt pavement systems. This back calculation model is influenced by IC measurement uncertainties and sensitivities of back calculation parameters (e.g., E1/E2, and d1/d2 or ratios of layer stiffness and thicknesses).

Normalizing ICMV to a Referenced Temperature: For asphalt compaction, an improved ICMV model is recommended to normalize ICMV to a referenced temperature. ICMV represents a relative stiffness of pavement materials during compaction at elevated temperatures. The asphalt stiffness is dependent on temperature, while the asphalt density is independent of temperature. During compaction, the ICMVs are associated with the asphalt surface temperature measurements. If the master curve of the asphalt mixture is known, the ICMV can be shifted along the curve to represent a value at a desired reference temperature.

Geospatial Analysis for ICMV: The geostatistical analysis of the ICMV is recommended to account for the influence of geospatial dependency in order to improve the correlation study. The commonly adopted linear regression analysis is based on the generalized regression without considering the effects of geographical dependency such as autocorrelation.

3 METHODOLOGY

3.1 *Technical framework*

The IC-density model is based on IC data and other in-situ density measurements. The model development makes use of statistical approaches. The IC data include IC Measurement Values (ICMV)—accelerometer-based measurements, vibration frequencies/amplitudes, and asphalt surface temperatures during compaction at vibratory mode during break-down and/or intermediate rolling. There are no ICMV for accelerometer-based measurements during static rolling. The densification is mainly achieved during vibratory compaction at elevated temperatures (during breakdown and intermediate rolling) while the increase of density due to static compaction (finishing rolling) is minimal, as displayed in Figure 2. However, different densification curves were observed in the field where the same equipment and materials were used with the proximity of tests (i.e., spatial differences). Therefore, the densification characteristic is very complex.

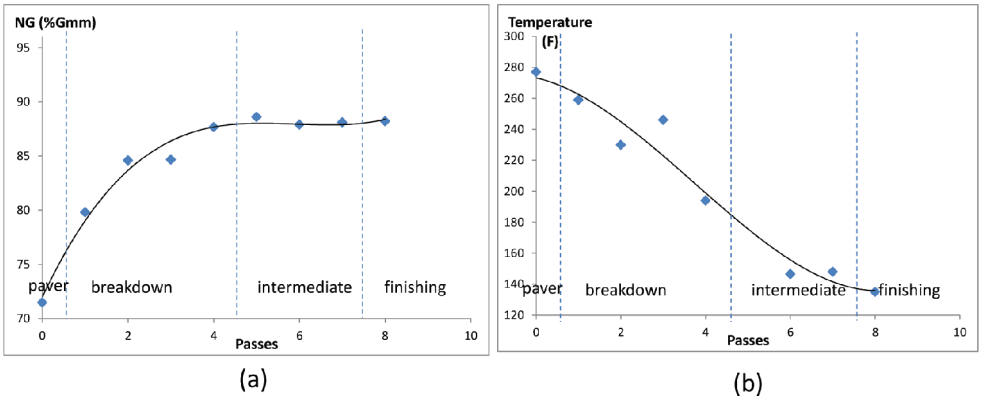

Figure 2. (a) Density growth and (b) temperature drops during compaction (FHWA IC demo in Maine, test point 1).

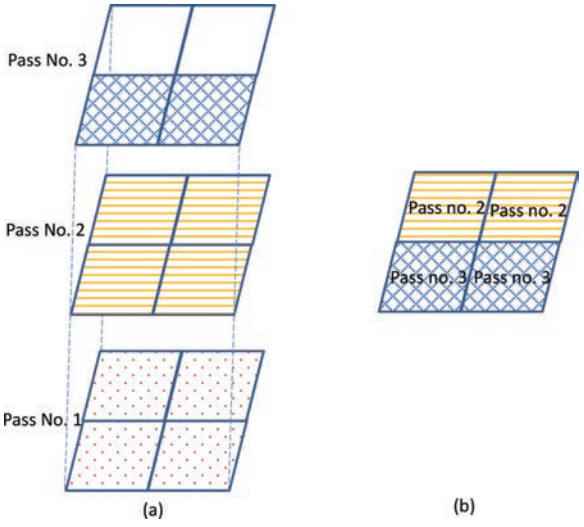

Figure 3. (a) Gridded all-passes IC data and (b) final coverage IC data.

The IC data, in terms of roller passes, include gridded all-passes data and final coverage data at 1 ft. (300 mm) by 1 ft. (300 mm) data meshes as displayed in Figure 3. The all-passes data include all IC measurements from every single roller pass at a given data mesh. The final coverage data include the last roller pass data. Currently, ICMV reflects the pavement layers up to 4 ft. (1.2 m) deep. ICMV is also categorized in two types: compaction indexes (e.g., CMV, HMV, and CCV) and stiffness/modulus values (Kb and Evib). Machine Drive Power (MDP) systems, which are not accelerometer-based, are not included in this study. Although there are researches on decoupling the ICMV, there are no prototype or commercial products available. The IC data analysis was conducted using the Veda software (Veda 2013) as displayed in Figure 4.

In addition to IC data, asphalt density measurements are normally conducted with NG as well as laboratory bulk density tests from field core samples in a calibration test strip. Under this study, NG data were collected after each IC roller pass at selected locations. Cores were then taken after the finishing rolling. NG measurements were also taken at the core locations prior to coring operation as displayed in Figure 5. Together, all the above IC measurements are tied with precise GPS measurements for density-IC model development.

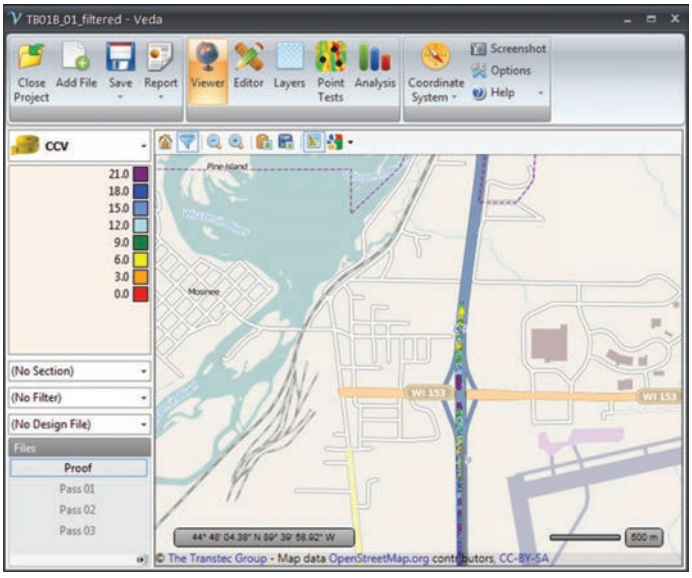

Figure 4. Veda software for IC data viewing and analysis (Veda 2013).

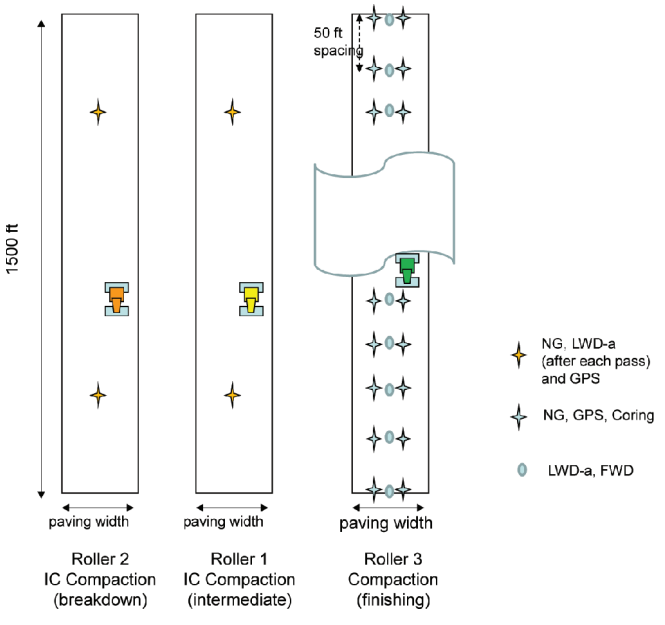

Figure 5. Calibration test strip with IC compaction and in-situ density measurements (FHWA IC demo in California, Test plan).

IC data and asphalt density measurements (using nuclear density gauge and cores) were collected in a calibration test strip. Both data were analysed using the Veda software and the results were extracted for the model development. IC data (ICMV, roller vibration frequencies/amplitudes, speeds, and asphalt surface temperatures) with respect to asphalt density measurements were extracted for both all-passes and final coverage data. Pass-by-pass data and portions of the final coverage data set were used to fit the IC-density model using the Excel Solver function. During the solving process, all unconstrained variables were made

positive and the evolutionary method was used to find a good solution to a reasonably well-scaled model. The fitted model was then validated using the remaining data set. The resulting model can then be used for the rest of the production compaction. The above IC-density model development framework is displayed in Figure 6.

The IC data capture compaction history including ICMV, surface temperatures, roller passes, vibration frequencies/amplitudes, roller speeds, etc. Although other factors can also influence in-place density (such as: nominal aggregate size to layer thickness ratios, aggregate shapes and gradation, binder and binder additives, reclaimed asphalt pavements, material transfer vehicles, pavers, etc.), the IC-density model is based on the IC data during breakdown and intermediate compaction in order to capture the most dominating factors, assuming the above factors being equal for a given lift at a given paving section. The data gap during static rolling (if IC is not equipped for the entire rolling train) would be considered as a random variable term fitted spatially with IC data and density measurements (including pass-by-pass data) in a calibration test strip. A simplification of the calibration process can be done by reducing the density measurements and coring. Therefore, the resulting IC-density model is locally calibrated for project-specific application in order to be a practical assurance tool for real-time in-place asphalt density prediction in the production compaction areas.

3.2 *IC Measurement Values (ICMV)*

The IC Measurement Values (ICMV) used in the US include Compaction Meter Value (CMV), Hamm Measurement Value (HMV), Compaction Control Value (CCV), vibration modulus (E_{VIB}), soil stiffness value (K_b), and Machine Drive Power (MDP). The Hamm Measurement Value (HMV) is identical to CMV. The K_b and MDP are not included in the second phase of the FHWA IC study due to the machine availability for asphalt IC.

Compaction Meter Value (CMV): CMV is a dimensionless compaction parameter developed by Geodynamik based on the phenomenon that different harmonic components of drum rebounds occur when compacting materials of different stiffness, displayed in Figure 7. CMV is influenced by roller dimensions, (i.e., drum diameter and weight) and roller operation parameters (e.g., frequency, amplitude, speed) (Sandström 1994).

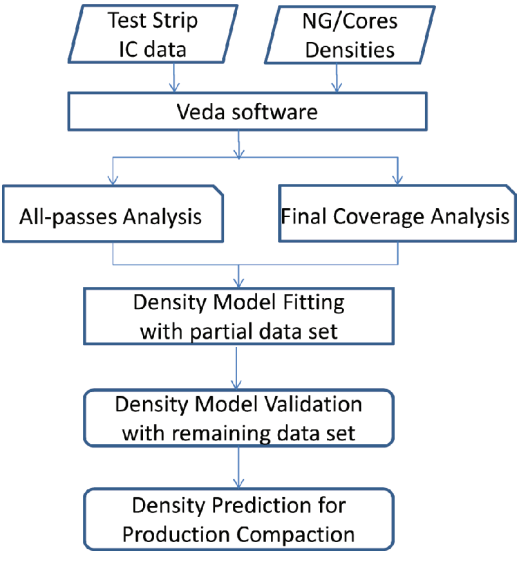

Figure 6. IC-density model development framework.

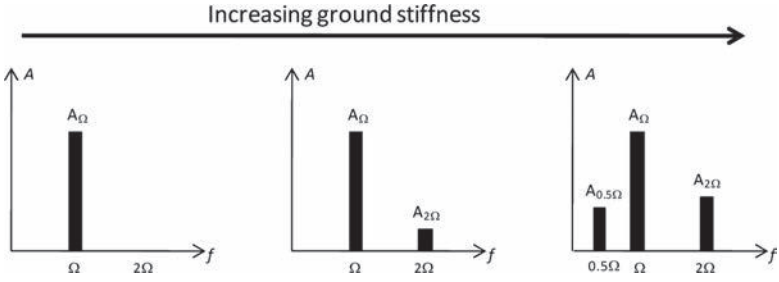

Figure 7. Changes in amplitudes of harmonics with increasing ground stiffness (Thurner and Sandström 1980).

CMV is calculated using Equation 1 (Sandström and Pettersson 2004).

$$CMV = C_1 \cdot \frac{A_{2\Omega}}{A_{\Omega}} \tag{1}$$

where
C_1: a constant (e.g., 300);
$A_{2\Omega}$: amplitude at the second order harmonic frequency;
A_{Ω}: amplitude at fundamental frequency.

The Geodynamik system also measures the Resonant Meter Value (RMV) which provides an indication of the drum behavior (e.g., continuous contact, partial uplift, double jump, rocking motion, and chaotic motion) and is calculated using Equation 2. Dynapac reports this value as Bouncing Value (BV). Under the drum jumping condition, the drum behavior affects the CMV measurements (Brandl and Adam 1997) and therefore must be interpreted in conjunction with the ICMV measurements (Vennapusa et al. 2010).

$$RMV = C_2 \cdot \frac{A_{0.5\Omega}}{A_{\Omega}} \tag{2}$$

where
C_2: a constant;
$A_{0.5\Omega}$: Acceleration at a sub-harmonic frequency caused by drum jumping movement (i.e., the drum skips every other cycle).

Dynapac uses a preselected threshold BV as an indicator of roller jumping to adjust the amplitude in compaction under the Auto-Feedback Control (AFC) mode. Similarly, Caterpillar uses RMV to adjust amplitude in compaction (White et al. 2008b). It was found that CMV increases monotonously with the stiffness of soil.

Compaction Control Value (CCV): CCV is developed by Sakai based on a similar concept that as the ground stiffness increases the roller drum starts to enter into a "jumping" motion which results in vibration accelerations at various frequency components displayed in Figure 8.

CCV is calculated using Equation 3.

$$CCV = \left[\frac{A_{0.5\Omega} + A_{1.5\Omega} + A_{2\Omega} + A_{2.5\Omega} + A_{3\Omega}}{A_{0.5\Omega} + A_{\Omega}} \right] \times 100 \tag{3}$$

where
$A_{1.5\Omega}, A_{2.5\Omega}$: amplitudes at sub-harmonic frequencies;
$A_{3\Omega}$: amplitude at the third order harmonic frequency.

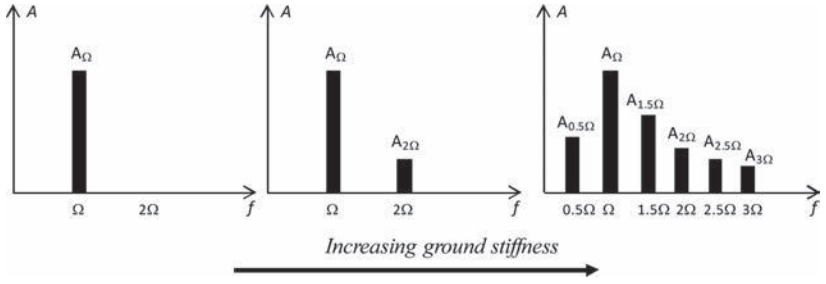

Figure 8. Changes in amplitude of spectrum with increasing ground stiffness (Scherocman et al. 2007).

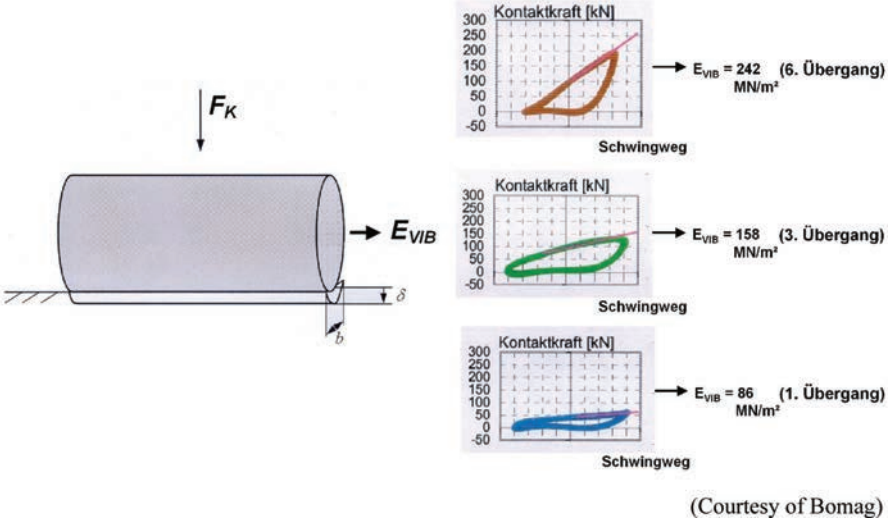

Figure 9. The drum-on-grade model and changes of slopes of the drum loading curves.

Vibratory modulus (E_{VIB}): Vibratory modulus (E_{VIB}) value is developed by Bomag based on the one-degree-of-freedom lumped parameter model and Lundeberg's theoretical solution for a rigid cylinder sitting on an elastic half-spaced earth, displayed in Figure 9 (Hertz 1895, Lundberg 1939, Kröber et al. 2001).

The E_{VIB} value is back-calculated using Equation 4. The E_{VIB} value is related to the modulus determined from a static plate load test (Krober 1998 and Krober et al. 2001).

$$z_d = \frac{(1-\eta^2)}{E_{VIB}} \cdot \frac{F_s}{L} \cdot \frac{2}{\pi} \cdot \left(1.8864 + \ln \frac{L}{W_d} \right) \tag{4}$$

where,
η: Poisson's ratio of the material;
L: length of the drum;
F_s: roller-soil interaction force;
W_d: contact width of the drum, $W_d = \sqrt{\frac{16}{\pi} \cdot \frac{R'(1-\eta^2)}{E_{VIB}} \cdot \frac{F_s}{L}}$
R': radius of the drum.

Correlation Studies: When performing regression analysis and model development between IC data and point test data (such as core densities), care shall be taken to understand the mechanism, footprints, and influence depths of different measurements displayed

in Figure 10. Depending on its weight and operational settings, a full size IC roller may measure up to 4 ft. (1.2 m) of influence depth with a 6 ft. (2 m) wide footprint.

3.3 *Decoupling of IC measurements*

ICMV is accelerometer-based under drum vibrating at around 20 Hz and the measured values are not decoupled or separated to represent individual pavement layers. The influence of underlying layers to the overall stiffness measurement can be simplified and modelled with Hook's law. The simplification is needed due to the short time frame of about 0.1 second (10 Hz) for the IC system to complete a computation cycle. A static two-layer single-degree freedom lumped system is displayed in Figure 11 and followed by the details of the model derivation for decoupling.

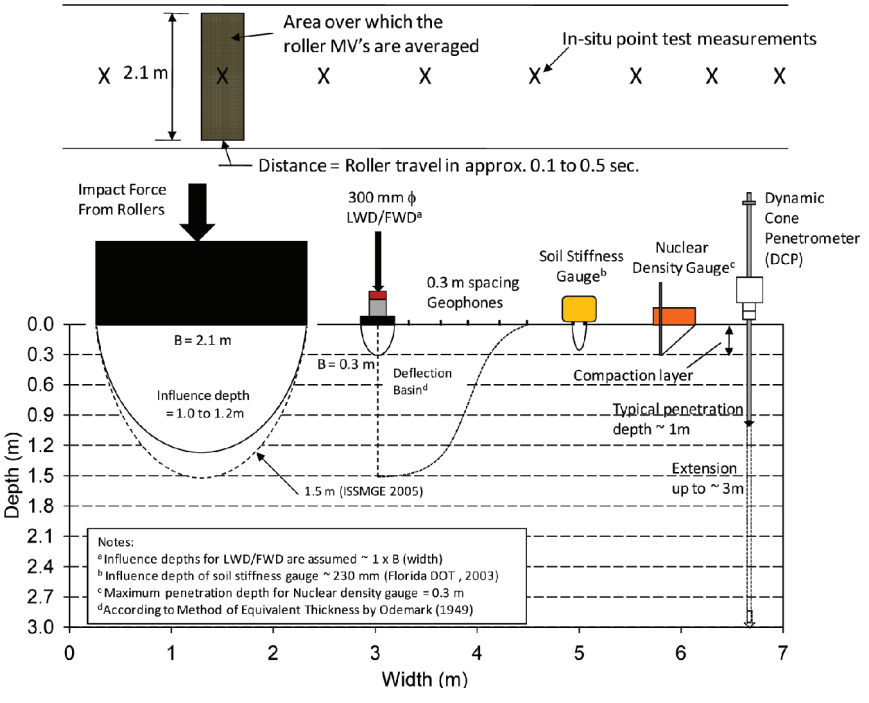

Figure 10. Influence depths for different measurements (White 2008).

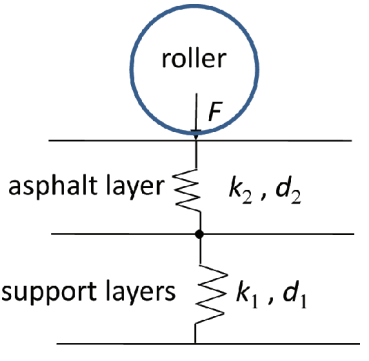

Figure 11. A static two-layer single-degree freedom lumped system under roller loading.

$$\begin{cases} F = k(d_1 + d_2) \\ F = k_1 d_1 \\ F = k_2 d_2 \end{cases} \tag{5}$$

where,
F: force exerted by the roller;
k: composite stiffness of the entire layer system;
k_1: stiffness of the support layers;
k_2: stiffness of the asphalt layer;
d_1: thickness of the base and underneath layers;
d_2: thickness of the asphalt layer.

The stiffness of the asphalt layer (k_2) can be derived as follows:

$$F = k\left[\frac{F}{k_1} + \frac{F}{k_2}\right] \tag{6}$$

$$k_2 = \frac{k \times k_1}{k_1 - k} \tag{7}$$

If the IC mapping data for the supporting layers of a two-layer system are available, the k_1 value can be determined. During the subsequent asphalt compaction, k value can be obtained at the same location as k_1. Therefore, the k_2 value for the top asphalt layer can be computed or re-coupled.

The above can also be extended to multi-layer linear elastic systems as follows:

$$\frac{1}{k} = \frac{1}{k_1} + \frac{1}{k_2} + \cdots + \frac{1}{k_n} \tag{8}$$

where,
k_n: stiffness of the top asphalt layer of a multilayer system.
$k_{i\ (i=1\ to\ n-1)}$: stiffness of the ith support layer of a multilayer system.

Therefore, the stiffness of the top asphalt layer can be solved as:

$$k_n = \frac{k k_1 k_2 \cdots k_{n-1}}{k_1 k_2 \cdots k_{n-1} - k k_2 k_3 \cdots k_{n-1} - \cdots - k k_1 k_2 \cdots k_{n-2} k_{n-1} - k k_1 k_2 \cdots k_{n-2}} \tag{9}$$

The above k values can be expressed in units or unitless based on the corresponding ICMV. With the above consideration in mind, regression analysis and model development between ICMV and core densities can be interpreted properly.

3.4 *Statistical approaches for IC-density model development*

Four (4) statistical models were considered during the development of the IC-density models, including Model I—multivariate linear model, Model II—multivariate nonlinear model, Model III—multivariate linear panel model, and Model IV—multivariate nonlinear panel model. Models III and IV were excluded after the initial screening study. The details of development for Models I and II using the SI units are described as follows.

3.4.1 *Model I—multivariate linear model*

A multivariate linear regression density model based on IC measurements can be expressed as follows:

$$\rho = B_0 + B_1 \cdot ICMV_a + B_2 \cdot W + B_3 \cdot T + B_4 \cdot f + B_4 \cdot Amp + B_5 \cdot ICMV_b + \epsilon \tag{10}$$

where,
ρ: asphalt density;
B_i: model intercept when $i = 0$ and coefficients when $i = 1$ to m, where m is total number of coefficients;
$ICMV_a$: ICMV during asphalt compaction;
W: roller weight;
T: asphalt surface temperature;
f: roller vibration frequency during asphalt compaction;
Amp: roller vibration amplitude during asphalt compaction;
$ICMV_b$: ICMV during base layer compaction or mapping;
$\in$: residual.

3.4.2 *Model II—multivariate nonlinear model*
A multivariate nonlinear IC-density model based on IC measurements can be expressed as follows:

$$\rho_n = \rho_0 + (G_{mm} - \rho_0) \times e^{-\left[\frac{a_1 \cdot k_{ac} + a_2 \cdot f + a_3 V + a_4 (T - T_r)}{n}\right]^{\beta}} + \Delta\rho_n \quad (11)$$

where,
ρ_n: density at pass count, n;
n: roller pass number;
ρ_0: density behind the paver;
a_1, a_2, a_3, a_4, and β: fitted parameters;
k_{ac}: asphalt stiffness expressed in ICMV;
f: roller vibration frequency during asphalt compaction;
V: roller speed;
T: asphalt surface temperatures;
T_r: a reference temperature;
$\Delta\rho_n$: difference between density at pass count, n, and the final density.

After the second screening process, Model II was selected to be used in the subsequent model calibration and field validation.

4 FIELD VALIDATION

The selected IC-density model was calibrated and validated using the field data from the first three (3) of the nine (9) field sites under Phase II of the FHWA IC project.

The Utah site is a project with asphalt overlay at US-89 in Lehi, UT. The test section for this study is approximately 3 miles (4.8 km) of US-89 conducted during nighttime paving. The project consisted of a mill-and-fill asphalt paving project with one lane in the northbound and southbound directions. 4 in. (100 mm) of the existing pavement were milled from the existing pavement prior to the asphalt overlay. The new layers include an asphalt base course (2.5 in. or 64 mm) and an SMA wearing course (1.5 in. or 38 mm) with a cross slope of 2%. The focus for this demonstration is the base course construction. Test Bed 02 that includes the coring section is located at the northbound of US-89. A Hamm IC roller was used at the breakdown position and a Sakai IC roller was used at the intermediate position.

The Florida site is located at I-95 in Brevard County, FL. The paving was operated on the outside lane behind construction barrels in two lifts between Stations 2432 and 2452 for 2,000 ft. (610 m) during night time. The project consisted of a mill-and-fill asphalt paving job for the travel lane in the northbound direction. Based on the core information of the existing pavement before paving, the average asphalt layer thickness is 7.81 in. (198 mm), and the base layer thickness is 7 in. (175 mm). The top 0.75 in. (19 mm) of existing friction course along with 3 in. (75 mm) of the existing structural layer for a total of 3.75 in. (95 mm) were milled off followed by two 1.5 in. (37 mm) lifts of HMA structural layer or base course. The bottom

Table 1. Description of IC field sites.

States	Location	Dates	Asphalt layer	IC rollers
Utah	US-89, Lehi, UT	August 6–9, 2012	2.5″ base course	Hamm, Sakai
Florida	I-95, Brevard, FL	October 15–18, 2012	1.5″ base course	Hamm, Sakai
Ohio	I-71, Morrow, OH	June 24–27, 2013	1.75″ base course	Hamm, Sakai

lift of the structural base course is the focus of this IC study. Test Bed 02 that includes the coring section is on the northbound travel lane of I-95. A Hamm IC roller was used at the breakdown position and a Sakai IC roller was used at the intermediate position.

The Ohio site is located at I-71 in Morrow County, OH. The paving was operated on the north lanes with traffic closure between junctions with SR 95 and Mt. Gilead-Fredericktown road during day time. The project consisted of a new asphalt construction for two 24ft. (7.3-m) wide sections and an inside shoulder in the northbound direction. The pavement layers are (from the bottom up): 6 to 8 in. (150 to 200 mm) 304 aggregate stone base, 10 in. (250 mm) 302 asphalt concrete base, 1.75 in. 19 mm intermediate course, and 1.5 in. 12.5 mm surface course. The 1.75 in. (45 mm) 19 mm intermediate course is the focus of this IC study. The Test Bed 02 location that includes the coring section is in the northbound direction of I-95. The Sakai IC roller was used as the breakdown roller with the front drum vibrating at the high frequency and low amplitude settings. The Hamm IC roller was used as the intermediate/finishing roller with the front drum vibrating at the high frequency and low amplitude settings.

4.1 *Density compaction curves and pass-by-pass IC data analysis*

The Nuclear density Gauge (NG) measurements after each roller pass were used to build density compaction curves that show the growth trend of asphalt densification. The main purpose of compaction curves is to identify the compaction characteristics for specific materials and roller(s) used in a paving project in order to determine the optimal rolling pattern. The NG measurements can also be correlated to ICMV to evaluate whether there is a linear relationship between the two.

The compaction curves and linear correlation for the Utah site are presented in Figure 12. The compaction curve from the breakdown compaction indicates a monotonic growth of densification. The temperature drop also follows a similar monotonic but reverse trend. The R^2 for the correlation between NG measurements and HMV from the breakdown compaction is 0.50 which is consistent with the observations by IC vendors.

The compaction curves and linear correlation for the Florida site are presented in Figure 13. The compaction curve indicates a rapid growth of densification during the breakdown compaction then levelling off during the intermediate compaction. The temperature drop also follows a similar but reverse trend. The R^2 for the correlation between NG measurements and CCV during the breakdown compaction is 0.97 while R^2 is 0.20 between the NG measurements and asphalt during the intermediate compaction. The significant difference between the two correlations is due to the nature of accelerometer-based ICMV that reflects the changes of internal aggregate structure or densification during breakdown compaction at elevated temperatures while the ICMV would reflect the hardening of asphalt binder during the cooling off stage of intermediate compaction.

The compaction curves and linear correlation for the Ohio site are presented in Figure 14. Three locations within a 100 ft. (30 m) section were surveyed. The compaction curves indicate different patterns even though the same equipment, materials, and compaction method were used. The temperature drop also follows a similar but reverse trend. At T1, the pattern of the compaction curve is similar to that from the Utah site, which is monotonic growth. At T2 and T3, the pattern is similar to that from the Florida site, which the density grows rapidly during the breakdown compaction then levels off during the intermediate compaction. Contrary to

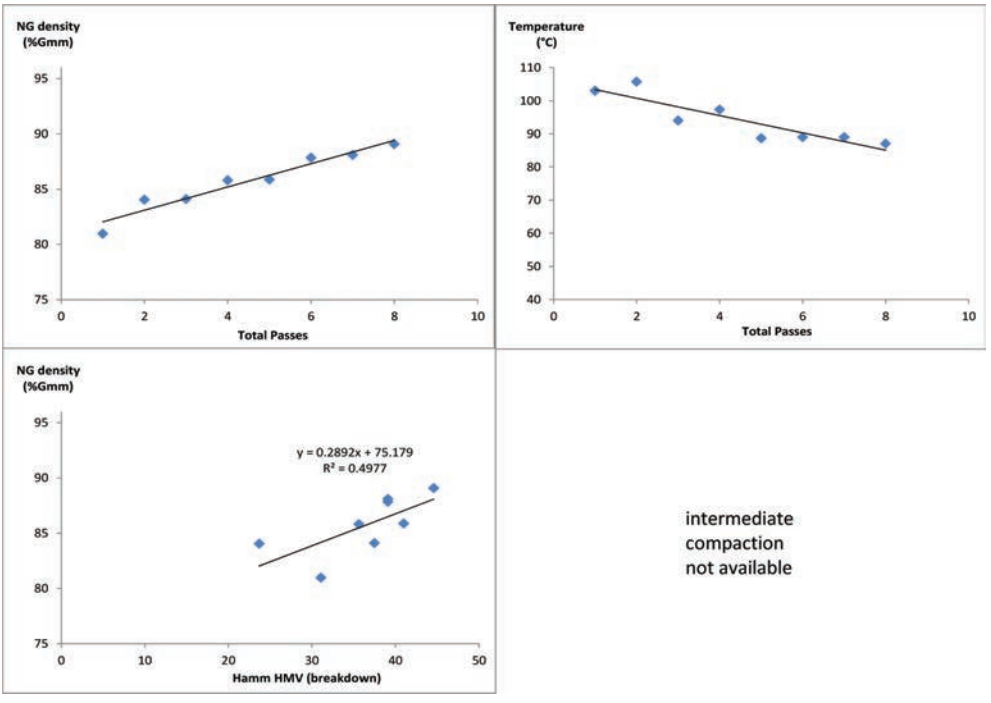

Figure 12. Compaction curves and linear correlation between NG measurements and Hamm HMV from breakdown compaction at a location in Test Bed 03 (UT site).

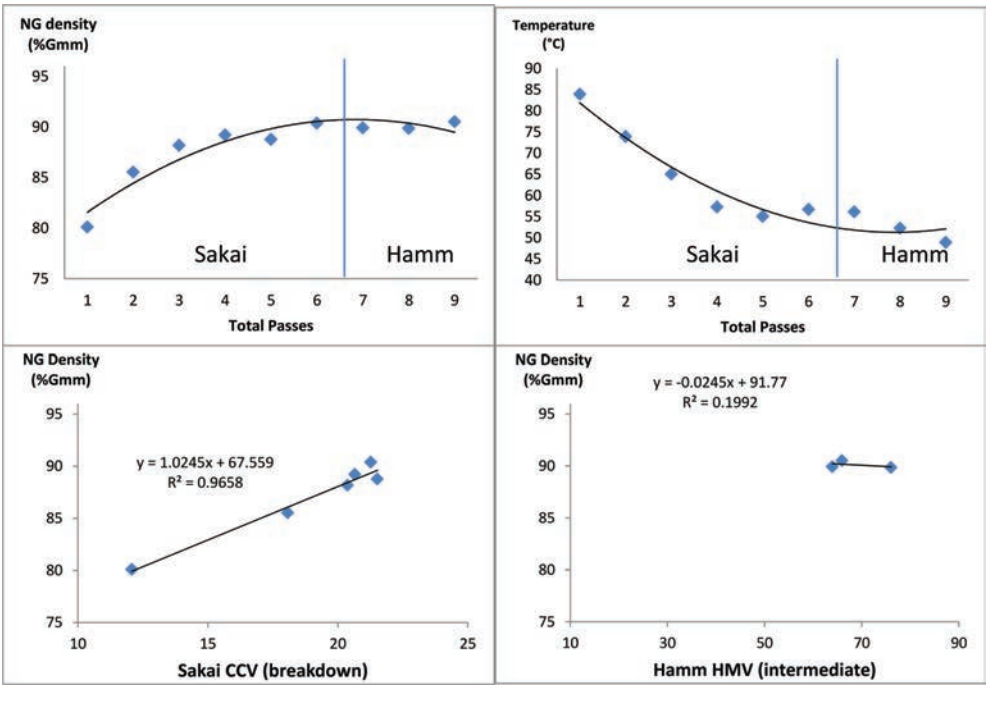

Figure 13. Compaction curves and linear correlation between NG measurements and Sakai CCV from breakdown compaction; and between NG measurements and Hamm HMV during intermediate compaction at a location in Test Bed 03 (FL site).

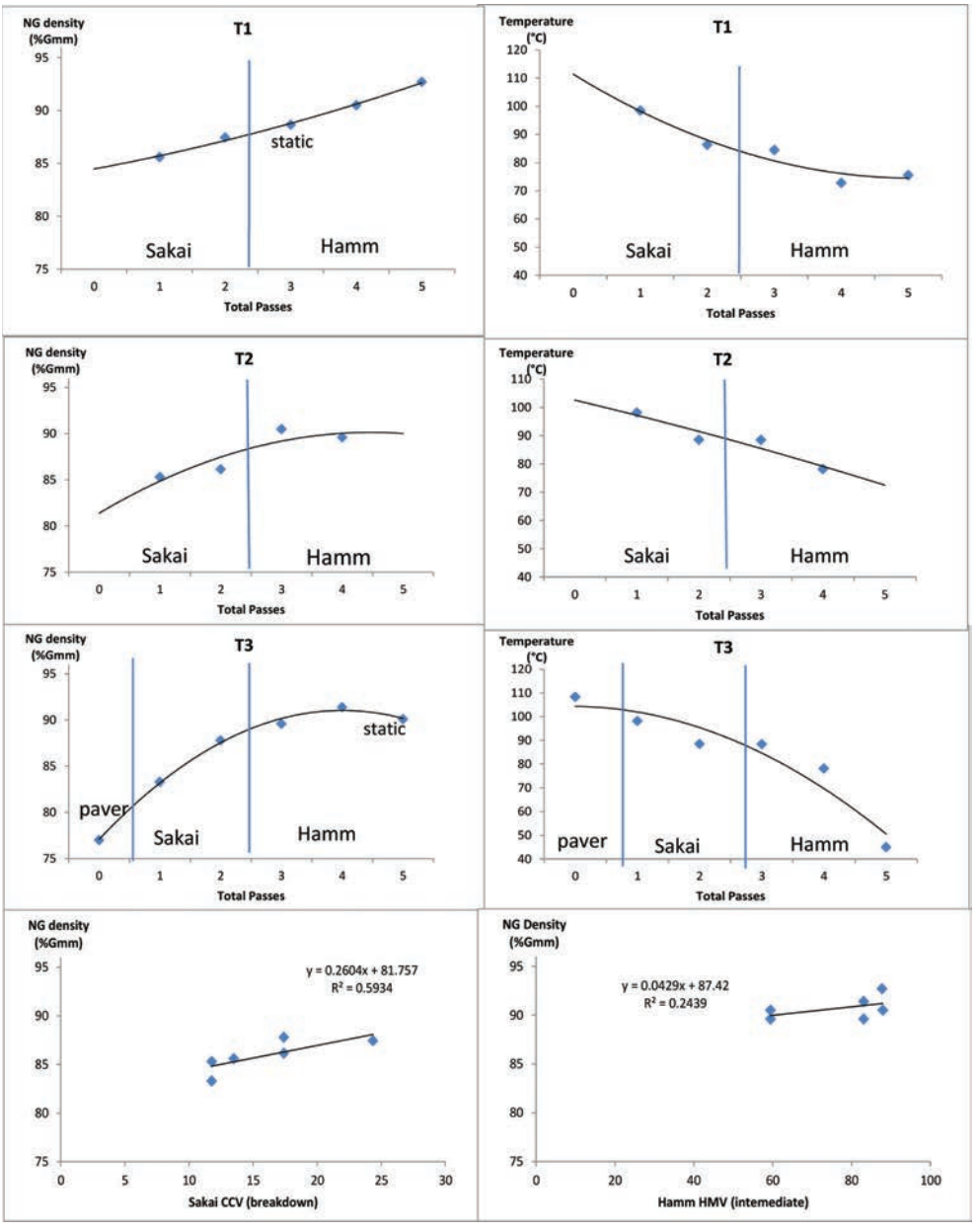

Figure 14. Compaction curves and linear correlation between NG measurements and Sakai CCV and Hamm HMV from breakdown and intermediate compaction at three locations in Test Bed 01 (OH site).

conventional belief that the optimal window for compaction is within higher temperatures, the comparison between T1 and T2/T3 present a different scenario. As the densification growth is slower within the breakdown compaction at T1, the densification continues during the intermediate compaction and eventually reaches higher density than these at T2 and T3. Therefore, compaction behavior is more complex than it was previously thought. This phenomenon also poses challenges to modelling efforts for predicting asphalt density. As for the ICMV-density relationship, The R^2 for the correlation between NG measurements and CCV during the breakdown compaction is 0.59, while it is 0.24 between the NG measurements and

HMV during the intermediate compaction. The comparison is consistent with that from the Florida site.

The above compaction curves and correlation analyses show that compaction characteristics may vary even within the same paving operation. It verifies the daily (or nightly) challenges that paving industry has been facing. It also calls for improved technology in order to achieve better quality control of consistent asphalt paving products. The above also shows that pass-by-pass ICMV and NG measurements are correlated well with R^2 from 0.49 to 0.97 during breakdown compaction. The correlation, however, is less satisfactory during intermediate compaction. It is postulated that ICMV during breakdown compaction reflects on the internal structure (or aggregate-to-aggregate contacts) of compacted mixture as the accelerometer-based measurements reflect the changes of the roller drum rebounds when the compacted materials stiffen due to aggregate re-arrangements. During intermediate compaction or later, the stiffening of compacted materials may be due to binder hardening while the density or internal aggregate structure stays mostly constant. Thus, the ICMV would be less correlated to densities at the later stages of compaction.

4.2 *Final coverage IC data vs. core density analysis*

There were sixty (60) cores taken during each field validation which is considered unprecedented and valuable for correlation study with IC. However, there may be a gap between what the IC measures and the final core results including any gains (further compaction) or loss (de-compaction) of density due to subsequent intermediate or finishing compaction. As postulated in the above pass-by-pass analysis, ICMV would be less correlated with density during later stages of compaction. The following analyses using the final coverage data present further such evidence.

The correlation of the final coverage IC data (i.e., last passes or final product data) and core density for the Utah site is presented in Figure 15. As expected, the correlation of ICMV with core density is poor during the latter stages of breakdown and intermediate compaction.

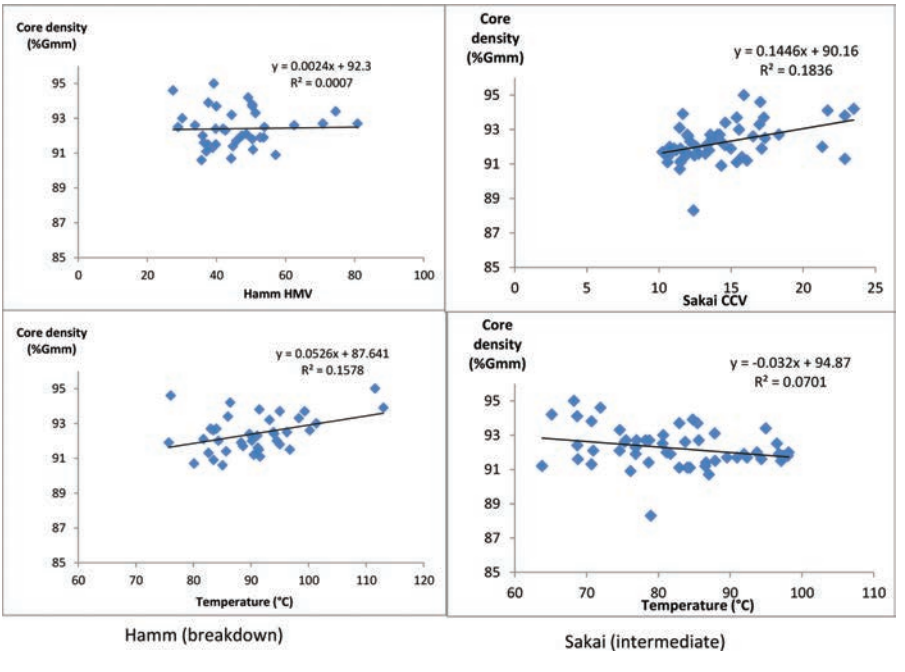

Figure 15. Core density data vs. Hamm HMV and Sakai CCV from breakdown and intermediate compaction in Test Bed 02 (UT site).

Even though there was no finishing compaction, the rolling patterns were erratic at Test Bed 02 which may pose issues for correlation. The erratic rolling patterns would produce non-uniform compaction, and thus density. As IC data were extracted within 6.6 ft. (2 m) diameter (i.e., approximately the full-size roller drum width) surrounding a core location and averaged for the processes, the averaged IC data may not be reflecting the density value of within a 4 in. (100 mm) diameter coring location.

The correlation of the final coverage IC data (i.e., last passes or final product data) and core density for the Florida site are presented in Figure 16. Similar to the Utah site, the correlation of ICMV with core density is poor during the latter stages of breakdown and intermediate compaction. The rolling patterns are also erratic at Test Bed 02.

The correlation of the final coverage IC data (i.e., last passes or final product data) and core density for the Ohio site are presented in Figure 17. Similar to the Utah and Florida sites, the correlation of ICMV with core density is poor during the latter stages of breakdown and intermediate compaction. There was no finishing compaction at Test Bed 02.

From the above observations, the correlation between final coverage IC data and the core density is poor. This is a different observation from the pass-by-pass analysis where ICMV does have good correlation with NG density measurements. Based on the NG-core density correlation analysis (not presented in this paper due to limited space), it can be deduced that ICMV measurements during breakdown compaction do reflect the actual in-place asphalt density. However, the final coverage IC measurements do not represent the eventual in-place density due to the measurements under cooler condition when binder stiffens in addition to the IC data averaging over a varied in-place density within the width of a roller drum.

4.3 *IC-density model validation*

The IC-model validation was conducted to explore the possibility of using such a model to overcome the limitation of the final coverage ICMV to correlate to in-place asphalt density.

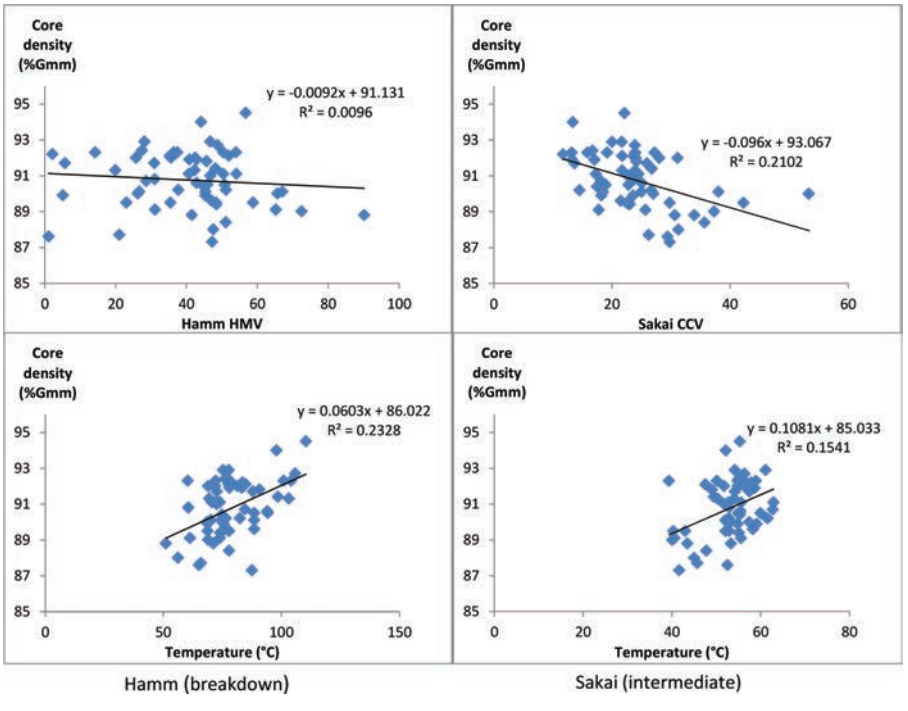

Figure 16. Core density data vs. Hamm HMV and Sakai CCV from breakdown and intermediate compaction in Test Bed 01 (FL site).

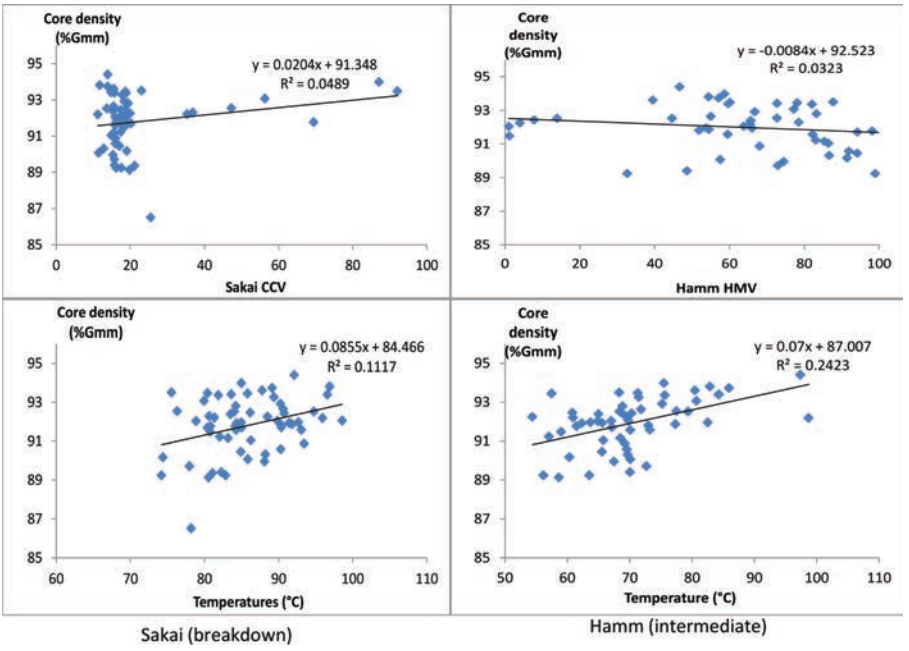

Figure 17. Core density data vs. Sakai CCV and Hamm HMV from breakdown and intermediate compaction in Test Bed 02 (OH site).

Since only three out of nine field sites are completed under the Phase II FHWA IC study, the following discussion serves as a preliminary model trial at this stage. The pass-by-pass IC-NG measurements, when available, were used along with the core-IC data for the IC-density model fitting. Then, the fitted model was used to correlate its density prediction with actual core density data and NG measurements.

The IC-density model fitting and validation for the Utah site are presented in Figure 18. This process used the Sakai IC final coverage data during breakdown compaction at TB02, but no pass-by-pass Sakai IC data were available. The correlation between a portion of the core/NG density data and ICMV (CCV) is surprisingly good with R^2 of 0.56. On the other hand, the results of IC-density model fitting and validation are relatively poor. This phenomenon is unusual and further investigation is warranted.

The IC-density model fitting and validation for the Florida site are presented in Figure 19. This process used the Sakai final coverage data within intermediate compaction at TB01 and the Sakai pass-by-pass data within breakdown compaction at TB02. The correlation between a portion of the core/NG density data and ICMV (CCV) is poor. On the other hand, the results of the IC-density model fitting and validation are improved with R^2 of 0.52 and 0.46, respectively.

The IC-density model fitting and validation for the Ohio site are presented in Figure 20. This process used the Sakai final coverage data within breakdown compaction at TB02 and the Sakai pass-by-pass data within breakdown compaction at TB01. The correlation between a portion of the core/NG density data and ICMV (CCV) is poor. On the other hand, the IC-density model fitting and validation are improved, but still low, with R^2 of 0.37 and 0.29, respectively.

For the above observations from the three field sites in Utah, Florida, and Ohio, the preliminary conclusion is that the IC-density model produced improved correlation with core/NG density by overcoming the limitation of accelerometer-based ICMV.

There are other considerations for the above observations. The current form of the IC-density model is deterministic to predict density at a given condition (ICMV, frequency, pass

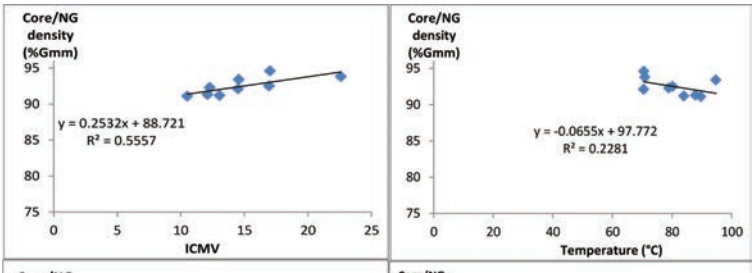

ρ_0	Gmm	α1	α2	α3	α4	β	k1	Tr
84.73075	100	0	0	0	0.001222	0.107065	26	80

Figure 18. IC-density model fitting and validation based on Sakai final coverage data during breakdown compaction at TB02 (UT site).

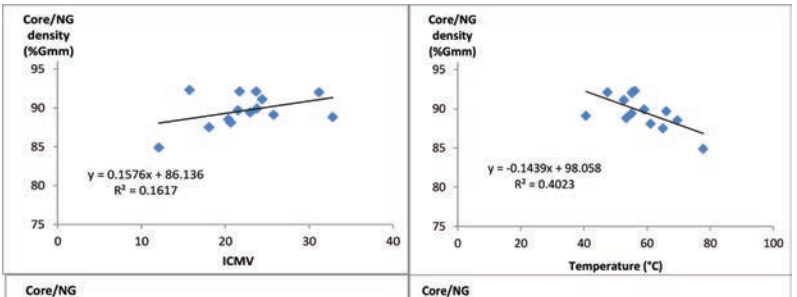

ρ_0	Gmm	α1	α2	α3	α4	β	k1	Tr
79.49051	90.473353	0.018725	0	0	0.008424	2.068956	26	80

Figure 19. IC-density model fitting and validation based on Sakai final coverage data within intermediate compaction at TB01 and Sakai pass-by-pass data at TB02 (FL site).

count, roller speed, and temperature). The model fitting with both pass-by-pass and final coverage IC data makes the model equal to a family of compaction characteristic curves in order to capture the entire compaction history, from immediately behind the paver to the finishing rolling. IC data from a single system were for model fitting and validation due to IC systems and ICMV varying from one vendor to another. As observed from the above

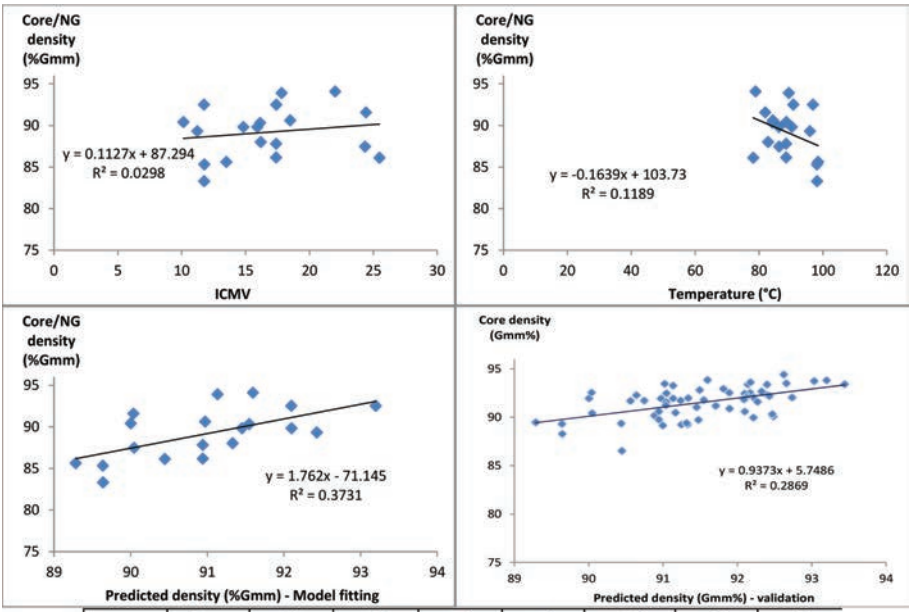

ρ_o	Gmm	k1	α1	α2	α3	α4	β	Tr
78	99	26	0.021479	0.001503	0	0.00001	0.501787	80

Figure 20. IC-density model fitting and validation based on the Sakai final coverage data within breakdown compaction at TB02 and the Sakai pass-by-pass data within breakdown compaction at TB01 (OH site).

pass-by-pass IC data analysis, the compaction curves can vary from one location to another even with the same equipment, materials, and paving method. Therefore, a single IC-density model, no matter how well-calibrated, would face the challenge to match a variety of compaction curves. Mathematically, the narrow range of core density values would also pose challenges to the correlation between the IC-density model prediction and core/NG measurements. Therefore, a technique to look beyond the least square (R^2) correlation is warranted.

At this stage, neither ICMV nor the IC-density model can be reliably used for acceptance. Further enhancements of the IC-model are desired in future studies to raise its confidence level for predicting in-place density using ICMV data.

5 SUMMARY AND FUTURE RESEARCH

5.1 *Summary and conclusions*

Under Phase II of the FHWA IC study, specific efforts were focused on evaluating IC technologies for acceptance of asphalt densities. Three (3) of nine (9) planned field validations were conducted in Utah, Florida, and Ohio to collect IC data, nuclear density measurements, and extensive coring with sixty (60) cores taken from each site. A series of model iterations were performed to select the candidate multivariate nonlinear IC-density model for subsequent model validation. The preliminary conclusions from the three field validation sites are as follows:

- The compaction characteristic curves may vary even within the same paving operation. The compaction process is thus more complex than originally thought.
- Pass-by-pass ICMV and NG measurements are reasonably correlated with R^2 from 0.49 to 0.97 during breakdown compaction. The correlation between pass-by-pass ICMV and NG measurements is less satisfactory during intermediate compaction.

- The final coverage ICMV measurements do not represent the eventual in-place density due to the ICMV measurements increasing at cooler condition when binder stiffens while internal aggregate structure stays constant. In addition, the ICMV were averaged within the width of a roller drum (approximately 6 ft. or 1.8 m) where in-place density may vary from one coring location to another (e.g., 4 in. or 100 mm cores), especially when the rolling patterns are erratic.
- The IC-density model improved the correlation between core/NG density and predicted density from no correlation up to R^2 of 0.50 by overcoming the limitation of accelerometer-based ICMV. However, neither ICMV nor IC-density model can be reliably used for acceptance at this stage based on limited field data and model development. Further enhancements of the IC-density model are desired in future studies with extended field data validation to raise its confidence level for predicting in-place asphalt density.

5.2 *Research refinements*

The following are recommended for the remaining six (6) field validations under Phase II of the FHWA IC study:

- More pass-by-pass nuclear density gauge measurements are needed to be conducted within the entire compaction history from zero-pass (immediately behind the paver), breakdown compaction, intermediate compaction, to finishing rolling.
- One IC roller should be limited for each of the breakdown and intermediate compaction to obtain cleaner data for IC-density model validation. A third IC roller can also be running at static mode at the finishing position to collet passes and temperature data.
- Further IC-density model enhancements may consider multiple IC roller data, incremental model form, and robust modeling tools such as the IMSL computing library.
- As the IC-density model matures, simplification of the model form and calibration is recommended in order to apply it to real-world paving operations.

ACKNOWLEDGEMENT

The authors would like to acknowledge the following who made this IC-density study possible: financial support from the US FHWA, technical support and equipment supplies from IC and GPS vendors (Hamm, Sakai, TopCon, and Trimble/Sitech), local DOT and contractors' supports for field validation (Utah DOT, Staker & Parson; Florida DOT, Hubbard; Ohio DOT, Kokosing).

REFERENCES

Carl, G. and Kuhn, I., Analyzing spatial ecological data using linear regression, Stoch Environ Res Risk Access, 22: pp. 315–324, 2008.

Chang, G., Xu, C., Horan, R., Michael, L., White, D., Vennapusa, P., FHWA/Transportation Pooled Fund (TPF) No. 954: Accelerated Implementation of Intelligent Compaction Technology for Embankment Subgrade Soils, Aggregate Base and Asphalt Pavement, Final Report, 2011.

Commuri, S., Intelligent asphalt compaction analyzer, Highways for life, technology partnerships program, Federal Highway Administration, DTFH61-08-g-00002, 2010.

Commuri, S., Mai, A., Zaman, M., Calibration Procedures for the Intelligent Asphalt Compaction Analyzer, Journal of Testing and Evaluation, 37(5), 2009.

Gallivan, V.L. and Chang, G.K., Harmonization and Standardization of Intelligent Compaction Technologies for Practical Implementation, Proceedings of Canadian Technical Asphalt Association (CTAA) Conference, 2012.

Gallivan, V.L., Chang, G.K., Horan, R., "Practical Implementation of Intelligent Compaction Technology in Hot Mix Asphalt Pavements", Asphalt Paving Technology 2011, Journal of Association of Asphalt Paving Technologists, Volume 80, pp. 1–32, 2011.

Hertz, H., Über die Berührung fester elasticscher Körper (On the Contact of Elastic Body), Gesammelte Werke, Bd. 1. Leipzig, 1895.
Johnson, G., Intelligent Compaction (history, projects, and analysis), presentation at the 57th Minnesota Association of Asphalt Paving Technologists (MAAPT) Conference, December 8, 2010.
Kitamura, Y., Fujioka, K., Fuchiyama, K., Nishio, T., Nakajima, S., "Evaluation of the highway subgrade strength with the acceleration wave of the vibration roller" Iowa Intelligent Compaction conference, (PowerPoint presentation), 2007.
Kröber, W. "Untersuchung der dynamischen Vorgänge bei der Vibrationsverdichtung von Böden," Ph.D. Dissertation, Schriftenreihe, Heft 11, Lehrstuhl und Prüfamt für Grundbau, Bodenmechanik und Felsmechanik der Technischen Universität München (in German), 1988.
Kröber, W., Floss, E., Wallrath, W. "Dynamic soil stiffness as quality criterion for soil compaction," Geotechnics for Roads, Rail Tracks and Earth Structures, A.A. Balkema Publishers, Lisse/Abingdon/Exton (Pa)/Tokyo, 189–199, 2001.
Lundberg, G., Elastische Berührung zweier Halbräume, Forschung, auf dem Gebiete des Ingenieurwesens, Band 10, Göteborg, 201–211, 1939.
Mooney, M.A. and Facas, N.W., Extraction of Layer Properties from Intelligent Compaction Data, National Cooperative Highway Research Program, NCHRP Highway IDEA Project 145, 2013.
Quintus, V., Rao, C., WHRP Study #00092-08-07, Intelligent Compaction Technology, final report, 2010.
Scherocman, J., Rakowski, S., Uchiyama, K., Intelligent compaction, does it exist? 2007 Canadian Technical Asphalt Association (CTAA) Conference, Victoria, BC, pp. 1–25, 2007.
Veda Software, http://www.IntelligentCompaction.com, 2013.
White, D.J., Vennapusa, P., Gieselman, H., Iowa DOT Intelligent Compaction Research and Implementation—Phase I, ER10-06, November, 2010.

This page intentionally left blank

Microstructural characterization and micromechanics of asphaltic materials—I

This page intentionally left blank

Asphalt Pavements – Kim (Ed)
© 2014 Taylor & Francis Group, London, ISBN 978-1-138-02693-3

Automatic generation of micromechanical numerical simulation model of asphalt concrete with visco-elastic properties

Xiaojun Li
College of Geological and Environmental Engineering of Xi'an University of Science and Technology, Xi'an City, Shaanxi Province, China

Laibin Li & Yuxian Huo
Xingtai Highway and Bridge Construction Company, Xingtai City, Heibei Province, China

Xiaoua Wang
College of Geological and Environmental Engineering of Xi'an University of Science and Technology, Xi'an City, Shaanxi Province, China

Chengying Shi
Xingtai Highway and Bridge Construction Company, Xingtai City, Heibei Province, China

ABSTRACT: In present research, two-dimensional boundary coordinates of 99 irregular aggregates were extracted after digital process of X-ray CT Images of asphalt concrete specimen. The modified Fast Fourier Transformation method (FFT) is used to obtain the fitting functions of those coordinates. With the boundary database from the functions, a method for developing two-dimensional asphalt concrete virtual model with irregular aggregates form is presented. Using the method, virtual models with different aggregate grading are generated. Brazil split tests of asphalt concrete are simulated with the samples by taking into account the actual inhomogeneities and microstructures, especially voids distributions, as the visco-elastic properties of the sand mastic and elastic properties of the aggregates are inputted into the FEM model. The test results show that the presented method can generate 2-D virtual mechanical simulation model of asphalt concrete automatically and the generated micromechanical models are capable of predicting the mixture behavior based on ingredient properties. It is believed that the proposed method can be extended to predict the mixture behavior based on ingredient properties.

Keywords: asphalt; mix; virtual test; CT; inner structure; visco-elastic properties

1 INTRODUCTION

Asphalt mixture is a composite material of graded aggregates combined with asphalt binder and a certain amount of air voids. Current mix design procedures are empirical and are based on trial-and-error methods. It will be time and energy consuming to completely evaluate the asphalt mixture properties with those methods and may sometimes lead to costly pavement failures. Recent research results show that the mechanical behaviors of asphalt mixture are far more complex than what we have recognized. The properties of asphalt mixes are affected not only by the volume fractions of asphalt binder, aggregates and air voids, but also the spacial distributions of these components. Both deformation and strength of asphalt mixture has a strong relationship with aggregate structure, mastic and air voids spacial distributions. By developing techniques to image and to quantify the structure of aggregates in asphalt concrete, and by applying granular mechanics to account for the aggregate structure and rheological methods to explain the dynamic mechanical responses of asphalt binder or mastic,

in such a scientific way as virtual test, it will be possible to quantitatively relate the raw material properties to the performance of pavements. This will develop the foundations to building more durable pavements. Virtual test, an important way to design modern structure and material, is actually a digital simulation process, the best advantage of which is not limited by test facilities and boundary conditions.

In present research, two-dimensional boundary coordinates of 99 irregular aggregates were extracted after digital process of X-ray CT Images of asphalt concrete specimen. The modified Fast Fourier Transformation method (FFT) is used to obtain the fitting functions of those coordinates. With the boundary database from the functions, a method for developing two-dimensional asphalt concrete virtual model with irregular aggregates form is presented. Using the method, virtual models with different aggregate grading are generated. Brazil split tests of asphalt concrete are simulated with the samples by taking into account the actual inhomogeneities and microstructures, especially voids distributions, as the visco-elastic properties of the sand mastic and elastic properties of the aggregates are inputted into the FEM model.

The test results show that the presented method can generate 2-D virtual mechanical simulation model of asphalt concrete automatically and the generated micromechanical models are capable of predicting the mixture behavior based on ingredient properties. It is believed that the proposed method can be extended to predict the mixture behavior based on ingredient properties.

2 CT IMAGE AND DIGITAL IMAGE PROCESS

The hollow cylinder asphalt concrete sample is used in this test. The diameter of the sample is 150 mm and the wall thickness and height of the sample is both 50 mm. This nondestructive technique provides a method to produce gray level images at different depths within a specimen. The material intensity at one point is reflected by the pixel gray intensity. The images acquired by X-ray CT were processed to produce binary images, as it is shown in Figure 1, the black color represents granular particles and white represents asphalt and voids.

2.1 *Theory of Fourier analysis*

There are two possible ways to describe an aggregate particle. One expression can be presented as the following Fourier series:

$$R(\theta) = a_0 + \sum_{m=1}^{M} (a_m \cos m\theta + b_m \sin m\theta) \tag{1}$$

In this function, $R(\theta)$ is the radius at angle θ, $0 < \theta < 2\pi$, a_0 represents the average radius of a particle and M is the total number of the coefficient. a and b, which change when m is

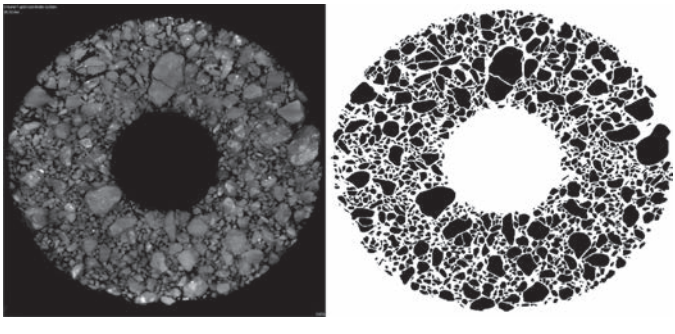

Figure 1. X-ray CT image and binary image.

different, are coefficients giving magnitude and phase for each harmonic. The origin of the coordinate system is usually in the center of the gravity.

Another possible method to quantify the characteristics of aggregates is the Fourier descriptor method. The granular boundaries, defined by the function x(θ) and y(θ), can be analyzed using the following Fourier series:

$$\begin{cases} x(\theta) = \frac{1}{2}A_{01} + \sum_{p=1}^{N}(A_{pi}\cos p\theta + B_{pi}\sin p\theta) \\ y(\theta) = \frac{1}{2}A_{02} + \sum_{p=1}^{N}(A_{pi}\cos p\theta + B_{pi}\sin p\theta) \end{cases} \quad (2)$$

In this expression, x(θ) and y(θ) are coordinates describing the particle, N is the total number of the coefficients, A_{01} and A_{02} reflect the average value of x and y, A_{pi} and B_{pi} reflect the coefficient of the harmonics, pi stands for the pi-th coefficient.

Because the first method could cause some miscalculation which shown as Figure 2, in this research, x and y, which are related to the particle shape, are studied, and the feature of the particle can be described while the problems mentioned before can be avoided.

A_{pi} and B_{pi} can be approximately estimated as following:

θ is a number belong to [0, 2π], the value of θ is

$$\theta_i = \frac{2\pi}{2n+1}(i+0.5) \quad (i= 0, 1, 2, 3..., 2n) \quad (3)$$

u_1 and u_2 are defined in order to compute A_{pi} and $B_{pi.}$

$$\begin{cases} u_{2n+2} = u_{2n+1} = 0 \\ u_j = f_j + 2\cos p\theta\, u_{j+1} - u_{j+2} \quad (j = 2n, 2n-1, 2n-2, \ldots, 2, 1) \end{cases} \quad (4)$$

In Equation (3) $\theta = \frac{2\pi}{2n+1}$. The trigonometric function can be calculated as following

$$\cos p\theta = \cos\theta\cos(p-1)\theta - \sin\theta\sin(p-1)\theta$$
$$\sin p\theta = \sin\theta\cos(p-1)\theta + \cos\theta\sin(p-1)\theta$$

Thus, the value of A_{pi} and B_{pi} can be evaluated using the following formulas:

$$\begin{cases} A_{pi} = \frac{2}{2n+1}(f_0 + u_1\cos p\theta - u_2) \\ B_{pi} = \frac{2}{2n+1}u_1\sin p\theta \end{cases} \quad (5)$$

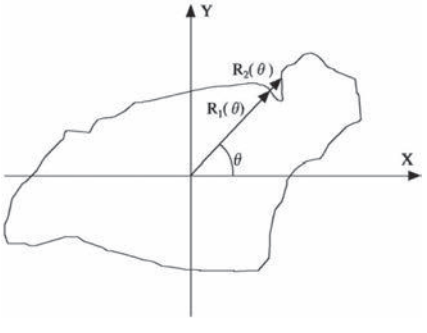

Figure 2. Typical miscalculation.

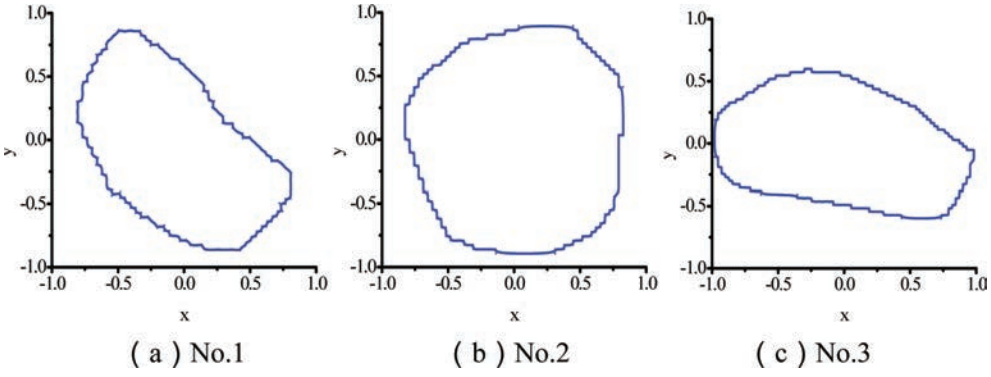

Figure 3. Digital shape of aggregate.

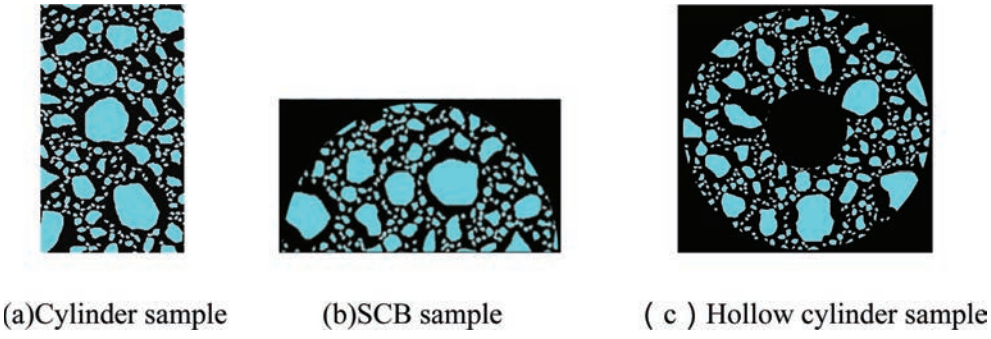

Figure 4. Geometry model of typical specimen particle.

2.2 *Database of 2D aggregate shape*

99 images of different aggregates were selected from the slices of X-Ray CT images of asphalt concrete sample. After digital image process, the coordinates of 2D aggregate skeleton were obtained. The coordinates were analyzed with Fourier analysis method and 99 different formulas were determined with different coefficients.

After normalization of the simulations results, the shape of aggregate can be quantified as Figure 3 with the formula, it is easy to make 2D micromechanical simulation Finite element model of asphalt concrete.

With the established database and PFC2D software, a program for two-dimensional virtual mechanical simulation of asphalt concrete with irregular particles was written. Some typical models are shown as Figure 4.

3 VIRTUAL SIMULATIONS OF SPLIT TEST

3.1 *Mesh generation*

Usually, there are three ways for mesh generation: Octree method; Delaunay method and Advancing front method. The Delaunay mesh generation algorithm is adopted in this paper. The process of its generation is firstly to generate the finite nodes and then to generate the nodes within the region. Due to the very irregular aggregate and complex mastic distribution, both the three-node triangle elements as four-node quadrilateral elements were used in the FE mesh for the complex geometry.

3.2 *Parameters for calculations*

Finite element simulations are conducted to predict the mixture behavior by combing aggregate and mastic properties with consideration of air void distribution.

Coarse aggregates are assumed as elastic material. The used sand mastic consists of asphalt and fine aggregates passing sieve size 1.18 mm and is assumed as visco-elastic material described by Burgers constitutive model. The model parameters are determined by experiments and transformed into Prony series.

Uniaxial creep tests are performed under the controlled-stress 0.2 MPa and viscoelastic parameters of Burgers model is achieved. The relax modulus of Burgers model is fitted with six-term Prony series and can be expressed as follows:

$$G(t) = G_{\infty} + \sum_{i=1}^{n_G} G_i \exp\left(-\frac{t}{\tau_i^G}\right) \tag{6}$$

where

$G(t)$ = relax modulus of Burgers model expressed as Prony series;

G_i = elastic spring constants of Burgers model;

τ_i = viscosity constants of Burgers model

The fitted parameters for six-term Prony series of relax modulus of Burgers model are as follows: $G_{\infty} = 2102868.53135$pa; $G_1 = 285843.50205$ Pa; $\tau_1 = 1807.06941$s; $G_2 = 129943.75591$ Pa; $\tau_2 = 16.77813$s; $G_3 = 291239.25846$ Pa; $\tau_3 = 1974.47877$s; $G_4 = 112455.47173$ Pa; $\tau_4 = 16.77812$s; $G_5 = 295994.1695$ Pa; $\tau_5 = 1682.12124$s; $G_6 = 295270.22585$ Pa; $\tau_6 = 1856.99569$s.

Modulus of 84.4 GPa is used for the aggregate and 84.4 GPa, 8.44 GPa, 2.81 GPa are used for sand mastic separately in the study. Poisson's ratio of 0.3 and 0.25 are input for the aggregate and sand mastic separately.

3.3 *Calculation results*

The tensile stress distributions are present as Figure 5. The numerical results show that the material inhomogeneities can have significant effects on the tensile stress concentration and

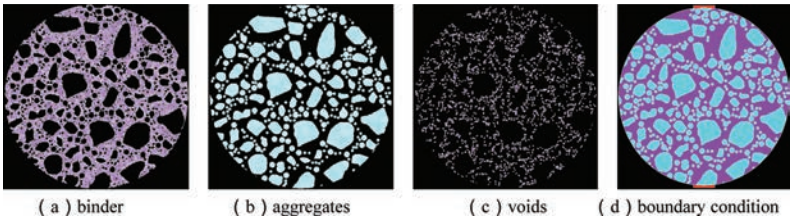

Figure 5. Finite element mesh of AC-16 specimen with 9% voids,150 mm in diameter.

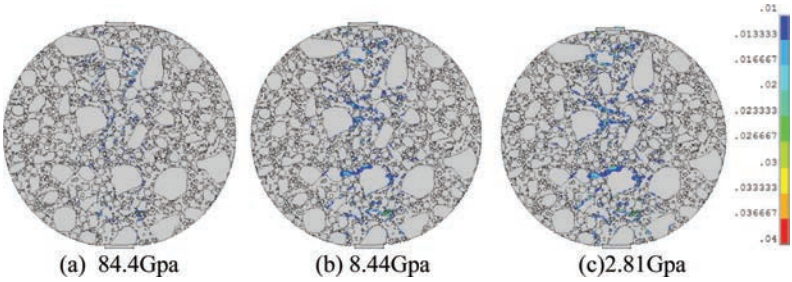

Figure 6. Splitting test results for different binder modulus.

the coarse aggregates skeleton has greater influence on mechanical properties of asphalt concrete. The calculation results also show the tensile stress decrease with the increasing of binder modulus. The presented method can automatically generate digital specimen and the generated digital specimen can satisfy the requirements of micro mechanical properties numerical analysis of asphalt concrete.

4 CONCLUSION

Two-dimensional boundary coordinates of 99 irregular aggregates were extracted after digital processing of asphalt concrete CT images. The modified Fast Fourier Transformation method (FFT) was used to obtain the fitting functions of those coordinates and the irregular particle form database was established. With the established database and PFC2D software, a program for two-dimensional virtual mechanical simulation of asphalt concrete with irregular particles was written. Taking three gradations as an example, under the same void,virtual simulations of Split test were carried out. The test results show that the presented method can automatically generate digital specimen and the generated digital specimen can satisfy the requirements of micro mechanical properties numerical analysis of asphalt concrete. It is believed that the proposed method can be extended to predict the mixture behavior based on ingredient properties.

REFERENCES

[1] Eyad Masad, Shadi Saadeh, Taleb Al-Tousan, Edward Garboczi, Dallas Little. Computations of particle surface characteristics using optical an X-ray CT image. Computational Materials Science. 2005, 10:407–411.

[2] Linbing Wang, Xingran Wang, Louay Mohammad, Chris Abadie. Unified Method to Quantify Aggregate Shape Angularity and Texture Using Fourier Analysis. Journal of Materials in Civil Engineering. 2005, 09:498–502.

[3] Elisabeth T. Bowman, Kenichi Saga & Tom W. Drummond. Particle Shape Characterization using Fourier Analysis. Geotechnique. 2000.

[4] Taleb Al-Rousan, Eyad Masad, Erol Tutumluer, Tongyan Pan. Evaluation of image analysis techniques for quantifying aggregate shape characteristics. Construction and Building Materials, 2006.

[5] Abbas A.R, Papagiannakis A.T, Masad E.A (2004) Linear and nonlinear viscoelastic analysis of the microstructure of asphalt concretes. Journal of Materials in Civil Engineering, 16(2): 133–139.

[6] Dai Q, You Z (2007). Prediction of creep stiffness of asphalt mixture with micromechanical finite-element and discrete-element models. Journal of Engineering Mechanics, 133(2): 163–173.

[7] Wang L.B., Frost Naga Shashidhar J.D. (2001) Microstructure Study of WestTrack Mixes from X-ray Tomography Images. TRB 80th Annual Meeting. (Paper No: 01-2632) Washington DC.

[8] You Z. Dai Q. (2007) Dynamic Complex Modulus Predictions of Hot-Mix Asphalt Using a Micromechanical-Based Finite Element Model, Canadian Journal of Civil Engineering, 34(12): 1519–1528.

[9] Yue Z.Q, Chen S, Zheng H, Tham L.G. (2003) Finite element modeling of geometrical using digital image processing. Computers and Geotechnics, (30): 375–397.

[10] Yue Z.Q, Chen S, Zheng H, Tham L.G. (2004) Digital Image Proceesing Based on Finite Element Method for Geomaterials. Chinese Journal of Rock Mechanics and Engineering, 23(6): 889–897.

Asphalt Pavements – Kim (Ed)
© 2014 Taylor & Francis Group, London, ISBN 978-1-138-02693-3

Understanding the microstructure of bitumen: A CLSM and fluorescence approach to model bitumen ageing behavior

Florian Handle, Josef Füssl, Susanna Neudl, Daniel Grossegger,
Lukas Eberhardsteiner, Bernhard Hofko, Markus Hospodka,
Ronald Blab & Hinrich Grothe
Vienna University of Technology, Vienna, Austria

ABSTRACT: Confocal Laser Scanning Microscopy (CLSM) allows the detailed study of the microstructure of bitumen and is capable of the visualization of fluorescent centers in bitumen. The origin of this fluorescence has been the subject of ongoing debate in the community. However, by the use of chromatographic separation and fluorescence spectroscopy, we were able to obtain new evidence regarding the composition and ageing behavior of asphaltene micelles. In fact, the aromatic mantle, serving as a stabilizing agent around the micelle, is responsible for high intensity fluorescent emissions in the visible range, and not the asphaltenes themselves. These facts serve as the basis for an updated micelle model, capable of describing both the visualized microstructure and the ageing behavior of asphalt concrete in respect to thermal healing of asphalt.

Moreover, based on this micelle structure model a new mechanical model for bitumen ageing was derived, in the framework of continuum micromechanics. Thereby, the bitumen is considered as a viscoelastic four-phase composite, consisting of an asphaltene phase embedded in a maltene phase. A third phase, built up by resins and highly polar aromatic structures, triggers the interaction between asphaltenes, and mechanically describes the age-dependent microstructure of bitumen. This model could be validated by means of shear rheometer tests on differently aged bitumen.

Keywords: Fluorescence spectroscopy, bitumen micro-structure, bitumen ageing, bitumen modeling, Confocal Laser Scanning Microscopy

1 INTRODUCTION

Asphalt concrete is one of the most prominent materials in road engineering. Due to rising crude oil prices and increased manufacturer liability the economic situation for producers, engineering companies, and customer become less and less favorable. Additionally, mineral concrete as a competitive material has become ever more popular over the last decade. This leads to the exploration of new technical processes, like warm mix asphalts and advanced recycling strategies that enable the production recycling asphalt mixes of equal quality levels compared to the original product. However, all these strategies depend on the understanding of bitumen microstructure, which is the defining factor for ageing properties of asphalt.

Bitumen is broadly defined as a *virtually not volatile, adhesive and waterproofing material derived from crude petroleum, or present in natural asphalt, which is completely or nearly completely soluble in toluene, and very viscous or nearly solid at ambient temperatures* [1]. This definition is as exact as possible, given the diversity of bitumina.

Since materials researchers started investigating bitumen several models for the bitumen microstructure and asphalt concrete were developed. This study is based on the micelle theory [2], [3] and the extended 5+1 scales of asphalt observation model [4], which points out the importance of the molecular and bitumen scale analysis for the material properties (Fig. 1).

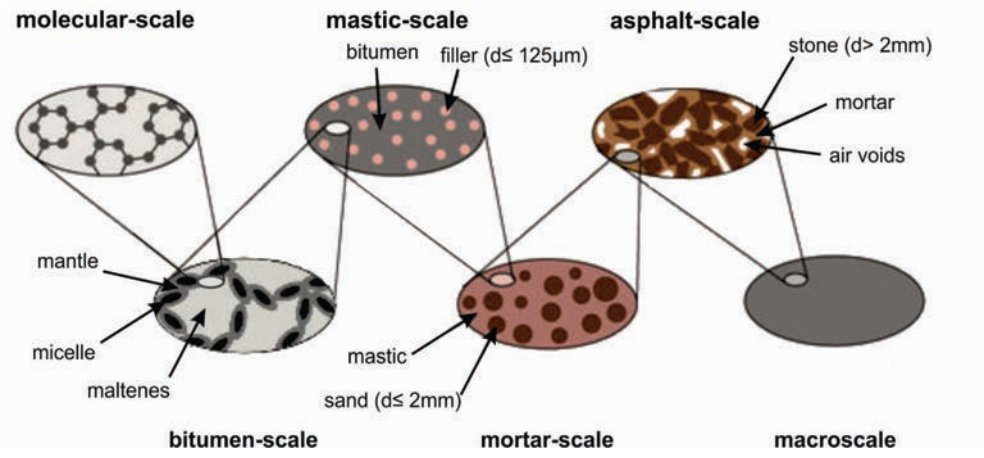

Figure 1. The 5+1 scales of asphalt observation, explaining the relations of material properties to the different scales of study [4].

Basically, this model assumes bitumen to be a colloidal system of asphaltenes micelles dispersed in a maltene matrix.

CLSM is an imaging technique capable of analyzing highly localized fluorescence emission and was used to visualize the bitumen microstructure. Additionally, fluorescence spectroscopy was employed to obtain integrated spectra of bitumen and bitumen fractions. By combining the information, we were able to develop a new model hypothesis for bitumen ageing.

Previous studies employing CLSM on bitumen have mainly been focused on SBS-modified bitumina [3], [5], [6], [7], [8]. The analysis of pure bitumen with this intriguing method was seldom conducted [9], [10], [8]. The discussion of the nature of the fluorescent centers that can be visualized by CLSM is an ongoing debate in bitumen research [11]. Contradictory identifications range from asphaltenes [10], [9] to waxes [12]. Some of these hypotheses can be discarded easily, since certain constituents are not capable of fluorescent emission in the visible range due to their very physical and chemical nature. This study has identified the origin of these fluorescent centers and found conclusive evidence that the aromatics fraction is the source of the strong fluorescent signals in bitumen that can be visualized by CLSM.

2 MATERIALS AND METHODS

2.1 *Bitumen and bituminous specimen*

The materials used in this study were carefully chosen for their material properties and their respective position in the production cycle of bitumen (Table 1). The precursors were studied to examine, if they exhibit a similar structural composition to their respective end products. Bitumen B50/70 was chosen as a typical material used in road construction, while B70/100 bitumina are often used for the production of SBS-modified bitumina.

2.2 *Analytical equipment*

We employed an ECLIPSE TE2000 (Nikon Corporation, Tokyo, Japan) as a confocal laser scanning microscope. The microscope hosts both a transmission and a CLSM (Confocal Laser Scanning Microscope) array. The light source for the transmission array is a T-DH 100 W Illumination Pillar (Koehler Type). An Argon-ion laser is used as source of excitation radiation. Typical for CLSM, laser optics is configured to allow a scanning of the surface and the image is created point by point and line by line. The advantages mentioned above in combination with the highly sensitive detector are key features for the successful application.

Table 1. Samples and description.

Sample	Description
Precursor 1	Vacuum flashed, cracked residuum
Precursor 2	Residuum of vacuum distillation
B50/70	Bitumen for asphalt concrete production
B70/100 1	Bitumen for asphalt concrete production or for production of SBS-modified Bitumina
B70/100 2	Bitumen for asphalt concrete production or for production of SBS-modified Bitumina

However, the capability to scan volumes below the surface, a key advantage of the CLSM technique, cannot be applied here, because of the high absorption cross section in the visible range of all bitumina. For sample preparation, the bitumen was heated to about 150–200°C as necessary for melting the sample. Then a small quantity of bitumen was applied to a glass slide with a piece of wire and a second glass slide was placed onto the sample. After a short period of cooling, the sample was measured. Early experiments showed that this procedure had to be modified. The first step towards a significant improvement in picture quality is the replacement of the standard object carriers by extremely thin glass slides (<0,5 mm). Second, an additional heating period was implemented, allowing the bitumen film to spread and become thinner. These very thin films could then be examined by CLSM.

For fluorescence spectroscopy, an Edinburgh Instruments FSP920 photoluminescence spectroscopy setup was at our disposal. As an illumination source, a XE900 Xenon Arc Lamp is used, which provides high intensity radiation on a broad spectrum. The setup employs double Czerny-Turner monochromators (type TMS300) at both excitation and emission arms, guaranteeing a very narrow spectral bandwidth. The detector is a S900 single-photon photomultiplier (type R928). The spectrometer was used to conduct both excitation and emission measurements. For sample preparation, the bitumina were heated to 150°C and a drop of bitumen was applied to a standard microscopic slide. This slide was stored at the same temperature for 5 minutes to allow the drop to spread and increase its surface. Afterwards the samples were cooled to room temperature and subjected to fluorescence spectroscopy. For bitumen fractions, this treatment was not necessary, because the maltene phase and its components are viscous liquids at room temperature and can be applied directly to the glass slide. The asphaltenes were taken up with toluene and then dripped slowly on the warm glass surface (80°C) to allow the formation of a thin film.

Chromatographic separation was conducted according to ASTM Standard 4124 [13], which is the most prominent and widely used method [11] and based on the Corbett procedure [14]. However, the nomenclature was changed to fit the SARA (Saturates Aromatics Resins Asphaltenes) scheme, deviating from the standards nomenclature (aromatics—naphthene aromatics; resins—polar aromatics). First bitumen was separated into maltene and asphaltene phase by extraction with n-heptane. However, the n-heptane extraction was conducted in a Soxhlet-extractor. The further separation is conducted in a 1000 mm chromatographic column with alumina as the stationary phase with three different solvents/solvent combinations. The eluate was collected in 50 ml beakers, which were sealed, cooled, and then stored at −15°C to slow oxidative degradation. Then each fraction was warmed to room temperature and subjected to distillative separation under vacuum. The sample was then cooled to room temperature before breaking the vacuum. Afterwards, the fraction was weighed. The sample was then again subjected to escalating distillation (max 185°C, 10 mbar, 10 min) and weighing until constant weight was reached to assure gravimetric exact measurements. Then the sample specimens were prepared for fluorescence spectroscopy.

3 RESULTS

3.1 *Microstructure of bitumen, bitumen precursors*

It was possible to obtain new and enhanced pictures of the bitumen microstructure by application of CLSM to pure bitumina. These images proof the existence of a microstructure, which

implicates agglomeration processes and phase separation processes in bitumen, as implicated in the micelle model. The fluorescent centers detected are of roughly ellipsoid shape, vary in size and amount, and their spatial distribution seems to be statistical and unordered. Exemplary, two images are shown in Figure 2. Their exact size distribution and population density varies for each sample and is characteristic for specific bitumina. The micelle model describes bitumen as a colloidal system of dispersed asphaltenes in a continuous maltene phase, which makes the spatial distribution of the fluorescent centers an important issue [3], [11]. Thus, a strong connection to the mechanical and rheological properties can be assumed. Preliminary experiments with picture analysis software have been conducted to assess the particle size distribution for the tested bitumina and whether significant differences between the samples can be found. Although the necessary picture processing is a rather complicated task due to high background fluorescence in bitumen, first results are promising and future experiments and process automation could provide a powerful tool for bitumen analysis.

3.2 *Fluorescence analysis and chromatographic separation*

Initially, fluorescence experiments have been conducted to support the use of CLSM as an imaging technique on bitumen. However, this study found that besides the distribution of fluorescent centers, the fluorescent behavior of bitumen and bitumen fractions can provide additional evidence regarding the actual microstructure of bitumen. Fluorescence spectroscopy yields an integrated spectrum that is not capable of visualizing spatial distributions. Information about the fluorescent centers and their composition in bitumen must be obtained indirectly through inference. A closer look on the basic physicochemical properties of bitumen reveals that bitumen contains only three fractions that could theoretically be the origin of the fluorescent signal. The asphaltenes, the resins, and the aromatics are, based on their general description, capable of fluorescence. Saturates can easily be dismissed as a source of fluorescent emission, due to the well defined chemical nature of fraction. There are two kinds of spectra presented here, excitation scans (variable excitation, fixed detection wavelength) and emission scans (fixed excitation, variable detection wavelength). For the excitation scans, the same detection wavelength as used at the microscope was chosen, 515 nm, and a spectral range of 200–500 nm was observed. For the emission spectra, two wavelengths have been studied carefully. First the excitation wavelength of 488 nm was selected, because this is one of the excitation wavelengths available in the CLSM setup. To check for high energy fluorescence transitions, we employed a wavelength of 280 nm (Fig. 3).

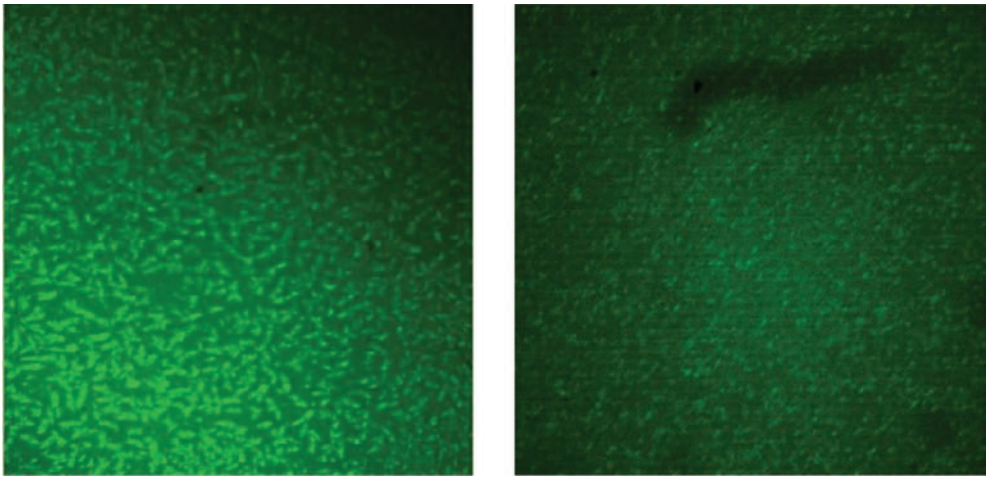

Figure 2. CLSM images of bitumen precursor PE1005 (left) and bitumen B70/100 (right), fluorescent centers characteristic for the respective sample.

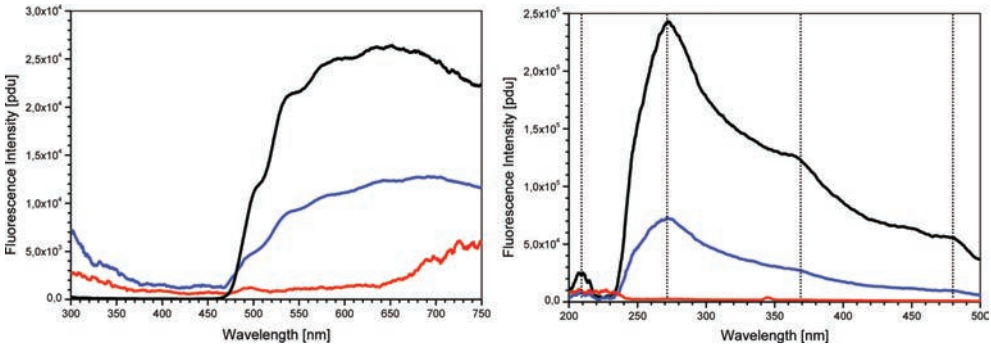

Figure 3. Emission fluorescence spectra of bitumen B50/70 (blue), asphaltenes (red) and maltenes (black) at 280 nm excitation wavelength (left) and excitation spectrum of bitumen B50/70 at 515 nm detection wavelengths.

The excitation fluorescence spectrum of pure bitumen allows the identification of four wavelength of particular interest (Fig. 3, right): 210 nm, 270 nm, 370 nm, 480 nm (dotted lines) for CLSM at a detection wavelength of 515 nm. These are a local and the absolute maximum, as well as the two shoulders visible in the excitation scan of the pure bitumen. The distribution of the fluorescent centers excited at these wavelengths would be of particular interest. Since fluorescence transitions can also be triggered by wavelengths lower than the necessary minimum, it is impossible to visualize the higher energetic transitions exclusively. For the CLSM studies, an excitation wavelength of 488 nm was chosen, because it is very close to the shoulder at 480–490 nm. Also it is one of the spectral lines providing the highest intensity available at the Argon-ion laser and is frequently used for CLSM. The technique was capable of revealing the origin of the fluorescence signals of the different species spatially distributed.

After the completion of the CLSM imaging, soon investigating the source of the fluorescence became a primary goal of further experiments. Usually a detailed interpretation of the fluorescence spectra could be attempted, but for bitumen, this is a rather difficult task. The dependency of fluorescence phenomena on the chemical vicinity of the molecules is very well documented and the effects of the surroundings are hardly assessable for bitumen [15]. Hence, a more empirical approach was chosen. The fractionation by chromatography is a well-known and reliable standard method in bitumen analysis [14], [13], [11]. It is often employed for characterization of bitumina by their relative contents of fractions. The fractions themselves again are complex mixtures of molecules, but exhibit similar chemical/physical behavior. In previous publications, the origin of fluorescence emission was suspected to be the asphaltenes fraction. This theory was explored to full extent. In general asphaltenes are defined as insoluble in n-heptane. While the basic extraction protocol for standardized testing is based on a simple extraction with n-heptane [13], for these experiments, a Soxhlet-extractor was used for the removal of asphaltenes, which guarantees as pure asphaltenes as reasonably possible. The fluorescence spectra of these fractions were surprising. Our experiments strongly indicated that the origin of the fluorescent centers can be found in the maltene phase and not in the asphaltenes phase, as proposed by other researchers [10]. The spectra of the asphaltenes show almost no fluorescent capabilities at either the detection wavelength or the excitation wavelength used by the CLSM (Fig. 3). The maltene phase exhibits strong fluorescence in these areas. The absolute intensity ratings, although being only general tendencies, suggest that the residuum somehow dampens the fluorescence of the pure bitumen 50/70 as it dilutes the extract. Obviously, the fluorescence of the asphaltenes is shifted to wavelengths higher than 750 nm, into the near infrared region, which is not accessible to the fluorescence spectroscope used in this study.

Further fractioning of the maltene phase into saturates, aromatics, and resins, was conducted to obtain their respective spectra. Although the spectra differ within reasonable

bounds, all bitumina show the same behavior: Only the aromatics fraction shows significant fluorescence in the relevant areas. Taking into account the micelle model and that the fluorescent centers are spatially distributed and the fluorescent species seem to agglomerate, they can be interpreted as a stabilizing mantle, composed mainly of aromatics, surrounding the asphaltenes micelles. Figure 4 shows the normalized spectra of the bitumen fractions and show that the aromatics exhibit very strong fluorescence at 480 nm excitation. However, it has to be added that normalization removes the information of fluorescent emission intensity, which is by several orders of magnitude higher for the aromatics than for both resins and saturates.

3.3 *The micelle model and ageing*

Considering this new information about the chemical structure of the micelle we formulated a new thesis regarding bitumen ageing. This model is a refinement of the micelle model and takes the research conducted upon the oxidative properties of bitumen and bitumen fractions [16], [11] into special consideration. The saturated fraction is considered the least reactive, almost inert by comparison, of all fractions. The asphaltenes seem to have a very strong capability for oxidation in liquid state (i.e. melted or in solution), but show low reactivity at ambient conditions due to their highly associated and solid state. Both aromatics and resins show significant susceptibility for oxygen uptake [16]. Due to this research, for mixing and construction, i.e. the first short term ageing step, oxidation can take place across all phases, with the exception of saturates, but for long term ageing, the oxidation of the asphaltenes fraction has to be considered insignificant. Based on the micelle structure model and its structural and chemical constraints, a pathway for oxidative species diffusing through the material can be plotted (Fig. 5, left).

The continuous phase is largely inert, so the first contact between oxidative species and reactive material happens at the surface of the micelle mantle, which is composed of aromatics and resins. There oxidation can occur and the ammount of reactive oxidative species reaching the asphaltenes has to considered reduced strongly by the oxidation happening in the mantle. This is also conclusive with studies on asphalt oxidation which generally show a declining amount of nonpolar aromatics and a buildup of resins and asphaltenes as a result of ageing. This oxidation process has to be considered very slow in nature, due to the low temperature and the stability of most carbohydrates to oxidation at ambient conditions. However, experience in road engineering show that road damages due to asphalt ageing can occur few months after the construction. Furthermore, experiments regarding asphalt heal-

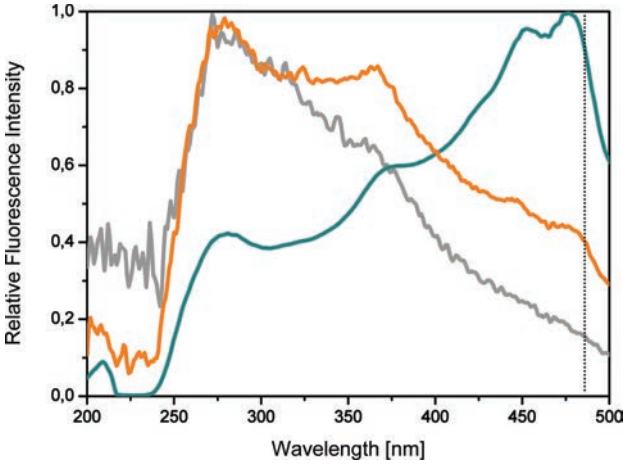

Figure 4. Fluorescence spectra of bitumen fractions: saturates (grey), aromatics (green), resins (yellow), detection wavelength of CLSM: 488 nm.

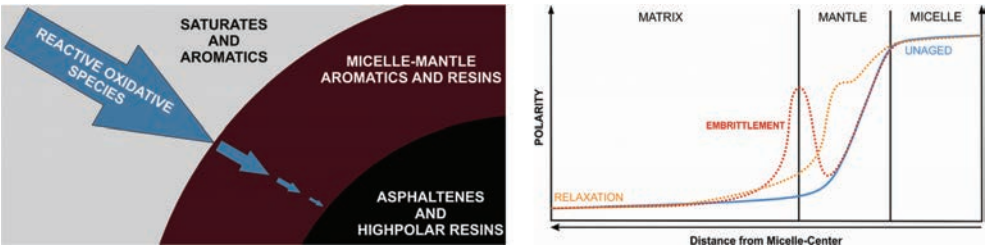

Figure 5. Reactive Oxidative Species (ROS) pathway in bitumen (left). Polarity of bitumen in the micelle structure in fresh (blue), long term aged (red), and relaxed (orange) state (right).

ing in lying asphalt concrete roads show that heating the asphalt can significantly increase road lifetime by enabling self healing [17]. Based on this research we developed a new model hypothesis for asphalt ageing. If the low mobility of molecules at ambient conditions is taken into account, it can be understood that oxidation leads to the formation of a high polar layer on the outside of the micelle mantle. If the polarity reaches a certain limit, then phase separation at this new boundary occurs and the whole, larger micelle plus mantle particle basically forms another immobile center. This reduces transduction of elastic properties and leads to a hardening of the material. If the asphalt is heated, then the diffusion rate significantly increases and the now highly polar resins/aromatics migrate into the center of the micelle and the functionality of the mantle is restored. This also explains why the ageing at road construction is not as destructive as it would have to be considered. At the high temperatures, the high polar oxidation products can simply be transported into the inside of the micelle. However, the increase in micell volume means that the mantle becomes thinner and thus the polarity gradient more extreme and micelle mobility in the matrix decreases. This limits the capability of relaxation by inclusion of high polar molecules in the micelles.

4 MICROMECHANICAL MODELING OF BITUMEN MICROSTRUCTURE

Based on the micelle model introduced before, delivering a basic concept of the bitumen microstructure, and the knowledge gain through the proposed results of chemical analysis, a mechanical model which takes the bitumen microstructure into account could be derived. Therefore, the framework of continuum micromechanis was chosen, allowing for a description of the viscoelastic response of bitumen depending on the volumetric composition and the physical properties of its constituents. Moreover, the interaction between material phases can be taken into account through different so-called homogenization schemes [18], [19], [20], [21], [22], [23]. Thereby, a material is considered as a micro-heterogenous body filling a macro-homogenous Representative Volume Element (RVE). Quasi-homogenous subdomains [20], [21], [22], also known as material phases, with known physical properties describe the microstructure within such an RVE. Correlating the homogeneous deformations acting on the boundary of an RVE with the resulting (average) stress, the mechanical behavior of the overall material can be estimated. Such an approach is refered to as homogenization.

On the basis of the chromatographic separation mentioned before, a reasonable subdivision of bitumen into distinct material phases for the micromechanical modelling were possible (see Fig. 6). Therefore, an RVE of bitumen is built up by a contiguous matrix phase, representing aromatics and resins, in which spherical inclusions are embedded, describing the saturates. While the asphaltenes, acting in the center of micelles, are also modelled by spherical inclusions, the micelle mantles are assumed to form a network-like structure and for this reason are represented by needles with randomly distributed orientations.

Identification of the viscoelastic behavior of the maltene phase (matrix phase and the inclusions representing the saturates) was done by static shear creep tests using a Dynamic Shear Rheometer (DSR). As asphaltenes and their mantle material (highly polar resins and

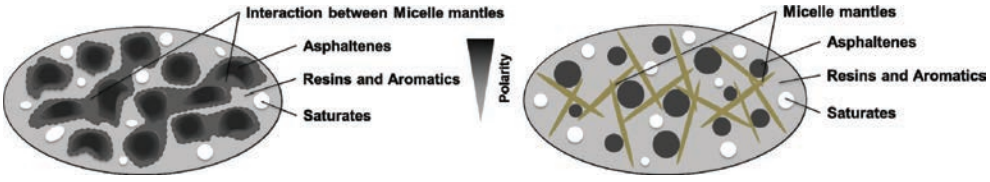

Figure 6. Concept of bitumen microstructure based on micelle model and therefrom derived RVE considered in micromechanical model.

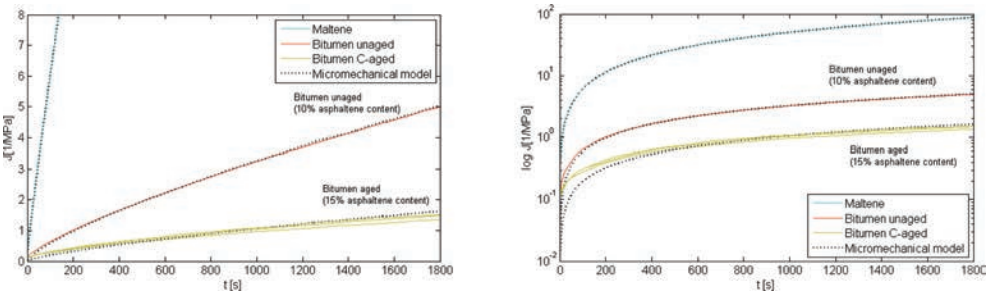

Figure 7. Comparison of experimental results on aged and unaged bitumen (B70/100 at +5°C) from static shear creep tests with predictions from micromechanical modelling.

aromatics) act together in the micelle structure, the same effective viscoelastic behavior is assigned to both phases. To access this effective behavior, static shear creep tests on bituminous mixtures with different (known) asphaltene contents were carried out and by comparison of experimental and model results on a best-fit basis the material behavior could be obtained. In addition, the increase of needles, representing the interaction between micelles, with increasing asphaltene content could be determined, revealing an exponential relationship for asphaltene contents between 0% and 20%. For a detailed validation of these assumptions and the introduced micromechaincal model we refer to further publications.

The influence of longterm ageing was investigated on B70/100 bitumen samples, aged in laboratory using PAV and RTFOT equipment [24]. From static shear creep tests on these samples it was found, that the mechanical behavior of asphaltenes as well as maltenes due to ageing is negligible. However, a significant increase in asphaltene content, and consequently the micelle mantle content, could be observed (detailed information also presented in further publication). This increase, and thus the effect of ageing, can be described satisfactorily by the derived micromechanical model, as can be seen in Figure 7.

5 CONCLUSION

Confocal laser scanning microscopy is an important tool for bitumen analysis, because of its capability to visualize the microstructure of bitumen. It proves the existence of two separate phases in bitumen, as predicted by the micelle theory. Also, it was possible to identify the fluorescent phase in bitumen by chromatography and fluorescence spectroscopy as the aromatics fraction. The aromatic phase contains the molecules that exhibit strong fluorescence capabilities at 488 nm excitation and 515 nm detection and seem to agglomerate. Although other phases also show activity under these conditions, it is by several orders of magnitude lower in intensity, if compared to the aromatics. Thus, an ongoing debate in the scientific community has found its end.

The realization that the fluorescent phase in bitumen is actually the aromatics phase indicates that this is a critical phase regarding ageing and embrittlement. Basically, we developed an enhanced micelle theory for ageing that is capable of explaining the different effects of

short term and long term ageing as well as thermal healing of asphalt concrete. This is an early step on the road to upstream recycling of asphalt concrete and bitumen, because the identification of problematic structural and chemical changes is necessary to overcome their effects.

Based on the introduced micelle model, a mechanical model is derived in the framework of continuum micromechanics considering bitumen as a four-phase composite consisting of asphaltenes, micelle mantles, and saturates embedded in a contiguous matrix of aromatics and resins. The microstructure was implemented in a homogenization scheme to predict the overall viscoelastic response. An increase of asphaltene content, and thus volume content of the micelles, is identified to be responsible for ageing effects, which can be described by the micromechanical model very well.

REFERENCES

[1] European Committee for Standardization. EN 12597: Bitumen and bituminous binders—Terminology. Brussels: European Committee for Standardization, 2012.

[2] Sheu E.Y. Physics of asphaltene micelles and microemulsions—theory and experiment, Journal of Physics: Condensed Matter, 8/1996, pp. A125–A141. 1996.

[3] Loeber L., Muller G., Morel J., Sutton O. Bitumen in colloid science: a chemical, structural and rheological approach, Fuel, 77/13, pp. 1443–1450. 1998.

[4] Lackner R., Spiegl M., Blab R., Eberhardsteiner J. Is Low-Temperature Creep of Asphalt Mastic Independent of Filler Shape and Mineralogy?—Arguments from Multiscale Analysis, Materials in Civil Engineering, 17/5, 2005, pp. 485–491. 2005.

[5] Sengoz B., Isikyakar G. Analysis of styrene-butadiene-styrene polymer modified bitumen using fluorescent microscopy and conventional test methods, Journal of Hazardous Materials, 150/2008, pp. 424–432. 2008.

[6] Topal A. Evaluation of the properties and microstructure of plastomeric polymer modified bitumens, Fuel Processing Technology, 91/1, 2010, pp. 45–51. 2009.

[7] Fawcett, A.H., McNally, T. Polystyrene and asphaltene micelles within blends with a bitumen of an SBS block copolymer and styrene and butadiene homopolymers, Colloid and Polymer Science 281/3, 2003, pp. 203–213. 2003.

[8] Handle F., Grothe H., Neudl S. Confocal Laser Scanning Microscopy—Observation of the Microstructure of Bitumen and Asphalt Concrete, 5th Eurasphalt & Eurobitume Congress, Istanbul, Turkey, P5EE-188. 2012.

[9] Forbes A., Haverkamp R.G., Robertson T., Bryant J., Bearsley S. Studies of the microstructure of polymer-modified bitumen emulsions using confocal laser scanning microscopy, Journal of Microscopy, 204/3, 2001, pp. 252–257. 2001.

[10] Bearsley S., Forbes A., Haverkamp R. Direct observation of the asphaltene structure in paving-grade bitumen using confocal laser-scanning microscopy, Journal of Microscopy, 215/2, 2004, pp. 149–155. 2004.

[11] Lesueur D. The colloidal structure of bitumen: Consequences on the rheology and on the mechanisms of bitumen modification, Advances in Colloid and Interface Science, 145. pp. 42–82. 2009.

[12] Lu X., Langton M., Olofsson P., Redelius P. Wax morphology in bitumen, Journal of Materials Science, 40, 2005, pp. 1893–1900. 2005.

[13] American Society for Testing and Materials. ASTM D4124-01—Standard Test Methods for Separation of Asphalt into Four Fractions, ASTM International, 2010.

[14] Corbett L.W. Composition of asphalt based on generic fractionation, using solventdeasphaltening, elution-adsorption chromatography and densimetric characterization. Analytical Chemistry, 41, pp. 576–579. 1969.

[15] Tucker S., Jason M., Acree W., Zander M., Mitchell R. Spectroscopic Properties of Polycyclic Aromatic Compounds Part IV: Effect of Solvent Polarity and Nitromethane on the Fluorescence Emission Behaviour of Select Bipolyciclic Aromatic Hydrocarbons, Applied Spectroscopy, 48(4), pp. 458–464. 1994.

[16] Peterson J.C. A Review of the Fundamentals of Asphalt Oxidation—Chemical, Physicochemical, Physical Property, and Durability Relationships. Transporation Research Board, Washington, DC 20001, 2009.

[17] Qiu J., Molenaar A.A.A., van de Ven M.F.C., Wu S., Yu J. Investigation of self healing behaviour of asphalt mixes using beam on elastic foundation setup, Materials and Structures, 45, pp. 777–791. 2012.

[18] Hill R. Elastic properties of reinforced solids: some theoretical principles, Journal of the Mechanics and Physics of Solids, 11, pp. 357–362. 1963.
[19] Hill R. Continuum micro-mechanics of elastoplastic polycrystals, Journal of the Mechanics and Physics of Solids, 13(2), pp. 89–101. 1965.
[20] Suquet P. Continuum micromechanics, Edition 1997, Wien—New York, Springer, 1997.
[21] Zaoui A. Structural morphology and constitutive behavior of microheterogeneous materials. in[20] Wien—New York, Springer. pp. 291–347. 1997.
[22] Zaoui A. Continuum micromechanics: survey. Journal of Engineering Mechanics (ASCE), 128(8), pp. 808–816. 2002.
[23] Scheiner S., Hellmich C. Continuum microviscoelasticity model for aging basic creep of early-age concrete. Journal of Engineering Mechanics, 135(4), pp. 307–323. 2009.
[24] Huang S.C., Tia M., and Ruth B.E. Laboratory Aging Methods for Simulation of Field Aging of Asphalts, Materials in Civil Engineering, 1996.

Asphalt Pavements – Kim (Ed)
© 2014 Taylor & Francis Group, London, ISBN 978-1-138-02693-3

A constitutive model for simulation of water to ice phase change in asphalt mixtures

Aikaterini Varveri
Delft University of Technology, Delft, The Netherlands

Stavros Avgerinopoulos
De Montfort University, The Gateway, Leicester, UK

Cor Kasbergen & A. (Tom) Scarpas
Delft University of Technology, Delft, The Netherlands

Andy Collop
De Montfort University, The Gateway, Leicester, UK

ABSTRACT: Frost damage is one of the major concerns in pavement design particularly in cold regions. During their service life, asphalt pavements are continuously exposed to various environmental conditions such as oxidation, ultraviolet radiation and moisture. The joint effects of mechanical and environmental loading progressively degrade the mechanical properties of asphalt pavements, resulting thus to frost damage when ice crystals form in the asphalt concrete. In this contribution a 3D energy based micromechanical finite element model is presented for simulation of the volume expansion that occurs during the water-to-ice phase change in the macro pores of the mixture. For the simulations, the internal microstructure of asphalt mixtures was captured with X-Ray Computed Tomography (CT) imaging techniques. The analyses enable the quantification of the contribution of asphalt mixture characteristics such as air voids and pore connectivity in the damage developed in the asphalt binder due to the volume change of water-to-ice in the pores.

Keywords: Frost damage, asphalt mixtures, constitutive modelling, X-ray computed tomography, phase change

1 INTRODUCTION

The detrimental effects of freeze-thaw cycles in Asphalt Concrete (AC) pavements are manifested by stripping of aggregates from the asphalt mixture, which ultimately results to pothole formation and deterioration of the pavement surface. For frost damage to occur, low temperatures and water in the pores have to be concurrently present in an AC pavement.

Depending on the design characteristics, air void content in an asphalt mixture can vary from 3–5% for a dense-graded mixture and up to 20% for an open-graded one. Because of precipitation and other reasons, moisture can accumulate inside the air voids and the microcracks in the top layers of the pavement, Figure 1(b). As the temperature drops below zero, the pavement freezes from the surface downwards and a phase change of water-to-ice takes place, followed by volume expansion, Figure 1(c). The expanding ice crystals impose compressive stresses to the adjacent aggregates, Figure 1(d), which can cause cohesive and/or adhesive damage.

Unlike the majority of substances, water expands upon freezing and its volume increases approximately by 9% under atmospheric pressure. On the basis of thermodynamics, volume expansion of water-to-ice is the result of a phase change from a liquid state to a solid one,

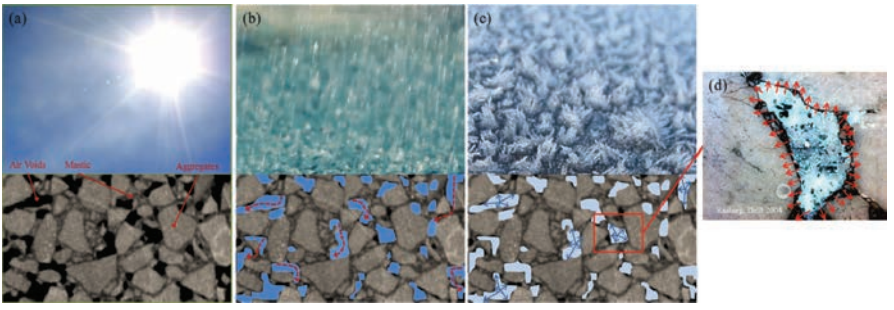

Figure 1. Frost damage: (a) asphalt mixture components, (b) moisture infiltration, (c) ice expansion, (d) developed stresses.

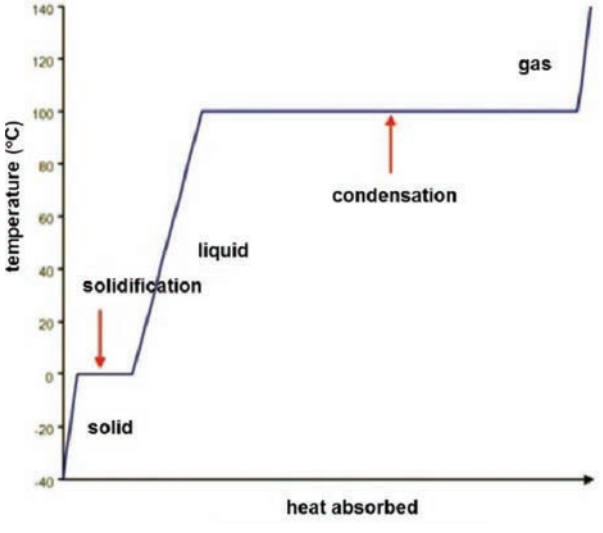

Figure 2. Heating curve for water.

Figure 2. Phase change takes place in a very narrow temperature range around zero degrees and for this reason temperatures below zero have very little influence on volume change.

Several models were proposed for the simulation of freeze-thaw damage mechanisms over the past years for soils [1–3] and cement concrete [4]. However, to the knowledge of the authors, there is no attempt in literature to model binder damage due to frost damage for asphalt mixtures. For asphalt concrete, previous studies focused on the characterization of AC mixtures performance under the influence of freeze-thaw cycles [5–7].

In the present study, a thermal-phase change micromechanical model capable of simulating the phase change driven volume expansion of water is combined with a thermal diffusion algorithm and a binder damage model to investigate the influence of AC mix characteristics on frost damage susceptibility. All Finite Element (FE) simulations were performed by the CAPA-3D FE system developed at Delft University of Technology [8] on 3D micromechanical meshes obtained by X-Ray Computed Tomography (CT) scans of actual asphalt cores.

2 WATER-TO-ICE PHASE CHANGE MODEL

The constitutive model utilized for the simulation of water-to-ice phase change is presented in this section. As shown in Figure 3, the model consists of a hyperelastic component

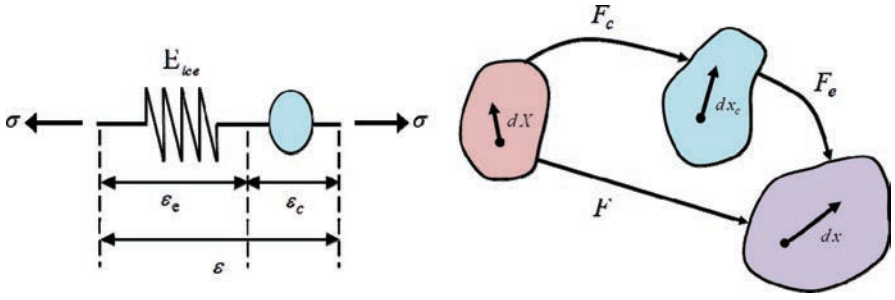

Figure 3. Schematic of the phase change material model.

representing the mechanical stiffness of the ice crystal and a swelling element which, when active, simulates the phase change driven expansion ε_c. For a constrained total deformation case (i.e. $\varepsilon = cnst$), as ε_c in the swelling component increases due to phase change, the hyperelastic spring is compressed and hence it exerts compressive stresses in the surrounding. The evolution equation for the water-to-ice expansion is postulated as

$$\frac{\partial \xi}{\partial t} = \frac{1}{t_c}(1-\xi) \tag{1}$$

where t_c is the characteristic time of the phenomenon. And ξ is the expansion in time. Assuming the initial condition $\xi|_{t=0} = 0$ the ice expansion in time is defined as

$$\xi = 1 - \exp\left(\frac{t}{t_c}\right) \tag{2}$$

A large deformation framework on the basis of multiplicative decomposition is utilized, where the total deformation tensor F is split into an elastic part F_e and an 'ice expansion' component F_c, so that it holds

$$F = F_e F_c \tag{3}$$

Here the ice expansion function as stated in Eq. (3) is incorporated into the 'ice expansion' deformation component as

$$F_c = (1 + k\xi) I \tag{4}$$

where k is the maximum expansion and I the second order identity tensor. By combining Eqs. (3–4) an expression for the elastic deformation tensor results

$$F_e = F F_c^{-1} = \frac{F}{1 + k\xi} \tag{5}$$

With regard to the reference configuration, the right Cauchy-Green strain tensors for the hyperelastic and the swelling component are described by

$$C_c = F_c^T F_c \tag{6}$$

$$C_e = F_e^T F_e \tag{7}$$

For a purely mechanical case, the Clausius-Planck dissipation inequality defines the dissipation of energy D, as

$$D = P : \dot{F} - \dot{\Psi} \geq 0 \tag{8}$$

where P is the first Piola-Kirchhoff stress, Ψ is the time derivative of the Helmholtz strain energy function. For the proposed model the Helmholtz free energy is defined as

$$\Psi = \Psi_c(\xi) + \Psi_e(C_e) \tag{9}$$

in which Ψ_c is the strain energy function of the swelling component, Ψ_e is the strain energy function for the single spring. Substituting Eq. (9) into the dissipation inequality of Eq. (8) results to

$$D = P : \dot{F} - \frac{\partial \Psi_e}{\partial C_e} : \dot{C}_e - \frac{\partial \Psi_c}{\partial \xi} \cdot \dot{\xi} \geq 0 \tag{10}$$

After some mathematical elaboration, the stress tensor and the dissipation inequality are obtained as

$$P = 2F_e \frac{\partial \Psi}{\partial C_e} F_c^{-T} \quad \text{and} \quad 2C_e \frac{\partial \Psi}{\partial C_e} : L_v + q \cdot \dot{\xi} \geq 0 \tag{11}$$

in which L_v is the velocity gradient and Σ is the Mandel tensor. To solve the above inequality, the following minimization problem is defined

$$\text{minimize } -\left(\Sigma : L_v + q \cdot \dot{\xi}\right) \tag{12}$$

$$\text{subject to } g(\Sigma, q) \leq 0 \tag{13}$$

To satisfy the above minimization problem, the following evolution laws can be postulated

$$\Sigma : L_v \geq 0 \tag{14}$$

$$\frac{\partial \Psi}{\partial \xi} \frac{\partial \xi}{\partial t} \geq 0 \tag{15}$$

where the following form for the velocity gradient of the ice component is defined

$$L_v = \dot{F}_c F_c^{-1} = \frac{\kappa \dot{t}_c (1 - \xi)}{1 + \kappa \xi} I = d\, I, \quad d \geq 0 \tag{16}$$

3 THERMAL CONDUCTION MODEL

On the basis of a staggered algorithm, the above phase change model is coupled to a thermal conduction model capable of simulating the conductive flow of heat into the components of the asphalt mixture. Conduction is governed by the following equation

$$q = -k \nabla T \tag{17}$$

where q is the heat flux vector ($W \cdot m^{-2}$), k is the thermal conductivity ($W \cdot m^{-1} \cdot °C^{-1}$) and T is the temperature (°C) at a point within the medium.

By combining Fourier's law for the conduction of heat (Eq. (17)) and the law for conservation of energy, assuming a constant thermal conductivity k, one can obtain the heat conduction equation

$$\frac{\partial T}{\partial t} = \alpha \nabla^2 T \tag{18}$$

where ∇^2 is the Laplace operator in three dimensional rectangular Cartesian coordinates and α is defined as the thermal diffusivity ($m^2 \cdot s^{-1}$) of the material according to Eq. (19)

$$\alpha = \frac{k}{\rho C_s} \tag{19}$$

where ρ is the mass density ($kg \cdot m^{-3}$) and C_s is the specific heat capacity of the conductive medium ($J \cdot kg^{-1} \cdot °C^{-1}$).

4 ENERGY BASED VISCO-ELASTIC DAMAGE MODEL

An energy-based constitutive model for the simulation of mechanical damage is employed for simulation of the damage in the binder. The model falls within the general framework of Continuum Damage Mechanics (CDM) and introduces material damage as an internal state variable representing the irreversible physical processes within the microstructure of the material.

On the basis of energy arguments and multiplicative decomposition of the total deformation gradient, the stress tensor of the damaged material has been derived in Varveri et al. [9] as

$$P = \left(2F_e \frac{\partial \Psi_v}{\partial C_e} F_e^{-T} + 2F_\infty \frac{\partial \Psi_\infty}{\partial C_\infty} F_\infty^{-T} \right) F^{-T} \tag{20}$$

in which F_e and F_∞ are the deformation gradients of the viscous and the hyperelastic components of the model and F is the total deformation gradient.

In the model, damage is a scalar quantity which varies from the undamaged state $(d = 0)$ to the fully damaged one $(d = 1)$. The evolution law for damage is defined as a function of the total dissipated viscous work W

$$d = 1 - e^{-k \cdot W^r} \tag{21}$$

where k and r are calibration parameters.

5 DEVELOPMENT OF 3D MICROMECHANICAL MESHES

The accurate representation of the internal structure of the asphalt specimens is quite significant in micromechanical modelling, since each mixture component has its particular thermal and mechanical properties. For that reason, in this study, three dimensional micromechanical Finite Element (FE) meshes were produced from X-Ray CT scans by means of Simpleware, a specialized 3D-based image processing software [10].

In this study, X-Ray CT scans from a porous (PA) and a dense (SMA) asphalt mixtures were utilized. After cropping the segmented data to the desired dimensions, a robust meshing algorithm was applied to enable the conversion of the 3D images into FE meshes that were used for computational analyses in the CAPA-3D FE system. The FE meshes comprised three phases i.e. aggregates, asphalt binder and (water filled) air voids, as shown in Figure 4. For the spatial discretization of the meshes, 3D linear four-node tetrahedral elements were used. Specifically, the PA and the SMA meshes consist of 412,304 and 1,286,806 elements, respectively.

6 MICROMECHANICAL FINITE ELEMENT SIMULATIONS

The phase change FE model developed was applied to examine the mechanical degradation of AC mixtures due to damage development in the asphalt binder as a result of phase-driven

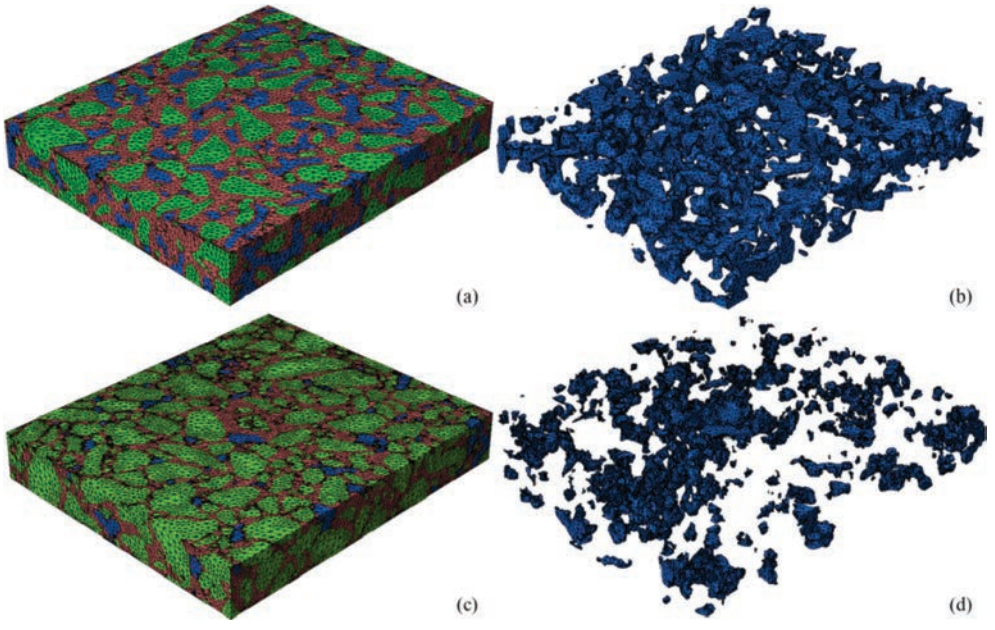

Figure 4. Volume renderings of (a) three-phase material and (b) air void phase in the PA mixture; (c) three-phase material and (d) air void phase in the SMA mixture.

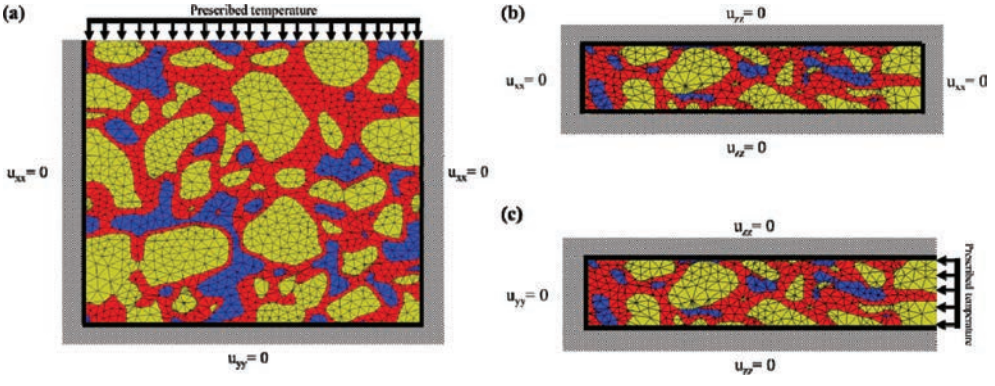

Figure 5. Specified boundary conditions in (a) X-Y, (b) X-Z and (c) Y-Z Plane.

volume expansion of water in the macro pores. Figure 5 shows the boundary conditions imposed during the FE simulations. A constant temperature $T = -2°C$ was applied at the top face to simulate top-down freezing. Adiabatic thermal flow conditions were specified at all other boundaries together with displacement restraints, Figure 5.

The thermal properties governing temperature propagation in AC pavements are volumetric heat capacity ρC_s and thermal conductivity k. In this study, the values of both properties differed for every constituent of the mixture i.e. aggregates (ag), asphalt binder (ab), air voids (av). The thermal conductivity and the volumetric heat capacity for each phase were chosen as $k^{ag} = 0.576$, $k^{ab} = 0.6173$ and $k^{av} = 0.09$ ($J \cdot mm^{-1} \cdot hr^{-1} \cdot °C^{-1}$) and $\rho C_s^{ag} = 2.024 \cdot 10^{-3}$, $\rho C_s^{ag} = 2.275 \cdot 10^{-3}$ and $\rho C_s^{ag} = 1.189 \cdot 10^{-6}$ ($J \cdot mm^{-3} \cdot °C^{-1}$), respectively.

For the viscoelastic asphalt binder, a viscosity of 2200 MPa·s was specified. Furthermore, aggregates were assumed hyperelastic and their mechanical properties were selected based on a study by Artamendi et al. [11]. An elastic modulus of 18.1 GPa and a Poisson's ratio of

0.171 were specified. For the ice material, the elastic modulus and the Poisson's ratio were specified 9.0 GPa and 0.31 (at 0 °C), respectively.

Figures 6(a) and 6(c) show the PA and SMA FE meshes in their undamaged condition, i.e. before freezing; for both meshes, aggregates are in yellow, asphalt binder in red and air voids in blue color. Figures 6(b) and 6(d) illustrate the damage distribution due to the action of the expanding ice crystals for the porous and the dense mixture, respectively.

The results show that damage accumulates in those areas of the binder located around the macro pores of the mixtures. It is observed that damage is more pronounced for the porous mixture than for the dense one. This finding is fairly obvious because the high air void content and interconnectivity of porous mixtures make them more susceptible to frost damage.

Figure 7 shows the expansion of the specimen in the vertical y direction as a result of the ice expansion in the pores. The black horizontal line indicates the height of the specimen in its initial configuration. As shown in Figures 7(a)–(c), damage evolution progresses as the phase-change process takes places and until the volumetric expansion reaches the terminal value of 9% water-to-ice volume expansion.

In Figure 8, the average displacement u_{yy} of the top surface is plotted against the compressive reaction forces developed in the horizontal x boundary direction of the specimen. The

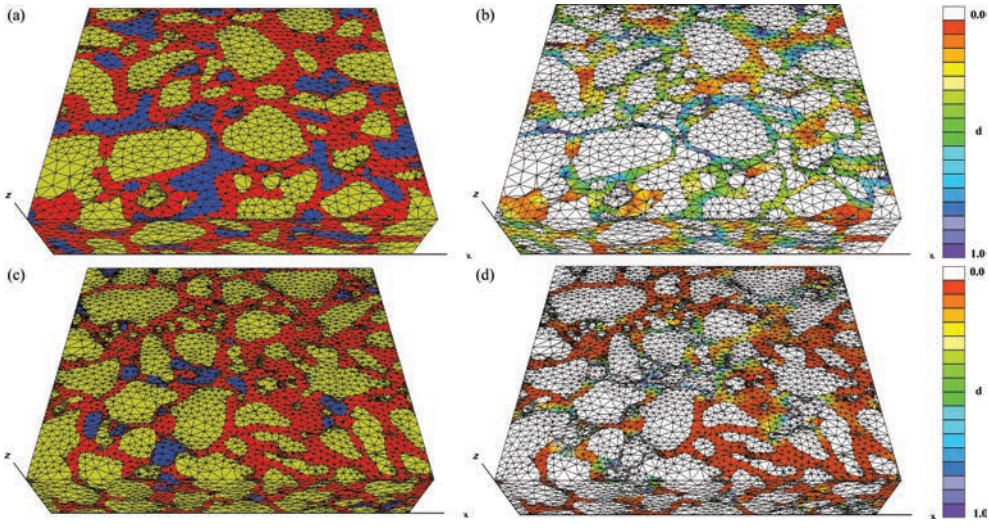

Figure 6. Three-phase finite element mesh and damage distribution due to water expansion in the PA (a–b) and the SMA (c–d) mixture.

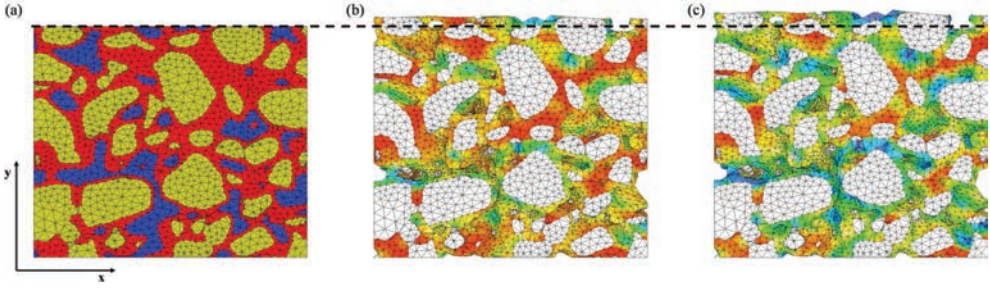

Figure 7. Displacement in vertical direction after (a) 0, (b) 3 and (c) 5 hrs of freezing for the PA mixture.

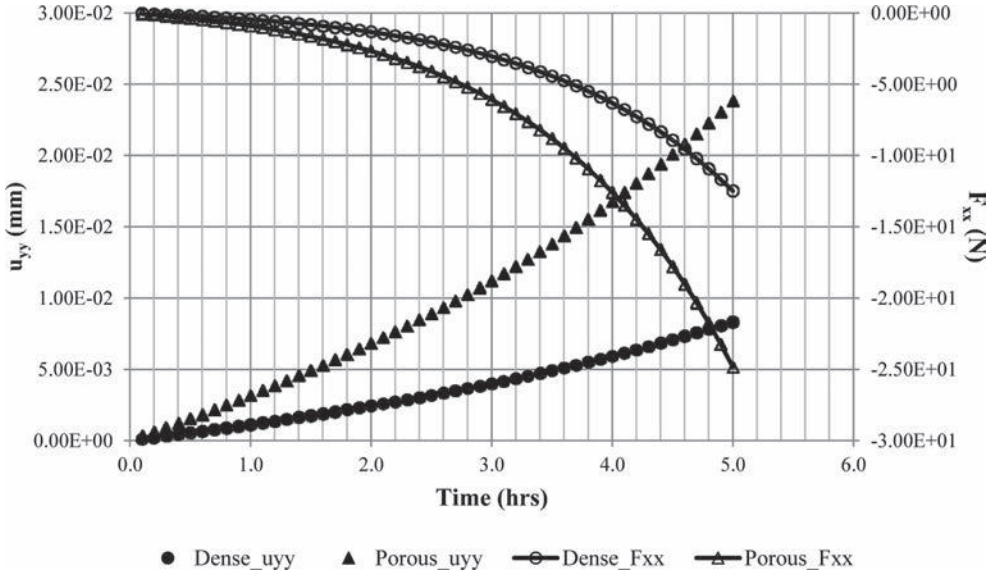

Figure 8. Influence of phase-driven volume expansion on the AC mixtures.

u_{yy} values at any given time correspond to the average shift in the y direction of all nodes for the aggregate and asphalt binder phases.

Calibration of the model is currently performed on the basis of micro-mechanical tests on AC samples similar to those shown in Figure 5 with analogous thermal and restraint boundary conditions [12].

7 CONCLUSIONS

The newly developed water-to-ice phase change model in combination with a thermal conduction algorithm and a viscoelastic damage model for binders are capable of capturing the intrinsic characteristics of frost damage in AC specimens and constitute a useful tool in the quantification of the influence of mix characteristics on the susceptibility of a mix to frost damage.

REFERENCES

[1] R.L. Michalowski and M. Zhu. A Constitutive Model of Saturated Soils for Frost Heave Simulations. Cold Regions Science and Technology, 22, pp. 47–63, 1993.
[2] A.P.S. Selvadurai, J. Hu and I. Konuk. Computational Modelling of Frost Heave Induced Soil-Pipeline Interaction I. Modelling Frost Heave. Cold Regions Science and Technology, 29, pp. 215–228, 1999.
[3] W.J. Fourie, D.L. Barnes and Y. Shur. The Formation of Ice From Infiltration of Water Into a Frozen Coarse Grained Soil. Cold Regions Science and Technology, 48, pp. 118–128, 2007.
[4] Z.P. Bazant, J.C. Chern, A.M. Rosenberg and J.M. Gaidis. Mathematical Model for Freeze-Thaw Durability of Concrete. Journal of the American Ceramic Society, 71 (9), pp. 776–783, 1988.
[5] D. Feng, J. Yi, L. Wang and D. Wang. Impact of Gradation Types on Freeze-Thaw Performance of Asphalt Mixtures in Seasonal Frozen Region. Ninth International Conference of Chinese Transportation Professionals (ICCTP), Harbin, China, pp. 1–7, 2009.
[6] D. Wang, J. Yi, and D. Feng. Impact of Freeze-thaw Cycles on the Performance of Asphalt Mixture Based Permeability. Advanced Testing and Characterization of Bituminous Materials, Rhodes, Greece, pp. 205–213, 2009.

[7] C. Maudit, F. Hammoum, J.M. Piau, V. Maudit, S. Ludwig and D. Hamon. Quantifying Expansion Effects Induced by Freeze-Thaw Cycles in Partially Water Saturated Bituminus Mix. Road Materials and Pavement Design, 11 (1), pp. 443–457, 2010.
[8] Scarpas, A. *CAPA-3D: A mechanics based computational platform for pavement engineering*, PhD dissertation. Delft University of Technology, Netherlands, 2005.
[9] A. Varveri, S. Avgerinopoulos, C. Kasbergen, A. Scarpas and A. Collop. Influence of Air Void Content on Moisture Damage Susceptibility of Asphalt Mixtures: Computational Study. Proceedings of the 93rd Annual Meeting of the Transportation Research Board, Washington, D.C., 2014.
[10] *Simpleware,* ScanIP, +ScanFE, 2011.
[11] Artamendi, I., Kane, M., Scarpas, A. and Villani, M.M. Measurement of the interface component characteristics. EU FP7 SKIDSAFE project report 1.1, 2011.
[12] A. Varveri. Coupled Environmental-Mechanical Causes of Damage in AC Mixtures. Dissertation thesis in preparation. Delft University of Technology, 2014.

This page intentionally left blank

Asphalt Pavements – Kim (Ed)
© 2014 Taylor & Francis Group, London, ISBN 978-1-138-02693-3

Comparing image processing techniques for asphalt concrete X-ray CT images

Tom Papagiannakis
University of Texas at San Antonio, San Antonio, TX, USA

Habtamu Zelelew
ESCINC/FHWA, Washington, DC, USA

Sos Agaian
University of Texas at San Antonio, San Antonio, TX, USA

ABSTRACT: This paper presents a comparison between two image segmentation techniques for processing asphalt concrete microstructure X-ray CT images; the Adaptive Enhancement-based Thresholding Algorithm (AETA) and the watershed segmentation embedded into the Volumetric-based Thresholding Algorithm (VTA). Both these methods were used to process the X-ray CT images of nine asphalt concretes. These consisted of three mix types, each prepared with three aggregate types. The mix designs included a Coarse Matrix High Binder Type C (CMHB) mix, a gap-graded Porous Friction Course (PFC) mix, and a fine-graded Superpave Type C (Superpave) mix. The three aggregate types included hard limestone, granite, and soft limestone. All mixtures were prepared with a PG 76-22 modified binder. The comparison of the two methods was carried out both visually and quantitatively. The later was accomplished by comparing the gradation estimated from the images using purpose-designed software to the gradation obtained from mechanical sieving. The results show that the inherent over-segmentation problem with the VTA technique is effectively reduced using the AETA method. Overall, the AETA method outperforms the VTA watershed image segmentation method by producing better separation between connected and overlapping aggregates. Its drawback is that it does not preserve the volumetric properties of the mixtures, as done by the VTA technique.

Keywords: asphalt; microstructure; segmentation; watershed; adaptive threshold

1 INTRODUCTION

High resolution X-ray Computed Tomography (CT) is a non-destructive imaging technique that has become increasingly popular for capturing the microstructure of asphalt concretes. It provides a unique insight into the makeup of mixture constituents and their spatial arrangement allowing detailed analytical modelling of their macroscopic behaviour (e.g., response to various forms of loading). Microstructure images allow the study of a variety of asphalt concrete properties and their distribution, including aggregate structure, air voids, permeability, degree of compaction, and state of damage. A variety of such studies is available in the literature (e.g., Masad et al., 1999; Shashidhar 1999; Tashman et al., 2002; Al-Omari and Masad 2004; Wang et al., 2004; Kutay et al., 2007; Khan and Collop 2010; Partl et al., 2007; Wu et al., 2011; and Zelelew and Papagiannakis 2011a, 2011b).

Processing X-ray CT images involves solving a number technical problems:

- Account for the different absorption rate of X-rays through each of these three phases, caused by their different densities.

- Account for the weakening of X-rays from the outside to the interior of the specimen being scanned.
- Establish grey level thresholds separating the three asphalt concrete phases, (i.e., air binder and aggregate).
- Difficulty in establishing the boundaries between aggregates, especially when they touch or overlap.

Hence, processing images to accurately represent the aggregates morphology, (e.g., size, shape, angularity) and the mixture physical properties (e.g., volumetric properties) remains challenging. This paper presents and compares two alternative X-ray image processing techniques for processing asphalt concrete X-ray images.

2 OBJECTIVE

The objective of this paper is to illustrate the technical highlights of two alternative X-ray imaging techniques for capturing the microstructure of asphalt concrete, highlight their differences and compare their accuracy.

3 THE ASPHALT CONCRETES ANALYZED

3.1 *Mix characteristics*

A total of nine asphalt concretes were included in this study. The mix designs consisted of a coarse-graded Coarse Matrix High Binder Type C (CMHB) mix, a gap-graded Porous Friction Course (PFC) mix, and a fine-graded Superpave Type C (Superpave) mix. Each of these mix designs was prepared with three aggregate types (hard limestone, granite, and soft limestone) and a PG 76-22 modified binder meeting the Texas DOT specifications. The aggregate gradations for each of the mix designs are shown in Figure 1. The design Equivalent Single Axle Loads (ESALs) for the project location was between 3 and 10 million and therefore a design gyrations of 100 (N_{design} = 100) was used. The AASHTO PP60 "Preparation of Cylindrical Performance Test Specimens using the Superpave Gyratory Compactor (SGC)" was followed to fabricate the asphalt concrete test specimens. The CMHB and Superpave

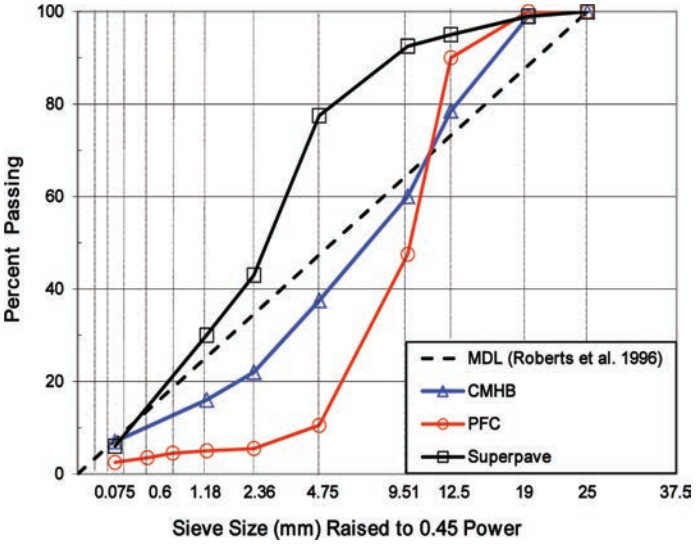

Figure 1. Aggregate gradations from mechanical sieving.

Table 1. Coarse aggregate angularity and texture using AIMS (Zelelew 2008).

Aggregate type	AI	TI	Description
Hard Limestone (HL)	2323	193	Sub-rounded and smooth aggregate
Granite (G)	2791	221	Sub-rounded and smooth aggregate
Soft Limestone (SL)	2195	80	Sub-rounded and polished aggregate

Angularity Index (AI) Range: Rounded (0–2100), Sub-rounded (2100–4000), Sub-angular (4000–5400), and Angular (5400–10,000).
Texture Index (TI) Range: Polished (0–165), Smooth (165–275), Low Roughness (275–350), Moderate Roughness (350–460), and High Roughness (460–1,000).

mixtures were compacted in the gyratory compactor to achieve a target air voids of 7.0% while the PFC mixtures were fabricated using a target air voids of 20%. Detailed mix design data and experimental test plan as well as numerical modeling of creep performance can be found elsewhere (Zelelew 2008).

3.2 *Aggregate characteristics*

The first generation of the Aggregate Image Measurement System (AIMS) (Masad 2005) was used to quantify the gradient angularity and surface texture of the coarse aggregates, retained on sieve size 4.75 mm (i.e., Sieve No. 4), used for the asphalt concretes tested. The gradient Angularity Index (AI) defines the sharpness of the corners of 2D images of aggregate particles. It quantifies changes along a particle boundary with higher gradient values indicating a more angular shape. AI has a relative scale of 0 to 10,000 with a perfect circle having a small but non-zero value. The Texture Index (TI) describes the relative smoothness or roughness of surface features less than roughly 0.5 mm in size. TI has a relative scale of 0 to 1,000 with a smooth polished surface approaching a value of 0. The aggregate shape characteristics can be classified into different sub-categories. Angularity was divided into rounded, sub-rounded, sub-angular, and angular. A higher angularity index indicates a higher aggregate angularity and may yield better aggregate interlocking. Similarly, texture was classified as polished, smooth, low, medium and high roughness. Aggregates with higher surface texture may provide better wheel friction and may improve skid resistance. The AIMS test results are presented in Table 1.

4 VOLUMETRIC-BASED THRESHOLDING ALGORITHM (VTA)

The Volumetric-based Thresholding Algorithm (VTA) utilizes the average volumetric properties of a particular asphalt concrete core to establish threshold levels for the boundary between mastic-aggregate and mastic-air. Prior to carrying out the VTA, the raw X-ray images are processed to enhance contrast and remove noise. Contrast enhancement is performed through histogram equalization using the MATLAB® function *histeq*, (Misiti et al., 2006). Noise removal is done using the median filtering technique and a kernel size of 3×3 pixels.

After this preliminary image treatment, the VTA is carried out in two steps, first for establishing the grey level mastic-air threshold and second for establishing the grey level aggregate-mastic air threshold referred to as T_1 and T_2, respectively. For the mastic-air threshold T_1, a seed (or initial) grey level value is assumed, the volume of the air voids computed for each of the X-ray CT sections and then averaged over the volume of the sample. The mastic-air grey level threshold T_1 corresponds to the grey level that minimizes the error between the laboratory measured air-voids and the X-ray CT image air voids. This process is repeated in establishing the mastic-aggregate grey level threshold T_2. Finding these threshold values involves an iterative process, whereby the grey level of a pixel is compared to the seed threshold values to establish whether it is an 'object' (pixel value equal to 1) or 'background' (pixel

value equal to 0). An example is shown in Figure 2. At the conclusion of this image processing step, the three phases of the asphalt concrete microstructure have been identified, while preserving the average volumetric properties of the mixture.

The images obtained with the VTA are further refined to improve separation between aggregates that are in contact or overlap. This is done through edge detection and segmentation. Edge detection enhances the physical boundaries between the three asphalt concrete phases. It is carried out using the gradient approach. The gradient of an image is the magnitude of the first-derivative of its image function, i.e., gray level $f(i,j)$. A Sobel operator is used to define the gradient:

$$|\nabla f| = \begin{bmatrix} \frac{\partial f}{\partial i} \\ \frac{\partial f}{\partial j} \end{bmatrix} = \sqrt{\left(\frac{\partial f}{\partial i}\right)^2 + \left(\frac{\partial f}{\partial j}\right)^2} \tag{1}$$

The first-order derivatives along the two Cartesian coordinates i and j are given by:

$$\frac{\partial f}{\partial i} = \nabla_i f = \frac{1}{2}[f(i+1,j) - f(i-1,j)] \tag{2a}$$

$$\frac{\partial f}{\partial j} = \nabla_j f = \frac{1}{2}[f(i,j+1) - f(i,j-1)] \tag{2b}$$

The direction of the gradient vector (i.e., the orientation of a unit normal vector perpendicular to the specified edge location), is used to quantify the orientation of the sharpest gray-level intensity change.

The steps involved in the VTA algorithm are summarized as follows:

- Step 1: Analyse the raw X-ray CT asphalt concrete two-dimensional images (i.e., circular slices) one at a time.
- Step 2: Apply the histogram equalization technique to enhance image contrast. This is accomplished through the use of the MATLAB® built-in function called *histeq*.
- Step 3: Apply a median filtering technique with a kernel size of 3 × 3 to remove image noise.
- Step 4: Perform thresholding to establish the threshold grey value T_1 between that separates mastic from air by minimizing the error between the core air voids and the average air voids considering all the two-dimensional images for this core.
- Step 5: Repeat Step 4 for establishing the grey level threshold T_2 that separates mastic and aggregates.

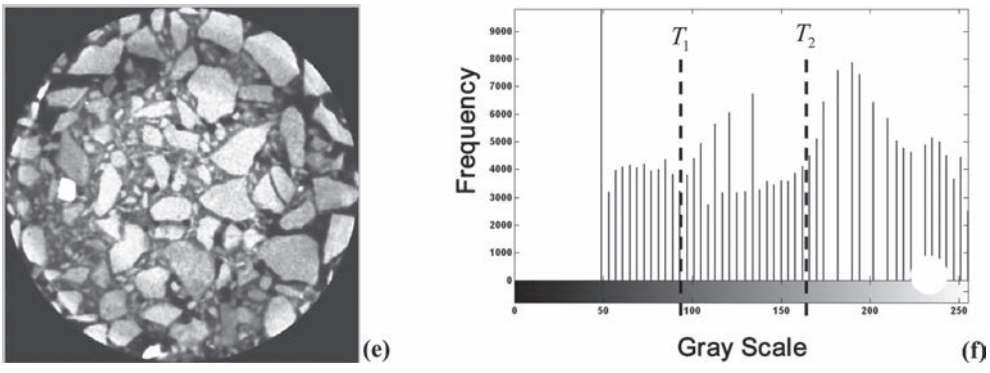

Figure 2. Illustration of VTA thresholding (Zelelew and Papagiannakis, 2011a).

- Step 6: Perform edge detection using the gradient method to separate adjacent and overlapping objects.
- Step 7: Enhance object segmentation using the watershed technique.

These steps were implemented into a MATLAB® code that automates the processing of X-ray CT images of asphalt concrete cores. More details on this technique were given by Zelelew and Papagiannakis (2011a).

5 ADAPTIVE ENHANCEMENT-BASED THRESHOLDING ALGORITHM (AETA)

An alternative to the VTA approach was developed by adapting the Human Visual System (HVS) originally developed for processing medical images (DelMarco and Agaian 2009). This involves an image Enhancement Measure (EME) that allows selecting automatically optimal processing of the best parameters and transforms of the HVS. The method is described next by considering an image $x(n, m)$ being split into $k_1 k_2$ blocks $w_{k,l}(i, j)$ of sizes $l_1 \times l_2$ for a given class of orthogonal transforms. EME is defined as:

$$EME = \frac{1}{k_1 k_2} \sum_{l=1}^{k_2} \sum_{k=1}^{k_1} 20 \log \left| \frac{I^w_{max;k,l}}{I^w_{min;k,l}} \right| \tag{3}$$

where, $I^w_{max;k,l}$ and $I^w_{min;k,l}$ are respectively the minimum and maximum grayscale intensities of the image $x(n, m)$ inside the block $w_{k,l}(i, j)$. This visibility operator was extended in the form of its second derivative (DelMarco and Agaian, 2009 and Zhou et al., 2010) and called the Second-Derivative-like Measure of Enhancement (SDME). It uses an HVS-type image decomposition, which defines SDME as follows:

$$SDME = \frac{1}{k_1 k_2} \sum_{l=1}^{k_1} \sum_{k=1}^{k_2} 20 \ln \left| \frac{I^w_{max;k,l} - 2I^w_{center;k,l} + I^w_{min;k,l}}{I^w_{max;k,l} + 2I^w_{center;k,l} + I^w_{min;k,l}} \right| \tag{4}$$

where, $I^w_{center;k,l}$ is the grayscale intensity of the center pixel in each block; $I^w_{min;k,l}$ and $I^w_{max;k,l}$ are defined earlier. The size of the blocks in Equations 3 and 4 includes odd kernels (e.g., 3×3, 5×5, 7×7, and 9×9).

The SDME measure is used to quantify adaptive grayscale thresholds for the asphalt concrete X-ray CT images. The algorithm seeks to establish an adaptive aggregate threshold (T_{Agt}) to separate aggregates from non-aggregate objects and another threshold to separate mastic from air objects (T_{Air}). The aggregate grayscale threshold T_{Agt} is related linearly to the SDME measure through:

$$T_{Agt} = M - \alpha(SDME) \tag{5}$$

where, M is the maximum grayscale intensity and α is a constant representing the level of details of interest. For establishing the aggregate-mastic boundary, a seed value of $\alpha = 1$ is used based on preliminary results of image processing. Combining Equations 4 and 5, gives:

$$T_{Agt} = M - \alpha \left[\frac{1}{k_1 k_2} \sum_{l=1}^{k_1} \sum_{k=1}^{k_2} 20 \ln \left| \frac{I^w_{max;k,l} - 2I^w_{center;k,l} + I^w_{min;k,l}}{I^w_{max;k,l} + 2I^w_{center;k,l} + I^w_{min;k,l}} \right| \right] \tag{6}$$

In summary, the AETA algorithm for establishing T_{Agt} involves the following steps:

- Step 1: Analyse the raw X-ray CT asphalt concrete two-dimensional images (i.e., circular slices) one at a time.

- Step 2: Apply the histogram equalization technique to enhance image contrast. This is accomplished through the use of the MATLAB® built-in function called *histeq*.
- Step 3: Apply a median filtering technique with a kernel size of 3×3 to remove image noise.
- Step 4: Compute the SDME value.
- Step 5: Define the level of detail of interest by selecting the α value for the aggregates (a value of 1.0 was selected).
- Step 6: Determine T_{Agt}.
- Step 7: Segment connected and overlapping aggregates.
- Step 8: Finally, generate a binary image by labeling white objects (grayscale of 255) for aggregates and black objects (grayscale of 0) for non-aggregates.

Note that the first 3 steps in the AETA method comprise image pre-processing and are identical to those described in the VTA method. The same procedure can be followed for establishing the air voids-mastic threshold (i.e., T_{Air}). More details on the AETA method were given by Zelelew et al., (2013).

6 RESULTS AND DISCUSSION

The two image processing techniques described above, namely the VTA and the AETA were compared in terms of their ability to realistically capture the microstructure of the nine asphalt concrete cores described under Section 3. This comparison involved both visual means, as well as quantitative means. The latter was based on the accuracy of these two methods in yielding the aggregate gradation obtained through mechanical sieving. The aggregate gradation was estimated from the microstructure using established imaging techniques.

6.1 *Visual comparison*

Although qualitative, visual comparisons of images obtained by the two image techniques presented provide valuable information as to their ability to realistically capture the microstructure of asphalt concretes. Figure 3 gives an example of such compassions for the PFC mixtures obtained with Hard Limestone (HL), Granite (G) and Soft Limestone (SL). Similar sets of images were produced for the CMHB and the Superpave mixtures. These images suggest drastic improvements in clarity between the pre-processed images (i.e., end of step 3) and the finished product for both the VTA and AETA methods. Visual inspection yielded no conclusive results as to the relative quality of these two methods, although the AETA-processed images appear to show aggregates with more naturally-shaped edges. On the other hand, the VTA-produced images appear to show a better separation between aggregates.

6.2 *Quantitative comparison*

The quantitative comparison of the two image processing methods, namely the VTA and the AETA, was carried out with reference to the aggregate gradations obtained through mechanical sieving (Fig. 1). The aggregate gradation of the asphalt mixture X-ray CT images was estimated using a purpose-designed MATLAB® program. This involved the *bwboundaries* and *regionprops* built-in functions. They were used to quantify the aggregate morphological and shape properties, such as the area, equivalent diameter, perimeter, major axis length, minor axis length, and orientation. This paper focuses on aggregate size comparisons only. This was defined as the equivalent diameter of an aggregate. These calculations were performed by considering all possible vertical slices by rotating the axis and averaging the equivalent diameter estimates. These in turn were translated to sieve sizes. Past studies also utilized this approach to estimate aggregate gradations in asphalt concrete images (Masad et al., 1999; Brandes and Hirata 2009; Kutay et al., 2010; and Coenen et al., 2012). The aggregate gradation obtained with the 3D statistic is more representative of the entire volume of the mixtures and therefore it was selected for comparisons with the laboratory-measured gradations.

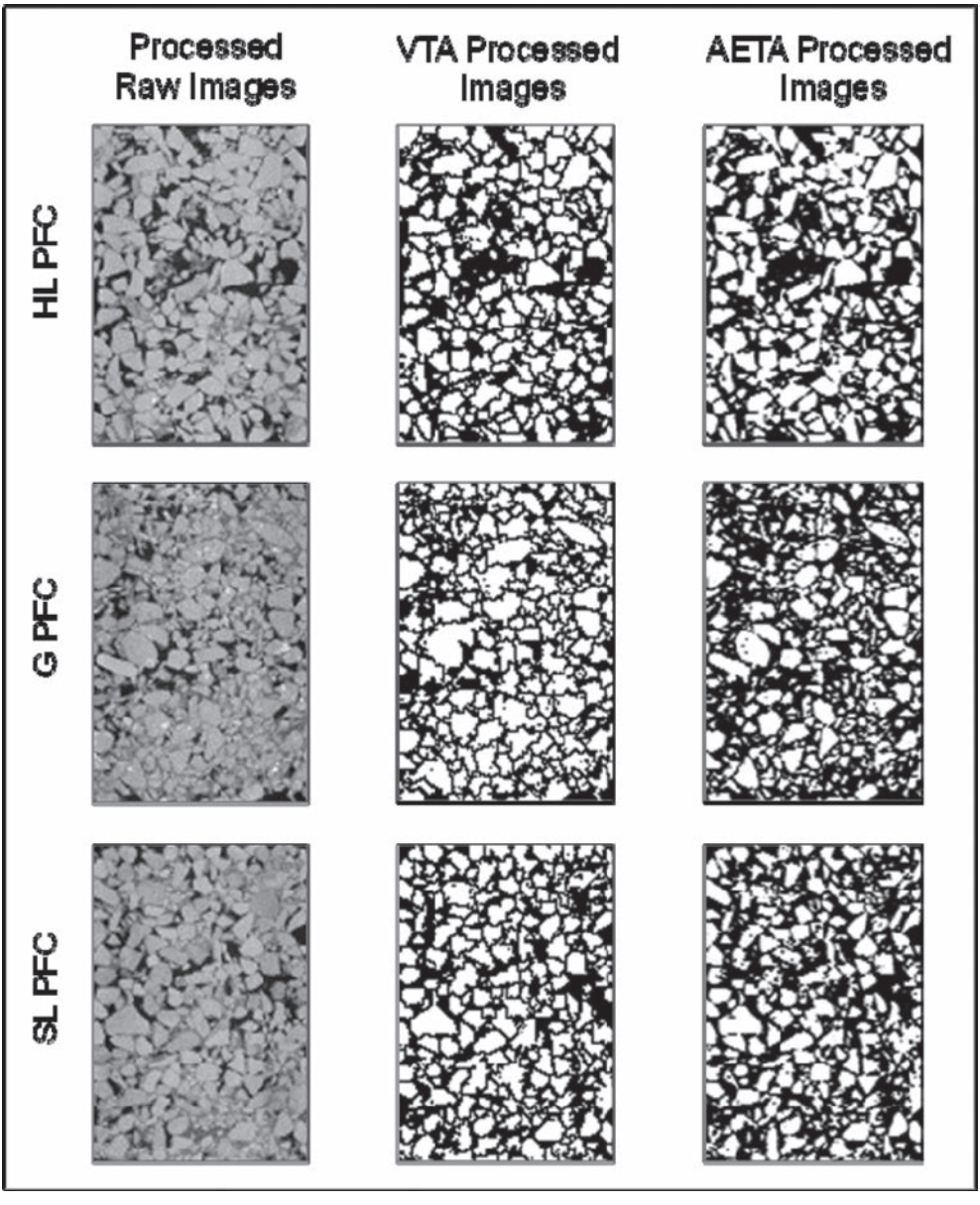

Figure 3. Comparison of VTA and AETA processed images; PFC mix.

An example comparing the image-based aggregate gradations obtained from the VTA and AETA methods versus the laboratory gradation is presented in Figure 4 for the PFC mix. Similar gradation comparisons were obtained for the CMHB, and Superpave mixtures. It is noted that for both the methods the smallest particle size that can be detected given the image resolution is 1.18 mm (i.e., Sieve No. 16). Hence, particle sizes finer than 1.18 mm could not be considered in this comparison.

These estimated gradations were compared in terms of absolute percent error with reference the gradations obtained through mechanical sieving. The results of the percent absolute error for individual particle sizes are shown in Figure 5. The general trend observed is that these errors increase as the particle sizes decrease for the CMHB and PFC mixtures while the

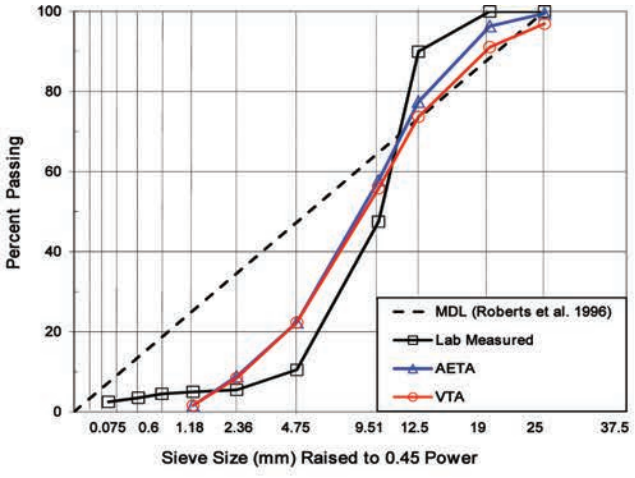

(a)

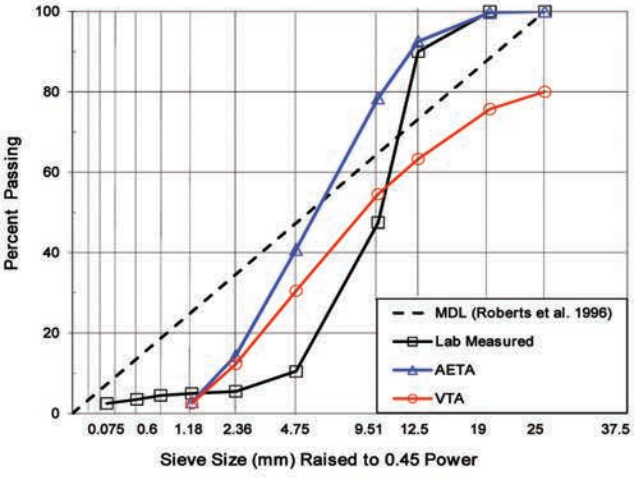

(b)

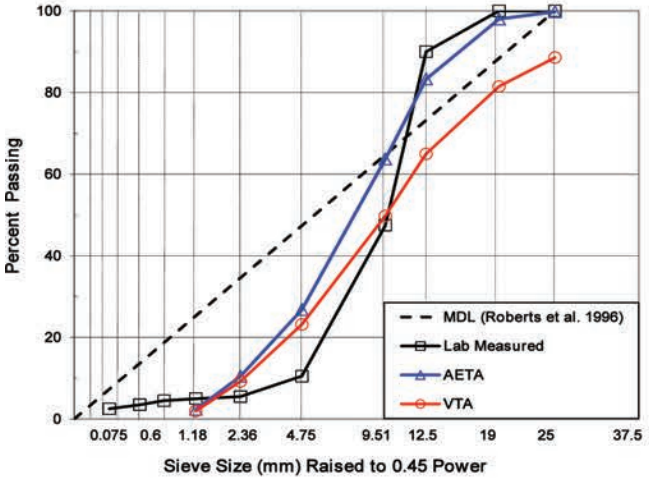

(c)

Figure 4. Comparison of gradations; (a) HL PFC, (b) G PFC, and (c) SL PFC.

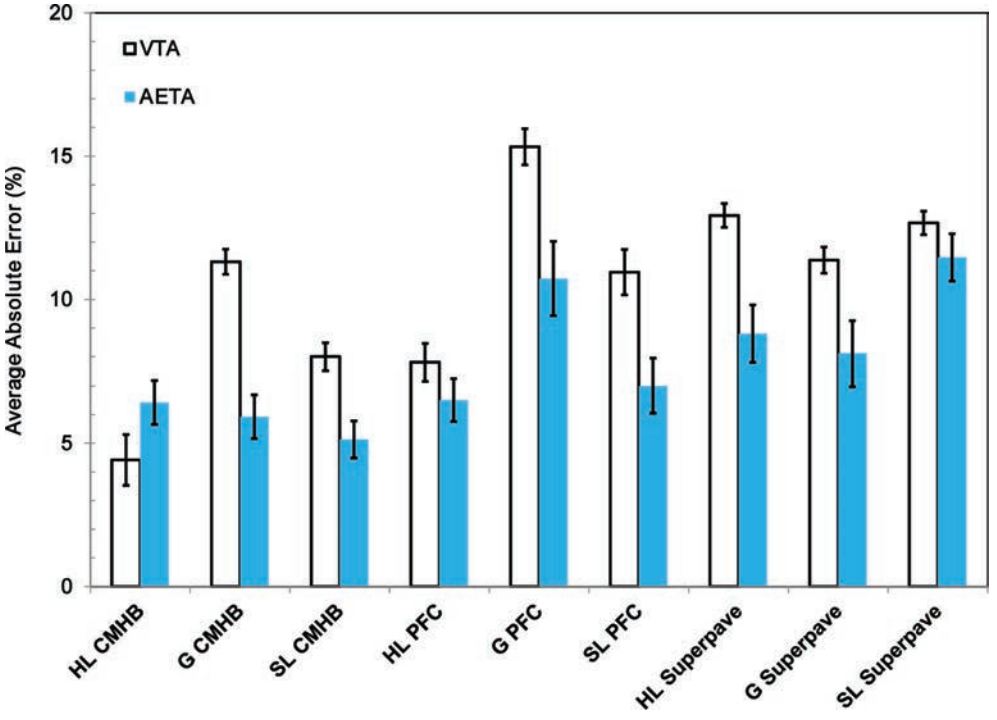

Figure 5. Comparison of gradation average absolute errors.

opposite was observed for the Superpave mixtures. This is likely due to the fine-graded nature of the mixtures. Figure 12 also summarizes the overall average absolute errors for all the samples analysed. The bars shown in this figure reflect the Coefficient of Variation (COV) of these errors. The average absolute error observed for the PFC mixture with granite aggregate type is substantially higher than those observed for the other mixtures. This is likely due to the large errors observed in multiple sieve sizes as well as the gap-graded nature of the mixture. The overall maximum absolute error observed for both methods among the nine mixtures was not higher than 16%. In general, the AETA method resulted in lower absolute errors when compared to the VTA method. For HL CMHB mix, however, the VTA method measured slightly lower absolute error (6.4%) compared to the AETA method (4.4%).

7 CONCLUSIONS

Based on these findings, it is evident that the AETA method outperforms the VTA method by producing more accurate aggregate gradations and more realistic aggregate shapes. Its disadvantage is that it does not preserve the volumetric properties of the samples. Additional objective comparisons are needed in terms of the ability of these two methods to capture other aggregate properties (e.g., orientation, shape, angularity) before deciding which method is best suited in processing asphalt concrete images.

REFERENCES

[1] Masad, E., Muhunthan, B., Shashidhar, N., and Harman, T. Internal structure characterization of asphalt concrete using image analysis. *Journal of Computing in Civil Engineering,* 13(2), 88–95, 1999.
[2] Shashidhar, N. X-ray tomography of asphalt concrete. Transportation Research Board, Transportation Research Record 1681, 186–192, 1999.

[3] Tashman, L., Masad, E., D'Angelo, J., Bukowski, J., & Harman, T. X-ray tomography to characterize air void distribution in Superpave gyratory compacted specimens. *International Journal of Pavement Engineering,* 3(1), pp. 19–28, 2002.
[4] Al-Omari, A., & Masad, E. Three dimensional simulation of fluid flow in X-ray CT images of porous media. *International Journal for Numerical and Analytical Methods in Geomechanics,* 28, 1327–1360, 2004.
[5] Wang, L., Paul, S., Harman, T., & D'Angelo, J. Characterization of aggregates and asphalt concrete using X-ray computerized tomography: state-of-the-art report. *Journal of the Association of Asphalt Paving Technologists,* 73, 467–500, 2004.
[6] Kutay, E., Aydilek, H., & Masad, E. Estimation of directional permeability of HMA based on numerical simulation of micro-scale water flow. *Transportation Research Board, Transportation Research Record 2001,* 29–36, 2007.
[7] Khan, R., & Collop, A. The Use of x-ray computed tomography to characterize microdamage in asphalt. *Journal of Road Materials and Pavement Design,* 11, Iss. sup 1, 89–109, 2010.
[8] Partl, M., Flisch, A., & Jönsson, M. Comparison of laboratory compaction methods using x-ray computer tomography. *Journal of Road Materials and Pavement Design,* 8(2), 139–164, 2007.
[9] Wu, W., Wang, D., & Zhang, X. Estimating the gradation of asphalt mixtures using x-ray computerized tomography and stereology method. *Journal of Road Materials and Pavement Design,* 12(3), 699–710, 2011.
[10] Zelelew, H., & Papagiannakis, A.T. A Volumetrics thresholding algorithm for processing asphalt concrete X-Ray CT images. *International Journal of Pavement Engineering,* 12(6), 543–551, 2011a.
[11] Zelelew, H., & Papagiannakis, A.T. Wavelet-based characterization of aggregate segregation in asphalt concrete X-ray computed tomography images. *International Journal of Pavement Engineering,* 12(6), 553–559, 2011b.
[12] Zelelew, H., (2008). Simulation of the permanent deformation of asphalt concrete mixtures using discrete element method (DEM). PhD Dissertation, Department of Civil and Environmental Engineering, Washington State University, Pullman, WA, 2008.
[13] Masad, E., (2005). *Aggregate imaging system (AIMS): basics and applications.* Texas Transportation Institute, Report No. FHWA/TX-05/5-1707-01-1, Texas A&M University System College Station, Texas, 2005.
[14] DelMarco, S., & Agaian, S. The design of wavelets for image enhancement and target detection. Mobile Multimedia/Image Processing, Security, and Applications. *Proceedings of the Society of Photo-Optical Instrumentation Engineers (SPIE),* 7351, 1–12, 2009.
[15] Zhou, Y., Panetta, K., & Agaian, S. Human visual system based mammogram enhancement and analysis. *IEEE International Conference on Image Processing Theory Tools and Applications (IPTA2010), Paris, France,* 229–234, 2010.
[16] Brandes, H., & Hirata, J. An automated image analysis procedure to evaluate compacted asphalt sections. *International Journal of Pavement Engineering,* 10(2), 87–100, 2009.
[17] Kutay, E., Arambula, E., Gibson, N., & Youtcheff, J. Three-dimensional image processing methods to identify and characterize aggregates in compacted asphalt mixtures. *International Journal of Pavement Engineering,* 11(6), 511–528, 2010.
[18] Coenen, A., Kutay, E., Sefidmazgi, N., & Bahia, H. Aggregate structure characterization of asphalt mixtures using two-dimensional image analysis. *Journal of Road Materials and Pavement Design,* 13(3), 433–454, 2012.

Long-term pavement performance prediction—I

This page intentionally left blank

Asphalt Pavements – Kim (Ed)
© 2014 Taylor & Francis Group, London, ISBN 978-1-138-02693-3

Effect of saturated ageing on fatigue behavior of asphalt pavements

Abhilash Bommerla & K. Sudhakar Reddy
IIT Kharagpur, Kharagpur, West Bengal, India

ABSTRACT: Top-down cracking is a commonly occurring distress in asphalt concrete pavements. Ageing of binder and effect of moisture, besides traffic loading parameters, contribute significantly to the top-down fatigue cracking of asphalt layers. Experimental investigations were conducted in this study to evaluate the effect of these parameters (ageing and moisture) on the fatigue crack initiation and propagation. Saturated Ageing Tensile Stiffness test (SATS), which is a protocol introduced recently in the European standards, has been used for ageing the asphalt mixtures. The ageing of the asphalt mix has been done for different periods: 25, 45 and 65 hours. Ageing indices of the aged mixes were calculated based on the resilient moduli of un-aged and aged mixes. Indirect Tensile Fatigue Test (ITFT) was conducted on aged and un-aged mixes. Fatigue life (load repetitions to crack initiation) of the mix aged under the combined action of temperature and moisture for 25 hours was found to be 30 percent of that of un-aged mix. Ageing the specimens for longer durations did not significantly reduce the fatigue life any further. Laboratory fatigue performance of mixes has been explained in terms of binder rheology and ageing index of mix.

Keywords: Saturated ageing, SATS test, ageing index, crack initiation, crack propagation

1 INTRODUCTION

Fatigue cracking is one of the major distresses in bituminous pavements. Fatigue cracking is not an instantaneous failure but starts as a micro crack at the top of surface layer (Top–down cracking) or at the bottom of asphalt course (Bottom–up cracking) by the action of traffic loads. With continuation of application of wheel loads the micro-crack slowly increases and intensifies to propagate to the entire depth of asphalt layer.

Ageing of binder and effect of moisture, besides traffic loading parameters, contribute significantly to the top-down fatigue cracking of asphalt layers. Ageing reduces binder's ductile property thereby increasing susceptibility of asphalt mixture to crack [1]. On the other hand moisture reduces the adhesion of the asphalt mastic causing easy propagation of crack [2]. So the combined effect of temperature and moisture on the properties of pavement materials has to be understood.

Research has been conducted in the past to understand the effect of ageing and moisture, individually, on the fatigue behaviour of asphalt pavements. But behaviour of the asphalt mixture subjected to different conditions is different from its behaviour under the combined condition. With the growing importance of perpetual or long life pavements, there is need to understand the combined effect of temperature and moisture on the fatigue behaviour of asphalt pavements. Saturated ageing is the term used to denote the combined effect of moisture and temperature.

Saturated Ageing Tensile Stiffness (SATS) Test [3] was used in this research work for observing the combined effect of moisture and temperature on the asphalt mixtures. SATS test is a new ageing method developed in UK. The test conditions represent the properties of asphalt mixture in field conditions (observed in UK) after 8 years of construction [4] [5].

SATS test includes pre-saturation of asphalt samples before placing them into a moist, high temperature and pressure chamber. As per EN 12697-45:2012, the compacted Marshall samples encased in the test specimen holders are placed in pressure and temperature vessel. Sufficient amount of water is added to completely immerse the bottom asphalt sample. The specimens are maintained at a temperature of 85°C and at a pressure of 2.1 MPa for a period of 65 hours before the temperature is reduced to 30°C. The specimens are maintained at 30°C for 24 hours with the pressure being unchanged.

Evaluation of resilient modulus can capture the change in the viscosity of bitumen caused due to ageing [6] and reduction in adhesion/surface energy of bitumen due to diffusion of water into bitumen mastic at high temperatures [7]. Ageing Index, which is the ratio of resilient modulus of asphalt sample before ageing and that after ageing, is used to determine the degree of saturated ageing.

To determine the combined effect of ageing and moisture, asphalt has to be aged in presence of moisture to different levels before evaluating it for fatigue life and crack propagation characteristics.

Experimental investigations were conducted in this study to evaluate the effect of these parameters (ageing and moisture) on the fatigue crack initiation and propagation. Saturated Ageing Tensile Stiffness test has been used for ageing the asphalt mixtures. Ageing of the asphalt mix has been done for different periods—25, 45 and 65 hours. Ageing indices of the aged mixes were calculated based on the resilient moduli of un-aged and aged mixes. Indirect Tensile Fatigue Test (ITFT) was conducted on aged and un-aged mixes. Fatigue life (load repetitions to crack initiation) of the mix aged under the combined action of temperature and moisture for 25 hours was found to be 30 percent of that of un-aged mix. Ageing the specimens for longer durations did not significantly reduce the fatigue life any further. Laboratory fatigue performance of mixes has been explained in terms of binder rheology and ageing index of mix.

2 MATERIALS

Two surface layer gradations, AC11DS and SMA13 have been chosen for carrying out project work, as the saturated ageing will affect mainly the surface layers. The AC11DS is asphalt concrete surface layer (DS—deckschischt) used in Germany. The second mixture is a Stone Matrix Asphalt layer used in India. The gradations selected are shown in Figure 1.

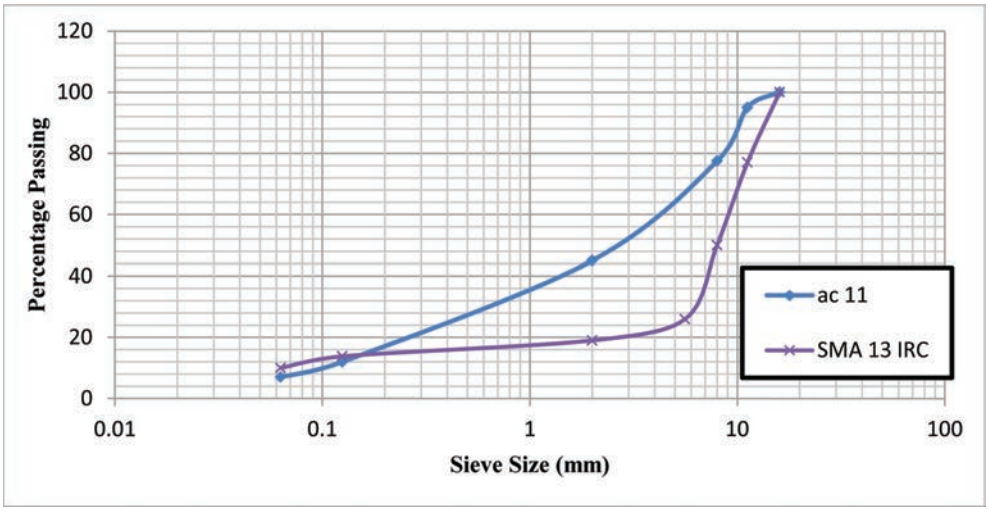

Figure 1. Selected gradations for AC11DS and SMA13.

Table 1. Volumetric properties of AC11DS and SMA13 mixtures.

	AC11DS	SMA13
Bitumen content (%)	5.7	5.7
Bulk density (g/cc)	2.450	2.340
Maximum density (g/cc)	2.526	2.542
Air voids (%)	2.9	8
Voids in mineral aggregate (%)	16.2	19.96
Voids filled with bitumen (%)	81.48	62.42
Bitumen film thickness (μm)	8.26	8.54

Asphalt mixtures are prepared with a bitumen content of 5.7% which is the optimum bitumen content for AC11DS. Table 1 gives the average values of various volumetric parameters. The same bitumen content has been used for both the mixtures. The mixtures developed different VMA and there by different air void content. Average film thickness values, estimated using surface area factors given by Asphalt Institute Manual Series 2, are also given in the table. The film thicknesses obtained for the two mixes are nearly the same.

The effect of saturated ageing on asphalt sample depends on the bitumen content and film thickness, saturated ageing conditions and amount of exposure of bitumen [8] [9]. As same film thickness has been produced by using same bitumen content and similar saturated ageing conditions have been used or both mixes, the degree of saturated ageing in two mixtures shall mainly differ due to the extent of bitumen exposure which depends on the air void content in mixture.

3 EXPERIMENTATION AND RESULTS

3.1 *Indirect tensile strength test*

Indirect Tensile strength test was conducted at 20°C on SMA13 and AC11DS samples before and after saturated ageing. Table 2 shows the values of Ultimate load and deformation, measured during Indirect Tensile Strength (ITS) test. Ageing ratio was also calculated (ageing ratio is the ratio of ultimate load after saturated ageing to that before saturated ageing) as a measure for comparing the change in ITS values with saturated ageing. Ageing ratio values are given in Table 2.

The ultimate tensile load, for both asphalt mixtures (AC11DS and SMA) reduced with ageing period and change is more significant upto 25 hrs of ageing beyond which the ageing ratio did not change appreciably.

3.2 *Resilient modulus test*

Resilient modulus of the asphalt samples has been determined at a temperature of 20°C before and after saturated ageing. Table 3 shows the average resilient modulus values obtained for each ageing period. Values of ageing index, ratio of resilient modulus before and after saturated ageing are given in the table.

3.3 *Indirect tensile fatigue test*

The fatigue testing on asphalt sample was conducted using Indirect Tensile Fatigue Testing (ITFT). The test has been conducted at 20°C with a load frequency of 10 Hz and rest period of 0.1 s. Loads of 3000 N and 1500 N were applied for AC11DS and SMA13 respectively. Micro crack and macro crack initiations were identified by plotting load repetitions against product of load repetitions and stiffness [10]. Table 4 gives the number of load repetitions corresponding to micro and macro crack initiation obtained for various periods of ageing for asphalt concrete and SMA mixes.

Table 2. Indirect tensile strength test results.

	Ultimate load (kN)		Deformation (mm)		Ageing ratio	
Ageing period	AC11	SMA	AC11	SMA	AC11	SMA
0 hrs ageing	16.33	11.13	2.6	2.8	1.000	1.000
25 hrs ageing	11.33	7.00	4.1	4.8	0.694	0.629
45 hrs ageing	10.10	5.70	3.1	5.3	0.618	0.512
65 hrs ageing	9.80	5.60	3.3	4.5	0.600	0.503

Table 3. Resilient modulus and ageing index values for AC11DS and SMA13.

	Resilient modulus (MPa)		Ageing index	
Ageing period	AC11	SMA	AC11	SMA
0 hrs ageing	4584	4975	1.000	1.000
25 hrs ageing	3009	1666	0.596	0.291
45 hrs ageing	2833	1187	0.575	0.253
65 hrs ageing	1782	1120	0.472	0.241

Table 4. Number of load repetitions in ITFT for micro and macro-crack initiation.

	Micro-crack initiation		Macro-crack initiation	
Ageing period	AC11	SMA	AC11	SMA
0 hrs ageing	18024	22126	52767	60493
25 hrs ageing	3541	7736	11341	20552
45 hrs ageing	5698	6468	16060	12968
65 hrs ageing	4463	6916	12958	22817

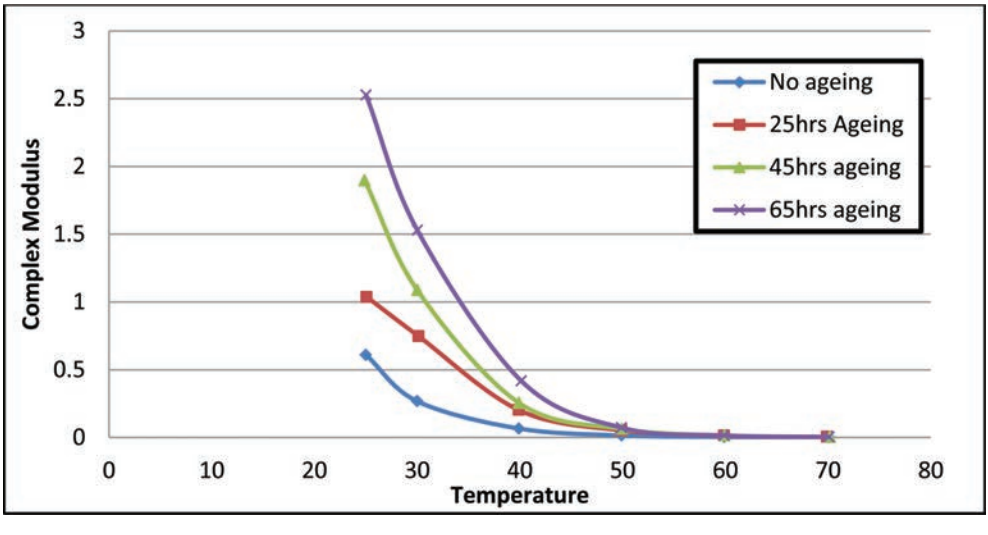

Figure 2. Variation of complex modulus with temperature for AC11DS.

3.4 *Dynamic shear rheometer*

3.4.1 *Stress sweep test*

The stress sweep test was conducted on bitumen sample extracted from asphalt aged for 65, 45 and 25 hours and also on the original binder. The stress sweep test has been conducted to select a single torque value, for all samples, which lie within the linear viscoelastic range of bitumen. A shear stress of 1000 Pa was chosen for the testing for bitumen samples for all degrees of ageing.

3.4.2 *Temperature sweep test*

The temperature sweep test was conducted to understand the behaviour of extracted bitumen sample at various temperatures. The test was conducted on bitumen samples extracted from asphalt mixtures aged to 25 hrs, 45 hrs and 65 hrs. The results were compared with those of original binder. Figures 2 to 4 show the results obtained from temperature sweep tests.

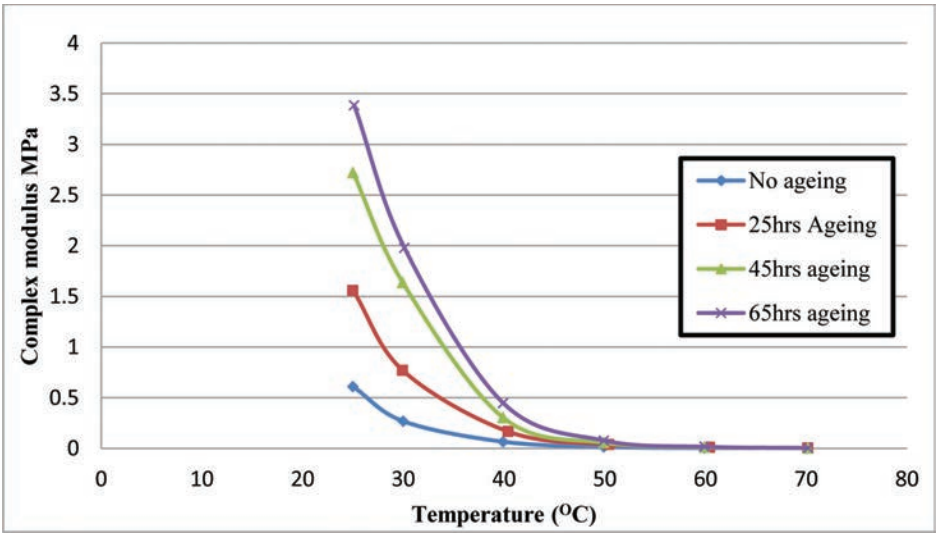

Figure 3. Variation of complex modulus with temperature for SMA13.

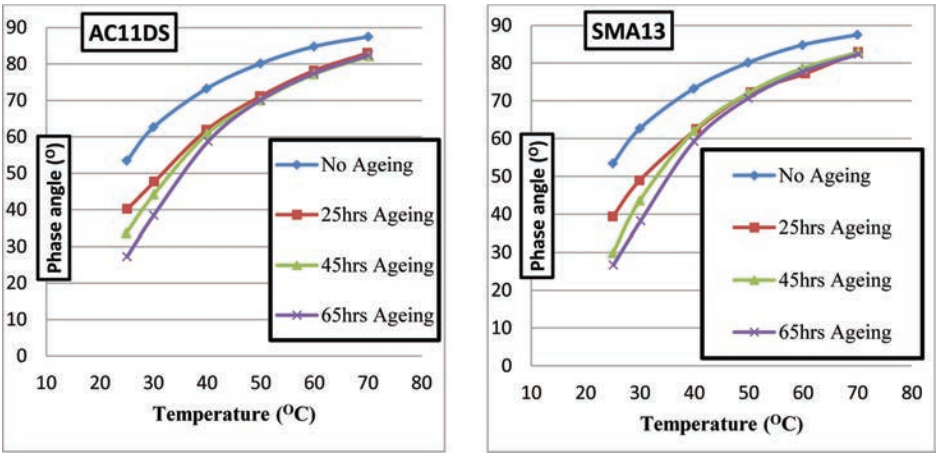

Figure 4. Variation of phase angle with temperature for AC11DS and SMA13 mixes.

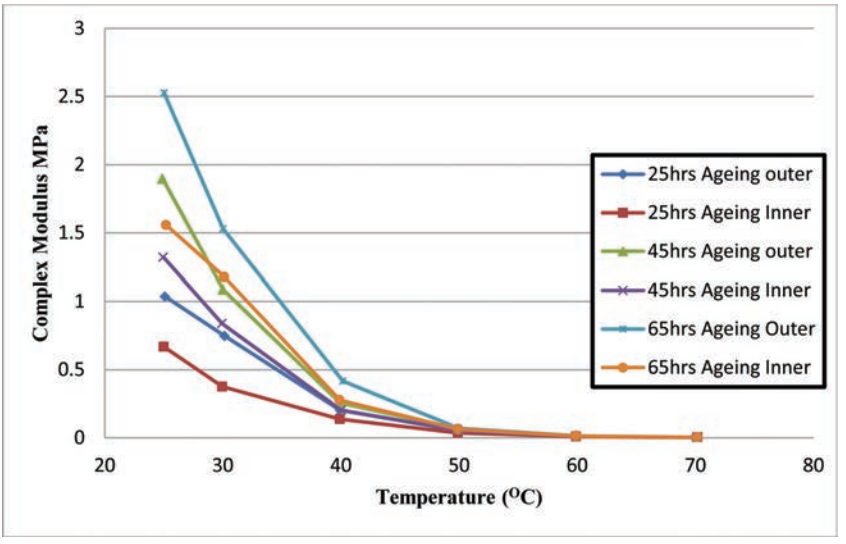

Figure 5. Variation of complex modulus with temperature for inner and outer material.

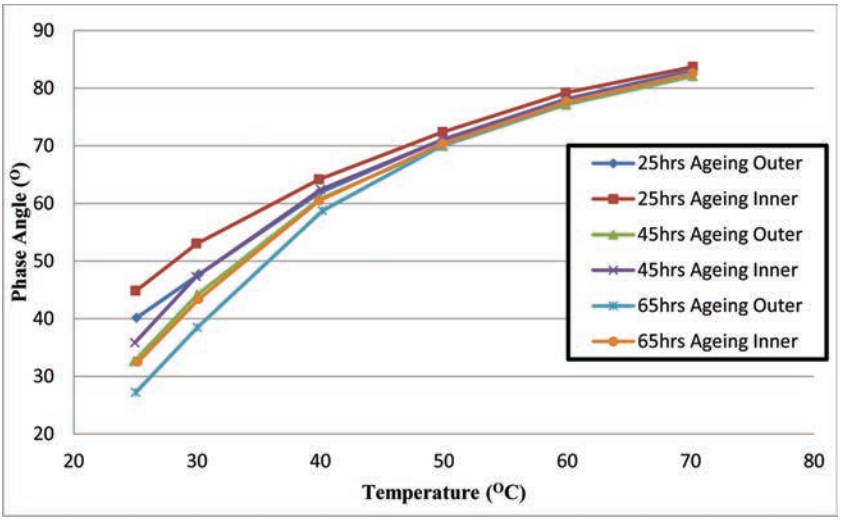

Figure 6. Variation of phase angle with temperature for inner and outer material.

The DSR test has also been conducted on the bitumen samples extracted separately from the outer shell and inner core of asphalt sample. Figures 5 and 6 shows the difference in the degree of ageing of outer and inner samples.

4 DISCUSSION OF RESULTS

4.1 *Indirect tensile strength*

Indirect tensile strength of asphalt mixture or more specifically that of asphalt mastic reduced with increase in the saturated ageing period. The effect of temperature and moisture is more

during the first 25 hrs of ageing after which the effect is reduced. While the binder and as a result of which the mix get stiffer with aging, moisture which leads to loss of adhesion of mastic appears to be more predominant in reducing the ultimate load of asphalt sample, as it reduces the adhesion of asphalt mastic. Katware [11] did not find much variation of tensile strength of asphalt mixtures after dry ageing.

4.2 *Resilient modulus test*

As the exposure of binder to air in SMA mix is more than that expected in AC11DS mix, lower ageing index values were observed for SMA, which indicates greater damage in SMA samples compared to AC11DS mix. It can be understood by the results that air void content has an important role in durability of asphalt mixture. Also after 65 hours of ageing, both the mixtures have very low ageing index values suggesting that the standard test condition of 65 hours of saturated ageing is too severe.

4.3 *Temperature sweep test*

Change in phase angle values represents inter-conversion of viscous and elastic components in the bitumen. The DSR results indicate that with 25-hr ageing most of the viscous component has converted to elastic component. With 45-hr and 65-hr ageing there is not much additional conversion into elastic component. As the phase angle values for AC11DS and SMA13 are similar, it can be concluded that the transition of viscous component to elastic component is influenced by period of ageing rather than exposure of bitumen (air voids).

The complex modulus of the bitumen extracted from SMA13 is more than that obtained for AC11DS extracted binder. This increase in complex modulus is mainly due to the change in exposure. Comparison of the DSR parameters of inner and outer shells of specimens shows that the inner part of the asphalt is ageing at a lower rate than the outer shell.

4.4 *Indirect tensile fatigue test*

The load repetitions for micro as well as macro crack initiation decreased with ageing period. Like other mix parameters, reduction in fatigue life was significant up to 25 hours of ageing. Eq.1 gives the relation between the number of load repetitions to macro-crack initiation and ageing index, G*Cosδ of binder.

$$N = 73636AI + 0.003407\mathrm{G}' + 2.529N_0 - 163091 \tag{1}$$

Table 5. Models for estimation of dL/dN.

Asphalt mixture	Ageing period (hrs)	dL/dN
AC11DS	0	$9.98 \times 10^{-22} * e^{\left(\frac{N}{1973.45}\right)}$
	25	$5.59 \times 10^{-11} * e^{\left(\frac{N}{1613.45}\right)}$
	45	$1.22 \times 10^{-10} * e^{\left(\frac{N}{2800.23}\right)}$
	65	$5.32 \times 10^{-10} * e^{\left(\frac{N}{2537.06}\right)}$
SMA13	0	$2.39 \times 10^{-18} * e^{\left(\frac{N}{3225.97}\right)}$
	25	$1.06 \times 10^{-09} * e^{\left(\frac{N}{5629.08}\right)}$
	45	$1.67 \times 10^{-09} * e^{\left(\frac{N}{2136.48}\right)}$
	65	$1.06 \times 10^{-09} * e^{\left(\frac{N}{10205.22}\right)}$

where, N—number of load repetitions to produce macro-crack after ageing
AI—Ageing Index
G'—G^*Cosδ value of binder after ageing
N_0—Number of load repetitions to produce macro-crack before ageing.

The relationship between compliance (inverse of stiffness) and load repetitions was examined. The rate of change of compliance with number of load repetitions (dL/dN) has been determined and models for estimating dL/dN are given in Table 5.

5 CONCLUSIONS

The effect of saturated ageing on bituminous mixes has been evaluated in this investigation by conducting different tests on two different mixes. The following conclusions are drawn.

- Moisture ageing is found to have similar effect on indirect tensile strength, resilient modulus and fatigue characteristics of the bituminous mixes investigated
- The reduction in strength of the mix with moisture ageing has been found to be significant only up to 25 hours of ageing. This suggests that the 65 hour of ageing period considered in the recently introduced saturated ageing tensile test may be unduly severe
- The reduction in indirect tensile strength of the mix due to 25 hours of moisture ageing is about 31 to 37% while the resilient modulus reduced by 40% and 71% respectively for AC11 and SMA mixes for similar period of aging
- The number of load repetitions required to initiate micro as well as macro cracks reduced by 65% for SMA mix and 80% for AC11 mix
- As in-service mix is subjected to ageing not exactly under dry conditions, moisture ageing represents more realistically the damage that is likely to be caused to the mix in an in-service pavement.

REFERENCES

[1] Chen, J.S.; Huang, L.S. Developing An Ageing Model To Evaluate Engineering Properties Of Asphalt Paveing Binders. Materials And Structures, Vol.33, P. 559–565, 2000.
[2] Kim, Y.; Little, D.N.; Lytton, R.L. Effect Of Moisture On Material Properties And Fatigue Resistance Of Asphalt Mixtures. Transport Research Record, V. 1891, P. 48–54, 2004.
[3] Din En 12697–45 Saturated Ageing Tensile Stiffness (Sats) Conditioning Test, 2012.
[4] Collop. A.C; Choi. Y; Airey. G.P. Efffect Of Pressure And Ageing In Sats Test. Journal Of Transportation Engineering, Asce, P. Vol-133, 618–624, 2007.
[5] Collop. C.A; Choi. Y.C; Airey. G.P. Development Of Sats Test. Institute Civil Engineers Transportation, 157(3), P. 163–171, 2004.
[6] Xiaoge, T.; Jianlong, Z.; Qisen, Z. Effect Of Ageing On Viscoelastic Performance Of Asphalt Binder. Proceedings Of The 23rd Southern African Transport Conference. Pretoria, South Africa: [S.N.]. 2004. P. 226–232.
[7] Cheng, D.X. Et Al. Moisture Damage Evaluation Of Apshalt Mixtures By Considering Both Moisture Diffusion And Repeated Load Conditions. Transportation Research Record, V. 1832, P. 42–49, 2003.
[8] Lu, X.; Isacsson, U. Effect Of Ageing On Bitumen Chemistry And Rheology. Construction And Building Materials 16, P. 15–22, 2002.
[9] Majidzadeh, K.; Brovold, F.N. State Of The Art: Effect Of Water On Bitumen-Aggregate Mixtures. Washington D.C. 1968.
[10] Hopman, P.; Kunst, P.; Pronk, A. A Renewed Interpretation Model For Fatigue Measurement. Verification Of Miner's Rule, 4th Eurobitume Symposium, Vol: 1. Madrid: [S.N.]. 1989. P. 557–561.
[11] Katware, A.V. Evaluation Of Effect Of Ageing On Fatigue Characteristics Of Bituminous Mixes. Iit Kharagpur. 2012.

Asphalt Pavements – Kim (Ed)
© 2014 Taylor & Francis Group, London, ISBN 978-1-138-02693-3

Military pavement subgrade problems

Raymond Rollings
Rollings Consulting, LLC, Beaufort, SC, USA

Nathaniel Rollings
U.S. Military Academy, West Point, NY, USA

Marian Rollings
Rollings Consulting, LLC, Beaufort, SC, USA

ABSTRACT: The subgrade is a major factor in structural design of flexible asphalt pavements. Although this is well understood, problems continue to occur on military pavements where designers have failed to properly deal with subgrade issues. Invariably, poor pavement performance results. This paper will examine six issues encountered with subgrades for military pavements and provide a brief case study illustrating the problem. The topics will be:

1. Assessment of geologic conditions. A runway and parallel taxiway suffered major structural failures because of misreading geology of the subgrade deposits.
2. Proper sampling and testing. A major military road system failed dramatically because the subgrade was improperly characterized by unrepresentative sampling and engineers failed to properly interpret laboratory tests.
3. Expansive soils. These are among the most difficult subgrade conditions with which we must deal, and an airfield taxiway failed because of incorrect testing, improper QC and QA processes, and construction failure.
4. Mitigation of sulfate attack. Techniques commonly used to deal with sulfate attack on concrete prove unable to prevent similar chemical attack on stabilized soils.
5. Permafrost. Pavement construction on permafrost is difficult and expensive. Attempts to shortcut these expensive requirements have led to unfortunate outcomes.
6. Tropical soils with allophane and halloysite clay minerals. Failure to recognize the unique characteristics of these soils has led to difficulties in the field.

Keywords: Subgrade, geology, expansive soil, soil strength, permafrost, tropical soil

1 INTRODUCTION

In recent years there has been an outburst of renewed interest in long-life or perpetual pavement concepts. However, such promising new concepts will reach fruition only when every aspect of the pavement is properly assessed, including the most basic one: the subgrade.

The strength of the subgrade dominates the thickness design of flexible airfields and particularly of military airfields with their large aircraft wheel loads and high tire pressure [1, 2, 3]. Regardless of the specific methodology used for thickness design, selection of the appropriate design strength is crucial to achieving a satisfactory result. However, many factors are involved in selecting appropriate strength values for design, and factors other than strength may determine success or failure of a pavement under traffic.

This paper will examine six specific areas where both government and civilian designers failed to adequately understand the subgrade soils in the design of flexible military pavements, and the consequences of these misunderstandings led to pavement failure.

2 GEOLOGY: MASIRAH AIR BASE (AB) RUNWAY AND TAXIWAY, OMAN

Past masters of the art of geotechnical engineering such as Terzaghi, Peck, and Casagrande often wrote of the importance of geology in geotechnical engineering, and such views are often quoted in textbooks and other professional literature. Yet in reviewing military pavement design documents, one often sees no mention of geology of a site, or if mentioned, it is simply a verbatim quote from a geologic survey with no interpretation as to what the geology means to the project site and design. Geology provides the framework upon which we hang our other data such as borings, testing results, and field observations to help us grasp the range of soil problems that must be addressed in design. Bad assumptions concerning the site geology tend to come back to haunt the designer.

Masirah Island lies in the Arabian Sea off the coast of Oman; it is remote and arid with an average annual rainfall of 100 mm. The island consists of a core of eroded hills rising to a maximum of 256 m surrounded by broad plains cut by wadis. In 1982–1983, the existing small Masirah AB was expanded to include a new runway and taxiway designed to meet U.S. Air Force (USAF) requirements for a medium load airfield capable of supporting major logistical missions. The design was by a U.S. engineering firm in the Midwest, and construction was by a U.S.-Omani joint venture. By the early 1990s the southern portions of the runway and taxiway had suffered massive rutting and surface distortions and were closed to USAF missions until the runway and taxiway were completely rebuilt in 2002 by a USAF RED HORSE engineering squadron. Normally, a flexible airfield pavement designed for USAF missions will require a resurfacing at approximately 15 to 20 years because of weathering and environmental damage to the asphalt binder, but the structural cross section will normally last 35, 40, or more years before reconstruction is needed. In the case of Masirah AB complete structural failure occurred in only ten years.

The original pavement design called for the in-situ gravelly residual soil to be excavated to the weathered igneous bedrock upon which the runway and taxiway pavement structure would be founded. The designer's borings suggested the existing residual soil varied from a few centimetres to over a meter thick and typically classified as GM or SM silty, gravelly, sandy soils. The design runway and taxiway pavement cross-section consisted of

- 100 mm asphalt concrete—75-blow Marshall mix design for airfields
- 150 mm base course—crushed limestone, California Bearing Ratio (CBR) 100
- 200 mm subbase—processed local GM residual soil, CBR 50
- Select fill subbase—if needed, processed local GM, SM residual soil, CBR 20
- Subgrade—weathered igneous bedrock, CBR 20 (assumed value of CBR).

Construction of the pavement proceeded without major incident except for periodic disputes between the contractor and the government representatives over "excessive" excavation depths to the weathered rock when removing the residual soil.

Unfortunately, the southern portion of the runway and taxiway that failed did not lie on residual soils and weathered rock as assumed by the designer. Instead they were located on a playa or dry desert lake bed. Post-failure borings in this area to a depth of 8 m found lacustrine deposits of silts and clay and a high water table only 100 mm or so below the ground surface. The design CBR for these lacustrine materials for the reconstructed pavement was 5, not the 20 used in the original design calculations.

There were ample warnings available at the time of design and construction:

- Observation of the site shows it is a closed basin warning that playa deposits may exist.
- Local on-base records reveal that periodically since the 1930s the area flooded following rains.
- Twice during construction the site was flooded by rain. The designer was flown to the site, but upon examining the situation, determined that such rare "acts of God" in such an arid environment did not require any adjustment in the design. The southern end of the runway and taxiway would also be closed several times after construction by flooding.

– The original borings used for the design have not been located, and one must wonder how the stratigraphy could be misinterpreted. Perhaps there were no borings taken in this portion of the airfield, but this would be most irregular.
– Finally, observations in the field should have quickly revealed to the contractor, the contractor's quality control inspectors, and the government quality assurance staff that the subgrade below the southern portions of the runway and taxiway were silts and clays with a high water table and not the specified weathered bedrock.

A simple understanding of desert geology and local observations and interpretation of the terrain would have warned of the danger of weak soils in the area, and there were ample opportunities for this fact to become known during design and construction.

3 TESTING: FT. LEONARD WOOD ROAD AND PARKING COMPLEX, MISSOURRI

Ft Leonard Wood was selected to be the Department of Defence (DOD) centralized training site for truck and similar heavy equipment operators as part of a Base Realignment and Closure (BRAC) program. New pavements for the mission required expansion of the motor pool to accommodate 462 additional vehicles ranging from 2-1/2-ton to 14-ton trucks, refuelling vehicles, combat transport vehicles, and tractor trailers, construction of 4 new large vehicle training areas, and an addition to the base road system. The government agency responsible for the project estimated the cost of construction as approximately 20 million dollars, but this was rejected by the BRAC committee in Washington D.C. as excessive. An aggressive redesign of the project was undertaken. A sample of the subgrade soil was obtained, a modified compaction curve and soaked CBR was developed in the laboratory (Fig. 1), a design CBR of 30 was selected from the laboratory data, a sophisticated layered elastic pavement design analysis was conducted, and the final full-depth asphalt concrete

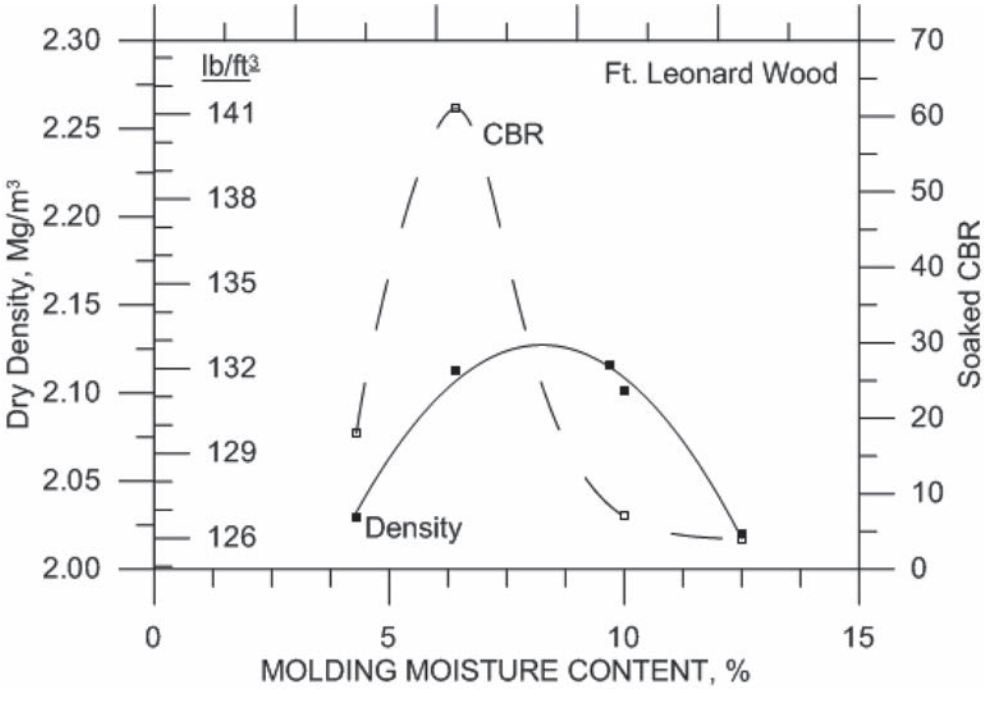

Figure 1. Subgrade compaction and CBR laboratory curves, Ft. Leonard Wood.

pavement for the required facilities cost approximately 14 million dollars. This was viewed by all as a major achievement, and the design was hailed in an industry trade journal as an example of how superior design and use of materials could achieve major cost savings. As soon as the pavements were opened to traffic, they suffered massive shear failures (Fig. 2). Repairs would cost approximately 9 million dollars, and the user's access to the training facilities would be delayed for a year.

Post-failure investigations found the typical subgrade soil CBR was 4 or less, not the 30 that the designer had used. Several elements came together to lead to this design misconception:

- An adequate geologic assessment was not done. The project site subgrade consisted of residual soils developed from weathering of interbedded cherty dolomite and sandstone producing a silty, clayey plastic soil matrix containing chert gravel particles. Such bedrock and weathering conditions do not produce soils with a 30 CBR.
- The U.S. Department of Agriculture (USDA) soil map identifies six soil series in two soil associations occurring as pavement subgrade in different portions of the motor pool, training areas, and road systems for the project area. Five of these six soil series are rated by the USDA as having severe problems when used as foundations for roads because of the clayey nature of the soil.
- A single soil sample is inadequate to assess subgrade conditions for this project, particularly in light of the six different soil series present in the project area.
- The compaction/CBR test series that was run was inadequate for selecting subgrade strength for the one sample that was tested. Military and ASTM guidance requires using three compaction curves of varying compaction energies and details specific methodology to follow to select an appropriate design CBR [1,4,5,6]. These procedures were not followed, and the designer's attempt to estimate an appropriate design CBR from the data was a failure.
- A design CBR of 30 is representative of select subbase material [1, 4, 5]; such a value is almost unheard of for a natural subgrade soil. Laboratory compacted soil specimens with appreciable gravel content give artificially high measurements of CBR because of the confining effects of the compaction mold [1]. For that reason, military pavement design assigns a design CBR to subbase and base course aggregates based on gradation and plasticity characteristics [1, 4, 5]. The tested sample of subgrade soil classified as a GC clayey gravel that failed to meet requirements for a 30 design CBR subbase because of plasticity

Figure 2. Subgrade shear failures, Ft. Leonard Wood.

characteristics and excess fines. Post-failure sampling throughout the project area found that subgrade soils typically classified as gravelly CH clays.

Improper selection of a design subgrade strength in this case was caused by a failure to assess local geologic conditions, inadequate sampling, use of an unrepresentative sample for testing, inadequate laboratory testing, and improper interpretation of test results.

4 EXPANSIVE SOILS: RANDOLPH AIR FORCE BASE (AFB) TAXIWAY, TEXAS

Expansive soils with their volume changes driven by soil moisture changes provide one of the pavement designer's most challenging subgrade soils. The military provides a variety of guidance for the designer [4,5,7,8], but there is no single solution to the problem. The designer must adapt the pavement design to the specific requirements of the site.

A Midwestern A-E firm prepared the design for a new connecting taxiway at Randolph AFB, and a local branch office of the firm had the contract to provide Quality Assurance (QA) services for the Air Force. The subgrade was an expansive, montmorillonite—rich alluvial CH-clay. To deal with the expansive subgrade, the design required the upper 200 mm of subgrade to be lime stabilized and placed and maintained wet of optimum until subsequent layers were placed. This approach has been used successfully for a number of military facilities on expansive clays in Oklahoma and northern Texas. The greatest moisture change under an expanse of airfield pavement occurs in the upper subgrade over the course of 2 to 5 years, and the moisture content then generally stabilizes to an equilibrium that is usually not affected by local environmental variations [1].

The project specifications required the contractor to select and use a stabilization lime content that would reduce the subgrade soil plasticity index to 10 or less. The contractor proposed that the design lime content be selected based on the Eads and Grim pH test [9] in accordance with local practice. The designer concurred, and the Eads and Grim test provided a 4% design lime content. Shortly after construction expansion in the subgrade soil damaged the taxiway pavement and required replacement of the pavement. Several factors contributed to this initial failure:

– The Eads and Grim test identifies the lime content at which the maximum pore fluid pH is achieved optimizing the environment for stabilization. However, the Eads and Grim Test provides no information on actual engineering properties that might be achieved, it underestimates the lime content for some soils, especially for tropical and subtropical weathered soils, and leaching has been a problem for the Eads and Grim predicted lime contents [9, 10, 11, 12]. The plasticity index is often used as an indicator of a soils swelling potential, but it is not always a failsafe indicator. Post-failure testing by several laboratories found the following typical results for this soil:

Lime, %	PI	Expansion, %	
0	45	12.0	
4	15	8.9	(Eads & Grim test result was 4% lime)
7	13	0.1	
13	12	0.4	(specified PI of ≤10 not met)

At the Eads and Grim lime content of 4%, the subgrade remains highly expansive. A soil that swells 3% in laboratory testing is typically considered expansive in the military guidance, and when appropriately lime stabilized, expansions are typically well below 1%. PI is often used as a surrogate to indicate swell potential which is suitable for many but not all soils. In this case, the PI could not be lowered to the specified 10 or less, but lime stabilization could reduce swell to acceptable levels. Military guidance for stabilization to control swelling soils requires the lime content to be based on actual laboratory swell tests [8].

– During construction, two QC tests were run on the lime-stabilized subgrade. The PI of the stabilized material was 30 and 34; these values are within the range of PI considered to be potentially expansive [7]. Neither the contractor's QC nor the designer's QA program identified that the lime stabilization was ineffective and that potentially expansive material was being placed directly under the pavement structure.
– The specification required the stabilized subgrade to be placed and maintained wet of optimum moisture content. However, the lime-stabilized soil was placed dry of optimum and was allowed to dry out after placement. Expansive soils placed dry of optimum have a fabric more prone to swelling than if placed wet of optimum, and the dry conditions allow an increased amount of water to be absorbed by the stabilized material. Both of these conditions increase the soil's swell potential.

In the end, this failure can be ascribed primarily to selection of too low a lime content through improper testing, failure to place and maintain the stabilized material wet of optimum, and failure of the QC and QA programs to recognize high PI test results that showed the lime stabilization was not effective and swelling was likely.

5 SULFATE ATTACK MITIGATION: TEXAS AND NEW MEXICO AIRFIELDS

Calcium-rich stabilized materials, notably those that contain portland cement or lime, can react with sulfates to form the sulfoaluminate mineral *ettringite* which can result in expansion and damage to pavements [13, 14, 15]. The USAF has had two airfield pavements in Texas and New Mexico damaged by this reaction known as sulfate attack (Fig. 3). Conventional concrete technology has well-established methods of coping with sulfate attack.

For conventional concrete, resistance to sulfate attack is commonly provided by using sulfate-resistant cements (Type II or V) which are lower in alumina content than cnvntional portland cement. Without sufficient alumina in the concrete, ettringite cannot form. However, use of sulfate-resistant cement fails in soil stabilization because the alumina needed for ettringite formation is readily provided by clay minerals in the soil, negating the effect of the low-alumina content sulphate-resistant cement.

Addition of fly ash and slag have been effective in combating sulfate attack in conventional portland-cement concrete where it appears that the fly ash and slag react with free calcium hydroxide to form calcium-silicate-hydrate (C-S-H) that is less vulnerable to sulfate

Figure 3. Swelling from sulfate attack on Type V cement-stabilized subgrade, Holloman AFB.

attack [16]. Class F fly ash has been found generally more effective than Class C fly ash for concrete sulfate resistance, and fly ash contents of at least 25–35% of the cementitious mass are needed for concrete sulfate resistance [16,17]. When calcium based stabilizers such as lime or portland cement are used for soil stabilization, addition of fly ash with the stabilizing agent may perform a similar function and tie up calcium ions that would not then be available to form ettringite. On the other hand, stabilized soils have less cementitious material, are far more permeable, and are weaker than portland-cement concrete which all would enhance vulnerability to sulfate attack. Consequently, the benefits of fly ash or slag for protection against sulfate attack may be less pronounced for stabilized soils compared to conventional concrete.

In 2008, the authors conducted a limited scope laboratory trial to examine the effect of fly ash addition with cement stabilization when exposed to soaking in a sulfate solution. Beams were prepared with a Clayey Sand (SC) soil mixed with 10% Type I/II portland cement and with Class F fly ash replacement levels of 0%, 15%, 30%, and 50% by weight of cementitious material. Samples were cured for 7 days and then placed in a saturated sulfate solution. Specimen expansion and cracking were rapid, and all specimens were badly damaged by the sulfate exposure in one to fourteen days of soaking. Specimens with fly ash deteriorated more quickly than samples without fly ash, and deterioration rate increased as fly ash content increased. This limited study suggests fly ash may not be effective for combating sulfate attack of cement-stabilized soils; however, sulfate attack and the role of fly ash is complex and multi-faceted and the topic needs further exploration.

The NCHRP Recommended Practice for stabilization of sulfate-rich soils [15] noted that research on use of fly ash and slag as potential mitigating measures for sulfate attack on stabilized soils was underway. Some success with use of fly ash to combat sulfate attack on lime stabilized soils had been reported earlier when the fly ash addition was combined with other mitigating methods [18]. Use of slag has also been reported as more effective than fly ash for resisting sulfate attack of cement-stabilized soils [19].

Sulfate attack on stabilized materials remains an unresolved issue, and proven methods of dealing with sulfate attack in conventional concrete are not effective in stabilized materials.

6 PERMAFROST: ARCTIC CONSTRUCTION

The need for military airfields in Alaska, northern Canada, and Greenland during World War II and the ensuing Cold War led to a number of airfield facilities being constructed on permafrost. From experience, it was learned the only effective way to deal with permafrost was to keep the permafrost from melting. Thick layers of non-frost susceptible material were required over the permafrost so the active layer of thawing would never reach the permafrost. It was also learned that maintaining the surface organic layer as an insulator was prudent. If ice-rich permafrost melted large settlements invariably resulted.

Thule Airbase was built in Greenland in 1951 and has undergone various expansions at different times. The thaw depth in unimproved areas at Thule with a mean annual air temperature of −11 °C varies from 1.2 to 2.4 m. Pavement designs at Thule AB initially required a minimum of 2 m of non-frost susceptible fill and base course to minimize any melting of the permafrost. During a 1952 expansion of the runway, this was changed to 1 m as an economy move. There was pronounced subsidence in the thinner sections within a year and several of the older 2-m thick sections also suffered settlement. Further studies found that painting the pavement surface white could reduce surface temperatures about 5 °C and reduced thaw penetration about 0.6 m. Recommended pavement design for future Thule AB pavements was a painted white surface and minimum 2.4-m thick pavement section. This design concept has proven effective in avoiding melting of the permafrost with resulting settlement. It has also apparently led to rise in the permafrost under the runway which served as a dam to subsurface flow and contributed to surface flooding of the airfield in 2002. Use of insulating material has been considered for reducing required thicknesses over the permafrost; however, types of materials that can withstand the structural loads applied by aircraft are limited, and

there have been unresolved issues with icing of insulated pavements compared to adjacent uninsulated pavements that do not ice.

Permafrost subgrades have special requirements. Trying to cut corners to save money leads to trouble, and the complexity of the situation makes solutions difficult and expensive.

7 ALLOPHANE AND HALLOYSITE-RICH TROPICAL SOILS: SOUTH PACIFIC

Residual soils developed from igneous rocks, and particularly volcanic ashes, under tropical weathering and constant high humidity are fine-grained and typically classify as MH soils. These soils exist at very high moisture contents and may contain high amounts of allophane and halloysite clay minerals. Allophane is generally considered an amorphous noncrystalline clay material, but this has been the subject of some debate. Halloysite exists as hydrated and unhydrated forms; there are also intermediate levels of hydration. The hydrated form has a distinct elongate tubular structure that may collapse, split, or unroll on drying and drying is irreversible. The irreversible drying characteristics of allophane—and halloysite-rich soils have a dramatic impact on laboratory test results, design, and construction. A sample of such soils that is oven dried, as is routinely done for laboratory testing, and then has moisture added to the sample for testing will be a completely different material from the sample that is air dried to the same test moisture content. Engineering test results from the two samples will be dramatically different so laboratory testing must replicate field conditions to achieve meaningful results.

A major road was to be built on an island in the South Pacific under a military contract. The subgrade was a halloysite-rich residual soil formed on basalt and classified as an MH soil. The continental-U.S.-based design engineer for the project had soil samples shipped back to a laboratory where they were dried, and laboratory compaction curves were run. Modified maximum laboratory dried density averaged around 1,280 kg/m^3, and optimum moisture content averaged around 34 percent. The designer specified the subgrade and embankments made from the subgrade were to be compacted to 85 percent of the modified density at the optimum moisture condition.

Attempts by the contractor to meet this requirement turned into a fiasco. The soil commonly existed at a moisture content of around 60%, and the annual 3.5 m rainfall without any dry season made drying the soil impossible. Occasionally, the 85 percent maximum density could almost be reached, but then a few more passes of the compaction equipment would see the density plummet. Generally, densities were well below the specified level. The oven dried laboratory samples that formed the basis of the designer's requirements were a different soil from the undried in-situ soil, and the specification requirements were meaningless. In contrast, some years before, another engineer familiar with tropical soils had been retained to oversee construction of an airfield on the same soils. This engineer had used test fills and field measurements to develop workable compaction requirements for the soil at the in-situ moisture contents and to select stable slopes for the embankments. He was working with the actual soil as it existed in the field and not an imaginary soil formed artificially by oven drying.

8 CONCLUSIONS

The subgrade soil is ultimately the foundation upon which all pavements must rest, and the design must recognize all of the strength and performance issues that the subgrade may pose. The Masirah AB and Ft. Leonard Wood examples illustrate how failure to appreciate the impact of geology on soil stratigraphy and properties can be catastrophic. Perhaps Karl Terzaghi expressed the role of geology in engineering best [20]:

> *"The geological origin of a deposit determines both its pattern of stratification and the physical properties of its constituents …Therefore, the knowledge of the relation between physical properties and geological history is of outstanding practical importance."*

For any engineering tests to be meaningful, the sample tested must be representative of the actual subgrade soil. The sample tested for the Ft. Leonard Wood example and upon which the entire design was predicated had strengths much higher than the actual subgrade resulting in immediate failure of the system under traffic. For the test results to be useful, the right tests must be run, they must be run correctly, and the results must be interpreted correctly. These were all contributing factors to the Ft. Leonard Wood, Randolph AFB, and tropical soil failure examples.

We can sample only a miniscule portion of the in-situ subgrade soil, and only when construction has revealed the soil to direct observation are we likely to have a good picture of the real situation. This underscores the importance of QC and QA programs to test and verify actual field conditions and also the crucial importance of the designer observing the site during construction to verify design assumptions are actually met in the field. At Masirah AB, Ft. Leonard Wood, and Randolph AFB expensive and embarrassing failures could have been avoided had information revealed during construction been acted upon.

Soils tend to be variable—there is no one real design strength or stiffness. Instead the designer must select a reasonable value recognizing the range of possible values and impact of future changes in moisture content. The analytical design procedure demands a single precise value; Mother Nature provides a variable. Finally, soils are complex and refuse to obey the assumptions we must make to allow tractable analytical solutions. The examples with expansive soils, sulfate attack, permafrost, and tropical soils illustrate that there are other factors besides subgrade strength that can dominate how well or poorly a pavement may perform.

Pavements can perform no better than their subgrade characteristics will allow; an engineer neglects this fact at his or her peril. Only if the subgrade effects are properly accounted for in design and construction will our concepts for long-life and perpetual pavements become possible.

REFERENCES

[1] R.G. Ahlvin. Origin of Developments for Structural Design of Pavements, Technical Report GL-91-1, USAE Waterways Experiment Station, Vicksburg, MS. 1991.

[2] R.S. Rollings. Evolution of Airfield Design Philosophies, Proceedings of XXII World Road Congress, Permanent International Association of Road Congresses, Durban, South Africa. 2003.

[3] L. Fine. and J. Remington. Chapter XIIX: Airfields for Very Heavy Bombers, The Technical Services, The Corps of Engineers: Construction in the United States, http://publications.usace.army.mil/publications/misc/un20/, Office of the Chief of Military History, U.S. Army, Washington, D.C. 1972.

[4] Department of Defense. Pavement Design for Roads, Streets, Walks, and Open Storage Areas, UFC 3-250-01FA, Washington, D.C. 2004.

[5] Department of Defense. Pavement Design for Airfields, UFC-3-260-02, Washington, D.C. 2001

[6] American Society for Testing and Materials. Standard Test Method for CBR (California Bearing Ratio) of Laboratory-Compacted Soil, ASTM D1883, Philadelphia, PA. 2007.

[7] Department of Defense. Foundations in Expansive Soils, UFC 3-220-07, Washington, D.C. 2004.

[8] Department of Defense. Soil Stabilization for Pavements, UFC 3-250-11, Washington, D.C. 2004.

[9] American Society for Testing and Materials. Standard Test Method for Using pH to Estimate the Soil-Lime Proportion Requirement for Soil Stabilization, ASTM D6276, Philadelphia, PA. 2006.

[10] M.P. Rollings. and R.S. Rollings. Geotechnical Materials in Construction, McGraw-Hill, New York, NY. 1996.

[11] D.N. Little. Handbook for Stabilization of Pavement Subgrades and Base Courses with Lime, The Lime Association of Texas, Austin, TX. 1995.

[12] L. McCallister. and T. Petry. Property Changes in Lime Treated Expansive Clays Under Continuous Leaching, Technical Report Gl-90-17, USAE Waterways Experiment Station, Vicksburg, MS. 1990.

[13] J.K. Mitchell. Practical Problems from Surprising Soil Behavior, Journal of Geotechnical Engineering, American Society of Civil Engineering, New York, NY, 112(3), pp. 259–289. 1986.
[14] R.S. Rollings. J.P. Burkes. and M.P. Rollings. Sulfate Attack on Cement-Stabilized Sand, Journal of Geotechnical and Geoenvironmental Engineering, American Society of Civil Engineers, New York, NY, 125(5), pp. 364–372. 1999.
[15] D. Little. and S. Nair. Recommended Practice for Stabilization of Sulfate Rich Subgrade Soils, NCHRP web-only document 145, National Cooperative Highway Research Program, Washington, D.C. 2009.
[16] M. Thomas. and J. Skalny. Chapter 24: Chemical Resistance of Concrete, Significance of Tests and Properties of Concrete & Concrete-Making Materials, Joseph Lamond and James Pielert editor, ASTM STP 169D, pp. 253–273. 2006.
[17] American Concrete Institute. Guide to Durable Concrete, Committee Report ACI 201.2R-08, Farmington Hills, MI. 2008.
[18] M. McCarthy. L. Csetenyi. A. Sachdeva. and M. Jones. Role of Fly Ash in the Mitigation of Swelling in Lime Stabilized Sulfate Bearing Soils, Proceedings of 2009 World of Coal Ash Conference, http://www.flyash.info/2009/106-mccarthy2009.pdf, Lexington, KY. 2009.
[19] L. Wang. Cementitious Stabilization of Soils in the Presence of Sulfates, PhD dissertation, Department of Civil and Environmental Engineering, Louisiana State University, Baton Rouge, LA. 2002.
[20] K. Terzaghi. Influence of Geological Factors in the Engineering Properties of Sediments, Economic Geology, Fiftieth Anniversary Volume, Society of Economic Geologists, Littleton, CO, pp. 557–618. 1955.

Asphalt Pavements – Kim (Ed)
© 2014 Taylor & Francis Group, London, ISBN 978-1-138-02693-3

Influence of moisture on Resilient Deformation behaviour of Unbound Granular Materials

Mohammad Shafiqur Rahman
Swedish National Road and Transport Research Institute, VTI, Linköping, Sweden
KTH Royal Institute of Technology, Stockholm, Sweden

Sigurdur Erlingsson
Swedish National Road and Transport Research Institute, VTI, Linköping, Sweden
University of Iceland, Reykjavik, Iceland

ABSTRACT: This study investigated the influence of moisture on the Resilient Deformation (RD) properties of Unbound Granular Materials (UGMs). A typical UGM used in pavement constructions with three different grain size distributions were tested with a range of moisture contents using Repeated Load Triaxial tests (RLTTs). From the European standard, the procedure for the study of the RD behaviour was used where each stress path is applied for 100 cycles. Additionally, the Multi-Stage (MS) loading procedure for the study of the permanent deformation behaviour were used where each stress path is applied for 10,000 cycles, to compare the results using the two test procedures. Results showed that resilient modulus (M_R) generally decreased with increase in moisture, where the finer grading was more affected. However, for the MS RLTTs, after a large number of load applications, some increase in M_R with increasing moisture was observed. This happened when the moisture content increased up to close to the optimum; above the optimum, M_R always decreased. This may be due to Post-Compaction (PC) aided by moisture in MS RLTTs where a large number of load cycles were applied.

Keywords: Unbound Granular Materials, resilient modulus, moisture, Repeated-Load Triaxial Test

1 INTRODUCTION

In thin flexible pavements, the base and sub-base layers, comprised of Unbound Granular Materials (UGMs), play a vital role in maintaining the structural integrity. The deformation behaviour of UGMs under external loading can be characterized as complex elasto-plastic with a recoverable or Resilient Deformation (RD) part and a small plastic or Permanent Deformation (PD) part [1]. RD of the base layer is associated with fatigue resistance of the asphalt layer while PD is responsible for the development of rutting. Analytical design of flexible pavement structures requires proper understanding and modelling of these deformation properties. Besides stress levels, moisture is considered to be one of the factors that have a substantial impact on the deformation behaviour of UGMs [2–6]. Predictions of variations of these properties with seasonal variation of moisture are therefore essential for a sustainable design approach.

The Repeated-Load Triaxial Test (RLTT) is considered to be the most convenient way of studying the deformation properties of UGMs. The European standard [7] prescribes two different test methods for study of the RD and PD behaviour of UGMs, respectively. The test protocol for study of the RD consists of applying a set of different stress paths for 100 cycles each. On the other hand, the protocol for study of the PD consists of applying a set of different stress paths for 10,000 cycles each. For the both kinds of tests, the standard prescribes two sets of different combinations of stress levels, namely 'High Stress Level' (HSL) and 'Low

Stress Level' (LSL). Since in RD test, only 100 load cycles are applied for each stress path, the accumulated permanent strain and Post-Compaction (PC) in this case are negligible. Thus this test is suitable for the analysis of pure RD behaviour of the material. On the other hand the PD test involves significant amount of PD and PC. The advantage of this latter test is that both RD and PD characteristics can be evaluated from the same test. Further, this test reflects the long term performance of the structure.

The aim of this work was to study the influence of moisture on the RD properties of UGMs. The effect of grain size distribution on the moisture sensitivity and the influence of the number of load cycles (N) and PC were also investigated. For this, RLTTs were performed on a typical UGM used in Swedish pavement construction where the grain size distributions and the moisture contents (w) were altered. Both the RD test and the PD tests were performed and the results were compared to investigate the effect of N and PC.

2 DEFORMATION BEHAVIOUR OF UGMS

In a UGM, the total induced strain due to single load pulse consists of elastic and plastic strains which can be expressed as:

$$\varepsilon_{tot} = \varepsilon_r + \varepsilon_p \tag{1}$$

where, ε_{tot} is the total axial strain, ε_r is the axial elastic strain and ε_p is the axial plastic strain. Usually, the elastic strain consists of the largest part of the total strain with only a small part due to the plastic strain [1]. However, pavements experience a large number of N and plastic strain accumulates ($\hat{\varepsilon}_p$) with N. In a RLTT, the cylindrical specimen is subject to a constant confining pressure, σ_c (constant confining pressure method) and a cyclic deviator stress, σ_d. Thus, the principal stresses acting on the specimen are: $\sigma_1 = \sigma_3 + \sigma_d$ and $\sigma_2 = \sigma_3 = \sigma_c$.

2.1 *Resilient deformation characteristics*

The RD characteristics are quantified using the resilient modulus, M_R which is an estimate of the stiffness modulus of the specimen for rapidly applied loads, calculated as [8]:

$$M_R = \frac{\sigma_d}{\varepsilon_r} \tag{2}$$

where, ε_r is the resilient (recoverable) axial strain, taken after several N, when the deformations have stabilized. M_R is dependent on the state of stress, measured as the sum of the principal stresses, called the bulk stress, $\theta = \sigma_1 + \sigma_2 + \sigma_3$. The variation of M_R with θ can be expressed with the well-known $k - \theta$ model [9–11] in its dimensionless form as:

$$M_R = k_1 p_a \left(\frac{\theta}{p_a} \right)^{k_2} \tag{3}$$

where, k_1 and k_2 are non-dimensional regression parameters and p_a is a reference pressure or atmospheric pressure taken as 100 kPa.

The effect of moisture on M_R can be expressed using the M_R-Moisture model proposed by Andrei [12] which is a slight modification to the current Mechanistic Empirical Pavement Design Guide (MEPDG) model by AASHTO (The American Association of State Highway and Transportation Officials) [13]. This model simplifies the MEPDG model by eliminating density as a variable and using gravimetric moisture content as predictor variable instead of degree of saturation:

$$\log_{10} \frac{M_R}{M_{Ropt}} = \log_{10} a + \frac{\log_{10} b - \log_{10} a}{1 + EXP(\beta + k_w (w - w_{opt}))} \tag{4}$$

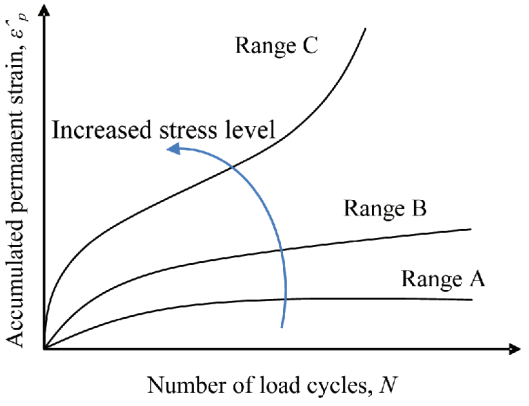

Figure 1. Different types of PD behaviour, depending on stress level [15].

where,

w = gravimetric moisture content expressed as decimal
w_{opt} = gravimetric optimum moisture content expressed as decimal
M_{Ropt} = resilient modulus at optimum moisture content
a = the minimum value of the ratio M_R/M_{Ropt}
b = the maximum value of the ratio M_R/M_{Ropt}
k_w = regression parameter dependent on material properties
and β is expressed as,

$$\beta = \ln_e\left(\frac{-\log_{10}(b)}{\log_{10}(a)}\right) \tag{5}$$

2.2 *Permanent deformation characteristics*

PD in UGMs accumulates with N and its development is very much dependent on the stress level. Werkmeister et al. [14] investigated the development of PD in UGMs using the shakedown concept. For cyclic loading of any constant magnitude, they identified three shakedown ranges for UGMs, shown in Figure 1, depending on the stress level. In shakedown range A (Plastic shakedown), at a relatively low stress level, after a PC period, the material stabilizes and the deformation becomes entirely resilient with no further accumulation of permanent strain. At an increased stress level, range B (Plastic creep) represents an intermediate response where the permanent strain per cycle continuously decreases or becomes constant without complete stabilization. In range C (Incremental collapse), when the stress level is increased even more, the permanent strain rate continues to increase leading to failure. The criteria to calculate the different shakedown ranges from RLTT data can be found in [7, 14].

3 EXPERIMENTAL STUDY

The RLTTs were carried out on cylindrical specimens of 150 mm in diameter and 300 mm in height. The specimens were prepared with target moisture contents and densities applying vibrocompaction. The axial deformations were measured using three Linear Variable Displacement Transducers (LVDTs), 120° apart, anchored to the middle third of the specimen. The loadings used for the tests were haversine pulses with a frequency of 10 Hz with no rest period. The confining pressure was applied through compressed air. Further details of the RLTT setup can be found in Rahman and Erlingsson [4].

The test for resilient modulus at constant confining pressure from the European standard EN-13286-7 [7] with HSL was followed. To minimize experimental scatter and to investigate the influence of moisture on the resilient stiffness, one specimen with a specific grain size distribution and degree of compaction was prepared with the minimum target moisture content. The conditioning from the standard was applied to the specimen. Then the first resilient test was performed. If during the resilient tests, any water drained out through the system, it was measured and the total amount of water required to reach the next target moisture content was added. The drainage was locked and sufficient time was allowed to achieve a uniform moisture distribution. In this way, more resilient tests were performed on the specimen by adding water in steps to achieve the target moisture contents.

For the PD tests, the Multi-Stage (MS) loading method from the European standard with HSL was used. In this case, several specimens identical to that used for the RD tests, with a range of moisture contents were prepared. Then each specimen was tested individually.

The moisture contents were measured after the final RD test with one specimen and after each PD test. The final moisture contents were a little less than the initial due to some losses during the procedure. In this paper, only the target moisture contents have been reported.

4 MATERIAL CHARACTERISTICS

The material used for this study is a crushed rock aggregate, typically used as base course material, obtained from Skärlunda in Sweden. It is characterized as foliated medium-grained granite with quartz, K-feldspars and plagioclase as main constituents [6]. The grain size distributions used were derived using the equation:

$$P = \left(\frac{d}{D_{max}} \right)^{n} \tag{6}$$

where, P is the percentage smaller than sieve size d, D_{max} is the maximum particle size and n is the grading coefficient describing the shape of the curve [16]. For this study, the grain size distributions were altered by varying n, shown in Figure 2. Except for the grading with $n = 0.35$, the other two conforms to the Swedish specifications [17]. The grading with $n = 0.35$ was used to investigate the influence of relatively high amount of fines on the moisture

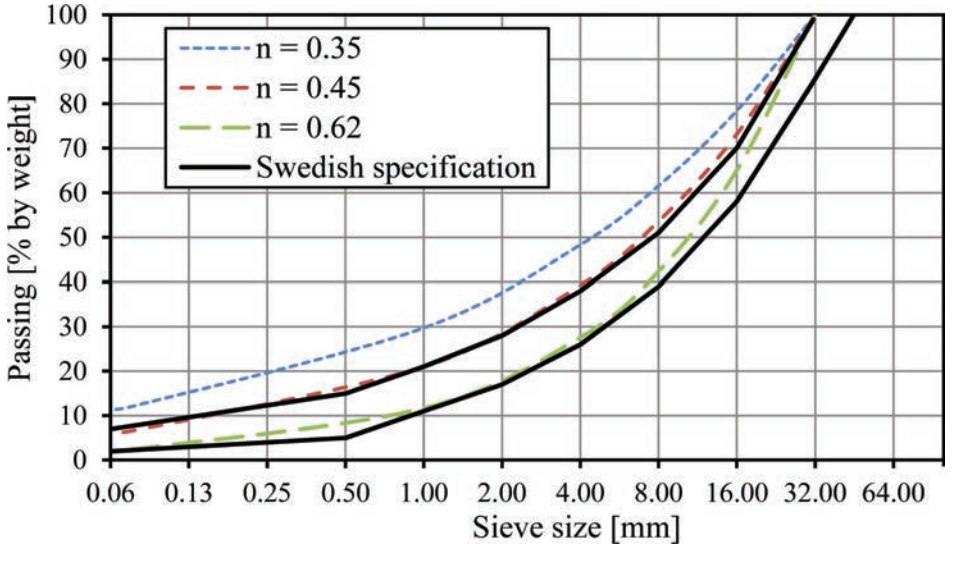

Figure 2. Particle size distributions.

Table 1. Material properties.

Grading coefficient, n	Optimum moisture content (% by weight)	Maximum dry density (g/cm^3)	Fine content (%) (< 0.075 mm)	Specific gravity [–]
0.35	6.5	2.22	12	2.64
0.45	6.0	2.26	6.5	2.64
0.62	5.5	2.11	2	2.64

sensitivity. The maximum particle size used was 31.5 mm. The modified Proctor method according to the European Standard EN 13286-2 [18] was used to determine the optimum moisture contents and the maximum dry densities. The specimens were compacted to 97% of the maximum dry density. Properties of the specimens have been summarized in Table 1.

5 RESULTS

5.1 *Resilient Deformation tests*

The resilient tests were performed with gravimetric moisture contents (w) starting at 1% with an increment of 1% each time up to close to saturation, where it was possible to carry on the tests with sufficient accuracy. For clarity, only a few of the results for $n = 0.35$ are plotted in Figure 3. Results showed that M_R decreased as w increased. The $k - \theta$ model, presented in Equation 3, was fitted to each measurement (with a specific w and n) using the least square curve fitting method. The parameters of the model were optimized employing the Solver add-in in Microsoft Excel. Plots of these parameters as a function of w are shown in Figure 4. It is observed that, the values of the parameter k_1 decreased with increasing w. This decrease was more pronounced for the finer grading indicating greater sensitivity to moisture. On the other hand, the parameter k_2 was less affected by moisture. The values of both the parameters k_1 and k_2 were also influenced by the grading coefficient.

A plot of the resilient moduli (normalized as M_R/M_{Ropt}) as a function of change in w with reference to the optimum is shown in Figure 5. The M_R-moisture model, stated in Equation (4), was calibrated using these data by optimizing the parameters with Solver, in a similar manner as for the $k - \theta$ model. For this, the values of M_R at a typical state of stress $\theta = 550$ kPa were used. These fitted models are also shown in Figure 5. The parameters of the model are presented in Table 2. Visual observation and the coefficient of determination (R^2) values in Table 2 suggest that good quality of fits were obtained with the M_R-moisture model. It is also reflected that the finer grading was more sensitive to moisture variation. From Table 2, it is observed that the values of the parameters a and k_w decreased while b and β increased as the grading went finer (decreasing n).

5.2 *Permanent Deformation tests*

From the PD test data, the M_R values as functions of θ were calculated. It was observed that in the initial stage of the tests, M_R generally decreased when w increased. But in contrast to the RD tests, after a certain N and at higher θ values, M_R started to increase with increase in w for all the cases. This increase was observed for w up to close to w_{opt} and above that, M_R started to decrease again. This behaviour was again more pronounced for the finer gradings. The plots of M_R versus θ for the different moisture contents are shown in Figure 6. For clarity, this is shown only for the grain size distribution with $n = 0.35$. The missing data is due to failure of the specimen having higher w undergoing excessive PD.

The k-θ model was calibrated for these tests and the variations of the parameters k_1 and k_2 with respect to w were plotted in Figure 7. As in the case of RD tests, k_1 was found to decrease with increase in w. On the other hand, in contrast to the RD tests k_2 was not constant. It was found to increase with w up to roughly close to w_{opt} and then it started to decrease. Since

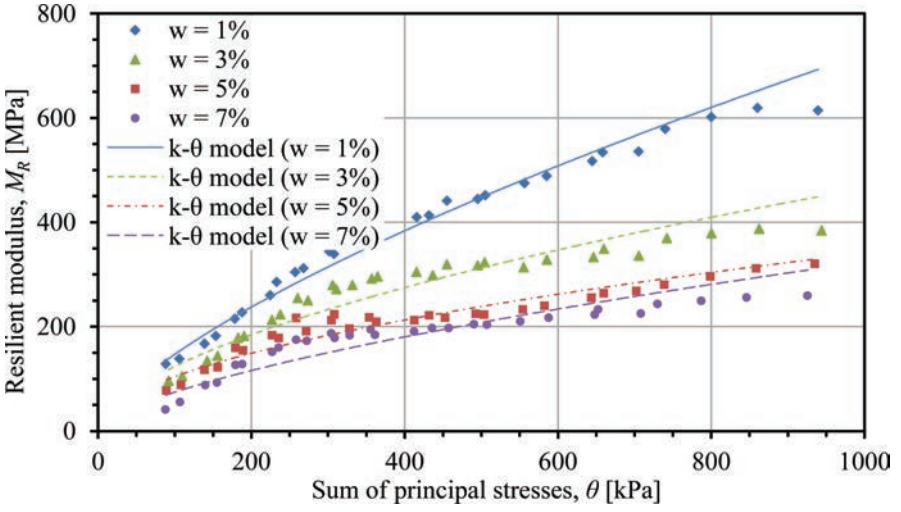

Figure 3. M_R as a function of θ for various moisture contents from RD test ($n = 0.35$).

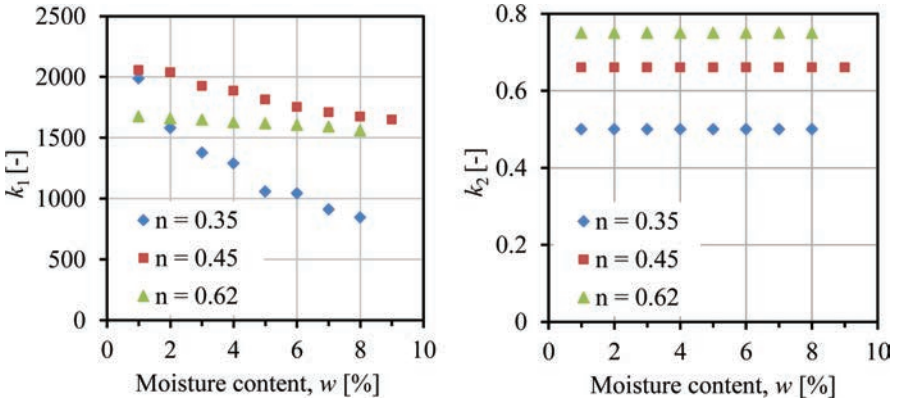

Figure 4. The parameters k_1 and k_2 as a function of moisture content from RD test.

the curves in Figure 6 cross each other, the results from the PD tests did not fit well to the sigmoidal M_R-moisture model, stated in Equation (4) for a reasonable θ value.

This behaviour was further investigated by plotting M_R as a function of N. This was studied for the three different shakedown range conditions, calculated as prescribed by the European standard [7]. An example is shown in Figure 8. The left part of the figure illustrates the accumulation of PD with N and the shakedown ranges for the different stress paths. The right part of the figure illustrates the change in M_R with N for three selected stress paths experiencing the three different shakedown ranges. It was found that when the shakedown range is A or B, M_R remained relatively constant with the number of load applications. But in case of shakedown range C, it increased with N. For the example in Figure 8, this increase was about 11% from 2,000th to 10,000th load cycle. This was the case for all the five C ranges, with different percentages of increase. Similar trend was found by Werkmeister et al. [14]. The explanation may be that M_R increased due to increased degree of compaction arising from PC due to large N. Since the tests were run as long as the materials survived, it may be assumed that any loss in M_R from shear failure did not come into play. Thus all the materials may be considered to be in a stage of PC during the tests. This led to the overall increase of the degree of compaction and M_R of a specimen as the test progressed. With the increase in

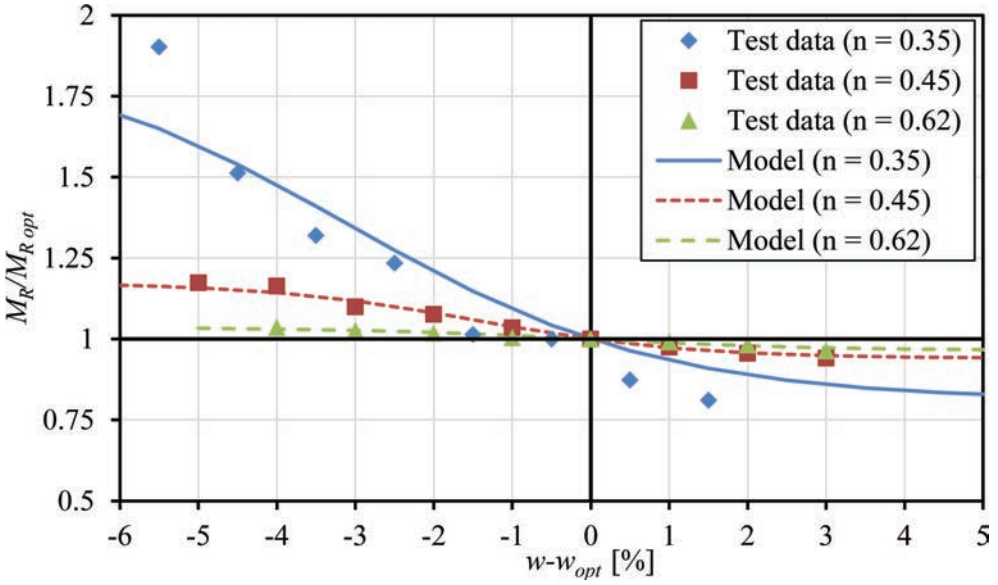

Figure 5. Resilient modulus ratio as a function of moisture content variation (for $\theta = 550$ kPa) from RD test.

Table 2. Parameters of the M_R-moisture model.

	Parameters				
Grading coefficient, n	a	b	β	k_w	R^2
0.35	0.810	1.902	1.118	49.545	0.887
0.45	0.941	1.174	0.961	74.473	0.984
0.62	0.964	1.036	–0.036	84.842	0.955

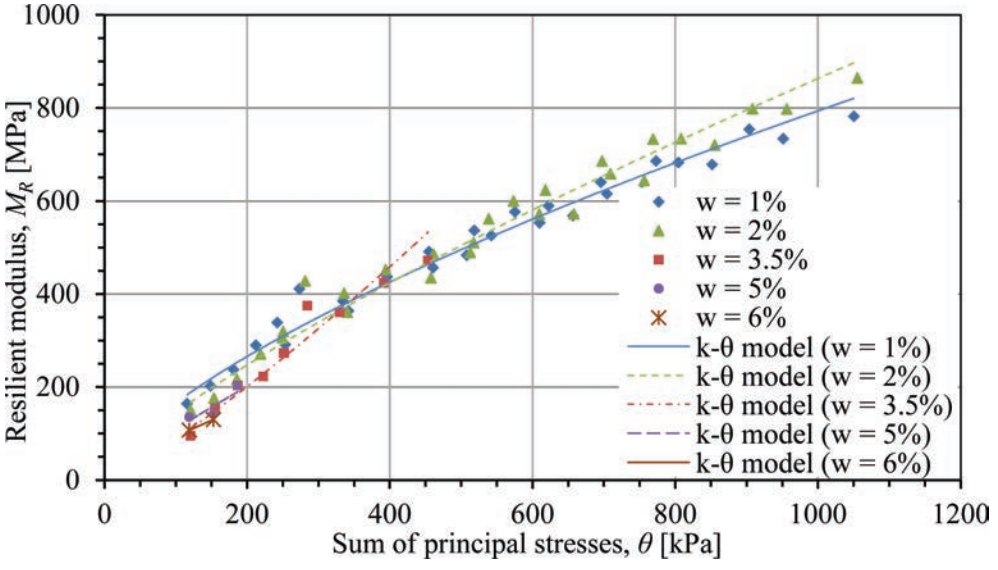

Figure 6. M_R as a function of θ at various moisture contents from PD test ($n = 0.35$).

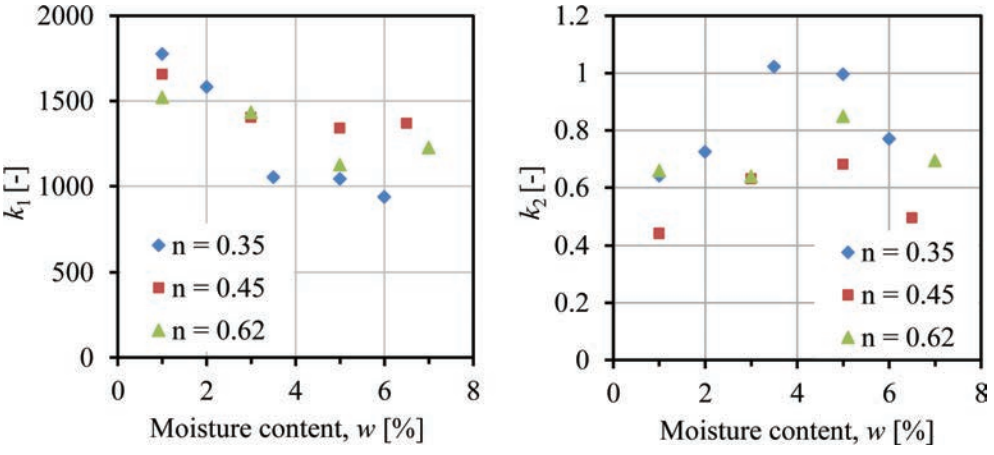

Figure 7. The parameters k_1 and k_2 as a function of moisture content from PD test.

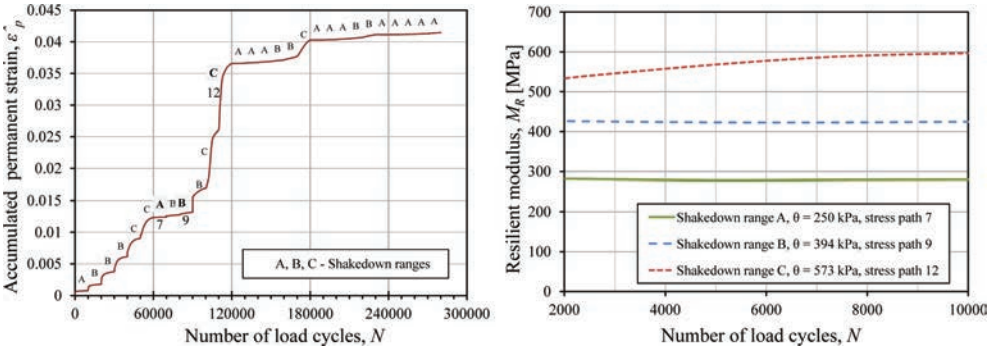

Figure 8. Evolution of M_R with N and PD for different shakedown ranges ($n = 0.35$, $w = 2\%$).

moisture, accumulation of PD increases [19] resulting in increased PC. Since it was easier for the specimen to achieve PC when it had higher w, its M_R increased earlier than the materials with lower w. Close to the optimum, the degree of PC was the maximum and the material reached the maximum dry density. After that this effect started to minimize. This resulted in the increase in M_R with w up to w_{opt} for the PD tests. Regarding the $k - \theta$ model, since it was found that k_2 increased with w for the PD tests, this implies that k_2 is dependent on accumulated PD and PC. Thus k_2 may be considered to be constant when the number of load applications are relatively low and when the accumulated PD and PC are negligible. But for higher N, resulting in considerable PD and PC, k_2 may be increasing up to a certain limit.

6 DISCUSSIONS

It was found from this study that moisture has a negative impact on pure resilient behaviour of UGMs. However, when RD is accompanied by significant amount of accumulation of PD due to PC, this may lead to some increase in M_R with w, depending on the degree of PC. The increase in stiffness was observed for shakedown range C. Since shakedown range C should not be permitted to occur in a well-designed pavement [14], the apparent increase in M_R may not be of practical benefit because the pavement then experiences a large amount of PD.

The PD tests were carried out using HSL from the European standard [7] which gave rise to many stress paths with shakedown range C. This increased the M_R with N. If LSL was

used, there would have been fewer stress paths with shakedown range C. In that case, the results from the RD and PD tests might have been more similar. Again, M_R should decrease if shearing of the specimen occurs. These need further investigation.

The results presented here were based on RLTTs where the variables are better controlled compared to field conditions. In reality there are many factors that may influence the results. For example, the UGMs may lose confinement with time and the grading may change due to crushing of the particles. Results from field studies by Salour and Erlingsson [20] using Falling Weight Deflectometer (FWD) showed that M_R decreased with increase in moisture. Thus this reflected similar results using the RD tests. The reasons may be that the FWD generally applies a limited number of N which is very similar to RD tests where the pure resilient behaviour is analysed. In the study by Salour and Erlingsson, the pavement section was open to traffic which might have led to some amount of PC, but might not have been significant enough to cause any increase in M_R. Generally, the stress levels prescribed by the European standard are relatively high, designed to test the material under a broad range of stress conditions. All of these stress paths may not be experienced by the UGM in reality.

The advantage of the PD test protocol is that it is possible to achieve information on both the PD and RD properties of UGMs from the same test, saving time and effort. This is also closer to reality and an indicator of long term performance of the material. The M_R obtained using this test reflects on its variation with load applications. However, the practical applicability of the value of M_R obtained using the PD test needs to be investigated.

7 CONCLUSIONS

This study was carried out to investigate the influence of moisture on the deformation behaviour of UGMs and the effect of grain size distribution, N and PC on the moisture sensitivity. It was based on RLTTs on a typical Swedish UGM with three different grain size distributions. From this study, the following were observed:

- M_R of the UGMs decreased with increasing w when the deformation was purely resilient with the degree of compaction remaining relatively constant, as in the case of RD tests. M_R increased with increase in w when there was significant amount of PC aided by moisture. This generally happened for the PD tests.
- UGMs with finer grading were more sensitive to variation in w.
- In all the cases, the parameter k_1 of the $k - \theta$ model decreased with increasing moisture. This was more pronounced for finer grading.
- The parameter k_2 was relatively insensitive to moisture for the RD tests with negligible PC. But it increased with moisture in the PD tests. Thus k_2 was found to be dependent on the accumulated PD and PC since these increase with increased moisture.
- The M_R-Moisture model yielded reasonable fit to the data from the RD tests. In that case, the parameters of the model were influenced by the grain size distribution. This model did not fit well to the PD test data.
- In shakedown range A and B, M_R remained constant with N. But in shakedown range C, M_R was found to increase with N.

Since the M_R-moisture model, stated in Equation (4) did not work for the PD tests, it may need to be improved to consider the effect of PC. However, this study was carried out only on one crushed rock aggregate with RLTTs. The conclusions drawn here should be verified with more tests with different materials. It should be further investigated to see which test condition between the RD and PD test protocols better represents reality.

ACKNOWLEDGEMENTS

This work was sponsored by the Swedish Transport Administration (Trafikverket).

REFERENCES

[1] Erlingsson, S. and Magnusdottir, B. Dynamic Triaxial Testing of Unbound Granular Base Course Materials. Proceedings from the 6th International Conference on the Bearing Capacity of Roads, Railways and Airfields, BCRRA'02, Lisbon, Portugal, pp. 989–1000. 2002.

[2] Cary, C.E. and Zapata, E.C. Resilient Modulus for Unsaturated Unbound Materials, Road Materials and Pavement Design, Vol. 12/13, pp. 615–638. 2011.

[3] Erlingsson, S. Impact of Water on the Response and Performance of a Pavement Structure in an Accelerated Test. Road Materials and Pavement Design, Vol. 11/4, pp. 863–880. 2010.

[4] Rahman, S. and Erlingsson, S. Moisture Sensitivity of Unbound Granular Materials, Proceedings of the 4th European Pavement and Asset Management Conference (EPAM4), CD-ROM, Malmö, Sweden. 2012.

[5] Lekarp, F. Resilient and permanent deformation behavior of unbound aggregates under repeated loading, Doctoral thesis, TRITA-IP FR 99-57, KTH Royal Institute of Technology, Stockholm, Sweden. 1999.

[6] Ekblad, J. Influence of Water on Coarse Granular Road Material Properties, Doctoral thesis, TRITA-VT FR 07:01, KTH Royal Institute of Technology, Stockholm, Sweden. 2007.

[7] CEN-European Committee for Standardization. EN 13286-7 Cyclic load triaxial test for unbound mixtures, European Standard, Brussels. 2004.

[8] Huang, Y.H. Pavement Analysis and Design, Second Edition, pp. 279, Prentice Hall, Inc., Englewood Cliffs, NJ. 2004.

[9] Seed, H.B., Chan, C.K. and Lee, C.E. Resilient characteristics of subgrade soils and their relations to fatigue in asphalt pavements, Proceedings of the International Conference on Structural Design of Asphalt Pavements, Ann Arbor, USA, Vol 1, pp. 611–636. 1962.

[10] Hicks, R.G. and Monismith, C.L. Factors Influencing the Resilient Response of Granular Materials, Highway Research Record 345, Highway research Board, Washington DC, USA, pp. 15–31. 1971.

[11] Uzan, J. Characterization of Granular Material, Transport Research Record 1022, Transportation Research Board, Washington DC, USA, pp. 52–59. 1985.

[12] Andrei, D. Development of a Predictive Model for the Resilient Modulus of Unbound Materials, Doctoral thesis, Arizona State University, USA. 2003.

[13] ARA. Guide for the Mechanistic Empirical Design of New and Rehabilitated Pavement Structures, Final report, NCHRP1-37A, Transportation Board of the National Academies, Washington D.C. 2004.

[14] Werkmeister, S., Dawson, A.R. and Wellner, F. Permanent Deformation Behavior of Granular Materials and the Shakedown Concept, Transport Research Record 1757, Transportation Research Board, Washington DC, USA, Paper No. 01-0152, pp. 75–81. 2001.

[15] Arnold, G.K., Dawson, A.R., Hughes, D., Werkmeister, S. and Robinson, D. Serviceability Design of Granular Pavement Material, Proceedings of the 6th International Conference on Bearing Capacity of Roads and Airfields, BCRRA'02, Lisbon, Portugal, pp. 957–966. 2002.

[16] Fuller, W.B. Proportioning concrete, A treatise on concrete, plain and reinforced, Taylor F.W. and Thompson, S.E., pp. 183–215. 1905.

[17] Trafikverket—The Swedish Road Administration. TRVKB 10 Obundna lager—Trafikverkets Krav Beskrivningstexter för Obundna material i vägkonstruktioner, TDOK 2011:265, Borlänge, Sweden. 2011. (In Swedish).

[18] CEN-European Committee for Standardization. EN 13286-2 Test methods for the determination of the laboratory reference density and water content—Proctor compaction, European Standard, Brussels. 2004.

[19] Rahman, M.S. and Erlingsson, S. Moisture Sensitivity of the Deformation Properties of Unbound Granular Materials, Proceedings of the 9th International Conference on Bearing Capacity of Roads and Airfields, BCRRA'13, Trondheim, Norway, pp. 777–786. 2013.

[20] Salour, F. and Erlingsson, S. Investigation of a Pavement Structural Behaviour during Spring Thaw Using Falling Weight Deflectometer, Road Materials and Pavement Design, Vol. 14, Issue 1, pp. 141–158. 2013.

Asphalt Pavements – Kim (Ed)
© 2014 Taylor & Francis Group, London, ISBN 978-1-138-02693-3

Determination of the preferred intervention point for rehabilitation of dense graded asphalt wearing courses on the sand sub-grades of the Swan Coastal Plain in consideration of the triple bottom line (ecological, economic and social impacts)

Martyn Glover
Curtin University, Perth, Western Australia, Australia
Roads2000 Pty Ltd., Perth, Western Australia, Australia

ABSTRACT: In most cases, decisions made by pavement engineers on the rehabilitation of a road pavement wear course are based on a simple economic model. The model compares the cost of replacing the wear course compared to ongoing maintenance of the existing wear course. There seems to be very little consideration for either the ecological impact (excessive fuel use, tyre wear) or social impacts (personal injury and excessive road noise).

The sand sub-grades of the Swan Coastal Plain provide some of the best road pavement foundations in the world. When combined with Perth's Mediterranean climate without any freeze/thaw it is considered that road pavements on the Swan Coastal Plain have much longer life spans than roads elsewhere in Australia and the world.

The published deterioration models for road pavements and the wear courses from around the world do not take consideration for either the beneficial sub-grade or environment that exists on the Swan Coastal Plain. The paper presents the preliminary findings for a PhD thesis to:

- establish the deterioration model for dense graded asphalt wear courses on the Swan Coastal Plain;
- determine the ecological, economic and social impacts during the deterioration of the dense graded asphalt wear courses;
- propose an appropriate point of intervention for rehabilitation of the dense graded asphalt wear course in consideration of the ecological, economic and social impacts; and
- consider the relative balance between negative environmental inputs during maintenance versus environmental impacts of a delayed response.

Keywords: Intervention point for rehabilitation of dense grade asphalt, sand sub-grades, Swan Coastal Plain, ecological, economic and social impacts, wear course deterioration

1 INTRODUCTION

In Western Australia there has been minimal research on the optimum intervention point for replacing dense graded asphalt wear courses on the Swan Coastal Plain. In the few cases that exist, the modelling has been based on an economic rationale only. Where pavement management systems have been employed by pavement engineers and asset managers, the deterioration models have generally been similar to those in the Eastern states of Australia or elsewhere in the world and these do not take into consideration the unique road building environment of the Swan Coastal Plain. It is anticipated that this research will provide a guide for engineering students, pavement engineers and asset managers who operate on the Swan

Coastal Plain so that the maintenance of dense graded asphalt wear courses is optimised in terms of the ecological, economic and social impacts of the deteriorating pavement.

2 THE SWAN COASTAL PLAIN

The Swan Coastal Plain is a 30 kilometre wide strip on the Indian Ocean coast directly west of the Darling Scarp uplands running from Cape Naturaliste in the south to above the City of Perth. This study will look specifically at the northern section of the Swan Coastal Plain, geologically referred to as the Perth Basin and aligned with most of the Perth metropolitan area.

In the area of the Perth basin, the Swan Coastal Plain is about 34 kilometres wide in the north, 23 kilometres in the south, and is bounded to the east by the Gingin and Darling Fault Scarps, which rise to over 200 metres above sea level. The scarps represent the eastern boundary of Tertiary and Quaternary marine erosion. The Swan Coastal Plain consists of a series of distinct landforms [1], roughly parallel to the coast. The most easterly landform comprises the colluvial slopes which form the foothills of the Darling and Dandaragan Plateaus and which represent dissected remnants of a sand covered, wave-cut platform known as the Ridge Hill Shelf. To the west of the colluvial slopes lies the Pinjarra Plain, a piedmont and valley-flat alluvial plain consisting predominantly of clayey alluvium that has been transported by rivers and streams from the Darling and Dandaragan Plateaus. The plain is generally about 5 kilometres wide west of the colluvial slopes, but along the Serpentine River it is about 15 kilometres wide in an east–west direction. To the west of the Pinjarra Plain, the Bassendean Dune System forms a gently undulating aeolian sand plain about 20 kilometres wide with the dunes to the north of Perth generally having greater topographic relief than those to the south. The dunes probably accumulated as shoreline deposits and coastal dunes during interglacial periods of high sea level and originally consisted of mostly lime (calcareous) sand with quartz sand and minor fine-grained, black, heavy-mineral concentrations. Apart from a small local area to the south of Perth, the carbonate material has been completely leached leaving dunes consisting entirely of quartz sand. West of the Bassendean Dune System are two systems of dunes which fringe the coastline. The most easterly of these is the Spearwood Dune System, which consists of slightly calcareous aeolian sand remnant from leaching of the underlying Pleistocene Tamala limestone. The most westerly dune system, which flanks the ocean, is the Quindalup Dune System (Safety Bay Sand), consisting of wind-blown lime and quartz beach sand forming dunes or ridges that are generally oriented parallel to the present coast, but which may also occupy blowouts within the Spearwood Dune System (see Fig. 1).

These sandy soils have particularly good road sub-grade qualities which along with the Mediterranean climate contribute significantly to the longevity of road pavements constructed upon the soils. These attributes will be discussed in further detail later in the paper.

3 RESEARCH DATA SETS

There are two key data sets that will be utilised for the research. The first is the Roman II dataset which is the Road Management System utilised by 134 of the 140 Western Australian Local Governments. The basic road data recorded in this dataset includes road lengths, widths, construction date and resurfacing dates. The second dataset is the financial information contained in the annual Report on Local Government Road Assets and Expenditure published by the Western Australian Local Government Association (WALGA). This publication provides information on annual Local Government road rehabilitation expenditure which has been consistently reported in the same format for the past 15 years.

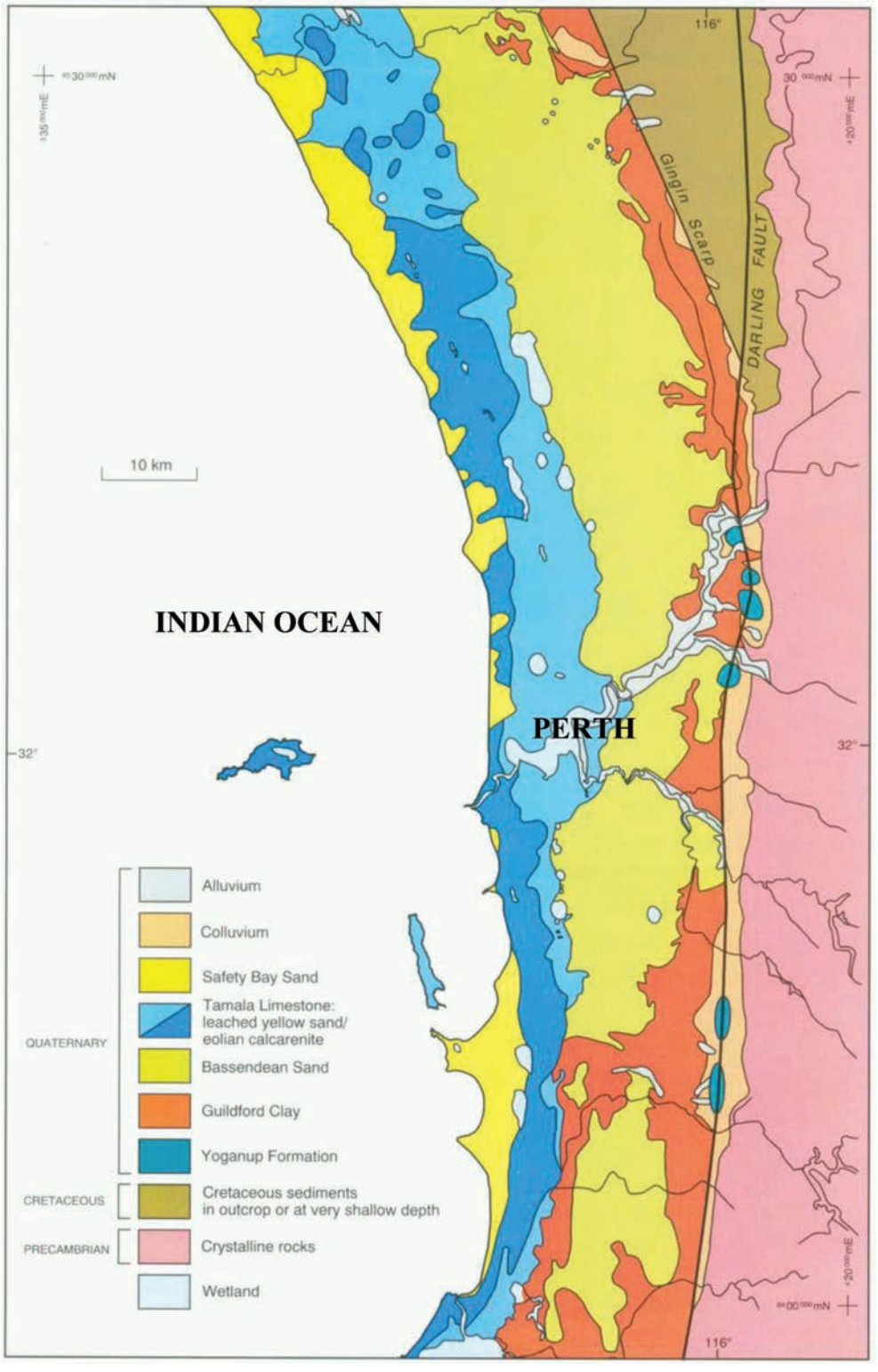

Figure 1. Swan coastal plain geomorphology [2].

4 PARTICIPATING LOCAL GOVERNMENTS

To provide further more detailed data all metropolitan Local Governments were contacted seeking permission to access their data and the following Local Governments provided that permission:

- City of Armadale,
- City of Belmont,
- Town of Cottesloe,
- City of Gosnells,
- City of Joondalup,
- Shire of Kalamunda,
- City of Mandurah,
- City of Melville,
- Shire of Mundaring,
- City of Nedlands,
- City of Rockingham,
- City of South Perth,
- City of Swan, and
- City of Wanneroo.

Because the project is specific to the Swan Coastal Plain it was decided to split the participating Councils into three distinct groups as follows:

- Swan Coastal Plain Group including Belmont, Cottesloe, Joondalup, Melville, Nedlands, South Perth and Wanneroo.
- Darling Range Group (local comparison) including Armadale, Gosnells, Kalamunda, Mundaring and Swan.
- Murray Coastal Group (southern Swan Coastal Plain) comprising of Mandurah and Rockingham.

5 PAVEMENT MANAGEMENT SYSTEM

Most Local Governments in Western Australia utilise the Roman II Pavement Management System. The six Local Governments which don't have Roman II have an alternative system of managing their road asset. All of the participating Local Governments use Roman II. This system and its predecessors have provided asset management tools for Local Government since the 1970's and the oldest data on asphalt was recorded in 1914 (Town of Cottesloe).

6 ROAD PAVEMENTS

Most pavements constructed on the Swan Coastal Plain are extremely thin by international standards and consist of a relatively thin unbound sub-base and basecourse overlaid with an extremely thin asphalt wear course. The Institution of Public Works Engineering Australia (WA Division Inc) Subdivision Guidelines Edition No 2.2, 2012 (the Guidelines) prescribes that pavement thickness is designed in accordance with:

- Pavement Design—A Guide to the Structural Design of Road Pavements (Austroads, 2004);
- A Guide to the Design of New Pavements for Light Traffic (APRG Special Report No. 21, 1998); and
- Main Roads WA Engineering Road Note 9—Procedure for the Design of Flexible Pavements.

The Guidelines [3] also prescribe the design life of pavements as follows:

Unless specified otherwise by the local government, the permanent deformation of the granular pavement must have a minimum design life of 40 years. Unless specified otherwise by the local government asphalt must have the following minimum design life:

- open graded asphalt—10 years;
- dense graded asphalt 50 millimetres total thickness or less—20 years fatigue life; and
- dense graded asphalt greater than 50 millimetres total thickness—40 years fatigue life.

Because the sands of this area of the Perth including the Safety Bay sand, Tamala Limestone and Bassendean Sand formations have California Bearing Ratios (CBRs) in excess of 12.0, the designed pavements are thin. The Guidelines provide three typical pavements ranging from 250 mm to 280 mm thick including an asphalt layer between 25 mm and 65 mm thick overlaying an unbound base of crushed rock and/or crushed limestone between 200 mm and 250 mm thick. Pavements constructed before the 1970's have used limestone spalls and/or lateritic gravels as the unbound portion overlaid by bituminous Macadam of varying thickness. These pavements tend to be even thinner than the more modern pavements with total pavement thicknesses recorded at less than 200 mm however they still perform well today as both residential and distributor pavements.

7 ASPHALTS

In the recent past almost all metropolitan roads were paved with dense grade asphalt. The design was generally a maximum size of 10 mm granite with a class 170 bitumen binder and at 50 blow marshal. The thickness was generally a minimum of 25 mm. Resurfacing activity has predominantly utilised dense grade asphalts although more recently Stone Mastic Asphalt (SMA) has become popular especially where the existing pavement is heavily cracked. Roman II does not differentiate between types of asphalt surface and the use of SMA is a new treatment as well as still at a low proportion of all asphalts, consequently this paper assumes that the great majority of road surfaces requiring resurfacing are dense graded asphalts.

Most of the metropolitan Perth Local Governments in Western Australia now utilise the IPWEA/AAPA Technical Specification, Tender Form and Schedule for Supply and Laying of Hot Asphalt Road Surfacing [4] for their asphalt paving works. The Specification includes mix designs with provision for stiffer bitumen eg class 320, and use of the specification has resulted in a very consistent quality of asphalt surface especially in the metropolitan area.

8 CLIMATE

The climate in the South West of Western Australia plays a substantial part in the longevity of road pavements. The long term average maximum temperature in Perth is 24.7°C (76.5°F) and the average minimum temperature is 12.8°C (55°F). The average rainfall is 731 mm (29 inches) over an average period of 104.9 days [5]. There is no freeze-thaw in Western Australia consequently the climate contributors to the aging of asphalt pavements are limited to the sun and rain. Freeze-thaw or frost weathering is a collective term for several mechanical weathering processes induced by stresses created by the freezing of water into ice. The term serves as an umbrella term for a variety of processes such as frost shattering, frost wedging and cryofracturing [6]. The process may act on a wide range of spatial and temporal scales, from minutes to years and in the case of road pavements from accelerating surface raveling to splitting entire pavements. Frost weathering is mainly driven by the frequency and intensity of freeze-thaw cycles and the properties of the materials subject to weathering. The Local Government Association of South Australia has recently commissioned a comprehensive study by the National Climate Change Adaption Research Facility titled Quantifying the cost of climate change impacts on local government assets. The report

includes predictions on the impact of climate change on Perth road pavements. The prediction is that in the year 2100 the average pavement life will increase as the average rainfall reduces [7].

9 TRIPLE BOTTOM LINE

The triple bottom line (abbreviated as TBL or 3BL, and also known as people, planet, profit or "the three pillars") captures an expanded spectrum of values and criteria for measuring organizational (and societal) success: economic, ecological, and social. With the ratification of the United Nations and International Council for Local Environmental Initiatives (ICLEI) TBL standard for urban and community accounting in early 2007, this became the dominant approach to public sector full cost accounting. Similar United Nations standards apply to natural capital and human capital measurement to assist in measurements required by TBL, e.g. the EcoBudget standard for reporting ecological footprint [8].

In this report, it is recognised that the decision to replace the wear course on a pavement is generally an economic decision based on the deterioration of the existing wear course versus the cost of replacing it and available funding. What is not considered and should be [9] are the ecological impacts of a deteriorating wear course relate to the increased pollution predominantly generated from increased tyre wear and fuel use while the social impacts are increased crashes and road noise. The WesTrack study conducted by the Federal Highway Administration in 2000 indicated that trucks running on smooth surfaces could reduce fuel consumption by 4.5 percent [10], other research has cited increased consumption due to roughness between 10 and 20 percent [11]. Nakamura and Ihara demonstrated that road noise from tyres increases as the asphalt ages [12]. Research in Texas between 2008 and 2009 has realised that poor pavement condition scores and ratings were associated with proportionally more severe crashes [13].

10 ROAD NETWORK

The key road network information for the participating Local Governments is included in Table 1.

Table 1. Local government road network key information [14–23].

			Asphalt road totals		
Group	Local government	Length of sealed road (km)	Area (m^2)	Area reseal (m^2)	Percentage resealed
Swan coastal plain	City of Belmont	229.28	220890	67350	30.49%
	Town of Cottesloe	48.47	29120	22780	78.23%
	City of Joondalup	1009.64	2627560	89785	3.42%
	City of Melville	733.65	521344	189480	36.34%
	City of Nedlands	147.00	131210	173290	132.07%
	City of South Perth	197.77	193480	38250	19.77%
	City of Wanneroo	1291.52	1028770	147140	14.30%
Murray coastal group	City of Mandurah	667.16	441322	9140	2.07%
	City of Rockingham	961.42	895201	46722	5.22%
Darling range group	City of Armadale	683.66	549108	103567	18.86%
	City of Gosnells	855.05	689125	147564	21.41%
	Shire of Kalamunda	645.00	209450	100240	47.86%
	Shire of Mundaring	602.75	129200	122970	95.18%
	City of Swan	1306.97	691640	139117	20.11%

Table 2. Road condition.

Group	Local government	Road condition												
		2000/01	2001/02	2002/03	2003/04	2004/05	2005/06	2006/07	2007/08	2008/09	2009/10	2010/11	2011/12	Average
Swan coastal plain	City of Belmont	0.65	0.66	0.66	0.66	0.65	0.65	0.66	0.66	0.75	0.75	0.76	0.76	0.69
	Town of Cottesloe	0.67	0.65	0.65	0.65	0.65	0.64	0.65	0.67	0.64	0.64	0.56	0.56	0.64
	City of Joondalup	0.79	0.81	0.81	0.81	0.81	0.81	0.80	0.70	0.65	0.65	0.68	0.69	0.75
	City of Melville	0.69	0.68	0.67	0.67	0.67	0.67	0.68	0.66	0.56	0.56	0.58	0.58	0.64
	City of Nedlands	0.67	0.65	0.65	0.65	0.65	0.65	0.66	0.66	0.64	0.64	0.54	0.54	0.63
	City of South Perth	0.69	0.68	0.68	0.68	0.68	0.68	0.68	0.68	0.67	0.67	0.70	0.70	0.68
	City of Wanneroo	0.75	0.74	0.74	0.74	0.73	0.73	0.74	0.71	0.77	0.77	0.79	0.79	0.75
Averages		**0.70**	**0.70**	**0.69**	**0.69**	**0.69**	**0.69**	**0.70**	**0.68**	**0.67**	**0.67**	**0.66**	**0.66**	**0.68**
Murray coastal group	City of Mandurah	0.75	0.64	0.75	0.75	0.75	0.75	0.75	0.68	0.67	0.68	0.77	0.77	0.73
	City of Rockingham	0.74	0.74	0.74	0.74	0.74	0.74	0.74	0.67	0.82	0.82	0.75	0.75	0.75
Averages		**0.75**	**0.69**	**0.75**	**0.75**	**0.75**	**0.75**	**0.75**	**0.68**	**0.75**	**0.75**	**0.76**	**0.76**	**0.74**
Darling range group	City of Armadale	0.70	0.68	0.69	0.69	0.69	0.69	0.68	0.68	0.73	0.73	0.74	0.74	0.70
	City of Gosnells	0.70	0.70	0.70	0.70	0.70	0.69	0.69	0.64	0.71	0.71	0.68	0.68	0.69
	Shire of Kalamunda	0.71	0.69	0.70	0.70	0.70	0.69	0.69	0.68	0.72	0.72	0.72	0.72	0.70
	Shire of Mundaring	0.70	0.70	0.70	0.70	0.70	0.70	0.69	0.60	0.60	0.60	0.62	0.62	0.66
	City of Swan	0.71	0.70	0.69	0.69	0.70	0.69	0.68	0.64	0.62	0.63	0.68	0.68	0.68
Averages		**0.70**	**0.69**	**0.70**	**0.70**	**0.70**	**0.69**	**0.69**	**0.65**	**0.68**	**0.68**	**0.69**	**0.69**	**0.69**

Table 3. Preservation performance.

Group	Local government	Preservation performance												
		2000/01	2001/02	2002/03	2003/04	2004/05	2005/06	2006/07	2007/08	2008/09	2009/10	2010/11	2011/12	Average
Swan coastal plain	City of Belmont	1.76	1.59	1.29	1.12	1.10	1.23	1.03	0.87	1.27	1.43	1.56	1.62	1.32
	Town of Cottesloe	1.66	2.38	2.48	2.26	1.75	1.94	1.64	1.88	1.77	1.73	1.67	1.79	1.91
	City of Joondalup	0.91	0.96	0.93	0.90	0.71	0.81	0.49	0.53	0.79	0.81	0.95	1.03	0.82
	City of Melville	1.32	2.04	1.04	0.83	0.87	0.88	0.93	0.92	1.02	1.00	1.53	1.28	1.14
	City of Nedlands	2.47	2.90	2.16	2.24	2.07	2.04	1.35	1.71	2.19	1.93	2.26	2.13	2.12
	City of South Perth	0.32	1.35	1.11	0.88	0.83	0.71	0.91	1.00	1.32	1.24	1.22	1.63	1.04
	City of Wanneroo	0.68	0.70	0.66	0.63	0.60	0.44	0.55	0.58	0.48	0.47	0.57	0.49	0.57
Averages		**1.30**	**1.70**	**1.38**	**1.27**	**1.13**	**1.15**	**0.99**	**1.07**	**1.26**	**1.23**	**1.39**	**1.42**	**1.28**
Murray coastal group	City of Mandurah	0.81	0.85	0.79	0.78	0.76	0.46	0.46	0.49	0.71	0.77	0.65	0.80	0.69
	City of Rockingham	0.65	0.56	0.63	0.65	0.51	0.61	0.78	0.72	0.74	0.54	0.80	1.06	0.69
Averages		**0.73**	**0.71**	**0.71**	**0.72**	**0.64**	**0.54**	**0.62**	**0.61**	**0.73**	**0.66**	**0.73**	**0.93**	**0.69**
Darling range group	City of Armadale	1.09	1.26	1.08	1.27	1.16	0.97	1.01	0.85	0.97	0.88	0.52	0.73	0.98
	City of Gosnells	0.46	0.85	0.78	0.90	0.57	0.69	0.61	0.58	0.81	0.96	0.91	0.84	0.75
	Shire of Kalamunda	0.67	0.71	0.80	0.72	0.72	0.53	0.72	0.83	0.56	0.62	0.60	0.42	0.66
	Shire of Mundaring	0.92	1.02	0.88	0.83	0.78	0.65	0.68	0.73	0.91	0.85	0.71	0.87	0.82
	City of Swan	0.87	0.72	0.83	0.88	1.07	0.92	1.04	1.02	0.90	0.90	1.05	1.31	0.96
Averages		**0.80**	**0.91**	**0.87**	**0.92**	**0.86**	**0.75**	**0.81**	**0.80**	**0.83**	**0.84**	**0.76**	**0.83**	**0.83**

Table 4. Expenditure per lane kilometre in built up areas.

		Expenditure per lane km in $,000s (built up areas)												
Group	Local government	2000/01	2001/02	2002/03	2003/04	2004/05	2005/06	2006/07	2007/08	2008/09	2009/10	2010/11	2011/12	Average
Swan coastal plain	City of Belmont	$13,730	$13,165	$10,105	$8,966	$8,933	$11,033	$9,907	$9,240	$10,242	$11,524	$12,019	$13,663	$11,044
	Town of Cottesloe	$9,715	$14,175	$15,164	$14,129	$11,244	$15,668	$14,142	$17,474	$13,838	$13,533	$12,738	$14,866	$13,891
	City of Joondalup	$3,604	$4,338	$4,227	$4,168	$3,359	$4,253	$2,750	$3,167	$6,000	$6,124	$6,859	$8,189	$4,753
	City of Melville	$5,243	$8,420	$4,854	$3,982	$4,237	$4,729	$5,313	$5,628	$7,765	$7,545	$11,212	$10,158	$6,591
	City of Nedlands	$13,729	$16,314	$13,522	$14,355	$13,600	$15,335	$11,031	$14,689	$16,184	$14,146	$16,096	$16,346	$14,612
	City of South Perth	$1,910	$8,200	$7,584	$6,163	$5,966	$5,610	$7,777	$9,152	$10,518	$9,934	$9,387	$13,673	$7,990
	City of Wanneroo	$2,152	$2,234	$2,330	$1,557	$2,004	$1,652	$2,275	$2,948	$3,023	$3,140	$3,484	$3,328	$2,511
Averages		**$7,155**	**$9,549**	**$8,255**	**$7,617**	**$7,049**	**$8,326**	**$7,599**	**$8,900**	**$9,653**	**$9,421**	**$10,256**	**$11,460**	**$8,770**
Murray coastal group	City of Mandurah	$3,565	$4,572	$4,733	$3,528	$3,986	$3,572	$2,260	$3,000	$4,920	$5,546	$5,134	$6,753	$4,297
	City of Rockingham	$3,241	$2,965	$3,351	$3,928	$3,229	$3,301	$4,135	$4,955	$5,167	$4,325	$6,571	$9,044	$4,518
Averages		**$3,403**	**$3,769**	**$4,042**	**$3,728**	**$3,608**	**$3,437**	**$3,198**	**$3,978**	**$5,044**	**$4,936**	**$5,853**	**$7,899**	**$4,408**
Darling range group	City of Armadale	$4,946	$7,307	$6,076	$7,078	$7,221	$6,803	$6,274	$7,127	$9,389	$7,882	$4,615	$5,476	$6,683
	City of Gosnells	$2,614	$5,456	$5,165	$6,655	$4,375	$5,873	$5,857	$5,685	$6,725	$6,518	$7,495	$7,405	$5,819
	Shire of Kalamunda	$3,734	$3,473	$5,170	$3,552	$4,922	$3,341	$5,892	$5,650	$3,020	$5,129	$4,021	$3,738	$4,304
	Shire of Mundaring	$4,160	$3,924	$3,478	$4,941	$2,951	$3,756	$3,555	$4,832	$6,602	$5,639	$5,952	$4,261	$4,504
	City of Swan	$3,547	$3,598	$4,528	$4,993	$5,597	$5,141	$7,977	$6,534	$3,023	$7,217	$9,130	$11,510	$6,066
Averages		**$3,800**	**$4,752**	**$4,883**	**$5,444**	**$5,013**	**$4,983**	**$5,911**	**$5,966**	**$5,752**	**$6,477**	**$6,243**	**$6,478**	**$5,475**

The annual Report on Local Government Road Assets and Expenditure published by the WALGA [14–23] provides key performance indicators for pavement performance based on a financial model. The three key financial values are:

- Current Replacement Value—is the current cost of replacing the road assets. It provides a datum from which the consumption of roads can be assessed.
- Written Down Value—is the current value after allowing for depreciation. The difference between replacement value and written down value represents the amount consumed.
- Status Quo Cost—is the estimated cost of maintaining the roads at their current condition. It provides a datum against which actual expenditure performance can be compared.

This paper considers two indicators based on the above financial values. The Road Condition Indicator is the ratio between the Written Down Value and the Current Replacement Value. The Preservation Performance Indicator is the ratio between the actual expenditure on preservation and the Status Quo Cost. These two key performance indicators for the road network since 2000–2001 are included in the Tables 2 and 3.

To provide a measure of the actual cost, Table 4 provides annual expenditure per linear kilometre in built up areas, that is, the roads which have most likely been asphalted.

11 DETERIORATION MODELS

The Roman II data has provided indications of the typical life of thin asphalts on the Swan Coastal Plain. The average resurfacing period for any Local Government has varied from as low as 10.3 years to as high as 27.3 years. The average resurfacing periods are presented in Table 5.

Further research will be required to determine the reasons for the different resurfacing periods including dominance of particular classes of road, Local Government asset policy, traffic volumes etc, however the Group averages are relatively consistent between 17 and 18 years with Swan Coastal Plain Group the longest at 18.2 years.

Table 5. Average resurfacing periods.

Group	Local government	Length of sealed road (km)	Resurfacing Period
Swan coastal plain	City of Belmont	229.28	12.7
	Town of Cottesloe	48.47	27.3
	City of Joondalup	1009.64	23.9
	City of Melville	733.65	16.2
	City of Nedlands	147.00	16.7
	City of South Perth	197.77	10.3
	City of Wanneroo	1291.52	20.5
	Average resurfacing period		18.2
Murray coastal group	City of Mandurah	667.16	22.0
	City of Rockingham	961.42	12.7
	Average resurfacing period		17.4
Darling range group	City of Armadale	683.66	18.9
	City of Gosnells	855.05	14.7
	Shire of Kalamunda	645.00	13.9
	Shire of Mundaring	602.75	22.3
	City of Swan	1306.97	19.5
	Average resurfacing period		17.9

12 CONCLUSION

The initial research indicates that road construction conditions in terms of quality subgrades and a Mediterranean climate on the Swan Coastal Plain are conducive to long lasting pavements. The research has provided an actual average resurfacing period which has maintained a favourable road condition. This still needs to be compared with theoretical deterioration models. We have also established that the available data sets are of good quality providing long term data for road pavements in metropolitan Perth. The research is yet to quantify the cost of tyre wear, fuel use, crash risk and road noise to the community and whether this will impact on the optimal intervention point.

ACKNOWLEDGEMENTS

The author wishes to thank the staff of the participating Local Governments, ARRB and WALGA for their contribution to date. The research could not take place without the support of Curtin University and my employer, Roads 2000 Pty Ltd.

REFERENCES

[1] McArthur, W.M. and Bettenay, E. (1960), The Development and Distribution of the Soils of the Swan Coastal Plain, Western Australia, CSIRO Soil Publication No. 16. CSIRO, Melbourne.
[2] Davidson, W.A. (1995). Hydrogeology and groundwater resources of the Perth region, Western Australia. Western Australia Geological Survey, Bulletin 142.
[3] IPWEA (2012), Local Government Guidelines for Subdivisional Development Edition 2.2, Institute of Public Works Engineering Australia (WA Division) Inc.
[4] IPWEA/AAPA (2002), Technical Specification, Tender Form and Schedule for Supply and Laying of Hot Asphalt Road Surfacing, Institute of Public Works Engineering Australia (Western Australia Division) Inc.
[5] http://www.weatherzone.com.au/climate/station.jsp?lt=site&lc=9225.
[6] http://en.wikipedia.org/wiki/Frost_weathering.
[7] Balston, J. et al (2012) Quantifying the Costs of Climate Change on Local Government Assets. National Climate Change Adaption Research Facility.
[8] http://en.wikipedia.org/wiki/Triple_bottom_line.
[9] Martin, T.C. (2005), Refinement of Road Deterioration Models in Australasia. AUSTROADS Research Report; AP-R267/05.
[10] Sime, M. et al. (2000) Techbrief: WesTrack track roughness, fuel consumption and maintenance cost. Federal Highway Administration, FHWA-RD-00-052.
[11] Marks, H. (2009) Smoothness Matters: The Influence of Pavement on Fuel Consumption. Hot Mix Asphalt Technology-November/December 2009.
[12] Nakamura, H. and Ihara, T. (2010). Tyre/Road Noise Characteristics of Several Asphalt Pavements. 11th International Conference on Asphalt Pavements, Nagoya.
[13] Yingfeng, L. et al. (2013). Impact of Pavement Conditions on Crash Severity. Accident Analysis & Prevention Volume 59.
[14] WALGA (2012), Report on Local Government Road Assets and Expenditure 2010/11, Western Australian Local Government Association Publication.
[15] WALGA (2011), Report on Local Government Road Assets and Expenditure 2009/10, Western Australian Local Government Association Publication.
[16] WALGA (2010), Report on Local Government Road Assets and Expenditure 2008/09, Western Australian Local Government Association Publication.
[17] WALGA (2009), Report on Local Government Road Assets and Expenditure 2007/08, Western Australian Local Government Association Publication.
[18] WALGA (2008), Report on Local Government Road Assets and Expenditure 2006/07, Western Australian Local Government Association Publication.
[19] WALGA (2007), Report on Local Government Road Assets and Expenditure 2005/06, Western Australian Local Government Association Publication.

[20] WALGA (2005), Report on Local Government Road Assets and Expenditure 2003/04, Western Australian Local Government Association Publication.
[21] WALGA (2004), Report on Local Government Road Assets and Expenditure 2002/03, Western Australian Local Government Association Publication.
[22] WALGA (2003), Report on Local Government Road Assets and Expenditure 2001/02, Western Australian Local Government Association Publication.
[23] WALGA (2002), Report on Local Government Road Assets and Expenditure 2000/01, Western Australian Local Government Association Publication.

Experimental characterization of asphaltic materials—III

This page intentionally left blank

Asphalt Pavements – Kim (Ed)
© 2014 Taylor & Francis Group, London, ISBN 978-1-138-02693-3

Discrete Element Modelling and experimental study on dilation behaviour of asphalt mixtures

Jiantong Zhang, Jun Yang & Keli Wang
School of Transportation, Southeast University, Nanjing, Jiangsu, China

ABSTRACT: This paper investigates the use of Discrete Element Modelling (DEM) to simulate the behavior of a highly heterogeneous nature under triaxial compressive test. The laboratory triaxial compressive test is conducted to capture the dilation of asphalt mixture. Dilative mechanism is analyzed through the microstructure using DEM. Digital specimens are prepared with random generator algorithm that would generate an irregular closed space to incorporate the balls inside of the space for each clump according to the graded mixture. Statistical regression method is developed to capture varying air void distributions along pavement depth. Based on this method, the air void phase of virtual specimen was built, which is close to the real asphalt pavement. Results show that the virtual specimen is similar to the actual triaxial compression test specimen and has the correct volumetric proportions. The dilatancy behavior and shear resistance are simulated by using DEM to investigate the variance of aggregate-binder-aggregate contact under triaxial compressive tests. The results of laboratory triaxial compressive test were in agreement with the result of DEM simulation. Both of these methods show that there was obvious dilation when the specimen was loaded. At the same time, the aggregate-binder-aggregate contact was fractured and formed a shear band.

Keywords: Asphalt mixture, Discrete Element Modelling, dilation, triaxial compression test, Particle Flow Code (PFC), permanent deformation, mechanism

1 INTRODUCTION

Dilatancy behavior plays a key role in asphalt mixture rutting. Dilation is a phenomenon of the volume increase that occurs in the particulate media when loaded beyond the elastic limit [1]. The dilatancy has significant implication; it means that the granular skeleton becomes loose during the shearing [2]. The property of soil dilatancy was first described by Osborne Reynolds [3–4] embodied in the well known "interlocking saw-tooth" analogy of Taylor. Rowe [5–7] developed a basic theory which explains how the geometrical interlocking of the particles influences the strength of the material, and provided a simple relationship between stress ratio and dilatancy factor which basically quantifies the geometrical effect. Within the framework of plasticity theory, Rowe's stress dilatancy relationship represents in fact a flow rule which determines the direction of plastic strains. Nova and Wood [8] later on proposed a stress invariant form of the relationship for addressing general stress and strain conditions. Wan and Guo [9–10] proposed a model which hinges upon concepts of coupled plastic hardening-softening and stress dilatancy in order to address both the void ratio and pressure dependency behaviour of granular soils. However, very little work has been done to address the effect of the dilatancy process on the quality of pavement. The challenges in the modeling of asphalt mixture contain the highly heterogeneous nature including aggregate internal structure and air void distribution, the time, temperature and rate-dependent behavior of the matrix and the limited computation capacity for very precise prediction. Digital specimen and test techniques permit investigation of strength and deformation mechanisms of asphalt

concrete going in a microscopic way that integrates mechanism identification, numerical simulation, and experimental observations. It represents the trend for the future mix design [11]. Virtual test can be utilized to simulate the laboratory test and make microstructure analysis of asphalt concrete under a specific load condition [12–15]. The micro-fabric discrete element method for the microstructure of asphalt mixture in two-dimensional was proposed by Buttlar and You [16]. Then the idealized model in three-dimensional was established to simulate the dilation behavior of asphalt concrete [17].

The aim of this paper is to further study the mechanism of dilation of asphalt mixture, which helps to explain the rutting mechanism of asphalt pavement. Also, the microstructure of asphalt mixture is analyzed using DEM, which can be used to explain the fundamental material properties of asphalt mixture. It is beneficial for designing and testing of asphalt pavements.

2 MECHANICAL MODELS FOR DISCRETE ELEMENT MODELING

There are three kinds of contact interaction effects: (1) interactions within aggregates; (2) interactions within sand mastic; (3) interactions between aggregate and sand mastic. In the DEM model, four contact models are used to represent the rheological characteristics of asphalt: Burger's model, the linear elastic contact model, the slip model, and the contact-bond model. These contact models are available in the PFC3D (Particle Flow Code in three Dimension). Burger's model and the linear elastic contact model are used as the contact-stiffness models for asphalt sand mastic and aggregate particles, respectively. The slip model represents the slip behavior at the two contacting entities and the contact-bond model can specify shear and normal tensile strength. The contact models are distributed according to interaction mechanic characteristics in this paper as shown in Table 1.

3 LABORATORY TESTING

3.1 *Test materials and sample preparation*

The Superpave Gyratory Compactor (SGC) is used to produce compacted specimens for volumetric analysis and determination of mechanical properties. The asphalt mix specimens of 150 mm (diameter) by 165 mm (height) were fabricated using the Superpave Gyration Compactor, and then 100 mm (diameter) by 150 mm (height) specimens were cored from compacted specimens for the test.

The selected aggregates were used in this test and limestone was employed as filler. Three types of asphalt mixture known as AC13, SMA13 and Sup13 which are the most common used mix types used for wearing course construction in China, were studied in details to serve as the baseline case in this study. The properties of SBS modified asphalt can be referred to the research of Zhang et al. [18], but the PG (performance grade) isn't measured. The mix proportions and aggregate gradations for the three mixtures are shown in Table 2.

3.2 *Triaxial compression test*

The three type of mixtures (SMA13, AC13 and Sup13) triaxial compression test results are shown in Table 3.

Table 1. Contact model distributions in DEM.

Contact types	Contact model
Interactions within aggregates	Contact-stiffness model
Interactions within sand mastic	Contact-bond model + Burger's model
Interactions between aggregate and sand mastic	Contact-bond model + Burger's model

Table 2. Compositions and aggregate gradations of asphalt mixtures.

Type of mix max stone size (mm)	AC13	SMA13	Sup13
Sieve size (mm)	% passing by weight		
16	100	100	100
13.2	95.9	93.4	97.1
9.5	76.8	62.2	78.8
4.75	50.7	24.8	53.0
2.36	34.4	21.4	32.5
1.18	25.2	18.1	19.9
0.6	18.3	15.3	15.3
0.3	13.5	13.2	9.4
0.15	10.6	12.0	7.2
0.075	7.2	11.2	5.5
Aggregate type	Limestone	Limestone	Limestone
Type of asphalt	SBS modified	SBS modified	SBS modified
Optimum binder content (%)	5.6	6.0	5.0
Air void content (%)	4.0	4.0	4.0

Table 3. Experimental results under triaxial compression test.

Mix type	σ_3 (KPa)	σ_1 (KPa)	C (KPa)	φ (^{0})	τ (KPa)
SMA13	0	1130.6	197.68	39.47	408
	138	1783.4			
	276	2183.4			
	0	1075.8			
	138	1700.2			
	276	2358.6			
AC13	0	770.7	207.52	33.30	395
	138	975.7			
	276	1521.2			
	0	792.9			
	138	1081.5			
	276	1383.7			
Sup13	0	859.4	212.90	37.52	416
	138	1296.6			
	276	1593.1			
	0	850.7			
	138	1326.5			
	276	1835.0			

4 DEM SIMULATION

4.1 *Numerical sample preparation procedure*

Discrete Element Modeling (DEM) for simulating movement and interaction of assemblies of rigid particles was developed by Cundall and Strack [19]. Reference to the study conducted by Lu [20], particles simulated by clumps of balls would be able to introduce the heterogeneity of materials and interlocking among particles from the shape or angularity perspective rather than by only a single ball into the model as shown in Figure 1. At first, a cylinder mold surrounded by walls needs to be created with the size identical to the sample size (height = 150 mm, diameter = 100 mm) for triaxial compression test. A simple model with gradation identical to that of mixtures but consisting of regular shape balls is created. Using the model developed by You et al. [21] and the consideration

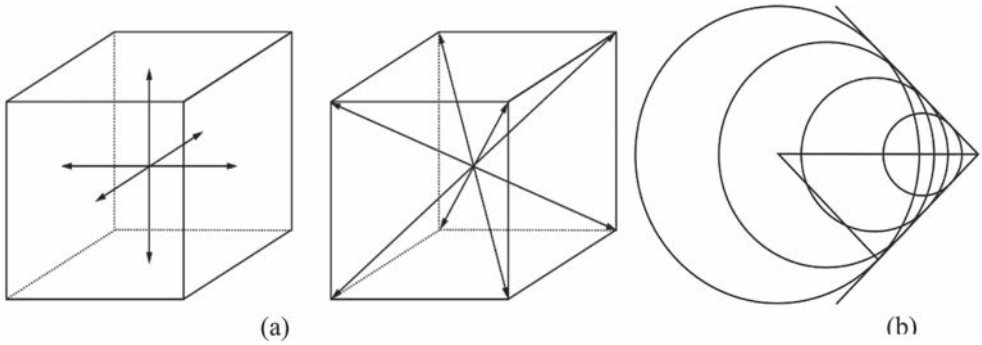

Figure 1. Method of fabricating irregular shaped aggregate. (a) Ball generation along one direction; (b) Directions of ball generation for clumps.

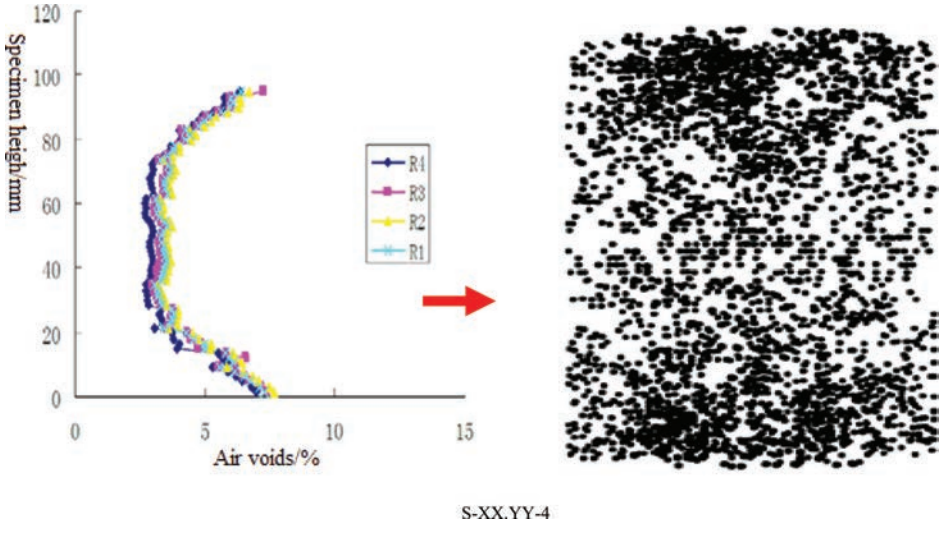

Figure 2. Fabrication process of air void phase of asphalt mixture. The left picture is the distribution of air void along the depth of asphalt mixture under triaxial compression test (The digital specimen's radii are 1 cm, 2 cm, 3 cm, and 4 cm represented by R1, R2, R3, R4, respectively) [22]; The right picture is the distribution of air void (Air voids represented by black spheres) of virtual specimen based on the data of the left picture.

of computing efficiency, the ball's radius (element size) is chosen as one millimeter. The physical information of clumps (balls' locations and radii) is already kept in storage at the former step. Traverse every ball in the new model and the ball with its center located in the same closed space would be added to the same clump. When all clumps had been delineated, the next stage's work is to delete a certain amount of balls to meet the void requirement as shown in Figure 2. It should be noted that the deleted ball should be a "free" one, namely it belonged to no clump. After performing stage two, the rest of the free balls will form the asphalt mastic phase. Finally, it is needed to check the volume ratio between coarse aggregate and asphalt sand mastic. Figure 3 depicts the mechanism for this final DEM model.

Air void distribution inside the specimen is studied using X-ray scanner, according to [23–24]. A statistical model is proposed to establish the air void phase instead of a model with random distribution shown in Figure 2. The air void phase of microstructure for the virtual specimen is established as shown in Figure 3(d).

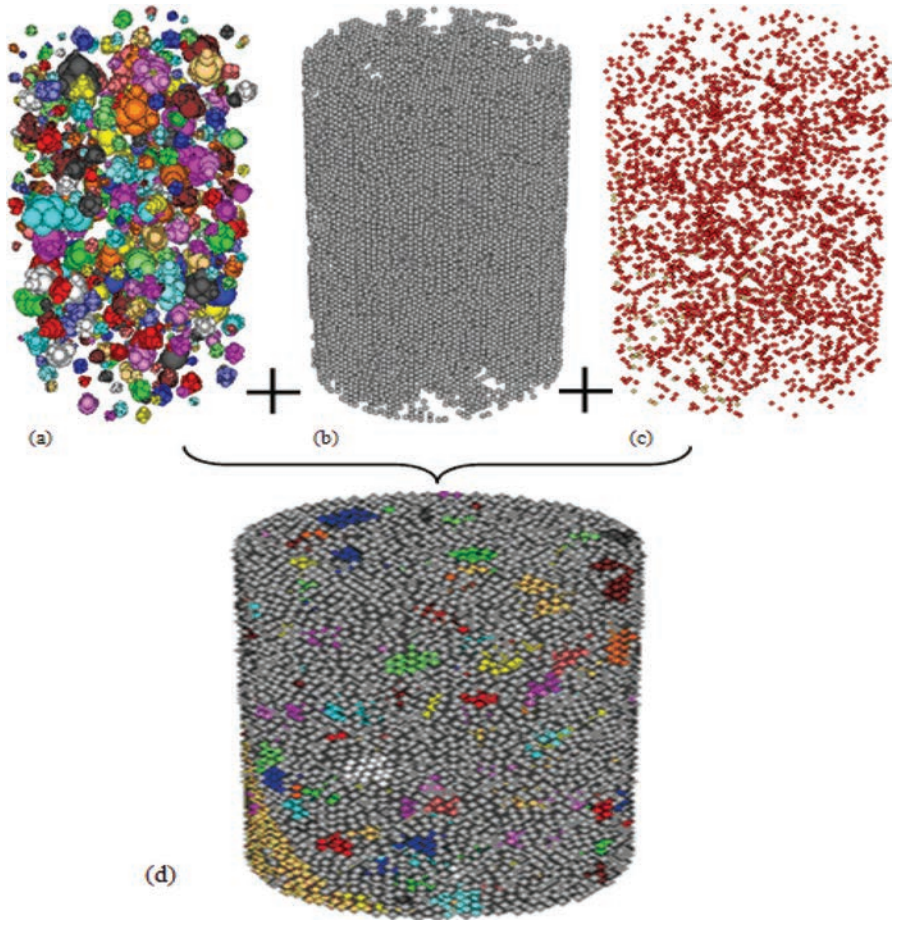

Figure 3. Schematics of mechanism of fabricating virtual specimen. (a) Coarse aggregate phase (>=2.36 mm); (b) Asphalt binder mortar (<2.36 mm); (c) Air void phase (VV = 4%, air voids are represented by red spheres); (d) Testing virtual specimen.

Finally, the information of physical components in the virtual specimen is calibrated by actual gradation of asphalt concrete. So far, the microstructure of asphalt concrete has been established based on DEM. To improve computational efficiency of the three dimensional model, the size of virtual cylindrical specimen is reduced to 60 mm by 40 mm (height by diameter) and the radius of the unit sphere is reduce to 0.5 mm. The coarse aggregate in virtual specimen can be calibrated, for example the coarse aggregate of Sup13 virtual specimen is as show in Figure 4. Also, the volume ratio of aggregate grading in virtual and actual specimen can be calculated (for instance, the Sup13 and AC13 specimen's volume ratio). Results for volume ratio against aggregate grading are plotted in Figure 5. It can be seen that the volume ratios are almost equal. It indicates that both virtual specimen and actual specimen have similar aggregate properties.

4.2 *Parameter determination*

The parameters of burgers model can be calculated by the equation (1) [17].

$$\varepsilon(t) = \frac{\sigma_0}{E_1} + \frac{\sigma_0}{E_2} + \frac{\sigma_0 t}{\eta_1} - \frac{\sigma_0}{E_2} e^{\frac{E_2}{\eta_2} t} \tag{1}$$

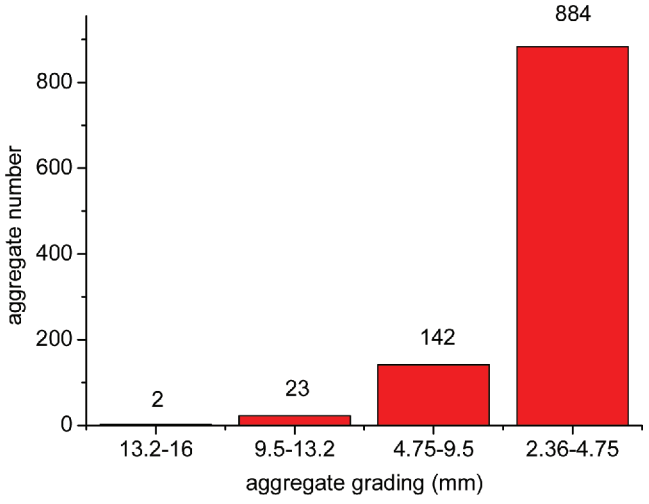

Figure 4. Distribution of coarse aggregates for virtual specimen Sup13.

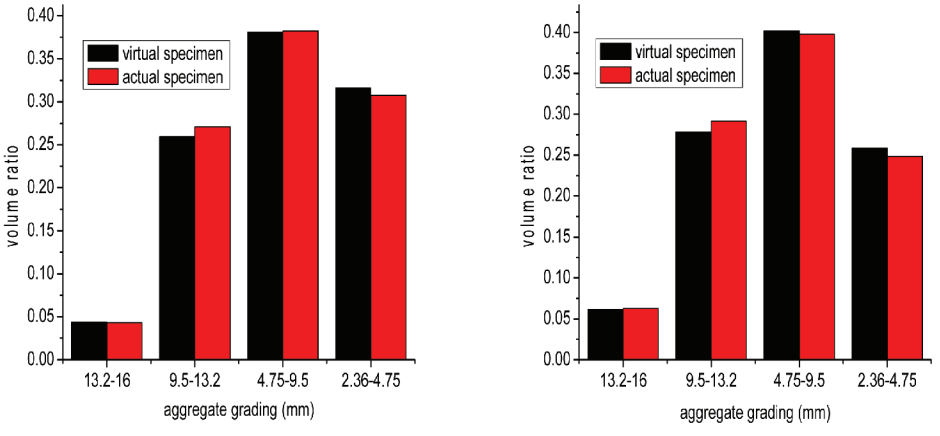

Figure 5. Volume ratio of aggregate grading in virtual and actual specimens. The left picture Is Sup13 specimen and the right picture Is AC-13 specimen.

where σ_0 is the creep loading, 40 KPa, and t is the test time. It can be seen from Figure 6 that the parameters of burgers model can be captured by fitted regression line under triaxial compression test of asphalt mortar of Sup13 and AC13. The parameter of burgers model is shown in Table 4.

4.3 *Virtual triaxial compression test*

The virtual specimen has been build and its parameters have been captured through triaxial compression of asphalt mortar in abovementioned parts. Also, the particle and contact model are ready for DEM model, the next step is to make an assembly of them, namely assign every contact a corresponding contact model and its properties according to the former tables. A FISH program is compiled to finish this task. The Burger's contact model is updated every timestep, and the creation of a new contact would automatically trigger the calling of a FISH function and install Burger's model and its properties dynamically. When a new contact is created, the FISH function would be triggered and all the contact properties within the digital sample would be updated. The bond contact parameters need to take into account.

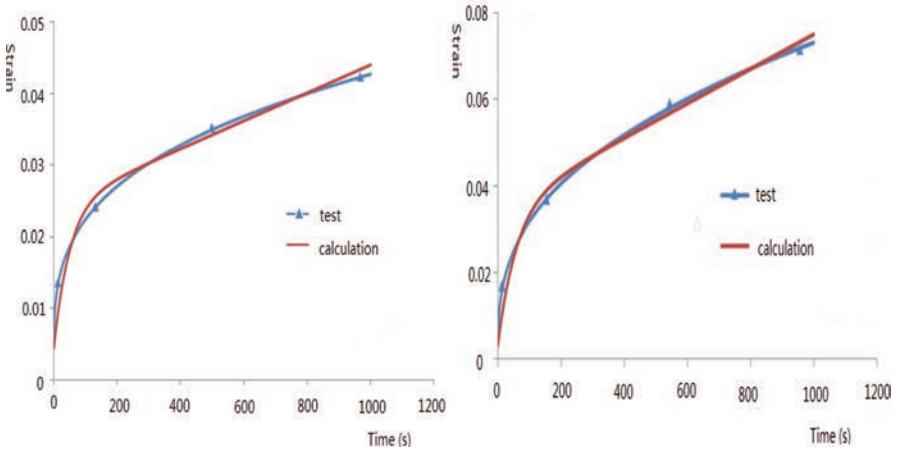

Figure 6. Fitted regression line for triaxial compression test of asphalt mortar of Sup13 (left) and AC13 (right).

Table 4. Parameters of burgers model for AC13 and Sup13 mix.

Mix type	E_1 (Pa)	η_1 (Pa·s)	E_2 (Pa)	η_1 (Pa·s)
Sup13	8.882E+06	2.043E+09	2.012E+06	1.005E+08
AC13	1.248E+07	1.000E+09	1.254E+06	7.416E+07

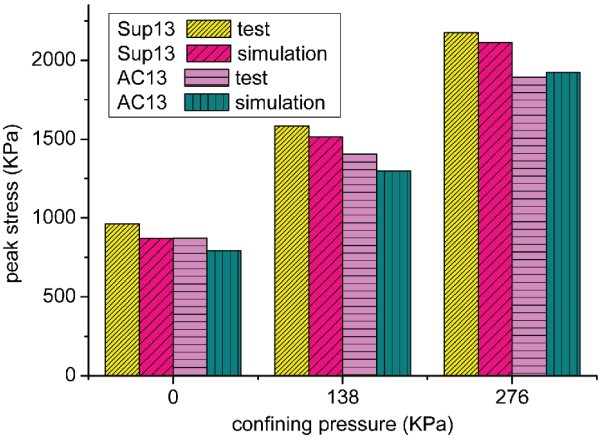

Figure 7. Comparison peak stresses obtained from DEM simulation and the actual test.

Therefore, it's better to develop concrete laboratory tests to assist obtaining the values as accurate as possible though it never obtains the real values because of many limitations. In this paper, the value of bonds contact parameters is obtained by regressing the DEM simulation and measured laboratory results.

5 DILATION ANALYSIS UNDER TRIAXIAL TEST AND DEM SIMULATION

The top plate is loaded at a strain rate of 8.47 mm/mm/min. And some variables are obtained once every 50 time-steps by calling "History" command, including the stress enforced. All

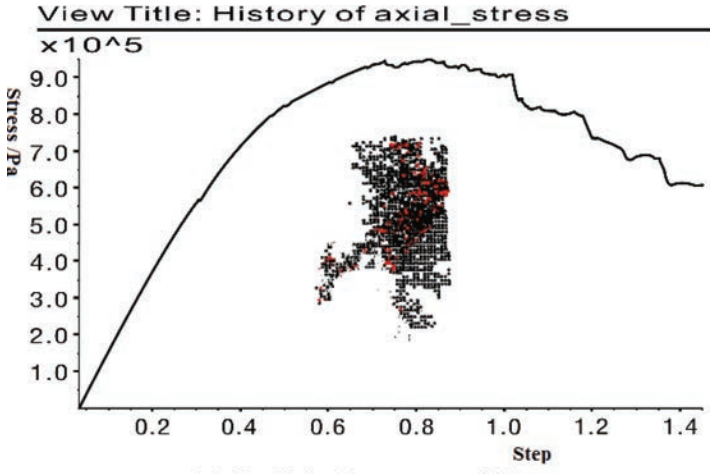

(a) Confining Pressures = 0KPa

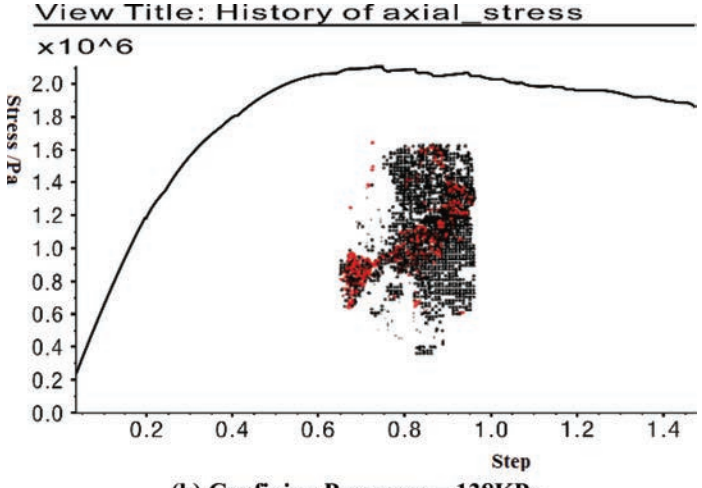

(b) Confining Pressures = 138KPa

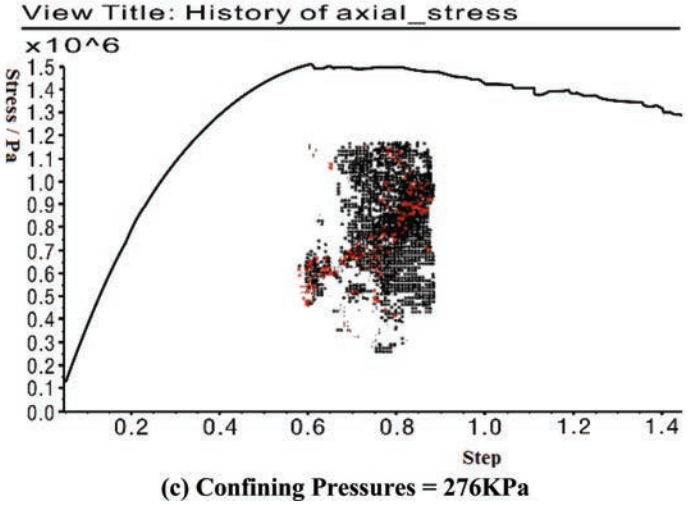

(c) Confining Pressures = 276KPa

Figure 8. Stress (Pa) versus step (10^7). DEM simulation results of Sup13 mix under triaxial compression test at different confining pressures (That Is 0 KPa, 138 KPa and 276 KPa, from (a) to (c)).

of variables can be predicted with 3D discrete element simulations under cyclic loading conditions. For comparison with laboratory test result, the axial stress is obtained at two confining pressure levels (20 and 40 psi), while the peak stresses were 1.815 MPa and 2.166 MPa. Average values of the laboratory test are shown in Figure 7.

The virtual specimen is subjected to DEM triaxial compression at 0 KPa, 138 KPa and 276 KPa of confining compression. For the sake of brief, here just the results for the Sup13 specimens are presented. Other two types compacted mixes, have the same deformation. Figure 8 shows stress changes in each step. Under the stress-time curves, the change of aggregate-binder-aggregate contacts in virtual specimen is presented. It indicates that the deformation of DEM specimen was calculated under triaxial compression test at different confining pressures. It should be noted that the red dots represent aggregate-binder-aggregate contacts that being destroyed by extend stress, and the black represents aggregate-binder-aggregate contact being destroyed by compression stress. Results from Figures 7 and 8 show that the peak stresses obtained from of DEM simulation are in agreement with the results obtained from laboratory test.

Figure 9 shows the change of specimens before and after loading for DEM simulation and laboratory test. It is obvious that both DEM specimen and laboratory test specimen, in

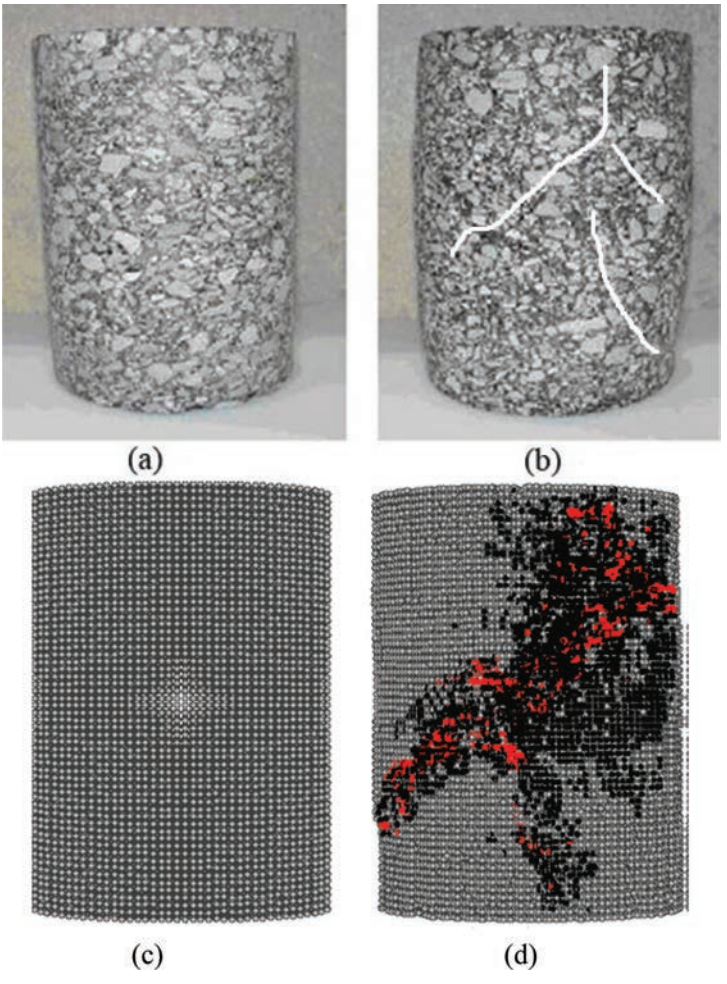

Figure 9. Specimens before and after loading for DEM and laboratory test. The original state of laboratory test specimen is shown in (a) Original state, and (b) The dilatancy state after loading; The original state of DEM specimen is shown in (c) Original state, and (d) Shows the dilatancy state after loading.

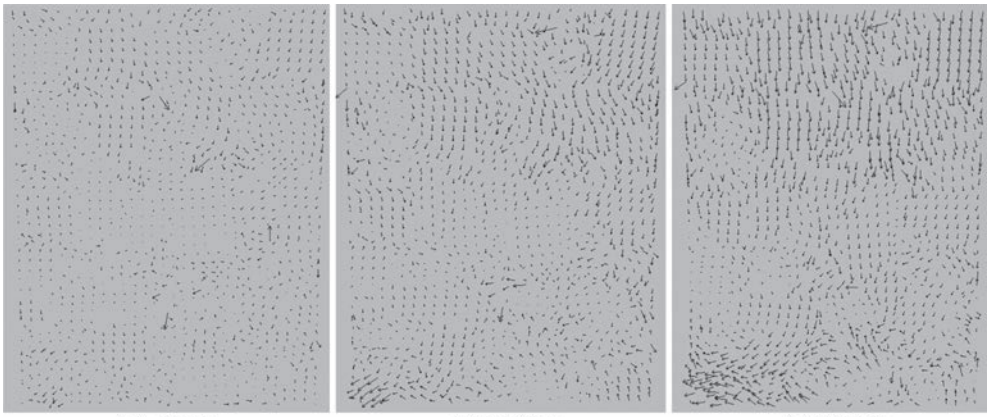

Figure 10. Displacement of digital specimen under 69 KPa, 138 KPa and 276 KPa confining pressures at the middle plane of sample.

original state didn't have the dilative behaviour, on the contrary, there was obvious dilatancy after the specimen was loaded. This result verifies the rationality of modeling processes. The shape change in the specimen also can be observed using simulation. Meanwhile, a shear band can be differed from the contact failure distribution zone. And the red dots represent the tension failure while the black dots represent the compression failure. This result indicates that the change or responses inside the specimen can be easily measured by means of testing the virtual specimen instead of the laboratory testing. A micromechanical analysis will be made by virtue of this advantage of the virtual test.

Figure 10 shows that the displacement plots are seen from the middle plane along the digital specimen height (Fig. 9d) under difference confining pressure. From Figure 10 we can see that the as larger confining pressure is applied to the sample the less dilation occurs. It is obvious that the dilative behaviour can be intuitively simulated by DEM. Therefore, DEM can simulate the dilation of asphalt mixture and it has a very good prospect in the pavement materials field although asphalt mixture has complex heterogeneous nature and mechanic characteristics.

6 CONCLUSIONS

It is important to understand the mechanism of dilation for asphalt pavement design, which helps to explain the rutting mechanism of asphalt pavement. This paper further studies the mechanism of dilation of asphalt mixture through analyzing the microstructure of asphalt mixture using DEM. Several conclusions are reached as following.

A microstructure model of asphalt mixture is established including irregular shape aggregate, asphalt binder mortar phase and air void phase. Digital samples are prepared with random generating algorithm represented by clump, and asphalt mastic is simplified as unit particles. Results show that the virtual specimen behaves similar to the actual specimen in triaxial compression test and has the correct volumetric proportions.

Statistical regression method is developed to capture varying air void distributions along pavement depth. Based on this method, the air void phase of virtual specimen was built, which is close to the real asphalt pavement.

In the mechanical model, Burger's viscoelastic contact model has been used in the DEM viscoelastic simulations. The parameter of Burgers was regressed under triaxial compression test to capture the microstructure parameters.

Based on the sieving mechanism analysis, an algorithm for coarse aggregate structure was developed. This algorithm can create irregular shapes based on a polyhedron unit.

By adjusting the orientations and lengths of the line segments, an aggregate with more variable irregular shapes can be obtained without changing its size.

The result of laboratory triaxial compression test was in good agreement with the result of DEM simulation. Both of these methods show that there was obvious dilation when the specimen was loaded. At the same time, the aggregate-binder-aggregate contact was fractured and formed a shear band.

A bit effective FISH code was developed to capture the microstructure response during loading, such as the aggregate-binder-aggregate contact. Therefore, the dilatancy behavior of asphalt mixture can be calculated by this method and the skeleton of aggregate can be captured.

ACKNOWLEDGEMENTS

The authors gratefully acknowledge the financial assistance provided by National Natural Science Foundation (NO. 51078089) and the Excellent Doctoral Dissertation of Southeast University (NO. YBJJ1347).

REFERENCES

[1] Song J., Pellinen T., Dilation Behavior of Hot Mix Asphalt Under Triaxial Loading, Road Materials and Pavement Design, 2007, 8 (1): 103–125.
[2] Wang Linbing, Hoyos Laureano R., Mohammad Louay, Chris Abadie, 2005. Characterization of Asphalt Concrete by Multi-Stage True Triaxial Testing. Journal of ASTM International, 2(10): Paper ID: JAI12276.
[3] O. Reynolds, On the dilatancy of media composed of rigid particles in contact with experimental illustrations, Philos. Mag. Ser. 5 20 (1885): 469–481.
[4] O. Reynolds, Experiments showing dilatancy, a property of granular material, possibly connected with gravitation, Proc. R. Inst. G.B. 11 (1886): 354–363.
[5] Rowe P.W. The Stress-Dilatancy Relation for Static Equilibrium of an Assembly of Particles in Contact. Proceeding Royal Society, 1962, 269 (1339): 500.
[6] Rowe, P.W., The stress dilatancy relation for static equilibrium of an assembly of particles in contact. Proc. of Royal. Sot. A, 1962, 269, 50&527.
[7] Rowe, P.W., Theoretical meaning and observed values of deformation parameters for soil. In *Stress-Strain Behaviour of Soils, Roscoe Memorial Sysposium.* ed. R.H.G. Parryh, Cambridge University, The Whitefriars Press Ltd., London and Tonbridge, 1971, pp. 143–194.
[8] Nova, R. and Wood, D.M., A constitutive model for sands in triaxial compression. *Int. J. Numer. and Anal. Methods* Geomech., 1979, 3, 255–278.
[9] Wan R.G., Guo P.J. (1998) A simple constitutive model for granular soil: Modified stress—dilatancy approach, Computers and Geotechnics, 22 (2): 109–133.
[10] Wan, R.G. and Guo, P.J., Coupled dilatancy-compaction model for homogeneous and localized deformation of granular materials. *Numerical Models in Geomechanics VI: NUMOG VI:* ed. S. Pietruszczak and G.N. Pande, 1997, 3–8.
[11] Robert F.L., Mohammad L.N., and Wang L.B., History of hot mix asphalt mixture design in the United States, ASCE 150th anniversary civil engineers paper, journal of materials in civil engineering, 2002, 14 (4): 279–293.
[12] Fu, Y., Wang, L., and Tumay, M.T. Experimental quantification and DEM simulation of irregular particle kinematics and local strains. Journal of Mechanics and Materials, 134 (2), 143–154, 2008.
[13] Habtamu Z., Tom P. Simulation of Asphalt Concrete Uniaxial Creep using Discrete Element Method (DEM). ASCE Geotechnical Special Publication Pavement Mechanics and Paving Materials, pp. 99–110, 2010.
[14] Chen Jun, Pan Tongyan, Huang Xiaoming. Micromechanical Modeling of Asphalt Concrete Fracture Using a Three-Dimensional Discrete Element Method. Journal of Wuhan University of Technology-Mater. Sci. Ed., pp. 1215–1221, 2011.
[15] You, Z, Liu, Y., and Qingli, D. Three-dimensional Micro structural-based Discrete Element Viscoelastic Modeling of Creep Compliance Tests for Asphalt Mixtures. J. of Materials in Civil Eng. 23(1), pp. 79–87, 2011.

[16] Buttlar, W.G., and You, Z. (2001). Discrete element modeling of asphalt concrete: Microfabric approach. Transportation Research Record. 1757, Transportation Research Board, National Research Council, Washington, D.C., 111–118.
[17] Liu Yu and You Zhanping. Visualization and Simulation of Asphalt Concrete with Randomly Generated Three-Dimensional Models. Journal of Computing in Civil Engineering, ASCE, 23 (6), pp. 340–347, 2009.
[18] Zhang Jiantong, Yang Jun*, Zhu Haoran. Research on shear dilation behavior of asphalt mixture, Journal of Building Materials, 2014, 17 (1): 97–102 (in Chinese).
[19] Cundall, P.A., Strack, O.D.L.: Adiscrete numerical model for granular assemblies. Géotechnique **29**(1), 47 (1979).
[20] Lu M., McDowell G.R. The importance of modeling ballast particle shape in the discrete element method. Granular Matter, 9: 69–80, 2007.
[21] You, Z., and Adhikari, S. Models for Asphalt Mixtures Using X-Ray Computed Tomography Images. International Journal of Pavement Research and Technology, 1(3), pp 94–99, 2008.
[22] Hu Chichun, Wang Duanyi, Zhang Xiaoning. Characterization of Asphalt Mixture Homogeneity Based on X-ray Computed Tomography. Journal of Testing and Evaluation, 40 (7), pp 1103–1111, 2012.
[23] Masad Eyad, Castelblanco, A, Birgisson, B. Effects of air void size distribution, pore pressure, and bond energy on moisture damage, Journal of Testing and Evaluation, 2006, 34(1), Paper ID: JTE13112.
[24] Masad Eyad, Dessouky Samer, and Little Dallas, Development of an Elastoviscoplastic Microstructural-Based Continuum Model to Predict Permanent Deformation in Hot Mix Asphalt, International Journal of Geomechanics, 2007, 7 (2): 119–130.

Asphalt Pavements – Kim (Ed)
© 2014 Taylor & Francis Group, London, ISBN 978-1-138-02693-3

Fatigue characters of asphalt multilayer surfacing system on steel bridge deck based on the five-point bending tests

Xueyan Liu, George Tzimiris, Tom Scarpas & Jinlong Li
Section of Road and Railway Engineering, Delft University of Technology, Delft, The Netherlands

ABSTRACT: Orthotropic steel deck bridges become popular the last decades due to lightweight and flexibility but then again several problems were reported in relation to asphalt surfacing materials such as rutting, cracking and loss of bond between the surfacing system and the steel deck. In The Netherlands a surfacing structure for orthotropic steel bridge decks mostly consists of five structural layers: top porous asphalt layer, guss asphalt layer, steel deck and two membrane layers.

The five-point bending (5PB) beam test is the standard device in France for characterization of fatigue response of asphalt concrete used on steel orthotropic deck bridges. In this investigation, the 5PB test was employed in order to evaluate the fatigue life of the asphalt multilayer structure on steel deck and also to evaluate the mechanical properties of both top and bottom membrane and the influence they have on the structure. Four membrane products were utilized as the top and bottom membrane layers in the 5PB beams. Furthermore, in the last part of this paper, the dissipated energy has been utilized to explain the incremental damage during the testing.

Keywords: Five-point bending beam test, orthotropic steel deck bridge, membrane, fatigue life, dissipated energy

1 INTRODUCTION

The world-wide reported distress problems between the surfacing layers and the Orthotropic Steel Deck Bridges (OSDB) indicate the need for further research on the interaction between them. The severity of the problem is enhanced by the considerable increase in traffic in terms of number of trucks and heavier wheel loads. Innovative methodologies offer opportunities to mitigate material response degradation and fatigue related problems in this type of structures contributing thus to significant extension of the service life of steel bridges [1].

The fatigue life assessment of OSDB hasn't yet been sufficiently investigated. The inspection results of orthotropic steel decks have shown that their working life can be shorter than other members of steel bridges due to fatigue [1], [2]. This means that particular details of orthotropic decks can be critical regarding the service life of a bridge.

Preliminary investigations have shown that the adhesive strength of the membrane between the surfacing layers and the decks of steel bridges has a strong influence on the structural response of OSDB. The most important requirement for the application of membrane materials on OSDB is that the membrane adhesive layer shall be able to provide sufficient bond to the surrounding materials.

Recently, the Transport Research Centre (DVS) of the Dutch Ministry of Transport, Public Works and Water Management (RWS) has initiated a research project for the evaluation of the performance of modern surfacing systems on steel deck bridges. The research project focuses mainly is on membrane performance and the effects hereof on the structure as a whole.

The Five Point Bending (5PB) beam test is a laboratory scale test that allows studying the fatigue resistance of surfacing layers on orthotropic bridge decks [1]. [3] in 1981 reported the most severe load case for surfacing layers of OSDB is when they are subjected to negative moments. The 5PB beam test has become a French standard test method (NF-P98-286, 2006) [1].

For the purposes of this paper 5PB beam tests were performed at TU Delft in order to understand if this type of test can be directly used to evaluate the performance of the multilayer asphalt surfacing system on OSDB and also to perform a laboratory scale test that would allow studying the fatigue resistance of surfacing layers on OSDB.

In the first part of this paper the experimental device of the 5PB, the test conditions and the instrumentation are described. In the second part, four membrane products ranked by the Membrane Adhesion Test (MAT) [4] were utilized as the top and bottom membrane layers in the 5PB beams. The results of the 5PB beam tests at two temperatures –5°C and +10°C are demonstrated. The results show that the in time deformation measurements are allowable to evaluate the fatigue response of the entire structure. The stiffness and the bonding characteristics of the intermediate membrane sheet as well as the wearing course behaviour seem to have great influence on the mechanical response of multilayer bridge surfacing system. The findings of the 5PB beam tests will assist the verification and the calibration of the finite element predictions and will allow for the further ranking of the best performance of the multilayer surfacing systems for Dutch OSDB.

Furthermore, in the last part of this paper, the fatigue damage in 5PB beam test is related to the amount of dissipated work computed by using the measurement of the actuator load and the loading plate deformation during the loading cycle. The dissipated work, which is equivalent to the lost part of the total potential energy of the beam, has been utilized to explain the incremental damage during the testing.

2 DESCRIPTION OF THE FIVE-POINT BENDING TEST

In order to assess the fatigue resistance of the multilayer asphalt surfacing system on OSDB, the French Five-Point Bending (5PB) beam test has been used. It was developed by the "Laboratoire Central des Ponts et Chausse´es" (LCPC) in the 70s, and its main advantage is the ability to safely represent the conditions on a real steel deck applying negative moments [5]. This occurs at the alignment of the stiffener web when each of the wheels of a double tyre is positioned at each side of the web Figure 1.

In The Netherlands, an asphaltic surfacing structure for OSDB mostly consists of two structural layers, Figure 1. The upper layer consists of Porous Asphalt (PA) for noise hindrance related reasons. For the lower layer, a choice between Mastic Asphalt (MA) and Guss Asphalt (GA), can be made [6]. Therefore, in order to study the fatigue response of the typical Dutch steel deck bridge, 5PB beam sample with the two wearing course bonded by two membrane sheets are investigated.

The 5PB beam sample consists of a 10 mm-thick steel plate, a 2 to 4 mm-thick bottom membrane, a 30 mm Guss asphalt layer, a 4.7~4.8 mm-thick top membrane and a 40 mm thick porous asphalt layer. The test samples is 100 mm wide, see Figure 2.

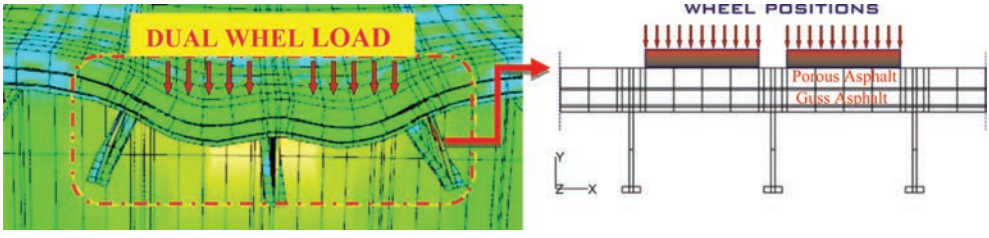

Figure 1. Schematic representation of the area of concern.

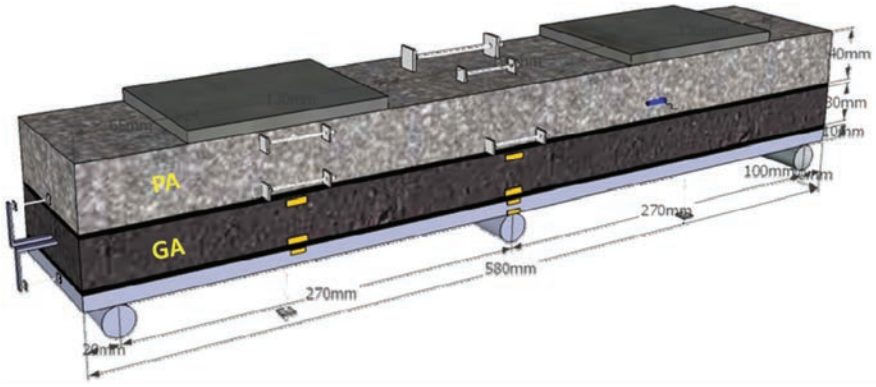

Figure 2. Specimen geometry and composition.

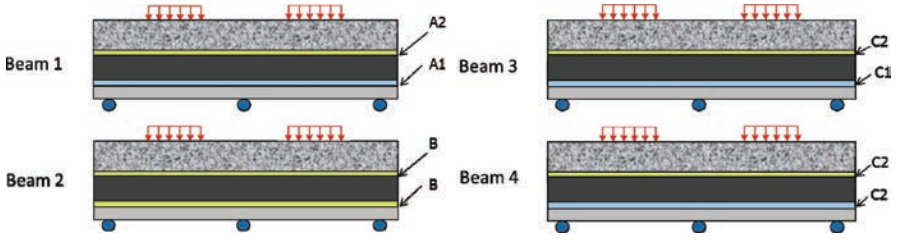

Figure 3. Four different types of specimen.

For the sample preparation a steel plate with 580 mm × 100 mm × 10 mm was used. Four different types of samples have been prepared, named as beam 1 bonded with membrane product A1 and A2 from company A, beam 2 bonded with membrane products B from company B, beam 3 bonded with membrane product C1 and C2 from company C and beam 4 bonded by membrane C2 from company C, see Figure 3.

2.1 *Experimental set up*

Both static and fatigue loading tests were performed under two temperatures ranges (–5°C and +10°C), Figure 4. The static loading tests were performed prior to the fatigue tests by using ramping load. The maximum ramp load is 18.4 kN and the ramp time to maximum load is 40 sec. For the fatigue tests, sinusoidal compression loading P ranging between F_{max} and $0.1 \times F_{max}$ at a frequency of 4 Hz was applied for two million cycles. In order to perform the tests under controlled temperature conditions, the set up was properly insulated and enclosed within a climate chamber.

The test samples are 100 mm wide and therefore each loading shoe print is 130 mm long and 100 mm wide. The pressure load applied on each shoe is 0.707 MPa. This load pressure corresponds to 9.2 kN on each shoe (0.707 MPa × 130 mm × 100 mm), which means a total of 18.4 kN were applied on the sample, see Figure 5. If the same load pressure is applied on a wheel print type B (double tyre 220 mm by 320 mm), it corresponds to 100 kN wheel load which is the typical truck load utilized in The Netherland.

2.2 *Tested membrane materials*

Product A1 and A2 are waterproof membranes manufactured with SBS elastomeric bitumen and internally reinforced with a non-woven polyester textile. These two products are implemented on concrete decks, steel decks, sand asphalt or asphalt concrete. Product A1 is

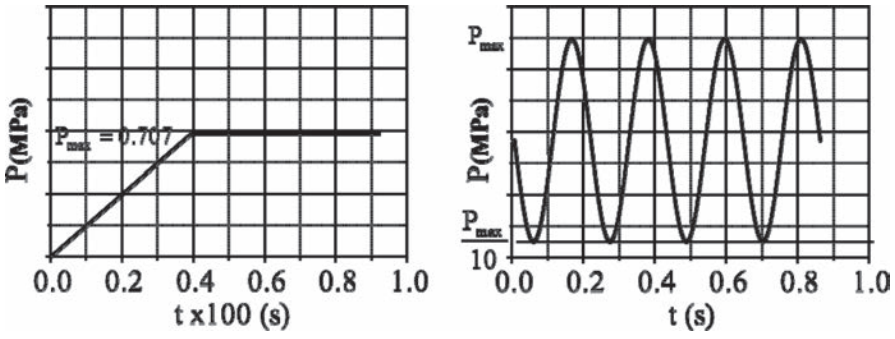

Figure 4. Static and dynamic loading scheme.

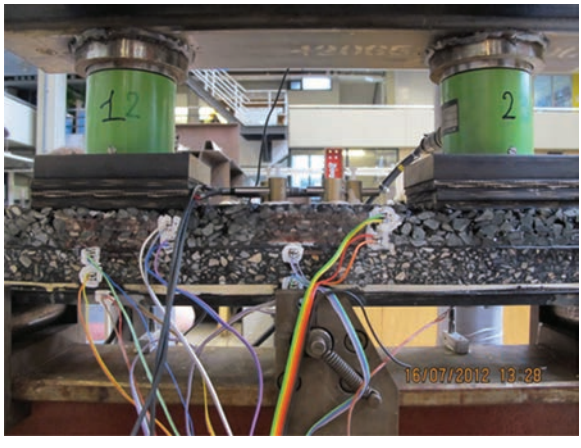

Figure 5. The five-point bending beam test set up.

applied on the steel plate, while product A2 is applied on the Guss aspahlt. Product A1 and A2 can be bonded to the prepared substrate by melting the film on the membrane surface and softening of the bitumen.

Another membrane product is manufactured by company B. This product B can be used as both bottom membrane and top membrane in steel bridge systems. Product B is used as moisture insulation layer on the surfacing system. This membrane is made of a high SBS modified isolation diaphragm which is reinforced with a strong support of polyester.

There are two types of membranes from company C. Product C1 is used only as bottom membrane, whist product C2 can be used both as top and bottom membranes in asphalt surfacing systems on a steel bridge decks. Product C1 is a 2.4 mm single-Ply membrane, with non-woven polyester fleece. This product is used for the single-play sealing under stone mastic asphalt, mastic asphalt or bituminous concrete.

Product C2 is a 4.7 mm single-Ply membrane with 1.5 mm strong fleece. This membrane is provided with a modified bituminous mass of 1.6 mm thickness on both sides. Product C2 is a waterproofing membrane for bridges, and it can provide high resistance to traffic.

3 RESULTS AND DISCUSSIONS

3.1 *Static tests*

The static tests were performed prior the fatigue tests until a maximum total load of 18.1 kN was reached, corresponding to a load pressure 0.707 MPa on each shoe The ramp time to

maximum load is 40 sec. The strains recorded by the strain gauges during the static test can be compared with the strain predictions from the FE simulations but also can give an indication about the integral response of the beam layers.

Figure 6 indicates the two cross sections where the strains have been recorded. Figures 7 and 8 show the transversal strains recorded during the static tests along the thickness of the tested beam. As it can be seen all tested beams produce higher strain values at 10°C rather than at –5°C. The influence of the temperature on the strain of the steel deck plate is not significant. Maximum tensile strain for all tested beams is recorded at the top face of the PA while maximum compressive strain at the bottom of the PA close to the top membrane.

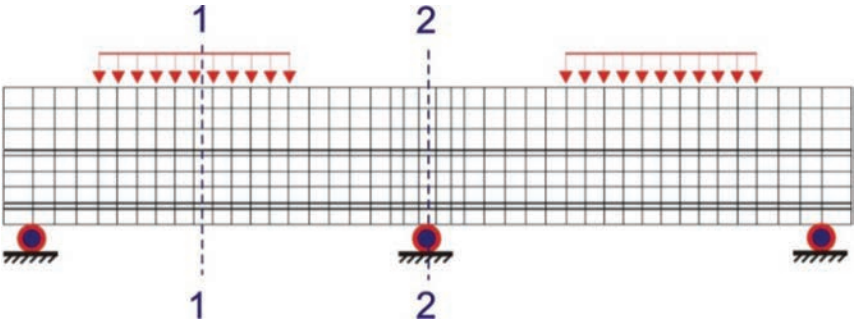

Figure 6. The area of concern.

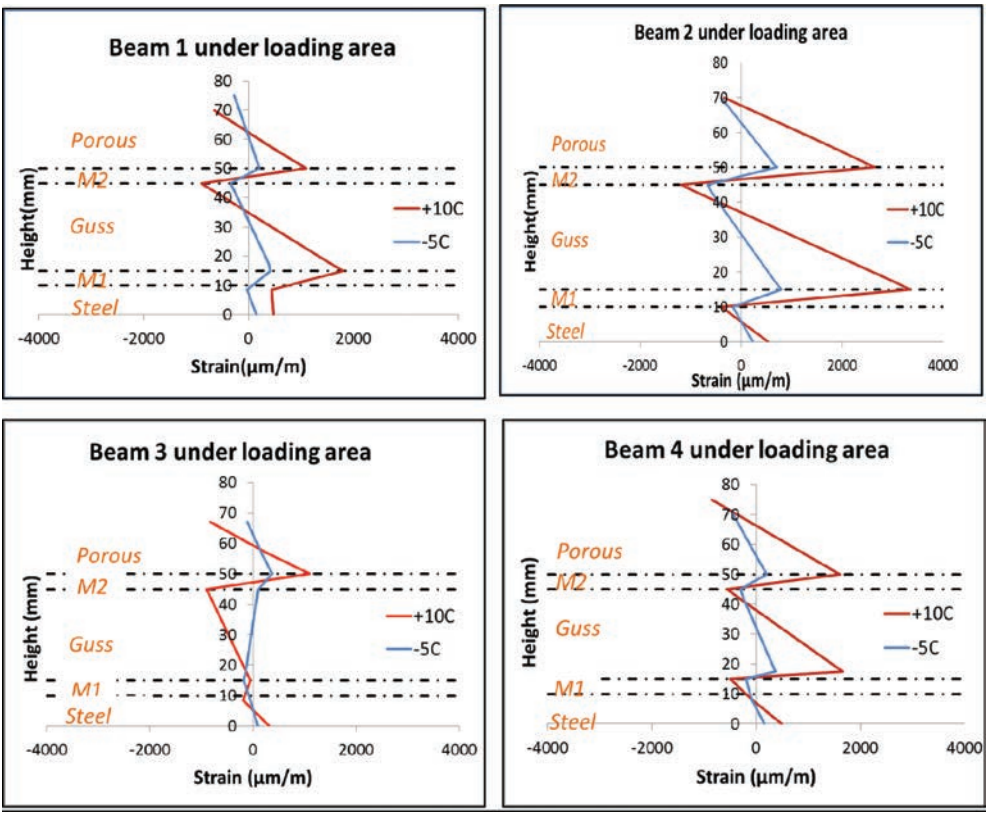

Figure 7. Strain distribution below the loading area, cross section 1-1.

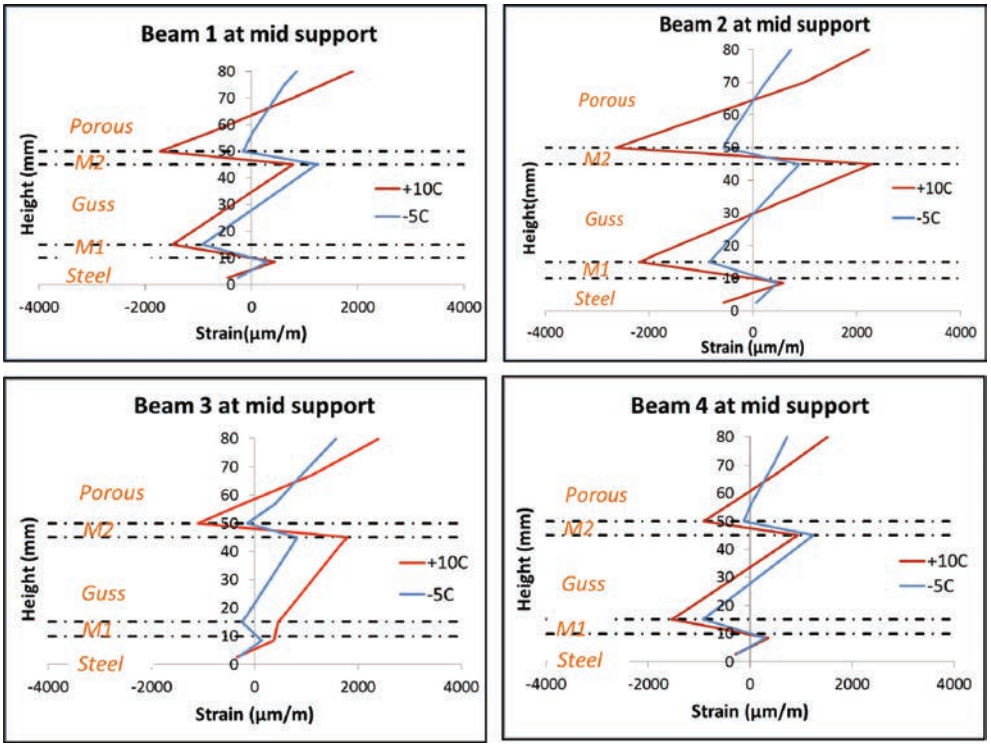

Figure 8. Strain distribution above the middle support, cross section 2-2.

3.1.1 *At cross section 1-1*

Beam 2 was found to be the most vulnerable one with higher strain amplitude compared with the rest of the tested beams at 10°C. High strain concentration was also recorded on beam 4 with high tensile strain at the bottom of GA at 10°C. Beam 3 was found to have the lower strain concentration especially at the area close to steel plate both at 10°C and −5°C. Finally, beam 1 has shown good response with low strain values particularly at −5°C.

3.1.2 *At cross section 2-2*

The same observation can be made at the location above the central support, Figure 7. Beam 2 was found to have higher strain both in compression and tension at 10°C. The influence of temperature is obvious for all cases. Beam 3 and 4 were found to be in the same range in term of the strain distribution. At −5°C, beam 3 was found to have the lowest strain values in GA. Beam 3 demonstrates a higher bonding effect between the GA and the steel plate both at −5°C and 10 °C.

3.2 *Fatigue tests*

Extensive effort was directed towards using dissipated work (energy) in the study of fatigue behaviour of asphalt concrete ([7], [8], [9]). The dissipated work approach has many advantages. For example, it is simple in principle and easy to use, requiring only the dissipated energy in each load cycle.

The dissipated work concept has been widely utilized for Four-Point Bending (4PB) beam test to characterize the fatigue life of asphalt concrete mixture. In most cases, the four-point bending beam consists of only one layer of the same mixture. Assuming that the deflection due to the shear is neglected in 4PB, this produces a uniform bending moment and zero-shear between the loading platen. The horizontal normal stress in the beam between the loading

platen can be directly computed by using the bending moment and the geometry of the beam and this results a simplified analysis.

The 5PB test is essential for the design of the asphalt layers on steel orthotropic decks: essential because the metallic structure is very flexible, and as a consequence, the asphalt concrete is submitted to very high levels of strains under traffic load as compared to asphalt on classic roads. The main advantage of 5PB test is the ability to safely represent the conditions on a real steel deck applying negative moments at the alignment of the stiffener web when each of the wheel of a double tyre is positioned at each side of the web. The disadvantage is that, due to the multi-surfacing layered structure and the presence of the middle support, the shear stress in the centre of the beam cannot be neglected. This makes the analysis become more complicated than the one required for the 4PB beam test. Also the fatigue damage can occur not only at asphalt concrete surfacing layers but also at the interface between the membrane bonding layers and the surfacing layers.

In this investigation, the fatigue damage of the 5PB beams is related to the amount of Dissipated Work (DW) computed by using the measurement of the actuator load and the loading plate deformation during the loading cycle. The dissipated work, which is equivalent to the lost part of the total potential energy of the beam, can be used to explain the incremental damage during the testing. The amount of dissipated work (energy) per loading cycle changes throughout the fatigue test. The average Ratio of Dissipated Work Change (RDWC) is used to relate damage accumulation in 5PB beams. The theoretical background of dissipated work can be found in [8], [10] and [11].

3.2.1 *Experimental results*

Under the controlled load mode of the 5PB tests, with a limited number of load cycles, the development of dissipated work in the four types of 5PB beams show two distinctive stages in Figure 9: (I) The dissipated work increases by decreasing the dissipated work reduction rate, (II) The dissipated work increases gradually with almost a constant slope (constant energy change rate). At higher temperature, under the same loading condition, all the tested beams show higher dissipated work than those at lower temperature. Since the value of the dissipated work can be used to explain the incremental damage during the testing, beam 3 bonded with membrane C1 and C2 shows less damages than the other three beams. The highest damage occurs for beam 2 bonded with membrane B at higher temperature.

In Figure 10, it can be observed that at both test temperatures the RDWC values for the four types of beam at two different temperatures are almost constant after 8000 load cycles. This proves that the second stage is reached (the plateau stage) where the plateau value can be found. This plateau value characterizes a period where a constant percentage of input energy is turned into beam damage. The analysis of the testing data indicates that such a plateau stage starts from approximately the 20% initial structure stiffness reduction until the 50% initial structure stiffness reduction. At higher temperature, the 5PB beams show higher RDWC values than those with lower temperature. Beam 3 with membrane product C1 and C2 at lower temperature shows almost no energy being turned into beam damage.

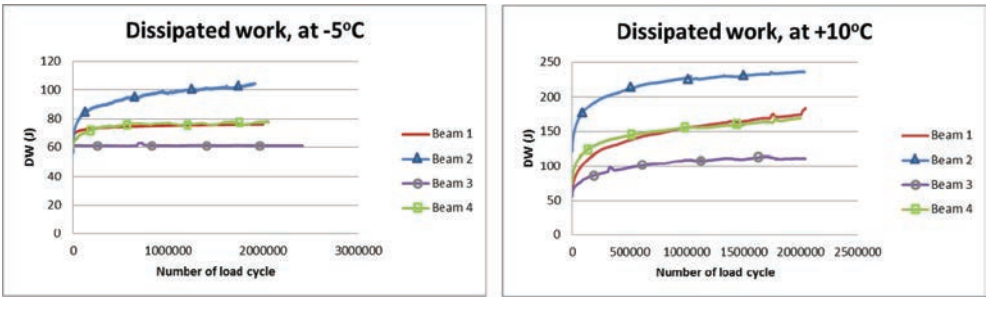

Figure 9. Comparison of dissipated work of 5PB beams.

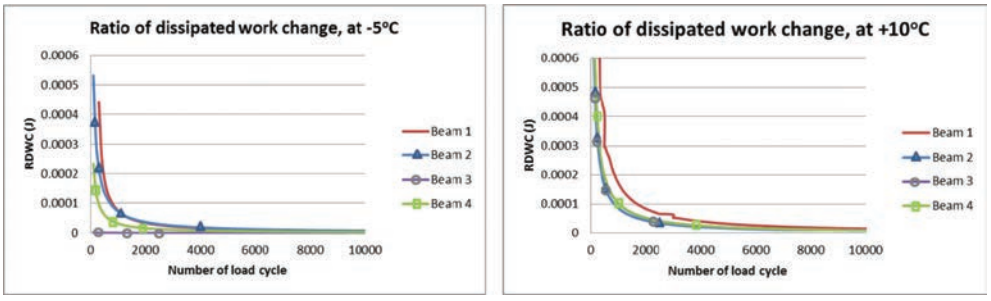

Figure 10. Comparison of ratio of dissipated work change of 5PB beams.

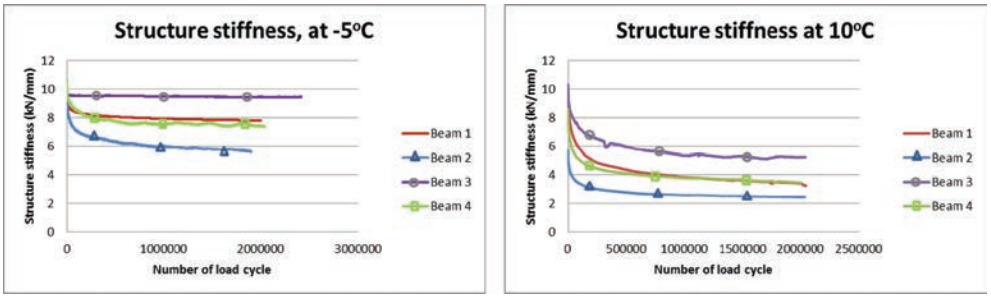

Figure 11. Comparison of structure stiffness in four types of 5PB beams.

Table 1. Comparison of fatigue life of 5PB beams at temperature of 10°C.

Failure criterion	Nf_{50}	DW (J)	RDWC (J)
Beam 1	300000	126.95	5.35e-07
Beam 2	260000	197.91	3.65e-07
Beam 3	2000000	114.52	5.83e-08
Beam 4	350000	137.69	3.25e-07

In this study, similar as the traditional failure definition, the structure stiffness of the 5PB beam is used instead of the material complex modulus. Figure 11 shows the decreasing structure stiffness of the 5PB beam with increasing number of load cycles. The structure stiffness of the 5PB beam is calculated by dividing the total measured actuator load over the load platen deformation during the loading cycle. It can be observed that temperature has important effects on the structure stiffness of the 5PB beams. At higher temperatures, the asphalt concrete layers together with its membrane layers become more flexible. The structure stiffness of the 5PB beam decreases faster at higher temperatures than at lower temperatures.

By a reasonable extrapolation of the testing data, Tables 1 and 2 show the cycles to failure of the 5PB beams with four types of membrane products at 10°C and –5°C respectively. The corresponding values of DW and RDWC at failure are also presented in these tables. It is noticed that using the traditional stiffness approach the predicted fatigue life of the 5PB beam varies from approximately 260,000 to 2 million load repetitions at the temperature of 10°C. Greater load repetitions are predicted for 5PB beam tested at –5°C.

By comparing Figure 9 to 11 along with the data presented in Tables 1 and 2, it can be observed that beam 3 bonded with membrane products C1 and C2 performs better than beams bonded with other membrane types at the two different testing temperatures, proving

Table 2. Comparison of fatigue life of 5PB beams at temperature of −5°C.

Failure criterion	Nf_{50}	DW (J)	RDWC (J)
Beam 1	2.5e+12	97.34	2.47e-14
Beam 2	6.0e+06	112.22	1.34e-08
Beam 3	1.0e+100	65.4	1.2e-102
Beam 4	1.0e+10	103.36	4.03e-12

that this is the best performing mult-surface layer system for the Dutch orthotropic steel deck bridges.

4 CONCLUSIONS

The main findings that can be drawn from the results presented in this paper are summarized as follows:

- The Five-Point Bending (5PB) beam test is a good tool for the study of the composite behavior of multilayer surfacing systems on orthotropic steel deck bridges.
- The response of the 5PB beam with different surfacing systems differs significantly with temperature due to the high temperature sensitivity of the asphaltic materials and the membranes.
- The results of the 5PB beam tests can be utilized for calibration and validation of the finite element tools and allow additional insight into the overall ranking of multilayer surfacing systems.
- 5PB beam 3 with membrane products C1 and C2 has shown the longer fatigue life in comparison to the other three beams with different surfacing systems. Beam 1 and 4 can be recommend as a second option.
- The concept of dissipated energy/work provides a means to quickly estimate the fatigue life of laboratory 5PB fatigue tests. The procedure introduced in this paper presents a simple method of fatigue behaviour analysis at different temperatures based on an energy approach.

ACKNOWLEDGEMENTS

This work is part of the research program of InfraQuest. InfraQuest is a collaboration between Rijkswaterstaat, TNO and the Delft University of Technology. This research project is partially funded by the Dutch Transport Research Centre (DVS) of the Ministry of Transport, Public Works and Water Management (RWS). Their financial support is highly appreciated.

REFERENCES

[1] Mangus, A.R. and Sun, S., *Orthotropic Bridge Decks. Bridge Engineering Handbook*, ed. W. Chen and L. Duan, Boca Raton: C.R.C. Press. 1999.

[2] Medani, T.O., Liu, X., Huurman, M., Scarpas, A & Molenaar, A.A.A. *Characterisation of surfacing materials for orthotropic steel deck bridges—Part 1: experiment work*. The International Journal of Pavement Engineering, (ISSN 1029-8436), vol. 11(3), pp. 237–253, 2010.

[3] Hameau, G., Puch, C., Ajour, A.M: *Fatigue Behaviour due to Negative Bending Moments* (in French), Revétments de Chaussées sùr platelages métalliques, 1981.

[4] Liu, X., and Scarpas, A. *Experimental and Numerical Characterization of Membrane Adhesive Bonding Strength on Orthotropic Steel Deck Bridges, Part 1*. Project report CITG2012-1, Delft University of Technology, The Netherlands, 2012.

[5] Houel, A., N'Guyen, T.L. and Arnaud, L. *Monitoring and Designing of Wearing Courses for Orthotropic Steel Decks Throughout the Five-point Bending Test*. Advanced Testing and Characterisation of Bituminous Materials, Vols 1 and 2, 2009, pp. 433–442.
[6] Liu, X., Medani, T.O., Scarpas, A., Huurman, M. and Molenaar, A.A.A. *Experimental and Numerical Characterization of a Membrane Material for Orthotropic Steel Deck Bridges: Part 2—Development and Implementation of a Nonlinear Constitutive Model,* Finite Elements in Analysis and Design, vol. 44, pp. 580–594, June 2008.
[7] Van Dijk, W. *Practical Fatigue Characterization of Bituminous Mixes*. Proceedings of the Association of Asphalt Paving Technologists, vol. 44, pp. 38–74. 1975.
[8] Van Dijk, W. and Visser, W. *The Energy Approach to Fatigue for Pavement Design*. Proceedings of the Association of Asphalt Paving Technologists, vol. 46, pp. 1–40. 1977.
[9] Carpenter, S.H., and Jansen, M. *Fatigue Behavior Under New Aircraft Loading Conditions*. In Aircraft/Pavement Technology: In the Midst of Change, seattle, Washington, 17–21 August 1997. Edited by F.V. Hermann. American Socity of Civil Engineers, New York. pp. 259–271. 1997.
[10] Ghuzlan, K. *Fatigue Damage Analysis in Asphalt Concrete Mixtures Based upon Dissipated Energy Concept*. PHD thesis. University of Illinois at Urbana-Champaign, August, 2001.
[11] Shen, S., Carpenter, S.: *Dissipated Energy concept for HMA Performance: Fatigue and Healing, Department of Civil and Environmental Engineering*. University of Illinois at Urbana-Champaign: Urbana, Illinois. 2007.

Asphalt Pavements – Kim (Ed)
© 2014 Taylor & Francis Group, London, ISBN 978-1-138-02693-3

Determination of binder-aggregate adhesion by contact angle measurement

Robert Aranowski & Przemysław Wojewódka
Gdansk University of Technology, Gdansk, Poland

Krzysztof Błażejowski
ORLEN Asfalt Sp. z o.o., Plock, Poland

ABSTRACT: The key factor in asphalt pavement durability, especially in the presence of water, is adhesion of the bituminous binder to mineral aggregates. There are currently no standard laboratory test procedures that can quickly and accurately measure the strength of the interaction (bond) between the binder and aggregate. In this regard, to evaluate the adhesion force measurements based on the contact angle between the binder and the aggregate by goniometric method were conducted. Contact angles at the mineral-binder-air interface were measured using a high temperature contact angle goniometer by a sessile drop technique. The influence of five adhesion promoters at different temperature (40 to 200°C, 104 to 392°F) for two minerals, granite and limestone, has been investigated. The road binder 35/50 (pen@25°C or @77°F) was used as the bituminous phase. Obtained results show that for granite, for nearly all used promoters, adhesion is better than for pure binder. In case of limestone, the difference of measured contact angles between pure binder and binder with additives is not evident and one can say that activity of some promoters is neutral or adhesion could be even worse. The results of contact angle tests at the full range of temperature can be used also for adhesion assessment for Warm Mix Asphalt (WMA) technologies.

Keywords: binder, aggregate, adhesion, contact angle

1 INTRODUCTION

The key factor in asphalt pavement durability, especially in the presence of water, is adhesion of the bituminous binder to mineral aggregates. However, the important role of adhesion between binder and aggregate has been recognized for almost one hundred years (Nicholson, V. 1932), but still no standard laboratory test procedures, that can quickly and accurately measure or estimate the strength of the interaction (bond) between the binder and aggregate.

In the recent studies it has been well documented that the work of adhesion between binder and aggregate is an important parameter determining the resistance of asphalt mixtures to fatigue cracking and moisture-induced damage. Many methods and techniques were used to determine the adhesive bond strength between aggregate and bituminous binder [2, 3, 9, 10]. Hefer et al. [1, 7] determined the surface free energy of binders and aggregates individually using the contact angle method using the Wilhelmy plate device.

Already in the seventies Ensley and Scholz [4, 5, 6] measured the work of adhesion between the binder and the aggregate using a microcalorimeter.

Also many estimations of surface free energy of aggregates were computed using the acid-base theory [12, 13] or were determined using the vapor adsorption method with a Universal Sorption Device (USD) manufactured by Rubotherm of Germany.

All of these methods are time consuming and require expensive test equipment. Therefore we evaluated the adhesion force by measuring the contact angle between the binder and the aggregate with goniometric method. Contact angles at the mineral-binder-air interface were measured using a high temperature contact angle goniometer by a sessile drop technic [8].

For testing the road binder paving grade 35/50 acc. to European Standard EN 12591 was used. This type of binder is usually used for building lower layers of road pavement structures, i.e. binder courses and asphalt bases. As an aggregate (mineral) material two types of rock were used: limestone and granite, representing different types of rock in respect of silica dioxide (SiO_2) content.

2 EXPERIMENTAL

2.1 *Fine binder spherical particles preparation*

The road binder paving grade 35/50 (range of needle penetration @25°C or @77°F, acc. to EN 1426), detailed properties of which are presented in Table 1, was used as the bituminous phase in the contact angle measurements. The binder samples with mass between 80 to 100 g were heated to 105°C (221°F) and the commercially available adhesive promoters were added and continuously mixed. The concentration of additives was 0.50 ± 0.01% by mass. The chemical composition of additives is presented in Table 2. In the next step the mixtures were heated to 170°C (338°F) and intensively mixed for 5 min with a rotational speed of 500 min^{-1}.

After mixture preparation, spherical binder particles were formed by rolling a small quantity of binder between two stainless steel plates at ambient temperature (about 20°C, 68°F). The range of binder particle size was from 0.5 mm to 1 mm. The spherical shapes of the binder particles were then checked by analyzing photos made with digital camera of particles in the Image Tools software to ensure that shapes are correct.

2.2 *Mineral aggregate samples preparation*

Mineral aggregates (granite and limestone grains 8–11 mm fraction), were crushed to an average particle size of 5–8 mm. Few particles with cubic shapes of the aggregate were dry ground using several abrasive materials with decreasing granulation (180, 220 mesh), then were wet ground with granulation 400, 500, 600, 800, 1000 mesh. The time period of polishing for each granulation was 5 min. Following this the polished aggregate samples were washed in an ultrasonic bath and examined in detail under an optical microscope for surface defects and scratches. Selected aggregate samples were boiled in distilled water for 20 min, and were

Table 1. Properties of binder 35/50.

Parameter		Road binder 35/50
Penetration at 25°C (@77°F), 0,1 mm (EN 1426)		45
Softening point ring & ball, (EN 1427)		54°C (129.2°F)
Fraass breaking point (EN 12593)		–9°C (15.8°F)
Viscosity, Pa · s	60°C, 140°F [1 s^{-1}]	815
(EN 13302)	90°C, 194°F [100 s^{-1}]	23.98
	135°C, 275°F [100 s^{-1}]	0.91
	150°C, 302°F [100 s^{-1}]	0.41
Acid number, mg KOH/g		0.3
Group composition, % of mass	Asphaltenes	20.8
	Alkanes/saturates	5.7
	Aromatics	27.7
	Resins	41.1

Table 2. Chemical composition of adhesion promoters.

Additive	Chemical composition
A	Fatty amines, amines, tallow alkyl[3-(tetrahydropyrimidinyl)propyl]: >25%
B	Phosphonic esters: >50% Ethoxylated fatty alcohol: <10% Phosphonic acid: <5%
C	Amidoamine >90% Ethylene amine <10% Glycerol <10%
D	Amidoamines, fatty acid C8-22, products of reaction polyalkyl amines and ethanolamines with fatty acid: 70–90% Diethanolamine <10% Have oils: <10%
E	Octylphosphonic acid

Table 3. Period of time needed to reach temperature equilibrium of the samples.

Temperature [°C]	Temperature [°F]	Period of time needed to reach contact angle equilibrium [min]
40	104	30
50	122	30
60	140	30
75	167	15
100	212	15
125	257	15
150	302	10
175	347	10
200	392	5

washed with acetone and dried at 105°C (221°F). The aim of the polishing of aggregates was to obtain a flat surface of the grain's face and eliminate the influence of mechanical adhesion on the contact angle measurements. The surface should be without any defects which can influence on the binder's wetting power.

2.3 *Contact angle measurement*

The polished and cleaned aggregates sample was glued to the measuring goniometer table and, using the optical system within the goniometer, the level was adjusted until horizontal. The prepared spherical sample of binder was carefully placed on the polished surface of the aggregates and the whole sample was placed in the goniometer heated chamber. The sample was heated at 2°C/min (35.6°F/min). When adjusted temperature was reached the photo of the sample has been taken after the period of time shown in Table 3. Different periods of time needed to reach contact angle equilibrium comes from viscosities of the binder at specified temperatures (earlier evaluated). The schematic diagram of contact angle measurement system is shown on Figure 1, photo of the system on Figure 2.

The contrast and brightness of obtained digital pictures were corrected. Using Image Tools software the binder drops shape were approximated by circle as is shown on Figure 3. Next, the line representing interfacial surface area between aggregate and binder drop was set. The contact angle calculation was performed using following equations:

$$\theta = \arccos(2R/d) \tag{1}$$

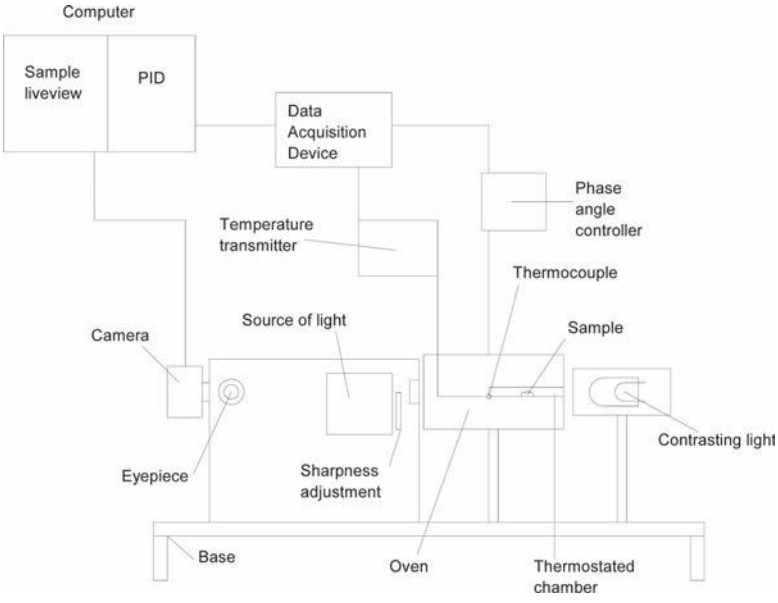

Figure 1. Schematic diagram of contact angle measurement system.

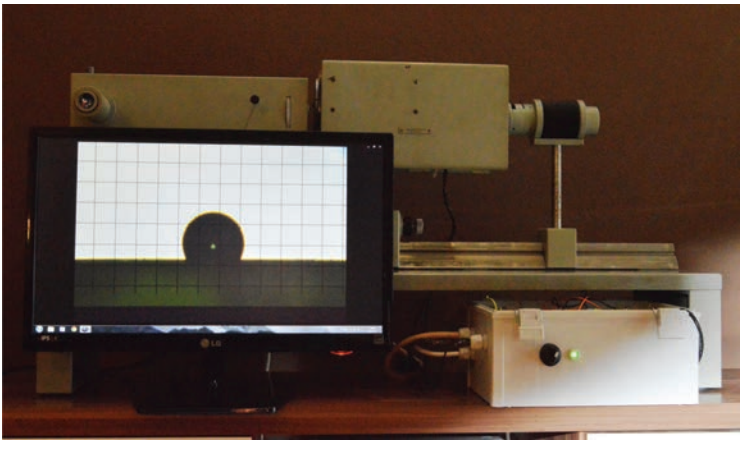

Figure 2. Photo of contact angle measurement system.

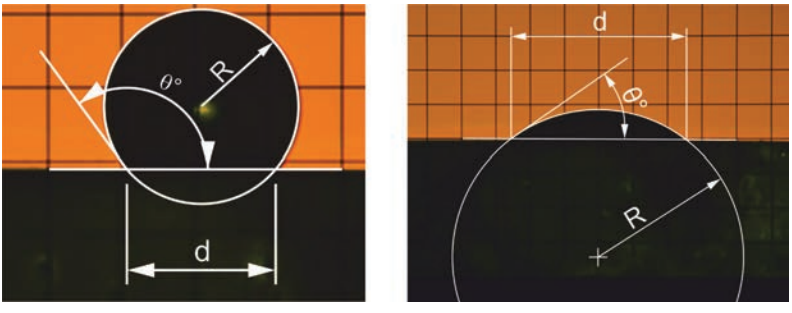

Figure 3. The examples of contact angle measurements methodology.

When the $\theta > 90°$ the contact angle was calculated from Eq. (2).

$$\theta = \arccos(2R/d) + \pi/2 \tag{2}$$

where:

R—radius of circle

d—length of circle diameter of interfacial surface area between aggregate and binder drop.

3 RESULTS

The results of wettability of granite and limestone by unmodified asphalt binder 35/50 are very similar at low temperature ranges (up to 120°C, 248°F). The contact angle was higher than 10 deg in both minerals. In the temperature range 120–200°C (248–392°F) it is clearly evident that the wettability of limestone by bituminous is better than granite (Fig. 4).

The modification of asphalt binder with commercially available additive based on fatty amines (with code A) improved the wettability of the minerals (granite and limestone) especially at higher temperature ranges. The decreasing of the contact angle is much more evident for granite than for limestone which was expected. The repulsive force caused by the hydroxyl group on granite surface is neutralized by the fatty amines, and therefore make the granite surface more hydrophobic (Fig. 5).

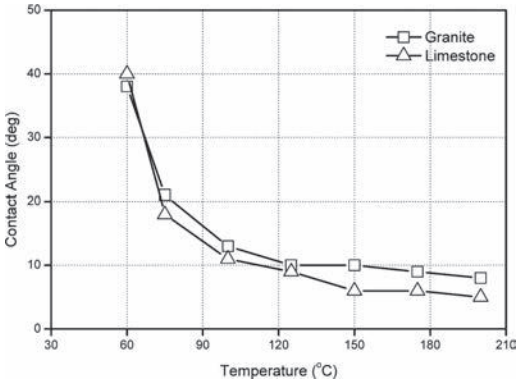

Figure 4. Contact angle of unmodified binder on granite and limestone vs. temperature.

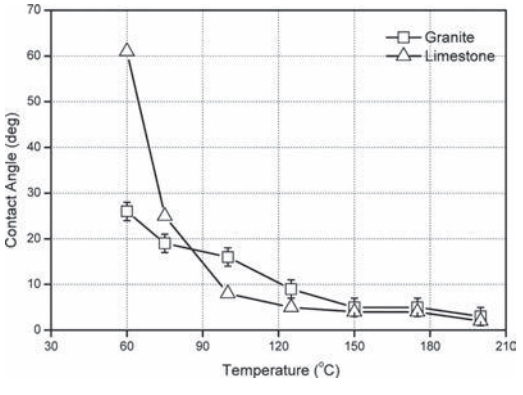

Figure 5. Contact angle of binder modified by A adhesion promoter on granite and limestone vs. temperature.

The opposite effect was observed for asphalt binder modified by additive based on phosphonic acid and its esters mixed with ethoxylated fatty alcohol (code B). Increase of the contact angle was evident for granite samples especially at high temperature ranges and is larger than for unmodified binder.

Alkaline additives containing amidoamine, ethylene amine and glycerol increased the wettability of limestone by asphalt binder significantly (Fig. 7). In the case of granite the contact

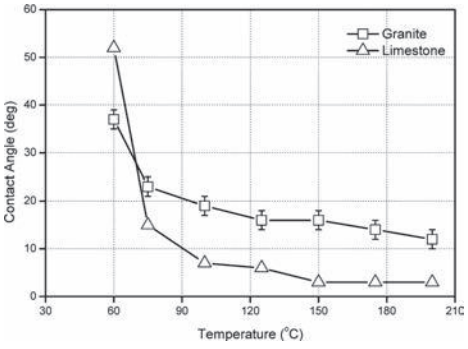

Figure 6. Contact angle of binder modified by B adhesion promoter on granite and limestone vs. temperature.

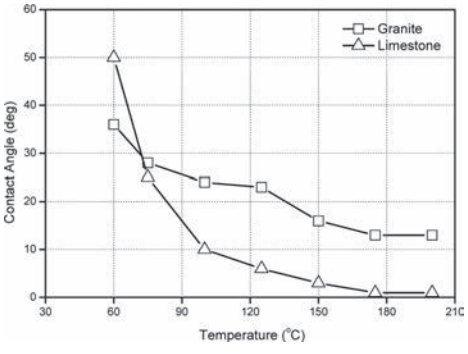

Figure 7. Contact angle of binder modified by C adhesion promoter on granite and limestone vs. temperature.

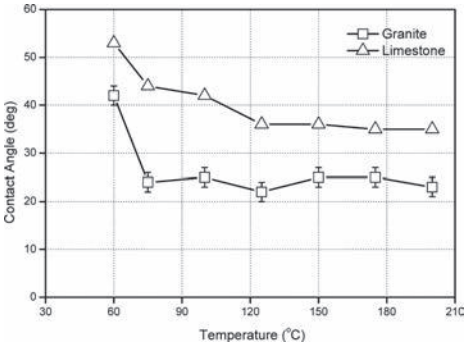

Figure 8. Contact angle of binder modified by E adhesion promoter on granite and limestone vs. temperature.

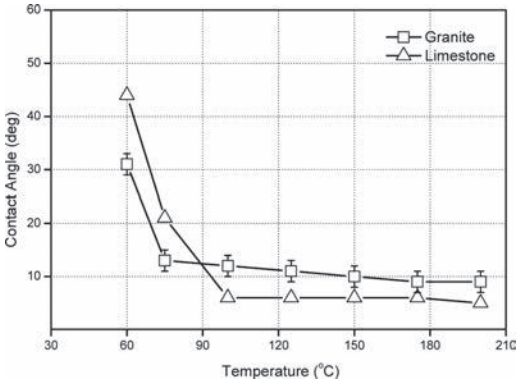

Figure 9. Contact angle of binder modified by D adhesion promoter on granite and limestone vs. temperature.

angle does not change at lower temperature ranges but increased above 120°C (248°F) in comparison to unmodified binder. The same effect was observed for additive D (Fig. 9).

The worst result is observed for pure octylphosphonic acid (Fig. 8), which in both cases (granite and limestone) decreased the wettability by asphalt binder dramatically.

4 CONCLUSIONS

We have developed here a fast low cost technique using the sessile drop. Contact angle measurement by sessile drop can be used to select the most compatible bitumen for a specific aggregate type. The system of contact angle measurements by a sessile drop technique is not so complicated as other techniques and consumes less time and doesn't need high qualified personnel.

Results of granite wettability by modified bitumen show that all based commercial additive except C decreasing contact angle and all acid modifiers increase contact angle, especially one with code E containing octylphosphonic acid.

The smallest contact angle was observed for bitumen modified by amine additives and limestone aggregates especially for A additives.

The worst results of limestone and granite wettability were observed for additives containing octylphosphonic acid. The contact angle decrease was five times higher than for unmodified bitumen. In case of limestone the influence of additives on wettability by asphalt binder much less evident except E modifier.

ACKNOWLEDGMENTS

The authors appreciate the financial support for the ORLEN Asfalt sp. z o.o., Poland.

REFERENCES

[1] Arno W. Hefer, Amit Bhasin and Dallas N. Little, P.E. (2006) "Bitumen Surface Energy Characterization Using a Contact Angle Approach" *Journal of Materials in Civil Engineering* Vol. 18 (6), 756–767.

[2] Bhasin, A., Masad, E., Little, D.N., and Lytton, R.L. (2006) "Limits on adhesive bond energy for improved resistance of hot mix asphalt to moisture damage" *Transportation Research Record, Transportation Research Board, Washington, D.C.*

[3] Bhasin, A., and Little, D.N. (2007) "Characterization of aggregate surface energy using the universal sorption device" *J. Mater. Civ. Eng.*, Vol. 19 (8), 634–641.

[4] Ensley, E.K., and Scholz, H.A. (1972). "A study of asphalt aggregate interactions by heat of immersion" *J. Inst. Pet.*, 58 560, 95–101.
[5] Ensley, E.K. (1973) "A study of asphalt aggregate interactions and asphalt molecular interactions by microcalorimetric methods: Postulated interaction mechanism" *J. Inst. Pet.*, 59 570, 279–289.
[6] Ensley, E.K., Petersen, J.C., and Robertson, R.E. (1984) "Asphalt aggregate bonding energy measurements by microcalorimetric methods" *Thermochim. Acta*, 77, 95–107.
[7] Hefer, A.W., Bhasin, A., and Little, D.N. (2006) "Bitumen surface energy characterization using a contact angle approach" *J. Mater. Civ.Eng.*, Vol. 18 (6), 759–767.
[8] Kwok D.Y., Gietzelt T., Grundke K., Jacobasch H.-J., and Neumann A.W. (1997) "Contact Angle Measurements and Contact Angle Interpretation. 1. Contact Angle Measurements by Axisymmetric Drop Shape Analysis and a Goniometer Sessile Drop Technique" *Langmuir*, Vol. 13, 2880–2894.
[9] Little, D.N., and Bhasin, A. (2006) "Using surface energy measurements to select materials for asphalt pavement." *Final Rep. for Project* 9-37, Texas Transportation Institute.
[10] Masad, E., Zollinger, C., Bulut, R., Little, D.N., and Lytton, R.L. (2006) "Characterization of HMA moisture damage using surface energy and fracture properties" *Asphalt Paving Technol*., Vol. 75, 713–754.
[11] Nicholson, V. (1932) "Adhesion tension in asphalt pavements, its significance and methods applicable in its determination" *Proc., Association of Paving Technologists*, Vol. 3, 28–48.
[12] van Oss, C.J., Good, R.J., and Chaudhury, M.K. (1988) "Additive and nonadditive surface tension components and interpretation of contact angles" *Langmuir*, 4, 884–891.
[13] van Oss, C.J. (1994) Interfacial forces in aqueous media, Marcel Dekker, New York.

Asphalt Pavements – Kim (Ed)
© 2014 Taylor & Francis Group, London, ISBN 978-1-138-02693-3

Investigation of asphalt mixture strength statistics at low temperature based on size effect analysis

Augusto Cannone Falchetto
Technical University of Braunschweig, Braunschweig, Germany

Jia-Liang Le & Mihai Marasteanu
University of Minnesota, Minneapolis, MN, USA

ABSTRACT: Low temperature cracking of asphalt pavements is a major distress in cold climates. Asphalt mixture strength is a fundamental parameter when designing pavements with increased durability. At low temperatures, asphalt mixtures have quasibrittle behavior with nominal strength strongly dependent on the structure size. In this paper, a simple method to relate the probability distribution function of strength of quasibrittle materials to the mean strength size effect is proposed. This is based on the finite weakest link model, which relates the cumulative distribution function of structural strength to the size dependence of the mean strength curve. A comprehensive experimental set of tests, which includes both mean size effect tests and strength histograms on specimens of asphalt mixture at low temperature, is used to verify the proposed method. The predicted mean strength curve obtained with this method is found to be in very good agreement with the experimental measurements on asphalt mixture specimens of different sizes, providing evidence of the validity of the proposed formulation. In the meanwhile, the effect of the size of the asphalt mixture Representative Volume Element (RVE) on the strength size effect prediction is also evaluated.

Keywords: Strength statistics, histogram testing, scaling, weakest link model

1 INTRODUCTION

Cracking due to low-temperature stresses is a prominent failure mode in asphalt pavements built in cold climates. Therefore, good strength properties are an essential requirement for asphalt mixture used in cold regions. The Indirect Tensile test (IDT) [1] is currently used for measuring strength on cylindrical specimens of asphalt mixtures. In the past different authors [2,3] demonstrated that IDT test presents non-unique strength size effect, which significantly limits the extrapolation of IDT experimental strength results to larger specimen sizes. At low temperatures, asphalt mixture exhibits quasibrittle behavior [4], and for this type of material size effect can be very significant. Therefore, strength size effect needs to be understood, especially when the field performance of asphalt pavement has to be predicted.

Quasibrittle materials, such as concrete, ceramics and asphalt mixture, are brittle heterogeneous materials characterized by inhomogeneities having dimensions not negligible compared to the structure size [5]. For structures made of quasibrittle materials, and without any pre-existing notches (indentations) or stress-free (fatigued) cracks, the associated size effect on structural strength can be described by the, so-called, Type-I size effect. This type of size effect is generally applicable to quasibrittle structures that fail at macro-crack initiation from one Representative Volume Element (RVE), which represents the smallest volume of material containing enough statistical information about the specific material property, in this case strength. Type I size effect is typical of flexural failure, for which the depth of the microcracking layer, where stress redistribution and energy release occur before the formation of a

macrocrack, is comparable to the RVE size. For small structures, this results into an energetic size effect while, for larger structures, the randomness of the materials leads to a statistics size effect [6]. For small and intermediate-size structures, Type-I size effect can be derived from the equivalent linear elastic fracture mechanics, where the distributed damage zone is replaced by a sharp crack [5,6]. The size effect at the large-size limit can be purely described by the classical Weibull statistics.

The size dependence of strength (Type I) for quasibrittle materials can be also obtained with finite Weakest Link Model (WLM) [5,6]. Due to the non-negligible dimension of the RVE, the structure is statistically modeled as a finite chain of RVEs, where the strength distribution of one RVE is obtained through multi-scale transition models and atomistic fracture mechanics [6]. Based on this theoretical framework, the cumulative distribution function (cdf) of the RVE strength is described by a Weibull distribution grafted on the left of a Gaussian cdf [5,6]. Therefore, the failure cdf of the RVE has to be known for obtaining the strength cdf and the mean strength of the entire structure. The RVE cdf can be obtained through strength histogram testing: strength tests are performed on a single-size specimen over a large number of replicates. Results can be analyzed on the Weibull scale [6] to identify the type of failure distribution (brittle, quasibrittle, ductile), and, hence, used to predict the strength size effect with the WLM.

This paper proposes a simple method to determine the mean strength size effect curve of asphalt mixture at low temperature. This approach is based on the WLM and on histogram strength testing of single-size beams in three-point bend configuration. The strength prediction is experimentally validated by further histogram testing on a smaller beam size and by mean strength tests on specimens of different sizes and geometry. The effect of RVE size on the strength cdf and on the prediction of the mean strength curve is also discussed.

2 THEORETICAL BACKGROUND

According to the finite WLM a structure can be modeled as a finite chain of RVEs having failure probability P_1. Assuming the statistical independence of the random RVE strengths and based on the joint probability theorem, the failure probability of the entire structure P_f can be computed as [6]:

$$P_f(\sigma_N) = 1 - \prod_{i=1}^{N} \left[1 - P_1(s_i \sigma_N)\right] \tag{1}$$

where P_1 is the cdf of strength of one RVE having characteristic size l_0, $\sigma_N = cP_{max}/bD$ is the nominal strength of the structure, P_{max} is the maximum load at failure, D is the structure characteristic size (scaling dimension), b is the third dimension of the structure, c is a constant and s_i is the field of the dimensionless maximum principal stress at the center of ith RVE.

It has been recently demonstrated that the failure cdf of one RVE can be approximated by a Gaussian cdf (core) with a Weibull distribution grafted on its left tail within a probability range of 10^{-4}–10^{-2} [5,6]. The grafted cdf of strength of one RVE can be mathematically expressed as:

$$P_1(\sigma) = 1 - \exp[-(\sigma/s_0)^m] \approx \langle \sigma/s_0 \rangle^m \quad (\sigma_N \le \sigma_{gr}) \tag{2}$$

$$P_1(\sigma) = P_{gr} + \frac{r_f}{\delta_G \sqrt{2\pi}} \int_{\sigma_{gr}}^{\sigma_N} \exp\left\{-\left[\frac{(\sigma' - \mu_G)^2}{2\delta_G^2}\right]\right\} d\sigma' \quad (\sigma_N > \sigma_{gr}) \tag{3}$$

where σ is the maximum elastic principal stress at the center of the RVE, s_0 is the scale parameter of the Weibull tail, m is the Weibull modulus (material constant), $\langle x \rangle = \max(x, 0)$, μ_G and δ_G are the mean and the standard deviation of the Gaussian core. $P_{gr} \approx (\sigma_{gr}/s_0)^m$ is the grafting probability between the Gaussian and the Weibull parts of the distribution, σ_{gr} is the grafting

stress and r_f is a scaling factor ensuring that Weibull-Gaussian grafted cdf is normalized: $P_1(\sigma \to \infty) = 1$. The continuity of the probability density function (pdf), $p_1(\sigma) = \mathrm{d}P_1(\sigma)/\mathrm{d}\sigma$, of the grafted distribution requires $p_1(\sigma_{gr}^{+}) = p_1(\sigma_{gr}^{-})$. Based on Eqs. (2,3), six statistical parameters, μ_G, δ_G, m, s_0, r_f and σ_{gr} are used to describe the failure distribution of one material RVE, $P_1(\sigma)$; however, with the normalization and continuity conditions, only four parameters are independent and, thus, fully define the RVE strength cdf.

The weakest link model, Eq.(1), together with Eqs. (2,3) can be used to calculate the strength distribution of the entire structure, which consists of two parts: a Weibull distribution up to the grafting stress followed by a distribution given by a chain of Gaussian elements. As the structure size increases the Weibull cdf extends into the Gaussian part eventually becoming completely dominant. From the strength cdf of one RVE, the mean structural strength for structures of different sizes can be obtained according to equation Eq. (4):

$$\bar{\sigma}_N = \int_0^1 \sigma_N \mathrm{d}P_f = \int_0^\infty [1\text{-}P_f(\sigma_N)]\mathrm{d}\sigma_N \tag{4}$$

However, a closed form does not exist for Eq.(4), and the effect of structure size, D, on the mean strength of geometrically similar specimens has to be determined numerically. Based on asymptotic matching, Bažant and co-workers [6,7] proposed an approximate expression for the size dependence of the mean strength:

$$\bar{\sigma}_N = \left[\frac{C_1}{D} + \left(\frac{C_2}{D}\right)^{rn/m}\right]^{1/r} \tag{5}$$

where C_1, C_2, and r are constant to be calibrated, m is the Weibull modulus, n is the number of dimensions to be scaled (n = 1, 2 and 3). C_1, C_2, and r can be determined using the following asymptotic conditions for small and large-size domains $[\bar{\sigma}_N]_{D\to l_m}$, $[d\bar{\sigma}_N/dD]_{D\to l_m}$ and $[\bar{\sigma}_N/D^{n/m}]_{D\to\infty}$, where l_m is the smallest structure size used in the scaling.

3 MATERIALS AND TESTING

In the experimental investigation, the asphalt mixture was prepared using a PG 64-34 asphalt binder (7.4% by weight) and a blend of taconite aggregates (55% of MIN TAC tailings and 10% of ISPAT tailings) and pit sand (35%). The Nominal Maximum Aggregate (NMAS) Size was 4.75 mm. Recently it was found that, for quasibrittle materials, the RVE size is about 2–3 times the size of the material inhomogeneities [5]. Based on sieve size analysis, the dimension of the asphalt mixture RVE was estimated as double of the size of the material inhomogeneities, which corresponds to the average aggregate size [4]. For the specific asphalt mixture used in this study, an average aggregate size of 1.22 mm and an RVE volume of $V_0 = 14.4$ mm^3 were estimated.

Four parameters are necessary to describe the entire RVE strength distributions: these can be conveniently chosen to be μ_G and δ_G, for the Gaussian cdf core and m and s_0, for the Weibull tail. Histogram strength testing can be performed to obtain these statistical parameters [5] and next used to predict the mean strength curve. Therefore, a comprehensive set of tests, consisting of both histogram strength testing on beam specimens in three-point bend (3PB), and mean strength on both three-point bend beams and Direct Tension (DT) prisms, were performed at low temperature. Table 1 presents a summary of the specimens details, while Figure 1 shows the four types of specimens used.

Specimens were obtained from twenty-six slabs of asphalt mixture (size 380 mm by 200 mm) compacted by mean of a Linear Kneading Compactor (LKC) at target air voids of 7%. Asphalt mixture beams for three-point bend tests were prepared with 1:$\sqrt{3}$:3 size ratio and thickness to span ratio equal to 1:6; since 2D scaling was selected for the beam specimens and to maximize the use the compacted slabs, a constant width b = 40 mm was imposed. DT specimens were also prepared by cutting one-size asphalt mixture prisms (Table 1). The width of the prism and thickness, D, of the beams were set as scaling dimensions of the DT and

Table 1. Specimens' details.

Specimen ID	Test type	Mean/ histogram	Replicates #	Dimensions ($L \times D \times b$)
A	3PB	Mean	12	$100 \times 16.7 \times 40$ mm
B	3PB	Histogram	28	$173 \times 28.9 \times 40$ mm
C	3PB	Histogram	30	$300 \times 50 \times 40$ mm
D	DT	Mean	7	$255 \times 55 \times 55$ mm

Figure 1. DT and beam specimens.

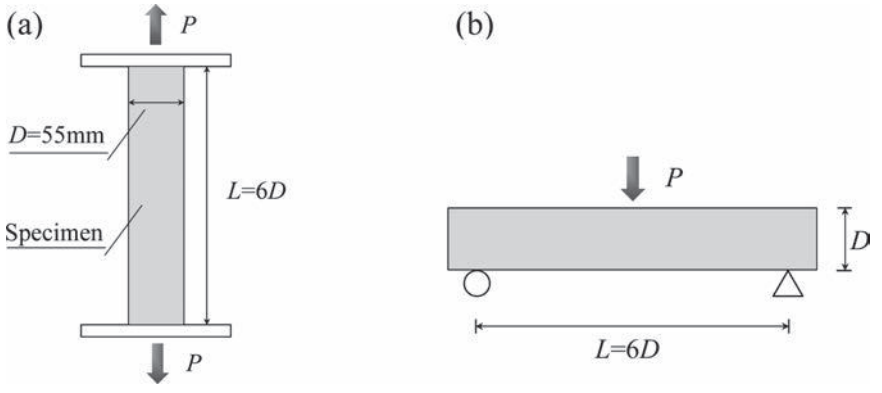

Figure 2. (a) Direct tension strength tests and (b) three-point bend.

three-point bend specimens respectively (Figure 2a and 2b). The overall dimensions of the specimens were chosen based on the dimensions of the compacted slabs and on the limitation imposed by the climatic chamber and loading frame.

Three-point strength histogram tests were first performed on the larger single-size beam specimens (Specimen C in Table 1) to determine the four parameters (m, s_0, μ_G and δ_G) of the RVE cdf. Based on the WLM the obtained RVE parameters were verified with a second strength histogram performed on beams with smaller size (Specimen B in Table 1). Mean strength tests were also run on specimens of different size and geometry (Table 1) to experimentally verify the mean strength curve predicted with the WLM. This is because the size of the three-point bend specimens was limited by the dimensions of the climatic chamber. Therefore, DT tests were selected as alternative test type to achieve a sufficiently large range of sizes to fully verify the ductile-to-brittle transition of material behavior as structure size

increases (Table 1 and Figure 2a). DT tests were performed by gluing the specimens to a set of plates with an epoxy compound, and then attached to loading frame through a set of screws.

Such an approach was used because by varying geometry and test type both failure probability and stress field change; given the same mean strength, it is possible to convert the dimensions of a structure for a specific geometry and stress field into a structure with different geometry and stress field [5]. In this study, the DT specimen was chosen to have the largest possible size that could fit into the climatic chamber to maximize the number of RVEs in the specimen so that the strength cdf of DT specimen would follow the two-parameter Weibull distribution. By doing so, a closed-form expression for calculating the equivalent size of the three-point bend beam can be easily developed. In order to reduce the viscoelastic effect of the binder component, testing temperature was set to $T = -24°C$ (low PG + 10°C) and tests duration was kept sufficiently short in order to avoid significant relaxation effects. The desired testing temperature was achieved through a controlled flow of nitrogen inside the climatic chamber of the servo-hydraulic machine used for testing; a conditioning time of three hours was imposed to all the type of specimens (3PB and DT) before testing.

Both 3PB and DT tests were conducted in load-control mode since only the peak load was of interest for this study. A time to failure of about 5 minutes was set for all the specimens with the aim of achieving a similar loading rate for the Fracture Process Zone (FPZ). Different authors in the past [8,9] used this loading procedure to limit the rate dependence of the FPZ. Therefore, different loading rates were used for different specimen sizes and geometries. Before the actual tests, several preliminary tests were performed to determine the loading rate for each specimen geometry and size.

4 SIZE EFFECT ANALYSIS

The nominal strength of three-point bend and direct tension was calculated as:

$$\sigma_N^B = \frac{3P_{\max}L}{2bD^2} \quad \text{and} \quad \sigma_N^T = \frac{P_{\max}}{bD} \tag{6}$$

where $P_{\max}$ is the peak load, L is the length of the beam, D is the scaling dimension (the thickness of the beam or the width of the DT prism) and b is the width of the beam for three-point bend (40 mm) or the depth of the prism (55 mm) for DT specimens.

In order to evaluate the size dependence of the mean nominal strength, the results obtained from the DT mean strength need to be converted into the corresponding equivalent 3PB beam. The DT prisms has a volume of 756,000 mm^3 (Table 1), which consists of almost 5.25×10^4 RVEs ($V_0 = 14.4$ mm^3). Given such a large number of RVEs, the strength cdf of DT specimens must follow the two-parameter (m, s_0) Weibull distribution [3, 5]. Therefore, the mean strength of DT, $\bar{\sigma}_N^T$, can be written as:

$$\bar{\sigma}_N^T = N_T^{-1/m} s_0 \Gamma\left(1 + \frac{1}{m}\right) \tag{7}$$

where N_T is the number of RVEs in the direct tension specimen. The mean strength of the 3PB beam, $\bar{\sigma}_N^B$, can be written as:

$$\bar{\sigma}_N^B = N_{eq,B}^{-1/m} s_0 \Gamma\left(1 + \frac{1}{m}\right) \tag{8}$$

where $N_{eq,B}$ is the equivalent number of RVEs [5] of the beam, which can be calculated based on the elastic stress distribution:

$$N_{eq,B} = \frac{b}{l_0^3} \int_V [(\sigma(\mathrm{x}) / \sigma_N^B)]^m \, \mathrm{d}V(\mathrm{x}) \tag{9}$$

where V is the volume of the beam. Based on Eqs. (7–9), it is possible to convert the DT specimen to the equivalent three-point bend beam by equating $\bar{\sigma}_N^T$ to $\bar{\sigma}_N^B$, which gives the equivalent depth of the three-point bend beam:

$$D_{eq} = \sqrt{\frac{(m+1)^2 N_T V_0}{3b}} \tag{10}$$

The Weiubll modulus, m, is the only unknown parameter in Eq. (10); together with s_0, μ_G and δ_G, it defines the failure cdf of one RVE. This set of four parameters can be obtained by fitting the WLM and the grafted RVE cdf, Eqs. (1–3), to the experimental strength histogram which, on the Weibull scale, consists of a low straight line (i.e. a Weibull distribution) and an upper curved part. At structure level the Weibull component of the failure distribution becomes more and more significant as the structure size increases. Therefore, in order to reduce the error in the estimation of the Weibull modulus m, and, hence, of the remaining statistical parameters of the RVE cdf, the WLM was fitted to the strength histogram of the larger beam series (beam C in Table 1). The experimental strength failure distribution and histogram plots of beams series B and C were obtained by first ranking the strength values in ascending order, $p = 1 \ldots N_t$, where p is the rank and N_t is the total number of tested specimens. Based on the midpoint position method [10] the strength cdf was calculated as $P_f(\sigma_N^B) = (p - 0.5)/N_t$.

Figure 3 shows the measured strength histograms on the Weibull scale (square and round markers). It is seen that the lower portion of the histograms follows a straight line with similar slope governed by the Weibull modulus, while the upper portion exhibits a clear nonlinearity given by a chain of Gaussian elements. Such a two-segment strength cdf has also been seen in other quasibrittle materials, such as Portland cement mortar, engineering and dental ceramics [11,12]. This also confirms what was found in a different study on asphalt mixture [4], indicating a clear dependence of the failure distribution on the structure size [5,6].

Finally, the histogram of beam size C (Table 1) can be fitted by the WLM, Eq. (1). Based on the 2D scaling used for beams, it was assumed that the macro-crack, causing the structure failure, develops across the entire width of the beam [6]. This implies that one side of the RVE must have the length equal to the beam width [4,5]; therefore, the effective RVE size for 2D beam can be calculated as $l_0 = \sqrt{V_0 / b} = 0.6$ mm. Figure 3 shows the fitted strength histogram for beam size C (solid line).

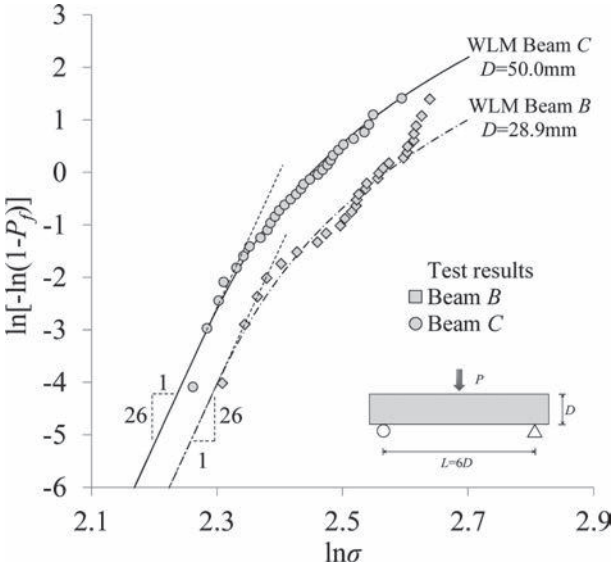

Figure 3. Experimental strength histogram and WLM fitting.

The following values of the four statistical parameters for the cdf of RVE strength were obtained with the WLM: $m = 26$, $s_0 = 12.68$, $\mu_G = 44.49$ and $\delta_G = 14.89$. Based on this set of values, the Coefficient of Variation (CoV) is approximately 33%, which is higher than what is normally observed in the laboratory tests. Nevertheless, it should be noted that the CoV estimated here is for one RVE whereas conventional laboratory test specimens usually consists of more RVEs, which would lead to a smaller CoV. The experimental strength histogram of beam size B was next used to verify the values of the parameters of the RVE cdf. Figure 3 shows that the WLM prediction (dashed line) agrees very well with the measured strength histogram of beam series B, further confirming the validity of the calibration of the strength cdf of one RVE and the finite WLM. Moreover, Figure 3 clearly shows that Weibull modulus is a material constant (Bažant and Pang, 2007) and independent of the structure size.

Given the value, $m = 26$, of the Weibull modulus, Eq. (10) can be finally used to convert the DT mean strength to its equivalent 3PB beam which results in a in a $D_{eq} = 2143$ mm; this is significantly larger than the specimen scaling size of DT prism (55 mm). Table 2 summarizes the mean strength for each specimen type. CoV stands for coefficient of variation.

The type of size effect of asphalt mixture can be finally evaluated by using the mean strength values of Table 2, together with the strength prediction obtained with the WLM and Eq. (5), which provides an approximate expression of the structural strength as function of the scaling size (D) [7]. This type of function does not require computational-demanding solutions, as would be when solving Eq. (4), and can be easily fitted to the experimental data or to the strength values obtained through the WLM for predicting the strength of larger or smaller structures. Figure 4 presents the experimental data, the mean strength predicted by the WLM and the mean size effect curve given by Eq. (5) (where $n = 2$ indicates two-dimensional scaling and $m = 26$ the Weibull modulus).

Figure 4 shows that the WLM predicts very well the mean structural strength of the experimental data. Eq. (5) provides a very good approximation of the size effect curve and, at the

Table 2. Mean strength results.

Specimen ID	Test type	Mean/histogram	Mean strength (MPa)	CoV (%)
A	3PB	Mean	14.3	7.0
B	3PB	Histogram	12.4	8.9
C	3PB	Histogram	11.4	8.4
D	Equivalent DT Beam	Mean	8.2	13.4

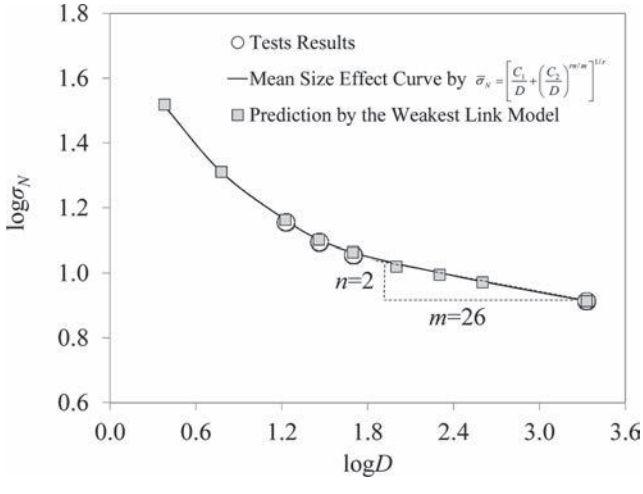

Figure 4. Mean strength curve.

same time, a more convenient formulation of the strength dependence on the structure size. Based on the asymptotic conditions for small and large size limits (see section 2), the following parameters of the mean strength curves, Eq. (5), were obtained: $C_1 = 45.34$, $C_2 = 1.56 \times 10^{15}$ and $r = 1.00$, which is in the typical range of 0.5–2 [7]. Moreover, Figure 4 clearly shows that asphalt mixture behave as a quasibrittle material having Type I mean strength size effect: for small specimen size it presents a ductile failure, while, as structure size increases, it changes toward a brittle failure, characterized by the Weibull distribution.

5 DISCUSSION ON THE RVE SIZE

In section 3, the RVE size of asphalt mixture was selected as double of the size of the material inhomogeneities which corresponds to the average grain size [4]. Nevertheless this differs with what used for other materials such as concrete for which RVE size is estimated to be about 2–3 times the size of the maximum material inhomogeneities [5]. The dissimilarity can be associated to the fact that the previous estimation of the RVE size was based on the size of distributed cracking zone of flexural beam for concrete. This may not be entirely applicable to asphalt mixtures, which may have a different size distribution of aggregates compared to concrete. Furthermore, the distributed cracking zone is defined as the zone experiencing strain-softening in a deterministic model [13], whereas the RVE here is defined as the smallest material volume whose failure causes the failure of the entire structure.

In order to further investigate the effect of RVE size on the materials strength distribution and on the mean strength size effect curve, two larger l_0 values were used for fitting the WLM to the experimental strength histograms. The two values were selected to be $1 \times \text{NMAS} = 4.75$ mm and $2 \times \text{NMAS} = 9.50$ mm which correspond to an RVE volume of $V_{0-1\text{xNMAS}} = 107.2$ mm^3 and $V_{0-2\text{xNMAS}} = 837.4$ mm^3 respectively. By using the same 2D scaling analysis previously selected for beam specimens, the effective RVE sizes was rescaled to $l_{0-1\text{xNMAS}} = \sqrt{V_{0-1\text{xNMAS}}/b} = 1.64$ mm and $l_{0-2\text{xNMAS}} = \sqrt{V_{0-2\text{xNMAS}}/b} = 4.63$ mm. WLM was then fitted to the experimental histograms. Figure 5 presents the WLM fitting for the original RVE size l_0, $l_{0-1\text{xNMAS}}$ and $l_{0-2\text{xNMAS}}$.

The plot of Figure 5 indicates there is a deviation from the optimum fitting as the RVE size increases resulting in a significant under prediction of the mean strength for smaller

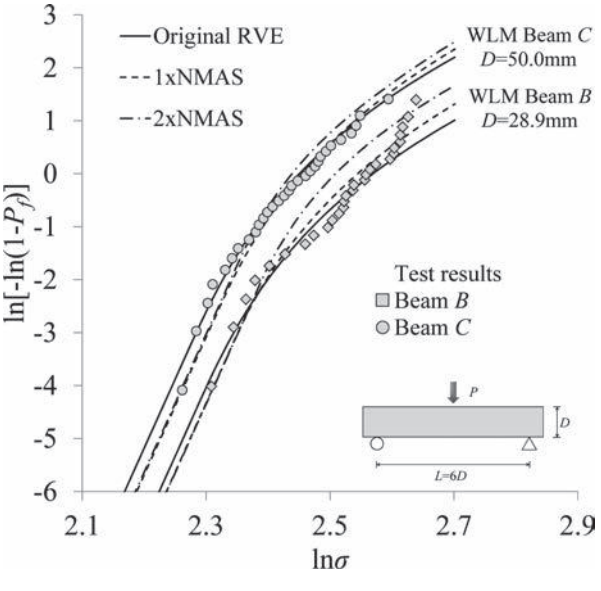

Figure 5. Strength histogram and WLM fitting for different RVE sizes.

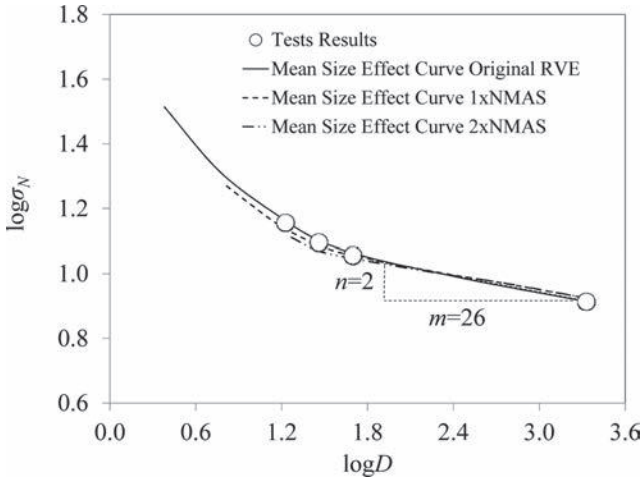

Figure 6. Mean strength curve for different RVE sizes.

structures while it leads to an over prediction for large sizes. This trend is visible in Figure 6, where, for small structures sizes, the mean strength curves become shorter due to the larger RVE size.

The curves obtained from the different fittings confirm that the selected RVE size, l_0, which is based on the average grain size, results in better mean strength predictions and, at the same time, suggest that smaller particles, such as filler, may play an important role in the failure of the material. However, this hypothesis need to be further investigated and verified through additional experimental work and analysis on asphalt mixture having different mix design, including larger NMAS.

6 SUMMARY AND CONCLUSIONS

In this paper a method to obtain the size dependence of mean strength of asphalt mixture at low temperature was presented. This approach is based on finite WLM and on flexural strength histogram testing of beams of a single size. The parameters characterizing the strength cdf of one RVE were first obtained from the experimental results and then used to predict the size dependence of asphalt mixture strength which was finally compared with the experimental values obtained on specimens of different sizes and geometry. The effect of the size of the asphalt mixture RVE on strength distribution and mean strength was addressed at the end. Two main conclusions can be drawn based on the experimental work and theoretical analysis performed:

- Experimental strength histogram confirms that asphalt mixture has quasibrittle failure behavior while mean strength curve follows a typical Type I size effect. Weibull-Gaussian grafted model can be used to statistically describe the RVE cdf of structural strength and together with the WLM can be used to predict strength and cdf of larger structures.
- The choice of the size of the material RVE is critical when applying this method. The fitting results obtained by selecting different RVE size indicate that the use of the average grain size is consistent with the experimental results, while larger RVE results in cdf and strength predictions which significantly deviate from values obtained from testing. The relatively small size of the RVE also suggests that fine particles are crucial for understanding the material failure. Nevertheless, the effect of RVE size on the cdf and mean strength requires additional analysis and experimental research, since, this type of scale effect modeling and investigation was never attempted before for asphalt mixture.

The proposed approach, based on histogram testing, is very promising and offers a tests procedure and an analysis solution to extrapolate small-scale test results to full-scale design without relying on the size effect tests, which is not possible with the current indirect tensile test method. This is attractive for testing asphalt mixtures at low temperatures due to the size limit of climatic chambers. In addition, such a model may become a simple analysis tool for practitioners when a wider range of asphalt mixtures, including different mix design, aggregate size, will be investigated and evaluated to provide a broader validation of the proposed modeling solution.

ACKNOWLEDGMENTS

The support provided by NCHRP-IDEA 151 is gratefully acknowledged. The results and opinions presented do not necessarily reflect those of the sponsoring agency. The authors would also like to acknowledge Dr. Chris Williams at Iowa State University for providing accesses to their laboratory and Linear Kneading Compactor (LKC), and the Minnesota Department of Transportation for providing the materials used in this study.

REFERENCES

[1] AASHTO T322-07-UL, Standard Method of Test for Determining the Creep Compliance and Strength of Hot Mix Asphalt (HMA) Using the Indirect Tensile Test Device, 2007.
[2] Rocco C., Guinea G.V., Planas J. and Elices M., The Effect of Boundary Conditions on the Cylinder Splitting Strength, Fracture Mechanics of Concrete Structures., pp. 75–84, F.H. Wittmann Edition, Freiburg, Germany, 1995.
[3] Bažant Z.P. and Planas J., Fracture and Size Effect in Concrete and Other Quasibrittle Materials, CRC Press, US, 1998.
[4] Marasteanu M.O., Cannone Falchetto A., Turos M. and Le J.-L., Development of a Simple Test to Determine the Low Temperature Strength of Asphalt Mixtures and Binders, IDEA Program Final Report NCHRP 151, December 2012.
[5] Le J-L., Bažant Z.P. and Bažant M.Z., Unified Nano-Mechanics Based Probabilistic Theory of Quasibrittle and Brittle Structures: I. Strength, Static Crack Growth, Lifetime and Scaling. Journal of the Mechanics and Physics of Solids, 59, pp. 1291–1321, 2011.
[6] Bažant Z.P. and Pang S-D., Activation Energy Based Extreme Values Statistics and Size Effect in Brittle and Quasibrittle Fracture, Journal of the Mechanics and Physics of Solids, 55, pp. 91–131, 2007.
[7] Bažant Z.P. and Novák D., Energetic-Statistical Size Effect in Quasibrittle Failure at Crack Initiation, ACI Materials Journal, 97(3), pp. 381–392, 2000.
[8] Swartz S.E. and Siew H.C., Is Load Control Suitable for Fracture-Energy Measurements for Concrete, Experimental Mechanics, 27(4), pp. 359–365, 1987.
[9] Cannone Falchetto A., Turos M.I. and Marasteanu M.O., Investigation of Asphalt Binder Strength at Low Temperature, Road Materials and Pavement Design, 13(4), pp. 804–816, 2012.
[10] Rinne H., The Weibull Distribution. A handbook, CRC Press, London, 2009.
[11] Salem J.A., Nemeth N.N., Powers L.P. and Choi S.R., Reliability Analysis of Uniaxially Ground Brittle Materials, Journal of Engineering for Gas Turbines and Power, 118, pp. 863–871, 1996.
[12] Lohbauer U., Petchelt A. and Greil P., Lifetime Prediction of CAD/CAM Dental Ceramics, Journal of Biomedical Materials Research, 63(6), pp. 780–785, 2002.
[13] Bažant Z.P., Scaling of Structural Strength. Elsevier, London, 2005.

Mineral aggregate in asphalt concrete/mix design methodology/novel methods to aid mix design

This page intentionally left blank

Asphalt Pavements – Kim (Ed)
© 2014 Taylor & Francis Group, London, ISBN 978-1-138-02693-3

Effect of fine aggregate form, angularity and texture on the viscoelastic properties of asphalt mortar

Yiqiu Tan, Hong Zhang & Huining Xu
School of Transportation Science and Engineering, Harbin Institute of Technology, Harbin, China

Yizhuang Wang
Department of Civil, Construction, and Environmental Engineering, North Carolina State University, Raleigh, USA

Xing'ao Yao
School of Transportation Science and Engineering, Harbin Institute of Technology, Harbin, China

ABSTRACT: Asphalt mortar is a kind of dispersion system combined asphalt mastic with fine aggregates. Fine aggregates properties have a significant effect on the viscoelastic properties of asphalt mortar. Effect of fine aggregate form, angularity, and texture on the viscoelastic properties of asphalt mortar were studied in this paper. Image analysis procedures consisting of diploid microscope and surface light source were developed to capture fine aggregate properties. Six indices were measured for 10 aggregate samples to describe these properties. The samples were related to the viscoelastic properties of asphalt mortar measured by DSR. The results showed that the form, angularity and texture of fine aggregate exercise a remarkable influence on instantaneous elasticity, viscous component and low temperature performance of asphalt mortar. Resistance to deformation decreased with a flat, elongated shape and a decrease in aggregate angularity and texture. Abundant angularity and texture are beneficial for an increase of viscous component and low temperature performance.

Keywords: fine aggregate, asphalt mortar, morphologic properties, viscoelastic properties, image analysis procedures

1 INTRODUCTION

Asphalt mortar is a matrix of fine aggregate and asphalt binder, including the fillers. Approximately 80 percentage of the total volume of asphalt mortar consists of fine aggregate. It is not surprising that the properties of fine aggregate play an important role in the performance of asphalt mortar, such as shape characteristic. Shape characteristics of fine aggregates are expressed as three independent properties: form, angularity and texture. With the development of Digital Image Processing (DIP) techniques because of its direct and quantitative, it has been a research hotspot to quantify aggregate shape characteristics and their relationship to the behaviour of asphalt mortar or asphalt mixture based on image technique.

Johnson (1998) [1] found that some additional parameters from digital imaging also predicted modulus and rut resistance very well and should be included in future research. Kwan (1999) [2] proposed a method to determine the flakiness and elongation index based on the DIP technique. In Brazil, Oliveira (2004) [3] developed a DIP method to measure the shape of fine aggregate particles based on the concept of volumetric coefficient.

Masad has done a lot of works in this field [4–6]. In 2000 [7], he proposed that images were captured at two resolutions of high resolution and low resolution to describe aggregate texture and angularity, respectively. In his next works (2001) [8], Masad provided procedures used to capture images to analyse form and angularity. A form index FI, an index AI to

represent angularity and a Texture Index (TI) were developed and tests results showed that among the different aggregate shape properties, texture had the strongest correlation with rutting resistance values. In 2006 [9], he evaluated image analysis techniques for quantifying aggregate shape characteristics and recommended some analysis methods.

Thomas (2007) [10] designed and developed a unified computer-automated system, which included the ability to analyse fine and coarse aggregates and to quantify texture, angularity, and the three dimensions of form. Prudencio (2013) [11] carried out experimental tests on mortar samples produced with three different manufactured fine aggregates with distinct shape index. The results showed that mortar flow is strongly influenced by the particle shape.

This study focus on applying image processing techniques to investigate the effects of fine aggregate form, angularity and texture on the viscoelastic properties of asphalt mortar. In order to simplify the imaging approach for measuring fine aggregate shape characteristics, sensitive size of fine aggregate shape characteristics was proposed in this study. Grey relation method was used to determine the sensitive size of fine aggregate shape characteristics based on the results of three standard FAA tests. Image acquisition system was developed to obtain the value of quantitative indices, which described the form, angularity and texture of the sensitive size particles. According to the analysis results of fine aggregate shape characteristics, two indices, E and SP, was proposed to evaluate shape characteristics of fine aggregates. At last, the correlation of E and SP values of different fine aggregates with asphalt mortars were conducted.

2 MATERIALS

2.1 *Fine aggregates*

Thirteen different fine aggregate samples were analysed in this study. Their properties were tested according to *Test Methods of Aggregate for Highway Engineering* (*JTG E42-2005*) and results were given in Table 1.

2.2 *Mineral fillers*

The limestone fillers properties were tested according to *Test Methods of Aggregate for Highway Engineering* (*JTG E42-2005*) and results were shown in Table 2.

2.3 *Asphalt binder*

The properties of asphalt binder were tested according to Standard *Test Methods of Asphalt and Asphalt Mixtures for Highway Engineering* (*JTJ 052-2000*) were given in Table 3.

Table 1. Properties of fine aggregates.

Sample ID	Type of aggregate	Source	Fineness modulus	Apparent relative gravity/(g · cm^{-3})	Lithology
1	Natural sand	Heilongjiang	2.9	2.618	Quartzite
2	Chips	Jilin	2.6	2.740	Limestone
3	Chips	Jilin	2.4	2.747	Limestone
4	Chips	Shandong	2.7	2.861	Limestone
5	Chips	Heilongjiang	2.9	2.708	Andesite
6	Chips	Gansu	3.4	2.730	Limestone
7	Manufactured sand	Gansu	3.0	2.642	Granite
8	Manufactured sand	Jilin	3.2	2.742	Limestone
9	Manufactured sand	Jilin	2.8	2.755	Limestone
10	Manufactured sand	Shandong	3.0	2.844	Basalt
11	Manufactured sand	Heilongjiang	2.5	2.778	Basalt
12	Manufactured sand	Heilongjiang	3.2	2.826	Basalt
13	Manufactured sand	Heilongjiang	4.2	2.822	Basalt

Table 2. Properties of mineral fillers.

Apparent relative gravity/(g · cm^{-3})	The percentage of passing sieve/%			
	<0.6 mm	<0.3 mm	<0.15 mm	<0.075 mm
1.629	100	100	97.3	84.4

Table 3. Properties of asphalt binder.

Properties	Results
Penetration (25°C, 100 g, 5 s)/0.1 mm	89.8
Ductility (15°C)/cm	133
Softening point (R&B)/°C	51.4
Density/(15°C)	1.03

3 TESTS

3.1 *FAA tests*

The underlying fact is that the shape characteristics of fine aggregate are affected by gradation composition. And it is a large work to measure each size particles of fine aggregates based on image analysis method. Therefore, sensitive size of fine aggregate shape characteristics, which mean that shape characteristics of the sensitive size particles can represent shape characteristics of the fine aggregate sample, was proposed in this study to establish a simple way for measuring the shape characteristics of fine aggregates.

In this study, three standard test methods for FAA (Fine Aggregate Angularity) were applied to determine the sensitive size of fine aggregate shape characteristics. They are AFNOR P18-564, the aim of which is to measure the flow time of fine aggregate in seconds through an orifice under specified conditions, AASHTO TP 33 (ASTM C1252) "Uncompacted void content of fine aggregate", in which FAA is defined as the percentage of air voids present in loosely compacted aggregates, and ASTM D3398 "Index of aggregate particle shape and texture", which provides an index value to the relative particle shape and texture characteristics of aggregates. Three fine aggregates samples (2#, 8# and 11#) composed of single size particles (2.36 mm, 1.18 mm, 0.6 mm, 0.3 mm, 0.15 mm and 0.075 mm) and three gradations (shown in Table 4) were measured according to the three standard test methods.

Grey relation analysis [12], which calculates the grey relation degree between target value and effect factors and looks for the primary affecting factors, was applied to determine the sensitive size of fine aggregate shape characteristics.

3.2 *Imaging acquisition and analysis tests*

Image acquisition system was developed to measure fine aggregate shape characteristics, which is shown in Figure 1. This system was consisted of four parts, which were stereo microscope, video camera, and area source, image analyser. Stereo microscope has the advantage of high image resolution and direct observation of objects. The stereo microscope was equipped with the video camera; therefore particle images could be real-time captured on the computer. Area source was used to create accurate definition of the particle boundary. The images were captured and analysed by the image analyser, which contained image captured software and image analysis software.

In this section, 10 kinds of samples were used and the objects of this test were the sensitive size particles. In order to describe different shape characteristics of fine aggregate, images were captured at two resolutions (0.003 mm/pixel high resolution and 0.015 mm/pixel low resolution) according to Masad's work [7]. Shown in Figure 2 are binary images of fine aggregates captured at two different resolutions.

Table 4. Percentage of passing sieve of three gradations (%).

	Sieve size/mm					
Gradations	2.36	1.18	0.6	0.3	0.15	0.075
a	100	76	53	35	12	0
b	80	50	25	8	0	0
c	89	62	38	21	5	0

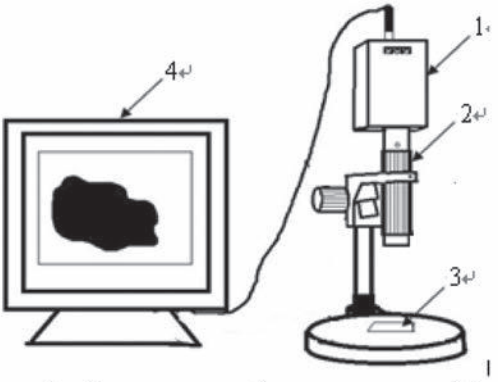

1-stereo microscope; 2-video camera; 3-area source; 4-image analyser

Figure 1. Image acquisition device of fine aggregate.

a) 0.003mm/pixel resolution

b) 0.015mm/pixel resolution

Figure 2. Fine aggregate particle images in two resolutions.

Six indices were selected for quantifying the different characteristics of fine aggregate shape, the diagrams of which were showed in Figures 3 and 4, and the calculation methods were presented in Table 5.

3.3 *Frequency sweep test by DSR*

Asphalt mortars with four kinds of fine aggregates (2#, 3#, 11#, 13#) were prepared with 11.17% asphalt content and 0% of air voids. The aggregate gradation of asphalt mortar was shown in Table 6. Cylindrical specimens with 100 mm diameter, 100 ± 2 mm height were prepared by Gyratory Compactor. Then the cylindrical specimens were cut into rectangular specimens with 4 mm × 13 mm × 60 mm size, which were used to determine the viscoelastic properties asphalt mortar by DSR.

The frequency sweep test by DSR (Dynamic Shear Rheometer) was applied to determine the viscoelastic properties of asphalt mortar. The procedure consisted of applying

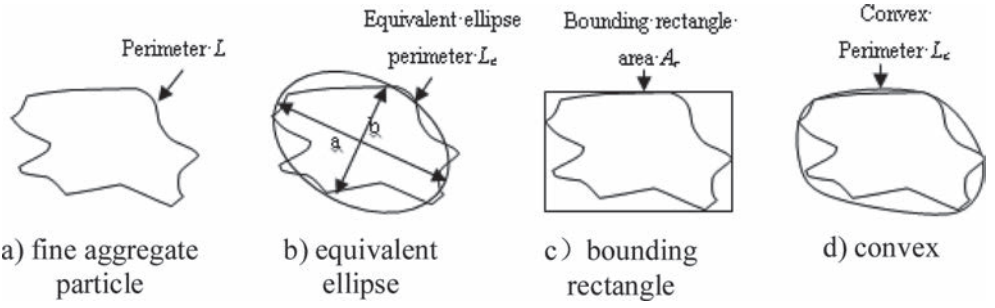

Figure 3. Diagrams of fine aggregate particle characteristic parameters.

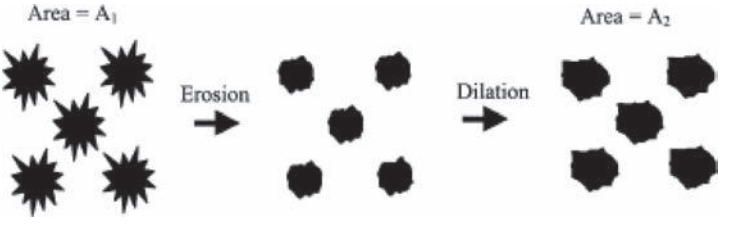

Figure 4. Diagram of erosion-dilation method.

Table 5. Quantitative indices of fine aggregate shape characteristics.

	1	2	3	4	5	6
Indices	$R = S/A_r$	$E = a/b$	$C_R = L/L_c$	$A_I = L/L_e$	$FF = L^2/4\pi S$	$SP = A_1 - A_2/A_1$

Table 6. Gradation of asphalt mortar.

Sieve size/mm	2.36	1.18	0.6	0.3	0.15	0.075	<0.075
The percentage of passing sieve/%	100	71.7	51.4	36.5	27.0	16.2	–

constant shear strain of 0.1% to avoid damaging the specimen over a range of loading frequencies (from 0.1 to 25 Hz). And this was performed at 30, 40, 50 and 60°C. With the resulting data, CAM model (Eq.(1)) was used to relate dynamic shear modulus to reduced frequency.

$$|G^*|(f') = |G^*|_e + \frac{|G^*|_g - |G^*|_e}{[1 + (f_c/f')^k]^{m_e/k}} \tag{1}$$

4 RESULTS AND DISCUSSION

4.1 *Sensitive size of fine aggregates shape characteristics*

The FAA test results of the three fine aggregates samples are shown in Table 7 through 9. And Table 10 presents the grey relation analysis results.

Table 7. Flow time of each size and three gradations (s).

Samples	2.36 mm	1.18 mm	0.6 mm	0.3 mm	0.15 mm	0.075 mm	Gradation a	Gradation b	Gradation c
2#	–	58.7	43.6	34.2	32	59.4	34.6	45.3	38.1
8#	–	55.2	42.5	34.8	32.5	43	33.1	42.1	36.6
11#	–	55.4	43.7	35.4	36.4	–	38.2	43.7	40.5

'–' The FAA value could not be measured and grey relation degree was considered as zero.

Table 8. Uncompacted void content of each size and three gradations (%).

Samples	2.36 mm	1.18 mm	0.6 mm	0.3 mm	0.15 mm	0.075 mm	Gradation a	Gradation b	Gradation c
2#	48.1	50.4	52.6	52.8	51.9	53.0	44.3	43.3	44.5
8#	45.7	47.7	51.8	53.6	53.6	54.4	43.2	43.0	44.7
11#	47.1	49.7	51.7	54.2	54.8	55.7	44.3	43.6	44.9

Table 9. Mean particle index of each size and three gradations (%).

Samples	2.36 mm	1.18 mm	0.6 mm	0.3 mm	0.15 mm	0.075 mm	Gradation a	Gradation b	Gradation c
2#	15.31	16.29	16.48	15.80	14.66	15.45	15.93	15.85	15.77
8#	13.01	13.90	16.10	17.19	17.05	17.06	15.08	15.55	16.11
11#	14.75	15.27	15.65	16.73	17.62	18.01	15.70	16.06	16.49

Table 10. Grey relation degree of each size.

FAA tests	2.36 mm	1.18 mm	0.6 mm	0.3 mm	0.15 mm	0.075 mm
AFNOR P18-564	0	0.43	**0.76**	0.75	0.72	0.37
AASHTO TP33	**0.79**	0.63	0.50	0.45	0.46	0.43
ASTM D3398	0.56	0.65	**0.77**	0.73	0.54	0.59
Sum of grey relation degree	1.35	1.71	**2.03**	1.93	1.72	1.39

According to Table 9, the grey relation degree of 0.6 mm size is the maximum from the result of AFNOR P18-564 test, which is the same as the ASTM D3398 test result. However, from the results of the AASHTO TP33 test, the grey relation degree of 2.36 mm size is the maximum. In order to determine the most sensitive size of fine aggregate shape characteristics, the grey relation degrees of each size from the three tests were added. The grey relation degree order of each size after adding is 0.6 mm > 0.3 mm > 0.15 mm > 1.18 mm > 0.075 mm > 2.36 mm. It is evident that the grey relational coefficients of 0.6 mm size is the maximum, as a result, 0.6 mm is selected as the sensitive size of fine aggregate shape characteristics.

4.2 *Analysis of fine aggregate shape characteristics based on imaging approach*

The results of shape characteristics indices value using image analysis technique are shown in Table 11.

In order to study the shape characteristics differences between manufactured sand and chips, one-way ANOVA was applied to analyse the differences of the indices value between manufactured sand and chips, and the results are shown in Table 12.

4.2.1 *Form*

On the basis of the results in Table 11, it is evident that the R value of 1# sample (natural sand), which is up to 0.713 and close to $\pi/4$, is greater than other samples. And the fact is that the more R is close to $\pi/4$, the more aggregate particle is nearly round. So compared with manufactured sand and chips, natural sand is more nearly round. However, according to the One-way ANOVA results in Table 12, the F value of R between manufactured sand and chips is 0.15 and smaller than $F_{0.05} = 5.59$ with a 95 percent confidence interval, which indicates that there are no significant differences of R between manufactured sand and chips.

From the point of E, E value of 1# (natural sand) is no marked different from other fine aggregates, especially manufactured sand. On the other hand, the F value of E between manufactured sand and chips is 8.18 and greater than $F_{0.05} = 5.59$ with a 95 percent confidence interval, which indicates that there are significant differences of E between manufactured sand and chips. And the E values of chips are greater than those of manufactured sand. Considering that greater E means more elongated aggregates, chips are more elongated than manufactured sand in terms of form characteristic.

4.2.2 *Angularity*

From the point of A_I,C_R and FF, which values of natural sand are obviously smaller than chips and manufactured sands, we can come to that natural sand is less angular. However, there is no obvious contrast of A_I,C_R and FF between chips and manufactured sands according to the result of Table 12, because all of the F value of A_I,C_R and FF between manufactured sand and chips are smaller than $F_{0.05} = 5.59$.

On the other hand, the SP value of natural sand is obviously smaller than the other fine aggregates, and the One-way ANOVA results in Table 12 show that the F value of SP is 5.98, which is greater than $F_{0.05} = 5.59$. As a result, there are remarkable contrast in terms of SP values among natural sand, chips and manufactured sands, and the SP value of natural sand is the smallest, which followed by chips and manufactured sands are the greatest. In consideration of the fact that the greater SP value is, the more angular fine

Table 11. Quantitative indices value of 10 samples.

	Form		Angularity				Texture			
Samples	*R*	*E*	*SP*	A_I	C_R	*FF*	*SP*	A_I	C_R	*FF*
1#	0.713	1.249	0.559	1.06	1.015	1.162	0.123	1.052	1.012	1.15
2#	0.695	1.365	0.644	1.077	1.023	1.284	0.163	1.097	1.026	1.288
3#	0.685	1.318	0.738	1.099	1.024	1.291	0.257	1.106	1.028	1.318
5#	0.665	1.341	0.846	1.093	1.024	1.276	0.244	1.098	1.023	1.318
6#	0.678	1.242	0.827	1.091	1.029	1.266	0.305	1.106	1.028	1.269
7#	0.673	1.27	0.827	1.097	1.03	1.251	0.245	1.113	1.029	1.304
8#	0.677	1.221	0.876	1.063	1.02	1.217	0.196	1.087	1.026	1.253
10#	0.691	1.214	0.947	1.097	1.029	1.271	0.298	1.107	1.027	1.285
11#	0.655	1.264	0.846	1.091	1.023	1.232	0.23	1.085	1.022	1.253
13#	0.665	1.295	0.827	1.073	1.015	1.232	0.156	1.097	1.019	1.263

Table 12. Analytic results of one-way ANOVA.

	Form		Angularity					Texture				
Indices	*R*	*E*	*SP*	A_I	C_R	*FF*	*D*	*SP*	A_I	C_R	*FF*	*D*
F	0.15	**8.18**	**5.98**	0.002	0.57	3.01	2.71	0.21	0.18	0.25	1.02	0.44

aggregate is, natural sands are smooth, chips are subangular and manufactured sands are more angular.

4.2.3 *Texture*

The results of Table 11 shows that the *SP*, A_I, C_R, *FF* value of natural sand (1#) is also smaller than other samples, which indicates that natural sands are smooth compared with chips and manufactured sands. And based on the One-way ANOVA results in Table 12, in which the *F* value of *SP*, A_I, C_R, *FF* value is less than $F_{0.05} = 5.59$, there are no obviously contrast between chips and manufactured sands in terms of texture.

The foregoing analysis shows that the differences of shape characteristics between natural with chips and manufacture sand are in terms of form, angularity and texture. Natural sand is nearly rounded, less angular and texture. And the difference of shape characteristics between chips and manufacture sand is in terms of shape and angularity. Chips are elongated or flaky and less angular than manufacture sand. Form index *E* and angularity index *SP* can describe the differences among different kinds of fine aggregates, so we propose the two indices as the evaluating indices of fine aggregate shape characteristics.

5 CORRELATION OF SHAPE INDICES TO LABORATORY ASPHALT MORTAR VISCOELASTIC PROPERTIES

The master curves of four kinds of asphalt mortars consisted of different fine aggregates are shown in Figure 5. Table 13 shows the fitting results of CAM model parameters.

5.1 *Influence of fine aggregates shape characteristics on* $|G^*|_e$

Equilibrium dynamic modulus $|G^*|_e$ is an index describing asphalt mortar high temperature resistance to deformation. The greater $|G^*|_e$ is, the stronger asphalt mortar ability to resist deformation is. Figure 6 showed the changes of equilibrium dynamic modulus $|G^*|_e$

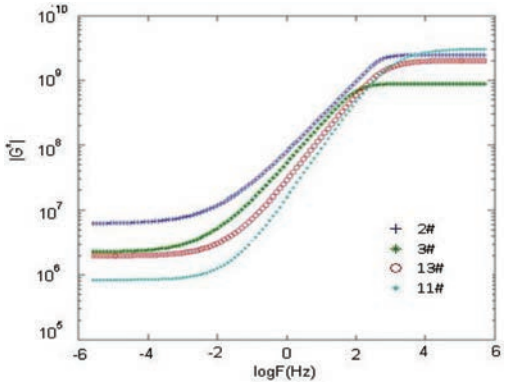

Figure 5. Master curves of four kinds of asphalt mortars.

Table 13. Fitting results of CAM model parameters.

Stockyard	Samples	E	SP	G_e^*/MPa	G_g^*/MPa	f_c/Hz	k	m_e	R	f'_c/Hz
A	2#	1.365	0.644	1.738	3683	544	0.541	0.584	0.324	0.0011
	3#	1.318	0.738	5.927	6380	1284	0.443	0.548	0.372	0.0037
B	13#	1.295	0.827	4.091	1347	171	0.836	0.698	0.251	0.0016
	11#	1.264	0.846	1.796	5045	894	0.442	0.664	0.452	0.0054

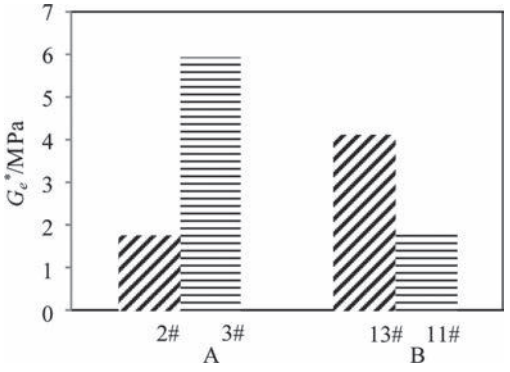

Figure 6. Equilibrium dynamic modulus $|G^*|_e$ of different asphalt mortars.

of asphalt mortar consisted of fine aggregate with different shape characteristics. Figure 6 and Table 13 showed that, for stockyard A, the $|G^*|_e$ of asphalt mortar consisted of fine aggregates with greater E value and smaller SP value is greater, however, for stockyard B, the conclusion is on the contrary. This shows that there is no significant correlation between Equilibrium dynamic modulus $|G^*|_e$ and fine aggregate shape characteristics. The effect of fine aggregate shape characteristics on asphalt mortar at high temperature or low frequency is not notable.

5.2 *Influence of fine aggregates shape characteristics on* $|G^*|_g$

For asphalt mortar, glassy dynamic modulus $|G^*|_g$ describes the ability to resist deformation at low temperature, and greater $|G^*|_g$ means stronger ability to resist deformation. The changes of glassy dynamic modulus $|G^*|_g$ of asphalt mortar consisted of fine aggregate with

different shape characteristics are shown in Figure 7. According to the results of Figure 7 and Table 13, glassy dynamic modulus $|G^*|_g$ of asphalt mortar, which is consisted of fine aggregates with smaller E value and greater SP value, is greater. This result indicates that, fine aggregate particles, which are more elongated and have less angularity, create smaller glassy dynamic modulus $|G^*|_g$. In the other word, fine aggregates with low content of elongated particles and abundant angular can increase asphalt mortar modulus and ability of deformation resistance at low temperature and high frequency.

5.3 *Influence of fine aggregates shape characteristics on shape parameters m_e*

m_e describes the sensitivity of asphalt mortar to temperature and frequency, and smaller m_e means that asphalt mortar is less sensitive to temperature and frequency. The changes of shape parameters m_e with different shape characteristics of fine aggregates are shown in Figure 8. The results of Figure 8 and Table 13 show that fine aggregates with smaller E value and greater SP value create greater m_e. This indicates that asphalt mortar composed of fine aggregates, the form of which is nearly cube and the angularity of which is plentiful, is more sensitive to temperature and frequency.

5.4 *Influence of fine aggregates shape characteristics on f_c*

f_c is the threshold frequency of rheometer zone and elastic zone at low temperature. On the other hand, f_c represents the frequency when storage modulus is equal to loss modulus. Great f_c signifies that asphalt mortar has a high phase angle and show more viscous

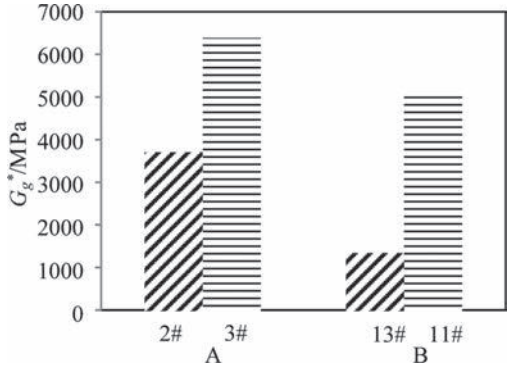

Figure 7. Glassy dynamic modulus $|G^*|_g$ of different asphalt mortars.

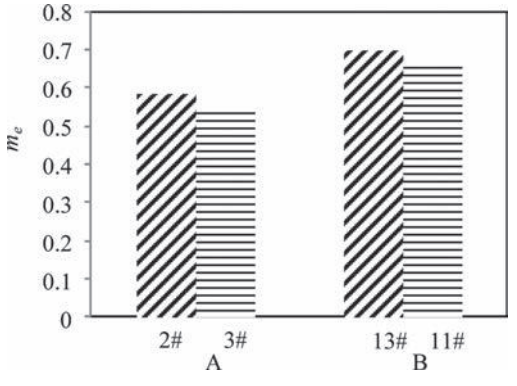

Figure 8. Shape parameters m_e of different asphalt mortars.

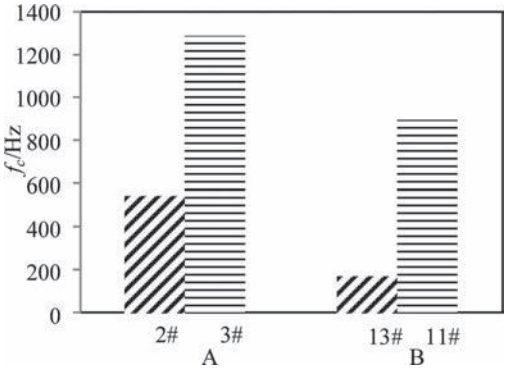

Figure 9. Threshold frequency f_c of different asphalt mortars.

component. As a result, the performance of asphalt mortar at low temperature is good. Figure 9 shows the changes of threshold frequency f_c with different shape characteristics of fine aggregates. In Figure 9, asphalt mortars consisted of fine aggregates with small E value and great SP value have a great threshold frequency f_c, which implies that fine aggregates with less elongated particles and more angular create greater f_c of asphalt mortar. This means that asphalt mortar consisted of fine aggregates, which are closed to cube in form and more abundant in angularity, has more viscous component and better low temperature performance.

In summary, the study about the influence of fine aggregates shape characteristics on the viscoelastic properties of asphalt mortar shows that, fine aggregates with less elongated particles and more angular are helpful to improve the viscous component and low temperature performance for asphalt mortar. However, for the high temperature performance of asphalt mortar, the results of the study don't show a good relationship with fine aggregates shape characteristics.

6 CONCLUSION

This study focused on measuring fine aggregates form, angularity and texture and their correlation with viscoelastic properties of asphalt mortar. The following observations can be made:

1. The grey relation degree of 0.6 mm size is the maximum; as a result, 0.6 mm is selected as the sensitive size of fine aggregate shape characteristics.
2. The image acquisition system, consisted of stereo microscope, video camera, area source and image analyser, can be used to obtain images and indices of fine aggregates shape characteristics.
3. The differences of shape characteristics between natural with chips and manufacture sand is in terms of form, angularity and texture. Natural sand is nearly rounded, less angular and texture. And the difference of shape characteristics between chips and manufacture sand is in terms of shape and angularity. Chips are elongated or flaky and less angular than manufacture sand.
4. Form index E and angularity index SP can describe the differences among different kinds of fine aggregates, and was proposed as the evaluating indices of fine aggregate shape characteristics.
5. Fine aggregates with less elongated particles and more angular are helpful to improve the viscous component and low temperature performance for asphalt mortar. However, for the high temperature performance of asphalt mortar, the results of the study don't show a good relationship with fine aggregates geometric characteristics.

REFERENCES

[1] Johnson E., Li X.J., Adam Z., et al. Investigation of Superpave Fine Aggregate Angularity Criterion for Asphalt Concrete[J]. Transportation Research Record, 2007, 1998:75–81.

[2] Kwan A.K.H., Mora C.F and Chan H.C. Particle shape analysis of coarse aggregate using digital image processing[J]. Cement and Concrete Research, 1999, 29(6):1403–1410.

[3] Oliveira A.L. Contributions to Mix Design and Production of Concrete Pavers[D]. Floriano´polis. PhD Thesis, Federal University of Santa Catarina, Brazil (in Portuguese), 2004.

[4] Masad E. Development of a Computer Controlled Image Analysis System for Measuring Aggregate Shape Properties[R]. Transportation Research Board, Washington DC IDEA Programs, 2003.

[5] Zelelew H.M., Papagiannakis A.T., Masad E. Application of Digital Image Processing Techniques for Asphalt Concrete Mixture Images[C]//12th International Conference on Computer Methods and Advances in Geomechanics 2008. International Association for Computer Methods, 2008, 1:119–124.

[6] Fletcher Thomas, Chandan Chandan, Masad, Eyad, et al. Aggregate Imaging System for Characterizing the Shape of Fine and Coarse Aggregates[J]. Transportation Research Record, 2003(1832):67–77.

[7] Masad E., Button W.J. Unified Imaging Approach for Measuring Aggregate Angularity and Texture[J]. Computer-Aided Civil and Infrastructure Engineering, 2000, 15:273–280.

[8] Masad E., Olcott D., White T., et al. Correlation of Fine Aggregate Imaging Shape Indices with Asphalt Mixture Performance[J]. Journal of Transportation Research Record, 2001, 1757:148–156.

[9] Taleb Al-Rousan, Eyad Masad, Erol Tutumluer, et al. Evaluation of image analysis techniques for quantifying aggregate shape characteristics[J]. Construction and Building Materials, 2007(21):978–990.

[10] Thomas B., Ali1 M., Matthew B., et al. Comparing Fine Aggregate Angularity with Aggregate and Hot-mix Asphalt Performance Tests[J]. 2006, 1962:79–89.

[11] Prudencio Jr R.L., Oliveira L.A., Weidmann D.F., et al Particle Shape Analysis of Fine Aggregate Using a Simplified Digital Image Processing Method[J]. Institution of Civil Engineers, 2013, 65(1):27–36.

[12] Liu Qinan1, Ma Tao, Li Chunlei. Analysis of Factors Affecting High-temperature Stability of Asphalt Mixture Based on Grey Relation Entropy[C]. 2010 International Conference on Optoelectronics and Image Processing, 2010(1):239–242.

Asphalt Pavements – Kim (Ed)
© 2014 Taylor & Francis Group, London, ISBN 978-1-138-02693-3

Research on fractal features of basalt aggregate surface topography

Jianzhong Pei
School of Highway, Chang'an University, South Erhuan Middle Section, Xi'an, Shaanxi Province, China

Yanwei Li
Transport Agency of Shijiazhuang City, Shijiazhuang, Hebei Province, China

Dongdong Zhang
CCCC First Highway Consultants Co., Ltd., Xi'an, Shaanxi Province, China

Yu Liu & Jiupeng Zhang
School of Highway, Chang'an University, South Erhuan Middle Section, Xi'an, Shaanxi Province, China

ABSTRACT: The main purpose of this research is to evaluate the fractal features of aggregate surface topography through capturing three-dimensional aggregate images with a three-dimensional optical dense point cloud measurement system and a newly-developed Matlab program calculating fractal dimensions of aggregate surfaces and sizes. Through analysis and comparison on fractal features of both fine and coarse basalt aggregate, it was observed that fractal dimensions of aggregates had an obvious size. Fractal dimension gradually increased along with the measurement size increasing. No fractal feature was shown when measurement size exceeds a certain limit, and the threshold value reflected the complexity of aggregate surface morphology. For basalt aggregates of 13.2 mm, the threshold value was 12.8 mm. Fractal feature was not necessarily shown with measurement size ranged from 0.8 mm to 12.8 mm. Obvious fractal features were shown when measurement size was less than 0.8 mm.

Keywords: basalt, surface topography, fractal feature, optical dense point cloud, newly developed Matlab program

1 INTRODUCTION

In road materials, the proportion of aggregates is the largest. The percentage is 70% to 85% for cement concrete, in hot asphalt mixture, the percentage could reach 90% to 95% [1]. Therefore, one of the most important factors affecting mixture performance is characteristics and quality of aggregates. Studies has been showed that the asphalt mixture's pavement performance is connected with Deformation, fatigue resistance, surface friction of Asphalt, which is affected by size, shape, size distribution and morphology of aggregates [2,3]. Therefore, in order to design a long-life pavement, aggregates must have a reasonable morphology. At present, the most relative experiments on mechanics including aggregates abrasion test, endurance test and polishing value test, chemical experiments including aggregate robustness test and organic content test, physical experiments including aggregate screening test, shape characteristic and surface texture measurement. There is a series of detail test methods in ASTM D3398, which is an indirect measurement method and it can be used for each particles aggregates. In the text, particle shape and macro-texture are used as the test object needing long time and more workload [4–7].

Fractal is a new theory to solve the problem of aggregate surface morphology. This theory was introduced into engineering surface morphology at 1986. Majumdar pointed out that

engineering surface showing different features, such as unstable randomness, disorder, self-similarity and multi-scale [8]. Furthermore, Majumdar infer out self-correlation function based on fractal dimension by Weierstrass-Mandelbrot fractal function. In china, it is not until 1994 that applying fractal theory to engineering surfaces. In connection with Engineering surface sectional profile curve, Ge made research about the changing processes of surface morphology by fractal dimension [9–10]. Cheng pointed out that fractal dimension could also clearly report surface roughness. In particular, it could overcome the lacking of scale in traditional roughness parameters [11].

In recent years, Image Analysis Techniques has been used to analysis material microstructure in different areas of Materials Science and Geotechnical engineering. The Image Analysis Techniques was lead into measure shape characteristics of aggregates in road projects as following. The techniques could measure different sizes of aggregates shape features fast, accurately and objectively. In the Image Analysis Techniques, aggregate shape features can be characterized by three indicators: Form, Angularity and Surface Texture. Therefore, the paper selects fractal dimension as parameter and makes the research of aggregate surface texture by Digital Image Analysis Techniques.

2 THREE-DIMENSIONAL CHARACTERIZATION OF AGGREGATE MORPHOLOGY

XJTUOM measurement system is a three-dimensional optical measurement technology which is based on the latest international technology. Three-dimensional optical measurement technology in this paper is a three-dimensional optical dense point cloud measurement system marking XJTUOM (Fig. 1). The systemic model is XJTUOM-I that includes two 1.3 million to 6.6 million pixel cameras and format size of a single measurement is 150 mm*110 mm to 400 mm*300 mm.

2.1 *3D scanning and three-dimensional coordinates obtaining of aggregates*

In order to acquire three-dimensional coordinates, we should scan aggregates to obtain three-dimensional images and three-dimensional coordinates. Four steps as follows:

1. Selected aggregates. In the study, two different particle size aggregates as the Table 1 shows.
2. Spray painting

As darker of aggregates surface, it is hard to distinguish fine aggregate surface characteristics in the process of scanning and lead data missing easily in the progress. To avoid this situation, during the experiment, aggregates surface was painted (Fig. 2).

3. Three-dimensional optical scanning

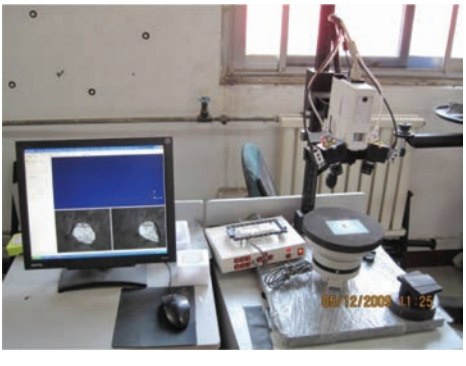

Figure 1. XJTUOM-I.

Table 1. Type and size of aggregates.

Aggregate	Particle size (mm)			
Species	19	16	13.2	9.5
Basalt-1	√	√	√	√
Basalt-2			√	√

Figure 2. Spray painted aggregates.

Aggregates after the spraying is placed on the stage, projection grating projects many fringes for different spatial frequency to the surface of aggregates and then cameras deformed fringe pattern. Phase method used to obtain the phase of the main values of various stripes and then we can obtain the true phase stripes. Cameras and Projection grating on aggregates surface is showed in Figures 3 and 4.

In order to obtain three-dimensional surface characteristics of aggregates more conveniently, aggregates should be tested according to three vertical mutually perpendicular surfaces marked A, B, C for scanning (Fig. 5).

4) Three-dimensional coordinates obtaining

As restricted by scanning image format, we had to scan two times for a aggregate and then automatic splicing would be need for results by Geomagic Studio 8 one of image data processing. Getting the entire three-dimensional aggregates coordinates for next. After stitching processing is completed, there will be an ASC document for 3-dimensional coordinate. This file is converted to TXT format then and each aggregate corresponds to a TXT file.

2.2 *Three-dimensional visualization of aggregates*

After completing three-dimensional optical scanning and obtaining three-dimensional characteristics of aggregates, we need to use appropriate procedures to achieve three-dimensional visualization of aggregates for next, so that we can observe the surface morphology and textures of aggregates more intuitively. It's also providing the basis for data processing and calculating next.

Currently, three-dimensional visualization of aggregates can be achieved by a lot of software. Geomagic Studio and MATLAB are most often used. Geomagic Studio is mainly used to generate three-dimensional model of aggregates and build aggregates complex surfaces. Because of powerful data processing capabilities and superior graph processing capabilities, MATLAB is very suitable for program calculating and feature extraction calculating of aggregate Morphology later. For the reason that, in this paper, Geomagic Studio was chosen as three-dimensional structure software of aggregates and MATLAB was chosen as analysis software of aggregate morphology later.

Geomagic Studio can create three-dimensional models by 3D point cloud data in the scanning before. In our study, Geomagic Studio was used to read TXT point cloud data of 13.2 mm diameter basalt-1 and generating six-sided view of three-dimensional aggregates.

Figure 3. Cameras.

Figure 4. Projection grating on aggregates surface.

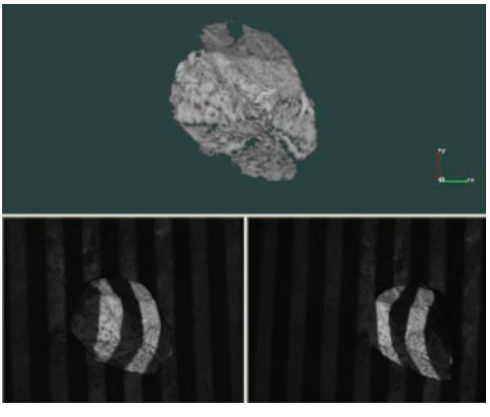

Figure 5. Software interface in scanning.

3 AGGREGATE MORPHOLOGY CHARACTERISTICS OF TWO-DIMENSIONAL PRRSING

With diameter of 13.2 mm basalt-1 and 4.5 mm basalt-2 the research object, three randomly particles selected from each of the aggregate particles. Aggregate particles is generated by the software Geomagic Studio 8 sides view, as shown in Figure 6, the three-dimensional figure available aggregate surface three coordinates of point cloud, and in the MATLAB generated three-dimensional topography on the surface of the coarse aggregate, the comparative study of the characteristics of aggregate surface topography.

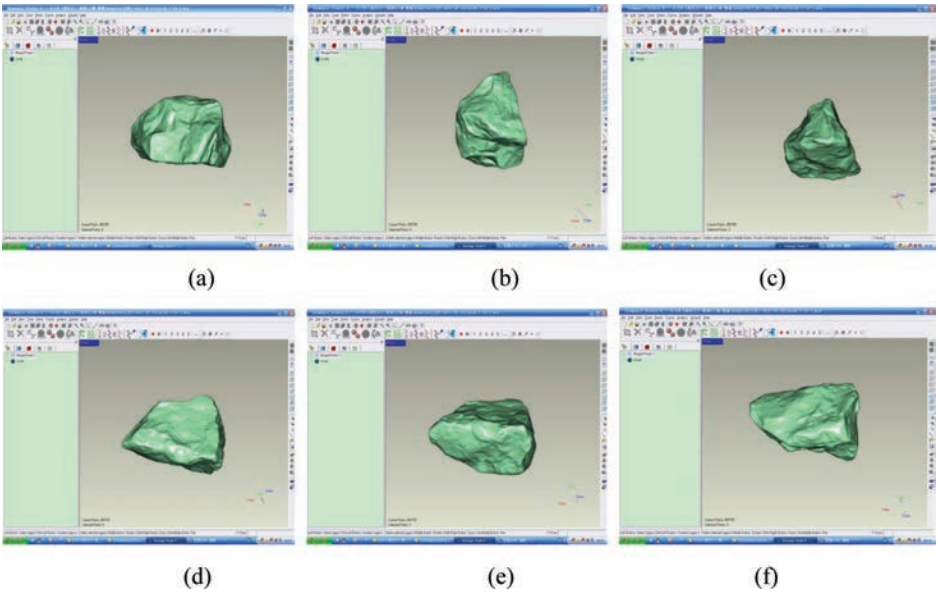

Figure 6. Aggregate particles hexahedral view.

3.1 *Coarse aggregate surface morphology analysis*

In order to understand the characteristics of coarse aggregate surface morphology, the 13.2 mm basalt-1 and basalt-2 of three optical is used to scan data, the calculation process of cube cover method use MATLAB software to write, in the random selection of material surface coverage, the relationship between the establishment and basalt-1–2 calculation data are shown in Tables 2 and 3 reflects the relation of double logarithmic coordinate diagram as shown in Figures 7 and 8.

Combining with the analysis in Table 2 and Figure 7 13.2 mm appearance characteristics of basalt-1 are as follows:

1. Figure 7 (a), for number one, when the delta of the range is 0.1~0.1 mm, coarse aggregate surface fractal dimension is 2.863, when the delta the range is 0.8~3.2 mm, the aggregate surface fractal dimension is 3.68, greater than 3 for unqualified data.
2. Figure 7 (b), for number two, when the delta of the range is 0.1~0.1 mm, coarse aggregate surface fractal dimension is 2.428; When the delta the range is 1.6~1.6 mm, the aggregate surface fractal dimension is 2.669.
3. Figure 7 (c), for number three when the delta of the range is 0.1~0.1 mm, coarse aggregate surface fractal dimension is 2.861; When the delta the range is 3.2~6.4 mm, the aggregate surface fractal dimension is 3.123, the influence of other factors lead to the results of fractal dimension mutation, causing its scope beyond the maximum limits.

Above all, we can draw a conclusion that, for a 13.2 mm basalt-1, when the measurement scale is greater than 12.8 mm, it does not show the aggregate surface fractal, When the measurement scale is between 0.8~12.8 mm, rough surface does not necessarily show the fractal; Only when it is less than 0.8 mm, surface showed the fractal nature.

According to Table 3 and Figure 8, analysis of the 13.2 mm basalt-2 appearance characteristics as follows:

1. Analysis diagram (d), when the delta of the range is 0.1~0.8 mm, coarse aggregate surface fractal dimension is 2.934, when the delta the range is 0.8~0.8 mm aggregate surface fractal dimension is 3.111, it is greater than the scope of the surface fractal dimension for the appearance characteristics of variation points.

Table 2. The relationship between N(δ) and δ of the 13.2 mm Basalt-1.

No. 1		No. 2		No. 3	
Scale δ/mm	Total cube $N(\delta)$	Scale δ/mm	Total cube $N(\delta)$	Scale δ/mm	Total cube $N(\delta)$
0.1	189899	0.1	1515982	0.1	780088
0.2	25924	0.2	308726	0.2	104870
0.4	3805	0.4	52357	0.4	14432
0.8	493	0.8	7429	0.8	2015
1.6	40	1.6	1108	1.6	280
3.2	3	3.2	179	3.2	32
6.4	0	6.4	32	6.4	2
12.8	0	12.8	4	12.8	0
25.6	0	25.6	0	25.6	0
51.2	0	51.2	0	51.2	0

Table 3. The relationship between vand δ of the 13.2 mm Basalt-2.

Basalt-2: No. 1		Basalt-2: No. 2		Basalt-2: No. 3	
Scale δ/mm	Total cube $N(\delta)$	Scale δ/mm	Total cube $N(\delta)$	Scale δ/mm	Total cube $N(\delta)$
0.1	575198	0.1	618108	0.1	45436
0.2	76045	0.2	82561	0.2	5928
0.4	9862	0.4	10783	0.4	797
0.8	1290	0.8	1444	0.8	83
1.6	155	1.6	195	1.6	5
3.2	18	3.2	30	3.2	0
6.4	2	6.4	3	6.4	0
12.8	0	12.8	0	12.8	0
25.6	0	25.6	0	25.6	0
51.2	0	51.2	0	51.2	0

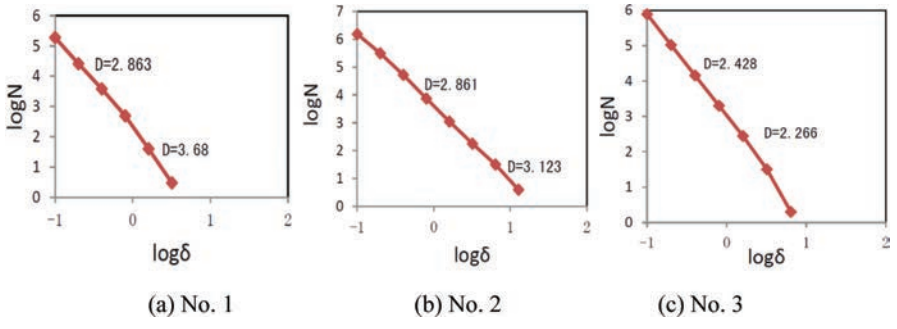

Figure 7. Surface fractal dimension results of the 13.2 mm Basalt-1.

2. Analysis diagram (e), when the delta of the range is 0.1~0.1 mm, coarse aggregate surface fractal dimension is 2.866; When the delta the range is 3.2~3.2 mm, the aggregate surface fractal dimension is 3.322.
3. Analysis diagram (f), when the delta of the range is 0.1~0.1 mm, coarse aggregate surface fractal dimension is 2.917; When the delta the range is 0.4~0.4 mm, the aggregate surface

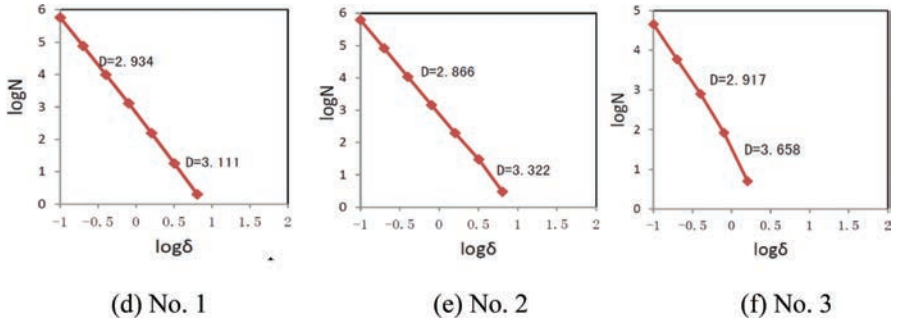

(d) No. 1 (e) No. 2 (f) No. 3

Figure 8. Surface fractal dimension results of the 13.2 mm Basalt-2.

fractal dimension is 3.658, when the measurement scale is larger than a certain value, the fractal dimension of the result beyond boundaries.

To sum up, we can draw a conclusion that, for basalt-1, when the measurement scale is greater than 3.2 mm, it doesn't show the aggregate surface fractal; When the measurement scale is between 0.4~3.2 mm, rough surface does not necessarily show the fractal; Only when it is less than 0.4 mm, surface to show the fractal nature.

Contrast of basalt-1 and basalt-2 of fractal features, we can draw the following conclusion:

1. Through comparing the following table (Table 4), it can be concluded that basalt-2 coarse aggregate surface topography is more sophisticated, the range of measurement scale is relatively smaller, aggregate morphology details showed more superior in the asphalt mixture of road performance.
2. By the Figure 8 (a) to Figure 8 (f), the value of fractal dimension is mainly between 2.5~3.0, range interval preference for the upper, the value of fractal dimension D is big. Thus can explain that basalt-1-2 surface morphology intense changing, aggregate on the surface is of high frequency component, morphology is rich in details, the space wavelength of the surface is relatively short. With this kind of coarse aggregate paving asphalt pavement, coarse aggregate can embedded squeeze each other better and forming stable pavement structure relatively. It's good for resistance to rut at high temperature and extending the life of the road.
3. Analysis diagram (a)~(f), measurement scale is smaller, the value of fractal dimension D is smaller; the measurement scale is larger, with larger value of fractal dimension D until it tends to infinity. Coarse aggregate surface morphology of fractal dimension in all scale does not exist a exact value, smaller measuring scale to calculate the fractal dimension is relatively smaller, when the measurement scale δ tends to zero, the fractal dimension of surface topography is more close to the real value.

3.2 *Fine aggregate surface morphology analysis*

In order to avoid affecting the mechanical properties of the interface, because of measured spacing is too small, we come up with a new parameter Scale fractal dimension R_d to analysis surface morphology of fine aggregates that could balance the interaction between measuring distance and fractal dimension.

Calculating scale fractal dimension parameters of fine aggregate, with a particle size of 4.75 mm basalt-1 and basalt-2 for example (Table 5) to analysis surface morphology of fine aggregates. Scale fractal distribution is shown in Figures 9 and 10.

We can conclude from the figure above, in the three basalt-1 aggregates, the change of the frequency of normal distribution curve fitting of scale fractal dimension is mitigatory, and data is continuous and concentrated, there is a relatively small difference among the

Table 4. Fractal features comparison between Basalt-1 and Basalt-2.

	Not exhibit fractal	Exhibit fractal uncertain	Exhibit fractal
Basalt-1	More than 12.8 mm	0.8~12.8 mm	Less than 0.8 mm
Basalt-2	More than 3.2 mm	0.4~3.2 mm	Less than 0.4 mm

Table 5. Basalt scale fractal dimension parameters for diameter of 4.75 mm.

	Scale fractal dimension parameter					
	Basalt-1			Basalt-2		
Grade	Aggregate-1	Aggregate-2	Aggregate-3	Aggregate-1	Aggregate-2	Aggregate-3
1	12.8764	13.0200	14.3696	10.7597	51.2798	56.6267
2	11.4587	20.4688	30.9697	26.5605	33.5506	78.9085
3	27.9051	9.8049	13.0597	28.0634	26.2798	78.1182
4	10.5657	7.9276	39.8177	13.0427	46.0051	38.8603
5	11.1443	1.2749	6.2705	11.1267	29.8184	76.8416
6	6.6912	4.9003	18.5331	25.2606	30.4387	69.6506
7	29.5784	36.8330	2.3544	6.6462	27.6612	97.3447
8	5.6122	8.6196	7.3117	24.8694	27.7011	78.3655
9	30.4049	31.4573	28.5306	13.6914	43.7404	76.9328
10	22.7774	1.6412	25.4658	24.8666	40.0636	78.4238

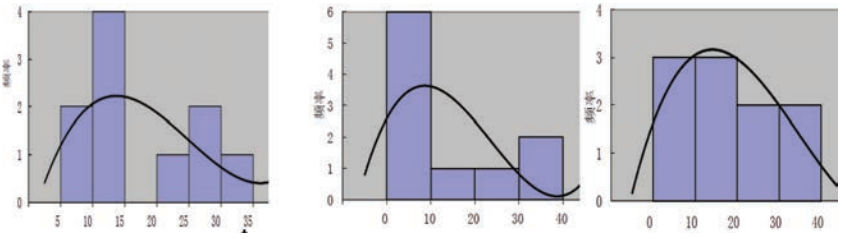

Figure 9. 4.75 mm Basalt-1 scale fractal dimension.

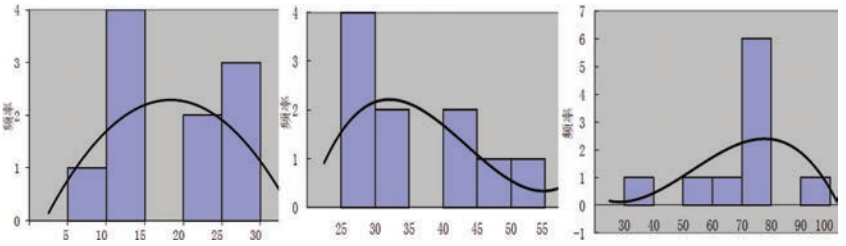

Figure 10. 4.75 mm Basalt-2 scale fractal dimension.

fractal dimension values of aggregates; in the scale fractal dimension frequency curve of basalt-2, the difference of scale fractal dimension values of different aggregates is relatively big, the distribution of data is relatively discrete. The scale fractal dimension of basalt-2 and aggregate-3 is shown in box Figure 11.

According to the drawing 11,we can know that in the aggregate-3 the scale fractal dimension of number 4 and 7 random faces are far away to the mean, they are the change points in

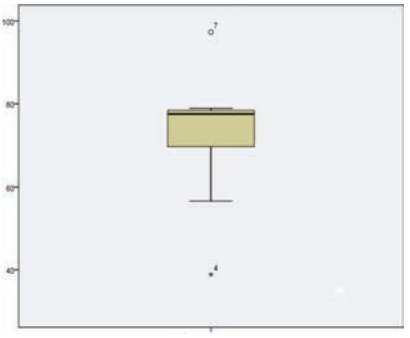

Figure 11. Scale fractal box diagram of aggregates-3 in 4.75 mm Basalt-2.

Table 6. Scale fractal statistics for 4.75 mm Basalt.

	Scale fractal dimension parameters					
	Basalt-1			Basalt-2		
Statistics	Aggregate-1	Aggregate-2	Aggregate-3	Aggregate-1	Aggregate-2	Aggregate-3
Random surface						
Effective	10	10	10	10	10	10
Missing	0	0	0	0	0	0
Average	16.901	13.595	18.668	18.489	35.654	73.007
Standard deviation of the average	3.072	3.870	3.860	2.562	2.822	4.930
Midpoint	12.168	9.212	16.451	19.279	31.995	77.526
Standard deviation	9.715	12.239	12.206	8.103	8.925	15.589
Variance	94.385	149.796	148.985	65.659	79.648	243.003
Minimum value	5.610	1.270	2.350	6.650	26.280	38.860
Maxima	30.400	36.830	39.820	28.060	51.280	97.340

statistic, it indicates that the aggregate's broken is unreasonable, which lead that surface scale fractal dimension have a big change, fine aggregates' morphology inhomogeneity.

Choosing three aggregates of whinstone-1 and whinstone-2, in every aggregate random choose 10 faces, comparing the difference of scale fractal dimension, hunting the morphology feature distribution regulation of fine aggregate, Table 6 shows the whinstone's scale fractal dimension of 4.75 mm.

According to Table 6, we can know that the mean values of scale fractal dimension three whinstone-1 aggregates are 16.901, 13.595 and 18.668. Meanwhile, the mean values of scale fractal dimension three whinstone-2 aggregates are 18.489, 35.654 and 73.007. Comparing the means, we can easily obtain that the scale fractal dimension R_d of whinstone-1 is mostly distributed between 1.27 and 39.82, and it is uniform. At the same time, we can see that scale fractal dimension R_d of whinstone-1 is mostly distributed between 6.65 and 97.34, the data are random and discrete. This indicates that whinstone-2 fine aggregate scale fractal dimension is larger than whinstone-1, also, whinstone-2 surface morphology roughness is fickle, the fine aggregate has a big size effect, which have a big effect to mixture's pavement performance.

But it is conditional that if the scale fractal dimension R_d is reasonable, which depends the rationality of the measuration distance. To fine aggregate the rationality of the measuration distance have a big effect to the scale fractal dimension R_d, if the measuration distance is oversize, the small scale information will be ignored, this is because the small percents in

the fine aggregates would easily cover up by big scale. Meanwhile, because singleness index covers limited information, combined with other index, it is more reasonable to building multi-index.

4 CONCLUSIONS

1. The 3D optical dense point cloud measurement system of XJTUOM type is employed to scan the surface of each aggregate, and the soft geomagic Studio 8 is used to achieve automatic splicing processing and get the 3D free-space diagram of aggregate particles, therefore 3D free-space diagram can obtain the 3D coordinates of point cloud of aggregate surface, in the matlab, 3D appearances of coarse aggregate surface are obtained, using self-similarity fractal dimension and dimension fractal description parameter of fine aggregate as evaluation indexes, we compare and research the feature of aggregate surface.
2. Taking basalt-1 and basalt-2 with the 13.2 mm particle size for example, we can find from the test results, the superficial appearances of coarse aggregate of basalt-2 are more subtle, the measurement scale of every range is relatively small, and appearance details of aggregates are more abundant, they will show up more superior pavement performance in asphalt mixture.
3. Taking basalt-1 and basalt-2 with the 4.75 mm particle size as research objects, statistical analysis software PASW is applied to analyze the appearance of fine aggregate of basalt. We can conclude from the test results, the discreteness of dimension fractal description parameters of basalt-2 is big, the variation of rough details of superficial appearance is big, relative to the basalt-1, the size effect of the fine aggregate is obvious, which will has relatively big influence on the pavement performance of the mixture.

ACKNOWLEDGMENTS

We wish to express our thanks to National Natural Science Foundation of China (Grant No. 51378073), Program for Innovative Research Team in University (Grant No. IRT1050), Research Project from Department of Transportation in Hebei Province (Grant No. Y-2010089) and Major State Basic Pre-research Development Program of China (973 Program, Grant No. 2012CB626814).

REFERENCES

[1] Hyoungkwan Kim. Automation of aggregate characterization using laser profiling and digital image analysis [D]. Austin: Univ. of Teas, 2002.

[2] Sheng Jinan. Asphalt and asphalt pavement performance [M]. Beijing: People's Communications Publishing House, 2001.

[3] wu Qihong. The impaction of aggregate to asphalt pavement [J]. Journal of Foreign Highway, 1998, 18 (1): 39–47.

[4] NH Maerz, M Lusher. Measurement of flat and elongation of coarse aggregate using digital image processing. In: Proc of Transportation Research Board, 80th Annual Meeting, Washington D.C, 2000, Paper No. 01-0177.

[5] ASTM D3398-2000, Standard Test for Index of Aggregate Particle Shape and Texture [S].

[6] Taleb A.R, Eyad M.L. Aggregate shape classification system using AIMS [A]. 83rd Transportation Research Board Annual Meeting [C]. Washington DC: The National Academies, USA, 2004.

[7] Tongyan P, Erolt, Samuel H. Carpenter. Effect of coarse aggregate morphology on the resilient modulus of hot mix asphalt [A]. 85rd Transportation Research Board Annual Meeting [C]. Washington D.C: The National Academies, USA, 2006.

[8] Brown C.A, Charles P.D, Johnsen W.A, et al. Fraetal analysis of topographic data by the patchwork method [J]. Wear, 1993, 161(1–2): 61–67.

[9] Ge Shirong, Suo Shuangfu. The Computation Methods for the Fractal Dimension of Surface Profiles. Tribology. 1997, 17(4): 354–362.
[10] Ge Shirong. Characterization of Surface Topography Changes During Running-In Process with Characteristic Roughness Parameter. Journal of China University of Mining & Technology. 1999, 28(3): 204–207.
[11] Chen Guoan Ge Shirong. Fractal Interpolation Simulation of Rough Surface Profiles. Tribology. 1998, 18(4): 346–350.
[12] Eyad Masad, Dana Olcott, Thomas White, and Laith Tashman Correlation of Imaging Shape Indices of Fine Aggregate with Asphalt Mixture Performance [C] Transportation Research Board 80th Annual Meeting January 7–11, 2001 Washington, D.C.
[13] Barrett, P.J. The Shape of Rock Particles. A Critical Review. Sedimentology, 27, 1980, pp. 291–303.

This page intentionally left blank

Asphalt Pavements – Kim (Ed)
© 2014 Taylor & Francis Group, London, ISBN 978-1-138-02693-3

Design of cement stabilized full depth reclaimed mixes using Superpave Gyratory Compactor

Ilker Boz & Mansour Solaimanian
Pennsylvania State University, University Park, PA, USA

ABSTRACT: Full Depth Reclamation (FDR) is a popular technique in rehabilitating distressed pavements. The technique is very effective and economical when the pavement problems extend beyond the surface layers and when base repair is essential in renewing the pavement. Engineering design of the FDR mix is important to ensure strength and durability of the FDR mix. Most of the existing mix design procedures for chemically stabilized FDR are based on laboratory compaction of specimens in a Proctor mold and determination of unconfined compressive strength of the mix. A procedure is proposed here to use the Superpave Gyratory Compactor (SGC) for preparation of compacted specimens and utilizing the indirect tensile strength of the compacted specimens for mix design. As part of this research, correlation between the strength of Proctor prepared specimens and SGC prepared specimens was evaluated. The strength of Proctor specimens was determined using unconfined compressive strength and that of SGC specimens was determined using indirect tensile strength. A total of 18 cement stabilized samples were prepared and tested. Test results indicated that there is a strong correlation between the two procedures.

Keywords: Superpave Gyratory Compactor, cement stabilization, Full Depth Reclamation, unconfined compressive strength, indirect tensile strength

1 INTRODUCTION

As for all structures, pavement structures deteriorate over time due to several factors, mainly by weather and traffic. Thus, there is a need for deteriorated pavements to be rebuilt or reconstructed in order to provide a smooth and safe ride. Economical and environmental reasons in today's world have led recycling or reclaiming of pavements to become convenient and attractive alternatives to rebuilding roads completely. Advantages of recycling or reclaiming can include saving natural resources such as aggregate and asphalt, using less energy, having less pollution, less construction cost, and having landfill spaces not filled by old pavement materials [1].

Full Depth Reclamation (FDR) is one of the most common recycling techniques and a popular one in rehabilitating distressed pavements. The technique is very effective and economical when the pavement problems extend beyond the surface layers and when base repair is essential in renewing the pavement. As it can be readily seen from Figure 1, FDR provides significant benefits in the form of the savings in natural resources and money when compared to a new base. Figure 1 results are based on a 2-lane road that is 1 mile long and 24 foot wide with 6 inches base [1].

FDR process requires pulverization of the existing pavement layers, stabilizing the pulverized material through the use of chemical or emulsion additive, compaction and curing of the mix.

Engineering design of the FDR mix is important to ensure strength and durability of the FDR mix, and compaction in the FDR process is one of the important factors in performance of the reclaimed mix. Poorly compacted mixes can result in pavement failures such as rutting

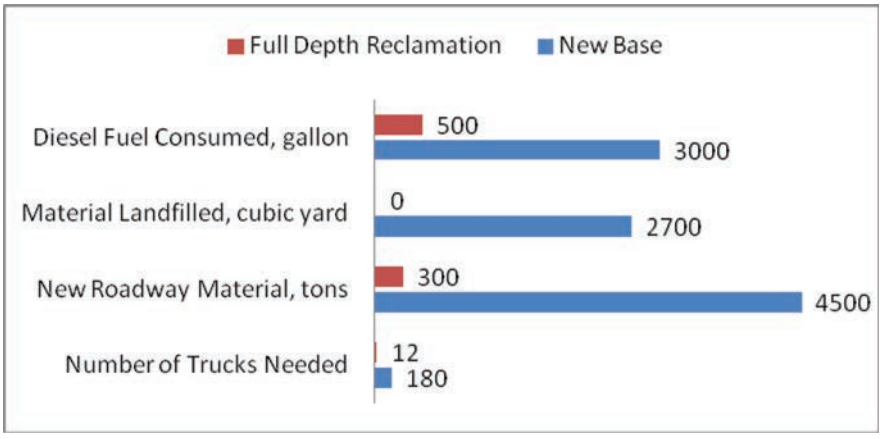

Figure 1. Energy and materials use for FDR and new base [1].

due to more densification under traffic [2]. Most of the existing mix design procedures for chemically stabilized FDR are based on laboratory compaction of specimens in a Proctor mold and determination of Unconfined Compressive Strength (UCS) of the mix. Strength retained after the UCS test can be used to quantify the amount of additive required and to ensure if enough strength is attained for the reclaimed mixes. For example, as indicated in Lewis et al. (2006), minimum strength of 450 psi is necessary for lab-fabricated specimens to have strength of 300 psi or greater achieved in the field [3]. Portland Cement Association recommends the unconfined compressive strength levels to be from 300 to 400 psi after seven days of curing [4].

Superpave Gyratory Compactor (SGC) has been also used in FDR mix design procedures. Mallick et al. (2002) have performed research on the compactive effort of the FDR mixes and suggested 50 gyrations to be used for the FDR mixes [5]. Lee et al. (1999) used the SGC to determine the optimum moisture content and asphalt emulsion content for cold in place recycling mixes [6]. Cross (2003) recommended the use of 30 and 35 gyrations for the reclaimed mixes [7]. Martinez et al. (2007) have studied effect of varying the standard conditions of gyration angle and vertical pressure and recommend a new mix design based on indirect tensile strength test [8].

The purpose of this research was to develop a procedure for cement stabilized FDR mixes to use the SGC for preparation of compacted specimens and utilizing the indirect tensile strength of the compacted specimens for mix design. Thus, correlation between the strength of Proctor prepared specimens and SGC prepared specimens was evaluated.

2 EXPERIMENTAL METHODOLOGY

The research in this study was conducted at Northeast Center of Excellence for Pavement Technology (NECEPT) at Penn State University, and the materials for this research were provided by Pennsylvania Department of Transportation. Specimens were prepared with 40% Reclaimed Asphalt Pavements (RAP), 60% stabilized earth, and determined amount of cement and water. Once specimens were compacted with in a Proctor mold and with a Superpave Gyratory Compactor, Unconfined Compressive Strength (UCS) testing and Indirect Tensile strength Testing (IDT) were performed in order to establish correlation between the strength results from the two compaction procedures.

2.1 *Material procurement*

In this project, Reclaimed Asphalt Pavement (RAP) materials were collected from a low traffic volume road in Dauphin County, PA and stabilized soil base materials were taken from

the road in Butler County, PA. Before collecting the RAP from the road, core samples were taken from arbitrarily determined sections of the road in order to determine the thickness of asphalt layer and the thickness of soil base. Wet coring was used, and during the coring process, a gas powered drill was used with a 6 inch diamond tipped coring bit (Fig. 2). The drill was connected to a water supply to help cool the sample and drill bit during the coring. Drilling was taken to sufficient depth to capture materials of different layers including the subbase. Cores were examined to determine the thickness of various layers (Fig. 2). It was determined that, on the average, the thickness of the asphalt and base layers were 40 mm and 60 mm respectively. This ratio of 2:3 for the asphalt thickness to base thickness layer was key in deciding proportioning materials from different layers in providing laboratory specimens.

In addition to coring, test pits were excavated at the site to verify thickness of layers and to obtain sufficient material for testing and characterization. Figure 3 shows samples from one of the test pits.

2.2 *Specimen preparation*

Following the RAP procurement and transportation to the laboratory, the RAP material was placed in an oven for 30 minutes at 135°C in order to loosen the material to the fullest extent possible. The loosened material was then blended with the base material after cooling. The blend consisted of 40 percent of the RAP (asphalt mix) and 60 percent the base material by the mass of dry weight of total mix. Sieve analysis was performed for the blend.

Figure 2. Coring and a core sample, Dauphin, PA.

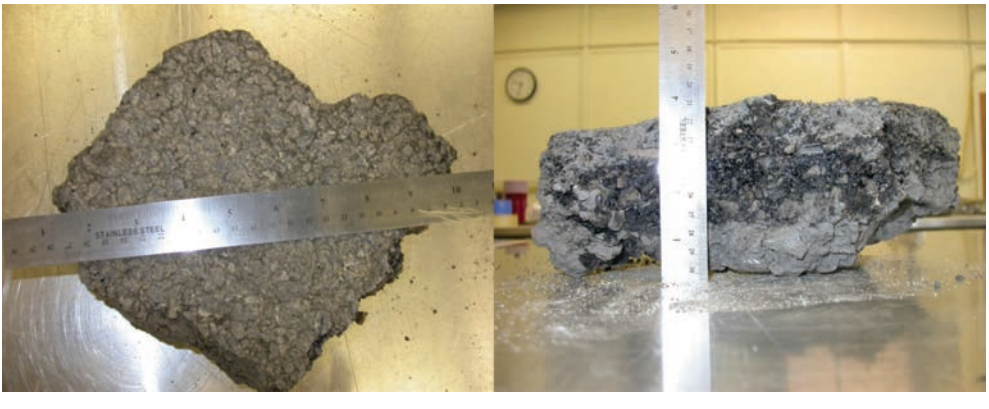

Figure 3. Test pit samples from Dauphin, PA.

The gradation is shown in Figure 4. The blend can be considered a coarse gradation as having a 19-mm nominal maximum size gradation.

2.3 *Mixing*

The optimum cement content was determined to be 7 percent with the corresponding optimum water content of 9.5 percent. Details of establishing optimum water and cement content are provided elsewhere (9). A sample of prepared mixes with cement and water is shown in Figure 5.

Nine specimens, three groups of three, were prepared and compacted in a Proctor for UCS test. Similarly, nine specimens, three groups of three, were also prepared and compacted using the SGC for IDT test. The specimens consisted of X percent cement and Y percent water by dry weight of the mix. Percentages for cement and water are shown in Table 1 for each group.

As it can be seen from Table 1, cement content was lowered and increased by 3 percentage points for the groups. That has resulted in decreasing or increasing water content by 0.75 percentage point for each 3% cement removal from or addition to the mix. The reason for that is to modify corresponding water demand caused by removal or addition of cement.

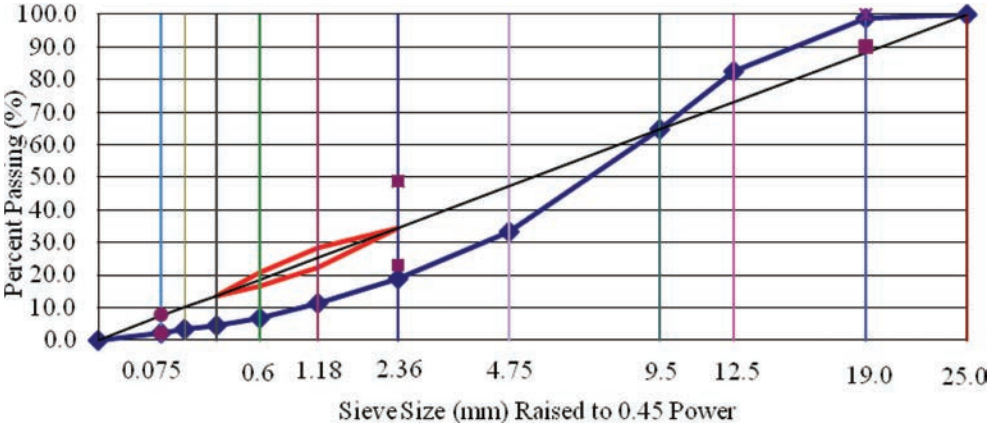

Figure 4. Gradation plot for FDR mix used in this study.

Figure 5. A sample mix after blending with cement and water.

Table 1. Water and cement contents of specimens.

Group	Water content, % (Y)	Cement content, % (X)
1	8.75	4
2	9.5	7
3	10.25	10

Figure 6. From left to right; proctor specimen and the steel mold, rammer for the proctor test, one day cured specimen, capped specimen after 7 day curing.

2.4 *Compaction*

A 4 in.-diameter steel mold with a collar attached was used for compaction of the UCS specimens according to AASHTO T 134, Standard Method of Test for Moisture-Density Relations of Soil-Cement Mixtures. The compaction was done in three layers in the mold and a total of 75-blow, 25-blow at each layer, was applied to each specimens. Average height of 6.86, 6.73 and 6.92 in. was achieved for Group 1, 2 and 3, respectively. After compaction, specimens were left in front of a fan overnight, and then were cured for 7 days in a moist room at 100% humidity. The specimens were then capped with a high strength hydro-stone material following the procedure outlined in ASTM C617-10, Standard Practice for Capping Cylindrical Concrete Specimens. After capping, the specimens were subject to curing in an oven at 40 Celsius degree for a day. Figure 6 shows the tools and the steps for Proctor specimens.

The SGC specimens were compacted right after mixing with 600 kPa of vertical pressure and a gyration angle of 1.16°. A 150-mm. diameter steel mold with holes (perforated), shown in Figure 7, was used for group 1 and 2 specimens and compacted to a target height of 52 mm. The recorded number of gyrations and average heights are shown in Table 2.

The SGC molds were perforated to allow water escape from the mold during compaction, and to dissipate pore water pressure. However, the perforated mold was not a successful application for the group 3 specimens, due to high moisture content. There was loss of very fine material through the holes during the gyration process. Thus, a steel mold with no holes was used for the group 3. As the reason for using perforated mold was to prevent water pressure built-up, compaction for the group 3 specimens was conducted in 3 stages. After completion of each stage of compaction, 3 minutes wait time was included to allow dissipation of the induced pressure. Table 3 summarizes gyration data for group 3 specimens.

Following compaction, specimens were left in front of a fan overnight, and then cured for 7 days in a moist room at 100% humidity. Specimens were subject to curing in an oven at 40°C for one full day right after the 7 day curing in the moist room.

Figure 7. A perforated compaction mold and covered with rag.

Table 2. Average number of gyrations and average height for the SGC specimens.

Group	Average gyration number	Average height (mm)
1	38	52.1
2	82	52.3
3	154	54.3

Table 3. Gyration numbers and heights for group 3.

Group	Specimen ID	Stage	Gyration number	Average height (mm)
3	S16	1	6	57.1
		2	9	55.9
		3	136	54
	S17	1	9	57.5
		2	19	55.9
		3	116	53.9
	S18	1	6	57.1
		2	26	55.9
		3	150	54.3

3 TEST RESULTS

3.1 *Unconfined compressive strength testing*

Specimens compacted by the proctor underwent unconfined compressive strength testing at a constant loading rate of 1 mm/min as per ASTM D1633, Standard Test Methods for Compressive Strength of Molded Soil-Cement Cylinders. Table 4 summarizes UCS test results. Unconfined compressive strength results presented in Table 4 are based on averaging three replicates for each group.

3.2 *Indirect tensile strength testing*

Specimens compacted by Superpave Gyratory Compactor underwent Indirect Tensile strength Test (IDT). Equation 1 was used to determine the indirect tensile strength. The IDT results are shown in Table 5. Similar to UCS testing, the IDT results presented are average of three replicates per each group.

$$S = \frac{2000P}{\pi * t * D} \tag{1}$$

where:
S = Tensile Strength, kPa
P = Maximum Load, N
t = Specimen thickness, mm
D = Specimen diameter, mm

Table 4. Unconfined compression tests results.

Group	Water content, % (Y)	Cement content, % (X)	Wet density, g/cm³	Bulk specific gravity	Average measured strength, kPa	Coefficient of variation
1	8.75	4	2.0	1.997	1069	9.05
2	9.5	7	2.1	2.099	1873	4.45
3	10.25	10	2.1	2.101	2095	9.11

Table 5. Indirect tensile test results.

Group	Water content, % (Y)	Cement content, % (X)	Wet density, g/cm³	Bulk specific gravity	Average measured strength, kPa	Coefficient of variation
1	8.75	4	2.21	2.206	252	16.74
2	9.5	7	2.25	2.252	595	4.04
3	10.25	10	2.26	2.259	708	14.2

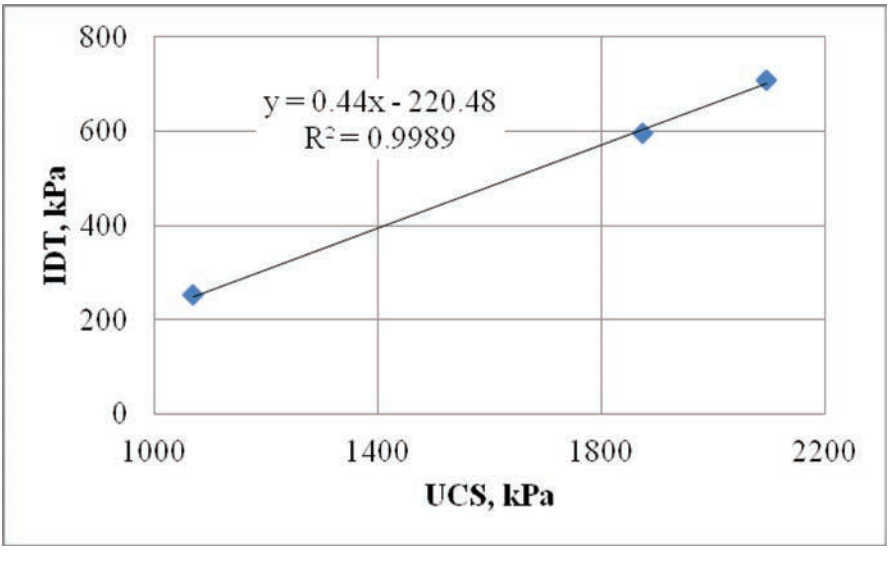

Figure 8. The correlation between IDT and UCS.

3.3 *Analysis*

The correlation between indirect tensile strength and unconfined compressive strength of specimens prepared with cement stabilized full depth reclaimed material is presented in Figure 8. The coefficient of determination, R-Squared, indicates a very strong correlation between the strengths obtained from these two different procedures. This is an indication of the potential for SGC compaction and indirect tensile testing of cement stabilized materials to replace the traditional design using the Proctor procedure. The advantage will be simplicity of compaction, the need for less material (as thinner specimens are prepared for indirect tensile test compared with unconfined compressive test, and a faster testing procedure.

A disadvantage of Proctor specimens prepared with reclaimed material is the surface roughness, especially if the reclaimed material is coarse graded. Uneven or rough surface of the specimen can cause problems during axial compressive loading of the specimens as the loading head may not perfectly sit on the top of the specimen. Sometimes, as was observed in this research, the surface is too rough to be ignored, and smoothening of the surface through capping (for example, with hydro-stone as used in this research) is needed, or the end must be trimmed to provide a smooth parallel surface. These problems are eliminated with the use of SGC and indirect tension.

4 SUMMARY AND CONCLUSION

Environmental and economical reasons have let asphalt recycling or reclaiming gain popularity in the pavement rehabilitation. As one of recycling techniques, Full Depth Reclamation (FDR) is mainly used in pavements for base associated problems. To date, there is no unified standard for design of FDR mixes. Most design procedures take advantage of standard or modified Proctor for compaction of specimens, following ASTM D558 or AASHTO T134.

The main purpose of this research was to find correlation between two different compaction and testing procedures: one using Proctor compaction and unconfined compressive strength testing, and the other using a Superpave gyratory compactor and indirect tensile strength testing. A total of 18 cement stabilized samples were prepared and tested. Test results indicated a very good correlation between the two procedures, and the potential of SGC/IDT process to replace the Proctor/UCS process for designing cement stabilized FDR mixes.

REFERENCES

[1] Full-Depth Reclamation: Recycling Roads Saves Money and Natural Resources, SR 995, Portland Cement Association, 2005.

[2] Basic Asphalt Recycling Manual. Asphalt Recycling and Reclaiming Association, 2001.

[3] Lewis, D.E., D.M. Jared, H. Torres, and M. Mathews. Georgia's Use of Cement-Stabilized Reclaimed Base in Full Depth Reclamation. Transportation Research Record: Journal of the Transportation Research Board, No. 1952, Transportation Research Board of the National Academies, Washington, D.C., pp. 125–133, 2006.

[4] Luhr, D. Recycling Roads Saves Money and Natural Resources. Public Works, Vol. 136, No. 5, pp. 115–117, 2005.

[5] Mallick, R.B., D.S. Bonner, R.L. Bradbury, J.O. Andrews, P.S. Kandhal, and E.J. Kearney. Evaluation of Performance of Full-Depth Reclamation Mixes. Transportation Research Record: Journal of the Transportation Research Board, No. 1809, Transportation Research Board of the National Academies, Washington, D.C., pp. 199–208, 2002.

[6] Lee, K.W., T.E. Brayton, D. Gress, and J. Harrington. Laboratory Evaluation of Mix Design Methods for Cold In-Place Recycling. In Proc., Fifth ASCE Materials Engineering Congress (L.C. Banks, ed.), American Society of Civil Engineers, Reston, Va., pp. 756–769, 1999.

[7] Cross, S.A. Determination of Superpave Gyratory Compactor Design Compactive Effort for Cold In-Place Recycled Mixtures. Research Record: Journal of the Transportation Research Board, No. 1819, Transportation Research Board of the National Academies, Washington, D.C., pp. 152–160, 2003.

[8] Martinez, H.A., R. Miro, and F. Perez-Jimenez. Spanish Experience with Gyratory Compactor and Indirect Tensile Test in Design and Control of Cold Recycled Asphalt Pavement. Transportation Research Record: Journal of the Transportation Research Board, No. 2001, Transportation Research Board of the National Academies, Washington, D.C., pp. 163–168, 2007.
[9] Morian, D., M. Solaimanian, B. Scheetz, and S. Jahangirnejad. Developing Standards and Specifications for Full Depth Pavement Reclamation. Final Report, Pennsylvania Department of Transportation, Report No. FHWA-PA-2012-004-090107, May 2012.

This page intentionally left blank

Asphalt Pavements – Kim (Ed)
© 2014 Taylor & Francis Group, London, ISBN 978-1-138-02693-3

Hot Mix Asphalt for airfield pavements—moving from Marshall mix design to Superpave

Navneet Garg
FAA Airport Pavement R&D Section, Atlantic City International Airport, NJ, USA

Qiang Li, Harkanwal Brar & Injun Song
SRA International Inc., Linwood, NJ, USA

ABSTRACT: Hot Mix Asphalt (HMA) design for commercial airports in the United States (U.S.) is performed in accordance with the Federal Aviation Administration (FAA) Advisory Circular (AC) 150/5370-10F, "Standards for Specifying Construction of Airports," Item P-401—Plant Mix Bituminous Pavements. Currently, P-401 asphalt material is designed using the Marshall mix design procedure and has performed satisfactorily. In 2006, the FAA started a research study to develop an updated P-401 specification based upon Superpave technology. The first phase of the study determined number of gyrations required to produce similar volumetrics as a 75-blow Marshall mix design. The study concluded that mix compacted to 70 gyrations in a gyratory compactor produced a mix with similar volumetric properties to that designed using 75-blow Marshall mix design procedure. The second phase of the study concentrated on laboratory performance tests to be included in the updated P-401 specifications. Performance tests included modified Asphalt Pavement Analyzer (APA) tests, high temperature Indirect tensile Test (IDT), flow number tests, and fatigue tests. This paper will summarize the results from Phase-I and present Phase-II results in detail.

Keywords: Marshall mix design, Superpave, airport pavements, performance tests

1 INTRODUCTION

Approximately 90 percent of the U.S.'s paved runways are paved with Hot Mix Asphalt (HMA) [1]. However, only a small percentage of the total HMA placed in the U.S. is used for airfields. HMA for airfield flexible pavements have been designed using the Marshall mix design method in accordance with FAA AC 150/5370-10 [2].

Marshall mix design procedure has performed satisfactorily. Since the highway industry has converted to superior performing asphalt pavement (Superpave) methodology, it is becoming more difficult to find contractors who are willing to perform mix design according to the Marshall mix design methodology. Hence, it is important that the Superpave method be adopted for HMA design for airfield pavements. Before the Superpave methodology can be adopted by the FAA, the number of gyrations required to provide an adequate compactive effort for airfield pavements must be determined. FAA sponsored three parallel efforts to evaluate the number of gyrations required to provide a density similar to 75 blows with the Marshall hammer. Since the 75-blow Marshall mixes have performed well on airfields in the past, it is believed that providing a density with the gyratory compactor equal to that obtained with Marshall compaction would be a good approach to adopt Superpave and still have confidence of good performance. To date,

three studies have been completed with assistance from FAA funding. The objectives of study were to:

- Determine number of gyrations required to produce an airfield quality HMA;
- Recommend a laboratory performance test to accompany the P401 Superpave specification.

The study is in its final stages and the findings are presented in this paper.

2 PREVIOUS RESEARCH

The FAA had three parallel efforts going on to achieve the above mentioned objective. Work was performed by

- SRA International, Inc. (FAA's support contractor);
- Engineer Research and Development Center (ERDC) at Vicksburg, MS (Interagency Agreement); and
- Parallel project under Airfield Asphalt Pavement Technology Program (AAPTP).

Additional details about these studies can be found elsewhere [3]. Dr. Don Christensen (Advanced Asphalt Technologies), working under FAA contract, summarized the results from three studies [4] and is presented below.

The ERDC research [5] focused on determining the number of gyrations required to achieve the same air void content as produced using 75-blow Marshall compaction. A wide range of mixes were included in this research. The mixes were designed with and without 10% natural sand. Two different binders were used: a Performance Grade (PG) 64-22, and a polymer-modified PG 76-22. The various combinations of aggregate type, size, gradation, natural sand content, and binder resulted in a total of 52 different mix designs. Few mixes that did not meet P401 specifications were included for comparative purposes. This study recommended that 70 gyrations be used to compact specimens in the gyratory compactor when designing HMA for airfield pavements.

In the AAPTP 04-03 project [1], in addition to N-equivalent, the researchers also examined how the mixes selected for the study compacted under traffic, and how much compaction effort was needed to provide adequate rut resistance for the intended application. Eleven primary mixes were used in the study, including seven designed using Marshall compaction and four designed using gyratory compaction. These mixes replicated mixes used in existing airfield pavements from a wide geographic area, and represented a variety of aggregate types, sizes, gradations, and binders. The AAPTP 04-03 researchers based their recommendations on the relationship between the number of gyrations and rutting resistance, as measured using the flow number test, as performed on the asphalt mixture performance tester. Specimens were prepared using two to four gyration levels with varying binder contents, and were then subjected to the flow number test. From these data, the minimum number of gyrations required to prepare specimens passing the flow number test was determined. The final recommendations were given in table form, giving design gyrations as a function of aircraft tire pressure. At tire pressures below 100 lb/in^2, 50 gyrations are to be used; at tire pressures from 100 to 200 lb/in^2, 65 gyrations are to be used; and at tire pressures above 200 lb/in^2, 80 gyrations are to be used in preparing specimens.

FAA/SRA approach was very similar to the ERDC study. However, in the FAA/SRA study, all the mixes used to determine N-equivalent were based on HMA designs used in airfield pavements that have exhibited good performance (mixes used in the ERDC study were not based on ones from actual airfield pavements). The FAA/SRA study also performed laboratory tests to compare the rut resistance and fatigue resistance of mixes designed using both Marshall and gyratory compaction. The average value of N-equivalent was 62; the researchers recommend using 70 gyrations to prepare specimens, since the difference between 62 and 70 gyrations is probably negligible. The rutting resistance of mixes designed using 70 gyrations was found to be slightly better overall than the same mixes designed using 75-blow Marshall compaction. The fatigue resistance of the mixes designed using the two procedures were found to be similar.

3 PERFORMANCE TESTS

Phase II of the study has just been completed. The main objective of the Phase II study is to examine the variability in performance that occurs when designing HMA mixtures using the two different compaction methods and recommend a performance test to accompany the P401 Superpave specification. The objective of the study was not only to evaluate differences in the overall level of performance between the two mix design methods, but more importantly to evaluate differences in the variability in performance between the two methods. The general research approach in Phase II was to prepare specimens from each mix design and perform both rut resistance and durability tests using laboratory procedures. The performance of mixes designed using the 75-blow Marshall mix method was compared to designs prepared using the N_{design} of 70 gyrations. A more effective design method would show a lower degree of variability in performance.

The mix performance was evaluated using the following laboratory tests: Asphalt Pavement Analyzer (APA) (AASHTO TP 63-09) tests, Asphalt Mixture Performance Tester (AMPT) flow number test (AASHTO TP 79-09), and uniaxial fatigue tests. Flow number and APA tests characterize the rut resistance of the mix, and uniaxial fatigue tests characterize the fatigue behavior at low temperatures.

3.1 *Asphalt Pavement Analyzer (APA) tests*

The rutting resistance of asphalt mixture was evaluated using the APA. The loading conditions in the APA are more commonly associated with highway conditions. The APA purchased by the FAA is shown in Figure 1. This APA has been customized to apply 260 psi hose pressure and up to 500 psi with an aluminium wheel with variable rate of loading to simulate different aircraft speeds.

The APA tests were conducted at 0.69 MPa (250 psi) at 64°C (147°F) (high temperature for the binder grade used in mix PG 64-22) to simulate the effects of high tire pressures and high pavement temperatures in airport pavements. Samples were prepared by the U.S.

Figure 1. FAA customized APA.

Army Engineer Research and Development Center (ERDC) at 70 gyrations using three different aggregate types (limestone, granite, and chert gravel), two different aggregate sizes (12.7 and 19.05 mm (0.50 and 0.75 inch)), and two different gradations (fine and coarse). PG 64-22 binder was used in all the mixes. Mixes contained sand content ranging from 0 to 30 percent. Data analysis was performed by direct rut depth measurements.

More details about materials, test procedure, and data analysis can be found elsewhere [6]. Figure 2 shows the results from APA tests for all mixes.

Weak mixes (containing high percentage of natural sand) show rapid accumulation of rutting during the initial load cycles and the samples failed (rut depth > 8 mm) in fewer than 4000 load cycles. Mixes containing chert gravel rutted comparatively quicker than the mixes containing granite and limestone. Based on the results of this study, Rushing et al. recommended a preliminary criterion of less than 10 mm rut depth after 4000 load cycles using 250 psi hose pressure at 64°C (high temperature for the binder grade used in mix PG 64-22) [5]. These were initial findings of the study.

This is an on-going study, and additional tests are being performed by the FAA at their laboratory on eight HMA mixes. These mixes have been used at airport pavements across the U.S. and have performed well under heavy aircraft traffic. These mixes contain different aggregate geologies (granite, dolomite, basalt, limestone, and argillite) and gradations. Both neat and Polymer Modified Asphalt (PMA) binders were used in these mixes. Preliminary tests performed by the FAA showed that Superpave Gyrator Compactor (SGC) mixes showed slightly better rut resistance compared to mixes design using the 75-blow Marshall mix design procedure.

3.2 *Flow number tests*

The AMPT flow number test is used to evaluate the rutting resistance of asphalt mixes. In a flow number test, the sample is subjected to repeated compressive stress of 600 kPa at high temperatures using an AMPT device. The test is performed on specimens that are cored and trimmed (100 mm diameter and 150 mm high) from SGC specimens prepared at the expected in-place air void content. Typical test setup and results are shown in Figure 3. Flow number

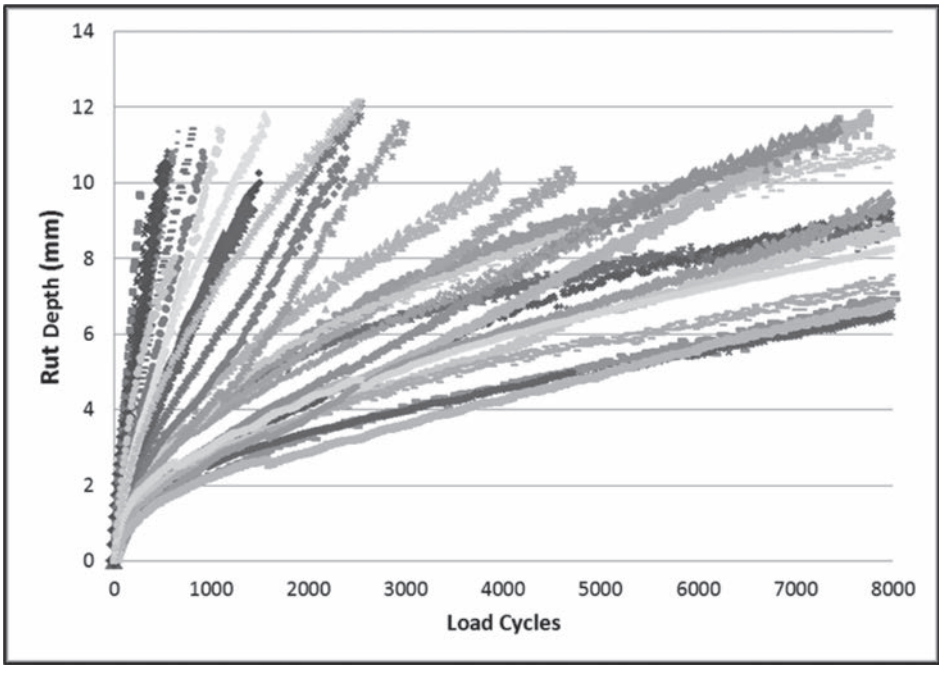

Figure 2. The APA test results on samples prepared by ERDC.

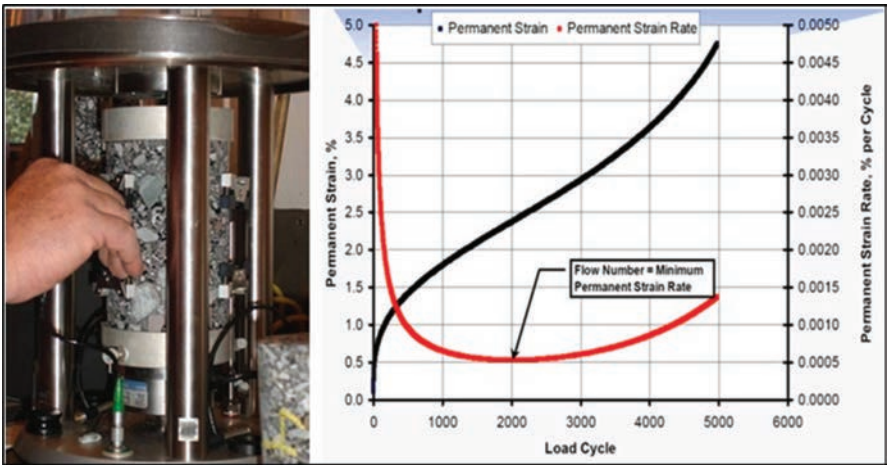

Figure 3. Flow number test.

Table 1. Summary of rut resistance tests (APA and flow number tests).

Mix ID #	FAA aggregate size (mm)	Design compaction method	Design gyrations	Binder grade	Test temperature (deg. C)	Flow number	APA rutting (mm)
1	19	Marshall	40	PG 64-22	50.9	88	4.6
		Gyratory	70	PG 64-22	50.9	120	4.9
2	25	Marshall	70	PG 64-22	51	75	5.6
		Gyratory	70	PG 64-22	51	75	5.6
3	19	Marshall	53	PG 64-22	52.1	120	5.3
		Gyratory	70	PG 64-22	52.1	100	4.6
4	19	Marshall	70	PG 70-22	54.8	190	3.4
		Gyratory	70	PG 70-22	54.8	190	3.4
5	25	Marshall	70	PG 64-22	48.5	120	6.0
		Gyratory	70	PG 64-22	48.5	120	6.0
6	19	Marshall	45	PG 64-22	52.1	56	7.9
		Gyratory	70	PG 64-22	52.1	74	5.7
7	25	Marshall	46	PG 64-22	55	150	4.2
		Gyratory	70	PG 64-22	55	220	5.5
8	19	Marshall	50	PG 70-22	55.4	130	6.1
		Gyratory	70	PG 70-22	55.4	150	4.9

tests are run at the average 7-day maximum pavement temperature 20 mm below the surface, at 50 percent reliability as determined using LTPPBind version 3.1. The number of cycles corresponding to the minimum permanent strain rate is defined as the flow number. Better asphalt mix designs will have higher flow number.

The flow number tests generally followed the trends shown by APA test results and appear suitable for evaluating the rut resistance of HMA for airfield pavements. The SGC mixes showed slightly better rut resistance, probably because of the slightly lower binder contents that were achieved with SGC designs (to provide same volumetrics as Marshall designs). Table 1 summarizes the results from APA and flow number tests performed in the study.

3.3 *Uniaxial fatigue tests*

Uniaxial fatigue tests were performed at 20°C and 4°C on all Phase II mixes shown in Table 4. In the uniaxial fatigue test, a completely reversed sinusoidal load was applied to the specimen

for an extended period of time. The complex modulus (|E*|) of the specimen was constantly monitored during the test, and the rate at which it declined was considered a measure of fatigue damage. Results were analyzed using continuum damage theory. Based on the test results obtained to date, shown in Figure 4, the HMA mixes designed using both the Marshall mix and SGC tend to have similar levels of fatigue resistance.

3.4 *Indirect tensile strength tests*

Indirect Tensile Strength (IDT) was measured at design air void content in accordance with ASTM D6931 at a temperature of 40°C and deformation rate of 5 mm/minute. Tests were performed on three different well performing HMA mixes used at airports and National Airport Pavement Test Facility. Figure 5 shows the relationship between IDT strength and the temperature difference between the high-temperature performance grade and the test temperature.

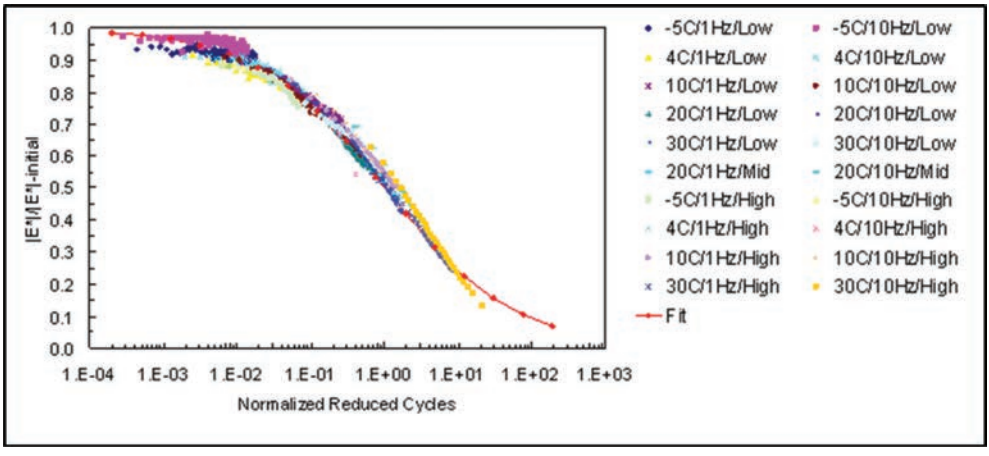

Figure 4. Final master curve for fatigue damage.

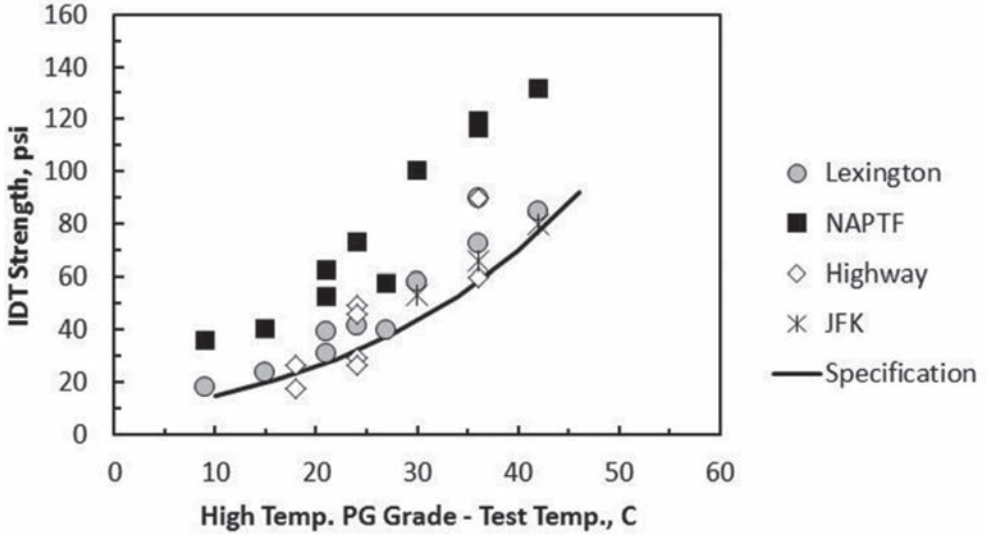

Figure 5. IDT strength as a function of difference between high temperature performance grade and test temperature.

The relationship is fairly reasonable, although the NAPTF mixture exhibits significantly higher IDT strengths than the other mixes. The reason for this difference could be the relatively low air void content of samples of the NAPTF mixes that was tested.

3.5 *Selection of performance test for P401 specification*

There is a need to have an engineering property test for airfield HMA that is simple, quick and inexpensive but still effective. The high temperature Indirect Tensile Test (IDT) meets all these requirements. It is in some ways even simpler than a Marshall stability and flow test, and can be performed using the Marshall press. Based on previous research studies [7–9] it has exhibited excellent correlation to other performance tests in a number of different research projects, including the current research. Other performance tests in the current research (APA, Flow Number Tests, Uniaxial Fatigue Tests) were able to quantify the performance of the mixes but were complicated and time consuming to perform. APA is a simple test, but the availability of equipment capable of loading upto 250-psi is limited and may be considered in the future. In the proposed P401 Superpave Specification, High Temperature IDT test has been recommended as the performance test.

4 SUMMARY

The FAA is in the process of developing an updated P-401 specifications based on the Superpave mix design technology. The Phase-I of the study recommended 70 gyrations for mix designs. The recommendation was based on the fact that HMA volumetrics of mixes designed using 70 gyrations were similar to volumetrics of mixes designed using 75 blow Marshall mix design. High temperature IDT test was recommended as the performance test to accompany the proposed P401 Superpave specification. The main issue with implementing the IDT test for airfield HMA is establishing specification requirements. Because only limited data have been collected on airfield mixtures, lenient IDT design criteria are included in this version of the P-401 Gyratory specification and IDT testing during production is included as a quality control item. This will allow the FAA to use the specification and collect additional data on IDT strengths and production variability to refine the design criteria and ultimately include the IDT test as an acceptance criterion.

ACKNOWLEDGEMENTS

The work described in this paper was supported by the FAA Airport Technology Research and Development Branch, ANG-E26, United States of America, Dr. Satish K. Agrawal, Manager. Acknowledgements are also due to Dr. Ray Bonaquist and Dr. Don Christensen, Jr. (Advanced Asphalt Technologies, LLC), Dr. Thomas Bennert (Soiltek Laboratory), Mr. Roy McQueen (Consultant), Mr. Frank Fee (Consultant), and Mr. John Rushing (ERDC) for their efforts. The contents of this paper reflect the views of the authors, who are responsible for the facts and accuracy of the data presented within. The contents do not necessarily reflect the official views and policies of the FAA, USA. The paper does not constitute a standard, specification, or regulation.

REFERENCES

[1] Cooley, Jr. L.A., Ahlrich, R.C., James, R.S., Prowell, B.D., Brown, E.R., Kvasnak, A., Implementation of Superpave Mix Design for Airfield Pavements. Final Report, AAPTP Project 04-03, 2009.
[2] Federal Aviation Administration (FAA) Advisory Circular (AC) 150/5370-10F, "Standards for Specifying Construction of Airports," Item P-401—Plant Mix Bituminous Pavements, 2011.
[3] Garg, N., Song, I., Brar, H. HMA-Related Research Activities for Airfield Pavements at the Federal Aviation Administration, 11th ISAP Conference on Asphalt Pavements, Nagoya, Japan, 2010.

[4] Christensen, D.W. Review of Recent Research on Using Gyratory Compaction to Design Hot Mix Asphalt for Airfield Pavements. Publication DOT/FAA/TC-13/48. FAA, U.S. Department of Transportation, November 2013.
[5] Rushing, J.F., Development of Criteria for Using the Superpave Gyratory Compactor to Design Airport Asphalt Pavement Mixtures. Publication DOT/FAA/AR-10/35. FAA, U.S. Department of Transportation, 2011.
[6] Rushing, J.F., Little, D.N., Garg, N., Using the Asphalt Pavement Analyzer to Assess Rutting Susceptibility of HMA Designed for High Tire Pressure Aircraft. Transportation Research Record 2296 Volume-4, Journal of the Transportation Research Board, 2012.
[7] Christensen, D.W., R. Bonaquist, and D.P. Jack. Evaluation of Triaxial Strength as a Simple Test for Asphalt Concrete Rut Resistance. Final Report to the Pennsylvania Department of Transportation, Report No. FHWA-PA-2000-010+97-04 (19), PTI Report 2K26, University Park: The Pennsylvania Transportation Institute, August 2000, 80 pp.
[8] Christensen, D.W., R.F. Bonaquist, D.A. Anderson and S. Gohkale. Indirect Tension Strength as a Simple Performance Test. New Simple Performance Tests for Asphalt Mixes, Transportation Research Circular E-C068, Washington, D.C.: Transportation Research Board, 2004.
[9] Zaniewski, J.P., and G. Srinivasan, Evaluation of Indirect Tensile Strength to Identify Asphalt Concrete Rutting Potential, Morgantown, W.V.: West Virginia University, Department of Civil and Environmental Engineering, May 2004.

Asphalt Pavements – Kim (Ed)
© 2014 Taylor & Francis Group, London, ISBN 978-1-138-02693-3

Implementation of a static strength test for evaluating the rutting resistance of asphalt mixtures and its application for quality controls

Silvia Angelone, Marina Cahuape Casaux & Fernando Martinez
Road Laboratory, School of Engineering, University of Rosario, Riobamba and Berutti, Rosario, Argentina

ABSTRACT: There is great concern in Argentina about the rutting resistance of asphalt mixtures mainly related to the high temperatures in summer and the number of overloaded trucks. As a standard, the Marshall mix design procedure is used and improvements have been introduced in order to reduce the risks associated with this kind of damage. Nowadays, the exclusive use of crushed aggregates and harder bitumen are mandatory. Also, the proposed job formula must be tested with the wheel tracking device in order to check the rutting behavior of the mixture. However, during the construction stage, the tests that are carried out for the quality control are not directly related to this issue. Hence, a static strength test named as "the Kim test" has been proposed to be included as a routine using the same equipment and the type of specimens that are currently taken during the works after the asphalt mixture has been placed in the field. This paper presents a brief description of the fundamentals of the test, the correlation between this static strength property and the rutting resistance for different mixtures used in Argentina and the implementation of the Kim test as a rutting quality indicator.

Keywords: asphalt mixtures, rutting resistance, Kim test, wheel tracking test, quality control

1 INTRODUCTION

In Argentina there is a great concern about the rutting resistance of asphalt mixtures mainly related to the high temperatures registered in asphalt pavements during the summer and the increasing number of overloaded trucks. As a standard, the Marshall Mix design procedure is used and, in order to reduce the risk associated with this kind of damage, several improvements have been introduced in the last years. For example, the exclusive use of crushed aggregates and harder bitumen are now mandatory.

However, according to the standards used in Argentina for road construction, the asphalt mixtures are considered with different level of details at the laboratory when the mix is formulated, at the asphalt plant when it is produced and in the field when it has been already placed.

First at the laboratory, the different mixture components are carefully controlled determining mechanical and physical properties for the aggregates and the bitumen. Then, the aggregates are combined in order to have the gradation between the specified limits for the selected kind of mixture and the optimum asphalt content is determined.

Physical (Marshall Density, air voids content, VMA and VFA) and mechanical (Marshall Stability, Flow, Stability/Flow Quotient and moisture susceptibility) properties are determined according to the standard mix requirements and a job formula is finally adopted.

Recently and due to the apprehension about the rutting performance of the mixtures designed according to the Marshall procedure, other complementary tests are carried out like the dynamic modulus test and the Wheel Tracking Test (WTT).

At the asphalt plant, two or three samples of the produced mixture are taken from the trucks every day and the gradation of the recovered aggregates, the bitumen content and other volumetric properties are controlled, verifying if these values are within certain limits of tolerance referred to the values obtained for the job formula. Also, samples are compacted and the Marshall density, stability and flow are determined.

Finally when the mix has been placed, cores are taken and the thickness and density are measured. Finally, if the density of the mixture is greater than a specified value related to the density obtained during the corresponding production day in the asphalt plant, the mixture is considered acceptable.

Briefly, if the results obtained in the asphalt plant are comparable with those obtained in the laboratory for the job formula and, the density of the cores taken from the pavement are also comparable with those obtained in the asphalt plant, it is supposed, by this indirect way, that the placed mixture have the required properties as determined originally during the formulation process. As can be observed, this quality control procedure does not take into account the real rutting behavior of the placed mixture.

Currently, tests of evaluating rut resistance of asphalt mixtures in the laboratory include different types of wheel tracking, repeated loading, dynamic modulus, flow number or flow time tests but these procedures are relatively complex, need sophisticated equipments, well trained technician and in general, are not available in the field laboratories.

The Marshall test is the most used worldwide test and the Marshall stability, the most well known static property of asphalt mixtures. However, several studies have shown that this result or even, the Marshall Quotient Stability/Flow (S/F) have little correlation with rutting characteristics of the mixtures [1].

Hence, this paper presents the use of a static strength test named as the Deformation Strength Test (DST) that could be included as a routine control for evaluating the rutting resistance of asphalt mixtures using the same equipment as for the Marshall Test. The main advantage of this test is that it can be applied for samples compacted at the laboratory or cores currently taken during the works after the asphalt mixture has been placed in the field.

In this study, the ability of the DST for estimating the rutting performance of asphalt mixtures has been evaluated through a correlation analysis with results obtained with the Wheel Tracking Test (WTT) for 20 different asphalt mixtures produced in different construction projects in Argentina. Also, the use of this static strength test for quality controls is proposed as a simple tool for a direct evaluation of the placed asphalt mixture against this kind of damage.

The background of this investigation is the research conducted by Professor K. W. Kim at the Kangwon National University in the Republic of Korea who developed a static test protocol for characterizing the deformation resistance of asphalt concretes and found that the property determined by this test, the deformation strength S_D, has relatively high correlation with the rutting parameters of asphalt mixtures when tested according to the Wheel Tracking and APA Tests.

2 EXPERIMENTAL PROGRAM

2.1 *Materials*

In this study, 20 different asphalt mixtures used in different construction projects in Argentina for base and surface layers were considered. These mixtures were Dense (D) and Semi-dense (S) asphalt concretes with two different maximum nominal aggregate sizes (12 or 20 mm) made with conventional (AC30) and polymer modified bitumen (AM3). Table 1 shows a detail of these mixtures and the main parameters obtained with the conventional Marshall mix design procedure.

Mixtures 9 to 17 were prepared with different percentages of Recycled Polyethylene (RP) from silo bags added by a dry process with two different types of recycled polyethylene, Chopped (C) and in Pellets (P). Details of these mixtures could be found in another paper

Table 1. Asphalt mixtures.

Mixture	Type	Bitumen	Marshall parameters							
			AC (%)	Vb (%)	Density (kg/dm^3)	Vv (%)	VMA (%)	Stability (kN)	Flow (mm)	St/Fl (kN/mm)
1	D12	AC30	4.9	11.9	2.436	3.1	15.0	13.9	3.6	3.9
2	D20	AM3	4.9	12.1	2.465	3.6	15.7	13.3	4.1	3.2
3	D20	AC30	4.9	12.1	2.465	3.6	15.7	13.3	4.1	3.2
4	D12	AC30	4.8	12.1	2.528	2.0	14.3	11.9	3.3	3.6
5	D20	AC30	4.6	11.6	2.516	3.5	15.1	11.3	3.8	3.0
6	D20	AC30	4.7	11.8	2.520	3.9	16.0	11.6	3.5	3.3
7	S20	AM3	5.0	12.2	2.442	3.1	15.3	16.8	5.3	3.2
8	S20	AM3	5.1	12.4	2.441	2.8	15.2	17.2	5.2	3.3
9	D20	AC30 + RPC	4.9	11.6	2.364	5.5	17.1	16.7	5.6	3.0
10	D20	AC30 + RPC	4.9	11.2	2.281	5.4	16.6	23.8	10.6	2.2
11	D20	AC30 + RPC	4.9	10.9	2.217	5.0	15.8	28.5	11.1	2.6
12	D20	AC30 + RPC	5.0	12.0	2.390	4.5	16.5	18.4	5.9	3.1
13	D20	AC30 + RPC	5.0	11.5	2.299	5.1	16.6	19.3	8.1	2.4
14	D20	AC30 + RPP	5.0	11.2	2.232	5.6	16.8	22.7	8.6	2.6
15	D20	AC30 + RPP	4.9	11.7	2.391	3.3	15.0	17.3	6.4	2.7
16	D20	AC30 + RPP	4.9	11.3	2.306	5.1	16.4	21.4	7.4	2.9
17	D20	AC30 + RPP	4.9	11.0	2.242	3.9	14.9	22.2	9.3	2.4
18	D20	AM3	4.8	11.6	2.414	4.2	15.8	13.9	2.7	5.2
19	D20	AC30	4.8	12.6	2.620	4.0	16.6	11.2	4.0	2.8
20	D20	AM3	4.8	12.0	2.500	3.9	15.8	17.6	3.6	4.9

[2]. All the mixtures without recycled polyethylene meet the mechanical requirements used in Argentina. With these mixtures, slabs were compacted to be used in the following tests as described below.

2.2 *Deformation Strength Tests (DST)*

The Deformation Strength Test, developed by Professor K. W. Kim at the Kangwon National University in the Republic of Korea, is a static test for measuring the deformation resistance of asphalt mixtures at a high temperature. In this test, also named as "Kim Test", a static load is applied to a small area at the top centre of a specimen through a round edge loading head (rod) as it is shown in Figures 1 and 2.

During the test, the applied load and the vertical displacement of the loading head are registered as it is shown in Figure 3. The parameter evaluated by this test is considered as the strength against deformation or the deformation strength designated as "S_D" based on the uniaxial peak load P and the vertical deformation Y at the peak load point.

The deformation strength S_D is calculated as:

$$S_D = \frac{4P}{\pi[D - 2(r - \sqrt{2rY - Y^2})]^2} \tag{1}$$

where:
S_D : Deformation strength (MPa)
P : Maximum load at failure (N)
Y : Vertical displacement of the loading head at failure if $Y < r$. Otherwise, $Y = r$ (mm)
r : Radius of edge curvature of the loading head (mm)
D : Diameter of the loading head (mm).

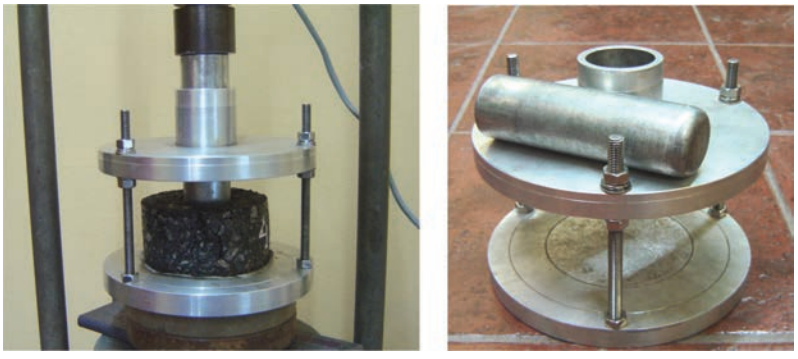

Figure 1. Testing device.

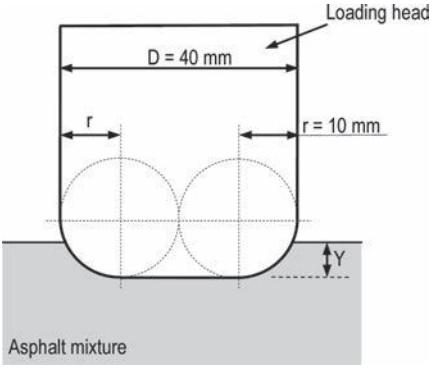

Figure 2. Details of the loading head.

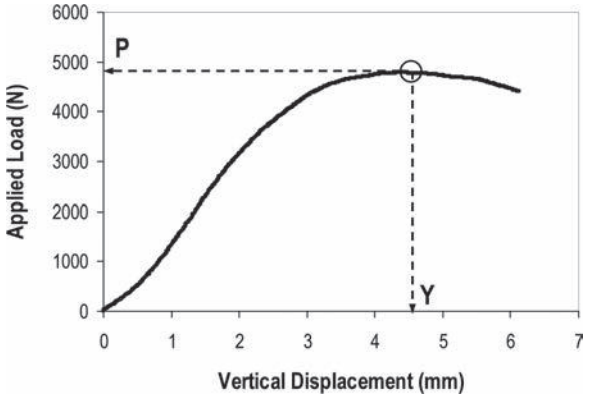

Figure 3. Measured load and vertical displacement.

A detailed description of the test can be found elsewhere [3–5]. After a sensitivity analysis, Dr. Kim has proposed the dimensions of the loading head ($r = 10$ mm; $R = 40$ mm), the testing temperature equal to 60 ºC and a loading rate equal to 30 mm/minute in order to obtain the best correlations between S_D and the rutting resistance of the mixtures. However, a loading rate equal to 50.8 mm/minute was adopted in this study allowing the use of conventional Marshall loading frames.

2.3 *Wheel tracking tests*

Wheel Tracking Tests (WTT) were carried out according to the EN 12607-22:2003 Standard "Bituminous mixtures—Test methods for hot mix asphalt—Part 22: Wheel tracking" for small testing devices, Procedure B. Based on an extensive experience developed in several European countries [6], USA [7] and Argentina [8] showing that the WTT results are good indicators of the observed rutting performance of in-service pavements, this procedure has been adopted as the standard to determine the susceptibility of asphalt mixtures against this kind of damage. In this test, a compacted slab of an asphalt mixture is moved backwards and forwards at a fixed frequency under a loaded wheel and the resulting rut depth at the centre of the slab is measured as a function of the number of loading cycles. Figure 4 shows the typical evolution of the rut depth as a function of the applied number of cycles for this test.

The proportional rut depth at 10000 cycles, PR_{10000}, is calculated as:

$$PR_{10000} = \frac{d_{10000}}{h} \times 100\% \tag{2}$$

with:
d_{10000} : rut depth after 10000 load cycles (mm)
h : specimen thickness (mm).

The wheel tracking slope WTS in millimeters per 10^3 load cycles, is calculated as:

$$WTS = \frac{(d_{10000} - d_{5000})}{5} \tag{3}$$

with:
d_{5000} : rut depth after 5000 load cycles (mm).

The asphalt mixtures used in this study were compacted in slabs with the required dimensions (300 × 300 × 50 mm) using a vibratory hammer. In many cases, the compaction energy was varied in order to obtain, for a given asphalt mixture, slabs with different degrees of compaction. At least, two slabs were prepared for each condition.

If it was verified that the mix was not laterally displaced after the WTT was completed on the centre testing line, a second line was tested on the same slab in order to obtain an additional set of data. A previous paper has shown that comparable results are obtained with this testing methodology [9].

2.4 *Experimental procedures*

The WTT were carried out at 60 ºC in air with a loading frequency of 26 cycles per minute and a wheel load of 700 N. The test ends when 10000 load cycles are applied or a rut depth of 20 mm is reached whichever is the shorter.

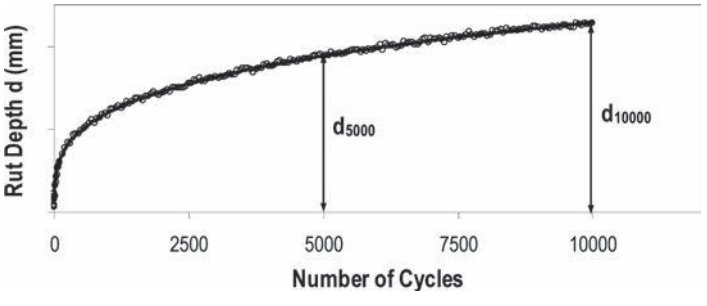

Figure 4. Evolution of the rut depth.

Figure 5. Specimens cored from the slab.

After the WTT was completed on one or two testing lines, two cores with 100 mm diameter were taken from each slab to be tested according to the Deformation Strength Test (DST) as shown in Figure 5. The DST were executed a 60 ºC and a loading rate equal to 50.8 mm/minute.

The averaged values of the PR_{10000}, WTS and S_D were considered for the following analysis.

3 OBTAINED RESULTS

Figures 6(a) and 6(b) show the variation of the deformation strength S_D as a function of the proportional rut depth at 10000 cycles, PR_{10000}, and the wheel tracking slope WTS for all the samples considered in this study.

Regression analysis was performed to evaluate correlation of WTT and DST test results. The best fit curve showing highest R^2 was selected among five regression models: linear, polynomial, exponential, power and logarithm.

As can be observed, a fairly good correlation exists between S_D and the rutting resistance of the mixtures evaluated through the PR_{10000} and WTS values, even for the materials used in this analysis with a wide variety of gradation, maximum nominal aggregate size and bitumen type.

A greater value of S_D implies a better rutting performance with smaller PR_{10000} values and lower WTS slopes.

Figure 7 presents the proportional rut depth PR_{10000} against the wheel tracking slope WTS for the wheel tracking tests carried out in this study.

In this figure, it is seen that a very good correlation exists between the proportional rut depth at 10000 cycles and the wheel tracking slope. Since both values have been considered as good indicators of the rutting resistance of the asphalt mixtures, it is evident that it is enough to consider only one of them because the other result strongly correlated.

In Argentina, several previous studies have shown that for warm climates and heavy traffic, it has been observed a good rutting performance of pavements with asphalt mixtures exhibiting wheel tracking slopes lower than 0.100 mm/10^3 cycleswhen tested in air according to the EN 12607-22:2003 Standard using small size devices [8, 10, 11]. Thus, from Figure 6(b), this acceptable rutting performance could be related with a minimum S_D value in the order of 3.5 to 4.0 MPa as a first approximation for all the asphalt mixtures with similar characteristics than those used in this study.

As a reference, the Ministry of Land, Infrastructures and Transport of the Korean Government has adopted as specification limits for hot-mix asphalt surface course mixtures the following values: $S_D > 3.2$ MPa for secondary road asphalt pavement and $S_D > 4.25$ MPa for first class highways *(Kim K. W., personal communication, 2013)*.

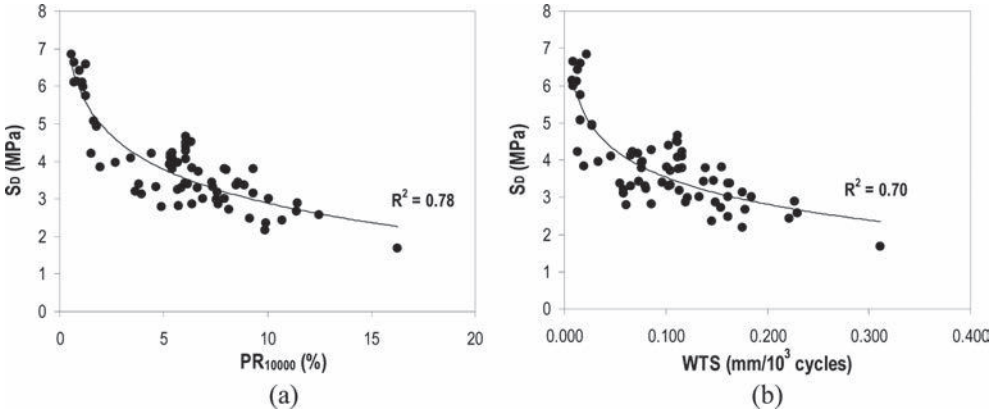

Figure 6. Relationships between WTT and S_D results.

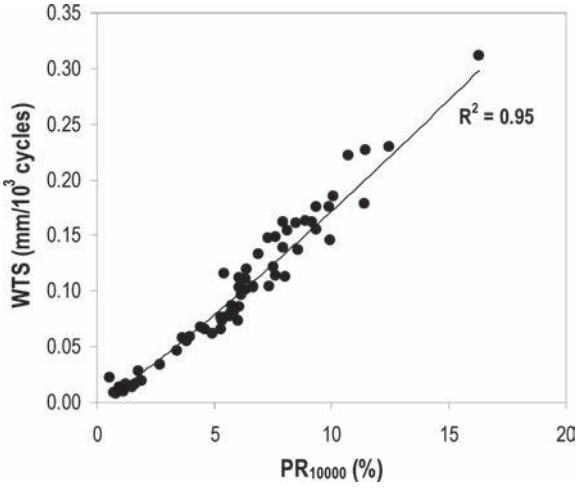

Figure 7. Relationship between PR_{10000} and WTS.

In general, the WTT procedures are relatively complex, need well trained technicians, require special equipments for the compaction and the testing of the slabs and are not widely used in field laboratories. Therefore, this Deformation Strength Test is a good option evaluating the rutting resistance of asphalt mixtures because it requires an inexpensive loading device and conventional testing equipments that can be found in almost all laboratories allowing the use of compacted samples or cores taken from in service pavements.

Based on the obtained correlations, the DST could be used as an indicator of the rutting resistance of asphalt mixtures when the WTT is not available.

4 APPLICATION OF THE DST FOR QUALITY CONTROL

Given that the DST is an inexpensive and simple testing procedure that can provide valuable information about the rutting resistance of asphalt mixtures, its application to the quality control of pavement sections is proposed.

After the optimum asphalt content has been adopted following the conventional mix design procedure, a couple of slabs are compacted in the laboratory and tested in air according to

the EN 12607-22:2003 Standard using a small size device. If the resulting average WTS is lower than 0.100 mm/10^3 cycles, the designed mix is considered as acceptable. Three additional samples are compacted following the Marshall procedure and tested according to the DST. The average of the obtained S_D for each sample is considered as a first reference value designated as S_{DREF1}. Also, two cores with 100 mm in diameter are taken from each slab used for the WTT and subjected to the DST. A second reference value for the Deformation Strength is calculated as S_{DREF2}.

At the construction site during the production of the asphalt mixture, loose mixture is taken from the trucks and Marshall samples are compacted at the field laboratory. Three of them are used for the conventional Marshall test as in the routine quality control but other three additional samples are used for the DST. If the average of the S_D results for these samples, S_{DLAB}, is greater than the S_{DREF1}, the production continues. Otherwise, the production is stopped and the cause for the observed difference is investigated.

When a pavement section is finished, cores are taken from this section in order to verify the density and the thickness of the layer. Then, these cores are subjected to the DST and the average of the S_D of this section, S_{DFIELD}, is compared to the S_{DREF2}. If S_{DFIELD} is greater than S_{DREF2}, the section is approved and the construction process continues.

Otherwise, the rutting susceptibility of the placed mixture must be checked through the WTT.

In this case, the authors have proposed a simple procedure producing susceptible cores to be used in a conventional WTT device. Three cores with 150 mm in diameter are taken along a line and with a special location as is shown in Figure 8. First, the core C is taken and then, two other cores (A and B) are taken on each side in order that the total length L be equal to 300 mm.

If it is necessary, the cores must be trimmed to obtain specimens with the required thickness for the WTT. These "three parts" specimens are constrained in a specially designed support and tested in a conventional WTT device as shown in Figure 9. A detailed description and validation of this procedure can be found in a previous paper [12].

WTS results with no substantial differences have been obtained for the "three parts" and monolithic specimens showing that this coring procedure is able to easily obtain samples for the conventional WTT apparatus. Other option is coring 200 mm specimens from the pavement according to the EN 12607-22:2003 Standard.

If the wheel tracking slope WTS is lower than 0.100 mm/10^3 cycles, the asphalt mixture is considered acceptable. Otherwise, the mixture is considered as not acceptable and corrective measures should be adopted.

Thus, this study proposes the use of the DST as a filter:

- If $S_{DLAB} > S_{DREF1}$ and $S_{DFIELD} > S_{DREF2}$, the asphalt mixture "Pass"
- If $S_{DLAB} < S_{DREF1}$ or $S_{DFIELD} < S_{DREF2}$, the asphalt mixture "No Pass" and other tests are necessary in order to arrive to a final decision.

With this purpose, the Deformation Strength Test is a simple tool that could be used to estimate the rutting resistance of an asphalt mixture when it is produced and placed in the field using conventional testing equipment with important savings in money and time reducing the number of the required Wheel Tracking Tests.

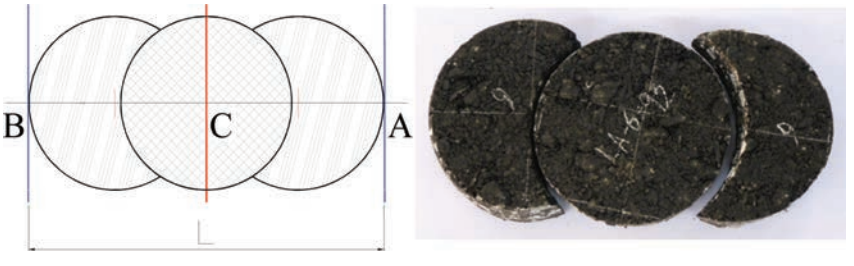

Figure 8. Coring procedure.

Figure 9. WTT with cores taken from the pavement.

5 CONCLUSIONS

In this paper, the use of a simple static strength test, the Deformation Strength Test DST or "Kim Test", has been evaluated to estimate the rutting potential of asphalt mixtures.

The main advantage of this test is that it uses conventional loading equipments that can be found in the field laboratories and compacted samples or cores taken from in service pavements. The resulting parameter of this test is the Deformation Strength S_D.

Correlation analysis were carried out between the results obtained with this test and the WTT for 20 different asphalt mixtures formulated with a great variety of gradation, maximum nominal aggregate size and bitumen type. It was found that S_D has a fairly good correlation to the Proportional Rut Depth at 10000 cycles, PR_{10000}, and the Wheel Loading Slope, WTS, obtained with the WTT. For the asphalt mixtures considered in this study, a strong correlation was found between the PR_{10000} and WTS values.

In Argentina, several previous studies have shown that for warm climates and heavy traffic, it has been observed a good rutting performance of pavements with asphalt mixtures exhibiting WTS values lower than 0.100 mm/10^3 cycles. Thus, a corresponding minimum value of S_D around 3.5 to 4.0 MPa could be adopted as a first approximation for mixtures with an acceptable rutting resistance.

Finally, the DST is proposed as a complementary test to be included in the quality control plans to estimate the rutting potential of the asphalt mixtures when they are produced and placed in the field. Even though the DST has an empirical basis that do not evaluate the real mechanistic response of the mixture, its simplicity and the use of conventional equipments show that it could allow for a better insight about the rutting performance of the asphalt pavements.

As this investigation is part of an ongoing research project, other asphalt mixtures are being tested in order to improve the obtained correlations. It is also planned that in a upcoming stage, the proposed quality control procedure will be implemented to verify its applicability, produce the necessary refinements and adjust the minimum S_D value through the performance monitoring of several roads that are being constructed in Argentina.

REFERENCES

[1] Li S.F., Kim J.Y., Lee K.H. and Kim K.W. Prediction of rutting based on volumetric and tensile properties of asphalt concrete. 4th Intl. Conference on Road & Airfield Pavement Technology, Kunming, China. 2002.

[2] Angelone S., Cahuape Casaux M., Borghi M. and Martinez F. Reuse of waste polyethylene from "Silo bags" in asphalt mixtures, 2nd. International Symposium on Asphalt Pavements & Environment, Fortaleza, Brazil, pp. 1–12. 2012.

[3] Doh Y.S., Yun K.K., Amirkhanian S.N. and Kim K.W. Framework for developing a static strength test for measuring deformation resistance of asphalt concrete mixtures, Construction and Building Materials, 21, pp. 2047–2058. 2007.

[4] Kim K.W., Amirkhanian S.N., Kim H.H., Lee M. and Doh Y.S. A New Static Strength Test for Characterization of Rutting of Dense-Graded Asphalt Mixtures, Journal of Testing and Evaluation, Vol. 39 (1), pp. 1–10. 2011.

[5] Baek S.H., Kim, J.C., Doh, Y.S. and Kim, K.W. Optimum loading speed for deformation strength test of bitumen mixtures. 7th Intl. RILEM Symposium on Advanced Testing and Characterization of Bituminous Materials, Rhodes, Greece, pp. 349–356. 2009.

[6] Kandhal P. y Cooley L. Evaluation of permanent deformation of asphalt mixtures using loaded wheel tester.—NCAT Report No. 2002–08. 2002.

[7] SAMARIS, Sustainable and Advanced Materials for Road Infra Structure Group. Permanent deformation of bituminous bound materials in flexible pavements evaluation of test methods and prediction models. SAM-05-D32. Final Summary Report 2006.

[8] Agnusdei J., Iosco O., Jair M. and Morea F. Correlación entre medidas de Ahuellamiento "in situ" y ensayos de laboratorio (2da Parte), 14th Congreso Ibero Latinoamericano del Asfalto. La Habana, Cuba. 2007. *(In Spanish)*.

[9] Angelone S., Martinez F., Cauhapé Casaux M., Andreoni R. and Lostumbo D. Influencia de los factores de carga y de servicio en el ensayo de rueda cargada, 14th Congreso Ibero Latinoamericano del Asfalto. La Habana, Cuba. 2007. *(In Spanish)*.

[10] Angelone S.M. Comportamiento de materiales viales. Diseño y control de mezclas asfálticas frente a la deformación permanente, PhD. Thesis, Universidad de Rosario, Rosario, Argentina. 2013. *(In Spanish)*.

[11] Morea F. Deformaciones Permanentes en mezclas asfálticas. Efecto de la reología de los asfaltos, la temperatura y las condiciones de carga. PhD. Thesis, Universidad de La Plata, La Plata, Argentina. 2011. *(In Spanish)*.

[12] Angelone S., Martinez F., Cauhapé Casaux M. and Borghi M. On-Site control of performance under plastic deformation of bitumen mixtures, 185, pp. 32–41. Madrid, Spain. 2012. *(In Spanish)*.

Warm mix asphalt technologies—I

This page intentionally left blank

Asphalt Pavements – Kim (Ed)
© 2014 Taylor & Francis Group, London, ISBN 978-1-138-02693-3

Moisture susceptibility of Warm-Mix Asphalt

Lorena Garcia Cucalon & Amy Epps Martin
Zachry Department of Civil Engineering, Texas A&M University, College Station, TX, USA

Edith Arambula, Fan Yin, Cindy K. Estakhri, Eun Sug Park & Jon Epps
Texas A&M Transportation Institute, College Station, TX, USA

ABSTRACT: Economic, environmental, and engineering benefits led to the rapid implementation of Warm-Mix Asphalt (WMA) during the past decade. While WMA technologies are generally performing well to date, development of standard mix design protocols continues and performance questions remain. This study evaluated laboratory conditioning protocols for WMA to simulate early life when they are more moisture susceptible and proposed 2 hours at 116°C for mix design and reheating to this temperature for quality assurance for all WMA technologies except foaming which requires reheating to 135°C. Next, WMA was shown to be more moisture susceptible as compared to Hot-Mix Asphalt in the early life based on a comprehensive analysis of three standard laboratory tests (wet and dry indirect tensile strengths and resilient modulus and their ratios and Hamburg Wheel Tracking Test stripping parameters) from four field projects that included nine WMA mixtures. Finally, an evaluation of performance evolution showed that WMA can overcome this vulnerability to moisture after a summer of aging and proposed 5 days oven aging at 85°C to capture this effect in the laboratory. Proposed conditioning protocols, aging protocols, and criteria for the tests utilized are provided for WMA mix design and analysis to preclude moisture susceptibility.

Keywords: warm-mix asphalt, moisture susceptibility, conditioning, aging

1 INTRODUCTION

Past efforts to reduce placement and production temperatures of asphalt mixtures date back to the late 1950s, including binder foaming processes, asphalt emulsification, and incomplete aggregate drying [1–2]. The latest technology adopted to reduce placement and production temperatures is Warm-Mix Asphalt (WMA). This technology offers a number of benefits, including decreased energy consumption, reduced emissions and fumes at the plant, improved working conditions at the construction site, extended haul distances, longer pavement construction season, improved workability and compactability, and reduced aging. Widespread use of this technology and realization of its benefits requires producing WMA with similar performance and durability as Hot-Mix Asphalt (HMA) at substantially reduced production and placement temperatures [3–5].

Despite the attractive economic, environmental, and safety advantages of WMA there are several barriers to its extensive implementation; such as imprecise correlation between laboratory and field performance, incomplete mix design procedures, and a wide variety of WMA technologies that entail a number of changes in the mixture production process as compared to HMA. In addition, several factors related to the lower production temperature of the WMA and the use of certain foaming and additive technologies can increase the moisture susceptibility of WMA, including:

- Introduction of additional moisture with the free water foaming WMA technologies,
- Use of wet/damp aggregates in the production process.

- Reduced binder absorption by the aggregates at lower production temperatures, and
- Reduced binder-aggregate bond strength in the presence of certain WMA additives.

From performance evaluations of various WMA technologies in the laboratory using mainly the Indirect Tensile (IDT) strength test before and after moisture conditioning (Lottman, AASHTO T283) and/or the Hamburg Wheel Tracking Test (HWTT) (AASHTO T324), the conclusion of several laboratory studies is that WMA is more moisture susceptible as compared to HMA [6–11]. However, minimization strategies such as adding anti-stripping agents or recycled materials have been shown to enhance WMA moisture susceptibility [12–21].

Despite the concerns raised by the laboratory test results that indicate that WMA is more susceptible to moisture damage, the documented field performance indicates that moisture susceptibility related distresses are not prevalent in WMA pavements and that the performance between WMA and HMA pavements is equivalent [10,11,22]. This discrepancy between the laboratory and field observations could be due to the relative limited monitoring time of the field sections or other causes that are not adequately represented in the laboratory evaluations.

A number of recent studies have been conducted to evaluate the effect of conditioning and aging protocols on WMA performance. The majority of these studies concluded that an increase in laboratory conditioning temperature and/or time may reduce the gap between WMA and HMA performance [22–25], but an appropriate conditioning protocol for WMA for Laboratory-Mixed Laboratory-Compacted (LMLC) specimens and Plant-Mixed Laboratory Compacted (PMLC) specimens for mix design and Quality Assurance (QA) purposes, respectively, is needed to simulate these mixtures in early life when they are more moisture susceptible. Current recommendations for WMA mix design include conditioning the loose mix two hours at the compaction temperature based on volumetrics and dry IDT strength to simulate Plant-Mixed Field-Compacted (PMFC) cores after construction [26]. Others recommend four hours at 135°C for conditioning prior to performance testing based on HWTT results which revealed WMA becomes equivalent to HMA after longer conditioning time at high temperature [24]. Recent research also indicated that reheating loose mix when compacting off-site PMLC specimens for QA purposes produced stiffer and stronger specimens than those compacted on-site [27]. HWTT results performed on PMFC cores from WMA pavements after one month and one year in-service revealed significant improvement in terms of rutting potential and suggested that the gap between WMA and HMA becomes negligible after a year in service for a specific climate [29]. The stiffening of asphalt mixtures due to field aging can be simulated in the laboratory through a combination of aging time and temperature which can be achieved by subjecting the compacted specimens to Long Term Oven Aging (LTOA) protocols [30–31].

2 RESEARCH APPROACH

The main objective of this research is to provide guidelines for mix design and QA to preclude moisture susceptibility in WMA. Three laboratory experiments were conducted on materials from field sections monitored with time for further correlation of laboratory testing and field performance. The selected field projects, testing protocols, and designs for the WMA laboratory conditioning, WMA moisture susceptibility (including anti-stripping), and WMA performance evolution experiments are described in this section; and detailed results can be found elsewhere [32].

2.1 *Field projects*

Table 1 provides details on location, climate, mixtures including WMA technologies, component materials, field compaction temperatures, coring dates, and corresponding laboratory experiments for the four selected field projects. Three of the four field projects represent the three extreme climates for moisture susceptibility: wet and Freeze/Thaw (F/T) in Iowa, cold and multi-F/T in Montana, and hot and wet in Texas. The fourth field project in New Mexico

Table 1. Summary of field projects.

Location and climate	Mixtures	Aggregates	Asphalt binder	Additives		Field compaction temperature (°C)	Coring dates	Experiment
				RAP	Anti-strip agent			
Iowa (Wet, Freeze)	HMA + RAP	Quartzite, limestone, field sand	PG 58-28	17%	None	146–149	Sep. 2011* Mar. 2012 Sep. 2012	LC MS AS PE
	Evotherm 3G + RAP					116–120		
	Sasobit + RAP					113–116		
Montana (Dry, Freeze)	HMA	Siliceous	Modified PG 70-28	None	1.4% lime	154–157	Oct. 2011* Apr. 2012	MS
	Evotherm 3G					132–138		
	Sasobit					135–138		
	Foaming					132–135		
Texas (Wet, No-Freeze)	HMA	Limestone, field sand	Modified PG 70-22	None	None	135–141	Jan. 2012* Sep. 2012	LC MS AS PE
	Evotherm DAT					110–113		
	Foaming					116–121		
New Mexico (Dry, No-Freeze)	HMA + RAP	Siliceous gravel	Modified PG 64-28	35%	1% versabind	141–143	Oct. 2012*	MS PE
	Evotherm 3G + RAP					124–127		
	Foaming + RAP					129–132		

*Coring right after construction was completed.
LC: Laboratory Conditioning; MS: Moisture Susceptibility; AS: Anti-Stripping; PE: Performance Evolution.

represents a climate that combines aspects of these three extreme climates (dry, cold during the winter, and relatively hot during the summer).

2.2 *Laboratory tests*

Three laboratory tests were utilized to meet the needs of this research. The Indirect Tensile (IDT) Strength Test (AASHTO T283) and the Resilient Modulus (M_R) Test (modified ASTM D-7369) were performed to determine mixture strength and stiffness, respectively. In order to evaluate moisture susceptibility of WMA mixtures as compared to HMA, both tests were also performed after subjecting the mixtures to the Lottman moisture conditioning protocol as described in AASHTO T283 with one freeze-thaw cycle.

In this study, dry M_R was used for comparing mixture stiffness and the wet M_R stiffness and M_R-ratio together with the wet IDT strength and the Tensile Strength Ratio (TSR) values were used as test parameters to compare WMA and HMA in terms of moisture susceptibility for each mixture, specimen type, and aging condition. An Analysis of Variance (ANOVA) followed by Tukey's Honest Significant Differences (HSD) test were performed on the dry M_R, wet M_R, and wet IDT strength values with a 5% significance level to discriminate differences between the mixtures, specimen types, or aging conditions. As only one TSR value is produced from each set of six specimens, the TSR results were compared based on the precision and bias statement for AASHTO T283 that indicates a d2 s acceptable range of two results with more than a 95% confidence level of 9.3% [33]. The same situation applies to M_R-ratio, where only one value is obtained, therefore a d2 s value of 10% was assumed for comparing results.

Additionally, to capture the effect of moisture under extreme conditions, the HWTT was performed and the Stripping Inflection Point (SIP) and stripping slope were calculated. Since

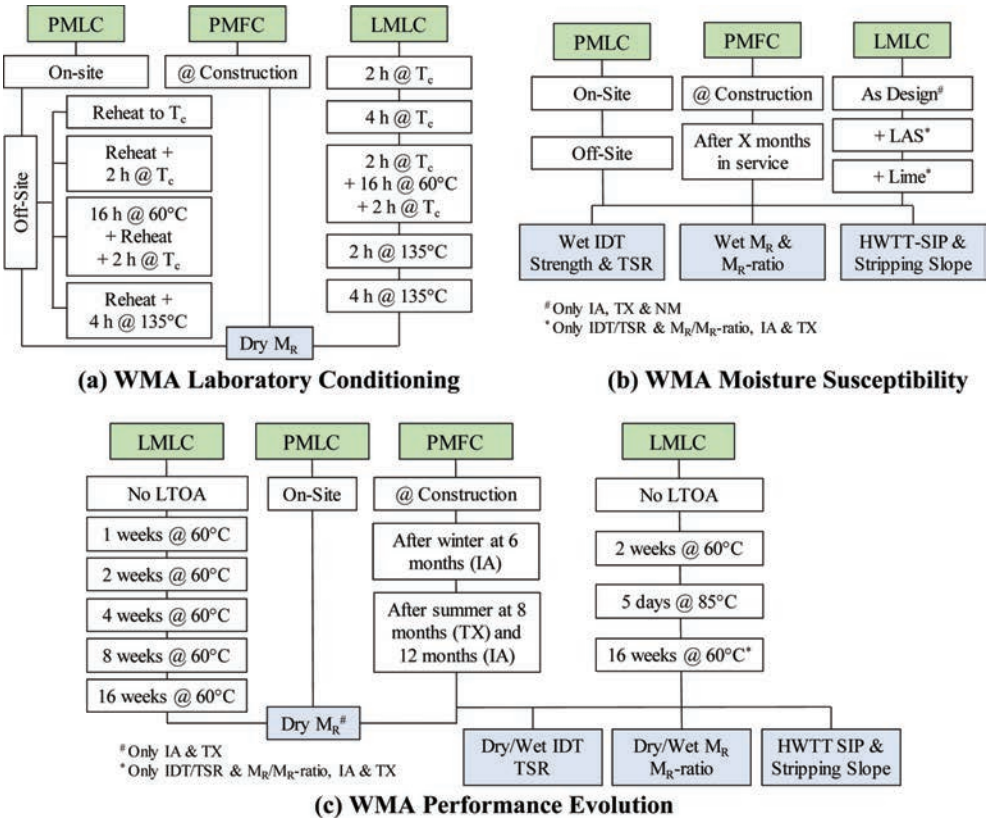

Figure 1. Experiment designs.

a precision and bias statement is not available for the selected HWTT test results, the average differences in SIP and the stripping slope for 20 different mixtures (all corresponding to the Texas field project) that exhibited stripping were calculated and 2,000 load cycles and 0.2 μm/cycle were utilized as d2s values for SIP and stripping slope, respectively.

2.3 *Experiment designs*

To assess the potential for moisture damage in WMA, three laboratory experiments were defined to satisfy the following objectives:

- Reproduce in the laboratory the early life aging condition in which WMA is more prone to moisture susceptibility related distresses in the field by evaluating multiple Short-Term Oven Aging (STOA) protocols as described in Figure 1(a) WMA Laboratory Conditioning
- Compare WMA versus HMA in terms of moisture susceptibility and evaluate the effect of anti-stripping additives as a possible moisture susceptibility minimization strategy as described in Figure 1(b) WMA Moisture Susceptibility.
- Study the effect of field aging in WMA and reproduce this effect in the laboratory by evaluating multiple Long-Term Oven Aging (LTOA) protocols as described in Figure 1(c) WMA Performance Evolution.

3 FINDINGS

This section provides a summary of the findings for each of the three experiments conducted in this study: WMA laboratory conditioning, WMA moisture susceptibility, and WMA performance evolution. In addition, laboratory results are compared to field performance as a precursor to development of guidelines for WMA mix design focused on preventing moisture susceptibility.

3.1 *WMA laboratory conditioning*

Based on the results of the WMA laboratory conditioning experiment that included evaluation of almost 250 LMLC specimens, on-site and off-site PMLC specimens, and PMFC cores from the Iowa, Texas, and Montana field projects; the significant increase of stiffness for LMLC specimens with longer conditioning times and higher temperatures (with the increase in temperature more significant) and the significant effect of reheating plant mix when fabricating off-site PMLC specimens were verified. To meet the main objective of providing guidelines for mix design and QA to preclude moisture susceptibility in WMA, specimens must be fabricated in the laboratory to reproduce the early life aging condition in the field when WMA is most vulnerable. Conclusions from this experiment for conditioning loose mix prior to laboratory compaction of specimens for evaluating moisture susceptibility are as follows:

- For LMLC specimens 2 hours at 135°C and 116°C were proposed as the standard laboratory conditioning protocol for HMA and WMA specimens, respectively.
- For PMLC specimens, compacting on-site after 1 hour at 135°C and 116°C for HMA and WMA, respectively, is proposed to stabilize the temperature.
- When compacting PMLC specimens on-site is not viable, the proposed conditioning protocol for off-site PMLC specimens is to (1) reheat to 135°C for HMA and WMA with foaming process and (2) reheat to 116°C for WMA with additives. Off-site PMLC specimens of WMA with foaming process require a different conditioning protocol as compared to WMA with additives because the foaming effect during production is assumed lost after mixing and cooling of the loose mix.

3.2 *WMA moisture susceptibility*

Based on the results of the WMA moisture susceptibility experiment that included evaluation of more than 850 LMLC specimens, on-site and off-site PMLC specimens, and PMFC

cores from the Iowa, Texas, Montana, and New Mexico field projects; the following conclusions can be made:

- The selected laboratory conditioning protocols simulate the early life of the pavement and produce laboratory compacted mixtures with performance in terms of moisture susceptibility equivalent to that of PMFC cores at construction and/or after winter as indicated by the selected laboratory tests.
- Based on laboratory moisture susceptibility tests, WMA can be more moisture susceptible in the early life (prior to a summer of aging) as compared to HMA, but equivalent performance is shown after a summer of aging for the field projects used in this study.
- When WMA is more moisture susceptible in the early life (prior to a summer of aging) based on laboratory testing, the use of anti-stripping agents may improve WMA performance. Compatibility of the anti-stripping agent with the WMA technology and component materials should be considered for optimizing performance.
- The differences identified between on-site and off-site PMLC specimens in terms of stiffness are also reflected in laboratory measured moisture susceptibility, with off-site PMLC specimens exhibiting improved resistance to moisture.

3.3 *WMA performance evolution*

Based on the results from the evaluation of more than 500 LMLC specimens, on-site PMLC specimens, and PMFC cores from the Iowa, Texas, and New Mexico field projects; the following conclusions can be made:

- For HMA and WMA PMFC cores there was a significant increase in M_R stiffness, IDT strength, and stripping resistance due to field aging after a summer. The difference between PMFC cores acquired after the first winter versus the ones at construction was insignificant for most cases for the field projects used in this study.
- Evaluating the change in dry M_R stiffness with laboratory aging at 60°C, it was observed that somewhere between 4–16 weeks of laboratory aging (different for WMAs and HMA mixtures) was representative of the field aging experienced by PMFC cores after the first summer. Additionally, the laboratory aging protocol of 2 weeks at 60°C was able to represent the time period where the stiffness of WMA was equivalent to the initial dry M_R stiffness of HMA without LTOA (for the Iowa pavement) or where the dry M_R stiffness of WMA and HMA converged (for the Texas pavement).
- As with field aging, the laboratory LTOA protocols used in this study also had a significant effect on performance, not only increasing dry M_R stiffness but also improving moisture susceptibility of the mixtures. In addition, the comparison of mixture performance measured in the laboratory between PMFC cores after several months in-service and LMLC specimens with LTOA indicated that laboratory aging of 16 weeks at 60°C as well as 5 days at 85°C were representative of the field aging that PMFC cores experienced after the first summer in the field.

3.4 *Summary of field performance*

This section focuses on the overall field performance of the HMA and WMA mixtures from the different field projects, comparing limited field performance data to the laboratory results previously discussed. For this purpose *common thresholds* were identified, including minimum 80% for TSR and M_R-ratio, minimum SIP of 10,000 based on the current Iowa specification, and minimum wet IDT strengths of 448 kPa and 552 kPa for unmodified (Iowa) and modified (Montana, New Mexico, and Texas field projects) binders based on averages from the current Nevada, Tennessee, and Texas specifications.

The four field projects exhibited generally good performance through the end of this study in March 2013. The Montana and New Mexico field projects which were characterized as good mixtures based on the laboratory testing and common thresholds did not exhibit any distress related to moisture susceptibility. Common factors for these mixtures include the use

of anti-stripping agents and a relatively elevated high-temperature performance grade binder (Montana) or RAP with a lower high-temperature performance grade binder (New Mexico) (Table 1). The Iowa field project did exhibit some localized raveling in both WMAs (WMA Sasobit® with RAP and WMA Evotherm® 3G with RAP) that was likely exacerbated by paver segregation at the crown and subsequent snow plow damage. The Iowa HMA with RAP did not exhibit raveling. In addition to possible construction issues, the Iowa field project did not include an anti-stripping agent. As for the Montana and New Mexico field projects with good performance for all mixtures in the laboratory and the field, agreement was shown for the Iowa field project between the relatively poor field performance and inadequate laboratory performance for the two WMAs with RAP for all three standard laboratory tests when compared to common thresholds. The Texas field project performed well and did not exhibit distresses related to moisture susceptibility despite construction in January 2012 and heavy truck traffic. This field project did not utilize RAP or an anti-stripping agent but did use a relatively elevated high-temperature performance grade binder, and agreement between the field and laboratory performance as predicted based on common thresholds is not as complete across the different specimen types or across the three standard laboratory tests. Unfortunately, all four field projects were constructed in fall or winter, and thus the overall hypothesis that WMA will exhibit adequate moisture susceptibility after a summer of aging was not fully tested.

4 GUIDELINES TO PRECLUDE MOISTURE DAMAGE IN WMA

Based on laboratory test results, field observations, and considering the common thresholds previously described; the guidelines for mix design and QA of WMA to preclude moisture susceptibility were developed as shown in Figure 2. After mixing WMA LMLC specimens according to the AASHTO R35 Appendix, loose mix STOA for 2 hours at 116°C is proposed prior to compaction. Next, a test to evaluate moisture susceptibility must be selected from the following three choices: wet and dry IDT strengths at 25°C and TSR by AASHTO T283, wet and dry M_R stiffness at 25°C (Modified ASTM D-7369) and M_R-ratio after moisture conditioning by AASHTO T283, or HWTT SIP and stripping slope per AASHTO T324 at 50°C. Two criteria

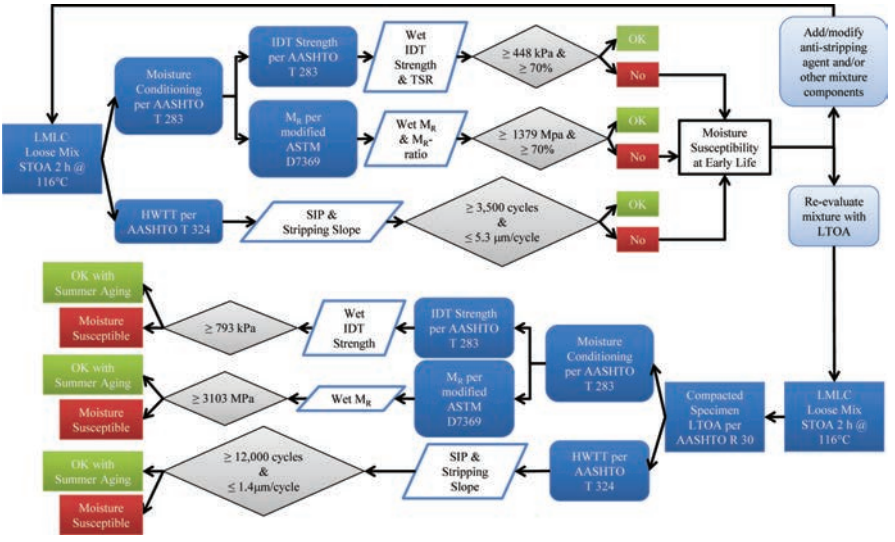

Figure 2. Guidelines for WMA moisture susceptibility evaluation.
Note: [a]LMLC specimens for mix design. For QA purposes use on-site PMLC or off-site PMLC with minimal reheating; [b]select a single test method and use it throughout the mix design verification; [c]If off-site PMLC specimens are used, employ the following thresholds (TSR and M_R-ratio remain unchanged): Wet IDT ≥ 690 kPa, Wet M_R ≥ 2068 MPa, SIP ≥ 6,000 cycles, stripping slope ≤ 2.0 µm/cycle.

for each test for these STOA specimens are shown in Figure 2. If off-site PMLC specimens are utilized to evaluate WMA moisture susceptibility, the thresholds are decreased for stripping slope and increased for wet IDT strength, wet M_R stiffness, and SIP to reflect the reheating effect. If the WMA passes both criteria for the selected test, the mixture is expected to have adequate performance in terms of moisture susceptibility; otherwise, moisture susceptibility in the early life is probable. Mixture modification in terms of adding/modifying anti-stripping agents and/or changing other mixture components (e.g. binder type, RAP, RAS, etc.) is proposed prior to a second evaluation of the modified WMA with these same criteria.

If the original WMA or modified WMA does not pass one or both criteria for the selected test, moisture susceptibility in the early life is probable but the mixture may be capable of overcoming this vulnerable period after a summer of aging prior to exposure to winter conditions. Therefore, a second evaluation is suggested after LTOA of compacted specimens for 5 days at 85°C per AASHTO R30, for which the same selected laboratory test is used with modified criteria that reflect the stiffening effects from aging. As shown in Figure 2, for this second evaluation of aged specimens, only wet properties are specified for IDT strength and M_R stiffness, but two HWTT criteria remain.

These criteria were developed based on separating the results from the relatively good field and laboratory performance of the Texas WMAs and the relatively poor field and laboratory performance of the Iowa WMAs as shown in Table 2 with an example for STOA specimens. Table 2 also shows verification of these criteria through examination of the WMAs from the Montana and New Mexico field projects. For the Montana field project where LMLC specimens were not available, on-site PMLC specimens were utilized. This verification resulted in a prediction of adequate performance in terms of moisture susceptibility for the majority of the standard laboratory tests for the STOA WMAs from both the Montana and New Mexico field projects, which agree with observed field performance.

The alternatives of adding anti-stripping agents and re-evaluating the moisture susceptible mixtures or LTOA to verify if the mixture will possibly overcome this susceptibility with aging were also explored. For the Iowa field project, even with the addition of two different anti-stripping agents, the majority of the Iowa STOA mixtures are likely still moisture susceptible in the early life, except for the WMA Sasobit® with RAP which was improved in terms of wet M_R stiffness and M_R-ratio with the addition of hydrated lime. WMA Foaming from the Texas field project and WMA Evotherm® 3G with RAP from the New Mexico field project (Table 2) marginally did not meet the criteria for M_R-ratio, but after LTOA in the laboratory, these mixtures passed the respective criteria. Adding hydrated lime to WMA Foaming from the Texas field project also produced a mixture that passed the criteria.

Table 2. Example of criteria development and verification for WMA moisture susceptibility evaluation (LMLC STOA 2 h at 116°C).

Test Parameter	Iowa		Texas		Montana[a]			New Mexico	
	Evotherm	Sasobit	Evotherm	Foaming	Evotherm	Sasobit	Foaming	Evotherm	Foaming
Wet IDT (kPa)	345	324	607	531	524	510	531	558	496
TSR (%)	84	77	79	66	59	57	72	73	70
Wet M_R (MPa)	917	1131	1944	1648	1800	2213	1613	2041	2206
M_R-ratio (%)	72	77	80	62	83	86	80	69	76
SIP (cycles)	1,677	2,176	6,256	4,111	>20000	>20000	>20000	>20000	>20000
Stripping Slope (μm/cycle)	10.0	6.6	1.7	2.9	0	0	0	0	0
Key	Does not meet criteria				Meets criteria				

[a]For Montana, no LMLC specimens are available and thus values of on-site PMLC specimens were used.

As shown in these mixtures passed the respective criteria. Adding hydrated lime to WMA Foaming from the Texas field project also produced a mixture that passed the criteria.

Table 2, two of the three STOA WMAs from the Montana field project (WMA Evotherm® 3G and WMA Sasobit®) did not meet the criteria for TSR. Unfortunately, data were not available to assess the effect of modifying the mixture components or aging.

Before being considered for adoption, the proposed guidelines that are suggested based on a limited number of field projects should be utilized on a trial basis. This will provide additional data to further refine the moisture susceptibility criteria and the laboratory conditioning and aging protocols that capture the time period when WMA may be most susceptible to this type of distress. Data from additional field projects will provide increased confidence in the guidelines provided with possible revisions to the framework proposed in this study. In addition, further information should be gathered toward resolving any differences between generally adequate field performance and laboratory assessment that indicates potential for moisture susceptibility for some mixtures. Continued field performance monitoring of the limited number of field projects is also suggested toward further improvement of the guidelines produced.

ACKNOWLEDGEMENTS

The research reported herein was performed under NCHRP Project 09-49 by the Texas A&M Transportation Institute. The research team gratefully acknowledges the cooperation and assistance provided by the agencies and contractors where field samples were collected. In addition, the partnership with the Federal Highway Administration (FHWA) Mobile Asphalt Laboratory and other NCHRP WMA Projects was integral to this work and is greatly appreciated.

REFERENCES

[1] Kristjansdottir, O., "Warm Mix Asphalt for Cold Weather Paving", University of Washington, Seattle, Washington, *M.S. Thesis* (2006).

[2] Zettler, R., "Warm Mix Stands Up to Its Trials" *Better Roads*, James Informational Media, Inc., Des Plaines, Illinois (February 2006).

[3] Button, J.W., C. Estakhri, and A. Wimsatt, *A Synthesis of Warm-Mix Asphalt* Report No. FHWA/TX-07/0-5597-1, Texas Transportation Institute, College Station, Texas (October 2007) 94 pp.

[4] Jones, W., "Warm Mix Asphalt Pavements: Technology of the Future" *Asphalt Magazine*, Asphalt Institute, Lexington, Kentucky (Fall 2004) pp. 8–11.

[5] Prowell, B.D., G.C. Hurley, and B. Frank, *Warm-Mix Asphalt: Best Practices*, Quality Improvement Publication, 2nd Edition, National Asphalt Pavement Association (2011).

[6] Austerman, A.J., W.S. Mogawer, and R. Bonaquist, "Evaluating the Effects of Warm Mix Asphalt Technology Additive Dosages on the Workability and Durability of Asphalt" 88th Annual Meeting of the Transportation Research Board, *Proceedings* (2009).

[7] Buss, A., M. Rashwan., and C. Williams. *Investigation of Warm-Mix Asphalts Using Iowa Aggregates*, Report No. IHRB Project TR-599, Institute for Transportation Iowa State University, Ames, IA (April 2011) 301 pp.

[8] Kim, Y-R., C. Baek, J. Lee, and C. Bacchi, "Evaluation of Moisture Susceptibility in a Warm Mix Asphalt Pavement: US 157, Hurdle Mills, NC" 2nd International Warm-Mix Asphalt Conference, St Louis, Missouri, *Proceedings*, (October 2011).

[9] Goh, S.W., Z. You, "Moisture Damage and Fatigue Cracking of Foamed Warm Mix Asphalt Using a Simple Laboratory Setup", ASCE T&DI Congress, Proceedings, (2011).

[10] Diefenderfer S.D., and T.M. Clark. "Warm-Mix Asphalt Heating Up in Virginia" *TR News 274*. (May-June 2011).

[11] Kim, Y-R., J. Zhang, and H. Ban, "Moisture Damage Characterization of Warm-Mix Asphalt Mixtures Based on Laboratory-Field Evaluation" 91th Annual Meeting of the Transportation Research Board, Washington, D.C., *Proceedings* (2012).

[12] Hearon, A., and S. Diefenderfer, "Laboratory Evaluation of Warm Asphalt Properties and Performance" Airfield and Highway Pavements: Efficient Pavements Supporting Transportation's Future, Bellevue, Washington, *Proceedings* (October 2008) pp. 182–194.

[13] Xiao, F., J. Jordan, and S.N. Amirkhanian, "Laboratory Investigation of Moisture Damage in Warm-Mix Asphalt Containing Moisture Aggregate" *Transportation Research Record*, No. 2126 (2009) pp. 115–124.
[14] Hurley, G.C., and B.D. Prowell, "Evaluation of Potential Processes for Use in Warm Mix Asphalt" *Journal of the Association of Asphalt Paving Technologists*, Vol. 75 (2006) pp. 41–90.
[15] Abbas, A.R., and A. Ayman, *Mechanical Properties of Warm Mix Asphalt Prepared Using Foamed Asphalt Binders*, Report No. FHWA/OH-2011/6, The University of Akron, Akron, OH (March 2011) 132 pp.
[16] Alavi, M.Z., E.Y. Hajj, A. Hanz, and H.U. Bahia, "Evaluating Adhesion Properties and Moisture Damage Susceptibility of Warm-Mix Asphalts, Bitumen Bond Strength and Dynamic Modulus Ratio Tests" *Transportation Research Record,* No. 2295, (2012), pp. 44–53.
[17] Bennert, T., A. Maher, and R. Sauber, "Influence of Production Temperature and Aggregate Moisture Content on the Performance of Warm Mix Asphalt" *Transportation Research Record,* No. 2208, Washington, D.C. (2011) pp. 97–107.
[18] Prowell, B.D., G.C. Hurley, and E. Crews, "Field Performance of Warm Mix Asphalt at the NCAT Test Track" *Transportation Research Record*, No. 1998 (2007) pp. 96–102.
[19] Mogawer, W.S., "WMA Activities and Research", Warm Mix Asphalt Technical Working Group Meeting, Irvine, CA, *Technical Presentation* (May 2011).
[20] Mogawer, W.S., A.J. Austerman, R. Kluttz, M. Rousse. "High-Performance Thin-Lift Overlays with High Reclaimed Asphalt Pavement Content and Warm-Mix Asphalt Technology" *Transportation Research Record*, No. 2293, Washington, D.C. (2012) pp. 18–28.
[21] Mejías-Santiago M., Doyle J., Howard I., Brown R. "Moisture Damage Potential for Warm Mix Asphalt Containing Reclaimed Asphalt Pavement" 2nd International Warm Mix Conference, *Proceedings*, (October 2011).
[22] Jones, D., R. Wu, B.W. Tsai, "Key Results from a Comprehensive Accelerated Loading, Laboratory, and Field Testing Study on Warm-Mix Asphalt in California" 2nd International Warm-Mix Asphalt Conference, University of California Pavement Research Center, St Louis, Missouri, *Proceedings* (October 2011).
[23] Clements, T., P.B. Blankenship, and K.C. Mahboub, "The Effect of Loose Mix Aging on the Performance of Warm Mix Asphalt" *Journal of the Association of Asphalt Paving Technologist*s, No. 81 (2012) pp. 541–567.
[24] Estakhri, C., J. Button, J., and A.E. Alvarez, *Field and Laboratory Investigation of Warm Mix Asphalt in Texas*, Report No. FHWA/TX-10/0-5597-2, Texas Transportation Institute, College Station, Texas (July 2010) 144 pp.
[25] Estakhri, C., Laboratory and Field Performance Measurements to support the Implementation of Warm Mix Asphalt in Texas, Report No. FHWA/TX-12/5-5597-01-1, Texas Transportation Institute, College Station, Texas (February 2012) 77 pp.
[26] Bonaquist, R., *NCHRP 9-43: Mix Design Practices for Warm Mix Asphalt*, NCHRP Report 691, ISSN 0077-5614 (2011).
[27] Al-Qadi, I.L., J. Kern, J. Baek, and M. Doyen, "Short-term Characterization and Performance of Warm Mix Asphalt" Illinois Bituminous Paving Conference, *Proceedings*, (2010).
[28] Hanz. A, E. Mahmoud, and H. Bahia, "Impacts of WMA Production Temperatures on Binder Aging and Mixture Flow Number" *Journal of the Association of Asphalt Paving Technologists*, Vol. 80 (2011).
[29] Estakhri C.K., R. Cao, A. Alvarez-Lugo, and J.W. Button, "Production, Placement, and Performance Evaluation of Warm Mix Asphalt in Texas" GeoHunan International Conference on Challenges and Recent Advances in Pavement Technologies and Transportation Geotechnics, Hunan, China, Proceedings (August 2009).
[30] Bell, C.A., A.J. Wieder, and M.J. Fellin, *Laboratory Aging of Asphalt-Aggregate Mixtures: Field Validation*, Report No. SHRP-A-390, Strategic Highway Research Program, National Research Council (1994).
[31] Brown, S.F., and T.V. Scholz, "Development of Laboratory Protocols for the Ageing of Asphalt Mixtures" Second Euroasphalt and Eurobitume Conference, Barcelona, Spain, *Proceedings*, Book 1, (2000), pp. 83–90.
[32] Epps Martin, A., E. Arambula, F. Yin, L. Garcia Cucalon, A. Chowdhury, R. Lytton, J. Epps, C. Estakhri, and E.S. Park, *NCHRP 9-49: Moisture Susceptibility of WMA Technologies*, NCHRP Report 763, National Cooperative Highway Research Program, Washington, D.C. (2014).
[33] Azari, H, *Precision Estimates of AASHTO T283: Resistance of Compacted Hot Mix Asphalt to Moisture-Induced Damage*, NCHRP Web-Only Document 166, National Institute of Standards and Technology, Gaithersburg, MD (September 2010).

Asphalt Pavements – Kim (Ed)
© 2014 Taylor & Francis Group, London, ISBN 978-1-138-02693-3

Evaluation of Warm Mix Asphalt technology for surface mixtures

Dinesh Ayyala, Haritha Malladi, N. Paul Khosla & Akhtarhusein A. Tayebali
North Carolina State University, Raleigh, NC, USA

ABSTRACT: Warm Mix Asphalt (WMA) has been a major sustainability initiative of the asphalt industry in the recent years. The widespread implementation of WMA has been hindered by concerns over its performance with respect to moisture and rutting susceptibility, and its long term performance. In this study, three WMA technologies—Sasobit, Advera WMA and Foamer device were evaluated in the laboratory and their performance was compared to conventional Hot Mix Asphalt (HMA). The control HMA mix used in this study was a 9.5 mm NMAS surface mixture with PG 64-22 asphalt binder. Mixing and compaction temperatures for WMA mixes used were 136 °C and 120 °C, respectively, representing a 28 °C reduction compared to HMA production temperatures. Moisture susceptibility and rutting evaluations were conducted using various performance tests—AASHTO T283 Tensile Strength Ratio (TSR), Asphalt Pavement Analyzer (APA) and Dynamic Modulus tests. Moisture conditioning of APA and Dynamic Modulus test specimens was also done to study its effect on performance. Although Advera and Foamer mixtures failed the minimum criterion of 85 percent TSR, E* Stiffness Ratio (ESR) test results for all mixtures were greater than 90 percent, indicating that the loss in dynamic modulus is much lower than that indicated by TSR values. APA test results show satisfactory performance for all WMA mixtures with respect to rutting.

Keywords: Warm Mix Asphalt, moisture susceptibility, rutting, ESR, pavement performance

1 INTRODUCTION

Warm Mix Asphalt (WMA) refers to the use of technology and additives to lower the mixing and compaction temperatures during the production of asphalt concrete [1]. Potential benefits of WMA use include energy-cost savings, extended paving season, increased hauling distances and improved compaction in the field [2, 3]. Various technologies currently used to produce warm asphalt mixes are broadly classified into categories based on how they modify the production of the mix [4]. Several other warm mix production methods have been studied to date [4, 5], a few of which are listed below according to type of modification:

- Asphalt foaming technology—Astec Double Barrel Green, Foamer, WAM-Foam
- Asphalt Foaming by Zeolite—Natural zeolites, Synthetic zeolites—Aspha-Min (Aspha-Min GmbH, Germany), Advera (PQ Corporation, USA)
- Bitumen Viscosity Modifiers—Sasobit (Sasol Wax GmbH, Germany), Licomont BS 100 (Clariant, Switzerland)
- Chemical Additives—Evotherm (MeadWestvaco, USA)

Use of WMA in asphalt pavement construction has raised two primary performance issues—moisture damage and low stiffness leading to rutting [5, 6]. Other factors that affect warm mix asphalt use are issues with workability and compactability [4, 6], determination of mixing and compaction temperatures for different binder types, aggregate compatibility with WMA modifier, extent of modification (modifier quantity or water percentage for foamed asphalt), use of anti-stripping additives amongst others [5–13]. The research study presented in this paper sought to evaluate the performance of warm asphalt mixtures prepared using

three types of WMA technology—Sasobit (viscosity modifier), Advera (zeolite) and the Foamer device (asphalt foaming technology).

Sasobit is a crystalline, long-chain aliphatic polymethylene hydrocarbon (paraffin wax) manufactured by Sasol Wax [14]. It modifies the asphalt binder by reducing its viscosity, thereby improving its flow. It has a melting point of 100°C below which it recrystallizes to form a lattice structure in the binder and imparts additional stability to the mixture [7]. Sasobit WMA has been produced in the laboratory at mixing temperatures of 124°C—157°C and compacted at temperatures as low as 88°C [6, 8, 9]. Studies have shown that Sasobit modified WMA exhibited better moisture damage resistance when used with granite aggregate [6] as compared to crushed stone [8] or limestone aggregate [9], and the moisture resistance further improved with the use of liquid anti-strip agent.

Advera is a synthetic zeolite manufactured by PQ Corporation, USA [16]. It is a hydrated aluminosilicate which contains 18 to 21 percent water and is obtained as a fine white powder. This hydro-thermally crystallized water is released upon heating above 100°C. When added to the asphalt concrete mixture, the released water causes micro-foaming making the mixture more workable at lower temperatures. PQ Corporation recommends addition of Advera WMA at a rate of 0.25 percent by weight of the mixture [15]. Due to release of moisture during mixing and lower production temperatures, WMA produced using zeolites results in significant loss of specimen strength after moisture conditioning [6, 8, 10]. These studies [6, 8, 10] have reported an increase in the strength of moisture conditioned mixtures (AASHTO T-283 tensile strength ratio [6] and E* Stiffness Ratio [8]) when hydrated lime was used as an anti-strip additive. Pavement sections constructed in the state of Massachusetts using Advera have showed no signs of moisture damage [8] even though research studies showed that laboratory mixtures failed to satisfy the AASHTO T-283 Tensile Strength Ratio test criteria.

The Foamer is a device manufactured by Pavement Technology, Inc., USA [16]. The device sprays water onto hot asphalt binder in a pressurized reaction chamber to produce foamed asphalt. Reduction in mixing and compaction temperatures are achieved as a result of the increased volume of asphalt foamed at lower temperatures leading to effective coating of aggregate particles. Similar to zeolites, foaming technology also imparts additional moisture to the asphalt concrete mixture increasing its susceptibility to moisture damage and rutting. Performance tests on WMA were conducted on mixtures containing foamed asphalt produced using various foaming devices such as WLB-10 [11], Gencor Green [12] and Astec Double-Barrel Green [13]. Moisture susceptibility tests using the AASHTO T-283 procedure showed variable results depending on the type of aggregate used and inclusion of Recycled Asphalt Pavement (RAP) material in the mixture.

Based on the results from several literature studies, it can be concluded that the performance of WMA mixtures with respect to moisture damage and rutting is a function of several parameters, the most important of which is the WMA technology used.

2 OBJECTIVES

The objectives of this research were to evaluate three warm mix technologies—Sasobit, Advera and the Foamer device and their effect on workability, moisture susceptibility and rutting resistance of asphalt concrete surface mixtures. Sasobit was added at 1.5 percent by weight of asphalt binder [6, 14], Advera was added at 0.25 percent by weight of mixture [8, 15] and the Foamer device was used to produce foamed asphalt by using water at 2 percent by weight of the binder, according to the manufacturer's recommendation.

In this study, the control mixture used was a 9.5 mm nominal maximum aggregate size Superpave mixture and the asphalt binder used was PG 64-22. A liquid anti-strip additive, AdHere LOF-6500 was used in all WMA mixtures as well as control mixture at a rate of 0.75 percent by weight of binder. The mixing and compaction temperatures for the control mix were 163°C and 149°C, respectively as determined from rotational viscometer tests on virgin binder [17]. Mixing and compaction temperatures could not be determined from standard rotational viscometer tests on asphalt binders modified using WMA technologies [5].

Therefore, 136°C for mixing and 120°C for compaction temperatures were selected based on a thorough study of typical values used in several past studies [5–13] and manufacturer recommendations [14–16].

Moisture damage was measured in terms of the Tensile Strength Ratio (TSR) and Dynamic Modulus (E*) Stiffness Ratio (ESR) of WMA mixtures. Rutting was measured using the Asphalt Pavement Analyzer (APA) device for specimens in dry and wet conditions to identify potential damage due to stripping of aggregate.

3 MIXTURE DESIGN

The control mix used in this study was a 9.5 mm nominal maximum size mixture, conforming to Superpave specifications [18] for surface mixtures designed to handle 0.3–3 million Equivalent Single Axle Loads (ESALs).

Superpave mix design was conducted for HMA mixture at the appropriate mixing and compaction temperatures stated previously. A short-term oven aging period of two hours was used for all mixtures according to AASHTO R-35, and mixtures were compacted using Superpave gyratory compactor to a design gyration (N_{des}) level of 65 gyrations. The design asphalt content was determined as 6.0 percent for the control mixture. The same asphalt content was also

Table 1. Mixture volumetrics and superpave specification limits.

Mix properties at N_{des}	Asphalt concrete mix technology				Superpave specifications [18]
	HMA	Sasobit	Advera	Foamer	
G_{mb} at N_{design}	2.328	2.329	2.325	2.316	
Max. specific gravity, G_{mm}	2.432	2.427	2.432	2.417	
% Air voids	4.4	4.0	4.1	4.2	4.0 ± 0.5
% Solids—Total mix	95.7	96.0	95.9	95.8	
% Solids—Vol. of agg. only	83.0	83.5	83.7	83.0	
% VMA	17.0	16.5	16.3	17.0	>15.0%
% VFA	74.2	75.5	75.0	74.3	65–78%
% G_{mm} at N_{ini} (7)	83.3	83.7	83.4	88.4	≤89.0%
% G_{mm} at N_{des} (65)	95.6	96.0	95.9	95.8	96%

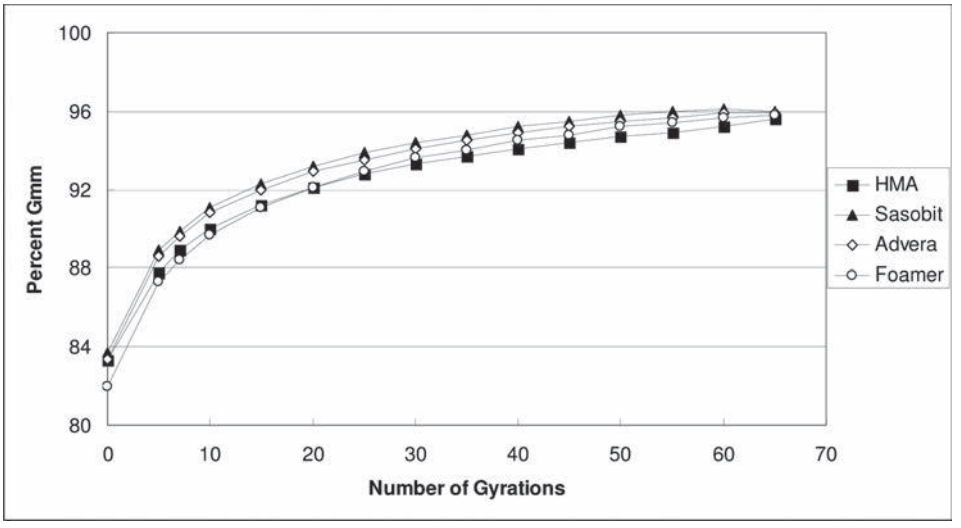

Figure 1. Percent G_{mm} versus number of gyrations.

used for design of WMA mixtures [5, 6]. Table 1 shows the Superpave mix volumetrics for the mixtures used in this study. All mixtures satisfied the volumetric requirements.

Compaction readings for specimen heights at different gyrations were recorded during the compaction of mix design specimens. The trends of decrease in specimen heights with an increase in the number of gyrations did not show any significant difference amongst the four mixtures. This indicates that the compactability of WMA mixtures was comparable to that of HMA. Figure 1 shows the plot of percent G_{mm} values versus number of gyrations for the four mixtures.

4 MOISTURE DAMAGE CHARACTERIZATION

Moisture damage susceptibility of WMA mixtures was analyzed using two test methods—Tensile Strength Ratio using a modified AASHTO T283 test procedure and E* Stiffness Ratio (AASHTO TP79-09). The specimens for the stiffness ratio test were conditioned using the same procedure as the modified AASHTO T283 procedure.

4.1 *Specimen preparation*

Preparation of specimens for TSR testing was done according to the modified AASHTO T283 procedure [18]. Asphalt concrete mixtures were conditioned at room temperature (25°C) for two hours after mixing and then subjected to long-term oven aging at 60°C for 24 hours. The mixtures were then subjected to short-term oven aging at the compaction temperature (149°C for control HMA and 120°C for WMA) before compaction. The specimens were compacted to an air void content of 7 ± 0.5 percent.

Specimens for ESR test were prepared according to the AASHTO R-35 procedure for HMA and WMA mixtures [5, 8]. The short-term oven aging time for the control HMA mixture was 4 hours at 135°C, followed by conditioning the mixture for an additional 45 minutes at 149°C for compaction. WMA mixtures were subjected to short-term oven aging for two hours at compaction temperature (120°C) before compaction. The specimens for ESR test were also compacted to an air void content of 7 ± 0.5 percent in order to directly compare the results with the TSR test. The mixtures did not exhibit any signs of damage or disintegration due to the high air void content in both dry and conditioned states. The original specimens were compacted in a 150 mm diameter mould to a height of 178 mm, and were later cored to a reduced diameter of 100 mm and cut to produce test specimens of height 150 ± 2.5 mm.

4.2 *Conditioning procedure*

Specimen conditioning for both TSR and ESR tests was done according to the modified AASHTO T283 procedure. Two subsets of three specimens each were prepared for the four mixtures. One subset was tested in dry condition and the second set was subjected to moisture conditioning by saturating the specimens to 70–80 percent saturation using vacuum saturation. The specimens after saturation were submerged in a water bath at 60°C for 24 hours. TSR test specimens were conditioned for two hours under water at 25°C after removal from the 60°C water bath, whereas ESR test specimens were air-dried overnight at room temperature (25°C). The reason for air-drying of ESR test specimens was to ensure that specimens were completely surface-dry to allow proper mounting of brass targets for strain measurement using LVDTs.

4.3 *Tensile strength ratio test results*

Table 2 shows the tensile strength ratios for HMA and WMA mixtures. The Tensile Strength Ratio (TSR) was calculated as a ratio of the average indirect tensile strength of specimens in conditioned (wet) state to that of specimens in dry state, as shown in Eq. (1).

$$\text{TSR} = \frac{\text{Average indirect tensile strength of wet specimens}}{\text{Average indirect tensile strength of dry specimens}} \quad (1)$$

Table 2. AASHTO T-283 tensile strength ratio test results.

Mixture type	Anti-strip dosage*	Average indirect tensile strength, kPa		TSR, % (min. 85)
		Dry	Wet	
Control (HMA)	0.75	1036.9	909.1	88
Sasobit	0.75	850.7	826.9	97
Sasobit	1.50	798.0	812.0	102
Advera	0.75	858.2	476.8	56
Advera	1.50	760.5	484.2	64
Foamer	0.75	888.3	700.3	79
Foamer	1.50	886.6	721.3	81

*Liquid anti-strip Ad-Here LOF6500 dosage by weight of binder.

Table 3. E* Stiffness Ratio (ESR) test results.

Mixture type	Temp. °C	Dynamic modulus, MPa						Average ESR, %
		Dry conditioned			Wet conditioned			
Freq., Hz		10	1	0.1	10	1	0.1	
HMA	4	13300	9670	6210	12600	9020	5790	93.7
	20	5560	3040	1460	5260	2810	1330	92.6
	40	1120	438	214	1100	456	240	104.7
Sasobit	4	12100	8400	5170	11700	8160	5120	97.7
	20	4760	2420	1130	4480	2260	1040	93.0
	40	962	395	226	890	364	199	90.9
Advera	4	11600	7910	4700	10800	7240	4170	91.2
	20	4350	2030	819	3790	1910	724	89.9
	40	802	280	132	646	226	105	80.3
Foamer	4	12600	8670	5190	11700	7930	4700	91.6
	20	4680	2250	957	4670	2310	999	102.2
	40	861	335	191	916	359	194	105

The results in Table 2 show that HMA and Sasobit mixtures satisfy the minimum TSR requirement of 85 percent, with Sasobit showing almost no signs of reduction in tensile strength due to moisture damage. This observation is consistent with other studies [6] which observed that Sasobit mixtures show excellent compatibility with chemical anti-stripping agents and granite aggregate, both of which were used in this study. Advera and Foamer mixtures resulted in average TSR values of 58 and 80 percent, both of which fail the minimum criterion of 85 percent. Therefore, the test was repeated with an increased anti-strip dosage of 1.5 percent by weight of binder in an effort to improve the TSR values. The repeated test results showed slight improvement in the TSR values, but this was due to reduced tensile strength of specimens in both dry and wet conditions as opposed to the desired increase in the wet tensile strength.

4.4 *E* Stiffness Ratio Test Results (ESR)*

The E* stiffness ratio or ESR test is based on evaluating the effect of moisture conditioning on the dynamic modulus of an asphalt concrete mixture, and has been reported as an alternative to the TSR test [8, 19]. Unconfined dynamic modulus test was conducted on specimens prepared at 7 ± 0.5 percent air voids according to AASHTO TP79-09, Standard Method of Test for Determining the Dynamic Modulus and Flow Number for Hot Mix Asphalt (HMA) Using the Asphalt Mixture Performance Tester (AMPT). Since the dynamic modulus test is a

non-destructive test, the same specimens were first tested dry and later subjected to moisture conditioning. The test was conducted at three temperatures—4, 20 and 40°C and at three frequencies—0.1, 1 and 10 Hz. ESR was calculated using Eq. (2).

$$\text{ESR} = \frac{\text{Dynamic modulus of wet specimens at test temperature and frequency}}{\text{Dynamic modulus of dry specimens at test temperature and frequency}} \quad (2)$$

Table 3 shows the average dynamic modulus measured in the dry and wet conditions for the four mixtures at the three test temperatures and frequencies, and the average ESR for each mixture at each test temperature.

It was observed that the dynamic modulus of all four mixtures after conditioning was greater than 90 percent of that in the dry condition at all the test temperatures, except for Advera mixture at 40°C. In this test, the difference between mixture stiffness in dry and wet conditions is not as prominent as it was in the TSR test.

5 RUTTING RESISTANCE CHARACTERIZATION

Rutting resistance of mixtures was evaluated using the Asphalt Pavement Analyzer (APA) device. The specimens used for this test were prepared according to AASHTO-R35 with four hours of short-term oven aging for HMA followed by 45 minutes at compaction temperature, and two hours of short-term oven aging for WMA at compaction temperature. The test specimens were prepared at an air void content of 7 ± 0.5 percent with 75 ± 2 mm height. Additional sets of Advera and Foamer specimens were prepared and moisture-conditioned using the modified AASHTO T-283 procedure to evaluate the effect of moisture damage due to stripping. Since HMA and Sasobit mixtures exhibited passing TSR values, they were tested only in the dry condition.

For asphalt concrete mixtures with 9.5 mm nominal maximum aggregate size, the maximum allowable rut depth according to North Carolina specifications is 9.5 mm for the traffic level under consideration. The APA test was conducted at the PG high-temperature of the binder at 64°C and final rut depths at the end of 8000 cycles were measured. Average rut depth of HMA specimens was measured to be 5.1 mm and that of Sasobit specimens was 4.2 mm. Average rut depth for Advera specimens in dry condition was measured as 5.0 mm

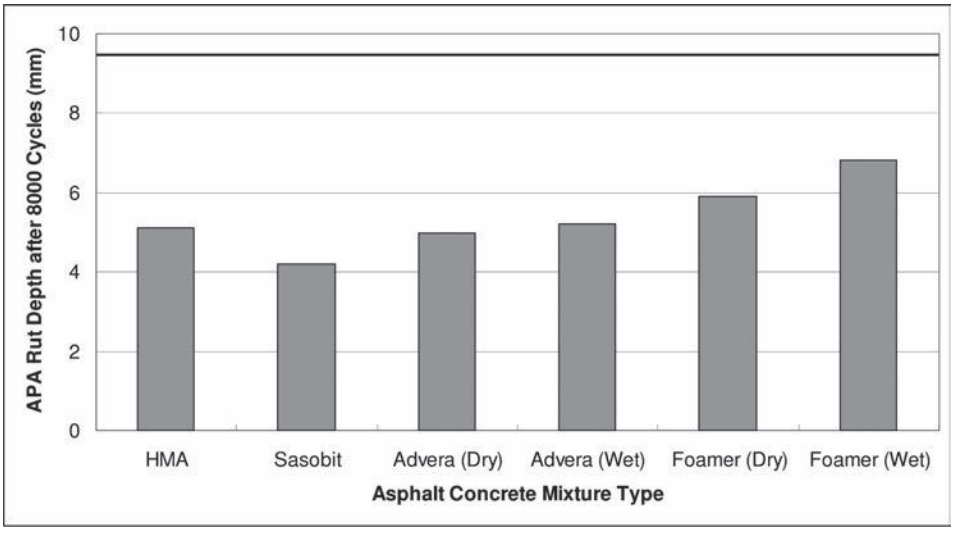

Figure 2. APA rut depth values.

and wet condition as 5.2 mm. For Foamer specimens, rut depth increased from 5.9 mm in dry condition to 6.8 mm in wet condition. Figure 2 shows the APA test results for the mixtures.

The results show that the average rut depth for all mixtures is lower than the allowable value, indicating that the mixtures did not show significant rutting damage. The tests conducted on moisture-conditioned specimens showed an increase in rutting, but the average rut depth was still lower than the allowable limit. Visual inspection of the specimens' broken surfaces did not show signs of aggregate stripping, which signifies that the WMA mixtures exhibited adequate resistance to rutting.

6 SUMMARY AND CONCLUSIONS

This study focused on investigation of performance characteristics of WMA mixtures prepared using three different warm mix technologies—Sasobit, Advera and the Foamer device. Performance characteristics of WMA was compared to a control HMA mixture with respect to moisture damage and rutting. Moisture damage susceptibility was evaluated using the AASHTO T-283 and ESR test methods, and rutting susceptibility of mixtures was evaluated using the Asphalt Pavement Analyzer.

TSR test results showed that WMA mixtures containing Sasobit did not exhibit any moisture damage, whereas Advera and Foamer mixtures failed to satisfy the failure criterion of minimum 85 percent TSR. The test was repeated by increasing the dosage of anti-strip additive to 1.5 percent by weight of binder, which did not affect the TSR values significantly.

Rutting resistance was measured using the Asphalt Pavement Analyzer device for all mixtures in both dry and saturated conditions. Rut depth values at the end of 8000 cycles were less than the specified limit of 9.5 mm for all the mixtures, indicating adequate resistance of the mixtures to rutting. The APA test results for saturated specimens also showed no significant stripping of aggregate from the specimen surfaces, indicating that low TSR values cannot be directly used as a parameter to assess moisture damage, especially for WMA mixtures produced using moisture-inducing technology such as zeolites and foaming devices.

ESR test results showed that all WMA mixtures retained more than 90 percent of their stiffness after moisture conditioning at most test temperatures. This conclusion supports evidence from literature that TSR test is not adequate to characterize the moisture damage resistance of WMA.

ACKNOWLEDGEMENTS

The authors would like to thank the North Carolina Department of Transportation for funding this research project. Special thanks are due to personnel at the NCDOT Materials & Tests Division, especially to Mr. James Budday, PE and Mr. Todd Wittington, PE. Support of PQ Corporation in the supply of materials for the study is also acknowledged.

REFERENCES

[1] Federal Highway Administration, US Department of Transportation. Warm Mix Asphalt Technologies and Research. Website: http://www.fhwa.dot.gov/pavement/asphalt/wma.cfm, Accessed 4 July, 2012.

[2] D. Brown, "Warm Mix: the Lights are Green," Hot Mix Asphalt Technology, vol. January/February, pp. 20–32, 2006.

[3] B. D. Prowell, "Warm Mix Asphalt Scan Summary Report," The International Technology Scanning Program, 11 July 2007. Website: http://www.international.fhwa.dot.gov/pubs/wma/summary.cfm, Accessed 4 July 2012.

[4] Audrius Vaitkus, Viktoras Vorobjovas, Laura Ziliute. The Research on the Use of Warm Mix Asphalt for Asphalt Pavement Structures. XVII International Baltic Road conference, Riga, Latvia, 2009.

[5] Ramon Bonaquist. NCHRP Project 9-43: Mix Design Practices for Warm Mix Asphalt. National Highway Cooperative Research Program Report 691, Transportation Research Board, Washington D.C., 2011.
[6] Graham C. Hurley, Brian D. Prowell. Evaluation of Potential Processes for Use in Warm Mix Asphalt. Journal of the Association of Asphalt Paving Technologists, 2006, Volume 75, pp 41–90.
[7] Damm K., Abraham J., Butz T., Hildebrand G., Riebsehl G. Asphalt Flow Improvers as Intelligent Fillers for Hot Asphalts—A New Chapter in Asphalt Technology. Journal of Applied Asphalt Binder Technology, 2002–4, Volume 2., pp 36–69.
[8] Walaa S. Mogawer, Alexander J. Austerman, Emad Kassem, Eyad Masad. Moisture Damage Characteristics of Warm Mix Asphalt Mixtures. Journal of the Association of Asphalt Paving Technologists, 2011, Volume 80, pp 491–526.
[9] Wasiuddin N. M., Selvamohan S., Zaman M. M, Guegan M. Comparative Laboratory Study of Sasobit and Aspha-Min Additives in Warm-Mix Asphalt. Journal of the Transportation Research Board, Transportation Research Record, 1998, pp. 82–88.
[10] Jun Zhang. Effects of Warm Mix Asphalt Additives on Asphalt Mixture Characteristics and Pavement Performance. Master of Science Thesis, University of Nebraska, Lincoln, Nebraska, November 2010.
[11] Ala R. Abbas, Ayman W. Ali. Mechanical Properties of Warm Mix Asphalt Prepared Using Foamed Asphalt Binders. FHWA Report No. FHWA/OH-2011/06, Ohio Department of Transportation, Columbus, Ohio, March 2011.
[12] Kvasnak A., Taylor A., Signore J., Bukhari S. Evaluation of Gencor Green Machine Ultrafoam GX. NCAT Report 10-03, National Center for Asphalt Technology, Auburn, Alabama, 2010.
[13] Middleton, B. and Forfylow, R.W. Evaluation of Warm Mix Asphalt Produced With the Double Barrel Green Process. Journal of the Transportation Research Board, Transportation Research Record, 2010, Volume 2126, pp. 19–26.
[14] Sasol Wax, "Sasobit," Sasol Wax, Website: http://www.sasolwax.us.com/sasobit.html, Accessed 25 October 2010.
[15] PQ Corporation, "Advera WMA Information Sheet," Website: http://www.adverawma.com/WMArev.pdf, Accessed 25 October 2010.
[16] Pavement Technology, Inc., Website: http://www.pavementtechnology.com/aboutus/index.asp, Accessed 25 October 2010.
[17] AASHTO T316–06: Standard Method of Test for Viscosity Determination of Asphalt Binder Using Rotational Viscometer, American Association of State Highway and Transportation Officials, February 2007.
[18] Contract Standards and Development Unit. Standard Specifications for Roads and Structures, North Carolina Department of Transportation, 2010.
[19] A.A. Nadkarni, K.E. Kaloush, W.A. Zeiada and K.P. Biligiri, "Using Dynamic Modulus Test to Evaluate Moisture Susceptibility of Asphalt Mixtures," Transportation Research Record: Journal of the Transportation Research Board, vol. No. 2127, pp. 29–35, 2009.

Asphalt Pavements – Kim (Ed)
© 2014 Taylor & Francis Group, London, ISBN 978-1-138-02693-3

Study on the improved recycled asphalt mixtures by microbubble-foamed asphalt

Kentaro Koshi & Hirochika Moriyasu
Technical Department, Maeda Road Construction Co., Ltd., Oosaki, Shinagawa, Tokyo, Japan

Keita Saito & Yasunari Shimizu
Technical Research Institute, Maeda Road Construction Co., Ltd., Oobatake, Tsuchiura, Ibaraki, Japan

ABSTRACT: In Japan, recycled asphalt mixtures have accounted for around 75% of the total asphalt production volume in recent years, and the percentage is expected to remain at the same rate. Thus efforts must be made to secure good working environments through measures to reduce asphalt fumes produced during the manufacture of asphalt mixtures and construction, and improve the workability. In reviewing such measures, we focused on a mechanical warm-mix technique (foamed asphalt) carried out in the U.S. and Europe, and introduced it to Japan. When applying foamed asphalt to the recycled asphalt mixtures used in Japan, as the recycled asphalt aggregate content of the mixtures is too high compared to the U.S. and Europe. (50–70%), high effectiveness cannot be obtained if the foamed asphalt is used as it is.

Therefore we reviewed methods for microfoaming foamed asphalt and adding a recycling agent (asphalt softening agent). This succeeded in reducing the temperature and improving the quality of recycled asphalt mixtures.

This paper reports details of the reviews we studied.

Keywords: Microfoaming, foamed asphalt, recycled asphalt mixture, recycling agent, asphalt foam

1 INTRODUCTION

In recent years, soaring prices of asphalt binders and aggregates in Japan have led to the promotion of the recycling of asphalt, and now recycled asphalt mixtures have accounted for around 75% of the total asphalt production volume. For this reason, there is a need to implement measures to reduced CO_2 emissions during manufacturing, improve workability, and reduced asphalt fumes, for recycled asphalt mixtures. One method for implementing these measures is the use of warm-mix asphalts. Considering the needs for mass manufacturing and costs, foamed asphalt which is commonly used in the U.S. and Europe is considered the most suitable. However, in Japan, the percentage (recycling rate) of recycled contained in recycled asphalt mixtures is still as high as 75%, and 46% on average which is a high level. Thus, even if foamed asphalt is used, the amount of foamed asphalt (amount of new asphalt) is small, and the effects of the warm-mix asphalt will also be small. Thus, to apply foamed asphalts to recycled asphalt mixtures with high recycling rate, there is a need to improve the foamed asphalt so that the effects of the warm-mix asphalt also become higher than before. Furthermore, in Japan, there is a regulation requiring the recycled asphalt or recycled asphalt mixture to be returned to the designated properties using recycling agent during manufacture at recycling rates higher than the designated levels. For this reason, a high recycling rate means more recycling agents must be used.

From this background, the authors attempted to enhance the effects of warm-mix asphalt by microfoaming foamed asphalt into even finer foam (microfoam) using a foaming enhancer, and succeeded in applying this technique even to recycled asphalt mixtures with high recycling rate. Furthermore, by applying the technique to recycling agents, the properties of mixtures were also improved.

This paper discusses the performance of recycled asphalt mixtures applying microfoaming foamed asphalt, and reports the results of verifying the effects of foaming recycling agents.

2 FOAMED ASPHALT

Foamed asphalt is made by mixing hot asphalt with water and foaming the mixture. As the asphalt volume increases and the apparent viscosity decreases, miscibility improves during manufacture. The asphalt returns to the original volume during construction work, but the bearing effects of the residual foam improves compaction. If the temperature further decreases after construction, the influence of the foam disappears, ensuring the quality of the mixture. However, increasing the recycling rate of recycled asphalt mixtures decreases the amount of new asphalt, resulting in reduced effects of applying the foamed asphalt. Since foamed asphalt is applied for reducing the manufacturing temperature of recycled asphalt mixtures and improving workability, there is a need to enhance the bearing effects of the foamed asphalt. Figure 1 shows the conceptual drawings of conventional foamed asphalt and improved foamed asphalt by microfoaming. It can be seen that after the conventional foamed asphalt foams and expands, bubbles with relatively large particle size bind together, expand, and then disappear, thus the residual foam amount tends to decrease during construction. Microfoaming is considered an ideal method for increasing the residual amount of this foam and enhancing bearing effects.

3 IMPROVEMENT OF FOAMED ASPHALT

Foamed asphalt was improved using a foaming enhancer. As we have already confirmed the relation between the Foam Index (FI), which uses expansion ratio and half period in a previous study[1)], and diameter of foam, FI was applied in this study to evaluate the performance of the foamed asphalt. Table 1 shows the properties of the straight asphalt used in this study.

Table 2 shows the foaming state of each type of foamed asphalt and state of bubbles under a microscope. With conventional foamed asphalt, as bubbles bind together, expand,

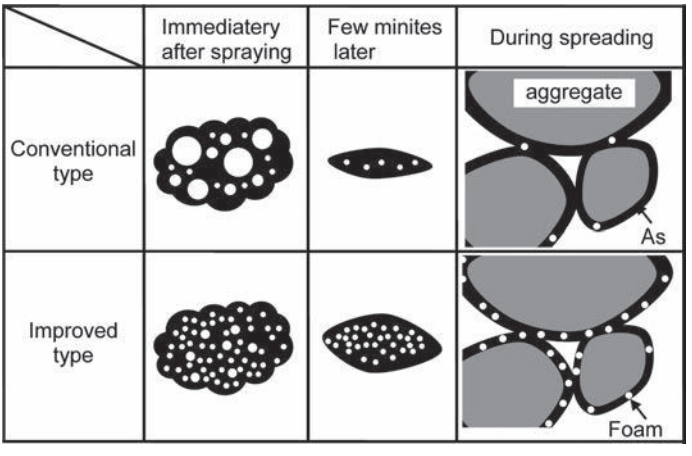

Figure 1. Conceptual drawing of foamed asphalt.

Table 1. Properties of asphalt.

Item	Name	Penetration (25°C) (1/10 mm)	Softening point (°C)	Ductility (15°C) (cm)	Density (15°C) (g/cm^3)
Property	Straight asphalt 60/80	71	47.5	100+	1.039

Table 2. Properties of foamed asphalt.

	Temporal change of expansion ratio	Foaming state	Microscopic image
Conventional foamed asphalt	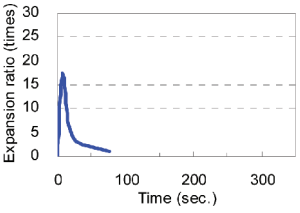	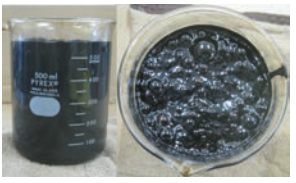	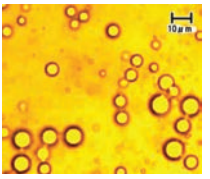
Improved foamed asphalt	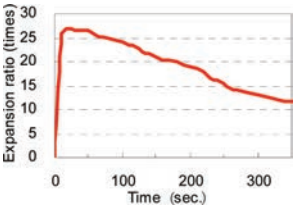	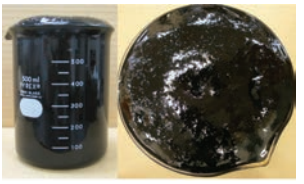	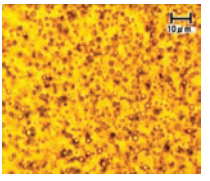

and then disappear, FI is low and there are very little bubbles remaining. In contrast, with the improved foamed asphalt, the foaming amount is greater. As this prevents the binding and expansion of the bubbles, many micro bubbles are seen to remain. These results indicate that the improved foamed asphalt can improve bearing effects during construction. It was also confirmed that as FI increases, the diameter of the individual bubbles decreases, resulting in the increase in residual bubbles.

4 VERIFICATION OF PROPERTIES OF MIXTURE APPLYING IMPROVED FOAMED ASPHALT

To verify the compaction and workability of mixtures to which the improved foamed asphalt are applied, property tests of various mixtures were conducted at recycling rates of 0, 20, 40, and 60%. Table 3 shows the test items.

The workability evaluation testing device shown in Figure 2 was used to verify workability. The testing device consists of a test container (A) for holding the mixture, rotating paddle for receiving resistance (B), and torque meter (C). The test container can hold 10 liters and is compatible with mixtures of various particle sizes. The test procedure and data test procedure consists of first placing the manufactured mixture inside the test container and then rotating the paddle in the mixture. The resistance is then detected using the torque meter and output to a PC every second. As shown by the waveform in Figure 3, the output torque data stabilizes several ten seconds after the start of measurement. Therefore one measurement completes in about two minutes. The average of the agitation torque values taken 20–40 seconds after the start of the test is used for evaluating workability. Mixtures with good workability have small torques while those with poor workability have large torques.

Table 3. Evaluation items and test methods.

Evaluation item	Test method
Compaction characteristics	Marshall method Gyratory Compaction (GC)
Workability	Workability evaluation test device
Sustenance of foamed effects	Marshall test
Basic properties	Marshall test, immersion Marshall test WT test, immersed WT test, bending test

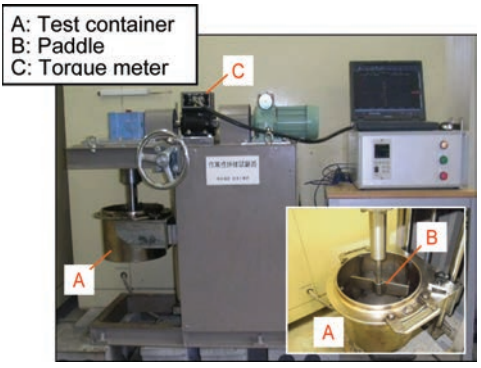

Figure 2. Workability evaluation test device.

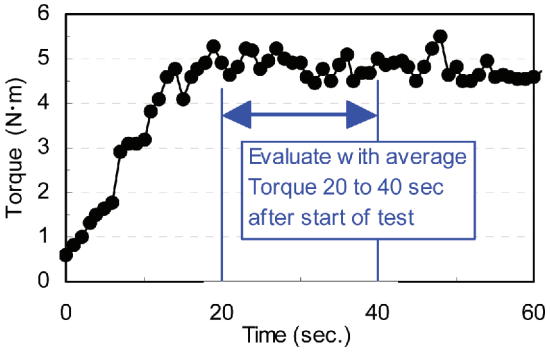

Figure 3. Evaluation method of workability evaluation test device.

4.1 *Study mixtures*

In Japan, two methods are used to design the composition of recycled asphalt mixtures: one is by adjusting the penetration and the other is by adjusting the recycled hot mix asphalt to the target split coefficient[2]. When adjusting to the design reference value, either the recycling agent or new asphalt (high penetration asphalt) is used or both are used. The amount of recycling agent added is determined by adjusting to the designed penetration using the recycling agent. Table 4 shows the composition of the mixtures used in this study and Table 5 shows the properties of the recycled aggregates.

4.2 *Compaction characteristics*

Figure 4 shows the relation between the mixture temperature and compaction degree by Marshall compaction at the recycling rate of 60%. The improved foamed asphalt showed

Table 4. Mixture proportion.

Mixture	Recycled asphalt aggregate content (%)	All asphalt (%)	New asphalt (%)	Recycled asphalt aggregate asphalt (%)	Recycling agent (%)
Recycled dense graded asphalt mixture (13)	0	5.7	5.70	–	–
	20		4.73	0.88	0.09
	40		3.76	1.76	0.18
	60		2.81	2.63	0.26

Table 5. Properties of recycled asphalt aggregates.

Recycled asphalt aggregate asphalt amount (%)		4.43						
Penetration (1/10 cm)		21						
Gradation	Sieve opening (mm)	13.2	4.75	2.36	0.60	0.30	0.15	0.075
	Percentage passing (%)	100.0	72.2	50.6	29.6	22.1	16.0	12.7

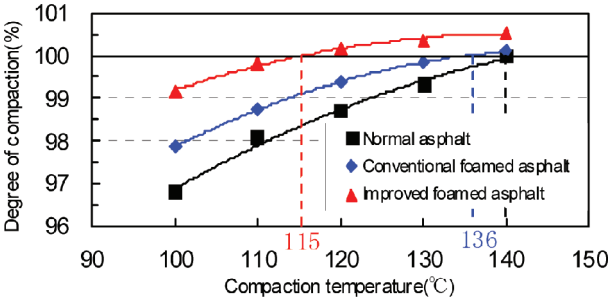

Figure 4. Relation between compaction temperature and compaction degree (recycling rate: 60%).

high compaction degree compared to normal asphalt at the same temperature. The same compaction degree as normal asphalt compacted at 140°C was obtained at 115°C (25°C reduction). The reduction effects of the improved foamed asphalt were 19°C higher than conventional foamed asphalt, and the improved foamed asphalt with many micro bubbles showed remarkable improvement in compaction due to bearing effects.

In consideration of the mechanism of the improvement effects of the compaction of the foamed asphalt, it is expected that the kneading by the roller will show higher compaction degree than the hammering of the Marshall rammer, therefore verifications were carried out using a Marshall rammer and Gyratory Compacter (GC). The number of gyrations of the GC was set the same as the Marshall compaction density of normal asphalt at 140°C. Figure 5 shows the relation between the mixture temperature and compaction degree at the recycling rate of 60% for different compaction methods. These results confirm that compaction tends to be better with GC for both foamed asphalt and improved foamed asphalt and in improved foamed asphalt the tendency is remarkable. Improved foamed asphalt thus promises to be effective for improving compaction even with roller compaction in the construction. The same tendency was seen at the recycling rates of 0, 20, and 40%.

4.3 *Workability*

Figure 6 shows the relation between the mixture temperature and agitation torque at the recycling rate of 60%. The improved foamed asphalt showed lower torque values compared to normal asphalt at the same temperatures, and the same torque as 150°C normal asphalt

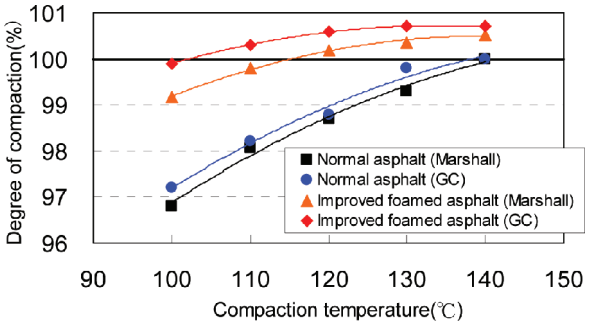

Figure 5. Compaction according to compaction method (recycling rate: 60%).

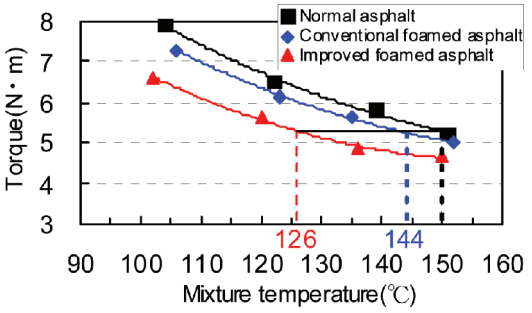

Figure 6. Relationships between mixture temperature and agitation torque (recycling rate: 60%).

was obtained at 126°C (24°C reduction). In the evaluation of workability, the same tendencies were seen at the recycling rates of 0, 20, and 40% as done with compaction.

Table 4 summarizes the improvement effects confirmed in the above study. For improved foamed asphalt, at high recycling rates which means that the amount of new asphalt is less, the improvement effects for compaction and workability decreased. Even at the recycling rate of 60%, improvement effects of about 25°C were seen. In addition, improving the foamed asphalt provided additional improvement effects of about 15°C. These results confirm that improved foamed asphalt can be applied for reducing the manufacturing temperature of recycled asphalt mixtures and improving workability.

4.4 *Continued effects of improved foamed asphalt*

To verify the sustenance of bearing effects using improved foamed asphalt, changes in the compaction degree with time after manufacture of the mixtures were investigated. The curing temperature was set at 150°C, the compaction temperature at 140°C, and the compaction degree at 100% taking 0 hours elapsed time as the reference for each mixture. Figure 7 shows the relation between the elapsed time and compaction degree. It was confirmed that as a result of the microfoaming of the improved foamed asphalt, bearing effects continued for a longer time than conventional foamed asphalt and were the same as normal asphalt.

4.5 *Basic properties of mixtures*

Using the improved foamed asphalt, mixture properties when compaction was carried out at lower mixture temperature were verified. The compaction temperature of the improved foamed asphalt was set at 104°C for the recycling rate of 0% and at 115°C for the recycling rate of 60% based on the results in Table 6. Table 7 shows the test results. No decrease in mixture properties was found as a result of decreasing the compaction temperature from that

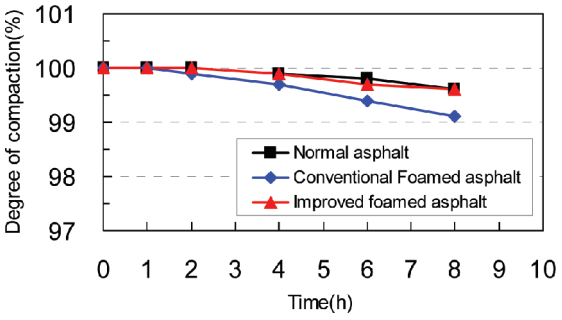

Figure 7. Relation between elapsed time and compaction.

Table 6. Improvement effects of improved foamed asphalt.

Item		Mixture	Recycled aggregate content (%) 0	20	40	60
Improvement effects* (°C)	Compaction	Conventional foamed asphalt	21	15	9	6
		Improved foamed asphalt	36	32	29	25
	Workability	Conventional foamed asphalt	19	15	10	6
		Improved foamed asphalt	31	28	27	24

*Compaction was analyzed at 140°C in normal asphalt and workability was analyzed at 150°C in normal asphalt.

Table 7. Mixture property.

Recycled aggregate content		0%		60%	
Item		Normal asphalt	Improved foamed asphalt	Normal asphalt	Improved foamed asphalt
Compaction temperature	(°C)	140	104	140	115
Marshall stability	(kN)	11.5	11.4	13.8	13.5
Flow value	(1/100 cm)	34	33	31	33
Residual stability	(%)	93.9	93.7	90.4	91.0
Dynamic stability	(time/mm)	600	600	1500	1400
Dynamic stripping rate	(%)	3.2	3.1	4.5	4.0
Bending strength (–10°C)	(MPa)	6.7	6.7	8.3	8.3
Bending fracture strain	($\times 10^{-3}$)	2.5	2.6	2.1	2.1
Bending stiffness	(10^3 MPa)	2.6	2.6	4.0	4.0

of normal asphalt. In addition, although reduced stripping resistance due to the use of water and foaming enhancer was feared for improved foamed asphalt, no such drop was seen.

5 VERIFICATION OF APPLICABILITY IN MANUFACTURING AND CONSTRUCTION

5.1 *Verification of manufacturing mixture on manufacturing plant machine*

As a result of measuring the FI of improved foamed asphalt using a calibration nozzle installed on manufacturing plant, it was confirmed that the same FI as obtained by a lab foamer can be obtained. Table 8 shows the properties of the recycled dense graded asphalt

Table 8. Mixture properties on laboratory machine and plant (recycling rate: 60%).

Item	Mixing place			
	Laboratory		Plant	
	Normal asphalt	Improved foamed asphalt	Normal asphalt	Improved foamed asphalt
Mixing temperature (°C)	160	138	163	137
Compaction temperature (°C)	140	115	141	114
Degree of compaction (%)	100 (reference)	100.1	100 (reference)	99.8
Torque (140°C) (N · m)	5.42	4.63	5.61	4.78
Marshall stability (kN)	13.8	13.5	12.8	13.0
Flow value (1/100 cm)	31	33	30	31
Residual stability (%)	90.4	91.0	91.2	90.8
Dynamic stability (time/mm)	1500	1400	1700	1700

Table 9. Compaction degree at site aiming at reduced mixing/paving temperature.

Aim	Mixture type	Mixing temperature (°C)	Measured sites	Degree of compaction (%)	
				Mean	Standard deviation
Reduced mixing temperature	Normal asphalt	155	14*	99.3	1.2
	Improved foamed asphalt	125		99.5	1.1
Improved workability	Normal asphalt	165	10	98.2	1.7
	Improved foamed asphalt			99.4	1.0

*Sampled 3 cores per site.

mixture (13) with a recycling rate of 60% made on the plant. The improved foamed asphalt was made with 25°C lower than normal asphalt, but it demonstrated more or less the same properties as normal asphalt.

5.2 *Verification in construction*

To verify performance in construction, compaction degree was investigated in the construction site using a recycled dense graded asphalt mixture (13) with recycling rate of 50%. Table 9 shows the compaction degree of asphalt shipped at temperatures reduced from normal asphalt by 30°C to decrease manufacturing temperature during summer, and that of asphalt shipped at the same temperature as normal asphalt in the aim to improve workability during winter. As a result, it was confirmed that the same compaction degree as normal asphalt was obtained in the shipment where the manufacturing temperature was decreased in summer, and workability improved and high compaction degree versus normal asphalt was obtained in winter.

6 RECYCLING AGENTS

Reviews to date have confirmed that improving foamed asphalt by microfoaming is effective for enhancing compaction and workability for recycled asphalt mixtures. Given that the

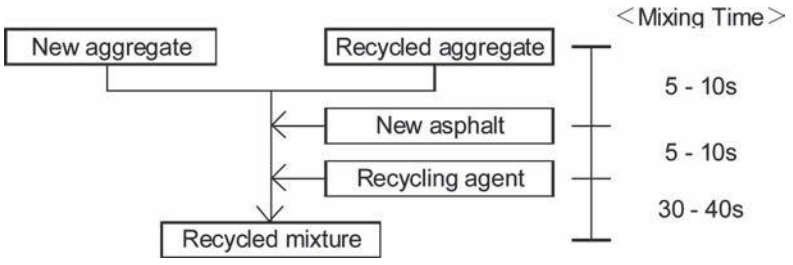

Figure 8. Example of mixing procedure at plant.

amount of new asphalt contained decreases with increasing recycling rate, high recycling rate also means less effectiveness of improving foamed asphalt. Thus it is difficult to achieve the desired effects when improved foamed asphalt is applied to mixtures with high recycling rate and some other methods for applying to high recycling rates are required.

Of the materials used for recycling mixtures, we have been focusing on recycling agents. Figure 8 shows examples of mixing methods used by Japanese manufacturing plants. Investigations were carried out based on the idea that in addition to foaming the asphalt, foaming the recycling agent further enhances bearing effects, allowing foaming techniques to be applied to mixtures with high recycling rate.

7 FOAMED PROPERTIES OF RECYCLING AGENT

Conditions enabling foaming and foamed properties were verified at various conditions. The recycling agents generally used in Japan were employed. Table 10 shows the properties of the recycling agents used. FI was applied for evaluating foamed properties and the foaming device used is similar to one for asphalt.

7.1 *Temperature of recycling agent*

Foamed properties were verified by varying the temperature of the recycling agent. The amount of water added was tentatively set at 3%. It was confirmed that the expansion ratio and half period became maximum at about 130°C, and no changes were found at 130°C or above. It was also clarified that no foaming occurs at around 100°C.

7.2 *Amount of water added*

Foamed properties were verified by varying the amount of water added. Figure 9 shows the maximum expansion ratio and FI. Both expansion ratio and FI were maximum when the amount of water added was about 2%.

Based on this review, the standard recycling agent temperature was set at 130°C and the standard amount of water added was 2.0%.

8 EFFECTS OF FOAMED RECYCLING AGENT ON MIXTURE PROPERTIES

The properties of recycled mixtures with recycling rate of 75% were verified using a foamed recycling agent. Table 11 shows the mixtures studied, namely normal mixture, mixture in which only the asphalt is foamed (As-foamed), mixture where both the asphalt and recycling agent are foamed (W-foamed), and improved foamed asphalt was used.

The split test is a test for evaluating the stiffness of recycled mixtures. The stiffness is known to have a high correlation with the deterioration level of mixtures (penetration of recovered asphalt) and the number of damage (fatigue damage resistance) in flex tests[4]. Recycling

Table 10. Properties of recycling agent.

Density (15°C)	0.905
Flash point (°C)	264

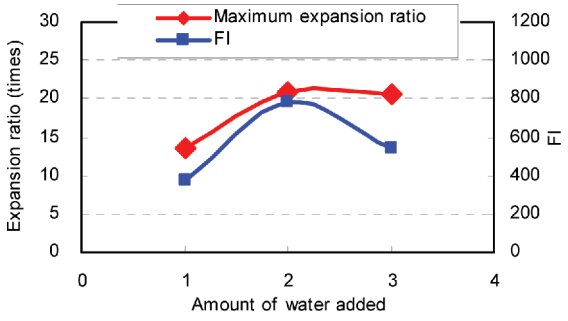

Figure 9. Maximum expansion ratio and FI.

Table 11. Mixture proportion.

Mixture	Recycling rate (%)	All asphalt (%)	New asphalt (%)	Recycled asphalt (%)	Recycling agent added (%)
Recycled dense graded asphalt concrete (13)	75	5.7	2.08	3.29	0.33

agents are added to recover appropriate stiffness values for recycled asphalt mixtures, and it is thought that if the foaming of the recycling agent enhances the effects of recovering stiffness, the mixture will have improved fatigue damage resistance.

8.1 *Compaction*

Compaction was verified in Marshall compaction test. Figure 10 shows the relation between the mixture temperature and compaction degree. Compared with normal asphalt and As-foamed, W-foamed showed a high compaction degree at the same temperatures. When W-foamed showed the same compaction degree as As-foamed, temperature reduction effects were about 5°C higher, resulting in improved compaction by the foaming of the recycling agent.

8.2 *Workability*

Figure 11 shows the results of the workability evaluation test of the mixture. Compared with normal asphalt and As-foamed, W-foamed showed a low torque at the same temperature. When W-foamed showed the same torque as As-foamed, temperature reduction effects were 5°C higher, resulting in improved compaction by the foaming of the recycling agent.

8.3 *Splitting test*

Table 12 shows the results of the split test. Compared with normal asphalt and As-foamed, W-foamed had a lower split coefficient. Foaming the recycling agent was found to increase

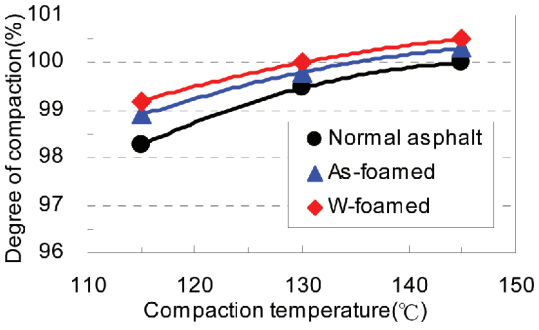

Figure 10. Marshall test results.

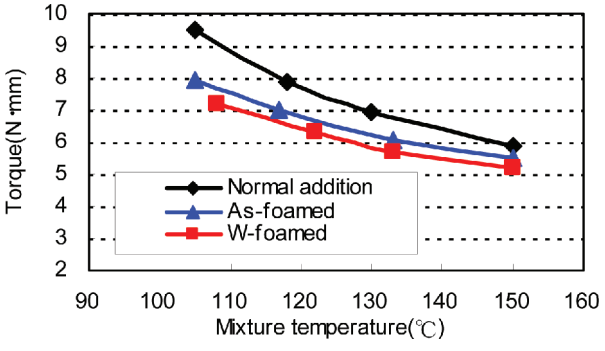

Figure 11. Workability evaluation test.

Table 12. Split test results.

Type of mixture	Normal addition	As-foamed	W-foamed
Split coefficient (MPa/mm)	0.71	0.70	0.64

the effects of lowering the split coefficient and bringing the split stiffness closer to the appropriate value.

From the above results, foaming the recycling agent and applying foaming technique to recycled asphalt mixtures with a recycling rate of 75% were found to enhance both compaction and workability. It was also confirmed to enhance the split stiffness improvement effects of recycled asphalt mixtures and the effects of adding the recycling agent.

9 SUMMARY

The following findings were obtained from the results of the verifications conducted.

1. By realizing foam finer than conventional bubbles using a foaming enhancer, the foaming index could be improved sharply.
2. It was confirmed that improving bearing effects by the microfoaming of foamed asphalt further enhances the compaction and workability of recycled asphalt mixtures with high recycling rates, and bearing effects further increase in roller compaction by kneading in construction.

3. Construction on actual roads demonstrated that the improved foamed asphalt is effective for reducing the paving temperature of recycled asphalt mixtures and improving workability.
4. Foaming the recycling agent was confirmed to improve compaction and workability, and the properties of recycled asphalt mixtures with high recycling rates.

10 CONCLUSION

The results of this study demonstrated the effectiveness of improved foamed asphalt for improving quality by reducing the manufacture temperature of recycled asphalt mixtures with high recycling rate and improving workability. We started full-scale manufacturing and shipment from June 2012. In addition, it was also revealed that the foaming of the recycling agent added may also further decrease manufacturing temperature, improve workability, and enhance mixture properties. Currently, we are verifying the results of manufacturing experiments conducted at our plant. In the future, we plan to verify these effects in construction, and develop a manufacturing system for recycled asphalt mixtures with high recycling rates in the aim to improve the working environment and improving product quality.

REFERENCES

1) KJ Jenkins: Characterisation of Foamed Bitumen, 7th Conference on Asphalt Pavements for Southern Africa, 1999.9.
2) Japan Road Association: Handbook for Pavement Recycling (2010 edition).

Asphalt Pavements – Kim (Ed)
© 2014 Taylor & Francis Group, London, ISBN 978-1-138-02693-3

Workability and coatability of foamed Warm-Mix Asphalt

Fan Yin, Edith Arambula & David Newcomb
Texas A&M Transportation Institute, TX, USA

Amit Bhasin
The University of Texas at Austin, Austin, TX, USA

ABSTRACT: Foaming of asphalt binders has become the most popular method for producing Warm-Mix Asphalt (WMA) in the United States. Mixing cold water and hot binder results in an expansion of the binder, a reduction in binder viscosity, and improved workability of the mixture and better coating of the aggregates by the foamed binder. The objectives of this study are to develop laboratory test methods to determine workability and coatability of asphalt mixtures and to validate the improved workability and coatability of foamed WMA as compared to Hot-Mix Asphalt (HMA). In the study, the maximum shear stress obtained during compaction using a Superpave Gyratory Compactor (SGC) is proposed as workability parameter. For mixture coatability evaluation, a testing procedure based on aggregate absorption is used and a coating parameter, coatability index, is proposed. Foamed WMA with different binder sources and grades and various water contents as well as control HMA are produced and evaluated in the study. Test results indicate that there is an optimum foaming water content that produces foamed WMA with the best workability and coatability characteristics when compared not only to other foamed WMA but also to control HMA.

Keywords: warm-mix asphalt, foaming process, workability, coatability

1 INTRODUCTION

Economic, environmental, and engineering benefits have led to the rapid implementation and widespread use of Warm-Mix Asphalt (WMA). Currently, the most popular method for producing WMA is foaming asphalt binder with water. The foamed WMA can be produced by the injection of water, water-bearing mineral additives, or wet aggregates. In the most popular foaming process, small amounts of cold water are injected into a hot asphalt stream ranging from 320°F (160°C) to 360°F (182°C). The mixing of cold water and hot binder results in the formation of steam resulting in an expansion of binder volume, a subsequent reduction in binder viscosity, and therefore, an improved workability of the mixture and better coating of the aggregate by the foamed binder.

Workability of asphalt mixtures is a property that describes the ease with which the mixture can be placed, worked by hand, and compacted. It is a function of temperature, binder properties (e.g., viscosity, grade, polymer modification, etc.), aggregate properties (e.g. size, angularity, etc.), among other factors.

Coatability of asphalt mixtures is defined as the degree of coating of the aggregates by the asphalt binder. This parameter is important to the performance of asphalt mixtures, since well-coated aggregates are likely to have a stronger bond between the particle and the binder, and thus a better resistance to moisture damage and other distresses.

The objectives of this study are to:

- Develop laboratory test methods to measure workability and coatability of asphalt mixtures.

- Evaluate the effect of different binder types and foaming water contents on the workability and coatability of foamed asphalt mixture.
- Compare the workability and coatability of foamed WMA against HMA.

In this study, an analysis method is proposed to evaluate the workability of foamed WMA using Superpave Gyratory Compactor (SGC) compaction data (i.e., shear stress versus number of gyrations). The maximum shear stress is proposed as mixture workability parameter. A modified procedure based on the aggregate absorption method originally developed by Velasquez et al. [1] is used to measure mixture coatability. The coatability index is proposed as the mixture coating parameter.

2 LABORATORY TEST METHODS

2.1 *Workability*

A SGC was used in this study to prepare the asphalt mixtures, which was operated based on a "shear-compaction" principle [2]. During compaction, the loose mix particles reoriented under the vertical and shear pressure for a target number of gyrations (i.e., 300) to ensure that a maximum shear stress was achieved [3].

After sieving, the aggregates were combined into individual batches according to the volumetric mix design and pre-heated in the oven to the mixing temperature. The asphalt binders were heated in the oven for 2 to 3 hours prior to transfer to the laboratory foamer. The laboratory foamer (i.e., Wirtgen WLB 10S) was calibrated according to the manufacturer's recommendation. The pre-heated aggregate batch was introduced into the mixer bucket and the portable mixer was placed under the laboratory foamer, as shown in Figure 1. The specific amount of foamed binder was dispensed into the bucket mixer as it was running. The mixer was stopped after 60 seconds and the loose mix was placed back into the oven for two hours at 275°F (135°C) for HMA and 240°F (116°C) for foamed WMA to achieve the proper short-term aging [4].

The loose mix was divided into individual specimen size batches (4,700 g per batch) after the short-term aging and then compacted. During compaction, the shear stress was continually monitored and plotted for each gyration. As shown in Figure 2, compaction was stopped after a significant reduction in shear stress was observed, which usually occurred between 200 and 300 gyrations.

Figure 2 shows a typical curve of the shear stress versus number of SGC gyrations during compaction. As illustrated, the curve can be divided in three phases. In the first phase, the

Figure 1. WMA foaming process in the laboratory.

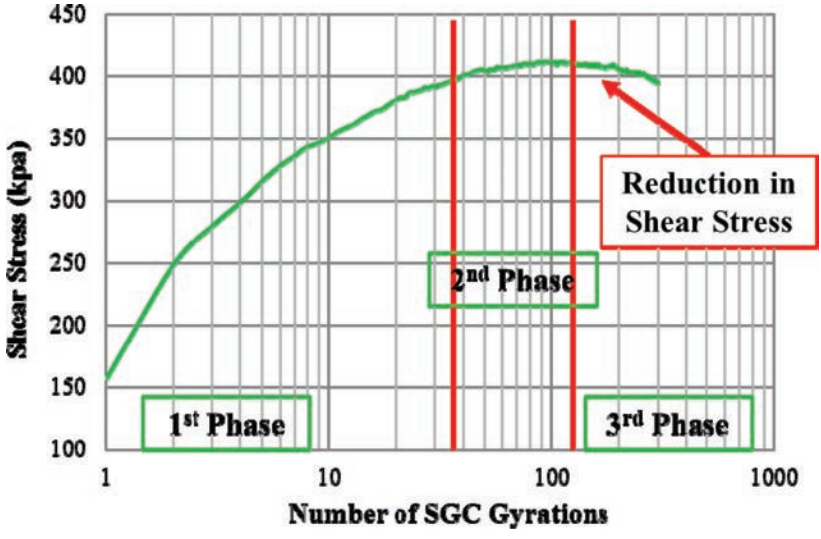

Figure 2. Typical shear stress vs. number of SGC gyrations curve showing the three phases of compaction.

slope of the shear stress curve is steep. The loose mix particles are being reoriented due to the initial compaction, and there is a significant increase in the internal friction within the mix due to the stone-on-stone contact resulting from loose mix particles reorientation. The shear stress starts to level off in the second phase. The density of the mix is expected to be near or at the target value somewhere in this phase. The third phase starts when a decrease in shear stress is observed. The reduction in shear stress is partially attributed to the dominant effect of pore pressure. For practical applications, the third phase in the compaction process should be avoided to prevent aggregate crushing after the maximum density is achieved.

According to Sombre et al., the shear stress versus SGC gyration curve can be used to determine the compaction characteristics of different asphalt mixtures [3]. Specifically, asphalt mixtures which compact more rapidly (steeper slope in loose mix height versus number of gyration curve) in the first few gyrations are expected to have a higher shear stress level afterwards, due to the increased internal friction within the mix. In addition, mixtures with a lower shear stress levels are expected to have better workability than those with a higher shear stress level. Therefore, maximum shear stress in the SGC compaction curve is proposed as the parameter to evaluate mixture workability.

2.2 *Coatability*

The method used in this study for determining the coatability of foamed WMA is primarily based on the aggregate absorption method originally developed by Velasquez et al. [1]. The method is based on the assumption that a completely coated aggregate has no access to water absorption when submerged in water for a short period (i.e., 1 hour), as water cannot penetrate through the asphalt film surrounding the aggregate surface. On the other hand, a partially coated aggregate is expected to have detectable water absorption, as water is able to penetrate and be absorbed by the uncoated particle. The following procedure was used to determine coatability of the asphalt mixtures.

After sieving, coarse aggregate fractions were combined into two individual batches (4,000 g per batch) following mix design, with one batch pre-heated in the oven at the mixing temperature while the other was stored at the room temperature. The amount of binder for the coarse aggregate fraction batch was determined based on the total binder content specified in the mix design and the surface area distribution of the coarse aggregate fraction.

The amount of binder for mixing with the 4,000 g coarse aggregate fraction batch was calculated using Equation 1:

$$W_b = 4{,}000 * \frac{P_b}{1 - P_b} * \frac{SA_{coarse}}{SST} * \frac{1}{P_{s-coarse}} \quad (1)$$

where:
W_b, amount of binder for mixing with a 4,000 g coarse aggregate batch (g)
P_b, optimum binder content from mix design (%)
SA_{coarse}, surface area of the combined coarse aggregates (m^2/kg)
SST, total surface area of mix design combined aggregates (m^2/kg)
$P_{s\text{-}coarse}$, percentage of coarse aggregates retained on 3/8 inch by the combined aggregates (%).

The same mixing and short-term aging procedure as those used in the workability evaluation were used to mix the coarse aggregate fraction batch with foamed binder and to short-term age the loose mix. The loose mix was taken out of the oven after short-term aging and cooled down to room temperature. The loose mix batch and the coarse aggregate fraction were each submerged under water for 1 hour. Afterwards, these two batches were damp-dried with a terry cloth to achieve the saturated Surface Dry (SSD) condition. The SSD weights of the loose mix batch and coarse aggregate fraction batch were recorded as $W_{loose\text{-}SSD}$ and $W_{agg\text{-}SSD}$, respectively. The water absorption for the loose mix batch and the coarse aggregate fraction batch using Equation 2 and Equation 3:

$$Abs\%_{loose} = \frac{W_{loose-SSD} - (4{,}000 + W_b)}{4{,}000 + W_b} * 100\% \quad (2)$$

$$Abs\%_{agg} = \frac{W_{agg-SSD} - 4{,}000}{4{,}000} * 100\% \quad (3)$$

The coatability index for the foamed asphalt mixture was calculated using Equation 4:

$$Coatability\ Index = \frac{Abs\%_{agg} - Abs\%_{loose}}{Abs\%_{agg}} * 100\% \quad (4)$$

Asphalt mixtures with a higher coatability index value are expected to have a better aggregate coating by the asphalt binder than those with a lower coatability index value. Therefore, coatability index is proposed as the parameter to evaluate mixture coatability.

3 EXPERIMENTAL DESIGN

A preliminary laboratory study conducted as part of the National Cooperative Highway Research Program (NCHRP) project 09-53 was performed to validate the workability and coatability test methods described in the previous section and compare the workability and coatability of foamed WMA against those of HMA. The experimental design for the study is shown in Table 1.

The materials used in the study correspond to a field project located on IH-25 in New Mexico. Three fractions of siliceous aggregates were combined following the mix design gradation shown in Figure 3. The optimum binder content by the weight of mix was 5.4%. For the coatability evaluation, the volumetrics for the coarse aggregate fraction were calculated based on the combined aggregate gradation and optimum binder contents from the mix design, as summarized in Table 2.

The Wirtgen WLB 10S laboratory foamer was used in this study to produce foamed WMA and control HMA, using an air-atomized foaming process. The temperature of the asphalt chamber in the foamer was at 320°F (160°C), and the air and water pressure were set to 72 psi

Table 1. Experimental design for workability and coatability evaluation.

Binder source	Mixture/foaming water contents			
	HMA/ 0%	Foamed WMA/1%	Foamed WMA/2%	Foamed WMA/3%
N64-22	X	X	X	X
O64-22	X	X	X	X
Y64-22	X	X	X	X
N70-22		X		
O70-22		X		

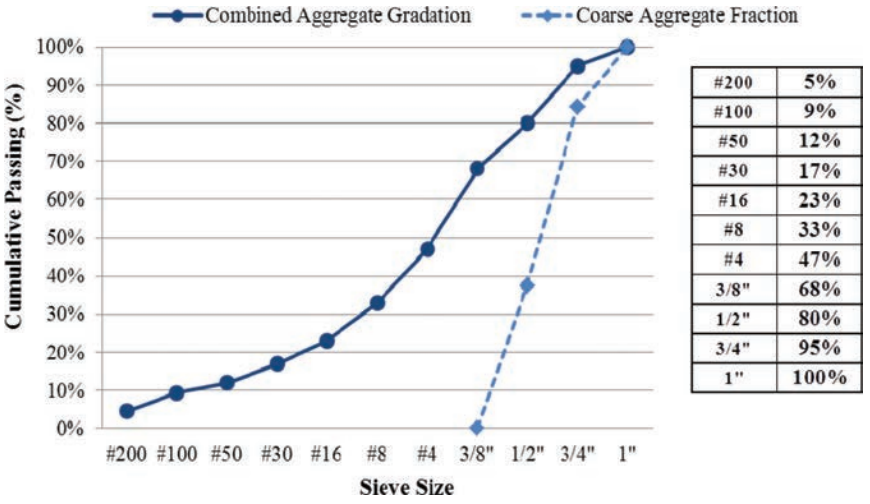

Figure 3. Design aggregate gradation for the New Mexico field project.

Table 2. Volumetrics calculation for New Mexico coarse aggregate fraction.

Volumetrics	Values	Reference
P_b	5.4 (%)	Mix design
SST	5.093 (m^2/kg)	Mix design & [5]
SA_{coarse}	0.410 (m^2/kg)	Mix design & [5]
W_b	57 (g)	Equation 1

per the manufacturer's recommendation. Foamed WMA using three neat binders, N64-22, O64-22, and Y64-22 were produced at three different foaming water contents, 1%, 2%, and 3%. To explore the foaming characteristics of polymer modified binders versus neat binders, foamed WMA with two polymer modified binders (N70-22 and O70-22) were also produced at 1% foaming water content, which was the optimum foaming water content providing foamed WMA with the neat binders with the best workability and coatability, as discussed in the following section. The workability and coatability comparison of those mixtures were used to validate the proposed methods.

In addition, the control HMA using the neat binders was also included in the study. The control mixtures were produced by the same laboratory foamer at 0% foaming water content. The production temperatures for foamed WMA and control HMA are summarized in Table 3.

Table 3. Summary of production temperatures for HMA and foamed WMA.

Foaming water contents	Mixing temperature	Short-term aging protocol	Compaction temperature
0% (HMA)	290°F (143°C)	2 hours at 275°F (135°C)	275°F (135°C)
1% (foamed WMA)	275°F (135°C)	2 hours at 240°F (116°C)	240°F (116°C)
2% (foamed WMA)	275°F (135°C)	2 hours at 240°F (116°C)	240°F (116°C)
3% (foamed WMA)	275°F (135°C)	2 hours at 240°F (116°C)	240°F (116°C)

The mixing temperature for the control HMA was determined based on the binder PG grade and foamed WMA production was at a temperature 25°F (8°C) lower than that for HMA. The comparison of workability and coatability by foamed WMA versus HMA was used to verify whether the foaming process produced WMA mixtures with better workability and coatability characteristics as compared to the control HMA.

4 RESULTS AND DISCUSSION

The workability and coatability results for the control HMA and the foamed WMA mixtures produced using three different neat binders at 1%, 2%, and 3% water contents are shown in Figures 4 and 5. In these figures, the control HMA results are compared against the foamed WMA values within each binder source. Each bar in Figure 4 represents the average value of two replicates and the error bars represent ± one standard deviation from the average value. Based on the span of the error bars, good repeatability for the workability test method was achieved.

A significant difference in workability (Fig. 4) and coatability (Fig. 5) was observed for the various foamed WMA mixtures and as compared to the control HMA for asphalt sources N and O. However, there was relatively little difference for source Y. Therefore, the workability and coatability test methods proposed in this study were validated as valid tools to capture the characteristics of the different mixtures depending upon the asphalt source.

As shown in Figures 4 and 5, foamed WMA mixtures employing N64-22 and O64-22 binders at 1% water content had better workability and coatability characteristics (indicated by a lower maximum shear stress and a higher coatability index) as compared to both the WMA mixtures foamed at higher water contents and the control HMA. This was true despite the fact that the production temperature for the WMA mixtures was approximately 30°F (17°C) lower than the production temperature for HMA. Therefore, a water content of 1% was optimum for these WMA foamed mixtures. Contrary to expectations, however, WMA mixtures foamed at higher water contents (i.e., 2% and 3%) yielded mixtures with equivalent or worse workability and coatability characteristics as compared to the control HMA.

A different workability and coatability trend is shown for mixtures employing the Y64-22 binder. These WMA mixtures had equivalent workability and coatability as compared to the control HMA despite of the amount of water used during foaming. Foaming measurements made outside the scope of this paper showed that this binder did not appreciably foam at any water content (i.e. 1% to 5%). The reduced foaming abilities of the Y64-22 binder are possibly due to the presence of an anti-foaming agent that is sometimes introduced during the crude refining or binder production process [6,7,8]. Further investigation in detecting possible anti-foaming agents in this particular binder using Fourier Transform Infrared Spectroscopy (FTIR) is currently ongoing.

As foamed WMA using N64-22 and O64-22 binders at 1% foaming water content had the best workability and coatability, foamed WMA using the polymer modified binders N70-22 and O70-22 were also produced at this water content. Workability and coatability results for foamed WMA using polymer modified versus neat binders are compared and summarized in Figures 6 and 7, respectively. As illustrated, better workability and coatability are shown for

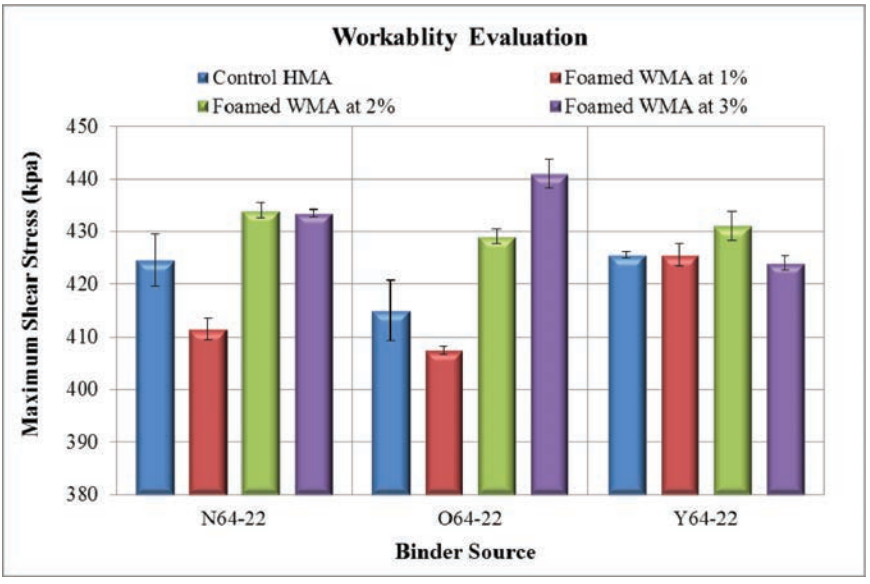

Figure 4. Workability test results for foamed WMA versus HMA.

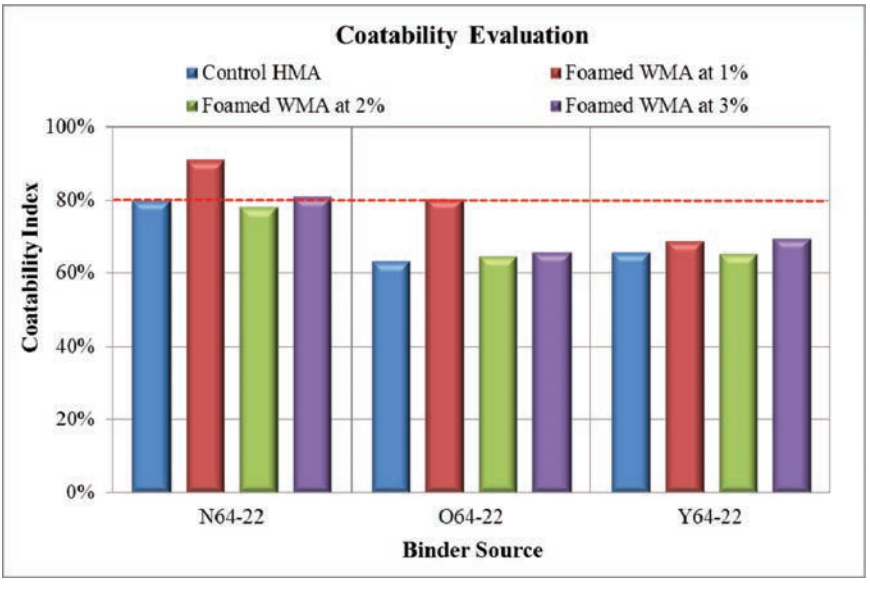

Figure 5. Coatability test results for foamed WMA versus HMA.

foamed WMA using neat binders than those using polymer modified binders. The reduced properties of foamed WMA using polymer modified binders are possibly attributed to the higher viscosity of the binder at the WMA production temperature, which was approximately 40°F (22°C) lower than the production temperature recommended by manufacturers. Thus, it may be advantageous to increase the production temperature for foamed polymer modified binders.

Additionally, the incorporation of polymer modifiers may have an effect on the binder foaming characteristics. Further investigation in workability and coatability of foamed WMA using polymer modified binders produced at higher temperatures is currently ongoing.

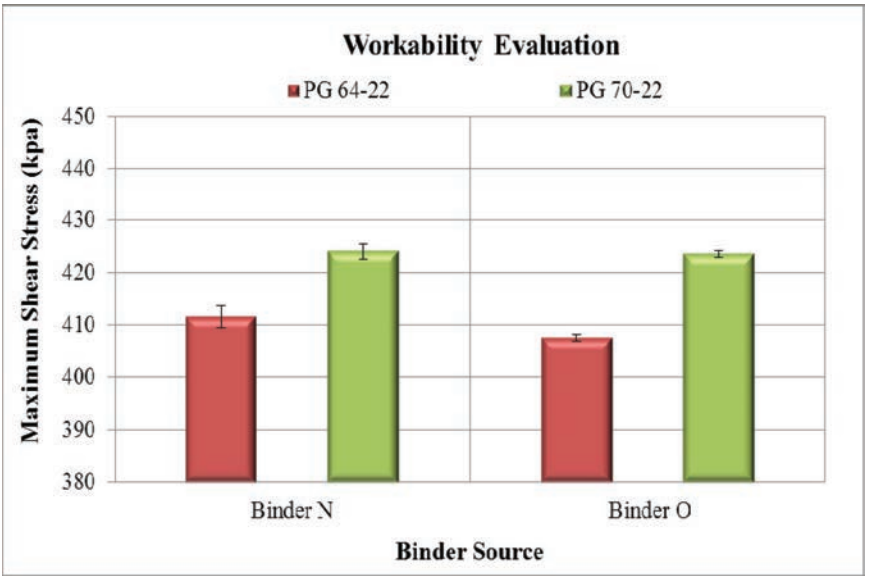

Figure 6. Workability test results for foamed WMA with neat versus polymer modified binder.

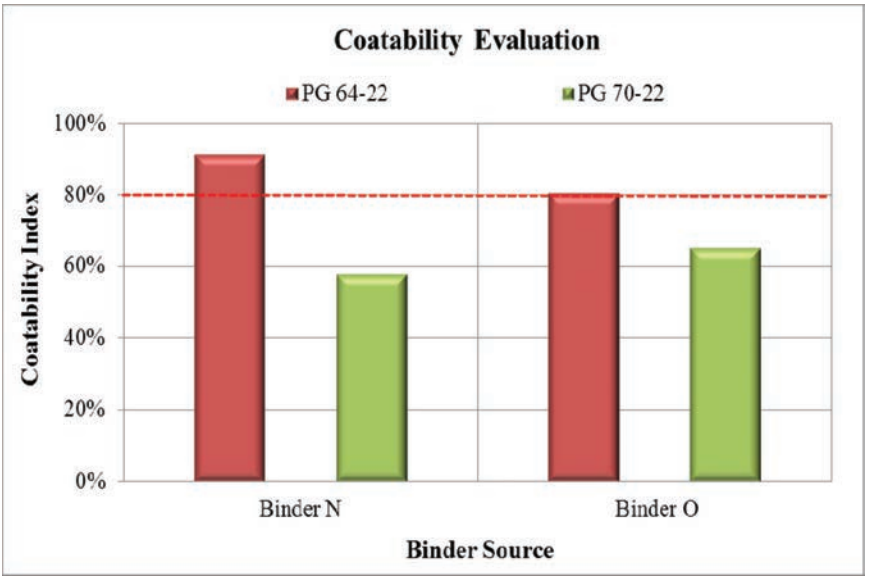

Figure 7. Coatability test results for foamed WMA with neat versus polymer modified binder.

5 CONCLUSIONS AND FUTURE WORK

Economic, environmental, and engineering benefits motivate the reduction of production and placement temperatures for asphalt concrete paving materials. The latest technology adopted for temperature reduction is WMA. The most popular method of producing WMA in the United States is by foaming the asphalt binder. The mixing of cold water and hot binder results in binder volume expansion, a subsequent reduction in binder viscosity, and

therefore, an improved workability of the mixture and better coating of the aggregates by the foamed binder.

In this study, test methods for evaluating mixture workability and coatability were developed using SGC compaction data and a modified aggregate absorption method, respectively. Maximum shear stress and coatability index were proposed as mixture workability and coatability parameters. For the coatability evaluation, only coarse aggregates retained on the 3/8 inch sieve are used. The relative difference in water absorption by the uncoated aggregates versus the loose mix is used to calculate the coatability index.

Foamed WMA using three different binders at three different foaming water contents were produced using a laboratory foamer. In addition, to validate the improved workability and coatability of foamed WMA, a control HMA mixture was also produced using the same laboratory foamer at 0% water content. The workability and coatability of the foamed WMA mixtures were compared against the characteristics of the HMA mixtures. In addition, the effect of binder source, binder grade and foaming water contents on mixture workability and coatability was investigated. The following conclusions were made based on the results of study:

1. Significant differences in the maximum shear stress and coatability index for foamed WMA mixtures versus the control HMA was observed for two of the three asphalts. Thus, the test methods proposed in this study seem promising in evaluating the workability and coatability of asphalt mixtures.
2. Foamed WMA mixtures produced with N64-22 and O64-22 binders had better workability and coatability when 1% foaming water content was used as compared to higher foaming water contents (i.e., 2% and 3%). Thus, for these two binders, 1% was considered the optimum foaming water content. However, equivalent workability and coatability was observed for the WMA mixtures that employed the Y64-22 binder as compared to the control HMA regardless of the foaming water content used. The possible presence of an anti-foaming agent in the Y64-22 binder is currently under investigation.
3. Comparison of foamed WMA versus control HMA mixtures showed that WMA produced at 1% foaming water content had better workability and coatability characteristics, despite the fact that the WMA mixtures were produced at temperatures approximately 30°F (17°C) lower than the control HMA. However, the WMA mixtures foamed at higher foaming water contents (i.e., 2% and 3%) had equivalent or worse characteristics as compared to the control HMA. This finding highlights the importance of identifying the best materials and foaming conditions to maximize the workability and coatability of foamed mixtures.
4. At WMA production temperatures, foamed WMA employing N64-22 and O64-22 had better workability and coatability as compared to those with N70-22 and O70-22. The higher viscosity of polymer modified binders is possibly attributed to the reduced mixture workability and coatability. Further investigation for foamed WMA using polymer modified binders produced at higher production temperature is currently undergoing.

For future work, it is recommended to explore the effect of foaming temperature and the presence of polymer in polymer modified binders on the workability and coatability characteristics of foamed WMA mixtures.

REFERENCES

[1] Velasquez, R., G. Cuciniello, D. Swiertz, R. Bonaquist, and H. Bahia, "Methods to Evaluate Aggregate Coating for Asphalt Mixtures Produced at WMA Temperatures." *Canadian Technical Asphalt Association (CTAA) Proceedings* (2010).

[2] Oy, I., "Operating Instructions Manual—Intensive Compaction Tester." Espoo, Finland (1995).

[3] Sombre, R.D., D.E. Newcomb, B. Chadbourn, and V. Voller, "Parameters to Define the Laboratory Compaction Temperature Range of Hot-Mix Asphalt." Journal of the Association of Asphalt Paving Technologies, Vol. 67 (1998).

[4] Yin, F., L. Garcia Cucalon, A. Epps Martin, E. Arambula, A. Chowdhury, and E.S. Park, "Laboratory Conditioning Protocols for Warm-Mix Asphalt." Journal of the Association of Asphalt Paving Technologies, Vol. 82 (2013) Forthcoming.
[5] Kandhal, P.S., K.Y. Foo, and R.B. Mallick, "A Critical Review of VMA Requirements in Superpave." NCAT Report No. 98-1 (1988).
[6] Abel, F., "Foamed Asphalt Base Stabilization." Proceedings. 6th Annual Asphalt Paving Seminar. Colorado State University. Loveland (1978).
[7] Fu, P., "Foamed Asphalt 101." http://foam101.info/Science/Asphalt.html Sustainable Transportation Center. University of California Davis. Accessed December 5, 2011.
[8] Kekevi, B., H. Barber, and H. Yildrim, "Synthesis and Characterization of Silicone-Based Surfactants as Anti-Foaming Agents." Journal of Surfactants and Detergents. pp. 1–9 (2011).

Asphalt Pavements – Kim (Ed)
© 2014 Taylor & Francis Group, London, ISBN 978-1-138-02693-3

Cleaner Warm-Mix Asphalt (CWMA) at macro level: Case study for the United States

Ali Jamshidi & Meor Othman Hamzah
School of Civil Engineering, Universiti Sains Malaysia—USM, Engineering Campus, Seberang Perai Selatan, Pulau Pinang, Malaysia

ABSTRACT: Although Warm-Mixture Asphalt (WMA) is a great step towards constructing a sustainable pavement, it is still a high energy-intensive technology. More energy-efficient WMA is required to fulfil stricter environmental regulations that might be prescribed by environmental policy makers in future. In this study, the effects of aggregate characteristics on WMA are evaluated in the terms of energy consumption and greenhouse gas (CO_2) emission on a large scale. The paper proposes a method of aggregate source selection to produce a Cleaner WMA (CWMA). The results showed that energy consumption and CO_2 emission of CWMA are lower than those of traditional WMA in the United States as a case study. The results also indicate that the amount of energy savings due to use of CWMA is sufficient to fuel 24,330 to 341,525 American households per annum, depending on aggregate type, source and asphalt type.

Keywords: Energy efficiency, greenhouse gas emission, sustainable infrastructures

1 INTRODUCTION

Asphalt mix production depends on energy resources in two ways: (1) energy required to produce asphalt binders in oil refineries; and (2) carbon-based energy carriers that are used as industrial fuels in asphalt mixing plants [1]. Moreover, energy demand is increasing consistently, and can be expected to do so in the future. For example, The United States Energy Administration (USEA) predicted that by the year 2020, total energy consumption from petroleum, natural gas, coal, electricity and renewable energy will increase by 32%, 33%, 62%, 22%, 45%, and 26% respectively [2]. Meanwhile, asphalt production was the second most energy-intensive manufacturing industry in the United States [3]. Therefore, it is necessary to quench the asphalt mix production's thirst for fossil fuels consumption with development of less energy-intensive construction technologies.

The two prevailing strategies by which the energy sectors in many countries are trying to cope with this problem are the following: searching for inexhaustible and non-polluting new energy sources and generating cleaner production of energy by the development of low-carbon technologies [4]. The challenges of the first strategy are clear: new infrastructure for the production and distribution of new energy sources needs to be constructed, while costs must decrease significantly. Even if new non-polluting energy sources are found, it will be many years before they can be produced on a large industrial scale. The second strategy affords energy producers to achieve results within a shorter period of time. The asphalt industry also needs to abide by environmental restrictions. Warm Mix Asphalt (WMA) technology is one of most important steps taken to reduce energy-intensive characteristics of the asphalt industries. However, it seems that the asphalt industries are thirstier than expected for more environmental-friendly technologies in pavement construction. Hence, new or more improved WMA additives should be developed to reduce the construction temperatures of asphalt mixture more than the current additives without sacrificing structural and functional

asphalt mix performances. Therefore, an extensive research infrastructure, including well-qualified human resource such as highly-educated and experienced researchers and pavement engineers, and well-equipped laboratories, are needed to develop such additives. Moreover, a plenty of raw materials and supporting infrastructures are necessary for mass production. For instance, in 2003 Sasol Wax invested $360 million to pipe natural gas from Mozambique to Sasolburg, South Africa, for the production of Sasobit® [5]. So, a great budget or a reliable line of credit should be provided to support this WMA additive project financially for field investigation and study from the cradle to the grave, such as development of initial version of an additive type, laboratory study of asphalt binder and mixture, long-term field investigation and recycling, as well as environmental impact studies. Under the shadow of this current financial crisis, it would not be free-risk investments for industrial owners and private sectors. Meanwhile, it is impossible to stop doing research on sustainability in asphalt industries. One solution is that the fundamental properties of asphalt mix material, aggregate and asphalt binders being evaluated in terms of energy intensive. For example, WMA technology reduces construction temperatures of asphalt mixes via various mechanisms; hence reduce fuel consumption and greenhouse gas emission. A question rises in the mind that it is possible to produce cleaner warm using current additives without any modification in WMA technology or not. To address this issue, Jamshidi et al. [1] proposed specific heat capacity coefficient of aggregate (C) as indicator of Environmental Polluting Parameter (EPP) in Superpave™ mix design method. In addition to consensus and source properties of aggregate, the Superpave™ will have parameter that enable pavement engineers, researchers and environmental policy makers to study environmental-friendliness of aggregate materials in the paving projects. More details were discussed by Jamshidi [6].

It should be noted that the effects of C of same aggregate type supplied from various sources can be different. It may affect the energy consumption and CO_2 emission in the asphalt mixing plants, specifically on a national scale.

2 MATERIAL AND METHODS

The asphalt binders used for this study were PG 64 and PG 76. Table 1 shows the rheological properties of the control asphalt binder (without WMA additives).

Two aggregate types, granite and limestone, were selected from 2 sources. Table 2 presents the properties of the aggregates in this study. Table 3 shows construction temperatures of hot and warm mixtures.

The amount of required heat energy, fuel requirement, and CO_2 emissions for a 10 km road length were computed using user-friendly computational software developed by Jamshidi [6], called EFEAS (Energy, Fuel and Emission Analyzing Software). Based on the mix design results, the optimum binder content is 5.0% while the corresponding mixture density was 2.38 g/cm^3. Therefore, the mass of mixture required to pave a 10-km dual carriageway with 3 lanes per direction, assuming lane width is 3.65 m and a 5-cm thick wearing course is 27,000 ton.

It is also supposed that the industrial fuel utilized in the asphalt mixing plants is natural gas. The ambient temperature of the environment was assumed to be 25°C. The outputs of

Table 1. Rheological properties of asphalt binders.

Asphalt binder				
Aging state	Test properties	PG 64 value		PG 76 value
Unaged	Viscosity at 135°C (mPa·s)	465.0		2587.5
(original state)	G*/sin (δ) at 64°C (kPa)	1.23	at 76°C (kPa)	1.51
Short-term-aged	G*/sin (δ) (kPa) at 64°C	2.68	at 76°C (kPa)	3.07
Long-term-aged	G*sin (δ) at 25°C (kPa)	2959		1650

Table 2. Aggregate properties at 25°C.

Aggregate type	Specific gravity (gr/cm^3)	Specific heat capacity (J/kg/°C)	Source
Granite	2.620	1188	1
	2.65	608	2
Limestone	2.770	880	1
	2.76	690	2

Table 3. Construction temperatures of WMA and HMA.

Mix type	Binder type	Construction temperature (°C)	
		Mixing	Construction
HMA	PG 64	160	150
WMA		145 and 130	135 and 120
HMA	PG 76	180	170
WMA		165 and 150	155 and 140

software are the energy and fuel requirements, and greenhouse gases, CO_2, CH_4 and N_2O, emitted to heat materials from ambient temperatures to the mixing points of the asphalt mixtures. Only CO_2 was considered in this study.

3 RESULTS AND DISCUSSION

Tables 4 and 5 show the required heat energy and natural gas to produce HMA and WMA for the assumed paving project. As expected the fuel requirements and CO_2 emissions for WMA production is less than those of HMA, irrespective of aggregate type, source and binder performance grade. For example, the WMA mixed at 130°C and incorporating granite aggregate supplied from source 1 and PG 64 binder requires 23.94% fuel lower than HMA produced using the same material type and source, as shown in Table 4.

Tables 4 and 5 also show the effects of aggregate source in terms of reduction percentages in the fuel requirements. Although the asphalt mixtures were produced using the same type of aggregate, fuel requirements and CO_2 emissions are significantly different. As an instance, WMA produced at 145°C using granite from source 1 requires 110,048 m^3 natural gas, while WMA produced at the same mixing temperature and containing granite from source 2 needs 58,220 m^3, which is 47.09% lower than source 1. It means that granite aggregate supplied from source 2 can be more sustainable as compared to those of source 1 due to lower specific heat capacity indicated in Table 2. Moreover, Tables 4 and 5 show that HMA containing aggregate from source 2, irrespective of aggregate type and binder types, requires less fuel as compared to WMA mixed at 145°C and 165°C for PG 64 and PG 76, respectively and containing aggregate from source 1. As an example, HMA produced using limestone from source 2 and PG 76 requires 93,156 m^3 natural gas as highlighted in grey, while 103,457 m^3 natural gas is needed to produce the WMA at 165°C using limestone from source 1, highlighted in yellow. Therefore, the HMA produced may be more sustainable than some WMA in terms of fuel consumption and CO_2 emissions.

The asphalt mixtures produced using aggregate with high specific heat capacity may meet many problems at various stages of the pavement life, including construction, utility and recycling as follow:

- More fuel is required to raise the temperature of aggregate from the ambient temperature to the mixing point, which translates to more emission and costs. Moreover, more time

Table 4. Heat energy and fuel requirements for production of HMA and WMA using PG 64.

Mix temperature (°C)	Mix type	Aggregate type	Aggregate source	Q_T[a] (TJ)	Fuel requirement (m^3)	CO_2 emission (kg)	Effects of WMA technology	Effects of aggregate source
							Reduction (%)	Reduction (%)
160	HMA	Granite	1	4.79	125,167	253,213	–	–
145	WMA			4.22	110,048	222,627	12.07	–
130				3.65	95,201	192,592	23.94	–
160	HMA		2	2.54	66,196	133,915	–	47.1139
145	WMA			2.23	58,220	117,779	12.06	47.0958
130				1.93	50,385	101,929	23.92	47.0751
160	HMA	Limestone	1	3.60	93,851	189,861	–	–
145	WMA			3.16	82,525	166,948	12.1	–
130				2.76	71,402	144,446	23.91	–
160	HMA		2	2.86	74,533	150,780	–	16.9863
145	WMA			2.51	65,548	132,604	12.05	16.9764
130				2.17	56,721	114,747	23.89	16.9665

[a]:Total required heat energy (Tera Joule) to raise the temperature of asphalt mix materials, including aggregate and asphalt binder, from 25°C to the mixing temperature; [b]:Difference in the fuel requirement between HMA and WMA; [c]:Difference in the fuel requirement between sources 1 and 2 2 and 3.

Table 5. Heat energy and fuel requirements for production of HMA and WMA using PG 76.

Mix temperature (°C)	Mix type	Aggregate type	Aggregate source	Q_T[a] (TJ)	Fuel requirement (m^3)	CO_2 emission (kg)	Effects of WMA technology	Effects of aggregate source
							Reduction (%)	Reduction (%)
180	HMA	Granite	1	5.82	152,137	307,773	–	–
165	WMA			5.21	136,053	275,235	10.51	–
150				4.60	120,225	243,215	20.86	–
180	HMA		2	3.19	83,444	168,807	–	45.1521
165	WMA			2.86	74,672	151,062	1051	45.1155
150				2.52	66,031	133,580	20.93	45.0771
180	HMA	Limestone	1	4.42	115,659	233,978	–	–
165	WMA			3.96	103,457	209,294	10.18	–
150				3.50	91,446	184,995	20.91	–
180	HMA		2	3.56	93,156	188,455	–	16.0159
165	WMA			3.19	83,350	168,617	10.57	15.999
150				2.82	73,693	149,081	20.97	15.9801

[a]:Total required heat energy (Tera Joule) to raise the temperature of asphalt mix materials, including aggregate and asphalt binder, from 25°C to the mixing temperature; [b]:Difference in the fuel requirement between HMA and WMA; [c]:Difference in the fuel requirement between sources 1 and 2.

is required to heat the aggregate in the asphalt mixing plants. Therefore, production time increase and efficiency of the mixing plants decrease.

- More mixing time is required that the asphalt mixture's temperature reaches to the equilibrium temperature (ambient temperature) after compaction. Therefore, it can delay to open the paved surfaces using such mixtures to traffic.
- The extra heat energy due to high specific heat capacity is absorbed by asphalt binder coated the aggregate particles, making asphalt binder more prone to aging. Hence, the

asphalt mixture containing aggregate with high specific heat capacity become brittle and failures, including alligator, and thermal cracklings, during the design life of the pavement. Therefore, the utility expenses of the asphalt pavement increase.

- Since the pavement is supposed as a statically indeterminate structure system and the heat energy distribute in the three dimensions, the extra heat creates internal-residual stresses and deformation in the pavement structure. The each individual deformation due to expansion creates extra stresses and strains that are not predicted during the asphalt mix design and the structural response evaluation in the test of the current asphalt mix. It can lead to accelerate development of cracking and decrease serviceability of the HMA and WMA pavement. It is obvious that the patterns of development and distribution of the cracks depend on many variables, such as asphalt mix materials, traffic loading and environmental factors.
- Meanwhile, a stiff asphalt mix material increases the required energy to the milling during recycling, increasing the fuel consumption, the emissions, and the operational costs, including the precipitation costs.

As a consequence, use of aggregate with high specific heat capacity to produce asphalt mixture can mean spending more money for lower quality, while more energy-efficient as well as high sustainability with a desired performance are required as a perfect pavement. In the other words, specific heat capacity can be considered as an important parameter to evaluate environmental impacts. Therefore, use of aggregate materials posses low specific heat capacity can be suggested as a strategy to select sustainable source of aggregate materials. It would be possible that the selected sustainable sources of the aggregate materials are located far from the asphalt mixing plants and paving projects. The haulage of the sustainable aggregate may increase total costs and emissions of asphalt mix production. The effects of transportation should be included in life cycle analysis of a paving project. Meanwhile, the long-term performance of asphalt mixes produced using low specific heat capacity is needed to study by field investigation. Even though no relationship was found between the specific heat capacity of aggregate and the engineering properties of HMA in terms of the resilient modulus, mix density, Marshall stability and flow [7, 8]. In addition, it is also necessary to study the profile of heat distribution at various depths of the HMA and WMA with compromising thermal diffusity after laying the mixtures as illustrated schematically in Figure 1. It can provide function of cooling rate over the time.

From Tables 4 and 5, it can be seen that mixtures containing granite and limestone from sources 2 require minimum heat energy and fuel. Therefore, an alternative to reduce the requirements of heat energy and fuel as well as CO_2 emission is by substituting the high specific heat capacity aggregate with aggregate possessing lower specific heat capacity. For instance, a fraction of granite aggregate with specific heat capacity of 1188 J/kg°C in mixture is suggested to be replaced by another granite aggregate with lower specific heat capacity, 608 J/kg°C. In other words, the optimum aggregate mixture is a blend of two aggregates from the same aggregate type but with different specific heat capacity values. This suggestion can be industrially feasible but the aggregate with lower specific heat capacity may be unavailable or expensive. Therefore, it may be economically impractical to replace the whole aggregate with those of lower specific heat capacity. Since the minimum specific heat capacity values were attributed to the aggregates extracted from source 2 for both granite and limestone, these sources are considered as the most environmentally friendly sources of substitutes, for

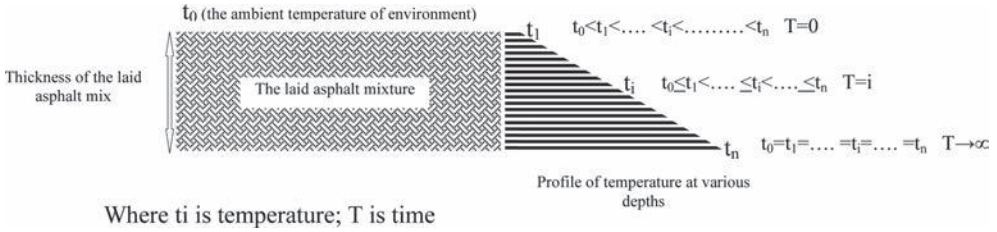

Figure 1. Schematic illustration of heat profile at various depths of the laid mixture.

Table 6. Aggregate blends incorporating aggregate with different C coefficients.

Asphalt mix code	Aggregate type	Percentage from source 1	Percentage from source 2
A	Granite	25	75
B		50	50
C		75	25
D	Lime stone	25	75
E		50	50
F		75	25

Table 7. Fuel requirement and CO_2 emission for heating aggregate and binder to produce of WMA and HMA using PG 64.

Asphalt mix code	Mix type	Mixing temperature	Fuel requirement	CO_2 emission (kg)
A	HMA	160	110,424	223,388
	WMA	145	97,091	196,415
		130	83,997	169,926
B	HMA	160	95,681	193,563
	WMA	145	84,134	170,203
		130	72,793	147,260
C	HMA	160	80,939	163,739
	WMA	145	71,177	143,991
		130	61,589	124,594
D	HMA	160	89,022	180091
	WMA	145	78,281	158363
		130	67,732	137021
E	HMA	160	84,192	170321
	WMA	145	74,037	149776
		130	64,062	129596
F	HMA	160	79,363	160550
	WMA	145	69,792	141189
		130	60,391	122171

a fraction of aggregates with high specific heat capacities. Table 6 shows different mixtures indicating blends of aggregate with lower specific heat capacity to produce more energy-efficient and Cleaner HMA (CHMA) as well as WMA (CWMA).

Tables 7 and 8 shows that the fuel requirement and CO_2 emissions of the asphalt mixture decreases as percentages of aggregate with low capacity increases, irrespective of aggregate and binder types as well as mixing temperature. As an example, HMA produced using granite aggregate from source 1 and PG 64 binder requires 125, 167 m^3 natural gas (under lined in Table 4), while the HMA produced using suggested the aggregate blend A or the aggregate blend containing 25% low specific heat capacity granite needs 110,424 m^3 natural gas at the same mixing temperature (underlined in Table 7). Another example, WMA produced using limestone supplied from source 1 and mixed at 145˚C requires 82,525 m^3 natural but the same WMA produced using 50% low specific heat capacity limestone requires (the aggregate blend E in Table 6) requires 74,037 m^3 natural gas (as shown in Table 7).

4 CASE STUDY: THE UNITED STATES

In the United States, transportation infrastructure investments account for 7% of the Gross Domestic Product (GDP) according to the National Asphalt Pavement Association [9].

Table 8. Fuel requirement and CO_2 emission for heating aggregate and binder to produce WMA and HMA using PG 76.

Asphalt mix code	Mix type	Mixing temperature	Fuel requirement	CO_2 emission (kg)
A	HMA	180	117,481	237,664
	WMA	165	103,527	209,435
		150	89,814	181,693
B	HMA	180	102,738	207,839
	WMA	165	90,571	183,225
		150	78,609	159,026
C	HMA	180	87,995	178,013
	WMA	165	77,613	157,011
		150	67,405	237,664
D	HMA	180	96,078	194,365
	WMA	165	84,718	171,384
		150	73,548	148,787
E	HMA	180	91,249	184,596
	WMA	165	80,473	162,796
		150	69,878	141,363
F	HMA	180	86,419	174,825
	WMA	165	76,229	154,211
		150	66,208	133,938

And, asphalt mixture is one of the most common materials used to construct pavements in transportation infrastructures, with almost 96% of hard-surfaced roads constructed using the material [10–12]. Meanwhile, approximately 500 million tons of asphalt mixtures are produced annually in the United States [13]. Therefore, the energy saving due to use of low specific heat capacity aggregate in the asphalt mix production can be significant. In this study, it was assumed that total aggregate and total asphalt binder mass are 475,000,000 tons ($0.95*500*10^6$) and 25,000,000 ton ($0.05*500*10^6$), respectively. Tables 9 and 10 show that heat energy and fuel requirements for HMA and WMA produced using various aggregate type and asphalt binders. It is obvious that PG 64 or PG 76 binder and one type aggregate from a given source are not used to produce the total asphalt mixture in the United States. It is just a simplifying to show the effects of high specific heat capacity of the aggregate on the asphalt industries on a large scale.

Although use of WMA technology reduces the fuel requirements, more sustainable WMA can be produced using low specific heat capacity aggregate on a national scale as presented in the Tables 9 and 10. For example, WMA produced at 145°C using PG 64 reduces the fuel requirement 23.94% as compared to HMA, while use of the granite aggregate with the low specific heat capacity decrease almost 47% for the both WMA and HMA without further technology and any modification in the current asphalt mixing plants. Moreover, use of the low specific heat capacity aggregate on national scale can be supposed as a strategy to reduce the share of the asphalt industries in the CO_2 production, hence the carbon tax of such industries reduce. It is obvious that all the mix production could not be WMA produced using PG 64 or PG 76 and aggregate types shown in Table 2. Moreover, all the asphalt mixing plants do not utilize the natural gas. It is emphasized that this study only tends to shows the effects of thermal properties of aggregate on the fuel requirement and CO_2 emission.

Meanwhile, the considerable reduction in the fuel requirements is even more interesting, in light of the fact that a 1% increase in the growth in the economy requires a 1.5% increase energy supply of a developing country, while crude oil production is declining at the rate of 4.5% per year[14]. A number of households that can be energized are computed based on the Annual Energy Consumption per Household (AECH). The amount of AECH is 107 GJ for the United States [15]. Figure 2 shows number of American households that can be fuelled using the proposed strategies.

Table 9. Heat energy and fuel requirements for production of HMA and WMA using PG 64 in the United States.

Mix temperature (°C)	Mix type	Aggregate type	Aggregate source	Q_T[a] (MJ)	Fuel requirement (m^3)	CO_2 emission (kg)	Effects of WMA technology	Effects of aggregate source
							Reduction (%)	Reduction (%)
160	HMA	Granite	1	88,780,577,487	2,317,904,624	4,689,121,055	–	–
145	WMA			78,056,473,133	2,037,917,134	4,122,706,362	12.07	–
130				67,525,969,627	1,762,984,221	3,566,517,080	23.94	–
160	HMA		2	47,000,000,000	1,380,239,984	2,479,885,254	–	47.06
145	WMA			41,300,000,000	1,213,845,182	2,181,106,796	12.10	47.08
130				35,700,000,000	1,050,386,119	1,887,561,543	24.01	47.13
160	HMA	Limestone	1	66,568,390,731	1,737,983,522	3,515,940,664	–	–
145	WMA			58,535,165,284	1,528,250,144	3,091,650,041	12.06	–
130				50,645,347,872	1,322,260,897	267,4933,795	23.91	–
160	HMA		2	52,900,000,000	1,380,239,984	2,792,225,488	–	20.53
145	WMA			46,500,000,000	1,213,845,182	2,455,608,803	12.09	20.56
130				40,200,000,000	1,050,386,119	2,124,931,119	24	20.62

[a]:Total required heat energy (Mega Joule) to raise the temperature of asphalt mix materials, including aggregate and asphalt binder, from 25°C to the mixing temperature; [b]:Difference in the fuel requirement between HMA and WMA; [c]:Difference in the fuel requirement between sources 1 and 2.

Table 10. Heat energy and fuel requirements for production of HMA and WMA using PG 76 in the United States.

Mix temperature (°C)	Mix type	Aggregate type	Aggregate source	Q_T[a] (MJ)	Fuel requirement (m^3)	CO_2 emission (kg)	Effects of WMA technology	Effects of aggregate source
							Reduction (%)	Reduction (%)
180	HMA	Granite	1	1.079E+11	2,817,367,333	5,699,534,115	–	–
165	WMA			9.65E+10	2,519,505,343	5,096,959,308	10.57	–
150				8.528E+10	2,226,398,921	4,504,005,018	20.97	–
180	HMA		2	59,186,809,656	1,545,263,431	3,126,067,922	–	45.15
165	WMA			52,964,807,670	1,382,817,910	2,797,440,632	10.51	45.11
150				46,836,026,318	1,222,806,216	2,473,736,974	20.86	45.07
180	HMA	Limestone	1	82,036,793,581	2,141,836,296	4,332,934,826	–	–
165	WMA			73,382,392,681	1,915,885,120	3,875,835,598	10.54	–
150				64,862,916,382	1,693,456,588	3,425,862,678	20.93	–
180	HMA		2	66,075,407,751	1,725,112,604	3,489,902,797	–	19.45
165	WMA			59,120,109,034	1,543,521,995	3,122,544,997	10.52	19.43
150				52,270,603,470	1,364,693,460	2,760,774,870	20.89	19.41

[a]:Total required heat energy (Mega Joule) to raise the temperature of asphalt mix materials, including aggregate and asphalt binder, from 25°C to the mixing temperature;
[b]:Difference in the fuel requirement between HMA and WMA; [c]:Difference in the fuel requirement between sources 1 and 2.

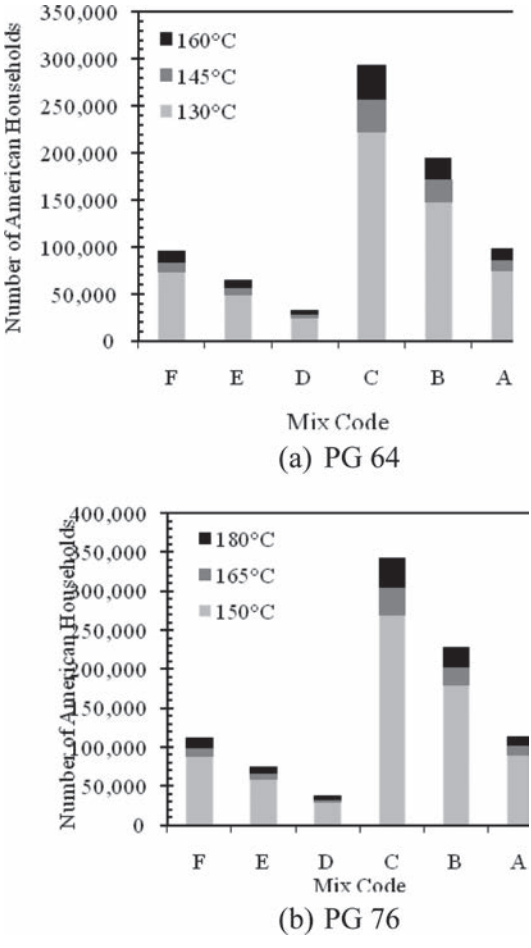

Figure 2. Number of American households that can be fuelled using the proposed strategies.

This can serve a sharp justification for environmental policy makers and energy planning experts to promote the development of WMA using less energy-intensive materials, such as aggregate materials with low-specific heat capacity on a large scale. Analysis of energy saving based on the provision of annual household energy would encourage asphalt industries to save more energy and subsequently reduces the energy cost in asphalt mixing plants, stimulates economic growth and conform to the Kyoto protocol limit on GHG emissions [6]. Therefore, it can be suggested a data bank of the aggregate sources can be developed based on the specific heat capacity to choose the sources of the aggregate materials with low specific heat capacity to produce CWMA and CHMA.

5 CONCLUSION

Although WMA technology reduce the fuel requirements and CO_2 emission via reduction of construction temperatures, selection of less energy-intensive aggregate materials can be led to produce cleaner warm and hot asphalt mixtures without modification of current technology of asphalt mixture construction in a paving projects. The asphalt mixtures produced using aggregate materials with the high specific heat capacity can have many problems for the asphalt mixtures from the cradle to the grave. Moreover, amount of fuel

saving and CO_2 reduction due to use of the low specific heat capacity can be more promising when they were analyzed on national scale in terms of number of American household can be fuelled using the energy saving. The results showed that energy savings due to use of the low specific heat capacity aggregate was enough to fuel 24,330 to 341,525 American households per annum, depending on aggregate type, source and asphalt type, based on the current standard of the life.

However, long-term performance, the costs and environmental impacts of the transportation of the aggregates with the low specific heat capacity to produce CHMA and CWMA should be included in the life cycle analysis of the paving projects to ensure that use of such aggregates is consistent with standards prescribed to construct the sustainable pavements.

REFERENCES

[1] Jamshidi A. Hamzah M.O. and You Z. Performance of warm mix asphalt containing Sasobit®: state-of-the-art, Journal of Construction and Building Materials, 38, pp. 530–53. 2013.
[2] USEA, 2004. Toward a National Energy Policy. United States Energy Administration.
[3] Zapata P. and Gambatese J.A. Energy consumption of asphalt and reinforced concrete pavement materials and construction, Journal Infrastructure System (ASCE), 11(1), pp. 9–20. 2005.
[4] Jamshidi A. Hamzah M.O. and Aman M.Y. Effects of Sasobit® content on the rheological characteristics of unaged and aged asphalt binders at high and intermediate temperatures, Journal of Materials Research, 15(4), pp. 628–38. 2012.
[5] Aurilio V. and Michael L.L. Sasobit®-warm mix asphalt technology: Victoria Street Trial in the city of Ottawa. In: Proceedings of the 53rd annual conference of the Canadian Technical Asphalt Association (CTAA). Saskatoon Saskatchewan, Canada, pp. 249–265. 2008.
[6] Jamshidi A. Rheological properties of asphalt binders, performance and sustainability of warm asphalt mixtures incorporating Sasobit®, Universiti Sains Malaysia (USM), PhD thesis; 2013.
[7] Luca J. and Mrawira D. New measurement of thermal properties of Superpave™ asphalt concrete, Journal of Materials in Civil Engineering, 17(1), pp. 72–79. 2005.
[8] Mrawira D.M. and Luca J. Effect of aggregate type, gradation, and compaction level on thermal properties of hot-mix asphalts. Canadian Journal Civil Engineering, 33(11), pp.1410–1417. 2006.
[9] NAPA. National asphalt roadmap: a commitment to the future. Lanham, MD: National Asphalt Pavement Association; 2007.
[10] Roberts F.L. Mohammad L.N. and Wang L.B. History of hot mix asphalt mixture design in the United States, Journal of Materials in Civil Engineering, 14(4), pp. 279–293. 2002.
[11] Kim, R.Y. Modelling of asphalt concrete, p.460, McGraw-Hill, United States. 2009.
[12] Druta C. Wang L. and Zhu T. Laboratory investigation of reclaimed asphalt pavement mixed with pure binder using X-Ray CT scanner, 9th International Conference of Chinese Transportation Professionals (ICCTP), Harbin, China. pp. 1–10. 2009.
[13] Keches, C. and LeBlank, A. Reducing greenhouse gas emissions from asphalt materials. Worcester Polytechnic Institute, the United States. 2007.
[14] Armstrong F.A. and Blundell K.M. Energy beyond oil, p. 240. Oxford University Press. United Kingdom. 2007.
[15] Zhang Q. Residential Energy consumption In China and its comparison with Japan, Canada and USA. Energy and buildings, 36(12), pp. 1217–1225. 2004.

This page intentionally left blank

Innovative pavement analysis and design—I

This page intentionally left blank

Asphalt Pavements – Kim (Ed)
© 2014 Taylor & Francis Group, London, ISBN 978-1-138-02693-3

Retrofitted fully permeable shoulders as a stormwater management strategy on highways

David Jones, Hui Li & John Harvey
University of California Pavement Research Center, Davis, CA, USA

ABSTRACT: This paper summarizes the results of laboratory testing, computer performance modeling, and life-cycle cost analysis of fully permeable shoulder retrofits as a stormwater management strategy for highways. The use of these types of pavement is being considered as a potential best management practice for managing stormwater in a number of states. The deliverables from this research are a preliminary design procedure and an example set of catalogue-type design tables that can be used to design pilot and experimental fully permeable pavement test sections. The results obtained from the analyses in this study indicate that fully permeable pavements could be a cost-effective stormwater best management practice alternative as a shoulder retrofit on highways, as well as for maintenance yards, parking lots, and other areas with slow moving truck traffic. However, these results need to be validated in controlled experimental test sections and pilot studies before wider-scale implementation is considered. The findings from these full-scale experiments will be used to identify situations where fully permeable pavements are an appropriate best management practice, validate and refine the design method, undertake detailed life-cycle cost and environmental life-cycle assessments, and to prepare guideline documentation for the design and construction of fully permeable pavements.

Keywords: Fully permeable pavements, stormwater management, shoulder retrofit

1 INTRODUCTION

Fully permeable pavements are defined for the purposes of this study as those in which all layers are intended to be permeable and the pavement structure serves as a reservoir to store water during storm periods in order to minimize the adverse effects of stormwater runoff.

Since the late 1970s, a variety of fully permeable pavement projects have been constructed in a number of U.S. states for low traffic areas and light vehicles. Most of the information available in the literature is about successes *[1]*, while few failures have been reported for these applications. Observations of several projects by the authors indicate that failures have occurred in localized areas due to clogging of the permeable surface, and to construction processes that have resulted in severe raveling (loss of particles from the surface) or cracking. Structural design methods have been empirical in nature, with little or no long-term monitoring data to support the empiricism. Purely empirical design methods require good comprehensive empirical data for all of the expected design conditions, which has limited the speed of technology development for fully permeable pavements because of the high cost of learning from inevitable failures. For this reason it is difficult for purely empirical design methods to consider different materials, climates, subgrades, and structural cross sections because of the need for a large factorial set of performance data that considers all of these design variable permutations. A review of design practice across the United States *[2]* shows the very limited scope of current applications for fully permeable pavements, even by the leading design firms specializing in this type of design. The limited scope of current applications is also reflected in the recently produced National Asphalt Pavement Association

(NAPA) *[3]*, American Concrete Pavement Association *[4]*, and Interlocking Concrete Pavement Institute *[5]* manuals for design of porous asphalt, pervious concrete pavements, and permeable interlocking concrete pavements, respectively.

2 PROJECT OBJECTIVES

The study discussed in this paper was part of a larger development program being undertaken by the University of California Pavement Research Center (UCPRC) for the California Department of Transportation (Caltrans), with the objective of developing guidelines and inputs for specification language, for the appropriate use of fully permeable pavements as a potential Best Management Practice (BMP) for controlling stormwater runoff from highways, maintenance yards, rest stops, and other pavements that Caltrans owns and manages. This objective would be met after completion of laboratory testing to characterize the mechanical and hydrological properties of fully permeable pavement materials; structural and hydrological performance modeling to develop initial designs; life-cycle cost analyses and environmental life-cycle assessment studies; and full-scale testing in the field and/or using accelerated load testing (using the Caltrans Heavy Vehicle Simulator [HVS]) to validate the structural and hydrological designs, or if necessary, to calibrate them to match the observed field performance. This paper covers the materials characterization and structural performance modeling components of the first phase of the study completed prior to full-scale testing. The hydrological performance modeling is discussed elsewhere in the literature *[6,7]*.

3 MATERIALS CHARACTERIZATION

3.1 *Subgrade materials*

On most pavements, subgrade materials are usually compacted as densely as possible to provide a platform for the overlying pavement layers and to provide added structural integrity to the pavement. However, on fully permeable pavements, compaction of the subgrade is generally restricted where possible to facilitate infiltration of water. This requires a thicker overlying pavement structure to compensate for the reduced subgrade strength. In this study, testing of subgrade materials focused on the influence of different levels of compaction and different moisture contents on the stiffness of those materials.

Initial studies of the properties of clays in California revealed that there is little difference in the strength and permeability characteristics of these materials. Consequently, only one clay and one silt material were tested. The testing of CH clay was considered unnecessary given the known poor bearing capacity and permeability characteristics of these materials, and the unlikelihood that a fully permeable pavement would be constructed on this type of material. Sand and gravel subgrades were also not included because they are expected to perform well in terms of both structural capacity and permeability, and are not as sensitive to the saturation levels expected in permeable pavements in California. A broad range of moisture contents and compaction levels were assessed. Tests on subgrade materials included standard indicator tests as well as permeability, resilient modulus (AASHTO T-307) and repeated load triaxial tests.

Test results *[8]* indicated that both soil types would add very little support to a pavement structure, and that the stiffness and the associated strength of the materials would decrease significantly as the moisture content increases. Any fully permeable pavement structure on these materials would need to compensate for this poor bearing capacity with thicker base and surfacing layers. Testing was not undertaken in the saturated condition given the already poor performance recorded at compaction moisture contents, and the difficulty in preparing specimens for testing (i.e. specimens "failed" before the test could be started).

3.2 *Permeable concrete subbase materials*

This phase of testing was included to determine whether an "inverted pavement design" approach would be suitable for fully permeable pavements. A stiff subbase would theoretically compensate for the loss of structural stiffness resulting from not compacting the subgrade and provide a stiff platform to confine the base course materials. It might also reduce the overall thickness of the pavement. Testing was limited to compressive strength only (ASTM C-35). Fatigue resistance and flexural strength testing were not undertaken given that cracks in this lower pavement layer would not significantly influence the pavement performance, and would actually improve the flow of water through the structure.

As expected, test results indicated a clear relationship between aggregate grading, cement content, water-to-cement ratio, and strength and permeability *[8]*. All specimens tested exceeded the anticipated permeability requirements, indicating that aggregate gradings and cement contents could be adjusted to increase the strength of the material whilst still retaining adequate water flow through the pavement. The water-to-cement ratio appeared to be critical, as expected, in ensuring good constructability and subsequent performance of the pavement.

3.3 *Base course materials*

The testing of fully permeable base course materials focused on four commercially available aggregates in the state with different geological origins. Performance of these materials was then compared with the results obtained by other researchers elsewhere in the United States. The aggregate gradations of three of the aggregate sources used smaller stone than is currently recommended by the National Asphalt Paving Association's (NAPA) permeable pavement guidelines. Discussions with northern California aggregate producers revealed that the larger stone gradations (approximately 38 mm to 50 mm maximum aggregate size) in the guidelines are generally not widely commercially available in California or are much more expensive to produce than products with a maximum aggregate size of approximately 19 mm to 25 mm. Tests on base course materials included standard indicator, permeability, and resilient modulus tests (AASHTO T-307).

Test results *[8]* on the different commercially available permeable base-course aggregates indicated that these materials would probably provide sufficient support for typical traffic loads in parking lots, basic access streets and driveways, and on highway shoulders, whilst serving as a reservoir layer for the pavement structure. Although three of the four materials tested had smaller maximum aggregate sizes than those typically discussed in the literature, the permeability was still adequate for California rainfall events.

3.4 *Asphalt wearing course materials*

A total of 19 mixes, including a dense-graded control, were assessed. Limited testing was carried out on a European mix, specimens of which were provided to UCPRC from a test track in Spain. These 19 mixes included five different binders and three different aggregates. A range of aggregate sizes, gradations, and air-void contents were covered in the mixes. Tests included standard indicator tests, permeability (ASTM PS129), flexural stiffness and fatigue resistance (AASHTO T-321), rutting resistance (AASHTO T-320), moisture sensitivity (AASHTO T-324) and raveling resistance (ASTM D7064).

Test results *[8]* indicated that the aggregate particle size distribution in the mix and the binder type will be the two most critical factors in designing permeable asphalt concrete wearing courses. Sufficient permeability for anticipated needs in California *[9]* was obtained on a range of mixes tested. Adequate resistance to rutting of the surface material appeared to be mostly a problem for the 9.5 mm mixes with conventional and rubberized binders, based on shear modulus. The 9.5 mm rubberized asphalt and 12.5 mm Georgia-gradation mixes had better rutting resistance in the Hamburg Wheel Tracking Test (which also considered moisture sensitivity), in particular the 12.5 mm mix containing polymers and fibers. Some moisture sensitivity was evident, but this could be overcome by the use of appropriate

anti-strip treatments. Most of the mixes of interest had adequate durability (resistance to raveling) compared to the dense-graded control. Fatigue cracking resistance at a given strain was better for the 9.5 mm rubberized and 12.5 mm polymer-modified mixes compared with the conventional mixes at a given strain. The polymer-modified 12.5 mm mix was stiffest at higher temperatures and under slower traffic (lower frequency of loading), while the conventional 9.5 mm mix had similar stiffness to the 12.5 mm mix at lower temperatures and under faster traffic. The rubberized 9.5 mm mix generally had lower stiffness than the other two mixes.

4 PERFORMANCE MODELING

A mechanistic-empirical design approach was used to evaluate a range of permeable pavements to produce a set of designs for different truck traffic, climate, and soil conditions. A full factorial considering asphalt material types, layer thickness, material properties, climate zone, season, diurnal peak temperature, axle type, axle load, traffic speed, and traffic volume resulted in a total of 15,552 different cases being run *[1,10,11]*. The results of the analyses were used to produce a catalog of designs, similar to the catalog designs prepared by the UCPRC for the Caltrans Rigid Pavement Design Catalog currently used in the Caltrans *Highway Design Manual (HDM)*.

All calculations considered two subbase options, namely no subbase and a 150 mm thick open-graded portland cement concrete subbase to provide support to the granular layer, and help protect the saturated subgrade. Material properties for each of the layers were obtained from the laboratory study. Three types of open-graded asphalt were considered in the calculations. Climate details were obtained from a database of California climatic data, and the temperatures at one-third of the depth of the asphalt layer were calculated from 30 years of data (1961 to 1990) using the *Enhanced Integrated Climate Model (EICM)*. The maximum, minimum, and average of the 30-year temperatures at one-third depth at each hour in each day for January, April and July were calculated. The maximum and minimum of the average day for each of those three months were chosen as the day and night temperatures, respectively for layer elastic theory calculations.

Axle loads were obtained from a database of California Weigh-In-Motion (WIM) stations. The allowable truck traffic (ESAL or Traffic Index) during the design life was calculated using a set of factors, including seasonal factor, day/night factor, axle type factor, ESAL factor (the average ESALs per axle), and load bin factor (percent of total axles in each load range). The value for each factor was determined based on the statistical analysis of statewide traffic information from the UCPRC/Caltrans WIM database. Axle loads less than half the legal load were ignored in order to keep the number of required calculations to an acceptable value, which was considered reasonable since they contribute very little to fatigue damage.

Two truck traffic speeds (7 and 40 km/h) were included in the calculations. The slower speed was selected to represent truck operations during traffic congestion on highways (in this case a detour onto the shoulder) and in maintenance yards or parking areas. The faster speed was selected to represent truck operations on a street or on a shoulder which has had traffic diverted on to it but which is not severely congested.

The stiffness at one-third thickness of the asphalt was calculated from the master curves for each combination of temperature and load frequency corresponding to loading time from flexural beam frequency sweep testing during the laboratory study. The stiffness of each type of asphalt material was averaged for the thickness of each layer to reduce the number of calculation combinations. Consequently, the stiffness of the asphalt used in the calculations was independent of the thickness of the layer.

The distresses analyzed included fatigue cracking of the asphalt layer associated with the tensile strain at the bottom of the asphalt layer, and unbound layer rutting associated with the vertical stresses at the top of the base, subbase (where included) and subgrade. Mechanical responses in terms of the tensile strains from different load configurations were determined using the layer elastic model in the *LEAP* software package *[12]*. Prior to the layer elastic

analysis, the stiffness of the granular base was evaluated using non-linear elastic models in the *GT-Pave* software package *[13]*. A range of values for different structural factors were selected for the structural response values of the granular base stiffness. The Uzan model *[14]* was used to consider the non-linear behavior of the granular base using *GT-Pave.* The procedure proposed by Tutumuller and Thompson *[15]* was used to obtain cross-anisotropic parameters of the granular base for *GT-Pave*. Based on the results of these calculations, three representative values of granular base stiffness, namely 60 MPa, 90 MPa, and 120 MPa, were chosen for the final structural calculations.

These data were then used as input in a Miner's Law equation to calculate the fatigue performance of the asphalt in terms of an allowable traffic index *[1,10]*. The actual repetitions to failure were calculated using this equation to determine the number of ESALs (later converted to Traffic Index) for each combination of asphalt type, thickness, and climate region.

5 PROPOSED STRUCTURAL DESIGN PROCEDURE

A preliminary catalogue-type design procedure based on region (rainfall), storm event design period, design, traffic, design truck speed, surfacing, subbase type, and the shear stress-to-shear strength ratio at the top of the subgrade was developed for preliminary design of fully permeable pavement test sections in California. Example design tables *[1]* were prepared from the computer modeling cases and calculations run as part of the computer modeling task described above. The example hydraulic design table includes 2-year, 50-year, and 100-year storm design events (considering infiltration and draw down for full storm duration and repeat storm events) for three California regions (north coast, Central Valley, and Los Angeles Basin). These three storm design events were selected to test the sensitivity of the design to a wide range of events (e.g., effect of storm intensity, storm duration, geometry, draw down, and degree of clogging on infiltration) and were not necessarily intended to be representative of typical Caltrans storm event design procedures. Example design tables for the asphalt concrete include three different open-graded mix designs (conventional 9.5 mm, 9.5 mm asphalt rubber, and 12.5 mm polymer modified), two truck speeds (7 km/h and 40 km/h), and two subbase options (no subbase and PCC-O subbase). All example tables assume a shoulder width of 3.0 m and cover designs up to a Traffic Index of 18 (~300 million ESALs). The shoulder is considered as a lane for drainage design purposes. The design tables have **not** been validated in full-scale experiments and are currently only intended for the design of experimental test sections. The proposed procedure generally entails the following:

1. **Select the permeability of the subgrade, subbase type, region, storm design event period, and number of lanes drained.** This information is used to determine the thickness of the gravel base/reservoir layer in terms of hydraulic performance. Consideration should be given to whether occasional overflows are permitted (e.g., during a series of heavy storms on consecutive days, prolonged rainfall, etc.) or not, as this will influence the choice of storm design period and dictate the thickness of the base/reservoir layer. Permeability should be measured for each project at a range of depths around the expected depth of the top of the subgrade after excavation of material for the reservoir layer(s). The lowest permeability should be used in the design. It should be noted that clay lenses between silt layers are common in the Central Valley of California, and these will influence permeability.
2. **Select the surface type.** Base thickness, design traffic, and design speed are used to identify the thickness of the HMA layer. Once the HMA layer thickness has been determined, this and base thickness are used to determine whether the shear stress-to-shear strength ratio at the top of the subgrade is adequate to prevent permanent deformation in the subgrade.

The design method assumes that water should only reach the top of the granular base layer for the design storm, and not be stored in the surface layer during the infiltration period, in order to improve the durability of the surface material.

The preliminary tables can be used for designs of test sections for both shoulder retrofit of highways and for parking lots, maintenance yards, and similar facilities. Two typical cross sections for shoulder retrofits were developed (one shown in Fig. 1) and two contractors asked to review them in terms of constructability. Both contractors indicated that construction appeared to be feasible and that they would be comfortable to bid on projects with similar designs. The selection of the most appropriate structure will depend on whether the existing pavement structure can maintain a vertical cut face equal to the height of the fully permeable pavement shoulder structure or not. A drain between the existing travelled way and the new fully permeable shoulder will need to be installed to allow any water in the travelled way to drain away from the road, while not allowing any water from the permeable area to flow into the pavement structure. An impermeable composite liner is included in the diagrams to prevent water flowing sideways from the reservoir layer and causing a slip failure in the embankment. The inclusion of this liner will be project dependent and not always required.

5.1 *Example*

An example design for a rubberized open-graded asphalt shoulder retrofit with no subbase to a three lane highway in Sacramento, CA is discussed below. The project design includes compacted subgrade permeability of 10^{-4} cm/s, a storm design of 50 years, design traffic index of 13 (~22 million ESALs), design truck speed of 7 km/h (due to congestion), and a surface layer of 9.5 mm Nominal Maximum Aggregate Size (NMAS) open-graded Rubberized Hot-Mix Asphalt (RHMA-O).

- **Step 1: Choose the base thickness based on hydraulic performance.**
  Using the appropriate table (Table 1 [Table B.1 in Appendix B in Reference 1]), the minimum thickness of granular base is selected for a subgrade soil permeability of 10^{-4} cm/s and 50-year design storm in the Sacramento region. These variables require a minimum

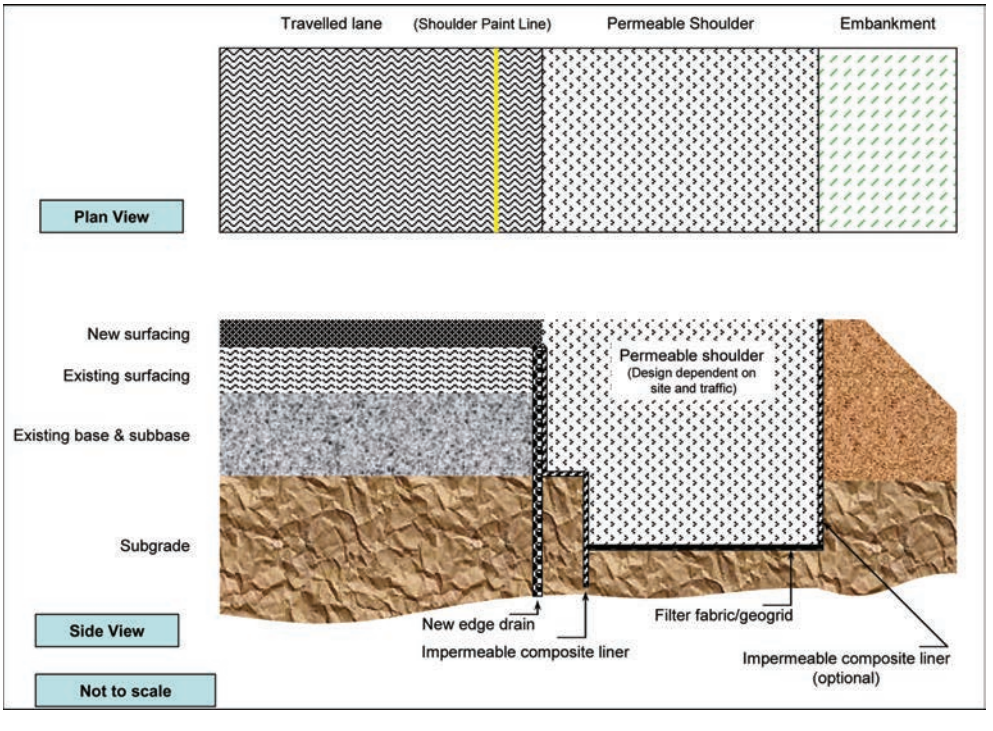

Figure 1. Example fully permeable pavement shoulder retrofit.
(Permeable shoulder placed against pavement layers with fabric separator).

Table 1. Preliminary granular base thickness based on hydraulic performance simulations.

Subgrade soil permeability (cm/s)[1]	Storm design (years) (Full storm duration)	Rainfall Region											
		Sacramento (Sac)				Riverside (LA)				Eureka			
		Thickness of Granular Base + PCC-O Subbase (mm)				Thickness of Granular Base + PCC-O Subbase (mm)				Thickness of Granular Base + PCC-O Subbase (mm)			
		Number of highway lanes[2]				Number of highway lanes[2]				Number of highway lanes[2]			
		2	3	4	5	2	3	4	5	2	3	4	5
1.00E-05	2	270	450	600	700	270	400	480	680	600	900	1270	1570
1.00E-04		130	180	250	420	130	150	320	400	350	650	850	1200
1.00E-03		130	130	130	130	130	130	130	130	130	130	130	150
1.00E-05	50	480	700	1050	1250	580	860	1180	1600	800	1270	1720	2150
1.00E-04		190	420	680	950	360	700	950	1350	500	850	1300	1770
1.00E-03		130	130	130	130	130	130	130	230	130	130	220	500
1.00E-05	100	600	800	1150	1430	680	1050	1300	1800	1150	1720	2300	2900
1.00E-04		210	500	750	1070	400	850	1200	1450	830	1300	1890	2500
1.00E-03		130	130	130	150	130	130	150	320	130	220	650	950

[1] Note that draw down times will vary significantly and are dependent primarily on subgrade soil permeabilities, but also on other factors such as number of lanes drained, storm recurrence interval, etc as well. Draw down times could vary between one hour for subgrades with a permeability of 1.00E-03 to several months for subgrades with a permeability of 1.00E-05 and higher. Refer to Reference 4 for discussion on the calculation of drain down times.

[2] The number of highway lanes must include the shoulder. Shoulder width is 10 ft. (3.0 m).

Table 2. Design chart for selecting RHMA-O thickness.

HMA Layer Thickness (mm)	Granular Base (GB) Layer Thickness (mm)																					
	500	550	600	650	700	750	800	850	900	950	1000	1050	1100	1150	1200	1250	1300	1350	1400	1450	1500
200	7.0	7.0	7.0	7.0	7.0	7.0	7.0	7.0	7.0	7.0	7.0	7.0	7.0	7.0	7.0	7.0	7.0	7.0	7.0	7.0	7.0
215	7.5	7.5	7.5	7.5	7.5	7.5	7.5	7.5	7.5	7.5	7.5	7.5	7.5	7.5	7.5	7.5	7.5	7.5	7.5	7.5	7.5
230	8.0	8.0	8.0	8.0	8.0	8.0	8.0	8.0	8.0	8.0	8.0	8.0	8.0	8.0	8.0	8.0	8.0	8.0	8.0	8.0	8.0
245	8.5	8.5	8.5	8.5	8.5	8.5	8.5	8.5	8.5	8.5	8.5	8.5	8.5	8.5	8.5	8.5	8.5	8.5	8.5	8.5	8.5
260	9.0	9.0	9.0	9.0	9.0	9.0	9.0	9.0	9.0	9.0	9.0	9.0	9.0	9.0	9.0	9.0	9.0	9.0	9.0	9.0	9.0
275	9.5	9.5	9.5	9.0	9.5	9.5	9.5	9.0	9.5	9.5	9.5	9.5	9.5	9.0	9.5	9.5	9.5	9.0	9.5	9.5	9.5
290	9.5	9.5	9.5	9.5	9.5	9.5	9.5	9.5	9.5	9.5	9.5	9.5	9.5	9.5	9.5	9.5	9.5	9.5	9.5	9.5	9.5
305	10.0	10.0	10.0	10.0	10.0	10.0	10.0	10.0	10.0	10.0	10.0	10.0	10.0	10.0	10.0	10.0	10.0	10.0	10.0	10.0	10.0
320	10.5	10.5	10.5	10.5	10.5	10.5	10.5	10.5	10.5	10.5	10.5	10.5	10.5	10.5	10.5	10.5	10.5	10.5	10.5	10.5	10.5
335	11.0	11.0	11.0	11.0	11.0	11.0	11.0	11.0	11.0	11.0	11.0	11.0	11.0	11.0	11.0	11.0	11.0	11.0	11.0	11.0	11.0
350	11.5	11.5	11.5	11.5	11.5	11.5	11.5	11.5	11.5	11.5	11.5	11.5	11.5	11.5	11.5	11.5	11.5	11.5	11.5	11.5	11.5
365	12.0	12.0	12.0	12.0	12.0	12.0	12.0	12.0	12.0	12.0	12.0	12.0	12.0	12.0	12.0	12.0	12.0	12.0	12.0	12.0	12.0
380	12.5	12.5	12.5	12.5	12.5	12.5	12.5	12.5	12.5	12.5	12.5	12.5	12.5	12.5	12.5	12.5	12.5	12.5	12.5	12.5	12.5
395	13.0	13.0	13.0	13.0	13.0	13.0	13.0	13.0	13.0	13.0	13.0	13.0	13.0	13.0	13.0	13.0	13.0	13.0	13.0	13.0	13.0
410	13.5	13.5	13.5	13.5	13.5	13.5	13.5	13.5	13.5	13.5	13.5	13.5	13.5	13.5	13.5	13.5	13.5	13.5	13.5	13.5	13.5
425	14.0	14.0	14.0	13.5	14.0	14.0	14.0	13.5	14.0	14.0	14.0	14.0	14.0	14.0	14.0	14.0	14.0	14.5	14.5	14.5	14.5
440	14.0	14.0	14.0	14.0	14.0	14.0	14.0	14.0	14.0	14.0	14.0	14.5	14.5	14.5	14.5	15.0	15.0	15.0	15.0	15.5	15.5
455	14.5	14.5	14.5	14.5	14.5	14.5	14.5	14.5	14.5	14.5	14.5	15.0	15.0	15.0	15.5	15.5	15.5	16.0	16.0	16.0	16.5
470	15.0	15.0	15.0	15.0	15.0	15.0	15.0	15.0	15.0	15.0	15.0	15.5	15.5	15.5	16.0	16.0	16.5	16.5	17.0	17.0	17.0
485	15.5	15.5	15.5	15.5	15.5	15.5	15.5	15.5	15.5	15.5	15.5	16.0	16.0	16.5	16.5	17.0	17.0	17.5	17.5	18.0	18.0
500	16.0	16.0	16.0	16.0	16.0	16.0	16.0	16.0	16.0	16.0	16.0	16.5	16.5	17.0	17.0	17.5	18.0	18.0	18.0	18.0	18.0

Table 3. Design chart for checking stress-to-strength ratio at top of subgrade.

HMA Layer Thickness (mm)	Granular Base (GB) Layer Thickness (mm)																					
	500	550	600	650	700	750	800	850	900	950	1000	1050	1100	1150	1200	1250	1300	1350	1400	1450	1500
200	Y	Y	Y	Y	Y	G	G	G	G	G	G	G	G	G	G	G	G	G	G	G	G
215	Y	Y	Y	Y	G	G	G	G	G	G	G	G	G	G	G	G	G	G	G	G	G
230	Y	Y	Y	Y	G	G	G	G	G	G	G	G	G	G	G	G	G	G	G	G	G
245	Y	Y	Y	G	G	G	G	G	G	G	G	G	G	G	G	G	G	G	G	G	G
260	Y	Y	Y	G	G	G	G	G	G	G	G	G	G	G	G	G	G	G	G	G	G
275	Y	Y	G	G	G	G	G	G	G	G	G	G	G	G	G	G	G	G	G	G	G
290	Y	G	G	G	G	G	G	G	G	G	G	G	G	G	G	G	G	G	G	G	G
305	G	G	G	G	G	G	G	G	G	G	G	G	G	G	G	G	G	G	G	G	G
320	G	G	G	G	G	G	G	G	G	G	G	G	G	G	G	G	G	G	G	G	G
335	G	G	G	G	G	G	G	G	G	G	G	G	G	G	G	G	G	G	G	G	G
350	G	G	G	G	G	G	G	G	G	G	G	G	G	G	G	G	G	G	G	G	G
365	G	G	G	G	G	G	G	G	G	G	G	G	G	G	G	G	G	G	G	G	G
380	G	G	G	G	G	G	G	G	G	G	G	G	G	G	G	G	G	G	G	G	G
395	G	G	G	G	G	G	G	G	G	G	G	G	G	G	G	G	G	G	G	G	G
410	G	G	G	G	G	G	G	G	G	G	G	G	G	G	G	G	G	G	G	G	G
425	G	G	G	G	G	G	G	G	G	G	G	G	G	G	G	G	G	G	G	G	G
440	G	G	G	G	G	G	G	G	G	G	G	G	G	G	G	G	G	G	G	G	G
455	G	G	G	G	G	G	G	G	G	G	G	G	G	G	G	G	G	G	G	G	G
470	G	G	G	G	G	G	G	G	G	G	G	G	G	G	G	G	G	G	G	G	G
485	G	G	G	G	G	G	G	G	G	G	G	G	G	G	G	G	G	G	G	G	G
500	G	G	G	G	G	G	G	G	G	G	G	G	G	G	G	G	G	G	G	G	G

Note: G--Stress-to-Strength Ratio <0.3; Y--0.3= < Stress-to-Strength Ratio < = 0.7; R--Stress-to-Strength Ratio > 0.7

base/reservoir layer thickness of 680 mm for a shoulder retrofit of a highway draining three lanes plus the shoulder (i.e., 4 lanes are selected in the table).

- **Step 2: Choose RHMA-O layer thickness based on RHMA-O fatigue damage for TI.** Using the appropriate table (Table 2 [Table E.5 in Appendix E in Reference 1]), select the minimum RHMA-O layer thickness for a base thickness of 700 mm (rounded up

from 680 mm from Step 1), and a traffic index of 13. The minimum required thickness of RHMA-O is 395 mm.

- **Step 3: Check the stress/strength ratio at the top of the subgrade.**
  Using the appropriate table (Table 3 [Table E.6 in Appendix E in Reference 1]), check the shear stress-to-shear strength ratio at the top of the subgrade based on the minimum required thickness of granular base of 700 mm and minimum required thickness of RHMA-O of 395 mm. The stress/strength ratio is "G," which implies that the shear stress is less than 0.3 of the shear strength. Consequently, permanent deformation in the subgrade should not be a problem for this pavement design.

Therefore, in this example, the minimum required thickness of granular base is 700 mm and the minimum thickness of RHMA-O is 395 mm for the design requirements and site conditions.

6 LIFE-CYCLE COST ANALYSIS

Example Life-Cycle Cost Analysis (LCCA) comparisons with conventional stormwater Best Management Practices (BMPs) for the Sacramento region *[16]* indicated that fully permeable pavements should cost less than conventional BMPs over a 40-year life-cycle. However, LCCA should be undertaken on a project-by-project basis because alternatives and costs for different types of fully permeable pavement will vary by region and over time.

A framework for environmental Life-Cycle Analysis (LCA) was reviewed; however, it was found that insufficient data were available at this time to complete an example LCA for fully permeable pavements.

7 CONCLUSIONS

Key findings from the computer modeling of structural capacity and development of structural designs phase of the fully permeable pavement study include:

- The use of mechanistic-empirical pavement design equations developed in this project was effective in estimating required structural thicknesses for fully permeable pavements to carry slow moving (between 7 and 40 km/h) truck traffic. Tens of thousands of layer elastic theory calculations to find critical stresses and strains in fully permeable asphalt pavements were performed in order to estimate thicknesses required for structural capacity. Statewide truck axle load spectra from Caltrans Weigh-In-Motion (WIM) measurements (captured in a UCPRC database) were used to select representative axle loads. Representative pavement temperatures were selected from a database of *Enhanced Integrated Climate Model (EICM)* calculations to estimate asphalt stiffnesses.
- The results of strain calculations in asphalt were used to estimate the required thicknesses for preventing fatigue cracking. Nonlinear layer elastic theory calculations were used to estimate the stiffness of the granular base, which were then used to estimate shear stress-to-strength ratios in the subgrade. Together, these results were used to develop structural design tables that can be used with hydraulic design calculations to determine required layer thicknesses. The pavement structures were considered feasible, with all pavement structures less than 1.5 m in total thickness for the heaviest traffic. The use of an open-graded portland cement subbase offers considerably greater protection against the risk of subgrade rutting for asphalt pavements.
- Preliminary design tables for pilot studies were developed considering structural and hydraulic performance based on the following design input variables:
  - Subgrade permeability,
  - Truck traffic level in terms of Traffic Index or ESAL,
  - Two temperature climate regions (Sacramento and Los Angeles),
  - Three design storms (2, 50, and 100 years) for three climate regions,

  - Two traffic speeds (7 km/h and 40 km/h), and
  - Various numbers of adjacent impermeable lanes.
- Design cross sections developed for shoulder retrofit of highways as well as low-speed trafficked areas such as parking lots and maintenance yards were reviewed by construction and maintenance experts and were considered to be feasible to construct and maintain.

REFERENCES

1. JONES, D., Harvey, J., Li, H., Wang, T., Wu, R. and Campbell, B. 2010. **Laboratory Testing and Modeling for Structural Performance of Fully Permeable Pavements: Final Report.** Davis and Berkeley, CA: University of California Pavement Research Center. (UCPRC-RR-2010-01).
2. HANSEN, B. 2007. Storm-Water Management: Porous Pavement Increases Storage Area at Portland Marine Terminal. **Civil Engineering, Vol. 77, No. 3.** Reston, VA: American Society of Civil Engineers.
3. HANSEN, K. 2008. **Porous Asphalt Pavements for Stormwater Management.** Lanham, MD: National Asphalt Pavement Association. (Information Series 131).
4. **Stormwater Management with Pervious Concrete Pavement.** 2009. Skokie, IL: American Concrete Pavement Association.
5. SMITH, D.R. 2011. **Permeable Interlocking Concrete Pavements.** Herndon. VA: Interlocking Concrete Pavement Institute.
6. KAYHANIAN, M., Anderson, D., Harvey, J.T., Jones, D. and Muhunthan, B. 2011. Permeability Measurement and Scan Imaging to Assess Clogging of Pervious Concrete Pavements in Parking Lots. **Journal of Environmental Management, Vol. 95(1).** pp 114–123.
7. CHAI, L., Kayhanian, M., Givens, B., Harvey, J. and Jones, D. 2012. Hydraulic Performance of Fully Permeable Highway Shoulder for Storm Water Runoff Management. **ASCE Journal of Environmental Engineering, 138(7).** pp 711–722.
8. JONES, D., Harvey, J., Li, H. and Campbell, B. 2009. **Summary of Laboratory Tests to Assess Mechanical Properties of Permeable Pavement Materials.** Davis and Berkeley, CA: University of California Pavement Research Center. (UCPRC-TM-2009-05).
9. KAYHANIAN, M., Chai, L. and Givens, B. 2010. **Hydraulic Performance Evaluation of Permeable Pavement under Heavy Load and Heavy Traffic.** Davis, CA: University of California, Davis. (CTSW-RT-10-247.03D).
10. LI, H., Harvey J. and Jones, D. 2010. **Summary of a Computer Modeling Study to Understand the Performance Properties of Fully Permeable Pavements.** Davis and Berkeley, CA: University of California Pavement Research Center. (UCPRC-TM-2010-04).
11. LI, H., Jones, D. and Harvey, J.T. 2012. Developing a Mechanistic-Empirical Design Procedure for Fully Permeable Pavement under Heavy Traffic. **Transportation Research Record, Journal of the Transportation Research Board, No 2305.** Washington, DC: National Academy of Sciences.
12. **LEAP 2.0: A Layered Elastic Analysis Program**. 2004. Berkeley, CA: Symplectic Engineering Corporation. (Release 2.0, March 2004).
13. TUTUMLUER, E. 1995. **Predicting Behaviour of Flexible Pavements with Granular Bases.** Atlanta, GA: Georgia Institute of Technology. (Ph.D. dissertation).
14. UZAN, J. 1985. Characterization of Granular Material. In **Transportation Research Record 1022**. Washington, D.C.: Transportation Research Board, National Research Council. pp. 52–59.
15. TUTUMLUER, E. and Thompson, M.R. 1998. **Anisotropic Modeling of Granular Bases**. Champaign, IL: University Illinois at Urbana Champaign. (Final Report to Federal Aviation Administration Center of Excellence for Airport Pavements. COE Report No. 2).
16. WANG, T., Jones, D. and Harvey, J. 2010. **A Framework for Life-Cycle Cost Analyses and Environmental Life-Cycle Assessments for Fully Permeable Pavements.** Davis and Berkeley, CA: University of California Pavement Research Center. (UCPRC-TM-2010-05).

This page intentionally left blank

Asphalt Pavements – Kim (Ed)
© 2014 Taylor & Francis Group, London, ISBN 978-1-138-02693-3

Laboratory characterization of North Carolina base course aggregates for permanent deformation model development and calibration

Liang Chern Chow, Debakanta Mishra & Erol Tutumluer
Department of Civil and Environmental Engineering, University of Illinois at Urbana-Champaign, Urbana, IL, USA

ABSTRACT: This paper presents partial findings from an ongoing research study at the University of Illinois aimed at laboratory characterization of North Carolina base course aggregates for permanent deformation model development and calibration. Monotonic triaxial shear strength tests were first conducted on four different aggregate types to establish the Mohr-Coulomb failure envelopes. Repeated load triaxial tests were then conducted on the aggregate materials at shear stress/strength ratios of 0.25, 0.50, and 0.75, to comparatively evaluate the permanent deformation accumulation trends, and subsequently develop improved rutting models for use in mechanistic-empirical pavement design methodologies. Experimental results clearly emphasize the importance of applied stress states, material's shear strength, and number of load repetitions as the most significant factors affecting unbound aggregate permanent deformation behavior. A new model is proposed to adequately capture the effects of applied stresses and shear stress/strength ratios in predicting permanent deformation behavior of base course aggregates. This proposed model can potentially be used to improve the rutting models currently used in AASHTO's mechanistic-empirical flexible pavement design procedure the Pavement ME software.

Keywords: Unbound aggregates, base course, permanent deformation, applied stress states, shear strength

1 INTRODUCTION

Rutting or permanent deformation accumulation is the primary damage/distress mechanism for unbound aggregate base/subbase layers in flexible pavements. Accordingly, rutting resistance is a major performance measure for designing pavements with granular base/subbase layers. Low strength granular materials are generally more susceptible to high permanent deformation accumulation, whereas "good quality" aggregate materials mobilize high shearing resistance to prevent settlement and lateral movement within the layer. Although the influence of stress state on unbound aggregate resilient modulus is relatively well understood, its influence on permanent deformation accumulation is usually not considered while designing flexible pavement structures.

Proper assessment of unbound aggregate layer rutting or permanent deformation behavior is critical to ensure the structural adequacy of flexible pavements. From an extensive review of published literature, Lekarp et al. [1] listed (a) stress levels, (b) principal stress reorientation, (c) number of load applications, (d) moisture content, (e) stress history, (f) density, (g) grading and fines content, and (h) aggregate type as primary factors governing the permanent deformation accumulation in unbound aggregate materials. The relationship between permanent deformation and applied stress was confirmed and different rutting models have been proposed by several researchers. Some of the more commonly used and noteworthy ones were proposed by Lekarp et al. [1], Barksdale [2], Monismith [3], Tseng and Lytton [4], Sweere [5],

Wolff and Visser [6], Paute et al. [7], Bonaquist and Witczak [8], Pappin [9], Huurrman [10], and van Niekerk and Huurman [11]. Moreover, as opposed to resilient modulus (M_R), shear strength properties have shown better correlations with unbound aggregate permanent deformation behavior for predicting field rutting performance [12–14]. Accordingly, characterization of unbound aggregate permanent deformation behavior in conjunction with shear strength properties is one of the primary objectives of an ongoing research effort at the University of Illinois.

This paper presents laboratory test results aimed at characterizing the permanent deformation behavior of four different aggregate materials. Note that the overall scope of the research study involves laboratory characterization of sixteen different aggregate materials used for unbound aggregate base/subbase applications in the state of North Carolina. Accordingly, laboratory tests for only the first four of the sixteen materials are presented in this paper to establish a framework for developing a new unbound aggregate permanent deformation damage model. Each of the presented aggregate materials consisted of different aggregate types such as granitic, basalt and limestone particles. Monotonic triaxial shear strength tests were first conducted on each aggregate material to establish the Mohr-Coulomb failure envelopes. Repeated load triaxial tests were subsequently performed on each material to characterize the permanent deformation behavior under different applied stress states, which were quantified according to certain established ratios of the applied shear stress with the shear strength under same confinement. In addition, multi-stage permanent deformation tests were also performed on each aggregate material to study the effects of stress history on permanent deformation accumulation. As a result, a new permanent deformation model has been proposed to adequately consider the effects of applied stress states and material shear strength while predicting the permanent deformation behavior under repeated loading.

2 AGGREGATE MATERIALS TESTED

The four (4) different crushed aggregate materials discussed in this paper were selected from different quarries, and are commonly used for pavement unbound base/subbase applications in the state of North Carolina. Two of the four aggregate materials comprised granitic particles (labeled as materials G1 and G2); the third aggregate material comprised limestone particles (labeled as material L) whereas the forth aggregate material comprised basalt (labeled as material B) particles. Figure 1 shows the gradation boundaries (black dotted lines) specified

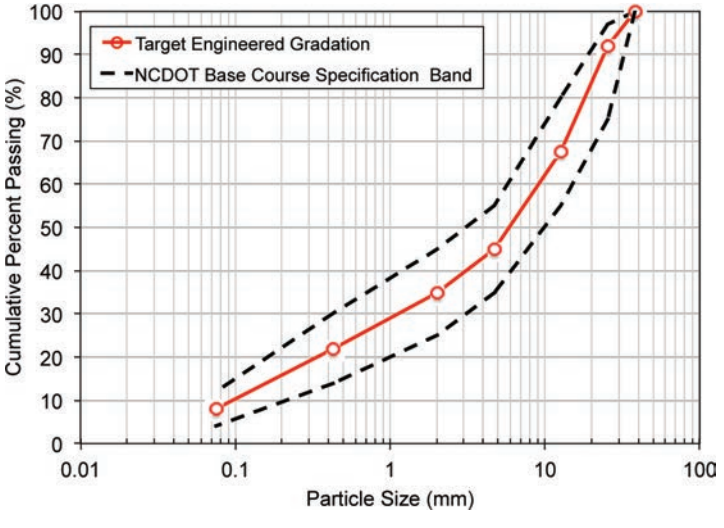

Figure 1. Engineered gradation for tested materials.

Table 1. Aggregate and shear strength properties of tested materials.

Label	Aggregate type	Max. dry density, $\gamma_{d,max}$ kN/m^3	Opt. moisture content, ω_{opt} %	Cohesion c kPa	Friction angle ϕ degree	Compaction water content %
Material G1	Granite	24.1	4.2	85.1	50	$\omega_{opt} \pm 0.1$
Material G2	Granite	21.9	5.5	59.4	45	$\omega_{opt} \pm 0.8$
Material B	Basalt	23.3	5.2	1.1	51	$\omega_{opt} \pm 0.2$
Material L	Limestone	21.1	5.9	2.4	45	$\omega_{opt} \pm 0.1$

by the North Carolina Department of Transportation (NCDOT) for typical unbound base course materials. All laboratory tests in the current study were conducted on specimens blended to achieve the mid-range curve shown in Figure 1.

Aggregate index property tests such as Atterberg's limits for the fines fraction, as well as the moisture-density tests were conducted by the NCDOT Material and Test Unit. Fines from these aggregate materials were found to be nonplastic in nature. The moisture-density characteristics for each aggregate material were established using a modified approach similar to the modified compaction procedure specified in AASHTO T-180. However, aggregate specimens in the NCDOT procedure were compacted in four equal lifts by applying 86 blows per lift (compared to 56 blows per lift specified by the AASHTO T-180 method) with a 4.5-kg (10-lb) hammer dropped from a height of 450-mm (18 in.). Resulting Optimum Moisture Content (OMC) and Maximum Dry Density (MDD) values for the each of the aggregate materials are listed in Table 1. Comparing the MDD values, the four aggregate types can be listed in the following order, from low to high: L, G2, B, and G1.

3 EXPERIMENTAL FRAMEWORK

Monotonic triaxial shear strength tests were first conducted on each aggregate material to establish the Mohr-Coulomb failure envelopes. These Mohr-Coulomb envelopes were then used to compute stress level combinations that would result in applied stress/shear strength ratios of 25%, 50% and 75% being applied on a specimen during repeated load triaxial tests. This was the main approach taken to characterize aggregate permanent deformation accumulation trends under different applied stress/shear strength ratios.

3.1 *Monotonic triaxial shear strength testing*

The primary objective behind this task was to establish the maximum shear stress levels that each material could be subjected to without undergoing shear failure. Cylindrical test specimens, 152-mm (6-in.) in diameter by 305-mm (12-in.) in height, were compacted in six (6) equal lifts targeting the OMC and MDD values listed in Table 1. The specimens were then sheared through the application of 1% strain per minute (0.05-mm/sec for a 305-mm long specimen) at all-around constant confining pressure levels of 35 kPa (5 psi), 69 kPa (10 psi) and 103 kPa (15 psi), respectively. The shear strength properties (cohesion intercept c and friction angle ϕ) for each aggregate material are listed in Table 1. From the table, material B recorded the highest friction angle value of 51 degrees, followed by material G1 ($\phi = 50$ degrees). Both materials G2 and L had a friction angle value of 45 degrees. As previously mentioned, all four materials comprised nonplastic fines; therefore the cohesion (c) values listed in Table 1 are primarily the result of linear interpretation of a nonlinear Mohr-Coulomb failure envelope. Comparing the peak deviator stress values at failure (see Table 2), the four aggregate materials can be listed in the increasing order of shear strengths as: L, B, $G2$, and $G1$.

The Mohr-Coulomb failure envelopes for each material were used to establish the stress state combinations to achieve certain Shear Stress Ratio (SSR or τ_f / τ_{max}) values during

Table 2. Stress states corresponding to different target SSR levels selected for repeated load triaxial testing (SSR: Shear Stress Ratio).

	Confining Pressure, σ_3		$\tau_f/\tau_{max} = 0.25$				$\tau_f/\tau_{max} = 0.50$				$\tau_f/\tau_{max} = 0.75$				*Deviator stress at failure, $\sigma_{d,\,failure}$	
			σ_f		σ_d		σ_f		σ_d		σ_f		σ_d			
	psi	kPa	psi	kPa	psi	kPa	psi	kPa	psi	kPa	psi	kPa	psi	kPa	psi	kPa
Material G1	3.0	20.7	4.6	31.7	13.9	95.8	6.7	46.2	31.6	217.7	9.4	64.8	55.1	379.6	87.5	603.0
	5.0	**34.5**	**6.9**	**47.5**	**16.0**	**110.2**	**9.3**	**64.1**	**36.4**	**250.8**	**12.4**	**85.4**	**63.3**	**436.1**	**100.6**	**693.2**
	7.0	48.2	9.1	62.7	18.1	124.7	11.8	81.3	41.1	283.2	15.4	106.1	71.6	493.3	113.7	783.5
	10.0	68.9	12.5	86.1	21.2	146.1	15.6	107.5	48.2	332.1	19.8	136.4	83.9	578.1	133.4	918.8
	15.0	103.4	18.1	124.7	26.4	181.9	22.0	151.6	60.0	413.4	27.2	187.4	104.6	720.7	166.1	1144.4
Material G2	3.0	20.7	4.3	29.6	9.2	63.4	6.0	41.3	20.7	142.6	8.2	56.5	35.8	246.7	56.1	386.6
	5.0	**34.5**	**6.6**	**45.5**	**10.7**	**73.7**	**8.6**	**59.3**	**24.3**	**167.4**	**11.1**	**76.5**	**41.9**	**288.7**	**65.8**	**453.1**
	7.0	48.2	8.8	60.6	12.3	84.7	11.1	76.5	27.9	192.2	14.0	96.5	48.1	331.4	75.4	519.7
	10.0	68.9	12.2	84.1	14.7	101.3	14.9	102.7	33.2	228.7	18.4	126.8	57.3	394.8	89.9	619.5
	15.0	103.4	17.7	122.0	18.6	128.2	21.2	146.1	42.1	290.1	25.6	176.4	72.7	500.9	114.1	785.8
Material B	3.0	20.7	3.4	23.4	3.4	23.4	3.9	26.9	7.9	54.4	4.5	31.0	13.7	94.4	21.8	150.4
	5.0	**34.5**	**5.6**	**38.6**	**5.7**	**39.3**	**6.4**	**44.1**	**12.9**	**88.9**	**7.5**	**51.7**	**22.5**	**155.0**	**35.8**	**246.5**
	7.0	48.2	7.9	54.4	7.9	54.4	9.0	62.0	17.9	123.3	10.5	72.3	31.2	215.0	49.7	342.6
	10.0	68.9	11.2	77.2	11.2	77.2	12.8	88.2	25.4	175.0	14.9	102.7	44.4	305.9	70.6	486.8
	15.0	103.4	16.9	116.4	16.7	115.1	19.2	132.3	38.0	261.8	22.4	154.3	66.3	456.8	105.5	727.0
Material L	3.0	20.7	3.4	23.4	2.6	17.9	3.9	26.9	6.0	41.3	4.5	31.0	10.3	71.0	16.2	111.4
	5.0	**34.5**	**5.6**	**38.6**	**4.2**	**28.9**	**6.4**	**44.1**	**9.5**	**65.5**	**7.4**	**51.0**	**16.5**	**113.7**	**25.8**	**177.9**
	7.0	48.2	7.8	53.7	5.8	40.0	8.9	61.3	13.1	90.3	10.3	71.0	22.6	155.7	35.5	244.5
	10.0	68.9	11.2	77.2	8.2	56.5	12.7	87.5	18.5	127.5	14.7	101.3	31.8	219.1	50.0	344.3
	15.0	103.4	16.8	115.8	12.1	83.4	19.0	130.9	27.4	188.8	21.9	150.9	47.2	325.2	74.1	510.6

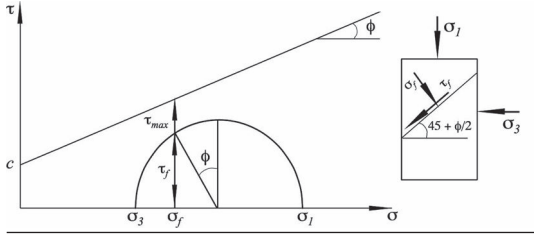

$$\text{Shear Stress Ratio (SSR)} = \frac{\text{Applied Shear Stress}}{\text{Shear Strength}} = \frac{\tau_f}{\tau_{max}}$$

*Deviator stress at failure also corresponds to shear stress ratio of 1.0.

repeated load triaxial testing. The concept of SSR has been diagrammatically illustrated in Table 2, and represents the ratio between the applied shear stress and the material shear strength at a particular applied normal stress level [see Eq. (1)]. At a certain constant confining pressure (σ_3), the shear strength of an aggregate material can be defined when Mohr-Coulomb circle is tangent to the failure envelope. Shear strength (τ_{max}) at this confinement is ϕ degree counter-clockwise rotation from the invariant (center of circle). The normal and shear stresses (represented by σ_f and τ_f, respectively) acting on the failure plane (oriented at an angle of $45° + \phi/2$ with the horizontal), therefore can be computed using Eqs. (2) and (3). The ratio between τ_f and shear strength of the material corresponding to that particular normal stress ($\tau_{max} = c + \sigma_{f*}\tan\varphi$) is defined as the shear stress ratio (SSR = τ_f / τ_{max}).

A list of σ_d and σ_f values corresponding to different confining pressure (σ_3) and SSR combinations are listed in Table 2. Each aggregate material was characterized for permanent deformation behavior by subjecting cylindrical triaxial specimens to SSR values of 0.25, 0.50 and 0.75, representing low, intermediate and high stress/strength ratios, respectively. For instance, an SSR value of 0.50 indicates that the specimen is subjected to stress levels that mobilize only 50% of the aggregate shear strength at that particular confining pressure. For a particular stress state, a limiting value of SSR is believed to control the permanent deformation behavior of unbound aggregate materials [15]. Lower SSR values essentially indicate that the material is subjected to a low stress state, and is less likely to undergo bearing capacity type shear failure. However, high SSR values (typically SSR ≥ 0.7) have been found to result in rapid permanent deformation accumulation, ultimately leading to shear failure [16, 17]. Accordingly, a unity value of SSR (SSR = 1.0) represents shear failure of the material.

$$\text{Shear Stress Ratio (SSR)} = \frac{\text{Applied shear stress}}{\text{Shear strength}} = \frac{\tau_f}{\tau_{\max}} \tag{1}$$

$$\sigma_f = \frac{2\sigma_3 + 2\sigma_3 \tan^2\phi + \sigma_d + \sigma_d \tan^2\phi - \sqrt{\sigma_d^2 \tan^2\phi(1+\tan^2\phi)}}{2(1+\tan^2\phi)} \tag{2}$$

$$\tau_f = \sqrt{(\sigma_d/2)^2 - [\sigma_f - (\sigma_3 + \sigma_d/2)]^2} \tag{3}$$

where

τ_f = Applied shear stress acting on failure plane;
$\tau_{\max}$ = Shear strength determined by $c + \sigma_f \tan\phi$;
σ_f = Normal stress acting on failure plane;
σ_3 = Applied confining pressure;
σ_d = Applied deviator stress, $\sigma_1 - \sigma_3$; and
ϕ = Friction angle determined from shear strength tests.

3.2 *Repeated load triaxial testing*

Permanent deformation accumulation trends of the four aggregate materials were investigated through repeated load triaxial testing at the three different SSR levels listed in Table 2. A confining pressure (σ_3) level of 34.5 kPa (5 psi) was selected, as highlighted in bold in Table 2, for the repeated load permanent deformation tests to ensure that deviator stress levels required for achieving the target SSR values remained within the equipment capabilities.

Cylindrical specimens having equal dimensions of 150-mm height and 150-mm diameter were prepared by following a procedure similar to that previously described, and were subjected to 10,000 load applications at each selected SSR level. Note that the application of only 10,000 load pulses per SSR level may represent a limitation of the test protocol, as it may not capture the transition from plastic creep (Range B) to incremental collapse (Range C) under very high number of load applications as defined by Werkmeister [18]. Nevertheless, the selection of 10,000 load applications per stress level in this study was primarily governed by time constraints associated with conducting tests to a higher number of load applications

(e.g. 100,000 cycles or more per stress level). All specimens tested exhibited "stable" behavior after 10,000 load applications without accumulating rapid and significant permanent strain. Accordingly, multi-stage permanent deformation tests were performed at SSR levels of 0.25, 0.50 and 0.75 by sequentially subjecting each specimen to 10,000 load applications at the different stress level combinations listed in Table 2.

3.2.1 *Characterization of permanent deformation behavior*

Figure 2(a) combines both the laboratory-measured and model-predicted permanent deformation accumulations for the four aggregate materials subjected to different SSR levels. As shown in the figure, higher applied stress levels (higher SSR values) consistently corresponded

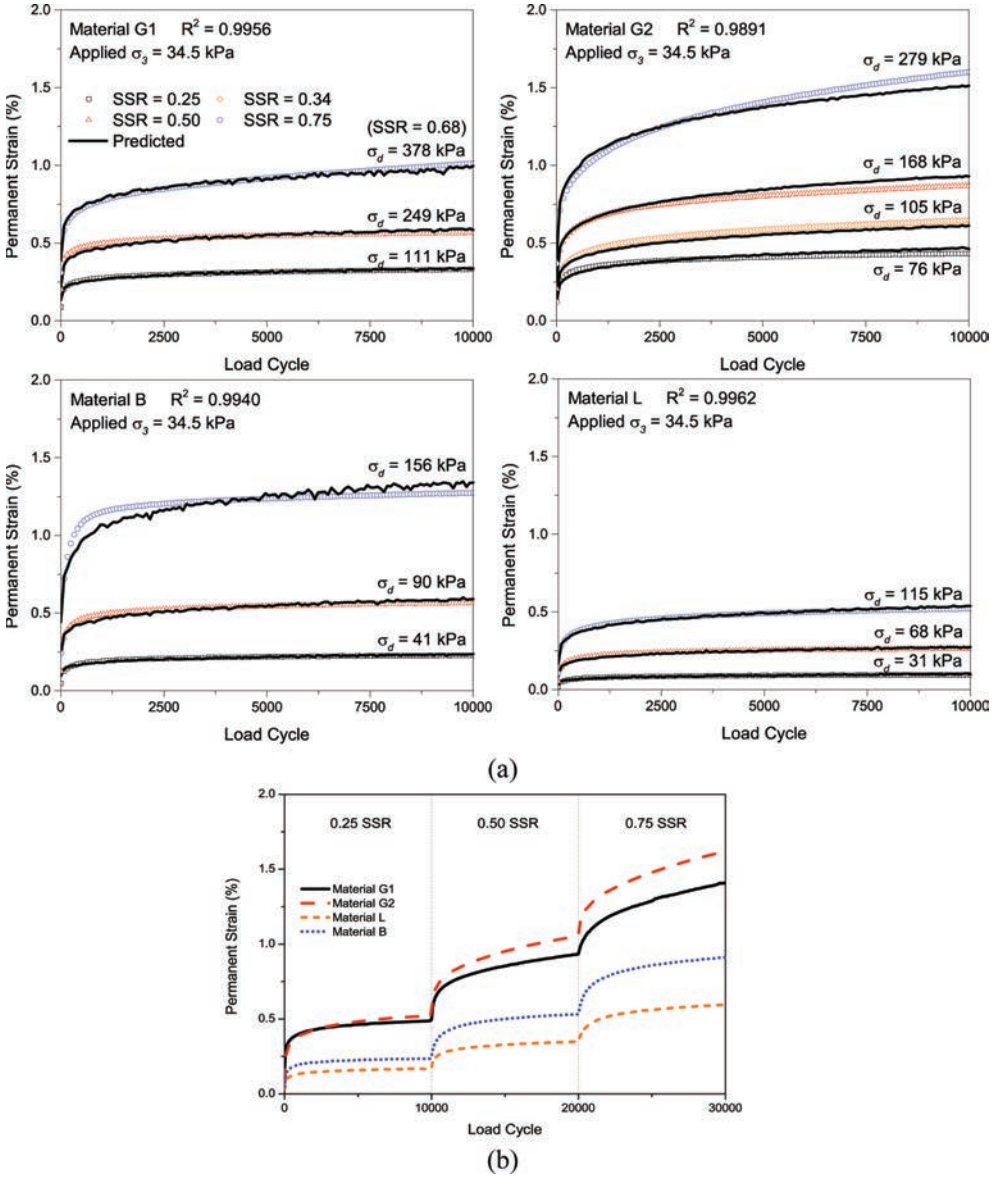

Figure 2. (a) Single-stage measured (symbols) and model predicted (solid lines) permanent strains and (b) multi-stage loading (SSR = 0.25, 0.50, 0.75).

to higher permanent strains accumulations. Note that the highest achieved SSR value for material G1 was limited to 0.68 (instead of 0.75), due to the test equipment loading limits. It is important to note that both the applied stress levels (represented by the deviator stress or σ_d) and SSR values need to be considered while comparatively evaluating the permanent deformation behavior of different aggregate types. For instance, at SSR of 0.50, material G2 records the highest permanent strain accumulation ($\varepsilon_p = 0.89\%$), whereas both materials G1 and B accumulated permanent strain levels of $\varepsilon_p = 0.57\%$, with material L accumulating the lowest permanent strain ($\varepsilon_p = 0.41\%$). However, applied deviator stresses at this level of SSR were 249, 168, 90 and 68 kPa for materials G1, G2, B and L, respectively. Comparing the permanent deformation accumulation trends of different aggregate types solely based on the SSR levels, without considering the applied deviator stress levels, may therefore lead to erroneous conclusions regarding material quality.

One multi-stage permanent deformation test was conducted for each material by sequentially subjecting a compacted specimen to 10,000 load applications each at stress states corresponding to SSR levels of 0.25, 0.50, and 0.75, respectively. Results from the multi-stage permanent deformation tests are shown in Figure 2(b). It is important to note that the permanent deformation accumulation curves shown in Figure 2(b) correspond to different applied deviator stress levels for different aggregate materials even for the same target SSR values. Figure 2(b) clearly highlights the effects of stress history on permanent deformation accumulation. By comparing the single-stage (Fig. 2a) and multi-stage (Fig. 2b) permanent deformation test results, it can be seen that gradually increasing repeated deviator stress levels lead to lower permanent deformation accumulations compared to singe-stage loading tests. Permanent deformation trends for the different aggregate types are unclear at lower applied stress states, and become distinctive as the SSR levels are increased. Similar observations have been reported in the past by Tutumluer et al. [16].

4 DEVELOPMENT OF PERMANENT DEFORMATION MODEL

The primary objective of this research effort is to develop an improved rutting model that can adequately capture the effects of aggregate shear strength and applied stress levels while predicting the permanent deformation behavior of unbound aggregates. Based on the phenomenological model originally proposed by Monismith et al. [3], a new model was developed to incorporate the effects of applied normal stress and SSR [see Eq. (4)]. As shown in Figure 2(a), the developed model was successful in consistently predicting the permanent deformation trends observed in the laboratory, with coefficient of determination (R^2) values of 0.99 or greater.

$$\epsilon_p(N) = AN^B \sigma_d^C \left(\frac{\tau_f}{\tau_{\max}} \right)^D \tag{4}$$

where
$\epsilon_p(N)$ = Permanent strain corresponding to N load applications;
σ_d = Applied deviator stress;
τ_f = Shear stress at failure;
$\tau_{\max}$ = Shear strength at failure; and
A, B, C, D = Regression parameters.

Note that in its current form the proposed model does not incorporate the effects of moisture content on permanent deformation accumulation. This is primarily because all shear strength and permanent deformation tests under the scope of the current study were conducted on specimens compacted at OMC and MDD conditions. Moreover, accuracy of the model has been verified at one confining pressure level only [all repeated load triaxial tests were conducted at a confining pressure level (σ_3) of 34.5 kPa or 5 psi], and further laboratory testing is required to confirm its applicability at different confining pressures. Although

confining pressure (σ_3) is not directly used as a parameter in the model formulation, it should be noted that the effects of confining pressure are indirectly reflected in the calculations for both σ_f as well as τ_f [see Eqs. (2, 3)]. Another mathematical limitation of the proposed model can be realized by assigning a unity (1.0) value to SSR. By definition, an SSR value equal to 1.0 indicates shear failure of the material, and therefore should lead to infinite permanent deformation accumulation. However, the proposed model in its current form fails to capture this phenomenon. The effects of moisture content, particle shape and surface texture, as well as stress history on permanent deformation accumulation will need to be further incorporated into the framework established for developing more comprehensive rutting models based on selected aggregate property databases in the future.

5 CONCLUSIONS

This paper presented partial findings from an ongoing research project at the University of Illinois aimed at laboratory characterization of North Carolina aggregates for permanent deformation model development and calibration. The following conclusions can be drawn from findings reported in this paper:

1. Aggregate shear strength properties and applied stress levels are important factors governing the permanent deformation accumulation in unbound aggregate base/subbase layers.
2. Adequate consideration needs to be given to both the shear Stress-to-Strength Ratio (SSR) and applied deviator stress (σ_d) levels to comparatively evaluate the permanent deformation behavior of different aggregate materials.
3. A "nearly perfect" match between measured and predicted permanent strain values was obtained using a proposed rutting damage model that captures the effects of number of load repetitions, SSR and applied deviator stress.

ACKNOWLEDGEMENTS

This research study has been made possible through insightful discussions with Dr. Judith Corley-Lay and the financial support from the North Carolina Department of Transportation (NCDOT). All laboratory tests were conducted utilizing the resources at the Illinois Center for Transportation, and the University of Illinois Advanced Transportation Research and Engineering Laboratory (ATREL). The help of Chunkun Su and Suriyati B. Supa'at of NCDOT are acknowledged for providing the preliminary laboratory test results. North Carolina aggregate producers are also acknowledged for supplying the materials used in the laboratory test matrix. Finally, sincere thanks to Yu Xie, graduate student at the University of Illinois for his support in conducting the laboratory tests reported in this paper.

REFERENCES

[1] F. Lekarp, U. Isacsson, and A. Dawson, "State of the art. II: Permanent Strain Response of Unbound Aggregates," *ASCE Journal of Transportation Engineering*, vol. 126, no. 1, pp. 76–83, 2000.

[2] R.D. Barksdale, "Laboratory Evaluation of Rutting in Base Course Materials," presented at the Proceedings of the 3rd International Conference on Structural Design of Asphalt Pavements, pp. 161–174, 1972.

[3] C.L. Monismith, N. Ogawa, and C.R. Freeme, "Permanent Deformation Characteristics of Subgrade Soils Due to Repeated Loading," *Transportation Research Record: Journal of the Transportation Research Board*, vol. 537, pp. 1–17, 1975.

[4] K.-H. Tseng and R.L. Lytton, "Prediction of Permanent Deformation in Flexible Pavement Materials," *Implication of Aggregates in the Design, Construction, and Performance of Flexible Pavements, ASTM STP*, vol. 1016, pp. 154–172, 1989.

[5] G.T. Sweere, "Unbound Granular Bases for Roads," Delft University of Technology, Delft, Netherlands, 1990.

[6] H. Wolff, A.T. Visser, and M. Coulomb, "Incorporating Elasto-plasticity in Granular Layer Pavement Design," *Proceedings of the ICE-Transport*, vol. 105, no. 4, pp. 259–272, 1994.
[7] J.L. Paute, P. Hornych, and J.P. Benaben, "Repeated Load Triaxial Testing of Granular Materials in the French Network of Laboratories des Ponts et Chaussées," Proceedings of the European Symposium Euroflex, Lisbon, Portugal, 20–22 September 1993.
[8] R.F. Bonaquist and M.W. Witczak, "A Comprehensive Constitutive Model for Granular Materials in Flexible Pavement Structures," Proceedings of the 8th International Conference on Asphalt Pavements, vol. 1, 1997.
[9] J.W. Pappin, "Characteristics of a Granular Material for Pavement Analysis," University of Nottingham, Nottingham, England, 1979.
[10] M. Huurman, "Permanent Deformation in Concrete Block Pavements," Delft University of Technology, Delft, Netherlands, 1997.
[11] A.A. Van Niekerk and M. Huurman, "Establishing Complex Behavior of Unbound Road Building Materials from Simple Material Testing," Delft University of Technology, Delft, 1995.
[12] M.R. Thompson, "State of the Art: Unbound Base Performance," Porceedings of the 6th Annual Symposium of the International Center for Aggregate Research (ICAR), pp. 1–10, 1998.
[13] M. Tao, L.N. Mohammad, M.D. Nazzal, Z. Zhang, and Z. Wu, "Application of shakedown Theory in Characterizing Traditional and Recycled Pavement Base Materials," *ASCE Journal of Transportation Engineering*, vol. 136, no. 3, pp. 214–222, 2010.
[14] Y. Xiao, E. Tutumluer, Y. Qian, and J. Siekmeier, "Gradation Effects Influencing Mechanical Properties of Aggregate Base-Granular Materials in Minnesota," *Transportation Research Record: Journal of the Transportation Research Board*, vol. 2267, pp. 14–26, 2012.
[15] U. Seyhan and E. Tutumluer, "Anisotropic Modular Ratios as Unbound Aggregate Performance Indicators," *Journal of Materials in Civil Engineering, ASCE*, vol. 14, no. 5, pp. 409–416, 2002.
[16] E. Tutumluer, I.T. Kim, and R.L. Santoni, "Modulus Anisotropy and Shear Stability of Geofiber-stabilized Sands," *Transportation Research Record: Journal of the Transportation Research Board*, vol. 1874, no. 1, pp. 125–135, 2004.
[17] I.T. Kim and E. Tutumluer, "Field Validation of Airport Pavement Granular Layer Rutting Predictions," *Transportation Research Record: Journal of the Transportation Research Board*, vol. 1952, no. 1, pp. 48–57, 2006.
[18] S. Werkmeister, A.R. Dawson, and F. Wellner, "Pavement Design Model for Unbound Granular Materials," *ASCE Journal of Transportation Engineering*, vol. 130, no. 5, pp. 665–674, 2004.

This page intentionally left blank

Asphalt Pavements – Kim (Ed)
© 2014 Taylor & Francis Group, London, ISBN 978-1-138-02693-3

Towards a sustainable surfacing system for the long-spanned orthotropic steel bridge deck in China Part I: State-of-the-practice

Xianhua Chen
School of Transportation, Southeast University, China

Xueyan Liu
CITG, TU Delft, Delft, The Netherlands

Zhendong Qian
ITS Center, Southeast University, China

Jun Yang
School of Transportation, Southeast University, China

ABSTRACT: Long-lasting asphalt surfacing systems still remain desirable for long-spanned stele as the deck pavement on many long-spanned steel bridges have exhibited severe distresses of cracking, rutting, shoving and de-bonding. Based on ten-year research works, this paper presented the state-of-the-practice of deck pavement on long-spanned steel bridges in mainland China. The typical distresses, their characteristics and the propagation have been figured out based on long-term field observation. Potential materials and structure solutions have been proposed according to field survey.

Keywords: long-spanned steel bridge, orthotropic steel decks, asphalt surfacing system, performance

1 INTRODUCTION

Orthotropic steel deck systems with cross-beams and longitudinal ribs have been widely used in modern long-span bridges to reduce the weight and depth of the girders [1]. The orthotropic steel deck plate of highway bridges requires a wearing surface not only to provide a smooth and safe riding surface for the vehicles passing through the bridges, but also for the purpose of loading dispersion layer to reduce the fatigue stresses in deck plate system caused by heavy traffic loading and corrosion protection of steel. The surfacing system on steel orthotropic decks act compositely with the steel deck plate and must be regarded as an integral part of the structural deck system [1–3]. It should be watertight, develop no cracks, be well bonded to steel deck plate, and long-lasting [3–8].

The application of orthotropic steel deck plate in highway bridges in China can be dated back to 1970s. However, it is only in recently fifteen years that experienced a rapid development of long-spanned steel bridges with orthotropic deck plates. Bituminous materials, such as gussasphalt, SMA and epoxy asphalt are commonly candidate surfacing materials. Their performances vary from excellent to poor, even a successful system in one bridges applied to another bridges with the similar weather conditions and traffics [9]. Many of pavements on the orthotropic steel decks of long-spanned steel bridges have exhibited cracking, rutting, shoving and de-bonding. The surfacing system on many long-spanned steel bridges can last no more than five years, some are reported to fail even within two or three years and visible fatigue cracks have been observed in the steel superstructure of deck plate system. It is thus

Table 1. Cable-supported steel bridges in the mainland of China [10].

Bridge name	Year	Main span (m)	Steel box-girder			Deck plate (mm)	Trapezoidal ribs					Original deck pavement
			Length (m)	Height (m)	Width (m)		Rib wall (mm)	Depth (mm)	Width at top (mm)	Rib spacing (mm)	Rib span (m)	
Suspension bridges												
Taizhou	2012	1080 × 2	2160	3.5	39.1	14/16	6/8	280	300	600	3.2	–
Xihoumen*	2009	1620	2220.8	3.51	36	14	8	280	300	600	3.6	Figure 1b
Zhujiang Huangpu	2008	1108	1108	3.5	38.6	16	8	280	300	600	3.2	Figure 1b
Runyang-South	2004	1490	1490	3	38.7	14/12	6	280	300	600	3.22	Figure 1b
Yichang Yangtze	2001	960	1187	3	30	12	6	280	300	590	4.02	Figure 1c
Haicang	2000	648	2000	3	28.8	12	6	280	300	600	3.5	Figure 1c
Jiangyin	1999	1385	1385	3	36.9	12	6	280	300	600	3.2	Figure 1a
Humen	1997	888	1997	3	33.6	12	8	260	320	620	4	Figure 1c
Xiling	1996	900	900	3	21.4	12	6	–	320	640	2.54	–
Cable-stayed bridges												
Edong	2010	926	901	3.8	38	16	8	300	300	600	3.0	Figure 1b
Jingyue	2010	816	1204	3.8	38.5	14/16	8	300	300	600	3.0	Figure 1b
Minpu***	2010	708	708	9	43.6/27	14/16	8	300	360	700	15.1	Figure 1b
Shanghai Yangtze	2009	730	1430	4	51.5	16	8	300	300	600	3.75	Figure 1b
Jingtang	2009	620	1210	3	30.1	14	8	280	300	600	3.5	Figure 1b
Sutong	2008	1088	2088	4	41	16/14	8	300	300	600	4	Figure 1b
3rd Nanjing	2005	648	1288	3.2	37.2	14/16	8	280	300	600	3.75	Figure 1b
2nd Nanjing	2001	628	1238	3.5	37.2	14	6	280	300	600	3.75	Figure 1b
Bashazhou	2000	618	904	3	30.2	12	8	260	320	640	6**	Figure 1c

*1. Twin-box girder;
**2. With a transverse rib in between two adjacent cross-beams;
***3. a.) Main girder is truss beam with double decks for highway traffic;
b.) With three transverse ribs in between two adjacent cross-beams.

of paramount importance to summarize the state-of-the-practice not only for a contribution towards a long-lasting surfacing system, but also for pro-longing fatigue life of superstructure of long-spanned steel bridges.

2 LONG-SPANNED STEEL BRIDGES IN CHINA

Within recently twenty years, more than twenty long-spanned steel bridges with orthotropic deck plates have been constructed to meet the requirements of rapid economy developments and travel demands. The deck system of long-spanned steel bridges in China normally consists of a deck plate, 12–14 mm thick and longitudinal trapezoidal or rounded closed ribs, supported with cross beams spaced from 3.2 to 4.5 m apart, as listed in Table 1. The steel decks are sand-blasted and then coated with zinc primer and waterproof membrane/bonding coat prior to the construction of 50–80 mm thick asphalt surfacing layers.

Typical structures of deck pavement used in China are shown as in Figure 1. Gussasphalt or Mastic Asphalt (MA), Epoxy Asphalt Concrete (EAC) and Stone Matric Asphalt (SMA) are the commonly candidate surfacing materials for those steel bridges. These materials are different in composition as illustrated in Figure 2. Their properties are also different according to the research results of Southeast University, as illustrated in Table 2.

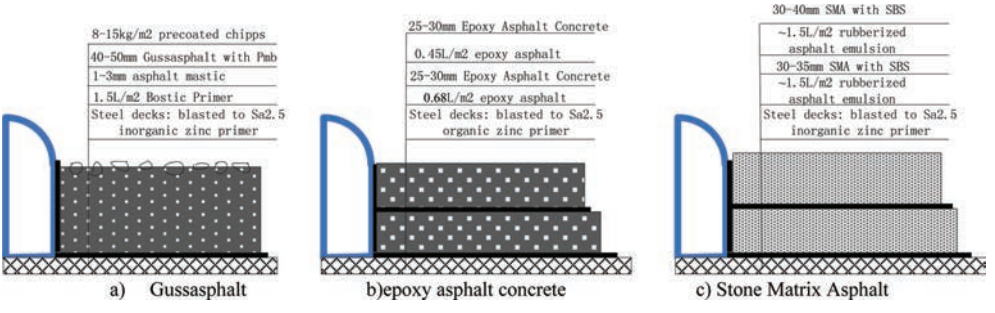

Figure 1. Basic pavement structures for long-spanned steel bridge decks in China.

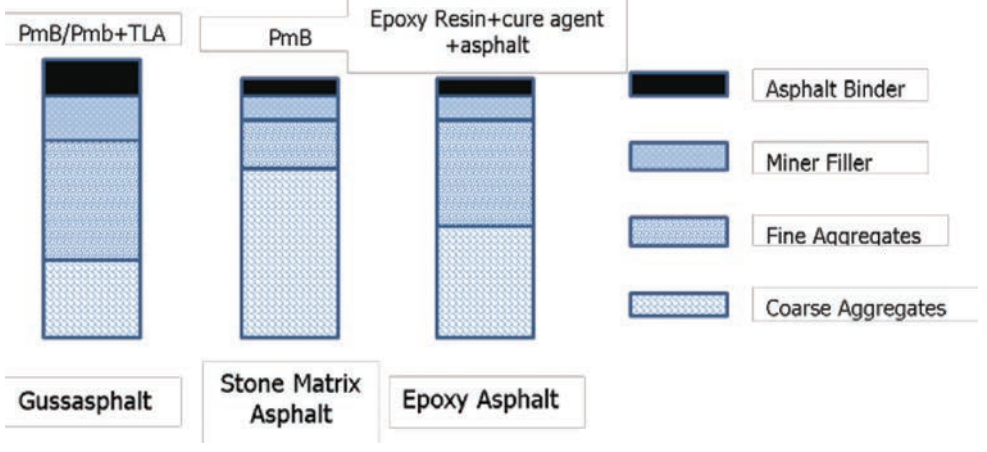

Figure 2. Composition of the commonly used surfacing materials.

Table 2. Properties of commonly used asphalt surfacing materials in China.

Properties	SMA10	GA	EAC	Test methods
Binder content	6.2	8.2	6.1	–
Air void/%	3.0	0.6	2.2	T0706-2011
Marshall stability	8.3	9.7	58	T0709-2011
Dynamic stability@60°C (0.7 MPa, cycle/mm)	4846	1276	17671	T0719-2011
Flexural strength@−15°C (1 mm/min, MPa)	10.31	13.72	24.18	T0715-2011
Flexural strain@−15°C (1 mm/min, 10^{-3})	3.09	8.26	3.72	T0715-2011
TSR (%)	88.3	95.7	91.8	T0729-2000
Expansion@15°C~−15°C (10^{-5}/°C)	2.25	2.14	1.52	T0720-1993

3 THE TYPICAL DISTRESSES AND THEIR PROPAGATIONS

The performances of asphalt surfacing on steel bridge decks in China vary from excellent to poor depending largely on local climate, deck plate flexibility, volume of heavy truck traffic, and the type and structure of the surfacing. The main distresses are fatigue cracking, slippage and de-bonding, rutting and shoving, and pothole. The performance of EAC systems is generally better other types of asphalt surfacing and its mean service life is longer than other systems.

3.1 *Fatigue cracking*

Fatigue cracking has been recorded in all type of pavement on orthotropic steel bridges decks. These cracks are located on the surface of the pavements near the conjunction ribs of the longitudinal and transverse stiffeners. The cracks were observed to propagate in depth and in length firstly, several weeks later, a second parallel longitudinal cracks could be initiated if the original one be not been sealed or repaired on time. And alligators or block cracking will be inevitable within several months, as summarized in Figure 3.

3.2 *Slippage and de-bonding*

Slippage of deck pavements were mainly observed in the surfacing system of SMA and MA at hot summer. The U-shaped cracks occur with the corrugation and shoving of the pavement. The cracks generally have a width of 2 cm to 10 cm covering at least lane, as shown in Figure 4.

Localized de-bonding has also been observed in the surfacing system of GA and SMA as shown in Figure 5. According to the repairing practice, asphalt layer adjacent the alligators or potholes will lose bonding as water can penetrate down to steel deck plate surface. Experiences also indicate that large area of the pavements will soon fail once the deck pavements system loses bond strength at the interface.

3.3 *Rutting, shoving and corrugations*

Rutting, shoving, and corrugations are typical distresses of the surfacing systems with thermal-plastic binder such as MA and dense graded asphalt concrete with polymer modified asphalt. Severe rutting has also occurred in the surfacing system of SMA. These problems could become even worse as the occurrence of fatigue cracking, the rapid increase of heavy duty traffic and the absence of efficient fighting against overloading, despite of higher performance grade polymer modified asphalt was adopted or natural hard asphalt was blended.

3.4 *Bubbles and hair cracks*

Bubbles and irregular micro-cracks were mostly found in the surfacing system of EAC. The bubble can be easily recognized with two or three radial micro-cracks. A ring crack of 15 cm to 30 cm in diameter will then develop within several weeks if the bubble crack be not properly repaired and sealed, and consequently, a pothole will form from bubbles as shown in Figure 6.

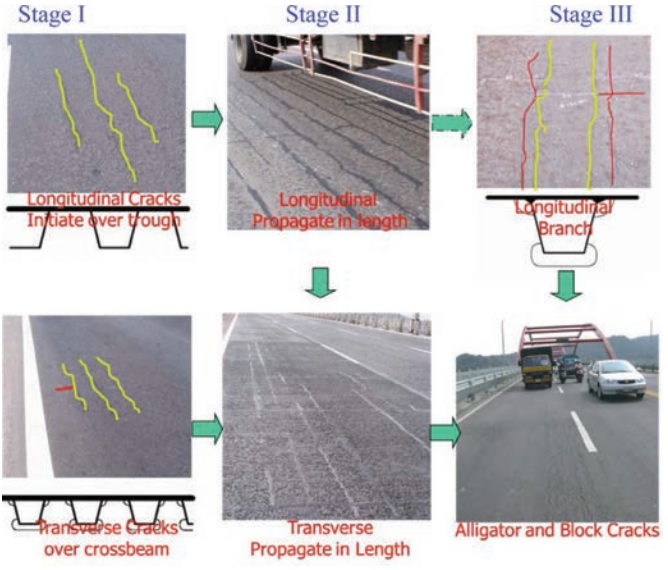

Figure 3. Fatigue cracking of pavements on orthotropic steel decks and its propagation.

Figure 4. Slippage cracking of SMA asphalt layer.

Figure 5. Debonding at the interface of asphalt surfacing and steel bridge decks.

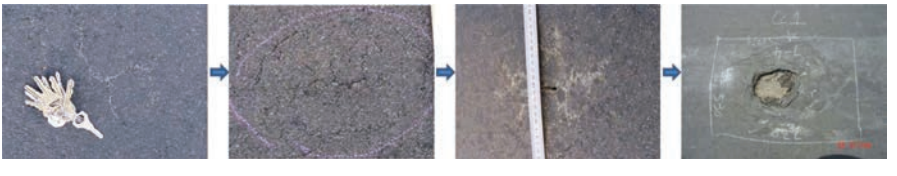

Figure 6. Bubble cracking and development of pothole.

4 CANDITATE MATERIALS AND STRUCTURES FOR DECK PAVEMENTS

4.1 *Gussasphalt*

Gussasphalt for road surfacing was developed principally by German engineers in the 1950s. It is estimated that some 45% of all existing autobahn surfaces in Germany are surfaced in gussasphalt and that many of them are 30 years old or more [11]. The application of GA on long-spanned steel bridge in the mainland of China begins from Jiangyin Bridge in 1999, with the paving technology introduced from England. The bridges opened to traffic 28th, September, 1999. Cracking was soon been founded in the first winter and visible rutting can been seen in the next summer. The whole system failed in the spring of 2002.

A schematic survey by Southeast University [12] has been launched soon after the first cracking and rutting have been observed in the deck pavement of Jiangyin bridge. According to the report, GA as a single layer cannot meet the requirements under the local traffic conditions and environments, although the use of pre-coated chips on the top can contribute to some content of rutting resistance. New binders with high viscosity at service temperature while low viscosity at construction temperature is desirable for a better rutting resistance against heavy duty traffic [13]. And the construction temperature should be lowered to decrease the reverse effect on primer coat, bonding and waterproofing layers below, as well as to shorten the aging effects of the binder itself. A new method for proportioning the gussasphalt is proposed based on workability, rutting resistance and low temperature flexibility [14]. The gradation is re-designed with a little bit higher content coarse aggregates and mineral filler used. The binder is a blend of 70% specially designed SBS-modified bitumen and 30% Trinidad lake asphalt. A polyolefin wax of Sasobit is added to the cooker to ensure that the gussasphalt is constructed at 180~200°C [15], which is relative low compared to conventional construction temperature up to 240°C. The new gussasphalt is proved to be successful in the test bridge of Runyang Bridges (2002), and in the test section of Jiangyin Bridge (2004), both are act as binder courses with a wearing courses of epoxy asphalt concrete. As the test section in Jiangyin Bridge lasted over than six year and developed only few longitudinal cracks and the test bridge of Runyang Bridges is still in very good condition up to now. Considering the flexibility and mechanization construction requirement of Taizhou Bridge [16], a blend of 70% straight bitumen with a penetration grade of 30–50 dmm and 30% TLA is adopted, and the content of limestone filler content decreases to 23%. A special blending system was designed to pre-blend before pumped into batch plant. Manufacture is in a batch plant with an output of 600 tonnes/day suitable for bridge deck work. The gussasphalt is held in the cookers for at best one hour with the mixing temperature (200°C) raising to 220°C for application by means of a small non-vibrating screed working on a 5 m width. An amount of 8 kg/m^2 of basaltic chips with the particle size of 13.2~19 mm was sprayed immediately the machine-laid surface of gussasphalt and compacted into the surface with a 2 tonnes steel roller, to increase the rutting resistance and interfacial shear strength.

4.2 *Epoxy asphalt concrete*

Epoxy asphalt concrete is a thermal-setting polymer concrete that is composed of a slow curing, Epoxy Asphalt binder mixed together with specially manufactured basaltic aggregates in the pug mill of an asphalt plant. The binder of Epoxy Asphalt is a two-phase chemical system in which the continuous phase is a thermoset epoxy resin and the discontinuous phase is a mixture of specialized asphalts. Epoxy Asphalt was first developed by Shell Oil Company in the late 1950's as a jet fuel and jet blast resistant specialty pavement for airfield applications.

In 1998, epoxy asphalt imported from United State (Type-C) has been introduced into China and firstly been used in 2nd Nanjing Yangtze River Bridge in 2000. In 2006, first commercial product of epoxy asphalt was manufactured with the patent developed by the deck pavement group of Southeast University (Type-N). The local epoxy asphalt has been applied successfully on Tianxinzhou Bridge in Wuhan, Minpu Bridge, Shanghai Yangtze

River Bridge and many other steel bridges in China. The viscosity of those two kind of epoxy asphalt and their hauling time are compared as shown in Figure 7 and Figure 8 [17].

Epoxy asphalt is a thermoset polymer-it will not melt after cured-rather than a thermoplastic material like SBS modified bitumen. It does not soften as much as bituminous materials and has shown no signs of rutting and shoving on previous projects in China that experience very high temperature up to 68°C in hot summer. Epoxy asphalt concrete is proved to be the super durable surfacing material for heavy duty traffic and extreme high temperature. It is widely used as surfacing materials not only for newly constructed long-spanned steel bridges, but also for resurfacing materials used in many rehabilitation applications in China. Epoxy Asphalt concrete is applied and compacted with conventional asphalt concrete paving equipment. The most difference of construction is that the mixture should been compacted before gel point. As mixing temperature and blending ration can both affect the time for the reactive system reaching the gel point, it is critical to ensure that the whole construction process are well organized and controlled. In order to avoid the hauling trucks running directly on the sticky surface of epoxy asphalt bonding coat, feeding machine has been adopted in Sutong Bridge. Full width paving technique, is employed in Taizhou Bridge to improve the construction efficiency and avoid potential cracking on longitudinal cracking that observed in the construction joints. Due to the specially designed bonding materials of two-stage reactive epoxy resin, hauling trucks can running on the surface of the bonding coat with no membrane removed by wheel, as shown in Figure 9. The cure reaction of epoxy resin will be activated during the paving process of the hot mixed epoxy asphalt concrete, which will contribute to a strong bonding at the interface of the two layers.

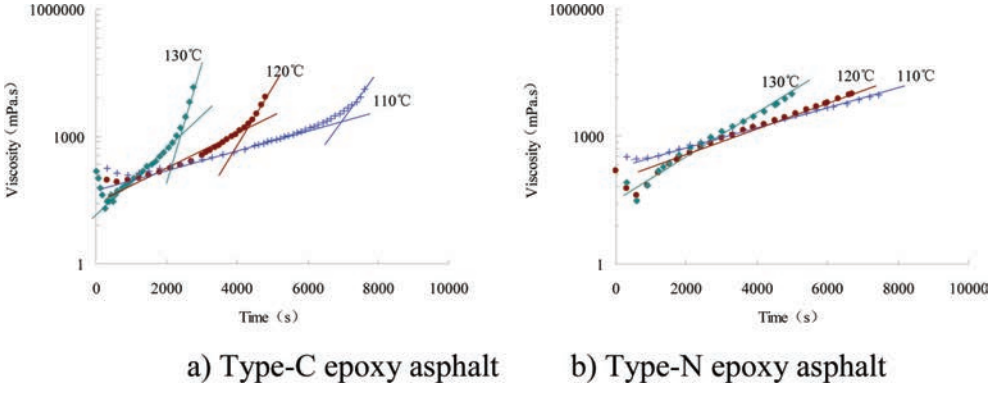

Figure 7. Viscosity curve of epoxy asphalt at isothermal cure condition.

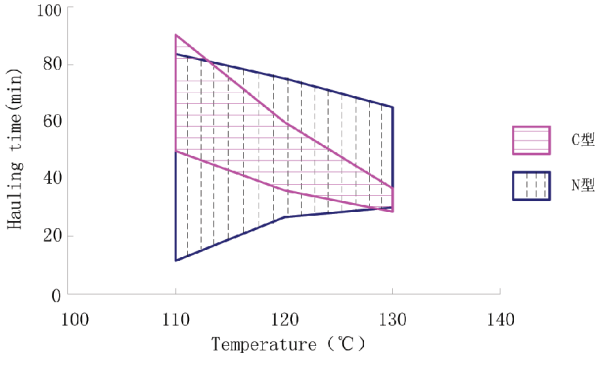

Figure 8. The time of tolerance for mixing and hauling epoxy asphalt.

Figure 9. Jointless epoxy asphalt concrete.

5 CONCLUSION

This paper presented state-of-the practice of asphalt surfacing on long-spanned orthotropic steel bridge decks in China. Fatigue cracking, de-bonding and rutting are main premature distresses on the deck pavements of long-spanned steel bridges. To overcoming the problems, we recommend that double layered epoxy asphalt for cable-stayed steel bridge with heavy duty traffic. SMA with high viscosity binder could also be used in the upper layer for cable-stayed steel bridge with light traffic loading. For the pavement on long-spanned suspension bridge with heavy duty traffic, the structure of epoxy asphalt constructed upon gussasphalt is recommended. The upper layer could be changed into SMA of dense grade asphalt concrete with high viscosity binder for suspension bridges with light traffic loading. It is also critical to improve the interfacial properties of deck pavement for both type of long-spanned steel bridges.

ACKNOWLEDGEMENT

The authors would thank National Natural Science and Foundation of China for the foundation project 50908053 and Key Technologies R&D Program of China for the project 2009BAG15B03.

REFERENCES

[1] Sukhen C., The Design of Modern Steel Bridges, *Boston: London Edinburgh*. 1992.
[2] AASHTO, LRFD Bridge Design Specifications, *American Association of State Highway and Transportation Officials, Washington, D.C.,* 1994.
[3] Roman W., Structural behaviour of surfacings on steel orthotropic decks and considerations for practical design, *Structural Engineering International*, (2): 124–129, 2002.
[4] Huang W., Theory and Method of deck paving design for long-span bridges, *Construction Industry Press, Beijing*, China, Oct., 2006 (in Chinese).
[5] Medani T.O., Design principles of surfacings on orthotropic steel bridge decks, Ph. D Dissertation. *Netherland: Delft University of Technology*, Jan, 2006.
[6] Chen X.H., Huang W., Yang J., et al, Cracking of wearing courses on steel orthotropic bridge decks, *6th RILEM International Conference on Cracking in Pavements*, Chicago USA, June 16–18, 2008.
[7] Chen X.H. The bending behaviours of asphalt surfacing on orthotropic steel bridge decks: a multi-scale approach, *Nanjing: Southeast University*, 2011, NSFC50908053. (in Chinese).
[8] Huang W., Ji Lin., Cheng G. et al, Runyang Construction Series: Asphalt surfacing for steel orthotropic decks, 1st Ed, Beijing, Communication, 2005. (in Chinese).
[9] Chen X.H., Fatigue Characters of deck pavement on steel orthotropic bridge decks based on composite beam, Ph D Dissertation, *Nanjing: Southeast University*, 2006, April. (in Chinese).

[10] Chen X.H., Qian Z.D., Liu X.Y., Zhang L., State-of-art of Asphalt surfacings on long-spanned orthotropic steel deck in China, *Journal of Testing and Evaluation*, 40(7): 1252–1259, 2012.
[11] Cliff Nicholls. Asphalt surfacings, Taylor & Francise-Library, 2004.
[12] Chen, X.H.; Huang, W.; Wang, J.W.; Cheng G. Damage causes of mastic asphalt pavement on orthotropic steel deck plate, *Journal of Traffic and Transportation Engineering*, 4(4), 5–9, 2004. (in Chinese).
[13] Chen, X.H.; Huang, W.; Li, H.T. High temperature stabilities of gussasphalt for orthotropic steel bridges. *Journal of Chongqing Jiaotong University*, 22(1), 32–35, 2003. (in Chinese).
[14] Chen, X.H.; Huang, W.; Wang, J.W. On design method of asphalt mixtures for orthotropic deck plates of long spanned steel bridges. *Highway*, (8), 34–38, 2004. (in Chinese).
[15] The deck pavement group of Southeast University, Asphalt surfacing for Runyang Yangtze River Bridges and the construction technologies, Southeast University, 2004. (in Chinese).
[16] The deck pavement group of Southeast University, Asphalt surfacing for Taizhou Yangtze River Bridges and the construction technologies, Southeast University, 2012. (in Chinese).
[17] Chen X.H., Qian Z.D., Equivalent factors of multi-axle loads for asphalt surfacing on steel bridge decks, *China Civil Engineering Journal*, 42(12), 197–202, 2009. (in Chinese).

This page intentionally left blank

Asphalt Pavements – Kim (Ed)
© 2014 Taylor & Francis Group, London, ISBN 978-1-138-02693-3

Rutting and cracking modeling of asphalt pavements considering nonlinear viscoelasticity and cohesive zone fracture

Soohyok Im
Texas A&M Transportation Institute, College Station, TX, USA

Hoki Ban
Hanyang University, Seoul, South Korea

Yong-Rak Kim
University of Nebraska-Lincoln, Lincoln, NE, USA

ABSTRACT: This study investigates the mechanical impact of the constitutive material behavior of asphalt layer (both nonlinear viscoelastic and fracture) for the prediction of pavement performance. In this study, a cohesive zone model was utilized to consider the fracture behavior of an asphalt mixture. The Semi-Circular Bend (SCB) fracture test was conducted to characterize the fracture properties of the asphalt mixture. Fracture properties were then used to simulate mechanical responses of pavement structures. In addition, Schapery's nonlinear viscoelastic constitutive model was implemented into the commercial finite element software ABAQUS via a user defined subroutine (user material, or UMAT) to analyze asphalt pavements subjected to heavy truck loads. A series of creep-recovery tests were conducted at various stress levels to obtain the stress-dependent viscoelastic material properties of the asphalt mixture. Utilizing the derived viscoelastic and fracture properties and the UMAT code, a typical pavement structure was modeled to investigate the effect of nonlinear viscoelasticity and fracture damage due to repeated heavy truck loads. Mechanical responses from two-dimensional finite element simulations of the pavement structure are presented and discussed.

Keywords: Asphalt pavement, nonlinear viscoelasticity, cohesive zone fracture, rutting, cracking

1 INTRODUCTION

Distresses in asphalt pavements, such as rutting and fatigue cracking, are critical safety issues affecting roadway users. Rutting, or, permanent deformation, is surface depression resulting from the accumulation of vertical displacements in asphalt pavement layers. The presence of this distress is even more dangerous for roadway users when the surface depression is filled with water. Accumulation of water in surface depressions increases the risk of vehicle hydroplaning, and, as a result of freezing and thawing cycles in cold regions, weakens pavement layers. Large damage areas, such as potholes, result from severe fatigue cracking in the pavement, combined with thermal stress. Pavement design methods should account for the combination of multiple factors that cause these distresses (i.e., traffic loads, environmental effects, and composite material constituent's combinations and interactions), in order to improve the reliability of the structures.

Recently, several studies including [1,2] have conducted viscoelastic analyses that consider the asphalt layer as linear viscoelastic and the other layers as elastic, using the finite element method in two-dimensional (2-D) or three-dimensional (3-D) models for predicting the time-dependent

response of flexible pavement. However, nonlinear response was not taken into consideration for their models in spite of abundant experimental observations [3,4] that present nonlinear response of asphalt binders and mixtures at certain levels of stress and strain.

The recent mechanistic-empirical (M-E) design guide predicts fatigue cracking resistance of asphalt pavements by considering various factors mentioned above. However, the M-E design guide is known to be limited in its ability to accurately predict mechanical responses in asphaltic pavements due to the use of empirically developed prediction models. Recently, the fracture behavior of asphalt mixtures has been studied by several researchers through fracture tests and numerical analysis by means of a cohesive zone model [5–8]. However, most studies were conducted at low temperature conditions, since fracture behavior at intermediate service temperatures is sensitive to loading rates. This study considered the fracture behavior of asphalt mixtures at an intermediate temperature condition (30˚C) using the cohesive zone model.

The primary objective of this study is to investigate more realistic pavement responses considering nonlinear-inelastic damage behavior of pavement structures. To this end, the SCB fracture test and creep and recovery test were performed to characterize the fracture properties and viscoelastic properties (linear and nonlinear) of an asphalt mixture. Then, the resulting test data were incorporated into relevant theories (such as Schapery's nonlinear viscoelastic model and the cohesive zone model) and numerical techniques (i.e., ABAUQS) to model a two-dimensional pavement structure subjected to heavy truck loads.

2 THEORY

2.1 *Schapery's nonlinear viscoelasticity*

Schapery's nonlinear viscoelastic single-integral constitutive model [9] for one-dimensional problems can be expressed in terms of an applied stress (σ) as follows:

$$\varepsilon(t) = g_0 D_0 \sigma + g_1 \int_0^t \Delta D\left[\psi(t) - \psi(\xi)\right] \frac{d\left(g_2\sigma\right)}{d\xi} d\xi \tag{1}$$

where,

ψ is the reduced time given by:

$$\psi(t) = \int_0^t \frac{d\zeta}{a_\sigma} \tag{2}$$

where,

g_0, g_1, g_2 and a_σ are the nonlinear viscoelastic parameters associated with stress level, t is the time of interest, and ξ is the integration variable. These parameters are always positive and equal to 1 for the Boltzmann integral in linear viscoelasticity. It is noted that Eq. (2) can include not only stress effect, but also effects such as temperature, moisture, and physical aging with each shift factor. D_0 and ΔD are uniaxial instantaneous and transient creep compliance at linear viscoelasticity respectively. The Schapery's nonlinear viscoelastic constitutive model was numerically implemented into the well-known commercial finite element software ABAQUS [10] via a user-defined subroutine called UMAT using recursive integration scheme developed by Haj-Ali and Muliana [11]. The UMAT subroutine code has been verified in the authors' previous study [12].

2.2 *Cohesive zone model*

Cohesive zone models regard fracture as a gradual phenomenon in which separation takes place across an extended crack tip (or cohesive zone) and where fracture is resisted by cohesive tractions, as illustrated in Figure 1. The cohesive zone effectively describes the material

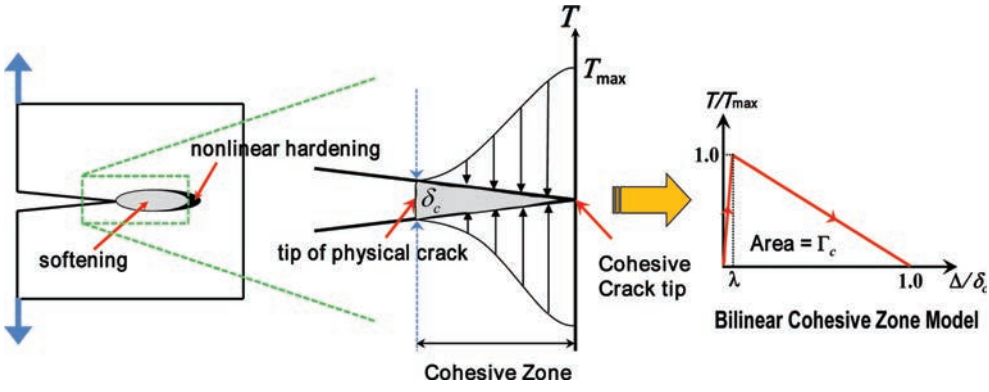

Figure 1. Illustration of cohesive zone model.

resistance when material elements are being displaced. Equations relating normal and tangential displacement jumps across the cohesive surfaces with the proper tractions define a cohesive zone model. Among numerous cohesive zone models developed for various specific purposes, this study used an intrinsic bilinear cohesive zone model [13–15]. The cohesive zone fracture energy (Γ_c), which is the locally estimated fracture toughness, can then be calculated by computing the area below the bilinear traction-separation curve with peak traction (T_{max}) and critical displacement (δ_c) as follows:

$$\Gamma_c = \frac{1}{2}\delta_c T_{max} \tag{3}$$

3 MIXTURE AND SPECIMEN FABRICATION

Table 1 summarizes mixture information, including Superpave PG asphalt binder grade, aggregate gradation of the mixture, and resulting binder content to satisfy mixture volumetric requirements. Binder content of 6.00% was determined as an appropriate value that satisfied all key volumetric characteristics of the asphalt mixture including the 4% ± 1% air voids.

To conduct the uniaxial static creep-recovery tests, a Superpave gyratory compactor was used to generate the cylindrical samples with a diameter of 150 mm and an approximate height of 170 mm. The compacted samples were then cored and sawn to produce testing specimens targeting an air void of 4% ± 0.5% with a diameter of 100 mm and a height of 150 mm after the compaction and coring-sawing process. To measure the axial displacement of the specimen under the static compressive force, epoxy glue was used to fix mounting studs to the surface of the specimen so that the three Linear Variable Differential Transformers (LVDTs) could be attached to the surface of the specimen at 120° radial intervals with a 100 mm gauge length. Next, the specimen was mounted in the UTM-25kN testing station for creep-recovery testing. Figure 2 illustrates overall laboratory processes to obtain a specimen for the uniaxial static creep and recovery test.

Figure 3 demonstrates the specimen production process for the SCB fracture test using the Superpave gyratory compactor and saw machines. The Superpave gyratory compactor was used to produce tall compacted samples: 150 mm in diameter and 175 mm in height. Five slices (each with a diameter of 150 mm and a height of 25 mm) were obtained by removing the top and bottom parts of the tall sample. Finally, the slice was cut into two identical halves, and the saw machine was used to make a vertical notch 25 mm long and 2.5 mm wide.

Table 1. Mixture information.

Mixture ID	Binder PG	Aggregate gradation (% passing on each sieve)									% Binder	% Voids
		19.0 mm	12.5 mm	9.5 mm	# 4	# 8	# 16	# 30	# 50	# 200		
AC mixture	64-28	100	95	89	72	36	21	14	10	3.5	6.00	4.09

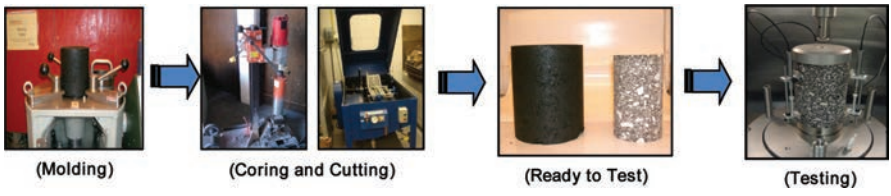

Figure 2. A specimen production process.

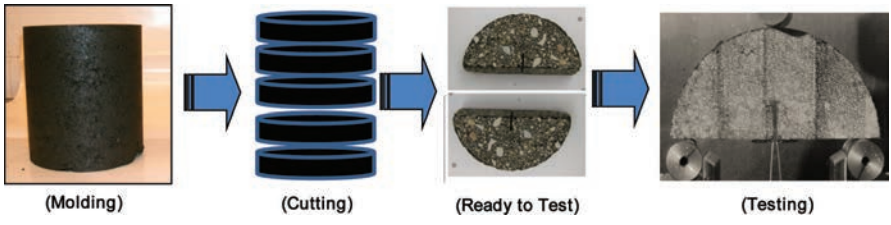

Figure 3. SCB specimen fabrication and fracture testing configuration.

4 LABORATORY TESTS AND MATERIAL PROPERTIES

4.1 *Creep-recovery test and viscoelastic material properties*

The static creep-recovery test was conducted on replicate specimens of the asphalt mixture at 30°C. Based on several preliminary tests conducted to find an appropriate creep loading time and recovery time, a creep stress for 30 seconds followed by recovery time of 500 seconds was applied to the specimens. A large range of stress levels was applied to identify the level of (stress-independent) linear viscoelastic range and to characterize stress-dependent nonlinear behavior of the mixture. Repeated preliminary tests indicated that the asphalt mixture was linear viscoelastic up to 700 kPa uniaxial creep stress. In other words, nonlinear viscoelasticity starts when the stress level is greater than 700 kPa. Therefore, a creep-recovery curve at the threshold stress level within the linear viscoelastic range was used to find linear viscoelastic properties, and other creep-recovery curves obtained from higher stress levels than the threshold stress were used to characterize the stress-dependent nonlinear viscoelastic properties. Figure 4 presents repeated creep-recovery test results. As shown in the figure, the higher stress level generated larger creep strain and provided less recovery at the testing temperature (30°C).

Using creep-recovery test results, the linear viscoelastic properties at the threshold stress level were identified, as were the nonlinear viscoelastic properties at higher stress levels. The procedure to obtain viscoelastic material properties of the asphalt mixture is well described in the authors' previous study [12]. Table 2 summarizes the viscoelastic parameters of the asphalt mixture: linear viscoelastic Prony series coefficients and nonlinear viscoelastic parameters.

4.2 *SCB fracture test and fracture properties*

In this study, the SCB fracture test was adopted. Even if the SCB geometry has some limitations such as complex stress state [6], it is practically attractive in that it is very repeatable,

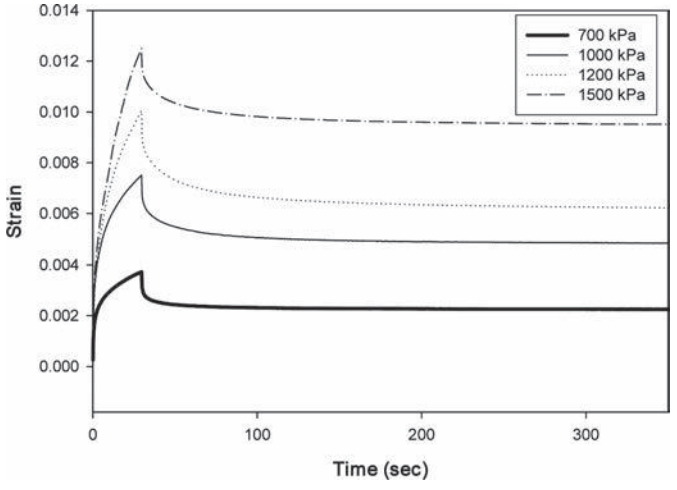

Figure 4. Creep-recovery test results at various stress levels.

Table 2. Viscoelastic properties determined through the characterization process.

Linear viscoelastic properties (Prony series coefficients)			Nonlinear viscoelastic parameters			
				Polynomial constants, *i*		
N	λ_n (s^{-1})	D_n (MPa^{-1})	Parameters	1	2	3
1	10^2	6.70×10^{-4}	g_0 (α_i)	0.05	0.77	–0.54
2	10	8.91×10^{-5}	g_1 (β_i)	0	0.01	–0.01
3	1	5.17×10^{-4}	g_2 (γ_i)	0.36	0.83	–0.71
4	10^{-1}	6.45×10^{-4}	a_σ (δ_i)	–0.14	0.84	–0.83
5	10^{-2}	9.47×10^{-4}				
6	10^{-3}	2.60×10^{-4}				
7	10^{-4}	2.73×10^{-4}				
8	10^{-5}	7.54×10^{-4}				

simple to perform, and that multiple testing specimens can be easily prepared through a routine process of mixing and Superpave gyratory compacting of asphalt mixtures. Furthermore, the SCB geometry is even more attractive considering the fracture characteristics of field cores, which are usually circular. Based on these practical benefits, the SCB testing configuration has become a popular geometry for evaluating the fracture behavior of bituminous mixtures.

Multiple SCB specimens of the asphalt mixture were prepared and tested with four different monotonic displacement rates (i.e., 1, 5, 10, and 50 mm/min.) at a testing temperature of 30˚C. As shown in Figure 3, metallic rollers separated by a distance of 122 mm (14 mm from the edges of the specimen) were used to support the specimen. Reaction force at the loading point was monitored by the data acquisition system installed in the mechanical testing machine. In addition, this study utilized the Digital Image Correlation (DIC) system incorporated with the SCB fracture test to more accurately capture the displacements at the mouth (denoted as Notch Mouth Opening Displacements [NMOD]) and at the tip (denoted as Notch Tip Opening Displacements, [NTOD]) of the initial notch. The accuracy of the DIC test results was well verified in the authors' previous study [16].

Fracture properties of the asphalt mixture were then determined by numerical simulations of the SCB fracture tests. This was implemented to identify fracture characteristics along the

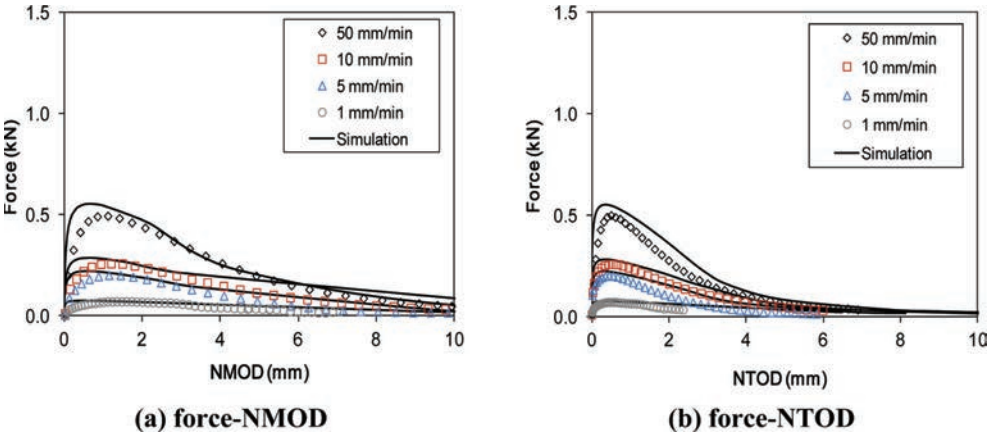

Figure 5. SCB test results vs. cohesive zone model simulation results.

Table 3. Cohesive zone fracture parameters determined.

Temperature (°C)	Loading rate (mm/min.)	Cohesive zone fracture parameters	
		T_{max} (kPa)	Γ_c (J/m^2)
30	1	8.0E+01	220
	5	2.5E+02	400
	10	3.2E+02	550
	50	6.5E+02	900

Fracture Process Zone (FPZ), which is locally associated with initiation and propagation of cracks through the SCB specimens. The cohesive zone fracture properties (two independent values of the three: T_{max}, δ_c, and Γ_c) in the bilinear model were determined for each case through the calibration process until a good match between test results and numerical simulations was observed. Figure 5 presents good agreements between the test results (average of the three SCB specimens per case) and finite element simulations. Resulting fracture properties (T_{max} and Γ_c) at each loading rate are presented in Table 3.

5 FINITE ELEMENT ANALYSIS OF PAVEMENT

A standard asphalt pavement was modeled through the 2-D finite element method in order to investigate the mechanical performance behavior of the pavement when subjected to heavy truck loading. The 2-D finite element modeling was conducted using a commercial package, ABAQUS Version 6.8 [10], which was incorporated with the cohesive zone fracture and the developed nonlinear viscoelastic UMAT.

Figure 6 illustrates a four-layered asphalt pavement structure (101.6 mm thick asphalt layer, 254 mm Portland Cement Concrete (PCC) layer with PCC joints, 101.6 mm Bituminous Foundation Course (BFC) and 152.4 mm subgrade). Both sides of the vertical edge of the finite element pavement model were fixed in the horizontal direction, and the bottom of the model was fixed in the vertical direction to represent a rock foundation. The red line in the figure indicates the region where cohesive zone elements were inserted in the mesh to allow cracking (reflective and/or top-down). The underlying layers (i.e., PCC, BFC, and subgrade) were modeled as isotropic linear elastic, while viscoelastic response was considered to

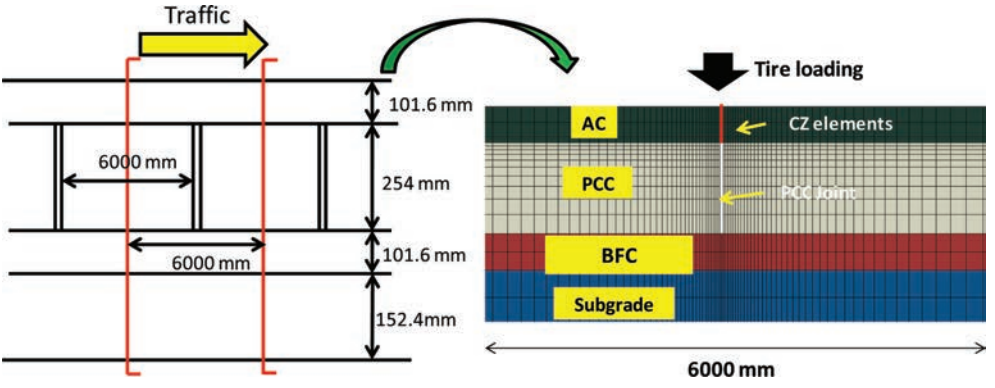

Figure 6. A pavement geometry and boundary conditions for fe modeling.

describe the behavior of the asphalt concrete surface layer: Prony series coefficients and nonlinear viscoelastic parameters presented in Table 2. Also, cohesive zone fracture parameters, Γ_c = 400 J/m^2 and T_{max} = 250 kPa presented in Table 3, were used for the fracture behavior of the asphalt concrete surface layer. Correspondingly, the surface layer can dissipate energy due to its viscoelastic nature and cohesive zone, which results in permanent deformation (rutting) and fracture of the layer.

A tire pressure of 720 kPa and axial load of 35.5 kN were applied to the pavement based on a study by Yoo [17]. The loading configuration of the Class 9 truck was used in this study. A 15.4 m Class 9 truck trailer traveling at 80 km/h takes 0.692 seconds to pass over a fixed point on the pavement. Therefore, the first truck passes the fixed point for 0.692 seconds and after 30 seconds a second truck passes through the same point. The passage of a total of 50 trucks was simulated in this study. The details of the truck loading conditions and properties of the underlying layers can be found elsewhere [18].

6 SIMULATION RESULTS

Among many mechanical responses, the vertical displacement from the pavement surface and the crack opening (horizontal) displacement through the depth of the asphalt concrete layer were examined since they are strongly related to the two primary distresses of asphaltic pavement: rutting and cracking.

Figure 7 compares permanent deformation (rut depth) accumulated from each truck loading up to the 50 cycles obtained from the four modeling approaches: linear viscoelastic with or without the cohesive zone fracture and nonlinear viscoelastic with or without the cohesive zone fracture. It clearly shows the increasing difference in the rut depth from the all four cases as the number of loading cycles increases. At the end of the 50 cycle simulation, the total rut depth predicted from the nonlinear viscoelastic with the cohesive zone fracture was the greatest, while the rut depth simulated from the linear viscoelastic without cohesive zone was the smallest. Figure 8 shows crack opening displacements from the top surface to the bottom of the asphalt layer at the end of 50th loading cycle from the two modeling approaches: linear and nonlinear viscoelastic with the cohesive zone fracture. As shown in the figure, the two modeling cases presented significant differences in the fracturing of the asphalt at the bottom of the layer. This is because the nonlinear viscoelastic case with cohesive zone fracture experienced tensile stresses approximately four times greater than those from the linear viscoelastic case at the bottom of the asphalt layer. The figures clearly demonstrate the effects of material characteristics on the overall pavement performance.

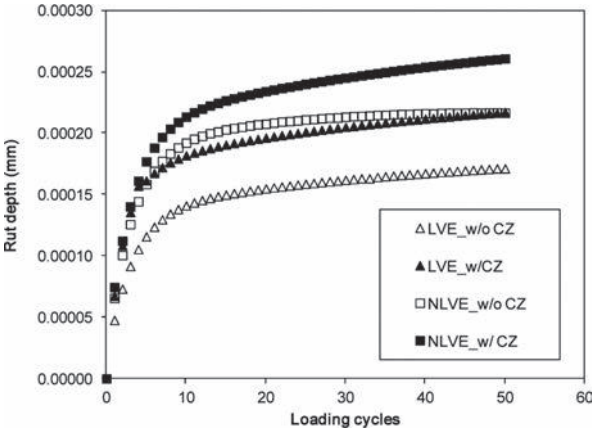

Figure 7. Comparison of permanent deformation up to 50 loading cycles.

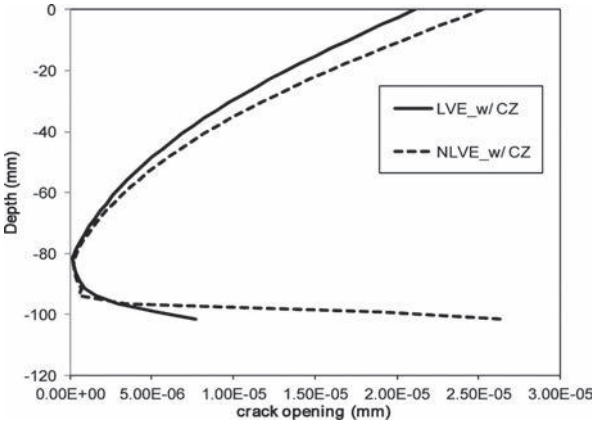

Figure 8. Depth-crack opening: LVE vs. NLVE.

7 SUMMARY AND CONCLUSION

More realistic pavement responses were attempted by considering the nonlinear-inelastic damage behavior of an asphaltic pavement structure subjected to repeated heavy truck loads in this study. The following bullet points summarize the conclusions that can be drawn:

- Schapery's nonlinear viscoelastic model was implemented into the ABAQUS via a user material subroutine UMAT.
- Creep-recovery tests at varying stress levels were conducted to identify viscoelastic mixture characteristics. As expected, test results clearly demonstrated stress-dependent mixture characteristics.
- At intermediate service temperatures such as 30°C, cohesive zone fracture properties of asphalt mixtures varied as the loading rate changed.
- Two-dimensional finite element simulations of a pavement structure showed significant differences among the cases (linear viscoelastic vs. nonlinear viscoelastic with and without fracture damage) in the prediction of pavement performance (both rutting and cracking).

- Although test results and numerical simulations presented in this study are limited to make any definite conclusions, performance differences observed between individual cases are considered significant and should be addressed in the process of performance-based pavement design. This further implies the importance of proper and more realistic characterization of paving materials.

ACKNOWLEDGEMENTS

The authors would like to thank the Mid-America Transportation Center (MATC) and US Department of Transportation (US-DOT) for their financial support.

REFERENCES

[1] Al-Qadi, I.L., Yoo, P.J., and Elseifi, M.A. Characterization of pavement damage due to different tire configurations, Journal of the Association of Asphalt Paving Technologists, 74, pp. 921–962. 2005.
[2] Kim, J., Roque, R., and Byron, T. Viscoelastic analysis of flexible pavements and its effects on top-down cracking, Journal of Materials in Civil Engineering, 27(7), 324–332. 2009.
[3] Masad, E. and Somadevan, N. Microstructural finite-element analysis of influence of localized strain distribution of asphalt mix properties. Journal of Engineering Mechanics, 128, pp. 1105–1114. 2002.
[4] Collop, A.C., Scarpas, A., Kasbergen, C., and Bondt, A. Development and finite element implementation of stress-dependent elastoviscoplastic constitutive model with damage for asphalt. Transportation Research Record, 1832, 96–104. 2003.
[5] Marasteanu, M.O., Dai, S.T., Labuz, J.F., and Li, X. Determining the low-temperature fracture toughness of asphalt mixtures. Transportation Research Record 1789, 191–199. 2002.
[6] Wagoner, M.P., Buttlar, W.G., and Paulino, G.H. Development of a single-edge notched beam test for asphalt concrete mixtures, Journal of Testing Evaluation, 33(6), pp. 452–460. 2005.
[7] Wagoner, M.P., Buttlar, W.G., and Paulino, G.H. Disk-shaped compact tension test for asphalt concrete fracture, Society for Experimental Mechanics, 45(3), pp. 270–277. 2005.
[8] Kim, H., Wagoner, M.P., and Buttlar, W.G. Simulation of fracture behavior in asphalt concrete using a heterogeneous cohesive zone discrete element model, Journal of Materials in Civil Engineering, 20(8), pp. 552–563. 2008.
[9] Schapery, R.A. On the Charcaterization of Nonlinear Viscoelastic Materials, Polymer Engineering and Science, 9, pp. 295–310. 1969.
[10] ABAQUS User's Manual Version 6.8. Hibbit, Karlsson & Sorenson, Inc., Pawtucket, R.I. 2008.
[11] Haji-Ali, R. and Muliana, A. Numerical finite element formulation of the Schapery non-linear viscoelastic material model, International Journal for Numerical Methods in Engineering, 59, pp. 25–45. 2004.
[12] Ban, H., Im, S., and Kim, Y. Impact of Truck Loading on Design and Analysis of Asphaltic Pavement Structures-Phase II, Mid-America Transportation Center, MATC-UNL:321, Final Report, 2011
[13] Geubelle, P. and Baylor, J. Impact-induced delamination of laminated composites: A 2D simulation, Composites Part B—Engineering, 29(5), pp. 589–602. 1998.
[14] Espinosa, H.D. and Zavattieri, P.D.A grain level model for the study of failure initiation and evolution in polycrystalline brittle materials, Part I: Theory and numerical implementation, Mechanics of Materials, 35, pp. 333–364. 2003.
[15] Song, S.H., Paulino, G.H., and Buttlar, W.G.A bilinear cohesive zone model tailored for fracture of asphalt concrete considering viscoelastic bulk material, Engineering Fracture Mechanics, 73(18), pp. 2829–2847. 2006.
[16] Im, S., Ban, H., and Kim, Y. Rate- and Temperature-Dependent Fracture Characteristics of Asphaltic Paving Mixtures, Journal of Testing Evaluation, 41, no 2: doi:10.1520/JTE20120174. 2012.
[17] Yoo, P.J. Flexible pavement dynamic responses analysis and validation for various tire configurations, PhD Dissertation, University of Illinois at Urbana-Champaign, 2007.
[18] Im, S., Ban, H., and Kim, Y. Impact of Truck Loading on Design and Analysis of Asphaltic Pavement Structures-Phase III, Mid-America Transportation Center, MATC-UNL:427, Final Report, 2012.

This page intentionally left blank

Asphalt Pavements – Kim (Ed)
© 2014 Taylor & Francis Group, London, ISBN 978-1-138-02693-3

The application of strain limit based design to heavy industrial pavements

Dennis Morian
Quality Engineering Solutions Inc., Conneaut Lake, PA, USA

Guangming William Wang
Quality Engineering Solutions Inc., Gainesville, FL, USA

Douglas Frith
Quality Engineering Solutions Inc., Reno, NV, USA

ABSTRACT: The concept of strain limit design as applied to heavy industrial pavements is discussed. The strain limit approach has been applied following the mechanistic design methodology provided in the Asphalt Institute's MS 23 document. This design approach has been found to be beneficial in some cases when used in the design of flexible pavement sections for heavy duty industrial asphalt pavements with high load repetitions.

Several multilayer pavement systems are considered when subjected to various heavy wheel load configurations, to assess the potential benefit to pavement cost and performance. The paper assesses how the design input conditions of subgrade support, applied wheel load stress, and load repetitions influence the effectiveness of the strain limit design approach. Under some combinations of design conditions the strain limit design approach shows promise for use in the design of these heavily loaded pavements.

Keywords: heavy industrial pavements, multi-layer mechanistic analysis, strain limit design of flexible pavements, applied wheel load stress

1 BACKGROUND

The concept of improving the design life by incorporating a fatigue resistant asphalt base has been recognized for around 20 years. Numerous studies indicate that fatigue life is increased with higher asphalt binder content in the rich-bottom mix [1–7]. Coupled with the long life pavement concept, the fatigue resistant asphalt base has enabled pavement designers to significantly improve the cost effectiveness of asphalt pavement sections for many highways. The concept is to produce a layer at the bottom of the asphalt layer which is more flexible and less susceptible to the initiation of fatigue cracking at the bottom of the asphalt layer system that consequently is effective in increasing the fatigue life of the pavement section. The practice has been to increase the asphalt content of an asphalt base layer by about 0.5% from the target mix design value. This has the effect of decreasing the effective air voids in the mix, and improving mix compactability. This approach, sometimes called a rich asphalt base, can also be achieved by reducing the design air voids of the asphalt base material, resulting in an increase in effective asphalt content.

This design approach has also been shown to be effective in improving the cost effectiveness of industrial asphalt pavement sections designed for heavy wheel loads. While the use of a fatigue resistant base typically does not result in a long life pavement at conventional thicknesses in these cases, it can result in the effective design of a thinner, less costly pavement section due to the ability to better resist the higher stresses produced from heavy wheel loads.

Our experience over the past dozen years with heavy wheel load design projects has been that in some cases this approach to a reduced pavement thickness works in some cases, but not in others. So the objective of this paper is to present additional assessment of these designs to better identify when the fatigue resistant base concept is effective, and when it is not.

2 SENSITIVITY ANALYSIS

Several input factors are of great importance in pavement design. These include, in addition to the wheel load factors, the subgrade stiffness, number of load repetitions, and layer thickness. Multiple analyses were conducted evaluating the effect of these input parameters on the effectiveness of a fatigue resistant asphalt base. Analyses were performed using an elastic layer tool, following the design methodology of the asphalt institute, and specifically MS 23. The analysis of each input factor follows.

The flexible pavement design principle is based upon multilayered elastic design concepts developed by the Asphalt Institute (AI). This procedure assumes that the application of a load to the pavement produces two critical elastic strains, horizontal tensile strain at the bottom of the asphalt concrete layer, and the vertical compressive strain at the top of the subgrade layer. Design criteria, in terms of maximum allowable values for both critical strains, are used as the basis for designing pavement thickness.

A storage area failure model has been used for the pavement damage analysis. This military storage model is considered to be suitable as it was developed specifically for heavy, slow moving vehicles with large tires.

AI equations for fatigue and rutting are expressed as follows:

$$N_f = f_1(\varepsilon_t)^{-f_2}(E_1)^{-f_3} \tag{1}$$

$$N_d = f_4(\varepsilon_c)^{-f_5} \tag{2}$$

where ε_t is the tensile strain at the bottom of the AC layer, and ε_c is the compressive strain on the top of the subgrade. The constants f_1, f_2, f_3, f_4 and f_5 are coefficients, whose valuese for the milirary storage model are presented below:

$$f_1 = 479; f_2 = 5; f_3 = 2.665; f_4 = 1.0E-17; f_5 = 7.10227 \tag{3}$$

2.1 *Subgrade modulus*

The importance of subgrade stiffness is even greater for heavy wheel load design than for conventional roadway design. An assessment of the effect of subgrade modulus illustrates this importance. In this analysis, the subgrade modulus value is varied from 12,500 to 22,500 psi. When the subgrade modulus is 22.5 ksi, pavement failure is controlled by fatigue. Decreasing the elastic modulus of the bottom AC layer will result in an increase in pavement life. When the subgrade modulus is 15.0 ksi, the pavement failure is controlled by rutting. Increasing the elastic modulus of the bottom AC layer will result in an increase in pavement life. When the subgrade modulus is 18 ksi, pavement failure is first controlled by rutting, and then switches to fatigue, which as pavement life is first increased with the increase in the modulus of the lower asphalt layer and then decreased once the pavement failure is controlled by fatigue. Results of this assessment are illustrated in Figure 1.

2.2 *Base modulus*

As shown in Figure 2, when the base modulus is 65 ksi, pavement failure is controlled by rutting. Increasing the elastic modulus of the bottom AC layer will result in an increase in pavement life. When the base modulus value is set at 50 ksi and 40 ksi respectively, pavement

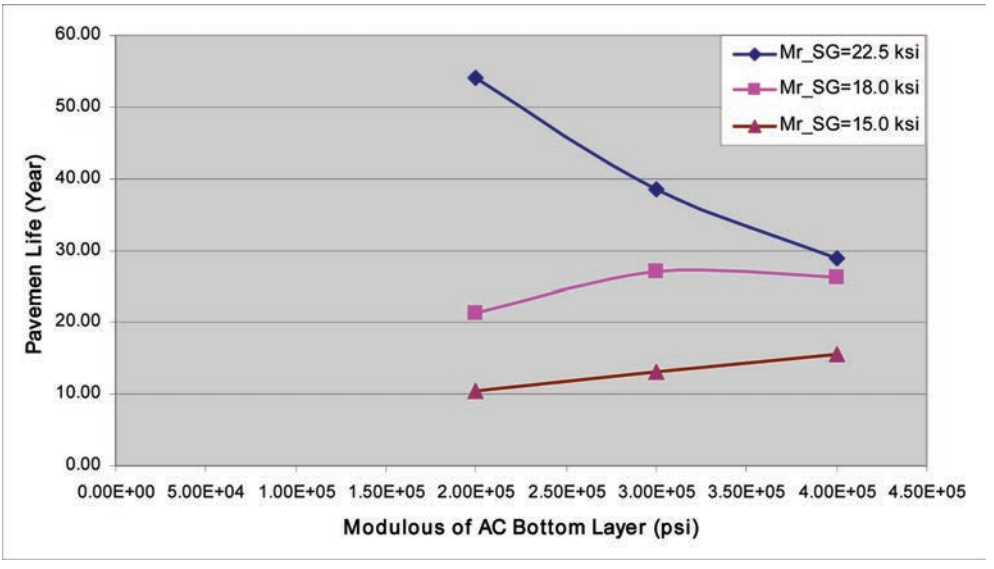

Figure 1. Effect of rich bottom AC layer on pavement life due to subgrade moduli.

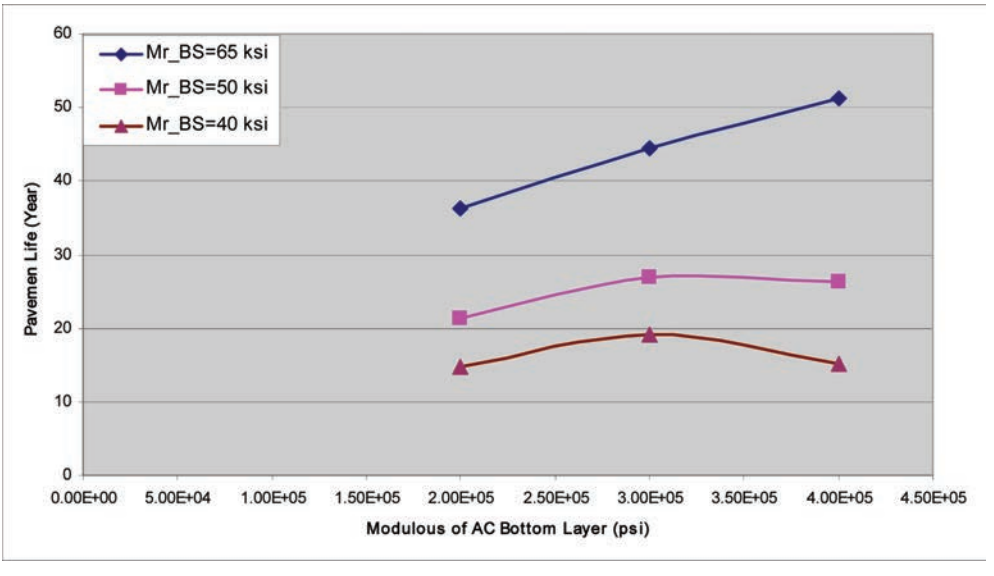

Figure 2. Effect of rich bottom AC layer on pavement life due to base moduli.

failure is first controlled by rutting, and then switches to fatigue, as the pavement life is first increased with the increase in the elastic modulus of the bottom AC layer and then decreased once the pavement failure is controlled by fatigue.

2.3 *Asphalt base thickness*

As shown in Figure 3, when the base thickness is 15″, the pavement failure is controlled by rutting. Increasing elastic modulus of the bottom AC layer will result in an increase in pavement life. When the base thickness is increased to 18″, the pavement failure is first controlled

by rutting as pavement life is first increased as the elastic modulus of bottom AC layer is increased, and then decreased as the failure mode switches to fatigue.

2.4 *Wheel load*

As shown in Figure 4, when the wheel load is light (for both 35,000 lbs and 25,000 lbs cases), pavement failure is controlled by fatigue. Increasing the elastic modulus of the bottom asphalt layer will result in a decrease in pavement life. When the wheel load is increased to 45,000 lbs, pavement failure is first controlled by rutting with a low AC modulus, and then switches to

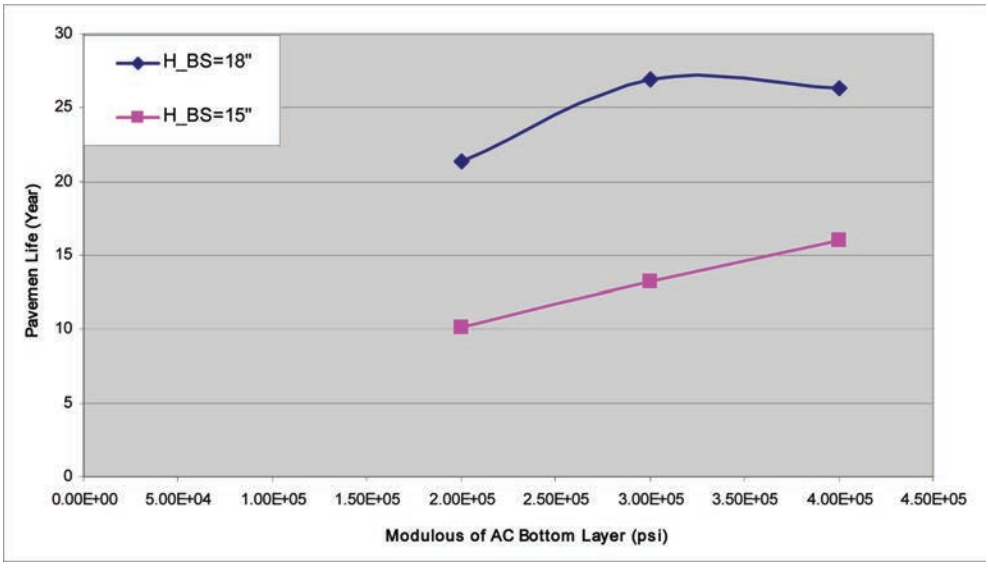

Figure 3. Effect of rich bottom AC layer on pavement life due to base thickness.

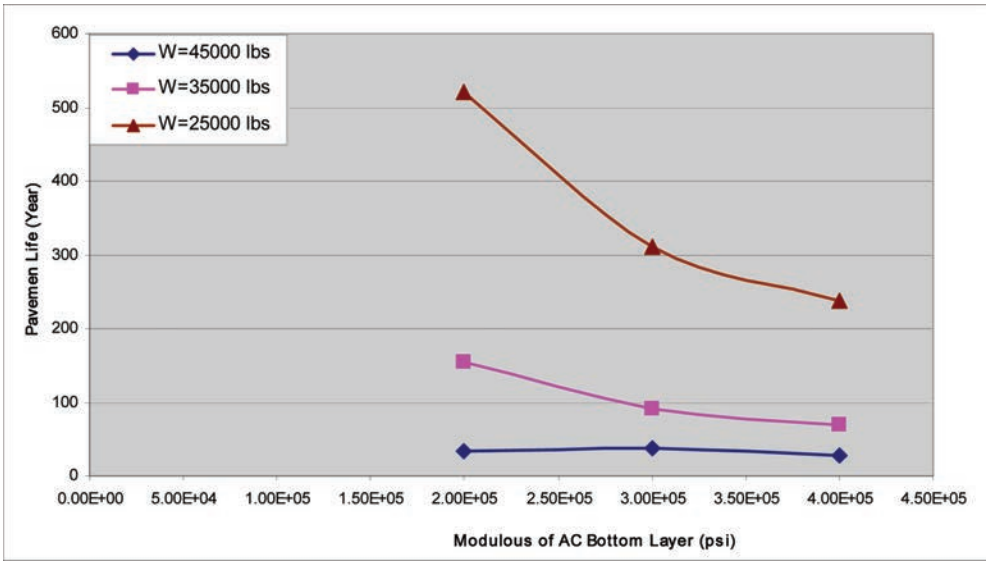

Figure 4. Effect of rich bottom AC layer on pavement life due to wheel load.

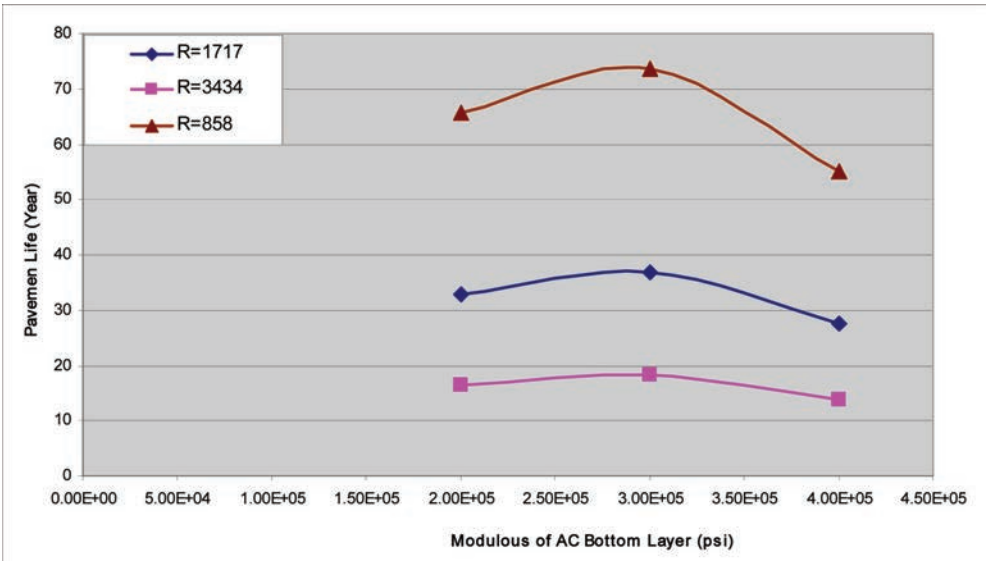

Figure 5. Effect of rich bottom AC layer on pavement life due to load repetitions.

fatigue as the AC modulus increases. This results in the pavement life first increasing with an increase in the elastic modulus of the bottom AC layer, and then decreasing once the pavement failure is controlled by fatigue.

2.5 *Load repetitions*

As shown in Figure 5, changes of load repetitions have no effect on the change in failure model. In general, increasing load repetitions will result in reduced pavement life.

By examining the above analysis of individual parameters, it can be observed that the contribution of a rich bottom asphalt layer to increased pavement life is only effective when failure is controlled by the fatigue design criteria. In this case, decreasing the elastic modulus of the asphalt rich bottom will have the effect of increasing pavement life. If pavement failure is controlled by the rutting criteria, a rich bottom will result in a decrease in pavement life.

3 DYNAMIC RESPONSE

In order to check the dynamic response on the tensile stress at the bottom of the asphalt layer, and vertical compressive stress on the top of the subgrade, a dynamic analysis was conducted using the 3D-Move software to compare the different stress responses between a conventional bottom asphalt mix and rich asphalt bottom mix. Five percent (5.0%) asphalt content by weight is assumed for the conventional bottom asphalt mix, and 5.5% asphalt content is assumed for the rich bottom asphalt mix. The loading configuration used in the analysis is shown in Figure 6, where x is the vehicle travel direction. The dynamic responses of the tensile stress at the asphalt bottom are presented in Figures 7 through 12 at three critical locations; A, B, and C. The results indicate the rich bottom asphalt mixture will result in less tensile stress than the conventional asphalt base mixture. Considering the vertical compressive stress on the top of the subgrade, the rich asphalt bottom mix has very little impact, as shown in Figure 13. This may be attributed to the thick thickness of the asphalt pavement. Table 1 summarizes the results of the dynamic response. As shown, the maximum tensile stress was reduced by around 3% when rich-bottom asphalt mix is used.

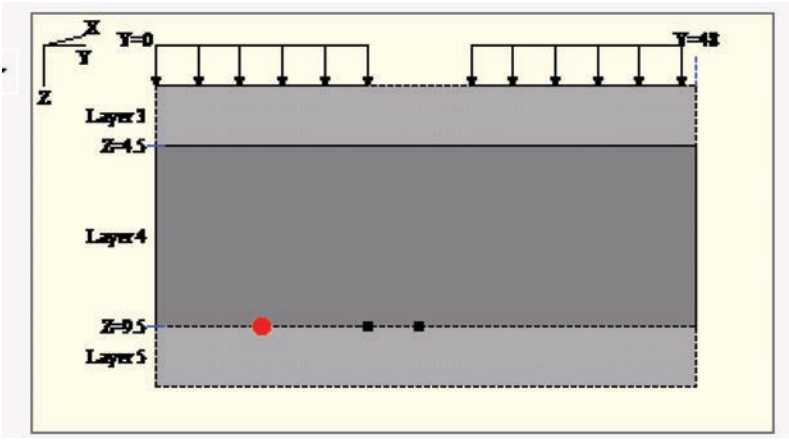

Figure 6. Loading configuration used in the dynamic analysis.

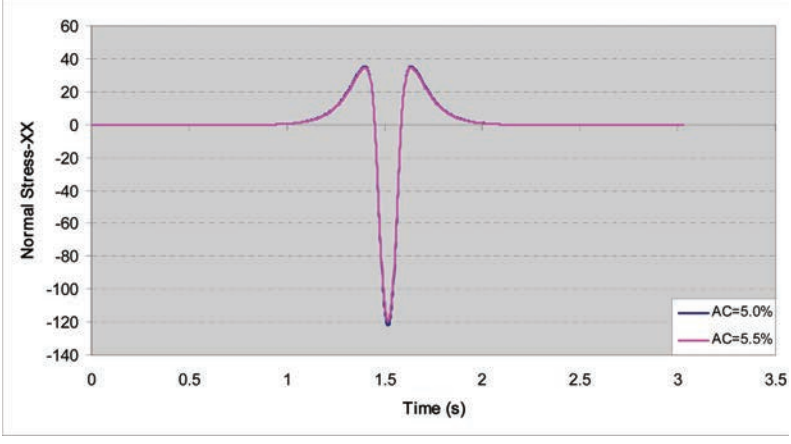

Figure 7. Dynamic response of normal stress-xx at location A.

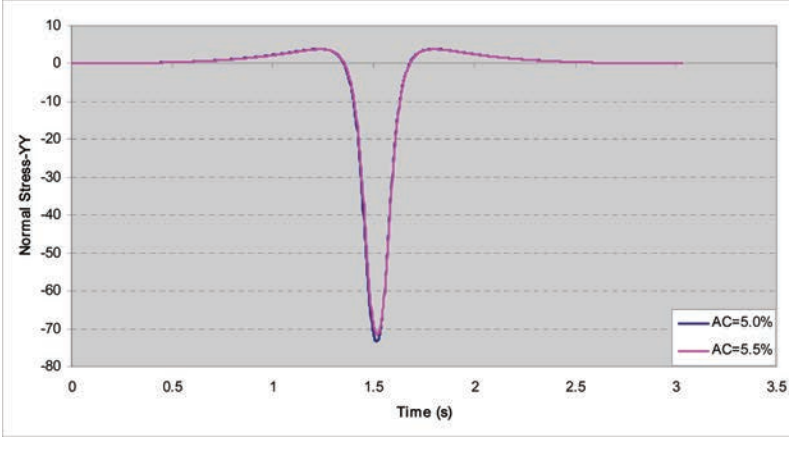

Figure 8. Dynamic response of normal stress-yy at location A.

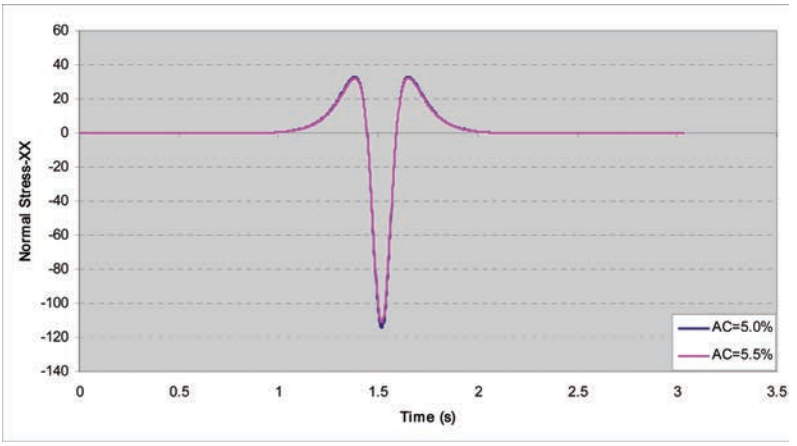

Figure 9. Dynamic response of normal stress-xx at location B.

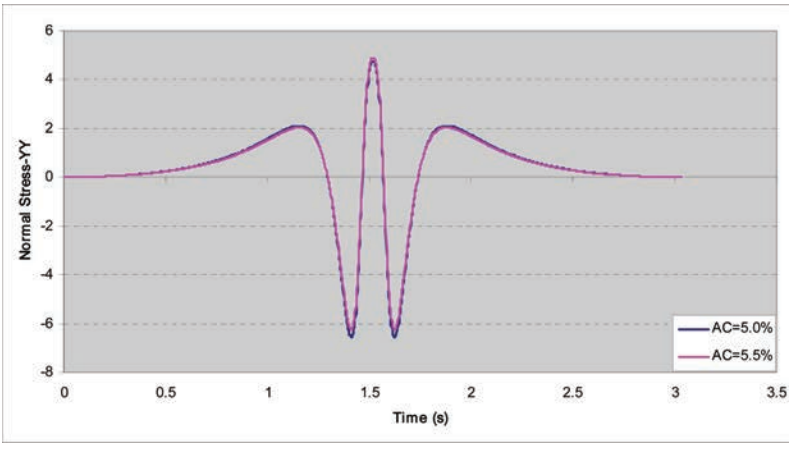

Figure 10. Dynamic response of normal stress-yy at location B.

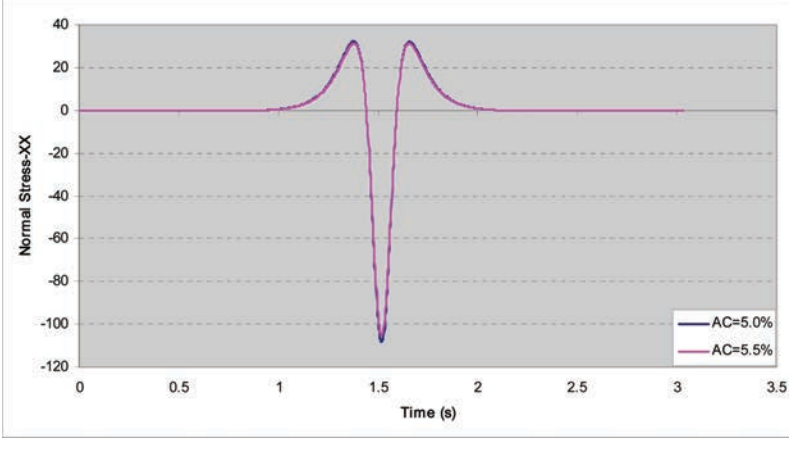

Figure 11. Dynamic response of normal stress-xx at location C.

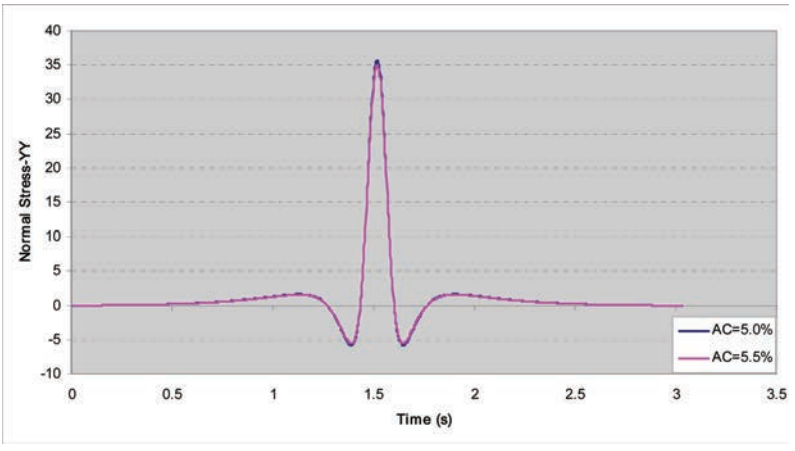

Figure 12. Dynamic response of normal stress-yy at location C.

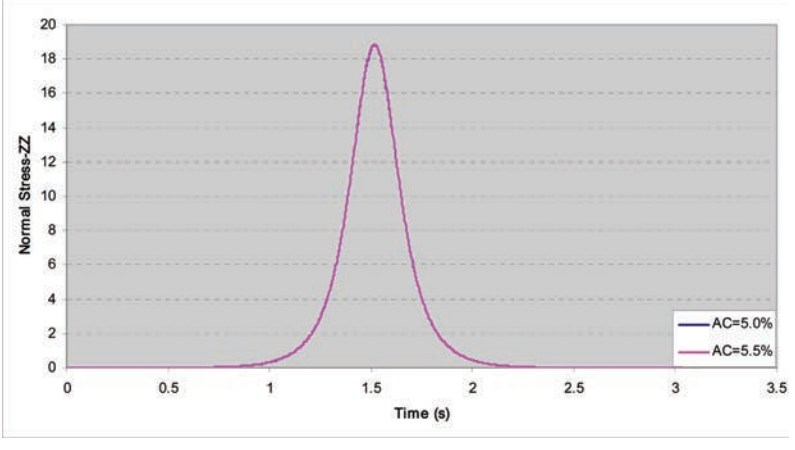

Figure 13. Dynamic response of normal stress-zz on the top of subgrade below location A.

Table 1. Summary of dynamic analysis.

	Asphalt content					
	5.00%		5.50%		Difference	
Location	Stress-xx (psi)	Stress-yy (psi)	Stress-xx (psi)	Stress-yy (psi)	Stress-xx	Stress-yy
A	–122.27	–73.45	–119.05	–71.47	2.63%	2.69%
B	–114.35	–6.56	–111.26	–6.26	2.70%	4.53%
C	–108.21	–5.79	–105.26	–5.57	2.73%	3.89%

4 CONCLUSIONS

The results of the analysis indicate that the inclusion of a fatigue resistant asphalt base in the design will improve pavement life for heavily loaded pavements only when the design is

controlled by the fatigue criteria. This finding is consistent with a rational understanding of the design methodology when typical design life of 20 years is the objective.

To further quantify the effect of the use of a fatigue resistant asphalt base, results of the dynamic analysis indicate that the inclusion of an asphalt rich base layer can increase pavement life by 3% for the parameters investigated. The increase in life could be greater if it is determined that a larger increase in asphalt content is practical. This effect in increasing pavement life is evident in the design of pavements for heavy wheel loads, as the balance between rutting and fatigue control is achieved.

REFERENCES

1. Monismith, C.L., F. Long, and J.T. Harvey. California's Interstate-710 Rehabilitation: Mix and Structural Section Designs, Construction Specifications. *Journal of the Association of Asphalt Paving Technologists,* Vol. 70, Clearwater Beach, FL, 2001, pp. 762–799.
2. Hajj, Elie, Y., Ulloa, A., Sebaaly, Peter E. and Gabriel Bazi. Impact of Rich-Bottom Design in Asphalt Pavements. International Journal of Pavement Research and Technology, Vol. 4 No. 6 Nov. 2011, pp. 313–323.
3. Abou-Jaoude, Grace G. and Ghauch, Ziad G. *Numerical Investigation of Design Strategies to Achieve Long-Life Pavements.* In TRB CD-ROM, Transportation Research Board 90th Annual Meeting, Washington DC, USA, 2012.
4. Harvey, J.H., Long, F., and Prozzi, J.A. Application of CAL/PAV Results to Long Life Flexible Pavement Reconstruction, *Accelerated Pavement Testing Conference*, Paper No. GS3-2, Reno, NV. 1999.
5. Harvey, J.H., Deacon, J.A., Tsai, B-W., and Monismith, C.L. Fatigue Performance of Asphalt Concrete Mixes and Its Relationship to Asphalt Concrete Pavement Performance in California, *UCB Report No RTA-65W485-2,* Asphalt Research Program, CAL/APT Program, Institute of Transportation Studies, University of California at Berkeley, Berkeley, CA, USA. 1996.
6. Anderson, R.M. and R. Bentsen. Influence of Voids in Mineral Aggregate (VMA) on the Mechanical Properties of Coarse and Fine Asphalt Mixtures. *Journal of the Association of Asphalt Paving Technologists,* Vol. 70, Clearwater Beach, FL, 2001, pp. 1–37.
7. Harvey, J., C. Monismith, R. Hornjeff, M. Berjarano, B.W. Tsai, and V. Kannekanti. Long-Life AC Pavements: A Discussion of Design and Construction Experience Based on California Experience. In *Proceedings of International Symposium on Design and Construction of Long Lasting Asphalt Pavements,* National Center for Asphalt Technology, Auburn, AL, 2004, pp. 285–333.

This page intentionally left blank

Pavement response analysis under static and moving wheel loads—I

This page intentionally left blank

Asphalt Pavements – Kim (Ed)
© 2014 Taylor & Francis Group, London, ISBN 978-1-138-02693-3

Determination of an equivalent elastic system to a multilayer viscoelastic structure: Application to the case of thick flexible pavement

Chupin Olivier & Chabot Armelle
LUNAM Université, IFSTTAR, France

Bodin Didier
ARRB Group Ltd., Vermont South, VIC, Australia

Piau Jean-Michel
LUNAM Université, IFSTTAR, France

ABSTRACT: Bituminous pavements are known to exhibit a thermo-viscoelastic behavior which is strongly dependent on temperature and load velocity. However, for many applications (pavement design, FWG analysis …) it is more convenient to deal with elastic calculations which facilitate parametric studies. But to be accurate such an approximation requires rules defining the right choice of elastic data sets. In this context, this paper presents a method to derive an equivalent elastic system to a multilayer viscoelastic pavement under given conditions of temperature and subject to loads moving at constant speed. Thus, the tool proposed hereafter should ease the elaboration of such rules. This paper explains the proposed method and illustrates its use on the case of a thick flexible pavement. By the way, we reexamine the "10 Hz rule" of the French pavement design method within this framework. We recall that this rule assumes that the equivalent modulus of a bituminous layer is approximately equal to the norm of its complex modulus computed at 10 Hz and at the temperature of the layer.

Keywords: thick flexible pavement, viscoelasticity, equivalent elastic system

1 INTRODUCTION

It is well known that the resilient behavior of asphalt concrete under traffic load is viscoelastic and highly sensitive to temperature, these features being inherited from those of bitumen binders. To take account of these features numerical programs such as ViscoRoute© 2.0 were developed more or less recently [1–5]. The high accuracy potential of these tools was demonstrated by way of comparison with experimental measurements stemming from instrumented pavements under simulated traffic, when varying amplitude and velocity of the loads, the pavement geometry or the profiles of temperature. Nevertheless for many applications such as pavement design or survey and back analysis, the use of elastic-based programs still remains at first step a very easy, fast and useful mean of modeling, which is also capable of providing an accurate quantitative description of pavement behavior. However the main condition for this is to make the right choice of the "equivalent elastic moduli" to be affected to the viscoelastic layers of the structure. In this context, the present paper aims at developing a methodology based on viscoelastic simulations and back calculation for determining these moduli. In addition, the results obtained from the method developed are eventually compared to the choice of modulus recommended by the French design method [6].

2 CALCULATION METHOD

The calculation method relies on the use of software ViscoRoute© 2.0 dedicated to the computation of the dynamic response (3D) under moving loads of pavements incorporating viscoelastic material layers. The software program is based on a semi-analytical solution technique described in other references to which the reader is referred for a comprehensive description [3–5]. The viscoelatic model is considered as the reference to simulate the pavement response at a given temperature and loading speed. The same tool is then used to calculate the response of the associated elastic structure of same geometry and subject to similar loading. The Young moduli of the different layers will be determined in order to obtain, in "some sense", comparable responses for the two structures. For this purpose, we define a mathematical function $\phi(\boldsymbol{E})$ to minimize which expresses the "distance" between the two models:

$$\phi(\boldsymbol{E}) = \sqrt{\sum_{i=1}^{n}\left(\frac{c_{i,\max}^{ve}(V,\theta,z_i) - c_{i,\max}^{e}(\boldsymbol{E},z_i)}{c_{i,\max}^{ve}(V,\theta,z_i)}\right)^2} \tag{1}$$

$c_{\max}^{ve}$ and $c_{\max}^{e}$ denote the selected quantities (e.g. deflection, strain, etc.) that we wish to be close in the viscoelastic and the elastic cases, respectively. The "equivalence criterion" ϕ is defined using n quantities which may be calculated at different depths z in the structure. $c_{\max}^{ve}$ represents the reference computed using ViscoRoute© 2.0 in which asphalt layers are modeled through the Huet-Sayegh model [7–9] (Fig. 1). $c_{\max}^{ve}$ is thus a function of speed V and temperature θ so the minimization technique is run for given values of these parameters. $c_{\max}^{e}$ depends on $\boldsymbol{E}$ which is an array of size *nve* (number of viscoelastic layers) composed of the unknown elastic moduli.

The minimization is performed according to a gradient method with respect to $\boldsymbol{E}$ for which an increment of modulus, $d\boldsymbol{E}$, is computed at each iteration as follows:

$$d\boldsymbol{E} = -\lambda\frac{\partial\phi(\boldsymbol{E})}{\partial\boldsymbol{E}} \quad \text{with} \quad \lambda = \frac{\alpha\phi(\boldsymbol{E})}{\left|\partial\phi(\boldsymbol{E})/\partial\boldsymbol{E}\right|^2} \tag{2}$$

The minimization process is stopped when $\left|\nabla\phi(\boldsymbol{E})\right| \le \varepsilon$. α and ε are small positive quantities.

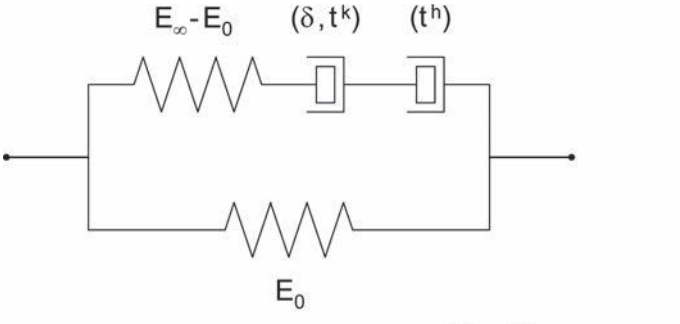

Figure 1. Schematic of the Huet-Sayegh rheological model and its complex modulus as a function of pulsation and temperature ($h > k > 0$; $j^2 = -1$).

For pavement design applications, the important issue is to obtain comparable true and equivalent critical strains or stresses governing the material damage criteria. Thus here we define ϕ as a function of the maximal strain and stress at the bottom of the asphalt layers, considered as the most relevant quantities for asphalt fatigue prediction. Note that this function can be extended to other quantities. For instance, if the application is focused on deflections or curvature then the whole deflection bowl could be used in the ϕ function.

3 STUDY OF A THICK FLEXIBLE PAVEMENT

The calculation method is applied to the study of a typical thick flexible pavement modeled with either two or three viscoelastic layers. In the first case, only two unknown moduli must be determined. This case will be used to illustrate the shape of the ϕ function and evaluate the calculation method. On the other hand, the case with three viscoelastic layers aims at illustrating a complicated situation involving thermal gradient in the structure. For both cases, we also examine the validity of the "10 Hz rule" used in the French pavement design method [6] to assess the elastic stiffness of bituminous layers (see further).

A schematic representation of the pavement structure is shown in Figure 2. It is composed of viscoelastic layers supported by a semi-infinite elastic foundation. For the analysis of the two-viscoelastic-layer case we consider that the two GB3 layers are melded. Table 1 gives the values of the Huet-Sayegh parameters of the different viscoelastic layers.

Two loading configurations are considered further. The imprints of these configurations are represented in Figure 3. These are composed of two or three identical circular loads.

3.1 *Case of a two-viscoelastic-layer structure*

In this section, the pavement is subjected to the French standard dual-wheel moving at constant speed V = 72 km/h = 20 m/s. The weight of each wheel (32,5 kN) is assumed to be uniformly distributed at the surface of the pavement over a disk of radius 0.125 m (Fig. 3).

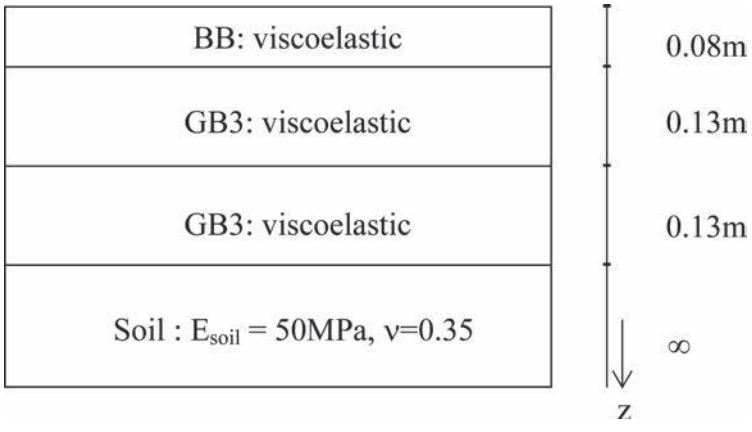

Figure 2. Cross-section of the pavement structure considered.

Table 1. Values of the Huet-Sayegh parameters.

	E_0 (MPa)	E_∞ (MPa)	δ	k	h	A0	A1	A2
GB3	11	28000	2.0	0.18	0.5	2.8	–0.4	1.7E-3
BB	11	18000	2.0	0.18	0.45	2.3	–0.4	1.7E-3

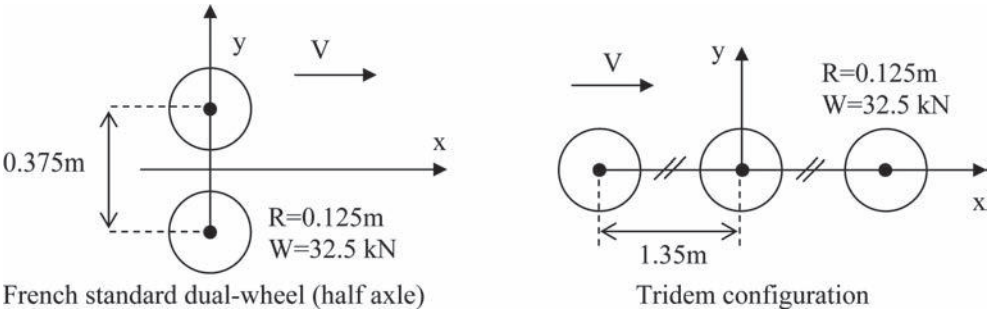

Figure 3. Top views of the loading configurations applied to the pavement.

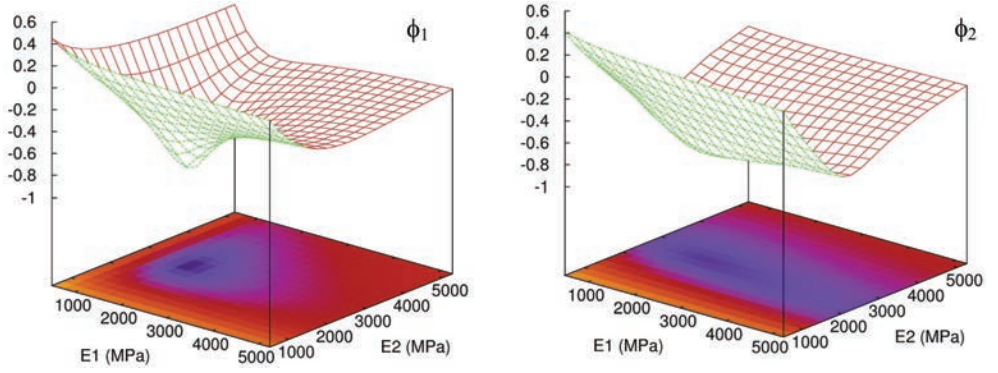

Figure 4. Plot of function $\phi_1(E_1,E_2)$ and $\phi_2(E_1,E_2)$ for the two-viscoelastic-layer pavement.

3.1.1 *Choice of ϕ and validation of the calculation method*

In the present case, function ϕ depends on two elastic moduli and its minimum can be graphically determined in a simple way. To validate the calculation method these moduli can be compared to those obtained by minimization. To evaluate the impact of the selected function ϕ on the back-calculated moduli, two functions composed of three quantities ($n = 3$) are used below.

The first function ϕ_1 includes ε_T and σ_T computed at the bottom ($z = 0.33$ m) of the pavement as well as ε_T computed at the top ($z = 0.04$ m) (see Fig. 2). ε_T denotes the maximum between the absolute values of the longitudinal strains ε_{xx} and ε_{yy}; σ_T is the equivalent for stress. In the second function denoted ϕ_2, ε_T in $z = 0.04$ m is replaced by ε_{zz} calculated at the top of the soil foundation ($z = 0.35$ m). Figure 4 shows a plot of the logarithm ($\log_{10}$) of these two functions. In this figure, E_1 and E_2 are respectively the values of the Young modulus of layer 1 and 2 attributed for elastic structure. Besides the viscoelastic computation is performed for $V = 20$ m/s and $\theta = 30$°C (temperature is uniform in both layers).

These two functions exhibit a single minimum which is more apparent for ϕ_1 in contrast with ϕ_2. Consequently, function ϕ_1 is probably more conducive to determining numerically the equivalent moduli by means of gradient descent. Note that depending on its definition, function ϕ may have several local minima and the choice of the quantities included in ϕ should be made with caution. For instance, ϕ_2 has not a well defined minimum probably because the value of ε_{zz} in $z = 0.35$ m is more sensitive to the mechanical properties of the soil foundation than to E_1 and E_2. In the rest of the paper, we use function ϕ_1 (ϕ=ϕ_1). Under the present conditions, this function leads to values of the equivalent moduli obtained by minimization of 1625 and 2712 MPa for E_1 and E_2, respectively. These values match those of the minimum shown in Figure 4 thus validating the calculation method.

3.1.2 *Detailed comparison between the viscoelastic and elastic equivalent solutions ($\theta = 30°C$)*
The viscoelastic response of the pavement is compared to that obtained in the elastic case using the equivalent moduli computed before (i.e. for $V = 20$ m/s and $\theta = 30°C$). For that purpose, Figure 5 shows horizontal profiles in the x- or y-direction (at a given depth z) of the mechanical fields used to define the equivalence criterion, i.e. to calculate function ϕ. We observe that these profiles provide as expected a good estimate of the maximal values ε_T and σ_T. Nonetheless, the shapes of the profiles are somehow different since creep/relaxation inherent to viscoelasticity leads to non-symmetric profiles in the moving direction and to a shifting of the maximum positions.

Besides, Figure 6 shows profiles of other signals which were not incorporated in the function ϕ. For these fields, in addition to some differences in shape between the elastic and the viscoelastic response non negligible differences are also observed at peak values. This could be expected since no constraint is imposed to match these components of the viscoelastic response. Nevertheless, the maximum of these fields remain lower than ε_T and σ_T and in the present example this difference would not impact design based on maximum strain or stress. Globally, the elastic calculation leads to quite acceptable results.

3.1.3 *Equivalent moduli as a function of temperature ($V = 20$ m/s)—the "10 Hz rule"*
The variation of the equivalent moduli with respect to temperature is now studied. The minimization is run for different temperatures which are assumed to be homogeneous with the same value in both viscoelastic layers. The temperature is varied successively from 0 to 40°C. Figure 7 shows the results obtained for the BB and the GB3 layers. As expected the equivalent moduli decrease with temperature ($V = 20$ m/s), i.e. as the viscoelastic materials soften. At $\theta = 30°C$ the equivalent moduli are those already computed in the previous section

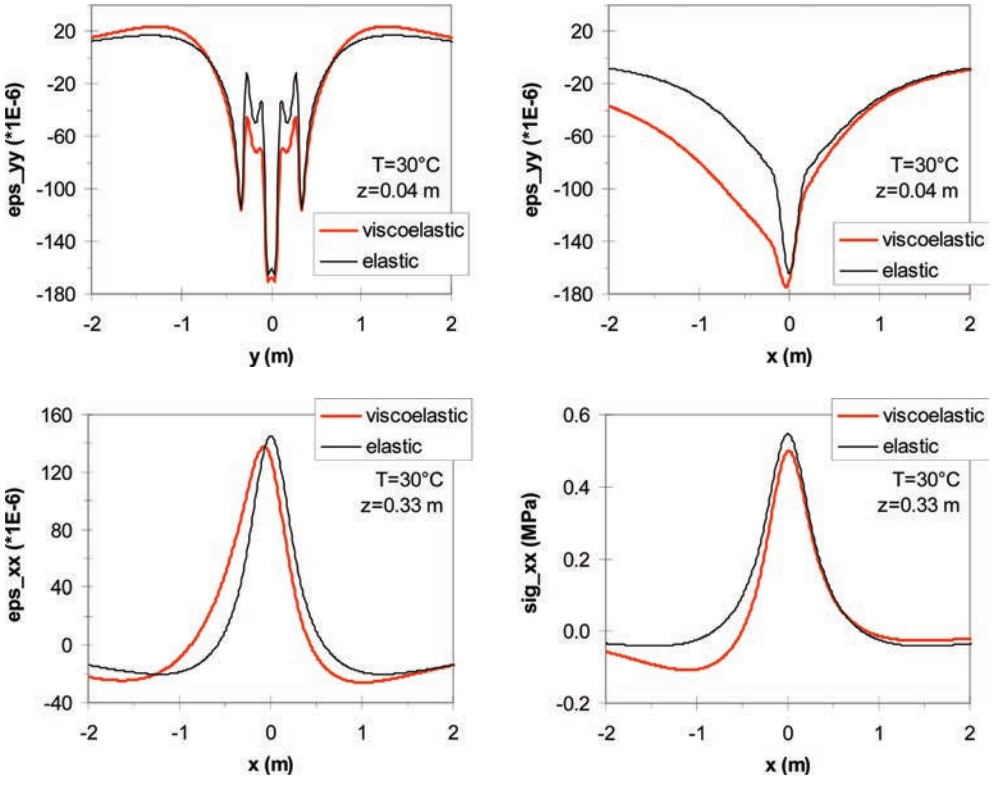

Figure 5. Profiles in the x- or y-direction of the fields used in the minimization process: comparison between elastic and viscoelastic computations.

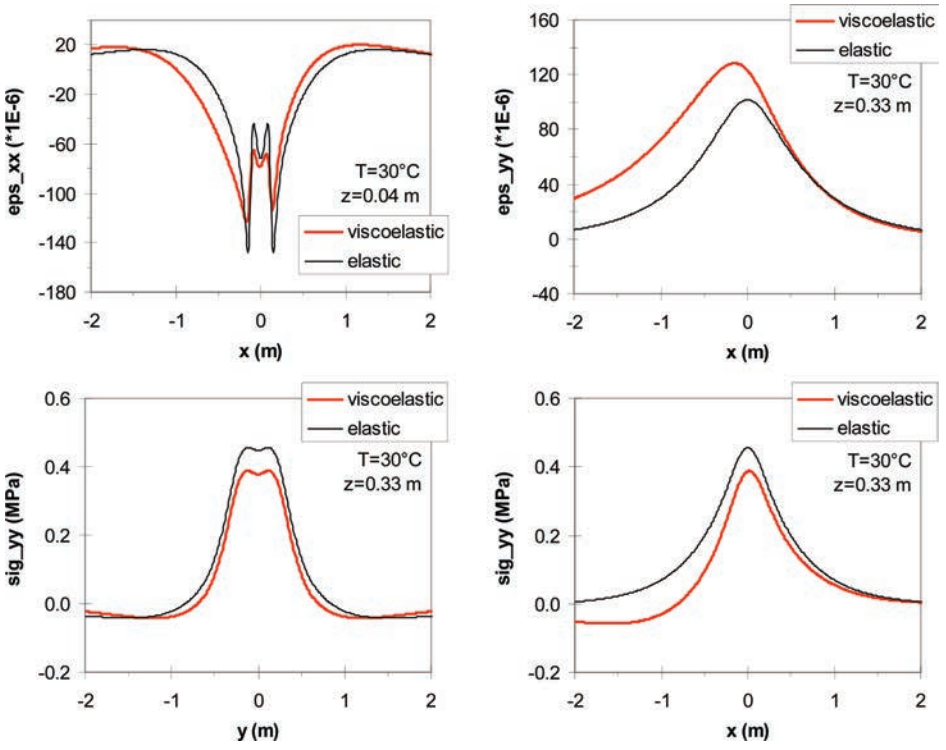

Figure 6. Profiles of fields not incorporated in function ϕ: comparison between elastic and viscoelastic computations.

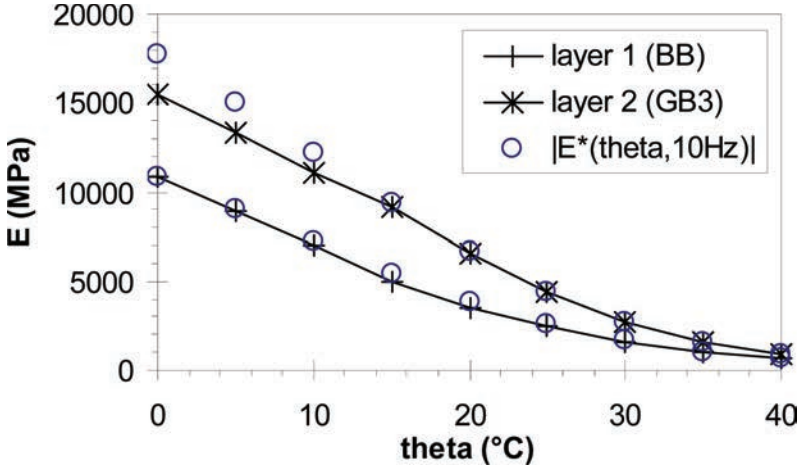

Figure 7. Variation of the equivalent moduli with respect to temperature and comparison with the norm of the complex modulus computed for θ and 10 Hz.

(E_1 = 1625 MPa and E_2 = 2712 MPa). For the different temperatures, the equivalent moduli are also compared to the magnitude of the complex modulus of the corresponding layer computed at temperature θ and frequency $f = \omega/2\pi = 10$ Hz, which is the rule applied in the design of pavements in France to account for variations of temperature. The values of the complex modulus for each layer are plotted using circle markers in Figure 7. These values are

in good agreement with the equivalent back-calculated moduli indicating that the rule under consideration performs well in the present case.

3.2 *Case of a three-viscoelastic-layer structure*

We consider in this section a three-viscoelastic-layer structure subjected to a tridem loading configuration. A thermal gradient is imposed in the asphalt concrete part of the structure. The temperature in the viscoelastic materials is assumed uniform per layer and equal to 35, 25 and 15°C for layer 1 (BB), 2 (GB3) and 3 (GB3), respectively. The same function ϕ as previously is used in the minimization. Figure 8 shows profiles of the selected fields used to compute function ϕ. The comparison between the viscoelastic and the elastic equivalent responses leads to similar conclusions as evoked for the two-viscoelastic-layer structure, i.e. a good match of the maximum values with some differences in the shape of the profiles. However, the back calculated moduli obtained and summarized in Table 2 are much lower

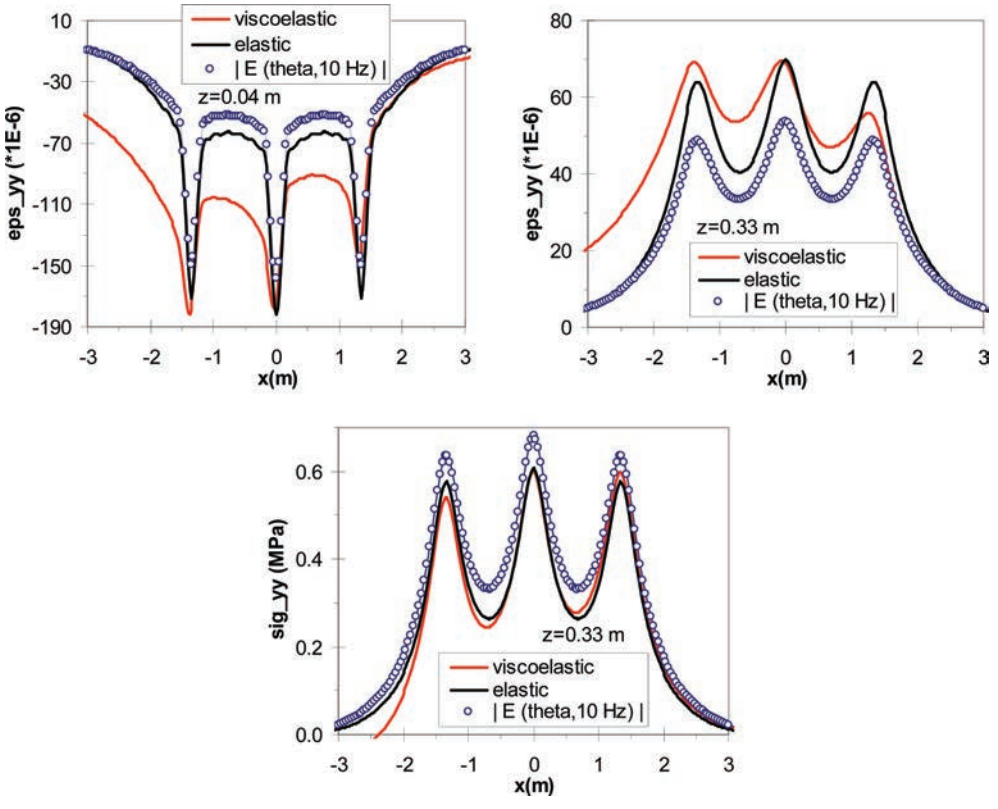

Figure 8. Profiles versus x of the fields used in the minimization process of the three-viscoelastic-layer structure: comparison between viscoelastic, elastic equivalent, and "10 Hz rule" computations.

Table 2. Back calculated moduli for the different layers and design moduli from the "10 Hz rule".

	Layer 1—BB (35°C)	Layer 2—GB3 (25°C)	Layer 3—GB3 (15°C)
Eeq (Mpa)	929	2695	6379
|E(theta,10 Hz)| (MPa)	1029	4461	9375

than the current design moduli stemming from the "10 Hz rule". In terms of mechanical response shown in Figure 8, this yields underestimation of ε_T in $z = 0.04$ m and 0.33 m, and overestimation of σ_T in $z = 0.33$ m when considering the design rule. The application of this rule is thus not well adapted to the present case whereas the elastic calculation still performs well provided that the equivalent elastic moduli are correctly chosen.

The differences observed could be attributed to a change of the appropriate loading frequency (load pulse duration) to be selected at different depth [10] for the thick asphalt pavements. As a remark, the loading frequencies corresponding to the back calculated moduli (inversion of the Huet-Sayegh law) are 7.6, 2.0 and 1.5 Hz for the layers 1, 2 and 3, respectively.

4 CONCLUSION

The aim of this paper was to present a method intended to help the setup of rules for defining equivalence between viscoelastic and elastic calculations of pavements, depending on the context of use and of a desired accuracy. In this framework, the proposed method was used to compute the equivalent moduli to be affected to bituminous layers of a thick flexible pavement subject to moving loads. This method has proven to provide accurate estimate of the equivalent moduli for various conditions of loading and temperature. The back calculated moduli obtained using the developed tool have also been compared to those recommended by the French pavement design method. Depending on the situation under consideration, the difference between these moduli was found more or less important. Nevertheless, to conclude on this aspect it would be necessary to define an acceptable difference after integrating weighting of the results to account for traffic, weather conditions, etc. which are elements considered in the design method. Finally, the type of approach presented here could be used to extrapolate the pavement design method to other contexts as done already for airfield pavements in France for which the equivalent moduli are determined as a function of temperature, load speed and thickness of the layers.

REFERENCES

[1] Hopman P.C. VEROAD: A Viscoelastic Multilayer Computer Program, Transportation Research Record 1539, 72–80. 1996.

[2] Siddharthan R.V., Yao J., Sebaaly P.E. Pavement strain from moving dynamic 3D load distribution, Journal of Transportation Engineering 124 (6) 557–566. 1998.

[3] Duhamel D., Chabot A., Tamagny P., Harfouche L. ViscoRoute: visco-elastic modeling for asphalt pavements. Bulletin des Laboratoires des Ponts et Chaussées (http://www.lcpc.fr/en/sources/blpc/index.php), 258–259:89–103. 2005.

[4] Chabot A., Chupin O., Deloffre L., Duhamel D. Viscoroute 2.0: a tool for the simulation of moving load effects on asphalt pavement, RMPD Special Issue on Recent Advances in Numerical Simulation of Pavements, 11 (2):227–250. 2010.

[5] Chupin O., Chabot A., Piau J.-M., Duhamel D. Influence of sliding interfaces on the response of a layered viscoelastic medium under a moving load, International Journal of Solids and Structures, 47:3435–3446. 2010.

[6] Corte J.-F., Goux M.T. Design of pavement structures: the French technical guide, Transport Research Report, 1539:116–124. 1996.

[7] Huet C. Etude par une méthode d'impédance du comportement viscoélastique des matériaux hydrocarbonés, Université de Paris (France), Ph.D. thesis. 1963.

[8] Huet C. Coupled size and boundary-condition effects in viscoelastic heterogeneous and composite bodies, Mechanics of Materials, 31:787–829. 1999.

[9] Sayegh G. Contribution à l'étude des propriétés viscoélastiques des bitumes purs et des bétons bitumineux, Faculté des Sciences de Paris (France), Ph.D. thesis. 1965.

[10] Denneman E. Improved Design Procedures for Asphalt Pavements: Pavement Temperature and Load Frequency Estimation, Report AP-T248-13, Austroads, Sydney. 2013.

Asphalt Pavements – Kim (Ed)
© 2014 Taylor & Francis Group, London, ISBN 978-1-138-02693-3

Best sensing location in pavement to compare loading conditions

Wenjing Xue & Linbing Wang
Department of Civil and Environmental Engineering, Virginia Tech, Blacksburg, VA, USA

Eric J. Weaver
Turner-Fairbank Highway Research Center, Federal Highway Administration, McLean, VA, USA

ABSTRACT: In the past decades, both the number of tire models and tire inflation pressure are increasing to transport oversized and overweight loads on highways. In-situ monitoring is an effective and reliable way to evaluate the influence of various complicated loading condition to the pavement. Since pavement instrumentation, experiment and following data analysis are expensive. Therefore, a study was made to find suitable locations of sensors in the pavement to evaluate the influence of various loading conditions. Based on the data analysis of the measured strain responses, the best sensing location is in the longitudinal plane at the bottom of pavements, because the responses were more stable and convergent, and the responses match with viscoelastic analysis the best.

Keywords: pavement instrumentation, sensing location, loading condition, pavement monitoring, 3D-move simulation

1 INTRODUCTION

The pavement is one of the very important assets of the society, and designed to carry the predicted traffic without exhibiting failure during its design life. So it is important for pavement engineers to understand the pavement responses induced by the traffic loads, then the material and structure of the pavement can be determined to stand the traffic loads. In the conventional calculation method, traffic loads are simplified to be uniform, circular and static, and so the distribution of pavement responses can be calculated using traditional plate theories. However, the results from this simplification are far from the actual responses, especially with the complicated traffic loading conditions on today's highways.

With the development of truck industry, more and more tire models have been supplied in the market to meet various tire requirements for different vehicles. Different tire models might induce different impacts to the pavement. Since the early 1990s, the conventional wide-base tires (385/65R22.5 and 425/65/R22.5) were proved to induce higher strain/stress to pavement structures and more cracking and rutting damage compared with dual tire assemblies [1–3].

At the same time, the last several years have seen an increase in the tire inflation pressure to transport oversized and overweight loads on highway. Based on the research conducted in the last several decades, TIP was proven to influence the tire-pavement contact stresses and pavement responses. As early as 1971, Seitz and Hubmann indicated that Tire Inflation Pressure (TIP) is an important factor which influences the distribution of the contact stresses [4]. In 1999, the experiment of Sime and Ashmore [5] indicated that TIP may affect the distributions of the contact pressure between tire and pavement obviously. In 2006, Fernando and his colleagues [6] evaluated the effect of tire size and inflation pressure on tire contact stresses and pavement responses.

As described above, the loading conditions on highways are far from the conventional simplification with numerous kinds of tires and different tire inflation pressures. In this case, in-situ monitoring is a good way to tell the influence of different loading conditions

on pavement responses under various circumstances. In the recent decades, many scholars in transportation field embedded sensors in pavements to study the influence of various loading conditions on pavement responses. In 2002, Al-Qadi and his colleagues measured pavement responses to different tire configurations with climatic parameters monitored at Virginia Smart Road [7]. In 2013, Xue and Weaver developed a methodology to compare the pavement responses induced by different tire configurations [8]. This methodology was also used to evaluate the influence of tire inflation pressure on pavement responses and distress predictions [9].

Based on the previous research, it is effective and reliable to instrument pavement sections and use the collected responses to evaluate the influence of various loading conditions. However, pavement instrumentation, experiment and following data analysis are very expensive. Therefore, a study, as presented in this paper, was made to find suitable locations of sensors in the top layer of pavement to evaluate the influence of loading conditions.

2 EXPERIMENT

The controlled load test was performed on the 100-mm and 200-mm thick Asphalt Concrete (AC) sections of the SPS-8 replacement sections: sections 39A803 and 39A804. These AC sections were constructed over a dense graded aggregate base at the Specific Performance Sections Experiment Number Eight (SPS-8) Ohio Strategic Highway Research Program (SHRP) Test Road. During the construction, Dynatest and Canadian strain gauges [10, 11] were placed; and after the construction, strain gauge Rosettes were retrofitted into 100-mm square holes cut through the AC surface layer as shown in Figure 1(a). After affixing the rossettes to the existing pavement, the removed part was back-filled and affixed to the pavement. X represents the direction of traffic, and Y represents the direction transverse to the traffic. One set of rosettes was placed 25 mm below the surface (referred as "top") and another 25 mm above the bottom of the AC layer (referred as "bottom"), each set in both the direction of, and transverse to, the direction of traffic, as shown in Figure 1 (b). For the purposes of this paper, the rosettes strains were used in the following data analysis because of their high survival rate, consistent signal quality, great conformability with the pavement structure and minimal effects from discontinuities. Based on Dynamic Cone Penetration Tests, the modulus of the base layer is 513 MPa; the modulus of the subgrade is 769 MPa.

A single-unit two-axle truck was used to conduct the load tests, as shown in Figure 2. The total weight of the loaded truck was 85.63 kN for the test series; the wheel base was 6.477 m. Four tire types and two configurations were used in the experiment: two wide-base and two duals. Tires were changed on-site as necessary. Table 1 lists the configuration parameters of the four involved tires.

The test runs of the experiment used three speeds (8, 40 and 89 km/hour), three tire inflation pressures (483, 689 and 827 kPa) on two pavement structures (100-mm and 200-mm thick). As a result, there were 18 test series (3 speeds $\times$ 3 tire inflation pressures $\times$ 2 thicknesses) for each kind of test tire listed in Table 1. Each test series was repeated at least three times or until three different tire prints around the gauges were achieved.

3 NUMERICAL SIMULATION

A new pavement analysis software 3D-Move, which is released by the University Nevada Reno, was used to calculate the strain responses in pavement. 3D-Move uses the continuum-based finite-layer approach to compute pavement responses. The software can take moving loads, three dimensional localized contact stress distribution of any shape, and viscoelastic material characterization for the pavement layers into consideration. The interface of 3D-Move is shown in Figure 3.

Due to the many advantages, 3D-Move was used to simulate the whole loading process numerically. In 1999, Sime and Ashmore [5] measured the localized stress distribution

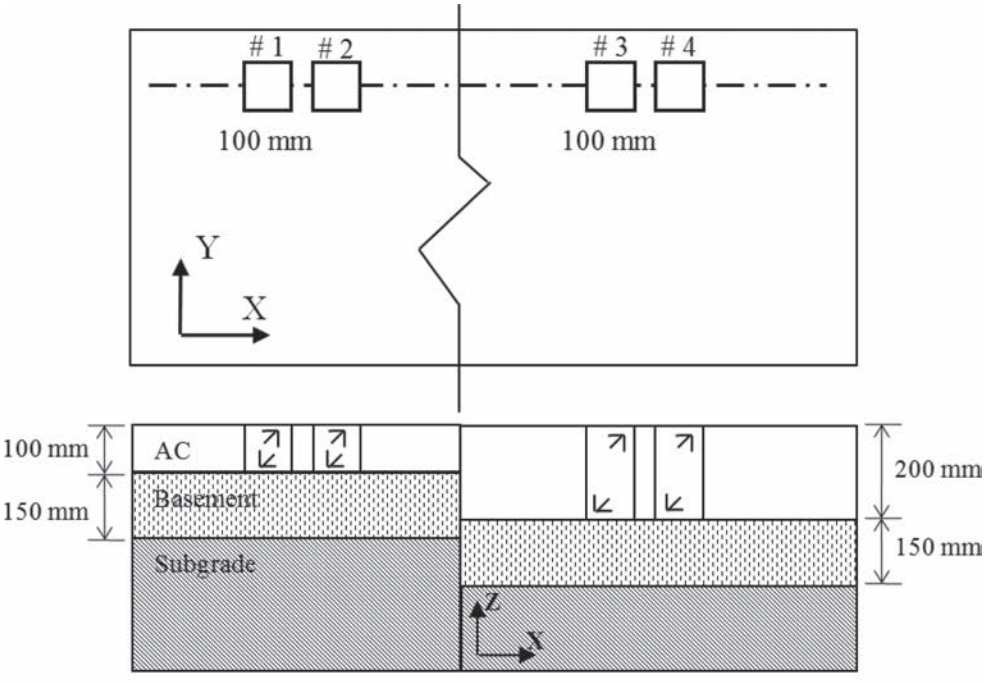

(a) 100-mm and 200-mm sections

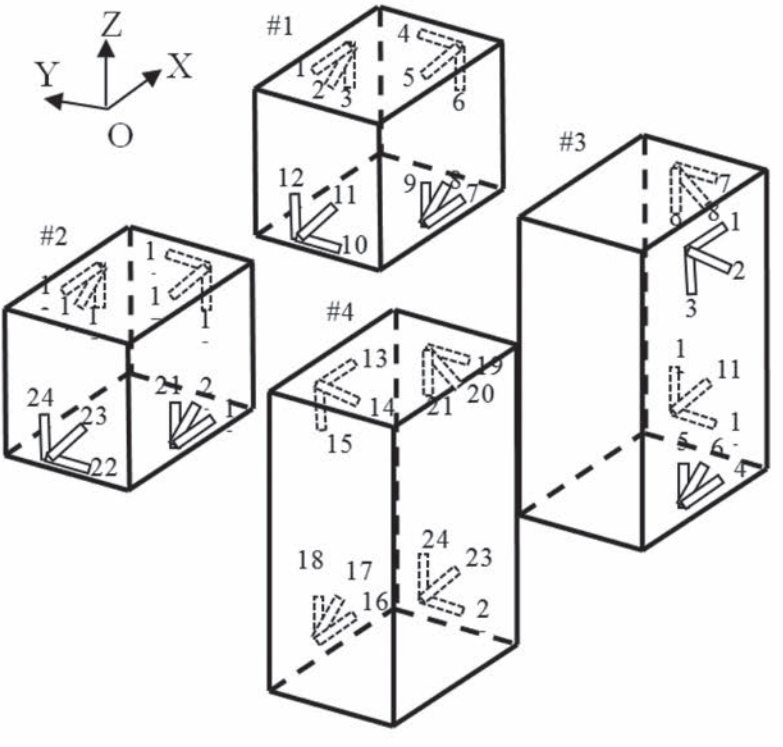

(b) Strain Gauge Locations

Figure 1. Pavement sections and Rosette strain gauge locations.

Figure 2. Test truck.

Table 1. Test tires specifications.

Manufacture	Type	Profile	Width of tire[(1)] (mm)	Width of tire footprint[(2)] (mm)
GoodYear	Wide base	65R22.5	425	330
GoodYear	Dual	75R22.5	295	222
Michelin	Wide base	45R22.5	495	438
Michelin	Dual	80R22.5	275	229

Note 1: "Width of Tire" refers to the width parameters provided by the manufacturers.
Note 2: "Width of Tires Footprint" refers to the width measurement of tire-pavement interface from a previous FHWA study [5].

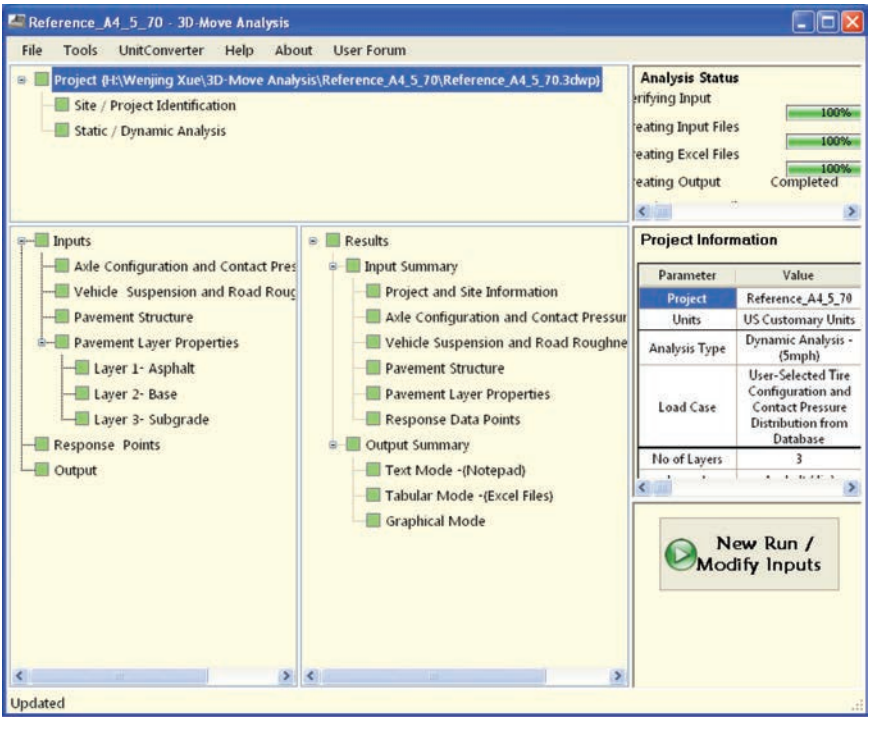

Figure 3. User interface of the software 3D-Move.

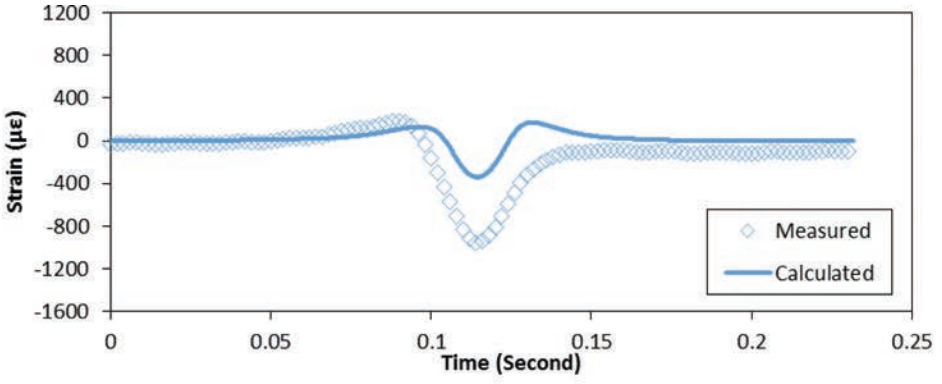

(a) Horizontal Strain Response $\varepsilon_X^{(Y)}$

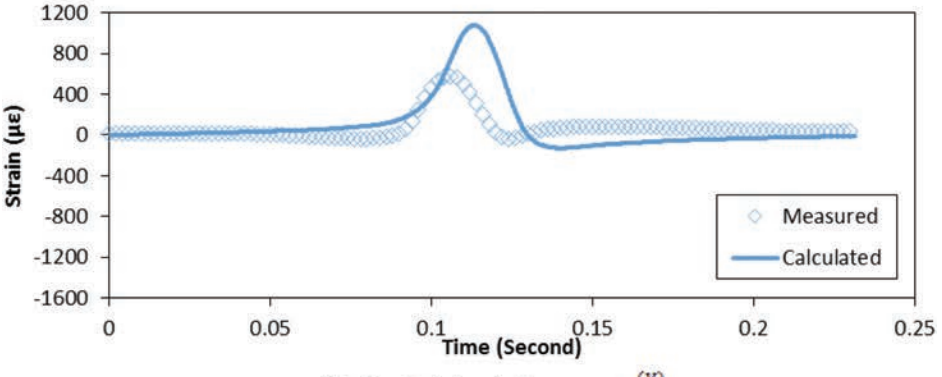

(b) Vertical Strain Response $\varepsilon_Z^{(Y)}$

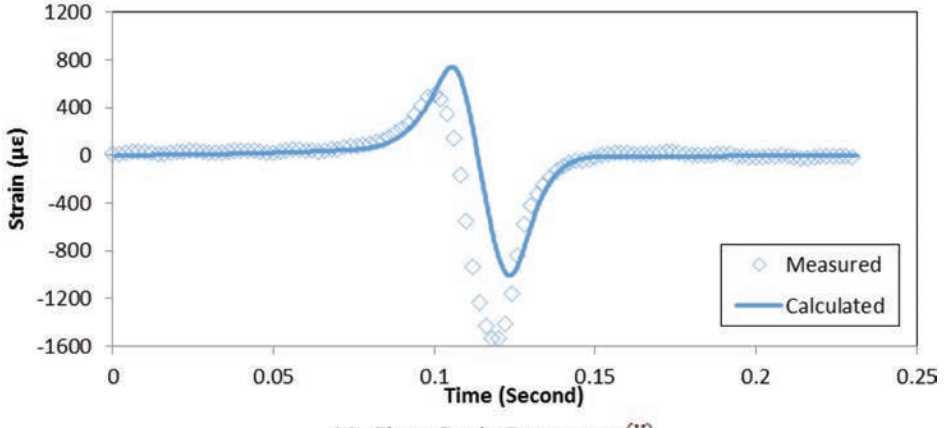

(c) Shear Strain Response $\gamma^{(Y)}$

Figure 4. Comparison between measured and 3D-Move calculated strain traces. *Bottom of 4'' AC, OSD = 3'', Temp =101.5^{0}F, GoodYear Wide-Base, Run#6.*

under several tire models with different tire inflation pressure, including the two GoodYear tires in this experiment (Table 1), and the measured stress distributions were incorporated in the database of 3D-Move. The pavement structures, shown in the previous section, was modeled in 3D-Move, and the tire-vehicle interface pressure distribution, measured by Sime and Ashmore [5] in similar loading conditions (load and TIP), was applied on the viscoe-

lastic pavement model with the corresponding temperature and speed. The calculated strain responses are compared with the measured ones in Figure 4.

As shown in Figure 4, the calculated horizontal strain was smaller than the measured data, but calculated vertical strain was bigger than the measured one. In general, the distribution of strain responses calculated by 3D-Move match well with the measurement in shape, with obvious differences in magnitude. The main reason might include the inaccuracy of the modulus of the base material, the anisotropy of asphalt concrete and various uncontrollable conditions during the experiment.

The research group in UIUC leaded by Professor Al-Qadi [12] has been conducting lots of Finite Element simulations in the past decades and matched very well with experimental results in both shape and magnitude. Their computations and measurements are not presented and compared in this paper because the loading and environmental conditions in their experiment were totally different. Two reasons are proposed to explain that the 3D-Move simulation in this paper doesn't match with experimental measurements as well as the numerical simulation they conducted. The experiment described in this paper was conducted with manually driven individual truck instead of the accelerated loading equipment used in the UIUC's experiment [12], and so many loading conditions (wheel load, speed, wandering position, and so on) couldn't be controlled as well as in the UIUC's experiment. As a result, it is understandable that the comparison in Figure 4 is not as good as the one conducted in [12]. At the same time, it is also possible that Finite Element model developed by Al-Qadi is more accurate than the Finite Layer model used in 3D-Move in simulating pavement responses, but more research is necessary to compare 3D-Move with Finite Element method on computation accuracy and efficiency.

4 DATA ANALYSIS

Since the experiment was conducted in a hot weather (averaged 32 ºC), and shear deformation is the dominant cause of rutting in asphalt concrete when temperature is high [12], shear strain was chosen to reveal the difference between different locations in pavements. Comparisons about shear strain responses at different locations in the pavements are made in Figure 5.

As shown in Figure 5 (a-b), the shear strain in the transverse plane was much smaller and sharper than the longitudinal one, which meant that a little error in the original measured strain would be enlarged a lot when it was adjusted to the maximum value in the whole loading area. So according to the distribution of longitudinal and transverse shear strain, the conclusion was that the shear strain in the longitudinal plane is better to tell the difference of loading, in other words, the effect of various tires to the pavement.

Comparing the strain distributions at different depth in Figure 5, the distribution curves of shear strain at the bottom of the pavements were much milder than the ones at the top. The drastic fluctuations at the top might induce unreasonable error during the process of the offset distance adjustment. So theoretically, the adjustments with the distribution curve at the bottom of the pavement might have higher accuracy.

According to theoretical calculation, the shear strain in 4 inch pavement is larger than that in 8 inch pavement both at the top and the bottom, as shown in Figure 5, because of the stress transfer over the depth of the pavement.

To verify the conclusion above, all the available shear strains (two longitudinal and 2 transverse) under various tires loading were adjusted with 3D-Move simulation, and the statistics of the results are concluded as in Table 2. A few unbelievable results, which were far beyond reasonable range, were caused by the small error enlargement and deleted as outliners. The less was the average standard deviation; the better was the adjustment, since it means the adjustments for temperature, offset distance and speed, match well between different runs.

As shown in Table 2, the average standard deviation of adjusted shear strain in longitudinal plane was much lower than that in transverse plane for all the monitoring points throughout 4 inch and 8 inch pavements. At the same time, the standard deviations of the

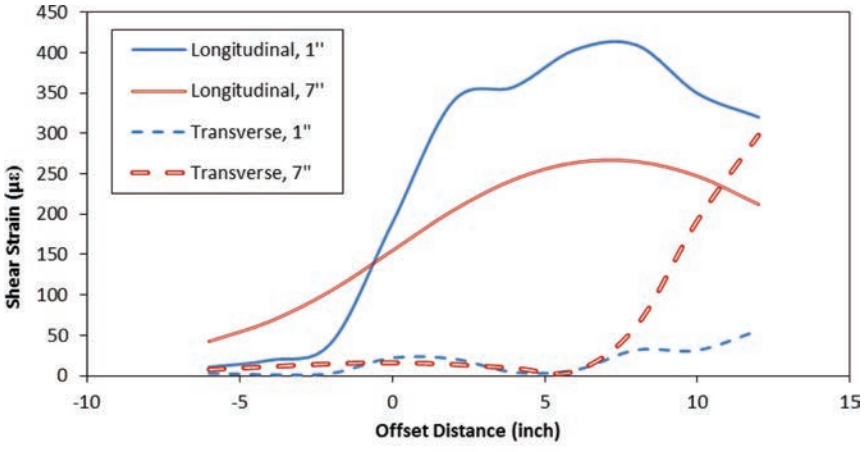

(a) Wide-base Tire

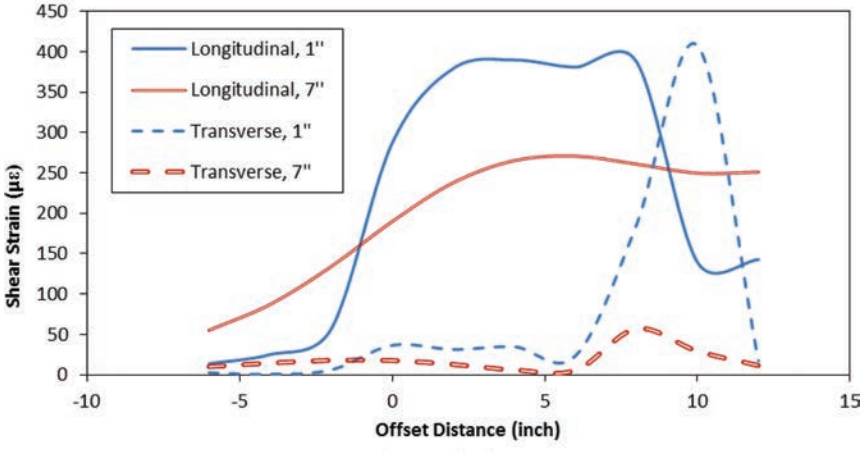

(b) Dual Tires

Figure 5. The distribution of shear strain predicted by 3D-Move. *200-mm pavement section, load distribution from GoodYear wide-base and dual tires, 25 mph, 100 psi.*

Table 2. Standard deviation of adjusted shear strain with 3D-Move (10^{-6}).

	100-mm section				200-mm section			
	Longitudinal		Transverse		Longitudinal		Transverse	
	Top	Bottom	Top	Bottom	Top	Bottom	Top	Bottom
GoodYear widebase	216.3	133.5	288.1	454.7	164.6	152.9	650.8	515.3
GoodYear duals	163.7	115.5	314.3	256.6	279.1	78.0	836.6	363.9
Michelin widebase	263.8	106.4	729.2	256.5	308.9	76.3	674.5	144.1
Michelin duals	105.2	114.8	216.8	584.1	114.0	86.6	529.7	336.0

adjusted shear strain at the bottom of the pavement were much less than those at the top. The standard deviation of adjusted measurements validated the assumptions above: the strain distribution in the longitudinal plane at the bottom of pavements is the most stable and wild with the least drastic fluctuations, and most suitable to tell the differences between loading conditions.

5 CONCLUSIONS

This paper presents a study to find the best sensing location in pavement to evaluate loading conditions. Based on the data analysis of the measured strain responses, the best sensing location is in the longitudinal plane at the bottom of pavements, because the responses were more stable and convergent, and the responses match with viscoelastic analysis the best.

ACKNOWLEDGMENTS

The authors appreciate the funding support from Eisenhower Transportation Scholarship. The authors also thank to the scholars at Ohio University for the assistance during the experiment and the laboratory tests.

REFERENCES

[1] Bonaquist, R. An assessment of the increased damage potential of wide base single tires. *Proceeding of the 7th International Conference on Asphalt Pavements, Design and Performance*, Nottingham, UK, pp. 1–16. 1992.
[2] Myers, L., et al. Measurement of Contact Stresses for Different Truck Tire Types To Evaluate Their Influence on Near-Surface Cracking and Rutting, Transportation Research Record: Journal of the Transportation Research Board, 1655(-1), pp. 175–184. 1999.
[3] Kim, D., R. Salgado, and AG. Altschaeffl. Effects of supersingle tire loadings on pavements, Journal of Transportation Engineering-Asce, 131(10), pp. 732–743. 2005.
[4] Yousefzadeh, M., S. Azadi, and A. Soltani. Road profile estimation using neural network algorithm, Journal of Mechanical Science and Technology, 24(3), pp. 743–754. 2010.
[5] Sime, M. and SC. Ashmore, Tire pavement interface pressure patterns. 1999, Federal Highway Administration.
[6] Fernando, E.G., et al. Evaluation of effects of tire size and inflation pressure on tire contact stresses and pavement response. 2006.
[7] Al-Qadi, I.L., et al. Pavement response to dual tires and new wide-base tires at same tire pressure. 2002, Transportation Research Board Natl Research Council. p. 38–47.
[8] Design and performance validation of a wireless sensing unit for structural monitoring applications, Struct. Eng. Mech., 17, pp. 393. 2004.
[9] A two-tiered self-powered wireless monitoring system architecture for bridge health management, Proc. SPIE, 7649, pp. 76490K. 2010.
[10] Christison, J.T., KO. Anderson, and BP. Shields. In-Situ Measurements of Strains and Deflections in Full-Depth Asphalt Concrete Pavement, J. Association of Asphalt Paving Technologists, 47, pp. 36. 1978.
[11] Christison, J.T. Insitu Measurement of Pavement Behavior Under Load, in *Annual Conference of the Roads and Transportation Association of Canada*. 1983: Edmonton, Alberta.
[12] Al-Qadi, I.L., et al. Dynamic analysis and in situ validation of perpetual pavement response to vehicular loading, Transportation Research Record: Journal of the Transportation Research Board, 2087(1), pp. 29–39. 2008.

Asphalt Pavements – Kim (Ed)
© 2014 Taylor & Francis Group, London, ISBN 978-1-138-02693-3

Structural and functional deterioration of porous asphalt pavement under moving wheel load in laboratory

Nobuyuki Yoshida & Syunpei Tani
Kobe University, Nada, Kobe, Japan

ABSTRACT: In Japan, the structural design method of porous asphalt pavement is presently empirical, and in order to apply porous asphalt pavement to heavy traffic roads in urban areas, the progress of both structural and functional damage to porous asphalt pavement due to traffic loads needs to be grasped. This paper describes an attempt that was made to understand the damage progress of porous asphalt pavement by carrying out a moving wheel load test on an instrumented small-scale porous asphalt pavement. The pavement consisted of a porous asphalt surface/binder layer, an asphalt-treated porous base-course, a crusher-run subbase-course and a sandy subgrade. The test was conducted in series with four conditions of (a) room temperature, (b) pavement surface temperature of 60°C, (c) room temperature after watering and (d) pavement surface temperature of 60°C after watering. It is shown that the load transmission function deteriorates with the number of wheel passing, especially under the higher temperature, that permeability in the rutted track is smaller than that in the other locations, and so on. This permeability deterioration is attributed to accumulated plastic deformation in the pavement but it is not easy to identify which layer controls this.

Keywords: Porous asphalt pavement, small-scale experiment, moving wheel load, earth pressure, permeability

1 INTRODUCTION

In Japan, porous asphalt pavement is used roughly in two ways: one is so-called "drainage" asphalt pavement and the other is "permeable" asphalt pavement as schematically shown in Figure 1. The former allows rainwater to enter from the road surface into the pavement but

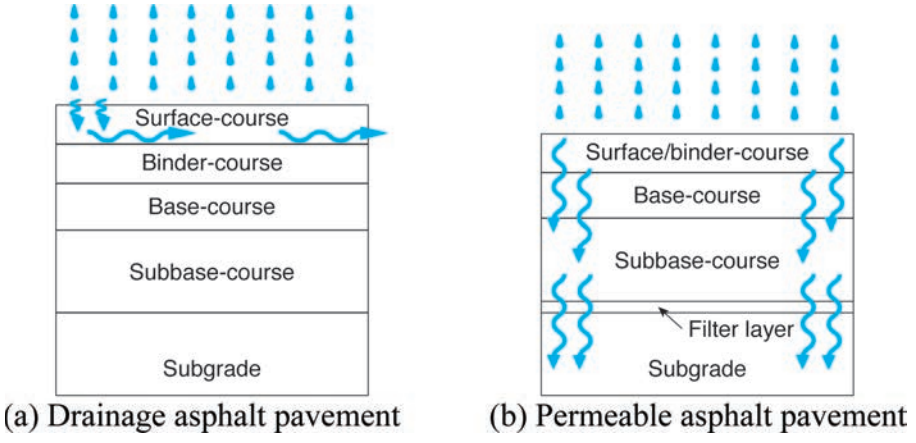

Figure 1. Typical porous asphalt pavements in Japan.

drains it laterally on the top or bottom faces of binder-course and the latter permits rainwater to flow further down to subbase-course, subgrade or further down. Drainage asphalt pavement was first adopted at an arterial road in Tokyo in 1987 and since then its construction is steadily increasing: for instance, about 25% of the area of national roads directly controlled by the government was replaced by the drainage asphalt pavement as of 2005 [1].

Regarding the permeable asphalt pavement on which this paper specifically focuses, its application to sidewalks was first explored around 1972 in Tokyo for improving soil conditions for roadside trees and walking difficulty in rainy days in urban areas and also for serving as flood control measures. From about 1984, then, the application of permeable asphalt pavement to sidewalks started in earnest. Presently, permeable asphalt pavements on sidewalks and parking areas are growing across the country. Meantime, some trial applications of permeable asphalt pavement to heavy traffic roads have been made in Japan mainly for flood countermeasure and groundwater recharge. In 2004, a law called Act on Countermeasures against Flood Damage of Specified Rivers Running Across Cities was put in force; by this, urban areas susceptible to flood damage had to take any measures. One of the measures is to replace existing usual asphalt pavements by permeable asphalt pavements. Since then, trial constructions of permeable asphalt pavement have gradually increased in national roads and some prefectural roads with limited follow-up investigations [2].

Permeable asphalt pavement is also used in other countries, but to the authors' knowledge, it is not too much to say that, unlike drainage asphalt pavement, most of them are as flood measures and a way of runoff management [3–6]. It has been favorably applied to sidewalks, car parks, pedestrian access, container yards, etc. but its application to heavy traffic roads seems scarce probably because there is no necessity of such.

The structural design method of porous asphalt pavement is empirical regardless of drainage or permeable one in Japan [7]. Considering the situation stated above, as long as permeable asphalt pavements concerned, it is urgent that a mechanistic design method be established. For this, it is needed to grasp the progress of structural damage and also functional deterioration such as permeability. This drove the authors to initiate a research program. In the research program, which has just started lately, a moving wheel load test on an instrumented small-scale permeable asphalt pavement has been carried out. In the followings, a brief outline of the moving wheel load test is presented first. Then, some of the results are described focusing on the vertical earth pressure, rut depth and permeability since the first two items reflect the structural damage and the third item the functional deterioration.

2 MOVING WHEEL LOAD TEST ON SMALL-SCALE PAVEMENT

2.1 *Test apparatus*

The test apparatus consists of three main components: a moving wheel load unit, a small-scale pavement unit and a control and data acquisition unit. Figure 2 is a bird's eye view of the moving wheel load unit together with the small-scale pavement. Regarding the moving wheel load unit, along the two guide rails of aluminum beams fixed on the high-strength steel frame, which are anchored to the concrete floor of the laboratory, a loaded wheel is moved back and forth on the small-scale pavement surface by a ball screw connected to an AC servomotor. The wheel is composed of a 100 mm-thick aluminum disk with a radius of 85 mm, of which outer periphery a 15 mm-thick hard rubber is bonded to. The wheel load is 1.37 kN. The wheel travel distance is 780 mm: a 110 mm from the both ends of the 1000 mm long small-scale pavement is marginal. The wheel speed is 19.22 m/min, which corresponds to twice the speed of the standard wheel tracking test in Japan [8]. Here, one travel counts the number of load applications as one.

The small-scale pavement tested here is a four-layered permeable asphalt pavement. Its structure is shown in Figure 3 together with installed sensors. The small-scale pavement is 800 mm wide and 1000 mm long but its height can vary depending on the thickness design. Here, the four-layered permeable asphalt pavement consists of a surface/binder-course and base-course of porous asphalt, a crusher-run subbase-course underlain by a sandy subgrade.

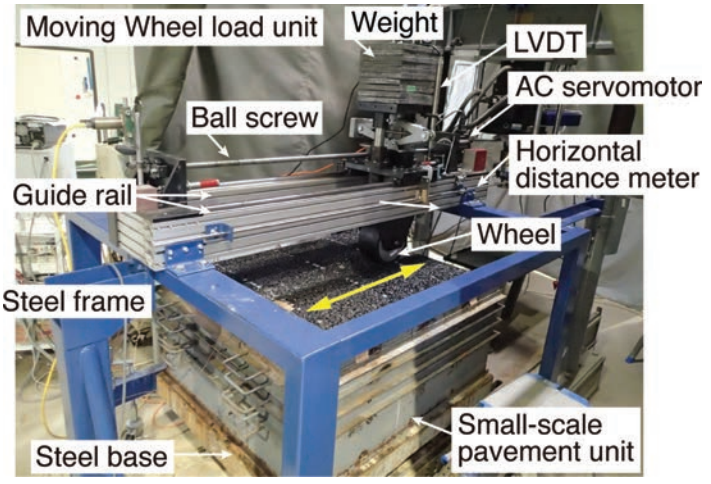

Figure 2. Moving wheel load test apparatus.

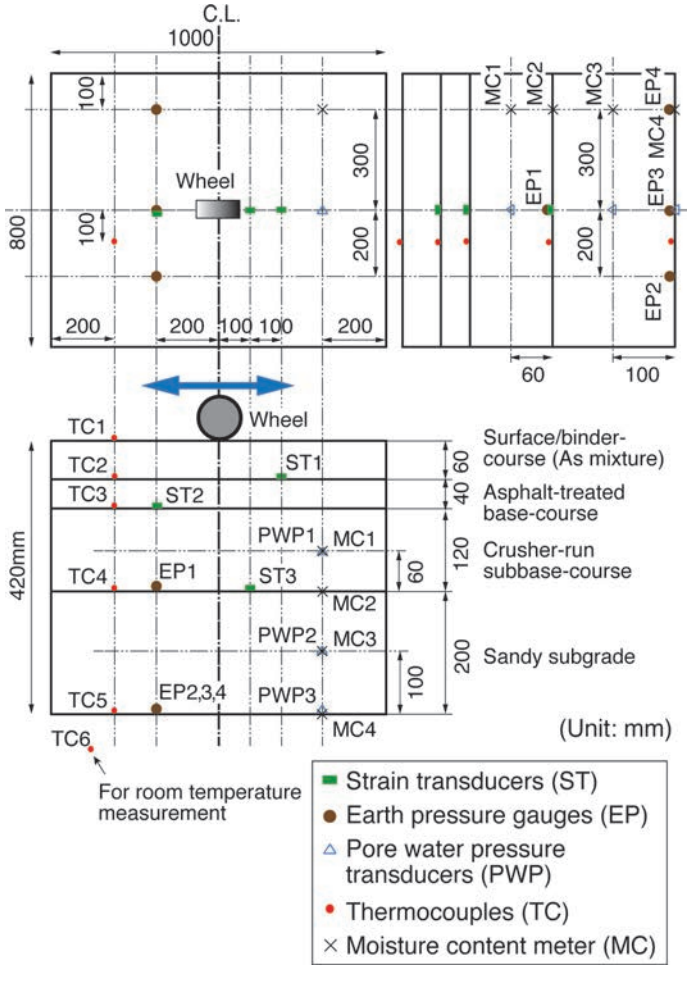

Figure 3. Small-scale asphalt pavement.

An actual empirical structural design of permeable asphalt pavement was first carried out with the conditions that: the design CBR is 12%, the design period is 10 years, the traffic volume class is N_7 (more than 3000 heavy vehicles per direction per day; the heaviest class) and the amount of seepage water per 15 seconds is greater than 1000 ml. Then, each thickness of the constituent layers was scaled down by being multiplied by 0.4, considering the size limit of the moving wheel load unit.

The surface/binder-course is 60 mm thick and made of a Type-H polymer-modified porous asphalt mixture (max. aggregate size of 13 mm) and the base-course is a 60 mm thick Type-II polymer-modified porous asphalt mixture (max. aggregate size of 20 mm). The grain size distributions and the Marshal stability test results of these two asphalt mixtures are given in Table 1. The subbase-course is 120 mm thick and made of a crusher-run (max. aggregate size of 30 mm) and the subgrade is 200 mm thick Toyoura sand. For the crusher-run, the maximum dry density and optimum water content are 2.267 g/cm^3 and 5.2%, respectively. The Toyoura sand has a maximum dry density of 1.584 g/m^3 and an optimum water content of 14.2%.

2.2 *Constuction of small-scale pavement*

The four-layered small-scale pavement was constructed as follows. First, a steel rectangular frame for the subgrade layer was fixed onto the steel base (Fig. 2); and at the same time, three earth pressure transducers, a pore water pressure transducer, a moisture content meter and a thermocouple were installed at the prescribed locations on the steel base shown in Figure 3. Then, Toyoura sand with its optimum water content was placed in the frame and compacted using a hand tamper and a 1 kN vibratory roller compactor till the amount required to achieve its maximum dry density was poured in. Meantime, at the specific locations on the face of 100 mm from the bottom, a pore water pressure transducer and a moisture content meter were carefully installed (Fig. 3). The surface roughness of the subgrade was then confirmed by using a straight edge ruler.

Next, the subbase-course was constructed in the similar way to the subgrade. A steel rectangular frame for subbase-course was stacked on the one for subgrade. After placing an earth pressure transducer, a strain transducer, a moisture content meter and a thermocouple

Table 1. Properties of porous asphalt layers.

Locations	Surface/binder-course	Base-course
Percentage finer by mass (%)		
31.5 mm		
26.5		100.0
19	100.0	98.1
13.2	97.3	55.3
4.75	18.6	27.6
2.36	14.1	14.8
0.6	10.6	10.0
0.3	8.0	7.0
0.15	5.5	4.6
0.075	4.5	3.5
Types of asphalt binders	Polymer modified asphalt (Type-H)	Polymer modified asphalt (Type-II)
Asphalt content (%)	5.0	3.5
Density (g/cm^3)	2.003	2.084
Theo. max density (g/cm^3)	2.511	2.571
Air void (%)	20.2	18.9
Marshal stability (kN)	5.21	5.31
Marshal flow (1/100 cm)	30	28
Dynamic stability (times/mm)	$\geqq 6000$	–
Permeability (m/sec)	11.57×10^{-4}	$\geqq 1.0 \times 10^{-4}$

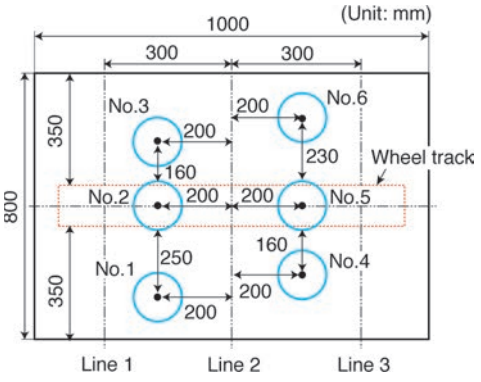

Figure 4. Locations of on-site permeability tests.

at the specific locations of subgrade surface, a prescribed amount of crusher-run with its optimum water content was poured in and compacted in the same way as for the subgrade; at the same time, a pore water pressure transducer and a moisture content meter were installed at a face of 60 mm from the subgrade surface.

Then, after stacking a steel rectangular frame for base-course on the one for subbase-course, a strain transducer and a thermocouple were installed at the prescribed locations of the subbase-course. The porous asphalt mixture for the base-course was carefully placed in and compacted using the hand tamper and 1 kN vibratory roller compactor so as not to cause a detrimental influence on the installed sensors.

Finally, the surface/binder-course was constructed in the same manner as the base-course after placing a strain transducer and a thermocouple at the prescribed locations on the base-course.

All the steel rectangular frames used in the preparation of small-scale pavement have an inner width of 800 mm, an inner length of 1000 mm and a variable height ranging from 20 to 50 mm depending on the thickness of the corresponding layer and the number of stacks.

2.3 *Test conditions*

The moving wheel load test was carried out sequentially under four environmental conditions: (a) room temperature, (b) 60°C pavement surface, (c) room temperature after watering the pavement surface and (d) 60°C pavement surface after watering the pavement surface. The test proceeded from the conditions (a) to (d): moving wheel load test continued till the number of load applications reached 10000 in each condition. Increasing the pavement surface temperature up to 60°C and maintaining it were done by turning on and off 6 pieces of 500-watt reflect lamps. Regarding the conditions (c) and (d), the pavement surface was watered evenly using a hose till the water seeped out at the bottom of subgrade without paying an attention to the flow rate and amount.

During all the tests, the room and pavement temperatures were monitored and at prescribed numbers of load applications, vertical earth pressure, horizontal strain, pore water pressure and surface roughness were measured. Moreover, after the completion of moving wheel load test at each condition, an on-site permeability test was carried out at six locations on the pavement surface shown in Figure 4, following the test method designated in the Manual of Pavement Investigation and Testing Method [9].

3 TEST RESULTS AND DISCUSSIONS

3.1 *Pavement temperature*

Figure 5 shows variations in the pavement temperature during the moving wheel load tests. Since all the tests were carried out in the mid December of 2012, the room temperature

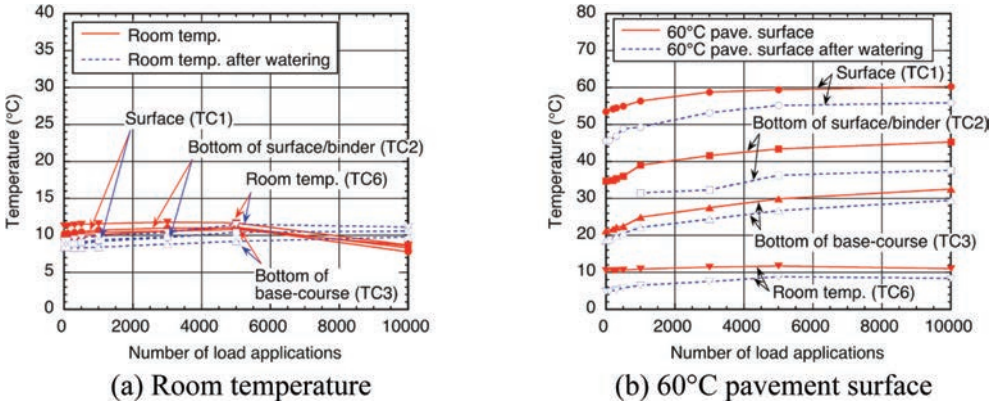

Figure 5. Pavement temperature variations during test.

was as low as about 10°C and showed little change for all the cases as can be seen in the figure.

In the case of the room temperature with or without watering, it is seen from Figure 5(a) that the pavement temperature shows only a little variation from the bottom of base-course to the pavement surface and is kept at about 10°C during the test. On the other hand, in the case of 60°C pavement surface without watering, the temperature control takes some time due to inexperienced handling of the six reflect lamps; that is, the surface temperature is about 54°C at the beginning but after the number of load applications of 3000, it is maintained at about 60°C as expected. It is also understood that there is a significant gradient in the vertical distribution of pavement temperature. At 10000 load applications, the temperature is 60°C at the pavement surface, 45°C at the bottom of surface/binder-course, 33°C at the bottom of base-course; the temperatures at the mid-depth of surface/binder-course and of base-course are about 53°C and 39°C, respectively.

In the case of 60°C pavement surface after watering, heating-up of the pavement surface using reflect lamps was conducted in the same way as for the 60°C pavement surface without watering; nonetheless, as seen in Figure 5(b), the pavement surface temperature does not reach 60°C even at the number of load applications of 10000 and is low by about 4°C. This is probably attributed to that the heating energy was consumed in evaporating water retained in the pavement. Thus, it is indicative that a surface temperature reduction effect can be expected in the permeable asphalt pavement.

3.2 *Vertical earth pressure*

Every time the test wheel passes over the embedded earth pressure gauges, vertical earth pressure is recorded in a waveform, from which the peak value is read out. Figure 6 shows changes in vertical earth pressure measured at the top and bottom of subgrade with the number of load applications for the four test conditions. At first glance, the cases of 60°C pavement surface with or without watering develop a larger vertical earth pressure than the cases of room temperature. This seems reasonable because the stiffness of both surface/binder and base-course becomes smaller due to a higher temperature, resulting in deterioration of their load transfer capability. At the top of subgrade, the vertical earth pressure increases rapidly in the early stage, then gradually; the ratios of vertical earth pressure at 1000-load applications to the initial value are 1.76 for the case of 60°C pavement surface and 1.80 for the 60°C pavement surface after watering.

In the case of room temperature without watering, it is seen in Figure 6(a) that the vertical earth pressures at the top and bottom of subgrade are about 6 kPa and 5 kPa, respectively and little change during the test. On the other hand, in the case of room temperature after watering, the vertical earth pressure gradually increases with the number of load applications

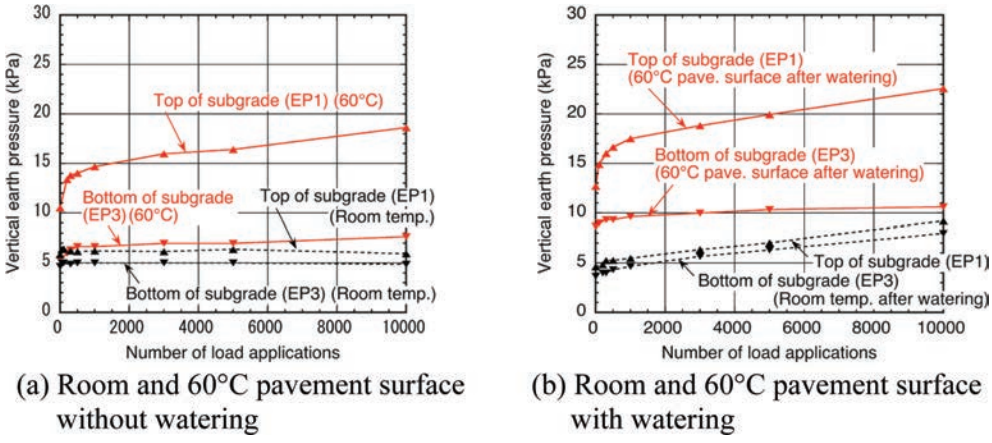

Figure 6. Changes in vertical earth pressure with number of load applications.

as seen in Figure 6(b). Taking into account the facts that the pavement temperature little changes (Fig. 5(a)) and that rut depth little increases during the test (see the next subsection and Fig. 8), this increase of vertical earth pressure can be attributed to the gradual deterioration of load transfer capability with an accumulation of wheel passes.

The horizontal distributions of vertical earth pressure measured at the bottom of subgrade are given in Figure 7 for the test conditions without watering. It is seen that, in the room temperature case, the magnitude of vertical earth pressure just below the wheel center is about 5 kPa and a vertical earth pressure of almost the same magnitude develops at a horizontal distance of 200 mm from the wheel center but at a distance of 300 mm, the vertical earth pressure drops down to about 2.5 kPa. The ratio of the vertical earth pressure just below the wheel center to that at a distance of 200 mm is about 1.0 initially and it little changes during the test. Similarly, the ratio of the vertical earth pressure just below the wheel center to that at a distance of 300 mm is about 0.5 and it remains almost unchanged. It can be said that, in the case of room temperature, the asphalt mixture layers (surface/binder-course and base-course) provide an excellent load transfer capability and it is sustained during 10000 load applications.

In the case of 60°C pavement surface, on the other hand, the vertical earth pressure is the largest just below the wheel center and decreases with distance from the wheel center, regardless of the number of load applications. Moreover, the vertical earth pressure at all three locations tends to increase with the number of load applications: for instance, from 5.3 kPa to 7.7 kPa just below the wheel center and from 3.5 kPa to 4.5 kPa at a distance of 200 mm. The ratio of the vertical earth pressure just below the wheel center to that at a distance of 200 mm is about 0.66 initially and it decreases asymptotically to 0.59 at the end. The ratio of the vertical earth pressure just below the wheel center to that at a distance of 300 mm is about 0.30 and it varies a little around 0.30 without any trend. Since the stiffness of asphalt mixture layers (surface/binder-course and base-course) decreases due to the elevated temperature and its load transfer capability deteriorates, the influence of wheel load on the pavement appears localized beneath the wheel. Furthermore, as the number of load application increases, the load transfer capability lowers with an accumulation of wheel passes.

Although not shown here, in the two cases with watering, the vertical earth pressure measured just below the wheel center and at a distance of 200 mm was larger than those without watering, especially just below the wheel center.

3.3 *Rut depth*

Changes of rut depth measured at three measurement lines (Fig. 4) on the centreline of wheel track during each test are plotted in Figure 8 in a consecutive manner. Note that for the cases

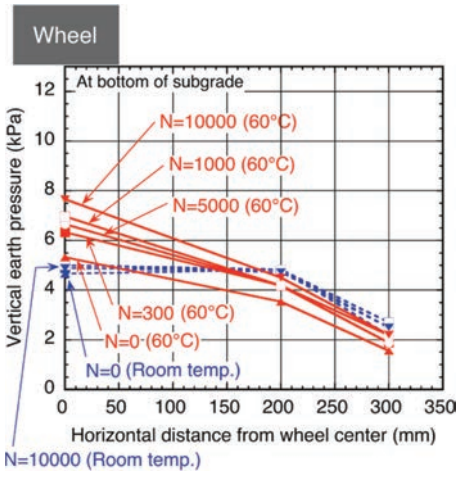

Figure 7. Horizontal distribution of vertical earth pressure in cases without watering.

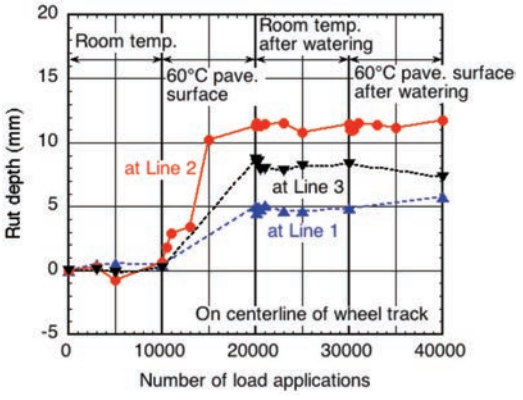

Figure 8. Changes of rut depth during test.

of 60°C pavement surface with and without watering, measurements of rut depth at Lines 1 and 3 were taken only at the beginning and end of each test because of avoiding a cumbersome operation of removing and attaching the reflect lamps. As seen in the figure, there is only a little rut developed in the room temperature condition but in the 60°C pavement surface condition, relatively large rut occurs: from 0.43 mm initially to 5.0 mm at the end at Line 1, from 0.65 mm to 11.3 mm at Line 2 and from 0.22 mm to 8.7 mm at Line 3. Figure 9 is a photo of pavement surface taken during the test, giving an image of rutting around Lines 2 and 3. After the 60°C pavement surface condition, rut depth seems not to increase as a whole, though only a little increase in rut depth may be noticed during the condition of the 60°C pavement surface after watering.

Rutting (vertical permanent displacement of pavement surface) is considered as an outcome of the accumulation of plastic deformation of each pavement constituent layer and it is speculated that beneath the rutted portion, void could be somewhat reduced.

3.4 *Permeability*

An on-site permeability test was carried out at the six locations shown in Figure 4 for the cases of room temperature and 60°C pavement surface. The two locations, 2 and 5, are in the

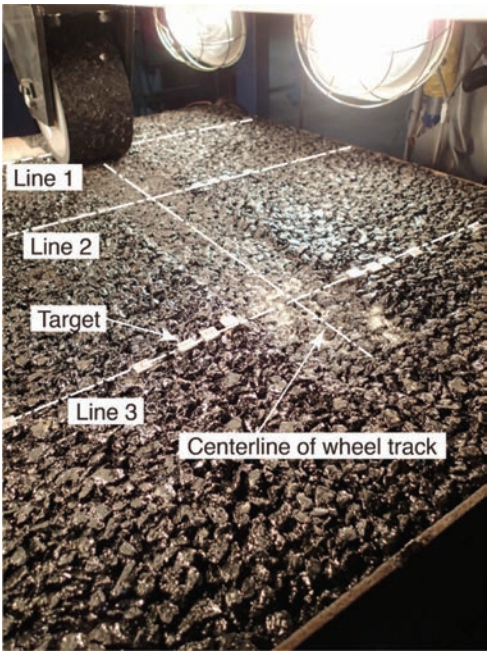

Figure 9. Rut along wheel track (60°C pavement surface condition).

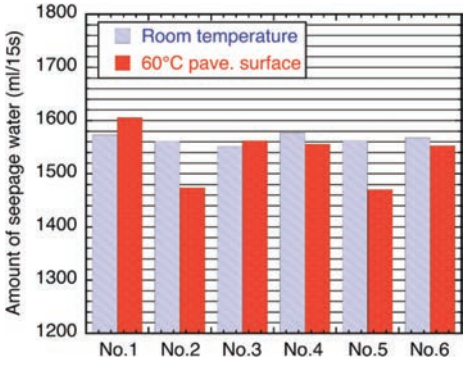

Figure 10. On-site permeability test results.

rutted portion. The test is a kind of falling head permeability test and measured is the time required for 400 ml of water to seep into pavement from its surface under an initial water head of 600 mm. Using the measured time and the amount of water, the amount of seepage water in ml/15 s is computed. Here, the test was carried out three times at each location and their average value was obtained.

Figure 10 summarizes the average amount of seepage water obtained at each location for the two cases. In the case of room temperature, it is seen that there is not much difference among the locations and the average value is 1566 ml/15 s which is almost the same as the value obtained immediately after the pavement was constructed. This is expected since there is little rut developed during the test. On the other hand, in the case of 60°C pavement surface, there is little difference in the amount of seepage water among the locations, 1, 3, 4 and 6, which are outside of the rutted portion: the average amount of seepage water is 1569 ml/15 s which is comparable to the value in the case of room temperature. The amount of seepage water at the location 2 is the same as that at the location 5, their average value

being 1472 ml/15 s; this is noticeably smaller than the other locations' values. Since these two locations are in the rutted portion as stated above, this reduced amount of seepage water seems to reflect a possible reduction of void at least in the surface/binder-course.

4 CONCLUSIONS

This paper describes a moving wheel load test on an instrumented small-scale permeable asphalt pavement conducted under four test conditions, the room temperature and 60°C pavement surface with or without watering, and some of the results are presented. The followings can be pointed out based on the study.

As expected, the influence of wheel load on the pavement is greater in the case of 60°C pavement surface than in the room temperature. At the elevated temperature, the stiffness of porous asphalt mixture layers decreases, leading to deterioration of load transfer function. It is further worsened by accumulation of wheel passes. As demonstrated in the test results, by these effects, the vertical earth pressure exerted on subgrade increased and rutting progressed. The permeability measured at the rutted portion of pavement surface was noticeably smaller than that at the other locations. This permeability deterioration seems to be attributed to accumulated plastic deformation in the pavement but it was not easy to identify which layer controls this. The permeability outside of the rutted portion of pavement surface was pretty much unchanged from the initial state. In reality, however, dust, tire rubber shavings, etc. would clog the near surface voids of permeable asphalt pavement, resulting in a long-lasting deterioration of permeability; it was outside the scope of this experimental study.

REFERENCES

[1] T. Kanou. The current state and agenda of recycling in the field of pavement. Public Works Management Journal, June Issue, Economic Research Association, pp. 12–15. 2008. (in Japanese).

[2] Japan Road Association (JRA). Permeable Pavement Guidebook 2007. Japan Road Association, Maruzen, 53p. 2007. (in Japanese).

[3] U.S. Environmental Protection Agency. Storm Water Technology Fact Sheet: Porous Pavement, EPA 832-F-99-023. 1999.

[4] W.F. Hunt and K.A. Collins. Permeable pavement: research update and design implications, Urban Waterways, North Carolina Cooperative Extension Service, North Carolina State University, 11p. 2007.

[5] M. Scholz and P. Grabowiecki. Review of permeable pavement systems, Building and Environment, 42, pp. 3830–3836, Elsevier. 2007.

[6] B. Shackel, S. Beecham, D. Pezzaniti and B. Myers. Design of permeable pavements for Australian conditions, 23rd ARRB Conference—Research Partnering with Practitioners, Adelaide, Australia, pp. 1–14. 2008.

[7] Public Works Research Institute (PWRI). Road surface rain water treatment manual (draft). Public Works Research Institute, Sankaido, 134p. 2005. (in Japanese).

[8] Japan Road Association (JRA). Method of wheel tracking test. Manual of Pavement Investigation and Testing Methods, Part 3, Japan Road Association, pp. [3]39–[3]56. 2007. (in Japanese).

[9] Japan Road Association (JRA). Method of on-site test for water permeability of porous pavement materials. Manual of Pavement Investigation and Testing Methods, Part 1, Japan Road Association, pp. [1]122–[1]126. 2007. (in Japanese).

Asphalt Pavements – Kim (Ed)
© 2014 Taylor & Francis Group, London, ISBN 978-1-138-02693-3

Heavy Vehicle Simulator tests at VTI

Thorbjorg Saevarsdottir
Faculty of Civil and Environmental Engineering, University of Iceland, Reykjavik, Iceland

Sigurdur Erlingsson
Faculty of Civil and Environmental Engineering, University of Iceland, Reykjavik, Iceland
Pavement Engineering, VTI, Linköping, Sweden

Håkan Carlsson
Pavement Engineering, VTI, Linköping, Sweden

ABSTRACT: Flexible test road structures have been built and tested in Accelerated Pavement Tests (APT) using a Heavy Vehicle Simulator (HVS) at VTI in Sweden for 15 years. The objectives have been to investigate pavement responses and pavement performance behaviour which can be used to validate mechanistic performance schemes. The pavement structures have been instrumented to measure their responses and performance and the surface profile was estimated. Here the accuracy of the measurements was estimated and a performance prediction was carried out. The registrations of the measurements were rather smooth with good repeatability and acceptable accuracy. The response, performance and accumulation of permanent deformation were modelled and generally good agreement was established between the measurements and calculations. From the analysis a performance prediction can be carried out as a function of time to evaluate the performance of new road concepts and maintenance strategies. The performance prediction provides the option of performing a life cycle cost analysis which can decrease both costs and environmental impacts.

Keywords: Accelerated Pavement Testing, Heavy Vehicle Simulator, instrumentation, response modelling, performance prediction

1 INTRODUCTION

For the development of mechanistic designing methods to proceed, the behaviour and properties of the pavement materials have to be properly understood under various traffic loadings and environmental conditions. The Accelerated Pavement Test (APT) is a test performed on full scale instrumented test roads, where the magnitude and location of the applied loads, the number of load repetitions and the environmental conditions are controlled. At regular intervals condition surveys and pavement response measurement are performed giving valuable validation data for the mechanistic designing methods. The development of APT with instrumented pavement structures has increased the understanding of pavement behaviour and built a foundation for new, more sophisticated design methods [1].

At the Swedish National Road and Transport Research Institute (VTI) flexible road structures have been built and tested in an APT using a Heavy Vehicle Simulator (HVS) for the last 15 years. The HVS machine operated at VTI (HVS Mark IV) is a mobile linear full-scale accelerated road-testing machine with a heating/cooling chamber system to keep a constant pavement temperature during testing. The objectives have been to investigate pavement responses and degradation development to understand pavement behaviour. This information can be used to validate mechanistic performance schemes. The pavement structures have been instrumented to measure their responses and performance and the surface profile was

also measured. From the data the response, performance and accumulation of permanent deformation can be calculated and a performance prediction done as a function of time for different materials, structures, climate conditions and traffic. The HVS machine can be used to evaluate new road concepts and maintenance strategies by assessing the total cost of constructing, maintaining and operating different road constructions under various conditions. A life cycle cost assessment comparison between investment alternatives of feasible designs can then be performed to decrease costs and environmental impact of road structures [2–6].

2 THE PAVEMENT STRUCTURE AND TESTING PROCEDURE

2.1 *The pavement structure*

Several pavements have been tested at VTI during the 15 years of operation. The main focus has been on flexible pavement structures with high quality base and subbase material. Tested pavements, both in the field and at VTI's test facility are constructed by normal road construction machinery. The VTI indoor full scale test facility has three test pits that are 3 m deep, 5 m wide and 15 m long, but the length of the monitored structure is normally 6 m. One of the tested structures referred to as SE10 is described here; it represents a typical flexible pavement structure according to the Swedish Road Administration [7–10]. The structure was equipped with the present instrumentation used at VTI: εMU coils, Soil Pressure Cells (SPC), Linear Variable Differential Transducers (LVDT's), and Asphalt Strain Gauges (ASG) to measure their response and performance, as well as moisture content sensors (Fig. 1). A laser beam on a straight edge was also used to measure the surface profile [2–6].

The structure (Fig. 1) consisted of a Hot Mix Asphalt (HMA) divided into a surface course (AC pen 70/100; d_{max} = 16 mm) and a bituminous road base (AC pen 160/220; d_{max} = 32 mm). Under the asphalt were two layers of unbound crushed rock (granite), a base layer (0–32 mm) and a subbase layer (0–90 mm). The subgrade consisted of silty sand. The structure was instrumented to measure stress, strain and deflection responses as a function of load repetitions as well as permanent deformation manifested on the surface as rutting (Fig. 1) [2].

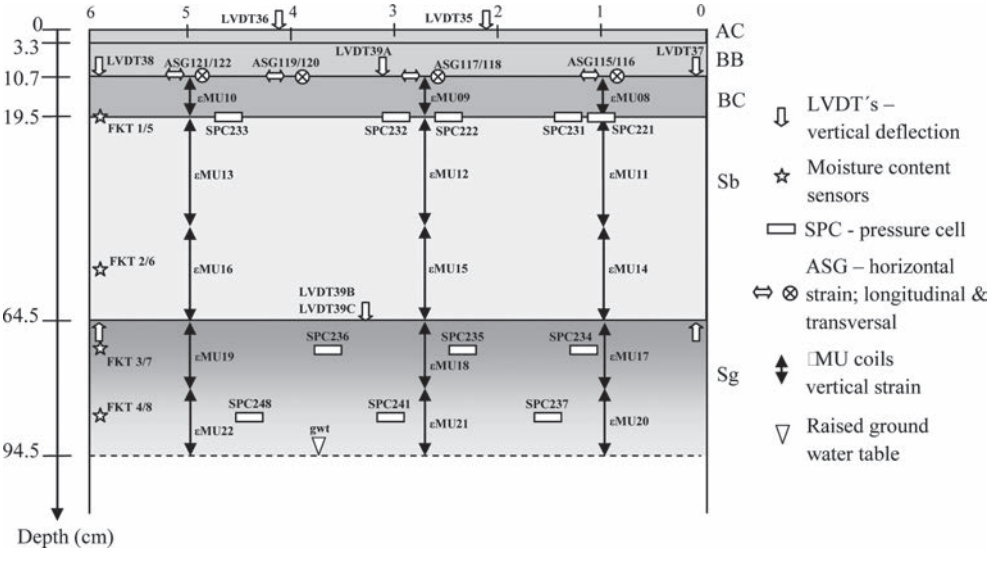

Figure 1. Cross section of the pavement structure SE10 (AC—asphalt concrete, BB—bituminous base, BC—granular base course, Sb—granular subbase and Sg—subgrade), along with its instrumentation. SPC221 and SPC222 are from the University of Nottingham, other pressure cells were from Geokon. Profile measurements are taken for 5 sections at one meter intervals (1 to 5).

2.2 *The testing procedure*

The test procedure was typical for the HVS testing performed at VTI. The test was divided into three phases with bidirectional loading applied in all the phases [2]:

- Pre-loading phase: for post-compaction, 20,000 load repetitions applying light loading (30 kN single wheel load and 700 kPa tyre pressure).
- Response phase: where responses are estimated from single and dual wheel configuration using various tyre pressures and axle loads.
- Main accelerating loading test: with more than one million load cycles applied, dual wheel configuration, 120 kN axle load (60 kN dual wheel load) and 800 kPa tyre pressure.

The dual wheel configuration had a centre to centre spacing of 34 cm. The lateral distribution of the loading followed a normal distribution where the wander was divided into eleven segments in steps of 5 cm, from plus to minus 25 cm. Half-way through the test water was added to the level of approximately 30 cm below the top of the subgrade, which is supposedly the worst case in Sweden (Fig. 1). No other alternations are usually made [2–5].

3 ACCURACY OF THE MEASUREMENTS

In the following figures a dual tyre loading was used; the registration taken under the centre of one of the wheels at a 120 kN axle load, 800 kPa tyre pressure, the speed of a rolling wheel of 12 km/h, and a constant temperature of 10°C. The responses are shown for both "moist", before the groundwater table was raised, and "wet" state, after the groundwater table was raised. The registrations of the measurements were rather smooth with some exceptions in the εMU coils, where the signal showed some noise. To assure reliability, in most cases multiple sensors were used at each depth, but it is recommended to have at least three sensors at each measured depth due to difficulties in measuring the response of unbound materials. This is due to the inhomogeneous nature of the materials and other variants influencing the results such as compaction and quality of the contact between the material and the meters.

3.1 *Moisture content sensors*

Water content reflectometer, CS616, from Campbell Scientific [11] was used to measure the volumetric water content in the pavement structure. In Figure 2 the water content of the structure (SE10) over the testing time is shown as well as the average moisture content with depth. In the figure MM1 and MM2 represent the measurements from meters 1 and 2. The measurements were stable and good correlation was observed between sensors, with the least correlation in the coarse subbase layer.

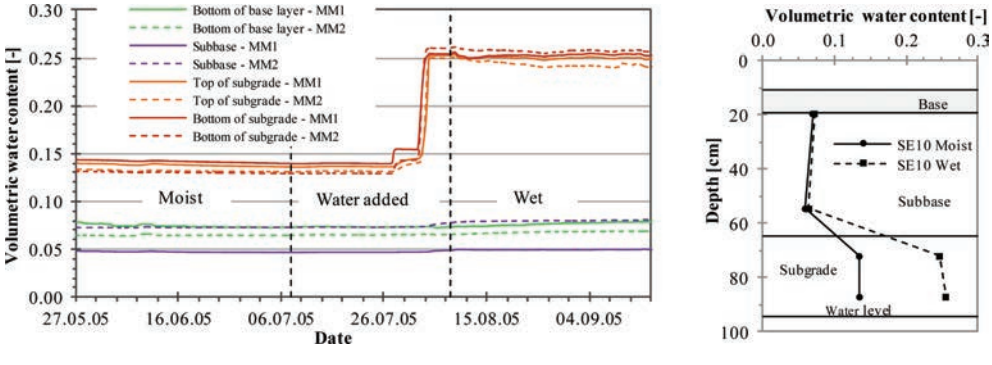

Figure 2. Change in the volumetric water content with time and as a function of depth.

3.2 *εMU coils*

Strain measuring unit or εMU coils (inductive coils) were used to measure the vertical strain, both elastic and permanent [12]. In Figure 3 the strain development is shown. The measurements were fairly constant over the "moist" and "wet" phases but all the sensors showed higher readings once the groundwater table was raised, indicating a softer structure. Typical values of the induced vertical strain registration of the εMU sensors are shown in Figure 4, with the measurements taken approximately in the middle of the "moist" and "wet" phases.

Individual sensors showed reasonable performance with most of them having less than 10% variation and only two around 20%, which is less variation than observed in previous tests. There was a slightly higher difference between sensors at the same depth in SE10 compared to previous tests. The difference varied from 8.8% up to 42.7%, but two sensors out of three were often close to one another, indicating the importance of having at least three sensors at each depth.

3.3 *Soil Pressure Cells (SPC)*

Soil Pressure Cells (SPC) or earth pressure cells are used to obtain the vertical stresses in the unbound pavement layers and subgrade soil. In SE10 earth pressure cells from Geokon

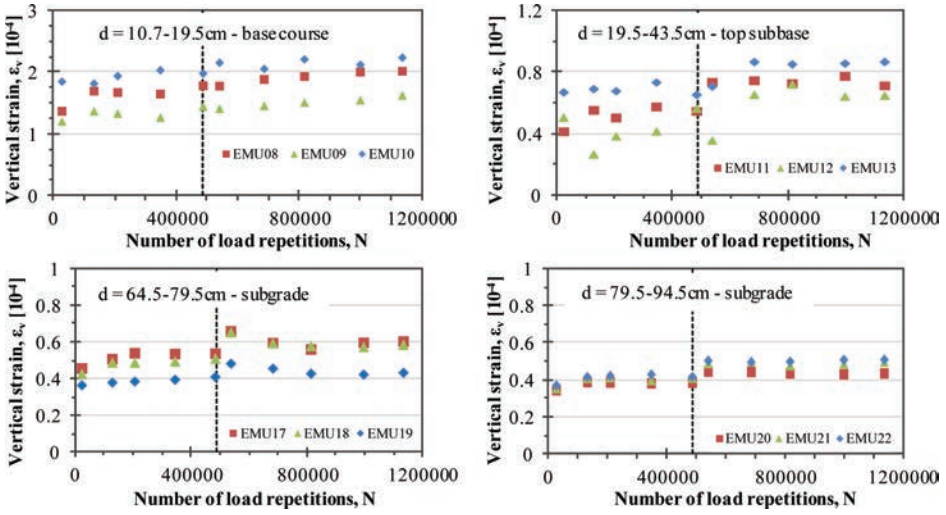

Figure 3. Induced vertical strain as a function of load repetitions for SE10 at depths from 10.7–19.5 cm, 19.5–43.5 cm, etc. (see Fig. 1). The vertical dotted lines indicate when the groundwater table was raised.

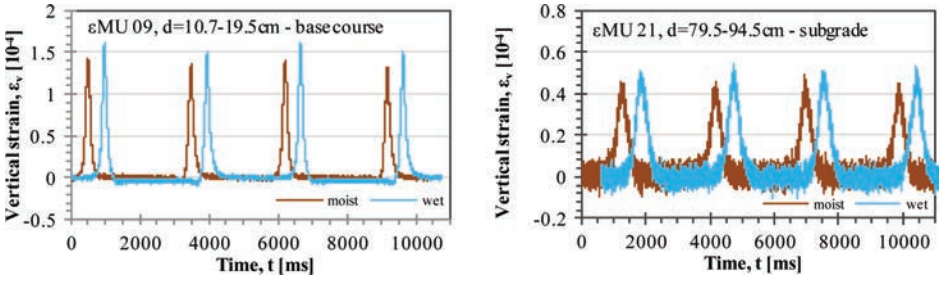

Figure 4. Induced vertical strain registration of εMU sensors at depths from 10.7–19.5 cm and 79.5–94.5 cm for SE10 in "moist" and "wet" states.

(Geokon 3500 pressure cells) were mainly used, but some older ones from the University of Nottingham were also included (Fig. 1) [13, 14]. In Figure 5 the vertical stress as a function of load repetitions is shown; the stress was reasonably constant during the first part of the main testing phase with a gradual increase as the test continued, indicating some post-compaction. The stress values decreased as the water was added, indicating a softer structure. Individual sensors in SE10 showed better performance than observed in previous tests. All the sensors in SE10 were under 8% variation in the "moist" state but the difference was higher in the "wet" state with a maximum of 28%. When examining the difference between sensors at the same depth the importance of having at least three SPC sensors at each depth is clearly visible.

3.4 *Linear Variable Differential Transducers (LVDT's)*

Linear Variable Differential Transducers (LVDTs) were used to measure the vertical deflection within a pavement structure in relation to the bottom of the test pit and over the base and subbase layers (Fig. 1). The development of resilient deformation measured with LVDTs is presented in Figure 6. The deformation was reasonably constant in the "moist" and "wet" phases, but it increased when the groundwater table was raised. A maximum of two LVDTs were placed at each depth and in some cases only one meter was in place due to practical limitations, but LVDTs are known for its accuracy.

3.5 *Asphalt Strain Gauges (ASG)*

Asphalt concrete Strain Gauges (ASG) (H-bar) of type PAST II AC produced by Dynatest were used to obtain the in-situ tensile strain at the bottom of the asphalt bound layers. In Figure 7 the tensile strain as a function of load repetitions is shown. The registered values were reasonably constant for individual sensors in the "moist" and "wet" states but the difference between sensors was great. The shape of the signal was as expected but the tensile

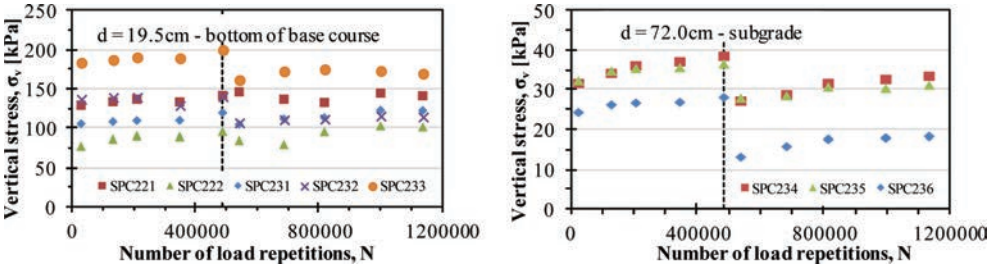

Figure 5. Vertical stress as a function of load repetitions for SE10, at depths 19.5 and 72.0 cm (see Fig. 1). The vertical dotted lines indicate when the groundwater table was raised.

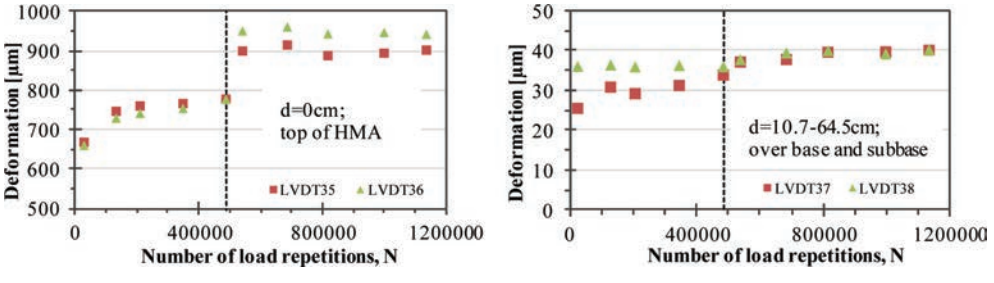

Figure 6. Induced deformation measure with LVDTs for SE10; from the bottom of the testing pit to the top of the HMA layers and over the base and subbase layers (see Fig. 1). The vertical dotted lines indicate when the groundwater table was raised.

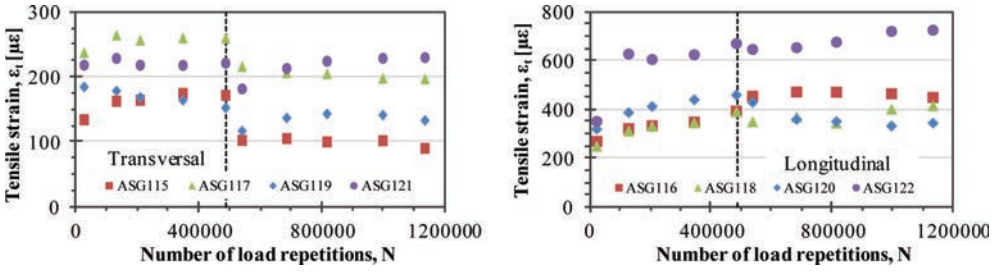

Figure 7. Induced tensile strain registration of ASG gauges at the bottom of the bituminous base for SE10 (see Fig. 1). The vertical dotted lines indicate when the groundwater table was raised.

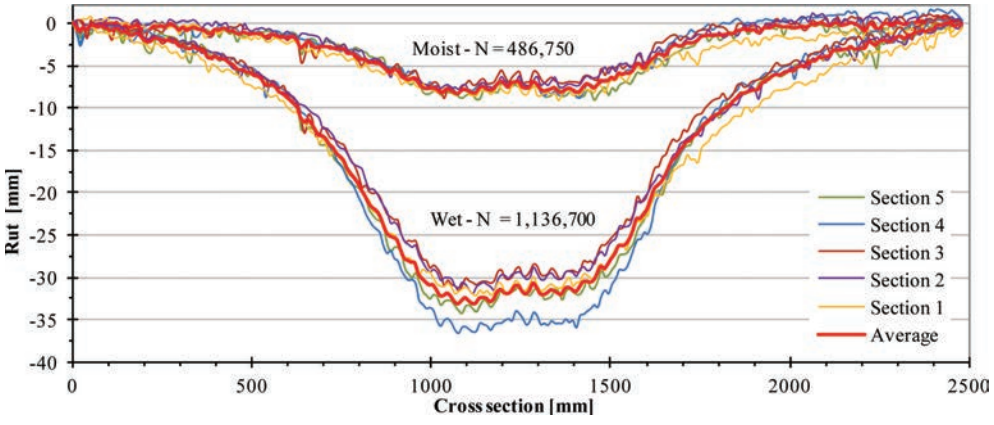

Figure 8. Cross section of the rutting profile after 486,750 load repetitions in the "moist" state and in the "wet" state after 1,136,700 load repetitions. Measurements were taken at 5 different sections, indicated by profiles 1–5 (Fig. 1).

strain was higher in the longitudinal direction than the transversal. For a single wheel the transversal tensile strain is normally higher but the situation is more complex with a dual wheel configuration. There are many factors that affect the tensile strain such as the wheel configuration, the tyre type and pressure, the material properties, the speed of the loading wheel and the applied load [15–17]. Generally the tensile strain increases with increased moisture content but here a decrease was observed in most cases. This should not have happened and indicates some error in the installation of the devices or, for example, a change in the properties of surrounding materials, some post-compaction or insufficient binding [6].

3.6 *Laser to measure the profile*

A custom-made laser beam on a straight edge has been used to measure the pavement profile. The laser measures the transverse profile of the pavement and then the data are converted to calculate the rut depth development under the straight-edge. The use of a laser has been proven to be reasonably accurate to estimate the amount of rutting at the surface. In Figure 8 the rutting profile at all measured sections for SE10 is shown at the end of the "moist" phase after 487,500 load repetitions and at the end of the "wet" phase after 1,136,700 load repetitions. The registered values were reasonably constant in the "moist" and "wet" states and a reasonable correlation between profiles was observed. The big impact water had on the structure can clearly be seen in the figure, with a great increase in rutting once the water was introduced.

4 RESPONSE MODELLING AND ANALYSIS

The response, performance and accumulation of permanent deformation are modelled to demonstrate a typical data process. From the analysis a performance prediction can be carried out as a function of time to evaluate the performance of new road concepts and maintenance strategies [18].

The pavement structure was modelled in an axisymmetric analysis where the responses were calculated using a Multi-Layer Elastic Theory (MLET) with the computer program ERAPAVE (EP) [19, 20]. The analysis was carried out with the asphalt bound layers and the subgrade treated as linear elastic materials. The stiffness modulus for granular materials (base and subbase) was treated as stress dependent [21, 22]:

$$M_r = k_1 p_a \left(\frac{3p}{p_a} \right)^{k_2} \tag{1}$$

where k_1 and k_2 are experimentally determined constants, p is the mean normal stress level of the loading, i.e. $p = \frac{1}{3}(\sigma_1 + \sigma_2 + \sigma_3)$ where σ_1, σ_2 and σ_3 are principal stresses, and p_a is a reference pressure, $p_a = 100$ kPa. This relationship has been shown to be able to capture the main behaviour characteristics of unbound granular materials under various rolling wheel loading situations [8, 9, 23].

The material parameters used in the numerical analyses of the responses are given in Table 1. When estimating the material parameters results from Plate Load (PL) tests, Falling Weight Deflectometer (FWD) tests, Indirect Tension Tests (ITT) of the bituminous layers and Repeated Load Triaxial (RLT) tests of the unbound layers were considered [2, 9, 18, 24]. The material parameters for the HVS testing were optimized for dual wheel configuration, under the centre of one of the tyres, with an applied axle load of 120 kN and 800 kPa tyre pressure. In all layers Poisson's ratio (ν) was set to 0.35. The parameters used in the permanent deformation predictions were estimated based on the materials being used as well as compaction, degree of saturation and stress state, where appropriate. The cohesion, c, was reduced by 10% from "moist" to "wet" state in the base and subbase layers and by 50% in the subgrade [18, 25–27].

Table 1. Material parameters of different layers used in the response analyses and of the unbound layers to predict the permanent deformation with the KT model.

		Response analysis				Permanent deformation			
SE10		E/M_r [MPa]	k_1 [–]	k_2 [–]	γ[kN/m^3]	c [kPa]	ϕ [°]	C [10^{-4}]	b [–]
Asphalt concrete	Moist	3500	–	–	24	–	–	–	–
	Wet					–	–	–	–
Bituminous base	Moist	3500	–	–	24	–	–	–	–
	Wet					–	–	–	–
Unbound base	Moist	–	500	0.6	20	40	43	1.1	0.35
	Wet		400			36		75	0.05
Unbound subbase									
Upper half	Moist	–	1450	0.6	19	40	43	0.6	0.33
	Wet		1150			36		440	0.05
Lower half	Moist	–	2850	0.6	19	40		0.5	0.31
	Wet		1550			36		330	0.05
Subgrade	Moist	50	–	–	16	14	35	0.05	0.55
	Wet	45				7		1.3	0.3

In table, E—Young modulus of bound materials; M_r—Resilient stiffness of unbound materials; γ—Unit weight.

The accumulation of the vertical strain in the unbound pavement materials was modelled according to a procedure developed by Korkiala-Tanttu (KT) [28, 29]. The KT model is a simple work hardening material model for unbound material:

$$\hat{\varepsilon}_p(N) = C \cdot N^b \cdot \frac{R}{A - R} \tag{2}$$

where $\hat{\varepsilon}_p$ is the accumulated vertical permanent strain, C is a material parameter depending on the compaction and saturation degree, N stands for the number of load repetitions, b is a shear ratio parameter depending on the material and stress state, R is the deviatoric stress ratio defined as, $R = q/q_f = \sigma_1 - \sigma_3/q_0 + Mp$, where $M = 6 \cdot \sin\phi/3 - \sin\phi$ and $q_0 = c \cdot 6 \cdot \cos\phi/3 - \sin\phi$, defined by the static Mohr Coulomb failure envelope, and A is the maximum value of R (here taken as 1.05).

The permanent deformation of the granular layers is gained by multiplying the permanent strain with the thickness of the layer (sublayer). Each layer has been divided into sublayers and the total deformation occurring in each layer is determined by summing up the permanent deformation over the sublayers. The lateral wander of the traffic is further accounted for by using the time-hardening summation approach, taking the calculated principal stresses representing the field conditions in the middle point of each layer over the area the wheels travel over [18, 20, 30, 31]. The calculations in Figures 9 and 10 were performed by using the KT model and the responses from MLET (ERAPAVE). The measured deformation of the asphalt bound layers was less than 1 mm, as the test was performed at a constant temperature of 10°C, and therefore not taken into account. In Figure 9 the rutting profile is displayed after 5 different load repetitions; two profiles are in the "moist" state and three in the "wet" state. The rutting profile in the "moist" state is overestimated, as well as the predicted rutting first after the water was added, but a fairly good correlation is reached in the end with a slight underestimation of the amount of rutting.

The Measurement (MM) of accumulated permanent deformation as a function of load repetition and the predicted deformation are displayed in Figure 10. In the figure the permanent deformation is shown for the base course, the subbase, and the top 30 cm of the subgrade, as well as the total deformation of the structure. In all layers the raised groundwater table accelerated the development of the permanent deformation, with the base layer showing the smallest increase whilst the subgrade showed the largest and greatest extent of increase in permanent deformation.

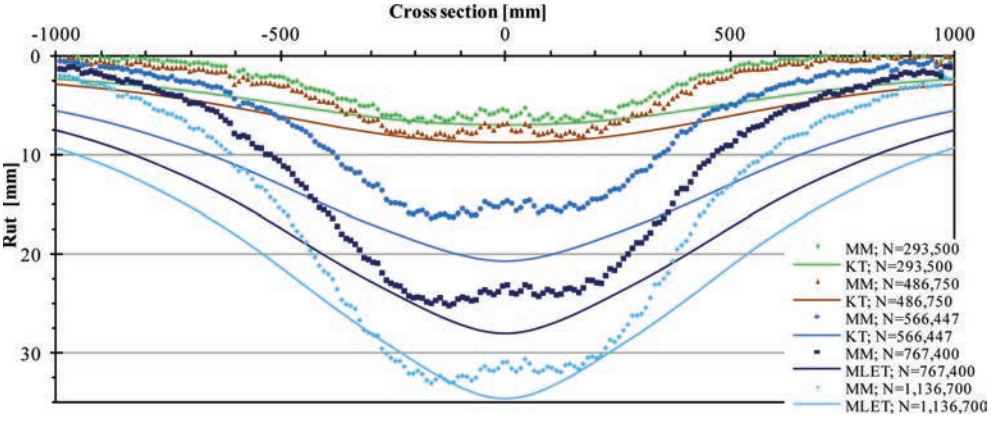

Figure 9. Cross section of the rutting profile after different numbers of load repetitions, two in the "moist" state (N = 293,500 and N = 486,750) and three in the "wet" state (N = 566,447, N = 767,400 and N = 1,136,700).

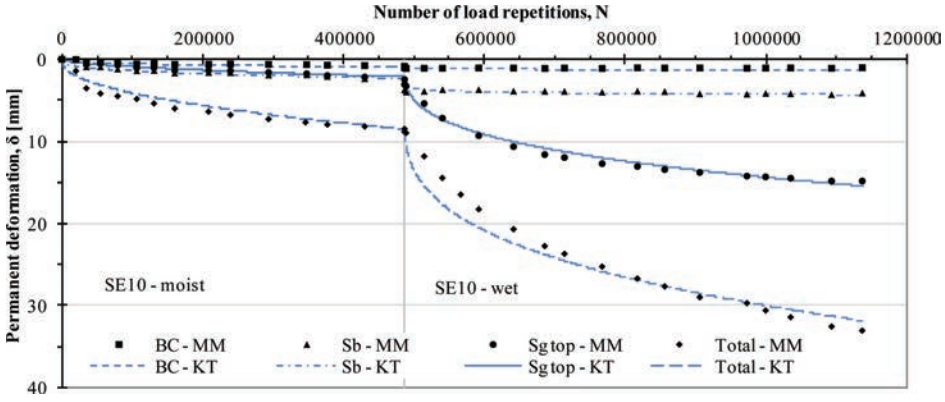

Figure 10. Permanent deformation in the unbound layers.

5 CONCLUSIONS

After 15 years of operating the HVS machine the test procedure and instrumentation have become quite robust. Test road structures have been built and tested to investigate their performance behaviour. The performance behaviour can thereafter be used for validation in a mechanistic performance scheme. A good correlation is observed between the measurements and calculations giving trustworthy results. These results can improve our understanding of pavement materials under a moving wheel loading.

It is believed that the accuracy of the pavements instrumentation is acceptable. In general the agreements were better for vertical strains than for stresses, but often it is more difficult to measure the vertical stresses in granular materials because of the complex inherent intergranular interactions between the aggregate particles and the sensors. The variation of the measurements for all sensors decreased as their location depth increased, most likely due to the fact that the influence of the dynamic loading diminishes with depth as well as having finer and more homogenous material in the subgrade. The ASG sensors performed fairly well but this was the only meter where a better performance was gained in previous tests compared to SE10, described here. As two sensors out of three at the same depth often gave good correlation it is recommended that at least three sensors be used at each depth. Due to the inhomogeneous nature of unbound materials it can be hard to measure their responses, with many factors influencing the results such as compaction and the quality of the contact between the meter and the material being measured.

REFERENCES

[1] Nokes, W.A., Mahdavi, M., Burmas, N.I., Holland, T.J., du Plessis, L. & Harvey, J.T. (2012). Developments in evaluating the benefits of implemented accelerated pavement testing results in California. In Harvey, J., Jones, D., Mateos, A. & Al-Qadi, I. (eds.) *Advances in Pavement Design through Full-scale Accelerated Pavement Testing*. Taylor & Francis Group, London. 529–540.

[2] Wiman, L.G. (2010). *Accelererad provning av vägkonstruktioner; Referensöverbyggnad enligt ATB Väg, VTI rapport 628*. Linköping, Sweden: Swedish National Road and Transport Research Institute (väg- och transportforskningsinstitut—VTI). (*In Swedish*).

[3] Wiman, L.G. (2006). *Accelerated load testing of pavements; HVS-NORDIC tests at VTI Sweden 2003-2004, VTI rapport 544A*. Linköping, Sweden: Swedish National Road and Transport Research Institute (väg- och transportforskningsinstitut—VTI).

[4] Wiman, L.G. (2001). *Accelerated load testing of pavements; HVS-NORDIC tests in Sweden 1999, VTI rapport 477A*. Linköping, Sweden: Swedish National Road and Transport Research Institute (väg- och transportforskningsinstitut—VTI).

[5] Wiman L.G. & Erlingsson S. (2008), Accelerated Pavement Testing by HVS—a Trans-national Testing Equipment, *Transport Research Arena Europe 2008*, Ljubljana, 21–24 April, 2008, CD ROM.
[6] Saevarsdottir, Th., Erlingsson, S. & Carlsson, H. (2014). Test procedure, instrumentation and modelling of a Heavy Vehicle Simulator Test at VTI in Sweden. Submitted to International Journal of Pavement Engineering.
[7] Vägverkets anvisningar (2004). ATB VÄG2004. Vägverkets publication 2004:111, Borlänge, Sweden. (*In Swedish*).
[8] Erlingsson, S. (2007). Numerical modelling of thin pavements behaviour in accelerated HVS tests. *Road Materials and Pavement Design*. 8/4, 719–744.
[9] Erlingsson, S. (2010). Impact of water on the response and performance of a pavement structure in an accelerated test. *Road Materials and Pavement Design*. 11/4, 863–880.
[10] Oscarsson, E. (2011). Evaluation of the Mechanistic-Empirical Pavement Design Guide model for permanent deformations in asphalt concrete. *International journal of Pavement Engineering*, 12/1, 1–12. doi:10.1080/102984 30903578952.
[11] Campbell Scientific, Inc. (2012). *CS616, Water content reflectometer*. Utah, USA: Campbell Scientific.
[12] Dawson, A. (1994) *The ε-mu system, users manual. 2nd ed*. Nottingham, UK: University of Nottingham.
[13] Geokon (2013). Instruction manual, Model 3500, 3510, 3515, 3600 earth pressure cells. Geokon, Inc. Lebanon, New Hampshire, USA.
[14] Nottingham Transportation Engineering Centre (NTEC) (2013). *Testing equipment*. Taken 23.03 2013 of http://www.nottingham.ac.uk/engineering-rg/infrastructureandgeomatics/ntec/facilities/equipment.aspx.
[15] Said, S.F. (1997). Variability in roadbase layer properties conducting indirect tensile test. *Proceedings of the 8th International Conference on Asphalt Pavements*, 10–14 August 1997. Seattle, Washington, USA.
[16] Loulizi, A., Al-Qadi, I.L. & Elseifi, M. (2006). Difference between in situ flexible pavement measured and calculated stresses and strains. *Journal of Transportation Engineering, ASCE*. 132/7, 574–579.
[17] Wang, H., Al-Qadi, I.L., Portas, S. & Coni, M. (2013). Three-dimensional finite element modeling of instrumented airport runway pavement responses. *Proceedings of the 92nd annual meeting of the Transportation Research Board (TRB)*, 13–17 January 2013. Washington D.C., Washington, USA, CD-ROM.
[18] Saevarsdottir, Th. & Erlingsson, S. (2013). Water impact on the behaviour of flexible pavement structures in an accelerated test. *Road Materials and Pavement Design*. doi:10.1080/14680629.20 13.779308.
[19] Erlingsson, S. & Ahmed, A.W. (2013). Fast layered elastic response program for analysis of flexible pavement structures. *Road Materials and Pavement Design*. 14/1, 196–210. doi:10.1080/14680629. 2012.757558.
[20] Ahmed, A.W. & Erlingsson, S. (2013). Evaluation of permanent deformation models for unbound granular materials using accelerated pavement tests. *Road Materials and Pavement Design*. 14/1, 178–195. doi:10.1080/14680629.2012.755936.
[21] Uzan, J. (1985). Characterization of granular materials. *Transportational Research Record 1022, TRB*. Washington, D.C.: National Research Council, 52–59.
[22] Lekarp, F., Isacsson, U. & Dawson, A. (2000). State of the art. I: Resilient response of unbound aggregates. *Journal of Transportation Engineering, ASCE*. 126/1, 66–75.
[23] Huang, Y.H. (2004). *Pavement analysis and design*. 2nd ed. Upper Saddle River, New Jersey, USA: Pearson Education Inc., Prentice Hall and Education Inc.
[24] Rahman, S. & Erlingsson, S. (2012). Moisture sensitivity of unbound granular materials. *Proceedings of the 4th European pavement and asset management conference (EPAM4), 5–7 September 2012*. Malmö, Sweden, CD-ROM.
[25] Theyse, H.L. (2002). *Stiffness, strength and performance of unbound aggregate material: Application of South African HVS and laboratory results of California flexible pavements*. Report for the California Pavement Research Program, University of California, Pavement Research Center.
[26] Matsushi, Y. & Matsukura, Y. (2006). Cohesion of unsaturated residual soils as a function of volumetric water content. *Bulletin of Engineering Geology and the Environment.* 65/4, 449–455.
[27] Fredlund, D.G. & Rahardjo, H. (1993). *Soil Mechanics for Unsaturated Soils*. New York: John Wiley & Sons, Inc.
[28] Korkiala-Tanttu, L. (2008). *Calculation method for permanent deformation of unbound pavement materials.* Espoo, Finland: VTT Technical Research Centre of Finland.

[29] Korkiala-Tanttu, L. (2009). Verification of rutting calculation for unbound road materials, *Transport, Proc. of the Institution of Civil Engineers*, 162/TR2, 107–114.
[30] Lytton, R.L., Uzan J., Fernando, E.G., Roque, R., Hiltumen, D. & Stoffels, S.M. (1993). Development and validation of performance prediction models and specifications for asphalt binders and paving mixes. *The Strategic Highway Research Program Project Rep. No. SHRP-A-357.*
[31] Hu, S., Zhou, F. & Scullion, T. (2011). Development, calibration and validation of a new M-E rutting model for HMA overlay design and analysis. *Journal of Materials in Civil Engineering*. 23/2, 89–99.

This page intentionally left blank

Experimental characterization of asphaltic materials—IV

This page intentionally left blank

Asphalt Pavements – Kim (Ed)
© 2014 Taylor & Francis Group, London, ISBN 978-1-138-02693-3

Effect of asphalt binder oxidation on the modulus of asphalt concrete mixtures

B. Shane Underwood
Arizona State University, Tempe, AZ, USA

Cheol-Min Baek
Korea Institute of Construction Technology, Korea

Y. Richard Kim
North Carolina State University, Raleigh, NC, USA

ABSTRACT: Oxidative aging of asphalt binder is a well-known phenomenon that has been studied by numerous researchers. Significant breakthroughs have been made in the fundamental understanding of this phenomenon at the asphalt binder level, and practicing engineers now have the tools needed to quantitatively assess the oxidative aging potential of these materials. Conversely, pavement engineers do not have a reliable method to assess the oxidative aging potential of an asphalt mixture because it is unclear exactly how aging in the asphalt binder affects the behaviour of asphalt mixture. Analysis that supports the use of existing models for this purpose is shown in this paper. The study begins with an examination of the effects of oxidative aging on binder and mixture moduli. Then, four existing predictive models that relate these moduli are examined. It is found that all four models do an adequate job of predicting the effect of asphalt binder oxidation on asphalt mixture modulus, but that two of the models, the Witczak models, match the trends observed in mixture experiments the best.

Keywords: oxidative aging, asphalt binder, asphalt mixture, dynamic modulus

1 INTRODUCTION

Aging has long been recognized as a major distress mechanism for asphalt concrete and by extension asphalt pavements, but the term aging can have multiple meanings. For some it is applied to mean the overall deterioration of an asphalt pavement from exposure to both climatological and load factors. In other cases, aging is meant to describe only the effects of climate, which includes oxidative aging, ultraviolet radiation, and moisture related damage [1]. The more common usage of the term aging, and the meaning of the term as used in this paper, is as a descriptor for the process of asphalt binder oxidation. This process causes the material to stiffen and embrittle, which leads to a higher potential for cracking.

The issue of oxidative aging in asphalt binder has been recognized and studied for almost a century. Hubbard and Reeve [2] published the results of a study examining the effect of a year of outdoor weathering on the physical and chemical properties of paving grade asphalt cements. Subsequent historical studies confirmed the basic findings that oxidation, and not volatilization alone, was responsible for the changes in asphalt properties which occurred due to exposure [3–5]. Significant literature has also been produced on the chemical aspects of the aging process and excellent reviews of these studies are given in the literature [1, 6, 7]. In some of the cited studies, researchers have used sophisticated experimental studies to propose conceptual, empirical and/or analytical models for the aging phenomenon in asphalt binder [8–11].

Probably the most well-known binder based aging model is the Global Aging System (GAS) model [12]. This empirical model includes relationships to predict the change in viscosity within an asphalt mixture both with time and with depth in an asphalt pavement structure. While certain aspects of this model have been criticized, the model predicts two trends that most agree to be fact; 1) aging occurs most quickly after initial construction and 2) aging effects are greatest near the pavement surface. An alternative to the GAS model is the transport model, developed through several independent research efforts under the direction of Dr. Charles Glover [8, 9, 11]. In comparison to the GAS model, the transport model treats the asphalt binder aging phenomenon with more scientific rigor and is thus believed to produce a more reliable aging to depth relationship.

A review of the pertinent literature shows that while significant research has been devoted to better understanding and modelling the aging phenomenon of asphalt binder, relatively little has been devoted to aging in asphalt mixtures [13–16]. The lack of significant research in this area, particularly in the years since the Strategic Highway Research Program (SHRP) concluded, is a reflection of the complexity involved in asphalt binder aging alone. When additional factors, like physico-chemical interactions between asphalt binder and aggregates occur and when the material becomes structured and contains air voids, the aging process becomes more complex. However, to date, there exists no comprehensive study that links the known behaviour of an asphalt binder to those of the asphalt mixtures. The lack of such a study makes it almost impossible to rigorously judge the impact of certain conditions on asphalt mixture behaviour simply by measuring the impacts of those changes on the properties of asphalt binder. Without such a study, and given the current state of understanding of this relationship, it is argued that the only way to determine the impact of aging on mixture properties is direct experimentation of the mixtures [17–19]. The complexity of the problem is quite staggering when one considers that in mixtures; 1) the aging kinetics are highly binder specific and dependent upon temperature; 2) physico-chemical interactions may be significant, 3) thermal exposure during the mixing and placement operations can be highly variable and in some cases not very well controlled; and 4) void content can vary. With these issues in mind, the objectives of this paper are to report on and demonstrate the following;

1. The effect of oxidative aging on the apparent viscosity of asphalt binder and how this effect compares with changes in the asphalt binder LVE properties after oxidative aging,
2. The effect of oxidative aging on the LVE response of asphalt mixture over the range of typical in-service temperatures, and
3. The ability of existing analytical models that relate asphalt binder and asphalt mixture LVE behaviours to capture the effect of asphalt binder aging on asphalt mixture modulus, and

This work is not intended to develop a new model, but rather to provide quantified evidence that existing tools can be used to provide insight into the effects of asphalt binder oxidation on asphalt mixture modulus. While this may be expected, the authors have been unable to identify any existing literature that attempts to confirm the hypothesis. Additionally, it should be understood that oxidation impacts behaviours beyond the LVE range (cracking, permanent deformation, etc.), but it is believed that before such impacts can be fully understood that the relationships within the LVE range must be first studied.

2 MATERIALS

The materials used in this study have been compiled from numerous studies and separated into two databases; one for asphalt mixtures (Table 1) and one for asphalt binders (Table 2). Both databases represent a broad range in material characteristics and together afford a unique opportunity to compare and contrast viscosity and rheological based aging characteristics over the range of conditions typically experienced in-service.

Viscosity data are available for all of the asphalt binders in the form of the viscosity temperature susceptibility relationship (A and VTS) coefficients. The dynamic shear modulus,

Table 1. Mixture database used for aging study.

Project	Mixture name	Aging conditions					Testing temperatures (deg. C)	
		Unaged	STOA	Plant mix	LTOA	Field	Max	Min
NCHRP 9-36	Airblown	✓	✓				4	40
	AAC-1	✓	✓					
	AAF-1	✓	✓					
	AAM-1	✓	✓					
	ABL-1	✓	✓					
	ABM-2	✓	✓					
	Citgoflex	✓	✓					
	Elvaloy	✓	✓					
	ALF PG 64	✓	✓					
	Novophalt	✓	✓					
	EVA	✓	✓					
ALF	ALF AC5		✓			✓	–10	54
	ALF AC5-base		✓			✓		
	ALF AC10		✓			✓		
	ALF AC20		✓			✓		
	ALF AC20-base		✓			✓		
	ALF Novophalt		✓			✓		
	ALF Styrelf		✓			✓		
NCSU	AL		✓		✓		–10	54
	A		✓		✓			
AAT	Citgo		✓		✓		4	40
WRI Kansas	Coastal Eldorado			✓	✓		4	40
	Koch Muskogee			✓	✓			
	Royal Trading			✓	✓			
	Sinclair Tulsa			✓	✓			
WRI Nevada	Crown Nevada			✓	✓		4	40
	Crown Canada			✓	✓			
	Sinclair, Wyoming			✓	✓			
	Crown Venezuela			✓	✓			

$|G^*|$, has been measured using the Dynamic Shear Rheometer (DSR) and is available for the combination of temperatures between 15°C and 115°C and frequencies between 0.1 and 100 radians per second. Some of the asphalt binders have beam stiffness measured with the Bending Beam Rheometer (BBR) for temperatures between approximately –30° and –10°C and for times between 8 and 240 seconds. Available binder conditions include; Original (unaged), RTFO aged, PAV aged at the standard temperature, PAV aged at 110°C (PAV110), and recovered from an asphalt mixture (REC). Mixture data is available for the unaged, STOA, LTOA, plant mixed, and field aged conditions. Since the binder RTFO and mixture STOA are meant to represent the materials after placement, they serve as the datum for comparison between and among materials.

3 AGING AND ASPHALT BINDER PROPERTIES

It is well known that asphalt binder becomes stiffer as oxidative aging occurs. Historically, this effect is quantified with aging indices defined as shown in Equation (1).

Table 2. Binder database used for aging study.

Project	Binder name	Aging conditions					Viscosity based analysis	LVE based analysis
		Original	RTFO	PAV	PAV110	REC		
ALF	AC 5	✓	✓	✓		✓	✓	✓
	AC 10	✓	✓	✓		✓	✓	✓
	AC 20	✓	✓	✓		✓	✓	✓
	Novophalt	✓	✓	✓		✓	✓	✓
	Styrelf	✓	✓	✓		✓	✓	✓
MnRoad	AC 20	✓	✓	✓		✓	✓	✓
	Pen 120/150	✓	✓	✓		✓	✓	✓
Westrack	Westrack	✓	✓	✓			✓	✓
Arizona DOT	Para. PG 58-22	✓	✓	✓	✓		✓	
	Para. PG 64-16	✓	✓	✓	✓		✓	
	Nav. PG 70-10	✓	✓	✓	✓		✓	
	Nav. PG 76-16	✓	✓	✓	✓		✓	
	Chev. PG 64-22	✓	✓	✓	✓		✓	
	Chev. PG 76-16	✓	✓	✓	✓		✓	
Witczak	Citgo PG 64-22	✓	✓	✓		✓	✓	
Maryland port authority	Citgo PG 70-22	✓	✓	✓			✓	
	TLA	✓	✓	✓			✓	
	Stylink	✓	✓	✓			✓	
	Novophalt	✓	✓	✓			✓	
	PMB	✓	✓	✓			✓	

$$AR = \frac{A_{age}}{A_{ref}} \tag{1}$$

where, A_{ref} is the binder property, viscosity or $|G^*|$, at some reference condition and A_{age} is the same binder property determined at a different aging condition but the same temperature-rate/frequency combination. The advantage of AR is its simplicity and that it works well to quickly show the aging sensitivity of a given material. Its disadvantage is that when defined at a single temperature, it does not provide a full picture of the effects of oxidative aging over the range of conditions that would be experienced under service [20]. In this analysis, ARs will be calculated based on both viscosity and $|G^*|$, using the basic form in Equation (1), but at various temperatures and frequencies of loading. In both cases the RTFO aged binder will serve as the reference condition.

3.1 *Aging effects on viscosity*

Viscosity values are determined for all of the asphalt binders in the database using the A and VTS function, Equation (2). This equation has been characterized for each material by using viscosity measures such as kinematic viscosity, absolute viscosity, penetration, etc. It is assumed, based on the work of others [12], that a maximum viscosity of 2.7×10^{12} cP exists for all materials.

$$\log\left(\log(\eta)\right) = A + VTS\log\left(T_R\right) \tag{2}$$

where, η is the viscosity in cP, A is the intercept of the temperature susceptibility relationship, VTS is the slope of the temperature susceptibility relationship, and T_R is the temperature in Rankine.

The results of viscosity based aging analysis are shown in Table 3 for 5° and 54°C. Although 5° and 54°C are shown, the *AR* values have been computed for −10°, 5°, 20°, 40° and 54°C, which together represent the range of in-service conditions. Through the analysis, it is found that the *AR* can be strongly dependent on temperature, see for example the MnRoad binders at the PAV aging condition. The aging characteristics are also found to depend on the specific binder and aging condition examined, but no clear correlation exists for predicting how the *AR* will manifest itself for the PAV condition given the behaviour of the Original binder. In some cases asphalt binders that show significant effect from the RTFO aging, show little effect from the PAV aging, see the Maryland PMB. In other cases, such as the MnRoad Pen 120/150 asphalt binder, significant Original to RTFO aging is observed and a large RTFO to PAV change is also observed. Note that several asphalt binders are found to have *AR* of 1 at −10°C (not shown), due to the assumption that the maximum viscosity of the asphalt binder is 2.7×10^{12} cP.

3.2 *Aging effects on linear viscoelastic properties*

Superpave binder specifications have caused $|G^*|$ to replace viscosity as the primary asphalt binder property. The *AR* calculated from $|G^*|$, unlike that calculated from viscosity, is a function of both frequency and temperature. Since the low end of the temperature range of interest (−10°C) cannot be accurately measured using the DSR, an analytical technique, presented elsewhere, that combines the results from the BBR and DSR tests is utilized in this study [21]. The *AR* results are shown for different aging levels and for all of the asphalt binders in Figure 1. Note that asphalt binders with BBR data available are plotted for −10°, 5°, 20°, 40° and 54°C whereas the other asphalt binders are shown for only 20°, 40°, and 54°C. The recovered asphalt binder samples do not have BBR data and thus their results are plotted at only 20°, 40° and 54°C.

To properly interpret Figure 1, it must be recognized that $|G^*|$ decreases as either the temperature increases or the frequency decreases. Thus, the $|G^*|$ based ratios show a larger effect from aging at higher temperatures and/or slower frequencies. For the highest frequencies

Table 3. Viscosity based aging ratios for study binders at selected temperatures.

		5°C				54°C			
Project	Binder	Orig.	PAV	PAV110	REC	Orig.	PAV	PAV110	REC
ALF	AC 5	0.21	7.08	–	0.91	0.44	3.70	–	1.12
	AC 10	0.06	3.22	–	0.69	0.19	2.30	–	0.89
	AC 20	0.22	9.37	–	2.07	0.39	4.52	–	1.72
	Novophalt	0.36	4.32	–	4.69	0.41	3.72	–	0.76
	Styrelf	0.49	2.17	–	1.05	0.49	5.39	–	1.66
MnRoad	AC 20	0.20	11.47	–	4.66	0.39	4.70	–	2.82
	Pen 120/150	0.20	12.17	–	9.21	0.40	4.38	–	4.08
Westrack	Westrack	0.22	2.29	–	–	0.42	1.63	–	–
Arizona DOT	Para. PG 58-22	0.24	8.30	27.05	–	0.41	3.45	8.88	–
	Para. PG 64-16	0.38	2.90	2.90	–	0.44	3.00	7.06	–
	Nav. PG 70-10	0.28	1.00	1.00	–	0.59	4.99	6.06	–
	Nav. PG 76-16	0.25	2.76	3.90	–	0.40	2.02	1.86	–
	Chev. PG 64-22	1.14	13.78	19.43	–	0.51	3.20	5.40	–
	Chev. PG 76-16	0.56	2.55	2.55	–	0.58	4.49	8.14	–
Witczak	Citgo PG 64-22	0.22	7.64	–	1.31	0.43	3.30	–	1.29
Maryland port authority	Citgo PG 70-22	0.32	7.64	–	–	0.47	3.40	–	–
	TLA	0.17	1.68	–	–	0.34	3.50	–	–
	Stylink	0.37	4.39	–	–	0.44	3.80	–	–
	Novophalt	0.26	1.12	–	–	0.31	1.71	–	–
	PMB	0.23	1.83	–	–	0.17	1.46	–	–

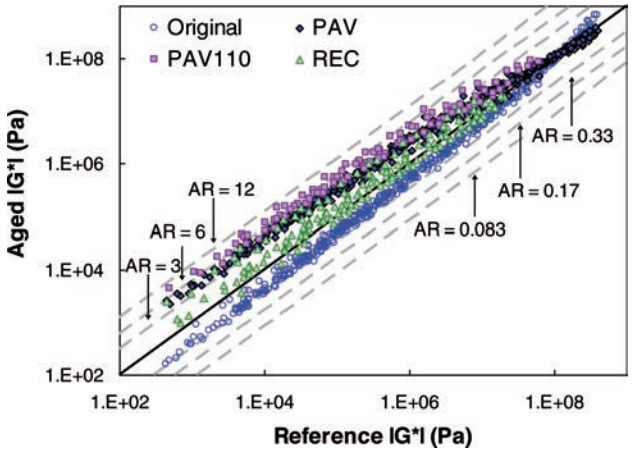

Figure 1. Effect of aging on asphalt binder $|G^*|$.

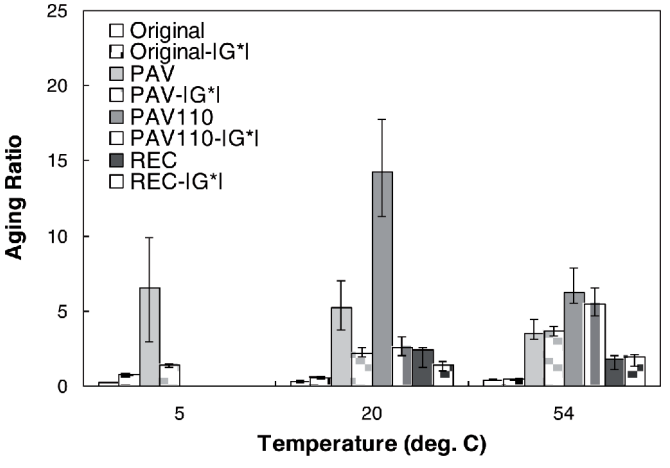

Figure 2. Comparison of viscosity based and $|G^*|$ based aging ratios at selected temperatures.

at −10°C some of the asphalt binders have the largest modulus for the Original aging condition. This is a result of extrapolation in the fitting procedure. Although BBR data is measured at temperatures as low as −30°C, the times at which measurements are taken are sufficiently long so that the equivalent frequency is slower than 10 Hz at −10°C. This issue could be avoided by strictly defining the glassy modulus of each binder and aging level at a constant value, some have suggested a value of 1 GPa [19]. Such an approach was not followed because the difference in AR from the chosen procedure was generally small and only affected a few frequencies at −10°C. Further, a better representation of the modulus at other temperatures was obtained by not assuming a constant glassy modulus.

A comparison of the $|G^*|$ and viscosity based aging ratios at some selected temperatures is shown in Figure 2. In this figure, the average AR, both $|G^*|$ and viscosity based, for all study materials is plotted. For the $|G^*|$ based quantity the value is computed by averaging the results at frequencies between 1 and 100 radians per second for a given temperature. Error bars are shown to represent the 75th and 25th percentiles. The agreement between the $|G^*|$ and viscosity based ratios is mostly favourable for the case of the Original and Recovered asphalt, but not for the PAV and PAV110 conditions. In these latter two aging conditions, the viscosity AR may be as large as 10 to 18, but the $|G^*|$ ratio never exceeds 7. This difference

may be attributed to the fact that some of the viscosity measurements used to generate the A and VTS relationships are non-fundamental quantities. At high temperatures, when kinematic or rotational viscosities are measured, the material is mostly Newtonian and a viscosity measurement may be a fundamental characteristic. However, at lower temperatures, where penetration is measured, the material is shear rate dependent and thus viscosity is an engineering quantity rather than a fundamental one. It is hypothesized that these shear rate effects will become more significant as the material becomes stiffer and thus overemphasize the true effects of oxidative aging. Examining only the data at 54°C, where non-Newtonian effects are reduced (although not eliminated), the agreement between the $|G^*|$ and viscosity based quantities improves.

4 AGING AND ASPHALT MIXTURE PROPERTIES

The standard LTOA aging procedure affects the LVE properties of asphalt concrete in the following ways [22]:

1. Aging universally increases mixture stiffness at high and intermediate temperatures and shows little effect at the lowest temperatures;
2. Increased aging has little effect on the t-T shift factors except for at higher temperatures;
3. The maximum phase angle is delayed to a slower reduced frequency upon further aging, which causes the elasticity to be greater at intermediate temperatures, but less at high temperatures;
4. The overall impact of aging is most noticeable in the intermediate temperature range.

Observations 1 and 2 are consistent with what is observed in the asphalt binder while observations 3 and 4 are not, which is an indicator of the complicated mechanisms that dictate how asphalt binder influences behaviours of asphalt mixtures. These mechanics have not yet been fully described with analytical or computational methods. Nevertheless, in the subsequent sections of this paper existing simplified tools will be shown to sufficiently capture some of these fundamental differences.

The impact of laboratory and in-service aging of asphalt concrete mixtures is summarized for the study materials in Figure 3. This figure conveys the same type of oxidative aging effect information shown for the asphalt binder in Figure 1. In Figure 3 the reference modulus (STOA or plant mixed) is plotted on the x-axis and the moduli at different aging levels (noted in the legend) are plotted on the y-axis. For convenience, lines at aging ratios of 2, 1.5, 0.67, and 0.5 are also shown. From this figure it is first observed that the field sections have a significant amount of variability. This variability is attributed to three primary factors; 1) the specimen-to-specimen variability were higher than usual for these materials, 2) the field sections were exposed to aging for only a very short period of time, less than five years, and 3) the well-known, but hard to quantify effects of lab-to-field compaction differences are

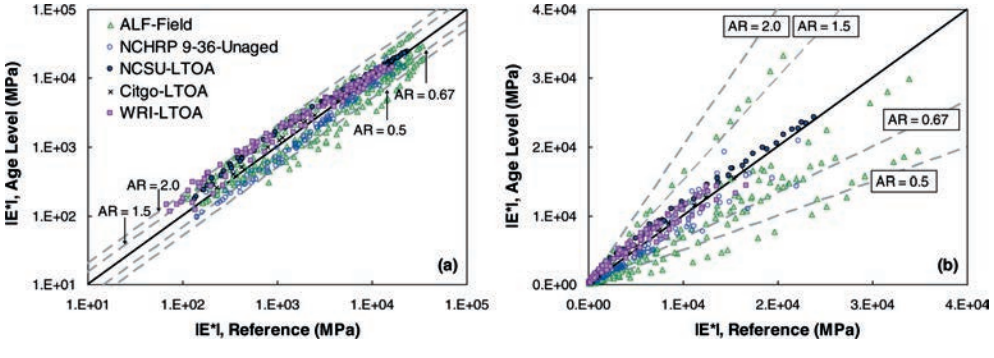

Figure 3. Effect of aging on measured $|E^*|$ in; (a) logarithmic space and (b) arithmetic space.

present. Comparisons of the different laboratory aged materials show that the unaged samples are almost consistently softer and the LTOA aged samples are almost consistently stiffer than the reference. Cases that do not follow this trend are likely the result of experimental variability since the differences are small. Some mixtures also show a trend towards a reduced aging effect at the extremely low modulus values.

Comparing Figures 1 and 3 it is seen that the mixture aging ratios are smaller in magnitude than those found for the asphalt binder. This effect could be related to the mismatch in aging conditions between binder and mixture because *unaged* asphalt mixture may not necessarily be the same as Original binder, STOA may not equate to RTFO, and LTOA may not equate to PAV. However, numerous research studies have concluded and engineering practice suggests an approximate and *on the average* agreement in material states at these aging conditions [16, 17, 23]. As noted in the introduction, the exact aging time correspondence is dependent upon many confounding factors, but in taking the general guidelines as truth or near truth, then it can be concluded that oxidative aging has a less noticeable effect on the mixture modulus than it does on the binder modulus.

5 COMPARISON OF OBSERVED MIXTURE LVE AND PREDICTED LVE FROM MODELS

The relationship between the mechanical properties of an asphalt mixture and its asphalt binder is highly complex and dependent upon many diverse factors such as aggregate gradation, void content, thermal history, etc. Some existing analysis methods exist for predicting this relationship and they have been applied to assess their ability to match the quantitative observations in the preceding sections of this paper. In total, four different analytical methods are used; 1) the Original Witczak model, 2) the Modified Witczak model, 3) the Hirsch model, and 4) the NCSU ANN model. Each of these models is explained in substantial detail in the literature and interested readers are referred to the review in [21] for more information and the equations.

The measured Original, RTFO, PAV, PAV110, and REC asphalt binder properties are used as input in these models to predict the effect of aging on mixture modulus. Plots similar to that shown in Figure 3 (a) are created to qualitatively and quantitatively examine the given model's ability to match the trends observed in mixture testing. These plots are shown in Figure 4 for each of the models. In Figure 4 (c) shaded areas are shown to represent conditions where the Hirsch model has not been fully calibrated [21]. These extrapolation areas are included since users would likely apply the model irrespective of extrapolative errors. Long term aged mixture moduli are predicted using only the Original Witczak model because it is the only model that utilizes viscosity (the output from the GAS model) as an input variable.

The predictions in Figure 4 shows that while each model predicts different values for the mixture modulus, each captures the fact that a given amount of stiffening in the asphalt binder does not directly translate to an equivalent amount of stiffening in asphalt mixture. The relationship between asphalt binder and mixture stiffness is not linear, and as such a major change in the properties of the asphalt binder does not necessarily mean a big change in the mixture modulus. In application, any of these models can be used irrespective of the magnitude of their prediction by using the model as a normalized formulation, i.e., use the model to predict AR instead of the modulus directly. Comparisons between Figure 3 (a) and Figure 4 (a)–(d) show that each predictive model matches the magnitude of the aging effect observed in the experiments. Recall that the influence of aging on the asphalt binder alone was shown in Table 3 and Figure 1 to regularly result in AR greater than 12 and less than 0.2. These observations are independent of the exact agreement between mixture and binder aging conditions and reflect a larger difference in behaviour of the two materials.

All models except the Original Witczak predict that aging is the most significant at intermediate conditions and becomes less significant at the extremes. This behaviour gives a characteristic elliptical shape to the plots in Figure 4 (b)–(d), but is most pronounced for the Hirsch and NCSU ANN models. Both of these models utilize only the $|G^*|$ and mixture

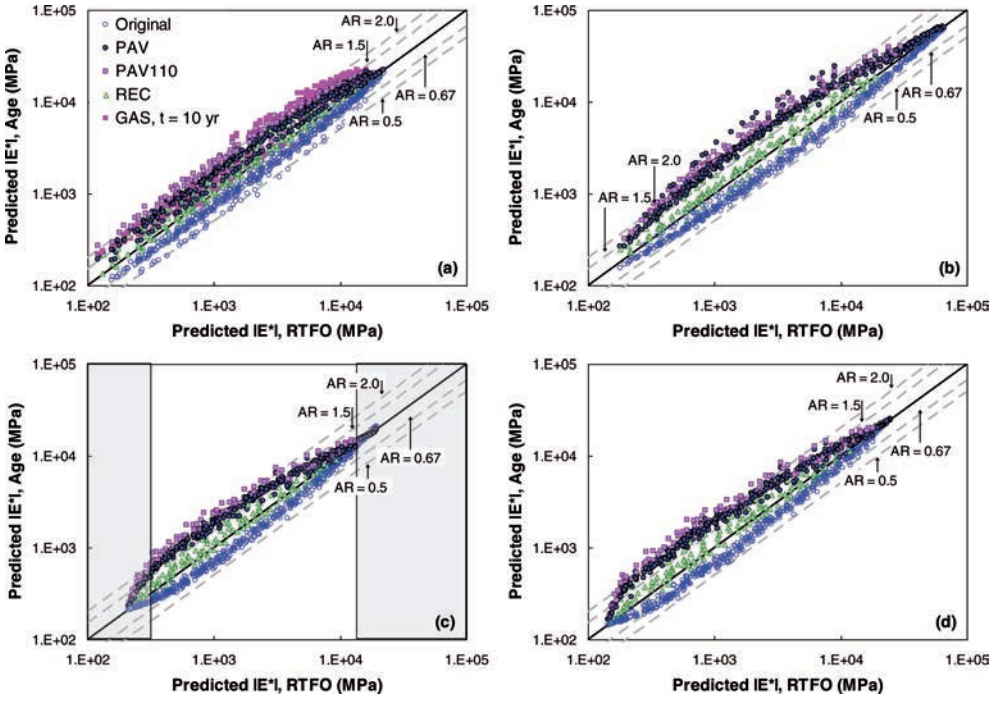

Figure 4. Predicted aging susceptibility with existing $|E^*|$ prediction models; (a) Original Witczak model, (b) Modified Witczak model, (c) Hirsch model, and (d) NCSU ANN model.

volumetrics as input parameters, but have no parameters to account for aggregate gradation. The Original Witczak model suggests that the effect of aging increases as the material softens, but it does not show the characteristic elliptical shape and instead this model predicts that the influence of aging is very similar at the intermediate and low modulus conditions, e.g. a parabolic shape. The characteristic shape from Figure 3 (a) varied from slightly elliptical (NCSU-LTOA and Citgo-LTOA series) to parabolic (WRI-LTOA and NCHRP 9-36). The better match from the two Witczak models may be related to the fact that they include parameters to directly account for the aggregate gradation, which may indirectly capture some of the influence of aggregate surface characteristics on the aging phenomenon.

6 CONCLUSIONS AND SUMMARY

The influence of oxidative aging on the viscosity and modulus of asphalt binder and on the modulus of asphalt mixtures has been studied. It was found that very little experimental data has been gathered on the influence of oxidative aging in asphalt mixtures. Surprisingly, no studies were found wherein researchers have attempted to study the effects of aging in asphalt binder and asphalt mixture at a consistent aging level and over the entire range of in-service conditions. Since data for direct comparison is not available, an indirect method was adopted wherein materials with vastly different properties were examined at many different aging levels. Using qualitative and quantitative methods it was shown that oxidative aging may influence the viscosity and linear viscoelastic modulus of asphalt binder by a factor of 10 or more. However, it was also observed that this influence does not directly translate to increases in the modulus of asphalt concrete mixtures. Such a direct translation does not occur due to the complex interactions that can occur within an asphalt concrete mixture including the mitigating effects of aggregate particles and the fact that asphalt binder typically represents only about 10–15% of the total volume of an asphalt concrete mixture. A rational method

that utilizes existing analytical models was shown to predict the influence of asphalt binder aging on mixture modulus with a reasonable degree of accuracy. With this method, engineers can better assess the influence of asphalt binder aging on the modulus of asphalt concrete mixtures.

ACKNOWLEDGEMENTS

This research is part of work sponsored by the Federal Highway Administration under Project No. DTFH61-02-D-00139—Task Order #10. The authors gratefully acknowledge the help from Dr. Ramon Bonaquist at AAT, Dr. Michael Harnsberger at WRI, Dr. Matthew Witczak, and Dr. Javed Bari for providing data for the database developed in this study.

REFERENCES

[1] Wright, J.R. Weathering: Theoretical and Practical Aspects of Asphalt Durability. Chapter 8 in *Bituminous Materials: Asphalts, Tars and Pitches Volume II*, Ed. A.J. Hoiberg. Interscience Publishers, New York. 1965.

[2] Hubbard, P. and C.S. Reeve. The Effect of Exposure on Bitumens. *Journal of Industrial and Engineering Chemistry*. Vol. 5, No. 1, 1913, pp. 15–18.

[3] Thurston, R.R. and E.C. Knowles. Oxygen Absorption tests on Asphalt Constituents. *Industrial and Engineering Chemistry*. Vol. 28, No. 1, 1936, pp. 88–91.

[4] Van Oort, W.P. Durability of Asphalt—It's Aging in the Dark. *Industrial and Engineering Chemistry*. Vol. 48, No. 7, 1956, pp. 1196–1201.

[5] Corbett, L.W. and R.E. Merz. Asphalt Binder Hardening in the Michigan Test Road After 18 Years of Service. In *Transportation Research Record: Journal of the Transportation Research Board*, No. 544, Transportation Research board of the National Academies, Washington, D.C., 1975, pp. 27–34.

[6] Lee, D.Y. and R.J. Huang. Weathering of Asphalts as Characterized by Infrared Multiple Internal Reflection Spectra. *Applied Spectroscopy*, Vol. 27, No. 6, 1973, pp. 419–490.

[7] Jemison, H.B., B.L. Burr, R.R. Davison, J.A. Bullin, and C.J. Glover. Application and use of the ATR, FT-IR Method to Asphalt Aging Studies. *Petroleum Science and Technology*, Vol. 10, No. 4, pp. 795–808.

[8] Lunsford, K.M. *The Effect of Temperature and Pressure on Laboratory oxidized Asphalt Films with Comparison to Field Aging*. Ph.D. Dissertation, Texas A&M University, College Station, Texas, 1994.

[9] Liu, M., K.M. Lunsford, R.R. Davison, C.J. Glover, J.A. Bullin. The Kinetics of Carbonyl Formation in Asphalt. *AlChE Journal*, Vol. 42, No. 4, 1996, pp. 1069–1076.

[10] Petersen, J.C. and P.M. Harnsberger. Asphalt Aging: Dual Oxidation Mechanism and Its Interrelationships with Asphalt Composition and Oxidative Age Hardening. In *Transportation Research Record: Journal of the Transportation Research Board*, No. 1638, Transportation Research board of the National Academies, Washington, D.C., 1998, pp. 47–55.

[11] Glover, C.J., A.E. Martin, A. Chowdhury, R. Han, N. Prapaitrakul, X. Jin, and J. Lawrence. *Evaluation of Binder Aging and its Influence in Aging of Hot Mix Asphalt Concrete: Literature Review and Experimental Design*. Publication 0-6009-1. Texas Transportation Institute, College Station, Texas. 2008.

[12] Mirza, M.W. and M.W. Witczak. Development of Global Aging System for Shrot and Long Term Aging of Asphalt Cements. *Journal of the Association of Asphalt Paving Technologists*. Vol. 64, 1995, pp. 393–430.

[13] Bell, C.A. *Aging of Asphalt Aggregate Systems*. Publication SHRP-A-305. Strategic Highway Research Program. National Research Council. Washington, D.C. 1989.

[14] Brown, S.F. and T.V. Scholz. Development of Laboratory Protocols for the Ageing of Asphalt Mixtures. *2nd Eurasphalt and Eurobitume Congress*, Barcelona, Spain. 2000.

[15] Airey, G.D. State of the Art Report on Ageing Test Methods for Bituminous Pavement Materials. *International Journal of Pavement Engineering*, Vol. 4, No. 3, 2003, pp. 165–176.

[16] Houston, W.N., M.W. Mirza, C.E. Zapata, and S. Raghavendra. *Environmental Effects in Pavement Mix and Structural Design Systems*. Publication NCHRP Web-Only Document 113. National Cooperative Highway Research Program, Washington, D.C. 2005.

[17] Bell, C.A. and D. Sosnovske. *Aging: Binder Validation*. Publication SHRP-A-384. Strategic Highway Research Program. National Research Council. Washington, D.C. 1994.
[18] Bell, C.A., M.J. Fellin, and A. Wieder. Field Validation of Laboratory Aging Procedures for Asphalt Aggregate Mixtures. *Journal of the Association of Asphalt Paving Technologists*. Vol. 63, 1994, pp. 45–80.
[19] Anderson, D.A., D.W. Christensen, H.U. Bahia, R. Dongre, M.G. Sharma, C.F. Antle, and J. Button. *Binder Characterization and Evaluation Volume 3: Physical Characterization*. Publication SHRP A-369. Strategic Highway Research Program. National Research Council. Washington, D.C. 1994.
[20] Petersen, J.C., R.E. Robertson, J.F. Branthaver, P.M. Harnsberger, J.J. Duvall, S.S. Kim, D.A. Anderson, D.W. Christensen, H.U. Bahia. *Binder Characterization and Evaluation Volume 1*. Publication SHRP-A-367. Strategic Highway Research Program. National Research Council. Washington, D.C. 1994.
[21] Kim, Y.R., B.S. Underwood, M. Sakhaei Far, N. Jackson, and J. Puccinelli. *LTPP Computed Parameter: Dynamic Modulus.* Final Report for Project: DTFH61-02-D-00139. Federal Highway Administration. Washington, D.C. 2009.
[22] Roque, R., J. Zou, Y.R. Kim, C. Baek, S. Thirunavukkarasu, B.S. Underwood, M.N. Guddati. *Top-Down Cracking of Hot Mix Asphalt Layers: Models for Initiation and Propagation*. Publication NCHRP Report 667. National Cooperative Highway Research Program, Washington, D.C. 2010.
[23] Von Quintus, H.L, J.A. Scherocman, C.S. Hughes, and T.W. Kennedy. *Asphalt-Aggregate Mixture Analysis System*. Publication NCHRP Report 338. National Cooperative Highway Research Program, Washington, D.C. 1991.

This page intentionally left blank

Asphalt Pavements – Kim (Ed)
© 2014 Taylor & Francis Group, London, ISBN 978-1-138-02693-3

Evaluation of cracking resistance of Superpave mixtures in Kansas

Syeda Rubaiyat Aziz & Mustaque Hossain
Department of Civil Engineering, Kansas State University, Manhattan, KS, USA

Greg Schieber
Bureau of Construction and Materials, Kansas Department of Transportation, Topeka, KS, USA

ABSTRACT: Reclaimed Asphalt Pavement (RAP) is a useful alternative to virgin aggregates in Hot-Mix Asphalt (HMA) as it reduces cost, conserves energy and enables reuse of existing asphalt pavement. However, use of higher percentage of RAP sometimes leads to drier mixes that are often susceptible to early cracking. In this study, cracking resistance of Superpave mixtures with varying asphalt and RAP contents were investigated. HMA specimens were prepared based on Superpave mix design criteria for 12.5-mm (1/2-inch) nominal maximum aggregate size. Specimens were compacted using the Superpave gyratory compactor. Repeated load Semi-Circular Bending (SCB) tests and Texas Overlay Tests (OT) (TEX-248-F) were performed to evaluate cracking resistance of Superpave mixtures containing three asphalt contents (5.2%, 4.9%, and 4.6%) and three RAP percentages (20%, 30%, and 40%) from two distinct sources. Results from both crack tests showed that, with the decrease in asphalt content, cracking propensity increases. Thus conclusions regarding proper RAP percentage use were drawn depending upon the binder content and grade of the RAP source.

Keywords: Semi-Circular Bending test, Texas Overlay Test, cracking resistance, Reclaimed Asphalt Pavement (RAP), Superpave mixtures

1 INTRODUCTION

Recent rise in crude oil price, emphasis on sustainability, and limited virgin aggregate availability have increased RAP material usage. Nationwide, approximately 100 million tons of RAP are produced each year. Approximately 80 million tons are reused in various aspects of pavement construction [1]. RAP contains long-term aged binder, thus asphalt mixes containing RAP could be a matter of concern, especially from the aspects of durability and long-term pavement performance. Asphalt binder present in RAP is stiffer than the virgin binder. Stiffer mix has benefits, such as being less susceptible to permanent deformation or rutting. However, it decreases fatigue life and thermal cracking resistance. There is a limitation to the maximum amount of RAP that could be used in surface layers, certain mixture types, and, in some instances, large or critical projects. Traditionally, the amount of RAP used has been limited to 15% or lower so no binder-grade changes are necessary. Current national guidelines indicate that a softer binder will be required if more than 15% RAP is used in the HMA mix [2]. Softer binders are expensive. Henceforth, it is necessary to come up with a certain percentage of RAP which would be cost effective as well as provide sufficient cracking resistance. In this study, Semi-Circular Bending (SCB) and Texas Overlay (OT) tests were selected to evaluate the cracking resistance of Superpave mixtures.

1.1 *Problem statement*

Some HMA mixtures are produced in Kansas, with asphalt content lower than the design asphalt content. As a result, relatively "drier" mixture is obtained, often leading to early cracking. This type of phenomena is severe for mixtures with Recycled Asphalt Pavement (RAP). Recently, the Kansas Department of Transportation (KDOT) took some initiatives to ensure sufficient amount of asphalt in their mixtures. The contractors, however, instead of adding extra binder, introduced dust into the mixtures with lower number of design gyrations. The rutting and moisture susceptibility of mixtures with lower binder content have already been investigated, but cracking resistance is yet to be evaluated.

1.2 *Objectives*

The main objective of this research was to evaluate the effect of increasing percentage of RAP and varying asphalt content on the cracking resistance of Superpave mixtures. The secondary objective was to establish the minimum asphalt content and maximum RAP content while ensuring acceptable cracking resistance.

2 MATERIALS AND MIX DESIGN

To achieve the objectives of this study, 12.5-mm Nominal Maximum Aggregate Size (NMAS) Superpave mixtures were evaluated. The design binder content of the base SM-12.5A (no RAP) mixture is 5.2%. SM-12.5A mixtures with 4.9% and 4.6% asphalt content were also included, to study the effect of varying asphalt content. In order to control the effect of the RAP source on HMA performance, all tests of SR-12.5A (Superpave mixture with RAP) have been conducted on two different sources of RAP. Both RAP sources were locally owned asphalt contractors and are mentioned here after as Shilling and Konza. The asphalt contents of Shilling and Konza RAP are 5.8% and 4.2%, respectively. The PG binder grade of Shilling RAP is 84-16, whereas the Konza RAP asphalt grade is PG 90-10. From each RAP source, mixtures with three RAP contents, 20%, 30%, and 40%, were evaluated. In order to compare the effect of RAP source on HMA performance, same virgin aggregates were used for all Superpave mixtures. The combined blend had five different virgin aggregates including coarse-crushed limestone (CS-1), fine-crushed limestone (CS-1A), manufactured sand (MSD-1), crushed gravel (CG-5), and natural/river sand (SSG). Table 1 shows the percentages of aggregates used in each blend. Figures 1(a) and 1(b) show the 0.45-power chart for SM-12.5A and SR-12.5A mixture with both sources of RAP materials, respectively. Table 2 tabulates the gradation of both sources of RAP.

Table 1. Percentage of aggregates and asphalt in superpave mixtures.

		Total asphalt content (%)				Virgin aggregates (%)					
		Shilling RAP		Konza RAP							
Mixture	RAP content (%)	Total asphalt	Virgin asphalt	Total asphalt	Virgin asphalt	CS-1	CS-1A	MSD-1	CG-5	SSG	Lime stone dust
SM-12.5A	0		5.2			25	15	15	20	25	0
	0		4.9			24	15	15	20	25	1
	0		4.6			24	15	15	20	25	1
SR-12.5A	20	4.7	3.6	4.3	3.5	20	12	12	16	20	0
	30	4.8	3.1	4.4	3.2	16	15	13	12	14	0
	40	4.3	2.1	4.1	2.5	12	13	13	12	10	0

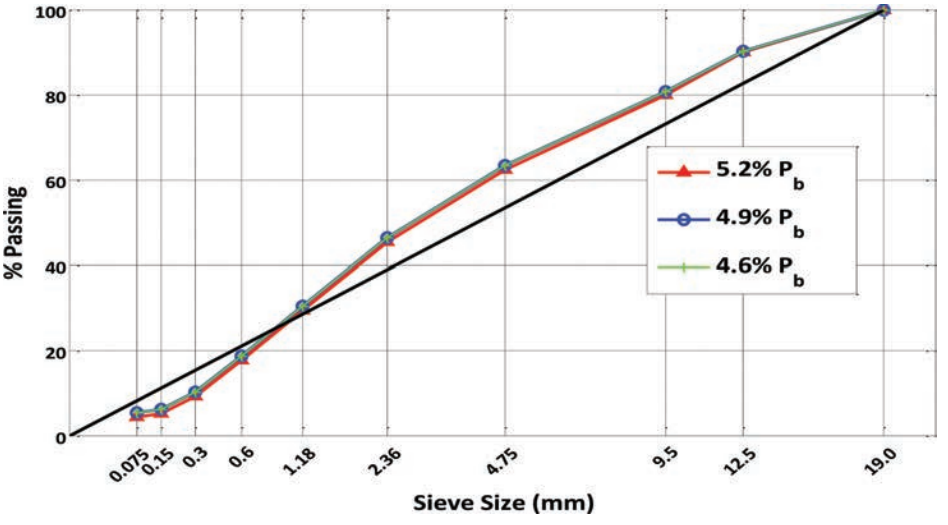

Figure 1(a). 0.45 power gradation chart for SM-12.5A mixture.

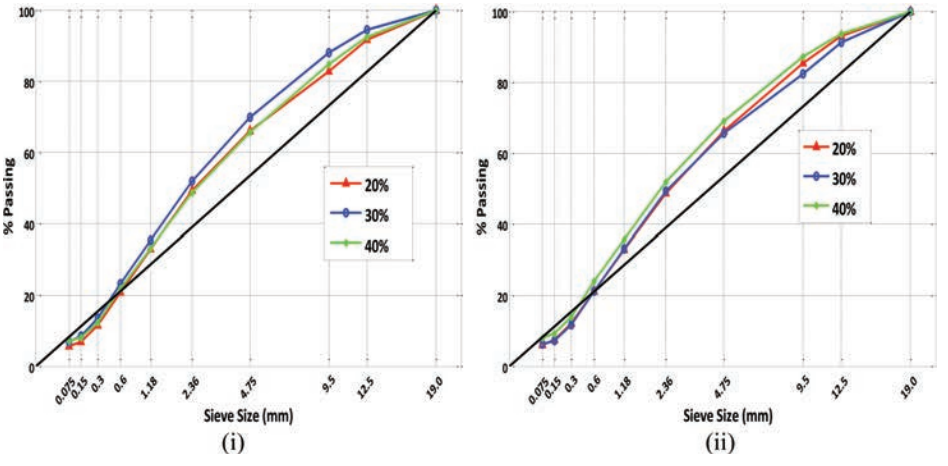

Figure 1(b). 0.45 power gradation chart for SR-12.5A mixture with (i) Shilling RAP and (ii) Konza RAP.

Table 2. Gradation of both sources of RAP.

Sieve size	3/4	1/2	3/8	#4	#8	#16	#30	#50	#100	#200
Shilling RAP	100	98	94	80	64	47	33	20	13	10
Konza RAP	100	96	92	78	64	48	35	21	15	12

3 PERFORMANCE TESTING

3.1 *Repeated load Semi-Circular Bending (R-SCB) test*

The Semi-Circular Bending (SCB) test was used in this study to evaluate the cracking resistance of HMA mixtures. The test is conducted on a half disc-shaped HMA specimen subjected to a three-point loading in compression. The specimen is typically 150 mm in diameter and 50 mm thick with a 6-mm notch at the bottom to initiate cracking there.

Repeated load SCB (R-SCB) test is a two-step process which involves establishing the input compressive load via monotonic or static SCB testing and then using a fraction of the maximum SCB failure load as the R-SCB input load. Repeated load of 10 Hz frequency with no rest period is applied to the specimen at 25 °C. Three replicates were tested for each RAP and asphalt content.

The cracking resistance potential of a mix under this test setup is characterized by the number of SCB load repetitions to cracking failure, where failure is tentatively considered as full crack propagation through the HMA specimen [3]. The R-SCB test setup in UTM-25 environment is shown in Figure 2(a).

Four fractional peak load (static SCB) levels obtained at 30%, 40%, 50%, and 60% of the maximum load were arbitrarily tried as the R-SCB input loads. The test continued until a crack propagated through the entire specimen. The final parameter for comparison was the number of load cycles to failure. The more the specimen could withstand cycles prior to fracture failure, the better cracking resistant it would possess. According to previous studies [4–5], approximately 50% of static SCB peak load should be considered as the R-SCB input load.

3.2 *Texas Overlay (OT) test*

Texas Overlay Tester (OT) test has been used for mix screening and for evaluating cracking (reflective) resistance of HMA overlays. Past research has shown that there is a strong correlation between OT test results and field performance [6]. OT test continues until the initial load decreases by 93%. The number of cycles to this load reduction represents the number of cycles to failure and is an indicator of HMA mixture cracking resistance. The test was conducted at 25 °C, consistent with the Tex-248-F test procedure. Test specimen is 150 mm long, 75 mm wide and 37 mm thick. The Asphalt Mixture Performance Tester (AMPT) machine was used to perform the test. Loading configuration of this test consists of a cyclic triangular displacement-controlled waveform at a standard maximum opening displacement of 0.635 mm and 10 seconds load cycle (5 seconds of loading and 5 seconds of unloading). Three replicates were tested for each varying RAP and asphalt content. Figure 2(b) shows the typical test setup. During testing, only one plate was pulled at the specified displacement rate and pushed to return to its original position. This load simulates the movement of the overlay and directly produces tensile stress in the specimen.

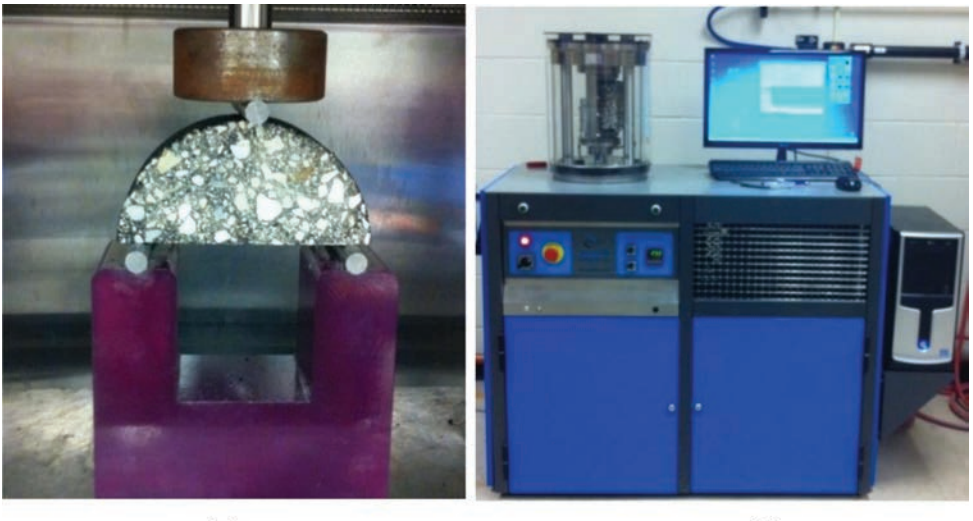

Figure 2. (a) R-SCB test setup in UTM-25; (b) OT test setup in AMPT.

4 TEST RESULTS AND ANALYSIS

4.1 *Repetitive load SCB test results*

The results of R-SCB test are shown in Figures 3, 4 and 5. Figure 3 shows that SM-12.5A mixture with 5.2% asphalt content provides the best cracking resistance because it can resist high R-SCB load repetitions before fracture failure when compared to two other mixtures. Performance deteriorated with decreasing amounts of asphalt content.

Figure 4 shows that SR-12.5A mixture with 20% RAP content has the best cracking resistance when Shilling RAP is used. This mixture demonstrated the highest number of load repetitions before fracture failure compared to the other two mixtures. Performance of these mixtures deteriorated with increasing RAP content and had trends similar to results of static SCB test of the SR-12.5A mixture. On the other hand, Figure 5 shows that SR-12.5A mixture with 40% RAP content has the best cracking resistance, when Konza RAP is used. This mixture endured the highest number of load repetitions before fracture failure compared to the other two mixtures. Konza RAP was relatively aged and drier as mentioned earlier, which could be the reason behind such behaviour.

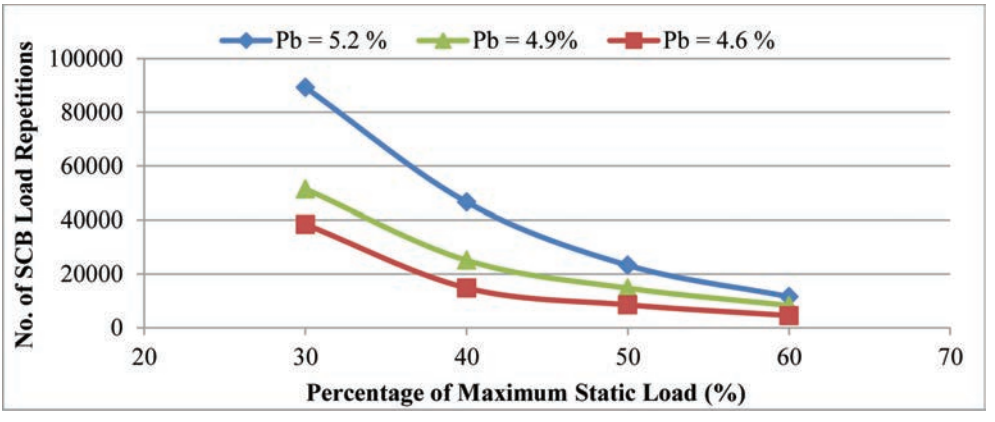

Figure 3. R-SCB percent load relationship vurves for SM-12.5A.

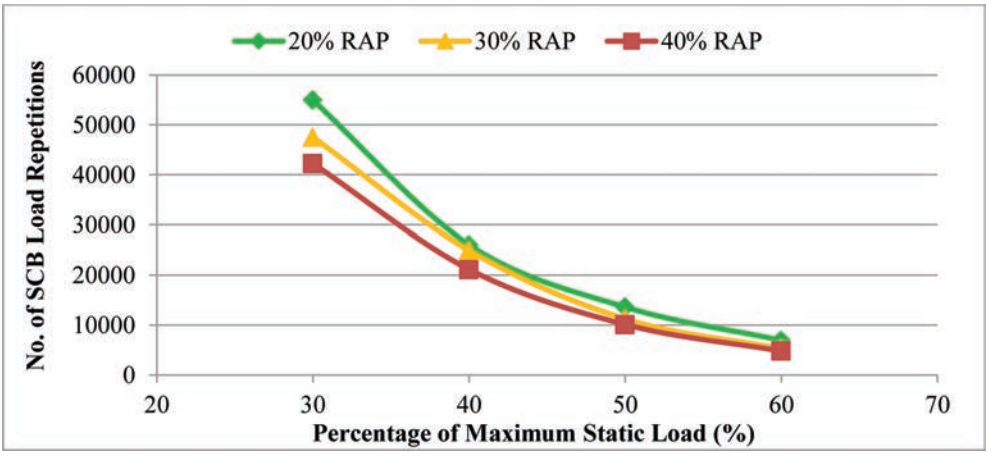

Figure 4. R-SCB percent load relationship curves for SR-12.5A with Shilling RAP.

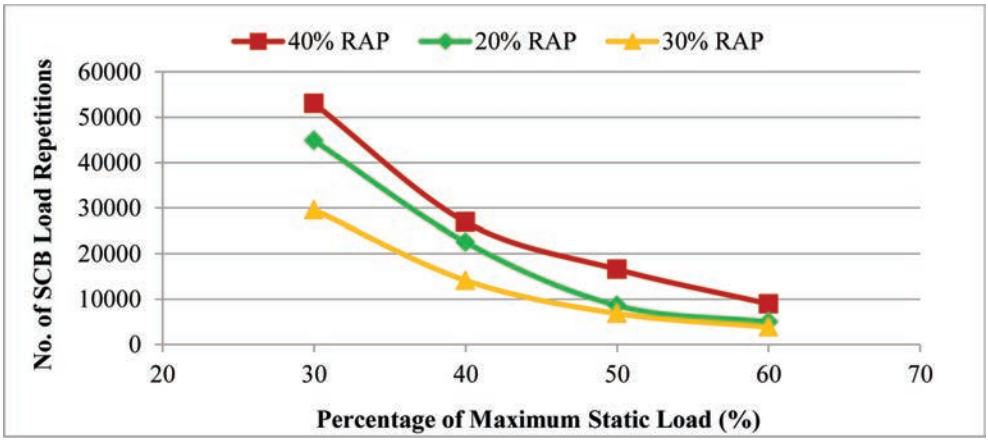

Figure 5. R-SCB percent load relationship curves for SR-12.5A with konza RAP.

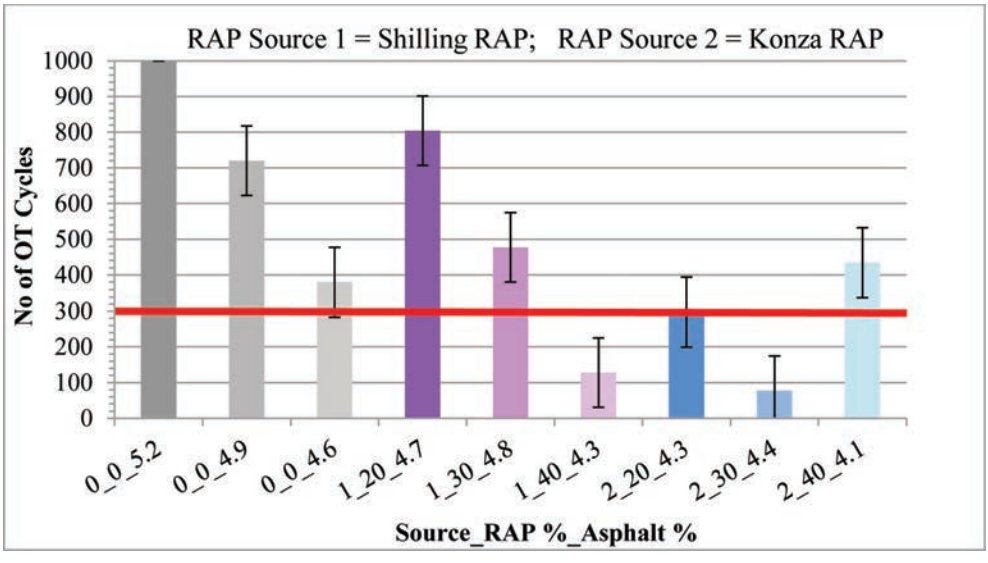

Figure 6. Summary of OT test results.

4.2 *Texas Overlay (OT) test results*

OT test was the other laboratory test performed for characterizing the cracking resistance of the Superpave mixtures. As a mix screening criteria, mixtures that last over 300 cycles are considered satisfactory with respect to the laboratory fatigue resistance [7]. With this criterion, in Figure 6 the best cracking resistance is shown by the mixture with 5.2% asphalt content. All replicates of this mixture passed 1,000 cycles (maximum threshold) before reaching 93% load reduction. The mixture with 4.9% asphalt had a fairly good performance. SM mixture containing 4.6% binder had a satisfactory performance, but it still was the worst among three.

For the SR-12.5A mixture with Shilling RAP, the mixture with 20% RAP content had the best cracking resistance among the three mixtures. The mixture containing 30% RAP had a somewhat satisfactory performance; however, SR mixture with 40% RAP was below 300 cycles. Thus, this mixture can be considered to have unsatisfactory fracture resistance.

For the SR-12.5A mixture with Konza RAP, the mixture with 40% RAP content had the best cracking resistance among the three mixtures. The mixture containing 20% RAP portrayed an average number of 296 OT cycles, which was marginal when compared to the threshold value (300 cycles). SR mixture prepared with 30% RAP from the second source also performed poorly.

4.3 *Statistical analysis*

Mean results obtained from both R-SCB (50% of $F_{static\ SCB}$ as input) and OT tests were compared to check if differences were significant. In addition, comparisons were done to find a combination of minimum asphalt content and maximum RAP content based on the test results, which would be able to ensure a satisfactory cracking resistance. Initially, using Tukey's adjustment method, means from both cracking resistance tests were compared as a whole. The adjusted *p*-value from the test output was compared with the level of significance (0.05). If *p*-value was less than or equal to 0.05, then it was considered that there were statistically significant difference between the means. In this study, the statistical analysis was performed using a software package, Statistical Analysis System (SAS)®. Tables 3 and 4

Table 3. Summary of Tukey's multiple comparisons (R-SCB test).

Source	2	0	2	1	1	1	0	2	0
RAP %	30	0	20	40	30	20	0	40	0
Asphalt %	4.4	4.6	4.3	4.3	4.8	4.7	4.9	4.1	5.2
2_30_4.4	**a**								
0_0_4.6		**a**							
2_20_4.3			**a**						
1_40_4.3				**ab**					
1_30_4.8					**abc**				
1_20_4.7						**bcd**			
0_0_4.9							**cd**		
2_40_4.1								**d**	
0_0_5.2									**e**

Table 4. Summary of Tukey's multiple comparisons (OT test).

Source	2	1	2	0	2	1	0	1
RAP %	30	40	20	0	40	30	0	20
Asphalt %	4.4	4.3	4.3	4.6	4.1	4.8	4.9	4.7
2_30_4.4	**a**							
1_40_4.3		**a**						
2_20_4.3			**ab**					
0_0_4.6				**b**				
2_40_4.1					**b**			
1_30_4.8						**b**		
0_0_4.9							**c**	
1_20_4.7								**c**

*Mix types not connected by same letter are significantly different.

demonstrate the multiple comparisons performed using the mean test results obtained from all mixtures in this study. Source 1 and 2 denote Shilling RAP and Konza RAP, respectively. Though Tukey's multiple comparisons of means for the R-SCB test results (Table 3) showed groupings, several overlaps did not allow formation of distinctive group. Mixtures with no RAP and 5.2% asphalt content had statistically significant different means than all other mixture types.

Table 4 shows the summary of the Tukey's multiple comparisons for the OT test results. Mixtures enclosed by the same colour border denote that they did not have any statistically significant difference among them. Results from the OT test showed almost clear groups.

Cracking test results of the SR-12.5A mixtures portrayed completely opposite patterns, which could be due to the intrinsic properties of various sources of RAP materials used in the mixtures. Therefore, without considering at least another source of RAP, it would not be possible to make a general conclusion about such asphalt content and RAP content combination by overall multiple comparison between the treatments.

Because of such limitations, the Bonferroni method of mean comparison was later used for simultaneously planned comparisons within different sources. This method controls family-wise type-I error [8]. Tables 5(a) and 5(b) show summaries of pairwise comparisons from the Bonferroni method for the R-SCB and OT tests, respectively. SM and SR mixtures are shown in ascending order of number of cycles. *p*-value obtained from the SAS® outputs were compared to the Bonferroni adjusted level of significance which was the ratio of level of significance to the number of comparisons from each test (n = 9 for SCB test and n = 7 for OT test). If the obtained *p*-value was less than or equal to the Bonferroni adjusted level of significance, then the means were considered to have statistically significant difference.

Pairwise mean comparisons (R-SCB test results) within the Shilling RAP indicate that there was no statistically significant difference among the mean number of cycles obtained for mixtures with 20%, 30%, and 40% RAP. Though the mixture with 20% RAP and 4.7% asphalt showed the best performance, it does not provide the maximum RAP and minimum asphalt combination. Henceforth, the mixture with 40% RAP and 4.3% asphalt can be considered to provide good cracking resistance performance under such conditions. For mixtures with Konza RAP, results were even clearer. The combination of 40% RAP content and 4.1% asphalt content had significantly different mean compared to the other two mixtures. Therefore, this mixture can provide good performance, especially when Konza RAP is used. When analysing the OT test results, a minimum threshold level of 300 OT cycles was taken into consideration. For mixtures with Shilling RAP, all result means were significantly different. However, the combination of maximum RAP and minimum asphalt portrayed the poorest performance and was below the threshold level. Thus, from OT test results of SR-12.5A

Table 5. Summary of Bonferroni method of comparisons.

(a) R-SCB test				(b) OT test			
SM-12.5A				*SM-12.5A*			
RAP %	0	0	0	RAP %	0	0	0
Asphalt %	4.6	4.9	5.2	Asphalt %	4.6	4.9	5.2
Groups*	a	b	c	Groups*	a	b	–
SR-12.5A (Shilling RAP)				*SR-12.5A (Shilling RAP)*			
RAP %	40	30	20	RAP %	40	30	20
Asphalt %	4.3	4.8	4.7	Asphalt %	4.3	4.8	4.7
Groups*	a	a	a	Groups*	a	b	c
SR-12.5A (Konza RAP)				*SR-12.5A (Konza RAP)*			
RAP %	30	20	40	RAP %	30	20	40
Asphalt %	4.4	4.3	4.1	Asphalt %	4.4	4.3	4.1
Groups*	a	a	b	Groups*	a	b	b

*Mix types not connected by same letter are significantly different.

Table 6. Virgin asphalt as a percentage of total asphalt content for both RAP source.

Shilling RAP			Konza RAP		
Total asphalt (%)	Virgin asphalt (%)	Virgin asphalt as a percentage of total asphalt (%)	Total asphalt (%)	Virgin asphalt (%)	Virgin asphalt as a percentage of total asphalt (%)
4.7	3.6	77	4.3	3.5	81
4.8	3.1	65	4.4	3.2	73
4.3	2.1	49	4.1	2.5	61

mixture with the Shilling RAP, it can be concluded that 30% RAP and 4.8% asphalt can provide satisfactory cracking resistance at the 95% confidence interval since the mean estimate of passing cycles is clearly above 300 (minimum threshold).

For mixtures with Konza RAP, test means did not show any statistically significant difference. Also, the mixture with 40% RAP and 4.1% asphalt was able to exceed the threshold level of 300 OT cycles. Therefore, this mixture has the potential to ensure good cracking resistance when material similar to Konza RAP is used.

Thus, with the results obtained from this study, conclusions can be made based on what type of RAP is used. If the RAP considered for the mixture is more binder rich, then results from the Shilling RAP should be considered. On the other hand, for a drier RAP, results from the Konza RAP should be taken into account. Statistical analysis suggests SR-12.5A mixture with Shilling RAP have two best cracking resistant mixtures: 40% RAP with 4.3% total asphalt content (from the R-SCB test results), and 30% RAP with 4.8% asphalt content (from the OT test results). For the Konza RAP, mixtures with 40% RAP and 4.1% asphalt content performed best in both cracking tests. Table 6 shows that proportion of virgin asphalt content in the best cracking resistant mixtures from the Shilling RAP are 49% and 65% of total asphalt content, while the best mixture from Konza RAP contains 60% virgin binder. Henceforth, it can be concluded that, based on statistical analysis, Superpave mixtures containing 30%–40% RAP and virgin asphalt content between 50%–65% of total asphalt should be able to provide good cracking resistance. A range for Asphalt and RAP content was concluded instead since the opposing results from both RAP sources indicate that study requires results from few more RAP source.

5 CONCLUSION

The objectives of this study were to evaluate the effect of increasing the percentage of RAP and asphalt content on the performance of Superpave mixtures in terms of cracking resistance; to compare the performance of Superpave mixtures when only the source of RAP is changed; and to establish the minimum asphalt and maximum RAP content while ensuring acceptable cracking resistance. Based on the test results obtained from this study, following conclusions can be made:

(a) Results from both static load SCB test and repeated load SCB test indicate that SM-12.5A mixture with design asphalt content (5.2%), SR-12.5A mixture with 20% Shilling RAP, and 40% Konza RAP demonstrate the best cracking resistance among the SM and SR mixtures, respectively.
(b) Performance deteriorated with decreasing asphalt content and increasing RAP content (for the Shilling RAP). However, the Konza RAP, which contained less asphalt, performed in the opposite manner.
(c) Results of the OT tests showed that the SM-12.5A mixture with 5.2% asphalt passed 1,000 cycles (maximum threshold) but still did not reach 93% load reduction. SR-12.5A mixture with 20% Shilling RAP and 40% Konza RAP, respectively, passed the minimum level of 300 OT cycles. Thus, these mixtures are expected to show less crack propensity.

(d) Using Tukey's method of multiple comparisons, test means were compared. Though the overlay test results formed almost distinct groups, R-SCB test results showed similarity within groups. Because of such overlaps and completely opposite behaved RAP sources, a general conclusion regarding minimum asphalt and maximum RAP content could not be done.
(e) Bonferroni's method was finally considered to draw conclusions within each source of RAP. For the Konza RAP, both R-SCB and OT test suggested a combination of 4.1% asphalt content and 40% RAP content which can provide satisfactory cracking resistance while using the least possible asphalt and maximum allowable RAP content. On the other hand, for the Shilling RAP, conclusions were split between 4.8% asphalt with 30% RAP content and 4.3% asphalt with 40% RAP content.
(f) Superpave mixtures containing 30% to 40% RAP and virgin asphalt content between 50% to 65% of total asphalt content should be able to provide good cracking resistance.

REFERENCES

[1] "Asphalt Pavement Recycling Facts." <http://moasphalt.org/facts/environmental/facts.htm> (accessed on Jan. 11, 2013).
[2] A. Copeland. Reclaimed Asphalt Pavement in Asphalt Mixtures: State of the Practice, Report No. FHWA-HRT-11-021, Federal Highway Administration, McLean, Virginia, USA. 2011.
[3] L.F. Walubita, V. Umashankar, X. Hu, B.P. Jamison. F. Zhou. T. Scullion, A.E. Martin. and S. Dessouky. New Generation Mix-Designs: Laboratory Testing and Construction of the APT Test Sections, Report No. FHWA/TX-10/0-6132-1, Texas Transportation Institute, College Station, Texas, USA. 2010.
[4] L.F. Walubita, A.N. Faruk, A.E. Alvarez and T. Scullion. The Overlay Tester (OT): Using the Fracture Energy Index Concept to Analyse the OT Monotonic Loading Test Data, Construction and Building Materials, Vol. 40, pp. 802–811. 2013.
[5] R.C. van Rooijen and A.H. de Bondt. Crack Propagation Performance Evaluation of Asphaltic Mixes Using a New Procedure Based on Cyclic Semi-Circular Bending Tests, Proceedings, 6th RILEM International Conference on Cracking in Pavements, Chicago, Illinois, USA, pp. 437–446. 2008.
[6] C. Von Holdt and T. Scullion. Methods of Reducing Joint Reflection Cracking: Field Performance Studies, Technical Research Report FHWA/TX-06/0-4517-3, Texas Transportation Institute, College Station, Texas, USA. 2005.
[7] L.F. Walubita, A.E. Martin, S.H. Jung, C.J. Glover, A.E. Chowdhury, S. Park. and R.L. Lytton. Preliminary Fatigue Analysis of a Common TxDOT Hot Mix Asphalt Concrete Mixture, Technical Research Report FHWA/TX-05/0-4468-1, Texas Transportation Institute, College Station, Texas, USA. 2004.
[8] R.O. Kuehl. Design of Experiments: Statistical Principles of Research Design and Analysis, 2nd Edition, pp. 107–111, Duxbury Press, California, USA, 2000.

Asphalt Pavements – Kim (Ed)
© 2014 Taylor & Francis Group, London, ISBN 978-1-138-02693-3

An experimental study on viscoelastic behaviour of bituminous mastics

Marco Pasetto, Stefano Damiano Barbati & Giovanni Giacomello
Department of Civil, Environmental and Architectural Engineering, University of Padua, Padua, Italy

ABSTRACT: The viscoelastic properties of asphalt mastics are influenced by the type of aggregate that is mixed with the bitumen. The objective of the investigation reported in this paper is to explore the use of an inorganic municipal waste filler (WBA) in bituminous mixtures. These materials are available in large quantities and provided at shipping cost, because of landfill problems. However, their use is still limited due to the intrinsic variability of the electrochemical relationship that occurs between aggregates and bitumen.

A comparative study on the viscoelastic performance of bituminous mastics is presented. The bitumen were free of polymer modification. All adhesive mastics were prepared using a single type of filler. The filler-bitumen mass ratio was varied in order to analyse its influence on material response. The filler is homogeneous; particles larger than 0.063 mm were excluded.

The programme of laboratory tests evaluated both the rheological and empirical properties, according to the European Standard. The results obtained demonstrate that the slag filler can be used as a replacement for the standard filler. The composition of the structure of the aggregates in bituminous mixtures was noticeably altered. However, the variation of the filler-bitumen mass ratio can determine some advantages on mechanical response, strength and yield level of the mastic.

Keywords: Bituminous mastics, inorganic fillers, viscoelastic properties, complex modulus, dynamic shear rheometer

1 INTRODUCTION

Two commercial strategies dominate the maintenance and construction of road pavements: the recycling of previously used raw materials; the use of marginal materials, collected from the wastes of other industrial processes. The interest in these sectors is due to environmental reasons, as it reduces the demand for raw materials of natural origin. On the other hand, their success is determined by the reduction of the unitary fixed costs and depends on the maintenance of an acceptable performance level for a sufficient length of time. Different studies have tackled this question in the last sixty years and recently, with the proliferation of refuse incinerators in Europe, research has begun into the use of slag from the combustion of Solid Municipal Wastes (SMW) [1–15]. In general these materials can be classified according to the dominant component: combustible, metallic, hazardous and mixed waste. However, not all parts of the slags may be used in road construction. This is because serious problems arise if there are phenomena of release, for example of heavy metals or fine and very fine particles, which can affect the working performances of bituminous mixtures or even leach and pollute the groundwater. Materials can be incompatible with the bitumen, in consequence of electrochemical profile (glass), or they can have the role of solvent. In most cases combusted SMW slags are partially utilizable, therefore an operation of selection of the acceptable fractions is necessary [16]; although partitioning is possible, the result may vary over time. Vitrification processes, even if costly, do not provide an acceptable improvement [16]. For this reason

alternative solutions are searched in order to use the product as it is or, at least, without expensive treatments.

One option is represented by bituminous mastics. They are the result of the physical and chemical pairing of bitumen and filler ($\varnothing < 0.075$ mm) and therefore offer an intermediate mechanical response between the bitumen and a concrete [17]. It has been demonstrated that the presence of fines can lead to important increases in the mixture performance: mechanical resistance, plasticity, voids content and water resistance. However, there are intrinsic critical qualities: the variability of the product of origin, potential toxicity of the fumes and polluting residues. Some cases documented in the literature report a reduction in the performance (sensitivity to temperature variations, functional and structural stability, fatigue and rutting resistance) and service life of the mix containing marginal materials compared to an analogous conventional one [17–26].

There are different variables of the composition that regulate the behaviour of these mastics: bitumen, i.e. the asphaltene content, fractional voids, particle size, chemical composition etc. [17]. Although the rheological characterization of mixtures can be complex, there are various studies in the literature that demonstrate the potentials of the use of incinerator slag, particularly when compared with conventional filler and cement. A rheological characterization of the bitumen is not sufficient to guarantee a result for the same tests done on the mastics and on the derived mixtures [27,28]. When the structure of the material allows it, the viscoelastic response of these mixtures can be represented by means of a Dynamic Mechanical Analysis (DMA) in an oscillatory regime, often of a sinusoidal type, with a Dynamic Shear Rheometer (DSR). Under the hypothesis of the principle of time-temperature equivalence, a dynamic analysis allows the problems of the viscoelastic characterization of the original bitumens and mastics to be dealt with, determining the main rheological properties (complex modulus, phase angle, viscosity) in a wide range of temperatures and loading times (or frequencies) [17–26].

The sensitivity of the analysis to the variation of the dominant factors is such that there is still no technical standard with indications on mastics (performance-based or prescriptive). An empirical characterization is also speedy and economical, enough to obviate any other determination, however advanced and robust. In the economics of the product and its application, the content and the cost of the bitumen are also important; for this reason the binder must be selected with care, choosing the best compromise between performances and unit cost. This paper describes the result of an experimental analysis on the use of the slags in the production of bituminous mastics, identifying the effects of filler content on the mechanical behaviour, and on the consistency of rheometric and empirical tests. The analyses were supported by laboratory activities aimed at gathering the data from the tests and limiting the storage times of the original materials. The analyses of the results are aggregated in order to present the mechanical response of the mastic in the preliminary phases of preparation of the mixtures and in the initial periods of use on the road, excluding the accelerated thermal treatments that substitute the different levels of aging.

2 EXPERIMENTAL PROGRAMME AND RESEARCH SET UP

The research studied the viscoelastic behaviour of mastics in the initial preparation and operating phases of mixtures of filler and bitumen. This paper presents the results obtained with the pairing of an inorganic non-conventional aggregate, composed of slags from the combustion of municipal waste, with a bituminous binder for road uses (EN 12597, EN 12591). The experimental proposal was in two phases. In the first, an empirical characterization was made of the binders to verify the penetration class and select them for the project, and of the bituminous mastics, to define the general and operational characteristics of specimen preparation. In the second phase the test protocol of the viscoelastic properties of the bitumen and its mixtures was developed, varying the dose of filler.

2.1 *Materials*

The trial followed a market survey of the main producers and suppliers of bitumen in Italy. Different traditional bitumens (unaged, unmodified and without additives) were offered for the study, with a variety of origins and performances. For this reason, an experimental phase was necessary to select the binders. Following the empirical analysis a single producer was identified: the bitumen was supplied in at least three penetration classes: 35/50, 50/70 and 70/100 0.1 mm (UNI/TR 11361), coming from the same plant and same production line. Products with different (or undeclared) origins and binders with intermediate behaviour between two adjacent penetration classes were excluded from the study.

The bitumens were sampled, placed in containers of approximately 75 g (±5 g) and stored at a constant temperature of 20 °C (±2 °C) for the entire period of the trial (EN 58). The aggregate was collected from the plant, placed in 10 kg containers, and transported to the laboratory. It was then heated to 105 °C until it reached a constant weight. The material was sieved and reduced to the fraction passing through a sieve with a nominal diameter of ∅ = 0.075 mm (mechanical sieving with an average yield of 4.38% in dry weight of slag). Table 1 gives details of the chemical analyses conducted on a representative sample of filler.

The filler, bitumen and mixing tools were placed in an oven at a temperature of 130 °C (±5 °C). The mastics were prepared using different doses of filler: 25%–50%–75%–100% of the weight of mastic. These values are in line with the typical prescriptions for bituminous mixtures for road use, and are consistent with traditional products and other research done in this field [27]. The binders were heated twice to a temperature above that of storage: when they were taken to the laboratory, on the reduction into small-sized samples, and during the mixing for specimen preparation. The additional thermal treatments are those necessary for the execution of the tests and included in the standard protocols (EN 1426; EN 1427; EN 12593; EN 13702; EN 12607/1; EN 14770). All the preparation and mixing phases were monitored using an infrared thermal camera (T-IR). This study is based on the characterization of the mastic in the phases immediately after preparation (condition: unaged); it was therefore decided not to give any thermal treatment to the bitumens and mastics.

2.2 *Empirical analysis*

The rheological characterization and preparation of the mastics was preceded by an analysis of the consistency of the binder and mastics. The selection was done on the basis of the tests in the Italian technical standard (Table 2) and the viscosity, to guarantee a workable product in the mixing phase.

Table 1. Basic analysis of municipal waste filler properties.

Test description	[Unit]	Method	Result (SD)
Mass residue at 105 °C	%	EN 14346	86.0
Mass residue at 700 °C	%	CNR IRSA 2	84.2
Specific gravity	g/cm^3	CEN ISO/TS 17892	1.10 (0.15)
pH	–	CNR IRSA 1	12.3 (0.7)
Chloride	mg/kg	–	2832 (272)
Organic carbon	%	EN 13137	0.78
Chlorine	%	EN 15309	3.60
Zinc	mg/kg	EN 13657	2366 (320)
Sulphur	%	EN 15309	0.33
Hydrocarbons	mg/kg	EN 13657	<0.18
Lead	mg/kg	EN 13657	1293 (394)
Copper	mg/kg	EN 13657	3072 (439)

Table 2. Empirical limits of bitumen, mean values.

Penetration grade	[Unit]	Method	35/50	50/70	70/100
Penetration at 25 °C (SD)	0.1 [mm]	EN 1426	38	65	77
Softening point temperature	[°C]	EN 1427	48	46	43
Fraass breaking point	[°C]	EN 12593	–7	–9	–13
Dynamic viscosity (at 135 °C)	[Pa·s]	EN 13702	~0.185	~0.203	~0.271
Mass-loss on heating (LOH)	%	EN 12607/1	<0.5	<0.5	<0.5
Penetration at 25°C (after LOH)	0.1 [mm]	EN 1426	55	58	54

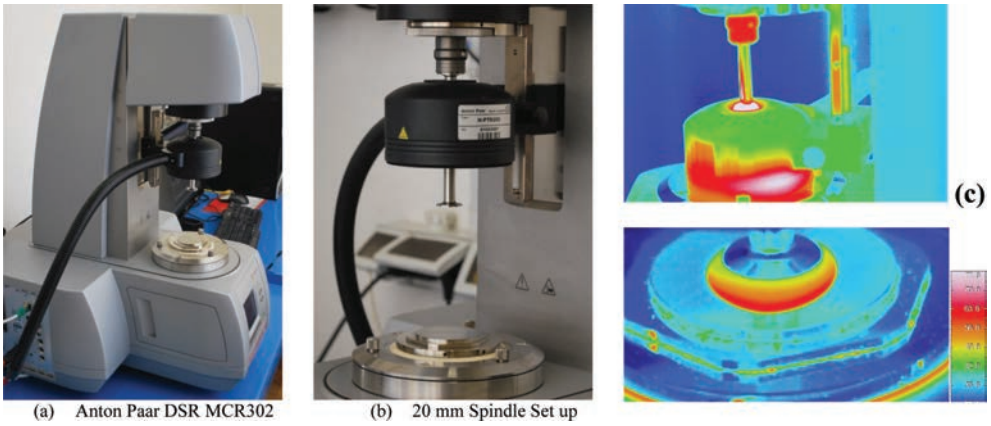

Figure 1. Dynamic shear rheometer (a), testing configuration (b) and thermal IR (c).

Table 3. Test conditions and spindle geometry.

Testing geometry	Diameter [mm]	Gap width [mm]	Temperature [°C]	Step. temp. ΔT [°C]	Red. frequency [Hz]
PP08	8	2	From 10 to 35	5	From 0.016 to 16
PP20	20	1	From 30 to 80	5	From 0.015 to 16

2.3 *Dynamic and rheological analysis*

The mechanical properties of the materials prepared for this study were determined in the region of the prevalent mechanical behaviour of a viscoelastic type. A test protocol was used that allows both the temperature and frequency to be varied, in an oscillatory regime of the sinusoidal type. The tests were conducted with an AntonPaar MCR 302 Dynamic Shear Rheometer (DSR, Fig. 1), taking into account the necessity to also test the mastics and in expectation of a possible problem of "spindle compliance".

The geometric characteristics of the tests of the two testing plate geometries are presented in Table 3. To verify the "spindle compliance", produced with two different geometries (spindles), it was decided to check the curves in a frequency sweep at temperatures of 30 and 35 °C.

The test in the oscillatory regime was conducted according to the prescriptions in the technical standard (EN 14770), pouring the bitumen onto the lower plate at a temperature of 130 °C (±10 °C). The gap is established, but the descent of the upper plate stops 20 μm above the value of the gap required by the test (Table 3). During the descent of the upper plate the normal force N_f must be no more than 0.5 N to avoid pre-stressing the bitumen due to

excess material. The control of the perpendicular force also continues during the "trimming" phase and, immediately after, when the upper plate is lowered by 20 μm, to be placed in the position required by the test. During each test the plate-bitumen contact is maintained with the control of the perpendicular force at $N_f = 0$ N.

The first series of tests involved the characterization of the region of Linear Viscoelastic (LVE) mechanical behaviour in an oscillatory regime (amplitude sweep, controlled strain), in the point in which the value of the complex modulus |G*| is equal to 95% of its initial value $|G_0|$ [21, 22, 27]. The limit value of the strain was determined on the average of five samples of bitumen, taken from different points of the original container to represent the entire supply. The second series of tests regarded the construction of the isothermal curves of the complex modulus (Fig. 2, left) and phase angle (Fig. 3, left) in an oscillatory sinusoidal regime and frequency sweep, with gradual 5 °C (ΔT) temperature increments between one cycle and the next.

For the construction of the "Master Curves" of the "standard complex modulus" |G*| (Fig. 2, right) and the phase angle δ (Fig. 3, right), an arbitrary reference temperature of 25 °C was chosen (Fig. 2 and 3, black curve). The individual isothermal curves represent the response of the material to a loading cycle in frequency sweep (see Figs. 2 and 3: PP08-void grey dot; PP20-bulk grey dot). These were shifted utilizing a form of shift factor (Williams, Landel and Ferry Method—WLF) present in the literature for bitumens [31] and mastics [27].

In this relationship the principle of overlapping Time-Temperature (TTS) is accepted as valid and the materials are "thermo-rheologically simple": an increase in temperature reduces the resting times of the structural processes associated to the strain and flow. If this reduction

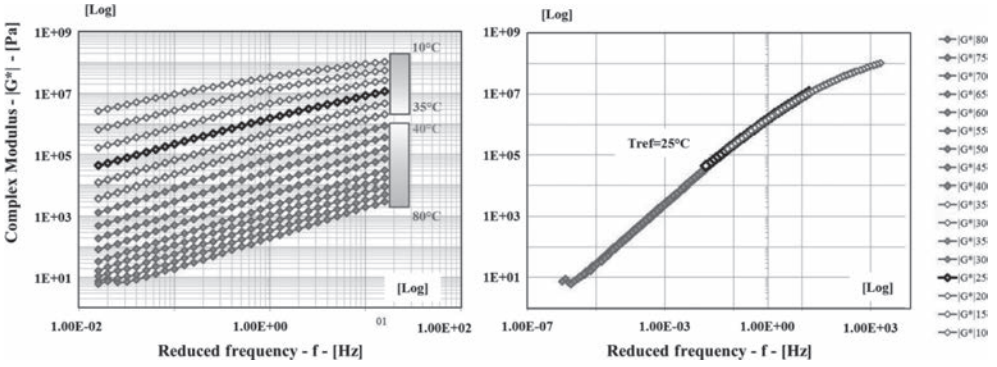

Figure 2. Isothermal plot of complex modulus for two spindle geometries. Bit. 50/70.

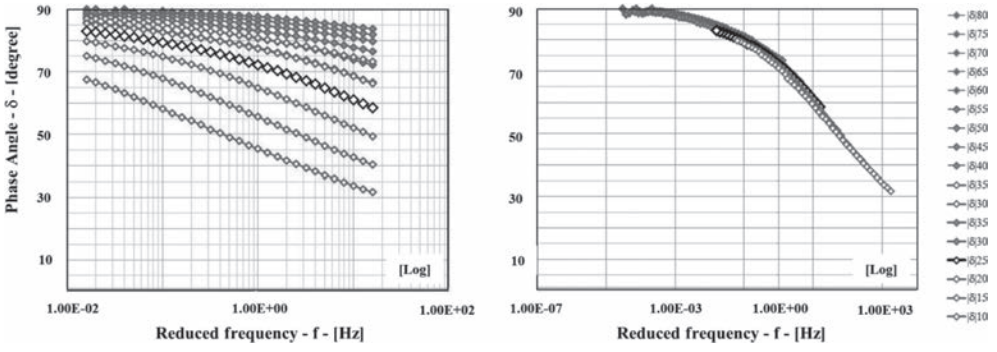

Figure 3. Isothermal plot of phase angle δ for two spindle geometries. Bit. 50/70.

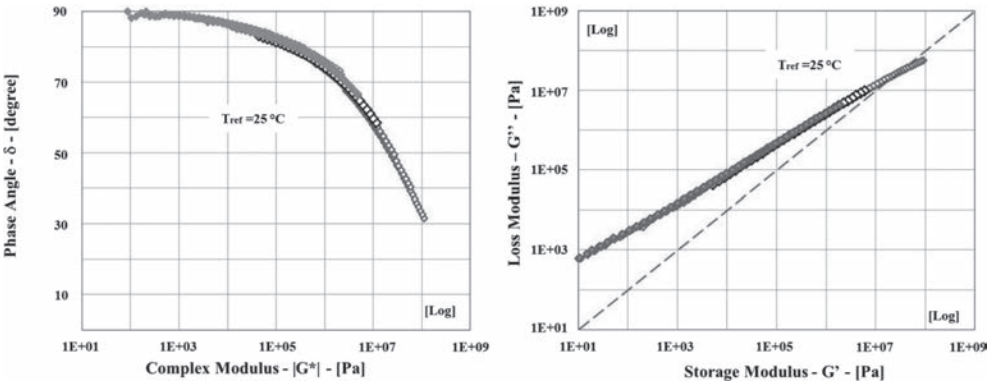

Figure 4. Extended plot: black (left) and Huet-modified (right) diagrams. Bit. 50/70.

is equal for all the times of the resting spectrum, an increase in temperature determines a horizontal shift of the response G(f) in the diagram log(|G*|) – log(f) towards shorter times and without substantial vertical shifts [29]. The values of the complex modulus |G*| and phase angle δ were introduced in the diagrams of Black (Fig. 4, left, phase angle versus complex modulus) and Huet-modified (Fig. 4, right, loss modulus versus storage modulus). This representation points out some typical characteristics of the mechanical behaviour, any problems deriving from the use of the DSR and the two testing plate geometries; influences less visible on the diagrams of the "Master Curves" [28].

3 RESULTS AND DISCUSSION

3.1 *Empirical test results*

The empirical analyses played a dominant role for the preliminary selection phase of the bitumen. They were also used to delineate the consistency of the bitumen and mastics produced with different doses of filler. Tables 4 and 5 show the results obtained in the checks of the softening point temperature (T_{Sp}) and penetration (P_{25}).

The values obtained are in line with those supplied by the producer (Table 2). A general increment was observed in the consistency of the mixture with the increase in the dose of filler: the increase in softening point temperature is not linear with respect to the increase in dose and is more marked for the 35/50 bitumen; penetration reduces with the dose of filler and is less marked for the harder bitumens; in the case of the 35/50 bitumen the effects of the addition of filler are shown for doses of 50% and above. Statistical analysis of the results, also taking into account the low number of specimens, did not provide a trend of the dispersion, expressed in terms of filler dose or consistency.

3.2 *DSR test results, master curves and viscoelastic behavior*

The limits of the region of the mechanical linear viscoelastic behaviour of the binders (35/50, 50/70 and 70/100), at various temperatures and frequencies, were determined with the objective of defining a common working condition for all the materials (Table 6). It should be pointed out that all the bitumens examined have demonstrated quasi-fluid characteristics of the pseudo-plastic polymer, also in the case of the mastics with a high dose of filler. The LVE limit, while depending on the consistency of the bitumen, does not appear to be noticeably linked to the dose of filler. The presence of filler clearly leads to an increase of the initial modulus $|G_0|$ in the "amplitude sweep" tests and, in the best observations, this value is about 10 times higher than the original bitumen. This effect is dominated by the reduction of the distance between the particles of filler, with the consequent increase in the number of points

Table 4. Softening point temperature for unaged bitumens and mastics [in °C].

Bitumen	Original		25% Filler		50% Filler		75% Filler		100% Filler	
Constant	T_{Sp}	SD	T_{Sp}	SD	T_{Sp}	SD	T_{Sp}	SD	T_{Sp}	SD
35/50	47.6	0.29	50.4	0.21	52.1	0.31	57.6	0.39	63.6	0.30
50/70	45.2	0.46	46.8	0.36	48.7	0.70	53.3	0.47	59.2	0.20
70/100	43.9	0.37	46.7	0.26	48.6	0.44	52.1	0.32	58.7	0.23

Table 5. Penetration for unaged bitumens and mastics [T=25 °C, pen. in mm/10].

Bitumen	Original		25% Filler		50% Filler		75% Filler		100% Filler	
Constant	P_{25}	SD	P_{25}	SD	P_{25}	SD	P_{25}	SD	P_{25}	SD
35/50	37	0.47	39	0.47	30	0.49	25	0.47	22	0.10
50/70	65	0.47	53	0.38	43	0.47	37	0.41	29	0.94
70/100	75	1.89	67	0.47	49	1.25	40	0.82	31	0.47

Table 6. Linear viscoelastic strain limits (%).

Penetration grade	35/50	50/70	70/100
8 mm (10 °C)	0.80	1.40	1.60
2 mm (35 °C)	1.50	1.80	3.00

Table 7. Mean values of WLF constants for unaged bitumens and mastics.

Bitumen	Original		25% Filler		50% Filler		75% Filler		100% Filler	
Constant	C_1	C_2	C_1	C_2	C_1	C_2	C_1	C_2	C_1	C_2
35/50	19	105	19	107	18	110	17	112	15	105
50/70	20	112	19	110	19	110	17	121	15	105
70/100	22	126	22	126	22	130	20	138	17	111

of contact efficacious for the distribution of internal stresses. Further research on the values of the mass ratio between filler and bitumen are planned for the future.

Due to problems linked to the timetable of the research project, it was not possible in this phase to completely define the two Newtonian plateaux (for $d\gamma/dt \rightarrow 0$ and $d\gamma/dt \rightarrow \infty$) and the dynamic viscosity curves in the oscillatory regime and plate-cone configuration (EN 13702). The results of the shift of the isotherms (frequency sweep) with the "WLF law" are summarized in Table 7 (see the mean value of the C_1 and C_2 coefficients). The values were calculated with the data of six tests: three specimens per geometry (PP08 and PP20). The WLF coefficients increase with the penetration grade; for some doses the mastic with 35/50 bitumen is analogous to 50/70. The general increase in the C_2 values suggests less sensitivity of the mastics to the temperature variations, in a more obvious way for the curves relating to the softer bitumen (70/100 mm/10).

Figure 5 reports the results of the viscoelastic analysis of the 35/50 bitumen and relative mastics, with the varying of the dose of filler.

The filler-bitumen pairing has improved the general performances of the mastic, reducing the dominant effect of the viscose component: the filler determines a general increase of both the stiffness (complex modulus $|G^*|$) and elasticity (phase angle δ) in the entire field

of frequencies. The result is included in the Black diagram, which also shows the problems of coherence caused by the filler and phenomena of non-linearity. These data partially complete the information obtained from the WLF: with the increase in the dose of filler, the mastic results as being more sensitive to the thermal variations at high working temperatures and lengthy loading times.

Figure 6 reports the results for the 50/70 bitumen and different mastics. In this case, the stiffening effect is less marked than in the 35/50 bitumen and is greater at the low frequencies. This indicates that the variation of the stiffness is dominated by the structure assumed by the solid skeleton in the bitumen matrix. The elasticity also apears to be less influenced compared to the 35/50 bitumen, and the thermal effect at high temperatures and low frequencies is absent. The action of partial modification of the bitumen, shown by the mastic with most filler in the case of the 35/50 bitumen, is attenuated in both the Black and Huet-modified diagrams. However, on the whole, the results obtained with the first two binders are comparable.

Figure 7 summarizes the results relating to the 70/100 bitumen (most widespread class in Italy), modified most by the contribution of the inorganic filler. The effect on the stiffness and elasticity is amplified by the structure of the filler: both improve with the reducing of the loading frequency and increase of the test temperature. Nonetheless, it should be observed

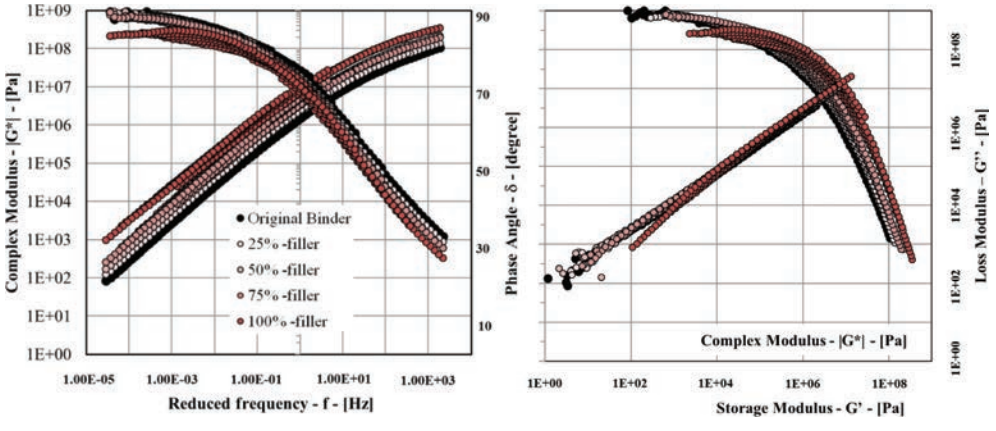

Figure 5. Extended plot: master curve |G*| and δ, black diagram and Huet-modified diagrams (right). Bit. 35/50.

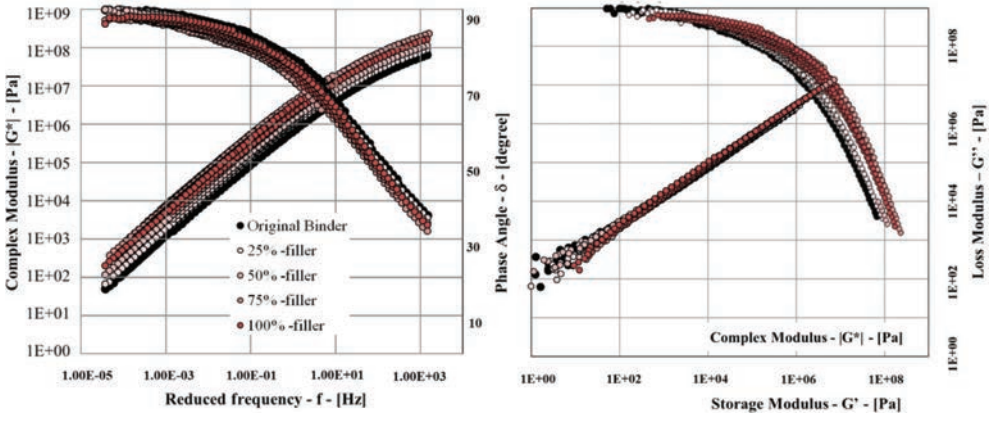

Figure 6. Extended plot: master curve |G*| and δ (left), black diagram and Huet-modified diagrams (right). Bit. 50/70.

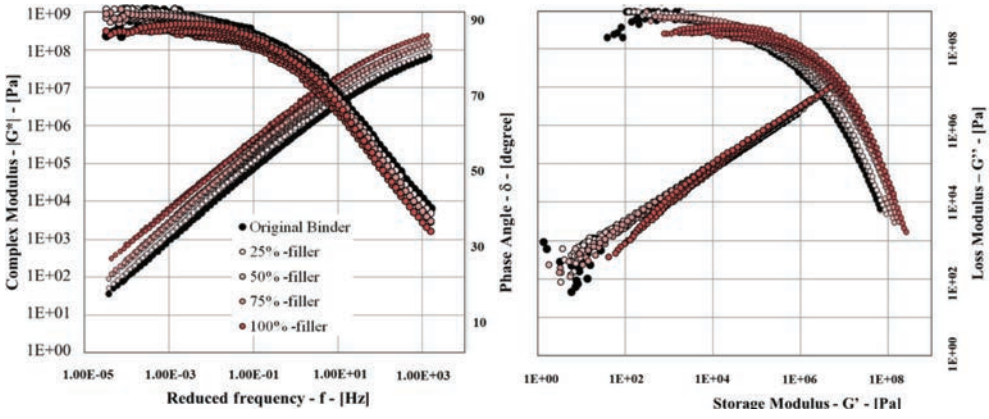

Figure 7. Extended plot: master curve |G*| and δ (left), black diagram and Huet-modified diagrams (right). Bit. 70/100.

that the problems of inconsistency of the rheological data are located in this same region of the mechanical response, linked to the relation between instrument and studied material, to phenomena of non-linearity and partial modification of the bitumen.

The phenomenon of "spindle compliance" is instead attenuated and the overlapping of the isotherm of the two geometries, at 30 and 35 °C, is positive. It is worth remembering that the evaluations produced on the Black and Huet-modified diagrams are totally independent of the operations of shifting of the isothermal curves, therefore of the law chosen for the shift factors and the model identified to build the master curves, as they eliminate the relation with the frequency and temperature. The disjointed shape of the curves of the mastic with the maximum dose demonstrates, at the same time, the increasing importance of the non-linear phenomena linked to the presence of large quantities of slag.

4 CONCLUSION

The mixtures, produced varying the unconventional filler-bitumen mass ratio, offer performances in line with the traditional products and a low sensitivity to temperature. The filler determines an increment in stiffness (G*) and elasticity (δ), increasingly evident with its dosage. The increment in stiffness is highest with the maximum dose (100%) of filler and is about 10 times the initial modulus, for the three bitumens considered. However, this mixture presents the biggest problems of "spindle compliance" and non-linearity, with a significant separation of the response to the stresses induced by the testing geometries.

With the increment in the dose of filler the contribution of the viscose component of the mechanical response is attenuated and the sensitivity of the instrument becomes a significant factor. In the conditions of maximum dose, the effect of the filler tends to depend also on the frequency of loading, as the lithic skeleton forms a more efficient and interconnected structure. The monotone, continuous and uniform shape of the curves (Black and Huet) demonstrates an acceptable equivalence between frequency and temperature.

Lastly, if the results offered by the 8 mm spindle are satisfactory, the 20 mm spindle shows problems at low frequencies/high temperatures (above 60 °C), where the sensitivity of the instrument is dominant.

5 STATEMENT

The research has been performed with the economic support of University of Padua, CPDA114132/11 funding, approved by Academic Senate in January 31, 2012 session.

REFERENCES

[1] Garrick NW., Chan KL. Evaluation of domestic incinerator ash for use as aggregate in asphalt concrete. Transport Research Record, 1418, pp. 30–34, 1993.

[2] Styron R.W., Gustin F.H., Viness T.L., MSW ash aggregate for use in asphalt concrete. ASTM Special Technical Publication, 1193, pp. 129–144, 1993.

[3] Federal Highway Administration (FHWA). User Guidelines for Waste and By-product Materials in Pavement Construction. FHWA-RD-97-148, Washington, DC, 1997.

[4] Zhang X., Gress D., Karpinski S., Eighmy T.T. Utilization of municipal solid waste combustion bottom ash as a paving material. TRRecord, 1652, pp. 257–263, 1999.

[5] Ogunro V.O., Inyang H.I., Hooper F., Young D., Oturkar A. Gradation control of bottom ash aggregate in Superpave bituminous mixtures. Journal of Materials in Civil Engineering, 16(6), 604–613, 2004.

[6] Forteza R., Far M., Seguí C., Cerdá V. Characterization of bottom ash in municipal solid waste incinerators for its use in road base. Waste Manage, 24, pp. 899–909, 2004.

[7] Hassan H.F. Recycling of municipal solid waste incinerator ash in hot mix asphalt concrete. Construction and Building Materials, 19, pp. 91–98, 2005.

[8] Flyhammar P., Bendz D. Leaching of different elements from sub-base layers of alternative aggregates in pavement constructions. Journal of Hazardous Materials, B137, 2006.

[9] Huang C.M., Chiu C.T., Li K.C., Yang W.A. Physical and environmental properties of asphalt mixtures containing incinerator bottom ash. Journal of Hazardous Materials, B137, 2006.

[10] Pasetto M., Baldo N. Laboratory Investigation on Foamed Bitumen Bound Mixtures made with Steel Slag, Foundry Sand, Bottom Ash and Reclaimed Asphalt Pavement. Road Materials and Pavement Design, iFirst, 2012, Taylor & Francis, pp. 1–22.

[11] Birgisdóttir, H., Bhander, G., Hauschild, M.Z., Christensen, T.H. Life cycle assessment of residues from municipal solid waste incineration: Recycling of bottom ash in road construction or landfilling in Denmark evaluated in the ROAD-RES model. Waste Manage, 27, 2007.

[12] Chen J.S., Chu P.Y., Chang J.E., Lu H.C., Wu Z.H., Lin K.Y. Engineering and environmental characterization of municipal solid waste bottom ash as an aggregate substitute utilized for asphalt concrete. Journal of Materials in Civil Engineering, 20(6), pp. 432–439, 2008.

[13] Xue Y., Hou H., Zhu S., Zha J. Utilization of municipal solid waste incineration ash in stone mastic asphalt mixtures: Pavement performance and environmental impact. Construction and Building Materials, 23, pp. 989–996, 2009.

[14] Dabo, D., Badreddine, R., De Windt, L., Drouadaine, I. Ten-year chemical evolution of leachate and municipal solid waste incineration bottom ash used in a test road site. Journal of Hazardous Materials, 172, pp. 904–913, 2009.

[15] Pasetto M., Baldo N. Mechanical characterization of bituminous mixtures with bottom ash from Municipal Solid Waste Incineration (MSWI), 3rd International Conference on Engineering for Waste and Biomass Valorisation—WasteEng 10, Beijing (RPC), CD-ROM, pp. 6, 2010.

[16] Bassani M., Santagata E., Baglieri O., Ferraris M., Salvo M., Ventrella A. Use of vitrified bottom ashes of municipal solid waste incinerators in bituminous mixtures in substitution of natural sands. Advances in Applied Ceramics, 108-1, pp. 33–43, 2009.

[17] Anderson, D.A., Christensen, D.W. and Bahia, H. Physical Properties of Asphalt Cement and the Development of Performance-Related Specifications. Journal of the Association of Asphalt Paving Technologists, 60; pp. 437–532, 1991.

[18] Christensen D.W. and Anderson D.A. Interpretation of Dynamic Mechanical Test Data for Paving Grade Asphalt. Journal of the Association of Asphalt Paving Technologists, 61, pp. 67–116, 1992.

[19] Anderson D.A., Christensen D.W., Bahia H.U, Dongré, R., Sharma M.G, Antle C.E and Button, J. Binder Characterization and Evaluation. Volume 3: Physical Characterization. SHRP-A-369. National Research Council, Washington D.C., 1994.

[20] Merusi F. Metodi reologici avanzati per l'analisi del comportamento dei bitumi stradali negli stati critici di esercizio. PhD Thesis submitted to the University of Parma, 2009.

[21] Airey, G.D., Hunter, E. Dynamic Mechanical Testing of Bitumen: Sample Preparation Methods. Proceedings of the Institution of Civil Engineers: Transport 156. TR2, pp. 85–92, 2003.

[22] Airey, G.D., Rahimzadeh, B., Combined bituminous binder and mixture linear rheological properties. Construction and Building Materials, Vol-18, pp. 535–548, 2004.

[23] Bari, J. and Witczak, M.W. New Predictive Models for Viscosity and Complex Shear Modulus of Asphalt Binders: for use with Mechanistic-Empirical Pavement Design Guide. Transportation Research Record, 2001, pp. 9–19, 2007.

[24] Delaporte, B., Di Benedetto, H., Chaverot, P. and Gauthier, G. Linear Viscoelastic Properties of Bituminous Materials; from Binders to Mastics. Journal of Association of Asphalt Paving Technologists. 76, pp. 455–494, 2007.
[25] Mezger, T.G., Rheology Handbook 2nd Edition. William Andrew Publ., 2006.
[26] Delaporte, B., Di Benedetto, H., Chaverot, P. and Gauthier, G. Linear Viscoelastic Properties of Bituminous Materals Including New Products Made with Ultrafine Particles. Road Materials and Pavement Design, Vol. 10(1), pp. 7–38, 2009.
[27] Yusoff, N.I.Md., Modelling the Linear Viscoelastic Rheological Properties of Bituminous Binders. PhD Thesis submitted to the University of Nottingham, 2012.
[28] Airey, G.D. Use of Black Diagrams to Identify Inconsistencies in Rheological Data. Road Materials and Pavement Design, 3(4), pp. 403–424, 2002.
[29] Chailleux, E., Ramond, G., and De La Roche, C.A., Mathematical-based Master Curve Construction Method Applied to Complex Modulus of Bituminous Materials. Journal of Road Materials and Pavement Design, Vol. 7, pp. 75–92, 2006.
[30] Yusoff, N.I.Md., Monieur, D., Ginoux, M.S., Hainin, M.R., Airey, G.D. and Di Benedetto, H., Modelling the Rheological Properties of Bituminous Binders using the 2S2P1D Model. Construction and Building Materials, 38, pp. 395–406, 2013.
[31] J.D. Ferry. Viscoelastic Properties of Polymers, 3rd Edition. 1980.

Technical standards

[33] EN 58 Bitumen and bituminous binders. Sampling bituminous binders.
[34] EN 1426 Bitumen and bituminous binders. Determination of needle penetration.
[35] EN 1427 Bitumen and bituminous binders. Determination of the softening point—Ring and Ball method.
[36] EN 12591 Bitumen and bituminous binders. Specifications for paving grade bitumens.
[37] EN 12593 Bitumen and bituminous binders. Determination of the Fraass breaking point.
[38] EN 12594, Bitumen and bituminous binders—Preparation of test samples.
[39] EN 12597 Bitumen and bituminous binders—Terminology.
[40] EN 13702 Determination of dynamic viscosity of modified bitumen by cone and plate method.

This page intentionally left blank

Asphalt Pavements – Kim (Ed)
© 2014 Taylor & Francis Group, London, ISBN 978-1-138-02693-3

Viscoplastic strain modeling of asphalt binder based on repeated creep recovery test

Chao Wang & Jinxi Zhang
Transportation Research Center, Beijing University of Technology, Chaoyang District, Beijing, P.R. China

ABSTRACT: The viscoelastic and viscoplastic properties of asphalt binder are valuable to the performance research on the asphalt mixture and pavements. Especially at high-temperature condition, the viscoplastic characteristics of binder play an important role in rutting-resistant performance. This paper presents a viscoplastic modeling method, which originates from the strain-hardening model, to study the unrecoverable strain response for binder in a repeated shear creep recovery test using a Dynamic Shear Rheometer (DSR). Two types of asphalt binders were evaluated in this study, namely the neat binder PG58-28 and the SBS polymer-modified binder PG70-28. In order to fit the model coefficients, a series of 10 cycles repeated creep recovery test were designed to conduct under multiple stress levels 25 Pa, 50 Pa, 100 Pa, doubled to 6400 Pa and three different time durations which included 0.1 s creep + 0.9 s recovery and 1 s + 9 s as well as 10 s + 90 s. Test results and modeling work indicate that, compared with the measured viscoplastic strain, the strain-hardening viscoplastic model can work well on the binder unrecoverable strain response prediction in repeated creep recovery test under lower stress levels and shorter creep duration and it is necessary to take the damage factor into consideration in the future work.

Keywords: Asphalt binder, high-temperature characteristic, repeated creep recovery, viscoplastic strain modeling

1 INTRODUCTION

Asphalt mixture performance prediction is crucial for pavement structure design based on the laboratory test and mechanical analysis. The common prediction approach used today is to develop the constitutive equations which can describe the material behaviour accurately under different temperature and loading conditions. The asphalt mixture modeling has been under research for many years to capture and characterize the rutting and cracking distresses. For rutting evaluation, the NCHRP Project 9–19 proposed the Flow Number (FN) test, in which method repeated creep loading and recovery test is conducted on a Universal Testing Machine (UTM) or Asphalt Mixture Performance Tester (AMPT), to assess the HMA mixture permanent deformation resistance under traffic load. In the FN test analysis proceeding, the permanent strain curve can be divided into three zones: primary, secondary, and tertiary. The cycle number where tertiary flow starts is regarded as the key parameter associated with the mixture rutting potential. Based on FN test data, several statistics modeling work were carried out to investigate the influences of dynamic modulus, gradation and short-term aging as well as long-term aging on the rutting performance of asphalt mixture [1, 2]. But it is still a challenging task to model the mixture strain responses in a three phases creep recovery test like the FN procedure. In order to complete this objective, a viscoelastic-viscoplastic constitutive model with damage is required for characterizing asphalt mixture behaviour.

It is has been widely accepted that the asphalt materials response to load is composed of four components, the elastic and plastic components which are time-independent and

Viscoelastic (VE) and Viscoplastic (VP) components which are time-dependent. Generally, the elastic portion is included in the viscoelastic one and the plastic portion is either very small or hardly distinguished from the viscoplastic response. So the model can be simplified to viscoelasticity and viscoplasticity. A nonlinear VE model with damage was developed by Schapery in 1990 [3]. Later, a combination of this VE model and an undamaged strain-hardening VP model was applied to describe asphalt mixture behaviour under uniaxial loading either in tension or compression [3–8]. Recently, Uzan supplemented the strain-hardening VP model with damage function consideration on viscoplastic components [9, 10]. Therefore, the completed VE-VP model with different types of damage evolution laws for different deformation components are formulated to enable the advanced constitutive model more powerful to characterize the asphalt mixture behaviour.

At the same time, the correlations between asphalt binder properties and mixture testing performance are also under investigation. Although it is still hard to accurately quantify the asphalt binder contributions to the core performance of asphalt mixture and pavement, it is also a fact that the VE-VP properties of asphalt mixtures are exactly derived from the asphalt binder components. So a better understanding of viscoelastoplastic fluid behaviour like asphalt binder will be of great help for the research on viscoelastoplastic solid like asphalt concrete. Recently, some studies revealed an interesting but key test finding that tertiary flow may also occur during a static creep test for asphalt binder on a DSR. And tertiary flow has been proved to be an intrinsic property of asphalt binders, which is similar to that in mixture, and should be considered in modeling the permanent deformation characteristics of asphalt binders [11–14]. Although the loading conditions in binder test and mixture test are different, shear loading and pull-push loading respectively, the common phenomenon of tertiary flow still seems to be a promising link between binder and mixture. Besides, it is the truth that most of the rutting failures are caused by a lack of sufficient shear-resistance in asphalt mixture.

This paper attempts to check the possibility of applying the strain-hardening VP constitutive equation on modeling binder unrecoverable shear strain responses under a series of Repeated Creep Recovery (RCR) tests. This effort is part of a larger research work devoted to development of a VE-VP model with growing damage for simulating the tertiary flow of asphalt binder.

2 THEORETICAL BACKGROUND

Based on the fundamental formulation proposed by Uzan (1985) and Schapery (1999), the theoretical strain-hardening VP model is employed to characterize the unrecoverable strain responses behaviour [15, 5]. The VP constitutive function form is as follows:

$$\dot{\varepsilon}_{vp} = \frac{g(\sigma)}{\eta_{vp}} \tag{1}$$

where $\dot{\varepsilon}_{vp}$ is the VP strain rate, $g(\sigma)$ is the constant-stress loading function, and η_{vp} is the material's coefficient of viscosity. When η_{vp} is assumed a power law of the measured VP strain (6), the following equation is obtained:

$$\dot{\varepsilon}_{vp} = \frac{g(\sigma)}{A\varepsilon_{vp}^{p}} \tag{2}$$

In which A and p are material model parameters. Then Equation (2) can be integrated and rearranged to:

$$\varepsilon_{vp} = \left(\frac{p+1}{A}\right)^{\frac{1}{p+1}} \left(\int_0^t g(\sigma)dt\right)^{\frac{1}{p+1}} \tag{3}$$

For the constant-stress loading condition, $g(\sigma)$ is independent of time so the Equation (3) turns to be:

$$\varepsilon_{vp} = \left(\frac{p+1}{A}\right)^{\frac{1}{p+1}} g(\sigma)^{\frac{1}{p+1}} t^{\frac{1}{p+1}} \tag{4}$$

Assuming a power law of the form $g(\sigma) = B\sigma^q$ where B and q are material coefficients, then Equation (4) becomes:

$$\varepsilon_{vp} = \left(\frac{p+1}{A}\right)^{\frac{1}{p+1}} (B\sigma^q)^{\frac{1}{p+1}} t^{\frac{1}{p+1}} \tag{5}$$

Coupling coefficients A and B into one coefficient C, the Equation (5) can simply reduce to:

$$\varepsilon_{vp} = \left(\frac{p+1}{C}\right)^{\frac{1}{p+1}} \sigma^{\frac{q}{p+1}} t^{\frac{1}{p+1}} \tag{6}$$

So there are totally three material parameters p, q, and C existed in the ultimate VP model formulation.

3 EXPERIMENTAL PROGRAM

Two types of asphalt binders were used in this study, one is neat binder PG58-28 and the other one is SBS modified binder PG70-28. Ignoring the aging effect on binder properties, only original binder samples were tested using a DSR under a constant temperature at 60 °C. In order to determine the coefficients in Equation (6), a series of 10 cycles Repeated Creep Recovery (RCR) tests with different stress levels and loading-unloading time durations were designed to conduct respectively. The details of the materials and test plan were summarized and provided in Table 1.

The 10 cycles RCR tests were conducted on each binder using nine stress levels and three time durations to measure the unrecoverable strain responses for the next binder VP modeling work. A typical RCR data for SBS binder PG70-28 from DSR is given in Figure 1.

4 VISCOPLASTIC MODELING

When applying the VP constitutive function shown in Equation (6) on the shear strain modeling of asphalt binder. It should firstly convert the mechanical symbol from compression or tension mode to shear mode. So the equation can be expressed as follows:

$$\gamma_{vp} = \left(\frac{p+1}{C}\right)^{\frac{1}{p+1}} \tau^{\frac{q}{p+1}} t^{\frac{1}{p+1}} \tag{7}$$

Table 1. Repeated creep recovery test plan.

	Neat binder PG58-28
Binder types	SBS binder PG70-28
Stress levels (Pa)	25, 50, 100, 200, 400, 800, 1600, 3200, 6400
Creep + recovery time durations (s)	0.1 + 0.9
	1 + 9
	10 + 90
Test cycles	10 cycles
Temperature	60 °C

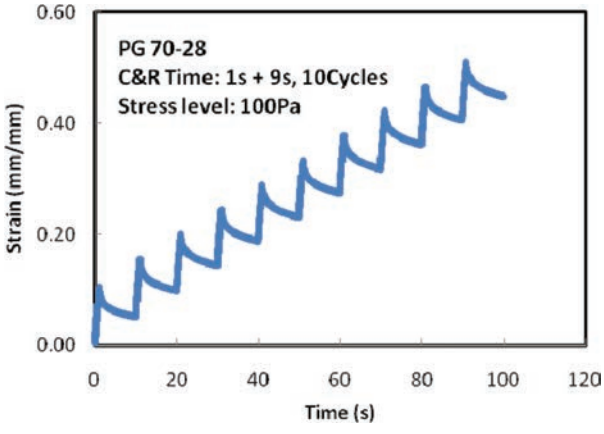

Figure 1. Typical RCR test data on DSR.

In order to fit the material coefficients p, q and C, it is need to respectively separate the stress variable and time variable, and the RCR test program given in Table 1 can be regarded as two series: (i) constant stress RCR tests at fixed stress level but varying the loading-unloading time duration. This series is to determine the parameter p with the Equation (7) reduced to:

$$\gamma_{vp} = C_1 t^{\frac{1}{p+1}} \tag{8}$$

Performing a logarithmic transformation, the Equation (8) becomes the common form of a linear equation $y = b + a \cdot x$, where a is the slope and b is intercept, as shown in Equation (9). Hence, $1/p+1$ is the slope of a line formed as Log γ_{vp} versus Log t and Log C_1 is the intercept of this line. Solving for the slope and the intercept of the plot is easily accomplished by model fitting using the test data.

$$Log\,\gamma_{vp} = Log\,C_1 + \frac{1}{p+1} Log\,t \tag{9}$$

Another test series is: (ii) Constant time RCR tests at fixed loading-unloading time duration but varying the stress levels, which aims to calculate the material parameter q and C. Similar to the transformation used above, Equation (10) and (11) are easily available to fit the test data and determine the q and C with the solved p value.

$$\gamma_{vp} = C_2 \tau^{\frac{q}{p+1}} \tag{10}$$

$$Log\,\gamma_{vp} = Log\,C_2 + \frac{q}{p+1} Log\,\tau \tag{11}$$

Next sections specifically present the model fitting and parameters calculating proceeding as well as the verification work for the two used asphalt binders.

4.1 *Determination of parameter p*

Based on the RCR tests at fixed stress level but varying the loading-unloading time duration, the plot of Log γ_{vp} versus Log t for the two binders are provided in Figures 2 and 3, respectively. In fact, plotting the line at any one fixed stress condition from the totally nine stress levels, for example the line of 800 Pa, is enough to fit the line slope because the slope value should be theoretically independent on the stress level according to the Equation (9). This point could

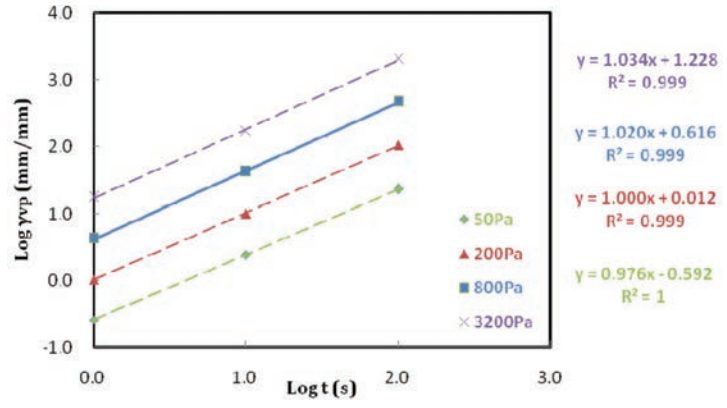

Figure 2. Neat binder linear fitting of Log γ_{vp} versus Log t.

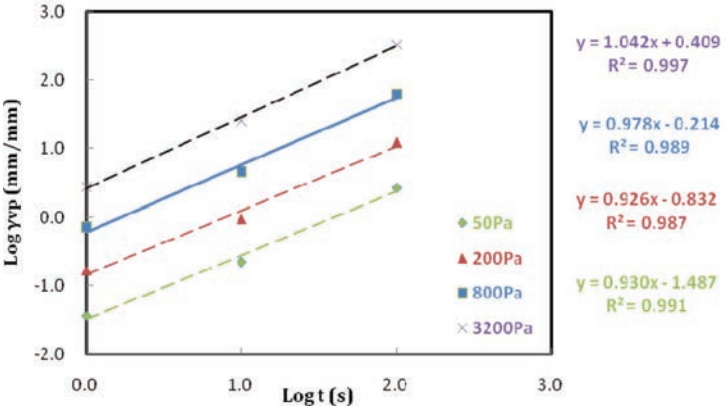

Figure 3. SBS binder linear fitting of Log γ_{vp} versus Log t.

also be proven by the extra three lines of 50 Pa, 200 Pa and 3200 Pa shown in the two figures and it was observed that the four lines at different stress levels exhibited the similar slope.

Using the fitting line of 800 Pa in this paper, the values of parameter p were respectively calculated as –0.0196 and 0.02249 for the two binders.

It should be noted that parameters q and C can also be determined since additional results at other stress levels are available. But using this method the q value is sensitive to parameter p during the calculating process. The slop shown in Figures 2 and 3 is similar but not exactly the same, which is more obvious for SBS binder. So it is still recommended to using the Equation (11) to determine the more accurate value of parameter q.

4.2 *Determination of parameters q and C*

For the RCR tests conducted at fixed loading-unloading time duration but varying the stress levels from 50 Pa to 3200 Pa, Log γ_{vp} versus Log t were plotted respectively in Figures 4 and 5 for the two binders. Similarly, the line of one time duration can work sufficiently but the extra two lines are also given to demonstrate the independence of the line slope on the time factor in accordance with the Equation (11).

Based on the line fitting of 1 s + 9 s loading-unloading time duration and the solved p values, the parameters q and C can be determined and then the ultimate calculated results of the model coefficients are summarized in Table 2.

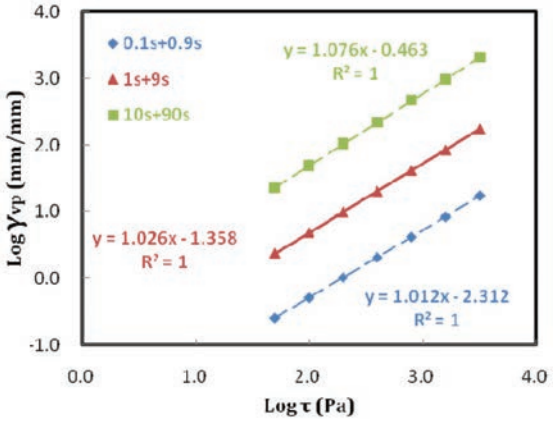

Figure 4. Neat binder linear fitting of Log γ_{vp} versus Log τ.

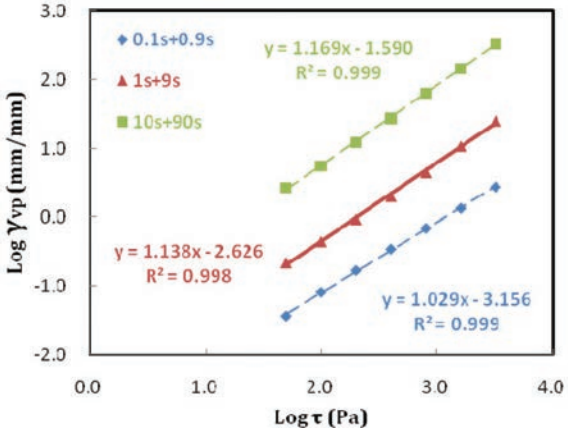

Figure 5. SBS binder linear fitting of Log γ_{vp} versus Log τ.

Table 2. Values of the viscoplastic model parameters.

Binder types	Neat binder PG58-28	SBS binder PG70-28
VP model	$\gamma_{vp} = \left(\frac{p+1}{C}\right)^{\frac{1}{p+1}} \frac{q}{\tau^{p+1}} \frac{1}{t^{p+1}}$	
Model coefficients		
p	–0.0196	0.02249
q	1.00588	1.16359
C	210.25	4939.57

4.3 *Model verification*

Figure 6 presents the comparison of measured and predicted unrecoverable strain using the VP strain-hardening model for the SBS binder PG70-28 in an arithmetic scale. The figure shows that the VP model is able to provide a reasonable prediction across all time duration. Meanwhile, increasing the stress level was found to negatively impact the prediction accuracy, which might be caused by the damage effect on binder under larger creep stress. Hence, on the basis of the

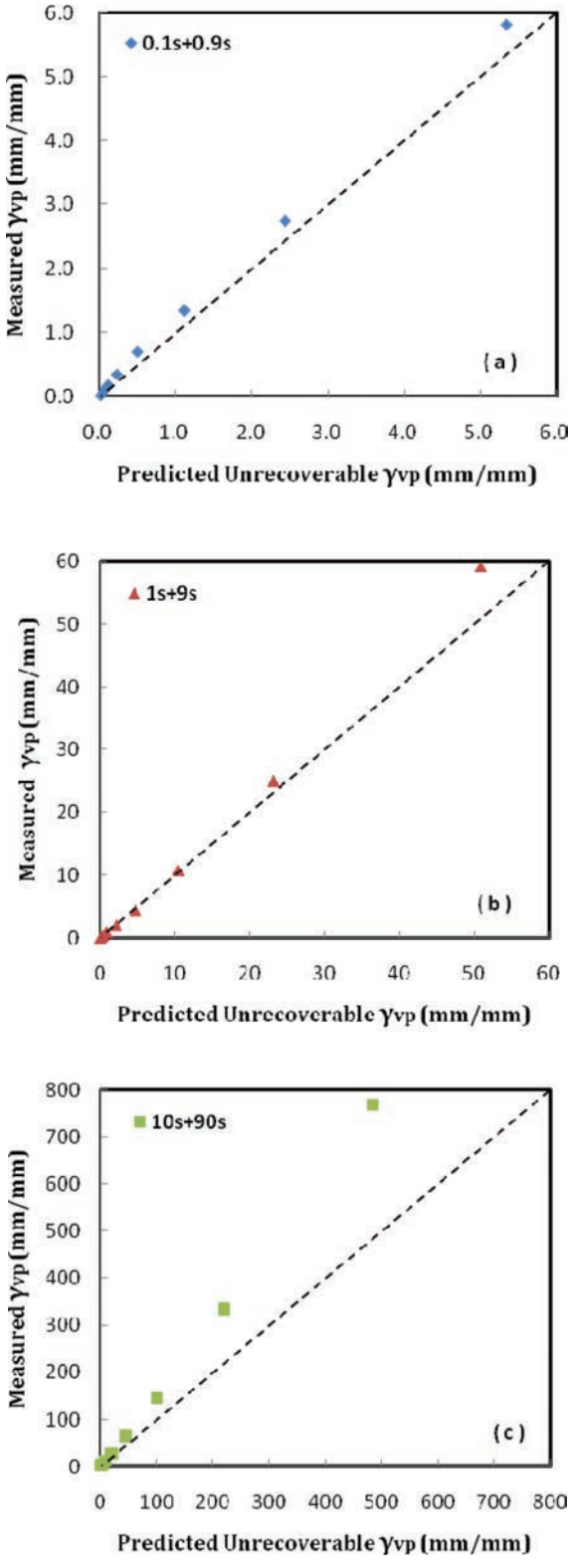

Figure 6. Predicted vs. measured unrecoverable VP strain in arithmetic scale.

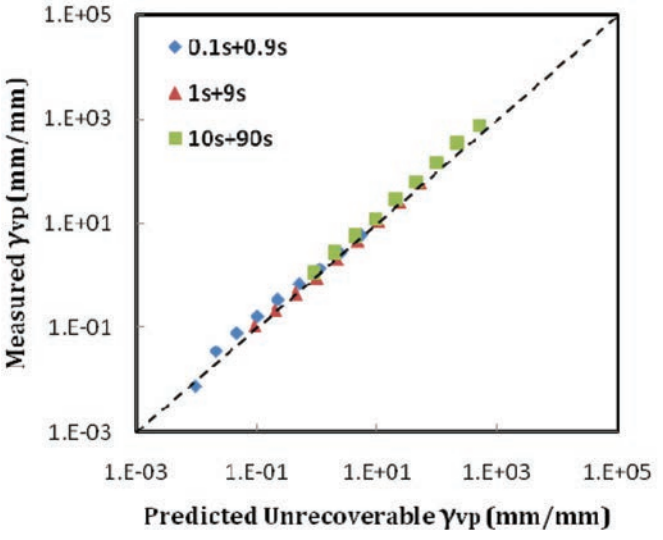

Figure 7. Predicted vs. measured VP strain for all cycles data in logarithmic scale.

undamaged VP model used in this paper, further study need to cover the damage influence on the VP modeling of asphalt binder under high stress levels and longer loading duration.

The comparison data of SBS binder plotted in a log scale is given in Figure 7. Besides, the neat binder P58-28 also exhibited the similar prediction results so they are not included.

5 SUMMARY

This study focused on applying the viscoplastic stain-hardening model on the characterization of asphalt binder. This model has been successfully employed to predict the asphalt mixture behaviour in compression and tension. Findings in this paper indicate that the VP model can also be used to describe the asphalt binder unrecoverable strain responses in a shear loading test on a DSR under lower stress levels and shorter loading duration.

In order to predict the binder behaviour more accurately, it may be possible take the damage impact into consideration and supplement the undamaged VP constitutive function with damage modification. This effort will contribute to develop a VE-VP model with growing damage to modeling the tertiary flow of asphalt binder, which is a promising approach linking the binder property to mixture permanent deformation performance.

ACKNOWLEDGEMENTS

This research was sponsored by the Beijing Natural Science Foundation Grant 8100001 from Beijing government and Hebei Transportation Technology Project Grant Y-2010154 from Hebei Department of Transportation. These supports are gratefully appreciated.

REFERENCES

[1] Apeagyei A. Rutting as a Function of Dynamic Modulus and Gradation, Journal of Materials in Civil Engineering, 23(9), pp. 1302–1310. 2011.

[2] Azari H. and Mohseni A. Effect of Short-term Condition and Long-term Aging on Permanent Deformation Characteristics of Asphalt Mixtures. Proceedings from the 88th Association of Asphalt Paving Technologists Annual Meeting, Denver Co., April 2013.

[3] Schapery R.A. A Theory of Mechanical Behaviour of Elastic Media with Growing Damage and Other Changes in Structure. Journal of the Mechanics and Physics of Solids, 38(2), pp. 215–253. 1990.
[4] Schapery R.A. Nonlinear Viscoelastic and Viscoplastic Constitutive Equations Based on Thermodynamics. Mechanics of Time-Dependent Materials, 1, pp. 209–240. 1997.
[5] Schapery, R.A. Nonlinear Viscoelastic and Viscoplastic Constitutive Equations with Growing Damage, International Journal of Fracture, 97, pp. 33–66. 1999.
[6] Gibson N.H., Schwartz C.W., Schapery R.A., and Witczak M.W. Viscoelastic, Viscoplastic, and Damage Modeling of Asphalt Concrete in Unconfined Compression, Transportation Research Record, 1860, pp. 3–15. Transportation Research Board, Washington, D.C., 2003.
[7] Chehab G.R., Kim Y.R., Schapery R.A., Witczak M.W., and Bonaquist, R. Characterization of Asphalt Concrete in Uniaxial Tension Using a Viscoelastoplastic Model, Journal of Association Asphalt Paving Technologists, 72, pp. 326–370. 2003.
[8] Chehab G.R. and Kim Y.R. Viscoelastoplastic Continuum Damage Model Application to Thermal Cracking of Asphalt Concrete, Journal of Materials in Civil Engineering, 17(4), pp. 384–392. 2005.
[9] Uzan J. Viscoelastic–Viscoplastic Model with Damage for Asphalt Concrete, Journal of Materials in Civil Engineering, 17(5), pp. 528–534. 2005.
[10] Uzan J. and Levenberg E. Advanced Testing and Characterization of Asphalt Concrete Materials in Tension, International Journal of Geomechanics, 7(2), pp. 158–165. 2007.
[11] Delgadillo R. Nonlinearity of Asphalt Binders and the Relationship with Asphalt Mixture Permanent Deformation, Ph.D. Dissertation, Department of Civil and Environmental Engineering, University of Wisconsin at Madison, Madison, WI. 2008.
[12] Motamed A. and Bahia H.U. Influence of Test Geometry, Temperature, Stress Level, and Loading Duration on Binder Properties Measured Using DSR, Journal of Materials in Civil Engineering, 23(10), pp. 1422–1432. 2011.
[13] Biligiri K., Kaloush K., Mamlouk M., and Witczak M.W. Rational Modeling of Tertiary Flow for Asphalt Mixtures, Transportation Research Record, 2001, pp. 63–72. Transportation Research Board, Washington D.C., 2007.
[14] Wasage T., Statsna J., and Zanzotto L. Repeated Loading and Unloading Tests of Asphalt Binders and Mixes, Road Materials and Pavement Design, 11(3), pp. 725–744. 2010.
[15] Uzan J., Sides A., and Perl M. Viscoelastoplastic Model for Predicting Performance of Asphaltic Mixtures, Transportation Research Record, 1043, pp. 78–89. Transportation Research Board, Washington D.C., 1985.

This page intentionally left blank

Asphalt Pavements – Kim (Ed)
© 2014 Taylor & Francis Group, London, ISBN 978-1-138-02693-3

Fatigue performance and stiffness properties of Stone Mastic Asphalts with steel slag and coal ash

Marco Pasetto
Department of Civil, Environmental and Architectural Engineering, University of Padua, Padua, Italy

Nicola Baldo
Chemistry, Physics and Environment Department, University of Udine, Udine, Italy

ABSTRACT: This paper describes the results of an experimental investigation and a theoretical study on the fatigue behaviour of Stone Mastic Asphalt (SMA) mixes, determined by the four-point bending test, according to the EN 12697-24 Annex D standard. The testing was performed on SMA mixes with Electric Arc Furnace (EAF) steel slag and Coal Bottom Ash, used at different proportions, in partial substitution for natural limestone and filler. The mix design method was based on the volumetric properties, as well as on the moisture resistance of the asphalt concretes. Both the Bailey's method and a conventional approach were used in order to identify the design grading curves of the mixes. Fatigue life was evaluated by means of the empirical approach, related to a 50% reduction in the initial stiffness modulus, as well as using more rational concepts, related to the macro-structural damage condition of the mixtures, in terms of dissipated energy and damage accumulation. With respect to the control SMA with limestone aggregates, the asphalt concretes with EAF slag and Coal Ash presented improved fatigue properties and delayed macro-crack initiation.

Keywords: Stone Mastic Asphalt, steel slag, coal ash, volumetric mix design, fatigue life

1 INTRODUCTION

Fatigue in asphalts, which is the type of damage caused by the repeated transit of vehicles at medium-low temperatures, leads to the development of crackings that may degenerate into the complete fracture of the road pavement. It is, therefore, a primary failure mode of flexible pavements, that has to be properly investigated in relation to the design of bituminous mixtures for road superstructures. The paper discusses the results of a laboratory testing concerning the fatigue and stiffness properties of Stone Mastic Asphalts designed by means of a conventional trial and error procedure, as well as a volumetric procedure, namely the Bailey method. The SMA mixes investigated were partially made with Electric Arc Furnace (EAF) steel slag and coal ash (up to 20% and 10% by weight of the aggregate, respectively), in order to valorize the environmental sustainability of the designed mixes.

The purpose was to evaluate the stiffness properties and the fatigue behavior of the SMA mixtures, by means of the four-point bending test, according to EN 12697-26 Standard, Annex B and EN 12697-24 Standard, Annex D, respectively.

2 MATERIALS

Three granular materials were used in the study: EAF slag, coal ash and natural aggregate (crushed limestone). The grading curves of the aggregates are presented in Figure 1, whereas Table 1 reports their physical-mechanical properties, as well as the specific road test protocols adopted.

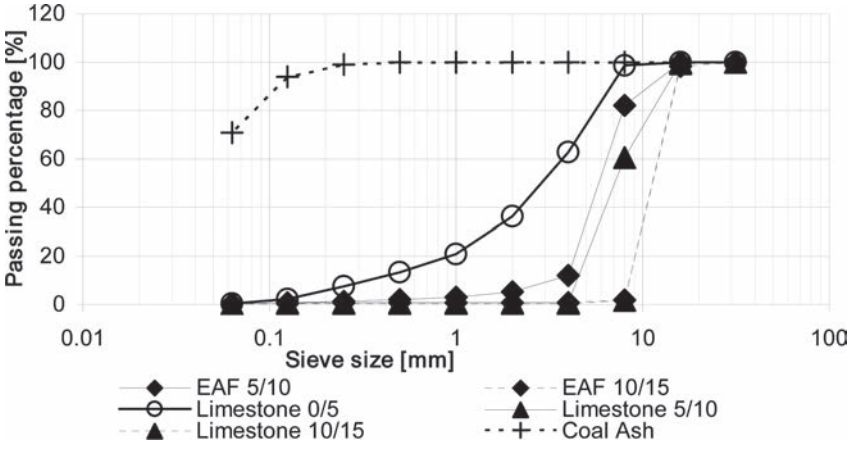

Figure 1. Grading curves of the aggregates.

Table 1. Physical and mechanical characteristics of the aggregates.

Physical ÷ mechanical properties	Crushed limestone 0/5	Crushed limestone 5/10	Crushed limestone 10/15	EAF 5/10	EAF 10/15	Coal ash
Los Angeles coefficient [%] EN 1097-2	–	–	30	–	8	–
Equivalent in sand [%] EN 933-8	69	–	–	–	–	–
Shape Index [%] EN 933-4	7	5	5	11	1	–
Flakiness Index [%] EN 933-3	6	8	6	9	5	–
Loose unit weight [g/cm^3] AASHTO T-19	1.47	1.25	1.26	1.72	1.67	0.85
Rodded unit weight [g/cm^3] AASHTO T-19	1.57	1.38	1.40	1.87	1.88	–

The binder used was a SBS polymer modified bitumen for all the mixtures investigated. It was characterized by a 46 dmm penetration (EN 1426), a Ring & Ball softening point of 75°C (EN 1427) and a Fraass breaking point of –13°C (EN 12593). The elastic recovery value, certified by the bitumen manufacturer, is higher than 50% at 25°C (EN13398).

3 MIXTURES

Four different SMA mixes were studied: two with both recycled and natural aggregates (S/RA, B/RA) and two, used as a control, with limestone only (S/LS, B/LS). For the control LS mix (all natural) various amounts of marginal materials are substituted by limestone with an equivalent grading fraction; instead of the coal ash, a conventional Portland Cement (PC) has been used as filler.

3.1 *Grading and composition of the mixes*

The particle size distribution of the mixes S/RA and S/LS was optimized by means of a conventional trial and error procedure, with reference to the design grading envelope of SITEB [1], in order to identify a curve as close as possible to its centre, but compatible with

the availability of the different aggregates in the sizes necessary to construct this "ideal" grading.

The aggregate skeleton of the mixes B/RA and B/LS has been developed following the Bailey method [2], in order to ensure aggregate interlock and suitable aggregate packing. The present study have been focused on 12.5 mm Nominal Maximum Particle Size (NMPS). Therefore, according to the Bailey criteria, Half Sieve, Primary Control Sieve (PCS), Secondary Control Sieve (SCS) and Tertiary Control Sieve (TCS) resulted equal to the 6.25 mm, the 2.36 mm, the 0.60 mm and the 0.150 mm sieve, respectively [2].

To achieve the level of coarse aggregate interlock desired in the SMA mix, the rodded unit weight, which is determined for each specific coarse aggregate, is used as the reference for the chosen unit weight of the coarse aggregate. With regards to different coarse aggregates, the Bailey Method combines them by volume mathematically, using the corresponding chosen unit weights. The chosen unit weight for the coarse aggregates (namely EAF 10/15 and Limestone 10/15) has been fixed to 125% of their corresponding rodded unit weight.

The Bailey procedure, have been implemented in an electronic spreadsheet, on the basis of the equations reported in the Transportation Research Circular No. E-C044 [3]. Table 2 reports the composition of the mixtures with (RA) and without (LS) marginal aggregates; the corresponding grading curves are presented in Figure 2.

Table 2. Aggregate type and particle size distribution of the mixtures.

Aggregate type	S/RA content [%]	S/LS content [%]	B/RA content [%]	B/LS content [%]
EAF slags 5/10	20	0	10.92	0
EAF slags 10/15	0	0	8.54	0
Coal ash	10	0	10.37	0
Limestone 0/5	25	25	20.79	22.56
Limestone 5/10	45	65	49.38	60.22
Limestone 10/15	0	0	0	6.89
Synthetic filler PC	0	10	0	10.33

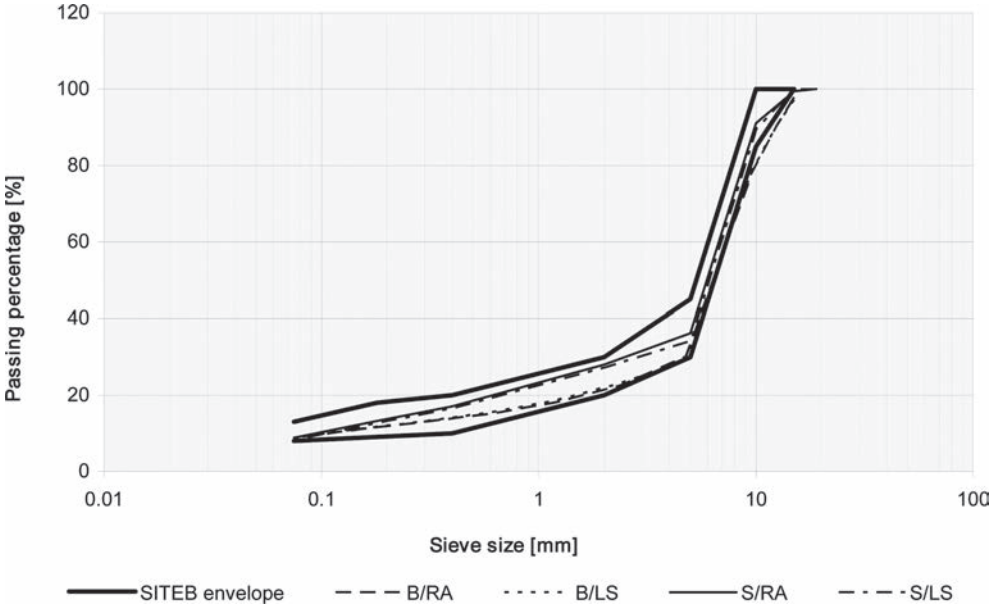

Figure 2. Design grading curves of the mixes.

The aggregate ratios, computed according to Eqs (1, 2, 3), have been reported in Table 3. The recommended ranges for the aggregate Ratios in SMA mixtures [2] are also evidenced.

The aggregate ratios requisites, recommended in the Transportation Research Circular No. E-C044 [3], for SMA mixes with a 12.5 mm NMPS, were completely satisfied for the B/RA as well as for the B/LS.

$$\text{CA Ratio} = \frac{\%\text{Passing Half Sieve} - \%\text{Passing PCS}}{100\% - \%\text{Passing Half Sieve}} \tag{1}$$

$$\text{FA}_c = \frac{\%\text{Passing SCS}}{\%\text{Passing PCS}} \tag{2}$$

$$\text{FA}_f = \frac{\%\text{Passing TCS}}{\%\text{Passing SCS}} \tag{3}$$

However, a partial noncompliance of the Bailey design grading curves with respect to the SITEB reference envelope, is worth mentioning. The discrepancies are related to the passing percentages at the largest sieves (greater than 4.75 mm), so denoting a coarser gradation for the design curves obtained by the Bailey method.

3.2 *Optimization of the mixture*

According to CIRS-Italian Ministry of Infrastructure Specifications [4], a mix design method based on the gyratory compaction and the Indirect Tensile Strength (ITS) test at 25°C, on both dry and wet cylindrical specimens, was adopted in order to optimize the bitumen content, for all the SMA mixes. Regarding the main gyratory test parameters, a speed of 30 revs/minute, a pressure of 600 kPa, an angle of rotation of 1.25° and a diameter of the mould of 150 mm, were adopted.

For each SMA mix, the Optimum Bitumen Content (OBC) was identified with respect to specific volumetric requisites: a residual air voids content (Va) at 10, 100 and 180 revs, of 8–12%, 2–4% and over 2%, respectively [4]. Then, for the optimal mixes, the dry indirect tensile strength at 25°C and the Tensile Strength Ratio (TSR) were determined and compared with the CIRS acceptance requisites. The TSR was calculated as the ratio between the indirect tensile strength of the samples conditioned by means of 15 days of immersion in a thermostatic bath at 25 °C (ITS_{wet}) and unconditioned (ITS_{dry}), respectively. The ITS_{dry} and the TSR values of the optimal SMA mixtures should result higher than 0.6 MPa and 75%, respectively. The results of the mix design procedure are presented in Table 4, which

Table 3. Aggregate Ratios for the design mixes.

Aggregate Ratio	B/RA	B/LS	Recommended range
CA Ratio	0.389	0.390	0.250–0.400
FAc Ratio	0.675	0.672	0.600–0.850
FAf Ratio	0.734	0.725	0.600–0.850

Table 4. Mix design results.

Mixtures	VMA [%]	VFB [%]	Va @ 10 res [%]	Va @ 100 res [%]	Va @ 180 res [%]	Bulk density [g/cm^3]	ITS_{dry} [MPa]	ITS_{wet} [MPa]	TSR [%]
S/RA	17.75	78.66	9.13	3.79	3.67	2.59	1.24	1.08	87
S/LS	17.00	78.00	9.08	3.74	3.55	2.46	1.13	0.85	75
B/RA	17.76	79.23	8.79	3.69	3.36	2.61	1.31	1.16	89
B/LS	17.02	78.56	8.22	3.65	3.13	2.48	1.25	0.98	78

details for each SMA mixture: Air Voids (Va) at 10, 100 and 180 revs, ITS for dry and wet conditions, Voids in the Mineral Aggregate (VMA), Voids Filled with Bitumen (VFB) and bulk density at 100 revs.

The Air Voids requisites prescribed by CIRS mix design procedure, at 10, 100 and 180 revs, were completely fulfilled, for all the SMA mixes, in correspondence of a bitumen content equal to 5.5% of the weight of the aggregate. For SMA mixtures a percentage of Voids in the Mineral Aggregate (VMA) higher than 17% and a percentage of Voids Filled with Bitumen (VFB) between 75% and 85% [5] are needed. According to data in Table 4, all the additional volumetric requisites are verified for the designed mixes. The mechanical requisites, in terms of ITS_{dry} and TSR were also satisfied, for all the designed SMA mixes (Table 4).

The SMA mixes designed by the Bailey method (B/RA and B/LS) showed improved ITS values, with respect to the reference asphalt concretes (S/RA and S/LS), varying from 5% to 18%, depending on the dry/wet condition.

Focusing the attention on the comparison between mixes with and without marginal aggregates, it is possible to observe higher ITS values for the SMA concretes made with EAF steel slag and coal ash. The highest TSR values recorded for the mixes with marginal aggregates, with respect to the corresponding natural SMA concretes, confirm the strong affinity between EAF steel slag and the modified binder, already observed in other investigations [5–8].

Given the high specific weight of the EAF slags, the bulk density of the mixes with Recycled Aggregates (RA) resulted higher than the limestone-only mixtures (LS), for both the aggregate skeleton design method.

4 PERFORMANCE TEST PROGRAMME

Four-point bending tests were conducted using the protocol described in Annex B of the European EN 12697-26 Standard for stiffness evaluation, as well as that reported in Annex D of the European EN 12697-24 Standard for fatigue analysis. The latter have been performed in a regime of stress control, with a wave of sinusoidal loading without rest periods. As reported by Artamendi and Khalid [9], the stress control procedure has to be preferred to the controlled strain testing, in the fatigue evaluation, for high stiffness materials, as the SMA. The fatigue tests were all conducted at a temperature of 20 °C, frequency of 10 Hz, and at three stress levels: 0.9, 1.4 and 1.9 MPa. For each test, in addition to the stress and strain values, the angle phase and energy dissipated at each loading cycle were also monitored, in order to be able to analyze the experimental data with an energy approach. The beam specimens submitted to the bending tests, with dimensions of 400 mm × 50 mm × 60 mm, were cut from 300 mm × 400 mm × 50 mm slabs, prepared using a laboratory compacting roller in accordance with the EN 12697-33 Standard.

4.1 *Stiffness test results*

Table 5 reports the results of the Stiffness Modulus evaluation, at different temperatures (0 °C, 10 °C, 20 °C, 30 °C), in correspondence of a frequency of 10 Hz.

Table 5. Stiffness modulus data [MPa].

Mixture	0 °C	10 °C	20 °C	30 °C
S/RA	12,863	10,647	6,916	3,376
S/LS	13,287	11,087	7,224	3,611
B/RA	10,917	8,465	6,030	3,205
B/LS	12,583	9,929	6,458	3,359

As it was expected, given the visco-elastic nature of the mixes investigated, the higher the temperature, the lower the Stiffness Modulus. The Bailey mixtures presented lower stiffness than SITEB concretes; the asphalt concretes made with marginal materials recorded lower Modulus in comparison with the correspondent natural mixes.

4.2 *Fatigue test results*

The classical fatigue curves, elaborated according to the initial value of strain ε_0 and number of cycles N_f, at which a 50% reduction of the initial stiffness is registered, are presented in Figure 3. The initial strain was evaluated at the 100th cycle (EN 12697-24, Annex D), since as generally recognized in the literature, this is the stage of the test when the material shows a stress-strain response that reliably represents the initial conditions, without yet being significantly affected by damage phenomena. The regression analysis of the fatigue data was performed using a power law model of the type:

$$\varepsilon_0 = \mathrm{a} N_f^{\mathrm{b}} \tag{4}$$

where a and b are regression coefficients depending on the type of material. Figure 3 presents, for the different mixtures, the experimental data and the Fatigue Curves (FC), while Table 6 report the regression coefficients and coefficient of determination R^2.

With reference to a fatigue resistance of 1,000,000 loading cycles (as indicated in Standard EN 12697-24, Annex D), and using Eq. (4), it was possible to calculate the corresponding tensile strain $\varepsilon(10^6)$, which was higher for the asphalts designed by means the Bailey method; in particular the highest value, 44 μm/m, was obtained for B/LS (Table 6).

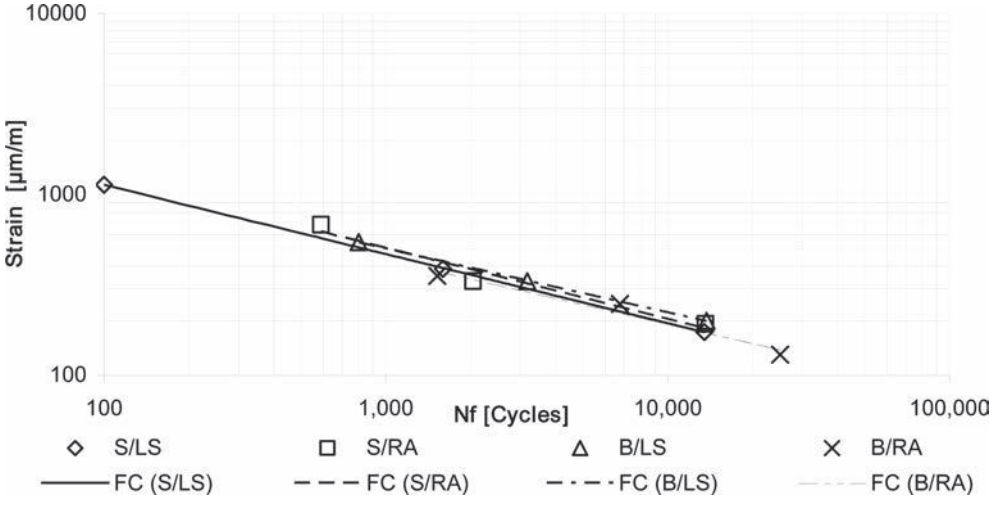

Figure 3. Fatigue life N_f versus initial strain.

Table 6. Fatigue curves—regression coefficients.

Mixture	a [μm/m]	b [–]	$\varepsilon(10^6)$ [μm/m]	R^2 [–]
S/RA	7601.9	–0.392	34	0.9594
S/LS	6571.5	–0.383	33	0.9999
B/RA	5088.0	–0.356	37	0.9581
B/LS	5712.0	–0.352	44	0.9997

4.3 *Dissipated energy analysis*

The data gathered in the fatigue tests were also analyzed with Carpenter's energy approach [10, 11], recently also utilized by other Authors [12, 13, 14]: the Plateau Value (PV) of the Ratio of Dissipated Energy Change (RDEC) is assumed as a fundamental damage parameter. This approach defines the RDEC as the ratio of the change in dissipated energy between two cycles and the dissipated energy of the first cycle, according to the formula:

$$\mathrm{RDEC} = \frac{\mathrm{DE}_{n+1} - \mathrm{DE}_n}{\mathrm{DE}_n} \tag{5}$$

where DE_n and DE_{n+1} represent the dissipated energy produced in load cycle n and n+1, respectively.

The RDEC is considered as a reliable indicator of the damage being done to the asphalt concrete from one cycle to another, as a function of how much dissipated energy was involved in the previous cycle [10, 11]. It results to be independent from other types of dissipated energy, due to mechanical work or heat generation and therefore it represents a true indicator of the internal damage developed into the material, during a fatigue test.

As discussed by Carpenter et al. [10, 11], the damage curve represented by the evolution of RDEC with the varying of the load cycles, can be divided into three different zones. RDEC decreases with the number of cycles in zone 1, then it is almost constant in zone 2, representing a stage during which there is a constant percent of input energy turned into internal damage. The third zone is characterized by a consistent and rapid increase of the RDEC with the load cycles; it describes the onset of true failure of the mixture. The stage of relevant interest in the Carpenter's approach is zone 2. The approximately constant RDEC value in zone 2 is named Plateau Value (PV) of RDEC and it is assumed as a fundamental damage parameter; a lower PV value corresponds to a longer fatigue life of the mixture [10, 11]. Figure 4 reports an example of the determination of PV value for the mix S/LS at 0.9 MPa.

Shu et al [12] have already used the PV value in order to compare different bituminous mixtures, but with regards to four point bending tests in a regime of strain control and using a single strain level for each asphalt concrete.

In this study, the damage curves (PV curves—PVC) have been elaborated, in order to compute the PV value for a 1,000,000 loading cycles (PV_6). Figure 5 shows the damage curves, determined as a function of N_f (load cycles that correspond to a 50% stiffness reduction) and the PV value.

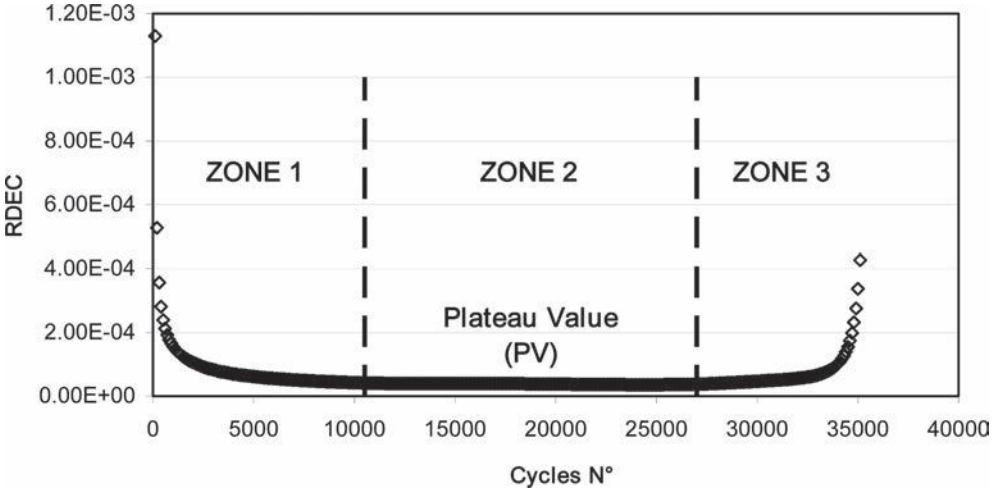

Figure 4. Determination of PV value for mix S/LS at 0.9 MPa.

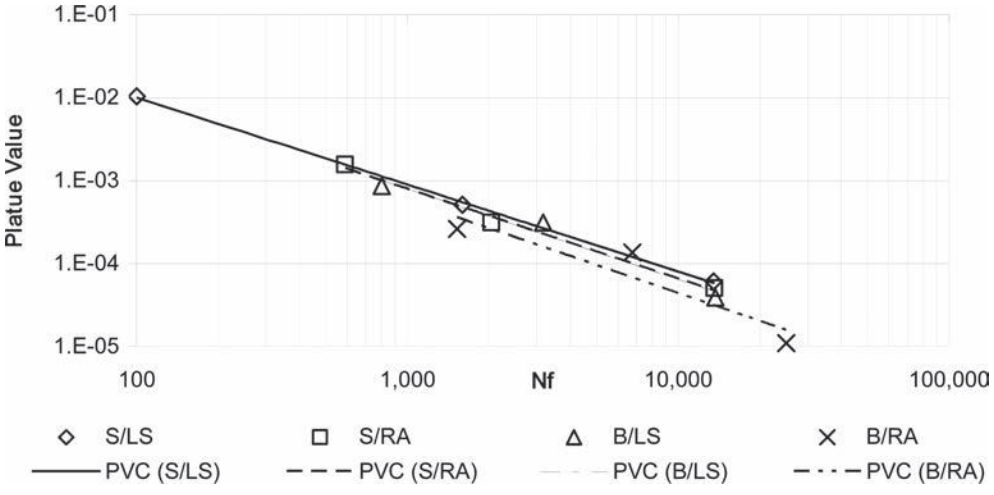

Figure 5. Plateau Value (PV) versus cycles to failure (N_f).

Table 7. Damage curves—regression coefficients.

Mixture	a [MPa]	b [–]	R^2 [–]	PV_6 [–]	ΔPV_6 [%]
S/RA	1.3715	–1.079	0.9925	4.60464E-07	76
S/LS	1.2458	–1.048	0.9994	6.41872E-07	50
B/RA	1.2798	–1.115	0.8741	2.61302E-07	–
B/LS	1.4808	–1.090	0.9688	4.27067E-07	–

For the analytical interpolation of the damage curves, a power law model was used:

$$PV = aN_f^b \tag{6}$$

where a and b are regression coefficients depending on the type of material. Table 7 reports the coefficients of regression and determination, as well as the PV value computed using Eq. (6) with reference to a 1,000,000 loading cycles. The percentage variations of the PV_6 of the SITEB mixtures, compared to the corresponding Bailey concretes (named ΔPV_6) have been also reported.

The analysis of the PV_6 values, determined with the energy based approach, allows the different types of mixtures to be compared. The Bailey's mixtures presented lower PV values and therefore lower damage, with respect to correspondent mixes studied with the conventional skeleton design approach. SITEB mixes developed consistent damage increments, expressed in terms of ΔPV_6, up to 76% for the S/RA mix. Comparing the two Bailey mixtures, it can be observed the higher damage developed for the mix with limestone (B/LS), 64% more than the B/RA asphalt. Therefore, according to the experimental results (Table 7), it has been verified the beneficial effect of the Bailey method in order to improve the fatigue behaviour of the bituminous mixtures investigated.

However, a relevant difference in the ranking of the mixtures, using the two methodologies, is worth mentioning. The energy based analysis led to rank the B/LS mix as less resistant to fatigue, whereas the conventional approach identified the B/RA mix as that characterized by the lower fatigue life. Such a discrepancy was already observed in a previous study regarding crumb rubber asphalt concretes and SBS polymer modified mixes [8]. As observed by several researchers [9–14], in the standard approach the failure of the sample is empirically based on the 50% stiffness reduction, whereas the energy based analysis can be considered more

reliable and effective, since the key parameter considered, the Plateau Value of the Ratio of Dissipated Energy Change, is rationally related to the internal state of damage achieved into the material during the fatigue test.

5 CONCLUSIONS

The four point bending fatigue tests, conducted on bituminous concretes of SMA type, have demonstrated the superior performance of the Bailey mixtures when compared with those designed with a conventional approach.

The better performance of the Bailey mixes is also fully confirmed by means of the Carpenter's energy based approach.

The effectiveness of the Bailey method in the increase of fatigue life was also clear for the mixtures made with EAF steel slag and coal ash up to 20% and 10% on the weight of the aggregates, respectively.

In this study a discrepancy emerged between the empirical fatigue evaluation and the energy based analysis, therefore it is recommended to approach very carefully the fatigue characterization based on the 50% stiffness reduction criterion.

It is has been verified a complete congruence between the different performance tests used in the investigation, in fact, the lower the stiffness at 20°C and 10 Hz, the higher the fatigue life of the mix at the same testing conditions.

REFERENCES

[1] SITEB, Capitolato d'appalto per pavimentazioni stradali con bitume modificato, Roma. 2000 [in Italian].

[2] Vavrik, W.R., Pine, W.J., Huber, G.A. and Carpenter, S.H. Aggregate Blending for Asphalt Mix Design: The Bailey Method, Transportation Research Record, 1789, pp. 147–153. 2002.

[3] Transportation Research Board. Bailey Method for Gradation Selection in Hot-Mix Asphalt Mixture Design, Transportation Research Circular N. E-C044, Washington, DC. 2002.

[4] Ministero delle Infrastrutture e dei Trasporti—CIRS, Norme tecniche di tipo prestazionale per capitolati speciali d'appalto, Roma. 2001 [in Italian].

[5] Pasetto, M. and Baldo, N. Performance comparative analysis of stone mastic asphalt with electric arc furnace steel slag: a laboratory evaluation, Materials and Structures, 45, pp. 411–424. 2012.

[6] Pasetto, M. and Baldo, N. Experimental Evaluation of High Performance Base course and Road Base Asphalt Concrete with Electric Arc Furnace Steel Slags, Journal of Hazardous Materials, 181, pp. 938–948. 2010.

[7] Pasetto, M. and Baldo, N. Mix design and Performance Analysis of Asphalt Concretes with Electric Arc Furnace Slag, Construction and Building Materials, 25, pp. 3458–3468. 2011.

[8] Pasetto, M. and Baldo, N. Fatigue Performance of Asphalt Concretes made with Steel Slags and Modified Bituminous Binders, International Journal of Pavement Research and Technology, 6 (4), pp. 294–303. 2013.

[9] Artamendi, I. and Khalid. H. Characterization of fatigue damage for paving asphaltic materials, Fatigue Fracture Engineering Materials and Structure, 28, pp. 1113–1118. 2005.

[10] Shen, S. And Carpenter, S.H.. Application of the dissipated Energy concept in fatigue endurance limit testing, Transportation Research Record, 1929, pp. 165–173. 2005.

[11] Carpenter, S.H. and Shen, S. Dissipated energy approach to study hot-mix asphalt healing in fatigue, Transportation Research Record, 1970, pp. 178–185. 2006.

[12] Shu, X., Huang, B. and D. Vukosavljevic. Laboratory evaluation of fatigue characteristics of recycled asphalt mixture, Construction and Building Materials, 22, pp. 1323–1330. 2008.

[13] Yoo, P.J., and Al-Qadi, I.L. A strain-controlled hot-mix asphalt fatigue model considering low and high cycles, International Journal of Pavement Engineering, 6, pp. 565–574. 2010.

[14] Maggiore, C., Grenfell, J., Airey, G. and Collop, A.C. Evaluation of fatigue life using dissipated Energy methods, 7th RILEM International Conference on cracking in pavements, Delft, The Netherlands, pp. 643–652. 2012.

This page intentionally left blank

Additives and modifiers for asphalt concrete—III

This page intentionally left blank

Asphalt Pavements – Kim (Ed)
© 2014 Taylor & Francis Group, London, ISBN 978-1-138-02693-3

Comparison between SBS and crumb rubber modified asphalt—laboratory and field study

Erik Nielsen
Danish Road Directorate, Hedehusene, Denmark

ABSTRACT: A modification concept called ROAD+, which combines crumb rubber granulate and an additive, Vestenamer®, has been studied in a huge laboratory and trial section study in Denmark. The objective has been to bridge gaps in existing documentation for the product and to gain experience with its application among Danish asphalt concrete producers.

A comparison study has been performed in 2011–2012 with trial and reference sections on a Danish highway with Stone Mastic Asphalt with nominal aggregate size 11 mm and a recipe not optimized for noise reduction. Three variations of Stone Mastic Asphalts differed only by the bituminous binder: SBS modified bitumen 40/100-75 according to European binder specification EN 14023 and a standard paving grade 70/100 modified with either 15% or 8% of ROAD+ by the "dry" mixing process.

Numerous samples have been taken from asphalt plant production and cores and slabs from the different sections for in depth study in the laboratory. Field tests for noise reducing effects have been performed by SPB and CPX measurements approx. 0, 2 and 12 months after paving. Various properties have been analysed in several laboratories: resilient modulus, creep, fatigue, cold temperature properties (TSRST) and rutting resistance (both laboratory and full scale).

Keywords: crumb rubber; SBS modified bitumen; Stone Mastic Asphalt; durability; noise reduction; laboratory and field trials

1 INTRODUCTION

The application of Ground Tyre Rubber (GTR) from old scrap tyres in bituminous materials for road applications has been introduced in Denmark more than 30 years ago. The first tests were performed in the late 1970s and early 1980s. In the early attempts GTR was utilized as both powder and granulates in order to produce an ice repellent road surface. The Board of Technology sponsored a literature study at the asphalt contractors' association [1] to examine the potential for reuse of rubber in asphalt pavements. The conclusion was that introduction of GTR would on short term mean substantial extra expenditure for road maintenance and on long term "more research was needed". The available quality of GTR in that period gave some problems with respect to technical issues and occupational health. Some test sections had been performed on national highways in 1986 showed premature failures in 1992 and were replaced [2]. The parallel development of alternative additives (polymers like Styrene-Butadiene-Styrene (SBS) and Ethylene-Vinyl-Acetate (EVA) did not show the same problems, and the interest in GTR declined.

In the last 15 years the re-use of GTR (0/2 mm and 0/4 mm fractions) have popped up from time to time related to the development of noise reducing pavement. But again the trials resulted in poor durability, technical problems associated with the production and the distance from "success" to "failure" was smaller compared to other alternative pavements.

The introduction of different technologies for reducing the mix temperature in asphalt production ("Warm Mix Asphalt") has accelerated in the last decade. Some of the technologies use additives that facilitate the incorporation of GTR in hot asphalt materials at "normal" mixing temperatures. Such a modification concept is called ROAD+. The product is a polymer bitumen and asphalt modifier produced by a process patented by Degussa. It has been used for many paving jobs in USA since 1998, and was later introduced in Europe.

2 ROAD+ —PRODUCT DESCRIPTION

The introduction of ROAD+ to the Danish road professionals coincided more or less with the Eurasphalt & Eurobitume Conference in Copenhagen in 2008, where the product description [3] was on display at the exhibition. ROAD+ combines crumb rubber particles having a size below 1.4 mm with 4.5% of an additive, Vestenamer®, described by the producer Degussa as a semicrystalline polyoctanamer.

The product description mentioned that both wet and dry process can be used with equal result. Wet process means that ROAD+ is added to the bituminous binder in a percentage between 8 and 15 and "digested" to create a modified binder that later can be used in asphalt production. The dry process means the ROAD+ is added at the asphalt plant together with aggregates, filler and bituminous binder in similar percentages as for the wet process; during hot storage and hauling the asphalt matures to create the modified asphalt.

The product description for ROAD+ stated—as a rule of thumb—that a standard bitumen modified with 10% ROAD+ as a minimum performs on level with a similar bitumen modified with 4% SBS (polymer; Styrene-Butadiene-Styrene). Among other characteristics it was mentioned that ROAD+ reduces traffic noise.

3 PREAMBLE AND OBJECTIVES OF THE DANISH COMPARATIVE TRIALS

It was decided by the national road administration, the Danish Road Directorate (DRD), in 2010 to perform an internal review on the documentation of ROAD+ supplied by the Danish crumb rubber producer GENAN A/S. This documentation consisted mainly of reports from Germany where several activities (research and trials) had been on-going recently. Supplementary information from other sources either on ROAD+ or crumb rubber modified asphalt was added to the review. One of the major contributions of additional information came from the Swedish Transport Administration which in a seminar [4] reported the findings of a huge three year study of crumb rubber modified asphalt after the wet process.

The review resulted in defining the objectives and focus points of Danish comparative trials with ROAD+ modified asphalt in order to provide confirmation or verification:

1. Gain practical experience with application of ROAD+ in Denmark
2. Verify the rule of thumb—"2.5% ROAD+ equals 1% SBS"
3. Obtain comparative characteristic properties of SBS and ROAD+ modified bitumen/asphalt to assess durability and other important properties for a road administration responsible for a heavily loaded road network.
4. Verify the statement that "ROAD+ reduces traffic noise."

The first three bullets are perhaps obvious points but the fourth requires some explanation. Noise reducing pavement has been a high prioritised subject for the Danish road administration for several years. The documentation on noise reduction for provided by GENAN included various test reports on a huge project [5] in Cologne, Germany (site: Konrad Adenauer Ufer) where ROAD+ modified binder was used in a noise reducing asphalt, LOA 5 D [6], developed by Ruhr University, Bochum, Germany [7]. Martin Radenberg states in [7] that "the open surface texture of the pavement is responsible for the noise reduction, and that modified binder is needed to obtain a durable surface texture". He gives no preference to the

type of modified binder. Wolfgang Fuchs [8] states in an article on the trials in Cologne that "the noise reducing potential of rubber modified asphalt is approx. 1–2 dB(A) compared to polymer modified asphalt". He offers no reference to document that claim.

4 ORGANISATION OF THE TRIALS AND SELECTIONS OF SITES

A project group was set up to follow the study and participate in its evaluation. The group consisted of representatives of

- the different levels of road administrations in Denmark (national and local including the city of Copenhagen),
- the Technical Committee of the Danish asphalt contractors' association (Asfaltindustrien),
- GENAN A/S, the Danish crumb rubber producer representing ROAD+
- Colas Danmark A/S, the asphalt contractor to perform the trials.
- The Research and Development department of the Danish Road Directorate.

The intended test protocols—especially for the noise measurement (acoustic environment and composition of traffic) and the full scale rutting experiment—meant that study had to accommodate a pre-trial before the actual trial sections where produced on a rural highway. The reference section was also not just intended to be used for this project but be part of a reference group for future pavement studies in noise and texture.

A suitable site (4 km) on Highway 411 was found in the North of Jutland between the cities Viborg and Aalborg for the main trials, and lorry parking lot on a recreational area on the motorway leading towards Aalborg was selected for the pre-trials. The contractor Colas Danmark A/S had the maintenance contract for the Danish Road Directorate in that area. The company had the main research laboratory nearby and was very experienced in handling SBS modified bitumen and asphalts. The Highway 411 had a new binder layer paved prior to the trial sections in order to ensure the best conditions for the comparison between the different surfaces and avoid that bearing capacity variations could interfere with the interpretation.

5 MATERIAL SELECTION

5.1 *Stone Mastic Asphalt (SMA)*

The optimal choice of asphalt type that would fulfil the objectives and conditions on the two trial sites was a Stone Mastic Asphalt (SMA) with a Nominal Maximum Aggregate Size (NMAS) of 11 mm. The aggregate gradation was chosen to be a standard gradation (meaning not optimised for noise reduction).

5.2 *Selected bituminous binders*

In the comparative study the three variants were intended to have the same surface texture and only differ by the applied bituminous binder. The compared binders have in this paper the following description (the subparagraph headings will be used to identify the various binders respectively asphalts in this comparative study):

5.2.1 *40/100-75*

The reference bitumen is SBS polymer modified bitumen in accordance with the European Modified binder specification EN 14023. The grade designation 40/100-75 means that the penetration is 40 – 100 × 0.1 mm and the softening point ring and ball is above 75 °C.

5.2.2 *ROAD+ 15%*

This modified binder consists of paving grade bitumen 70/100 mm with addition of 15% ROAD+. Under the assumption stated in [3] ("2.5% ROAD+ = 1% SBS") this binder shall be

directly comparable to the reference bitumen and represents a high level of binder modification for road application in Denmark.

5.2.3 *ROAD+ 8%*

This modified binder consists of paving grade bitumen 70/100 mm with addition of 8% ROAD+. Under the same assumption this binder represents the typical medium-low level of binder modification used in Denmark.

6 CONDITIONS THAT INFLUENCED THE EXPERIMENTAL PROGRAM

The initial experimental program had presumed that the wet process should have been used, since that would have provided the largest amount of information in testing the binder "before and after" paving. Facilities to produce the crumb rubber modified binder was available, but the practical configuration of Danish asphalt plants seemed to give problems with respect to handling the modified binder. During the preparation stage GENAN A/S offered information and technical expertise from the German experience and two obstacles were identified.

1. Virtually all Danish asphalt plants are equipped with horizontally placed binder storage tanks with internal heating pipes, and agitation is achieved by pumping to circulate the binder. The lack of internal propellers and the presence of heating pipes would lead to precipitation of crumb rubber particles on the pipes. This would create heat transfer problems and lack of control of binder properties (composition and ageing).
2. The viscosity of ROAD+ (crumb rubber) modified binder demands pipes with approx. 100 mm internal diameter in order to be pumped. Many of the Danish asphalt plants capable of handling highly SBS polymer modified bitumen have internal diameter not larger than approx. 75 mm.

For these reasons we were forced to use the dry process, since major investments in plant equipment had not been anticipated. This means that the study will compare crumb rubber modified asphalt with asphalt produced with a SBS polymer modified bitumen.

7 EXPERIMENTAL PLAN

7.1 *Division of experimental plan*

Instead of an experimental plan on the materials used for the trial sections we had to add an initial model study on the binder part in order to gain some experience for comparison of the properties of binders assumed to be present in the trial mixes. But the main focus was on the properties of the asphalt materials. Some properties were tested at the asphalt contractor (Colas) and some at the road administration (DRD). A few properties were even tested both places in order to gain experience on the variability in testing. This could prove to be useful information in future quality control efforts at contractors' and third parties level as larger standard deviation was anticipated than for ordinary paving grades.

7.2 *Model experiment for bituminous binders*

The model binders of ROAD+ were produced in the laboratory according to procedure found in ROAD+ documentation [9]. The paving grade 70/100 was heated to 180 °C and appropriate amount of ROAD+ was added during steering by a propeller. When ROAD+ after a short period was blended in the bitumen the temperature was reduced to 170 °C and steering continued for 2 hours before the sample was divided into subsamples. These were later treated in accordance with EN 12594 "Sample preparation" before each binder test which is stated in Table 3 together with the results (to avoid repetitions).

7.3 *Experimental plan for the asphalt materials*

The experimental plan for the asphalt material was based on full scale asphalt plant production, and not on laboratory mixed samples. The specification from the contractor on the individual mixes can be found in Table 1.

Samples of loose mix were taken directly from the plant. These samples were used for mix control and mechanical tests that required special laboratory compaction procedures (Marshall compaction, gyratory compaction, wheel tracking test, Temperature Stress Restrained Specimen Test and trapezoidal fatigue test). Numerous cores and plates were either drilled or cut from the pre-trial sections in order to test resilient modulus, dynamic creep, indirect tensile fatigue and full scale permanent deformation.

The total plan for testing of the asphalt materials can be found in Table 2, divided with the laboratory to perform the test. The full report can be found in [10], but indirect tensile fatigue will be reported in this paper as a measure of durability.

7.4 *Experimental plan for road inventory of the trial sections*

Apart from normal quality control for a pavement (e.g. coring for determination of compaction degree and voids) the trial sections on Highway 411 were intended to be as undisturbed as possible. The purpose was to facilitate road inventory measurements for years to come (friction, evenness and bearing capacity) but especially to provide the conditions for acoustic measurements of noise reductions and texture profiles.

The comparative noise reduction between the trial sections was assumed to be small. For this reason two methods were chosen; a spot measurement ISO 11819-1:2001 Statistical Pass By (SPB) and a continuous measurement of the entire length of the pavement with trailer ISO/CD 11819-2 Close Proximity (CPX) at 50 and 80 km/h. The measurements would be repeated frequently from paving the trial sections to the normal period for reference measurements for the Danish Noise classification of surface layers. This is after approx. 80 days for SPB and approx. 50 days for CPX. These periods are intended to obtain a representative surface texture after the traffic has removed the surplus bituminous mortar on top of the newly paved sections. The time difference needed for the two methods lies in the fact that the CPX trailer is running in the worn wheel tracks as opposed to the SPB measurement that is more dependent of the surface area in the vicinity of the location of the measurement point.

Table 1. Specification for gradation (percentage passing), binder content and some volumetric characteristics for Stone Mastic Asphalt 11 paved at Highway 411.

SMA 11	ROAD+ 8%	ROAD+ 15%	40/100-75 (Reference)
11.2 mm	100%	100%	100%
8 mm	52%	52%	52%
5.6 mm	35%	35%	35%
4 mm	30%	30%	30%
2 mm	22%	22%	22%
1 mm	18%	15%	18%
0.5 mm	15%	12%	15%
0.250 mm	13%	9%	13%
0.125 mm	9%	8%	10%
0.063 mm	6.5%	6.0%	7.5%
Binder content	5.6% 70/100 + 0.448% ROAD+	5.6% 70/100 + 0.84% ROAD+	5.6% 40/100-75
Asphalt density	2.630 Mg/m^3	2.630 Mg/m^3	2.640 Mg/m^3
Void volume	2.9%	2.3%	3.3%
Voids filled with bitumen	84.0%	88.0%	81.7%
Voids in mineral aggregate	18.4%	18.8%	17.8%

Table 2. Experimental plan for asphalt materials with reference to property, test methods and performing laboratory [10].

Property	Test method	Road directorate (DRD)	Contractor (Colas)	Third party laboratory
Compactability	Marshall Compaction (EN 12697-30) at 145 °C	+	+	
	Gyratory compaction (EN 12697-31) at 145 °C 150 mm Ø	+		
Stiffness	Resilient modulus (EN 12697-26 Annex F) at 2 °C, 10 °C and 20 °C	+	+	
	Stiff modulus (EN 12697-26 Annex A) at 15 °C			+
Fatigue	Resistance to fatigue (EN 12697-24 Annex E) at 15 °C	+	+	
	Resistance to fatigue (EN 12697-24 Annex A) at 15 °C			+
Permanent deformation	Dynamic creep (EN 12697-25 Test Method A) at 40 °C	+		
	Wheel Tracking Test (EN 12697-22 Model B in water) at 60 °C		+	
	Full scale wheel tracking (DART [11]), 5 kN load, 900 kPa, Super single tyre, temperature gradient 40 °C–20 °C, 110,000 passages	+		
Low temperature	Temperature Stress Restrained Specimen Test (AASHTO TP-10)			+

The surface texture can also be determined like Mean Profile Depth (MPD) or texture spectrum as the CPX trailer is equipped with a laser measuring device recording the profile of the wheel track simultaneously. The acoustical measurements are repeated approx. one year after paving.

For this paper the acoustical measurements (CPX and SPB) will be reported, but the full study can be found in [10].

8 EXTRACT OF RESULTS FROM THE COMPARATIVE STUDY

8.1 *Results of model experiments for bituminous binders*

The obtained results from the model experiment in the laboratory are stated in Table 3.

The model study leads to the following conclusions:

- Addition of ROAD+ and reaction with the bituminous binder will in asphalt lead to a modified concept.
- The effect is dependent of the added amount (and presumably of the base bitumen).
- Modification of paving grade 70/100 with 15% ROAD+ gives much higher viscosity than the SBS polymer modified reference bitumen even though the softening point R&B is much lower.
- The examined combination of 70/100 an 8% addition of ROAD+ shows an elastic recovery above 50%, but the test could not be performed according to the standard for addition of 15% ROAD+ due to premature failure.
- Ductility at 25 °C shows that ductile properties of ROAD+ modified binders are not good. This is presumably due to the presence of crumb rubber particle that act as crack initiators.

Table 3. Properties of the bituminous binders in the model study of properties.

Test	Reference	Unit	70/ 100	40/ 100-75	ROAD+ 8%	ROAD+ 15%
Penetration @ 25 °C	EN 1426	× 0.1 mm	77	64	47	42
Softening point R&B (water)	EN 1427	°C	46.4	–	55.4	63.0
Softening point R&B (glycerol)	EN 1427	°C	–	83.5	–	–
Penetration index, I_P	EN 12591		–1.1	5.5	–0.1	1.2
Dynamic viscosity @ 135 °C	EN 13302	mPa s	431	1,920	1,028	3,860
Dynamic viscosity @ 160 °C	EN 13302	mPa s	146	620	283	1,097
Elastic recovery @ 10 °C	EN 13398			84%	69%	Failure at 88 mm
Ductility @ 25 °C	ASTM D-113	cm		73	17	16
Rolling Thin Film Oven Test (RTFOT) EN 12607-1						
Change of mass	EN 12607-1	%		0.041	0.053	–0.013[a]
Penetration @ 25 °C	EN 1426	× 0.1 mm		47	37	35[a]
Softening point R&B (water)	EN 1427	°C		–	63.0	75.6[a]
Softening point R&B (glycerol)	EN 1427	°C		82.5	–	–
Penetration index, I_P	EN 12591			4.5	0.9	2.8[a]

[a]The values are only indicative. The binder ROAD+ 15% was too "structured" at 163 °C at RTFOT (EN 12607-1 Rolling Thin Film Oven Test) to spread out in a uniform film during conditioning. In this comparative study it was not relevant to raise the temperature for this binder to 180 °C as prescribed in the standard as an option.

8.2 *Results from asphalt materials*

The fatigue test was performed by Danish Road Directorate with Nottingham Asphalt Tester in accordance with EN 12697-24 Annex E. The results indicate that the fatigue performance of ROAD+ 15% is poorer than the comparable SBS polymer modified bitumen 40/100–75, while ROAD+ 8% gave results on the same level. Similar findings were obtained at the contractors' laboratory, but the trapezoidal two point bending fatigue showed that both ROAD+ combinations gave poorer fatigue life than the reference [10]. These results and the ductile properties (ductility and elastic recovery) of ROAD+ in Table 3—especially in high contents—can indicate that some of the remaining crumb rubber particles may act as crack initiators.

8.3 *Results of noise reduction from the trial sections on Highway 411*

The trial sections on Highway 411 are placed in a rural area, where the speed limit is 80 km/h. In order to compare the CPX (Close Proximity) measurements with other test sections in city streets, the CPX trailer measurements have been performed at both 50 and 80 km/h. The results of the noise level the three types of binder for both speeds can be seen in Figure 2a and b as a function of the number of days after paving.

The reference level for the Danish noise declaration of noise reducing pavement is also given in the two figures. The two figures indicate that the used SMA mix—as intended—is not a noise reducing asphalt for urban application, but for 80 km/h roads the three variations could pass when new as a noise reducing type. There is a significant increase in noise levels within the first two weeks after paving, but with a CPX measurement accuracy of approx. 0.5 dB there is no significant difference between the three binders. The minute decline in noise level from the 1st to the 2nd year which is most dominant in Figure 2b at 80 km/h can partly be explained by renewal of the test tyre and the fact that the rubber in the new tyre is softer than the old, and thereby a decrease in noise.

The results for the SPB measurements (Statistical Pass By) are shown in Figure 3a and b for passenger cars at 80 km/h and multi axle trucks at 70 km/h respectively.

The SPB measurements for passenger cars at 80 km/h show in Figure 3a the same type of increase in noise level the first weeks after paving as the CPX measurements in Figure 2a and b.

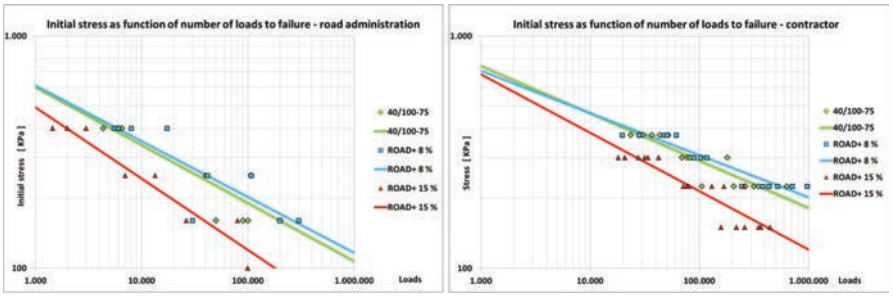

Figure 1a and 1b. Indirect tensile fatigue performed at 15 °C on cores (diameter 100 mm; thickness 23–40 mm) from pre-trial sections of SMA with three different bituminous binders.

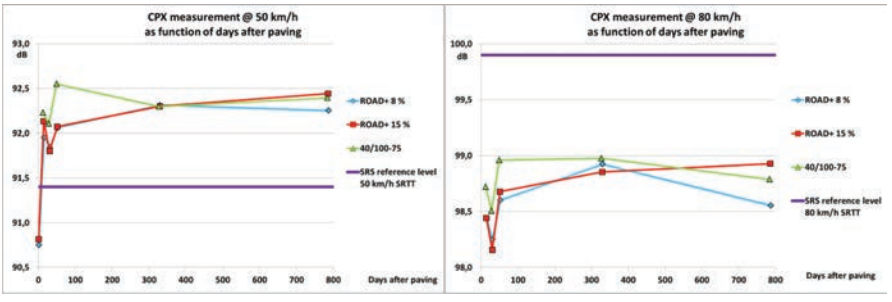

Figure 2a and 2b. CPX measurements on Highway 411 on the trial sections of SMA mixes with the three different bituminous binders as function of number of days after paving. The relevant noise reference level of the Danish noise declaration of noise reducing pavement are given as information.

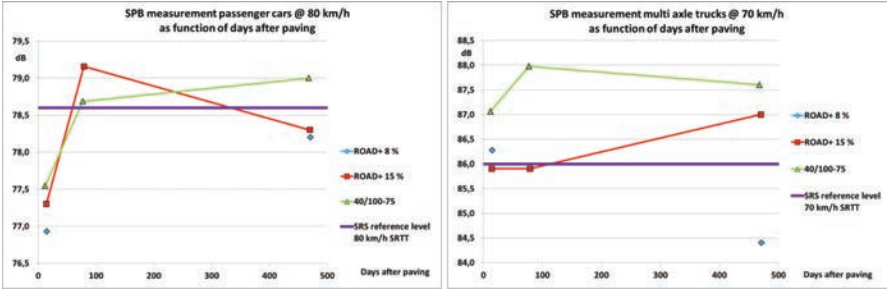

Figure 3a and 3b. SPB measurements on Highway 411 on the trial sections of SMA mixes with the three different bituminous binders as function of number of days after paving for passengers cars and multi axle trucks respectively. The relevant noise reference level of the Danish noise declaration of noise reducing pavement are given as information.

The results for multi axle trucks at 70 km/h in Figure 3b must only be taken as indicative since the extract of this category of vehicles on the highway trials is below the number recommended in the standard.

The noise measurements (CPX and SPB) lead to the following conclusions:

- Stone Mastic Asphalt with 11 mm as nominal maximum aggregate size and a aggregate gradation which has not optimised for noise reduction has been used in a study where ROAD+ in 8% and 15% have been compared to SBS polymer modified bitumen. Within the accuracy to the test methods the noise reduction of the three binder variations cannot significantly be distinguished.

- Wolfgang Fuchs' [8] stated potential improvement of "approx. 1–2 dB(A)" on noise reduction by using ROAD+ as opposed to SBS polymer modified bitumen cannot be verified.

9 ANSWER TO THE OBJECTIVES OF THE DANISH COMPARATIVE TRIALS

This paper presents parts of the documentation of the Danish comparative trials which has been organised to gain experience with ROAD+ modified asphalt including its characteristics and application in Denmark. In paragraph 3 the objectives and focus points of the study were defined and the overall conclusions from the whole study [10] can be summed up in the following statements:

1. ROAD+ (Ground tyre rubber and Vestenamer®) can be utilised by the "dry" process for the production of modified asphalt with the present level of technology at the Danish asphalt contractors.
2. The rule of thumb—"2.5% ROAD+ equals 1% SBS"—could not be verified.
3. ROAD+ with 15% addition do not give quite the same level as SBS modified bitumen 40/100–75 with respect to durability (fatigue) and other characteristics; among others ductile properties.
4. The use of ROAD+ modified binder as opposed to SBS polymer modified bitumen do not significantly by itself reduce traffic noise.

ACKNOWLEDGEMENT

This project was sponsored by the Maintenance Department of the Danish Road Directorate. The author will like also to thank Lars Ladehoff, Colas Danmark A/S, and Michael Hvam, Genan A/S, for their contributions to the project.

REFERENCES

[1] J.M. Kirk, Genanvendelse af gummi i bituminøse vejmaterialer, Asfaltindustriens Vejforskningslaboratorium (Asfaltindustrien), 1984.
[2] N. Lundberg and P.J. Andersen, Prøvestrækninger på hldv. 348, 411 og 416, VD notat 46, Vejdirektoratet 1997.
[3] ROAD+ product description; ROAD+_longer_lasting_roads.pdf, pamphlet on display 2008, GENAN A/S.
[4] Swedish Transpoort Administration (Trafikverket), seminar on the 29th–30th September 2010, Gothenburg Sweden, (http://www.trafikverket.se/Foretag/.....).
[5] Carsten Rickers, Lärmoptimierter Asphalt mit Gummimodifikation zur Reduktion von Straßenlärm, Power Point presentation Stadt Köln 29.09.2010—http://www.ft.dk/samling/20101/almdel/tru/bilag/5/898275/index.htm.
[6] IFTA-Erstprüfungsbericht Nr.: 1005036-1, LOA 5 D—("Spurbindungsversuch—Ruhr-Universität Bochum") 17-06-2010.
[7] Martin Radenberg: Hinweise zur Umsetzung—Lärmoptimierter Asphaltdeckschichten für den kommunalen Straßenbau, Ruhr-Universität Bochum, Germany, 29. Juni 2009.
[8] Wolfgang Fuschs, Gummimodifizierter Asphalt zur Lärmreduzierung, Strasse und Autobahn, 1/2011, p26–28, 2011.
[9] Zielke and Manhke: Binder tests of bitumen modified with ROAD+, Test Report No. 48/2005, HEIDEN LABOR für Baustoff- und Umweltprüfung GmbH, Germany 2005.
[10] Erik Nielsen: Gummimodificeret asfalt—rapport for demonstrationsstrækninger med gummimodificeret asphalt med produktet ROAD+ (GENAN A/S). Danish Road Directorate (Vejdirektoratet), VD-report No. 432, 2013.
[11] E. Nielsen and C.B. Nielsen, Danish Asphalt Rut Tester—Bridging the gap between laboratory and real life, Eurasphalt & Eurobitume Congress 2008, Copenhagen, Denmark.

This page intentionally left blank

Asphalt Pavements – Kim (Ed)
© 2014 Taylor & Francis Group, London, ISBN 978-1-138-02693-3

Mechanical influence of mineral fillers on asphalt mixture cracking behaviour

Elena Romeo, Riccardo Roncella, Silvia Rastelli & Antonio Montepara
Parco Area delle Scienze, University of Parma, Parma, Italy

ABSTRACT: The role of asphalt modifiers and/or modified fillers on the cracking behaviour of asphalt mixtures is extremely complex and has not been fully explained. To characterize the mechanical influence of fillers on asphalt mixture cracking behaviour it is essential to assess the viscoelastic properties of the mastic. Accurate description of strain evolution and distribution in mastics is essential for revealing significant information on mixtures macroscopic behaviour.

In this study, 16 different mastics composed by the combination of four different fillers and four asphalt binders, were evaluated on the basis of test results and their mechanical analyses. The Dynamic Shear Rheometer (DSR) and the Bending Beam Rheometer (BBR) were used to characterize the rheological properties of the different mastics. Their cracking behaviour was investigated using a Modified Direct Tension Test (MDTT). Strain localization and damage distribution were observed using a completely redesigned in-house developed Digital Image Correlation System (DIC) capable of accurately capturing localized or non-uniform stress distributions in asphalt materials. The role of fillers in cracking resistance was quantified, and induced mechanisms due to filler addition were investigated. The effect of hydrated lime was further discussed by comparing test results from hydrated lime filler and test results from limestone and clay fillers.

Keywords: HMA mixtures; mineral filler; mastic; direct tension test; digital image correlation

1 INTRODUCTION

Cracking in flexible pavements is widely recognized as a mastic-related distress meaning that fracture in asphalt mixture is governed by the properties of the asphalt binder and the filler [1–2]. The stiffness of the mastic affects the ability of the mixture to resist permanent deformation at higher temperatures, influences stress development and fatigue resistance at intermediate temperatures, and influences stress development and fracture resistance at low temperatures [3].

As discussed by many authors [4–7], the effect of the filler is based on a volumetric effect and/or a physico-chemical interaction between the filler and the asphalt binder. Polymer modifiers in the binder and/or hydrated lime in the filler are commonly introduced in attempt to enhance the mechanical performance of asphalt mixtures. However, previous studies [8–10] have shown that the addition of the same modifier to different asphalt binders may lead to contrasting results in terms of fatigue resistance and low-temperature cracking. Similarly, it was shown that hydrated lime reacts quite differently as a filler with different asphalts (SHRP AAD-1 and SHRP AAM-1), leading to great discrepancies in terms of cracking resistance and fatigue life [11–13]. In summary, the role of asphalt modifiers and/or modified fillers on the cracking behaviour of asphalt mixtures is extremely complex and has not been fully explained.

Accurate description of strain evolution and distribution in mastics is essential for revealing significant information on the influence of microstructure properties on asphalt

mixture macroscopic behaviour. The analysis of strain development requires appropriate experimental techniques. Very few studies in the past have been focused on the evaluation of the strain magnitudes within the mixture microstructure [14]. Masad et al. [15–17] used both digital imaging and X-ray computed tomography techniques to evaluate the microstructure of asphalt mixture in terms of aggregate orientation and air voids concentration, as well as strain distribution, finding that the percent of air voids is the main factor that controls strain distribution. However, the influence of strain evolution in the mastic on mixture crack initiation and propagation has not been addressed previously. Therefore, it is of considerable interest to investigate how filler particles and their interaction with asphalt binder affect mixture's cracking behaviour.

The present study evaluates the influence of mineral fillers on asphalt mixture macroscopic cracking response by analysing the localized strain distribution within the mastic microstructure. Four different fillers where associated to four asphalt binders (two unmodified and two polymer modified) to obtain 16 asphalt mastics. The rheological properties of the mastics were evaluated conducting Superpave testing procedures, including the DSR and BBR over a wide range of temperatures. The cracking behaviour of the mastics was investigated using a Modified Direct Tension Test (MDTT). Strain localization and damage distribution were observed using a completely redesigned in-house developed DIC software code called DICe, which was initially designed to facilitate the quantification of strains in the mastic in between the aggregates in a typical asphalt mixture [18]. The DIC-based system was employed to obtain 2D full-field strain maps of mastic specimens during tensile loading.

2 MATERIALS

Sixteen asphalt mastics were used in this study. The mastics were composed by four different asphalt binders, labeled as NV, N2, MR and ML. NV and N2 are two unmodified binders, graded as PG64-28 and PG58-22 respectively. MR and ML, graded as PG64-22 and PG70-22, are two polymer modified binders obtained blending the N2 unmodified one with a 3.5% of SBS cross-linked and SBS linear polymers, respectively. The SBS was blended with the base asphalt by the manufacturer using high shear milling.

Four fillers were associated to the four binders: a limestone filler, a clay filler, and two combinations of limestone + hydrated lime (20% weight) and clay filler + hydrated lime (20% weight). The selected filler concentration was 60% by weight for all mastic formulations. Following are the properties of the three materials:

- Limestone filler is composed of $CaCo_3$ with a density of 2.65 g/cm^3, a specific surface area of 0.28 m^2/g and a 9 pH.
- Clay filler is composed of SiO_2 (66.06%), Al_2O_3 (16.57%), Fe_2O_3 (7.1%), K_2O (2.69%), CaO (2.46%) and MgO (1.99%) with a density of 2.8 g/cm^3, a specific surface area of 0.32 m^2/g and a 7 pH.
- Hydrated lime is composed of $Ca(OH)_2$ with density of 2.34 g/cm^3, a surface area of 13.5 m^2/g and a 12.5 pH.

3 RHEOLOGICAL PROPERTIES

The Dynamic Shear Rheometer (DSR) and the Bending Beam Rheometer (BBR) were used in this study to determine the rheological properties of asphalt mastics. The DSR was used to measure the complex dynamic shear modulus (G*) at 25°C and 60°C. The appropriate applied stress amplitude for each test temperature was determined by conducting a stress sweep at a constant frequency of 10 radians/s. With known stress and measured shear strain values, the linear range of the materials behavior was determined. The testing was conducted with an 8-mm plate with a 2-mm gap and a 25-mm plate with a 1-mm gap at 25°C and 60°C, respectively.

The BBR was used to determine the stiffness of the binder and mastics at –25°C, –12°C and –5°C. A constant load of 980 mN was applied for 240 s, and the creep stiffness at 60 s was determined.

Figure 1 shows the results obtained from DSR at 60°C and 25°C. The mastic properties at high temperature are more affected by the asphalt binder rather than the filler composition. The combination of clay filler and hydrated lime makes the mastic very stiff decreasing significantly its workability. Similar results were obtained at intermediate temperatures. The most important role is played by the base asphalt binder. N2 performs better than the NV one and the addition of SBS modifier does not increase the performance of the mastic.

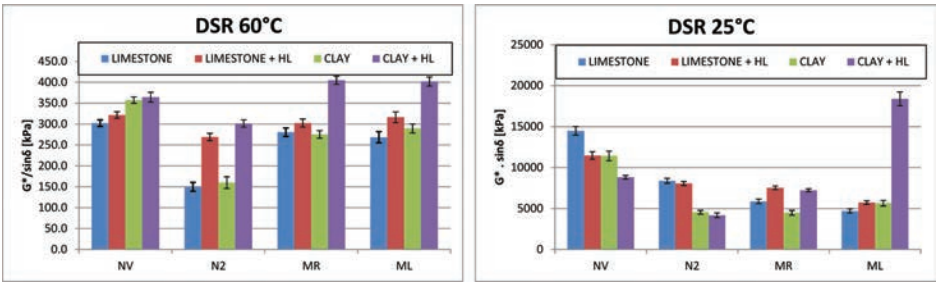

Figure 1. DSR results at 60°C and 25°C.

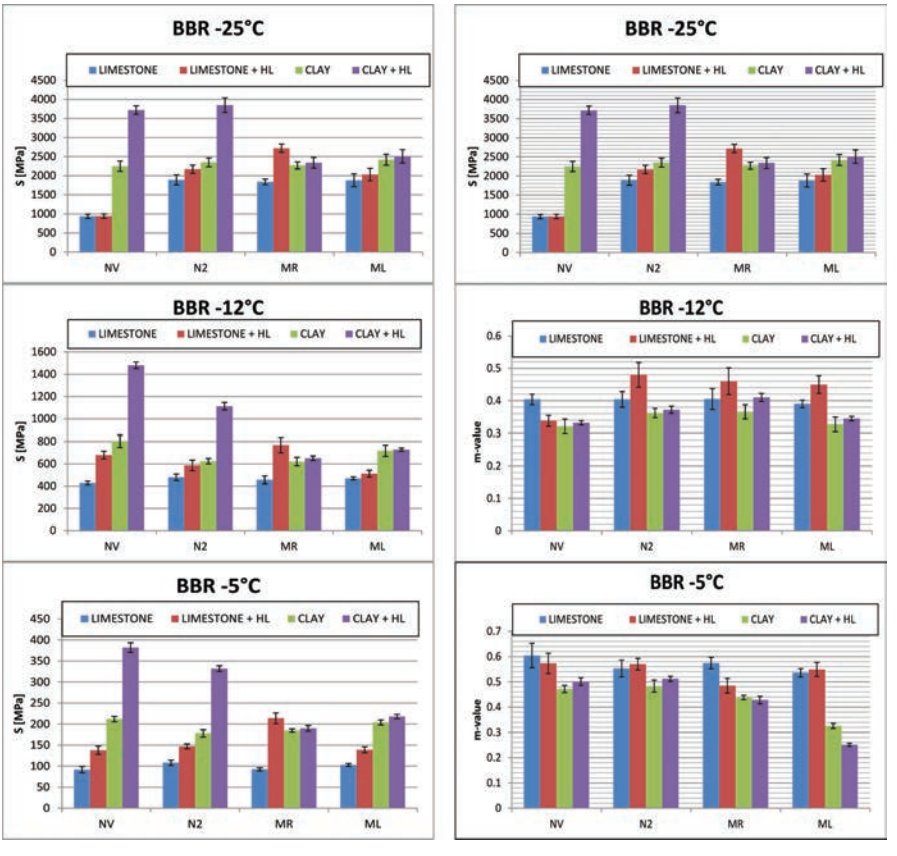

Figure 2. BBR results at –25°C, –12°C and –5°C.

Conversely, the results obtained from BBR, shown in Figure 2, highlight that the stiffness at low temperatures is more affected by the type of filler. The trend is similar at different temperatures.

Clearly, the clay filler and the addition of hydrated lime provide the most overall stiffness to the mastic. The surface activity of hydrated lime and hence physiochemical stiffening potential seems to be quite high.

4 CRACKING BEHAVIOR

4.1 *Modified Direct Tension Test (MDTT)*

The cracking behaviour of the mastics was investigated using a Modified Direct Tension Test (MDTT) performed in a servo-hydraulic load frame to allow the material to stretch up to rupture.

The specimen geometry was optimized to meet the following criteria: uniform stress distribution within the specimen web, adequate gauge length for accurate strain measurements, ease of specimen preparation. A Finite Element (FE) analysis was conducted to determine adequate specimen dimensions (specimen total length, web length, flange length and width) in order to obtain uniform stress distribution within the specimen web. The material property was assumed as viscoelastic; fixed boundaries were assumed at one end of the specimen, while a pulling load was applied at the other end. The final specimen dimension was determined to be 106 mm long, 20 mm wide and 10 mm thick, with an effective gauge length of 46 mm.

A further critical point was identifying the correct testing speed to assure correct data analyses. Different constant strokes were tested: from 0.084 mm/sec to 3.36 mm/sec. It was observed that, at lower speeds, the mastic exhibits extreme strain before rupturing as well as a significant reduction in the cross-sectional area, leading to not reliable calculation of stresses. Conversely, higher loading rates have shown to fracture the asphalt mastic before it reaches the minimum extension not allowing for a representative differentiation among the different mastic compositions. The optimum speed was identified as 1.68 mm/sec.

4.2 *Mastic specimen preparation*

The mastic specimens were prepared following the improved SuperPave™ binder testing specimen preparation procedure suggested by Ho and Zanzotto [19]. For each specimen, 28 g of asphalt binder and 42 g of filler were prepared and heated at mixing temperature (150°C for unmodified binders and 175°C for modified ones) in separate tins for 30 minutes. Then, the filler was slowly added to the asphalt in the oven. A mechanical mixer, with a maximum nominal angular speed of 8,000 rpm, was used to blend the materials at mixing temperatures. The mixing process was carefully followed so that the filler was homogeneously dispersed in the binder.

The mastic was continuously stirred as it cooled to prevent settling and then was poured to the preheated dog-bone shaped aluminum mold. The specimen is allowed to cool to room temperature for one hour and de-molded. It is then placed in the environmental control chamber for one hour at testing temperature before the test is performed.

4.3 *Strain analysis*

The influence of mineral fillers on mastic strain localization and damage distribution is simplified by field measurements of deformation over an area of finite extent through a Digital Image Correlation (DIC)-based method. The method is based on the application of a photogrammetry-based technique together with a properly designed laboratory test configuration. MDTT strains were evaluated using a completely redesigned in-house developed DIC software code called DICe, which was initially designed to facilitate the quantification of strains in the mastic in between the aggregates in a typical asphalt mixture. In this study, the method

was for the first time employed to measure and observe strain evolution and crack initiation in mastics.

The new DICe software code implements, for the image correlation step, a fairly innovative Least Squares Matching approach [20] that uses higher order polynomial shape functions to model the displacement field between the reference and the measured image of the DIC sequence: proposed also by other authors in different application fields [21][22]. The technique is, for the first time, applied to this kind of DIC scenario. The most important issue addressed by the new code is that, with high strain phenomena, especially just before crack initiation, is rare that the strain distribution in the area evaluated by the punctual Least Squares Matching measure can be considered strictly constant, even if that area is small. Hence, with lower order shape function (e.g. with (linear) affine transformation models) higher residuals can be expected in the estimation process, statistical error rejection techniques (i.e. observation data snooping) are harder to be applied, and lower levels of accuracy can be expected.

The previous DIC system has shown to achieve satisfactory accuracy compared to strain gauges, resulting in 0.04% accuracy in compressive/tensile strains and 0.03% accuracy in shear strains (further details on the method are discussed elsewhere [18]). In this case, due to the peculiar, localized, behavior of the mastic, it's hard to perform the same comparison with the new technique. Nonetheless, assuming that the nonlinearity of the displacement field can be considered similar to the ones obtained in the schematic (and general) tests performed in [22], smaller errors (up to a factor of 4) can be expected. Further investigation and a rigorous evaluation of the accuracy performance of the new algorithm should be performed in the future.

A digital camera Basler piA1600-35 gm (resolution 1608 × 1308, focal length 8 mm, pixel size 7.4 micrometers, 35 fps@max resolution), directly connected to the testing control system, is located on a support inside the climatic chamber where tests are performed. The chamber is provided with a proper LED lighting system which assure good illumination without heating up the specimen. Since the crack phenomenon is very fast and short-lasting (1÷2 seconds), the camera was properly set up to acquire the images in a smaller area of the sensor (1600 × 500 pixel) reducing the bandwidth required for transmitting each frame and, consequently, allowing a higher frame rate (ca. 80 fps). Thanks to the elongated shape of the specimen, once provided an optimal imaging geometry, the reduced size of the images still allowed the complete acquisition of the whole specimen surface. The images are automatically processed by the software, providing accurate displacement/strain fields. To achieve high accuracies in the strain field measurements, the specimen surface must present a well-contrasted grey scale speckle pattern, easily obtainable by a water paint-based treatment [14][18].

4.4 *Test procedure*

MDTT tests were performed on three replicates at 10°C using an MTS closed-loop servo-hydraulic loading system adopting a 2.5 kN load cell. The specimen was fixed at one end and pulled from the other end applying a constant stroke of 1.68 mm/sec until rupture occurs.

The engineering stress was computed according to the SuperPave™ binder specification:

$$\sigma_f = \frac{P_f}{A_0} \tag{1}$$

where: s_f = failure stress; P_f = measured load at failure; A_0 = original cross-sectional area

Failure is defined as the point on the stress-strain curve where the load reaches its maximum. The rapid loading rate and the interpretation of the test only up to fracture allow for a continuum representation. Strains were obtained from DIC system, interpolating all the strain values of the grid points located at the 46 × 20 mm specimen central cross-sectional area. The test configuration is shown in Figure 3.

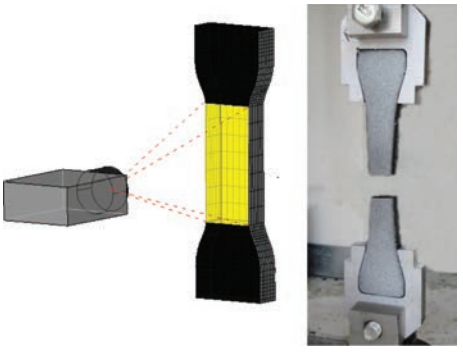

Figure 3. Mastic modified direct tension test configuration.

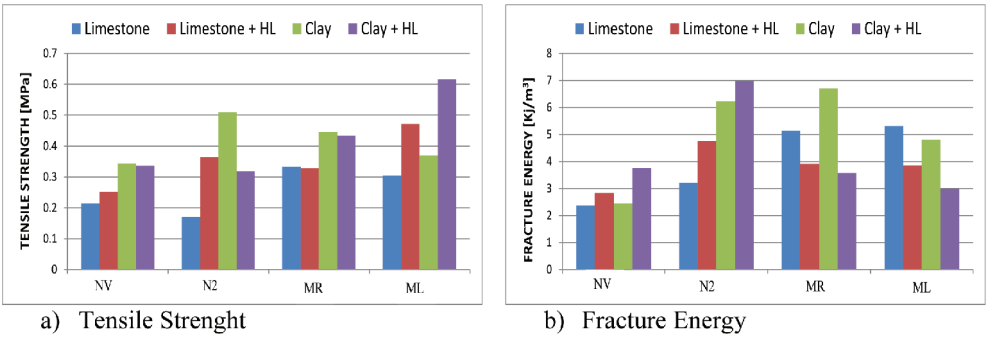

Figure 4. Effect of filler on mastics tensile limits.

4.5 *Results*

Tensile strengths and Fracture Energy (FE) densities computed as the area under the stress-strain curve at fracture initiation [23] were compared. Tensile strengths of the mastics are shown in Figure 4a. The results clearly show that the nature of filler influences the resistance of the mastics, since all the clay-composed materials result in a higher tensile strength. Conversely, the influence of hydrated lime on ultimate strength is not clear: it seems capable of either enhancing/decreasing (+50% for MLA; –38% for N2LA) the mastic resistance not making any difference (for NV and MR).

More significant are the fracture energy results shown in Figure 4b. The filler nature plays an important role in defining this failure parameter: clay-filler mastics exhibit higher fracture energies. Moreover, the presence of hydrated lime in unmodified mastics significantly enhances the fracture limit, while in polymer modified ones gives a negative contribution.

Figures 5–8 show full-field tensile strain maps at crack initiation for the 16 mastics, obtained from NV, N2, MR and ML asphalt binders, respectively. It can be observed that the unmodified mastics containing limestone fillers (with and without hydrated lime) exhibit distributed damage in the all area, showing different points of microcrack coalescence. Conversely, the unmodified mastics containing clay fillers, show high strains localized solely along the fracture path. The opposite behaviour was observed in modified mixtures. In detail, the modified mastic containing only limestone filler results in a more localized damage concentration, while the mastic containing clay filler and hydrated lime exhibits different areas of excessive damage.

The most likely reason for the observed trends is attributable to the physico-chemical interactions between binders and fillers and thereby to the particular network established within the mastic. Indeed, while the result of the reaction between unmodified binders and clay

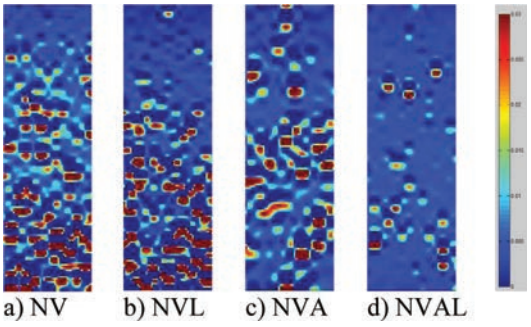

Figure 5. Full-field strain maps for mastics containing NV binder.

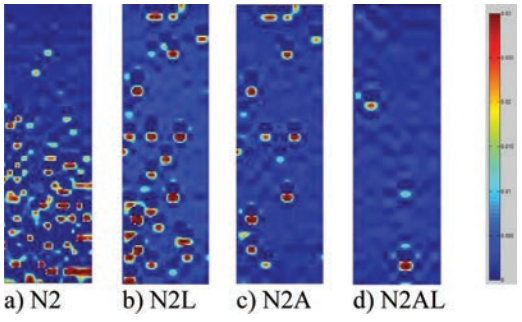

Figure 6. Full-field strain maps for mastics containing N2 binder.

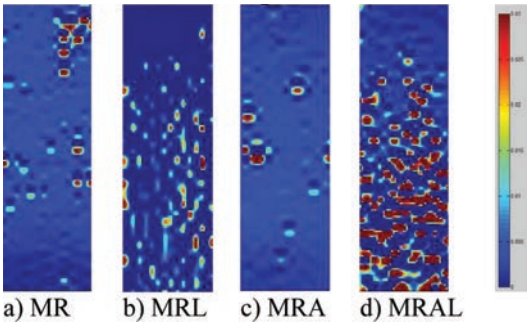

Figure 7. Full-field strain maps for mastics containing MR binder.

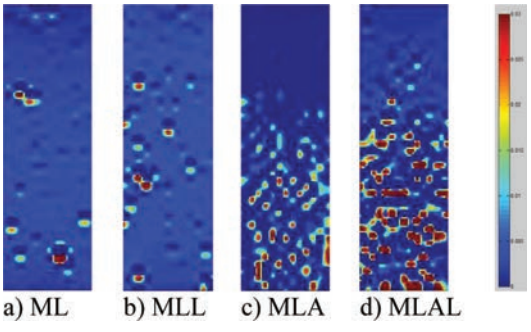

Figure 8. Full-field strain maps for mastics containing Ml binder.

fillers is a toughened matrix capable of redistributing part of the stress, modified binders combined with the same clay fillers result in a weaker matrix which allows for the development of highly distributed microcrack.

5 SUMMARY AND CONCLUSIONS

Rehological properties and cracking behaviour of 16 asphalt mastics composed by the combination of four asphalt binders (two unmodified and two SBS polymer modified) and four different fillers, were examined. A Modified Direct Tension Test (MDTT) was employed to estimate the failure limits of mastics. A completely redesigned in-house developed Digital Image Correlation (DIC) system was used to observe strain development and damage distribution in mastics. From rheological and MDTT results, it was observed that the filler nature influences the stiffness and the resistance of the mastics, since all the clay-composed materials results stiffer and exhibit higher tensile strengths. Conversely, the mastic rheological properties at high and intermediate temperatures are more affected by the base asphalt binder rather than the filler composition and/or the addition of SBS polymer modification. DIC analyses revealed that the nature of filler has a great influence on mastic cracking patterns. In detail, clay fillers seem to improve unmodified mastics cracking behavior leading to strain localization, while decreasing the performance of polymer modified mastics, resulting in the development of different areas of excessive damage.

Conversely, when limestone filler is employed, the damage distribution depends uniquely on the properties of asphalt binders: unmodified mastics show highly distributed damage in the critical area, while modified mastics exhibit high strain concentrations around the point of fracture.

ACKNOWLEDGEMENTS

This research has been supported by the Italian Ministry of University and Research within the project "FIRB—Futuro in Ricerca 2010"—Subpixel techniques for matching, image registration and change detection.

REFERENCES

[1] D.A. Anderson, W.H. Goetz. Mechanical Behavior and Reinforcement of Mineral Filler-Asphalt Mixtures. Journal of The Association of Asphalt Paving Technologists, 42, pp. 37–66, 1973.

[2] J. Craus, I. Ishai, A. Sides. Some Physiochemical Aspects of the Effect and Role of the Filler in Bituminous Paving Mixtures. Journal of The Association of Asphalt Paving Technologists, 45, pp. 558–588, 1976.

[3] W.G. Buttlar, D. Bozkurt, G.G. Al-Khateeb, A.S. Waldhoff. Understanding Asphalt Mastic Behavior Through Micromechanics. Transportation Research Record: Journal of the Transportation Research Board, 1681, pp. 157–169, 2007.

[4] Y.K. Kim, D.L. Little, I. Song. Effect of Mineral Fillers on Fatigue Resistance and Fundamental Material Characteristics: Mechanistic Evaluation.Transportation Research Record, 1832, pp. 1–8, 2003.

[5] A.F. Faheem, U.H. Bahia. Conceptual Phenomenological Model for Interaction of Asphalt Binders with Mineral Fillers. Journal of the Association of Asphalt Paving Technologists, 78, pp. 680–717, 2009.

[6] B.J. Smith, S. Hesp. Crack Pinning in Asphalt Mastic and Concrete: Regular Fatigue Studies. Transportation Research Record, 1728, pp. 75–81, 2000.

[7] B. Delaporte, H. Di Benedetto, P. Chaverot, G. Gauthier. Effect of Ultrafine Particles on Linear Viscoelastic Properties of Mastics and Asphalt Concretes. Transportation Research Record, 2051, pp. 41–48, 2008.

[8] J.T. Harvey, J.A. Deacon, B. Tsai, C.L. Monismith. A Fatigue Performance of Asphalt Concrete Mixes and its Relationship to Asphalt Concrete Pavement Performance in California. Report No. Rta-65 W485-2. California Department of Transportation, 1995.
[9] J.T. Harvey, J.A. Deacon, A.A. Tayebali, R.B. Leahy, C.L. Monismith. A Reliability-Based Mix Design and Analysis System for Mitigating Fatigue Distress. Eighth International Conference on Asphalt Pavements, Seattle, Washington, 1997.
[10] H.U. Bahia, D.I. Hanson, M. Zeng, H. Zhia, M.A. Khatri, R.M. Anderson. Characterization of Modified Asphalt Binders in Superpave Mix Design. NCHRP Report 459, 2001.
[11] D.N. Little, J.C. Petersen. Unique Effects of Hydrated Lime Filler on the Performance-Related Properties of Asphalt Cements: Physical and Chemical Interactions Revisited. Journal of Materials in Civil Engineering, 17(2), pp. 207–218, 2005.
[12] P. Hopman, A. Vanelstraete, A. Verhasselt, D. Walter. Effects of Hydrated Lime on the Behaviour of Mastics and on Their Construction Ageing. International Conference on Durable and Safe Road Pavements, Kielce, Poland, Vol. I, 1999.
[13] W.G. Buttlar, D. Bozkurt, G.G. Al-Khateeb, A.S. Waldhoff. Understanding Asphalt Mastic Behavior Through Micromechanics. Transportation Research Record, 1681, pp. 157–169, 1999.
[14] E. Romeo. Two-dimensional digital image correlation for asphalt mixture characterisation: interest and limitations. Road Materials and Pavement Design DOI:10.1080/14680629.2013.815128, 2013.
[15] E. Masad, B. Muhunthan, N. Shashidhar, T. Harman. Aggregate orientation and segregation in asphalt concrete. Geotech. Spec. Publ. 85, pp. 69–80, 1998.
[16] E. Masad, B. Muhunthan, N. Shashidhar, T. Harman. Internal structure characterization of asphalt concrete using image analysis. Journal of Computing in Civil Engineering, 13(2), pp. 88–95, 1999.
[17] E. Masad, N. Somadevan, H.U. Bahia, S. Kose. Modeling and Experimental Measurements of Strain Distribution in Asphalt Mixes. Journal of Transportation Engineering, 127(6), pp. 477–485, 2001.
[18] B. Birgisson, A. Montepara, E. Romeo, R. Roque, R. Roncella, G. Tebaldi. An Optical Strain Measurement System for Asphalt Mixtures Materials and Structures. 42, pp. 427–441, 2009.
[19] S.M.S. Ho, L. Zanzotto. Sample Preparation for Direct Tension Testing—Improving Determination of Asphalt Binder Failure Stress and Test Repeatibility. Transportation Research Board, 1766, pp. 15–23, 2000.
[20] A. Grün. Adaptive least squares correlation—a powerful image matching technique. South African J. Photogramm. Remote Sensing and Cartography, 14(3), pp. 175–187, 1985.
[21] C. Re, G. Cremonese, E. Dall'Asta, G. Forlani, G. Naletto, R. Roncella. Performance evaluation of DTM area-based matching reconstruction of Moon and Mars. Proc. SPIE 8537, Image and Signal Processing for Remote Sensing XVIII, 85370V Edinburgh, United Kingdom, September 24, 2012.
[22] F. Bethmann, T. Luhmann. Least-squares matching with advanced geometric transformation models. International Archives of Photogrammetry, Remote Sensing and Spatial Information Sciences, Vol. XXXVIII, Part 5 Commission V Symposium, Newcastle upon Tyne, UK, pp. 86–91, 2010.
[23] R. Roque., B. Birgisson, B. Sangpetgnam, Z. Zhang. Hot Mix Asphalt Fracture Mechanics: A Fundamental Crack Growth Law for Asphalt Mixtures. Journal of the Association of Asphalt Paving Technologist, 71, pp. 816–827, 2002.

This page intentionally left blank

Asphalt Pavements – Kim (Ed)
© 2014 Taylor & Francis Group, London, ISBN 978-1-138-02693-3

Decay law of Cement-Emulsified-Asphalt-Cold-Recycled Mixture (CEACRM) in recycling process

Lei Huang
China Merchants Chongqing Communications Research and Design Institute Co., Ltd., Chongqing, China
School of Civil Architecture, Chongqing Jiaotong University, Chongqing, China

Yu Gu
School of Transportation Engineering, Tongji University, Shanghai, China

Boming Tang
School of Civil Architecture, Chongqing Jiaotong University, Chongqing, China

Zengheng Hao
Chongqing Zhixiang Road-Paving Technology Engineering Co., Ltd., Chongqing, China

ABSTRACT: Based on the failure mechanism under the limit load of the pavement and long-term aging mechanism of the asphalt mixture, taking the residual value as the constraint condition for termination, the decay law of road performances of Cement-Emulsified-Asphalt-Cold-Recycled Mixture (CEACRM) in the recycling process by comprehensive tests of mechanical properties, water stability, high and low temperature performance, modulus performance, and fatigue performance were studied. Results showed: 1) The decay of road performance of cold recycled mixture caused by circulatory recycling is nonlinear; 2) New-aged asphalt membranes generated in the multiple recycling sharply lower the cohesion of the binder, which leads to a negative effect on mechanical properties and the modulus performance of the mixture; 3) The adding of the cement reduces the sensitivity of the recycled mixture to water and temperature. Though the water stability and high temperature performance is obviously attenuated, it can still meet application requirements. 4) With the increase of the cement and the aging of the asphalt, the attenuation of the low temperature crack resistance of the mixture is obvious. 5) As asphalt membranes and cement slurries generated in the multiple recycling are stress concentration positions for fatigue failure, the decay of the fatigue life is the most remarkable in road performances. The research defined a relation between the cycle period of recycled mixture and the performance decay, which laid foundation for sustainable reusing of the recycled mixture in the future.

Keywords: Cement-Emulsified-Asphalt-Cold-Recycled Mixture (CEACRM); cold recycle; decay law; residual value; road performance

1 INTRODUCTION

With the proposition of the sustainable development strategy and the low-carbon concept, the cold recycling technique of asphalt pavement, as a green maintenance technique, which is energy-efficient and environmentally friendly, is gradually being focused on, and has been widely used in overhaul engineering of every highway. Since 1980s, it has been started on research and applications of the cold recycling technique of asphalt pavement in China, and till now, thousands of kilometers of cold recycled pavements have been built. However, under the effect of the load and natural factors, these completed and opened cold recycled

pavements start to be close to or have reached their service life, and whether they can be cold-recycled twice even many times, has become a difficulty that the development of the cold recycling technique of asphalt pavement must encounter and need to be addressed urgently.

Through the analysis of the current situation of the application of the cold recycled asphalt pavement and the properties of the recycled material it can be known that, the residual value of the recycled material is still huge, which makes the reusing of cold recycled pavements possible when they reach their service life. Two main existing process forms of cold recycling of asphalt pavement are the cold recycling with cement-foamed-asphalt and the cold recycling with cement-emulsified-asphalt, of which the cold recycling essences are both to make up for losses of performances of original pavements, and this kind of making up is merely an approximation instead of a recovery of the original level. Accordingly, along with the increase of recycling times of the cold recycled mixture, its residual value will undoubtedly decrease gradually until it can not reach the request of the road performance. In order to maximize recycling times and to achieve the goal of circulatory cold recycling, the developmental state of the decay law of the cold recycled mixture must be grasped; thereby the foundation could be laid for research of later improvement measures.

2 DECAY LAW OF THE PERFORMANCE OF THE OLD MATERIAL ON THE ASPHALT PAVEMENT

According to effects on the long-term aging of the old material on the asphalt pavement from external conditions such as the coupling of the light, the heat and the water, the traffic load and so on, the simulating test method of the multiple cold recycling in door of the old material on the asphalt pavement was developed, and then experimental studies were done about the gradation and the performance of the old material in the multiple cold recycling, of which the results are as follows:

From Table 1 it is seen that, in the multiple cold recycling, the old material on the pavement is presented to be the trend that the coarse aggregate decreases while the fine aggregate increases. Through observation, the fine aggregate can be gradually filled into structural poles of the coarse aggregate, which proves that the residual value of the old material after experiencing the multiple recycling is still very huge.

From Table 2 it is seen that, along with the increase of recycling times, the anti-pressure ability and the wear resistance ability of the old material decrease gradually. Researches

Table 1. The changing rule of the gradation of the old material in the multiple cold recycling.

Grain size (mm)	Old material after primary recycling	Old material after secondary recycling	Old material after tertiary recycling
37.5	100.00	100.00	100.00
31.5	100.00	100.00	100.00
26.5	100.00	100.00	100.00
19.0	100.00	100.00	99.75
16.0	98.81	95.90	95.73
13.2	96.93	88.20	85.81
9.50	84.71	70.10	61.83
4.75	48.02	35.90	28.54
2.36	22.06	16.80	12.46
1.18	10.02	9.10	6.94
0.60	6.18	5.40	5.17
0.30	0.94	2.40	3.11
0.15	0.76	1.30	2.09
0.075	0.35	0.80	1.39

Table 2. The changing rule of the performance of the aggregate in the old material in the multiple cold recycling.

Technical index	Crushing value (%)	Los Angeles abrasion value (%)	Apparent density (10 g/cm^3)	Water absorption ratio (%)	Adhesion level with the asphalt
Primary recycling	19.3	21.1	2.52	1.76	5
Secondary recycling	21.6	23.2	2.53	1.88	5
Tertiary recycling	27.8	29.0	2.55	1.92	4
Four times recycling	34.3	38.8	2.59	2.25	3
Code requirement	≤28	≤30	≥2.5	≤2	≥4

show that, the continuity presented by the gradation of the multiple recycling old material, is mainly caused by discrete asphalt micelles, which contribute less to mechanical properties of the old material and is the main factor leading to the pavement cracking. Hence, the residual value of the old material after the multiple cold recycling, meanwhile, is limited.

3 DECAY LAW OF THE CEACRM (CEMENT-EMULSIFIED-ASPHALT-COLD-RECYCLED MIXTURE)

Through research on the decay law of the old material on the asphalt pavement it can be found that, the residual value of the old material on the pavement is limited, so during the process of the multiple cold recycling, how to make full use of its residual value, depends on research on the decay law of the road performance of the cold recycled mixture.

3.1 *Proportion design of the circulatory cold recycled mixture*

In order to avoid effects on the decay law of the mixture during the process of circulatory cold recycling from factors like the proportion of the material, in this test, the same design proportion was adopted in every cold recycling proportion design:

- The proportion of the old material is 100% (Full utilized);
- The gradation of the old material is selected to be the "A" gradation of the fine-grained type of the emulsified-asphalt-cold-recycled mixture in *Technical Specifications for Highway Asphalt Pavement Recycling*;
- The optimum asphalt content is 3%, which means the asphalt content in the emulsified asphalt is 3% of the total mass of the cold recycled mixture;
- The solid content of the asphalt in the emulsified asphalt is 62%;
- The proportion of the cement is 1%.

3.2 *Decay law of the mechanical performance*

The mechanical performance of the cold recycled mixture is the evaluation index that indicates the bearing capacity of the structural layer of the cold recycled pavement, and it is the most fundamental request of the road performance of the cold recycled mixture that it can meet the requirement of the bearing capacity of the pavement after being treated by the cold recycling technique. Based on the technical regulation for the emulsified-asphalt-cold-recycled mixture in *Technical Specifications for Highway Asphalt Pavement Recycling* (JTG F41-2008), in this test, 15° Csplitting strength and 40°C Marshall stability were adopted as evaluation indexes.

From Figure 1 it is seen that, in the multiple cold recycling, along with the increase of recycling times, the air void of the cold recycled mixture is gradually enlarging. This variation of the skeletal structure, when reflected on the mechanical performance of the mixture, is that the Marshall stability and the splitting strength decay simultaneously, and along with the

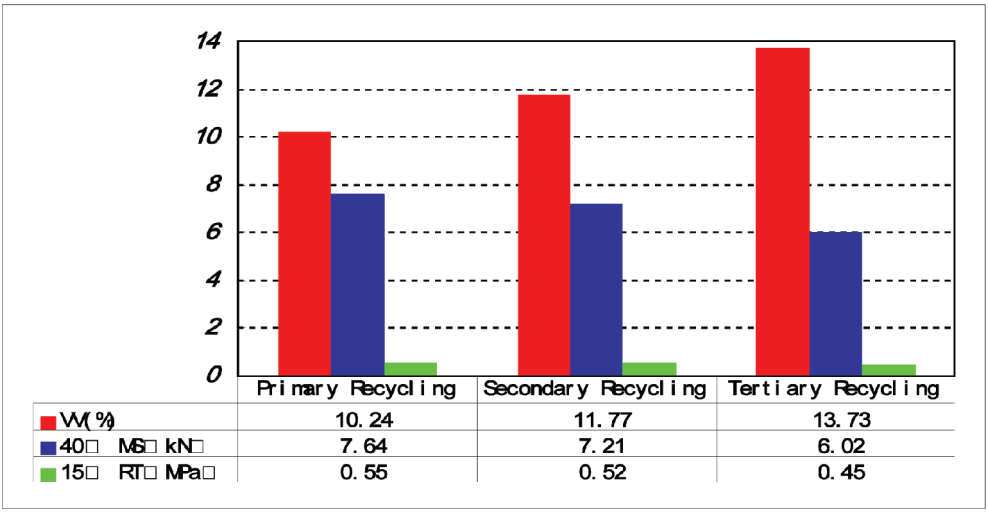

Figure 1. The variation trend of the mechanical performance of the mixture after the multiple cold recycling.

increase of circulatory recycling times, the range of the decay is also enlarging; in addition, when it is circulated to the third time, its Marshall stability has already decayed to the lower limit requested by the specification, while the splitting strength has not reached the operating requirement of the asphalt surface.

In order to preferably indicate the decay law of the mechanical performance of the CEACRM in the multiple cold recycling, here introduces the concept of the decay ratio of the mechanical performance. Taking the mechanical performance index after the primary recycling as the reference value, of which the difference with the later mechanical performance of the recycled mixture divided by the reference value is the decay ratio of the mechanical strength, which can also be worked out by the following equation.

$$R_{decay} = \frac{R_1 - R_i}{R_1} \times 100\% \tag{1}$$

where

R_{decay}= the strength decay ratio of the mechanical performance;

R_1= the strength value after primary circulatory cold recycling (Marshall stability: kN; splitting strength: Mpa);

R_i= the strength value after i times circulatory cold recycling (Marshall stability: kN; splitting strength: Mpa).

After data processing of test results according to the equation above, the decay ratio of the mechanical strength of the CEACRM in every cold recycling cycle was worked out, and this is shown in Table 3 in detail.

From Table 3 it is seen that, with the increase of recycling times, the decay ratio of its strength performance is presented to be the downward trend. Researches show that, the asphalt added during the process of the multiple cold recycling may form repeatedly wrapped new-aged asphalt membranes on the surface of the old material, which may become a weak surface in the bonding system of the recycled mixture, making the cohesion of the binder decline sharply. Meanwhile, the wrapping effect of added emulsified asphalt on the aggregate comes into play, under which the fine aggregate bonds together to form the aggregate micelle with a certain grain size. The increase of recycling times causes the soaring of the amount of the aggregate micelle, and then leads to the change of the skeletal structure of the whole mixture. The formation of the aggregate micelle also causes the lack of enough fine aggregate

Table 3. The decay ratio of the mechanical strength of the multiple cold recycled mixture.

Test content	Primary recycling	Secondary recycling	Tertiary recycling
Decay ratio of 40° C Marshall stability (%)	–	5.62	21.20
Decay ratio of 15° C splitting strength (%)	–	5.45	18.18

to fill into the skeletal structure, which causes that the air void of the cold recycled mixture starts to enlarge. However, because the bond force on the surface of the new-aged asphalt membrane is limited, the aggregate micelle, meanwhile, is unstable, which may be easily separated under the effect of the traffic load. Therefore, it may cause the instability of the skeleton, and then leads to the decline of the mechanical performance.

3.3 *Decay law of the water stability*

Because the cold recycled mixture is compacted and formed under normal temperature environment, the problem of its large air void is unavoidable. Because of this material characteristic, the cold recycled pavement may be easily eroded by the water and then generate damages such as the stripping of the asphalt membrane, the raveling, the pothole and so on. Accordingly, for the CEACRM surface, the water stability is similarly a significant factor that influences the road performance. The water stability of the asphalt mixture is finally indicated by the declining degree of the physical and mechanical performance of the asphalt mixture under the water-immersion condition. In this test, the decay law of the water stability is shown in the following figure.

From Figure 2 it is seen that, in the multiple cold recycling, along with the increase of recycling times, three evaluation indexes that reflect the water-resisting performance of the mixture, which are the emersion retained Marshall stability, the tensile strength ratio after the freeze-thaw cycle and the tensile strength ratio after the wetting-drying cycle, decline simultaneously, and with the increase of circulatory times, the degree of this decay is also increasing gradually, and when it is circulated to the third time, its performance index has already decayed to approach to the lower limit requested by the specification. It indicates that, with the increase of circulatory times, especially in the later period of the multiple cold recycling, the water damage of the mixture may easily occur when the mixture is in the service period.

In order to preferably indicate the decay law of the water stability of the CEACRM in the multiple cold recycling, here introduces the concept of the decay ratio of the water stability. Taking the water stability index after the primary recycling as the reference value, of which the difference with the later water stability of the recycled mixture divided by the reference value is the decay ratio of the water stability, which can also be worked out by the following equation.

$$S_{wd} = \frac{S_1 - S_i}{S_1} \times 100\% \tag{2}$$

where

S_{wd}= the strength decay ratio of the water stability;

S_1= the strength value after primary circulatory cold recycling (Marshall stability: kN; splitting strength: Mpa);

S_i= the strength value after i times circulatory cold recycling (Marshall stability: kN; splitting strength: Mpa).

After data processing of test results according to the equation above, the decay ratio of the water stability of the CEACRM in every cold recycling cycle was worked out, and this is shown in Table 4 in detail.

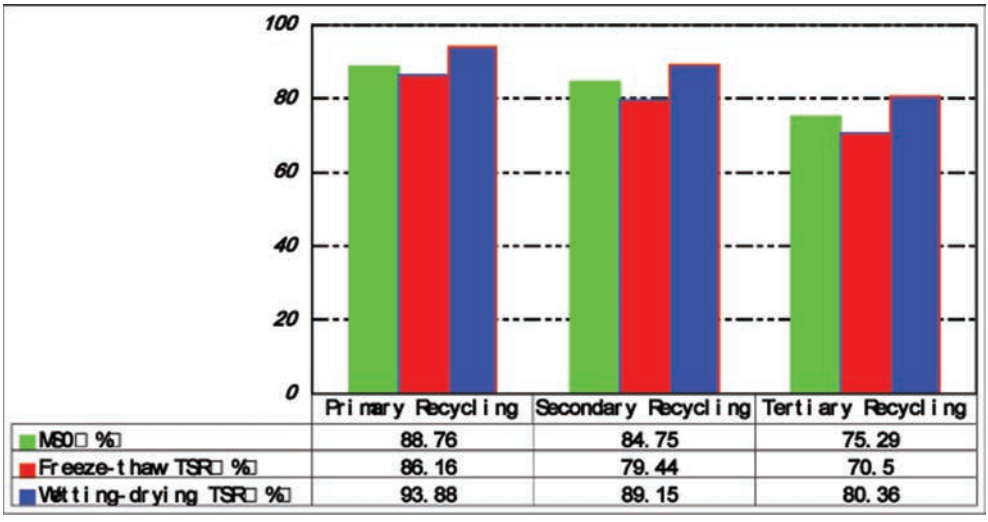

Figure 2. The varying trend of the water stability of the mixture after the multiple cold recycling.

Table 4. The decay ratio of the water stability of the multiple cold recycled mixture.

Test content	Primary recycling	Secondary recycling	Tertiary recycling
Decay ratio of the emersion retained Marshall stability (%)	–	9.02	20.81
Decay ratio of the tensile strength ratio after the freeze-thaw cycle (%)	–	7.80	18.18
Decay ratio of the tensile strength ratio after the wetting-drying cycle (%)	–	5.04	14.40

From Table 4 it is seen that, with the increase of recycling times, the decay ratio of its strength performance is also presented to be the upward trend; however, it can still meet the using requirement of the specification. The reason is that, the adding of the cement causes the decline of the sensibility of the emulsified asphalt cold recycled mixture to the water; Through the hydration reaction, to a certain degree, the cement can absorb a part of the water, while the humid environment formed by the residual water is also beneficial for the formation of the cement strength, which is somewhat helpful to the water-resisting performance of the emulsified asphalt cold recycled mixture. However, during the circulatory process from the secondary cold recycling to the tertiary cold recycling, the decay ratio of the water stability increases sharply. After the tertiary cold recycling, the water stability of the material has already been close to the critical point that can meet fundamental using requirement. The reason is that, during the process of the circulatory cold recycling, the air void of the molded specimen is enlarging gradually, which leaves enough space for the water to enter into, and the increasing water greatly influences the aggregate and the asphalt binder. Besides, the aggregate micelle in a free state is also a main factor that influences the water stability of the cold recycled mixture.

3.4 *Decay law of the durability*

For the service life of the CEACRM surface in the process of the multiple cold recycling, this study adopted four-point bending fatigue test to do the evaluation. By the fatigue test, its

Table 5. The testing result of the fatigue performance of the multiple cold recycled mixture.

Test content	Strain level (10^{-6})	Fatigue life (times)	Original stiffness modulus (Mpa)	Phase angle (deg)	Cumulative dissipated energy (kJ/m)
Primary cold recycling	100	458646	4628	23.7	34.2
	200	418562	4470	22.6	32.4
Secondary cold recycling	100	305867	3964	21.8	25.8
	200	276545	3703	20.5	21.1
Tertiary cold recycling	100	135682	3002	13.6	13.8
	200	106332	2985	10.2	9.8

Table 6. The decay ratio of the fatigue life of the multiple cold recycled mixture.

Test content	Primary recycling	Secondary recycling	Tertiary recycling
Decay ratio of the fatigue life under the strain level of 100 (%)	–	33.31	70.42
Decay ratio of the fatigue life under the strain level of 200 (%)	–	33.93	74.60

loading times at the fatigue life were worked out, which was considered to be the quantitative index to evaluate the service life of the mixture during its circulatory cold recycling period.

From the result of the fatigue performance test of the CEACRM in the multiple cold recycling in Table 5, it is seen that, along with the increase of recycling times, its fatigue performance is presented to be remarkable downward trend, and with the increase of the strain, the downward trend becomes more remarkable.

In order to preferably indicate the decay law of the fatigue performance of the CEACRM in the multiple cold recycling period, here introduces the concept of the decay ratio of the fatigue life. Taking the fatigue life after the primary recycling as the reference value, of which the difference with the later fatigue life of the cold recycled mixture divided by the reference value is the decay ratio of the fatigue life, which can also be worked out by the following equation.

$$F_{decay} = \frac{F_1 - F_i}{F_1} \times 100\% \tag{3}$$

where

F_{decay} = the decay ratio of the fatigue life;

F_1= the fatigue life after primary circulatory cold recycling;

F_i= the fatigue life after i times circulatory cold recycling.

After data processing of test results according to the equation above, the decay ratio of the fatigue of the CEACRM in every cold recycling cycle was worked out, and this is shown in Table 6 in detail.

Researches show that, the new-aged asphalt membrane and the new-aged cement paste are the stress concentration point where the fatigue failure occurs, which directly causes remarkable influences on the fatigue performance of the circulatory cold recycled mixture as a result of the increase of recycling times.

4 CONCLUSIONS

1. Through the research on the decay law of the old material on the asphalt surface it is found that, the residual value of the old material of the cold recycled asphalt pavement that has achieved the service life is still very huge.

2. The proposed decay ratio index can quantitatively indicate the decay trend of the cement emulsified asphalt in the process of the circulatory cold recycling.
3. Through the experimental research on multiple cold recycling of the cement emulsified asphalt mixture it is found that, with the increase of recycling times, its mechanical performance and its water stability decline gradually. In the later period of the multiple cold recycling, a number of performance indexes such as the mechanical performance of the mixture can not meet application requirements in the specification; the addition of the cement has declined the water sensibility of the circulatory recycled mixture, and even though its water stability can meet the application requirement in the specification, it has already been close to the lower limit in the specification, which is on the critical point where the failure occurs.
4. Through the fatigue test on the CEACRM it is found that, totally speaking, the four-point blending fatigue performance of the CEACRM is poor, and the increase of the strain level and recycling times has a great influence on the fatigue performance of the cold recycled mixture. At the same strain level, with the increase of cold recycling times, the fatigue performance is presented to be a downward trend, and in a high strain level, this trend is more obvious.
5. The results has quantitatively evaluated decay trends presented by every road performance of the CEACRM during different circulatory recycling periods, which have great guiding significance on promoting measures specifically proposed in the late period.

REFERENCES

[1] Research on the key paving technology of sustainable composite cold recycled pavement [M], Chongqing: China Merchants Chongqing Communications Research & Design Institute Co., Ltd., Scientific and technological key research project.

[2] Ministry of Transport of the PRC. Technical Specification for Highway Asphalt Pavement Recycling (JTG F41-2008) [S], Beijing: China Communications Press, 2008.

[3] Lei Huang, Xiangming Liu, Chao Lan, Huiqiang Chen, Quan Feng. The proportion design and implement of the asphalt pavement with C-ETM semi-flexible base course [J], Road Machinery & Construction Mechanization, 2008(9): 57–59.

[4] Quan Feng, Chao Lan, Lei Huang. The application of the emulsified asphalt-cement stabilized gravel semi-flexible base course material in the maintenance of the old road [J], Road Machinery & Construction Mechanization, 2008(10): 60–63.

Asphalt Pavements – Kim (Ed)
© 2014 Taylor & Francis Group, London, ISBN 978-1-138-02693-3

Investigating effect of amine based additives on asphalt rubber rheological properties

Amadou Bocoum
Civil Engineering, North Carolina A&T State University, Greensboro, NC, USA

Shahrzad Hosseinnezhad
Energy and Environmental Sustainability, North Carolina A&T State University, Greensboro, NC, USA

Elham H. Fini
Civil Engineering, North Carolina A&T State University, Greensboro, NC, USA

ABSTRACT: This paper investigates merits of introducing bio-binder and liquid Warm Mix Asphalt (WMA) additives to asphalt rubber to enhance its rheological properties. It is hypothesized that amine-based liquid additives can facilitate rubber devulcanization and speed up the release of rubber polymer into the asphalt matrix. This in turn can enhance asphalt rubber rheological properties including high temperature properties. This paper specifically focuses on high temperature properties and temperature susceptibility of the asphalt rubber modified by amine-based additives. High temperature properties were investigated by quantifying the effect of warm mix asphalt additives (Rediset and Evotherm) and bio-binder on the shear susceptibility and temperature susceptibility of asphalt rubber. Ambient crumb rubber with 10% and 15% concentrations by the weight of asphalt binder was used in this study. The rotational viscometer was used to evaluate the effect of additives on the asphalt rubber high temperature properties and pumpability. FT-IR analysis was studied to determine presence of devulcanized rubber polymer inside the asphalt matrix. It was found that all three additives reduced the viscosity and improved the pumpability significantly. In addition, the effect of additives found to be more significant when higher percentages of rubber were used. Additives with higher perecentages of amine compunds found to be more effective in devulcanizing rubber.

Keywords: crumb rubber; devulcanization; asphalt binder; bio-binder; warm mix additive

1 INTRODUCTION

Asphalt binder resistance to deformation at intermediate temperature and hot summers significantly affects overall pavement resistance to rutting deformation under heavy traffic at high temperature. Such deformation is more pronounced during the summer season when the asphalt reaches temperatures closer to its softening point. Recent studies indicate that when the air temperature is 30°C, the surface temperature of asphalt can reach up to 50°C thus reaching or exceeding the softening point of asphalt [1]. Also, the softening point of asphalt can be correlated with its viscosity: asphalt with a higher softening point tends to have higher viscosity and higher resistance to deformation [1]. To enhance asphalt resistance to deformation, researchers have used various modifiers and additives such as Styrene Butadiene Styrene (SBS) block copolymer, Ethylene Vinyl Acetate (EVA), Polyvinyl Acetate (PVA), Styrene Butadiene Rubber (SBR) and natural rubber latex [2, 3]. The last two of these additives have been identified as constituents of crumb rubber, a recycled rubber produced from scrap tires [4]. Crumb Rubber (CR) is produced by removing steel and fluff and using

a granulator and/or cracker mill (aided by cryogenic or mechanical means) to reduce the size of the tire particles [5]. The rubber particles are then sized by passing them through a set of sieves. It has been found that the application of rubber in asphalt can enhance high temperature properties and rutting resistance of asphalt pavement while improving asphalt pavement skid resistance, noise and construction cost [6].

Crumb Rubber Modified asphalt (CRM) has two diffrent effects on the asphalt matrix: one can be characterized as filler effect and is the impact of of rubber particles or physical filler effect and the second one is due to the release of rubber polymer into the asphalt matrix [7]. The physical effect of rubber is the main player in increasing rubber visosity and in some case reduce CRM pumbability and the resulting mixture's workability which makes its application problematic. Such problems include the reduction in asphalt workability and the difficulty of pumping asphalt containing high percentages of crumb rubber [8]. It has been documented that interaction environment could significantly affect devulcanization of CRM and consequencly releasing backbone polymer of rubber. This phenomenon reduces the viscosity of asphalt and enhances its physical properties [9]. It has been well documented that the interaction of amine-based compounds with rubber particles at high temperature could significantly speed up devulcanization [9]. In addition, existence of alkali metal such as sodium or potassium within the medium can facilitate the breakage of the cross-linkages in the rubber particles releasing the rubber polymer. However, it has been reported that this process is highly sensitive to temperature and heating rate; as such, thermal cracking of rubber polymer could occur due to excessive heating [9, 10].

Ever since the sixties when Charles McDonald employed the dry processes to produce a rubberized asphalt mixture named Overflex TM, a number of researchers have studied the benefits of applying Crumb Rubber Modified (CRM) binders into asphalt pavements [11]. It has been well documented that rubber asphalt shows better resistance to rutting. Rutting is one of the common pavement distresses which can occurs due to traffic loading, especially under hot climatic conditions [12]. It has been reported that the rutting resistance parameters of CRM binders improves as the CRM percentages increases. Introducing some additives to CRM has been studied. Golzin and his collaborator used Poly Phosphoric Acid (PPA) to evaluate the effect of CR on the performance of unmodified asphalt binder at different temperature; they showed that by increasing the PPA content, the values of softening point was increased while the penetration grade was decreased. Furthermore, it has been reported that increasing the PPA content from 1.5% to 2% could improve the binder performance at high temperature [13]. Their test results showed that adding crumb rubber, reduced penetration, temperature susceptibility, ductility and increased the softening point, elastic recovery and adhesion [13].

Wang et al. measured viscosity of several asphalt rubber at different temperatures using a rotational viscometer; these researchers found that the addition of crumb rubber can greatly increase the binder viscosity, and that in order to meet the Superpave maximum viscosity threshold of 3.00 Pa.s, CR asphalt needs to be heated to higher temperature. In addition, it was found that to maintain same viscosity, one has to continuously increase the mixing temperature as the percentages of rubber increase. As such, when 15%, 20% and 25% crumb rubber were introduced to the base asphalt (viscosity > 3.0 Pa.s at 135°C), the temperature had to be increased from the original 135°C to 147°C, 162°C and 174°C, respectively, in order to maintain viscosity below the 3.0 Pa.s threshold [14]. Therefore, the mixing temperatures and compaction temperatures of rubberized asphalt binders were much higher than those of non-modified asphalt mixtures. This in turn, can cause further challenges in the construction schedule as well as increase the fuel consumption used for heating purposes [14]. More importantly, it can damage the rubber structure and cause disintegration of rubber particles [15].

In this paper, certain amine-based liquid additives are used to facilitate rubber asphalt interaction so that the dramatic increase in viscosity due to introduction of rubber is prevented. Amine compounds facilitate release of rubber polymer into asphalt, thus softening the overall asphalt-rubber matrix. As a result, the viscosity threshold could be met at relatively lower temperatures. This not only prevents disintegration of rubber particles due to reduction in

the mixing temperature but also facilitates pumping and hence allows for application of higher percentages of rubber into the asphalt.

In this paper bio-binder is used as an amine based additives. Bio-binder is produced under the thremechemichal conversion of swine manure. The efficiency of this process is 70% meaning a swine farm with 10,000 hogs per year could produce 5,000 barrels of crude oil per year [16]. The estimated cost for bio-binder production using this method is only estimated to be $0.54/gallon while the cost of petroleum-based asphalt is reported to be $2.5/gallon [17]. Chemichal analysis of bio-binder showed that it has high amine content [18]. Rheological properies of asphalt binder improved by introdicing 5–20% of bio-binder [19]. By comparision of the price of petroleum based binder with bio-binder, considering the fact that bio-binder has higher amine content and improvment in rheologichal properties of asphat binder, bio-binder has been selected as one of the amine based additives.

In this paper merits of application of bio-binder and liquid warm mix amine based additives to enhance asphalt rubber workability by reducing its shear viscosity at high temperatures is investiagted [18–20]. It is expected that introduction of such additives can produce rubberized asphalt mixtures with desirable properties at lower mixing temperature. Therefore, this paper evaluates the effects of these three specific amine based additives on high temperature properties of CRM asphalt by conducting selected Superpave binder tests.

2 MATERIALS AND METHODS

2.1 *Asphalt binders*

The base binder for this study was PG64-22 which is commonly used as an asphalt binder in the state of North Carolina.

2.2 *Crumb Rubber (CR)*

Crumb rubber is produced by mechanical shredding at the ambient temperature. The crumb rubber was provided by re-Rubber LLC of Ontario, Canada. Table 1 shows the grading of the rubber particles and has 200-80 mesh size.

The rubber characteristics are given in Table 1. The asphalt rubber was produced in the laboratory incorporating an ambient CRM source at two percentages of 10% and 15%, (by the weight of asphalt binder) into commonly-used PG64-22. The blending of the CRM with the base asphalt (PG64-22) was done mechanically using a 1600 rpm drill equipped with a mixing blade. The CRM (200-80 mesh) was gradually poured into the PG64-22, as the shear was conducted at 250°C by the usage of a hot plate for 30 minutes, following California Department of Transportation specification. The drill speed was maintained at 800 rpm, and the blade on the mixer was completely submerged into the sample to prevent the whipping of air into it and subsequent bubbling. The same procedure was used for both rubber concentrations.

Table 1. Crumb rubber gradation.

Sieve no.	mm	Weight retained	Individual % retained	Cumulative % passing
80	0.177	42	41.50%	58.50%
100	0.149	13.7	13.60%	44.90%
120	0.125	16.5	16.30%	28.60%
140	0.105	13.9	13.70%	14.80%
170	0.088	7.2	7.10%	7.70%
200	0.074	7.8	7.70%	0.00%
Pan		3.1	0.00%	
Total		104.2	100.00%	

2.3 *Amine based additives*

Three amine-based liquid additives were investigated in this study. These include Bio-binder, Evotherm and Rediset. Bio-binder was produced in NC A&T University's Sustainable Infrastructure laboratory and Evotherm and Rediset were provided by MeadWestvaco (MWV) and Akzonobel, respectively. These additives were added to the rubber asphalt at the dosages recommended by manufacturers. Bio-binder was added at 5% and 10% dosages by weight of asphalt binder to create the bio-modified binder. Accordingly, Evotherm and Rediset were added at dosages of 0.5% and 1.5% to the rubberized asphalt binders, respectivly [21].

The bio-binder was derived from swine manure manufactured at the NC A&T farm. It was produced from the thermochemical conversion of swine manure to bio-oil followed by distillation and filtration [20]. In this method, the animal waste is charged in the reactor. Nitrogen gas is used as a processing gas to purge the residual air in the reactor three times and the reactor is heated up to the setting temperature which is maintained at a constant level for a specific time. After the reaction is complete, the reactor is rapidly cooled down to room temperature using a recycled ice-water cooling coil. The gas is then released from the autoclave reducing the pressure in the autoclave to atmospheric pressure. The sticky residue is then separated from the aqueous solutions by filtration followed by polymerization and vacuum distillation to produce bio-binder.

2.4 *Viscosity measurement*

To study effects of rubber and various amine based additive on rheological properties of asphlat binder as well as pumpability, each rubberized binder sample (un-aged) was tested using Brookfield viscometer following ASTMD4402 specification to evaluate its viscosity, and high temperature properties. Viscosity was measured at four different temperatures (105°C, 120°C, 135°C, 150°C), and six different speeds (rpm) (5, 10, 20, 25, 50 and 100). A smooth spindle SC4-27 was used for measurements. The testing specimen was prepared by pouring 10.5 g of each material into an aluminum chamber. At each temperature, the reading was recorded after the specimen was preheated for 30 minutes.

2.5 *Temperature susceptibility*

Temperature susceptibility is a measure of variation of asphalt binder viscosity with temperature change [22]. Follwing Eq. (1) has been commonly used to calculate the Viscosity-Temperature Susceptibility (VTS) [23].

$$VTS = \frac{[\log(\eta T_2)] - \log[\log(\log(\eta T_1)]}{\log(T_2) - \log(T_1)} \tag{1}$$

T_1 and T_2 are the temperatures of the binder at known points; ηT_1 and ηT_2 are the viscosities of the binder at the same known points (cP). The dimension of the VTS is directly proportional to the temperature susceptibility of the binder.

2.6 *Shear susceptibility*

The rate of change in viscosity with the shear rate is called Shear Susceptibility [24].

The shear susceptibility or also known as the shear index is determined by calculating the slope of the line formed by a log of rotational speed versus the log viscosity graph using Eq. (2)

$$SS = \frac{\log(Viscosity)}{\log(speed)} \tag{2}$$

2.7 *Attenuated Total Reflectance Fourier Transform Infrared Spectroscopy (ATR-FTIR)*

A FTIR spectrometer, Shimadzu, 1.30(2005) single reflection zinc selenide prism was used in transmission mode to acquire the spectra of asphalt samples in wave-numbers ranging from 4000 cm^{-1} to 500 cm^{-1}. The prism was cleaned with methylene chloride and back ground spectrum was taken. To consider the effect of dissoltion part of rubber, before each measurment, the asphalt samples were dissoved in methylene chloride, fitrated to separate the rubber particles and then dried to make sure removal of solvent.

3 RESULTS AND DISCUSSIONS

The influence of the amine-based additives (Rediset, Evotherm and Bio-binder) as well as rubber concentration, temperature and shear rate on viscosity of modified and non-modified rubber asphalt was investigated. Figures 1a and 1b show the amount of viscosity change with the increase in temperature for the rubber asphalts at the two different rubber concentrations. As it can be seen, the viscosity of all specimens decreases with the increase in temperature. However, the change in viscosity is more significant in rubber asphalt compared to that for control asphalt. It was also shown introduction of 10% Bio-binder could compensate the stiffening effect of the rubber. As such the blends with both 10% and 15% rubber with 10% bio-binder showed significant improvemnet in pumpability.

In addition, the effects of the three additives on rubber asphalt are shown in Figure 2. It can be observed that the effect of additive on viscosity change is more pronounced in 15% rubber dosage compared to 10% rubber cases. Furthermore, 10% bio-binder was found to be most effective in reducing viscosity.

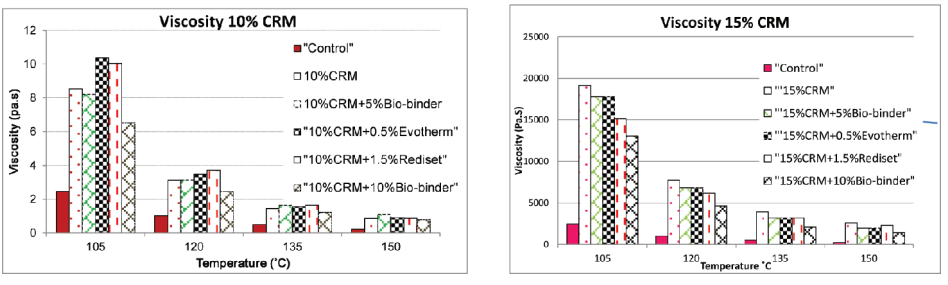

Figure 1. a) (10% CRM) and b) (15% CRM). Viscosity vs. temperature for control, 10% and 15% CRM, with WMA at 10 rpm.

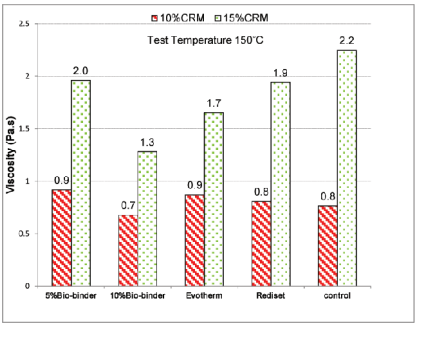

Figure 2. Viscosity comparisons of the CRM at the two concentration levels with the different WMA, and 150°C test temperature.

It was also found that the viscosity at 150°C was increased between 100% and 214.28% by increasing the rubber content from 10 to 15%. The test temperature was found to be the most dominant factor affecting asphalt rubber viscosity. However, it should be noted at all temperatures (105°C to 150°C) the viscosity was below the Superpave specification threshold (maximum asphalt binder viscosity no greater than 3 Pa.s at 135°C) designated to ensure mixture workability.

3.1 *Viscosity temperature susceptibility*

Figures 4a and 4b; are a graphical plot of Log (temperatures) versus Log (Log (viscosity)) for the control binder, 10, 15% CRM binder, with and without additive. It can be observed that the control binder has higher slope than all the CRM binder at different rubber concentration level with or without additive, as the results showed the temperature susceptibility of control binder was reduced by incorporating the additives. Also Figure 3a shows that the 10% CRM binder with Evotherm and Bio-binder has the same slope as the 10% CRM binder without any additive while the slope found to be lower than 10% CRM binder with Rediset. The same trend holds true for the 15% CRM binder. Consequently, it can be stated that with the incorporation of amine-based additives and Bio-binder into CRM binder, one can achieve higher rubber concentration in rubberized asphalt while reducing the modified asphalt temperature susceptibility.

3.2 *Shear susceptibility*

The shear susceptibility is illustrated in Figure 4a for 10% CRM and Figure 4b for 15% CRM which show plots of log (shear rate) versus Log (viscosity) at 150°C temperature. From the

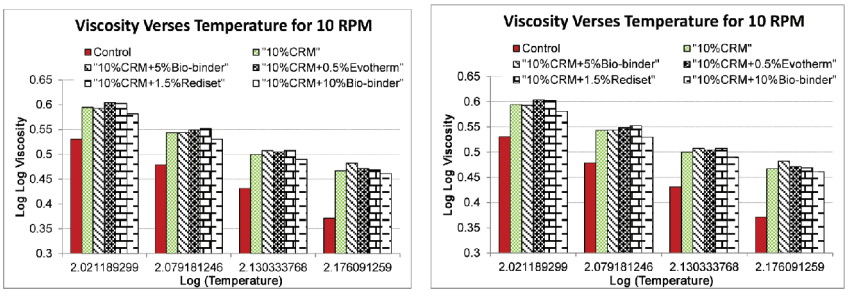

Figure 3. a) (10% CRM) and b) (15% CRM). Viscosity Temperature Susceptibility (VTS) for CRM with additives and bio-binder at 150°C.

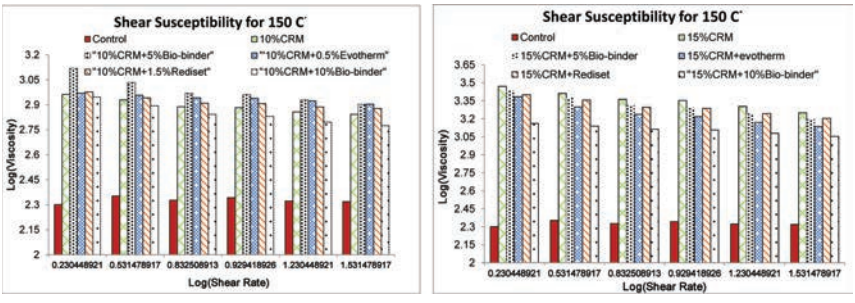

Figure 4. a) (10% CRM) and b) (15% CRM) Shear Susceptibility (SS) for CRM with additives and bio-binder at 150°C.

analysis of Figure 4, it can be seen that the shear susceptibility of the control binder is considerably reduced by modifying it with bio-binder and rubber. Furthermore, it is seen that the higher is the rubber concentration; the lower is the shear susceptibility. This can be due to the chemical interaction of additive, Bio-binder, and the rubber particles with the control binder.

3.3 *FT-IR analysis*

To analyze effect of additives and presence of polymer in asphalt matrix, characterization of molecular structure was done using Fourier Transform Infrared Attenuated Total Reflectance Spectroscopy (FTIR-ATR). This technique operates the Mid-Infrared (MlR) range, where all organic compounds interact with infrared radiation (4000 cm^{-1} to 400 cm^{-1}) providing direct information about the specific elements in the sample, as well as their molecular structure and chemical composition. In this method, total internal reflectance of infrared light in a non-absorbing prism is used. Contact of absorbing substances with the prism surface will attenuate the internally reflected light and provides an infrared absorption spectra, corresponding to a spectra recorded if the light passed through the surface layer of the material [25]. To remove the filler effect of rubber from devulcanization effet, all the samples dissolved in methylene chloride and rubber particles separated by filteration. To conduct the test, after removing the solvent, thin layers of each specimen were applied on top of a Zinc Selenide (ZnSe) ATR prism. It was shown that FTIR analysis can be used to monitor appearance of new molecules from devulcanized rubber inside the asphalt which is known as "capture presence of rubber" on the IR spectra.

For investigation of the effect of amine compounds on devulcanization of the rubber particles, neat asphalt and CRM samples with three different types of addtive were tested. Figures 5a, 5b and, 5c compare the spectra for 15% rubber without additive (control), 15% CRM with three amine additives (1.5% rediset, 0.5% Evotherm and 10% bio-binder). Figure 6 is the spectra for neat asphlat and crumb rubber asphalt without additive.

The main polymer components of crumb rubber are Nature rubber, Butadiene styrene rubber and Cis-butadiene Rubber [4]. Each of these polymers has special related peaks, these

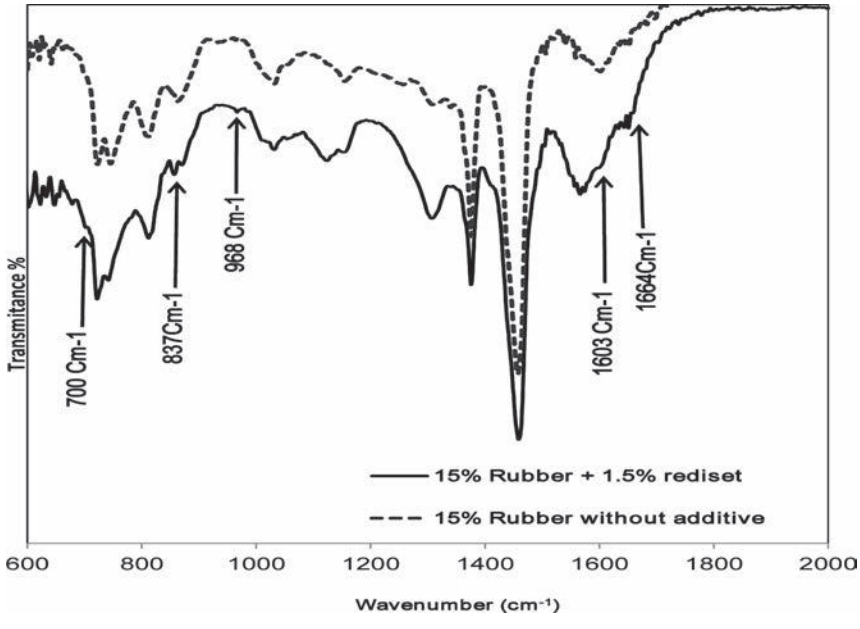

Figure 5a. FT-IR spectra of 15% rubber + 1.5% rediset.

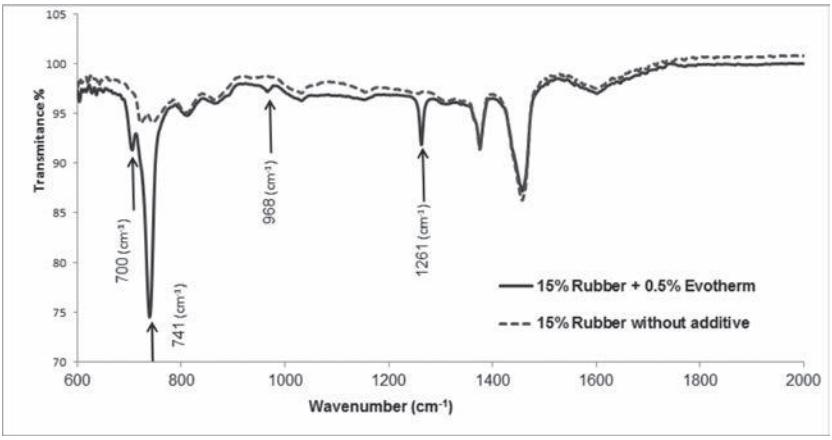

Figure 5b. FT-IR spectra of 15% rubber + 0.5% evotherm.

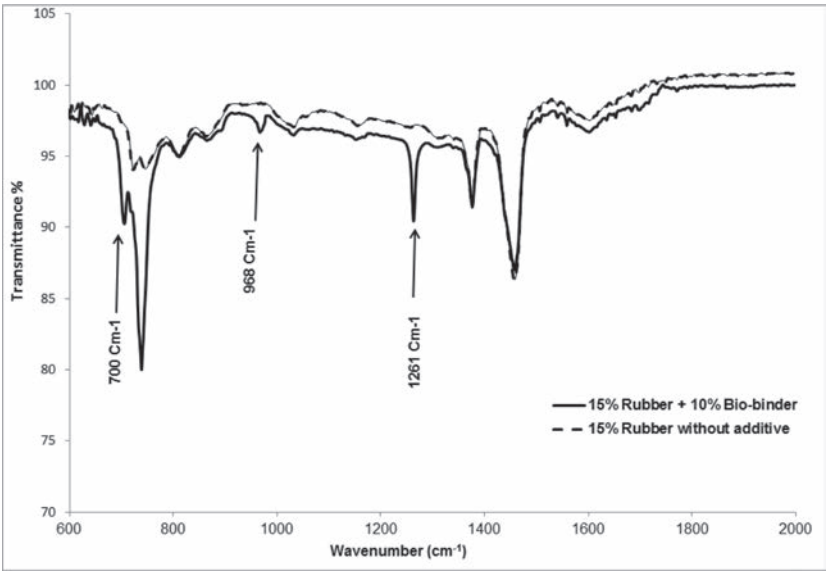

Figure 5c. FT-IR spectra of 15% rubber + 10% bio-binder.

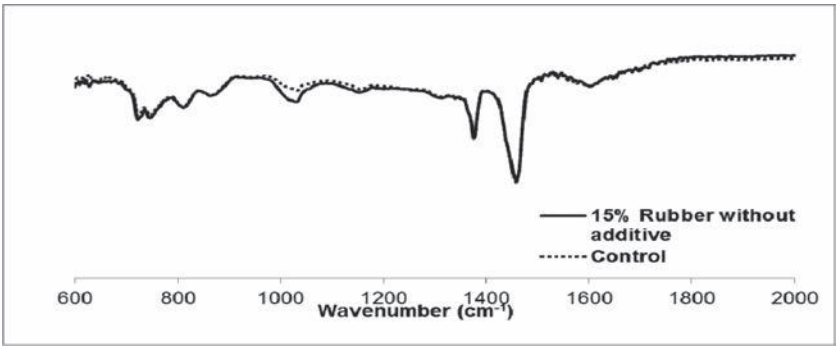

Figure 6. FT-IR spectra of 15% rubber without additive.

spectra helps to better understand devulcanization of rubber and releasing the polymer to the asphalt matrix. The presence of the peak around 968 cm^{-1} is attributed to the trans and vinyl double bond out-of-plane C-H bending of poly butadien, this peak was observed in all three addtives [26].

One of the dominant infrared peaks is due to the out-of-plane aromatic C-H deformation at 700 cm^{-1} which indicates the prsence of poly styrene butadiene rubber. This peak was appeared in the three additive [27]. Other significant peak is related to the aromatic ring breathing mode at 1,603 cm^{-1}, this peak was appeared in samples containing Rediset and it is an indication of releasing Styrene butadiene polymer.

Appearance of a peak in1664 cm^{-1} for the C=C stretch and 837 cm^{-1} is related to =C-H out-of-plane wag for poly isoprene (natural rubber backbone) which was observed in the sample prepared with rediset [26, 27].

Figure 6 represent the spectra for crumb rubber modified asphalt without any additives. It was clear that there is not any siginificant differences with neat asphalt spectra and rubber modified one. This spectra is the witness for devulcanization of rubber to realse polymer in the asphlat matrix by application of amine based compounds.

4 SUMMARY

This paper investigates effect of amine-based additives on the viscosity of asphalt rubber. It was shown that the viscosity increases with the increase of the percentage of rubber in asphalt binder. However, when amine-based additives were introduced, the viscosity was reduced significantly. It can be observed that the asphalt rubber with Rediset has the lowest viscosity at 10% rubber concentration, followed by Evotherm and bio-binder. At 15% rubber concentration level, asphalt rubber with 10% bio-binder showed the lowest viscosity followed by Evotherm and Rediset. Considering that reduced viscosity is one of the main factors affecting the pumpaing and workability, the additives used in this study could be promising candidates for enhancing the workability of asphalt rubber. This is important because reductions in viscosity can allow for reduction of mixing and compaction temperature of asphalt rubber. It has been reported that, high temperature exposure of asphalt rubber leads to rubber degradation [28]. In addition, utilizing such additives can facilitate the application of higher percentage of rubber in asphalt without exceeding viscosity threshold. This paper demonstrates that introducing the aforementioned additives to rubber asphalt mixes can significantly improve the Viscosity Temperature Susceptibility (VTS) and shear susceptibility of binders, thereby enhancing the high temperature performance of asphalt binders.

FT-IR studies revealed devolcanization of rubber inside the asphlat matrix by releasing polymer component. From this studies, the trace of poly styren butadien was seen when either of the additives were intoduced. But trace of natural rubber was captured just by rediset. The study results showed significant imporvment in viscosity of 15% CRM asphalt when bio-binder and evotherm were introduced. This in turn promotes application of bio-based additives with high amine content to faciliate devulcanization while improving CRM pumbpability.

By considering the effect of bio-binder on devulcanization of rubber, our future work would be based on replcement of bio-binder with regular asphalt binder and mixing with crumb rubber to improve binder performance. This approach will have benefit to pavement industry including reduction in cost of asphalt production while increasing the perfomance of bio-binder on road construction.

ACKNOWLEDGMENTS

This research is sponsored by the National Science Foundation (Award No: 1150695) and NCHRP IDEA Project 171. The authors would like to acknowledge the invaluable assistance provided by Daniel Oldham and Farrokh Mirzaefard of North Carolina A&T State

University. The contents of this paper reflect the view of the authors, who are responsible for the facts and the accuracy of the data presented. This paper does not constitute a standard, specification, or regulation.

REFERENCES

[1] Ping, L., and K. Jiang, H. Li, *High Temperature Stability of Asphalt Mixture with influence styrene butadiene styrene.* Journal of Procedia-social behavioral sciences, 2012. 43: p. 842–848.

[2] Zhao, Y.G., Fan; Xu, Jing; Jin, Jing, *Analysis of aging mechanism of SBS polymer modified asphalt based on Fourier transform infrared spectrum.* Journal of Wuhan University of Technology-Mater. Sci. Ed., 2010. 25(6): p. 1047–1052.

[3] Baochang Zhanga, M.X., Dewen Zhanga, Huixuan Zhanga, Baoyan Zhang, *The effect of styrene–butadiene–rubber/montmorillonite modification on the characteristics and properties of asphalt.* Construction and Building Materials, 2009. 23(10): p. 3112–3117.

[4] Fan, P. and C. Lu, *A Study on Functionalization of Waste Tire Rubber Powder Through Ozonization.* Journal of Polymers and the Environment, 2011. 19(4): p. 943–949.

[5] Takallou, H.B.T., Mojie B., Recycling tires in rubber asphalt paving yields cost, disposal benefits. Elastomerics, 1991. 123: p. 19–24.

[6] MacLeod, D.H., Susanna; Wirth, Ryan; Zanzotto, Ludo, *Study of crumb rubber materials as paving asphalt modifiers.* Canadian Journal of Civil Engineering, 2007. 34(10): p. 1276–1288.

[7] Jeong, K.-D.L., Soon-Jae; Amirkhanian, Serji N.; Kim, Kwang W., *Interaction effects of crumb rubber modified asphalt binders.* Construction and Building Materials, 2010. 24(5): p. 824–831.

[8] Thodesen, C., K. Shatanawi, and S. Amirkhanian, *Effect of crumb rubber characteristics on crumb rubber modified (CRM) binder viscosity.* Construction and Building Materials, 2009. 23(1): p. 295–303.

[9] John B. Macleod, M.E.M., Ronald D. Myers, Peter Nicholson, *Rubber devulcanization process*, 1995, Exxon Research And Engineering Company: USA.

[10] Van Duin; Martin, N.J.W.M., Verbruggen; Miriam A.L., Van Der Does; Leen, *Method for devulcanizing rubber with an amine*, in *Grant*March 27, 2002.

[11] U. Bahia, H. and R. Davies, *Effect of Crumb Rubber Modifiers CRM on Performance Related Properties of Asphalt Binders.* Journal of the Association of Asphalt Paving Technologists, 1994. 63.

[12] Carl. T, F.X., S.N. Amirkhanian, *Modeling viscosity behavior of crumb rubber modified binders.* Journal of Construction and Building Materials, 2009. 23: p. 3053–3062.

[13] Golzin Y, a.H.S.M., Improving the performance of Crumb Rubber bitumen by means of Poly Phosphoric Acid (PPA) and Vestenamer additives. Journal of Construction and Building Materials, 2011. 25: p. 3108–3116.

[14] Hainian. W, Z.D., Z. You, D. Cao, Effect of warm mixture asphalt (WMA) additives on high failure temperature properties for crumb rubber modified (CRM) binders. Journal of Construction and Building Materials, 2012. 35: p. 281–288.

[15] Abdelrahman, M., Monitoring the interaction of asphalt with crumb rubber modifier (CRM), in Engineering Research and Innovation Conference2011: Atlanta, GA.

[16] Zhang, Y. *Converting Swine Manure to Oil: U of I Makes the Process Faster, Easier*. MARCH 23, 2004 [cited 2013 September]; Available from: http://news.aces.illinois.edu/news/converting-swine-manure-oil-u-i-makes-process-faster-easier.

[17] Transportation, N.Y.D.o. [cited 2014 February]; Available from: https://www.dot.ny.gov/main/business-center/contractors/construction-division/fuel-asphalt-steel-price-adjustments.

[18] Aurangzeb, E.H.F.E.W.K.A.S.M.B.Z.Y.H.O.Q., *Chemical Characterization of Biobinder from Swine Manure: Sustainable Modifier for Asphalt Binder.* Journal of Materials in Civil Engineering, 2011. 23: p. 1506–1513.

[19] Fini, E.H.A.-Q., Imad L.; You, Zhanping; Zada, Boubacar; Mills-Beale, J., *Partial replacement of asphalt binder with bio-binder: characterisation and modification.* International Journal of Pavement Engineering, 2011: p. 1–8.

[20] Fini, E.H.O., Daniel J.; Abu-Lebdeh, Taher, *Synthesis and Characterization of Bio-Modified Rubber (BMR) Asphalt: A Sustainable Waste Management Solution for Scrap Tire and Swine Manure.* Journal of Environmental Engineering, 2013: p. 130712223113003.

[21] Turner, Z.A.A.B.A.M.a.F., Influence of Warm-Mix Additives and Reduced Aging on the Rheology of Asphalt Binders with DifferentNatural Wax Contents. A.M.ASCE2, 2011.

[22] P.M. Claudy, J.M.L., D. Martin, J.P. Planche, *Thermal behavior of asphalt cements, Thermochimica Acta.* Thermochimica Act, 1998. 324: p. 203–213.
[23] Rasmussen, R.O., L. Robert L., and C. George K., *Method to Predict Temperature Susceptibility of an Asphalt Binder.* Journal of Materials in Civil Engineering, 2002. 14: p. 246–252.
[24] Roberts, F.L., P.S. Kandhal, E.R. Brown, D.Y. Lee, and T.W. Kennedy, *Hot Mix Asphalt Materials, Mixture, Design, and Construction*, in *National Asphalt Pavement Association Research and Education Foundation* 1996: Lanham, Md.
[25] Karlsson, R., U. Isacsson, and J. Ekblad, *Rheological characterisation of bitumen diffusion.* Journal of Materials Science, 2006. 42(1): p. 101–108.
[26] J-F. MASSON, L.P., P. COLLINS, *Rapid FTIR method for quantification of styrene-butadiene type copolymers in bitumen.* Journal of Applied Polymer Science, 2001. 79(6): p. 1034–1041.
[27] O'Keefe, J.F. *Identification of polymers by IR spectroscopy*. Jun 1, 2004; Available from: http://www.thefreelibrary.com/Identification+of+polymers+by+IR+spectroscopy.-a0119376722.
[28] Ghavibazoo, A., A. Magdy, and R. MohyElDin, *Mechanism of Crumb Rubber Modifier (CRM) dissolution into asphalt matrix and its effect on final physical properties of CRM binder.* 92th Annual Meeting of the Transportation Research Board 2013.

This page intentionally left blank

Microstructural characterization and micromechanics of asphaltic materials—II

This page intentionally left blank

Asphalt Pavements – Kim (Ed)
© 2014 Taylor & Francis Group, London, ISBN 978-1-138-02693-3

Micro-scale investigation of oxygen diffusion on bitumen surfaces

Prabir Kumar Das, Niki Kringos & Björn Birgisson
Division of Highway and Railway Engineering, KTH Royal Institute of Technology, Stockholm, Sweden

ABSTRACT: This study investigates the evolution of microstructures due to oxygen diffusion on bitumen surface and its effect on bulk properties utilizing Atomic Force Microscopy (AFM) and Differential Scanning Calorimetry (DSC). The bitumen specimens were conditioned in four different modes: both light and air, only air but no light, only light but no air and neither light nor air, for 15 and 30 days. From the AFM investigation after 15 and 30 days of conditioning period, it was found that the percentages of microstructure on the surface reduced with ageing. The DSC heating scan showed that the amount of wax remains constant even after the systematic conditioning. Interestingly, during the cooling cycle, crystallization of wax molecules started earlier for the oxidized specimens than the non-oxidized one. The analysis of the obtained results indicated that the oxidation created a thin film upon the exposed surface, which acts as a barrier and creates difficulty for the wax induced microstructures to float up at the surface. From the DSC analysis, it can be concluded that the oxidation product induced impurities in the bitumen matrix, which acts as a promoter in the crystallization process.

Keywords: Wax induced microstructure, diffusion, bitumen, Atomic Force Microscopy

1 INTRODUCTION

The viscoelastic behaviour of bitumen plays a prominent role in asphalt mixture durability, such as cracking (thermal or traffic induced) and raveling. Being an organic substance, with time its viscoelastic property can deteriorate due to exposure to the environment, which is known as age hardening. Oxidative ageing, which takes place within the top layer of exposed bitumen surface, can be noted as a dominant part in the ageing process of bitumen in asphalt mixtures [1]. Ageing involves chemical and/or physical property changes that usually make the bitumen harder and more brittle, consequently increasing risks of premature pavement failure.

The existing accelerated ageing tests [2], make use of the time-temperature superposition principle in which artificially severe conditions are created to replicate the ageing process. Aging of bitumen by using high temperature and pressure is, however, a fundamentally different process from long-term aging at (normal) lower temperatures and (ambient) pressures. So, an investigation on accelerated test residue bitumen might not give the true information of what happens due to ageing in the field [3]. To understand the actual changes of bitumen properties due to the slow oxidation process, it is important to investigate the bitumen through a controlled test environment. For this reason, and given recent advanced, the Atomic Force Microscopy (AFM) has been employed in this study.

AFM is an imaging tool that can deliver the surface topography, stiffness and tackiness information of materials [4]. AFM has gaining in popularity over the past years for examining bitumen samples [5–13] because of relatively simple sample preparation and operates under ambient conditions. While operated in the simplest mode, the tapping mode, imaging of the surface topology and phase signal information can be obtained. Topography image can provide insight on the phase separation information and any presence of topography

features, whereas phase signal can indicate areas that differ in stiffness and tackiness. One specific focus point of several studies has been the appearance of structures, named 'bees' given their black and yellow stripes under the AFM. The earliest studies mainly explained the appearance of these structures on the 'asphaltene' phase in bitumen (i.e. the phase that is not soluble in n-heptane and is often referred to as the more heavy and polar molecules in the mixture) [6,7]. Recent studies have, however, conclusively shown that the bee structures are directly linked to the presence of crystalline fractions in the material, often referred to as the waxes [9–13]. The presence of such microstructures will dictate, if not heavily influence, the macro scale properties of bitumen, such as stiffness, viscoelasticity, plasticity, adhesion, fracture and healing characteristics. Having a better understanding of how these microstructures are evolved with ageing and related to the resulting mechanical response thus opens a large potential for tailoring and enhancing the long term properties of asphalts.

Any chemical changes due to the surface oxidation process may have some effect on the crystalline fractions present in bitumen. To investigate such effects, Differential Scanning Calorimetry (DSC) can be a useful tool. DSC is the thermo-analytic method that can determine any physical changes in bitumen associated with heat exchange. If there are any crystalline molecules present in the bitumen then during the heating scan these molecules needs more heat to melt and thus once the bitumen absorb extra heat and be cooler than the furnace, causes the flow curve point down which is known as endothermic event. The reverse logic applies to exothermic events where energy is released. Since AFM is only applicable for the surface investigation, to study the surface ageing effect on bulk crystalline fractions, DSC has also been employed.

In this paper, the oxygen diffusion on bitumen surface has been investigated utilizing the AFM and the DSC, where the evolutions of microstructures on the bitumen surface due to the oxidation were studied.

2 EXPERIMENTAL

An unaged and unmodified straight run bitumen was used in this study provided by Nynas AB, Sweden. The physical-chemical properties of this bitumen are presented in Table 1. The penetration, softening point, dynamic viscosity, kinetic viscosity and Fraass breaking point were measured in accordance with the European standards EN 1426, EN 1427, EN 12596, EN 12595 and EN 12593, respectively. The chemical characterization (SARA analysis) of bitumen was done by using the thin-layer chromatography with flame ionization detection (TLC-FID) technique.

Specimen preparation: Using material from the top of a can is not recommended for a representative sample as more aging occurs at the surface. Therefore, the bitumen was first stirring

Table 1. Bitumen properties.

Property	Value
Physical properties	
Penetration (25°C, 0.1 mm)	86
Softening point (°C)	46.4
Dyn. Viscosity @ 60°C	96
Kin. Viscosity @ 135°C	181
Fraass breaking point (°C)	–16
DSC Wax content (%)	6.2
Chemical components	
Saturates (%)	11
Aromatics (%)	55
Resins (%)	19
Asphaltenes (%)	15

properly at 120°C to avoid such bias. For AFM scanning, approximately 30 mg of hot liquid bitumen was carefully placed on a rectangular aluminum plate (10 mm × 10 mm × 1 mm) and kept for 5 minutes on a hot plate at the same temperature to allow the bitumen to spread out and create a smooth surface. In the preparation process, the specimens were left horizontally and covered to prevent dust pick-up. During the preparation, the specimen surfaces were exposed to the air. Since all specimens went through same preparation process, this minor oxidation during specimen preparation can be ignored.

Right after the specimen preparation, specimens were exposed to the following four different levels of conditioning: both light and air, only air but no light, only light but no air and neither light nor air, for 15 and 30 days. One specimen was kept unconditioned to give a reference measure.

The light source used in this study was normal commercial fluorescent lamp, which does not emit ultraviolet radiations. Since argon is one of the noble gas and heavier than the ambient air, it was used to create an oxygen free (no air) environment. To create oxygen free environments, specimens were placed in glass containers in which argon gas was introduced via an inlet. In this process, argon gas was allowed to spread in the container until the air was pushed out completely leaving for an airtight environment. For the dark (no light) conditioning, specimens were placed inside containers, carefully wrapped in multiple layers of aluminum foil and kept in a dark place.

After 24 hours, the unconditioned bitumen specimen was scanned with the AFM to investigate the topography features. The 15 and 30 days conditioned specimens were investigated by using AFM and the percentage of observed microstructures at the surface compared to investigate the ageing propensity. Thereafter, the 30 days conditioned specimens were investigated furthermore utilizing DSC and compared to study any change of the crystalline fractions due to the systematic conditioning. More details on AFM and DSC will be given in the following sections.

2.1 *Atomic Force Microscopy (AFM)*

In this study, AFM (using a VECO Dimension 3100 device) was used for the microstructural characterization of the conditioned specimens. The scanning of size 50 × 50 μm was carried out in tapping mode at room temperature (25°C) and scan rate was 1 Hz. In this process, cantilevers with spring constant of 40 N/m were used at the resonance frequency of 300 kHz, with a minimum of damping of the amplitude signal.

Depending on the type, source, time-temperature history of bitumen, microstructures may be observed (Fig. 1a) on the bitumen surface from the AFM scans [5–13]. To quantify these microstructures, the open source Gwyddion 2.3 software was utilized. For this, at first the AFM topography image was analyzed using a Laplacian of Gaussian edge detection technique [14] as shown in Figure 1b. Once the microstructures were marked then the marked grains were extracted (Fig. 1c) and thereafter, used for pixel area quantification to calculate

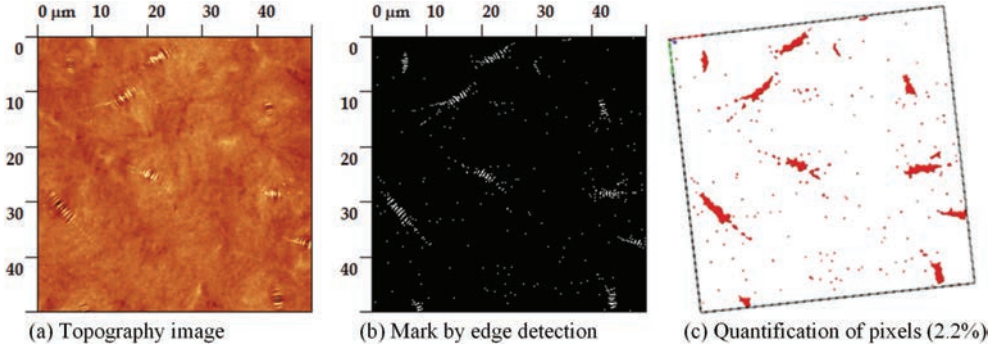

Figure 1. Quantification of microstructures.

the percentage of microstructure present in the frame. For each specimen, AFM scans were conducted at three different locations and the average percentage from these was used as representative average of the percentage of microstructure present at that specimen's surface.

2.2 *Differential Scanning Calorimetry (DSC)*

To investigate any change in the crystalline fractions of specimens due to the previously described conditioning procedures, the DSC analysis was conducted on the 30 days conditioned specimens. The tests were performed using a METTLER instrument (model METTLER TOLEDO DSC 1) equipped with a refrigerated cooling system.

Approximately 15 mg of bitumen was scraped from the each AFM specimens into the DSC sample pans, which were sealed with lids with a small hole to prevent pressure build up and possible deformation of the cups during the tests. The sample pan was then placed horizontally on a hot plate at 80°C for 10 minutes to let the bitumen touch the pan bottom and also level out the surface. Afterwards, the sample pan was placed in DSC furnace and cooled from 25°C to −70°C and kept at this temperature for 5 minutes. Data was recorded during heating from −70°C to +110°C and cooling from +110°C to −70°C, where the heating and cooling rate was 10°C/min. Bitumen were melted completely during the heating, which means the oxidized surface layer also been homogenized in the bulk. If there are any changes in the crystallization process due to the conditioning of the specimens, thus, can be observed in the cooling cycle.

3 RESULTS AND DISCUSSIONS

Figure 2 shows the typical topography image with the computed percentages of microstructure of the unconditioned bitumen specimen. Typical bee structures can be seen since this bitumen contains 6.2% natural wax (Table 1). This topography information of the unconditioned specimens can be used as a benchmark, to detect any change due to the systematic conditioning.

The AFM topography images of the bitumen under four different levels of exposures are shown in Figure 3. In this figure, top row images were aged over 15 days and images in the bottom row over 30 days. To investigate the microstructure evolution due to increased exposure intensity, all the exposed specimens were compared with the reference specimens (unexposed one). After 15 and 30 days, the combined effect (Air + light) caused a reduction of 100%. The oxidation caused a reduction of microstructures by 38% and 58%, and the light caused a reduction of 19% and 14%, respectively. Comparing the specimen exposed to air during 15 and 30 days of exposure (i.e., (b) vs. (f)), it can be observe that the percentage

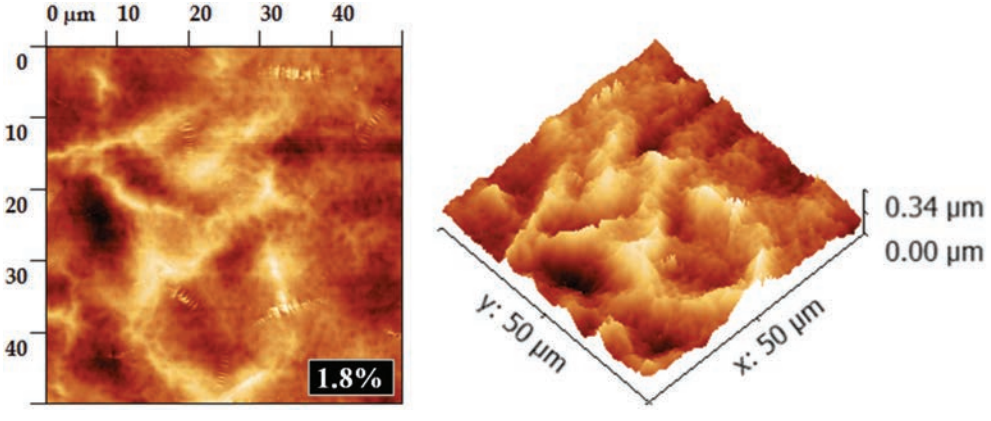

Figure 2. Topographic 2D (left) and 3D (right) AFM image.

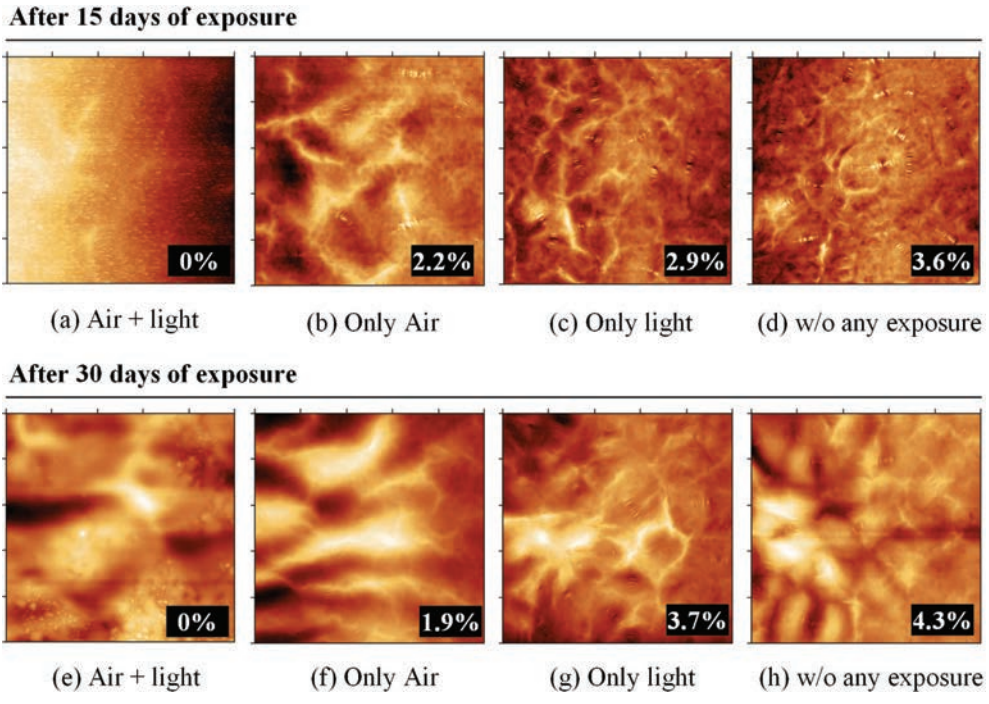

Figure 3. Topography images of conditioned specimens after 15 and 30 days.

of microstructure decreases. In case of non-oxidized specimens, however, the percentage of microstructure increases with time.

From this analysis, it was observed that the visible microstructures at the surface decrease with an increasing degree of oxidation and time. In the case of only light exposed and unexposed specimens, with the time the percentage of microstructure at the surface increases. This confirms that the thin film at the specimen surface caused due ageing may create a barrier, which restricts the microstructures to float towards the surface, and if there is no such barrier at the surface, the percentage of microstructure increases with time.

From the aforementioned AFM topography analysis, it has been observed that there are certainly changes on the bitumen surface caused by the different ageing history. To investigate any change in crystalline molecules due to this thin film surface ageing, DSC analysis has been conducted. Since DSC can determine any physical changes in bitumen associated with heat exchange, it can determine any changes in melting and crystallization phenomena due the systematic conditioning.

The heat flow characteristics of all the specimens with 30 days of exposures have been investigated. Since this is a 'waxy' bitumen (Table 1), both endothermic and exothermic effect was observed as shown in Figure 4a-b. The correspondent zones to the endothermic and exothermic event of the specimens are zoomed in as shown in the figure (right). In the figure, the areas under the wide endothermic peaks represent the enthalpy absorbed due to melting of wax. One may observe that all the four curves in Figure 4a have almost same starting-ending points, and can be superimposed into one curve. This indicates that there is no change in enthalpy due to the different exposures which means the percentage of wax in the bitumen remains constant after 30 days of exposures. Since the percentage of wax remains constant, then the total area under the exothermic peaks in Figure 4b should also have a constant value. It can be observed that during the cooling the shape and the starting-ending point of the exothermic peak somehow differ from each other. The starting point of exothermic event represents the starting of crystallization process. The crystallization starts earlier for oxidized specimens than the unaged one. In this crystallization process, any presence of impurities

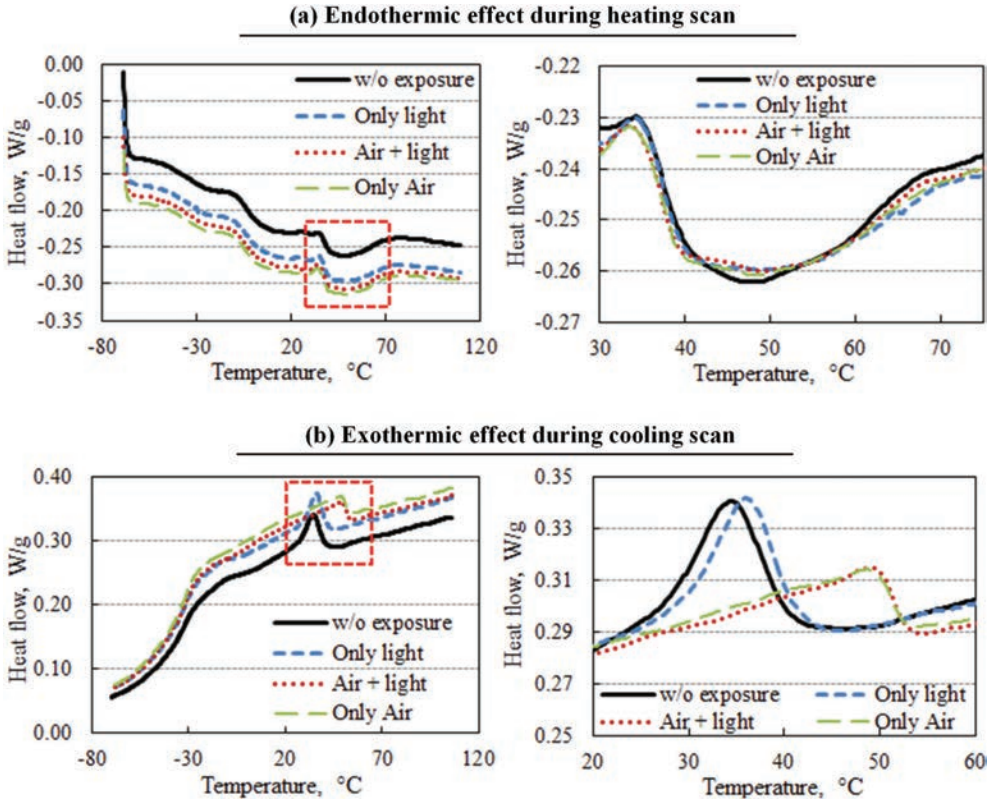

Figure 4. Heat flow analyses of different levels of exposure.

may act as a promoter that may accelerate the process. The product due to the oxidation process may introduced such impurities in the bitumen matrix and thus the crystallization process starts earlier than the without oxidized one.

4 SUMMARY OF FINDINGS

Since bitumen was exposed to air, the oxidation created a thin film upon the exposed surface. This thin film acted as a semipermeable barrier that created difficulty for the wax induced microstructures to float up at the surface. As film becomes thicker or denser with time and increasing degree of exposure, thus the percentage of microstructure seen at the surface was decreased as depicted in Figure 5. For without exposed specimen, with time the percentage of microstructure was increased at the surface, since there was no such thin film caused due to oxidation.

5 LABORATOTY VS. FIELD AGEING

One may notice from aforementioned results and discussions that with oxidation the percentage of bee-shaped microstructures reduces on the surface and the amount of wax remains constant. However, the previous AFM studies [15–17] on PAV aged bitumen had reported the increase of bee-shaped microstructure compared with unaged bitumen.

The hydrocarbons in bitumen react with atmospheric oxygen, where the reaction type and rate depends on the surrounding temperature and pressure. Thus, the type of chemical reac-

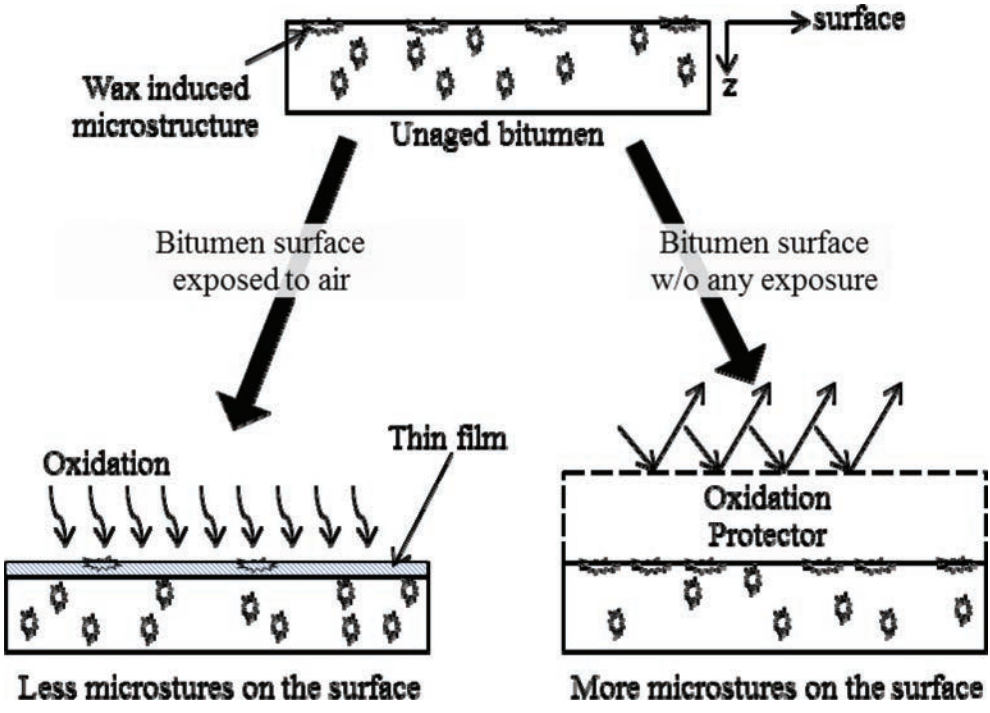

Figure 5. Microstructures evolution due to thin film surface ageing.

tions may vary with the change of pressure and temperature. In the accelerated ageing simulations, especially the PAV test, bitumen gets exposed to extremely high pressure and elevated temperatures for a short time. There is the possibility that the product after the accelerated aging test may differ from the slow but long ageing process with different temperature and pressure history (field ageing). This would then lead to the conclusion that 'ageing' from a PAV tests is indeed a completely different process from ageing in the field [3].

Moreover, AFM is only capable to provide surface information not the bulk. The PAV residue bitumen undergoes heating and cooling for several times during sample collection and specimen preparation for AFM. Due to this thermal history, the aged surface layer (which acts as a barrier) melts down homogeneously in the matrix. In this way, the surface changes entirely and shows completely different surface information than that observed in this study. Thus, the surface information one gets from the disturbed PAV residue bitumen is not even representing the bitumen surface right after the PAV ageing.

6 CONCLUSIONS

The evolution of microstructure due to oxygen diffusion on bitumen surface and its effect on bulk properties has been investigated utilizing Atomic Force Microscopy (AFM) and Differential Scanning Calorimetry (DSC), respectively. The bitumen specimens were subjected to four different environmental conditions: both light and air, only air but no light, only light but no air and neither light nor air, for 15 and 30 days.

From the analyses it was found that the percentage of microstructure on the surface reduced with ageing. For the specimens exposed in oxygen environments, the quantity was lowest and with the time it became even lower. Since it was previously concluded that the microstructures are linked directly to the wax content, one would expect the wax content to also become less. From the DSC results, however, it was proven that this is not the case, as the wax content stayed in fact the same. From this, it can be concluded that a thin film forms

at the specimen surface caused due ageing thus creating a barrier, which restricts the microstructures to float towards the surface.

Though the thermo-analytical investigation showed that the crystalline fractions in the bitumen remain constant even after been exposed to air, crystallization of wax molecules did start earlier for the exposed specimens than the without exposed one. This implies that the chemical reaction product due to the exposures creates impurities in material and causes the acceleration of the crystallization process.

ACKNOWLEDGEMENTS

This research was sponsored by Swedish Road Administration and KTH Royal Institute of Technology, Sweden. The authors acknowledge Måns Collin and Per Redelius for many valuable discussions around the table. Nynas AB is thanked for providing the bitumen.

REFERENCES

[1] Petersen JC. Asphalt oxidation—an overview including a new model for oxidation proposing that physicochemical factors dominate the oxidation kinematics, Fuel Science and Technology International, 11, pp. 57–87. 1993.
[2] Airey GD. State of the Art Report on Ageing Test Methods for Bituminous Pavement Materials, International Journal of Pavement Engineering, 4(3), pp. 165–76. 2003.
[3] Lu X. Talon Y. and Redelius P. Ageing of bituminous binders—laboratory tests and field data, Proceedings of the 4th Eurasphalt and Eurobitume congress, May, Copenhagen, Denmark. 2008.
[4] Bellitto VJ. Atomic Force Microscopy—Imaging, Measuring and Manipulating, Surfaces at the Atomic Scale, InTech, Croatia. 2012.
[5] Lesueur D. Gerard JF. Claudy P. Létoffé JM. Planche JP. and Martin D. A structure-related model to describe asphalt linear viscoelasticity, Journal of Rheology, 40(5), pp. 813–36. 1996.
[6] Loeber L. Sutton O. Morel J. Valleton JM. and Muller G. New direct observations of asphalts and asphalt binders by scanning electron microscopy and atomic force microscopy, Journal of Microscopy, 182(1), pp. 32–39. 1996.
[7] Jäger A. Lackner R. Eisenmenger-Sittner C. and Blab R. Identification of four material phases in bitumen by atomic force microscopy, Road Materials and Pavement Design, 5, pp. 9–24. 2004.
[8] Masson JF. Leblond V. Margeson J. and Bundalo-Perc S. Bitumen morphologies by phase detection atomic force microscopy, Journal of Microscopy, 221, pp. 17–29. 2006.
[9] de Moraes MB. Pereira RB. Simao RA. and Leite LFM. High temperature AFM study of CAP 30/45 pen grade bitumen, Journal of Microscopy, 239(1), pp. 46–53. 2010.
[10] Schmets A. Kringos N. Pauli AT. Redelius P. and Scarpas T. Wax induced phase separation in bitumen, International Journal of Pavement Engineering, 11(6), pp. 555–63. 2010.
[11] Allen RG. Little DN. and Bhasin A. Structural Characterization of Micromechanical Properties in Asphalt Using Atomic Force Microscopy, Journal of Materials in Civil Engineering, 24(10), pp. 1317–27. 2012.
[12] Fischer HR. Stadler H. and Erina N. Quantitative temperature-depending mapping of mechanical properties of bitumen at the nanoscale using the AFM operated with PeakForce TappingTM mode, Journal of Microscopy, 250(3), pp. 210–7. 2012.
[13] Das PK. Kringos N. Wallqvist V. and Birgisson B. Micromechanical investigation of phase separation in bitumen by combining AFM with DSC results, Road Materials and Pavement Design, 14(S1), pp. 25–37. 2013.
[14] Marr D. and Hildreth E. Theory of edge detection, Proceedings of the Royal Society, February, London: B Biological Science, 207, pp. 187–217. 1980.
[15] Huang SC. and Pauli AT. Particle Size Effect of Crumb Rubber on Rheology and Morphology of Asphalt Binders with Long-term Aging, Road Materials and Pavement Design, 9(1), pp. 73–95. 2008.
[16] Wu S. Pang L. Mo L. Chen Y. and Zhu G. Influence of aging on the evolution of structure, morphology and rheology of base and SBS modified bitumen, Construction and Building Materials, 23(2), pp. 1005–10. 2009.
[17] Zhang HL. Yu JY. Feng ZG. and Xue LH. Effect of aging on the morphology of bitumen by atomic force microscopy, Journal of Microscopy, 246(1), pp. 11–19. 2012.

Asphalt Pavements – Kim (Ed)
© 2014 Taylor & Francis Group, London, ISBN 978-1-138-02693-3

Multiscale modeling of asphaltic media considering heterogeneity, viscoelasticity, and nonlinear fracture damage

J.E.S. Lutif
Universidade Federal do Espírito Santo, Vitória, ES, Brazil

Y. Kim
University of Nebraska, Lincoln, NE, USA

F.V. Souza
Multimech R&D, LLC, Omaha, NE, USA

D.H. Allen
PSI Technologies Inc., Saskatchewan, Canada

ABSTRACT: This study presents a multiscale computational model with its verification and validation efforts for predicting damage-dependent mechanical behavior of asphaltic media that are subject to fracture damage. Two length scales (global and local) are two-way coupled in the model framework by linking a homogenized global scale to a heterogeneous local scale representative volume element. Based on the two-way coupled concurrent multiscaling and the use of the finite element technique incorporated with material viscoelasticity and cohesive zone fracture, the model approach can successfully account for the effect of mixture heterogeneity, material viscoelasticity, and damage accumulation due to cracks in the small scale on the overall performance of larger scale mixtures or structures. Along with the theoretical model formulation, two example problems are shown: one to verify the model and its benefits through comparisons with analytical solutions and single-scale simulation results, and another to validate the model for various cases where material viscoelasticity, mixture heterogeneity, and cohesive zone fracture are involved.

Keywords: multiscale model, asphalt, heterogeneity, viscoelasticity, cohesive zone fracture, finite element method

1 INTRODUCTION

Asphalt materials are classical examples of multi-phase composites consisting of aggregate particles surrounded by a cementitious phase. The understanding of the mechanical behavior of asphalt materials has been a challenge to the civil engineering community due to multiple complexities related: mixture heterogeneity, anisotropy, nonlinear inelasticity, and damage growth in multiple forms.

Microstructure-based computational modeling has been actively pursued by many researchers as a means of overcoming the aforementioned challenges, since the microstructure-based computational modeling can readily account for the geometric complexities and inelastic constitutive relations of mixture components. Even though various computational techniques based on the mixture microstructure and its component characteristics have demonstrated sufficient modeling feasibility in addressing the challenges, solutions for the mixture problems are sometimes limited because they usually require a tremendous amount of computational time and effort, which is rarely feasible with currently available computing power. Asphalt mixtures and pavement structures typically contain thousands of irregularly-shaped,

randomly-oriented aggregate particles along with thousands of potential cracking sites which would require a highly refined microstructure with enormous degrees of freedom. These clear limitations have led researchers to seek alternative approximate approaches that can account for the hierarchical structure of heterogeneous materials without having to model every microstructural detail, but still considering the most important ones.

One approach, which has been receiving increasing attention from many different engineering-science disciplines, is that of multiscale modeling as demonstrated in many studies [1–11]. In this approach, different length scales within the macroscopic body are separately analyzed and then linked together. When statistical homogeneity on the smaller scale Representative Volume Element (RVE) is satisfied, constitutive equations for the larger scale can be produced using a homogenization principle [12–15]. Therefore, the global constitutive behavior of heterogeneous objects can be determined by the solution of a smaller scale RVE boundary value problem.

In this paper, we present the modeling framework developed so far and its verification and validation with model calibrated. At this stage of model development, only two length scales (called herein global and local scales) with material elasticity, viscoelasticity, and damage due to cohesive zone fracture are considered.

2 TWO-WAY COUPLED MULTISCALE MODEL

The multiscale model developed has been implemented into a finite element code. At this stage of the model development, two length scales (i.e., global and local) are considered together with material viscoelasticity and cohesive zone fracture.

As presented in Figure 1, a global scale solid object (length scale l^G) with evolving microcracks (length scale l_c^L) on the local scale (length scale, l^L) RVE is modeled. The object is statistically homogeneous at the global scale where the continuum is represented by a heterogeneous local scale RVE. The RVE is the smallest object size that is sufficiently large so that the estimation of the effective properties is independent of the object size. As illustrated in the figure, in the local scale RVE, various sources of heterogeneity such as particles, voids, and cracks can be considered.

The primary variables in the model are the displacement vector, the strain tensor, and the stress tensor. It should be noted that in order to produce reasonably accurate predictions through the multiscale process, the global length scale needs to be much larger than the local length scale, and the local length scale should be much larger than the length scale of microcracks. Theoretical details on the multiscale model presented in this paper can be found elsewhere [15–17].

The multiscale model herein is termed two-way linked because the applied displacements on the boundary of the local scale are computed from the global scale strain tensor

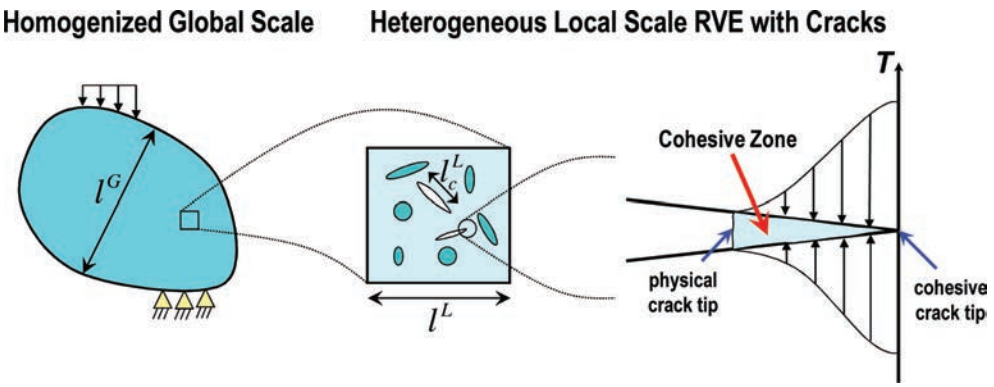

Figure 1. A schematic illustration of a general object with global-local linking.

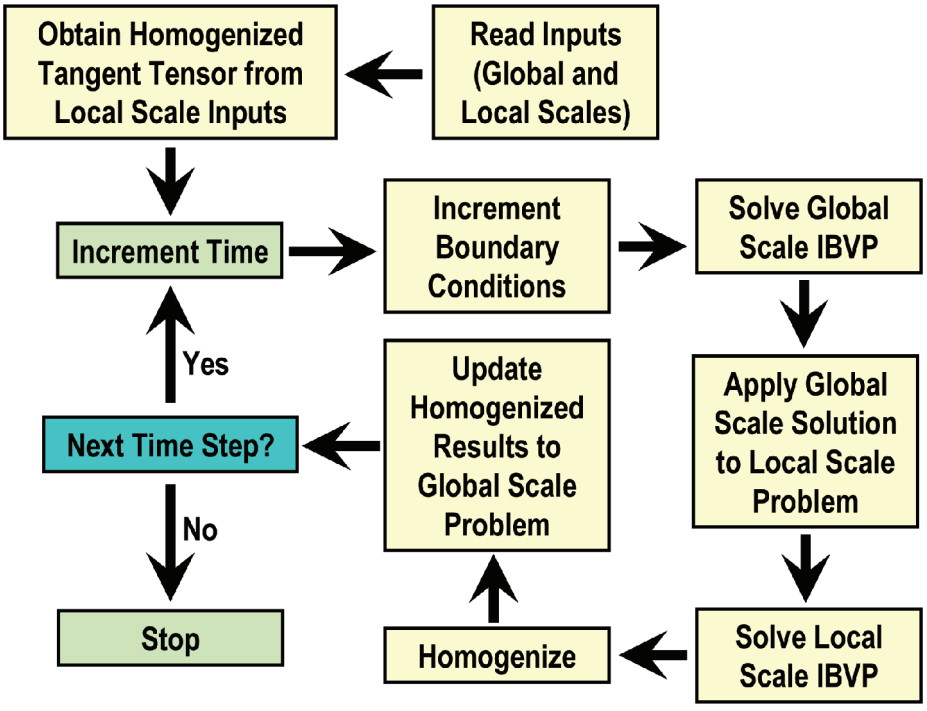

Figure 2. Two-way linked multiscale modeling process.

(global-to-local linking), and the homogenized constitutive quantities are obtained from the solution of the local scale problem (local-to-global linking). A simple description of the two-way coupled multiscale modeling algorithm is given in Figure 2. Basically, the model is operated in seven primary steps: 1) read inputs for global and local scales; 2) obtain initial homogenized tangent tensor for global Initial Boundary Value Problem (IBVP); 3) solve the global IBVP at a given time step; 4) apply global scale solution to local scale IBVP; 5) solve the local scale IBVP at the time step; 6) homogenize local scale results; and 7) update homogenized local scale results to the global scale object at each integration point for the next time step. The two-way linking is essentially necessary when the problem is subjected to material viscoelasticity and evolved microstructure such as microcracks, since the problem with material viscoelasticity and cracking is typically time-, history-, and spatial-dependent. In the multiscale modeling process, the global scale can be discretized with a homogeneous finite element mesh, which dramatically reduces the time required for mesh refinement and computation, while the local scale considers mixture heterogeneity. A local scale RVE is attached to each global scale integration point of selected global scale finite elements.

As illustrated in Figure 2, global scale response can be obtained by performing a local scale analysis, and using homogenization principles, relationships connecting both length scales can be established. In other words, the constitutive relationship at the global length scale is based on the constitution of the local scale RVE.This indicates that there is no need to determine the global scale constitutive functional *a priori*, since it is determined concurrently as the analysis of local scale is performed.

3 MULTISCALE MODEL VERIFICATION

In order to verify the multiscale computational model developed, a heterogeneous tapered bar as presented in Figure 3 is introduced. The tapered bar is a general composite consisting

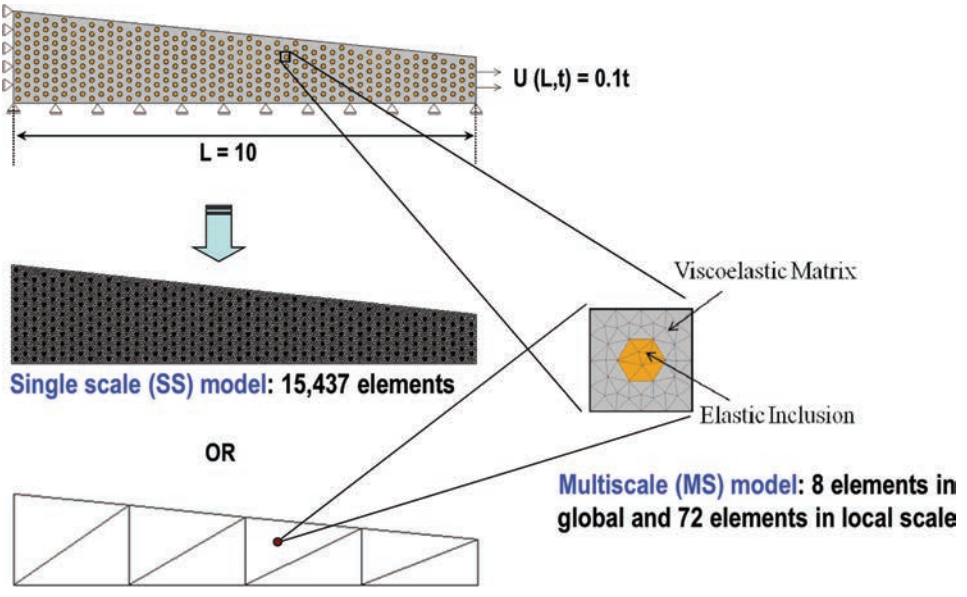

Figure 3. Elastic-viscoelastic tapered bar problem for model verification.

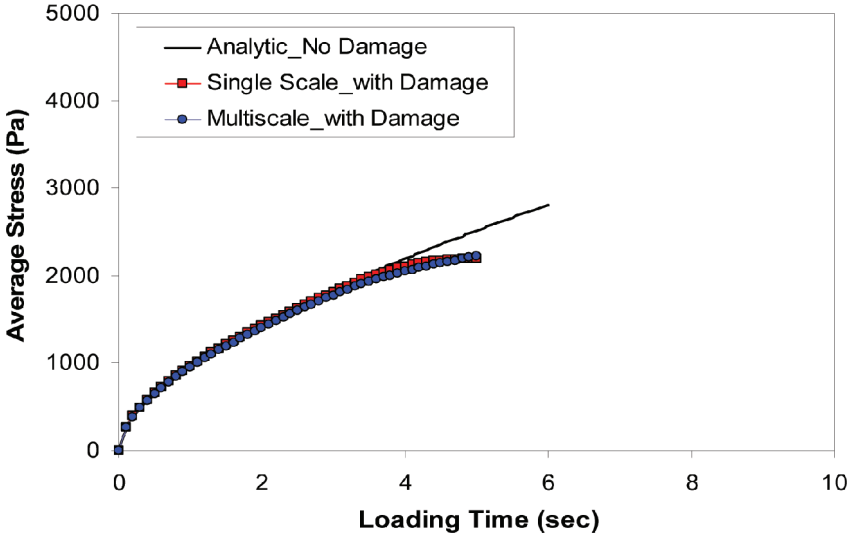

Figure 4. Model verification results.

of viscoelastic matrix and elastic particles. Due to the axis of symmetry, only half of the bar is modeled, and monotonically increasing displacements are applied at the right end of the bar, as shown in the figure.

For the multiscale analysis, a local scale microstructure describing the important geometric heterogeneities is needed. In the present verification problem, a unit cell is selected which possesses the same volume fraction and equal level of mesh refinement obtained from the single scale reference mesh. Model verification was performed by comparing multiscale simulation results to single scale results and analytical solutions available.

Figure 4 plots the average stresses of the tapered bar as loading time increases. Due to the formation of cohesive zones followed by cracks, it can be noticed that the average stress

deviates from the non-damage (linear viscoelastic) case (presented by analytical solution). The multiscale solution was considered satisfactory when compared to the single scale simulation results. The accuracy of the multiscale model with only 8 elements for the global scale and 72 elements for each local scale RVE suffice, as opposed to 15,437 elements needed by the single scale reference simulation. In terms of computational time required to run this problem, the multiscale solution was obtained approximately 250 times faster than the single scale case. With only one processor (2.50 GHz CPU with 4 GB RAM) 26,700 seconds were necessary to complete the single scale case, whereas only 105 seconds were used to run the multiscale problem. Furthermore, the multiscale model can also run in parallel computing environments, which highlights the benefit of multiscale modeling approach. The parallel computing can vastly reduce simulation time, since individual local scale problem can be solved in parallel by multiple processors. Clearly, this example demonstrates the accuracy and efficiency of the multiscale model. This benefit will further be noticeable when one models typical multiphase composites and structures that present very complicated geometry and material inelasticity.

4 MULTISCALE MODEL VALIDATION-CALIBRATION

To validate the two-way linked multiscale model for predicting the mechanical behavior of asphalt mixtures, three-point bending beam tests of asphalt mixture specimens were performed at 21 °C, and test results were compared to model simulation results. As presented in Figure 5(a), the rectangular beam specimens were placed inside a three-point bend fixture and loaded by a UTM-25 kN machine at a constant displacement rate (0.83 mm/s) until the specimens failed completely. Three replicates were tested. Figure 5(a) shows the experimental setup.

Figure 5(b) presents the two-way linked multiscale simulation accomplished by linking the heterogeneous local scale RVE (10.0 mm by 10.0 mm square) to a homogeneous global scale beam specimen (150 mm by 40 mm rectangle). The global scale bending performance was modeled as a damage-induced, non-linear viscoelastic continuum by a two-way linking strategy. For the modeling, the loading configuration was simulated in the same manner as the test setup. It is important to mention that at this point the numerical model simulations were performed allowing microcraks and their coalescence to macrocracks only at the local scale. The damage in the global scale was then accounted indirectly by the loss of stiffness of the homogenized constitutive tensor, due to the cracking at the local scale.

The selected local scale RVE was discretized into a finite element mesh with triangular elements with 0.5 mm size as presented in Figure 5(c). The aggregate particles were modeled as isotropic and linear-elastic, and the surrounding mastic was modeled as isotropic, viscoelastic with cohesive zone fracture. To determine the global mesh refinement which is a primary factor that affects total computing efforts, a mesh convergence study was also performed. Different global meshes were linked to the local scale RVE until the finite element numerical solution converged to an analytical solution. A set of homogeneous global scale meshes in a different level of mesh refinement (10-mm element size to 2.5-mm element size) was evaluated. Considering a balance between the level of accuracy desired and the computational time spent, in this study, the global mesh with 5-mm triangular elements (Fig. 5(d)) was finally selected since it required a reasonable computing time by providing a relatively fair level of accuracy.

The model validation-calibration was accomplished by comparing the model simulation results with analytical and experimental results. To that end, three scenarios were attempted: i) multiscale w/o cracks, where no damage was considered in the analysis, ii) multiscale w/cracks (validation), where the damage parameters used in the simulation were directly obtained from the semicircular bend fracture tests [18,19], and iii) multiscale w/cracks (calibration), where one of the damage parameters (m-value) used in the simulation was calibrated for a better agreement with experimental results. Figure 6 shows the results.

Model simulation results showed a fairly good agreement with the analytical solution when damage was not involved (i.e., multiscale w/o cracks). This verifies the accuracy of the model

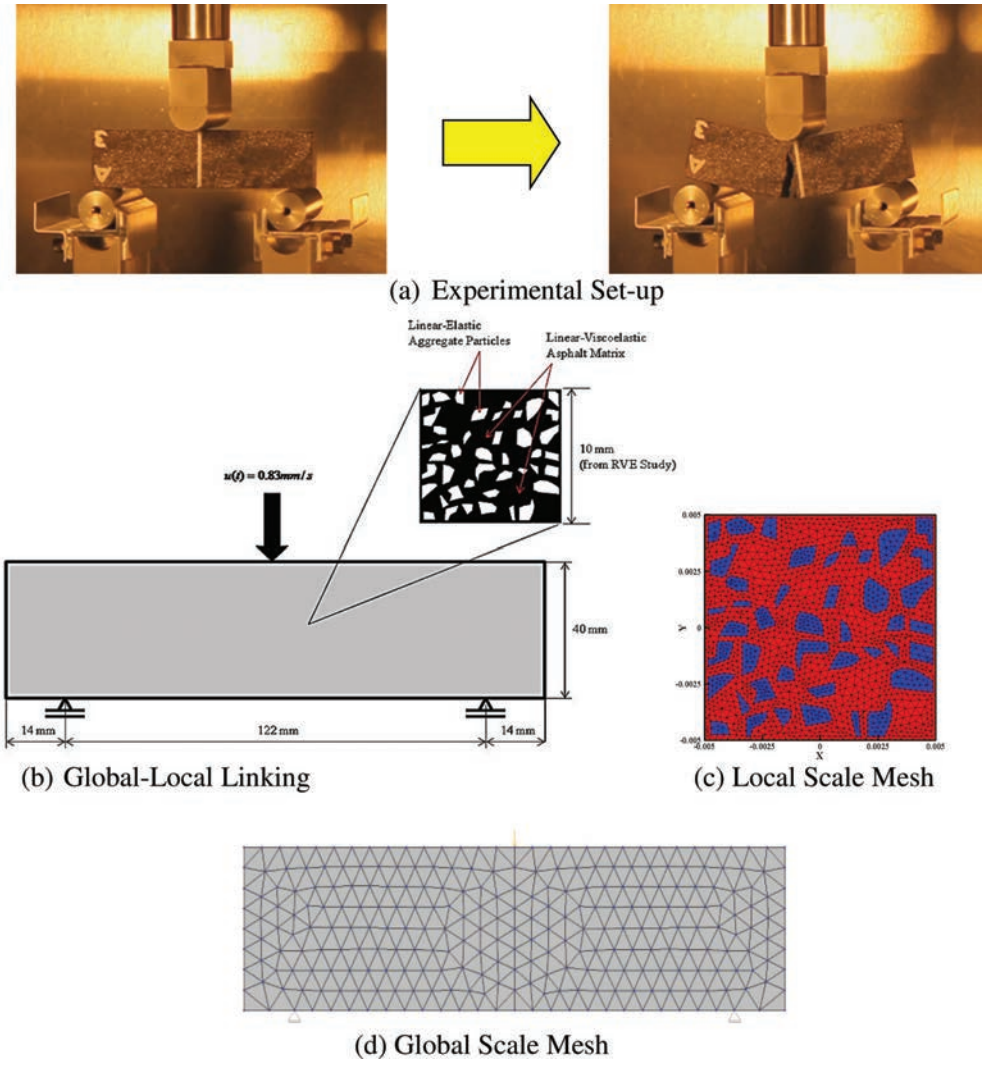

Figure 5. Multiscale model validation-calibration.

when damage is not associated. In addition, the model simulation results without damage seemed to follow the experimental test results nicely up to 1.2 seconds (stage 1) by representing some energy being dissipated due to the material viscoelasticity. The initial slope from model simulations matched very well with the experimental results, which demonstrates that, along with the appropriate constitutive model and the properly defined properties of mixture components, the multiscale model can satisfactorily capture the mixture response when damage is not induced. After passing the stage 1, due to the formation of cohesive zones followed by microcracks, it can be noticed that the average stress deviates from the non-damage (linear viscoelastic) curve. After 1.5 seconds of loading, the three-point bend test results started to deviate from simulation results with cracks. The rate of damage propagation seemed to be underestimated in the numerical simulations (case of multiscale w/cracks_validation_m = 2.5) using the damage parameters determined from the semicircular bend fracture test incorporated with the viscoelastic cohesive zone model. The mismatch between the simulation results and test results can be from multiple sources including the approximated finite element meshes, limited model capabilities at the current stage, and the assumed constitutive

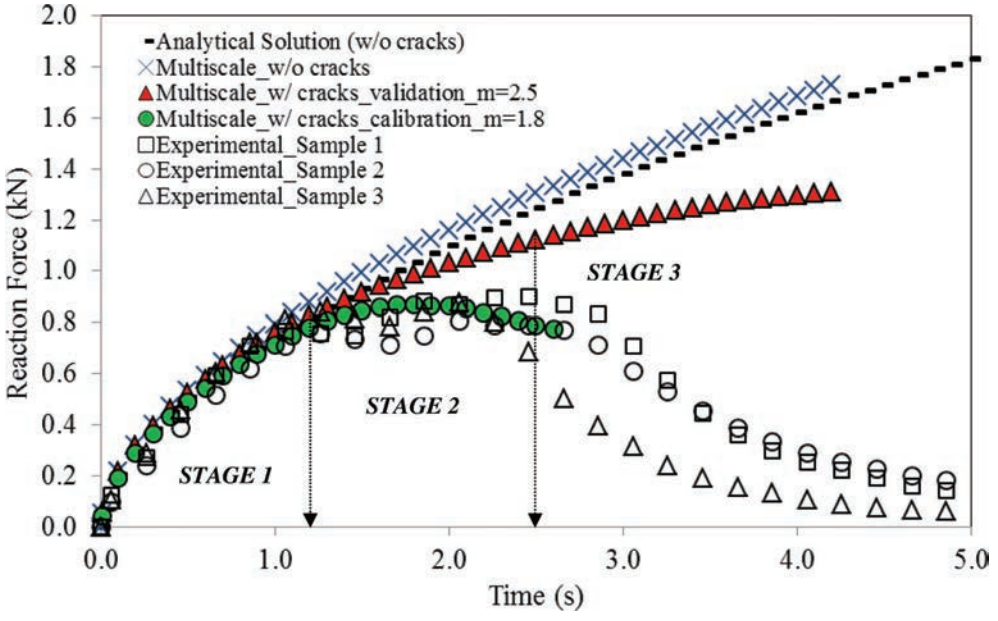

Figure 6. Multiscale simulations vs. experimental tests and analytical results.

relations (i.e., linear elastic behavior of aggregates and viscoelastic behavior of asphalt mastic with cracking) for the mixture, etc.

Since it is not feasible to identify the sources of mismatch at the current stage, model calibration was attempted in a simple way by merely varying one of the cohesive zone damage parameter, *m*-value. In this way, it can be investigated how the model represents the effects of damage characteristics of component properties on entire mixture/structure performance. In the damage evolution law, the damage parameter *m* significantly changes the damage evolution rate. By varying the *m*-value from 2.5 to 1.8, which induces a faster degradation of the mixture, model calibration was achieved. All other material characteristics were kept the same as the ones used in the validation case. The simulations results with the calibrated *m*-value (multiscale w/cracks_ calibration_m = 1.8) showed a good agreement with experimental results, as demonstrated in Figure 6.

Aside from the efficiency of the multiscale model, another clear benefit is the capability of the model to visualize the small-scale phenomena. To do this, three local scale RVEs (21, 156, and 451) were selected. Each local scale RVE was named accordingly with the global element it was linked. The deformed mesh and elemental stresses at both global and local scale structures at 2.5 seconds (stage 3) were selected and presented in Figure 7 for the validation case ($m = 2.5$) and the calibration case ($m = 1.8$), respectively. Clearly, at the same loading stage, the case with $m = 1.8$ presented severe damage evolution from the local RVEs and correspondingly, greater stiffness reduction in its global scale. It can also be noted that the mixture behavior with damage phenomenon can be captured by the model, as seen by the different stress responses in the selected RVE microstructures. The microstructure linked to the global element 21 (RVE 21) showed the highest tensile stress compared to the other elements. This result was expected as the highest tensile strains developed at the bottom of the three-point bending beam test. Similarly, highest compressive stresses were observed from the local RVE linked to the global element 451.

The level of damage in the microstructure linked to the global elements from the region of higher stresses was noticeably pronounced, and microcracks began to connect to each other, forming macrocracks. The insertion of cohesive zone elements, which was eventually converted to a crack, reduced the stresses on the sample compared to the case with no damage. With the unique model capability to visualize the smaller length scales, damage

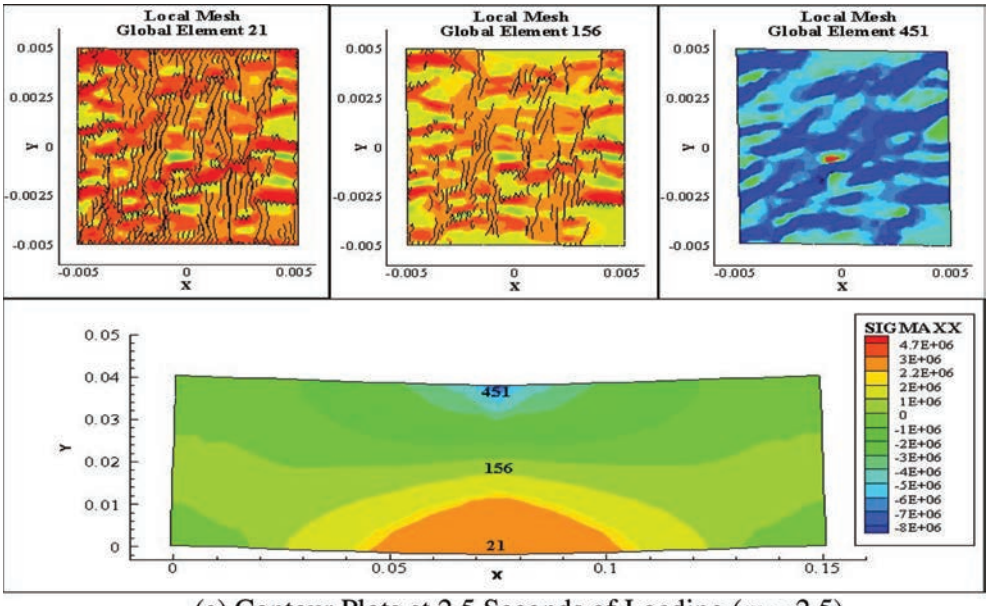

(a) Contour Plots at 2.5 Seconds of Loading ($m = 2.5$)

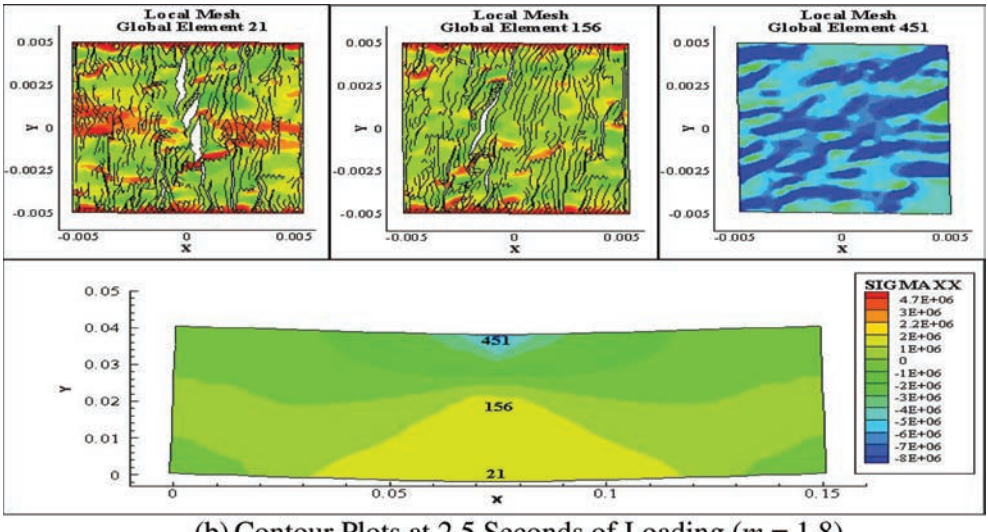

(b) Contour Plots at 2.5 Seconds of Loading ($m = 1.8$)

Figure 7. Snapshots of contour plots at 2.5 seconds from model simulations.

evolution could be analyzed in a more detailed manner than traditional approaches that did not account for microstructural details.

5 SUMMARY AND CONCLUSIONS

A computational multiscale model for predicting mechanical behavior of heterogeneous, inelastic asphaltic media was presented. The model can account for mixture heterogeneities by taking into account individual mixture constituents through the unique scale-linking technique: a local scale in a form of the heterogeneous RVE and a global scale which has been homogenized from the local scale responses. The model was implemented using the finite

element formulation, so that geometric complexities and material inelasticity with physical cracks can be properly handled without any significant loss of accuracy.

Verification of the model was conducted by simulating a simple tapered bar where two distinct phases (i.e., elastic particles and viscoelastic matrix) exist. By comparing multiscale simulation results to single scale results and analytical solutions available, model verification was confirmed. Moreover, a significant reduction in computational effort by using the multiscale approach compared to the single scale simulation was observed.

The multiscale model was also validated and calibrated by comparing laboratory test results with model simulation results of the three-point bending beam specimens, where elastic fine aggregate particles are surrounded by viscoelastic mastic that was subjected to fracture. Clearly, the model can simulate the laboratory tests by capturing the formation of microcracking and the propagation in the heterogeneous local scale RVE and update the local scale fracture process to the global scale damage-dependent performance.

The clear understanding of the small scale phenomena can then be guidelines to select mixture constituents in a more appropriate way and to improve current asphalt mixture design methodology so that better-performing and longer-lasting roadway mixtures can be produced. In addition, since only small scale material properties are required in the model, this modeling approach can reduce the amount of laboratory testing required, thereby providing substantial additional cost savings. Although many challenges still exist, and further improvements are necessary remain for the future studies, this study demonstrates the potential power and efficacy of this modeling approach as a purely mechanistic method for the analysis and design of various asphaltic media.

ACKNOWLEDGEMENTS

The authors are grateful for the financial support received from the National Science Foundation (Grant No. CMMI-0644618) and the Texas A&M Research Foundation. We also appreciate MultiMech Research and Development, LLC for providing courtesy license of multiscale software package MultiMech™ during performance of this work.

REFERENCES

[1] F. Feyel, Multiscale FE^2 elastoviscoplastic analysis of composite structures. Computational Materials Science, 16, pp. 344–354, 1999.

[2] F. Feyel and J.L. Chaboche, FE^2 multiscale approach for modeling the elastoviscoplastic behavior of long fibre SiC/Ti composite materials. Computer Methods in Applied Mechanics and Engineering, 183, pp. 309–330, 2000.

[3] J. Fish and A. Wagiman, Multiscale finite element method for a locally non-periodic heterogeneous medium. Computational Mechanics, 12, pp. 164–180, 1993.

[4] J. Fish and V. Belsky, Multigrid method for periodic heterogeneous media, Part II: multiscale modeling and quality control in multidimensional cases. Computer Methods in Applied Mechanics and Engineering, 126, pp. 17–38, 1995.

[5] J. Fish, and K. Shek, Multiscale analysis of composite materials and structures. Composites Science and Technology, 60, pp. 2547–2556, 2000.

[6] S. Ghosh, K. Lee, and P. Raghavan, A multi-level computational model for multiscale damage analysis in composite and porous materials. International Journal of Solids and Structures, 38, pp. 2335–2385, 2001.

[7] K. Lee, S. Moorthy, and S. Ghosh, Multiple scale computational model for damage in composite materials. Computer Methods in Applied Mechanics and Engineering, 172, pp. 175–201, 1999.

[8] J.T. Oden, and T.I. Zohdi, Analysis and adaptive modeling of highly heterogeneous elastic structures. Computer Methods in Applied Mechanics and Engineering, 172, pp. 3–25, 1997.

[9] J.T. Oden, K. Vemaganti and N. Moes, Hierarchical modeling of heterogeneous solids. Computer Methods in Applied Mechanics and Engineering, 148, pp. 367–391, 1999.

[10] P. Raghavan, S. Moorthy, S. Ghosh and N.J. Pagano, Revisiting the composite laminate problem with an adaptive multi-level computational model. Composites Science and Technology, 61, pp. 1017–1040, 2001.

[11] R.M. Haj-Ali and A.H. Muliana, A multi-scale constitutive formulation for the nonlinear viscoelastic analysis of laminated composite materials and structures. International Journal of Solids and Structures, 41, pp. 3461–3490, 2004.
[12] R.M. Christensen, Mechanics of composite materials, Wiley, New York, 1979.
[13] T. Mura, Micromechanics of defects in solids, 2nd Edition, Martinus Nijhoff Publishers, Dordrecht, 1987.
[14] S. Nemat-Nasser and M. Hori, Micromechanics: overall properties of heterogeneous materials, North Holland, New York, 1993.
[15] D.H. Allen, Homogenization principles and their application to continuum damage mechanics. Composites Science and Technology, 61, pp. 2223–2230, 2001.
[16] F.V. Souza. Multiscale modeling of impact on heterogeneous viscoelastic solids with evolving microcracks. Ph.D. dissertation, University of Nebraska, Lincoln, Nebraska, 2009.
[17] F.V. Souza and D.H. Allen. Multiscale modeling of impact on heterogeneous viscoelastic solids containing evolving microcracks. International Journal for Numerical Methods in Engineering, 82(4), pp. 464–504, 2010.
[18] F.T.S. Aragão and Y. Kim. Mode I fracture characterization of bituminous paving mixtures at intermediate service temperatures. Experimental Mechanics, 52(9), pp. 1423–1434, 2012.
[19] Y. Kim and F.T.S. Aragão. Microstructure modeling of rate-dependent fracture behavior in bituminous paving mixtures. Finite Elements in Analysis and Design, 63, pp. 23–32, 2013.

Asphalt Pavements – Kim (Ed)
© 2014 Taylor & Francis Group, London, ISBN 978-1-138-02693-3

Structuralization as characteristic to link the mechanical behaviours of asphalt concrete at different length scales

B. Shane Underwood
Arizona State University, Tempe, AZ, USA

Y. Richard Kim
North Carolina State University, Raleigh, NC, USA

ABSTRACT: Multiscale characterization and modelling is an increasingly popular technique for the investigation of asphalt concrete due to limitations with the level of insight possible from macroscale mechanistic models with respect to certain key performance characteristics. Four key questions arise in the multiscale experimental/mechanical evaluation of asphalt concrete; 1) what are the different characteristic length scales within asphalt concrete, 2) how should these materials be constructed in the laboratory for experimentation 3) what are the characteristic behaviours of these different scales, and 4) how are these behaviours linked across the scales. In this paper the authors present research findings concerning the fourth question. A characteristic index, the structuralization index, is identified as a scale independent characteristic that explains the stiffening characteristics of asphalt concrete across length scales. The definition and basis for the development of this structuralization index is presented. Next, the application of this structuralization index to two different materials is shown. It is the authors' belief that this structuralization index can serve as a means to link the characteristic behaviours of asphalt concrete for analytical upscaling of the modulus, and perhaps other properties as well.

Keywords: asphalt, multiscale, mastic, structuralization

1 INTRODUCTION

In previous papers the issues of defining the characteristic length scale in asphalt concrete and how these should be constructed in the laboratory as well as evaluated the characteristic behaviours of these materials has been evaluated [1–3]. In this document the multiscale modelling issue of linking the behaviours across scale is examined. The ultimate vision and goal for this line of research is in articulating an alternative framework with which to investigate the mechanical behaviours of asphalt concrete and to develop new insights that may lead to improvements in the engineering of this material. Existing methods have proven useful in the field of asphalt technology, but fundamental limitations with respect to their ability to more fundamentally understand cause and effect relationships is becoming apparent. The concept of internal structuralization within asphaltic composites was introduced by Rigden [4], when he applied the fractional compaction, *FC*, quantity to asphalt mastics. This value evolved from empirical packing studies and from analytical studies on the stiffening of dilute solutions. Although the term itself was, apparently, first coined by Rigden, it has been used by others without specific reference to Rigden's work or the term fractional compaction. The mathematical definition of *FC* is given in Equation (1). Its value generally varies from 0 to approximately 3 with 0 indicating infinite space between particles and the upper value corresponding to a void less condition.

$$FC = \frac{100 - \%Voids}{100 - \%Void_{ref}} \quad (1)$$

where $\%Voids$ is the void volume in a given material expressed as a percentage of total volume and $\%Voids_{ref}$ is the void volume in a given material expressed as a percentage of total volume and determined from a separate experiment. Keep in mind that $\%Void_{ref}$ is determined from dry compacted filler whereas $\%Voids$ is from the filler plus asphalt. The addition of asphalt facilitates compaction and hence the ability of mastic to have $\%Voids$ lower than $\%Voids_{ref}$.

The concept of *FC* is used to normalize materials with respect to their basic packing characteristics under some standardized compactive effort. It follows from the hypothesis that materials of different composition behave similarly when the internal structure is under a similar state of inter-particulate interaction. The reference void content can be chosen at any condition, but it is typically taken as the dry compacted density of the material. Since the concept has been historically applied to fillers in mastics, this compacted void content is usually that determined by the Rigden apparatus and is referred to as the Rigden voids. For real materials this void content may range from 20% to 40% or more depending on the characteristics of the material.

The concept also suggests that it is important and necessary to understand the way that particles pack and assemble within a body at a particular volumetric concentration. Experimental evidence shows that for most materials a rapid change in mechanical properties begins to occur at a *FC* of approximately 0.6, e.g., at particle volume concentrations of 40% to 60%. At this point the modulus begins to qualitatively change from a liquid-like response to a solid-like response and to rapidly increase in magnitude [1, 5–8]. It is hypothesized that the transition from liquid-like (e.g., binder-like) to solid-like (e.g., mixture-like) behaviours within only the mastic scale as particle concentration increases suggests a universal linkage between scales through the internal structuralization within the composite. This index, termed the structuralization index, would quantify the effects of internal structure and inherently supposes that the internal structure is responsible for much of the stiffening observed in the high concentration mastics, Fine Aggregate Matrix (FAM), and the mixture. It is further supposed that this index, like the *FC*, should be based upon the packing characteristics of the raw aggregates since these properties give an *indication* of the surface texture, particle shape, frictional characteristics, etc. of the aggregates as they exist within the material. Each of these properties is expected to contribute to either how the structure forms within a given scale, or how the structural skeleton reacts to loading. In this paper, this hypothesis is evaluated.

2 STRUCTURALIZATION INDEX

The definition of the structuralization index, *SI*, is given in Equation (2), which is very similar to the definition of *FC* except the reference void content is now the void content when the *internal structure* just forms. Thus, Equation (2) represents a more functional definition of the concept of *FC*. It is supposed that this void content is between the loose and compacted void ratios ($\%Voids_{loose}$ and $\%Voids_{comp}$ respectively) measured via the standard laboratory methods.

$$SI = \frac{100 - \%Voids}{100 - \%Voids_{str}} \quad (2)$$

In Equation (2), $\%Voids$ is the void volume in a given material expressed as a percentage of total volume. It is not simply the air void content, but rather it is the volume content of all space that exists between aggregate particles. It is very similar to the VMA value that is typically computed for an asphalt concrete mixture. In fact, for the mastics, the $\%Voids$ is the VMA. However, in the case of mix and FAM the $\%Voids$ is slightly different than VMA because it does not include the volume of space occupied by the filler. To calculate the $\%Voids$

for Equation (2) requires one to carry out volumetric calculations using known aggregate size distribution, bulk specific gravity and effective specific gravity for each aggregate size or range of sizes, asphalt content, and air void content. The $\%Voids_{str}$ is the structuralized void ratio and is computed by Equation (3), where B is a theoretical parameter ranging from 0 to 1 that indexes the void ratio where structuralization onset occurs with respect to the compacted and loose void ratios.

$$\%Voids_{str} = B\left(\%Voids_{loose} - \%Voids_{comp}\right) + \%Voids_{comp} \tag{3}$$

Structural onset is an abstract term, but it is functionally considered to be the point at which interparticulate contacts are sufficient enough in number and/or in strength to support the structure and resist substantial deformation under load. One might consider this characteristic as the cumulative contact strength and it is a function of both the number of contacts and the individual strength of each contact. The compaction level needed to create a stable structure should be aggregate specific and it likely depends on the physical properties of the aggregate (texture, angularity, shape, etc.), the mineralogical composition (physico-chemical properties), and the gradation. The relative importance of these factors is not known, but each is believed to contribute at least somewhat to the observed structuralization potential. The following are hypothesized based on literature review and the authors' experience;

- The physical properties are the most important factors affecting the achievement of a stable skeleton structure and these factors are similar at all scales for a given source.
- The void structure in a loose and compacted voids test, i.e., the void structure at any fixed compactive effort, is influenced to a significant enough amount by each of these factors that none can be ignored.
- The amount of compaction effort needed to reach a stable configuration is constant for a given aggregate source, but the actual void structure at this stable configuration will depend on scale specific factors (gradation, physico-chemical influences, etc.). Thus B is a material constant but since $\%Voids_{comp}$ and $\%Voids_{loose}$ change, $\%Voids_{str}$ is scale dependent.
- The loose and compacted void contents serve as consistent markers for these additional influences and provide reliable measures by which one can find this stable structure.

The hypotheses regarding bounding of the structuralized void ratio by the coarse and fine void contents is accounted for by the B parameter in Equation (2). If the B parameter is 0.5 then the structuralized void ratio is the average of the loose and compacted void ratios. When B is zero then the SI is equivalent to the FC. Based on the hypotheses above, more angular and rough surface textured stone should lead to a B that is closer to 1 than it is for rounded and smooth aggregate. Since the critical cumulative contact strength is the physical parameter that dictates whether a given microstructure is structuralized ($SI = 1$), under structuralized ($SI < 1$), or over structuralized ($SI > 1$), it is believed that the more angular and rough sources will reach the structuralized configuration with less compaction effort. In this work, the goal is to identify the existence of a structuralization index and quantify its value for two different materials. If this concept is verified then an experiment to measure its value may be developed in later work.

3 MATERIAL

Two highly granular and generally cubical, granite-based AC mixtures with no deleterious materials are utilized. The primary AC mixture is well-graded with a Nominal Maximum Size of Aggregate (NMSA) of 9.5 mm. The secondary mixture consists of a blend of aggregates with a NMSA of 19.0 mm. These mixtures are respectively referred to as the 9.5 mm and 19.0 mm mixtures throughout this paper. Aggregate Imaging Measurement System (AIMS) parameters have been measured for these aggregates. It is found that they have statistically similar angularity (sub-rounded), Form 2D (Semi-Elongated), and Sphericity (low) and significantly different texture (primary mixture shows high-moderate roughness and the

secondary mixture shows low-low roughness properties) [9]. More details on these materials are given elsewhere [2].

From these two study mixtures various materials have been created to support this study. These materials include: mastic at different volumetric concentrations; FAM with different maximum aggregate size, gradation, asphalt content, and air void content; and full scale asphalt concrete mixture. These materials are summarized in Table 1 (Primary mixture) and Table 2 (secondary mixture). These tables also include the structuralization index values for each material, the $\%Voids_{str}$ used to compute this quantity is described later.

4 TEST METHODS

Temperature and frequency sweep tests were conducted on the materials at different length scales; binder, mastic, FAM, and mixture. The strain levels for the tests shown in this paper

Table 1. Structuralization indices for S9.5B materials.

Material	Blend ratio	Asphalt content (%)	Air void (%)	SI
Binder and mastic				
UA	0	100	–	0.00
AA	0	100	–	0.00
MS10	0.1	76.3	–	0.22
MS20	0.2	58.9	–	0.44
MS255	0.255	51.4	–	0.56
MS26	0.261	50.4	–	0.58
MS30	0.3	45.6	–	0.66
MS40	0.4	35.1	–	0.88
MS50	0.5	26.5	1.5	1.09
MS52	0.52	25	2.8	1.12
MS55	0.55	22.8	4.3	1.16
			3	1.29
			4	1.27
MS60	0.6	19.5	5.5	1.25
			6.7	1.24
			10.4	1.19
C-FAM				
FLH	0.34	8.27	9.1	1.19
FMH	0.3	9.7	9.1	1.15
FMM	0.3	9.7	6.5	1.18
FML	0.3	9.7	4.5	1.21
FHH	0.261	11.16	9.1	1.10
FHM	0.261	11.16	6.5	1.14
VF-FAM				
VFCL	0.2	11.6	12.4	1.25
VFCL-HV	0.2	11.6	19.4	1.15
VFCM	0.261	8.5	21	1.23
VFFM	0.261	15.6	4.4	1.12
VFFH	0.32	12.2	9.5	1.16
VF-A	0.255	16.5	3.3	1.08
VF-B3	0.255	15.2	3.9	1.14
VF-B7	0.255	15.2	7.8	1.09
VF-C3	0.255	13.2	4.5	1.23
VF-C7	0.255	13.2	8	1.19
Mixture				
MX1	0.255	5.9	4	1.25

Table 2. Structuralization indices for I19.0C materials.

Material	Blend ratio	Asphalt content (%)	Air void (%)	SI
Binder and mastic				
MS19-AA	0	100	–	0.00
MS19-10	0.1	77.5	–	0.22
MS19-20	0.2	60.5	–	0.45
MS19-309	0.309	46.2	–	0.69
MS19-40	0.4	36.6	–	0.89
MS19-50	0.5	27.9	0.2	1.11
MS19-55	0.55	24.1	3.2	1.19
MS19-60	0.6	20.6	5.8	1.26
Fine FAM				
FF19-A0	0.309	13.1	1.9	1.05
FF19-A4	0.309	13.1	3.7	1.03
FF19-B5	0.309	11.7	5	1.08
FF19-B9	0.309	11.7	8.2	1.04
Mixture				
MX19	–	4.5	4.4	1.22

were confirmed to be low enough so as not to induce any permanent damage or significant nonlinear viscoelastic behaviours [10]. The experiments were performed using either a parallel plate shear geometry (binder and mastic at particle concentrations below 50%), a torsional cylinder geometry (mastic at particle concentrations of 50% and above and FAM), or an axial tension-compression geometry (mixture). Tests were performed to confirm that the geometrical inconsistencies between the parallel plate and torsional cylinder did not contribute to the differences in mechanical behaviours observed across the length scales. The axial and radial strains were measured in the axial tension-compression geometry tests and used to compute the shear properties. Experiments were performed over the range of 10° to 54°C. Details of the analysis procedures can be found elsewhere [1].

Void content tests were performed to identify both the loose and compacted voids at different length scales and combinations of scales: filler, fines, filler+fines, etc. For the filler, the kerosene voids test was performed to determine the compacted voids content. The kerosene method has been reported to yield similar values to those measured by the Rigden apparatus (R^2 of 0.96) [11, 12], here they are treated as equivalent to the Rigden voids. The compacted voids for other scales were determined by AASHTO T 19 (dry rodded void content). The loose voids content for all scales was determined according to either AASHTO T 304 (filler, fines, and filler+fines) or AASHTO T 326 (materials with coarse aggregates).

5 TEST RESULTS

Results of temperature and frequency sweep tests are summarized with dynamic shear modulus, $|G^*|$, mastercurves in Figure 1 [1]. The modulus increases with the material length scale. This increase is not consistent between the different phases or with respect to temperature and frequency. The modulus is most affected by the changes occurring between the mastic and FAM scales. Between these two scales the material stiffens by a factor of 10 to 10,000 (depending on the specific condition of interest), and the time-dependence, which can be observed through the log-log slope of the mastercurve, qualitatively changes from liquid-like to solid-like. From the binder to the mastic and the FAM to the mixture the material modulus also increases, but the stiffness factor only varies between approximately 2 and 7 in both cases. These differences are statistically significant as the repeatability of the tests was very good, with coefficient of variations of all tests less than 10% and in many cases closer to 2–5%.

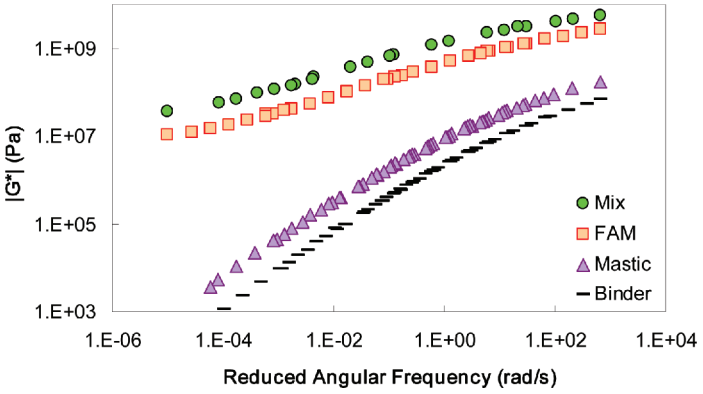

Figure 1. Comparison of |G*| values for each characteristic element in an asphalt mixture.

Table 3. Void contents for study materials.

Material	Compacted voids (%)	Loose voids (%)
Primary mixture materials		
12.5 mm—Pan	28.7	–
12.5 mm–2.36 mm	42.1	47.1
12.5 mm–0.6 mm	40.1	45.0
12.5–0.075 mm	31.4	40.8
1.18 mm–0.075 mm	41.1	48.6
0.3 mm–0.075 mm[a]	47.3	56.0
1.18 mm—Pan	36.2	47.8
0.3 mm—Pan[b]	41.7	55.3
Filler	33.2	65.3
VFFM & VFFH + Filler	47.1	56.8
VFFM & VFFH + Filler	42.6	56.2
VFCL, VFCL-HV, VFCM – Filler	46.7	56.3
VFCL, VFCL-HV, VFCM + Filler	43.3	55.6
VF-B3 & VF-B7 + Filler	42.0	55.8
VF-C3 & VF-C7 + Filler	42.4	55.8
Secondary mixture materials		
25.0 mm—Pan	25.9	35.0
25.0 mm–1.18 mm	37.7	42.3
25.0 mm–0.6 mm	34.2	39.2
25.0 mm–0.075 mm	29.1	36.5
0.6 mm–0.075 mm[c]	38.6	48.4
0.6 mm—Pan[d]	34.7	48.8
Filler	38.6	71.8

[a]Used in VF-A, VF-B3, VF-B7, VF-C3, and VF-C7, [b]Used for VF-A, [c]Used in FF19-A0, FF19-A4, FF19-B5, and FF19-B9, [d]Used in FF19-A0 and FF19-A4.

A compilation of loose and compacted void contents is shown for different particle size distributions in Table 3. These void contents are used to calculate the *SI* via Equation (2). The importance of gradation in determining the void content at the two compaction bounds can be clearly observed. For a fixed maximum aggregates size, the void content reduces as finer aggregates are included. This trend occurs even though the actual void content of these smaller scales may be larger than the scale that they are being added to. For example in the primary mixture, the 12.5 mm–0.6 mm range contains a compacted void content of 40.1% and the 0.3 mm–0.075 mm contains a compacted void content of 47.3%. However, when

these two are combined (12.5 mm–0.075 mm) the combination produces a compacted void content of 31.4%. This trend occurs in both materials.

6 APPLICATION OF STRUCTURALIZATION CONCEPT TO ASPHALTIC COMPOSITES

The first step in evaluating the existence of the *SI* is to examine how the *FC* concept applies across length scales. If *FC* is a sufficient index then these resulting curves should appear continuous with no major breaks or disruptions. The stiffening ratio for mastic is defined by taking the mastic $|G^*|$ as the numerator and the binder $|G^*|$ as the denominator. The stiffening ratio for the mixture and FAM is defined with by using the appropriate mastic $|G^*|$ as the denominator. This approach best matched the concepts of the microstructural hypothesis where the numerator is the $|G^*|$ of the target scale and the denominator is the $|G^*|$ of the material which coats the particles in this target scale [2, 3]. For the modulus ratio, test data was examined at many temperatures and frequencies, but was only compiled and presented at a few specific temperatures and at 18.85 rad/s. The trends shown are representative of all other conditions evaluated.

Figure 2 shows the results of this analysis for the primary mixture. Each data point represents one of the different mastic and FAM materials (Table 1). From this figure a consistent and smoothly varying curve is seen within the mastic phase and within the FAM phases. However, between the phases the curves are disjointed and do not form a consistent trend, which means that either *FC* is not an appropriate *SI* or that the entire concept of *SI* is flawed. *FC* may not be an appropriate *SI* because in taking the dry compacted density as the reference void content suggests that structural onset occurs at the densest possible dry aggregate configuration. However, one can clearly see a stable structure forming, i.e., one with contacting particles and internal load paths, at void contents greater than this value.

It is believed that the onset of a stable structure should be accompanied by a rapid change in mechanical properties, and that this rapid change can serve as a marker for structuralization onset. As seen in Figure 2 the mastic shows a bilinear relationship with respect to *FC*, and the point of inflection in this relationship indicates a structural change. This inflection can be used to identify the value of *B* by adjusting *B* until the intersection of the two bilinear curves corresponds to an x-value of 1. Since *B* does not depend on the scale, the inflection point can be used to define the $\%Voids_{str}$ and thus *SI* for all scales. This process is demonstrated for the primary mixture in Figure 3. The relationship between *FC* at structuralization onset, FC_S, and the *B* parameter is given in Equation (4). This *B* value can subsequently be substituted in Equations (2) and (3) to determine the *SI* value for each material. The analysis shows that *B* is 0.68 for the primary mixture and 0.50 for the secondary mixture. Thus, according to the discussion above it takes more compactive effort to reach a stable configuration for the secondary mixture than it does for the primary mixture. The AIMS data suggests

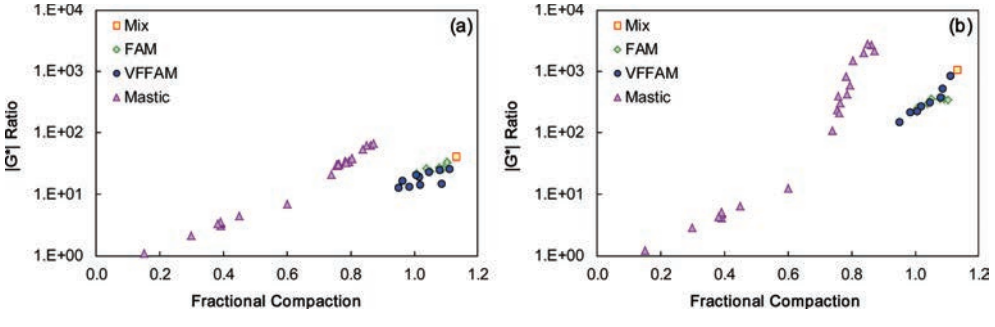

Figure 2. |G*| ratio of different characteristic length scales for primary mixture with respect to FC at; (a) 10°C and (b) 54°C.

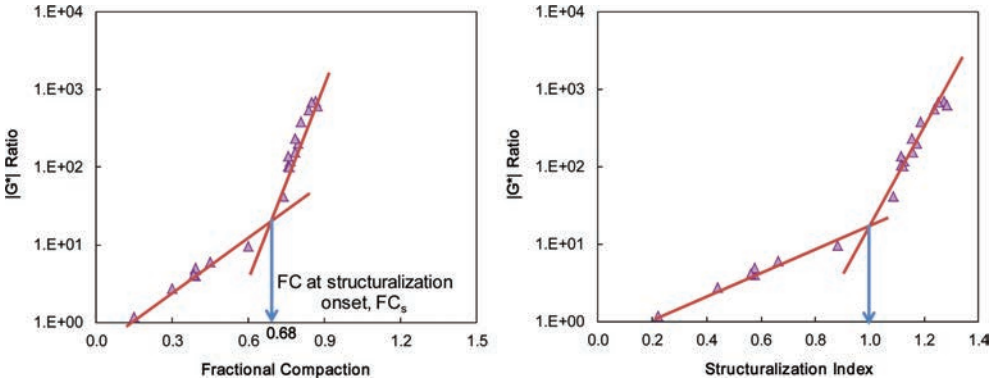

Figure 3. Identification of *B* parameter from measured mastic behaviors.

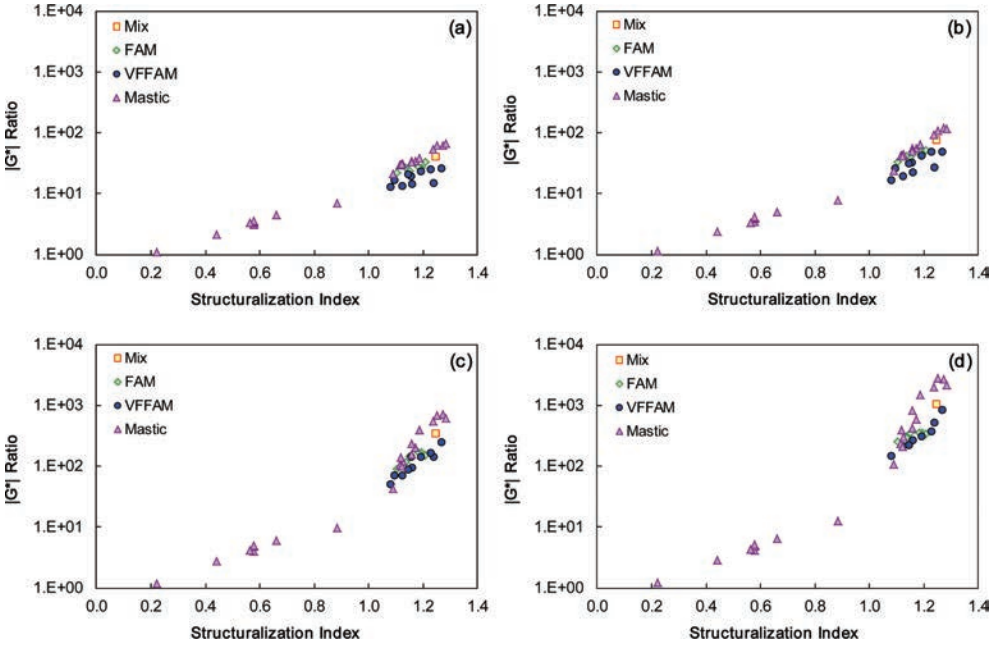

Figure 4. Structuralization plots for the |G*| ratio of the primary mixture materials at; (a) 10°C, (b)20°C, (c) 40°C and (b) 54°C.

that the primary mixture is more angular and so a higher compactive effort for the secondary mixture is not unexpected.

$$B = \frac{\left(1 - FC_s\right)\left(100 - \%Voids_{comp}\right)}{\%Voids_{loose} - \%Voids_{comp}} \tag{4}$$

The resulting modulus ratio plots using the *SI* are shown for the study mixtures in Figures 4 and 5. Note that modulus alone does fully capture the LVE response (and thus does not comprehensively prove a linkage between scales). The authors also examined the log-log slope of the measured data and although not shown here the same trends and continuous curves occur. The agreement is not perfect and it is surmised that the structuralization is only a first order approximation that may not be accounting for interactive effects between the

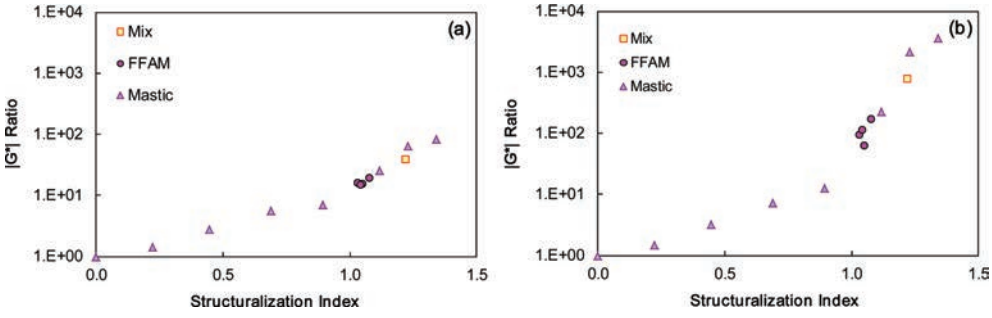

Figure 5. Structuralization plots for the |G*| ratio of the secondary mixture materials; (a) 10°C and (b) 54°C.

structure and asphalt binder or mastic and how this may affect the forces present at particle interfaces.

The fact that consistent temperature and frequency dependent slope (not shown in this paper) and modulus ratio curves could be defined across all scales for both study materials indicates that the assumptions put forth in the previous paragraphs are reasonably accurate. Independent evaluation and quantification of the aggregate characteristics aid in interpreting the reasonableness of the characterized *B* parameter. It should be noted that the authors evaluated many different potential indices to link the behaviours of these composites across length scales including some based on percolation theory. None of these methods produced as consistent of trend as the *SI* value defined here.

7 CONCLUSIONS AND SUMMARY

The reasonableness of internal structuralization as a linking concept for the mechanical behaviors of asphaltic composites across length scales has been evaluated. It is found that the traditional measure of structuralization, the *FC*, is not sufficient enough to describe the behaviors across length scales even though it can describe the effects of structure within a single scale. A new index, the structuralization index is subsequently postulated and defined based on a more general interpretation of the onset of structuralization and this index is found to capably explain the change in modulus and time-dependence of these composites across length scales. The existence of what is deemed to be a first order approximate linking index, which consists of a singular factor, *B*, and the void contents at different compaction efforts, suggests that a form of self-similar structuralization occurs in these composites. More study is needed to understand this phenomenon with better clarity. However, it appears based on this work and additional study that could not be presented within the limitations of this volume that this self-similarity is different than what is explained by existing statistical physics theories such as percolation.

REFERENCES

[1] Underwood, BS and Kim, YR Experimental investigation into the multiscale behavior of asphalt concrete, *International Journal of Pavement Engineering*, 12(4), pp. 357–370. 2011.

[2] Underwood, BS and Kim, YR. Microstructural association model for multiscale evaluation of asphalt concrete, *Journal of Materials in Civil Engineering*, 25(9), pp. 1153–1161. 2013.

[3] Underwood, BS and Kim, YR. Microstructural investigation of asphalt concrete for performing multiscale experimental studies, *International Journal of Pavement Engineering*, 14(5), pp. 498–516. 2013.

[4] Rigden, PJ. The use of fillers in bituminous road surfacings: a study of filler-binder systems in relation to filler characteristics, *Journal of the Society of Chemical Industry*, 66(9), pp. 299–309. 1947.

[5] Buttlar, WG, Bozkurt, D, Al-Khateeb, GG, Waldhoff, A. Understanding asphalt mastic behavior through micromechanics, In *Transportation Research Record: Journal of the Transportation Research Board*, 1681, pp. 157–169. 1999.
[6] Delaporte, B, DiBenedetto, H, Chaverot, P, Gautheier, G. Linear viscoelastic properties of bituminous materials: from binders to mastics, *Journal of the Association of Asphalt Paving Technologists*, 76, pp. 445–494. 2007.
[7] Shashidhar, N and Shenoy, A. On using micromechanical models to describe dynamic mechanical behavior of asphalt mastics, *Mechanics of Materials*, 34(10), pp. 657–669. 2002.
[8] Yin, HM, Buttlar, WG, Paulino, GH, DiBenedetto, H. Assessment of existing micro-mechanical models for asphalt mastics considering viscoelastic effects, *Road Materials and Pavement Design*, 9(1), pp. 31–57. 2008.
[9] Masad, E. (2004) Aggregate imaging system (AIMS): basics and applications, Final Report for Project 5-1707-01, TXDOT, Austin, TX.
[10] Underwood, BS and Kim, YR Comprehensive evaluation of small strain viscoelastic behavior of asphalt concrete, *Journal of Testing and Evaluation*, 40(4), pp. 99–110. 2012.
[11] Grabowski, W and Wilanowicz, J. The structure of mineral fillers and their stiffening properties in filler-bitumen mastics, *Materials and Structures*, 41(4), pp. 793–804. 2008.
[12] Heukelom, W. The role of filler in bituminous mixes, *Journal of the Association of Asphalt Paving Technologists*, 34, pp. 396–429. 1965.

Asphalt Pavements – Kim (Ed)
© 2014 Taylor & Francis Group, London, ISBN 978-1-138-02693-3

Simulation of drying aggregate in asphalt plants

Haifang Wen & Kun Zhang
Department of Civil and Environmental Engineering, Washington State University, Pullman, WA, USA

Andrew Hobbs
Astec Inc., Chattanooga, TN, USA

Steven Lee Edburg
Department of Civil and Environmental Engineering, Washington State University, Pullman, WA, USA

ABSTRACT: Lowering production temperature in warm mix asphalt technology may lead to inadequate drying of aggregates, resulting in low-quality asphalt production. Due to difficulty in direct observation of drying and heating process and measurement of aggregate temperature inside the dryer, numerical analysis offers an alternative way to study heat transfer and aggregate temperature evolution. In this paper, coupled Computational Fluid Dynamics (CFD) and Discrete Element Method (DEM) is used to simulate aggregate movement and heat transfer in a simple drum. The effects of aggregate size and drum rotation speed on aggregate temperature evolution and fluid temperature on the heating efficiency are studied. The results show that coupled CFD-DEM technique is an appropriate approach to study aggregate movement and temperature evolutions in the drum directly. Small particles can be heated more easily than large particles. Determination of optimal drum rotation speed needs to consider particle movement models as well as resident time in a real drum with inclined angle. High fluid temperature could reduce heating time of particles to reach the target mixing temperature. The preliminary results may provide some guidelines for operating the mixing drum efficiently and designing drum to control quality of asphalt mixes and save energy.

Keywords: Coupled CFD and DEM, granular drying, rotation drum, heat transfer

1 INTRODUCTION

The increased awareness of sustainability has encouraged the use of low energy and low emission technologies for pavement design, such as Warm Mix Asphalt (WMA). WMA refers to a technology that reduces the mixing and compaction temperatures in order to lower energy consumption and reduce the emissions of greenhouse or other toxic gases [1]. However, one of the concerns of the use of low production temperatures for producing WMA is that the aggregate does not always dry adequately, which could lead to the susceptibility of the asphalt mix to moisture stripping or raveling [2–6].

In order to produce high quality, well-coated asphalt mixes, the aggregate particles need to be dried thoroughly and heated to mixing temperature, which can be achieved by counter-flow or parallel-flow drying in a plant. Currently the degree to which the aggregate is dried cannot be quantified precisely because it is not realistic to measure the aggregate temperature directly [7]. Therefore, a method of estimation of the degree of drying of the aggregates is needed to determine whether the aggregate is sufficiently dried before it is mixed with the asphalt binder. Based on the coupling of the Discrete Element Method (DEM) and Computational Fluid Dynamics (CFD), this study attempts to simulate the

heating process of aggregate as an essential step in estimating the degree of drying during the production.

The DEM is employed to simulate the movement of granular particles, and the CFD can model the behavior of a fluid, such as gas or liquid. Coupled CFD-DEM simulations have been used widely in many industry areas, such as studying the granular behavior in a fluidized bed [8], heat and mass transfer in a lime shaft kiln [9], and tablet coating in pharmaceuticals [10]. Therefore, a numerical simulation of the coupled CFD-DEM technique is a viable way to study the phenomena that occur inside an asphalt mix drum. The coupled CFD-DEM technique also shows a promising way to study aggregate behavior, such as moisture and temperature evolution, in the rotary drum dryer [7, 11].

In this paper, heat convection between hot gas and granular particles and heat conduction among particles are simulated to demonstrate the feasibility of the approach. A simple counter-flow drum model with four flights attached symmetrically around the inner chamber is used to demonstrate the aggregate particle movement and temperature evolution through the coupled CFD-DEM method. The effects of particle size, drum rotation speed, on aggregate temperature evolution, and fluid temperature on the heating efficiency are studied. The results could provide useful guidelines to optimize drum design and operation.

2 SIMULATION METHOD

The coupled CFD-DEM approach used in this paper is based on an open source program developed by Christian Doppler Laboratory [12] called the CFDEM project [13]. The CFD part of the simulations was conducted within OpenFOAM® [14], and the DEM part of the simulations was conducted by LIGGGHTS, an open source software package for modeling granular material based on LAMMPS, which is an open source molecular dynamics code developed by Sandia National Laboratories [15].

2.1 *Governing equations of the DEM*

The DEM was first developed by Cundall and Strack [16]. All of the particles in the computational domain follow Newton's laws of motion and are tracked in a Lagrangian way. The forces that act on the particles in this simulation include normal force and tangential force from the particle contacts, drag force from the fluid part, and gravity. The kinematic function is expressed as Eq. (1):

$$mi\frac{dv_i}{dt} = \sum_j F_{ij}^n + \sum_j F_{ij}^t + F_i^f + F_i^g \tag{1}$$

where F_{ij}^n is the normal contact force; F_{ij}^t is the tangential force; F_i^f is the drag force, and F_i^g is gravity.

Hertz-Mindlin contact model is adopted to calculate normal and tangential contact force [17]. Drag force is expressed as Eq. (2):

$$F_i^f = \frac{V_p^\beta}{\varepsilon_p}(u_f - u_p) \tag{2}$$

where β represents the interphase momentum transfer coefficient due to drag, which is calculated using a drag relationship proposed by Koch and Hill [18] that is based on the lattice-Boltzman simulation.

2.2 *Governing equations of CFD and CFD-DEM coupling*

The motion of a fluid phase is governed by the volume-averaged Navier-Stokes equations for compressible fluid, which can be written as Eqs. (3, 4):

$$\frac{\partial \alpha_f}{\partial t} + \nabla \cdot (\alpha_f u_f) = 0 \tag{3}$$

$$\frac{\partial (\alpha_f u_f)}{\partial t} + \nabla \cdot (\alpha_f u_f u_f) = -\alpha_f \nabla \frac{p}{\rho_f} - R_{sl} + \nabla . \tau \tag{4}$$

where α_f is the volume fraction occupied by the fluid; ρ_f is the fluid density; u_f is the fluid velocity; τ is the stress tensor for the fluid phase; and R_{sl} represents the momentum exchange with the particulate phase.

2.3 *Governing equations of heat transfer*

Particle temperature evolutions due to heat conduction among particles are shown as Eq. (5) [19]:

$$m_p c_p \frac{dT_{p,i}}{dt} = \sum \dot{Q}_{pi-pj} + \dot{Q}_{pi,source} \tag{5}$$

where $\dot{Q}_{pi-pj}$ is the rate of heat conduction flux by particle contacts; $\dot{Q}_{pi,source}$ is the rate of heat conduction flux by other sources; m_p, c_p $T_{p,i}$, are the particle mass, specific thermal capacity, and temperature respectively.

The model for heat convection between hot gas and particles is based on Li and Mason [20], which can be modeled by a solver of "cfdemSolverPisoScalar" developed by Christian Doppler Laboratory [21]. The rate of heat transfer Q_s from the gas to the particle can be calculated as Eq. (6):

$$Q_s = h_i A_i (T_g - T_{pi}) \tag{6}$$

where h_i is the heat transfer coefficient of the particles; A_i is the surface area of the particles; T_g is the gas temperature; and T_{pi} is the particle temperature.

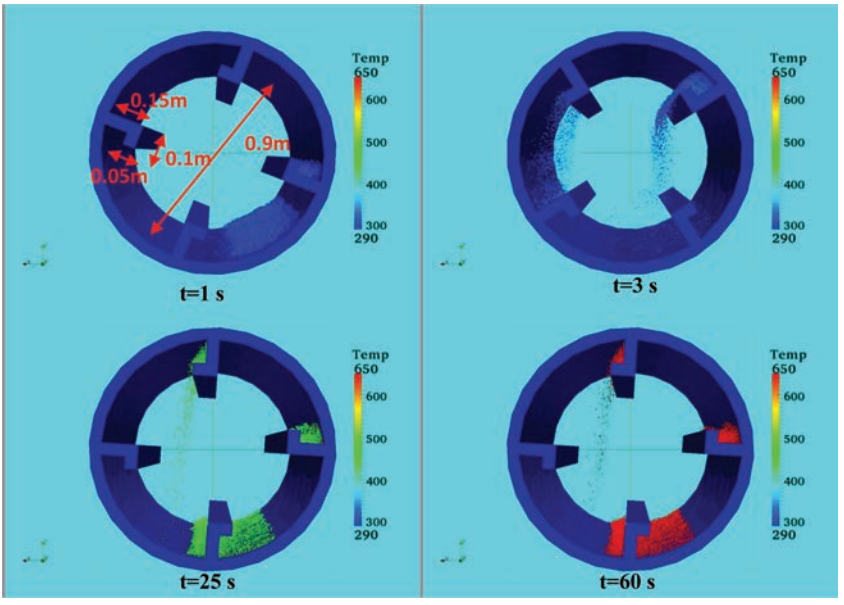

Figure 1. Snapshot of particle movement at t = 1 s, 3 s, 25 s and 60 s.

Table 1. Parameters used in drum simulation.

DEM		CFD	
Particle density (kg/m^3)[2]	2900	Fluid density (kg/m^3)[1]	1.188
Particle diameter (m)	0.01, 0.02, 0.03	Fluid specific thermal capacity (J/kg · K)[3]	1010
Particle young's modulus (N/m^2)[2]	1.38e7		
Particle poisson's ratio[2]	0.25	Fluid thermal conductivity (J/K · s · m)[3]	0.0457
Coefficient of restitution[2]	0.45		
Coefficient of sliding friction[2]	0.55	Kinematic viscosity (m^2/s)[3]	5.1e-5
Coefficient of rolling friction[2]	0.3		
Particle specific thermal capacity (J/kg · K)[3]	800	Initial velocity of gas (m/s)	1
Particle thermal conductivity (J/K · s · m)[3]	5		
Initial particle temperature (K)	293 (20ºC)	Initial fluid temperature (K)	1000, 2000, 3000
DEM time step (s)	0.00001	CFD time step (s)	0.005
Coupling intervals	500		
Drum rotation speed (second per round)	0.8, 2, 5, 10	Total simulation time (s)	60

Notes: [1]Fluid density is set to be constant in this study. [2]Parameters are from reference (7). [3]Parameters are from: http://www.engineeringtoolbox.com/.

2.4 *Drum geometry, simulation parameters and initial conditions*

In this study, a simplified drum with four flights is simulated, shown in Figure 1. The length of the drum is 1 m. Table 1 presents the parameters and initial conditions used in this simulation. As drum rotates, the flights pick up the aggregate particles that cascade due to gravity. Hot gas enters one end of the drum and exits from the other end where the aggregate particles enter. In order to study the effects of particle size, drum rotation speed, and fluid temperature on the heating efficiency, these three parameters are varied.

3 RESULTS AND DISCUSSION

3.1 *Particle movement and fluid characterization*

Figure 1 shows snapshots of the particle movement and temperature distribution at times of 1 s, 3 s, 25 s, and 60 s in the simulated drum with the rotation speed of 5 seconds Per Revolution (SPR). The particle size is 0.01 m in diameter, and the number of particles in the drum chamber is 13,500. This figure illustrates that the coupled CFD-DEM method is able to capture the escalation and cascading modes of the particle movement in the drum and the formation of veiling lift by the flights.

Also, the evolutions of the particle temperature can be observed directly from color of particles and studied by statistic data. Figure 2 shows the evolution of the maximum, minimum, and average temperature of two particles heated in the drum during 3600s under fluid temperature of 1000 K (727ºC). The initial temperature of the aggregate is set to 293 K (20ºC) and then is increased to temperature of 1000 K to reach the state of equilibrium with fluid temperature. It is seen that the aggregate temperature increases quickly at the early heating time, and then approaching to fluid temperature slowly.

Figure 3 shows the temperature and velocity of the fluid along the horizontal cross-section at 60 s. The arrows indicate the fluid flow direction. The temperature profiles show that the outlet temperature of the fluid is lower than the inlet temperature of the fluid due to the heat convection from the fluid phase to the particles. As for velocity, the gas at the center of the drum flows faster than the gas at the right edge of drum where the particle bed probably hinders the flow of fluid. Therefore, the coupled CFD-DEM method captures the mode of particle movement and fluid flow characterization.

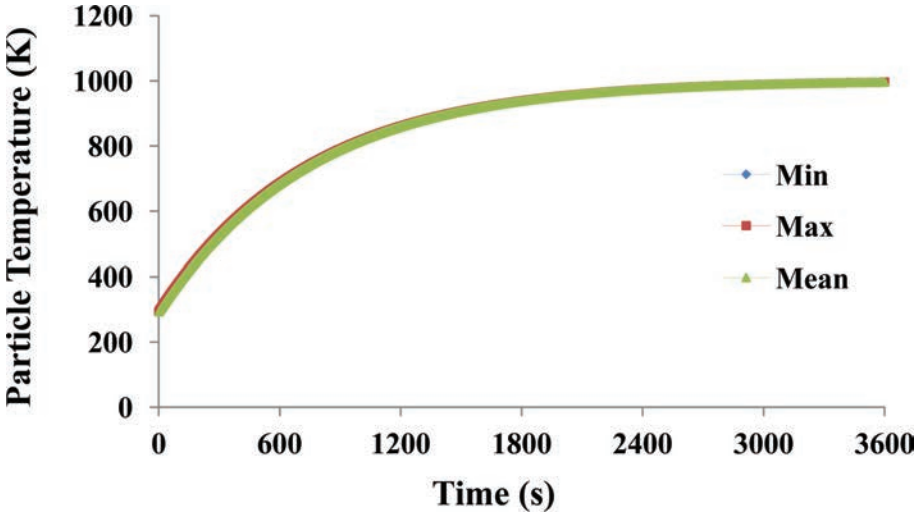

Figure 2. Particle temperature versus time.

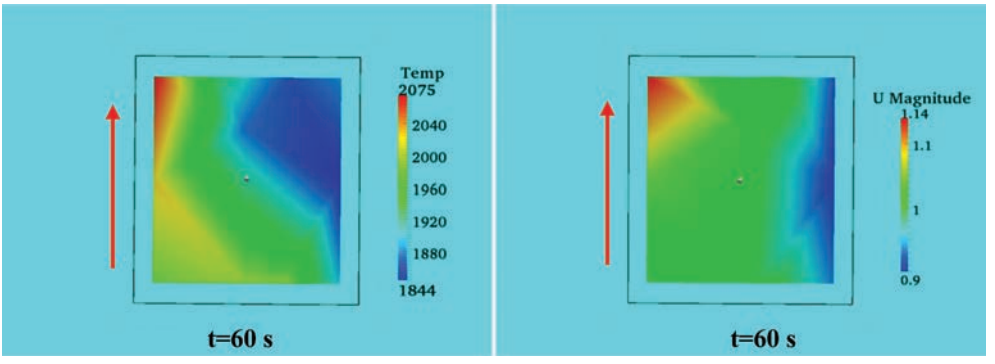

Figure 3. Profiles of fluid phase: temperature (left) and velocity (right).

3.2 *Effects of particle size*

In order to study the effect of particle size on the temperature changes of the particles, three particle diameters, 0.01 m, 0.02 m, and 0.03 m, are used for the simulation. The total mass of each size of particle is controlled equally to 20.5 kg. That is, the particle numbers used in the simulation are 13,500, 1,688 and 500 for the 0.01 m, 0.02 m, and 0.03 m particles, respectively. The fluid temperature is set to 2000 K (1727ºC). Figure 4 shows the relationship of particle temperature to particle size. It is seen that the small particles are much easier to heat than the large particles. A possible reason for this phenomenon is that the small particles have a large specific surface area, which is instrumental in absorbing heat energy from the hot gas and the heat conduction among the particles, which depends on the amount of contact area.

3.3 *Drum rotation speed*

Figure 5 illustrates the effect of the drum rotation speed on the particle temperature changes. Four different rotation speeds are used in the simulation: 0.8, 2, 5, and 10 SPR. It should be noted that smaller value of SPR means faster rotation speed. A comparison of the results of the rotation speeds of 2, 5, and 10 SPR shows that as the rotation speed increases, the

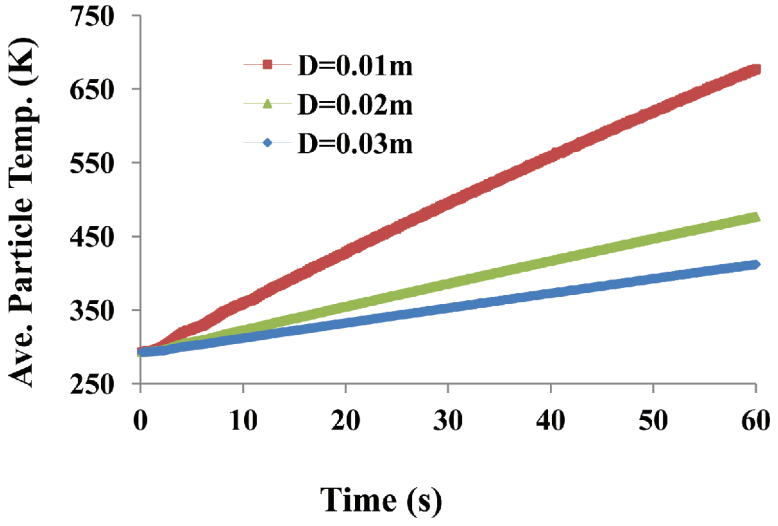

Figure 4. Average particle temperatures versus particle size.

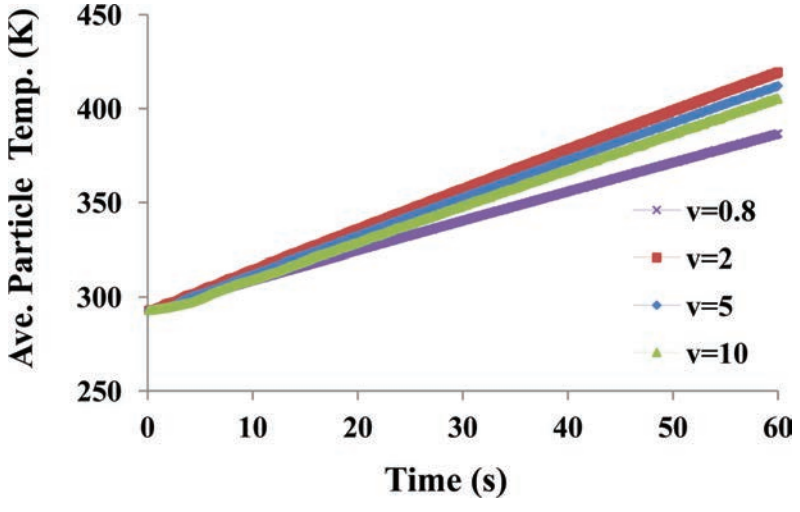

Figure 5. Average particle temperature versus rotation speed.

particles heat up faster. This phenomenon results from the veiling formation of the particles created by the flights in the drum. The fast rotation leads to more frequent exposure of the particles in the heat convection areas where the particles can be heated efficiently by the hot gas. Hobbs observed that a rapid increase in particle temperature corresponds to the start of veiling [7]. Therefore, a fast rotation speed is beneficial for heating aggregate particles quickly. However, this discussion is within the cascading mode of particle movement. If the rotation speed is set to 0.8 SPR, the mode of granular motion in this drum will be centrifuging without the veiling formation. In this case, the final temperature of the particles in centrifuge mode is lower than temperature of the particles in cascade mode. However, in a real drum with an inclined angle, although higher rotational speed might increase veiling frequency, it also will decrease the overall residence time. Therefore, determination of optimal rotation speed needs to consider balancing veiling frequency and residence time to achieve complete drying.

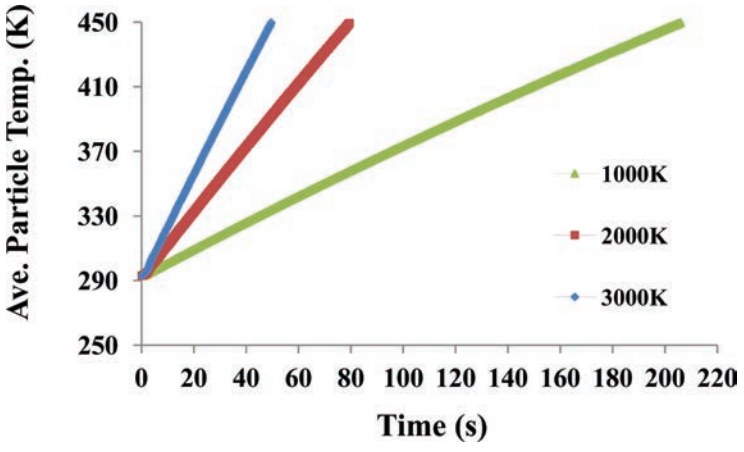

Figure 6. Average particle temperature versus heating time.

3.4 *Heating efficiency*

In agreement with common sense, higher fluid temperature will result in higher particle temperatures during the same heating time. If particles are designed to be heated up to certain mixing temperature, such as 450 K (177ºC), the heating time should be different under different fluid temperatures. Figure 5 shows heating time needed to heat particle to temperature of 450 K under different fluid temperature. For fluid temperature of 1000 K (727ºC), it takes 206 s to heat the particles to the target mixing temperature, and 80 s and 50 s under 2000 K (1727ºC) and 3000 K (2727ºC) respectively. It is as expected that shorter heating time is need under higher fluid temperature so that in an inclined drum operation, determining optimum heat time shall be based on fluid temperature and energy saving perspective, as well as without compromising the quality of hot mixes.

4 CONCLUSIONS

The adequate drying of aggregate particles is critical for WMA to achieve good performance. A methodology to quantify the drying process of aggregate is currently lacking. The coupled CFD-DEM technique is used here to study the aggregate movement and temperature evolutions in a simulated simplified rotating drum with flights. Hot gas is used to heat the aggregate while the drum is rotating. It is found that:

1. Particle size affects the heating efficiency. Small aggregate particles heat quickly compared to large particles, which is likely due to the relatively large specific surface area of the smaller particles.
2. With an increase in the drum rotation speed, the heating efficiency increases. However, an excessively fast rotation speed causes the particles to centrifuge, which reduces the heating efficiency. Determination of optimal rotation speed needs to consider particle movement model, and balance veiling frequency and residence time to achieve complete drying in a real drum with certain inclined angle.
3. Shorter heating time is needed under higher fluid temperature. Determination of optimum heat time shall be based on inlet fluid temperature and energy saving perspective, as well as without compromising the quality of hot mixes. This finding indicates the importance of the proper design of asphalt drums.

As a preliminary effort, this paper studies the feasibility of using the coupled CFD-DEM technique to simulate the drying process of aggregate. The simulation does not consider the heat transfer from the hot gas and particles to the drum wall, and the heat loss from the drum wall to the ambient environment. Also, a mass transfer and moisture evaporation model are

not included in this study. These factors will contribute largely to the heat transfer and temperature evolution of the particles in the drum. In addition, scale-up models should be used in the simulation, and experimental calibration needs to be carried out to verify the results from the numerical analysis.

REFERENCES

[1] Corrigan, M. *Warm Mix Asphalt Scan*. http://www.warmmixasphalt.com/submissions/76_20080325_2007WarmMixAsphaltSCAN_NAPA2008.pdf. Accessed July. 16, 2013.

[2] Diefenderfer, S. and A. Hearon. *Laboratory Evaluation of a Warm Asphalt Technology for Use in Virginia.* Virginia Transportation Research Council research report, Charlottesville, VA, 2008.

[3] Xiao, F., S.N. Amirkhanian, and B.J. Putman. Evaluation of rutting resistance in warm mix asphalts containing moist aggregate. *Transportation Research Record: Journal of the Transportation Research Board*, No. 2180.1, Transportation Research Board of the National Academies, Washington, D.C. pp. 75–84. 2010.

[4] Wielinski, J., A. Hand, and D.M. Rausch. Laboratory and field evaluation of foamed warm mix asphalt projects. *Transportation Research Record: Journal of the Transportation Research Board*, No. 2126.1, Transportation Research Board of the National Academies, Washington, D.C. pp. 125–131. 2009.

[5] Kvasnak, A., R. West, J. Moore, P. Turner, and N. Tran. *Case Study of Warm Mix Asphalt Moisture Susceptibility in Birmingham*. CD-ROM, No. 09-3703, Transportation Research Board of the National Academies, Washington, D.C. 2009.

[6] Kvasnak, A., B. Prowell, G. Hurley, R. West, T. Kreich, L. Osborn, B. Frank, K. Peregrine, and D. Jones. *Engineering Properties, Emissions, and Field Performance of Warm Mix Asphalt Technologies*. NCHRP 9-47 A Interim Report, NCAT, Auburn, AL. 2010.

[7] Hobbs, A. Simulation of an aggregate dryer using coupled CFD and DEM methods. *International Journal of Computational Fluid Dynamics*, Vol. 23(2), pp. 199–207. 2009.

[8] Fries, L., S. Antonyuk, S. Heinrich, and S. Palzer. DEM–CFD modeling of a fluidized bed spray granulator. *Chemical Engineering Science*, Vol. 66(11). pp. 2340–2355. 2011.

[9] Bluhm-Drenhaus, T., E. Simsek, S. Wirtz, and V. Scherer. A coupled fluid dynamic-discrete element simulation of heat and mass transfer in a lime shaft kiln. *Chemical Engineering Science,* Vol. 65(9). pp. 2821–2834. 2010.

[10] Suzzi, D., S. Radl, and J.G. Khinast. Local analysis of the tablet coating process: Impact of operation conditions on film quality. *Chemical Engineering Science*, Vol. 65(21). pp. 5699–5715. 2010.

[11] LeGuen, L., F. Huchet, and P. Tamagny. Drying and heating modelling of granular flow—application to the mix-asphalt processes. *Journal of Applied Fluid Mechanics*, Vol. 4. pp. 71–80. 2011.

[12] Goniva, C., C. Kloss, A. Hager, and S. Pirker. An open source CFD-DEM perspective. In *Proceedings of OpenFOAM Workshop*, Gothenburg, Sweden, 2010.

[13] CFDEMproject. CFDEM-Open source CFD, DEM and CFD-DEM. http://cfdem.dcs-computing.com/. Accessed July 3, 2013.

[14] OpenCFD Ltd. OpenFOAM-The open source CFD toolbox. http://www.openfoam.com/. Accessed July 3, 2013.

[15] Plimpton, S.J. Fast parallel algorithms for short-range molecular dynamic. *Journal of Computational Physics*, Vol. 117, 1995, pp. 1–19. (LAAMPS homepage: http://lammps.sandia.gov, Accessed July 7, 2013).

[16] Cundall, P.A., and O.D. Strack. A discrete numerical model for granular assemblies. *Geotechnique*, Vol. 29. pp. 47–65. 1979.

[17] LIGGGHTS Document. LIGGGHTS/LIGGGHTS-PUBLIC/doc/pair_gran. Html, 2013.

[18] Van Buijtenen, M.S., W.J. Van Dijk, N.G. Deen, J.A.M Kuipers, T. Leadbeater, and D.J.J. Parker. Numerical and experimental study on multiple-spout fluidized beds. *Chemical Engineering Science*, Vol. 66(11). pp. 2368–2376. 2011.

[19] LIGGGHTS Document. LIGGGHTS/LIGGGHTS-PUBLIC/doc/fix_heat_gran_conduction. html, 2013.

[20] Li, J. and D.J. Mason. A computational investigation of transient heat transfer in pneumatic transport of granular particles. *Powder Technology*, Vol. 112(3). pp. 273–282. 2000.

[21] CFDEM Document. CFDEM/CFDEMcoupling-PUBLIC-2.2.x/doc/cfdemSolverPisoScalar. html, 2013.

Experimental characterization of asphaltic materials—V

This page intentionally left blank

Asphalt Pavements – Kim (Ed)
© 2014 Taylor & Francis Group, London, ISBN 978-1-138-02693-3

Evaluation of gradation-based criteria for cracking performance

Marco Isola, Jian Zou & Reynaldo Roque
Department of Civil and Coastal Engineering, University of Florida, Gainesville, FL, USA

Sanghyun Chun
Florida Department of Transportation, State Materials Office, Gainesville, FL, USA

George Lopp
Department of Civil and Coastal Engineering, University of Florida, Gainesville, FL, USA

ABSTRACT: It is well documented that performance of asphalt mixture is related to aggregate structure. The Dominant Aggregate Size Range-Interstitial Component (DASR-IC) model provides a framework of gradation-based parameters and associated criteria to link gradation characteristics and volumetric properties to aggregate structure, mixture properties, and field performance. Primary interlocking of coarser aggregate is characterized by DASR parameters, which have been used to establish performance-based criteria based on extensive field rutting data. Studies have also shown that mixtures with acceptable DASR criteria may result in acceptable cracking performance, indicating that IC characteristics strongly influence fracture resistance. Therefore, IC parameters have been used to establish and evaluate preliminary criteria for optimal cracking performance based on limited data. This paper presents the basis and early results for the evaluation and, if necessary, modification of IC criteria, through an extensive laboratory experiment. The challenge was to realistically isolate the effects of the IC, given that all DASR-IC components are interrelated. The results to date indicate that IC parameters have a strong effect on damage rate and fracture energy in a manner consistent with expected trends.

Keywords: Aggregate structure, gradation-based criteria, cracking performance, damage rate, fracture energy

1 INTRODUCTION

Asphalt mixture is a heterogeneous multiphase material comprising aggregates of various sizes, asphalt binder, and air voids. Thus, proportions and properties of the mixture constituents, as well as their chemical and physical interactions, dictate the content and spatial distribution, (generally referred to as the internal structure) of the mixture. Internal structure significantly influences asphalt mixture's mechanical properties and resistance to major distresses, such as rutting and cracking. Most mixture design methods recognize the importance of internal structure by imposing requirements for aggregate type, size, gradation, and volumetrics, as well as limits on density during compaction. For instance, aggregate gradation is generally selected to meet Superior Performing Asphalt Pavements (Superpave®) mix design specifications. However, Superpave® mixtures that meet all existing design criteria have exhibited highly variable cracking performance [1]. Research has not reached a consensus on rational design guidelines for achieving optimal cracking performance.

Research over the past ten years has emphasized on developing methods for quantitatively or qualitatively characterizing aspects of the internal structure of asphalt mixtures. With the development of computer technology, several researchers have used image analysis techniques to characterize mixture microstructure, and to directly quantify the internal structure distribution.

Researchers have also used digital imaging techniques to analyze digitized mixture images and quantitatively study the internal structure distribution of Hot Mix Asphalt (HMA). 2D images of the internal structure can be captured using a microscope and a camera, or through X-ray Computed Tomography (CT). X-ray CT is a unique nondestructive tool that obtains a series of 2D images of the internal structure of the specimen at fixed intervals through the entire thickness of the specimen, based on differences in density among the mix constituents. The system then combines this series of scanned images to produce a three-dimensional (3D) reconstructed image of the specimen's internal structure. Masad and Button summarized the ways in which imaging methods are used for characterizing and quantifying the internal structure of HMA [2]. The two main uses are performing aggregate orientation analysis [3, 4] and studying the size, connectivity, and distribution of air voids [5, 6]. Sefidmazgi, Tashman and Bahia used image analysis to implement a set of internal aggregate structure analysis features for asphalt mixtures, and proposed new indices to relate rutting performance to aggregate structure [7]. Specifically, they developed the iPas software, to quantitatively characterize the length and orientation of the stone-to-stone contact areas of asphalt mixtures. The software includes an Internal Structure Index (ISI) parameter function of contact length characteristics that correlates internal aggregate structure characteristics to mixture rutting performance.

Several theories have been proposed to characterize internal structure and link gradation to aggregate structure and mixture performance. In the early 1980s, the Bailey method was developed at the Illinois Department of Transportation with the main purpose of controlling the volumetric properties of mixtures during construction as a means of combatting the rutting of asphalt mixtures, while also maintaining proper durability characteristics. The Bailey method of mix design provides a set of tools to evaluate aggregate blends, to better understand the relationship between aggregate gradation and mixture voids, and design the aggregate structure in an asphalt mixture [8, 9]. The method is a systematic approach that provides aggregate interlock as the backbone of the aggregate structure and a balanced continuous gradation with adequate packing based on Voids in Mineral Aggregate (VMA) to complete the mixture and ensure optimal asphalt binder content. The design approach relies on coarse aggregate density as a measure of aggregate interlock. In addition the method defines gradation parameters that characterize packing of the aggregates and are related to air voids and VMA.

Numerous research projects have focused on characterizing aggregate structure and its relationship to mixture performance. In particular, several researchers have identified relationships between the primary coarse aggregate structure and mixture resistance to rutting based on interactive coarse particles (e.g., density, contact length characteristics). However, research has yet to properly characterize the volume within the interstices of the coarse aggregate structure. Recently, a conceptual and theoretical approach to evaluate aggregate structure based on packing theory named Dominant Aggregate Size Ratio—Interstitial Component (DASR-IC) model was developed at University of Florida, as described below, which is promising in addressing coarse aggregates structure and interstitial volume.

1.1 *DASR-IC model*

The DASR-IC model provides a framework for the design and modification of gradations to ensure that mixtures will have sufficient aggregate interlock to resist permanent deformation, as well as adequate durability and fracture resistance. According to the model, mixture behavior is influenced by two primary components: DASR, the coarse aggregate that forms the structural interactive network of aggregate and resists shear; and IC, the combination of fine aggregate, binder, and air voids, which fills the Interstitial Volume (IV) within DASR and resists primarily tension and to a lesser extent, shear. DASR can be composed of one size or multiple contiguous sizes of coarse particles. The composition can be determined by conducting particle interaction analysis based on packing theory. Particles larger than DASR will simply float in the DASR matrix and will not play a major role in the aggregate structure. On the other hand, particles finer than DASR are identified as the aggregates that do not interact with the coarser portion and fill the IV. Figure 1(a) illustrates these concepts.

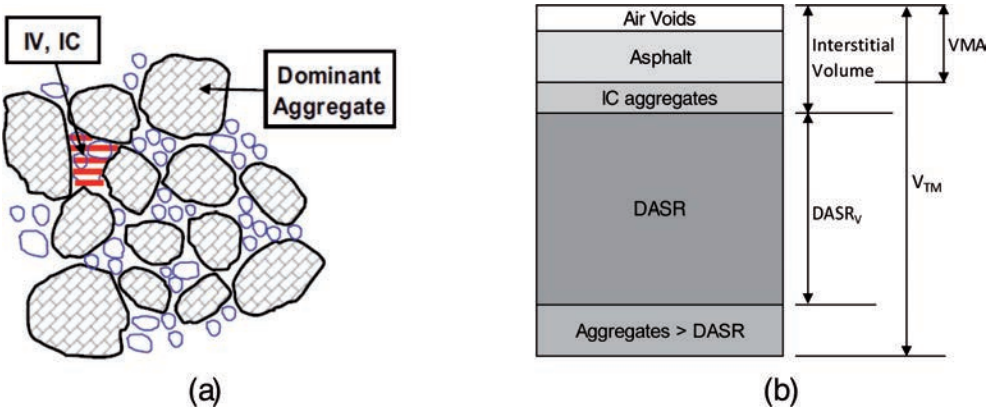

Figure 1. Schematic representations of the DASR-IC model.

Kim, Roque, and Birgisson indicate that the porosity of DASR can be used as a criterion to ensure contact between DASR particles and provide adequate interlocking [10]. Field and laboratory results clearly showed that DASR porosity can be used as an indicator of mixture resistance to permanent deformation (rutting). It is a well-known fact in soil mechanics that the porosity of granular materials should be no greater than 50% for particles to have contact with each other [11]. Porosity can be calculated for any single size, or any set of contiguous sieve sizes within a mixture, by assuming that a mixture has certain effective asphalt content and air voids for a given gradation and, therefore, VMA is comparable to the volume of voids in soil. Porosity can be calculated using the below equations.

$$V_{T(DASR)} = V_{TM} - V_{AGG>DASR} \tag{1}$$

$$V_{V(DASR)} = V_{ICagg} + VMA \tag{2}$$

$$\eta_{DASR} = \frac{V_{V(DASR)}}{V_{T(DASR)}} = \frac{V_{ICagg} + VMA}{V_{TM} - V_{AGG>DASR}} \tag{3}$$

where η_{DASR} = DASR porosity, $V_{V(DASR)}$ = volume of voids within DASR, $V_{T(DASR)}$ = total volume available for DASR particles, V_{ICagg} = volume of IC aggregates, V_{TM} = total volume of mixture, and $V_{AGG>DASR}$ = volume of particles larger than DASR (Fig. 1(b)).

Guarin indicates that IV bonds the coarse aggregate structure together, thereby providing resistance to tension, as well as a secondary structure to help DASR resist shear [12]. IC characteristics and properties strongly influence asphalt mixture cracking resistance. IC characteristics are expected to have a strong influence on key mixture properties, including fracture energy and creep rate as well as how they change with aging. IC should fill the IV, forming a secondary structure that helps resist deformation and fracture without disrupting the DASR structure. Guarin developed a new parameter, the Disruption Factor (DF), to determine the potential of fine aggregates to disrupt the DASR structure. The DF, which can be calculated as the ratio of potentially disruptive particles over the volume of DASR voids, is determined through a 3D packing analysis using spherical particles and single size DASR.

Studies have shown that mixtures with acceptable DASR criteria may or may not result in acceptable cracking performance, indicating that IC strongly influences fracture resistance [1]. For this reason, the DASR-IC model has been expanded to include Fine Aggregate Ratio (FAR) and Effective Film Thickness (EFT) parameters for more defined characterization of the IV. FAR (the ratio between the coarse and fine portions of the IC) is an indicator of the relative coarseness of the IC particle distribution. EFT (a durability-related measure of binder distribution in the IV) is calculated using the effective volumetric properties of fine

aggregate portion (i.e., passing 2.36 mm sieve size) of asphalt mixture using the following equation:

$$\text{EFT(microns)} = \frac{V_{be}}{\text{SA} \cdot W_T \cdot PF_{AGG}} = \left[\frac{P_b - \left(\frac{\text{Abs}}{100} \right) \cdot P_{AGG}}{\text{SA} \cdot PF_{AGG} \cdot G_b} \right] \times 1000 \quad (4)$$

where V_{be} = effective volume of asphalt binder, SA = surface area of fine aggregate, W_T = total weight of mixture, PF_{AGG} = percent of fine aggregate by mass of total mixture, P_b = percent of asphalt content by mass of total mixture, Abs = absorption, P_{AGG} = percent of aggregate by mass of total mixture, and G_b = specific gravity of asphalt binder.

Chun, Roque, and Zou [1] identified preliminary acceptable ranges of each parameter based on both laboratory and field data [12, 13] for optimal mixture property performance in terms of rutting and cracking:

- DASR porosity: 38–52% (48–52%: marginal)
- DF: 0.50–0.95
- EFT: 12.5–25.0 microns
- FAR: 0.28–0.36

Chun et al indicate that EFT, FAR, and the DF criteria can be used together to enhance the cracking resistance of asphalt mixtures [1]. However, the current IC parameters (EFT and FAR) were identified and evaluated using limited field data, and, therefore, may not fully characterize the interstitial volume, resulting in a need for further evaluation and possible modification of the IC criteria.

1.2 *Objectives*

The primary objectives of this study are:

- Develop an approach to evaluating IC criteria for cracking performance.
- Present the results of testing and analysis to date.

2 RESEARCH APPROACH

The DASR-IC model provides a framework of gradation-based parameters and associated criteria to characterize mixture structural characteristics and to link gradation and volumetric properties to field performance. The model uses (a) DASR porosity to ensure contact between larger particles within the mixture to provide suitable resistance to deformation, (b) DF to evaluate the degree of disruption of the IC on the DASR structure, (c) EFT to characterize binder distribution within the IV, and (d) FAR to estimate the relative coarseness of IC particles.

DASR porosity and DF criteria have been evaluated through a wide range of field and laboratory test results. Therefore, as long as the asphalt mixture design meets both criteria, it will have adequate coarse aggregate interlocking undisrupted by fine aggregates, which will ensure good rutting performance. EFT and FAR parameters and associated criteria play an important role in cracking performance; however, past research evaluated these elements with limited data, leaving a need for validation and refinement. This need led to the design of an experimental testing plan that will provide the data necessary to identify IC's effect on the cracking performance of asphalt mixture.

Given that all DASR-IC components are interrelated, realistically isolating the IC effects was challenging. The DASR porosity governs the coarse aggregate structure, which also affects the sizes and distribution of IV. Therefore, in order to isolate IC and its effects on performance, it was necessary to design first the coarse aggregate structure with adequate interlocking and then vary the fine portion of the gradation. This can be done by fixing the

DASR porosity and DF within the acceptable range, and then designing the IC gradation with varying EFT and FAR parameters.

This approach involved the design of mixture gradations that were not associated with actual mixtures; however, any alternative approaches involving only realistic mixture gradations would have required changing the gradation of the coarse portion in order to maintain the proposed ranges of IC parameters. This adjustment would have altered the DASR porosity and the DF, and would have led to complicated testing results involving the effects of both DASR and IC. Furthermore, it should be noted that the existing ranges for IC parameters were established using varying DASR characteristics representing varied levels of coarseness, which implies that the IC parameter criteria are applicable for varied DASR characteristics, as long as the mixture meets all gradation-based criteria. Therefore, the proposed approach appears to be viable for isolating IC and determining its effects on the cracking performance of asphalt mixtures.

2.1 *Materials and testing matrix*

In order to obtain the data necessary to meet the objectives of this study, an experimental testing plan was developed, which includes a wide range of mixtures subjected to different varying conditioning levels. Two aggregate types widely used in the state of Florida for road construction and rehabilitation projects were used to produce mixtures for laboratory testing: Georgia granite and Florida oolitic limestone. Two binder types: an unmodified binder (PG 67-22) and a polymer-modified binder (PG 76-22) were included in the testing plan to evaluate the interactive effects of binder type and interstitial volume characteristics. All mixtures were fine dense-graded and were designed using the Superpave® system with 12.5 mm Nominal Maximum Aggregate Size gradations and traffic level C, which corresponds to 3–10 million Equivalent Single Axle Loads over 20 years.

The DASR-IC model was used to design the range of mixtures to be tested. As stated previously, although a wide range of laboratory and field data was used to evaluate the DASR porosity and the DF, the acceptable ranges of EFT and FAR were determined based on limited data. For this reason, mixtures were designed by maintaining DASR porosity and DF values within the acceptable ranges, while broader ranges were used for EFT and FAR parameters. Two levels of DASR porosity within the acceptable range were selected for each aggregate type. Four different combinations of IC parameters were determined for each DASR porosity level by fixing the DASR and changing only the composition of the IC portion (particles smaller than the DASR), including one combination with both EFT and FAR outside (or near) the bounds, one with both parameters within the range, and the remaining two with either EFT or FAR near the bounds (Table 1). This led to eight gradations per aggregate type, as shown in Figures 2 and 3, respectively. Two binder types were adopted in this study. The optimal asphalt contents determined based on the unmodified binder for all sixteen gradations were employed to produce the other sixteen mixtures of the same gradations with the polymer-modified binder. As a result, a total of sixteen gradations and thirty-two mixtures were encompassed in this study.

These thirty-two mixtures were subjected to three conditioning levels in order to evaluate the changes in fracture properties at different ages and to assess the relationship between IV characteristics, cracking performance, and conditioning level, including (a) Short Term Oven Aging (STOA—AASHTO R30 [14]), (b) Long Term Oven Aging (LTOA—AASHTO R30 [14]), and (c) A combination of LTOA and Cyclic Pore Pressure Conditioning (CPPC). STOA simulates the aging effects that occur during the mixing and construction processes. LTOA simulates the aging of mixtures subjected to in-situ conditions of approximately 5 to 10 years. LTOA plus CPPC was employed to simulate the combined effects of oxidative aging and repeated internal water pressure [15]. Figure 4 shows the flowchart for the experimental testing program.

2.2 *Specimen preparation*

Specimens were produced for Superpave Indirect Tensile (IDT) tests at each of the three conditioning levels. All mixtures were designed using the Superpave mix design procedure. All

Table 1. Calculated DASR-IC parameters for granite and limestone mixtures.

	DASR I				DASR II			
	IC 1	IC 2	IC 3	IC 4	IC 1	IC 2	IC 3	IC 4
Granite								
Porosity (%)	41.0	42.3	42.4	42.7	44.3	44.6	45.2	45.6
DF	0.49	0.77	0.69	0.65	0.56	0.82	0.69	0.70
FAR	0.22	0.41	0.35	0.33	0.25	0.41	0.32	0.33
EFT	13.3	21.7	23.7	27.0	14.1	20.4	23.6	27.6
AC (%)	4.5	4.8	5.4	5.8	4.8	4.9	5.3	5.7
VMA (%)	12.9	14.9	14.9	12.9	13.3	13.8	14.6	15.2
VFA (%)	69.0	73.2	73.2	69.0	69.9	71.0	72.6	73.7
DP	1.14	0.93	0.91	0.87	1.09	1.04	0.95	0.89
Limestone								
Porosity (%)	40.7	41.2	41.2	42.3	45.9	45.2	46.4	47.1
DF	0.65	0.79	0.85	0.90	0.61	0.67	0.74	0.84
FAR	0.25	0.31	0.35	0.38	0.25	0.29	0.32	0.38
EFT	13.2	19.5	21.3	27.9	15.5	15.4	22.3	29.2
AC (%)	5.7	5.9	6.0	6.9	6.1	5.7	6.6	7.3
VMA (%)	11.4	12.3	12.2	13.9	12.9	11.9	13.6	14.7
VFA (%)	65.0	67.5	67.3	71.3	69.1	66.4	70.6	72.7
DP	0.91	0.81	0.82	0.67	0.75	0.86	0.69	0.62

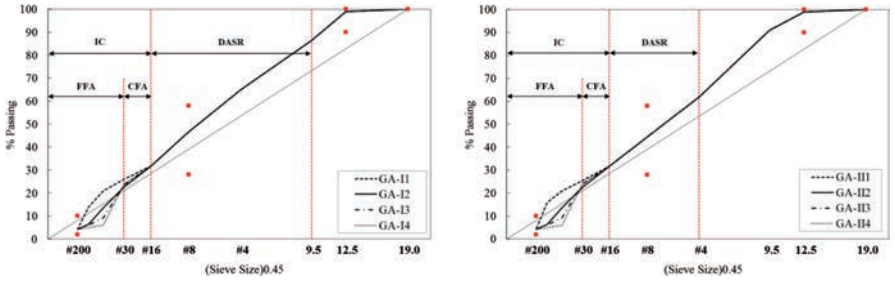

Figure 2. Gradation design of granite mixtures (DASR I and II).

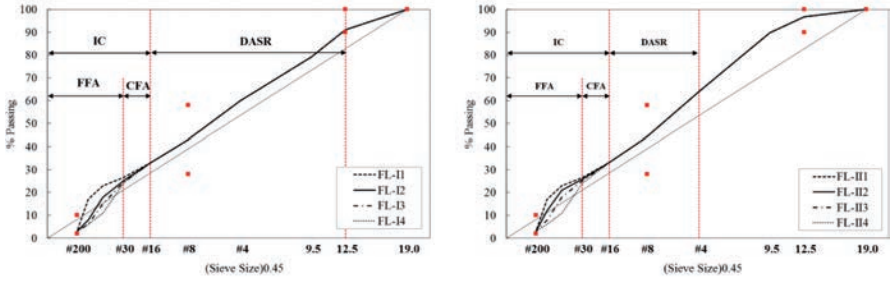

Figure 3. Gradation design of limestone mixtures (DASR I and II).

three mixtures were subjected to STOA and then compacted to 7% (± 0.5%) air voids using the Superpave gyratory compactor. For each type of mixture, two thirds of the compacted pills were further aged using LTOA. All pills were then sliced into specimens of the desired thickness (approximately 1.5 inches), and gage points were attached to each face of the prepared specimens for deformation measurements during the Superpave IDT tests described below. Next, half of the LTOA aged specimens were subjected to CPPC [15].

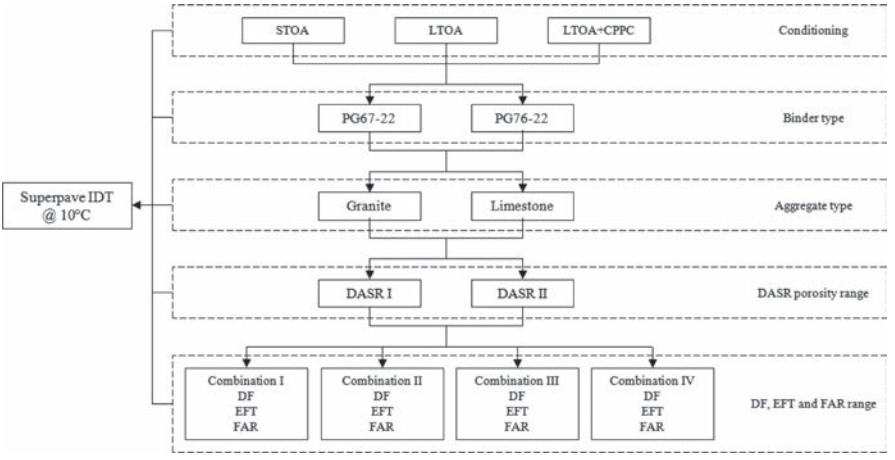

Figure 4. Flowchart for experimental testing plan.

2.3 *Superpave IDT*

Superpave IDT tests were performed at 10°C to obtain HMA fracture properties for each mixture at each conditioning level. The Superpave IDT is composed of a sequence of three tests (resilient modulus, creep compliance, and strength), from which damage and fracture-related mixture properties are determined, including resilient modulus, creep rate, and fracture energy limit [16–18]. Resilient modulus (M_R) is the ratio of the applied stress to recoverable strain when repeated loads are applied. It is a measure of the elastic stiffness of asphalt mixture. Creep rate is the rate of change of the creep compliance curve at 1000 seconds, which has been shown in prior work to be related to the rate of damage accumulation of a mixture. Fracture Energy limit (FE) is the total energy necessary to induce fracture, and represents the tolerance of the mixture to fracture.

3 PRELIMINARY RESULTS

Results to date obtained from Superpave IDT tests were used to evaluate the effect of the IV characteristics on asphalt mixture cracking performance. The main fracture properties of granite mixtures with unmodified binder subjected to STOA and LTOA conditions are summarized in Figures 5 and 6. More specifically, fracture energy limit and creep rate results are presented, since these properties have been found to be closely related to the cracking performance of the asphalt mixture. To further quantify the effects of IV characteristics on fracture resistance, the energy-based criterion called Energy Ratio (ER) was used, which includes an ER parameter and the associated minimum values of ER required for adequate cracking performance [19]. The ER parameter, defined as the ratio of Dissipated Creep Strain Energy limit ($DCSE_f$) over the minimum Dissipated Creep Strain Energy ($DCSE_{min}$) required for good top-down cracking performance, is expressed in the following equation:

$$\mathrm{ER} = \frac{DCSE_f}{DCSE_{min}} = \frac{a \times DCSE_f}{m^{2.98} \times D_1} \tag{5}$$

where

$$a = 0.0299\sigma^{3.1} \times (6.36 - S_t) + 2.46 \times 10^{-8} \tag{6}$$

where, σ (in psi) is tensile stress in the asphalt layer, S_t (in MPa) is tensile strength, $DCSE_f$ (in kJ/m^3) is dissipated creep strain energy limit, D_1 (in 1/psi) and m are power law parameters

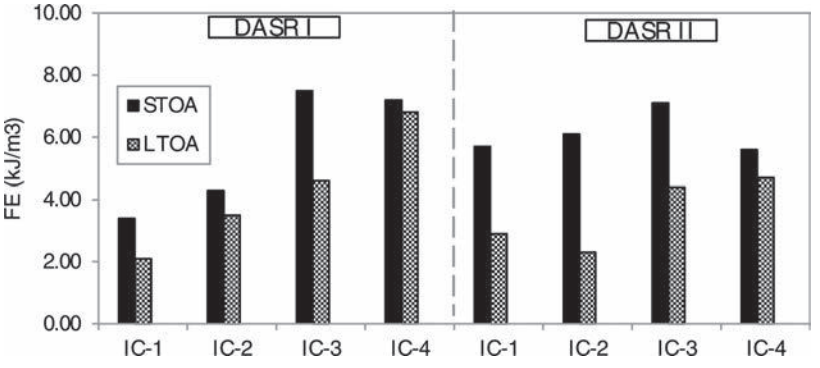

Figure 5. Effect of IV characteristics on FE (PG 67-22).

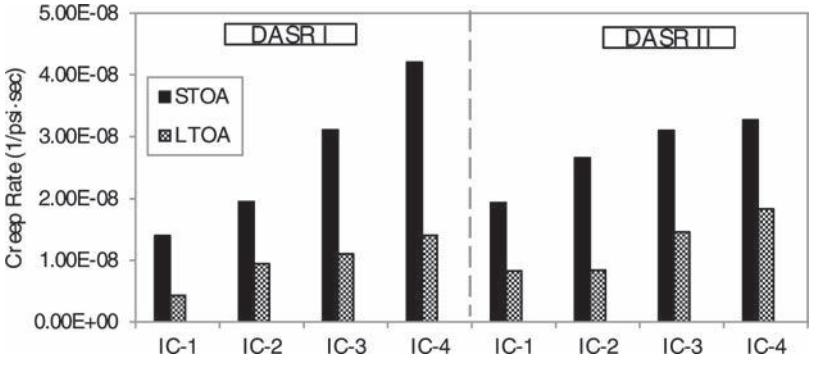

Figure 6. Effect of IV characteristics on creep rate (PG 67-22).

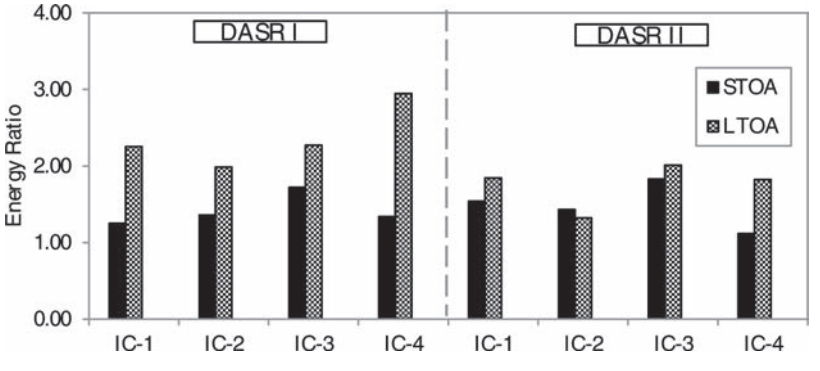

Figure 7. Effect of IV characteristics on ER (PG 67-22).

from creep compliance test. Figure 7 summarizes the effects of IV characteristics on ER. As shown in Figures 5 and 6, results indicate that different IC gradations within each DASR resulted in significant changes in mixture properties. In particular, the results of mixtures at STOA condition reveal that FE increased as IC coarseness increased (Fig. 5), which indicates an increase in fracture tolerance. A similar trend occurred in the creep rate results (Fig. 6), indicating that coarser IC gradation tend to accumulate damage at a faster rate. This trend was expected, as mixtures with coarse IC have higher asphalt content, as reflected by a higher EFT, and therefore a higher creep rate. Consistent with expectations, LTOA was able to

embrittle and stiffen all mixtures as manifested by loss of FE and decrease in creep rate. In particular, both IC-4 mixtures, which are characterized by the highest EFT and coarseness level for each DASR porosity level, exhibited a relatively small reduction in FE compared to the other mixtures but significant reduction in creep rate when subjected to LTOA. Results of further analysis, with respect to the effects of different IC gradations, indicate that both DASR porosity levels (i.e. DASR I and DASR II) of granite mixtures exhibited similar trends of changes in fracture properties at both heat oxidation levels.

The effects of IC characteristics on fracture performance were evaluated using the ER approach. A higher ER generally implies better cracking resistance, which relates to a higher FE and/or lower creep rate; however, it should be noted that a higher ER resulting from higher levels of heat oxidation does not necessarily imply better fracture performance since ER was calibrated based on pavement sections subjected to a similar level of oxidative aging. Therefore, ER was used in this research for relative comparison of the fracture performance of mixtures subjected to similar levels of heat oxidation. ER results indicate that both IC-3 mixtures with all four DASR-IC parameters within the preliminary acceptable ranges (i.e. IC-3 (DASR-I) and IC-3 (DASR-II)) outperformed the other mixtures under STOA conditions (Fig. 7). Under LTOA condition, ER was able to capture the behavior of IC-4, which exhibited the greatest increase in ER among all mixtures. This greater gain in ER of these two mixtures may be explained by the higher effective film thickness which helped retain the FE at a higher level.

4 DISCUSSION

As described above, preliminary testing results showed that FE increased as IC coarseness increased. These results indicate that IC coarseness significantly influences mixture cracking resistance, regardless of DASR porosity level. One possible explanation for this influence is that coarse IC aggregates filling the IV tend to leave more space among them, as indicated by higher asphalt content and higher EFT (Table 1), which decreases the stress concentration between IC aggregates. In order to achieve a better understanding of the relative effects of IC characteristics on stress and strain distribution within the IV, further studies using finite element models are concurrently being performed. The goal of this numerical analysis is to support the findings obtained from the laboratory study and to draw conclusions for a broader range of mixture gradations. A set of 2D linear elastic models using a schematic representation of the IV has been developed. Results to date showed that stress concentration along the gaps between IC aggregates decreased as IC coarseness increased. Details on the development of the finite element models, as well as complete results of numerical simulations, will be presented in a separate paper.

5 CONCLUSIONS

This study sought to evaluate the DASR-IC model with particular focus on the evaluation and possible modification of IC criteria. In order to isolate IC and its effects on mixture performance, the gradations included in the study were designed by fixing DASR porosity at two different levels within the acceptable range. The IV was then designed to encompass broad ranges for IC parameters (DF, EFT, and FAR). Based on the testing results to date, a summary of findings is presented as follows:

- Different IC gradations within each DASR resulted in significant changes in fracture properties of granite mixtures with unmodified binder.
- The trends of change in fracture properties (i.e., FE and creep rate) observed at STOA and LTOA conditions were almost the same for both DASR levels. In particular, both FE and creep rate increased as IC coarseness increased.
- LTOA caused the material to become stiffer and more brittle, which resulted in lower FE and decreased creep rate.

- ER results indicated that, for STOA condition, both IC-3 mixtures with all DASR-IC parameters within the preliminary acceptable ranges outperformed the other three mixtures regardless of DASR porosity level.
- Under LTOA condition, both IC-4 mixtures with the highest IC coarseness and the largest EFT for each DASR porosity level exhibited greater increase in ER than the others. This greater gain in ER of these two mixtures may be explained by the higher effective film thickness which helped retain the FE at a higher level.

REFERENCES

[1] Chun, S., Roque, R., Zou, J., "Effect of Gradation Characteristics on Performance of Superpave Mixtures in the Field", Transportation Research Record 1540, Transportation Research Board, Washington, D.C., pp. 43–52, 2012.

[2] Masad, E., Button, J., "Implications of Experimental Measurements and Analysis of the Internal Structure of Hot-Mix Asphalt", Transportation Research Record 1841, Transportation Research Board, Washington, D.C., pp. 212–20, 2004.

[3] Masad, E., Tashman, L., Somedavan, N., Little, D., "Micromechanics-Based Analysis of Stiffness Anisotropy in Asphalt Mixtures", Journal of Materials in Civil Engineering, 14(5), pp. 374–383, 2002.

[4] Tashman, L., Masad, E., Little, D., Zbib, H., "A Microstructure-Based Viscoplastic Model for Asphalt Concrete", International Journal of Plasticity, 21(9), pp. 1659–1685, 2005.

[5] Arambula, E., Masad, E., Martin, A.E., "Influence of Air Void Distribution on the Moisture Susceptibility of Asphalt Mixture", Journal of Materials in Civil Engineering, 19(8), pp. 655–664, 2007.

[6] Kutay, E.M., Aydilek, A.H., "Pore Pressure and Viscous Shear Stress Distribution due to Water Flow within Asphalt Pore Structure", Computer-Aided and Civil Infrastructure Engineering, 24(3), pp. 212–224, 2009.

[7] Sefidmazgi, N.R., Tashman, L., Bahia, H., "Internal Structure Characterization of Asphalt Mixtures for Rutting Performance Using Imaging Analysis," Journal of the Association of Asphalt Paving Technologists, Vol. 81, 2012.

[8] Vavrik, W., Pine, W.J., Huber, G., Carpenter, S.H., Bailey, R., "The Bailey Method of Gradation Evaluation: The Influence of Aggregate Gradation and Packing Characteristics on Voids in the Mineral Aggregate", Journal of the Association of Asphalt Paving Technologists, Vol. 70, pp. 132–175, 2001.

[9] Vavrik, W., Pine, W.J., Huber, G., Carpenter, S.H., Bailey, R., "Bailey Method for Gradation Selection in HMA Mixture Design", Transportation Research Circular, E-C044, E-C044, 2002.

[10] Kim, S., Roque, R., Birgisson, B., "Identification and Assessment of the Dominant Aggregate Size Range (DASR) of Asphalt Mixture", Journal of the Association of Asphalt Paving Technologists, Vol. 75, pp. 789–814, 2006.

[11] Lambe, T.W., Whitman, R.V. Soil Mechanics, John Wiley & Sons, New York, 1969.

[12] Guarin, A. Interstitial Component Characterization to Evaluate Asphalt Mixture Performance, Ph.D. Dissertation, University of Florida, Gainesville, FL, 2009.

[13] Roque R., Chun S., Zou J., Lopp G., Villiers C., "Continuation of Superpave Projects Monitoring", Final Report of Florida Department of Transportation, University of Florida, Gainesville, Florida, 2011.

[14] AASHTO, Standard Practice for Mixture Conditioning of Hot-mix Asphalt, AASHTO R 30, Washington, D.C., 2001.

[15] Roque, R., Isola, M., Chun, S., Zou, J., Koh, C., Lopp G., "Effects of Laboratory Heating, Cyclic Pore Pressure, and Cyclic Loading on Fracture Properties of Asphalt Mixture", Final Report of the FDOT, University of Florida, Gainesville, FL, 2012.

[16] Roque, R., Buttlar, W.G., "The Development of a Measurement and Analysis System to Accurately Determine Asphalt Concrete Properties Using the Indirect Tensile Mode", Journal of the Association of Asphalt Paving Technologists, Vol. 61, pp. 304–32, 1992.

[17] Buttlar, W.G., Roque, R., "Development and Evaluation of the Strategic Highway Research Program Measurement and Analysis System for Indirect Tensile Testing at Low Temperatures", Transportation Research Record 1454, Transportation Research Board, Washington, D.C., pp. 163–71, 1994.

[18] Roque, R., Buttlar, W.G., Ruth, B.E., Tia, M., Dickson, S.W. and Reid, B., "Evaluation of SHRP Indirect Tension Tester to Mitigate Cracking in Asphalt Pavements and Overlays", Final Report of the Florida Department of Transportation, University of Florida, Gainesville, FL, 1997.

[19] Roque, R., Birgisson, B., Drakos, C., Dietrich, B., "Development and Field Evaluation of Energy—Based Criteria for Top-Down Cracking Performance of Hot Mix Asphalt", Journal of the Association of Asphalt Paving Technologists, Vol. 73, pp. 229–60, 2004.

Asphalt Pavements – Kim (Ed)
© 2014 Taylor & Francis Group, London, ISBN 978-1-138-02693-3

Characterization of nonlinear viscoelastic material properties of asphalt materials in multiple length scales

Soohyok Im
Texas A&M Transportation Institute, College Station, TX, USA

Hoki Ban
Hanyang University, Seoul, South Korea

Yong-Rak Kim
University of Nebraska-Lincoln, Lincoln, NE, USA

ABSTRACT: It is well known that asphaltic materials present complicated viscoelastic behaviour that is significantly affected by the rate of loading and time as well as by temperature conditions. To improve accuracy in the analysis and design of asphaltic materials and pavement structures, the viscoelastic constitutive model has been considered by many studies. However, abundant experimental observations have presented nonlinear response of asphaltic materials at certain levels of stress and strain, and the nonlinear behaviour is not considered in the current pavement design methods. This study develops testing-analysis methods to rigorously define the stress-dependent nonlinear viscoelastic material characteristics at various stress levels. To this end, Schapery's nonlinear viscoelastic model is employed to characterize the nonlinear viscoelastic behaviour of asphaltic materials in two different length scales, i.e., mixture scale and component scale. The test and analysis results discussed in this paper provide a better understanding and identification of the true mechanical behaviour of asphaltic materials in pavements.

Keywords: Asphalt materials, nonlinear viscoelasticity, multiple scales, modeling

1 INTRODUCTION

An asphalt pavement is typically a multilayered system consisting of asphalt concrete, base, subbase, and subgrade layers. Multilayered elastic theory has been widely used for analysis and design of flexible pavements. As an example, the new pavement design guide, Mechanistic-Empirical Pavement Design Guide (MEPDG), has been developed and is currently under applications by many US states. The MEPDG basically uses layered elastic theory to determine the mechanical responses in conjunction with empirically developed failure criteria called transfer functions. Although the MEPDG employs various design parameters (climate, traffic, materials, etc.) to predict the performance of flexible pavements, it is known to be limited in its ability to accurately predict mechanical responses in asphaltic pavements. This limitation is due to the use of simplified structural analysis methods, a general lack of understanding of the fundamental constitutive behaviour and damage mechanisms for paving materials, and the use of circular tire loading configurations. Asphalt mixtures are typically considered viscoelastic; their stress and strain response is time-rate-temperature dependent. Therefore, the assumption of elasticity for an asphalt layer is misleading in predicting the performance of flexible pavements.

Recently, several studies [1–3] have conducted viscoelastic analyses that consider the asphalt layer as linear viscoelastic and the other layers as elastic, using the finite element method in two-dimensional (2-D) or three-dimensional (3-D) models for predicting the time-dependent

response of flexible pavement. However, nonlinear response was not taken into consideration for their models in spite of abundant experimental observations [4,5] that present nonlinear response of asphalt binders and mixtures at certain levels of stress and strain. When asphalt pavements are subjected to heavy truck loads, asphalt materials may present nonlinear viscoelastic behavior due to high stress (or strain) levels. Therefore, the nonlinear viscoelastic response of asphaltic pavement subjected to heavy truck loads should be taken into account for more accurate design and analysis.

The primary objective of this study is to investigate stress-dependent nonlinear viscoelastic characteristics of asphalt mixtures so as to identify the significance of nonlinear response for the more accurate analysis and design of asphalt pavements that are typically subjected to heavy vehicle loads. To that end, Schapery's single integral viscoelastic theory was applied with repeated creep-recovery tests in two different length material scales: the Fine Aggregate Matrix (FAM) scale and its corresponding asphalt concrete scale.

2 SCHAPERY'S NONLINEAR VISCOELASTICITY

Schapery's nonlinear viscoelastic single-integral constitutive model [6] for one-dimensional problems can be expressed in terms of an applied stress (σ), as follows:

$$\varepsilon(t) = g_0 D_0 \sigma + g_1 \int_0^t \Delta D\left[\psi(t) - \psi(\xi)\right] \frac{d\left(g_2 \sigma\right)}{d\xi} d\xi \tag{1}$$

where ψ is the reduced time given by:

$$\psi(t) = \int_0^t \frac{d\zeta}{a_\sigma} \tag{2}$$

where g_0, g_1, g_2, and a_σ are the nonlinear viscoelastic parameters associated with stress level, t is the time of interest, and ξ is the integration variable.

These nonlinear viscoelastic parameters are always positive and equal to 1.0 in linear viscoelasticity. It should be noted that Eq. (2) can include not only the stress effect but also other effects such as temperature, moisture, and physical aging with each shift factor. D_o and ΔD represent uniaxial instantaneous and transient creep compliance at linear viscoelasticity, respectively.

The uniaxial creep compliance in a form that combines the instantaneous and transient part can be expressed as a generalized power law, as follows:

$$D(\psi) = D_o + \Delta D(\psi) = D_o + D_c \psi^p \tag{3}$$

where D_o, D_c, and p values are material parameters representing the uniaxial linear viscoelastic creep behavior.

In the case of torsional shear loading, Schapery's nonlinear viscoelastic constitutive model can be expressed in terms of an applied shear stress (τ) and responsive shear strain (γ) with a different set of nonlinear viscoelastic parameters (with superscript *), as follows:

$$\gamma(t) = g_o^* J_0 \tau + g_1^* \int_0^t \Delta J\left[\psi(t) - \psi(\zeta)\right] \frac{d\left(g_2^* \tau\right)}{d\xi} d\xi \tag{4}$$

As in Eq. (3), the torsional creep compliance in a form combining the instantaneous and transient part can be expressed as follows:

$$J(\psi) = J_o + \Delta J(\psi) = J_o + J_c \psi^q \tag{5}$$

where J_o, J_c, and q values are material parameters representing the torsional linear viscoelastic creep behavior.

3 MATERIALS AND SPECIMEN FABRICATION

Three aggregates were selected and blended in this study: 16 mm limestone, 6.4 mm limestone, and screenings to produce an Asphalt Concrete (AC) mixture. All three aggregates are limestone with the same mineralogical origin. The Nominal Maximum Aggregate Size (NMAS) of the final aggregate blend was 12.5 mm. The asphalt binder used in this study was Superpave performance graded binder PG 64-28. With the limestone aggregate blend and the binder, a volumetric design of the AC mixture was accomplished; this resulted in a binder content of 6.0% by weight of the total mixture to meet the 4.0% target air voids and other necessary volumetric requirements. Along with the AC mix design, its FAM mix design was then conducted based on the volumetric mix design of its corresponding AC mixture. The FAM mixture consisted of the same PG 64-28 binder and fine aggregates passing No. 16 sieve (mesh size of 1.19 mm). The mix design of FAM was determined by considering that the coarse aggregates in the corresponding AC mixture could be separated from the FAM by virtually picking them out of the compacted AC mixture microstructure. Asphalt binder absorbed into coarse aggregates was subtracted from the total amount of binder used in the AC mixture, and the resulting remaining binder content was calculated to mix FAM. This approach resulted in a binder content of 8.0% by total weight of aggregates in the FAM mixture. A detailed description on specimen fabrication can be found elsewhere [7]. Table 1 illustrates gradation, bulk specific gravity (G_{sb}), and consensus properties (i.e., Fine Aggregate Angularity [FAA], Coarse Aggregate Angularity [CAA], Flat and Elongated [F&E] particles) of the aggregates used in this study.

As illustrated in Figure 1, AC and FAM specimens were fabricated to conduct the uniaxial and torsional creep-recovery tests, respectively. To fabricate AC specimens, a Superpave

Table 1. AC and FAM mix design and consensus properties of aggregates used.

Sieve analysis (wash) for gradation (AC mixture)										
Aggregate sources	19 mm	12.7 mm	9.5 mm	#4	#8	#16	#30	#50	#100	#200
16-mm limestone	100.0	95.0	89.0	–	–	–	–	–	–	–
6.4-mm limestone	100.0	100.0	100.0	72.0	–	–	–	–	–	–
Screenings	100.0	100.0	100.0	100.0	36.0	21.0	14.0	10.0	7.0	3.5
Combined gradation	100.0	95.0	89.0	72.0	36.0	21.0	14.0	10.0	7.0	3.5
Sieve analysis (wash) for gradation (FAM mixture)										
Gradation	100.0	100.0	100.0	100.0	100.0	100.0	66.7	47.6	33.3	16.7
Physical and geometrical properties										
Consensus properties	FAA(%) = 45.0, CAA (%) = 89.0, F&E (%) = 0.0, Gsb = 2.577									

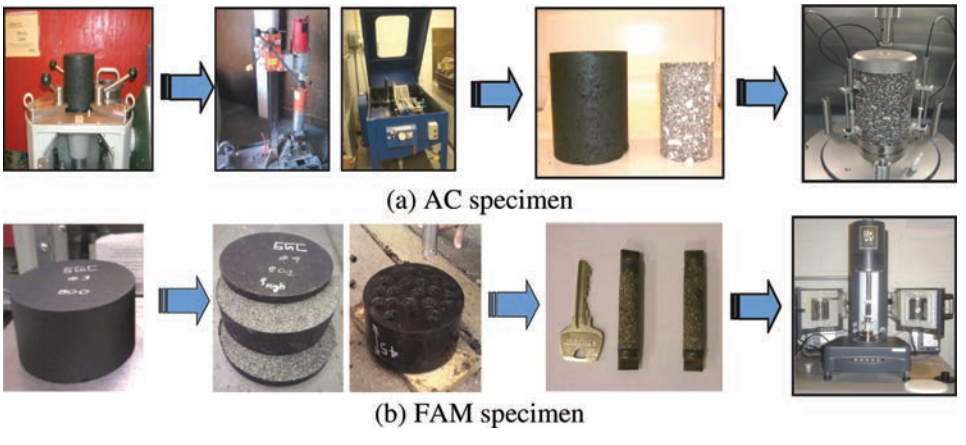

Figure 1. Specimen fabrication process for the repeated creep-recovery tests.

gyratory compactor was used to produce the cylindrical samples with a diameter of 150 mm and an approximate height of 170 mm. Then, the compacted samples were cored and sawn to produce testing specimens targeting an air void of 4% ± 0.5% with a 100-mm diameter and 150-mm height. To measure the axial displacement of the AC specimens, mounting studs were glued to the surface of the specimens so that three Linear Variable Differential Transformers (LVDTs) could be installed on the surface of the specimens through the studs at 120° radial intervals with a 100-mm gauge length. The AC specimen was then mounted in a mechanical testing station equipped with an environmental chamber for the uniaxial static creep-recovery tests.

Along with the AC mixture, the Superpave gyratory compactor was also used to produce a cylindrical FAM sample with a diameter of 150 mm and a height of 80 mm. The sample was then sliced into three pieces to obtain a middle section of 45 mm height. Then, cylindrical specimens 45 mm long and 12.25 mm in diameter were cored out of the middle 45 mm section of the bulk FAM sample. Special care was taken while coring, since the geometry and surface quality of the top and bottom parts of the core are very important when subjected to torsional loads. The FAM specimen was then installed into a rheometer to conduct torsional shear static creep-recovery tests in order to characterize viscoelastic deformation of the FAM mixture.

4 LABORATORY TESTS AND RESULTS

The static creep-recovery test was conducted on replicate specimens of AC mixture and FAM mixture at an identical testing temperature of 30 °C. Based on several preliminary tests conducted to find an appropriate creep loading time and recovery time, a creep stress for 30 seconds followed by recovery time of 500 seconds was applied to the specimens. The vertical deformation (in compression mode) from the AC specimens was monitored with the three LVDTs, while the torsional displacements (in pure shear mode) from the FAM specimens were measured with transducers installed in the rheometer. A large range of stress levels was applied to identify the level of (stress-independent) linear viscoelastic range and to characterize stress-dependent nonlinear behaviour of each mixture. Repeated preliminary tests indicated that the AC mixture was linear viscoelastic up to 700 kPa uniaxial creep stress, and the FAM specimens were generally subjected to linear viscoelastic behaviour up to 15 kPa torsional creep stress. In other words, nonlinear viscoelasticity starts when the stress level is greater than 700 kPa and 15 kPa for the AC specimens and the FAM specimens, respectively. Therefore, a creep-recovery curve at the threshold stress level within the linear viscoelastic range was used to find linear viscoelastic properties, and other creep-recovery curves obtained from higher stress levels than the threshold stress were used to characterize the stress-dependent nonlinear viscoelastic properties of each mixture.

Figure 2 presents repeated creep-recovery test results obtained from the AC mixture and FAM mixture, respectively. Each strain curve at a specific creep stress level was averaged from three replicates. Test results between replicates were similar, so that the averaged curves presented in Figure 2 could be reasonably used to estimate deformation characteristics of each asphalt mixture. As shown in the figure, the higher stress level generated larger creep strain and provided less recovery at the testing temperature (30 °C).

5 CHARACTERIZATION OF NONLINEAR VISCOELASTIC PROPERTIES

The approach most often described in the literature to obtain nonlinear viscoelastic material properties is based on Schapery's procedure using numerical fitting of laboratory test data both in the linear viscoelastic range and in the nonlinear viscoelastic range at each stress level [8,9]. As mentioned earlier, the repeated creep-recovery test results were used to identify linear and nonlinear viscoelastic material properties. The procedure to define nonlinear viscoelastic properties starts with the identification of linear viscoelastic material properties

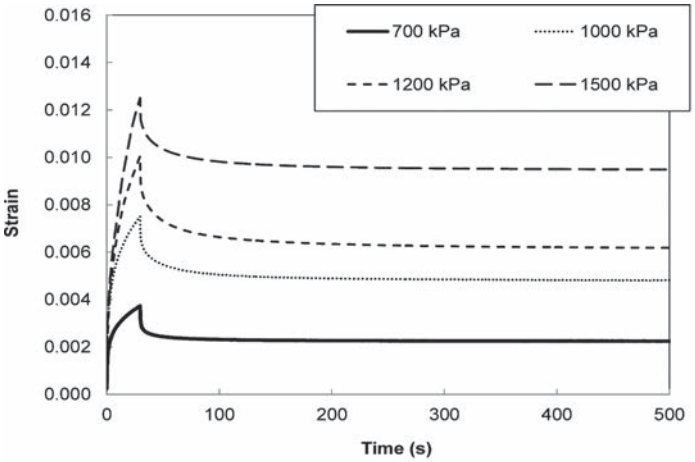

(a) AC mixture

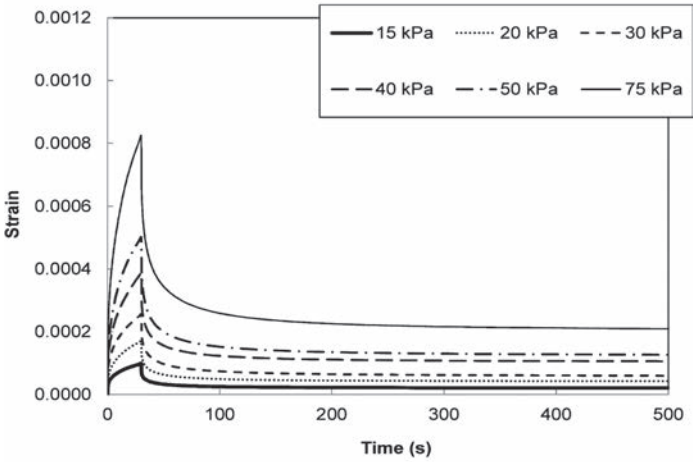

(b) FAM mixture

Figure 2. Repeated creep-recovery test results.

using the test results at the threshold stress level. The linear viscoelastic properties are then used to find nonlinear viscoelastic properties by using creep-recovery test data resulting from higher stress levels than the threshold level. To better illustrate the characterization process, a schematic view of a single creep-recovery test is introduced in Figure 3 for a constant stress (σ_o) loading-unloading condition.

For the loading time period, (i.e., $0 < t < t_1$), Eq. (1) can be expressed as:

$$\varepsilon_c(t) = g_0 D_0 \sigma_0 + g_1 g_2 \sigma_0 \Delta D\left(\frac{t}{a_{\sigma_o}}\right) \tag{6}$$

For the unloading time period, that is, $t > t_1$, it can be expressed as:

$$\varepsilon_r(t) = g_2 \sigma_0 \left[\Delta D\left(\frac{t_1}{a_{\sigma_o}} + t - t_1\right) - \Delta D(t - t_1)\right] \tag{7}$$

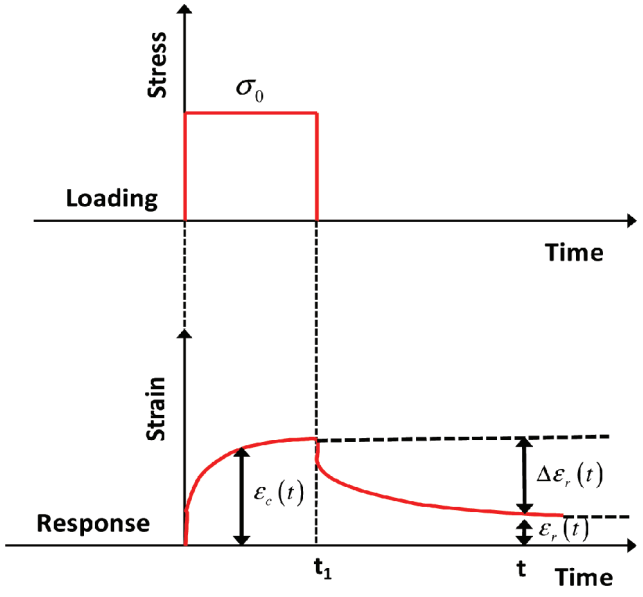

Figure 3. Schematic illustration of a single creep-recovery test.

The first step is to obtain linear viscoelastic material properties (D_o, D_c, and p for uniaxial creep and J_o, J_c, and q for torsional creep) from the generalized power law (Eq. (3), Eq. (5)) at the threshold stress level. Since the recoverable response is linear viscoelastic ($g_o = g_1 = g_2 = a_\sigma = 1.0$) at the threshold stress level, the recovered strain $\Delta\varepsilon_r$ shown in Figure 3 can be used to obtain the linear viscoelastic material properties. Linear viscoelastic material properties in the form of generalized power law are determined by minimizing errors between experimental measurements and predicted strains. Once the linear viscoelastic properties have been obtained, the nonlinear viscoelastic parameters at higher stress levels can then be determined. To do this, the recovered strains at higher stress levels than the threshold level are used again with the notion that the transient creep compliance is expressed in the form of a power law [8]. The resulting recovered strain $\Delta\varepsilon_r$ as a function of time is expressed as follows:

$$\Delta\varepsilon_r(t) = \varepsilon_c(t_1) - \varepsilon_r(t) = \alpha - \beta\left[\left(1 + a_{\sigma_o}\lambda\right)^n - \left(a_{\sigma_o}\lambda\right)^n\right] \tag{8}$$

where

$$\alpha = g_0 D_0 \sigma_0 + g_1 g_2 D_c \sigma_0 \left(\frac{t_n}{a_{\sigma_0}}\right)^n \tag{9}$$

$$\beta = g_2 D_c \left(\frac{t_1}{a_{\sigma_0}}\right)^n \tag{10}$$

$$\lambda = \frac{t - t_1}{t_1} \tag{11}$$

Fitting Eq. (8) to the recovered strain data $\Delta\varepsilon_r$ can determine constants: n, α, β, and a_σ. It is also noted that n is almost stress-independent and can be obtained at a low stress level; therefore, the n value can be fixed as a material constant, and the values of α, β, and a_σ are obtained by repeating the fitting process. Next, from Eq. (10), g_2 is determined by minimiz-

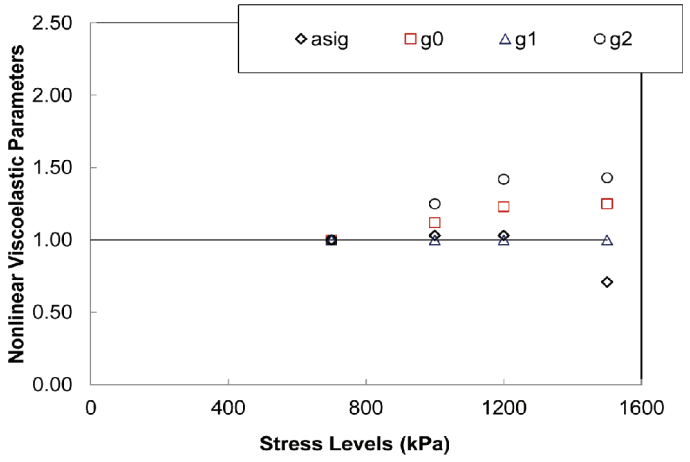

(a) AC mixture

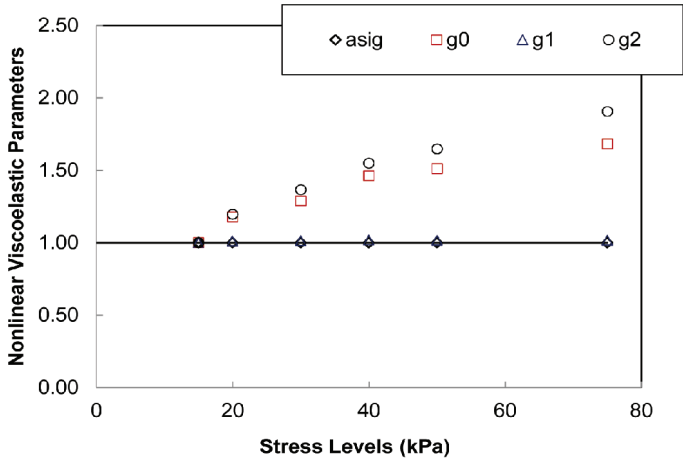

(b) FAM mixture

Figure 4. Nonlinear viscoelastic material parameters as a function of stress levels.

ing errors between experimental data and Eq. (10). Similarly, g_0 and g_1 are determined from Eq. (9). Based on this fitting process, all nonlinear viscoelastic parameters of the AC mixture and FAM mixture were found and are presented in Figure 4 plotted as a function of stress levels. The figures show that, for both AC and FAM mixture, parameter g_1 is not significantly related to nonlinearity, whereas other parameters such as g_0 and g_2 are affected by stress levels when the mixtures are subjected to nonlinear viscoelastic deformation. Both parameters generally increased as higher stresses were involved. Regarding a_σ, with the limited data available at the current stage, it does not seem to be highly related to the stress levels for both mixtures, except the value of AC mixture at the stress level of 1,500 kPa. However, this observation needs extended tests and relevant analyses to confirm.

6 SUMMARY AND CONCLUSION

This study developed testing-analysis methods to properly define the stress-dependent nonlinear viscoelastic material characteristics of asphalt materials. Schapery's single integral

viscoelastic theory was applied with repeated creep-recovery tests. Based on the test results and data analysis, the following bullet points summarize the conclusions that can be drawn:

- The repeated creep-recovery test and analysis method based on Schapery's single integral viscoelasticity were applied to both torsional FAM testing and uniaxial AC testing.
- Creep-recovery tests at varying stress levels were conducted to identify viscoelastic mixture characteristics. Test results were generally reasonable and repeatable, and analyses of test results were straightforward.
- Asphalt mixtures (in both length scales) clearly presented stress-dependent nonlinear viscoelastic responses at stress levels greater than the linear viscoelastic range. For both mixtures, nonlinear viscoelastic parameter g_1 did not show any significant nonlinearity, while parameters g_0 and g_2 increased with greater stresses. This indicates that the stress-dependent nonlinear viscoelastic behavior should be considered for the more accurate analysis and design of asphalt pavements that are typically subjected to heavy vehicle loads.
- With the test data and analysis results at this stage, a strong correspondence between the FAM and AC mixtures exits in their viscoelastic deformation characteristics. This implies that the viscoelastic characteristics of typical AC mixtures could potentially be estimated and/or predicted from the FAM testing, which can significantly reduce experimental-analytical efforts required to conduct AC testing. The authors currently investigate a correlation between the AC mixture and the FAM mixture. Any visible findings will be presented.
- This study was limited in its scope by testing only one type of asphalt mixture at one testing temperature (30 °C). A follow-up study is recommended to conduct the extended tests with different mixtures and testing temperatures to confirm the findings and observations obtained from this study.

ACKNOWLEDGEMENTS

The authors gratefully acknowledge the financial supports received from the Mid-America Transportation Center (MATC), the Nebraska Department of Roads (NDOR), and the National Research Foundation of Korea (Grant No. 2012K1A3A1A12054814).

REFERENCES

[1] Al-Qadi, I.L., Yoo, P.J., and Elseifi, M.A. Characterization of pavement damage due to different tire configurations, Journal of the Association of Asphalt Paving Technologists, 74, pp. 921–962. 2005.
[2] Kim, J., Roque, R., and Byron, T. Viscoelastic analysis of flexible pavements and its effects on top-down cracking, Journal of Materials in Civil Engineering, 27(7), 324–332. 2009.
[3] Elseifi, M.A., Al-Qadi, I.L., and Yoo, P.J. Viscoelastic modeling and field validation of flexible pavements, Journal of Engineering Mechanics, 132(2), pp. 172–178. 2006.
[4] Masad, E. and Somadevan, N. Microstructural finite-element analysis of influence of localized strain distribution of asphalt mix properties, Journal of Engineering Mechanics, 128, pp. 1105–1114. 2002.
[5] Collop, A.C., Scarpas, A., Kasbergen, C., and Bondt, A. Development and finite element implementation of stress-dependent elastoviscoplastic constitutive model with damage for asphalt, Transportation Research Record, 1832, 96–104. 2003.
[6] Schapery, R.A. On the characterization of nonlinear viscoelastic materials, Polymer Engineering and Science, 9(4), pp. 295–310. 1969.
[7] Kim, Y., Karki, P., and Im, S. Dynamic modulus prediction of asphalt concrete mixtures through mixture microstructure characteristics and mechanical properties of constituents, Transportation Research Board, CD-ROM 2011.
[8] Lai, J. and Bakker, A. 3-D Schapery representation for non-linear viscoelasticity and finite element implementation, Computational Mechanics, 18, pp. 182–191. 1996.
[9] Zaoutsos, S.P. and Papanicolaou, G.C. On the influence of preloading in the nonlinear viscoelastic-viscoplastic response of carbon-epoxy composites, Composites Science and Technology, 70, pp. 922–929. 2010.

Asphalt Pavements – Kim (Ed)
© 2014 Taylor & Francis Group, London, ISBN 978-1-138-02693-3

Usage of advanced functions of Dynamic Shear Rheometer for the selection of a suitable binder for asphalt mixtures

Ondřej Dašek, Petr Hýzl, Michal Varaus & Pavel Coufalík
Faculty of Civil Engineering, Brno University of Technology, Veveří, Czech Republic

Petr Špaček & Zdeněk Hegr
Skanska a.s., Praha, Czech Republic

ABSTRACT: Asphalt pavements often have a tendency to creation of cracks and potholes, which can be associated with a decrease of the functional properties of asphalt binder. This decrease can be caused either by inadequate use of binders for the intended application, or undesirable change of binder properties during usage, most often due to excessive oxidative aging of asphalt binders in the asphalt mixtures.

One of the progressive functions of Dynamic Shear Rheometer (DSR) is the possibility to analyse the relaxation of shear stress of asphalt binders in dependence on time. This parameter is suitable to differ the appropriateness of the binder usage for the relevant application.

The results of advanced tests of Dynamic Shear Rheometer conducted on several types of asphalt binders, such as paving grade bitumen, polymer modified bitumen and asphalt rubber binder are introduced in the paper. The methodology describing the selection of the suitable binder for the presumed application using DSR device with the describing of Rolling Thin Film Oven Test (RTFOT) aging of binders is also presented.

Keywords: Bituminous binder, asphalt mixture, rheology, dynamic shear rheometer, relaxation of shear stress

1 INTRODUCTION

The relaxation of shear stress measured in the bituminous binder can become an important indicator of the level of material ability to diminish the imposed stress, as well as the quality of the modifying system. The ability to absorb the thermically induced stress is a significant property of the real bitumen layer that leads to the reduction of its cracking potential and can influence the transfer of tensile stresses in the bituminous mixture. This ability is primarily determined by the properties of the bituminous binder and bituminous film thickness that is used for the binder. The Czech systems of road testing specifications, particularly the technical regulations TP 151 [1] describe a method that enables the measurement of the aforesaid relaxation in bituminous mixtures. The test has proved to be very time-consuming and not always optimized in terms of instrumentation to ensure mutual consistency of inter-laboratory results. The basic idea for measuring the relaxation of shear stress of the bituminous binder using DSR is to describe the relaxation behaviour of the bituminous binder itself under given temperature conditions to predict the subsequent relaxation behaviour of bituminous mixtures, and thus to eliminate complex laboratory testing. When a bituminous binder shows a fast relaxation of imposed stress, the finished bitumen layer is assumed to have a reduced tendency to the formation and propagation of cracks. [2]

Table 1. Basic binder characteristics.

Binder	Penetration [0.1 mm]	Softening point [°C]
Paving grade bitumen 50/70	54	48.9
PmB 45/80-50	45	54.2
PmB 25/55-55	30	65.7
PmB 25/55-65	25	78.2
CRmB 25/55-60	38	62.3

2 MATERIALS USED

The following materials were chosen for laboratory testing: paving grade bitumen (gradation 50/70), three Polymer modified Bitumens (PmB) from the same producer (gradation 45/80-50, 25/55-55, and 25/55-65), and one Crumb Rubber modified Bitumen (CRmB, asphalt rubber) prepared in the laboratory by mixing paving grade bitumen 50/70 with 15.5% crumb rubber with a grain size of 0/1 mm (gradation 25/55-60). The basic properties of individual binders are given in Table 1.

3 APPLIED TEST PROCEDURES

To evaluate the properties of selected bituminous binders and the effects of ageing using the Rolling Thin Film Oven Test (RTFOT), empirical tests of binders (needle penetration according to the EN 1426 standard, softening point—ring and ball method according to the EN 1427 standard, and elastic recovery according to the EN 13398 standard) and a performance test of shear stress relaxation using DSR (dynamic shear rheometer) were chosen.

3.1 *Rolling Thin Film Oven Test (RTFOT)*

The Rolling Thin Film Oven Test is described in the EN 12607-1 standard. The ageing of bituminous binders is influenced by atmospheric oxygen only up to small thicknesses (approx. 50 μm); therefore, a rolling thin film of the binder is applied in the test. The test simulates binder ageing during the coating of aggregates in the mixing plant of bituminous mixtures. [3–5]

For the binder ageing test, an oven with a doubled wall and electric heating at a temperature of 163 °C is used. The binder is placed in eight cylindrical glass vessels supplied with heated air from a nozzle. The combined effect of heat and air is determined from the change of the binder weight in the vessels or from the change in the bituminous binder properties measured prior to and after the ageing. To describe the changes of properties, the tests of needle penetration, softening point or dynamic viscosity are used. The changes in binder properties after the ageing can also be expressed by rheological properties detected using a dynamic shear rheometer.

3.2 *Measurement of the shear stress relaxation in DSR*

There is a variety of rheometers, i.e. instruments to detect the rheological properties of materials. Rotary (oscillatory) rheometers (referred to as dynamic shear rheometers—DSR in road engineering) are complex instruments for characterising the rheological behaviour of a wide spectrum of materials. They are designed to describe the dynamic viscosity and also allow for measurements of the other rheological properties, i.e. in both stable shear and oscillating modes. For rheological measurements, the Kinexus rotational rheometer by Malvern was used in the Road Laboratory of Brno University of Technology, see Figure 1.

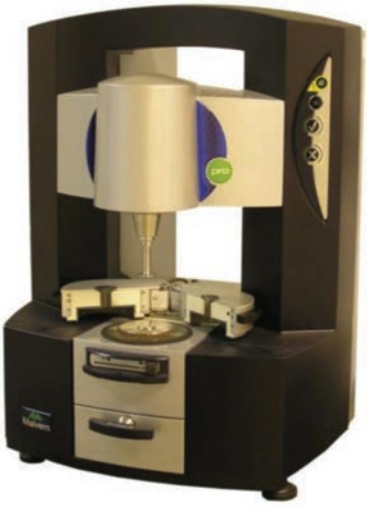

Figure 1. Kinexus rotational rheometer.

To determine the rate of shear stress relaxation in DSR, the following procedure has so far been used: at first, shear strain at a given shear rate is applied on the bituminous binder sample at a given temperature—the shear strain should be chosen in the linear viscoelastic region. For the whole testing period, the applied strain is maintained at a constant value. After the initial increase in shear stress that corresponds to shear strain and shear rate is achieved, the decrease in stress over time is monitored. The test result involves a relaxation curve of shear stress, which represents the dependency of shear stress decrease on time.

For ideally elastic materials, no shear stress relaxation will occur after the shear strain introduced, and the shear stress remains constant. In the case of a substance with ideally viscous behaviour, the internal stress will be eliminated practically immediately after the shear strain is introduced. When the shear strain is introduced to a viscoelastic material, a delayed relaxation of shear stress takes place, i.e. partial or full relaxation occurs after a certain period of time. The relaxation curve has an exponential shape, and the level of shear stress relaxation depends on the viscous component of the material.

When the shear strain is applied on a viscoelastic liquid, the complete relaxation of shear stress will be achieved (provided that the relaxation time is sufficient). For viscoelastic solids, no relaxation of shear stress to zero will take place even after a very long time interval. The relaxation curve will asymptotically near the final value referred to as equilibrium stress. This means that at least a part of the molecules are chemically or physically linked and, therefore, not able to move freely. At any moment of the test it is possible to determine the relaxation modulus as a ratio of instantaneous shear stress and set initial shear strain. [6]

4 TEST RESULTS

Below are presented the results of individual laboratory tests of binders and the description of the influence of the Rolling Thin Film Oven Test (RTFOT) on individual properties of tested bituminous binders.

4.1 *Needle penetration, softening point and elastic recovery*

The resulting values of needle penetration, softening point and elastic recovery of tested binders are given in Table 2, including the description of the influence of RTFOT ageing on the aforesaid characteristics. Paving grade bitumen showed the highest penetration value

Table 2. Basic binder characteristics prior to and after the short-term ageing (RTFOT).

	Penetration [0.1 mm]		Softening point [°C]		Elastic recovery [%]	
Binder	–	RTFOT	–	RTFOT	–	RTFOT
Paving bitumen 50/70	54	35	48.9	52.5	–	–
PmB 45/80-50	45	30	54.2	58.5	52.3	58.5
PmB 25/55-55	30	27	65.7	70.4	84.0	66.8
PmB 25/55-65	25	16	78.2	81.3	85.3	76.0
CRmB 25/55-60	38	28	62.3	68.4	61.5	77.0

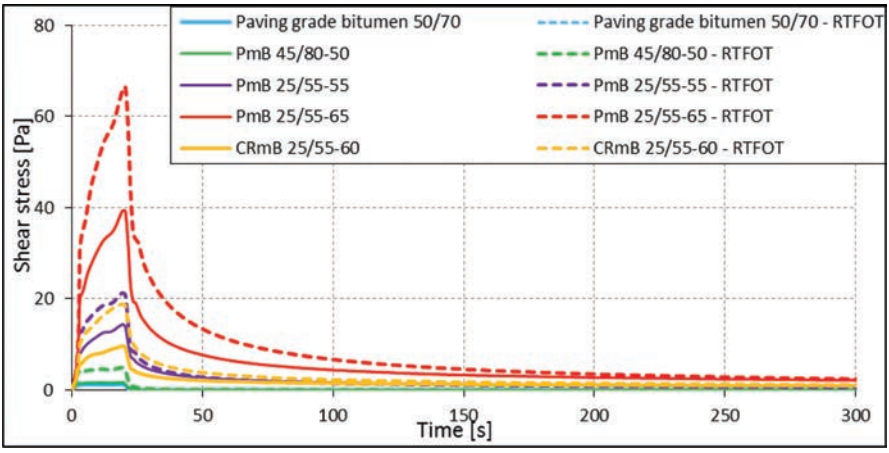

Figure 2. Relaxation of shear stress of individual binders (shear strain 1% after 20 s).

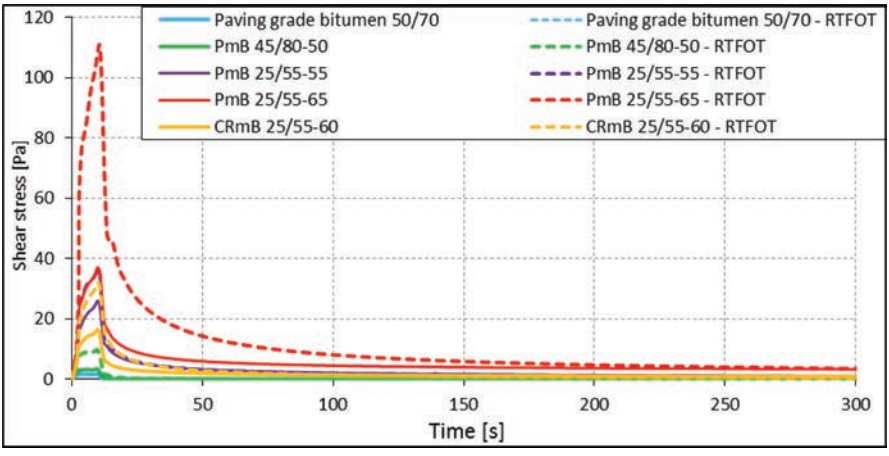

Figure 3. Relaxation of shear stress of individual binders (shear strain 1% after 10 s).

and the lowest softening point. Penetration of polymer modified bitumens decreases and the softening point increases with the increasing degree of modification of polymer modified bitumen. Short-term ageing resulted in a reduced penetration in all binders ranging from 3 to 19 penetration units. The PmB 25/55-55 showed the least influence of ageing on the value of penetration. The softening point of all binders increased due to RTFOT ageing by 3.1 °C

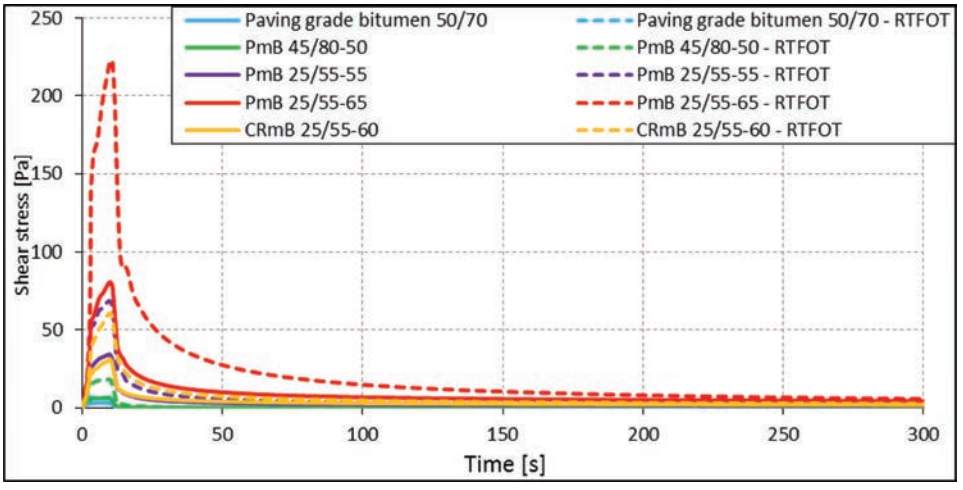

Figure 4. Relaxation of shear stress of individual binders (shear strain 2% after 10 s).

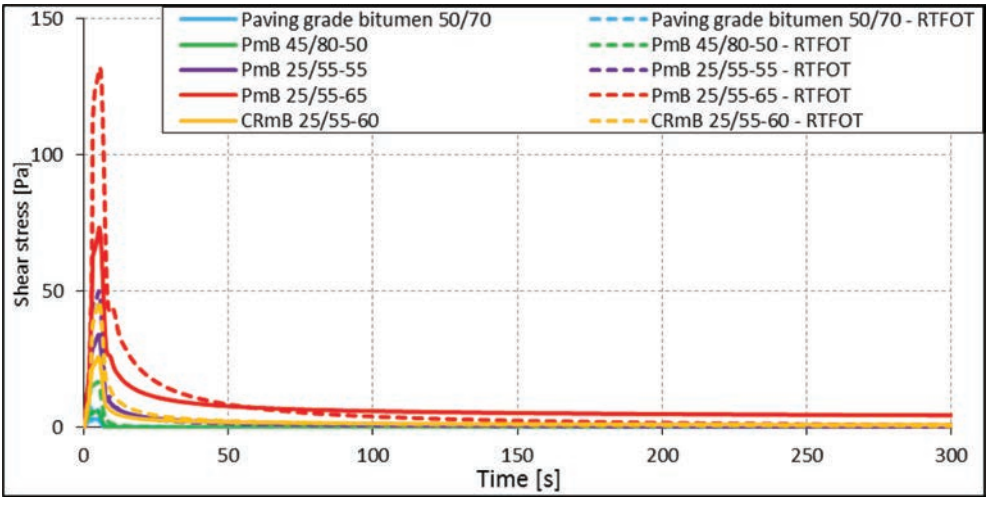

Figure 5. Relaxation of shear stress of individual binders (shear strain 1% after 5 s).

to 6.1 °C. The greatest change of the softening point value could be observed in case of crumb rubber modified bitumen. Naturally, the change in test values of the aged crumb rubber modified bitumen could be caused by the additional reaction of crumb rubber particles with bitumen at a high temperature. Due to ageing the elastic recovery decreased in the PmB 45/80-50 and CRmB 25/55-60 binders and increased in the two remaining polymer modified bitumens.

4.2 *Relaxation of shear stress*

The relaxation of shear stress of binders in DSR has been determined at a temperature of 50 °C using parallel measuring plates with a diameter of 25 mm and a gap size of 2.0 mm. The relaxation tests were carried out in the mode of controlled strain. The initial shear strain achieved a value of 1% and 2% of sample thickness, and the time to achieve the shear strain was 5 s, 10 s and 20 s, and a relaxation time 300 s was used.

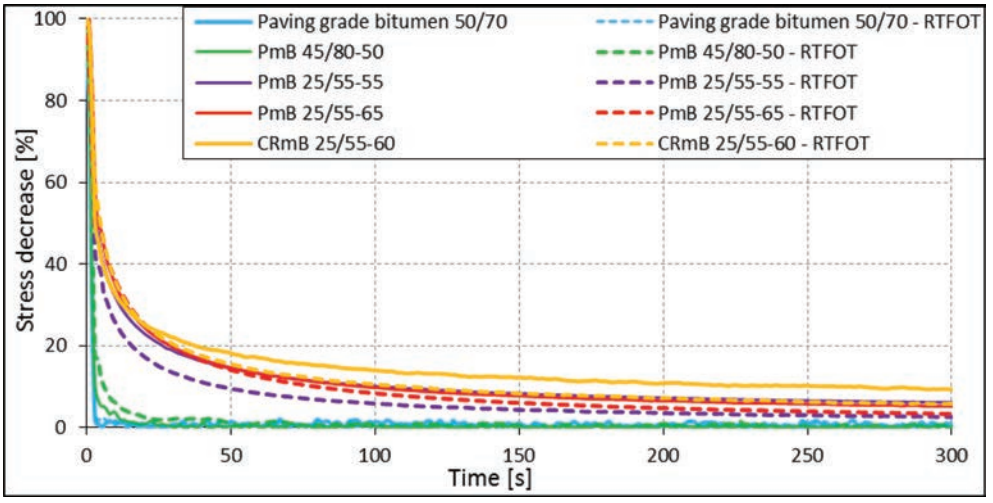

Figure 6. Decrease in shear stress of binders, in % (shear strain 1% after 20 s).

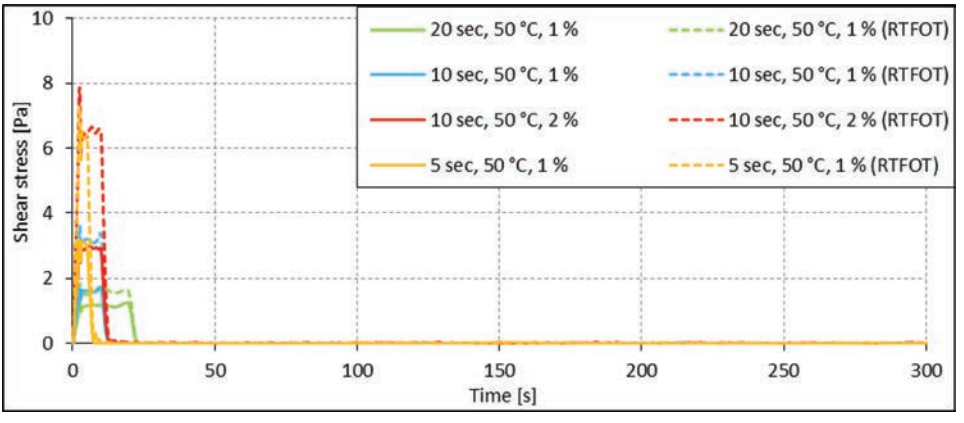

Figure 7. Relaxation of shear stress of paving grade bitumen 50/70.

Figures 2–5 compare the relaxation of shear stresses of individual binders depending on the time for various boundary test conditions. PmB 25/55-65 and paving grade bitumen 50/70 showed the highest and the lowest shear stresses, respectively. When testing the relaxation of shear stress of the paving grade bitumen 50/70 at 50 °C, the shear stress decreases practically immediately to zero once the shear strain ceased to be introduced on the bitumen sample. The negligible elastic response corresponds to great phase angles measured using the dynamic shear rheometer (80 ° to 85 °). Besides, when shear stress is introduced at 50 °C, the sample has already become flexible to such a degree that the pseudoviscosity of the plate/plate system is more likely to be measured. The decrease in shear stress of the PmB 45/80-50 sample was only slightly slower. For PmB 25/55-50, PmB 25/55-65 and CRmB 25/55-60, shear stress did not relax fully after 300 seconds; the relaxation curve is asymptotically nearing the final value (equilibrium stress). The RTFOT ageing caused an increase in initial maximum shear stresses of all binders. From Figure 6 it is obvious that the relaxation of shear stress is faster for aged binders than for non-aged ones when maximum shear stress equalling 100% is applied.

Figures 7–11 compare the relaxation curves of individual binders with various conditions applied during the testing of shear stress relaxation. The magnitude of maximum

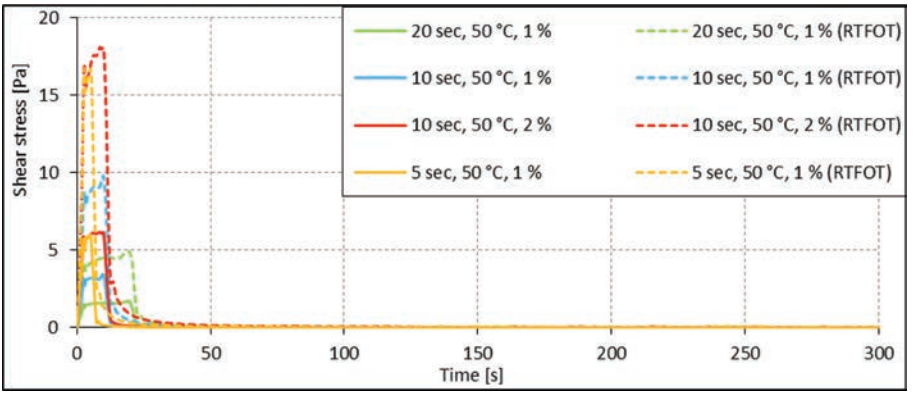

Figure 8. Relaxation of shear stress of PmB 45/80-50.

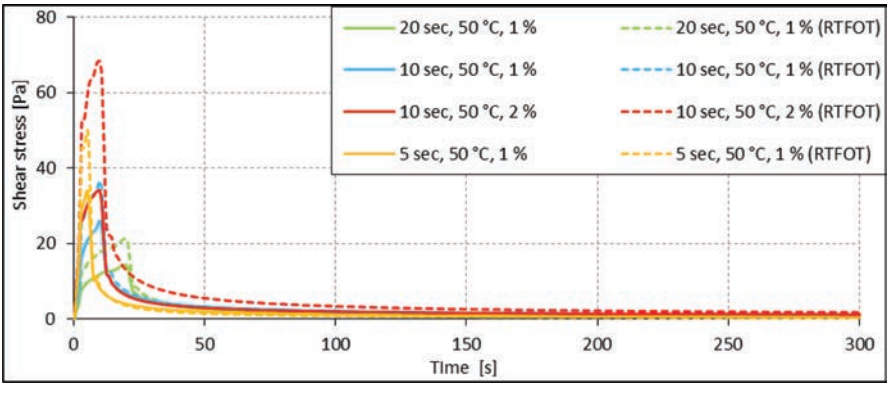

Figure 9. Relaxation of shear stress of PmB 25/55-55.

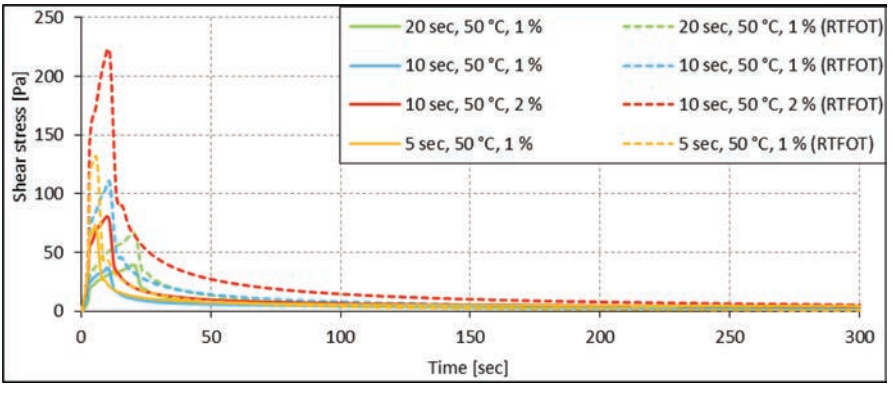

Figure 10. Relaxation of shear stress of PmB 25/55-65.

shear stress depends on the rate of shear strain change (shear rate). At the same shear rate, the loading line showed an approximately identical pattern (e.g. 1% after 5 s and 2% after 10 s). At a double shear rate, the produced shear stress also became doubled (e.g. 1% after 10 s and 2% after 10 s). The slowest relaxation of shear stress occurred in binders after a low shear rate had been applied (1% after 20 s), while the greatest

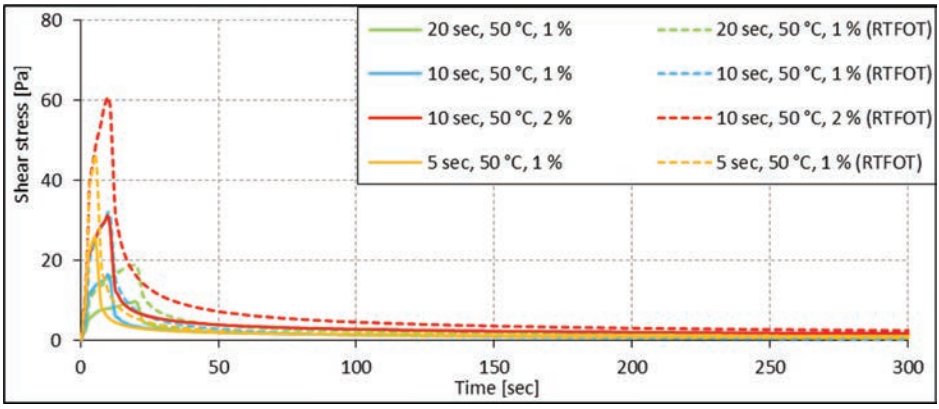

Figure 11. Relaxation of shear stress of CRmB 25/55-60.

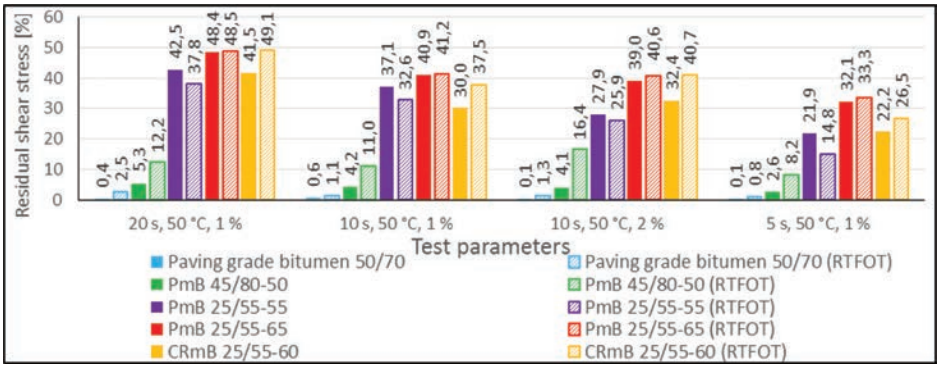

Figure 12. Residual shear stress of individual binders after 5 seconds of relaxation.

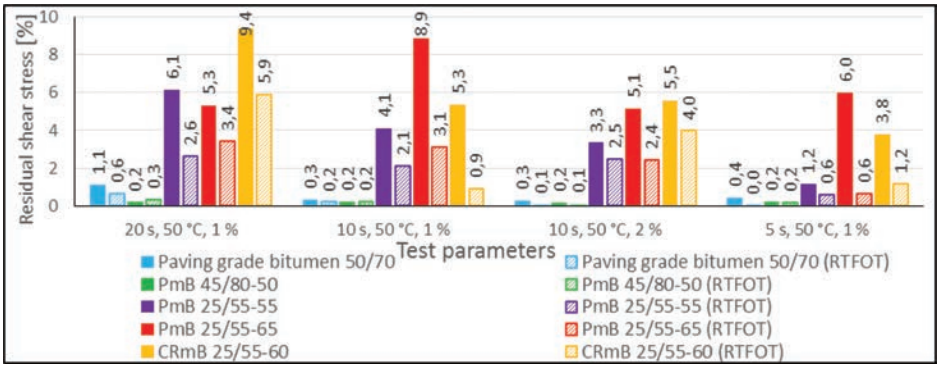

Figure 13. Residual shear stress of individual binders after 300 seconds of relaxation.

relaxation of binders was observed after a fast shear strain had been introduced (1% after 5 s).

Figure 12 summarizes residual shear stresses of binders after 5 seconds of relaxation in dependence on test conditions. Figure 13 shows residual values of shear stress of individual binders after 300 seconds of relaxation depending on the set test conditions. After 300 seconds

of relaxation, the crumb rubber modified bitumen CRmB 25/55-60 and polymer modified bitumen PmB 25/55-65 achieved the highest equilibrium stresses. Here again, the considerable influence of simulated ageing on the behaviour of bituminous binders could be observed. Probably due to crosslinking processes caused by thermo-oxidative reactions of radicals, the measured maximum shear stress increases and the percentage relaxation of shear stress of binders decreases in DSR.

5 CONCLUSIONS

The results of selected tests made on a spectrum of non-aged and RTFOT aged bituminous binders are presented in this article. For laboratory testing, 50/70 paving grade bitumen, three different polymer modified bitumens, and one crumb rubber modified bitumen (asphalt rubber) were chosen.

During the testing of shear stress relaxation in DSR made at 50 °C, the degree of modification system is likely to be employed. The relaxation of shear stress of binders has been determined in DSR at a temperature of 50 °C using parallel plates with a diameter of 25 mm and a gap size of 2.0 mm. The magnitude of maximum shear stress depends on the rate of shear strain change (shear rate). For PmB 25/55-50, PmB 25/55-65 and CRmB 25/55-60, shear stress did not relax completely after 300 seconds; the relaxation curve asymptotically approached the final value (equilibrium stress). The RTFOT ageing resulted in increasing the initial maximum shear stresses of all binders. When a maximum shear stress equalling 100% is applied, the relaxation of shear stress is faster in aged binders than in non-aged ones.

The relaxation of shear stress measured in the bituminous binder using DSR can be an important indicator of the level of material ability to diminish the applied stress, as well as the quality of the modification system. The basic purpose of the measurement of shear stress relaxation of bituminous binders using DSR is to describe the relaxation behaviour of the binder itself under given temperature conditions to predict the subsequent relaxation behaviour of bituminous mixtures. When a bituminous binder shows a fast relaxation of shear stress applied, it is assumed that the tendency of the finished bituminous layer to create and propagate cracks will be decreased.

Modern dynamic shear rheometers enable not only oscillation tests but also tests in stable shear flow as well as measurements of normal sample force to be carried out. The new test equipments allow for increasingly more precise descriptions of the behaviour of paving materials. In combination with the laboratory simulation of ageing, it is possible to describe the development of performance characteristics of bituminous binders and to predict their behaviour in a real pavement.

ACKNOWLEDGEMENT

The article has been prepared with the support of TA03030381 “New Test Methods for Asphalt Binders and Mixtures Allowing the Extension of Asphalt Pavements Performance”, support of TA02030639 “Durable acoustic asphalt pavement courses with utilization of bituminous binders modified by rubber microfiller including innovative technology of rubber milling” and TA02030549 “The most effective utilization of reclaimed asphalt pavement layers for production of new asphalt mixes”.

REFERENCES

[1] TP 151. Asphalt Mixtures with High Stiffness, Technical Conditions by the Ministry of Transport of the Czech Republic, Prague. 2010.

[2] C.S. Clopotel and H.U. Bahia. Importance of Elastic Recovery in the DSR for Binders and Mastics, Engineering Journal, 16(4), pp. 99–106. ISSN 0125-8281. 2012.

[3] J. Plitz. Ageing of bituminous binders, Asphalt Pavements '97, Ceske Budejovice, Czech Republic, pp. 125–129. 1997.
[4] A. Shalaby. Modelling short-term aging of asphalt binders using the rolling thin film oven test, Canadian Journal of Civil Engineering, 29, pp. 135–144. 2002.
[5] G.A.J. Mturi and J. O'Connell. Monitoring Ageing of Bituminous Binders, 31st Annual Southern African Transport Conference, Pretoria, South Africa, pp. 1–13. 2012.
[6] T.G. Mezger. The Rheology Handbook, For Users of Rotational and Oscillatory Rheometers, 3rd revised edition, ISBN 978-3-86630-864-0, Germany. 2011.

Asphalt Pavements – Kim (Ed)
© 2014 Taylor & Francis Group, London, ISBN 978-1-138-02693-3

Possibilities of a hollow cylinder tester for asphalt mixtures

Eduardo J. Rueda, Silvia Caro, Bernardo Caicedo & Julieth Monroy
Department of Civil and Environmental Engineering, Universidad de los Andes, Bogotá, Colombia

ABSTRACT: The characterization of asphalt concrete materials continues being a crucial area of work in the field of pavement engineering. As part of the efforts to improve the current knowledge of this complex material, a novel laboratory equipment has been recently designed and constructed at Universidad de Los Andes (Bogotá, Colombia). This device, named "Hollow Cylinder Tester for Hot Mix Asphalt (HMA) materials" (HCT-HMA), is a multipurpose apparatus equipped with an environmental conditioning chamber and a versatile loading system able to apply axial and/or torsional loads. The main feature of this equipment is the geometry of the specimen, which consists of a 12.7 cm in height hollow cylinder with 2.54 cm wall thickness. This paper describes the components of the HCT-HMA and some of the possibilities of this device to characterize asphalt concrete materials. It is expected that this machine will provide new and valuable information regarding the complex response of asphalt mixtures.

Keywords: Asphalt mixture, hollow cylinder tester, mechanical characterization

1 INTRODUCTION

There exist several different standardized experimental methodologies that are applied worldwide to determine the mechanical properties of asphalt mixtures. Some of these techniques include, among others, the dynamic modulus test [1], the shear modulus test [2], and the indirect tensile test [3]. Most of these methodologies, however, are restricted to narrow stress paths. This situation constrains the acquisition of data regarding the response of the material under more complex conditions. For this reason, geotechnical and pavement engineers have found that the "Hollow Cylinder" methodology is an efficient tool to improve the possibilities of material characterization.

The hollow cylinder methodology has been used to study the properties of different materials, ranging from wood and metals to soils and polymers. The advantage of this methodology is that it enables the use of a wide range of stress paths that are typically limited in regular triaxial testing. This is partially due to the fact that the geometrical configuration of the specimens (i.e., hollow cylinders) promotes a more uniform stress distribution within samples subjected to torsional loading than that obtained in solid specimens. Additionally, as it will be explained in this paper, for the specific case of asphalt mixtures, this methodology could also be used to efficiently characterize the effect of environmental conditions on the mechanical response of the material.

Geotechnical engineers have used hollow cylinder testing procedures to study the response of clays and granular unbound materials subjected to the combined effect of axial and shear stresses (i.e., to simulate the rotation of principal stresses) [4]. The first experimental experience using this methodology intended to quantify the resistance of unconfined clays in pure shear [5]. Similar studies on clays continued with Geuze and Tan [6], and later by Saada and Zamani [7].

Based on the positive results obtained on clays, the use of the hollow cylinder methodology was expanded to study several effects of sands, including its undrained anisotropy behaviour,

liquefaction phenomena, and the effect of large amplitude vibrations on the shear modulus and damping of these materials [8], [9], [10]. Additionally, Di Benedetto et al. [11] used the hollow cylinder technique to describe the constitutive viscous and non-viscous behaviour of sand materials. Finally, a hollow cylinder machine was developed by the group of Geomaterials and Infrastructure Systems at Universidad de los Andes (Bogota, Colombia) to study the mechanical response of coarse aggregates used as part of base and subbase layers in pavement structures [12].

In contrast to the broad experience in geotechnical engineering, the application of hollow cylinder methodologies to characterize asphalt concrete is limited. The first experience was conducted in 1986 when a hollow cylinder apparatus was designed at the University of California at Berkeley to study the dynamic properties of asphalt concrete under axial and torsional loads [13] [14]. In 1999 the University of Illinois at Urbana-Champaing developed a new hollow cylinder apparatus to evaluate rheological properties of asphalt concrete like creep compliance, tensile strength and dynamic modulus [15]. In this case, however, the mechanism of load application consisted of applying pressure in the inner cavity of the hollow cylinder specimen. More recently, Brown et al. [16] at University of Nottingham designed a hollow cylinder apparatus to study the susceptibility of asphalt concrete to permanent deformation.

The experiences mentioned previously were the motivation for this work. This paper describes the characteristics of a new hollow cylinder machine, named "Hollow Cylinder Tester for Hot Mix Asphalt materials" (HCT-HMA), and explores some possible applications of the HCT-HMA to conduct novel characterization testing on this material. The HCT-HMA is a multipurpose device equipped with an environmental conditioning chamber and a versatile loading system able to combine different load applications.

This paper contains four sections. The first section presents the basic principles used in hollow cylinder tests. Next, the main features of the hollow cylinder device are described, followed by an explanation of the possibilities of the new machine to evaluate the performance of asphalt materials, as well as some calibration activities. Finally, the main conclusions of this work are presented.

2 HOLLOW CYLINDER TESTER FOR ASPHALT MATERIALS

The HCT-HMA is a laboratory equipment developed with the objective of conducting comprehensive characterization of asphalt materials. It was designed to test hollow cylinder samples in both torsional and axial loads. These loads can be applied using different combinations (e.g., axial and/or torsional load under monotonic, cyclic, and other conditions), at the point that the device can be used to reproduce tridimensional state of stresses that occurs in asphalt concrete materials subjected to moving loads. Additionally, it can be used to determine the linear and non-linear viscoelastic material properties of the mixtures, as well as to characterize its fatigue and permanent deformation susceptibility. In addition, the HCT-HMA was created to provide valuable information about the response of asphalt mixtures subjected to realistic field conditions. Within this context, the use of a hollow cylinder geometry accelerates environmental conditioning processes, due to the double exposed walls that characterize testing specimens. Therefore, the new HCT-HMA has been also designed to quantify the role of controlled environmental conditions, such as relative humidity and oxidation process, in the response of asphalt mixtures. Figure 1 illustrates the equipment and its components.

2.1 *Sample characteristics and fabrication procedure*

The specimen geometry for the HCT-HMA consists of a 12.7 cm height hollow cylinder with 2.54 cm wall thickness and 12.7 cm outside diameter. These dimensions were defined based on the recommendations provided by Saada and Townsend [17], who suggested a geometrical criterion shown in Eq. (1) to reduce the non-uniformity distribution of shear stresses.

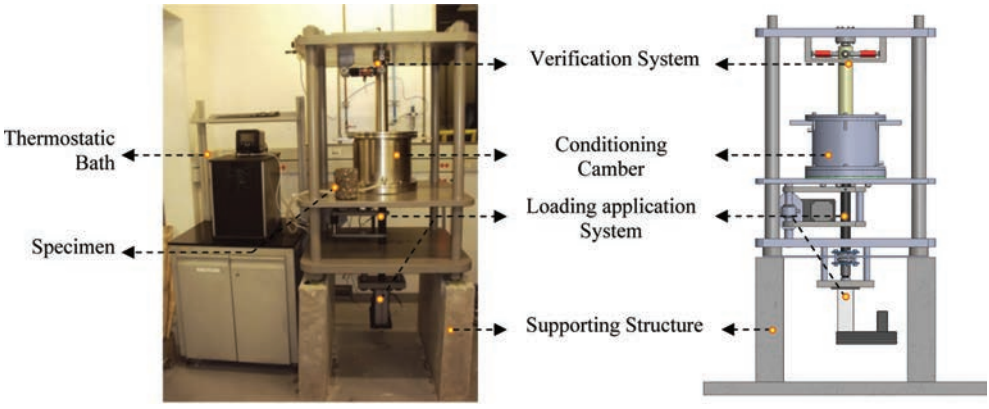

Figure 1. Hollow cylinder tester for hot mix asphalt materials: HCT-HMA.

Figure 2. (a) coring process, and (b) specimen geometry (centre).

According to these dimensions, the use of mixtures with a maximum nominal size of the aggregates equal or smaller than 12.5 mm (1/2 inch) is recommended.

$$\frac{r_{inner}}{r_{outer}} \geq 0.65 \text{ and } H \geq 5.44\sqrt{r_{inner} - r_{outer}} \quad (1)$$

where r_{inner} is the inner radius of the sample, r_{outer} is the outer radius of the specimen and H is the height of the sample.

The specimen preparation initiates with the fabrication of an asphalt mixture sample with 15 cm in height and 15 cm in diameter using the Superpave Gyratory Compactor. These samples are subsequently cored to remove the external shell of the specimen, using a 12.7 cm drill core, and to remove the inner cylindrical part of the specimen, using a 7.62 cm drill core. Finally, the hollow samples are trimmed 1 cm at the top and bottom edges of the specimen to produce smooth surfaces. Figure 2 presents the coring process and the final specimen configuration.

2.2 *Main components of the HCT-HMA*

Besides the testing specimen, the HCT-HMA has four main components: 1) a conditioning chamber, 2) a load application system, 3) a displacement and loading measurement system,

and 4) a software that controls the aforementioned component to perform specific operations. The following sections describe each one of these components.

2.2.1 *Conditioning chamber*

The conditioning chamber of the HCT-HMA is comprised of a base that holds the specimens between two rigid plates, and a pressure-temperature container able to generate specific environmental conditions (Fig. 3a and b). These environmental conditions are obtained by controlling the magnitude of the temperature, relative humidity and air pressure; parameters that can be applied either independently or simultaneously. Additionally, the conditioning chamber was equipped with a lifting system that was designed to displace the pressure-temperature container vertically in order to open or close the chamber (Fig. 3c).

The conditioning chamber has different subsystems to control each environmental parameter. Thermal conditioning, for example, is achieved by means of a thermostatic-bath that allows water, at a specific temperature, to recirculate through a double wall located within the container. The bath capacity ranges from –14 to 175 °C.

The chamber also has the ability to create environments that promote oxidative aging in asphalt mixtures. The aging subsystem consists of the application of high air pressure to the inner and outer parts of the specimen. The maximum pressure that can be applied to the specimen is 2000 kPa (20 Bar), which is similar to the value used in the Pressure Aging Vessel (PAV) procedure [18].

Finally, a constant relative humidity condition can be obtained within the chamber using a vapour equilibrium technique. This technique consists of locating a vessel containing a saturated saline solution outside the chamber. Depending of the salt used, the solution creates a controlled relative humidity environment that is transmitted into the chamber using a peristaltic pump.

2.2.2 *Loading application system*

The axial and torsional loads are applied to the specimen using the loading application system presented in Figure 4. This system has two electric linear actuators able to apply 20 kN. The actuators consist of a load cell and an accurate roller screw mechanism that permits the application of heavy loads at high speeds.

The system of axial loading application comprises an axial actuator with a stroke length of 6.0 cm and a force capacity of 20 kN. On the other hand, torsional loading is applied through an actuator connected to a 30.0 cm arm that is fixed to the extension shaft. The torsional actuator can apply a maximum torque of 6 kN-m.

2.2.3 *Displacement and loading measuring system*

In order to measure, verify and control all the variables and parameters involved in the characterization process, the HCT-HMA has a sophisticated instrumentation system that can be

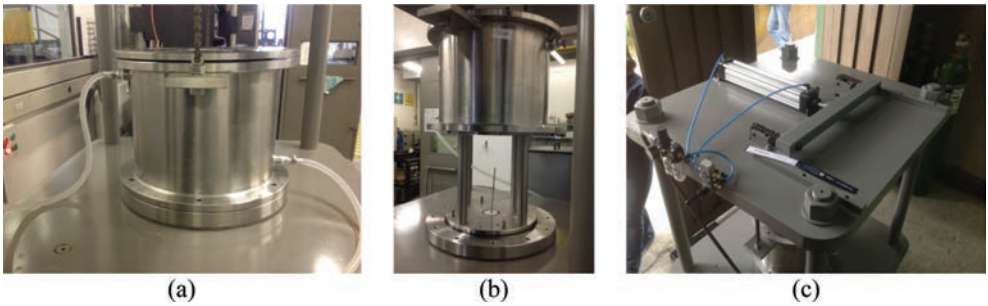

Figure 3. (A) HCT-HMA conditioning chamber, (b) base and pressure-temperature container in the highest position, and (c) lifting system.

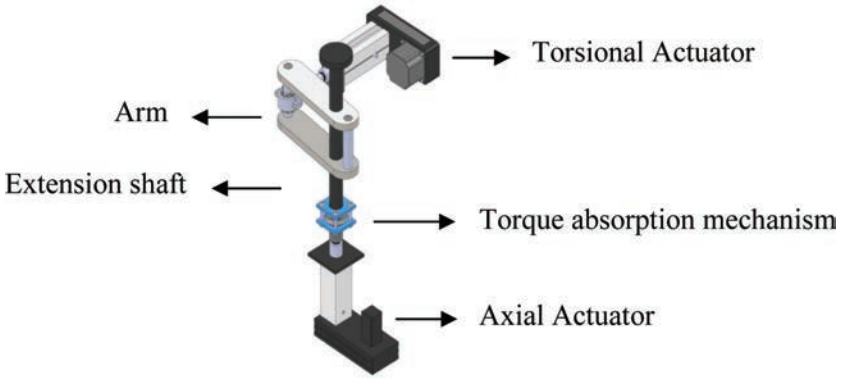

Figure 4. Loading application system.

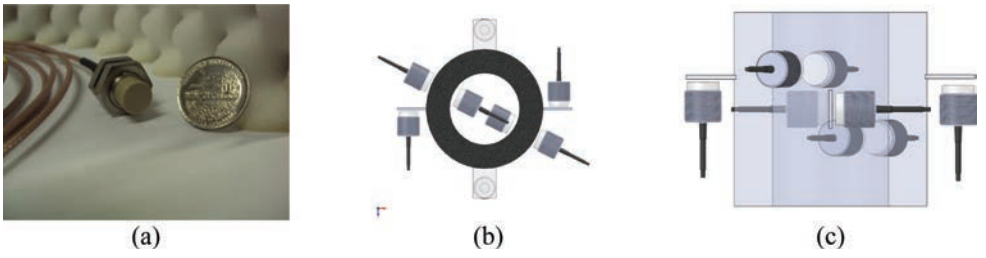

Figure 5. Positions of the displacement sensors: (a) eddy current displacement sensors, (b) top and (c) transverse view of the sensors located in the specimen.

divided into three components. The first component is in charge of measuring the specimen displacement, the second controls the environmental parameters and the last component is used to verify the magnitude of the applied loads.

The displacement measurement component consists of eight non-contact displacement sensors that use the eddy current principle (Waycon T3-G-KA with a precision of 0.006 mm). The displacement sensors are fixed at different points surrounding the specimen in accordance to the direction of measurements (Fig. 5). Thus, the axial strain is obtained using two sensors located at the top of the second third of the sample on either side (Fig. 5c). The measurement of the shear strain uses a similar technique. The difference in this case is the horizontal position of the sensors, since the radial displacement is measured in the inner and the outer walls of the sample by a pair of sensors that face each other.

The system designed to control the environmental conditions within the chamber and the testing specimen is composed by a couple of thermocouples (National Instruments 745691-01), moisture sensors (Honeywell HIH4602C) and pressure sensors (Futek QSH01450) (Fig. 6). These sensors are placed in the inner and the outer part of the specimen. The thermocouples are located in the walls of the sample to control the specimen's temperature, while the pressure and the moisture sensors are placed within the conditioning chamber to control the environment that surrounds the specimen.

Finally, two types of load cells are used to verify the magnitude of the load applied to the specimen. The applied axial load is measured using a "Pancake" load cell (Futek FSH01493). This cell has a maximum capacity of 22240 N and is able to resist tension and compression stresses. The applied torsional load is measured and verified using two "Tension-Compression" load cells (Futek FSH00711), based on the principle of a "pair of forces".

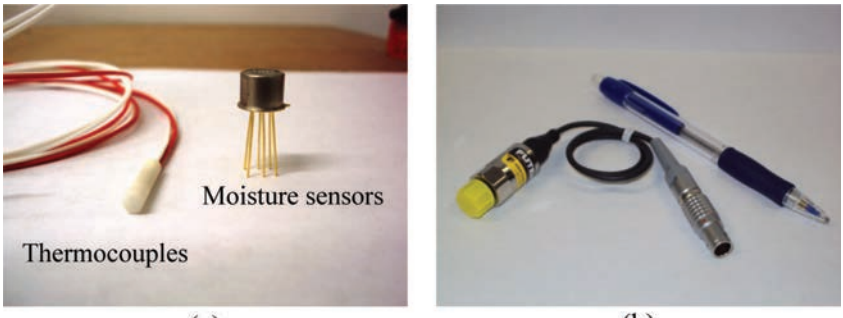

Figure 6. Components of the environmental control system: (a) thermocouples and moisture sensor, and (b) pressure sensor.

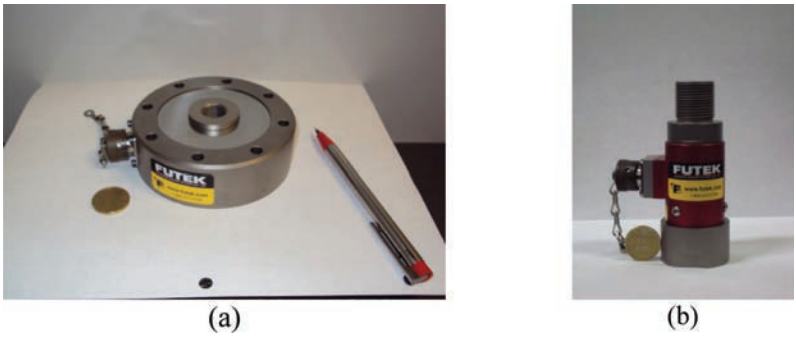

Figure 7. Load cells used to verify the axial and torsional loads: (a) pancake load cell, and (b) tension-compression load cell.

2.2.4 *Software to control the HCT-HMA*

As a complementary component of this equipment, a software was developed to enable communication between the HCT-HMA and the user. The HCT-HMA software was developed in the visual programming language "LabVIEW", and it contains four sections: 1) the "Settings" of the system, 2) the "Input Signal", in which the user can define the type of loading (e.g., cyclic axial load with certain amplitude and frequency) and the type of test (i.e., strain-controlled or stress-controlled), 3) the description of the "Previous Procedures" required before the experimental test initiates, and 4) the "Output Signal", in which the response of the material can be monitored in real time during the experiment.

3 POSSIBILITIES OF THE HCT-HMA

As observed in the previous sections, the HCT-HMA offers a wide range of possibilities for the characterization of HMA materials, as described in the following sections.

3.1 *Evaluation of viscoelastic properties of asphalt materials subjected to controlled environments*

Depending on the characteristic of the applied load, the HCT-HMA can be used to determine the linear and non-linear viscoelastic material properties of asphalt mixtures in the time and in the frequency domain (e.g., creep compliance, relaxation modulus and dynamic modulus).

Additionally, the use of the climatic chamber of the HCT-HMA enables the study of the influence of different environmental conditions (temperature, relative humidity, oxidative aging or a combination of them) on the viscoelastic properties of HMA materials.

3.2 *Evaluation of the performance and degradation of hot mix asphalt materials*

The HCT-HMA also provides the possibility to determine the fatigue life of asphalt mixtures and their susceptibility for permanent deformation. In the case of fatigue deterioration and failure, the equipment permits the characterization of this degradation process not only under the classical oscillatory axial stress/strain configuration, but also under oscillatory shear or torsional stress/strain. Besides, the equipment could be used to characterize the susceptibility of the material to permanent deformation using torsional shear stress configurations. In addition, the characterization of these deterioration processes using the HCT-HMA can be conducted under any defined environmental conditions. Thus, this machine can be used to evaluate the influence of environmental conditions on the performance and deterioration of the material (e.g., influence of moisture conditions or oxidative aging on the fatigue deterioration of asphalt mixtures).

4 CALIBRATION ACTIVITIES

Currently, the main structure of the HCT-HMA has been built, the components of the machine have been acquired, the task of verifying and calibrating the individual components of the machine has been finalized, and the assembling all the parts of the system has been completed. In terms of the verification of the HCT-HMA components, this task included the calibration of the load cells, the thermostatic bath, and the displacement, temperature, moisture and pressure sensors, among others activities. In the case of the thermostatic bath, for example, the calibration consisted of determining the maximum temperature that could be obtained within the conditioning chamber based on a temperature values assigned to the bath, as well as the time required for temperature stabilization within the chamber. Figure 8 presents the preliminary results of this calibration process.

Similarly, the operation of the load actuators, the capacity of the load cells to provide accurate values, and the correct response of the displacement sensors were also verified. In the case of the tension-compression load cell, for example, this was achieved by using a reference load cell and a servo-controlled press. The process consisted of applying a specific load using the servo press, verifying this load value with the reference load cell and comparing

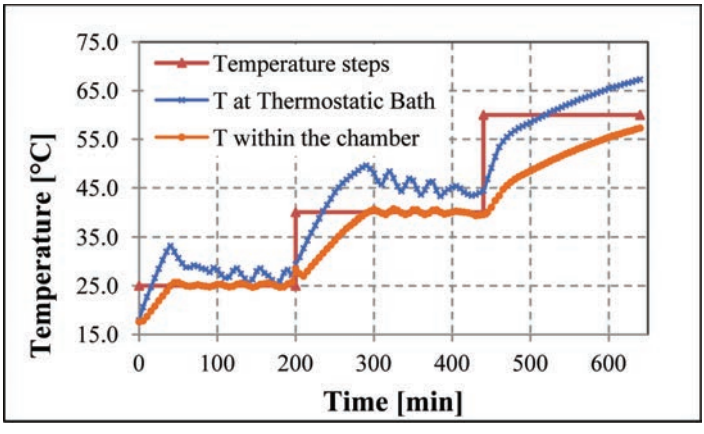

Figure 8. Calibration of the temperature at thermostatic bath and the temperature within the conditioning chamber.

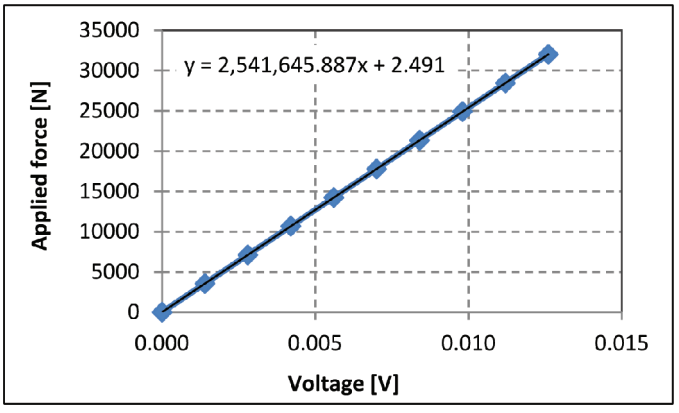

Figure 9. Calibration of the load cells (calibration parameters: K(N/V) = 2,541,645.8 and offset = 2.491 N).

it with the voltage values measured by the target cell. The final output of this procedure is the calibration constant (*K*) and its corresponding offset value, which in this particular case were defined as 2,541,645.8 N/V and 2.491 N, respectively (Fig. 9).

In the near future, several activities will be conducted on the recently assembled HCT-HMA to corroborate the proper operation of the machine. This includes, among others, checking the capacity of HCT-HMA to apply a requested load configuration, and verifying if the device can accurately measure the response of the specimen and capture this information using the developed software. Besides, it would be necessary to compare the results of the HCT-HMA machine with those obtained from standardized tests; for example, the dynamic modulus will be determine using both the HCT-HMA and the MTS testing system, in order to calibrate the testing procedure. Only after accomplishing these activities, it would be possible to design different experimental plans to conduct advance characterization of asphalt mixtures that, as mentioned previously, would include the relationship between the environment and the mechanical response of these materials.

5 CONCLUSIONS

This paper describes a new machine named "Hollow Cylinder Tester for HMA materials" or HCT-HMA. The machine counts with a versatile loading system and a sophisticated conditioning system that will improve the current testing possibilities to characterize asphalt mixtures. Among other characteristics, the HCT-HMA could be used to determine linear and non-linear viscoelastic properties and deterioration process of asphalt mixtures (e.g., fatigue and permanent deformation) that are subjected to a variety of environmental conditions and a wide range of stress paths (axial and/or torsional loads). Thus, the HCT-HMA will provide information regarding the role of different environmental parameters (i.e., temperature, relative humidity and air contact) in the deterioration of the HMA properties.

Currently, the calibration of most components of the machine (load application system, load verification system and environmental sensors) has been finalized, as well as the assembly of these components into the structure of the machine.

It is expected that the Hollow Cylinder Tester for Hot Mix Asphalt will became an efficient tool to achieve a more comprehensive characterization of the behaviour of this material.

ACKNOWLEDGEMENTS

This publication was made possible by the call for proposals "Research Program 2012" from the Office of the Vice President for Research—Universidad de los Andes (Bogotá, Colombia).

Its contents are solely the responsibility of the authors and do not necessarily represent the official views of the Universidad de los Andes (Bogotá, Colombia).

REFERENCES

[1] AASHTO T 342-11, "Standard Method of Test for Determining Dynamic Modulus of Hot-Mix Asphalt Concrete Mixtures," American Association of State and Highway Transportation Officials, pp. 1–18, 2011.

[2] ASTM Standard D7312, "Standard Test Method for Determining the Permanent Shear Strain and Complex Shear Modulus of Asphalt Mixtures Using the Superpave Shear Tester (SST)," www.astm.org, pp. 1–9, 2010.

[3] ASTM Standard D 6931, "Standard Test Method for Indirect Tensile (IDT) Strength of Bituminous Mixtures," www.astm.org, pp. 1–5, 2012.

[4] A.S. Saada, "Hollow Cylinder Torsional Device: Their Advantages and Limitations," Advanced Triaxial Testing of soil and rock, pp. 766–795, 1988.

[5] L.F. Cooling and D.B. Smith, "The Sheating Resistance of Soils," Journal of the Institution of Civil Engineering, vol. 3, no. 7, pp. 333–343, 1936.

[6] E.C.W.A. Geuze and T.T. Tan, "The Shearing Properties of Soils," Proceeding 2nd International Congress on Rheology, 1953.

[7] A.S. Saada and K.K. Zamani, "The Mechanical Behavior of Cross Anisotropic Clays," Seventh International Conference on Soil Mechanics and Foundation Engineering, pp. 351–359, 1969.

[8] D.W. Hight, A. Gens, and M.J. Symes, "The Development of a New Hollow Cylinder Apparatus for Investigating the Effects of Principal Stress Rotation in Soils," Géotechnique, vol. 33, no. 4, pp. 355–383, 1983.

[9] J. Buchheister and J. Laue, "Two Directional Cyclic Loading Experiments in a Hollow Cylinder Apparatus," First European Conference on Earthquake Engineering and Seismology, 2006.

[10] V.P. Drnevich and F.V. Richart, "Soil Mechanics and Foundations Division," Proceedings of the American Society of Civil Engineers, vol. 96, pp. 453–469, 1970.

[11] H. Di Benedetto, H. Geoffroy and C. Sauzéat, "Viscous And Non Viscous Behaviour Of Sand Obtained From Hollow Cylinder Tests," Advanced laboratory stress-strain testing of geomaterials, vol. 29, pp. 217–226, 2001.

[12] B. Caicedo, M. Ocampo, L. Vallejo, and J. Monroy, "Hollow Cylinder Apparatus for Testing Unbound Granular Materials of Pavements," Road Materials and Pavement Design, vol. 13, no. 3, pp. 455–479, Sep. 2012.

[13] J.B. Sousa and C.L. Monismith, "Dynamic Response of Paving Materials," Transportation Research Record, no. 1136, pp. 57–68, 1987.

[14] S.H. Alavi and C.L. Monismith, "Time and Temperature Dependent Properties of Asphalt Concrete Mixes Tested as Hollow Cylinders and Subjected to Dynamic Axial and Shear Loads," Journal of the Association of Asphalt Paving Technologists, vol. 63, pp. 152–181, Sep. 1994.

[15] W.G. Buttlar, G.G. Ai-khateeb, and D. Bozkurt, "Development of a Hollow Cylinder Tensile Tester to Obtain Mechanical Properties of Bituminous Paving Mixtures," *Asphalt Paving Technology*, pp. 369–403, 1999.

[16] S.F. Brown, B.V. Brodrick, K. Tekieli, and a.C. Collop, "A torsional hollow cylinder research apparatus for studying the permanent deformation characteristics of asphalt," *Road Materials and Pavement Design*, vol. 14, pp. 65–85, Apr. 2013.

[17] A.S. Saada and F.C. Townsend, "State of the Art: Laboratory Strength Testing of Soils. Laboratory Shear Strength of Soil," *A Symposium, American Society for Testing and Materials*, pp. 7–77, Dec. 1981.

[18] ASTM Standard D 6921, "Standard Practice for Accelerated Aging of Asphalt Binder Using a Pressurized Aging Vessel (PAV)," *www.astm.org*, pp. 1–6, 2008.

This page intentionally left blank

Recycling—I

This page intentionally left blank

Asphalt Pavements – Kim (Ed)
© 2014 Taylor & Francis Group, London, ISBN 978-1-138-02693-3

Rutting and cracking potential of HMA consisting of RAP

G. Bharath
IIT Kharagpur, Kharagpur, West Bengal, India

Vivek Tandon
University of Texas at El Paso, El Paso, TX, USA

M. Amaranatha Reddy & K.S. Reddy
IIT Kharagpur, Kharagpur, West Bengal, India

ABSTRACT: This paper presents the details of a study conducted to evaluate rutting and cracking potential of mixes consisting of Reclaimed Asphalt Pavements (RAP). Texas (Type B) and Indian (DBM-2) mix specifications were reviewed and a mix design that meets both specifications was selected for evaluation purpose. Hot mix asphalt specimens consisting of 0%, 15%, 25% and 35% RAP were prepared in the laboratory using PG64-22 asphalt as a virgin binder. Design binder content of mix was estimated by conducting Superpave volumetric mix design. Performance of mixes was evaluated using dynamic modulus test, Hamburg wheel tracking device, and Texas overlay test. In addition, binder tests such as multiple stress creep recovery, linear amplitude sweep test and Complex modulus were performed on virgin as well as reclaimed binders to identify the influence of virgin and reclaimed binders on mix performance. Laboratory test results suggest that addition of RAP enhances rutting resistance in comparison to conventional mixtures, while cracking/fatigue resistance deteriorated. The results indicated that fatigue/cracking potential should be the governing factor in the selection of optimal percentage of RAP.

Keywords: Reclaimed Asphalt Pavement, fatigue, Texas overlay tester, binder rheology

1 INTRODUCTION

Reclaimed Asphalt Pavement (RAP) is asphalt concrete that has been removed from an existing pavement and is generally subjected to some degree of long-term aging as well as traffic loading. RAP can be recycled into new mixture by heating and mixing with virgin aggregate and asphalt binder. The recycling process can be conducted at conventional hot mix temperatures. The use of Reclaimed Asphalt Pavement (RAP) has become more prevalent with the rising cost of virgin materials and with the recent emphasis being laid on developing more environment friendly and sustainable roadways. Some studies [1–3] have shown that the percentage of RAP has a significant effect on the performance of asphalt mixture with RAP. To perform well in the field, the asphalt concrete overlay mixture must be both rut and reflective crack resistant. Thus, both rutting and reflective cracking must be considered during the mixture design. For the surface layer, rutting in the presence of moisture is the main concern, which has been successfully addressed in Texas using the Hamburg Wheel Tracking Test (HWTT). Though generally considered to be secondary to rutting in terms of its effect on performance, it is necessary that the issue of reflective cracking is given due consideration. The Overlay Tester is recommended for this issue in Texas. This paper presents the details of a study conducted to evaluate rutting and cracking potential of mixes consisting of Reclaimed Asphalt Pavement (RAP) material.

2 OBJECTIVE AND SCOPE

2.1 *Objective*

The main objective of this study is to evaluate the impact of RAP content on the properties of the final mixes in terms of resistance to rutting and fatigue cracking.

2.2 *Scope*

In this study, Texas (Type B) and Indian (DBM-2) mix specifications were reviewed and a mix design that meets both specifications was selected for evaluation purpose. Hot mix asphalt specimens consisting of 0%, 15%, 25% and 35% RAP were prepared in the laboratory using PG64-22 asphalt as a virgin binder. Design binder content of mix was estimated by conducting Superpave volumetric mix design. Performance of mixes was evaluated using dynamic modulus test, Hamburg wheel tracking device and Texas overlay tester. Rheological tests such as Dynamic Shear Rheometer, Multiple Stress Creep Recovery and Linear Amplitude Sweep Test were performed on PG64-22 and recovered binders to evaluate the influence of virgin and recovered binders on asphalt mixes.

3 MATERIAL CHARACTERISATION AND MIX DESIGN

3.1 *Virgin materials*

A single source of aggregate was used for this research. PG64-22 grade binder was used as virgin binder. Binders were aged as per SHRP protocols of short term and long term aging [4]. Dynamic Shear Rheometer (DSR) testing was completed on the virgin binder according to AASHTO TP5-93 [5]. The DSR testing produced rheological properties for the binders including and phase angle (δ). Master curves were developed for the complex modulus (G*) parameter using the results of rheological tests conducted using DSR on binders at different temperatures and frequencies.

Bending Beam Rheometer (BBR) testing was carried out on the virgin binder according to AASHTO T 313-09 [6] and creep stiffness (S) and slope (m) were determined. Tables 1 and 2 contain the rheological data obtained from the DSR and BBR tests respectively. The Performance Grade (PG) of the binder was confirmed according to AASHTO R-29 "Standard Practice for Grading or Verifying the Performance Grade of an Asphalt Binder" [7].

3.1.1 *Multiple stress creep recovery test*

The Multiple Stress Creep Recovery (MSCR) test is the latest development to the Superpave Performance Graded (PG) Asphalt Binders specification. Using the Dynamic Shear

Table 1. DSR test results for virgin binder.

	G*/Sinδ (kPa) for	
Temperature (°C)	Un-aged	RTFO-aged
64	1.67	3.50
70	0.79	1.68
76	0.39	0.82

Table 2. BBR test results for PAV-aged virgin binder.

Virgin binder grade	Creep stiffness (MPa)	Slope (m)
PG64-22	148	0.301

Rheometer (DSR), a one-second creep load is applied to the asphalt binder sample. After the 1-second load is removed, the sample is allowed to recover for 9 seconds. The test is started with the application of a low stress (0.1 kPa) for 10 creep/recovery cycles after which the stress is increased to 3.2 kPa and repeated for an additional 10 cycles. The material response in the MSCR test is significantly different than the response in the existing PG tests. In the PG system, the high temperature parameter, G*/sinδ, is measured by applying an oscillating load to the asphalt at very low strain. Due to the low strain level, the PG high temperature parameter does not accurately represent the ability of polymer modified binders to resist rutting.

In the MSCR test, higher levels of stress and strain are applied to the asphalt, better representing the condition which occurs in pavements. By using higher levels of stress and strain the MSCR test captures not only the stiffening effects of the polymer, but also the delayed elastic effects. Results of MSCR test conducted on virgin PG64-22 binder are given in Table 3.

3.2 *RAP materials*

The RAP material was collected from Jobe mix plant, El Paso, TX. The basic tests conducted include the gradation, binder content and specific gravities. Table 4 shows RAP gradation. The binder from the RAP was extracted as per ASTM D 2172 [8]. The Rotavapor method was used to recover the binder from the solvent as per AASHTO T170 [9]. Average binder content in the RAP was found to be 4.2% (by weight of mix).

DSR test was conducted on the binder extracted from RAP. Test results are given in Table 5.

3.2.1 *Linear amplitude sweep test*

Linear Amplitude Sweep (LAS) test indicates the ability of asphalt binders to resist fatigue damage due to cyclic loading. The amplitude sweep test was conducted on PAV-aged virgin and RAP binders using dynamic shear rheometer at intermediate temperatures identified corresponding to a G*Sinδ value of 5000 kPa. The intermediate temperatures have been identified as 16°C and 22°C respectively for virgin and RAP binders.

Frequency sweep was performed at constant amplitude of 0.1% over a range of frequencies varying from 0.1 to 30 Hz. Complex modulus and phase angle were recorded at each frequency. Amplitude sweep was also run at the intermediate temperatures using oscilla-

Table 3. MSCR test results for virgin binder.

		Creep compliance (Jnr) at stress level of		% recovery at stress level of	
Grade	Temperature (°C)	3.2 kPa^{-1}	0.1 kPa^{-1}	3.2 kPa^{-1}	0.1 kPa^{-1}
PG64-22	64	2.56	2.08	2.99	13.74

Table 4. Average RAP aggregate gradation.

Sieve size (mm)	% passing
19	100.0
9.5	86.0
4.75	55.0
2.36	36.1
0.6	18.9
0.3	12.2
0.075	3.0

Table 5. DSR test results for un-aged and PAV-aged RAP binder.

Un-aged RAP binder		PAV-aged RAP binder		PAV-aged virgin binder	
Temp (°C)	G*/sin δ (kPa)	Temp (°C)	G*sin δ (kPa)	Temp (°C)	G*sin δ (kPa)
64	148	31	2120	31	890
70	79.3	28	2700	28	1200
76	43	25	3390	25	1630
82	23.6	22	4250	22	2220
88	13.3	19	5240	19	3000
–	–	16	6390	16	3970
–	–	–	–	13	5040

Table 6. LAS fatigue model parameters.

Binder type	A	B	Nf (5% strain)
Recovered binder	446466342.4	8.608	429.5908
Virgin binder (PG64-22)	147610246.9	7.592	728.679
15% RAP	131559071.1	6.589	3262.928
25% RAP	149264033.6	6.465	4519.747
35% RAP	250954684.7	7.943	704.1685

tory shear at constant frequency of 10 Hz. Amplitude was varied from 0.1% to 30% [10]. Table 6 shows the Binder fatigue model parameters.

The binder fatigue performance parameter Nf can be estimated as

$$Nf = A(\gamma_{\max})^{-B} \tag{1}$$

where $\gamma_{\max}$ is the maximum expected binder strain for a given pavement structure and A and B are empirical coefficients derived from LAS test data. A and B values obtained for virgin, recovered binders (both PAV-aged) and at various RAP contents from are given in Table 6. From the results it shows that fatigue life of binder increases up to 25% RAP content.

3.3 *Development of master curve for DSR parameters*

The rheological nature of bituminous binders over wide temperature and frequency ranges can be characterized by Time-Temperature Superposition (TTS) [11]. TTS is the procedure of shifting of the test data collected at different temperatures to frequencies that correspond to a reference temperature, so that various curves can be aligned to form a single master curve applicable for a reference temperature.

In the present study, Williams-Landel-Ferry (WLF) relationship [12] given as Eq. (2) was used to estimate the shift factors.

$$\log f_{red} - \log f = \log \alpha_t = -\frac{C_1(T - T_{ref})}{(C_2 + T - T_{ref})} \tag{2}$$

where, f_{red} is the reduced frequency (Hz) at which the master curve should be read, f is loading frequency (Hz), T is the experimental temperature, T_{ref} is the reference temperature for which master curve is developed and C_1 and C_2 are empirical constants.

Master curve can be developed using different models. For low and intermediate temperatures, a generalized power law is suitable to describe the frequency dependant behavior of bituminous materials [13]. For a full temperature range, a sigmoidal fitting function is considered to be more appropriate [14]. In the present study, sigmoidal function, represented by Eq. (3), was used to develop the master curve for G* [15].

$$\log|G^*| = \delta + \frac{\alpha}{1 + e^{\beta - \gamma \log f_{red}}} \quad (3)$$

where, δ is minimum complex modulus, $\delta + \alpha$ is maximum modulus or span of the data, β and γ are respectively the location and slope steepness parameters of the sigmoidal curve, f_{red} is the reduced frequency obtained from shift factor (Eq. 2) and test frequency.

The experimental data was analysed using solver function of Excel spreadsheet to determine the values of C_1, C_2, α, β, γ and δ used in the Equations 2 and 3. The reference temperature was chosen to be 64°C. This temperature was selected to correspond to a high service temperature. Figure 1 shows the sigmoidal fit for PG64-22 binder.

3.4 *Asphalt concrete mix design*

Virgin aggregate, RAP and Virgin binder were collected from Jobe plant in El Paso. The asphalt content in the RAP was found to be 4.2%. Texas (Type B) and Indian (DBM-2) aggregate gradations were reviewed and a gradation that meets both specifications was selected for evaluation purpose. The gradation is shown in Figure 2. Mix specimens were prepared with

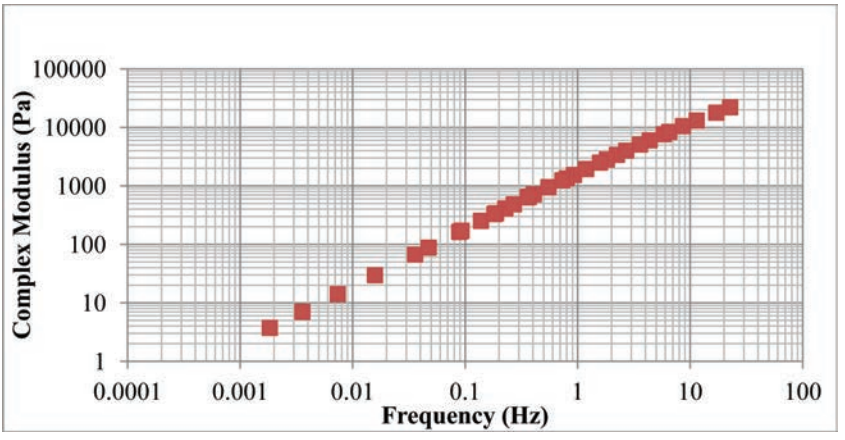

Figure 1. Complex modulus master curve for un-aged PG64-22.

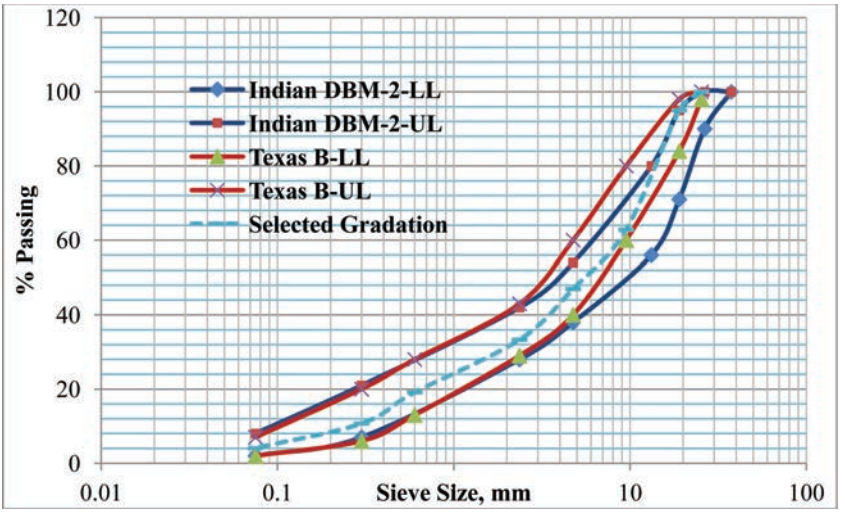

Figure 2. Selected aggregate gradation.

Table 7. Mix design parameters.

Mix type	OBC (%)	% binder replacement	VMA (%)	VFA (%)	Dust proportion
0% RAP	4.6	0	14.4	72	0.96
15% RAP	4.4	14.3	14.3	72.5	1
25% RAP	4.3	24.3	14.05	71	1.05
35% RAP	4.25	34.5	14.4	72	1.1

0, 15, 25 and 35% RAP content. A design compaction effort (design number of gyrations, N_{design}) of 50 was selected.

Virgin aggregates were batched by individual sieve size and heated at the mixing temperature for a minimum of 4 h before mixing. The RAP was batched as a stockpile and heated at the mixing temperature for 2 h before mixing. The RAP stockpile was heated for less time so that the RAP stockpile attained compaction temperature while minimizing aging of binder. The asphalt, aggregates, and RAP were mixed in a bucket mixer, short-term aged at the compaction temperature for 2 h, and then compacted using a Superpave Gyratory Compactor (SGC). After compaction, the bulk specific gravity of all specimens was measured using a Corelok vacuum sealing system according to ASTM D6752 (16). Design binder contents were selected to yield design air void content of 4% and to satisfy other volumetric parameters such as Voids in Mineral Aggregates (VMA) and Voids Filled with Asphalt (VFA) as per the Superpave mix design specifications (SP 2) [4]. Table 7 gives the mix design parameters for each of the RAP contents.

4 PERFORMANCE CHARACTERISTICS

4.1 *Dynamic modulus*

For linear viscoelastic materials, the dynamic modulus is defined by the stress-strain relationship under continuous sinusoidal loading. Temperatures, rate of loading, age, and mixture characteristics (i.e. binder stiffness, binder content, air voids, and aggregate gradation) are all factors that affect the dynamic modulus values of asphalt concrete. By applying a uniaxial sinusoidal load to a specimen and measuring the strain, the dynamic modulus of asphalt concrete can be calculated

$$E^* = \sigma/\varepsilon \tag{4}$$

σ = peak maximum stress
ε = peak maximum strain

The dynamic modulus test is conducted over a range of temperatures and frequencies. The Mechanistic-Empirical Pavement Design Guide—MEPDG (17) recommends performing the test at the following temperatures: –10°C, 4.4°C, 21.1°C, 37.8°C, and 54.4°C. For each temperature, the following frequencies should be tested: 25 Hz, 10 Hz, 5 Hz, 1 Hz, 0.5 Hz, and 0.1 Hz. The properties that are obtained from this test provide insight into the viscous properties of the material and can be correlated with in-service rutting measurements.

Individual dynamic modulus master curves for each group of samples are used as raw data to construct the master curves. An Excel Solver was used to develop master curves. Figure 3 shows the master curves for different asphalt concrete mixtures.

4.2 *Rutting characteristics*

The effect of high RAP content and production parameters on the rutting susceptibility of the mixtures was evaluated in accordance with AASHTO T324 'Hamburg Wheel-Track Testing of Compacted Hot-Mix Asphalt (HMA)' (18). Gyratory specimens were fabricated from loose lab-produced mixture to an air void level of 7.0 ± 1.0% as required by AASHTO T324.

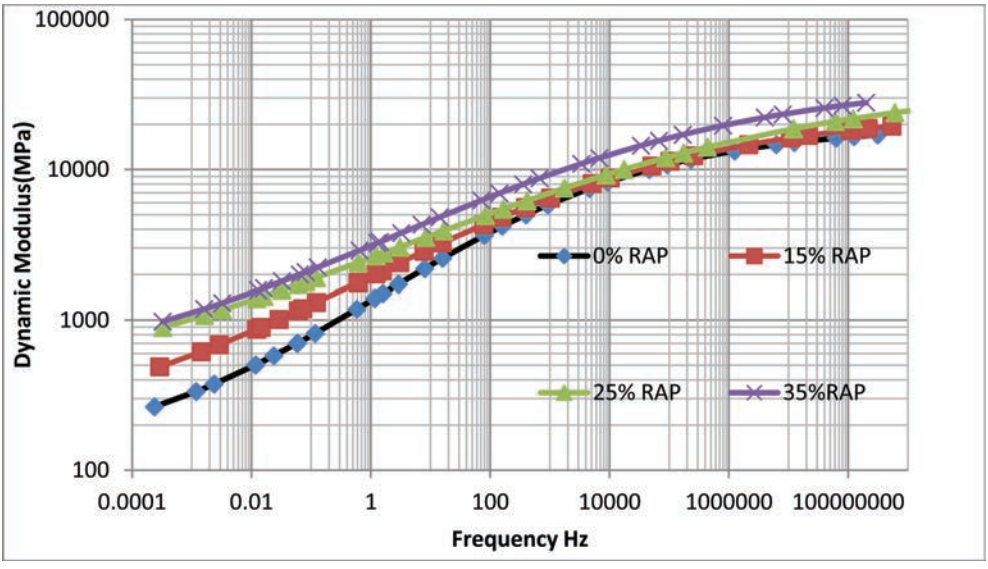

Figure 3. Dynamic modulus master curves.

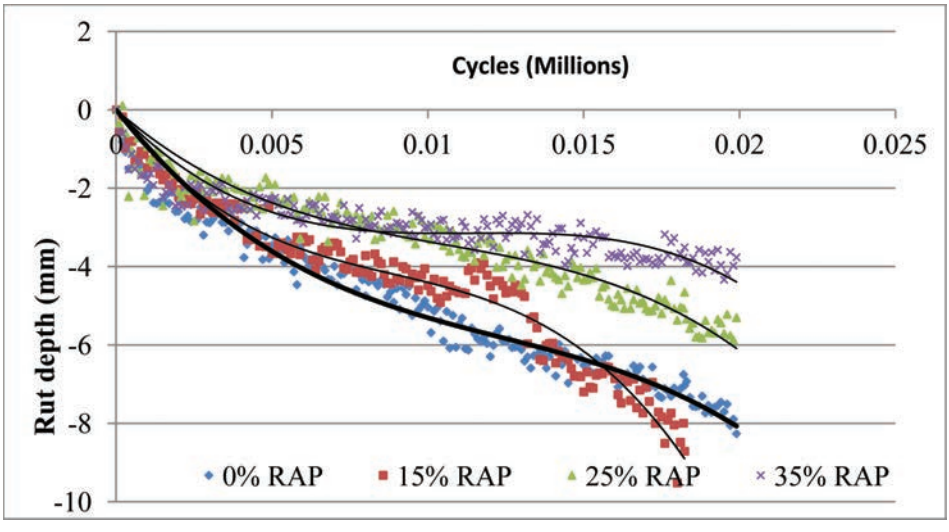

Figure 4. Rut test results at 50°C.

Testing in the HWTT was conducted at a test temperature of 50°C. Testing terminated at 20,000 wheel passes. Rutting potential of the mixes decreased as the amount of RAP in the mixture increased. Figure 4 shows the variation of rut depth with number of load passes.

4.3 *Fatigue characteristics*

Reflective cracking susceptibility of mixes with and without RAP was evaluated using the Texas Transportation Institute (TTI) Overlay Tester which was designed by F.P. Germann and R.L. Lytton in the late 1970's to simulate the opening and closing of joints or cracks. The device is a computer-controlled electrohydraulic system that applies repeated direct tension loads to HMA specimens. The machine features two steel blocks, one is fixed and the

other slides horizontally. The sliding block applies tension in a cyclic triangular waveform to a constant maximum displacement of 0.025 inches. The sliding block reaches the maximum displacement and then returns to its initial position in 10 seconds. Testing is performed at a constant temperature of 77 ± 3°F. This test method measures the number of cycles to failure. The overlay tester can be run on standard size samples, typically 6 in (150 mm) long by 3 in (75 mm) wide by 1.5 in (38 mm) high. These specimens can be prepared from either field cores or from Superpave Gyratory Compactor (SGC) molded specimens. During OT testing, the measurable parameters include the applied load, opening displacement, time, number of load cycles, and test temperature. All these data are automatically recorded in the computer attached to the OT machine as an Excel spreadsheet. The primary output of the OT test is the crack-resistance potential of an HMA mix, which is essentially quantified in terms of the number of cycles for the sample to fail (i.e., 93 percent drop of the first cycle peak load).

Fatigue test results are given in Figure 5. As different layers in the overlay have different critical issues, it is appropriate to set different criteria for each. Based on the substantial overlay tester results, TxDOT's specification on the HWTT [19], the preliminary criteria for the overlay tester and the HWTT, are presented in Table 8.

HWTT tests showed that rutting resistance increased with RAP percentage in the mix. However, the Texas overlay tester suggests that fatigue life will decrease with increase in RAP content. Based on data obtained from RAP mixtures, it is concluded that the maximum percentage of RAP is approximately 20% without the addition of rejuvenating agent. Fatigue life of binder increases up to 25% of RAP from LAS test, were results are shown in Figure 6.

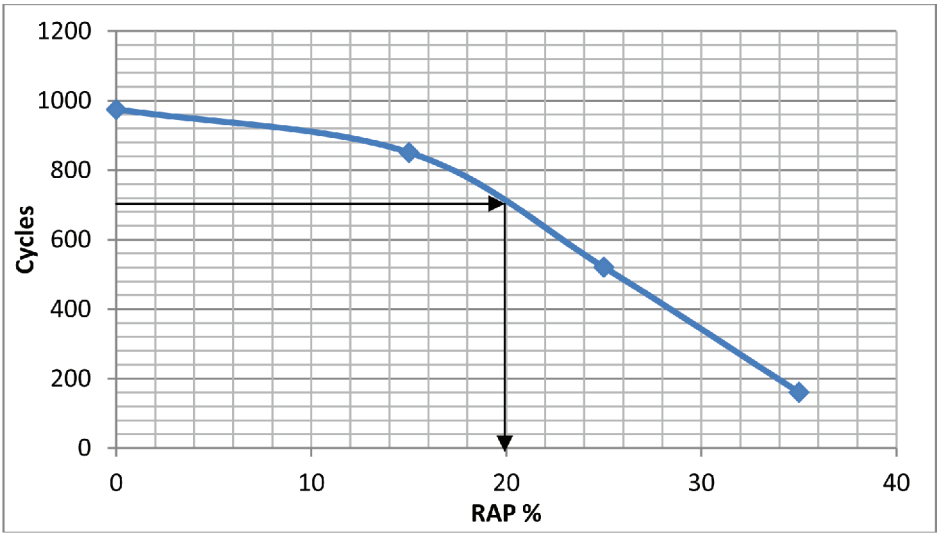

Figure 5. Variation of fatigue life with RAP content.

Table 8. Preliminary criteria for asphalt overlay mixtures.

Tests	Indicator	Bottom layer	Top layer
Overlay Tester @ 77 °F (25 °C) and 0.025 in opening	Reflective cracking life	750 cycles, min.	300 cycles, min.
HWTT @ 50 °C	Rut Depth (RD)	N/A	PG64-22, RD@10,000 < 12.5 mm PG70-22, RD@15,000 < 12.5 mm PG76-22, RD@20,000 < 12.5 mm

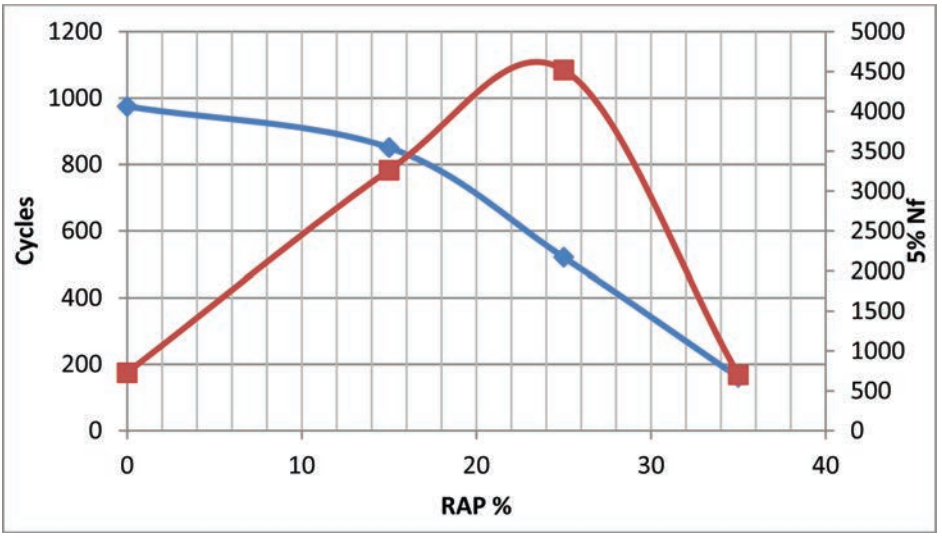

Figure 6. Fatigue life variations in binder and mix with RAP content.

5 CONCLUSIONS

The main objective of this work was to examine the effect of addition of RAP on the fatigue and rutting performance of asphalt mix. The significantly higher G*/Sinδ values of the binder extracted from RAP compared to those of virgin binder suggest that addition of RAP will improve the rutting performance of the mix. The higher dynamic values and the significantly better rutting performance of mixes with RAP determined using HWTT also prove the highly beneficial effect of adding RAP to reduce rutting in asphalt mix.

The relatively larger G*Sinδ values of RAP binder compared to those of virgin binder indicate that mixes with RAP are expected to have inferior fatigue performance. Linear amplitude sweep test results obtained for virgin and RAP binders show that mixes with RAP will have inferior fatigue performance for larger bending strains. Overlay tester results reveal that addition of RAP is likely to reduce the fatigue of the mix. 20% RAP appears to be an appropriate RAP content to be added to the mix from fatigue consideration.

REFERENCES

[1] Ren Shuan-zhe, Wang Yong-qi, Yin Ran. The Research on Recycled Asphalt Mixture Design. Highway Traffic Science and Technology, (10): 35–39, 2007.
[2] Paul, H.R. Evaluation of Recycled Projects for Performance. Baton Rouge: Louisiana Transportation Research Center, 82–91, 1998.
[3] Xiong Chu-hua, Ling Tian-qing, Zhang Yong-xing, Wu Zhi-hui. The Use of Central Plant Hot Recycling Technology in Chengdu-Chongqing Highway Maintenance Project. Journal of China & Foreign Highway, (2): 193–197, 2008.
[4] SP-2. Superpave Series No.2, Superpave Mix Design, Asphalt Institute, 4th edition, Research Park Drive, Lexington, KY, 2004.
[5] AASHTO TP5-93 “Test Method for Determining the Rheological Properties of Asphalt Binder Using a Dynamic Shear Rheometer”.
[6] AASHTO T 313-09 “Standard Method of Test for Determining the Flexural Creep Stiffness of Asphalt Binder Using the Bending Beam Rheometer (BBR)”.
[7] AASHTO R-29 “Standard Practice for Grading or Verifying the Performance Grade of an Asphalt Binder”.
[8] ASTM D 2172, “Standard Test Methods for Quantitative Extraction of Bitumen from Bituminous Paving Mixtures”.

[9] AASHTO T170, “Recovery of Asphalt from Solution by Rotavapor Method”.
[10] AASHTO TP 101-12, “Standard Method of Test for Estimating Fatigue Resistance of Asphalt Binders Using the Linear Amplitude Sweep”.
[11] Christensen J.D.W., and Anderson D.A, Interpretation of Dynamic Mechanical Test Data for Paving Grade Asphalt Cements, Proceedings of Association of Asphalt Paving Technologists 61, pp. 67–99, 1992.
[12] Williams, M.L., Landel, R.F., and Ferry, J.D. The Temperature Dependence of Relaxation Mechanism in Amorphous Polymers and other Glass Forming Liquids, Journal of ACS, Volume 77, pp. 3701, 1955.
[13] Christensen, D. W. Analysis of Creep data from Indirect Tension Test on Asphalt Concrete, Asphalt Paving Technologists, Vol. 67, pp. 458–489, 1998.
[14] Pellinen, T.K., Witczak, M.W., and Bonaquist, R.F. Asphalt Mix Master Curve Construction using Sigmoidal fitting Function with Nonlinear Least-Squares Optimization Technique, Proc., 15th ASCE Engg Mechanics Conf., Columbia Univ., New York., USA, 2004.
[15] Biswas, K.G., and Pellinen, T.K. Practical Methodology of Determining the In Situ Dynamic (Complex) Moduli for Engineering Analysis, Journal of Materials in Civil Engineering, Vol. 19 (No. 6), 2007.
[16] ASTM D 6752, “Standard Test Method for Bulk Specific Gravity and Density of Compacted Bituminous Mixtures Using Automatic Vacuum Sealing”.
[17] NCHRP (2004a). “Guide for Mechanistic Empirical Design of New and Rehabilitated Pavement Structures”. NCHRP 1-37A, Final Report, Part 1, Introduction. National Cooperative Highway Research Program, Washington, DC.
[18] AASHTO T324 “Hamburg Wheel-Track Testing of Compacted Hot-Mix Asphalt”.
[19] Manual of Test Procedure, Tex-242-F, Hamburg wheel-tracking test, TxDOT, Aug. 2002.

Asphalt Pavements – Kim (Ed)
© 2014 Taylor & Francis Group, London, ISBN 978-1-138-02693-3

Workability of WMA and WMA-RAP mixtures and relationship to field compaction

Mariely Mejias-Santiago, Jesse D. Doyle & John F. Rushing
U.S. Army Engineer Research and Development Center, Vicksburg, MS, USA

ABSTRACT: The terms workability and compactability have been applied to asphalt mixtures to describe the relative ease with which material can be placed, hand worked, or compacted. A number of methods described in literature have been investigated to quantify this parameter, including devices that measure the torque required to rotate a mixing paddle through a sample of asphalt mixture. An improved workability measurement device based on that concept is described in this paper. Data collected with this device for seventeen mixtures are presented. The mixtures included both Hot Mix Asphalt (HMA) and Warm Mix Asphalt (WMA). WMA was produced with Sasobit® additive, Evotherm™ 3G additive, and by asphalt binder foaming. Reclaimed Asphalt Pavement (RAP) contents of 25 and 50% were also investigated for HMA and WMA. Four of the mixtures without RAP, including HMA and one of each WMA, were produced at an asphalt plant and placed into test strips with full scale construction equipment. Compaction of the pavement mat was monitored by embedded thermocouples, and nuclear density gauge measurements were taken between successive roller compactor passes. The relationship between laboratory measurement of workability and the relative ease of field compaction is investigated.

Keywords: Warm Mix Asphalt, WMA, RAP, workability, compactability

1 INTRODUCTION

The workability of asphalt mixtures is related to the compaction properties of the mixture. The same material properties that affect the compaction characteristics of a mix also affect its workability. Workability of asphalt mixes has been defined by Celik and Atis [1] as the property that allows producing, handling, placing, and compacting a mixture with the minimum application of energy. It can also be thought of as a mixture's resistance to shear in an unconfined condition once movement of mix particles has been initiated. Workability can be defined from a field perspective as the asphalt mixture property that describes the ease with which the asphalt mixture can be placed, worked by hand, and compacted to the desired density [2]. Workability is affected by both aggregate properties and binder properties [3]. While the workability of asphalt mixtures is an important property in the construction of Hot Mix Asphalt (HMA) pavements, it has not been widely studied.

The primary purpose of this paper is to present test results from an asphalt mixture laboratory workability test device and to investigate its relationship to field compactability for HMA and Warm Mix Asphalt (WMA) mixtures. The secondary purpose of this paper is to investigate the laboratory workability of HMA and WMA mixtures containing 25 and 50% Reclaimed Asphalt Pavement (RAP).

2 LITERATURE REVIEW

One of the earliest laboratory studies of hot mix workability was conducted by Marvillet and Bougault [4]. They developed a device to measure workability of asphalt mixtures in the

laboratory. The device consisted of a heated and insulated testing chamber which held the hot mix and a mixing paddle that was inserted into the mix. The mixing paddle was rotated at a constant angular velocity, while the resistance of a spring was measured. The spring resistance was converted to a workability value that could then be used to compare mixture's relative workability. This measurement was then repeated at a series of temperatures to investigate the temperature dependence of the workability measurements. The workability value was defined such that as viscosity decreased and temperature increased, the workability value for the mixture would increase. The research results indicated that the workability measurements were strongly dependent not only on temperature and binder viscosity but also on aggregate shape (angularity) and particle size distribution (gradation) [4]. An increase in the filler content decreased the workability as well. Asphalt content was not found to significantly affect the measured workability values.

A study conducted by Gudimettla et al. (2003) expanded on the work of [4] in developing a device to measure asphalt mixture workability. The introduction of the Superpave mix design procedure and increased use of polymer modified binders reinforced the need for quantitative laboratory measurement of asphalt mixture workability. The researchers developed a prototype workability meter based on the designs of [4]. A workability index was determined from measurements of the torque required to rotate a paddle at constant speed (15 rpm) in a mixture sample. Data were collected for a range of temperatures as the sample was allowed to cool. The results indicated similar trends to the work previously done by [4]. Aggregate type was found to significantly affect the workability of mixtures; aggregate with high angularity exhibited lower workability values than semi angular aggregates. Workability was found to increase as the Nominal Maximum Aggregate Size (NMAS) was decreased. Mixtures made with polymer-modified PG 76-22 binder demonstrated significantly lower workability values than mixtures produced with neat PG 64-22 asphalt binder. Temperature also significantly affected workability values. Gudimettla et al. [3] suggested that the workability device they developed could be used to determine laydown and compaction temperatures for mixtures made with polymer modified asphalt binders but were unable to draw significant conclusions on what those temperature ranges should be based on the available data.

One purported benefit of WMA is the increased workability at lower (and at conventional) compaction temperatures. Bennert et al. [2] evaluated different methods to quantify workability for WMA. Of the six methods investigated (three binder and three mixture), the most rational rankings of data were obtained by binder lubricity testing, workability measurements with an Asphalt Workability Device (AWD) similar to the device developed by [3], and air voids of Marshall compacted specimens. Howard et al. [5] investigated workability of HMA and of mixtures with foamed asphalt and Evotherm™ 3G made at HMA temperatures. Workability was evaluated by the AWD on reheated samples of plant produced mixture. Results indicated that there was initially little difference in the mixtures, but that the mixture with Evotherm™ 3G additive remained more workable than the others after an extended haul time. Wang et al. [6] found the workability of WMA mixtures to be better than that of HMA and suggested that mixing and compaction temperatures can be established based on ranges of workability torque.

An additional purported benefit of WMA is the ability to improve workability for mixtures containing RAP. For a given virgin binder grade and mixing temperature, the addition of RAP generally decreases mixture workability [7, 8]. Austerman et al. [9] evaluated workability of WMA containing 10 to 25% RAP and observed improved workability with respect to HMA. Other researchers [10, 11] have evaluated workability of 100% RAP mixtures with WMA additives for in-place recycling applications and found improved workability relative to mixtures without the WMA additives.

3 EXPERIMENTAL PROGRAM

3.1 *Mixtures tested*

The asphalt mixtures used in the study consisted of an aggregate blend designed to meet Job Mix Formula (JMF) gradation requirements for a 12.5 mm nominal maximum aggregate size

mixture according to Unified Facilities Guide Specification 32-15-15.13, "Hot Mix Asphalt for Airfields". The aggregate blends used in this study are summarized in Table 1. The aggregate sources and blend used for the field produced mixtures (Gradation 1) were selected based on materials available for plant production. The base binder for all mixtures was PG 67-22 from a single refinery. Sasobit® was added at a rate of 1.5% of virgin binder mass and Evotherm™ 3G was added at a rate of 0.5% of virgin binder mass. Water added during foaming was 2% of binder mass and was not considered part of the binder mass for calculation of asphalt content. Asphalt mixtures were designed using 75 gyrations in a Superpave gyratory compactor to achieve 4.0% air voids. Additional mixture details are provided in [12, 13].

3.2 *Field compaction*

Data from full-scale field tests of ongoing research studies were used to evaluate field compaction of one HMA and three WMAs. The pavement structure consisted of 100 mm of asphalt concrete over 250 mm of limestone base course with a California Bearing Ratio (CBR) of 100 over a 300-mm-thick clay-gravel subbase course with a CBR of 30. The subgrade was high-plasticity clay and had an average CBR of 15. The test item was 15.2 m long and 3.7 m wide.

Asphalt for the full-scale tests was produced by APAC Mississippi, Inc. from a local drum mix plant in Vicksburg, MS, and delivered to the construction facility. Samples of the mixtures were collected from elevated platforms at the plant to verify that the mix design had been achieved. Plant production temperatures for the HMA and WMA were 143 °C and 121 °C, respectively.

The asphalt concrete pavement layer was constructed on a prepared crushed limestone base course using conventional paving equipment in two 50-mm lifts. The asphalt layer was placed with a Caterpillar AP655D asphalt paver. Breakdown rolling was performed using

Table 1. Properties of mixtures tested.

Mixture ID	Percent passing by sieve size (mm)					RAP (%)	LST (%)	Gravel (%)	Sand (%)	CAA (%)	Virgin AC (%)	Total AC (%)
	12.5	9.5	4.75	2.36	0.075							
H00G1-LP	96	85	68	54	4.9	0	60	25	15	92	5.3	5.3
H00G1-FP	96	85	68	54	4.9	0	60	25	15	92	5.3	5.3
S00G1-FP	96	85	68	54	4.9	0	60	25	15	92	5.2	5.2
E00G1-FP	96	85	68	54	4.9	0	60	25	15	92	5.2	5.2
F00G1-FP	96	85	68	54	4.9	0	60	25	15	92	5.1	5.1
H00G2-LP	99	90	71	45	7.2	0	100	0	0	100	4.9	4.9
S00G2-LP	99	90	71	45	7.2	0	100	0	0	100	4.9	4.9
E00G2-LP	99	90	71	45	7.2	0	100	0	0	100	4.8	4.8
F00G2-LP	99	90	71	45	7.2	0	100	0	0	100	5.0	5.0
H25G3-LP	98	87	61	39	6.8	25	75	0	0	98	3.9	5.3
S25G3-LP	98	87	61	39	6.8	25	75	0	0	98	3.9	5.3
E25G3-LP	98	87	61	39	6.8	25	75	0	0	98	3.9	5.3
F25G3-LP	98	87	61	39	6.8	25	75	0	0	98	3.9	5.3
H50G4-LP	98	88	61	41	6.2	50	50	0	0	97	3.1	5.9
S50G4-LP	98	88	61	41	6.2	50	50	0	0	97	3.3	6.1
E50G4-LP	98	88	61	41	6.2	50	50	0	0	97	3.3	6.1
F50G4-LP	98	88	61	41	6.2	50	50	0	0	97	3.3	6.1

H: Hot Mix Asphalt; S: Sasobit®; E: Evotherm™ 3G; F: Foamed Asphalt.
00: 0% RAP; 25: 25% RAP; 50: 50% RAP.
G1: Gradation 1; G2: Gradation 2; G3: Gradation 3; G4: Gradation 4.
LP: Laboratory Produced Mixture; FP: Field Produced Mixture; LST: Limestone; CAA: Coarse Aggregate Angularity.

a Caterpillar CB-534D XW vibratory steel-wheel asphalt compactor. An Ingersol Rand PT125R pneumatic roller was used for intermediate rolling. The steel-wheel roller with no vibration was used for finish rolling. A CRS-2 asphalt emulsion tack coat was applied between lifts. In-place volumetric properties are provided in the descriptions of each full-scale test. The average volumetric properties of the asphalt layer were determined from ten 100-mm-thick cores.

The asphalt mixtures were monitored during placement and compaction to determine the compaction behaviour. Data collected during these processes included temperature of the mixture during paving and compaction, density of the asphalt layer during compaction using a nuclear density gauge, and the number and type of roller passes required to achieve adequate mat density.

3.3 *Workability testing*

Mixture workability was evaluated using the Prototype Workability Device shown in Figure 1. This device was built specifically for this project by Instrotek, Inc., in Riley, NC, based on the work of [3]. The method consists of immersing a paddle into a sample of loose asphalt mixture and measuring the torque required to keep the paddle rotating at a constant speed within the sample. Workability is defined as the inverse of the measured torque.

The paddle configuration used had a roller attached to the shaft to push down the material that the auger normally moves up during the mixing process (Fig. 1). This configuration showed continuous sample remixing and did not create a shear plane through the mixture. A shear plane created within the sample would show a consistent workability (torque) over a given temperature range because of a lack of resistance [3]. This paddle configuration also

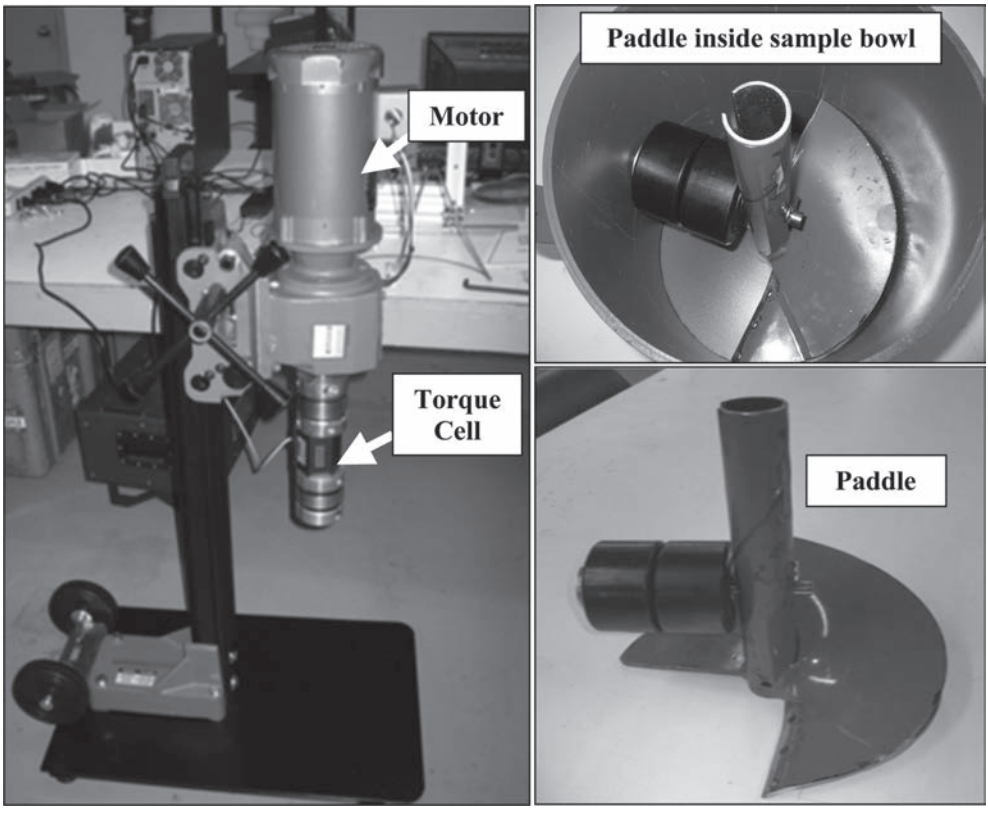

Figure 1. Prototype workability device.

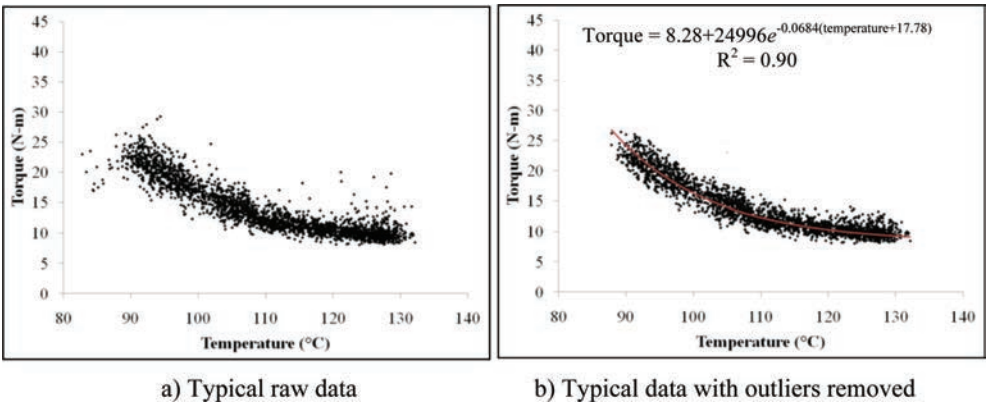

Figure 2. Typical data reduction from workability test.

provided a consistent temperature throughout the sample, and no aggregate breakage was observed. The sample bowl used was 25 cm in diameter and 28 cm deep and it is shown in Figure 1 with the paddle inserted.

For workability testing, two 11 kg samples per mixture were tested, and results were averaged to be used for comparisons. Laboratory-produced mixtures were prepared at a standard mixing temperature of 160 °C for HMA and 130 °C for WMA. For consistency, the field produced mixtures were reheated in the laboratory at the same temperatures prior to testing. For each test, the bowl and the paddle were heated to the corresponding mixing temperature. Each sample was placed into the bowl with the paddle already inserted inside the bowl, since the paddle configuration used did not allow for the opposite procedure of inserting the paddle in the sample mixture. The device was set to a constant rate of paddle revolution of 15 rpm as recommended by [3]. This rate was considered reasonable to produce a wide range of torque (workability) for the temperature range tested. Mixture temperature was measured using a miniature infrared sensor attached to the device. Torque and temperature were monitored and recorded continuously at a data collection rate of 48 Hz using a program written in National Instruments' Labview program.

Data reduction was performed using regressions between torque and temperature and evaluating standardized residuals for each test to identify outliers. Regressions were of the exponential form given in Eq. (1). Where: *Torque* = torque required to rotate the paddle, N-m; *Temperature* = mixture temperature, °C; and *a, b, c* = regression constants.

$$Torque = a + be^{-c(temperature+17.78)} \quad (1)$$

Figure 2 shows an example of the typical raw data from the workability device and the final data and regression model without outliers. The regression analysis and the identification of outliers through evaluation of standardized residuals were performed using the software Table Curve 2D. Once the data from each test were analysed, the final regression models of the two samples per mixture were averaged and used to compare the workability of the different mixtures.

4 RESULTS

4.1 *Field compaction*

Figures 3a and b show temperature and air void content measurements taken during break down rolling (vibratory steel wheel compactor). The air void content was determined using the wet density reading from the nuclear density gauge and the measured theoretical

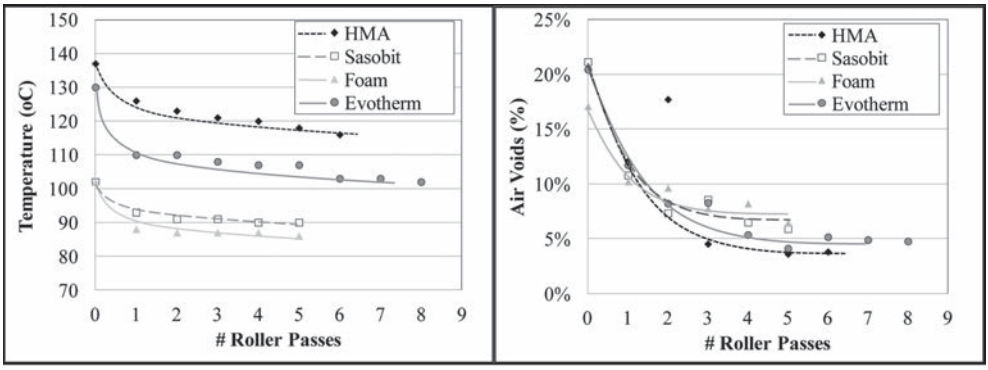

a) Pavement Temperature b) Air Voids

Figure 3. Compaction measurements taken during break down rolling.

maximum density of each mixture. Density measurements were taken with a Troxler nuclear density gauge in backscatter mode. The values reported were adjusted so that the terminal air void content was equal to the average of the extracted cores. The temperature measurements are from thermocouples attached to small metal rods and embedded in the center of the surface layer immediately after paving. The temperature reading at the start of compaction is reported, along with the readings taken after different number of passes of the breakdown roller.

The roller pattern was very similar for each of the mixtures. The number of roller passes for breakdown rolling varied between five and eight on the different items. The HMA had the highest initial mat temperature of 137 °C. The Evotherm™ 3G mixture was produced hotter than expected, and compaction began with the mat temperature at 130 °C. The Sasobit® and foamed asphalt mixtures had initial mat temperatures of 102 °C.

Figure 3 shows that the temperature of the HMA was approximately 10 °C warmer than the Evotherm™ 3G and approximately 30 °C warmer than the Sasobit® and foamed asphalt during compaction. The air void content during compaction (Fig. 3b) was similar for the Sasobit® and foamed asphalt. These items did not densify as much as the HMA and Evotherm™ during breakdown rolling. The HMA had the lowest terminal air void content.

4.2 *Workability relationship to compactability*

Mixtures sampled during construction were reheated and tested using the workability device to determine how the laboratory measured torque values compared to field observations. The results of testing are given in Figure 4. The laboratory-produced HMA is also provided for comparison. Workability testing indicates a slight stiffening of the HMA produced in the asphalt plant as evidenced by higher torque values at equivalent temperatures. Mixture stiffening is known to occur during asphalt production. In addition, all field-produced mixtures were reheated in the laboratory prior to testing, which could have caused additional stiffening. The torque value measured for the HMA at the field placement temperature of 137 °C is 12.3 N-m. The measured torque value for the WMAs was 19.5, 11.3, and 18.5 N-m for the Sasobit®, Evotherm™ 3G, and foamed asphalt, respectively, at their field placement temperatures. These results indicate that the Evotherm™ 3G has similar or better workability than the HMA when 7 °C cooler. The foamed asphalt and Sasobit® exhibited reduced workability due to their low compaction temperature (102 °C).

Field compaction results directly correlate with the laboratory workability testing. The HMA and Evotherm™ 3G compacted to very similar air voids, even though the Evotherm™ was produced at a lower temperature. The air void content of the foamed asphalt and Sasobit® was approximately 2% higher with the same compaction effort. Their reduced workability at lower temperatures caused less densification to occur. Given that the density

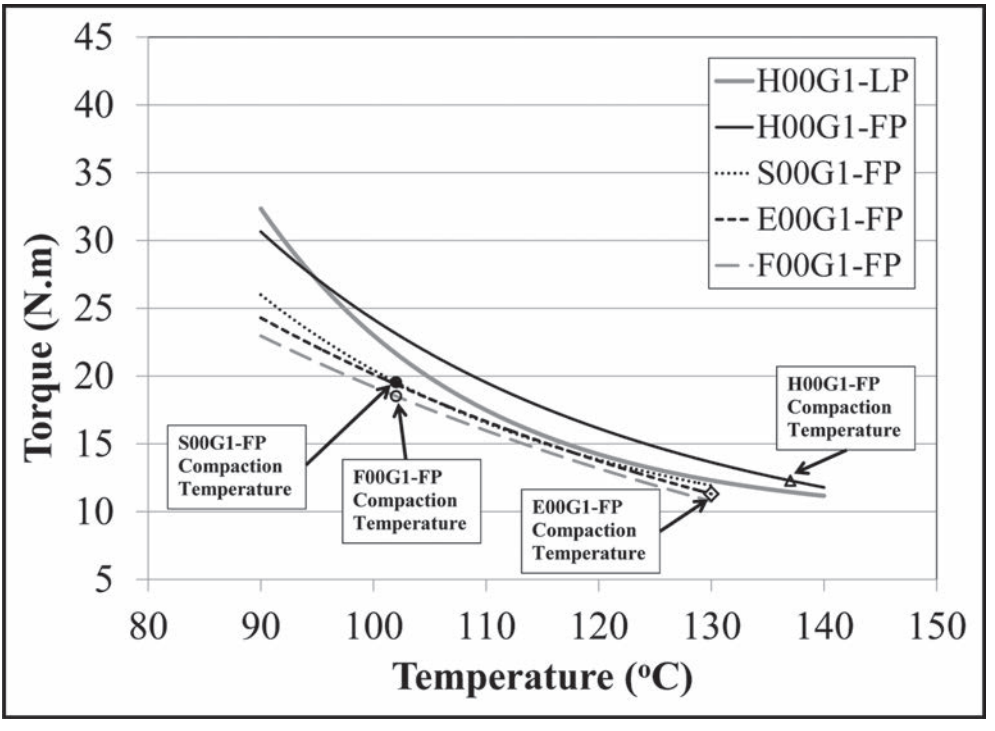

Figure 4. Workability test results from field mixtures.

of these mixtures was near the lower limits accepted by the construction specifications, the corresponding torque values measured for these mixtures can be used as a threshold for which to deem a mixture temperature suitable for compaction. An example would be to recommend laboratory torque values not exceed 20 N-m at the compaction temperature, which represents the minimum workability (maximum torque) measured on mixtures that still met minimum allowable field compaction requirements. Using this minimum workability limit, the minimum temperature for compaction of the HMA mixtures would be 110 °C, while for the WMA mixtures it would be 100 °C.

4.3 *Laboratory workability of HMA and WMA mixtures containing RAP*

Additional workability testing was conducted on laboratory-produced mixtures to evaluate the workability of mixtures containing RAP. RAP contents of 25% and 50% were evaluated in three WMA mixtures and one HMA. The results are presented in Figure 5a–c. The H00G1-LP mixture is also provided for comparison. At 0% RAP, the H00G2-LP mixture behaved very similarly to the H00G1-LP mixture. The differences in torque at a given temperature could be attributed to the difference in aggregate type and angularity. All the WMA mixtures were more workable than the two HMA mixtures at 0% RAP. Increasing the RAP content decreased the workability of all mixtures. However, WMA increased the workability at all RAP contents, which indicates that compaction temperature can be reduced when using WMA without compromising the workability.

The lower workability of all high-RAP mixtures as compared to the H00G1-LP mixture suggests that the minimum compaction temperatures need to be adjusted when RAP is used. To evaluate this, the workability data was examined to determine the temperature at which the torque was equal to 20 N-m. This is presented in Figure 5d. To meet the maximum torque requirement of 20 N-m the minimum compaction temperature needs to be increased by at least 10°C and 20 °C for 25% and 50% RAP mixtures, respectively, for both HMA and

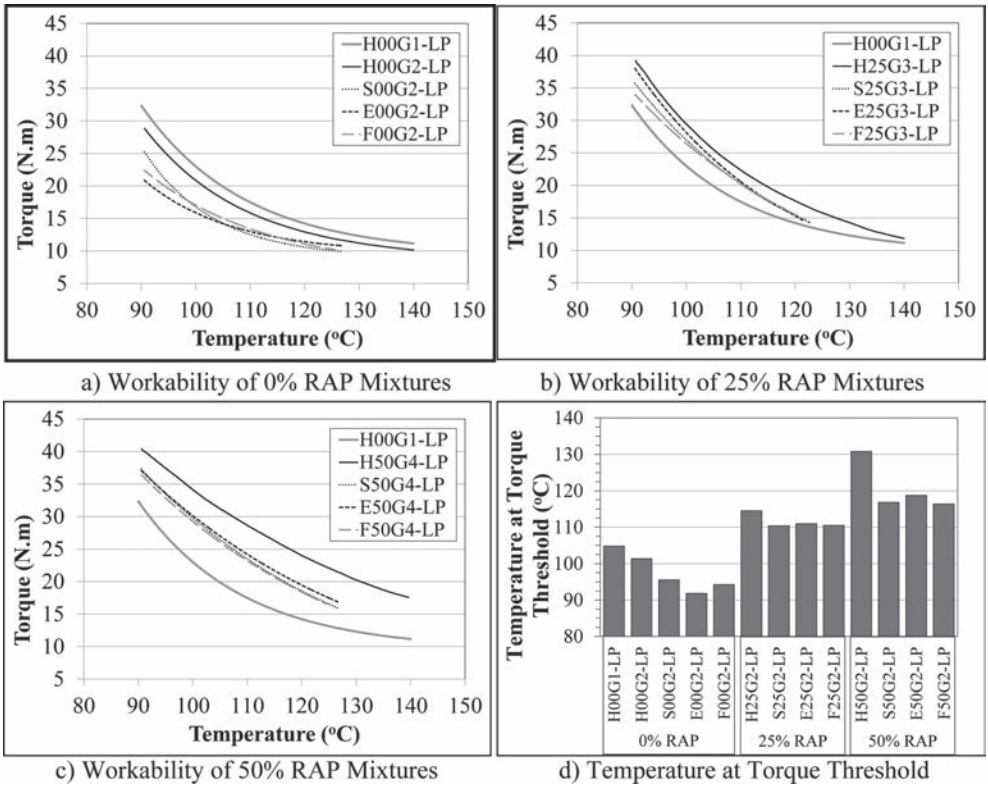

Figure 5. Laboratory workability of HMA and WMA mixtures containing rap.

WMA. For the mixtures evaluated in this paper, at 25% RAP, the minimum compaction temperatures of the HMA and WMA would be 120 °C and 110 °C, respectively. At 50% RAP, the minimum compaction temperatures of the HMA and WMA would be 130 °C and 120 °C, respectively.

5 SUMMARY AND CONCLUSIONS

In the field, WMA showed similar compactability to HMA when approximately 10 °C cooler and reduced compactability at lower temperatures. For example, Evotherm™ 3G compacted to air voids very similar to HMA, even though the Evotherm was produced and compacted at lower temperatures. When WMA was compacted at very low temperatures, as was the case for foamed asphalt and Sasobit®, the air voids were higher with the same compaction effort.

Field compaction results showed a direct correlation with the laboratory workability results. WMA showed to have similar workability to HMA when approximately 10 °C cooler. At temperatures cooler than these, WMA exhibited reduced workability. The reduced laboratory workability at lower temperatures causes less densification to occur in the field. Since the densities of the mixtures evaluated met the construction specifications, and since there is a direct correlation between the laboratory workability and field compaction, a maximum torque value of 20 N-m is recommended to be used as a threshold to estimate a mixture minimum compaction temperature. From the workability results on the field mixtures, the minimum compaction temperatures recommended for the HMA and the WMA mixtures are 110 °C and 100 °C, respectively.

High-RAP-WMA has better workability than high-RAP-HMA. However, overall the workability is reduced when RAP is added; this agrees with the results of [7, 8].

Therefore, for high-RAP mixtures (25–50% RAP), the minimum compaction temperatures need to be increased by 10–20 °C to meet the maximum torque recommendation of 20 N-m.

In general, workability results showed that the torque method evaluated is efficient in determining the workability of different mixtures and that the laboratory workability can be used to predict mixture compactability.

DISCLAIMER AND ACKNOWLEDGEMENTS

Citation of trade names does not constitute an official endorsement or approval of the use of such commercial products. All product names and trademarks cited are the property of their respective owners. The findings of this paper are not to be construed as an official Department of the Army position. This research was funded by the U.S. Air Force Civil Engineering Center. Tim McCaffrey, Lance Warnock, and Kevin Taylor are thanked for their efforts in collecting laboratory data for this paper. Permission to publish was granted by the Director, Geotechnical and Structures Laboratory, U.S. Army Engineer Research and Development Center.

REFERENCES

[1] Celik, O.N. and Atis, C.D. Compactibility of Hot Bituminous Mixtures made with Crumb Rubber-Modified Binders, Construction and Building Materials, 22(6), pp. 1143–1147. 2008.

[2] Bennert, T., G. Reinke, W. Mogawer, and K. Mooney. Assessment of Workability and Compactability of Warm-Mix Asphalt, Transportation Research Record No. 2180, pp. 36–47. 2010.

[3] Gudimettla, J.M., L.A. Cooley, Jr., and E.R. Brown. Workability of Hot Mix Asphalt. NCAT Report 03–03. Auburn, AL: National Center for Asphalt Technology. 2003.

[4] Marvillet, J., and Bougault, P. Workability of Bituminous Mixes: Development of a Workability Meter, Proceedings of the Association of Asphalt Technologists, Vol. 48, pp. 91–110. 1979.

[5] Howard, I.L., Baumgardner, G.L., Jordan III, W.S., Menapace, A.M., Mogawer, W.S., and Hemsley Jr., J.M. Haul Time Effects on Unmodified, Foamed, and Additive Modified Binders Used in Hot Mix Asphalt, Transportation Research Board 92nd Annual Meeting Compendium of Papers, (DVD-ROM), Washington, DC, USA, Paper No. 13–3093. 2013.

[6] Wang, C., Hao., P., Ruan, F., Zhang, X., and Adhikari, S. Determination of the Production Temperature of Warm Mix Asphalt by Workability Test, Construction and Building Materials, 48(Nov 2013), pp. 1165–1170. 2013.

[7] Mogawer, W.S., Austerman, A.J., and Bonaquist, R. Determining the Influence of Plant Type and Production Parameters on Performance of Plant-Produced Reclaimed Asphalt Mixtures, Transportation Research Record No. 2268, pp. 71–81. 2012.

[8] Mogawer, W., Bennert, T., Daniel, J.S., Bonaquist, R., Austerman, A., and Booshehrian, A. Performance Characteristics of Plant-Produced High RAP Mixtures, Asphalt Technology: Journal of the Association of Asphalt Technologists, Vol. 81, pp. 403–440. 2012.

[9] Austerman, A.J., W.S. Mogawer, and R. Bonaquist. Evaluating the Effects of Warm Mix Asphalt Technology Additive Dosages on the Workability and Durability of Asphalt Mixtures Containing Recycled Asphalt Pavement, Transportation Research Board 88th Annual Meeting Compendium of Papers, (DVD-ROM), Washington, DC, USA, Paper No. 09–1279. 2009.

[10] Mallick, R.B., P.S. Kandhal, and R.L. Bradbury. Using Warm Mix Asphalt Technology to Incorporate High Percentage of Reclaimed Asphalt Pavement Material in Asphalt Mixes. Transportation Research Record No. 2051, pp. 71–79. 2008.

[11] Tao, M., and R.B. Mallick. Effects of Warm-Mix Asphalt Additives on Workability and Mechanical Properties of Reclaimed Asphalt Pavement Material, Transportation Research Record No. 2126, pp. 151–160. 2009.

[12] Doyle, J.D., Mejias-Santiago, M., Brown, E.R., and Howard, I.L. Performance of High RAP-WMA Surface Mixtures. Asphalt Paving Technology: Journal of the Association of Asphalt Paving Technologists, Vol. 80, pp. 419–457. 2011.

[13] Rushing, J.F., Mejias-Santiago, M., and Doyle, J.D. Assessment of Warm Mix Asphalt (WMA) for Heavy Traffic Airfields. Transportation Research Record: Journal of the Transportation Research Board, No. 2371, pp. 41–48. 2013.

This page intentionally left blank

Asphalt Pavements – Kim (Ed)
© 2014 Taylor & Francis Group, London, ISBN 978-1-138-02693-3

Effect of lime on short-term bearing capacity of bitumen emulsion recycled mixtures

Giacomo Betti
Department of Civil and Industrial Engineering, University of Pisa, Pisa, Italy

Andrea Cocurullo
NTEC, University of Nottingham, University Park, Nottingham, UK

Alessandro Marradi
Department of Civil and Industrial Engineering, University of Pisa, Pisa, Italy

Gabriele Tebaldi
Department of Civil and Environmental Engineering and Architecture, University of Parma, Parma, Italy
Department of Civil and Coastal Engineering, University of Florida, Gainesville, FL, USA

Gordon Airey
NTEC, University of Nottingham, University Park, Nottingham, UK

Kim Jenkins
Department of Civil Engineering, University of Stellenbosch, Matieland, South Africa

ABSTRACT: Cold recycling is one of the most employed rehabilitation techniques for asphalt pavements and it is becoming more and more important as the reduction of emissions becomes a priority in the reduction of the greenhouse effect. The main advantages of asphalt cold recycling techniques are the use of reclaimed materials and the lack of need to heat the aggregates to make the mixtures: these possibilities allow for reduced consumption of natural aggregates and emissions providing, at the same time, many technical and economical benefits. The reduction of emissions in the use of reclaimed materials is due to a reduction of transport, in particular that reduction is bigger when the reclaimed materials are used in place. Nevertheless, the so-called cold in place recycling has challenges to control the water content in the mixtures and of quickly achieving a sufficient bearing capacity to allow the completion of the re-paving work. Generally the solution is provided by the use of active fillers, mainly Portland cement, able to absorb water and stiffen the mixtures. Sometimes the in place working conditions make necessary (presence of clay soils) or suggest (high moisture content) the addition of lime, but its effect on cold mixtures performances is, at the moment, not completely understood.

In an effort to improve on-site performance of recycled mixtures, the authors developed an extensive research programme aimed to investigate the effects provided by the introduction of lime in cold recycled mixtures as active filler. The basic idea was to analyse the bearing performance of pavement layers made with bituminous emulsion cold recycled mixes with different blends of active fillers (cement, lime). This paper evaluates the short term bearing capacity of recycled mixtures: assessment provided are based on results of deflectometric tests carried out on a trial section specifically built in Italy, close to Florence. Tests have been undertaken using LWD (Lightweight Deflectometer) and FWD (Falling Weight Deflectometer) immediately after compaction and after 24 hours of curing. The obtained results, even though they need to be confirmed by the analyses of long-term behaviour, positively support the use of lime as an active filler.

Keywords: Cold Recycling, Lime, Lightweight Deflectometer, Falling Weight Deflectometer

1 INTRODUCTION

Asphalt mixtures are the most common materials employed in the road pavements around the world, so "how to employ?" and "how to manage?" the material produced in the demolition of damaged pavements at the end of the service life (the so-called RAP—Reclaimed Asphalt Pavement [1]) is one of the main issues for road agencies and road administrations.

Among the different options, the focus on cold recycling techniques is nowadays increasing due to the enormous contribution that they can give to increase sustainability of road constructions.

As reported in literature, the main benefits provided by cold recycling of asphalt pavements are, general, related to [2]:

- consumption reduction of natural materials;
- reduction of amount of waste materials to be disposed;
- reduction of energy consumption and greenhouse emissions due to cold production process.

In the case of in-place recycling another beneficial aspect of this technique is related to the reduction of heavy vehicle movements to provide fresh materials on construction site.

On the side of the advantages, the cold recycling techniques have to face the challenges related with mix design:

- the control of mixture's water content;
- quickly achieving a sufficient bearing capacity that allows completion of the repaving work.

Generally the solution is provided by the use of an active filler (a filler that chemically alters the mix properties): Portland cement appears to be the most used mainly due to the possibility to absorb the excess water, as a results of its setting reaction, and to quickly provide an increase of the mixture stiffness after compaction.

The in place recycling techniques in some situations may have some additional problems related to the specific pavement conditions. Two very common situations that engineers have to solve are the presence of clay soil inside of the granular materials of unbounded layer, mainly in during on site stabilization of distressed pavement, both with foam bitumen or bitumen emulsion, and when the amount of water greatly exceeds the optimum water content (or fluid content) for compaction. A practical solution frequently use in the work places to overcome these problems it is to add calcium oxide (quicklime) [3]. In the cases of clayey soils, the calcium oxide induces the flocculation of montmorillonitic components of soils making them insensible to the water. In the case of a large amount of water, the mechanism to dry the mixtures come from the reaction of hydration of calcium oxide to become calcium hydroxide with the production of a large amount of heat.

The question associated with this practical procedure is related to the global amount of active filler and whether the lime used for drying can be considered as an active filler? Or, in other words, can the lime be used instead of the cement or can the lime partially replace the cement in the global amount of active filler?

In general, limited literature exists regarding the effect on short and long term performance of cold recycled mixture made using different blends of active fillers including cement and lime. In an effort to assess the possible benefit of substitution of cement with lime in cold recycling, the Universities of Pisa, Parma, Stellenbosh and Nottingham designed and tested a full scale trial section to evaluate, under real traffic conditions, the short and long term performance of cold recycled mixtures made with multiple blends of active fillers.

Results presented in this paper are part of the extensive research work mentioned above and focussed on the short term performance of two bitumen emulsion recycled mixtures with and without addiction of lime to replace part of the mineral filler. Tests have been undertaken by means of Light Weight Deflectometer (LWD) and Falling Weight Deflectometer (FWD) immediately after compaction and after 24 hours of curing.

2 OBJECTIVE AND SCOPE

The objective of this research work is to investigate the influence of introducing lime as active filler in cold recycled mixtures on the short term bearing capacity of a bituminous emulsion recycled mixture.

A mixture made with 100% of RAP, with 1% of Portland cement by weight of aggregates as active filler was selected as a reference mixture and it was compared with a similar mixture where 2% (by aggregates weight) of lime was used to replace 2% of mineral filler (by weight of aggregates).

The bearing capacity of the two mixtures was investigated immediately after compaction with Light Weight Deflectometer (LWD) and 24 hours after compaction with Falling Weight Deflectometer (FWD). The possibility to use LWD immediately after compaction is related to the low stiffness of the mixtures: any component with binding action (cement, lime and emulsion) has no time to have a considerable effect hence the bearing capacity of the layer is mainly provided by the aggregate interlocking. After 24 hours of curing deflectometric tests were performed by means of FWD tests due to the achieved stiffness of recycled mixtures.

3 MATERIALS AND TRIAL SECTION CHARACTERISTICS

Trial section was built using two recycled mixtures with bitumen emulsion and different blends of active filler. Two different fractions of RAP aggregates have been selected to form the stone skeleton of the mixes: RAP fraction 0–10 mm and RAP fraction 10–20 mm. The two recycled mixtures had the same grading composition (100% RAP) and a cationic ultraslow setting bitumen emulsion was used as stabilizing binder. The total amount of filler in the mix was optimized to reach the OMMC (Optimum Moisture Mixing Content); the proportion of the three components, mineral filler, cement and lime, was optimized in order to investigate their influence on short term performances. Mixes were designed as reported in the following Table 1. The percentages of fillers, both active and mineral filler, should be considered as theoretical values; in the field a moderate variation occurs due to the inherent variability of recycled mixtures production process. For these reasons, the effective amount of fillers contained in the mixes are also presented.

To analyze the evolution in time of recycled mixtures performance, a specific trial section have been designed, realized and tested on a local road under construction near Florence (Italy). Recycled materials have been produced following the in-plant recycling techniques, laid with a paver and compacted using a combination tandem roller (front rubber tires and rear metallic drum). Dimensions of the trial section and pictures taken during construction process are hereinafter presented.

The trial section pavement at the moment of testing campaign consists of a 17 cm layer of recycled material over a lime stabilized subgrade (Fig. 2). The pavement will be completed with additional 4 cm of asphalt concrete wearing course type, to be laid directly over the recycled layer. The entire pavement structure were designed with the only aim to reach the

Table 1. Specification of mix composition.

		Theoretical value		
Mix ID	% bitumen emulsion	% cement	% lime	% mineral filler
2A	3	1	2	1.5
2B	3	1	0	3.5
		Real value		
2A	3	1.1	2.1	1.6
2B	3	1.2	0	4.3

Figure 1. Pictures taken during laying and compaction on the left. Dimensions of trial section on the right.

	4 cm of wearing course (not present at the moment of test campaign)
	17 cm of bitumen emulsion recycled layer
	Subgrade

Figure 2. Pavement structure of the trial section.

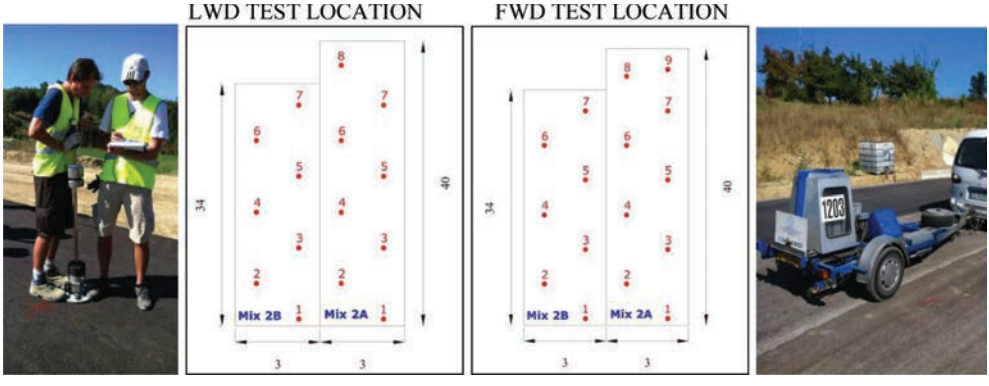

Figure 3. Test location scheme for LWD and FWD.

stress and strain distribution under load allowing researchers to clearly underline the different performances of the two investigated materials.

Test locations, both with LWD and FWD, were distributed to cover the entire trial section and can be shown in the subsequent schemes. Due to a fixed amount of material produced for the different mixtures and different paving layout (pavement shoulders, paver width setup, road curvature, etc.), the two sections have a different length and, consequently, a different number of test locations.

LWD tests were also carried out to characterize the subgrade of the pavement trial sections, prior to laying the recycled mixtures, in order to take into account the subgrade bearing capacity in data evaluation and to better understand test results carried out after compaction (zero curing). The test location used to characterize the pavement subgrade was exactly that used for the recycled mixture (Fig. 3). Results were also reported in the form of coloured maps for the entire trial field (Fig. 4—grid of data was created using the kriging algorithm) to underline the spatial variation of subgrade Surface Modulus

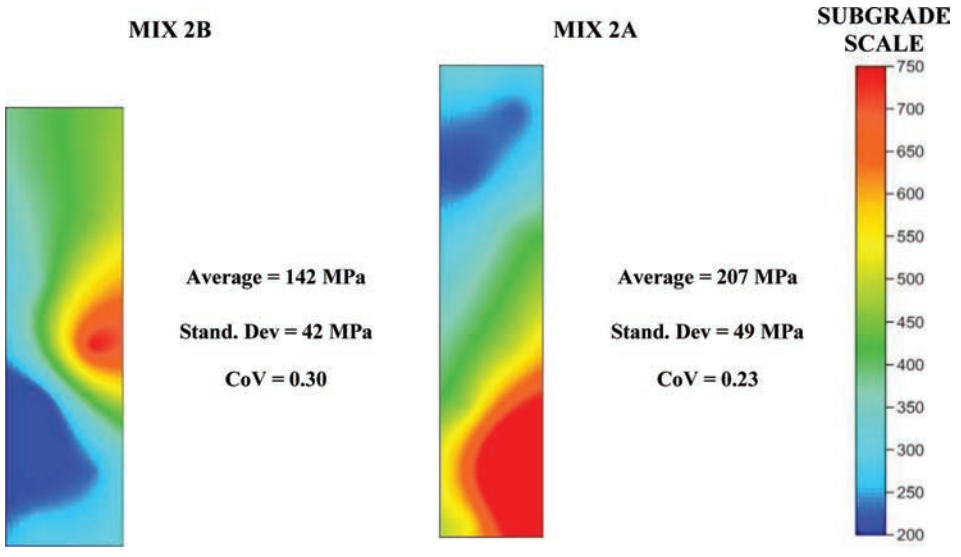

Figure 4. Colour maps of surface modulus for subgrade.

(Equation 1). Average value, Standard Deviation and Coefficient of Variation are also reported in Figure 4.

4 INVESTIGATION METHOD

4.1 *Light weight deflectometer LWD*

The dynamic load plate test in the form of Light Weight Deflectometer (LWD) was firstly introduced as mechanistic (or analytical) approaches to pavement engineering found increased support internationally, as a new method to determine the E-modulus of unbound and cement-bitumen stabilized materials in pavements [4].

The LWD testing device is used to characterize a half-space bearing capacity in terms of surface deflection and consequently through the Surface Modulus calculated using Boussinesq equation: stress distribution and Poisson's ratio is used to calculate elastic moduli. The effect on the calculated surface deflection modulus is seen from the equation:

$$E = \frac{f\ (1\ \nu^2)\ \sigma_0\ a}{d_0} \tag{1}$$

where the factor "f" (plate rigidity factor) is 2 for uniform distributions and π/2 for the rigid case, which may be more correct for cohesive materials, "a" is the load plate radius, "σ_0" and "d_0" are respectively the maximum value of the applied stress and the measured deflection.

During the field test with the LWD, an impact-like load is applied to the surface via a circular steel plate (load plate). The load set consists of a falling weight and a guide rod. After release, the falling weight slides down along the guide rod and hits a spring-damper element made of synthetic material.

A geophone installed in a centerplate hole records the speed of the ground subjected by the test load, allowing calculation of the plate displacement; at the same time, load applied during the impact is measured via a load cell. The data obtained can be used to estimate the surface modulus of the tested surface. The advantages of these types of instruments are the portability (small size and weight) and the speed of the tests, allowing the implementation for QC/QA on a large scale.

The Light Weight Deflectometer is becoming more and more used worldwide thanks to the new performance based approaches, such as the one introduced in UK with the IAN 73. In Italy, LWD on-site controls of compaction level are included since 2009 in the set of technical specifications for roadwork assigned by ANAS, the Italian Road Authority. LWD standard practice in the ANAS technical specifications are suggested to be used for embankment, granular foundation and cement stabilized layers; for cold recycled layers (in plant or in situ, with emulsion or foam bitumen) the LWD dynamic load plate test according ASTM E2583-07 is the only field test requested during construction.

In the present study short term bearing capacity of tested mixes was evaluated immediately after compaction by means of LWD (0 hours tests). Tests were carried out by applying a load able to induce on the surface a deflection higher than 100 μm in order to avoid problems due to the sensor accuracy [5].

4.2 *Falling weight deflectometer*

Today's most common testing equipment for evaluation of structural condition of pavements is the Falling Weight Deflectometer (FWD) which is a trailer-mounted device capable of transmitting a specified load to the pavement surface comparable with a heavy vehicle moving on the pavement with a speed ranging in the 60–80 km/h interval [6]. The falling mass, the spring system (rubber buffers), and drop height can each be adjusted to achieve the desired impact loading on the pavement. Vertical deflection peaks are measured at the centre of the loading plate and at multiple radial positions by a series of deflection sensors. The impulse load acting on the pavement causes a "wave front" of recoverable deformations, or deflections, that spread out from the centre of the load. Both the peak impulse load (force) and maximum vertical deflections of the "wave front" are measured at multiple radial distances from the load centerplate. These deflections, considered as a function of the applied impulse load, provide an indication of the structural strength of the pavement [7].

Since the theoretical approaches used to determine the stress–strain relationships in pavement layers calculate the deflections for given mechanical properties, it is necessary to make an inversion using a backcalculation tool. Several methods have been developed to backcalculate the mechanical properties of pavement; these methods vary in analysis type, material model, and optimization algorithm [8].

In the present study FWD tests have been undertaken after 24 hours of curing applying to the surface a pressure if about 1000 kPa. Centerplate deflection were used to calculate the Surface Modulus while the other deflection measurements allow the pavement layers modulus to be backcalculated following the structure presented in Figure 2. The pavement structure will be completed with the wearing course in the following months.

5 RESULTS AND DISCUSSION

Results of the test campaign are firstly presented in terms of Surface Modulus (Equation 1). This parameter can be defined as a measure of "Stiffness Modulus" based on the application of a known load at the top of the tested material. It can be considered a composite value with the contribution of all the underlying layers [9]; for LWD test, due to the load applied, the stiffness of the closest layer to the loading plate appear to be predominant. Regarding FWD a specific test setup able to reach a load corresponding to 1000 kPa was selected, rending the centreplate deflection, the one used to calculate Surface Modulus, significantly dependent on the stiffness of all the underlying layers. Results are reported comparing performances of the two mixes. Threshold values provided by technical prescription of Italian road authority ANAS are also reported: subbase layers realized with the in plant cold recycling technique should reach a Surface Modulus higher than 45 MPa after 4 hours from laying and compaction and higher than 170 MPa after 24 hours. These prescriptions are mainly devoted to evaluate the density achieved after compaction and avoid distresses due to the transit of delivery vehicles.

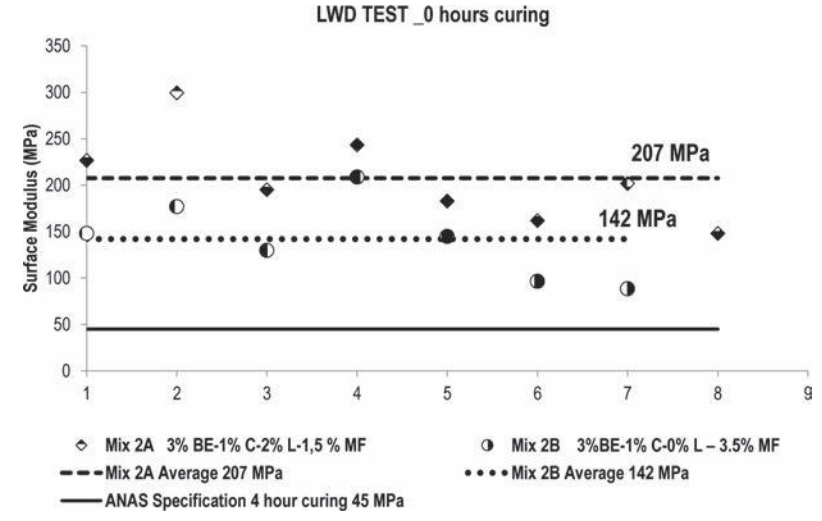

Figure 5. LWD surface modulus comparison.

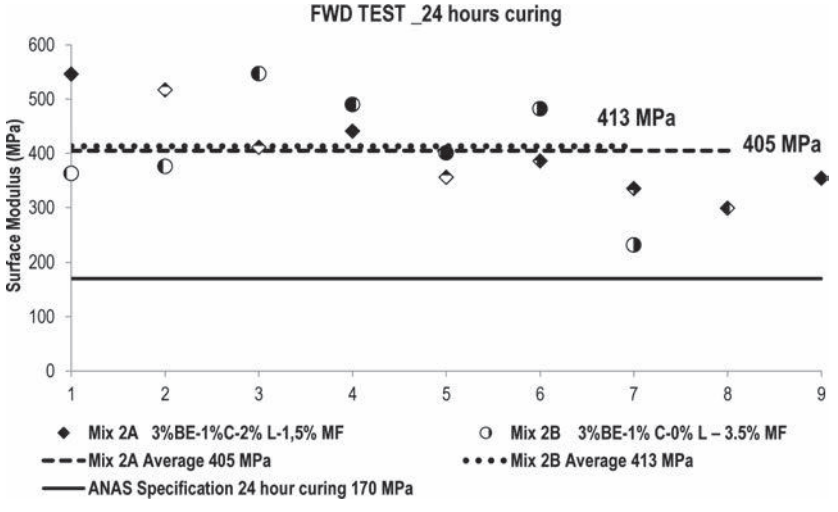

Figure 6. FWD surface modulus comparison.

In the subsequent pictures results of LWD tests are reported. The graph is organized plotting the Surface Modulus versus the number of test location (for example in the Mix 2A field 9 test location have been analysed).

The two mixes showed high values of Surface Modulus, both after compaction and after 24 hours of curing, more than two times greater than the threshold value required by ANAS technical specification. To better understand the spatial variation of LWD and FWD tests results, a colour map have been created for Surface Modulus using a specific spatial interpolation algorithm (grid of data was created using the kriging algorithm). Results are reported in the subsequent Figure 7 where x-axis represent the cross amplitude of the field and the y-axis the length of the field; average value, standard deviation and coefficient of variation (ratio of standard deviation and average value) are also presented.

FWD Deflection recorded after 24 hours from compaction have also been used to backcalculate the elastic equivalent modulus of the recycled layers. The pavement

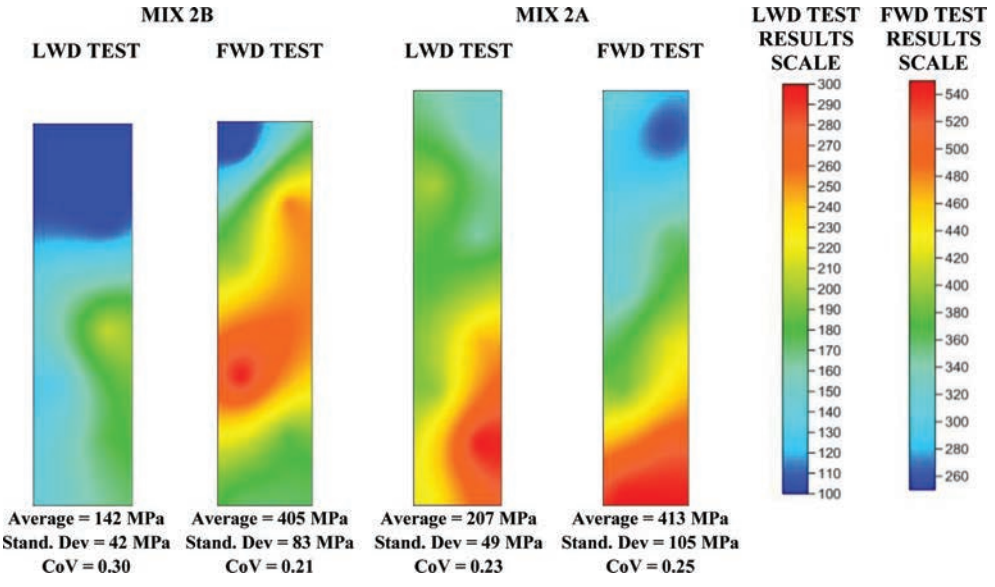

Figure 7. Colour map of surface modulus of recycled layers.

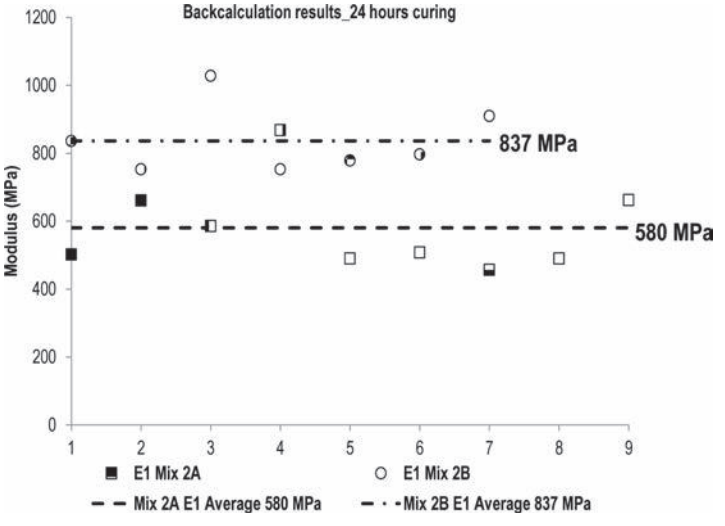

Figure 8. Comparison of E1 modulus of recycled mixtures from backcalculation process.

structure was assumed to be as reported in Figure 2 except for wearing course (laying of wearing course will be done in the next couple of weeks) and the Odermark-Buossinesq backcalculation method (MET Method of Equivalent Thickness) has been used. Results are subsequently reported in terms of modulus of recycled layer (E1) in order to separate the influence of the subgrade stiffness and then underline the recycled mixtures performance.

Results presented in Figure 8 can be considered an absolute measure of mixes stiffness after 24 hours of curing and allow to model the pavement response to applied loads. More information about that response will be provided by monitoring the stiffness evolution of the mix in the next month.

To provide a more detailed analysis and evaluate the influence of active fillers on mixtures strengthening, a comparison of modulus after compaction and after 24 hours of curing has been done, treating each mixture alone. To reach this goal the Surface Modulus calculated from LWD tests after compaction have been compared with the E1 modulus resulting from backcalculation of deflection recorded with FWD tests after 24 hours curing (FWD centreplate deflection after 24 hours of curing results too much dependent on subgrade stiffness than not useful to investigate the performance on the recycled mixture alone). In this regard it worth noting that, from a theoretical point of view, a Surface Modulus, which is a measure of the half space bearing capacity, cannot be compared with a layer modulus. Furthermore, the influence depth of the LWD tests can be assumed to be 1÷1.5·D (D = diameter of the loading plate) depending on different boundary conditions of the testing process. On the other hand, due to the stiffness of the materials, the deflection measured after compaction (LWD tests) appears to be strictly dependent on behaviour of only the upper layers, rending the Surface Modulus a preliminary indication on bearing capacity of the recycled layer alone.

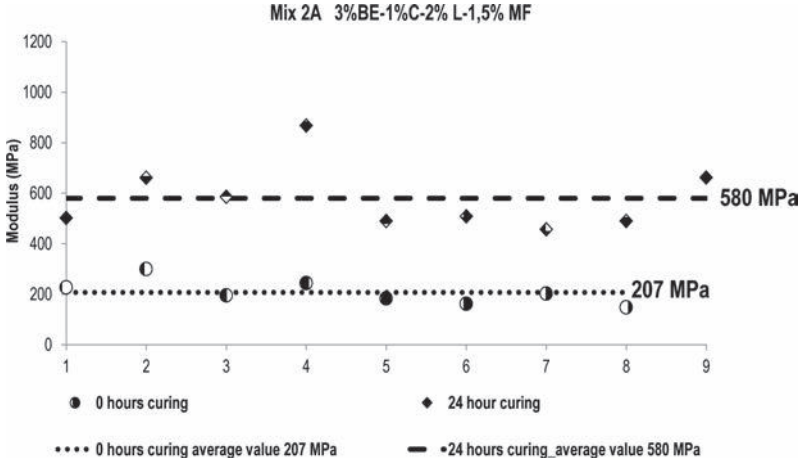

Figure 9. Comparison of modulus at 0 curing and 24 hours curing—mix 2A.

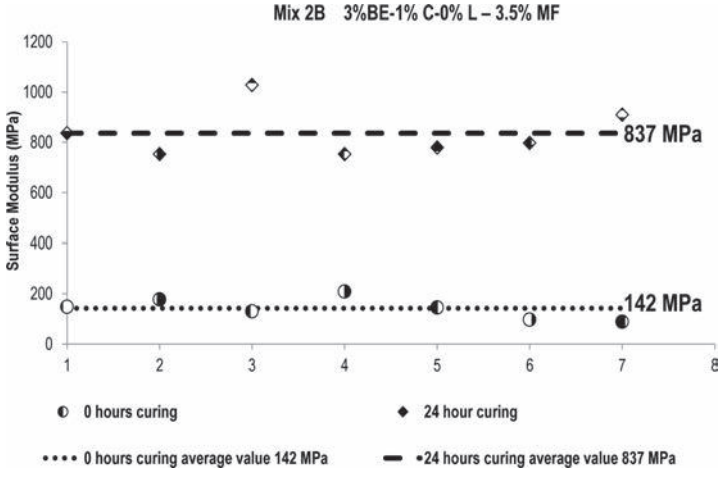

Figure 10. Comparison of modulus at 0 h curing and 24 h curing—mix 2B.

Results shows that a significant increase of mixtures stiffness occurs after only 24 hours of curing. Since the trial section is placed on a real road, no problems are recognized for the road authority to complete the pavement structure construction by placing the wearing course.

6 SUMMARY AND CONCLUSIONS

In this paper the short term performances of recycled mixtures made using different blends of active fillers have been analysed. The effect of using lime as active filler has been investigated by means of LWD and FWD tests after compaction and after 24 hours of curing.

Tested mixtures appear to perform well; threshold values provided by the ANAS technical specification significantly exceeded both after compaction and after 24 hours of curing.

As reported in the introduction, lime can be used to stabilize clay particles or to aid the drying process of RAP aggregates. Mix 2A can be considered to be this second situation with lime being used to substitute a certain amount of mineral filler (1% of cement is however added to the mix). In that case, comparing results to those obtained with a reference mix (mix 2B with only 1% of cement and no lime in the mix), no negative effect on material bearing capacity can be recognized due to the use of lime as active filler. On the other hand, lime seems to affect the strengthening process decreasing the rate of strength evolution in the mixes, even though tests carried out over a long term period will be needed to clarify this aspect.

To conclude, results obtained appear to be very promising regarding the short term performance of recycled mixtures. Further research is on-going with the aim to investigate the effect on long term performance of introducing lime in cold recycled mixture as active filler.

REFERENCES

[1] Tebaldi G., Dave. E., Marsac P., Muraya P., Hugener M., Pasetto M., Graziani A., Grilli A., Marradi A., Wendling L., Gaudefroy V., Jenkins K., Loizos A., Bocci M., "*Classification of Recycled Asphalt (RA) material*". 2nd International Symposium on Asphalt Pavements & Environment, ISAP TC APE, Fortaleza, Brazil, October 1–3 2012.

[2] Pereira P., Santos L.P., *Technical-Economical Evaluation of Pavement Recycling Alternatives,* Proceedings of the Third Gulf Conference on Road 2006.

[3] Asphalt Academy "*Technical Guideline: Bitumen Stabilized Materials. A guideline for the Design and Construction of Bitumen Emulsion and Foamed Bitumen Stabilized Materials*" Asphalt Academy, Pretoria South Africa, 2009.

[4] Marradi A., *Dynamic Field Assessment of short term bearing capacity for cold recycled layer*, PEAT Journal of Pavement Engineering and Asphalt Technology, Volume 12, Issue 1, Liverpool May 2011.

[5] Fleming P.R., Edwards J.P. *LWD Best Practice Guide*, 2010.

[6] Ullidtz P., *Pavement Analysis*, pp 256, Elsevier Science Publisher, Netherland 1987. ISBN 0-444-42817-8.

[7] Plati C., Loizos A., Papavasiliou V., Kaltsounis A., *Investigation In Situ Properties of Recycled Asphalt Pavement with Foamed Asphalt as Base Stabilizer*, Advance in Civil Engineering, volume 2010, Article ID 565924, 10 pages, Soheil Nazarian, 2010.

[8] Goktepe B.A., Agar E., Hilmi A.L., *Advance in backcalculating the Mechanical Properties of Flexible Pavements*, Advance in Engineering Software, volume 37 pp 421–431, Elsevier 2005.

[9] Draft HD25 Interim Advice Note IAN73/06, Revision 1, *Design Guidance for Road Pavement Foundation*, 2009.

Asphalt Pavements – Kim (Ed)
© 2014 Taylor & Francis Group, London, ISBN 978-1-138-02693-3

Performance evaluation of Cement Grouted Bituminous mixes

G. Manikantha Raju, D. Sita Rami Reddy & K. Sudhakar Reddy
IIT Kharagpur, Kharagpur, West Bengal, India

ABSTRACT: Cement Grouted Bituminous (CGB) mix is a semi flexible type of pavement material which essentially is an open graded (porous) bituminous mix grouted with cement mortar. CGB mixes have the advantages of both flexible and rigid pavements. This hybrid mixture provides good rutting and top-down cracking resistance. In the present study, an effort was made to evaluate the performance of CGB mixes. The study consists of selection of an appropriate gradation, design of cement mortar and performance evaluation of CGB mix. Performance of CGB and normal mixes was evaluated by conducting beam fatigue and static indentation creep tests. Correlations developed between the quantity of grout penetrating the mix with the air voids in dry aggregates and voids in mix will be useful for selecting suitable aggregate gradations. Different strength parameters of the mix improved significantly due to grouting. Resistance to moisture damage also improved. CGB mixes had much longer fatigue lives compared to unmodified mixes. Rutting performance of CGB mix, as observed in the static indentation creep test, was observed to be significantly better than that of normal mix. Results obtained from the investigations suggest that cement grouted bituminous mix can be a promising material for surface layers.

Keywords: Semi flexible, cement grouted, grouting, rut resistant, fatigue performance

1 INTRODUCTION

Bituminous (flexible) and concrete (rigid) are the two common types of pavement built. Flexible pavements are characterized by their lower initial cost, higher maintenance costs while rigid pavements have higher initial cost and longer life span. Concrete pavements require better construction skills and maintaining the joints in concrete pavement is also not easy. The main modes of failure in bituminous pavements are fatigue cracking, rutting and moisture damage of bituminous layers. Cement grouted bituminous mix, which is expected to have better rutting and moisture damage resistance, has been investigated in this study.

Cement grouted bituminous mix basically has two components: bituminous mix and cement grout. Aggregate gradation in the bituminous mix is selected in such a way that the mix will contain more voids compared to traditional dense-graded mixes. The volume of voids, thus created, will be sufficient for adequate quantity of grout to penetrate. Oliveira et al., [1] suggested that 25 to 35% voids are required in bituminous mix to allow proper penetration of cement grout. The cement grout is spread over the bituminous mix and made to flow through the voids of the bituminous mix. This type of grouted bituminous mix offers high rut resistance, fuel and oil spill resistance and acts as water impervious layer to underlying layers. It will also be free from the requirement of maintaining joints and offers a surface which has better wearing resistance.

The study methodology broadly consists of (i) design of gradation of aggregates by examining the relationship between the voids in the gradation and the quantity of grout penetrating the mix (ii) design of cement grout for proper penetration into the mix and for adequate strength of the grouted mix and (iii) evaluation of the performance of cement grouted bituminous mixes.

2 MATERIALS USED IN THE STUDY

2.1 *Aggregates*

Crushed coarse aggregate, fine aggregate and mineral filler used in this study were procured from the Shelda quarry in the state of West Bengal, India and these aggregates satisfy the requirements of the Ministry of Road Transport and Highways (MoRTH), Government of India [2].

Six trial gradations were chosen for the present study in which the first 3 gradations are selected in such a way that the fraction of filler retained between the following pairs of sieves: –0.6 μm to 0.3 μm, 0.3 μm to 0.15 μm and 0.15 μm to 0.075 μm is 1% for each pair and similarly the fraction of sand fraction retained between the following pairs of sieves: –4.75 mm to 2.36 mm, 2.36 mm to 1.18 mm and 1.18 mm to 0.6 mm is 2% for each pair of sieves. Fourth gradation has only 26.5 mm to 4.75 mm size coarse aggregates. Fifth gradation is similar to that of Surface dressing specified by MoRTH [2]. Sixth gradation is similar to bituminous macadam [2] aggregate gradation. Details of selected aggregate gradations are given in Table 1.

2.2 *Binder*

Two unmodified viscosity grade binders, VG-30 and VG-10, were used to study the effect of binder type on cement grouted bituminous mixes.

2.3 *Cement grout*

Cement used in the grout was satisfying the Specification as per IS-12269-1987 [3]. Sand used was graded as given in Table 2. Fly ash and Silica were used in the present study to increase the flow of cement grout at lower water cement ratio.

Table 1. Aggregate gradations used.

	% Passing for gradation number					
Sieve size (mm)	1	2	3	4	5	6
26.5	100	100	100	100	100	100
19	95	95	95	66.7	92.5	95
13.2	80	75	45	33.3	20	72
9.5	60	25	25	16.7	3.5	
4.75	10	10	10	0		26
2.36	8	8	8		1	
1.18	6	6	6			
0.6	4	4	4			
0.3	3	3	3			6
0.15	2	2	2			
0.075	1	1	1		0.75	4

Table 2. Sand gradations adopted.

Sieve size in microns	Retained between the sieves (%)
600-300	43
300-150	47
<150	10

3 EXPERIMENTAL INVESTIGATIONS

3.1 *Void ratios in dry aggregate gradations*

The volume of voids available for cement grout penetration can be related to void ratio of dry aggregate gradations. For this, three different methods were adopted. In all the three methods the principle for finding the void ratios is similar. Only the volume and compaction effort is different. In Method 1, a three-liter metal cylindrical measure was taken and aggregates were filled in 3 layers. Each layer was tamped 25 times with a 16 mm diameter and 60 mm long steel rod. In Method 2, California Bearing Ratio test mould of volume 2250 cc was taken and aggregates were compacted in 3 layers by Marshall compaction hammer applying 25 blows over each layer. Method 3 consisted of determining the percentage voids in a manner similar to that adopted in method 2 but the Marshall hammer used for compaction has projections on the surface so that the compaction can be done more effectively. Void ratio in the compacted aggregate is computed using the bulk specific value of aggregates. The void ratios obtained with different gradations are tabulated in Table 3.

3.2 *Preparation of bituminous samples*

Cylindrical samples of bituminous mix were prepared using split Marshall mould. Effort was made to produce specimens of 50 mm height. The mixture of heated aggregates and binder was compacted by 25 blows of Marshall compaction hammer applied on one side only to have more air voids to facilitate penetration of adequate quantity of cement mortar. The quantity of binder required was estimated for each gradation separately based on the quantity required for a film thickness of 8 microns. Film thickness was estimated using the surface area factors given in Asphalt Institute manual MS-2 [4]. Binder contents adopted for different gradations are given in Table 4. Average volumetric parameters of the mixes produced with different gradations are also given in Table 4.

Table 3. Void ratios for different gradations.

	Void ratios by		
Gradation type	Method 1	Method 2	Method 3
1	0.55	0.36	0.35
2	0.59	0.41	0.39
3	0.60	0.49	0.46
4	0.56	0.45	0.45
5	0.63	0.46	0.45
6	0.47	0.30	0.30

Table 4. Binder content in gradations and volumetric parameters.

Gradation type	Binder content (%)	G_{mm}	G_{mb}	VMA	Va
1	4.43	2.714	2.204	26.1	18.8
2	4.43	2.718	2.159	27.7	20.6
3	4.43	2.724	2.031	33.1	26.7
4	1.26	2.769	1.979	31.5	28.6
5	2.03	2.774	1.890	36.7	31.9
6	6.65	2.657	2.212	25.2	13.1

3.3 *Grout penetration*

The amount of grout penetrating the specimen was obtained by measuring the weights of the specimen before and after grouting. The amount of grout penetrating different specimens prepared using different gradations is given in Table 5. The corresponding aggregate void ratio values computed by the three different methods are also given in the table. Water cement ratio of 0.75 and a cement:mortar proportion of 1:1 were used for preparing mortar. VG-30 binder was used to prepare bitumen mix specimens.

Table 5 indicates that the trends of variation of voids are similar for methods 2 and 3. Method 1 also gives nearly similar results with minor variations. In view of this, it has been decided to use the void ratio values obtained with method 3 for further analysis. The relationship between aggregate void ratio (obtained by method 3) and cement grout penetrated is shown in Figure 1.

3.4 *Effect of binder type on grout penetration and strength parameters*

Cement grouted bituminous mix samples were prepared with 3, 4 and 6 gradations. VG-30 and VG-10 binders were used. The samples were cured for 7 days and tested for Marshall stability and flow and Indirect Tensile Strength (ITS). Marshall and ITS parameters and the quantities of grout penetrated are tabulated in Table 6.

Mixes with VG3-0 binder yielded marginally more Marshall stability and ITS values compared to mixes having VG-10 binder. The amount of grout penetration is also slightly more with VG30 mixes.

Table 5. Void ratio in aggregates and quantity of grout penetrated.

Gradation type	Void ratios by			Cement grout penetrated (g)
	Method 1	Method 2	Method 3	
1	0.55	0.36	0.35	258.3
2	0.59	0.41	0.39	298.6
3	0.60	0.49	0.46	311.6
4	0.56	0.45	0.45	340.5
5	0.63	0.46	0.45	345.2
6	0.47	0.30	0.30	154.7

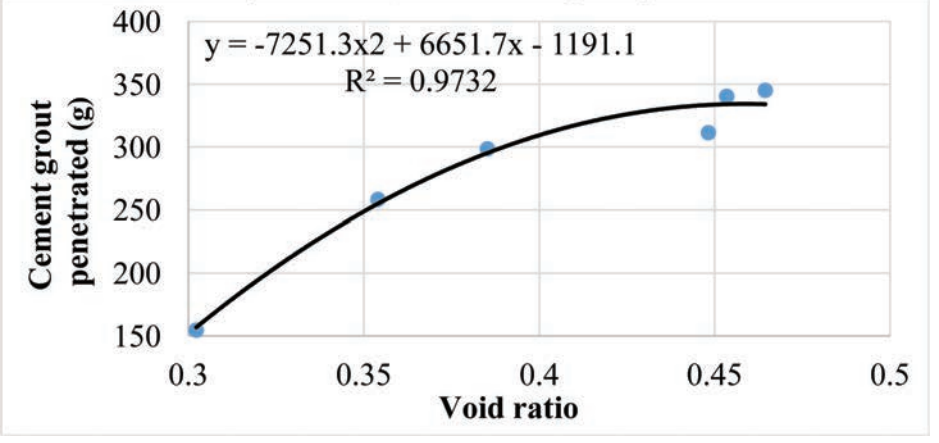

Figure 1. Void ratio vs grout penetrated.

Table 6. Details of grout penetration, marshall and ITS test results.

Gradation type	Binder type	Grout penetrated (g)	Marshall stability (kN)	Flow (mm)	ITS (kPa)
3	VG-10	274.0	28.4	4.5	1023.9
3	VG-30	309.0	30.4	5.8	1031.4
4	VG-10	317.0	33.4	3.9	982.6
4	VG-30	340.5	34.2	4.6	1107.6
6	VG-10	148.7	7.8	8.4	478.1
6	VG-30	152.0	8.2	9.2	590.8

Table 7. Compressive and flexural strengths of grout.

Fly ash content (%)	Compressive strength (MPa)	Flexural strength (MPa)
0	19.3	1.39
10	22.5	1.68
20	18.5	1.41

Figure 2. Cement grouted bituminous sample before and after grouting.

4 GROUT

For increasing the flow of mortar, fly ash was introduced in the cement mortar. Three different fly ash contents, 0%, 10% and 20% by weight of cement, were used. Super plasticizer was also used in the water to increase the flow at lower water cement ratios. Trials were made with different water cement ratios for each fly-ash content. Water cement ratios of 0.68, 0.65 and 0.63 were found to be appropriate for 0%, 10% and 20% fly ash contents respectively. Details of compressive and flexural strengths of 7-day cured specimens prepared with different fly-ash contents are given in Table 7.

5 PREPARATION OF CEMENT GROUTED BITUMINOUS MIXES

Aggregates and bitumen were heated to the mixing temperature and were mixed uniformly and poured into split moulds at compaction temperature. The mix was compacted by Marshall hammer by applying 25 blows on one face only to have more voids to allow

Table 8. Marshall, ITS and moisture damage test results.

Gradation type	Marshall stability (kN)	Flow (mm)	ITS value (kPa)	Soaked ITS value (kPa)	Retained ITS (%)
3	30.2	2.3	1034	1019	98.57
4	34.5	1.8	1108	1093	98.62

Figure 3. Beam sample.

sufficient penetration of the grout. The mix was allowed to cool for one day. Next day, cement grout was prepared as per design proportions and was poured on the surface of the bituminous mix sample which was retained inside the mould and vibrated with electrical plate vibrator to allow the grout to penetrate into the voids of bitumen mix. The grouted bituminous samples were allowed to cure. Weights of the samples before and after the grout has penetrated were measured to determine the quantity of grout penetrated. Figure 2 shows the bituminous mix sample before grouting and after grouting.

6 PERFORMANCE TESTS ON CEMENT GROUTED BITUMINOUS MIXES

Tests conducted on the grouted bituminous mix samples are Marshall Test, Indirect tensile strength test, Fatigue test and Static indentation test. VG-30 binder, aggregate gradations 3 and 4, cement mortar (cement sand ratio of 1:1) and water-cement ratio of 0.65 were used to prepare the specimens. 10% of the sand was replaced by Silica fume. 10% of Cement was replaced by fly-ash. Super plasticizer was also used to improve grout penetration. Marshall Stability and flow, and indirect tensile strength were determined. Moisture damage test was also performed. The results are given in Table 8. ITS test was conducted at 25°C temperature.

The Indirect tensile strength values of the grouted bituminous mix are significantly larger compared to typical ITS value that can be expected for normal bituminous mixes. Retained ITS values are also high which shows that cement grouted bituminous mixes are less susceptible to moisture damage.

7 FATIGUE PERFORMANCE OF CEMENT GROUTED BITUMINOUS MIXES

Fatigue failure is one of the major load-related distresses experienced in pavements. Modulus of rupture values of different combinations of grouted bituminous mixes were determined by conducting flexure test on beams of 360 mm × 75 mm × 50 mm size. Samples were cured for 7 days in wet gunny bags after which they were removed from the moulds. Figure 3 shows a

grouted beam along with mould. Modulus of Rupture values were used to select appropriate stress levels for the fatigue test.

To evaluate the fatigue performance of the cement grouted bituminous mixes, beams were tested at different stress ratios. The load was applied at a frequency of 110 rpm. The test was conducted under constant stress mode. Fatigue failure of the cement grouted bituminous mix was identified as the point at which the specimen is unable to take any further load. The load was applied on top of the beam with a repeated load arrangement. Load was measured using a load cell. Fatigue equations were developed for the two aggregate gradations (3 and 4). Results of fatigue test are given in Table 9. Figures 4 and 5 show fatigue relationships between stress ratio and load repetitions to failure for gradations 3 and 4 respectively.

Fatigue relationship for cement grouted bitumen mix prepared using gradation 3 is given as Eq. (1).

$$N = 1136.56\left(\frac{1}{SR}\right)^{11.91} \tag{1}$$

Fatigue relationship for cement grouted bitumen mix prepared using gradation 4 is given by Eq. (2).

Table 9. Beam fatigue test results.

	No of repetitions to failure	
Stress ratio	Gradation 4	Gradation 3
0.965	1650	2200
0.911	5500	5720
0.857	6930	8800
0.804	19800	24420
0.750	39600	43120

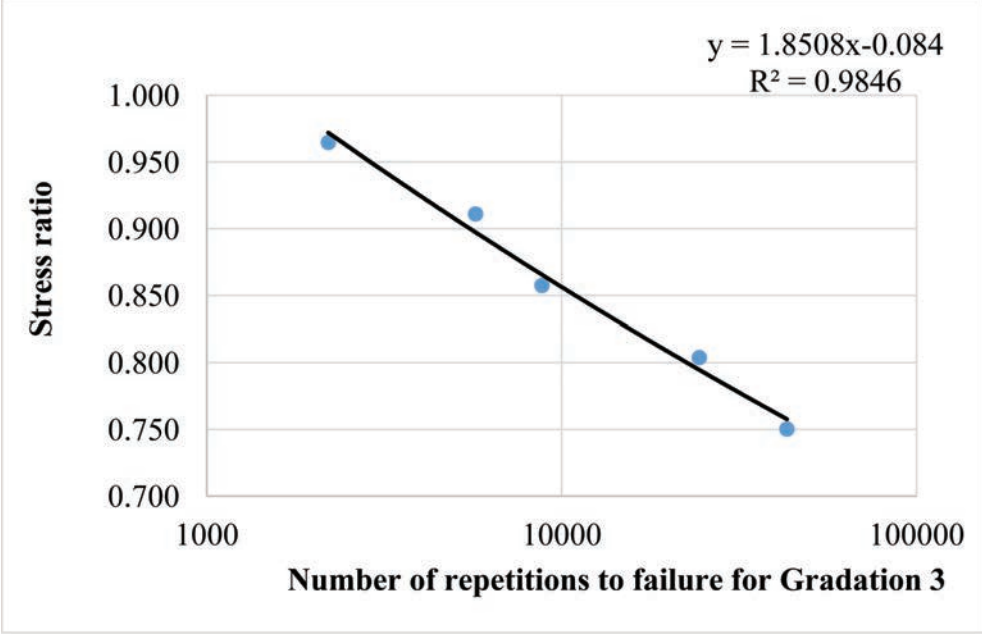

Figure 4. Stress ratio vs no of repetitions to failure for gradation 3.

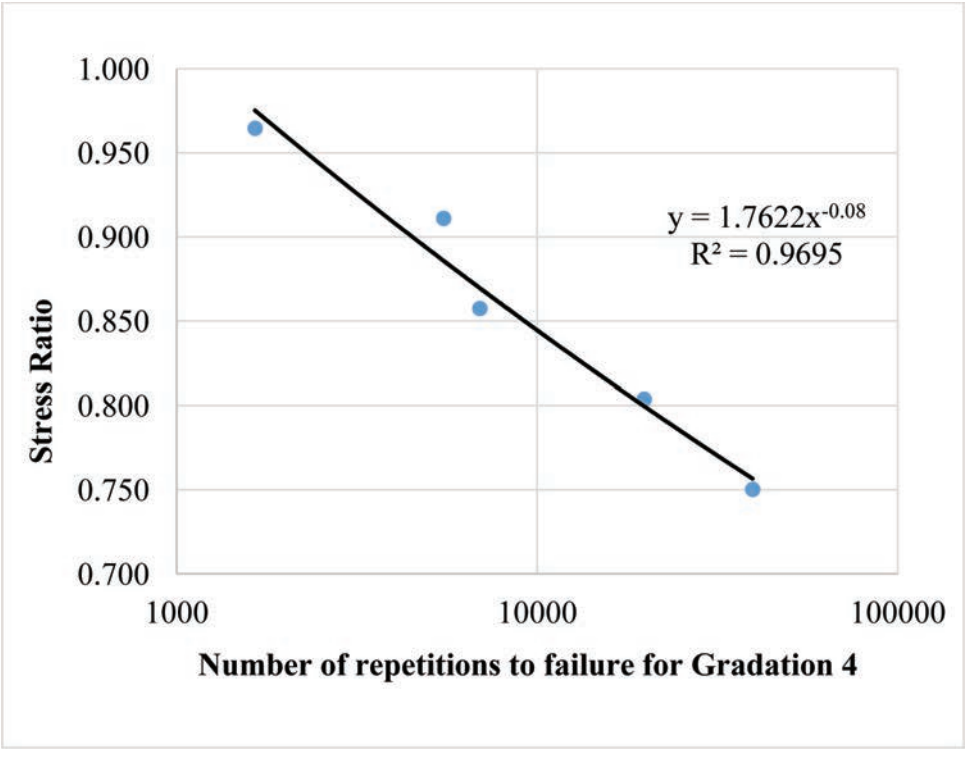

Figure 5. Stress ratio vs no of repetitions to failure for gradation 4.

$$N = 1190.30\left(\frac{1}{SR}\right)^{12.5} \tag{2}$$

8 ELASTIC MODULUS

Elastic modulus of grouted bituminous mix was obtained by measuring the mid-span deflection of the beam in the beam fatigue test. Average elastic moduli of the mix obtained with gradations 3 and 4 are 10575 and 10285 MPa respectively.

9 RUTTING PERFORMANCE OF BITUMINOUS MIXES

Cement grouted bituminous mixes are expected to have good rut resistance. Rutting performance test was conducted using static indentation test. This test was also conducted on traditional Bituminous Concrete (BC) mix for comparing with cement grouted bituminous mixes. This test was conducted at a temperature of 50°C.

9.1 *Static indentation test*

A variety of tests are used to evaluate the rutting resistance of bituminous mixes in laboratory. Creep test is the simplest one to study the permanent deformation characteristics of bituminous materials. In the present study, indentation test was used to determine the permanent deformation behavior of bituminous concrete mixes. In the indentation test [5], a constant load of 0.8 kN is applied through a loading plate of 38 mm diameter which produces a

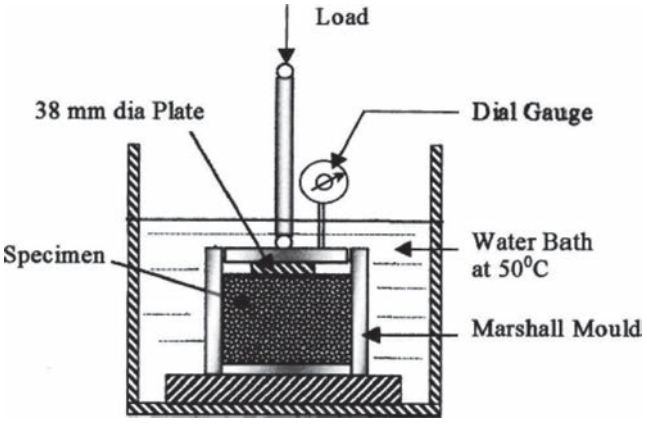

Figure 6. Schematic arrangement of static indentation test method.

Table 10. Static indentations test results.

Gradation type	Total deformation in 0.01 mm (TD)	Permanent deformation in 0.01 mm (PD)	Elastic deformation 0.01 mm (ED)	PD as % of ED	PD as % of TD
BC	35	7.5	27.5	27.2	21.4
Gradation 3	21	2	19	10.6	9.6
Gradation 4	23.5	2.5	21	11.9	10.6

vertical pressure of 700 kPa on one of the flat faces of a cylindrical specimen. A dial gauge was used to measure the vertical deformation of the specimen. Figure 6 shows the schematic arrangement of Static Indentation test method. The results of static indentation test are shown in Table 10.

It can be seen from Table 10 that not only the total deformation got reduced in grouted mixes but the permanent deformation components have also been reduced significantly.

10 CONCLUSIONS

The present investigation clearly demonstrated the superior performance of grouted mixes in terms of rutting, fatigue cracking and moisture damage. The following specific observations are made from the present study.

- The penetration of cement grout in the mix is directly proportional to the air voids in dry aggregates.
- The effect of binder hardness on grout penetration was very less.
- The Marshall stability and Indirect tensile strength values of grouted mixes are significantly larger than typical values obtained with normal mixes.
- High tensile strength ratio suggests satisfactory moisture resistance.
- The rutting performance of cement grouted bituminous mixes very high compared with that of normal bituminous mix.

REFERENCES

[1] Oliveira, J.R.M., Sangiorgi, C., Fattorini, G., and Zoorob, S.E. Investigating the fatigue performance of grouted macadams, Journal of Transport, 162(2), pp. 115–123. 2009.

[2] Ministry of Road Transport and Highways. Specifications for road and bridge works, Fourth revision. Indian Roads Congress, New Delhi, 2001.
[3] IS-12269, Indian Standard specification for 53 grade ordinary Portland cement, The Bureau of Indian standards, New Delhi, 1987.
[4] Asphalt Institute, Mix design method for asphalt concrete and other Hot-Mix types, Asphalt Institute, Lexington, 1995.
[5] Palit, S., Reddy, K., and Pandey, B. Laboratory Evaluation of Crumb Rubber Modified Asphalt Mixes. J. Mater. Civ. Eng., 16(1), pp. 45–53. 2004.

Modeling of asphaltic materials and pavements

This page intentionally left blank

Asphalt Pavements – Kim (Ed)
© 2014 Taylor & Francis Group, London, ISBN 978-1-138-02693-3

Aging and constitutive modeling of asphalt mixtures: Research developments in Brazil

Lucas F. de A.L. Babadopulos, Jorge Barbosa Soares & Verônica T.F. Castelo Branco
Laboratório de Mecânica dos Pavimentos da Universidade Federal do Ceará (LMP/UFC), Departamento de Engenharia de Transportes, Fortaleza-CE, Brazil

ABSTRACT: The use of complex modulus for asphalt mixture characterization is still restricted to special projects in Brazil. Nevertheless it is recognized the importance of leveling ongoing national research efforts towards a new pavement design methodology with international state-of-the-art developments. The work presented herein concentrates on testing and analysis procedures for characterizing stiffness of asphalts mixtures considering its properties dependency on aging evolution. It uses an existing aging phenomenological model and it also proposes an aging experimental procedure. The referred model utilizes an internal state variable and four materials constants. Coupling the aging and well-established linear viscoelastic models, storage and loss moduli results at two different aging states are predicted. A simulation of the change in dynamic modulus with time (aging) is also presented to illustrate the potential of the modeling approach. This work is part of a continuing research at *Universidade Federal do Ceará*, at Fortaleza, Brazil, involving extended aging times, methodology, materials and further modeling efforts.

Keywords: aging, asphalt mixture, stiffness, complex modulus, modeling

1 INTRODUCTION

Asphalt mixture mechanical characterization in Brazil is today primarily based on resilient modulus and indirect tensile strength tests. There is still no national standard for fatigue or permanent deformation mixture characterization. In some specific situations, especially in road concessions to the private industry, controlled-stress diametral compression test at only room temperature is used for the former, and laboratory traffic simulators or dynamic creep (Flow Number) is used for the latter. Brazil is currently undergoing a national effort to develop its own mechanistic-empirical pavement design method, based on a national pavement material database and on the performance of test sections monitored around the country. A first version of the design guide is planned for 2016.

When it comes to mixture characterization in Brazil, the use of complex modulus is still restricted to academia and research centers. Therefore, it should not be considered in this first phase of the design method, which is being planned in such a way to be systematically updated. For that reason, it is recognized the importance of leveling the country's research with international state-of-the-art developments. In this context, the present work deals with the improvement of test and analysis procedures for the characterization of asphalt mixtures considering their properties dependency on aging evolution.

There is no worldwide consensus on a procedure for the characterization of fatigue in asphalt mixtures, although it is considered a major pavement distress. There is also no widely accepted aging model or experimental procedure to take into account this phenomenon in fatigue characterization, despite extensive literature comments on its influence. This paper is focused in modeling the behavior of asphalt mixtures under small strains, aiming at the stiffness characterization and at the incorporation of aging considerations. The authors believe

that the presented approach is an important step towards more sophisticated stiffness and fatigue characterization of mixtures in the Brazilian pavement design procedure. The research is part of a broader project related to the development of the new Brazilian mechanistic-empirical pavement design method. At this point, only data for early ages (2 days of aging) at two different temperatures (85 and 135ºC) were available. Aging was induced to loose asphalt mixture, in a procedure adapted from Partl et al. [1].

In literature, some works have presented viscoelastic models which included aging time as a variable (Daniel et al., [2]; Michalica et al., [3]) in addition to loading time (or frequency). However, these models are not conceived to allow easy coupling of aging to other mechanical characteristics of the asphalt mixture, such as viscoplasticity or damage. This has motivated the use of the aging phenomenological model proposed by Al-Rub et al. [4]. The referred approach couples aging to linear viscoelastic, viscoplastic and damage responses of asphalt mixtures. The model utilizes an internal state variable, whose evolution depends on oxygen availability, temperature, and four materials parameters. Those parameters are related to aging susceptibility, reaction kinetics, and aging history and temperature dependency. It allows to establish a relation between the difference of aging time and the difference of temperature in two different aging processes under the same oxygen availability. The material constants are obtained by minimizing model prediction square errors with respect to experimental results. Complex modulus results can be used to fit linear viscoelastic models at different aging states. The comparison between the linear viscoelastic parameters obtained at the different aging states allows the identification of the aging model parameters along with the linear viscoelastic parameters aging sensitivity. With the fitted aging model parameters, the nonlinear and the damage aging sensitivity can be estimated comparing experimental results obtained at different aging states, as shown by Al-Rub et al. [4]. This is the object of an ongoing research project conducted by the authors, and this paper presents the first aging results obtained. An aging experimental procedure is also proposed for asphalt mixtures herein as a contribution of the present research under development in Brazil.

2 LITERATURE REVIEW

2.1 *Linear viscoelasticity*

In this paper, mechanical analogs are used to fit linear viscoelastic models to experimental data. The Generalized Maxwell-Wiechert model was fitted to storage modulus following a Linear Least Squares Method, and then the Generalized Kelvin-Voigt model was generated by an interconversion procedure (Park and Schapery, [5]). These models are commonly referred to as Prony series models, and are often used to represent the linear viscoelastic behavior of solid continuum media, e.g., bituminous materials. The Maxwell-Wiechert model gives a Prony series for the relaxation modulus defined by the parameters E_∞, E_i's, and ρ_i's, while the Kelvin-Voigt does the same for the creep compliance, whose Prony series is defined by the parameters D_0, D_j's, and τ_j's. These properties are given in the time domain, and designated transient. However, it is more practical to perform experiments in the frequency domain, due to time consuming and difficulty with respect to linearity limits typical from time domain tests. In such case, the complex modulus (E^*) is used. For viscoelastic materials, the strain signal is delayed from the stress signal by a quantity known as the phase angle (φ). Using Euler's formula for complex exponentials, E^* is given by the ratio between stress and strain during a harmonic oscillation:

$$E^* = \frac{\sigma^*}{\varepsilon^*} = \frac{\sigma_0 e^{i(\omega t-\varphi)}}{\varepsilon_0 e^{i\omega t}} = \frac{\sigma_0}{\varepsilon_0} e^{i\varphi} = |E^*| e^{i\varphi} = |E^*|(\cos\varphi + i\sin\varphi) = E' + iE'' \quad (1)$$

where $i = \sqrt{-1}$.

$E' = |E^*| \cos\varphi$, known as the storage modulus, is associated to the stored portion of mechanical energy during harmonic loading. $E'' = |E^*| \sin\varphi$ is the loss modulus, associated

to the dissipated portion. The angular frequency ω represents the pulsation (rad/s), and it is directly related to the loading frequency f (Hz), as $\omega = 2\pi f$. The parameter $|E^*|$ is referred to as the dynamic modulus, although it does not deal with inertial properties. It grows with the increase in loading frequency and decreases with growing temperature. $|E^*|$, along with φ, describes the behavior of linear viscoelastic materials in the frequency domain.

For an asphalt mixture, a composite heterogeneous material, the interlocking provided by the aggregates provides to the phase angle a non monotonic trend with the change in temperature (or frequency). Generally, for low frequencies and high temperatures, φ grows with loading frequency, whereas for high frequencies and low temperatures the inverse occurs (Clyne et al., [6]; Flintsch et al., [7]). This phenomenon can be explained by the fact that the elastic behavior ($\varphi = 0°$) of the aggregates influences more the material's response when the asphalt binder is softer, i.e., at low frequencies and high temperatures. At those conditions, a decrease in frequency leads to a more elastic response, because aggregates participation in the material's behavior becomes more important: φ decreases.

Assuming the generalized Maxwell model, the storage (E') and the loss (E'') moduli are calculated from Eq. (2) and Eq. (3), respectively.

$$E' = E_\infty + \sum_{i=1}^{n} E_i \frac{\omega^2 \rho_i^2}{1 + \omega^2 \rho_i^2} \tag{2}$$

$$E'' = \sum_{i=1}^{n} E_i \frac{\omega \rho_i}{1 + \omega^2 \rho_i^2} \tag{3}$$

In this paper, a least squares optimization based on Eq. (2) was used with assumed relaxation times (ρ's) and long-term modulus (E_∞). It consists of the minimization of the Cost Function described by $C(E_i) = \left[E'_{experimental} - \left(E_\infty + \sum_{i=1}^{n} E_i \frac{\omega^2 \rho_i^2}{1 + \omega^2 \rho_i^2} \right) \right]^2$. This is presented in detail by Babadopulos [8] and it is analogous to equations provided in Silva [9]. The resulting equation from the optimization of the cost function leads to a system of linear equations. Eq. (4) summarizes the fitting procedure:

$$\sum_{i=1}^{n} \sum_{k=1}^{n} \left[\left(\frac{\omega k^2 \rho_i^2}{1 + \omega k^2 \rho_i^2} \right) \cdot \left(\frac{\omega k^2 \rho_j^2}{1 + \omega k^2 \rho_j^2} \right) \cdot E_i \right] = \sum_{k=1}^{M} \left[(E_k - E_\infty) \cdot \left(\frac{\omega k^2 \rho_i^2}{1 + \omega k^2 \rho_i^2} \right) \right] \tag{4}$$

The value of the long-term modulus (E_∞) is meant to be assumed lower than the lowest obtained modulus. Eq. (4) represents the algebraic linear system whose solution is the set of stiffness constants associated to the preestablished time constants in order to fit E' (frequency domain) experimental results using a linear least squares method. It is capable of considering all M experimental points (ω_k, E_k). The dummy variable (index) j represents the lines of the linear system to solve, and it varies from 1 to n (number of elements in the Prony series). Although E'' is not used in the fitting procedure, it can be used to verify the goodness of fit, comparing experimental to predicted results from Eq. (3). Then, the procedure proposed by Park and Schapery (1999) to interconvert the relaxation modulus discrete spectrum (E_∞, E_i's, ρ_i's) into a creep compliance discrete spectrum (D_0, D_j's, τ_j's) can be applied. Having both Prony series (relaxation and creep), allows one to model both strain input and stress input problems in linear viscoelasticity.

2.2 *Aging*

Since the production, asphalt binders are subjected to conditions which induce a change in their mechanical properties. Volatilization of light fractions produces physical aging. There is also oxidative aging, induced by irreversible chemical reactions of the binder with diffused oxygen in its volume. Binder aging is largely reported in the open literature, with relevant contributions made four decades ago (Lee and Huang, [10]; Lau et al., [11]; Petersen et al.,

[12]). On the other hand, constitutive modeling of asphalt mixtures aging is a relatively undeveloped subject. In Brazil, an attempt to include aging in constitutive modeling of asphalt mixtures is undergoing at *Universidade Federal do Ceará*. Different laboratory mixture aging methods are being considered, and mixture properties are subsequently obtained.

Al-Rub et al. [4] proposed a phenomenological mechanistic-based aging model which is conceptually similar to the chemical pressure- and temperature-dependent aging models for binders, which predict the basic carbonyl reaction rate. It establishes a general law for the evolution of an aging internal state variable and, then, couples its value to the effects of aging, i.e., change in mechanical properties such as viscoelastic, viscoplastic and damage characteristics. The general expression for the model is as follows:

$$\dot{A} = \Gamma^{\alpha}\theta^{k_1}(1-A)k_2 exp\left[-k_2\left(1-\frac{T}{T_0}\right)\right] \tag{5}$$

where A is the aging internal state variable, $\dot{A}$ its time derivative, θ is the normalized oxygen content (between 0 and 1), T_0 the reference aging absolute temperature, and T the actual absolute temperature. The four aging model parameters are the aging dependency on normalized oxygen content k_1, the aging history dependency k_2, the aging temperature dependency k_3, and the aging fluidity parameter Γ^{α}. The last one is given in s^{-1} and its inverse can be interpreted as a relaxation time for the aging process, i.e., time necessary for a fixed change in the original value of the aging variable. The aging internal state variable ranges from zero to 1, with $A = 0$ representing an unaged material, whereas $A = 1$ represents a completely aged material. This model can be simplified, assuming the material to be saturated ($\theta = 1$), $k_2 = 1$, and integrating it. The result is shown in Eq. (6).

$$A = 1 - (1 - A_0)e^{-ct} \tag{6}$$

where A_0 is the value of the aging state variable in the beginning of the aging process ($A_0 = A(t)_{t=0}$) and $c = \Gamma^{\alpha} exp[-k_2(1 - T/T_0)]$. The product $t' = ct$ can be seen as a reduced aging time, taking aging temperature into account. This simplified model is the one used to fit the experimental data in this paper.

The aging model can be coupled in the constitutive modeling of asphalt mixtures as shown by Al-Rub et al. [4]. For the coupling to linear viscoelasticity, the referred authors used the creep compliance discrete spectra at different aging states. In the present paper, the relaxation modulus discrete spectra were used. Eqs. (7a, 7b, 7c) represent the coupling between linear viscoelasticity and the aging of the material.

$$(E_{\infty})_A = (1 - A_0)^{-\alpha_1} \cdot E_{\infty}; (E_i)_A = (1 - A_0)^{-\alpha_1} \cdot E_i; \tag{7a,7b}$$

$$(\rho_i)_A = (1 - A_0)^{-\alpha_1} \cdot \rho_i \tag{7c}$$

The subscript A indicates the aged state. The model parameters represent the relaxation spectrum susceptibility with respect to aging (α_1 for the elastic modulus, α_2 for the transient modulus, and α_3 for the relaxation times).

3 MATERIALS AND METHODS

3.1 *Reference asphalt mixture*

The asphalt mixture investigated is a dense asphalt concrete with 12.5 mm nominal maximum aggregate size. The binder is classified by penetration as a 50/70. For the designed air voids content (4%), the required binder content was 6.0% (by weight). The resulting maximum theoretical density (Gmm) determined by the Rice test was 2.3915 g/cm³ (average results for three samples).

The materials tested in this paper are the reference unaged mixture (Age Zero), and two mixtures resulting from aging (designated Age 2, because of the 2 days aging time in the oven) at different temperatures (Age 2, 85ºC and Age 2, 135ºC). Testing different temperatures allows to identify the mixture aging sensitivity with respect to aging temperature, which constitutes a contribution with respect to the results originally presented by Al-Rub et al. [4], where aging temperature dependency was not evaluated. The Gmm changed with aging, resulting in 2.4025 g/cm³ for Age 2, 85ºC and 2.4017 g/cm³ for Age 2, 135ºC.

3.2 *Aging procedure*

Short-term aging was simulated at 150ºC, for 2 h. For the long-term aging simulation, aging was induced to the loose asphalt mixture, using a procedure inspired by a RILEM protocol described in the work edited by Partl et al. [1]. In order to normalize aging conditions, identical cooking trays (30 × 50 × 8 cm) containing asphalt mixture were maintained in the oven at the desired aging temperature. Equal quantities of material (three batches of 3.5 kg, i.e., 10.5 kg) were stored in each tray, in order to have always approximately the same height.

Sample preparation in the Superpave Gyratory Compactor was set to stop at a fixed height, targeting 150 mm, as the number of gyrations necessary to produce samples with 4% air voids could change due to the bitumen viscosity variation induced by aging. Final heights near to 150 mm were obtained, using approximately 2.630 kg of mixture to prepare each sample. Samples were not cored or cut, but used directly from gyratory compaction in the mechanical tests. For each aging condition (Age Zero; Age 2, 85ºC; and Age 2, 135ºC), 15 samples were prepared following the described procedure. The obtained mean air void contents were 4.3, 4.5 and 4.7%, respectively.

4 RESULTS AND DISCUSSION

In this section, the experimental results (dynamic modulus and phase angle) are described and compared. The procedure to fit the adopted linear viscoelastic and aging models is also described, and the resulting parameters are presented. A comparison is made between model prediction and experimental results. At the end, a brief aging simulation is performed, showing the estimated change of the mixture stiffness, according to the fitted aging model.

4.1 *Stiffness characterization*

AASHTO TP62-03 [13] was the test protocol adopted for HMA stiffness characterization. The results are shown in master curves for both $|E^*|$and φ, as indicated in Figures 1a and 1b, respectively. Mean results were obtained from four tests in samples of 100 mm diameter by

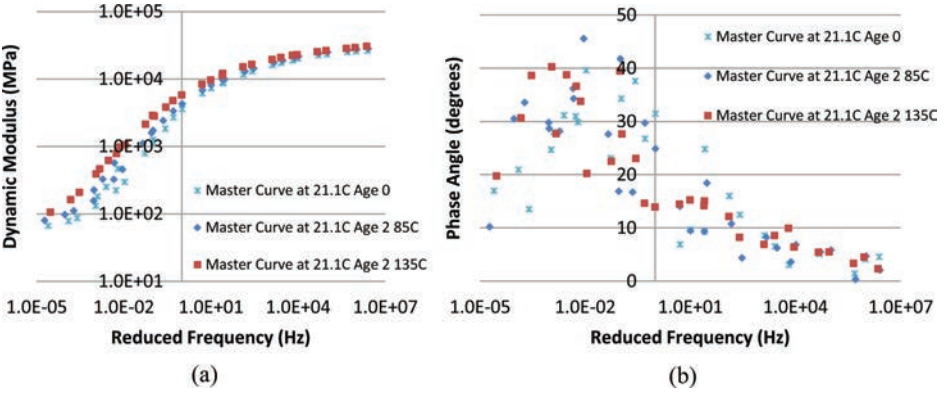

Figure 1. Dynamic modulus (a) and phase angle (b) master curves for the three tested aging states.

150 mm height, using three axial LVDTs mounted 120º apart on the surface of the sample, around its circumference. Fingerprint tests (short-time complex modulus tests, at very small strain amplitudes) were conducted in order to select the load pulse to be tested. A strain amplitude of 67.5 με was the target, expecting to reach strain amplitudes in the interval between 60 and 75 με. At this strain levels, linearity conditions should be respected and negligible strain dependency (nonlinearity) observed. The master curves for each aging state were obtained after horizontally shifting the isotherms, using a WLF Law (Williams et al., [14]).

In Figure 1a, it can be seen that $|E^*|$ gradually increases as aging evolves. In logarithmic scale (Fig. 1a), the dynamic modulus at low reduced frequencies (or high temperatures) seems to be much more affected by aging then at high reduced frequencies, as observed by other authors (Glover et al., [15]). This means that the percentage change in dynamic modulus is higher at low reduced frequencies. The scatter of φ results may not present a clear trend for the phase angle as aging evolves, as seen in Figure 1b, at least for the beginning of the aging process. The expected trend with respect to aging evolution was a decrease in φ.

4.2 *Linear viscoelasticity modeling*

The fitting procedure for linear viscoelasticity experimental data was the one presented in the Literature Review. At first, a pre-smoothing procedure using a sigmoidal function was tried, but significant prediction inaccuracy was observed for frequencies below 10^{-3} Hz at 21.1ºC. So, direct fitting to the data was used and resulted in acceptable results for the cases analyzed. One elastic term (long-term modulus, E_∞) and eleven transient terms (pairs E_i, ρ_i) were used to fit the storage modulus ($E'' = |E^*| \cdot cos\varphi$) experimental data. The same set of relaxation times (ρ_i), a decade apart one from another, was used for fitting all asphalt mixtures data, varying only the stiffness parameters (E_i's). The results are the discrete relaxation spectra of the tested asphalt mixture at different aging conditions, which describe its linear viscoelastic behavior, and can be used to simulate any kind of loading path that do not cause material nonlinearities (such as plasticity or damage). Then, the procedure proposed by Park and Schapery [5] to interconvert the relaxation modulus discrete spectrum (E_∞, E_i's, ρ_i's) into a creep compliance discrete spectrum (D_0, D_j's, τ_j's) was applied. The obtained discrete spectra (relaxation modulus and creep compliance) for the three aging states tested in this work are presented in Table 1.

The linear viscoelastic models summarized in Table 1 presented a satisfactory fitting to the experimental data. The good fitting was observed both for the storage modulus E' (fitting input) and the loss modulus E'' (not the fitting input), as seen in Figure 2. This indicates that linearity limits were respected during laboratory tests.

Table 1. Discrete spectra for the three evaluated aging states.

	Age Zero	Age 2, 85ºC	Age 2, 135ºC		Age Zero	Age 2, 85ºC	Age 2, 135ºC
E_∞ (MPa) =	60	75	90	D_0 (MPa^{-1}) =	3.74E-05	3.48E-05	3.15E-05
ρ_i (s)	E_i (MPa)	E_i (MPa)	E_i (MPa)	τ_j (s)	D_j (MPa^{-1})	D_j (MPa^{-1})	D_j (MPa^{-1})
1.00E-07	1.62E+03	1.90E+03	3.29E+03	1.00E-07	2.21E-06	2.25E-06	3.24E-06
1.00E-06	2.65E+03	2.78E+03	2.88E+03	1.00E-06	4.34E-06	4.01E-06	4.11E-06
1.00E-05	3.87E+03	4.20E+03	3.66E+03	1.00E-05	8.00E-06	7.58E-06	5.69E-06
1.00E-04	4.67E+03	4.66E+03	4.09E+03	1.00E-04	1.47E-05	1.32E-05	9.53E-06
1.00E-03	4.82E+03	4.89E+03	5.17E+03	1.00E-03	3.01E-05	2.47E-05	1.75E-05
1.00E-02	2.84E+03	3.48E+03	4.50E+03	1.00E-02	4.27E-05	3.92E-05	3.45E-05
1.00E-01	4.42E+03	4.11E+03	3.70E+03	1.00E-01	7.79E-05	8.00E-05	6.18E-05
1.00E+00	1.32E+03	1.81E+03	2.87E+03	1.00E+00	4.44E-04	2.88E-04	1.50E-04
1.00E+01	3.02E+02	6.35E+02	9.51E+02	1.00E+01	1.59E-03	8.50E-04	5.44E-04
1.00E+02	1.45E+02	1.54E+02	4.52E+02	1.00E+02	3.63E-03	3.10E-03	9.95E-04
1.00E+03	3.02E+01	6.05E+01	7.08E+01	1.00E+03	1.04E-02	7.34E-03	7.64E-03

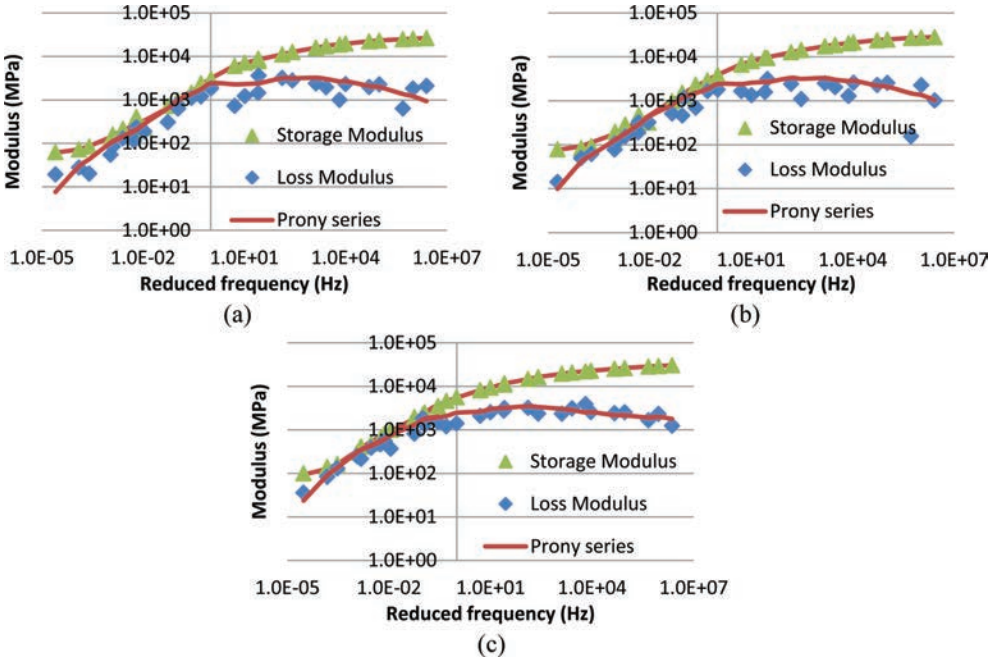

Figure 2. Measured and modeled (Prony series) storage and loss moduli for (a) Age Zero, (b) Age 2, 85ºC and (c) Age 2, 135ºC.

4.3 *Aging modeling*

In this section, the previously obtained viscoelastic models are considered as inputs for the aging modeling. In this work, aging modeling consists in determining the best set of parameters, with respect to experimental data, for the simplified model presented in the Literature Review: the reference temperature (T_0), the aging fluidity parameter (Γ^{α}), the initial aging state (A_0), the aging temperature dependency (k_3), and the relaxation spectra susceptibility with respect to aging (α_1 for the elastic modulus, α_2 for the transient modulus and α_3 for the relaxation times). The optimization of the aging oxygen availability dependency (k_1) and the aging history dependency (k_2) were not pursued for this work. They were assumed to be equal to 0.15 (as Al-Rub et al., [4] assumed) and 1 (to simplify calculation), respectively. The reference temperature (T_0) was taken as 21.1ºC.

The first step for the aging model fitting is the estimation of the values of the aging state variable (A), to which the aging process has led the asphalt mixtures to present at each aging condition. In this work, the initial aging state (A_0) was assumed to be zero, as Age Zero was taken as the beginning of the aging process. However, A_0 could be assumed to have a value different from zero, accounting for short-term aging (Al-Rub, [4]), and this would mean that the initial aging state occurred before the one referred to in this paper as Age Zero.

The parameter α_3, which accounts for the aging susceptibility of the relaxation time, was assumed to be zero ($\alpha_3 = 0$), as the magnitudes of the discrete spectra were obtained at exactly the same relaxation times, in a manner that they did not vary with respect to the aging state. As the elastic (E_∞) and the transient (E_i's) magnitudes did vary with respect to the aging state (A), the ratios between aged and unaged magnitudes were used as indicators of the aging state change. In addition, the aging susceptibility of the elastic and the transient relaxation magnitudes are given by α_1 and α_2, respectively.

Therefore, if the relaxation magnitudes are to be modeled using the unaged relaxation spectra and the aging model, the least squares method can be applied to minimize the error in the model prediction, varying the values of the aging state variable ($A_{2,85ºC}$ and $A_{2,135ºC}$) and the elastic and transient aging susceptibility. The procedure was carried out using Solver

and the obtained results were $\alpha_1 = 0.58$, $\alpha_2 = 0.94$, $A_{2,\ 85°C} = 0.228$ and $A_{2,135°C} = 0.449$. With the obtained aging state variable values ($A_{2,\ 85°C} = 0.228$ and $A_{2,135°C} = 0.449$), the aging model could be fitted by the determination of optimal $\Gamma^{\alpha</I>} = 9.95 \times 10^{-7}\ s^{-1}$ *and* $k_3 = 3.03$. The summary of the results is presented in Table 2.

Combining the aging model, whose parameters are presented in Table 2, with the linear viscoelastic model, whose parameters are presented in Table 1, one can represent all data of this paper. Figure 3 presents the comparison between experimental storage and loss moduli results at both aging states and the results predicted by the combination of Prony series and aging model.

It can be seen that the aging model, combined with the unaged discrete relaxation spectrum, can fit stiffness experimental data for asphalt mixtures, at least for early ages. Al-Rub et al. [4] used experimental data from the work done by Walubita [16], fitting an aging model for data covering up to 6 months of aging of compacted mixtures at 60ºC. Those authors evaluated two asphalt mixtures, obtaining Γ^{α} of 3.33 and $9.30 \times 10^{-7}\ s^{-1}$, i.e., the same order of magnitude found in the present paper. Al-Rub et al. [4] stated that Γ^{α} is used as an indicator of mixtures susceptibility to oxidative aging, because $1/\Gamma^{\alpha}$ could be regarded as a "relaxation time" for the aging. In this paper, temperature dependency was captured, because data was generated using aging at two different temperatures. Data for longer aging times will soon be available as part of the ongoing research effort at *Universidade Federal do Ceará*, at Fortaleza, Brazil.

4.4 *Aging simulation*

To present the main contribution of an aging model representing asphalt materials mechanical properties evolving with aging time, a few analytical simulations were performed. In the simulations the percent change in the Dynamic Modulus is presented as time passes during aging at a constant temperature. Different aging temperatures were evaluated, from 40 to 150°C. Results were summarized in Figure 4.

It can be seen that the fitted model predicts that a 40% increase in $|E^*|$ occurs at approximately 2.8×10^5, 2.4×10^5, 1.9×10^5, 1.1×10^5 and 0.9×10^5 s, for 40, 60, 85, 135 and 150°C, respectively. This corresponds to the following aging times, in days: 3.2, 2.8, 2.2, 1.3 and 1 day. For a given aging time, for example, 2 days, the predicted percent increases in $|E^*|$ are approximately 22, 26, 36, 68 and 75. In other words, it can be said that, based on some observations of the consequences of aging (change in moduli master curves in the case of this paper) at few aging states, a phenomenological aging model based on an internal state

Table 2. Result for the fitted aging model to the studied mixture.

Γ^{α} (1/s)	A_0 ( )	k_1 ( )	k_2 ( )	k_3 ( )	α_1 ( )	α_2 ( )	α_3 ( )	T_0 (ºC)
9.95×10^{-7}	0.00	0.15	1.00	3.03	0.58	0.94	0.00	21.1

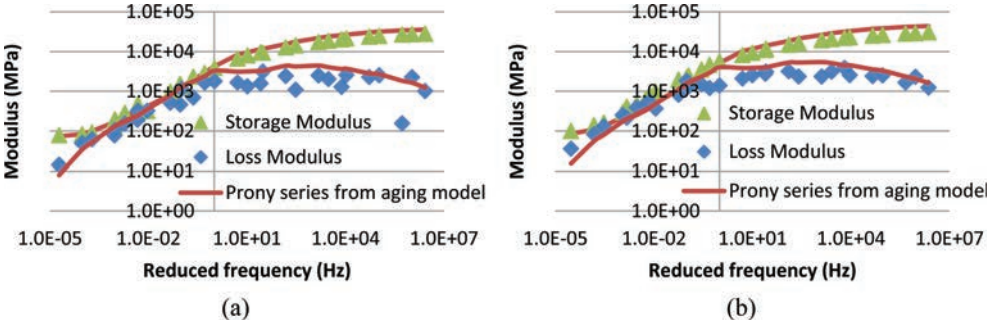

Figure 3. Measured and modeled (Prony series combined to aging model) storage and loss moduli for (a) Age 2, 85ºC and (b) Age 2, 135ºC.

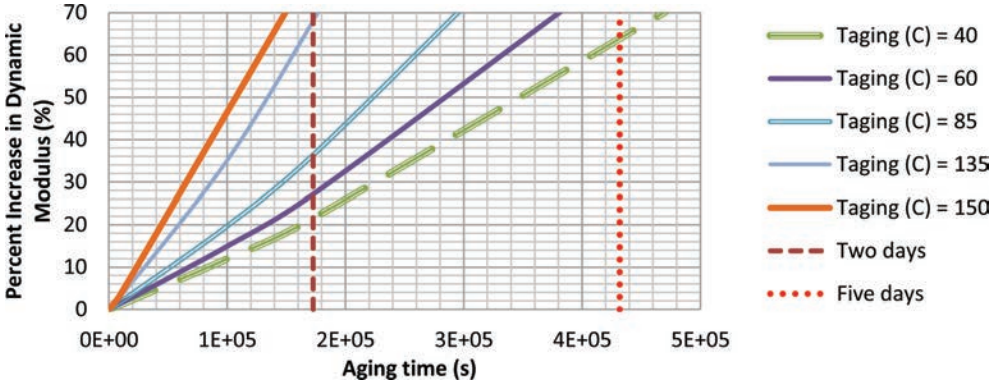

Figure 4. Aging simulation at constant aging temperatures: 40, 60, 85, 135, 150ºC.

variable can associate aging time and aging temperature. The aging model predicts the value of the aging internal state variable (A) and it is then coupled to the aging consequences using the susceptibility parameters (α_i's). This gives the aging model the ability to predict the evolution of the mechanical properties, such as the Storage and the Loss Moduli, of asphalt mixtures. It is observed that this could be analogously done for viscoplasticity and damage as well, as presented by Al-Rub [4]. It is to be noticed that only two aging times were evaluated to this point of the research and could lead to prediction errors. A more comprehensive fitting will be produced with further data.

5 CONCLUSIONS

This paper uses an existing phenomenological model to study the aging effect on linear viscoelastic properties of asphalt mixtures. The referred aging model utilizes an internal state variable and four materials parameters. An aging experimental procedure inspired by a RILEM protocol is presented as part of a broader research effort under development in Brazil related to the country's new mechanistic-empirical pavement design method to be launched in 2016. Different aging temperatures allowed to identify the mixture aging sensitivity with respect to aging temperature, which constitutes a contribution with respect to the results originally presented by Al-Rub et al. [4], where aging temperature dependency was not evaluated. Concerning the aging model fitted in this paper, the material constants were obtained by minimizing square errors of the model compared to dynamic modulus experimental results at different aging states. A well-established procedure was used to fit the curves (Prony series) directly to experimental results (linear viscoelastic model), without pre-smoothing the data. The same relaxation times (ρ_i) were used for fitting all storage moduli (E')—aged and unaged mixtures—varying only the stiffness coefficients (E_i's). Combining the aging and the linear viscoelastic models, storage and loss moduli results at two different aging states were satisfactorily predicted. At the end, a simulation of the change in dynamic modulus with time (aging) was performed to show the potential of the coupled modeling approach. Data for extended aging times are being collected at *Universidade Federal do Ceará*, Brazil, and will be presented along with further modeling efforts in future papers by the authors and their research group.

REFERENCES

[1] Partl, M.N.; Bahia, H.U.; Canestrari, F.; de la Roche, C.; Di Benedetto, H.; Piber, H.; Sybilski, D. (Eds.). Advances in Interlaboratory Testing and Evaluation of Bituminous Materials. Report STAR 206-ATB. Unedited version of State-of-the-Art Report of the RILEM Technical Committee 206-ATB. p. 417. 2012.

[2] Daniel, J.S.; Kim, Y.R.; Lee, H.J. Effects of Aging on Viscoelastic Properties of Asphalt-Aggregate Mixtures. Transportation Research Record, 1630, Transportation Research Board, National Research Council, Washington, D.C. pp. 21–27. 1998.
[3] Michalica, P.; Kazatchkov, I.B.; Stastna, J.; Zanzotto, L. Relationship between chemical and rheological properties of two asphalts of different origins, Fuel, 87, pp. 3247–3253. 2008.
[4] Al-Rub, R.K.A.; Darabi, M.K.; Kim, S-M.; Little, D.N.; Glover, C. J. Mechanistic-based constitutive modeling of oxidative aging in aging-susceptible materials and its effect on the damage potential of asphalt concrete. Construction and Building Materials. 41, pp. 439–454. 2013.
[5] Park, S.W., Schapery, R.A., 1999. Methods of interconversion between linear viscoelastic material functions. Part I—a numerical method based on Prony series. International Journal of Solids and Structures, 36, pp. 1653–1675.
[6] Clyne, T.R.; Li, X.; Marasteanu, M.O.; and Skok, E.L. Dynamic and Resilient Modulus of MN/DOT Asphalt Mixtures. MN/RC-2003-09. Minnesota Department of Transportation, Minneapolis. 2003.
[7] Flintsch, G.W.; Al-Qadi, I.L.; Loulizi, A.; Mokarem, D. Laboratory Tests for Hot-Mix Asphalt Characterization in Virginia. VTRC 05-CR22. Virginia Transportation Research Council, Charlottesville. 2005.
[8] Babadopulos, L.F.A.L. Avaliação do Modelo Viscoelástico Linear Aplicado a Misturas Asfálticas Utilizadas em Revestimentos de Pavimentos no Brasil. Projeto de Graduação. Curso de Engenharia Civil da Universidade Federal do Ceará. Fortaleza. 2013. In Portuguese.
[9] Silva, H.N. Caracterização viscoelástica linear de misturas asfálticas: Operacionalização Computacional e Análise pelo Método dos Elementos Finitos. Dissertação de Mestrado, Programa de Pós-Graduação em Engenharia de Transportes, UFC. 2009.
[10] Lee, D.Y.; Huang, R.J. Weathering of Asphalts as Characterized by Infrared Multiple Internal Reflection Spectra. Anal. Chem., 46, p. 2242. 1973.
[11] Lau, C.K.; Lunsford, K.M.; Glover, C.J.; Davison, R.R.; Bullin, J.A. Reaction Rates and Hardening Susceptibilities as Determined from POV Aging of Asphalts. Transp. Res. Rec., 1342, pp. 50–57. 1992.
[12] Petersen, J.C., Branthaver, J.F.; Robertson, R.E.; Harnsberger, P.M.; Duvall, J.J.; Ensley, E.K. Effects of Physicochemical Factors on Asphalt Oxidation Kinetics. Transp. Res. Rec., 1391, pp. 1–10. 1993.
[13] AASHTO TP 62-03 Standard Method of Test for Determining Dynamic Modulus of Hot Mix Asphalt (HMA), American Association of State Highway and Transportation Officials, Washington, D.C. 2005.
[14] Williams, M.L.; Landel, R.F.; Ferry, J.D. The Temperature Dependence Relaxation Mechanism in Amorphous Polymers and other Glass Forming Liquids. Journal of ACS, 77, pp 3701. 1955.
[15] Glover, C.J.; Martin, A.E.; Chowdhury, A.; Han, R.; Prapaitrakul, N; Jin, X.; and Lawrence, J. Evaluation of Binder Aging and its Influence in Aging of Hot Mix Asphalt Concrete: Literature Review and Experimental Design. Report No. FHWA/TX-08/0-6009-1. 2008.
[16] Walubita, L.F. Comparison of Fatigue Analysis Approaches for Predicting Fatigue Lives of Hot Mix Asphalt Concrete Mixtures (HMA). Ph.D. Dissertation, Texas A&M University, College Station, TX. 2006.

Asphalt Pavements – Kim (Ed)
© 2014 Taylor & Francis Group, London, ISBN 978-1-138-02693-3

Evaluation of the fatigue performance of asphalt mixtures with high RAP content

Amirhossein Norouzi, Mohammadreza Sabouri & Y. Richard Kim
Department of Civil, Construction and Environmental Engineering, Raleigh, NC, USA

ABSTRACT: Reclaimed Asphalt Pavement (RAP) has been used successfully in asphalt pavements at percentages up to 20 percent. The main problem that prevents transportation agencies from incorporating higher percentages of RAP is that high RAP contents may result in mixtures that are overly stiff and prone to fatigue cracking. In this study, the previously developed fatigue failure criterion for the Viscoelastic Continuum Damage (VECD) model, the G^R method, is used to evaluate the effect of incorporating high percentages of RAP on the fatigue cracking behavior of two different sets of plant-produced mixtures, referred to in this study as the VTe and MIT mixes. Incorporating high percentages of RAP into the VTe mixtures did not lead to a significant difference in fatigue resistance, which may suggest that the blending of RAP binder and virgin binder works as well as virgin binder alone. However, for the MIT mixtures, an increase in the percentage of RAP to 50 percent led to a considerable decrease in fatigue resistance, which was mitigated in this case with the use of a softer base binder.

Keywords: Reclaimed Asphalt Pavement (RAP), failure criterion, fatigue, damage

1 INTRODUCTION

During recent decades, the need for Reclaimed Asphalt Pavement (RAP) has increased. Some of the advantages of utilizing RAP include the preservation of the existing pavement profile, conservation of asphalt and aggregate resources, conservation of energy, and reduction in life-cycle costs [1]. However, many transportation agencies are not willing to use more than 10 percent to 20 percent RAP in Hot Mix Asphalt (HMA) [2]. One reason for this unwillingness is that RAP contains asphalt binder that has been aged, and incorporating higher RAP contents into HMA can produce mixtures that are stiffer than the same mixtures without RAP. Consequently, such mixtures would be less workable and more susceptible to field failure, such as fatigue cracking [3, 4]. Also, certain production factors, such as the RAP source, the virgin binder Performance Grade (PG), production temperature, and plant type, can affect the degree of blending RAP and virgin asphalt and consequently affect the performance of the resultant asphalt mixture [5].

Regardless of these concerns, Departments Of Transportation (DOTs) in the United States have been forced to increase the amount of RAP up to 50 percent in flexible pavements because of economic considerations, increases in the cost of asphalt binder, and environmental concerns.

Their primary objective is to encourage the use of recycled materials in the construction of highways to the maximum economical and practical extent possible with equal or improved performance [6].

Because fatigue cracking is one of the most common distresses in asphalt concrete pavements, it is extremely important to define or predict the fatigue cracking behavior of HMA in flexible pavement design and preservation. Therefore, an effective fatigue performance model is needed that can represent both fatigue damage growth and the fatigue failure criterion in

order to define the fatigue life of the pavement. Furthermore, in order to meet the demands for using RAP in HMA to the extent that is possible, the model should be able to incorporate RAP mixtures as well.

The Simplified Viscoelastic Continuum Damage (S-VECD) model is a continuum damage mechanics-based model that has been applied effectively to predict the performance of asphalt concrete mixtures under different loading conditions [7–12]. Zhang et al. [13] developed a new energy measure that represents the rate of damage growth using the S-VECD model and that can predict fatigue failure. However, Zhang et al. developed this approach based on controlled Crosshead (CX) mode of loading test data only. Later, Sabouri and Kim [14] applied Zhang et al.'s failure criterion to different modes of loading and found it to be mode of loading-dependent. They proposed a new failure criterion (the G^R method) that remedies the problems associated with Zhang et al.'s failure criterion. This new failure criterion is considered to be independent of mode of loading, strain amplitude, and temperature. According to this criterion, a characteristic relationship exists between the rate of change of the averaged released pseudo strain energy during fatigue testing and the final fatigue life, and is proved to be present in both RAP and non-RAP mixtures. This failure criterion combines the advantages of the S-VECD model and this characteristic relationship, which both originate from fundamental mixture properties.

Given the above considerations, the objective of this paper is to investigate the effect of incorporating high percentages of RAP in asphalt mixtures on the mechanical properties and the performance of those mixtures in terms of fatigue cracking using the S-VECD failure criterion and in comparison with standard (non-RAP) mixes.

2 MATERIALS AND SPECIMEN PREPARATION

2.1 *Materials*

For this study, a total of eight mixtures from two main sources were selected to be evaluated for their mechanical properties and fatigue performance. The first four mixtures are Superpave 9.5 mm plant-produced mixtures obtained from Pike Industries in Williston, Vermont (VT). These mixtures incorporate four different percentages of RAP: 0%, 20%, 30% and 40%. The VT mixtures are designated as VTeXXLC, with XX representing the percentage of RAP. The second source, Manitoba Infrastructure and Transportation (MIT), provided 16 mm plant-produced mixtures obtained from provincial Highway 8 in Manitoba, Canada. For the MIT mixtures, loose mixtures were sampled during paving of the top lift of each section at the project site. These sections were constructed in September 2009 and consisted of two 2-inch lifts with conventional HMA (i.e., 0% RAP), 15% RAP, and 50% RAP with no PG grade change for the new asphalt and 50% RAP with a PG grade change for the new asphalt.

2.2 *Binder*

PG 64-28 asphalt binder from a regional supplier was utilized for all the Vermont mixtures. The Manitoba mixtures that were evaluated in this study were manufactured using an asphalt binder of Pen grade 150/200. According to the study by Hajj et al. [15], the binder PG for the softer binder used in the Manitoba mixtures is specified as 52-34 whereas it is defined as 58-28 for the other mixes. Table 1 presents a summary of the properties of these eight mixtures.

2.3 *Specimen preparation*

All the specimens were compacted using the Superpave Gyratory Compactor (SGC) to a diameter of 150 mm and a height of 178 mm. To obtain specimens of uniform air void distribution, these samples were cored and cut to a 100 mm diameter and a height of 150 mm for the dynamic modulus tests and a height of 130 mm for the CX cyclic direct tension tests.

Table 1. Summary of mixture properties.

Mix type	Binder	Total AC (%)	RAP (%)	Compaction temp. (°C)	AV (%)
VTe00LC	PG64-28	6.5	0	149	6.0
VTe20LC	PG64-28	5.7	20	149	6.0
VTe30LC	PG64-28	5.1	30	154	6.0
VTe40LC	PG64-28	4.5	40	146	6.0
MIT-C	PG58-28	5.2	0	124	5.4
MIT-15R	PG58-28	5.2	15	124	4.9
MIT-50R	PG58-28	5.0	50	124	5.9
MIT-50RSB	PG52-34	5.0	50	129	5.7

The air void content was measured using the CoreLok method for each specimen before testing. All the samples selected for this study have the target air void of ±0.5%. All of the direct tension test specimens were glued to metal plates using DEVCON steel putty. Vertical deformations were measured using four Linear Variable Differential Transducers (LVDTs) with the gauge length of 70 mm at intervals of 90 degrees for both the dynamic modulus and CX cyclic tension tests.

3 TESTING METHODS

Two main tests were carried out in this study: (1) dynamic modulus tests were performed to determine the linear viscoelastic characteristics using the Asphalt Mixture Performance Tester (AMPT), and (2) CX cyclic direct tension tests were performed to determine the viscoelastic damage characteristics using the Material Testing System (MTS).

3.1 *Dynamic modulus testing*

Dynamic modulus testing was carried out in compression under load-controlled mode following the protocol given in AASHTO TP 79 [16]. The tests were performed for all mixtures at 4°C, 20°C, 40°C, and 54°C and at frequencies of 25, 10, 5, 1, 0.5, and 0.1 Hz. The load levels were specified by trial and error so that the strain amplitudes were between 50 and 75 microstrain to prevent damage to the specimens. The dynamic modulus (|E*|) values were fitted for the coefficients of the sigmoidal function and time-temperature shift factors by optimizing the dynamic modulus mastercurve. After determining the shift factors, the dynamic modulus was converted to the relaxation modulus, E(t), of the Prony series form to obtain a constitutive relationship between the strain and stress in the time domain. Finally, a power term, alpha (α), used in VECD theory, was calculated from the maximum log-log slope, m, of the relaxation modulus and time using the relationship, $\alpha = 1 + (1/m)$.

3.2 *Controlled Crosshead (CX) cyclic direct tension tests*

The CX cyclic direct tension tests were performed at 10 Hz at different temperatures based on the binder PG to determine the viscoelastic damage characteristics. All tests were performed at three to four different strain amplitudes (high, medium and low). The strain amplitudes were selected in such a way to create a spread of numbers of cycle to failure (N_f) in the range of 1,000 to 100,000 cycles. Fingerprint dynamic modulus tests were conducted to check the variability of the test specimens before running the CX cyclic direct tension tests. The dynamic modulus value measured from this test is specified as $|E^*|_{fingerprint}$ and is used to calculate the Dynamic Modulus Ratio (DMR) via Equation (1). $|E^*|_{LVE}$ is the linear viscoelastic dynamic modulus of the material at the particular temperature and frequency of the test. A DMR value in the range of 0.9 to 1.1 guarantees that the linear viscoelastic

properties obtained from the dynamic modulus tests can be used effectively in S-VECD analysis.

$$DMR = \frac{|E^*|_{fingerprint}}{|E^*|_{LVE}} \tag{1}$$

The fatigue failure for each of the specimens tested in the CX cyclic tests was determined by Reese's approach, which is based on the change in phase angle [17]. The phase angle increases until strain localization occurs, and then drops suddenly. This sharp decrease occurs around the failure point, which makes the determination of the number of cycles to failure accurate and consistent in a laboratory testing.

3.3 *Fatigue failure criteria*

The S-VECD failure criterion is based on the total released pseudo strain energy during a cyclic test. The maximum stored pseudo strain energy at each cycle reflects the material's ability to store energy at that particular time. As the damage grows, the material loses the stored energy for the same magnitude of applied pseudo strain due to the reduction in pseudo stiffness. The difference between the current stored maximum pseudo strain energy and the corresponding undamaged state is referred to as the *total released pseudo strain energy.*

The rate of change of the averaged released pseudo strain energy values throughout the history of the test is denoted as G^R. Sabouri and Kim [14] showed that G^R and the final fatigue life (N_f) are highly correlated, because the faster the damage accumulates, i.e., releasing higher amounts of energy during fewer numbers of cycles, the quicker the material should fail.

In order to minimize the effect of viscoplasticity, Sabouri and Kim suggested using the PG of the base binder to determine a proper testing temperature, as shown in Equation (2).

$$T(°C) \leq \frac{High\ temperature\ binder\ PG\ grade + Low\ temperature\ binder\ PG\ grade}{2} - 3 \leq 19°C \tag{2}$$

4 RESULTS AND DISCUSSION

Figure 1 presents the results of the linear viscoelastic characterization of the VTe and MIT mixes in both log-log and semi-log scales. The points in the graphs are the averaged dynamic modulus values of three replicates for each mixture. As Figure 1 (a) and (b) show for the VTe mixes, the addition of RAP into the VTe mixtures does not seem to have a significant effect on the dynamic modulus values, as no major differences are found in the dynamic modulus values when the RAP content is increased from 0 percent to 40 percent. On the other hand, as Figure 1 (c) and (d) indicate for the MIT mixes, incorporating RAP into the MIT mixtures has a more pronounced effect on the dynamic modulus values. In this case, the dynamic modulus values have increased significantly when 15% RAP is added to the mixture. One possible reason for this different behavior between the VTe and MIT mixes could be the greater difference in the PGs of the RAP binder and virgin binder in the MIT mixtures. The MIT RAP binder is PG 76-10 whereas the VTe RAP binder is PG 70-22.

Figure 2 presents the results of the S-VECD fatigue characterization of both the VTe and MIT mixtures. These plots illustrate how fast the material integrity (C) decreases as the damage (S) increases. These damage characteristic curves are each plotted up to the cycle when the phase angle starts to decrease. This cycle is considered to be the point of localization, i.e., the point where a single dominant macro-crack forms.

As Figure 2 (a) shows for the VTe mixes, all the C vs. S characteristic curves collapse almost on the same line, except for the 30% RAP mix for which the line stays a little above the

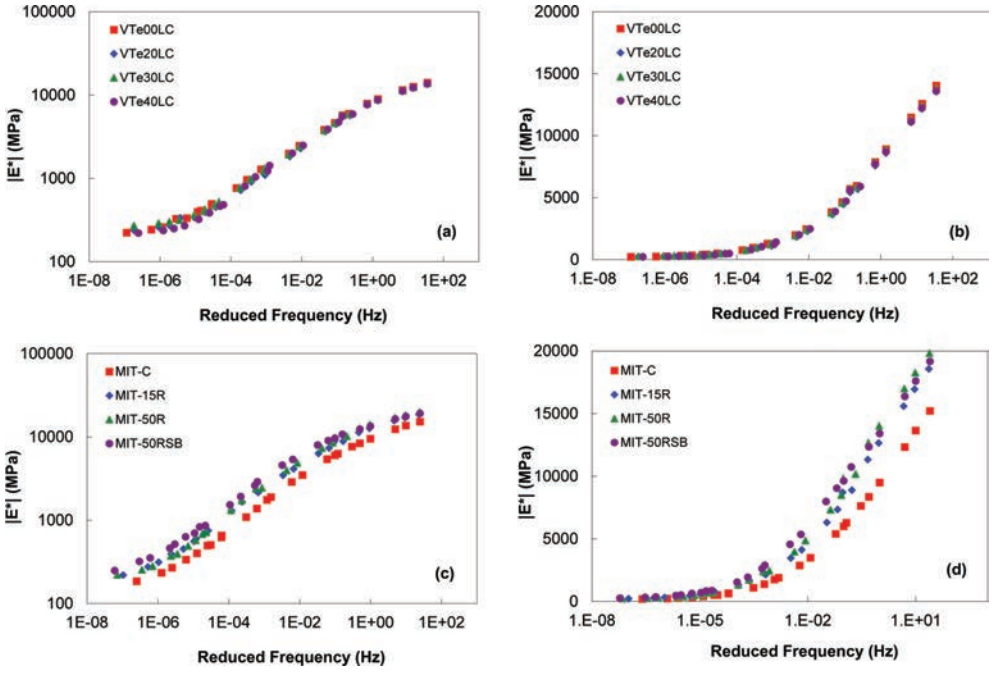

Figure 1. Dynamic modulus mastercurves: (a) VTe in log-log scale, (b) VTe in semi-log scale, (c) MIT in log-log scale, and (d) MIT in semi-log scale.

other lines. As Figure 2 (b) shows for the MIT mixes, the non-RAP mix and also the mix with soft binder show a rapid decrease in material integrity with an increase in damage compared to the mixtures with 15% and 50% RAP content.

The last point on each curve indicates the C value at failure (C_F). The results for the MIT mixtures confirm observations by Hou et al. [7] that suggest that the inclusion of RAP increases the material integrity at failure, though not to the same degree. The higher material integrity at failure value suggests that RAP mixtures cannot tolerate as much damage before failure as non-RAP mixtures. This ability is due to the mixture becoming more brittle once the RAP is incorporated into the mix. However, a comparison of only the damage characteristic curves cannot yield reliable information about the different mixtures' fatigue resistance, because the energy that is input by mechanical force is consumed not only in creating and propagating cracks in the material, but also in deforming the material. Therefore, it is important to include both stiffness and damage characteristics of a material when determining fatigue cracking resistance.

Figure 3 presents the characteristic relationships developed for both the VTe and MIT mixtures. A strong power law relationship exists between the failure criterion, G^R, and the number of cycles to failure, which is evident for all eight mixtures, according to the high coefficient of variance (R^2) values shown in Figure 3. One interesting observation to be made from Figure 3 (a) is the collapse of the failure criterion for all four VTe mixtures with different RAP contents. As discussed in the previous section, the dynamic modulus mastercurves and also the damage characteristic curves of this set of RAP mixtures are very close to those of the virgin mixture, indicating that the fatigue performance of the RAP and virgin mixtures would be similar. These similarities between the RAP and virgin mixtures seem to suggest that the materials (RAP binder grade, virgin binder grade, and type, etc.) and the mix design used for these RAP mixtures result in RAP mixtures with fatigue performance characteristics that are similar to those of the virgin mixture.

However, Figure 3 (b) demonstrates that incorporating high percentage RAP into the mix deteriorates the mixture fatigue resistance, as the failure criterion line for 15% RAP is a little

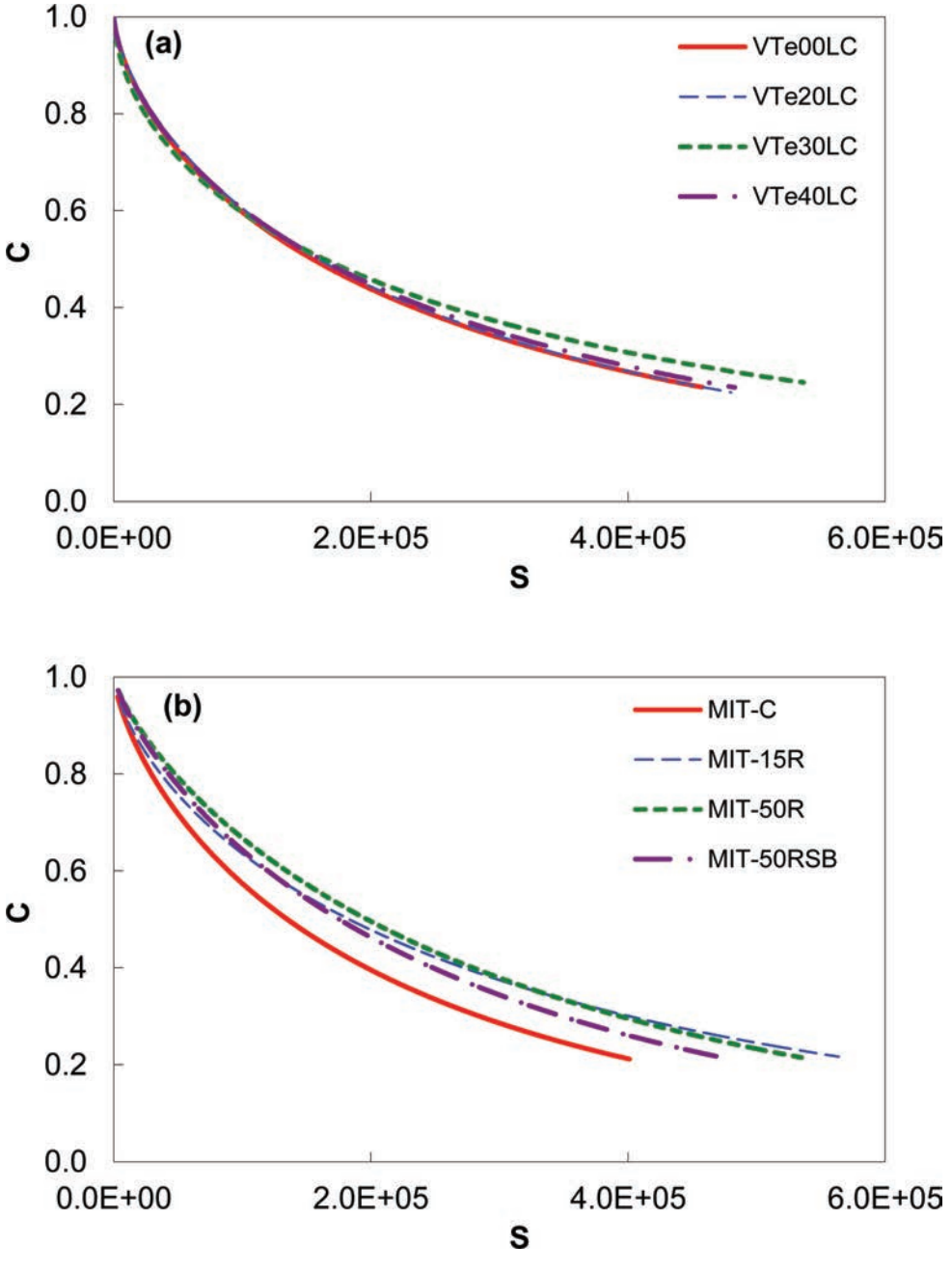

Figure 2. Characteristic curves for: (a) VTe and (b) MIT mixes.

below the virgin mix line, but the line for 50% RAP deviates from those two considerably, suggesting that at the same G^R value, the mix with 50% RAP results in fewer numbers of cycles to failure. This outcome may be due to the increase in the virgin binder stiffness as 50% aged binder is added to the mix, which makes the pavement system experience lower strains and consequently lower G^R values under the same loading history.

Another interesting observation from Figure 3 (b) is that the use of the softer binder (PG 52-34) can improve fatigue resistance, as the line for 50% RAP with the softer binder stays

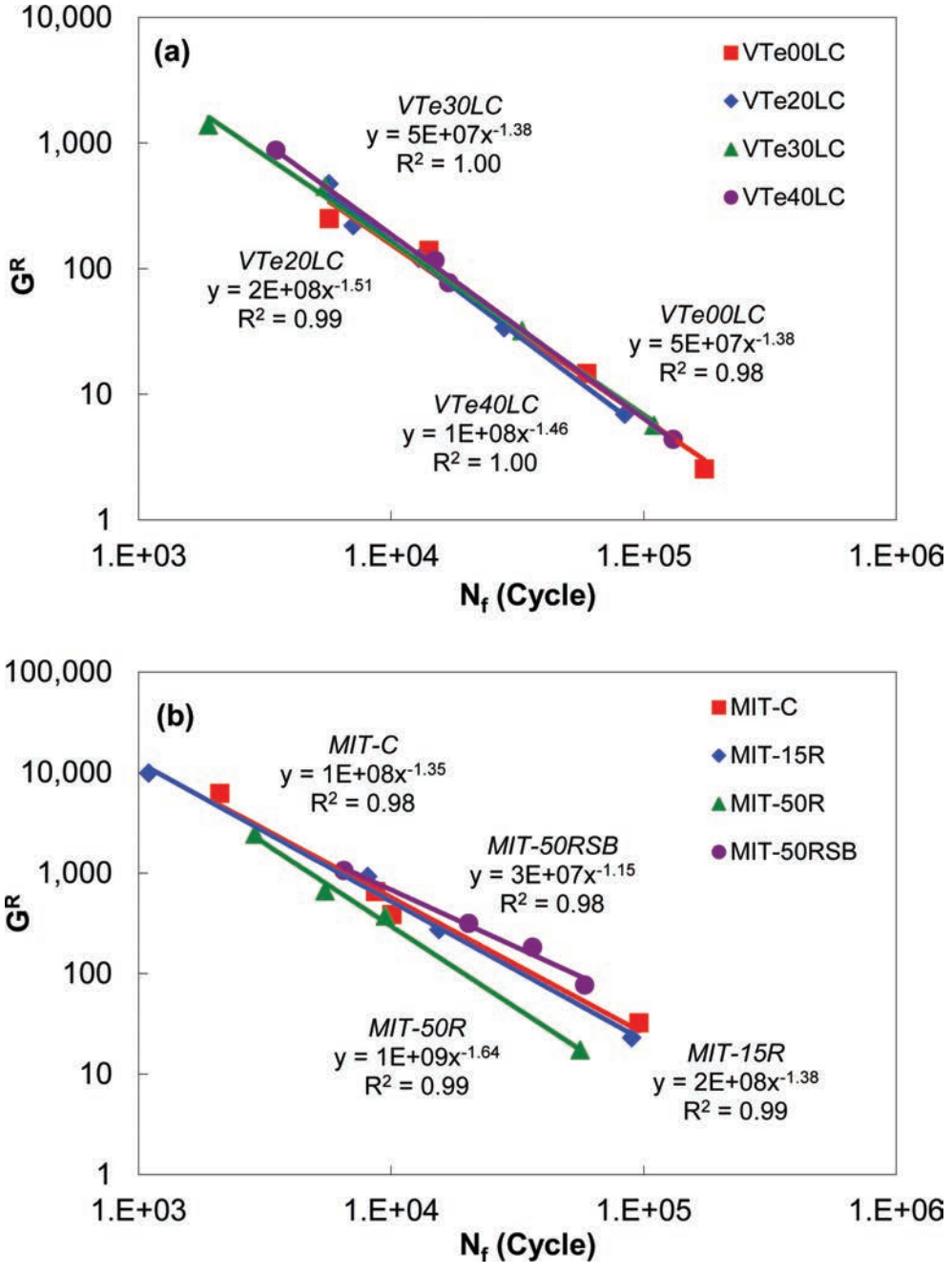

Figure 3. Relationship between G^R and N_f for: (a) VTe and (b) MIT mixes.

even higher than the line of the non-RAP mix. This finding suggests that using soft binder in high RAP content mixes can compensate for the decrease in fatigue resistance. Also, as expected, the MIT-C mix, which has the lowest stiffness (Fig. 1 (c)) and deepest fatigue characteristic curves (Fig. 2 (b)) among all the MIT mixtures with the same base binder, shows the best fatigue resistance, as its corresponding failure criterion line in Figure 3 (b) stays above the lines of the RAP mixtures with the same base binder.

5 CONCLUSIONS

This research conducted a laboratory evaluation of plant-produced mixtures from Vermont and Manitoba with RAP contents up to 50 percent. The impact of high RAP content on the fatigue cracking resistance of HMA mixtures was evaluated using a pseudo strain energy-based failure criterion. A different fatigue behavior trend was observed from the mixtures obtained from the two projects. The following summary presents the findings of this study for the evaluated mixtures.

- In general, the use of RAP, especially high RAP content, in HMA decreases the fatigue resistance, probably due to the addition of aged binder that stiffens the asphalt mixture.
- The data indicate no significant change in dynamic modulus values as the RAP content was increased for the VTe mixtures, whereas the mixture stiffness increased up to 25% when 15% RAP was added to the virgin MIT mix. One reason for this increase could be the difference in PG grades of RAP binders that were used in the VTe and MIT mixtures.
- The use of 50% RAP without a grade change for the virgin binder resulted in a reduction of the fatigue life of the MIT mixtures. However, the use of a softer virgin binder with the 50% RAP mixture improved fatigue resistance.
- Based on the findings of this study, it is concluded that it is possible to design high-quality HMA with up to 50% RAP that meets the desired fatigue resistance performance.
- This study's failure criterion (G^R) and the S-VECD model seem to be effective when used to compare the fatigue resistance of RAP and non-RAP asphalt concrete mixtures.

ACKNOWLEDGEMENTS

The authors would like to acknowledge the financial supports from the Transportation Pooled Fund 5(230) study, *Evaluation of Plant-Produced High-Percentage RAP Mixtures in the Northeast*, and from the FHWA DTFH61-08-H-00005 project, *Hot Mix Asphalt Performance-Related Specifications Based on Viscoelastoplastic Continuum Damage* (*VEPCD*) *Models*.

REFERENCES

[1] Kennedy, T.W., W.O. Tam, and M. Solaimanian. *Effect of Reclaimed Asphalt Pavement on Binder Properties Using the Superpave System*. Research Report 1250-1, Center for Transportation Research, Bureau of Engineering Research, Austin, TX, September 1998.

[2] Copeland, A. *Reclaimed Asphalt Pavement in Asphalt Mixtures: State of the Practice*. Publication FHWA-HRT-11-021, Turner-Fairbank Highway Research Center, Federal Highway Administration, McLean, VA, April 2011.

[3] Bonaquist, R. *Laboratory Evaluation of Hot Mix Asphalt (HMA) Mixtures Containing Recycled or Waste Product Materials Using Performance Testing.* Publication FHWA-PA-2005-006-98-32(19), Pennsylvania Department of Transportation, Office of Planning and Research, 2005.

[4] McDaniel, R., A. Shah, G. Huber, and V. Gallivan. Investigation of Properties of Plant-Produced RAP Mixtures. *Transportation Research Record: Journal of the Transportation Research Board*, No. 1998, Transportation Research Board of the National Academies, Washington, D.C., 2007, pp. 103–111.

[5] Mogawer, W.S., T. Bennert, J.S. Daniel, R. Bonaquist, A. Austerman, and A. Booshehrian. Performance Characteristics of Plant Produced High RAP Mixtures. *Road Materials and Pavement Design*, Vol. 13, Supplement 1, 2012, pp. 183–208.

[6] Al-Qadi, I.L., Q. Aurangzeb, and S.H. Carpenter. *Impact of High RAP Content on Structural and Performance Properties of Asphalt Mixtures*. Research Report FHWA-ICT-12-002, Illinois Center for Transportation, Rantoul, IL, June 2012.

[7] Hou, T., B.S. Underwood, and Y.R. Kim. Fatigue Performance Prediction of North Carolina Mixtures Using Simplified Viscoelastic Continuum Damage Model. *Journal of the Association of Asphalt Paving Technologists*, Vol. 79, 2010, pp. 35–80.

[8] Kim, Y.R. and D.N. Little. One-Dimensional Constitutive Modeling of Asphalt Concrete. *ASCE Journal of Engineering Mechanics*, Vol. 116, No. 4, 1990, pp. 751–772.

[9] Lee, H.J. and Y.R. Kim. A Viscoelastic Continuum Damage Model of Asphalt Concrete with Healing. *ASCE Journal of Engineering Mechanics*, Vol. 124, No. 11, 1998, pp. 1224–1232.
[10] Daniel, J.S. and Y.R. Kim. Development of a Simplified Fatigue Test and Analysis Procedure Using a Viscoelastic Continuum Damage Model. *Journal of the Association of Asphalt Paving Technologists*, Vol. 71, 2002, pp. 619–650.
[11] Chehab, G.R., Y.R. Kim, R.A. Schapery, M. Witczack, and R. Bonaquist. Characterization of Asphalt Concrete in Uniaxial Tension Using a Viscoelastoplastic Model. *Journal of the Association of Asphalt Paving Technology*, Vol. 72, 2003, pp. 315–355.
[12] Underwood, B.S., Y.R. Kim, and M.N. Guddati. Characterization and Performance Prediction of ALF Mixtures Using a Viscoelastoplastic Continuum Damage Model. *Journal of the Association of Asphalt Paving Technologists*, Vol. 75, 2006, pp. 577–636.
[13] Zhang, J., M. Sabouri, Y.R. Kim, and M.N. Guddati. Development of a Failure Criterion for Asphalt Mixtures under Fatigue Loading. *Road Materials and Pavement Design*, Vol. 14, Supplement 2, 2013, pp. 1–15.
[14] Sabouri, M. and Y.R. Kim. Development of Failure Criterion for Asphalt Mixtures under Different Modes of Fatigue Loading. *Transportation Research Record: Journal of Transportation Research Board*. In press.
[15] Hajj, E.Y. et al. *Impact of High RAP Content on the Performance Characteristics of Asphalt Mixtures in Manitoba*. 2011 Annual Conference of the Transportation Association of Canada, Edmonton, Alberta, CA.
[16] American Association of State Highway Transportation Officials (AASHTO). *AASHTO TP 79-10, Standard Method of Test for Determining the Dynamic Modulus and Flow Number for Hot Mix Asphalt (HMA) Using the Asphalt Mixture Performance Tester (AMPT)*. Washington, D.C., AASHTO, 2011.
[17] Reese, R. Properties of Aged Asphalt Binder Related to Asphalt Concrete Fatigue Life. *Journal of the Association of Asphalt Paving Technologists*, Vol. 66, 1997, pp. 604–632.

This page intentionally left blank

Asphalt Pavements – Kim (Ed)
© 2014 Taylor & Francis Group, London, ISBN 978-1-138-02693-3

Three dimensional behaviour of bituminous mixtures in the linear viscoelastic and viscoplastic domains: The DBN model

Pierre Gayte, Hervé Di Benedetto & Cédric Sauzeat
ENTPE-University of Lyon, LGCB & LTDS (UMR 5513), Vaulx-en-Velin, France

ABSTRACT: Behaviour of bituminous mixtures is very complex. Their rheological properties depend on strain amplitude level and temperature. We can observe linear viscoelasticity properties for very small strain amplitudes and non-linearities for larger strain levels. Fatigue and rutting (permanent deformation) can appear for a great number of cycles. Moreover brittle or ductile failure can occur. All of these properties strongly temperature and time dependant.

The DBN (Di Benedetto-Neifar) model developed at LGCB laboratory (*University of Lyon/ENTPE "Ecole Nationale des TPE"*) aims at describing the complex behaviour of bituminous mixtures with an unified formalism. The model is also versatile and may be adapted to take into account some specific properties of bituminous materials. First, equations describing the whole three-dimensional DBN model in the linear domain are proposed. Then the visco-plastic formalism is introduced in the Elastic-Perfectly Plastic (EPP) case which is a simplified version of the model proposed for numerical finite element calculations.

Calibration of the model in the viscoelastic and viscoplastic domains as well as simulation are proposed based on experiments made at LGCB laboratory for different loading paths in the small and large strain domains.

Keywords: Bituminous mixtures, 3D behaviour, 3D modelling, DBN model, viscoelasticity, viscoplasticity

1 INTRODUCTION

1.1 *Background*

Several external solicitations (mechanical, thermal, physical, chemical) can be identified when considering the behaviour of roadway structures. We can also observe that a coupling between these effects often appears. A main difficulty is then to model these effects (and their coupling) so as to be able to get a realistic performance prediction of bituminous pavements.

Mechanical properties of bituminous mixtures have to be modelled considering these four main properties [1–2]:

- Stiffness and stiffness evolution with time in the linear domain
- Fatigue and damage law evolution,
- Permanent deformation and accumulation of this deformation,
- Crack and crack propagation, in particular at low temperature.

Indeed they allow to characterize the structural effect of bituminous layers of the road and its evolution with time (not true for very thin surface layers). Being able to represent these properties is a way to model the behaviour of roads and then to indroduce this knowledge in pratical design methods using finite element methods.

Each of theses properties appears for a given domain of loading and corresponds to a specific type of behaviour for the mixtures. Thanks to Figure 1 it is possible to identify the domains corresponding to the different aspects introduced previously and the corresponding

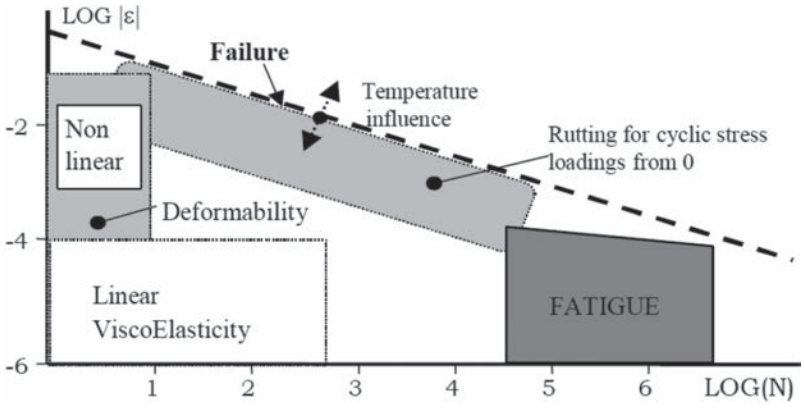

Figure 1. Domains of behaviour for bituminous mixtures (Strain amplitude (ε) above number of cycle (N)) by Di Benedetto (1990).

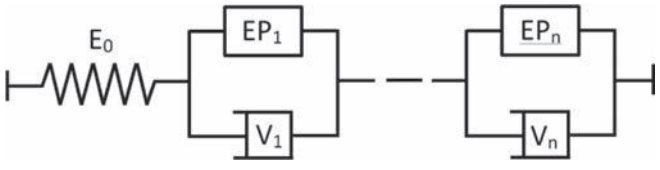

Figure 2. Analogical 1D representation of the DBN model.

"typical" type of behaviour for mixtures. Boundaries of domains are informative and transition from one domain to another is made in a smooth and continuous way.

1.2 *The DBN (Di Benedetto-Neifar) model*

Former works made at ENTPE (*Ecole Nationale des Travaux Publics de l'Etat*) leads to the development of the DBN model which is an attemp to describe with one formulation the different types of behaviour observed for bituminous mixtures. The main goal of this paper is to introduce a new version of the DBN model which aims at describing both the linear viscoelasticity and non linear domains. The general concept, equations and calibration process of the DBN model are more precisely described in [2]. Only the main aspects are recalled here.

This model is based on simple rheological elements and its calibration is made from experimental results on bituminous mixtures. Due to its high versatility this model is able to describe the behaviour in a wide range of strain amplitude, temperature and number of cyclic loadings. As a result this model can be very simple to use (linear viscoelastic domain) or more complicated (when introducing nonlinearity, fatigue) following required refinement.

The 1D representation of the DBN model is composed of one spring (modulus E_0) and n elementary bodies (each of them composed by an elastoplastic (*ie.* non viscous) body (EP) in parallel with a dashpot (linear V body) as shown on Figure 2. The number of elementary bodies can be chosen arbitrarily as the calibration procedure always needs the same number of constants. If n is high, simulations calculus are close to the experimental data. But also calculations take more time. Calibration of the n elementary bodies is made from parameters of the 2S2P1D model (also developed at LCGB-ENTPE) in the linear domain.

From the general structure of the model (Fig. 2) the total strain[1] $\underline{\varepsilon}$ is given by the sum of the strain in each body $\underline{\varepsilon_i}$ (Eq. (1)), while all bodies are subjected to the same stress $\underline{\sigma}$.

[1]Second order tensors are denoted with simple underline ($\underline{\varepsilon}$) and fourth order tensors with double underline ($\underline{\underline{M}}$).

Stresses in the EP_i and V_i body are denotedv $\underline{\sigma}_i^f$ and $\underline{\sigma}_i^v$ and verify the relationship (Eq. (2) and Fig. 3).

$$\underline{\varepsilon} = \sum_{i=0}^{n} \underline{\varepsilon}_i \tag{1}$$

$$\underline{\sigma} = \underline{\sigma}_i^f + \underline{\sigma}_i^v \tag{2}$$

1.3 *Visco-plasticity for body "i"*

Plasticity phenomenon appears when sollicitation applied to a given non viscous material create non-reversible deformations. A classical elastoplastic formulation is chosen to simulate plasticity. The yield surface $f(\underline{\sigma}_i^f) = 0$ (Fig. 4) is the limit between the elastic and the plastic domain for body EP_i. It is obtained from experimental tests. While the stress $\underline{\sigma}_i^f$ remains "inside" the yield surface only elastic strains occur in body EP_i. Once $\underline{\sigma}_i^f$ reaches the yield surface plastic (non-reversible) strains may appear involving viscoplasticity for body "i".

1.4 *Objectives*

The developments introduced in this article focus on the modelling of linear and non linear (deformability in Fig. 1) behaviours. Rutting and fatigue are not introduced yet. A simplified version of the DBN model is presented. This version is developped to facilitate introduction of the model in finite elements methods calculations considering that each EP_i body is Elastic-Perfectly Plastic (EPP) which means linear elastic (E) behaviour within the yield surface

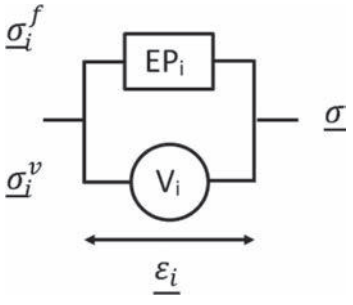

Figure 3. Representation of stress and strain in body "*i*".

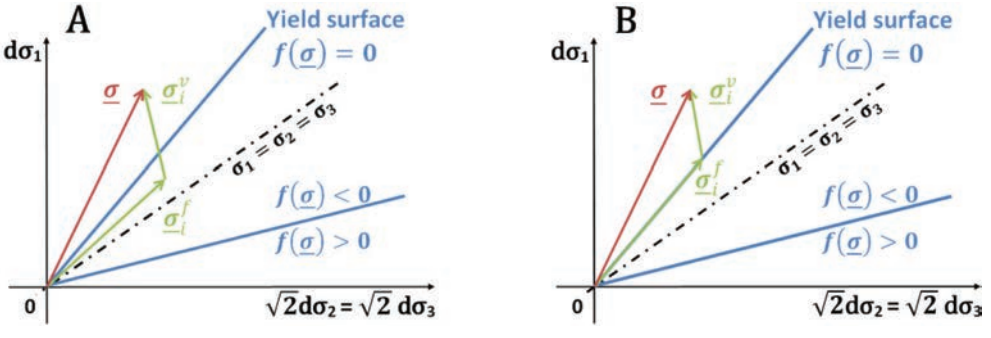

Figure 4. Representation of two possibles cases for $f(\underline{\sigma}) > 0$ considering $\sigma_2 = \sigma_3$ (A) elastic behaviour ($f(\underline{\sigma}_i^f) = 0$) and (B) visco-plastic behaviour ($f(\underline{\sigma}_i^f) < 0$).

and Perfect Plasticity (PP) for larger strain amplitudes. As explained previously the goal is to develop a rheological model which is able to correctly take into account some complex features of bituminous materials and simple enough to be implemented into a finite elements calculation software. Let's remind that it could be improved thanks to the high versatility of the model. Simple or more complex version can be considered depending on the studied phenomena.

2 FORMULATION OF EP_i BODIES FOR THE EPP (ELASTIC—PERFECTLY PLASTIC) VERSION OF THE DBN MODEL

Formulation of the EPP version of the DBN model is introduced for the 3D case. Figure 5 gives the analogical representation for the three-dimensional case.

2.1 *Elastic part of EP type body*

In the linear domain stress and strain of EP body are linked by the elastic tensor $\underline{\underline{M}}_i^e$ with components $M_{i_{mjkl}}^e$ using Equation 3

$$\varepsilon_{i_{mj}} = M_{i_{mjkl}}^e \sigma_{i_{kl}}^f \tag{3}$$

The elastic part of EP body is considered to be isotropic. Then elastic tensor can be written (Equation 4) as a function of the Young modulus E_i and the Poisson's ratio υ_i. These coefficients are both obtained from the optimisation process used in the unidirectional case from the 2S2P1D model. More details are available in [2] concerning the calibration process and experimental data needed.

$$M_{i_{mjkl}}^e = \frac{\left(1+\upsilon_i\right)\delta_{mk}\delta_{jl} - \upsilon_i\delta_{kl}\delta_{mj}}{E_i} \tag{4}$$

2.2 *Plastic strains of EP type body for the EPP version*

2.2.1 *General equations*

The stain $\underline{\varepsilon_i}$ of an EP_i body is considered as the sum of an elastic strain $\underline{\varepsilon_i^e}$ and a plastic strain $\underline{\varepsilon_i^p}$ (Fig. 5):

$$\dot{\underline{\varepsilon}}_i = \dot{\underline{\varepsilon}}_i^e + \dot{\underline{\varepsilon}}_i^p = \underline{\underline{M}}_i^{ep} \dot{\underline{\sigma}}_i^f \tag{5}$$

where $\dot{}$ denotes the objective time derivative. Equation (5) can be rewritten considering the elastoplasticity framework. Then for plastic loading it comes:

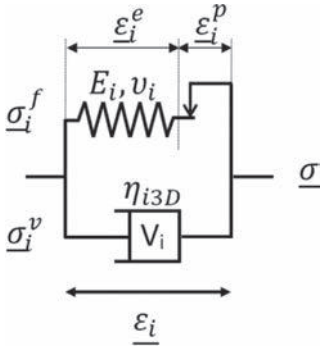

Figure 5. Analogical 3D representation of the EPP version of the DBN model.

$$\dot{\underline{\varepsilon}}_i = \underline{\underline{M}}_i^{ep}\,\dot{\underline{\sigma}}_i^f = \underline{\underline{M}}_i^{e}\,\dot{\underline{\sigma}}_i^f + \underline{\underline{M}}_i^{p}\,\dot{\underline{\sigma}}_i^f = \dot{\underline{\varepsilon}}_i^e + \dot{\underline{\varepsilon}}_i^p \tag{6}$$

And for unloading case:

$$\dot{\underline{\varepsilon}}_i = \underline{\underline{M}}_i^{e}\,\dot{\underline{\sigma}}_i^f \tag{7}$$

where $\underline{\underline{M}}_i^{ep}$ and $\underline{\underline{M}}_i^{p}$ are respectively the elastoplastic and the plastic tensors given by:

$$\underline{\underline{M}}_i^{ep} = \underline{\underline{M}}_i^{e} + \underline{\underline{M}}_i^{p} \tag{8}$$

$$\underline{\underline{M}}_i^{p} = M_i^p\left(\underline{n}_f \otimes \underline{n}_g\right) \tag{9}$$

And $\underline{n}_f$ and $\underline{n}_g$ are unit normal vectors to the yield surface f and the plastic potential surface g. M_i^p is the norm of the plastic tensor $\underline{\underline{M}}_i^p$ which is infinite because of the perfect plasticity property of the model. In this case Equation 6 can be rewritten:

$$\dot{\underline{\varepsilon}}_i^p = \underline{\underline{M}}_i^{p}\,\dot{\underline{\sigma}}_i^f = \dot{\varepsilon}_i^p\,\underline{n}_g \tag{10}$$

2.2.2 *Yield surface f*

The chosen yield surface is adapted from equations given by S. Maïolino in [3]. It is a general smooth, convex and cone-shaped function.

$$\begin{aligned} &f\left(R, L_s, I_0, I_1, J_2, J_3\right) \\ &= sign\left(I_1 + I_0\right)\left[L_s^2\left(I_1 + I_0\right)^3 R^3 - 3\left(L_s^2 - L_s + 1\right)\left(I_1 + I_0\right)J_2 R + 9\sqrt{2}\left(1 - L_s\right)J_3\right] \end{aligned} \tag{11}$$

where parameters R and L_S are respectively the "opening" and the "shape ratio" of the yield surface, I_0 gives the summit of the cone which is on the first trisect. I_1, J_2, J_3 are three invariants[2] of tensor $\underline{\sigma}^f$ (Fig. 6). This formulation of the yield surface needs to be calibrated for the case of bituminous mixtures.

From a series of triaxial compression and extension tests Di Benedetto and Yan [4] establish that the yield surface is a cone, whose axis is the trisect. Sections in deviatoric planes

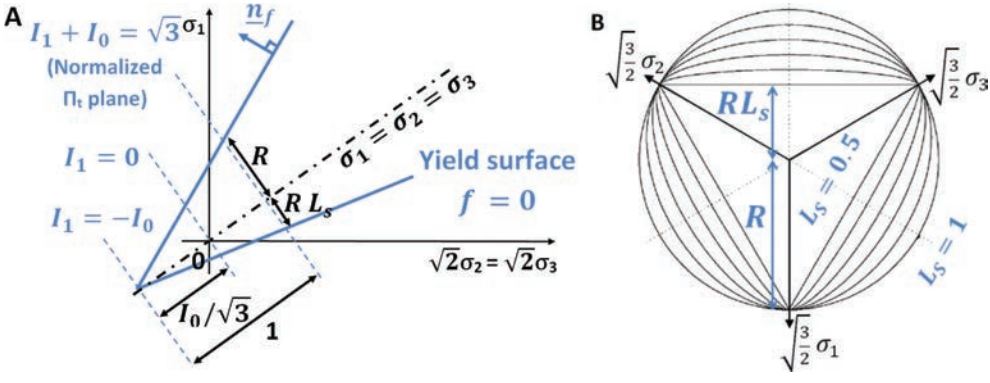

Figure 6. Representation of the yield surface (A) Section in the axis $\sigma_1 - \sqrt{2}\sigma_2 = \sqrt{2}\sigma_3$—(B) Section by the normal plane to the first trisect given by equation $I_1 + I_0 = \sqrt{3}$ in the principal axis.

[2] $I_1 = tr(\underline{\sigma}^f)$; $J_2 = tr(\underline{s}^{f^2})$, $J_3 = tr(\underline{s}^{f^3})$ where $\underline{s}^f = \underline{\sigma}^f - 1/3\,tr(\underline{\sigma}^f)$.

(perpendicular to the first trisect) are equilateral triangles (Fig. 7). It is supposed that yield surfaces of all bodies "i" have the same shape. From these considerations and using the function Eq. (11) the yield surface for bituminous material is proposed. The yield surface $f(\underline{\sigma}^f) = 0$ of the EPP version of the DBN model is then given by:

$$f\left(\underline{\sigma}^f\right) = \begin{cases} f^t\left(R_t, L_s, I_{0t,i}, I_1, J_2, J_3\right) & when\ I_1 \leq I_{p,i} \quad (12.1) \\ f^c\left(R_c, L_s, I_{0c,i}, I_1, J_2, J_3\right) & when\ I_1 > I_{p,i} \quad (12.2) \end{cases}$$

In order to approximate the Di Benedetto and Yan criterion (Fig. 7) with a smooth surface (to simplify computations) the shape ratio L_s has been chosen equal to 0.55 for each DBN body (Fig. 8). It remains the same for the two functions. Surfaces are thus given by continu-

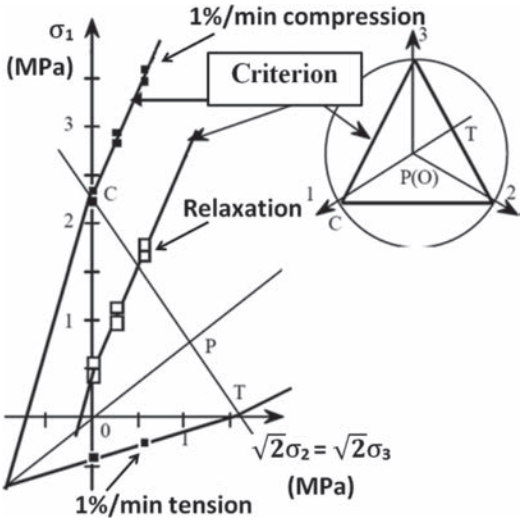

Figure 7. Failure stress for triaxial compression and tension tests at 1%/min and relaxation values (experimental data), and proposed failure surface (from [4]).

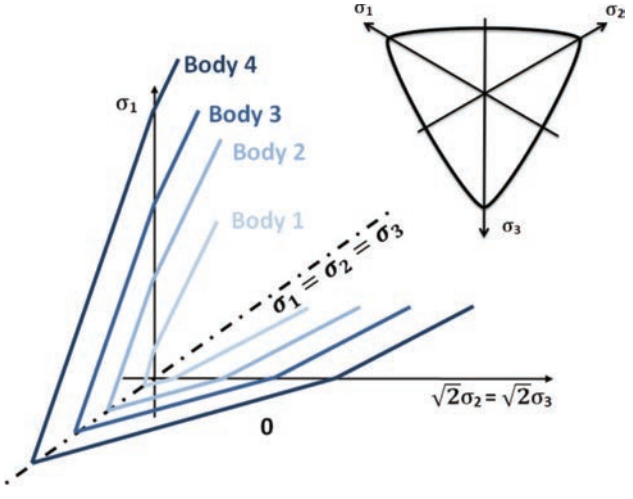

Figure 8. Representation (2D) of yield surfaces of the EPP version of the DBN model (only four EP bodies drawn).

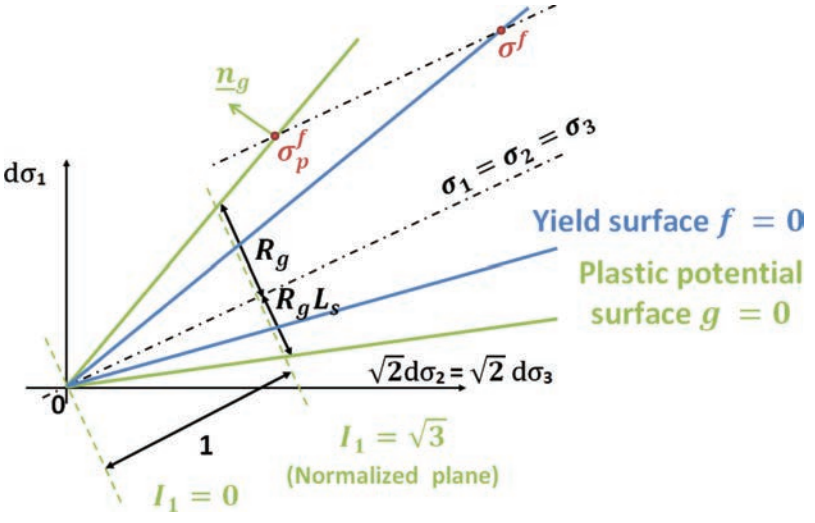

Figure 9. Representation of the plastic potential surface with parameters (R_g, L_{sg}).

ous and differentiable functions. Calibration of parameters R_t, R_c, $I_{0t,i}$, and $I_{p,i}$ is obtained from experimental data. R_t and R_c are not denoted with subscript "i" they take the same value for each EP_i body.

2.2.3 *Plastic potential g*

Direction of plastic strain is given by the unit normal vector to the plastic potential surface. In the EPP version of the DBN model introduced in this article it is decided to keep the same equation as the one used for the yield surface but with a different shape ratio L_{sg} and opening R_g.

$$g\left(R_g, L_{sg}, I_1, J_2, J_3\right) = sign\left(I_1\right)\left[L_{sg}{}^2\left(I_1\right)^3 R_g^3 - 3\left(L_{sg}{}^2 - L_{sg} + 1\right)\left(I_1\right)J_2 R_g + 9\sqrt{2}\left(1 - L_{sg}\right)J_3\right] \tag{13}$$

where I_1, J_2, J_3 are the three invariants of the tensors $\underline{\sigma}$. Parameters R_g and L_{sg} are obtained from experimental data of tension/compression tests by a calibration process. Poisson's ratios in tension and compression in the plastic domain are needed. R_g and L_{sg} are the same for each EP_i body. Then plastic potential surface is given by (Fig. 9):

$$g\left(R_g, L_{sg}, I_1, J_2, J_3\right) = constant \tag{14}$$

3 FORMULATION OF LINEAR V_i BODIES AND MAPPING RULE

3.1 *General V body behaviour*

Behaviour of V type body is given by:

$$\dot{\varepsilon}_{mj} = N_{i_{mjkl}}\, \sigma^v_{kl} \tag{15}$$

where $\underline{\underline{N}}_i$, with components $N_{i_{mjkl}}$, is the viscous rheological tensor which is a function of the temperature T. Thermo-susceptibility of bituminous material is thus taken into account in the model. It can be shown that the Time Temperature Superposition Principle is verified even in the nonlinear domain [2].

3.2 *Linear viscoelastic case*

This section deals with the LVE behaviour of V_i bodies *ie.* when $f(\underline{\sigma}^f) < 0$ or $f(\underline{\sigma}^f) < 0$ with no plastic strains ($\underline{\sigma}^f \cdot \underline{n}_f \leq 0$). A basic hypothesis formulated and interpreted in Di Benedetto (1987) is that the rate of the elastoplastic stress tensor ($\dot{\underline{\sigma}}^f$) is collinear and in the same direction as the viscous stress tensor ($\underline{\sigma}^v$) (Fig. 10). Considering this hypothesis and Eq. (15), let ζ_i be the ratio between norms of tensor $\underline{\underline{N}}_i$ and $\underline{\underline{M}}_i^e$:

$$\underline{\underline{N}}_i = \zeta_i \underline{\underline{M}}_i^e \tag{16}$$

Only one scalar is then needed to complete the description of the behaviour of the body V. The scalar parameter η_{i3D} is introduced:

$$\left\| \underline{\underline{N}}_i \right\| = \frac{1}{\eta_{i3D}} = \zeta_i \left\| \underline{\underline{M}}_i^e \right\| \tag{17}$$

where $\left\| \underline{\underline{A}} \right\| = \sqrt{A_{ij} A_{ij}}$ is the norm of tensor $\underline{\underline{A}}$. From equations 16 and 17 it comes:

$$\dot{\varepsilon}_i = \underline{\underline{N}}_i \underline{\sigma}_i^v = \zeta_i \underline{\underline{M}}_i^e \underline{\sigma}_i^v = \frac{\underline{\underline{M}}_i^e \underline{\sigma}_i^v}{\eta_{i3D} \left\| \underline{\underline{M}}_i^e \right\|} \tag{18}$$

Taking the case of a one dimensional loading (only σ_{11} is not nil), it comes:

$$\dot{\varepsilon}_{11i} = \frac{\sigma_{11i}^v}{\eta_{i3D} E_i \left\| \underline{\underline{M}}_i^e \right\|} = \frac{\sigma_{11i}^v}{\eta_i} \tag{19}$$

where η_i is the one dimensional viscosity constant of body "*i*". Then:

$$\eta_{i3D} = \frac{\eta_i}{E_i \left\| \underline{\underline{M}}_i^e \right\|} \tag{20}$$

Finally constant ζ_i which allows describing the whole behaviour of the V body is given by the relation:

$$\zeta_i = \frac{1}{\eta_{i3D} \left\| \underline{\underline{M}}_i^e \right\|} = \frac{E_i}{\eta_i} \tag{21}$$

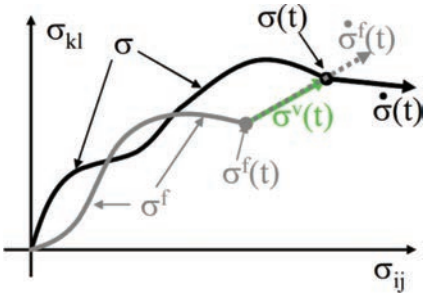

Figure 10. Evolution of the non-viscous (or elastoplastic) stress $\underline{\sigma}^f$ and of the viscous stress $\underline{\sigma}^v$ in the case without plastic strains (LVE behaviour).

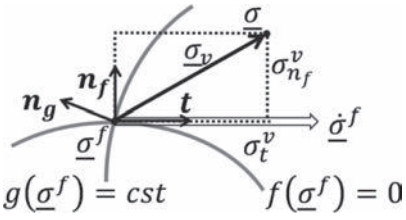

Figure 11. Representation of tensors when reaching the yield surface in the case of perfect plasticity.

3.3 *Viscoplastic case*

The EPP-version introduces a perfectly plastic model for EP_i bodies. This section deals with the viscoplastic case *ie.* $f\left(\underline{\sigma}_i^f\right) = 0$ with plastic strains $\left(\underline{\sigma}_v \cdot \underline{n}_f > 0\right)$. When non viscous stress $\left(\underline{\sigma}_i^f\right)$ reach the yield surface two complementary phenomena appear:

- As stress $\underline{\sigma}_i^f$ is on the yield surface the rate $\dot{\underline{\sigma}}_i^f$ can only be tangent to the surface $f\left(\underline{\sigma}_i^f\right) = 0$. In others words $\dot{\underline{\sigma}}_i^f$ is only pointing in the orthogonal directions of vector $\underline{n}_f$ which means $\dot{\underline{\sigma}}_i^f \cdot \underline{n}_f = 0$. Consequently $\dot{\underline{\sigma}}_i^f$ and $\dot{\underline{\sigma}}_i^v$ are no more collinear when plasticity is activated (Fig. 11).
- Plastic strain rate $\dot{\underline{\varepsilon}}_i^p$ is collinear to the unit normal vector $\underline{n}_g$ to the plastic potential surface. Its norm is denoted $\dot{\varepsilon}_i^p$ and given by the Mapping rule presented hereafter. Then $\dot{\underline{\varepsilon}}_i^p = \dot{\varepsilon}_i^p \underline{n}_g$.

From Equation 15 it comes:

$$\dot{\underline{\varepsilon}}_i = \underline{\underline{N}}_i \underline{\sigma}_i^v = \underline{\underline{N}}_i \left(\underline{\sigma}_{i\,n_f}^v + \underline{\sigma}_{i\,t}^v \right) \tag{22}$$

where $\underline{\sigma}_{i\,n_f}^v$ and $\underline{\sigma}_{i\,t}^v$ are respectively the projection of $\underline{\sigma}_i^v$ on the unit normal vector $\underline{n}_f$ to the yield surface and $\underline{\sigma}_{i\,t}^v = \underline{\sigma}_i^v - \underline{\sigma}_{i\,n_f}^v$. From this equation elastic and plastic part can be identified:

$$\begin{cases} \dot{\underline{\varepsilon}}_i^e = \underline{\underline{N}}_i \underline{\sigma}_{i\,t}^v \\ \dot{\underline{\varepsilon}}_i^p = \underline{\underline{N}}_i \underline{\sigma}_{i\,n_f}^v \end{cases} \tag{23}$$

Finally the norm of the rate of plastic strain is equal to:

$$\dot{\varepsilon}_i^p = \left\| \underline{\underline{N}}_i \right\| \left\| \underline{\sigma}_{i\,n_f}^v \right\| \tag{24}$$

And the expression of the rate of plastic strains is given by:

$$\dot{\underline{\varepsilon}}_i^p = \left\| \underline{\underline{N}}_i \right\| \left\| \underline{\sigma}_{i\,n_f}^v \right\| \underline{n}_g \tag{25}$$

4 EXAMPLES OF SIMULATION

Figure 12 presents the results of a complex modulus test performed on Mix6%5070[3] (from [5]) and the simulations with the linear viscoelastic model having continuum spectrum 2S2P1D [6] and the DBN model having 5, 15 and 25 bodies. The influence of the number of chosen elementary bodies "*n*" can be observed. The calibration procedure is presented in [5].

[3]Mix6%5070 is a mix with 6% (aggregate weight) of 50/70 penetration grade pure bitumen and a continuous 0/10 mm aggregates grading.

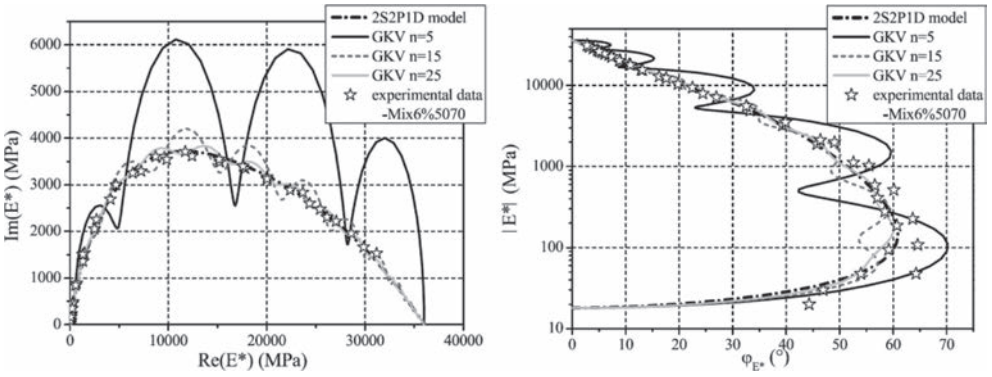

Figure 12. Experimental results of complex modulus test on Mix6%5070 and simulations with 2S2P1D and DBN models (5, 15, 25 elements)—Left: Cole-Cole diagram; Right: Black diagram—of complex modulus E* (from [5]).

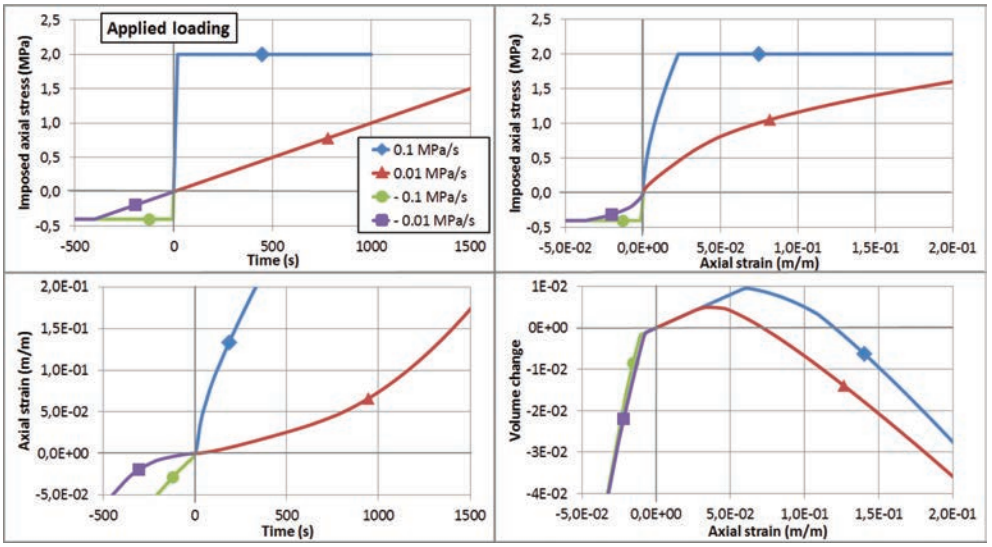

Figure 13. Simulations of compression and tension tests at two axial stress rates (0.1/0.01 MPa/s) followed by a creep period, using EPP version of the DBN model.

Results of a simulation based on the presented EPP version of the DBN model is plotted on Figure 13. Compression and tension tests are performed at two rate of stress (0.1/0.01 MPa/s) followed by a creep period. Calibration is made using 20 DBN bodies and is given in Annex A.

5 CONCLUSIONS AND PERSPECTIVES

This paper presents a version of the DBN model developed at LGCB laboratory (*ENTPE "Ecole Nationale des TPE"*) called the Elastic—Perfectly Plastic (EPP) version. DBN model is known to be versatile. This version is used to describe the linear viscoelastic and the visco-plastic domain. It can be upgraded to take into account more phenomena such as fatigue, rutting, brittle failure. Due to the limited number of pages these aspects are not developed in this paper.

The calibration of the EPP version of the BDN model needs twenty constants for the isotropic case. Nine of these constants are obtained in the small strain domain (linear viscoelastic behaviour) from the 2S2P1D model. Two constants are considered to stand for thermo-susceptibility of the material using the William-Landel-Ferry equation. The Time-Temperature Superposition Principle (TTSP) is respected in the linear and nonlinear domains. The plastic domain (yield and plastic potential surfaces) needs the last nine constants to be calibrated. Although few new constants are introduced this version has a good potential. Its formulation is easy-to-use. This law will be implemented further in a finite elements methods program.

REFERENCES

[1] Di Benedetto H., Corté, "Matériaux routiers bitumineux 1", Hermes Sciences Publications, Traité Mécanique et Ingénierie des Matériaux, France, 2004. [In French].

[2] Di Benedetto H., Mondher N., Sauzéat C., Olard F., "Three-dimensional thermo-viscoplastic behaviour of bituminous materials: the DBN model", Road Materials and Pavement Design, Vol. 8, Issue 2, pp. 285–316, 2007.

[3] Maïolino S., "Proposition of a general yield function in geomechanics", Comptes Rendus Mecanique 333, pp. 279–284, 2005.

[4] Di Benedetto H., Yan X., "Comportement mécanique des enrobés bitumineux et modélisation de la contrainte maximale", Matérials and Structures, Vol. 27, pp. 539–547, 1994. [In French].

[5] Tiouajni S., Di Benedetto H., Sauzéat C., Pouget S., "Approximation of linear viscoelastic model in the 3 dimensional case with mechanical analogues of finite size—Application to bituminous materials", Road Materials and Pavement Design, Vol. 12, No. 4/2011, pp. 897–930, 2011.

[6] Di Benedetto H., Delaporte B., Sauzéat C., "Three-dimensional linear behaviour of bituminous materials: experiments and modeling", ASCE International Journal of Geomechanics, Volume 7, Issue 2, pp. 149–157, March/April 2007.

[7] Di Benedetto H., Nguyen H.M., Pouget S., Sauzéat C., "Time-temperature superposition principle for bituminous mixtures: three dimensional approach and extension in the nonlinear domain", First ICTI Conference, organizers CATS & ISMARTi, Beijing, pp. 178–188, April 2008.

[8] Di Benedetto H., Olard F., "DBN law for the thermo-visco-elasto-plastic behaviour of asphalt concrete", Modeling of Asphalt Concrete, Y. Richard Kim, ASCE Press, Mc Graw-Hill Construction, 2009.

[9] Di Benedetto H., Olard F., Sauzéat C., Delaporte B., "Linear viscoelastic behaviour of bituminous materials: from binders to mixtures", Road Material and Pavements Design, Volume 5 Special Issue, EATA, pp. 163–202, 2004.

[10] Mondher N., Di Benedetto H., "Thermo-viscoplastic law for bituminous mixtures", Road Materials and Pavement Design, Volume 2, Issue 1, 2001.

[11] Mondher N., "Comportement thermomécanique des enrobés bitumineux: expérimentation et modélisation", Ph.D. Thesis, Ecole Nationale des Travaux Publics de l'Etat, 1997. [In French].

[12] Nguyen M.L., "Etude de la fissuration et de la fatigue des enrobes bitumineux", Ph. D. Thesis, Ecole Nationale des Travaux Publics de l'Etat, 2003. [In French].

[13] Nguyen Q.T., "Comportement thermomécanique des enrobés bitumineux sous solicitations cycliques dans les domains linéaire et non-linéaire", Ph.D. Thesis, Ecole Nationale des Travaux Publics de l'Etat, 2011. [In French].

[14] Olard F., "Comportement thermomécanique des enrobes bitumineux à basses temperatures", Ph.D. Thesis, Ecole Nationale des Travaux Publics de l'Etat, 2003. [In French].

[15] Pouget S., "Influence des proprieties élastiques ou viscoélastiques des revêtements sur le comportement des ponts à dalle orthotrope", Ph.D. Thesis, Ecole Nationale des Travaux Publics de l'Etat, 2011. [In French].

[15] SETRA-LCPC, Guide technique, "French design manual for pavement structures", Ed. LCPC et SETRA, Paris, 1997.

[16] Tatsuoka F., Ishihara M., Di Benedetto H., Kuwano R., "Time-dependent shear deformation characteristics of geomaterials and their simulation", Soils and foundations Vol. 42, No. 2, pp. 103–129, April 2002, Japanese Geotechnical Society.

[17] Tran Q.D., "Modèle simplifié pour les chausses fissures multicouches", Ph.D. Thesis, Ecole Nationale des Ponts et Chaussées, 2004. [In French].

ANNEX A

Calibration of the EPP version of the DBN model used to perform compression and tension simulations tests:

No.	Modulus E_i (MPa)	Poisson's coefficients v_i	Viscosities n_i (MPa · s) at tref	Stress threshold s_i^+ (MPa)	Stress threshold s_i^- (MPa)
0	36000	0,182			
1	2200000	0,420	1,76E-06	22,6	–3,7
2	1365000	0,420	1,73E-05	20,5	–3,4
3	782100	0,420	1,57E-04	18	–3,0
4	448300	0,420	1,42E-03	15,7	–2,6
5	254800	0,420	1,28E-02	13,45	–2,2
6	141300	0,420	1,13E-01	11,1	–1,8
7	73330	0,420	9,27E-01	9,05	–1,5
8	32650	0,420	6,54E+00	7,3	–1,2
9	10930	0,420	3,47E+01	5,64	–0,9
10	3019	0,420	1,52E+02	4,65	–0,8
11	756	0,420	4,79E+02	3,55	–0,6
12	227	0,420	1,44E+03	2,85	–0,5
13	93	0,420	2,94E+03	2,35	–0,4
14	58	0,420	4,66E+03	1,6	–0,3
15	70	0,420	8,88E+03	0,65	–0,1
16	94	0,420	1,89E+04	0,42	–0,1
17	208	0,420	6,59E+04	0,26	–0,04
18	527	0,420	3,75E+05	0,17	–0,03
19	1679	0,420	2,67E+06	0,13	–0,02

Asphalt Pavements – Kim (Ed)
© 2014 Taylor & Francis Group, London, ISBN 978-1-138-02693-3

Accelerated pavement testing for verification of DARWin-ME models for superpave pavements

Stefan Romanoschi
Department of Civil Engineering, University of Texas, Arlington, TX, USA

Mustaque Hossain
Department of Civil Engineering, Kansas State University, Manhattan, KS, USA

ABSTRACT: APT tests were conducted on 12 lanes of Superpave pavements with various thickness and mix design. The objectives of this research were to validate the pavement response models and fatigue relationship used in DARWin-ME. All pavement sections were instrumented with asphalt strain gages to measure transverse and longitudinal tensile strains and thermocouples for temperature measurements. Companion beam samples of the Superpave mix with the same air voids as the test lanes were tested in an IPC beam-fatigue test machine under controlled strain mode at three different strain levels till they reach 50% of the initial stiffness. The sections were loaded with a 100 kN (22.5-kip) single axle traveling at a uniform travel speed of 11.2 km/h (7 mph). The pavement responses were also independently calculated by the response software, JULEA. The results show that DARWin-ME structural response model for flexible pavements under-predicts the longitudinal strains at the bottom of the asphalt concrete layers, the structural response used for predicting alligator cracking. The computed strains were two to three times smaller than the measured strains. The laboratory beam fatigue test results show that a single model for the fatigue life of asphalt concrete, such as the one incorporated in DARWin-ME, does not effectively predict the fatigue life for all mixes.

Keywords: Superpave, DARWin-ME, fatigue life, Accelerated Pavement Testing

1 INTRODUCTION

The National Academy of Science, through its NCHRP Program, has developed a user-friendly procedure capable of executing mechanistic-empirical design while accounting for local environmental conditions, local highway materials, and actual highway traffic distribution by means of axle load spectra [1]. The resulting procedure was adopted by the American Association of State Highway and Transportation (AASHTO) as the new AASHTO design method (DARWin-ME) for pavement structures. It should be noted that all mechanistic design approaches produce "*theoretical structural designs*" that should be adjusted or *"calibrated"* to actual conditions using data originated from in-service pavement structures. DARWin-ME is a procedure with (i) national correlations to estimate selected inputs, (ii) national default values, and (iii) national calibration factors developed from the LTPP sites [2]. It is clear that all these need to be validated and/or calibrated for each specific state and/or region. Without region/state specific calibration, the new guide will be ineffective and of limited use for design purposes. Also, assessment of the design reliability can only be attempted after the guide has been calibrated and validated. This paper describes research work that aimed to contribute to the pavement performance models by conducting accelerated pavement tests at the Civil Infrastructure Systems Laboratory (CISL) Laboratory of Kansas State University. Due to the limited number of pavement sections that can be constructed and tested at CISL, the

research work focused on verification of the DARWin-ME models for representative flexible pavement structures in three Midwestern states: Iowa, Kansas and Missouri.

2 ACCELERATED PAVEMENT TESTING (APT) AT THE CIVIL INFRASTRUCTURE SYSTEMS LABORATORY (CISL)

The APT facility at CISL of Kansas State University is an indoor facility with about 651 m^2 (7,000 ft^2) of floor space [3]. The laboratory allows full-scale accelerated testing on pavement structures. The test pavements are constructed in three, 1.83 m (6.0 ft) deep test pits of varying width and 6.1 m (20 ft) in length. The accelerated loading is provided by the APT machine that can be moved on rails between the testing pits. The main components of the machine are the steel frame, which has two main girders with a 12.8 m (42-ft) center-to-center span; and the bogie, that is supported by the frame. The bogie is pulled back and forth by a rubber belt attached to an electric motor fixed on the frame. The wheel-load assembly consists of a single or tandem axle mounted on the bogie. Loading of the axle assembly is accomplished with a two hydraulic cylinders mounted on the bogie, above the single axle. The hydraulic pump pressurizes the oil in the hydraulic circuit and thus, the two cylinders push the bogie into the steel frame and the axle on the top of the test pavement. The cylinders also raise the bogie when uni-directional loading is applied. The axle load is controlled by the pressure in the hydraulic circuit. Load cells mounted on each wheel are used to measure the instantaneous wheel loads [3].

The bogie moves with a constant speed of 11 km/h (7 mph) on the test pavement; acceleration and deceleration are done outside the test area. The bogie takes approximately 5.8 seconds to complete its travel distance in one direction. In bi-directional loading mode, approximately 620 passes of the bogie are applied in one hour of operation, and about 100,000 passes in one week. The operation is typically stopped for several hours weekly for maintenance of the machine and measurement of pavement response and performance. Typically, two test pavements are constructed in each pit and loaded simultaneously with one wheel of the axle passing above each test pavement. The machine is equipped with a lateral wandering device that moves the entire frame in a lateral direction, with a maximum lateral wander of ±0.3 m (±12 inch). The lateral movement is applied in steps of 12.5 mm (0.5 inch) using screw jacks. A temperature-control chamber was built to encase the entire steel frame such that the temperature in the asphalt concrete layers could be controlled within ±3°C (±6°F). For this project, target testing temperatures were 20°C (68°F) and 35°C (95°F).

2.1 *CISL 14 experiment*

The objective of this experiment was to verify the models used in the Mechanistic Empirical Pavement Design Guide (now DARWin ME) for the design of new flexible pavements through Accelerated Pavement Testing (APT). Twelve experimental pavement structures were constructed and tested. Three pairs were 'fatigue cracking' sections aimed to study fatigue-cracking behavior of flexible pavements. The remaining three pairs were 'rutting' sections aimed to study rutting behavior of asphalt concrete pavements. In total, six Superpave HMA mixes were used, two for each of the three states. One 'fatigue-cracking' and one 'rutting' pavement were built for each mix.

Figure 1 shows an example of four test sections, a fatigue-cracking pair and rutting pair of test sections, built in two pits to test the two Superpave mixes of one state. The pavement sections were constructed in three layers: a Hot-Mix Asphalt (HMA) surface layer, a 0.15 m (6.0 in.) unbound granular base course, and a 1.5 m (5.0 ft), A-7-6 clay subgrade. The 'fatigue-cracking' sections had a 100 mm (4.0 in.) nominal thickness for the HMA layer and were loaded at a pavement surface temperature of 20°C (68°F). The 'rutting' sections had a 178 mm (7.0 in.) nominal thickness for the HMA surface layer and were loaded at a pavement surface temperature of 35°C (95°F).

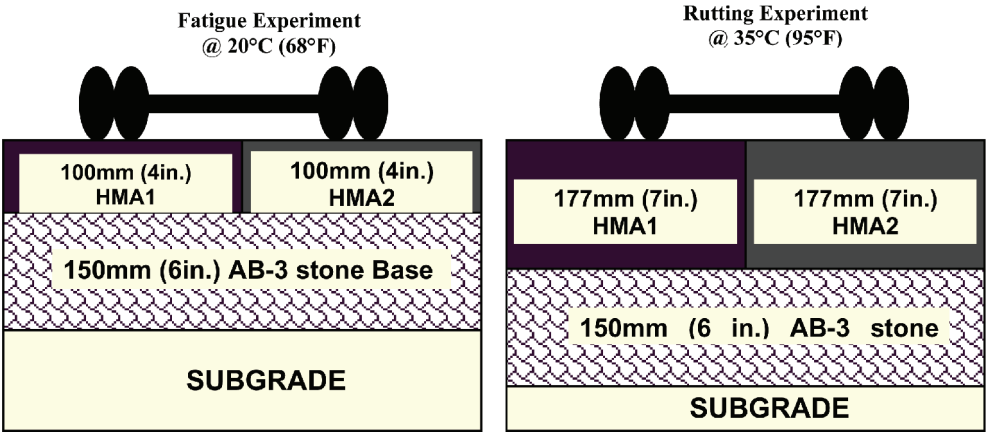

Figure 1. Cross section of the experimental pavement sections.

The sections were loaded with a 100-kN (22,500 lb) single axle applied at a uniform travel speed of 7 mph (11 km/hr). Lateral movement was provided by a lateral wandering device that moved the entire frame of the APT machine in the lateral direction, with a maximum lateral wander of ±0.305 m (±1.0 ft). Transverse profiles at the pavement surface were measured periodically during APT loading to record the evolution of rut depth with the number of load repetitions.

Instrumentation was embedded in the experimental pavement sections during construction. Strain gages were used to measure horizontal and vertical strains at the bottom of the HMA layer. Linear Variable Differential Transformers (LVDTs) were used to measure the dynamic and permanent vertical deformation in each layer. Pressure (stress) cells were used to measure the vertical compressive stress at the top of the subgrade layer. Thermocouples were used to measure the temperature at the surface and at two additional depth points in each pavement structure.

The Departments of Transportation (DOT) of Kansas, Missouri, and Iowa provided the mix designs for the six Superpave mixes used for test section construction. A local contractor, Schilling Construction Inc., constructed the pavement sections at CISL with materials transported from the three states. The six asphalt mixes consisted of a Kansas course mix (KS1) with 19-mm Nominal Maximum Aggregate Size (NMAS); a Kansas fine mix (KS2) with 12.5-mm NMAS; two 12.5-mm NMAS Missouri mixes with different binders (PG 70-22 for MO1 mix and PG 64-22 for MO2 mix), and two 12.5-mm NMAS Iowa mixes with the same binder but different design Equivalent Single Axle Loads (ESALs) (30 million for mix IA1 and 3 million for mix IA2). The mix design information, including aggregate gradation, PG binder grade, gravimetric binder content, and measured *in-situ* air voids can be found elsewhere [4].

3 FLEXURAL FATIGUE OF ASPHALT CONCRETE MIXTURES

In order to determine flexural fatigue properties of HMA mixes used for this research project, approximately 500 mm (20 inch) square slabs were cut from the HMA pads built outside the CISL laboratory with the mixes at the same time the experimental pavement test sections were constructed. The pads were compacted with the same rollers and at the same density as for the test sections. A Troxler nuclear density gage was used to measure the as-compacted density. Six beams were cut from each slab. Before testing, the beams were placed in the environmental chamber for at least two hours at 20°C (68°F), the test temperature. This test temperature was controlled by a heating and cooling unit and was maintained for all tested samples.

Each asphalt specimen was placed in the IPC beam-fatigue test machine and fixed in position with clamps (Fig. 2). After the input parameters were selected (dimensions of the beam, microstrain level, etc.) and all readings were zeroed, the fatigue test was started. After the test was initialized, the IPC beam-fatigue computer displayed the initial stiffness, measured after 200 cycles, and computed the termination stiffness as half of the initial stiffness. The applied cyclic load used was sinusoidal, with a frequency of 10 Hz and with no rest periods. The peak-to-peak load amplitude was recorded. The specimens were tested under controlled strain mode at three different strain levels: 100, 200, and 300 microstrain (10^{-6} in/in). Mixes KS1 and KS2 were also tested at 400 and 500 microstrain. Failure of the specimen was considered when the beam reached 50% of the initial stiffness.

The test loading time, cycle number, maximum and minimum applied load and deflection, tensile stress, strain, phase angle, flexural stiffness, modulus of elasticity, and dissipated energy data were recorded periodically. A typical test output, given in Figure 3, showed that

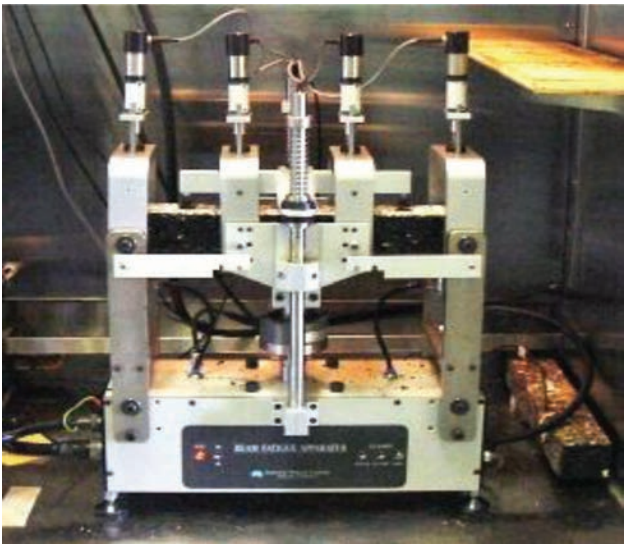

Figure 2. Beam fatigue testing apparatus.

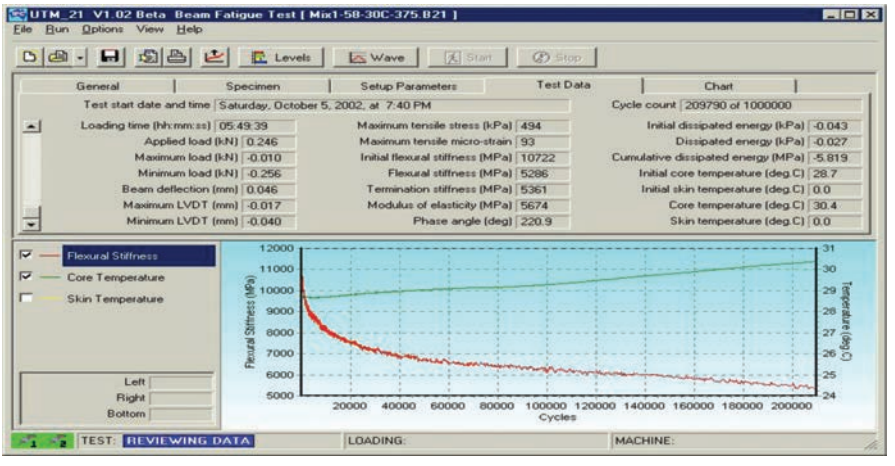

Figure 3. Typical output screen of beam fatigue test.

flexural stiffness decreased with an increasing number of loading cycles. This trend was observed for all beams tested in this experiment.

Some HMA specimens in this test did not reach the termination stiffness of 50% of the initial stiffness after maximum number of 2 million cycles, especially the specimens tested at low strain levels. For time consideration, these tests were stopped after 2 million loading cycles. This limited cycle number was input in to fatigue test control software as it was deemed that the stiffness data collected in the first 2 million cycles would allow estimation of the number of cycles to failure, considered as the number of cycles where the stiffness reaches half of the initial values. For these specimens an assumption was made that after 500,000 load cycles, flexural stiffness decreases linearly with the number of applied cycles:

$$S = b_0 + b_1 N \tag{1}$$

where
S = stiffness (MPa), N = is the number of cycles, and b_0 = is the intercept of the Y axis, and b_1 is the slope.

The final modulus, which is half of the initial modulus, has the following equation:

$$S_{fin} = b_0 + b_1 N_{fin} = 0.5 * S_{initial} \tag{2}$$

Therefore, the fatigue life N_{fin} was determined as follows:

$$N_{fin} = (S_{fin} - b_0)/b_1 \tag{3}$$

The coefficients b_0, b_1, R^2, and N_{fin} were computed using Microsoft Excel. A graphical example of the use of linear regression to estimate the number of cycles to failure for the specimens that did not fail up to 2 million cycles is shown in Figure 4.

The number of cycles to failure was also calculated considering an exponential evolution of the stiffness with the number of cycles, as follows:

$$S = c\ N^d \tag{4}$$

The coefficients c and d were computed using Microsoft Excel from the stiffness data recorded during the first 2 million cycles. Then, the number of cycles to failure, N_{fin}, was calculated. However, engineering judgment dictated that the linear regression provided a much

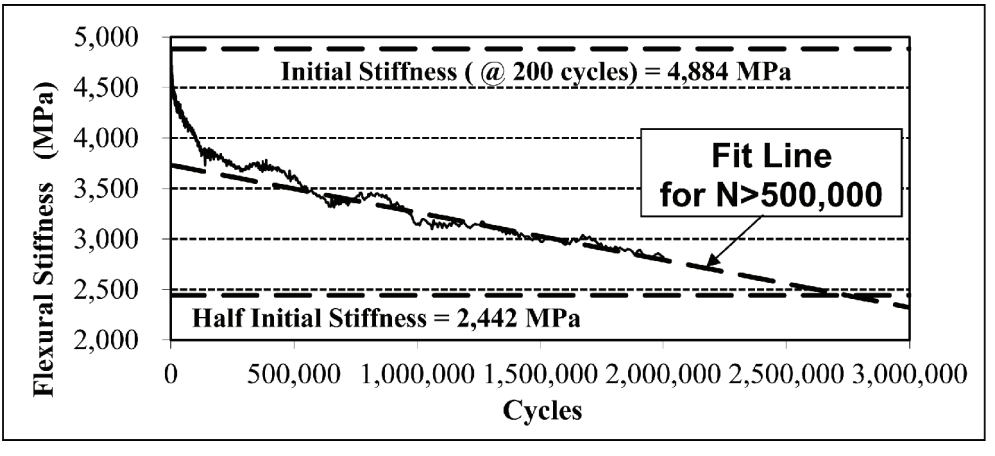

Figure 4. Estimation of loading cycles to failure by extrapolation.

better fit than the exponential model, and therefore, the fatigue lives obtained with the linear model were used for further analysis.

Models expressing the relationship between the number of cycles to failure and loading strain were developed after the number of cycles to failure was determined for each tested sample. Table 1 presents, for each of the six mixes subjected to flexural fatigue tests, two models relating the number of cycles to failure and loading strain. The models are very similar from a mathematical standpoint. However, a slightly better fit is obtained with Model 1.

Figure 5 shows, on the same chart, the Model 1 fit curves for all six mixes. The figure indicates that for loading stains higher than 100 micro-strains and at 20°C (68°F), HMA mix

Table 1. Models relating the number of cycles to failure and loading strain.

Mix	a	b	c	R-squared
Model 1: $N = a * (micro\text{-}strain)^b$				
KS1	1.61E+11	–2.10978		0.922867
KS2	9.41E+08	–1.06065		0.374794
MO1	3.71E+10	–1.53314		0.357193
MO2	4.77E+10	–1.72622		0.763139
IA1	1.09E+13	–2.82145		0.635796
IA2	1.29E+12	–2.61847		0.947428
Model 2: $log_{10}(N) = a + b * log_{10}(micro\text{-}strain)$				
KS1	11.19836	–2.07084		0.866162
KS2	8.963334	–1.0955		0.446746
MO1	10.57472	–1.54622		0.592261
MO2	10.68022	–1.7123		0.816795
IA1	13.03939	–2.83302		0.843026
IA2	12.0887	–2.60335		0.921726
Model 3: $N = 10^M * a * (strain)b * (E^*)^c$				
	7.89	–1.59697	0.070324	0.09
Model 4: $log_{10}(N) = M + log_{10}(a) + b * log_{10}(strain) + c * log_{10}(E^*)$				
	8.44	–1.6095	0.045636	0.330

Note: E^* is measured in MPa.

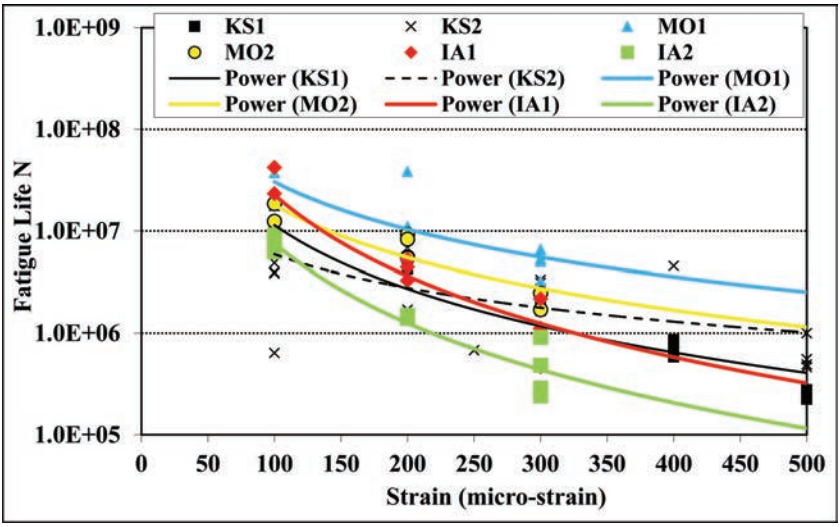

Figure 5. Flexural fatigue lives predicted by model 1.

MO1, with a polymer-modified binder, has the highest fatigue life, while mix IA2 has the shortest fatigue life. The difference in fatigue life increases with increased strain level.

In order to incorporate the effect of mix stiffness and volumetric properties, two overall fatigue models (Models 3 and 4) were developed from the fatigue data recorded on all samples. These models are similar to Equation 5 (shown later), the fatigue model incorporated in AASHTO DARWin ME, with $M = 4.84*[V_b/(V_a + V_b) - 0.69]$. A better fit of the overall model was obtained for Model 4.

4 FATIGUE CRACKING

CISL test sections were monitored to observe surface cracking every time the pavement response and surface profile measurements were performed. The only crack observed was for section KS2-4 at 1,300,000 passes of the APT machine; no other cracks were observed on other 11 sections. That crack was in the longitudinal direction, was located very close to the centerline of the section, and had a length of approximately 1.06 m (27 inches). The crack grew to approximately 1.08 m (43 inch.) in the following 100,000 load repetitions. However, the crack was not observed anymore when the next measurements were performed at 1,500,000 load repetitions, and after that.

5 MEASURED STRAIN AT THE BOTTOM OF THE HMA LAYER

Strain values were recorded for at least four cycles (eight passes) of the CISL APT machine, at a sampling frequency of 100 Hz. Recording was started when the axle was at the west end of the travel and had started traveling east. Strain measurements were performed for two lateral positions of the wheels: (1) Position 0: The symmetry axis of the wheel was right above the gages and the tires were straddling the gages. (2) Position +6: With one tire passing right above the strain gages; the symmetry axis of the wheel was 0.15 m (6 inches) to the side from the location gages. Figure 6 shows and example of measured strain signals. Figures 7 and 8 show the evolution of measured strains with the number of applied passes.

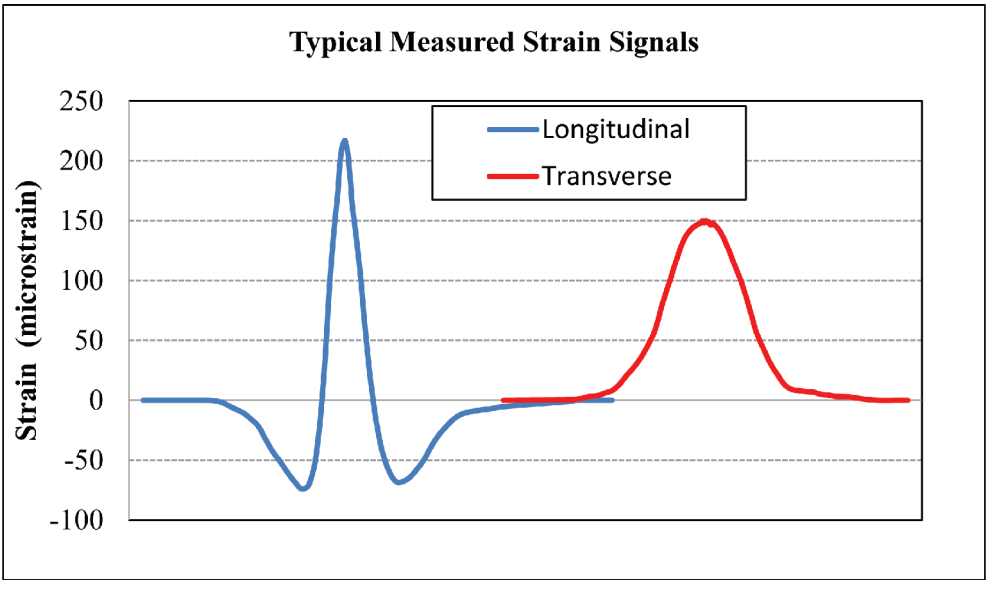

Figure 6. Typical signals for the measured horizontal strains at the bottom of the asphalt concrete layer.

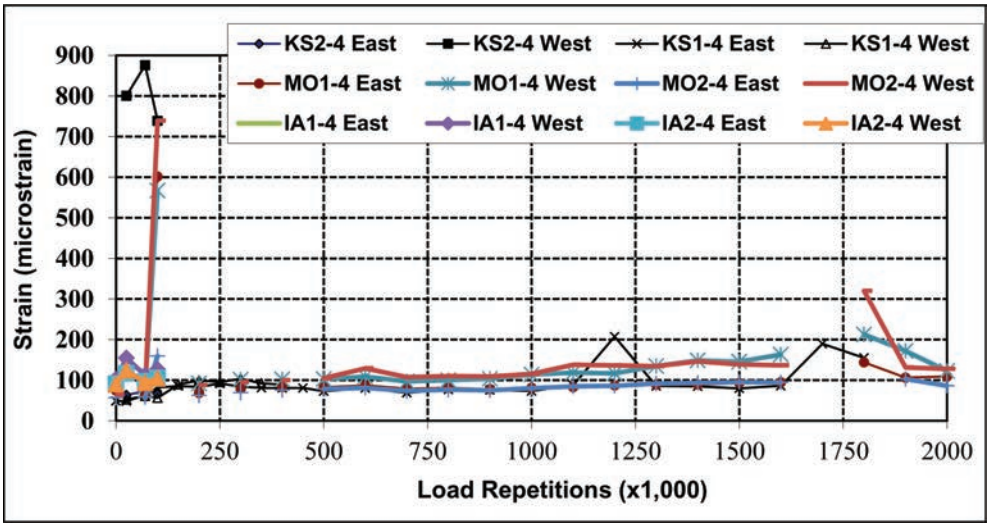

Figure 7. Transverse strains for the fatigue-cracking sections (4″ HMA).

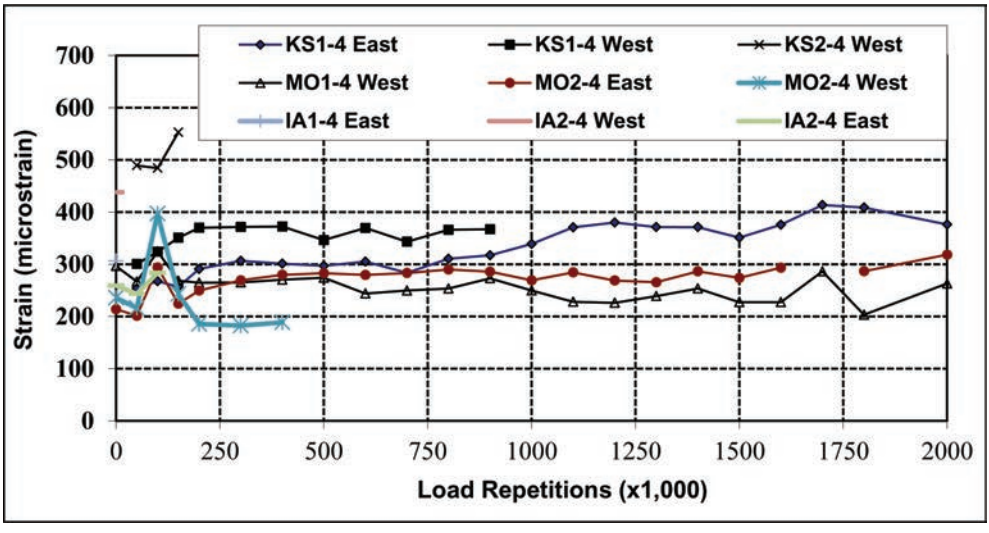

Figure 8. Longitudinal strains for fatigue cracking sections.

A few observations can be made regarding the measured strains at the bottom of the HMA layer:

- The measured longitudinal strains are almost always larger than the corresponding transverse strains.
- In the Kansas fatigue-cracking sections, the longitudinal strains recorded before loading commenced were very high. However, once loading commenced, the recorded strains were comparable to but remained higher than those recorded for the other fatigue-cracking sections.
- Differences between corresponding strains measured by replicate gages (east and west) installed in the same test sections can be significant, in many cases larger that the difference between corresponding strains measured on two sections with mixes from the same state.

- In general, when two mixes of the same state are compared, the ranking of the corresponding measured strains matches the expected ranking. Strains measured on the KS1, MO1, and IA1 sections are smaller than those measured on the KS2, MO2, and IA2 sections.
- For most cases, strains measured after the first 200,000 load repetitions seem to remain stable, exhibiting only small fluctuations after that.

6 VERIFICATION OF PAVEMENT RESPONSE MODEL

The response model that calculates the stresses and strains that develop in the pavement structure under truck wheel loading is of paramount importance in the MEPDG (predecessor of DARWin ME software) model since distresses and thus, pavement performance, are estimated based on the computed stresses and strains. The MEPDG software does not yield computed stresses and strains as outputs. Rather the software output contains accumulated fatigue-damage parameters for bottom-up fatigue cracks. This fatigue damage is calculated from the value of the longitudinal strain found at the bottom of the asphalt concrete layer in incremental fashion using Miner's law [1]. The fatigue model calculates the allowable repetitions to failure as

$$N_f = 0.00432 * k_1' * C(1/\varepsilon_t)^{3.9492}(1/E)^{1.281} \quad (5)$$

where
ε_t = longitudinal strain at the bottom of the asphalt concrete layer;
E = stiffness of the asphalt concrete;
$C = 10^M$ and $M = 4.84*[V_b/(V_a + V_{bef}) - 0.69]$;
V_a and V_{bef} = air voids and effective binder volumetric content (%); and
k_1' = a parameter that depends only on the thickness of the asphalt layers.

For each of the 12 months, the total duration of simulated APT trafficking used in this study, the MEPDG output obtained listed the fatigue damage in percentages, the number of trucks passing over the designed pavement structure, and the estimated stiffness of the asphalt concrete layers. Simulation of the APT testing was conducted with MEPDG software for level 1 and 3 analyses, at a 50% reliability level. In both analyses, all pavement materials were assumed to be linear elastic. However, the value of the modulus of asphalt concrete was selected depending on the speed of loading. Since the number of trucks in the simulations was the same as the number of axle passes in the APT experiment, it was possible to compute the damage calculated by the MEPDG model for a single pass of the APT axle for each month. The damage values were then used to "back-estimate" the longitudinal strain at the bottom of the asphalt concrete with Equation 5.

Figure 9 shows the correspondence between the measured longitudinal strains and the corresponding values "back-estimated" from the MEPDG output in the level 1 and level 3 analyses. The figure suggests that for the "rutting" sections, the measured strains were between two and three times higher than the computed strains, at both levels 1 and 3. For the thinner sections, the computed strains were closer to the measured strains in some cases, but in many cases they were two to three times higher than the measured strains. This suggests the algorithms for computing the response in the MEPDG model should be reviewed and further validated. The under-prediction of strains may result in under-designed pavement structures for fatigue resistance.

In addition to back-estimating the longitudinal strains from the MEPDG software output, the MEPDG-calculated pavement response was obtained by performing runs with the JULEA software. JULEA is the linear-elastic model incorporated in the MEPDG software for computing response of new flexible pavement structures. The JULEA software models the wheel load as uniformly distributed over circular areas.

The calculation of the theoretical strains with the JULEA software was done assuming the loading configuration shown in Figure 10. The figure also shows the points where the stresses

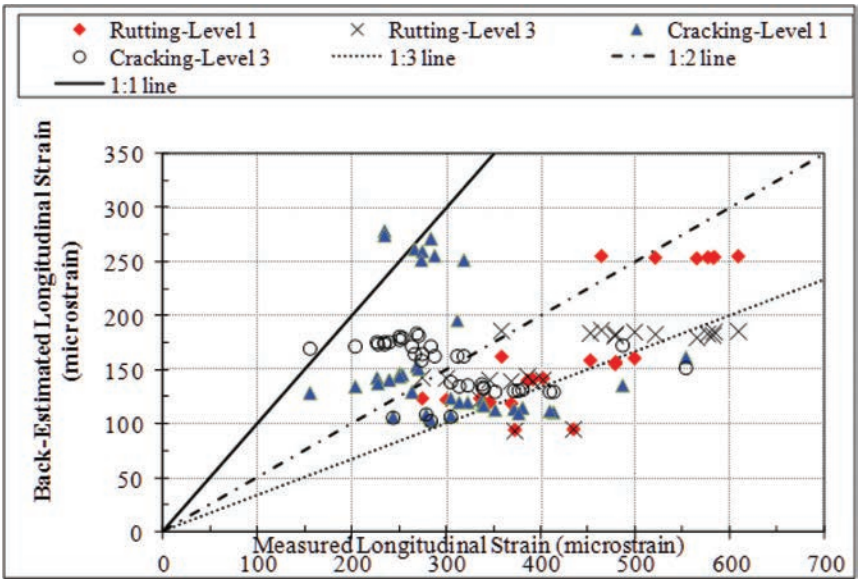

Figure 9. Measured and back-estimated longitudinal strains.

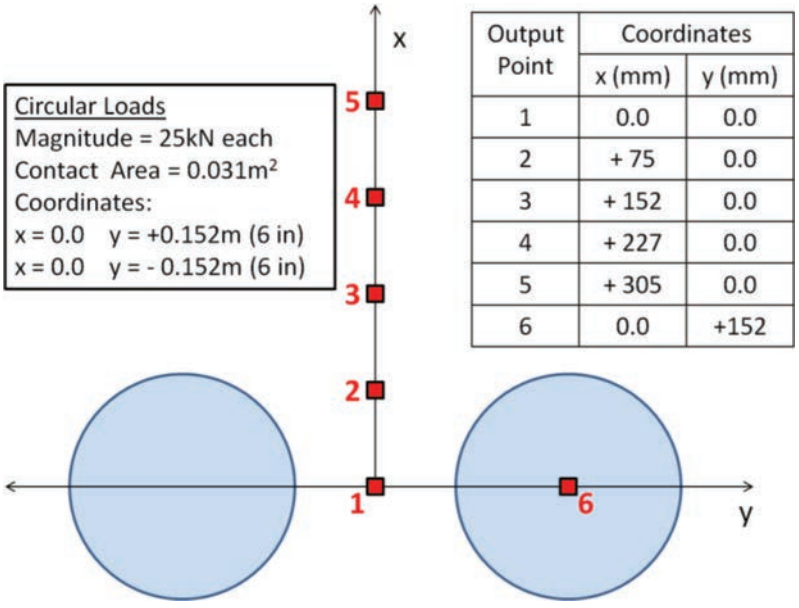

Output Point	Coordinates	
	x (mm)	y (mm)
1	0.0	0.0
2	+ 75	0.0
3	+ 152	0.0
4	+ 227	0.0
5	+ 305	0.0
6	0.0	+152

Figure 10. Loading model for JULEA calculations.

and strains were computed (output points). The layer moduli were the same as those used in the MEPDG inputs for Level 3 design analysis [5].

Results of the JULEA calculations are shown in details elsewhere [5]. They suggest the following:

- The computed maximum longitudinal strains at the bottom of the HMA layer are not always in between the two wheels. Depending on pavement layer thickness and stiffness, they can also develop right underneath the center of one circular loading area.

- Longitudinal strains computed by JULEA are different from those back-estimated from the MEPDG output. This suggests that the MEPDG software code should be reviewed.
- With a very few exceptions, the longitudinal strains computed by the JULEA model and back-estimated from the MEPDG output are smaller than the corresponding measured strains. This can lead to severe under-estimation of the fatigue damage for the bottom-up cracking and thus, to over-estimation of the fatigue cracking lives of the flexible pavement structures.

7 CONCLUSIONS

The following can be concluded from this research study:

- The MEPDG structural response model for flexible pavements under-predicts the longitudinal strains at the bottom of the asphalt concrete layers, the structural response used for predicting fatigue/alligator cracking. The computed strains were two to three times smaller than the measured strains.
- The laboratory beam-fatigue tests performed at 20°C (68°F) indicate that a single model for the fatigue life of asphalt concrete, such as the one incorporated in MEPDG, does not effectively predict the fatigue life of all mixes.
- The experiment could not verify either the bottom-up or top-down fatigue-cracking models incorporated in the MEPDG, since only one of the twelve tested sections exhibited cracking. Moreover, the longitudinal crack that appeared in that section healed before the load repetitions ended.
- With a very few exceptions, the longitudinal strains computed by the JULEA model and back-estimated from the MEPDG output were smaller than the corresponding measured strains. This can lead to severe under-estimation of the fatigue damage for the bottom-up cracking and to over-estimation of the fatigue-cracking lives of the flexible pavement structures.

ACKNOWLEDGEMENTS

The authors would like to acknowledge the sponsorship of this study by the Midwest States Accelerated Pavement Testing Pooled-Funds program financed by the Departments of Transportation in Iowa, Kansas and Missouri.

REFERENCES

[1] NCHRP. *Guide for Mechanistic-Empirical Design of New and Rehabilitated Pavement Structures*. Final Report, NCHRP Project 1-37A. Transportation Research Board, National Research Council, Washington, DC, webdocument: http://www.trb.org/mepdg/guide.htm accessed August 2004.

[2] Quintus, H.V and L. Scofield. *2002 Design Guide—Implementation*. Presented at the Workshop on 2002 AASHTO Design Guide, 82nd Annual Meeting of the Transportation Research Board, Washington, DC, January 11, 2003.

[3] Melhem H.G. *Development of an Accelerated Testing Laboratory for Highway Research in Kansas*, Report No. FHWA-KS-97/5, Kansas Department of Transportation, Topeka, November 1997.

[4] Onyango M. *Verification of Mechanistic Prediction Models for Permanent Deformation in Asphalt Mixes Using Accelerated Pavement Testing,* Doctoral Dissertation, Kansas State University, Manhattan, 2009.

[5] Romanoschi S.A., Lewis, P., Gedafa, D. and M. Hossain. *Verification of Mechanistic-Empirical Design Models for Flexible Pavements Through APT Testing*. (CISL EXPERIMENT NO. 14), Draft Final Report, Midwest States Accelerated Pavement Testing Pooled Fund Program, December 2011.

This page intentionally left blank

Asphalt Pavements – Kim (Ed)

Power law viscoelastic contact model for Discrete Element Method simulation of asphalt binder

Bo Peng & Linbing Wang
Virginia Tech, Blacksburg, VA, USA

ABSTRACT: The Discrete Element Method (DEM) has been extensively used for modelling the behavior of asphalt concrete, cement concrete and other geomaterials with discontinuous structure. As one of the most important materials for pavements, asphalt has very complex characteristics. Unlike existing linear viscoelastic contact models, this paper provides a detailed exploration of the contact model for thin film power-law creeping materials based on C.Y. Chueng's work. This model is aimed at simulating the thin film asphalt layer between two aggregates, which is a common structure in asphalt mixture. The new contact model was implemented on software PFC 3D and is numerically verified. Experiments with specimens containing a thin film asphalt between two aggregates are employed to validate the new contact model.

Keywords: Discrete Element Method, contact model, power law viscoelastic, viscoelastic, thin film

1 INTRODUCTION

Asphalt, an adhesive, low-cost and waterproof material discovered as early as 3800 B.C., is extensively used in pavement construction. However, asphalt is also acknowledged as a complex material which is not able to be well analysed by solid mechanics directly, because of its inelasticity, temperature sensitivity, load sensitivity and complex polymer structure. Some theoretical models have been developed for asphalt, such as dynamic models, temperature dependence models, and pressure dependence models. For more practical applications, the linear viscoelastic model is widely used in DEM, especially when it comes to asphalt mixtures.

DEM was proposed by Cundall in 1979 [1]. Since then, the method has been studied worldwide. DEM can be applied in a varied range of research, including soil and rock simulation, fluidization of cohesionless and cohesive particles flow, confined or unconfined particle flow, particle packing, compaction of particles, etc. The advantage of DEM is that it can simulate heterogeneous materials through discretization. Setting different parameters to the contributing materials in the simulation helps to distinguish their interaction. Those characteristics ensure DEM is a good method to simulate asphalt concrete (AC), which consists of various components such as asphalt binder, aggregates and air void.

In DEM, a contact model is the key to defining material and interaction type within a specimen. As the most frequently used DEM platform to develop asphalt application, Particle Flow Code (PFC) [2] has implemented several contact models, such as the linear elastic model [3], Hertz model [4], and soft-placement model; however, there are only two viscoelastic contact models—the linear viscoelastic and the Burger model, which are all linear models. Because of that, most recent asphalt simulation problems studied, such as prediction of mixture dynamic modulus [5], creep stiffness [6], mixture failure [7], are all based on linear viscoelastic contact models.

Asphalt is a complex material, and a linear viscoelastic model might not be accurate enough to describe its behavior. In this case, a high-order non-linear contact model is needed to improve simulation results. Considering the fact that asphalt often exists as a thin film layer between aggregates in mixture, the primary objective of this research is to develop a rational power law viscoelastic contact model. A corresponding DLL file that can be used as contact model and applied directly into PFC 3D is developed. The DEM simulation results are verified by theoretical results, and force-displacement simulation results from the contact model are validated with experiments.

2 POWER LAW CONTACT MODEL

2.1 *Theoretical model*

Asphalt binder is usually considered as a viscous fluid at relatively high temperatures, and an elastic medium at relatively low temperatures. In the temperature range of pavement, asphalt is regarded as a viscoelastic material. A viscoelastic model is usually comprised of an elastic part and an energy dissipation part, which is presented by a spring and dashpot. There are two types of common combinations—the Kelvin model which connects spring and dashpot in parallel and the Maxwell model which connects spring and dashpots in series. Different combinations of the Maxwell and Kelvin models can be assembled to come up with various viscoelastic models.

To simulate the complexity of a real viscous material, a nonlinear Maxwell model that theoretically assumes unidirectional flow in a uniform passage was developed by C.Y. Chueng and D. Cebon in 1997 [8]. This solution is aimed at acquiring the relationship between force and displacement of a thin-film asphalt layer sandwiched between two aggregates. Simplifying the two aggregate surfaces as two parallel rigid planes, the specimen employed is shown in Figure 1. Chueng verified his solution in compression, shear and combined compression and shear by comparison with experimental results. The following theoretical content is based on a paper of Chueng's in 1997 [8].

This solution assumes that the width of the layer is much larger than the height of the layer. As Figure 1 shows, *2a* is the width, *2h* is the height and *2l* is the length. Due to the large aspect ratio, *a*/*h*, this model can be regarded as a plane strain problem. Influenced by surrounding temperature and the characteristics of creeping material itself, pure bitumen in a thin film would follow a power-law relationship as:

$$\frac{\sigma'_{ij}}{\sigma_0} = \frac{2}{3}\left(\frac{\dot{\varepsilon}_e}{\dot{\varepsilon}_0}\right)^{1/n} \frac{\dot{\varepsilon}_{ij}}{\dot{\varepsilon}_e} \tag{1}$$

where σ_{ij} is the deviatoric stress tensor; $\dot{\varepsilon}_{ij}$ = strain rate sensor; $\dot{\varepsilon}_e$ = effective strain rate; and σ_0, $\dot{\varepsilon}_0$ are constants, which are related to the ambient temperature. If $n = 1$, then this solution

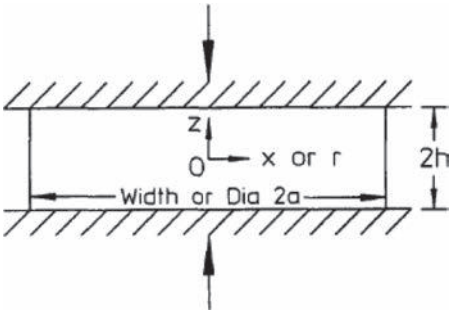

Figure 1. Geometry information of the thin layer [8].

becomes linear viscosity; while in the case of $n > 1$, the power law creep behaviour is assigned to the material layer. Parameter n is also related with temperature. Using the equation above, the constitutive equation can be written as:

$$\sigma_{xx} - \sigma_m = \frac{2}{3}\frac{\sigma_0}{\dot{\varepsilon}_0^{1/n}}(\dot{\varepsilon}_e)^{(1-n)/n}\left(\frac{\partial \dot{u}}{\partial x}\right) \tag{2}$$

$$\sigma_{zz} - \sigma_m = \frac{2}{3}\frac{\sigma_0}{\dot{\varepsilon}_0^{1/n}}(\dot{\varepsilon}_e)^{(1-n)/n}\left(\frac{\partial \dot{w}}{\partial z}\right) \tag{3}$$

$$\tau_{xz} = \frac{1}{3}\frac{\sigma_0}{\dot{\varepsilon}_0^{\frac{1}{n}}}(\dot{\varepsilon}_e)^{\frac{1-n}{n}}\left(\frac{\partial \dot{u}}{\partial z} + \frac{\partial \dot{w}}{\partial x}\right) \tag{4}$$

where σ_m is the mean stress. Besides the constitutive condition, the equilibrium conditions are:

$$\frac{\partial \sigma_{xx}}{\partial x} + \frac{\partial \tau_{xz}}{\partial z} = 0 \tag{5}$$

$$\frac{\partial \sigma_{zz}}{\partial z} + \frac{\partial \tau_{xz}}{\partial x} = 0 \tag{6}$$

Then, let's take a look at strain rate sensor for this situation:

$$\dot{\varepsilon}_{ij} = \begin{bmatrix} \partial \dot{u}/\partial x & 0 & 1/2\left(\partial \dot{u}/\partial z + \partial \dot{w}/\partial z\right) \\ 0 & 0 & 0 \\ 1/2\left(\partial \dot{u}/\partial z + \partial \dot{w}/\partial z\right) & 0 & \partial \dot{w}/\partial z \end{bmatrix} \tag{7}$$

where $\dot{u}$ is the deformation rate in x direction, and $\dot{w}$ is the deformation rate in z direction.

Because of the large aspect ratios in the thin film model, $\partial \dot{u}/\partial z$ strain rate would be much larger than the deformation rates in other directions. Therefore, the strain rate tensor can be rewritten as:

$$\dot{\varepsilon}_{ij} = \begin{bmatrix} 0 & 0 & 1/2\left(\partial \dot{u}/\partial z\right) \\ 0 & 0 & 0 \\ 1/2\left(\partial \dot{u}/\partial z\right) & 0 & 0 \end{bmatrix} \tag{8}$$

The effective stress in the case can be simplified as:

$$\dot{\varepsilon}_e = \left(\partial \dot{u}/\partial z\right)/\sqrt{3} \tag{9}$$

Simplify the Eq. (4) and equilibrium Eq.(5) by Eq.(9), we can get:

$$\frac{\tau_{xz}}{\sigma_0} = \left(\frac{1}{\sqrt{3}}\right)^{(n+1)/n}\left(\frac{|\partial \dot{u}/\partial z|}{\dot{\varepsilon}_0}\right)^{1/n}\operatorname{sign}\left(\frac{\partial \dot{u}}{\partial z}\right) \tag{10}$$

$$\frac{\partial P}{\partial x} = \frac{\partial \tau_{xz}}{\partial z} \tag{11}$$

where $P = -\sigma_m$. Because of the symmetry of structure, $\partial\tau_{xz} = 0$ when $z = 0$ and ignorance of the changing of pressure in the direction of z, the combination of the Eqs. (10, 11) can be written as:

$$\frac{\partial \dot{u}}{\partial z} = \left(\frac{\sqrt{3^{n+1}}\dot{\varepsilon}_0}{(n+1)\sigma_0^n} \right) |Z|^n \left| \frac{\partial P}{\partial x} \right|^n \operatorname{sign}\left(\frac{\partial P}{\partial z} \right) \tag{12}$$

The boundary conditions include $\dot{u} = 0$ at $z = \pm h$, $P = 0$ at the location $x = \pm a$, and:

$$F = 2l\int_{-a}^{a} P\, dx \tag{13}$$

where F is the force load on the surface.

For the overall thin film, compression of the material would lead to a flow from the center to the sides. Take $\dot{Q}$ as volumetric flow in the x-direction, the flow equation is:

$$\frac{\dot{Q}}{2l} = -2\dot{h}x \tag{14}$$

Consider the boundary condition and flow equation, then integrate the Eq.(12), the viscoelastic material force-displacement relationship is obtained as:

$$\frac{dh}{dt} = -h\dot{\varepsilon}_0 \left(\frac{1}{n+2} \right) \left(\frac{2n+1}{n} \right)^n \left(\frac{\sqrt{3}}{A} \right)^{n+1} \left(\frac{F/(4al)}{\sigma_0} \right)^n \tag{15}$$

where a and l are the relevant width and length of the layer; here, only h is a variable, other parameters are all constant. Regarding $\sigma_n = F/4al$, $\dot{\varepsilon}_n^v = -\dot{h}/h_0$, Eq. (15) can be rewritten as:

$$\dot{\varepsilon}_n^v = \dot{\varepsilon}_0 \left[\left(\frac{1}{n+2} \right) \left(\frac{2n+1}{n} \right)^n \left(\frac{\sqrt{3}}{A} \right)^{n+1} \right] \left(\frac{\sigma_n}{\sigma_0} \right)^n \tag{16}$$

Eq. (16) shows the pure viscosity of a material when elasticity is taken into consideration. The constitutive model is composed of a spring in series with the nonlinear dashpot denoted as:

$$\dot{\varepsilon}_n^0 = \dot{\varepsilon}_n^e + \dot{\varepsilon}_n^v = \frac{\dot{\sigma}_n}{E_n} + \dot{\varepsilon}_0 \left[\left(\frac{1}{n+2} \right) \left(\frac{2n+1}{n} \right)^n \left(\frac{\sqrt{3}}{A} \right)^{n+1} \right] \left(\frac{\sigma_n}{\sigma_0} \right)^n \tag{17}$$

where $\dot{\varepsilon}_n^0$ is the total strain which includes elastic and viscous parts. This is the microscopic constitutive model for a thin film viscoelastic material.

2.2 *DEM contact model development*

On the basis of Eq. (17), a constitutive contact model is deduced to apply in the DEM:

$$\dot{u} = \frac{\dot{f}}{E_n} + \dot{\varepsilon}_0 \left[\left(\frac{1}{n+2} \right) \left(\frac{2n+1}{n} \right)^n \left(\frac{\sqrt{3}}{A} \right)^{n+1} \right] \left(\frac{f}{\sigma_0} \right)^n \tag{18}$$

where u is the contact deformation between two spheres and f is the contact force. Then applying a backward difference approximation of a finite difference scheme, we can obtain the final equation applied in the DEM contact model:

$$\frac{u^{t+1} - u^t}{\Delta t} = \frac{f^{t+1} - f^t}{\Delta t \times E_n} + \dot{\varepsilon}_0 \left[\left(\frac{1}{n+2} \right) \left(\frac{2n+1}{n} \right)^n \left(\frac{\sqrt{3}}{A} \right)^{n+1} \right] \left(\frac{f^{t+1} + f^t}{2\sigma_0} \right)^n \tag{19}$$

where u^{t+1} is the current contact overlap which has been updated by Newton's Second Law automatically; u^t and f^t are obtained from the previous time step; and f^{t+1} is the only unknown variable—a contact force, needed to be calculated through contact model in the current time step. Therefore, Eq.(19) is a solvable equation that can be applied in DEM directly.

This power law user-defined contact model is written into PFC 3D with the C++ language. After the key equation—Eq.(19)—is written into the interface between C++ and FISH, which is the official coding language for PFC 3D, a DLL file is generated by compiling the C++ project, and this DLL file allows the new contact model to be loaded in PFC 3D directly. When the user contact model is running, the updated contact force would be obtained through Eq.(19) using the velocity, displacement and force in the previous time step and the Newton method is applied to solve the high order equations.

2.3 *Numerical verification*

To verify this contact model, a PFC 3D model of two fixed balls with constant overlap is developed, as shown in Figure 2. The computed normal contact force changing with time is recorded in the DEM simulation, and the analytical results are compared with computed results. In this case, since the overlap u is a constant, Eq.(19) can be simplified as:

$$\dot{f} = -kf^n \tag{20}$$

where $k = E_n \dot{\varepsilon}_0/\sigma_0^n [(1/n+2)(2n+1/n)^n(\sqrt{3}/A)^{n+1}]$.

Take $n = 2$ as test case, the analytical solution for Eq.(20) would be:

$$f(t) = \frac{1}{kt + (1/F_0)} \tag{21}$$

where F_0 is the initial contact force when $t = 0$.

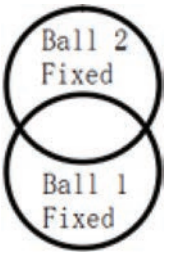

Figure 2. DEM verification model.

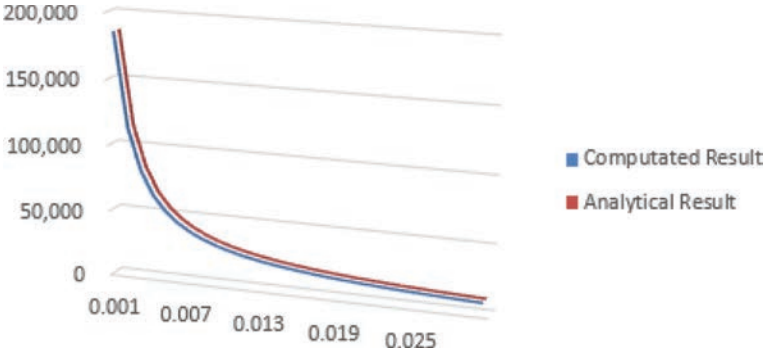

Figure 3. Comparison between computed result and analytical result.

The red line in Figure 3 shows the analytical results calculated by Eq.(21), and the blue line is the contact force obtained from the two fixed ball model in PFC 3D. Analytical results and computed DEM results from the power law contact model match well, verifying the power law's solution is successfully integrated into the DEM contact model. Both lines demonstrate that the force vanishes to zero with time, which is consistent with a viscosity material under constant loading.

3 EXPERIMENT VALIDATION FOR CONTACT MODEL

3.1 *General experiment description*

In order to develop the experimental situation consistent with power law theory—a thin film layer between two rigid planes, a sample is prepared as a thin film asphalt sandwiched between two cubic aggregates. Unakite aggregates are used in this experiment. In comparison with the stiffness of asphalt, the stiffness of Unakite aggregates is very large and can be considered as rigid. PG70-33 binder is used in the tests. After the binder was heated to 300 °F, a slight amount of softened binder was positioned over one aggregate, and another aggregate is used to cover the other surface of asphalt binder immediately. When the temperature goes down, asphalt shrinkage is inevitable. To neutralize the tension caused by shrinkage during the asphalt cooling down, the sample is pressed gently. This pressure assists in the formation of a thinner and more evenly distributed asphalt layer.

The size of the sample is mainly limited by the size of container in SKYSCAN 1174. The SKYSCAN is a micro X-ray CT machine that has the capability to measure dimension information of specimen, such as the asphalt thickness, asphalt width and aggregate size. The X-ray picture for a sample is shown as Figure 4.

Besides measuring dimensions, SKYSCAN also has a micro-processor, which controls the application of torsion, tension and pressure. After asphalt samples are placed in the loading stage, a uniaxial compression load is applied to samples from top and bottom stages. Because of the high energy of X-ray, the temperature within the machine will slightly increase. In this case, it is very important to finish the tests as soon as possible to keep testing times the same. Testing parameters are set through software controlling the X-ray system. With a constant speed of 0.7 μm, the force-displacement relationship is recorded during uniaxial compression process.

3.2 *Experiment parameter and data analysis*

To verify the correctness and accuracy of power law contact model, two sets of tests are performed. The parameters are provided in Table 1.

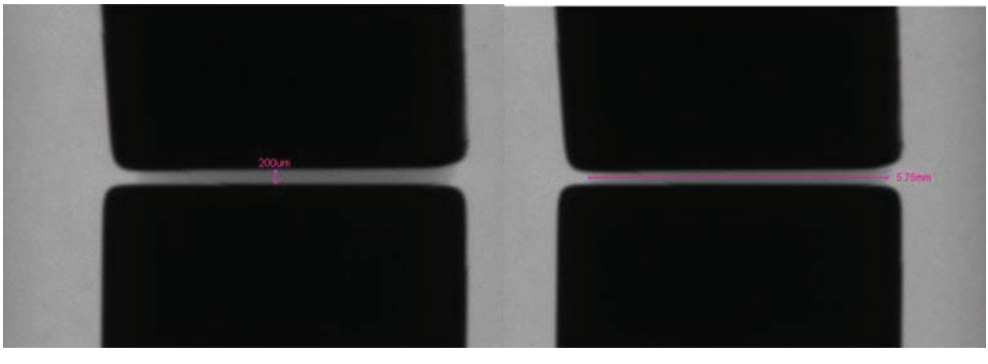

Figure 4. Test sample.

Table 1. Sample information.

	Thickness of asphalt lay (μm)	Width of asphalt lay (mm)	Aspect ratio of asphalt layer	Aggregate material	Plane size of stone (mm)
Experiment 1	156	3.92	25.13	Unakite	4.29*4.29
Experiment 2	156	3.5	22.44	Unakite	4.29*4.29

After the force-displacement data is obtained from SKYSCAN, a curve fitting method is applied to obtain the parameters of the contact model in Eq.(19). To simplify the process, three reorganized parameters are estimated:

$$a_1 = E_n$$
$$a_2 = \frac{\dot{\varepsilon}_0}{\sigma_0^n}$$
$$a_3 = \left[\left(\frac{1}{n+2}\right)\left(\frac{2n+1}{n}\right)^n\left(\frac{\sqrt{3}}{A}\right)^{n+1}\right]$$

The curve fitting solution employs an Ordinary Differential Equation (ODE) solver and a fmincon function in MATLAB to find the minimal difference between experimental results and computational ODE results. To acquire accurate fitted curve and estimated parameters, the initial values of the parameters are very important. Without a reasonable initial value, the fmincon function has a high possibility to find a local minimum, whereas only the global minimum is the desired answer. Supposing $n = 2$, this process will only obtain material-related parameters a_1, a_2, because a_3 can be directly calculated when the geometry information is known.

To evaluate the accuracy of power law model, material parameters a_1, a_2 estimated from test 2 and geometric parameter a_3 from test 1 are applied in DEM model, which is used for comparison with experimental data 1. Vice versa, DEM data by a_1, a_2 from test 1 and a_3 from test 2 are compared with experimental data 2.

In Figures 5 and 6, the blue dashed line presents the experiment results, the green dots represent the fitted curve where the material parameters are obtained from the same test and the red line demonstrates the numerical results with material parameters from another experiment. For the experimental data, the general trend of force-displacement obeys the viscoelastic law, which is near elastic at the beginning, and gradually plateaus. In terms of how well the power law model fits with the experimental results, an average error is calculated—average absolute value of force difference between experimental data and power law numerical data:

$$F_{err} = \frac{1}{n}\Sigma_{i=1}^{n} \mid F_{simulation} - F_{experiment} \mid \tag{22}$$

and relative error percentage is defined as force error divided by maximum experimental force after its increasing rate stabilized:

$$P = F_{err}/F_{stable} \tag{23}$$

The detailed results are shown in Table 2. The columns in the table represent the experiment results used for comparison, and the rows describe the data sets used for material parameters estimation, which are applied to numerical results. As the table shows, errors are relatively small when the same test data is used for parameter estimating and error testing—7.8% for test 1 and 3.36% for test 2. The maximum numerical force error is 5.3 N, after divided by the stable force in the experiment—30.1 N, the relative error does not exceed 17%.

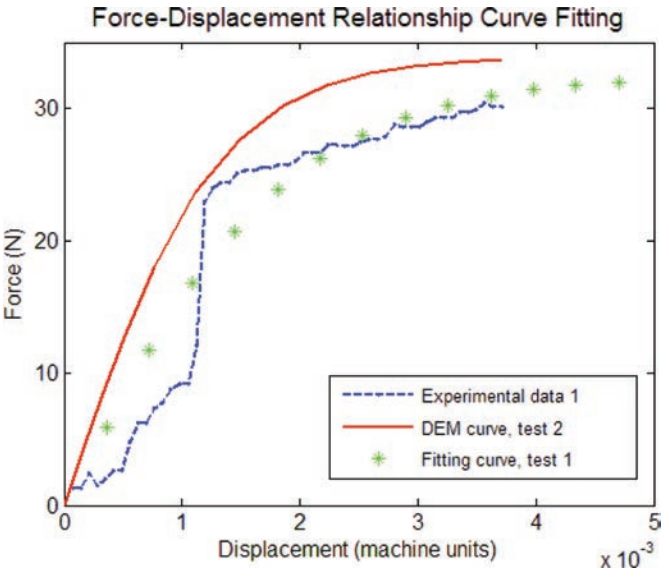

Figure 5. Experiment, numerical, DEM results for experiment 1.

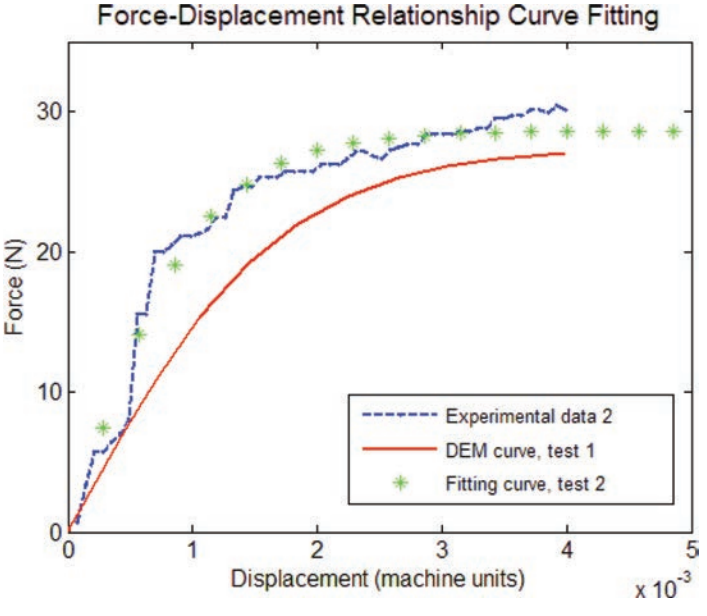

Figure 6. Experiment, numerical, DEM results for experiment 2.

Table 2. Error information between experiment results and DEM results.

Parameter from test data	Force error (N)		Error percentage	
	Test 1	Test 2	Test 1	Test 2
Test 1	2.357	5.314	7.83%	17.65%
Test 2	3.551	1.0117	11.80%	3.36%

There are several reasons that cause the error. First, the two planes of aggregates sandwiched asphalt binder are not strictly parallel to each other. Second, the friction of aggregate surface is not large enough to ensure the theoretical boundary condition. Third, the lateral deformation in both directions along the plane is not even.

4 CONCLUSION AND FUTURE WORK

As a new alternative contact model for asphalt binder simulation, the power law model shows a good potential to solve thin film asphalt problems. With the corresponding power law DLL file generated by C++ code, the new contact model is able to be loaded directly into PFC 3D to apply to more complex problems. However, some interesting problems are also raised during this research. How does film thickness influence the accuracy of power law model? How does aggregate stiffness and friction affect experimental results? What is the force (stress) range that the power law model is good for? Can we use more parameters to calibrate power law model and improve model accuracy? This paper provides a foundation for further exploration and future work.

REFERENCES

[1] Cundall, P.A. and Strack, O.D.L. A Discrete Numerical Model for Granular Assemblies, Geotechnique, 29 (1), pp. 47–65, 1979.

[2] Itasca. Particle flow code 3D manual: Background and theory. Minneapolis, Minnesota, 2008.

[3] F. Miao, and A. Renzo. Modelling Particle Contacts in Distinct Element Simulations: Linear and Non-Linear Approach, Chemical Engineering Research and Design, 83 (11), pp. 1287–1297, 2005.

[4] H. Hertz. On the Contact of Elastic Solids. Journal fur die Reine und Angewandte Mathematik, 92, pp. 156–171, 1882.

[5] Abbas, A., Masad, E., Papagiannakis, T. and Harman, T. Mcriomechanical modeling of viscoelastic behavior of asphalt mixtures using finite element method. International Journal of Geomechanics, 7(2), pp.131–139. 2007.

[6] Ullidtz, P. Distinct element Method for study of failure in cohesive particle media. Transportation Research Record, 1757, pp. 127–133. 2001.

[7] Liu, Y., Dai, Q. and You, Z. Viscoelastic model for discrete element simulation of asphalt mixture. Journal of Engineering Mechanics, 135(4). Pp. 324–333. 2009.

[8] C.Y. Cheung, D. Cebon, Thin Film Deformation Behavior of Power Law Creeping Material. Eng. Mech., 123, pp. 1138–1152, 1997.

[9] C.Y. Cheung, Mechanical behavior of bitumen and bituminous mixes, dissertation, Cambridge University Engineering Department, 1995.

[10] Linbing Wang, Mechanics of Asphalt: Microstructure and Micromechanics, McGraw Hill, New York, c2011.

This page intentionally left blank

Pavement response analysis under static and moving wheel loads—II

This page intentionally left blank

Asphalt Pavements – Kim (Ed)
© 2014 Taylor & Francis Group, London, ISBN 978-1-138-02693-3

Inverted pavement versus semi-rigid pavement: Comparison of dynamic response in field test via mobile loading simulator

Jiayin Liu & Jingyun Chen
Dalian University of Technology, Dalian, Liaoning, P.R. China

Yunquan Liu
The Communications Research Institute of Liaoning Province, Shenyang, Liaoning, P.R. China

Changhong Zhou
Dalian University of Technology, Dalian, Liaoning, P.R. China

ABSTRACT: Dynamic response is an important indicator in estimating long-term performance of a pavement structure. To obtain dynamic responses, field measurement is a direct and realistic method. In this study, a multidirectional strain measurement is performed in a highway section paved by two structures: an inverted pavement and a semi-rigid pavement. Accelerated loads are imposed by a full-scale Mobile Load Simulator (MLS). A comparison on dynamic responses from the two structures is made. Two loading positions, central and eccentric loading, are performed alternately. The strains are measured by strain gauges. The results show the maximum tensile strain at the bottom of asphalt mixture in the inverted pavement is higher than that in the semi-rigid pavement at both loading positions. It is concluded that the bottom-up fatigue crack would be the potential failure mode of inverted pavement since the introduction of graded crushed stone interlayer decreases the material stiffness under asphalt mixture. Crack observation from the inverted pavement confirms this failure. The measurement under various axle amplitudes shows that there is a good agreement between strain increments and tire contacted pressure increments. Therefore, when the heavy vehicles are concerned, the tire contacted pressure, rather than the load amplitude, should be the primary parameter in fatigue prediction.

Keywords: Dynamic response, inverted pavement, strain gauge, MLS, ALF

1 INTRODUCTION

Reflective cracking is a common distress type in semi-rigid asphalt pavement. Crack often occurs in the semi-rigid base, and then extends to the pavement surface subsequently. To eliminate reflective cracking, inverted pavement was advanced as an alternative pavement structure. An unbound aggregate interlayer on top of the semi-rigid base was used to prevent surface asphalt pavement from cracking. Extensive studies have been conducted to evaluate the performance of inverted pavement.[1] However, the use of inverted pavement is still limited by the lack of field experiments. Question arises from contractors about whether the long-term performance of the inverted pavement is superior to that of the semi-rigid pavement when the total thicknesses are the same. Since the unbounded interlayer exhibits a nonlinear constitutive relationship under loading, current design methods are unsuitable for the analysis of inverted pavements. Therefore, there is an urgent requirement to make a field comparative study between the inverted pavement and the semi-rigid one.

The dynamic response of field test has always been a prevailing and efficient indicator in evaluating the performance of a pavement structure.[2–4] In these field tests, the responses were

commonly collected under the load of a specific truck.[5–6] It will provide a realistic reflection of multi-axle configuration. However, it is not an alternate opinion for long-term load application. In contrast to vehicles, the Accelerated Loading Facility (ALF) provides a cyclic load with high stability. Previous ALF tests performed on special built test sections.[8–10] As the advancement of movable ALF, the equipment is able to move at a maximum speed of 1 km/h under its own power. As a result, a long-term field test could be performed on real road. MLS-66 is one of this movable ALF which designs and manufactures in South Africa. As a single axle dual-tire version of TxMLS, this machine implements a unidirectional wheel load with six load units. The maximum loading rate is up to 6000 times/hour which is the highest one among all the ALFs. Since MLS is much smaller than that of TxMLS, it is convention to perform tests on field. Given the advantages above, MLS66 is an appropriate machine for field test.

2 OBJECTIVES

The objective of this study is to provide field performance data for both semi-rigid pavement and inverted pavement. An accelerate pavement test on semi-rigid pavement and inverted pavement has been carried on in field section in Liaoning, P.R. China. The multidirectional dynamic responses have been collected and compared under the loads from MLS66. The differences on mechanical response and potential failure mode are highlighted. It also provides data to understand the pavement responses under variable loading amplitude.

3 TEST ROAD DESIGN AND INSTRUMENTATION

3.1 *MLS66 accelerated loading facility*

Figure 1 shows the appearance of the new full-scale accelerate loading faculty MLS66. Before test, its four corner jacks were adjusted to the correct working height.

Figure 2 shows the loading system. Inside the machine, six sets of bogies were assembled to a loading system. Each bogie is consisted with two set of hydraulic actuator, and a pressurized nitrogen accumulator to control the load application on pavements. Dual tires representing half of an axle are installed on each bogie. A guide rail carrying the six bogies is linked by chains. The bogies driving by chains perform a circular movement along rail in the vertical cross section (as shown in Fig. 2(a)). Therefore, a continuous unidirectional load is created in pavement of 6.6 m length under the equipment. Since the hydraulic system on each bogie runs individually, a repeated load spectrum with up to six load amplitudes (G1–G6) would be provided by MLS66.

3.2 *Pavement structure*

Figure 3 shows the two pavement structure being tested. The first one is the semi-rigid pavement. The semi-rigid pavement is consisted of a 17.5 cm asphalt mixture course, a 40 cm

Figure 1. Appearance of the MLS66 facility.

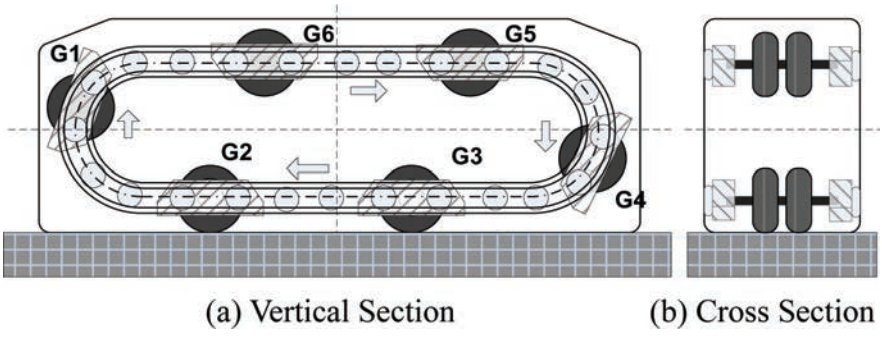

Figure 2. Load system of MLS66 facility.

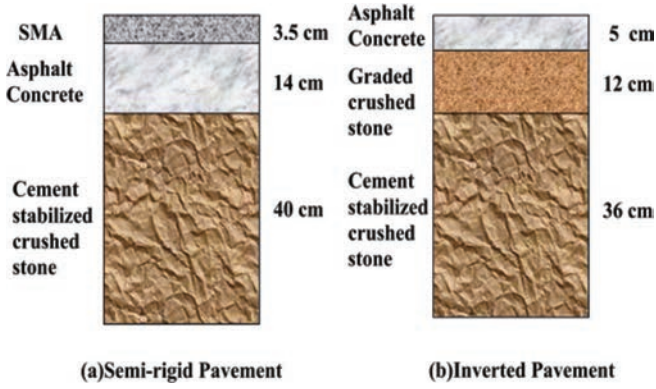

Figure 3. Structures of two kinds of pavement.

semi-rigid base and 15 cm graded sand subbase. The structure has been widely used in case of heavy load traffic in highway construction of China. The typical failure mode of this structure is reflective cracking. The second is the inverted pavement. A 12 cm unbounded stone under the surface course is advanced as the interlayer. Under the interlayer, there is a 36 cm semi-rigid base. A 5 cm layer of flexible pavement was placed over the interlayer.

The test field is located at an unopened highway section. All of the pavements were constructed on prepared subgrade with its modulus above 70 MPa. All construction works were followed the requirement of local specification.

3.3 *Device instrumentation*

The arrangements of devices are shown in Figure 4. It is to be noticed that the two pavement structures are total different. Therefore, the devices were instrumented at the bottom of each layer to obtain the maximum tensile strain for each material. Strain gauges were instrumented during the pavement construction. To measure the dynamic responses at different layers, the devices lined up along the direction of travel at the bottom of asphalt mixture layer and base layer separately. In the surface layer, FBG-FRP (Fiber Bragg Grating-Fiber Reinforced Polymer) sensors were used to measure the vertical strain, and PP-OFBG (Polypropylene-Optic Fiber Bragg Grating) sensors were used to measure the longitudinal and transversal strains. In the base layer, only longitudinal and transversal responses were measured. All devices were aligned along the track of loading wheels. In the asphalt mixture layer, a 600 mm distance between the sensors was kept to avoid interference. In the base layer, the distance was 900 mm. The construction of test road and the instrument of the gauges were done alternatively. The work of Timm et al.[11]

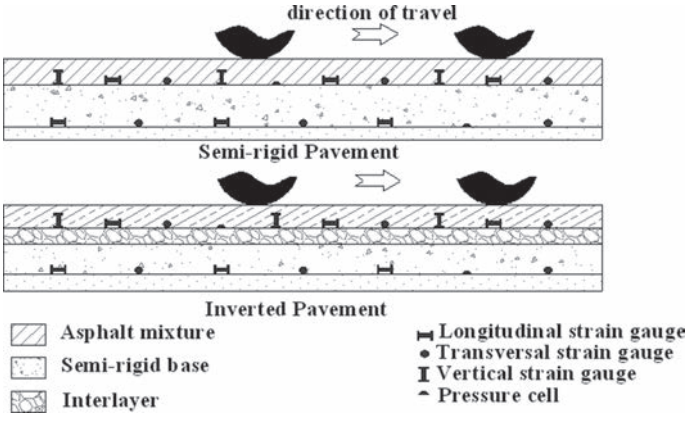

Figure 4. Arrangements of sensors in two kinds of pavement.

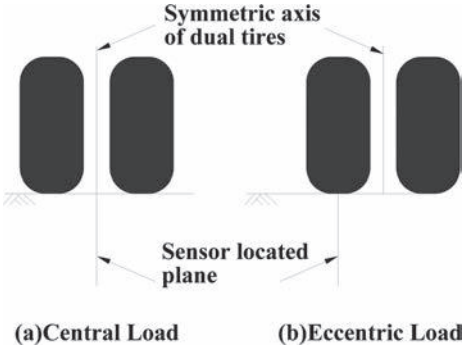

Figure 5. Two loading positions.

was referenced as a guide for the instrumentation in order to prevent the device from damage.

The data acquisition system was capable of recording fast dynamic responses up to 200 Hz. The frequency is accurate enough to obtain successive dynamic responses. Since the amount of data was huge, a three-minute dynamic response was recorded for every one hundred thousand load application.

3.4 *Load applications*

Figure 5 shows the two kinds of transversal load location for field test. In the first one, the symmetric axis of dual tires is right on the top of the plane strain devices located (central loading). In the second one, the symmetrical axis of a single tire is right on the top of the device plane (eccentric loading).

In order to simulate the traffic flow consisted by various load levels, a spectrum with multiple amplitude axle loads was imposed. The loads of six wheels G1 to G6 were set to three different values as shown in Table 1. G1 represents half of a 100 kN rear axle of a truck. G2 and G3 represent half of a rear axle in a 30% and 50% overloaded truck, respectively. The tire contacted area for each load level was measured. The measured contacted areas A, and the calculated tire contacted pressures P are all listed.

In spite of the increments of wheel load range from 30% to 50%, the increments of contacted area are 21.2% and 40.5%, respectively. The increments of tire contacted pressure are only 3% and 7%, respectively. The increment of axle amplitude results in a significant

Table 1. Parameters of six loading units (G1 to G6).

Items	G1	G2	G3–G6
Load L/kN	50	65	75
Percentage/100%	1	1.3	1.5
Contacted area A/mm^2	51876	62854	72893
Tire pressure P/MPa	0.96	0.99	1.03
Percentage/100%	1	1.03	1.07

increment in tire contacted area. Compared to the tire contacted area, the increments of tire pressure are not significant.

4 TEST RESULTS

An accumulated loading over 2.2 million times has been applied on each pavement. From all the results, the primary-stage dynamic responses, which are taken as the first quarter of the entire data, are focused on for the following analyses. During this stage, the primary densification is finished and the pavement is still undamaged. Therefore, data from this stage is appropriate to represent the normal working condition of pavement.

4.1 *Dynamic responses of semi-rigid pavement*

Figure 6 shows the three directional dynamic responses at the bottom of asphalt mixture in one load cyclic from two load locations. In each cycle, six peak values appear in terms of the six loading units. The difference in peak-value time is caused by the different longitudinal locations of sensor. In the transversal direction, strain was compressive under central loading. Then it changed into a tensile one under eccentric loading. The results show there is a switch in strain from negative to positive while the loading point moves transversal from the inner to the outer side. When the wheel moves towards and away from the sensor, the longitudinal strain exhibits a compression-tension-compression response. The maximum tensile strain is discovered when tire is directly on top of sensor. The maximum vertical compression strain is found under central loading. Since in all conditions, the maximum tensile strain is less than 100×10^{-6}, fatigue cracking would not start from the bottom of asphalt mixture.

Figure 7 shows the dynamic responses at the bottom of semi-rigid base. Unlike asphalt mixture, the responses of cement stabilized stone are not time-dependent. The strain curves are symmetry when wheel moves towards and away. The strain responses at the bottom of cement stabilized stone layer are wider than that of asphalt mixture. The value from central loading is higher than that from the eccentric loading because of the superposition of two loading regions. The maximum tensile strain is 169.1×10^{-6} from longitudinal direction. Since the tensile strain at the bottom of semi-rigid base is higher than that at the bottom of asphalt mixture, the bottom of semi-rigid base would be the location where reflective cracks start.

4.2 *Dynamic responses of inverted pavement*

Figure 8 shows the three directional dynamic responses in inverted pavement. Similar shapes of curve are observed. That means the load creates the same compressive or tensile strain in inverted pavement as it does in semi-rigid pavement. However, there are significant differences among strain values. The result shows that the tensile strains in inverted pavement were much higher than those in semi-rigid pavement in longitudinal and transversal direction. The maximum value is 543.9×10^{-6} from transversal direction under 50 kN load. The high tensile strain will be the reason of fatigue cracking in inverted pavement. Based on the result, we may conclude that transversal crack would be found at the bottom of the asphalt mixture under long-term cyclic loads.

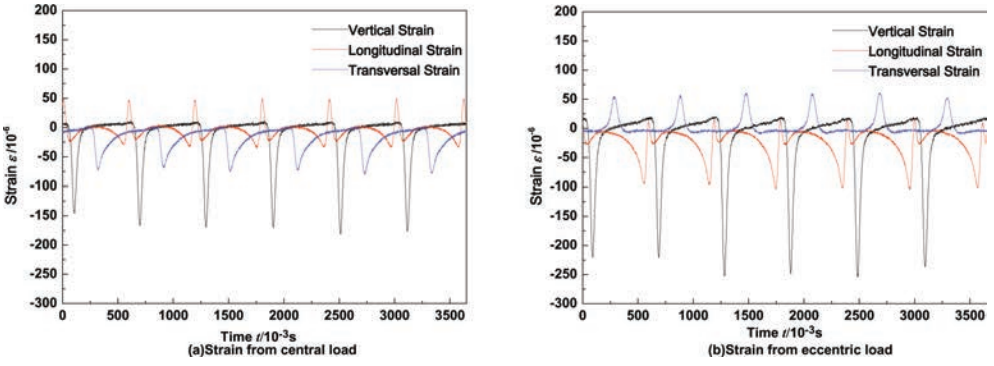

Figure 6. Strains at the bottom of asphalt mixture in semi-rigid pavement.

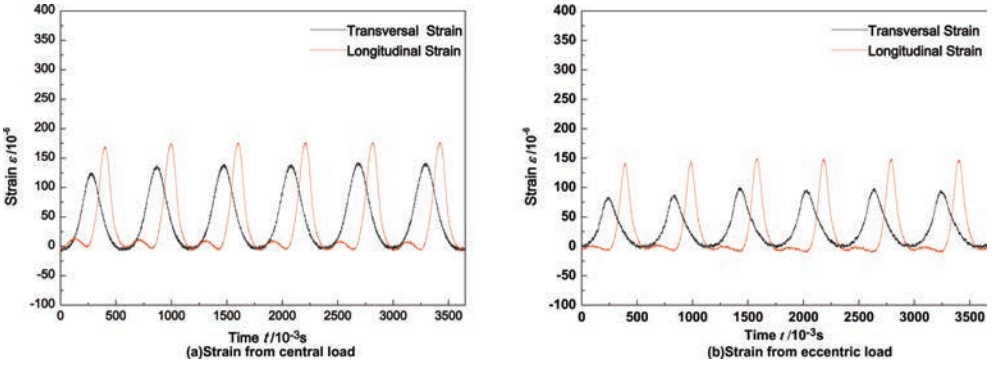

Figure 7. Strains at the bottom of base in semi-rigid pavement.

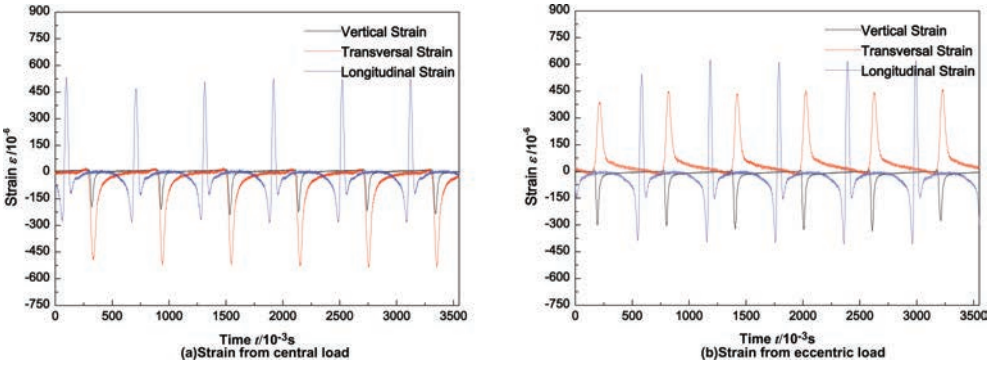

Figure 8. Strains at the bottom of asphalt mixture in inverted pavement.

4.3 *Crack observation*

At the end of the test, when 2.2 million equivalent load passes have been imposed in the semi-rigid pavement, the observation showed that the pavement was still undamaged. The results show that the fatigue life of semi-rigid pavement is much higher than 2.2 million times. While the same numbers of load have been exerting on the inverted pavement, surface cracks were observed after 1.7 million passes from the 8 m^2 loading area (6.6 m*1.2 m). Distress surveys were taken to reveal the growth of cracks. Figure 9 shows the relationship between

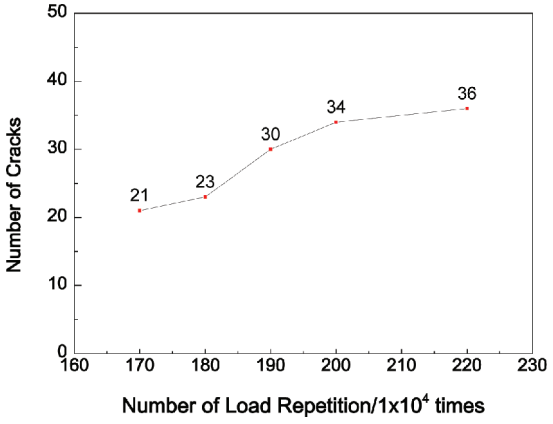

Figure 9. Numbers of cracks vs. load repetitions in inverted pavement.

the number of cracks and the number of load repetition. The result shows that the crack density was 0.9 m/m^2. For all the 36 cracks, 82% of them were transversal crack. This observation shows a good agreement with the result predicted based on the field-measured strain in the inverted pavement.

5 DISCUSSIONS

Based on the field-measured dynamic responses, the critical mechanical state of both pavements was obtained. Figure 10 shows the three-dimensional strain vectors at the bottom of asphalt mixture for both pavements. The compressive or tensile status of bulk strain is also shown.

The introduction of interlayer causes the differences between mechanical statuses. In semi-rigid pavement, since the stiffness of cement stabilized stone is close to that of asphalt mixture. The asphalt mixture and semi-rigid base bend together. The bottom of the cement stabilized stone layer bears higher tensile strain than the asphalt mixture layer does. Since the thickness of base layer is greater than asphalt mixture, the bottom of asphalt mixture will be in compression which will not initiate crack. The crack may start from the base layer, and it may result in reflective cracking.

In the inverted pavement, the introduction of interlayer increases the differences in modulus between the top two layers. In inverted pavement, the asphalt mixture is in a mechanical state of bending. The bottom of asphalt mixture bears majority of tensile stress. The results suggest that transverse fatigue crack may initiate at the bottom of asphalt pavement. The percentage of transversal crack in all cracks (Fig. 9) has confirmed this result. Since inverted pavement is vulnerable to fatigue load, it would be appropriate for highway with low traffic volume. The indicator of strain at the bottom of asphalt mixture would be decisive in the pavement design. The fatigue failure could be avoided by increasing the thickness or increasing the tensile strength of asphalt mixture.

The relationship between contacted pressure and field measured strain is analyzed. Table 2 shows strain ratio collected from 16 gauges under different axle loads. Based on the result, the average strain under 65 kN load and 75 kN are 1.07 and 1.11 times as the strain under 50 kN load, respectively. The results show that, the field measured strain is in good correlation with the contacted pressure, regardless the non-linear behavior of materials. Therefore, an accurate estimate of fatigue responses should be made in considerate contacted pressure, rather than load level. If the enlarged contacted area is ignored, the calculation based on a fixed contacted area would be overestimated the fatigue strain when overload is concerned.

It is to be noticed that the heavier loads affect the pavement through two aspects: higher contacted pressure and larger contacted area. The increment in contacted pressure will

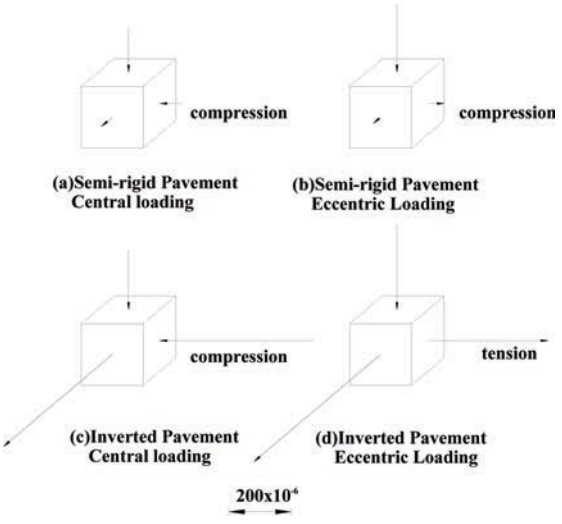

Figure 10. Three-dimensional strain vectors at the bottom of asphalt mixture.

Table 2. Strains statistics at various load levels.

No.	ε_{50kN}:ε_{65kN}:ε_{75kN}	No.	ε_{50kN}:ε_{65kN}:ε_{75kN}	Average
1	1:1.128:1.058	9	1:1.043:1.165	$\varepsilon_{50\,kN}$: $\varepsilon_{65\,kN}$: $\varepsilon_{75\,kN}$ = 1:1.07:1.11
2	1:0.994:1.100	10	1:1.081:1.121	
3	1:1.031:1.156	11	1:1.056:1.066	
4	1:1.006:1.043	12	1:1.084:1.183	
5	1:1.032:1.037	13	1:1.091:1.167	
6	1:1.099:1.117	14	1:1.144:1.147	
7	1:1.010:1.046	15	1:1.151:1.141	
8	1:1.128:1.058	16	1:1.043:1.165	

Note: $\varepsilon_{50\,kN} = \varepsilon_{G1}$, $\varepsilon_{65\,kN} = \varepsilon_{G2}$, $\varepsilon_{75\,kN} = (\varepsilon_{G3} + \varepsilon_{G4} + \varepsilon_{G5} + \varepsilon_{G6})/4$.

decrease the fatigue life of pavement by generating a higher tensile strain. The way contacted area affecting fatigue growth is complex and needs further studies.

The distress survey, as well as the measured tensile strain, shows that the inverted pavement is more vulnerable to fatigue cracking compared to semi-rigid pavement. The result is found to be different with the conclusion drawn by Rasoulian et al.[1,12] The difference causes from the pavement configuration. Rasoulian replaced the semi-rigid layer by crushed limestone base. In China, an important issue confronting the contractors is the soft subgrade. To eliminate the pavement damage induced by soft subgrade, a thick semi-rigid base was commonly used. When the inverted pavement was constructed, a 36 cm semi-rigid base was kept. After the introduction of interlayer, the asphalt mixture was replaced by graded crushed stone. Since the thickness of asphalt mixture decreased, the inverted pavement was sensitive to fatigue load. The fatigue performance of inverted pavement would be improved when the thickness of asphalt mixture increases.

6 CONCLUSIONS

Directly measured dynamic responses have been obtained from field test of semi-rigid and inverted pavement. Comparison shows that the maximum tensile strain exists in the longitudinal direction of the inverted pavement. The transversal crack would result from the

maximum tensile strain. This corresponding type of cracks was discovered during the test. Since the inverted pavement is sensitive to the load application, the thickness design is vital indicator for inverted pavement.

The results show that, in both pavements, the vertical compression strain under eccentric loading is higher than that under central loading during a cyclic period. A sign convention of transversal strain may result while the measurement point moves transversal from the inner side to the outer side. A compression-tensile-compression pattern is observed in longitudinal strain during the procedure of load wheel moving towards and away from the sensor.

The results under different load amplitudes show that the strain responses have a directly impact from the tire contacted pressure rather than load level. The estimation without consideration of contacted area would lead to inaccuracy of fatigue life. The tire contacted pressure should be the primary concerned in estimating fatigue strains.

ACKNOWLEDGEMENT

The authors would like to express their thanks to the Liaoning Department of Transportation for the support in field construction, to fellows of the Communications Research Institute of Liaoning Province for adjusting test equipment and accomplish the field test. The authors also want to acknowledge all others not mentioned here who contributed to this project.

REFERENCES

[1] Rasoulian, M., Becnel, B., & Keel, G. Stone interlayer pavement design. *Transportation Research Record: Journal of the Transportation Research Board*, 1709(1), pp. 60–68. 2000.

[2] Bayat, A., & Knight, M. Investigation of hot-mix asphalt dynamic modulus by means of field-measured pavement response. *Transportation Research Record: Journal of the Transportation Research Board*, 2154(1), pp. 138–145. 2010.

[3] Zafir, Z., Siddharthan, R., & Sebaaly, P.E. Dynamic pavement-strain histories from moving traffic load. *Journal of Transportation Engineering*, 120(5), pp. 821–842. 1994.

[4] Bhattacharjee, S., Gould, J.S., Mallick, R.B., & Hugo, F. An evaluation of use of accelerated loading equipment for determination of fatigue performance of asphalt pavement in laboratory. *International Journal of Pavement Engineering*, 5(2), pp. 61–79. 2004.

[5] Mollenhauer, K., Wistuba, M., & Rabe, R. Loading frequency and fatigue: In situ conditions & impact on test results. In *2nd Workshop on Four Point Bending*, University of Minho, Pais, pp. 261–276. 2009.

[6] Mulungye, R.M., Owende, P.M.O., & Mellon, K. Finite element modelling of flexible pavements on soft soil subgrades. *Materials & Design*, 28(3), pp. 739–756. 2007.

[7] Dong, Z.H., X Q.L.,& Lu P.M. Dynamic response of semi-rigid base asphalt pavement based on accelerated pavement test. *China Journal of Highway and Transport*, 24(2), pp. 1–5, 11. (In Chinese). 2011.

[8] Nilsson, R.N., Oost, I., & Hopman, P.C. Viscoelastic analysis of full-scale pavements: validation of VEROAD. *Transportation Research Record: Journal of the Transportation Research Board*, 1539(1), pp. 81–87. 1996.

[9] Elseifi, M.A., Al-Qadi, I.L., & Yoo, P.J. Viscoelastic modeling and field validation of flexible pavements. *Journal of Engineering Mechanics*, 132(2), pp. 172–178. 2006.

[10] Chen, D.H., Zhou, F., & Yuan, X. Verification and calibration of VESYS5W fatigue cracking model using results from accelerated pavement testing. *Journal of Testing and Evaluation*, 35(5), pp. 544–552. 2007.

[11] Timm, D.H., & Priest, A.L. Dynamic pavement response data collection and processing at the NCAT test track. *National Center for Asphalt Technology*. 2004.

[12] Titi, H., Rasoulian, M., Martinez, M., Becnel, B., & Keel, G. Long-Term Performance of Stone Inter-layer Pavement. *Journal of Transportation Engineering*, 129(2), pp. 118–126. 2003.

This page intentionally left blank

Asphalt Pavements – Kim (Ed)
© 2014 Taylor & Francis Group, London, ISBN 978-1-138-02693-3

Pavement responses as function of truck tire type

Jaime A. Hernandez, Imad L. Al-Qadi & Hasan Ozer
University of Illinois at Urbana-Champaign, Champaign, IL, USA

James Greene & Bouzid Choubane
Florida Department of Transportation, USA

Rongzong Wu & John Harvey
University of California at Davis, Davis, CA, USA

Eric J. Weaver
Federal Highway Administration, USA

ABSTRACT: An experimental program to compare pavement responses caused by new-generation Wide-Base Tires (WBT) with the conventional Dual-Tire Assembly (DTA) is presented. Four pavement sections were built, tested, and instrumented at two test sites: two sections at Florida DOT facility and two sections at UC-Davis. H-type strain gauges at the bottom of the Asphalt Concrete (AC) and pressure cells on top of the base and the subbase were installed at each test site. Instrumentation also included surface foil gauges in Florida and a multi-depth deflectometer at UC-Davis. All sections were subjected to the same test loading: five tire loads (26.2, 36.2, 44.4, 62.1, and 79.9 kN) and four tire inflation pressures (552, 690, 758, and 862 kPa) at three temperatures using the two types of tires considered. In addition, two cases of differential tire inflation pressures were included for DTA (552/758 and 414/758 kPa). Pavement responses to a tire loading of 44 kN and tire inflation pressure of 758 kPa for both tires are presented. Data analysis and impact of tire type on pavement responses is discussed. This paper is part of the pooled-fund project TPF-5(197), The Impact of Wide-Base Tires on Pavement Damage: A National Study.

Keywords: New-generation wide-base tires, accelerated pavement testing, pavement instrumentation, pavement responses

1 INTRODUCTION

The use of Wide-Base Tires (WBT) as an alternative to the conventional Dual-Tire Assembly (DTA) has advantages for trucking operations (fuel economy, hauling capacity, and tire cost and repair) and the environment (gas emission and tire recycling) [1]. The First-Generation (FG-WBT) was introduced in North America in the early 1980s, but it proved to be more detrimental than DTA to flexible pavements [2–6]. The new-generation WBT (NG-WBT) began to be used in 2000, and some research has been performed comparing the damage caused to Asphalt Concrete (AC) by WBT with damaged caused by DTA. What follows is a short summary of the main studies that experimentally compared WBT and DTA.

Major research was conducted at Virginia Tech to assess the pavement damage caused by different tire types and axle configurations [7–10]. Twelve pavement structures were built, heavily instrumented and tested with DTA (275/80R22.5) and NG-WBT (445/50R22.5). During the first test session (May 2000) and based on strain at the bottom of AC, it was determined that NG-WBT produced almost the same fatigue damage as DTA. For vertical

compressive stress, the difference between DTA and NG-WBT decreased with depth, even though it was higher for NG-WBT near the surface. Similar results were obtained during November 2000 and July 2001.

The effect of different tire types has also been studied in Canada [11]. An experimental section with a thickness of 4 in was built at Laval University in Québec City, and it was instrumented to measure longitudinal and transverse strains at different levels as well as vertical strain. It was found that at an inflation pressure of 106 psi, DTA produced less strain at the base than the WBT, and 455/55R22.5 produced less strain than 385/65R22.5. By contrast, when the tire inflation pressure was increased to 130 psi, 385/65R22.5 and 455/55R22.5 produced lower vertical strain than that of the DTA. In addition, WBT provided better performance with regard to rutting.

DTA and WBT were mechanically compared by the National Center for Asphalt Technology (NCAT) in 2006 [12]. A pavement section 6.73 in thick was subjected to accelerated pavement testing using two types of tires: 275/80R22.5 and 445/50R22.5. The test section was instrumented with longitudinal and transverse strain gauges at the bottom of the AC layer with pressure cells on top of the base and subgrade. The readings from the instrumentation were compared with analytical results calculated with WESLEA software. The study concluded that there is insignificant difference between WBT and DTA in the horizontal strain at the bottom of the AC layer and the stress on top of the subgrade.

Response of and damage to pavement by DTA and WBT have been also compared in pavements with different thicknesses [13, 14]. Flexible pavement sections with thicknesses varying between 6 and 16.5 in were instrumented and tested at the Advanced Transportation Research Engineering Laboratory (ATREL) at the University of Illinois at Urbana-Champaign. Thermocouples and strain gauges (two longitudinal and one transverse) were installed. The test sections were subjected to moving loads (5 and 10 mph) using conventional DTA (11R22.5), NG-WBT (455/55R22.5), and FG-WBT (425/65R22.5). The measurements showed that the lowest longitudinal strain at the bottom of the AC is created by DTA. Also, WBT-425 presented a higher response than WBT-455 for all testing conditions. Based on the experimental measurements, it was possible to conclude that WBT-425 is the most damaging tire with regard to fatigue cracking, followed by WBT–455.

A similar study focusing on the damage caused by DTA and WBT-455 on roads with low traffic volume was conducted by Al-Qadi and Wang [15]. Three sections with the same surface layer (75- and 125-mm thick) but different base thickness (200, 300, and 450 mm) were instrumented and modeled. The investigation found that WBT caused more damage than DTA to roads with low traffic volume.

The results of an additional study of WBT and pavement damage were published in 2009 by Greene et al. [16]. The focus of that project was to evaluate pavement rutting. Two types of pavement were subjected to accelerated loading until a rut depth of 12.5 mm was reached. The type of tire with the greatest number of passes to create a 12.5-mm rut depth was the DTA, while WBT-425 required the fewest. In addition, WBT-455 required a similar number of repetitions as DTA on an open-graded surface and slightly less on a dense-graded one. Based on the readings of two surface sensors installed 125 mm from the edge of the tire, it was concluded that WBT-425 generated the highest surface transverse strain. Finally, WBT-445 was found to cause more rutting damage than DTA and WBT-455, while the damage caused by WBT-455 and DTA were similar.

Although solid research has been conducted, no final conclusions have been drawn about pavement performance when WBT and DTA are considered. This paper discusses the instrumented pavement sections subjected to accelerated loading that are part of the pooled-fund project TPF-5(197), The Impact of Wide-Base Tires on Pavement Damage: A National Study. This pooled-fund study approaches the problem in a holistic way, using tools such as an advanced numerical model, artificial neural networks, and pavement instrumentation. The details of the pavement structures as well as their instrumentation are described. In addition, the typical reading of installed sensors is provided along with some results for a specific loading case [44 kN (10 kips) applied load and 758 kPa (110 psi) tire inflation pressure].

2 TEST SECTIONS

2.1 *Pavement structure*

2.1.1 *Pavement structure at Florida DOT*

Two pavement structures were built and instrumented at Florida DOT's State Materials and Research Park in Gainesville (test pit and test track section). The structure under the AC layers is the same for both sections: A-3 subgrade according to the AASHTO classification method: 305 mm of a mixture of limerock and subgrade soils on top of the subgrade; and 267 mm of limerock base directly underneath the AC layers.

The AC layers are different for each structure. The section on the test track has an existing 38-mm-thick AC with PG 67-22 binder and 12.5-mm Nominal Maximum Aggregate Size

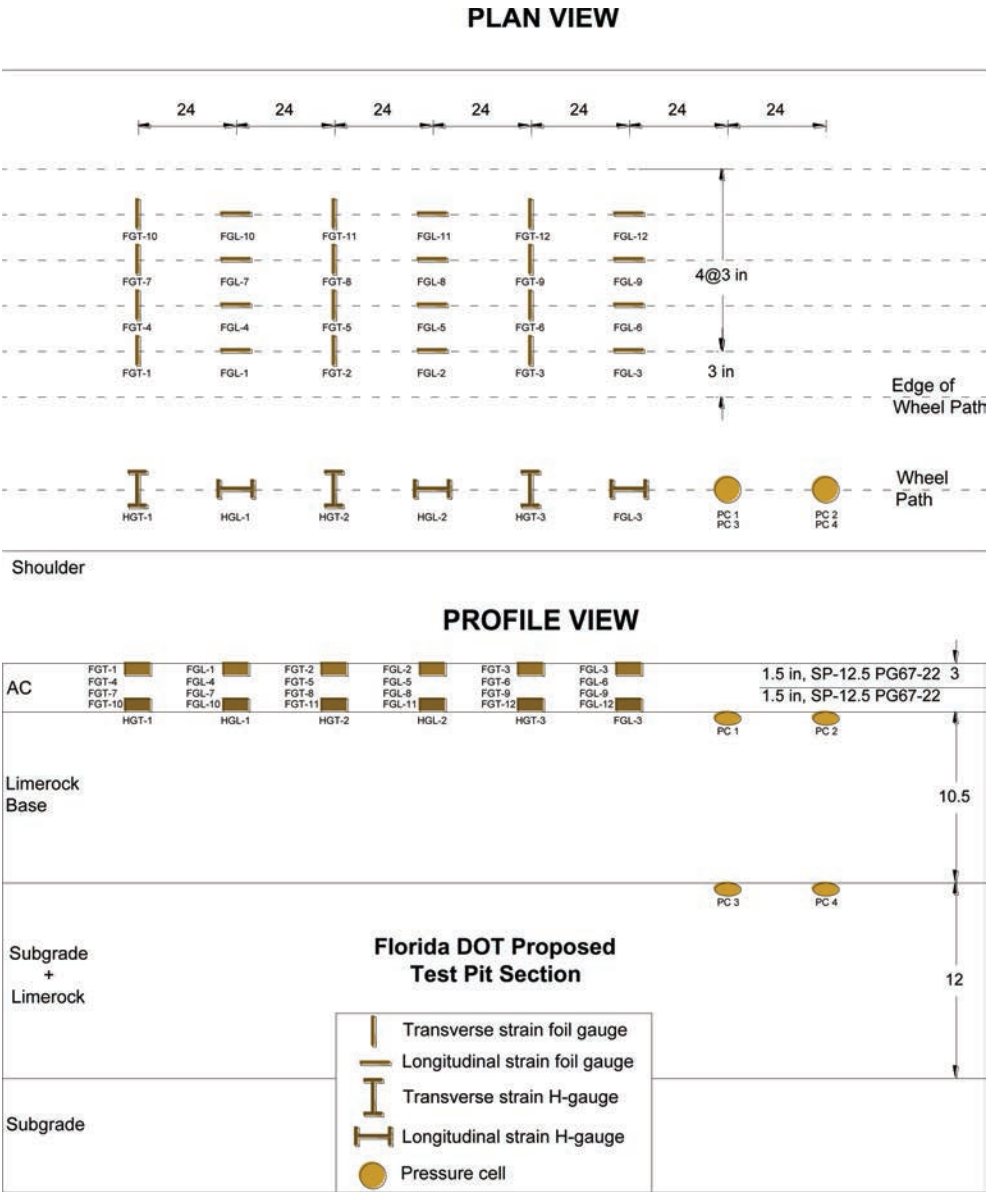

Figure 1. Pavement structure and instrumentation for the test pit section at florida DOT facility.

(NMAS), which is overlaid by two lifts of AC. The first lift is 38-mm-thick, and the surface lift is 25-mm-thick of 4.75-mm NMAS. The binder for these two layers was PG 76-22, and the NMAS was 12.5 and 4.75 mm, respectively. The thickness of the AC layer of the section in the test pit was 76 mm and was built using two lifts of equal thickness. The AC of the test pit has a NMAS of 12.5 mm and PG 67-22 binder. Figure 1 details the pavement structure of the test pit section.

2.1.2 *Pavement structure at UC-Davis*

As with the sections in Florida, the layer configuration under the AC is the same for the two pavement structures built and instrumented at UC-Davis. The top 200 mm of the clay subgrade were ripped and recompacted, and the thickness of the base was 270 mm. Between the AC and the base layer, 250 mm of recycled base were constructed. The two sections differ in the thickness of the AC layer: one at 60 mm, and the other at 120 mm. In addition, the AC layer contained 15% RAP.

2.2 *Instrumentation*

2.2.1 *Florida DOT*

Three types of sensors were used to measure pavement responses of the test sections built at the Florida DOT facility: 48 foil strain gauges, 12 H-type strain gauges, and four pressure cells. The foil gauges were installed on the surface of the pavement and were arranged in six sets. Each set was placed 610 mm in the traveling direction, and it was composed of four foil gauges. At the same time, each of these four gauges was located every 76.2 mm perpendicular to the wheelpath (see Fig. 1). The H-type strain gauges were placed at the bottom of the AC of each section in the longitudinal (traffic) and transverse direction. As in the case of the foil gauges, the separation between two consecutive H-type strain gauges was 610 mm. Finally, four pressure cells were installed in the test pit section: two at the interface between the AC and base and two on top of the subbase.

2.2.2 *UC-Davis*

H-type strain gauges, Multi-Depth Deflectometers (MDD), pressure cells, and thermocouples were installed in the pavement sections at UC-Davis. For the thick section, four strain gauges were installed at the bottom of each lift (eight total). Out of these four, two were installed in the longitudinal direction and two in the transverse. In addition, two pressure cells were placed at the recycled-base/existing-base and AC/recycled-base interfaces. In the case of the thin section, six strain gauges (three in each direction) and one pressure cell were placed at the bottom of the AC. Both sections were equipped with MDD to measure deflection at various locations in the pavement structure.

3 LOADING

All pavement structures were subjected to accelerated loading using the same testing matrix. The values of applied load and tire inflation pressure were intended to cover a wide range, varying from very low (552 kPa and 26.8 kN) to very high (862 kPa and 80.0 kN). In addition, differential tire inflation pressure was considered in the case of DTA. All the values used in the testing matrix are summarized in Table 1.

The described testing matrix was performed at three temperatures at each testing site: Florida at 25°C, 40°C, and 55°C (77°F, 10°F4, 131°F); and UC-Davis at 20°C, 35°C, and 50°C (68°F, 95°F, 122°F). Furthermore, the load was applied unidirectionally at the Florida DOT site and bidirectionally at the UC-Davis site. Test at different offsets With Both Tires (WBT and DTA) were also performed at UC-Davis for a specific case: temperature = 50°C (122°F), tire inflation pressure = 552 and 862 kPa (80 and 125 psi), and load = 44 kN (10 kip). The offsets were 178 and 305 mm. The location of the tires with respect to line of sensors was different

Table 1. Experimental matrix for tire contact stress measurement.

Tire inflation pressure (kPa*)	Load (kN*)				
552	26.7	35.6	44.5	62.3	80.0
690					
758					
862					
414/758**					
552/758**					

*1 kPa = 0.145 psi; 1 kN = 0.225 kip; **Differential tire inflation pressure (DTA only).

at each testing site. At UC-Davis, the center of each of the tires matched the line of sensors, while at the Florida site, the edge of each tire was placed 76 mm from the first longitudinal foil gauge (which means that the center of the tires did not line up with the line of sensors).

4 TYPICAL READINGS

Typical readings of the sensors installed in Florida are presented in Figure 2. Because the instrumentation in both testing sites differs only with regard to the MDD, these measurements are considered to be representative of all the sections. The curves shown correspond to the sensors in the test pit section for DTA with an applied load of 44 kN (10 kip) and tire inflation pressure of 758 kPa (110 psi).

Figure 2a presents the variation of the longitudinal strain at the bottom of the AC with time. Three distinctive segments of the plot can be clearly distinguished. In the first one, the tire creates compressive longitudinal strain as it approaches the sensor. When the tire reaches the strain gauge, tensile strain is generated and the maximum longitudinal strain is experienced by the pavements. When the tire leaves the sensor, compressive strains are read once more. The variation with time of the transverse strain at the bottom of the AC does not exhibit compressive strain (see Fig. 2b). There is a chance that the strain gauge experiences compressive strain if the tire does not travel on top of the line of sensors (with offset). Good repeatability was observed in at least two of the three strain gauges installed in each direction. It should be noted that the alignment of the sensors plays a significant role in the uniformity of their readings, and this alignment might easily be altered during installation of the sensor and compaction of the AC layers.

Figure 2c and 2d show the change of the surface strain in the direction of traffic and perpendicular to traffic (negative sign indicates tension). The area directly underneath the tire has high compressive stresses in the in-plane directions. This creates high compressive strains in the longitudinal and transverse directions at the points close to the surface and in the vicinity of the contact patch. The longitudinal surface strain decreases as the distance transverse to the traffic direction increases until its value completely vanishes, as illustrated in Figure 2 where the peak of each curve decreases as the location of the foil gauge changes from 76.2 mm to 304.8 mm. This is not exactly the case for the transverse surface strain, where the highly compressed zone close to the tire becomes tension before the magnitude of the strain becomes zero. In summary, longitudinal surface strain magnitude monotonically decreases from the loaded area, while transverse surface strain changes its sign before becoming zero. As a consequence, at some points on the pavement surface, the sign of the peak transverse and longitudinal surface strain are opposite, as seen in Figure 2c and 2d. Furthermore, the peak increases when the location of the foil gauge changes from 76.2 mm to 152.4 mm. The reason for this behavior cannot be gener-

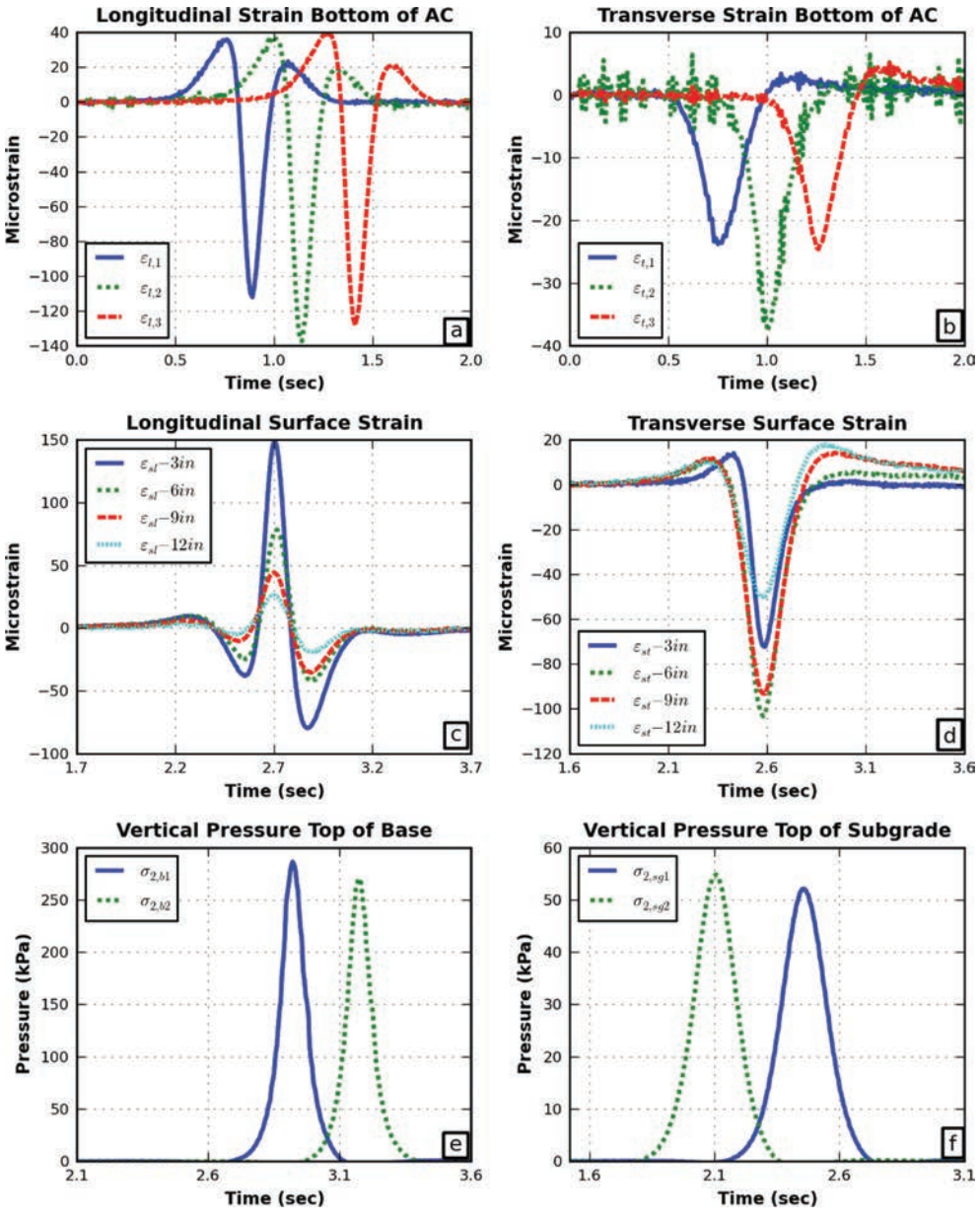

Figure 2. Typical measurements of florida DOT's instrumentation: (a) longitudinal strain at the bottom of the AC; (b) transverse strain at the bottom of the AC; (c) longitudinal strain at the pavement's surface; (d) transverse strain at the pavement's surface; (e) vertical pressure on top of the base; and (f) vertical stress on top of the subgrade.

alized because it might change for a different pavement structure, loading condition, and sensor location.

Finally, Figure 2e and 2f present the typical readings of the pressure cells on top of the base and subbase. The readings from this type of sensor are commonly used to determine the loading time and how this load duration changes with depth. As can be seen in the figure, not only does the peak decrease with depth, but the loading time also increases.

5 COMPARISON OF WBT AND DTA

The comparison between the measurements of both tire types at 44 kN (10 kips) applied load and 758 kPa (110 psi) tire inflation pressure is presented in Figure 3. The longitudinal and tensile strain at the bottom of the AC in Florida and the longitudinal tensile strain at the bottom of each lift in Davis are shown in Figure 3a and 3b, respectively. In each of these cases,

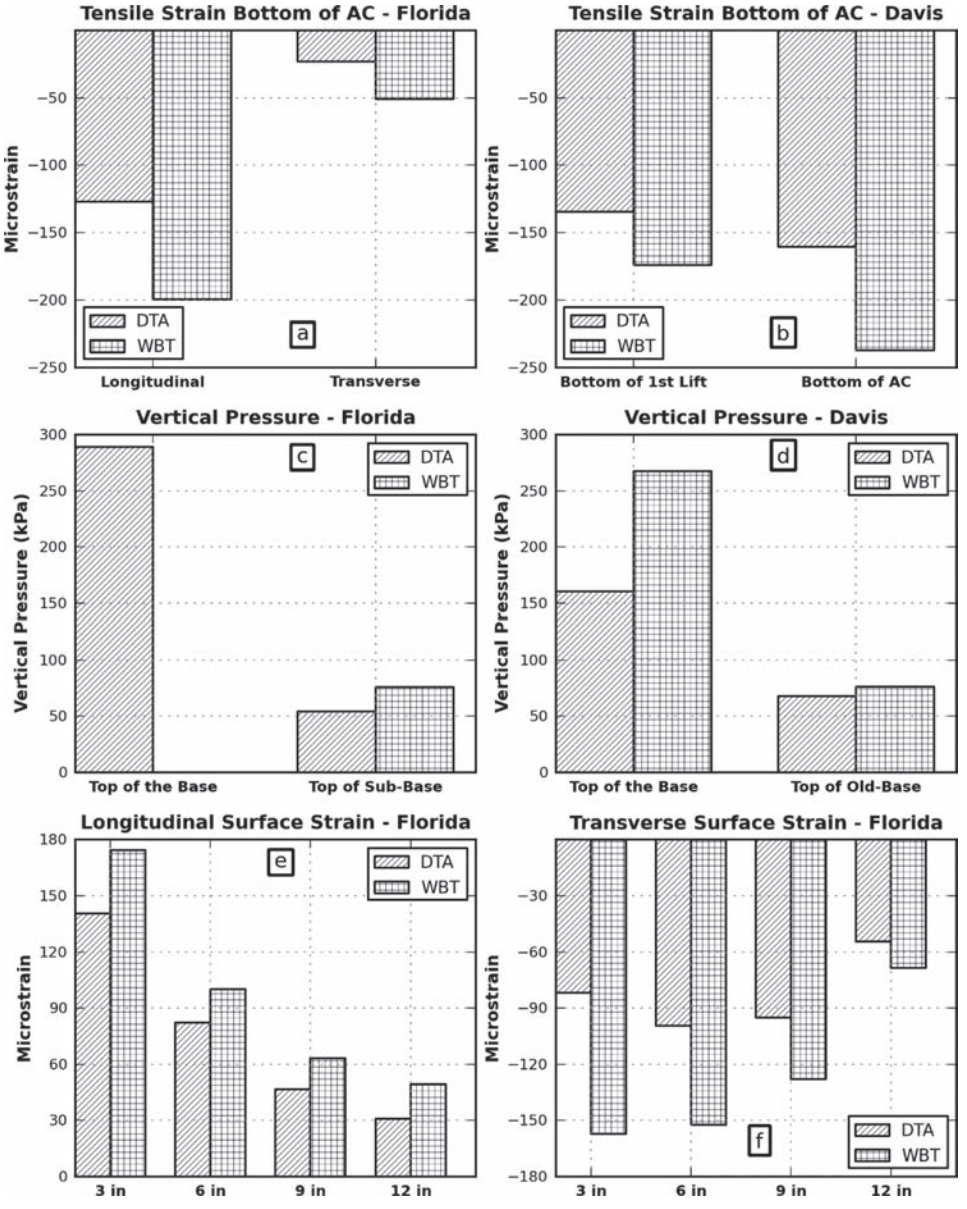

Figure 3. Experimental measurements for 44 kN applied load and 758 kPa inflation pressure: (a) longitudinal and transverse tensile strain at bottom of AC in Florida; (b) longitudinal strain at bottom of each lift in Davis; (c, d) vertical pressure on top of the base and subgrade for both sections; and (e, f) longitudinal and transverse surface strain at various distances from tire's edge in Florida.

WBT created more strain than DTA. Analysis of the load-transfer mechanism of the tires considered in this research showed that the contact area of WBT is smaller (not to mention that there is a spacing between the tires of the dual assembly), although the contact length is longer for WBT. However, the maximum vertical contact stresses are similar for both tires for the specific loading case considered [17]. This indicates that the distribution of the applied load is more concentrated for WBT than for DTA, which translates into higher longitudinal and transverse tensile strains in the AC.

It is important to consider that strain gauges read strain at a single point, and the strain might not be maximum at any specific point. This fact is more relevant in the Florida section, where the center of the DTA was not aligned with the line of sensors. To find the actual maximum, a calibrated finite element model can be developed, so all the points in the pavement structure can be analyzed.

Figure 3a and 3b also show a higher longitudinal strain compared with the transverse. In the extreme case of circular contact area subjected to uniform vertical contact stresses, the strain in both directions would be equal at any depth under the center of the tire–pavement contact patch. However, this is not the case for the actual tire–pavement contact. Relevant differences are seen in the strains along the longitudinal and transverse directions, indicating that the circular contact area with uniform pressure in the vertical direction only is not a good approximation for pavement analysis.

Figure 3b compares in-plane tensile strains at two depths, and it can be seen that the difference between WBT and DTA increases with depth. This result can be explain by taking into account the area used by each tire to distribute the applied load. Because WBT load distribution is more localized, its effects have a greater variation with depth. This is observed not only with the longitudinal tensile strain but also with the vertical pressure (see Fig. 3d). On the contrary, DTA not only has greater contact area but also is composed of two tires with space between them. As a consequence, depth has a greater influence on longitudinal tensile strain that is caused by WBT than DTA.

This argument cannot be generalized to other loading conditions, responses, or pavement structures. A good example of this caveat is the vertical pressure. As can be seen in Figure 3d, the difference between the vertical pressures caused by each tire decreased with depth, indicating that the effects of tire–pavement contact become less relevant as the vertical distance from the pavement surface increases. It is worth noting that the measurements of the deepest pressure cells in each section were not very different, as can be inferred from the readings on top of the subbase and on top of the old base in Florida and Davis, respectively.

The variation of the longitudinal and transverse surface strains with the distance perpendicular to the traveling direction for WBT and DTA is presented in Figure 3d and 3e, respectively. As briefly discussed above, there is a highly compressed zone caused by the confinement provided by the pavement structure surrounding the area where the tire is in contact with the pavement. The longitudinal surface strain decreases from the highly compressed region around the tire–pavement contact zone until it becomes zero without changing to tension. In contrast, the transverse surface strain changed from compression under the tire to tension before fully vanishing away from the tire. This finding suggests that there is a point with maximum surface transverse tensile strain.

The shape of the variation of the longitudinal surface strain from the tire's edge is very similar for both tires. This is not the case, however, for the transverse surface strain. After analyzing readings for DTA, it was seen that the mentioned transverse surface strain is higher at 152.4 mm than at 76.2 mm from the tire's edge and then decreases until it vanishes. This result indicates that the transverse foil gauges are in the zone in tension; it also indicates that the first gauge is located before the peak tensile strain and the other three after. Conversely, for the case of WBT, all the foil gauges are located after the peak transverse tensile surface strain. Because all foil gauges are located at the same distance from each tire's edge, it can be concluded that the peak transverse tensile strain is located closer to the WBT.

In general, Figure 3d and 3e show higher surface strains for WBT than for DTA. Because the tire–pavement contact stresses are more localized for WBT (smaller contact area and single tire), a point at a fixed distance from the edge of each tire will experience higher surface

strain from WBT than from DTA. The difference between the strain values from tires is higher in the transverse direction than the longitudinal one. It is worth recalling that loading was carried out by maintaining the distance from the tire's edge to the closest foil gauges at 76.2 mm.

6 CONCLUSIONS

Pavement structures, instrumentation, and loading details of four accelerated pavement testing sections that are part of the pooled-fund project TPF-5(197), The Impact of Wide-Base Tires on Pavement Damage: A National Study were discussed. In addition, the typical readings of the sensors used, along with some results for a specific loading case (applied load = 44 kN and inflation pressure = 758 kPa) were provided and analyzed.

The results presented indicate that WBT create greater responses than DTA on the pavement at the studied locations (longitudinal and transverse tensile strains on the surface and at the bottom of the AC, and vertical pressure) and for the loading case that was considered. It is concluded that depth has greater influence on the measurements caused by WBT than DTA. It was also observed that the stress/strain state near the contact between the tire and the pavement is a relevant factor in pavement behavior close to the surface and at the surface itself.

It should be emphasized that the results discussed in this paper are not conclusive. The findings are from only a portion of extensive tests performed at a wide range of temperatures, loads, and tire inflation pressures and currently being analyzed.

ACKNOWLEDGMENT

This paper discusses some results from an ongoing pooled-fund study, DTFH61-11-C-00025: The Impact of Wide-Base Tires on Pavement—A National Study. The project is being conducted in cooperation with the Illinois Center for Transportation; the U.S. Department of Transportation, Federal Highway Administration; Rubber Manufacturers Association, and the following state departments of transportation: Illinois, Minnesota, Montana, New York, Ohio, Oklahoma, Texas, and Virginia. The feedback and input of the following are greatly appreciated: David Lippert, Shongtao Dai, Dan Hill, Wes Yang, John Bowman, Brian Diefenderfer, and Larry Buttler. This project is managed by Eric Weaver, who has been instrumental in providing directions and input.

The contents of this paper reflect the view of the authors, who are responsible for the facts and the accuracy of the data presented herein. The contents do not necessarily reflect the official views or policies of the Illinois Center for Transportation, the Federal Highway Administration, or the participating partners. This paper does not constitute a standard, specification, or regulation.

REFERENCES

[1] Elseifi, M.A., Al-Qadi, I.L., and Yoo, P.J. "Viscoelastic Modeling and Field Validation of Flexible Pavements." Journal of Engineering Mechanics, 132(2), 172–178. 2006.

[2] Huhtala, M., Philajamaki, J., and Pienimaki, M. "Effects of Tires and Tire Pressures on Road Pavements." Transportation Research Record: Journal of the Transportation Research Board, 1227, 107–114. 1989.

[3] Huhtala, M. "The Effect of Different Trucks on Road Pavements." Proc., International Symposium on Heavy Vehicle Weights and Dimensions, Kelowna, British Columbia. 1986.

[4] Bonaquist, R. "An Assessment of the Increased Damage Potential of Wide-Base Single Tires." Proc., 7th International Conference on Asphalt Pavements, International Society for Asphalt Pavements, Lino Lake, Minnesota, 1–16. 1992.

[5] Sebaaly, P.E., and Tabatabaee, N. "Effect of Tire Parameters on Pavement Damage and Load-Equivalency Factors." Journal of Transportation Engineering, 118(6), 805–819. 1992.
[6] Harvey, J., and Popescu, L. "Accelerated Pavement Testing of Rutting Performance of Two CAL-TRANS Overlay Strategies." Transportation Research Record: Journal of the Transportation Research Board, 1716, 116–125. 2000.
[7] Al-Qadi, I.L., Elseifi, M.A., and Yoo, P.J. *Pavement Damage Due to Different Tires and Vehicle Configurations*. Virginia Tech Transportation Institute, Blacksburg, Virginia. 2004.
[8] Al-Qadi, I.L., Elseifi, M.A., Yoo, P.J., and Janajreh, I. "Pavement Damage Due to Conventional and New Generation of Wide-Base Super Single Tires." Tire Science and Technology, 33(4), 210–226. 2005.
[9] Al-Qadi, I.L., Yoo, P.J., Elseifi, M.A., and Janajreh, I. "Effects of Tire Configurations on Pavement Damage." Journal of the Association of Asphalt Paving Technologists, 84, 921–962. 2005.
[10] Elseifi, M.A., Al-Qadi, I.L., Yoo, P.J., and Janajreh, I. "Quantification of Pavement Damage Caused by Dual and Wide-Base Tires." Transportation Research Record: Journal of the Transportation Research Board, 1940, 125–135. 2005.
[11] Pierre, P., Dore, G., and Vagile, L. *Characterization and Evaluation of Tire-Roadway Interface Stresses, Ministry of Transport*. University of Laval, Québec City, Québec. 2003.
[12] Priest, A.L., and Timm, D.H. "Mechanistic Comparison of Wide-Base Single Versus Standard Dual Tire Configurations." Transportation Research Record: Journal of the Transportation Research Board, 1949, 155–163. 2006.
[13] Al-Qadi, I.L., and Wang, H. "Full-Depth Pavement Responses Under Various Tire Configurations: Accelerated Pavement Testing and Finite Element Modeling." Journal of the Association of Asphalt Paving Technologists, 78, 645–680. 2009.
[14] Al-Qadi, I.L., and Wang, H. *Evaluation of Pavement Damage Due to New Tire Design*. Illinois Center for Transportation, Rantoul, Illinois. 2009.
[15] Al-Qadi, I.L., and Wang, H. *Pavement Damage Due to Different Tire and Loading Configurations on Secondary Roads*. NEXTRANS University Transportation Center, West Lafayette, Indiana. 2009.
[16] Greene, J., Toros, U., Kim, S., Byron, T., and Choubane, B. *Impact of Wide-Base Single Tires on Pavement Damage*. Florida Department of Transportation. 2009.
[17] Hernandez, J.A., Al-Qadi, I.L., and De Beer, M. "Impact of Tire Loading and Tire Pressure on Measured 3D Contact Stresses." Proc., 2013 T&DI Airfield and Highway Pavement Conference, Los Angeles, California. 2013.

Asphalt Pavements – Kim (Ed)
© 2014 Taylor & Francis Group, London, ISBN 978-1-138-02693-3

Effect of geotextile-reinforced base on fatigue life of Hot-Mix Asphalt pavement

Milad Saghebfar, Mustaque Hossain & Nassim Sabahfar
Department of Civil Engineering, Kansas State University, Manhattan, KS, USA

ABSTRACT: Geotextiles have been widely promoted for pavement structures over the past 30 years. Previous studies show that a geotextile placed at the subgrade-base course interface of a paved road can increase the number of load repetitions before rutting failure. Thus, reduction of base and/or asphalt thickness may be possible. However, there is a lack of well-instrumented full-scale experiments to investigate effect of geotextile reinforcement on other possible mechanisms of pavement failure like fatigue of the Hot-Mix Asphalt (HMA) layer. In this study, full–scale accelerated pavement testing was done on eight pavement test sections. Six out of these eight sections had base layers reinforced with different types of woven geotextiles. The reinforced sections and the control sections (with unreinforced base) were paved with Superpave HMA layers. Base and subgrade materials were the same for all sections while some test sections had different asphalt and base layer thicknesses. Each test section was instrumented with six H-bar strain gages at the bottom of the HMA layers to measure longitudinal and transvers strains. The mechanistic response of each section was monitored and analysed at the selected number of wheel passes. Predicted fatigue lives of the test sections were calculated based on the Asphalt Institute and Shell models. Results indicate that fatigue life of test sections did not increase due to geotextile reinforcing although rutting performance of some reinforced sections did improve. This may indicate geotextiles may not improve fatigue performance of HMA layers in pavements.

Keywords: Geotextile, Hot-Mix Asphalt, fatigue life, Accelerated Pavement Testing

1 INTRODUCTION

One of the persistent problems involved with Hot-Mix Asphalt (HMA) pavements is fatigue cracking. The repeated traffic loads result in tensile stress repetitions in the bound layers. Under these repeated strains, fatigue cracks initiate at locations where the largest tensile strains and stresses develop. These critical locations depend on many factors such as pavement structural configuration, layer stiffness, and load configuration (area of load distribution, magnitude of stresses at the tire-pavement interface, etc.). After crack initiation at critical locations, repeated traffic loads can cause the cracks to propagate throughout the entire layer. These cracks allow water infiltration, which can negatively affect pavement performance. Many pavement structural models assume that cracks initiate at the bottom of the asphalt concrete surface layer and then propagate upward. These cracks are aptly named bottom-up fatigue cracks. The newly released AASHTO mechanistic-empirical design procedure (DARWin ME) considers the alligator cracking as bottom-up fatigue cracking [1]. DARWin ME also recognizes another type of fatigue cracking, now known as top-down cracking, which are longitudinal cracks in the wheel path. The cause of top-down cracking is highly debated but they do seem to exist, especially in hot-weather locations and pavement constructed on moisture sensitive subgrades [1].

Classical fatigue analysis directly correlates the fatigue life of asphalt mixtures with the critical pavement responses (stresses or strains). A number of fatigue analysis approaches

have been proposed by researchers over the last few decades. The point of failure is normally defined as the moment at which the stiffness of the specimen is reduced to a certain value [2]. While dissipated energy theory was introduced by Hopman and Pronk [3] in the fatigue analysis, dissipated energy ratio was used to describe the fatigue damage of asphalt mixtures. Ghuzlan et al. [4] and Shen and Carpenter [5] developed models that can predict the fatigue life from material properties and loading conditions. Kim et al. [6] and Lundstrom [7] applied Viscoelastic Continuum Damage (VECD) approach to simulate the damage evolution under cyclic loading tests. According to SHRP-A-404, pavements with different mix stiffness, thickness, subgrade modulus, air void and asphalt content exhibit different fatigue behaviour [8]. A literature review was done by Carpenter [9] on fatigue cracking models. In the majority of models, the number of load applications to fatigue crack appearance (N_f) is related to the strain at the bottom of the HMA layer (ε_t). Thus, this strain was measured and analyzed in this study to assess fatigue life of HMA pavements under accelerated pavement testing.

2 ACCELERATED PAVEMENT TESTING (APT)

The Civil Infrastructure Systems Laboratory (CISL) at Kansas State University is one of only six such university-owned facilities in the nation that is capable of testing large-scale asphalt and concrete pavement sections under full-scale loading. CISL houses an Accelerated Pavement Testing (APT) machine and three pits for constructing test sections. The reaction frame of the APT machine covers a distance of 12.8 m and applies axle load with air-bag suspension on dual tires. The wheel assembly is belt driven by a 20-HP electric motor, while the load is controlled by hydraulic pressure. The pits are each approximately the same size at 6.1-m long, 4.9-m wide, and 1.8-m deep [9].

Loading mechanism at CISL APT can be controlled via hydraulic pressure, tire pressure, and test speed. In this testing, an 80-kN single axle load with air-bag suspension was applied on dual tires. Tire pressure was 627 kPa and testing speed was 11 km/h. The APT machine has the ability to wander laterally during passes simulating realistic traffic load distribution across the lane. A ±150 mm wander was applied in a truncated normal distribution. The number of passes for one full wander cycle is 676.

2.1 *Test sections*

Two pits at CISL were divided into two lanes each for a total of four lanes. In the first series of tests, each lane had a length of 6.1 m (20 ft.), width of 2.45 m (8 ft.) and depth of 1.83 m (6 ft.). In the second series of tests, the width of the test sections was increased to simulate expected geotextile behavior (full-width mobilization) in the field. In the second test series, each section had a length of 3.05 m (10 ft) in the direction of trafficking and 4.9 m (16 ft) width in the direction perpendicular to traffic. The second series configuration was created to accommodate the full-width of the geotextiles. Figure 1 shows the cross sections of the test pavements.

Sections A and E are the unreinforced (control) test sections with a deep (305 mm) crushed aggregate base. Other test sections have crushed aggregate bases with varying thickness and reinforced with different types of woven geotextiles. HMA, base course aggregate and subgrade materials for all sections were the same but their thicknesses varied.

2.2 *Material properties*

2.2.1 *Subgrade*

An AASHTO A-7-6 clay was used in subgrade construction. The maximum dry density of the subgrade soil was 1.61 g/cm^3 at an optimum moisture content of 21%. However, 24% moisture content was used to produce a CBR of 2.6 (corresponding subgrade resilient modulus of 4,700 psi). The subgrade was placed and compacted in five lifts. Dynamic Cone Penetrometer (DCP) testing was done on each lift to evaluate subgrade strength.

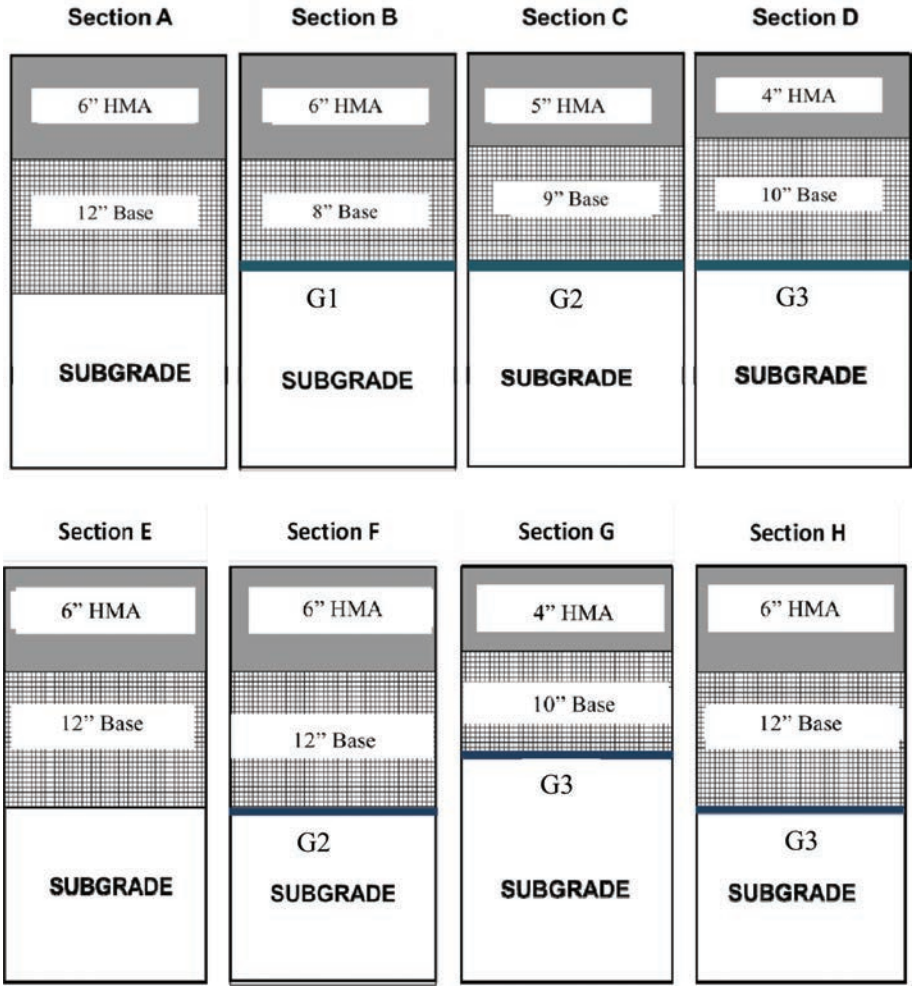

Figure 1. Cross sections of the test pavements.

2.2.2 *Base course*

Well-graded crushed limestone, known as AB-3 in Kansas, was used as the base layer material for all sections. The AB-3 had a mean particle size of 4.4 mm, coefficient of curvature of 1.55 and coefficient of uniformity of 21. The optimum moisture content of the base material was 10.2% and the maximum dry density was 2.13 g/cm^3. Base course layers were compacted at 95% of the maximum dry density. DCP and Light Falling Weight Deflectometer (LFWD) tests were done to assess layer strength and stiffness, respectively, to ensure base courses for the test sections are comparable.

2.2.3 *Hot-Mix Asphalt (HMA)*

All sections were paved with a 12.5-mm Nominal Maximum Aggregate Size Superpave mixture with fine gradation. This HMA mixture with 25% of Recycled Asphalt Pavement (RAP) materials is known as SR-12.5 A by the Kansas Department of Transportation (KDOT). A PG 58-28 virgin binder was used in SR-12.5 A.

2.2.4 *Geotextile*

Three types of woven reinforcement/stabilization geotextiles were used. The geotextiles were composed of high-tenacity polypropylene yarns, which are woven into a network such

that the yarns retain their relative position. The wide width tensile strengths of the geotextiles based on ASTM D4595 testing are shown in Table 1. Geotextile type G1 was used in section B and G2 was used in sections C and F. Sections D, G and H were reinforced by geotextile G3.

2.3 *Instrumentation*

2.3.1 *Sensor preparation*

Each section was equipped with six strain gages (three in the longitudinal and three in the transverse direction) and two thermocouples. Sensors were placed just below the HMA layer and under the wheel path. A Data Acquisition (DAQ) system was used to collect instrument responses. The DAQ system interfaced with a PC equipped with LabVIEW 2009 through a simple USB 2.0 connection. The strain gauge responses were recorded for a full wander cycle (676 passes) each time. The top 20 peak strain measurements were averaged.

Four types of strain gages were used to measure strain in the hot mix asphalt: foil strain gages; strain coils; and H-bar gages. Foil strain gages are placed in carrier blocks or extracted pavement cores [11]. Among different types of strain gages, H-bar gages are more accurate and have been successfully used in previous experiments [12,13]. In this study, PML-60-2 L strain gages from Tokyo Sokki Kenkyujo Co. were used. Each strain gage was connected to two aluminium rods (Fig. 2). Strain gages come with wires; however the original wires cannot tolerate the high temperature of asphalt during construction. Thus, conductor wires of 22 AWG types with braided shields were soldered to the H-bars. The solder was covered by

Table 1. Properties of Geotextiles used.

	Strength (kN/m)		
Strain	G_1	G_2	G_3
2% (MD)	7	9	7
2% (XD)	9	15	26
5% (MD)	18	26	21
5% (XD)	20	33	64
Ultimate (MD)	39	66	70
Ultimate (XD)	39	53	70

Note: MD: Machine Direction; XD: Cross Machine Direction.

Figure 2. H-bar strain gages.

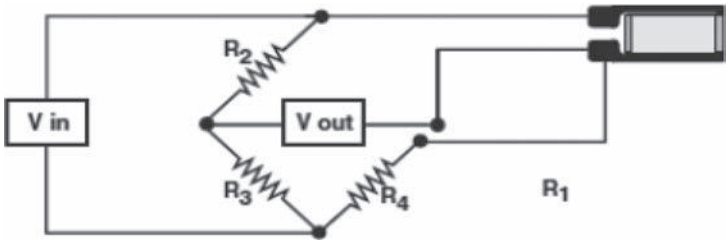

Figure 3. Completed quarter-bridge Wheatstone bridge circuit for strain gage [14].

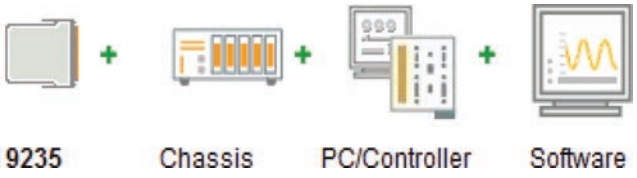

Figure 4. Schematic of data acquisition system (NI 9235 module shown for example [14]).

a heat shrinking sheath. Then the resistance of the gages was checked to make sure it was close to 120 ohms. The calibration factor provided by the manufacturer was used as the gage factor.

2.3.2 *Data acquisition system*

A compact DAQ (cDAQ) system from National Instruments was used for data collection. The cDAQ system allows multiple interchangeable modules to be used with an electronic chassis, with a simple USB interface and a Personal Computer (PC). For this setup, three types of terminal block modules were used with the cDAQ-9178 chassis. A thermocouple module (NI 9211, 4 channel, +/–80 mV, 24 bit differential analog input), two quarter-bridge input modules (NI 9235, 120 ohm, 8 channel, 24 bit, 2.5 ex) and an analog input module (NI 9205, 32 channel, +/– 10 V, 16 bit) were installed in the chassis for data collection during the experiments. The quarter-bridge modules complete the Wheatstone bridge circuit for the strain gages as shown in Figure 3. Applying the necessary excitation voltage, and the strain gage factor can be applied via software.

The cDAQ system interfaced with a PC equipped with LabVIEW 2009 through a simple USB 2.0 connection. A custom Virtual Instrument (VI) was constructed in LabVIEW in order to collect necessary data for the study. The VI creates a *.csv file (or appends onto an existing file) with specified column headers and then acquires data from the cDAQ system at a rate of 100 readings per second using the built-in DAQ Assistant VI. The pulse for each sensor is displayed in a chart (in pairs to show sensors which lie under the moving wheel on the same chart, to simplify the observation). The data for each sensor is output to a specific column in the *.csv file created (or appended to it). This file is continuously saved and after the VI is stopped, the file may be opened and viewed. Figure 4 shows this acquisition and display process. Within the DAQ Assistant VI settings, the input from a strain gage is read as strain gage input and the correct strain gage factor is applied.

3 TEST RESULTS

Six H-bar strain gages were placed at different locations in each test section to measure longitudinal and transvers strains at the bottom of the HMA layer. Results are shown in Tables 2 and 3. Average longitudinal and transverse strains at the bottom of the HMA layer are plotted in Figures 5 and 6. These strain responses fluctuate widely up to about 100,000 repetitions. This is most likely due to the consolidation of the HMA and base

Table 2. Longitudinal strains at the bottom of HMA layer.

	Section A			Section B		
Reps.	No. of readings	Ave. strain (10^{-6})	Std. Dev.	No. of readings	Ave. strain (10^{-6})	Std. Dev.
676	2	308	–	3	422	92
10,000	2	369		3	426	32
20,000	2	261		3	649	202
50,000	2	587		2	335	124
75,000	2	228		2	401	290
100,000	2	246		2	362	315
250,000	2	293		2	364	357
	Section C			Section D		
676	3	490	210	2	185	
10,000	3	675	154	2	400	
20,000	3	460	113	2	678	
50,000	3	763	43	2	597	
75,000	3	576	127	2	517	
100,000	3	750	178	2	522	
250,000	3	750	107	2	679	
	Section E			Section F		
676	2	436	–	2	276	
10,000	2	228		2	152	
20,000	2	296		2	677	
50,000	2	363		2	578	
100,000	2	309		2	423	
250,000	2	484		2	582	
300,000	2	553		2	596	
400,000	2	577		2	619	
	Section G			Section H		
676	2	636		2	116	
10,000	2	370		2	563	
20,000	2	518		2	36	
50,000	2	681		2	261	
100,000	2	622		1	693	
250,000	2	664		1	569	
300,000	2	725		1	613	
400,000	2	746		1	585	

layers. After about 100,000 repetitions, the results were analyzed and showed a clear trend among the sections. In the first test, both transverse and longitudinal strains at the bottom of HMA are lower in the control section (Section A) than in the reinforced sections (sections B, C and D). Control and Section B have the same HMA thickness (150 mm). Strain at the bottom of the HMA layer in the control section is less that for the geotextile-reinforced Section B.

In the second test, the thinnest section (section G) experienced highest transverse and longitudinal strains. After 200,000 repetitions of loading, both transverse and longitudinal strain in the control section (section E) and test sections F and H (reinforced sections, thickness same as the control section) are very close. Thus, geotextile reinforcement at the interface of the base and the subgrade did not reduce strains at the bottom of the HMA layer.

Table 3. Transverse strains at the bottom of HMA layer.

	Section A			Section B		
Reps.	No. of readings	Ave. strain (10^{-6})	Std. Dev	No. of readings	Ave. strain (10^{-6})	Std. Dev
676	2	439	–	3	395	209
10,000	2	334		3	390	255
20,000	2	341		3	370	30
50,000	2	339		3	484	62
75,000	2	307		3	470	170
100,000	2	224		3	370	226
250,000	2	215		3	436	145
Rep.	Section C			Section D		
676	3	480	287	3	466	65
10,000	3	572	465	3	550	68
20,000	2	317	–	2	551	–
50,000	2	297		2	443	
75,000	1	445	–	2	447	
100,000	2	598	–	2	408	
250,000	2	610		2	407	
Rep.	Section E			Section F		
676	2	366	–	2	179	–
10,000	2	409		2	326	
20,000	2	417		2	472	
50,000	2	510		2	637	
100,000	1	276	–	2	399	
250,000	2	528	–	2	527	
300,000	2	583		2	503	
400,000	2	596		2	578	
Rep.	Section G			Section H		
676	2	–	304	2	553	–
10,000	2		196	2	471	
20,000	2		168	1	650	–
50,000	2		113	1	171	
100,000	2		185	1	183	
250,000	2		109	1	643	
300,000	2		116	1	623	
400,000	2		180	1	631	

4 FATIGUE LIFE

In the majority of fatigue life models, the number of load applications to fatigue crack appearance (N_f) is related to the tensile strain at the bottom of the asphalt layer (ε_t) and elastic modulus of asphalt layer (E_1). The Asphalt Institute expressed following formula as failure criterion for fatigue cracking [15]:

$$N_f = f_1(\varepsilon_t)^{-f_2}(E_1)^{-f_3}$$

f_1, f_2 and f_3 are constants determined from fatigue tests. Table 4 shows f_1, f_2 and f_3 values suggested by the Asphalt Institute and Shell models.

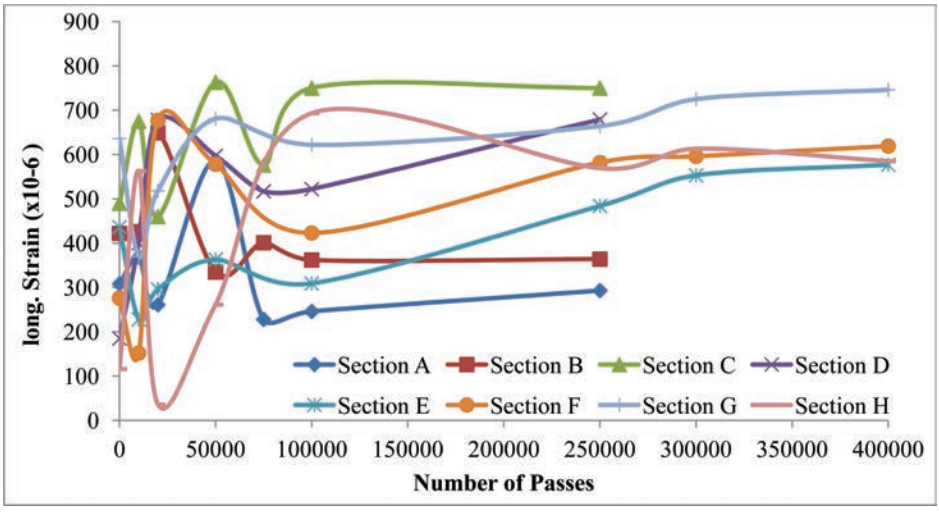

Figure 5. Longitudinal strains at the bottom of HMA.

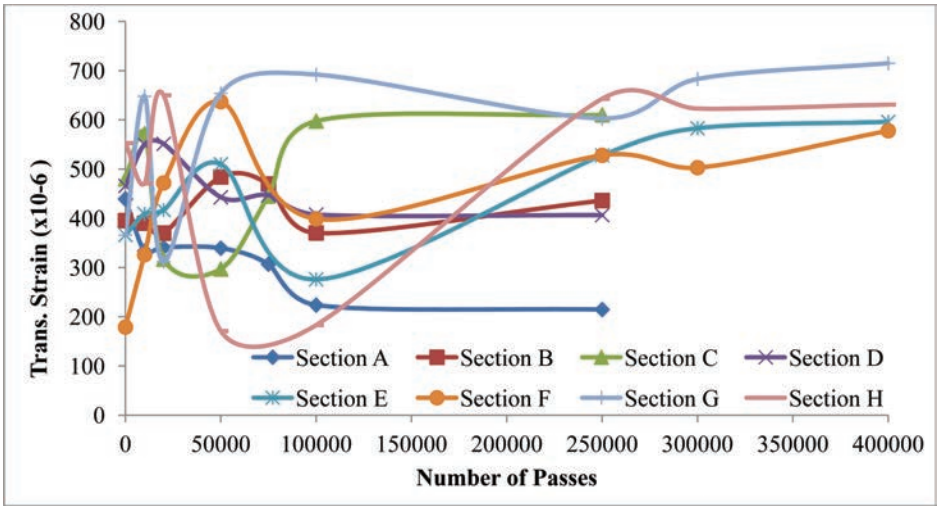

Figure 6. Transverse strains at the bottom of HMA.

Table 4. Parameters in fatigue cracking models [15].

Parameters	Asphalt institute	Shell
f_1	0.0796	0.0685
f_2	3.291	5.671
f_3	0.854	2.363

In this study, fatigue lives of the test sections were calculated based on the measured strains at the bottom of HMA layer and layer moduli were back calculated from FWD testing. FWD testing was done after construction of the test sections, and also after 250,000 and 400,000 wheel load repetitions. Table 5 shows the predicted remaining fatigue life of test sections for 676, 250,000, and 400,000 wheel load repetitions.

Table 5. Predicted fatigue life.

Section	E1 (ksi)	Tensile strain (10^{-6})	Asphalt institute	Shell model
	Remaining fatigue life after 676 load repetitions			
Section A	300	308	602,048	640,740
Section B	300	422	213,574	107,425
Section C	307.3	490	127,967	43,499
Section D	300	185	3,222,474	11,537,778
Section E	300	436	191,823	89,274
Section F	300	270	928,610	1,352,039
Section G	308	636	54,139	9,859
Section H	300	316	553,326	554,023
	Remaining fatigue life after 250,000 load repetitions			
Section A	300	293	709,562	850,446
Section B	300	364	347,430	248,455
Section C	313.3	750	31,012	3,718
Section D	314	679	42,939	6,500
Section E	366	484	114,782	30,862
Section F	325	582	69,247	14,363
Section G	325	664	44,876	6,801
Section H	325	569	74,592	16,326
	Remaining fatigue life after 400,000 load repetitions			
Section E	300	577	76,282	18,223
Section F	310	619	58,862	11,322
Section G	325	746	30,590	3,514
Section H	305	585	71,880	16,209

After 676 repetitions, strain at the bottom of the HMA layer in the section D was less than other sections, so predicted fatigue life for this section is higher than other sections. When consolidation of the HMA and base layers had completed and strains were recorded, there appeared to be no significant improvement in fatigue life of the test sections constructed with a geotextile. In both experiment series, remaining fatigue life for the unreinforced section (section A or E) was higher than the reinforced sections after 250,000 and 400,000 repetitions.

4 CONCLUSIONS

Eight test sections including six geotextile-reinforced sections and two unreinforced control sections were subjected to full-scale accelerated pavement testing. Transverse and longitudinal strains at the bottom of the HMA layer were measured at regular loading intervals. Predicted fatigue life for the test section was calculated based on the Asphalt Institute and Shell models. Apparently, HMA fatigue life was not increased by using a geotextile reinforcing layer below the base. Therefore, geotextile-reinforced bases did not improve the fatigue resistance of these sections. It is expected that a reinforced HMA layer will results in lower strain at the bottom of the HMA layer, and that in turn will increase the fatigue life.

REFERENCES

[1] NCHRP. Guide for Mechanistic-Empirical Design of New and Rehabilitated Pavement Structures. Final Report, NCHRP Project 1–37 A. Transportation Research Board, National Research Council, Washington, DC, web document: http://www.trb.org/mepdg/guide.htm.

[2] Ning Lia„ A.A.A. Molenaara, M.F.C. van de Vena, Shaopeng Wu, Characterization of fatigue performance of asphalt mixture using a new fatigue analysis approach, Construction And Building Materials, Volume 45, August 2013, Pages 45–52.

[3] Hopman PC, Kunst PA, Pronk AC. A renewed interpretation method for fatigue measurements-verification of Miner's rule. In: Proc. of the 4th eurobitume symposium, Madrid, Spain; 1989.
[4] K.A. Ghuzlan, S.H. Carpenter, Fatigue damage analysis in asphalt concrete mixtures using the dissipated energy approach, Can J Civil Eng, 33 (7) (2006), pp. 890–901.
[5] S. Shen, S.H. Carpenter, Development of an asphalt fatigue model based on energy principles, Assoc Asphalt Pav Technol (2007), p. 76.
[6] Y.R. Kim, H.J. Lee, D. Little, Fatigue characterization of asphalt concrete using viscoelasticity and continuum damage theory, Assoc. Asphalt Pave. Technol. (AAPT), 66 (1997), pp. 520–569.
[7] R. Lundstrom, Characterization of asphalt concrete deterioration using monotonic and cyclic tests, Pav Eng (2003), p. 4.
[8] F. Moghadas Nejad, E. Aflaki, M.A. Mohammadi, Fatigue behavior of SMA and HMA mixtures, Construction And Building Materials, 2010, Vol. 24(7), pp. 1158–1165.
[9] Carpenter, S.H. "Fatigue performance of IDOT mixtures." Carpenter, S.H., "Fatigue Performance of IDOT Mixtures," ICT Research Report FHWA-ICT-07-007, University of Illinois, Urbana (2006).
[10] Lewis, P. Lessons Learned From the Operations Management of an Accelerated Pavement Testing Facility. Proceedings of the 3rd Intl. Confc. On Accelerated Pavement Testing, Madrid, Spain, October 2008.
[11] Perkins, S.W. "Mechanical Response of Geosynthetic-Reinforced Flexible Pavements," *Geosynthetics International*, Vol. 6, No. 5, 1999, pp. 347–382.
[12] Webster, S.L. *Geogrid Reinforced Base Courses for Flexible Pavements for Light Aircraft: Literature Review and Test Section Design.* Miscellaneous Paper GL-92-6. U.S. Army Corps of Engineers Waterways Experiment Station, Vicksburg, Miss., 1992.
[13] Tang, X. A Study of Permanent Deformation Behavior of Geogrid Reinforced Pavement Using Small Scale Accelerated Pavement Testing. Ph.D. Dissertation, The Pennsylvania State University, 2007, State College, PA.
[14] Saghebfar, m., Bortz, B., Frink, E. and M. Hossain. Instrumentation Experience at the Kansas Accelerated Pavement Testing Facility of Geocell Reinforcement. Proceedings of the ASCE Airfield and Highway Pavements Conference, Los Angeles, Calif., June 9–12, 2013.
[15] Huang, Yang Hsien. Pavement analysis and design. 1993.

Asphalt Pavements – Kim (Ed)
© 2014 Taylor & Francis Group, London, ISBN 978-1-138-02693-3

Resilient modulus modeling of unsaturated subgrade soils with matric suction control

Farhad Salour
Pavement Technology, Swedish National Road and Transport Research Institute, VTI, Linköping, Sweden
Division of Highway and Railway Engineering, Royal Institute of Technology, KTH, Stockholm, Sweden

Sigurdur Erlingsson
Pavement Technology, Swedish National Road and Transport Research Institute, VTI, Linköping, Sweden
Faculty of Civil and Environmental Engineering, University of Iceland, Reykjavik, Iceland

Claudia E. Zapata
Faculty of Sustainable Engineering and the Built Environment, Arizona State University, Tempe, AZ, USA

ABSTRACT: Stiffness of pavement subgrade materials that is commonly determined by the resilient modulus parameter is an important component in the mechanistic design of flexible pavement structures. Environmental effects such as seasonal variations in pavement moisture content can considerably influence this material property which should be properly considered in any realistic pavement design. The seasonal changes in moisture condition affects the stress state in the subgrade due to changes in the matric suction which is an important stress state variable in unsaturated soil mechanics. In this study, a modified test procedure and a predictive resilient modulus model that takes into account the subgrade soil matric suction as a stress state variable is presented. Two different silty sand subgrade materials were tested in unsaturated conditions using a series of Repeated Load Triaxial (RLT) tests. The tests were performed under various matric suctions (moisture contents) to enhance the understanding of its effect on the resilient modulus. The results showed a considerable influence of the moisture content (matric suction) on the subgrade resilient modulus. The resilient modulus data together with the suction measurements were used and a set of parameters for the enhanced predictive model were developed. This model accounts for seasonal variation of subgrade material stiffness by incorporating suction as a stress state variable.

Keywords: subgrade, resilient modulus, unsaturated soil, matric suction, environmental effects, moisture content

1 INTRODUCTION

The Swedish Traffic Administration has initiated a research program to develop a comprehensive Mechanistic-Empirical analysis and design procedure of pavements. The aim is to develop and calibrate enhanced design models for flexible pavement structures that are calibrated for the materials, construction practices, traffic loads and climatic conditions of the road network in Sweden.

One of the important input parameters in the analysis and design of any flexible pavement structure is the stiffness of the unbound layers. This material property is widely characterized by the resilient modulus (M_R), which depends on many factors such as gradation and texture, stress state, compaction energy, dry density, number of load cycles and moisture content [1].

Large part of the road network in Sweden consists of relatively thin flexible pavement structures that are located in cold regions. These pavement structures are subjected to significant seasonal variations in pavement environmental condition that influences the material properties and pavement performance. In unbound pavement materials and subgrade soils, moisture content is known to be the major environmental factor which can be affected by seasonal changes in water table condition, water infiltration from precipitation as well as the frost-thaw action.

Since moisture content in unbound pavement materials is one of the main factors that have a significant role in their mechanical response, proper consideration to this factor should be given in any sustainable pavement design approach. As a consequence, the essential role of the environmental factors has been substantially emphasized in the latest design guide procedures in pavement engineering [2,3].

Over the recent years, a number of experimental studies has been carried out to understand the influence of moisture content on the resilient response of pavement unbound materials and to develop models that can properly predict this parameter and its variation due to seasonal effects [4–8]. Most of the models developed from these studies are based on triaxial testing on unbound materials at different moisture contents and use a total stress approach. These models incorporate an environmental factor that represents the influence of the changes in the moisture content on the resilient modulus for the set of stress levels applied during the triaxial testing.

From unsaturated soil mechanics, it is known that variations in the moisture content of fine-grained subgrades (seasonal environmental variations) result in changes in the stress state of the soil which is explained by changes in the soil matric suction, which is the pressure difference between the pore-air and the pore-water phases in the soil matrix. Therefore, a more rational approach to incorporate seasonal effects in the resilient modulus predictive models would be to consider matric suction as a fundamental variable in the stress state of the subgrade soil [9–11].

The overall objective of this study was to investigate the influence of moisture content on the mechanical response of silty sand subgrade materials and to further calibrate model parameters of a suction-dependent resilient modulus model.

In this study, two different silty sand subgrade soils were tested. Silty sand subgrade materials appear frequently in Nordic countries due to the heterogeneous sedimentation process of glacial origin. The proposed model was validated and the regression parameters were determined for the silty sand subgrade soils commonly found in Sweden.

The materials were tested at the Arizona State University (ASU) Geotechnical Laboratory using a custom built advanced triaxial cells and control units. The system enables full control/measurement of pore-water and pore-air pressure of the cylindrical test specimen during the Repeated Load Triaxial (RLT) test. The load sequences used for this purpose were in accordance to the NCHRP 1-28A [12] protocol "Harmonized Test Methods for Laboratory Determination of Resilient Modulus for Flexible Pavement design" after some modifications to the procedure that would allow for testing soil in unsaturated conditions with matric suction control. More details on the modification to the NCHRP 1-28A loading procedure and triaxial cell control unit can be found in Cary and Zapata (2011) [11].

2 MODELING OF RESILIENT MODULUS

It is widely recognized that the resilient modulus can properly characterize the mechanical stiffness of pavement unbound materials and subgrade soils. This parameter is measured under conditions representative of the stress state and the environment that is experienced by the unbound materials in the pavement system. Many researchers have proposed mathematical models that describe the stress dependence of the resilient modulus using a total stress approach. These models are mainly developed from curve fitting of the laboratory triaxial data and do not directly account for environmental factors [1].

To overcome this drawback, Cary and Zapata (2011) [11] proposed an enhanced resilient modulus model that accounts for seasonal environmental variations by incorporating matric suction as stress state variable. They obtained sets of regression constants from triaxial experiments on granular base and subgrade materials that are commonly used in the state of Arizona. Their proposed model is presented in Eq. (1):

$$M_R = k_1 p_a \left(\frac{\theta_{net} - 3\Delta u_{w-sat}}{p_a} \right)^{k_2} \left(\frac{\tau_{oct}}{p_a} + 1 \right)^{k_3} \left(\frac{(\psi_{m_0} - \Delta\psi_m)}{p_a} + 1 \right)^{k_4} \quad (1)$$

where,
p_a = atmospheric pressure (here chosen as 100 kPa)
$\theta_{net} = \theta - 3u_a$ = the net bulk stress (θ = bulk stress = $\sigma_1 + \sigma_2 + \sigma_3$ and u_a = pore-air pressure)
Δu_{w-sat} = pore-water pressure build up under saturated condition ($\psi_m = 0$)
τ_{oct} = octahedral shear stress = $1/3\sqrt{(\sigma_1 - \sigma_2)^2 + (\sigma_1 - \sigma_3)^2 + (\sigma_2 - \sigma_3)^2}$
ψ_{m_0} = initial matric soil suction and $\Delta\psi_m$ = relative change in soil matric suction with respect to ψ_{m_0} due to pore-water pressure build up under unsaturated condition ($\Delta u_{w-sat} = 0$)
$k_1 \geq 0, k_2 \geq 0, k_3 \leq 0$ and $k_4 \geq 0$ are regression constants.

In RLT tests, the principal stresses acting on the specimen are: $\sigma_1 = \sigma_3 + \sigma_d, \sigma_2 = \sigma_3$ and $\sigma_3 = \sigma_c$ where σ_c = confining pressure and σ_d = deviator stress. Therefore, $\theta = \sigma_d + 3\sigma_c$ and $\tau_{oct} = \sqrt{2}/3\ \sigma_d$.

3 TEST MATERIAL INDEX PROPERTIES

Two silty sand subgrade soils commonly encountered in Sweden were selected for testing in this study. The subgrade soils were obtained from two different sites in Sweden; the southern part (near Torpsbruk in the Småland province) and the northern part (near Luleå in Norrbotten province) of the country. Wet sieve analysis, specific gravity, maximum dry density, optimum moisture content and Soil-Water Characteristic Curve (SWCC) tests were performed on the selected materials. A summary of the test results is presented in Table 1. Figure 1 shows the grain size distribution curves for the subgrade soils used in this study.

The SWCC for the subgrade materials were determined using the Fredlund SWCC device which is an oedometer-type apparatus for applying matric suctions from near zero values up to 1500 kPa under various stress paths [13]. A saturated ceramic stone with a High Air Entry (HAE) value of 500 kPa was used for this test, which allowed applying suction values up to 450 kPa. This was found to be suitable for the non-plastic subgrade soils tested. The subgrade soils specimens were compacted in the brass ring of the apparatus to reach the maximum dry density that was obtained from the standard Proctor test and then were fully saturated. Thus, the drying paths of the SWCCs for the subgrade soils were obtained by applying air pressure to the specimens. For each soil, the equilibrium moisture contents at six different matric suctions were measured. These graphs were further used to apply the matric suction levels required to reach the target moisture contents for the resilient modulus tests. The SWCCs and test apparatus are presented in Figure 2.

Table 1. Summary of the subgrade soil index properties.

Subgrade soil	USCS class.[1]	Passing No. 200 (%)	Max. dry unit weight (kN/m³)[2]	Opt. moisture content. (%)	Specific gravity	Plasticity index
Luleå	SM	42.2	19.6	10.1	2.68	Non plastic
Torpsbruk	SM	27.4	20.3	7.6	2.67	Non plastic

[1]USCS = Unified Soil Classification System.
[2]Maximum dry unit weight is based on standard Proctor compaction test (ASTM D698).

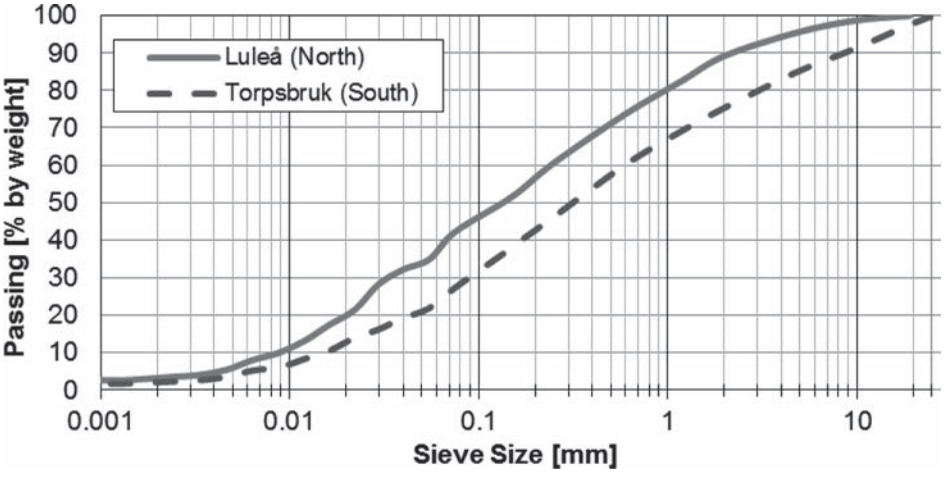

Figure 1. Subgrade soils grain size distributions.

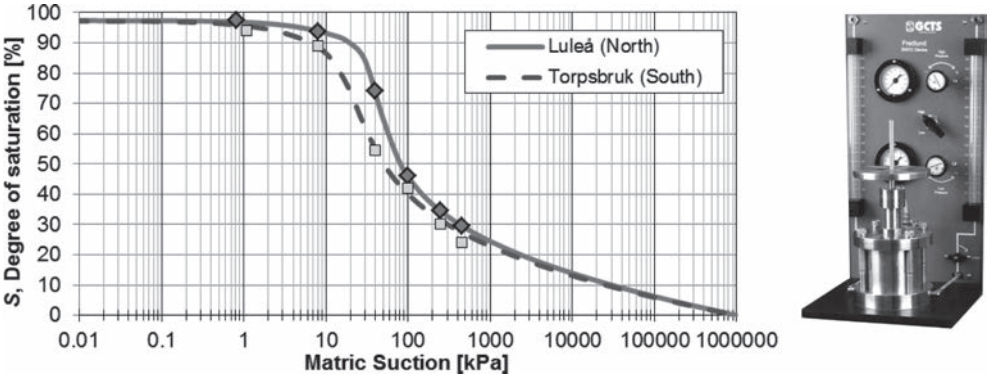

Figure 2. SWCC for subgrade materials (left), Fredlund SWCC apparatus (right).

4 EQUIPMENT SETUP AND TESTING SYSTEM

The triaxial cell and control unit for unsaturated soils testing at ASU is a custom-built electro-hydraulic system with fully digital servo controllers that is capable of adjusting pore-water and pore air pressure of the soil specimen during the test. In the triaxial cell, the bottom platen is built-in with a 500 kPa HAE ceramic disk similar to the one used in the Fredlund SWCC device. The top loading platen is built-in with a porous stone that allowed for application of air pressure to the specimen. In order to eliminate erroneous diffusion of air bubbles that might be trapped in the lines and under the bottom ceramic disk, the bottom platen is also equipped with a flushing device. For the confinement of the specimen during the test, air was used. The vertical deformations on the test specimen were measured using two Linear Variable Differential Transformers (LVDTs) mounted directly on the studs that were buried into the specimen during the compaction process. Schematic overview of the triaxial system is depicted in Figure 3.

5 TRIAXIAL SPECIMEN PREPARATION

Preparation of the specimens was in accordance with the NCHRP 1-28A test protocol [12]. In order to obtain a homogeneous mix, the subgrade materials were thoroughly mixed at

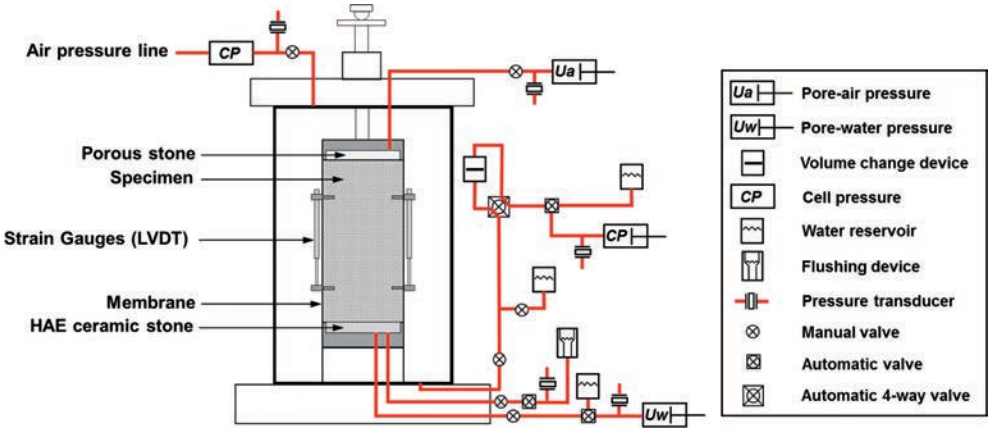

Figure 3. Schematic overview of the triaxial testing system at ASU.

Table 2. Target degrees of saturation, corresponding moisture contents and calculated matric suctions for resilient modulus testing of the subgrade soils.

	Luleå subgrade				Torpsbruk subgrade			
Degree of saturation, S (%)	30.0	50.0	79.3[1]	94.3	30.0	50.0	70.1[1]	97.1
Moisture content, w (%)	3.8	6.4	10.1[1]	12.0	3.6	5.4	7.6[1]	10.4
Matric suction, ψ_{m_0} (kPa)	443.9	81.0	35.0[1]	6.7	316.0	51.6	23.3[1]	0.0

[1]Measurement corresponding to the optimum moisture content.

their optimum moisture content and stored in a sealed container in a controlled temperature room for approximately 48 hours. Subsequently, the materials were compacted to reach their maximum dry density as per the standard Proctor tests. These specimens were cylindrical and were 102 mm in diameter and 203 mm in height (4 × 8 inch). The two subgrades were tested at 4 different moisture contents with two replicates that add up to a total number of 16 successful tests. The four different target moisture contents for resilient modulus tests were the optimum moisture contents as well as the moisture contents corresponding to 30, 50 and near 100% degrees of saturation.

In the preconditioning process, to reach the target moisture content for the resilient modulus tests, the specimen were compacted at optimum moisture content and subsequently, they were either saturated or dehydrated to the target moisture content. This was controlled by regular measurement of the weight of the specimens. Once the specimen was close to the target moisture content, the latex membrane was assembled and the specimen was stored in a moisture-sealed bag for about 24 hours. During this period, the specimen was intermittently turned over upside down to retain the homogeneity in moisture distribution.

The specimen was then mounted on the triaxial cell pedestal. Any possibly entrapped air under the ceramic stone and in the connection lines was flushed out and after applying a suitable confinement pressure the target matric suction value was imposed. In this procedure, under the applied matric suction, the specimen is supposed to absorb or release water unless moisture equilibrium is reached. This was the last phase of the moisture equilibration process. Once the equilibration process was completed, the resilient modulus test was started.

It should be mentioned that the specimens could have reached the desired moisture content by only performing the last part of the equilibration process mentioned above (only applying suction to the compacted specimen that correspond to the target moisture content). However, this would be a relativity long process due to the dimension of the specimen and the fine content of the soils. Therefore and as stated earlier, preconditioning of the specimens was performed prior to the final equilibration phase which expedited the process.

6 TEST RESULTS

Examples of the resilient modulus test results for the two subgrade soils are presented in Figures 4 and 5. These figures show the resilient modulus changes with respect to changes in the bulk stress and the moisture content (degree of saturation) of the specimens. Higher moisture contents correspond to lower matric suction values in the subgrade. It should be mentioned that loading sequences for the two subgrades were not fully identical. In the NCHRP 1-28A test protocol [12], loading sequence procedure for the resilient modulus testing of subgrades are divided into two different procedures; Procedure Ib for granular subgrades and Procedure II for fine-grained subgrades. According to the test protocol specification, the Torpsbruk subgrade is categorized as granular subgrade and the Luleå subgrade is categorized as fine-grained subgrade. The specifications for the material classifications and the corresponding test sequences can be found in NCHRP 1-28A [12]. Figure 4 shows variations in the resilient modulus for the two subgrades with respect to changes in degree of saturation and bulk stress. The data plotted in this figure correspond to cyclic deviator stress of 28 kPa.

As expected, increase in the bulk stress resulted in increase in the resilient modulus and increase in the moisture content (matric suction reduction) resulted in decrease in the resilient modulus. It can be observed that both subgrades exhibited higher sensitivity to the bulk

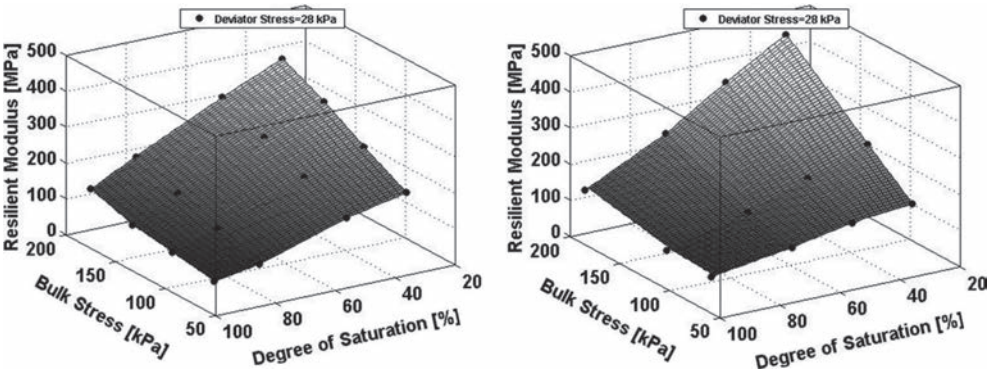

Figure 4. Examples of data; resilient modulus variations with change in moisture content and bulk stress for Luleå Subgrade (Left) and Torpsbruk Subgrade (Right).

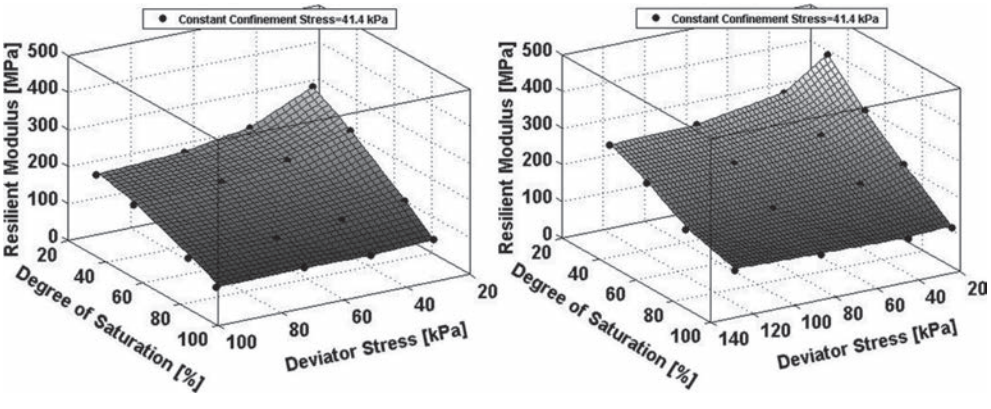

Figure 5. Example of data; resilient modulus variations with change in moisture content and deviator stress under constant confinement stress (41.4 kPa) for Luleå subgrade (left) and Torpsbruk subgrade (right).

stress values at lower degree of saturations. That is, at lower degrees of saturation, resilient modulus of the subgrade increased at higher rate with increase in the bulk stress.

Figure 5 illustrates variations in the resilient modulus as a function of changes in degree of saturation and deviator stress. The data in these figures correspond to a constant confinement stress of 41.4 kPa. From these figures, it can be seen that the subgrades generally exhibited a softening behaviour with respect to increase in the deviator stress. For a constant confinement stress, increase in the deviator stress resulted in decrease in the resilient modulus. However, this softening behaviour was diminished as the moisture content of the subgrade was increased. At high degree of saturations, the magnitude of the deviator stress had no or insignificant influence on the resilient modulus.

7 MODEL PARAMETERS

The regression parameters for the model presented in Eq. (1) were calculated by least square curve fitting on the resilient modulus test data. In total, 123 data points for the Luleå and 150 data points for the Torpsbruk subgrade that correspond to different combinations of stress invariants and matric suctions were used for this statistical analysis. The Solver function in Microsoft Excel was used for the model parameters optimization. The coefficient of determination (R^2) and the adjusted coefficient of determination (R^2_{adj}) were also calculated to evaluate the goodness of fit for the proposed model. The calibrated model parameters and the goodness of fit statistics are summarized in Table 3. Figure 6 shows the prediction results from the Cary and Zapata model presented in Eq. (1) together with the measurements for the two subgrade materials.

The regression of the test data yielded R^2_{adj} values of 0.76 and 0.78 for Luleå and Torpsbruk subgrades, respectively. This is considered to be good for unbound subgrade materials which

Table 3. Resilient modulus model regression parameters for the subgrade soils.

	Model parameters				Goodness of fit	
	k_1	k_2	k_3	k_4	R^2	R^2_{adj}
Luleå subgrade	1489	0.746	–2.633	0.434	0.761	0.759
Torpsbruk subgrade	1524	0.774	–1.470	0.475	0.785	0.784

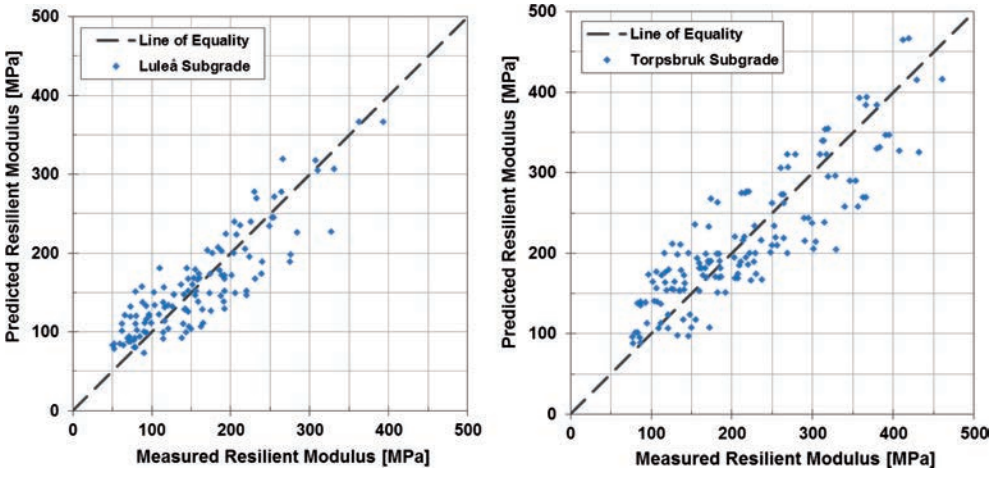

Figure 6. Actual versus predicted resilient modulus obtained from the Cary and Zapata model for Luleå subgrade (left) and Torpsbruk subgrade (right).

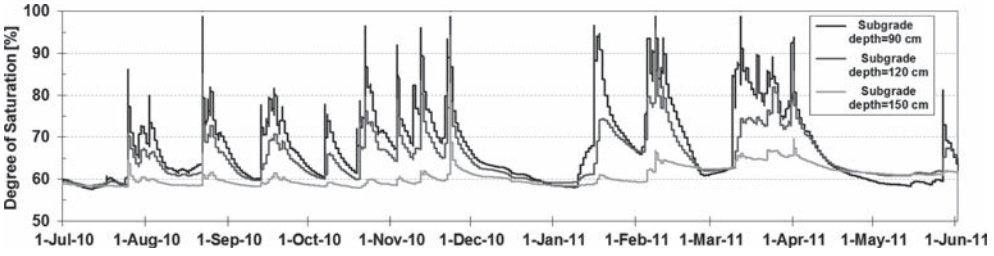

Figure 7. Degree of saturation variations in the subgrade soil of a road structure in torpsbruk (measurements from the unpaved shoulder of the pavement).

generally show high data scatters in experimental tests such as the resilient modulus. From the graphs plotted in Figure 6 and given the goodness of fit parameters presented in Table 3, it can be concluded that the proposed model that includes matric suction as a fundamental stress variable might be a realistic approach for taking into account effect of change in the environmental conditions.

8 FIELD MOISTURE VARIATION IMPACT ON RESILIENT MODULUS

In the recent years, considerable improvements have been made in techniques and instrumentations that can measure in-situ moisture content of pavement unbound layers. Often, considerable variation in the moisture content has been observed, mainly due to water infiltration after heavy rainfalls and spring thaw action in cold regions. This has called the attention of the researchers to further investigate moisture effects on the performance of the pavement structures.

Figure 7 shows variations in degree of saturation in the subgrade layer of the test road section in Torpsbruk (southern Sweden), over a one year period (July 2010 to June 2011). The Torpsbruk subgrade soil samples that were used in this study were taken from this road section. This figure is based on in-situ measurements from two moisture rods, each consisting of four moisture probes [14]. Figure 7 shows the considerable variation in the subgrade moisture content particularly in the upper section. The subgrade degree of saturation deviates from an equilibrium state of approximately 60% to more than 90% due to the autumn heavy rainfalls as well as the thawing action in the spring. From the Torpsbruk subgrade SWCC presented in Figure 2, this change in moisture content corresponds to matric suction variations from about 35 kPa to about 5 kPa. Concerning the impact on the resilient modulus of the subgrade, for a confinement stress of 27.6 kPa and a deviator stress of 13.8 kPa, increase in the degree of saturation from 60% to over 90% resulted in resilient modulus decrease from 205 MPa to 118 MPa. This corresponds to 42% reduction in the resilient modulus.

9 SUMMARY AND CONCLUSIONS

Proper accounting for the environmental effects on the resilient modulus of the unbound materials can result in more cost effective pavement design. Variation in the moisture content of unbound materials is known to be the major driving factor for seasonal changes in the resilient modulus.

Any change in the moisture content affects the soil matric suction that can be considered as an independent stress state variable in the resilient modulus prediction models of subgrade soil materials. Several resilient modulus tests were conducted on two silty sand subgrade soils and at four different degrees of saturation (matric suctions). The test data were then used to determine regression parameters of a model that take account of matric suction as a stress state variable. The prediction model showed a relatively good correlation with the

experimental data. Given the goodness of fit of the prediction model, it can be concluded that considering matric suction as a stress state variable that incorporates environmental effects into the resilient modulus predictive model might be a rational approach.

Reconstructing the field moisture variations of the Torpsbruk subgrade that was monitored over a one-year period revealed 42% reduction in the resilient modulus when the moisture content increased from the natural equilibrium state during heavy rainfalls and the spring thaw. This illustrates the importance of the environmental effects and the necessity for developing models that can properly account for the seasonal environmental variations.

It is believed that a more extensive database with more tests and materials is required to validate the approach and improve or calibrate the model presented in this study. The major concern for this methodology is that triaxial systems that are capable of measuring matric suction under cyclic loading are mainly limited to research institutes. The authors recommend more research works to be carried out to further develop the approach that is believed to be a step forward to a realistic pavement design.

ACKNOWLEDGEMENTS

This study was sponsored by the Swedish Transport Administration (Trafikverket) and the Fredrik Bachmans memorial foundation (Stiftelsen Fredrik Bachmans Minnesfond). The authors wish to thank Peter Goguen, laboratory manager, and Kenneth Witczak, laboratory coordinator, at Arizona State University, School of Sustainable Engineering and Built Environment for their technical support and assistance.

REFERENCES

[1] Lekarp, F., Isacsson, U. and Dawson, A. State of the Art. I: Resilient Response of Unbound Aggregates. Journal of Transportation Engineering, 126(1), 2000, pp. 66–75.

[2] ARA, Inc., ERES Consultants Division. Guide for Mechanistic–Empirical Design of New and Rehabilitated Pavement Structures. Final report, NCHRP Project 1-37A. Transportation Research Board of the National Academies, Washington, D.C., 2004. (Available at: http:// www.trb.org/mepdg/).

[3] Zapata, C.E., Andrei, D., Witczak, M.W. and Houston, W.N. Incorporation of Environmental Effects in Pavement Design, International Journal of Road Materials and Pavement Design, Vol. 8, No 4, 2007, pp. 667–693.

[4] Doucet, F. and Doré, G. Resilient Modulus and Resilient Poisson Coefficient of the C-LTTP Granular Materials. Proceedings of the Annual Conference of the Canadian Geotechnical Society, Canadian Geotechnical Society, Quebec City, Canada, 2004.

[5] Santha, B.L. Resilient Modulus of Subgrade Soils: Comparison of Two Constitutive Equations, Transportation Research Record: Journal of the Transportation Research Board, Vol. 1462, Transportation Research Board of the National Academies, 1994, pp. 79–90.

[6] Cary, C.E. and Zapata, C.E. Enhancement of the Model for Resilient Response of Soils due to Seasonal Environmental Changes Implemented in the M-EPDG. Transportation Research Record: Journal of the Transportation Research Board. Vol. 2170, 2010, pp. 36–44.

[7] Andrei, D. Development of a Predictive Model for the Resilient Modulus of Unbound Materials, Doctoral Dissertation, Arizona State University, Tempe, Arizona, 2003.

[8] Rahman, M.S. and Erlingsson, S. Moisture Sensitivity of Unbound Granular Materials. Proceedings of the 4th European Pavement and Asset Management Conference (EPAM 4). CD-ROM., Malmö, Sweden, 2012.

[9] Khoury, N.N. and Zaman, M. Correlation among Resilient Modulus, Moisture Variation and Soil Suction for Subgrade Soils, Transportation Research Record: Journal of the Transportation Research Board, Vol. 1874, Transportation Research Board of the National Academies, 2004, pp. 99–107.

[10] Yang, S.R., Huang, W.H. and Tai, Y.T. Variation of Resilient Modulus with Soil Suction for Compacted Subgrade Soils. Transportation Research Record: Journal of the Transportation Research Board, Vol. 1913, Transportation Research Board of the National Academies, 2005, pp. 99–106.

[11] Cary, C.E. and Zapata, C.E. Resilient Modulus Testing for Unsaturated Unbound Materials, International Journal of Road Materials and Pavement Design, Vol. 12, No. 3, 2011, pp. 615–638.
[12] National Cooperative Highway Research Program, Laboratory Determination of Resilient Modulus for Flexible Pavement Design, In Research Results Digest, No. 285, Transportation Research Board of the National Academies, Washington, D.C., 2004, 52 p.
[13] SWC-150 Fredlund Soil Water Characteristic Device, User's Guide and Reference Manual, Version 1.1, GCTS Testing Systems, 2007. (Available at: www.gcts.com).
[14] Salour, F. and Erlingsson, S. Moisture Sensitive and Stress Dependent Behavior of Pavement Unbound Materials from Insitu Falling Weight Deflectometer Tests. Transportation Research Record: Journal of the Transportation Research Board, No. 2335, Transportation Research Board of the National Academies, 2013, pp. 121–129.

Asphalt Pavements – Kim (Ed)
© 2014 Taylor & Francis Group, London, ISBN 978-1-138-02693-3

Influence of saturation and repeated loading on mechanical behavior of permeable asphalt pavement

Yusuke Kawaguchi, Shinichiro Nakashima & Norikazu Shimizu
Yamaguchi University, Tokiwadai, Ube, Japan

ABSTRACT: In this study, a cyclic plate load test was conducted for a pavement model in the laboratory to evaluate the mechanical behavior of permeable asphalt pavement with different degrees of saturation. A four-layer pavement model was prepared, and 49 kN was loaded repeatedly through a steel plate, 300 mm in diameter, at a frequency of 1.0 Hz. A total of 100,000 repetitions were applied alternating the saturation conditions of the model between drained (dry) and saturated (wet). The test results showed that the repeated loading under a saturated condition caused a remarkable increase in the elastic deformation of the pavement surface. The normal stress on the subgrade surface showed a decrease in the saturating process, and changed to an increase in the following loading process. Based on a series of elastic analyses for a simple three-layer model, softening of the subbase course and the subgrade occurred in the saturating process, followed by softening of the subbase course and the surface course in the repetition process.

Keywords: permeable asphalt pavement, saturation degree, mechanical behavior, repeated plate load test, elastic multi-layered analysis

1 INTRODUCTION

Permeable asphalt pavement is a special type of pavement that allows rainwater to pass through it, as shown in Figure 1, thereby reducing the runoff from a site. This type of pavement has been applied to areas with light traffic, such as parking lots and sidewalks, since the mid-1970s. However, recent changes in storm water regulations, established to counteract urban flooding in Japan [1], have prompted us to expand the application to areas with heavier traffic.

In the practical application of permeable asphalt pavement to roadways with heavy traffic, mechanical durability is of great concern. On the one hand, many researchers [e.g., 2–10] have

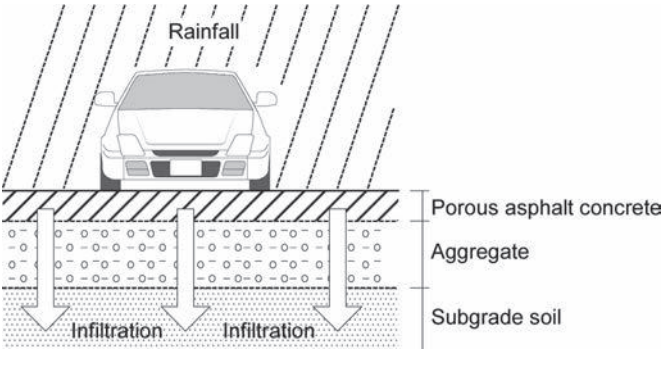

Figure 1. Typical structure of permeable asphalt pavement.

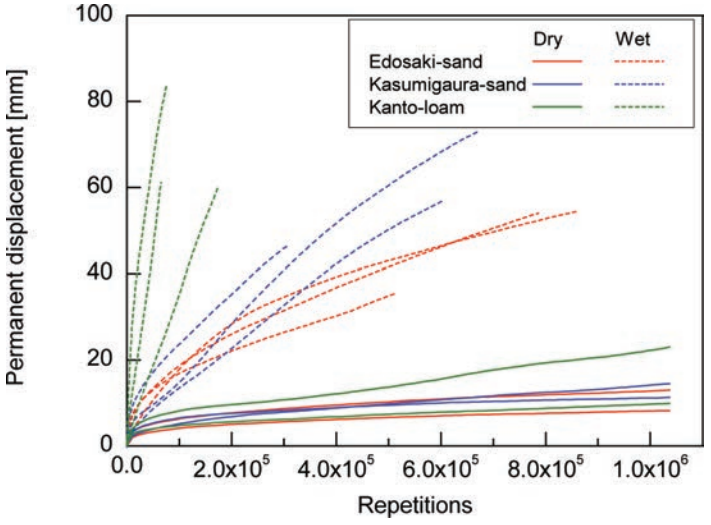

Figure 2. Permanent displacement of loading surface by repeated plate load test for permeable asphalt pavement models with different subgrade materials and different saturation conditions.

reported the negative effects of water saturation on the stiffness and the strength of unbound granular materials through material tests. Therefore, we can easily expect the premature failure of pavement structures, if the thickness of the permeable pavement is designed in the same way as conventional (impervious) asphalt pavement. On the other hand, the results of some field tests [11] that have been conducted on real roadways in service indicate no notable damage to the permeable pavement sections relative to the impervious pavement sections within a period of several years. Therefore, for the proper assessment of permeable asphalt pavement on roadways with heavy traffic, further tests and simulations are needed using reasonable layered models under properly controlled mechanical and hydrological boundary conditions.

The authors [12, 13] have developed indoor cyclic plate load testing equipment to evaluate the performance of permeable asphalt pavement sections with different subgrade materials and different saturation conditions. The results of the model tests have revealed that under a highly saturated condition, rutting (permanent deformation of pavement surface) grew over a few times or more rapidly than under a dry condition, as shown in Figure 2. Based on the test results, the authors of this paper conducted an additional model test to study the deterioration mechanism of permeable asphalt pavement. The degree of saturation was controlled in the middle of the load repetitions by raising and lowering the water level in the model. A series of elastic analyses was also carried out for a simple three-layer model. Based on the experimental and analytical results, we will discuss the influence of the saturation degree and the load repetitions on the mechanical behavior of permeable pavement.

2 OUTLINE OF MODEL TEST

An indoor cyclic plate load testing device was used in this study. Figure 3 shows the cross section of the pavement model. This model was a 1 m × 1 m cylinder, consisting of a 50-mm-thick surface course, a 50-mm-thick base course, a 200-mm-thick subbase course and a 600-mm-thick subgrade. The bottom layer (100 mm) was a filter layer (a mixture of crushed gravel and coarse sand) that allows water to flow smoothly into and out of the model.

A repeated load, namely, a 1.0 Hz sine-wave load ranging from 0.1 to 49 kN, which results in a loading pressure of 694 kPa, was applied through a steel rod on the load plate that sits on the model surface. The load plate was a steel plate, 50 mm in thickness and 300 mm in diameter.

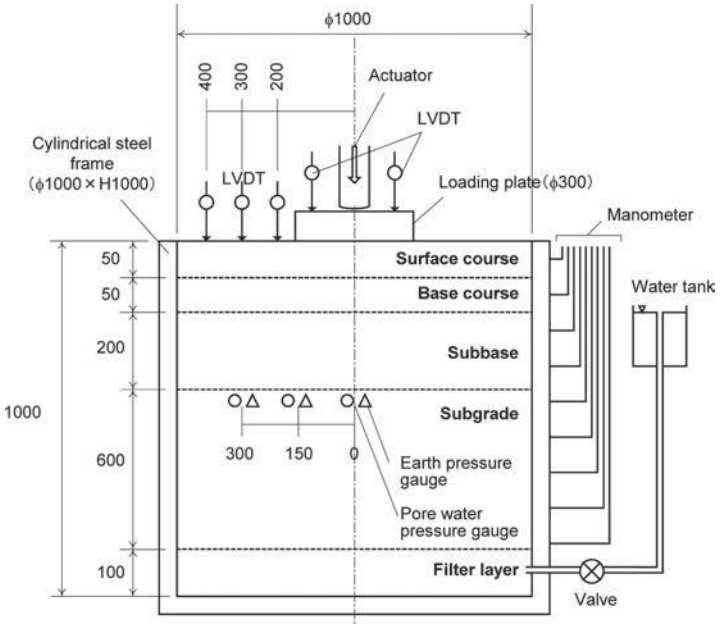

Figure 3. Cross section of permeable pavement model.

The pavement materials and their conditions are shown in Table 1. They were chosen based on the Japanese interim manual for permeable asphalt pavement design [14]. The subgrade soil was local Masa sand, a well-graded type of sand with gravel having a CBR-value of 27.1% in the laboratory.

The construction procedure for the model is shown in Figure 4. The compaction ratios (relative densities) of the subgrade and the subbase course were 90% and 95%, respectively, under their optimum moisture contents. After the completion of the subgrade preparation, pressure gauges and piezometers were installed within the subgrade (about one centimeter below the subgrade/subbase interface) at three locations, or along the centerline (X = 0 mm) and 150 and 300 mm away from the centerline. After the load plate was placed on the pavement surface, two LVDTs were set on the plate to monitor the vertical displacement; another three LVDTs were set on the pavement surface 200, 300 and 400 mm away from the centerline to monitor the surface deformation.

Figure 5 illustrates the test procedure. 20,000 repetitions under a drained (dry) condition and the same number under a saturated (wet) condition were alternated, and consequently, 100,000 repetitions were done in total. In the saturating process, we raised the water level of the model over two weeks, providing water from the model bottom, until the water level reached the base/subbase interface. In the draining process, we released the outflow valve and kept it open for over two weeks. No loading was conducted during the saturating/draining processes.

Before and after every 20,000 repetitions, a Static Plate Load (SPL) test was carried out, as indicated by "K" in Figure 5, using the same equipment as in the repeated plate load test. The aim of the SPL test in this study was to monitor the change in stiffness of the pavement model throughout the experiment. Relatively smaller loads (5, 10 and 20 kN) were applied in the SPL test to minimize the plastic deformation of the model, and the modulus of pavement reaction K_{30} was calculated using the following equation:

$$K_{30} = P/A\ s \tag{1}$$

where P = applied load (5, 10 and 20 kN), A = area of the loading plate (70,650 mm^2) and s = vertical displacement of the loading plate.

Table 1. Material and properties of each layer.

	Surface course	Base course	Subbase course	Subgrade
Thickness	(50 mm)	(50 mm)	(200 mm)	(600 mm)
Material and properties	Open-graded asphalt mix Binder: High viscosity modified asphalt type-H Binder content: 4.8% Bulk density: 1.981 g/cm^3 Theoretical max density: 2.482 g/cm^3 Air void: 20.2% Marshall stability: 6.40 kN Flow value (1/100 cm): 30 Permeability: 1.5×10^1 cm/s	Asphalt treated aggregates Binder: Polymer modified asphalt binder type-II Binder content: 4.3% Bulk density: 2.087 g/cm^3 Theoretical max density: 2.503 g/cm^3 Air void: 16.6% Marshall stability: 7.10 kN Flow value (1/100 cm): 29 Permeability: 6.6×10^2 cm/s	Crusher-run Max. dry density: 2.194 g/cm^3 Opt. moisture content: 3.6% Water absorption: 0.79% Abrasion loss: 23.1% Modified CBR: 63.8% Plastic Index: NP Permeability: 5.7×10^{-2} cm/s	Masa sand Particle density: 2.616 g/cm^3 Opt. moisture content: 11.8% Max. dry density: 1.930 g/cm^3 CBR: 27.1% Permeability: 5.0×10^{-3} cm/s
Sieve size	Passing %	Passing %	Passing %	Passing %
37.5 mm		100	100	
31.5 mm		99.2	98.6	
26.5 mm		95.7	–	
19.0 mm	100	86.2	68.4	
13.2 mm	96.4	55.2	–	100
9.5 mm	65.3	–	–	–
4.75 mm	18.7	19.8	27.5	98.77
2.36 mm	13.9	16.1	18.4	73.00
0.6 mm	8.2	11.4	–	32.82
0.3 mm	7.0	8.8	–	18.72
0.15 mm	5.9	6.1	–	8.87
0.075 mm	4.3	4.3	–	3.34

Figure 4. Construction procedure of pavement model.

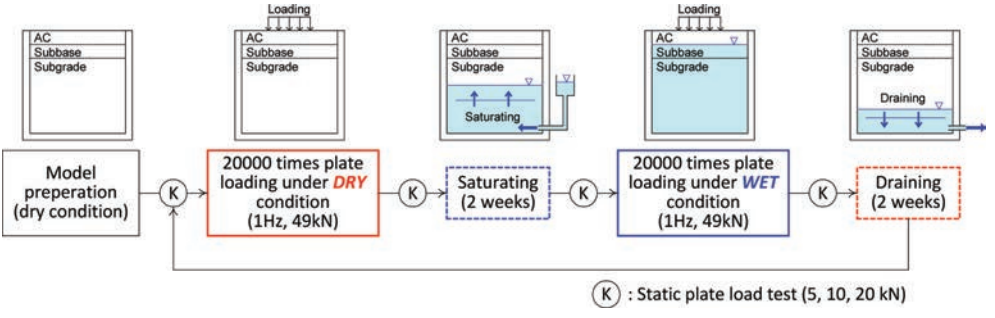

Figure 5. Test procedure.

3 EXPERIMENTAL RESULTS

Figure 6 presents the entire histories of the measurements. Figures 6(a) and (b) show the permanent displacement and the resilient displacement, respectively, of the load plate and the pavement surface (outside of the load plate) obtained from the LVDT measurements. Here, the permanent displacement is defined as the residual component of the vertical displacement that remains after unloading, while the resilient displacement is defined as the displacement amplitude at each loading cycle. From Figure 6(a), the permanent displacement of the load plate shows a continuous increase. However, contrary to our previous experiments shown in Figure 2, we cannot find a remarkable difference in the increasing ratio between the dry and the wet cases. One reason is that the number of repetitions in this study was so small (less than one-tenth of the previous experiments) that plastic deformation was not generated visibly in the pavement model within this range of repetitions. Figure 6(c) shows the normal stress on the subgrade by the earth pressure gages. This figure shows that the pressure acting on the subgrade in this experiment was about half the amount of the loading pressure by the load plate (694 kPa). Figure 6(d) shows the excessive pore water pressure within the subgrade by the piezometers. We can see that pore water pressure was activated in the saturated cases, but that the amount is less than 0.2% of the loading pressure by the plate load and that it shows stability during the repetitions.

Figure 7 presents a comparison of the growth of the resilient displacement of the load plate and the normal stress on the subgrade within each set of 20,000 repetitions. The resilient displacement of the load plate in the wet cases increased more rapidly than that in the dry cases. Also, the normal stress on the subgrade showed a significant increase with the repetitions in the wet cases, while the stress remained constant (or showed a small decrease) in the dry cases. From these results, we find that repetitions under a wet condition increase the elastic deformation of the pavement model, which results in the increase in pressure acting on the subgrade surface.

Figure 8 shows the results of the SPL tests that were conducted before and after each set of 20,000 repetitions. From Figure 8(a), overall, the modulus of pavement reaction K_{30} gradually dropped with the progress of the test, which implies the deterioration of the stiffness of the

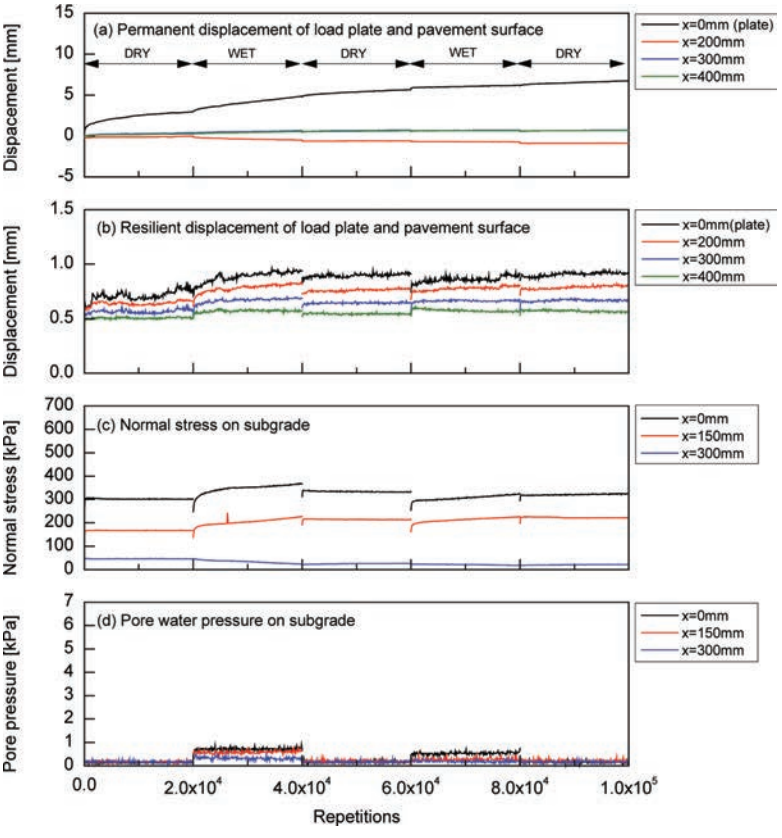

Figure 6. Histories of measurements by repeated plate load test.

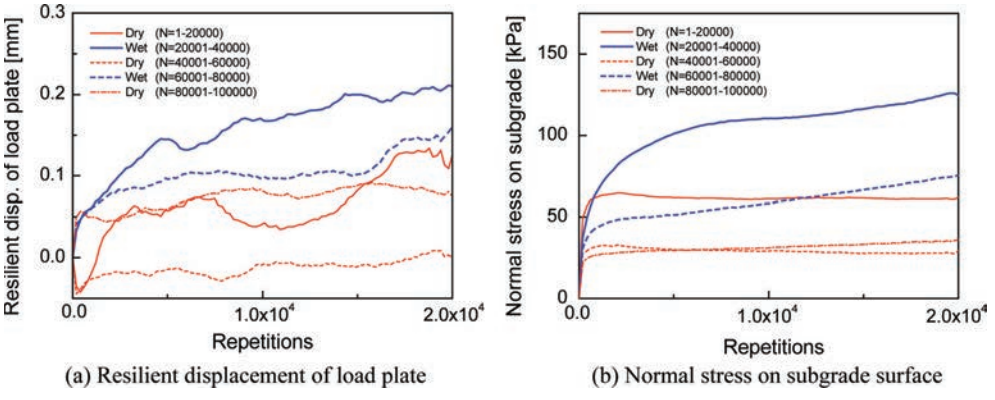

Figure 7. Change in resilient displacement of load plate and normal stress on subgrade within each 20000 repetitions.

pavement model. At the same time, we can clearly see that modulus K_{30} largely dropped after experiencing 20,000 repetitions under a wet condition, and it recovered after draining. On the other hand, K_{30} did not show any remarkable change after 20,000 repetitions under a dry condition or following the saturating process. Figure 8(b) shows the normal stress on the subgrade along the centerline when 20 kN was applied in the SPL tests. From this figure, we can see that

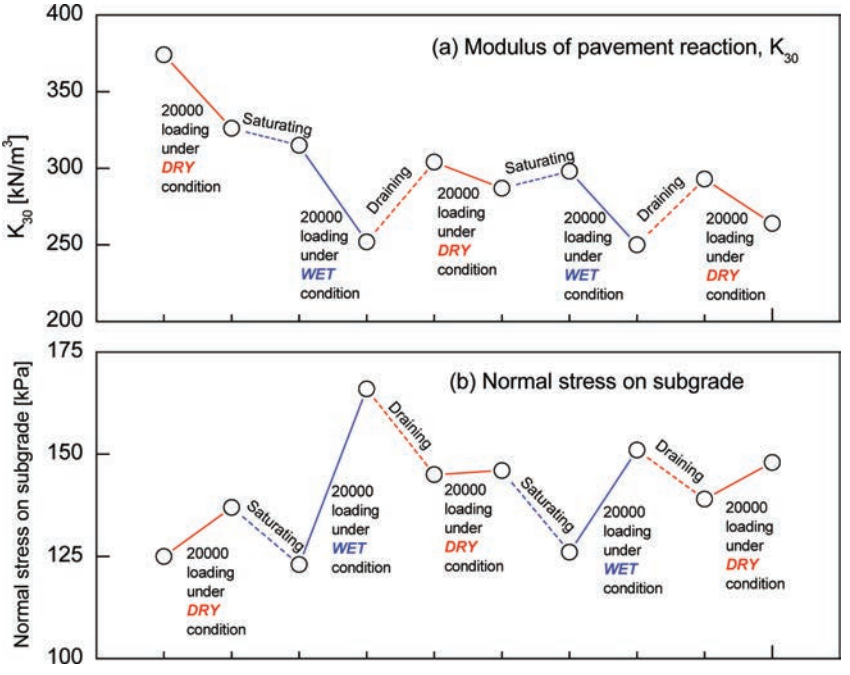

Figure 8. Results of static plate load tests.

Table 2. Change in response of pavement surface and stress on subgrade.

Type of external impact	Displacement of plate		Normal stress on subgrade
	Permanent displacement	Resilient displacement	
a) 20000 repetitions under DRY condition	Small increase	Small increase	Small increase
b) 20000 repetitions under WET condition	Small increase	Increase	Increase
c) Saturating (from dry to wet)	–	Small increase	Decrease
d) Draining (from wet to dry)	–	Decrease	Decrease

the normal stress on the subgrade largely increased after experiencing 20,000 repetitions under a wet condition, while the change was small under a dry condition. In addition, the normal stress on the subgrade showed a decrease after both saturating and draining processes.

Table 2 summarizes the changes in the vertical displacement of the load plate and the normal stress on the subgrade at each stage of the experiment. The growth of the permanent displacement with repetitions seems reasonable, but the reasons for the changes in the resilient displacement and the normal stress on the subgrade are not clear. They might be associated with the change in the elastic behavior of the pavement. Therefore, we carried out a series of elastic analyses in the following section to evaluate which layer was softened (or hardened) by the loading and saturating/draining processes.

4 SIMULATION OF MODEL TEST USING ELASTIC-LAYERED THEORY

Based on the traditional layered elastic theory, a simple three-layer model was analyzed. As shown in the right column of Table 3, the model consists of a top layer, 100 mm in thickness,

Table 3. Simulation model and cases of elastic analysis.

	Case name					
	HHH	HSH	SSH	HHS	HSS	SSS
1st layer AC (E_1)	E_0	E_0	0.1 E_0	E_0	E_0	0.1 E_0
2nd layer Subbase (E_2)	E_0	0.1 E_0	0.1 E_0	E_0	0.1 E_0	0.1 E_0
3rd layer Subgrade (E_3)	E_0	E_0	E_0	0.1 E_0	0.1 E_0	0.1 E_0

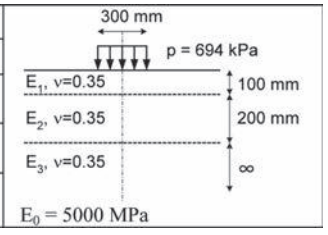

which represents the asphalt concrete layers in the experiment, a second layer, 200 mm in thickness, which represents the subbase course, and a bottom layer, with a half-space, which represents the subgrade. A circular uniformly distributed load of 694 kPa, 300 mm in diameter, was loaded on the surface of the top layer. The aim of this analysis was to understand the pavement response (resilient displacement of the pavement surface and normal stress on the subgrade) associated with the elastic moduli of the layers. Therefore, to simplify the problem, only two kinds of elastic moduli were used, E_0 = 5000 MPa (relatively hard) and 0.1 E_0 (relatively soft). Poisson's ratio was 0.35 for all the layers. Table 3 shows the calculation cases. Regarding the model with all layers E_0 (HHH) as the basic model, the elastic moduli of part or all of the layers were replaced with the soft value (0.1 E_0). For example, model HHS has a hard modulus (E_0) in the top and second layers and a soft modulus (0.1 E_0) in the third layer.

Figure 9 presents the analytical results of the vertical displacements of the top surface. The displacements were normalized by the value of the basic model (HHH) at the load center (X = 0 mm). The red plots indicate the models with "soft" subgrade, while the black plots indicate the models with "hard" subgrade. The figure shows that the displacement of model HHH is smaller than that of any other models. This means that the surface displacement always increases if the elastic modulus of any layer is reduced. The figure also shows that the red and the black plots exist separately forming each group at X = 500 mm or farther. This means that the elastic modulus of the subgrade determines the spread of the surface deformation. Moreover, from a comparison of the results of the three models, HHS, HSH and SHH, if the elastic modulus of just one layer is reduced, the softening of the upper layer brings about a larger displacement at the load center (X = 0 mm).

Figure 10 shows the normal stresses on the subgrade. The plots for model HHH exist just behind those for model SSS, because their stress levels are completely consistent with each other. Regarding the normal stress of the subgrade surface along the load center (X = 0 mm), all the red plots are lower than the black plots. This means that if the elastic modulus of the subgrade is reduced, the normal stress of the subgrade surface always decreases. At the same time, the figure shows that the normal stress of the subgrade surface shows an increase in the cases where the elastic modulus of the AC or the subbase course is reduced. From the analytical results, we find that a reduction in stress of the subgrade surface indicates the softening of the subgrade material, while an increase in stress indicates the softening of the upper layers (AC and/or subbase course).

Based on the above analytical results, we try to explain the experimental phenomena shown in Table 4. Here, we select the results of the elastic behavior, or the resilient displacement of the load plate and the normal stress on the subgrade. Firstly, in the process of repeated loading under a dry condition, the elastic moduli are thought to change little at all layers, because the resilient displacement of the pavement surface and the normal stress of the subgrade surface were almost the same during the process. Next, in the process of repeated loading under a wet condition, both the pavement surface displacement and the subgrade surface stress rose in the experiment. This corresponds to the analytical results of model HSH or SSH or to a reduction in the elastic modulus occurring only at the subbase or at both the subbase and the AC layers, while maintaining the subgrade elastic modulus. Through the saturating process of the experiment, the resilient displacement increased a

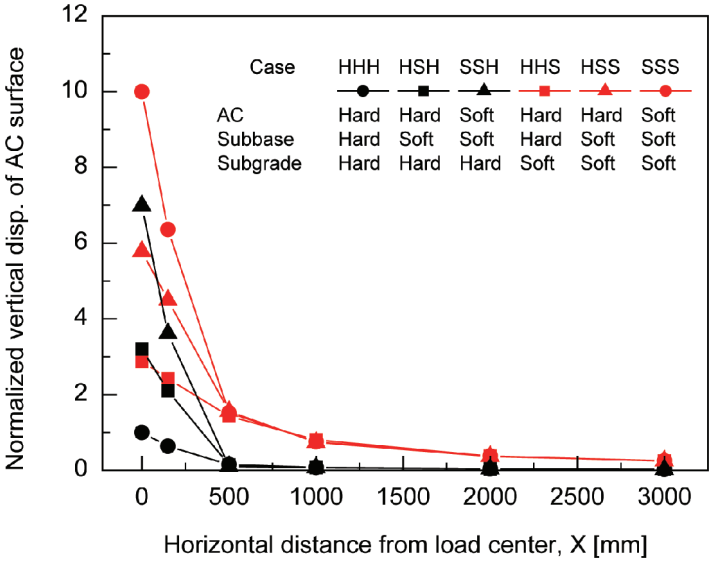

Figure 9. Vertical displacement of model surface by elastic analysis.

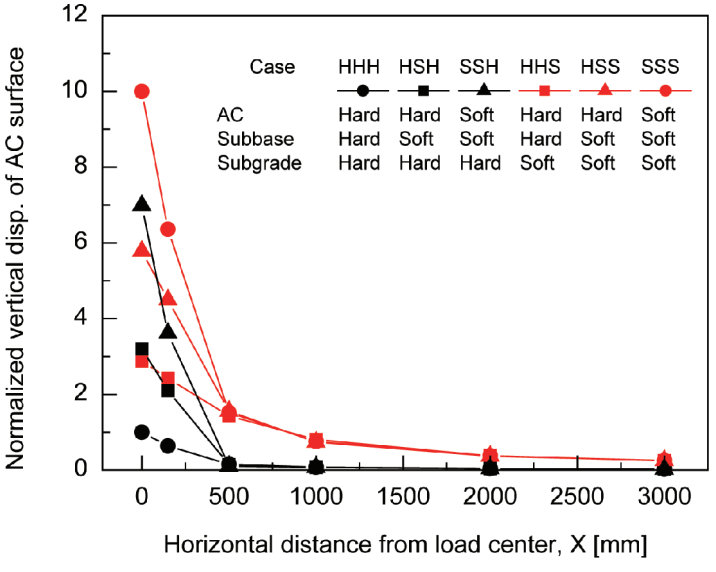

Figure 10. Normal stress on subgrade surface by elastic analysis.

little and the subgrade stress decreased. This corresponds to model HSS or HHS or to the elastic modulus of only the subgrade or both the subgrade and the subbase decreased. Finally, draining was the only process during which the resilient displacement showed a decrease. Based on the analytical results, this indicates that an increase in the elastic modulus occurred at a layer during the draining process. On the other hand, the subgrade stress decreased in the draining process of the experiment. Considering the analytical fact that hardening of subgrade caused an increase in subgrade stress, it can be said that the increase in elastic modulus occurred not at the subgrade, but at the upper layer or at the subbase and/or the AC layer.

Table 4. Possible reasons for experimental results.

Type of external impact	Experimental results (table 2)		Possible reason for experimental result estimated from elastic analysis
	Resilient displacement of pavement surface	Pressure on subgrade surface	
a) 20,000 repetitions under DRY condition	Small increase	Small increase	Small decrease in stiffness of ACor subbase
b) 20,000 repetitions under WET condition	Increase	Increase	Decrease in stiffness of AC or subbase
c) Saturating (from dry to wet)	Small increase	Decrease	Decrease in stiffness of subbase and subgrade
d) Draining (from wet to dry)	Decrease	Decrease	Increase in stiffness of AC or subbase

5 CONCLUSIONS

In this study, a cyclic plate load test has been conducted for a permeable pavement model in the laboratory to grasp the deformational characteristics of permeable pavements under saturated and unsaturated conditions. A series of elastic analyses was also carried out for a simple three-layered model to evaluate the model test results.

From the results of the model tests, in the cases of the saturated pavement model, the resilient displacement of the pavement surface and the normal stress on the subgrade surface grew progressively larger with the load repetitions, while they were almost stable in the unsaturated cases. Based on the elastic analyses, this means that the load repetitions under saturated conditions caused the softening (elastic modulus reduction) of the subbase course or the AC layer, while the subgrade remained relatively stable.

The results of the static plate load tests showed that the saturation of the model brought about a significant drop in the normal stress on the subgrade surface against a static load, with a constant modulus of pavement reaction K_{30}. The analytical results explained this drop as a reduction in elastic modulus occurring at the subgrade or at both the subgrade and the subbase course. On the other hand, the draining water from the model resulted in an increase in the modulus of pavement reaction K_{30} and a decrease in the normal stress on the subgrade surface against a static load. The analytical results explain this as an elastic modulus recovered in the draining process.

From the above results, it is evident that the subbase course is a key layer of permeable pavement because its mechanical properties change remarkably due to the water flow into and out of the pavement and the load repetitions.

REFERENCES

[1] Specified urban river inundation countermeasures, 2003, Act No. 77, 2003.
[2] Lekarp, F., Isacsson, U. and Dawson, A., State of the art. I: Resilient response of unbound aggregates, ASCE Journal of Transportation Engineering, pp. 66–75, 2000.
[3] Lekarp, F., Isacsson, U. and Dawson, A., State of the art. II: Permanent strain response of unbound aggregates, ASCE Journal of Transportation Engineering, pp. 76–83, 2000.
[4] Haynes, J.G. and Yoder, E.J., Effects of repeated loading on gravel and crushed stone base course materials used in the AASHO Road Test, Highway Research Record, No. 39, pp. 82–96, 1963.
[5] Hicks, R.G. and Monismith, C.L., Factors influencing the resilient properties of granular materials, Highway Research Record, No. 345, pp. 15–31, 1971.
[6] Barksdale, R.F. and Itani, S.Y., Influence of aggregate shape on base behaviour, Transportation Research Record, No. 1227, Transportation Research Board, Washington, D.C., pp. 173–182, 1989.

[7] Dawson, A.R., Thom, N.H. and Paute, J.L., Mechanical characteristics of unbound granular materials as a function of condition, Flexible Pavements, Proceedings of the Europeans Symposium Euroflex, A.G. Correia, ed., Balkema, Rotterdam, The Netherlands, pp. 35–44, 1993.
[8] Barksdale, R.D., Laboratory evaluation of rutting in basecourse materials, Proceedings of the 3rd International Conference on Structural Design of Asphalt Pavements, pp. 161–174, 1972.
[9] Maree, J.H., Freeme, C.R., Van Zyl, N.J. and Savage, P.F., The permanent deformation of pavements with untreated crushed stone bases as measured in heavy vehicle simulator tests, Proceedings of the 11th ARRB Conference, Part 2, pp. 16–28, 1982.
[10] Thom, N.H. and Brown, S.F., Effect of moisture on the structural performance of a crushed-limestone road base, Transportation Research Records, No. 1121, Transportation Research Board, Washington, D.C., pp. 50–56, 1987.
[11] Itoh, M., Ayabe, T. and Kubo, K., Performance of permeable pavements under heavy traffic, Journal of Pavement Engineering, JSCE, pp. 91–98, 2007 (in Japanese).
[12] Nakashima, S. and Kohashi, H., Influence of seepage water on deformational behavior of permeable asphalt pavements, Proceedings of the 13th Conference of the Road Engineering Association of Asia and Australasia, CD-ROM, 9-017, 2009.
[13] Ikeda, A. and Nakashima, S., Effect of soil type and moisture content of subgrade soils on permanent deformation of asphalt pavement, Proceedings of the 14th Conference of the Road Engineering Association of Asia and Australasia, pp. 319–326, 2013.
[14] Public Works Research Institute, Technical manual for roadway stormwater storage and infiltration facilities, 2006 (in Japanese).

This page intentionally left blank

Recycling—II

This page intentionally left blank

Asphalt Pavements – Kim (Ed)
© 2014 Taylor & Francis Group, London, ISBN 978-1-138-02693-3

Utilization of municipal solid waste Incinerator Bottom Ash Aggregate in asphalt mixture

Dong Liu, Lihan Li & Huajie Cui
Key Laboratory of Road and Traffic Engineering of Ministry of Education, Tongji University, Shanghai, P.R. China

ABSTRACT: The objective of this paper is to analyze the physical and chemical properties of natural weathered municipal solid waste Incinerator Bottom Ash Aggregate (IBAA) within 6 months, and in the following the physical properties of asphalt mixture containing different amounts of IBAA as aggregate substitution. The Marshall mix design method was carried out to determine the design asphalt content. Dynamic creep test, moisture susceptibility test, and low-temperature bending test were performed to evaluate the engineering properties of mixture. Results showed that the weathering treatment increased the apparent density and decreased the pH, water absorption and crushing value of IBAA. The most obvious changes occurred in the first 3 months. Results showed that IBAA improved the resistance of permanent deformation, water resistance and anti-crack performance of asphalt mixture containing IBAA no more than 30%. It is recommended that IBAA be subjected to weathering treatment for at least 3 months before being used, and the amount of IBAA be limited to 30%, by total weight of the aggregate to ensure satisfactory pavement performance.

Keywords: Incinerator Bottom Ash Aggregate (IBAA), asphalt mixture, weathering treatment, properties, mixing amount

1 INTRODUCTION

Incinerator Bottom Ash Aggregate (IBAA) is the most common by-product after incinerating municipal solid waste in combustor facilities. It is estimated annual production of IBAA is 2 million tons in Shanghai, China. Although landfill may cause ground-water contamination due to inadequate monitoring system, it is the most common treatment measure in Shanghai at present. However, there is not enough space for landfill. Besides, the mining of aggregate is becoming an ecological problem as the demand for aggregate is increasing rapidly due to rapid infrastructure activities in Shanghai. IBAA has a potential for utilization in road construction [1,2]. Such utilization would decrease the amount of IBAA for landfill and the natural aggregate used, which avoids the damage to the environment.

The major chemical components of IBAA are silica (SiO_2), alumina (Al_2O_3), ferric oxide (Fe_2O_3), and lime (CaO). According to the previous researches [3,4], freshly quenched IBAA has a high reactivity, mainly because of high contents of amorphous and highly reactive silica and lime. During the natural weathering process, some of the chemical and mineralogical characteristics undergo significant changes including oxidation, dissolution and precipitation, carbonation, and the neoformation of clay-like minerals. As a consequence, the properties of IBAA may change. However, there are few studies about the properties of IBAA undergoing natural weathering treatment. Researches have proven that a one-to-three month exposure to natural weathering decreases dramatically the release of heavy metals from IBAA [3,4]. Natural weathering is the most cost-effective treatment method [5].

Regarding the utilization of IBAA in asphalt mixture, a number of trails have been conducted. In these studies, different amounts of IBAA were used as an aggregate substitute.

Chen [6] evaluated the engineering properties of asphalt mixture containing IBAA up to 40%. It is recommended that the mixing amount of IBAA be limited to 20% in base course and 10% in surface mix to ensure satisfactory pavement performance. Garrick [7] used up to 32% IBAA. Walter [8] recommended using IBAA up to 40–55% with an asphalt content of 5.5–6.5%. Based on previous research works, it can be concluded that IBAA is potential material which can be utilized in asphalt mixture. However, there is no consistent conclusion about the amount of IBAA could be used and the pavement performance of IBAA-mix. More researches should be done to understand the properties of IBAA and its mixture.

The main focus of the present investigation was directed towards the weathering treatment of IBAA and properties of asphalt mixture containing IBAA. The aim of this paper is to evaluate the properties of weathered IBAA and asphalt mixture containing 0, 10, 20, 30 and 40% IBAA by aggregate weight in terms of:

1. pH value, crushing value, apparent specific gravity and water absorption of IBAA with different weathering time;
2. Marshall properties, permanent deformation, moisture susceptibility and anti-crack performance of asphalt mixture containing IBAA.

2 MATERIALS AND METHODS

2.1 *Materials*

2.1.1 *IBAA*

IBAA used in this study were derived from a single incinerator in Shanghai. It was stored and weathered outdoor. During the weathering process, the IBAA was turned over several times a week with a shovel to ensure homogenization of the moisture content and to improve the air contact. The sieve sizes of IBAA were shown in Figure 1. To understand the effect of weathering treatment on IBAA, basic properties of IBAA were tested at different time. Specific gravity test (JTG E42, T0328-2005), water absorption ration (JTG E42, T 0330-2005) and crushing value test (JTG E42, T0350-2005) were carried out according to China standard. The pH was determined for the suspension after 24 h equilibration period with liquid-to-solid ration of 5.

2.1.2 *Aggregate and mineral filler*

The basalt aggregates and mineral filler were chosen from local engineering. Four different sizes of basalt aggregate were used, and they were 0–4.75 mm, 4.75–9.5 mm, 9.5–13.2 mm and 13.2–19 mm, respectively. The sieve sizes of basalt aggregate and mineral filler were shown in Figure 1. Table 1 gives the basic physical properties of basalt aggregates and mineral filler.

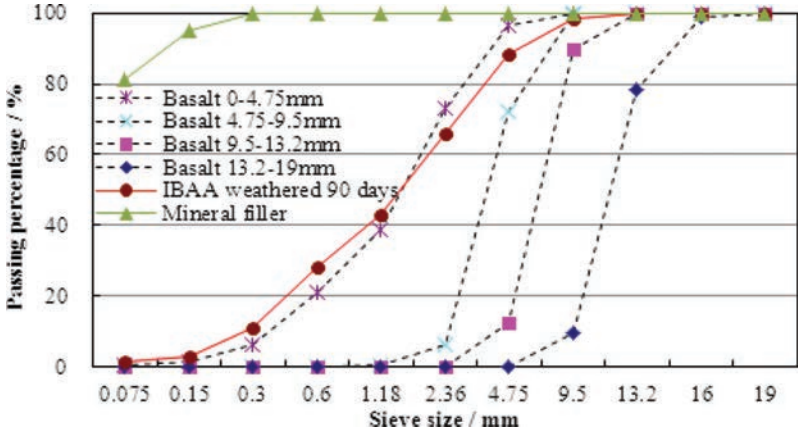

Figure 1. Gradation curves of basalt aggregate, mineral filler and IBAA.

Table 1. Basic properties of basalt aggregate and mineral filler.

Properties	Basalt aggregate/mm				Mineral filler
	0–4.75	4.75–9.5	9.5–13.2	13.2–19	
Apparent specific gravity (g/cm^{-3})	2.911	2.776	2.776	2.823	2.720
Absorption (%)	–	2.65	2.52	1.93	–
Crushing value (%)	–	21	22	22	–

Table 2. Basic properties of AH-70.

Properties	Measured values	Requirements
Penetration at 25°C (0.1 mm)	75.2	60~80
Ductility, 5 cm/min, 15°C (cm)	>100	≥100
Softening point (°C)	48.2	44~54

Table 3. Basalt aggregate and IBAA blending percentages.

IBAA blending percentages (%)	Percentage in the aggregate blend (%)				
	Basalt aggregate				Mineral filler
	13.2–19 mm	9.5–13.2 mm	4.75–9.5 mm	0–4.75 mm	
0 (Control)	37	13	6	35	9
10	37	12	7	25	9
20	37	10	8	17	8
30	37	9	9	7	8
40	37	8	8	0	7

All properties of basalt aggregates and mineral filler satisfied the requirement of Chinese norm JTG F40-2004.

2.1.3 *Asphalt binder*

Base asphalt (AH-70) was used to prepare asphalt mixture. All the testing results of AH-70 were shown in Table 2 and within specification (Chinese norm JTJ052-2000) limits.

2.1.4 *Mixture design*

IBAA was used as a substitute for natural aggregate in asphalt mixture. Basalt aggregates and IBAA were blended to meet the China specification. AC-16 asphalt mixture was used in this study. The contents of IBAA used were 0, 10, 20, 30, and 40% by mass of the total mix, whereas the 0% IBAA-mix was used as the control group. This resulted in the blending percentages shown in Table 3 and the gradation curves of mixture shown in Figure 2. Mix design was carried out according to the Marshall mix design method (ASTM D 1559) at different IBAA substitution ratios. Air voids, Voids in the Mineral Aggregate (VMA), Voids Filled with Asphalt (VFA), Marshall stability and flow value of marshal specimens were used to decide the optimal asphalt content of asphalt mixture. The optimum asphalt content was determined considering 4% of air voids.

2.2 *Pavement performance test*

2.2.1 *Dynamic creep test*

Dynamic creep tests were conducted to characterize the deforming resistance of asphalt mixture. The specimens of 100 mm in diameter and 100 mm in height were prepared and

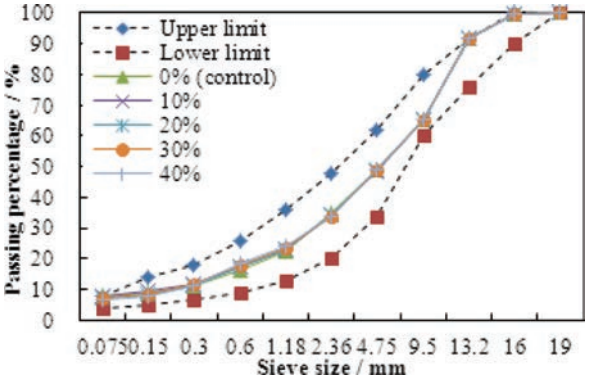

Figure 2. Aggregate blend gradation curves for different IBAA content.

then tested at 60°C. The tests were carried out using MTS 810 to apply axial stress to specimens.

The conditions under which the unconfined dynamic uniaxial creep test is performed are: (a) preloading for 10 min at 0.01 MPa, as a conditioning stress; (b) haversine wave stress pulse for 7200 s with frequency of 1 Hz (by allocating 100 ms for pulse width and 900 ms for rest period); (c) maximum axial stress was 100 kPa. During the test, the accumulated strain of specimens was calculated by Eq.(1). The growth rate of creep strain of asphalt mixture also shows the resistance of asphalt mixture to permanent deformation, which was calculated by Eq.(2).

$$\varepsilon = h/H_0 \quad (1)$$

$$s = \Delta\varepsilon/\Delta n \quad (2)$$

where ε is the accumulated strain of specimen during the test time, 1 mm/mm; h is the axial deformation, mm; and H_0 is the initial specimen height, mm; s is the growth rate of creep strain during the test time, ε/time; Δε is the accumulated strain between 3600 loading cycles to 7200, 1 mm/mm; and Δn is the loading cycles, time.

2.2.2 *Moisture susceptibility test*

Tensile Strength Ration (TSR, water freeze at –18°C for 16 h and thaw at 60°C for 24 h as a cycle) of Marshall specimens were tested at the loading rate of 50 mm/min according to JTG E20-2011 of China.

2.2.3 *Low-temperature bending test*

In order to investigate the low-temperature flexibility of asphalt mixture, the three-point bending beam test was conducted. According to JTG E20-2011 of China, specimens of 250 mm × 30 mm × 35 mm were prepared. And the tests were carried out using MTS 810 to apply stress to specimens with span length of 200 mm at the loading rate of 50 mm/min at –10°C. Failure strain of asphalt mixture was calculated based on the bending deflection of beams.

3 RESULTS AND DISCUSSION

3.1 *IBAA properties*

The pH values of IBAA as a function of weathering time were given in Figure 3. As can be observed, the pH value decreased rapidly with weathering time up to about 90 days, and then levelled off. The freshly quenched IBAA had a high pH of 12.4, which was controlled by the formation and solubility of portlandite according to the previous studies [3,4]. Atmospheric CO_2 was absorbed by the alkaline IBAA in the following time. After weathering time of 90 d, the pH value of IBAA maintained at about 8.4.

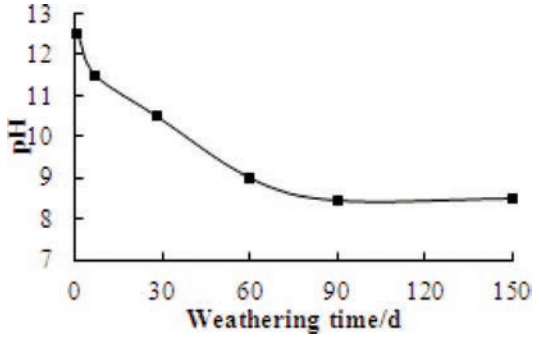

Figure 3. pH of IBAA with weathering time.

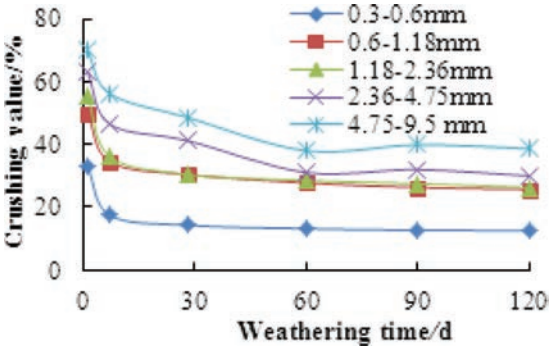

Figure 4. Crushing value of IBAA.

Table 4. Specific gravity and water absorption of IBAA.

	Apparent specific gravity (g/cm^{-3})		Water absorption (%)	
	Weathering time (d)		Weathering time (d)	
IBAA	1	90	7	180
0–2.36 mm	2.280	2.433	–	–
2.36–4.75 mm	2.404	2.410	8.5	8.2
4.75–9.5 mm	2.403	2.577	9.4	8.7

Crushing value reflects the crushing strength of aggregate. Figure 4 shows the variation of crushing value of IBAA with different particle sizes during weathering. As can be observed, the natural weathering treatment decreased the crushing value of IBAA. The formation of neoformed phases including calcite, gypsum, and ettringite improved the mechanical properties of IBAA. Figure 4 also shows that the IBAA with smaller particle size had a lower crushing value, which means its ability of resisting crushing was better. Crushing value of IBAA larger than 4.75 mm is over 30%. Because of low strength of coarse IBAA, the asphalt mixture containing coarse IBAA is expected to show low strength. This is why particle size of IBAA larger than 9.5 mm was not chosen to be used in the asphalt mixture in this study.

Table 4 shows the specific gravity and water absorption of IBAA. It illustrates that IBAA had higher water absorption and lower apparent specific gravity contrast to natural aggregate (Table 1). Meanwhile, with the weathering time, the neoformed phases filled the porous structure of IBAA, and this resulted in the decrease of absorption and the increase of specific

gravity. The higher water absorption of IBAA will lead to the higher design asphalt content of asphalt mixture, which will increase the cost of asphalt mixture. Therefore, it is recommended that IBAA be subjected to weathering treatment for at least 3 months before being used in asphalt mixture.

3.2 *Volumetric properties of mixture*

The Optimal Asphalt Content (OAC) and Marshall properties of prepared asphalt mixture are presented in Table 5. IBAA increased the OAC due to the higher absorptivity relative to natural basalt aggregate. The OAC increased linearly with about 0.67% increase for every 10% IBAA replacement. The addition of IBAA caused increase in VMA and VFA. The Marshall stability of mixture with IBAA was higher than control mixture. The Marshall stability increased with the increase of mixing amount of IBAA no more than 20%. While IBAA was more than 20%, the Marshall stability decreased. The flow value remained within the range of 2.3–4.0 mm for the different mixes. All Marshall properties satisfied the China specification except the VFA of IBAA-mix.

3.3 *Pavement performance*

3.3.1 *Dynamic creep test*

The results of dynamic creep test at 60°C are shown in Figure 5 and Table 6. As seen in Figure 5, the accumulative creep strain of asphalt mixture increased with load cycles. 10% IBAA-mix had the lowest accumulative creep strain. Meanwhile, the growth rate of creep strain of 10% IBAA-mix was lowest, which means that the accumulative creep strain of 10% IBAA-mix grew slowest and it had the strongest resistance to permanent deformation. 40% IBAA-mix both had the highest accumulative strain and growth rate of creep strain.

Table 5. Marshall properties of mix.

Parameters	IBAA content (%)					China specification
	0	10	20	30	40	
Optimal asphalt content (%)	4.0	4.8	5.7	6.3	6.6	–
Air voids (%)	4.1	4.0	4.0	3.9	4.0	3.5~5
VMA (%)	15.7	16.4	18.4	20.5	25.0	≥13.5
VFA (%)	70.5	75.0	77.8	82.8	86.2	65~75
Marshall stability (kN)	8.7	10.2	11.1	10.4	10.2	≥8
Flow value (mm)	3.6	2.4	4.0	2.3	3.3	1.5~4

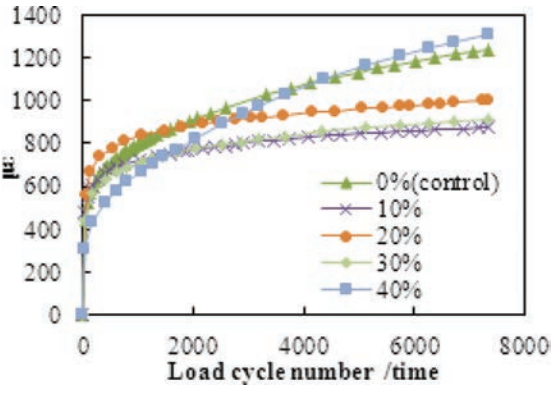

Figure 5. Accumulated strain versus load cycle number.

Table 6. Dynamic creep test results.

	Mixtures with different IBAA contents (%)				
Index	0	10	20	30	40
ε/(10^{-6})	1227	878	999	913	1305
s/(με/time)	3.35	1.05	1.11	1.32	4.57

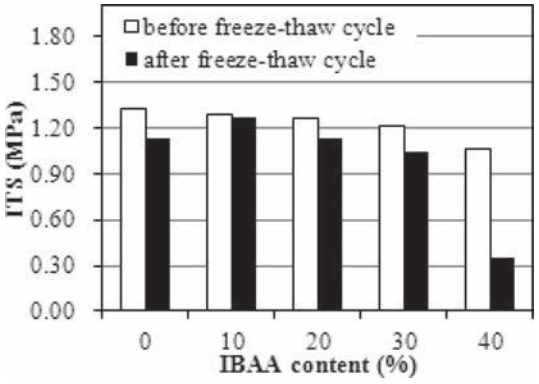

Figure 6. ITS of asphalt mixture.

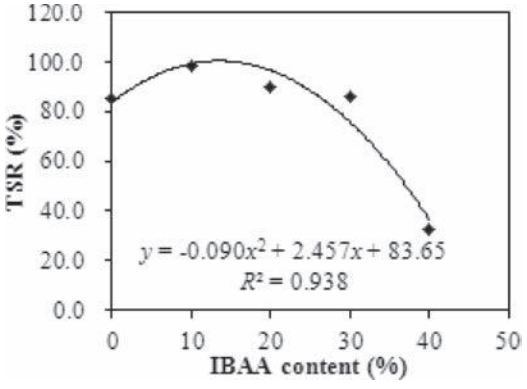

Figure 7. TSR versus IBAA content.

This proved that the asphalt mixture containing IBAA had stronger resistance of permanent deformation at high-temperature than control asphalt mixture except 40% IBAA-mix.

3.3.2 *Moisture susceptibility test*

Indirect Tensile Strength (ITS) test results before and after freeze-thaw cycle are given in Figure 6. As shown in Figure 6, the ITS values of asphalt mixture before freeze-thaw cycle decreased with the increase of IBAA percentages. Meanwhile, the ITS values after freeze-thaw cycle increased from 0% to 10% IBAA replacement. At higher IBAA substitutions, similar to the asphalt mixture before freeze-thaw, a gradual decrease was noticed. Figure 7 illustrates the TSR value of asphalt mixture. It shows that the TSR of 10% IBAA-mix was higher than the control mixture. 20% IBAA-mix was approximately the same with the control mixture. At higher IBAA replacements, the TSR value declined significantly. The TSR value of 40% IBAA-mix was only 32.9%, which could not satisfy the Chinese specification.

Table 7. Failure strain of asphalt mixture.

Mixtures with different IBAA contents (%)	0	10	20	30	40
Failure strain/(10^{-6})	2523	2691	2944	3196	3288

3.3.3 *Low-temperature bending test*

Results of bending test at −10°C are shown in Table 7. Failure strains of asphalt mixture increased with the increase of IBAA percentages. This means the asphalt mixture containing more IBAA showed better anti-crack properties at low temperature. However, this doesn't mean more IBAA should be used in asphalt mixture to improve its resistance to crack. The more IBAA used in mixture, the more asphalt will be used. It is easy to understand that the more asphalt provide better flexibility of mixture at low temperature. Considering the more asphalt will cost much more, it is not economical to improve mixing amount of IBAA just for enhancing anti-cracking property of asphalt mixture.

4 CONCLUSIONS

On the basis of the results of this study, the following conclusions are made:

1. The natural weathering treatment of IBAA deceased the chemical activity (pH value), and improved the physical properties including the decrease of water absorption and increase of crushing strength. Natural weathering time of 90d was necessary for IBAA being used in asphalt mixture.
2. Optimal asphalt content of mixture increased with the increase of IBAA used. The IBAA resulted in the higher VMA, VFA, Marshall stability, and lower flow value than natural aggregate.
3. Asphalt mixture containing IBAA had stronger resistance of permanent deformation at high-temperature than control asphalt mixture except 40% IBAA-mix.
4. Mixtures containing IBAA no more than 30% met the requirement of moisture susceptibility. Mixture containing 40% IBAA had poor moisture susceptibility.
5. Asphalt mixture containing more IBAA showed better anti-crack properties at low temperature due to more asphalt used.

On the basis of the performance analysis in this study, it is recommended that the mixing amount of IBAA is no more than 30% in asphalt mixture.

REFERENCES

[1] Forteza R. Far M. Seguí C. et al. Characterization of bottom ash in municipal solid waste incinerators for its use in road base, Waste Management, 24(9), pp.899–909. 2004.

[2] Huang C.M. Yang W.F. Ma H.W. et al. The potential of recycling and reusing municipal solid waste incinerator ash in Taiwan, Waste Management, 26(9), pp.979–987. 2006.

[3] Yao J. Li W.B. Tang M., et al. Effect of weathering treatment on the fraction and leaching behavior of copper in municipal solid waste incinerator bottom ash. Chemosphere, 81(5), pp.571–576. 2010.

[4] Chimenos J.M. Fernández A.I. Miralles L. et al. Change of mechanical properties during short-term natural weathering of MSWI bottom ash. Environmental Science & Technology, 39(19), pp.7725–7730. 2005.

[5] Todorovic J. and Ecke H. Treatment of MSWI residues for utilization as secondary construction minerals: a review of methods. Minerals and Energy-Raw Materials Report, 20(3–4), pp.45–59. 2006.

[6] Chen J.S. Chu P.Y. Chang J.E. et al. Engineering and environmental characterization of municipal solid waste bottom ash as an aggregate substitute utilized for asphalt concrete. Journal of Materials in Civil Engineering, 20(6), pp.432–439. 2008.

[7] Garrick N.W. Chan K.L. Evaluation of domestic incinerator ash for use as aggregate in asphalt concrete. Transportation Research Record, 1418, pp.30–34. 1993.

[8] Walter C.E. Practical refuse recycling. Journal of the Environmental Engineering Division, ASCE, 102(1):139–148. 1976.

Asphalt Pavements – Kim (Ed)
© 2014 Taylor & Francis Group, London, ISBN 978-1-138-02693-3

An investigation into the effects of accelerated curing on Cold Recycled Bituminous Mixes

Chibuzor Ojum, Kranthi Kuna, Nick H. Thom & Gordon Airey
Nottingham Transportation Engineering Centre (NTEC), The University of Nottingham, Nottingham, UK

ABSTRACT: Compared to Hot Mix Asphalts (HMA), the behaviour of Cold Recycled Bituminous Mixes (CRBM) is more complex due to the presence of water in the mix. CRBMs develop strength and stiffness with time and this relates to the rate at which curing occurs in the mix. Various accelerated laboratory curing and conditioning regimes exist for CRBM and are used in a variety of ways by researchers although the underlying question remains: how realistic are these curing and conditioning regimes in simulating pavement conditions as experienced in the field? The ideal curing regime for these mixture types would be to simulate conditions similar to those experienced in the field. Most accelerated curing regimes fail to reproduce the actual condition of the mix that is expected in the pavement and tests are therefore conducted at superior conditions. This results in overestimating the mix performance in the field. This is especially true when the fundamental properties of the CRBM are compared with other mixes such as HMA and Warm Mix Asphalt (WMA). Hence, there is a need to develop a curing regime that simulates as realistically as possible actual pavement conditions. This paper investigates the need for accelerated curing and the degree of acceleration that is realistic by studying different curing regimes and their effect on mechanical and performance behaviour of CRBMs. The experimental design is carefully selected in such a way that the curing conditions include regimes that are followed by different highway agencies and also conditions that are expected to simulate different climatic zones. The investigation includes both bitumen emulsion and foamed bitumen treated mixes with and without cement.

Keywords: Bitumen emulsion, foamed bitumen, cold recycled bituminous mixes, accelerated curing, performance testing, field performance

1 INTRODUCTION

There are significant benefits of incorporating Reclaimed Asphalt Pavements (RAP) in the production of bituminous mixtures and these benefits include considerable savings in cost, energy and environmental gains that arise as a result of the reduction in the disposal of waste materials from rehabilitation and maintenance of road structures. The mechanical and performance properties of CRBM are intimately related to the curing condition [1]. The strength development of CRBM is very important as it is dependent on the rate at which curing occurs. This plays a major role in relation to traffic opening time and the long term performance of the road [2]. The absence of well-established and defined specifications for CRBM that realistically simulate pavement conditions as experienced in the field has resulted in varied curing regimes being used that can potentially overestimate the performance of the asphalt pavement. Therefore knowledge of the most appropriate curing regime is crucial. The research presented in this paper highlights the need for accelerated curing and the effect on degree of acceleration by examining different curing regimes and how they affect the mechanical and performance properties of the CRBM by direct comparison of mixtures produced using bitumen emulsion and foamed bitumen with and without cement.

2 MATERIALS

The materials used are typical of those used in recycling of asphalt pavements for road applications. The RAP was sourced from a contractor engaged in CRBM production. The RAP was characterised prior to mix design and the gradation ascertained in accordance with BS EN 933-2:2012. A composition analysis was conducted and the binder in the RAP was separated using a fractionating column in accordance with BS 598-102:2003. The residual binder content of the RAP was obtained as 5.5%. The gradation of the RAP including that of the extracted RAP aggregate is shown in Figure 1. The virgin aggregate used comprised limestone supplied in nominal sizes as follows: 20 mm, 14 mm, 10 mm, 6 mm, dust (0.075 mm–4 mm) and filler.

Further to this, to ascertain if the bitumen in the RAP could be classified as "active" or "inactive", an indicative test was conducted currently under investigation by the International Union of Laboratories and Experts in Construction Materials, Systems and Structures (RILEM). This involved conditioning a sample of RAP for 4 hours at 70°C followed by the manufacture of three 100 mm diameter by 63.5 mm high specimens using Marshall Compaction with 50 blows per face. After compaction, Indirect Tensile Strength (ITS) tests in accordance with BS EN 12697-23 were carried out at 20°C and then in wet conditions, soaked at 20°C for 24 hours. If the soaked ITS ≤ 100 kPa or the specimens do not hold together at 70°C, the RAP is considered to be inactive. For comparison, the test was also conducted with RAP conditioned at 140°C. In all cases, the values exceeded 100 kPa indicating that the binder in the RAP used in the study can be classified as active. The results are presented in Figure 2.

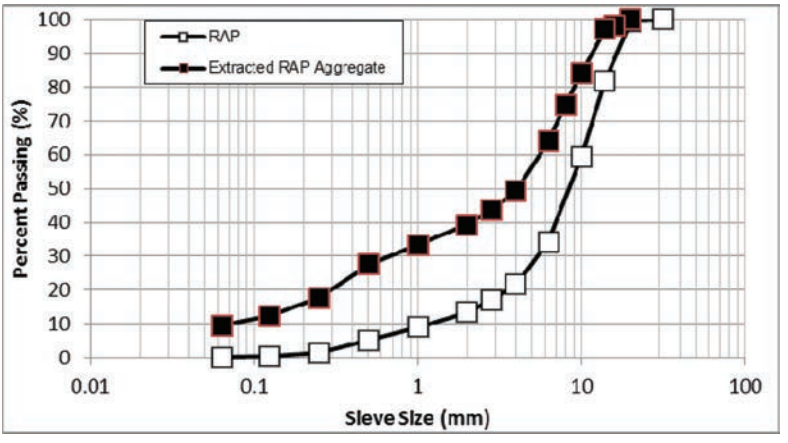

Figure 1. Aggregate gradations of RAP and residual RAP after binder extraction.

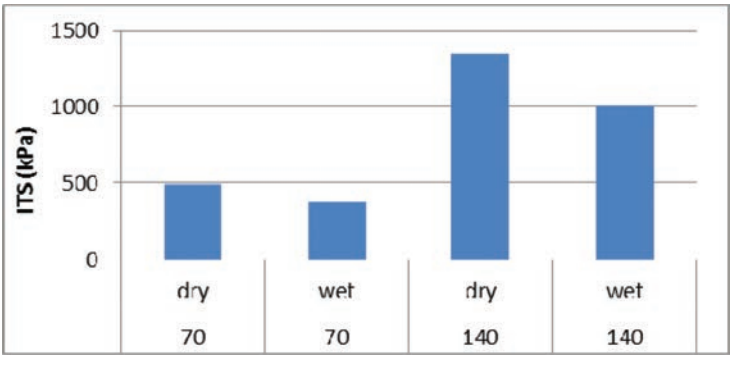

Figure 2. Test to ascertain state of binder in RAP.

Table 1. Bitumen emulsion formulation and properties.

Property	Value
Particle surface electric charge	Positive
Binder level (%)	60
Water level (%)	40
Softening point (°C)	52
Penetration (dmm)	47
Density (g/cm³)	1.016

The bitumen emulsion used is a cationic bitumen emulsion containing 60% bitumen and 40% water. The formulation and properties of the bitumen emulsion are shown in Table 1. The penetration grade for the foamed bitumen as supplied was obtained as 70/100 with specific gravity of 1.03 and softening point of 45°C. The cement used conformed to CEM II/A-L 32.5 R in line with BS EN 197-1.

3 EXPERIMENTAL PLAN

3.1 *Introduction*

It is a well-established fact that curing has a significant effect on the mechanical and performance properties of CRBM [3]. This research aimed to provide a valid investigation into the behavior of CRBM taking into account (1) the effect of temperature, curing conditioning and curing duration (2) the influence of cement with different curing regimes and (3) the difference in terms of the mechanical and performance properties of CRBM between bitumen emulsion and foamed bitumen. Table 2 states the plan for the experimental study.

3.2 *Mix design procedure*

The composition of aggregates used in the research study comprised 50% RAP and 50% virgin aggregates. The limits and gradation used are as depicted in Figure 3. The aggregate gradation limits are based on Table 9/12 Zone C of the UK Manual of Contract Documents for Highway Works Volume 1 Series 900 Clause 948 [4]. To further optimise the aggregate gradation, a fuller curve was targeted in order to obtain the gradation that gives the maximum density and ensures smaller particles are adequately packed together with larger particles thereby reducing voids and creating better particle to particle contact, stability and better water resistance for the produced mixtures.

Tables 3 and 4 state design parameters used as obtained from mix design studies conducted on both mixture types. It should be noted that the residual binder content for the bitumen emulsion mixtures is 3.25%. In both cases, the mix proportions are typical of those used in reality.

3.3 *Specimen preparation*

100 mm diameter CRBM specimens were produced using bitumen emulsion and foamed bitumen. Mixing for the bitumen emulsion mixtures was done using a Sun & Planet mixer while the foamed bitumen mixtures were produced in a dual shaft pug mill mixer using a Wirtgen WLB 10 S foam rig. The specimens were compacted using a Coopers Gyratory Compactor in accordance with BS EN 12697-31, at a constant pressure of 600 kPa, a speed of 30 rpm, an angle of gyration of 1.25° and 110 gyrations for all cores prepared. The selection of 110 gyrations was made following comparisons with specimens made using modified Proctor compaction. After compaction, the specimens were left in the mould for 24 hours

Table 2. Experimental study.

Phase	Curing temperature (°C)	Curing duration (days)	Curing condition	Cement content (OPC)
1	5	28	Fully Wrapped (FW)	0%
	20			
	40			
2	5	28	Unwrapped (UW)	0%
	20			
	40			
3	5	28	Fully Wrapped (FW)	1%
	20			
	40			
4	5	28	Unwrapped (UW)	1%
	20			
	40			
5	20	21	Combination* (COMBO)	0%
6	20	21	Combination* (COMBO)	1%
7	40	3	Fully Wrapped (FW)	0%
8	40	3	Fully Wrapped (FW)	1%

*Partially wrapped for 7 days + fully wrapped for 14 days.

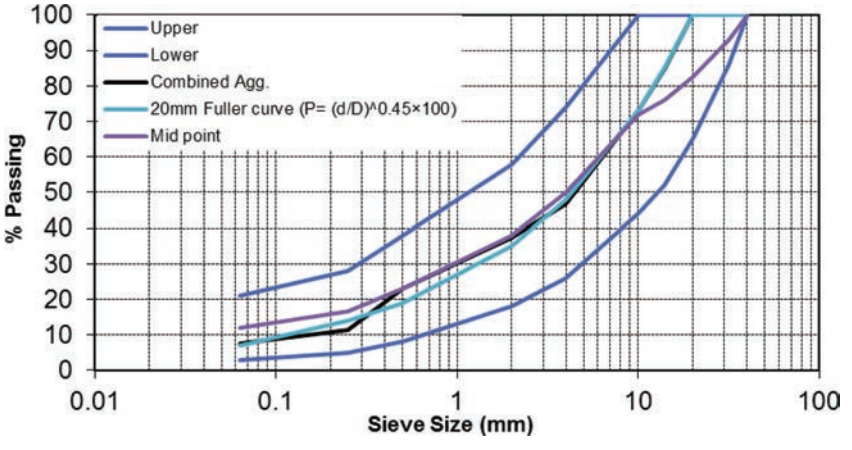

Figure 3. Aggregate gradation.

Table 3. Bitumen emulsion mix parameters.

Bitumen emulsion mixtures	
Bitumen emulsion content	5.42%
Pre-wet water content	2.63%
Optimum Total Fluid Content (OTFC)	8.05%

Table 4. Foamed bitumen mix parameters.

Foamed bitumen mixtures	
Bitumen content	3.25%
Mixing water content	4.80%
Optimum Total Fluid Content (OTFC)	8.05%

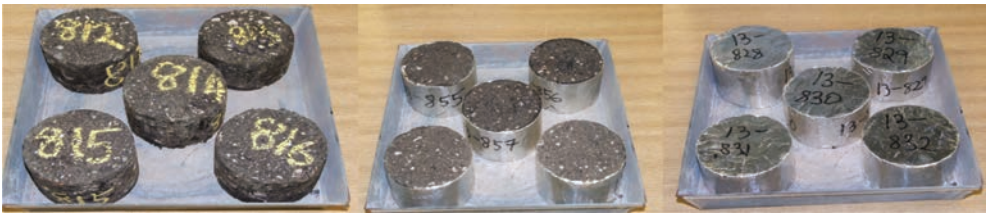

Figure 4. (L-R)—unwrapped, partially wrapped and fully wrapped.

and this was followed by curing according to the regime as stated in Table 2. Figure 4 shows the cores in their respective curing conditions.

4 TESTING METHOD AND RESULTS

4.1 *Stiffness modulus and ITS test results*

4.1.1 *Introduction*

In this study, the stiffness modulus was determined using a servo-pneumatic testing machine (NU-14) by applying indirect tension to the cylindrical specimens. A rise time of 124 ms and a target horizontal deformation of 5 μm were used. Ten conditioning pulses were applied to the specimens followed by five test pulses. The measurements were repeated along two diameters and the average stiffness values calculated. The test was conducted at 20°C according to BS EN 12697-26 specifications. Three specimens were tested in each condition.

The ITS test involved applying compressive loads to the samples between two loading strips which creates tensile stresses along the vertical diametric plane causing a splitting failure [5]. The test was conducted at 20°C using the INSTRON test equipment located at the Nottingham Transportation and Engineering Centre (NTEC) in accordance with BS EN 12697-23. In each case, the same three specimens used for ITSM testing were also tested for ITS.

4.1.2 *Effect of curing conditioning*

Figures 5–7 present stiffness modulus results as obtained for CRBM produced using bitumen emulsion and foamed bitumen conditioned for 28 days at three different temperatures with and without the inclusion of 1% OPC. The results as seen in Figures 5–7 show that the Fully Wrapped (FW) specimens had the lowest stiffness values especially those cured at 5°C with values of 929 MPa and 648 MPa respectively for both bitumen emulsion and foamed bitumen mixtures with 0% OPC. The highest stiffness values for the FW mixtures with 0% OPC were observed on specimens cured at 40°C with values of 1791 MPa and 1554 MPa for bitumen emulsion and foamed bitumen. At all curing temperatures, UnWrapped (UW) specimens with 0% OPC reached a stiffness 2–2.5 times the FW specimens.

ITS test results are presented in Figures 8–10. The trend observed for the ITS test results is identical to that for stiffness. The lowest strength values were observed also for the FW specimens cured at 5°C for both bitumen emulsion and foamed bitumen. At 0% OPC, UW specimens achieved 1.5–2.5 times the strength of FW specimens.

4.1.3 *Temperature influence on curing*

The influence of curing temperature on the stiffness modulus and strength development of the mixtures is illustrated in the case of 0% OPC specimens in Figures 11–12. The stiffness modulus and strength development increases with increase in curing temperature. This was evident irrespective of the curing conditioning employed. Higher curing temperatures resulted in higher rates of stiffness and strength increase which led to higher maximum values.

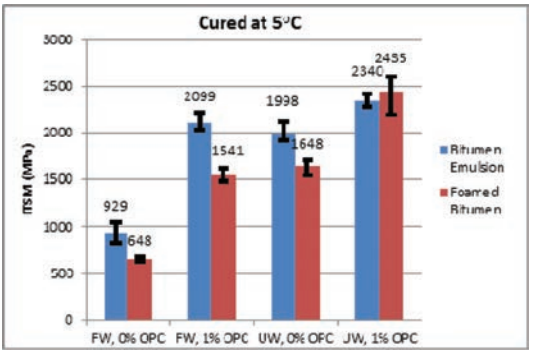

Figure 5. ITSM of specimens cured at 5°C.

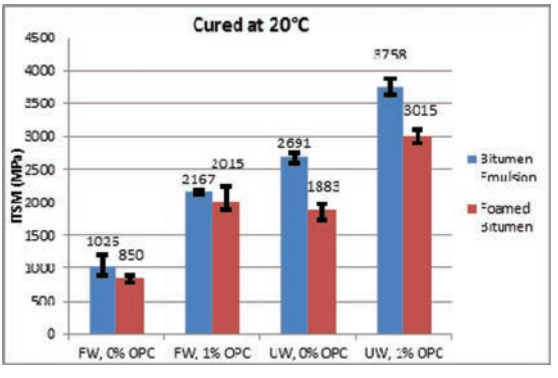

Figure 6. ITSM of specimens cured at 20°C.

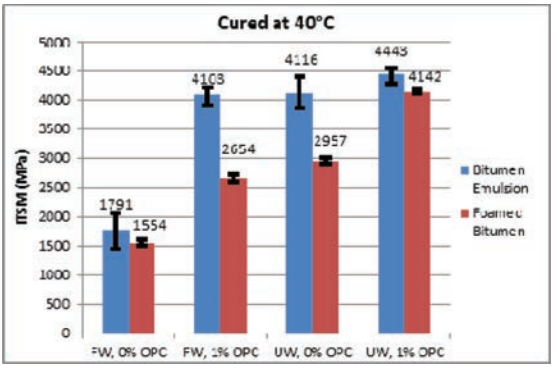

Figure 7. ITSM of specimens cured at 40°C.

A major phenomenon occurring during the curing process is moisture loss. As shown in Figures 13 and 14, there is naturally a significant difference between FW and UW specimens particularly with bitumen emulsion. Nevertheless, it is apparent from the relatively modest difference between final water contents at different curing temperatures that moisture loss is not the only mechanism involved in 'curing'. High temperature is clearly responsible for additional strength/stiffness gain, possibly by facilitating binder adhesion during the curing process.

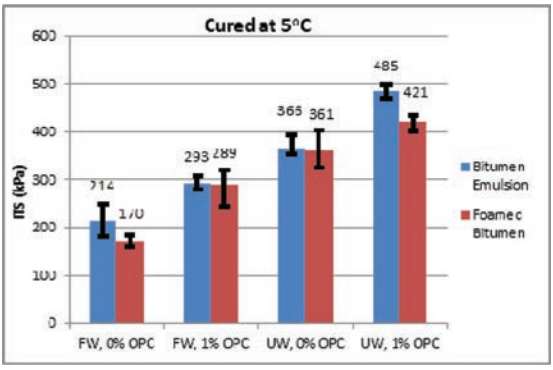

Figure 8. ITS of specimens cured at 5°C.

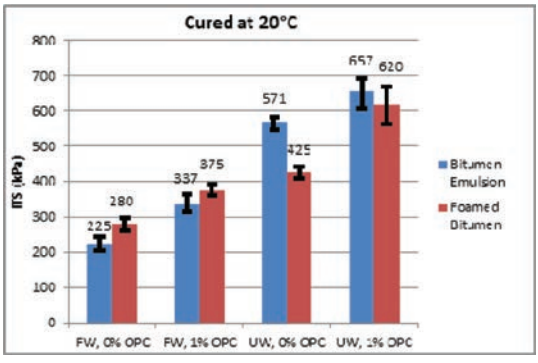

Figure 9. ITS of specimens cured at 20°C.

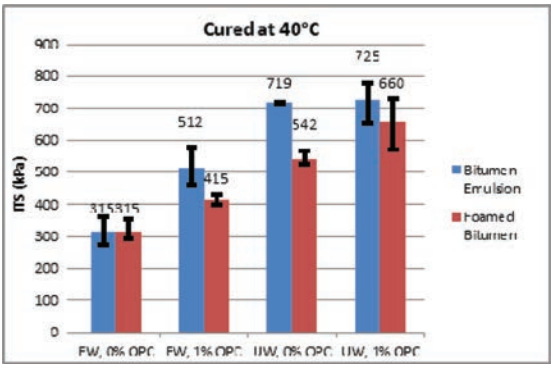

Figure 10. ITS of specimens cured at 40°C.

4.1.4 *Influence of cement*

The addition of cement increased the stiffness and strength at all curing temperatures for both FW and UW conditions. This increase is partly due to the removal of water from the system during hydration and partly due to the formation of cementitious bonds. In terms of stiffness, the addition of 1% OPC to FW specimens increased the 28 day values to those of 0% OPC UW specimens, illustrating the usefulness of cement in countering adverse weather during curing. The effect in terms of strength was slightly less but still significant.

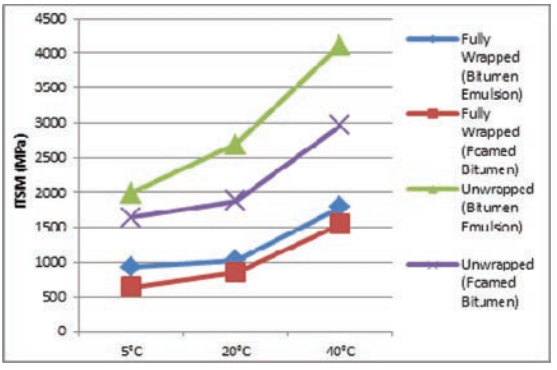

Figure 11. Stiffness trend.

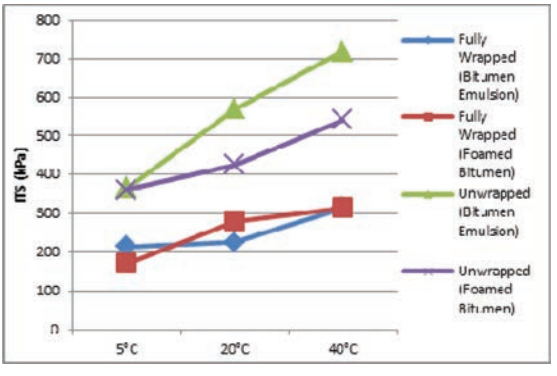

Figure 12. Strength trend.

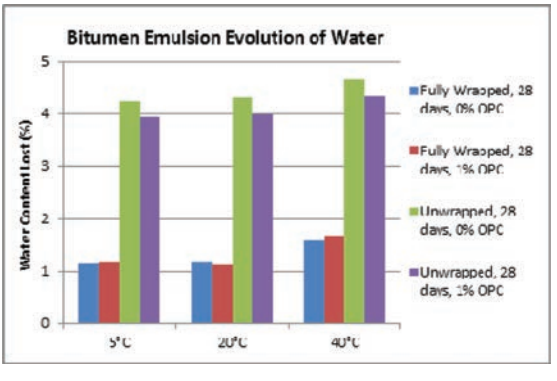

Figure 13. Bitumen emulsion moisture evolution.

Addition of cement to UW specimens also led to strength and stiffness increase. However, it is noticeable that with curing at 40°C, the effect of cement is minor. This suggests that its primary role, at least at 1%, is to remove water and facilitate bitumen bond formation rather than to create cementitious bonds.

4.1.5 *Influence of curing time*

This can be seen in Figures 15 and 16 where the 3 day and 28 day data are compared. Typically, it may be found that the stiffness values for the FW specimens, cured at 40°C for 3 days were

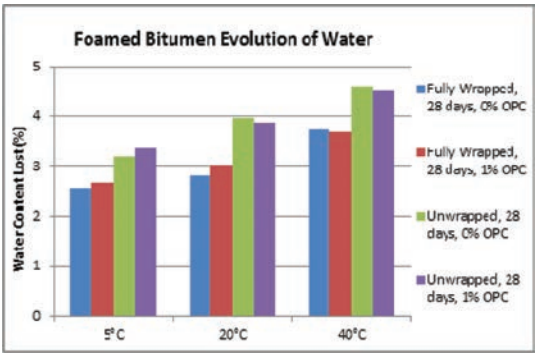

Figure 14. Foamed bitumen moisture evolution.

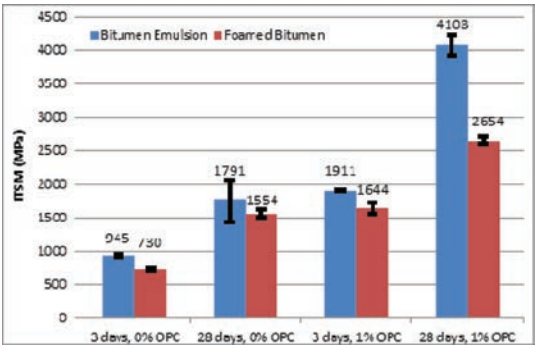

Figure 15. ITSM (3 days and 28 days).

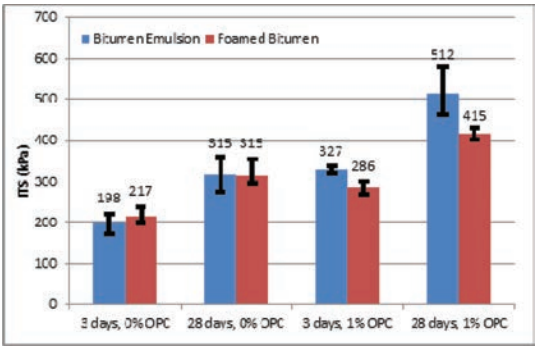

Figure 16. ITS test results (3 days and 28 days).

about 50% of those achieved at 28 days and with respect to the ITS results, the proportion is about 70%.

The combination of 7 days partially wrapped and 14 days fully wrapped (COMBO) was introduced to simulate typical field conditions with a surface course applied 7 days after construction of the base layer and trafficking commencing 14 days later. Figures 17 and 18 below compare this curing condition to the 28 day curing period of FW and UW curing conditions at 20°C. It is observed that in every case, the COMBO lies in between the FW and UW curing conditions. This reinforces the view that 28 days UW may result in an overestimate of actual performance and also suggests that 28 days FW may be appropriately conservative.

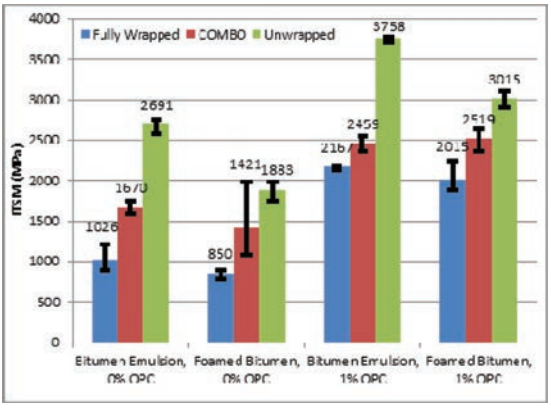

Figure 17. ITSM (COMBO).

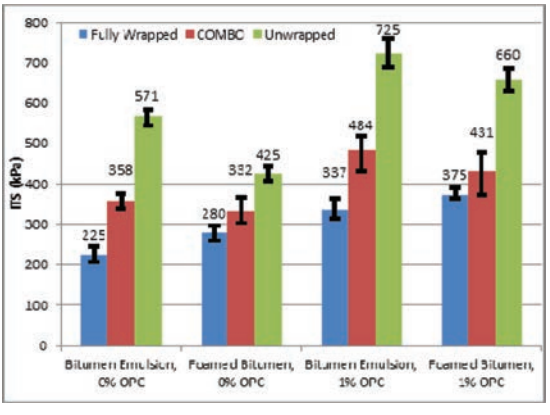

Figure 18. ITS (COMBO).

4.1.6 *Comparison of bitumen emulsion and foamed bitumen*

On average, it is clear that the emulsion specimens were generally stiffer and stronger than the foamed bitumen specimens. However, it should be noted that the grade of bitumen used in the emulsion was harder, reflecting common practice since hard binders tend not to foam so effectively. The binding effectiveness was probably similar in both cases since there was no significant difference between the two binders in terms of the relative effect of temperature, time, curing condition (FW or UW) or cement addition. Thus, in these cases, the two binders may be considered as having extremely similar types of action.

4.2 *Resistance to repeated loading*

To complete this study the resistance to permanent deformation was carried out using the Repeated Load Axial test (RLAT) in accordance to BS DD 226 as the guide. Test specimens were subjected to repeated load axial pulses that simulate loading conditions in road pavements. The parameters used are stated below:

- Conditioning stress: 10 kPa
- Conditioning period: 600 s
- Test stress: 100 kPa
- Test duration: 1800 pulses
- Test temperature: 30°C

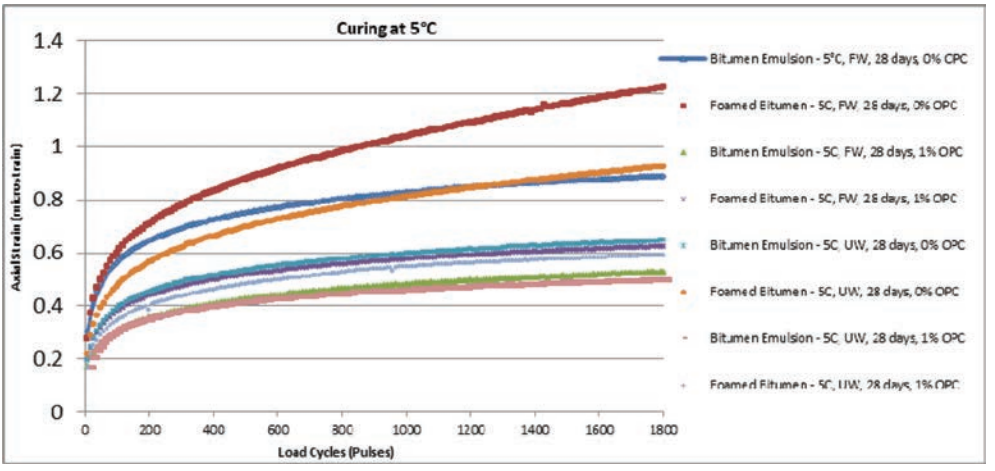

Figure 19. Permanent deformation at 5°C.

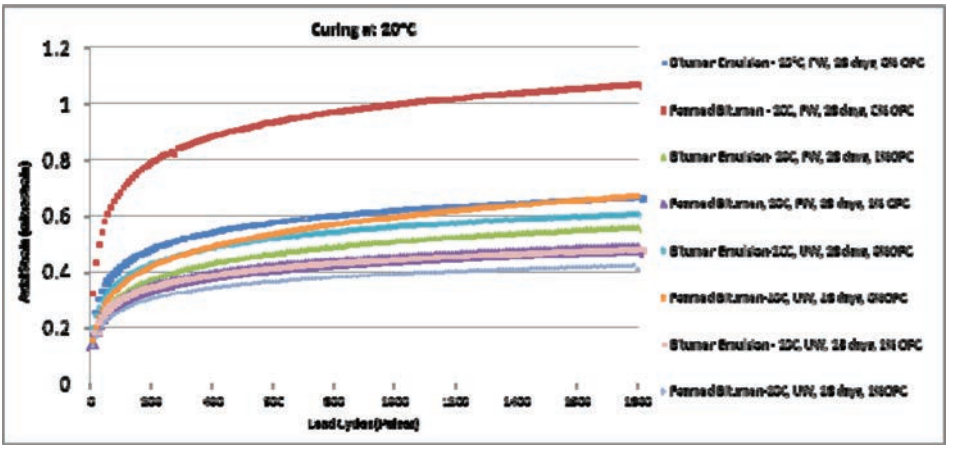

Figure 20. Permanent deformation at 20°C.

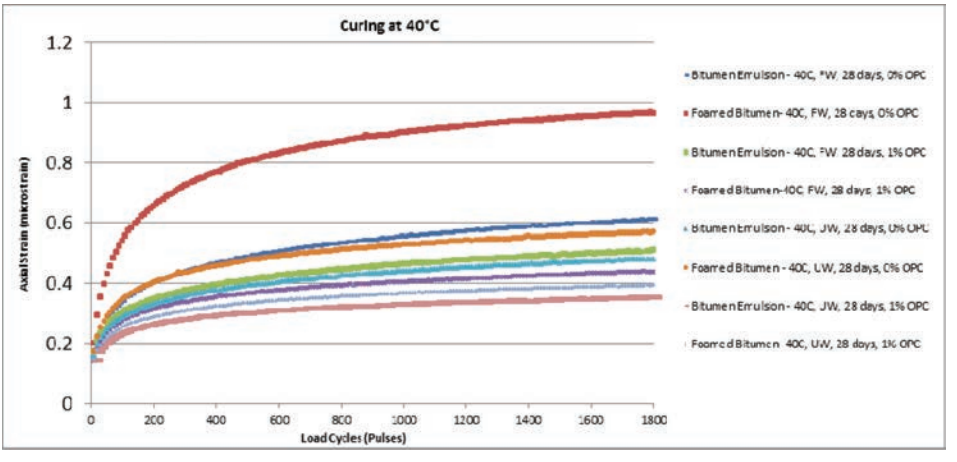

Figure 21. Permanent deformation at 40°C.

Analysing the permanent deformation results as presented Figures 19–21, the effect of curing temperature is moderate while the addition of cement greatly affects the performance of the CRBMs. Overall, the UW CRBMs had better resistance to deformation at the different temperatures but the difference is relatively slight. Similarly, the CRBMs produced with bitumen emulsion outperformed those produced with foamed bitumen as expected due to their harder binder.

5 CONCLUSIONS

The suite of tests carried out on CRBMs for this paper has resulted in several interesting conclusions with practical repercussions, namely:

- Curing temperature dramatically affects the rate of curing and the 28-day strength and stiffness values despite final water contents being similar.
- The ratio of 28-day stiffness results of specimens cured unwrapped to those cured fully wrapped is typically 2–2.5, independent of curing temperature. The equivalent indirect tensile strength ratio is 1.5–2.5.
- The inclusion of 1% cement in the fully wrapped case leads to strength and stiffness results approximately equal to those of unwrapped specimens without cement, suggesting that 1% cement addition is an appropriate means of avoiding the effects of adverse weather during curing.
- Strengths and stiffness results at 3 days are approximately 50–70% of those at 28 days, illustrating the danger of damage due to early trafficking.
- A 2-stage curing regime intended to simulate site practice produced strength and stiffness data that lay between the wrapped and unwrapped 28-day results.
- The behaviors of emulsion-bound and foamed-bitumen bound materials were very similar in terms of the relative effects of curing time and temperature, specimen wrapping and cement addition. However, the emulsion bound materials had consistently better performance as expected due to the harder grade of binder used.
- Exactly the same trends appeared from tests for permanent deformation resistance as for strength and stiffness.

REFERENCES

[1] Batista, F., and Antunes, M. (2003). "Pavement rehabilitation using asphalt cold mixtures." Proc., MAIRPAV'03 Conf., 3rd Int. Conf. on Maintenance and Rehabilitation of Pavements and Technical Control, International Society for Concrete Pavements, Bridgeville, PA, 653–662.

[2] Jenkins, K. Mix Design Considerations for Cold and Half-Warm Bituminous Mixes with Emphasis on Foamed Bitumen. PhD Thesis, Stellenbosch University, 2000.

[3] Jenkins KJ, Moloto PK. Updating bituminous stabilized materials guidelines: mix design report. Phase II—Curing protocol: improvement. Technical memorandum task 7; 2008.

[4] Manual of Contract Documents for Highway Works Volume 1 (MCHW), Specification for Highway Works. Highways Agency, Welsh Assembly Government, Transport Scotland and the Department of the Environment for Northern Ireland. The Stationery Office, London.

[5] Kavussi, A., and Modarres, A. (2010). "A model for resilient modulus determination of recycled mixes with bitumen emulsion and cement from ITS testing results." Construction and Building Materials, Volume 24, Issue 11, PA 2252–2259.

Asphalt Pavements – Kim (Ed)
© 2014 Taylor & Francis Group, London, ISBN 978-1-138-02693-3

Forensic analysis of long term aged Hot Mix Asphalt field cores containing Reclaimed Asphalt Pavement

Kelly Barry
Vanasse Hangen Brustlin Inc., North Ferrisburgh, VT, USA

Jo Sias Daniel
University of New Hampshire, Durham, NH, USA

Denis Boisvert
New Hampshire Department of Transportation, Concord, NH, USA

ABSTRACT: The practice of incorporating Reclaimed Asphalt Pavement (RAP) into Hot Mix Asphalt (HMA) is common within the paving industry as a cost effective source of quality paving binder and aggregate. These mixtures incorporate already aged asphalt binder into new mixtures, which can impact the performance of the mixture in the field in terms of cracking, rutting and aging. This paper presents the results of a forensic study on cores from 23 year old pavements; the objective was to determine if a difference in aging between high and low RAP mixtures existed. Binders were extracted and recovered from field cores taken along New Hampshire Department of Transportation (NHDOT) paving projects that were constructed in 1987. This included 35% RAP mixtures from I-93 and virgin and low RAP mixtures along I-89. Field cores were obtained from the travel and shoulder lanes of the pavement sections and asphalt binder was extracted and recovered from different depths in the pavement structure. The results indicate that the 35% RAP mixtures age more uniformly through depth and between travel and shoulder lanes compared to the virgin and 15% RAP mixtures.

Keywords: High RAP, recycling, aging, extracted binder, field cores

1 INTRODUCTION

Hot Mix Asphalt (HMA) is comprised of three main components: aggregate, asphalt binder and recycled materials. While recycled materials can come from several different sources, the most commonly used in HMA is Reclaimed Asphalt Pavement (RAP), which is asphalt concrete from millings or plant waste that is processed for inclusion in new mixtures. RAP is a source of paving quality asphalt binder, as well as paving quality aggregate. The primary concern with use of RAP is the asphalt binder, which has been aged and is stiffer and more brittle than a virgin binder, which may lead to a higher susceptibility to cracking in the field. Based on experience and research, transportation agencies have been comfortable using 15–20% RAP (by total weight) in their mixtures [1–4] before any modifications to the mixture, such as changing binder grade, are required to offset the impact of the RAP binder.

Many research projects have evaluated the performance of asphalt mixtures containing various amounts of RAP compared to virgin mixture performance [1–8]. However, most of the research has been conducted on laboratory mixtures or field mixtures that have been in place for only a few years. This paper presents the results of a forensic analysis on 23 year old field cores that contained 35% RAP in the surface and intermediate binder layers. Companion virgin or low RAP (15%) field cores were also obtained. The binders were extracted and recovered from the field cores and tested in the laboratory to determine if the high RAP

mixtures aged differently than the low RAP or virgin mixtures in the field. The aging that occurred along the depth of the core as well as comparison between travel and shoulder lane cores are evaluated in this study.

2 MATERIALS AND METHODS

2.1 *Field cores*

Field cores were obtained from 23 year old pavements in two locations: Interstate 93 and Interstate 89 in New Hampshire. The I-93 cores contained 35% RAP; the I-89 surface cores were a virgin mix and the intermediate course contained 15% RAP. An intermediate course pavement of that age with virgin mix was not available, so the comparisons are between high and low/no RAP mixtures. The mixtures used a ¾ in. maximum aggregate size gradation with AC-10 binder. More details on the mixtures can be found in [9]. The two pavement sections had Average Daily Traffic (ADT) counts of approximately 20,000 vehicles per day for I-93 and 36,000 vehicles per day for I-89.

Volumetric information for the cores is presented in Table 1. The field cores had a large range in air void contents, with average values varying significantly at the surface between the travel and shoulder lanes and between the surface and intermediate layers.

2.2 *Asphalt binder extraction and testing*

The asphalt binder was extracted and recovered from three layers of each field core: the top 0.5 in., the next 1.0 in., and the next 1.0 in. For most of the cores, the top two layers were surface course materials and the bottom layer was the intermediate course. The exception is the I-89 travel lane middle layer that contains both surface and intermediate course material. Figure 1 shows the extraction layers and mixtures with depth, where the surface course is indicated in light grey and intermediate course is indicated in dark grey, and each unit

Table 1. Average volumetric properties of field cores.

Location	RAP Content (% by total weight)	Min. Air Void	Max. Air Void	Ave. Air Void	Ave. VMA	Ave. VFA
I-93 Travel surface	35%	1.1%	4.2%	2.2%	15.7	88.8
I-93 Travel intermediate		3.6%	6.5%	5.1%	17.5	69.4
I-93 Shoulder surface	35%	3.6%	4.0%	3.8%	16.7	77.1
I-93 Shoulder intermediate		4.5%	5.4%	5.0%	16.9	70.7
I-89 Travel surface	0%	3.5%	4.5%	4.0%	13.8	71.5
I-89 Travel intermediate	15%	1.7%	3.7%	2.6%	14.6	82.5
I-89 Shoulder surface	0%	6.6%	8.6%	7.6%	20.1	62.4
I-89 Shoulder intermediate	15%	4.3%	5.9%	5.1%	17.0	70.1

Figure 1. Schematic of layer and binder extraction depths.

represents 0.5 in. The binder was extracted from each layer following AASHTO T-164 using trichloroethelyne as the solvent and recovered following AASHTO T-170.

Binder testing included the Bending Beam Rheometer (BBR) (AASHTO T 313), Direct Tension Test (DTT) (AASHTO T 314) and Dynamic Shear Rheometer (DSR) (AASHTO T 315) testing. Only one specimen was tested at each location and depth, so a typical statistical analysis could not be performed. In order to quantify the differences between binder results, percent differences were calculated to compare stiffness, m-values and critical cracking temperatures. To compare the shear modulus and phase angle master curves, a ratio of the modulus and phase angle values at various reduced frequencies were calculated and plotted on a log scale. The control specimens for percent differences are displayed as the numerator in the legend of each graph.

3 RESULTS AND DISCUSSION

3.1 *Naming scheme*

The specimen name starts with the route number from which the sample was cored, followed by a "T" or "S" for travel lane or shoulder lane, respectively, followed by a number which indicates the % RAP in the layer, followed by a "t", "m", or "b" for the top 0.5 in., middle 1 in., and bottom 1 in. respectively. Binder specimens that contained a mixture of surface and intermediate course binder are noted with a "*" at the end of the name.

3.2 *BBR M-Value and stiffness*

Figure 2 presents the BBR stiffness measured at several temperatures while Figure 3 through Figure 5 present the percent difference comparisons at –18C for the stiffness values. Figure 6 shows the m-value results at different temperatures and Figure 7 through Figure 9

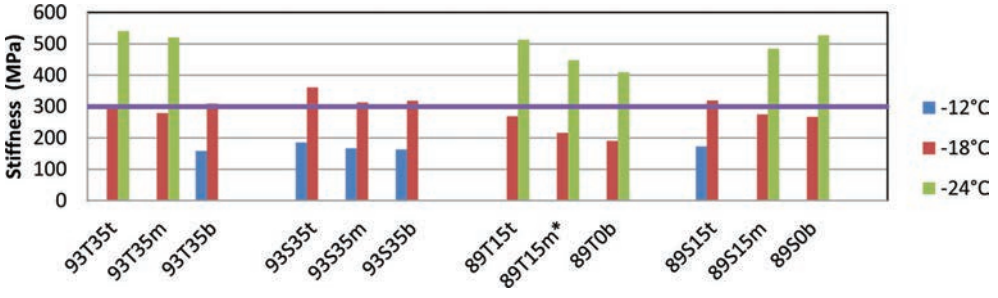

Figure 2. Stiffness of all binder specimens.

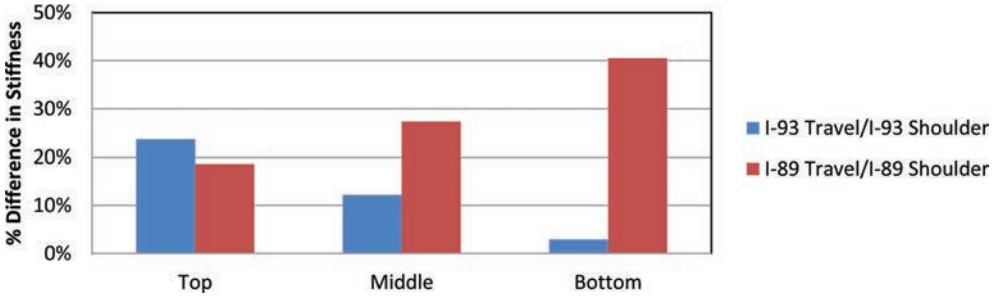

Figure 3. Percent difference between stiffness of travel and shoulder lanes with depth.

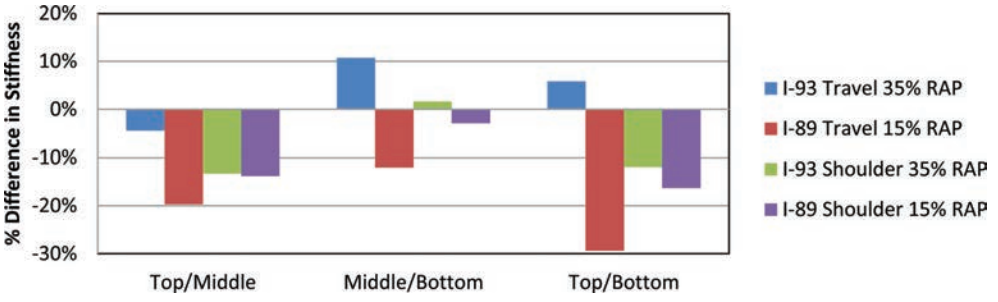

Figure 4. Percent difference between stiffness of lanes with depth.

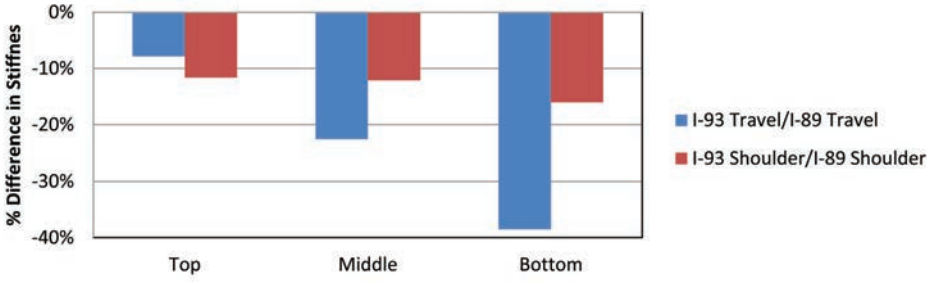

Figure 5. Percent difference between stiffness of high and low RAP with depth.

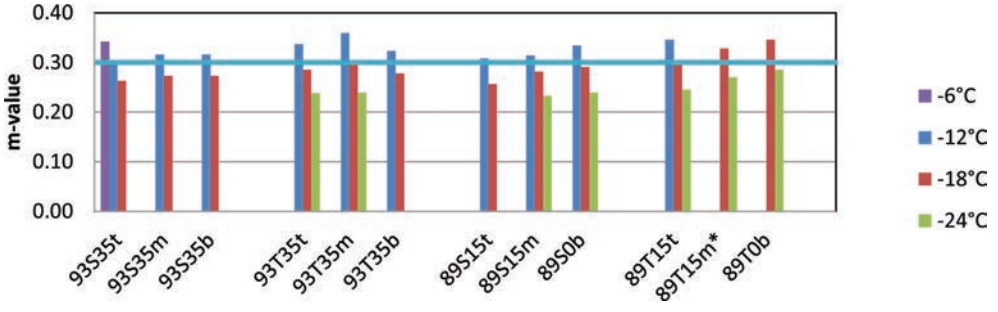

Figure 6. M-Values for all binder specimens.

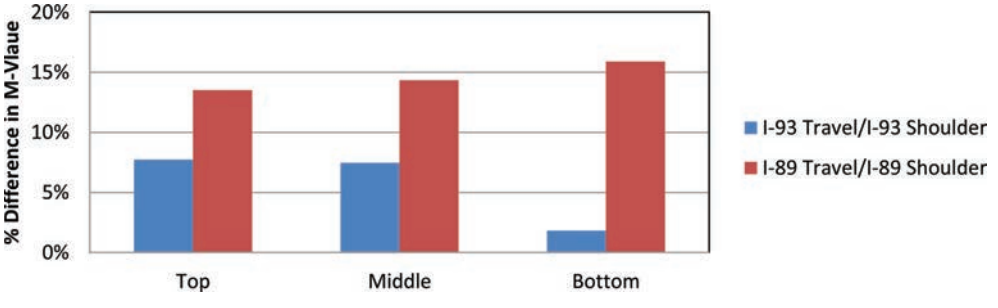

Figure 7. Percent difference between M-Value of travel and shoulder lanes with depth.

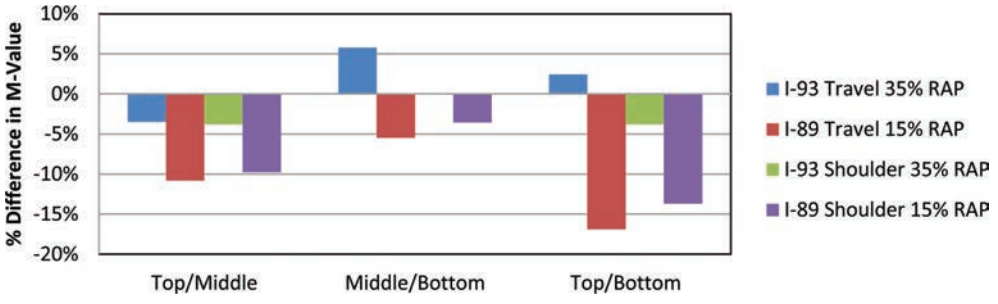

Figure 8. Percent difference M-Value of lanes with depth.

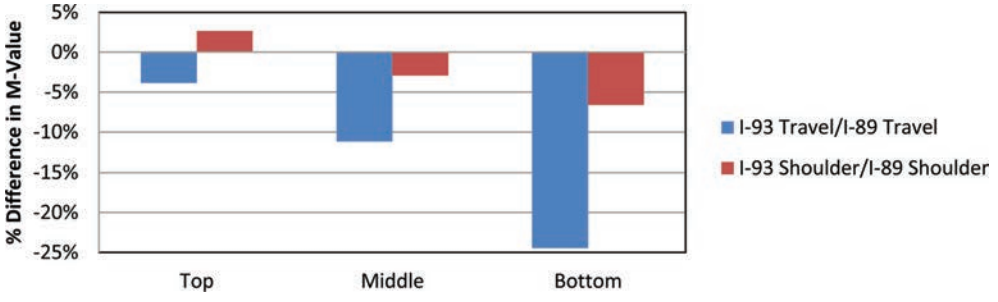

Figure 9. Percent difference between M-Value of high and low RAP with depth.

present the percent differences at –18C for the m-value results. In both cases, there is a larger percent difference among the low RAP cores compared to the high RAP cores between lane types. The low RAP cores have a much higher percent difference throughout lane types than the high RAP cores. There is an increasing percent difference with depth between the RAP contents and a much greater variability in the low RAP cores, especially with depth from the surface particularly in the travel lane. The results indicate that high RAP cores aged differently from the low RAP cores because the low RAP cores have greater changes in stiffness and m-value through the pavement depth and between lane types.

It is expected that the high RAP cores have higher stiffness and lower m-value due to the already aged binder. Increased exposure to oxidation at the surface is expected to cause higher stiffness at the surface and decrease through the middle and bottom layers. The m-value is expected to increase through the middle and bottom layers. Traffic action is shown to decrease the effects of aging at the surface, so it is probable that there are lower stiffness values in the travel lane compared to the shoulder lane, and higher m-values in the travel lane. Higher air voids are shown to increase the aging process by allowing oxygen to flow through the pavement layers, however, since the higher air voids were in the intermediate course it likely had less of an impact. The stiffness and m-value trends follow the predicted behaviors, indicating these specimens are good candidates for determining if RAP has an impact on aging as there are no unexpected trends.

3.3 *Critical cracking temperature*

Critical Cracking Temperature (CCT) values were calculated following AASHTO MP 1a-04 and are presented in Figure 10. Figure 11 through Figure 13 present the percent differences between CCT value results. Similar to the stiffness and m-value results, there is a larger percent difference between low RAP cores compared to the high RAP cores. This larger difference in CCT values in the low RAP cores is observed when comparing depth from surface

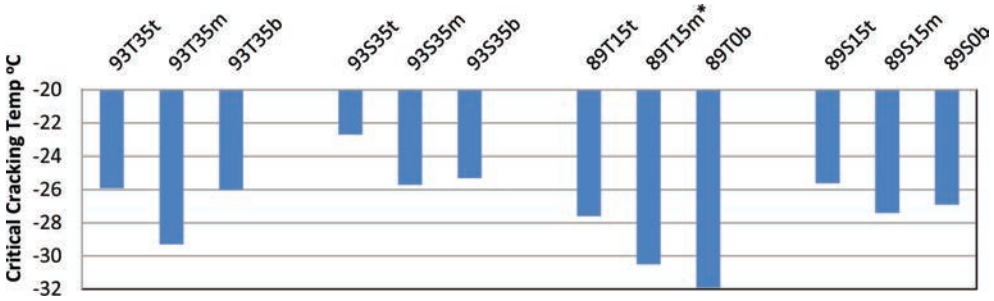

Figure 10. Critical cracking temperature of all binder specimens.

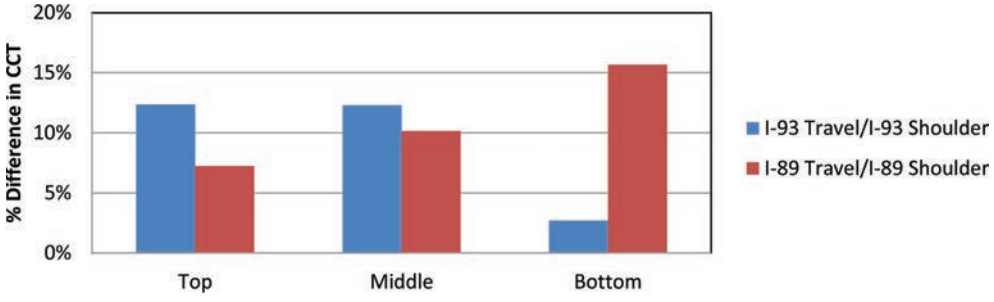

Figure 11. Percent difference between CCT of travel and shoulder lanes with depth.

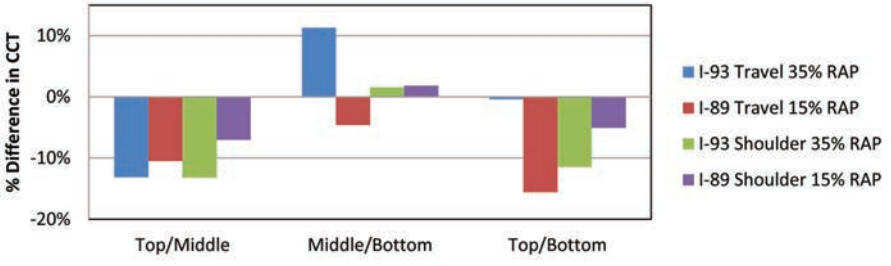

Figure 12. Percent difference CCT of lanes with depth.

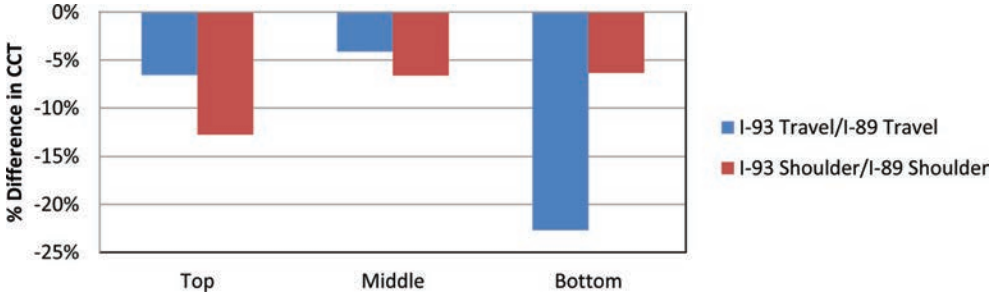

Figure 13. Percent difference between CCT of high and low RAP with depth.

and when comparing lane type. It is important to notice the high RAP mixture middle specimens for both lanes had lower CCT values than the top and bottom depths, which caused an increase in the percent difference that is not observed in the previous results from stiffness and m-value. The top and bottom layers of the high RAP cores, however, have similar CCT values that are consistent with previous results which may indicate the middle layer is an outlier. These results indicate that the high RAP cores have aged more uniformly during their service life when compared to low RAP cores both with depth and lane type.

It is expected that the high RAP cores have higher CCT than the low RAP cores due to the already aged binder. Increased exposure to oxidation at the surface is expected to cause higher CCT at the surface and decrease through the middle and bottom layers. The CCT values trends follow expected behaviors with respect to traffic and air void content, indicating these specimens are good candidates for determining if RAP has an impact on aging as there are no unexpected trends.

3.4 *Dynamic shear modulus |G*|*

Figure 14 presents the dynamic shear modulus, |G*|. In general, the master curves follow trends observed from the stiffness, m-value and CCT results, with the top sections having highest (stiffest) master curves and stiffness decreasing with depth and RAP content. The shoulder lanes also have stiffer master curves than the travel lanes. Air void contents were not consistent, which may have affected aging over the lifespan of the pavement, however the air voids are lowest at the surface, decreasing the impacts of aging in the intermediate layers.

Figures 15 and 16 present ratios of the |G*| master curves (20°C reference temperature) by depth, lane type and RAP content. The legend indicates the numerator and

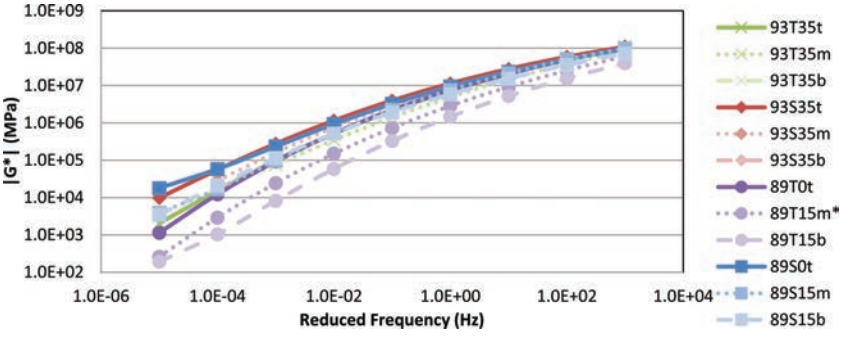

Figure 14. Summary of all binder's |G*| master curves.

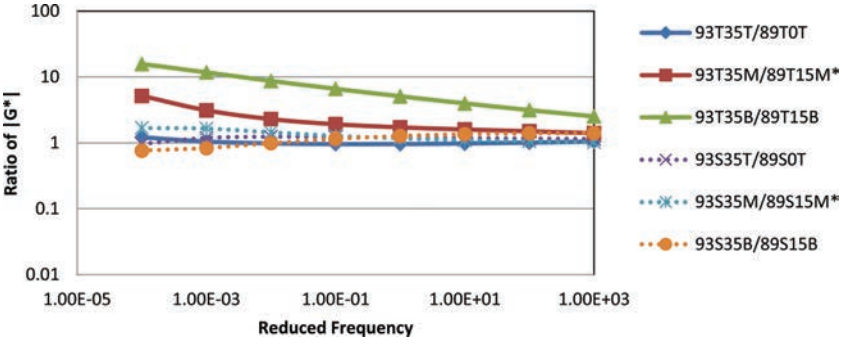

Figure 15. Ratio of |G*| for travel and shoulder lanes.

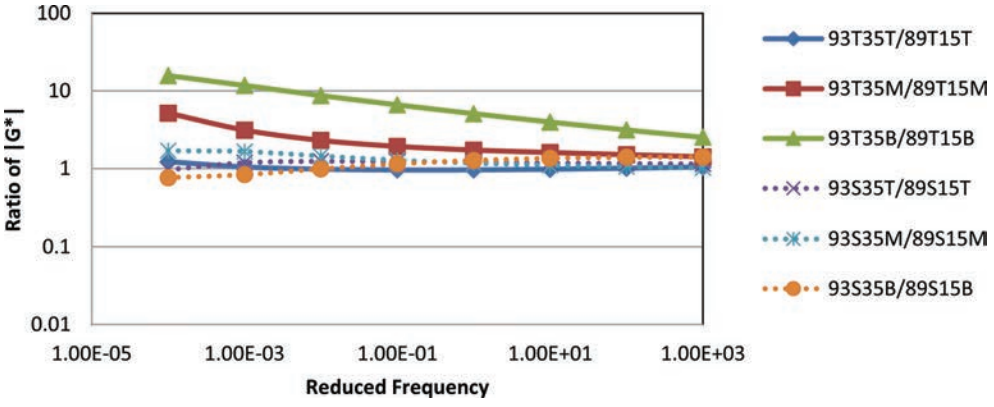

Figure 16. Ratio of |G*| for high RAP and low RAP cores.

denominator in the ratio. With few exceptions, the low RAP mixtures have larger ratios, indicating a larger difference in stiffness. At all depths and frequencies the ratio of high RAP specimens are close to 1, indicating very similar stiffness while the low RAP travel lane ratios are close to 12 times greater between the top and bottom specimens and close to 5 times greater for the shoulder lane at low frequencies. This greater difference suggests the low RAP mixtures are not aging uniformly with depth, while the high RAP mixtures are aging at a more similar rate. There is also more uniform aging indicated between shoulder and travel lane for the high RAP mixtures when compared with the low RAP mixtures.

4 SUMMARY AND CONCLUSIONS

The research goal for this project was to determine if high RAP mixtures age differently than mixtures with low or no RAP. Field cores that had been in service for 23 years with varying amounts of RAP were obtained. The binder was extracted and recovered from surface and intermediate courses and tested for shear modulus, phase angle, stiffness, m-value and critical cracking temperature. The binder testing, in general, yielded trends among RAP contents, lane types and depths that were consistent with previous research, with increase in stiffness at the surface, in the shoulder lanes compared to travel lanes, and in high RAP mixtures compared to low RAP mixtures.

By quantifying the difference between the high and low RAP performance using percent differences and ratios, the following conclusions are drawn regarding the effects of RAP content on aging based on the pavements evaluated in this study:

- High RAP mixtures appear to age differently than low RAP mixtures;
- High RAP mixtures have more uniform properties along pavement depth and between shoulder and travel lanes than low RAP mixtures.

While this research, as well as previous research, has shown that high RAP mixtures are stiffer and thus more susceptible to cracking than low RAP or virgin mixtures, this research has also shown that they age at a more uniform rate. It is also indicated that aging in the high RAP mixtures cause smaller differences from initial conditions over time. Oxidation of the RAP material that occurred during its initial service life is likely the reason for the smaller changes observed. Knowing that high RAP mixtures will age less over time means that transportation agencies can better predict material properties over design life, and thus better predict pavement performance.

5 RECOMMENDATIONS FOR FUTURE WORK

The following items are recommendations for future work to evaluate the effect of high RAP on asphalt pavement performance in field aged mixtures:

- Include test sections of wider range of RAP contents;
- Evaluate initial mixture and binder performance;
- Evaluate mixture and binder performance at regular time intervals throughout pavement service life; and
- Eliminate as many sources of error between test sections possible by selecting roadways with similar ADT and consistent aggregate gradation, layer thickness and air void content.

ACKNOWLEDGEMENTS

The authors acknowledge NHDOT for providing funding for this work and Materials and Research Bureau of NHDOT for performing much of the binder extractions and binder testing for this project.

REFERENCES

[1] McDaniel, R.S., Shah, A., & Huber, G. "Investigation of Low- and High-Temperature Properties of Plant-Produced RAP Mixtures." FHWA FHWA-HRT-11-058 (2012).
[2] Singh, D., Zaman, M., & Commuri, S. "A Labratory Invesitgation into the Effect of Long-Term Oven Aging on RAP Mixes Using Dynamic Modulus Test." *International Journal of Pavement Research and Technology* Volume 5 (2012): 142–152.
[3] West, R., Kvasnak, A., Tran, N., Powell, B., & Turner, P. "Testing of Moderate and High Reclaimed Asphalt Pavement Content Mixes." *Transporation Research Record* No. 2126 (2009): 100–108.
[4] Zhao, S., Huang, B., Shu, X., Jia, X., & Woods, M. "Labratory Performance Evaluation of Warm Mix Asphalt Containing High Percentages of RAP." *Transprotation Research Board* Report 12-4542 (2012): 98–105.
[5] Al-Qadi, I., Aurangzeb, Q., Carpenter, S.H., Pine, W.J., & Trepanier, J. "Impact of High RAP Content on Structural and Performance Properties of Asphalt Mixtures." *Illinois Center for Transportation* Series No. 12-002 (2012).
[6] Barry, Kelly. "Forensic Analysis of Long Term Aged Hot Mix Asphalt Field Cores Containing Reclaimed Asphalt Pavement." MA thesis of University of New Hampshire, Durham, 2013. Print.
[7] Christensen, D. "Analysis of Creep Data from Indirect Tension Test on Asphalt Concrete." *Journal of the Asphalt Paving Technologists* Volume 67 (1998): 458–492.
[8] Tarbox, S., & Daniel, J.S. "Effects of Long Term Oven Aging on RAP Mixtures." *Journal of the Transportation Research Board* Report 12–1504 (2012): 1–15.
[9] Daniel, J.S., Kim, Y.R., & Lee, H. "Effects of Aging on Viscoelastic Properties of Asphalt Aggregate Mixtures." *Transportation Research Record* Volume 1630 (1998): 21–27.

This page intentionally left blank

Asphalt Pavements – Kim (Ed)
© 2014 Taylor & Francis Group, London, ISBN 978-1-138-02693-3

Resistance to permanent deformation of base courses asphalt concretes made with RAP aggregate and steel slag

Marco Pasetto
Department of Civil, Environmental and Architectural Engineering, University of Padua, Padua, Italy

Nicola Baldo
Chemistry, Physics and Environment Department, University of Udine, Udine, Italy

ABSTRACT: The results are presented of a laboratory investigation aimed at analyzing the rutting susceptibility of asphalt concretes with Reclaimed Asphalt Pavement (RAP) aggregate and Electric Arc Furnace (EAF) steel slag, used at different proportions (up to 70% of the weight of the aggregates), in partial substitution of limestone aggregates. The experimental study has been focused on the characterization of the physical-mechanical properties of the marginal materials, as well as on the mix design and the permanent deformation evaluation (by means of Creep Recovery Tests, Repeated Load Axial Tests, Wheel Tracking Tests) of bituminous mixtures for road asphalt concrete base courses. Since the requisites for acceptance in the Italian Specifications and Standards have been satisfied and given the positive mechanical performance (indirect tensile strength at 25°C on dry samples up to 2.35 MPa, depending on the mixture), it has been verified that the marginal aggregates investigated can be used as substitution of the lithic materials in the base courses, also with very high content (up to 70% on the weight of the aggregates).

Keywords: Base course asphalt concrete, steel slag, reclaimed asphalt pavement, permanent deformation resistance

1 INTRODUCTION

The accumulation of permanent deformations at high working temperatures and heavy loadings leads to the formation of surface ruts, i.e. longitudinal hollows with raised edges. This can be caused by the poor shear strength of the asphalt that forms the surface layer of a flexible pavement.

Resistance to permanent deformation in a bituminous mix is mainly influenced by the compaction level of the mixture, binder's rheological properties and content [1], and factors connected with the aggregate (angularity, particle size distribution, shape of the grains, texture, etc.) [2, 3]. For this reason, the use of unconventional aggregates deserves a particular attention in the design of bituminous mixtures, especially in the case of heavily trafficked pavements (e.g. in motorways and airport pavements).

The paper presents the results of a laboratory study aimed at verifying the influence of different types of aggregates (two recycled plus a natural one) on the permanent deformation resistance of base courses asphalt concretes.

Two artificial and recycled aggregates were used in the study: Electric Arc Furnace (EAF) steel slag, and Recycled Asphalt Pavement (RAP) aggregates. The use of these materials in the construction of transport infrastructures appears to be particularly promising. Although applications of each type of un-conventional aggregate for road pavements have been widely tested [4–7] in the past, their simultaneous utilization in an integrated lithic matrix of

bituminous mixtures for pavement layers is still the subject of research aimed at evaluating suitability and economy of the application.

2 MATERIALS

The artificial and recycled aggregates (EN 13043) considered in the study were what are known as marginal materials [8–11]; more specifically they are EAF steel slag and RAP aggregate. The marginal aggregates used in the study were supplied by different private companies in northern Italy, while the natural aggregate (limestone and sand) derived from a quarry in the same area.

The grading curves of the aggregates reported in Figure 1, show that the 10/15 mm fractions of the EAF slag and limestone had an almost identical particle size distribution, while a relevant difference can be noticed between the 15/20 fractions: the first slag had a finer composition that the corresponding fraction of the limestone. The 5/10 mm fraction of the EAF slag presented an intermediate grading distribution. RAP and natural sand represent the fine aggregates.

Table 1 reports the physical-mechanical properties of the aggregates, as well as the specific road test protocols adopted.

The Los Angeles test showed a good resistance of the EAF slag to abrasion and friction, with a LA coefficient lower than the acceptance requisites of SITEB—Italian Society of Bitumen Technologists Specifications [12], set at 25%. The Los Angeles coefficient of crushed limestone, as well as that of RAP aggregate, are higher than SITEB's threshold, with differences of 20% and 8%, respectively. The mechanical resistance of the marginal aggregates is anyway higher than that of the natural ones.

The cleanliness, expressed in terms of Equivalent in Sand, resulted extremely good for all the aggregates and largely above the minimum SITEB threshold, fixed at 50%. Both the limestone and the marginal aggregates, namely EAF slag and RAP, presented satisfactory

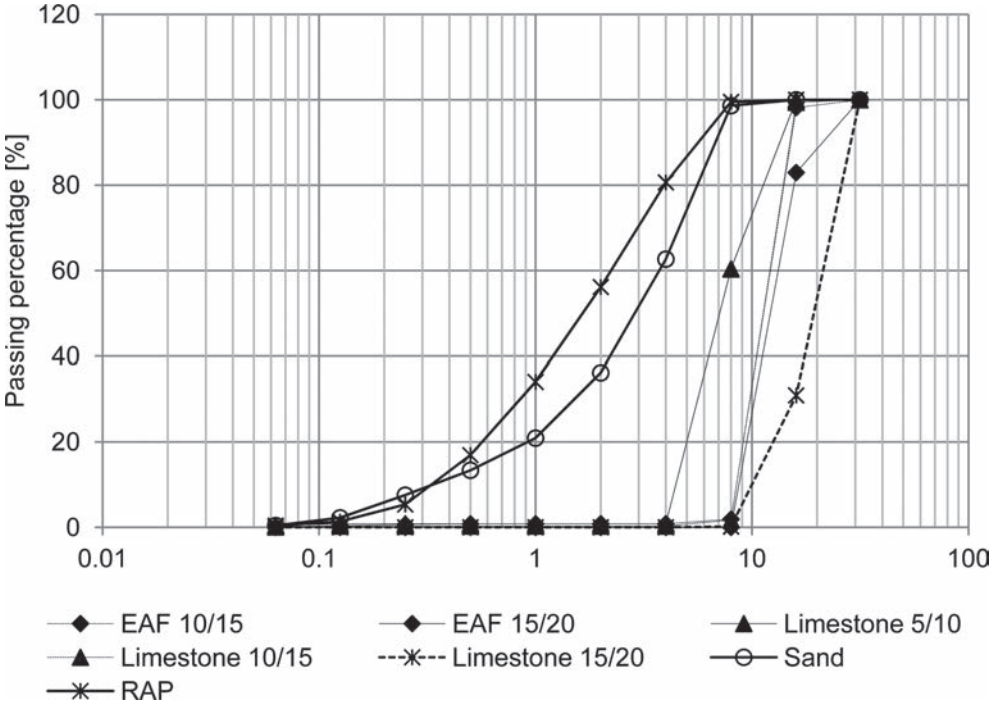

Figure 1. Grading curves of the aggregates.

Table 1. Physical and mechanical characteristics of the aggregates.

Physical ÷ mechanical properties	Natural sand	Crushed limestone 5/10	Crushed limestone 10/15	Crushed limestone 15/20	EAF 10/15	EAF 15/20	RAP aggregate
Los Angeles coefficient [%] EN 1097-2	–	–	30	–	7	–	27
Equivalent in sand [%] EN 933-8	86	93	–	–	–	–	98
Shape index [%] EN 933-4	–	9	2	4	8	3	10
Flakiness index [%] EN 933-3	–	10	2	5	6	4	7
Particle density [Mg/m^3] EN 1097-6	2.81	2.44	2.72	2.78	3.87	3.74	2.36
Plasticity index [-] CEN ISO/TS 17892-12	0	0	0	0	0	0	0

Table 2. Major heavy metal content of EAF slags.

Element	Initial concentration [mg/kg]	TCLP leaching concentration	Limit leaching concentration—legal thresholds
Copper (Cu)	221.0	0.004 mg/l	0.05 mg/l
Cadmium (Cd)	<0.5	<1.0 µg/l	5 µg/l
Lead (Pb)	37.7	19.5 µg/l	50 µg/l
Zinc (Zn)	589.0	<0.001 mg/l	3 mg/l
Chromium—total (Cr)	3534.0	32.7 µg/l	50 µg/l
Nickel (Ni)	37.6	<3.0 µg/l	10 µg/l
Mercury (Hg)	<0.5	<1.0 µg/l	1 µg/l
Selenium (Se)	17.4	<5.0 µg/l	10 µg/l
Vanadium (V)	554.0	32.2 µg/l	250 µg/l
Arsenic (As)	5.5	<5.0 µg/l	50 µg/l
Beryllium (Be)	<0.5	<1.0 µg/l	10 µg/l

morphological properties, given that the Flakiness Index values were consistently below the maxim requisite limit, fixed by SITEB at 25%. All the marginal aggregates resulted as practically unaffected by the action of water, presenting non-determinable Atterberg Limits (Liquid Limit and Plastic Limit), as prescribed in the Italian technical regulations. The particle densities of the RAP aggregates are quite similar to those of the natural materials, but decidedly lower than those of the steel slags.

By Italian Law, the steel slags considered are "non-hazardous, special non-toxic and non-noxious" refuse; their pH resulted equal to 11.5. The chemical composition of the EAF slags have been analyzed with XRF (X-ray fluorescence); their toxicological characteristics were checked in terms of initial concentrations of heavy metals, measured with the ICP-AES methodology (Inductively Coupled Plasma—Atomic Emission Spectrometer), whilst their leaching was determined by the TCLP (Toxic Characteristic Leachability Procedure) given in Appendix A of Standard UNI 10802, following the method in Standard EN 12457-2.

The slags, in terms of oxides, contain a prevalence of FeO (30.4%) and CaO (27.7%), as well as SiO_2 (17.5%), MgO (6.6%) and Al_2O_3 (4.8%). The SiO_2/CaO ratio characterizes the EAF slag as a substantially alkaline aggregate and therefore suitable to guarantee the necessary adhesion with the weakly acid bitumen. With regard to the initial concentration of heavy metals (Table 2), the steel slags present higher contents of vanadium, zinc and chromium, the

latter predominating over all the other metals; anyhow it is less than 0.4% of the total volume of slags.

The results in Table 2 demonstrate that, for the steel slag, the release of heavy metals by leaching is within the limits of the environmental regulations in force in Italy (Legislative Decree no. 152/2006). Therefore, given that the constituents of the mixtures do not present toxicological problems, it was considered unnecessary to proceed with leaching tests on asphalt specimens.

The steel slags investigated in the present research have been seasoned by the producer, exposing the material to weather for a period of at least six months, so that the unbound fraction of calcium oxide can be stabilized naturally, without being subject to a volumetric expansion. However, a volumetric stability test on the EAF slags, according to the Standard EN 1744/1 part 15.3, has been performed and it showed a null expansion after the 168 hours requested by the protocol. Lastly, neither the natural aggregates nor those of fusion demonstrated any problems of affinity with the bitumen, with no stripping of the grains coated with binder after 24 hours of immersion in water at 25 °C.

Cold extraction (by centrifugation) of the bitumen of the RAP aggregate revealed a binder content of 4.3% (EN 12697-1) on the weight of the aggregate. The extracted bitumen showed a penetration of 15 mm/10 at 25 °C (EN 1426) and a softening point, with the Ring & Ball Method, of 74 °C (EN 1427); it is therefore a decidedly aged and particularly hard binder. A conventional bitumen (50/70 dmm pen) was used as virgin binder for all the mixtures in the experiments.

RAP aggregates were preheated at mixing temperature for 2 hours, before the mixing. The virgin bitumen, RAP and the other aggregates (namely limestone and steel slags), have been mixed together in a heated lab mixer for one minute.

3 MIXTURES

Five mixes were designed with an integrated slag-RAP-limestone lithic matrix (S0R2, S0R4, S3R0, S3R2, S3R4) and one, used as control, with only natural aggregate (S0R0). Artificial and recycled aggregates were used up to 70% of the weight of the total aggregate.

3.1 *Grading and composition of the mixes*

The particle size distribution of the mixes with artificial and recycled aggregates was optimized with reference to the design grading envelope of SITEB [12] for asphalt concrete base courses, in order to identify a curve as close as possible to its centre, but compatible with the availability of the different aggregates in the sizes necessary to construct this "ideal" grading. For the control mix (all natural) various amounts of marginal materials are substituted by limestone with an equivalent grading fraction.

Table 3 reports the grading composition of the bituminous mixtures and proportions of the components, whereas the corresponding grading curves are presented in Figure 2. The design grading curves (Fig. 2) are all within the reference grading envelope [12] for base course asphalts with maximum aggregate size of 20 mm.

3.2 *Optimization of the mixture*

The volumetric mix design, according to CIRS-Italian Ministry of Infrastructure Specifications [13], based on the gyratory compaction procedure and the Indirect Tensile Strength (ITS) test at 25°C, on both dry and wet cylindrical samples, was used for the optimization of the bituminous mixtures. Regarding the main test parameters, a speed of 30 revs/minute, a pressure of 600 kPa, an angle of rotation of 1.25° and a diameter of the mould of 150 mm, were used in the gyratory compaction.

The Optimum Bitumen Content (OBC) for each mixture was determined in correspondence to the residual air voids content (Va) at 10, 100 and 180 revs, of 10–14%, 3–5% and

Table 3. Aggregate type and particle size distribution of the mixtures.

Mix composition	Fraction [mm]	Quantity [%]					
		S0R0	S0R2	S0R4	S3R0	S3R2	S3R4
Crushed limestone	5/10	25	15	12	29	21	14
	10/15	20	20	20	–	–	–
	15/20	12	12	11	–	–	–
Sand	0/2	40	30	13	38	26	12
RAP aggregate	0/10	–	20	40	–	20	40
EAF steel slag	10/15	–	–	–	10	18	18
	15/20	–	–	–	20	12	12
Filler (additive)	–	3	3	4	3	3	4

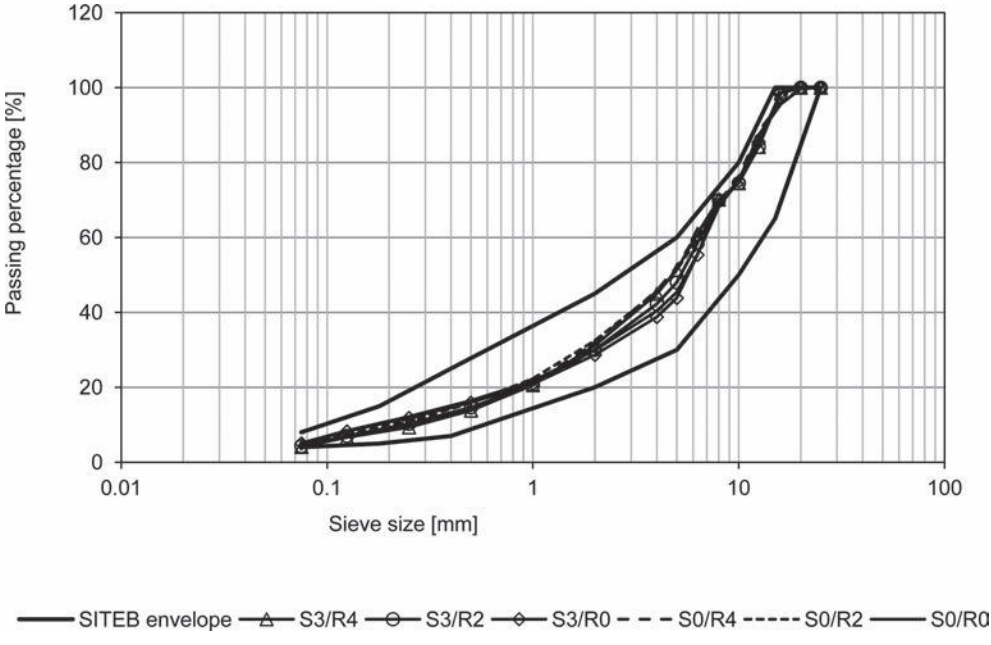

Figure 2. Design grading curves of the mixes.

over 2%, respectively [13]. The binder content determined regards the virgin bitumen added to the granular mixtures, therefore, for the mixes containing RAP aggregate, the total bitumen content is given by the sum of the aged bitumen of the RAP and the OBC.

The Tensile Strength Ratio (TSR) has been computed as the ratio between the indirect tensile strength of the specimens treated by means of 15 days of immersion in a thermostatic bath at 25 °C (ITS_{wet}) and untreated (ITS_{dry}), respectively. The ITS_{dry} and the TSR values of the mixtures prepared with the optimum bitumen content should result higher than 0.6 MPa and 75%, respectively, in order to fulfill the CIRS acceptance requisites.

For each of the 6 asphalt concretes, different mixtures were analyzed, in which, having defined the type of aggregate and grading composition, the amounts of binder were varied at intervals of 0.25% on the weight of the aggregate. To support the phase of mix design, four gyratory specimens were produced for each mix. The results of the mix design procedure are summarized in Table 4, which details for each material: OBC, Air Voids (Va) at 10, 100 and 180 revs, bulk density at 100 revs, ITS for dry and wet conditions.

Table 4. Mix design results.

Mixtures	OBC (%)	Va @ 10 res (%)	Va @ 100 res (%)	Va @ 180 res (%)	Bulk density (g/cm^3)	ITS dry (MPa)	ITS wet (MPa)	TSR (%)
S0R0	4.75	13.24	4.96	2.95	2.410	1.62	1.35	83
S0R2	3.90	13.09	4.89	2.89	2.433	1.88	1.61	86
S0R4	3.00	12.91	4.78	2.81	2.469	2.35	2.06	88
S3R0	4.85	12.20	4.27	2.48	2.626	1.74	1.46	84
S3R2	4.00	12.02	4.18	2.39	2.661	1.90	1.73	91
S3R4	3.10	11.88	4.03	2.27	2.714	2.18	2.01	92

The total bitumen content resulted to be within the typical range of base courses asphalt concretes, namely 4.5–5.5% by weight of the aggregates [12, 13], for all the mixes. As it was expected, the greater the RAP content, the lower the virgin bitumen content that is necessary in order to optimize the mixture made with RAP aggregate.

The bulk density of the mixtures was obviously heavily affected by the integration of the EAF slags in the aggregate skeleton, given the high grain densities of the steel slag particles.

The Air Voids requisites prescribed by CIRS mix design procedure, at 10, 100 and 180 revs, were completely satisfied, for all the mixes. The ITS values in dry conditions, resulted largely above the CIRS acceptance requisite (at least more than double) for all the asphalt concretes, as well as the ITS on wet samples, always higher than the 75% of the correspondent ITS dry value (up to 92%, depending on the mix composition), so coming to the conclusion of the acceptability of these base courses asphalt concretes.

The mixes with marginal aggregates showed improved ITS values, with respect to the reference limestone-only asphalt concrete (S0R0), varying from 7% to 53%, depending on the dry/wet condition and on the mix composition; the mixture made with 30% EAF slag and 40% RAP (S3/R4) was characterized by the highest mechanical strength and moisture damage resistance. The rough texture of the steel slags, as well as the presence of a bitumen film on the RAP particles (aged binder), enable a strong adhesion between the new bitumen added to the mixes and the marginal aggregates grains, that allows, to the optimized asphalt concretes, to achieve consistent mechanical strength. Moreover, the greater the RAP content, the higher the ITS value.

4 PERFORMANCE TEST PROGRAMME

Creep Recovery Tests (CRT, BS 598 Standard) and Repeated Load Axial Tests (RLAT, BS 226 Standard) at 40°C, as well as Wheel Tracking Tests (WTT, EN 12697-22 Standard, procedure B) at 60°C, have been performed on the six asphalt concretes optimized in the mix design procedure, in order to investigate the permanent deformation resistance of the mixes at high temperature. The CRTs were conducted setting both the loading time and rest period at 3600 s, respectively, and with a constant uniaxial stress equal to 100 kPa. The same stress level (100 kPa) have been applied also for the cyclic uniaxial stress in the RLAT, for 3600 pulses, with loading and unloading times were fixed at 1 s. Both the CRTs and RLATs were performed on cylindrical specimens prepared by gyratory compaction, whereas for the WTT, 300 mm × 400 mm × 50 mm slabs produced by a laboratory compacting roller, were used.

4.1 *Permanent deformation test results and discussion*

Figures 3–5 report the evolution of the permanent deformation curves during the tests conducted (CRT, RLAT and WTT respectively); the evolution of the permanent deformation, for all the mixes, is that typical of visco-elasto-plastic materials: a first phase with a decreasing creep rate, and a second with a constant creep rate can be clearly distinguished. For the CRT it is also possible to appreciate the recovery of the visco-elastic deformation after unloading.

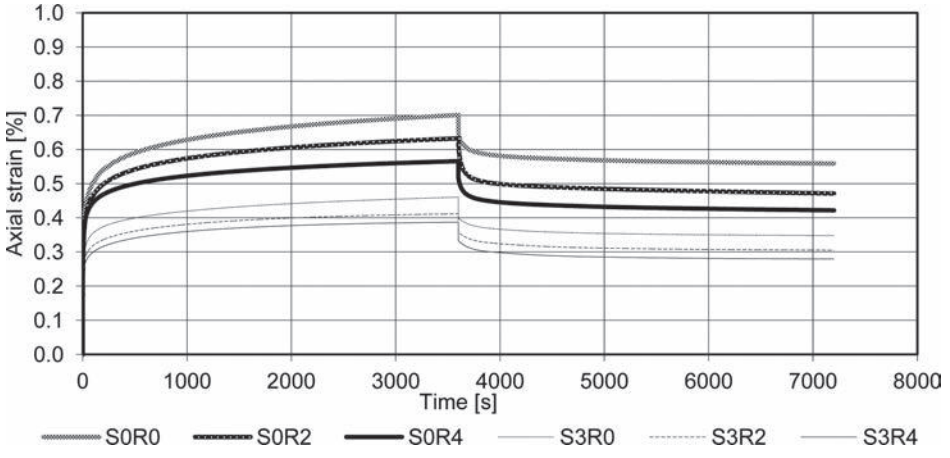

Figure 3. Permanent deformation curves by CRT.

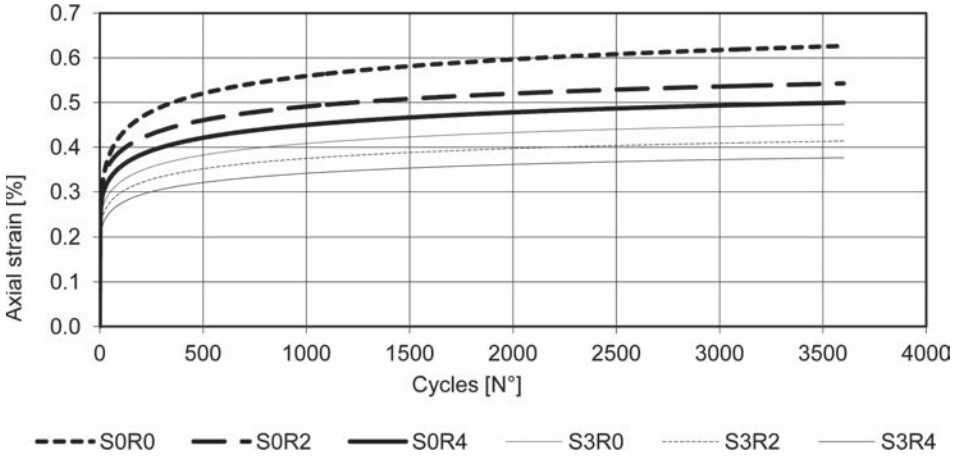

Figure 4. Permanent deformation curves by RLAT.

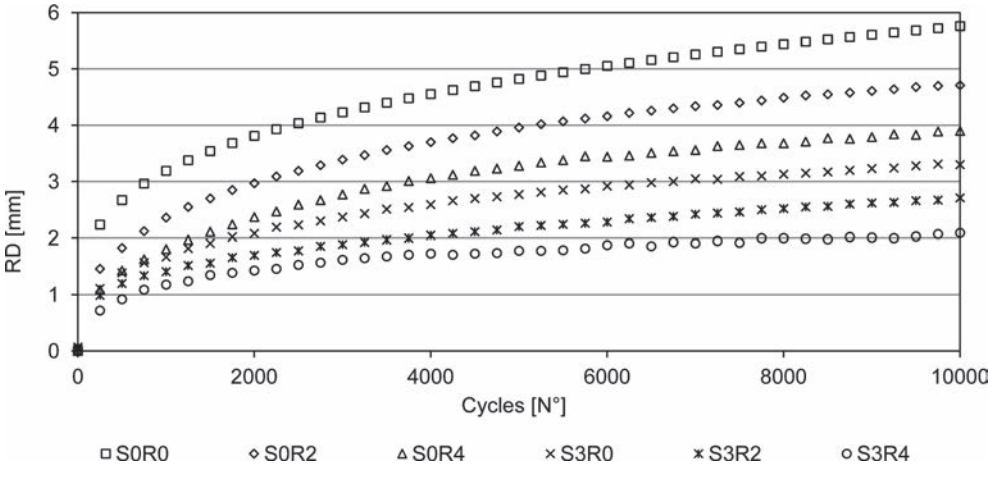

Figure 5. Permanent deformation curves by WTT.

Table 5 reports the permanent deformation for CRT and RLAT (unitary axial strain—ε_p), as well as for WTT (Rut Depth—RD), for each mixture; the Creep rate (for CRT and RLAT) and the Wheel Tracking Slope (for WTT) are also indicated. The Creep rate has been computed as the ratio between the cumulative axial strain in a defined range of load applications and the width of the interval (evaluated between 1,800 and 3,600 s for CRT; 1,800 and 3,600 cycles for RLAT). Similarly, the Wheel Tracking Slope (WTS) was determined as the ratio between the cumulative rut depth in a defined range of load applications and the width of such interval (evaluated between 5,000 and 10,000 cycles in the test period).

Given that the Standards in force provide no reference for defining the minimum value required for mixture's acceptance and that the permanent deformation tests are strongly influenced by the compaction technique, the results have to be evaluated in comparative rather than absolute terms, in order to identify, primarily, the influence of the marginal aggregates.

The asphalt concretes made with recycled aggregates showed lower permanent deformations, as well as lower Creep rate and WTS, than the mixtures with limestone, in all the tests (CRT, RLAT, WTT). The polyhedric shape, high angularity and rough texture of the EAF slag enhances the high internal friction and therefore a better densification condition of the base courses asphalt concretes, with a benefit for the resistance to permanent deformations. The integration of the RAP in the aggregate skeleton of the mixtures allows to substantially reduce the magnitude of the permanent deformations, as observed in all the tests, especially for the highest RAP content, namely 40%. The permanent deformation reduction of 33%

Table 5. Permanent deformation test results.

Mixtures	ε_p CRT [%]	Creep rate—CRT [microstrain/sec]	ε_p RLAT [%]	Creep rate—RLAT [microstrain/10^3 cycles]	RD [mm]	WTS [mm/(10^3 cycles)]
S0R0	0.559	0.022	0.626	0.020	5.77	0.198
S0R2	0.471	0.018	0.543	0.015	4.74	0.150
S0R4	0.422	0.013	0.500	0.014	3.88	0.124
S3R0	0.348	0.012	0.451	0.012	3.31	0.106
S3R2	0.305	0.008	0.414	0.011	2.70	0.102
S3R4	0.279	0.007	0.376	0.010	2.07	0.062

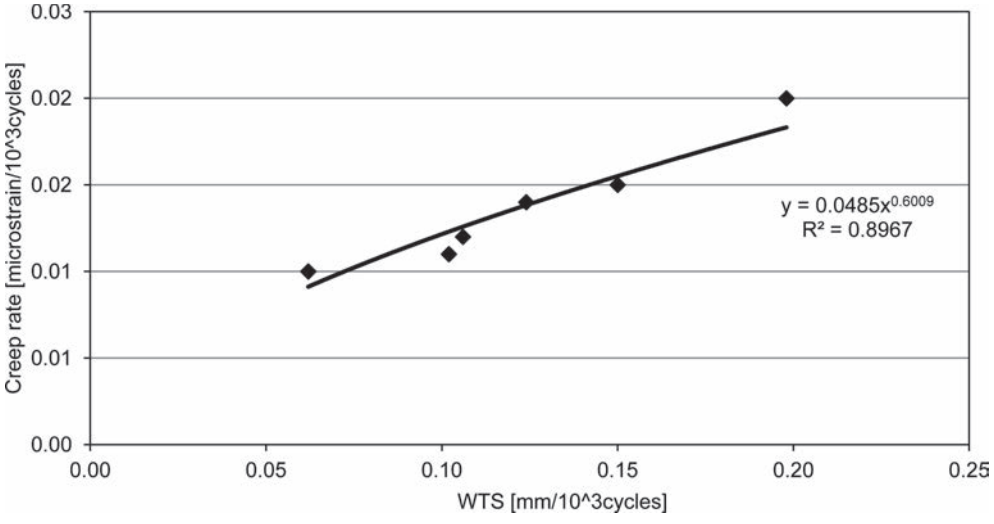

Figure 6. Correlation between the WTS and the Creep rate by RLAT.

recorded for the mix S0R4, with respect to the mix S0R0, is further increased for the mix S3R4 containing 30% EAF slags; in this case the rut depth recorded is less than half and the wheel tracking slope is about a third.

Even if Ozen et al. [14] have found a poor correlation between RLAT at 40°C and LCPC wheel tracking test at 60°C, for the mixtures investigated in this study it has been verified a satisfactory correlation between the Creep rate of the RLAT and the Wheel Tracking Slope of the WTT (Fig. 6), so confirming previous results of others researchers [11]. The data interpolation, by means a power function, gives good value of the coefficient of determination R^2 (0.89) and demonstrates a reasonable congruence between RLAT and WTT analysis, in spite of different test temperatures and stress level involved and the absence of confinement in the RLAT protocol adopted. However, further research and a larger data set are needed in order to formulate a conclusive judgment about the possibility to identify an effective correlation between RLAT and WTT data.

5 CONCLUSIONS

The marginal aggregates studied have shown physical-mechanical characteristics substantially equivalent to those of natural stone aggregates usually used in transport infrastructure construction and no hazardous leaching behaviour.

The experimental results are extremely satisfactory for all the mixtures made with marginal aggregates, especially for those prepared with RAP, in terms of both road technical acceptance requisites (Air Voids, ITS), and permanent deformation resistance.

The limited axial deformation registered during the Creep Recovery Tests and Repeated Load Axial Tests, lead to the conclusion that the RAP mixes have a little aptitude to develop excessive permanent deformations.

The Wheel Tracking Test, representative of loading conditions with slow channelled traffic at high temperature, has furtherly confirmed an extremely positive overall performance of the mixtures, in terms of rutting resistance.

The mixes with RAP and steel slags were characterized by low water damage, thus demonstrating a good durability.

Of the five mixes with marginal aggregates, S3R4, made with 30% EAF steel slags and 40% RAP, showed to be the best in all the mechanical and performance tests.

REFERENCES

[1] Ahmedzade, P., Tigdemir, M. and Kalyoncuoglu, S.F. Laboratory investigation of the properties of asphalt concrete mixtures modified with TOP-SBS, Construction and Building Materials, 21, pp. 626–633. 2007.

[2] Abo-Qudais, S. and Al-Shweily, H. Effect of aggregate properties on asphalt mixtures stripping and creep behaviour, Construction and Building Materials, 21, pp. 1886–1898. 2007.

[3] Shen, D.H., Kuo, M.F. and Du, J.C. Properties of gap-aggregate gradation asphalt mixture and permanent deformation, Construction and Building Materials, 19, pp. 147–153. 2005.

[4] Sorlini, S., Sanzeni, A. and Rondi, L. Reuse of steel slag in bituminous paving mixtures, Journal of Hazardous Materials, 209–210, pp. 84–91. 2012.

[5] Liapis, I. and Likoydis, S. Use of electric arc furnace slag in thin skid-resistant surfacing, Procedia—Social and Behavioral Sciences, 48, pp. 907–918. 2012.

[6] Chen, J.S., Huang, C.C., Chu, P.Y. and Lin, K.Y. Engineering characterization of recycled asphalt concrete and aged bitumen mixed recycling agent, Journal of Materials Science, 42, pp. 9867–9876. 2007.

[7] Xiao, F. and Amirkhanian, S.N. Laboratory investigation of utilizing high percentage of RAP in rubberized asphalt mixture, Materials and Structures, 43, pp. 223–233. 2010.

[8] Pasetto, M. and Baldo, N. Experimental Evaluation of High Performance Base course and Road Base Asphalt Concrete with Electric Arc Furnace Steel Slags, Journal of Hazardous Materials, 181, pp. 938–948. 2010.

[9] Pasetto, M. and Baldo, N. Mix design and Performance Analysis of Asphalt Concretes with Electric Arc Furnace Slag, Construction and Building Materials, 25, pp. 3458–3468. 2011.
[10] Pasetto, M. and Baldo, N. Performance comparative analysis of stone mastic asphalt with electric arc furnace steel slag: a laboratory evaluation, Materials and Structures, 45, pp. 411–424. 2012.
[11] Pasetto, M. and Baldo, N. Resistance to permanent deformation of road and airport high performance asphalt concrete base courses, Advanced Materials Research, 723, pp. 494–502. 2013.
[12] SITEB, Capitolato d'appalto per pavimentazioni stradali con bitume modificato, Roma, 2000 [in Italian].
[13] Ministero delle Infrastrutture e dei Trasporti—CIRS, Norme tecniche di tipo prestazionale per capitolati speciali d'appalto, Roma, 2001 [in Italian].
[14] Ozen, H., Aksoy, A., Tayfur, S. and Celik, F. Laboratory performance comparison of the elastomer-modified asphalt mixtures, Construction and Building Materials, 43, pp. 1270–1277. 2008.

Asphalt Pavements – Kim (Ed)
© 2014 Taylor & Francis Group, London, ISBN 978-1-138-02693-3

Effect of asphalt binder content and grade on transverse field cracking performance of Minnesota's Roadways

Eshan V. Dave, Chelsea Hanson & Benjamin Helmer
Department of Civil Engineering, University of Minnesota Duluth, Duluth, MN, USA

Luke Johanneck
Office of Materials and Road Research, Minnesota Department of Transportation, Minnesota, MN, USA

ABSTRACT: Cracking is a major distress mechanism in asphalt pavements. Thermal cracking is especially prevalent in Northern Minnesota and other areas with cold climates. Developing asphalt mix designs that are more resistant to cracking distresses is necessary to reduce maintenance and rehabilitation expenditures. The present study involves analysis of over 32,000 asphalt mixes and approximately 12,000 field sections available from Minnesota Department of Transportation (MnDOT).

The main objective of this work is to identify the effects of asphalt binder content and binder grade on the actual field cracking performance. A comprehensive database has been developed that includes mix design information (design traffic level, mix size, binder type, wear versus non-wear course), mix volumetrics and gradation (air voids, voids in mineral aggregates, voids filled with asphalt, adjusted asphalt film thickness, percent passing on control sieves, recycled fractions), and actual field performance data from MnDOT's pavement management system.

This database has made it possible to quantify the effects of binder content and grade on the actual field performance. A series of statistical tests were conducted to determine if significant relationships exist between the binder content and grade, and the field cracking performance. The results show that both binder content and grade have a significant effect on the transverse cracking of pavements and for Minnesota the PG XX-34 grade may be better suited than the PG XX-28 binder grade.

Keywords: Thermal Cracking, mix design parameters, comprehensive database, mix acceptance criteria, binder content, PG grade

1 INTRODUCTION

One of the main causes of asphalt pavement degradation in cold climate regions, specifically in the northern United States and Canada, is transverse cracking [1,2]. This is caused by the pavements contracting when they are subjected to low temperatures. The asphalt concrete also becomes brittle as well during the cooling process. The combination of both the thermal contraction and embrittlement of the asphalt mixture lead to transverse cracks forming and propagating within the pavement structure. These cracks lead to decreased serviceability of the pavement to the public. Current asphalt mix design specifications are highly based on mix volumetric measures and require no laboratory performance test as a means to predict field cracking performance of asphalt mix designs [3]. A laboratory performance test to supplement existing asphalt mix design specifications is needed to improve the performance of asphalt pavements throughout their lifetime. Pavement performance data has also been used as a means to improve ways of predicting field performance of asphalt pavements and refining the mix design process [4,5].

Analysis of the effect of mix design parameters (asphalt film thickness, voids in mineral aggregate, asphalt binder grade) on field cracking performance is also an important aspect of improving asphalt pavement performance. Creating a comprehensive database that includes both mix design information and pavement performance data will allow for continued analysis of mix design parameter effects on asphalt pavement field performance in the future. This continued improvement will refine the mix design process and result in pavements with decreased transverse cracking.

2 DATA SOURCES

The data sources that were combined to construct a comprehensive database of asphalt mix design parameters and pavement field cracking performance were obtained from MnDOT's Office of Materials and Road Research (OM&RR). The data was received in the form of Microsoft Excel spreadsheets. Four primary data sources were available. These data sources are comprised of:

1. Mixture Design Reports (MDR)
2. Laboratory Information Management Systems (LIMS)
3. Pavement Management Systems (PMS).

2.1 *Data mapping*

The computer software program used in this study to compile and build the comprehensive database of both mix design parameters and field performance data was Microsoft Access. This software program allows for importing different sets of data, such as Microsoft Excel Spreadsheets, and combining or "linking" the multiple data sets together into one comprehensive database. The five data sources described previously are imported as "Tables" into Access. The combination of these tables into one Access file creates a comprehensive database. This newly formed database allows for vital information from different sources to be combined together in one list. This list of data can then be used for analysis. For this study, asphalt mix design parameters from the LIMS data source were combined with the field performance data for conducting statistical analysis.

The "linking" of data sources will be referred to as "data mapping" throughout the rest of the report. The records that are common across various data sets are used for "linking" them. These common records are referred to as "mapping parameters". These are the means by which multiple data sources are combined together to allow for specific information to be extracted from each source. They also allow for traversing throughout multiple data sets when looking for specific mix parameters or field performance quantities. Searches conducted within Access for certain parameters are referred to as queries. These mapping parameters can be seen in Table 1.

The focus of this paper will be the field cracking performance of asphalt pavements and the effect of mix parameters on this distress measure. A description of the mapping parameters used to extract this data can be found in the following text of the report.

Table 1. Mapping parameters related to different data sources.

Data source	Mapping parameter
Material Data Records (MDR)	MDR, Mix Design
LIMS Database	Project Number (SP), MDR, Mix Design
Pavement Management Systems (PMS)	Route Type, Route Number, Year, Pavement Section Reference Points
Geographic Information Systems (GIS)	Route Type, Route Number, Year, Pavement Section Reference Points, Project Number (SP)

3 FIELD CRACKING PERFORMANCE

The field cracking performance was expressed in the form of twelve different measures of transverse cracking. The scope of this paper is limited to the transverse cracking amounts.

3.1 *Calculation of field cracking performance measures*

The PMS data source contains all of the field performance (distress) data, specifically cracking performance of different pavement sections. Information pertaining to route types (Interstates, State highways, and US highways) and route numbers are included in this data source which contains 188 unique routes. The distress information includes transverse cracking, longitudinal cracking, rutting, raveling, patching, and longitudinal joint deterioration. Due to the main focus of this study pertaining to cracking of asphalt pavements, only transverse and longitudinal cracking were included in the statistical analysis phase, and only the transverse cracking results are included in this report. Inclusion of this data source into the database allows for the ability to track the effect of different mix design parameters on field performance of the pavement over several years. This data contains information recorded between year 2004 and 2011.

The transverse cracking data in the PMS data is collected based on the severity of the cracks, namely low, medium and high. For each severity level, the data is reported in terms of percent cracking (% cracking). Percent cracking is calculated as 2 times the number of cracks per 500 feet length of the survey section. For purposes of conducting a statistical analysis between amount of cracking and laboratory tests as well as asphalt mix parameters, a number of measures of field cracking performances can be calculated. In this study, the researchers looked at transverse cracking amounts in two primary ways: (1) total cracking; and, (2) total weighted cracking. Total cracking is sum total of low, medium and high severity cracks, whereas weighted cracking amount is arbitrary cracking amount with weight factors of 1, 2 and 4 applied to low, medium and high severity crack amounts.

The total cracking and total weighted cracking amounts for a given PMS section for each year of distress survey can be used to calculate additional cracking measures that are representative of field cracking performance. This paper includes the results pertaining only to transverse cracking rates and results. These measures for transverse cracking are described in Table 2.

3.2 *Data mapping with transverse field cracking*

For cracking distress data that was combined and analysed with mix design information, the PMS data source needed to contain a mapping parameter that is common with the LIMS data source. The PMS data source contains distress information, it is the only source of field cracking data in the comprehensive database. Without a common mapping parameter between the LIMS and PMS data sources, no analysis of cracking data with mix parameters could be conducted. An illustration depicting this linking of mapping parameters together is seen in Figure 1.

The combining of the PMS and GIS data made it possible to pair and extract transverse cracking distress data with its respective project number. This project number then was used to link this data with mix parameter data, which was needed to statistically analyse and investigate any relationships between the transverse cracking amounts and mix design parameters. This is shown in Figure 2.

3.3 *Statistical analysis and presentation of results*

Once the data was exported from the database, it was able to be input to the SAS software. The analysis that was run on the data was an LS Means analysis. This type of analysis allows for investigating effects of multiple variables. An LS Means analysis was chosen as the proper analysis to run on the selected data. The null hypothesis in the LS Means analysis

Table 2. Field cracking measures.

Measure	Description	Unit
Maximum Total Transverse Cracking Amount (MTCTotal)	Maximum transverse cracking amount (low + medium + high) of all survey years for a pavement section normalized against number of years for which pavement section has been in service.	% cracking/year
Maximum Total Weighted Transverse Cracking Amount (MTCWeighted)	Maximum weighted transverse cracking amount (low + 2*medium + 4*high)/6 of all survey years for a pavement section normalized against number of years for which pavement section has been in service.	% cracking/year
Maximum Total Transverse Cracking Rate (MTCRTotal)	Maximum increase in total transverse cracking amounts (low + medium + high) between any two consecutive years of service.	% cracking/year
Maximum Total Weighted Transverse Cracking Rate (MTCRWeighted)	Maximum increase in total weighted transverse cracking amounts (low + 2*medium + 4*high)/6 between any two consecutive years of service.	% cracking/year
Average Total Transverse Cracking Rate (ATCTotal)	Difference between maximum and minimum total transverse cracking amounts (low + medium + high) divided by number of years that pavement section has been in service.	% cracking/year
Average Weighted Total Transverse Cracking Rate (ATCWeighted)	Difference between maximum and minimum total weighted transverse cracking amounts (low + 2*medium + 4*high)/6 divided by number of years that pavement section has been in service.	% cracking/year

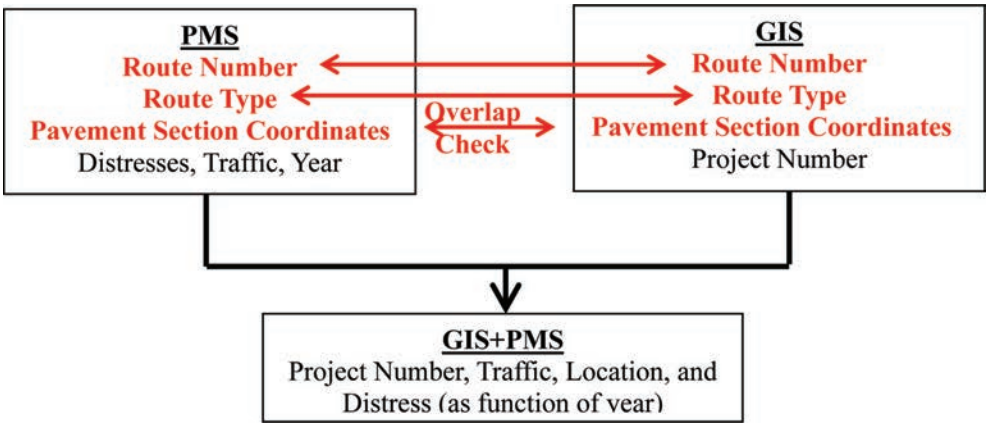

Figure 1. Linking and combining of PMS and GIS data sets in microsoft access.

is that the binder content and/or binder grade have no effect on the field cracking performance indicator (such as, MTCTotal). A p-value of > 0.05 indicates it can be said with 95% confidence that the null hypothesis is correct. A p-value of < 0.05 indicates that it can be said with 95% confidence that the null hypothesis is not true, and it can be rejected. This means that the binder content and/or binder grade does have a statistically significant relationship with field cracking performance.

To further investigate the effects of binder content and/or binder grade on the extent of transverse cracking, the data was converted to a normalized frequency. This was accomplished by first distributing the binder content in discrete intervals. Next, the data for all

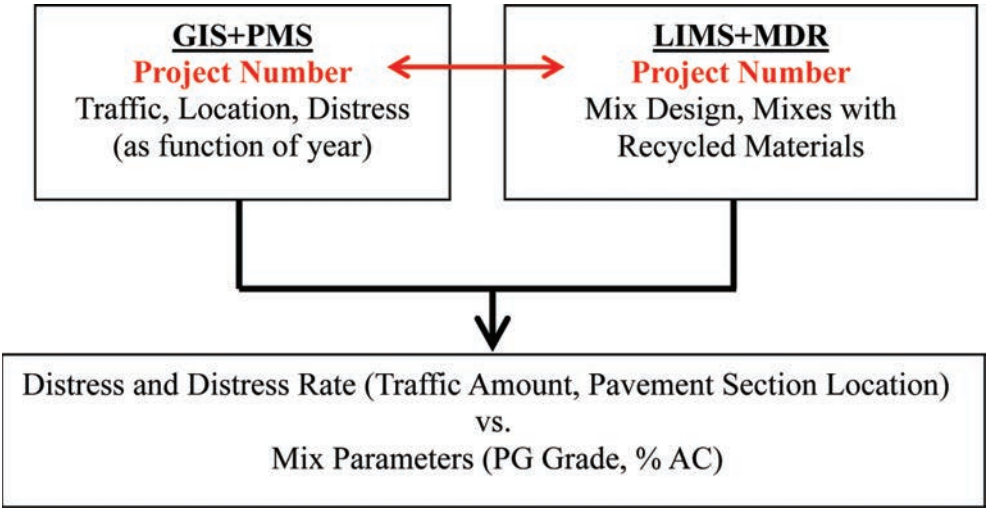

Figure 2. Linking and combining of PMS and GIS data sets to mix design parameter data.

pavement sections in each interval of binder content or each binder grade were analysed to determine the percent of sections that have no cracking (MTCWeighted of 0%/500 ft./year) and ones with cracking at 10, 20, 30, 40 and 50%/500 ft./year respectively. The database consists of very few pavements with cracking amounts above 50%, therefore cracking amounts above this percentage were not considered. Thereafter, the normalized frequencies for each of the cracking amounts were plotted for each interval of binder content and each binder grade.

4 TRANSVERSE CRACKING AND MIX DESIGN PARAMETER ANALYSIS

4.1 *Asphalt binder amount (percent binder)*

The asphalt binder contents were determined using chemical extraction and ignition oven methods. The binder contents were then used to determine their effects on the measures of transverse cracking. The statistical analysis for asphalt binder contents determined using both methods are presented in Table 3 and Table 4. The results show that irrespective of the measurement method, the asphalt binder content has significant effect on the amount of field cracking.

In order to further evaluate this effect, the MTCWeighted data was analyzed to determine the normalized frequencies. The normalized frequencies of the transverse cracking amounts for various ranges of asphalt binder contents are plotted in Figure 3 for chemical extraction and Figure 4 for ignition oven methods. In general, the results show a greater percent of pavements are free of transverse cracks for mixes with higher asphalt binder content. The data for mixes with greater than 6.0% asphalt binder content as determined using chemical extraction is the only outlier. The plots also show that the number of pavements with 20, 30 and 40%/500 ft./year cracking increase as the amount of asphalt binder in mixes decrease. Specifically, the asphalt mixes with binder contents between 4.0 and 4.5% represent almost 10% more pavements with 20 and 30%/500 ft./year cracking as compared to other mixes.

4.2 *Asphalt binder grade (PG, PGLT and PG spread)*

The asphalt binder grade (PG), the low temperature grading of the binder (PGLT) and the spread between the high and low temperature grading (PG Spread) information was used

Table 3. Effect of asphalt binder content (chemical extraction) on measures of maximum field cracking.

Cracking measure	*p*-value	Field cracking is related to percent binder?
MTCWeighted	<0.0001	Yes
MTCTotal	<0.0001	Yes
MTCRTotal	0.0005	Yes
MTCRWeighted	<0.0001	Yes

Table 4. Effect of asphalt binder content (ignition oven) on measures of maximum field cracking.

Cracking measure	*p*-value	Field cracking is related to percent binder?
MTCWeighted	<0.0001	Yes
MTCTotal	<0.0001	Yes
MTCRTotal	<0.0001	Yes
MTCRWeighted	<0.0001	Yes

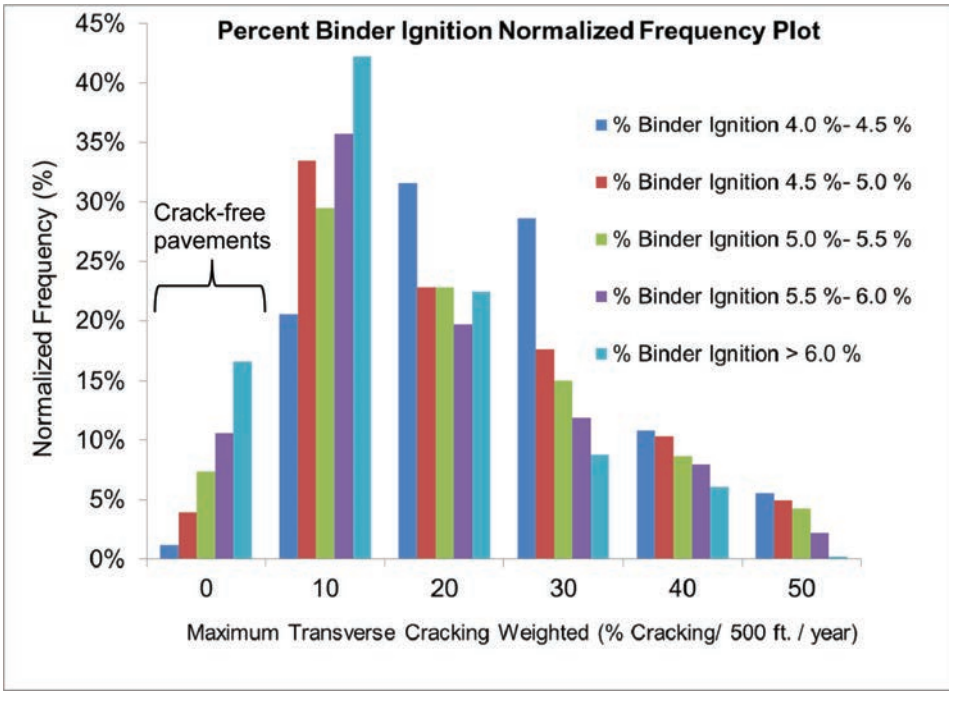

Figure 3. Normalized frequency plot of asphalt binder content (chemical extraction) with various ranges of weighted maximum transverse cracking amounts (MTCWeighted).

to conduct a statistical analysis. The results from the statistical analysis conducted to determine whether different field cracking measures depend on the asphalt binder grade and its derivatives are presented in Table 5, Table 6, and Table 7. The results show that the asphalt binder grade has a significant effect on the amounts and rates of transverse cracking.

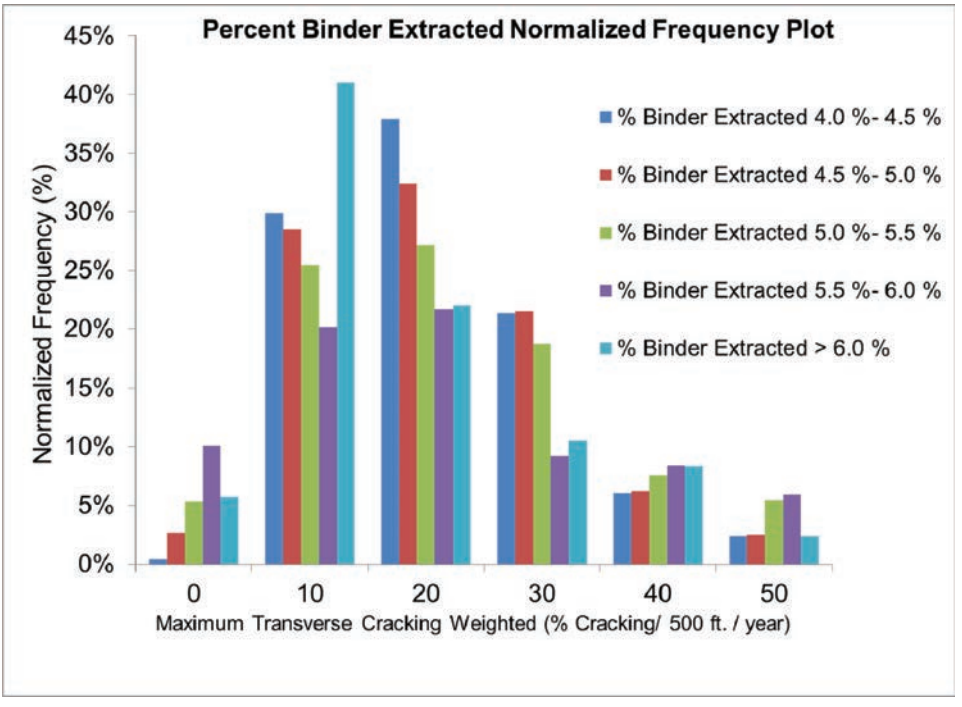

Figure 4. Normalized frequency plot of asphalt binder content (ignition oven) with various ranges of weighted maximum transverse cracking amounts (MTCWeighted).

Table 5. Effect of asphalt binder grade (PG) on measures of maximum field cracking.

Cracking measure	*p*-value	Field cracking is related to PG?
MTCWeighted	<0.0001	Yes
MTCTotal	<0.0001	Yes
MTCRTotal	<0.0001	Yes
MTCRWeighted	<0.0001	Yes

Table 6. Effect of asphalt binder low temperature grade (PGLT) on measures of maximum field cracking.

Cracking measure	*p*-value	Field cracking is related to PGLT?
MTCWeighted	<0.0001	Yes
MTCTotal	<0.0001	Yes
MTCRTotal	<0.0001	Yes
MTCRWeighted	<0.0001	Yes

Similar to analysis of previous mix parameters, in order to determine the effects of asphalt binder grade on the amount of cracking, the PGLT data was used to generate normalized frequencies of the maximum weighted transverse cracking (MTCWeighted). The frequencies are plotted for PGLT of –28 and –34 °C. These two were selected as a majority of pavements

Table 7. Effect of spread in asphalt binder grade (PG Spread) on measures of maximum field cracking.

Cracking measure	*p*-value	Field cracking is related to PG Spread?
MTCWeighted	<0.0001	Yes
MTCTotal	<0.0001	Yes
MTCRTotal	<0.0001	Yes
MTCRWeighted	<0.0001	Yes

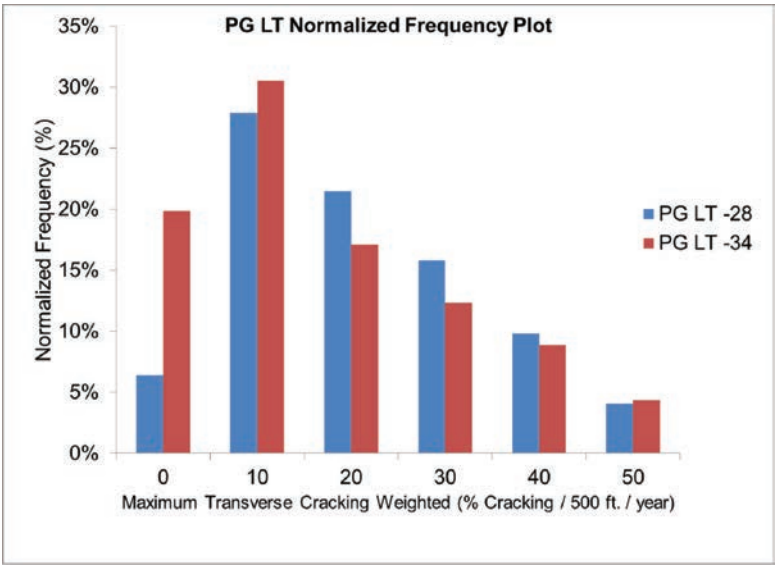

Figure 5. Normalized frequency plot of asphalt binder low temperature grade (PGLT) with various ranges of weighted maximum transverse cracking amounts (MTCWeighted).

in the database represent these types of binders. The results are plotted in Figure 5. The results show that a significantly greater amount of pavements are crack free when containing mix with PGLT of -34. Furthermore, a larger number of pavements with higher transverse cracking amounts (20, 30 and 40%/500 ft./year) have mixes with PGLT -28 binder.

5 CONCLUSIONS AND RECOMMENDATIONS

This study undertook task of combining various data sources corresponding to the asphalt mix designs and pavement performance that are available to Minnesota Department of Transportation into a single comprehensive database. The findings from this study resulted in several conclusions regarding the effects of mix design parameters on field cracking performance of asphalt pavements. The focus of this paper is on the evaluation of the effects of asphalt binder content and the asphalt grade on transverse cracking performance of the highways.

The key conclusions that can be drawn from the results presented herein are:

- The amount of asphalt binder, both calculated by means of chemical extraction and ignition oven, showed significant effect on transverse field cracking performance.
  - Mixes with higher asphalt contents corresponded to a greater percent of pavements with low transverse cracking. Specifically with pavements containing 20, 30, or 40 (%/ 500 ft./year), the cracking amounts are higher for with mixes containing low amounts of asphalt binder.

- The PG binder grade, PGLT, and PG Spread do have an effect on transverse cracking amounts.
  - Mixes with PGLT -34 have higher amounts of transverse crack free pavements as compared the mixes with PGLT -28. A higher amount of 20, 30, and 40 (%/ 500 ft./ year) cracking occurred for mixes with PGLT -28 binder.
- Asphalt binder grade has a significant effect on the pavement cracking performance. Mixes containing -34 asphalt binders have significantly greater amount of crack-free pavements as compared to mixes containing -28 binders. Fewer percent of pavements with significant amounts of transverse cracking are represented by mixes with -34 binder grades as compared to those with -28 binder grades.
- The amount of asphalt binder has a significant effect on field cracking performance. The mixes with higher asphalt content showed lower amounts of cracking.

Generating a comprehensive database and the subsequent statistical analysis in context of field cracking performance helped make several observations regarding future recommendations. The key recommendations from the research efforts of this study are as follows:

- The asphalt binder amount and grade play an important role in the cracking performance of bituminous pavements and overlays. The asphalt binder grade recommendations along with the potential for use of a minimum asphalt binder amount in the specifications should be reevaluated. The future tasks of the current project will provide additional information on this topic through field and laboratory evaluation of several pavement sections.
- The data analysis presented herein did not normalize the field cracking performance measured against the amount of traffic. The future data analysis should consider this effect to determine if the cracking amounts and rates are significantly affected by traffic level and whether the effects of mix design parameters on cracking are altered by the effects of traffic.

REFERENCES

[1] M. Marasteanu, S. Dai, J. Labuz and X. Li, "Determining the Low-Temperature Fracture Toughness of Asphalt Mixtures," *Transportation Reserach Record 1789,* 2002.

[2] M. Marasteanu, K.H. Moon, E.Z. Teshale, A.C. Falchetto, M. Turos, W. Buttlar, E. Dave, G. Paulino, S. Ahmed, S. Leon, A. Braham, B. Behnia, H. Bahia, H. Tabatabaee, R. Velasquez, A. Arshadi, S. Puchalski, S. Mangiafico, C. Williams, A. Buss, J. Bausano, A. Kvasnak, "Investigation of Low Temperature Cracking in Asphalt Pavements," National Pooled Fund Study—Phase II, Report No. MN/RC 2012-23, Minnesota Department of Transportation, August 2012.

[3] T. Bennert, *Implementation of Performance-Based HMA Mixtures in NJ.,* Presentation at the Annual Meeting of the Association of Asphalt Paving Technologists, Tampa, Florida, 2011.

[4] A. Hanna, "Sensitivity Evaluation of MEPDG Performance Prediction," National Cooperative Highway Research Program, Report No. 372, 2013.

[5] R. Bonaquist, "HMA Fatigue and Low Temperature Properties to Support MEPDG," Wisconsin Highway Research Program for the Wisconsin Department of Transportation, Madison, WI, 2011.

This page intentionally left blank

Warm mix asphalt technologies—II

This page intentionally left blank

Asphalt Pavements – Kim (Ed)
© 2014 Taylor & Francis Group, London, ISBN 978-1-138-02693-3

Temperature effects on Warm Mix Asphalt performance

Venon Jalali, James R.A. Grenfell & Andrew Dawson
Nottingham Transportation Engineering Centre, Department of Civil Engineering, The University of Nottingham, University Park, Nottingham, UK

ABSTRACT: Over the past few years, several Warm Mix Asphalt technologies have been developed to help lower asphalt production temperatures by up to 30°C. As part of this research, two different technologies were investigated; a wax additive using Sasobit and a chemical additive using Rediset LQ. The rheological behaviour of the base binders and the base binders with each additive was investigated over a range of temperatures using both a Dynamic Shear Rheometer (DSR) at lower temperatures and a rotational viscometer at higher temperatures. Then by performing the Dynamic Contact Angle (DCA) test using the Wilhelmy Plate apparatus, the effect of these additives was looked at in terms of the Surface Energy components of the binders.

Keywords: Warm Mix Asphalt (WMA); compaction temperature; rheology; surface energy

1 INTRODUCTION

Warm Mix Asphalt (WMA) refers to bituminous mixtures which are produced at temperatures approximately 25°C to 55°C lower than the typical production temperature of Hot Mix Asphalt (HMA) for the purposes of energy saving and lowering greenhouse gas emissions. However, as a replacement material for conventional HMA, WMA should have similar strength, durability and performance characteristics [1].

During the mixing, delivery or compaction processes, if the mixture's temperature drops below the minimum allowable production temperature at which adequate compaction can be achieved, then serious problems are expected. In the case of WMA mixtures, the effects of temperature decline on the properties of mixture may be more complicated than in HMA due to the presence of additives. This can refer to several factors such as the lower level of ageing in WMA binder due to the lower production temperatures, the effect of additives on the rheological, physical and mechanical characteristics of the binders, binder-aggregate adhesion properties and subsequently, the resultant mixture mechanical performance and properties [2].

The aim of this research is to study the effects and implications of temperature decline during mixing, delivery, placement and compaction phases on the mechanical performance of Warm Mix Asphalt along with the determination of the fundamental reasons for such performance changes.

2 MATERIALS IN USE

2.1 *Bitumen modifiers*

2.1.1 *Sasobit®*

Sasobit is a product of the Sasol Wax Company in South Africa. It is a crystalline, long chain aliphatic polymethylene hydrocarbon wax with a general formula of C_nH_{2n+2} whose carbon

chain length ranges from C_{45} to C_{100} plus. Sasobit results from coal gasification and is a by-product from the synthetic petrol production process called Fischer-Tropsch. Having a melting point of about 100°C, it can be totally dissolved in bitumen at above 115°C. Sasobit can be either in the form of a white powder or granules pills [3,4].

It is said that when added to the bitumen for producing WMA mixtures, it decreases the viscosity and improves the lubrication, both of which result in improving the mixture workability and compactability at temperatures lower than HMA [1,5]. According to the research of Liu et al. [5] adding 3% Sasobit to the binder can reduce the asphalt production temperature by 15°C.

When Sasobit cools down, it begins to crystallise at 110°C and below its congealing point, it forms regularly distributed, microscopic, stick-shaped particles. Such a crystallisation results in increasing the stiffness of the binder and the resistance against deformation. At service temperatures, Sasobit forms a lattice structure in the binder that provides stability for the mixture [6,7].

2.1.2 *Rediset® LQ 1102 CE*

Rediset LQ is a chemical Warm Mix Asphalt liquid additive which has recently been developed by AkzoNobel. It is said that it allows the production and compaction of asphalt pavements at temperatures typically 20 to 30°C lower than conventional HMA. The surfactants in Rediset LQ modify the properties of the binder in such a way that readily allows it to bond with the active sites on the aggregate surface. The surfactants also reduce the surface tension of the asphalt binder, which enables efficient coating of asphalt binder on the aggregate surface. This property enables the binder to readily coat the aggregate and eventually increases the workability of the mix and allows the mix to be more compactable at lower temperatures [8]. According to the producer, it will not change the penetration grade of the binder.

2.2 *Pure bitumen and modified binders*

The main neat binder used in this research was bitumen 70/100 pen made from blending 53.4% bitumen 160/220 pen with 46.6% bitumen 30/45 pen. The base neat binders which were used only in the case of supplementary tests were a 160/220 pen and 30/45 pen bitumen. The modified binders in the current research include Sasobit-modified and Rediset LQ-modified binders each of which have been produced by adding three different dosages of Sasobit (2, 3 and 10% of the weight of binder) and Rediset LQ (0.4, 0.5 and 0.6% of the weight of the binder) respectively to each of the three different neat binders.

The bituminous blends and modified binders have been prepared and made in accordance with BS EN 12594:2007 [9]. However, some modifications have been applied to the recommendations in bitumen sample preparation in terms of bitumen's heating temperature and time. Heating time and temperature for the modified binders have been considered the same as the base binder and not according to their softening point.

3 BINDER TESTS

In order to determine the physical, mechanical and rheological behaviour and behavioural characteristics of the binders and also to study the binding, coating and surface energy properties, a comprehensive matrix of laboratory tests has been devised and performed as shown in Table 1.

3.1 *Penetration grade and softening point determination*

The penetration grade and softening point tests were performed in accordance with BS EN 1426:2007 [11] and BS EN 1427:2007 [12], respectively, in order to have the basic physical characteristics of the binders and the effect of each additive and its dosage on the properties. The test specifications are as shown in Table 1 and the results are presented in Table 2. It can

Table 1. Binder testing matrix.

Test	Standard name	Standard no.	Test device	Description
1. Pen grade determination	Determination of needle penetration	BS EN 1426: 2007 [11]	Penetrometer	Test temperature = 25°C
2. Softening point determination	Determination of the softening point-ring and ball method	BS EN 1427: 2007 [12]	Ring and ball aparatus	N.A.
3. Brookfield viscometry	Determination of dynamic viscosity of bituminous binders using a rotating spindle apparatus	BS EN 13302: 2010 [13]	Brookfield viscometer	Temperature swept from 90°C to 180°C with 10°C intervals, meter reading = (50 ± 10)% spindle size = SC4-34
4. Bitumen wax content	Determination of the paraffin wax content-part 1: method by distillation part 2: method by filtration	BS EN 12606-1: 2007 [16]	Standard laboratory distillation and filtration setup	N.A.
5. Brookfield viscometry	Test methods for viscosity determinations of unfilled asphalts using the brookfield thermosel apparatus	SUPERPAVE ASTM D4402 [14]	Brookfield viscometer	Temperature swept from 90°C to 180°C with 10°C intervals, rotational speed = 20 rpm shear rate = 6.8 s^{-1} spindle size = SC4-27
6. Frequency-temperature sweep	Determination of complex shear modulus and phase Angle-Dynamic Shear Rheometer (DSR)	BS EN 14770: 2012 [17]	Bohlin's CVO Dynamic Shear Rheometer (DSR)	Frequency swept from 0.1 Hz to 10 Hz over the temperature range of 10°C to 75°C with 10°C intervals
7. DCA	Dynamic contact angle measurement	[18]	Wilhelmy plate	Test temperature = 23°C ± 2°C

be seen that while adding Rediset LQ has nearly no effect on penetration grade and softening point of the binders, adding Sasobit significantly increases the softening point and decreases the penetration grade.

3.2 *Brookfield viscometry test*

In order to study the effect of the additives on the rheological behaviour of the binders, Brookfield viscometry tests have been performed on the binders over the temperature range of 90°C to 180°C. This was done to investigate the viscosity of the binders at high temperatures and to study the changes in binder rheology in the presence of the additives around the mixing and compaction temperatures. It was also done to justify or find the correct production temperature of the WMA.

The Brookfield viscometry test in this research was performed twice, based on two different Standards, BS EN 13302:2010 [13] and ASTM D4402 [14]. The reason for this has been the considerable difference between the results of the test based on BS EN 13302:2010 [13] for the Sasobit-modified binders, with those of the NCAT Report 05-06 [3], Yero et al. [15] and Liu et al. [5], which had been done in accordance with the ASTM Standards.

BS EN Standards validate choosing any rotational speed (rpm) for the spindle at which the meter reading remains between 10% and 100%. In the current research, BS EN-based Brookfield viscometry has been performed by using spindle SC4-34. At each temperature,

Table 2. Penetration grade and softening point determination test results.

Bitumen/binder	160/220	160/220 +2%Sasobit	160/220 +3%Sasobit	160/220 +10%Sasobit	160/220 +0.4%Rediset	160/220 +0.5%Rediset	160/220 +0.6%Rediset
Sample no.	12-37	13-485	13-486	13-574	N.A.	13-487	13-488
Description	Base binder	98% (12-37) +2% (10-2757)	97% (12-37) +3% (10-2757)	90% (12-37) +10% (10-2757)	99.6% (12-37) +0.4% (13-451)	99.5% (12-37) +0.5% (13-451)	99.4% (12-37) +0.6% (13-451)
Pen grade	200	145	126	57	N.A.	186	184
Softening point	37	64.4	75	99.5	N.A.	37.6	37.6
Bitumen/binder	30/45	30/45 +2%Sasobit	30/45 +3%Sasobit	30/45 +10%Sasobit	30/45 +0.4%Rediset	30/45 +0.5%Rediset	30/45 +0.6%Rediset
Sample no.	12-38	13-489	13-490	13-575	N.A.	13-491	13-492
Description	Base binder	98% (12-38) +2% (10-2757)	97% (12-38) +3% (10-2757)	90% (12-38) +10% (10-2757)	99.6% (12-38) +0.4% (13-451)	99.5% (12-38) +0.5% (13-451)	99.4% (12-38) +0.6% (13-451)
Pen grade	36	27	26	17	N.A.	34	34
Softening point	54	67	82.5	102	N.A.	54	54.8
Bitumen/binder	70/100	70/100 +2%Sasobit	70/100 +3%Sasobit	70/100 +10%Sasobit	70/100 +0.4%Rediset	70/100 +0.5%Rediset	70/100 +0.6%Rediset
Sample no.	13-99	13-100	13-493	13-576	13-781	13-101	13-494
Description	53.4% (12-37) +46.6% (12-38)	98% (13-99) +2% (10-2757)	97% (13-99) +3% (10-2757)	90% (13-99) +10% (10-2757)	99.6% (13-99) +0.4% (13-451)	99.5% (13-99) +0.5% (13-451)	99.4% (13-99) +0.6% (13-451)
Pen grade	90	60	56	34	87	87	85
Softening point	44.8	71.6	81	101.5	44.8	45.2	45.6

the rotational speed was set to the value at which the meter reading stays between 10% and 100% with the preferred value of about (50 ± 10)%. However, SUPERPAVE (ASTM) recommends using spindle SC4-21 or SC4-27, rotating at a speed of 20 rpm to apply a shear rate of 6.8 s^{-1}. In this research the SUPERPAVE-based Brookfield viscometry has been performed using spindle size SC4-27.

From the test results, it can be observed that just after Sasobit's melting temperature (transition point), the viscosity of the modified binder drops and the viscosity curve shifts down afterwards. However, it seems that at the temperatures lower than the transition point the crystallisation phenomenon in the wax structure results in an increased viscosity of the binder. As can be seen in Table 3 and Figures 1 and 2, according to the Brookfield viscometry test results performed based on BS EN 13302:2010 [13], the viscosity of the 70/100 pen bitumen was not reduced as much as it could reduce the mixing and compaction temperature by 25°C as promised in NCAT Report 05-06 [3] or even by 15°C as shown by Liu et al. [5]. Even increasing the dosage of Sasobit up to 10% by the weight of the binder and also performing the test on both the 30/45 pen and the 160/220 pen binders did not show the promised level of reduction in the viscosity of the binders.

Table 3. BS EN-based brookfield viscometry test results.

	Viscosity (cP) [mPa.S]					
Bitumen	70/100 (13-99)	70/100 +2%Sasobit (13-100)	70/100 +3%Sasobit (13-493)	70/100 +10%Sasobit (13-576)	70/100 +0.5%Rediset (13-101)	70/100 +0.6%Rediset (13-494)
Temperature (°C)						
90	–	5815.0	15837.0	70545.0	5619.0	6539.0
100	2795.0	2052.0	4042.3	28833.0	2555.0	3034.0
110	1404.0	1064.0	989.1	775.0	1298.0	1485.0
120	736.6	601.1	557.9	394.5	712.6	783.8
130	431.9	344.9	322.3	250.5	394.9	449.9
140	258.5	211.2	197.4	159.0	240.5	269.9
150	163.2	142.2	133.2	105.2	158.4	166.0
160	113.4	96.0	89.1	75.6	104.7	115.0
170	78.6	66.0	62.1	54.6	72.1	80.0
180	56.4	48.6	46.5	40.8	53.1	61.0

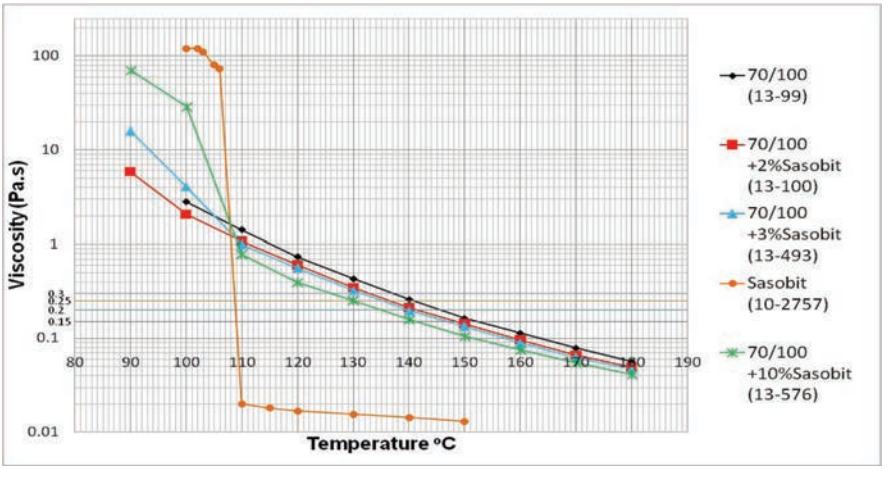

Figure 1. BS EN-based brookfield viscometry test results (Sasobit-modified binders).

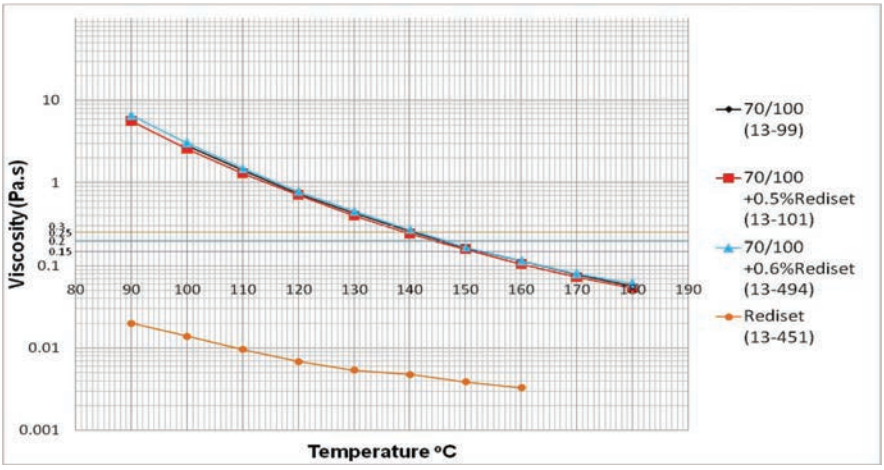

Figure 2. BS EN-based brookfield viscometry test results (Rediset LQ-modified binders).

Table 4. ASTM-based brookfield viscometry test results.

	Viscosity (cP) [mPa.S]					
Bitumen	70/100 (13-99)	70/100 +2%Sasobit (13-100)	70/100 +3%Sasobit (13-493)	70/100 +0.4%Rediset (13-781)	70/100 +0.5%Rediset (13-101)	70/100 +0.6%Rediset (13-494)
Temperature (°C)						
90	5565.0	3993.0	3355.0	4968.0	5030.0	4985.0
100	2336.0	1740.0	1449.0	2275.7	2118.3	2013.3
110	1176.0	905.7	765.0	1156.0	1077.0	1078.0
120	647.9	507.3	438.2	596.4	592.8	590.5
130	364.2	290.6	253.1	333.9	331.6	330.4
140	217.9	176.9	153.5	202.7	199.2	196.8
150	144.1	118.3	101.9	132.4	131.6	128.9
160	96.1	79.7	69.1	92.6	86.7	85.5
170	66.8	55.1	46.9	63.3	58.6	56.2
180	49.2	43.4	35.1	45.7	43.4	42.2

Therefore, in order to make sure about the repeatability of the results, the test was repeated again but this time, based on ASTM D4402 [14]. However, referring to the results of ASTM-based Brookfield viscometry test, as shown in Table 4 and Figures 3 and 4 it can be seen that using 3% Sasobit can decrease the mixing and compaction temperature by up to 10°C which is still less than the amount reported in the NCAT Report 05-06 [3], work by Liu et al. [5] and as promised by the producer.

It seems that according to the results, the ASTM-based Brookfield viscometry should be more reliable. The reason for such a difference in the test results could be due to the greater turbulent flow of the bitumen between the inner wall of the apparatus cup and the surface of the spindle in the BS EN-based test. Due to the greater gap between the inner wall of the cup and the surface of the spindle in the BS EN-based test compared to the ASTM-based test, the rotational flow of bitumen around the spindle will be less laminar and more turbulent at high temperatures and rotational speeds. This turbulent flow can result in applying some additional unwanted friction on the surface of the spindle and therefore show a greater value of the binder viscosity than it really is.

For the Rediset LQ chemical additive, nearly no effect on the viscosity of the binder can be seen, which was expected from the specifications according to the material producer.

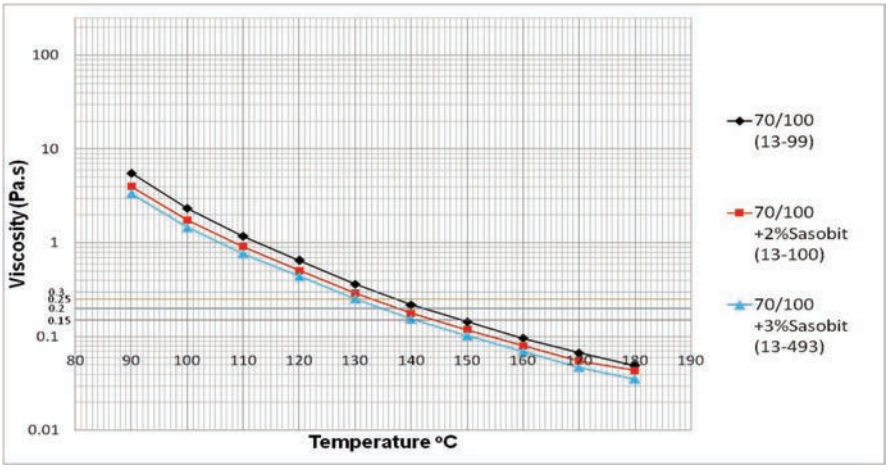

Figure 3. ASTM-based brookfield viscometry test results (Sasobit-modified binders).

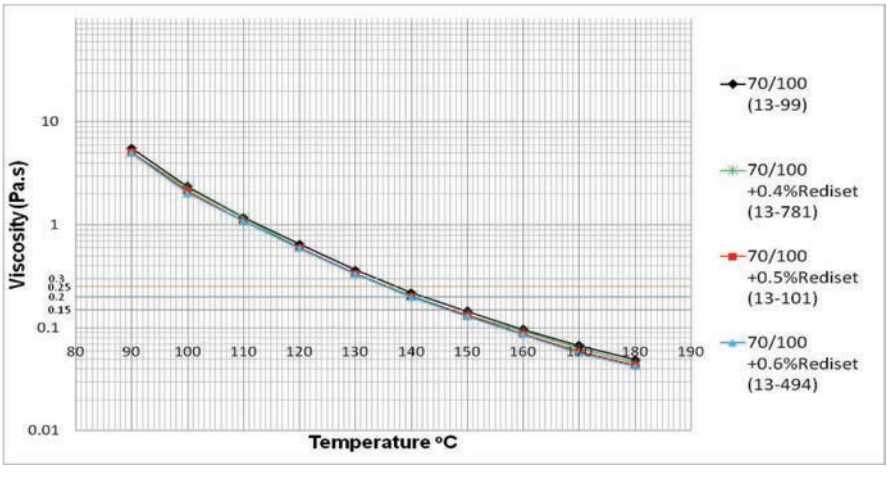

Figure 4. ASTM-based brookfield viscometry test results (Rediset LQ-modified binders).

3.3 *Bitumen wax content test*

In order to understand these differences, the Bitumen Wax Content test was performed on the base binders in accordance with BS EN 12606-1:2007 [16], because it was predicted that the bitumen might have been already waxy and adding more wax to the existing amount in the bitumen might have no significant effect. In the other words, bitumen samples might have been waxy, themselves, therefore, decreasing their viscosity sensitivity to the extra wax content. However, the Bitumen Wax Content test showed that the base bitumens were non-waxy types. As they contained no more than 0.06% and 0.02% of Paraffin wax for the 160/220 pen and 30/45 pen, respectively.

Thus, the unexpected results (small decrease in the viscosity of the modified binders compared to their neat bitumen) of Brookfield viscometry test might have been because the bitumen samples had nearly no wax initially and originally. Eventually, the added Sasobit (wax) might have been consumed by the non-waxy bitumen to increase its wax content to a normal balanced level.

To check this theory, it was necessary to add more Sasobit to modify the pure bitumen samples and 10% Sasobit-modified binders were produced. However, performing the same

Brookfield viscomety test on the 10% Sasobit-modified bitumen grades did not result in any significant decrease in the viscosity of the binders.

3.4 *Frequency-temperature sweep test*

The mechanical properties of the binders were studied by investigating their rheological behaviour by performing the Frequency-Temperature Sweep test using a Dynamic Shear Rheometer (DSR) over a range of different temperatures (5°C to 80°C) and frequencies (0.1 Hz to 10 Hz). The test was performed in accordance with BS EN 14770:2012 [17]. It should be mentioned that the rheological behaviour investigations have been carried out for two main reasons. Firstly, to study the mechanical properties of the binder itself in the presence of additives at different temperatures and loading frequencies and secondly, in order to have sufficient fundamental support to analyse and interpret the mechanical behaviour of the

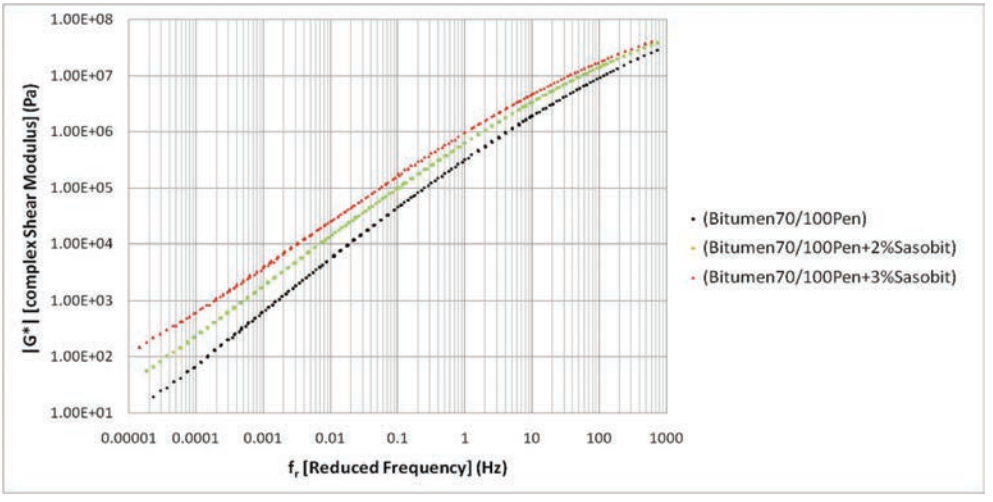

Figure 5. Comparative master curves for the complex shear modulus of the sasobit-modified 70/100 pen bitumen (Reference temperature = 25°C).

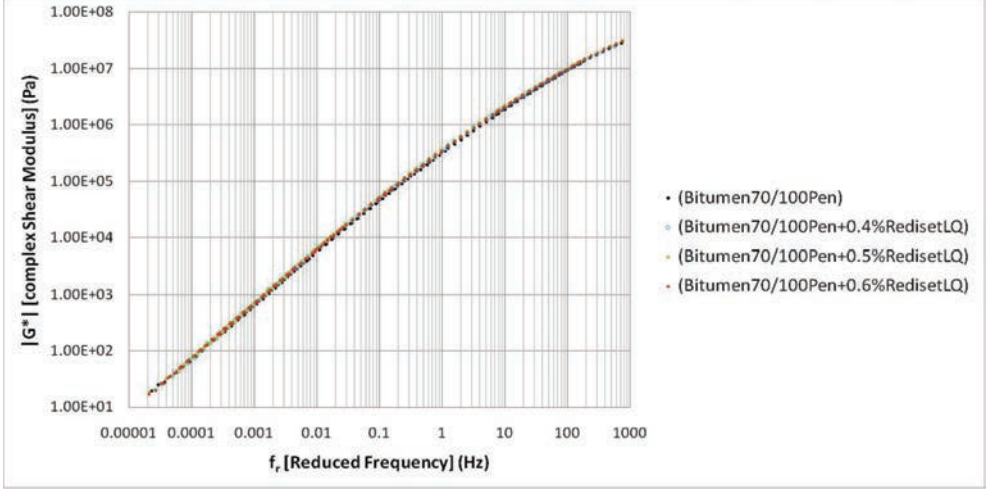

Figure 6. Comparative master curves for the complex shear modulus of the rediset LQ-modified 70/100 pen bitumen (Reference temperature = 25°C).

Table 5. DCA test results.

Binder sample	Probe liquid	Average advancing contact angle [θ] (°)	Known sueface energy components of the probe liquid (mJ/m^2)				Calculated sueface energy components of the tested binder (mJ/m^2)			
			γ^{LW}	γ^+	γ^-	γ	γ^{LW}	γ^+	γ^-	γ
(13-99)	Water	96.974	21.8	25.5	25.5	72.8	33.65498	0.13137	1.773095	34.62024
[Bitumen70/100Pen]	Glycerol	86.924	34	3.92	57.4	64.00053				
	Di-Iodomethane	51.106	50.8	0	0	50.8				
(13-100)	Water	103.76	21.8	25.5	25.5	72.8	22.25891	0.469704	0.199052	22.87045
[Bitumen70/100	Glycerol	87.16	34	3.92	57.4	64.00053				
Pen+2%Sasobit]	Di-Iodomethane	71.102	50.8	0	0	50.8				
(13-493)	Water	105.55	21.8	25.5	25.5	72.8	21.62833	0.154691	0.339383	22.08658
[Bitumen70/100	Glycerol	91.342	34	3.92	57.4	64.00053				
Pen+3%Sasobit]	Di-Iodomethane	72.242	50.8	0	0	50.8				
(13-781)	Water	101.682	21.8	25.5	25.5	72.8	33.46833	0.022859	0.303498	33.63491
[Bitumen70/100	Glycerol	86.994	34	3.92	57.4	64.00053				
Pen+0.4%RedisetLQ]	Di-Iodomethane	51.438	50.8	0	0	50.8				
(13-493)	Water	99.524	21.8	25.5	25.5	72.8	34.89661	0.022596	0.495519	35.10824
[Bitumen70/100	Glycerol	85.16	34	3.92	57.4	64.00053				
Pen+0.6%RedisetLQ]	Di-Iodomethane	48.88	50.8	0	0	50.8				

resulting mixtures at the operating temperatures. This will also allow linking the behaviour of the mixtures to the mechanical properties of their corresponding binders at the mixing and compaction temperatures at which the mixtures mechanical behaviour will be formed.

The Frequency-Temperature Sweep test, which has been characterised in Table 1, has been performed in strain-controlled mode applying a maximum strain value of 0.5%, 0.4% and 0.3% for 0%, 2% and 3% Sasobit-modified binders respectively to remain within the Linear Visco-Elastic Region (LVER). For the Rediset LQ-modified samples, the LVER has been set to the same value as for the neat binder. The results of the Frequency-Temperature Sweep tests are shown in Figures 5 and 6.

From the test results, it can be concluded that adding Sasobit increases the complex shear modulus (G*) and decreases the phase angle of the binders, while the Rediset LQ has nearly no effect on the parameters.

Adding 3% Sasobit to the 70/100 pen bitumen increases its complex shear modulus by nearly 8 times at about 10°C and 1.5 times at about 75°C. Adding 2% Sasobit has increased the complex shear modulus by about 3 times at 10°C and nearly 1.5 times at about 75°C.

3.5 *Dynamic Contact Angle test (DCA)*

This test has been performed to find out the changes in the values of the Surface Energy (SE) components of the binders, which may be caused by the additives. The measured values, when combined with the ones of aggregate, will be used to calculate the Bonding Energy. This is used to evaluate the work of adhesion when combined with aggregates and also to calculate the work of de-bonding in the presence of water in order to estimate the moisture sensitivity of the resulting mixtures.

Also, according to the Brookfield viscometry test results, as the viscosity issue may not be the only factor which is affected by Sasobit, the DCA test has been performed to find out the reasons why a lower production temperature of WMA can be used when Sasobit is added. Therefore, it is predicted that Rediset LQ should change the surface tension of the bitumen if it has no effect on the rheological issues such as viscosity.

The DCA test has performed using a DCA Analyser apparatus (Wilhelmy Plate method) according to NTEC laboratory protocol [18]. In order to increase the precision of the results, five slides per binder sample were prepared to perform the test by the use of three different probe liquids: water, glycerol and di-iodomethane. The test results and data can be found in Table 5.

Referring to Table 5, the relatively high value of the γ^{LW} component, which is representative of the Van der Waals non-polar interaction forces, confirms that the tested neat bitumen is basically a non-polar material as it naturally is. However, in contrast with the slightly acidic behaviour which is normally expected from any neat bitumen, the higher value of γ^- (basic component) compared to γ^+ (acidic component) indicates that the neat bitumen is slightly basic in nature. This means that this bitumen can give better adhesion if it is used with acidic aggregates (e.g. Granite).

In the case of the Sasobit-modified binders, it can be observed that adding Sasobit has decreased the non-polar component as well as the basic characteristics of the modified binder in comparison with the neat bitumen. At the same time it increases the acidic component of SE which can result in a better adhesion of the Sasobit-modified binders with a basic aggregate (e.g. Limestone).

According to the results reflected in Table 5, Rediset LQ has not changed the non-polar component of SE significantly. However, it has considerably decreased both γ^+ and γ^-, which can result in a better moisture resistance.

4 CONCLUSIONS

- While adding Rediset LQ has nearly no effect on the Penetration Grade and Softening Point of the binders, adding Sasobit significantly increases the Softening Point and decreases the Penetration Grade.

- According to the Brookfield viscometry test results which was performed based on BS EN 13302:2010 [13], the viscosity of the 70/100 pen bitumen was not reduced as much as it can lower the mixing and compaction temperature by 25°C as promised in the NCAT Report 05-06 [3] or by 15°C as shown in Liu et al.s research. Increasing the dosage of Sasobit up to 10% by the weight of the binder and performing the tests on the both base bitumen grades did not show the promised significant reduction in the viscosity of the binders.
- The results of ASTM-based Brookfield viscometry test showed 3% Sasobit can decrease mixing and compaction temperature by up to 10°C which is still less that the amount reported in NCAT Report 05-06 [3], the research of Liu et al. [5] and promised by the producer.
- Rediset LQ chemical additive has nearly no effect on the viscosity of the binder, which was expected from the specifications of the manufacturer. In fact, this additive, has nearly no influence on the rheological and mechanical properties of the binder.
- Adding Sasobit increases G* and decreases the phase angle of the binders while Rediset LQ has nearly no effect on the mentioned parameters.
- Adding 3% Sasobit to 70/100 pen bitumen increases its complex shear modulus by nearly 8 times at about 10°C and 1.5 times at about 75°C. Adding 2% Sasobit increased the complex shear modulus by about 3 times at 10°C and nearly 1.5 times at about 75°C.
- Adding Sasobit decreases the non-polar component as well as the basic characteristics of the modified binder in comparison with the neat bitumen. It also increases the acidic component of SE which can result in a better adhesion of the Sasobit-modified binders with a basic aggregate (e.g. Limestone).
- Rediset LQ does not affect the non-polar component of SE significantly. However, it has considerably decreased both γ^+ and γ^-, which can result in a better moisture resistance.

5 FUTURE WORK

Mixture compaction trials will be carried out for the different binder compositions over a range of temperatures to investigate the effect of temperature reduction on the compacted material properties. Stiffness, fatigue, rutting and water sensitivity tests will be performed in order to characterise the mechanical properties of the resulting mixtures which will be mixed at recommended mixing temperature and compacted at a number of temperatures lower than the recommended compaction temperature.

Binding/coating quality of the mixtures and also the post-failure structure of the tested mixtures will be observed through SEM or X-Ray CT to support the mechanical test results.

Finally, it is planned to develop approaches and guidelines to improve the mechanical deficiencies and reduce the potential distresses resulting from the time delay and temperature decline between mixing and compaction.

REFERENCES

[1] Bonaquist, R. (2011). Mix Design Practices for Warm Mix Asphalt, NCHRP Report 691. National Cooperative Highway Research Program, Washington.

[2] Jalali, Venon. (2012). "Temperature Effects on Warm Mix Asphalt Performance", NTEC Report No. 12114, First Year Postgraduate Research Report for Ph.D. Degree in Civil Engineering-Pavement, Nottingham Transportation Engineering Center (NTEC), Department of Civil Engineering, The University of Nottingham, Nottingham, UK.

[3] Hurley, G. & Prowell, B. (2005). Evaluation of Sasobit® for use in Warm Mix Asphalt, NCAT Report 05-06, National Centre for Asphalt Technology (NCAT), Auburn University, Alabama, U.S.

[4] www.sasolwax.com, (Accessed: 14th September 2013).

[5] Liu, J., Saboundjian, S., Li, P., Connor, B. and Brunette, B. (2011). Laboratory Evaluation of Sasobit-Modified Warm Mix Asphalt for Alaskan Conditions, Paper for Journal of Materials in Civil Engineering© ASCE.

[6] Jamshidi, A., Hamzah, M.O., You, Zh. (2013). Performance of Warm Mix Asphalt Containing Sasobit®: State-of-the-Art. ELSEVIER Journal of Construction and Building Materials 38, pp 530–553.
[7] Polacco, G., Filippi, S., Paci, M., Giuliani, F. and Merusi, F. (2011). Structural and Rheological Characterization of Wax Modified Bitumens. Fuel, Vol. 95, pp 407–416.
[8] www.akzonobel.com, (Accessed: 14th September 2013).
[9] BS EN 12594:2007, Bitumen and Bituminous Binders—Preparation of Test Samples.
[10] BS EN 13043:2013, Aggregates for Bituminous Mixtures and Surface Treatments for Roads, Airfields and Other Trafficked Areas.
[11] BS EN 1426:2007, Bitumen and Bituminous Binders—Determination of Needle Penetration.
[12] BS EN 1427:2007, Bitumen and Bituminous Binders—Determination of the Softening Point—Ring and Ball Method.
[13] BS EN 13302:2010, Bitumen and Bituminous Binders—Determination of Dynamic Viscosity of Bituminous Binder Using a Rotating Spindle Apparatus.
[14] American Society of Testing and Materials—ASTM. ASTM D4402: Standard Test Methods for Viscosity Determinations of Unfilled Asphalts Using the Brookfield Thermosel Apparatus.
[15] Yero, A.S., Hainin, M.R. (2011). Influence of Organic Wax on Bitumen Characteristics, American Journal of Engineering and Applied Science, 4 (2): pp 265–269.
[16] BS EN 12606-1:2007, Bitumen and Bituminous Binders—Determination of the Paraffin Wax Content—Part 1: Method by Distillation, Part 2: Method by Filtration.
[17] BS EN 14770:2012, Bitumen and Bituminous Binders—Determination of Complex Shear Modulus and Phase Angle—Dynamic Shear Rheometer (DSR).
[18] Ahmad, N., (2011) 'Asphalt mixture moisture sensitivity evaluation using surface energy parameters.' PhD Thesis, NTEC, The University of Nottingham, UK.
[19] BS EN 12697-31:2007, Bituminous Mixtures—Test Methods for Hot Mix Asphalt—Part 31: Specimen Preparation by Gyratory Compactor.

Asphalt Pavements – Kim (Ed)
© 2014 Taylor & Francis Group, London, ISBN 978-1-138-02693-3

Evolution of bubble size distribution during foam bitumen formation and decay

Biruk W. Hailesilassie
Division of Highway and Railway Engineering, Infrastructure Engineering, School of Architecture and the Built Environment, Royal Institute of Technology (KTH), Stockholm, Sweden

Philipp Schuetz & Iwan Jerjen
Laboratory for Electronics/Metrology/Reliability, EMPA, Swiss Federal Laboratories for Material Science and Technology, Duebendorf, Switzerland

Andrea Bieder
Ammann Schweiz AG, Langenthal, Switzerland

Martin Hugener
Road Engineering/Sealing Components, EMPA, Swiss Federal Laboratories for Material Science and Technology, Duebendorf, Switzerland

Manfred N. Partl
Division of Highway and Railway Engineering, KTH Stockholm, Stockholm, Sweden
Road Engineering/Sealing Components, EMPA, Swiss Federal Laboratories for Material Science and Technology, Duebendorf, Switzerland

ABSTRACT: The warm asphalt mixture process using foam asphalt technology allows mixing and compaction at lower temperature. Nevertheless the higher air void content and incomplete coating of large aggregates are issues that need improvement to reach the properties of hot mix asphalt. In order to improve the understanding and characterization of the bitumen foam, X-ray radiography was used to investigate the formation and decay of bitumen foam in 2D representation. Image segmentation analysis was used to determine the foam bubble size distribution as a function of time. The impact of water content on the process has been studied for two penetration grade bitumen. The water content showed considerable influence on the foam quality in terms of expansion ratio and bubble size distribution. Increasing the water content in the foaming process leads to a quicker collapse of the bubbles and favors coalescence of individual bubbles.

Keywords: Foamed bitumen, expansion ratio, half-life, X-ray radiography, image segmentation analysis

1 INTRODUCTION

Foamed asphalt technology, which allows lower mixing temperatures, has been used successfully in many countries. Energy saving, decreased emissions of fumes and odor, extending the paving season, compaction aid for stiffer mixes … etc., are main advantages of the foam asphalt (warm mix asphalt) over the conventional hot mix asphalt. Foam asphalt produced at ambient temperature needs improvement to reach the properties of hot mix asphalt for heavy duty roads. Higher void content and incomplete coatings of large aggregates are the main reasons for its lower performance. Foam bitumen is a mixture of air, water and bitumen. It is produced through the injection of small quantities of water typically 1–6.0% regarding the mass of the

bitumen into hot penetration grade bitumen (160–180°C) in an expansion chamber. The bitumen expands to about 5–15 times its original volume [1] and forms a foam, which is highly efficient in wetting and coating the surface of fine particles [2]. As the foam collapses most of the water is lost in the form of steam, leaving residual bitumen with properties similar to the original bitumen [3]. The time that the expanded bitumen takes to settle to half its expanded volume is called the half-life, τ [4]. The half-life is used to explain the stability of the foam bitumen in general. The desirable value of the half-life is difficult to determine since the addition of water varies the half-life. The Expansion Ratio (ER) is determined by taking the ratio of expanded volume in the foamed state to the non-foamed volume of bitumen in the container.

Foam bitumen allows to construct asphalt pavements at reduced temperature in terms of mixture production, transport, laying and compaction [5]. Reducing production and compaction temperatures by using WMA (Warm Mix Asphalt) in place of HMA (Hot Mix Asphalt) is environmentally beneficial since it decreases fuel or energy consumption, reduces emissions of CO_2 and reduces smoke from mixing plant and improves working conditions at the paving site [2, 6].

Foams may be classified as dry or wet depending on the liquid (bitumen) content, which is represented by the liquid volume fraction *f*. The amount of liquid may range from less than 1% to about 30% [7]. These characterizes only about the foamability of liquid foam (two-phase systems) in general. The higher the gas fraction the better the foamability. In the dry foam the films forming the interface between bubbles are not spherical since these bubbles are made of polyhedral cells [8].

Coarsening is a change of bubble morphology which mainly occurs in two way: by the rupture of the film between two adjacent bubbles or cells and or by gas diffusion driven Ostwald ripening [9]. The rupture of thin films is related to the drainage (redistribution of liquid) and stability of foam films [7], whereas the Ostwald ripening is caused by inter-bubble gas diffusion by which liquid foam comes in to thermodynamic equilibrium, where one large bubble is energetically more favorable than two smaller bubbles [10]. Because of the above mentioned processes, bubbles smaller than the average size shrink, while large bubbles become larger resulting in an increase of the average size of the bubbles over time [11].

Usually foam bitumen is characterized by two empirical parameters called expansion ratio and half-life. The two parameters only describes the volumetric property of the foam bitumen. However the relation of these parameter to foam properties, such as foam morphology, bubble size distribution, drainage, coarsening, … etc. remained still unclear due to the difficulty to study the unstable foam and its black color. Usually expansion ratio and half-life are determined using a foam ruler. However, foam bitumen is very unstable when foamed at higher water content and the measurement of the expansion using the foam ruler can be inaccurate.

Moreover, the rheology and stability of the foam are mainly depending on the foam's bubble size distribution and gas liquid fraction [12]. To determine the growth rate of bubbles in dry foam, the bubble size and shape are crucial. For wet foam the influence of the bubble shape is less significant since the bubble shape are expected to be more spherical [7]. Hence, determination of the bubble size distribution in foam is crucial for a better understanding of the foam properties and the stability of the foam. However, there is no work on how the foam bitumen is formed during the foaming process, how it changes with time and which mechanisms are responsible for this. The present paper intends to help in closing this gap.

The main objective of the study is to characterize the morphology of foam bitumen bubbles and the evolution of bubble size distribution with time during the foaming process for different foam bitumen parameters using X-ray radiography analysis. Hence, the influence of the water content and bitumen temperature on two different types of penetration grade bitumen has been studied.

2 EXPERIMENTAL METHOD

The foam bitumen was produced using a WLB10S lab foamer. To study the dynamic process of foam formation and decay, a special X-ray setup has been constructed. The idea was to cre-

ate a 2D cross-section through a container that is filled with foam. As shown in Figure 2(a), between X-ray source and detector, a test box was placed according to the field of view required for the experiment. The test box consisted of two parallel plate produced from a wooden frame and covered with silicon coated paper, having a size of 297 × 210 mm × 10 mm. An extension pipe made of fiber reinforced plastic, having internal diameter of 8 mm and length of 2000 mm was connected to the outlet nozzle of the lab foamer to take the foam bitumen in to the test box.

Both horizontal and vertical axis of the X-ray field of view had a resolution of 205 µm. The images were taken at 14.7 frames/s. The study was done for two types of bitumen of different origin. Bitumen A (supplied from Nynas, Germany) had a penetration value 80*0.1 mm and softening point of 45.3°C and the other harder bitumen type B (supplied from Grisard AG, Switzerland), had a penetration of 51*0.1 mm and softening point of 51.1°C.

Influence of the water content was investigated for 1 and 4% water content (W.C.) by weight of the bitumen in combination with 160°C foaming temperature as shown in Table 1.

Analysis of bubble size distribution was done for each experiment at three particular characteristic moment of time as shown in Figure 1, which includes

1. The time when the foam is close to maximum expansion, h_{max}. This corresponds to 4.2 s starting from the time of spraying.
2. The time at half of the expansion height, $h_{max}/2$; in this case the moment of time depends on the expansion height, i.e. the value is different for all different kinds of foaming conditions.
3. The time at the end of the decaying process, this time frame also depends on the water content and temperature of the bitumen.

As shown in Figure 2 (b) the total field of view of the X-ray was 195 mm*176 mm. In a single experiment hundreds of images were taken, since there is a limitation on showing all the results specific points selected. A rectangular section of 164.0 mm by 57.4 mm for foam analysis at the bottom of the images for analysis of bubble size distribution with time. In some cases the maximum expansion height of the foam was measured using a ruler at the end of the experiment, since the foaming height was above X-ray field of view. Zero time corresponds to the starting of the spray, when the foam comes out of the extension tube.

Table 1. Experimental plan.

Type of bitumen	Foaming temperature (°C)	Water content (mass-%)
A	160	1 and 4
B	160	1 and 4

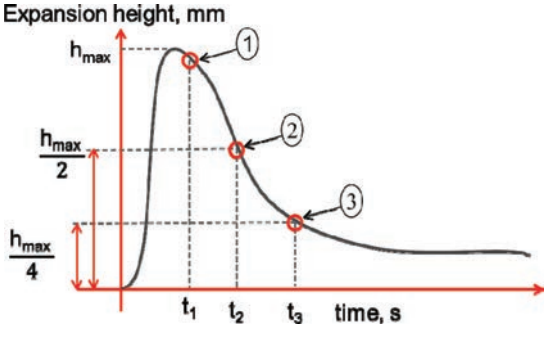

Figure 1. Analysis points for bubble size distribution on the decay curve.

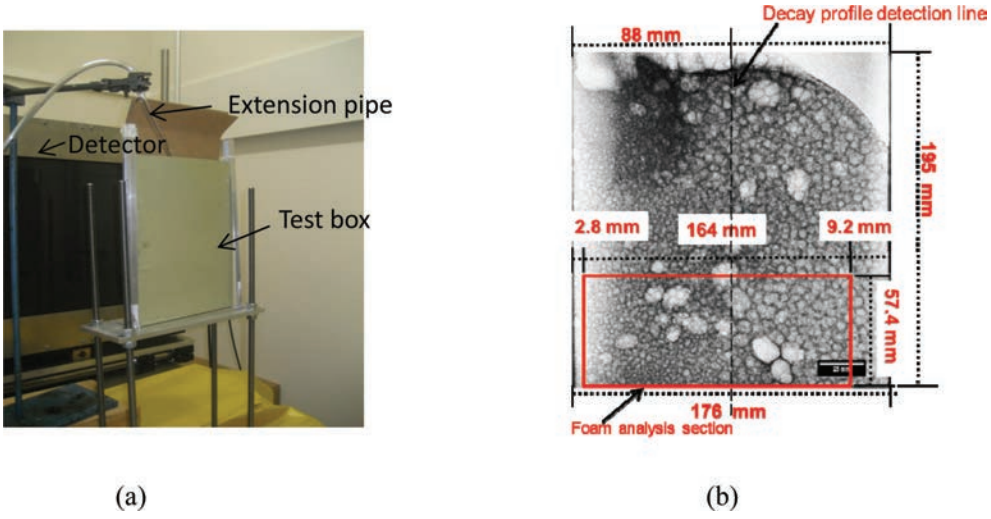

Figure 2. (a) Foam bitumen X-ray setup (b) X-ray analysis section, image at 5.2 s for 1% W.C at 160°C bitumen temperature for bitumen type "A".

3 DATA ANALYSIS

For the characterization of the bubble size distribution, an algorithm was developed using Matlab to perform image segmentation and bubble detection. Image thresholding was applied to find the boundary of the vapor and bitumen phase. Defining the boundary of bitumen and vapor was not trivial in the image segmentation due to possible overlapping of the bubbles as well as the noise from the X-ray measurements. After confirming the detection of possible bubbles from image segmentation, each bubble was counted and numbered from left to right within the image analysis section. For bubble detection, the minimum bubble size for image segmentation was set to 0.2 mm^2 which corresponds to approximately five pixels. Bubble sizes below this limit were not considered in this analysis.

4 RESULT AND DISCUSSION

4.1 *Influence of the water content on foamed bitumen bubble size distribution*

The foam bitumen decay profiles shown in Figure 3 (a) and (b) were determined by taking a cross section at the center of the field of view as indicated in Figure 2 (b) using "Fiji" image analysis software. As it is expected increasing the water content leads to higher expansion height for both investigated bitumen as indicated in Figure 3 (a) and (b). The expansion height was higher for the softer bitumen "A" compared to the harder bitumen "B" for the same water content. The pressure produced by water vapor inside the bubbles is counter balanced by forces of the thin film of each bubble, which has a direct relation to surface tension and viscosity. Hence for the same amount of water content, bitumen "A" has a higher expansion due to its lower viscosity and surface tension.

In order to understand the influence of the water content on the morphology of bubbles, 1% W.C. and 4% W.C. at 160°C foaming temperature are compared for bitumen "B" as shown in Figures 4 and 5. Enormous polydispersity of bubbles was observed during the foaming process as indicated in Figure 4 (a) and the coarsening continued even for longer period. The main destabilization mechanism of foam with viscous liquid matrix in the wet condition is coarsening [10, 13]. In the case of bitumen "B" it is found that the major decaying or destabilizing mechanism was coarsening and bursting of bubbles at the foam bitumen surface. Coarsening is caused by rupture of films between two adjacent bubbles. In addition

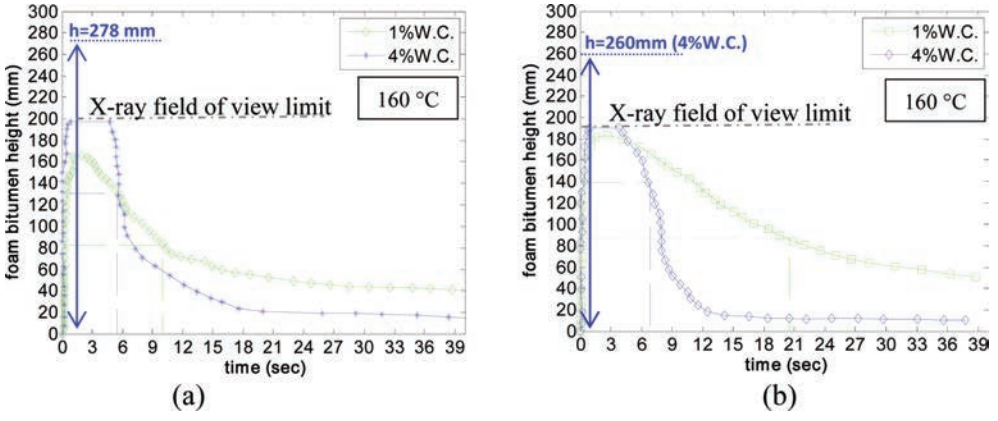

Figure 3. The foam bitumen height in the parallel plate during the decay process (a) bitumen "A" (b) bitumen "B" in the field of view.

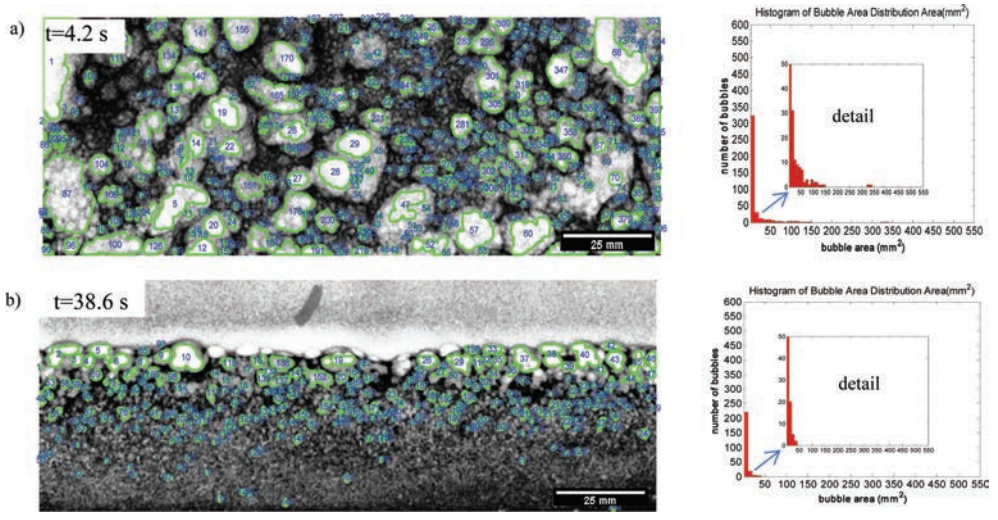

Figure 4. Foam bitumen bubble size distribution in the foam analysis section at different decay times, t_1 and t_3 (1% W.C., Bitumen "B", 160°C Temperature).

to this redistribution of the gas in bubbles, such as Ostwald ripening can cause coarsening [14]. Because of the polydispersity of foam bitumen, pressure difference between the inside and outside of the bubbles surface; a consequence diffusion of vapor occurs during the decaying process, hence Ostwald ripening can cause coarsening as well.

The surface energy which is proportional to the interaction surface area of the bubbles enables the individual bubbles to take up shape minimizing the surface energy [13]. Moreover, the surface tension tends to minimize the contact surface of bitumen and vapor, which leads to quicker coarsening. Increasing the viscosity and minimizing the surface tension plays a big role in stabilizing the foam and reducing the quick collapse of foam [12, 15]. Therefore, high surface tension can be one of the reasons for the quick collapse of bitumen "B". The surface energy of the foam will decrease with time as the foam decays.

Rising of the bubbles to the surface, in addition to subsequent drainage causes creaming [13]. This is also true in the case of bitumen type "B" where drainage of liquid bitumen from relatively dry zone of foam bitumen, near the surface towards the wet region was observed at the end of decaying process as shown in Figure 5 (b). The variation of liquid (bitumen) con-

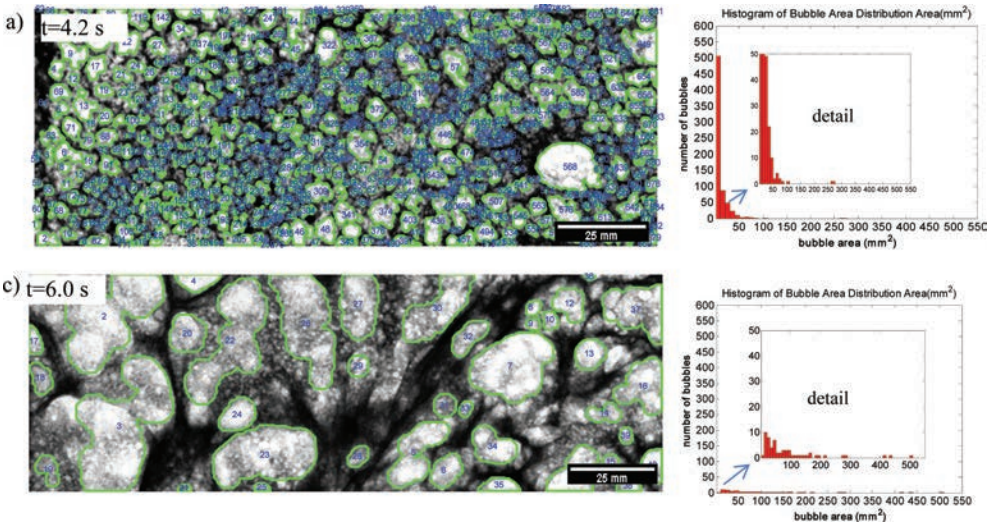

Figure 5. Foam bitumen bubble area distribution at different decay times, t_1 and t_3 (4% W.C., bitumen "B", 160°C temperature).

tent from the top surface to the bottom creates a density profile that helps the foam to remain in equilibrium under gravity [13]. During the experiment the sequence of images showed that liquid bitumen drained through the plateau borders during the decay process.

In the case of 4% W.C. the polydispersity of the bubbles is also significant, as shown in Figure 5 (a) and (b). The bubbles become larger and fewer during the decay process due to coalescence, triggered by excess pressure from the foam producing water. This made the 4% W.C. foam less stable compared to 1% W.C. as indicated in Figure 3 (b). Since heat exchange occurs between water and bitumen during the foaming process, more energy is required to evaporate the water. Hence, increasing the water content decreases the temperature of foam in general, therefore the viscosity of the bitumen will increase even at the beginning of the foaming process. The increase of the viscosity minimized the creaming effect compared to the foam with 1% W.C. Nevertheless the excess pressure from higher water content produces vapor that leads to quick collapse.

As presented in Figure 6 (a) and (b), for these characteristic moment of time the cumulative number of bubbles in percentage are plotted from the histograms. The cumulative bubble size distribution in Figure 6 (a) indicated that less water content produce smaller bubbles. In the case of 1% W.C. for bitumen type "A", the number of smaller bubbles (0.2–10 mm^2) decreased immensely during the decay process and the number of larger bubbles increased. This indicates the growth of smaller bubbles over time during the decay process. In the case of 4% W.C. the bubbles size distribution change was less after the half of the expansion height. For instance the number of smaller bubbles at 6.9 s (half of the expansion height) was comparable to the 9.6 s (one fourth of the expansion height). From observation during the experiment drainage of bitumen within this time range was less compared to bitumen "B" shown in figure 4(a), rather the bubbles were growing and coarsening due to surface tension effect. In addition fast coalescence was observed during the decay process. As shown in figure 6 (b), the influence of the water content on the bubbles size distribution at the beginning of the foaming process (4.2 s) was less for bitumen type "B". Nevertheless, as presented in figure 4 (a) and 5 (a) the morphology of the bubbles was different. At the end of the decay, bubbles remaining close to the surface of the foam were smaller in size compared to the 4% W.C. In this case, the decay of the foam appears to depend much on gas loss by diffusion into the surface of the foam including a gas loss due to bursting cell walls located at the foam surface.

From observing of the image sequences, the decay mechanism of bitumen type "A" for 1% W.C. and 160°C foaming temperature is mainly caused by coalescence, drainage and gas

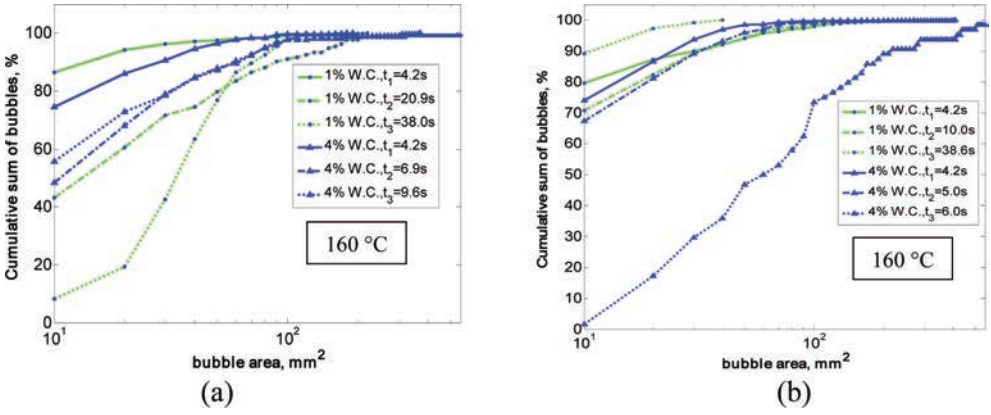

Figure 6. Cumulative sum of bubble area vs. number of bubbles (a) Bitumen "A" (b) Bitumen "B".

loss from bursting bubbles located on the surface of the foam; Whereas bitumen type "B" was more influenced from bitumen drainage and resulting separation between the dry foam of the surface and the wet zone at the bottom of the foam for 1% W.C. and 160°C foaming temperature. Therefore the decaying mechanism for bitumen type "B" was influenced by significantly creaming effect it was followed by the loss of gas through diffusion at the surface the bursting bubbles on the surface of the foam. Moreover, in the case where 4% W.C. and 160°C foaming temperature was used both bitumen types were influenced mainly from quick coalescence of individual bubbles.

5 CONCLUSIONS

Foam bitumen decay was found to be a dynamic process of coarsening of the foam bitumen bubbles. The coarsening takes place in a fraction of a second creating impacts on adjacent bubbles and eventually leading to sudden bubble coalescences. In all experiments it was observed that there is a redistribution of bubble size during the decaying process. During the decay of the bubble size distribution became progressively larger with time for 160°C bitumen temperature. In general, at the beginning of the foam formation, majority of the bubbles are small in size (0.2–10 mm^2) and the foam is relatively monodisperse, at latter stage the bubbles became polydisperse. Comparing different foaming conditions, it was observed that the majority of the bubble size distribution ranged between bubble area of 0.2–10 mm^2 regardless of the water content. For the harder bitumen "B" the cumulative bubble area and number of bubbles were less influenced by the water content at 160°C foaming temperature as compared to the softer bitumen "A". During the decaying process, at a time t_2 and t_3, bitumen "B" at 1% W.C. had a high percentage of small bubbles area (0.2–10 mm^2) compared to bitumen "A" for 1% W.C. Hence, the morphology and bubble size distribution depended on the origin of the binder.

The evaluation of foam bitumen formation and decaying mechanism with X-ray analysis was helpful to understand the influence of water on the foaming of bitumen from the experimental point of view. Understanding the decaying mechanism is certainly useful to identify and optimize the stabilizing mechanism. For instance at lower water content (1% W.C.) and 160°C foaming temperature uniform bubble size distribution was found but the foam was decaying due to drainage, creaming and bubble burst at the foam surface. Different literatures suggested that this decaying mechanism can be improved by increasing the viscosity of the bitumen and reducing the diffusion of gas between bubbles. Similarly other experiments performed in this research can be used to improve the different stabilizing mechanism of foam bitumen.

Formation and decaying of foamed bitumen is a complex mechanism which certainly needs further attention and research efforts. However, principles found and shown here appear

promising and may serve as an element for both more reliable practical tools for assessing foaming and decaying mechanisms of foam bitumen. This also helps to improve theoretical understanding and characterization of foam bitumen.

REFERENCES

[1] Koenders B.G., Stoker D.A., Bowen C., de Groot P., Larsen O., Hardy D., and Wilms K.P., "Innovative Process In Asphalt Production And Application To Obtain Lower Operating Temperatures," presented at the 2nd Eurasphalt & Eurobitume Congress Barcelona 2000, 2000.

[2] Jenkins K.J., "Mix Design Consideration for Cold and Half-Warm Bituminous Mixes with Emphasis on Foam Bituemn" Doctor of Philosphy, Department of Civil Engineering university of Stellenbosch, 2000.

[3] Namutebi M., "Some Aspects of Foamed Bitumen Technology," Licentiate Thesis, Division of Highway and Railway Engineering, Royal Institute of Technology, Stockholm, 2011.

[4] Muthen K.M., "Foamed Asphalt Mixes," CSIR TRANSPORTEK, 1998.

[5] van de Ven M.F., Sluer B.W., Jenkins K.J., and van den Beemt M.A., "New developments with half-warm foamed bitumen asphalt mixtures for sustainable and durable pavement solutions," *Road Materials and Pavement Design,* vol. 13, pp. 713–730, 2012.

[6] Chowdhury A. and Button J.W., "A Review of Warm Mix Asphalt," Texas Transportation Institute, 2008.

[7] Stevenson P., *Foam Engineering Fundamentals and Applications*, 2012.

[8] Matzke E.B., "Volume-shape relationships in variant foams. A further study of the role of surface forces in three-dimensional cell shape determination," *Am. J. Botany,* vol. 33, 1946.

[9] Lemlich R., "Prediction of Changes in Bubble Size Distribution due to Interbubble Gas Diffusion in Foam.," *Ind. Eng. Chem. Fundam,* vol. 17, pp. 89–93, 1978.

[10] Rami-shojaei S., Vachier C., and Schmitt C., "Automatic analysis of 2D foam sequences: Application to the characterization of aqueous proteins foams stability," *Image and Vision Computing,* vol. 27, 2009.

[11] Lambertm J., Cantat I., Delannay R., Mokso R., Cloetens P., Glazier J., and Graner F., "Experimental Growth law for Bubbles in a Moderately "wet" 3D Liquid Foam," *Phys. Rev. Lett.,* vol. 99, 2007.

[12] Körner C., Thies M., and Singer R.F., "Modeling of metal Foaming with Lattice Boltzmann Automata," *Advanced Engineering Materials,* vol. 4, pp. 765–769, 2002.

[13] Weaire D. and Hutzler S., *The Physics of Foams. Oxford University Press, Oxford.* Oxford: Oxford University Press, 1999.

[14] Denis W. and Stefan H., *The Physics of Foams*. oxford: clarendon press 1999.

[15] Korner C., "Foam formation mechanisms in particle suspensions applied to metal foams," *Materials Science and Engineering,* vol. 495, pp. 227–235, 2008.

Asphalt Pavements – Kim (Ed)
© 2014 Taylor & Francis Group, London, ISBN 978-1-138-02693-3

Evaluating the effects of Sasobit on characterization and workability of asphalt mixes containing reclaimed asphalt binders

Faramarz Safazadeh
Sharif University of Technology, Tehran, Iran

Ali Vahabi
Isfahan University of Technology, Isfahan, Iran

ABSTRACT: Use of Reclaimed Asphalt Pavement in HMA[1] is beneficial by reduction of initial costs. But the higher stiffness of aged binder may lead to workability issues in the field, therefore use of large percentages of RAP[2] impacts the HMA properties. Utilizing Sasobit is a solution to use more RAP at a relatively lower temperature in HMA mixes. This study investigates the effects of 2 percent Sasobit on the reduction of compaction temperature by measuring low shear viscosity and workability of mixtures containing RAP binder. Low and intermediate temperature properties of RAP binder using mix designs were compared to properties of artificially aged binders. Virgin binder was aged in PAV to make artificial RAP binder. Comparison between physical parameters of RAP binder and binder aged in PAV[3] was done and it was found that about 40 hours is sufficient for simulating the aging of RAP binder and making artificially aged binder. Results of this study on artificial RAP show that utilizing Sasobit is a feasible way to make HMA which contain 25% RAP. Utilizing RAP and Sasobit together in a HMA project would lead to select softer virgin asphalt binder with a lower performance grade.

Keywords: Recycling, reclaimed asphalt binder, HMA, WMA[4], mortar

1 INTRODUCTION

Asphalt recycling became popular since 1970s with shortage of resources, increase in binder price and environmental issues. Also utilization of RAP in HMA decreases the costs of disposals. The higher the percentage of RAP utilized in a job, the greater is the savings. Incorporating Warm Mix Asphalt (WMA) technologies like Sasobit into HMA mixes conserves fuel by reducing compaction and mixing temperature and will improve the flow of asphalt [1]. Both Aged binder from RAP and Sasobit will have some effects on resultant binder. For compensating the change of rheological binder properties caused by the aged binder and Sasobit, a virgin binder with a lower Performance Grade (PG) will be used [2].

To date, extraction with solvents and recovery of RAP binder is the only method to obtain binder from aggregates for physical characterization. The reaction of asphalt binder and solvent while in solution can alter the physical properties of the recovered asphalt binder like binder hardening. Residual solvent often remains in the recovered asphalt binder at the

[1]Hot Mix Asphalt.
[2]Reclaimed Asphalt Binder.
[3]Pressure Aging Vessel.
[4]Warm Mix Asphalt.

completion of the recovery process, which alters the physical properties of the asphalt binder. Also there would be possibilities that Asphalt binder is not completely extracted from the aggregate, leaving strongly adsorbed material that may have significantly different bulk physical properties than the remainder of the recovered asphalt binder [3]. To determine low temperature characterization of RAP binder properties, researchers have developed mix designs and back calculation of binder properties [4].

The higher stiffness of aged binder may lead to workability issues in the field, therefore use of large percentages of RAP impacts the HMA properties. Utilizing Sasobit is a solution to use more RAP at a relatively lower temperature in HMA mixes [5–7]. Sasobit lower the viscosity of asphalt, making the end product attaining sufficient workability and having the ability to be compacted to the desirable air void [5].

Workability is known as the ability of the asphalt mixture to be easily handled, placed, and be compacted. Measuring the workability of HMA mixtures is a matter of interest and many agencies determine mixture workability based on subjective visual field observations and other methodologies. To date, limited research has been conducted to identify a methodology to quantify HMA workability.

The concept behind workability testing devices for HMA appears to have begun with Marvillet and Bougault in 1979. Instrotek, Inc. took their ideas and developed the prototype equipment.

The general concept that they developed involved measuring the torque required to push a paddle through a bituminous mixture at different temperatures. Because the torque required moving the paddle would increase as the temperature decreased, a measurable indication of the workability of the mixture was determined [8].

The objectives of this study were to:

1. Investigate rheological properties of Warm Mix Asphalt (WMA) binders containing artificially long-term aged binder.
2. Evaluate the workability of mixtures that incorporate RAP and WMA technology.

2 EXPERIMENTAL PLAN AND TESTS

Addressing the need for non-solvent based RAP binder characterization, two procedures for simulating the aging of RAP binder is presented in this paper. At first virgin binder is aged in PAV for several hours (20, 25, 35 and 40 hr). Low and intermediate temperature properties of RAP binder using mix designs and back calculation of binder properties is compared to properties of artificially aged binders. At last there is a comparison between reduction of compaction temperature of mixtures containing RAP by considering workability index and binder viscosity. Figure 1 shows a flow chart of the experimental design used in this study. As been said artificially RAP is produced by aging the virgin binder in the PAV. The period of time being in the PAV for aging is determined by comparison between physical parameters of RAP binder and binder aged in PAV

1. Comparison between IDT[5] of HMA species containing RAP and IDT of HMA species containing burned RAP (RAP aggregates) and binder aged in PAV.
2. Comparison between stiffness of binder aged in PAV and extrapolated stiffness of RAP binder computed by Sweirtz et al. method.

Single gradation was used to make HMA species for IDT. For meeting the gradation requirement, the ASTM-D3515 specification (12.5 mm Nominal Maximum Aggregate Size Job Mix Specification) is used.

For this comparison RM denotes asphalt mixes prepared with virgin binder and RAP, while PM denotes asphalt mixes prepared with virgin binder, burned RAP and binder aged

[5]InDirect tension test.

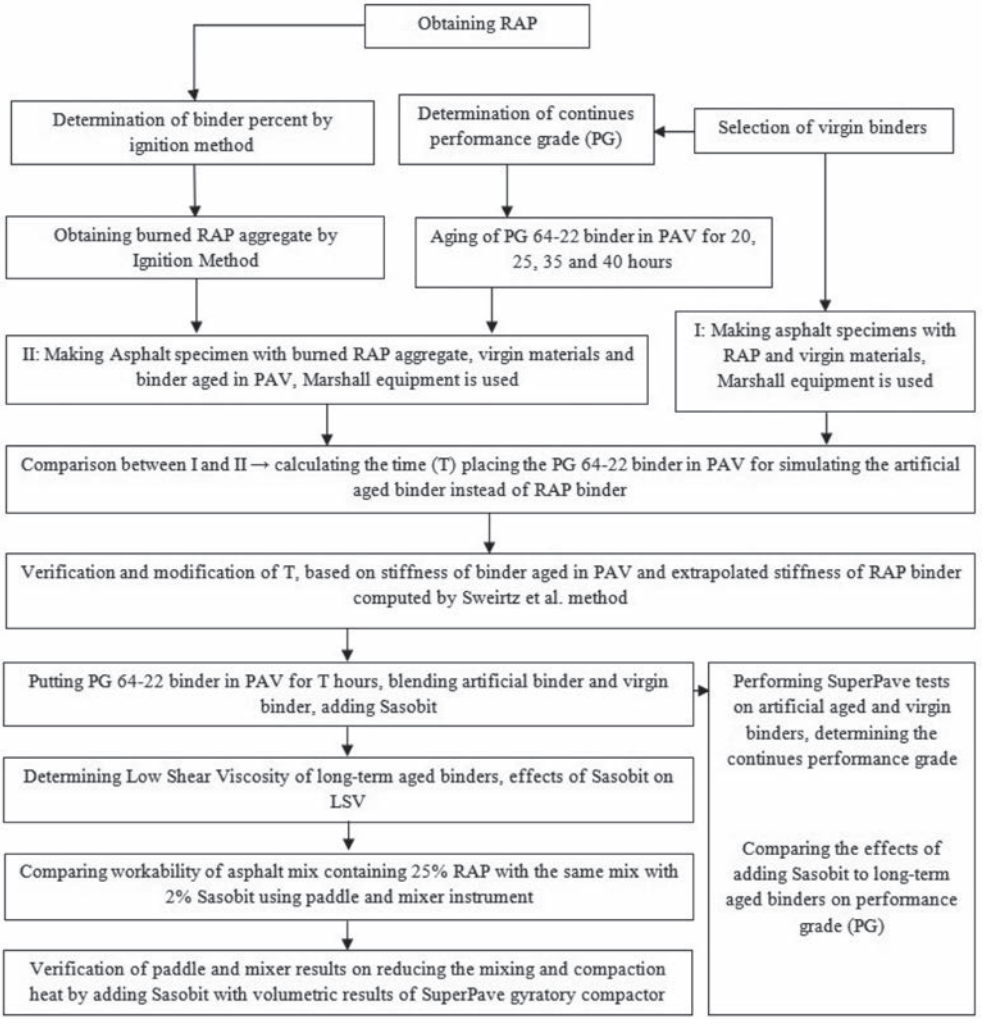

Figure 1. Diagram of experimental plan.

in PAV instead of RAP binder. For determination of asphalt content of RAP, it was ignited in furnace at 540°C in accordance with ASTM-D 6307-98 [9]. In order to create a mix design of 4% air voids, several different mixes were prepared and the air voids were calculated. The percent air voids was determined by modification to AASHTO T269 by determining the bulk specific gravity (G_{mb}) and theoretical maximum density (G_{mm}) of the mixes.

In the second method developed by Sweirtz et al. the proposed analysis procedure will require the preparation of two mortar samples from one RAP source and one fresh binder sample. SRAP denotes mortar sample that contains RTFO binder and R100 (passing No. 50 and retained on No. 100 sieve) RAP while RRAP denotes mortar sample that contains RTFO binder and burned R100 RAP. Both the total binder content and gradation of the mortar samples is equal, meaning that any difference in properties between the SRAP and RRAP mortar can be attributed to the RAP binder contained within the SRAP mortar. The analytical procedure is based on the assumption that the effect of RAP binder on the continuous grading curve for the fresh binder will simply be a shift in stiffness or m-value. The shift between the stiffness of SRAP and RRAP at –12°C and –18°C remains constant; respectively the same shift at the critical time (60 seconds) would be applied to the fresh binder at –12°C and –18°C. Based on this method the stiffness of fresh binder blended with

RAP binder is calculated and stiffness of RAP binder can be extrapolated on a diagram of stiffness and percent of RAP binder. With comparison between stiffness of RAP binder and virgin binder aged in PAV, the time of aging is predicted.

3 RESULTS AND DISCUSSIONS

In Figure 2 force—displacement curve is shown in order to compare the total fracture energy and fracture energy to failure [10]. In this figure RM mixes show less displacement in their maximum tensile strength in comparison with PM mixes. Therefore, for more simulating PM40 is placed in 135°C for about 2 hours in order to increase asphalt absorption by aggregates.

Table 1 presents indirect tensile strength properties of each specimen. It was observed that virgin binder aged around 40 hours in PAV can be used instead of RAP binder and its effects would be observed through SuperPave asphalt binder tests.

In Figure 3 stiffness of SRAP and RRAP mortar samples, containing 4, 7 and 10 percent RAP binder measured by BBR test at −12°C and −18°C are shown. Making mortar samples with higher percentages of RAP binder because of poor workability of them was impossible.

For a given temperature, higher percent of RAP binder have higher shift between the stiffness of SRAP and RRAP because of high stiffness of RAP binder in comparison with binder that is aged in RTFO. In BBR test stiffness reduces with time but the shift between

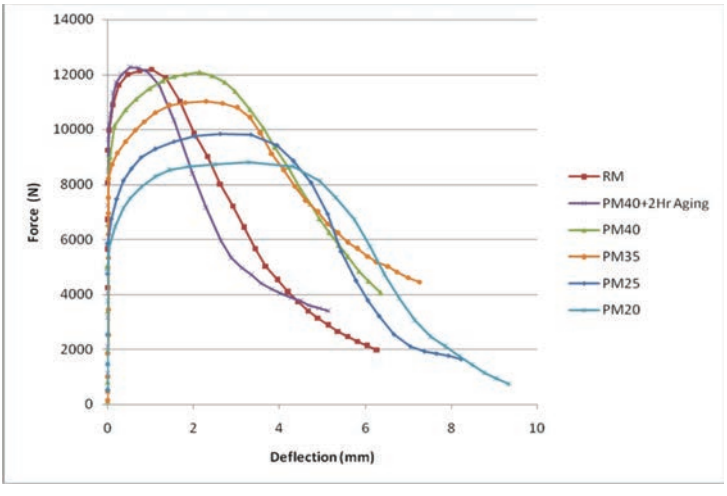

Figure 2. IDT results for different aging times.
*Binder in PM20, PM25, PM35 and PM40 has aged in PAV for 20, 25, 35 and 40 hours.

Table 1. Results of indirect tensile strength tests.

Specimen	Force (N)	Tensile strength (kpa)	Displacement (mm)	Fracture energy to failure (kj)	Total fracture energy (kj)
RM	12231	1036	0.87	12	43.8
PM20	8820	745	3.29	24.9	57.7
PM25	9841	795	2.62	23.7	56.3
PM35	11025	937	2.29	23.5	61.1
PM40	12021	1045	2.14	24.1	59.5
PM40+2h aging	12251	1069	0.53	6.1	37.6

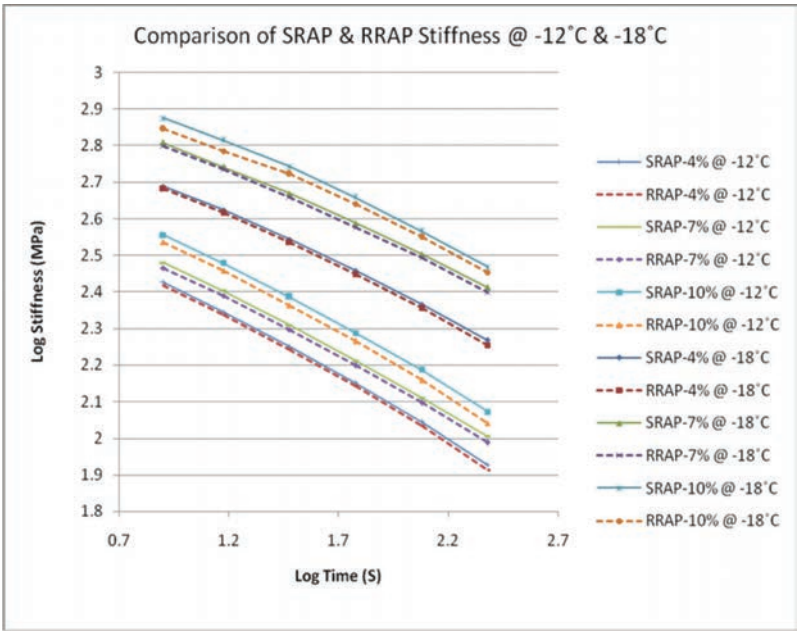

Figure 3. Stiffness diagrams of SRAP and RRAP mortars samples.

Table 2. Shift between SRAP and RRAP mortar binder.

		RRAP			SRAP			
Log time	Time (s)	Log stiffness	m-value	Stiffness (MPa)	Log stiffness	m-value	Stiffness (MPa)	Log δ between two stiffness
2.42	0.278	262	2.43	0.29	267	0.9	8	0.0082
2.33	0.301	217	2.34	0.312	221	1.18	15	0.008
2.24	0.326	175	2.25	0.336	178	1.48	30	0.0074
2.143	0.352	139	2.152	0.36	142	1.78	60	0.0093
2.03	0.377	108	2.04	0.384	111	2.08	120	0.0119
1.92	0.403	82	1.93	0.408	84.5	2.38	240	0.013
						δ mean value		0.0096
						Standard deviation		0.0023

Table 3. Applying the shift at the critical time.

Time (s)	Stiffness RTFO binder (MPa)	Log stiffness RTFO binder	δ	Log stiffness[1] RTFO + 4% RAP binder	Stiffness RTFO + 4% RAP binder (MPa)
60	92.6	1.97	0.0093	1.976	94.6

1—log stiffness RTFO + 4% RAP binder = log stiffness RTFO binder + δ.

SRAP and RRAP is constant except mortar samples which contain 10 percent RAP binder at −18°C. This could be of non-uniform or non-homogeneous blend of mortar binders and the sensitivity of stiffness in low temperatures. In Tables 2 and 3 stiffness of binder aged in RTFO and 4 percent RAP binder through applying the shift at the critical time (60 seconds) is calculated. Other cases are performed like the previous state.

After determining the stiffness of binders containing RAP binder at each temperature, stiffness of RAP binder is extrapolated on a diagram of stiffness and percent of RAP binder (Fig. 4). Then extrapolated stiffness at each temperature is compared with stiffness of virgin binder aged in PAV to estimate the time for stimulating the aging of RAP binder (Fig. 5). The resultant time is averaged between two temperatures and about 40 hours is quite enough for stimulating the aging of RAP binder and making artificially aged binder.

Continues performance grade of two virgin binders (PT[6] 60-70 and PT 85-100) and the artificial aged binder through SuperPave tests are presented in Table 4. Based on these continues performance grades, allowable percentage of RAP binder blending with virgin binder to obtain the binder which is specified by the agency depending on the project location and conditions can be represented by the following equation:

$$RAP = \frac{(T_{\text{Blend}} - T_{\text{Virgin}})}{(T_{\text{RAP}} - T_{\text{Virgin}})} \tag{1}$$

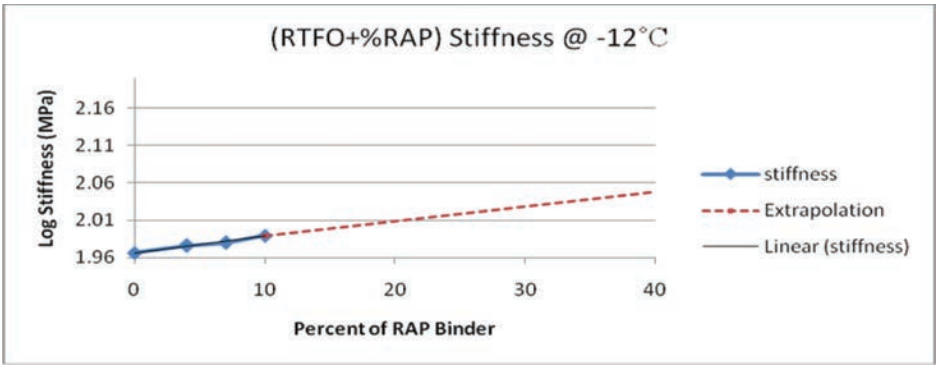

Figure 4. Stiffness of blended binder containing RAP binder.

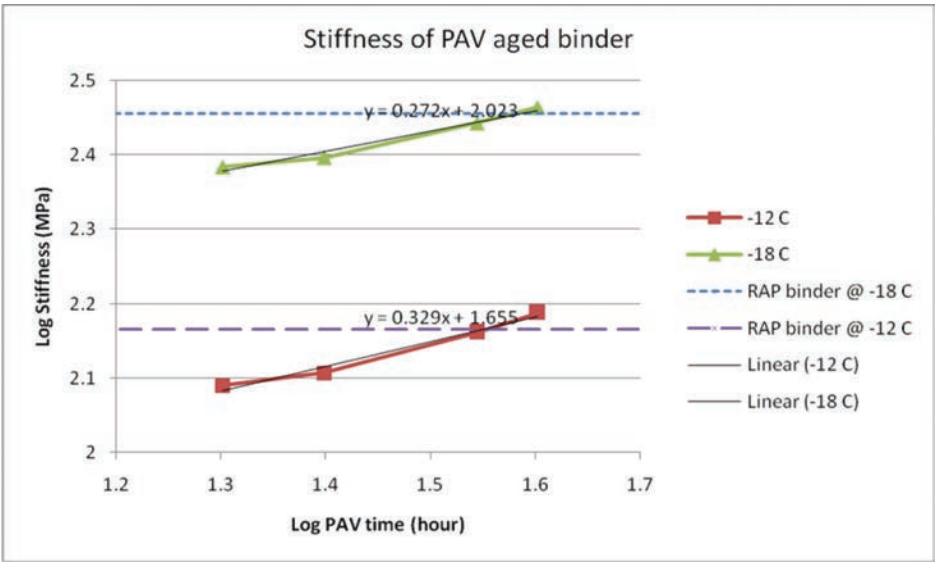

Figure 5. Stiffness of binder aged in PAV vs. extrapolated stiffness of RAP binder.

[6]Penetration test.

Table 4. Performance grade of virgin and artificial binders.

Performance grade	Aging condition	Test properties	Critical temperature °C		
			PT 60-70	PT 85-100	Artificial RAP
High temperature	None	G*/sinδ (kPa) = 1.0	67.3	61.5	76.4
	RTFO	G*/sinδ (kPa) = 2.2			
Intermediate temperature	RTFO+PAV	G*.sinδ (kPa) = 5000	21.8	20.2	24.5
Low temperature		m-value = 0.3	–25	–26.2	–15.6

Table 5. Performance grade of virgin PT 60-70 binder and 25% artificial RAP.

Performance grade	Aging condition	Test properties	Critical temperature °C	
			Virgin binder + 25% artificial RAP	2% sasobit added
High temperature	None	G*/sinδ (kPa) = 1.0	70.2	74.3
	RTFO	G*/sinδ (kPa) = 2.2		
Intermediate temperature	RTFO+PAV	G*.sinδ (kPa) = 5000	22.3	23
Low temperature		m-value = 0.3	–21.9	–21.7

Table 6. Performance grade of virgin 85–100 binder and 25% artificial RAP.

Performance grade	Aging condition	Test properties	Critical temperature °C	
			Virgin binder + 25% artificial RAP	2% sasobit added
High temperature	None	G*/sinδ (kPa) = 1.0	66.2	70.1
	RTFO	G*/sinδ (kPa) = 2.2		
Intermediate temperature	RTFO+PAV	G*.sinδ (kPa) = 5000	22.1	21.3
Low temperature		m-value = 0.3	–22.3	–22.1

where T_{virgin} is the critical temperature of the virgin asphalt binder; T_{blend} is the critical temperature of the blended asphalt binder; %RAP is the percentage of RAP to be used in the HMA expressed in decimal; and TRAP is the critical temperature of the recovered RAP binder. To satisfy the low-temperature grade of PG 64-22 when the virgin PT 60-70 binder is utilized, allowable percentage of RAP binder is 32% and when virgin PT 85-100 binder is utilized, 40% is the allowable percentage of RAP binder.

In Table 5 and 6 performance grade of 25% RAP blended with virgin binder and the influence of adding 2% percent Sasobit to this blend is presented.

SuperPave tests show that utilizing softer binder will help to have better performance in low temperatures and this will justify the increase in allowable percentage of RAP. From Table 5 it is observed that by adding Sasobit the performance grade of the blend will be PG 70-16. And for Table 6 it's PG 70-22, therefore adding Sasobit to the softer virgin binder is more economical by improving the performance grade from PG 66-22 to PG 70-22.

Viscosities of asphalt binder at different shear rates are obtained and by fitting Cross-Williamson, low shear viscosity is determined. The Cross-Williamson model is:

$$\eta = \eta_{\infty} + \frac{\eta_0 - \eta_{\infty}}{1 + (k\dot{\gamma})^n} \tag{2}$$

where η_∞ is the terminal viscosity, η_0 is the zero shear viscosity; k and n are constant models and $\dot{\gamma}$ is the shear rate. In this research low shear viscosity for virgin PG 64-22 binder, virgin binder with 25% artificial RAP and the same blend with 2% Sasobit is obtained. Table 7 presents viscosities at different shear rates at 145°C for virgin binder with 25% artificial RAP and all parameters by fitting Cross-Williamson are presented in Table 8. Other states are obtained likes this; for all of them mixture and compaction temperatures based on low shear viscosities are presented in Table 9.

Accuracy and validity of LSV is upon to measuring the viscosities near zero shears and also the model that is used for fitting. Viscosity is measured by the rotational viscometer as specified in AASHTO T-316 (TP48). Figure 6 presents viscosity curves at each shear rate for virgin binder with 25% artificial RAP. In Figure 7 low shear viscosity vs. temperature for virgin PG 64-22 binder (Pen 60-70), virgin binder with 25% artificial RAP and the same blend with 2% Sasobit is shown. Virgin binder containing 25% artificial RAP with 2% Sasobit has the biggest absolute value slope of reducing LSV; thus it could be concluded that it has temperature sensitivity. Also it could be seen that adding 25% artificial RAP to virgin binder increase its sensitivity to temperature. Viscosity at each shear rate in a constant temperature is measured and data which is fitted by Cross-Williamson shown in the next column. Different between measured and fitted viscosity is shown by dη and smaller the total square

Table 7. Viscosities of virgin binder with 25% artificial RAP at 145 °.

			Viscosity (cP)		
Temperature (°C)	Shear rate (1/s)	Torque (LV[1])	Measured	Fitted data	(dη)^2
145	0.68	1	1255.5	1277.5	484
	1.7	1.7	918	867.2	2583.4
	2.55	2	675	666.7	67.7
	3.4	2.2	540.5	543.7	3991
	5.1	2.5	422.3	409.9	156.1
	6.8	2.8	352.3	342.6	92.8
	17	6	303.5	235.6	4604.7
	34	10.6	265.5	209.6	3119
	47.6	12.1	215.5	203.8	135
	68	16.3	202.5	200.2	5.2

1—LV = 673.7 dyneocm.

Table 8. LSV parameters for virgin binder with 25% artificial RAP.

Temperature (°C)	N	K	η_0 = LSV =	η_∞ =	Sum (dη)^2
125	1.1	1.8	3014.7	610	10767
145	1.5	0.6	1559.6	195	15239
165	2	0.6	1017.5	112	2353

Table 9. Mixture and compaction temperatures based on low shear viscosities.

	Temperature (°C)	
Binder	Mixing	Compaction
Virgin PG 64-22	131	114
Virgin PG 64-22 + 25% RAP	148	124
Virgin PG 64-22 + 25% RAP + 2% sasobit	117	102

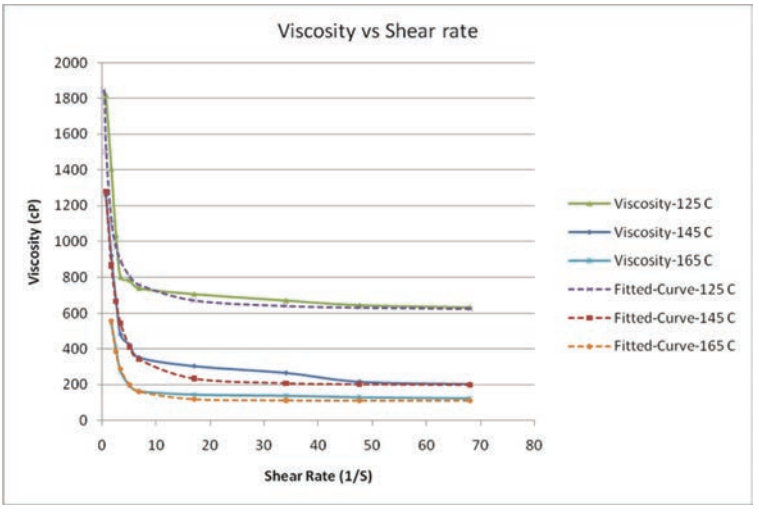

Figure 6. Viscosity curves for virgin binder with 25% artificial RAP.

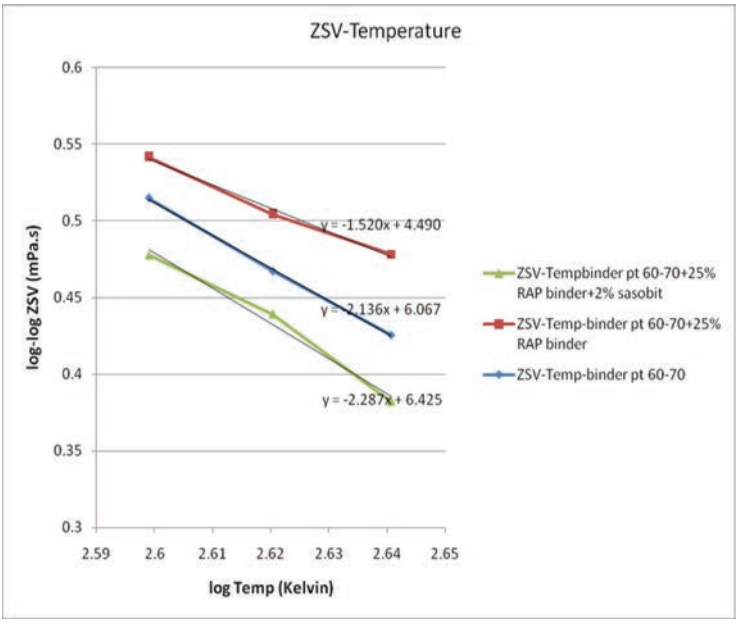

Figure 7. Low shear viscosities vs. temperature.

of that shows the accuracy of fitting. Brookfield apparatus Viscometer used in this study could measure viscosities that required torques between 1 to 100 LV; therefore by using spindle No. 27 viscosities at lower shear rates could be taken.

Another way for determining or make comparison between temperatures of mixture and compaction of asphalt mixes is evaluating the workability of the mix. For measuring workability a workability meter device is built in this study (Fig. 8). Device tools include a motor, a gearbox that reduces the rotating rate of the shaft from 1400 to 23.3, a shaft and two paddles at the end of the shaft, an instrument for measuring the torque and a bucket for mixing the asphalt according to what is made by Instrotek, Inc [8]. The more torque that asphalt mix causes to the device, it means that the mix has less workability. Evaluating the workability

Figure 8. Devices for evaluating workability of asphalt mix.

Table 10. Results of workability devices.

	Asphalt mix + 25% RAP		Asphalt mix + 25% RAP + 2% sasobit	
Mixing temperatures (°C)	Torque (N · m)	Workability (1/N · m)	Torque (N · m)	Workability (1/N · m)
150	14.7	0.068	12	0.083
140	17	0.059	12.8	0.078
130	26	0.038	14.7	0.068
120	29.7	0.034	22	0.045
110	31.9	0.031	28	0.036

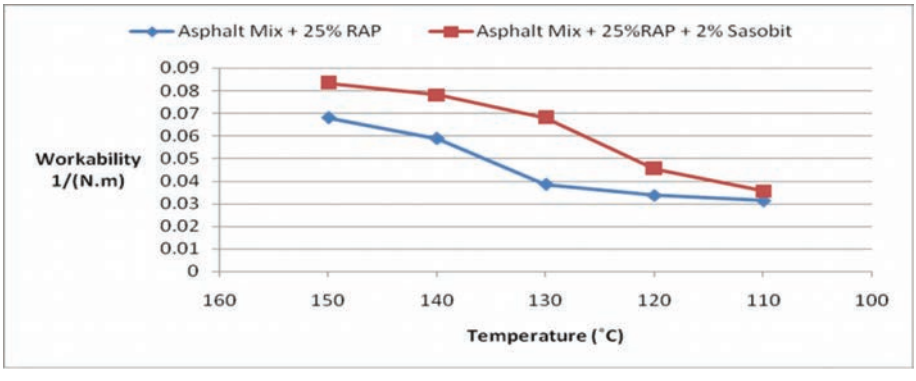

Figure 9. Graphs of workability.

criterion by this device is the reverse value of the torque. Asphalt mixture containing 25% RAP in comparison with the same mixture with 2% Sasobit are made and their workability are evaluated and presented in Table 10.

In Figure 9 the graphs of workability and temperature are shown, obvious improvement of workability by adding 2% Sasobit and about 20°C reduction in mixture temperature are seen. For confirmation of the workability evaluation, asphalt mixture with the same properties are made and compacted by SuperPave gyratory compactor in 150°C. Comparison is

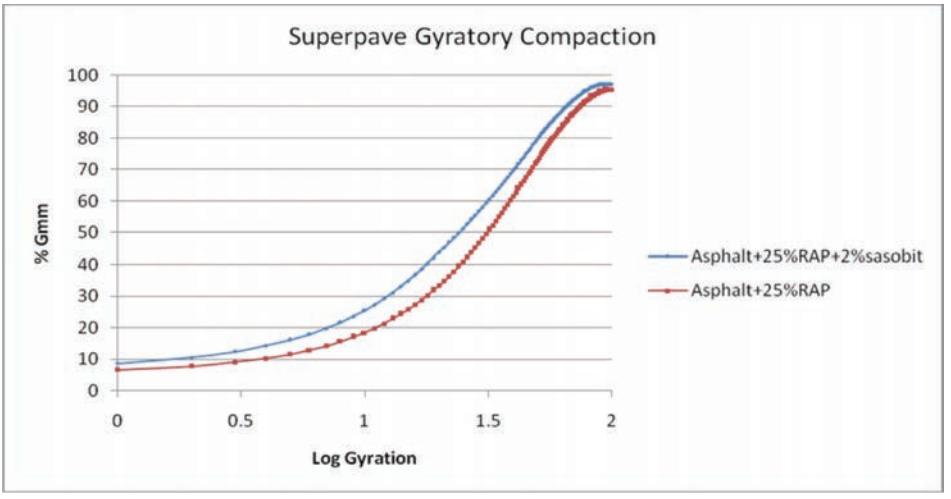

Figure 10. Graphs of % Gmm in SGC.

done based on the air trapped in the asphalt mix and it shows the capability of the asphalt compaction (Fig. 10). For better comparison, gradation and G_{mm} of two mixes are the same. Adding 2% Sasobit to the asphalt mix will improve the compact ability and reduces the air tapped from 4.5% to 2.8%. Thus it shows that the workability device compared two mixes approximately right.

4 CONCLUSION AND RECOMMENDATIONS

Based on this study, the following conclusions and recommendations can be made

1. Virgin binder aged around 40 hours in PAV can be used as artificial aged asphalt binder and its effects on stiffness and total fracture energy would be the same with RAP asphalt binder.
2. SuperPave tests show that utilizing RAP and Sasobit together in a HMA project would lead to select softer neat asphalt binder with a lower performance grade.
3. Using Sasobit with a softer neat asphalt binder is practical way of increasing allowable percent of RAP binder.
4. Use of Sasobit with asphalt binder at a mixing temperature of 130°C produced mixes with workability and compatibilities that are lower but close to those of a mix with virgin asphalt binder, mixed at 150°C.
5. There seems to be a significant advantage in using Sasobit in reducing temperature for using asphalt binder in recycling of HMA. The important advantages of using Sasobit are in terms of reduction of temperature and hence associated fuel cost and emissions, and the ability to recycle HMA at a lower temperature. This ability would lead to more widespread use of Reclaimed Asphalt Pavement.
6. Field project to evaluate Sasobit mixes with HMA should be initiated. The use of 2% Sasobit with asphalt binder is recommended.

REFERENCES

[1] Hurley G.C. and B.D. Prowell. Evaluation of Sasobit(R) for Use in Warm Mix Asphalt, National Center for Asphalt Technology, NCAT Report 05-06, 2005.
[2] Kim, H. and S.J. Lee. Rheology of Warm Mix Asphalt Binders with Aged Binders, Construction and Building Materials, No. 25, pp. 183–189. 2011.

[3] McDaniel, R. and R.M. Anderson. Recommended Use of Reclaimed Asphalt Pavement in the SuperPave Mix Design Method-Project 9–12, National Academies Press, NHCRP Report 452, 2001.
[4] Swiertz, D. and E. Mahmoud. Estimating the Effect of RAP and RAS on Fresh Binder Low Temperature Properties without Extraction & Recovery, Transportation Research Record, No. 2208, 2010.
[5] Mallick, R. and E. Bradley. An Evaluation of Heated Reclaimed Asphalt Pavement (RAP) Material and Wax Modified Asphalt for Use in Recycled Hot Mix Asphalt (HMA), the 86th Annual Meeting of the Transportation Research Board, 2007.
[6] Mogawer, W.S. and A.J. Austerman. Incorporating High Percentages of Recycled Asphalt Pavement (RAP) and Warm Mix Asphalt (WMA) Technology into Thin Hot Mix Asphalt Overlays to be Utilized as a Pavement Preservation Strategy, the 88th Annual Meeting of the Transportation Research Board, 2009.
[7] Tao, M. and R.B. Mallick. An Evaluation of the Effects of Warm Mix Asphalt Additives on Workability and Mechanical Properties of Reclaimed Asphalt Pavement (RAP) Material, Transportation Research Record, No. 2126, 2009.
[8] Gudimettla M. and L.A. Cooley. Workability of Hot Mix Asphalt, National Center for Asphalt Technology, NCAT Report 03-03, 2004.
[9] ASTM D 6307. Standard Test Method for Asphalt Content of Hot-Mix Asphalt by Ignition Method, American Society for Testing and Materials, West Conshohocken. 1999.
[10] Witczak, M.W. and K. Kaloush. Simple Performance Test for SuperPave Mix Design, National Academies Press, NHCRP Report 465, 2002.

Asphalt Pavements – Kim (Ed)
© 2014 Taylor & Francis Group, London, ISBN 978-1-138-02693-3

Towards a better understanding of Warm Mix Asphalt surface-active additives mechanism

Geisler Flavien
Laboratoire de Tribologie et Dynamique des Systèmes, UMR 5513 CNRS-ECL-ENISE, Ecole Centrale de Lyon, Ecully, France
Total Marketing Services, Centre de Recherche de Solaize, Solaize, France

Kapsa Philippe
Laboratoire de Tribologie et Dynamique des Systèmes, UMR 5513 CNRS-ECL-ENISE, Ecole Centrale de Lyon, Ecully, France

Lapalu Laurence
Total Marketing Services, Centre de Recherche de Solaize, Solaize, France

ABSTRACT: Although foaming, viscosity reduction and surface-active agents are now commonly used technologies to produce Warm Mix Asphalt (WMA), the mechanisms of such technologies are still not well understood. That is why this study aims to understand surface-active additives mechanism to further improve the chemistry of such additives. Literature shows that the studied additives have only a slight impact on the viscosity and allocates them lubricant and adhesion promoting properties. In order to evaluate possible reactions of WMA additives with mineral substrates and/or bitumen components, tribological experiments were conducted on the linear alternative tribometer available at the Laboratory of Tribology and System Dynamics (LTDS). Several parameters able to act on the friction coefficient were tested. Then Scanning Electron Microscopy with Energy Dispersive X-ray Spectroscopy (SEM-EDX) and X-ray Photoelectron Spectroscopy (XPS) will be used to show evidence of a tribo-chemical film on the aggregates surface. On the other hand, quantification of the bitumen containing additives-aggregate interaction was evaluated at mixing temperature by using the sessile drop method with several kinds of minerals.

Keywords: Warm Mix Asphalt additives mechanism, tribological film formation, surface tension measurements

1 INTRODUCTION

Over 100 Mt of bitumen are worldwide consumed every year, mainly for asphalt pavement applications [1]. Traditional asphalt concretes are composed of about 95 weight percent of aggregates and 5 percent of binder (bitumen). Because of its viscous-elastic properties at room temperature, bitumen should be heated to further coat the aggregates. In practice, for a better coating, both aggregates and bitumen are heated. This mixture is classically called Hot Mix Asphalt (HMA). It is traditionally manufactured at temperatures range from 150°C to 200°C and from 100°C to 135°C during the mixing and compaction steps respectively.

According to more severe regulations and with the aims to be more competitive, to improve the safety of workers, to reduce both costs and fuel consumption and to decrease pollutant (Polycyclic Aromatics Hydrocarbons, NOx, SOx, greenhouse gas) emissions, asphalt manufacturers try to reduce the asphalt mix temperatures without (significantly) affecting the properties of the mixes. For the last twenty years, manufacturers experiment Warm Mix Asphalt (WMA) technologies whose mixing temperatures are lower, typically ranged from 100°C to 140°C.

Literature reveals the existence of many different technologies, which are now commonly used to produce WMA. Some of them are called foaming technologies and results of the presence of water in the mix. Above 100°C, this small amount of water is responsible of a global mix volume expansion which improves the mixture workability [2–4]. Presence of water results of Water Based Process or is due to foaming additives such as zeolites. Others are called Non-Foaming (NF) technologies. Different kinds of NF-WMA are already available on the market and they do not contribute to the workability improvement in the same way: waxy components are thought to decrease the binder viscosity; others are thought to act as surface active agents [2–4].

In our work we are concerned by the question: "How do WMA non-foaming additives improve the workability of asphalt concretes?" The mechanisms by which they act are indeed currently not well understood.

Furthermore binder viscosity is a key parameter to explain the asphalt mix workability; so much that it has longtime been the only parameter into account. But it has been shown than some of the NF-WMA only slightly reduce the binder viscosity and it is believed that this small reduction cannot fully explain the reduction of temperatures for producing WMA rather than HMA [5].

Recently, tribological experiments have proved that WMA are effective in improving the bitumen lubrication of contact aggregate-aggregate [5–7]. Thus lubrication is a mechanism which can also contribute to improve the workability of asphalt concretes. In this study, we proposed to evaluate how WMA agents act on the binder viscosity, on the lubrication properties when two mineral surfaces are in contact and if they can improve the wettability.

2 EXPERIMENTATION

2.1 *Materials*

2.1.1 *Bitumen*

To understand how the addition of WMA additives to neat bitumen can improve the workability of the final asphalt mix a 35/50 neat bitumen was studied. The neat bitumen was provided by TOTAL. Some of its properties are summarized in Table 1. Three NF WMA additives with various chemistry were studied. Bitumens references are listed in Table 2.

2.1.2 *Aggregates*

Asphalt mixes are made of aggregates of various sizes, shapes, roughness, chemical/mineralogical compositions etc. To simplify the study flat samples of various materials were used to represent different kinds of aggregates: glass, limestone, marble and granite. Flat samples were polished prior the tests. Samples were provided by a marbler as 6 cm × 3 cm × 0.5 cm plates. More details are listed in Table 3.

Table 1. Penetration at 25°C and softening point of the control bitumen.

Penetration	Softening point
40 (1/10 mm)	51.4°C

Table 2. Reference statement of the studied bitumen.

Bitumen reference	A	B1	B2	C1	C2	D
Additive						
Name	–	Additive 1	Additive 1	Additive 2	Additive 2	Additive 3
Content	–	1% (wt)	3% (wt)	0.4% (wt)	1.2% (wt)	3% (wt)

Table 3. Details on the aggregates used in this study.

Type of aggregate	Limestone	Marble	Granite
SEM picture (magnification x72)	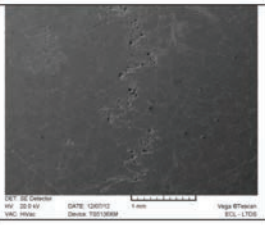	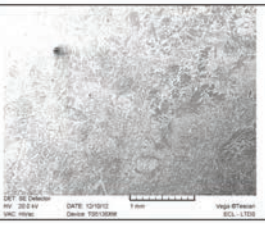	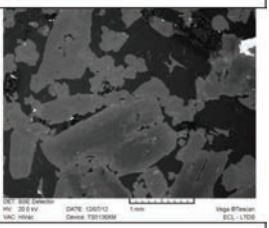
List of elements (determined by EDX)	Ca, O, Si, Mg (and C)	Ca, Mg, Si, O, Fe	Si, O, Na, Mg, Al, Ca, Fe, Ti
Compounds present	⇨ $CaCO_3$ ⇨ $CaMg(CO_3)_2$ ⇨ iron oxydes	⇨ $CaCO_3$ ⇨ $CaMg(CO_3)_2$ ⇨ $Mg_6[Si_4O_{10}](OH)$, H_2O ⇨ $(Mg,Fe)_3Si_2O_5(OH)_4$	⇨ quartz : SiO_2 ⇨ feldspath : SiO_2Al2O_3(Na/K/Ca) ⇨ Mica: $Si_6Al_2O_{20}$Mg/Fe and/or $Si_6Al_2O_{20}$Al/K ⇨ Pyroxene: Si_2O_6(MgFe)
Roughness (Ra) of flat samples (µm)	0.05	0.07	0.07

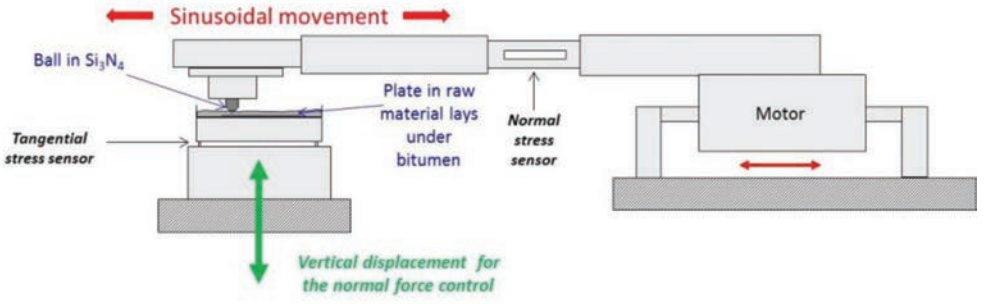

Figure 1. Ball on flat reciprocating tribometer.

2.2 *Test methods*

2.2.1 *Bitumen viscosity measurements*

A Brookfield rotational viscometer was used to determine the viscosity of virgin and WMA binders at three different temperatures (80°C, 100°C and 120°C). Then, the value at 160°C was extrapolated by semi-logarithmic regression between 100°C and 120°C. The temperature is controlled by the mean of a Peltier bottom plate.

2.2.2 *Tribological measurements*

To determine whether WMA additives are able to improve the lubricant properties of bitumen by reducing the friction coefficient of two in-contact aggregates, a pin on flat linear reciprocating tribometer was used (Fig. 1). A Si_3N_4 ball of radius 6.35 mm was chosen to slide against the mineral flats presented in section 2.1.

The experimental parameters consist in sliding distance and frequency of 10 mm and 0.1 Hz respectively, of a 50 N normal load (which creates a mean pressure of 0.7 GPa). 1600 cycles or more are generally performed during an experiment and the temperature was 120°C. Measured parameters are temperature, normal force (L), tangential force (T) and displacement. The Coefficient Of Friction (COF also noted µ) is then defined as COF = T/L (= µ).

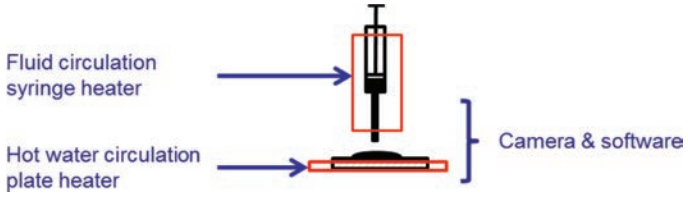

Figure 2. Scheme of the tensiometer.

Prior to experiments, mineral plates are washed three times ten minutes in a water ultrasonic bath and dried in an oven at 100°C overnight (to remove dust contaminations). Then both ball and plates are rinsed with heptane, acetone and propan-2-ol under ultrasonic conditions. Two hours before a tribological experiment, bitumen is heated at 140°C in an oven.

2.2.3 *Contact angle measurements*

Sessile drop experiments were performed in order to evaluate if WMA additives promote a better bitumen coating of aggregates. The tensiometer has been modified to allow high temperature contact angle measurements (Fig. 2). Prior experiments, all bitumens are heated at 180°C in an oven for 1 h 30 in order to pump bitumens in the syringe. In the same time, flats are washed with white-spirit and heated at 90°C thanks to the water circulation plate heater. Then the full bitumen syringe is clamped on the tensiometer and heated at 150°C via the oil circulation flat heater. After one hour, experiments are performed.

Experiments consist in laying a drop of bitumen on the mineral flat. Then, due to capillary effects, bitumens drops spread out on the plane. A camera records the process; a dedicated-software analyzed pictures by fitting the shape of the drops and gives contact-angles values. A minimum of five drops by flat sample are laid. Drop putting down is made manually. This leads to relative important initial contact angles variability.

3 RESULTS AND DISCUSSION

3.1 *Asphalt binder viscosity*

As expected, Figure 3 reveals that bitumen viscosity significantly decreases with temperature. On this figure, it can be seen that WMA additives are effective in decreasing the control binder viscosity; they acts as flow improvers. At 120°C, the most important control binder viscosity reduction is obtained by adjunction of additive D. In this case, a 27% decrease was measured. However, the control binder viscosity is reduced by 90% when temperature gets from 120°C to 160°C. As confirmed by literature review, NF-WMA agents' viscosity can therefore not fully explain the workability of WMA.

3.2 *Tribological behavior*

First friction experiments in various speed conditions have shown that, due to the relatively high viscosity of bitumen, a liquid film can be formed in the contact. Then, it is possible to distinguish 2 situations: friction with hydrodynamic film formation, friction in boundary lubrication conditions (without a liquid film in the contact).

3.2.1 *Experiments conducted in hydrodynamic lubrication regime*

Figure 4 presents results from the tribological experiments performed with glass flats. It can be seen that the COF decreases with increasing temperatures (due to viscous effects) and the curves shape confirms that experiments are conducted in the hydrodynamic range where a full film separates the ball and the flat and where the film thickness depends on the viscosity of the lubricant (bitumen in the present case). Some experiments conducted

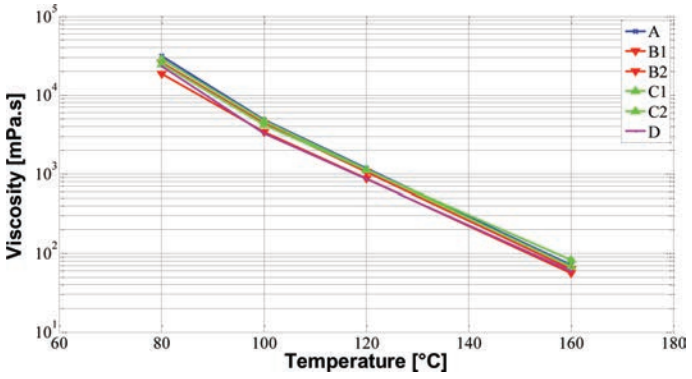

Figure 3. Viscosity of bitumen as a function of temperature; effects of WMA agents.

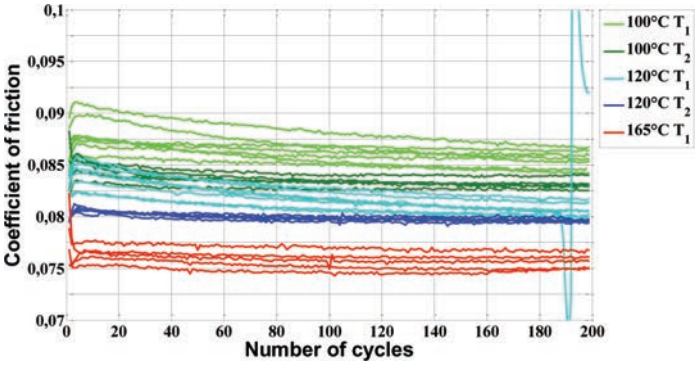

Figure 4. COF as a function of number of cycles in the case of a Si_3N_4 ball sliding against a glass flat.

at various frequencies (0.1 Hz, 0.5 Hz, 1 Hz and 2 Hz) confirm the hydrodynamic hypothesis.

This graph also reveals a time dependence of μ which can be attributed to a diffusion time of some chemical species to the sliding surfaces. The fact that the diffusion seems quicker at elevated temperatures seems corroborate this hypothesis.

One the other hand, experiments performed on glass samples at 120°C reveals that WMA agents do not modify the COF of the control bitumen under hydrodynamic conditions. This seems coherent with the fact that WMA agents imply small reduction of the binder viscosity (i.e. tribological experiments are not able to significantly differentiate these small viscosity variations).

We conclude that the sliding contact of a Si_3N_4 ball against perfectly smooth glass flat samples in presence of bitumen and with the experimental parameters we used are conducted in the hydrodynamic range where viscosity play a key role: enough to bring out the temperature influence but not strong enough to show the WMA additives influence. However this result does not imply that WMA agents do not get lubricating properties.

By using rougher materials, experiments can be performed under mixed or boundary conditions and should help to reveal the impact of WMA additives.

3.2.2 *Experiments conducted in boundary lubrication regime*

3.2.2.1 Limestone

Figure 5 shows results from tribological experiments conducted with limestone flats. This graph compares the mean COF of the control binder and those of the binder modified with various WMA chemical additives. Results seem relatively reproducible.

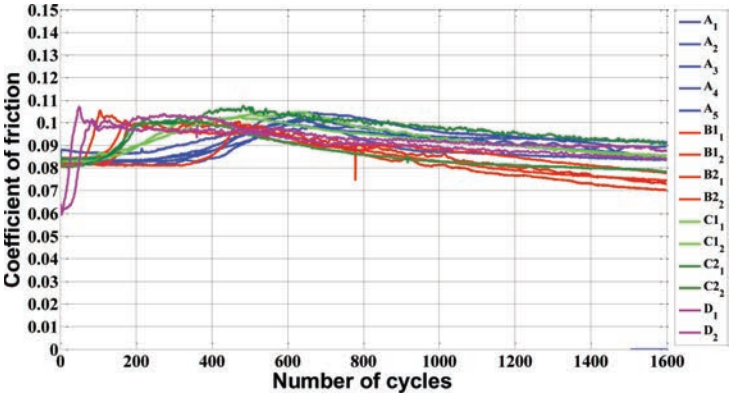

Figure 5. COF as a function of number of cycles in the case of a Si_3N_4 ball sliding against a limestone flat with bitumen in the contact.

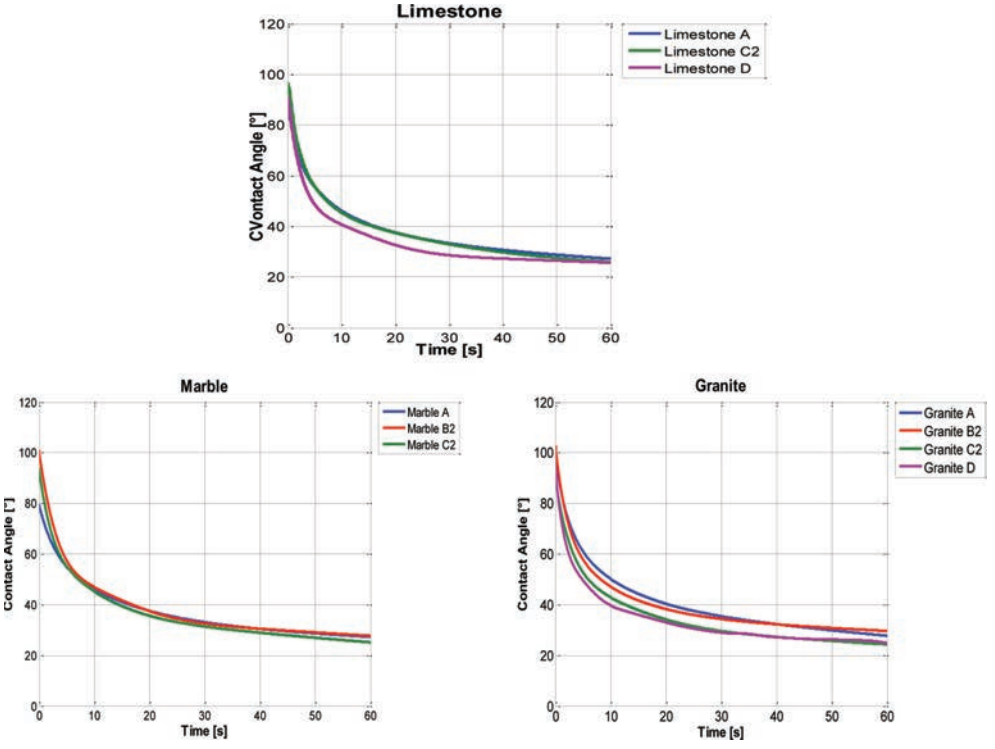

Figure 6. Contact angle measurements of bitumen droplets on various materials: limestone, marble and granite.

The control binder gets an initial 0.083 COF value for the 300 first cycles. Then μ increases up to 0.1. This increase is thought to correspond to wear of the plate. After that, the COF decreases and reaches a steady state with μ-values of 0.09.

WMA agent D leads to low value of COF in the early stage (μ = 0.06) and do not seem to act in the final stage where μ is equal to the COF-value of the control binder. It can also be noticed that wear occurs after a short initial period. This behavior suggests that this kind of components quickly move to the surface aggregate and is removed when wear occurs.

One can also suppose that the initial film thickness is thinner due to the presence of wax resulting in the short wear-induction time.

Contrary to bitumen D, bitumen containing Additive 1 do not promote COF modification in the early stage but seem to induce a COF reduction in the final stage.

3.3 *Bitumen-aggregates wettability*

Thermo-dynamical contact angle and the time necessary to reach this steady state are usually the two sought factors in wetting experiments. In some cases, the steady state time is short but it could sometimes be very long. Moreover, in our study, the bitumen's and the flat's temperatures are 150°C and 90°C respectively. That means the steady state is reached when the whole system is at 90°C and when the contact angle becomes constant. However, when the drop temperature falls from 150°C to 90°C, bitumen viscosity is dramatically increased. This can lead to very long equilibrium time (t_{eq}). That is why, our experiments were stopped at t = 40s which can further be called t_{eq}.

Figure 6 shows contact angles as a function of time for several bitumens and different kinds of plate's material. The drop spreads out very quickly for the fifteen first seconds. It could be attributed to the time at which the drop reaches the thermic equilibrium.

Plots reveal that marble and limestone plates, which are very similar in chemical composition and in roughness, get very similar contact angles at t_{eq}. On the opposite, the final contact angle measured with granitic samples is much higher confirming a better affinity of bitumen for limestone rather than granite substrates [8].

These graphs also reveal that bitumens with WMA-agents get lower contact angle than the control binder, especially in the case of granite materials.

Curves of bitumen D present rapid decrease initial contact angle to final contact angle values. This result confirms that Additive D moves to the surface of aggregate.

4 CONCLUSIONS AND PERSPECTIVES

In this study, we have shown that WMA-additives can play various roles:

- They slightly decrease the viscosity of bitumen. However, this minor phenomenon is not sufficient to explain why WMA are so workable at 120°C.
- They do not affect the COF in the hydrodynamic lubrication range (due to the small variations in binders viscosity).
- They are efficient in slightly decreasing the COF in the boundary lubrication range. This fall appears in different stage of the sliding experiments depending on the WMA-agents and on the nature of the sliding substrates.
- They facilitate the coating of aggregate as proved by contact angle measurements.

For a better understanding of the WMA additives mechanism, X-ray Photo-electron Spectroscopy (XPS) have to be used to show evidence of a tribo-chemical film on the aggregates surface.

Tribological experiments with other aggregate materials, granite and marble plates are in progress, in order to precise the role of the aggregate nature.

REFERENCES

[1] http://www.eurobitume.eu/fr/national/switzerland/qu%E2%80%99est-ce-que-le-bitume, read August 26, 2013.

[2] Capitão S.D., Picado-Santos L.G., Martinho F., Pavement engineering materials: Review on the use of warm-mix asphalt, Construction and Building Materials, 36, pp. 1016–1024, 2012.

[3] Estakhri C., Button J., Alvarez A.E., Field and Laboratory Investigation of Warm Mix Asphalt in Texas, Texas Transportation Institute, Report No FHWA/TX-10/0-5597-2, July 2010.

[4] Zaumanis M., Warm Mix Asphalt Investigation, Master of Science Thesis, 2010.
[5] Bahia H.U., Hanz A., Mahmoud E., Quantifying the Effects of Warm Miw Additives using the Asphalt Lubricity Test, Warm Mix Technical Working Group Meeting, Seattle, WA, December 16, 2009.
[6] Bahia H.U., Puchalski S., Effect of WMA Additives on Binders Workability and Performance, PMB's and WMA-binders—new experiences, NorBit seminar 2012, Grand Hotel, Oslo, October 16, 2012.
[7] Baumgardner G.L., Reinke G.R., Brown II J., Lubricity Properties of Asphalt Binders Used in Hot-Mix and Warm-Mix Asphalt Pavements, 5th Eurasphalt & Eurobitume Congress, Istanbul, June 13–15, 2012.
[8] Ardebrant, H., and R.J. Pugh. Wetting Studies on Silicate Minerals and Rocks Used in Bituminous Highways, Colloids and Surfaces 58, No. 1–2 (September 16, 1991): 111–130.

Asphalt Pavements – Kim (Ed)
© 2014 Taylor & Francis Group, London, ISBN 978-1-138-02693-3

Study on integrated application and durability of two warm-mix asphalt techniques

Liping Liu, Xiaofei Gao, Zhoucong Xu & Lijun Sun
Key Laboratory of Road and Traffic Engineering of the Ministry of Education, Tongji University, Shanghai, China

ABSTRACT: Warm-mix asphalt technique has been widely adopted by road departments in an increasing number of countries and regions due to its advantages in energy efficiency, environment protection, asphalt aging prevention, extended construction seasons, improvement of working environment for the workers and prompt opening to traffic. At present a number of warm-mix asphalt techniques have emerged. Performance of warm-mixed mixtures varies with mechanism and process of warm-mix techniques. Study shows that compared with hot mix technique, some warm-mix techniques such as warm-mix technique by adding organic viscosity reducers significantly improve stability of the mixture under high temperature, while other warm-mix techniques like surfactant-based warm-mix asphalt significantly improve the anti-fatigue performance. Therefore, the two warm-mix asphalt techniques were applied integrally to different asphalt layers on Shaoguan-Ganzhou Expressway based on their respective characteristics. 200 m test section was paved and tested in terms of compaction, evenness and other performance parameters. The test results demonstrate that all technical parameters of warm mix asphalt reach hot-mix asphalt standards. In addition, laboratory accelerated aging test on the warm and hot mix mixtures were conducted, and the durability evaluation reveals that compared with hot-mix asphalt mixture, warm-mix asphalt is more durable.

Keywords: Warm-Mix Asphalt, surfactant warm-mix asphalt technique, organic viscosity-reducing warm-mix asphalt technique, integrated application, durability

1 INTRODUCTION

Warm-mix asphalt mixture is a general term for a new kind of asphalt mixture whose construction temperature is between that of hot-mix and cold-mix (normal temperature) temperatures with performances equal to that of hot-mix asphalt mixture. Its working temperature can be 30–60°C lower than that of hot-mix asphalt mixture. It has such advantages as energy efficiency, environment-friendliness, asphalt aging prevention, extended construction season, improvement of working environment for workers and prompt opening to traffic. Therefore, warm-mix technique has aroused great interest of road workers worldwide since it emerged, and has become a hot topic for road technique researches in recent years[1,2,3,4]. At present, plenty of warm-mix techniques or products have emerged in international market, out of which warm-mix technique by foaming asphalt, surfactant-based platform warm-mixing technique and warm-mixing technique by adding organic additive etc. are representative[5,6]. The process of warm-mix varies with warm-mix mechanism of different warm-mix techniques. So do the results. The paper focuses on Surfactant-based platform warm-mixing technique and warm-mixing technique with addition of SAK organic viscosity reducers. The two warm-mix techniques were applied in different asphalt layers on Shao-Gan Expressway in consideration of their respective advantages[7]. The post-construction compaction effect and evenness and other performances were tested and compared to those of hot-mix asphalt mixture. Also,

long-term durability of the two warm-mix asphalt mixtures were evaluated through laboratory accelerated aging test and compared to that of hot-mix asphalt mixture. This paper will expound in these two aspects.

2 EVALUATION ON DESIGN AND PERFORMANCE OF MIXTURES PRODUCED BY TWO WARM MIXING TECHNIQUES

Different warm-mix asphalt techniques have different effects on performance of asphalt mixtures. The organic viscosity reducer-based SAK technique (abbreviated as S-WMA) and surfactant-based Evotherm technique (abbreviated as E-WMA) are adopted herein. Design and performance of mixtures at Gradation AC-20C and Gradation AC-13C were compared and evaluated. 70# common asphalt was used for Gradation AC-20C in the middle asphalt course, and SBS modified asphalt was used for Gradation AC-13C in the upper asphalt course. The dose of SAK added was 3% of the mass of asphalt. The dose of Evotherm DAT-H5 added was 11% of the mass of asphalt (effective ingredient: 0.5%). These two mixtures are mixed and moulded under temperature 30°C lower than that of hot-mixing.

2.1 *Comparison on performance of WAC-20C by two warm mixing techniques*

Granite and 70# common asphalt were used for Gradation WAC-20C. Warm-mix asphalt mixtures were prepared by SAK technique and Evotherm technique respectively. See Table 1 for composition of Gradation WAC-20C. The optimum asphalt-aggregate ratio and relevant parameters of asphalt mixture designed are as shown in Table 2. Results of mixtures performance test are as shown in Tables 3 and 4. Here, performances of the mixtures evaluated include stability of asphalt mixture at high temperature, crack-resistance at low temperature, water damage resistance and fatigue resistance. Relevant test methods and standards were executed per Technical Specification for Construction of Highway Asphalt Pavements (JTG F40-2004).

It can be seen from the above table that when 70# common asphalt was adopted, the optimum asphalt-aggregate ratio of both warm-mix techniques was 5.2%, 0.3% higher than that of hot-mix asphalt mixture at the same Gradation.

It can be seen from Table 3 that asphalt mixture prepared by SAK warm mix technique was significantly superior in terms of dynamic stability, while surfactant-based warm mix technique was significantly superior in terms of performance at low temperature. Water stability of both was inferior to hot-mix asphalt mixture. To improve their water stability, appropriate amount of cement or hydrated lime were added into mixtures prepared by the warm-mix

Table 1. Composition of gradation WAC-20C.

	Sieve sizes (mm)											
Type of gradation	26.5	19	16	13.2	9.5	4.75	2.36	1.18	0.6	0.3	0.15	0.075
Percent passing (%)	100	96.9	83.9	72.5	59.8	35.9	25.9	17.1	12.3	8.7	7.0	5.2

Table 2. Design results of different asphalt mixtures (AC-20C).

Type of mixture	Asphalt-aggregate ratio	Marshall stability (kN)	Flow value (mm)	Air void (%)	VFA (%)	VMA (%)
S-WMA	5.2	8.2	3.2	4.2	70.79	14.13
E-WMA	5.2	8.19	3.42	3.9	73.42	15.42
HMA	4.9	8.3	3.3	4.1	67.8	16.8
Requirement of code		≥8	1.5~4	3~6	65~75	≥13

Table 3. General performance of WAC-20C mixture.

Evaluation parameters	Dynamic stability/ time/mm, 60°C	Maximum flexure tensile strain/με	TSR (%)
Type of mixture			
S-WMA	3297	8493	76.6
E-WMA	1394	10126	76.9
HMA	1614	9916	87.7
Requirement of code	≥1000	≥2000	≥75
Test method	T0719	T0728	T0729

Table 4. Test results of warm-mix asphalt mixtures for water stability improvement.

Test option	TSR of S-WMA (%)	TSR of E-WMA (%)	TSR of HMA (%)
The original gradation	75.3 (0.89/0.67)	76.7 (0.90/0.69)	87.7
1% cement was added	86.9 (0.84/0.73)	74.7 (0.83/0.62)	–
1% hydrated lime was added	83.5 (0.97/0.81)	65.8 (0.79/0.52)	–

Note: the left parenthesized values indicate splitting-strengths before thawing, while the right parenthesized values indicate splitting-strengths after thawing.

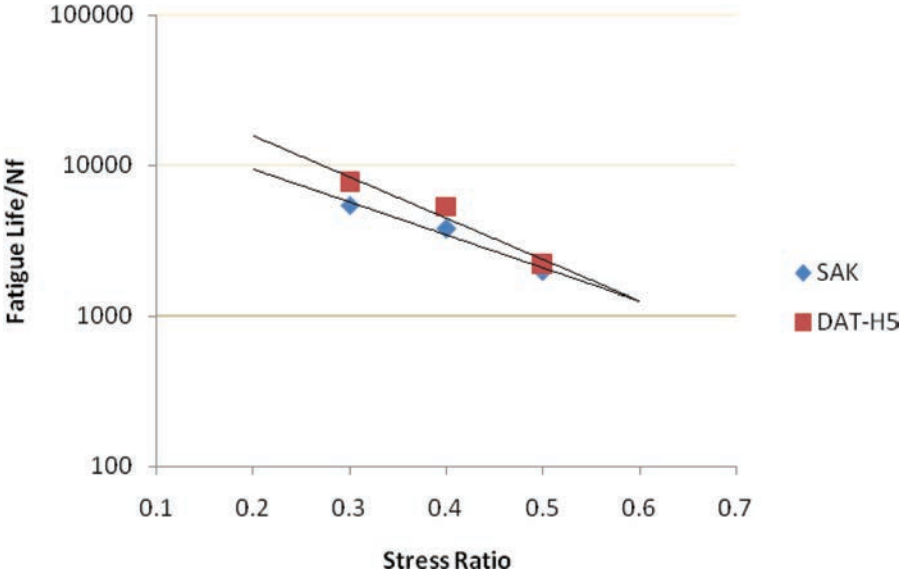

Figure 1. Fatigue curve of AC-20C mixture prepared by two warm mix techniques.

techniques respectively, in other words, 1% mineral powders in the gradation was substituted with cement or hydrated lime in equivalent mass. See Table 4 for test results.

It can be seen from Table 4 that TSR of S-WMA was significantly improved and has been close to that of hot-mix asphalt mixture after cement or hydrated lime was added. So both 1% cement and 1% hydrated lime can improve water damage resistance of S-WMA. For E-WMA, the water damage resistance drops slightly after cement was added, while TSR of E-WMA drops significantly after hydrated lime was added. Therefore, cement or hydrated lime shall not be used as admixture in production of E-WMA.

Fatigue resistance of asphalt mixture can be evaluated based on fatigue life of mixture at different stress ratios, the fatigue curve of which is as shown in Figure 1.

It can be seen from the fatigue curve that fatigue resistance of mixture prepared by Evotherm warm mix technique was higher than that of mixture prepared by SAK warm mix technique at the same stress ratio.

2.2 *Performance comparison of WAC-13C prepared by the two warm mixing techniques*

In Gradation WAC-13C, diorite was used as coarse aggregate, limestone as fine aggregate, and SBS modified asphalt as binding material. Warm-mix asphalt mixtures were prepared by SAK technique and Evotherm technique respectively. See Table 5 for composition of Gradation WAC-13C. The optimum asphalt-aggregate ratio and relevant parameters of asphalt mixture designed are as shown in Table 6. Results of performance test of the mixtures are as shown in Table 7.

It can be seen from the above table that when SBS modified asphalt was adopted, the optimum asphalt-aggregate ratio of both warm-mix techniques was 5.4%, 0.2% higher than that of hot-mix asphalt mixture at the same Gradation.

It can be seen from Table 7 that when SBS modified asphalt was adopted, stability of both Warm-mix asphalt mixtures at high temperature, particularly S-WMA, was higher than that of hot-mix asphalt mixture; Maximum flexure tensile strain of both Warm-mix asphalt mixtures at low temperature was slightly different but higher than HMA. Different from common asphalt, water damage resistance of both Warm-mix asphalt mixtures, particularly E-WMA technique, was higher than that of hot-mix asphalt mixture. Similar to WAC-20C, Fatigue life of WAC-13C was also compared. See Figure 2.

It can be seen from the fatigue curve that for modified asphalt, fatigue resistance of AC-13C mixture prepared by Evotherm warm mix technique was obviously higher than that of SAK warm mix technique at same stress ratio.

Table 5. Composition of gradation WAC-13C.

	Sieve sizes (mm)									
Type of gradation	16	13.2	9.5	4.75	2.36	1.18	0.6	0.3	0.15	0.075
Percent passing (%)	100	95.9	73.5	46.1	25.7	18.4	12	8.8	7.8	4.4

Table 6. Design results of different asphalt mixtures (AC-13C).

Type of mixture	Asphalt-aggregate ratio	Marshall stability (kN)	Flow value (mm)	Air void (%)	VFA (%)	VMA (%)
S-WMA	5.4	11.8	3.08	4.1	72.6	13.5
E-WMA	5.4	12.4	3.62	3.9	71.4	14.9
HMA	5.2	13.3	2.6	4.0	72.6	14.6
Requirement of code		≥8	1.5~4	3~6	65~75	≥13

Table 7. General performances of WAC-13C mixture.

Evaluation parameters	Dynamic stability/ time/mm, 60°C	Maximum flexure tensile strain/με	TSR (%)
Type of mixture			
S-WMA	6568	9736	90.6
E-WMA	5384	9876	95.8
HMA	5184	7556	88.6
Technical requirement	≥2800	≥2500	≥80
Test method	T0719	T0728	T0729

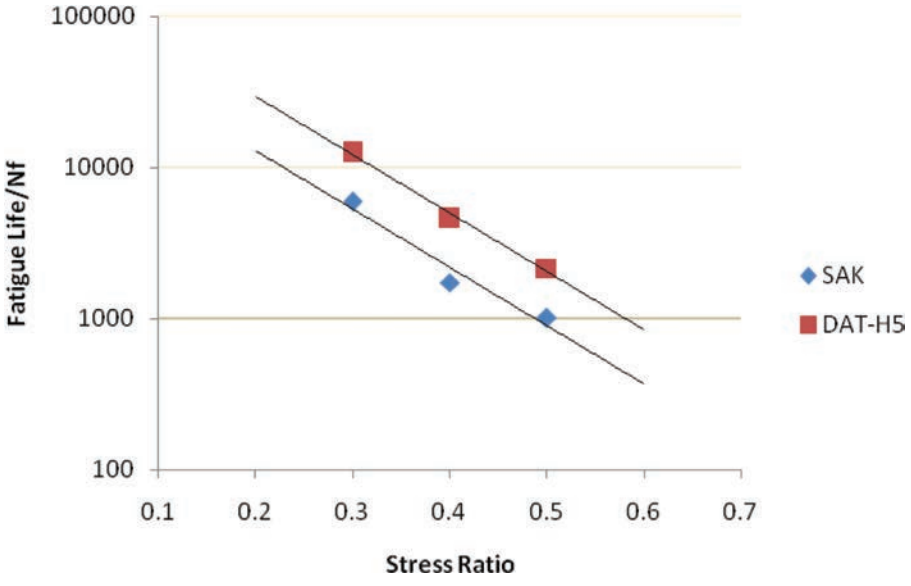

Figure 2. Fatigue curve of AC-13C mixture prepared by two warm mix techniques.

3 INTEGRATED APPLICATION OF TWO WARM MIXING TECHNIQUES IN PROJECTS

Considering respective advantages of two warm mixing techniques, the organic viscosity reduction technique and surfactant-based technique were integrally applied in Shaoguan-Ganzhou Expressway with total length at 200 m. Organic viscosity reduction—based warm-mix technique was used in the middle asphalt course due to its outstanding stability at high temperature; while surfactant-based warm-mix technique was used in bottom asphalt course due to its relatively fine fatigue resistance; and Evotherm modified asphalt warm mixing technique was used in surface asphalt course due to its excellent comprehensive performance. The test road structure is as shown in Table 8.

After construction, evenness, compactness, surface texture depth, friction coefficient, water permeability coefficient and rebound deflection were tested for the upper surface courses, and evenness, compactness, water permeability coefficient and rebound deflection were tested for the middle and bottom surface courses. See Tables 9 and 10 for the result.

It can be seen from the test results that when warm-mix asphalt mixture technique was adopted, all construction quality test indexes can fully meet corresponding technical requirements of hot-mix asphalt mixture technique.

4 EVALUATION ON DURABILITY OF TWO WARM MIXING TECHNIQUES

Gradation AC-13C warm-mix asphalt mixture was prepared by the two warm mixing techniques. The warm-mix asphalt mixtures undergo accelerated aging test, and then their high temperature performance after short-term aging and water damage resistance, crack resistance at low temperature and fatigue resistance after long-term aging were tested, studied and compared to those of hot-mix asphalt mixture to evaluate durability of warm-mix asphalt mixture.

4.1 *Stability of warm-mix asphalt mixture at high temperature after short-term aging*

The newly warm-mix asphalt mixture was placed in the baker at 135°C to age for 4 h before formation to simulate aging of asphalt mixture during construction. After short-term aging,

Table 8. Integrated application scheme of two warm mix techniques.

Structural course	Thickness and type	Remarks
Upper asphalt course	4 cm WAC-13C	SBS modified asphalt, surfactant-based warm-mix technique
Middle asphalt course	6 cm WAC-20C	SBS modified asphalt, organic viscosity reduction warm-mix technique
Bottom asphalt course	15 cm WAC-25F	70# common asphalt, surfactant-based warm mix technique

Table 9. Summary of test results of upper asphalt course (WAC-13C).

Type of structure	Evenness standard deviation (mm)	Surface texture depth (mm)	Friction coefficient (BPN)	Water permeability coefficient (ml/min)	Deflection (0.01 mm)	Average thickness (mm)	Compactness (%)
WAC-13C	0.85	0.79	68	51.3	15.3	41.0	93.7
Technical requirement	⩾1.2 mm	/	>45	⩾120 ml/min	/	–10% of designed value	≥93

Table 10. Summary of test results of middle and lower asphalt courses.

Type of structure	Evenness standard deviation (mm)	Water permeability coefficient (ml/min)	Deflection (0.01 mm)	Average thickness (mm)	Compactness (%)
WAC-20C	1.15	87	17.55	52.5	94.3
WAC-25F	1.37	Not leaky	25.38	162.0	96.9
Technical requirements	⩾1.5 mm	⩾120 ml/min	/	–8% of design value	≥93

Table 11. Comparison on stability of different mixtures at high temperature after short-term aging.

Type of mixture	HMA	S-WMA	E-WMA
Post-aging dynamic stability/time/mm	6826	21352	18652
Pre-aging dynamic stability/time/mm	5187	6568	5384

stability of asphalt mixture at high temperature was evaluated through rutting test, the results of which are as shown in Table 11.

It can be seen from above table that dynamic stability of different mixtures was significantly improved after short-term aging, particularly dynamic stability of warm-mixed mixture was improved by 2 to 3 times of the hot-mix asphalt mixture. So short-term aging contributes to improving rutting resistance of warm-mix asphalt mixture.

4.2 *Water stability of warm-mix asphalt mixture after long-term aging*

Specimen prepared with warm-mix asphalt mixture having undergone short-term aging test was placed in a baker at 85°C and heated for 5d in a ventilated manner to simulate status of the asphalt mixture after years. After long-term aging, water stability of asphalt mixture was evaluated through freeze-thaw split test (T0729-2000), the results of which are as shown in Table 12.

Table12 indicates that water damage resistance of all asphalt mixtures drops obviously after long-term aging, out of which organic viscosity reduction based warm mixing technique was slightly better. But generally speaking, water damage resistance of warm-mix asphalt mixture after long-term aging was equivalent to that of hot-mix asphalt mixture.

4.3 *Crack resistance of warm-mix mixture at low temperature after long-term aging*

The specimen after long-term aging also undergoes bending test at low temperature (–10°C). The test results are as shown in Table 13.

The above table indicates that crack resistance of different asphalt mixtures drops obviously after long-term aging, particularly the hot-mix asphalt mixture, while the organic viscosity reducer based warm mixed technique was relatively better.

4.4 *Fatigue resistance of warm-mix asphalt mixture after long-term aging*

Also post-long-term-aging specimen was tested on its bending fatigue life at low temperature in controlled stress method. Fatigue performance of different asphalt mixtures after long-term aging was reflected by remaining fatigue life of mixtures at different stress levels. Fatigue curves of different asphalt mixtures after long-term aging are as shown in Figure 3.

Table 12. Comparison on water stability of different mixtures after long-term aging.

Type of mixture	HMA	E-WMA	S-WMA
Pre-aging TSR (%)	92.4	95.8	90.6
Post-aging TSR (%)	77.1	76.7	79.8

Table 13. Comparison on performance of different mixtures at low temperature after long-term aging.

Type of mixture	HMA	E-WMA	S-WMA
Pre-aging maximum flexure tensile strain/με	12891	9876	9736
Post-aging maximum flexure tensile strain/με	3984	5999	7963

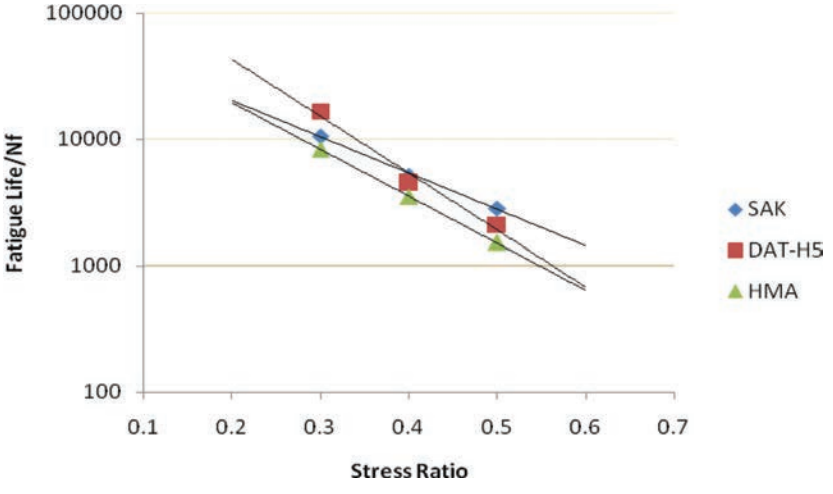

Figure 3. Fatigue curves of different asphalt mixture after long-term aging.

It can be seen from Figure 3 that fatigue resistances of two warm-mix asphalt mixtures were higher than that of hot-mix asphalt mixture under the same long-term aging conditions. By comparing the two warm-mix asphalt mixtures, it can be seen that remaining life of surfactant-based warm mix technique turns from advantageous to disadvantageous with increase of stress level, in other words, it drops quickly.

5 CONCLUSION

1. Different warm-mixing techniques have different effects on mixture performance, and can be used for particular purposes. Asphalt mixtures prepared by surfactant-based warm mixing technique shows great fatigue resistance and can be primarily used on occasions requiring better anti-fatigue capability. Modified asphalt can be used in surface courses as it shows good overall performance. Asphalt mixtures prepared by organic viscosity reducer based warm mixing technique was prominently stable under high temperature and can be primarily used on occasions requiring better stability under high temperature, e.g., the middle surface course.
2. Where common asphalt was used, water damage resistance of mixtures prepared by both warm mixed techniques drops significantly. For organic viscosity reducer based technique, 1% cement or hydrated lime can be added to substitute for mineral powder to improve water damage resistance of the mixture; but this method does not work on surfactant-based WMA technique, and even has counteraction.
3. The two WMA techniques were applied to different asphalt layers of Shaoguan-Ganzhou Expressway based on their respective performance. 200 m test section was paved and tested in terms of compactness and evenness. The test results demonstrate that all technical parameters fully meet technical requirements of HMA at the same gradation.
4. The two warm-mix asphalt mixtures undergo indoor accelerated aging and performance test for durability evaluation. Compared to hot-mix asphalt mixture at the same Gradation, they were superior in terms of low temperature performance and anti-fatigue property.

REFERENCES

[1] Yhang Jian-gang. Warm Mix Asphalt Application and Performance [J]. Highway and Transportation Research, 2006(8).
[2] Huang Wen-yuan. Warm Mix Asphalt Technology Application in China and Abroad [J]. Shanghai Highway, 2008(3).
[3] Zuo Feng, Ye Fen. Foreign Warm Mix Asphalt Technology and Performance Evaluation in Abroad, China and Foreign Highway, 2007(27).
[4] Xu Shi-fa, Yan Bin, Ji Jie, Gao Yuan. High Energy Save and Low Emissions Energy Mix Asphalt Technology Status and Prospects [J]. Highway, 2005(7).
[5] Qin Yong-chun. Warm Mix Asphalt Based Surfactant Mixture Design and Related Properties [D]. PhD thesis in Tongji University, 2009.
[6] Qing Yong-chun, Huang Song-chang, Xu Jian. Warm Mix Asphalt Technology and the Latest Research [J]. Bitumen, 2006, 20(4):18–21.
[7] Gao Xiaofei, Performance Research On Surfactant-based Warm-mix Asphalt and Warm-mix Asphalt Technique by Adding Organic Viscosity Reducers [D]. Tongji University. 2011.

Experimental characterization of asphaltic materials—VI

This page intentionally left blank

Asphalt Pavements – Kim (Ed)
© 2014 Taylor & Francis Group, London, ISBN 978-1-138-02693-3

Characterization of bituminous layers interfaces: From the mechanical behaviour to the modelling

Ktari Rahma, Leandry Ismaelle, Millien Anne, Fouchal Fazia, Pop Ion-Octavian & Petit Christophe
GEMH Laboratory, Civil Engineering and Durability, University of Limoges, Egletons, France

ABSTRACT: Even if, for composite materials, many experimental studies as well as behavior laws have been developed, evaluation of the behavior of interfaces between pavement layers is an actual scientific lock. The current French design method only takes into account interfaces, as conventional perfect bonding or slipping plane. In order to understand the behavior of the interface or interphase, the photomechanical tools are unavoidable. Global and local analysis, determined by two methods, includes tracking markers and Digital Images Correlation (DIC). The feasibility of this approach is presented for a direct tensile test on double-layered asphalt pavement specimen. The results (roughness, adhesion) will be input as parameters of a damage model interface.

Keywords: Interface, image analysis, field measurements, roughness, damage model

1 INTRODUCTION

In road construction, multi-layer composite material making up a road structure are subjected to traffic loading and environmental impacts. Sustainable development needs repairs works or fortification works. Proposed solutions use bituminous materials for the surface layer with optimized mechanical characteristics; layers are finer and finer. This strategy leads to an increase of thermo mechanical stresses on a part close to the surface of the pavement including more and more interfaces between pavement layers especially treated layers with hydraulic or hydrocarbon binders. Associated pathologies to layers unsticking are observed despite the obligation to use a sticking by interposition of a brush layer in tack coat. Sizing road method only considers sticking or a perfect sliding in interfaces conditions. International studies are based on mechanical responses for traction or shearing under monotone or fatigue stress [1, 2, 3, 4, 5]. Obtained results show a direct dependence between the stress, residual dosage of the brush layer and the applications conditions in the building site. Moreover, modelling of interfaces mechanical performances is not studied much in scientific publications. It is mainly expounded models based on elasto-plastic local laws like Mohr-Coulomb. This paper deals with the feasibility of a local approach based on the optical techniques use. This approach will allow the modelling parameters like damage variables and roughness profile.

2 MATERIALS AND FORMULATION: DESCRIPTION OF THE COATED

The tested material comes from an experimental board which has been made in relation to the RILEM ATB&SIB project [4]. It concerns a double-layered asphalt pavement. The lower and the upper layers consisted of an asphalt mixture type AC 12 with binder 35/50 content 4.75% (EN 13108-1), separated by a tack-coat SBS modified emulsion 50/70, binder

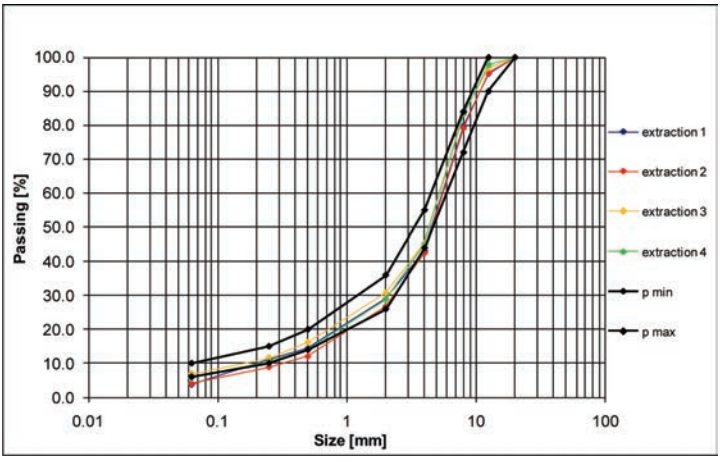

Figure 1. Particle sizes curve.

Table 1. Bitumen emulsion characteristics.

Penetration @ 25°C [dmm]	EN 1426	55 ÷ 65
Viscosity @ 160°C [Pa · s^{-1}]	EN 12595	0.200 ÷ 0.800
Softening point [°C]	EN 1427	65 ÷ 75
Breaking point (Fraass) [°C]	EN 12593	<–18

residual: 210 g/m^2. The particle sizes of the mixture are shown in Figure 1. Typical parameters of tack-coat emulsion are presented in Table 1.

3 EXPERIMENT INVESTIGATION

Simple traction tests have been realized with a plane-parallel form specimen (Fig. 2). To ensure the bonds between specimen and machine, metallic items are stock on the specimen surface (Fig. 2). Those items are screwed up on the electro mechanic press axis. The trial machine submits the specimen to a displacement speed about 0.5 mm/min. During feasibility tests, mechanical data and images speed acquisition are about a measurement per second. Experiment temperature is equal to room test temperature (22°C).

4 GLOBAL HOMOGENEOUS ANALYSIS

Global measurement fields are obtained on the one side by mark tracking using a software named DEFTAC developed by the scientific team PEM of P' Institute of Poitiers and on the other side by digital images correlation using another software named CORRELA developed by the same team [9]. To use the marks tracking method, white mark are placed on the items on both sides of the specimen (Fig. 2). This technic is based on the tracking of those marks in each acquired image by calculating their geometric center weighted by the light intensity. During the test position centers allow the global vertical variation ΔUy. Quotient between ΔUy and the initial specimen length is defined as the conventional deformation ε_{yy}.

Digital Images Correlation (DIC) consists in matching two images of the specimen plan surface. Those images correspond to two distinct mechanical states of the specimen. The first one is the reference state and the second the deformed state.

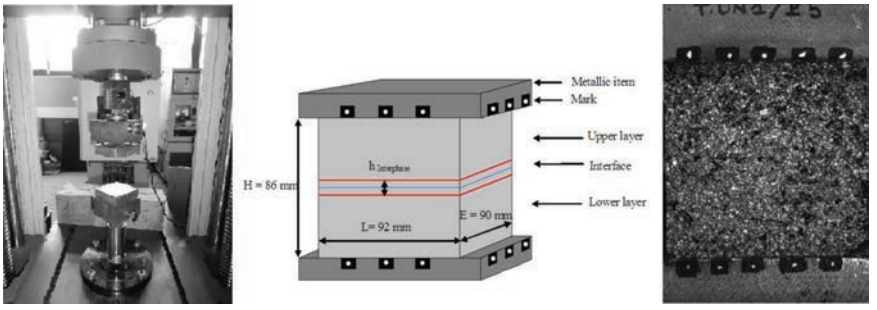

Figure 2. Trial machine, specimen geometry and preparation of surfaces for image analysis.

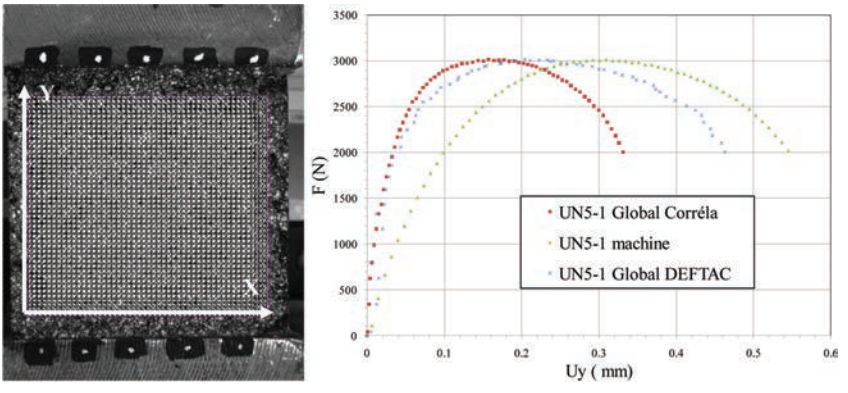

Figure 3. Global fields a) study area (reference, markers and correlation grid) b) overall load–displacement curve.

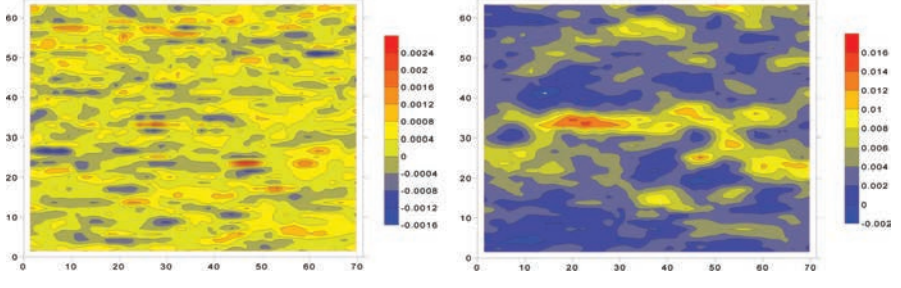

Figure 4. Global fields of strain ε_{yy} a) picture 13 b) picture 60.

When the image pattern of the deformed state is perfectly overlapped with those of the reference state image, displacements are determined.

Generally, pattern is either the objet natural texture, either an artificial pattern like painting projection. In this study case, specimen surface texture is not adequate, so a speckle is projected on its surface.

A correlation study is achieved with a rise of =0.202 mm/pixel and the correlation windows size is about 8 × 8 pixels (the shift is equal to 2 pixels). Global fields for each method cited above and the study area included the reference, markers and correlation grid are presented in Figure 3.

Two fields are presented on Figure 4: as the maximal stress is obtained for the 41st picture, the first field (a) corresponds to the initial linear part of the global stress-strain curve.

It allows the visualization of material heterogeneity. The second presented field has been captured after the stress pic and shows the strain localization on the interphase.

5 LOCAL ANALYSIS

Different evolution curves are plotted. It concerned the vertical displacement versus the vertical position for each picture. Figure 5 presents an example of results for a vertical line located in the middle of the analyzed specimen face. Those curves are used to evaluate the interphase local strain and the interphase size. In this study the interphase is 2.5 mm. Local strain is defined as the guiding coefficient of each curve median segment. In Figure 5, the observed local strain scatter in the neighborhood of the interface/interphase for different curves shows the roughness effect and the material heterogeneity.

6 COMPARISON OF LOCAL ANALYSIS WITH GLOBAL ANALYSIS

Figure 6 is the global and local curves over lapping. It shows difference of the behavior between the global specimen (usual data) and the interface (DIC data). The beginning of this difference seems to be early.

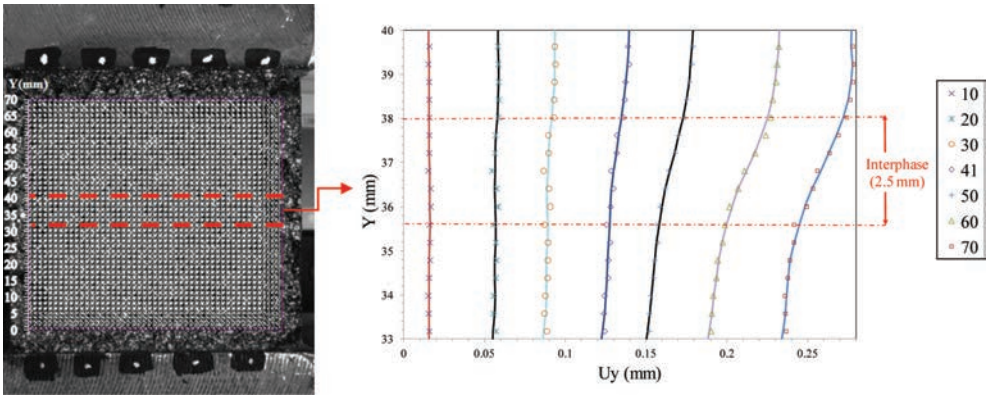

Figure 5. Localization of the interface during the essay with a correlation windows size 8 × 8 pixels.

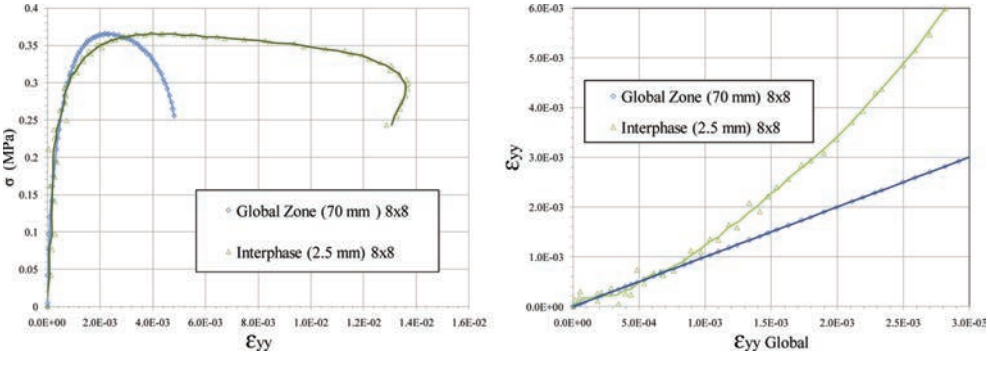

Figure 6. a) superposition of global and local behavior curves: Stress–strain curve—b) focus on the localization of the interface.

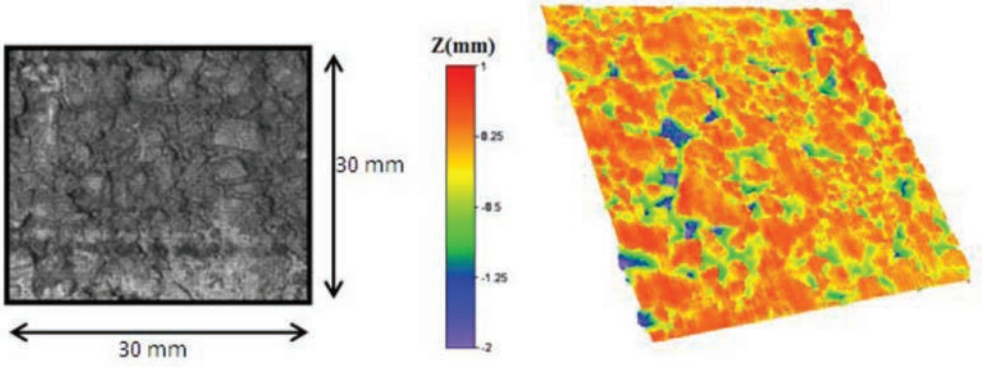

Figure 7. a) Sample before break—b) profile of interface roughness to the initial state.

Table 2. Average roughness of the study area.

	Initial state	Post break
Ra (mm)	0.32	0.50
Rq (mm)	0.44	0.67

7 MORPHOLOGY AND INTERFACE ROUGHNESS

Fringe projection principle is the same as shadow moiré which allows the visualization and the direct calculation of the relief of a studied object surface. For this study, a reference volume is employed instead of a reference plan for more accuracy [13]. The basic principle of the optical technique consists of projecting a pattern of fringes and in recording an image of the object from another point of view with a CCD camera. Even if the surface to be analyzed does no present large discontinuities, a specific image analysis is used to determine the phase of deformed pattern on the relief object surface [9]. For that purpose, the software Light 3D, developed by PEM team research of the GMSC department of the P' Institute of Poitiers, has been used.

Before the measurement, the surface to study must be prepared: white paint projection is carried (Fig. 7-a). Figure 7-b shows the rough state surface at the initial condition. The aim of this study is to introduce roughness parameters or roughness curves in a model.

To analyze the surface roughness, the roughness average (Ra) and the root Mean Square Roughness (Rq) are calculated in Table 2 [14, 15, 16]. Those parameters come from the ISO 4288 Standard (1996). For this specimen, partial statistic results are presented in following table. A global increase of means roughness can be observed due to the grain wrenching after breaking.

The local study performed with DIC method, presented in section 5, allows determining the thickness interphase which is close to 2.5 mm. This value is similar to the roughness value (Table 2).

8 INTERFACE MODELLING

The homogenization method consists of describing the average behavior for equivalent material by taking into account the microscopic parameters for each component.

In this study, homogenous model is proposed for the bituminous material. It's considered as a one-dimensional composite cell. The interphase is described by two material layers shown in Figure 8. Both layers are characterized by the same thickness.

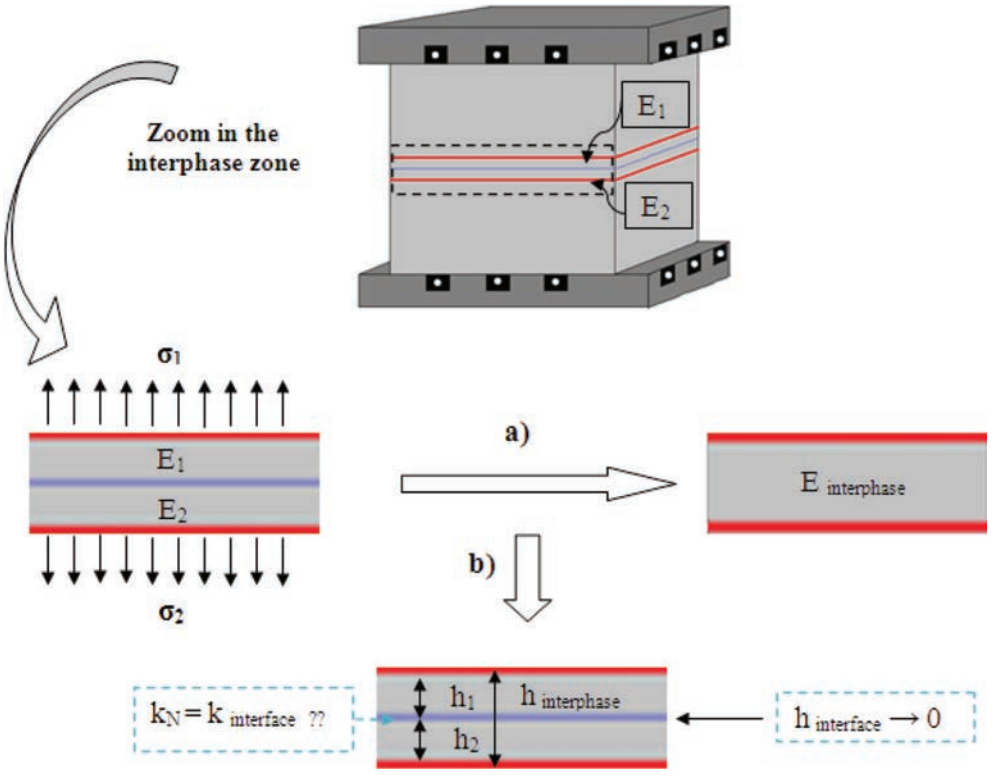

Figure 8. a) Homogenizing a bituminous double layer materials in parallel b) interface modelling.

Young's modulus for the upper layer in the samples is $\mathbf{E_1}$ and for lower layer is $\mathbf{E_2}$. These parameters are measured in two areas located on each side of the interface. Both thickness areas are equal to 13.5 mm chosen as they are greater than a grain size.

Also, Young's modulus secant $E_{interphase}$ can be determined experimentally from the stress-strain curves (see Fig. 6-a).

Young's modulus results for the different materials are given in Figure 9, for the maximum and minimum uncertainty bars of measurement for the experimental study.

This model allows us to calculate Young's $E_{interphase}$ modulus (Fig. 8-a) for the homogeneous material. The interphase behavior shown in Figure 9 is described in the following equations.

$$\sigma_{interphase} = E_{interphase} \times \varepsilon_{yy}^{interphase}, \sigma_1 = E_1 \times \varepsilon_{yy}^{1}, \sigma_2 = E_2 \times \varepsilon_{yy}^{2} \quad (1)$$

The equilibrium of the interphase involves Eq. (2):

$$\sigma = \sigma_{interphase} = \sigma_1 = \sigma_2 \quad (2)$$

The sum of the displacements U_y^1 and U_y^2 in the direction of y, calculated for the first and the second layer must be equal to the total material *"interphase"*

$$U_y^{interphase} = U_y^1 + U_y^2 \quad (3)$$

$$h_{interphase} = h_1 + h_2 \quad (4)$$

which: ε_{yy}^1, ε_{yy}^2: Mean strain in the upper and the lower layer respectively.
U_y^1, U_y^2: Relative displacement for each layers.

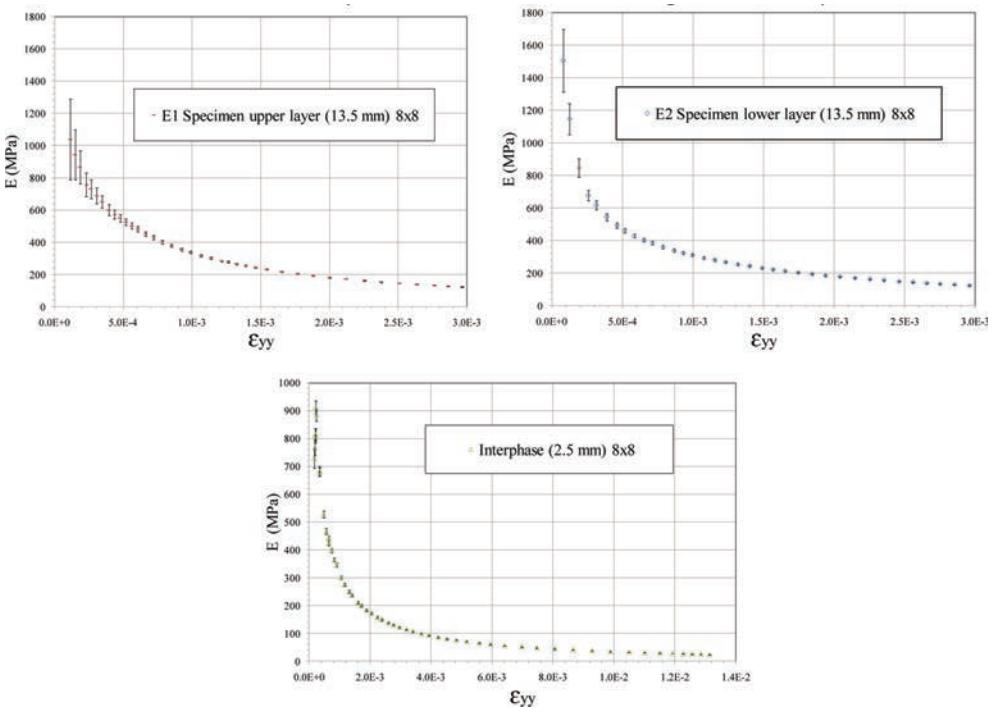

Figure 9. The secant modulus for the different materials: E_1 for upper layer, E_2 for lower layer and $E_{interphase}$ for interphase zone.

Finally Young's interphase modulus is obtained by Eq. (5)

$$E_{interphase} = \frac{E_1 \times E_2 \times (h_1 + h_2)}{E_1 h_2 + E_2 h_1} \tag{5}$$

The results shown in Figure 10, present Young's modulus $E_{interphase}$ measured (including the interface behavior) and calculated (perfectly bonded layers). It enables the user to get by difference of both curves the interface behavior.

If we opt for finite element modeling, we need to assume joint finite element (thickness tend to zero). The linear elastic joint behavior is reminded in Eq. 6.

$$\sigma_{interface} = k_{interface} \times [U_y] \tag{6}$$

where: $[U_y]$ is the relative normal displacement of the interface.

Now, if we include the interface behavior in Eq. (3) we get Eq. (7)

$$U_y^{interphase} = U_y^1 + U_y^2 + [U_y] \tag{7}$$

The normal stiffness k_N of the interface is then deduced from Eq. (1, 6, 7):

$$k_N = \frac{E_{interphase} \times E_1 \times E_2}{E_1 \times E_2 \times (h_1 + h_2) - E_{interphase} \times E_2 \times h_1 - E_{interphase} \times E_1 \times h_2} \tag{8}$$

The interface stiffness result is given in Figure 11-a. We can see with the error bars that incertainty depend on the level of displacement measurements. So for k_N calculation, we consider only displacements that are more than one micrometer in order to have an acceptable accuracy.

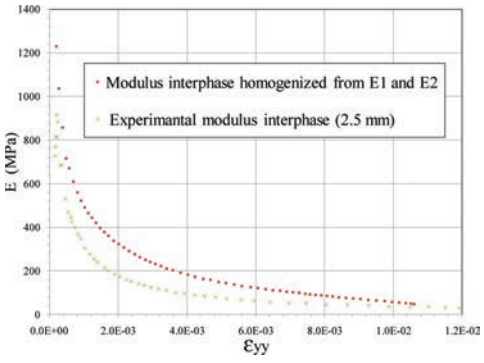

Figure 10. Comparison of the interphase modulus: experimental modulus data and modulus homogenized from E_1 and E_2.

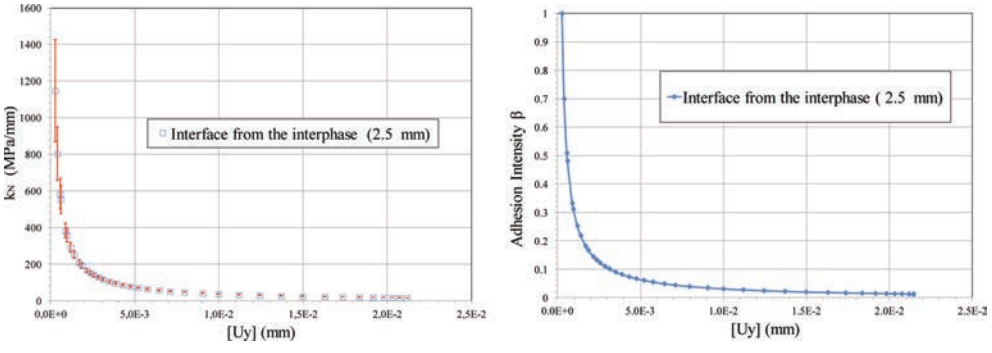

Figure 11. a) Normal interface stiffness b) evolution of the adhesion intensity with the relative displacement at the interface.

In the case of the modeling RCCM type [10, 11], the adhesion intensity variable β introduced by Fremond [12] can be experimentally determined from the normal stiffness of the interface (Fig. 11-b).

9 CONCLUSION AND PERSPECTIVES

This study confirms the possibility to determine the interface thickness by localization and to identify the parameters of the interface behavior such as roughness, stiffness, adhesion intensity. The goal of this work is to develop an interface modeling for the pavement structures by using the previous main parameters. This analysis concern only bonding test with tensile loading. Other tests are performed with shear loading in order to get a better understanding interface behavior such as interlocking effect depending on roughness for instance.

REFERENCES

[1] Diakhate M., Millien A., Petit C., Phelipot-Mardelé A., Pouteau B., Experimental investigation of tack coat fatigue performance: towards improved lifetime assessment of interfaces in pavement structures, Construction and Buildings, 25, (2), pp. 1123–1133. 2011.

[2] D'Andrea A., Tozzo C., Boschetto A. and Bottini L. Interface Roughness Parameters and Shear Strength, Modern Applied Science, Vol. 7, No. 10, Canadian Center of Science and Education. 2013.

[3] Raab C., Abd El Halim A.O. and Partl M.N. Interlayer bond testing using a model material. Construction and Building Materials. 26, pp. 190–199. 2012.
[4] Canestrari F., Ferrotti G., Lu X., Millien A., Partl M.N., Petit C., Phelipot-Mardelé A., Piber H. and Raab C. Mechanical Testing of Interlayer Bonding in Asphalt Pavements, Advances in Interlaboratory Testing and Evaluation of Bituminous Materials, State-of-the-Art Reports of RILEM Technical committee 206-ATB, chapter 6, pp. 303–360. 2013.
[5] Hun M., Chabot A. and Hammoun F. A four-point bending test for the bonding evaluation of composite pavement. 7th RILEM International Conference on Cracking in Pavement, Delft. 2012.
[6] Romanoschi S., Metcalf J., Characterization of Asphalt Concrete Layer Interfaces, Transportation Research Record, 1778, (1), pp. 132–139, 2001.
[7] Kim H., Arraigada M., Raab C., and Partl M., Numerical and Experimental Analysis for the Interlayer Behavior of Double-Layered Asphalt Pavement Specimens. J. Mater. Civ. Eng. 23, Special issue: Multiscale and Micromechanical Modeling of Asphalt Mixes, pp. 12–20. 2011.
[8] Ozer H., Al-Qadi I.L., Leng Z., Fracture-Based Friction Model for Pavement Interface Characterization, Transportation Research Record, 2057, (1), pp. 54–63. 2008.
[9] Brémand F., Cottron M., Doumalin P., Dupré J.C., Germaneau A., Valle V., Mesures en mécanique par méthodes optiques, Techniques de l'Ingénieur. 2011. (en anglais).
[10] Monerie Y., Raous M., A model coupling adhesion to friction for the interaction between a crack and a fiber/matrix interface, Z.A.M.M., 205–209. 2000.
[11] Raous M., Interface models coupling adhesion and friction, C.R. Mécanique, 333, (7–8), pp. 491–501. 2011.
[12] Frémond M., Adhérence des solides, J. Méc. Théor. Appl., 6, pp. 383–407. 1987.
[13] Léandry I., Brèque C., Valle V. Calibration of a structured-light projection system: Development to large dimension objects, Optics and Lasers in Engineering, 50,3, pp. 373–379. 2012.
[14] Santos P., Julio E. A state-of-art review on roughness quantification methods for concrete surfaces, Construction and Building Materials, 38, pp. 912–923. 2013.
[15] Ech M., Yotte S., Morel S., Breysse D., Pouteau B., Qualification of wearing course material surface evolution after durability test, Construction and Building Materials, 35, pp. 313–320. 2012.
[16] Raposeiras A.C., Vega-Zamanillo A., Calzada-Pérez M.A., Castro-Fresno D., Influence of surface macro-texture and binder dosage on the adhesion between bituminous pavement layers, Construction and Building Materials, 28, (1), pp. 187–192. 2012.

This page intentionally left blank

Asphalt Pavements – Kim (Ed)
© 2014 Taylor & Francis Group, London, ISBN 978-1-138-02693-3

Comparison of asphalt fatigue characteristics under different control modes

Hong Zhang, Liyan Shan, Yiqiu Tan, Yichen Feng & Hongsen He
School of Transportation Science and Engineering, Harbin Institute of Technology, Nangang District, Harbin, Heilongjiang, China

ABSTRACT: Fatigue cracking is a common form of distress in asphalt pavement. The ability of asphalt binder to resist accumulation of fatigue damage can have a profound effect on the service life of asphalt pavements. However, the fatigue characteristics of asphalt binder depend heavily on the loading modes. That is the fatigue characteristic of asphalt binder under controlled-stress mode is totally different from that under controlled-strain mode. The issue affects the establishment of universal fatigue evaluation index of asphalt binder. This study focused on analysing the fatigue performance difference between under controlled-stress and controlled-strain mode. The fatigue characteristics of two kinds of asphalt binders under different loading control modes were compared. And the fatigue performances relationship under different control modes was founds. Further, a method to transform accumulated dissipated energy curve from one loading mode to the other was proposed.

Keywords: asphalt binder, fatigue, controlled-stress mode, controlled-strain mode

1 INTRODUCTION

Fatigue cracking is one of the primary distresses in asphalt pavements. As one of the most important components of asphalt mixture, asphalt binder plays a critical role in the fatigue performance of asphalt mixture even asphalt pavement. So the fatigue characteristics of asphalt binder have always been focused in the past few decades.

The fatigue behavior of asphalt binder is complex as it is affected by many factors, such as temperature, loading level, loading control mode and so on. Among these, loading control mode is one of the most important effect factors. The fatigue behavior of asphalt binder under controlled-stress mode is totally different from that under controlled-strain mode. And the fatigue life rankings of different asphalt binders under different control modes are contradictory evaluated by the same index, which makes it different to choose binders with better fatigue performance. The common practice in fatigue analysis is to employ the controlled-strain mode for asphalt materials that are used in thin pavements and controlled-stress mode for asphalt materials used in thick pavements (1). However, changes in the structural design of pavements and complex traffic loading make it difficult to identify pavement systems that adhere strictly to either controlled-strain or controlled-stress conditions.

In order to address this problem and better evaluate the fatigue performance of asphalt binders, some researchers have attempted to unify the results from controlled-strain and controlled-stress modes of testing for the same asphalt materials using different methods. Monismith et al. (2) corrected for the mode of loading by introducing a mode factor in analysis of fatigue testing. Van Dijk et al. (3,4) were the first to suggest to use the dissipated energy concept to analyze fatigue behavior. During the fatigue process the material is damaged and energy is dissipated. Bonnetti, K.S. et al. (5) used K_1 (slope) and K_2 (intercept) for the curve of N_{p20} (the number of cycles at which the dissipated energy ratio shows 20% deviation from the no-damage ratio) versus initial dissipated energy per cycle to define fatigue performance

and it showed that these two values were not highly affected by the loading mode. Ghuzlan and Carpenter (6) attempted to unify the results from different control mode by using the ratio of the change in dissipated energy between consecutives cycles (i and i + 1) to the dissipated energy in the first of the consecutives cycles (i). There is a constant plateau value in the curve of the ratio versus the number of load cycles, which was independent of the mode of loading. Based on that energy principle, Shen and Carpenter (7) established a PV (plateau value) fatigue prediction model for asphalt mixture. Kim et al. (8) used the elastic–viscoelastic correspondence principle proposed by Schapery (9) to derive damage functions and stress–strain relationships for asphalt mixture under controlled-strain and controlled-stress cyclic loadings. After it has been successfully used for mixture, some researchers (10, 11) applied the theory to asphalt binder, and it showed that some binders did follow that and some not. Based on the elastic–viscoelastic correspondence principle, Kim et al. (12) also employed the concept of Dissipated Pseudo Strain Energy (DPSE) to evaluate the fatigue cracking life of Fine Aggregate Matrix (FAM) using the Dynamic Mechanical Analyzer (DMA). Masad et al. (13) separated the DPSE due to the change in phase angle (W_{R1}) and pseudo stiffness (W_{R2}) and permanent deformation (W_{R2}) and unified the results of the controlled-strain and controlled-stress modes of loading by the ratio of W_{R3} to W_{R1}. Based on the same theory and the principles of fracture mechanics, Castelo Branco et al. (14,15) also developed the crack growth index, and proved that this index can quantify fatigue cracking in an asphalt mixture independent of the mode of loading. Bhasin et al. (16) quantitatively compared different energy methods to characterize fatigue in asphalt materials, and showed the advantages and disadvantages of different methods. All these methods focus on unifying the results from different loading control modes in form, but the fatigue behavior difference still needs to be studied and the fatigue performance relationship between different control modes is seldom studied.

Based on the above analysis, the fatigue performances of two kinds of asphalt binders in different control modes were studied by analysing the dynamic modulus curve and accumulated dissipated energy curve. The relationship between the performances in these two kinds of control modes was established. Further, a method to transform accumulated dissipated energy curve from one loading mode to the other was proposed.

2 MATERIALS AND TEST METHODS

Two neat asphalt binders were selected for this study. For the remainder of this paper, these materials are labeled as generic binders A and B. Both of the materials are standard, unmodified asphalt binders. A is 60~80 "penetration" asphalt, and B is 80~100 "penetration" asphalt, according to the Chinese penetration grade. These binders were both aged in a rolling thin-film oven (i.e., RTFO-aged) prior to testing to simulate the effects of mixing and compaction. Laboratory testing was performed using a TA Instruments DHR-2 rheometer. All tests were conducted with an 8-mm diameter parallel plate geometry and 2-mm gap setting. Two types of test were conducted: stress sweep test and fatigue test. At least three replicates were performed for each condition. Although not shown in this paper, the variability for these tests is generally less than 10 percent.

2.1 *Stress sweep test*

Before the fatigue tests were conducted, the stress or strain levels for these experiments were chosen from the results of stress sweep test, as shown in Figure 1. The strain increases linearly with increase in stress level at first and increases sharply when the stress level gets to some level. When the strain is 3%, the stress is 0.3 MPa for binder A at 20°C, 0.25 MPa for binder B at 20°C, 0.14 MPa for binder A at 25°C and 0.11 MPa for binder B at 25°C. 0.3 MPa and 3% for binder A at 20°C, 0.25 MPa and 3% at 20°C for binder B, 0.14 MPa and 3% at 25°C for binder A, and 0.11 MPa and 3% at 25°C for binder B are named couples of loadings. In order to compare the fatigue performance of the studied asphalt binders in different loading

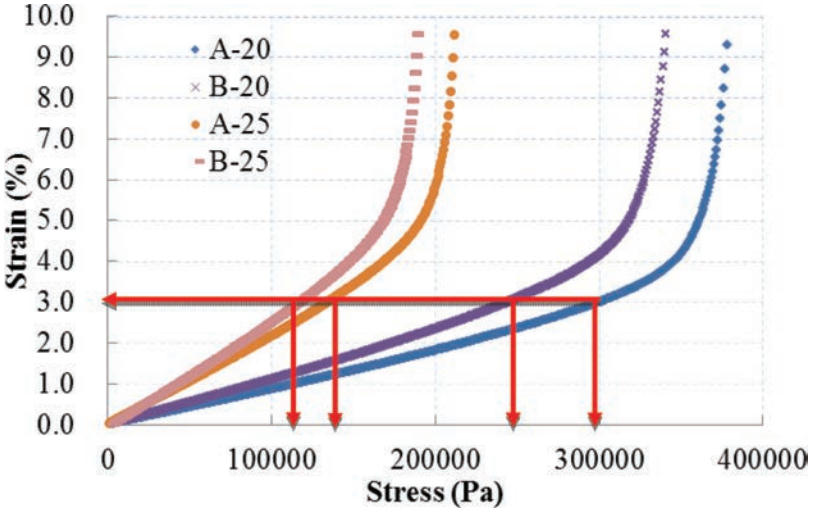

Figure 1. Stress sweep test results for the studied binders.

modes, it is necessary to choose the couples of loading. To round up or down the stress level a little bit, 0.3 MPa at 20°C and 0.15 MPa at 25°C were chosen for binder A, and 0.25 MPa 20°C and 0.1 MPa at 25°C were chosen for binder B. Besides that, In order to study the fatigue performance of the asphalt binders in different stress levels, the stress levels of 0.1 and 0.2 MPa at 25°C for binder A and 0.15 and 0.3 MPa at 20°C for binder B were also chosen.

2.2 *Fatigue test*

Because fatigue is generally a concern at intermediate temperatures, these tests were conducted at 20°C and 25°C. The fatigue tests were conducted in both controlled-stress and controlled-strain modes with a 10 Hz continuous sinusoidal loading until the dynamic modulus of the specimens gets to smaller than 20% of the initial value.

3 RESULTS AND ANALYSIS

3.1 *Analysis of the dynamic modulus curves in different loading modes*

Figure 2 presents the fatigue characteristics of the studied asphalt binders in terms of dynamic modulus versus number of cycles. In Figure 2, the data series that are labelled A-0.1 MPa indicate that the tested binder is A and the controlled stress is 0.1 MPa, with similar meanings for the other data series labels. Figure 2 shows that the dynamic modulus value decreases slowly at first, but then the degradation accelerates quickly as the specimen approaches failure in controlled-stress mode. In controlled-strain mode, the dynamic modulus value decreases slowly at first, then decreases quickly and decreases slowly again after attaining about 30% of its initial value. The figure also shows that the fatigue performance of asphalt binders worsens with an increased input magnitude and also with an increase in temperature.

If the fatigue process is divided into two phases (the demarcation point is the point after where the dynamic modulus decreases quickly), it is meaningful to find that if the strain and stress levels are a couple of loading, the curve in the controlled-stress mode almost coincides with the curve in the controlled-strain mode in the first phase. For example, 0.3 MPa and 3% are the couple of loading for binder A at 20°C, and the A-0.3 MPa dynamic modulus curve overlaps with the A-3% dynamic modulus curve at 20°C in the first phase. Same phenomenon can be found for another couple of loadings. It means that the effect of strain and the effect of stress are the same as in the first phase. Furthermore, under those conditions, the fatigue

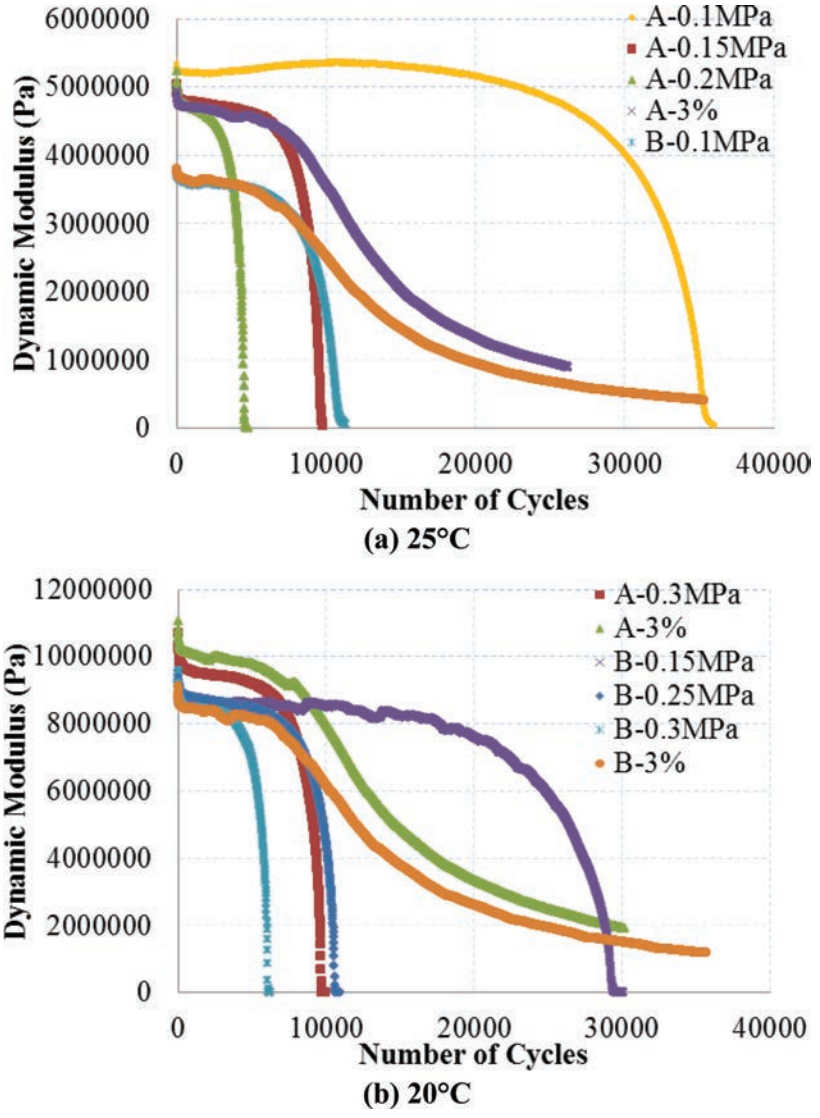

Figure 2. Fatigue performances of the studied binders.

behavior of the asphalt binders is the same in different control modes. The main differences between the fatigue behavior of the asphalt binder in controlled-strain mode and controlled-stress mode are in the second phase of the fatigue process. In controlled-stress mode, the dynamic modulus value decreases quickly in the second phase, but in controlled-strain mode, the dynamic modulus value decreases slowly. This phenomenon leads to the fatigue life of the same asphalt binder being different in different control modes evaluated by the same index.

3.2 *Analysis of the dissipated energy in different loading modes*

In order to compare the fatigue performance of asphalt binders in different loading modes and find the relationship between them, the dissipated energy of the binders under the couple of loading was studied.

The equation to calculate dissipated energy is shown as follow in Equation (1). After integrating Equation (1), Equation (2) was obtained. The dissipated energy per cycle changes

with increase in number of cycles. The accumulated dissipated energy is the sum of the dissipated energy from cycle one to cycle n, as shown in Equation (3). It can also reflect the fatigue performance of asphalt binders.

$$w_i = \oint \tau(dt)d\gamma(t) = \oint \tau(t)\frac{d\gamma(t)}{dt}dt \quad (1)$$

$$w_i = \pi\tau\gamma\sin\delta \quad (2)$$

$$W_n = \sum_{i=1}^{n} w_i \quad (3)$$

where: w_i = dissipated energy (Pa);
τ = shear stress (Pa);
γ = shear strain (%);
δ = phase angle;
W_n = accumulated dissipated energy (Pa).

Figure 3 presents the dissipated energy changing law of the asphalt binder A and B in terms of accumulated dissipated energy versus number of cycles. It shows that the accumulated dissipated energy increases with increases in number of cycles under both controlled-stress and controlled-strain modes. In controlled-stress mode, the accumulated dissipated energy increases linearly first then the increasing ratio increases when the dissipated energy accumulates to some level. In controlled-strain mode, the accumulated dissipated energy increases linearly first same to that in controlled-stress mode. After the dissipated energy accumulates to some level, the increase ratio decreases with increases in number of cycles. The curve of

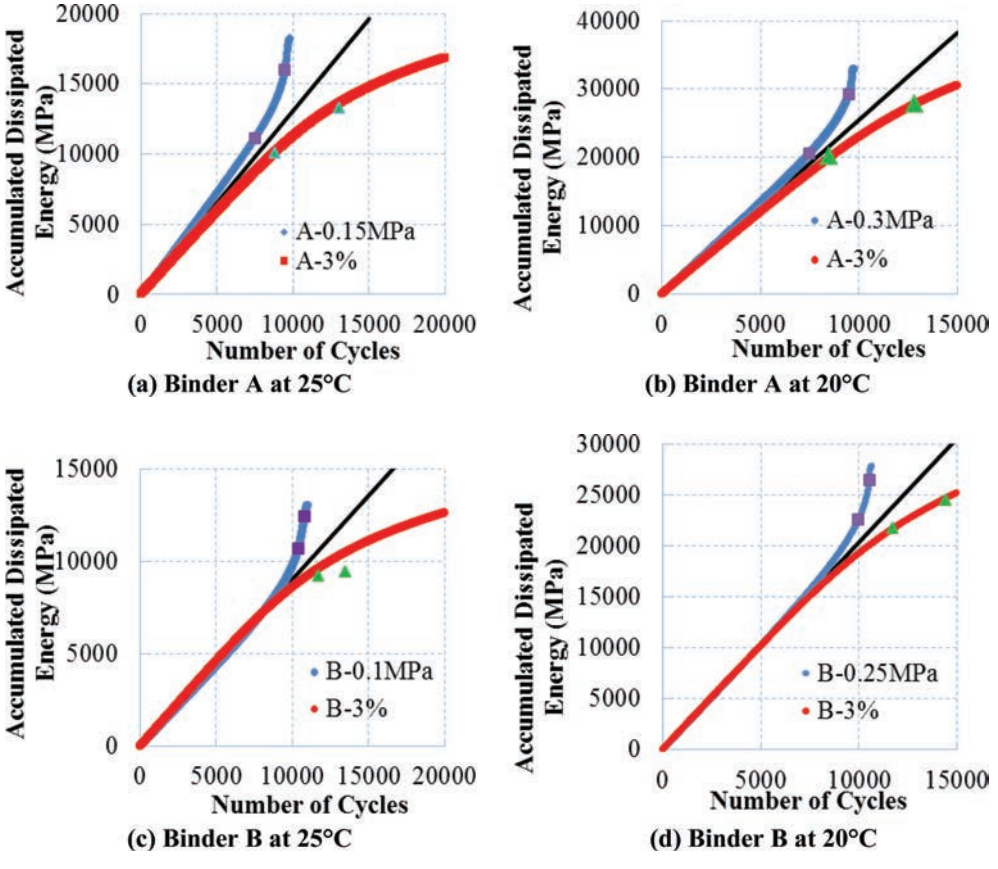

Figure 3. Accumulated dissipated energy under the four couples of loading.

accumulated dissipated energy versus number of cycles under controlled-stress mode almost coincides with that under controlled-strain mode in the linear part. Besides that, the curve of accumulated dissipated energy versus number of cycles under controlled-stress mode and that under controlled-strain mode seems to be symmetrical.

In order to prove these two kinds of curves were symmetrical or not, three steps were taken. First, the symmetrical axis was chosen and plotted. It is chosen based on the coincided part of the two curves. It is the linear line that goes through the coincided part (black linear line), as shown in Figure 3. Second, two points in the non-linear part of the controlled-stress curve were chosen, and the symmetrical points were calculated, as shown in Figure 3 and Table 1. Finally, the calculated points were compared to the points in the controlled-strain curve, and the symmetry was proved. It should be noted that the x-axis scale and y-axis scale are not the same, so the two points seems to be not symmetrical. But they are symmetrical in fact.

As shown in Table 1, the values in "In controlled-stress curve" column are the points selected by the authors, and two points were select for each condition. By calculating, the symmetrical points of the selected points can be found, as shown in "Calculated symmetrical points" column. The point in the controlled-strain curve that is the most closet to the calculated symmetrical point was found as shown in "In the controlled-strain curve". The symmetry of the controlled-stress curve and the controlled-strain curve was studied by comparing the values in the last two columns in Table 1. It can be seen in the table that the values in these two columns are very close. For example, for point 2 of binder A at 25°C, the calculated symmetrical point is (13008.48, 1.33×10^{10}) and the real point in controlled-strain curve is (13001.8, 1.36×10^{10}), these two points are very close, same to another points, except for point 1 at 25°C for binder B. For that point, the calculated symmetrical is (13455.97, 0.95×10^{10}), but the real point in the curve is (13448, 1.05×10^{10}). The differences between the y values of these two points are a little big but not huge. Based on the whole results, it can be say that the controlled-stress curve is symmetrical to the controlled-strain curve. If the controlled-stress curve was obtained, the controlled-strain curve can be obtained by symmetry calculation and vice verse.

3.3 *Accumulated dissipated energy curves transformation from one loading mode to the other*

Known from the analysis of the above, the controlled-stress curve is symmetrical to the controlled-strain curve. If the controlled-stress curve was obtained, the controlled-strain curve

Table 1. Calculated results for the symmetry.

Binders	Temperature	Point	Symmetrical axis	In controlled-stress curve	Calculated symmetrical points	In controlled-strain curve
Binder A	25°C	Point 1	$y = 1.3 \times 10^6 x$	7500.42, 1.11×10^{10}	8795.06, 1.01×10^{10}	8792.18, 1.01×10^{10}
		Point 2		9500.26, 1.60×10^{10}	13008.48, 1.33×10^{10}	13001.8, 1.36×10^{10}
	20°C	Point 1	$y = 2.55 \times 10^6 x$	7504.36, 2.06×10^{10}	8465.48, 2.02×10^{10}	8460.77, 1.98×10^{10}
		Point 2		9500.38, 2.92×10^{10}	12854.40, 2.78×10^{10}	12858.40, 2.78×10^{10}
Binder B	25°C	Point 1	$y = 9.0 \times 10^5 x$	10401.5, 1.07×10^{10}	11692.98, 0.92×10^{10}	11698, 0.96×10^{10}
		Point 2		10806.7, 1.24×10^{10}	13455.97, 0.95×10^{10}	13448, 1.05×10^{10}
	20°C	Point 1	$y = 2.04 \times 10^6 x$	10005.2, 2.26×10^{10}	11743.72, 2.18×10^{10}	11744.4, 2.17×10^{10}
		Point 2		10555.1, 2.65×10^{10}	14458.03, 2.46×10^{10}	14462.4, 2.47×10^{10}

can be obtained by symmetry calculation and vice versa. In this part, a method to transform accumulated dissipated energy curve from one loading mode to the other was proposed and three steps were taken as follows.

First, the accumulated dissipated energy curve of one controlled mode was got from fatigue experiments, and a function was chosen to fit the curve. For controlled-stress mode, the function which was shown in Equation (4) was used to fit the accumulated dissipated energy curve, and Equation (5) was used to fit the accumulated dissipated energy curve of controlled-strain mode.

$$W_{fit-stess} = \frac{w_0 \times (10t)}{\left(1 - \frac{t}{t_R}\right)^{1/(\nu+1)}} \tag{4}$$

$$W_{fit-stain} = w_0 \times (10t) \times \left(1 - \frac{t}{t_R}\right)^{1/(\nu+1)} \tag{5}$$

where: $W_{fit-stress}$ = fitted accumulated dissipated energy of controlled-stress mode (Pa);
$W_{fit-strain}$ = fitted accumulated dissipated energy of controlled-strain mode (Pa);
w_0 = initial dissipated energy without damage (Pa);
t = time(s);
$\left(1 - t/t_R\right)^{1/(\nu+1)}$ = damage evolution function;
t_R, ν = material parameters, obtained by fitting.

Second, the symmetrical axis was chosen and plotted based on the coincided part of the curve. The expression of the symmetrical axis was shown in Equation (6).

$$y = kt \tag{6}$$

where: $k = 10 \times w_0$;
w_0 = initial dissipated energy without damage (Pa).

If two curves are symmetrical about a straight line the expression of which is as Equation (6) shows, and the functional relationship of one curve is $y = f(t)$, then the functional relationship of the other curve is as Equation (7) shows.

$$\frac{2kt + (k^2 - 1)y}{1 + k^2} = f\left(\frac{2ky - (k^2 - 1)t}{1 + k^2}\right) \tag{7}$$

So on the basis of knowing the functional relationship of accumulated dissipated energy curve in one mode which was shown in Equation (4) or Equation (5), the functional relationship of accumulated dissipated energy curve in the other mode can be measured. Take the case of the controlled-stress mode, if the functional relationship of accumulated dissipated energy curve in controlled-stress mode was known, the functional relationship of accumulated dissipated energy curve in controlled-strain mode was shown in Equation (8).

$$\begin{aligned} \frac{2kt + (k^2 - 1)W_{measure-strain}}{k^2 + 1} = 10w_0 \times \frac{2kW_{measure-strain} - (k^2 - 1)t}{k^2 + 1} \\ \times \left(1 - \frac{\frac{2kW_{measure-strain} - (k^2 - 1)t}{k^2 + 1}}{t_R}\right)^{-1/(\nu+1)} \end{aligned} \tag{8}$$

where: $W_{measure-strain}$ = measured accumulated dissipated energy of controlled-strain mode (Pa).

Third, give the values of t and get the values of $W_{measure-strain}$. Because Equation (8) was a nonlinear equation, the values of $W_{measure-strain}$ were calculated by Matlab software. The results of the measured $W_{measure-strain}$ were shown in Figure 4.

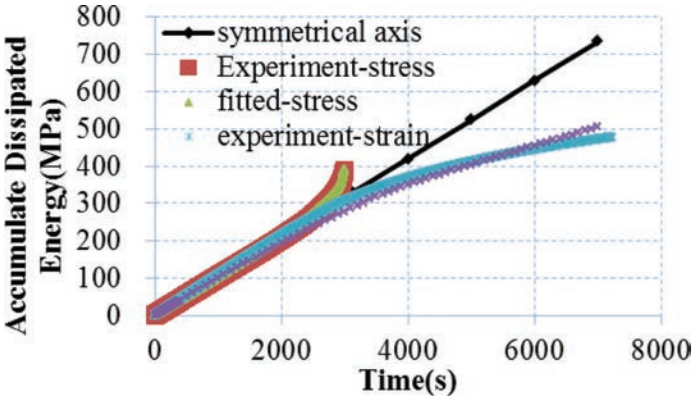

Figure 4. The measured results of accumulated dissipated energy of controlled-strain mode.

As shown in Figure 4, the fitted curve of accumulated dissipated energy in controlled-stress mode ("fitted-stress") is coincident with the experimental data ("experiment-stress"), which is indicated that Equation (4) can fit the accumulated dissipated energy in controlled-stress mode well. On the other hand, the measured curve of accumulated dissipated energy in controlled-strain mode ("measured-strain") is also relatively consistent with the experimental data ("experiment-strain"), which further demonstrates that the controlled-stress curve is symmetrical to the controlled-strain curve.

4 CONCLUSIONS

This paper analyses and compares the differences in the fatigue behavior of asphalt binders in different loading control modes in terms of dynamic modulus and accumulated dissipated energy. The fatigue behaviour relationship between different control modes is found. And the differences are explained by the cross-sections in different control modes. Based on the results presented, several conclusions can be drawn:

1. If the controlled stress and controlled strain is a couple of loading, the fatigue curves of asphalt binders in different control modes are the same in the first phase.
2. If the controlled stress and controlled strain is a couple of loading, the accumulated dissipated energy curve of asphalt binders in controlled-stress mode is symmetrical to that in controlled-strain mode.
3. The method to transform accumulated dissipated energy curve from one loading mode to the other proposed by the article is practicable.

To confirm these findings, more asphalt binders including modified asphalt binders should be tested and analyzed in the future.

ACKNOWLEDGEMENT

This study was sponsored by National Natural Science Foundation of China (51108138 and 51310105005), China Postdoctoral Science Foundation (2013M531050) and the Fundamental Research Funds for the Central Universities (Grant No. HIT. NSRIF. 2014081).

REFERENCES

1. Huang, Y.H. *Pavement Analysis and Design*. Prentice-Hall: Englewood Cliffs, NJ, 2004.
2. Monismith, C.L., and J.A. Deacon. Fatigue of Asphalt Paving Mixtures. *Journal of Transportation Engineering*, TE2, 1969, pp. 317–345.
3. Van Dijk, W. Practical Fatigue Characterization of Bituminous Mixes. *Journal of Association of Asphalt Paving Technologists*, Vol. 59, 1975, pp. 38–74.
4. Van Dijk, W., H. Moreaud, A. Quedeville, and P. Uge. The Fatigue of Bitumen and Bituminous Mixes. *Proceedings of the Third International Conference on the Structural Design of Asphalt Pavements*, Vol. 1, 1972, pp. 354–366.
5. Bonnetti, K.S., K. Nam, H.U. Bahia. Measuring and Defining Fatigue Bahavior of Asphalt Binders. In *Transportation Research Record: Journal of the Transportation Research Board, No.1810*, Transportation Research Board of the National Academies, Washington, D.C., 2003, pp. 33–43.
6. Ghuzlan, K.A. and S.H. Carpenter. Energy-derived, Damage-based Failure Criterion for Fatigue Testing. In *Transportation Research Record: Journal of the Transportation Research Board, No. 1723*, Transportation Research Board of the National Academies, Washington, D.C., 2000, pp. 141–149.
7. Shen, S. and S.H. Carpenter. Development of an Asphalt Fatigue Model Based on Energy Principles. *Journal of Association of Asphalt Paving Technologists*, Vol. 76, 2007, pp. 525–555.
8. Kim, Y.R., D.N. Little, and R.L. Lytton. Fatigue and Healing Characterization of Asphalt Mixtures. *Journal of Materials in Civil Engineering*, Vol. 15, 2003, pp. 75–83.
9. E.Masad, V.T.F. Castelo Branco, D.N. Little, and R. Lytton. A Unified Method for the Analysis of Controlled-strain and Controlled-stress Fatigue Testing. *International Journal of Pavement Engineering*, Vol. 9, 2008, pp. 233–246.
10. Castelo Branco, V.T.F., E. Masad, A. Bhasin, and D.N Little. Fatigue Analysis of Asphalt Mixtures Independent of Mode of Loading. In *Transportation Research Record: Journal of the Transportation Research Board, No. 2057*, Transportation Research Board of the National Academies, Washington, D.C., 2008, pp. 149–156.
11. Lytton, R.L., J. Uzan, E.G. Fernando, R. Roque, D. Hiltmen, and S. Stoffels. Development and Validation of Performance Prediction Models and Specifications for Asphalt Binders and Paving Mixtures. *SHRP Rep. No. A-357*, Strategic Highway Research Program, National Research Council, Washington, D.C.,1993.
12. Bahia, H.U., M. Zeng, H. Zhai, and A. Khatri. *Superpave Protocols for Modified Asphalt Binders*. 15th Quarterly Progress Rep. for NCHRP Proj. 9–10. National Cooperative Highway Research Program, Washington, D.C. 1999.
13. Bouldin, M.G., R. Dongré, and J. D' Angelo. Proposed Refinement to the Superpave High Temperature Specification Parameters for Performance Graded Binders. In *Transportation Research Record: Journal of the Transportation Research Board, No. 1766*, Transportation Research Board of the National Academies, Washington, D.C., 2001, pp. 40–47.
14. D'Angelo, J., R. Kluttz, R. Dongré, K. Stephens, and L. Zanzotto. Revision of the Superpave High Temperature Binder Specification: The Multiple Stress Creep Recovery Test. *Journal of the Association of Asphalt Paving Technologists*, Vol. 76, 2007, pp. 123–162.
15. Rodrigo Delgadillo, U.B. Hussain, and L. Rod. A Nonlinear Constitutive Relationship For Asphalt Binders. *Materials and Structure*, Vol 45, 2012, pp. 457–473.
16. Reyes, M., I.B. Kazatchkov, J. Stastna, and L.Zanzotto. Modeling of Repeated Creep and Recovery Experiments in Asphalt Binders. In *Transportation Research Record: Journal of the Transportation Research Board, No. 2126*, Transportation Research Board of the National Academies, Washington, D.C., 2009, pp. 63–72.

This page intentionally left blank

Asphalt Pavements – Kim (Ed)
© 2014 Taylor & Francis Group, London, ISBN 978-1-138-02693-3

Moisture sensitivity of interlayers between conventional and porous asphalt mixes

Emiliano Pasquini, Fabrizio Cardone & Francesco Canestrari
Università Politecnica delle Marche, Ancona, Italy

ABSTRACT: The use of geocomposites obtained combining bituminous membranes with reinforcing geosynthetics represents a promising option for asphalt pavement application. Thanks to their waterproofing effect, such geocomposites could be successfully used also underneath porous surface layers as an alternative of bituminous tack coat. In this sense, one of the major issue related to the use of geocomposites at the interface between porous surface layers and binder courses is the prolonged contact with drained rainfall water. Given this background, a specific research study was carried out in order to evaluate the moisture sensitivity of interlayers positioned between traditional dense graded asphalt concretes and porous asphalt concretes. Particularly, two geocomposite materials produced combining an elastomeric membrane with a polyester textile and a fiberglass grid, respectively, were investigated along with a traditional reference interlayer obtained by applying hot polymer modified asphalt at the interface. In order to evaluate moisture sensitivity of such interlayers, shear tests were carried out in both dry and wet conditions on double-layered samples prepared in the laboratory. Experimental results showed that the prolonged action of the water did not produce loss of performances of studied interlayers in terms of interface shear strength.

Keywords: Geocomposites, asphalt pavement, interface shear properties, moisture sensitivity, porous asphalt

1 INTRODUCTION

Nowadays, Porous Asphalt Concrete (PAC) is successfully worldwide used on the main highway systems as wearing course or overlay on top of existing pavements in order to improve the surface performance. PACs are bituminous mixtures characterized by a discontinuous grading (high amount of coarse aggregates and low sand and filler content), thus creating an open structure with high air void content (usually ≥ 20%). The particular arrangement of the voids is such that rainwater can drain through a system of interconnected voids to the sideways of the road pavement, thus improving wet weather driving conditions (reduced hydroplaning and splash & spray along with improved skid resistance). Moreover, the high air void content also allows the reduction of traffic induced noise emissions [1–4].

Despite its safety and environmental benefits, PAC can suffer and expose underlying asphalt courses to significant moisture damage due to its open structure, leading to a weakening and hence shortened durability of entire pavement [5–8]. Therefore, an adequate bituminous interlayer with waterproofing function is necessarily required underneath porous surface courses in order to prevent infiltration of water through underlying layers.

In this context, the use of geocomposites obtained by combining a bituminous membrane with a reinforcing geosynthetic can represent a promising option for interlayer systems. In fact, they simultaneously act as waterproofing barrier to control water flow as well as reinforcement systems improving structural response of pavements [5, 9–14].

This paper illustrates a part of an ongoing wider research project which aims at developing an optimized reinforced membranes for asphalt pavement applications on the basis of a performance-related approach [15, 16].

Particularly, the present research evaluated the use of specified geocomposites produced combining an elastomeric bituminous membrane with two different reinforcement types. Such materials could be placed underneath porous surface layers for waterproofing purpose as an alternative of traditional bituminous interlayer. The effectiveness of studied products was investigated in the laboratory with regard to the moisture sensitivity of interface shear behavior of layered systems.

2 MATERIALS AND METHODS

2.1 *Asphalt concrete*

In the present research, double-layered slabs were prepared in the laboratory. The lower layer consisted of a dense graded (conventional) mix AC20 prepared with limestone aggregates (D_{max} = 20 mm) and SBS polymer modified bitumen dosed at 4.0% by the weight of the aggregates. Whereas the upper layer consisted of an open graded (porous asphalt) mix PA 16 prepared with basaltic aggregates (D_{max} = 16 mm) and the SBS polymer modified bitumen dosed at 4.9% by the weight of the aggregates. The gradations and the main properties of the bitumen used for both mixtures are shown in Figure 1 and in Table 1, respectively.

2.2 *Interlayer systems*

Three different double-layered systems were considered depending on the type of interlayer material used: a bituminous material and two geocomposite systems. The reference interface configuration was prepared with an SBS polymer modified binder classified as PMB 45/80-70 according to EN 14023. Hot bitumen dosed at 0.6 kg/m^2 was applied at the interface of the double-layered slabs.

On the other hand, the studied geocomposites, having a thickness of 2.5 mm, were obtained combining an elastomeric bituminous membrane, modified with Styrene-Butadiene-Styrene (SBS) synthetic copolymers, and two different reinforcing materials (Fig. 2). The reinforcing materials were a polyester nonwoven textile and a fiberglass grid characterized by a square

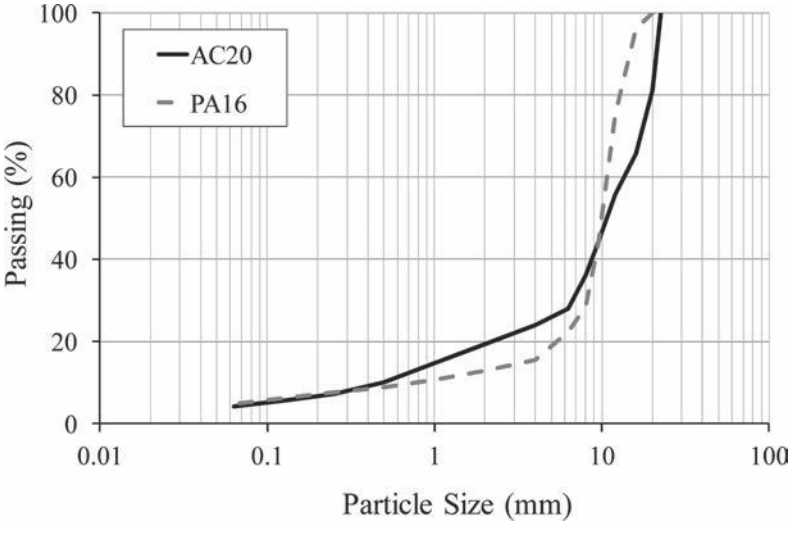

Figure 1. Asphalt concrete gradations.

Table 1. Main properties of the SBS polymer modified bitumen.

Properties	Standard	Unit	Value
SBS polymer content by weight	–	%	3.8
Penetration	EN 1426	0.1 mm	54
Softening point	EN 1427	°C	71
Elastic recovery	EN 13398	%	89
Dynamic viscosity @ 135°C	EN 12595	Pa · s	1.24
Mass loss after RTFOT	EN 12607-1	%	0.05
Penetration after RTFOT	EN 1426	0.1 mm	27
Softening point after RTFOT	EN 1427	°C	77

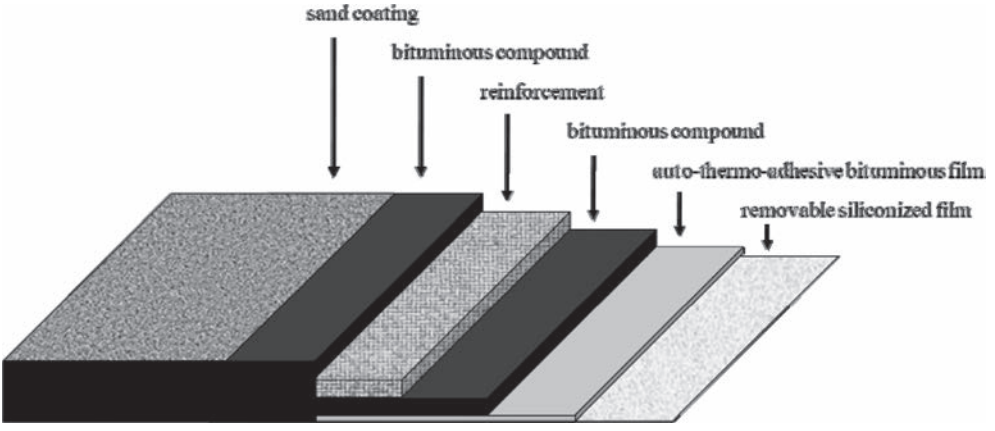

Figure 2. Typical cross-section of reinforced geomembrane.

12.5 mm mesh. It is worth mentioning that the upper side of both geocomposites was coated with a fine sand ($D_{max} < 0.5$ mm) whereas the lower side was characterized by an auto-thermo-adhesive SBS-modified bituminous film (Fig. 2).

2.3 *Laboratory specimen preparation*

Double-layered slabs with a plan dimension of 305×305 mm^2 were compacted in the laboratory by means of a Roller Compactor (EN 12697-33).

Each slab was prepared following different phases. First, the lower layer (binder course) was compacted with a thickness of 40 mm, assuming a target of 8.0% air void content. After cooling of slab at room temperature for 4 hours, depending on the required interface configuration, the appropriate interlayer system (hot bitumen or geocomposite) was applied. Then, a 40 mm thick upper layer (porous asphalt) was compacted with a target air void content of 21.0%. Finally, the compaction direction was marked on the slab surface in order to perform the shear tests in the same direction.

From each double-layered slabs, five 95 mm diameter cylindrical specimens to be evaluated by means of Ancona Shear Testing Research and Analysis (ASTRA) tests were obtained by coring.

2.4 *ASTRA test*

The ASTRA test allowed the evaluation of the interlayer (hot bitumen or geocomposites) influence on the interface shear behavior of the corresponding layered systems.

The ASTRA device (Fig. 3), compliant with the draft European Standard prEN 12697-48 and the Italian Standard UNI/TS 11214, is a direct shear box, similar to the device used in

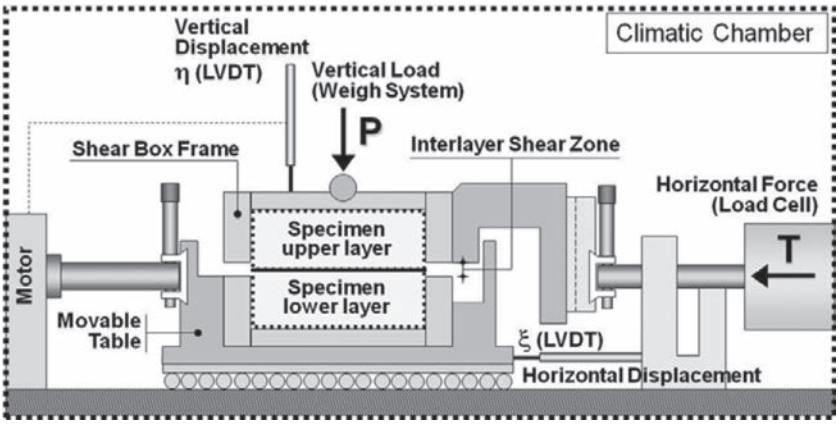

Figure 3. Scheme of ASTRA equipment.

soil mechanics, and the whole apparatus is located in a climatic chamber with temperature and relative humidity control. Single specimen, prepared in laboratory or cored from the field, is installed in two half-boxes (upper and lower) separated by an unconfined interlayer shear zone and the lower half-box is free to move with a fixed rate [17, 18]. During the test, a constant horizontal displacement rate of 2.5 mm/min occurs while a constant vertical load, normal to the interface plane, is applied on the upper half-box in order to generate a given normal stress (σ_n).

This test returns a data-set where interlayer shear stress (τ), horizontal (ξ) and vertical (η) displacement are reported, allowing the calculation of the maximum interlayer shear stress (τ_p), for each specimen. ASTRA tests, carried out at various stress levels σ_n, allow a complete assessment of failure and residual properties (post-peak) of interfaces to be obtained [17]. Previous studies [17, 18] have shown how residual friction, inner cohesion, dilatancy and tack coat adhesion affect the interlayer shear resistance in multi-layered bituminous systems.

3 EXPERIMENTAL PROGRAM

Three interface configurations were obtained using different interlayer materials. The reference configuration, prepared with hot applied bitumen at the interface, is hereafter named as REF whereas the configurations characterized by the presence of the geocomposites are labeled as GPT in the case of geocomposite reinforced with a nonwoven polyester textile and GFG in the case of the geocomposite reinforced with a fiberglass grid with a square 12.5 mm mesh.

The research aims to identify the studied geocomposites as suitable solution, alternative of bituminous tack coat, for interface waterproofing. Moreover, the geocomposites can assure anti-pumping and anti-reflective cracking performance. Because of prolonged contact between geocomposites (placed at the interface between porous surface layers and binder courses) and drained rainfall water during service life of pavement, the use of such geocomposites was evaluated in terms of moisture effects on interlayer shear properties.

To this end, ASTRA interface shear tests on cylindrical specimens cored from double-layered slabs were carried out at 20°C under three normal stresses ($\sigma_{n1} = 0.0$ MPa, $\sigma_{n2} = 0.2$ MPa and $\sigma_{n3} = 0.4$ MPa) performing three repetitions for each test configurations (Table 2).

The moisture sensitivity of interlayer systems was evaluated by carrying out shear tests on both dry and water exposed samples. Each sample of specified interface configurations was divided into two subsets: dry (9 specimens) and wet (9 specimens). Before testing, the dry subsets and the wet subsets were conditioned for 15 days at 20°C in air and fully immersed in water, respectively.

Table 2. Summary of test program.

	ASTRA test repetitions ($T = 20°C$)					
	Dry conditions			Wet conditions		
Configuration	σ_{n1}	σ_{n2}	σ_{n3}	σ_{n1}	σ_{n2}	σ_{n3}
REF	3	3	3	3	3	3
GPT	3	3	3	3	3	3
GFG	3	3	3	3	3	3

4 RESULTS AND ANALYSIS

The overall results of ASTRA tests are presented in Table 3 in terms of envelope characteristic parameters, where c_0 is the pure shear resistance, Φ_p is the peak friction angle, c_r is the pure shear resistance after the failure and Φ_r is the residual friction angle. These values come from the peak and friction envelopes, obtained as linear regression of the representative shear data measured applying different normal stresses σ_n (0.0, 0.2 and 0.4 MPa). The statistical overall quality of the adopted linear regression models is showed in Table 4 in terms of Standard Errors (SE) of c_0, c_r, Φ_p and Φ_r as well as of τ_p and τ_r.

First of all, it is interesting to note that tested double-layered systems exhibited a certain pure shear resistance after failure ($c_r \neq 0$), unlike results obtained in previous researches on different grid-reinforced and unreinforced interfaces [17, 19–21]. According to Canestrari et al. [22], this "residual cohesion" is provided by the presence of the thick bituminous interlayer which obstructs the real contact between the asphalt layers. This finding seems to be confirmed by the fact that the two layers of the specimens were still held together by the bituminous interlayer after testing.

Moreover, it was possible to note that the shear failure did not affect the interface between the interlayer and the asphalt layers but it was located within the interlayer: the deformable bituminous film caused the asphalt layers to slip each other without breaking and determined the residual cohesion of the double layered systems. Thus, in this case, also the residual friction angles Φ_r were influenced by interlayer characteristics in opposition to what found in several studies [17, 19–21] of unreinforced and grid-reinforced systems. In fact, such researches demonstrated that, once the failure condition is reached, the residual friction properties can be considered as an intrinsic characteristic of the asphalt materials. This assumption is still valid if a real contact between the two layers is allowed whereas it seems not applicable in the presence of interlayers.

Figure 4 illustrates peak envelopes for each testing condition. Results show that the reference configuration REF offered the highest shear resistance. This experimental finding proves that the presence of a reinforced membrane at the interface inevitably reduces the bonding between the asphalt layers, according to several previous investigations carried out on reinforced interfaces using various experimental devices [12, 16, 19, 20, 22–25].

On the basis of such results, the application of studied geocomposites has to be carefully verified for interfaces located close to the road surface where the shear stresses transmitted by vehicles remain still high. In fact, a too much low shear strength at the interface could imply the risk of debonding and consequent slippage between the wearing and the binder courses causing both structural and functional damage to the pavement. In any case, it can be asserted that GFG can be successfully applied for asphalt layers reinforcement (at least underneath the binder course); in fact, it was demonstrated, through static three-point bending tests, that the application of GFG geocomposite is able to provide an enhanced damage resistance of the double layered reinforced systems as regard to GPT geocomposite. On the other hand, the geocomposite GPT could be preferred to GFG thanks to the lower interface debonding as long as the required reinforcing contribution is limited.

Table 3. Envelope characteristic parameters of ASTRA tests.

	Dry conditions						Wet conditions					
	$\tau_p = c_0 + {}_n\mathrm{tg}\Phi_p$			$\tau_r = c_r + \sigma_n \mathrm{tg}\Phi_r$			$\tau_p = c_0 + {}_n\mathrm{tg}\Phi_p$			$\tau_r = c_r + \sigma_n \mathrm{tg}\Phi_r$		
	c_0 (MPa)	Φ_p (°)	R^2	c_r (MPa)	Φ_r (°)	R^2	c_0 (MPa)	Φ_p (°)	R^2	c_r (MPa)	Φ_r (°)	R^2
REF	0.383	37.05	0.88	0.069	39.84	0.98	0.355	34.70	0.88	0.063	38.01	0.95
GPT	0.246	39.75	0.91	0.083	37.51	0.99	0.254	39.92	0.90	0.090	32.06	0.97
GFG	0.199	32.35	0.88	0.081	28.52	0.98	0.234	31.76	0.85	0.116	27.69	0.96

Table 4. Statistical overall quality of linear regressions for ASTRA test results.

	Dry conditions						Wet conditions					
	$\tau_p = c_0 + {}_n\mathrm{tg}\Phi_p$			$\tau_r = c_r + \sigma_n \mathrm{tg}\Phi_r$			$\tau_p = c_0 + {}_n\mathrm{tg}\Phi_p$			$\tau_r = c_r + \sigma_n \mathrm{tg}\Phi_r$		
	SE_{c0} (MPa)	$SE_{\Phi p}$ (°)	$SE_{\tau p}$ (MPa)	SE_{cr} (MPa)	$SE_{\Phi r}$ (°)	$SE_{\tau r}$ (MPa)	SE_{c0} (MPa)	$SE_{\Phi p}$ (°)	$SE_{\tau p}$ (MPa)	SE_{cr} (MPa)	$SE_{\Phi r}$ (°)	$SE_{\tau r}$ (MPa)
REF	0.029	6.55	0.052	0.014	2.92	0.026	0.027	5.55	0.049	0.022	4.01	0.040
GPT	0.026	6.00	0.048	0.005	1.03	0.009	0.033	6.50	0.052	0.015	2.55	0.023
GFG	0.029	6.08	0.044	0.010	1.87	0.015	0.031	6.08	0.049	0.015	2.57	0.023

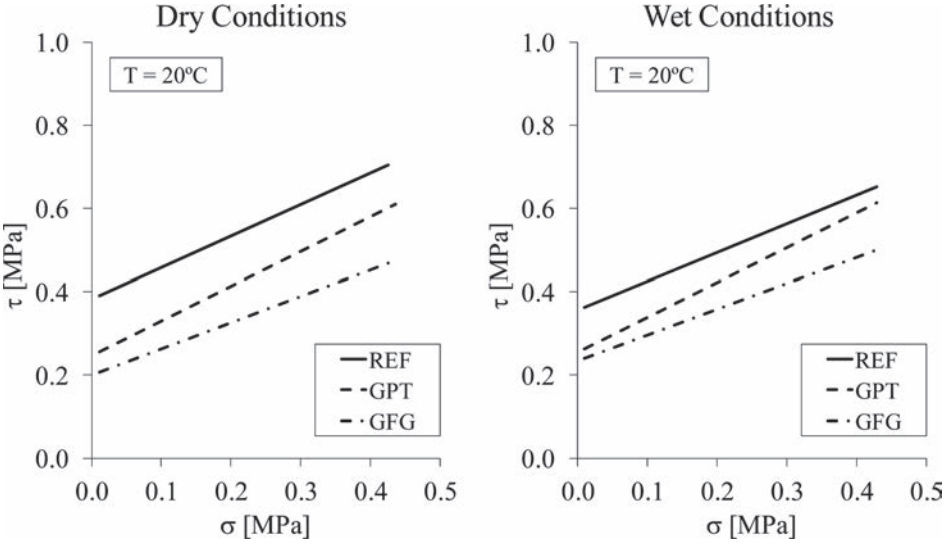

Figure 4. ASTRA test peak envelopes: dry (left) and wet (right) conditions.

As far as the water resistance of studied interlayers is concerned, the comparison between dry and wet configurations for each studied interlayer is shown in Figure 5 in terms of the peak envelopes. Results proved that only the reference interlayer REF exhibited a certain performance decrease due to the water exposure whereas interface treated with geocomposites GPT and GFG demonstrated identical or even improved performances in wet conditions. However, the difference between dry and wet conditioned samples was negligible and hence not directly related to real damage due to water. Thus, it can be asserted that the application of the studied geocomposites did not imply an increase in moisture sensitivity at the

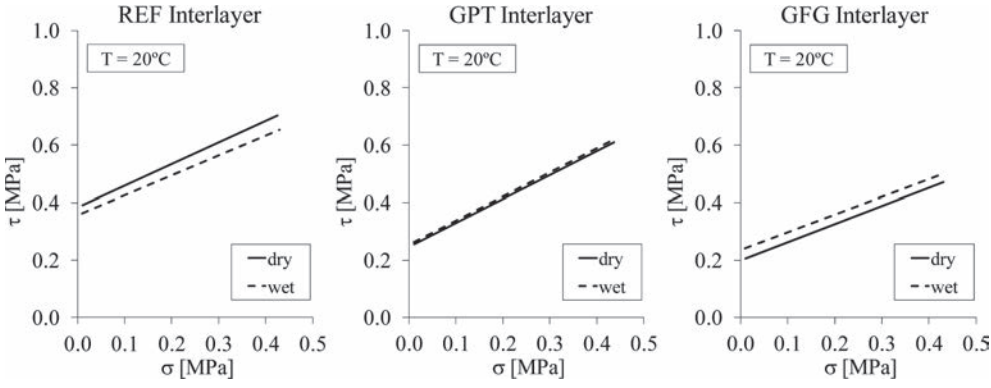

Figure 5. ASTRA test peak envelopes: moisture sensitivity of studied interlayers.

corresponding interfaces with respect to a traditional interlayer (hot applied polymer modified bitumen). It is also right to point out that, for a better comprehension of the moisture sensitivity of studied interlayers, a more severe water conditioning (e.g. higher temperature and/or time, repeated dry/wet cycles, etc.) should be selected for further studies in order to emphasize the water damage at the interface.

5 CONCLUSIONS

The research described in this paper has the objective of evaluating the potential application of reinforced membranes underneath porous surface layers as an alternative of traditional bituminous interlayer. An SBS polymer modified binder and two geocomposites were considered as interlayer systems. The geocomposites consisted of an elastomeric bituminous membrane reinforced with a polyester nonwoven textile (geocomposite GPT) and a fiberglass grid (geocomposite GFG), respectively. The effectiveness of studied products was investigated in the laboratory with regard to the moisture sensitivity of interface shear behavior of layered systems.

ASTRA tests carried out in dry and wet conditions allow the following conclusions to be drawn:

- Studied interlayers exhibit a "residual cohesion" after failure provided by the presence of a thick bituminous film which obstructs the real contact between the bituminous layers;
- The installation of geocomposites at the interface inevitably leads to lower interface bonding between the asphalt layers reducing peak strength. Particularly, geocomposite GPT showed slightly higher performances than GFG;
- The application of the studied geocomposites did not imply an increase in moisture sensitivity of the corresponding interfaces with respect to a traditional interlayer.

It is worth clarifying that, in order to avoid debonding and consequent slippage between the wearing and the binder courses due to the high shear stresses transmitted by vehicles, the application of studied geocomposites close to the road surface should be carefully designed as a function of predicted stresses and strains at the interface. In this sense, further studies evaluating the shear stresses typically generated as a function of the interface depth are currently in progress with the aim of a theoretical validation of the use of interlayers.

As far as results presented in this study concern, it is possible to state that the geocomposite GPT could be preferred to GFG thanks to the lower interface debonding as long as the required reinforcing contribution is limited.

Finally, as far as water sensitivity concerns, it is right to point out that the difference between dry and wet conditioned samples was negligible. Thus, for a better comprehension of the moisture sensitivity of studied interlayers, a more severe water conditioning should be selected for further studies.

ACKNOWLEDGEMENTS

This study was sponsored by INDEX Construction Systems and Products S.p.A. that gave both financial and technical support for the research project.

REFERENCES

[1] Molenaar AAA, Meerkerk AJJ, Miradi M and van der Steen T. Performance of Porous Asphalt Concrete, Journal of the Association of Asphalt Paving Technologists, 75, pp. 1053–1094. 2006.
[2] Kandhal PS and Mallick RB. Design of New-Generation Open Graded Friction Courses, NCAT Report No. 99–3. 1999.
[3] Suresha SN, Ravi Shankar AU and Varghese G. Effect of Aggregate Gradations on Properties of Porous Friction Courses Mixes, Materials and Structures, 43(6), pp. 789–801. 2010.
[4] Santagata FA, Canestrari F, Pasquini E, Ayr U and Pisciotta M. Acoustic Characterization of Different Road Materials, ISAP International Symposium on Asphalt Pavements and Environment, Zurich, Switzerland. 2008.
[5] Kim H, Sokolov K, Poulikakos LD and Partl MN. Fatigue Evaluation of Porous Asphalt Composites with Carbon Fiber Reinforcement Polymer Grids, Transportation Research Record, 2116, pp. 108–117. 2009.
[6] Alvarez AE, Martin AE and Estakhri C. A Review of Mix Design and Evaluation Research for Permeable Friction Course Mixtures, Construction and Building Materials, 25, pp.1159–66. 2011.
[7] Partl MN, Pasquini E, Canestrari F. and Virgili A. Analysis of Water and Thermal Sensitivity of Open Graded Asphalt Rubber Mixtures, Construction and Building Materials, 24, pp. 283–91. 2010.
[8] Partl MN and Poulikakos LD. A Multi-Scale Fundamental Investigation of Moisture Induced Deterioration of Porous Asphalt Concrete, Construction and Building Materials, 25, pp. 1025–35. 2012.
[9] Lytton RL. Use of Geotextiles for Reinforcement and Strain Relief in Asphalt Concrete, Geotextiles and Geomembranes, 8, pp. 217–237. 1989.
[10] Correia NS, Bueno BS. Effect of Bituminous Impregnation on Nonwoven Geotextiles Tensile and Permeability Properties, Geotextiles and Geomembranes, 29, pp. 92–101. 2011.
[11] Virgili A, Canestrari F, Grilli A and Santagata FA. Repeated Load Test on Bituminous Systems Reinforced by Geosynthetics, Geotextiles and Geomembranes, 27(3), pp. 187–195. 2009.
[12] Caltabiano MA and Brunton JM. Reflection Cracking in Asphalt Pavement, Journal of the Association of Asphalt Paving Technologists, 60, pp. 310–330. 1991.
[13] Prieto JN, Gallego J and Perez I. Application of the Wheel Reflective Cracking Test for Assessing Geosynthetics in Anti-Reflection Pavement Cracking Systems, Geosynthetics International, 14(5), pp. 287–297. 2007.
[14] Zamora-Barraza D, Caldaza-Perez M, Castro-Fresno D and & Vega-Zamanillo A. Evaluation of Anti-Reflective Cracking Systems using Geosynthetics in the Interlayer Zone, Geotextiles and Geomembranes, 29(2), pp. 130–136. 2011.
[15] Canestrari F, Pasquini E and Belogi L. Optimization of Geocomposites for Double-Layered Bituminous Systems, RILEM Bookseries, 4, pp. 1229–1239. 2012.
[16] Pasquini E, Bocci M and Canestrari F. Laboratory Characterization of Optimized Geocomposites for Asphalt Pavement Reinforcement, Geosynthetics International, 21(1), pp. 24–36. 2014.
[17] Canestrari F, Ferrotti G, Partl MN and Santagata E. Advanced Testing and Characterization of Interlayer Shear Resistance, Transportation Research Record, 1929, pp. 69–78. 2005.
[18] Canestrari F and Santagata E. Temperature Effects on The Shear Behaviour of Tack Coat Emulsions Used in Flexible Pavements, International Journal of Pavement Engineering, 6(1), pp. 39–46. 2005.
[19] Ferrotti G, Canestrari F, Virgili A and Grilli A. A Strategic Laboratory Approach for the Performance Investigation of Geogrids in Flexible Pavements, Construction and Building Materials, 25(5), pp. 2343–2348. 2011.
[20] Ferrotti G, Canestrari F, Pasquini E and Virgili A. Experimental Evaluation of the Influence of Surface Coating on Fiberglass Geogrid Performance in Asphalt Pavements, Geotextiles and Geomembranes, 34, pp. 11–18. 2012.

[21] Pasquini E, Bocci M, Ferrotti G and Canestrari F. Laboratory Characterisation and Field Validation of Geogrid-Reinforced Asphalt Pavements, Road Materials and Pavement Design, 14(1), pp. 17–35. 2013.
[22] Canestrari F, Grilli A, Santagata FA and Virgili A. Interlayer Shear Effect of Geosynthetic Reinforcements, 10th International Conference on Asphalt Pavements, Quebec City, Canada, pp. 811–820. 2006.
[23] Zamora-Barraza D, Caldaza-Perez M, Castro-Fresno D and Vega-Zamanillo A. New Procedure for Measuring Adherence between a Geosynthetic Material and a Bituminous Mixture, Geotextiles and Geomembranes, 28(5), pp. 483–489. 2010.
[24] Shukla SK and Yin JH. Functions and Installation of Paving Geosynthetics, 3rd Asian Regional Conference on Geosynthetics, Seoul, South Korea, pp. 314–321. 2004.
[25] Canestrari F, Ferrotti G, Lu X, Millien A, Partl MN, Petit C, Phelipot-Mardelé A, Piber H and Raab C. Mechanical Testing of Interlayer Bonding in Asphalt Pavements. Advances in Interlaboratory Testing and Evaluation of Bituminous Materials, State-of-the-Art Report of the RILEM Technical Committee 206-ATB, pp. 303–360, Springer, Dordrecht Heidelberg New York London. 2013.

This page intentionally left blank

Asphalt Pavements – Kim (Ed)
© 2014 Taylor & Francis Group, London, ISBN 978-1-138-02693-3

Fatigue behaviour of an asphalt concrete reinforced with glass fiber grid with 4PB test

I.M. Arsenie
Epsilon Ingénierie, Anse, France
ICUBE, UMR 7357, INSA de Strasbourg, Strasbourg, France

C. Chazallon
ICUBE, UMR 7357, INSA de Strasbourg, Strasbourg, France

J.L. Duchez
Epsilon Ingénierie, Anse, France

D. Doligez
6D Solutions, Sainte Foy les Lyon, France

ABSTRACT: Glass fiber grids or "geogrids" are geocomposite materials frequently employed in asphalt pavement design as reinforcement interlayer to delay the occurrence and propagation of cracks. This paper presents the study and the characterization of the fatigue behavior of a standard asphalt concrete and of the composite made of the asphalt concrete and a glass fiber grid. The aim of this study is to characterize the fatigue behavior of the different structures, to compare them and to quantify the increase in fatigue life due to the geogrid. This is achieved with the four point bending tests performed in the laboratory. The fully reverse fatigue tests were carried out on two different types of specimens: A non-reinforced asphalt concrete beam and a reinforced asphalt concrete beam with two fiber glass grids. The analytical damage model of Castro-Sanchez is calibrated on the bituminous mixture and on the geogrid reinforced bituminous mixture and we discuss the accuracy of this model. The reinforcement role of the glass fiber grid is evidenced by the four point bending test results and supported by the modeling results.

Keywords: fatigue cracking, asphalt concrete, geogrid, four point bending test, analytical damage model

1 INTRODUCTION

The service life of an asphalt pavement depends on its performance under the action of traffic loads and thermal stresses. The phenomenon known as "fatigue cracking" happens under the repeated loads induced by traffic and it is one of the major causes of pavement deterioration [2]. Fatigue cracking is initiated where the tensile stresses are significant, generally at the bottom of the asphalt surface course. One of the methods used to delay this phenomenon is to use a coated glass fiber grid called "geogrid" at the interface between surface course and base course. The geogrid is bonded to the base course with bitumen emulsion. The complex made of asphalt concrete and geogrid has a very good behavior under fatigue loading, delaying the fatigue crack initiation and propagation. In this way, the geogrid works as reinforcement of the asphalt concrete surface course, subjected to fatigue loading.

In this paper, we study the fatigue behavior of the complex made of an asphalt concrete and a geogrid. The study is organized in five sections as follow:

– Section 2 presents the materials and the sample preparation steps.
– Section 3 describes the fatigue test procedures and experimental device.
– Section 4 presents the Four Point Bending (4PB) fatigue tests results.
– Section 5 presents the simulation of the number of cycles at failure with the Castro-Sanchez damage model.

2 MATERIALS AND SAMPLE PREPARATION

2.1 *Tested materials*

The tested asphalt concrete is a standard Semi-Coarse Asphalt Concrete (SCAC) 0/10 class III according to the European classification [3], with the elasticity modulus of 9 GPa, obtained in four point bending tests performed at $T = 15°C$ with $f = 10$ Hz. The aggregate gradation is presented in Figure 1. The bituminous mixture is composed of the following aggregate fractions: 40.68% of 0/4 mm, 9.46% of 4/6 mm, 42.58% of 6/10 mm, 1.89% of filler and 5.39% bitumen 35/50.

The geogrid used as a reinforcement is the coated glass fiber grid CIDEX 100 SB of 6D Solutions, represented in Figure 2. The product is an elastic composite made of warp and filling yarns and nonwoven parts of polyester fiber (mesh: 40×40 mm^2). Both yarn types are made of continuous glass fiber and SBS resin. The mechanical strength at failure of this geogrid is 100 KN/m. In practice, the geogrid is bonded to the pavement layers by applying 600 g/m^2 of bitumen emulsion.

2.2 *Sample preparation*

Two types of samples are made in laboratory [3], respectively: Non-Reinforced (NR) and reinforced (R) asphalt samples. There are five steps in the making process of the reinforced asphalt slabs, as follows:

A. The compaction of the first asphalt concrete layer of 50 mm height,
B. The insertion of a geogrid with a bitumen emulsion applied at ambient temperature (23°C)

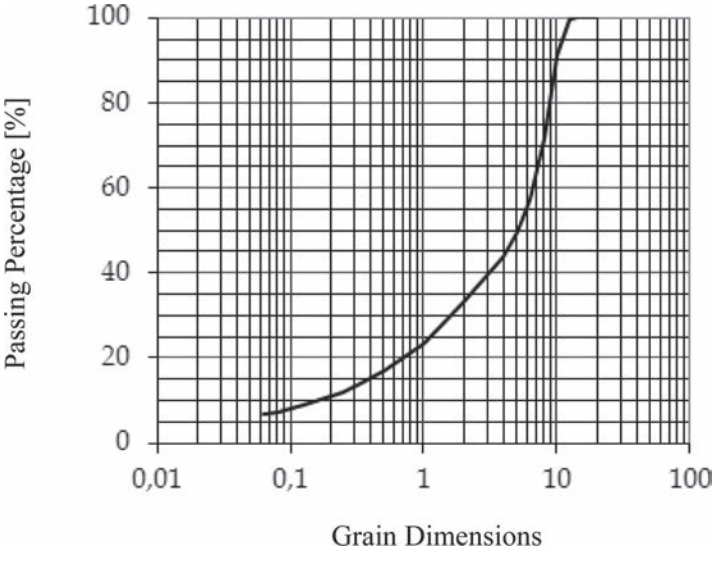

Figure 1. Aggregate gradation of SCAC 0/10 class III.

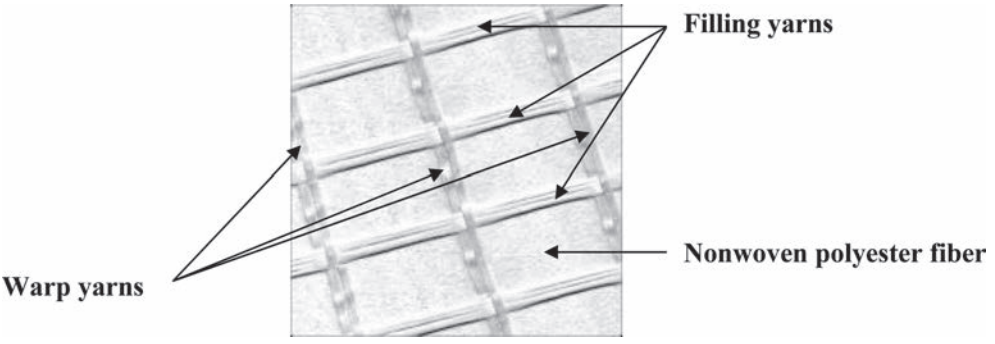

Figure 2. Geogrid CIDEX 100 SB, 6D Solutions.

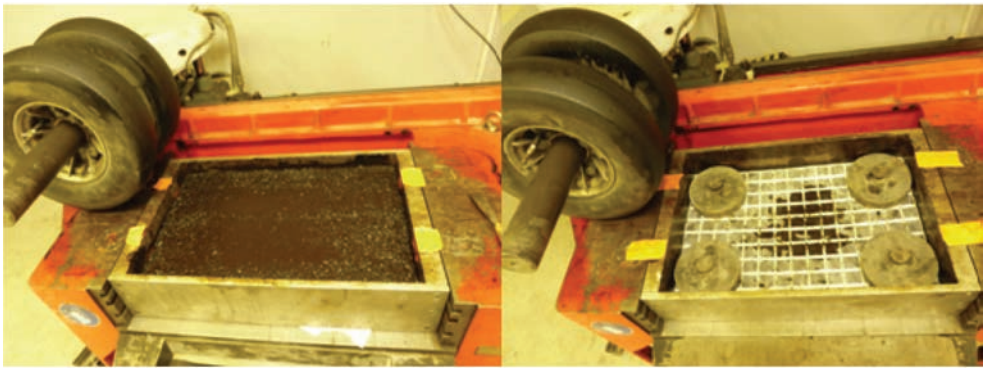

Figure 3. Fixation of the glass fiber grid with bitumen emulsion on the compacted asphalt layer, Epsilon laboratory.

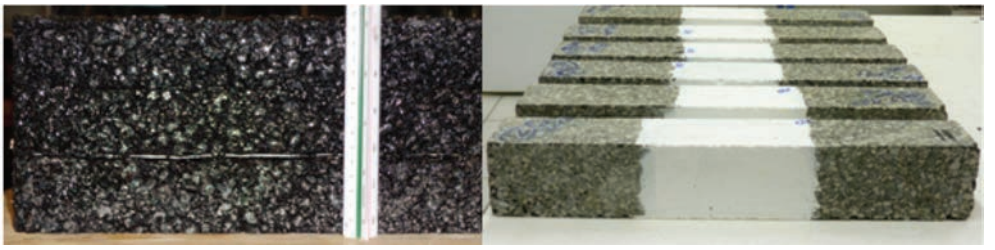

Figure 4. Reinforced asphalt slab and beams.

C. The compaction of the second asphalt concrete layer of 50 mm height,
D. The insertion of a second geogrid with a bitumen emulsion applied at ambient temperature (23°C),
E. The compaction of the third asphalt concrete layer of 50 mm height.

The slabs have the dimensions $600 \times 400 \times 150$ mm^3 (length × width × height). A quantity of 600 g/m^2 of bitumen emulsion was used to insert each geogrid in the R specimens. For the NR specimens, only 300 g/m^2 of bitumen emulsion was used between the asphalt layers. Once the slab is removed from the roller compactor mold, two blocks made of the same asphalt mixture are fixed with araldite at both ends of the slab (minimum 15 mm thickness each) in order to obtain a total slab length of 630 mm. The last operation is sawing the slabs. From each slab we

obtain three beams of $630 \times 100 \times 100$ mm^3. The reinforced asphalt beam vertical section from the bottom to the top is: 25 mm asphalt concrete layer, geogrid with bitumen emulsion, 50 mm asphalt concrete layer, geogrid with bitumen emulsion and 25 mm asphalt concrete layer.

3 FATIGUE TESTS PROCEDURES

The fatigue tests are performed using a four point bending device, specially designed for this study. The standard 4PB device was adapted to the dimensions of the samples, according to the standard [1]. The fatigue tests are fully reverse four point bending tests, performed with a controlled strain, with a frequency of 25 Hz at 10°C temperature [1]. In the French pavement design method [2], the admissible tensile strain at the bottom of asphalt layers is calculated in function of the tensile stress leading to failure after 1 million cycles in a standardized fatigue test with $f = 25$ Hz at $T = 10$°C. The tests are performed with the two types of beams presented in section 2: reinforced (R) and Non-Reinforced (NR) asphalt beams.

3.1 *Four point bending testing device*

The standard fatigue device corresponds to asphalt beams of $400 \times 50 \times 50$ mm^3. These dimensions are not sufficient to test the reinforced asphalt beams presented in section 2. The fatigue device was design to test asphalt beams of $630 \times 100 \times 100$ mm^3.

3.2 *Four point bending test configuration*

Figure 5 shows the principle of the fully reverse four point bending (4PB) test with sinusoidal waveform [1]. In the fully reverse 4PB bending test, the beam is bent from the initial position to the position corresponding to the amplitude of deflection in both senses of tension and compression. Failure happens in an area of uniform moment corresponding to the central part of the beam, between the two load lines.

The deflection is constant and the response of the material is the force, which decreases with the number of cycles. The imposed strain of 135 μm/m corresponds to a constant deflection of 0.1035 mm. This value was chosen to obtain a fatigue life for the non-reinforced asphalt mixture around 400 000 cycles.

The displacement of the beam is measured with a sensor-type Linear Variable Differential Transducer (LVDT) with a range of ± 1 mm. Material response and phase angle are measured during the test.

4 FOUR POINT BENDING FATIGUE TESTS AND RESULTS

A significant number of fatigue tests at three different strain levels (150 μm/m, 135 μm/m, 115 μm/m) were performed on Non-Reinforced (NR) and reinforced (R) asphalt specimens in order to determine the fatigue curves of the materials.

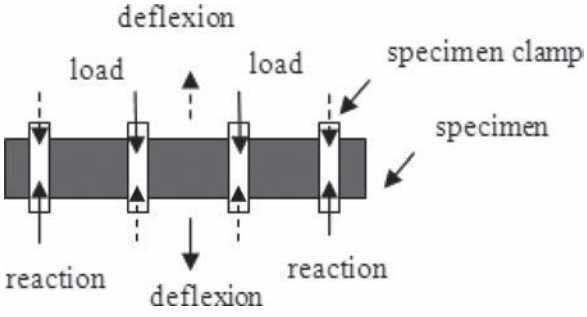

Figure 5. Principle of the fully reverse 4PB fatigue test [4].

The fatigue damage curves ($E/E_i - N$) at the strain level $\varepsilon = 135$ μm/m are presented in this paper (Fig. 6). Twelve 4PB fatigue tests were performed at 10°C with 25 Hz: 6 tests performed on NR asphalt specimens (1 NR .... 6 NR) and 6 tests performed on R asphalt specimens (1R .... 6R).

The 4PB fatigue test results presented in Table 1 show that the geogrid reinforces the asphalt mixture by the increase of the fatigue life. The average fatigue life for each group of specimens and the average fatigue life increase are calculated.

The indicator is the fatigue life, defined in [1],[2] as the number of cycles corresponding to a 50% decrease of the initial elastic modulus. This is represented by an evolution of the ratio $E/E_i = 0.5$ which corresponds to a damage "D" equal to 0.5, determined as $D = 1 - E/E_i$.

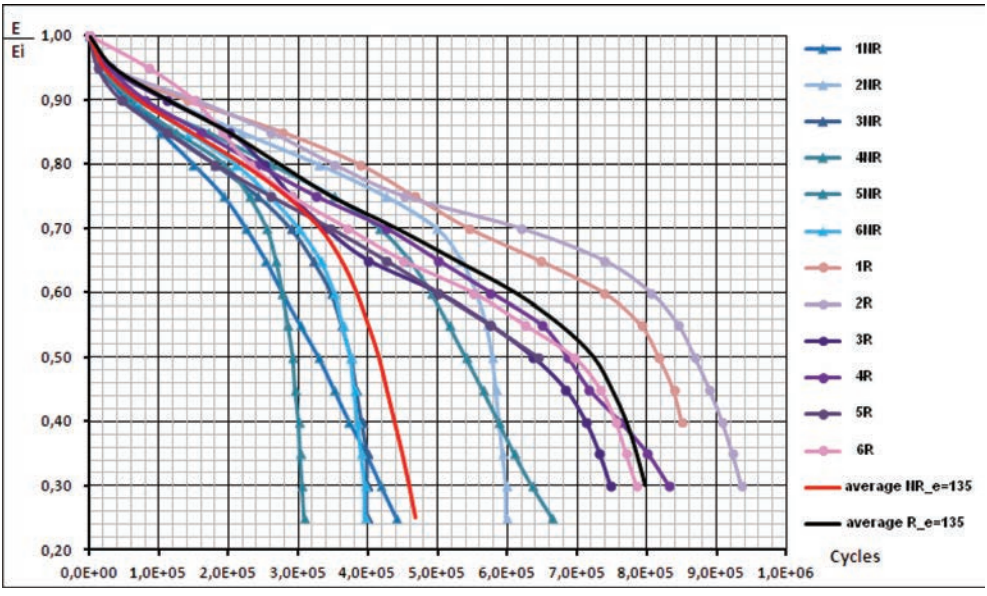

Figure 6. Fatigue damage curves ($E/E_i - N$) in the 4PB fatigue tests on *NR* and *R* specimens.

Table 1. Fatigue 4PB test results at $\varepsilon = 135$ μm/m, $T = 10$°C, $f = 25$ Hz.

Specimen name	Initial elastic modulus E_i	Fatigue elastic modulus E_f (50%)	Fatigue life $N_{f\,(50\%)}$
1 NR	13 976	6 988	328 210
2 NR	12 960	6 480	578 130
3 NR	13 728	6 864	374 550
4 NR	13 736	6 868	540 050 ($N_{f\,max}$)
5 NR	13 962	6 981	291 800 ($N_{f\,min}$)
6 NR	14 870	7 435	375 770
Average NR	13 872	6 936	414 752
1 R	13 470	6 735	817 200
2 R	12 692	6 346	868 210 ($N_{f\,max}$)
3 R	12 042	6 021	636 640 ($N_{f\,min}$)
4 R	12 222	6 111	685 650
5 R	11 864	5 932	643 584
6 R	12 000	6 000	695 210
Average R	12 382	6 191	724 416
Fatigue life increase			309 664 (74.66%)

Significance of the following terms:

NR—non reinforced asphalt beams,
R—reinforced asphalt beams,
E—elastic modulus in MPa,
E_i—initial elastic modulus, after 100 loading cycles,
$E_{f\ (50\%)}$—fatigue elastic modulus, $E_f = E_i/2$,
$N_{f(50\%)}$—fatigue life, number of cycles corresponding to E_f,
$N_{f,max}$—the maximum fatigue life in a group of specimens (NR and R),
$N_{f,min}$—the minimum fatigue life in a group of specimens (NR and R).

Observations on the 4PB fatigue tests results:

- The initial elastic modulus seems to be smaller for the R specimens in comparison with the NR specimens.
- Nevertheless, the fatigue life is considerably improved at the R specimens in comparison with the NR specimens. For the tested strain level $\varepsilon = 135$ μm/m, the average fatigue life increase due to the geogrid is 309 664 cycles, representing 74.66% of the average fatigue life of NR specimens.

5 ESTIMATION OF THE NUMBER OF CYCLES AT FAILURE WITH THE CASTRO-SANCHEZ DAMAGE MODEL

The disadvantage of the fatigue curve is the fact that it doesn't allow to estimate the number of loading cycles corresponding to failure (when damage $D = 1$).

The application of Castro-Sanchez analytical damage model [9] allows estimating the number of cycles at failure for the materials.

The fatigue curves have the general form [1]:

$$\ln N_{f(50\%)} = A_0 + A_1 \ln \varepsilon \tag{1}$$

where: $N_{f(50\%)}$ is the fatigue life, ε is the strain level, A_0, A_1 are material parameters identified from the fatigue tests results.

The Castro-Sanchez damage model is written as follow:

$$N = a\varepsilon^b D^c \tag{2}$$

where: N is the number of loading cycles, ε is the strain level, D is the damage, a, b, c are material parameters identified from the fatigue tests results.

For $D = 0.5$ the Eq. (3) becomes:

$$\ln N_{f(50\%)} = \left(\ln a + c \ln 0.5\right) + b \ln \varepsilon \tag{3}$$

From the association of the Eq. (1) with the Eq. (3) it results the parameter b as $b = A_1$ and the relation between parameters a and c:

$$\left(\ln a + c \ln 0.5\right) = A_0 \tag{4}$$

We firstly determine parameter c from Castro-Sanchez model and then parameter a results from the Eq. (4). For $D = 0.5$ it results the equation:

$$N_{f(50\%)} = a\varepsilon_0^b (0.5)^c \tag{5}$$

From the ratio $N/N_{f(50\%)} = (2D)^c$ it results:

$$c = \frac{\ln\left(\frac{N}{N_{f(50\%)}}\right)}{\ln(2D)} \tag{6}$$

The Eq. (6) is written at every strain level tested for the next values of D, respectively: 0.05; 0.1; 0.15; 0.20; 0.25; 0.30; 0.35; 0.40; 0.45; 0.55; 0.60; 0.65; 0.70; 0.75. The numbers of loading cycles corresponding to each D value are taken from the average fatigue damage curves ($E/E_i - N$). The parameter c is calculated as the average of the values obtained for each strain level (150 μm/m, 135 μm/m, 115 μm/m).

The parameters a, b and c are identified on the fatigue tests results and presented in Table 2.

The Eqs. (7, 8) are used to simulate the damage evolution presented in Figure 7 and Figure 8.

– Non reinforced asphalt concrete:

$$\ln N = 39.253 - 5.293 \ln \varepsilon + 0.47 \ln D \tag{7}$$

– Reinforced asphalt concrete:

$$\ln N = 43.008 - 5.905 \ln \varepsilon + 0.84 \ln D \tag{8}$$

Table 2. Parameters of the Castro-Sanchez damage model.

Parameters for the Castro-Sanchez damage model	Non reinforced asphalt mixture (specimens NR)	Reinforced asphalt mixture (specimens R)
a	39.253	43.008
b	5.293	5.905
c	0.470	0.840

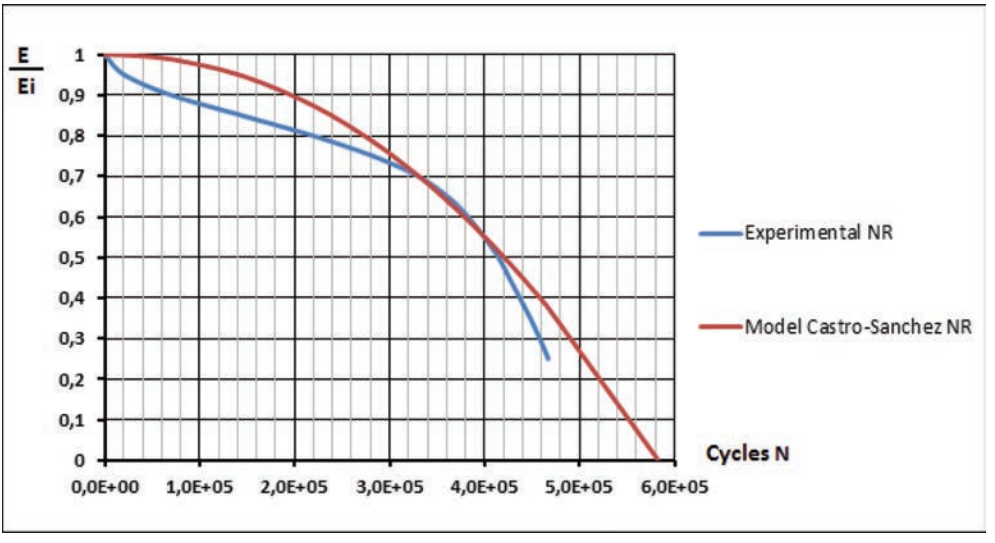

Figure 7. Experimental fatigue damage curve (average) versus simulated fatigue damage curve with Castro-Sanchez model, NR asphalt specimens at $\varepsilon = 135$ μm/m.

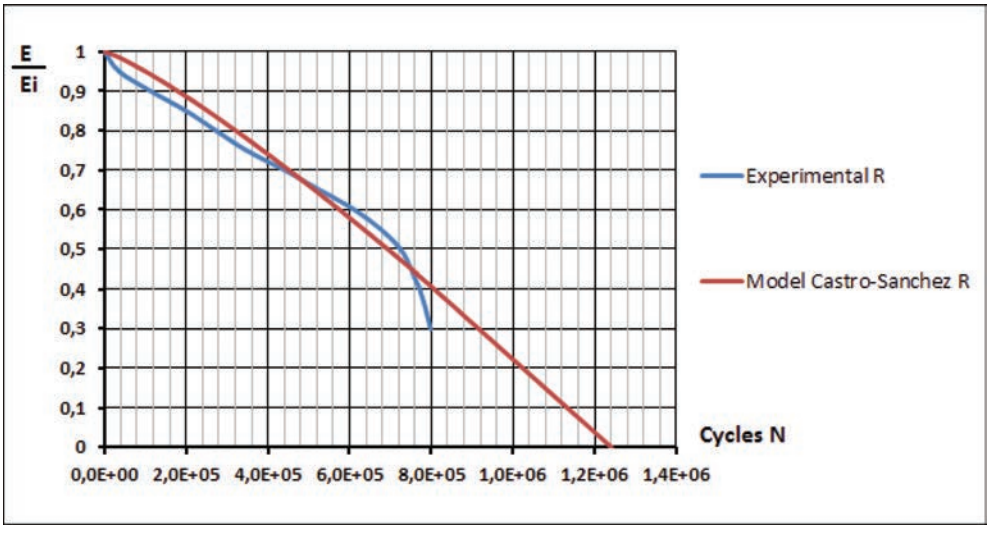

Figure 8. Experimental fatigue damage curve (average) versus simulated fatigue damage curve with Castro-Sanchez model, R asphalt specimens at $\varepsilon = 135$ μm/m.

Table 3. Estimation of the number of cycles at failure with Castro-Sanchez model.

Strain ε (μm/m)	Non reinforced asphalt mixture NR			Reinforced asphalt mixture R		
	$N_{f(50\%)}$	N_r	$N_{f(50\%)}/N_r$	$N_{f(50\%)}$	N_r	$N_{f(50\%)}/N_r$
135	414 752	590 887	0.702	724 416	1 254 631	0.577

At failure, damage $D = 1$, and the Eqs. (7, 8) become:

– Non reinforced asphalt concrete:

$$\ln N_r = 39.253 - 5.293 \ln \varepsilon \tag{9}$$

– Reinforced asphalt concrete:

$$\ln N_r = 43.008 - 5.905 \ln \varepsilon \tag{10}$$

where N_r is the number of loading cycles at failure.

Table 3 presents the number of cycles at failure, calculated with the Eqs. (9, 10). The comparison of the ratios $N_{f(50\%)}/ N_r$ between the non-reinforced asphalt concrete and the reinforced asphalt concrete shows that the glass fiber grid has a reinforcement role even after 50% stiffness loss (0.702 versus 0.577).

The simulated fatigue damage curves (D–N) at $\varepsilon = 135$ μm/m are presented versus the average (over 6 test results) experimental fatigue damage curves (D–N) in Figures 7 and 8. One can observe that the model fails to capture the trend of bituminous mixtures fatigue damage evolution. However, the simulated and experimental fatigue damage curves overlap for D in the range (0.3, 0.5) for NR specimens and D in the range (0.3, 0.55) for R specimens.

6 CONCLUSIONS

This paper presents a part of a laboratory study where an evaluation was done of the increase in fatigue life of asphalt by using the glass fiber grid. This was done using fully reverse Four

Point Bending tests (4PB), performed on Non-Reinforced (NR) and Reinforced (R) asphalt specimens.

The fatigue tests results were obtained at the strain level $\varepsilon = 135$ μm/m, at $T = 10$°C and $f = 25$ Hz, as recommended by the European fatigue standard. At this strain level, the average value (over 6 test results) of the fatigue life increase is 74.66% of the non-reinforced asphalt average fatigue life (over 6 test results). More 4PB fatigue tests must be performed in order to confirm this value.

Castro-Sanchez model was used to estimate the number of cycles at failure for both materials (NR and R). The ratios between the fatigue life and the number of cycles at failure show that the geogrid behavior is to reinforce the asphalt mixture even after the 50% decrease of its elastic modulus. Even if the model fails to capture the trend of bituminous mixtures fatigue damage evolution, the simulated and experimental fatigue damage curves overlap for D in the range (0.3, 0.5) for NR specimens and D in the range (0.3, 0.55) for R specimens. This is interesting because the simplicity of the model, which is easily applied and gives an idea of damage evolution.

REFERENCES

[1] EN 12697-24, (2012). Méthodes d'essai pour mélange hydrocarboné à chaud. Résistance à la fatigue, French version.

[2] Technical Guide, (1994). Technique, Conception et dimensionnement des structures de chaussées, SETRA-LCPC.

[3] EN 13 108-1, (2006). Spécification des matériaux Partie1. Enrobés bitumineux, French version.

[4] Arsenie I., Chazallon C., Themeli A., Duchez J.L., Doligez D., (2012). Study of the fatigue behavior of fiber glass reinforced bituminous mixture, 7th RILEM International Conference on Cracking in Pavements, Vol. 2, pp. 653–664, 21 Juin 2012, Delft, Holland.

[5] Bacchi, M. (2009). Analysis of the variation in fatigue life through four-point bending test, In: *2end Workshop on Four point Bending: From Theory to Practice*, Proceedings of the workshop, pp. 205–215, Pais (Ed.), University of Minho, Portugal. ISBN 978-972-8692-42-1.

[6] Chazallon C., Arsenie I., Themeli A., Duchez J.L., Doligez D., (2013). Study of the fatigue behaviour of an asphalt mixture reinforced by glass fiber grid, European Asphalt Technology Association conference (EATA), 12 p. 3–5 Juin 2013, Braunschweig, Allemagne.

[7] Huurman, P., Pronk, A.C. (2009). Theoretical Analysis of the 4 Point Bending Test. *Advanced Testing and Characterization of bituminous Materials*. Loizos, Partl, Scarpas and Al-Quadi (Eds), Taylor and Françis Group, London, ISBN 978-0-415-55854-9.

[8] Pronk A.C., (2009). Collaborative study with 4PB devices in Europe. Round Robin with three different beams, Proceedings of the second *4PB Workshop*, University of Minho, Portugal, pp. 71–91, 2009.

[9] Castro, M. and Sanchez, J.A. (2008). Estimation of asphalt concrete fatigue curves A damage theory approach. Construction and Building Materials, Vol. 22, pp. 1232–1238.

This page intentionally left blank

Asphalt Pavements – Kim (Ed)
© 2014 Taylor & Francis Group, London, ISBN 978-1-138-02693-3

An investigation into dynamic modulus of Western Australia Hot Mix Asphalt

Sarayoot Kumlai, Peerapong Jitsangiam & Hamid Nikraz
Department of Civil Engineering, Curtin University, WA, Australia

ABSTRACT: Most road networks in Western Australia (WA) are made of flexible pavement with a relatively thin asphalt wearing course and Dense Graded Asphalt (DGA), a commonly used asphalt mix with a continuous size distribution and a low design air-void of around 3% to 7%. Currently, the input parameters for asphalt material for pavement design in Australia still rely entirely on the resilient modulus which cannot incorporate the visco-elastic behaviour of such material into pavement analysis and design. Unlike resilient modulus, dynamic modulus can describe the stress-strain relationship of viscoelastic material across a wide range of temperatures and frequencies in the form of the Master Curve. The Master Curve is constructed through a sigmoidal function and the Time-Temperature Superposition principle (TTS) with a second-order polynomial shift factor function, according to AASHTO PP62-09. This study aims to investigate the dynamic modulus of Western Australian asphalt mixes, considering three different mixes with varying maximum aggregate sizes of 7 mm, 10 mm, and 14 mm. For this study, all test specimens were controlled to reach a 5% air-void with a Survopac gyratory compactor. Specimens were then tested with an Asphalt Mixture Performance Tester (AMPT) with a testing range of four temperatures: 4°C, 21°C, 37°C and 54°C, and six frequencies; 0.1 Hz, 0.5 Hz, 1 Hz, 5 Hz, 10 Hz, and 25 Hz, according to AASHTO TP62-07. Moreover, the dynamic modulus predictive equation proposed by NCHRP 1-37A MEPDG was modified and introduced to suit WA asphalt mixes.

Keywords: Asphalt concrete, dynamic modulus, master curve, AMPT, predictive equation

1 INTRODUCTION

Western Australia (WA) is the largest state in Australia, with an area of 2,529,875 square kilometres; one-third of the entire continent. Thus, road networks are crucial to such vast land areas in terms of connecting and maintaining communities and transporting goods. Consequently, the improvement of road network infrastructures, particularly pavement structures, is a fundamental responsibility for the WA government and road authorities. The first step to improving road infrastructures is to understand how pavement material behaves under real environmental and traffic conditions.

Most pavement structures in WA are made of flexible pavement with relatively thin asphalt wearing courses. Dense Graded Asphalt (DGA) is commonly used as a typical asphalt mix in which aggregate particle sizes are distributed evenly from coarse to fine, and the design air-void is relatively low, generally 3% to 7% [1]. This type of mix is suitable for wearing course applications as it has an enormous capacity for carrying traffic loads.

Currently, Australian pavement design approaches use the resilient modulus as an input parameter for performance criteria and structural analysis. This type of modulus can only represent the stiffness properties of asphalt concrete at a single temperature and frequency. It does not reflect real conditions and cannot incorporate the visco-elastic behaviour of asphalt concrete material into pavement analysis and design. Thus, the dynamic modulus was recently introduced as it has the ability to explain the stiffness and visco-elastic properties of asphalt

concrete across a wide range of temperatures and frequencies. It is therefore now possible for pavement engineers to effectively consider a wide range of environmental and traffic conditions that are as close to real conditions as possible.

2 MATERIAL CHARACTERIZATION

The stiffness of a material is always significant with regard to engineering purposes, as stiffness is an effective indicator of material strength. This information allows engineers to make decisions with regard to choosing suitable materials for particular applications. In the study undertaken here, asphalt concrete is characterised according to the dynamic modulus Master Curve with varying temperatures and frequencies.

2.1 *Shifting techniques*

The properties and the performance of asphalt concrete depend upon temperature and frequency (time), as illustrated by the multiple lines of the dynamic modulus in the frequency domains shown in Figure 1. However, there are also advantages in characterising the strength of asphalt concrete with a single smooth line, rather than multiple lines, in association with the Time-Temperature Superposition principle (TTS) [2–9]. This principle applies shift factors, $a(T)$, multiplied by frequencies, Eq.(1), to align multiple lines from different temperatures into one temperature reference line, the so-called the Master Curve. According to AASHTO PP62-09 [10], there are two recommended shift factor functions. They are the MEPDG shift factor and the Second-order polynomial function. Both functions rely on a reference temperature, but the first employs the viscosity of an asphalt binder, investigated with additional tests. Consequently, this study aims to investigate only the Second-order polynomial function, Eq.(2), due to its more practical purpose.

$$\log f_r = \log f + \log [a(T)] \tag{1}$$

$$\log[a(T)] = a_1 (T_R - T) + a_2 (T_R - T)^2 \tag{2}$$

where f_r is reduced frequency (Hz)
f is frequency (Hz)
$a(T)$ is shift factor

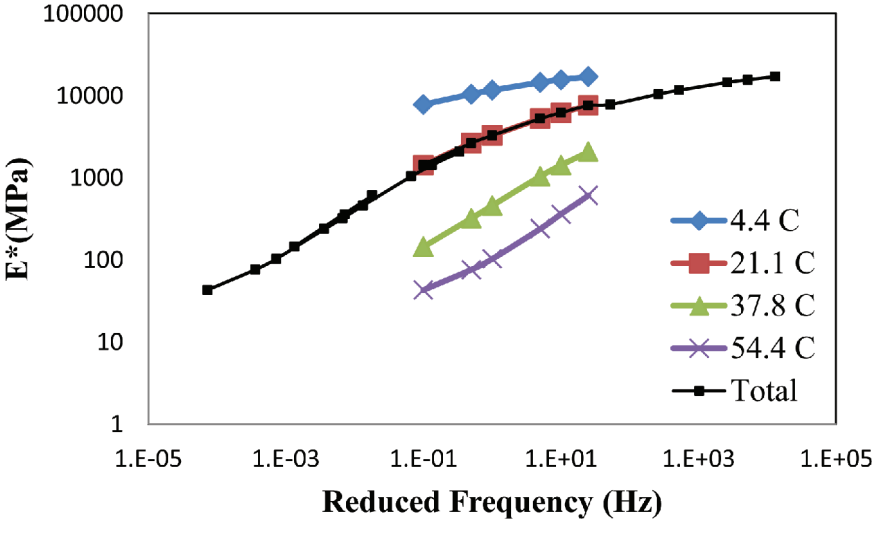

Figure 1. Dynamic modulus master curve.

T_R is reference temperature (°C)
T is temperature (°C)
a_1, a_2 is fitting coefficient

2.2 *Sigmoidal fitting function*

A single smooth line, known as the Master Curve, represents the dynamic modulus values over an observed range of temperatures. As a result, a single polynomial fitting function cannot be used to fit this curve. This is due to the fact that the polynomial swing at low and high temperatures causes irrational predictions of moduli for extrapolation outside a range of test data. Therefore, a sigmoidal function [2], Eq.(3), is usually applied to obtain greater accuracy in the model, and an optimisation technique is used to acquire each coefficient value in this function.

$$\log(|E^*|) = \delta + \frac{\alpha}{1 + e^{\beta - \gamma \log f_r}} \tag{3}$$

where $|E^*|$ is dynamic modulus (MPa)
$\delta, \alpha, \beta, \gamma$ is fitting coefficient

3 DYNAMIC MODULUS PREDICTIVE MODEL

To obtain the complex test data for constructing the Master Curve, a series of asphalt tests were performed, using a sophisticated testing machine, the Asphalt Mixture Performance Tester (AMPT). The Tester is generally unavailable in common asphalt and pavement engineering laboratories, leading to limitations of access to test results. Therefore, NCHRP 1-37A MEPDG [11] introduced a predictive equation which obtains the dynamic modulus of asphalt concrete over a range of temperatures, rates of loading, and ageing conditions. In this equation, Eq.(4), volumetric data of asphalt concrete mixture and bitumen viscosity are the main input parameters.

$$\log|E^*| = 3.750063 + 0.02932\rho_{200} - 0.001767(\rho_{200})^2 - 0.002841\rho_4 - 0.058097V_a - 0.802208\left[\frac{V_{beff}}{V_{beff} + V_a}\right] + \frac{3.871977 - 0.0021\rho_4 + 0.003958\rho_{38} - 0.000017(\rho_{38})^2 - 0.005470\rho_{34}}{1 + e^{(-0.603313 - 0.313351\log(f) - 0.393532\log(\eta))}} \tag{4}$$

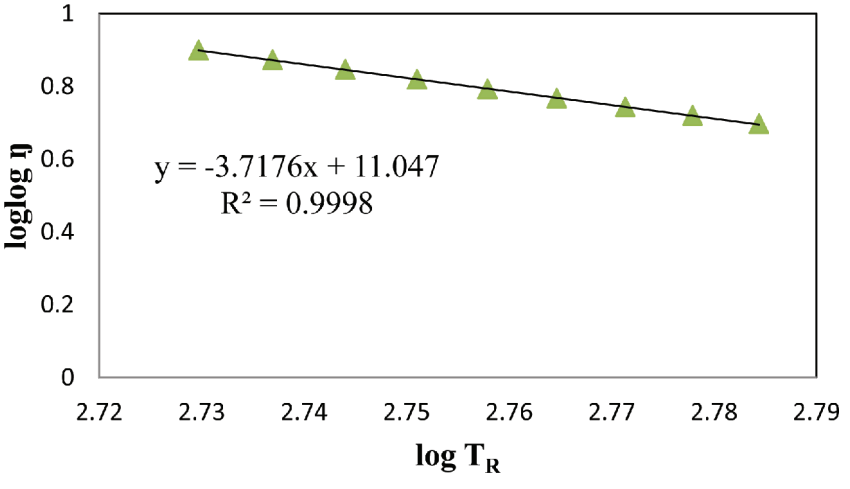

Figure 2. Bitumen binder properties.

where η is bitumen viscosity, 10^6 Poise
f is loading frequency (Hz)
V_a is air void content (%)
V_{beff} is effective bitumen content by volume (%)
ρ_{34} is cumulative % retained on the 3/4 in sieve
ρ_{38} is cumulative % retained on the 3/8 in sieve
ρ_4 is cumulative % retained on the No.4 sieve
ρ_{200} is % passing the No.200 sieve

Moreover, the bitumen binder viscosity, at the particular temperature of interest, is an important parameter which can be determined from the ASTM viscosity temperature relationship [12–13], Eq.(5)

$$\log \log \eta = A + VTS \log T_R \tag{5}$$

where η is bitumen viscosity (cP)
T_R is temperature (Rankine)
A is regression interception
VTS is regression slope of viscosity temperature susceptibility

4 EXPERIMENTAL WORK

4.1 *Materials*

This study used Dense Graded Asphalt (DGA) with three maximum sizes of 7 mm, 10 mm, and 14 mm, and the bitumen binder of class C170 [14] was selected, as it is a commonly used material in Western Australian hot mix asphalt mixes. The gradation details are shown in Table 1, and the bitumen viscosity can be estimated through Eq.(5) with values of A and VTS of 11.047 and –3.7176 respectively.

4.2 *Sample preparation*

According to AASHTO TP62-07 [15], a 150 mm diameter mould was selected for the sample preparation and a Survopac gyratory compactor [16] was utilised to compact samples until they reached a 5 ± 0.5% target air-void at 150 ± 5°C, in accordance with AS 2891.2.2-1995 [17].

Table 1. Gradation for this study.

	Percent passing (%)		
Size sieve (mm)	7 mm	10 mm	14 mm
26.5	100.0	100.0	100.0
19.0	100.0	100.0	100.0
13.2	100.0	100.0	98.0
9.5	100.0	97.9	83.8
6.7	98.3	81.0	68.2
4.75	83.1	65.5	52.8
2.36	57.6	44.2	35.7
1.18	41.9	30.6	25.1
0.6	31.4	20.9	17.4
0.3	18.4	13.4	11.5
0.15	8.6	8.0	7.2
0.075	4.8	5.2	5.1

Table 2. Recommended stress level, equilibrium time and number of cycles.

Temperature (°C)	Stress level (kPa)	Equilibrium time (hour)	Frequency (Hz)	Number of cycles
			25	200
			10	200
4	700–1400	4 hrs or overnight	5	100
21	350–700	3	1	20
37	140–250	2	0.5	15
54	35–70	1	0.1	15

Following this, sample-coring and top—bottom cutting was conducted to obtain a final diameter of 100 mm and a height of 150 mm.

4.3 *Testing procedures*

The Asphalt Mixture Performance Tester (AMPT), consisting of the testing machine, an environmental chamber, and a measuring system, was utilised for dynamic modulus testing. This study considered only four temperatures; 4°C, 21°C, 37°C, and 54°C, and six loading frequencies; 0.1 Hz, 0.5 Hz, 1 Hz, 5 Hz, 10 Hz, and 25 Hz, in accordance with AASHTO TP62-07 [15]. Stress levels, equilibrium time and the number of cycles were also recommended by this standard, as can be seen in Table 2.

5 TESTING RESULT AND MASTER CURVE

Two important parameters were obtained from the experimental work; the dynamic modulus ($|E^*|$), and phase angle (δ), but only the dynamic modulus values were applied to the Master Curve. As mentioned in section 2, the second-order polynomial and sigmoidal function were chosen for fitting shift factors and constructing the Master Curve by following the non-linear least square method. Optimised computer programs, for example the Solver function in MS EXCEL, and SPSS, were used to estimate the fitting coefficient; the details of each mix are shown in Table 3. The Master Curve can then be conducted by applying shift factors to generate reduced frequencies, as can be seen in Figure 3.

Some observations from the different asphalt mixes used in this study are presented below:

- Asphalt concrete material is temperature and frequency dependent; it was therefore stiffer at low temperatures and high frequencies and less stiff at high temperatures and low frequencies.
- Maximum size affects the stiffness properties of asphalt concrete at high frequencies (low temperature), as the 14 mm dynamic modulus Master Curve is above the others and this can be seen in Figure 3(a) and 3(b), with the fitting coefficient α, span of modulus value of the 14 mm mix, being the highest. This result is consistent with the recommendation of Australian standard [18] which states that the 14 mm mix is suitable for heavy-duty applications.
- The phase angle, representing the visco-elastic properties of asphalt concrete, gradually increases from low temperatures (4°C) to intermediate temperatures (37°C), but it starts decreasing at high temperatures (54°C), possibly due to aggregate interlocking effects.
- Maximum size does not affect the phase angle of asphalt concrete and the shift factor, which can be seen in Figure 3(c) and 3(d). There was a small difference among phase angle and shift factor values.

Table 3. Master curve fitting coefficients.

Parameter	Initial value	Estimated value		
		7 mm	10 mm	14 mm
δ	0.5	–0.25286	–0.2965	–0.29847
α	3	3.740696	3.842805	3.870229
β	–1	–1.31576	–1.42346	–1.36451
γ	–0.5	–0.55419	–0.51654	–0.54018
a_1	0.1	0.073573	0.073165	0.070497
a_2	0.0001	0.000353	0.000283	0.000257

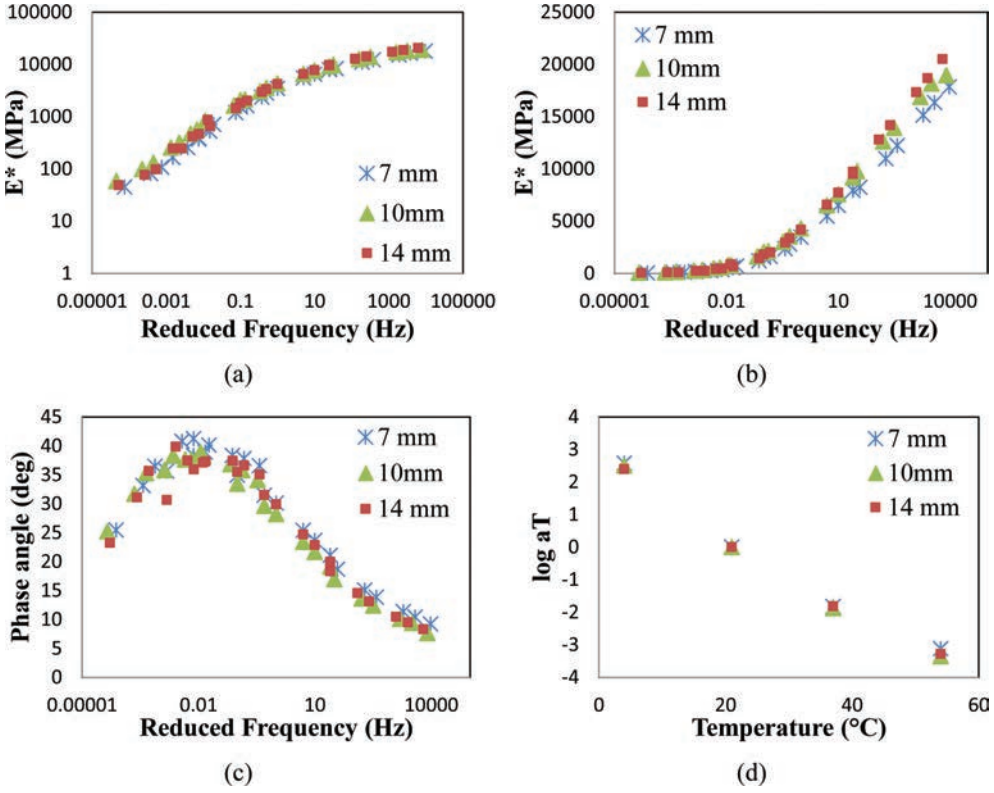

Figure 3. Characterization of asphalt concrete; (a) $|E^*|$ in logarithmic space, (b) $|E^*|$ in semi-logarithmic space, (c) Phase angle, and (d) Shift factor.

6 MODIFIED PREDICTIVE MODEL

NCHRP 1-37A MEPDG [11] introduced the predictive model for estimating the dynamic modulus in level 2 and level 3 analyses. All the data in this model, as shown in Table 4, was substituted to predict the dynamic modulus at the same temperature and frequency as conducted in the experimental work. As a result, it is obvious that the predictive model results over-estimated the dynamic modulus prediction, particularly at high temperatures. All predicted Master Curves of the dynamic moduli are lined above the experimental curve, shown in Figure 4(a), 4(b), and 4(c). The graph in Figure 4(d) shows that almost all of the data points are higher than the line of equality related to predictive $|E^*|$ and experimental $|E^*|$.

Table 4. Input parameters of NCHRP 1-37A predictive model.

Maximum size	Input parameters					
	ρ_{34}	ρ_{38}	ρ_{4}	ρ_{200}	Vb_{eff}	V_a
7 mm	0.0	0.0	16.9	4.8	11.558	4.957
10 mm	0.0	2.1	34.5	5.2	11.513	4.927
14 mm	0.0	16.2	47.2	5.1	11.446	4.825

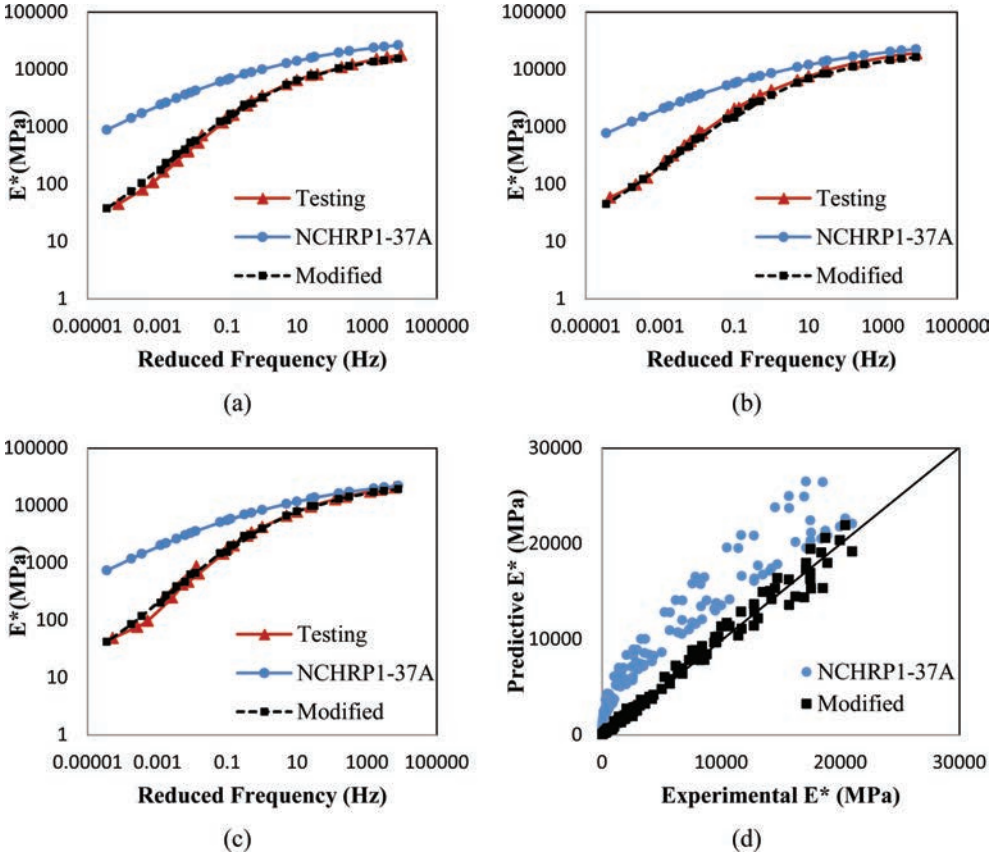

Figure 4. Master curve of $|E^*|$ from experiment and predictive model; (a) 7 mm, (b) 10 mm, (c) 14 mm, and (d) Comparison between NCHRP 1-37A and modified model.

$$\log|E^*| = 1157.579 + 80.63314\rho_{200} - 7.72723(\rho_{200})^2 - 0.15864\rho_4 - 66.7672V_a - 1471.54\left[\frac{V_{beff}}{V_{beff}+V_a}\right] + \frac{-110.51 + 6.756108\rho_4 - 62.2534\rho_{38} + 3.058393(\rho_{38})^2 - 0.005470\rho_{34}}{1+e^{(0.431204-0.5603\log(f)-0.65874\log(\eta))}} \quad (6)$$

In order to suit Western Australian HMA mixes, the NCHRP 1-37A MEPDG predictive model required modification. Within this model modification, the non-linear least square method and the optimisation computer program were employed to recalculate the model coefficient with the same function and the same parameters. A new modified predictive model is presented in Eq.(6). It can be seen that the predicted modulus results derived from this

modified model are very close to those of the testing modulus for all mixes, as the comparison between both moduli from the prediction and the tests is made as shown in Figure 4(a), 4(b), and 4(c). Moreover, the plotting between the predictive $|E^*|$ and the experimental $|E^*|$ illustrates that most of the data converges to the line of equality, shown in Figure 4(d). Consequently, it can be concluded that the modified predictive model from this study can be used to estimate the dynamic modulus value for typical WA mixes more effectively than the originally introduced model of NCHRP 1-37A MEPDG.

7 CONCLUSION

The Master Curve derived from the dynamic moduli and phase angles can be effectively used to characterise the stiffness and the visco-elastic properties of an asphalt concrete material across a wide range of temperature and frequencies. Dense Graded Asphalt (DGA) with three maximum aggregate sizes of 7 mm, 10 mm, and 14 mm is a typical mix for WA. The dynamic modulus results for all mixes in this study show that they are related to the aggregate size of mixtures at high frequencies (low temperature). Moreover, the traditional predictive model of the dynamic modulus, introduced by NCHRP 1-37A, does not suit predictions with regard to the WA mixes in this study due to trends of over-estimation. Thus, the predictive model modification was made to achieve a more appropriate prediction for WA hot mix asphalt mixes in particular. The modified predictive model for WA hot mix asphalt mixes was introduced, as in Eq.(6), to properly evaluate the WA dynamic moduli.

This study concentrated on only one typical hot mix asphalt mix. In fact, there are several asphalt mixes in use in Australia, for instance, Dense Graded Asphalt (DGA), Open Graded Asphalt (OGA), Stone Mastic Asphalt (SMA), and Fine-Gap Graded Asphalt (FGGA). Furthermore, only one original binder type was considered in this study, not including other types of binders such as modified binders. Therefore, investigation of the dynamic modulus for Australian mixes should take all these factors into account in future studies.

ACKNOWLEDGEMENT

The authors would like to thanks Western Australian Mainroads via Western Australian Asset Research Centre (WAPARC) for the financial support of this project, and the AARB Group Ltd for the supply of some relevant information. Moreover, the Australian Research Council (ARC) Linkage (LP110100634) is also gratefully acknowledged for its financial contribution to this work.

REFERENCES

[1] Austroads. Guide to Pavement Technology; Part 2: Pavement Structural Design, 249 pages, Austroads Incoporated, Sydney, 2010.

[2] Bonnaure, F., Gest, G., Gravois, A., and Uge, P. A New Method of Predicting the Stiffness of Asphalt Paving Mixtures. Journal of the Association of the Asphalt Paving Technologists, 46, pp.64–104, 1977.

[3] Pellinen, T., Witczak M.W., and Bonaqusit, R. Master Curve Construction Using Sigmoidal Fitting Function with Non-linear Least Squares Optimization Technique. Proceedings of the 15th ASCE Engineering Mechanics Division Conference, Columbia University, New York. 2002.

[4] Witczak M.W., Kaloush K., Pellinen T., El-Basyouny M., Von Quintus H. Simple performance test for superpave mix design, NCHRP Report 465, Transportation Research Board, National Research Council. Washington, D.C., 2002.

[5] Birgisson, B., Roque, R., Kim, J., and Viet Pham, L. The use of complex modulus to characterise the performance of asphalt mixtures and pavement in Florida. Final Report, University of Florida, 2004.

[6] Cross, S.A., Jakatimath, Y., and Sumesh, K.C. Determination of Dynamic Modulus Master Curves for Oklahoma HMA Mixtures. Final Report, Oklahoma State University, The Oklahoma department of transportation, 2007.
[7] Lee, K., Kim, H., Kim, N., and Kim, Y. Dynamic Modulus of Asphalt Mixtures for Development of Korean Pavement Design Guide, Journal of Testing and Evaluation (JTE), 35(2), 2007.
[8] Eyal, L., and Ayesha, S. Interpretation of Complex Modulus Test Results for Asphalt-Aggregate mixes, Journal of Testing and Evaluation, 36(14), 2008.
[9] Kim, Y.R. Modelling of Asphalt Concrete, 452, ASCE press, United states of America, 2009.
[10] American Association of State Highway and Transportation Officials (AASHTO). Developing Dynamic Modulus Master Curves for Hot Mix Asphalt (HMA): PP 62-09, AASHTO Provisional Standards, 2009.
[11] Transportation Research Board of the National Academies. Guide for Mechanistic-Empirical Design of New and Rehabilitated Pavement Structures. Final Report, NCHRP 1-37A, TRB, Washington, D.C., 2004.
[12] American Society for Testing and Materials. ASTM D2493 Viscosity-Temperature Chart for Asphalts, 1998 Annual book of ASTM Standards, Vol. 0.403, pp.230–234, 1998.
[13] Witczak, M.W., and Mirza, M.W. Development of a Global Aging System for Short and Long Term Aging of Asphalt Cements, Journal of the Association of the Asphalt Paving Technologists, 64, pp.393–430, 1995.
[14] Standards Australia. Residual bitumen for pavements, Standards Australia, Sydney, 1997.
[15] American Association of State Highway and Transportation Officials (AASHTO). Determining Dynamic Modulus of Hot Mix Asphalt (HMA): TP 62-07, AASHTO Provisional Standards, 2003.
[16] Servopac Monitor version 1.24. Servo-controlled gyratory compactor operating and maintenance manual, IPC PTY Ltd., Australia. 2000.
[17] Australia Standards. Methods of sampling and testing asphalt—Sample preparation—Compaction of asphalt test specimens using a gyratory compactor, 1995.
[18] Standards Australia. Hot mix asphalt—A guide to good practice, Standards Australia, Sydney, 2005.

This page intentionally left blank

Additives and modifiers for asphalt concrete—IV

This page intentionally left blank

Asphalt Pavements – Kim (Ed)
© 2014 Taylor & Francis Group, London, ISBN 978-1-138-02693-3

Composite stress analysis of fibre-reinforced Hot-Mix Asphalt mixtures

Pyeong Jun Yoo, Yeon-Bok Kim & Sang-Min Ham
KICT, Ilsan, Goyang, Republic of Korea

ABSTRACT: This study presented an experimental and analytic approach to predict the direct tensile bond strength of recycled plastic fibre-reinforced Hot-Mix Asphalt (HMA) mixtures. The toughening effects of recycled plastic fibre-reinforced HMA mixtures were characterized using the direct tensile loading test developed in this study. The direct tensile loading approach was based on a law of mixture that can separate the composite stress of the mixture into a matrix part and a fibre stress part. The approach showed good correlation among stresses within a limited range of experimental data. The interfacial bond strength could be predicted using this approach in view of the failure of the composite mixture partially due to fibre and matrix interfacial bond failure.

Keywords: Direct tensile loading, fibre-reinforced HMA, flexural strength, interfacial bond strength

1 INTRODUCTION

In recent years, increasing attention has been given to the possibility of improving the mechanical properties of Hot-Mix Asphalt (HMA) by incorporating fibrous reinforcement [1–3].

HMA mixtures with some types of plastic fibres, such as polyester, polypropylene, or nylon, have been reported to be superior to plain HMA in terms of toughness, indirect tensile strength, shear strength, and fracture energy. The improved toughness and fracture energy, which may increase the fatigue life of HMA, were the representative effects in the use of fibres with HMA [4–7].

In addition to HMA, steel fibres, polyesters, or nylon fibres in a short, discontinuous dimension were utilized to implement the enhanced toughness and fracture energy to concrete material by the fibre-bridging effect [8–10].

The toughening effects of the fibre composite are typically characterized using direct tensile tests associated with force-displacement curves or tension-softening curves; however, the fibre's random distribution and orientation require the use of assumptions regarding the probability density functions and randomly oriented effective fibres to calculate the effective composite stresses along the failure plane by accounting for the fibre's bridging forces [11].

The mechanical behaviour of the fibre reinforced composite typically depends on the fibre geometry, fibre contents, the relative stiffness of the matrix and fibre, and the fibre-matrix interfacial bond strength. However, the probabilistic approach to calculate the composite stress considers the bonding effect through an indirect parameter, such as the snubbing coefficient, that depends on the fibre geometry instead of through the interfacial shear stress or strength term [11, 12].

Not all fibres mixed in the composite are equally effective in their toughening with such randomness; however, if sufficient strength improvement can be obtained, the practical advantages of fibres in HMA will be confirmed. A promising cause of toughening may be that the fibres in HMA enhance the shear strength at the interface between the HMA matrix

and fibres, and the enhanced property can delay the initiation and propagation of damages [11, 12].

This study addresses the three-dimensional reinforcement of a HMA mixture using recycled plastic fibres to enhance the interfacial bond strength and proposed a method to calculate the effective fibre volume fraction along the failure plane. The effective fibre volume fraction estimated the interfacial bond strength along the failure plane.

The reinforcing effect by the fibres may occur through the fibre and matrix interfacial shear strength, and a law of mixture considering the matrix and fibre's contributions to enhancing the composite strength separately was adopted, and the interfacial bond strength, which depends on the various fibre contents, was also obtained using direct loading tests.

2 PLASTIC FIBRE-REINFORCED HMA

Plastic fibre-reinforced HMA is comprised of a fibre phase and HMA matrix phase. In addition to the HMA matrix, the fibre phase is also supposed to enhance the tensile strength of the composite. Plastic fibres that are randomly oriented in the matrix were used in this study; the fibres were manufactured through an extrusion process and have embossments on the surface of the fibre and a unique shape and dimensions depending on the rectangular or circular shape of extrusion nozzle.

To make the fibres, the recycled PET chips were first reproduced out of discarded PET bottles. A local recycling manufacturer provided the recycled PET chips. PET fibres having a unique dimension were produced through an extrusion process with a rectangular or circular nozzle. The dimensions of the recycled PET fibres for a coarse aggregate mixture are shown in Figure 1a and are 30 mm (length) × 1–1.5 mm (width) × 0.3–0.5 mm (thickness).

Figure 1a is the 30 mm PET fibres for an asphalt treated-base layer, which has the maximum aggregate size smaller than 19 mm. Figure 1a shows the embossments on the surface of rectangular fibre with a width of 1.5 mm. The colourless fibre, shown in Figure 1b, has one longitudinal groove for the additional separation of the fibre during dry mixing with the aggregate in a plant. The nozzle in this case has a sharp tip inside the rectangular extrusion nozzle to make the groove. The circular fibres, Figure 1c, are used in this study for the coarse aggregate gradation with the maximum aggregate size smaller than 19 mm; the circular nozzle can produce these fibres in the dimension of 0.5 mm wide and 30 mm.

This study only used PET fibres, shown in Figure 1c, to investigate the effect of the fibre content on the HMA toughness. For easiness of the mixing fibres with aggregates during the dry mixing process, the cylindrical fibre-packs as shown in Figure 1d were manufactured and the polypropylene cover-film of the pack was melted down during the dry-mixing process with aggregate because of its relatively lower melting temperature in the range of 150–160°C than the dry mixing temperature above 180°C in a plant.

The mechanical properties of the recycled PET fibres are as follows: the specific gravity of the recycled PET fibre is approximately 1.32, the tensile strength is 300–305 MPa, the elastic modulus at room temperature is approximately 13 GPa, and the elongation is 7.5%. All of the mechanical properties of a recycled PET fibre are equivalent to the typical values of a new PET fibre.

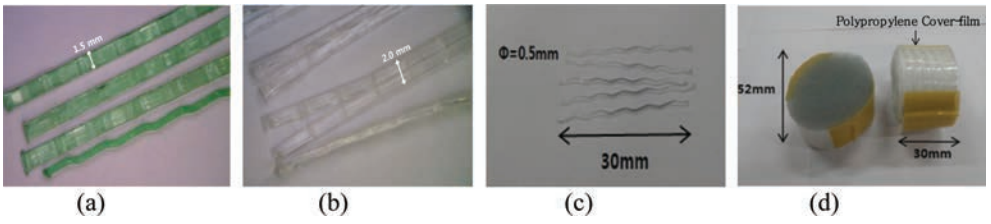

Figure 1. (a) Embossed PET fibres, (b) Grooved PET fibres, (c) Circular PET fibres, and (d) Cylindrical fibre packs.

The asphalt binders for all of the mixtures used in this study were the Superpave PG 64-22 grade with a penetration of 65 and a softening point of 49°C. The characteristics of the HMA mixtures are provided in Table 1, and the aggregate gradation of the mixtures is provided in Table 2. All HMA mixtures, both with and without fibres, were mixed with the optimum asphalt content according to the Marshall-Mix design process with a course aggregate gradation.

This study attempted to avoid the binder content's dependency on the mixture's behaviour, aiming to observe only variations due to the fibre contents. The fibre contents for the coarse aggregate gradation varied with values of 0.2, 0.4, 0.6, 0.8 and 1.0% to the specimen's weight. The aggregate gradation for the maximum aggregate size of 19 mm was in coarse gradation, as shown in Table 2. The lower G_{mm} of the fibre-reinforced mixes may due to the additional fibre volume and mass in the HMA.

Table 1. Mixture characteristics.

	Mix design data			
Mix type	Binder type	Design AC (%)	Air void (%)	G_{mm}
Control	PG 64-22	5.0 ± 0.02	4.5–5.0	2.521
Fibre mix	PG 64-22	5.0 ± 0.02	5.0–6.3	2.510

Table 2. Aggregate gradation.

Sieve analysis								
Sieves	1″	0.75″	0.5″	0.375″	No. 4	No. 8	No. 30	No. 200
% passing	100.0	94.5	77.3	59.7	31.9	24.1	12.3	3.0

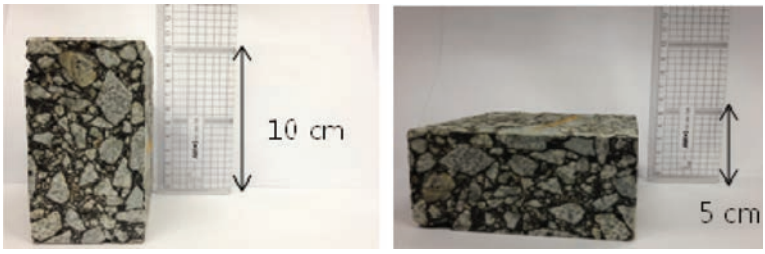

Figure 2. Direct loading test specimens.

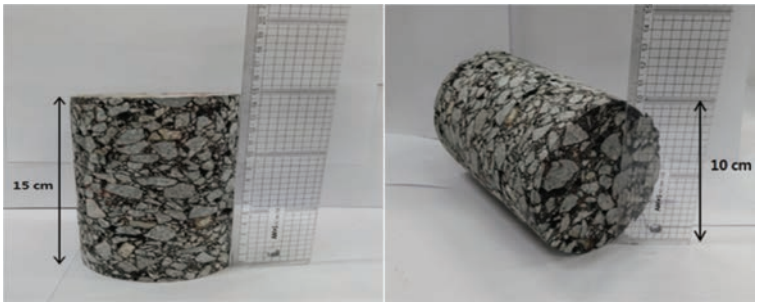

Figure 3. Dynamic modulus test specimens.

Without any balling of the fibres in the mixture, all of the specimens were compacted in a 150-mm-diameter mold at approximately 160°C using a gyratory compacter, with 100–120 gyrations applied to each specimen until the target height for each specimen (i.e., 120 mm) was achieved. The relatively higher air void content of the fibre-reinforced mixture required additional gyrations. The mass of each specimen was calculated as a function of the target air void content, such as 5%, the volume of the gyratory mold, and the theoretical specific gravity, G_{mm}. Two specimens with dimensions of approximately 100 mm (height) × 100 mm (width) × 50 or 70 mm (thickness), shown in Figure 2, were cut from each compacted specimen for direct tensile testing, as described in the following section. Figure 3 shows the specimens for the dynamic modulus tests with dimensions of 150 mm (height) × 100 mm (diameter).

3 LABORATORY TESTS

3.1 *Dynamic modulus tests*

The dynamic responses of PET fibre-reinforced HMA were investigated including 0.0, 0.2, 0.4, 0.6, 0.8, and 1.0% fibre contents by the total weight of asphalt mixture.

Asphalt mixture was well known as a viscoelastic material, which depends on loading time and temperature. For a linear viscoelastic material, the stress-strain relationship under a continuous sinusoidal loading can be explained in terms of the complex dynamic modulus (E*).

The dynamic modulus of asphalt mixtures was measured at five different temperatures and at six frequencies.

Figure 4 shows the test results of dynamic modulus at reference temperature of 10°C for specimens with or without fibres. The master curve describes the loading frequency and temperature dependent properties under linear viscoelastic condition.

It is indicated that the dynamic modulus increases with the increase of the frequencies, Figure 4. The dynamic modulus of fibre reinforced specimens in low temperature or high frequency are smaller than those of the plain HMA. This means that the stiffness of fibre reinforced HMA at low temperature can be reduced by the addition of fibres. Improved toughness due to the slightly greater value of phase angle by the decrease of dynamic modulus compared with the plain HMA can improve the resistance to fatigue damage after numerous cyclic loading at low temperature.

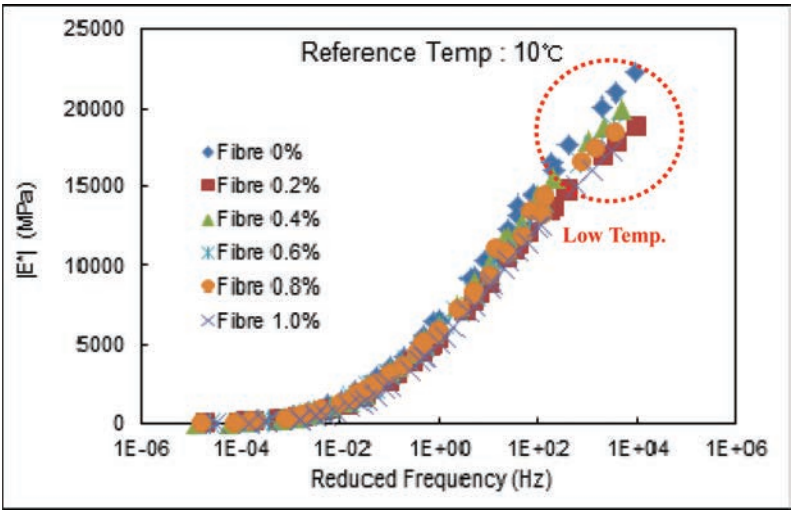

Figure 4. Dynamic modulus master curve in the semi-log scale.

In addition, the phase angles of the fibre reinforced specimens (5.7–45.6°) are greater than those of the plain HMA (5.1–39.5°). This may cause that the air voids in the fibrous HMA (5.0–6.3%) are higher than the values of the plain HMA (4.5–5.0%).

On the other hand, the fatigue parameters such as $|E^*|\sin\delta$ for the fibre reinforced specimens at the low and intermediate temperatures, such as −5, 5, and 10°C are smaller than the values for the plain HMA as shown in Figure 5. The loss modulus ($|E^*|\sin\delta$) could be a parameter to characterize the potential of fatigue cracking of asphalt mixture at low temperature.

The smaller fatigue parameters at the low and intermediate temperatures may indicate that the resistance to fatigue damage of fibre reinforced mixtures can be enhanced; this is due to the fibres can distract the stresses produced during cyclic loading.

In addition, the dynamic modulus data could be used to convert from dynamic frequency data to Prony series data, which is the linear viscoelasticity model to use in most finite element package for a future research purpose.

3.2 *Direct tensile loading test*

A new fixture with two clamping grips for a direct tensile test on HMA was presented. The new fixture makes it possible to use a rectangular specimen by imposing uniform tensile loading at the central area of the specimen. Using the new direct tensile test fixture, it was possible to determine the tensile force versus displacement curves of the various fibre contents.

The toughening effect of PET fibre-reinforced HMA is characterized by considering specimens subjected to uniaxial tension. Figures 6a–c illustrate the direct tensile loading test set-up, including the specimen mounting device, the plates that hold the test specimens, and the upper and lower loading jigs with two clamping grips. The specimen mounting device, shown in Figure 6a, holds the rectangular specimens and ensures identical test dimensions, such as the 1-mm gap between the plates and central point of the specimen, as shown in Figure 6b. The end of the mounted specimen is glued, whereas the middle of the specimen is not glued, as shown in Figure 6b; this schematic is used to induce a uniform uniaxial tension and a failure plane in the middle of the specimen. The glued portion of the specimen should not slip during the direct tensile loading test if a realistic force-displacement curve is to be obtained.

In addition to the specimen being glued to the plates, a uniform torque is applied at the end of a specimen to ensure that the plates do not slip and to obtain a uniform distribution of the tensile load in the middle of the specimen. A composite force-displacement curve was recorded

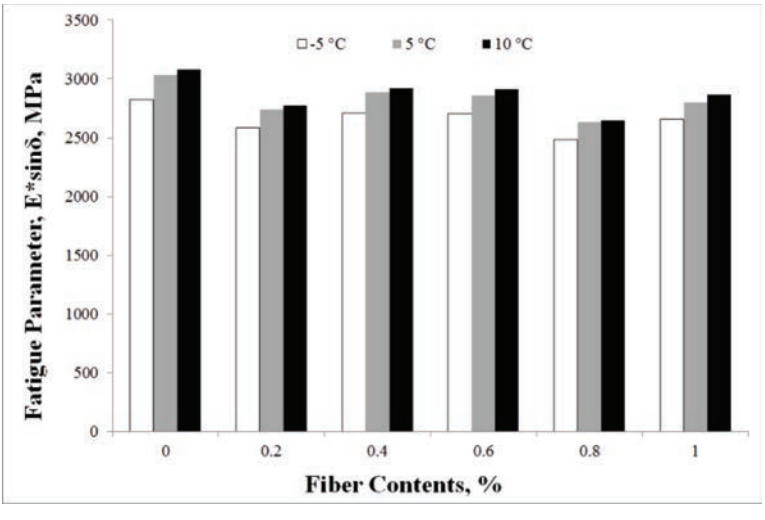

Figure 5. Maximum fatigue parameters.

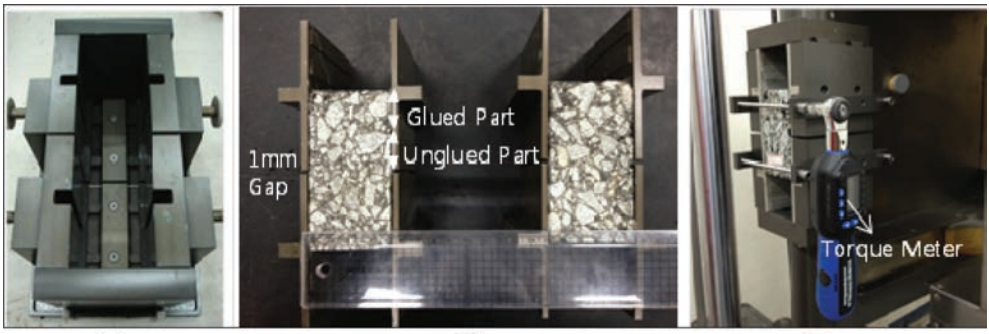

Figure 6. (a) Specimen mounting device, (b) Flanged test specimens, and (c) Test fixture with two clamping grips.

for each displacement-controlled test conducted at a rate of 0.02 mm/s at 20°C, which is a rather high loading rate compared to the rate of approximately 0.01 mm/s in the SHRP-A-641.

However, due to the maximum aggregate size of 19 mm and the coarse aggregate gradation in this study, the loading rate was arbitrarily increased without any mechanical consideration. The displacement at the center of each specimen's failure plane was monitored using a Linear Variable Differential Transducer (LVDT) in the Material Testing System (MTS), as shown in Figure 6c [13–15].

Failure occurred most often on the free part of the specimen, where the specimen was not glued to the inserts. In addition to the direct loading test set-up, analytic approaches were presented as practical applications of the use of short, discontinuous fibres; the fibres were randomly oriented and uniformly distributed without any balling of fibres in the matrix, although not all fibres were equally effective in strengthening. The approaches were based on a law of mixture in which the composite stress of the mixture is correlated with the tensile stress in the HMA matrix and the stress in the fibres, as described in the following section.

4 COMPOSITE STRESS ANALYSIS

This study presents a law of mixture that separates the composite stress into matrix and fibre components to calculate the tensile stress of fibre-reinforced HMA comprised of randomly oriented plastic fibres in a ductile HMA matrix with a lower tensile strength than the fibres.

Through regression analyses, the composite stress-displacement (σ–δ) curves were observed to make correlations among the composite stress (σ_c), the stress in the HMA matrix without fibres (σ_m), and the stress in the fibres (σ_f). The interfacial bond strength (τ) between the matrix and fibres was also determined. The interfacial bond strength resulted in additional tensile strengthening of the mixture whereby tensile load was transferred from the matrix to the fibres. As the tensile loading was transferred from the matrix to the fibres, the interfacial bond stress also began to increase until the composite failed when the fibre-matrix bond was broken. The critical fibre length, L_c, and the average interfacial bond strength of a fibre is given by Eq. (1) [9]:

$$L_c = \sigma_{fu} \frac{w}{2\tau} \tag{1}$$

where σ_{fu} is the ultimate tensile strength of HMA (2–5 MPa); w is the fibre width (1.0–2.0 mm); and τ is the average interfacial bond strength (0.1–0.5 MPa). For a fibre width of 1.5 mm and an average assumed interfacial bond strength of 0.1 MPa, as in this study, a fibre length of $L_f = L_c$ resulted in a length ranging from 1.5 to 3.75 cm [16, 17]. This study arbitrarily decided to use a fibre length of 3 cm.

The toughening of a fibre in Figure 7a, which bridges the matrix failure plane, depends on the centroid distance z from the matrix, the embedded length l, and the orientation angle φ. The orientation angle φ of the embedded fibre may result in a random value on the hemisphere, as shown in Figure 7b. If a fibre located along the failure plane is perpendicular to the loading axis ($\varphi = 90°$), no toughening effect is expected. Because of the randomness in φ, the probability density function $p(\varphi)$ is used, as illustrated in Figure 7c.

The immeasurable nature of the fibre's centroid distance of z in the matrix requires the use of the uniform random distribution function, $p(z)$, as follows [11]:

$$p(z) = \frac{1}{B - A}, \quad \text{for} \quad A = 0 \le z \le B = \frac{L_f}{2} \tag{2}$$

$$p(z) = \frac{2}{L_f} \tag{3}$$

The effective fibres enhancing the toughness along the failure plane have an equal probability of being located at any point on the semicircle that is one side of the failure plane in a three-dimensional view, as shown in Figure 7b. According to Figure 7c, the probability density function of the inclination angle to the matrix failure plane, $p(\varphi)$, is as follows [11, 13]:

$$p(\varphi) = \sin\varphi, \quad \text{for} \quad 0 \le \varphi \le \pi/2 \tag{4}$$

N_t is the total number of fibres in the failure plane of the volume in $A_c L_f$, which may include some fibres bridging the matrix failure plane in the middle of the direct loading specimen, and can be calculated as follows:

$$N_t = \frac{\text{Total fibre volume in failure plane}}{\text{Volume per fibre}} = \frac{A_c L_f \times V_f}{A_f L_f} = \frac{A_c V_f}{A_f} \tag{5}$$

where A_c is the cross-sectional area of the failure surface, A_f is the cross-sectional area of a fibre, and V_f is the volume fraction of the fibres in the HMA.

dN_e is the effective number of fibres along the failure plane, which increases the average bond strength. dN_e includes the randomness in the fibre's centroid distance and the fibre's orientation in terms of the uniform random distribution functions, such as $p(z)$ and $p(\varphi)$. The random number of fibres may be calculated using the orientation angle, from φ to $\varphi + d\varphi$, and the centroid distance, from z to $z + dz$, across the failure plane in the middle of the direct loading specimen as follows:

$$dN_e = N_t p(\varphi) d\varphi p(z) dz, \quad \text{for } 0 \le \varphi \le \frac{\pi}{2} \text{ and } 0 \le z \le \frac{L_f}{2} \tag{6}$$

Integrating Eq. (6) yields

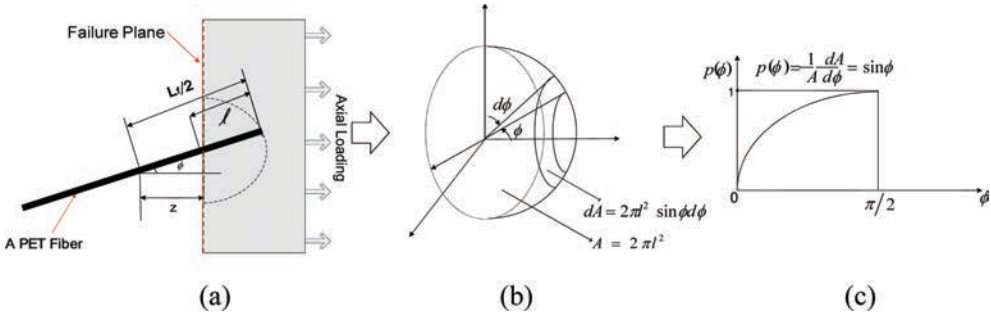

Figure 7. (a) Centroid distance of z, (b) Randomly oriented fibres, and (c) The probability density function of the fibre orientation [11].

$$N_e = \frac{A_c V_f}{A_f} \int_{z=0}^{\frac{L_f}{2}\cos\varphi} \frac{2}{L_f} \int_{\varphi=0}^{\pi/2} \sin\varphi d\varphi dz = \frac{1}{2}\frac{A_c V_f}{A_f} = \frac{1}{2} \times N_t \tag{7}$$

$$V_{fe} = \frac{1}{2} \times V_f \tag{8}$$

The effective number of fibres, N_e, describes the tensile stress along the failure plane. Substituting the effective number of fibres yields an expression for the tensile strength of the randomly oriented composite reinforced fibres. The tensile stress of the composite (σ_c), including the fibres (σ_f) in the matrix (σ_m), can be described by the law of mixtures as follows:

$$\sigma_c = \sigma_m\left(1 - V_{fe}\right) + \sigma_f \times V_{fe} = \sigma_m\left(1 - V_{fe}\right) + 2\tau\left(\frac{L_f}{w}\right) \times V_{fe} \tag{9}$$

$$\frac{\sigma_c}{V_{fe} \times L_f / w} = \frac{\sigma_m\left(1 - V_{fe}\right)}{V_{fe} \times L_f / w} + 2 \times \tau \tag{10}$$

where σ_m represents the stress in the unreinforced HMA matrix and σ_f is the stress in the fibre. A_c = 70 mm × 90 mm, A_f = 1.5 mm × 0.7 mm, L_f = 30 mm, and V_f = 0.0–1.0% are the cross-sectional areas of the matrix, the cross-sectional area of the fibre, the length of the fibre, and the volume fraction of the fibres, respectively.

The direct loading test of the fibre-reinforced HMA with the new fixture developed in this study yields distinguishable composite stress-displacement (σ_c–δ) curves that depend on various fibre volume fractions, as shown in Figure 8a. Eq. (10) can be used to predict both the tensile strength of the composite (σ_c) and the average bond strength of the composite (τ).

The total interfacial bond stress transmitted across the matrix failure plane could be regressed by Eq. (10) using the direct loading test results. Thus, Eq. (10) represents a combined strengthening composite relationship for the tensile failure of the fibre-reinforced HMA.

We defined the correlation among the experimental values of $\sigma_{cu}/(V_{fe} \times L_f/w)$, $(\sigma_m(1 - V_{fe}))/(V_{fe} \times L_f/w)$, and the average interfacial bond strength of τ for the composite reinforced with PET fibres, shown in Figure 8b, using the ultimate composite stresses (σ_{cu}) in each σ_c–δ curve, as shown in Figure 8a.

The composite stress model, Eq. (10), assumes that the frictional bond between the fibre surface and the matrix accounts for the interfacial shear force and neglects any effect of an elastic bond between them. The frictional resistance due to the fibres depends on the amount of slip on the interface between the matrix and fibre. The ultimate composite stress (σ_{cu}) exists before the slipping of the fibre in the matrix. During either the slipping or pulling-out process, the short embedded ends of the effective fibres at the matrix failure plane of the direct loading specimen are completely pulled out, whereas the longer embedded ends of the effective fibres may have had some slippage but are not fully pulled out.

Figure 8a shows the direct loading versus displacement curves. The P–δ curves are experimentally determined and depend on the various fibre contents, such as μ = 0.0, 0.2, 0.4, 0.6, 0.8, and 1.0%, relative to the specimen's weight. The 0.4% Fibre mixture resulted in the highest peak force (2.88 kN) and the displacements at the peak force for fibre mixtures were also extended more compared with the 0.9 mm for the unreinforced mixture as shown in Figure 8a. The 0.4% of fibre content for the coarse aggregate gradation in this study could be set as the optimum and the enhanced toughness compared with the plain HMA, such as the area under the P–δ curve, can extend the performance of fibre reinforced mixture.

The direct tension tests yield the following relationship from a regression analysis, as shown in Figure 8b:

$$\frac{\sigma_c}{V_f \times L_f / w} = 1.04 \times \frac{\sigma_m\left(1 - V_f\right)}{V_f \times L_f / w} + 0.23 \tag{11}$$

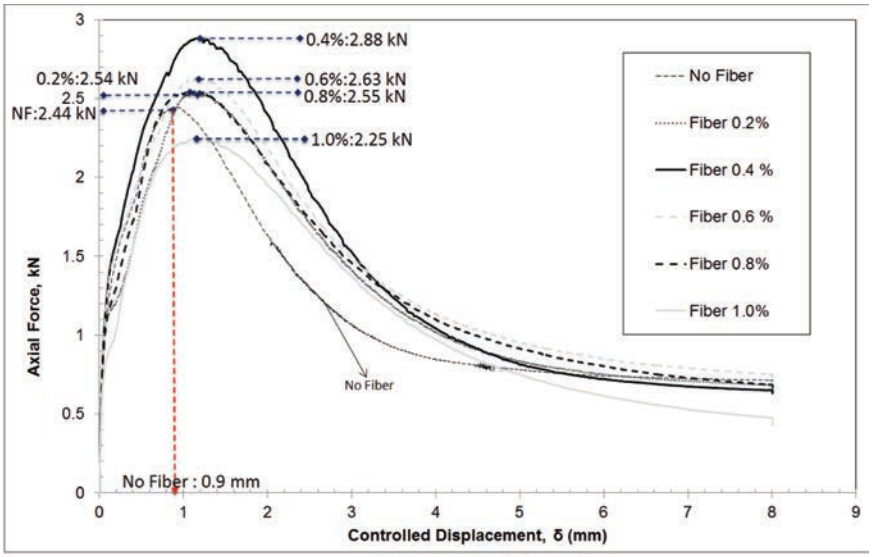

(a)

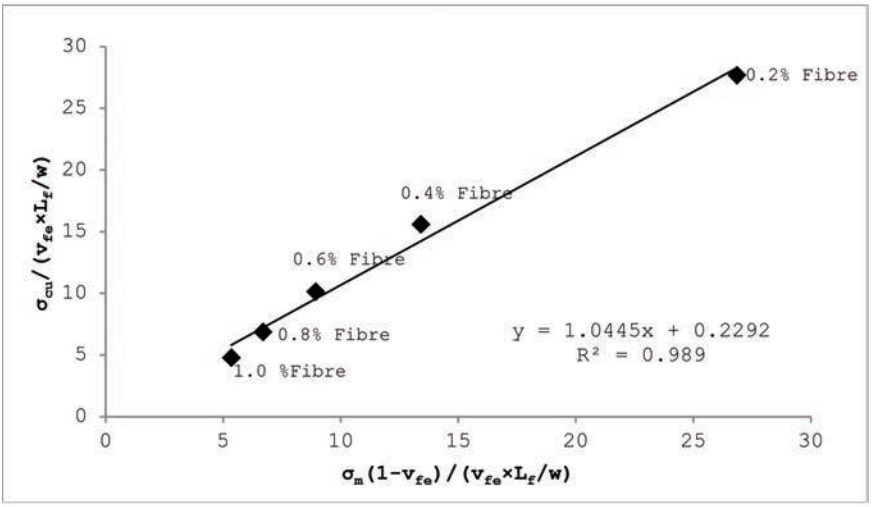

(b)

Figure 8. (a) Composite load-displacement curves and (b) Regression of the law of mixtures.

Eq. (11) shows a composite stress and strength relationship for the tensile failure of the fibre-reinforced HMA with randomly oriented fibres. The slope of the regression line is 1.04, which is close to unity, verifying that the matrix reaches its ultimate tensile strength at failure. Comparing Eqs. (10, 11) yields the average interfacial strength, $\tau = 0.12$ N/mm^2, compared to the maximum tensile stress at the peak, 0.47 N/mm^2 (0.4% Fibre), as shown in Figure 8a. The fibre's contribution to resisting the failure is approximately 25.5%, and the remaining portion of the resistance is due to the bond strength of the HMA matrix. The some fibres lying perpendicular to the axial loading axis along the failure plane led to the lower rate of the shear resistance.

Given the PET fibre material's axial strength, which ranged from 300 to 350 MPa, it was assumed that no fibre rupture occurred during the tests because of the maximum tensile stress in the specimens was approximately 470 KPa at the failure plane.

The regression in Figure 8b indicates that the strengthening effect of the fibres is below average if the fibre contents are greater than 0.6% or less than 0.4%. The fibre contents in both of these cases are below to the regression line, indicating that the optimum fibre content with the coarse aggregate gradation in this study is 0.4–0.6% of the specimen's weight. The test results around the optimum fibre contents are concentrated slightly above the regression line, indicating that a higher value of the average interfacial strength could be possible.

5 CONCLUSION

This study presented a law of mixtures that separates the composite stress into matrix and fibre components to estimate the tensile shear stress of fibre-reinforced HMA comprised of randomly oriented plastic fibres in a softer, ductile HMA matrix. Because not all fibres enhance the toughness along the failure plane, this study proposed a method to calculate the effective fibre volume fraction along the failure plane to estimate the composite stress and interfacial bond strength along the failure plane.

The approach found a correlation among stresses, such as the composite stresses, the stresses in the HMA matrix without fibres, and the stresses in the fibre, using direct tensile loading tests. The interfacial bond strength representing the intercept of the regression equation was predicted because of the composite mixture failure due to the failure of the fibre and matrix interfacial bond. The average interfacial bond strength was $\tau = 0.12$ N/mm^2, indicating that the fibre's contribution in resisting failure is approximately 25.5% of the maximum tensile stress at a peak of 0.47 N/mm^2, and the remaining portion of the resistance is due to the bond strength of the HMA matrix. This result indicates that the fatigue life of the fibre reinforced mixture could be enhanced by the interfacial bond strengthening effect of the fibres along the failure plane.

The regression exhibits an acceptable correlation; however, fibre contents greater than 0.6% or less than 0.4% fall below the regression line, indicating that the optimum fibre content with the coarse aggregate gradation is 0.4–0.6% above the regression line.

REFERENCES

[1] Agostinacchio, M. and Cuomo, G. Asphalt Concrete Pavement Reinforcement through the Addition of Micro-fibres and Steel Meshes, Proceedings of 4th International SIIV congress, University of Palermo, Italia, pp. 1–12. 2004.

[2] Kaloush, K.E., K.P. Biligiri, and W.A. Zeiada. Evaluation of FORTA Fibre Reinforced Asphalt Mixtures using Advanced Material Characterization tests-Evergreen drive, Tempe, Arizona, Research Report, FORTA Corporation, Grove city, PA, USA., 2008.

[3] Yoo, P.J., B.S. Ohm, and J.Y. Choi. Toughening Characteristics of Plastic Fibre-Reinforced Hot-Mix Asphalr Mixtures, KSCE Journal of Civil Engineering, Vol. 16, No. 5, pp. 751–758. 2012.

[4] Trottier, J.F., and N. Banthia. Toughness Characterization of Fibre Reinforced Concrete. In The Journal of Materials in Civil Engineering, Vol. 6, No. 2, pp. 264–289. 1994.

[5] Lee, S.J., J.P. Rust, H. Hamouda, Y.R. Kim, and R.H. Bordon. Fatigue Cracking Resistance of Fibre Reinforced Asphalt Concrete, In The Textile Research Journal, Vol. 75, No. 2, pp. 123–128. 2005.

[6] Bueno, B.S., W.R. Silva, D.C. Lima, and E. Minete. Engineering Properties of Fibre Reinforced Cold Asphalt Mixes. Technical Note, The Journal of Environmental Engineering, *ASCE*, Vol. 129, No. 10, 2003.

[7] Zahran, S.Z., and M.N. Fatani. Glass Fibre Reinforced Asphalt Paving Mixture: Fesibility Assessment, The Journal of King Absulaziz University, Vol. 11, No. 1, pp. 85–98. 1999.

[8] Swamy, R.N. and P.S. Magnet. A theory of the flexural strength of Steel Reinforced Concrete, Cement and Concrete Research, Vol. 4, pp. 313–325. 1974.

[9] Magnet, P.S. Tensile strength of steel fibre reinforced concrete, Cement and Concrete Research, Vol. 6, pp. 245–252. 1976.

[10] Yin, S.W. A Fibre Bridging Model for the Fracture of Brittle Matrix Composites, Engineering Fracture Mechanics, Vol. 46, No. 5, pp. 887–894. 1993.

[11] Li, V.C., Y. Wang, and S. Backer. A Micromechanical Model of Tension-softening and Bridging Toughening of Short Random Fibre Reinforced Brittle Matrix Composites, The Journal of Mechanics and Physics of Solids, Vol. 39, No. 5, pp. 607–625. 1991.
[12] Lawrence, P. Some Theoretical Considerations of Fibre Pull-Out from an Elastic Matrix, The Journal of Material Science, Vol. 7, pp. 1–6. 1972.
[13] Lange-Kornbak, D. and B.L. Karihaloo. Tension Softening of Fibre-Reinforced Cemetitious Composites, The journal of Cement and Concrete Composites, Vol. 19, pp. 315–328. 1997.
[14] Petersson, P.E. Direct Tensile Tests on Prismatic Concrete Specimens, Cement and Concrete Research, Vol. 11, pp. 51–56. 1981.
[15] Strategic Highway Research Program. Direct Tension Test Experiments. SHRP-A-641, National Research Council, Washington, D.C., 1993.
[16] Strategic Highway Research Program. Binder Characterization and Evaluation, Volume 1. SHRP-A-367, National Research Council, Washington, D.C., 1994.
[17] Roque, R., and W.G. Buttlar. Development of a Measurement and Analysis System to Accurately Determine Asphalt Concrete Properties using the Indirect Tensile Test. The Journal of the Association of Asphalt Paving Technologists, Vol. 61, pp. 304–332. 1992.

This page intentionally left blank

Asphalt Pavements – Kim (Ed)
© 2014 Taylor & Francis Group, London, ISBN 978-1-138-02693-3

Evaluation of Recycled Tire Rubber (RTR) modified binders to typical polymer modified binders for performance specifications

John A. D'Angelo
D'Angelo Consulting, LLC, Virginia, VA, USA

Gaylon Baumgardner
Paragon Technical Services, Jackson, MS, USA

ABSTRACT: The use of Recycled Tire Rubber (RTR) to produce PG modified binders has seen a tremendous increase in interest. Under the current economic conditions it is quite cost effective to produce RTR modified binders that will meet typical extended PG grades and Multi-Stress Creep and Recovery (MSCR) grades. One major question is, are RTR modified binders equivalent to typical polymer modified binders currently being used. To evaluate the binder properties new tools, such as the cup and bob Searle system, have been developed. This testing system is used to evaluate the binder properties of RTR modified binders under the AASHTO M 320 and MP 19 specifications.

This study evaluates binders modified with multiple RTR sizes and percentages to typical SBS modified binders. Sizes such as 60, 30 and 20 mesh RTR are blended with neat binders at zero, 5, 10, 15 and 20 percent to produce modified binders. The properties of the blends are being evaluated using both parallel plate and cup and bob geometries and M 320 and MP19 specifications against typical SBS modified binders. These blends will see further testing in asphalt mixtures to look at performance properties and make comparisons of these properties.

Keywords: Asphalt binders, recycled tire rubber, PG grading, MSCR, cup and bob

1 INTRODUCTION

With the introduction of Superpave and performance related asphalt binder specifications the use of binder modification has grown tremendously [1]. In some states in the US, such as Nevada, polymer modified binder is used almost exclusively. Styrene Butadiene Styrene (SBS) is the most commonly used polymer for modification because of its ease of use, relative stability and overall long term performance on the roadway [2]. Many tests and procedures have been developed to assure the SBS is in the asphalt binder; these are typically called SHRP + tests. Highway agencies in order to assure the polymer they want is in the binder have added these plus tests to the standard AASHTO M320 binder specification [3]. These developments have led to restrictive specifications that don't allow for innovation in the industry when it comes to performance enhancements to asphalt binders.

In the late 2000's the price of asphalt binder rose significantly. Highway agencies were use to prices of $150 to $200 dollars a ton in the 1990's, but today's prices are now in the range of $500 dollars per ton. There have been corresponding increases in the price of polymer also significantly increasing the final price of modified asphalt binder. In addition to the price increase there have also been shortages of polymer over the past few years. This increased cost and shortages of material has sparked an interest in looking for alternate materials to replace the polymer additives and reduce costs.

Recycled Tire Rubber (RTR) has been used as an asphalt binder additive for many years [4, 5]. Historically RTR had been blended with the asphalt binder at the mix plant and

directly pumped into the mixes or mixed dry with the hot aggregate in the plant. Over the past several years technologies and process have been developed that allow for blending of the RTR in a terminal facility and then shipping the modified asphalt binder to the mix plant similar to typical polymer modified asphalt binders. Additionally the cost of RTR in relationship to the cost of asphalt binder has reduced significantly. With increase in cost of SBS polymer and asphalt binder and the improvements in processing of RTR modified asphalt binder there has been a renewed interest in using RTR in paving projects.

This paper covers the evaluation of RTR modified asphalt binder to SBS modified asphalt binder using both the AASHTO M 320 specification tests and the AASHTO MP 19 specifications and tests. Multiple RTR sizes and percentages where use in the modification process to evaluate how the rubber modified binder compares to the typical SBS modified asphalt binder.

2 EXPERIMENTAL PLAN

In this study a Gulf Coast PG 64-22 asphalt binder was blended with various RTR size material and percentages. Table 1 shows the RTR size and blend percentages combinations. The 80 mesh RTR was only blended at 11 percent to produce a PG 76-22 material for comparison to the other blends. The properties of these various blends of RTR were then compared to typical SBS modified binder commercially blended to meet a PG 76-22 under the AASHTO M 320 specification. The SBS modified, PMBs 1 & 2, PG 76-22's were produced commercially with approximately 2.5 to 2.8 percent SBS polymer and approximately 0.25 to 0.4 percent Polyphosphoric Acid (PPA). A hybrid binder 76 AR HB was made with 7 percent 30 mesh rubber and approximately 1.5 to 2 percent SBS was also included in the study. Separation characteristics of the RTR binders were not evaluated.

The performance properties for each of the modified asphalt blends were tested using both the AASHTO M320 specification tests and the AASHTO MP 19 specifications tests. It has been shown that the M 320 tests and specifications do not accurately identify the performance characteristics of modified binders [6, 7, 8, 9]. The Multi-Stress Creep and Recovery (MSCR) test used in MP 19 has demonstrated a much better relationship to actual field rutting than $G^*/\sin\delta$ from the M 320 specification [10, 11]. In this study the results of the both specifications are compared.

Size and concentration of RTR in the asphalt blend will affect the final binder properties [12]. This is why several mesh sizes were used to account for the size and concentration affect. The gradations for the different mesh sizes are shown in Figure 1. Using several percentages of RTR for each mesh size allows for the evaluation of both the percent concentration and particle size on the binder properties. Each of the different mesh sizes have very different gradations clearly seen by looking at the 150 µm and 300 µm sieve sizes in Figure 1.

Standard test procedures for the DSR were adjusted to accommodate the addition of the RTR. For the 80, 60 and 30 mesh rubber the gap size was increased to 2 mm. The 20 mesh rubber was tested using the new cub & bob geometry [13]. The geometry uses a stationary cub with a rotational bob allowing a 6.5 mm gap. The cup & bob can be used in the typical oscillatory mode to measure G^* and δ and in creep and recovery to measure J_{nr} and % Recovery.

Table 1. The shaded area shows the blends of PG 64-22 with RTR mesh size and percentages evaluated in the study.

RTR mesh size	80	60	30	20
RTR % blend				
5				
10		■	■	■
15				
20				

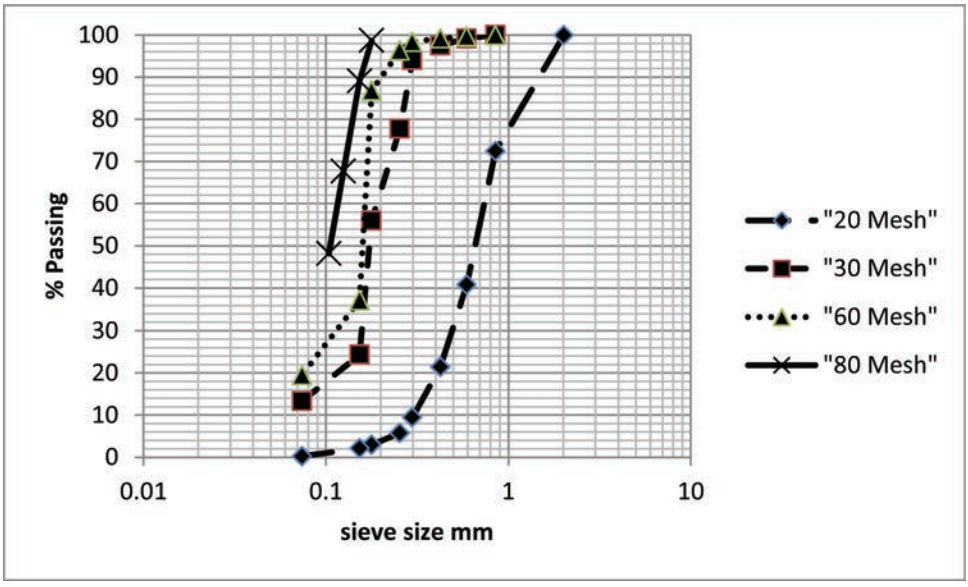

Figure 1. Plot of the RTR gradations for each mesh size.

3 RESULTS

The results from the binder grading, for both M 320 and MP 19 specifications, of the RTR blends is shown in Table 2. As the amount of RTR increased the PG grading in both specifications increased. The M 320 high temperature grade increases from a PG 70 for the 5% blends to a PG 88 for the 20% blends. The MP 19 grading varied from a 64H-22 to a 70E-22. The interesting item with the MP 19 grading is that in any temperature there are four individual grades which are achieved by reducing the creep compliance requirement at any specific temperature, 4.0 for S grades, 2.0 H grades, 1.0 V grades and 0.5 for E grades. This system indicates going from a 64H to a 70E is actually 7 grade changes while the M 320 only has 3 grade changes.

3.1 *High temperature properties*

To compare the RTR modified rubber blends to the SBS binders and hybrid the high, intermediate and low temperature binder properties were compared for both the M 320 and MP 19 test results. Figure 2 compares the $G^*/\sin\delta$ @ 76°C to J_{nr} 3.2 kPa^{-1} @ 64°C for the RTR blends and 2 SBS 76-22, PMB 1 & 2 and hybrid 76–22, RTR and SBS. Only the materials that would meet the M 320 PG 76-22 are compared here to make the performance comparison. The 10 and 15% RTR 80, 60 and 30 mesh blends all met the PG 76-22 grade. As the percentage of RTR increases and the mesh size becomes finer the $G^*/\sin\delta$ increases and the J_{nr} 3.2 kPa^{-1} decreases as expected. Where the differences become significant is between the two grading systems. While the $G^*/\sin\delta$ results show all the material to be a PG 76 the J_{nr} results indicated that results vary over three grades from a 64V to and 64E+ grade.

As previously noted it has been demonstrated that the MP 19 J_{nr} results more accurately differentiate between the rutting potential of binders. The PMB and Hybrid binders all have $G^*/\sin\delta$ values close to the top of the PG 76 range. This is due to the SHRP+ requirements imposed by the highway agencies. For the 15% 30 and 60 mesh RTR the $G^*/\sin\delta$ are basically the same as the SBS PMB 2 and the 76 AR HB binders. However, the J_{nr} values indicate that there is a significant difference in results for these binders. The J_{nr} values go from about 0.15 for the PMB and hybrid binders to a 0.3 for the 15% RTR blends. This is actually a doubling

Table 2. M 320 and MP 19 grading for each of the RTR blends.

RTR mesh size	80	60	30	20
RTR % blend				
5		PG 70-22 PG64H-22	PG 70-22 PG64H-22	PG 70-22 PG64V-22
10	PG 76-22 PG 64E-22	PG 76-22 PG 64V-22	PG 76-22 PG 64V-22	PG 76-22 PG 64V-22
15		PG 76-22 PG 64E-22	PG 76-22 PG 64E-22	PG 82-22 PG 70E-22
20		PG 88-22 PG 70E-22	PG 88-22 PG 70E-22	

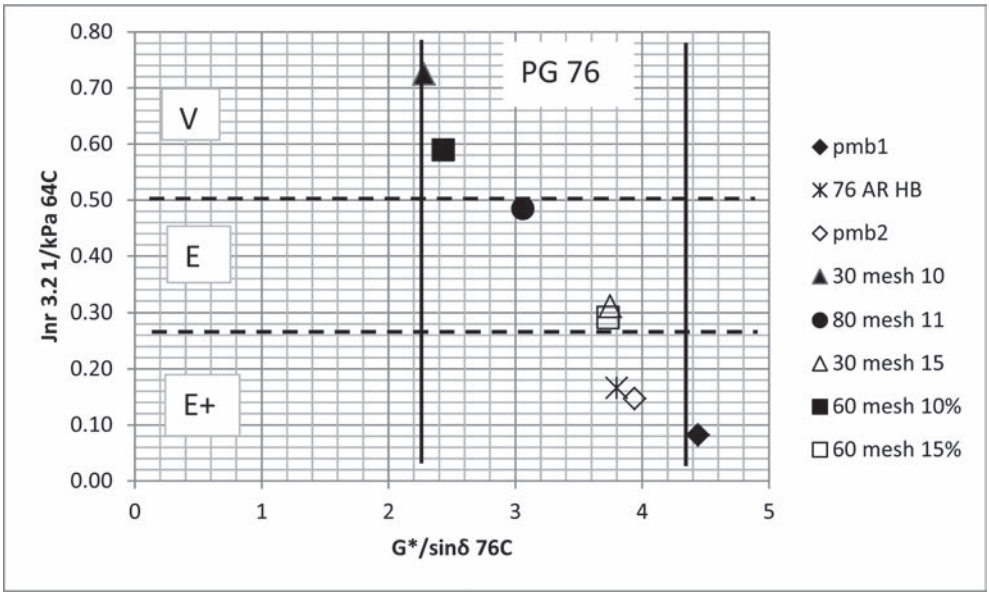

Figure 2. Comparison of M 320 $G^*/\sin\delta$ @ 76°C compared to the MP 19 J_{nr} 3.2kPa^{-1} @64°C.

of the J_{nr} value which indicates a full grade change even though the $G^*/\sin\delta$ value is the same. A similar difference in properties is seen for the 10% 30 and 60 mesh RTR. The $G^*/\sin\delta$ for the two blends are almost the same, but the J_{nr} properties are starting to show some differences from 0.72 to 0.59. This again demonstrates the difference in properties comparing M 320 and MP 19 requirements.

The evaluation of the change in properties with RTR mesh size and percentage clearly shows changes in the various blends. Figure 3 shows the J_{nr} 3.2 kPa^{-1} results for the various mesh sizes and blend percentages at 64°C. A reduction in the J_{nr} compliance is seen with the increase in percentage of RTR. The control PG 64-22 has a J_{nr} of 1.9 which decreases to 0.1 for the 20% RTR blends. In each of the RTR percentage there are also differences in properties based on mesh size. For the 5 and 10% RTR the 60 mesh material provides a lower compliance value than the 30 mesh material. Comparing the 80 mesh 11% RTR to both 10% RTR blends show that the finer 80 mesh material again reduces the compliance. At 15 and 20% RTR little difference can be seen between the 30 and 60 mesh materials. This is likely due to the overall high percentage of rubber in the blend and extremely low compliance values overwhelming the mesh size effect.

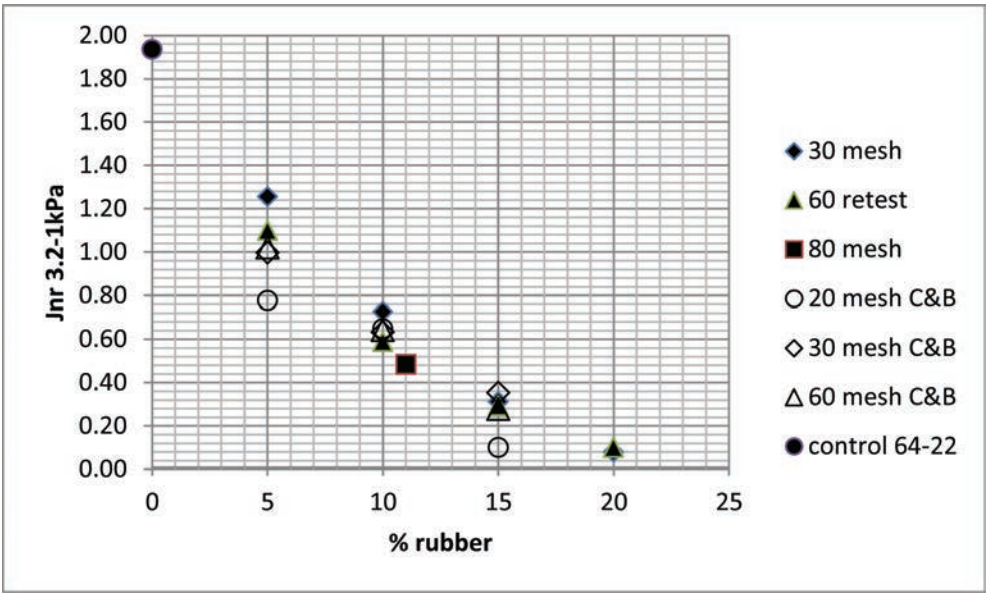

Figure 3. J_{nr} 3.2 kPa^{-1} results for the various RTR mesh sizes and percentages measured at 64°C.

Comparison of the cup and bob to parallel plate results for J_{nr} indicate that there are no significant differences. At 10 and 15% RTR the results fall right on top of each other. At 5% RTR the cup and bob results are slightly below the parallel plate results but well within the typical within lab differences. The cup and bob for the 20% RTR were not completed in time for this paper. There are no parallel plate results for the 20 mesh RTR because the large particle size would require the gap to be at least 6 mm. This is far greater than is practical for running parallel plate geometry in a dynamic shear rheometer at high grade temperatures. The cup and bob results for the 20 mesh RTR indicate that this material has a lower compliance value than the 30 or 60 mesh RTR. This is in contrast to the 30, 60 and 80 mesh samples which indicate that the finer mesh material produces lower compliance results. Further testing will have to be done to verify the results.

The second aspect of the MP 19 specification is the % Recovery measured during the MSCR test. Non-recoverable creep compliance J_{nr} is a measure of stiffness related to permanent deformation. The % Recovery from the test is a measure of the delayed elastic response of the material. The % Recovery for the various RTR blends is shown in Figure 4. The data mirrored what was seen with the compliance value J_{nr}. As the percent RTR in the mix increased the delayed elastic response increased from about 11% for 5% RTR to 65% for 20% RTR. At 5 and 10% RTR the finer mesh blends had higher % Recoveries than the courser mesh RTR. At 15 and 20% RTR the mesh size was either the same or the courser mesh had higher % Recovery. Again this is likely due to the high percentage of RTR overwhelming the size effect. While the parallel plate and C&B results were the same for the compliance results the % Recovery data indicated a difference. For each mesh size and percentage of RTR the C&B provided higher % Recovery than the parallel plate results. For the J_{nr} value to be the same for both geometries, but have the % Recovery to be higher the creep and recovery must be different. The unrecovered strain is the same, but the peak strain during the creep portion of the curve must be higher which would increase the recovery portion if the preeminent strain remains the same.

The cause for this difference is still under investigation, but one possible reason is the geometry. In the C&B the gap size between the bob and inside surface of the cup is 6.5 mm. The bob is also 25 mm high so with the applied stress the full gap for the height and circumference of the bob is moved. In the parallel plate geometry it is only the very outside edge of the plates that

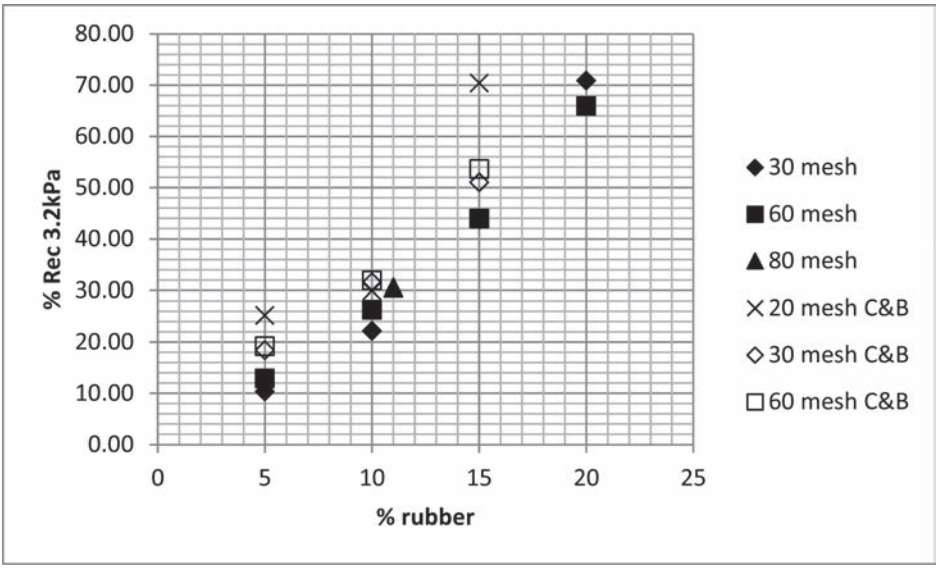

Figure 4. % Recovery results @ 3.2kPa^{-1} for the various RTR mesh sizes and percentages measured at 64°C.

sees any significant movement. The differences in geometry are shown in Figure 5. The effect of moving significantly more material in the sample, for the C&B geometry over the parallel plate, is likely causing the difference. This increase in volume of material moved in the C&B geometry will likely cause greater particle interaction than in the parallel plate geometry. Which geometry is more accurately measuring the properties on the material is still under investigation.

One approach to evaluate modified asphalt binders in the MP 19 specifications is to evaluate the J_{nr} 3.2 kPa^{-1} and the % Recovery together graphically. The % Recovery results were plotted against the J_{nr} results for each sample in the study. This data is shown in Figure 6. Samples with low J_{nr} values and high % Recovery plot to the upper left corner of the graph while samples with higher J_{nr} values and low % Recovery plot to the lower left corner of the graph. The SBS polymer modified binders are in the upper left hand corner of Figure 6. The control asphalt binder plots in the lower right hand corner of the mix. This plot again shows as the % RTR increases the J_{nr} reduces and the % Recovery increases. On the graph is also drawn a solid line labelled elastic response. This line was developed based on testing of polymer modified asphalt binders where binder with compatible polymers well blended and cross-linked would always plot above this elastic response line. The 15% RTR blends all easily meet the 64E grade, J_{nr} less than 0.5 and % Recovery greater than 35%. These results are very typical for commercial SBS modified asphalt binders. Though the specific pmb's used in this study were on the very stiff range for normal materials many would fall in the same range as the 15% RTR blends.

3.2 *Intermediate temperature properties*

The aged properties of the asphalt binder are evaluated by testing in the DRS at intermediate pavement temperatures. The Pressure Aging Vessel (PAV) conditioned binder blends were tested in the DSR to determine $G^*\sin\delta$ values. Aged binders become brittle and are prone to cracking at temperatures in the 15 to 25°C temperature range. Currently the cup and bob geometry cannot be used for intermediate temperature testing in the DSR. The large sample size and surface area of the bob cause significant machine compliance issues with the DSR. To address the RTR particle size the gap for the 8 mm parallel plate was increased from 2 mm to 4 mm. At the intermediate temperatures between 16 and 25°C the binder sample can maintain its shape in the DSR with the 4 mm gap without losing its edge integrity. The intermediate

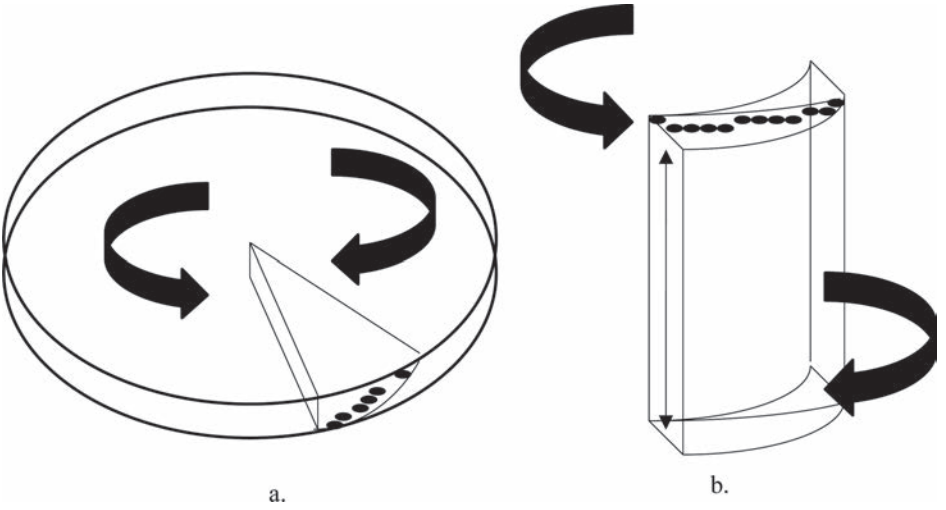

Figure 5. a) Parallel plate geometry with only significant movement at the outside edge of the plates, b) Cup & Bob geometry demonstrating the significant increase in volume of asphalt binder moved in the test.

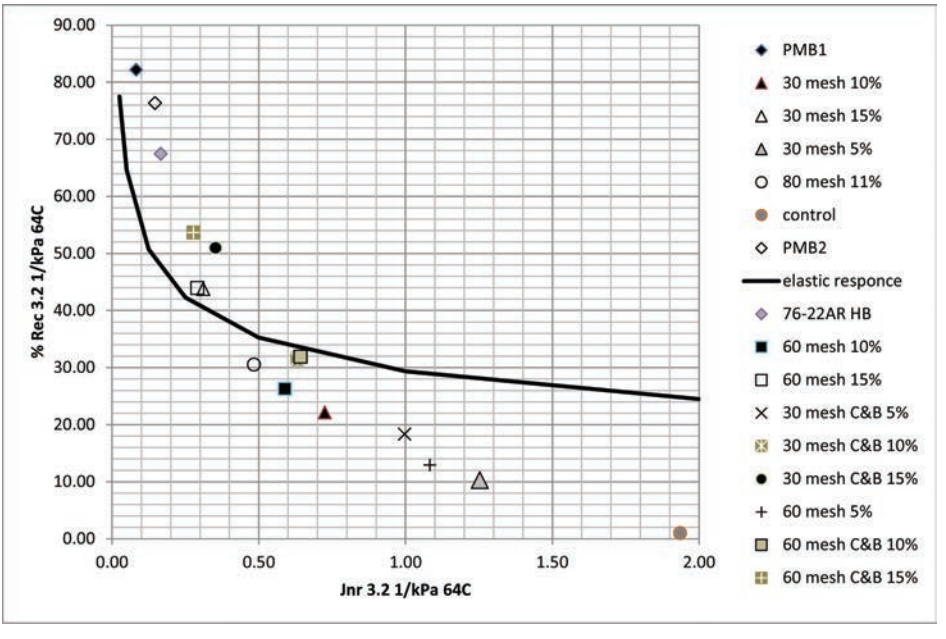

Figure 6. MSCR J_{nr} verses % Recovery comparison for the various RTR mesh sizes and percentages compared to the SBS PMB and hybrid binders.

DSR data at 22°C using the 4 mm gap is shown in Figure 7. Compared to the PG 64-22 control the finer mesh RTR blends 30, 60 and 80 mesh binders reduced the $G^*\sin\delta$ values. For the intermediate DRS properties the 20 mesh shows no effect on the control base binder.

The reduction in the $G^*\sin\delta$ for the 20, 30, 60 and 80 RTR is significant. At 5% rubber there is a 25% reduction the intermediate DSR value. At 20% RTR there is over a 50% reduction in the intermediate DSR value. This is likely due to the processing oils in the RTR defusing into the asphalt binder. Tire rubber typically will have approximately 17% process oils. While the

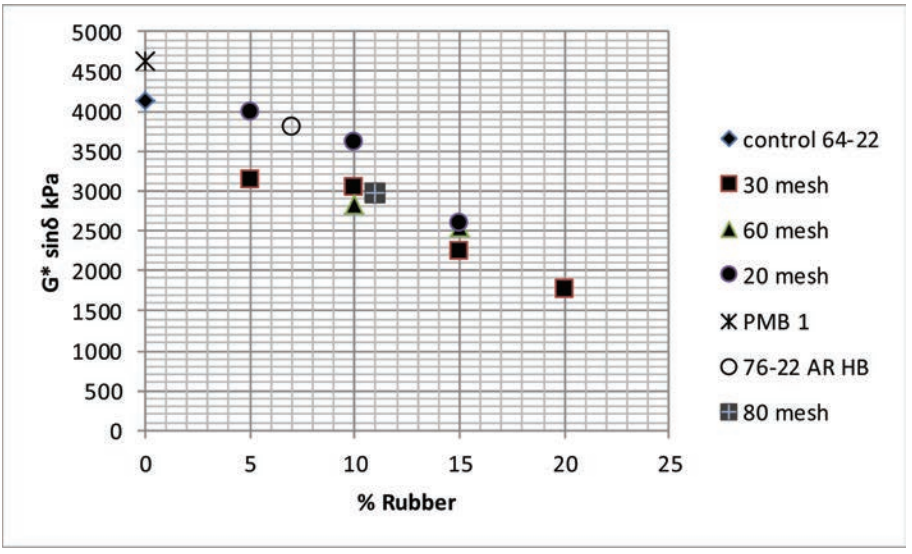

Figure 7. Intermediate PAV aged DSR test results for the various mesh sizes and percent RTR blends compared to the control PG 64-22.

RTR will absorb some of the maltene fraction of the asphalt binder the light processing oils will come out of the RTR defusing into the base asphalt lowers the intermediate properties. With typical SBS modified asphalt binders the intermediate DSR values of the base asphalt increase with the addition of the polymer. This is seen in Figure 7. This requires addition of other additives or a softer base asphalt to prevent the intermediate DSR value becoming too high and not meeting grade requirements. The softening effect of these RTR processing oils on the high temperature properties of the binder are likely overwhelmed by the particle interaction of the RTR particles.

3.3 *Low temperature properties*

Due to space limitations, details of the low temperature properties of the various blends will not be discussed in detail. The low temperature grades of the various blends were shown in Table 2. The Bending Beam Rheometer S values were slightly lower for the RTR blends and the m value had a slight increase. The property changes were not enough to actually change the low temperature grade of the base asphalt binder. The change that did occur is also, likely due the light processing oils in the rubber defusing into the base asphalt binder.

4 CONCLUSIONS

This study evaluated binder modified with multiple RTR sizes and percentages. Sizes such as 60, 30 and 20 mesh RTR are blended with neat binders at 5, 10, 15 and 20 percent to produce modified binders. The properties of the blends were evaluated using both parallel plate and cup and bob geometries and M 320 and MP 19 specifications against typical SBS modified binders.

- In cases where the M 320 high temperature RTFOT DSR indicated that the binders should have the same properties the MSCR J_{nr} properties indicated that the binders are not the same. The M 320 criteria indicate that all the 10 and 15 percent RTR blends would be graded as a PG 76-22. In the MP 19 MSCR the same blends indicated multiple grades

from a 64V to a 64E+ grade and that blends with the same $G^*/\sin\delta$ values would have different J_{nr} values. This indicates that the MP 19 specification is more discriminating than the M 320 specification.

- The RTR mesh size and blend percentage each had an effect on the blended binder properties. As the percentage of rubber increased and the mesh size decreased the binder high temperature properties would increase.
- The % Recovery from the MSCR testing indicates that the RTR does increase the delayed elastic response of the binder blends. An increase in RTR percentage or a reduction in mesh size both increased the % Recovery. The RTR blends could not reach the same magnitude of % Recovery as the SBS modified binders. Percent Recovery is not a performance indicator only an indicator of delayed elastic response. New criteria may have to be developed to evaluate the extent of response needed to evaluate RTR.
- The Cup & Bob geometry provide equivalent J_{nr} results to parallel plate testing for the 30 and 60 mesh size RTR. The % Recovery for the Cup & Bob was slightly greater than for parallel plate testing. This increase % Recovery is likely due to the increased rubber particle interaction in the larger Cup & Bob sample and the geometry effects of the movement of the bob to the outer wall of the cup as opposed to the movement at the outside edge of the parallel plate geometry.
- Processing oils from the RTR defuse into the asphalt binder reducing the intermediate and low temperature properties of the binder blend.
- Blends of RTR modified asphalt binder can be produced to provide equivalent properties to SBS modified binders.

ACKNOWLEDGMENTS

The authors would like to thank Dr. Isaac Howard and Mississippi State University for their help and support on the work.

REFERENCES

[1] "Quantification of the Effects of Polymer Modified Asphalt for Reducing Pavement Distress," Engineering Report 215, Asphalt Institute, ER-215.

[2] D'Angelo, J., Dongre, R, Reinke, G. "Evaluation of Repeated Creep and Recovery Test Method as an Alternative to Shrp+ Requirements for Polymer Modified Asphalt Binders" Proceeding, Canadian Technical Asphalt Association, November 2006.

[3] Epps, J. "Uses of Recycled Rubber Tires in Highways," Synthesis of Highway Practice 198, National Cooperative Highway Program, National Academy Press, 1994.

[4] Heitzman, M. "State of the Practice—Design and Construction of Asphalt Paving Materials With Crumb Rubber Modifier," Publication FHWA-SA-92-022, FHWA, U.S. Department of Transportation, May 1992.

[5] John D'Angelo, Raj Dongre, "Superpave Binder Specifications and their Performance Relationship to Modified Binders," Proceeding, Canadian Technical Asphalt Association, November 2002.

[6] Bahia, H.U., Hanson, D.L., Zeng, M., Zhai, H., Khatri, M.A., and Anderson, R.M., Characterization of Modified Asphalt Binders in Superpave Mix Design, Report No. 459, National Cooperative Highway Research Program, National Academy Press, Washington, D.C., 2001.

[7] Phillips, M.C. and Robertus, C., "Binder Rheology and Asphaltic Pavement Permanent Deformation; The Zero-shear Viscosity," 1st Eurasphalt and Eurobitume Congress, Strasbourg, 1996, Paper No. 5.134.

[8] Dongre, Raj, and D'Angelo, John, "Refinement of Superpave High Temperature Binder Specification Based on Pavement Performance in the Accelerated Loading Facility," Transportation Research Record 1829, TRB, Transportation Research Board, National Research Council, Washington D.C. (2003). pg. 39–46.

[9] D'Angelo J. Dongre R. "Development of a Performance Based Binder Specification in the United States." Proceedings 3rd Eurasphalt & Eurobitume Congress, Vienna, Austria, 2004, pg 339.

[10] D'Angelo, John, et al. "Revision of the Superpave High Temperature Binder Specification: The Multiple Stress Creep Recovery Test." Journal of the Association of Asphalt Paving Technologists, Vol. 76, 2007.
[11] Abdelrahman, M., Carpenter, S., "Mechanism of Interaction of Asphalt Cement with Crumb Rubber Modifier," Transportation Research Record No. 1661, 1999, pg. 106–113.
[12] Baumgardner, G., D'Angelo, J., "Evaluation of New Dynamic Shear Rheometer Testing Geometry for Performance Testing of Crum Rubber-Modified Binder." Transportation Research Record No. 2293, 2012, pg. 93–101.

Asphalt Pavements – Kim (Ed)
© 2014 Taylor & Francis Group, London, ISBN 978-1-138-02693-3

Investigating the evolution of emulsified binder nanorheology using Atomic Force Microscopy

Pooyan Kabir, Maryam S. Sakhaeifar & Dallas N. Little
Department of Civil Engineering, Texas A&M University, College Station, TX, USA

ABSTRACT: This study involves evaluating the evolution of rheological and nanorheological properties of asphalt emulsion residue and its control binder through the application of two different test methods, Dynamic Shear Rheometer (DSR) and Atomic Force Microscopy (AFM). This study also involves evaluating chemical properties by application of Fourier Transform Infrared Spectroscopy (FTIR). The adopted methods use the same evaporative techniques to recover the residue but involve different consecutive curing periods (procedure A: 24 hours at 25°C and 24 hours at 60°C and procedure B: 6 hours at 60°C in a forced draft oven based on ASTM specifications). The evolutions of rheological properties have been investigated as the emulsion transitions through various degrees or stages of aging. Furthermore, the impact of aging in terms of its thermal history on the bitumen microstructure is reported. It was observed that certain asphalt chemical parameters have a consistent and measurable effect, as determined by the AFM, on bitumen microstructure. This study focuses on evaluating whether the full recommended curing periods are required and identifying the causes of different behaviors relative to base binders. Results indicate that oxidative aging contributes different to the change in rheology and nanorheology with various times of curing, compared with unaged base binder.

Keywords: emulsified binder; recovered residue; nanorheological properties; Chemical composition; atomic force microscopy

1 INTRODUCTION

An increase in the use of emulsion-based surface treatments has generated the motivation and need to better characterize and understand properties of emulsions that impact their constructability and in-service performance (1). A number of researchers from around the world (2, 3) have reported microstructural properties of neat and modified asphalt binders based on the results of Atomic Force Microscopy (AFM). Some of the microstructural studies have investigated the impact of oxidative aging (2). One of the challenges in characterizing the emulsion is to establish a widely acceptable residue recovery method. There are concerns expressed about the applicability of procedures regarding their length and the possibility for reducing the time required. The recovery by distillation, as defined in ASTM D244 has been reported by a number of researchers to be inadequate due to high recovery temperatures and extended recovery time (4). A recovery method using temperatures more consistent with those experienced in the field is needed to provide a residue representative of the as-built material and maintain the integrity of binder systems. Recently developed residue recovery methods involve recovery of a thin film of emulsion in a forced-draft oven to address the needs of both recovery at more appropriate temperatures, and the ability to produce adequate emulsion for testing (4). The evaluations of the ASTM method conducted by Hanz et al. (1) and by Kadrmas involved evaluation of emulsion residue rheological properties and comparison with the unaged base binders (5, 6). A similar study was conducted by Hanz et al. (1), which focused on evaluating rheological properties at various times during the recovery procedure, for unmodified and modified

emulsions, commonly used for chip seals. The results show that the properties of emulsion residue do not reflect those of the unaged base binder, and the evaporative recovery method preserves the effects of modification (5). Residues produced by the method under development by the New Zealand Transport Agency were using its standard test methods of penetration, softening point, and torsional recovery on unmodified and polymer-modified emulsions. Results of both methods of characterization indicate that the residue produced has properties significantly different from those of the unaged base binder (7).

An important component of asphalt durability is defined as the resistance of asphalt to the detrimental effects of oxidative age hardening on its performance properties. In asphalt pavements, oxidative age hardening contributes significantly to pavement embrittlement, eventually resulting in excessive pavement cracking. Oxidative hardening is attributed primarily to the introduction of polar, oxygen-containing chemical functionalities on asphalt molecules causing increased molecular interactions. These changes in chemical composition would be expected to increase asphalt hardening (8). The four fractions produced by the Corbett separation scheme in the order of their increasing molecular polarity are saturates, naphthene aromatics, polar aromatics, and asphaltenes. The saturates fraction is generally a light straw-colored oil, primarily hydrocarbon in nature, with little aromaticity and a low heteroatom content except for sulfur. Corbett (9) described the effects on physical properties of the four generic fractions separated by his procedure as follows: the asphaltenes function as thickeners; fluidity is imparted by the *saturates* and naphthene aromatics fractions which plasticize the polar aromatics and asphaltenes fractions; the polar aromatics fraction imparts ductility to the asphalts, and the *saturates* and naphthene aromatics in combination with the asphaltenes produce complex flow properties in the asphalt. A proper balance in the amounts of the different chemical components is necessary to produce asphalt that is durable and resistant to detrimental physical property changes on oxidative aging (8). Jemison (10) showed the advantages of using FTIR-ATR method for asphalt analysis with respect to ease of analysis and repeatability.

In this study, the impact of aging in terms of its thermal history on the bitumen microstructure is reported. The goal was to further understand the link between asphalt chemistry and macroscopic performance by investigating the findings obtained from AFM, DSR, and FTIR testing. Therefore, it was focused to evaluate and compare the need for the 48-hrs versus 6-hrs recovery time specified in ASTM D7497 to identify the cause of different behaviors relative to base binders. Evaluation was conducted at high and intermediate temperatures on emulsion residues and base binders subjected to different aging conditions. It was revealed that certain asphalt chemical parameters have a consistent and measurable effect, as determined by the AFM, on bitumen microstructure. The initial rheological evaluation of emulsion residue indicates that residue properties from two different recovery procedures are different and they exceed those of the unaged base binder. This research provides new and supporting evidence concerning the influence of aging on properties that ultimately govern macroscopic behavior.

2 MATERIALS AND EXPERIMENTAL PLAN

Three different types of binders; control binder, residue recovered based on procedure A at 25ºC for 24 hours followed by recovery at 60ºC for 24 hours and residue recovered through procedure B at 60ºC for 6 hours. The three different samples were prepared and evaluated at three different aging conditions; original, short term aged (Rolling Thin Film Oven; RTFO) and long-term aged (Pressure Aging Vessel: PAV). These binders were selected to compare the difference of evaporative techniques at different aging conditions. The selected emulsion is a CSS-1H which represents a cationic slow set emulsion and the base (control) binder is PG64-22. The volumetric percentage of cationic emulsifier is approximately 3.

2.1 *Sample preparation*

The asphalt binders were aged for short term aging based on the AASHTO T 240 for Rolling Thin-Film Oven (RTFO) test and for long term aging based on AASHTO R28 using the

pressure aging vessel. The residues from emulsified binder were obtained using the ASHTO PP 72-11 including both procedure A (48 hours recovery) and procedure B (6 hours recovery), based on the recovery procedure from AASHTO M140 and AASHTO M208 respectively. The microscope slides were cleaned by methanol before preparing the samples for AFM testing. The slide was heated by 160 °C and then was cooled down by 30°C intervals and then was kept in ambient temperature to prevent aging and dust absorption. The amount of 0.2–0.3 grams of binders were spread on 0.5×3 (cm^2) area to prepare the samples.

2.2 *Equipment*

The Bruker Dimension Icon AFM and the data processing unit were used to measure mechanical properties at the room temperature (25 °C). All of the images were obtained by using Peak Force Quantitative Nano-Mechanics (PF-QNM) and MPP-12100-10 silicon cantilevers manufactured by Bruker. The calibrated cantilevers used for this study have an average resonant frequency of 150 kHz, and a tip radius of 8 nm and an average tip angle of 18°. The spring constant of the cantilever used for the experiment was calculated by Thermal Tune in Icon AFM (4.9 N/m).

A Tensor 27 Bruker™ Fourier Transform Infrared (FTIR) spectrometer was used to measure the infrared spectra. The Attenuated Total Reflectance (ATR) method was utilized to collect the spectrum as described by Jemison et al. (10).

2.3 *Test methods*

The test for characterization of rheological properties of binders at different aging and different evaporative techniques were conducted by using the DSR at intermediate and high temperatures. The Multiple Stress Creep and Recovery (MSCR) was selected to evaluate the permanent deformation criteria and the effects of different aging conditions. The test was performed based on the ASTM D7405. The test was conducted by a 25 mm plate and 1 mm gap setting. The sample was loaded for 1 second followed by 9 seconds of rest period. Ten creep and recovery cycles were conducted at 100 (Pa) creep stress level and ten creep and recovery cycles conducted at 3200 (Pa) creep stress level. The non-recoverable creep compliance (J_{nr}) and percent strain recovery were used to evaluate the binder modification properties. The fatigue resistance of the binders was evaluated by running a sweep strain test at an intermediate temperature (25°C) by varying the percentage of strain applied to the samples. The test comprises of evaluating the effects of increasing the strain on asphalt binder stiffness, $|G^*|$, at a constant frequency and temperature. This test was done by 8 mm parallel plate and gap setting of 2 (mm). The sweep strain tests were conducted at the frequency of 10 rad/s.

2.3.1 *Multiple Stress Creep and Recovery (MSCR) and sweep strain results*

The standard suggests use of nonrecoverable compliance (J_{nr}) and percent strain recovery to evaluate test results. Polymer modification allows the binder to accumulate less permanent deformation due to delayed elasticity so a portion of the deformation is recovered after unloading (12). Use of the J_{nr} quantifies this behavior and allows for evaluation of the impact of modification on performance. Furthermore, percent strain recovery provides a means to detect the presence of a polymer network and evaluate its development as a function of curing time. These behaviors cannot be captured using the current $|G^*|$ and delta testing protocols, therefore the MSCR test has been adopted and used for polymer-modified binders.

The permanent deformation of binders was evaluated using the MSCR test conducted at 60°C considering two sample replicates. The non-recoverable creep compliance of each samples were calculated based on ASTM D7405 and the averaged values of two replicates were used for further evaluation. The results presented in Figure 1 demonstrate the non-recoverable creep compliance (J_{nr}) of two residues using different recovery procedures and base binder at two different stress levels of 100 Pa and 3,200 Pa. It was found that the J_{nr} for the PAV aged material are identical regardless of the binder type and the adopted recovery

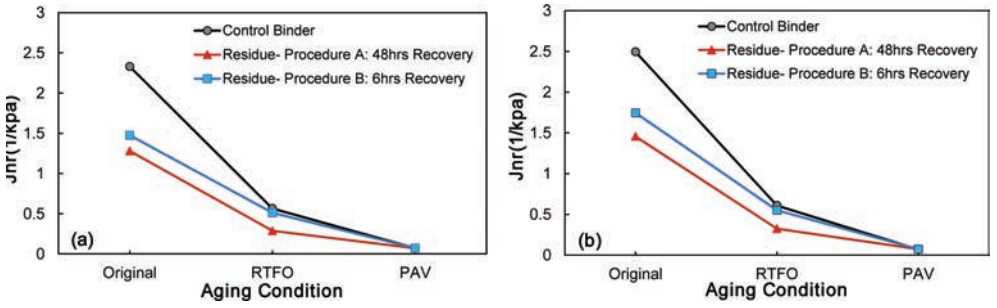

Figure 1. J_{nr} at different aging conditions for MSCR testing at 60°C testing temperature for (a) 100 Pa and (b) 3,200 Pa stress levels.

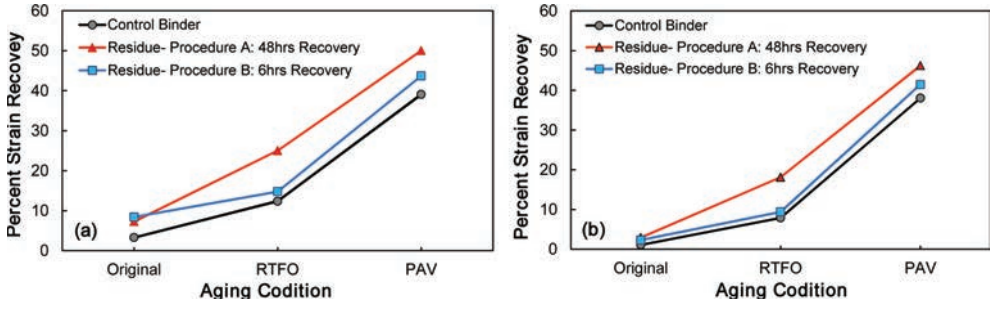

Figure 2. Average percent recovery at different aging conditions for MSCR at 60°C testing temperature for (a) 100 Pa and (b) 3,200 Pa stress levels.

procedure. The J_{nr} of control binder and recovered residue using procedure B are close and they both are different from the residue acquired using procedure A at short-term aging condition. The values of J_{nr} are different for both recovered residues and control binder at unaged condition (original). These results indicate that the recovery of the modified emulsion residues produces an aged material with rheological properties that approach those of the base binder subjected to the PAV aging. The benefit of modified emulsion is also noted by the significant increase in resistance to permanent deformation (lower J_{nr}) for emulsion relative to that of base binder at unaged and short-term aging conditions.

The average percent strain recovery was used to quantify development of the polymer network at various aging conditions in the emulsion residues and to compare results to the properties of the base materials. Percent strain recovery is defined as the difference in strain at the end of the creep and recovery cycles. In ASTM D7405, the average percent strain recovery over the 10 cycles of the test at a given stress level is reported (5). Figure 2 provides results of percent strain recovery evaluation at a 60 °C testing temperature at stress levels of 100 Pa and 3,200 Pa. The results demonstrate significant differences in the effect of recovery procedures and modification versus the base binder. At these testing conditions, both the control binder and two residues exhibited negligible percent recovery strain recovery. Both recovered residues show higher percent strain recovery that increases with aging time.

The failure properties of the control binder and two residues are presented in Figure 3. The results presented in this figure exhibit differing sensitivities to recovery procedures against the control binder. The procedure A exhibits significantly less strain tolerance after 48 hours curing by approximately 8% decrease in failure strain while procedure B leads to 4% decrease in failure strain comparing to control binder in original condition. The failure strain of the RTFO-aged binders are very close for both recovery procedures and base binder and is well below that of original condition which indicates the RTFO material demonstrate less strain tolerance. The PAV-aged residues demonstrate more strain tolerance comparing to the

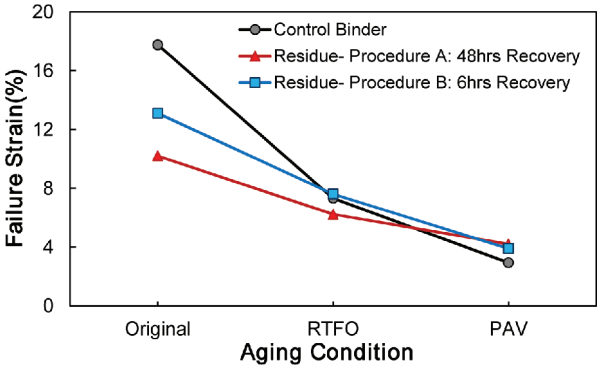

Figure 3. Failure strain as function of aging for sweep strain at 25°C.

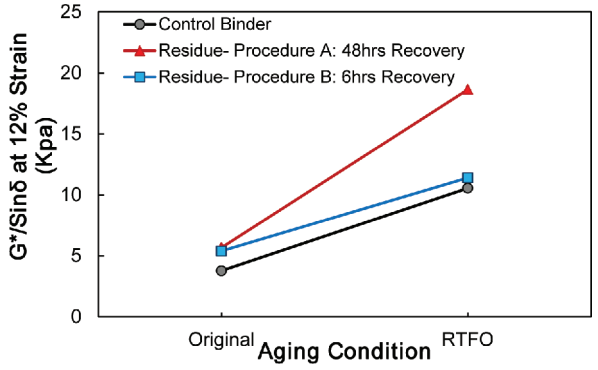

Figure 4. Resistance to permanent deformation criteria as function of aging.

control binder at the same condition. The deviation of behavior of residues from the control binder at different aging conditions indicate that in regard to strain tolerance, factors other than oxidative aging are affecting the performance of the emulsion residue.

Figure 4 provides the $|G^*|/\sin\delta$ values at different aging conditions. The results for the oven recovered emulsified binder for 48 hours indicate that the curing conditions produces levels of oxidative aging that are different from the other recovered binder for 6 hours and control binder. The largest increase in $|G^*|/\sin\delta$ was realized in RTFO aging condition for the residue recovered for 48 hours. From these results, the properties of the emulsion residues subjected to the ASTM recovery method reflect the effect of latex modification and aging.

2.3.2 *Atomic force microscopy results*

Asphalt chemical parameters have a measurable effect on the asphalt microstructure that can be observed with AFM to reveal the microstructure. Interesting findings can be derived through the interaction of the tip with the microstructure of the asphalt sample using the pull-off force curve (13). The atomic force microscopy was used in this study to image the surface and identify different phases and microstructures on the specimen surface. This was achieved in non-contact mode as the primary imaging mode. In addition, AFM was also used in Spectroscopy Mode (SM) to measure the nano-scale response of asphalt binders aged at different conditions. Therefore, a combination of these two techniques (AFM and SM) was used to map the microstructure of the asphalt binder and estimate microstructure mechanical properties as illustrated in Figure 5 and Figure 6 respectively. Different phases in an asphalt specimen were identified and a force measurement in each of the phases was performed at different aging conditions for control binder and emulsion residues. The tests consisted of

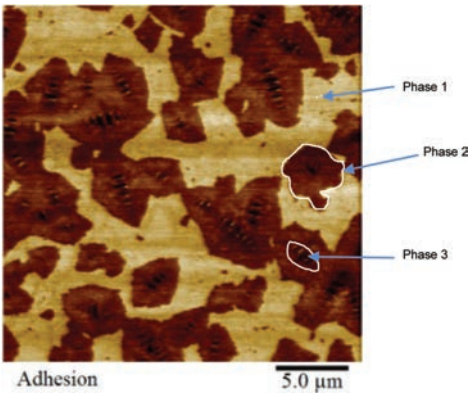

Figure 5. Adhesion image of control binder (color scale shows relative differences in phases based on tip adhesion during scanning).

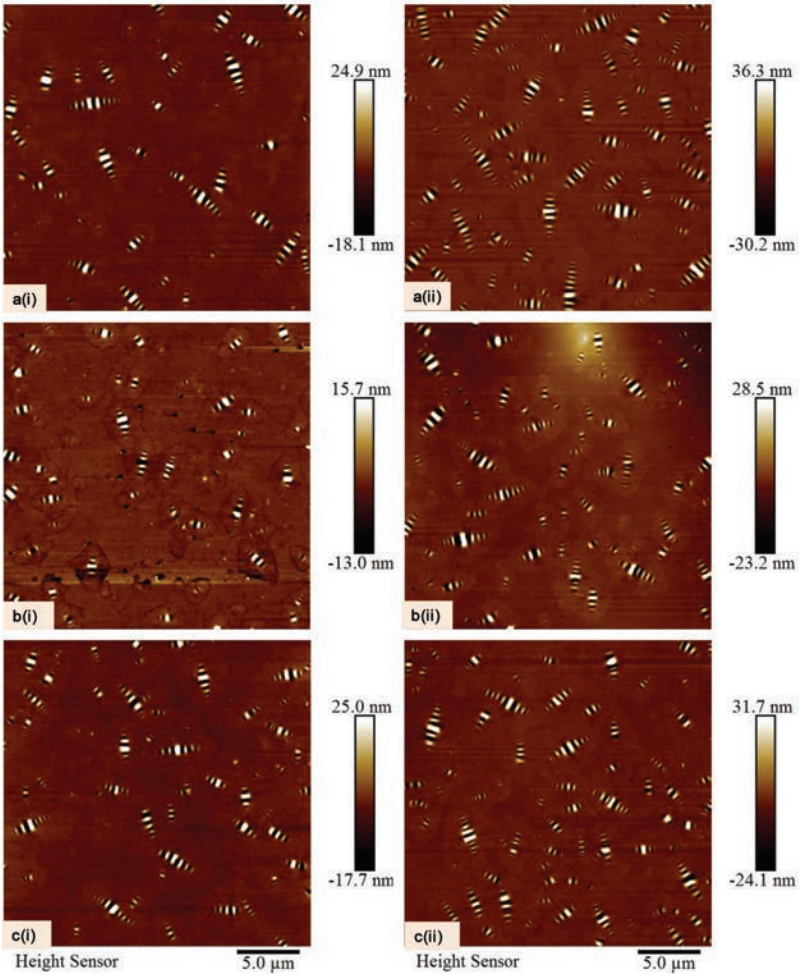

Figure 6. Topography images (25 µm × 25 µm) of control binder at a(i) Original, a(ii) PAV, residue using procedure A (after 48 hrs recovery: 24 hrs @ 25ºC and 24 hrs @ 60ºC) at b(i) Original, b(ii) PAV, and residue using procedure B (after 6 hrs recovery @ 60ºC) at c(i) Original and c(ii) PAV aging conditions.

three force measurements taken in each phase. An illustration of different asphalt phases and locations of each measurement is shown in Figure 5. A 25 μm × 25 μm topography image is presented for each asphalt binder, including identification of individual phases and a profile extraction of the corresponding phase topography.

Furthermore, evaluation of emulsification on asphalt calculated by conducting force distance curves and it has been shown in Figure 7 and mechanical properties were summarized in Table 1. From the results, it can be concluded that differences are mostly attributed to

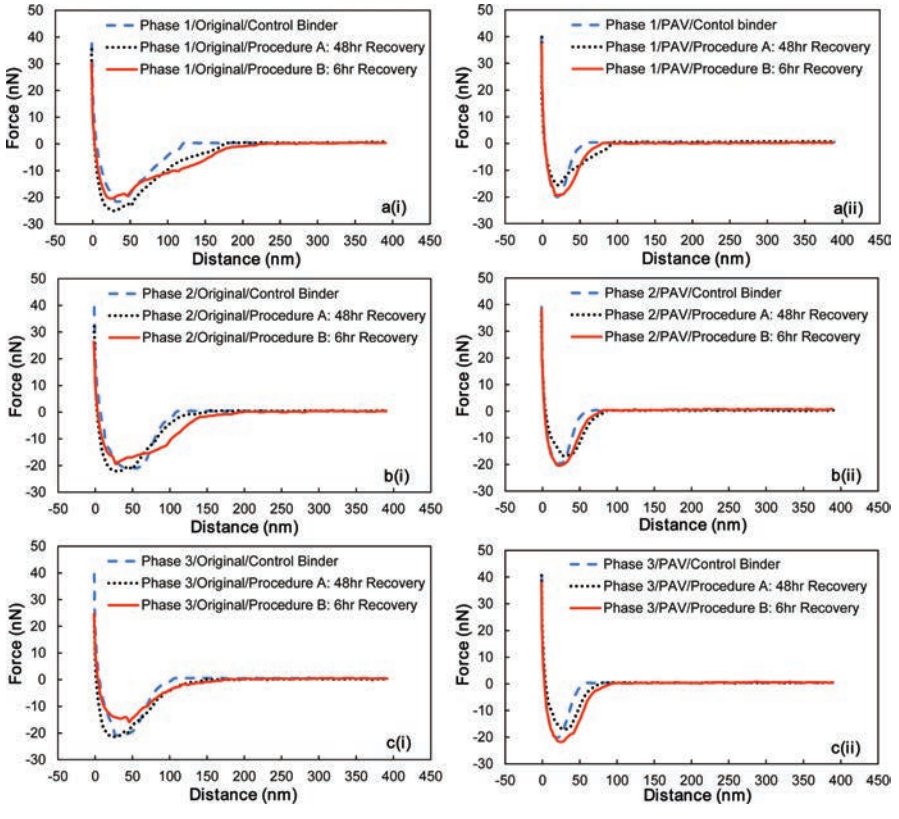

Figure 7. Results of force-distance curves from AFM testing.

Table 1. Summary of interpreted information from AFM test.

	Mechanical properties	Young's modulus (Mpa)		Energy dissipation (nm × nN)	
Binder type	Aging condition	Original	PAV	Original	PAV
Control binder	Phase 1	200	610	1354	553
	Phase 2	150	585	1339	623
	Phase 3	185	840	1137	600
Residue-procedure A	Phase 1	533	625	2138	705
(48 hrs recovery)	Phase 2	466	526	1583	754
	Phase 3	476	716	1482	677
Residue-procedure B	Phase 1	350	888	2061	786
(6 hrs recovery)	Phase 2	200	643	1730	839
	Phase 3	250	775	1110	1010

physical changes in the asphalt binder and emulsification process. Also hypothesized was that additional source of these differences are potentially oxidation, sample reheating, and residual water. The foaming of the residues during reheating might be another reason. Foaming during reheating indicates the possibility that a thin film was created over the emulsion residue during recovery. In the literature (14), this is referred to as *skinning*, a similar effect was noted by Takamura in development of the evaporative recovery method when recovery was attempted at high temperatures. This film has a significantly higher stiffness than conventional asphalts do; thus, the presence of the film with the remaining, partially cured, emulsion residue has the potential to increase DSR results.

The chemistry and microrheology of these microstructures within the asphalt binder influence its macroscopic properties, such as stiffness, viscoelasticity, adhesion, fracture and healing. Because the state of component dispersion (component compatibility) of an asphalt has a significant effect on asphalt oxidative hardening rate, the possibility is suggested by Peterson (8) that some of the antioxidants may have also reduced oxidative hardening by acting as a dispersant for the asphaltene-like components in the asphalt that leads to the improvement of component compatibility. Indeed, it has been reported by Dybalski (15) that *cationic asphalt additives*, commonly used as asphalt emulsifiers, augment the peptization of the asphaltenes constituent and thus reduces the asphalt hardening rate. According to their findings, of 82 asphalts tested, 81% were benefited by the additives, with a minimum of 15% and a maximum of 65% reduction in hardening rate during the rolling thin-film oven test (ASTM D2872-77). In another study (16), the hardening rate of a recycled pavement mixture during laboratory aging was reduced several fold by a high float emulsifying agent used to emulsify the recycling agent before recycling the pavement mixture in the laboratory.

In this study the Young's modulus and energy dissipation of different phases were calculated for the control binder and emulsion residues aged at different conditions. The findings have been summarized in Table 1. The young's modulus was calculated based on the Sneddon indentation theory by using the spring constant, tip radius, tip half angle and the sample Poisson's ratio. This parameter was used to compare the stiffness of different phases although the response was not purely elastic in this set of tests. The dissipated energy was also calculated based on the area under the force distance curves. As it is expected the dissipated energy decreases in more brittle materials like the control binder and recovered residues in PAV aging conditions compared to the unaged (or original) conditions. The interesting finding is that the dissipated energy was higher for recovered residues compared to the control binder at each aging conditions which indicates the dominant effect of emulsifying process in the residues obtained based on two adopted evaporative recovery procedures.

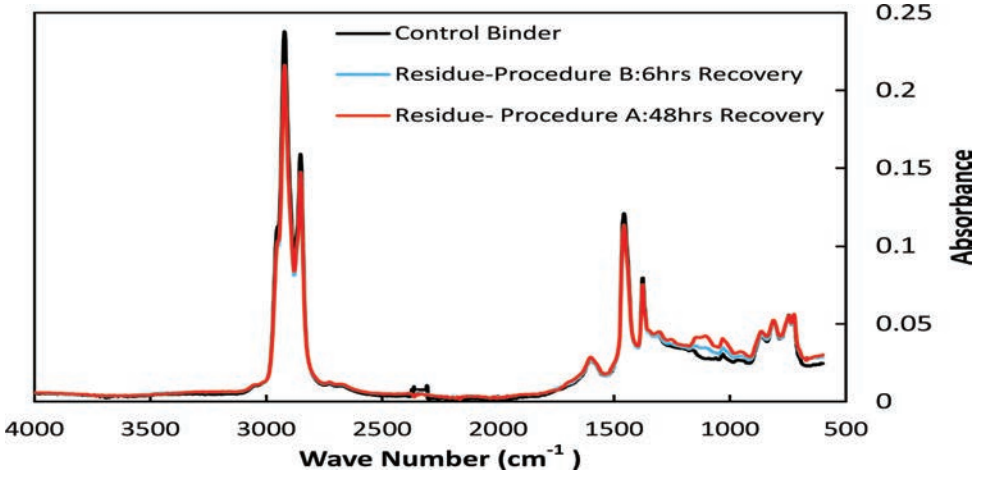

Figure 8. FTIR spectra for different recovery methods.

2.3.2 *Fourier transform infrared results*

Asphalt chemical parameters have a measurable effect on the aging of asphalt that can be observed with FTIR to reveal the chemical difference. Lau et al. (17) have showed that the carbonyl area would be a good measure of oxidation and the area under the peak between 1650 and 1820 wavenumber (cm^{-1}) was measured to determine if the asphalt was oxidizing during the curing processes. The Carbonyl areas were 0.69, 0.79, and 0.81 for control binder, 6 hours recovery, and 48 hours recovery respectively. The carbonyl area can be used as an indication of aging in binders. FTIR spectrum showed that longer process ages the binder more than shorter recovery method. The water was not observed in the specimens since there is no major peak around 3347 cm^{-1} wave number which can be related to the presence of water (18). The IR spectrum is shown in Figure 8 and the difference in spectrum should be related to recovery process and the emulsification process of binders.

3 CONCLUSIONS AND RECOMMENDATIONS

The objective of this study was to semi quantitatively characterize the micro-rheology and rheology of a control binder and emulsion residues obtained through different evaporative recovery procedures by using AFM, DSR, and FTIR testing. Based on the results obtained from the study the effects of long-term aging impact not only the material behavior of these microstructures, but also the distribution of each asphalt microstructure. The long-term aging clearly induces microstructural change in asphalt. The form and extent of these changes, however, were different for control asphalt versus emulsion residues. It is hypothesized that the remaining differences in rheological response as revealed through the evaluations of strain tolerance and percent strain recovery can be related to effects of emulsifier chemistry or different recovery methods. The strain sweep and MSCR produce results that are able to discriminate between recovery procedures and quantify the change in critical properties, as a function of aging time. It was observed that the properties of the emulsion residue do not correspond to those of the unaged base binder. Results support that residue be considered as rolling thin-film oven-aged or partially-aged material rather than unaged material. The theme of this research effort was to determine if these differences are due to oxidative aging, remaining moisture, chemistry of the emulsifier, or a combination of these factors. The findings of this study help the concerns that have been expressed about the length of long evaporative recovery procedure and the possibility for reducing the time required.

Further research is needed to understand the level of aging that occurs in the field relative to the aged state of the residue produced by the recovery method, to quantify the differences in performance between various emulsions and to correlate laboratory performance with actual field performance. The apparent relationships between component ratios and property changes on oxidative aging, as determined by the relationships of the generic fractions, are recommended to be acquired to enhance the results of this study to provide valuable insight into the chemical and physicochemical aspects of asphalt oxidative hardening.

REFERENCES

1. Hanz, A.J., Z.A. Arega, H.U. Bahia, "Rheological Behavior of Emulsion Residues Produced by Evaporative Recovery Method", Journal of the Transportation Research Board, No. 2179, Transportation Research Board of the National Academies, Washington, D. C., 2010, pp. 102–108.
2. Allen, R.G., D.N. Little, A. Bhasin, and R.L. Lytton, "*Identification of the Composite Relaxation Modulus of Asphalt Binder Using AFM Nanoindentation*", Journal of Materials in Civil Engineering, accepted June 2012.
3. Nahar, S.N., B. Dillingh, S. Erkens, A.J.M. Schmets, H.R. Fischer, A. Scarpas, and G. Schitter, "*Is Atomic Force Microscopy Suited as Tool for fast Screening of Bituminous Materials? An Interlaboratory Comparison Study*", Transportation Research Board, Washington, D.C. 2013.

4. *Transportation Research Circular E-C122: Asphalt Emulsion Technology: Review of Asphalt Emulsion Residue Procedures*. Transportation Research Board of the National Academies, Washington, D.C., 2007.
5. Hanz, A., Z. Arega, and H.U. Bahia. Rheological Evaluation of Emulsion Residues Recovered Using Newly Proposed Evaporative Techniques. Presented at 88th Annual Meeting of the Transportation Research Board, Washington, D.C., 2009.
6. Kadrmas, A., Using Dynamic Shear Rheometer and Multiple Stress Creep Recovery to Compare Emulsion Residue Recovery Methods. Presented at 88th Annual Meeting of the Transportation Research Board, Washington, D.C., 2009.
7. Waters, J.C., G.M. Bosma, and P.R. Herrington. *Residual Binder Extraction from Emulsions for Quality Assurance Testing*. New Zealand Transport Agency Research Report No. 360. New Zealand Transportation Agency, Wellington, New Zealand, 2008.
8. Petersen, J.C., "A Review of the Fundamentals of Asphalt Oxidation", Transportation Research Circular E-C140, October 2009.
9. Corbett, L.C., Relationships Between Composition and Physical Properties of Asphalts. *Proc., Association of Asphalt Paving Technologists*, Vol. 39, 1970, pp. 481–491.
10. Jemison, H.B., B.L. Burr, R.R. Davison, J.A. Bullin, and C.J. Glover. Application and use of the ATR, FT-IR method to asphalt aging studies. *Fuel science & technology international* 10, no. 4–6 (1992): 795–808.
11. Griffen, R.L., W.C. Simpson, and T.K. Miles, Influence of Composition of Paving Asphalts on Viscosity, Viscosity-Temperature Susceptibility, and Durability. *Journal of Chemistry and Engineering Data*, Vol. 4, 1959, pp. 349–354.
12. D'Angelo, J., Effect of Polymer-Asphalt Binder Compatibility and Cross-Link Density of Non-Recoverable Compliance in the MSCR Test Method. Presented at Southeast Asphalt User/Producer Group, San Antonio, Texas 2007.
13. Allen, R.G., D.N. Little, and A. Bhasin, "*Structural Characterization of Micromechanical Properties in Asphalt Using Atomic Force Microscopy*", Journal of Materials in Civil Engineering, ASCE, Vol. 24, No. 10, Oct. 1, 2012.
14. Takamura, K. Comparison of Emulsion Residues Recovered by Forced Air Flow and RTFO Drying. Presented at AEMA/ISSA Joint Annual Meeting. Asphalt Emulsion Manufacturers Association, Amelia Island, Fla., March 13–16, 2000.
15. Highway Chemicals Newsletter, Akzo Chimie America (formerly Armak Company), McCook, Illinois, Fall 1979.
16. Khosla, N.P., Effect of Emulsified Modifiers on the Characteristics of Recycled Mixtures. Proc., Association of Asphalt Paving Technologists, Vol. 51, 1982, pp. 522–539.
17. Lau, C.K., Lunsford, K.M., Glover, C.J., Davison, R.R., and Bullin, J.A. (1992). Reaction rates and hardening susceptibilities as determined from POV aging of asphalts. Transportation Research Record 1342(50):50–57.
18. Zofka, Adam. Evaluating applications of field spectroscopy devices to fingerprint commonly used construction materials. Transportation Research Board, 2013.

Asphalt Pavements – Kim (Ed)
© 2014 Taylor & Francis Group, London, ISBN 978-1-138-02693-3

Estimating the tensile strain at the bottom of the HMA layer using TSD deflection slope measurements

Samer Katicha, James Bryce & Gerardo Flintsch
Virginia Tech Transportation Institute, Blacksburg, VA, USA

ABSTRACT: In this paper, we use Traffic Speed Deflectometer (TSD) deflection slope measurements to estimate the tensile strain at the bottom of the HMA layer. The procedure we follow is essentially the one proposed by Thyagarajan et al. [1], which can be used to calculate the tensile strain at the bottom of the HMA layer using Falling Weight Deflectometer (FWD) measurements, modified to apply to the TSD deflection slope measurements. The TSD calculated tensile strains are compared to FWD calculated tensile strains. The results show that although the procedure was initially developed and tested for loading conditions corresponding to the FWD, when applied to TSD deflection slope measurements, the procedure gives similar results to those obtained from the FWD which suggest it is also applicable to the TSD. This shows that continuous deflection devices in general, and the TSD in particular, are viable devices that give reasonable results for at least network-level pavement management applications.

Keywords: Continuous deflection devices, Traffic Speed Deflectometer, tensile strain, HMA

1 INTRODUCTION

Measurement of the existing structural capacity of a pavement is a critical input for (1) structural analysis of in service pavements, (2) identification of sections with structural capacity deficiencies at the network level, and (3) design of pavement renewal or rehabilitation treatments at the project level. State Departments Of Transportation (DOT's) routinely use deflection measurements at the project level, using mainly the Falling Weight Deflectometer (FWD), and some are starting to use them also at the network level [2], [3]. Although the FWD provides a very useful tool to assess the pavement structural or bearing capacity of a pavement, and can be used to determine the moduli of the component layers, this technology has the limitation of only allowing stationary measurements at discrete points along the pavement sections. The need to stand on the road for a short period of time disturbs traffic and requires traffic control. This limits the productivity and the density of points at which data are collected and increases survey cost.

The use of continuous deflection measuring devices—that in some cases operate at traffic speed—allows a better spatial coverage with less negative impact on mobility compared to the FWD and potentially lower survey cost per unit length. Although the currently available "continuous" devices do not provide the same detailed information, accuracy, and repeatability as the FWD, they are becoming increasingly popular as a practical alternative, especially for network-level structural monitoring. These devices were evaluated in a recent Strategic Highway Research Program 2 (SHRP2) R06(F) project. The project surveyed user needs for a continuous deflection device, evaluated current technologies implemented in different types of continuous deflection measuring devices, identified the most promising devices for effectively supporting pavement management decisions, evaluated the capabilities of these devices, and identified and illustrated potential applications to support network-level pavement management [3].

As part of the SHRP2 R06(F) project, the Traffic Speed Deflectometer (TSD) was selected for further evaluation. Part of this evaluation included comparison of the TSD with the FWD. The Surface Curvature Index (SCI) and Base Damage Index (BDI) were two of the chosen parameters used in the comparison. The SCI and BDI were chosen because they can be calculated from measurements obtained from either the FWD or the TSD and because the two parameters have been shown to be good predictors of the tensile strain at the bottom of the HMA layer [1]. In this paper, we compare the calculated tensile strain at the bottom of the asphalt layer obtained from FWD deflection measurements and TSD deflection slope measurements.

2 OBJECTIVE

The objective of this paper is to compare the TSD and FWD calculated tensile strain at the bottom of the asphalt layer. TSD and FWD measurements were first converted to the SCI from which the tensile strain was calculated. Before we present the methodology followed and the results, a brief overview of the FWD and TSD are given.

3 EQUIPMENT DESCRIPTION

3.1 *Falling Weight Deflectometer (FWD)*

The FWD applies a load pulse that simulates the load of a rolling vehicle wheel to the pavement. The load is produced by dropping a weight onto a circular plate (generally of 300 mm diameter) placed on the pavement surface. The applied load and vertical pavement deflection at various radial distances (e.g. 0 mm, 200 mm, 300 mm, 450 mm, 600 mm, 900 mm, 1200 mm, and 1500 mm) from the center of the load are measured and recorded. The collected data obtained from FWD testing is used to determine the structural condition of the pavement.

3.2 *Traffic Speed Deflectometer (TSD)*

The TSD (Fig. 1) is mounted on an articulated truck with a rear axle load of 100 kN (22 kips) which, in the model evaluated, utilizes four Doppler lasers mounted on a servo-hydraulic

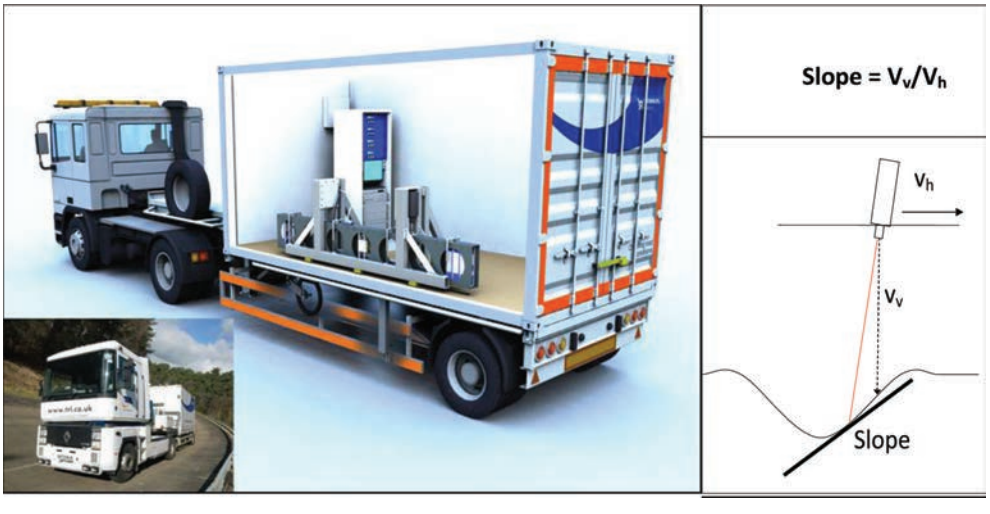

Figure 1. Computer render of the TSD, with the TSD in operation (inset).

beam to record the vertical deflection velocity of a loaded pavement under one of the dual wheel assemblies. Three Doppler lasers are positioned such that they measure deflection velocity at a range of distances in front of the rear axle. The fourth sensor is positioned 3.6 m in front of the rear axle largely outside the deflection bowl, acting as a reference laser. The beam on which the lasers are mounted moves up and down in opposition to the movement of the trailer in order to keep the lasers at a constant height from the pavement surface. To prevent thermal distortion of the steel measurement beam, a climate control system maintains the trailer temperature at a constant 20 °C. Two prototypes had been developed at the time of the evaluation by the manufacturer Greenwood Engineering A/S of Denmark. One is owned and operated by the Danish Road Institute (DRI) and the other is owned by the UK Highways Agency (HA) and operated on their behalf by the UK Transport Research Laboratory. Newer production devices have incorporated more Doppler laser sensors [3].

The lasers are mounted at a small angle to measure the horizontal vehicle velocity, the vertical and horizontal vehicle suspension velocity, and the vertical pavement deflection velocity. Due to its location, mid-way between the loaded trailer axle and the rear axle of the tractor unit, the reference laser is expected to measure very little vertical pavement deflection velocity, and its response can therefore be used to remove the unwanted signals from the three measurement lasers. When accurately calibrated, the TSD produces measurements of deflection velocity that depend on driving speed. To remove this dependence, the deflection velocity is divided by the instantaneous survey speed to give a measurement of deflection slope, as illustrated in the figure. Deflection velocity is measured in mm/s whilst survey speed is measured in m/s; therefore, deflection slope measurements are output in units of mm/m [4].

4 METHODOLOGY

The methodology followed in this paper is to first calculate the SCI from TSD and FWD measurements and then use the SCI to calculate the tensile strain at the bottom of the asphalt layer. For the measurements, the applied load for both the TSD and FWD was 40 kN and FWD deflection measurements were temperature corrected to the temperature at which the TSD tests were performed.

4.1 *Calculating the SCI and BDI*

The calculated SCI is SCI300 which is defined as d_0–d_{300}, while BDI is defined as d_{300}–d_{600}, where d_0, d_{300} and d_{600} are the deflections at 0 mm, 300 mm, and 600 mm from the applied load, respectively. For the FWD, d_0, d_{300}, and d_{600}, are directly measured and calculation of the SCI and BDI is straightforward. In the following section, we present the methodology used to calculate the SCI and BDI from TSD slope measurements.

The TSD measures the slope of the deflection bowl. Therefore, the deflection can in principle be obtained from the TSD slope by integration if a sufficiently detailed representation of the full deflection slope bowl is available. Integration is however only specified up to a constant value and therefore we cannot recover the deflection without a reference deflection measurement. We can however obtain the difference between two deflection readings (the constant cancels out) which gives the SCI or BDI. The relationship between slope, deflections and SCI and BDI is presented in Eq. (1).

$$\int_a^b s(x)dx = d(b) - d(a) = \text{SCI} \tag{1}$$

where, $s(x)$ is the slope at location x and $d(x)$ = deflection at location x. To calculate the SCI from TSD measurements, the TSD slope was integrated numerically. To calculate SCI, the integration interval is [0 mm; 300 mm] while for the BDI the integration interval is [300 mm; 600 mm]. TSD slope measurements were obtained at 100, 300 and 756 mm from the applied wheel load and the deflection slope at 0 mm was assumed to be equal to zero. This assumption

is valid if the load is uniformly (or approximately uniformly) applied over a specific area rather than being a point load, which is the case for a wheel load, and if viscoelastic effects are neglected. Note that viscoelastic effects will cause the response to the applied load to be slightly delayed so that the slope will actually be zero at a location slightly behind the applied wheel load. However, the calculation of SCI is not significantly affected by the location where the deflection slope is set to zero (see Fig. 3-41 and Fig. 3-42 in [3]).

4.2 *Calculating the tensile strain at the bottom of the asphalt layer*

Thyagarajan et al. [1] developed an equation to relate the tensile strain at the bottom of the asphalt layer with SCI and BDI using FWD deflection measurements. The relationships developed for determining the strain for aggregate base pavements are presented in Eq. (2), respectively:

$$Log(\varepsilon_{AC}) = 0.5492Log(SCI) + 0.3850Log(BDI) + 0.7812Log(H_{AC}) - 0.0017H_{AC} + 1.7353 \qquad R^2 = 0.994 \tag{2}$$

where:
ε_{AC} = strain at the bottom of the asphalt layer
H_{AC} = thickness (mm) of the asphalt layer
SCI = Surface Curvature Index (mm)
BDI = Base Distress Index (mm).

It is noted that these equations were developed for use with FWD measurements so may not be entirely appropriate when using deflections measured using a rolling-wheel load moving at traffic speed as with the TSD.

5 RESULTS

To demonstrate the applicability of the methods described earlier, the strain at the bottom of the asphalt layer was estimated for a tested pavement section approximately 2.2 km long. Figure 2 shows the TSD deflection slope measured 100 mm from the applied wheel load and the FWD d_0 both at 20 m intervals. Although the measurements from each device have

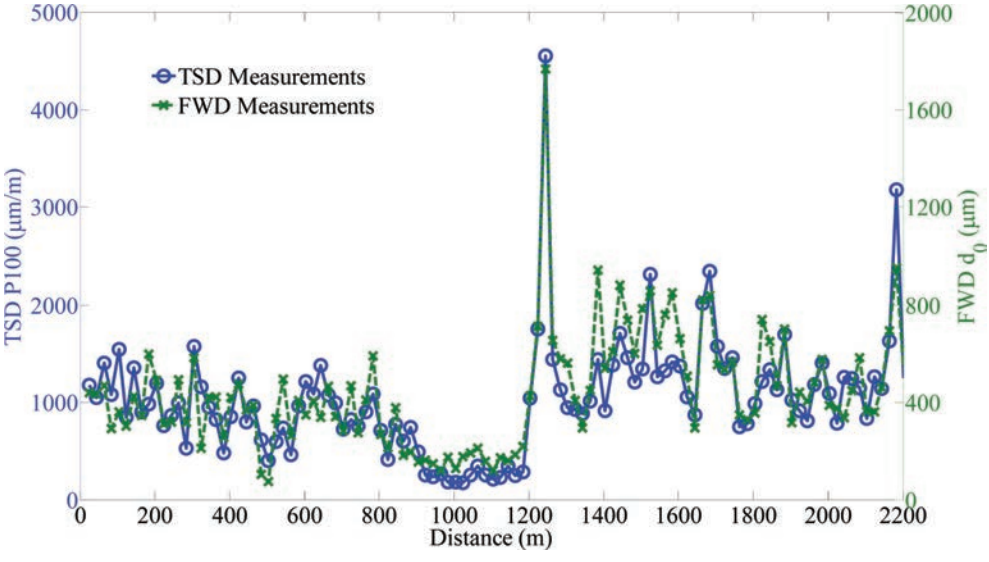

Figure 2. Comparison of TSD and FWD measurements.

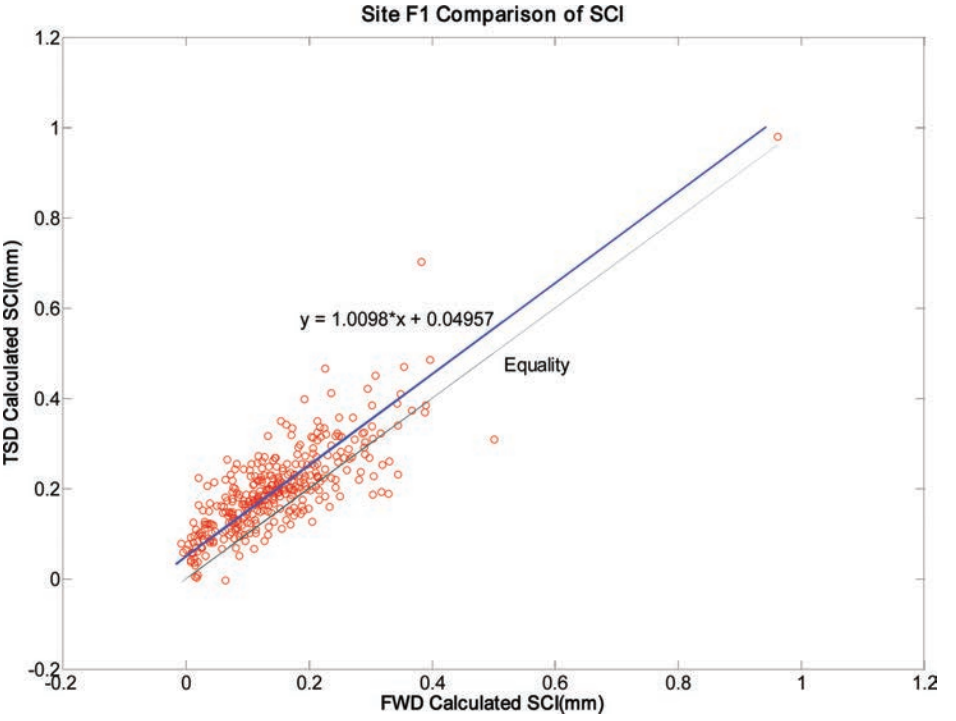

Figure 3. TSD calculated SCI versus FWD calculated SCI.

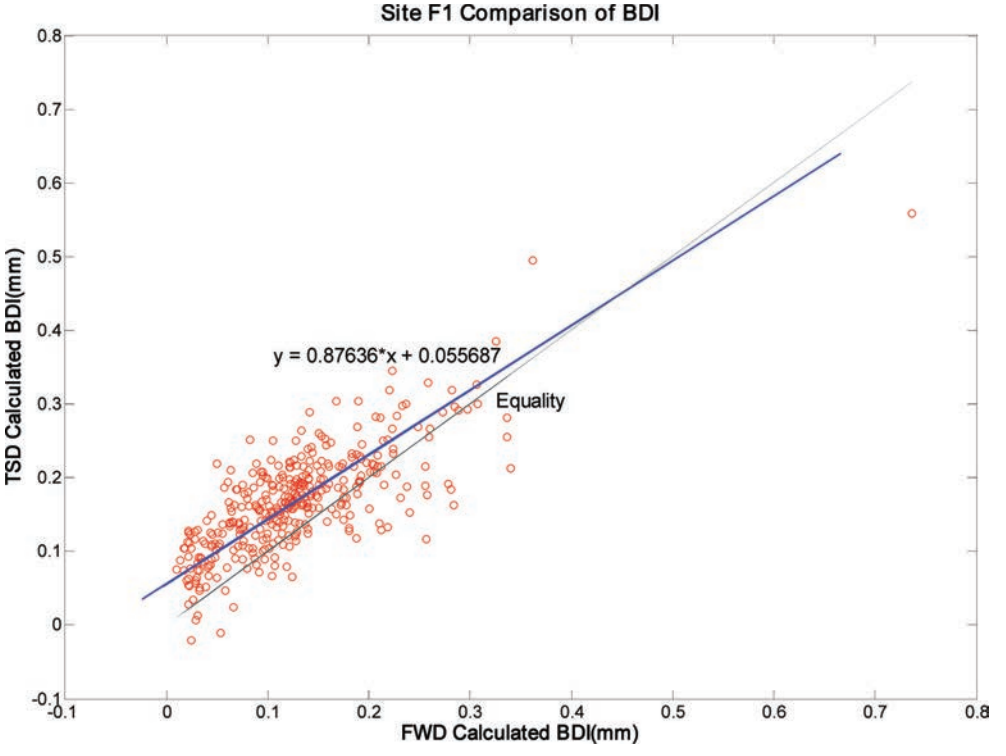

Figure 4. TSD calculated BDI versus FWD calculated BDI.

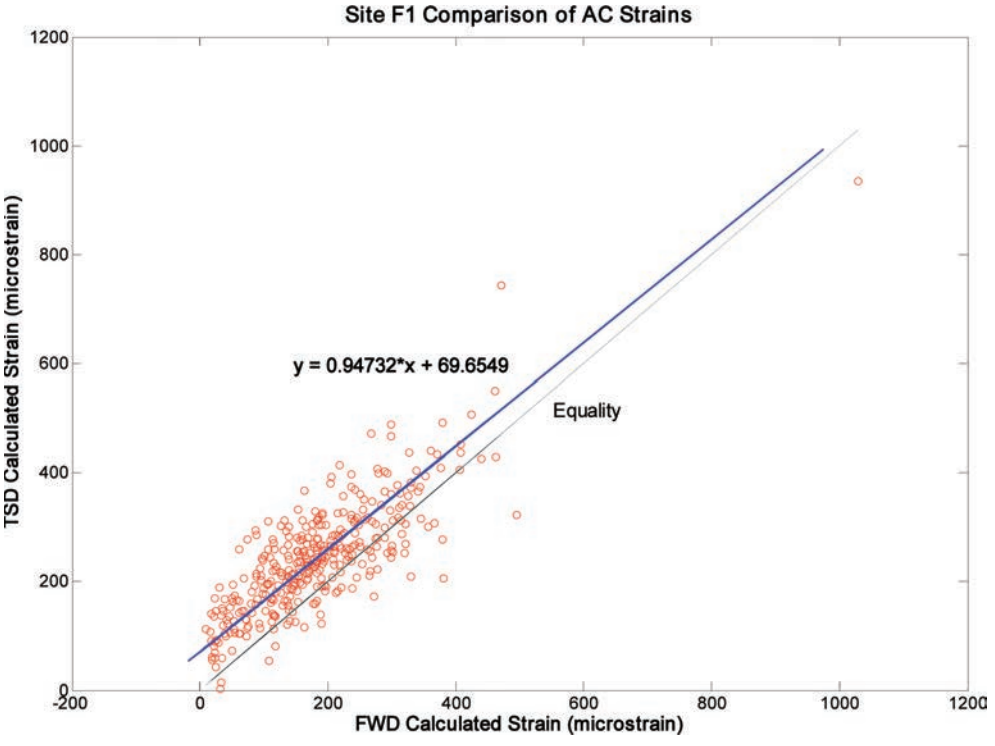

Figure 5. Strain at the bottom of the asphalt layer estimated by TSD and FWD.

different units, they both follow the same trends. The figure shows that like the FWD, the TSD was able to capture the structural variation in the pavement sections.

The comparison of the SCI calculated from data gathered by the TSD and FWD are presented in Figure 3, and the BDI calculated from data from each device are compared in Figure 4. The relationship shown in each case was determined using orthogonal regression, since both estimates contain measurement errors. For the SCI, the slope of the regression is close to 1 and the TSD calculated SCI is, on average, about 0.05 mm higher than the FWD calculated SCI. For the BDI, the two devices follow the same trends however the slope of the regression in this case is about 0.88 which suggests that the relationship between the TSD BDI and the FWD BDI while still good, is not quiet as good as the relationship in the case of the SCI. Similar to the case of the SCI, in general, the TSD calculated BDI values were larger than the FWD calcualted ones.

Using the SCI, BDI, and thickness of the pavement, the strain at the bottom of the asphalt layer was estimated along the site for each measuring device. The comparison of the strain at the bottom of the asphalt layer from the two devices is presented in Figure 5. The strains calculated from each device follow the same trends which shows the potential of using the TSD for network level applications; however, the TSD calculated strain was on average larger by about 65 microstrain than the FWD calculated strain and the variability around the trend line is still considerable compared to the accuracy required for detailed analysis such as is done at the project level. For example, the results presented in Figure 5 shows that there could be as much as 200 microstrain difference between the TSD and FWD calculated strain.

5 CONCLUSION

This paper compared the TSD and FWD estimated strain at the bottom of the asphalt layer. The results show that, in general, the calculated strain from either device follow the same

trends with TSD calculated tensile strain on average larger by about 65 microstrain than FWD calculated tensile strain. Furthermore, there is a significant variability in the relationship between the tensile strain obtained from each device. This variability could result in differences of as much as 200 microstrain.

The results here suggest that further investigation of the causes that lead to the TSD measuring higher strain levels is needed. Although the applied load was of the same magnitude (40 kN), the dynamics of how the load is applied in each case are much different. In the case of the FWD, the load is dropped onto the pavement whereas for the TSD the load is applied by a moving wheel.

REFERENCES

[1]. Xu, B., Ranjithan, S.R., and Kim, Y.R. (2002), "New Relationship Between Falling Weight Deflectometer Deflections and Asphalt Pavement Layer Condition Indicators, *Transportation Research Record*, Vol. 1806, pp. 48–56.

[2]. Flintsch, G.W., and McGhee (2009), "Managing the Quality of Pavement Data Collection," NCHRP Synthesis of Highway Practice 39-01, Transportation Research Board, Washington, D.C.

[3]. Flintsch, G.W., Ferne, B., Diefenderfer, B., Katicha, S.W., Bryce, J., Nell, S., and Clark, T. (2013), "*Assessment of Continuous Pavement Deflection Measuring Technologies*," Second Strategic Highway Research Program (SHRP2), Report S2-R06F-RW-1, The National Academies, Washington, D.C.

[4]. Ferne, B. W, Langdale, P., and Round N (2009), Development of a calibration procedure for the UK Highways Agency Traffic Speed Deflectometer. Transportation Research Board 88th Annual Meeting, January 2009. Washington D.C.

This page intentionally left blank

Microstructural characterization and micromechanics of asphalt materials

This page intentionally left blank

Asphalt Pavements – Kim (Ed)
© 2014 Taylor & Francis Group, London, ISBN 978-1-138-02693-3

Modeling the effects of constituent properties on the mechanical behavior of asphalt mixtures

Francisco Thiago Sacramento Aragão
Department of Civil Engineering, Universidade Federal do Rio de Janeiro-COPPE, Rio de Janeiro, RJ, Brazil

Yong-Rak Kim
Department of Civil Engineering, University of Nebraska-Lincoln, Lincoln, NE, USA

ABSTRACT: This study evaluates the influence of constituent properties on the mechanical behavior of asphalt mixtures. A computational microstructure model is used to simulate the overall behavior of the mixtures based on individual constituent properties. The heterogeneous mixtures are composed of linear elastic coarse aggregate particles that are embedded into a viscoelastic fine-aggregate asphalt matrix phase. To properly model the mechanical behavior of the composite, other complex mixture characteristics, such as geometrical properties of the aggregate particles and rate-dependent fracture characteristics of the fine aggregate asphalt matrix are taken into account in the model. Simulations are performed to demonstrate the ability of the model to identify the influence of mix constituents and design factors such as stiffness, volume fraction, and fracture characteristics on the overall mechanical behavior of the mixtures. Even if extra work is required to refine the model, the results demonstrate that carefully-developed computational microstructure models, such as the one presented herein, represent a promising strategy to model the complex behavior of asphalt mixtures in a scientifically-sound and efficient manner.

Keywords: Asphalt mixtures, mechanical behavior, mixture constituents, microstructural modeling, finite element method

1 INTRODUCTION

Asphalt concrete mixtures are particulate composites in which a rigid skeleton of aggregate particles is held together by a softer phase of Fine Aggregate Matrix (FAM) mixture that is composed of asphalt binder, air voids, and fine aggregates. To predict the mechanical behavior of these heterogeneous and viscoelastic composites that experience damage at different length scales, several researchers have proposed various computational predictive models based on the discrete and the finite element methods [1–10]. These computational microstructure models have stronger scientific basis than empirical methodologies that are based on statistical analyses of regional and case-specific databases. In comparison to other computational approaches, the computational microstructure models are also advantageous because they account for diverse complexities (*e.g.*, material inelasticity, heterogeneity, anisotropy, multiple damage forms). Computational microstructure models can also greatly reduce the costs associated with laboratory experiments because they generally only require individual mixture constituent properties as model inputs. Another advantage of the computational microstructure modeling approach is that it allows a comprehensive examination of the microstructural, inelastic material behavior so that stresses and strains within the microstructure can be analyzed more realistically.

In an attempt to characterize the microstructural fracture damage behavior of asphalt mixtures, Aragão [11] has recently proposed a computational microstructure model based on the finite element method that is incorporated with material viscoelasticity and rate-dependent Cohesive Zone (CZ) fracture. In 2010, Aragão *et al.* [8] successfully employed an earlier version of that model in numerical simulations of the dynamic modulus of asphalt mixtures and demonstrated the potential of the microstructural modeling approach to simulate the undamaged mechanical behavior of the material based on component properties.

Kim and Aragão [10] used the computational model proposed by Aragão [11] in fracture simulations of real microstructures of asphalt mixtures. In their work, Kim and Aragão [10] used component properties obtained from simplified testing programs [12] to simulate the individual component behavior within the microstructure of the mixtures and the corresponding overall mechanical responses of the composite. Kim and Aragão [10] observed that the rate-dependent fracture model generated considerably more accurate predictions than its rate-independent version, which clearly demonstrates the need for the consideration of this behavior in microstructure modeling of asphalt mixtures.

As demonstrated by Aragão *et al.* [8] and Kim and Aragão [10], the accuracy of microstructural models greatly depends on the level of understanding of the physics of the real problem and on how well the computational models simulate those physical characteristics. These characteristics include the heterogeneity and random distribution of aggregate particles, the inelasticity of the Fine Aggregate Matrix (FAM), the large size of the plastic zones around the crack tips of the damaged mixtures, and the rate-dependent characteristics of those fracture zones, among others.

In that sense, this paper presents the computational microstructure model proposed by Aragão [11] to simulate the effects of constituent properties on the mechanical behavior of asphalt mixtures. Parametric analyses are conducted in this paper to demonstrate the ability of the model to directly account for component characteristics, such as stiffness, volume fraction, and rate-dependent fracture on the overall mechanical behavior of the mixtures. The results presented in this paper demonstrate that carefully-developed models based on the computational microstructure approach have a great potential to become powerful design and analysis tools for asphalt mixtures and pavements. For that, only component properties and representative boundary conditions of the real problems are required to simulate the mechanical responses of the mixtures subjected to different loading conditions.

2 DYNAMIC MODULUS SIMULATIONS

As previously mentioned, Aragão *et al.* [8] have demonstrated the ability of the computational microstructure modeling approach to predict the dynamic modulus of asphalt mixtures. The predictive capabilities of different modeling methodologies typically used in the literature were compared and indicated the great potential of the numerical approach. In that study, the researchers also demonstrated that the computational microstructure methodology can directly account for the effects of constituent properties on the dynamic modulus of the mixtures. Figure 1a shows the virtual testing set-up (*i.e.*, mixture microstructure, boundary conditions and virtually-generated deformation sensors) used by Aragão *et al.* [8] to simulate the dynamic modulus of real mixture microstructures. Figures 1b and 1c show the results of the parametric analysis conducted by the researchers to evaluate the change in the overall mixture stiffness given changes in the asphalt content and aggregate stiffness, which are two important component properties that significantly affect the overall mixture stiffness. From the results shown in Figure 1b, it is clear that the computational model successfully captured the effect resulting from the addition of more asphalt binder in the mixture microstructure. The use of the matrix properties with a higher binder content resulted in lower dynamic modulus values, as expected. On the other hand, the stiffening effect resulting from the use of stiffer aggregate particles has also been successfully characterized, as shown in Figure 1c.

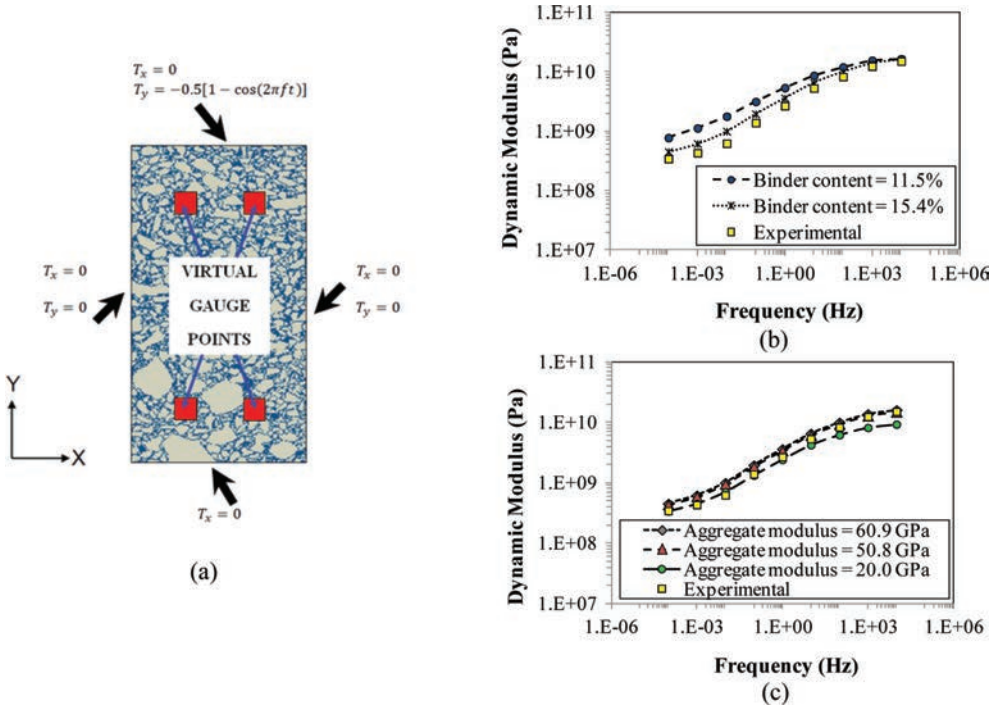

Figure 1. (a) Virtual testing set-up and parametric analyses on the effects of (b) binder content and (c) aggregate stiffness on the dynamic modulus of asphalt mixtures (Aragão *et al.*, 2010).

3 FRACTURE SIMULATIONS

Other important variables that affect the mechanical behavior of the mixtures include the volume fraction of aggregate particles, as well as the fracture characteristics of the FAM phase. Thus, this section presents a sensitivity analysis to illustrate the ability of the computational model to account for the effects of such important constituent properties on the overall fracture damage behavior of the mixtures. For that, virtually-generated mixture microstructures composed of linear elastic aggregate particles and viscoelastic FAM are simulated. Fracture is assumed to occur within the matrix phase and is modelled using the bilinear Cohesive Zone (CZ) fracture concept.

The bilinear CZ model was selected among several others due to its simplicity and interesting features, such as the ability to reduce the artificial compliance effect through the adjustment of the effective displacement, δ_t. As illustrated in Figure 2, the bilinear model postulates that there is a fully-recoverable, linear elastic behavior until the traction on the cohesive surface reaches the peak value, or cohesive strength, T_{max}, in the traction-separation curve. To the cohesive strength corresponds an effective displacement, δ_t, above which damage starts to take place and the ability of the CZ elements to sustain traction is gradually reduced until it reaches a critical displacement, δ_c. At that point, the complete dissipative and irreversible failure of the CZ element is reached, and the process is repeated for the next cohesive elements that are still active in the mesh.

The rate-dependence of the fracture properties is defined via Eqs. (1) and (2). Eq. (1) represents a simplification of the rate- and temperature-dependent expression for cohesive strength proposed by Espinosa and Zavattieri [13] because the consideration of thermal effects on the fracture properties is out of the scope of this study. A similar rate-dependent expression is assumed for the other CZ property, *i.e.*, the cohesive fracture energy, G_c.

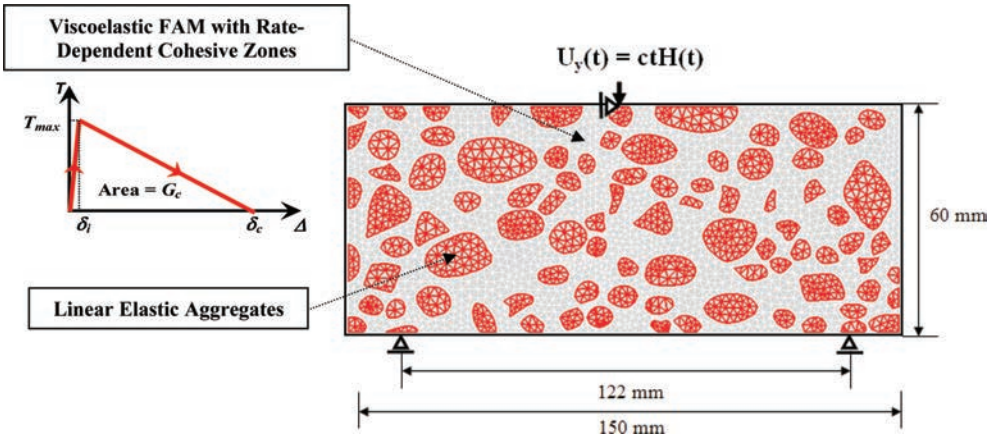

Figure 2. Bilinear CZ model and example of a virtual asphalt mixture microstructure used in the fracture simulations.

$$T_{max} = T_{max}^{ref}\left\{1+\beta_T \ln\left(\frac{\dot{\delta}_e}{\dot{\delta}_e^{ref}}\right)\right\} \tag{1}$$

$$G_c = G_c^{ref}\left\{1+\beta_G \ln\left(\frac{\dot{\delta}_e}{\dot{\delta}_e^{ref}}\right)\right\} \tag{2}$$

where $\dot{\delta}_e^{ref}$, T_{max}^{ref}, G_c^{ref}, and β_T and β_G = reference displacement jump rate, cohesive strength at $\dot{\delta}_e^{ref}$, cohesive fracture energy at $\dot{\delta}_e^{ref}$, and model parameters determined with the aid of experimental test results. δ_e represents the evolving effective displacement jump in each cohesive element and is calculated from the values of the normal and tangential displacement jumps, δ_n and δ_t, respectively, as shown in Eq. (3).

$$\delta_e = \sqrt{\delta_n^2 + \delta_t^2} \tag{3}$$

3.1 *Effects of aggregate volume fraction*

Two two-dimensional microstructures were generated to evaluate the effect of volumetric characteristics of aggregate particles on the fracture behavior of asphalt mixtures. The microstructures differed only on volume fraction of aggregate particles. For the analysis herein, two different values of aggregate volume fraction (qualitatively named as low and high volume fractions) were used to generate the two microstructures.

To simulate the complex geometry of the microstructures, finite-element meshes were generated with triangular elements measuring approximately 1 mm within the central region of the virtual beams and 2 mm outside that region. The objective of the higher refinement level at the central region was to maintain the geometric characteristics (*e.g.*, angularity) of the particles. Additionally, it is important to have a higher refinement level in the regions with higher potential for crack initiation and propagation because the possible crack paths are limited by the topology of the finite-element mesh. This mesh-dependence problem can be alleviated with the use of more refined meshes close to the evolving crack tips. However, the use of excessively refined meshes may result in very expensive computational cost and may also intensify the problem of artificial compliance that is inherent to intrinsic cohesive models.

The two finite-element meshes generated for the parametric analysis are shown in Figures 3a and 3b. To avoid the effects of the artificial compliance due to the use of an intrinsic

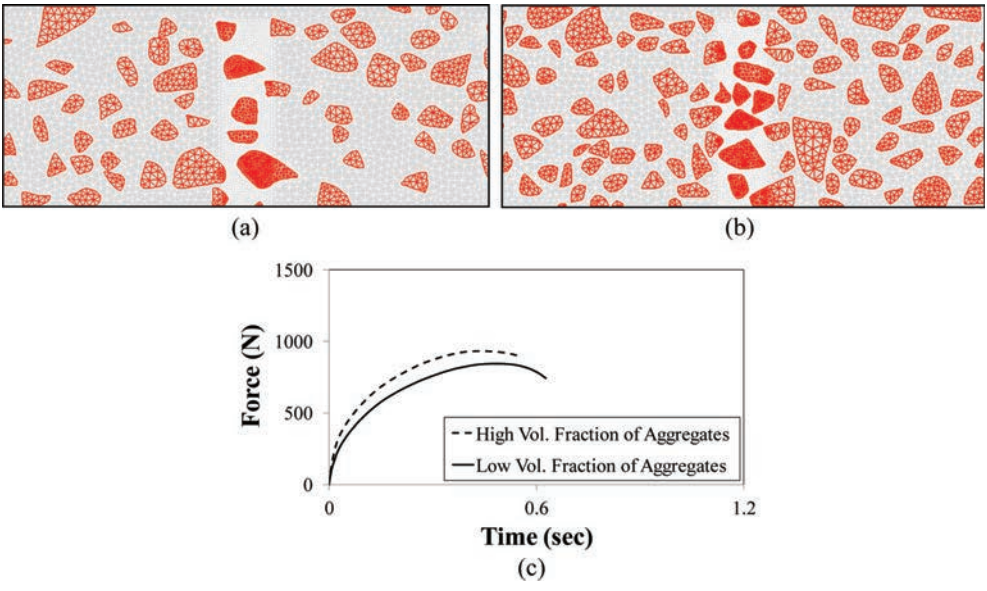

Figure 3. FEM mesh and microstructure of virtual HMA beam samples: (a) low and (b) high volume fraction of aggregates; and (c) simulation results.

CZ model, similar numbers of cohesive elements (2414 and 2170, respectively) were assigned to the meshes. Three-point bending tests were conducted and a monotonically-increasing displacement of 50 mm/min. was applied downwards to the node located at the middle of the top edge of the virtual specimens. Figure 3c presents the sensitivity of the force-time curve to the volume fraction of aggregate particles. From Figure 3c, it is clear that both initial stiffness and strength of the mixture increased as the volume fraction of aggregates increased.

Figure 4 shows snapshots of the virtual beams at a simulation time of 0.54 seconds and illustrates the different levels of microstructural damage experienced by the beams. Figure 4 also shows contour plots of the stress tensor horizontal component s_{11}. The contours reveal a higher concentration of stresses at rigid aggregate particles and around the crack tips, as expected. Such type of detailed information of the stress (and strain) distributions within the microstructures of the virtual specimens can be very useful during the asphalt mixture design process because components with appropriate characteristics may be selected based on the microstructural analysis.

3.2 *Rate-dependent fracture characteristics*

The two cohesive fracture parameters that mostly influence the overall mixture responses are the CZ strength and fracture energy. Therefore, this section presents sensitivity analysis results for the parameters T_{max}^{ref} and G_c^{ref} that define the functions relating cohesive strength and fracture energy to the rate of displacement jumps (Eqs. (1) and (2)) experienced by each cohesive element. For this parametric analysis, the beam shown in Figure 2 was used and the simulations were conducted at a rate of 50 mm/min.

Figure 5 presents the sensitivity of the force-time curve to the two rate-dependent parameters investigated. From the analysis of Figure 5a, it is clear that as T_{max}^{ref} increased, the peak load also increased. This was expected because damage initiation is retarded when larger strength values are specified to the cohesive elements. On the other hand, the analysis of Figure 5b reveals that as G_c^{ref} increased, the fracture resistance of the mixture also improved, which was demonstrated by the larger area under the force-time curve. This analysis clearly demonstrates that the rate-dependent fracture model developed herein successfully identified the influence of component fracture properties to the overall mixture damage behavior.

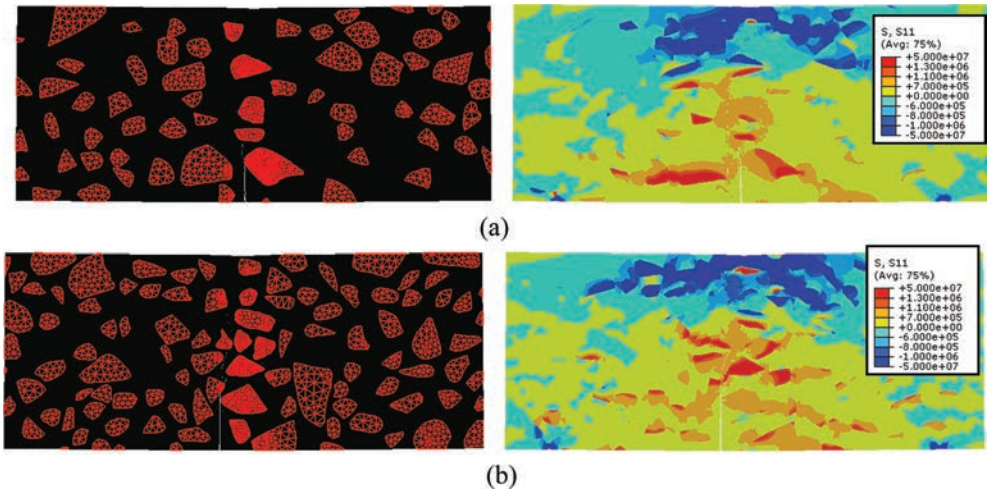

Figure 4. Microstructural damage and stress contour plots at for samples with (a) low and (b) high volume fraction of aggregates.

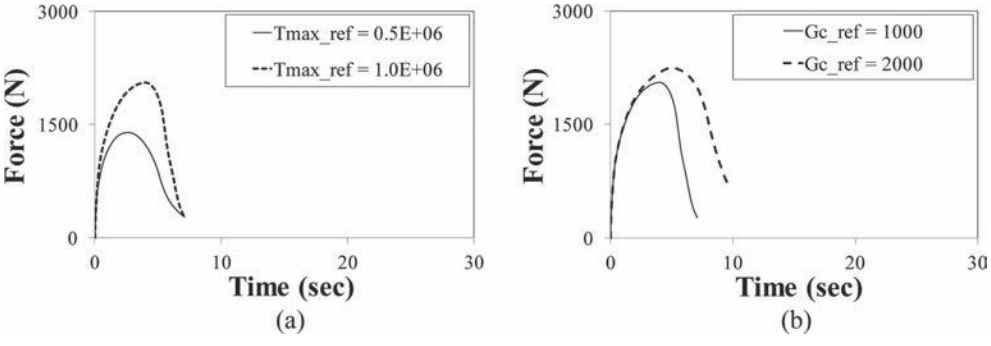

Figure 5. Parametric analysis for: (a) T_{max}^{ref} and (b) G_c^{ref}.

To further illustrate the effects of the rate-dependent fracture parameters on the fracture behavior of the mixtures, an additional analysis comparing progressive fracture damage levels experienced by the beam at different stages of the simulations was also conducted. Figure 6 shows comparisons for two different T_{max}^{ref}, *i.e.*, 0.5 MPa and 1.0 MPa. As expected, the analysis of Figures 6a and 6c reveals that the beam experienced premature damage initiation for a lower T_{max}^{ref} (0.5 MPa). Damage also propagated faster in the beam when a lower T_{max}^{ref} was assigned, as demonstrated in Figures 6b and 6d. Finally, Figure 7 shows comparisons for two different G_c^{ref}, 1000 J/m^2 and 2000 J/m^2. Damage initiated at similar simulation stages for both cases, as demonstrated in Figures 7a and 7c. However, as shown in Figures 7b and 7d, after the initiation of damage, crack propagation was much faster for the case with smaller G_c^{ref}, as less energy was required to fully separate the two faces of each CZ element in the mesh.

As previously mentioned, one interesting feature of the computational microstructure modeling approach is that it allows a more comprehensive examination of the microstructural, inelastic material behavior so that stresses and strains within the microstructure can be analyzed more realistically. To illustrate that capability, Figures 8b to 8e show progressive microstructural fracture and stress (s_{11}) contour plots at simulation times ranging between 4 and 14 seconds for the applied displacement rate of 25 mm/min. The corresponding force-time

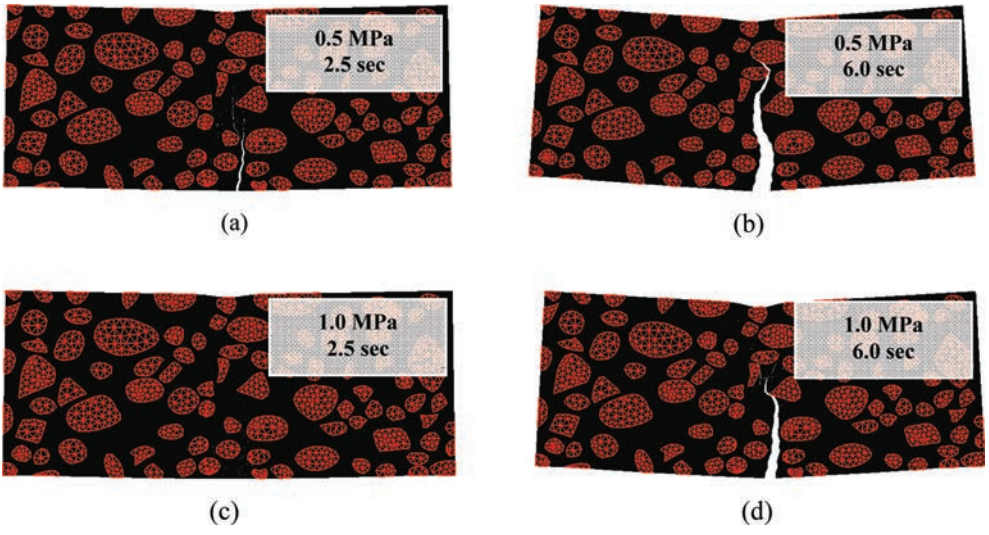

Figure 6. Progressive microstructural fracture at two simulation times, *i.e.*, 2.5 and 6.0 seconds, for two different T_{max}^{ref}: (a) and (b) 0.5 MPa; (c) and (d) 1.0 MPa.

Figure 7. Progressive microstructural fracture at two simulation times, *i.e.*, 2.5 and 6.0 seconds, for two different G_c^{ref}: (a) and (b) 1000 J/m^2; (c) and (d) 2000 J/m^2.

plot is shown in Figure 8a. The contour plots reveal that there is a higher concentration of stresses on the stiff aggregate particles. High stress levels were also observed around the tip of the crack. Stress levels were drastically reduced at the bottom of the beam after the formation and propagation of the macro-crack within the sample microstructure.

Another interesting observation can be made from the comparison between Figures 8c and 8d: in Figure 8c, two major cracks were initially formed, but only one has finally propagated, as shown in Figure 8d. Such behavior is typically observed in fracture tests conducted with real samples in the laboratory. Multiple cracks tend to coalesce from micro-cracks formed in the damaged sample, but the path that requires less energy to create new surfaces within the specimen microstructure is naturally chosen for the macrocrack propagation.

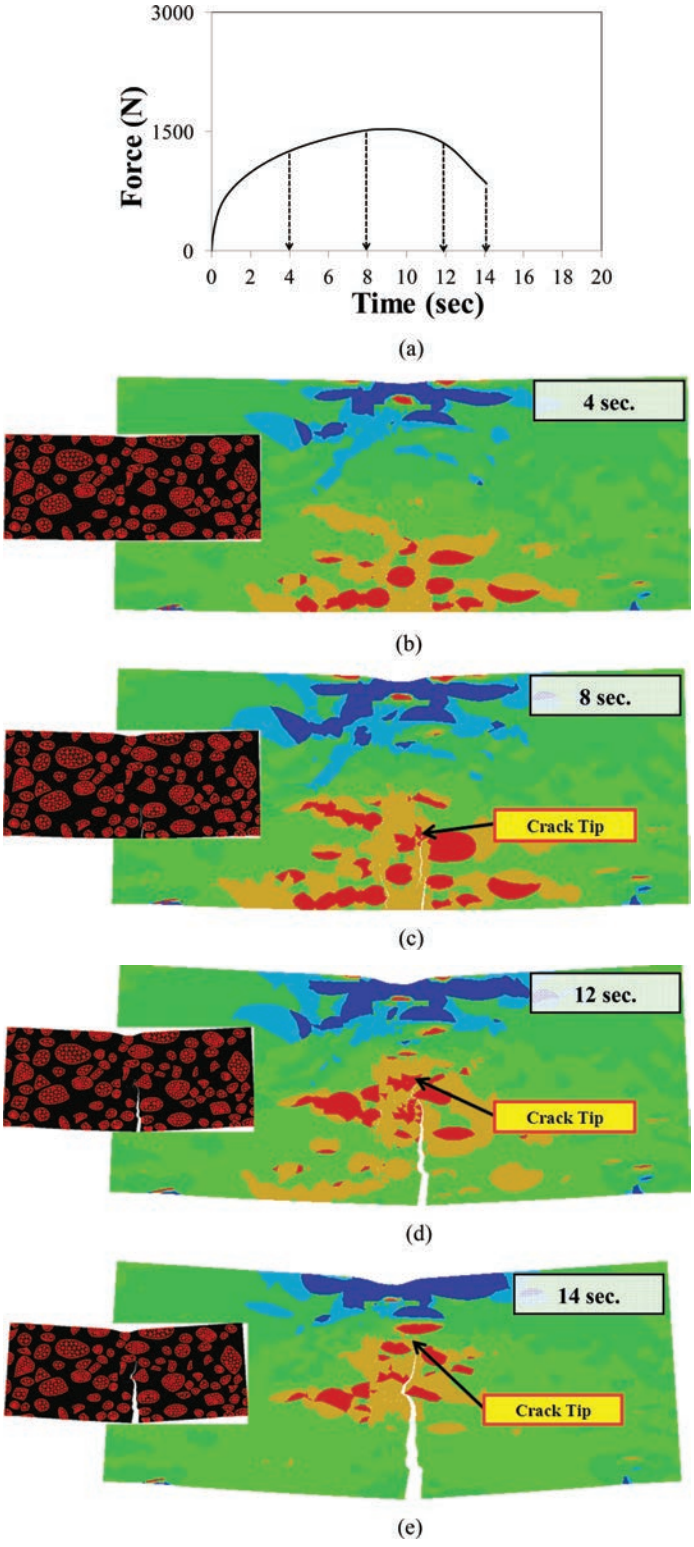

Figure 8. (a) Simulation results and progressive microstructural fracture and stress (s_{11}) contour plots at: (b) 4 sec.; (c) 8 sec.; (d) 12 sec.; and (e) 14 sec.

Such type of analysis can provide meaningful information that can be used during the mixture design phase and guide the process of material selection. Additionally, as demonstrated in this paper, carefully-developed computational microstructure models, such as the one presented herein, have a great potential to become efficient and comprehensive analysis tools that can be incorporated into the next generation of pavement design programs. The interesting features of the microstructural approach can also contribute to enhance the performance prediction capabilities of such design methodologies, which may result in significant savings on maintenance and rehabilitation of existing pavement structures.

4 CONCLUSIONS

Computational microstructure models have been regarded by the pavement mechanics community as a promising approach to model the mechanical behavior of asphalt mixtures. To demonstrate the potential of a well-designed microstructure model recently proposed by the authors of this study, numerical simulations were performed on virtual samples and several interesting results are presented in this paper. Based on the results and analysis, the following conclusions can be made:

- The computational microstructure modeling approach can directly account for the effects of diverse constituent properties on the overall mechanical behavior of asphalt mixtures;
- With the microstructural approach, detailed information about the stress and strain distributions within the mixture microstructure can be obtained from simulations and used for the selection of better engineered materials to compose the mixtures, as well as for further analysis of mixture performance;
- The microstructural methodology is also able to model the damage-dependent behavior of the heterogeneous mixtures in a realistic manner. As was exemplified in this study, an analysis of microstructural damage evolution demonstrated that the model could successfully capture the formation of multiple cracks within the microstructure and the choice for one path for the propagation of a macrocrack until complete failure of the virtual sample.

ACKNOWLEDGEMENTS

The authors are grateful for the financial support received from the Brazilian Coordination for the Improvement of Higher Education Personnel (CAPES) for the participation in the event.

REFERENCES

[1] Buttlar, W. and You, Z. Discrete Element Modeling of Asphalt Concrete: Microfabric Approach. *In Transportation Research Record: Journal of the Transportation Research Board, No. 1757*, *TRB*, National Research Council, Washington, D. C., pp. 111–118. (2001).

[2] Masad, E., Tashman, L., Somedavan, N., and Little, D. Micromechanics-Based Analysis of Stiffness Anisotropy in Asphalt Mixtures. *Journal of Materials in Civil Engineering*, 14 (5), pp. 374–383. (2002).

[3] Soares, J.B., Freitas, F.A., and Allen, D.H. Crack Modeling of Asphaltic Mixtures Considering Heterogeneity of the Material. *In Transportation Research Record: Journal of the Transportation Research Board, No. 1832*, *TRB*, National Research Council, Washington, D.C., pp. 113–120. (2003).

[4] You, Z. and Buttlar, W.G. Discrete Element Method to Predict the Modulus of Asphalt Concrete Mixtures. *Journal of Materials in Civil Engineering, ASCE*, pp. 140–146. (2004).

[5] Kim, Y.R., Allen, D.H., and Little, D.N. Damage-Induced Modeling of Asphalt Mixtures through Computational Micromechanics and Cohesive Zone Fracture. *Journal of Materials in Civil Engineering*, pp. 477–484. (2005).

[6] Kim, Y.R., Allen, D.H., and Little, D.N. Computational Model to Predict Fatigue Damage Behavior of Asphalt Mixtures under Cyclic Loading. *In Transportation Research Record: Journal of the*

Transportation Research Board, No. 1970, *TRB*, National Research Council, Washington, D.C., pp. 196–206. (2006).
[7] Dai, Q. and You, Z. Micromechanical Finite Element Framework for Predicting Viscoelastic Properties of Asphalt Mixtures. *Materials and Structures*, 41, pp. 1025–1037. (2007).
[8] Aragão, F.T.S., Kim, Y.R., Karki, P., and Little, D.N. Semi-Empirical, Analytical, and Computational Predictions of Dynamic Modulus of Asphalt Concrete Mixtures. *In Transportation Research Record: Journal of the Transportation Research Board, No. 2181*, *TRB*, National Research Council, Washington, D.C., pp. 19–27. (2010).
[9] Aragão, F.T.S., Kim, Y.R., Lee, J., and Allen, D.H. (Micromechanical Model for Heterogeneous Asphalt Concrete Mixtures Subjected to Fracture Failure. *Journal of Materials in Civil Engineering (Issue: Multiscale and Micromechanical Modeling of Asphalt Mixes)*, 23, No. 1, pp. 30–38. 2011).
[10] Kim, Y. and Aragão, F.T.S. Microstructure Modeling of Rate-dependent Fracture Behavior in Bituminous Paving Mixtures. Finite Element in Analysis and Design, 63, pp. 23–32. (2013).
[11] Aragão, F.T.S. Computational Microstructure Modeling of Asphalt Mixtures Subjected to Rate-dependent Fracture. *Ph.D. dissertation*. University of Nebraska—Lincoln. (2011).
[12] Aragão, F.T.S. and Kim, Y. Mode I Fracture Characterization of Bituminous Paving Mixtures at Intermediate Service Temperatures. *Experimental Mechanics*, 52 (9), pp. 1423–1434. (2012).
[13] Espinosa, H.D. and Zavattieri, P.D. A Grain Level Model for the Study of Failure Initiation and Evolution in Polycrystalline Brittle Materials, Part I: Theory and Numerical Implementation. *Mechanics of Materials,* 35 (3–6), pp. 333–364. (2003).

Asphalt Pavements – Kim (Ed)
© 2014 Taylor & Francis Group, London, ISBN 978-1-138-02693-3

Viscoelastic behavior of mastic phase of Asphalt Concrete

Mohammad Hossain
Department of Civil Engineering and Construction, Bradley University, Peoria, IL, USA

Hasan Faisal & Rafiqul Tarefder
Department of Civil Engineering, The University of New Mexico, Albuquerque, NM, USA

ABSTRACT: Asphalt Concrete (AC) is a well-known viscoelastic material. In AC, asphalt binder is mainly responsible for the viscoelastic behavior, as it consists of coarse aggregate, asphalt binder and fines. The asphalt binder creates an asphalt film around the coarse aggregate and fines. Indeed, fines are trapped inside the binder film, which is also known as mastic. As mastic governs most of the mechanical properties of AC, a nano mechanical characterization of mastic of AC is done using nanoindentation tests. Nanoindentation tests created the opportunity to indent on the thin sample as integral part of AC system. Fifty nanoindentation tests were conducted on the mastic phase of AC. In, nanoindentation tests an extended creep hold is used to obtain the creep data of mastic phase. A Burgers viscoelastic model is developed using the laboratory nanoindentation data. In addition, the viscoelastic model is used in the Finite Element Model (FEM) framework ABAQUS to simulate nanoindentation test. The force-depth curve acquired from FEM framework showed good agreement with laboratory test data.

Keywords: Viscoelastic, nanoindentation, mastic, creep, Finite Element Method

1 INTRODUCTION

Several laboratory testing protocols are available to evaluate and characterize Asphalt Concrete (AC) mix. Laboratory tests are performed on both compacted and loose AC mix. In recent years, many researchers are conducting tests by nanoindentation on asphalt mixture components such as asphalt binder and aggregates to understand materials behavior at micron scale [1–3]. In a nanoindentation test, an indenter is used to indent a sample surface and the movement of the indenter is measured with an increasing load or deformation [4]. It is a very powerful technique to measure hardness and Young's modulus of a material. Very few studies have been done on the AC mix such as on mastic and matrix materials using nanoindentation techniques [5]. Though extensive research have been done in materials science and composite materials using this novel approach [6–9]. In addition, biomedical engineers used this test to measure mechanical properties of organ and components of human body such as strength of bones and muscles [10,11]. In this study, nanoindentation test is done on mastic phase of AC.

Mastic materials or asphalt mastic is defined as mixture of asphalt binder with fines passing through # 200 sieve (0.075 mm) [12,13]. On the other hand, matrix materials are mixture of asphalt binder with fine aggregate passing through a # 4 sieve and retained on a # 200 sieve. When aggregates are heated and mixed with hot asphalt binder to produce AC, coarse aggregates are coated with mastic materials and surrounded by matrix materials. It is challenging to do nanoindentation tests on the asphalt binder since the binder attach at the tip of indenter at the ambient temperature. Despite this challenge, successful indentation tests have been performed on the aged asphalt binder [14,15]. This study is done to

understand the viscoelastic behavior of mastic materials at the ambient temperature using nanoindentation tests.

2 OBJECTIVES

The objectives of this study are:

1. Perform nanoindentation tests on mastic materials at the ambient temperature and understand the viscoelastic behavior.
2. Develop a viscoelastic mechanical model from the nanoindentation creep data.
3. Validate the viscoelastic mechanical model using Finite Element Method (FEM) modeling.

3 METHODOLOGY

Two fulfill the objectives; AC samples are made by mixing fine aggregates and fines with asphalt binder. Laboratory nanoindentation tests are performed only on the mastic phase of AC. To understand the viscoelastic behavior, a creep indentation is applied following loading and before unloading an indenter from the mastic materials. A viscoelastic mechanical model is developed from the laboratory creep indentation data. Finally, a FEM model is developed in ABAQUS and the viscoelastic mechanical model is used to define the material properties of mastic and the force-depth relationship is compared and validated with the laboratory indentation tests. The limitations of this study are: mastic materials are mix of fines with binder and under nanoindentation indenter hit either fines or binder, but in this study, it is assuming that despite the indenter hit either component, it is the mastic phase of AC; another limitation is to select only one mechanical viscoelastic model and not several models are compared; finally, a two dimensional axisymmetric FEM model is developed where as a three dimensional model would provide better results.

4 BACKGROUND

Both load control and displacement control indentation tests can be performed on the materials. Figure 1 shows schematics of conventional nanoindentation test. Figure 1(a) shows the depths measure during loading and unloading of the indenter and Figure 1(b) shows the typical load-displacement curve. A sitting load is typically applied initially to facilitate contact between the tip and sample surface. Next, the load is increased gradually from point A to B. The tip is unloaded at the maximum load point B. The unloading path is assumed to be elastic for most of the elastoplastic material. The unloading curve does not come back to point A due to plastic deformation in the elastoplastic materials. The slope of the unloading curve at point B is usually equal to the slope of the loading curve at point A. The surface profile as shown in Figure 1(a) is a function of the penetration depth during loading and unloading. It should be noted that mastic materials is a visco-elastic-plastic material. To overcome the viscous effect into the unloading part, a creep load is applied at the maximum load after point B.

As it mentioned earlier, nanoindentation is mostly applied to measure Young's modulus and Hardness of materials. The Oliver-Pharr method is the most widely used method for determining stiffness and hardness values from load-displacement data. The following Eqs. (1, 2) are used to measure the reduced elastic modulus and hardness respectively.

$$\frac{1}{E^*} = \frac{1-\nu^2}{E} + \frac{1-\nu_i^2}{E_i} \tag{1}$$

where E is Young's modulus of the material, ν is Poisson's ratio of the material, E_i is Young's modulus of the indenter and ν_i is Poisson's ration of the indenter, E^* is the reduced modulus.

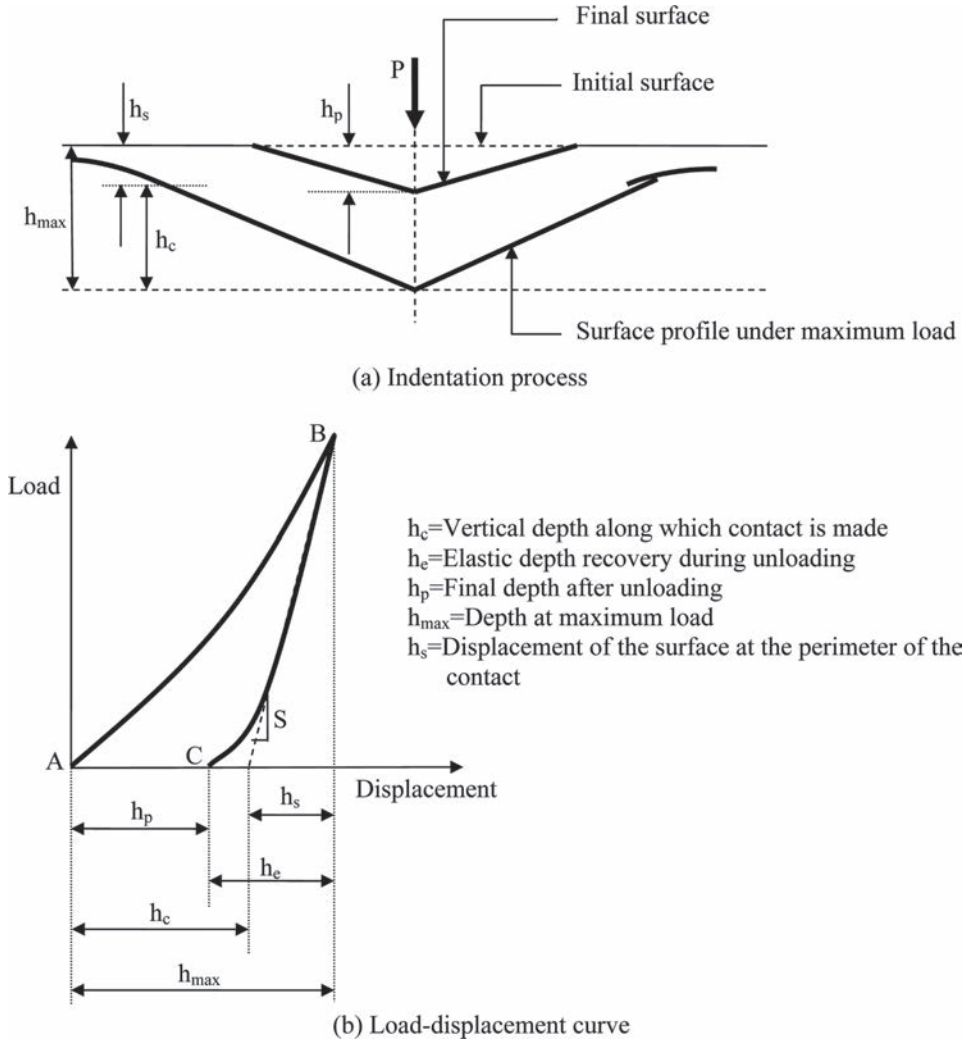

Figure 1. Schematic diagrams of indentation test.

$$H = \frac{P_{max}}{A} \tag{2}$$

where P_{max} is peak load and A is projected area of contact at peak load.

Young's modulus and hardness of mastic materials are already measured using nanoindentation [5]. Nanoindentation is performed on AC and claimed that Young's modulus of mastic materials are less than 3.0 GPa and for aggregate this value is greater than 12.0 GPa. They focused only on the loading and unloading part of the test data. In this study the test is done with loading and then creep and unloading and emphasis are given mostly on the creep indentation part to develop the viscoelastic mechanical model and later on loading, creep and unloading relationship is validated by the FEM modeling.

Nanoindentation on mastic materials has some challenges. The challenge arises due to use of fine aggregates in the AC mix. Fine aggregates are mixed to facilitate the compaction of AC to make thin samples for nanoindentation tests by cutting AC samples using laboratory saw. Schematics of nanoindentation tests are shown in Figure 2. Figure 2(a) shows the AC sample with fines, binder, micro voids, and fine aggregates; during indentation, indenter

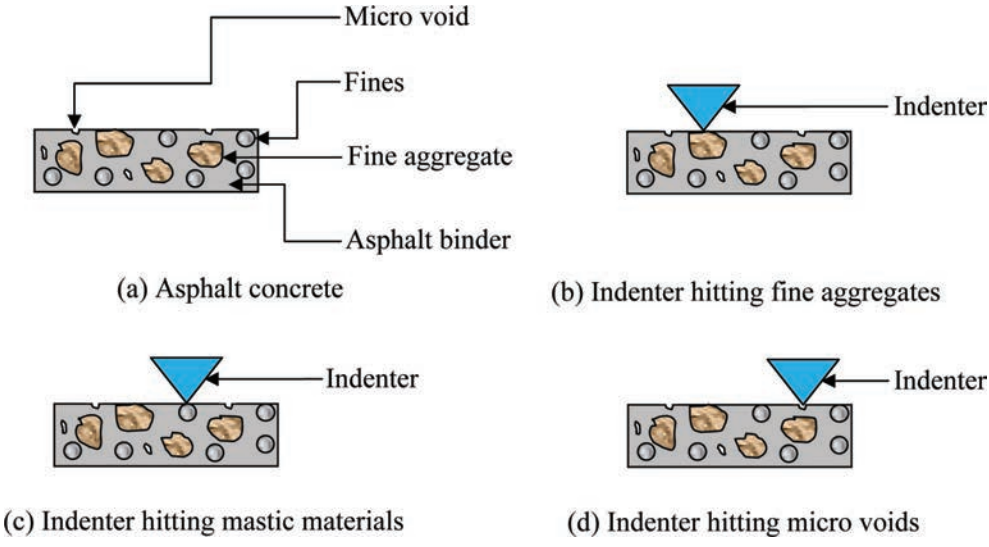

Figure 2. Schematic diagrams of nanoindentation on mastic materials.

might hit on the fine aggregates, which is shown in Figure 2(b); Figure 2(c) shows indentation on mastic materials and Figure 2(d) shows another limitation of this test that is indenter might hit on micro void. In this study, nanoindentation tests are done on such location that is free from fine aggregates and the test data is carefully analyzed to remove data that shows indentation on micro voids.

5 LABORATORY TEST

5.1 *Sample preparation*

Superpave mixes used with PG 70-22 and fine aggregates were collected from plant. Mixture was compacted into 150 mm (6 in) diameter cylinders by a Superpave Gyratory compactor using 600 KPa (87.02 psi) vertical pressure. The sample was prepared at a target low air voids of 4% to reduce voids in the sample. Using a fine laboratory saw, 6 mm (0.25 in) thick square shape of size 25 mm × 25 mm (1 in × 1 in) slices were prepared for the test. The slice that has minimum fine aggregates on the top of the sample was selected for the test. Many slices are discarded due to large voids, broken aggregates and parts and fracture face due to cutting by saw. Smooth surface of the cube is very important for nanoindentation experiment. Because the contact area is measured indirectly form the depth of penetration, a rough surface may cause errors in the determination of the area of contact between the indenter and the specimen. Therefore, the square samples were polished by a grinding machine rotating a angular speed of 150 rpm with sequence of SiC paper of decreasing abrasiveness (100, 200, 400, 800, 1000, 1200, and 1400 grit). Only one surface was polished. Finally the specimens were washed in a water bath to remove any remaining dusts. Figure 3 shows a sample on stud and substrate. Sample was fixed on substrate and stud with glue. The red box is shown to locate the location of indentation test, which is free from fine aggregates. It should be noted that the indentation on micro voids cannot be avoided during the test.

5.2 *Nanoindentation tests*

The nanoindenter device at the UNM nano test laboratory was used for indentation. More details on the nanoindentation testing equipment are given in this reference [14]. For this study, Berkovich indenter tip was used since some previous study shows than spherical

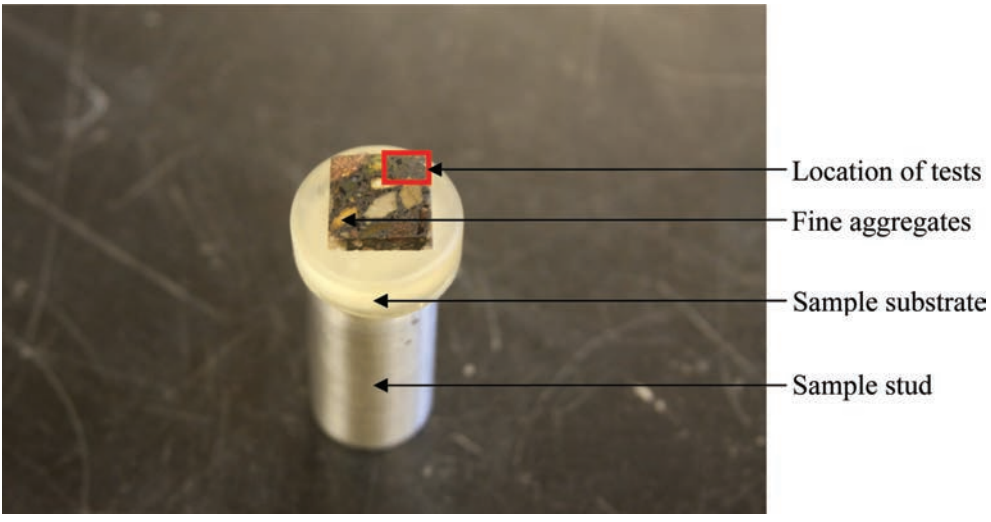

Figure 3. Laboratory sample for nanoindentation tests.

indenter glued with the unaged binder [5]. As a result, system compliance can be lost during indentation on asphalt. A Berkovich tip consists of three-sided pyramidal Berkovich tip with a semi angle of 65.27°. It has sharp and well-defined (pyramid defined by face angle 65.3°) tip geometry. In this study, a maximum load of 0.51 mN was applied with a loading and an unloading rate of 0.02 mN/sec. A sitting load of 0.01 mN was used for all the indentations. A creep time of 200 seconds was applied after reaching the maximum load. This creep time is also known as dwell time [16,17]. The viscous effects of the test results are reduced by using a fast unloading rate and applying an extended dwell time. Tarefder and Faisal have shown that a dwell time of 100–200 seconds can minimize the viscous effect of asphalt [14]. Mastic phase of the AC sample was indented at 50 locations to deal with the variability of nanoindentation results, considering the limitations as mentioned earlier, and due to material heterogeneity in the asphalt mastic.

6 RESULTS AND DISCUSSIONS ON LABORATORY TESTS

6.1 *Force-depth relationship*

Figure 4 shows the force-depth curves obtained from the nanoindentation tests on mastic materials. Forth indentations are plotted from the fifty indentation test results. Ten indentations are discarded due to fact that the indenter might hit on the micro voids. The force-depth curves are discontinuous or showing negative indentation depth for those discarded tests. It is observed that the force-depth curves widely ranges with indentation depth from 52.96 nm to 6392.30 nm for same load of 0.51 mN. This wide variation is due to the heterogeneous behavior of mastic materials. Also, as mentioned earlier, indenter might hit either fines or the asphalt binder. Though, all the indentations showed plastic depth after unloading. In addition, no negative slope is observed at the unloading curve, this means 200 sec holding time is appropriate to overcome the viscous effects of mastic materials. Due to this wide range of deformation, it would be practical to get an average value of the indentation depths.

6.2 *Creep behavior*

Figure 5 shows the creep behavior of mastic materials. The hold time was 200 sec for all indentations. Fourth creep indentations are plotted in Figure 5(a) and the average of the

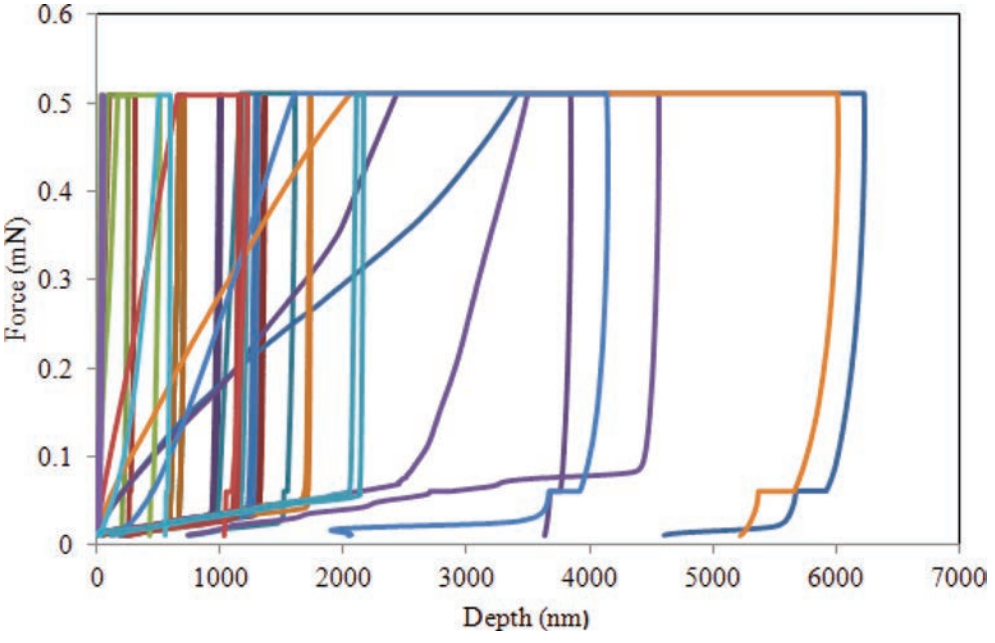

Figure 4. Force-depth relationships derived from nanoindentation test.

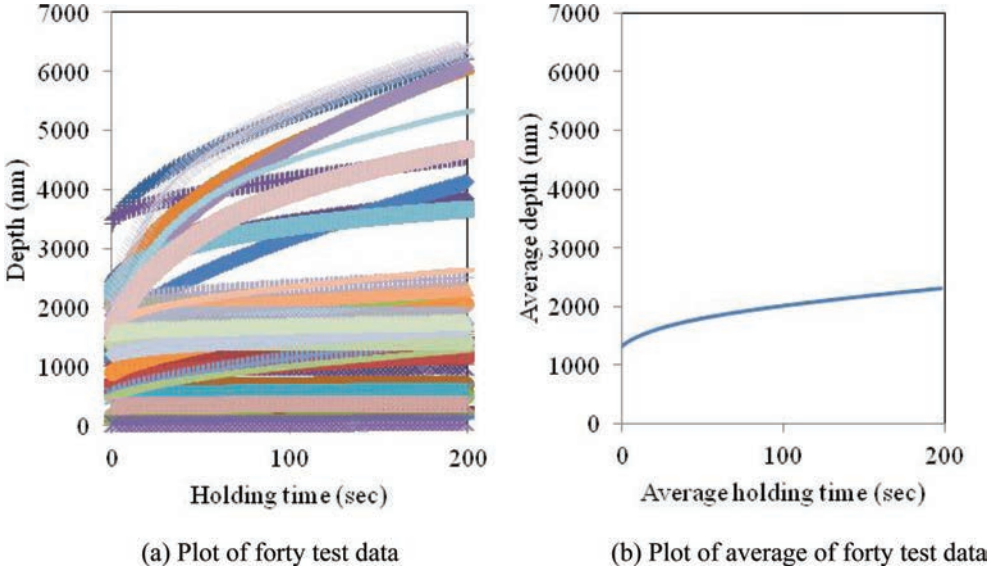

Figure 5. Creep behaviors of mastic materials under nanoindentation tests.

forty indentations are plotted in Figure 5(b). Creep data shows both linear and nonlinear indentation depth that increase with time. Again, the linear depth increase might be due to the fact that, indenter hits on the fines and the nonlinear depth increase caused by when indenter hits on the binder. Fines are elastic in nature, so indentation shows linear increasing lines; on the other hand, asphalt binder is viscoelastic and shows nonlinear increasing lines. Since fines mixed with binder and while indenter hits fine and pressed downward, underneath

the fines there are both binder and more fines and when indenter hits binder, underneath the binder there are fines or binder. So for mastic materials we have to consider combine effects of binder and fines. For this reason, to keep both linear and nonlinear creep behavior, the average depth is plotted in Figure 5(b). This average plot is further analyzed to develop viscoelastic mechanical model.

6.3 *Viscoelastic mechanical model*

Viscoelastic model can be expressed using several mechanical modes such as Maxwell, Kelvin, Burgers model, and generalized model. Figure 6 shows representations of Burgers model, which is a combination of Maxwell and Kelvin models. Burgers model best represents the viscoelastic materials [18]. The mechanical Burgers model for the nanoindentation tests can be represented by the following Eq. (3).

$$h^2(t) = \frac{\pi}{2} P_0 \cot\alpha \left[\frac{1}{E_1} + \frac{1}{E_2}\left(1 - e^{-\frac{t}{\tau_2}}\right) + \frac{t}{E_1 \tau_1} \right] \tag{3}$$

where h is the displacement due to applied load on a material, P_0 is the indentation load, α includes half angle of Berkovich indenter, E is the elastic modulus, t is time, and τ is retardation time. The total strain of the materials has three components, an instantaneous elastic strain, a viscous strain, and a retarded strain as shown in Figure 6(b). For the known value of h, P_0 and t, from the indentation test, the values of E_1, E_2, τ_1, and τ_2 can be obtained from the simplified Eq. (4).

$$h^2(t) = A_1 + A_2\left(1 - e^{-\frac{t}{\tau_2}}\right) + A_3 t \tag{4}$$

where $A_1 = \frac{\pi}{2} P_0 \cot\alpha \frac{1}{E_1}$, $A_2 = \frac{\pi}{2} P_0 \cot\alpha \frac{1}{E_2}$ and $A_3 = \frac{\pi}{2} P_0 \cot\alpha \frac{1}{E_1 \tau_1}$.

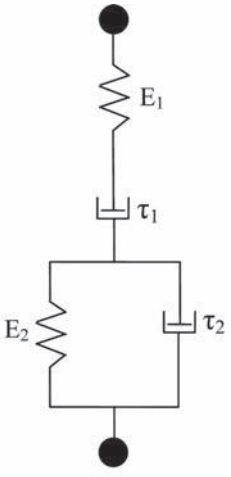

(a) Four elements Burgers spring and dashpot representation of viscoelastic material

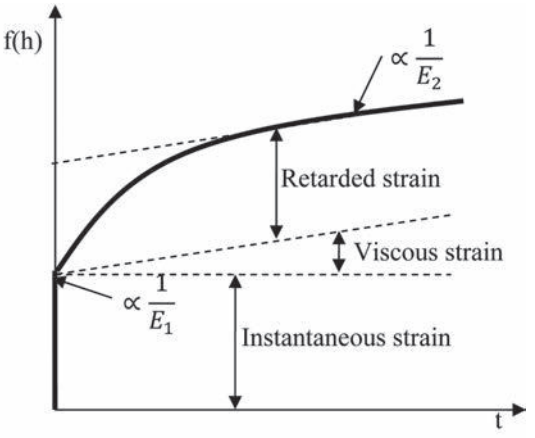

(b) Displacement response for steep increase in load for Burgers model

Figure 6. Mechanical model of viscoelastic materials.

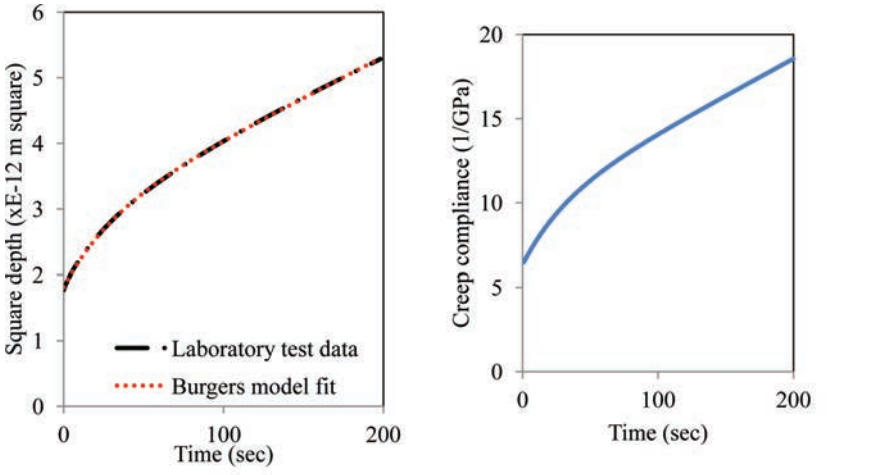

Figure 7. Mechanical model of mastic materials.

In this study, Eq. (4) is fitted with the Figure 5(b) to find A_1, A_2, and A_3. A nonlinear curve fitting algorithm is used in MATLAB to optimize those parameters.

Figure 7(a) shows the optimized Burgers model with the laboratory test results. The optimized values are: E_1 = 0.1580 GPa, E_2 = 0.2860 GPa, τ_1 = 144.85 sec, and τ_2 = 30.86 sec. Figure 7(a) shows very good fitting with laboratory average test data with R-square value 0.999. Using the Burgers model parameters, Creep compliance, $J(t)$ of the mastic materials is determined from the following Eq. (5):

$$J(t) = \frac{1}{E_1} + \frac{1}{E_2}\left(1 - e^{-\frac{t}{\tau_2}}\right) + \frac{t}{E_1 \tau_1} \tag{5}$$

The Creep compliance plot is shown in Figure 7(b). This is also known as contact creep compliance.

7 FEM MODEL DEVELOPMENT

Two dimensional axisymmetric FEM model is developed with ABAQUS/CAE 6.9-EF. The FEM model is shown in Figure 8. The rectangular block is 5.0 mm wide and 5.1 mm depth with 0.1 mm mastic materials on top of the 5.0 mm thick fine aggregate. The Burgers model is converted into Proney series parameters using the equations mentioned in the literatures [19]. The Poisson's ratio of mastic materials is considered as 0.40. The fine aggregate is considered as elastic materials with Young's modulus 48,264 MPa and Poisson's ratio 0.20 [20]. The indenter is considered as analytic rigid, the bottom of the model is hinged connected, the left side of the model is roller, and the right side is free. The elements are eight noded quadratic plane stress elements. The aspect ratio of the smallest element, under the indenter, is 1.63 and the aspect ratio of the largest element, at the bottom-corner of the model is 1.0. The loading is done similar to the laboratory tests, 25 sec loading, 200 sec hold time, 25 sec unloading. A 0.51 mN concentrated load is applied at the top of indenter tip.

One of the challenges in nanoindentation FEM simulation is to set contact between the indenter and the top of elements. Careful interaction modeling is performed to overcome this challenge. Interaction modeling required assigning master and slave surface and in this model, the indenter is assigned as master surface and top of mastic materials are assigned as slave surface.

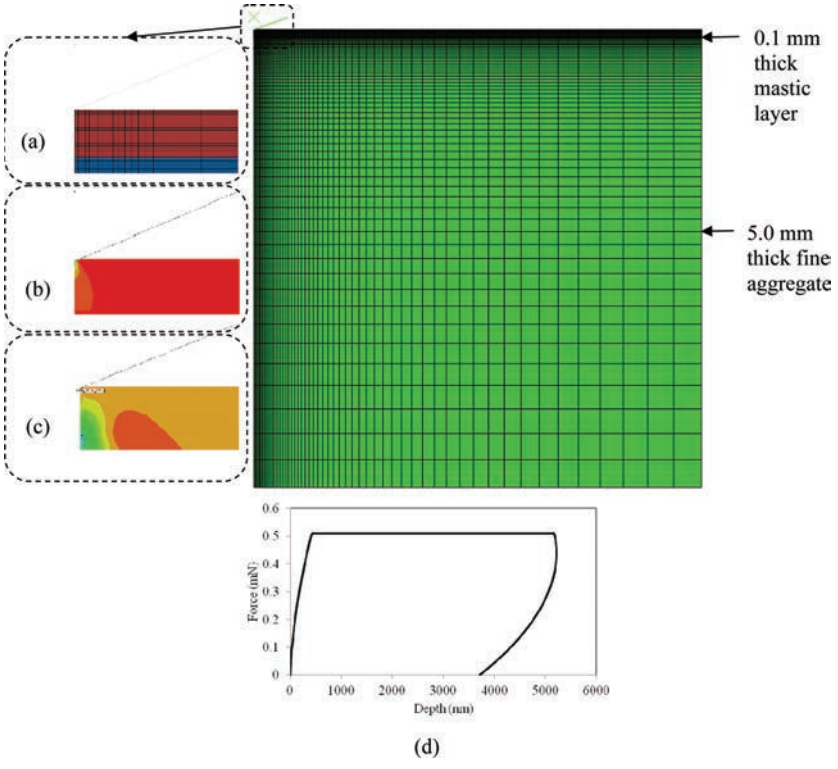

Figure 8. FEM model with (a) zoomed in section on mastic materials, (b) vertical strain distribution in mastic materials, (c) vertical stress distribution in mastic materials (d) force-depth relationship of mastic materials.

Only tangential behavior between master and slave surface is assigned. Contact control and contact initialization is also performed in the FEM simulation. Automatic over closure tolerance is assigned and the initial over closure is treated as interface fits. It should be noted that, deformation control nanoindentation automatically considered all the above mentioned contact properties.

Figure 8(a) shows a zoomed in view of the mastic materials with the indenter, Figure 8(b) shows the vertical strain (*E22*) distribution in mastic materials, and Figure 8(c) shows the vertical stress (*S22*) distribution in mastic materials. The stress and strain distributions are showed only for illustration purpose. Figure 8(d) shows the force-depth relationship of mastic materials measured at the element just under the indenter. The maximum depth measured is 5216.03 nm, which is measured at the end of holding time and before unloading. The maximum depth measured in the forty laboratory indentations is 6392.30 nm and that is 22.55% higher than the simulation results. So the maximum depth measured in the FEM simulation is in between the lowest and highest indentation measured in the laboratory. This validates the Burgers model developed in the previous sections. It should be noted that, Bercovich indenter is conical shape and the FEM model is axi-symmetric and the indenter is assumed as axi-symmetric as well and this assumption might cause some errors in the simulation results. In addition, only one Burgers model is assumed but in reality the mechanical model is a series of Burgers models or a generalized model might gives better results.

8 CONCLUSIONS

Nanoindentation tests are done to understand the contact creep behaviors of mastic materials and with the creep indentation data a Burgers model is developed. In addition, A FEM

model is simulated to validate the Burgers model. It has been observed that, the Force-depth curve acquired from FEM framework showed good agreement with laboratory indentation data. Nanoindentation is a novel approach to test materials and researchers are conducting these tests protocols for decades but this is new to pavement engineering. Though a limited study is done and more studies are required in this emerging field.

REFERENCES

[1] E.A. Ossa, V.S. Deshpande, D. Cebon, Spherical indentation behaviour of bitumen, Acta Materialia, 53(11), pp. 3103–3113. 2005.

[2] C. Schilde, A. Kwade, Measurement of the Micromechanical Properties of Nanostructured Aggregates via Nanoindentation, Journal of Materials Research, 27(4), pp. 672–684. 2012.

[3] R.G. Allen, D.N. Little, A. Bhasin, R.L. Lytton, Identification of the Composite Relaxation Modulus of Asphalt Binder Using AFM Nanoindentation, Journal of Materials in Civil Engineering, ASCE, 25(4), pp. 530–539. 2013.

[4] W.C. Oliver, G.M. Pharr, An Improved Technique for Determining Hardness and Elastic Modulus Using Load and Displacement Sensing Indentation Experiments, Journal of Materials Research, 7(6), pp. 1562–1583. 1992.

[5] R.A. Tarefder, A.M. Zaman, W. Uddin, Determining Hardness and Elastic Modulus of Asphalt by Nanoindentation, International Journal of Geomechanics, ASCE, 10(3), pp. 106–116. 2010.

[6] A. Hodzic, S. Kalyanasundaram, J.K. Kim, A.E. Lowe, Z.H. Stachurski, Application of Nano-Indentation, Nano-Scratch and Single Fibre Tests in Investigation of Interphases in Composite Materials, Micron, 32, pp. 765–775. 2001.

[7] C.A. Schuh, Nanoindentation Studies of Materials, Materialstoday, 9(5), pp. 32–40. 2006.

[8] J. Minster, M. Micka, Numerical Simulation of an Indentation Process for Defining the Viscoelastic Characteristics of Time-Dependent Materials, Journal of Materials Science and Engineering, 2(1), pp. 81–89. 2012.

[9] S.N.V.R.K. Kurapati, Elastic-Plastic Indentation Deformation in Homogeneous and Layerd Materials: Finite Element Analysis, University of Kentucky, 2008.

[10] S. Gupta, F. Carrillo, M. Balooch, L. Pruitt, C. Puttlitz, Simulated Soft Tissue Nanoindentation: A Finite Element Study, Journal of Materials Research, 20(8), pp. 1979–1994, 2011.

[11] Z. Wu, T.A. Baker, T.C. Ovaert, G.L. Niebur, The Effect of Holding Time on Nanoindentation MEasurements of Creep Bone, Journal of Biomechanics, 44(6), pp. 1066–1072. 2012.

[12] Y. Kim, D.N. Little, Linear Viscoelastic Analysis of Asphalt Mastics, Journal of Materials in Civil Engineering, ASCE, 16(2), pp. 122–132. 2004.

[13] N. Kringos, A. Scarpas, A. de Bondt, Determination of Moisture Susceptibility of Mastic-Stone Bond Strength and Comparison to Thermodynamical Properties, Journal of the Association of Asphalt Paving Technologists, 77, pp. 435–478. 2008.

[14] R.A. Tarefder, H. Faisal, Effects of Dwell Time and Loading Rate on the Nanoindentation Behavior of Asphaltic Materials, Journal of Nanomechanics and Micromechanics, ASCE, 3(2), pp. 17–23, 2013.

[15] R. Tarefder, H. Faisal, Nanoindenthation Characterization of Asphalt Concrete Aging, Journal of Nanomechanics and Micromechanics, ASCE, 2013.

[16] V. Sarihan, Energy Based Methodology for Damage and Life Prediction of Solder Joints Under Thermal Cycling, IEEE Transactions on Components, Packaging, and Manufacturing Technology: Part B, 17(4), pp. 626–631. 1994.

[17] R. Goodall, T.W. Clyne, A Critical Appraisal of the Extraction of Creep Parameters from Nanoindentation data Obtained at Room Temperature, Acta Materialia, 54(20), pp. 5489–5499. 2006.

[18] Y.H. Huang, Pavement Analysis and Design, Second Edi, Pearson Prentice Hall, Upper Saddle River, NJ, 2004.

[19] K. Juan, Y. Ju-yun, Application of Linear Viscoelastic Differential Constitutive Equation in ABAQUS, in: International Conference on Computer Design and Applications, IEEE, pp. 152–156. 2010.

[20] R. Roque, C. Koh, Y. Chen, X. Sun, G. Lopp, Introduction of Fracture Resistance to the Design and Evaluation of Open Graded Friction Courses in Florida, Tallahassee, FL, 2009.

Asphalt Pavements – Kim (Ed)
© 2014 Taylor & Francis Group, London, ISBN 978-1-138-02693-3

Uniaxial fatigue testing of diverse asphalt concrete mixtures

Waleed A. Zeiada, B. Shane Underwood & Kamil E. Kaloush
Department of Civil, Environmental and Sustainable Engineering, Arizona State University, Tempe, AZ, USA

ABSTRACT: The uniaxial fatigue test is a useful method for developing constitutive models to describe the fatigue behaviour of asphalt concrete mixture owing to the uniform states of stress across the specimen section. As part of the NCHRP 944-A project, a proposed uniaxial fatigue test protocol and software were developed to assess fatigue damage and healing. In this study, the protocol was used to evaluate a wide range of conventional and modified asphalt mixtures sampled from national and international projects as well as laboratory prepared mixtures with different volumetric properties. The study mixtures included those modified with rubber, polymer, fiber, warm mix additives, and combined rubber and warm mix. The fatigue analysis was performed using the simplified viscoelastic continuum damage (S-VECD) approach where the damage characteristic (C-S) curves were established for each mixture, and then used to obtain the fatigue relationships through simulated predictions. Overall, the proposed uniaxial fatigue test protocol was successfully used with respect to the S-VECD formulation to capture fatigue behaviour of all tested mixtures.

Keywords: Uniaxial, asphalt mixture, fatigue, viscoelastic, continuum damage

1 INTRODUCTION

Fatigue cracking, associated with repetitive traffic loading over time, is considered to be one of the most significant distress modes in flexible pavements besides thermal cracking and rutting. Fatigue cracking is a progressive distress and can be divided into three different stages. An early stage of fatigue cracking consists of intermittent longitudinal wheel path cracks. An intermediate stage of fatigue cracking called alligator cracking because the cracking pattern resembles an alligator's skin. A final stage of fatigue cracking is disintegration when potholes form.

The fatigue life of an asphalt pavement depends directly on the properties of the materials in the mix plus the complicated microstructure of asphalt concrete mixture, which is related to the aggregate size and gradation [1,2], binder grade [3], air voids and binder content [4,5], temperature [6,7], rest period [8,9,10,11], aging [12,13,14], and additives [15,16,17,18,19,20]. As a result, the fatigue properties of asphalt mixtures are very complicated and sometimes difficult to predict.

There are two main approaches that can be utilized to characterize the fatigue behavior of asphalt concrete mixtures: phenomenological and mechanistic. Mechanistic approach is inherently more complex than the Phenomenological one but it is more widely accepted because it uses material properties based on stress-strain relationships [21]. The mechanistic approach can be implemented through three main methods; dissipated energy [22,23,24], fracture mechanics [25,26,27], and continuum damage mechanics [28,29,30,31,32,33,34].

Different test methodologies have been developed over the past few decades for measuring the fatigue behavior of asphalt concrete mixtures such as the beam fatigue test [35,36], cantilever rotating beam test [37], trapezoidal cantilever beam test [38], supported flexure test [39], uniaxial direct-tension test [40,41,42,43], uniaxial tension-compression test [40,44,45], indirect diametrical test [46,47], triaxial test [48,49], and wheel track test [38].

As part of the NCHRP 9-44 A project, a uniaxial fatigue test protocol was developed to evaluate the fatigue damage and healing of asphalt concrete mixtures. The development test protocol includes several studies to identify appropriate sample fabrication procedures, gluing materials and procedures, alignment, machine compliance impacts, strain wave shape, and strain-controlled method [50]. The main objective of this study was to evaluate the fatigue behavior of diverse conventional and modified asphalt concrete mixtures tested by a developed uniaxial fatigue test method using the simplified-viscoelastic continuum damage (S-VECD) analysis. This analysis enables the prediction of the fatigue life relationships under both stain and stress controlled mode of loading with fewer experiments.

2 MIXTURES AND SPECIMENS PREPARATIONS

2.1 *Description of projects and mixtures*

In this study, the fatigue behavior of a diverse set of asphalt concrete mixtures from four main projects was evaluated by performing both dynamic modulus $|E^*|$ test and uniaxial fatigue tests. All the tested specimens were compacted in the laboratory using the Superpave gyratory compactor. Project 1 included the testing of four 19-mm conventional dense graded mixtures at combinations of two levels of air voids (4.5 and 9.5%) and two levels asphalt content (4.2 and 5.2%). The main objective of the first project was to investigate the effect of changing the volumetric properties on the fatigue behavior of asphalt concrete mixtures. Project two included the testing of three 19-mm gap graded Asphalt concrete mixtures. The first mixture was a control while the second and the third were polymer-modified and rubber-modified asphalt concrete mixtures respectively. The main objective of this project was to study the effect of polymer and rubber additives on the fatigue performance of asphalt concrete mixtures. Project three included the testing of two 9.5-mm dense graded mixtures. The first mixture was a standard dense graded mixture while the second mixture was the same mixture, but modified with 19-mm long fibers. The objective of project three was to evaluate the effect of adding fiber on the fatigue performance of asphalt mixtures. Project four included the testing of two asphalt mixtures. The first mixture was a regular 9.5-mm dense graded Warm Mix Asphalt (WMA) mixture using Evotherm additive while the second mixture was a newly used 12.5-mm gap graded rubber-modified WMA mixture. The main objective of this project was to compare the fatigue performance of both mixtures in order to investigate the replacement of the first mixture with the second newly used mixture. The asphalt mixtures of project one were mixed and short term aged in the laboratory while asphalt mixtures for the remaining projects were sampled from actual field projects and then compacted in the laboratory. Table 1 presents the aggregate gradation while Table 2 shows the design volumetric properties of the different mixtures.

Two different specimen geometries were manufactured for each test. For the $|E^*|$ test, gyratory plugs were compacted into 150 mm diameter and 170 mm tall specimens. Then, one 100 mm diameter sample was cored from each gyratory plug. The sample ends were sawn to arrive at typical test specimens of 150 mm in height. For uniaxial tension-compression fatigue test, the compaction height was increased to 180 mm and the final specimen dimensions were 150 mm height and 75 mm in diameter. The main reason to increase the compaction height was to allow for larger end cuts to produce a more homogeneous air void distribution which increases the chances to have a middle failure in the uniaxial fatigue test.

3 TEST METHODS

3.1 *Dynamic modulus test*

The $|E^*|$ tests, per AASHTO T342 were performed in the laboratory at five temperatures –10, 4.4, 21.1, 37.8, 54.4 °C and six load frequencies: 25, 10, 5, 1, 0.5 and 0.1 Hz. The stress levels were varied with the frequency to keep the specimen response within a linear viscoelastic limit

Table 1. Aggregate gradation of tested mixtures.

	% Passing					
	Project 1	Project 2		Project 3	Project 4	
Sieve size mm	19-mm dense graded conventional mixture	19-mm gap graded control and polymer–modified mixtures	19-mm gap graded rubber–modified mixture	9.5-mm dense graded conventional and fiber mixtures	9.5-mm dense graded WMA mixture	12.5-mm gap graded rubber WMA mixture
25.4	100.0			–	–	–
22.4		100	100			
19.0	95.0			–	–	100
16.0		98.0	98.0			
12.5	80.0			100	100	97.0
11.2		65.0	68.0			
9.5	59.0			96.0	95.0	84.0
8.0		38.0	44.0			
4.75	39.0			55.0	59.0	30.0
4.0		23.0	24.0			
2.38	29.0			38.0	45.0	22.0
2.0		21.0	22.0			
1.2	23.0			26.0	27.0	14.0
0.6	17.0			17.0	17.0	9.0
0.3	10.0			9.0	12.0	7.0
0.15	5.0			5.0	8.0	6.0
0.075	3.3			4.1	5.5	5.0
0.063		10.5	7.5			

Table 2. Design volumetric properties of tested mixtures.

Volumetric property	Project 1	Project 2			Project 3	Project 4	
		Control	Polymer	Rubber		WMA	Rubber–WMA
Binder grade	PG64-22	ABS16 70/100	ABS16 50/100-75	GAP16	PG64-22	PG76-22	PG64-22AP
Target asphalt content (%)	4.5	5.9	5.9	8.7	5.9	5.7	8.1
Theoretical max. Sp. Gr. (G_{mm})	2.467	2.464	2.456	2.359	2.397	2.498	2.407
Design air voids (%)	4.1	2.6	2.6	2.4	7.0	4	6

(recoverable microstrain below 150 microstrain). The test parameter values; dynamic modulus and phase angle, were measured at different temperatures and frequencies. The average dynamic modulus and phase angle values were summarized based on three replicates for each mixture. Figure 1 shows a typical instrumented test specimens and the applied wave shape.

3.2 *Uniaxial tension-compression test*

The first step prior to running the test included gluing end plates to the specimen using the jig shown in Figure 2. The applied glue was Devcon plastic steel 5 minutes epoxy putty. The test specimen was then instrumented with three LVDTs to monitor material response. The uniaxial tension-compression fatigue test was conducted to evaluate the fatigue damage of the

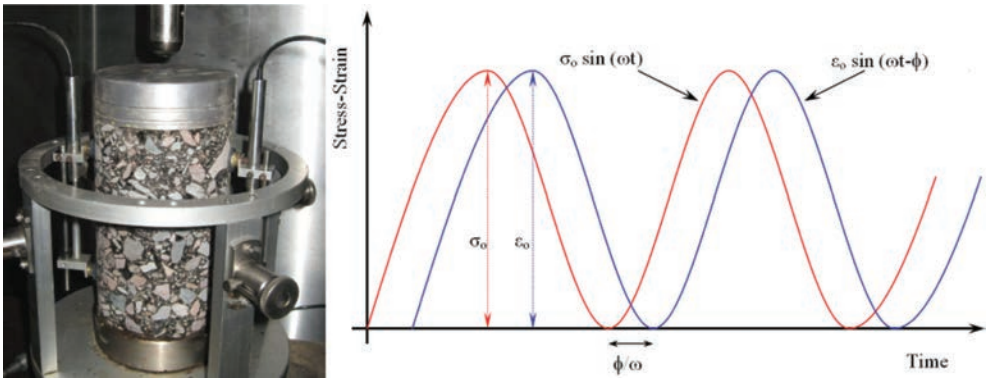

Figure 1. |*E**| Test setup and applied wave shape.

Figure 2. Specimen gluing jig and test setup with failed specimen.

tested mixtures using the viscoelastic and continuum damage model. A servo hydraulic testing machine was used to load the specimens under an on-specimen strain-control mode of loading (Fig. 2). A sinusoidal strain (continuous wave) was applied. The test software was capable of achieving and maintaining the target on-specimen strain based on the outputs from the three LVDTs by dynamically changing the actuator strain level to solve the machine compliance issue. New software was developed for Arizona State University by IPC (Industrial Process Control) company and is designated as UST032-v1.01b S-VECD fatigue test [50]. The uniaxial tension-compression fatigue tests were conducted using two or more specimens for each mixture at 21.1 °C. At each loading cycle, the software calculated the dynamic modulus and the phase angle plus the stress and the strain values from the actuator and the three LVDTs. The uniaxial tension-compression fatigue test was run until a sudden decrease in phase angle is reached as possible.

4 TEST RESULTS

4.1 *Dynamic modulus test results*

The |*E**| master curves were constructed for the tested mixtures from the four projects as shown in Figure 3. It can be observed from Figure 3(a) that the |*E**| values were more significantly

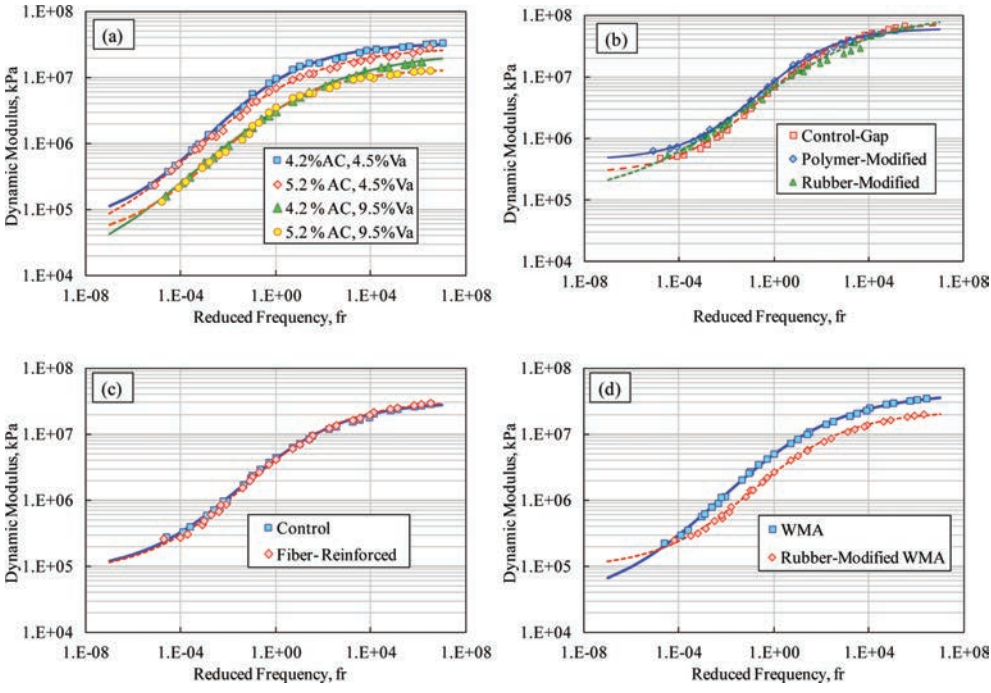

Figure 3. Dynamic modulus master curves of tested mixtures (a) Project 2; (b) Project 2; (c) Project 3; and (d) Project 4.

affected by varying the air voids from 4.5 to 9.5% than by varying the asphalt content from 4.2 to 5.2%. Figure 3(b) shows that at high test temperatures, the polymer-modified mixture expressed the highest stiffness followed by the reference and rubber-modified mixtures. In comparison, at low temperatures, the rubber-modified mixture had the highest stiffness followed by reference and polymer-modified. The rubber-modified mixture exhibited the lowest stiffness compared to the other two mixtures at 21 °C which is the test temperature used for the uniaxial tension-compression test. Figure 3(c) indicates that for the particular mixtures studied, the addition of fiber had almost no effect on the $|E^*|$ values. It can be observed from Figure 3(d) that at lower and intermediate temperatures the rubber-modified WMA mixture exhibits a lower $|E^*|$ values compared to the WMA mixture. However, at high temperatures, the $|E^*|$ values of both mixtures are closer. This unique behavior of rubber-modified mixtures would indicate an enhancement of their performance with respect to thermal and fatigue cracking at lower and intermediate temperatures with a sensible rutting resistance at high temperatures.

4.2 *Uniaxial fatigue test results*

Table 3 includes a summary of the uniaxial tension-compression fatigue tests. It is observed from this table that tensile strain levels were varied within the same project where it was expected that the tested mixture would give totally different fatigue behavior. That judgment was typically based on the relative difference in the dynamic modulus master curves. For only project three, both control and fiber-reinforced mixtures were tested on the same strain level as both exhibit similar dynamic modulus values. This issue does not affect the ability to make comparisons between mixtures as measured data can be interpolated and/or slightly extrapolated to the same conditions. The fingerprint data confirmed the findings from the dynamic modulus tests, which can be seen by observing the $|E^*|_{FP}$ column in Table 3. By comparing results of tests conducted at close strain levels, it can be observed

Table 3. Uniaxial fatigue test results for all mixtures.

Project number	Mixture type	Specimen ID	Air voids %	Tensile strain με	$\|E^*\|_{FP}$ MPa	Machine compliance factor, MCF	Initial stiffness MPa	Initial ϕ degree	Cycles to failure, N_f
Project 1	4.2% AC, 4.5% Va	D-401	3.77	75	7856	5.74	6785.8	29.2	221,168
		D-402	4.72	145	7598	5.29	5868.5	31.3	10,610
		D-490	4.44	90	7711	4.55	6628.7	27.9	67,786
		D-491	4.48	90	7295	4.50	6182.4	26.82	51,160
	5.2% AC, 4.5% Va	D+402	3.46	105	7163	4.80	5812.2	31.2	201,846
		D+404	3.37	175	6371	4.41	4624.1	34.3	28,404
		D+406	3.54	75	6775	4.80	5828.2	32.5	676,100
		D+449	4.79	122.5	6012	4.31	4684.3	33.0	140,182
		D+461	3.94	122.5	6917	4.69	5732.5	28.4	166,602
	4.2% AC, 9.5% Va	D-946	9.22	87.5	4468	3.46	3548.8	29.9	279,692
		D-978	9.45	90	4639	3.45	3842.7	28.2	79,032
		D-983	9.14	90	5301	4.27	3947.2	32.3	26,524
		D-969	9.52	115	3712	2.83	2989.8	28.1	21,892
		D-981	8.73	115	5030	3.58	4020.9	31.5	17,924
		D-984	8.76	115	4970	3.56	3799.4	30.1	57,402
	5.2% AC, 9.5% Va	D+943	9.52	95	3562	2.85	2822.4	31.4	213,804
		D+944	8.92	125	4437	3.57	3330.5	31.2	137,514
		D+948	9.34	200	4228	3.93	2460.6	36.3	2,940
		D+949	9.99	187.5	3465	2.97	2264.3	39.0	9,090
		D+961	9.66	155	4160	3.50	2986.3	34.6	57,402
		D+9B2	9.34	155	3725	2.66	2847	33.5	49,234
Project 2	Control-gap	SWC03	3.65	125	10,978	6.78	8,609	25.3	131,830
		SWC02	3.82	150	10,310	6.45	7,435	28.6	11,030
	Polymer-modified	SWP05	3.55	150	8,479	5.08	6,707	21.8	138,570
		SWP06	3.65	200	8,913	5.43	6,214	24.1	28,620
	Rubber-modified	SWR04	2.81	150	6,710	4.45	5,296	24.9	126,380
		SWR06	3.11	200	7,123	4.63	5,134	25.5	27,200
Project 3	Control	PAC10	5.98	225	6,305	3.39	4,337	28.8	5,710
		PAC11	6.07	225	6,613	4.06	4,888	26.4	10,000
	Fiber-reinforced	PAF08	5.60	225	6,643	4.10	4,592	29.0	74,000
		PAF09	5.51	225	6,084	3.86	4,261	29.2	134,000
Project 4	WMA	PACW03	5.71	175	8,206	4.91	5,730	30.2	250,000
		PACW11	6.42	250	6,708	4.09	4,873	31.2	98,480
	Rubber-WMA	PARW07	6.31	250	3,523	2.46	2,444	32.9	1,800,000[a]
		PARW11	5.74	450	3,915	2.87	1,821	39.6	130,000[b]

[a]Test did not show reduction in phase angle and test was stopped.
[b]450 με was stopped at approximately 130,000 cycles and then strain levels were increased repeatidly until failure.

that the fatigue response asphalt concrete mixtures in project one was not strongly affected by air void content (at a fixed strain level), but did exhibit observable asphalt content effects. In project two, the polymer-modified and rubber modified mixtures showed comparable fatigue performance and were better compared to the control mixture. The results of project three showed the fiber-reinforced mixture exhibits a superior fatigue resistance compared to the control mixture, however the dynamic modulus values for both mixtures were similar. For project four, the new rubber-modified WMA as expected showed an improved fatigue performance compared to the regular WMA mixture. It was also noticed that the rubber-modified WMA mixture tolerated the highest tensile strain levels among all the test mixtures with immense fatigue cycles.

5 DAMAGE CHARACTERISTIC (C-S) CURVE

The construction of C-S curves in this paper followed the most updated procedure to calculate damage parameter, *S* [33]. For each mixture, the C-S curves were established from each test sample. Then a single power model was fitted through the collapsed curves to represent the model C-S curve for the mixture. A more favorable damage characteristic curve is the one that has the greatest damage level for a given pseudo stiffness as it means that the rate of damage growth for a given pseudo energy input will be less and thus the incremental loss in pseudo stiffness will also be less. However, one cannot, or should not, use this curve alone to judge the fatigue resistance of the three mixtures. Figure 4 shows the C-S curves of the mixtures for four projects together. It can be observed from Figure 4(a) that, like the modulus response, the damage characteristic relationship is more strongly affected by the 5% change in air void content than it is by the 1% change in asphalt content. It can be also observed that mixtures with lower air voids and higher binder contents produce favorable damage characteristic curve. Figure 4(b) shows that the most favorably positioned damage characteristic curves are obtained from the reference-gap and polymer-modified mixtures.

It is interesting to observe in Figure 4(c) that both the control and the fiber-reinforced C-S curves are very similar; however, the pseudo stiffness at failure, $C_{failure}$, value for the control is higher compared to the fiber-reinforced mixture. This may imply that the addition of fibers does not appreciably change the internal structure of the mixture compared to other additives as polymer and rubber. What may support this argue is the fact that the fiber has almost no effect on the modulus obtained from either the dynamic modulus test or the uniaxial fatigue test. So, the fiber role is to hold the microcracks which consequently delay the formation of the macrocracks or the fatigue failure. For this particular mixture, microdamage that is affected by the fibers might occur relatively late in the fatigue process, e.g., after a *C* value of approximately 0.4 has been achieved. Figure 4(d) showed as anticipated that the rubber-modified WMA mixture showed a favorable C-S curve compared to WMA mixture.

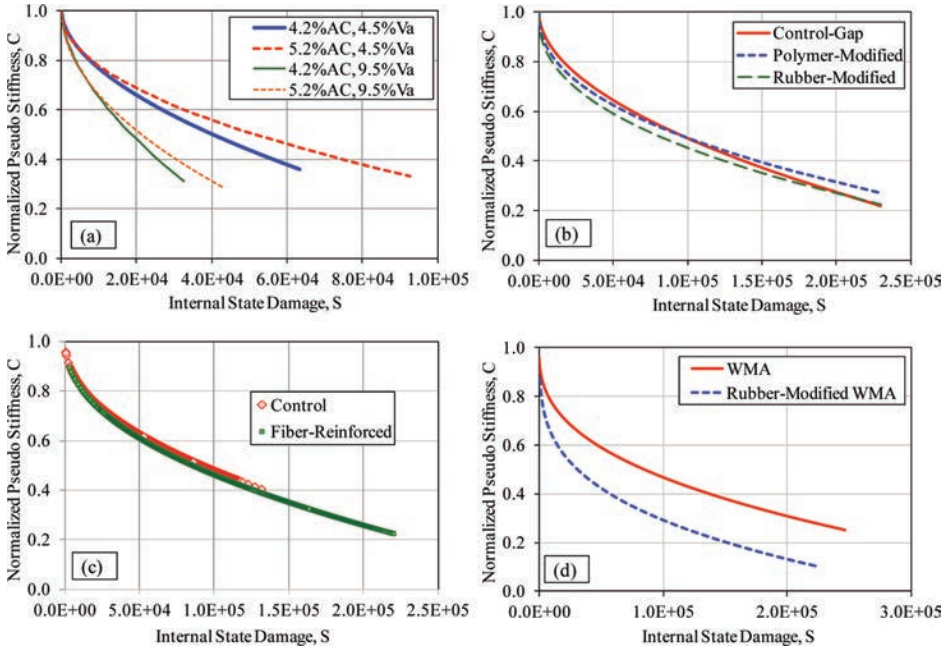

Figure 4. Comparison of damage characteristic curves for study mixtures (a) Project 2; (b) Project 2; (c) Project 3; and (d) Project 4.

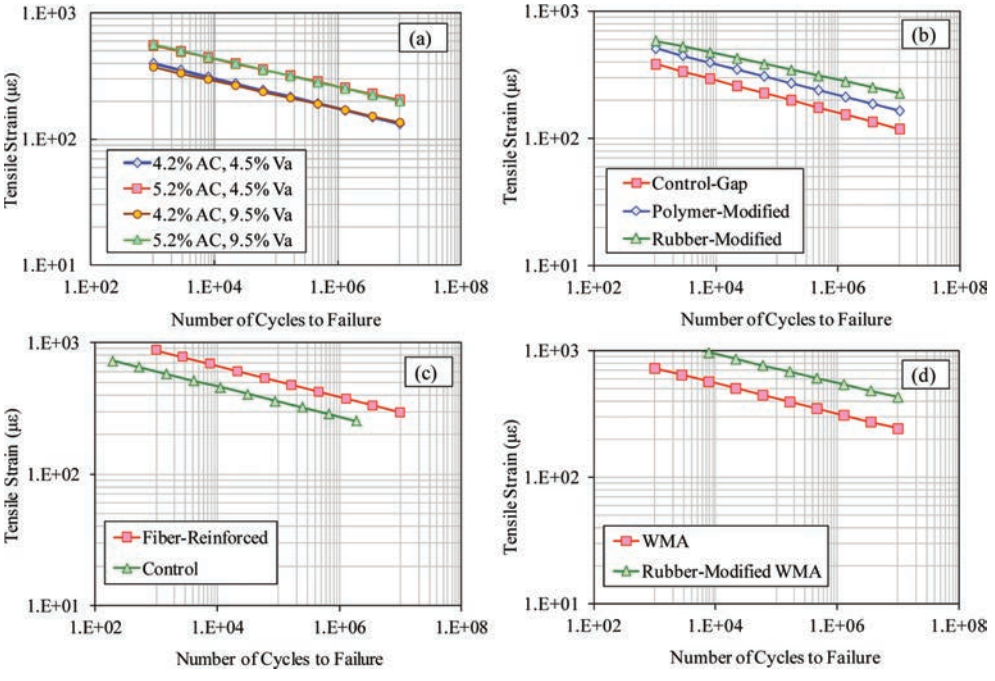

Figure 5. Simulation results for controlled strain test (a) Project 1; (b) Project 2; (c) Project 3; and (d) Project 4.

6 FATIGUE PERFORMANCE SIMULATION

Damage curves alone are not sufficient to judge the fatigue resistance of an asphalt concrete mixture since they only indicate the resistance to damage. Under a given external condition (i.e., load level or deformation magnitude, temperature, frequency of loading, and load shape) the amount of pseudo strain energy created will vary by mixture. Therefore, one must consider the damage curves and the $|E^*|$ of a mixture in order to evaluate its fatigue resistance. The implication of this situation is simply that in order to gain useful information on fatigue performance, one must perform simulated predictions of the fatigue life at specific conditions of interest. In this paper, the Simplified-Viscoelastic Continuum Damage (S-VECD) theory is used to derive formulas for predicting the material response to fully reversed constant stress and constant strain loadings [33]. There formulas were verified using independent laboratory experiments and showed good prediction of fatigue life [51].

In this paper, only the simulation results for the controlled strain condition at 21 °C and 10 Hz frequency are presented as shown in Figure 5. In Figure 5(a), it is seen that there is little overall effect from the 5% air void content change, but a noticeable effect from the 1% change in asphalt binder content. Since the conditions simulated for these figures are very similar to the experiments, this finding is not surprising. It is observed from Figure 5(b) that overall the asphalt rubber mixture is expected to yield a longer laboratory fatigue life. Figure 5(c) showed a superior fatigue resistance for the fiber-reinforced mixture compared to the control mixture however both showed similar modulus values and C-S curve. Figure 5(d) showed that the addition of the rubber to the WMA mixture enhance the fatigue behavior.

7 DISCUSSIONS AND CONCLUSIONS

This paper presented research performed to compare properties and fatigue performance characteristics of diverse asphalt mixtures from laboratory studies and field projects.

The data were used to compare the performance of the mixtures within each project using the Simplified-Viscoelastic Continuum Damage (S-VECD) approach.

Results from project one showed as expected that increases in asphalt content and air voids reduced the modulus of the material. A 5% change in air void content was found to more strongly affect the modulus of the study mixture than a 1% change in asphalt content. Controlled on-specimen strain fatigue tests were also showed that the fatigue performance of the study mixture was more strongly affected by the 1% change in asphalt content than the 5% change in air void. The simulated fatigue behavior predicted in accordance with the viscoelastic continuum damage theory supported the experimental findings for controlled strain loading.

For project two, dynamic modulus test results indicate that, at high test temperatures, the polymer-modified mixture expressed the highest stiffness followed by the reference and rubber-modified mixtures. In comparison, at low temperatures, the rubber-modified mixture had the highest stiffness followed by reference and polymer-modified. The S-VECD analysis clearly showed the benefits of the rubber modified mixture in terms of laboratory fatigue resistance.

It was interesting in project three that both fiber-reinforced and control mixture showed similar modulus and C-S curve, however the fatigue life of the fiber-reinforced mixture was higher compared to the control mixture. That was mainly due to the elongated C-S curve of the fiber-reinforced mixture compared to a shorter damage curve for the control mixture.

For the tested mixture in project four, the rubber-modified WMA mixture showed a tendency to resist cracking and rutting more than the regular WMA by showing lower dynamic modulus at low and intermediate temperature and meantime similar modulus to the WMA mixture at high temperature. Both the uniaxial test result and the S-VECD analysis showed that the rubber-modified WMA expressed much better fatigue resistance compared to the WMA mixture. Overall, the results showed that the rubber-modified WMA mixture is by far the best fatigue resistance mixture followed by the fiber-reinforced mixture.

In conclusion, the S-VECD analysis represents a more powerful tool to evaluate fatigue resistance than the traditional method of examining only the number of cycles necessary to reach a certain stiffness reduction. Such approaches inherently smear the effects of modulus and damage into the analytical result. The rationality of the model with regards to air void content and asphalt content changes as well as the effect of using different additives has been examined in this paper. In addition, these results showed that the developed uniaxial fatigue test method was successfully able to capture the true fatigue behavior of the assorted tested mixtures.

REFERENCES

[1] Abo-Qudais, S., Shatnawi, I. Prediction of Bituminous Mixture Fatigue Life Based on Accumulated Strain, Journal of Construction and Building Materials, vol. 21, pp. 1370–1376, 2007.

[2] Sousa, J.B., Paris, J.C., Prates, M., Barros, R., Langlois, P., and Leclerc, A.M. Effect of Aggregate Gradation on Fatigue Life of Asphalt Concrete Mixes, In Transportation Research record 1630, TRB, National Research Council, Washington, DC, 1998.

[3] Carpenter S.H, and Shen S. Dissipated energy approach to study hot-mix asphalt healing in fatigue. In Transportation Research record, National Research Council, Washington, DC, pp. 178–185, 2006.

[4] Harvey, J., Bor-Wen Tsai. Effect of Asphalt Content and Air Void Content on Mix Fatigue and Stiffness, Transportation Research Record No: 1543, Washington, D.C. pp. 38–45, 1996.

[5] Tayebali, A.A., Rowe, G.M., and Sousa, J.B. Fatigue Response of Asphalt Aggregate Mixtures, Journal of the Association of Asphalt Paving Technologists (AAPT) vol. 61, pp. 333–360, 1994.

[6] Nejad, F.M., Aflaki, E., and Mohammadi, M.A. Fatigue Behavior of SMA and HMA Mixtures, Journal of Construction and Building Materials, vol. 24: pp. 1158–1165, 2010.

[7] Verstraeten, J., Romain, J.E., and Veverka, V. The Belgian Road Research Center's Overall Approach Structural Design, Proceedings of Fourth International Conference Structural Design of Asphalt Pavements, Ann Arbor Michigan, U.S.A., Mallory Lithographing Inc./AnnArbor/vol.1, pp. 298–324, 1977.

[8] Raithby, K.D, and Sterling, A.B. The Effect of Rest Periods on the Fatigue Performance of a Hot-Rolled Asphalt under Reversed Axial Loading, Proceedings, the Association of Asphalt Paving Technologists (AAPT), vol. 39, pp. 134–52, 1970.

[9] Bonnaure, F., Huibbers, A.H.J.J., and Booders, A. A Laboratory Investigation of the Influence of Rest Periods on Fatigue Characteristics of Bituminous Mixes, Proceedings, the Association of Asphalt Paving Technologists (AAPT), vol. 51, pp. 104, 1982.
[10] Zeiada, W.A., Souliman, M.I., Kaloush, K.E., Mamlouk M.S., and Underwood, S.B. Comparison of Fatigue Damage, Healing, and Endurance Limit using Beam and Uniaxial Fatigue Tests, Submitted to the 93rd Annual Transportation Research Board Meeting, Washington, D.C., 2014. (under review 2013).
[11] Underwood, S.B., and Zeiada, W.A. Modeling Micro-damage Healing in Asphalt Concrete with a Smeared Continuum Damage Approach, Submitted to the 93rd Annual Transportation Research Board Meeting, Washington, D.C., 2014. (under review 2013).
[12] Raad L., Saboundjian S., and Minassian G., Field Aging Effects on Fatigue of Asphalt Concrete and Asphalt-Rubber Concrete, Transportation Research Record, No. 1767, Transportation Research Board, Washington, D.C., 2001.
[13] Molenaar, A.A.A., Hagos, E.T., and Van de Ven, M.F.C. Effects of Aging on the Mechanical Characteristics of Bituminous Binders in PAC, Journal of Materials in Civil Engineering, vol. 22(8), pp. 779–787, 2010.
[14] Koohi, Y., Lawrence, J.J., Luo, R., and Lytton, R.L. Complex Stiffness Gradient Estimation of Field-Aged Asphalt Concrete Layers Using the Direct Tension Test, Journal of Materials in Civil Engineering, vol. 24(7), pp. 832–841, 2011.
[15] Little, D.N. An Evaluation of Asphalt Additives to Reduce Permanent Deformation and Cracking in Asphalt Pavements: A Brief Synopsis of on-Going Research, In Association of Asphalt Paving Technologists Proceedings (AAPT), vol. 55. 1986.
[16] Kaloush, K.E., Biligiri, K.P., Zeiada, W.A., Rodezno, M., and Reed, J. Evaluation of Fiber-Reinforced Asphalt Mixtures Using Advanced Material Characterization Tests, Journal of Testing and Evaluation, ASTM International, vol. 38(4), pp. 400–411, 2010.
[17] Yan, J., Ni, F., Yang, M., and Li, J. An Experimental Study on Fatigue Properties of Emulsion and Foam Cold Recycled Mixes, Journal of Construction and Building Materials, vol. 24(11), pp. 2151–2156, 2010.
[18] Xiao, F., Wenbin Zhao, P.E., and Amirkhanian, S.N. Fatigue Behavior of Rubberized Asphalt Concrete Mixtures Containing Warm Asphalt Additives, Journal of Construction and Building Materials, vol. 23(10), pp. 3144–3151, 2009.
[19] Muniandy, R., and Huat, B.B. Laboratory Diameteral Fatigue Performance of Stone Matrix Asphalt with Cellulose Oil Palm Fiber, American Journal of Applied Sciences, vol. 3(9), 2005.
[20] Khattak, M.J., & Baladi, G.Y. Engineering Properties of Polymer-Modified Asphalt Mixtures. Transportation Research Record 1638, Journal of the Transportation Research Board, Washington D.C., vol. 1, pp. 12–22, 1998.
[21] Kim, Y.R., Little, D.N., and Lytton, R.L. Fatigue and healing characterization of asphalt mixtures, Journal of Materials in Civil Engineering, ASCE, Vol. 15, No. 1, pp. 75–83, 2003.
[22] Carpenter, S.H., and Shen, S. Application of the Dissipated Energy Concept in Fatigue Endurance Limit Testing, Transportation Research Record 1929, Transportation Research Board of National Academies, pp. 165–173, 2005.
[23] Ghuzlan, K., and Carpenter, S.H. An Energy-Derived/Damage-Based Failure Criteria for Fatigue Testing, Transportation Research Record 1723, Transportation Research Board of the National Academies, pp. 131–141, 2000.
[24] Shen, S. and Carpenter, S.H. Development of an Asphalt Fatigue Model Based on Energy Principles, Proceedings of The Association of Asphalt Paving Technologists (AAPT), vol. 76, pp. 525–574, 2007.
[25] Majidzadeh, K., Kauffmann, E.M., and Saraf, C.L., Analysis of Fatigue of Paving Mixtures from the Fracture Mechanics Viewpoint, Fatigue of Compacted Bituminous Aggregate Mixtures, ASTM STP, 508, pp. 67–84, 1972.
[26] Jacobs, M.M.J., Hopman, P.C., and Molenaar, A.A.A. Application of Fracture mechanics Principles to Analyze in Asphalt Concrete, Journal of the Association of Asphalt Paving Technologists (AAPT), vol. pp. 1–39, 1996.
[27] Roque, R., Birgisson, B., Sangpetngam, B., and Zhang, Z. Hot Mix Asphalt Fracture Mechanics: A Fundamental Crack Growth Law for Asphalt Mixtures, Journal of the Association of Asphalt Paving Technologists (AAPT), vol. 71, pp. 816–827, 2002.
[28] Schapery, R.A. A Theory of Mechanical Behavior of Elastic Media with Growing Damage and Other Changes in Structure, Journal of Mechanics and Physics of Solids, vol. 38, pp. 215–253, 1990.
[29] Park, S.W., Kim, Y.R., and Schapery, R.A. A viscoelastic Continuum Damage Model and Its Application to Uniaxial Behavior of Asphalt Concrete, Mechanics of Materials, vol. 24, pp. 241–255, 1996.

[30] Kim, Y.R. Lee, H.J., and Little, D. Fatigue Characterization of Asphalt Concrete Using Viscoelasticity and Continuum Damage Theory, Journal of the Association of Asphalt Paving Technologists, vol. 66, pp. 520–558, 1997.
[31] Lee, H-J., and Kim, Y.R. Viscoelastic Constitutive Model for Asphalt Concrete under Cyclic Loading, Journal of Engineering Mechanics, vol. 124(1), pp. 32–40, 1998.
[32] Kutay, M.E., Gibson, N., and Youtcheff, J. Conventional and Viscoelastic Continuum Damage (VECD)-Based Fatigue Analysis of Polymer Modified Asphalt Pavements, Journal of the Association of Asphalt Paving Technologists, vol. 77, pp. 395–434, 2008.
[33] Underwood, B.S. Kim, Y.R., and Guddati, M.N. Improved Calculation Method of Damage Parameter in Viscoelastic Continuum Damage Model, International Journal of Pavement Engineering, vol. 11(6), pp. 459–476, 2010.
[34] Underwood, B.S., Baek, C.M., and Kim, Y.R. Use of Simplified Viscoelastic Continuum Damage Model as an Asphalt Concrete Fatigue Analysis Platform. Transportation Research Record, Journal of the Transportation Research Board, vol. 4, pp. 36–45, 2012.
[35] Tayebali, A.A., Coplantz, J.S., Harvey, J.T., and Monismith, C.L. Interim Report on Fatigue Response of Asphalt-Aggregate Mixtures, SHRP project A-003A, TM-UCB-A-003A-92–1, Asphalt Research Program, Institute of Transportation Studies, University of California-Berkeley, Berkeley, CA, 1992.
[36] Tayebali, A.A., Rowe, G.M. and Sousa, J.B. Fatigue Response of Asphalt-Aggregate Mixtures, Journal of the Association of Asphalt Paving Technologists (AAPT), Vol. 61, pp. 333–360, 1992.
[37] Pell, P.S. and Hanson, J.M. Behavior of Bituminous Road Base Materials under Repeated Loading, Proceedings of Association of Asphalt Paving Technologists (AAPT), pp. 201–229, 1973.
[38] Van Dijk, W. Practical Fatigue Characterization of Bituminous Mixes, Proceedings, Journal of the Association of Asphalt Paving Technologists (AAPT), Vol. 44, p. 38, Phoenix, Arizona, 1975.
[39] Majidzadeh, K., Kauffmann, E.M., and Ramsamooj, D.V. Application of Fracture Mechanics in the Analysis of Pavement Fatigue, Journal of Association of Asphalt Paving Technologists (AAPT), pp. 227–246, 1971.
[40] Raithby, K.D. and Ramshaw, J.T. Effect of Secondary Compaction on the Fatigue Performance of a Hot-Rolled Asphalt, Transportation and Road Research Laboratory TRRL-LR 471, Crowthorne, England, 1972.
[41] Bolzan, P., Huber, G. Direct Tension Test Experiments, SHRP-A-661. Washington DC: Strategic Highway Research Program, 1993.
[42] Daniel, J.S., and Kim, Y.R. Development of a Simplified Fatigue Test and Analysis Procedure Using a Viscoelastic, Continuum Damage Model, Journal of the Association of Asphalt Paving Technologists, vol. 71, pp. 619–650, 2002.
[43] Erkens, S.M.J.G and Poot, M.R. The Uniaxial Tension Test—Asphalt Concrete Response (ACRe), Delft University of Technology Report 7–01–117–7, 2001.
[44] Soltani, A., and Anderson, D.A. New Test Protocol to Measure Fatigue Damage in Asphalt Mixtures, Journal of Road Materials and Pavement Design, vol. 6, pp. 485–514, 2005.
[45] Christensen, D.W., and Bonaquist, R.F. Analysis of HMA Fatigue Data Using the Concepts of Reduced Loading Cycles and Endurance Limit, Journal of the Associations of Asphalt Paving Technologists (AAPT), vol. 78, pp. 377–416, 2009.
[46] Roque, R. & Buttlar, W.G. The development of a measurement and analysis system to accurately determine asphalt concrete properties using the indirect tensile mode, Journal of the Association of Asphalt Paving Technologists (AAPT), vol. 61, 304–333, 1992.
[47] Navarro, D. and Kennedy, T.W. Fatigue and Repeated-Load Elastic Characteristics of In-service Asphalt-Treated Pavement, Research Report No.183–2, Center for Highway Research, the University of Texas at Austin, Austin, TX, 1975.
[48] Pell, P.S. and Cooper, K.E. The Effect of Testing and Mix Variables on The Fatigue Performance of Bituminous Materials, Journal of the Association of Asphalt Paving Technologists (AAPT), Vol. 44, pp. 1–37, 1975.
[49] Sousa, J.B. Dynamic Properties of Pavement Materials, Ph.D. Thesis, University of California, Berkeley, CA, 1986.
[50] Zeiada, W.A. Endurance Limit for HMA based on Healing Phenomenon Using Viscoelastic Continuum Damage Analysis, Doctoral Dissertation, Arizona State University, Tempe, AZ, United States, 2012.
[51] Underwood, B.S., Kim, Y.R., and Guddati, M.N. Characterization and Performance Prediction of ALF Mixtures Using a Viscoelastoplastic Continuum Damage Model, Journal of the Association of Asphalt Paving Technologists (AAPT), vol. 75, pp. 577–636, 2006.

This page intentionally left blank

Asphalt Pavements – Kim (Ed)

Quantitative nanomechanical property mapping of bitumen micro-phases by peak-force Atomic Force Microscopy

S.N. Nahar & A.J.M. Schmets
Road Engineering, Faculty of Civil Engineering and Geosciences, Delft University of Technology, Delft, The Netherlands

G. Schitter
Automation and Control Institute (ACIN), Vienna University of Technology, Vienna, Austria

A. Scarpas
Road Engineering, Faculty of Civil Engineering and Geosciences, Delft University of Technology, Delft, The Netherlands

ABSTRACT: It is commonly assumed that the two-phase morphology of bituminous materials at the micrometer length scale is the origin for the material's mechanical response at larger length scales. Usually this morphology, or microstructure, is observed by using Atomic Force Microscopy (AFM), providing height and phase maps of the material's surface. The aim of this work is to quantify the nanomechanical properties of the phases that constitute the microstructure of bitumen, using Peak-Force Tapping mode AFM. The mechanical properties, i.e. modulus, probe-sample adhesion force, dissipated energy and deformation are measured for four well defined bitumen grades from the SHRP library. It is found that the measured mechanical property maps possess similar morphological characteristics as the height and phase images from traditional AFM, i.e. they overlap. For all phases of the four bitumen the averaged mechanical properties could be obtained. After proper averaging, these properties could be compared between the four bitumen grades and with their documented macroscale properties. Such correlations were found to exits, but also anomalies have been found. These anomalies may originate from a different viscoelastic response of the material phases at the experimental loading rate of 2 kHz, while traditional mechanical tests are performed at much lower frequencies. Thus, a systematic study of the nanomechanical properties is presented, with promising results that shall enable a better understanding of the link between micro and macro-scale properties of bituminous materials.

Keywords: bitumen, nanomechanical properties, Peak Force AFM, Derjaguin–Muller–Toporov model

1 INTRODUCTION

Bituminous materials are known to be composed of a large range of dissimilar organic molecules. Upon solidification of the material from the melt, these molecules tend to locally order, or phase separate, giving rise to the material's microstructure. This microstructure has been characterized by Atomic Force Microscopy (AFM) [1–4]. The microstructural details are found to depend on the origin of the raw material and its thermodynamic history. Most bituminous binders are found to exhibit a two phase microstructural morphology, where domains of different sizes are dispersed throughout a matrix phase [2, 3, 5].

Phase images originating from one of the dynamic AFM imaging modes, tapping mode AFM, provide only qualitative evidence of the difference of mechanical properties between the domains and the continuous phase [2–5]. The mechanical property contrast observed in a

phase image is the cumulative contribution of all different mechanical responses like modulus, adhesion, deformation and energy dissipation. Therefore, it is very difficult to obtain micro scale mechanical properties from AFM phase images alone.

Usually the nanoindentation technique is used to characterize the viscoelastic properties of time dependent materials like bitumen at the nano to micro scale [6–8]. For example, the mechanical response of bitumen at the microstructural level was first studied using the grid indentation technique by Jaeger et al. [9]. However, this technique had several disadvantages such as its relatively poor spatial resolution (order of 5 μm). At this resolution it is impossible to obtain the separate mechanical properties of the various phases that have been identified by AFM, as these phases are typically found to be in the range of 1–10 μm.

With AFM, a spatial resolution of several nanometers is easily obtained. Employing a recently invented imaging mode of AFM (Peak Force QNM), quantitative mechanical property mapping of bituminous binders with nanoscale spatial resolution has become possible, e.g. Fischer et al. [10].

In the present work we focus on the identification of nanomechanical properties by utilizing the Peak Force AFM mode on four Strategic Highway Research Program (SHRP) bitumen: AAC, AAA, AAG and AAK. These four bitumen grades are known to possess rather distinct microstructure morphologies [3]. Meanwhile their macroscopic mechanical properties as well as chemical composition [11] are rather different. This suggests that the macroscopic mechanical properties of bitumen originate from the microstructural length scale. In order to establish the link between the microstructure of a bitumen and its macro-mechanical behaviour and performance, the first step is to quantify the mechanical properties of the various material phases observed. As mentioned before, some authors already reported some nanomechanical data for bitumen, though issues like repeatability, consistency and robustness of these data are yet not firmly established. Then these nanomechanical data are correlated with the well-established properties of these binders. If a correlation between these sets of data exists, it would allow for appraising the properties of bituminous binders by modification of its microstructure. This can be achieved by tailored processing conditions, application of additives etc.

2 MATERIALS AND METHODS

2.1 *Materials*

Four different bituminous binders were selected from the Materials Reference Library of the Strategic Highway Research Program (SHRP): AAC-1, AAA-1, AAG-1 and AAK-1. The binders were imaged and mechanically mapped using the Peak Force QNM mode of AFM. The materials were selected on the basis of their compositional and mechanical differences, which would ease the identification of possible correlations with nanomechanical properties. The characteristics of the selected bitumen are presented in Table 1.

2.2 *Sample preparation*

The samples were prepared by applying 20 mg of bitumen sample to the AFM sample substrate (steel sample disks with a diameter of 12 mm) with a spatula. And the specimens were

Table 1. Properties of SHRP bitumen [11].

Sample	Penetration in 1/10 mm units (25°C, 100 g, 5s)	Softening point (R & B) (°C)	Viscosity (at 60°C) (Pa·s)	Asphaltene (%)	Wax (%)
AAC-1	133	42.8	41.9	10.1	5.06
AAA-1	160	44.4	86.4	16.2	1.62
AAG-1	53	48.9	186.2	5.0	1.13
AAK-1	70	49.4	325.6	20.1	1.17

subsequently heated on a hot plate of 100°C for 30 seconds in order to create a thin flat film with thickness of 200–300 μm. Then the specimens were thermally conditioned inside an oven at 100°C for 60 minutes followed by cooling under ambient conditions. The specimens were later kept inside petri dishes to avoid any ambient particle pick-up, and stored at room temperature before AFM imaging.

2.3 *Peak-force QNM mode of AFM*

Peak Force QNM uses the Peak Force Tapping mode as principle of operation. In this scanning mode the probe is indirectly modulated by driving the AFM cantilever through a piezo-element in a sinusoidal waveform of 2 kHz and at an amplitude of 150 nm. This motion generates instantaneous force-distance curves each time the cantilever taps on the sample. The peak interaction force value of the force-distance curves is used as the imaging feedback parameter. The tip trajectory over time during a tapping cycle is portrayed in Figure 1. In Figure 1(a), the path 1-2-3 represents the approach part and 3-4-5 is the retract part of a single tapping cycle. At position 1, the tip is far from the sample surface. The probe then approaches the sample and experiences attractive forces until the contact point at 2 has been reached, and then slightly deforms the sample at 3. While going through the retract part, the probe is pulled off while the sample holds the probe momentarily with an adhesion force (at 4). Later the probe recovers back to its original position [12–15].

The force versus time curve is shown in Figure 1(b) which illustrates the Peak Force Tapping operation and the tip trajectory (note that the tip trajectory is in time versus tip location). By using the calibrated scanner settings, the system converts the force-time curve, Figure 1(b), into the force-distance curve as shown in Figure 1(c). These force-distance curves are comparable to the load versus penetration curves that are common in the context of nanoindentation studies. The analysis of the recorded data is done simultaneously by fitting with models from contact mechanics, resulting in a map of mechanical properties like elastic modulus, tip-sample adhesion, energy dissipation, and maximum deformation of the material.

2.4 *Instrumental settings and measuring environment*

The Dimension Icon Atomic Force Microscope from Bruker was used for Peak Force QNM imaging of the selected bitumen samples. RFESPA silicon AFM cantilevers (Bruker) were

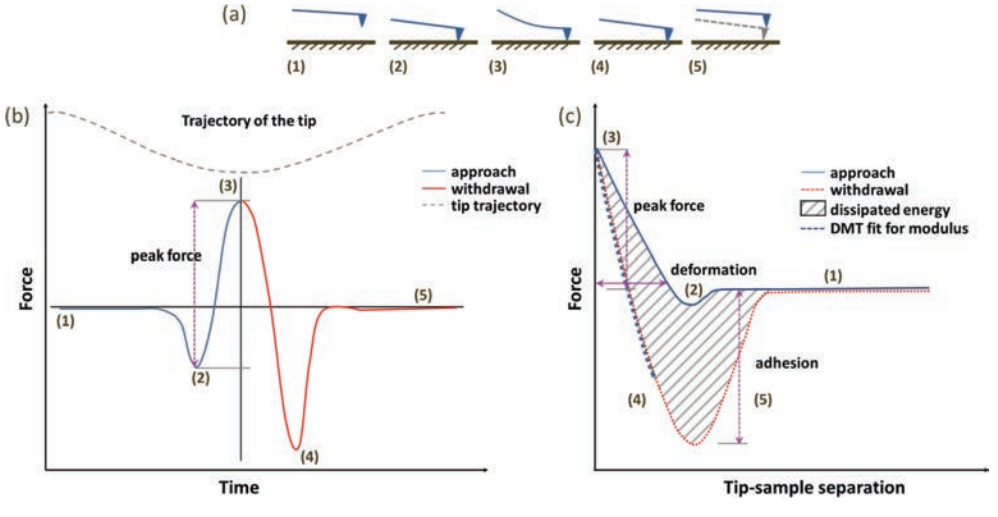

Figure 1. (a) Approach and withdrawal of the AFM-tip in a single tapping cycle (b) principle of Peak Force Tapping operation with the tip trajectory (c) schematic of force-distance curve obtained at each tapping cycle with the peak force as controlling parameter.

used as probe. These probes have a nominal resonance frequency of 75 kHz and a nominal spring constant of 3 N/m. The tip heights of these probes are in the range of 15–20 μm and have a nominal tip radius of 8 nm. The linear scanning rate was set to 1 Hz (1 line/s) and the mechanical mapping of the material was carried out at 30×15 μm^2 scan size with a pixel resolution of 512×256. The applied peak force was kept to 8 nN, leading to minimal and almost elastic deformation of the sample, which was iteratively found to be the best setting for optimal mechanical property mapping. The cantilever material is antimony (n) doped silicon which has a 40 ± 10 nm aluminium reflective coating on its backside. The nominal cantilever dimensions were $225 \times 35 \times 3$ μm. All the measurements were performed using the Peak Force QNM mode in air at ambient temperature (22°C).

The system was calibrated following the relative calibration method. The probe was selected and calibrated before every measurement series. The deflection sensitivity of the cantilever was measured by acquiring a force curve on a silicon wafer substrate. The spring constant was measured 2.8 N/m, using the 'thermal-tune' method. A reference sample of known modulus was used to measure the tip radius. The reference sample was imaged in Peak Force QNM mode and the tip radius was obtained by fitting with contact mechanics models until the known modulus value of the reference sample was obtained. This tip radius was later used in further fitting cycles.

As the applied force on the sample was very small (8 nN), the tip-sample contact geometry can be approximated by a hard sphere in contact with an elastic plane. Thus, the Derjaguin-Muller-Toporov (DMT) model from contact mechanics was used for real-time curve fitting to obtain the local value of the elastic modulus of the bitumen [12, 15, 16], Figure 1(c). Another mechanical property attained in the mapping is the adhesion force, illustrated by the minimum force in Figure 1(c). The origin of this force can be any attractive force between the tip and the sample. As the measurements were performed in air, Van der Waals forces, electrostatic forces, and forces resulting from a capillary meniscus between sample and AFM-tip, contribute to the adhesion force. The maximum deformation is defined as the penetration of the tip into the surface at the peak force. This property is calculated from the difference in separation from the point where the force is zero and the peak force point along the approach curve, Figure 1(c), and 70% of this value is recorded in the real-time mapping. The finally, the dissipated energy per tapping cycle is obtained by integrating the area between the approach and retract curves.

For the offline analysis of the AFM images the software package Gwyddion [17] was used. Offline analysis of the data was performed to obtain the statistical and spatial distribution of the measured mechanical properties at different regions of the imaged bitumen surface.

3 EXPERIMENTAL RESULTS AND DISCUSSION

The microstructural morphology along with the mechanical properties of thin film bituminous binders was obtained by Peak Force QNM mode AFM for specimens prepared according to the procedures described before. The mechanical properties of the bituminous binder's surface are obtained by analyzing the force curves in real-time. In the context of this research five different mechanical properties have been measured simultaneously: a) topography, which reveals the surface topography (height) of the bitumen sample, b) DMT modulus, which provides the local elastic modulus value of the material as derived from fitting with the DMT model, c) deformation, the maximum deformation occurring from the penetration of the tip into the surface at peak force, d) adhesion and e) the dissipated energy per cycle, obtained from the area enclosed by the loading and unloading curves.

In the following, first the complete set of measured local mechanical properties of a single binder, AAC, is presented and its qualitative features are discussed. Subsequently, the properties of the other binders are presented in a comparative setting. Finally, it is shown how overall consistent mechanical properties can be derived from the data, and how these relate to other microstructural and macro-mechanical properties.

3.1 *Morphology and mechanical properties of SHRP bitumen AAC*

The microstructure of the binder AAC, as presented in the height or topography image in Figure 2(a), displays the typical two phase features as observed by many other authors [2, 3, 9]. The microstructure is characterized by the presence of phase consisting of elongated, almost elliptical, domains. The size of these domains range from 3 to 8 μm along the long axes, along which also the typical undulating or wrinkling pattern is observed [2, 3, 5]. The domains are found to be dispersed in a continuous or matrix phase.

From the DMT modulus data channel, Figure 2(b), it is observed that the local modulus values vary over the scanned area, and these variations do show a similar pattern as observed in the height image, though not very pronounced in the case of AAC. Comparing Figures 2(a) and 2(b) one finds that the domains possess higher local modulus values than the surrounding matrix phase. This is consistent with the deformation results, Figure 2(c). The domains, possessing lower moduli, are expected to deform less than the matrix phase, which is also observed. One should note here that (elastic) modulus is a material property, while stiffness is defined as the resistance to deformation of a structure. As in the present experiment *local* mechanical properties, each pixel represents a 50×50 nm area, are probed, there is essentially no difference between stiffness and modulus. The local stiffness varies from 300 MPa to 800 MPa. At the centre of the domains the modulus is highest, and then gradually decreases towards the continuous phase. From the modulus point of view interfaces between the two phases are rather diffuse.

The adhesion and dissipated energy maps are shown in Figures 2(d) and 2(e). Here the interfaces are much sharper. For both, adhesion and dissipated energy, the domains display lower values than the matrix. The dissipated energy and adhesion data show similar trends. Therefore, for the other samples only the adhesion data will be presented.

3.2 *Morphology and mechanical properties of SHRP bitumen AAA, AAG, AAK*

Two phase morphology is also observed for the binders AAA and AAK, Figures 3(a) and 3(c). The size of the domains in AAA range from 0.3 to 3 μm and their shapes tend towards cir-

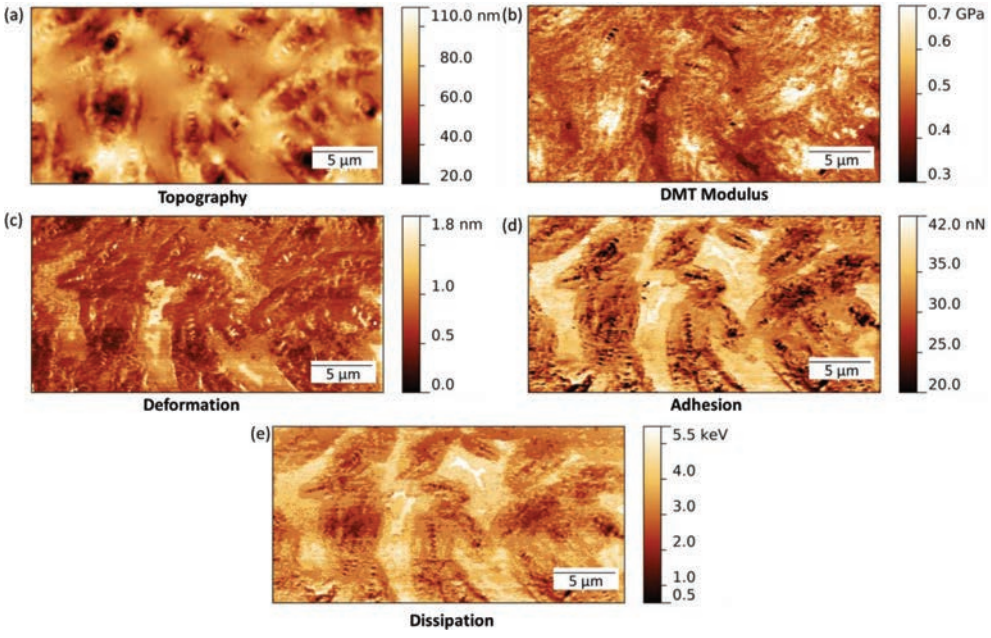

Figure 2. Quantitative nanomechanical property maps of SHRP bitumen AAC. 30×15 μm^2 Map of (a) Topography, (b) DMT modulus, i.e. the stiffness, (c) Deformation, (d) Adhesion and (e) Dissipation.

cular. The local mechanical properties of AAA, Figure 3(aii–iv), show that here the domains possess the lower modulus (~130 MPa and ~170 MPa), and that the material is overall softer than AAC. The domains are also found to be somewhat protruded from the matrix. Comparing this with the findings from AAC, suggests that the protruded phase is always the softer or lower modulus material. Surprisingly, the deformation of the softer domains is found to be lower than the deformation of the continuous phase. This may be explained by differences

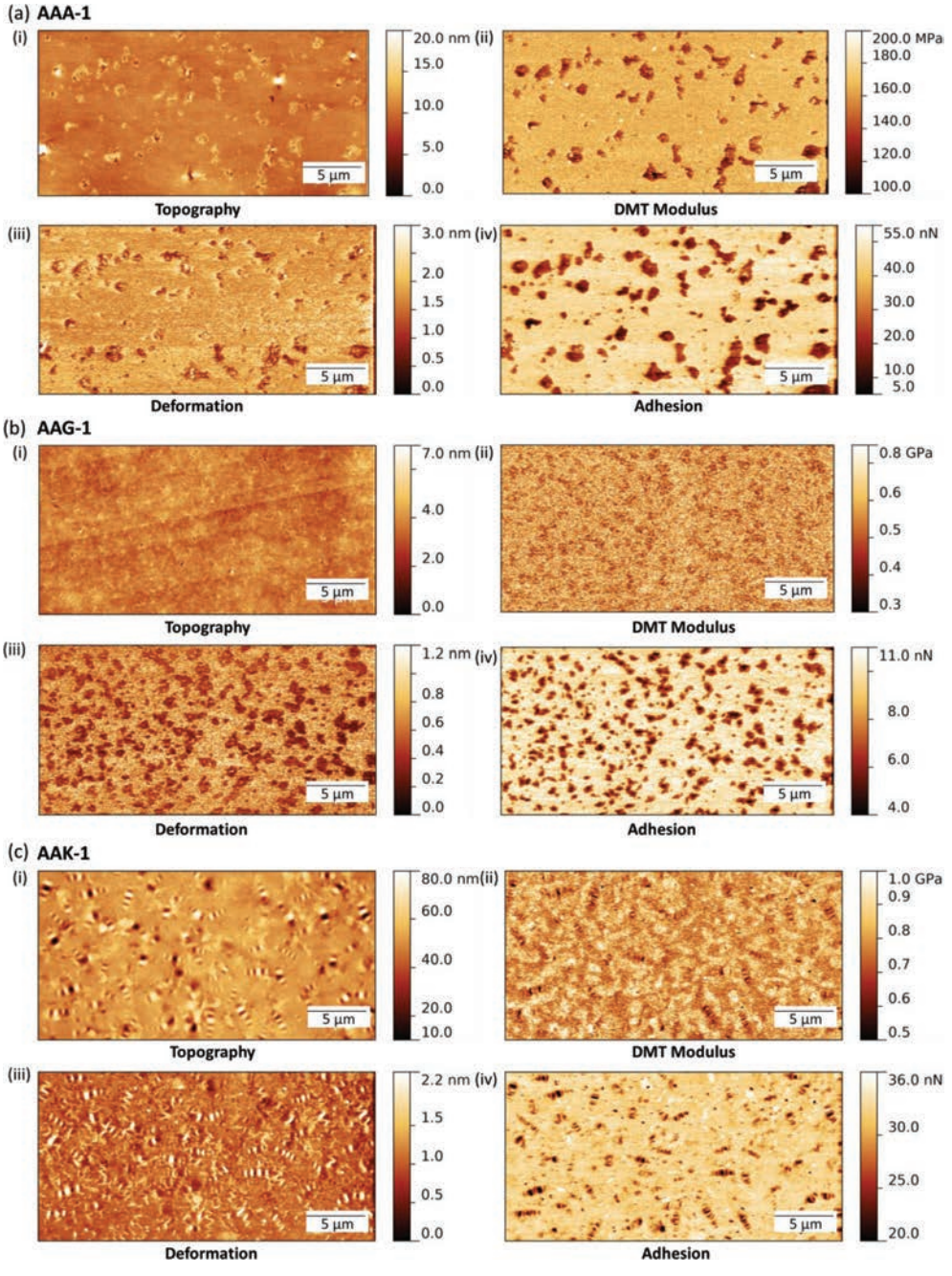

Figure 3. Quantitative nanomechanical property maps of (a) AAA-1, (b) AAG-1 and (c) AAK-1. 30×15 µm^2 maps of (i) Topography, (ii) DMT modulus, (iii) Deformation and (iv) Adhesion.

in viscoelastic properties of both phases. The QNM technique loads the material locally at a rate of 2 kHz, while viscoelastic response is known to be strongly frequency dependent. Finally, for AAA the domains are found to be the regions of lowest adhesion.

The topography image of the binder AAG, Figure 3(b), shows that the surface of this binder is extremely flat, with a z-range up to only 7 nm. From the height image alone, biphasic morphology is not apparent. Though, the mechanical property data presented in Figure 3(b) to 3 (e), the existence of two phases is obvious. The modulus data show structuring of regions with lower modulus (~500 MPa), sized from 0.2 to 1 µm. The modulus of the matrix phase is found to higher (~620 MPa). The 2-phase character is most apparent from the adhesion and deformation images. Both properties are found to be lowest for the domains. The contrast between phases in the latter images is much sharper than for the topography and modulus images.

The last bitumen selected for this study, AAK, is characterized by a dominant occurrence of the closely packed domains, which cover almost 90% of the scanned surface, Figure 3c. The domains are elliptical in shape with a wrinkling pattern along the long axis, leading to the well-known bee-like appearance of the domains. The size of the domains varies from 0.7 to 3 µm. The mechanical property data show that the (only slightly visible) matrix has the lowest modulus of about 780 MPa. The domains show a modulus minimum in the area that is wrinkled, surrounded by a region of highest modulus (~850 MPa). Future investigations with an ultra-sharp AFM cantilever tip should reveal whether the lower modulus in the domain centres is an imaging artefact caused by the wrinkling or represents the true local mechanical property. Lastly, the deformation and adhesion data reveal that the domains have lower values than the surrounding material.

3.3 *Translation of mechanical property maps to material characteristic values*

The mechanical maps as presented in the previous paragraphs provide an overview of properties over the scanned surface. In order to relate these maps to other properties of the studied binders, a proper averaging procedure has to be adopted. Firstly, the average value is taken over a square area that is completely within one phase, inset of Figure 4(a). In order to assure the statistical validity of the averaging procedure, the same procedure was followed at the same location of the sample surface but with averaging squares that were stepwise increased from 5×5 pixels to 30×30 pixels. For each of these square averaged properties also the standard deviation was calculated. It should be noted that each single pixel represents an independent measurement of a full force-distance curve, from which the presented properties are derived by analysis of these curves. In Figure 4(a) the result of this averaging procedure is demonstrated for the matrix phase of bitumen AAA. The averaged mean modulus appears to be independent of the averaging area, though the standard deviation initially decreases and flattens out at an averaging square of 30×30 pixels. Thus, to obtain a reasonable estimate of

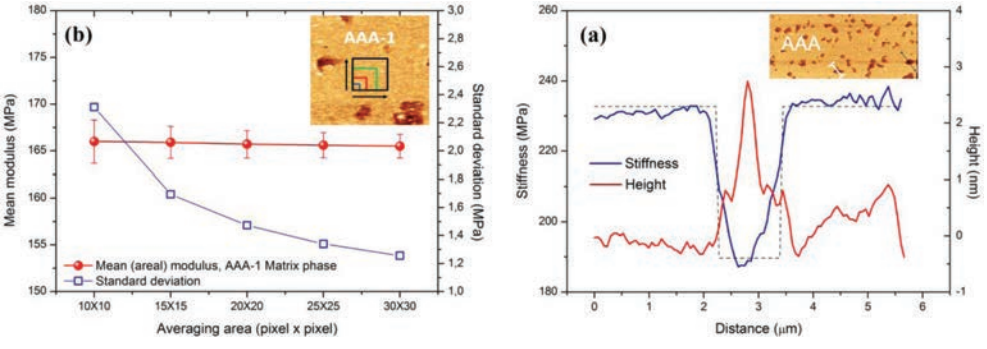

Figure 4. (a) Averaging procedure, and (b) correlation of height to modulus along a path (inset) for AAA.

the areal averaged mechanical properties from AFM images, averaging over a small square area is sufficient. Though, to obtain an idea of the precision, one has to find in an iterative way the averaging area where the standard deviation starts flattening out. It was also found that the averages are independent of the precise location of the averaging square within the phase.

Finally, in Figure 4(b) it is demonstrated how height variations of the sample surface correlate with variations in mechanical properties. In Figure 4(b) the height and modulus of AAA along the path is depicted in the inset. Here it appears that the softer phase is slightly elevated (4 nm) relative to the stiffer phase. As mentioned in the discussion of the individual material maps, this relation between phase stiffness and height is found consistently for all the materials examined in this study.

The results of the mean mechanical properties for both phases of the four bitumen grades have been summarized in Table 2. The areal averaging procedure as described earlier was followed throughout. Also some morphological features of the microstructure have been added. To facilitate comparison, for each material the phase with maximal modulus and deformation have been shaded (green).

From Table 2 one can conclude that AAA has phases with the lowest modulus: linear averaging using the phase fraction gives an average stiffness of 160 MPa at 22°C. This is in agreement with the information in Table 1. According to this latter table AAG should possess the highest modulus. However, for AAG one finds a modulus of 580 MPa, which is smaller than the same for AAK, 840 MPa. Further, for both AAC and AAK the domains constitute the phase with highest modulus, whereas for both AAA and AAG the matrix phase has the highest modulus. It should be noted that the assignment of phases (domains, i.e. 'bees' and matrix) was based on the universal appearance of an isolated, convex phase (the bees) embedded in a matrix that surrounds them. This distinction should possibly be adjusted, given the mechanical properties of these phases.

Another finding, that might explain the anomalies just mentioned, is that for AAC and AAK the stiffest phase experiences the lowest deformation at peak force. While for AAA and AAG the stiffest phase, surprisingly, shows also the largest deformation at peak force. Before it has been proposed that this might be due to very different viscoelastic properties of the two phases, which might lead to a switch in apparent modulus at the experimental frequency of 2 kHz, the loading rate. Applying the same linear approximation based on phase fractions for the adhesion data, AAA appears the stickiest bitumen, while AAG is the least sticky. These findings apparently correlate with the penetration and asphaltene fractions as given in Table 1.

Table 2. Averaged mechanical properties of bitumen phases at 22°C (per material the highest values are shaded green).

Materials/ phase	Modulus (MPa)	Deformation (nm)	Adhesion (nN)	Dissipation (keV)	Domain size (μm)	Phase fraction (%)
AAC-1						
Domain	650.7 ± 30.7	0.54 ± 0.05	26.2 ± 1.9	1.68 ± 0.18	3–8	75
Matrix	370.9 ± 11.3	1.58 ± 0.06	39.9 ± 0.9	5.11 ± 0.06		25
AAA-1						
Domain	130.6 ± 5.9	1.12 ± 0.19	17.6 ± 2.2	3.68 ± 0.45	0.3–3	20
Matrix	167.1 ± 1.5	1.85 ± 0.06	46.7 ± 1.4	9.75 ± 0.34		80
AAG-1						
Domain	509.5 ± 35.3	0.39 ± 0.04	6.01 ± 0.4	0.06 ± 0.008	0.2–1	35
Matrix	622.6 ± 25.5	0.80 ± 0.06	10.1 ± 0.3	0.78 ± 0.002		65
AAK-1						
Domain	845.9 ± 57.1	0.93 ± 0.09	31.7 ± 0.7	1.56 ± 0.001	0.7–3	90
Matrix	776.7 ± 10.8	1.58 ± 0.16	34.9 ± 0.4	2.32 ± 0.030		10

4 CONCLUSION

A novel AFM mode, Peak Force QNM, has been utilized to map simultaneously the topographical and mechanical properties of four bitumen from the SHRP materials library. This mode allows acquiring and analysing the individual force curves from each cantilever tap during the imaging process. These force curves are fitted in real time to obtain the local mechanical properties—modulus, adhesion, deformation and dissipated energy—of the bitumen sample. In this way the phase images of traditional tapping mode AFM are unravelled into the individual effects contributing to the phase signal.

It is shown that topographical features of the sample surface are reflected by the mechanical properties; the softest phase is always found to be 2–5 nm elevated relative to the higher modulus phase. Moreover, it is shown that phases as occur in topography images are observed as areas of constant mechanical properties in the mechanical maps. A method has been demonstrated that allows breaking down the mechanical property maps into averaged properties with standard deviation for each phase.

From this it is found that for two materials (AAC and AAK) the domains, or bee's, constitute the phase with higher modulus, while the opposite has been found for AAA and AAG. Moreover, an anomaly has been observed between the modulus and deformation for AAA and AAG. For these materials the stiffer phase displays at the same time the highest deformation. It is proposed that this may originate from viscoelastic effects that may be prominent at loading rates of 2 kHz.

By assuming a simple linear relation between the phase fractions and their mechanical properties, per bitumen (phase) averaged mechanical properties are obtained. Then, these phase averaged properties are compared with known properties of the binders as obtained by different means. Some properties like penetration (as a measure for 'stiffness') showed reasonable correlation with the nanomechanical results. Though a better understanding of the systems studied is required to formulate more sophisticated methods that allow for prediction of traditional bitumen properties from phase morphological and nanomechanical properties.

In conclusion, for the first time nanomechanical properties of distinct bitumen grades have been studied systematically. Phase morphology and nanomechanical maps appear to be congruent. Hence, the microstructure of bitumen can be safely identified as the property defining length scale. On-going and future research efforts are directed to explanations of the anomalies observed in this work. Thus it will contribute to a better understanding of bituminous materials from a more fundamental point of view, which should serve in the end the industrial, engineering and professional pavement communities.

ACKNOWLEDGEMENTS

The authors would like to acknowledge Troy Pauli from the Western Research Institute (Laramie, USA) for providing the bitumen. Financial support from the Dutch national IOP Self-Healing Materials program (AgentschapNL, The Netherlands) under grant no. SHM01056 is gratefully acknowledged.

REFERENCES

[1] Loeber L., Sutton O., Morel J., Valleton J.M., Muller G. New direct observations of asphalts and asphalt binders by scanning electron microscopy and atomic force microscopy. Journal of Microscopy. 1996;182(1):32–39.

[2] Masson J.F., Leblond V., Margeson J. Bitumen morphologies by phase-detection atomic force microscopy. Journal of Microscopy. 2006;221(1):17–29.

[3] Pauli A.T., Grimes R.W., Beemer A.G., Turner T.F., Branthaver J.F. Morphology of asphalts, asphalt fractions and model wax-doped asphalts studied by atomic force microscopy. International Journal of Pavement Engineering. 2011;12(4):291–309.

[4] Schmets A., Kringos N., Pauli T., Redelius P., Scarpas T. On the existence of wax-induced phase separation in bitumen. International Journal of Pavement Engineering. 2010;11(6):555–563.
[5] Nahar S.N., Schmets A.J.M., Scarpas A., Schitter G. Temperature and thermal history dependence of the microstructure in bituminous materials. European Polymer Journal. 2013;49(8):1964–1974.
[6] Cheng L., Xia X., Scriven L.E., Gerberich W.W. Spherical-tip indentation of viscoelastic material. Mechanics of Materials. 2005;37(1):213–226.
[7] Jäger A., Lackner R. Finer-Scale Extraction of Viscoelastic Properties from Nanoindentation Characterised by Viscoelastic–Plastic Response. Strain. 2009;45(1):45–54.
[8] Lu H., Wang B., Ma J., Huang G., Viswanathan H. Measurement of Creep Compliance of Solid Polymers by Nanoindentation. Mechanics of Time-Dependent Materials. 2003;7(3–4):189–207.
[9] Jäger A., Lackner R., Eisenmenger-Sittner C., Blab R. Identification of Microstructural Components of Bitumen by Means of Atomic Force Microscopy (AFM). PAMM. 2004;4(1):400–401.
[10] Fischer H., Stadler H., Erina N. Quantitative temperature-depending mapping of mechanical properties of bitumen at the nanoscale using the AFM operated with PeakForce TappingTM mode. Journal of Microscopy. 2013;250(3):210–217.
[11] Jones D.R. SHRP Materials Reference Library, Asphalt Cements: A Concise Data Compilation 1993.
[12] Pletikapić G., Berquand A., Radić T.M., Svetličić V. Quantitative nanomechanical mapping of marine diatom in seawater using PeakForce Tapping atomic force microscopy Journal of Phycology. 2012;48(1):174–185.
[13] Sweers K.K.M., Bennink M.L., Subramaniam V. Nanomechanical properties of single amyloid fibrils. Journal of Physics: Condensed Matter. 2012;24(24):243101.
[14] Wenger M.P.E., Bozec L., Horton M.A., Mesquida P. Mechanical Properties of Collagen Fibrils. Biophysical Journal. 2007;93(4):1255–1263.
[15] Young T.J., Monclus M.A., Burnett T.L., Broughton W.R., Ogin S.L., Smith P.A. The use of the PeakForce TM quantitative nanomechanical mapping AFM-based method for high-resolution Young's modulus measurement of polymers. Measurement Science and Technology. 2011;22(12):125703.
[16] Goldstein R.V., Gorodtsov V.A., Ustinov K.B. A mechanical model of the contact interaction between the atomic force microscope measuring element and a surface under investigation. Nanotechnologies in Russia. 2009;4(7–8):525–529.
[17] Nečas D., Klapetek P. Gwyddion: an open-source software for SPM data analysis. Centreurjphys. 2012;10(1):181–188.

Sustainable asphalt technologies—II

This page intentionally left blank

Asphalt Pavements – Kim (Ed)
© 2014 Taylor & Francis Group, London, ISBN 978-1-138-02693-3

Effective reduction of asphalt pavement temperatures

Rajib B. Mallick & Ryan K. Worsman
Civil and Environmental Engineering, WPI, Worcester, MA, USA

Hui Li & John Harvey
Civil and Environmental Engineering, University of California Pavement Research Center, University of California, Davis, CA, USA

Sankha Bhowmick
Mechanical Engineering, University of Massachusetts, Dartmouth, MA, USA

ABSTRACT: High surface temperatures increase the risks of rutting and top-down cracking in Hot Mix Asphalt (HMA) pavements. Reducing temperature extremes in asphalt pavements is a step towards building sustainable pavements. The objective of the research reported in this study was to evaluate the concept of using Geosynthetic Reinforced Chip Seal (GRCS) as an effective method to reduce temperatures in HMA pavements under different types of solar radiation conditions. Equipment was developed for simulating different levels of solar radiations, for different time periods, and determining temperatures at multiple depths of four pavement samples simultaneously. Temperature data at uniform depths of different types of HMA samples under a wide range of solar radiation conditions were collected. An instrumented test section was set up at the University of California Pavement Research Center site in Davis, CA. Temperature data from the GRCS and an adjacent Open Graded Friction Course (OGFC) section were compared. The major conclusion is that a GRCS reduces the temperature of HMA pavement, and the reduction in temperature at the different depths can be as high as 10C, which can result in an extension of pavement life substantially. The use of a GRCS is recommended for application in high temperature areas to reduce temperature and extend lives of asphalt pavements. Further study of reduction in temperature with higher albedo aggregates, double chip seals and concrete pavements is recommended.

Keywords: sustainable, temperature, geosynthetic, chip seal, solar

1 INTRODUCTION

High temperature related permanent deformation (rutting) is a major type of distress in HMA pavements. A rise in temperature leads to a reduction in stiffness and permanent deformation resistance under shear and compressive stresses in HMA and a consequent increase in potential of rutting [1, 2]. Also, higher temperatures lead to faster aging of asphalt binders, and hence accelerated deterioration of asphalt pavements due to low-temperature cracking, ravelling and top-down cracking [3]. One way to prevent high temperature related rutting is to modify the properties of asphalt pavement materials through the addition of stiffeners or modifiers, such as polymers, that make the asphalt binder stiffness less susceptible to a rise in temperature. Such an approach works well and has been commonly used; however there are two drawbacks, the use of polymers leads to an increase in cost, and the industrial supply of modifiers could be inconsistent. Furthermore, the use of polymer modified asphalt also necessitates the use of a higher temperature during production of HMA, which leads to greater energy consumption and higher amount of fumes and emissions.

An alternative approach could be to control the pavement temperatures through designing the pavement structure with specific layers such that the temperature of HMA could maintain a lower level (compared to conventional HMA pavements) at high ambient temperatures. This paper presents the results of a study that was carried out with that specific objective.

2 OBJECTIVE

The objective of this study was to evaluate a system of keeping the temperature of pavements at a lower level during high ambient temperature conditions through the use of GRCS with moderately high albedo aggregates.

3 THEORY

Temperatures in HMA pavements rise quickly and remain elevated in the summer season because of high absorption of solar radiation (less reflection, more absorption due to the low albedo of the asphalt) [4]. The temperature of the HMA layers becomes progressively hotter during hot spells, and typically the 7-day maximum temperature is considered for selecting the appropriate asphalt binder grade for prevention of rutting. Such temperatures can rise as high as 70–90 °C, depending on the location, and temperatures in the range of 60–70 °C are common in many parts of the US. Generally, if the span of temperature (high to low) is too large (>90 °C) a polymer modified asphalt is specified.

The hypothesis that is evaluated here is the following. If the amount of heat that reaches the HMA layer could be reduced, then the increase in temperature in the HMA layer could be lowered. This could be achieved by a two step process. First, a layer of geotextile, made of polypropylene, could be laid down on top of the HMA. Generally such layers are placed after the application of a thick layer of asphalt binder, such that the geotextile layer is "saturated". Since both polypropylene geotextile (0.1–0.22 W/mK) and asphalt binder (0.15–0.17 W/mK) have lower thermal conductivities compared to aggregates (2–7 W/mK) and HMA (0.8–1.5 W/mK) [5], the rate of heat transfer will be slowed down through the introduction of thermal insulation of the geotextile layer between the surface and the HMA layer. Secondly, a chip seal could be placed on top of the geotextile (resulting in a GRCS), in which the special aggregates have a high albedo (reflectivity) such that less of the solar radiation is absorbed by the pavement. The hypothesis is that the higher reflection at the chip seal surface and the lower conduction at the geotextile layer will jointly reduce the-temperature of the HMA layer though both solar reflection cooling and thermal insulation cooling [6]. It should be noted that asphalt mix layer has been recently evaluated as an insulating layer for concrete pavements by Khazanovich et al [7].

4 EXPERIMENTAL WORK

The experimental work consisted of two parts: laboratory and field. For the laboratory part, four pavement core samples (obtained from the field) consisting of four different types of HMA were instrumented, subjected to radiation, and tested for rise in temperature at different depths; GRCS was then applied on the top of each of the four samples, and they were retested for temperature under the same conditions of radiation. The temperature data from the samples with and without the GRCS were then compared. For the field part, temperature data from full scale test sections were obtained, as discussed in Section 4.3.

4.1 *Description of HMA samples*

The four samples (Table 1) have been characterized for their thermal properties earlier by the authors, and effective thermal conductivity and heat capacities have been reported in

Table 1. Description of samples.

Pavements	Sample/description	Layer composition	Bulk specific gravity
Highway-HMA layers over PMRAP base	S (9.5 mm over 12.5 mm NMAS over PMRAP base); PMRAP-RAP with 3.5% emulsion and 1.3% cement; 9.5 and 12.5 mm mixes	63 mm of HMA over 75 mm of Plant Mixed Reclaimed Asphalt Pavement (PMRAP)	Top layer + Middle layer 2.377 Bottom layer: 2.084
Highway-HMA layers over foamed asphalt base	M (9.5 mm over 9.5 mm over foamed asphalt base); foamed asphalt contained 3.1% binder and 1.4% cement; 9.5 mm mix	55 mm of HMA over 135 mm of foamed asphalt	Top layer + Middle layer 2.284 Bottom layer 2.067 1.975
Highway-HMA layers over cement treated base	R (9.5 mm over 12.5 mm over cement treated base); full depth reclaimed base with 4% cement; 9.5 and 12.5 mm mixes	70 mm of HMA over 165 mm of cement treated base	Top layer: 2.386 Middle layer: 2.209 Bottom layer: 2.033
Airport-HMA layers of different types two lifts	(FR) Fuel Resistant ½ inch NMAS mix over ¾ inch NMAS polymer modified (PM) binder mix over existing HMA or Macadam; FR—12.5 mm maximum size mix with 7% PG 88-22 binder PM—19 mm maximum size mix with 6% PG 82-22 PM binder	40 mm of FR and 53 mm of PM over 59 mm of existing P401 mix	Top layer: 2.549 Middle layer: 2.557 Bottom layer: 2.467

Chen et al [8]. Samples S, M and R are from highway pavements, while sample FR is from an airport pavement. The thermal properties, which were determined through a combined experiment, finite element analyses, and back calculation procedure, ranged from 1.3–1.8 W/mK for thermal conductivity, and 1,200–1,800 J/kgK for the heat capacity. For each sample, the temperature sensors [9] (thermistors, with an accuracy of ± 0.1C), were placed at 6 locations, as follows: 25 mm above the surface, on the surface, and 25, 50, 75 and 100 mm below the surface. The GRCS layers were created with PG 64–22 asphalt binder as tack coat, a non-woven fabric as the geotextile, and a locally available aggregate, with albedo of 0.24, with MS-2 emulsion as the chip seal. The gradation of the aggregates conformed to South Dakota Chip Seal Type 1A (100%, 40–70%, 0–15%, 0–5% and 0–1% passing the 12.5 mm, 9.5 mm, 4.75 mm, 2.36 mm and 0.075 mm sieves, respectively).

4.2 *Description of the solar radiation simulation equipment*

To test the samples under uniform conditions, a specialized piece of equipment called the "Solar Simulator" was developed. The frame of the Solar Simulator is essentially a wooden chamber; two of the sides are plywood secured with screws and wood glue, while the front and back are transparent polymer sheets, held in place with clamps (Fig. 1). One of the plywood sides has a port to which a chilled-air vent can be connected (for cooling, if required). The top of the chamber contains four round ports that serve to secure in place four halogen lamps (for heating). Beneath the lamps, the base of the cube is formed by insulation 'jackets' sitting atop plywood. Each jacket is a cube with a cylindrical opening; 4″ or 6″ × (up to) 8″ (100 or 150 × 200 mm) cylindrical asphalt mix samples sit inside the jackets, so that only the top surface is exposed. These asphalt mix samples contain sensors, in order to measure the temperature at the surface, as well as at varying heights throughout the sample. The halogen lamps (and chilled-air blower, when used) can be connected by computer and used to simulate a variety of real-world temperature profiles. The main components of the equipment consist of a microcontroller, a servo, a dimmer, and four halogen lamps. An algorithm (programmed with PuTTY software) in the microcontroller regulates the dimmer through the servo, to provide time dependent radiation from each of the four halogen lamps, allowing the simultaneous testing of four samples. The angle of rotation of the dimmer was calibrated

Figure 1. Four samples (with GRCS) being tested simultaneously (photo taken with side boards removed) in the solar simulator.

Figure 2. GRCS section at the UC Davis pavement research facility.

against radiation (kW/m^2) through test data acquired with a pyranometer (Brand: CMP3, Kipp and Zonen).

Essentially, once the user inputs the radiation as a function of time the dimmer setting versus radiation calibration curve is utilized to set a dimmer setting versus time function for the servo to control the dimmer. The microcontroller also collects data from the temperature sensors and provides them to the user as .csv files.

4.3 *Description of test section*

An approximately 4 m by 4 m section of GRCS was constructed over an existing HMA section (100 mm HMA + 150 mm Aggregate Base) at the University of California Pavement Center (UCPRC) test facilities in Davis, California in September 2013 (Fig. 2). The section was instrumented with a weather station and thermocouples, to obtain wind, solar radiation, air temperature and temperature at different depths of the pavements. Details of the existing sections are available in reference [10]. A PG 64-16 asphalt binder was applied on the existing surface at a rate of 1.3 liters per square meter. A non-woven geotextile layer was then rolled over the tack coat, first with a light (90 kg) hand roller and then with a side-walk roller (after application of sand). Next, a polymer modified cationic rapid set emulsion was applied at a rate of 2.7 liters per square meter, and then the chip seal aggregates were applied, which were rolled with a light hand roller first, and then using a pickup truck. The same aggregate/gradation that was used for the laboratory studies was used. Note that the temperature data for one day (from 4 pm, 9/18/13 to 5 pm, 9/19/13) from this section and an adjacent Open Graded Friction Course (OGFC) permeable pavement (100 mm OGFC + 300 mm Granular Base) with surface albedo of 0.08 [11] and permeability of 0.11 cm/s [12] were compared for this paper.

5 RESULTS AND ANALYSIS

The radiation intensity in the solar simulator was matched with solar radiation data that had been obtained earlier on a late spring/early summer day (outside the Civil Engineering department building, WPI, Worcester, MA, 42.2 N, 71.8 W) with a pyranometer, increasing from 0 to approximately 0.8 KW/m^2 in the first four hours, and then decreasing to 0 in the next four hours. The curve can be represented by the equation Radiation (kw/m^2) = -0.05(time, hour)^2 + 0.4(time, hour). The temperature data were collected for a

total time period of 16 hours, of which the simulated solar radiation was on for the first 8 hours and off for the next 8 hours. Figures comparing the temperature data at the different depths, between HMA and the GRCS sample are presented in Figures 3 through 6. In general, the temperatures were observed to be lower for the GRCS samples. The temperature is higher for GRCS in two cases—for 25 mm above surface in S sample, and for 25 mm above surface and the surface for the R sample. The higher temperature at the

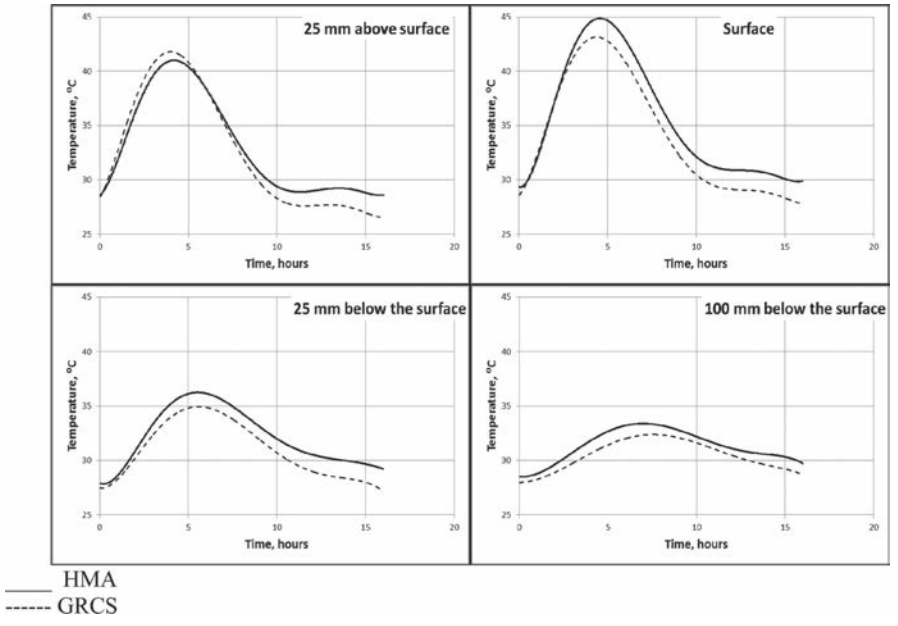

Figure 3. Temperature at different depths, S sample.

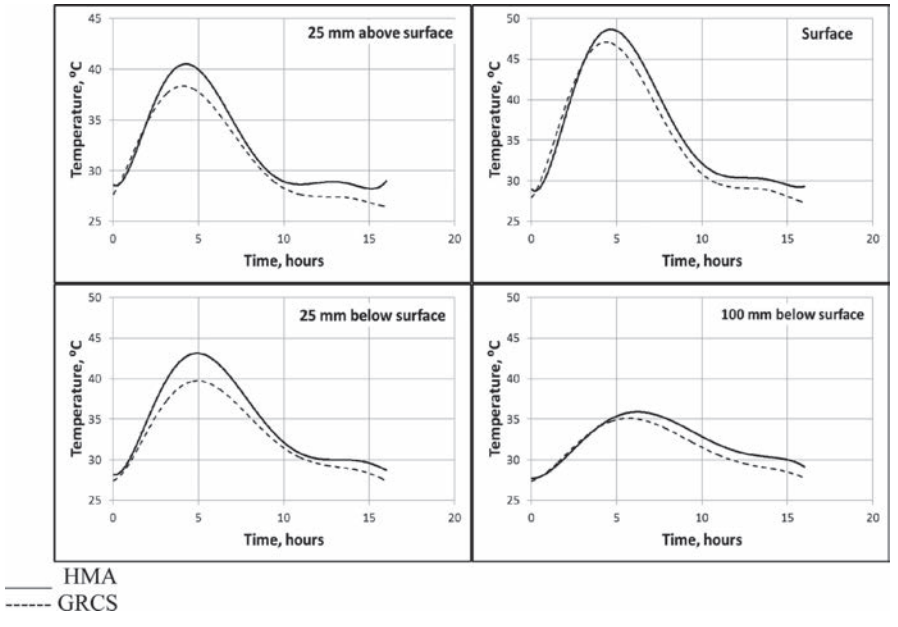

Figure 4. Temperature at different depths, M sample.

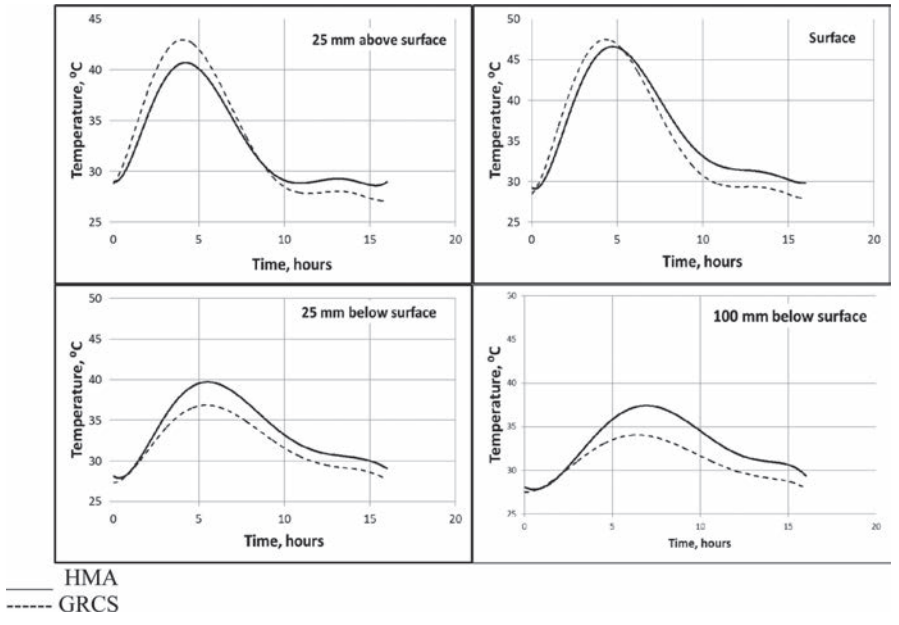

Figure 5. Temperature at different depths, R sample.

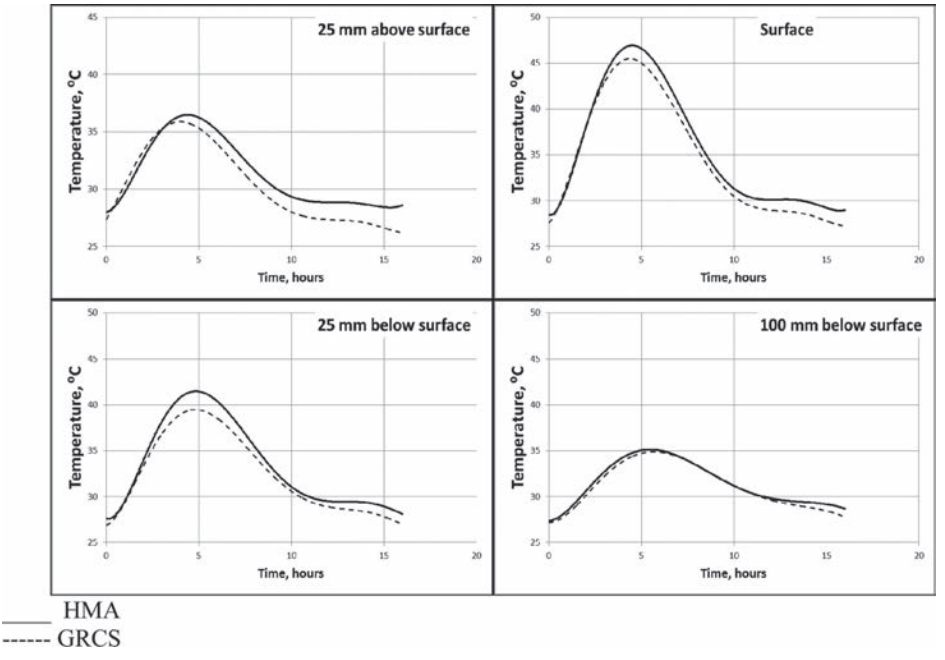

Figure 6. Temperature at different depths, FR sample.

surface of the chip seal (at the aggregate) should not be of concern regarding permanent deformation potential.

The temperatures throughout the depth of the samples are consistently lower for the GRCS samples, compared to the HMA sample. For the temperatures at a height of 25 mm above the surface, the difference at the end of the test (8 hours after the radiation is turned off)

is important. For all of the cases, a negative difference of 2 °C or higher is noted. In terms of percentage reduction in temperature at the end of the 16 hour period, throughout the various depths, the reduction in temperature with the use of GRCS ranges from 3.5–9%. The greatest reduction being noted near the surface of the samples, most of the reductions were between 5 and 7% (Fig. 7). This indicates that after sunset, the near surface temperature of the GRCS pavements would most likely be cooler than similar HMA pavements, and therefore will have a reduced effect on the environment/air quality, especially on warm days [13]. This also means that the cumulative effect of the high temperature would be much less in the case of the GRCS samples, and hence the average maximum 7-day temperature (at any depth) should also be much lower in the case of the GRCS samples. That is, throughout a large part of the HMA cross section, the overall rise in temperature, and the duration of rise in temperature will be much lower in the case of the GRCS samples. It is therefore expected that both (temperature related) aging and permanent deformation potential of HMA layers could be lowered by the use of GRCS. For example, analysis with the Mechanistic Empirical Pavement Design Guide/software has shown that a lowering of temperature of HMA layers from 70 °C to 60 °C can extend the rutting life of a pavement by more than 10 years [14].

If an aggregate with a higher albedo could be used then the benefits will be definitely greater. A reduction of temperature of 10 °C at a depth of 25 mm was confirmed with test of a HMA sample under a higher/longer (actual) solar radiation levels (Fig. 8); the tests have shown that the beneficial effects are enhanced at higher radiation levels/longer radiation periods (warmer days/summer time).

The temperature at the different depths for the GRCS test section and the adjacent OGFC test section at UC Davis (Fig. 9) show that the presence of the GRCS seems to be effective in signifcant lowering of temperature. The reductions range from 2 °C at 50 mm above the surface to 9 °C at a depth of 12.5 mm, as summarized in Figure 10. As Figure 9 shows, the temperaure fluctuations seem to be moderated by the presence of GRCS. Figure 11 shows the temperatures along the depths for the two sections for the entire time period of data collection. Note that the spread in temeprature is larger in the case of the OGFC section; for example, the temperature at 25 mm below the surface for the GRCS section ranges from 17 to 42 °C, wheras that for the OGFC section ranges from 15 to 51 °C; a reduction in high pavement temperature can extend the rutting service life, especially at the early part of its life. Also, for the GRCS section there is a greater reduction in temperature between the surface

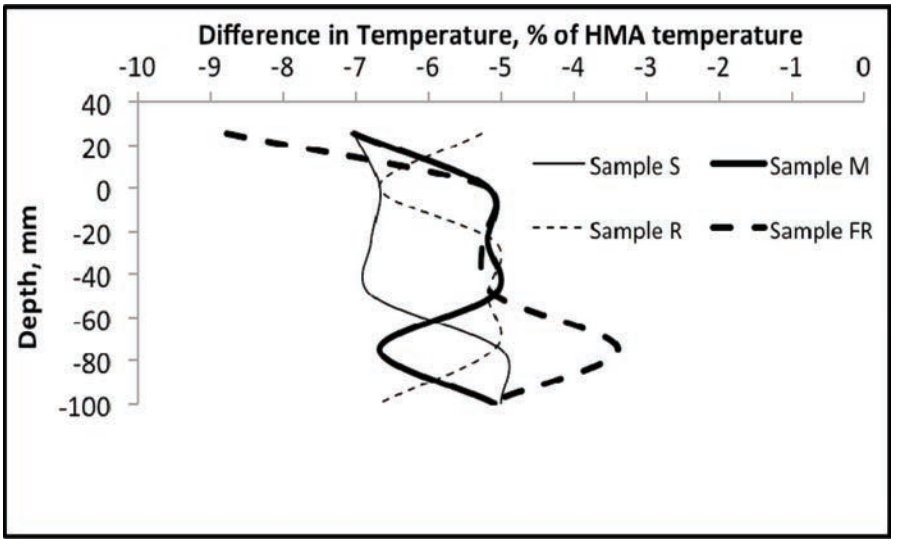

Figure 7. Temperature difference between GRCS and HMA sample (%) at 16 hours.

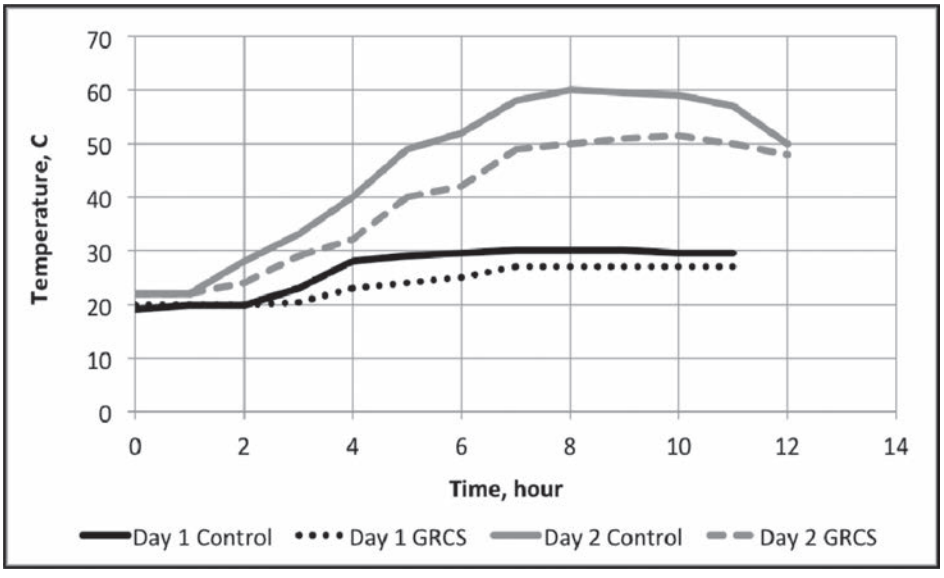

Figure 8. Results of tests on small samples conducted outdoors; solar radiation, Day 1: 0–0.7 kW/m^2, for a total duration of 11 hours, ambient temperature ranged from 14 to 23°C; Day 2: 0–0.9 kW/m^2, for a total duration of 12 hours, ambient temperature ranged from 20 to 38°C; 9.5 mm NMAS mix with 6% PG 64-28 binder.

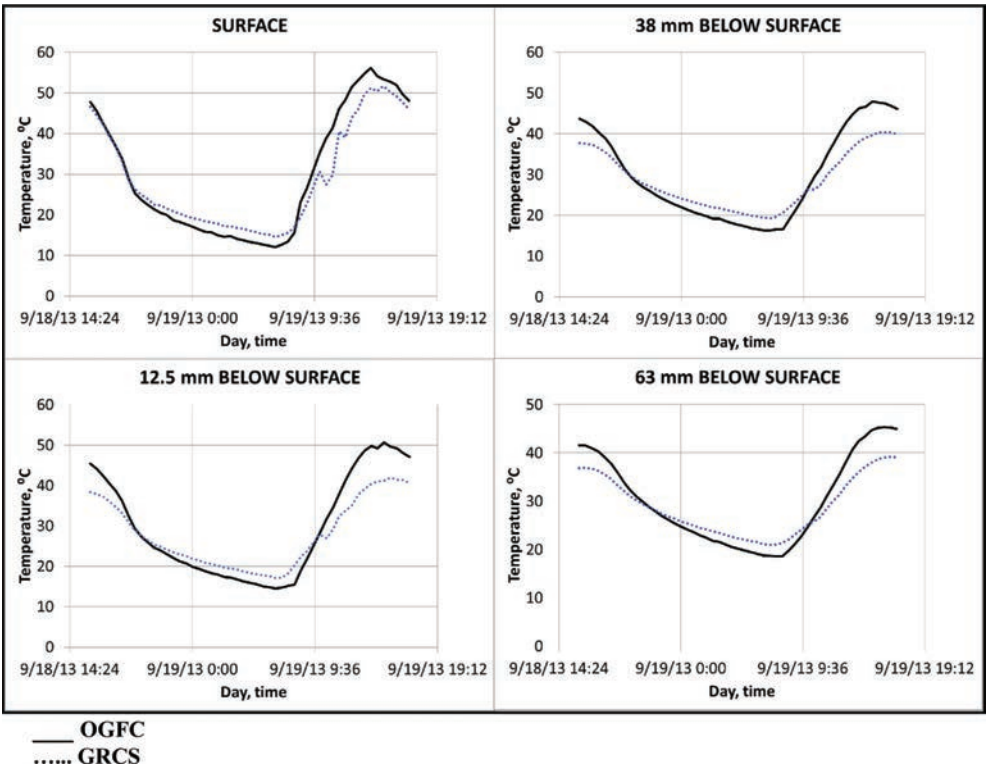

Figure 9. Temperature at different depths of the test sections.

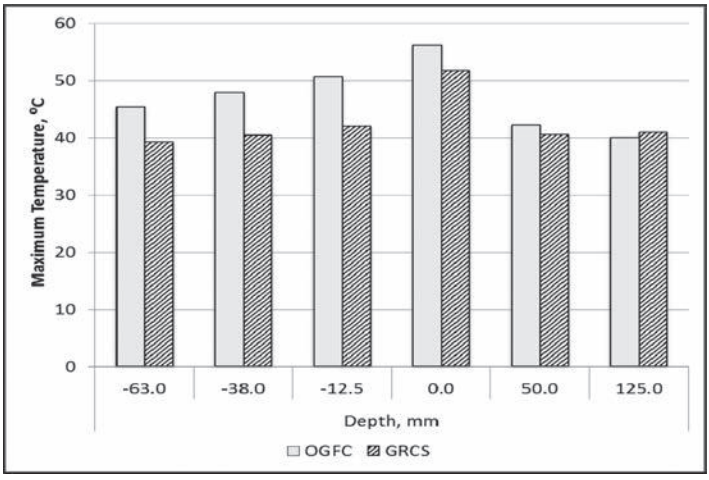

Figure 10. Comparison of maximum temperatures at different depths of test section.

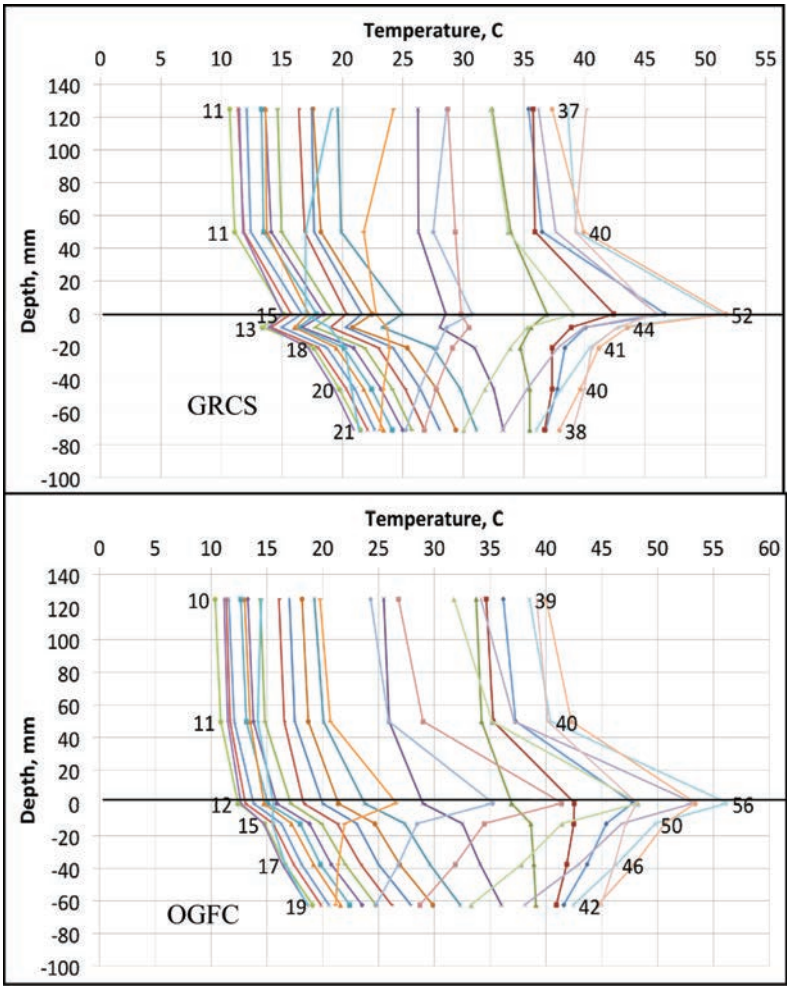

Figure 11. Range of temperatures for the entire time period.

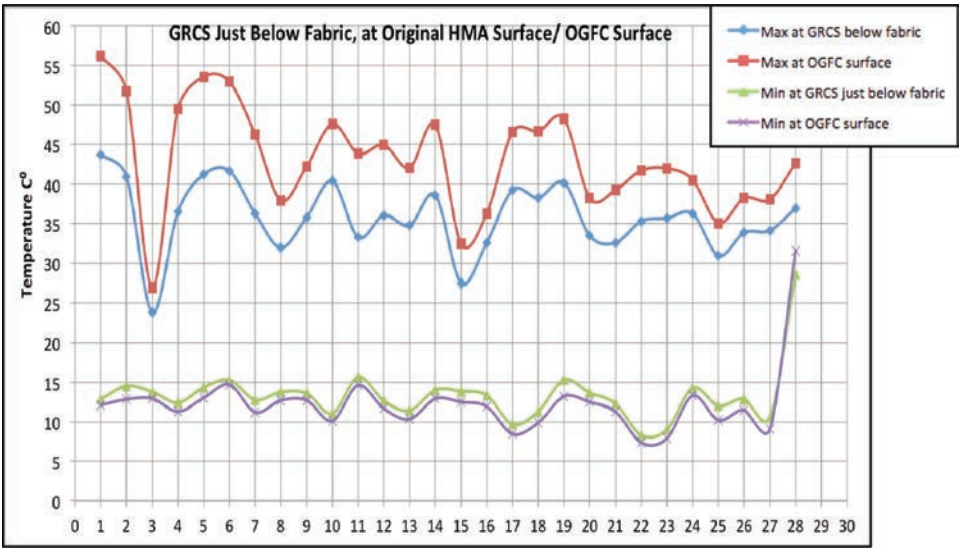

Figure 12. Maximum and minimum tenperatures, collected between 9/18/2013 and 10/15/2013.

and the lower layers. Figure 12 shows field data obtained from September–October: note the >10 °C reduction in temperature at the surface of the pavement.

6 CONCLUSIONS AND RECOMMENDATIONS

The following conclusions can be made on the basis of the laboratory and the field study that have been reported in this paper.

1. The use of geosynthetic reinforced chip seal can reduce the temperature of HMA pavements at different levels to different degrees.
2. The reduction of temperature depends on the intensity/duration of solar radiation.
3. Temperature reductions in the range of 10 °C are possible.
4. Daily fluctuations of temperature in pavements can be moderated through the use of GRCS.

The scope of further research with full-scale test pavement includes the use of the following: 1. Aggregates with higher albedo for chip seal; 2. Geotextile layer with different thicknesses; 3. Placement of double chip seals; 4. Use of GRCS on top of concrete pavements for lowering the temperature differential; 5. Durability of the GRCS to make it an effective and feasible treatment option for lowering pavement temperature, in both high and low traffic volume pavements.

ACKNOWLEDGEMENTS

The authors gratefully acknowledge the help of Don Pellegrino, Kevin Burns and Andrea Caprio of the Civil and Environmental Engineering department at WPI, David Jones of UC Davis and Steve Thaxton of Propex Operating Company, LLC in conducting this study.

REFERENCES

[1] Van de Loo, P.J. The creep test, a key tool in asphalt mix design and in the prediction of pavement rutting. Proceedings of the Association of Asphalt Paving Technologists, 47, 253–281, 1978.

[2] Monismith, C.L., Hicks, R.G., Finn, F.M., Sousa, J., Harvey, J., Weissman, S., Deacon, J., Coplantz, J., and Paulsen, G. Permanent Deformation Response of Asphalt Aggregate Mixes. SHRP-A-415, Strategic Highway Research Program, TRB, National Research Council, Washington, D.C., 1994.
[3] Bell, Chris. Summary Report on Aging of Asphalt-Aggregate Systems SR-OSU-A-003 A-89-2. SHRP A-305 Report. http://onlinepubs.trb.org/onlinepubs/shrp/SHRP-A-305.pdf.
[4] Bejan, Adrian, "Heat Transfer." John Wiley & Sons, 1993.
[5] National Cooperative Highway Research Program (NCHRP). "Guide for Mechanistic-Empirical Design." Transportation Research Board, Washington, DC, Design Inputs, March 2004.
[6] Li, H., et al., The Use of Reflective and Permeable Pavements as a Potential Practice for Heat Island Mitigation and Stormwater Management. *Environmental Research Letters*, 2013. 8(1): p. 14.
[7] Khazanovich, L., Balbo, J.T., Lederle, R., Marasteanu, M., Saxena, P., Tompkins D.,Vancura, M., Watson, M., Johanneck, L., Harvey, J., Santero, N.J., and Signore, J. Design and Construction Guidelines for Thermally Insulated Concrete Pavements. MN/RC 2013–02. http://www.lrrb.org/pdf/201302.pdf.
[8] Bao-Liang Chen, Laura Rockett and Rajib B. Mallick. Laboratory Investigation of Temperature Profiles and Thermal Properties of Asphalt Pavements with Different Subsurface Layers. Journal of Association of Asphalt Paving Technologists (AAPT), Volume 77, 2008.
[9] http://dlnmh9ip6v2uc.cloudfront.net/datasheets/Sensors/Temp/ntcle100.pdf.
[10] Li, Hui. Evaluation of Cool Pavement Strategies for Heat Island Mitigation, UC Davis, Institute of Transportation Studies. December 2012. https://merritt.cdlib.org/file/display?file=producer%2F2012_UCD-ITS-RR-12-33.pdf&object=ark%3A%2F13030%2Fm5ws8z00&version=1.
[11] Li, H., J. Harvey, and A. Kendall, Field Measurement of Albedo for Different Land Cover Materials and Effects on Thermal Performance. *Building and Environment*, 2013. 59(0): p. 536–546.
[12] Li, H., M. Kayhanian, and J. Harvey, Comparative Field Permeability Measurement of Permeable Pavements Using Astm and Ncat Methods. *Journal of Environmental Management*, 2013. 118 (0) p. 144–152.
[13] Akbari, H., Pomerantz, M. and Taha, H. Surfaces and Shade Trees To Reduce Energy Use and Improve Air Quality in Urban Areas. *Solar Energy* Vol. 70, No. 3, pp. 295–310, 2001.
[14] Mallick, Rajib B., Chen Bao-Liang and Sankha Bhowmick. Harvesting Energy from Asphalt Pavements and Reducing the Heat Island Effect. International Journal of Sustainable Engineering, Volume 2 Issue 3 2009.

Asphalt Pavements – Kim (Ed)
© 2014 Taylor & Francis Group, London, ISBN 978-1-138-02693-3

Evaluation of SMA containing RAP and RAS

Stacey Diefenderfer
Virginia Center for Transportation Innovation and Research, Charlottesville, VA, USA

ABSTRACT: The use of Recycled Asphalt Shingles (RAS) is generating interest among agencies and industry as a means of encouraging environmentally friendly practices and potentially reducing material costs. The Virginia Department of Transportation (VDOT) has allowed the use of manufacturing waste shingles since 2008 and tear-off shingles since 2010; however, use is restricted to dense-graded asphalt mixtures. In 2012, an asphalt producer asked to be allowed to use RAS in Stone-Matrix Asphalt (SMA), which had not been previously permitted by VDOT. This paper examines the impact of RAS on SMA mixture properties and performance.

The mixture evaluated was a 12.5 mm nominal maximum aggregate size SMA produced with a PG 76-22 binder. The control mixture included 15% Reclaimed Asphalt Pavement (RAP). The RAS mixture design incorporated 10% RAP and 5% RAS, resulting in a binder replacement of approximately 29%. Testing performed included volumetric analysis, dynamic modulus, flow number, rut, and fatigue testing of the mixtures.

Test results indicated that for the SMA mixtures evaluated in this study, the inclusion of RAS appears to improve high temperature/low frequency modulus values and rutting resistance. The inclusion of RAS had mixed effects on the mixture performance in laboratory fatigue testing. Additional testing is required to determine if in-service cracking or fatigue performance is significantly or practically affected. In general, additional evaluation is recommended to allow a better understanding of the impact of RAS use.

Keywords: Recycled Asphalt Shingles (RAS), Reclaimed Asphalt Pavement (RAP), Stone-Matrix Asphalt (SMA), performance testing

1 INTRODUCTION

Highway agencies have been using increasing amounts of reclaimed and recycled materials over the past number of years, as asphalt prices have continued to rise. The primary reclaimed and recycled materials used in asphalt materials are Reclaimed Asphalt Pavement (RAP) and Recycled Asphalt Shingles (RAS).

RAP has commonly been used in asphalt mixtures since the late 1970s. The use of RAS is more recent, having been introduced in the late 1980s and early 1990s [1–3]. However, with the introduction of Superpave in the 1990s, recycling became less prevalent as agencies learned to deal with a new design framework that was not particularly optimized for recycled materials. However, with increasing material prices and a greater emphasis on environmental stewardship, the interest in using increased amounts of these materials has grown rapidly. Recently, a large number of studies have investigated the increasing quantities of recycled and reclaimed material in asphalt mixtures, specifically RAP [4, 5] and RAS [6].

The Virginia Department of Transportation (VDOT) specifications for asphalt paving mixtures allow the use of up to 30% RAP in dense-graded surface mixtures. The percentage of RAP allowed in Stone-Matrix Asphalt (SMA) mixtures is dependent upon the binder type specified for the mixture: up to 20% when PG 70-22 binder is used; and up to 15% when PG 76-22 binder is used. In addition, the specifications allow up to 5% by weight of mixture of either post-consumer waste RAS or manufacturing waste RAS in dense-graded asphalt

mixtures. The percentage of binder contributed by the RAP or RAS or combination thereof must not exceed 30% of the total binder content of the mixture. Currently, the specifications do not allow the use of RAS in SMA mixtures; however, the effect of such use is being investigated through the mixtures evaluated in this study and other projects.

2 PURPOSE AND SCOPE

This study was initiated to evaluate the laboratory performance of two plant-produced SMA mixtures that incorporated 10% RAP and 5% RAS into the mixture. Testing included volumetric analysis, dynamic modulus, and flow number testing; rutting analysis using the Asphalt Pavement Analyzer (APA); and fatigue analysis. The results of the testing of these mixtures were compared with those for a plant-produced control SMA mixture that included 15% RAP. All mixtures were sampled at the plant during production, and all test specimens were produced in the laboratory.

3 MATERIALS AND METHODS

All mixtures were produced by the same contractor using the same source materials; however, mixture RAS A was produced in a different drum plant than mixtures RAS B and RAP Control. Mixture designs are shown in Table 1. Loose mixture samples were collected at the plant during production to provide materials for this study.

3.1 *Volumetrics*

Volumetric analyses were performed to determine fundamental mixture properties. Data collected included asphalt content and gradation; bulk and Rice specific gravities (G_{mb} and G_{mm});

Table 1. Mixture designs.

Mix designs	RAS A	RAS B	RAP control	VDOT specification [7]
Asphalt content, %	6.8	6.8	6.8	6.3 min.
Asphalt type	PG 76-22	PG 76-22	PG 76-22	
VTM, %	2.8	2.8	3.0	2.0–4.0
VMA, %	18.4	18.4	18.4	18.0 min.
VFA, %	84.6	84.6	83.4	
FA ratio	1.48	1.48	1.58	1.2–2.0
P_{be}, %	6.8	6.8	6.7	
G_{mm}	2.440	2.440	2.448	
VCA_{mix}, %	42.3	42.3	42.4	$<VCA_{DRC}$[a]
Aggregates				
Type	Percentage			
#7 quartzite	67	67	64	
–1/2 inch RAP	10	10	15	
#8 quartzite	10	10	10	
Limestone filler	8	8	11	
RAS	5	5	–	

[a]See Virginia Test Method 99 [8].
VTM = voids in total mix; VMA = voids in mineral aggregate; VFA = voids filled with asphalt; FA ratio = fines to asphalt ratio; P_{be} = effective binder content; G_{mm} = maximum theoretical specific density; VCA_{mix} = voids in coarse aggregate of mix; RAP = reclaimed asphalt pavement; RAS = recycled asphalt shingles.

Voids in Total Mix (VTM); Voids in Mineral Aggregate (VMA); Voids Filled with Asphalt (VFA); aggregate bulk and effective specific gravities (G_{sb} and G_{se}); Dust to Asphalt ratio (D/A ratio); percent binder absorbed (P_{ba}); and effective binder content (P_{be}).

3.2 *Dynamic modulus*

Dynamic modulus tests were performed with a Universal Testing Machine (UTM 100) (Industrial Process Controls, Inc. [IPC]) with a 25 to 100 kN loading capacity in accordance with AASHTO T 342 [9]. Tests were performed on 100-mm-diameter by 150-mm-tall specimens. Specimen air void levels of 7 ± 0.5% were obtained for each test specimen with the exception of one mixture, which averaged 8.0% air voids. Five testing temperatures ranging from –10.0ºC to 54.4ºC and six testing frequencies ranging from 0.1 to 25 Hz were used. Tests were conducted starting from the coldest temperatures to the warmest temperatures. In addition, at each test temperature, the tests were performed starting from the highest to the lowest frequency. Load levels were selected in such a way that at each temperature-frequency combination, the applied strain was in the range of 75 to 125 microstrain. All tests were conducted in the uniaxial mode without confinement. Stress versus strain values were captured continuously and used to calculate dynamic modulus. Dynamic modulus was computed automatically using IPC |E*| software. Results at each temperature-frequency combination for each mixture type are reported for three replicate specimens.

3.3 *Flow number*

The flow number test is used as a laboratory test to evaluate the rutting resistance of asphalt mixes. It is generally accepted that the higher the flow number, the lower the rutting susceptibility.

An IPC Universal Testing Machine (UTM 100) with a 25 to 100 kN loading capacity was used to conduct the flow number tests. Testing was performed on 100-mm-diameter by 150-mm-tall specimens having air void levels of 7 ± 0.5% with the exception of one mixture, which averaged 8.0% air voids. Tests were conducted at 54°C, which is based on LTPPBind software that represents the 50% reliability maximum high pavement temperature at locations in central Virginia. A repeated haversine axial compressive load pulse of 0.1 s every 1.0 s was applied to the specimens. The tests were performed in the unconfined mode using a deviator stress of 600 kPa and for two sets of specimens, 206 kPa. The tests were continued for 10,000 cycles or a permanent strain of 5%, whichever came first. During the test, permanent strain (εp) versus the number of loading cycles was recorded automatically, and the results were used to estimate the flow number. The flow number was determined numerically as the cycle number at which the strain rate is at a minimum based on the Francken model. All flow number testing at 600 kPa deviator stress was conducted on specimens previously tested for dynamic modulus. Testing using 206 kPa deviator stress was conducted on additional specimens.

3.4 *Asphalt pavement analyzer rutting analysis*

Rut testing was conducted using the APA and APA-Jr. (Pavement Technologies, Inc.) in accordance with Virginia Test Method 110 [8]. The APA was used to test a set of three replicate beams, and the APA-Jr. was used to test a pair of replicate beams. Other than the number of replicates, there were no differences in the manner in which the testing was performed in the two devices. Beams 75 mm thick by 125 mm wide by 300 mm long were tested at a test temperature of 49°C. Sets of beams were tested simultaneously. A vertical load of 120 lbf was applied through a rubber hose filled with compressed air at a pressure of 120 psi. The loading wheel speed was 2 ft/sec, and a total of about 135 min was required to complete 8,000 cycles of load applications. Total deformation after 8,000 cycles of load applications is considered the total rut depth. The reported test result is the average rut depth for the duplicate beams of each mixture type tested simultaneously.

3.5 *Fatigue analysis*

Four-point flexural beam fatigue tests were performed in accordance with AASHTO T 321 [9] using at least three replicate specimens at three strain levels (minimum total of nine beams) for each mixture type. IPC beam fatigue test equipment was used. All tests were conducted at a single temperature of 20ºC. The tests were conducted in the strain-controlled mode. Applied tensile strain levels ranging from 300 to 600 microstrain were used so that fatigue curves of strain versus number of cycles to failure could be developed. During the test, repeated application of the specified strain was continued until failure occurred in the test specimen. Specimen failure was defined as the number of cycles at which beam stiffness degraded to 50% of the initial flexural stiffness.

4 RESULTS AND DISCUSSION

Volumetric results for all mixtures are shown in Table 2. Most properties were fairly consistent among the mixtures. Mixtures RAS B and RAP Control had slightly low VMA and VTM for the compacted volumetric specimens. Volumetric values compared well with VDOT monitor data (not shown) except for the VMA results, in which case all monitor specimens passed the specification requirements.

Table 2. As-produced mixture properties.

Property	RAS A	RAS B	RAP control	VDOT specification [7]
Asphalt content, %	6.52	6.47	6.60	6.3 min.
Maximum theoretical specific gravity, G_{mm}	2.458	2.422	2.433	
VTM, %	5.4	1.7	1.6	2.0–4.0
VMA, %	20.0	16.5	16.8	17.0 min.
VFA, %	73.2	89.5	90.3	
VCA_{mix}, %	42.0	36.5	40.8	$<VCA_{DRC}$[a]
FA ratio	1.59	1.72	1.70	1.2–2.0
Mixture bulk specific gravity, G_{mb}	2.327	2.380	2.394	
Aggregate effective specific gravity, G_{se}	2.722	2.672	2.692	
Aggregate bulk specific gravity, G_{sb}	2.718	2.668	2.688	
Absorbed binder content, P_{ba}, %	0.06	0.06	0.06	
Effective binder content, P_{be}, %	6.47	6.41	6.54	
Effective film thickness, F_{be}, microns	9.6	8.8	9.0	
Density @ N_{ini}, %	83.9	88.2	87.3	
Gradation				
Sieve size	% passing			
3/4 in (19.0 mm)	100.0	100.0	100.0	
1/2 in (12.5 mm)	83.3	81.9	83.6	
3/8 in (9.5 mm)	63.2	59.0	60.9	
No. 4 (4.75 mm)	28.2	24.5	28.7	
No. 8 (2.36 mm)	19.8	20.8	22.0	
No. 16 (1.18 mm)	16.9	18.4	18.6	
No. 30 (600 µm)	14.9	16.2	16.5	
No. 50 (300 µm)	13.4	14.7	14.3	
No. 100 (150 µm)	12.2	13.4	12.9	
No. 200 (75 µm)	10.28	11.03	11.11	

[a]See Virginia Test Method 99 [8].
G_{mm} = maximum theoretical specific density; VTM = voids in total mix; VMA = voids in mineral aggregate; VFA = voids filled with asphalt; VCA_{mix} = voids in coarse aggregate of mix; FA ratio = fines to asphalt ratio; RAP = reclaimed asphalt pavement; RAS = recycled asphalt shingles.

4.1 *Dynamic modulus*

Dynamic modulus results for all mixtures are shown in Figure 1. It can be seen that at reduced frequencies above approximately 0.1, the mixtures show good agreement in moduli values. At reduced frequencies below approximately 0.1, the RAP Control mixture is less stiff than the RAS mixtures. Despite being produced at different plants, the two RAS mixtures have good agreement in moduli values.

Direct comparisons of the dynamic moduli for the RAS and control mixtures are shown in Figure 2, where the light dashed lines indicate a 20% difference from the line of equality. At moduli values below about 15000 MPa, the RAS mixtures are considerably stiffer than the

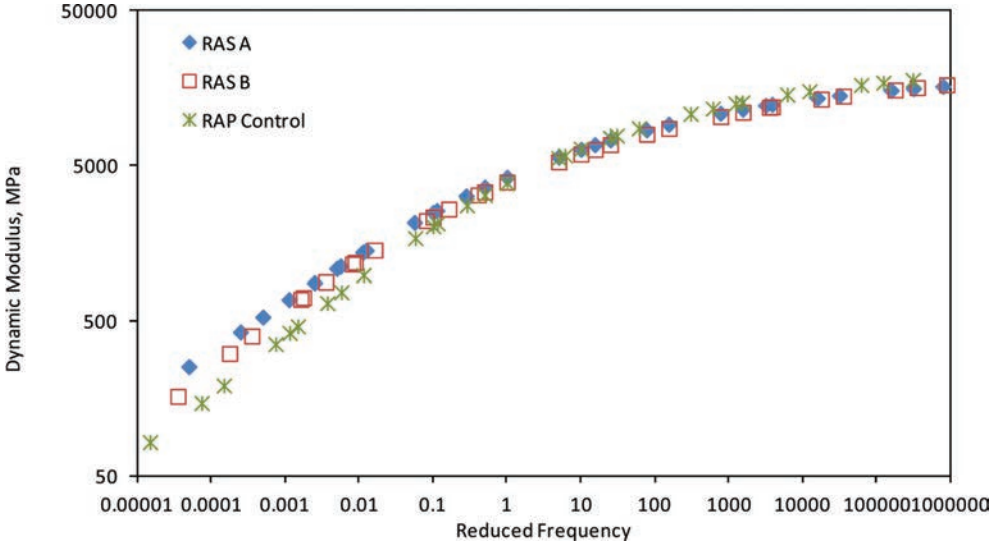

Figure 1. Dynamic modulus versus frequency for all mixtures.

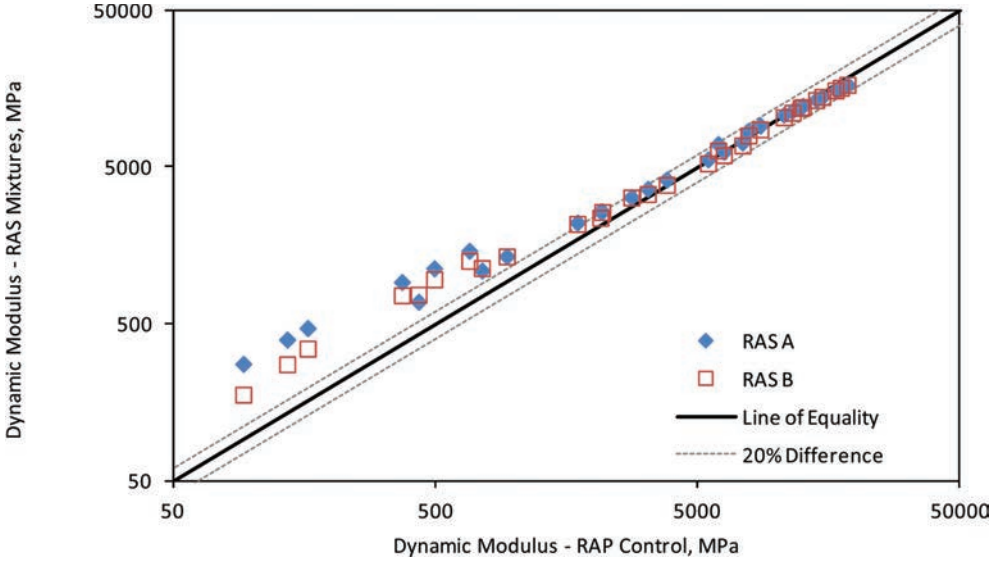

Figure 2. Comparison of modulus values for RAS mixtures versus RAP control mixture.

RAP Control mixture. These values correspond to tests performed at 54.4ºC at all frequencies and the 0.1, 0.5, and 1.0 Hz tests performed at 37.8ºC.

4.2 *Flow number*

Figure 3 presents the flow number values and air void contents for each specimen tested. The percentages at the base of each bar indicate the specimen air void content, and I-bars indicate one standard deviation about the average flow number. All mixtures were tested with a deviator stress of 600 kPa; however, material limitations prevented the testing of mixture 12-1006 at 206 kPa deviator stress. For the 600 kPa testing, the air voids for all specimens were consistent and were well within the acceptable test tolerance of 7.0 ± 0.5% air voids. Both RAS mixtures performed significantly better than the RAP Control mixture in the 600 kPa flow number test. In the 206 kPa deviator stress test, the RAS B mixture still performed better than the RAP Control mixture; however, the difference between the two (as well as the difference between the 600 kPa and 206 kPa tests) was also likely influenced by the difference in air voids, as it can be seen that the RAS B air voids were at the low end of the acceptable range whereas the RAP Control air voids were at the high end (with one specimen exceeding the acceptable tolerance).

4.3 *APA rutting analysis*

Rut testing was performed only on mixtures RAS A and RAS B because of a lack of material for the RAP Control mixture. The rut testing results are summarized in Table 3. Both mixtures rutted significantly less than the maximum VDOT criterion of 4.0 mm for SMA mixtures, despite the fact that the air void contents of all but one specimen were outside the specification requirement of 8.0 ± 0.5%. The rutting performance trend, with the RAS B mixture having a greater rut depth than the RAS A mixture, follows that shown by the flow number and indicates that RAS A mixture should be more rut resistant than the RAS B mixture.

4.4 *Fatigue analysis*

Fatigue testing was performed only on mixtures RAS B and RAP Control because of a lack of material for mixture RAS A. Figure 4 presents the fatigue curves and their regressed k-N

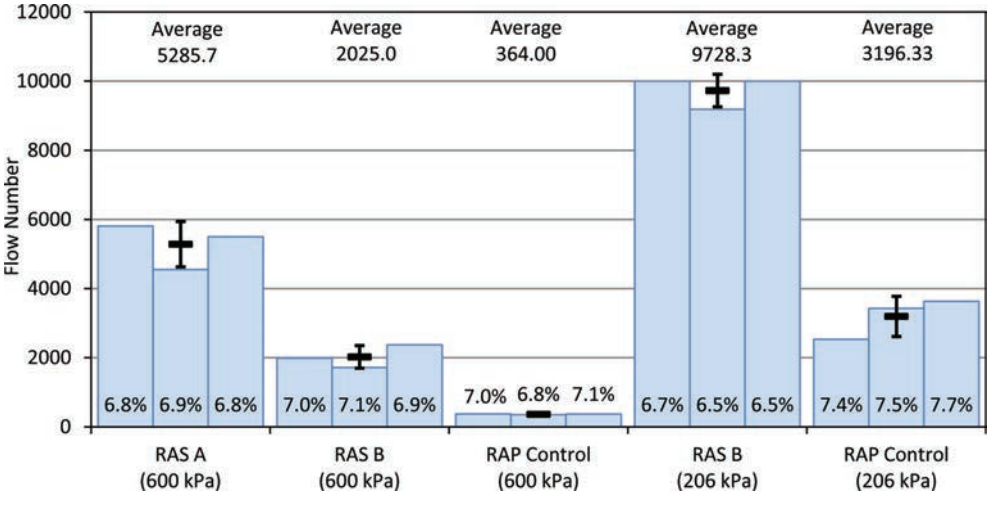

Figure 3. Flow number test results for all specimens. Black bars show average values, and I-bars indicate standard deviation. Specimen air void contents are shown near the base of each column.

Table 3. APA rut data.

	RAS A		RAS B	
Replicate	Air voids, %	Measured rutting, mm	Air voids, %	Measured rutting, mm
1	9.4	0.86	8.5	1.69
2	9.8	1.18	5.2	1.41
3	9.8	0.89	–	–
Average	9.7	0.98	6.9	1.55

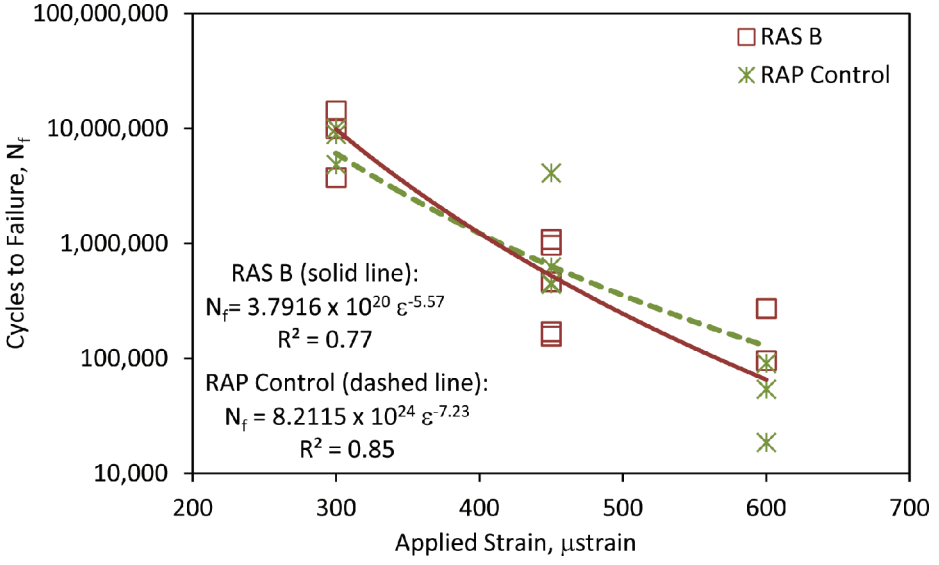

Figure 4. Fatigue curves.

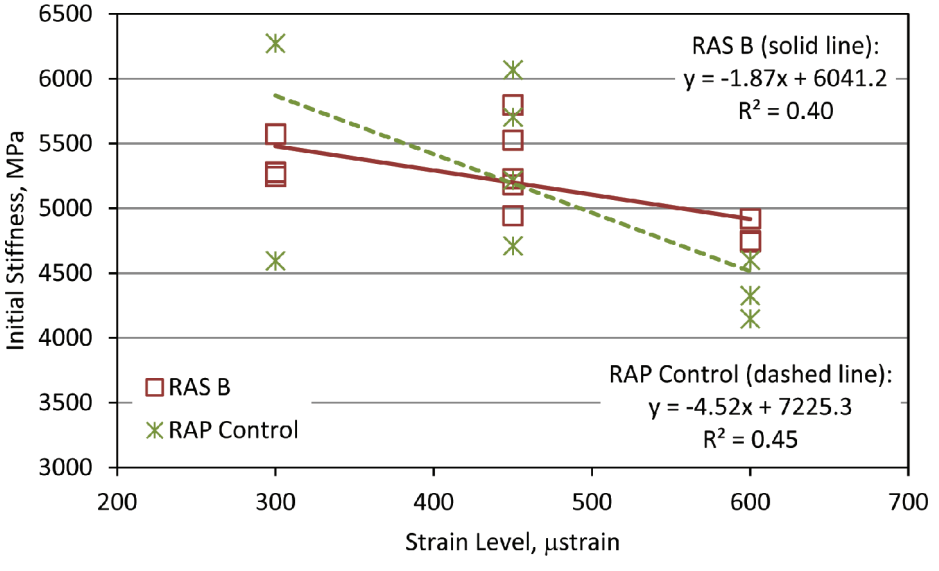

Figure 5. Applied strain versus initial stiffness for all fatigue specimens.

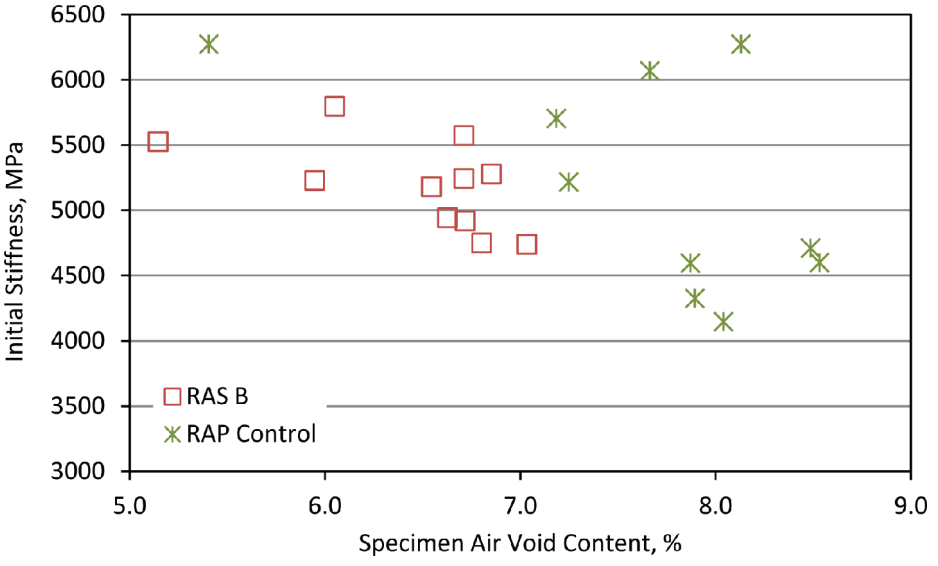

Figure 6. Specimen air void content versus initial stiffness for all fatigue specimens.

equations. The slope of the RAS B curve is greater than that of the RAP Control curve, indicating that at applied strains above approximately 400 microstrain, the RAS B mixture is expected to fail in fatigue sooner than the control mixture. Using the regressed k-N equations for each mixture and assuming a fatigue life of 50 million cycles, the fatigue endurance limit can be calculated to be 262 microstrain and 244 microstrain for the RAS B and RAP Control mixtures, respectively, indicating that under low applied strain loading, the RAS B mixture will outperform the RAP Control mixture.

In addition to the regression analysis of the fatigue data, the test results were investigated to determine if the initial stiffness of each mixture was particularly sensitive to applied strain level or specimen air void content. These results are shown in Figures 5 and 6. Figure 5 indicates a slight relationship between the applied strain and initial stiffness, although with R^2 values of only 0.40 and 0.44 for the RAS B and RAP Control mixtures, respectively, these relationships are not substantial. Figure 6 shows very little correlation in this study between the specimen air void contents and initial stiffness, with both data sets having R^2 values less than 0.35.

5 FINDINGS AND CONCLUSIONS

Based on the results of this study, the following findings are offered:

- RAS can successfully be incorporated into the design and production of SMA mixtures.
- The inclusion of RAS increased the stiffness and modulus of SMA mixtures at higher test temperatures and lower test frequencies. Very little effect on modulus was seen at temperatures below 37.8ºC.
- The inclusion of RAS significantly increased the rutting resistance of SMA mixtures as measured by the flow number test. The APA rut test indicated the same trend of rut resistance between the two RAS mixtures seen in the flow number results.
- The inclusion of RAS may adversely affect the fatigue resistance of SMA mixtures depending on the applied strains. However, this finding is based on laboratory testing of only two mixtures and additional mixtures should be evaluated both in the laboratory and in service to determine the extent to which this may affect in-service mixtures.

In conclusion, for the SMA mixtures evaluated in this study, the inclusion of RAS appears to improve high temperature/low frequency modulus values and rutting resistance as meas-

ured by the flow number test. This is likely to result in improved mixture performance and durability under conditions of heavy slow loading, such as with rest areas and truck climbing lanes, although in-service monitoring is recommended to verify this conclusion. The inclusion of RAS adversely affected the mixture performance in laboratory fatigue testing. Additional testing is required to determine if the in-service cracking or fatigue performance is significantly affected. In general, additional evaluation of RAS-containing SMA mixtures is recommended to allow a better understanding of the impact of RAS use.

ACKNOWLEDGMENTS

This research was supported by SPR funds through the Virginia Center for Transportation Innovation and Research. The author thanks Troy Deeds, Donnie Dodds, Ben Earl, Shane Moomaw, and Kim Snead of VCTIR for their outstanding efforts in specimen preparation and testing. Appreciation is extended to Adams Construction for materials. The author also thanks David Lee, Clyde Landreth, Travis Higgs, and Jeff Henderson of the VDOT Salem District; Bill Bailey of the VDOT Materials Division; and Tommy Schinkel of the VDOT Richmond District for their efforts in support of this work. Appreciation is also extended to Linda Evans of VCTIR for her editorial assistance.

REFERENCES

[1] Paulson, G.A, Stroup-Gardiner, M.A., and Epps, J.A. Recycling Waste Roofing Material in Asphalt Paving Mixtures. In Transportation Research Record No. 1115, Transportation Research Board, Washington, DC, pp. 171–182, 1987.

[2] Newcomb, D.E., Stroup-Gardiner, M., Weikle, B.M., and Drescher, A. Properties of Dense-Graded and Stone Mastic Asphalt Mixtures Containing Roofing Shingles. In Use of Waste Materials in Hot-Mix Asphalt, ASTM STP 1193, H.F. Waller, editor. American Society for Testing and Materials, West Conshohocken, PA, 1993.

[3] Button, J.W., Williams, D., and Schrocman, J.A. Roofing Shingles and Toner in Asphalt Pavements. Research Report 1344-2F. Texas Transportation Institute, College Station, 1995.

[4] Mogawer, W.S., Bennert, T., Daniel, J.S., Bonaquist, R., Austerman, A., and Booshehrian, A. Performance Characteristics of Plant Produced High RAP Mixtures. In Road Materials and Pavement Design, Vol. 13, Supplement 1, Taylor and Francis, Abingdon, Oxfordshire, UK, pp. 183–208, 2012.

[5] West, R., Willis, J.R., and Marasteanu, M. Improved Mix Design, Evaluation, and Materials Management Practices for Hot Mix Asphalt with High Reclaimed Asphalt Pavement Content. NCHRP Report 752. Transportation Research Board, Washington, DC, 2013.

[6] Williams, R.C., Cascione, A., Yu, J., Haugen, D., Marasteanu, M. and McGraw, J. Performance of Recycled Asphalt Shingles in Hot Mix Asphalt. Report TPF-5(213). Iowa State University, Ames, 2013.

[7] Virginia Department of Transportation. Special Provision Copied Notes, Special Provisions, and Supplemental Specifications for Plant Mix Schedules—Statewide. Richmond, 2013.

[8] Virginia Department of Transportation, Materials Division. Virginia Test Methods. Richmond, 2013.

[9] American Association of State Highway and Transportation Officials. Standard Specifications for Transportation Materials and Methods of Sampling and Testing, Part 2B: Tests. Washington, DC, 2012.

This page intentionally left blank

Asphalt Pavements – Kim (Ed)
© 2014 Taylor & Francis Group, London, ISBN 978-1-138-02693-3

The model for induction-healing asphalt concrete

Alvaro Garcia
Nottingham Transportation Engineering Centre (NTEC), University of Nottingham, University Park, Nottingham, UK
Empa, Swiss Federal Laboratories for Materials Science and Technology, Duebendorf, Switzerland

Moisés Bueno & José Norambuena-Contreras
Empa, Swiss Federal Laboratories for Materials Science and Technology, Duebendorf, Switzerland

Quantao Liu
State Key Laboratory of Silicate Materials for Architectures, Wuhan University of Technology, Wuhan, China

Manfred N. Partl
Empa, Swiss Federal Laboratories for Materials Science and Technology, Duebendorf, Switzerland
Highway and Railway Engineering, School of Architecture and the Build Environment, KTH Stockholm, Stockholm, Sweden

ABSTRACT: Induction heating of asphalt concrete is accomplished by adding electrically conductive particles to the asphalt mixture, and heating them with an induction heating device. When the temperature of the asphalt concrete is higher than 30–70 °C, cracks may start closing. In this article, the healing properties of 25 different mixtures, with the same aggregates distribution and amount of bitumen, but with 2 different lengths, 4 different quantities, and 4 different diameters of steel wool fibers have been considered. It has been found that the asphalt concrete studied can be healed up to 60% and that healing happens when the temperature is higher than 50 °C. Additionally, asphalt healing versus the increase of temperature has been fitted through an equation based on the capillary theory, showing that capillary flow is the main parameter affecting asphalt healing at high temperature.

Keywords: Healing asphalt concrete, induction heating, capillary flow

1 INTRODUCTION

Bitumen starts behaving like a Newtonian fluid at temperatures ranging from 30 °C to 70 °C, depending on the type of bitumen [1–4] (T_{newt}). Above these temperatures, bitumen may start flowing through any possible crack open in the pavement, in a sort of capillary flow [5]. This may happen naturally when the temperature is high enough, for example during summer, although it can be also promoted artificially by induction heating [6–9] or by microwave heating [10].

Induction heating of asphalt concrete is a technique that consists in heating electrically conductive particles, for example, steel wool fibers, previously mixed into the asphalt concrete mixture [7, 8]. Then, with the help of an induction heating device, it is possible to heat the particles locally and, through heat diffusion, heat the binder and heal the cracks.

The objective of this research is to find out the inductive healing properties of dense asphalt concrete. Asphalt healing via induction heating has been demonstrated for asphalt mastic and for porous asphalt concrete, although the influencing factors have not yet been quantified [5]. Moreover, until now, it is not clear how induction heating will affect the healing properties of dense asphalt concrete. With this purpose, 25 different asphalt concrete

mixtures, with the same aggregate distribution and amount of bitumen, but with 2 different average lengths of fibers, 4 different fiber contents, and 4 different diameters of steel wool have been prepared and their healing properties have been analysed. Moreover, a model has been explained and the healing properties of asphalt concrete explained.

2 EXPERIMENTAL METHOD

2.1 *Materials*

A dense asphalt concrete mixture was used in this research. The mixture composition is shown in ref. [11]. The aggregates consisted of crushed basaltic material (size between 0.063 mm and 11 mm) and limestone filler (size < 0.063 mm). Virgin bitumen 70/100 pen was used.

Additionally, steel wool fibers were added to the mixture. These fibers had 4 different diameters, 0.02855 mm, 0.03642 mm, 0.08389 mm and 0.15498 mm and an average length after mixing and compacting of approximately 1.5 mm. Finally, 4 different amounts of fibers were used: 0%, 2%, 4% and 6%, by total volume of bitumen in the mixture.

2.2 *Test specimens preparation*

The amount of material in each mixture was approximately 16 kg. 16 kg materials were first heated to 160 °C and then mixed in a laboratory planetary mixer, at a mixing speed of 312 rpm, during approximately 5 minutes. After the mixing, the mixtures were conditioned for 12 hours in an oven at 160 °C. This was done to simulate extreme bitumen ageing conditions.

The 16 kg batch was used to prepare specimens of 12 cm × 5 cm × 5 cm. Additionally, a 3 mm wide and 8 mm deep notch was created in the middle of the test samples. These test specimens had air void content between 4% and 10%.

2.3 *Temperature and induction heating measurements*

The temperature change in the asphalt concrete test samples was measured with a 640 × 480 pixels, infrared camera. The induction heating experiments were performed with a 30 kW induction heating generator at a maximum frequency of 78 kHz. The air temperature during the process was 20 °C.

In this research the total temperature of the 12 cm × 5 cm × 5 cm specimens has been calculated as an average between the temperature at the bottom of the test sample and the temperature at the top surface, after 1 minute heating. Moreover, the Newtonian cooling constants (ξ) of the 25 cm × 25 cm × 5 cm test specimens were calculated by observing their cooling rates during 20 minutes. The average value of the Newtonian cooling constants for all the mixtures was 0.0055 $(m^2 \cdot s)^{-1}$ and their standard deviation was 0.0012 $(m^2 \cdot s)^{-1}$.

2.4 *Bitumen rheology*

The asphalt binder of the mixtures was recovered by rotary evaporator in order to determine the temperature when Newtonian behaviour occurs. With this objective, the dynamic shear properties of bitumen were measured with a dynamic shear rheometer in a configuration with 25 mm diameter parallel plates, with a 1 mm gap. Oscillatory frequency sweeps were carried out over a range of 0.001 Hz to 0.1 Hz at temperatures from 30 °C to 70 °C under a constant strain of 0.1% within the linear viscoelastic region. The complex viscosity (η^*) as a function of frequency (ω) at different temperatures was recorded automatically during the tests.

2.5 *Healing measurements*

Induction healing of the asphalt concrete prismatic specimens was done as follows: first the tests specimens were numbered; then, they were randomly selected for heating during 0.5 minutes, 1 minute, 1.5 minutes, 2 minutes and 2.5 minutes, respectively. Later, they

were tested under three-point bending configuration at –20 °C at a deformation rate of 0.5 mm/min, stopping the tests when the force in the discharge curve of the beams reached 20 N. This load was enough to produce a crack of approximately 200 μm width crossing the specimen from the tip of the notch to the load application point. In this research, it was found that the average 3-point bending strength of the beams was 6.61 kN and the standard deviation 0.75 kN.

Once cracks were created, the test specimens were let to rest during 2 hours at 20 °C and heated during the time selected. Finally, the test samples were tested again under three-point bending. The healing level ($S(\tau)$) of asphalt mastic was defined as the relationship between the ultimate force of the test specimens during a three point bending test, F_0, and the ultimate force measured in the beams after the healing process $F_b(\tau)$, where τ is a parameter that gives an idea of the amount of energy in the asphalt concrete test sample during the healing process:

$$S(\tau) = \frac{F_b(\tau)}{F_0} \tag{1}$$

3 THEORETICAL BACKGROUND

3.1 *Temperature evolution of the test samples*

Healing does not happen only during the time induction heating, but also during the cooling time, as long as the temperature of asphalt concrete is above T_{newt} (see coloured area in Fig. 1). With this in mind, the cooling of a hot body can be described by the Newton's law of cooling [14]:

$$\frac{dQ}{dt} = \alpha A\left(T_{air} - T\right) \tag{2}$$

where Q is the thermal energy, α is a heat transfer coefficient, taken constant as a simplification, A is the surface area across which the heat is being transferred, T is the temperature of the asphalt surface and T_{air} is the temperature of the environment.

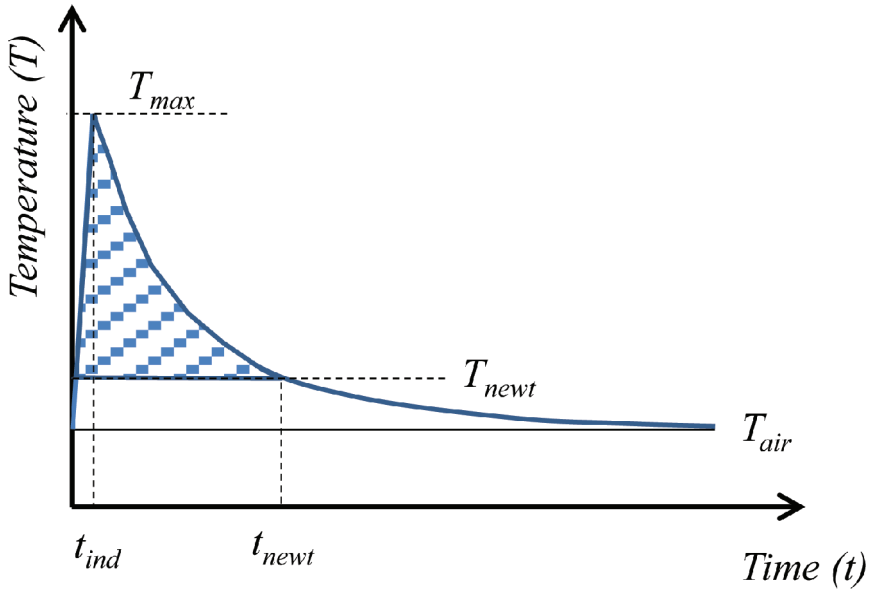

Figure 1. Temperature changes in dense asphalt concrete due to induction heating [12].

If the temperature T of the asphalt concrete surface is higher than the environmental temperature T_{air}, asphalt concrete will lose an amount of heat dQ in a time interval between t and $t + dt$, reducing its temperature T by dT.

$$dQ = -mcdT \tag{3}$$

where m is the mass of asphalt concrete and c is its specific heat.

The equation that shows the change in temperature as a function of time is

$$-mc\frac{dT}{dt} = \alpha A\left(T_{air} - T\right) \tag{4}$$

Integrating this equation, knowing that at time $t = 0$ s, the temperature of asphalt concrete will be T_{max} and introducing ξ to α/mc (m^{-2} s^{-1}), one obtains

$$\int_{T_{\max}}^{T} \frac{dT}{T_{air} - T} = -\xi A\int_{0}^{t} dt \tag{5}$$

and therefore

$$\ln\left(T - T_{air}\right) = -\xi A\cdot t + \ln\left(T_{\max} - T_{air}\right) \tag{6}$$

Hence, the time (T_{newt}) until the temperature of the test sample equals T_{newt}, i.e. when healing will be stopped is

$$t_{newt} = \frac{\ln\left(T_{\max} - T_{air}\right) - \ln\left(T_{newt} - T_{air}\right)}{\xi A} \tag{7}$$

With this in mind, the total time when the temperature of the test sample is above the environment temperature reads

$$t = t_{ind} + t_{newt} \tag{8}$$

where t_{ind} is the time of induction heating and t_{newt} is the time until the test sample comes back to the original temperature.

As the time of induction heating is very small (less than 2.5 minutes) compared to the total time when the temperature of the sample is above T_{newt} (can be more than 500 minutes), it can be eliminated from the equation, and the time healing can be approximated with Eq. (7) alone.

Finally, by solving T in Eq. (6),

$$T = T_{air} + \left(T_{\max} - T_{air}\right)e^{\left(-\xi A\, t\right)} \tag{9}$$

the area below the cooling curve (coloured area in Fig. 1), between $t = 0$ and $t = t_{newt}$, can be calculated:

$$\tau = \frac{T_{air}\xi A t_{newt} - \left(T_{\max} - T_{air}\right)\left(e^{\left(-\xi A t_{newt}\right)}\right)}{\xi A} - T_{newt}t_{newt} \tag{10}$$

This parameter will be called tau (τ) from now, its units are K · s and gives an impression of the total amount of heat in asphalt concrete during the healing process.

3.2 *Asphalt self-healing theory*

The capillary phenomena can be studied through a modification of the Lucas-Washburn equation [13] (see Fig. 2). As a simplification, in this research the crack has been assumed circular and vertical. The main forces that act in the crack are due to the surface tension (F_t),

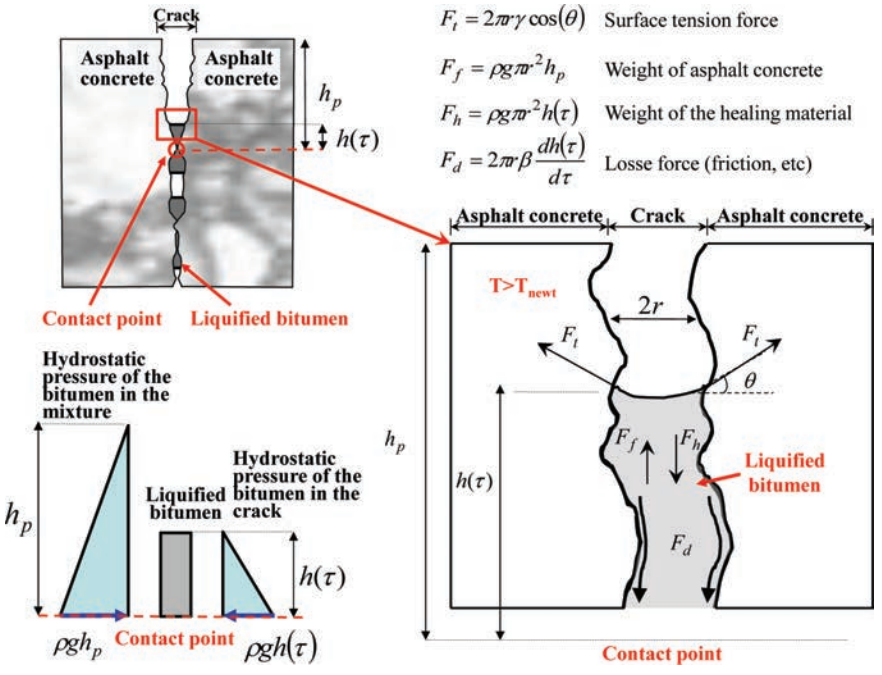

Figure 2. Scheme of the forces acting in an asphalt concrete crack during the healing process [12].

$$F_t = 2\pi r\gamma\cos(\theta) \tag{11}$$

where r is the capillary radius or half the crack width in this case; γ is the surface tension of the liquid and θ the contact angle in the wetting front. The contact angle is not constant, but will vary with the healing rate and with the different materials in the composite. To simplify the model, the contact angle has been assumed constant, and $\cos(\theta)$ equal to 1 in the calculations. Additionally, the force exerted by gravity (F_g) is considered in this model as the hydrostatic force in the zone where the binder is flowing into the crack (F_f) minus the force exerted by the weight of the healing material in the crack (F_h):

$$F_g = F_f - F_h = \rho g\pi r^2\left(h_p - h(\tau)\right) \tag{12}$$

where $\rho g\pi r^2 h_p$ is the positive hydrostatic force in the crack, being ρ the density of the binder, g the gravity and h_p the distance from the beam surface to the bottom of the healed zone being considered and $\rho g\pi r^2 h(\tau)$ the weight of the healed zone, which depends on the τ parameter. In this case, h_p is an artificial reference point which represents the distance of the crack to the surface. It is variable in time for each healed zone, but constant and equal to the height of the specimen (H) (see Fig. 2) when the whole length of the crack is being considered.

Moreover, a dissipation parameter β can be introduced in order to take into account possible sources of energy dissipation during healing, for example the force of friction by the movement bitumen against the crack faces (F_d):

$$F_d = 2\pi r\beta\frac{dh(\tau)}{d\tau} \tag{13}$$

With this in mind, the equation obtained by balancing the surface tension force, the gravity force and the energy dissipation force is:

$$2\pi r\left(\gamma - \beta\frac{dh(\tau)}{d\tau}\right) = \rho g\pi r^2\left(h(\tau) - h_p\right) \tag{14}$$

And the analytical solution for Eq. (14) is given by

$$h(\tau)=\left(h_p+\frac{2\gamma}{\rho gr}\right)\left(1-e^{-\frac{\rho gr\tau}{2\beta}}\right) \tag{15}$$

As the speed at which this process will happen will be constant in all directions, the effective area ($A_E(\tau)$) in the broken beam after some time heating, assuming a certain number of contact points (n) from where the healing process may happen, will be:

$$A_E(\tau)=\int_0^{\tau}2\pi nh(\tau)dh(\tau)=\frac{\rho grn}{2\beta}\left(h_p+\frac{2\gamma}{\rho gr}\right)^2\int_0^{\tau}\left(1-e^{-\frac{\rho gr\tau}{2\beta}}\right)e^{-\frac{\rho gr\tau}{2\beta}}d\tau \tag{16}$$

Solving the equation

$$A_E(\tau)=C\cdot e^{-D\tau}\left(-1+e^{\frac{D\tau}{2}}\right)^2, \tag{17}$$

where

$$C=\pi n\left(h_p+\frac{2\gamma}{\rho gr}\right)^2 \tag{18}$$

and

$$D=\frac{\rho gr}{\beta} \tag{19}$$

3.3 *Mechanical resistance estimation*

At the beginning of the healing, even when both faces of the crack are very close to each other, they are not completely in contact, only in certain points, randomly distributed through the crack. This means that for a complete recovery, the binder has to flow through these empty spaces and that healing will extend from the contact points through the crack.

After some time of healing (τ), during the three points bending tests, the maximum momentum ($M_F(\tau)$) in the middle of the beam is:

$$M_F(\tau)=\frac{F_b(\tau)\cdot L}{4} \tag{20}$$

where $F_b(\tau)$ is the force carried by the beam after some time heating and L is its span.

In addition, the maximum tension in the sample (σ_u), before breaking after some time of heating is given by:

$$\sigma_u=\frac{M_F(\tau)\cdot H}{2\cdot I(\tau)} \tag{21}$$

In this equation, σ_u is the maximum resistance capacity of the material, H is the height of the specimen, assuming that asphalt concrete cracks heal uniformly. Moreover, $I(\tau)$ is the moment of inertia for the area $A_E(\tau)$ given by (16):

$$I(\tau)=Ce^{-D\tau}\left(-1+e^{\frac{D\tau}{2}}\right)^2 \tag{22}$$

In addition, the force the beam resists after some specific time heating can be obtained by inserting Eq. (22) and Eq. (20) in Eq. (21),

$$F_b(\tau) = C_1 \cdot e^{-D\tau}\left(-1 + e^{\frac{D\tau}{2}}\right)^2, \tag{23}$$

where C_1 is

$$C_1 = 8\frac{\sigma_u \cdot C}{L \cdot H}, \tag{24}$$

Finally, substituting Eq. (23) in Eq. (1) leads to the following equation representing the healing level:

$$S(\tau) = \frac{C_1}{F_0} \cdot e^{-D\tau}\left(-1 + e^{\frac{D\tau}{2}}\right)^2. \tag{25}$$

4 RESULTS AND DISCUSSION

4.1 *Rheological properties of the bitumen extracted from dense asphalt concrete*

Figure 3 (a) shows the effect of frequency on the complex viscosity (η^*) of the extracted bitumen at different temperatures. To analyse the deviation of the bitumen behaviour from Newtonian, the rheological data were fitted through the following power law relationship [15]:

$$\eta^* = m \cdot |\omega|^{n-1}. \tag{26}$$

where ω is the frequency and η^* is the complex viscosity, with m and n denoting the fitting parameters. $n = 1$ corresponds to a Newtonian fluid and $n < 1$ reflects a higher degree of pseudoplastic properties of the fluid. In this study the bitumen properties were considered Newtonian when the flow behaviour index was higher than 0.9. This transition from $0.9 \leq n < 1$ is also known as near-Newtonian behaviour [16].

In Figure 3 (a), it can be seen that at the higher testing temperatures this bitumen presents a near-Newtonian behaviour, where the complex viscosity is relativity independent of the applied shear frequency. In contrast, at lower temperatures, the complex viscosity decreases with increasing frequency, exhibiting shear-thinning behaviour (pseudoplasticity).

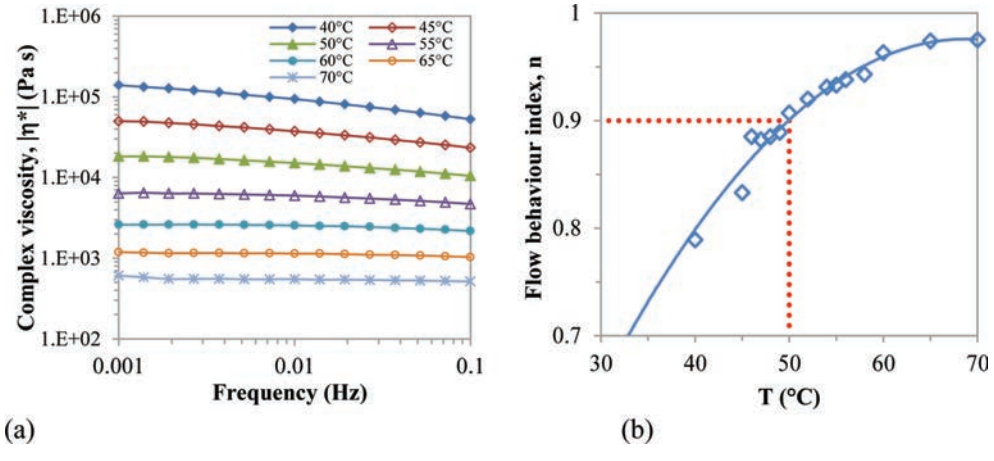

Figure 3. (a) Complex viscosity (η^*) as a function of shear frequency at temperatures from 40 °C to 70 °C and (b) flow behavior index (n) at different temperatures [12].

Moreover, the flow behaviour indexes (n) obtained at different temperatures are plotted in Figure 3 (b). It can be observed that the flow behaviour index increased with increasing temperature, getting close to 1 (ideal Newtonian behaviour). Hence, it can be concluded that the tested bitumen behaves like a near-Newtonian fluid at temperatures above 50 °C. This transition temperature is associated to the type of bitumen and ageing level, varying for other bitumens and ageing states.

4.2 *Asphalt healing results*

In Figure 4, the healing level of asphalt concrete versus the average temperature of the test samples is shown. All results obtained from different test samples, with different percentages and diameters of steel wool are shown. One of the most remarkable points is that all results for the different materials align in a single curve. In Figure 4, it can be observed that the healing, so as the point dispersion, starts at approximately 50 °C, when bitumen has a near-Newtonian behaviour. From this point, the healing levels increase with the temperature in the test samples until approximately 0.6, which happened at around 100 °C.

Since the test samples were heated without a mould, their shape changed constantly with temperatures above 50 °C. Therefore, the healing levels could not be 1, as in reference [5], where the test samples were contained in the same moulds where they had been made. Besides, these results are lower than those in reference [17] for porous asphalt concrete, where the highest healing levels reached approximately 0.8. A higher healing level was not reached because the geometry of these test samples was different. Additionally, to improve the understanding of the data, the healing results have been filtered by using a moving average filter (see solid points in Fig. 4).

Moreover, in Figure 1, the healing levels versus the τ parameter and the fitting corresponding to Eq. (25) are shown. For the fitting, only data at a temperature higher than near-viscoelastic threshold have been considered. The fitting by the model is relatively good, with an R^2 coefficient of 0.949, a maximum error of 0.1167 and an average error of 0.037. From the fitting of the equation, the maximum healing level possible with this material is approximately 0.60. This value is lower than others reported in previous researches [5] and may be caused by the different test samples geometries during healing. For future work it

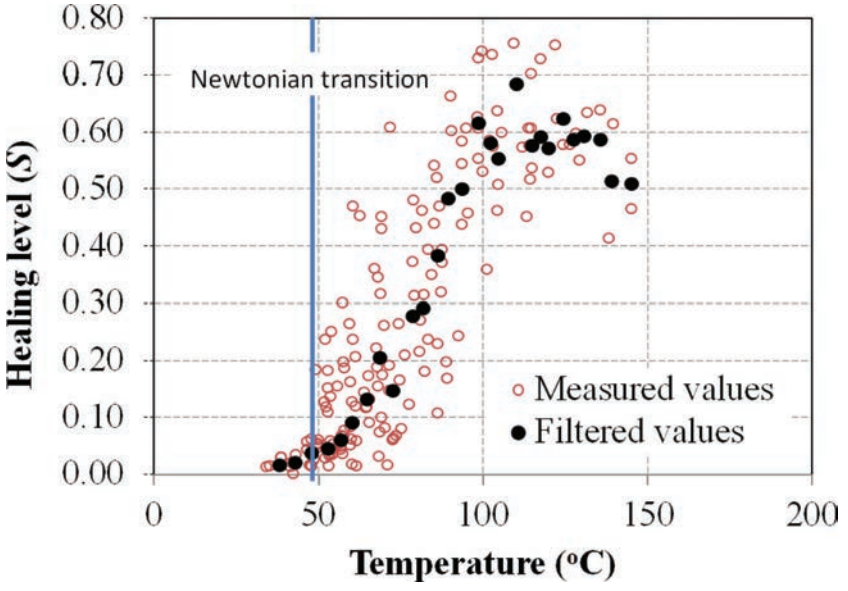

Figure 4. Healing data versus average temperature in the test samples [12].

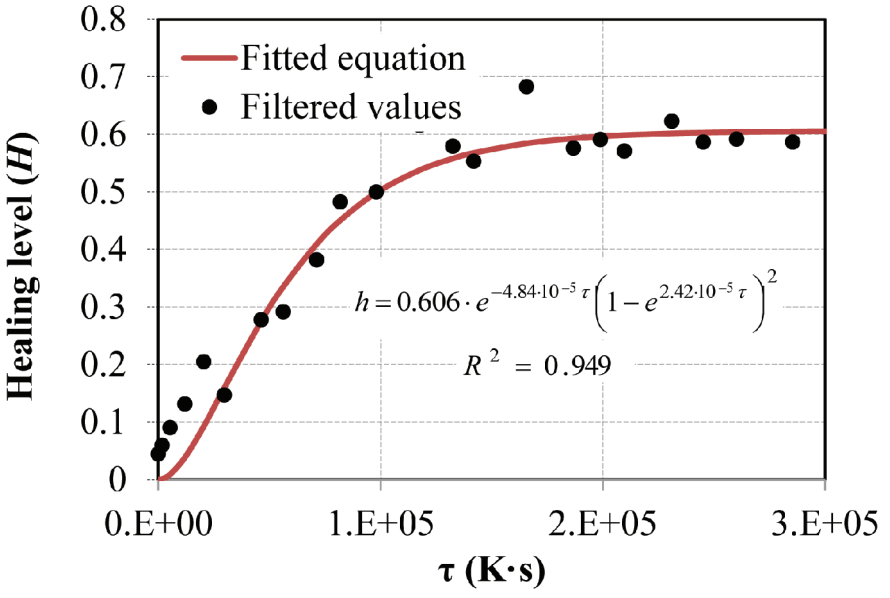

Figure 5. Healing level versus τ parameter and fitted equation [12].

will be very important to standardize a method for measuring the healing levels of asphalt concrete.

From these data, and after comparing them with those presented in reference [5] it can be concluded that the most appropriate way for healing asphalt concrete is to increase and maintain the temperature above the Newtonian transition (see Fig. 4) for a certain amount of time. If the temperature is very high during a long time, healing levels can be reduced [5], and if the temperature is too low, healing will not occur. For this reason, an optimum asphalt concrete material for self-healing applications should have a thermal conductivity as low as possible, such that the energy is not easily dissipated in the environment. With this, healing may happen at lower temperatures and the global efficiency of the system will be increased.

5 CONCLUSIONS

This article showed the effect of induction heating on the healing of damaged test samples of dense asphalt concrete. It has been found that the healing rates of dense asphalt concrete increase with increasing temperature.

Besides, the mechanical resistance of the test samples could be recovered up to 60% at around 100 °C. To reach a certain healing level, it is necessary to heat the samples above a certain temperature. If the heating time is less, damage will not be fully recovered.

Moreover, the healing recovery of dense asphalt concrete depends on the capillary flow of bitumen through the crack. This occurs above a certain temperature, in this case 50 °C, which corresponds to the near-Newtonian behaviour temperature. From the model deducted from the Lucas-Washburn equation and from the experimental results, it can be concluded that for the same bitumen and aggregates in a crack with constant width, healing recovery will depend only on the average temperature reached in the asphalt concrete specimen.

For this reason, the most appropriate way for healing asphalt concrete is to increase the temperature above the Newtonian transition and maintain it for a certain amount of time. Hence, asphalt concrete material should have a very low thermal conductivity, so that the energy is not easily dissipated in the environment.

A limitation of the model explained in the article is that it does not consider the cases where the total amount of energy introduced in the asphalt concrete is too high, i.e. at a level where the structure of asphalt concrete can be destroyed. Moreover, it is still unclear which is the exact amount of heat necessary for healing a crack in asphalt concrete, as with the induction heating method, the whole asphalt concrete volume, including the undamaged volumes are being heated.

REFERENCES

[1] Ukwuoma O, Ademodi B. The effects of temperature and shear rate on the apparent viscosity of Nigerian oil sand bitumen. Fuel Process Technol, 60, pp. 95–101. 1999.
[2] Zhao Y, Machel HG. Determination of the viscosities of Grosmong Reservoir Bitumen, Alberta, Canada. CSP CSEG CWLS Convention. Calgary, Canada. 2009.
[3] Sybilski D. Non-Newtonian viscosity of polymer-modified bitumens. Mater Struct, 26, pp. 15–23. 1993.
[4] Bazyleva AB, Anwarul H, Fulem M, Becerra M, Shaw J. Bitumen and heavy oil rheological properties: reconciliation with viscosity measurements. J Chem Eng Data; 55, 3, pp. 1389–1397. 2010.
[5] García A. Self-Healing of open cracks in asphalt mastic. FUEL;93, pp. 264–272. 2011.
[6] Liu Q, García A, Schlangen E, van de Ven M. Induction healing of asphalt mastic and porous asphalt concrete. Const Build Mat;25, pp. 3746–3752. 2011.
[7] Liu Q, Schlangen E, García A, van de Ven M. Induction heating of electrically conductive porous asphalt concrete. Const Build Mat;24(7), pp. 1207–1213. 2009.
[8] García A, Schlangen E, van de Ven M. Induction heating of mastic containing conductive fibers and fillers. Mat Struct;44(2), pp. 499–508. 2010.
[9] García A, Schlangen E, van de Ven M, Liu Q. A simple model to define induction heating in asphalt mastic. Const Build Mat;31, pp. 38–46. 2012.
[10] Gallego J, del Val MA, Contreras V, Páez A, Heating asphalt mixtures with microwaves to promote self-healing, Const Build Mat; 42, pp. 1–4. 2013.
[11] Garcia A, Norambuena-Contreras J, Partl MN, Schuetz P. Uniformity and mechanical properties of dense asphalt concrete with steel wool fibers. Const Build Mat, 43, pp. 107–117. 2013.
[12] Hamraoui A, Nylander T. Analytical approach for the Lucas-Washburn equation, J Colloid Interf Sci; 250, pp. 415–421. 2002.
[13] Garcia A., Bueno M, Norambuena-Contreras J, Partl M. Induction healing of dense asphalt concrete, Construction and Building Materials, 49, pp. 1–7. 2013.
[14] Arpaci VS, Selamet A, Kao SH. Introduction to heat transfer, Prentice Hall, New Jersey. 2000.
[15] Sung, Y.T., Kum, C.K., Lee, H.S., Kim, J.S., Yoon, H.G., Kim, W.N. Effects of crystallinity and crosslinking on the thermal and rheological properties of ethylene vinyl acetate copolymer. Polymer 46 (25), pp. 11844–11848. 2005.
[16] D. M. Heyes, P. J. Mitchell, P. B. Visscher Viscoelasticity and near-newtonian behaviour of concentrated dispersions by Brownian dynamics simulations Trends in Colloid and Interface Science VIII Progress in Colloid & Polymer Science Volume 97, pp. 179–182. 1994.
[17] Liu Q. Induction healing of porous asphalt concrete. PhD Thesis. TU Delft, the Netherlands 2012.

Asphalt Pavements – Kim (Ed)
© 2014 Taylor & Francis Group, London, ISBN 978-1-138-02693-3

Investigation on hardening mechanism and cement hydration of Cement Asphalt Emulsion Composites

Xing Fang
Empa, Swiss Federal Laboratories for Materials Science and Technology, Duebendorf, Switzerland

Alvaro Garcia
Nottingham Transportation Engineering Centre, University of Nottingham, Nottingham, UK
Empa, Swiss Federal Laboratories for Materials Science and Technology, Duebendorf, Switzerland

Manfred N. Partl
Empa, Swiss Federal Laboratories for Materials Science and Technology, Duebendorf, Switzerland
Highway and Railway Engineering, School of Architecture and the Build Environment, KTH Stockholm, Stockholm, Sweden

Pietro Lura
Empa, Swiss Federal Laboratories for Materials Science and Technology, Duebendorf, Switzerland
Institute for Building Materials, Swiss Federal Institute of Technology Zurich (ETHZ), Zurich, Switzerland

ABSTRACT: Cement Asphalt Emulsion Composites (CAEC) are mixtures of bitumen emulsion, cement, water and aggregates that harden at ambient temperature. They are mixed at ambient temperature and harden due to breaking of the emulsion, water evaporation and cement hydration. Potential advantages of CAEC are lower temperature susceptibility than asphalt concrete and higher flexibility than cement concrete. To quantify the effects of cement hydration on the mechanical properties of CAEC, two different emulsions (cationic and anionic) mixed with either 0%, 3% and 6% Ordinary Portland Cement (OPC) by mass of dry aggregates were studied by isothermal calorimetry and Marshall tests. By monitoring the mass of the specimens and estimating the amount of water bound by the cement, the water content was calculated. This study shows that bitumen emulsion has no significant effect on the degree of cement hydration. Cement hydration, however, significantly contributes to the hardening of CAEC. Moreover, a higher amount of cement added to the mixture results in a higher amount of bound, adsorbed and capillary water in the CAEC.

Keywords: CAEC, bitumen emulsion, Portland cement, isothermal calorimetry

1 INTRODUCTION

Cold mix asphalt consists of bitumen emulsion, water, unheated aggregates and filler. This material has low environmental impact and is cost-effective [1–3]. However, it has rarely been used as structural layer for heavy-duty pavements [2,3], mainly because of the long time (several weeks) required to reach its full strength [4], resulting in inadequate performance (inferior early strength and high porosity) compared with conventional Hot Mix Asphalt (HMA) [3,5,6].

In order to improve the early performance of cold mix asphalt, cement can be added to the mixture. The addition of 1% to 2% wt. of Ordinary Portland Cement (OPC) to cold mix asphalt may improve its early-life mechanical properties [7] and the fully cured material acquires comparable mechanical properties to an equivalent HMA [3,8,9]. Research on these

composite materials, often called CAEC (Cement-Asphalt Emulsion Composite) [10,11], started in the 1970s. CAEC shares characteristics of both cement and asphalt concrete [12]. In particular, compared with HMA, CAEC has higher deformation resistance, lower temperature susceptibility [10], and better resistance to water damage [11]. Additionally, the introduction of cement in cold mix asphalt accelerates emulsion breaking [5], because cement hydration consumes water in the emulsion and meanwhile it increases its alkalinity. This has a special impact when a cationic bitumen emulsion is used [13]. However, because of the long time required to reach its full strength and an inadequate understanding of this material, CAEC has rarely been used in pavements.

This research aims at obtaining a general perspective of CAEC. It focuses on OPC hydration and on water evaporation and their contribution to the mechanical properties of CAEC. With this purpose, two emulsions, one cationic and one anionic, have been mixed with Ordinary Portland Cement (OPC) in various amounts (0%, 3% and 6% by total mass of aggregates) and with aggregates to prepare CAEC. The evolution of the mechanical properties of the mixture with time was characterized with Marshall Stability tests. The effect of emulsion on the cement hydration has been investigated by means of Isothermal Calorimetry tests. Finally, the evolution of water content in CAEC has been quantified to characterize the hardening of the mixture.

2 MATERIALS AND METHODS

2.1 *Materials*

A dense CAEC mixture (0/8) was used in this research [14]. The aggregates used to make CAEC were quarry material (size between 2 and 8 mm and density 2770 kg/m^3), crushed sand (size between 0.063 and 2 mm and density 2688 kg/m^3), and filler (size < 0.063 mm and density 2638 kg/m^3). The total amount of filler in the mixture was 6% by mass of dry materials (aggregates + filler). Two types of commercially-available unmodified bitumen emulsion, with 60% of residual bitumen content, were used in this paper. The first one was a rapid-setting cationic emulsion, while the second one was a solvent-free, slow-setting anionic emulsion (Table 1). Additionally, to facilitate the mixture preparation, 2.52% wt. (by dry aggregates) tap water was added to the mixture. Ordinary Portland Cement (OPC) CEM I 42.5 N (chemical analysis and phase composition shown in Table 2) was added to the mixture, by replacing 0%, 3% and 6% (all filler replaced) of filler. Table 3 shows the mix compositions. In this paper, OPC designates ordinary Portland cement; 3 and 6 represent 3% and 6% cement by mass of dry aggregates, and A and C denote anionic and cationic bitumen emulsion, respectively. An example is OPC3C-7d, a cationic bitumen emulsion with 3% OPC by mass of dry aggregates 7 days after compaction.

2.2 *Test specimens preparation*

The raw materials were added to the bowl in this order: first the coarse aggregates, then water and emulsion, then the sand and finally the filler and cement. The materials were mixed during 1 minute. The temperature during the mixing process was 20 ± 1°C. One mix was used to make 9 cylindrical Marshall specimens with 101.6 mm diameter, approximately 7 cm height and 1190 g of mass. Immediately after placing the specimens in the mould, they were compacted with 100 blows of the Marshall hammer, 50 for each side of the specimens.

Table 1. Properties of bitumen emulsion and residual bitumen binder.

Properties	Anionic emulsion	Cationic emulsion
Softening point °C	58.5	63.6
Penetration, @ 25°C, 0.1 mm	41	24

Table 2. Chemical analysis and phase composition of OPC.

Chemical analysis	CaO	SiO_2	Al_2O_3	Fe_2O_3	MgO	K_2O	Na_2O	SO_3	TiO_2	P_2O_5	SrO	L.O.I.	Total
(wt. %)	62	20	5.1	2.9	2.3	1.01	0.26	3	0.28	0.2	0.15	2.68	99.4
Phase composition	C_3S	C_2S	C_3A	C_4AF	MgO	K_2SO_4	Na_2SO_4	K_2O	Na_2O	CaO free	$CaCO_3$	$C\underline{S}H_2$	
(wt. %)	56	16	4.8	11.5	1	1.6	0.26	0.1	0.15	0.27	4.8	4	100.1

Table 3. The amount of materials by 100 g of mixture.

Aggregate [g]	Water [g]	Emulsion [g]	Filler [g]	Cement [g]	Cement [%][a]
78.99	2.52	13.45	5.04	0	0
			2.52	2.52	3
			0	5.04	6

[a]Percentage of cement by mass of dry aggregate.

The specimens, still in the moulds, were left in a humidity-controlled room (relative humidity 90 ± 3% and temperature 20 ± 1°C) for one day. After this, the test samples were demoulded and the lateral and bottom surfaces were sealed with aluminum foil. Then, the specimens were left in the humidity-controlled room during the required curing time: 1, 3, 7, 14, 21 and 28 days. During the curing period, water in the specimens could evaporate from the specimens' upper side only. Additionally, 3 hot mix asphalt specimens (made by residual bitumen from both anionic and cationic emulsion) were prepared for comparison purposes.

2.3 *Isothermal calorimetry*

Isothermal calorimetry tests were conducted at 20°C with a Thermometric TAM Air instrument calibrated at 600 mW. The rate of heat release was measured on mixtures containing the three types of cement and the two types of bitumen emulsion, with duplicate specimens for each mixture. The water-to-cement ratio (w/c) of the CAEC mixtures was 3.14 for mixtures with 3% cement and 1.57, for mixtures with 6% cement, including both the water in the emulsions and the extra water added for workability. In addition to the CAEC mixtures, cement paste with w/c 1.0 and cold mix asphalt mixtures without cement were measured for comparison purposes. Cement paste with w/c 1.0 was used in order to avoid settlement of cement paste in the case of high w/c. Furthermore, it has been confirmed in reference [15] that the increase of w/c has no significant influence on cumulative heat released in the case when w/c is beyond 0.42. 20 g of freshly-mixed CAEC or 6 g of cement paste were inserted into glass vials of internal diameter 22.5 mm, sealed with a tight lid and placed in the measuring cell. The rate of heat release was then measured during 72 hours and integrated to obtain the cumulative heat release.

2.4 *Moisture losses and amount of trapped water*

The moisture loss of the Marshall specimens during curing was monitored by weighing them regularly during 28 days. Simultaneously, the Marshall specimens without cement were cured in a humidity-controlled room (relative humidity 90 ± 3% and temperature 20 ± 1°C) for 4 months until mass loss due to evaporation stopped. Then they were crushed and oven-dried at 105°C to obtain the trapped water content. The trapped water was defined as the water adsorbed on the surfaces of aggregate and filler as well as the water trapped in the closed pores within the bitumen and that cannot evaporate. In this study, the amount of trapped water was determined from the average of 20 duplicate samples.

Because the cationic emulsion broke immediately when fine aggregates were added to the mixture, a considerable amount of water was lost during the compaction process. For this reason, it was possible to quantify the water-content evolution only for the mixtures with anionic emulsion.

2.5 *Marshall tests*

The Marshall stability of cold mix asphalt samples was measured at 1, 3, 7, 14, 21 and 28 days. The tests were carried out immediately after the specimens had left the humidity-controlled room and were finished in approximately 10 min. The testing room temperature

was strictly controlled at 20 ± 1°C. Marshall tests were conducted in room temperature other than 60°C treatment in water bath. The reason is that the water bath will increase the cement hydration. Furthermore, the water bath will raise the water content in the samples which and thus decrease the strength of samples [9]. Every Marshall stability value was obtained from the average results of 3 specimens.

3 RESULTS AND DISCUSSION

3.1 *Isothermal calorimetry*

Mixtures without cement did not show any heat liberation, confirming that all the heat liberated from the CAEC mixture came from cement hydration. In addition to the CAEC, also the rate of heat liberation and the cumulative heat for the cement pastes are shown in Figure 1.

Compared with the cement paste, the main hydration peak of mixtures with anionic emulsion was wider and occurred significantly later, which reveals a retardation of the OPC hydration. However, the main hydration peak of OPC in the presence of cationic emulsion occurred slightly earlier than for the OPC paste. The cumulative heat release of OPC in the presence of anionic emulsion was initially lower than for cement paste, but increased steadily and eventually surpassed the heat released by the cationic mixture and by the cement paste. From Figure 1 it can be observed that cement with anionic emulsion samples showed a longer dormant period than cement with cationic emulsion samples, while there is no significant difference between cationic emulsion samples and the cement pastes. Similar conclusion has been made in reference [13]. In that paper, the author indicated that the addition of small percentage of cationic to cement paste didn't influence the rate of heat liberation or the cumulative heat released. However, the addition of anionic bitumen emulsion slightly increased the dormant period of cement hydration [13]. The initial retardation or acceleration observed in Figure 1 may be due to the pH of the bitumen emulsions [13], while no significant effect of the emulsion or of the bitumen could be observed on the later development of hydration. Similar conclusion has been made in reference [16] that emulsifier has no significant influence on cumulative heat released of cement hydration.

The degree of hydration reached by the cement was obtained as described in [17]:

$$\alpha(t_i) = \frac{H_{t_i}}{H_{cem}} \tag{1}$$

where $\alpha(t_i)$ is the degree of hydration at time t_i; H_{t_i} is the cumulative heat measured at time t_i (J/g of cement) and H_{cem} is the potential heat of OPC hydration which is 433.6 J/g of cement [18].

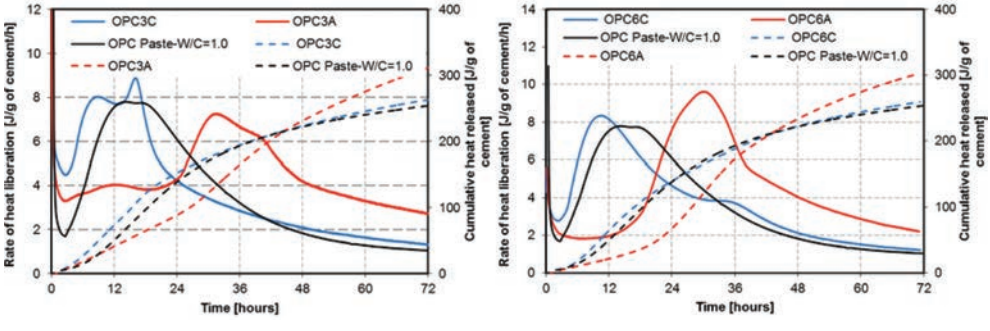

Figure 1. Isothermal calorimetry of OPC: 3% cement (left) and 6% cement (right) with cationic emulsion (blue) and anionic emulsion (red), cement paste (black—w/c = 1.0). Rate of heat liberation as continuous lines; cumulative heat as dashed lines.

Table 4. Degrees of OPC hydration at 24 h, 72 h and 28 d.

Mixtures	OPC3C	OPC6C	OPC3A	OPC6A	Cement paste
W/C	3.14	1.57	3.14	1.57	1.0
24 h [%]	35.1	32.2	20.3	15.4	32.0
72 h [%]	60.7	60.3	71.8	70.3	58.6
28 days [%]	60.7	60.3	71.8	70.3	58.6

The degrees of hydration of OPC at 24 h and at 72 h, obtained from Eq. 1 are shown in Table 4. Additionally, the influence of different types of bitumen emulsion on the hydration degree of mixtures with 3% and 6% OPC hydration are shown in Figure 1.

As the initial w/c in the CAEC is rather high (3.14 for 3% cement and 1.57 for 6% cement), it is assumed in this study that the loss of water due to evaporation in the Marshall specimens has little impact on cement hydration in the first few days. Thus, the degree of hydration reached in the first three days is assumed to be equal to that of the mixtures hydrating in sealed condition in the isothermal calorimeter (considering the moisture loss by evaporation for the OPC mixtures after 3 days the w/c of the Marshall specimens is approximately between 0.9 and 1.7).

After 3 days, the degree of hydration was considered to remain constant up to 28 days. Of course this approach will lead to an underestimation of the amount of bound water, which in reality will continuously grow, albeit at a low rate. However, since the degree of hydration at 3 days is already rather high, and considering the unknown effect of evaporation on the rate of hydration in the CAEC, this approach is considered to yield less uncertainties than a possible estimation of the degree of hydration at 28 days based on the rate of hydration in the first three days.

3.2 *Quantification of water content evolution*

The water in the mixture comes mainly from the bitumen emulsion and partly from the extra water used to wet the coarse aggregates. In reference [9] it has been shown that the water content has a significant effect on the mechanical properties of CAEC. Thus in this section, the amount of water evaporated, the amount of water trapped and the amount of water bound by the cement is quantified. The water in the specimens can be classified in three categories: *i)* residual water consisting of residual evaporable water at time t_i and of trapped water, *ii)* physically bound water on the surface of the cement hydration products and *iii)* chemically bound water within the hydration products [19]. Evaporable water refers to the capillary water within the capillary pores that are present in the hydration products of the cement and in the pores between the aggregates and the filler. The evaporated water is the water evaporated through the upper face of the specimens and is monitored by regular weighing. The driving force for water evaporation is the difference in the water potential between the interior of the CAEC specimens and the air in the climate chamber, which progressively decreases (due to evaporation and binding by cement hydration products) until an equilibrium with the ambient relative humidity is eventually reached.

In this paper, the bound water (both chemically bound and physically bound, see categories *ii)* and *iii)* above) was determined according to Powers model [19]. In particular, 1 g of OPC that has fully reacted binds a total amount of 0.42 g of water [19].

The mass loss from all the mixtures with anionic emulsion as a function of time, corresponding to the amount of evaporated water, was measured by regular weighting. The results revealed that the evaporated water increased rapidly during the first week after compacting and very small increase was observed afterward until 28 days. It is very clear that samples showed higher evaporated water content in the absence of cement. This is result from the consequences that cement hydration bound water and reduced the amount of evaporable water. The amount of trapped water was 1.21%; in this paper, it is assumed that the amount of trapped water is the same for all mixtures, independent of the amount of cement.

The residual evaporable water in specimens used for the Marshall tests was calculated by subtracting the water that had already evaporated at time t_i, the water bound by the cement and the trapped water from the initial water present in the samples. Thus the residual evaporable water content was quantified as:

$$p_{ev,res}(t_i) = p_{tot} - p_{bou}(t_i) - p_{trap} - p_{ev}(t_i) \quad (2)$$

where p_{tot} is the total initial water content in the mixtures. It was the same for every type of material with anionic emulsion and was obtained from the water in the emulsion plus the extra water used to wet the aggregates. Its value was 7.90%: 2.52% (tap water) + 13.45% (amount of emulsion) × 40% (water from the emulsion), see Table 3. $p_{ev}(t_i)$ is the percentage of water by initial mass of mixture that has evaporated at time t_i, $p_{bou}(t_i)$ is the percentage of water bound by the cement and p_{trap} is the water trapped in the mixture (1.21%). The residual evaporable water was quantified by Eq. 2 other than by oven drying is due to the reasons that the heating will accelerate cement hydration and the loss of volatile components of bitumen. Furthermore, $p_{bou}(t_i)$, the water bound by cement hydration, was quantified as:

$$p_{bou} = \lambda \cdot C \cdot \alpha(t_i) \quad (3)$$

where λ is the amount of water bound by 1 g of cement, which is 0.42 g/g; C is the percentage of cement in the mixture, 2.52% and 5.04% for mixtures with 3% and 6% of cement, respectively (see Table 3) and $\alpha(t_i)$ is the degree of hydration at curing time, t_i (Table 4).

According to this equation, the residual evaporable water left in the specimens, the water bound by cement and the water evaporated at after 1 day, 7 days and 28 days were quantified and are shown in Figure 2. In this Figure, it can be observed that OPC6A bound more water than OPC3A. But at the same time, OPC6C contained more residual evaporable water. This result partly explained why the modulus of CAEC steadily increases even after several months [4,12]. It should be noted that on one hand, a higher amount of cement in the CAEC mixture will definitely bind more water. On the other hand, the amount of water held by capillary forces may be higher in the mixtures with more cement. This will result in the decrease of the evaporation rate and also in a higher content of residual evaporable water at equilibrium. Although this is just a hypothesis and it is pending of further research.

3.3 *Marshall stability results*

In the case of the reference HMA, the Marshall stabilities of samples, made with the residual bitumen obtained from the anionic and cationic emulsions, were 25.9 kN and 36.5 kN, respectively.

The evolution of the Marshall stability with 0%, 3% and 6% of OPC is shown in Figure 4. A linear growth of the stability can be observed in the case of test samples made with cationic

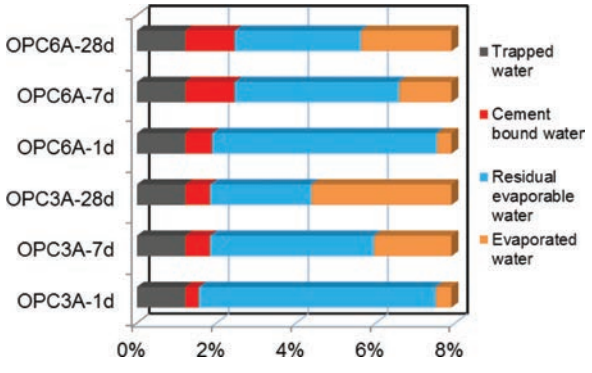

Figure 2. The water content evolution of Marshall specimens with anionic emulsion.

bitumen emulsion, without cement (OPC0C). However, in the case of anionic emulsion without cement (C0A), the bitumen emulsion broke too slowly to provide enough strength. The dimension changed during curing because of gravity. For this reason, the measured stability was presented here as a reference. The Marshall stability of mixtures with both cationic and anionic emulsions increased significantly with the addition of cement. The stability increased steadily during the 28 days curing period except for OPC3C, which remained almost constant after 7 days curing. The stability of OPC6C at 28 days was lower than that of the corresponding reference HMA, while the stability of test samples made with anionic emulsion (OPC3A and OPC6A) was similar to that of the reference HMA.

3.4 *The contribution of cement to CAEC*

In the case of mixtures without cement, only bitumen acts as a binder. The Marshall stabilities of mixtures with cationic emulsion are lower than the stabilities of those containing cement and, in the case of slow setting anionic emulsion, the test samples collapsed after demoulding.

When a small amount of cement was added to CAEC, it had an immediate effect on the mechanical properties of the cold mixed asphalt: the stability of mixtures containing 3% OPC and cationic emulsion was higher than for mixtures without cement 1 day after mixing (see Fig. 3a). However, in the case of mixtures with OPC and anionic emulsion, there was no significant difference in the Marshall stability after 1 day curing when compared to the test samples without OPC (see Fig. 3b). In Figure 1, it can be observed that in the presence of cationic emulsion, the main hydration peak of OPC occurred before 24 hours curing, while in the case of mixtures with anionic emulsion the main hydration peak took place after 24 hours curing. Besides, as the contribution of the emulsion to the Marshall stability

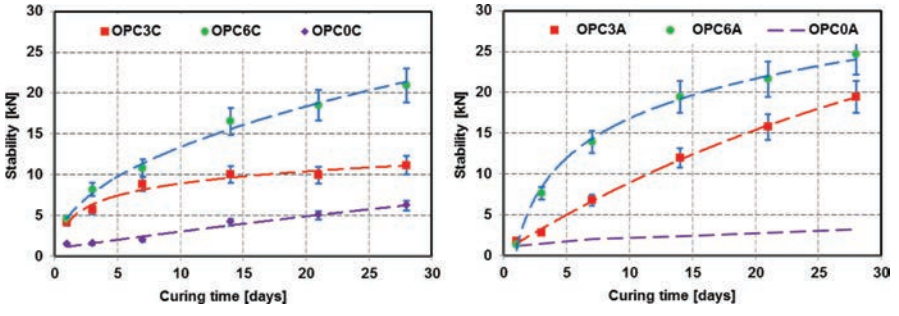

Figure 3. Evolution of the Marshall stability with curing time (a. OPC-C, b. OPC-A).

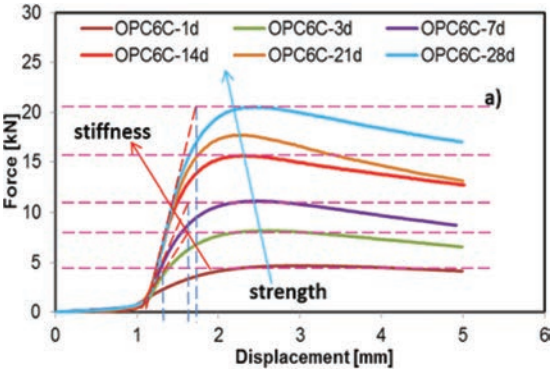

Figure 4. Marshall force-displacement curve of OPC6C (left) as a function of curing time.

Table 5. Degree of hydration VS Marshall stability of mixtures at 24 h.

Mixtures	OPC3C	OPC6C	OPC3A	OPC6A
Degree of hydration [%]	35.1	32.2	20.3	15.4
Marshall stability [kN]	4.1	4.6	1.8	1.4

is very limited (see OPC6C in Fig. 4), the increase of strength could be mainly attributed to cement hydration. Table 5 shows the degree of cement hydration versus the Marshall stability of anionic emulsion mixtures and cationic emulsion mixtures after 24 h curing. It indicated clearly that mixtures with higher degree of hydration clearly show higher Marshall stability. This can be confirmed by reference [6] and [20], in which rapid hardening cement was used to accelerate the hardening of CAEC.

3.5 *The contribution of bitumen emulsion to CAEC*

The most important contribution of bitumen emulsion to the mixture is to supply the bituminous binder for increasing the flexibility of CAEC and to provide water for the cement hydration. In this article it has been concluded that bitumen emulsion has no significant effect on the ultimate degree of cement hydration. On one hand, bitumen emulsion provides water for the cement hydration and on the other hand, cement particles consume the water and trigger the flocculation of bitumen droplets. By quantifying the moisture losses in the mixtures, it was found that the residual evaporable water content in the mixtures is relatively high after 28 days curing (from 2.5% to 3.5% by initial mass of mixtures). Thus, the increase of strength in these mixtures may be caused by the hardening of bitumen. The contribution of bitumen emulsion to the asphalt concrete mixture has however not been fully understood and needs to be characterized in detail in the future.

4 CONCLUSIONS

In this article, the cement hydration in the CAEC mixtures was characterized by isothermal calorimetry and the results indicated that bitumen emulsion may slightly retard or accelerate cement hydration, but has no significant effect on the ultimate degree of hydration of cement.

Cement hydration products act as a binder by forming bridges between aggregates and thus increasing the Marshall stability of cold mixed asphalt. Meanwhile, cement hydration products act as a stiffener of the binder substrate and consequently increase the stiffness of cold mixed asphalt. Bitumen emulsion provides water for cement hydration and some flexibility for the mixture.

The quantification of water content indicates that although cement hydration consumed a part of water, a relatively high amount of water still existed in CAEC mixtures after 28 days. This is the main reason for later development of strength and stiffness.

It can be concluded that CAEC has comparable mechanical properties to hot mix asphalt when cement is well distributed in the mixtures. The early strength of cold mixed asphalt can be substantially improved by adding a certain amount of cement. Although bitumen emulsion has no significant effect on the cement hydration process, the individual contributions of cement and bitumen emulsions to the mechanical properties of cold mix asphalt are still unclear.

ACKNOWLEDGEMENTS

The authors thank Hans Kienast, Walter Trindler, Axel Schöler and Dr. Mateusz Wyrzykowski for help with the experiments and CTW Strassenbaustoffe AG for providing bitumen emulsion. The first author was financed by a scholarship from the China Scholarship Council.

REFERENCES

[1] D. Swiertz, P. Johannes, L. Tashman, H. Bahia. Evaluation of Laboratory Coating and Compaction Procedures for Cold Mix Asphalt. AAPT 2012.

[2] T.A. Doyle, C. McNally, A. Gibney, A. Tabakovic. Developing maturity methods for the assessment of cold-mix bituminous materials. Construction and Building Materials 38 (2013) 524–529.

[3] S. Al-Busaltan1, H. Al Nageim, W. Atherton, G. Sharples. Mechanical Properties of an Upgrading Cold-Mix Asphalt Using Waste Materials. Journal of Materials in Civil Engineering, 2012.24:1484–1491.

[4] H. Al Nageim et al. A comparative study for improving the mechanical properties of cold bituminous emulsion mixtures with cement and waste materials. Construction and building materials 36 (2012): 743–748.

[5] D. Needham. Developments in bitumen emulsion mixtures for roads. Ph.D. thesis, University of Nottingham, Nottingham, UK.

[6] Y. Yao, H. Sun. Performance and microanalysis of cement asphalt mortar with admixture of coal fly ash. Journal of Materials Science Research, Vol. 1, No. 2; April 2012.

[7] I.N.A. Thanaya, S.E. Zoorob, J.P. Forth. A laboratory study on cold-mix, cold-lay emulsion mixtures. Proceedings of the Institution of Civil Engineers, ICE Publishing, London, UK, 47 55. Transport 162 February 2009 Issue TR1 Pages 47–55.

[8] S.F. Browm, D. Needham. A study of cement modified bitumen emulsion mixtures. In: AAPT 2000. Reno, Nevada; 2000.

[9] A. Garcia, P. Lura, M.N. Partl, I. Jerjen. Influence of cement and environmental humidity on asphalt emulsion and cement composites performance. Materials and structures 2012, in press. DOI 10.1617/s11527-012-9971-6.

[10] G. Li, Y. Zhao, S.-S. Pang, W. Huang. Experimental study of cement-asphalt emulsion composite. Cement and concrete research, Vol. 28, No. 5: 635–641, 1998.

[11] S. Oruc, F. Celik, M.V. Akpinar. Effect of cement on emulsified asphalt mixtures. JMEPEG (2007) 16: p. 578–583.

[12] R.L. Terrel, C.K. Wang. Early curing behaviour of cement modified asphalt emulsion mixtures, AAPT 1972.

[13] N. Pouliot, J. Marchand, M. Pigeon. Hydration mechanisms, microstructure, and mechanical properties of mortars prepared with mixed binder cement slurry-asphalt emulsion. J. Mater. Civ. Eng. 2003. 15: 54–59.

[14] The aggregate size distribution http://www.blzag.ch/pdf/20120412092641.pdf from Civil Engineering Offices of Zurich.

[15] P. Lura, F. Winnefeld, X. Fang. A simple method to estimate the amount of water bound by cement. Journal of Thermal Analysis and Calorimetry 2014, submitted.

[16] Y. Tan, J. Ouyang, J. Lv, Y. Li. Effect of emulsifier on cement hydration in cement asphalt mortar. Construction and Building Materials 47 (2013) 159–164.

[17] A.K. Schindler, K.J. Folliard. Heat of hydration models for cementitious materials, ACI Materials Journal, 2005.

[18] H.F.W. Taylor. Cement chemistry 2nd edition, pp 216–217, 1997.

[19] T.C. Powers, T.L. Brownyard. Studies of the physical properties of hardened Portland cement paste, Bulletin 22, Research Laboratories of the Portland Cement Association, Chicago, 1948.

[20] Y. Higuchi, Y. Harada, T. Sato, K. Nakagawa, A.I. Kawaguchi, Y. Kasahara. Quick hardending cement-asphalt composition. United States Patent 4084981, April 18, 1978.

Long-term pavement performance prediction—II

This page intentionally left blank

Asphalt Pavements – Kim (Ed)
© 2014 Taylor & Francis Group, London, ISBN 978-1-138-02693-3

Scottish Inspection Panel

Michael McHale
TRL, Edinburgh, UK

Dougie Millar
Transport Scotland, Glasgow, Scotland, UK

Ian Carswell
TRL, Wokingham, Berks, UK

ABSTRACT: In order to provide an indicator of the performance of SMA surface course, the Scottish Inspection Panel (SIP) was established in 2006. This paper describes the work undertaken by the SIP, including the development of a visual assessment procedure that has its roots in a system established in the 1950s. The SIP team comprises a group of widely experienced asphalt experts who represent a cross-section of the asphalt industry. The survey team record any features that appear to affect the service life of the surface course to establish initial causes and typical modes of failure. Sites of special interest are also inspected to assess the performance of new materials and to identify longer term deterioration trends. Based on the observations and results of SIP surveys, several recommendations have been made to improve material design, construction and aftercare. Examples of improvements include closing up the surface texture to improve durability, without compromising safety; improved joint construction techniques, advice on treatment selection; and promoting the importance of maintaining drainage systems. Recent SIP results (2012) have shown that year-on-year improvements are being made and the process has been successful in improving the performance of surface courses laid on the Scottish trunk road network.

Keywords: SMA, durability, defects, visual inspection, performance

1 INTRODUCTION

In order to provide an indicator of the performance of asphalt surface course, Transport Scotland established an annual monitoring procedure in 2006. Each year the Scottish Inspection Panel (SIP) is responsible for assessing the visual condition of a selection of surface courses (Fig. 1).

Sites are selected to provide an indication of early-life performance and estimates of service life. Prominent faults are recorded to establish initial causes and modes of failure. The SIP team comprises road experts representing Transport Scotland and the road industry.

This paper describes the development of the method used and how results have been used to steer research, document performance and promote and develop best practice.

2 VISUAL INSPECTIONS

Visual inspections have been used for many years to assess and record the general condition of a road surfacing, and compare new materials or techniques with existing ones. The original approach [1] was developed over many years by the Road Research Laboratory

Figure 1. Scottish inspection panel.

in the 1950s to inspect full-scale road experiments. Some properties such as resistance to deformation or skidding could be measured by suitable apparatus, but other features such as excess binder, disintegration and uniformity of appearance could only be determined by visual examination. A basic marking regime using a 6-point scale was applied by a panel of experienced road engineers.

2.1 *Present method*

The 1990s saw an influx of new materials and material types from mainland Europe. It was necessary to revise the assessment procedure so that it could encompass all the types of materials likely to be used. The present method involves a panel of experts following a laid down methodology that has been used since 1993. A basic mark is allocated from a 7-point scale with fault suffixes, if appropriate, and the mean of individual results is calculated by the panel Convener. The system has been fully utilised by Transport Scotland and the Highways Agency in England to assess the durability of asphalt surfacing over the last decade.

2.1.1 *Marking*

The panel members attribute marks to each surfacing site on the basis of its current serviceability irrespective of the elapsed time since it was laid. In considering the serviceability of the surfacing, the aspects given in Table 1 are considered. If any of the aspects are evident to a significant degree on the site, the relevant suffix from Table 1 is applied to the basic marking.

Once any appropriate fault suffixes have been assigned, the basic mark is allocated from the 7-point scale shown in Table 2. Only the panel mark is reported and this is based on an average consensus of the panel. When considering the markings, any sections that warrant a suffix cannot receive the basic mark of G or better. The exception to this rule is the use of joint open (j_o) or joint fretted (j_f) suffix, e.g. if given a G_{J_o} or G_{j_f} this reflects that the mat is fault free but there has been a problem in constructing the joint.

2.2 *Site selection*

Transport Scotland's integrated pavement management system is used to provide information on materials laid on the network. Schemes are chosen to represent a range of sites in terms of climate, terrain, geographical location, traffic and surfacing type. For the purposes of retaining supplier anonymity, sites inspected are allocated specific acronyms throughout reports. In certain instances sites are subdivided into separate parts. This is typically done when the

Table 1. Defects and associated suffixes.

Suffix	Description	Notes
v	Variable	Random variations from point to point within the section only, not "traffic laning" or of obvious variations from load to load
t	Variability with traffic intensity	Marked transverse differences caused by variations in traffic intensity between lanes
+	Fatting up	Macadam, surface dressing
–	Loss of chippings	Hot rolled asphalt
	Loss of aggregate	Porous asphalt, macadam, thin surfacings, slurry surfacing
	Loose chippings	Surface dressing
	Wearing causing substrate to "grin" through	High-friction surfacing
j_o/j_f	Joint issue	j_o = open joint/j_f = fretting at joint
f	Fretting of mortar	Hot rolled asphalt
g	Growth of vegetation	Porous asphalt
p	Ponding	Porous asphalt
d	Delamination from substrate	Porous asphalt, thin surfacings, surface dressing, high-friction surfacings, slurry surfacing
s	Stripping	All except high-friction surfacings
c	Cracking	Hot rolled asphalt, macadam, thin surfacing, high-friction surfacings

Table 2. Basic seven-point scale.

Mark	Description	
E ("Excellent")	No discernible defect	
G ("Good")	No significant defect	Termed serviceable
M ("Moderate")	Some defects but insufficient for serious problem	
A ("Acceptable")	Several defects but would usually be just acceptable	
S ("Suspect")	Seriously defective but still serviceable in the short term	
P ("Poor")	Requires remedial treatment	Termed unserviceable
B ("Bad")	Requires immediate remedial treatment	

site contains areas that are subject to different levels of traffic stress, e.g. bends, junctions, or display distinct differences in surfacing condition.

2.2.1 *Early-life performance*

A review of surfacing performance in 2006 looked at sites in both good and poor condition to establish the reasons behind their relative performance. This led to an annual review to assess the early-life performance of surface courses that have been in service for approximately two years. Due to the surfacing season typically running from September to March each year, the actual age of the schemes inspected varies between 18 and 30 months. The nominal period of two years is selected as it is generally accepted that the condition of a surfacing after two years is a good indicator of its potential to achieve its predicted design life. After two years the surfacing has carried a reasonable amount of traffic and has been subjected to the cyclic environmental effects of seasonal change. Importantly, the supplier also remains the guarantor for a period of two years. As a guide, it is generally acknowledged that a surfacing should be assessed as either Excellent or Good after two years in service, with little or no significant defects.

2.2.2 *Estimates of service life*

In addition to inspecting two year old sites, older sites are inspected to assess the long term durability of surface courses and provide further estimates of service life.

2.3 *Reporting*

An example of the visual assessment results for inspections undertaken in 2006 is summarised in Figure 2. In most instances, the panel mark represents the average of six individual assessments and the mean visual condition marks are plotted using the following transformation:

E = 6; G = 5; M = 4; A = 3; S = 2; P = 1; and B = 0.

Research carried out for the Highways Agency [2] estimated that the average typical service-life of a surface course was between 13 and 14 years. This service-life relates to surfacing that has been manufactured and installed correctly in accordance with the appropriate specification. The limit of serviceability for the surface course was defined as when the visual condition drops to below *Acceptable*. The line drawn on Figure 2 represents an idealised linear deterioration with time. A recommended requirement to ensure a reasonable design life is that the condition of the surfacing should be assessed as Good or better after two years.

The two circles superimposed onto Figure 2 highlight sites that were assessed to have particularly poor visual condition for their age in 2006. The circle on the left of the graph represents a cluster of sites that are less than two years old.

2.3.1 *Observations*

The SIP team also record features that affect service life. Survey results consistently show that aggregate loss is the most commonly occurring defect. The fault is described as either latent or severe. The former is associated with materials that have an open texture owing to a lack of fine aggregate or mortar (Fig. 3) and, although assessed to be serviceable at the time of the inspection, are predicted to have poor long-term durability. The second type of aggregate loss is commonly described as fretting. This is where both coarse and fine aggregate are seen to be lost from the mix under the action of trafficking.

2.3.2 *Quality of construction*

A visual inspection, in itself, cannot always attribute the cause of poor quality, but it can assess the quality of workmanship associated with parts of the installation process. A common SIP observation was that the construction of joints could be improved. All asphalt surfacing

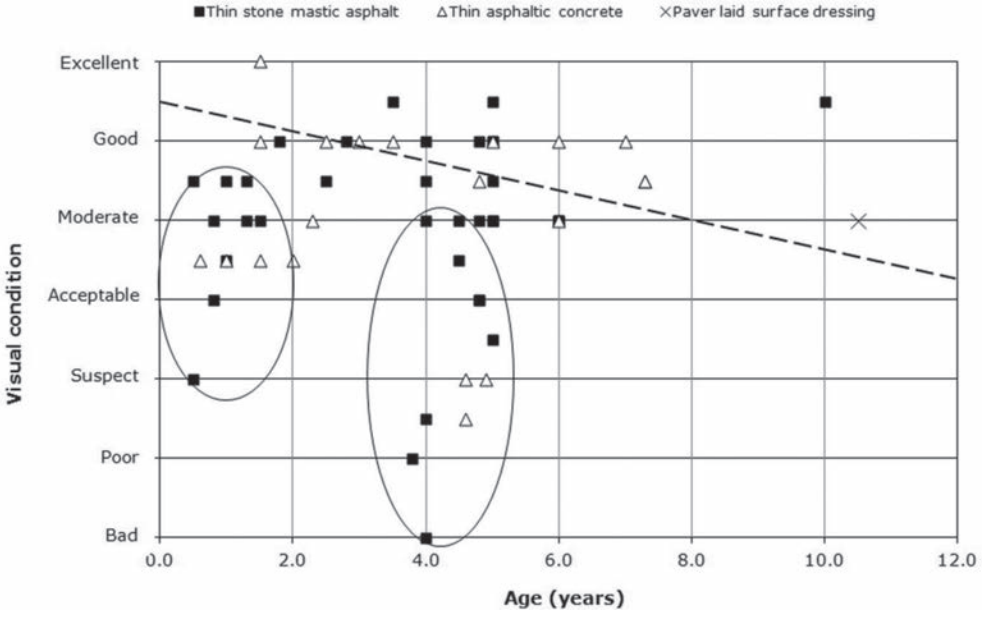

Figure 2. Average visual condition marks (2006).

Figure 3. Open texture.

joints are potential areas of weakness because they are likely to be less well compacted and can allow increased access to water penetration. It was evident from older sites that joints were often the first place to show the signs of deterioration which then start to migrate across the pavement. SIP surveys have recommended that steps should be taken to ensure that joints are well constructed and sealed to prevent water infiltrating and adversely affecting the lower pavement layers.

3 USE OF RESULTS

Examples of how SIP results have been used to steer research, document performance and promote and develop best practice are given below.

3.1 *Driver for new research*

The results of the SIP surveys carried out between 2006 and 2008 were a major driver in Transport Scotland commissioning a programme of research to adjust Scotland's domestic Specification to improve material durability, quality control and safety. The SIP surveys provided evidence that many existing surface courses were not providing good value for money. The open nature of the surface course and poor joint construction were highlighted to be of particular concern. The research led to the introduction of a new national specification in 2010 [3] that requires denser modified mixes using smaller stone sizes. It is expected that the dissemination of the research findings [4] and the new specification will improve the durability of new surface courses, extend service life and the value for money spent on road construction. It also addresses the Government's aim of reducing disruption to road users caused by road construction and maintenance.

3.2 *Benchmarking*

As an overseeing organisation, Transport Scotland strives to improve the performance of trunk road pavements. The SIP surveys play an important role in monitoring and tracking the technical performance of road surfacing. A comparison of the breakdown of average survey markings for SIP surveys 2008 to 2012 is shown in Figure 4. It can be seen that the surface courses examined in 2012 received the highest percentage of E and G markings. There was a marked improvement on 2011, and the results were better than earlier surveys.

The proportion of sites exhibiting defects over this period is presented in Figure 5. Compared to previous surveys, the 2012 survey recorded the lowest number of visual defects. Seventy per cent of the 2012 sites were assessed as being defect free.

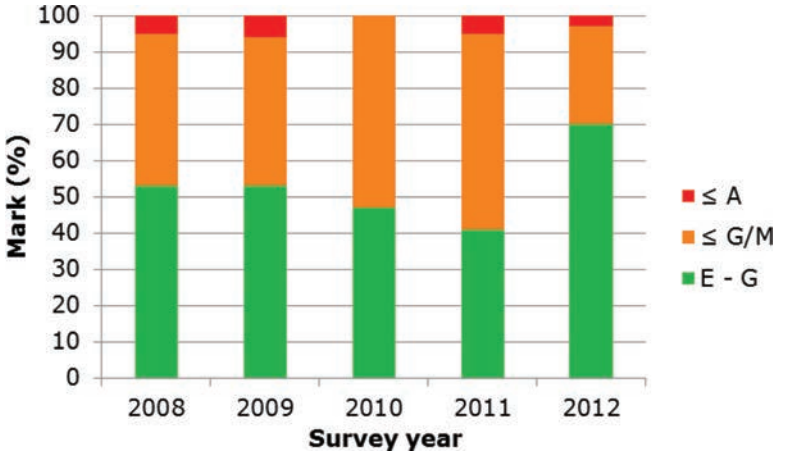

Figure 4. Comparison of average markings for SIP 2008–2012.

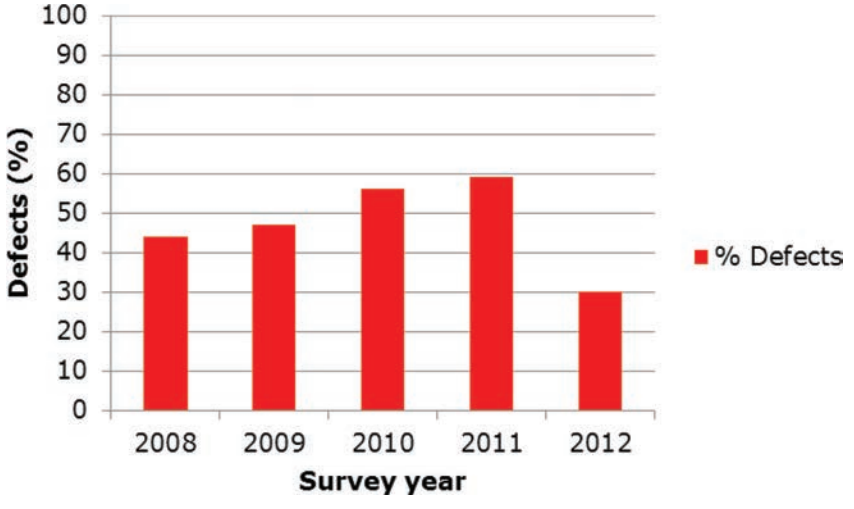

Figure 5. Comparison of recorded defects for SIP surveys.

Figure 6 shows a breakdown of the type of defect as a proportion of all the defects recorded for each SIP survey between 2008 and 2012.

Miscellaneous defects (coded red) include faults such as material variability, variability with traffic intensity, delamination and cracking. In 2010 it was decided to introduce a fault suffix for joint defects such as an open or fretted joint. Information on the specific condition of the joint was not recorded prior to 2011.

The improved results for 2012 are believed to be as a direct result of the implementation of recommendations from previous inspections. It is planned that future visual inspections will be continued on an annual basis to assist the process of further improving the performance of road surfacing.

3.3 *Developing best practice*

3.3.1 *Material selection*

Based on the poor performance of 0/14 mm surface course at highly stressed sites, such as roundabouts and busy junctions, it was recommended that the nominal aggregate size be

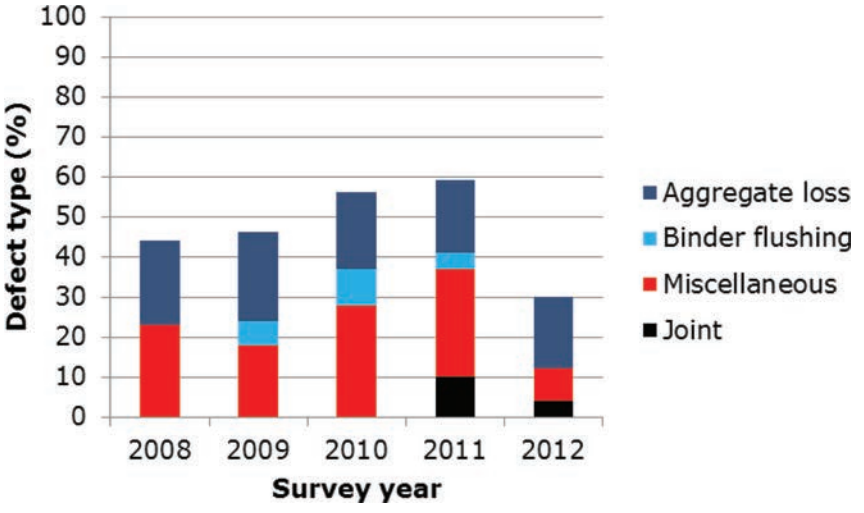

Figure 6. Type of defect recorded on SIP surveys.

Table 3. Extract from guidance on the selection of TS2010 SMA mixtures [3].

Mixture Description	Site Category/Description					
	Non-event	Medium Risk of Skidding	High Risk of Skidding	Noise Sensitive Area		High Stress
				High speed	Low speed	e.g. roundabouts
SMA 14						
SMA 10						
SMA 8 (Developmental)						
SMA 6						

reduced for high stress sites and new guidance was produced on selecting the correct material to suit the location (Table 3). Since 2011, the stress level of SIP sites has been assessed and designated as high, medium and low, e.g. junctions and roundabouts (High); crawler lanes and bends (Medium); and straight-run sections (Low).

3.3.2 *Joints*

In an attempt to elevate the importance of joints additional suffixes were introduced in 2010 as part of the visual assessment process. This raised the question of how joints were being constructed and how they could be improved in the future. On recent new build schemes echelon paving has been employed to remove joints altogether. For maintenance schemes a new approach to constructing longitudinal joints has been trialled with excellent results. The technique involves using a special cutting wheel that creates a chamfered joint (Fig. 7). The method appears to have several benefits that include reduced wastage of material, ease of coating joints and a better quality, well-sealed joint.

3.3.3 *Drainage*

SIP observations regularly highlight examples of poor or inadequate drainage and it has been highlighted that there is a continuing need to promote and generate dialogue on the importance of maintaining drainage systems. This has led to Transport Scotland funding

Figure 7. Chamfered joint.

new research to collect quantitative data on the impact that drainage has on the life of a road pavement.

4 SUMMARY

After the initial review of surfacing performance in 2006, Transport Scotland introduced an annual monitoring procedure to assess the visual condition of surface courses laid on the strategic network. The approach has been refined and has been successful in steering new research, documenting performance and promoting and developing best practice. The results from the annual surveys have demonstrated that the implementation of recommendations from previous inspections have made valuable improvements. Future visual inspections are planned to assist the process of continuing to improve the performance of Scotland's roads.

REFERENCES

[1] Lee, A.R. A Method of Assessing the Condition of Experimental Surfacings. Road Tar, Vol. 11, No 3, pp. 1–5, 1957.

[2] Nicholls, J.C, I. Carswell, C. Thomas and B. Sexton. Durability of Thin Asphalt Surfacing Systems. Part 4: Final Report after Nine Years' Monitoring. TRL Report TRL674, Transport Research Laboratory, Crowthorne, 2010.

[3] Transport Scotland. Surface Course Specification and Guidance Notes. TSIA No. 35, Transport Scotland, Glasgow, 2010. (http://www.transportscotland.gov.uk/files/documents/roads/TS2010_Ver_01_Dec_10_PDF.pdf).

[4] McHale, M.J., I. Carswell and P. Roe. New Surface Course Specification for Scotland. TRL Report TRL670, Transport Research Laboratory, Edinburgh 2011.

Asphalt Pavements – Kim (Ed)
© 2014 Taylor & Francis Group, London, ISBN 978-1-138-02693-3

The residual life of thin surfaced pavements

David Alabaster
NZ Transport Agency, Christchurch, New Zealand

Theunis Henning & Douglas Wilson
The University of Auckland, Auckland, New Zealand

ABSTRACT: The practice of applying thin wearing course layers of asphaltic concrete over unbound granular pavement layers is wide-spread in New Zealand. Determining the as-built life of new thin surfaced unbound granular pavements is becoming increasingly important for two reasons. The first is the increasing use of "design and construct" type contracts where the client is required to make some judgement of the length of life of the finished pavement at the end of the defects liability period. The second is the continual constraints on maintenance budgets making it imperative that all designs are as efficient and effective as possible.

Previous attempts to develop a residual life determination for thin surfaced pavements have used transient surface deflections. Equipment such as the Falling Weight Deflectometer (FWD) provide key inputs to the Mechanistic—Empirical pavement design models that estimate life. More advanced models have combined laboratory testing and deflection measurements effectively attempting to eliminate the more conservative empirical aspects of the modelling process. Both approaches have their limitations which will be discussed and illustrated with data from the Canterbury Accelerated Pavement Testing Indoor Facility (CAPTIF).

The aim of this paper is to report the issues surrounding existing residual pavement life models used in New Zealand and propose a methodology of research into addressing the gaps in knowledge and/or practice.

Keywords: Accelerated pavement testing, long term pavement performance, residual life, CAPTIF

1 INTRODUCTION

New Zealand's sealed roading network consists primarily of chipsealed or thin wearing course layers of asphaltic concrete over unbound granular pavement layers. Traditionally pavements have been designed by consultants and built by contractors, resulting in conservative designs and the average pavement life on the State Highway network is approximately 40 years. Routine maintenance is carried out promptly and periodic resurfacing is the only major treatment requirement. There is an increasing use of "design and construct" type contracts where the client is required to make some judgement of the length of life of the finished pavement at the end of the defects liability period and New Zealand Transport Agency is about to undertake its first Public Private Partnership with similar requirements. There has also been a strong drive to keep maintenance budgets at current levels making it imperative that all designs are as efficient and effective as possible. Thus determining the as-built life of new pavements is becoming increasingly important.

Three residual life models based on Mechanistic—Empirical pavement design and FWD measurements have been trialled in previous research [1]. The best model was "*plus or minus 500%. This means if the FWD predicts the pavement life of two million ESAs then the actual life could range from 400,000 ESAs to 10 million ESAs. The range of life predicted makes it*

difficult to use in compliance and if penalties are imposed then the 'greater' life of 10 million is taken as the achieved life."

2 EXISTING RESIDUAL LIFE DETERMINATIONS FOR UNBOUND GRANULAR MATERIALS

Mechanistic—Empirical pavement design based residual life determinations for unbound granular materials have been tested by New Zealand researchers [1]. The research reviewed the accuracy of the residual life predictions from three common methods to analyse FWD data. The methods were tested against New Zealand pavements where the life was known or could be estimated from rutting or roughness data.

The first method reviewed was a prediction based on the central deflection of the FWD. This method is used in the Austroads Guide to Pavement Technology [2] to infer the load carrying capacity of pavements that are being rehabilitated. The research found that this method was the most inaccurate and recommended that it not be used in the future.

The Austroads mechanistic pavement design method was used as the basis of the second method. The pavement life was estimated from the vertical compressive strain in the subgrade, back calculated from the FWD deflections. This method generally underestimated the life by 10 to 100 times. But the method was also capable of overestimating the life where the pavement failed in the granular layers.

In the third method tested, the Austroads mechanistic pavement design method was calibrated. Again, the pavement life was estimated from the vertical compressive strain in the subgrade back calculated from the FWD. But the subgrade strain criteria that links the elastic strain to life had been 'broadly' calibrated to the soil types. Calibrating the model resulted in the predictions ranging from 0.1 times the life to 10 times the life, but typically between 0.2 and 5 times the life.

Additional methods were investigated in the project, CAPTIF data [3] was reviewed in detail to determine whether a soil specific subgrade strain criteria could be developed. It was found that the variables of; assumed end of life rutting conditions, the timing of the FWD test (before trafficking or after an initial period) and the depth of the pavement, played a significant role in the determined subgrade strain criteria. Figure 1 below illustrates the effect of pavement depth on the subgrade strain criteria on the same Tod Clay subgrade

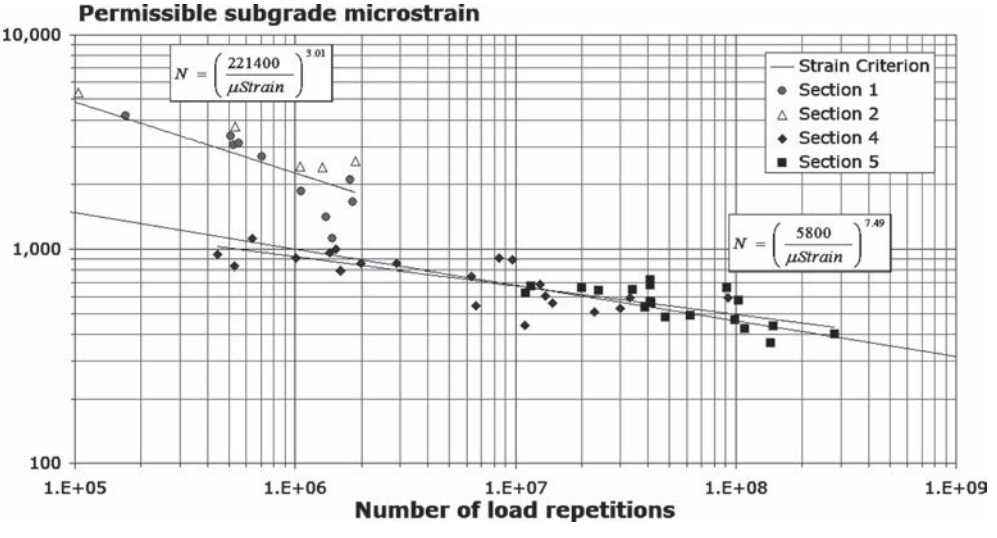

Figure 1. CAPTIF load cycles vs subgrade strain for 15 mm VSD for the mature pavement.

material constructed at different moisture contents, with State Highway Standard TNZ M/4 basecourses. Sections 1 and 2 were 150 mm deep basecourses on a subgrade CBR of 7 and 9 respectively, while sections 4 and 5 were 300 mm deep basecourses on a subgrade CBR of 3 and 8 respectively. The Figure suggests that thinner pavements built on stronger subgrades will perform better than softer subgrades with thicker pavements where the elastic strains are equal at the top of the subgrade. Reviewing the data, it is arguable that section 5 could be included in the thinner data set without difficulty and that in fact it was the weaker subgrade in section 4 that is creating the diverging result.

Supplementary checks were suggested to consider the performance of the basecourse but not considered in detail. They included a curvature check for near surface deformation similar to that used by Austroads for asphaltic concrete surfaces, a CBR check on near surface deformation by inferring CBR from modulus, a check on near-surface deformation by applying a strain criterion at the mid-height of granular layers and finally a check on the modular ratio of adjacent pavement layers.

Three key observations and recommendations were made:

- That a single project could have individual point reading with predicted lives ranging from 0.01 million ESA to 100 million ESA. The research recommended that the 10th percentile prediction of life be used as it is generally accepted that a pavement requires rehabilitation once 10% of a pavement needs repair.
- Analysis could follow the Austroads subgrade strain approach, generally with considering the basecourse layers and only need broad calibration based on past project experience.
- Contractor payment reductions should only be applied where the predicted life is 1/5th of the design life.

Clearly the existing techniques are not accurate enough to use in a contractual arrangement.

3 PAVEMENT PERFORMANCE CONSIDERATIONS

In developing a new model a review of parameters effecting pavement performance prediction is required. These can be broadly separated in Traffic Loading, Pavement Materials, Environment and Maintenance regime, Analysis Methods and finally the Definition of Failure.

3.1 *Traffic loading*

Despite the obvious need, accurate loading data is difficult to establish in most situations. The New Zealand Transport Agency (NZTA) has six Weigh in Motion (WIM) sites to develop loading parameters for 94,000 kilometres of road network. All of the 114 nationally managed traffic monitoring sites are on the 11,000 kilometres of State Highway network throughout New Zealand that are continuously counted. These sites classify the traffic composition by length by the use of dual inductive loops. The sites are then supplemented with 1500 count sites that are part of regional state highway traffic monitoring contracts. These include 127 continuously counted and 466 non-continuously dual inductive loops. Furthermore, 141 are continuously counted and 655 are non-continuous single inductive loops that provide counts only. 113 Pneumatic tubes that provide classification by axle and a further 328 "virtual" sites are used to assist in coverage of the full road network [4]. The NZTA's design guidance, contained in the 2007 New Zealand Supplement to the Austroads Pavement Design Guide, averages the number of Standard Axle Repetitions per heavy commercial vehicle axle across the WIM data. The supplement also provides the average number of heavy vehicle axles per heavy vehicle from the WIM data. Design loadings for pavement design are calculated from the Annual Average Daily Traffic and its growth, the percentage of heavy commercial vehicles calculated at the site or estimated from adjacent sites and the average WIM parameters for Standard Axle Repetitions. Directional and lane usage factors are applied where required [5].

Research in to network deterioration modelling has suggested that quality of traffic loading data is poor for model development. The research recommended installing telemetry sites

on the Long Term Pavement Performance (LTPP) sites with temporary "Weigh in Motion" loading samples to also be obtained [6].

Australia has some 200 Weigh in Motion sites and the data for each site is summarised in the Austroads Guide to Pavement Technology [7]. The guide lists the average number of heavy vehicle axles per heavy vehicle at each site and the number of standard axle repetitions per heavy commercial axle. Thus the number of standard axle repetitions per heavy commercial vehicle can be determined by multiplying the two together. Finding the highest and lowest values of the two parameters does not necessarily find the range of standard axle repetitions per heavy commercial vehicle. However, it certainly suggests it can range from 1 to 7 confirming, at least in part, that traffic loading data in New Zealand could be a major source of error in any subsequent residual life determination.

3.2 *Pavement materials*

Current residual life systems assume that elastic strain (deflection) can be related to plastic strain (rutting) with one relationship for all materials. While this may be approximately true for basecourse materials made and laid to highway standard specifications, such as the NZTA M/4 Basecourse Specification and TNZ B/2 Construction Specification, there are still other compliant materials such as Dacite where the current CAPTIF test suggests this doesn't appear to apply.

A constant relationship between elastic strain and plastic strain is less likely to be true for subbase materials that have wider specifications [8] and it is definitely untrue for subgrades such as volcanic ashes which appear to be very tolerant of high deflections [3, 9].

3.3 *The environment and maintenance regimes*

The Environment and Maintenance regimes play a significant role in the life of unbound granular pavements. HDM-4 provides two forms of rutting progression models. One for cracked sections and the other for uncracked sections, with default model coefficients provided for both chipseal and asphalt surfaced pavements. Attempts to calibrate the models using the New Zealand LTPP sites failed and a two phase model was then proposed. The first phase modelled stable rut progression and the second phase an accelerated progression defined as twice the average expected stable progression [6]. The rate of rut progression in the stable phase was able to be modelled from CAPTIF data as a function of the pavement thickness and the modified structural number and was validated on the Gisborne and Hawkes's Bay State Highway networks. CAPTIF data was also used to develop a logistic model to estimate the probability of accelerated rut progression; the model was a function of equivalent standard axle repetitions, modified structural number and pavement thickness. The research considered the mechanism was generally only seen on over loaded low strength pavements.

3.4 *Mechanistic analysis system*

Mechanistic—Empirical pavement design models are in themselves relatively simple approximations of reality. They are generally conservative (which serves their purpose) but they are not an adequate model for residual life predictions in a contractual environment. These systems involve the iterative mechanistic calculation of stresses and strains to fit the measured deflections. This generates a best fit model of the elastic performance of the pavement layers. The pavement life is then estimated by comparing the calculated elastic strains or stresses with empirical performance relationships at critical points in the pavement, such as the vertical strain at the top of the subgrade.

The existing models all analyse static loads using the theory of elasticity which is a gross but practical simplification of the real situation [10]. In fact the loads are dynamic, the materials are granular not solid and the behaviour at the stress levels we are considering contains some element of plastic movement. Better models exist; Finite Element Models provide the flexibility to consider non-linear material models, dynamic loads and material yielding.

Analysis at CAPTIF shows Finite Element Models certainly provide closer approximations to measured elastic strains. Distinct Element Methods provide a granular model however they too are simplifications with approximations required for at the least environmental conditions and the computational needs generally mean not all load cycles are modelled. However, there are no models that provide an exact replication of reality.

Current life prediction systems for unbound materials assume a constant or an increasing resilient strain within the pavement [1]. Results from CAPTIF have shown a third option with some pavements showing decreasing strain and deflection values, whilst plastic strains still gradually increase. This adds to the inaccuracy of current residual life predictions when the deflections are not measured at construction.

3.5 *Failure mechanisms*

A key part of any model predicting failure is to clearly define what failure is. In the New Zealand context, pavements are often noted to be rehabilitated due to excessive maintenance costs rather than having met some terminal fatigue condition.

Attempts have been made to create data driven models of the rehabilitation decision making process. Most recently an attempt was made to develop a model for maintenance costs and then develop criteria to define the "end of life" of State Highway pavements [11].

RAMM data was collect from the West Wanganui, Southland, Gisborne and Hawke's Bay networks to develop the models and the Nelson network was used to validate the results. The variables for the models included, Roughness, Shoving, Rutting, Potholes, Alligator cracking, Edge break, Scabbing, Pavement Maintenance Costs, Surfacing Maintenance Costs, Shoulder Maintenance Costs, Total Maintenance Costs (a summation of the previous three), Traffic Levels (AADT), Pavement Age (since construction or last rehabilitation) and Urban or Rural Environment.

A Total Maintenance cost model (Pavement, Surfacing, Shoulder costs) found the most significant variable to be roughness, which is intuitively sensible, followed by shoving, alligator cracking, traffic, rutting, age and potholes in prioritised order.

A Pavement Maintenance cost model also listed roughness as the most significant variable, which again is intuitively sensible, followed by shoving, traffic, rutting, alligator cracking, age and potholes in prioritised order.

A Pavement and Surfacing Maintenance cost model was also developed and not surprisingly roughness was again shown to be the most significant variable and intuitively sensible, followed by traffic rutting, shoving, alligator cracking, age and potholes.

While the parameters in all of the models where almost all statistically significant the overall low r-squared values (<0.25) suggested that that models would have difficulty accurately predicting maintenance costs at individual sites. The researcher suggested that there must be a substantial random element to maintenance costs, or an alternative view is that there are additional influences on the maintenance costs not considered in the data, be that other parameters (such as material type), sampling errors (cracking and potholes are a 10% sample) or simply sampling once a year is not fast enough to detect some modes of distress adequately (ie shoving, cracking and potholes).

Despite the setback of not finding a robust maintenance cost model the research went on to try and predict rehabilitation decisions with a logit model developed from the RAMM data available. A logit model allows the modeller to set a "threshold probability" above which rehabilitation is predicted to occur and below which it won't. Again the four networks were combined to produce a single network, but this time the networks were also separately modelled as well.

The model for all four networks and the total maintenance cost as the only cost parameter suggested that total maintenance was the most significant parameter in rehabilitation decisions with the traffic level and whether it was Urban or Rural also being highly ranked.

By setting the threshold at 11% the model has a 72% probability of correctly predicting rehabilitation and equally a 72% probability of correctly predicting no rehabilitation when the site does not need it.

Using the Pavement and Surfacing Maintenance costs as separate variables resulted in traffic being the most significant variable. Surfacing costs being more significant than pavement costs, that was also ranked below roughness and the urban/rural split. Rutting was not considered to be a significant parameter in the model.

The total maintenance cost model had a better log likelihood value and thus was likely to provide a better model to predict maintenance decisions.

The research also investigated individual models for the separate networks which were much simpler, suggesting some significant regional variance in either performance or the decision to rehabilitate.

The models with no traffic parameter imply that all that is required for rehabilitation is for the maintenance costs to rise over a predetermined value—irrespective of traffic volume. To a certain extent this is true as the State Highway decision making procedure for Rehabilitation is purely based on the Net Present Value (Present Worth of Costs) of the ongoing Maintenance cost vs the Net Present Cost of the Rehabilitation. The inclusion of the traffic parameter in the models is presumably a risk or priority adjustment made at the regional level—higher volume roads are more important and likely to deteriorate faster, thus earlier intervention may be needed. What is interesting is that keeping all others factors equal—the models suggest that Hawkes Bay would seem to need four times the maintenance cost that Southland intervenes at.

The Nelson network was used to validate the combined four network maintenance cost or rehabilitation models. The Nelson network had 408 treatment lengths, 14 of which had been rehabilitated.

The maintenance cost model had a poor fit to the actual data, which is not surprising as the R squared values of the model were low.

The research concluded that:

- A two tier model may have been better, the first tier triggering on condition such as rutting or roughness with the 2nd tier triggering rehabilitation on maintenance cost. But a two stage model was not investigated.
- Maintenance costs could not be accurately predicted from the data considered
- Maintenance costs did not appear to rise dramatically with time
- Maintenance costs, Traffic and Roughness, in that order, were the main drivers of rehabilitation.

The research demonstrates that defining the end of life of pavements is difficult and the end of a pavements life appears to be a function of the funding rules for rehabilitation and the local regions interpretation of those rules. Across all regions total maintenance costs, roughness and traffic volumes appear to be the key drivers of rehabilitation decisions.

Total maintenance costs, while difficult to model accurately with the available data, are a function of Roughness, Shoving, Alligator cracking, Traffic, Rutting, Pavement Age and Potholes. While Pavement Maintenance cost are subtlety different and are driven in order of importance by Roughness, Shoving, Traffic, Rutting, Alligator cracking, Pavement Age and Potholes.

4 PROPOSED METHODOLOGY

It is proposed that data from previous CAPTIF pavement tests could be used to develop a practical residual life determination. Previous CAPTIF projects contain data sets that would be ideal for this research work.

This methodological step would add a new and novel approach to the traditional analysis to encompass the fundamental limitations of the existing approach. The aim of the extra step is to provide a "site calibration of the model" to the analysis that would possibly be a combination of laboratory testing, QA data and early life performance data (during the defects liability period). The objective of the calibration would be to reduce the uncertainly in loading data, moisture conditions and elastic-plastic performance data and measures of construction quality. Figure 2 indicates how the process could enhance the determination of residual life.

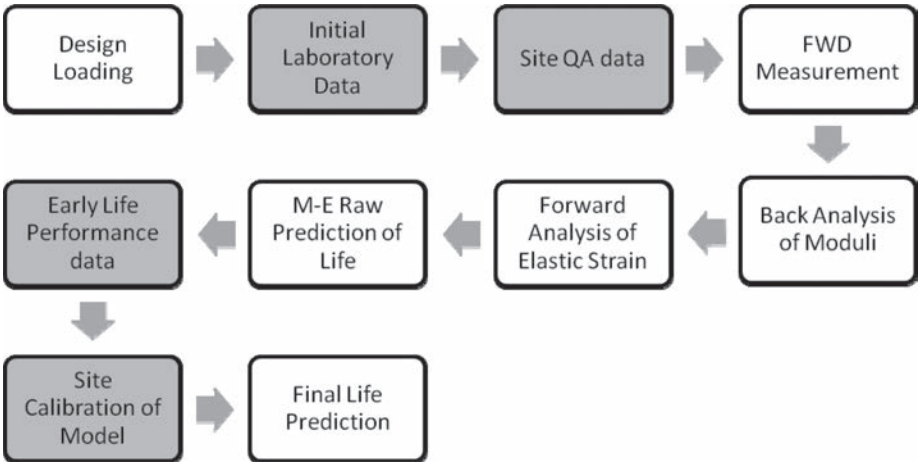

Figure 2. Proposed residual life determination process (non traditional steps grey shaded).

CAPTIF provides a data set that demonstrates why traditional approaches are inaccurate on State Highway strength pavements [12]. Two test sections with nearly identical FWD readings provide significantly different performance. The same project has pavements using the same basecourse materials but at different thicknesses which provides a measure of the sensitivity required in the model.

The current CAPTIF project "The relationship between vehicle axle loadings and pavement wear on local roads" will add a number of ideal data sets to test the model at local road strengths. With these data sets it will be possible to investigate the influence of traffic loading, pavement materials, analysis methods and the definition of failure.

The model would be validated against suitable LTPP sites to check that it works in the field; this will also confirm whether the environment and maintenance regimes need further consideration. This will ensure the quality and validity of this project, which will have significant impacts on future NZTA business processes.

5 CONCLUSIONS

An improved calibrated residual pavement life model that can be used at the project level to assess the remaining life in newly constructed pavements is needed. If a suitably flexible model can be developed it could also be used to determine the remaining life of all pavements. In that case it could be used to prioritise network level models that have identified pavements that are nearing the end of their lives.

A calibrated residual life determination has the following benefits:

- Accurate judgement of the likely life of "Design and Construct" pavements.
- It will provide a way to review all constructed pavements to ensure they are efficient and effective.
- Improved forward programme predictions.
- Improved asset valuations.
- Improved understanding of when to transfer to more expensive but low risk/low maintenance bound pavements.

More complex models that combine laboratory testing and deflection measurements with Finite Element Models will not alone produce good models—a number of practical limitations need to be addressed:

1. The real life loading situation is almost always unknown. For example New Zealand reports data from six weigh in motion sites for 94,000 km of road network.

2. Pavement material response to load becomes increasing complex with depth. Elastic strain to performance relationships need to be calibrated at each site.
3. The environment and maintenance regimes affect pavement performance. The quantity, quality and effect of future maintenance needs to be assumed, as does the future environment that pavement the will operate in.
4. All Mechanistic—Empirical design models are approximations to reality and need calibration.
5. Assumed failure conditions and real life decisions on rehabilitation need to be aligned.

It is clear that the proposed methodology to predict the life of new (and existing) pavements is needed.

REFERENCES

[1] G. Arnold, G. Salt, D. Stevens, S. Werkmeister, D. Alabaster and G. van Blerk, "Compliance testing using the falling weight deflectometer for pavement construction, rehabilitation and area wide treatments," *New Zealand Transport Agency Research Report,* pp. 85P, 2009.

[2] AUSTROADS, "Part 5: Pavement evaluation and treatment design," in *Guide to Pavement Technology*, AUSTROADS, Ed. Australia: AUSTROADS Publication, 2009.

[3] D. Alabaster and A. Fussell, "Fatigue design criteria for low noise surfaces on New Zealand roads," *Land Transport New Zealand Research Report,* pp. 90P IN 2 VOLS, 2006.

[4] G. Wen, "State highway traffic data booklet. 2008–2012." NZ Transport Agency, Wellington, 2013.

[5] Transit New Zealand, "New zealand supplement to the document, pavement design—A guide to the structural design of road pavements (AUSTROADS, 2004)," Transit New Zealand, Wellington, 2007.

[6] T. Henning, "The development of pavement deterioration models on the state highway network of New Zealand," 2008.

[7] AUSTROADS, "Part 2: Pavement structural design," in *Guide to Pavement Technology*, AUSTROADS, Ed. Australia: AUSTROADS Publication, 2012.

[8] G. Arnold and S. Werkemeister, "Pavement thickness design charts derived from a rut depth finite element model," 11. 2010.

[9] D. Alabaster, G. Fairless, R. Bailey and J. Patrick, "Characterisation of some New Zealand Subgrades," *TRANSFUND NEW ZEALAND RESEARCH REPORT,* pp. 53 p., 2000.

[10] P. Ullidtz, "Analytical tools for design of flexible pavements," in Copenhagen, Denmark, 2002, pp. 20p.

[11] M. Gribble, R. Ul-Islam and J. Patrick, "The Prediction of Pavement Remaining Life," *Land Transport New Zealand Research Report,* pp. 54p, 02, 2008.

[12] G. Arnold, B. Steven, D. Alabaster and A. Fussell, "Effect on pavement wear of increased mass limits for heavy vehicles: stage 3," *Land Transport New Zealand Research Report,* pp. 118P, 2005.

Asphalt Pavements – Kim (Ed)
© 2014 Taylor & Francis Group, London, ISBN 978-1-138-02693-3

Comparison of rutting performance between the PURWheel and the NCAT test track

Yu Tian, Ali Hekmatfar & John E. Haddock
School of Civil Engineering, Purdue University, West Lafayette, IN, USA

ABSTRACT: Continuously increasing traffic volumes, vehicle loads and tire pressures require asphalt mixtures to be designed to achieve better performance. This increased performance can be more easily obtained if asphalt mixture designs can be more closely tied to in-service performance. One way of doing so is with the use of laboratory tests tied directly to in-service asphalt pavements.

The Indiana Department of Transportation took the opportunity to establish rutting performance relationships between laboratory wheel tracking tests and the in-service pavement represented by the National Center for Asphalt Technology test track. Laboratory wheel tracking tests are performed in a relatively short time period. Conversely, pavements on the test track are typically trafficked over a period of years and thus subjected to seasonal and daily climate cycles in addition to traffic loads. Direct correlation between the two tests without considering the effects of temperature and aging is unrealistic.

In this research, applying temperature-aging modifications to the asphalt mixtures made comparisons between the laboratory wheel tracking and the full-scale test track more realistic. The findings show a good correlation between the two can be achieved by properly accounting for environmental factors.

Keywords: Test track, PURWheel, rutting, temperature, aging

1 INTRODUCTION

Over the past decades in-service pavements have seen increased traffic volume, vehicle loads and tire pressures. As a result, pavements often deteriorate more quickly than anticipated during the design phase, thus posing significant challenges to the design profession. Such challenges highlight the need for pavement design methods and materials selection that can link laboratory-scale testing with in-service pavement performance. Such methods could help to provide extended service life of asphalt pavements.

Design models must be calibrated and validated using actual traffic. The most desired way is utilizing in-service traffic loads and monitoring the pavement performance throughout the pavement service life. However, to do so is unrealistic in that it would take 10–20 years before enough data were collected. In order to represent the potential long-term performance within a relative short period of time, extensive efforts have been made to develop accelerated pavement testing techniques. In such tests, either full-or partial-scale traffic loads are applied in such a manner that the accumulation of damage is accelerated into a compressed time period. There are three levels of accelerated pavement tests: 1) Full-scale test track; 2) full-scale accelerated loading devices; and 3) laboratory wheel tracking devices. Full-scale test track and laboratory wheel tracking testing are discussed in this paper.

Full-scale test tracks apply controlled traffic loads to test sections, usually built for specific purposes. Such testing can duplicate real-world traffic loads, usually in an accelerated manner and is most representative of in-service pavements. However, accelerating the traffic load of a pavement test track also means the test sections are not exposed to the same amount of

varying seasonal temperatures. In late 1990s, the National Center for Asphalt Technology (NCAT), with the cooperation of several state departments of transportation, constructed a full-scale pavement test track in Alabama. The Indiana Department of Transportation (INDOT) took this opportunity to establish rutting performance relationships between the Purdue laboratory wheel tracking system (PURWheel) and the in-service pavement represented by the NCAT track.

The primary objective of the work described herein is to establish useful rutting relationships between in-service pavements, as represented by NCAT track and the PURWheel, Such relationships can help facilitate the development of pavement rutting performance predictions based on laboratory test results.

2 EXPERIMENTAL DESIGN

In order to validate the Superpave mixture design method and establish the desired relationships between the NCAT track and PURWheel, the experimental design shown in Table 1 was developed. Three factors were considered in the design, binder type, binder content and aggregate gradation); each factor had two different levels as shown in Table 1.

NCAT track sections N3 and N4 were sponsored by INDOT, sections N5-N8 by the Alabama Department of Transportation (ALDOT), sections N9 and N10 by the Federal Highway Administration (FHWA), and sections N1 and N2 by the track project. Specimens cut from track sections N1-N8 were transported to Indiana and tested in the PURWheel. While additional data is always better when making conclusions, in this particular experiment, the cost of producing and transporting samples made it difficult to increase the number of samples placed in the PURWheel device. Specimens tested in PURWheel were directly sampled from test track and hence represent as-constructed field conditions. The sample disturbance was minimized when taking samples and hence the reliability of testing results was increased.

Aggregates used in the mixtures were an Alabama limestone and a blast furnace slag. Gradations of the fine-graded mixtures plot above the Primary Control Sieve (PCS) while the coarse-graded mixture gradations plot below the PCS. The asphalt binders used in this study were an unmodified (neat) PG 67-22, a Styrene Butadiene Styrene (SBS) modified PG 76–22, and a Styrene Butadiene Rubber 63 (SBR) modified PG 76-22 binder. The HMA mixture designs were completed according to the Superpave volumetric mixture design method. Specimens for the design procedure were compacted with 100 gyrations of the SGC. The optimum binder content was chosen at 4 percent air voids. Detailed mixture design and test track construction information can be found in [1, 2, 3].

2.1 *NCAT test track*

The NCAT test track, as shown in Figure 1, is 2,743 m long and consists of 1,829 m tangents and 914 m curve sections. The original track construction was finished in the summer of

Table 1. Experimental design.

Binder	Binder content (%)	NCAT track section	
		Fine-graded	Coarse-graded
67-22 Unmodified	Optimum	N4	N6
	Optimum + 0.5	N3	N5
76-22 SBS	Optimum	N1	N9
	Optimum + 0.5	N2	N10
76-22 SBR	Optimum	–	N8
	Optimum + 0.5	–	N7

Figure 1. NCAT test track [3].

Figure 2. PURWheel testing device [1].

2000, and traffic application was started in the fall of that year. The test track includes 26 test sections on the tangents, 13 on the North (N) and 13 on the South (S), and 20 test sections in the curves, 10 West (W) and 10 East (E). The Alabama Department of Transportation (ALDOT), the Federal Highway Administration (FHWA), and the INDOT jointly sponsored sections N1 through N10. The ten mixtures shown in Table 1 were produced and placed on the track and subjected to 10 million Equivalent Single Axle Loads (ESAL) in approximately two years. Trafficking was accomplished using four tractor-trailer combinations operating at 72 km per hour. The individual single axles were loaded so that one truck pass applied approximately 10 ESAL [1]. Due to constraints at the time, and for the results reported in this paper, only the rutting data recorded from 18 September 2000 to 10 May 2002 were used. The number of ESAL applied in this time period was 7,102,106.

2.2 *PURWheel*

The PURWheel is a laboratory wheel-tracking device developed in the 1990's at Purdue University and has been implemented by Indiana DOT and Mississippi State University to simulate performance associated with rutting and stripping. As shown in Figure 2, the

PURWheel is in a self-contained temperature chamber where the desired test temperature can be maintained and wheel load and wheel speed can be controlled and rut depth measured. PURWheel specimens are 305 mm long, 286 mm wide and 50 mm thick. In this research, specimens were cut from the inside lane of NCAT track and trimmed to fit into the PURWheel., two replicates were tested for each NCAT track section. Two specimens were tested simultaneously at temperature of 50C. The PURWheel pneumatic tires were inflated to 690 kPa and loaded to 1.5 kN. One wheel pass consists of a forward and backward movement of the wheel with velocity of 33 cm/s. Tests were terminated after 20,000 passes or a 20 mm (0.8 in) rut was observed, whichever occurred first. Rut depth was measured over the entire length of a specimen using moving Linear Variable Differential Transducers (LVDT) [4, 5]. Sivasubramaniam [1] discovered a linear relationship between the logarithm of rut depth and the logarithm of number of PURWheel.

3 DIRECT CORRELATION

The first attempt at a relationship between the PURWheel and NCAT track rutting performance was direct correlation. This was done by comparing the total rut depths from the PURWheel at 20,000 passes to those of the NCAT track at approximately 7 million ESAL. As shown in Figure 3, overall there is a fair correlation; the coefficient of determination is 0.69. However, when the modified binder and unmodified mixture data are separated, the correlations are poor. The coefficient of determination for modified mixtures is 0.1; the coefficient of determination for the unmodified mixtures is 0.3. Perhaps even more disturbing

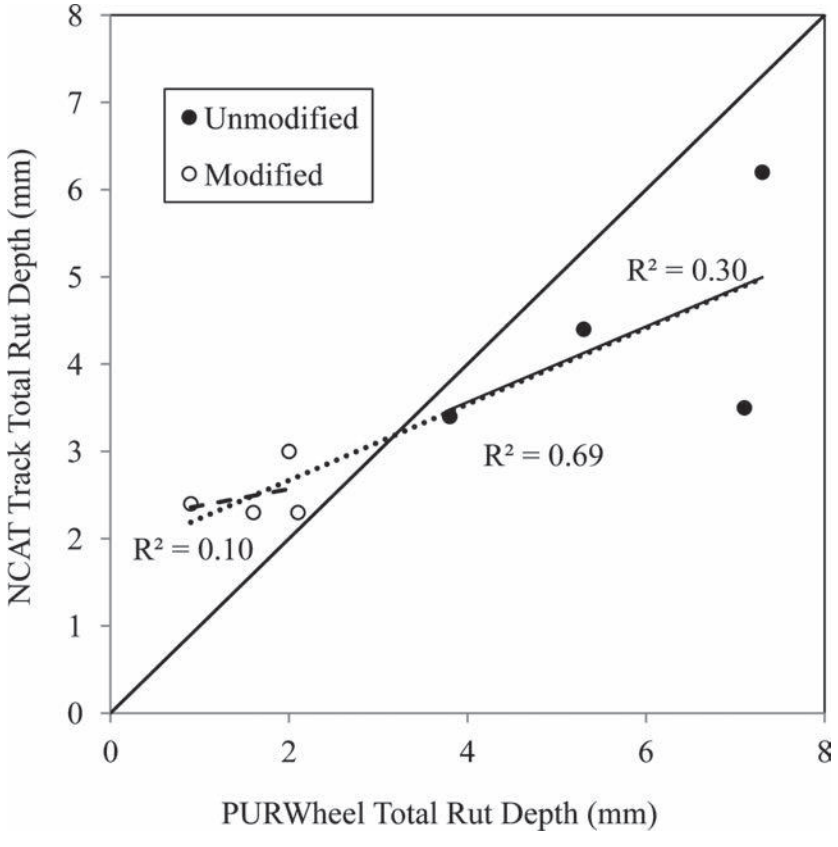

Figure 3. PURWheel and NCAT rut depth correlation [1].

than the poor correlations is the fact that for the modified asphalt mixtures the relationship between the NCAT track and the PURWheel might be negatively correlated, suggesting that as rut depths increase in the PURWheel, they decrease on the track. The relationship seems unlikely, at best.

The correlations displayed in Figure 3 are not entirely unexpected given that fundamental differences exist between the two tests [4]. More importantly, the NCAT track traffic was applied during two full calendar years. The mixtures were thus exposed to the environment, for two years, including the natural temperature cycling between day and night, as well as seasonal changes. Traffic applied during higher temperature days can result in more rutting than would occur with the same amount traffic applied during cooler temperatures. To the contrary, the PURWheel trafficking was conducted under a constant temperature of 50C.

Asphalt mixture aging can also make it difficult to compare the rutting performance between full-scale test tracks and laboratory wheel tracking devices. When asphalt mixtures are placed and trafficked on a full-scale test track, they are exposed to the environment and thus some aging of the asphalt binder occurs, even if the traffic loading is accelerated. The result can significantly alter the rutting performance of a mixture during the loading period; a load applied early in the traffic cycle can generate more damage to a test section as compared to an equivalent load applied late in the traffic cycle. This aging does not occur in laboratory wheel tracking tests as they are generally completed in only a few days.

The two factors, variations in rutting due to temperature cycles and variations in rutting due to asphalt binder aging, must be properly accounted for when comparing full-scale test track and laboratory wheel tracking results. If this is done, the results from the two methods should be more comparable.

3.1 *Temperature influence*

The NCAT track rutting data are shown in Figure 4. The basic idea of temperature influence is based on the fact that full-scale test track sections respond to same traffic loads differently depending on temperature of the asphalt mixture. In the case of the NCAT track, the ESAL applied to the pavement should be weighted differently, depending on the pavement temperature at which they were applied. This can be accomplished using a "load-temperature spectra" approach [3].

Since the asphalt pavement test section is softer at higher temperature and hence less resistant to rutting damage, it is expected that the stiffness of the asphalt mixture in the test section

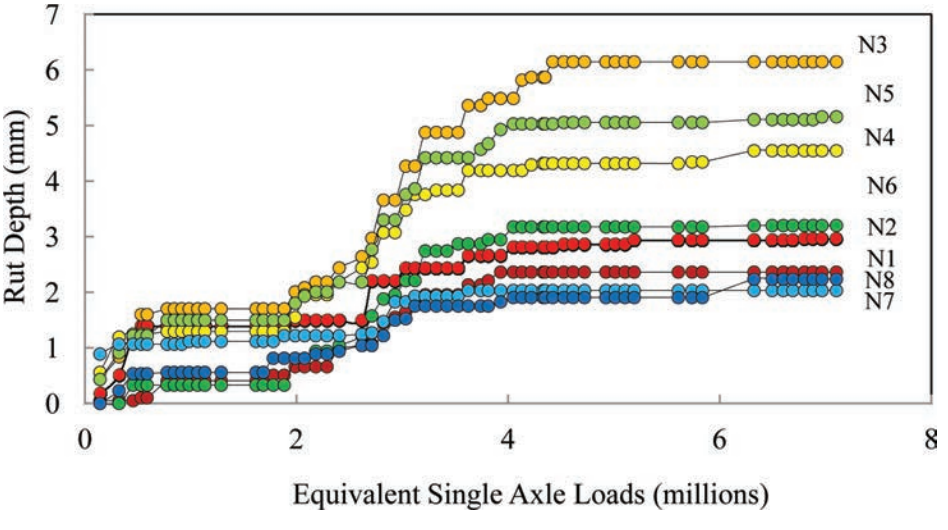

Figure 4. NCAT track rutting data.

can be used to generate a temperature modification factor. A statistical correlation between mixture temperature and mixture stiffness was developed based on data collected from the 2003 NCAT track trial. The mixture stiffness can be expressed as a function of temperature as shown in Equation (1), where T is the pavement surface temperature in Celsius [6]. Such a correlation provides an approach to modify the rutting results with consideration of the temperature effect; the stiffness serves as a temperature dependent indication of the mixture's rutting performance.

$$\text{Stiffness}_T = \frac{1}{\text{Compliance}_T} = \frac{2{,}793{,}344}{e^{0.05976T}} \tag{1}$$

The first step in applying the load-temperature spectra approach is to divide the NCAT track temperature data from the testing period into several temperature ranges. Temperature ranges were chosen based on the Performance-Graded (PG) asphalt binder grading system. Little rutting was observed on the NCAT track when the traffic was applied at pavement surface temperatures lower than 34C [1,6]. Therefore, the first range was chosen as 34–40C, with 37C being the range midpoint. This midpoint was selected as the standard point to develop the temperature modification factors, hereafter referred to as temperature factors. The temperature factors for each temperature range were then constructed using Equation (2), where T again is the pavement surface temperature in Celsius [6]. The temperature factors for all the PG temperature ranges were thus derived and are shown in Table 2. Since 37C is the standard point, the temperature factor for this temperature range is one.

$$\text{TemperatureFactor} = \frac{\text{Compliance}_T}{\text{Compliance}_{37C}} \tag{2}$$

Multiplying the number of ESAL applied by the proper temperature factor yields the modified number of ESAL applied. This "modified ESAL" number accounts for the pavement surface temperature when the original ESAL were applied; the traffic applied at higher pavement temperatures is weighted with a larger temperature factor. To accomplish this the plot of ESAL applied to the NCAT track as a function of time was examined and broken into increments based on the accumulated ESAL applied to the track at the time rut depth was measured. For each traffic increment, the average pavement surface temperature was calculated and the temperature factor corresponding to the temperature range was multiplied by the ESAL increment. After applying this process over the entire two-year period of traffic at the NCAT track, a sum of 16 million modified ESAL was the result. This is over twice the number of ESAL physically applied to the track and is the result of accounting for the temperature effects on rutting. The modified NCAT test track results are plotted in Figure 5.

For the PURWheel data the temperature modification is more straightforward. Since all testing was conducted at 50C, which corresponds to a temperature factor of 2.049 as shown in Table 2. This factor was applied to all PURWheel data, as shown Figure 6.

Table 2. Temperature factor.

Temperature range (C)	Midpoint of temperature range (C)	Temperature factor
<34	Not applicable	0
34–40	37	1.000
40–46	43	1.431
46–52	49	2.049
52–58	55	2.932
58–64	61	4.196

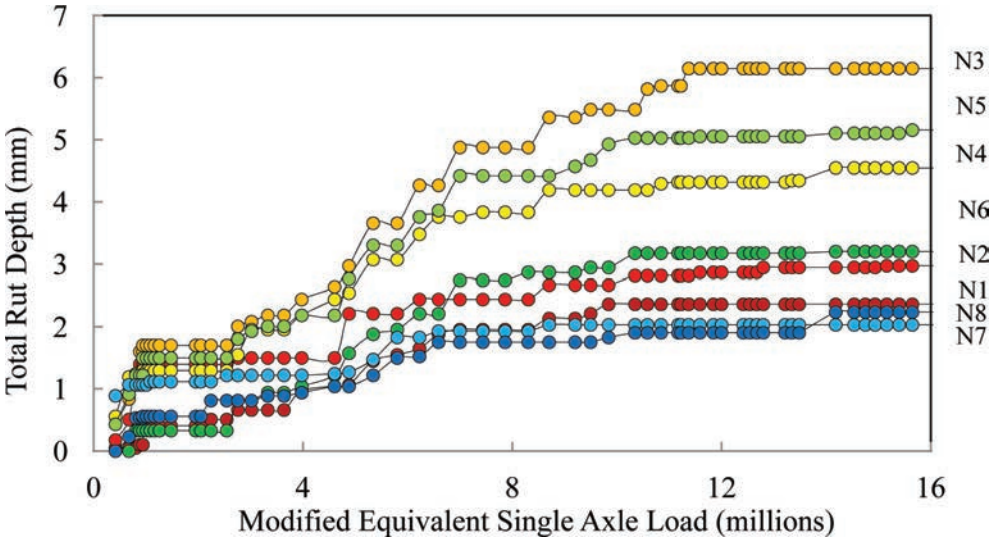

Figure 5. Temperature modified NCAT track rutting data.

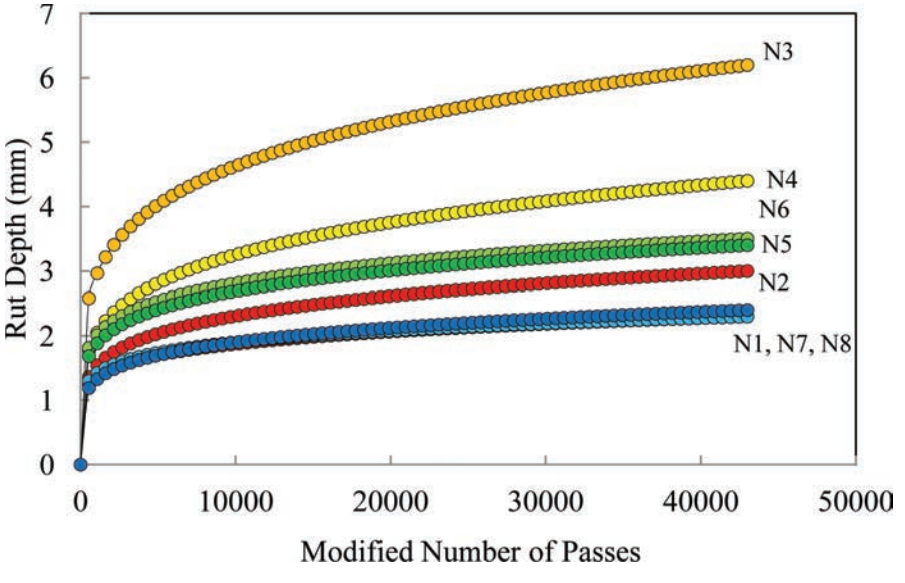

Figure 6. Temperature modified PURWheel rutting data.

3.2 *Aging influence*

Asphalt binder aging can make a direct comparison between the NCAT track and PURWheel more difficult. When an asphalt pavement is exposed to the environment, the asphalt binder in the mixture begins to age, making the binder and the pavement stiffer. Due to this aging, or stiffening of the asphalt pavement, the rate of rutting tends to decrease with pavement age; thus asphalt pavement performance can change between a pavement's early and later life. While the PURWheel is a laboratory test that can be completed in only a few days, testing on the NCAT track took approximately two years to complete. To account for potential rutting differences due to asphalt binder aging, a methodology was applied to both the NCAT track and PURWheel data.

Similar to accounting for temperature effect, the concept of aging modification is to convert rut depths measured at different pavement ages into rut depths at some standard time. To do so an aging factor is applied to the rutting data. The aging factor is defined as the ratio of the rutting rate at a given pavement age to the rutting rate at a standard time; the factor is larger than one before the standard time and smaller after. Dividing the rutting data by the aging factor thus makes the early age rut measurements smaller and the late age rut measurements larger. Powell suggested the standard time be chosen in the middle of the testing period for NCAT track, 301 days, to provide the best correlation between laboratory and field performance. A regression model was derived to calculate the aging factor as shown in Equation (3) [3].

$$\text{Aging factor} = 90.622 \times \text{days}^{-0.7397} \tag{3}$$

Since the field experiments in this research were also conducted at the NCAT track, Powell's aging factor was adopted. These aging modifications were applied to the already temperature modified NCAT track rutting data and are shown in Figure 7.

The aging modification method was also applied to PURWheel rutting data. As with the NCAT track data, it was decided the middle point of the testing period (9750 passes) should be chosen as the standard time. A regression model similar to the track model was developed and is shown in Equation (4). This aging modification was applied to temperature modified PURWheel data and is shown plotted in Figure 8.

$$\text{Aging factor} = 9074.4 \times \text{passes}^{-0.992} \tag{4}$$

3.3 *Modified data comparisons*

The correlation between the NCAT track and PURWheel data, when both sets of data have been temperature and aging modified is plotted in Figure 9. As shown in the figure, the correlations between NCAT track and PURWheel data have been significantly improved. The coefficients of determination for the overall, modified, and unmodified mixtures are improved from 0.69 to 0.84, 0.1 to 0.87, and 0.3 to 0.61 respectively.

Figure 9 also shows a fairly consistent bias in the data. The NCAT track consistently shows about 2 mm more rutting depth than does the PURWheel. This bias may be due to geometry, tires pressures, or mechanical reasons. Additional work will be needed to investigate reasons

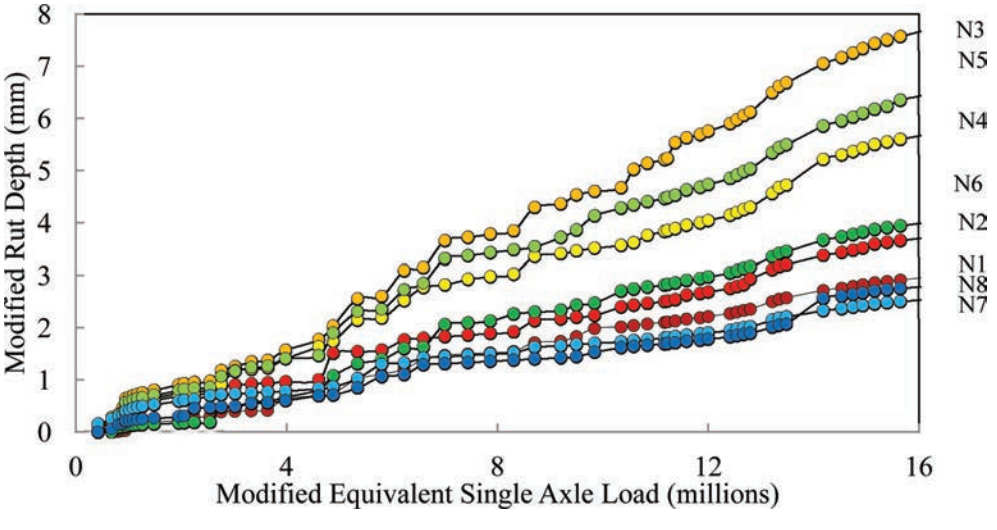

Figure 7. Temperature/aging modified NCAT rutting data.

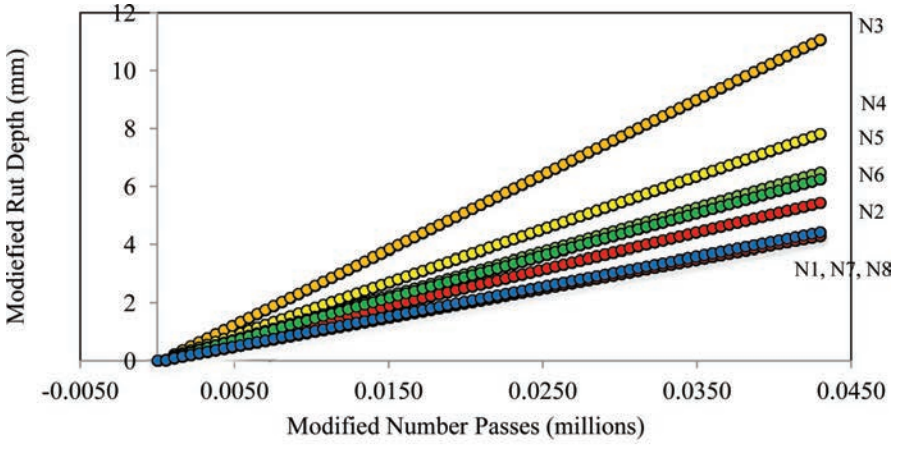

FIGURE 8 Temperature/aging modified PURWheel rutting data

Figure 8. Temperature/aging modified PURWheel rutting data.

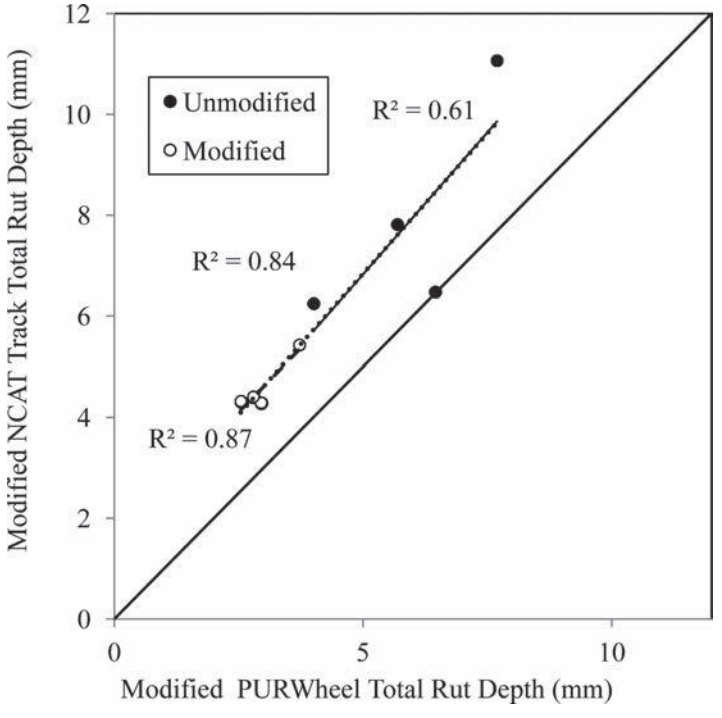

Figure 9. Correlation between modified NCAT track data and PURWheel data.

for the bias. However, although currently unexplained, the consistency of the bias can be dealt with by simply shifting the data.

4 CONCLUSIONS

Laboratory-scale wheel tracking tests have been used for years in the asphalt industry. However, in order to make them more useful they need to be more closely comparable to

in-service results. The work reported in this paper has sought to make the laboratory wheel tracking results from the PURWheel comparable to the in-service pavement of the NCAT track. Based on the data and analyses reported herein, it appears that comparisons between the NCAT track and the PURWheel are more valid when adjustments are made to account for the effects temperature and aging can have on asphalt mixtures.

REFERENCES

[1] Sivasubramaniam, Sivaranjan, Validation of Superpave Mixture Design and Analysis Procedures Using the NCAT Test Track, PhD Dissertation, School of Civil Engineering, Purdue University, 2006.

[2] Hua, Jianfeng. Finite element modeling and analysis of accelerated pavement testing devices and rutting phenomenon, PhD Dissertation, School of Civil Engineering, Purdue University, 2000.

[3] Powell, Raymond, Predicting field performance on the NCAT pavement test track, PhD Dissertation, Auburn University, 2006.

[4] Huang, H.M., Analysis of Accelerated Pavement Tests and Finite Element Modeling of Rutting Phenomenon, Ph.D. Thesis, Purdue University, 1995.

[5] Stiady, J.L., Validation of SHRP Asphalt Mixture Specifications Using Accelerated Testing, Ph.D. Thesis, Purdue University, 2000.

[6] Timm, David H., and Angela L. Priest., Material Properties of the 2003 NCAT Test Track Structural Study, NCAT Report 06-01, 2006.

Experimental characterization of asphaltic materials—VII

This page intentionally left blank

Asphalt Pavements – Kim (Ed)
© 2014 Taylor & Francis Group, London, ISBN 978-1-138-02693-3

Alternative methodologies to evaluate storage stability of rubberised bitumens

Davide Lo Presti, Naeem Memon, James R.A. Grenfell & Gordon Airey
Nottingham Transportation Engineering Centre, Pavement Research Building, University of Nottingham, Nottingham, UK

ABSTRACT: Tyre Rubber Modified Binders (TR-MBs), produced through the McDonald wet process and used worldwide (e.g. asphalt rubber), have demonstrated various benefits to pavements and, moreover, they represent a good opportunity for recycling tyre rubber. However this technology is still struggling to be fully adopted in Europe. One of the reasons is their poor stability during high temperature storage, which leads to high initial costs due to usage of specialised equipment. No-agitation (storage-stable) TR-MBs is proving to be a great alternative and its development could also be the key to increase the use of tyre rubber in paving applications in Europe. This paper presents the results of a study which focuses on investigating conventional and alternative methodologies to evaluate the storage stability of TR-MBs. Results have shown that an accurate binder design is fundamental to improve compatibility of TR-MBs. Furthermore, the study highlights that Dynamic Mechanical Analysis (DMA) and X-Ray CT scans are very suitable techniques to control the compatibility of tyre-rubber bitumen blends leading to the development of storage-stable TR-MBs.

Keywords: Tyre rubber, modified bitumen, storage stability, DMA, X-Ray CT

1 INTRODUCTION

Polymer modification of bitumens is not a new phenomenon, but interest of this technique has increased considerably during the past decade due to the increased performance-related requirements on asphalt pavements. One of the prime roles of a bitumen modifier is to increase the resistance of the asphalt to permanent deformation at high road temperatures without adversely affecting the properties of the bitumen or asphalt at other temperatures. As a matter of fact, processing compatible polymer-bitumen blends allows to greatly increase the high temperature end of paving grade, leaving the low temperature slightly better [1]. Another common practice in the more recent years consists in manufacturing modified bitumens by using recycled polymers. One of the most common is recycled Tyre Rubber (TR) and the relative method of modifying bitumen is referred to be as the "wet process". The major restriction encountered in polymer modifications of bitumen remains the incompatibility of the modifying polymer and the bitumen matrix. Tyre Rubber—bitumen blends are usually not compatible system and these forces contractors to adopt specialized expensive equipment to avoid phase separation during storage or transportation. For this reason most of the research in this field is focusing on developing technologies and methodologies to produce compatible tyre rubber—bitumen blends. The optimisations of these technologies pass also through the development of the assessment techniques and a better understanding of the phase separation during binder storage. This paper aims to enrich this field of research by providing techniques and results toward a better assessment of storage stability of tyre rubber modified bitumens.

2 BACKGROUND

2.1 *Compatibility (Stability) of polymer-bitumen blends*

In general, incorporating a polymer in a bitumen matrix results in a multiphase material with a great tendency to phase separate [2], (Fig. 1). If, without taking any special precautions, a road bitumen and a given thermoplastic polymer are mixed hot, one of the following three results may occur:

- *The mix is heterogeneous*: this is the most likely result (i.e., where the polymer and the bitumen prove to be incompatible). In this case, the constituents in the mix separate and the mix has none of the characteristics of a road binder.
- *The mix is totally homogeneous*, including at the molecular level: this is the infrequent case of perfect compatibility. In this case, the oils in the bitumen solvate the polymer perfectly and destroy any intermacromolecular interactions. The binder is extremely stable, but the modification of service qualities with respect to those of the initial bitumen is very slight. Only its viscosity increases. This is, therefore, not the desired result.
- *The mix is microheterogeneous* and is made up of two distinct finely interlocked phases. This is the compatibility sought and gives the bitumen genuinely modified properties. In such a system, the compatible polymer "swells" by absorbing some of the oily fractions of the bitumen to form a polymer phase distinct from the residual bitumen phase comprising the heavy fractions of the binder (the rest of the oils, plus the resins and asphaltenes).

A desirable system, therefore, has to be a blend of bitumen with a partially miscible polymer that is homogeneous as judged by eyesight but heterogeneous under the microscope [3]. As a consequence, even for compatible systems, the equilibrium situation is a macroscopic phase separation of the two-phases: the Asphaltene Rich Phase (ARP) being the denser phase and on the other hand the Polymer Rich Phase (PRP).

Since these binders consist of two distinct phases, they are subject to the same physical principles as those governing the separation or sedimentation of bitumen emulsions (Stokes' law). In other words, the velocity of displacement of dispersed particles (polymer phase in the case of a bitumen matrix and bitumen phase in the case of a polymer matrix) increases as:

- The particle size increases,
- The difference in density between the two phases increases, and
- The viscosity of the continuous phase decreases.

Thus the larger the density difference and the larger the particle size, the faster the separation rate. Polymer/bitumen compatibility is indeed a dynamic concept and compatible systems are

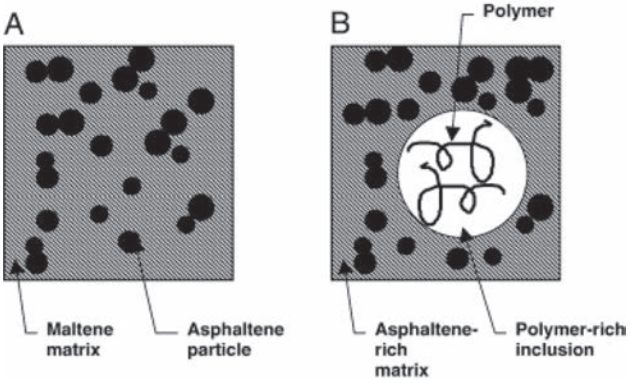

Figure 1. Effect of polymer-modification on the colloidal structure of a bitumen: original bitumen (A) and the corresponding PMB with increased asphaltenes content in the matrix (B) (adapted from Lesuer, 2009).

those with slow separation rate [1]. Usually this equilibrium is reached with a medium-high percentage of polymer, around 5–6% by weight, which creates a three-dimensional polymer network that radically changes the properties of bitumen; with lower percentages (<3–4%) a continuous bitumen phase with a dispersed polymer is obtained, with higher amounts (6–7%) instead it is the bitumen that is dispersed in a continuous polymer phase [1]. Tyre rubber—bitumen blends, are micro-heterogeneous mixes that in order to provide the desired level of modification need a very high amount of polymer (between 10–25%).

2.2 *Tyre rubber—bitumen blends*

Depending on the adopted processing conditions and on the selected materials, the wet process leads to different technologies. Caltrans [4], makes an important distinction between the various blends related to the rotational viscosity of the resulting Tyre Rubber Modified Bitumens (TR-MBs) at high temperature. Based on this distinction, it is possible to divide the wet process into two families: the "wet process–high viscosity" and the "wet process–no agitation". The High Viscosity—wet process is the original wet process, invented by Charles McDonald [5], and leads to a product with a series of benefits which are basically all linked to the binder's increase in elasticity and viscosity at high temperatures that allow greater film thickness in paving mixes without excessive drain down or bleeding [6]. Despite the fact that these types of technologies (e.g. asphalt rubber), have been demonstrated to provide various benefits to pavements, it is still struggling to be fully adopted in Europe, mainly because of their poor stability during high temperatures storage, which leads to high initial costs in modifying existing asphalt plants. In the wet process-no agitation, the characteristic swelling process of the wet process-high viscosity is replaced by the depolymerisation/devulcanisation and the optimised dispersion of the TR into the bitumen by using a high processing temperature (200–260°C) and high shear stress during the mixing (up to 8000 rpm), resulting in a smooth, homogeneous product. In this process, no modifications to the asphalt plant are required. In fact, these blends are manufactured with very fine TR particles that can be digested (broken down and melted in) relatively quickly and/or can be kept dispersed by normal circulation within the storage tank rather than with agitation by special augers or paddles. Although such binders may develop a considerable level of modification, rotational viscosity values rarely approach the minimum threshold of 1,500 cPs (1.5 Pa.s) at 177°C, that is necessary to significantly increase binder contents above those of conventional asphalt mixes without excessive drain down [4]. Hence, depending on the chosen materials and processing variables, the modification of bitumen with TR can provide different products and improving one aspect (e.g. storage stability) could compromise another (e.g. rheological properties).

3 EXPERIMENTAL PROGRAMME

The experimental programme consists of the application of different storage stability analysis techniques on some TR—bitumen blends. Conventional analysis is based on the sole estimation of the softening point of top and bottom sections of a "tube" sample of modified binder after hot storage. The proposed techniques make use of Dynamic Shear Rheometers (DSR) and X-Ray CT analysis with image processing to provide a better understanding of the phase separation process. This section will show details of the methodologies and the next will provide the reader with results and discussions.

3.1 *Materials*

Several Tyre Rubber Modified Bitumens (TR-MBs) were produced and then subjected to conventional storage stability analysis (EN 13399) together with two innovative methodologies involving a rheological investigation by means of Dynamic Shear Rheometer (DSR) and X-Ray CT together with image analysis techniques. The first two analyses were performed on TR-MBs made of a 50/70 pen bitumen and 18% by weight of 30# TR. These components have been blended for 120 minutes in high shear at two different processing

temperatures: 180°C and 210°C. This was performed to have a better understanding of the effect of the processing temperature on storage stability. The X-Ray CT analysis was performed on another TR-MB made with a 70/100 pen bitumen and 15% by weight of 40# TR. These components were blended in high shear at 180°C and for 180 minutes.

3.2 *Conventional softening point storage stability analysis*

Storage stability testing was undertaken based on European Standard EN 13399, but modified with several storage times in order to have a better understanding of the phase separation process. Aluminium toothpaste tubes were filled with TR-MB straight after production at 180°C. The tubes were then sealed and placed n a vertical orientation and holding them in an oven at 180°C (Fig. 2).

After different storage periods the tubes were taken from the oven and cooled down to ambient temperature, before placing into a freezer at –20°C. Once frozen the samples were cut into thirds and the top and bottom sections were subjected to Softening Point tests (EN 1427). In order to define a bituminous binders is stable under hot storage, EN 13399 prescribes a maximum ΔSP of 5ºC between the two sections.

3.3 *Storage stability analysis by means of DSR*

In order to obtain a complete rheological characterisation, a Dynamic Mechanical Analisys (DMA) of the top and bottom section of the blends was performed by making frequency sweep tests over a wide range of temperatures with an Antoon Paar Physica MCR 101 Dynamic Shear Rheometer (DSR). The tests were performed under the following conditions and making at least three repetitions:

- Loading Mode: controlled-strain
- Temperatures: 0ºC to 80ºC with 5ºC intervals (neat bitumen) 30ºC to 80ºC with 5 or 10ºC intervals (TR-MB)
- Frequencies: 0.10, 0.16, 0.25, 0.40, 0.63, 1, 1.6, 2.5, 4, 6.3 and 10 Hz
- Plate geometries: 8 mm ϕ and 2 mm gap (0–50ºC) (only neat bitumen) 25 mm ϕ and 1 and 2 mm gap (30–80ºC)
- Strain amplitude: 0.5% with 8 mm plates (within LVE dependent on G^*) 0.5% and 2%–12%@80°C with 25 mm plates (within LVE response dependent on G^*)

Figure 2. Toothpaste tubes in a rack prior to placing in the oven.

For each test, samples were prepared by means of a hot pour method, based on Alternative 1 of the AASHTO TP5 Standard (AASHTO, 1998). The gap between the upper and lower plates of the DSR was chosen such that the rheological properties taken at wider gap widths (2 mm for 25 mm) were independent of the gap. The rheological properties of the binders were measured in terms of their complex (shear) modulus, G^*; and phase angle, δ. Black diagrams, were used as the basis of all the rheological analyses in this paper. Furthermore, TR-MBs have been tested only at the higher temperature range, 30ºC to 80ºC, because high temperatures provide a major evidence of polymer networks within a bitumen matrix.

3.4 *Storage stability analysis by means X-Ray CT and image processing*

3.4.1 *X-Ray CT scans*

X-Ray CT imaging is a non-destructive method that allows the internal structure of a material to be imaged. This means that internal slices can be made near to the top and the bottom of the samples without damaging the internal structure of the TR-MB. The specimen is scanned by X-Rays at the desired location, which results in a series of linear attenuation coefficients, which are then reconstructed to form a cross-sectional image of the specimen. A CT image is called a slice and represents what an object would look like if it were sliced open along a plane. The grey levels in a CT slice correspond to the molecular weight of what is being imaged and is due to X-Ray attenuation. The X-Rays are scattered or absorbed as they pass through each volume element. The higher the molecular weight of the element the lighter it appears in the obtained image. In order to achieve the best possible image, a set of parameters are needed. These are based on current, voltage, exposure time and the use of filters. For this work the following parameters were selected; voltage 310 kV, current 2.1 mA, exposure time 90 ms, a 2 mm copper source filter and a 25 mm aluminium back filter.

3.4.2 *Image processing*

For the Image Processing, a minimum of two slices were taken through each section (top and bottom) and these were obtained as 16 bit digital images. The ImageJ programme was then used to separate the bitumen and crumb rubber phases in the captured image based on the densities of the materials. The Image J programme was then used to carry out also the thresholding of the CT image. In this technique, specific ranges of pixel greyscales were isolated for analysis. The images used are 16 bit images, meaning that they have 65536 (2^{16}) shades of grey. Each shade of grey represents a different density due to the specific attenuation properties. Different densities relate to different materials, which can therefore be isolated and quantified. Figure 3 shows the X-Ray CT image before and after thresholding.

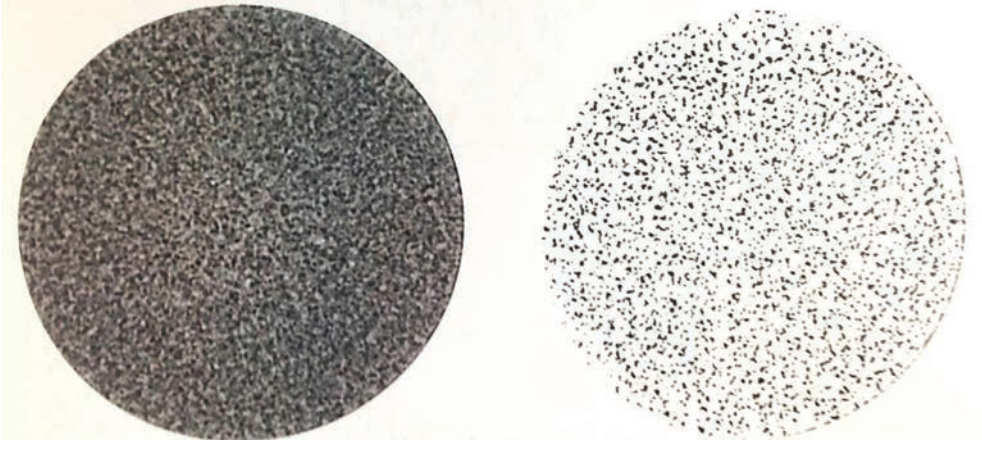

Figure 3. CT image of TR-MB (left), thresholded image of TR particles (right).

The right image shows a black and white TR-MB, where the bitumen is the white phase (higher density), while the left images shows only the isolation of TR particles (black).

4 RESULTS AND DISCUSSION

This section will show a comparison between the SP storage stability methodology and a Dynamic Mechanical Analysis (DMA) first. These results will be enriched by the outcome of another investigation aiming at understanding the mechanism of phase separation through X-Ray CT analysis coupled with image processing techniques.

4.1 *Dynamic mechanical analysis*

The first part of the investigation was focused on assessing the effect of the processing temperature on the stability of the blends. TR-MBs were produced and then subjected to a more conventional SP storage stability analysis together with DMA. SP analysis (Table 1) shows that rubber phase separation starts to be relevant after a few hours. The results do not show a clear trend, since TR-MB produced at 210ºC seems to have a higher separation rate after 4 hours, while after 24 hours of hot storage it is the TR-MB HS180 which shows the higher difference between the top and bottom sections. For this reason, all the binders were also characterised through rheological tests.

DMA was performed by frequency sweep tests at high service temperatures (30–80ºC) with conditions shown in section 2. The results of these analyses are shown in terms of Black diagrams and clearly highlight the differences between the two TR-MBs. After 1 hour (Fig. 4)

Table 1. Softening points of TR-MBs HS before and after hot storage.

Softening point (UNI EN 1427)	TR-MB HS 180 (°C)		TR-MB HS 210 (°C)		ΔSP (°C)	
	Top	Bottom	Top	Bottom		
Before hot storage	62.0		55.0			
After 1 h of hot storage	61.0	63.0	54.0	55.0	2.0	1.0
After 4 h of hot storage	59.0	61.5	55.0	59.0	2.5	4.0
After 24 h of hot storage	50.0	63.0	50.0	59.0	13.0	9.0

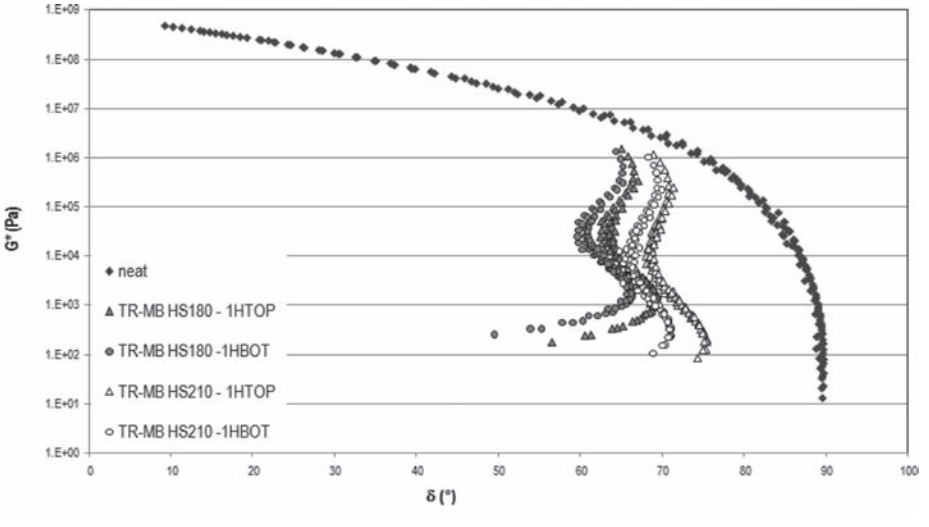

Figure 4. Black diagrams of top and bottom parts of the TR-MBs after 1 h of hot storage.

both TR-MBs show almost no separation, but already after four hours (Fig. 5) TR-MB HS 210 demonstrates a large difference in performance between the top and bottom sections. The majority of the rubber tends to settle towards the bottom and the Black diagram of the top part tends to have the properties of the base bitumen (neat). After 24 hours, (Fig. 6) TR-MB HS180 also shows a big gap between the upper and lower sections, but it is not comparable with the loss in properties of TR-MB HS210, which shows the rheology of the top section being extremely close to that of the neat bitumen.

Comparing these results with those of the conventional tests, shown in Table 1, it is possible to notice that from the SP test the TR-MB HS180 seemed to be the less stable while, on the contrary, the DMA results (Figs. 4–6) show that the TR-MB produced at 210ºC has a higher separation rate than the TR-MB produced at 180ºC. In fact, the results clearly show

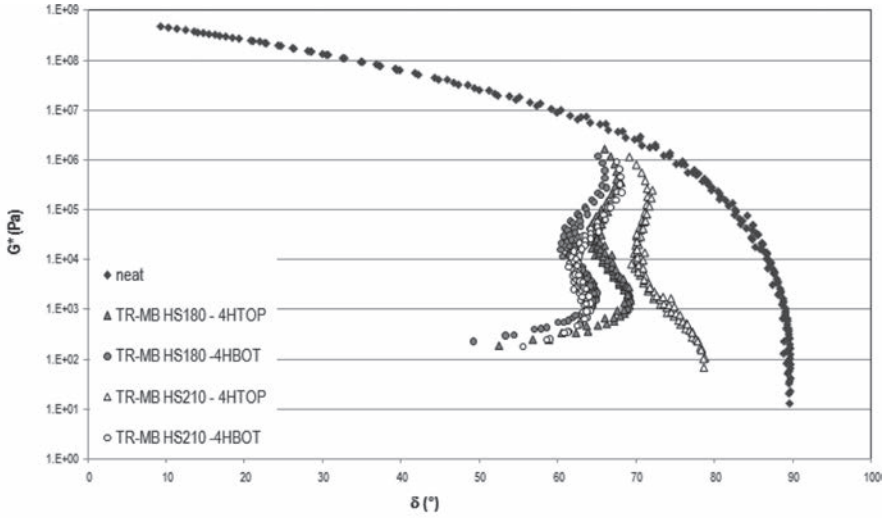

Figure 5. Black diagrams of top and bottom parts of the TR-MBs after 4 h of hot storage.

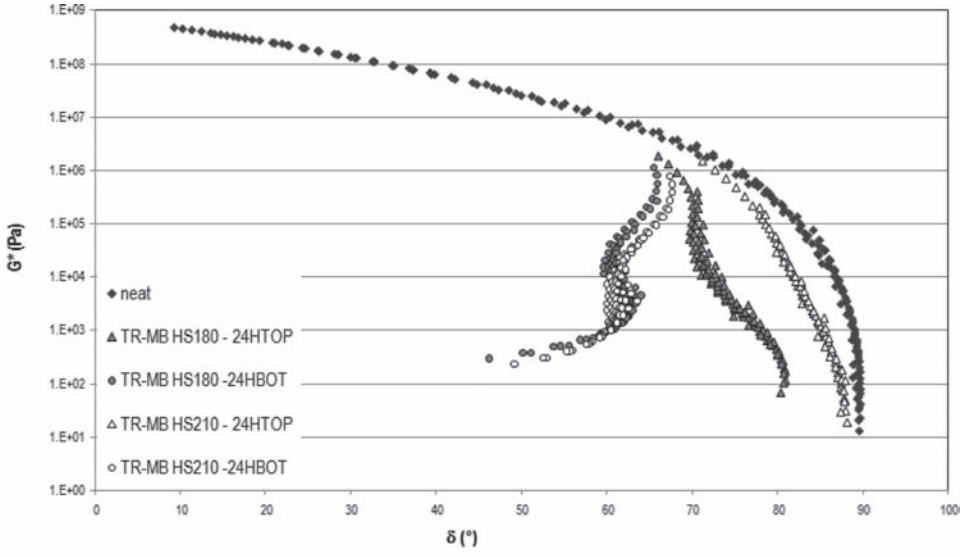

Figure 6. Black diagrams of top and bottom parts of TR-MBs after 24 h of hot storage.

that the difference in terms of Black curves between the top and bottom sections of the TR-MB HS210 is much higher than the difference measured for the TR-MB HS180.

4.2 *X-Ray analysis*

X-Ray CT images of TR-MB 70/100 blends with 15% of TR (40 mesh) are presented before and after storage in Figure 7. These images are representative sections at 100× magnification so that the clear distribution of the TR particles in the different sections before and after hot storage can be seen. So that the storage stability could be assessed, the amount of TR particles in both the top and the bottom of the samples were investigated separately. The particle area measurement was performed using X-Ray images at 50 times magnification using the Image J software.

Figure 1 shows the dispersion of the TR particles within the bitumen matrix after production and the top and bottom sections after 24 hours of the storage stability investigation.

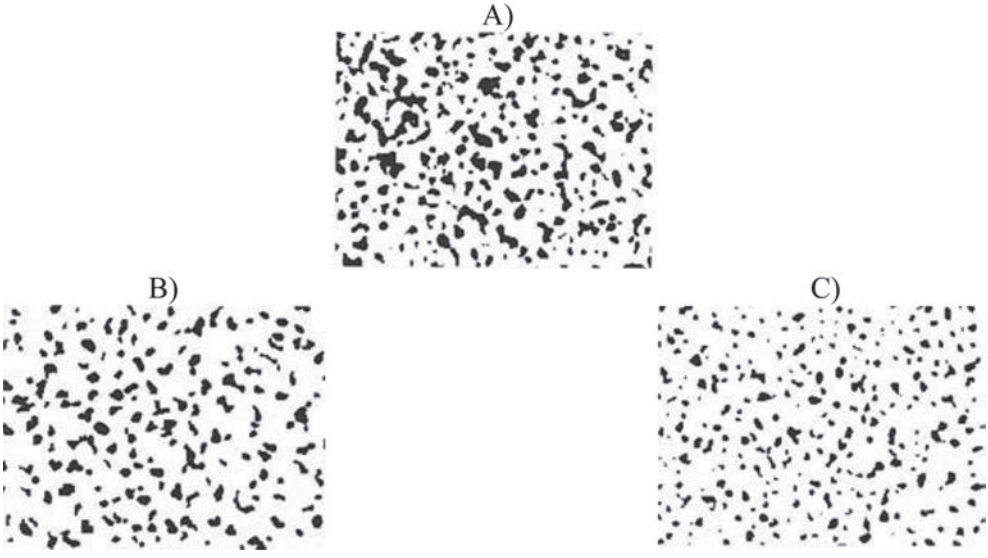

Figure 7. X-Ray CT images of A) TR-MB before storage, B) top after storage and C) bottom after storage at 200 × magnification.

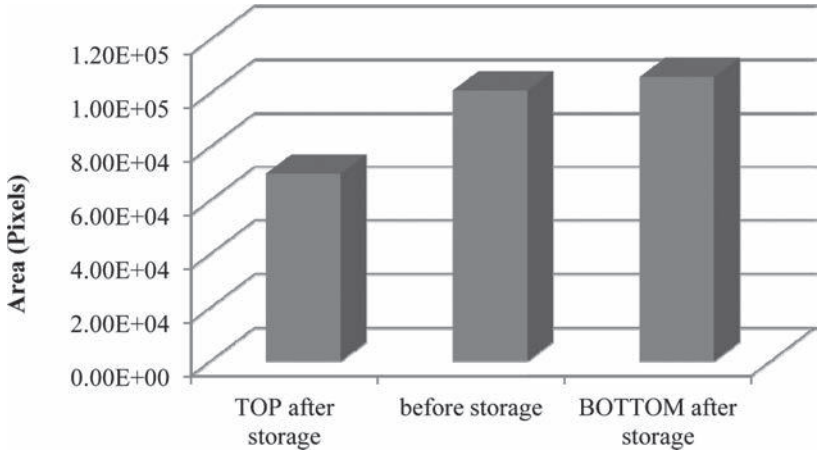

Figure 8. Area of TR particles in different sections of the storage tube before and after storage.

The X-Ray CT images indicate that the TR phase is evenly distributed after the production phase (Fig. 7a). However, a significant separation has occurred after prolonged hot storage. In general, the TR with a higher density than the bitumen (fine particles) has settled to the bottom third of the tube (Fig. 7c), whereas the lower density TR particles (coarse particles) have migrated to the top (Fig. 7b). The TR concentration in the blend has also affected the migration of the TR particles during the storage period.

Following these visual observations, the areas of the TR particles were also calculated in these sections taken from the storage tubes. This was done to confirm the observations quantitatively. These measurements, shown in Figure 8, demonstrate the between the values calculated before and after the hot storage, but also the clear difference between the amounts of TR particles in the top and bottom sections after hot storage. In fact, the bottom section has more TR compared to the top section, which now has less TR than after initial mixing. Also it can be seen that it is the smaller particles that in the bottom section that have led to this increase (Fig. 8).

5 CONCLUSION

This study presents two alternative methodologies for the assessment of a very complex phenomenon related to polymer modification of bitumen: the storage stability under high temperatures. In fact conventional tests such as the ring and ball test have not been designed for such complex materials as rubberised binders. A proof of this statement is provided by the fact that performing the test with such heterogeneous material is almost never problem-free, compared to the testing of neat bitumen. This may result in significant errors as shown by this study. On the other hand, Dynamic Mechanical Analysis proved to be a more effective tool and the authors believe that assessing the storage stability of modified binders through rheological characterisation gives a better understanding of the separation process. Furthermore, X-Ray CT and image analysis proved to be very useful to clarify a complex phenomenon, which had not yet been fully characterized, such as the behavior of modified binders under hot storage. This part of the investigation led to the clarification of the phase separation process of the rubberised binders after a long period of hot storage. As a result, the finer TR particles (higher density) tend to sink in the bottom section, also due to agglomeration, while the larger TR particles (lower density) tend to float the top. In addition, image analysis clarified that the sinking phenomenon is more relevant than floating, and this justifies the better rheological properties of the bottom section recorded through the dynamic mechanical analysis.

ACKNOWLEDGEMENTS

The authors wish to acknowledge the University of Palermo (IT) for the significant contribution to the experimental programme.

REFERENCES

[1] Lesueur, D., The colloidal structure of bitumen: Consequences on the rheology and on the mechanisms of bitumen modification. 1–2, s.l.: Advances in Colloid and Interface Science, Vol. 145, 2009,
[2] Hesp, S.A. and Woodhams, R.T., Polymer Modified Asphalt Binders, ASTM Publications, Vol. STP 1180, 1992.
[3] Pfeiffer, J.P., The Properties of Asphaltic Bitumen. Elsevier, pp. 1–12, Amsterdam 1950.
[4] Asphalt Rubber Usage Guide. State of California Department of Transportation, Materials Engineering and Testing Services, 2006.
[5] Lo Presti, D. Recycled Tyre Rubber Modified Bitumens for road asphalt mixtures: A literature review, Construction and Building Materials, Vol. 49, pp. 863–881, 2013.
[6] Lo Presti, D., Airey, G. and Partal, P., Manufacturing Terminal and Field Bitumen-Tyre Rubber Blends: The Importance of Processing Conditions. Procedia-Social and Behavioral Sciences, Vol. 53, pp. 485–494, 2012.

This page intentionally left blank

Asphalt Pavements – Kim (Ed)
© 2014 Taylor & Francis Group, London, ISBN 978-1-138-02693-3

Investigation of the effect of temperature on asphalt binder fatigue

Farinaz Safaei & Cassie Hintz
Department of Civil, Construction, and Environmental Engineering, North Carolina State University, Raleigh, NC, USA

ABSTRACT: Fatigue resistance of asphalt pavements is known to be a temperature dependent phenomenon. The temperature dependence of pavements is driven by its constituent asphalt binder. This study evaluates the effect of temperature on asphalt binder fatigue resistance using the Dynamic Shear Rheometer (DSR). Results were analyzed using a Simplified Viscoelastic Continuum Damage (VECD) analysis framework. Results demonstrate that damage during DSR testing only manifests as fatigue cracking below a certain critical temperature above which flow rather than fracture dominates failure. Similarly, at sufficiently low temperature, adhesive failure between the DSR plates and asphalt specimen is found to confound results. Over the range of temperatures where cohesive fatigue cracking is found to occur in the DSR, time-temperature superposition using linear viscoelastic time-temperature shift factors can be applied to VECD results, allowing for efficient fatigue characterization at multiple temperatures. Trends in fatigue life with varying temperature appear to be binder dependent.

Keywords: asphalt binder, fatigue, time-temperature superposition, viscoelastic continuum damage modeling

1 INTRODUCTION

Fatigue cracking in asphalt pavements results from the accumulation of damage under repeated traffic loading. It is generally assumed that fatigue damage in asphalt pavements is most critical at intermediate temperatures corresponding to springtime when layers underlying the asphalt concrete become saturated due to thawing of snow and ice and/or rain [1]. However, pavements are subjected to a variety of temperatures associated with seasonal and daily fluctuations in temperature and thus, fatigue damage does not accumulate not at a specific temperature but rather over a critical range of temperatures. Therefore, understanding and modeling temperature effects on fatigue is an area of great interest. At sufficiently high temperatures, fatigue damage is not expected to be of concern as the soft nature of the asphalt binder will lead to failure by plastic flow rather than cracking and also promote self-healing of existing microcracks. Similarly, at sufficiently low temperatures, asphalt binder becomes very stiff and brittle, which will lead to dominance of thermal cracking as opposed to fatigue.

Asphalt binder is weakest asphalt concrete constituent and is responsible for the temperature sensitivity of asphalt concrete. Thus, this study aims to investigate the effect of temperature on asphalt binder fatigue measured using the Dynamic Shear Rheometer (DSR). The effect of temperature on the failure mechanism of the asphalt binder (i.e., fracture versus plastic flow) is investigated. Additionally, application of Time-Temperature Superposition (TTS) to fatigue damage growth, quantified using simplified ViscoElastic Continuum Damage (VECD) framework is used to aid in interpretation of results and offers an efficient means to predict fatigue damage growth under varying climatic conditions.

2 BACKGROUND

2.1 *Binder fatigue testing*

In the current Superpave, Performance Grading (PG) specification for asphalt binders, the parameter $|G^*| \cdot \sin \delta$ measured within the linear viscoelastic regime at a single temperature is used to evaluate fatigue performance under the assumption that a softer and more elastic binder will be more fatigue resistant [2]. Recent research has shown that this parameter is not a good indicator of the damage resistance, particularly in the case of modified asphalts, since it is only a single point at a small strain level and does not take the traffic loading in to account [3]. Therefore, Bahia et al. introduced a new test method, called the time sweep, which consists of repeated cyclic loading in the DSR at constant loading amplitude as an alternative to the current specification [4]. One can change the amplitude of loading during the test to simulate differing pavement structures and calculate a fatigue life based on monitoring the changes in loading resistance with respect to number of loading cycles. The procedure has been shown to capture binder contribution to asphalt mixture fatigue resistance based on laboratory comparison of time sweep results and asphalt concrete fatigue test results [4].

However, the temperature at which the time sweep test is applicable and how to account for fluctuations in temperature in fatigue modeling has not been rigorously studied. Hintz and Bahia [5] studied the mechanism of fatigue failure of asphalt binders in the time sweep test. Their work demonstrated that fatigue failure in the DSR manifests as "edge cracks," which are circumferential cracks that initiate from the periphery of the specimen and propagate towards the specimen center as the number of loading cycles increases, effectively causing the reduction of sample radius and consistent with other materials fatigued under cyclic torsional loading. However, their study was only done over limited temperature range and others account in the literature have noted confounding effects of edge flow during time sweep testing in the DSR. Anderson et al [6] observed two mechanisms of failure in the time sweep test, depending on the test temperature. At low temperatures, the formation of cracks was noted as the failure mechanism but plastic flow at the periphery of the sample was found to occur when tests were conducted at relatively high temperatures. Soenen and Eckmann also reported as the stiffness of binder decreases as a result of testing temperature increase, edge flow occurs but as long as the modulus was sufficiently large fatigue cracks developed toward the center of the sample [7,8].

This study investigates the effect of binder temperature (and thus, $|G^*|$) on the failure mechanism of asphalt binder based on image analysis of specimens following testing.

2.2 *S-VECD model*

Fatigue test results were interpreted using a Simplified Viscoelastic Continuum Damage (S-VECD) model. VECD-based frameworks have been used extensively to characterize the complex behavior of asphalt mixtures [9,10] and more recently have been applied to binders [11]. Details on the S-VECD model development are provided elsewhere [12]. However, a brief overview is provided in the interest of the reader. Viscoelastic continuum damage modeling of asphalt materials is based on Schapery's work potential theory which utilizes an internal state variable, S, to quantify damage as a result of microstructural changes which lead to a reduction in effective stiffness. This internal state variable representing damage is derived from the following damage evolution law:

$$\frac{ds}{dt} = \left(-\frac{\partial W^R}{\partial s} \right)^{\alpha} \tag{1}$$

where W^R is the pseudostrain energy density defined in Eq. (1) and α is a material dependent constant. For the work herein, α is defined as $1/m$ where m is the steady-state slope of the dynamic shear modulus master curve in log space [11].

$$W^R = \frac{1}{2} C(S)\left(\gamma^R\right)^2 \tag{2}$$

where γ^R is pseudostrain and $C(S)$ is the pseudostiffness of the materials.

Effectively, pseudostrain is equivalent to the linear viscoelastic stress response to loading history of interest divided by an arbitrary reference modulus, often selected to be one as is the case here. In the case of cyclic loading applied in the DSR, peak pseudostrain can be calculated as:

$$\gamma_{pp}{}^{R}{}_{cycle\,i} = \frac{1}{G_R} \cdot \left(\gamma_{pp_{cycle\,i}} \cdot |G^*|_{LVE}\right) \tag{3}$$

where G_R is an arbitrary modulus, selected to be one, $\gamma_{pp_{cycle\,i}}$ is the peak pseudostrain in a given cycle I and $|G^*|_{LVE}$ is the linear viscoelastic $|G^*|$ at the fatigue testing temperature (i.e., reduced frequency).

The pseudostiffness is defined in Eq. (4). The value of $C(S)$ with no damage is one and $C(S)$ decreases as material integrity is lost. The Dynamic Modulus Ratio (DMR) is a parameter used to account for specimen to specimen variability equal to $|G^*|_{Initial}/|G^*|_{LVE}$. For each time sweep test the DMR value is generally between 0.9 and 1, indicating good repeatability.

$$C^*(S) = \frac{\tau_{pp}}{\gamma_{pp}{}^{R} \cdot DMR} \tag{4}$$

where τ_{pp} is the peak shear stress in cycle of interest. Damage, S, is derived through numerically solving Eq. (1) with input of Eq. (2) to arrive at:

$$S = \sum_{i=1}^{N} \left[\frac{DMR}{2} \left(\gamma_{pp}{}^{R}\right)^2 \left(C^*{}_{i-1} - C^*{}_{i}\right) \right]^{\frac{\alpha}{1+\alpha}} \cdot [t_i - t_{i-1}]^{\frac{1}{1+\alpha}} \tag{5}$$

where t is time, and i refers to the cycle number. The primary benefit of the S-VECD model is that it is found that the relationship between $C(S)$ is the same regardless of loading history. This is illustrated in Figure 1 for a binder tested in the DSR using initial strain amplitudes of 3% and 4%.

2.2.1 *Incorporation of temperature effects in the S-VECD model*

Temperature effects have been incorporated into the S-VECD model for asphalt mixtures through use of time-temperature superposition. It has been generally accepted that asphalt is a thermo-rheologically simple material [14]. Furthermore, it has been demonstrated that

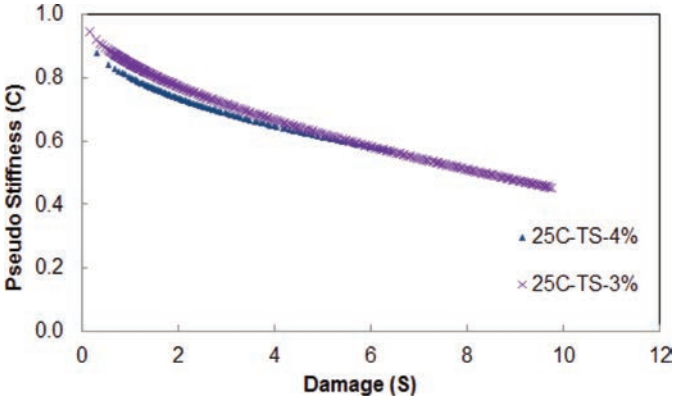

Figure 1. Damage characteristic curve for 370903 at 3 and 4% strain level.

thermorheological simplicity extends to the damage regime for asphalt mixtures. In 2001 Chehab et al [9] conducted uniaxial monotonic tests on mixture specimens at varying temperatures and loading rates and demonstrated that the time-temperature superposition can be used to collapse resultant VECD damage curves. Daniel and Kim [15] performed cyclic direct tension tests on mixtures at various cyclic crosshead displacement amplitudes, frequencies, and temperatures to investigate if predictions can be made from one temperature to another. These studies incorporated temperature effects into VECD models through replacing actual time with reduced time determined using linear viscoelastic time-temperature shift factors [9, 15].

In the case of the S-VECD framework for binders presented, time temperature is incorporated through the concept of reduced time by replacing t with reduced time, ξ (Eq. (6) and (7)). Reduced time is used in the damage calculation in order to shift to the reference temperature using time-temperature shift factors determined from linear viscoelastic characterization.

$$\xi = \frac{T}{a_T} \tag{6}$$

$$S = \sum_{i=1}^{N} \left[\frac{DMR}{2} \left(\gamma_{pp}{}^{R} \right)^2 \left(C^*_{i-1} - C^*_{i} \right) \right]^{\frac{\alpha}{1+\alpha}} \cdot \left[\xi_i - \xi_{i-1} \right]^{\frac{1}{1+\alpha}} \tag{7}$$

Similarly, pseudostrain and consequently pseudostiffness are calculated using reduced frequency.

2.2.2 *Fatigue life prediction from S-VECD model*

The VECD model can be extended to allow for fatigue life predictions. To do this, a power law model is fit to the unique $C(S)$ versus S curve:

$$C = 1 - C_1 \left(S \right)^{C_2} \tag{8}$$

where C_1 and C_2 are experimentally determined coefficients. Then, the following solution for fatigue life (N_f) can be derived:

$$N_f = \frac{\left(f_R \right) \left(2^{\alpha} \right) S_f^{\alpha - \alpha C_2 + 1}}{\left(\alpha - \alpha C_2 + 1 \right) \left(C_1 C_2 DMR \right)^{\alpha} \left(\gamma^R \right)^{2\alpha}} \tag{9}$$

where S_f = damage accumulation at failure, f_R = reduced loading frequency (Hz). Any pseudostrain amplitude of interest can be input into Eq. (9), allowing for prediction of results at any loading amplitude from results of a single test.

3 OBJECTIVES

The primary objectives of this research are to:

1. Evaluate the effect of temperature on the failure mechanism of asphalt binders tested under fatigue loading in the DSR
2. Evaluate applicability of time-temperature superposition to fatigue damage growth in the DSR.

4 EXPERIMENTAL PLAN

All tests were conducted in a TA ARG2 DSR using the 8 mm parallel plate-plate set-up. The tests were in the strain control mode. The binders tested are listed in Table 1. Two of

Table 1. Tested binders.

ID	Binder PG
30-0903	64-22
37-0903	70-22
C35	70-34

the binders were from the Long-Term Pavement Performance (LTPP) program, 30-0903 and 37-0903, which are from New Jersey and Oregon, respectively. Binder C35 is a polymer modified asphalt used in Minnesota. Thus, binders used in varying climates were selected which were anticipated to have very different behavior. All binders were aged in the Rolling Thin Film Oven (RTFO) prior to testing.

Frequency sweep tests were conducted to determine the linear viscoelastic properties of asphalt binders. In these tests, a constant load amplitude of 1% strain is applied to avoid damaging the specimen and the frequency changed between 0.1 to 30 Hz. Tests were performed at 50, 35, 20 and 5°C for all binders. Asphalt binder dynamic shear modulus and phase angle master curves were constructed from frequency sweep results and the Williams–Landel–Ferry (WLF) equation (Eq. (10)) was fit to the data to allow for prediction of the time-temperature shift factor at any temperature [2]:

$$\log \frac{a_T(T)}{a_T(T_o)} = -\frac{c_1(T - T_o)}{c_2 + (T - T_o)} \tag{10}$$

a_T = the shift factor at temperature T and, C_1, C_2 = experimentally determined coefficients.

Time sweep tests were conducted to study effects of temperature on fatigue resistance of asphalt binders. Tests were conducted at 5, 10, 15, 20, 25, and 35°C for all binders. Time sweep tests were all conducted in displacement controlled model at 10 Hz loading frequency and 3% initial strain amplitude.

5 RESULTS

5.1 *Linear viscoelastic master curves*

Dynamic shear modulus master curves for the three binders tested are presented in Figure 2. Moduli values for the fatigue testing conditions, 10 Hz frequencies with varying temperature are superimposed on the master curves, which show a wide range of $|G^*|$ values was covered by the temperatures considered.

5.2 *Analysis of failure mechanism and relation to binder $|G^*|$*

A depiction of samples following fatigue testing in the DSR at all test temperatures for binder 300903 is shown in Figure 3. The top pictures were obtained by freezing specimens following testing and then detaching the spindle using procedure proposed by Hintz and Bahia [4]. The bottom row of pictures is of the specimens in the DSR after testing before spindle detachment. It can be seen that as temperature increases, the failure mechanism translates from being fracture to flow. The radial lines emanating from specimen edge indicate the failed area and the smooth center of the specimens indicates the portion of the sample that remained intact. Similar observations were made for other binders and were made to judge failure mechanism. At 5°C it can be seen that the sample appears macroscopically flat. In this case, the binder had detached from the spindle rather than failing by cohesive fracture. For all binders, at 5°C adhesion loss between the DSR plates and the binder specimen occurred

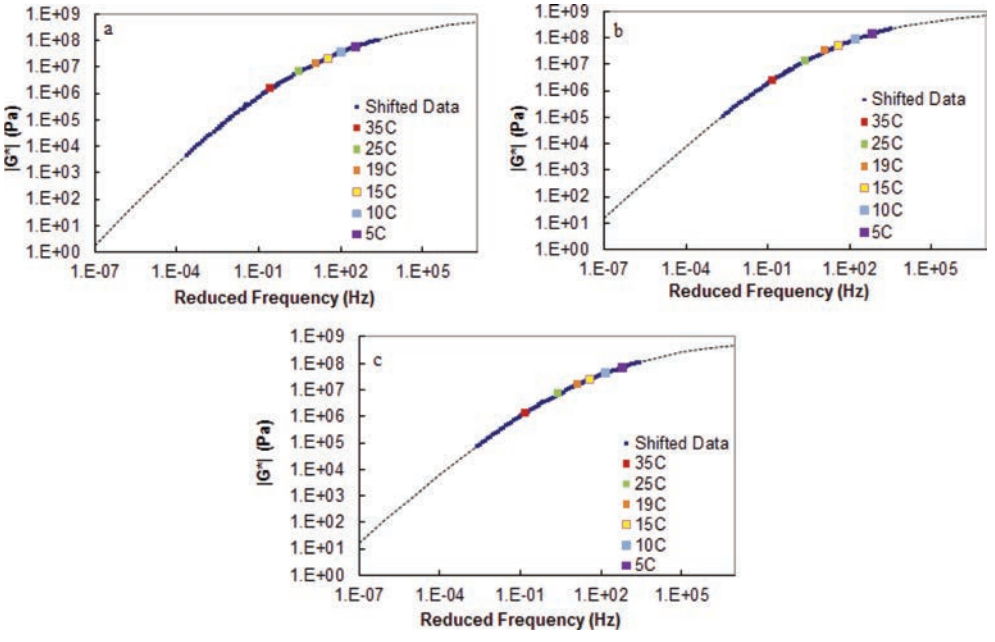

Figure 2. Master curves containing selected temperatures for a) 300903 b) 370903 c) C35.

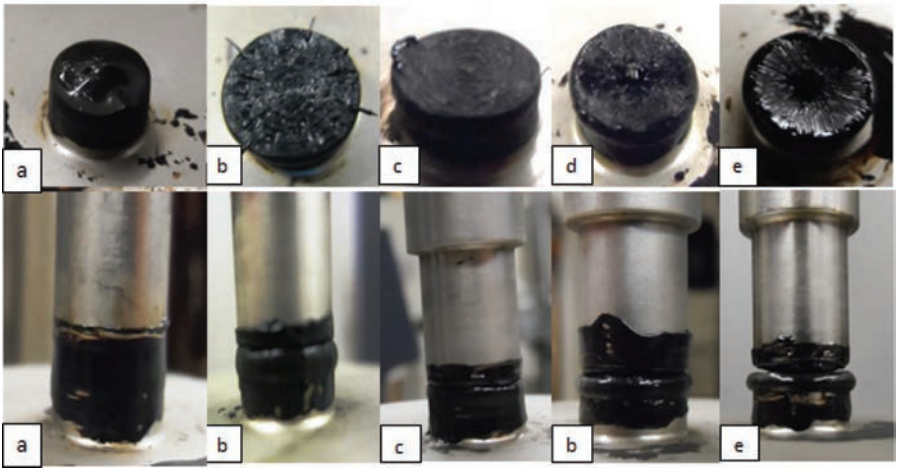

Figure 3. Specimen 300903 after testing at a) 5°C, b) 10°C, c) 15°C, d) 25°C, and e) 35°C.

rather than cohesive fracture of the specimen, determined based on a sudden drop in loading resistance during testing and visual observation of debonding following testing. The linear viscoelastic $|G^*|$ and phase angles determined from the master curves presented in Figure 2 at 10 Hz frequency and each testing temperature are provided in Table 2 with color coding to indicate the dominant failure mechanism. While only based on testing of three binders, these results suggest that cohesive fatigue fracture will occur during the time sweep test when the $|G^*|$ at the testing temperature and frequency is between 10 MPa and 50 MPa. It can be seen that above $|G^*|$ values of approximately 50 MPa, adhesive failure becomes a concern and that below values of 10 MPa, flow becomes evident with dominant flow rather than fracture at values below roughly 6 MPa.

Table 2. Complex modulus (|G^*|) and phase angle (δ) values for tested binders at tested temperatures.

Temperature (°C)	300903		370903		C35	
	|G^*| (MPa)	Phase angle (°)	|G^*| (MPa)	Phase angle (°)	|G^*| (MPa)	Phase angle (°)
35	1.49	58.51	2.44	34.73	1.38	35.90
25	6.50	48.16	13.15	48.15	6.70	46.34
19	13.90	45.68	30.99	42.81	15.21	42.57
15	21.95	46.96	51.07	36.80	24.87	38.00
10	36.83	51.18	88.23	31.22	43.26	33.81
5	58.33	56.63	140.36	27.37	70.45	30.88

= cohesive fracture, = cohesive fracture with moderate flow, = adhesive failure, = predominately flow failure.

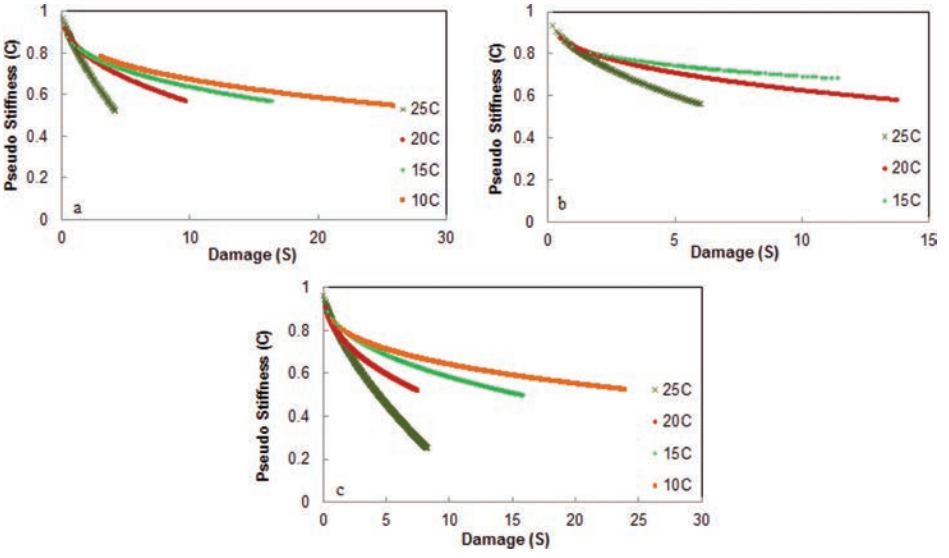

Figure 4. Time sweep damage curves for a) 300903 b) 370903 c) C35.

5.3 *Application of time-temperature superposition to S-VECD damage curves*

Based on the above presented results, S-VECD analysis was conducted for tests where cohesive fracture was found to be the dominant failure mechanism. S-VECD damage curves before and after application of time-temperature superposition are shown in Figures 4 and 5. Note that for Figure 5, a reference temperature of 20°C was used and linear viscoelastic time-temperature shift factors determined from frequency sweep testing were used. Trend is consistent with previous mixture findings.

Results demonstrate that by shifting the data to a reference temperature of 20°C, C vs. S curves collapse to a single curve, indicating time-temperature superposition is applicable in the range of temperatures where cohesive fracture is the dominant failure mechanism, indicating the S-VECD model can be used to efficiently characterize fatigue damage over the dominant range of temperatures where fatigue occurs.

5.4 *Fatigue life trends with temperature*

In defining a point for fatigue failure, besides the damage characteristic curves, the material integrity (i.e., C value) at failure is also important. Here, the peak in CxN (where N is number

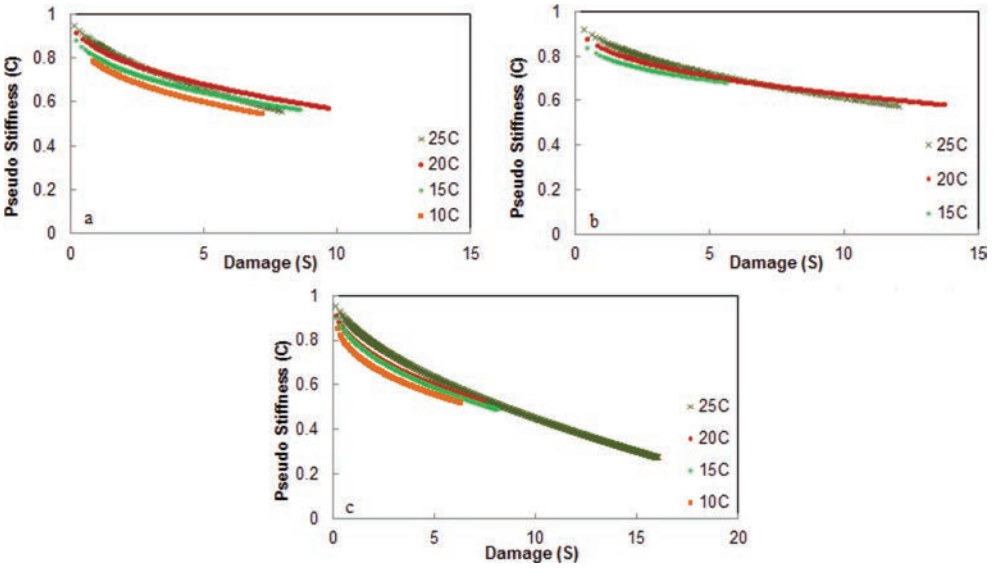

Figure 5. Shifted time sweep damage Curves for a) 300903 b) 370903 c) C35.

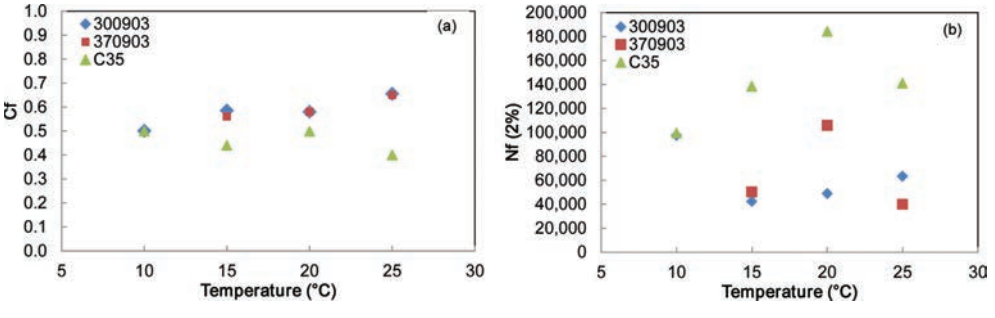

Figure 6. (a) PseudoStiffness at failure versus temperature and (b) fatigue life versus temperature.

of loading cycles) versus N is used to define failure, which is similar to the stiffness times N approach proposed by Rowe and Bouldin [16]. The peak in C times N corresponds to a marked change in the rate of loss in material integrity, as shown in, and is therefore considered a logical failure definition.

Trends in C_f with temperature for the three asphalt binders tested are shown in Figure 6(a). Note that data where flow or adhesion loss were found to be significant were excluded from analyses. Results show C_f is more or less stable with temperature. To determine the number of cycles to failure from the predicted results using the SVECD model, the C value at the failure cycle (C_f) is used as the failure criterion to determined S_f in Eq. (9). Results of fatigue life prediction at 2% strain amplitude are shown in Figure 6(b). Results show that binder C35 shows superior fatigue performance compared to other binders regardless of temperature, which is somewhat expected as this is a highly polymer modified asphalt. In addition, it can be seen that both binders 370903 and C35 show a peak in fatigue life at 20°C whereas binder 300903 shows a consistently increasing trend in fatigue life with increasing temperature. These results demonstrate that fatigue life is temperature dependent and the dependency of fatigue resistance on binder is also related to binder type.

6 CONCLUSIONS

- The time sweep appears to be applicable within the range of $|G^*|$ values of 10 to 50 MPa. Above this limit, adhesion loss becomes problematic. Below this limit, flow rather than cohesive fatigue fracture dominates failure.
- It can be seen that time temperature superposition applies to the time sweep results within the S-VECD framework in the range of temperature which cohesive fracture is the dominant fatigue failure mechanism.
- Results demonstrate no clear trend in fatigue life with temperature within the regime where cohesive fracture is observed. Thus, the effect of temperature on cohesive fatigue fracture in binders merits further study.

ACKNOWLEDGEMENTS

This research was supported by the University of Wisconsin–Madison. This support is greatly appreciated.

REFERENCES

[1] Huang. Pavement Design and Analysis. Englewood, N.J, Prentice Hall, 2004.
[2] Bahia, H.U., H. Zhai, M. Zeng, Y. Hu, and P. Turner. Development of Binder Specification Parameters Based on Characterization of Damage Behavior. Journal of the Association of Asphalt Paving Technologists, Vol. 70, pp. 442–470, 2002.
[3] Soenen, H. and Eckmann, B. Fatigue testing of bituminous binders with a dynamic shear rheometer. Proceedings of the 2nd Eurasphalt and Eurobitume Congress, Barcelona, 2000.
[4] Bahia, H.U., D.I. Hanson, M. Zeng, H. Zhai, M.A. Khatri, and R.M. Anderson. Characterization of Modified Asphalt Binders in Superpave Mix Design. NCHRP Report 459, TRB, National Research Council, Washington, D.C., 2001.
[5] Hintz, C., Bahia, H.U. Understanding mechanisms Leading to Asphalt Binder Fatigue in the Dynamic Shear Rheometer (DSR). In Press in Journal of the Association of Asphalt Paving Technologists, 2013.
[6] Andersen, D.A., Le Hir, M.Y., Marasteanu, M., Planche, J-P., Martin, D., and Gaauthier, G. Evaluation of Fatigue Criteria for Asphalt Binder. In Transportation Research Record, 1766:48–56, 2001.
[7] Soenen, H., and Eckmann, B. Fatigue Testing of Bituminous Binders with a Dynamic Shear Rheometer. Proc., 2nd Eurasphalt and Eurobitume Congress, Barcelona, Spain, 2000.
[8] Soenen, H., De La Roche, H., Redelius, P. Predict Mix Fatigue Tests from Binder Fatigue Properties, Measured with a DSR. 3rd Eurasphalt and Eurobitume Congress, Vienna, 2004.
[9] Chehab, G., Y.R. Kim, R.A. Schapery, M. Witczack, and R. Bonaquist. Time-Temperature Superposition Principle for Asphalt Concrete Mixtures with Growing Damage in Tension State. Journal of Association of Asphalt Paving Technologists, Vol. 71, pp. 559–593, 2002.
[10] Underwood, B.S., Y.R. Kim and M.N. Guddati. Characterization and Performance Prediction of ALF Mixtures Using a Viscoelastoplastic Continuum Damage Model. Journal of Association of Asphalt Paving Technologists, Vol. 75, pp. 577–636, 2006.
[11] Hintz, C., R.A. Velasquez, C.M. Johnson, and H.U. Bahia. Modification and Validation of the Linear Amplitude Sweep Test for Binder Fatigue Specification. Transportation Research Record, National Research Council, Washington, D.C., No. 2207, pp. 99–106, 2012.
[12] Underwood, B.S., C.M. Baek, and Y.R. Kim. Use of Simplified Viscoelastic Continuum Damage Model as an Asphalt Concrete Fatigue Analysis Platform. In Transportation Research Record: Journal of the Transportation Research Board, Issue 2296, Transportation Research Board of the National Academies, Washington, D.C., pp. 36–45, 2012.
[13] Safaei, F., Lee, J.S., Hintz, C., Kim, Y.R. Implications of Warm Mix Asphalt on Long Term Oxidative Aging and Fatigue Performance of Asphalt Binders and Mixtures. Under Review in Journal of the Association of Asphalt Paving Technologists,2013.
[14] Anderson, D.A., et al. Binder characterization and evaluation, Volume 3: Physical Characterization. Report SHRP-A-369, Strategic Highway Research Program, National Research Council, Washington, DC, 1994.

[15] Daniel, J.S. Development of a Simplified Fatigue Test and Analysis Procedure Using a Viscoelastic, Continuum Damage Model and Its Implementation to WesTrack Mixtures. Ph.D. dissertation. North Carolina State University, Raleigh, 2001.
[16] Rowe, G.M. and M. Bouldin. Performance of Asphalt Mixtures in the Trapezoidal Fatigue Test, Journal of Association of Asphalt Paving Technologists, Vol. 62, pp. 344–384, 1993.

Asphalt Pavements – Kim (Ed)
© 2014 Taylor & Francis Group, London, ISBN 978-1-138-02693-3

Effective temperature for permanent deformation testing of asphalt mixtures

Alaeddin Mohseni
Pavement Systems Inc., Bethesda, MD, USA

Haleh Azari
AASHTO Materials Reference Laboratory (AMRL), National Institute of Standards and Technology, Gaithersburg, MD, USA

ABSTRACT: Effective temperature for rutting (T_{eff}) is defined in the literature as a single testing temperature for asphalt mixtures to simulate rutting in the field. This temperature is essential in reducing the testing and analysis of asphalt mixture performance. Current procedures are developed during SHRP A-407 and NCHRP 9-22 projects which calculate T_{eff} from Mean Annual Air Temperature (MAAT). The objective of this study is to review the existing T_{eff} approaches for testing asphalt mixtures and to explore the possibility of developing a more robust and simplified T_{eff} procedure.

Comparison of the SHRP and NCHRP procedures with the calculated rutting determined that the test temperatures provided by these procedures were too low to cause rutting damage. Furthermore, the comparison of Degree-Days parameter, which correlated well with rutting, and MAAT revealed that MAAT is over-predicting T_{eff} in coastal areas due to mild winters while under-predicting it in desert areas due to colder nights. An enhanced T_{eff} approach was developed based on the incremental rutting damage concept that was used for the LTPP Bind high-temperature model. The proposed procedure is more accurate since it is calibrated to the field and experts' opinion, yet it is simpler and easier to use than the current approaches.

Keywords: Effective temperature, asphalt mixture performance, permanent deformation, degree-days, rutting

1 BACKGROUND

The determination of a single testing temperature for asphalt mixtures to simulate permanent deformation (rutting) is essential in reducing the testing and analysis of AC mixture performance. The presence of a single temperature at which AC mixtures can be evaluated has been termed the "Effective Temperature—T_{eff}" in the literature.

T_{eff} is defined by SHRP A-407 (1) as "a single test temperature at which an amount of permanent deformation would occur equivalent to that measured by considering each season separately throughout the year." T_{eff} is defined by SHRP A-415 (2) as "that temperature at which loading damage accumulates at the same average rate in service as in the laboratory. Thus, when testing at the effective temperature, there is a one-to-one correspondence between laboratory and in-service loading cycles."

1.1 *Existing effective pavement temperature models*

The SHRP effective pavement temperature was developed during SHRP A-407 (1) and is based on mean annual air temperature and critical depth as follows:

$$T_{eff} = 30.8 - 0.12\,(z) + 0.92\,(MAAT_{design})$$
$$MAAT_{\text{design}} = MAAT_{\text{Average}} + K_{\alpha}\sigma_{\text{MAAT}} \quad (1)$$

where:
T_{eff} = Effective pavement temperature for rutting, °C
z = critical depth down from pavement surface, mm
$MAAT_{\text{design}}$ = mean annual air temperature, °C
K_{α} = K at appropriate reliability level of 95% (1.645)
σ_{MAAT} = standard deviation of distribution of MAAT for site location.

Sotil and Witczak (3) proposed an extended equation that included loading frequency. This model is identical to SHRP A-407 model for the depth of 1.0 in. and frequency of 1 Hz. The model was utilized in NCHRP 9-30A (4), however, it was attributed to SHRP A-415. NCHRP 9-22 (5) introduced another T_{eff} model that introduced seasonal variability and three new climatic parameters into the model as follows:

$$T_{eff} = 14.62 - 3.36\,\text{Ln}(Freq) - 10.94\,z + 1.121\,MAAT - 1.7178\,\sigma_{\text{MAAT}} - 0.431\,Wind + 0.333\,Sun + 0.08\,Rain \quad (2)$$

where:
T_{eff} = modified Witczak effective temperature for rutting, °F
$Freq$ = effective loading frequency, Hz
z = desired pavement depth, inches
$MAAT$ = mean annual air temperature, °F
σ_{MAAT} = standard deviation of the mean monthly air temperature
$Wind$ = mean annual wind speed, mph
Sun = mean annual sunshine percentage, %
$Rain$ = cumulative annual rainfall depth, inches.

Note that σ_{MAAT} for SHRP and NCHRP equations are not the same. In the SHRP model, σ_{MAAT} is the yearly MAAT variation, however, in NCHRP it is the monthly variation of Mean Monthly Temperature (MMT) which indicates seasonal variation. Both models have a depth term which is linear with depth and results in about 3ºC (SHRP) and 6ºC (NCHRP) reduction in T_{eff} for every inch depth into the pavement. The NCHRP model is also used in NCHRP 9-33A (6) for specification criteria for Simple Performance Tests (SPT).

1.2 *SHRP temperature models*

In order to calculate the design temperatures for SUPERPAVE, equations were developed relating design air temperature to design pavement temperature for both high and low design air temperatures. During SHRP-A-637 (7) project, pavement surface temperature during the hottest 7-day period of the year was calculated for five sites in Maryland, New York, Virginia, Arizona and Saskatchewan using Integrated Climatic Model (ICM) software. Solar absorption, radiation transmission through air, atmospheric radiation, and wind speed data was used to estimate pavement temperatures at different depths within AC layer. SHRP-A-648A (8) used these calculations to determine high design pavement temperature with depths below the pavement surface. The model was utilized for the SHRP high temperature Performance Grade selection. Equation 3 includes the SHRP model for estimating pavement temperature at the depth of 20 mm below the pavement surface ($\boldsymbol{T_{20}}$) from air temperature ($\boldsymbol{T_{air}}$) and latitude (***lat***):

$$T_{20\text{mm}} = (T_{air} - 0.00618lat^2 + 0.2289lat + 42.2)\,(0.9545) - 17.78 \quad (3)$$

1.3 *LTPP Seasonal AC Pavement Temperature (SAPT) model*

FHWA initiated a project to utilize LTPP Seasonal Monitoring Program (SMP) data to validate and/or enhance the SHRP equations. The SMP data was measured from within the

pavement layer for 25 locations for up to 3 years which was significantly more data that SHRP had access to at the time. During this project, Mohseni (9, 10) developed new temperatures models from SMP data which were included in the LTPPBind V2.1 software. Following is the high temperature model:

$$T_d = 54.32 + 0.78\ T_{air} - 0.0025\ Lat^2 - 15.14\ log_{10}\ (d + 25) \quad (4)$$

where:
T_d = High AC pavement temperature below surface, °C
T_{air} = Air temperature during the hottest 7-day period of the year, °C
d = Depth to surface, mm.

1.4 *LTPPBind version 3.1 pavement temperature model*

SUPERPAVE binder Expert Task Group (ETG) initiated a project to address the concern from the Southern U.S. states that the SHRP high temperature grades did not correspond to their climate. During this project, Mohseni (11) determined that the SHRP high temperature determination (mean 7-day high pavement temperature) is short-sighted and does not consider the longevity of the high temperatures. Mohseni introduced a new parameter, the degree-days, to replace the SHRP high mean 7-day parameter. An incremental rutting damage model based on NCHRP 1-37A stiffness and permanent deformation models (12–14) was developed based on hourly calculation of temperatures and damage within pavement layer. The incremental rutting damage for different binder grades, aggregate gradations, and traffic levels were accumulated on hourly basis for 20 years for about 280 locations within the U.S. The calculated rutting correlated very well with pavement degree days at depth of 20 mm. A transfer function was developed to convert the pavement temperature to air degree days for easier implementation (Equation 5). Equation 5 was implemented in LTPPBind version 3.1.

$$T_{20} = 22.8 + 14\ DD - 0.96\ DD^2 \quad (5)$$

where:
T_{20} = Design high pavement temperature at 20-mm depth
DD = Annual Air Degree-Days > 10°C (×1000°C)
Accumulated Daily Air Temperature in Excess of 10°C for Entire Year
Statistics: R^2 = 90%, N = 1307, SEE = 2.5°C.

1.5 *Pavement temperature with depth*

Determination of the pavement temperature and heat exposure within the pavement layer is a critical part of effective pavement temperature model. Significant temperature gradient exist in the pavement, especially during afternoon hours when air temperatures peaks. Pavement surface temperature rises accordingly and the temperatures within the pavement also increase with time, but with some delay. During night, however, the process is reversed when surface temperature quickly drops but pavement temperatures are still high. Before the sunrise next day, however, the temperatures within the pavement layer stabilize. Different procedures have been developed to estimate the high pavement temperature with depth. SHRP (8) developed Equation 6 to estimate high mean 7-day pavement temperature from surface temperature.

$$T_d = T_s\ (1 - 0.063\ d + 0.007\ d^2 - 0.0004\ d^3) \quad (6)$$

where:
T_d = maximum pavement temperature (°F) at depth "d"
T_s = maximum pavement surface temperature (°F)
d = depth of critical location to surface, in.

Mohseni (9) developed a pavement temperature model (Equation 4) from LTPP using empirical climatic data from Seasonal Monitoring Program which was used in LTPPBind software for binder grade selection. Equation 7 is the depth term of Equation 4 previously mentioned:

$$T_d = T_s - (15.14\ log_{10}(d + 25) - 21.16) \quad (7)$$

where:
T_d = high AC pavement temperature below surface, °C
T_s = high pavement surface temperature, °C
d = depth of critical location to surface, mm

Figure 1 shows the estimated high pavement temperature gradient through a pavement using the LTPPBind depth term (dash line). The points in Figure 1 are annual pavement Degree-Days within asphalt layer estimated using ICM and hourly weather data (air temperature, wind speed, and sunshine) for four Arizona sites. It should be noted that the LTPPBind depth model, based on measured SMP data, and the calculated pavement temperatures for Tucson agree well. The LTPPBind depth term also agrees with other weather station locations shown in the figure since the depth term adjust itself with surface temperatures (the line shifts up and down).

1.6 *Objectives*

The objective of this study is to 1) review existing effective temperature approaches and 2) develop an enhanced approach for calculating the effective temperature (T_{eff}) for testing asphalt mixtures as part of prediction of in situ rutting performance. Specifically, the objective of this research study is to explore the possibility of developing a more accurate and simplified procedure for calculating effective temperature for asphalt mixture rutting performance prediction for any location in the U.S.

2 REVIEW OF THE CURRENT METHODOLOGIES

2.1 *White paper on effective pavement temperature for rutting*

Mohseni (15) reviewed existing effective temperature models in 2005 and proposed a simplified approach for FHWA. Mohseni employed the incremental hourly damage concept and

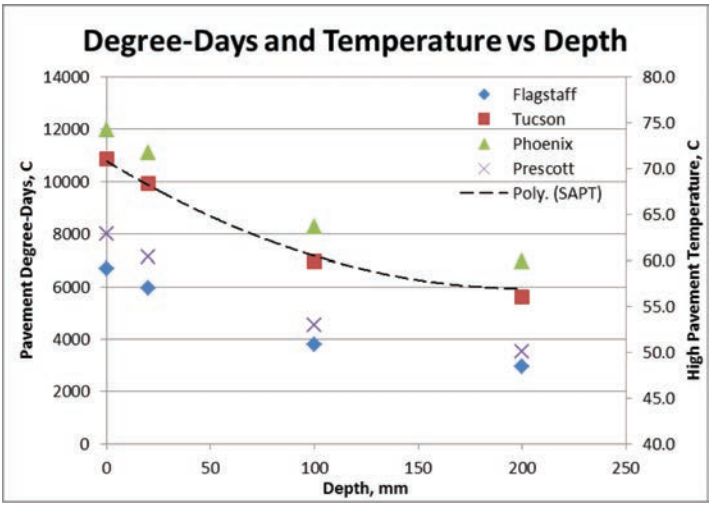

Figure 1. High pavement temperature versus depth from LTPPBind study.

the Degree-Day parameter to develop an effective temperature for Flow Number testing. The analysis showed that the effective temperature equation recommended by SHRP and NCHRP (based on Mean Annual Air Temperature) provided significantly lower temperatures than the incremental hourly damage approach. Subsequently, FHWA adopted 50% high temperature PG from LTPPBind version 3.1 (equation 5 above) as the test temperature for flow number testing.

2.2 *Test temperatures of asphalt ETG flow number study*

The FHWA Asphalt Expert Task Group (ETG) initiated a study in 2010 to examine different rutting tests in order to nominate the most promising for Asphalt Mixture Performance Tester (AMPT). Three different test temperatures were used in this study by several competing approaches. The details of the study are included in Reference 16. Most test temperatures were based on 50% high temperature PG from LTPPBind V3.1.

Test method 1 (from NCHRP 9-30), test methods 4 through 6 (proposed by MTE construction) and test method 7 (iRLPD method) all used 50% LTPPBind high temperature PG grade as the test temperature. Method 2 (by NCAT) used 50% PG minus 6°C and method 3 (from NCHRP 9-30A) used the effective pavement temperature algorithm developed by SHRP (1). Figure 2 shows the test temperatures versus Degree-Days from LTPPBind for the nine mixtures included in the study. As indicated from the figure, NCHRP 9-30A test temperatures were more than 20°C lower than the test temperatures for most other test methods.

Some adjustments were made to the LTPPBind-based temperatures and a lower temperature than 50% reliability PG was actually used. The final test temperatures were about 2°C lower than 50% reliability high-temperature PG from LTPPBind V3.1. This adjustment was done since the ETG study participants believed that 50% PG was a little too high for testing the mixtures. Furthermore, analysis of preliminary test data showed that the lowered test temperature agreed better with the mixture performance in the field. There were also confusion in using LTPPBind high-temperature model. Therefore, it was decided that a separate model was needed for calculating the effective temperatures instead of using LTPPBind 50% reliability PG.

2.3 *Review of the existing T_{eff} rutting equations*

Equation 1 was used by SHRP to estimate T_{eff} rutting using Mean Annual Air Temperature (MAAT) and critical depth. Since rutting occurs under pavement loadings at high

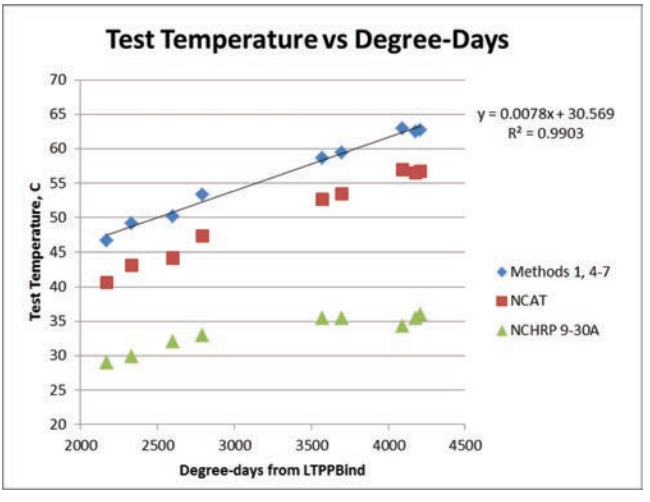

Figure 2. Test temperature versus degree-days for nine mixtures from ETG flow study.

temperatures, the analysis for rutting should also concentrate on the hot days of the year when the predominant rutting takes place. Mean Annual Air Temperature (MAAT), however, is an annual statistic and includes the temperatures of the cold winter days as well hot summer days. As a result, locations with hot summers days and cold winters days may have similar MAAT with areas with mild summer and mild winter. Conversely, in the desert environment MAAT is lowered by the lower temperatures of the nights. For this reason, MAAT did not seem to be a proper climatic parameter for estimating rutting damage at a site.

Equation 2, developed by NCHRP 9-22, tried to address this problem by incorporating the seasonal variations (σ_{MAAT}) and three additional climatic variables into the model. Apart from its complexity, the resulting T_{eff} of this model still has the above mentioned problems.

Furthermore, the depth term in the SHRP and NCHRP models is linear. Past research indicates that the control temperature that relates to rutting reduces with depth in a non-linear fashion and therefore the temperature change is reduced with depth. For this reason, Equation 1 (SHRP) may be underestimating and Equation 2 (NCHRP) may be overestimating the temperature at lower depths.

The 50% reliability high-temperature from LTPPBind seems to provide a reasonable test temperature for asphalt mixture testing. However, it may be fine tuned and better defined for wider use.

3 COMPARING DIFFERENT METHODS

3.1 *Comparing Mean Annual Air Temperature (MAAT) versus Degree-Days (DD)*

Mean Annual Air Temperature (MAAT) is utilized by several SHRP and later NCHRP projects as the temperature parameter for determining effective temperature for rutting. MAAT parameter was used in NCHRP 9-22 and 9-30A for determining the effective temperature. Degree-Days parameter has been used by LTPPBind for binder grade selection. The two climatic parameters (MAAT and Degree-days) are compared here to determine the differences. Figure 3 shows MAAT versus Degree-Days (DD) for 20 selected cities in the U.S. Figure 3 shows a relatively good agreement between the two parameters for most

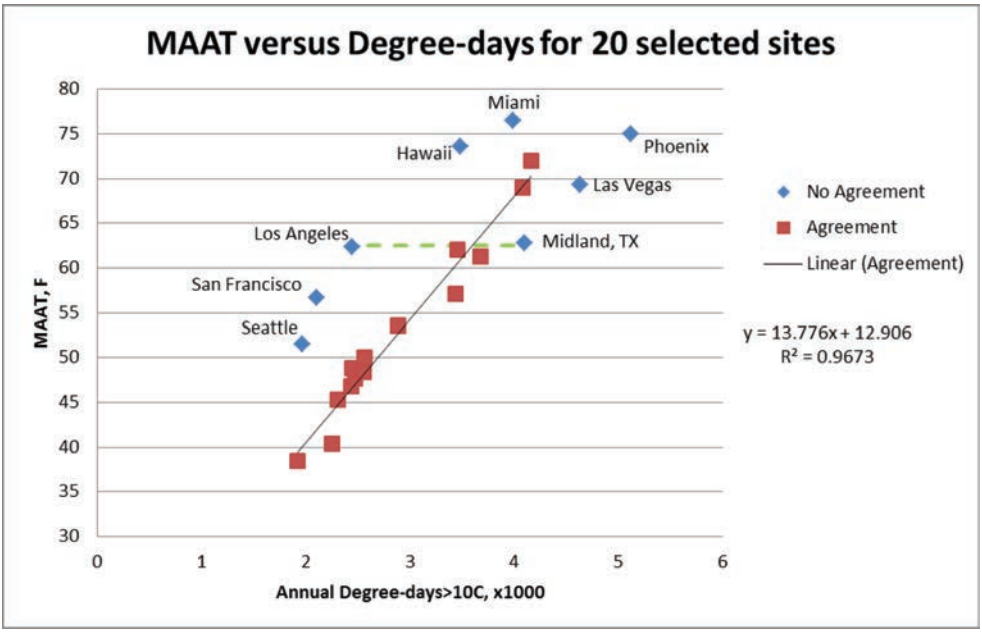

Figure 3. Mean Annual Air Temperature (MAAT) versus degree-days for selected cities.

locations within U.S. (points shown as red squares). However, for some sites (shown in blue diamond) the two parameters are significantly different. Figure 3 shows three locations (Los Angeles, Tulsa, and Midland) on a green dash line that have the same MAAT (about 62.5°F) but significantly different Degree-Days (2.5, 3.7 and 4.1 × 1000°C respectively). It appears that MAAT overestimates heat exposure in coastal areas by about 7°C and underestimates heat exposure in desert environments (Phoenix, Midland, Las Vegas) by at least the same amount.

The reason for the discrepancy of the two metrics for some locations was investigated. The points above the line in Figure 3 are locations that MAAT over-estimates the temperature compared to DD. These locations are all close to ocean and since coastal regions have milder winters than further inland, this fact has caused the increase in MAAT. Furthermore, the points below the line belong to desert locations where temperature drops drastically at night. MAAT is an average of temperatures for days and nights (high and low) and over seasons and as a result:

- MAAT is higher for coastal areas because of the milder nights and milder winters
- MAAT is lower for desert areas because of the colder nights

Therefore, including low temperatures in the temperature parameter is not feasible. Degree-days, which is based on the accumulation of higher temperatures than 10°C, does not include temperature at cold nights and cold winter months, therefore, it does not suffer from the shortcomings of MAAT.

3.2 *Comparing pavement temperature with depth algorithms*

Figure 4 shows the depth term for four procedures mentioned previously. The SHRP A-407 T_{eff} algorithm is a function of pavement surface temperature and for this purpose 55ºC was assumed. Figure 4 shows that the SHRP A-648 procedure and LTPPBind agreed up to the depth of 125 mm, however, SHRP temperature drops at higher rate than LTPPBind model at lower depths. SHRP A-407 and NCHRP 9-22 T_{eff} procedures are linear with depth and does not level out at lower depths. NCHRP 9-22 procedure provides much higher estimates of temperature drop with depth than SHRP A-648 and LTPPBind and is significantly

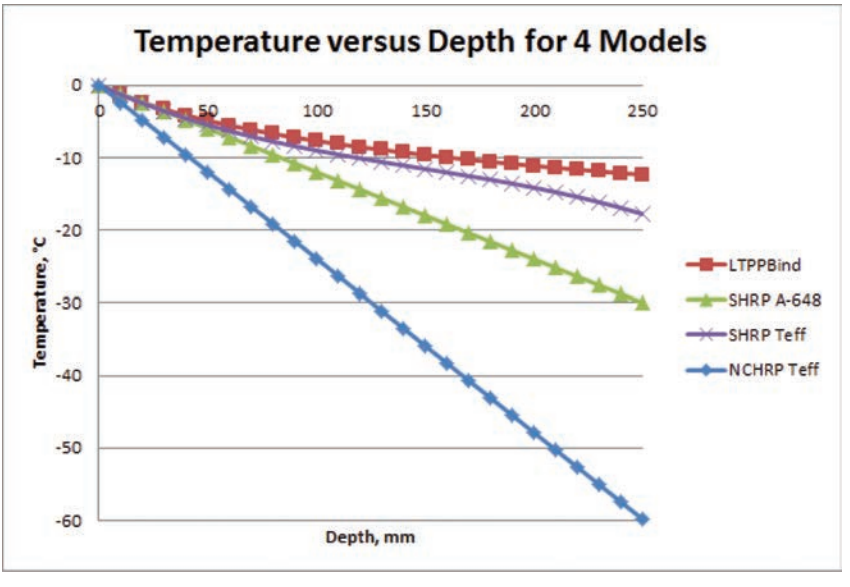

Figure 4. Depth term for different pavement temperature algorithms.

over-estimating the effect of depth on reduction of pavement temperature. The LTPPBind model has the best functional form and provides better estimate of maximum temperature with depth of AC layer.

4 DEVELOPMENT OF A SIMPLIFIED EQUATION FOR T_{eff}

A Mechanistic-Empirical approach similar to the approach used for the development of enhanced high temperature PG binder selection procedure (LTPPBind) (11) was utilized in this study to develop T_{eff} for asphalt mixtures based on rutting damage. Hourly pavement temperature frequencies at the critical depth of 20 mm which was developed under LTPPBind project was used in this study for a typical pavement structure and for 270 locations in the U.S. These data were developed using Integrated Climatic Model V 2.6 (ICM) and hourly climatic data for a 20-year period. Using NCHRP 1-37a (12–14) calibrated stiffness model, AC stiffness was estimated for every temperature and subsequently the rutting damage was calculated using NCHRP 1-37a final permanent deformation model. Several assumptions had to be made regarding pavement structure, traffic loadings and allowable rut depth.

A typical pavement structure (6 inch conventional Asphalt Concrete (AC) over 12 inch base course) with standard loading of 3 million standard axles and loading frequency of 10 Hz (for highway speed) and a limiting rut depth of 12.7 mm was considered. The binder parameter used in the NCHRP 1-37A AC stiffness model was consistent with the LTPPBind PG selection at 98% reliability. Rutting damage for all temperatures in a 20-year analysis period was accumulated on hourly basis to calculate the total rutting damage for every location. Effective Pavement Temperature was then calculated as the temperature that produces similar rate of rutting damage in laboratory as in the field (with climatic variations) under similar loading conditions.

4.1 *Develop proposed T_{eff} using degree-days*

As a result of the correlation analysis it was found that degree-days correlate best with T_{eff}. The derived model is shown in Equation 8.

$$T_{eff} = 33 + 7 * DD + \varepsilon \tag{8}$$

where:
T_{eff} = effective pavement temperature for rutting, ºC
DD = average yearly air degree-days over 10ºC, ×1000, °C
Accumulated Daily Air Temperature in Excess of 10°C for Entire Year
Statistics: $R^2 = 88\%$, $SEE = 1.43$, $N = 216$.

Equation 7 has a depth term $15.14\ log_{10}(d + 25)$ which is currently used in LTPPBind version 3.1 to determine temperature drop within the pavement. This term at depth of 20 mm ($d = 20$) was used to determine the temperature drop within the pavement layer for T_{eff}. Equation 9 includes the proposed procedures for calculating effective temperature for rutting with depth.

$$T_{eff} = 58 + 7.0 * DD - 15\ log_{10}(z + 45) \tag{9}$$

where:
z = depth of layer, mm (depth of layer to pavement surface)

4.2 *Comparing different effective temperature approaches*

Four different approaches for effective temperature that were discussed in this paper, is compared to show the differences. Figure 5 shows LTPPBind 50% reliability PG (Equation 5),

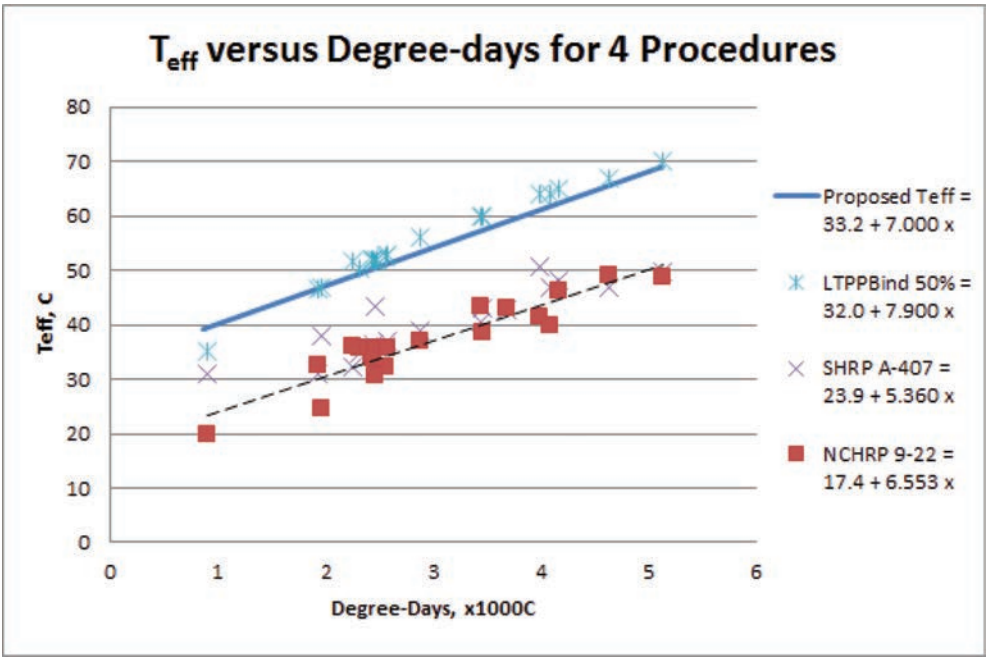

Figure 5. SHRP, NCHRP, 50% PG and new effective temperatures versus degree-days.

the proposed T_{eff} model (Equation 9), SHRP model (Equation 1), and NCHRP model (Equation 2) versus Degree-Days from LTPPBind. The proposed parameter is slightly lower than LTPPBind 50% PG which is currently used by several agencies. SHRP and NCHRP T_{eff} at the depth of 1 inch are similar except for four points, which are locations that are close to the ocean. On average, the proposed T_{eff} is about 20°C higher than SHRP and NCHRP T_{eff}.

Although effective temperatures similar to the proposed T_{eff} was used in the ETG flow number study as test temperature successfully, the main application of model was as the test temperature for the newly developed incremental Repeated Load Permanent Deformation test procedure introduced by Azari and Mohseni (17). The results of iRLPD tests performed on nine ETG specimens from eight different states (various design traffic and binder type) were used to estimate rutting (17) and it was found that the rutting damage parameter from iRLPD test using proposed T_{eff} and deviator stress of 600 kPa (to simulate standard axle loading) provided reasonable estimate of rutting and correlated well with the expected performance of the mixture in the field. However, the tests performed using the SHRP T_{eff} temperature (method 3 using NCHRP 9-30A) did not exhibit any noticeable damage mainly due to the low effective temperature. The proposed T_{eff} was judged for reasonableness by the experts and was also field calibrated to provide feasible rutting damage results.

5 FINDINGS AND RECOMMENDATIONS

Existing effective temperature models for rutting were reviewed and a simplified equation was developed in this study. A rational approach was developed for calculating the effective temperatures (T_{eff}) for rutting for asphalt mixture design. Although this procedure was utilized to establish the test temperatures for the incremental Repeated Load Permanent Deformation (iRLPD) tests, it can also be used for flow number tests. The result of this analysis was a simple procedure that estimates effective pavement temperature for rutting for any location in the U.S. as a function of a readily available climatic parameter (degree-days) and depth of asphalt layer.

The followings findings were made from this study:

1. Comparison of the SHRP and NCHRP procedures with the calculated rutting data and judgement of experts determined that the test temperatures provided by these procedures were too low to cause rutting damage at standard loading.
2. Mean Annual Air Temperature (MAAT), the climatic parameter used in SHRP and NCHRP models, is over-predicting T_{eff} in coastal areas with mild winters while under-predicting it in desert areas with colder nights.
3. Degree-Days, correlated with rutting damage, is significantly better than MAAT, which was used in the SHRP and NCHRP equations.
4. The linear depth term in SHRP and NCHRP models is different from actual pavement temperature profiles with depth which shows significant non-linearity.
5. The NCHRP depth term is significantly over-estimating the effective temperature with depth while SHRP A-648 and the proposed depth term is closer to the actual pavement temperatures with depth.
6. The proposed procedure is more accurate, calibrated to the field and experts' opinion, yet simpler and easier to use than the currently available approaches.

The following recommendations are given for the future studies:

1. SHRP and NCHRP T_{eff} concept should be revisited as these procedures may not provide reasonable temperatures for laboratory testing of AC specimens.
2. The proposed effective temperature seems to provide significantly better temperatures for high-temperature testing of asphalt specimens and is highly recommended for test temperature of iRLPD and flow number tests.
3. The depth term from LTPPBind high temperature model was used for effective temperature; however, this term is not validated below 100 mm (about 4 inch) depth. An improved depth term should be developed for T_{eff} using the Degree-Day concept using more data.

REFERENCES

1. SHRP-A-407 Report (1994), "The Superpave Mix Design Manual for New Construction and Overlays", Strategic Highway Research Program, National Research Council, Washington, DC.
2. SHRP-A-415 Report (1994), "Permanent Deformation Response of Asphalt Aggregate Mixes", Strategic Highway Research Program, National Research Council, Washington, DC.
3. Sotil and Witczak (2005), "Effective Temperature of Asphalt Mixtures for Permanent Deformation Analysis", AAPT 2005.
4. NCHRP 9-30A Final Report (2012), Report 719, "Calibration of Rutting Models for Structural and Mix Design", National Cooperative Highway Research Program.
5. NCHRP 9-22 Final Report (2011), Report No. 704, "A Performance-Related Specification for Hot-Mixed Asphalt", National Cooperative Highway Research Program.
6. NCHRP 9-33A Final Report (2011), Web-only Document 172, "Adapting Specification Criteria for Simple Performance Tests to HMA Mix Design", National Cooperative Highway Research Program.
7. SHRP-A-637 (1994), M. Solaimanian and P. Bolzan, "Analysis of the Integrated Model of Climatic Effects on Pavements: Sensitivity Analysis and Pavement Temperature Prediction".
8. SHRP-A-648A (1994), "Weather Data base for the SUPERPAVE Mix Design System".
9. Mohseni (1997), "LTPP Seasonal Asphalt Concrete (AC) Pavement Temperature Models", FHWA-RD-97-103.
10. Mohseni et al. (1998), "Improved AC Pavement Temperature Models from LTPP Seasonal Data", Presented at 77th Annual TRB Conference, Washington D.C., 1998.
11. Mohseni, Carpenter and D'Angelo (2005), "Development of SUPERPAVE High-Temperature Performance Grade (PG) Based on Rutting Damage", AAPT.
12. Andrei and Witczak (1999), "Development of a Revised Predictive Model for the Dynamic (Complex) Modulus of Asphalt Mixtures", NCHRP 1-37A Interim Technical Report, University of Maryland.

13. Kaloush and Witczak (2000), "Development of a Permanent to Elastic Strain Ratio Model for Asphalt Mixtures," Development of the 2002 Guide for the Design on New and Rehabilitated Pavement Structures, NCHRP 1-37A Inter Team Technical Report.
14. ARA, Inc. ERES Division. "2002 Design Guide. Design of New and Rehabilitated Pavement Structures.", Draft Final Document. NCHRP 1-37A Project, Champaign, IL August 2003.
15. Mohseni (2005), "Development of Simplified Approach for Calculating Effective Pavement Temperature for Asphalt Mixture Performance Prediction", White Paper Prepared for FHWA, Office of Pavement Technology.
16. Azari and Mohseni (January 2013), Report on incremental Repeated-Load Permanent Deformation Testing (iRLPD), FHWA Asphalt Expert Task Group, Flow Number Task Force.
17. Azari and Mohseni (2013), "Permanent Deformation Characterization of Asphalt Mixtures Using Incremental Repeated Load Testing", Accepted for publication in Transportation Research Journal, 2013.

This page intentionally left blank

Asphalt Pavements – Kim (Ed)
© 2014 Taylor & Francis Group, London, ISBN 978-1-138-02693-3

Possibility to utilize new natural rock asphalt for guss asphalt

Atsushi Kawakami, Iwao Sasaki & Kazuyuki Kubo
Public Works Research Institute, Tsukuba-shi, Ibaraki, Japan

Sadaharu Ueno
Nichireki Co., Ltd., Japan

Madi Hermadi & Willy Pravianto
Institute of Road Engineering, Indonesia

ABSTRACT: AsButon is natural rock asphalt and it has been used as granular material for macadam base course in actual pavement works in Indonesia. However, AsButon was expected to utilize as the alternative asphalt materials, because there are huge amount of AsButon deposit and it is estimated at 163 million tons. Institute of Road Engineering (IRE, Indonesia) and Public Works Research Institute (PWRI, Japan) has been conducting the cooperation researches to seek for better utilisation of AsButon since 2011. In this research, the physical properties and chemical properties of AsButon were analysed, and the AsButon can be expected to be more durable than straight asphalt at high temperatures. The tendencies of the compositions of AsButon were close to the tendency of the composition of Trinidad Lake Asphalt (TLA). Therefore the asphalt mixture tests for guss asphalt using AsButon were conducted. As the results, the guss asphalt mixture using AsButon ratio of 20% was met the Japanese standards of guss asphalt mixture for fluidity, dynamic stability and flexural strain. AsButon is regarded to be possible alternative for TLA as guss asphalt material for steel bridge deck pavement.

Keywords: AsButon, natural rock asphalt, alternative asphalt, guss asphalt, steel bridge deck pavement

1 INTRODUCTION

In Japan, the rising price and decreasing production of petroleum asphalt has become a problem in recent years, and so a technology for using natural asphalt as well as petroleum asphalt needs to be developed. A natural asphalt called AsButon is produced around Butung in Indonesia. AsButon can be mined directly from the surface of the earth and is converted into granular material by primary processing. This granular material contains 70–80% minerals. In Indonesia, AsButon is mainly used by being blended with subgrade material in the macadam construction method and petroleum asphalt. AsButon reserves have been estimated at 163 million tons, and so its use as a surface asphalt mixture would be advantageous in view of its abundance. Indonesia intends to study the complete extraction of asphalt from AsButon. Thus, the Institute of Road Engineering (IRE) in Indonesia and the Public Works Research Institute (PWRI) in Japan have been conducting joint research since 2011 on effective ways to use AsButon. Using AsButon from Kabungka and Lawele, where there are large reserves, the joint research clarified its chemical and physical properties [1]. The results indicated that as physical properties, AsButon was hard at ordinary temperatures and thick at high temperatures compared with straight asphalt, and was also more promising in fluidity resistance than straight asphalt. Especially, AsButon from Kabungka was much harder but more brittle than straight asphalt at low temperatures. Regarding chemical properties, AsButon was composed

of fewer aromatic series and more resin and asphaltene than straight asphalt. This is heavy asphalt, and is similar in composition to TLA, which is a type of natural asphalt.

In Japan, the guss asphalt mixture is used for the base of steel plate deck pavement, and TLA is employed as a binder of this guss asphalt mixture. As of 2012, there are 680,728 bridges over 2 m long in Japan [2]. Of these, 158,897 bridges are over 15 m long, of which 60,432 (38%) with a total length of 4,722 km are steel bridges. Therefore, a large quantity of AsButon could be used if it can be employed for the guss asphalt mixture.

In this research, mixture properties were studied in order to clarify the potential use of AsButon as a material of the guss asphalt mixture, and the results are reported here.

2 APPROACH

2.1 *Test materials*

AsButon used for the test is natural asphalt produced around Butung in Indonesia, and would be an inexpensive source of asphalt for pavement because it can be mined directly from the surface of the earth. AsButon is natural rock asphalt containing 70–80% minerals, is granular and is sold packed in bags for sandbags. Therefore, AsButon would eliminate the need to break up solid lumps, as required with TLA, resulting in improved workability.

In this research, AsButon from Kabugka and Lawele, where there are large reserves, was tested using TLA as a comparison sample. Table 1 shows the combined gradation of the mixtures used for the study. In Japan, it is common practice to use mastic asphalt mixtures composed of 75% of straight asphalt 20/40 and 25% of TLA. In this study, therefore, comparison was made between mixtures made by using 15, 20 or 25% of AsButon in place of TLA and mixtures made by using 25% of TLA.

2.2 *Test items*

The five items shown in Table 3, which are provided in the bridge deck pavement standard for Honshu–Shikoku bridge (proposal, hereinafter referred to as "HSBE standard"), the waterproofing handbook for highway bridges, pavement investigation and a testing methodology handbook, were tested. Evaluation was conducted to determine if the mixture using AsButon satisfies the standard values shown in Table 3.

2.2.1 *Study on workability*

The guss asphalt mixture must create a dense impermeable asphalt layer by spreading without rolling, differently from ordinary asphalt mixtures. The Luer fluidity test was conducted in order to evaluate the difficulty (workability) of spreading. After pouring the guss asphalt

Table 1. Combined gradation.

Sieve opening	Combined gradation	Gradation envelop
Percent passing by mass (%)		
19.0 mm	100.0	100.0
13.2	99.3	95~100
4.75	72.5	65~85
2.36	52.7	45~62
0.6	42.4	35~50
0.3	36.8	28~42
0.15	28.5	25~34
0.075	23.6	20~27
Asphalt content (%)	9.5	7~10

Table 2. Mixture ratio.

Mixed ratio of natural asphalt and petroleum asphalt (%)			
Natural asphalt			Straight-run asphalt (20/40)
AsButon	KABUNGKA	15	85
	LAWELE	20	80
		25	75
Trinidad Lake Asphalt (TLA)		25	75

Table 3. Test items and criteria.

Item	Test method	Test temperature	Standard-specified value	Compliance criterion
Workability	Luel fluidity test	240°C	20s or less	HSBE
Dynamic stability	Wheel tracking test	60°C	300 times/mm or more	
Flexibility at low temperature	Bending test (breaking strain)	–10°C	8.0×10^{-3} or more	
	Bending test (brittleness, small specimen)	–5, 0, 5, 10, 15, 20, 25°C	–	Source [3]
Adhesiveness	Tensile adhesive strength test (steel deck, mixture)	23°C	0.6 N/mm^2 or more	Source [4]
		–10°C	1.2 N/mm^2 or more	
Waterproof property	Permeability test by pressurized water	Temperature correction	No leakage	Source [5]

mixture at 240°C into a container of a certain depth and placing a 995 g heavy bob on the mixture, the time for the bob to penetrate 5 cm by its own weight was measured.

2.2.2 *Study on fluidity resistance*

To evaluate fluidity resistance, the dynamic stability (times/mm) was obtained by a wheel tracking test at a test temperature of 60°C. The test specimen was 300 mm long, 300 mm wide and 50 mm thick, and was created by pouring guss asphalt into the mold since compaction was not required.

2.2.3 *Study on deflection at low temperatures*

To evaluate the deflection at low temperatures, the fracture strain was measured by a bending test at a test temperature of –10°C and loading rate of 50 mm/min. The test specimen was 300 mm long, 100 mm wide and 50 mm thick. Moreover, to confirm the tendency of brittleness temperature, bending test using small specimen were conducted. This test specimen was 120 mm long, 10 mm wide and 10 mm thick. The loading speed of bending test was 20 mm/minutes, and test temperature was –5, 0, 5, 10, 15, 20, 25°C.

2.2.4 *Study on adhesiveness*

Not only the steel plate deck and the guss asphalt mixture layer but also the guss asphalt mixture layer and the surface course must adhere to and unite with each other. Therefore, the adhesive tensile test was conducted between a steel plate that imitated the steel plate deck and the guss asphalt mixture, and between the guss asphalt mixture and the mixture for surfaces. In this test, two kinds of primers were used in order to bond a steel plate and the guss asphalt mixture. Both were solvent adhesives: one was the conventional type (solvent type), and the other greatly shortened the drying time at low temperatures. For bonding between

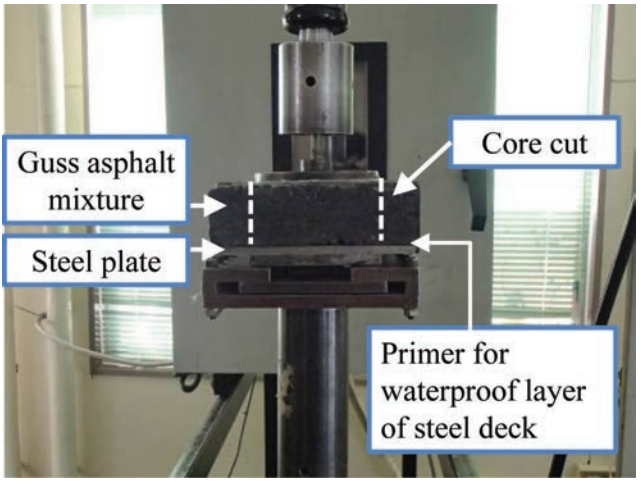

Figure 1. Method of adhesive tensile test.

the guss asphalt mixture and surface course, the emulsified rubberized asphalt was used as tack coat. The test specimen was created by pouring the guss asphalt mixture into a mold for a wheel tracking test with a 5-mm-thick steel plate placed on the bottom. In the adhesive tensile test, the tensile strength was measured using a universal tester with the φ10 cm core cut as shown in Figure 1.

2.2.5 *Study on waterproofing property*

The guss asphalt mixture is used as a waterproofing membrane in a steel plate deck. Therefore, waterproofness is one of the most important performance requirements, and was estimated by a permeability test by pressurized water. During the test, the permeability for 10 min was measured after pressurization at 1.5 MPa for 24 h.

3 TEST RESULTS

3.1 *AsButon ratio and fluidity*

Figure 2 shows the relationship between the AsButon ratio and fluidity. As the AsButon ratio increased, Luel fluidity showed a tendency to increase. All AsButons meet the standard specification (20 s or less) if the AsButon ratio is 20% or less, indicating that fluidity comparable to or higher than that obtainable at the TLA ratio of 25% can be obtained under the same conditions.

3.2 *AsButon ratio and dynamic stability*

Figure 3 shows the relationship between the Asbuton ratio and dynamic stability. As the Asbuton ratio increased, dynamic stability showed a tendency to increase. All Asbutons meet the standard specification (300 times/mm) if the Asbuton ratio is 20% or more. If the Asbuton ratio is 25%, dynamic stability of AsButon can be obtained higher than that obtainable at the TLA ratio of 25%.

3.3 *AsButon ratio and flexural strain*

Figure 4 shows the relationship between the Asbuton ratio and flexural strain. Flexural strain does not show any tendency to change significantly depending on the Asbuton ratio. The standard-specified requirement is met if the Asbuton ratio is in the 15–25% range.

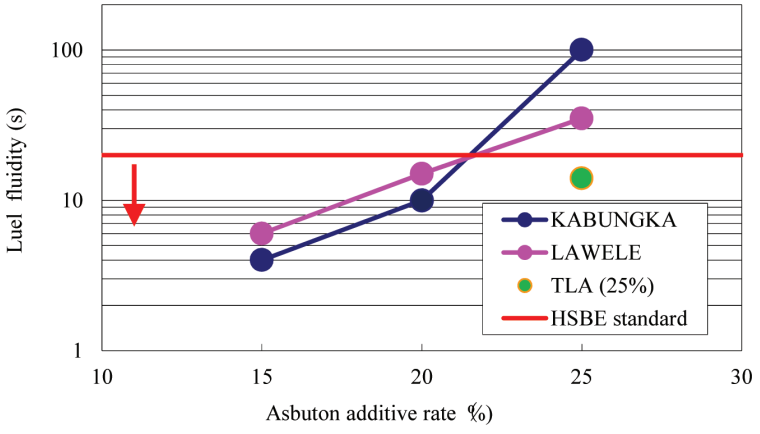

Figure 2. Relationship between the AsButon ratio and luel fluidity.

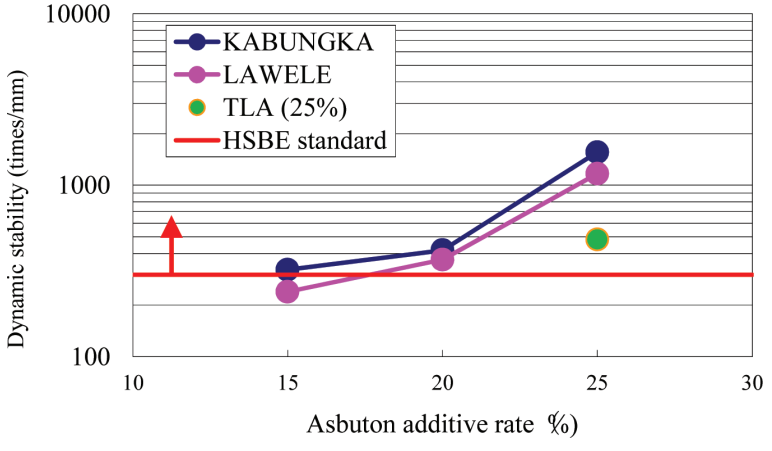

Figure 3. Relationship between the AsButon ratio and dynamic stability.

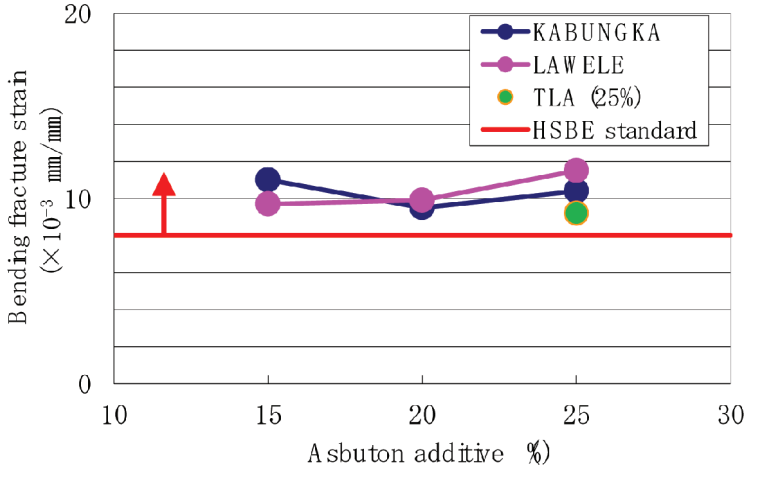

Figure 4. Relationship between the AsButon ratio and flexural strain.

Figure 5 shows the bending test results using small specimen of each mixture which indicate tendency of brittleness temperature. The inflection temperatures of bending strength of all AsButon were higher or same as that of TLA, therefore the AsButon have good flexibility at lower temperature than TLA.

3.4 *Results of adhesive tensile test*

The results of the adhesive tensile test between the steel plate deck and the guss asphalt mixture using primer-1 and primer-2 are shown in Figure 6. AsButon from Kabugka (20%) and Lawele (25%) met the target values in the waterproofing handbook for

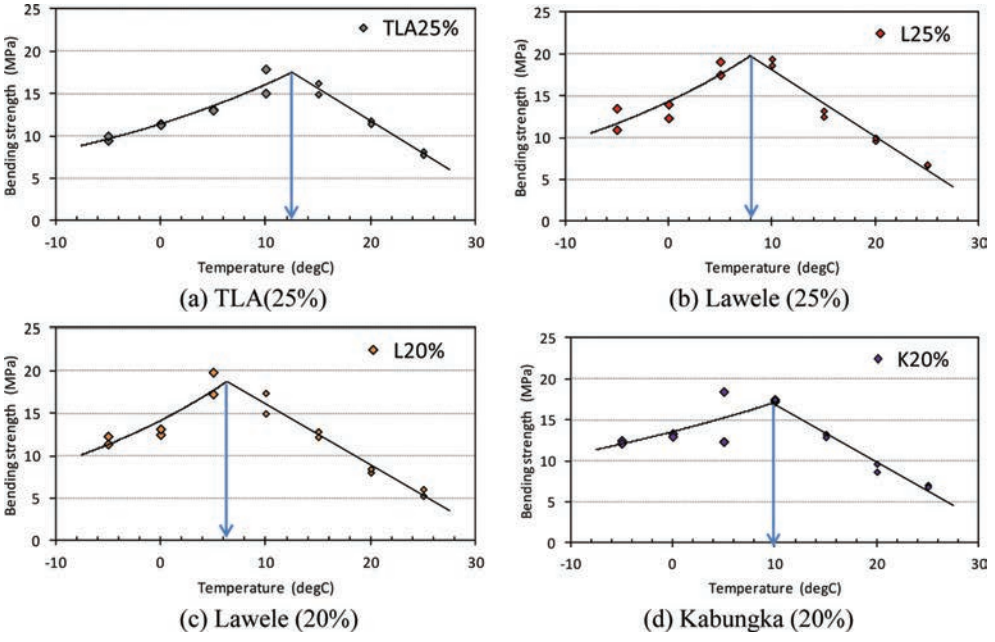

Figure 5. Bending test results using small specimen of each mixture.

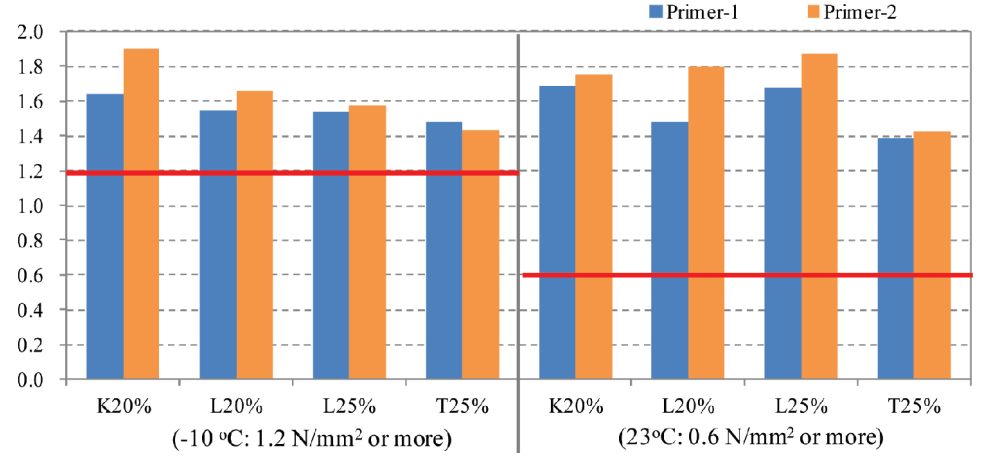

Figure 6. Results of adhesive tensile test between steel plate deck and guss asphalt mixture.

highway bridges under all measurement temperatures. Therefore, adhesion between the steel plate deck and the guss asphalt mixture using AsButon is considered to be quite good.

The results of the adhesive tensile test between the guss asphalt mixture and the mixture for surfaces using emulsified rubberized asphalt are shown in Figure 7. AsButon from Kabugka (20%) and Lawele (25%) met the target values in the waterproofing handbook for highway bridges under all measurement temperatures. Therefore, adhesion between the mixture for surfaces and the guss asphalt mixture using AsButon is considered to be quite good.

3.5 *Results of permeability test by pressurized water*

The results of the permeability test by pressurized water are shown in Table 4. Impermeability was confirmed because the amount of permeability for 10 min after pressurization for 24 h was 0 cm^3 under all conditions.

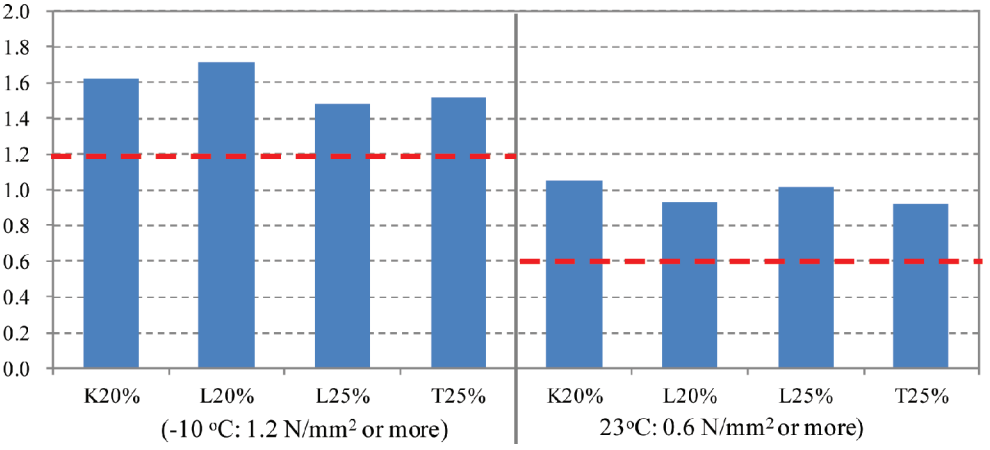

Figure 7. Results of adhesive tensile test between guss asphalt mixture and surfaces course mixture.

Table 4. Results of permeability test by pressurized water.

Test case	Natural asphalt	No.	Pressure	Pressurization time	Measuring time	Amount of permeable water	Result
1	*AsButon*						
	KABUNGKA (20%)	1	1.5 MPa	24 hours	10 minutes after 24 hours	0 cm^3	Impermeable
		2				0 cm^3	
		3				0 cm^3	
2	LAWELE (20%)	1				0 cm^3	Impermeable
		2				0 cm^3	
		3				0 cm^3	
3	LAWELE (25%)	1				0 cm^3	Impermeable
		2				0 cm^3	
		3				0 cm^3	
4	TLA (25%)	1				0 cm^3	Impermeable
		2				0 cm^3	
		3				0 cm^3	

4 CONCLUSION

It has been verified that all five requirements as a standard of the guss asphalt mixture in Japan, including the workability (Luel fluidity), fluidity resistance (dynamic stability), deflection at low temperatures (fracture strain), adhesiveness (adhesive tensile intensity), and waterproofness (for permeability test by pressurized water), are met by mixing the natural asphalt (AsButon, 20%) from Indonesia.

Therefore, AsButon can be used as a binder of the guss asphalt mixture. However, the optimal mixing ratio may vary somewhat with the location of production, mining site, etc., and thus it is necessary to consider quality control of AsButon in the future.

REFERENCES

[1] Hermadi, M., Kubo, K., et al.: Japan-Indonesia Cooperation on the Research in AsButon, Proceedings of 14th REAAA Conference, 2013.3.

[2] Japan Highway Users Conference: Road Statistics Yearly Report, 2009.

[3] Hiroyuki N., Atsushi K., Itaru N.,: Characteristics of bending test using small specimen and evaluation for warm mix asphalt, Annual conference of Japan society of civil engineers, 2002.9.

[4] Japan Road Association: Waterproofing handbook for highway bridges, 2007.3.

[5] Japan Road Association: Handbook of investigation and testing of pavement, 2007.6.

Additives and modifiers for asphalt concrete—V

This page intentionally left blank

Asphalt Pavements – Kim (Ed)
© 2014 Taylor & Francis Group, London, ISBN 978-1-138-02693-3

Improvement of asphalt concrete moisture damage resistance using Saline Coupling Agent

Meng Guo & Yiqiu Tan
Harbin Institute of Technology, Nangang District, Harbin, China

Rui Zhang
Tianjin Highway Engineering General Company, Tianjin, China

ABSTRACT: Moisture damage is one of the most common distresses of asphalt pavement. Silane Coupling Agent (SCA) has been used as an additive to prevent the moisture damage of asphalt pavement. This paper aims at investigating the effect of SCA on moisture sensitivity of asphalt mixture in the laboratory. The freeze-thaw cycle and the dynamic water flushing were applied to simulate the moisture damage conditions of asphalt mixtures. The effectiveness of SCA was confirmed by the hydrophilic coefficient test. The effects of SCA on moisture sensitivity of asphalt mixtures were evaluated by various methods, including indirect tensile strength (low-temperature and mid-temperature), high-temperature creep test and mid-temperature fatigue test. The results show that SCA can improve the moisture resistance of the granite filler obviously; SCA can effectively improve the moisture sensitivity of asphalt mixtures, and the significance is aggregate dependent. Freeze-thaw cycle and dynamic water flushing are two effective methods for simulating moisture damage.

Keywords: Asphalt mixture, moisture damage, silane coupling agent, freeze-thaw cycle, dynamic water flushing

1 INTRODUCTION

Moisture damage is a major failure mode in asphalt pavements. This failure can be defined as the loss of strength, stiffness and durability due to the presence of moisture leading to adhesive failure at the binder–aggregate interface and/or cohesive failure within the binder or binder–filler mastic [1,2]. The damage of water on asphalt mixture can be summarized into two forms, one is the freeze-thaw cycle, the other is dynamic water flushing under wheel loads. Recently, there are many researches about freeze-thaw cycle destruction, but little about dynamic water flushing under wheel loads. Shin-Che Huang et al. [3] indicated that the composition in the asphalt–aggregate interfacial region may change during repeated freeze–thaw cycling, and found that carboxylic acids play a major role in determining the moisture sensitivity of pavement mixtures. Raquel Moraes et al. [4] found that the bond strength of asphalt–aggregate systems was highly dependent on modification and moisture exposure time by using the Bitumen Bond Strength (BBS) test. E. Pasquini et al. [5] studied the fatigue property of open graded asphalt rubber mixtures in both dry and wet conditions with and without temperature cycles. They found that fatigue resistance of the studies materials was only little affected by water and temperature cycles and superior to traditional open graded mixtures produced with SBS modified bitumen only. And they validated and modeled the results by means of an elasticity-based damage model.

In fact, dynamic water flushing under wheel loads is one of the most important causes for moisture damage of asphalt pavement (Fig. 1). L.D. Poulikakos et al. [6] used an innovative test method to mechanically test 150 mm diameter cylindrical cores from eight materials in

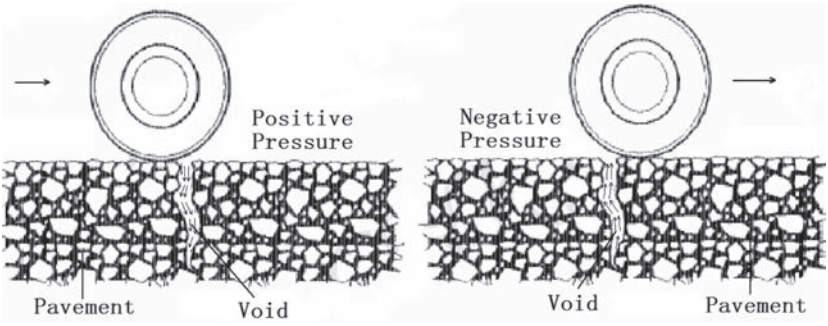

Figure 1. Dynamic water flushing induced by wheel loads.

dry state and while being submerged under water. They found that the application of Coaxial Shear Test (CAST) for a twin lay porous asphalt as well as conventional porous asphalt shows a reduction in complex modulus due to fatigue loading after each thermal cycle and due to detrimental effects of water submersion. Moisture susceptibility results using CAST reflected the field inspections of surface degradation.

Modifying materials or changing structure composition can improve the moisture sensitivity of asphalt pavement. Some studies have confirmed that the anti-stripping agent can improve the moisture damage resistance performance of asphalt mixture. F. Moghadas Nejad et al. [2] studied the effects of nanomaterial, namely Zycosoil, on the moisture damage of asphalt mixtures. They found that limestone has less moisture damage potential compared to granite. The ratio of wet/dry values of Indirect Tensile Strength Test (ITST) and Indirect Tensile Fatigue Test (ITFT) for mixes containing Zycosoil was higher than the control mix for two types of aggregate. Yong-Rak Kim [7] evaluated the effects anti-stripping additives on bituminous mixtures through multiple scale laboratory test results, they found that the mixes, where high-quality aggregates and polymer-modified binder are used, are fairly self-resistant to moisture damage without treating any anti-stripping additive and do not show any visible sensitivity between additives, whereas the effects of additives and their sensitivity are significant in the mixes that use the unmodified binder and low-quality aggregates. Jun Xie et al. [8] found that the asphalt mixture with Compound Fly Ash Modifier (CFAM) has excellent moisture sensitivity in terms of higher indirect tensile strength and tensile strength ratio during frost–thaw process. In addition, after specific moisture damage treatments, CFAM modified asphalt mixtures show better stiffness modulus, resistance to permanent deformation and fatigue life. Shu Wei Goh et al. [9] found that the addition of nanoclay and carbon microfiber would improve a mixture's moisture susceptibility performance or decrease the moisture damage potential in most cases. Xiao Qing-yi et al. [10] confirmed the silane coupling agent can form a coupling layer in surface of granite and basalt to by infrared spectroscopy. The cohesiveness between asphalt and granite or basalt can reach level 5 if asphalt is modified by SCA. In contrast, it can only reach level 2 or level 3 if the asphalt is not modified by the coupling agent. After being treated by silane coupling agent, Marshall stability can increase by 10%~20%, Marshall modulus can increase by 6%, and residual Marshall stability can increase by 18%~28%. TSR of asphalt mixtures after three freeze-thaw cycles can increase by 25%~33%. Wang Zhenjun et al. [11] found Si-O bond on the surface of aggregate modified by SCA, and Si-O-Si bond on the interface between asphalt mastics and aggregate modified by SCA by infrared spectrum. Saeed Ghaffarpour Jahromi [12] found that AC-20 have less moisture induced damages compared to AC-10 and dynamic modulus values for mixes with AC-20 were higher than the one with AC-10 for all the aggregate types. Addition of lime for river gravel samples showed significant difference between two types of bitumen but no major differences were found in crashed granite. Weibiao Wang et al. [13] investigated the use of strip-prone aggregates in hydraulic asphalt concrete, and they found that the significant detrimental effects of using strip-prone aggregates for open-grade porous asphalt, but that aggregate-bitumen adhesion

and tensile strength could be increased by adding amine or hydrated lime to the asphalt mix. Mohammad Zia Alavi et al. [14] demonstrated that the use of specific WMA additives has potential to improve the moisture resistance of the mixture by using Bitumen Bond Strength (BBS) and dynamic modulus ratio (ESR) tests. The above researches fully confirmed the potential of the anti-stripping agent in improving asphalt mixture moisture sensitivity, but the models simulating water behavior were too simple (only the freeze-thaw cycle), not considering the dynamic water flushing caused by wheel loads. The influence of water behavior (including freeze-thaw cycle and dynamic water flushing) on road performance (including high-temperature deformation resistance, low-temperature cracking resistance, and mid-temperature fatigue cracking resistance) is not clear.

2 MATERIALS

2.1 *Asphalt*

Asphalt binder with a penetration grade 90 was used in this study, whose basic properties are shown in Table 1.

2.2 *Aggregate and filler*

Aggregate used in this paper consists of basalt, andesite I, and andesite II.

As indicated by Roberts et al. [15], the mineral filler is used in HMA to: (i) meet aggregate gradation specifications, (ii) reduce the optimum asphalt content by filling voids in the granular skeleton, (iii) increase mixture stability and (iv) enhance "bond" of the aggregate–asphalt system. More recently, Prowell et al. [16,17] summarized that the addition of filler to HMA can be associated with the following main effects: (i) stiffen the asphalt, (ii) extend the asphalt–increase the asphalt volume in the HMA, or (iii) simultaneously extend and stiffen the asphalt.

Fillers used in this paper are divided into three categories, including limestone, andesite and granite, whose basic properties are shown in Table 2.

2.3 *Anti-stripping agent*

Anti-stripping agent used in this paper is Silane Coupling Agent, whose structure contained two kinds of functional groups, and one group can attract organic compounds of asphalt,

Table 1. Physical properties of asphalt.

Properties	Standard	Result
Penetration (100 g, 5 s, 25°C), 0.1 mm	ASTM D5-73	89
Softening point (°C)	ASTM D36-76	48
Ductility (15°C, 5 cm/min), cm	ASTM D113-79	>100
Ductility (5°C, 5 cm/min), cm	ASTM D113-79	16.4

Table 2. Physical properties of fillers.

Filler	Apparent relative density (g/cm^3)	Sieve passing percentage (%)		
		0.6 mm	0.15 mm	0.075 mm
Limestone	2.827	100	96.5	76.7
Andesite	2.864	100	98.7	76.7
Granite	2.614	100	85.7	74.2

the other group can react with compounds on the surface of inorganic materials. Coupling agent reaction process is as follows:

Firstly, some composition of the coupling agent experiences hydration reaction because of the water vapor existing in the air and stone surface pores, and the silicon alcohols is obtained. The chemical reaction is shown in function (1);

Secondly, condensation reaction happens between silicon alcohols and hydroxyl on stone surface, and a coupling layer (PDMS) is obtained. The coupling layer can reduce surface contact angle between asphalt and aggregate, improve the wetting and infiltration rate of asphalt in the stone surface. Therefore, silane coupling agent can effectively improve the interface bonding between asphalt and aggregate. The chemical reaction is shown in function (2);

Finally, a chemical bond or a chelate forms between R groups and organic material (asphalt), and physical bonding such as Van der Waals' force can also occur. So the coupling between two different chemically properties materials is completed. The chemical reaction is shown in function (3).

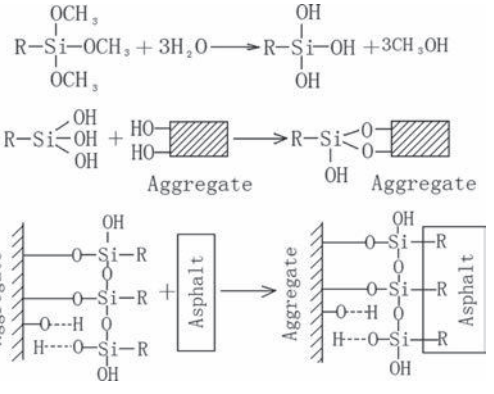

(1)

(2)

(3)

2.4 *Mixture design*

AC-16C mixture type was adopted according to China's specification. The grading curve for mixtures was shown in Figure 2. Marshall Tests were carried out to find the optimum asphalt binder content of mixtures, which was 4.6% by weight of aggregates.

Note:

1. The temperature heating asphalt can't be more than 160 °C, and the content of SCA is 0.3% of asphalt (mass ratio).
2. Asphalt mixtures need to be conditioned in 150 °C for 50 minutes before compaction.

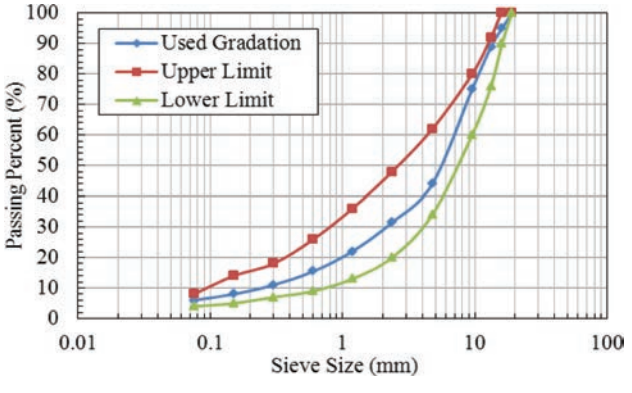

Figure 2. Aggregates gradation curves of asphalt mixtures.

Table 3. Test project.

Serial number	Aggregate	Filler	Treated by SCA
No. 1	Basalt	Limestone	No
No. 2	Basalt	Andesite	Yes
No. 3	Andesite I	Limestone	No
No. 4	Andesite I	Limestone	Yes
No. 5	Andesite I	Andesite	Yes
No. 6	Andesite I	Granite	Yes
No. 7	Andesite II	Limestone	No
No. 8	Andesite II	Andesite	Yes
No. 9	Andesite II	Granite	Yes

In order to study the improvement of SCA on road performance of asphalt mixtures, test project in this paper is shown in Table 3.

3 TEST METHODS

3.1 *Filler hydrophilic coefficient*

In order to study the improvement of SCA on asphalt mastics, hydrophilic coefficients of six kinds of fillers (including untreated limestone, untreated andesite, untreated granite, treated limestone, treated andesite and treated granite) were tested. The treat process is as follows: firstly, weigh the SCA (mass of SCA:mass of filler = 1.5:100), then disperse the SCA into water (mass of SCA:mass of water = 2:100); secondly, put the solution into filler, and stirring for 15 min; finally, remove moisture with the temperature 105 °C.

3.2 *Freeze-thaw cycle test*

3.2.1 *Freeze-thaw cycle procedure*

Compaction method of specimen is gyratory compacting, and the diameter of specimen is 100 mm, height is 63.5 mm ± 1.3 mm. The procedure of free-thaw cycle is as follows:

① The specimens were randomly divided into two groups. The first group of specimens were kept on the platform at room temperature; the second group of specimens were immersed in water with 97.3~98.7 kPa (730~740 mmHg) for 15 minutes, then open the valve, kept specimen in the water without pressure for 0.5 hours.
② The second group of specimens were removed into a plastic bag with 10 ml water, then maintain the condition temperature −18 °C ± 2 °C for 16 hours.
③ The specimens removed from the low-temperature case were immediately put in water tank with the temperature 60 °C ± 0.5 °C for 24 hours.

3.2.2 *Evaluation method*

3.2.2.1 Tensile Strength Ratio (TSR)

The specimens were kept in 15 °C ± 0.5 °C constant temperature water tank for 2 hours, then were removed and immediately applied splitting loading by MTS machine. The loading rate is 50 mm/min. The indirect tensile strength is calculated according to equation (4), and he TSR is calculated according to equation (5).

$$R_T = 0.006287 P_T / h \tag{4}$$

where:

R_T = Indirect tensile strength, MPa;
P_T = The maximum value of test load, N;
h = The specimen height, mm;

$$TSR = (R_{T_2} / R_{T_1}) \times 100 \tag{5}$$

where:

TSR = Tentile strength ratio,%;

R_{T_1} = Indirect tensile strength before freeze-thaw cycle, MPa;

R_{T_2} = Indirect tensile strength after freeze-thaw cycle, MPa;

3.2.2.2 High-temperature creep rate

High-temperature creep test was used to evaluate deformation resistance performance of asphalt mixture. Creep rate was selected as evaluation index. The lower creep rate should be, the better mixture high-temperature performance should be. Creep rate growth rate was selected as index evaluating the influence of freeze-thaw cycle on high-temperature of asphalt mixture. The lower creep rate growth rate should be, the better moisture sensitivity of mixture high-temperature performance should be.

(1) Creep indexes calculation method. Data in a stable deformation section was used to calculate the creep indexes. Creep rate was calculated according to function (6), and the creep rate growth rate was calculated according to function (7).

$$\varepsilon_s = \frac{\varepsilon_2 - \varepsilon_1}{(t_2 - t_1)/\sigma_0} \tag{6}$$

where:

σ_0 = Indirect tensile strength, MPa;

t_1 = The starting time of creep stability period, s;

t_2 = The ending time of creep stability period, s;

ε_1 = The creep strain corresponding to the starting time;

ε_2 = The creep strain corresponding to the ending time;

ε_s = The creep rate, 1/s/MPa.

$$\alpha = \frac{\varepsilon_{s_2} - \varepsilon_{s_1}}{\varepsilon_{s_1}} \times 100 \tag{7}$$

where:

α = Creep rate growth rate, %;

ε_{s_1} = Creep rate before freeze-thaw cycle, 1/s/MPa;

ε_{s_2} = Creep rate after freeze-thaw cycle, 1/s/MPa;

(2) Test condition. The forming method of specimens was Marshall compction test. The diameter of specimens is 101.6 mm, and height is 63.5 ± 1.3 mm. After compaction, half of specimens go through freeze-thaw treatment, the other half are as control samples. Before loading, all specimens need to be kept in 45 °C water tank for 1 hour, and then removed into 45 °C MTS environmental cabinet immediately. The constant loading is 0.04 MPa.

3.2.2.3 Low-temperature Indirect Tensile Strain (LITS)

This study evaluated the low-temperature anti-cracking performance by low-temperature indirect tensile test. The LITS was selected as the evaluation index of asphalt mixtures low-temperature performance. The bigger the LITS should be, the more excellent the low-temperature performance of asphalt mixtures should be. The LITS rate was selected as the evaluation index of moisture sensitivity of asphalt mixtures low-temperature performance. The bigger the LITS rate should be, the better the moisture sensitivity of asphalt mixtures low-temperature performance should be.

The forming method of specimens is Marshall compaction test, the diameter of specimens is 101.6 mm, and the height is 63.5 ± 1.3 mm. After compaction, half of the specimens need to go through the freeze-thaw cycle, the other half are selected as the control samples. The test temperature is –10 °C, and the loading rate is 1 mm/min.

3.2.2.4 Mid-temperature fatigue life

1. Evaluation Index. This research adopts the fatigue life to evaluate the fatigue performance of asphalt mixture. The higher the fatigue life should be, the better the anti-fatigue performance of asphalt mixtures should be. The fatigue life ratio was selected as evaluating the moisture sensitivity of fatigue performance of asphalt mixtures. The higher the fatigue life ratio should be, the better the moisture sensitivity of fatigue performance of asphalt mixtures should be.
2. Test conditions. The forming method of specimens is rotary compacting test. The diameter of specimens is 101.6 mm, and height is 63.5 ± 1.3 mm. The test temperature is 15 ± 1 °C. The loading frequency is 10 Hz. The load waveform is sine wave, and the minimum load is 2% of the maximum load. Before loading, 30 s preloading was applied on the specimens in order to make every part in good contact. The stress level is 30% of indirect tensile strength.

3.3 *Dynamic water flushing test*

In order to study the influence of dynamic water flushing on asphalt mixture, a device was developed to simulate the union impact of water, temperature and loading (Fig. 3).

The characteristics of the dynamic water flushing device are as follows:

1. It can provide excitation to simulate the dynamic water pressure caused by wheel loads;
2. It can control the pressure value and repeating frequency exactly;
3. The temperature of circulated water can be controlled exactly.

When the piston moves downward, the water in area A is pressed into specimen voids, some water can reach area B, which can simulate the case that water is pressed into the pavement under wheel loads. When the piston moves upward, the water in area B goes back into area A, which can simulate the pore water pumping action when the wheel loads go away. During the test, the piston does not contact the specimen. The test parameters are as follows:

Frequency: 10 Hz;
Water pressure: 0.4 MPa;
Water temperature: 45 °C;
Flushing time: 15 minutes;
The evaluation method is same as 3.2.2.

All the test values shown in this paper are averages of results from up to four individual experiments.

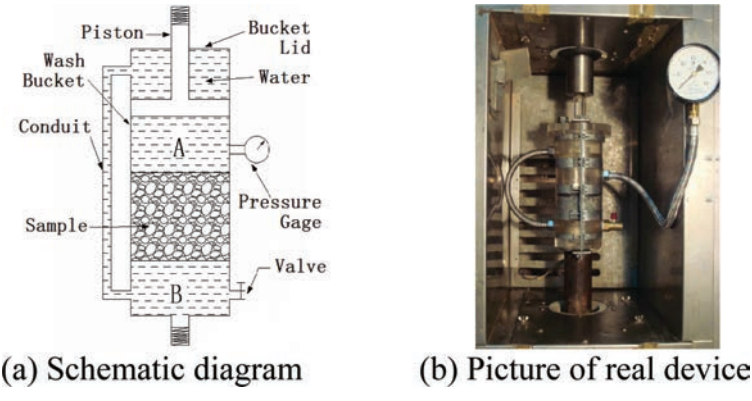

Figure 3. Dynamic water flushing device.

4 RESULTS AND DISCUSSION

4.1 *Hydrophilic coefficient test*

It can be seen from Figure 4 that the SCA effects little on limestone filler and andesite filler, but hydrophilic coefficient of granite filler treated by SCA decreases by 16%, that's because limestone and andesite are good at attracting oil, but granite is good at attracting water. It shows that SCA can improve the adhesion between acidic aggregate and asphalt.

4.2 *Freeze-thaw cycle test*

4.2.1 *TSR*

It can be seen from Figure 5 that, before freeze-thaw cycle, the strength of andesite aggregate I is highest, andesite aggregate II is minimum if the mixtures weren't treated by SCA. After adding SCA, the strength of andesite aggregate II is nearly the same with basalt aggregate, and the strength of andesite aggregate I increases by 13%. For andesite I aggregate and andesite II aggregate, modified andesite filler and modified granite filler show better performance than unmodified limestone. For basalt aggregate, the improvement of SCA on different fillers is not remarkable. Comparing No. 3 and No. 4, we can see that after freeze-thaw cycle, SCA can increase TSR of andesite I aggregate mixtures by more than 13%, which is corresponding to the hydrophilic coefficient test. TSR of modified andesite filler mixtures can catch up with the level of unmodified limestone filler mixtures. But SCA effects little on TSR of granite filler mixtures, which is different from the hydrophilic coefficient test. The reason is the effect of aggregate and the test scale dependence.

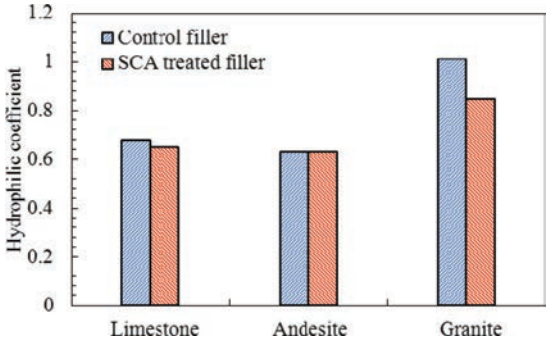

Figure 4. Hydrophilic coefficient of fillers.

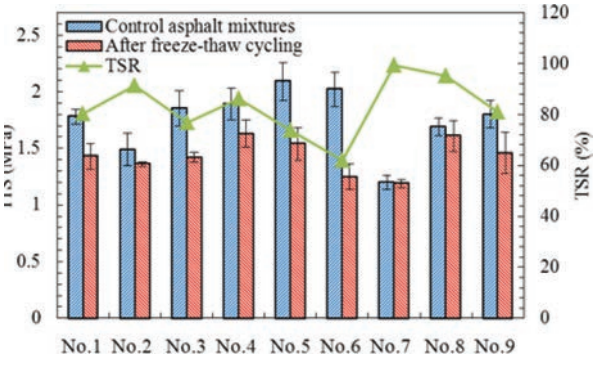

Figure 5. ITS and TSR results through freeze-thaw cycle.

4.2.2 *High-temperature creep test*

It can be seen from Figure 6 that, creep rate of andesite II aggregate is highest, and SCA can improve its high-temperature performance. SCA can decrease the creep rate growth rate of andesite I aggregate dramatically, but this phenomenon is not obvious for basalt aggregate and andesite II aggregate.

4.2.3 *Low-temperature indirect tensile strain*

It can be seen from Figure 7 that SCA effects little on LITS of all asphalt mixtures, which means SCA effects little on low-temperature of asphalt mixtures. After freeze-thaw cycle, SCA can increase the LITS rate of basalt aggregate and andesite II aggregate obviously, which means SCA can improve moisture sensibility of asphalt mixtures low-temperature performance.

4.2.4 *Mid-temperature fatigue life*

It can be seen from Figure 8 that SCA can increase fatigue life of basalt aggregate mixtures, but decrease fatigue life of andesite II aggregate mixtures. SCA effects little on fatigue life of andesite I aggregate mixtures. After freeze-thaw cycle, SCA can increase fatigue life of all asphalt mixtures. The above shows that SCA can improve moisture sensibility of asphalt mixtures mid-temperature fatigue performance.

4.3 *Dynamic water flushing test*

Dynamic water flushing can make the interface adhesive between asphalt and aggregate weaken, which can effects road performance of asphalt mixtures.

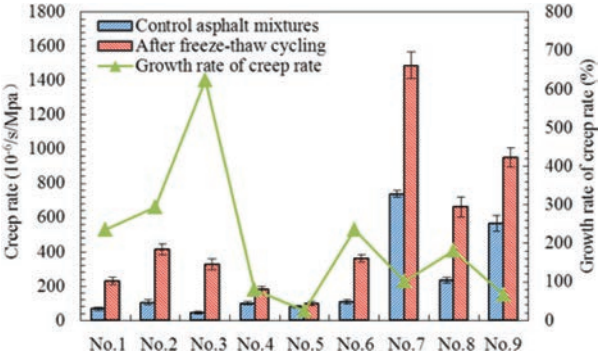

Figure 6. High-temperature creep results through freeze-thaw cycle.

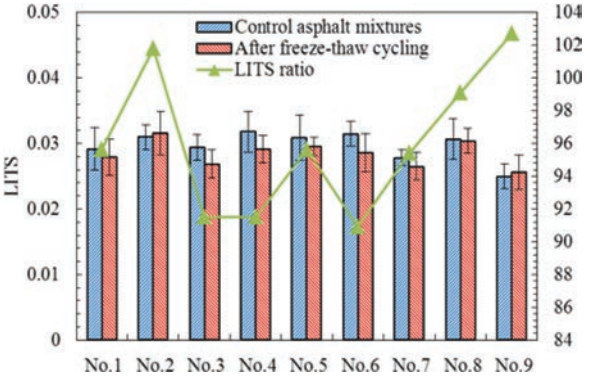

Figure 7. Low-temperature indirect tension results through freeze-thaw cycle.

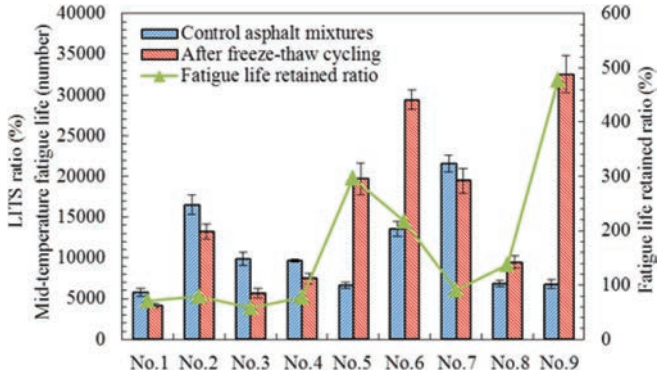

Figure 8. Mid-temperature fatigue life results through freeze-thaw cycle.

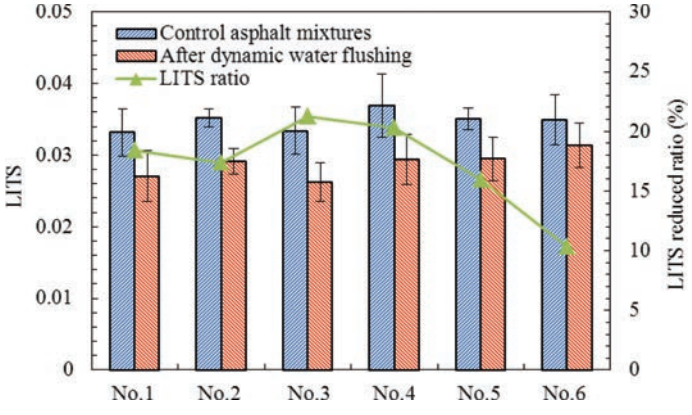

Figure 9. Low-temperature indirect tension results through dynamic water flushing.

(a) Fracture surface of control sample (b) Fracture surface through dynamic water flushing

Figure 10. Inner morphology variation of asphalt mixtures through dynamic water flushing.

It can be seen from Figure 9 that dynamic water flushing can damage the low-temperature performance of all asphalt mixtures. SCA can decrease the indirect tensile strain ratio of asphalt mixtures after dynamic water flushing. And SCA has the biggest effect on granite filler mixtures, the minimal effect on limestone filler mixtures. Inner morphology variation of asphalt mixtures under dynamic water flushing is shown as Figure 10.

Figure 10 shows that dynamic water flushing can strip the asphalt from the aggregate, which means the pore water pressure caused by wheel loads is one of the most important reasons on moisture damage of asphalt pavement. Figure 10 can demonstrate the device developed in

this paper can simulate the dynamic water flushing well. We can study the influencing factors of moisture damage, evaluate the moisture sensitivity of asphalt pavement, and reveal the mechanism of the moisture damage of asphalt pavement by using the method.

5 CONCLUSIONS

Based on the testing and analysis presented herein, the conclusions of the study are summarized as follows:

1. The hydrophilic coefficient tests indicate that SCA can improve the moisture sensitivity of the granite filler obviously, but the influence of SCA on strong lipophilic powder is not significant.
2. The freeze-thaw splitting test indicates that SCA can improve the moisture sensitivity of the andesite aggregates and three kinds of fillers, and SCA is more effective for acid aggregate or acid filler.
3. High-temperature creep tests show that SCA can improve the high-temperature stability of andesite aggregate mixtures and its moisture sensitivity obviously, but effects little on basalt aggregate mixtures.
4. Low-temperature indirect tensile tests show that SCA effects little on low-temperature of asphalt mixtures, but it can improve moisture sensibility of asphalt mixtures low-temperature performance.
5. Fatigue tests indicate that the influence of SCA on the fatigue life of asphalt mixtures is aggregate dependent. SCA can improve moisture sensibility of asphalt mixtures mid-temperature fatigue performance.
6. Dynamic water flushing can make the interface adhesive between asphalt and aggregate weaken. SCA can improve the performance of asphalt mixtures resisting dynamic water flushing.

Above all, freeze-thaw cycle and dynamic water flushing are two effective methods for simulating moisture damage. SCA can effectively improve the moisture sensitivity of asphalt mixtures, and the significance is aggregate dependent. Further researches on SCA treated asphalt mixture are highly recommended to understand the correlation between the laboratory and practical applications.

REFERENCES

[1] Lottman R.P. Predicting Moisture-Induced Damage to Bitumen Concrete Field Evaluation. NCHRP Report 246. Transportation Research Board, National Research Council, Washington, D.C., 1982.

[2] F. Moghadas Nejad, A.R. Azarhoosh, GH.H. Hamedi, M.J. Azarhoosh. Influence of using nonmaterial to reduce the moisture susceptibility of hot mix asphalt. Constr Build Mater, 31, pp. 384–388. 2012.

[3] Shin-Che Huang, Raymond E. Robertson, Jan F. Branthaver, J. Claine Petersen. Impact of lime modification of asphalt and freeze–thaw cycling on the asphalt–aggregate interaction and moisture resistance to moisture damage. J Mater Civ Eng, 17(6), pp. 711–718. 2005.

[4] Raquel Moraes, Raul Velasquez, and Hussain U. Bahia. Measuring the effect of moisture on asphalt-aggregate bond with the bitumen bond strength test. Transport Res Rec, 2209, pp. 70–81. 2011.

[5] M.N. Partl, E. Pasquini, F. Canestrari, A. Virgili. Analysis of water and thermal sensitivity of open graded asphalt rubber mixtures. Constr Build Mater, 24, pp. 283–291. 2010.

[6] L.D. Poulikakos, M.N. Partl. Evaluation of moisture susceptibility of porous asphalt concrete using water submersion fatigue tests. Constr Build Mater, 23, pp. 3475–3484. 2009.

[7] Yong-Rak Kim, Ingryd Pinto, Seong-Wan Park. Experimental evaluation of anti-stripping additives in bituminous mixtures through multiple scale laboratory test results. Constr Build Mater, 29, pp. 386–393. 2012.

[8] Jun Xie, Shaopeng Wu, Ling Pang, Juntao Lin, Zuhuang Zhu. Influence of surface treated fly ash with coupling agent on asphalt mixture moisture damage. Constr Build Mater, 30, pp. 340–346. 2012.

[9] Shu Wei Goh, Michelle Akin, Zhanping You, Xianming Shi. Effect of deicing solutions on the tensile strength of micro- or nano-modified asphalt mixture. Constr Build Mater, 25, pp. 195–200. 2011.
[10] Xiao Qingyi, Qian Chunxiang, Xie Jianguang. Experimental research on modification of asphalt concrete performance and asphalt-aggregate interface by coupling agent. J SE Univ (Nature Science Edition), 34(4), pp. 485–489. 2004.
[11] Wang Zhenjun, Wang Rui, Xiao Jingjing, Wang Xiao. Effects of silane coupling agent on road performances of composite asphalt mixtures. J Civ, Archit & Environ Eng, 32(5), pp. 41–46. 2010.
[12] Saeed Ghaffarpour Jahromi. Estimation of resistance to moisture destruction in asphalt mixtures. Constr Build Mater, 23, pp. 2324–2331. 2009.
[13] Weibiao Wang, Yingbo Zhang, Kaare Höeg, Yue Zhu. Investigation of the use of strip-prone aggregates in hydraulic asphalt concrete. Constr Build Mater, 24, pp. 2157–2163. 2010.
[14] Mohammad Zia Alavi, Elie Y. Hajj, Andrew Hanz, Hussain U. Bahia. Evaluating adhesion properties and moisture damage susceptibility of warm mix asphalts using bitumen bond strength (BBS) and dynamic modulus ratio (ESR) tests. Transport Res Rec, 4331. 2012
[15] Roberts FL, Kandhal PS, Lee DY, Kennedy TW. Hot Mix Asphalt Materials, Mixture Design, and Construction. NAPA Research and Education Foundation, Lanham, Maryland, 1996.
[16] Prowell BD, Zhang JB, Brown ER. Aggregate Properties and the Performance of Superpave-Designed Hot Mix Asphalt. NCHRP Report 539. Transportation Research Board, National Research Council, Washington, D.C., 2005.
[17] Brown ER, Haddock JE, Crawford C. Investigation of Stone Matrix Asphalt Mortars. Transport Res Rec, 1530, pp. 95–102. 1996.

Asphalt Pavements – Kim (Ed)
© 2014 Taylor & Francis Group, London, ISBN 978-1-138-02693-3

Estimation of the composition of rubber bitumen pellets using Thermogravimetric Analysis

Ignacio Artamendi, Paul Phillips & Bob Allen
R&D Department, Aggregate Industries UK, Hulland Ward, Derbyshire, UK

Gareth Evans
Billian UK Ltd., Sheffield, UK

ABSTRACT: Ground Tyre Rubber (GTR) bitumen pellets is a relatively new technology to deliver rubber modified binders to asphalt mixtures. The pellets are manufactured by producing a rubber modified binder by means of the wet process which is then pelletized by the aid of mineral filler. The resulting pellets are solid particles relatively hard produced in a range of individual sizes from 5 mm to 20 mm and consisting of a rubber-bitumen core coated with a thin layer of filler. These pellets can be incorporated directly into asphalt as a partial replacement of some of the bitumen to introduce a polymer (GTR) into the mixture, or as a rubber modified binder in hot mix recycling operations. In both applications, the total binder content of the asphalt mixture and the rubber content by weight of the total binder will depend on both the amount of pellets added and their composition. In this work, Thermogravimetric Analysis (TGA) has been used to estimate the amount of bitumen, rubber and filler in a pellet. TGA was carried out on the individual components of the pellets i.e. rubber, bitumen and filler and on the pellets before and after removal of the bitumen by means of solvent extraction. The pellets were then used to produce an asphalt mixture by replacing some of the bitumen. Binder content analysis of the mixtures was then carried out using standard techniques. It was found that the contribution from the pellet to the total binder content of the mixture reflected the composition of the pellet derived from TGA.

Keywords: Ground Tyre Rubber (GTR), rubber-bitumen pellet, Thermogravimetric Analysis (TGA), binder content

1 INTRODUCTION

The use of Polymer Modified Binders (PMBs) in asphalt has increased steadily during the last years. In Europe PMB consumption is estimated to be more than 10% of the total bitumen consumption [1]. This demand is also expected to grow during the coming years due to, among others, performance based specifications for asphalt. Elastomeric polymers such as SBS and SBR are, however, expensive and are not always readily available. As a result the use of more economical waste polymers particularly Ground Tyre Rubber (GTR) has gained considerable attention particularly in Europe.

Ground Tyre Rubber (GTR) has been used extensively in road pavement applications for more than 60 years. Two generic processes namely the 'wet process' and the 'dry process' have been developed for incorporating tyre rubber into asphalt mixtures. In the wet process the rubber particles are blended with bitumen at elevated temperatures to produce a rubber modified binder. In the dry process, on the other hand, the rubber particles are added directly into the aggregate blend before introducing the binder into the mixture.

The performance of bituminous mixtures containing tyre rubber has varied greatly. Mixtures produced with asphalt-rubber binders (wet process) have shown, in general, better over-

all performance than those produced by the dry process. Poor compaction, durability and resistance to permanent deformation have been generally associated with mixtures produced by the dry process [2]. Furthermore, most of the highways agencies in the USA recommend the use of the wet process.

In the US the term Asphalt Rubber as defined by ASTM D8 is used for rubberised binders produced by the wet process with at least 15% rubber by weight of total binder. Separation and settling of the rubber particles during storage and rubber degradation as a result of extended heating periods are however common problems associated to these types of binders. Alternatively, crumb rubber modified binder with lower concentration of rubber, between 5 to 15%, and therefore less prone to these issues are used by some agencies in the US.

Ground Tyre Rubber (GTR) bitumen pellets is a relatively new technology to deliver rubber-modified binders. The pellets are manufactured by producing an asphalt-rubber binder which is then pelletized using mineral filler. The resulting pellets are solid particles relatively hard of similar size as the aggregates consisting of a rubber-bitumen core coated with a thin layer of filler. These pellets can be incorporated directly into asphalt as a partial replacement of some of the bitumen to introduce a rubber polymer (GTR) into the mixture. The level of modification required can be easily adjusted by adding the correct amount of pellets and depends on the performance requirements for that specific mixture.

The level of polymer modification i.e. the amount of GTR by weight of total binder in the mixture is dependent on the amount of GTR and bitumen in the pellet thus in its overall composition. In order to estimate the composition of the pellets TGA analysis has been carried out on the individual components of the pellets i.e. rubber, bitumen and filler, and on the pellets before and after removal of the bitumen by means of solvent extraction. GTR bitumen pellets were then added to an asphalt mixture and the binder content of the mixture was determined using standard techniques.

2 GTR BITUMEN PELLETS

GTR bitumen paving pellets were manufactured by Billian UK Ltd. at their factory in Sheffield, UK. The manufacturing process consists of first producing a rubber-modified binder (asphalt-rubber binder) by blending fine GTR with bitumen and then pelletizing the modified binder with the aid of mineral filler. The base bitumen used to produced the rubber-modified binder was a 100/150 pen and the GTR had a maximum nominal size of 1.0 mm and was sourced from truck tyres.

A blending unit AR150M manufactured by Phoenix Industries was used to produce the rubber-modified binder. The unit consists of a bitumen heating tank, a mechanical mixer and a reaction tank. The heating tank is used to maintain the temperature of the bitumen at 175 °C before blending with the GTR using a mechanical high shear mixer. The bitumen and GTR are fed directly into the mixer at controlled rates to give 15–25% rubber by weight of total binder. Mixing continues until an homogenous blend is produced. The modified binder is then kept in a reaction tank for about 1 to 2 h. During this time bitumen components diffuse into the rubber causing it to swell [3]. Once produced, the rubber-modified binder is fed to a pelletizer through an insulated line. The pelletizer consists of a rotating disc where the filler is fed from a silo through a line at a controlled rate. The binder is applied by slow flowing line. As the binder makes contact with the filler on the rotating disc a small pellet is formed until it is large enough to be removed from the hood. After the pellets are formed they are transported to an air cooling unit by means of a vibrating conveyor belt. Once cooled, these are screened into different sizes typically 5 mm to 20 mm and stored in different size bags (10 kg, 25 kg and 1 tonne sacks). The mineral filler used to produce the pellets was Hydrated Lime (HL). The introduction of an adhesion promoter filler (HL) to the mixture via the pelletised binder is known to enhanced the durability of asphalt [4]. The effect of HL on mixture performance was, however, outside the scope of the paper.

The final pellets are solid particles relatively hard of similar size as the aggregate (typically around 10 mm maximum nominal size) consisting of a rubber-bitumen core coated

Figure 1. GTR bitumen paving pellets.

with a thin layer of filler (see Fig. 1). The pellets can be stored in bags without the need of heated storage tanks and can be incorporated directly in to the mixing box by conventional systems.

3 EXPERIMENTAL

3.1 *Thermogravimetric analysis of GTR bitumen pellets*

Thermogravimetric Analysis (TGA) is an experimental method widely used in composition analysis and it is particularly useful for multi-component materials [5]. In this method a sample is heated to extremely high temperatures of up to 2000 °C and its mass loss is monitored continuously as a function of temperature. As the temperature increases, various components of the sample are decomposed (volatilised) and the percentage mass loss of each component is measured. Results are plotted with temperature on the X-axis and mass loss on the Y-axis. Decomposition rates, i.e. first derivatives, are also plotted to determine decomposition temperature range of each component. The concentration of each component can then be determined from the mass loss and the temperature range of the decomposition of the component.

TGA of the pellets was carried out in two stages. The first stage was to analyse the individual components of the pellets i.e. GTR, bitumen and hydrated lime in order to determine the mass of the residue and find out at which temperature the decomposition of components take place. This was followed by TGA of the pellets as received. The second stage involved the removal of bitumen from the GTR bitumen pellets using solvent extraction. Carbon disulphide (CS_2) was used as a solvent as this solvent is specific to dissolving the bitumen without affecting the other components [6]. Portions of the GTR pellets were treated to dissolution in CS_2 by adding 20 cm^3 of the solvent onto approximately 0.8 g of solid. Three separate portions were treated with the solvent. The residues from the filtration were then dried in an oven at 75 °C for 24 hours before being analysed by TGA.

The GTR pellets and the rubber samples were ground using a SPEX Sample Prep Model 6850 Freezer/Mill. The bitumen sample was unsuitable for this preparation, and both the hydrated lime and the treated pellets after removal of the bitumen were deemed to not require any further grinding. The sample was placed into a polycarbonate vessel with a steel impactor and then lowered into a bath of freezing liquid nitrogen (about −196 °C). The frozen sample was then pulverised by the magnetically-driven impactor before retrieval and further analysis.

The TGA experiments were carried out using a Stanton Redcroft STA1500 apparatus. The mass of the samples was approximately 30 mg. Samples were placed in 70 µl platinum crucible. Heating rate applied was 10 °C/min and an atmosphere of air at a flow rate of 50 cm^3/min was employed.

Table 1. Composition of mixtures.

	Composition (%)	
Component	Control mixture	GTR pellet mixture
4/10 mm	39.6	39.6
2/6.3 mm	11.3	11.3
0/4 mm	39.5	39.3
Limestone filler	4.0	3.8
Binder (100/150)	5.6	4.6
GTR pellets	–	1.4
Total	100	100

3.2 *Compositional analysis of asphalt mixtures*

Two asphalt mixtures with and without the GTR bitumen pellets were prepared in the laboratory and used for compositional analysis. The control mixture was produced with a 100/150 pen bitumen and the bitumen content was 5.6%. The GTR pellet mixture, on the other hand, contained 4.6% bitumen (100/150 pen) and 1.4% GTR bitumen pellets. Mixture components and proportions are presented in Table 1.

Aggregates and bitumen were heated in an oven at 170 °C and mixed in a mechanical mixer. GTR pellets were incorporated directly to the hot aggregates before the bitumen was added. The mixtures were produced in 5 kg batches. Un-compacted loose material was used for analysis. In total, 3 identical samples of the control mixture and 9 samples of the GTR pellet mixture were manufactured.

Compositional analysis was carried out following standard tests method. These included binder content by ignition [7] and soluble binder content [8]. In the ignition method a sample of 1500 g approximately was heated in a furnace at 480 °C for 50 minutes. The binder content was then determined from the total mass of the mixture before and after ignition. A correction factor of 0.21 for the aggregate blend used was applied to counteract for mineral loss of mass during ignition, in accordance with the test method, Three different laboratories (A, B, C) tested a sample of each mixture using this method.

The soluble binder content method, on the other hand, involved binder extraction by dissolving in a solvent (dicholromethane), separation of the mineral matter from the binder solution, determination of the quantity of binder by difference and by binder recovery (direct) and finally calculation of the soluble binder content. Separation of the mineral matter was carried using bottle rotation machine and pressure filter (binder by difference). Bucket centrifuge-Type 1 and volume calculation from an aliquot portion was employed for soluble binder content by recovery method. Three different laboratories (D, E, F) tested the GTR pellet mixture using both binder by difference and by recovery methods.

4 RESULTS AND DISCUSSIONS

4.1 *Composition of GTR bitumen pellets*

The results from the TGA experiments are presented in Figures 2–6. Figure 2 shows the TGA results for the GTR. It can be seen that there were a series of overlapping mass losses starting at around 200 °C and reached completion at around 550 °C. The total mass loss was 92.1% and the amount of residue after completion of the test was 7.9%. At temperatures below 300 °C mass loss is due to the volatilization of lubricants, stabilizers and other small molecules in the rubber with relatively low boiling points. Main polymeric compounds of the rubber like polyisoprene and styrene-butadiene rubber decompose at temperatures between 300 and 600 °C. At these temperatures, the polymer chains break down into a variety of smaller molecular fragments that will eventually vaporize. The remaining mass of

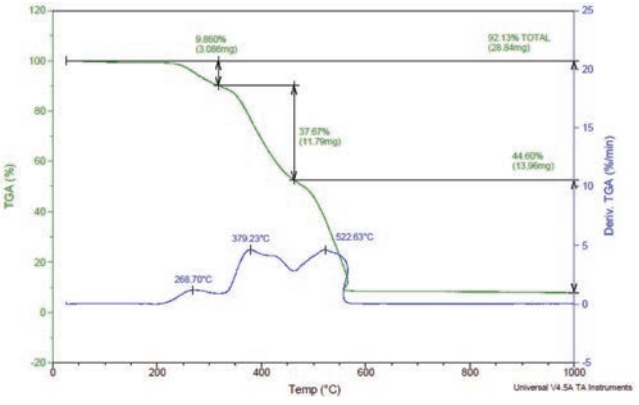

Figure 2. TGA of Ground Tyre Rubber (GTR).

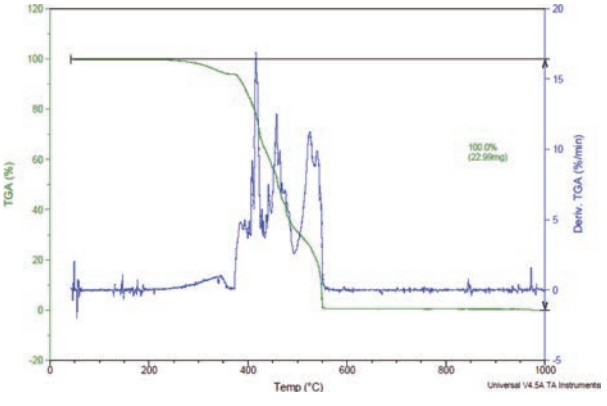

Figure 3. TGA of bitumen (100/150 pen).

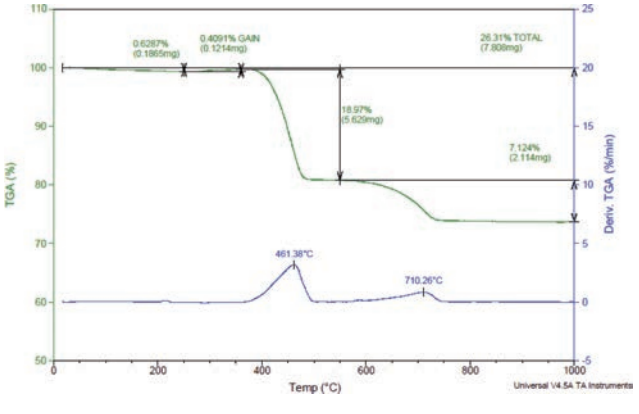

Figure 4. TGA of hydrated lime.

material at temperatures higher than 600 °C is carbon black and the remaining mineral ash residues. Similar thermal degradation curves for crumb rubber modifier have been reported elsewhere [9].

Figure 3 shows TGA results for the bitumen. The mass losses indicated decomposition of the different bitumen components from light molecular weight aromatics to high molecular

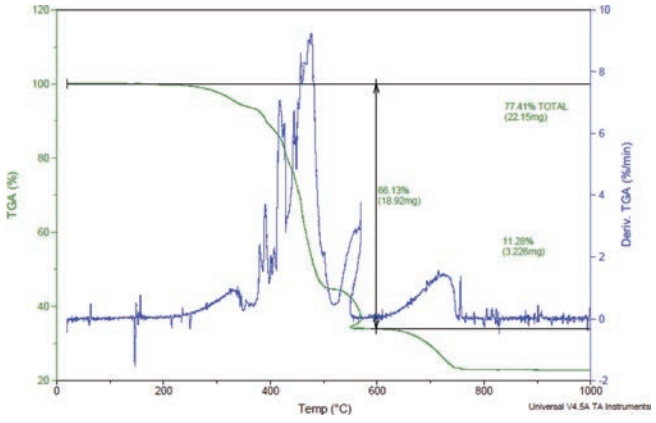

Figure 5. TGA of GTR bitumen pellets.

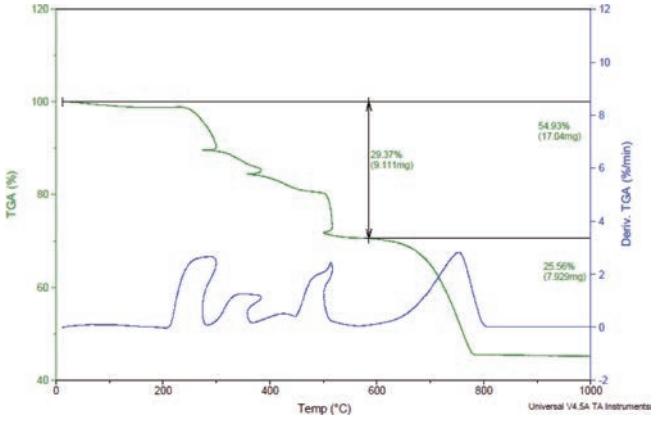

Figure 6. TGA of treated GTR bitumen pellets.

weight compounds. Furthermore, mass losses began soon after 200 °C and were completed in the region of 550 °C. A total mass loss of 100.0% was seen with no residue.

TGA results for the hydrated lime sample are shown in Figure 4. It can be seen that there were two main mass loss events with around 19.0% being lost by 500 °C followed by a smaller broad mass loss of 7.1% from around 550 °C to 750 °C. The residue was seen as a fine grey powder and amounted to 73.7%. The TGA profile for this material was not expected. The decomposition scheme for hydrated lime is $Ca(OH)_2 \rightarrow CaO + H_2O$ and as such would only expect a single mass loss step. The presence of the mass loss at around 400 °C overlaps with the bitumen and GTR mass losses.

TGA test results for the GTR bitumen pellets are presented in Figure 5. The GTR bitumen pellet showed a series of mass losses. The first section was the mass loss before 600 °C, while the second section was the mass losses occurring after 600 °C. It was assumed that the mass loss at temperatures higher than 600 °C were due solely to the decomposition of the hydrated lime. TGA tests were carried out in quadruplicate (see Table 2).

TGA test results of the residues from the samples treated with CS_2 are shown in Figure 6. It can be seen from the samples with the bitumen removed, that the oxidation of the remaining crumb rubber is very reactive under air, producing a large amount of heat. This sample generated heat increases the heating rate of the experiment distorting the TGA curve when plotted against temperature. However the triplicate determinations on the produced residue were all in good agreement as can be seen in Table 2.

Table 2. Mass losses of GTR bitumen pellets samples.

Material	Sample no.	Mass loss (%)			
		20–600 °C	600–1000 °C	Total	Residue
GTR bituminous pellets	1	66.5	11.1	77.6	22.4
	2	66.1	11.4	77.5	22.5
	3	66.0	11.3	77.3	22.7
	4	66.8	11.3	78.1	21.9
	Mean	66.4	11.3	77.6	22.4
	CoV	0.005	0.010	0.004	0.013
Treated GTR bituminous pellets	1	29.4	25.6	55.0	45.0
	2	26.7	26.3	53.0	47.0
	3	27.8	25.7	53.5	46.5
	Mean	28.0	25.9	53.8	46.2
	CoV	0.049	0.015	0.019	0.023

Due to the complexity of the hydrated lime mass loss profile and its overlapping with the GTR and bitumen decompositions, the estimation of the components of the GTR bitumen pellets is not straight forward. For the estimation of the composition of the pellets it was assumed that the mass loss from the heating above 600 °C was solely due to the hydrated lime.

The solvent treated GTR bitumen pellet samples showed an average mass loss of 28.0% between about 20 °C (ambient temperature) and 600 °C. Assuming that this mass loss was solely due to GTR and knowing the residual mass from the GTR was 7.9%, then the GTR content is: $28.0 \times (100/92.1)\% = 30.4\%$. The untreated GTR bitumen pellets showed an average mass loss of 66.4% between ambient temperature and 600 °C. Therefore, subtracting the mass loss occurring due to the GTR (28.0%) should yield the mass loss due to bitumen. In this case, the bitumen content is $(66.4 - 28.0)\% = 38.4\%$. Therefore, the level of hydrated lime present is, assuming that the composite consists of only three ingredients, 31.2%. Therefore the composition of the GTR bitumen pellet can be estimated at 38.4% bitumen, 30.4% GTR and 31.2% hydrated lime.

Typical or target pellet composition provided by the supplier of the pellets was 50% bitumen, 20% GTR and 30% hydrated lime. Results obtained from TGA showed lower bitumen content and higher rubber content that the target proportions. Estimated hydrated lime content, on the other hand, was close to the target value. The effect of such a change in composition was seen as an increase in the modification level i.e. rubber content while the binder content remained practically the same. Differences between the estimated and the target bitumen and rubber contents could be due to various causes. First, the TGA method used in this study provides just an estimation of the composition of the pellets as it is assumed that the mass loss at temperatures above 600 °C is solely the result of the decomposition of the hydrated lime. Also, the size of the samples used for the analysis is very small i.e. 30 mg approximately which could introduce some experimental error.

Higher rubber contents determined from TGA analysis might also suggest that during the manufactured of the rubber modified binder a higher amount of rubber than the target is blended with the bitumen. This could be monitored by adequate controls and calibration of the bitumen and rubber addition systems. Another possibility is that some rubber could have been deposited at the bottom of the reaction tank after a production run. This rubber could have then been blended with the freshly mixed rubber-bitumen binder increasing the overall rubber content of the binder. Nevertheless, quality control on the rubber—bitumen blends is carried out periodically at the plant and is primarily based on viscosity measurements. Viscosity values of the binders produced at the plant were determined using a digital viscometer (Haake VT-02) and were found to be between 20 to 60 dPa · s (2000–6000 cP) at 175 °C. It should be noted that viscosity values specified

for asphalt rubber in the US are 1500–5000 at 177 °C for binders containing a minimum of 15% rubber.

4.2 *Composition of asphalt with GTR bitumen pellets*

This section presents theoretical and experimental binder contents for the control and GTR pellet mixtures. As indicated before, the control asphalt mixture had 5.6% bitumen content whereas the GTR pellet mixture contained 4.6% bitumen and 1.4% GTR bitumen pellets by weight of the total mixture. The total binder content of the GTR pellet mixture can be calculated theoretically based on the composition of the GTR pellets and the percentage of pellets in the mixture. Table 3 shows the theoretical binder content and rubber content for two different GTR pellets composition, one based on the target GTR pellet composition (50% Bit, 20% GTR, 30% HL) and the other determined from TGA experiments (38.4% Bit, 30.4% GTR, 31.2% HL). It can be seen first that the total binder contents of the control and GTR pellets mixture were 5.6% and 5.5%, respectively. The percentage of GTR in the binder was, however, higher when the estimated GTR pellet composition from TGA were used.

Binder content determined by the ignition method and soluble binder content determined by different and by binder recovery (direct) methods are presented in Table 4. It can be seen that for the control mixture binder content by ignition was the same as the target value i.e. 5.6%. Binder content by ignition for the GTR pellet mixture was 5.3%, thus, lower than the target value for that particular GTR pellet composition. It should be noted that the binder content was determined by heating the samples in a furnace at 480 °C for 50 minutes. TGA of the GTR showed, however, that not all the components of the rubber decomposed below this temperature. It is believed that at this temperature some rubber compounds primarily synthetic rubber, carbon black and other ash mineral are still present in the sample. This can then introduce some errors in the calculation of the binder content determined from the total mass of the mixture before and after ignition. Larger variability was also found for the GTR pellets mixture. This could be the results of uneven distribution of the pellets within the mixture under laboratory conditions.

Soluble binder contents for the GTR pellet mixture determined by difference and by binder recovery (direct) methods showed lower binder content that the target value. It is known that vulcanised rubber as in tyre rubber does not completely dissolve in organic solvents. So, in the determination of the soluble binder content the bitumen dissolved in the solvent but not the GTR. The calculated soluble binder content was; therefore, lower than the actual total binder content which includes non-dissolve rubber compounds. If it

Table 3. Theoretical binder content of the GTR pellet mixture.

GTR pellets componets	GTR pellet composition (%)	GTR pellets by wt of total mixture (%)	Components in the mixture	Content by wt of total mixture (%)
Bitumen	50.0	1.4	Bitumen from pellet	0.7
GTR	20.0		GTR from pellet	0.3
Hydrated lime	30.0		HL from pellet	0.4
			Added bitumen	4.6
			Total bitumen	5.3
			Total binder	5.6
			(% GTR by wt of binder)	(5.3)
Bitumen	38.4	1.4	Bitumen from pellet	0.5
GTR	30.4		GTR from pellet	0.4
Hydrated lime	31.2		HL from pellet	0.4
			Added bitumen	4.6
			Total bitumen	5.1
			Total binder	5.5
			(% GTR by wt of binder)	(7.3)

Table 4. Experimental binder content of the asphalt mixtures.

Mixture	Method	Laboratory	Binder content (%)
Control mixture	Ignition	A	5.8
		B	5.5
		C	5.5
		Mean	5.6
GTR pellet mixture	Ignition	A	5.1
		B	5.7
		C	5.2
		Mean	5.3
	Direct	D	4.9
		E	5.2
		F	5.1
		Mean	5.1
	Difference	D	5.6
		E	5.2
		F	5.2
		Mean	5.3

is assumed that the rubber particles do not dissolve, the soluble binder content is just the bitumen content of the mixture. For the GTR pellet mixture the theoretical bitumen content was 5.1% which is close to the experimental soluble binder content. (5.1%—direct method and 5.3%—by difference).

5 CONCLUSIONS

- TGA was found to be a useful tool to characterise the individual components of the GTR bitumen pellets and to estimate their overall composition.
- The composition of the GTR bitumen pellets determined by TGA was estimated at 38.4% bitumen, 30.4% GTR and 31.2% hydrated lime.
- Percentage of rubber-binder in the pellet determined by TGA (68.8%) was similar to the target binder content provided by the supplier of the pellets (70.0%). Rubber concentration determined by TGA (30.4%) was, however, larger than the value provided by the supplier (20.0%).
- Binder content for the GTR pellet mixture determined by the ignition method (5.3%) was lower that the control mixture and the target value (5.6%). This was attributed to non-combusted rubber compounds at during oven ignition. Furthermore, TGA of the rubber confirmed that some rubber compounds volatilised at temperatures above the ignition oven temperature.
- Soluble binder contents for the GTR pellet mixture (5.2% direct method and 5.3% by difference method) were also lower than the target value (5.6%). This could be attributed to non-dissolve rubber particles during binder extraction.
- The level of polymer (rubber) modification i.e. the amount of GTR by weight of total binder in the mixture is dependent among others on the overall composition of the pellets. Hence, robust quality control measures are required during the manufacture of the GTR bitumen pellets to ensure consistence in the product and its composition.

REFERENCES

[1] Eurobitume. European Bitumen Consumption 2012. Brussels, Belgium. http://www.eurobitume.eu/system/files/EuropeanBitumenConsumption2012.pdf.

[2] Epps, J.A. Uses of Recycled Rubber Tyres in Highways, National Cooperative Highway Research Program (NCHRP), Synthesis of Highway Practice 198, Transportation Research Board, National Research Council, Washington, DC, 1994.
[3] Artamendi, I. and Khalid, H.A. Diffusion Kinetics of Bitumen into Waste Tyre Rubber, Journal of the Association of Asphalt Paving Technologists, 76, 133–164, 2006.
[4] Lesueur, D., Petit, J. and Ritter, H-J. The Mechanisms of Hydrated Lime modification of Asphalt Mixtures: State-of-the-Art Review, Road Materials and Pavement Design, 14(1), pp. 1–16, 2013.
[5] Menczel, J.D. and Prime, R.B. Thermogravimetric Analysis (TGA), Thermal Analysis of Polymers, Fundamental and Applications, John Wiley, New York, 2009.
[6] Morgan, P. and Mulder, A. The Shell Bitumen Industrial Handbook Shell Bitumen Chertsey, UK.
[7] Comité Européen de Normalisation (CEN), EN 12697-39: 2012 Bituminous Mixture—Test Methods for Hot Mix Asphalt—Part 39: Binder Content by Ignition.
[8] Comité Européen de Normalisation (CEN), EN 12697-1: 2012 Bituminous Mixture—Test Methods for Hot Mix Asphalt—Part 1: Soluble Binder Content.
[9] Ghavibazoo, A. and Adbelrahman, M. Compositional Analysis of Crumb Rubber during Interaction with Asphalt and Effect on Properties of Binder, International Journal of Pavement Engineering, 14(5–6), pp. 517–530, 2013.

Innovative pavement analysis and design—II

This page intentionally left blank

Asphalt Pavements – Kim (Ed)
© 2014 Taylor & Francis Group, London, ISBN 978-1-138-02693-3

Towards modeling rutting for asphalt pavements in hot climates

Aaron D. Mwanza & Mundia Muya
Department of Civil and Environmental Engineering, School of Engineering, University of Zambia, Lusaka, Zambia

Peiwen Hao
Highway College, Chang'an University, Shaanxi Province, Xi'an, China

ABSTRACT: Rutting is a chronic disease in asphalt pavements despite several mitigation measures. Although many attempts have been made by both researchers and practitioners to develop rutting prediction models, each model, however, has certain inherent limitations due to assumptions and data used during the development of the model. Placement of an asphalt overlay is the most common method used in Zambia to rehabilitate existing asphalt pavements. The objective of this research is to go towards developing a national rutting prediction model for use in tropical hot climates based on default finite element creep and elasto-visco-plastic analysis tools in abaqus. Dynamic modulus and repeated load tests are conducted on overlay mixtures designed based on the pavement residual structural adequacy from deflection tests to provide material properties for the constitutive rutting model. Unified, three dimensional linear viscoelastic boundary value problems were formulated for six national representative pavement sections. In general, the FE creep and elasto-visco-plastic rutting evolutions were in agreement with the measured laboratory scaled one third mobile load simulator's. Performance ranking of the validated models revealed optimal pavement system combination suitable for calibration. The study recommends future directions for local adoption of the South African mechanistic-empirical design method currently being developed.

Keywords: Finite element, rutting, creep, elasto-visco-plastic, overlay

1 INTRODUCTION

The use of asphalt overlays is one of the most common methods used in Zambia to rehabilitate deteriorated existing asphalt pavement roads. The type of an overlay and its required thicknesses are principally governed by the residual structural adequacy and strength of the existing pavement (PVMNT), determined mostly from non-destructive deflection tests such as the Falling Weight Deflectometer (FWD). Once adequately constructed, the satisfactory performance of an asphalt overlay is influenced by various factors including the existing PVMNT conditions, traffic loading, and environmental conditions (temperature, etc.).

Permanent Deformation (PD) in asphalt overlays is most severe in hot climates particularly under heavy traffic loading [1]. Estimation and prediction of the maximum distresses likely to occur within the PVMNT layers after construction of an overlay is critical to optimize PVMNT design and management [2]. Constitutive modeling of the PD behavior of asphalt pavement structures enables PVMNT engineers to evaluate the PVMNT deterioration progress and develop regional specific performance based asphalt mix specifications.

In this study, Finite Element (FE) analysis tools in ABAQUS were used to simulate a PVMNT model to predict PD that leads to rutting estimation. To validate the ABAQUS models and the related FE analysis, Accelerated Pavement Testing (APT) with the third-scale Mobile Load Simulator (MLS3) was used to measure the PD on laboratory scaled constructed overlay test sections of similar PVMNT structure and materials as the ABAQUS models.

2 STUDY OBJECTIVES AND METHODOLOGY

Given the above background, the objectives of the work documented in this paper were three-fold, namely:

- To evaluate the PD models in ABAQUS platform for the suitability of predicting rutting in hot tropical climates like Zambia.
- To characterize the Zambian roads asphalt mixes for PD response and rutting performance.
- To determine the regional temperature correction factors that adequately accounts for the effect of prolonged heat and high temperatures on deflection measurements.

The study methodology incorporated Nondestructive Testing (NDT) with the FWD conducted on in-service roads for a period of 2 years in different seasons to generate regional temperature correction factors and the overlay mix design data. In-situ characteristics of PVMNT layers in combination with dynamic modulus and repeated load testing on asphalt mixes provided material input parameters for the PD and rutting models. FE analysis in ABAQUS was executed to compare and validate the rutting performance of various laboratory-scaled PVMNT structures under accelerated trafficking with the MLS3.

3 EXPERIMENTAL PROGRAM

As discussed in the subsequent text, the experimental design plan comprised of FWD testing, modulus back-calculation and computations, sensitivity analysis, asphalt mix design and laboratory testing, accelerated PVMNT testing with the MLS3 and ABAQUS FE modeling.

3.1 *Falling Weight Deflectometer (FWD) testing*

Deflection response of a PVMNT to any applied load is an important indicator of the structural capacity, material property characterization, and subsequent PVMNT performance [3]. A Dynatest FWD model 8000 was used to collect deflection data, with typical test parameters, namely: 40 kN impulse load at one drop per point in the wheel path, 30 cm diameter circular foot plate, and seven geophones radially located at 0, 203, 306, 457, 610, 914, and 1534 mm, interspacing. Deflection measurements were taken at minimum 100 m interspacing on alternate lanes in the wheel path of a 45 km two-lane road, with one lane in each direction.

In order to account for the effects of seasonal temperature variations on deflection measurements, FWD tests were conducted over a period of 2 years spread over the three significant seasons of Zambia, namely rainy, cold, and hot season. Five representative PVMNT sections were selected based on the normal variation in the PVMNT cross-section, layer thickness, material type and quality, subgrade support, riding quality, and surface distresses for FE analysis.

3.1.1 *Modulus calculation-back analysis*

Based on the 90th percentile, a representative deflection basin was established for each PVMNT section for analyzing the representative moduli values. Raw deflection measurements were normalized and calibrated for regional temperature correction through a protocol model that was developed by taking into account a two years' seasonal temperature variation effects on deflection measurements before processing the elastic moduli back-calculations.

Back-calculation involves iterative and regression techniques to minimize errors between measured and calculated deflection values. This was computed using the following Eq.(1).

$$MSE = f(E,h) = \frac{1}{n}\sum_{i=1}^{n} We_i \left\{ D_i^c(E,h) - D_i^m \right\}^2 \quad (1)$$

where:
$D_i^c(E,h)$ = Calculated deflection at location i based on E and h,
D_i^m = Measured deflection at location i,
n = Number of FWD sensors,
E = {E1, E2, E3, ….., Em} (unknown moduli of the layers),
H = {h1, h2, h3 …… hm-1} (known layer thickness), and
We_i = Weighing factor for sensor i (We_i = 1 if all sensors are given the same importance).
MSE = Mean Square error

3.1.2 *Sensitivity analysis of modulus values*

A temperature correction model that was developed in this study based on moduli obtained from back-calculation analysis of the Evaluation of Layer Moduli (ELMOD) software at different temperatures was used to compare the moduli values obtained on each PVMT section throughout the temperature regime and season that the FWD tests were conducted. The default model format for temperature correction is expressed in Eq.(2).

$$D_{25} = D_0 e^{0.279T} \tag{2}$$

where:
D_0 = Measured center deflection
T = Temperature at the bottom of the wearing surface (approximately 40 mm from the surface)

In order to compare the deflections between sections, the deflection temperature models for each PVMNT section were normalized to the average HMA temperature during the testing period of 25 °C. An example of a generalized model for some PVMNT sections after nonlinear regression is shown in Figure 1.

Temperature correction factors can be read off from the relevant graph and applied to deflection measurements before in-putting into the ELMOD back-calculation software [6].

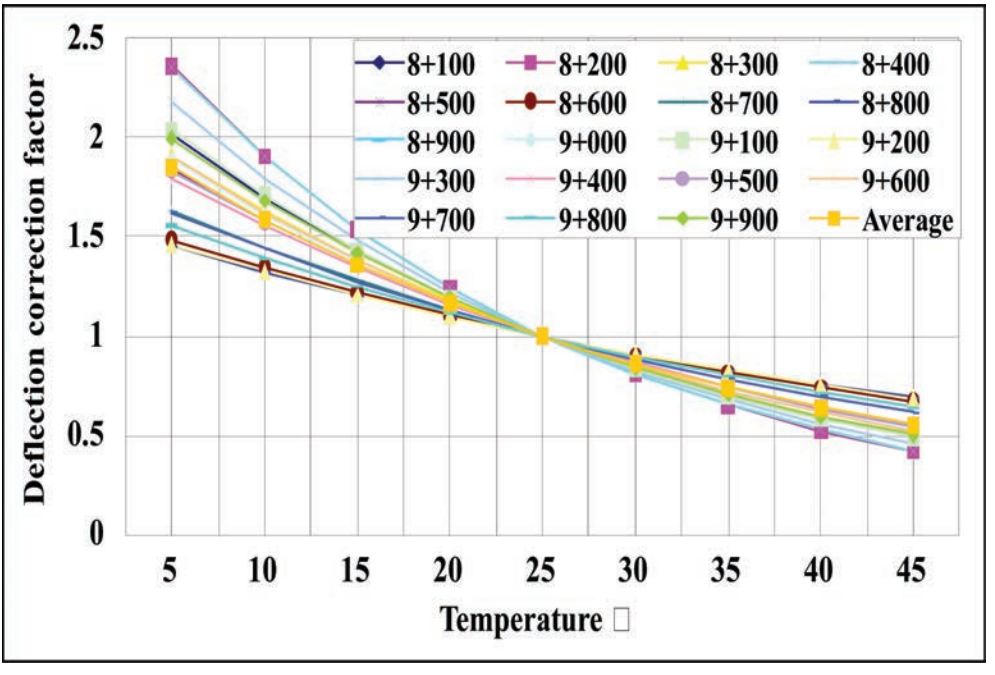

Figure 1. Temperature correction factors for deflection measurements.

Based on these adjustments, the corrected in-situ layer moduli were then utilized for development of PD and rutting prediction models. The residual life of each PVMNT section and the required overlay thickness were calculated based on the 1993 AASHTO PVMNT design guide. The 1993 AASHTO overlay thickness design method utilizes the effective thickness approach. The required thickness of the Asphalt Concrete (AC) overlay was determined and computed as a function of the structural capacity required to meet future traffic demands and the structural capacity of the existing pavement [7].

$$h_{oL} = \frac{SN_{OL}}{a_{OL}} = \frac{SN_f - SN_{eff}}{a_{OL}} \tag{3}$$

where:
h_{OL} = Required thickness of asphalt overlay,
SN_{OL} = Required structural number of asphalt overlay,
a_{OL} = Structural layer coefficient of asphalt overlay,
SN_f = Structural number required to carry future traffic; and
SN_{eff} = Total effective structural number of the existing pavement prior to overlay.

The design subgrade resilient Modulus (M_R value) was obtained from FWD measurements based on back-calculation analysis. The effective structural number (SN_{eff}) was obtained using the AASHTO residual life method [8].

3.2 *Asphalt mix design and laboratory testing*

The original and existing PVMNT structures were designed based on the South African standards and codes of practice [9]. Five asphalt mixes were prepared for use on each delineated PVMNT sections as seen in Table 1 and the SuperPave mix-design method was used to characterize the volumetric and engineering properties of the mixes. Laboratory tests on asphalt mixes that provided elastic- and viscoelastic-plastic properties included dynamic modulus (|E^*|) [10], repeated load testing, flow number (F_N), and static creep—flow time (F_t) [11]. Dynamic modulus test was performed on the overlay mixes to obtain the modulus parameters for the surfacing course material that was used in the analysis for the models. For the creep model, dynamic and static creep compliance tests were performed to obtain the flow number and flow time respectively for determining creep model parameters (*A, n,* and *m*).

Table 1. Basic material characteristics for the asphalt mixes.

PVMNT section	A	B	C	D & E
Chainages (km)	7.16–7.5	9.9–13.8	16.8–18.75	21.75–24.2
Binder type	60/70	PG64-22	PG70-22	PG58-40
Filler additive	Limestone	Portland cement	Hydrated lime	Limestone
Sample type	Core	Loose mix	Loose mix	Loose mix
Polymer modified	No	No	Yes	Yes
Paving date	May-09	May-09	Jun-09	Jun-09
Nominal aggregates size (mm)	19.0	12.5	12.5	12.5
N_{design}	100	75	100	100
AS—constructed volumetric properties				
AC (%)	5.61	5.2	5.3	5.4
AV@N_{design} (%)	4.08	3.33	4.4	4.4
VMA	18.4	15.8	18.862	17.4
VFA	55.2	59.1	51.8	57.1
%G_{mm}@N_{ini}	88.2	88.8	85.4	85.5
%G_{mm}@N_{des}	96.1	95.6		
%G_{mm}@N_{max}	97.2	99.9	97.2	97.3
In-situ AV (%)	6.00 ± 0.5	6.75 ± 0.5	9.38 ± 0.5	7.00 ± 0.5

The Frequency sweep at constant height test was performed to obtain the dynamic shear moduli (*G*, G'* and *G''*) and bulk moduli (*K*, K', K'')* as input parameters for the viscoelastic model.

Dynamic modulus for each mix was determined by conducting the test at two temperatures, thus 20 °C and 35 °C each at 0.1, 0.5, 1.5, 10, and 25 Hz frequencies, respectively and then generating $|E^*|$ master-curves at 35 °C as a reference temperature that is representative of the Zambian summer high temperature regime when asphalt PD and rutting are more critical. The shift factors were determined using a sigmoidal function [12]. Equation 4 shows the sigmoid function (master curve—fit equation) that was used in this study.

$$\log|E^*| = \delta + \frac{\alpha}{1 + e^{\beta - \gamma(\log(f_r) + S_T)}} \tag{4}$$

where:
$|E^*|$ = Dynamic modulus,
δ = Minimum modulus value,
$\delta + \alpha$ = Maximum value of $|E^*|$
β and γ = Sigmoid function fitting parameters
f_r = Reduced frequency at the reference temperature
S_T = Shift factors

The reduced frequency was computed using the equation below;

$$\log f_r = \log f + \frac{\Delta E_a}{19.14714}\left(\frac{1}{T} - \frac{1}{T_r}\right) \tag{5}$$

where:
f_r = Reduced frequency at the reference temperature
f = Loading frequency at the test temperature;
T_r = Reference temperature in °K;
T = Test temperature in °K;
ΔE_a = Activation energy (treated as a fitting parameter)

The temperature shift factors are given by Eq.(7).

$$\log a(T) = \frac{\Delta E_a}{19.14714}\left(\frac{1}{T} - \frac{1}{T_r}\right) \tag{6}$$

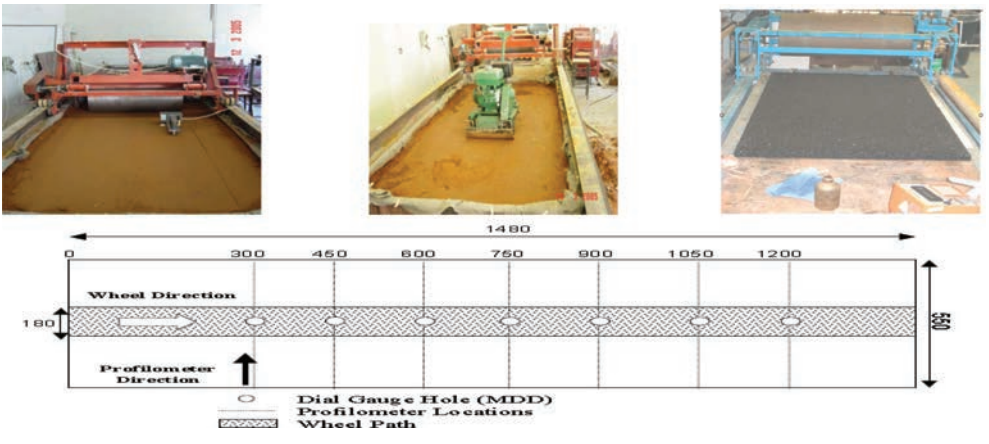

Figure 2. Schematic of PVMNT test preparation and profile marking.

where:
a(T) = Shift factor at temperature T,
T_r, T and ΔE_a = as defined in Equation 4 and 5

3.3 *Accelerated third-scale mobile load simulator (MLS3) testing*

A model mobile load simulator MLS3 (MMLS3) is a one-third scale of a full scale APT machine with the potential to test the effect of different environmental impacts to rutting such as temperature under wet and dry conditions [13]. It can be applied both in the laboratory and in the field. The MMLS3 consists of four axles, each with a 300 mm diameter inflated pneumatic wheel, circulating in a vertical closed loop. The nominal wheel speed is 2.5 m/s resulting in 7200 wheel loadings per hour. Slower speeds can be selected if desired. A series of accelerated load testing on laboratory scaled pavement sections were carried out and rut depth was recorded at profilemeter gauge positions of every 1000 incremental load applications under a one-third scaled value of the actual truck wheel. The tyre pressure was set at 750 kPa at a wheel load of 2.9 kN and temperature of 25 °C in conformity with the average HMA test temperature during the period of conducting the deflection tests on in service pavements.

3.3.1 *Test protocol*

The test method includes pre-conditioning of the laboratory scaled pavement test sections at the predetermined test temperature and measuring a set of cross section profiles before the MMLS3 is moved into position. Trafficking is applied to the pavement while maintaining the test temperature. At predetermined intervals the loading is stopped and cross-section profiles measured. After a predetermined number of repetitions the loading is terminated and a total depth of rutting is reported.

4 FINITE ELEMENT (FE) PROBLEM FORMULATION

Three models in ABAQUS Version 6.10 were selected; namely, creep, elasto-visco-plastic, and viscoelastic. The model selection criteria were based on the ability to conduct material characterization tests for the required input data. The PVMT configuration and boundary conditions adapted are shown in Figure 3. Representative PVMNT sections and material parameter models used in each FE analysis are shown in Table 2.

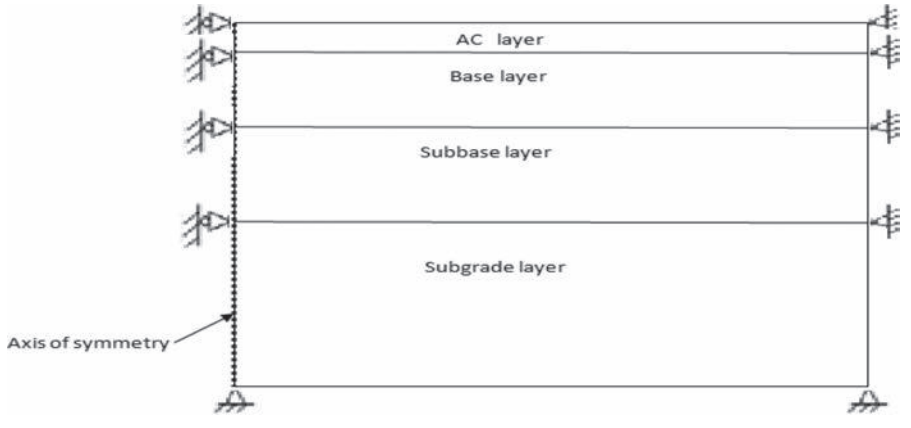

Figure 3. PVMNT configuration and boundary conditions for abaqus analysis.

Table 2. Finite element model and PVMT sections parameters.

Overlay mix type				A	B	C	D	E
Section Chainages (km)				7.16-7.5	9.9-13.5	16.8-18.7	21.8-24.2	36.7-38.5
Thickness of pavement layers (mm)	100mm			65mm	55mm	80mm	80mm	80mm
	200mm			180 mm	185 mm	175 mm	165 mm	165 mm
	300mm			190 mm	230 mm	230 mm	210 mm	210 mm
	400mm							
	500mm							
Material models parameters from experimental tests conducted at 35°C reference temperature								
Overlay asphalt hot mix material properties for modeling rutting	AC modulus (MPa)			3115	1619	2410	2437	1494
	Poisson ratio			0.35	0.35	0.35	0.35	0.35
	Creep model parameters		A	$1*10^{-9}$	$5*10^{-9}$	$4.5*10^{-9}$	$5*10^{-9}$	$6*10^{-9}$
			n	0.67	0.56	0.5	0.6	0.8
			m	-0.5	-0.5	-0.5	-0.5	-0.5
	Viscoelastic model parameters		K^*	1444.01	717.37	1304.28	1325.4	849.21
			K	1237.76	581.3	1010.83	976.4	684.0
			K''	946.82	518.1	781.08	919.3	566.0
	Elasto-visco-plastic	Type of analysis: Viscous	A	3*10-6	6*10-6	6.2*10-6	1*10-5	-
			n	0.7	0.7	0.7	1	-
			m	-0.5	-0.5	-0.5	-0.5	-
			f	0.5	0.5	0.5	0.5	-
		Plastic	σ_y	1434	1145.5	2110	1439	665.7
			γ	0.03013	0.0252	0.0254	0.0313	0.0381
FWD test results conducted at 25°C average HMA temperature								
Base layer	Elastic modulus(MPa)			1241	1250	1613	1127	1127
	Poisson ratio			0.4	0.4	0.4	0.4	0.4
Subbase layer	Elastic modulus(MPa)			305	542	331	200	220
	Poisson ratio			0.45	0.45	0.45	0.45	0.45
Subgrade layer	Elastic modulus(MPa)			257	309	292	157	180
	Poisson ratio			0.45	0.45	0.45	0.45	0.45
LEGEND				Hot mix asphalt (Overlay				
				Crushed stone base/dense macadam				
				Cement stabilized gravel				
				Unbound gravel fil				
				In-situ subgrade/selected fill				

5 RESULTS, ANALYSIS, AND DISCUSSIONS

PD prediction models implementation in ABAQUS showed that the viscoelastic model could not capture the PD response characteristics. The displacements measured were too small (2*E-11 mm) in magnitude, which can be considered negligible. Two models, the creep and elasto-visco-plastic, were able to capture the PD response characteristics of

Table 3. FE model and MLS3 results with mix ranking.

Elasto-visco—plastic model					Creep model			
Mix/ PVMT Id.	Load repetitions x1000	Permanent deformation (mm)	Rank	MLS3 (mm)	Mix/ PVMT Id.	Load repetitions x1000	Permanent deformation (mm)	Rank
A	300	6.23	3	7.18	A	300	6.84	4
B	300	5.54	2	6.02	B	300	5.79	2
C	300	3.49	1	4.45	C	300	2.81	1
D	300	7.32	4	8.50	D	300	6.17	3
E	300	10.1	5	14.0	E	300	12.3	5

the asphalt (AC) mixes. A linear formulation was subsequently used to predict the evolution of PD in the asphalt mixes. Ranking of the models for each asphalt mix is shown in Table 3 including comparisons of the models to the MLS3 results.

It can be seen from Table 3 that the two model predictions are very close to each other due to the complementary creep compliance found in both PD models. The APT prediction from the MLS3 is also comparable to the analytical model PD predictions, albeit that its PD values are about 5% higher than the analytical PD values. Overall, the results from laboratory testing, field FWD testing, APT, and numerical modeling were plausible and substantiated the significance of local temperature normalization of the FWD deflection measurements.

6 CONCLUSIONS

In-situ material tests were conducted using NDT techniques (i.e., FWD) to design overlay mixes. Laboratory tests were performed on the overlay mixes to generate model input parameters needed for FE ABAQUS analysis. In order to validate the models, APT trafficking with the MLS3 were performed on the scaled laboratory constructed PVMNT sections to further compare the PD performance of the five Overlay (AC) mixes. From the results and study findings, the following conclusions were drawn:

- The two models, *creep and elasto-visco-plastic*, predicted a total PD that is close to the APT (MLS3) measured values; hence, the models are considered reliable with modifications as suggested in this paper.
- The FWD tests provided reliable information for the PVMNT layer moduli values that can be used for PD analysis in ABAQUS.
- It has been demonstrated that back-calculation techniques in ELMOD software need temperature correction factors that are project specific to achieve reliable and representative PD predictions.
- Asphalt mixes were ranked for their PD and rutting performance; therefore, calibration of the rutting models can be carried out based on APT in the field or lab as well as observation of rutting performance in service.

ACKNOWLEDGMENTS AND DISCLAIMER

Part of the work presented in this paper was extracted from the primary author's PhD. Degree study thesis in China at Chang'an University. Special thanks go to the co-authors and the literature provided in support of this manuscript. This research was supported by the funds from the Natural Science Fund Committee (NSFC) of China (No. 50808023), (No. 51011120574) and the Special Fund for Basic Scientific Research of Central Colleges, Chang'an University (CHD2010JC061).

The contents of this paper reflect the views of the authors who are responsible for the facts and accuracy of the data presented herein and do not necessarily reflect the official views or policies of any agency or institute. This paper does not constitute a standard, specification, nor is it intended for design, construction, bidding, contracting, or permit purposes. Trade names were used solely for information and not for product endorsement.

REFERENCES

[1] Zambian Roads. "A Guide to the design of road pavements (Final Draft)." *A Roads Department Publication*, Lusaka, Zambia: pp 23–30. 1999.

[2] Yang H. Huang. Pavement analysis and design (2nd edition). Pearson Prentice Hall, Upper Saddle River, NJ07458. pp. 12–40. 2004.

[3] B. Choubane and R.L. McNamara. A practical approach to predicting subgrade moduli using falling weight deflectometer (FWD) data. Florida Dept. of Transportation: pp. 123–139. 2000.

[4] Alexander K. Appea. Validation of FWD Testing Results at the Virginia Smart Road: Theoretically and by Instrument Responses. "*PhD Dissertation*," Virginia Polytechnic Institute and State University, Blacksburg, Virginia. pp. 122–130. 2003.

[5] Aaron, D. Mwanza. Modeling of Rutting Prediction for Flexible Pavements in Zambia. "*PhD Dissertation,*" Chang'an University, Xi'an, China. pp. 118–230. 2013.

[6] P. Ullidtz N.F. Coetzee. Analytical procedures in Nondestructive Testing pavement evaluation and ELMOD 5 procedures. "*Transportation Research Record,*" No. 1482, Transportation Research Board. pp. 32–56. 1995.

[7] Wu, Chen, Garspard and Zhang. Structural Overlay Design of Flexible Pavement by Nondestructive Test Methods in Louisiana. "*87th Transportation Research Board Annual Meeting.*" Washington, D.C. pp. 7–9. 2008.

[8] American Association of State Highway and Transportation Officials (AASHTO). AASHTO Guide for Design of Pavement Structures. Washington, D.C. pp. 278–285. 1993.

[9] Southern Africa Transport and Communications Commission (SATCC). Draft Code of Practice for the Design of Road Pavements, Pretoria, South Africa: pp. 8–56. 1998.

[10] American Association of State Highway and Transportation Officials AASHTO:TP62-03. Standard Method of Test for Determining Dynamic Modulus of Hot-Mix Asphalt Concrete Mixtures. Washington, D.C. pp. 15–28. 2003.

[11] American Association of State Highway and Transportation Officials AASHTO T320-03. Standard Method of Test for Determining the Permanent Shear Strain and Stiffness of Asphalt Mixtures Using the Superpave Shear Tester (SST). Washington, D.C. pp. 3–10. 2007.

[12] Pellinen, T.K., M.W. Witczak and R.F. Bonaquist. Asphalt mix master curve construction using sigmoidal fitting function with non-linear optimization. "*American Society of Civil Engineers*," Reston, VA 20191-4400, United States: pp. 25–38. 2004.

[13] Yuchen Wang. Jan Grundling and Lizl Steynberg. Accelerating pavement testing for temperature changes and sustainability by model mobile load simulator (MMLS) in South Africa. "*The 16th Hong Kong Society for Transportation Studies (HKSTS) International Conference,*" Hong Kong, China. pp. 557–564. 2011.

[14] Asphalt Institute. Superpave mix design, Superpave Series No. 2 (SP-2). 2001.

[15] Shu Wei Goh. Development of Specifications for the Superpave Simple Performance Test. "*Master's Thesis,*" Michigan Technological University. pp. 13–26. 2009.

[16] Theyse, H.L., De Beer, M., Rust, F.C. Overview of South African mechanistic pavement design method. "*Transportation Research Record,*" No. 1539, Transportation Research Board. pp. 6–17. 1996.

[17] Park, D.W. Characterization of permanent deformation in asphalt concrete using a laboratory prediction method and an elastic visco plastic model. "*PhD Dissertation,*" Texas A&M University, College Station, Texas. pp. 134–158. 1996.

[18] Witczak, M.W., K. Kaloush, M. El-Basyouny and H.V. Quintus (2002). Simple Performance Test for Superpave Mix Design.

[19] Epps, A., Walubita, L.F. and Bangera, N.U. Pavement response and rutting for full-scale and scaled APT. "*Journal of Transportation Engineering,*" ASCE: pp. 451–461. 2003.

[20] Erkens, S.M.J.G., X. Liu and A. Scarpas. (2002). "3D Finite element model for asphalt concrete response simulation. "*International Journal of Geomechanics,*" ASCE, V2(3): pp. 305–330. 2002.

This page intentionally left blank

Asphalt Pavements – Kim (Ed)
© 2014 Taylor & Francis Group, London, ISBN 978-1-138-02693-3

Evaluation of low temperature stability of bitumen and hot mix asphalt pavement

Bagdat Teltayev, Yevgenya Kaganovich & Yerick Amirbayev
JSC "Kazakhstan Highway Research Institute", Almaty, Kazakhstan

ABSTRACT: Evaluation of low temperature stability of bitumen and hot mix asphalt pavement is actual in conditions of sharp continental climate of Kazakhstan.

In this paper low temperature stability of bitumen of grades BND 60-90 (BND means an oil road bitumen) and BND 90-130 has been carried out by testing on Bending Beam Rheometer (BBR) under Superpave method. Low temperature stability of hot mix asphalt pavement has been carried out by method based on integral equation of theory of linear viscoelasticity and applying tensile strength of hot mix asphalt.

The results of testing on BBR have shown that bitumen of grades BND 60-90 and BND 90–130 meet the requirements of Superpave specifications up to –39°C and –42°C respectively, which does not correspond to reality. Low temperature cracks on hot mix asphalt pavement occur during first years of operation and in future the distances between them reduce. In 3–5 years the distances between low temperature cracks on hot mix asphalt pavement correspond to 10–70 m.

Evaluation of low temperature stability of hot mix asphalt pavement considering volumetric indices and viscoelastic properties of hot mix asphalt and conditions of temperature falling has shown that such characteristics as cooling start temperature and cooling rate influence greatly over cracking of pavement. Unfavorable one is complex of high cooling start temperature and high cooling rate. Depending on cooling start temperature and cooling rate the first low temperature cracks can occur at the temperature of –1 to –24°C, which is close to reality.

Keywords: Bitumen, superpave, hot mix asphalt, low temperature cracking

1 INTRODUCTION

Study of low temperature stability of bitumen in sharp continental climatic conditions of Kazakhstan is actual due to the provision of stability to low temperature cracking of hot mix asphalt pavement.

Analysis of climatic characteristics of northern part of the Republic has shown that practically every year in winter months air temperature falls below –40°C several times. There are considerable differences not only in values of minimum temperature in regions, but also in character of temperature falling during cold season and its vaiations. Thus, for Astana city duration of temperature falls in winter season for 65% of measurements corresponds to 12–18 hours, temperature falling rate in 20% of measurements is more than 1.0°C per hour with maximum in 1.9°C per hour. It is obvious that such climatic characteristics influence greatly over low temperature stability of bitumen and hot mix asphalt pavement.

In this paper low temperature stability of bitumen of grades BND 60-90 and BND 90-130 of Pavlodar plant, which often has been applied in northern part of the country, has been determined by testing on BBR under Superpave method.

Evaluation of hot mix asphalt pavement temperature cracking stability has been carried out by method, based on integral equation of theory of linear viscoelasticity and using hot mix asphalt tensile strength.

2 MATERIALS APPLIED

In this paper bitumens of grades BND 60-90 and BND 90-130 have been used, meeting the requirements of Kazakhstan standard ST RK 1773-2005. Basic standard indices of the bitumens have been shown in the Table 1. The bitumens have been produced by Pavlodar plant from crude oil of Western Siberia (Russia) by direct oxidation.

Porous hot mix asphalt of type B under standard of Kazakhstan ST RK 1225-2003 has been prepared with the use of aggregate of fractions 5–10 mm (20%), 10–15 mm (13%), 15–20 mm (10%) from Novo-Alekseevsk rock pit (Almaty Oblast), sand fraction 0–5 mm (50%) from the plant "Asphaltconcrete-1" (Almaty city) and mineral powder (7%) from Kordai rock pit (Zhambyl Oblast). Content of bitumen of grade BND 90-130 in hot mix asphalt is 4.8% by weight of dry mineral material. Basic standard indices of aggregate and hot mix asphalt have been shown in the Tables 2 and 3 respectively. The grading curve of mineral part of hot mix asphalt has been shown in Figure 1. In this figure, lower and upper permissible limits of the passing of particles are designated by bold lines. As it is seen, grain composition of the hot mix asphalt meets the requirements.

3 LOW TEMPERATURE STABILITY FOR BITUMEN

The indices for low temperature stability of bitumen–creep stiffness (S) and the indicator, characterizing stress relaxation rate (m-value) of bitumen have been determined by testing on BBR at temperatures –18, –24, –30 and –36°C under standard ASTM D 6648-08 after double aging of bitumen under standards ASTM D 2872-08 and ASTM D 6521-08. The device has been produced by the company ATS (Applied Test Systems Inc., USA).

Table 1. Basic standard indices of bitumen.

Indice	Measurement unit	Requirements of ST RK 1773-2005		Value	
		BND 60-90	BND 90-130	BND 60-90	BND 90-130
Penetration, 25 °C, 100 gr, 5 s	0.1 mm	61–90	91–130	69	98
Penetration index PI	–	–1,0 … +1,0	–1,0 … +1,0	–0,26	–0,96
Ductility:	cm				
– 25°C		≥ 131	≥ 65	55	139
– 0°C		≥ 4,5	≥ 4,0	3,5	5,5
Softening point	°C	≥ 47	≥ 43	50,8	45,3
Fraas point	°C	≥ –18	≤ –20	–22,2	–24,6
Dynamic viscosity, 60°C	Pa · c	≥ 75	≥ 75	393,1	174,2
Cinematic viscosity	mm^2/s	≥ 230	≥ 180	593,0	409,0

Table 2. Basic standard indices of aggregate.

Indice	Measurement unit	Requirements of ST RK 1284-2004	Value	
			Fraction 5–10 mm	Fraction 10–20 mm
Average density	g/cm^3	–	2.55	2.62
Elongated particle content	%	≤ 25	13	9
Clay particle content	%	≤ 1.0	0.3	0.2
Bitumen adhesion	–	–	Satisf.	Satisf.
Water absorption	%	–	1.93	0.90

Table 3. Basic standard indices of hot mix asphalt.

Indice	Measurement unit	Requirements of ST RK 1773-2005	Value
Average density	g/cm^3	–	2.39
Water saturation	%	1.5–4.0	2.3
Voids in mineral aggregate	%	≤ 19	14
Air void content in hot mix asphalt	%	2.5–5.0	3.8
Compression strength:	MPa		
– 0°C		≤ 13.0	7.3
– 20°C		≥ 2.5	3.4
– 50°C		≥ 1.3	7.3
Water stability	–	≥ 0.85	0.92
Shear stability	MPa	≥ 0.38	0.40
Crack stability	MPa	4.0–6.5	4.1

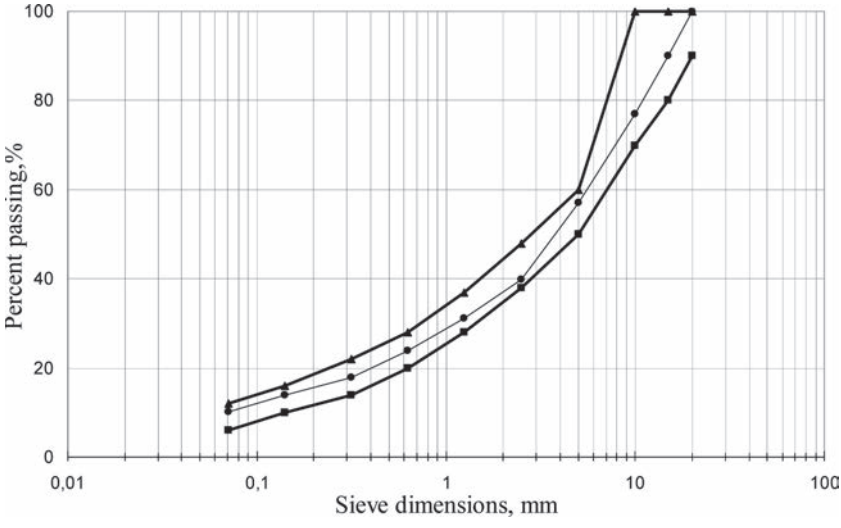

Figure 1. Asphalt mixture grading curve.

Sample of bitumen in the form of beam with dimensions 125 × 12.5 × 6.35 mm has been tested by applying load of 100 g (980 mN) to the center of the sample. Deflection of the center of the beam has been measured at 8, 15, 30, 60, 120 and 240 s. Stiffness has been calculated by Eq. (1):

$$S(t) = \frac{PL^3}{4bh^3\delta(t)'} \quad (1)$$

where, S(t)—stiffness at load time t;
P—applied load;
L—length of beam span;
b, h—width and height of beam;
δ(t)—deflection of center of beam span at time t.

The results of testing for bitumen have been represented in Figures 2 and 3. Superpave specifications require bitumen stiffness at load duration for 60 s not to exceed 300 MPa at

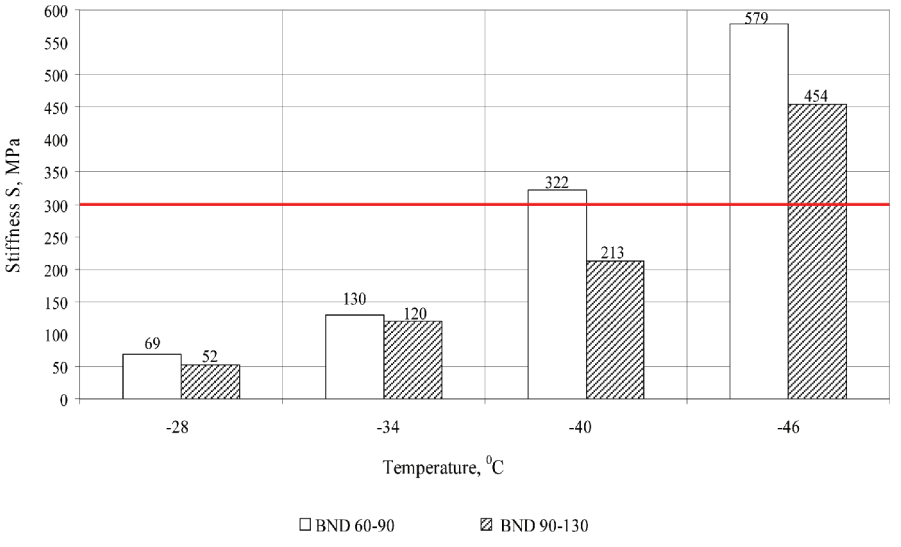

Figure 2. Bitumen stiffness at low temperatures.

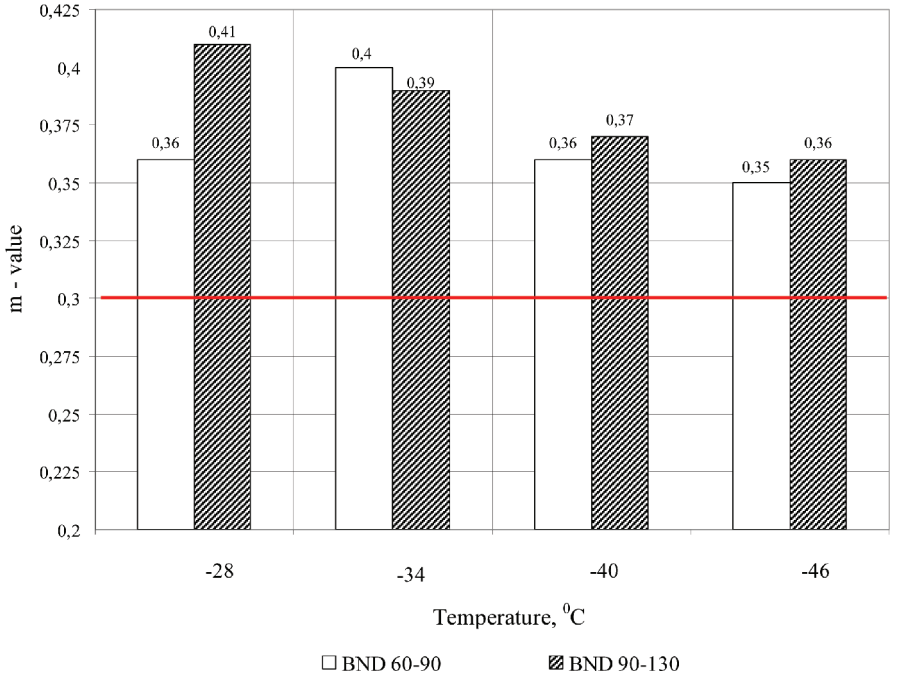

Figure 3. m-value for bitumen at low temperatures.

estimated minimum temperature, and m-value was not less than 0.3 [1]. We can note that except for bitumen of grade BND 60–90 at temperature –28°C, with temperature falling m-value decreases, but at all temperatures it exceeds minimum allowable value 0.3. As it could be expected, with temperature falling the bitumen stiffness increases. Bitumen of grade BND 60-90 meets the requirements of Superpave specifications up to –39°C inclusively, and BND 90-130—up to –42°C inclusively, which does not correspond to reality. Low temperature

cracks on hot mix asphalt pavement occur during first years of operation and in future the distances between them reduce. In 3–5 years the distances between low temperature cracks on hot mix asphalt pavement correspond to 10–70 m.

4 LOW TEMPERATURE CRACKING STABILITY OF HOT MIX ASPHALT PAVEMENT

4.1 *Calculation of temperature stress*

Road specialists believe that low temperature crack on hot mix asphalt pavement occur due to impossibility of free deformation of pavement in horizontal direction with temperature falling. Its neighboring sections hamper any section of continuous hot mix asphalt pavement to deform freely. Value of non-realized temperature deformation in hot mix asphalt pavement at time t one can determine under Eq. (2):

$$\varepsilon_T(t) = \alpha\left[T(t) - T_0\right], \tag{2}$$

where, α—linear temperature contraction coefficient of hot mix asphalt, 1/°C;
T_0—initial temperature, °C;
T(t)—temperature at time t.

Present paper considers hot mix asphalt pavement as infinite bar, lying on continuous homogeneous base, between which there is no friction. Temperature of hot mix asphalt pavement will be characterized by its value on the pavement surface, i.e. air temperature.

Temperature variation during time has been set by Eq. (3):

$$T(t) = T_0 - \frac{1}{3600} \cdot k \cdot t, \tag{3}$$

where, k—temperature falling (cooling) rate, °C/h;
t—time, s.

Hot mix asphalt is a typical viscoelastic material, mechanical properties of which depend on load duration and temperature [2–4]. Therefore temperature stress in hot mix asphalt pavement can be determined by the following integral equation of theory of linear viscoelasticity [5], i.e. Eq. (4):

$$\sigma_T(t) = \int_0^t E(t-\tau)d\varepsilon_T(\tau), \tag{4}$$

where, E(t)—hot mix asphalt relaxation function;
t—time, at which stress $\sigma_T(t)$ has been calculated;
τ—parameter of integration;
$\varepsilon_T(\tau)$—non-realized temperature contraction in hot mix asphalt pavement.

Hot mix asphalt relaxation function has been described by the correlation model of M.W. Witczak [6] and has been shown in Figure 4.

4.2 *Calculation of low temperature cracking stability of hot mix asphalt pavement*

Considering that air temperature falling in the area of Astana city often starts at the temperature of –8 to –12°C, temperature stress in hot mix asphalt pavement has been calculated at the cooling rate of 0.4, 0.8, 1.2, 1.6 и 2.0°C/h, starting from the cooling start temperature of $T_0 = -10$°C. The results obtained have been shown in Figure 5. As it is obvious, temperature falling under linear law causes the increase of temperature stress in hot mix asphalt pavement under non-linear law at all the considered cooling rates. Dependence of temperature stress at various cooling rates from low temperature has been shown in Figure 6. On diagrams of

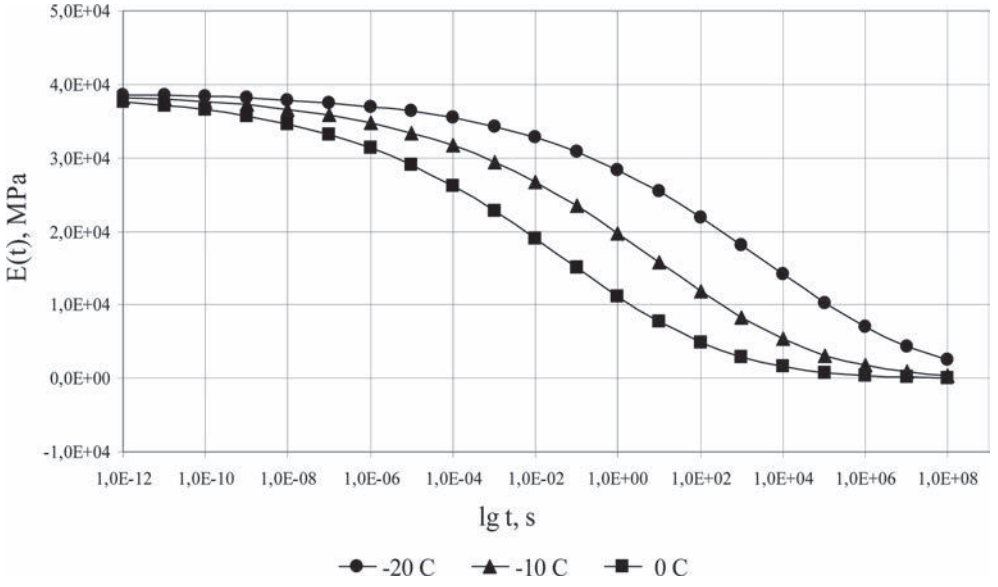

Figure 4. Hot mix asphalt relaxation function.

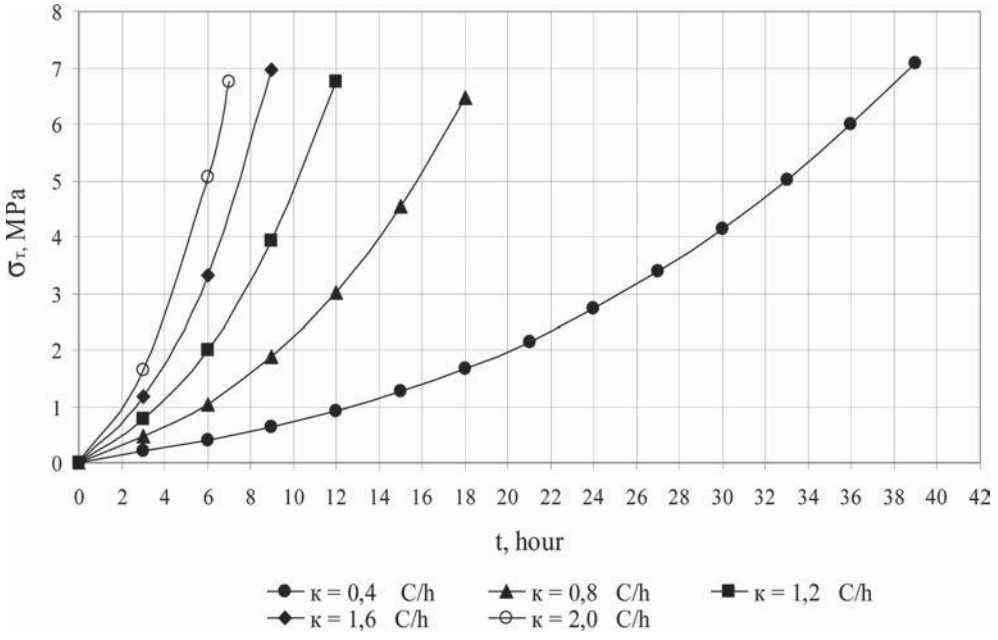

Figure 5. Temperature stress in hot mix asphalt pavement at cooling start temperature $T_0 = -10°C$.

this figure another diagram has been applied, showing the dependence of hot mix asphalt tensile strength on temperature R(T), which has been obtained by testing of samples in the form of beam with dimensions $40 \times 40 \times 160$ mm in special testing system TRAVIS under standard EN 12697-46. The device has been produced by the company InfraTest (Germany). Such combination of diagrams allows finding of important indices for cracking occurrence on hot mix asphalt pavement.

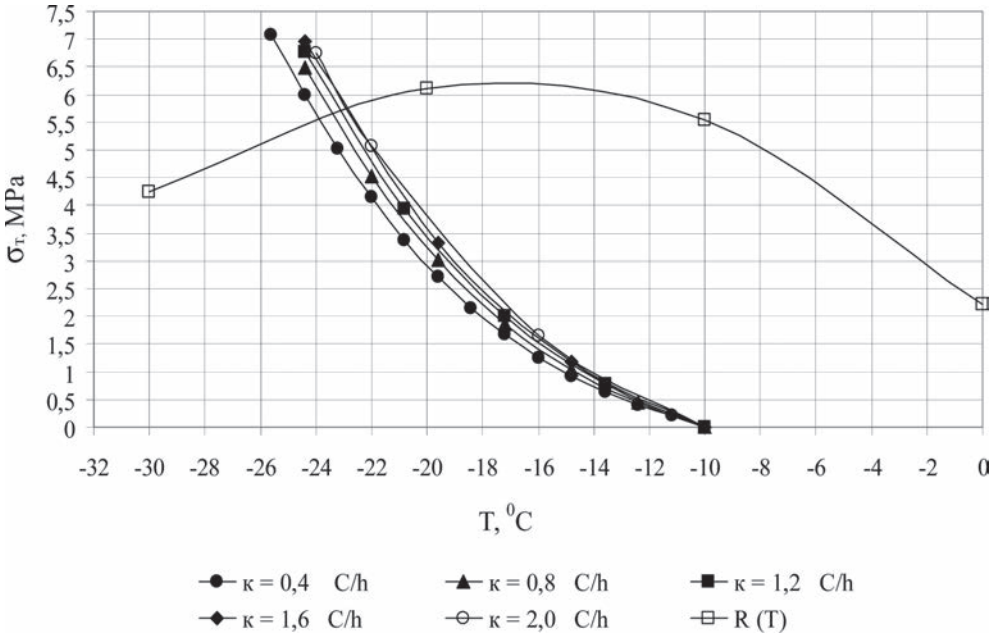

Figure 6. Combined diagrams of temperature stress in hot mix asphalt pavement at cooling start temperature $T_0 = -10$°C and tensile strength of hot mix asphalt.

Thus, dropping vertical line from cross point of diagrams, on horizontal axis one can find critical temperature T_{cr}, when low temperature cracks occur on pavement. Drawing horizontal line from cross point of diagrams, one can determine critical stress σ_{cr} on vertical axis, when low temperature cracks occur. Knowing values of critical stress, from diagram of Figure 5 one can determine values for critical time t_{cr} at various cooling rates. Critical time shows in what time since the commencement of low temperature crack occurs in pavement.

Obtained by the above methods the values of critical time, critical temperature and critical stress have been represented in the Table 4. Data of this Table show that critical time considerably depends on temperature falling rate. At low cooling rates occurrence of low temperature cracks on pavement has been expected after expiring of long time, and at high cooling rates the cracks can occur in relatively short time. Thus, at k = 0.4°C/h occurrence of low temperature crack can be expected approximately in 34 hours, and at k = 2.0°C/h—in 6 hours.

It has been found that critical temperature and critical stress at considered cooling start temperature and accepted hot mix asphalt do not practically depend on cooling rate: $T_{cr} = -23$ to −24°C, σ_{cr} = 5.5–5.8 MPa. In other words, regardless of rate and duration of cooling the first low temperature cracks on hot mix asphalt pavement can occur at temperature range of −23 to −24°C.

It has been found that in the considered climatic area at high rates of air cooling (for example at κ = 1.0°C/h) temperature falling starts from the temperature of $T_0 = -3$ to −10°C, and at low rates of cooling (for example at κ = 0.4°C/h)—from the startt temperature of $T_0 = +1$ to −20°C. Considering that further evaluations of low temperature cracking stability for hot mix asphalt pavement have been carried out at two cooling rates (κ = 0.4 and 1.0°C/h) and at three values of cooling start temperature ($T_0 = 0, -10, -20$°C). Specific values of critical time, critical temperature and critical stress obtained have been shown in Table 5. The results of analysis for the data of the Table have shown that cooling start temperature influences greatly over cracking stability of pavement. The increase of cooling start temperature provides the increase of critical time, critical stress and critical temperature. And reduce of cooling start temperature causes opposite phenomena: critical time and critical stress reduce, and critical

Table 4. Critical time, critical temperature and critical stress at cooling start temperature $T_0 = -10$°C.

Temperature falling rate κ,°C	Critical time t_{cr}, h	Critical temperature, T_{cr},°C	Critical stress, σ_{cr}, MPa
0.4	33.8	–24.0	5.5
0.8	16.5	–23.6	5.6
1.2	10.8	–23.4	5.7
1.6	7.2	–23.2	5.8
2.0	6.4	–23.0	5.8

Table 5. Critical time, critical temperature and critical stress at various cooling rates and cooling start temperatures.

Cooling rate κ,°C/h	Cooling start temperature T_0,°C	Critical time t_{cr}, h	Critical temperature T_{cr},°C	Critical stress σ_{cr}, MPa
0.4	0	52.0	–21.0	6.0
	–10	34.5	–24.0	5.6
	–20	19.5	–28.0	4.6
1.0	0	17.5	–17.5	6.2
	–10	13.0	–23.4	5.6

temperature falls. For example, in the case of increasing of cooling start temperature from –20°C to 0°C critical time increases 2.7 times, critical stress increases for 1.4 MPa, and critical temperature increases for 7°C. It has been found out that from the point of view for provision of temperature cracking stability for pavement, combination of high cooling start temperature and high cooling rate is unfavorable one. Thus, at cooling start temperature $T_0 = 0$°C and cooling rate $\kappa = 1.0$°C/h critical temperature is equal to –17°C.

5 CONCLUSIONS

The results of hot mix asphalt pavement low temperature stability evaluation obtained in this work allow making conclusions as follows:

1. Method, which uses integral equation of linear viscoelasticity theory and hot mix asphalt tensile strength, allows considering the hot mix asphalt properties, including bitumen properties, as well as conditions of cooling while evaluation of hot mix asphalt pavement low temperature cracking stability. With the help of this method one can determine important values of low temperature cracking stability of pavement—critical time, critical temperature and critical stress.
2. In those cases when cooling starts from similar initial temperature, equal to –10°C, without dependence on rate and duration of cooling, the first low temperature cracks on pavement can occur at the temperature range of –23 to –24°C.
3. Cooling start temperature influences greatly on temperature cracking stability of pavement. Its increase causes the increase of critical time and critical stress, as well as the increase of critical temperature.
4. From the point of view for provision of low temperature cracking stability of pavement combination of high cooling start temperature and high cooling rate is unfavorable one. Calculations show that in case of cooling from the temperature of 0°C and at cooling rate of 1.0°C/h the first low temperature cracks on pavement can occur at the temperature of –17°C.

REFERENCES

[1] Performance Graded Asphalt Binder Specification and Testing. Superpave Series No. 1. Asphalt Institute, 1999.

[2] Huang Y.H. Pavement Analysis and Design. Second Edition, 775 p., Pearson Education Inc., New Jersey. 2004.

[3] Papagiannakis A.T. and Masad E.A. Pavement Design and Materials, 542 p., John Wiley & Sons, Inc. New Jersey. 2008.

[4] Yoder E.J. and Witczak M.W. Principles of Pavement Design, 736 p., John Wiley & Sons, Inc., New Jersey. 1975.

[5] Tschoegl N.W. The Phenomenological Theory of Linear Viscoelastic Behavior. An Introduction, 769 p., Springer-Verlag, Berlin, 1989.

[6] ARA Inc., ERES Consultants Division. Guide for Mechanistic-Empirical Design of New and Rehabilitated Pavement Structures. Final Report. NCHRP Project 1-37 A. Transportation Research Board of the National Academies, Washington, D.C., 2004.

This page intentionally left blank

Asphalt Pavements – Kim (Ed)
© 2014 Taylor & Francis Group, London, ISBN 978-1-138-02693-3

Development of field-calibrated master curves for in-place modulus

Mary Robbins
National Center for Asphalt Technology at Auburn University, Auburn, AL, USA

David Timm
Auburn University, Auburn, AL, USA

ABSTRACT: This study developed a method for estimating in-place modulus of Asphalt Concrete (AC) by developing a master curve calibrated to strains measured at the National Center for Asphalt Technology Pavement Test Track. This innovative approach utilizes parameters that can be measured directly in the field, eliminating the need for a time-frequency conversion, a topic that has been heavily debated. Unlike dynamic modulus master curves that are reliant on testing frequencies and temperatures, the field-calibrated master curves developed in this study were constructed with vehicle speed and mid-depth pavement temperature, thereby more accurately representing field conditions of in-place AC modulus. Field-calibrated master curves were constructed for fourteen sections from the 2006 and 2009 research cycles utilizing strain measurements under heavy trucks. Although these trucks operate at a target speed of 45 mph (72.4 km/h), 95% of the speeds measured ranged from 42 to 52 mph (67.6–83.7 km/h). These master curves were found to accurately predict in-place modulus with coefficients of determination, R^2, ranging from 0.82 to 0.98. When applied to strains under much slower speeds (14–33 mph (22.5–53.1 km/h)), the field-calibrated master curve resulted in an R^2 of 0.97, indicating that this procedure is applicable at a wider range of vehicle speeds.

Keywords: Pavement design, pavement analysis, mechanistic-empirical, material characterization

1 INTRODUCTION

Pavement design has progressed over the years into the more robust and adaptable Mechanistic-Empirical (M-E) design framework. Central to M-E design is dynamic modulus (|E*|) of Asphalt Concrete (AC) which enables the prediction of critical stresses and strains within the pavement that are used to predict specific distresses. |E*| captures the viscoelastic nature of AC through its dependency on both temperature and frequency (time) and is meant to characterize how a particular mixture is likely to respond to a moving load under varying pavement temperatures and vehicle speeds in the field. |E*| can be determined in the laboratory through the application of sinusoidal compressive stress pulses applied at varying frequencies and temperatures. Although |E*| is measured at a wide range of frequencies and temperatures, it is difficult to capture the entire range of pavement temperatures a pavement may experience in-service, therefore master curves are constructed to enable the prediction of |E*| at any frequency (speed) and temperature.

As states look to adopt recently developed M-E design frameworks such as the Mechanistic-Empirical Pavement Design Guide (MEPDG) and the associated AASHTOWare® Pavement ME Design software, it is important to understand how the prediction of critical distresses compares to field performance. Because tensile strain is dictated by |E*|, it is necessary to investigate how |E*| relates to field conditions. To translate |E*| to field conditions

requires loading, frequency, and temperature to be accurately defined in the field. With this several challenges arise; frequency is difficult to measure in the field and furthermore, the testing parameters (loading and induced strain) in the laboratory differ from field conditions. Loading frequency is challenging, if not impossible, to measure in the field. However, loading frequency is necessary to capture the viscoelastic effect of truck speed on AC modulus. As a result, researchers have relied on time-frequency relationships to provide frequency since loading time can be measured from stress or strain pulses under traffic loading. Although time can be measured from either strain gauge responses or pressure plates embedded in the pavement, there has been disagreement on the definition of loading time.

|E*| testing in the laboratory includes the application of the compressive load pulses in a continuous fashion for each frequency tested, however, load pulses are not continuous in the field due to axle configurations and vehicle spacing. Furthermore, |E*| testing is completed at a range of frequencies; however, in the field, load is applied at a range of vehicle speeds. To translate laboratory conditions to field conditions would require the time of loading be determined in the field and converted to loading frequency. The proposed time-frequency relationship utilized in the MEPDG is simply $t = 1/f$, where f is loading frequency and t is loading time [1]. Some researchers propose that the correct conversion is $1/(2\pi f)$ based on the field of rheology [2–4], while others suggest alternative relationships [5–8].

An alternative to |E*| testing to characterize the AC modulus is to backcalculate moduli from deflections measured with a Falling Weight Deflectometer (FWD). Although FWD testing is a relatively quick way to assess the in-situ material properties and condition of the pavement layers, it is similar to |E*| testing in that FWD testing does not accurately represent traffic loading. Rather than applying a dynamic load similar to a truck traveling at highway speeds, FWD testing is completed with an impact load. Research at the National Center for Asphalt Technology (NCAT) Test Track has shown that the impact load applied during FWD testing is more representative of a truck traveling at 120 mph (193.1 km/h) [9].

In a recent study [10], a master curve was constructed for in-situ AC modulus considering vehicle speed and temperature. This study utilized backcalculated moduli from FWD to adjust dynamic modulus for damage. Although vehicle speed was considered, it was done by developing loading frequency-vehicle speed relationships which incorporated the $t = 1/f$ relationship to convert measured load durations into frequency at various vehicle speeds [10]. A previous study at the NCAT Test Track found that when this time-frequency conversion was used, an underprediction of strain relative to field measured strain resulted [11]. Therefore, there is a need to develop a method that predicts AC modulus directly from field conditions to more closely match strains measured in the field.

2 OBJECTIVES AND SCOPE

The primary objective of this study was to develop a method to construct master curves for in-place composite AC modulus calibrated to field measured strain, using vehicle speed and pavement temperatures.

To meet this objective, strain measurements were made under heavy loading in fourteen instrumented test sections at the National Center for Asphalt Technology (NCAT) Test Track. Mid-depth pavement temperature and actual vehicle speed was recorded at the time of each strain measurement. Additionally, in-place volumetrics were determined based on as-built properties at the time of construction. A Layered Elastic Analysis (LEA) program, WESLEA, was utilized to determine the in-place composite AC modulus that corresponded to tensile strain measurements in each test section.

3 METHODOLOGY

To develop master curves for in-place AC modulus, AC moduli were determined based on measured tensile strain. Tensile strain was measured at the bottom of the AC in fourteen

instrumented pavements. Using field measured strain, the modulus of the entire AC layer (as a composite of the individual AC layers) was determined based on a layered elastic analysis unique to each section using WESLEA. Since it has been well-established that strain is influenced by vehicle speed and pavement temperature, the AC modulus required to achieve that strain should reflect the field conditions at which the strain was measured. To do so, an AC modulus master curve calibrated to field conditions and field-measured strain was created for each test section. This was done by applying a sigmoidal fit function, consistent with the form described in AASHTO PP 61-09 for creating dynamic modulus master curves using vehicle speed (mph) rather than testing frequency (Hz) and mid-depth pavement temperature, to the moduli required to achieve the strain measured in the field.

3.1 *Test sections*

A total of fourteen instrumented test sections from the 2006 and 2009 test cycles at the NCAT Test Track were used to complete this study. The NCAT Test Track is a 1.7 mile (2.7 km) oval track located in Opelika, Alabama. Live traffic is applied at a target vehicle speed of 45 mph (72.4 km/h). Heavy trucks are manually operated for 16-hours a day, 5 days a week, totalling approximately 10 million Equivalent Single Axle Loads (ESALs) in the 2-year traffic period. Each of the five trucks used in daily operations have approximately a 12-kip (53.4 kN) steer axle, 40-kip (178 kN) tandem axle, and 5 trailing 20-kip (89.0 kN) single axles.

Four of the fourteen sections were constructed in the 2006 test cycle and included N1, N2, N8 and N9. Sections N1 and N2 were designed to mirror one another with identical aggregate skeletons in the AC layers and both were constructed with approximately 7 inches (178 mm) of AC atop the same limerock aggregate base typically used by Florida Department of Transportation (FDOT) placed at approximately 10 inches (254 mm). These sections differed by the Performance Grade (PG) of the asphalt binder (PG 67-22 and PG 76-22) used in the top two AC lifts. Sections N8 and N9 also complemented one another as both used the compacted Track soil as base material atop a compacted soft subgrade material all over top the uncompacted Track soil. The soft subgrade material was imported from Seale, Alabama and closely replicates subgrade materials typically encountered by the Oklahoma DOT. Both sections were composed of the same four AC mixtures including a Stone Matrix Asphalt (SMA) surface lift and rich bottom layer, with the difference being the AC thickness. Section N9 was designed at 14 inches (357 mm) of AC, whereas section N8 was designed at 10 inches (254 mm) of AC.

For this investigation nine of the ten newly constructed sections in the 2009 test cycle were evaluated in addition to the N9 section left in place from the 2006 test cycle. The compacted subgrade used in all nine newly constructed sections has been well-documented as an AASHTO A-4(0) metamorphic quartzite soil found on-site [12]. The aggregate base was also consistent among the nine newly constructed sections in the 2009 cycle and was a crushed granite material often used by the Alabama DOT [12]. Two sections sponsored by Shell Oil Products, USA [13], N5 and N6, were constructed of sulfur-modified Warm-Mix Asphalt (WMA) in the binder and base courses and were designed at 9 and 7 inches (229 and 178 mm) of AC, respectively. Section N7, sponsored by Kraton Performance Polymers, Inc. [14], was the thinnest section at 5.75 inches (146 mm) and constructed entirely with high polymer (7.5% Styrene Butadiene Styrene (SBS)) modified asphalt. Two sections, N10 and N11, were part of a larger group experiment [15] and included 50% Reclaimed Asphalt Pavement (RAP) in each lift and were designed at 7 inches (178 mm) thick. Section N11 was produced as a WMA using the foaming technique, while section N10 was produced at typical production temperatures for hot-mix asphalt. Section S9 was the control section of the group experiment, designed at 7 inches (178 mm) thick and containing typical Superpave AC mixtures. Sections S10 and S11 in the group experiment were 7-inch (178 mm) sections and both were constructed with warm-mix technologies. AC mixtures in section S10 were produced with foaming technology and the AC mixtures in S11 contained additives to reduce the viscosity during production. The last section, S12, was designed at 7 inches (178 mm) and utilized pellets of naturally occurring asphalt produced by Trinidad Lake Asphalt (TLA) to replace 25% of the virgin binder (PG 67-28) in all lifts throughout the AC cross-section.

3.2 *Instrumentation*

Each section was instrumented with a strain gauge array at the bottom of the AC, earth pressure cells at the top of the granular base and subgrade as well as embedded temperature probes. The strain gauge array consisted of six longitudinal (measuring strain in the direction of traffic) and six transverse (measuring strain perpendicular to traffic) strain gauges. The gauges were installed in groups of three with the center gauge along the outside wheelpath with the remaining gauges offset two-foot on-center, to the right and left, to account for wheel wander. Temperature probes were embedded in the shoulder of each section to capture pavement temperature at the surface, mid-depth and bottom of the AC in addition to 3-inches (76 mm) into the granular base. Mid-depth pavement temperatures associated with measured tensile strains in this study varied from mid-30s (1.6°C) to upwards of 120°F (48.9°C). Detailed information regarding the embedded instrumentation has been documented elsewhere [16].

Data were collected on a weekly basis, including strain measurements under 3 passes of each truck to capture the best-hit and in-situ pavement temperatures at the time of collection. Consistent with previous studies at the track [17], it was found that strain in the longitudinal direction was larger than in the transverse direction, therefore this study considered only longitudinal tensile strain at the bottom of the AC under single axle loads. The best-hit approach consisted of obtaining data from each of the working longitudinal strain gauges on a given date and selecting the maximum peak strain measured from all the passes of a given axle type.

Traffic at the Test Track operates at a target vehicle speed of 45 mph (72.4 km/h), however due to the manual operation of these heavy triple-trailer trucks, the speed is somewhat variable. Actual vehicle speed was calculated using raw strain traces and known distances between instrumentation, as previously documented [18]. This was necessary to associate actual speed with measured strain values. Tensile strains were measured under vehicle speeds ranging between 33 and 63 mph (53.1 and 101.4 km/h), although more than 95% of the strains measured were at vehicle speeds between 42 and 52 mph (67.6 and 83.7 km/h).

3.3 *In-place AC modulus*

To construct a master curve for in-place AC modulus, the in-place modulus was first determined through modulus-strain relationships. Modulus-strain relationships for each of the fourteen sections included in this study were developed using an LEA program, WESLEA version 3.0, as previously documented [18]. By using the field-measured strain with the modulus-strain relationship, the in-place modulus required to achieve that strain was determined. The number of iterations that were required to model all of the different AC lifts in each cross-section was unmanageable and the LEA program utilized for this analysis was limited to a maximum of 3 AC layers. Therefore, the AC was considered as one layer, as documented elsewhere [18], and relationships were developed for a composite AC modulus. Using section-specific surveyed thicknesses measured during construction and average backcalculated moduli for the aggregate base and subgrade layers (also section-specific); each section was simulated under a single axle load, representative of the Test Track traffic. By varying the AC modulus over a wide range of values while holding the aggregate base and subgrade moduli constant at their respective backcalculated values, maximum horizontal tensile strain at the bottom of the AC was predicted. By varying the AC moduli, a wide range of vehicle speeds and mid-depth pavement temperatures were accounted for inherently. The ranges of AC moduli were selected to achieve predicted tensile strains that were within the range of the maximum and minimum peak strain measured in the field for each section. This enabled the development of modulus-strain relationships in which tensile strain measured in the field at the bottom of the AC could be applied to determine the in-place (composite) AC modulus required to achieve that strain value. By using this method, the master curves developed were calibrated to field-measured strain under varying speeds and pavement temperatures, and thus circumvented the short-falls associated with FWD testing and backcalculated AC moduli, as were discussed previously.

In following layered elastic theory, the strain used to determine the in-place AC modulus must be elastic. Therefore, several steps were taken to ensure that the strains used in this investigation were elastic in nature and were measured in an un-damaged pavement. These steps, although documented elsewhere [18], included the evaluation of strain as a function of time, and temperature; assessing the difference between 95th percentile strain and maximum strain; and assessing the root mean squared error associated with backcalculated AC moduli.

3.4 *Master curve construction*

Because AC is a linear viscoelastic material that is time and temperature dependent, the time-temperature superposition principle can be applied. The time-temperature superposition principle allows for data to be shifted using a reference temperature. |E*| master curves are developed by first measuring |E*| in the laboratory at a range of frequencies and temperatures, following either the AASHTO TP 79-09 (specific for the Asphalt Mixture Performance Tester (AMPT)) or the AASHTO TP 62-07 specification. According to AASHTO PP 61-09 the dynamic modulus master curve is a sigmoidal fit function of the form shown in Equation (1). It should be noted that this provisional procedure is intended for use with the AMPT and |E*| measurements made in accordance with AASHTO TP 79-09. This procedure utilizes a modified Hirsch equation to determine the limiting maximum modulus by fixing the dynamic shear modulus of the binder at 145,000 psi (1 GPa), thus transforming the "$3|G^*|_{binder}$" term into 435,000 psi (3 GPa) as shown in Equation (2). It should also be noted that Equation (2) is presented differently in AASHTO PP 61-09, such that the parameter P_c is shown to be applied to the entire equation. The authors used the form of the equation shown in Equation (2) by verifying the original form of the Hirsch model presented in [19] and confirming this is the form of the equation used in the MasterSolver Excel spreadsheet developed by Bonaquist under the NCHRP 09-29 project [20]. To shift the data to one reference temperature, the Arrehenius shift factor is used according to AASHTO PP 61-09 and is shown in Equation (3), below. Essentially, the frequency corresponding to the |E*| measurement is transformed to reflect the frequency required to achieve the same |E*| value at said reference temperature. This is completed by applying the shift factor determined in Equation (3) to the test frequency, as described by Equation (4).

$$\log(|E^*|) = \delta + \frac{(Max - \delta)}{1 + e^{\beta + \gamma(\log \omega_r)}} \tag{1}$$

where:
$|E_*|$ = dynamic modulus, ksi
δ = fitting parameter, represents logarithm of limiting minimum modulus
β, γ = fitting parameters
ω_r = reduced frequency, Hz
Max = logarithm of limiting maximum modulus (ksi), see Eq. (2)

$$|E^*|_{\max} = \frac{1}{1000}\left[P_c\left[4{,}200{,}000\left(1 - \frac{VMA}{100}\right) + 435{,}000\left(\frac{VMA \times VFA}{10{,}000}\right)\right] + \frac{1 - P_c}{\left[\frac{\left(1 - \frac{VMA}{100}\right)}{4{,}200{,}000} + \frac{VMA}{435{,}000(VFA)}\right]}\right] \tag{2}$$

where:
$|E^*|_{max}$ = limiting maximum modulus, ksi

$$P_c = \frac{\left(20 + \frac{435{,}000(VMA)}{VFA}\right)^{0.58}}{650 + \left(\frac{435{,}000(VMA)}{VFA}\right)^{0.58}}$$

VMA = Voids in mineral aggregate (%)
VFA = Voids filled with asphalt (%)

$$\log a(T) = \frac{\Delta E_a}{19.17142}\left(\frac{1}{T} - \frac{1}{T_r}\right) \tag{3}$$

where:
$a(T)$ = shift factor
ΔE_a = activation energy, treated as a fitting parameter
T = temperature, °K
T_r = reference temperature, °K

$$\log(\omega_r) = \log(\omega) + \log[a(T)] \tag{4}$$

where:
ω_r = reduced frequency (Hz)
ω = test frequency (Hz)

In developing a master curve for in-place composite AC modulus, it was elected to use the same form of the sigmoidal fit function used for dynamic modulus, shown in Equation (1). Due to the previously noted issues surrounding load duration in the field and conversion to frequency, rather than using loading rate (frequency in Hz) and temperatures as applied in dynamic modulus testing, it was elected to utilize loading rates and temperatures associated with the measured tensile strains (from which composite modulus was determined). Therefore, the actual vehicle speed and pavement temperatures relative to the tensile strain measured at the bottom of the AC were used for the construction of in-place composite AC modulus master curve. Based on previous studies at the Test Track [17] which found strong correlations between strain and temperatures at the mid-depth of the AC, mid-depth pavement temperatures measured from the embedded temperature probes at the time of strain measurements were utilized for use in the field-calibrated master curves.

The form of the master curve equation used for in-place composite AC modulus is shown in Equation (5). The same Arrehenius shift factor (Equation (3)) was used but was applied to the actual vehicle speed associated with the in-place composite AC modulus (field-measured strain) as described by Equation (6) and for a reference temperature of 22°C. As applied here, the activation energy represents the activation energy of the composite AC layer. Consistent with the |E*| master curve construction, ΔE_a, β_{comp}, γ_{comp}, and $log\ E_{comp,min}$ (shown in Equation (1) as δ) were treated as fitting parameters and determined for each of the field-calibrated master curves. The values of these regression terms were determined using non-linear optimization as is done in the MasterSolver spreadsheet and recommended in AASHTO PP 61-09 for |E*| master curve construction. The initial estimates utilized in the MasterSolver spreadsheet developed by Bonaquist [20] for the fitting parameters, δ, β, γ, and ΔE_a were also utilized for the initial estimates for field calibrated master curve as well and were as follows: 0.5, –1, –0.5, 200,000, respectively. The Generalized Reduced Gradient (GRG) non-linear method was used in Excel solver to complete the non-linear optimization with the solver options identical to those used in MasterSolver as it also relies on Excel Solver. During the non-linear optimization, rather than continuing to alter the fitting parameters to converge on a solution for each, the first set of solutions was utilized. This is consistent with MasterSolver and if allowed to continue through several iterations the predictions worsen, in some cases resulting in a negative coefficient of determination. The goal of the non-linear optimization was to minimize the Sum of the Squared Errors (SSE). For each field-calibrated master curve,

the coefficient of determination (Equation (7)) as well as the ratio of standard error of the predictions (S_e) (Equation (8)) to standard deviation of measured values (S_y) was computed in arithmetic scale for evaluating the goodness of fit. Equations 7 and 8 are consistent with fit statistics used by Dongré et al. in a 2005 evaluation of the Witczak and Hirsch predictive models for dynamic modulus [21].

The parameters utilized in developing the field-calibrated master curve for in-place composite AC modulus must also represent a composite AC layer. Therefore in determining the limiting maximum composite modulus for the field-calibrated master curve, the AASHTO PP 61 procedure for limiting maximum dynamic modulus shown in Equation (2) was used; however, the VMA and VFA used to calculate the limiting maximum composite modulus represent the VMA and VFA of the in-place composite AC layer rather than VMA and VFA for one AC mixture. In-place VMA and VFA values for each AC lift were computed for each section based on as-built properties recorded at the time of construction. These values were then combined using the same method used for determining blended G_{sb}, this procedure is documented elsewhere [18].

$$\log(E_{comp}) = \log E_{comp,min} + \frac{\log E_{comp,max} - \log E_{comp,min}}{1 + e^{\beta comp + \gamma comp(\log v_r)}} \tag{5}$$

where:
E_{comp} = composite modulus, ksi
$\log(E_{comp,min})$ = fitting parameter
β_{comp}, γ_{comp} = fitting parameters
$E_{comp,max}$ = limiting maximum composite modulus, ksi

$$\log(v_r) = \log(v) + \log[a(T)] \tag{6}$$

where:
v_r = reduced vehicle speed (mph)
v = vehicle speed (mph)

$$R^2 = 1 - \frac{(n-k)}{(n-1)}\left(\frac{S_e}{S_y}\right)^2 \tag{7}$$

where:
n = number of observations
k = number of fitting parameters (4)
S_y = standard deviation of the measured values

$$S_e = \sqrt{\frac{SSE}{n-k}} \tag{8}$$

where:
S_e = standard error of the prediction
SSE = sum of squared errors = $\sum_i^n (E_{mi} - E_{pi})^2$
E_{mi} = ith Measured E_{comp}, ksi
E_{pi} = ith Predicted E_{comp}, ksi

4 RESULTS AND DISCUSSION

Field calibrated master curves were developed for each of the fourteen sections included in this investigation. An example of a field-calibrated master curve is shown in Figure 1 for section N5, a 9-inch (229-mm) sulfur-modified WMA section. Table 1 summarizes the fitting

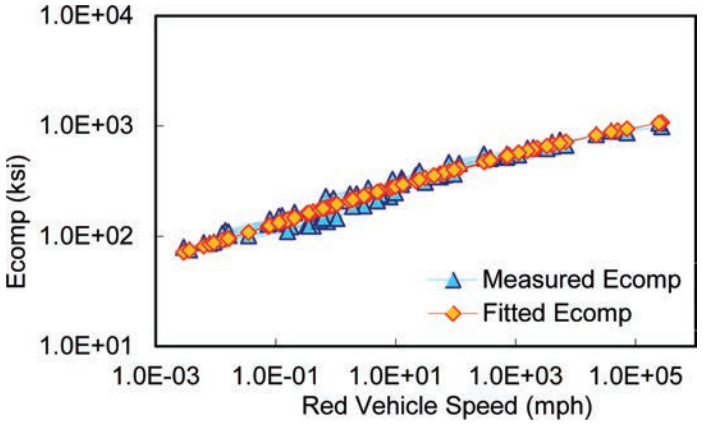

Figure 1. Field-calibrated master curve, N5.

Table 1. Master curve fitting parameters and fit statistics.

Section	log $E_{comp,max}$	log $E_{comp,min}$	β_{comp}	γ_{comp}	$\Delta E_{a\ comp}$	R^2	S_e/S_y
N1	3.502	0.079	–0.403	–0.217	292758	0.8246	0.5130
N2	3.511	0.723	0.094	–0.389	180300	0.9508	0.2651
N8	3.519	–0.897	–0.721	–0.248	261163	0.9293	0.3257
N9 (2006)	3.522	–0.069	–0.634	–0.210	314759	0.9546	0.2609
N5	3.497	0.776	–0.212	–0.250	285057	0.9823	0.1355
N6	3.497	0.400	–0.283	–0.199	311684	0.9566	0.2119
N7	3.502	0.511	–0.534	–0.251	228390	0.9143	0.3112
N9 (2009)	3.523	0.467	–0.711	–0.167	239440	0.8517	0.4067
N10	3.513	1.844	1.222	–0.283	318494	0.8699	0.4418
N11	3.509	0.259	–0.660	–0.182	251839	0.9621	0.2001
S9	3.498	0.044	–0.527	–0.237	242057	0.9106	0.3043
S10	3.499	0.664	–0.458	–0.225	291183	0.9338	0.2617
S11	3.497	1.817	0.528	–0.259	383847	0.9571	0.2123
S12	3.518	0.317	–0.595	–0.210	274946	0.9561	0.2204

parameters and fit statistics (in arithmetic scale) for each curve. It should be noted that the values in Table 1 are based on U.S. customary units. Sections N8 and N9 from the 2006 test cycle have negative values for the log $E_{comp,max}$ term, indicating that the limiting minimum modulus for each of these sections is greater than zero and less than 1 ksi. Overall, the master curves fit the data very well. Only three of the fourteen sections had R^2 values less than 0.9. However, as shown in Table 1, the field-calibrated master curves for each of these three sections, N1 (Florida, 2006), N9 from 2009 (Oklahoma) and N10 (High RAP), maintained acceptable coefficients of determination, with the lowest accounting for more than 82% of the variability in the data. These same sections are the only sections to have S_e/S_y ratios less than 0.35, a common threshold for defining excellent fit.

A speed study completed for section S9 was used to validate the application of the field-calibrated master curves to speeds beyond the narrow range at which they were developed. The speed study was conducted on four different test dates throughout the course of the 2009 test cycle to capture tensile strains at a variety of mid-depth pavement temperatures and vehicle speeds. On each test date four speeds were tested: 15, 25, 35 and 45 mph (24.1, 40.2, 56.3 and 72.4 km/h). For this evaluation, however, only the first three target speeds were used, as the strains at 45 mph (72.4 km/h) were already incorporated into this study. Actual vehicle speeds ranged from 14 to 33 mph (22.5 to 53.1 km/h) and mid-depth pavement temperatures

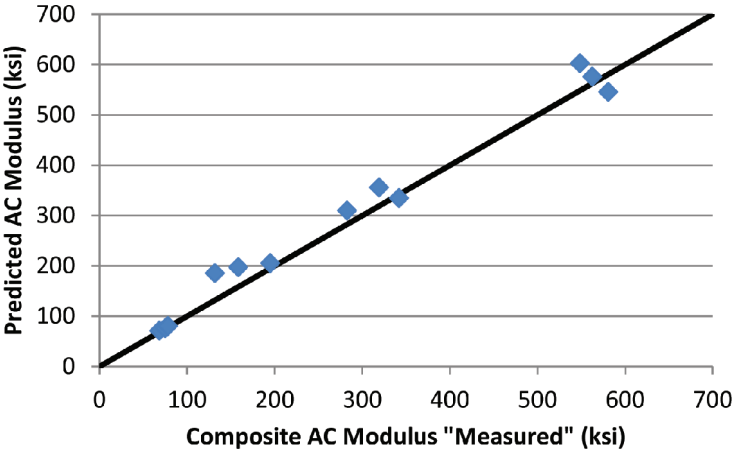

Figure 2. "Measured" vs. predict AC modulus for S9 Speed Study.

ranged from 48 to 113°F (8.9 to 45°C). The in-place AC moduli were predicted for S9 by applying the field-calibrated master curve for S9, with fitting parameters shown in Table 1, to the field conditions (vehicle speed and mid-depth pavement temperatures) at the time of the strain measurements. The tensile strains measured under varying speeds and temperatures were applied to the S9 modulus-strain relationship to determine "Measured" in-place composite AC moduli. Figure 2 plots the "Measured" in-place composite AC moduli against the AC moduli predicted by the field-calibrated master curve. Evident from this plot, as the data are approximately centered along the line of equality, the field-calibrated master curve is a very good predictor of in-place composite AC modulus at a range of vehicle speeds and pavement temperatures. This is reaffirmed by a very high coefficient of determination of 97%.

5 CONCLUSIONS AND RECOMMENDATIONS

This study aimed to develop a method for constructing master curves for in-place AC modulus using known field conditions such as vehicle speed and pavement temperature calibrated to field measured strain. Based on this study, the following conclusions can be drawn:

- Overall, the developed master curves fit the data very well, allowing for the estimate of in-place AC composite modulus specific to a test section, at a given mid-depth pavement temperature and vehicle speed. Therefore, it can be concluded that a master curve can be accurately calibrated to field measured strains to predict in-place AC modulus of the composite AC layer using known vehicle speed and mid-depth pavement temperature.
- This simple and straightforward method enables direct computation of modulus for undamaged pavement sections exhibiting elastic responses without relying on time-frequency conversions.
- Although master curves were constructed using a narrow range of vehicle speeds (42–52 mph (67.6–83.7 km/h)), based on the validation of the S9 speed study data, the master curves are applicable to speeds slower than 45 mph (72.4 km/h), down to 15 mph (24.1 km/h).
- Given the strong fit statistics reported for the field-calibrated master curves and the inability of FWD testing to capture the effect of real traffic speeds, this method for predicting in-place AC modulus has the capability of being an alternative to backcalculation of AC moduli through FWD testing for instrumented pavements.
- It is recommended that the field-calibrated master curves developed in this study be related to other known as-built properties of the pavement cross-section to create a model to predict in-place composite modulus for any cross-section, vehicle speed and mid-depth pavement temperature.

REFERENCES

[1] ARA Inc., Eres Consultants Division. Development of the 2002 Guide for the Design of New and Rehabilitated Pavement Structures; Appendix CC-3, Updated Traffic Frequency Calculation for Asphalt Layers, Final Document, NCHRP 1-37A, 2003.

[2] Van der Poel, C. A General System Describing the Viscoelastic Properties of Bitumens and its Relation to Routine Test Data. In Journal of Applied Chemistry, Vol. 64, pp. 221–236, 1954.

[3] Ferry, J.D. Viscoelastic Properties of Polymers. 3rd Ed., John C. Wiley and Sons, New York, 1980.

[4] Schwarzl, F.R. Numerical Calculation of Stress Relaxation Modulus from Dynamic Data for Linear Viscoelastic Materials. In Rheological Acta, Vol. 14, pp. 581–590, 1975.

[5] Christensen, R.M. Theory of Viscoelasticity, Academic Press, New York, 1982.

[6] Schapery, R.A. and S.W. Park. Methods of Interconversion between Linear Viscoelastic Material Functions. Part II-An Approximate Analytical Method. In International Journal of Solids and Structures, Vol. 36, pp. 1677–1699, 1999.

[7] Al-Qadi, I.L, W. Xie, and M.A. Elseifi. Frequency Determination from Vehicular Loading Time Pulse to Predict Appropriate Complex Modulus in MEPDG. In Journal of the Association of Asphalt Paving Technologists from the Proceedings of the Technical Sessions, Vol. 77, pp. 739–772, Philadelphia, PA, 2008.

[8] Daniel, J.S. and Y.R. Kim. Relationships Among Rate-Dependent Stiffnesses of Asphalt Concrete Using Laboratory and Field Test Methods. In Transportation Research Record: Journal of the Transportation Research Board No. 1630, Transportation Research Board of the National Academies, Washington, D.C., 1998, pp. 3–9.

[9] Leiva-Villacorta, F. Advanced Computing Techniques in Structural Evaluation of Flexible Pavement Using the Falling Weight Deflectometer. Doctoral Dissertation. Auburn University, 2012.

[10] Seo, J., Y. Kim, J. Cho and S. Jeong. Estimation of In Situ Dynamic Modulus by Using MEPDG Dynamic Modulus and FWD Data at Different Temperatures. International Journal of Pavement Engineering, Vol. 14, Issue 4, pp. 343–353, 2013.

[11] Robbins, M. and D. Timm. Effects of Strain Pulse Durations on Tensile Strain in a Perpetual Pavement. Proceedings of the International Conference on Perpetual Pavement, 2009. Columbus, OH, 2009.

[12] Taylor, A.J. and D.H. Timm. Mechanistic Characterization of Resilient Moduli for Unbound Pavement Layer Materials. Report No. 09-06, National Center for Asphalt Technology, Auburn University, 2009.

[13] Timm, D.H., M.M. Robbins, J.R. Willis, N. Tran and A.J. Taylor. Evaluation of Mixture Performance and Structural Capacity of Pavements Using Shell Thiopave: Phase II—Construction, Laboratory Evaluation, and Full-Scale Testing of Thiopave Test Sections—Final Report. Report No. 12-07, National Center for Asphalt Technology, Auburn University, 2012.

[14] Timm, D.H., M.M. Robbins, J.R. Willis and A.J. Taylor. Field and Laboratory Study of High-Polymer Mixtures at the NCAT Test Track: Final Report. Report No. 13-03, National Center for Asphalt Technology, Auburn University, 2013.

[15] Vargas-Nordcbeck, A. and D. Timm. Physical and Structural Characterization of Sustainable Asphalt Pavement Sections at the NCAT Test Track. Report No. 13-02, National Center for Asphalt Technology, Auburn University, 2013.

[16] Timm, D.H. and A.L. Priest. Material Properties of the 2003 NCAT Test Track Structural Study. Report No. 06-01, National Center for Asphalt Technology, Auburn University, 2006.

[17] Timm, D.H. and A.L. Priest. Flexible Pavement Fatigue Cracking and Measured Strain Response at the NCAT Test Track. Proceedings of the 87th Annual Meeting of the Transportation Research Board, Washington, D.C., 2008.

[18] Robbins, M.M. New Methods for Predicting Critical Tensile Strains in an M-E Framework. Doctoral Dissertation, Auburn University, 2012.

[19] Christensen, Jr., D.W., T. Pellinen, and R.F. Bonaquist. Hirsch Model for Estimating the Modulus of Asphalt Concrete. Journal of the Association of Asphalt Paving Technologists from the Proceedings of the Technical Sessions, Vol. 72, pp. 97–121, Lexington, KY, 2003.

[20] Bonaquist, R. MasterSolver Version 2.3. http://onlinepubs.trb.org/onlinepubs/nchrp/docs/NCHRP09-29_mastersolver2-2.xls.

[21] Dongré, R., L. Myers, J. D'Angelo, C. Paugh and J. Gudimetta. Field Investigation of Witczak and Hirsch Models for Predicting Dynamic Modulus of Hot-Mix Asphalt. Journal of the Association of Asphalt Paving Technologists, Vol. 74. Long Beach, CA, 2005.

Asphalt Pavements – Kim (Ed)
© 2014 Taylor & Francis Group, London, ISBN 978-1-138-02693-3

The development of pavement rehabilitation design guidelines for increasing the allowable axle load from 100 kN to 115 kN

Laszlo Petho
ARRB Group Ltd., Sustainable Infrastructure Management, Albion, QLD, Australia

Csaba Toth
Department of Highway and Railway Engineering, Budapest University of Technology and Economics, Budapest, Hungary

ABSTRACT: The road network in Hungary had to be improved and reconstructed due to the mutual EU agreement to increase the then allowable 100 kN axle load to 115 kN. This requirement was a challenge on an aged road network, where the pavement layers were designed and built to a lesser frequency and amplitude of vehicle loading.

The Instrument for Structural Policies for Pre-Accession (ISPA) was launched to assist the candidate countries with this issue. This paper provides a summary of the development of a series of guidelines for road pavement rehabilitation design in Hungary. The complex problem of the pavement structural design in a semi-empirical system is discussed; the EU does not provide harmonised standards for pavement design purposes. Also, the paper outlines how to incorporate existing asphalt layers prone to plastic deformation into the rehabilitated pavement structure, while maintaining a low risk of future distresses.

The guidelines were developed on a series of case studies of an overall length of 300 km. FWD tests and wheel tracking tests combined with visual inspections provided the basis for the work. Using this approach it was possible to develop a series of guidelines for cost-effective pavement rehabilitation design.

Keywords: pavement rehabilitation; semi-empirical; plastic deformation; design guidelines; cost-effective

1 INTRODUCTION

Due to the mutual agreement between the European Union (EU) and Hungary, (which joined the EU in May 2004), a significant section of the trunk road network had to be improved and reconstructed to a higher standard, which allowed increasing the then permitted 100 kN axle load to 115 kN. The Hungarian road network is 31 628 km in total (excluding local roads maintained by local Councils), of which 8297 km forms the trunk network [1]. The agreement for improvement applied to 7400 km in total. This requirement was a challenge on an aged road network, where the pavement layers were designed and built, mainly in the 80 s and 90 s, to a lesser frequency and amplitude of vehicle loading.

The Instrument for Structural Policies for Pre-Accession (ISPA) was launched by the EU to assist the candidate countries with this issue. This paper provides a summary of the development of a series of guidelines for road pavement rehabilitation design in Hungary as part of the ISPA II main framework. The ISPA program included a systematic road infrastructure upgrade, which involved road pavement rehabilitation and widening, upgrade of intersections, traffic calming measures, parallel bikeways and bridge rehabilitation or reconstruction works.

In order to address this issue, the Directorate for the Coordination of Road Transport Affairs–EU project division (the Client) commissioned the University of Technology,

Budapest, and the two largest commercial road material testing institutes, IMI and Bau-Teszt to develop specific Guidelines for the road rehabilitation program based on 115 kN axle loads. The ISPA II project included five sections of the trunk network, namely Main Roads no. 2 (38.8 km), no. 6 (121.9 km), no. 42 (55.1 km), no. 47 (29.3 km) and no 56 (54.6 km), a total length of 299.7 km. These road sections form part of the trans-European transport network (TEN-T) and the Transport Infrastructure Needs Assessment (TINA) network [2]. The Guidelines worked out for ISPA II was a pilot project and later formed the technical basis for tenders and technical investigations on the project level and other road rehabilitation projects under the 115 kN strengthening projects [3].

According to the scope of the preparation of the Guidelines the focus was on pavement rehabilitation and widening. It was necessary to include the following tasks:

- review of relevant function parameters
- review of the pavement design methodology, and harmonisation with the then current technical specifications
- development of a methodology for reconstruction, including, but not limited to the following main objectives:
  - incorporating existing asphalt layers prone to plastic deformation into the rehabilitated pavement structure, while maintaining a low risk of future distresses
  - minimising the amount of Recycled Asphalt Pavement (RAP) and developing options for re-use
  - developing a methodology for design of widening; focussed on avoiding longitudinal cracks and subsidence of the newly widened widening strip
  - as road sections within urban areas are often built with kerb and channel, this results in a major restriction on overlay treatments. The feasibility of the overlays and possible other options to address the structural capacity requirements had to be analysed.

The following documents and data were supplied by the Client:

- concept design documents, outlining alignment design and upgrade requirements
- existing pavement configurations from the road network database (OKA in Hungarian)
- traffic count data for each sub-section
- rut depth measured by the Road Surface Tester (RST)
- road surface condition, determined according to Roadmaster, a uniform methodology applied by Main Roads Hungary
- deflection results, measured by the KUAB Falling Weight Deflectometer (FWD)
- thickness of layers and wheel-tracking test results for each layer based on cores taken from the pavement at 1000 m frequency; in order to maintain cost-effectiveness, where the rut depth did not exceed 15 mm, sampling was not performed
- local treatments and rehabilitations of short sections, not yet transferred to the road network database.

2 ASPHALT OVERLAY DESIGN

2.1 *Pavement rehabilitation concept*

Hungary, as a member of the EU and the Comité Européen de Normalisation (CEN)—European Committee for Standardization—implement the EN standards on the national level. However, these standards apply for products and test methods, and the EU and CEN do not provide harmonised standards for pavement design purposes. The Hungarian approach in pavement structural design is semi-empirical (mechanistic-empirical) and the complex task, combined with technological considerations, had to be treated in the Guidelines.

In general, a pavement rehabilitation design seems to be a straightforward process today. The basic question is how to allocate the technically possible minimum and maximum asphalt overlay thickness in a particular situation (Fig. 1A); the minimum should be sufficient to be able to increase the bearing capacity of the existing pavement (say a minimum of 50 mm), but also should have a realistic maximum limit (which is around 200–250 mm).

The process is basically influenced by two major parameters, e.g. the number of traffic loading and the performance of the existing pavement. Low traffic volume combined with relatively good pavement condition would require a minimum overlay thickness, while heavy traffic combined with poor road condition requires significant overlay (Fig. 1B). This simplified approach is behind every pavement overlay design: empirical, semi–empirical or mechanistic; however, in order to avoid subjective decisions among the pavement engineers, the asset owner usually requires one of the above methods to provide consistency on the road network.

The refinement of the input parameters is vital. This is the driver of introducing innovative materials and technologies, and provides effective pavement configurations in the longer term. However, the effectiveness cannot be considered only from the structural capacity point of view, there are many other aspects, such as the increased axle loads and tyre contact pressure and consequently the plastic deformation of existing layers. Therefore, in the broader context it is necessary to analyse the cost-effectiveness by using a Pavement Management System (PMS). However, the thinking should not stop at the PMS level, it could be made even more complex considering the areas of energy balance, emissions and the impact on the natural and built environment (Fig. 1B).

The scope of the work outlined in this paper did not make it possible to consider the whole system and the boundaries of the work were identified at the advanced pavement rehabilitation design level (Fig. 1B).

2.2 *Asphalt overlay based on the deflection criteria*

A two layered system, transformed into an equivalent infinite layer was used for the overlay design [4–5]. The semi-empirical asphalt overlay design was developed on the basis of

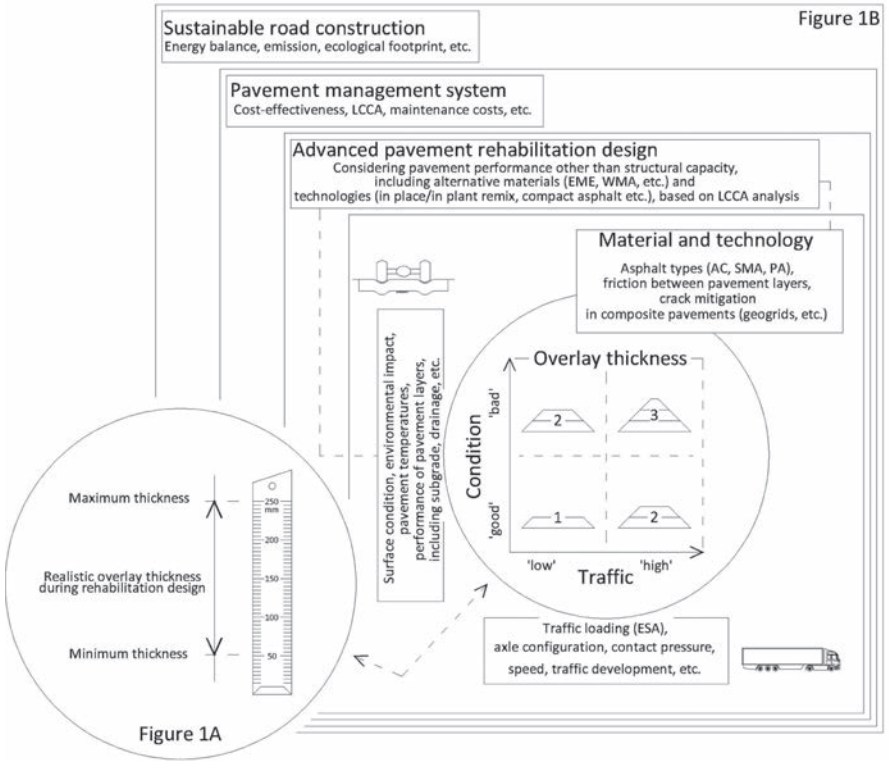

Figure 1. a) and b) Complex engineering assessment of the pavement design.

measured deflection of the existing pavement structure [5]. The overlay design was based on the deflection criteria; however the deflections in the pavement structure were calculated using the General Mechanistic Pavement (GMP) design approach. This method gives a unique tool in the overlay design. It has its constraints, but basically provides a rational tool for pavement engineers.

The characteristic value of the measured deflection ($s_{measured}$) should be compared to the allowable (tolerable) deflection ($s_{tolerable}$); the deflection of the overlaid pavement should not exceed the allowable deflection, which value depends on the traffic loading, expressed in Equivalent Standard Axle (ESA) repetitions. The performance of the existing pavement layers did not provide design input, and the layer properties were not back-calculated for further application; the pavement structures were be described by the characteristic deflection. The characteristic deflection was calculated from the D0 value derived from the FWD measurement, tested at 100 metres frequency per traffic lanes. The method provided a solution solely for the asphalt overlay design; unbound granular or concrete overlay was out of the scope for this method.

The design method can be summarised as follows: the representative deflection (*SM*) for a homogeneous section was determined by means of appropriate non-destructive testing [5]. The tolerable deflection (*SE*) was determined based on semi-empirical equations. Based on the two deflection values the required asphalt layer thickness (*HF*) was calculated as specified in Eq. (1).

$$SM \leq SE \tag{1}$$

The load in the pavement model was $F = 100$ kN axle load, which was distributed on single tyres. The assumption was that the load on each tyre was distributed on a circular area, and the contact pressure between the tyre and pavement had a value of $P = 0.65$ MN/m^2. The deflection of the two layered system (existing pavement structure and overlaying asphalt) was calculated according to Eq. (2), where *S* is the overall rebound deflection of the pavement structure after overlay (in mm), *SA* is the calculated deflection of the existing pavement (in mm) and *SF* is the calculated deflection of the overlaying asphalt (in mm).

$$S = SA + SF \tag{2}$$

The calculated deflection of the upper layer (*SF*) was computed using Eq. (3) [5], where *R* is the radius of the loading area (in mm), *P* is the contact stress between pavement and tyre (in MN/m^2), *EF* is the overlaying asphalt mix stiffness (in MPa), *MF* is the Poisson value of the overlaying asphalt and *ZF* is the corrected thickness of the upper layer, calculated according to Eq. (4) [5]. In the calculation of *ZF* in Eq. (4), *V* is the correction factor and *HF* is the thickness of the overlaying asphalt (in mm); *HF* is calculated in an iterative process. The calculations were performed using $EF = 7000$ MPa, $MF = 0.35$ and $V = 0.9$.

$$SF = \frac{P * R}{EF} * \left[\begin{array}{l} 2*(1-MF^2) - 2*(1-MF^2)*\left(1+\left(\frac{ZF}{R}\right)^2\right)^{\frac{1}{2}} \\ \quad + \dfrac{(1+MF)*\left(\frac{ZF}{R}\right)^2}{\left[1+\left(\frac{ZF}{R}\right)^2\right]^{\frac{1}{2}}} - \left(MF + 2MF^2 - 1*\left(\frac{ZF}{R}\right)\right) \end{array} \right] \tag{3}$$

$$ZF = V * HF \tag{4}$$

The calculated deflection of the lower layer (*SA*) was computed using Eq. (5) [5], where *EL* is the equivalent modulus of the existing pavement structure, calculated from the measured

deflection according to Eq. (6) [5] (in MN/m^2), ML is the Poisson value of the existing pavement structure (in this calculation 0.40), ZL is the corrected thickness of the lower layer, calculated according to Eq. (7) [5] (in mm), EL is the equivalent modulus of the existing pavement structure (in MPa) and SM is the representative deflection (in mm).

$$SA = \frac{P*R}{EL} * \left[\begin{array}{l} 2*(1-ML^2)*\left(1+\left(\frac{ZL}{R}\right)^2\right)^{\frac{1}{2}} + \left(ML+2ML^2-1\right)*\left(\frac{ZL}{R}\right) \\ -\left(1+ML\right)*\frac{\left(\frac{ZL}{R}\right)^2}{\left[1+\left(\frac{ZL}{R}\right)^2\right]^{\frac{1}{2}}} \end{array} \right] \tag{5}$$

The equivalent modulus of the existing pavement structure (EL) was calculated according to Eq. (6) and the corrected thickness of the lower layer ZL according to Eq. (7).

$$EL = 2*\left(1-ML^2\right)*\frac{P*R}{SM} \tag{6}$$

$$ZL = V*HF*\left(\frac{EF}{EL}*\frac{1-ML^2}{1-MF^2}\right)^{\frac{1}{3}} \tag{7}$$

The calculation of the overlay thickness (HF) is an iterative process, where the thickness of the overlaying asphalt is increased gradually by 5 mm increments until Eq. (1) is met. For the ISPA II project it was decided to continue using the above mentioned equivalent standard axle load and use a factor of 1.5 to account for the increased strains induced by the increased load magnitude. This decision was made by the executive group prior to commencing the works and it is not an outcome of the project in scope; however, this project fully utilised this methodology and it was considered a reasonable approach.

A key element of the design process was the correct calculation of the tolerable deflection. The original equation was based on the American Association of State Highway and Transportation Officials (AASHO) investigation, and it was used as an overall description of any type of pavement structure. However, in the 1970s Hungarian researcher proved [6] that the designer has to determine the actual pavement structure and accordingly a different equation should be applied during the pavement design as outlined in Eq. (8) [6–7] and in Table 1.

$$SE = a*(F100)^{\frac{-1}{b}} \tag{8}$$

The above calculation is summarised in nomographs [7]; also the authors of this paper developed a spreadsheet for the above procedure. The advantage of using a spreadsheet for such a procedure is that the input parameters of the new asphalt layer can be changed, and asphalt materials with higher performance, such as high modulus asphalt, can be readily implemented, resulting in cost-effective pavement design methods.

Table 1. Tolerable deflection calculation (F_{100} is the design axle load) [7].

Type of existing pavement	Constant a	Constant b
Fully-flexible pavement structure (unbound granular pavement)	25	4.00
Flexible pavement structure (full depth asphalt pavement)	14.5	4.55
Semi-flexible pavement structure (composite pavement)	9.0	5.00

2.3 *Homogeneous sub-sections*

The characteristic deflection (s_m), which is represented by the allowable deflections (*SE*) in the calculations, is expressed according to Eq. (9), where $\bar{b}$ is the mean value of the measured deflections within the homogeneous sub-section; homogenous sub-sections were determined using the cumulative sum method [8], s_b is the standard deviation within the homogeneous sub-section and μ is the factor for the level of risk.

$$s_m = \bar{b} + \mu \cdot s_b \tag{9}$$

The deficiency of this system is that the measured deflection, which relates to the full existing pavement, is a major input into the calculations and the method cannot consider the impact of removal of existing pavement layers by cold planing. If removal of existing layers is necessary, due to low resistance to plastic deformation, the method will result in overdesigned pavement structures, as the higher structural capacity of the back-filled layers will not be taken into consideration. Also, the deflection criteria may be misleading on composite pavements due to the higher structural capacity of the cement treated or concrete subbase layers.

3 ASPHALT TECHNOLOGY RELATED CONSIDERATIONS

3.1 *Risk of plastic deformation*

The increased axle load does not only have an influence on the pavement structural capacity, but also increases the risk of plastic deformation under the extremely high contact pressure generated by super single tyres. Many asphalt layers, built in the 70 s to 80 s consisted of river gravel and/or soft bitumen, and these asphalt layers could not withstand the shear forces of such a high contact pressure.

Realising this issue, the hot mix asphalt specification [9] had already required wheel tracking test for pavement rehabilitation, performed on cores extracted from the existing asphalt layers. Although the specification [9] provided threshold values, the action list of the specification was quite vague. As a result, in reality, layers prone to plastic deformation were always removed to avoid any risks. An outcome of the Guidelines was that it provided risk management for such a situation, returning cost-effective pavement structures, while maintaining a low risk of future distresses in terms of plastic deformation. A series of wheel tracking tests were performed for the above mentioned five road sections at a frequency of 1000 metres, where all asphalt layers were tested. The tests were performed according to EN 12697-22 [10] which was in prEN form at the time of preparation of the work.

In the road pavement the traffic load induces vertical (positive) stress and horizontal (negative) stress and the difference of these stresses results in the deviator stress. The plastic deformation is a result of a positive deviator stress, and the magnitude changes as a function of the depth. This theoretical consideration is in line with experience, i.e. the most vulnerable layers in terms of plastic deformation are the upper 100–120 mm of the pavement. Therefore, if the layer, which is prone to plastic deformation, is covered by suitable, rut resistant asphalt layers of more than 120 mm, the non-conforming layer may remain in the pavement structure without any major risks.

This consideration—supported by the project steering group—was based on experience; such a depth reduces the deviator stress and the temperatures so that plastic deformation cannot develop under traffic load. The temperature distributions in depth and its effect on the material properties are discussed elsewhere [11]. It should be noted that the above considerations are valid in the Central-European climate and other climatic regions may need thicker or thinner asphalt layers to overcome the risk of plastic deformation. If the risk of plastic deformation is eliminated, and the non-conforming layer remains in the pavement, additional benefits can be obtained. Layers, prone to plastic deformation, usually contain soft binders or have high binder content, which positively influences the fatigue properties of the pavement. It should be noted that in this study the term plastic deformation is not

exchangeable with post-compaction of the pavement layers, even though they sometimes show the same symptoms.

3.2 *Overlay design combined with plastic deformation problems*

Based on the above consideration, the following options can be applied, if the existing pavement contains asphalt layer(s) prone to plastic deformation:

a. Non-conforming subbase layer (3rd asphalt layer); if the total thickness of the conforming 2nd and 1st layer in the existing pavement are less than 130 mm, and there is no need for an overlay, the removal of the 3rd layer (including the 2nd and 1st layer) would be extremely costly. In this case, applying an overlay (even if it is not necessary from the structural point of view) may be more cost-effective.
b. Non-conforming intermediate layer (2nd asphalt layer); based on cost-effectiveness and risk acceptance, there are more options to consider:
   - applying a thick overlay, so that the existing intermediate layer will be overlaid by at least 130 mm of new asphalt. Such a solution can only be cost-effective, if there is already a need for structural strengthening and there are no height constraints. If the existing pavement does not require strengthening, this solution may not be cost-effective.
   - removal of the non-conforming 2nd layer (including the 1st layer) and back-filling with conforming asphalt layers.
   - removal of the 1st layer and apply Remix Add technology for the non-conforming 2nd layer—then back-filling the 1st layer.
c. Non-conforming wearing course (1st asphalt layer);
   - cold milling of the 1st layer and back-filling with suitable asphalt mix
   - apply Remix or Remix Plus technology for the 1st layer, if the existing asphalt layer is suitable for such a modification.
   - apply a thick overlay, so that the existing wearing course will be overlaid by at least 130 mm of new asphalt. Such a solution can only be cost-effective, if there is already a need for structural strengthening and there are no height constraints. If the existing pavement does not require strengthening, this solution may not be cost-effective.

It can be seen that the pavement designer has two major options, mill and replace, or significant overlay. In case there is a need for significant structural strengthening, the second option is very cost-effective. If there is a need for moderate strengthening (70 mm), the second option may still be cost-effective. Also, minimising the milling operation would not only result in less RAP, but would also shorten construction time, resulting in less impact on road users and overall costs. If it is more suitable to remove the layer prone to plastic deformation, it is paramount that the entire layer be removed from the pavement structure.

3.3 *Urban areas, height restrictions by kerb and channel*

Significant lengths of the five road sections, designed in the pilot project, were in urban areas, where height restrictions by existing kerb and channel had to be considered. Re-construction of existing kerb and channel alignment does not include only the removal and replacement of concrete kerbs and channels, but would also include adjustment of intersections, drainage, and verge and every driveway and road entry, which was out of scope. The cost implications were estimated to be enormous and therefore in urban areas it was considered not possible to apply overlay with significant thickness. If structural strengthening was not required, mill and replace was suggested (considering the options in Section 3.2) or a maximum thickness of 50 mm overlay was applied. The asset owner acknowledged that the design life was shorter than necessary (<15 years) on these sections. The Guidelines also discussed and included suggestions for the following topics:

- required asphalt types (wearing, intermediate and base course)
- allowable minimum and maximum layer thicknesses

- applied binder types
- allowable RAP content according to the asphalt type
- volumetric and performance related requirements for each asphalt type.

As a practical outcome, the pilot project provided detailed pavement design and technology considerations. For a better visualisation—including all input (see Section 1) and output data—longitudinal section were developed; an example is shown in Figure 2. Due to the limited available space only the methodology is provided in this paper. The background on data collection and analysis and verification of the methodology is discussed in details in the contract report provided to the Client [12].

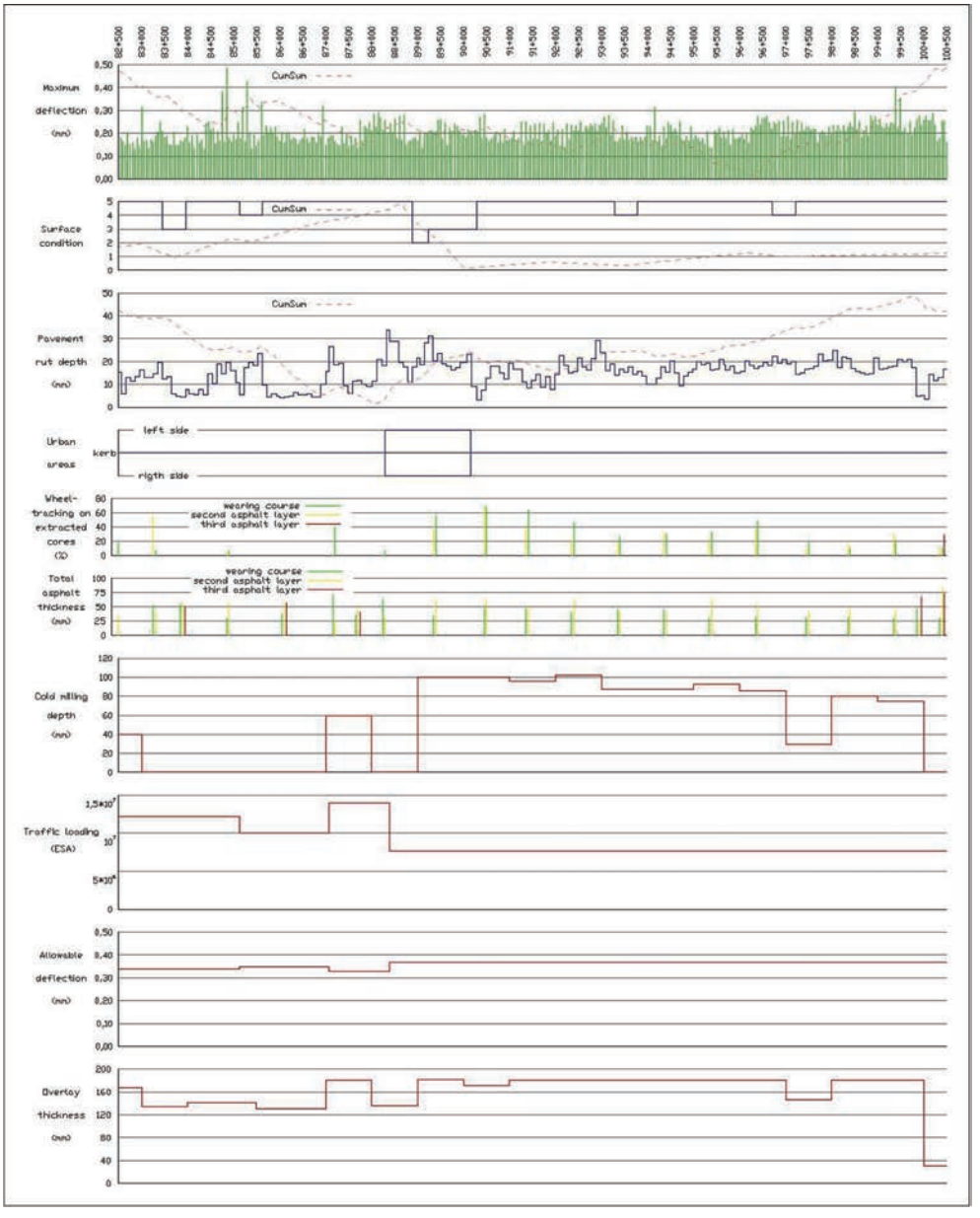

Figure 2. Longitudinal section of input and output data (example on road no. 6).

3.4 *Cost savings*

By using the above methodology which is based on semi-empirical pavement design, extensive FWD and wheel-tracking test, for the five road sections—a total length of 299.7 km -, 482 000 tonnes of asphalt were required; the estimated amount of RAP was 27 000 tonnes. These values were later refined in the detailed design phase; however, the authors were not involved in this phase of the works.

4 SUMMARY

A significant section of the Hungarian trunk road network had to be improved and reconstructed to a higher standard due to an agreement with the EU. Following reconstruction the allowable axle load was increased from 100 kN to 115 kN.

The Instrument for Structural Policies for Pre-Accession (ISPA) was launched to assist with this issue. This paper provides a summary of the development of a series of guidelines for road pavement rehabilitation design in Hungary as part of the ISPA II main framework. The ISPA program involved a systematic road infrastructure upgrade, including road pavement rehabilitation and widening, upgrade of intersections, traffic calming measures, parallel bikeways and bridge rehabilitation or reconstruction works.

The ISPA II project included five sections of the trunk network, a total length of 299.7 km. Development of the Guidelines for ISPA II was a pilot project and later formed the technical basis for tenders and technical investigations on the project level and other road rehabilitation projects under the 115 kN strengthening projects.

The complex problem of the pavement structural design in a semi-empirical system is discussed. Also, the paper outlines how to incorporate existing asphalt layers prone to plastic deformation into the rehabilitated pavement structure, while maintaining a low risk of future distresses. Using this approach it was possible to develop a series of guidelines for cost-effective pavement rehabilitation design.

As a practical outcome of the work presented here, detailed pavement designs and technology considerations, also visualised in longitudinal sections were developed, which provides practical help for considering all input parameters and understanding the complex nature of the road pavement rehabilitation design.

REFERENCES

[1] Hungarian Main Roads 2011, Road network length according to subcategories, [in Hungarian], viewed September 2013, http://internet.kozut.hu/szakmai/orszagos_kozutak_adatai/kozutakfojellemzoi/Documents/Országos%20közúthálózat%20útkategóriánkénti%20 megoszlása.pdf.

[2] European Commission, Directorate General for Mobility and Transport 2013, Infrastructure: TEN-T: What do we want to achieve?, webpage, European Commission, DG Mobility and Transport, Brussels, viewed September 2013, http://ec.europa.eu/transport/themes/infrastructure/index_en.htm.

[3] Pallos, I, Toth, C & Petho, L 2004, 'Pavement design options in the ISPA II project', Revue of Roads and Civil Engineering, vol. 6, pp. 7–10 [in Hungarian].

[4] Odemark, N 1949, Investigations as to the elastic properties of soils and design of pavements according to the theory of elasticity, meddlane 77, Statens Vaginstitut; Stockholm, Sweden.

[5] Nemesdy, E 1986, 'Calculation of the deflection and strains in multi-layers pavement structures', Review of Transportation Sciences, May 1986, pp. 193–201 [in Hungarian].

[6] Boromisza, T 1976, 'Bearing capacity of asphalt pavements based on deflection measurements', Revue of Roads and Civil Engineering, pp. 521–28 [in Hungarian].

[7] Hungarian Road Society 2005, Design of road pavement structures and overlay design with asphalt, ÚT 2-1.202, Hungarian Road Society, Budapest, Hungry, [in Hungarian].

[8] COST Transport 1998, COST 336: use of falling weight deflectometers at network level: information gathering report, task group 2, European Cooperation in Science and Technology (COST), Brussels, Belgium, viewed 27 May 2013, http://cordis.europa.eu/cost-transport/src/pub-336.htm.

[9] Hungarian Road Society 2002, Hot mixtures and asphalt pavement courses for road constructions, ÚT 2-3.301: 2002, Hungarian Road Society, Budapest, Hungry [in Hungarian].
[10] European Committee for Standardization 2003, Bituminous mixtures: test methods for hot mix asphalt: part 22: wheel tracking, EN 12697-22-2003, CEN, Brussels.
[11] Fi, I & Petho, L 2008, 'Calculation of the equivalent temperature of pavement structures', Civil Engineering, vol. 52, no. 2, pp. 91–6.
[12] IMI, BME, Bau-Teszt, October 2003, ISPA—project, 2nd phase, Guide to pavement rehabilitation design, Contract report, Budapest, Hungary [in Hungarian].

Maintenance and rehabilitation—II

This page intentionally left blank

Asphalt Pavements – Kim (Ed)

The crack resistance potential of sand asphalts subjected to thermal loading

O.M. Ogundipe
Civil Engineering Department, Ekiti State University, Ado-Ekiti, Nigeria

N.H. Thom
NTEC, University of Nottingham, UK

A.C. Collop
Faculty of Technology, De-Montfort University, UK

ABSTRACT: A test method which involves the use of thermal cycling rig was developed to evaluate crack resistance of three sand asphalt mixtures called Sand asphalts 1, 2, and 3. The specimens were three-layer beams. The bottom layer was 10 mm asphalt concrete with 10/20 penetration grade bitumen. The middle layer was the sand asphalt and the top (surface) layer was also made of 10 mm asphalt concrete, but 40/60 penetration grade bitumen was used in the mix. Also, the control specimen (without sand asphalt layer) was examined. The specimens were subjected to thermal loading by cyclic opening and closing of the crack at the centre of the specimen at a temperature of −3°C, increasing the magnitude of crack opening with each cycle, until it was deemed to have failed. It was found that the specimens with sand asphalt layer performed better than the one without the asphalt layer. Also, the tests showed that specimen with Sand asphalt 1 in the middle layer was more successful that either Sand asphalt 2 or Sand asphalt 3 and it allowed a crack opening approximately two times greater than the control case.

Keywords: Sand asphalt, cracks, thermal loading, overlay

1 INTRODUCTION

The rehabilitation of deteriorated pavement usually involves overlaying with a new surfacing material called overlays. The major problem with overlays is reflective cracking. Reflective cracking is simply the propagation of existing cracks in an old pavement through the underside of the overlay to the surface [1]. This allows water to infiltrate the pavement causing premature failure of the overlay. Researchers have identified that the two major causes of reflective cracking in overlays are the action of traffic loading and the daily/seasonal temperature variation resulting in thermal loading [2–7]. This study focuses on the thermal loading. The daily temperature variation causes a series of repeated temperature changes over a period with the temperature above the fracture temperature of the asphalt concrete, while the seasonal temperature variation causes a single drop in temperature below fracture temperature of the asphalt concrete.

Temperature variations induce stress in the overlay. The dissipation of the stress through the process called relaxation prevents the initiation of cracks. At high temperature, the stress is dissipated quickly because asphalt is visco-elastic. However, at low temperature, asphalt behaves more as elastic material and the stress induced are not fully dissipated, resulting in concentration of stress in the crack region. This causes initiation of cracks in the overlay.

A number of researchers have investigated the crack resistance potentials of different materials used with overlays to thermal loading. Cleveland et al [8] evaluated geosynthetics placed under or within a Hot Mix Asphalt (HMA) overlay to reduce the severity or delay the appearance of reflection cracks using Texas Transport Institute (TTI) overlay tester. The overlay tester evaluates the relative ability of a HMA beam ($3 \times 6 \times 20$-inch) with and without geosynthetics to resist thermal cracking. The geosynthetics used in the research were Bitutex composite, Pave-Dry 38, PetroGrid 4582, Ha Telit C40/17, Glass Grid 8501, and Star Grid G + PF. In the study, six beams were reinforced with geosynthetic materials, with the seventh unreinforced representing the "control" beam. The beams were tested to failure in the overlay tester. The results showed the best performance was recorded with grid and composites and the non-woven products performed better than the thin asphalt surface.

Also, Bhosale and Mandal [9] carried out laboratory study on Open Graded Asphalt Concrete (OGAC) as a crack relief layer using an asphalt concrete slab fatigue testing equipment. In the research, they investigated the conventional Dense Bitumen Macadam (DBM) and the OGAC overlay under simulated thermal and traffic loads with 5 mm differential deflection of zero load efficiency factor. They performed the experimental work in a strain-controlled environment with an average room temperature of 29°C. A gap of 5 mm was maintained between two pavement plates, representing the initial existing crack width in the old distressed pavement. Simulation of daily and seasonal thermal contraction and expansion cycle was achieved by cyclically opening and closing the initial existing crack by 1.83 mm at a strain rate of 4.547 mm/min. They also considered mixed mode of displacement. They found that the conventional overlay of DBM showed faster rate of decay with number of simulated thermal load cycle than OGAC overlay. They concluded that it did arrest the crack propagation.

Dempsey [10] developed and evaluated the use of ISAC to alleviate the problem of reflective cracking in asphalt pavements. The ISAC consisted of a low-stiffness geotextile as the bottom layer, a viscoelastic membrane layer as the core, and a very high stiffness geotextile for the upper layer. In his study, a laboratory pavement section with an AC overlay placed on a jointed Portland cement concrete slab was constructed and tested in an environmental section. The thermal strain was simulated using a mechanical device, opening and closing the joint at extremely low rate. The temperature of the chamber was maintained at –1.1°C. His results showed that the laboratory AC overlay section without ISAC (control) cracked and separated completely within seven cycles of joint movement. The AC overlay performed exceedingly well when it was treated with the ISAC system and tested under the same conditions as the control pavement, cracks appeared only when the slab movement had increased to 5.08 mm and over and the ISAC geotextile had been subjected to 158 cycles.

This study investigated the performance of three different sand asphalts used with a 10 mm asphalt concrete overlay subjected to thermal loading against reflective cracking.

2 MATERIALS AND METHODS

The materials used for this study, the characterization tests carried out on the materials and the methods adopted are presented in this section.

2.1 *Materials*

The materials used in this study are as follows:

10 mm asphaltic concrete with 40/60 and 10/20 penetration grade bitumen. The mix composition is as shown in Table 1 and the particle size distribution curve for the blend of aggregates is shown in Figure 1.

The Stress Absorbing Membrane Interlayers (SAMIs) mixtures used in this research were sand asphalts 1, 2 and 3. The mix compositions of the SAMIs are shown in Table 2. The Indirect Tensile Stiffness Moduli (ITSM) of the asphalt concrete mixtures and the sand asphalts were determined using the Nottingham Asphalt Tester (NAT) in accordance with (DD 213:1993) [11]. In the ITSM a load pulse was applied to the vertical diameter of a cylindrical

Table 1. Mix composition for 10 mm asphalt concrete.

Sample type	Percent by composition of aggregate
10 mm aggregate	37%
6 mm aggregate	26%
Dust	36%
Filler	1%
Binder type	10/20, 40/60 bitumen
Binder content	5.3% by mass of total mix
Target air void	5%

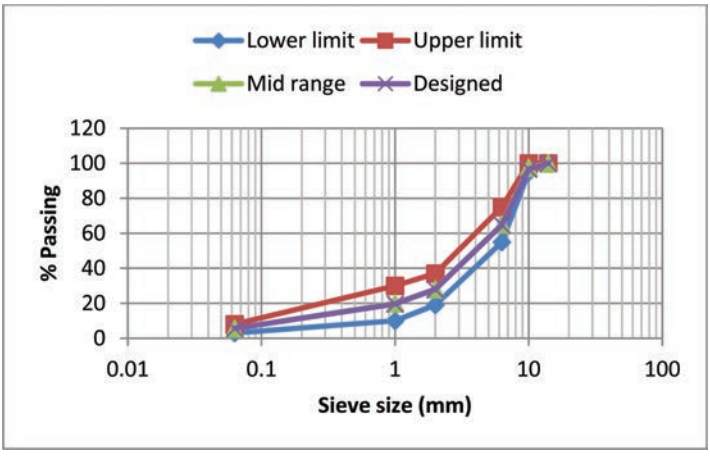

Figure 1. Particle size distribution curve for the blend of aggregates for 10 mm asphalt concrete.

Table 2. Mix compositions for sand asphalts 1, 2 and 3.

	% by composition of aggregate	% by composition of aggregate	% by composition of aggregate
Sample type	Sand asphalt 1	Sand asphalt 2	Sand asphalt 3
0/4 crushed rock fill	95%	74.5%	–
Fine sand	–	20%	84%
Filler	5%	5.5%	16%
Binder type	Polymer modified binder	Polymer modified binder	160/220 bitumen
Binder content	9% by mass of total mix	9.1% by mass of total mix	10.3% by mass of total mix
Target air void	2%	2%	5%

specimen (100 mm in diameter and 40 mm thick) positioned centrally between the upper and the lower platens and the resultant peak transient deformation along the horizontal diameter was measured. The ITSM results for the 10 mm asphalt concrete with 40/60 and 10/20 penetration grade bitumen and sand asphalts at 10°C, 20°C and 30°C are shown in Table 3.

2.2 *Methods*

The objective of this study was achieved using the thermal cracking simulation apparatus developed at the University of Nottingham. The thermal cracking testing device is shown

Table 3. Indirect tensile stiffness moduli.

Asphalt concrete (AC)/SAMIs	Stiffness (MPa)		
	Temperature		
	10°C	20°C	30°C
AC (40/60)	10035	3899	1098
AC (10/20)	15435	9591	5008
Sand asphalt 1	8548	2725	636
Sand asphalt 2	7564	2444	510
Sand asphalt 3	635	209	118

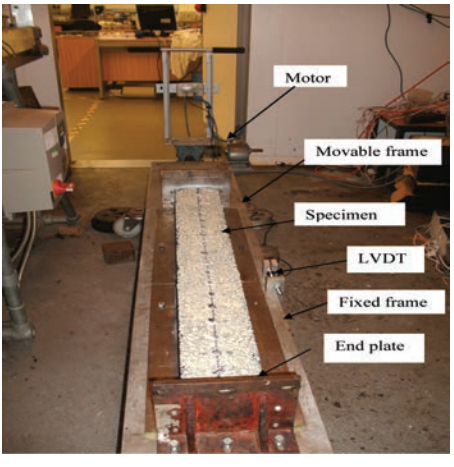

Figure 2. Thermal cycling device.

Figure 3. Thermal cycling device control unit.

in Figure 2. The mould and the control unit (see Fig. 3) were modified for the present study. The thermal cracking device is made up of a horizontal frame 2 m and 0.2 m in length and width, respectively. The horizontal frame is in two halves with one half fixed and the other half connected to a DC motor through a worm drive. This allows it to be opened and closed at a chosen rate.

It was modified such that the motor will provide selectable, variable extension and contraction rates between 1.0 mm in one hour and 1.0 mm in twenty four hours. To allow the motor to rest, the delay between individual operations varies between 5 and 95 seconds. The contraction/expansion rates were read from a Linear Variable Differential Transformer (LVDT). The indicator lights on the device control unit (see Fig. 3) were used to monitor the direction of movement of the movable plate, completion of selected operation and any fault encountered during the test.

2.2.1 *Specimen preparation and instrumentation*

The test specimens were made up of 3-layer beams of length 1000 mm and width 125 mm. The first (base) layer was a 40 mm thick 10 mm asphaltic concrete with 10/20 penetration grade bitumen, the middle layer (where present) was sand asphalt of 10 mm thickness. The top layer was a 30 mm thick 10 mm asphaltic concrete with 40/60 penetration grade bitumen. The control specimens were prepared in two layers without sand asphalt layer (the base and surface layers). In this case, the base and the surface layers were both 40 mm thick.

The beams for the first (base) layer were produced by manufacturing a slab of dimension 500 mm × 500 mm × 40 mm. The aggregates and binder were batched as shown in Table 1, mixed at 185°C and compacted in a mould 500 mm × 500 mm × 205 mm with a roller compactor at a temperature of 180°C just before compaction to a thickness of 40 mm. The slabs were cut into beams of 500 mm and 125 mm in length and width, respectively. Two steel and end plates were bolted on the frame; then the two beams were glued on the steel plates and the sides of the mould were bolted to the end plates as shown in Figure 2. The sand asphalts' materials were batched as shown in Table 2. The aggregates and binders for sand asphalt 3 were heated at 140°C and compacted at 130°C, while the aggregates and binder for sand asphalts 1 and 2 were batched and heated to a temperature of 180°C, and compacted on the bottom layer at a temperature of 150°°C. The compaction was done with a vibrating hammer (Kango). The surface layer aggregates were batched as shown in Table 1 and heated to 160°C and compacted to the required thickness at 150°C. All the mixtures were mixed in accordance with (BS EN 12697-35:2004) [12].

Demec pips were glued to the centre of the top layer 50.8 mm apart to measure the surface strain. Also, the expansion and contraction (opening and closing) of the frame was monitored using the LVDT readings. The top of the specimen was painted white to monitor the appearance of cracks.

3 TEST PROCEDURE

The thermal cycling testing device with the specimen in place was placed in a temperature controlled room at test temperature of −3°C for a minimum of five hours. The test was conducted by opening the movable part of the rig for a period of 6 hours and closing it for another 6 hours. This was achieved by setting the contraction (closing) or the expansion (opening) rate on the control box and the required travel distance. The appearance of a crack on the surface was monitored visually and the movement of the movable frame was read from the LVDT. The strain on the overlay (surface layer) was measured and recorded. The test was stopped when the sample was deemed to have failed completely. The criterion for failure was the appearance of a crack at the surface of the specimen.

4 TEST RESULTS

The surface strain was determined from the demec gauge readings. The results were presented as graphs of surface strain versus the distance from the centre of the specimen to the point the measurement was taken on the specimen.

4.1 *Control specimen (No SAMI)*

The specimen was tested by opening the movable frame for 6 hours and closing it for 6 hours at each prescribed travel distance. It failed after crack opening of 1 mm. The surface strains for 0.5 mm and 1 mm crack openings are shown in Figure 4. It shows that for 0.5 mm crack opening, the strains were almost uniformly distributed with peak strain developing at –50 mm (50 mm to the left of the beam's centre) and at the centre, no crack was seen on the specimen at this point. Also, at 1.0 mm crack opening, the strain concentration developed at the centre of the specimen directly above the centre of the split base and cracks appeared at the surface (centre) spanning the whole width of the specimen. The photographs of the specimen before and after the test are shown in Figure 5.

The reason for early appearance of a crack can be attributed to two major factors. The first is the bond between the surface layer (overlay) and the base layer, subjected to tensile loading. At low temperature, strong bond exists between the overlay and the base layer for the control specimen [1]. The strong bond provides restraint for the horizontal movement of the base layer, therefore resulting in tensile strain concentration at the base of the overlay. The second factor is the lack of any soft interlayer (sand asphalt) between the overlay and the base layer. The horizontal deformation of this layer allows dissipation of energy and the slip

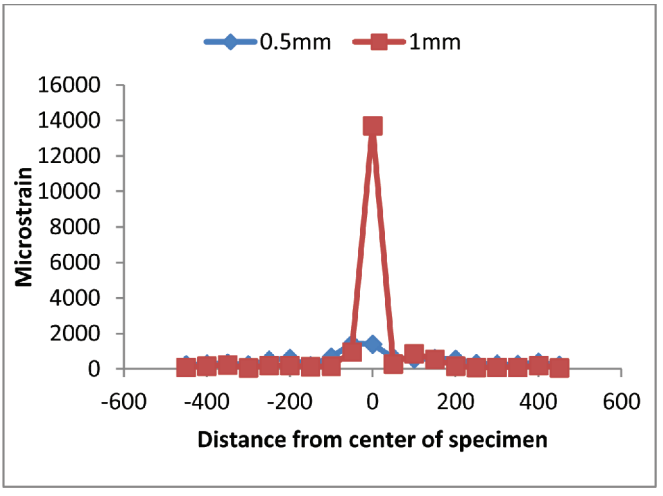

Figure 4. Strains at 0.5 and 1.0 mm opening.

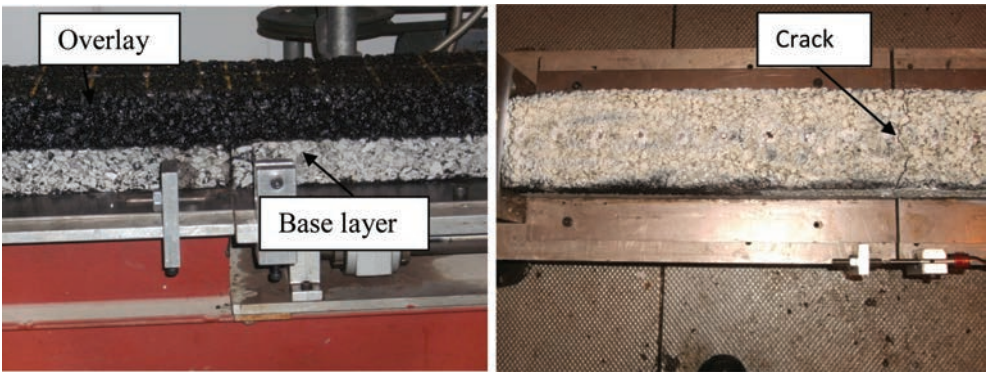

Figure 5. Photographs of the control specimen (a) before (b) after the test.

between the layer and the overlay isolates the overlay from the tensile strain concentration because of reduced restraint to the horizontal movement of the base layer, therefore reducing the tensile strains in the overlay. In the case of a control specimen with strong bond and no sand asphalt, high tensile strains developed in the overlay leading to rapid propagation of a crack when the fracture strength of the overlay is exceeded.

4.2 *Specimen with sand asphalt 1*

The specimen with sand asphalt 1 was subjected to thermal cycling and cracks appeared after 2.0 mm crack opening. The surface strain distribution in the specimen for crack openings of 0.5 mm, 1.0 mm, 1.5 mm and 2.0 mm are shown in Figure 6. The figure shows that the strain distribution was uniform at –150 mm to –400 mm while strain concentration developed at –100 mm to 450 mm. Cracks were seen after the device was opened by 1.5 mm at the part of the beam with high strain concentration, the test was stopped after crack opening of 2.0 mm when the specimen was deemed to have failed The photographs of the specimen before and after the test are shown in Figure 7. It can be seen from the figure that cracks developed in the area with high strain concentration, while no crack was seen in the area with uniform stress concentration.

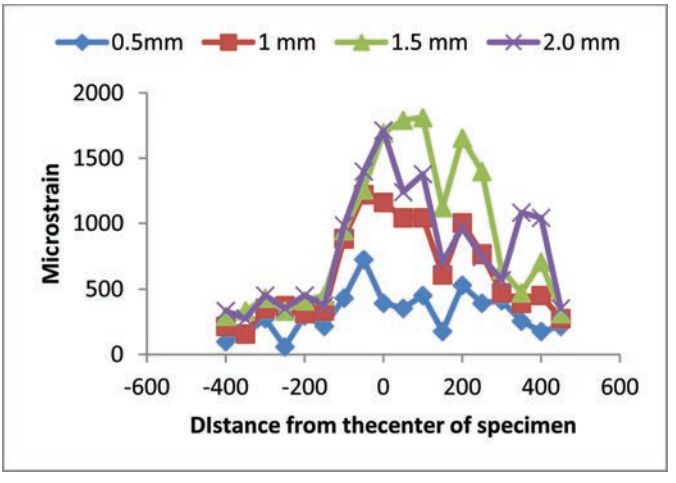

Figure 6. Strains at 0.5 mm and 1.0 mm, 1.5 mm and 2.0 mm opening.

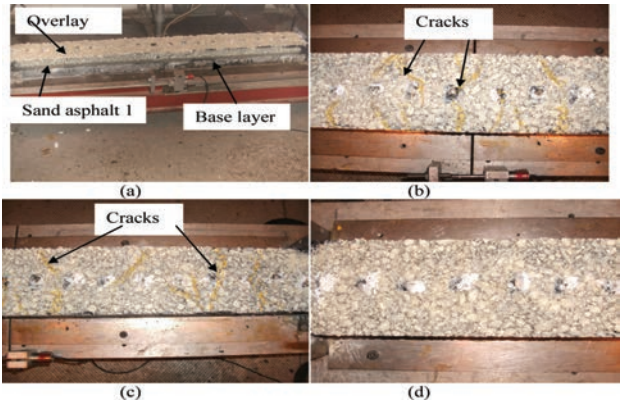

Figure 7. Photographs of the specimen incorporating sand asphalt 1 (a) before (b) after the test (center) (c) after the test (right) (d) after the test (left).

Also, as explained for the control specimen, two factors were responsible for the performance of sand asphalt 1. These are the bond between the overlay, the sand asphalt and the base layer and the crack resistance of the sand asphalt because of its stiffness. The sand asphalt 1 (SAMI layer) allows the dissipation of energy and in turn less tensile strain in the overlay. Cracks appeared after crack opening of 2.0 mm compared to 1.0 mm for the control specimen.

4.3 *Specimen with sand asphalt 2*

The same test procedure was carried out for the specimen with sand asphalt 2. The test was stopped after crack opening of 1.5 mm as cracked appeared at the surface. The surface strain distributions at 0.5 mm, 1.0 mm and 1.5 mm crack openings are shown in Figure 8. The figure shows that strain concentration developed at the centre of the specimen, while the strain distribution was uniform at the right and left of the specimen. Cracks appeared after opening the movable frame by 1.5 mm in the region of strain concentration. The photographs of the specimen before and after the test are shown in Figure 9.

Although the specimen failed at 1.5 mm crack opening, the strain distribution in the overlay was more uniform than that in specimen with sand asphalt 1. This is probably because sand asphalt 1 mixture is coarser, thus having greater stiffness and less flexibility than sand asphalt 2. Jung and Vinson [13] observed that mixture fracture strength depends on the aggregate type and sizes and the air voids of the mixture. It is clear like the specimen with sand asphalt 1 that the crack resistance is influenced by the presence of sand asphalt 2 with lower stiffness than the overlay and the base layer.

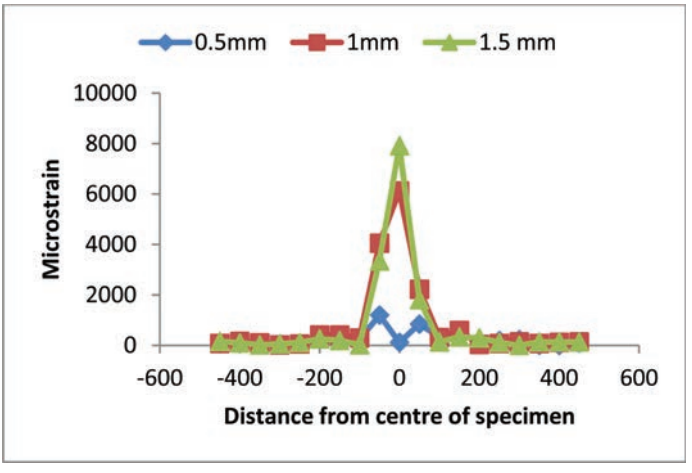

Figure 8. Strains at 0.5 mm and 1.0 mm, and 1.5 mm opening.

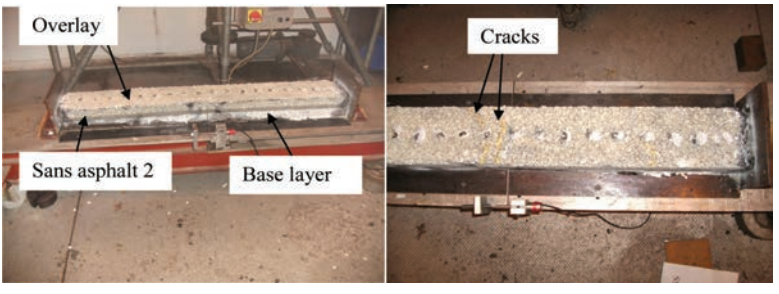

Figure 9. Photographs of the specimen incorporating sand asphalt 2 (a) before test (b) after test.

4.4 *Specimen with sand asphalt 3*

The test for the specimen with sand asphalt 3 was carried out like the other specimens. At 0.5 mm and 1 mm crack openings as shown in Figure 10, the strain distribution was uniform at the two ends with peak concentration developing around the centre of the specimen (crack region). Also, the figure shows that at 1.5 mm and 2.0 mm crack openings, the stress at this stage was concentrated at the centre and the test was stopped after 2.0 mm when a full width crack developed at the centre. Dave et al [14] found in their study that sections with highly modified sand asphalt placed under the overlay under thermo-mechanical loading cycle showed no crack, but that the bottom of the binder course (overlay-interlayer interface) was at the threshold of complete softening and separation. This shows the importance of the interface bond to the resistance of the SAMIs to crack developing at the surface of the overlay under thermal loading.

Also, in this case, the specimen benefits from the slip between the overlay and the sand asphalt 3 allowing relative movement of the base layer and isolating the overlay from stress concentration in the crack region. The photographs of the specimen before and after test are shown in Figure 11. However, the ineffectiveness of the sand asphalt against reflective cracking under traffic loading has to be taken into consideration [15]. This indicates that while the low stiffness of the interlayer aids retardation of cracks, their load carrying capacity must be considered before they are chosen for a particular purpose.

4.5 *Summary*

The summary of the surface strain results are presented in Figure 12. It shows the maximum measured strain at the surface of the specimen. These results are most revealing. Based on

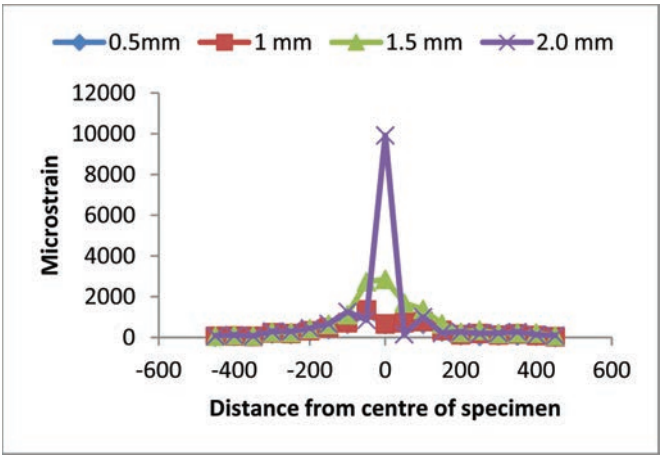

Figure 10. Strains at 0.5 mm and 1.0 mm, 1.5 mm and 2.0 mm opening.

Figure 11. Photographs of the specimen incorporating sand asphalt 3 (a) before test (b) after test.

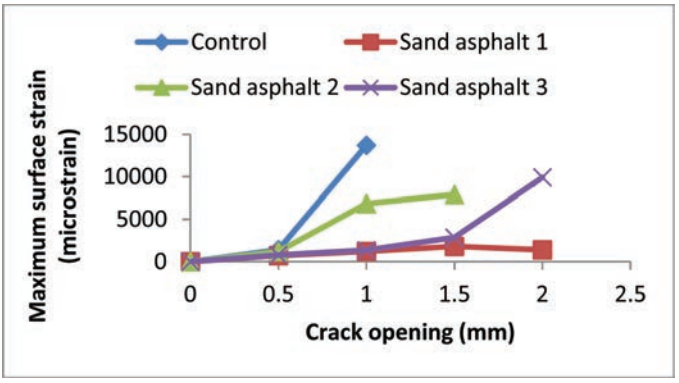

Figure 12. Summary of data from thermal cycling test.

experience from fatigue testing one would expect cracking to propagate rapidly once the strain level reached greater than about 2000–3000 microstrain and this does indeed appear to have been the case. Sand asphalt 1 has been the most successful and it is considered likely that the final point shown on the curve may be false, perhaps because the location of maximum strain was outside the strain measurement zone. Nevertheless sand asphalt 1 has clearly been more successful than either sand asphalt 2 or the sand asphalt 3 and it allowed a crack opening approximately two times greater than the control case.

5 CONCLUSION

This paper presents an evaluation method for performance of sand asphalt against reflective cracking under thermal loading. It can be seen from the tests that all the specimens with sand asphalt performed better than the control specimen with no SAMI. This indicates that having a soft interlayer like sand asphalt between the overlay and existing pavements retards/delays crack growth, thus increasing the life of the overlay. The strain distribution was more uniform in all the specimens with sand asphalt than the control specimen and they sustained greater crack opening than the control specimen. This established the importance of the slip between the overlay and SAMIs to the crack resistance of sand asphalts used as interlayer between overlay and existing pavement. The slip ensures that stress concentration around the crack region is not transferred to the overlay.

REFERENCES

[1] O.M. Ogundipe. Mechanical Behaviour of Stress Absorbing Membrane Interlayers. Ph.D Thesis, University of Nottingham, Nottingham, United Kingdom, 2011.
[2] Palacios C., Chehab G.R., Chaignon F. and M. Thompson. Evaluation of fibre reinforced bituminous interlayers for pavement preservation. Proceedings of 6th International RILEM Conference, Chicago, U.S.A. 721–729, 2008.
[3] Von Quintus H.L., Mallela J., Weiss W. and S. Shen. Techniques for Mitigation of Reflective Cracking. Applied Research Associates, Champaign, IL, USA. Interim Report AAPTP 05-04, 2007.
[4] Nesnas K. and M.E. Nunn M.E. A thermal pavement response model for top-down reflection cracking in composite pavement. 85th Annual Meeting of the Transportation Research Board. Washington D.C., 2006.
[5] Abe N., Maehara H., Maruyama T. and Ooba K. An Examination of Factor which affects Reflective Cracking. Proceedings of 4th International RILEM Conference, Ottawa, Canada. 464–474, 2000.
[6] Moleenar A.A.A. Evaluation of Pavement Structure with Emphasis on Reflective Cracking. Proceedings of 2nd International RILEM Conference, 21–48, 1993.

[7] Smith R.G. Laboratory Testing of Fabric Interlayers for Asphalt Concrete Paving: Interim Report. Transportation Research Record 916. 6–17, 1983.
[8] Cleveland G.S., Button J.W. and Lytton R.L. Geosynthetic in Flexible and Rigid Pavement Overlay. Texas Transport Institute, Texas A&M University System. Report 1777-1, 2002.
[9] Bhosale S.S. and Mandal J.N. Open Graded Asphalt Concrete for Mitigation of Reflection Cracking on Asphalt Concrete Overlays. 12th International Conference of International Association for Computer Methods and Advances in Geomechanics (IACMAG), India. 4409–4416, 2008.
[10] Dempsey B.J. Development and Performance of Interlayer Stress-Absorbing Composite in Asphalt Concrete Overlays. Transportation Research Record 1809. 175–183, 2002.
[11] British Standard. Method for determination of the indirect tensile stiffness modulus of bituminous mixture. British Standard Institution, London, UK, 1993. (DD 213:1993).
[12] British Standard. Bituminous Mixtures-Test Method for Hot Mix Asphalt: Laboratory Mixing. British Standard Institution, London, UK, 2004. (BS EN 12697-35:2004).
[13] Jung D.H. and T.S. Vinson. Low Temperature Cracking: Test Selection. Strategic Highway Research Program, National Research Council, Washington D.C. SHRP-A-400, 1994.
[14] Dave E.V., Song S.H., Buttlar W.G. and G.H. Paulino. Reflective and Thermal Cracking Modeling of Asphalt Concrete Overlays. Advanced Characterization of Pavement and Soil Engineering Materials. 1241–1252, 2007.
[15] Ogundipe O.M. Thom N.H. and A.C. Collop. Investigation of Crack Resistance Potential of Stress Absorbing Membrane Interlayers (SAMIs) under Traffic Loading. Construction and Building Materials Journal, Vol. 38, pp. 658–666, 2013.

This page intentionally left blank

Asphalt Pavements – Kim (Ed)

Sustainability metrics of flexible pavement preservation and rehabilitation in Canada

Susanne Chan
Pavement Design Engineer, Downsview, Ontario, Canada

Becca Lane
Materials Engineering and Research Office, Downsview, Ontario, Canada

Tom Kazmierowski
Pavement and Materials Engineering, Golder Associates Ltd., Mississauga, Ontario, Canada

ABSTRACT: The Ministry of Transportation Ontario (MTO) is committed to maintaining the provincial transportation infrastructure in a sustainable manner. One way to achieve pavement sustainability is through the combined use of environmentally sound pavement preservation and in-situ pavement recycling strategies. Pavement preservation is the use of proactive, planned strategies that extend the life of the pavement, providing a cost effective solution for asset management. In-place pavement recycling is a pavement rehabilitation strategy that reuses 100% of the existing roadway materials, conserving non-renewable resources, eliminating disposal costs, and reducing environmental impacts.

This paper outlines the various pavement preservation and in-place recycling strategies utilized in Canada to achieve sustainability. Pavement sustainability is quantified by comparing the energy consumption and Greenhouse Gas (GHG) emissions generated by the various pavement rehabilitation strategies using the PaLATE software. The results indicate that pavement preservation and in-place recycling strategies are cost competitive and provide a significant reduction in energy use, aggregate consumption, and GHG emissions when compared to traditional rehabilitation treatments. Detailed discussion on these technologies and their environmental impacts are presented, as well as a 10 years historical perspective of the Ministry's pavement preservation and in-place recycling program.

Keywords: Pavement preservation, in-place pavement recycling, greenhouse gas emissions, sustainable pavements, PaLATE

1 INTRODUCTION

The Ministry of Transportation Ontario (MTO) believes that the protection of air, water and land resources is necessary to sustain current and future generations. The main benchmarks established for sustainable pavements are reducing the use of natural resources, reducing energy consumption and minimizing Greenhouse Gas (GHG) emissions [1]. One way to achieve pavement sustainability is through the combined use of environmentally sound pavement preservation and in-place pavement recycling strategies.

This paper outlines the various pavement preservation and in-place recycling strategies utilized in Canada to achieve sustainability. Also, detailed discussion on these technologies and their environmental impacts are presented, together with the 10 years historical perspective of the ministry's pavement preservation and in-place recycling program.

2 PAVEMENT SUSTAINABILITY TREATMENTS

Pavement sustainability can be achieved through the combined use of pavement preservation and in-place recycling strategies. The following subsections outline the various pavement preservation and in-place recycling strategies utilized by MTO.

2.1 *Flexible pavement preservation treatments*

Pavement preservation is a proactive, planned strategy applied in a timely manner to extend the life of the pavement without adding structural strength to the pavement. The timeframe to apply pavement preservation is early in the pavement's life before the pavement has deteriorated past a certain condition; thereafter a more costly, less sustainable rehabilitation treatment is required. The various pavement preservation treatments used by MTO are summarized as follows: [2].

2.1.1 *Crack sealing*

Crack sealing treatments are used to prevent water and debris from entering cracks in Hot Mix Asphalt (HMA) pavement. Limiting water infiltration protects the underlying pavement layers and reduces the detrimental effects of freeze thaw cycles. Typically, the Ministry expects crack sealing to extend the life of a pavement by 3 years and as such, crack sealing is a cost effective treatment to prolong the pavement life.

2.1.2 *Slurry seal*

Slurry seal is a thin cold slurry treatment applied to the entire HMA surface. Typically it is used to seal the pavement surface, fill minor surface irregularities, address ravelling and oxidation, and to improve friction. It consists of a mixture of well-graded aggregate and slow setting emulsion and has an expected pavement extension life of 3–5 years.

2.1.3 *Micro-surfacing*

Micro-surfacing is a premium, polymer-modified cold slurry paving system applied to the entire HMA surface. Typically it is used to address ravelling and oxidation, fill ruts and minor surface irregularities, and to improve friction and ride. It consists of a mixture of dense-graded aggregate, asphalt emulsion, water and mineral fillers that is typically placed 10–12 mm thick, with an expected pavement life extension of 7–9 years. Micro-surfacing is a good example of preventive maintenance and the Ministry considers this treatment to be one of the most cost effective preservation treatments.

2.1.4 *Chip seal*

Chip seal is a mechanized spray patching application of asphalt and single-sized aggregate chips rolled onto the existing pavement surface. Typically it is used to seal the pavement surface, enrich hardened or oxidized asphalt, and to improve surface friction. It can be applied on a small patch area (Dynapatch) or the entire HMA surface, with an expected pavement life extension of 4–6 years.

2.1.5 *Ultra-thin bonded friction course*

Ultra-thin bonded friction course, also known as Novachip®, is a thin HMA treatment that is applied to the entire pavement surface. Typically it is used to address surface distress, seal the surface and increase surface friction. It consists of gap-graded polymer-modified HMA placed about 10 to 20 mm thick on a heavy, polymer-modified emulsified asphalt tack coat. This treatment has a relatively high initial cost and, subsequently, has shown limited use by the Ministry.

2.1.6 *Fibre modified chip seal*

Fibre Modified Chip Seal (FMCS), also known as FiberMat®, is a mechanized spray patch thin treatment that is applied over the existing HMA surface. It is a similar process

to regular chip seal with the addition of fibre to help prevent reflective cracking. FMCS incorporates chopped fibreglass strands on the polymer-modified emulsion which has been sprayed onto the existing surface, applies a second spray of polymer-modified emulsion and covers this with an aggregate layer. Typically it is used either to seal the surface to prevent water ingress and control reflective cracking or as a Stress Absorbing Membrane Interlayer (SAMI) to mitigate reflection cracking of a new overlay. This is a relatively new treatment utilized by the Ministry, and the results and performance are being monitored.

2.1.7 *Hot in-place recycling*

Hot In-place Recycling (HIR) is used by the Ministry as both a pavement preservation and pavement rehabilitation strategy for pavements that are generally free of major structural distress. HIR is used to address surface distress, and improve surface friction and ride. For the HIR process, the existing surface is heated and scarified in-place to a depth of 40–50 mm, rejuvenated and reprofiled to a new grade. This operation is carried out with an HIR train in a continuous operation. HIR is considered a sustainable preservation treatment since it recycles 100% of the existing HMA surface in-place, which minimizes material hauling to and from site. This preservation treatment has an expected pavement life extension of 7 to 9 years, similar to a conventional one lift HMA overlay.

2.1.8 *Warm mix asphalt*

Warm Asphalt Mix (WMA) is an environmentally friendly alternative to HMA. WMA is produced at temperatures about 30 °C lower than conventional HMA. Producing WMA at lower temperature uses less energy and also significantly reduces the emissions generated. Some other potential WMA benefits: mix can be transported over longer haul, easier to achieve compaction density, shorter time required for opening to traffic, potential to improve construction of transverse and longitudinal joints and reduced workers' exposure to fumes during placement and compaction of the WMA.

2.2 *In-place flexible pavement recycling strategies*

For over two decades, in-place pavement recycling technologies have been developed which enable an existing pavement surface to be rejuvenated and reprofiled in-place. This eliminates the need for off-site hauling and processing, enhancing the environmental benefits. The Ministry has successfully implemented a number of in-place pavement recycling technologies in the past, and they are performing well. Following outlines the various in-place recycling rehabilitation strategies used by MTO [3].

2.2.1 *Full Depth Reclamation (FDR)*

FDR is a pavement reconstruction technique where the existing HMA pavement and a predetermined portion of the underlying granular base are pulverized in-place to produce a well graded, homogenous base material [4]. A new HMA binder and surface courses are placed after FDR to complete the pavement rehabilitation. FDR is performed on the roadway without the addition of heat, and the treatment depths are typically 100 to 300 mm.

2.2.2 *Cold In-place Recycling (CIR)*

Conventional CIR is an established pavement rehabilitation technique that processes in-place the existing HMA pavement for depths up to 125 mm, mixes in a small amount of emulsified asphalt cement (about 1–1.5%) and then reprofiles the mix as a binder course in one continuous operation. A new HMA surface course is placed after the emulsion has set and the moisture and compaction specification requirements have been met, typically after 14 days [5].

CIR is a cold process that saves energy and reduces emissions. It is well suited to address a wide range of moderate to severe pavement distresses, and it has been found to mitigate reflective cracking and extend pavement life [6].

2.2.3 *Hot In-place Recycling (HIR)*

HIR is a pavement rehabilitation technique that consists of heating and softening the existing HMA surface, scarifying the heated pavement surface, adding rejuvenator, fine aggregates and/or admixture as required, mixing, reprofiling and then compaction as a binder or surface course in one continuous operation. Typical treatment depth is about 40 to 50 mm, with some multi-stage trains claiming to treat up to 75 mm depth. HIR is also considered as a preservation treatment because, when properly designed, it can act as a standalone surfacing not requiring a separate overlay.

2.2.4 *Full depth reclamation with Expanded Asphalt Stabilization (EAS)*

FDR with EAS is a reconstruction process that includes in-place full depth reclamation of the HMA and underlying granular with the addition of expanded (foamed) asphalt cement. To expand or "foam" the asphalt, a small amount of cold water is injected into the hot asphalt cement in the expansion chamber of a reclaimer/stabilizer. As the cold water turns to steam, the asphalt cement 'foams', facilitating mixing with the cold, damp, reclaimed material from the FDR process. With a minimum of two-day curing period after the stabilized material is graded and compacted, the expanded asphalt stabilized base can be overlaid with HMA [7].

EAS is an in-place process that allows for 100% cold recycling of the roadway material, resulting in fuel savings and reducing emissions. The stabilizing process, which typically involves the top 150 mm of the FDR layer, strengthens the recycled base, thus, reducing the thickness requirements of the HMA overlay.

2.2.5 *Cold In-place Recycling with Expanded Asphalt Mix (CIREAM)*

CIREAM is a recent development in CIR technology that uses expanded asphalt rather than emulsified asphalt to bind the mix. It adopts the same concept of adding 1% cold water into the heated asphalt cement to expand (foam) the asphalt for more efficient coating of the reclaimed asphalt material. In addition, the curing time required prior to overlay with a HMA surface course is significantly reduced from the conventional CIR of 14-days to 2-days with CIREAM, since less moisture is added during the process [5].

2.3 *Quantities of sustainable pavement treatments*

Over the years, MTO has carried out many pavement preservation treatments and in-place recycling strategies to extend the pavement life. Table 1 below summarizes the quantities of pavement preservation and in-place recycling treatments that were carried out in the past 10 years.

Micro-surfacing accounts for the vast majority of the Ministry's preservation treatment quantities (72%). The performance of the micro-surfacing has been very good and

Table 1. Summary of MTO sustainable treatments quantities (2003–2012).

Treatment	Quantities (m^2)
Preservation	
Slurry seal	906,050
Micro-surfacing	7,309,677
Chip seal	849,178
Fibre modified chip seal	578,878
Ultra-thin bonded friction course	450,223
In-place processing	
Hot in-place recycling	324,124
Full depth reclamation	16,097,880
Cold in-place recycling	4,388,508
Expanded asphalt stabilization	2,929,914
Cold in-place with expanded asphalt mix	3,758,829
Total sustainable treatment quantities	**37,593,261**

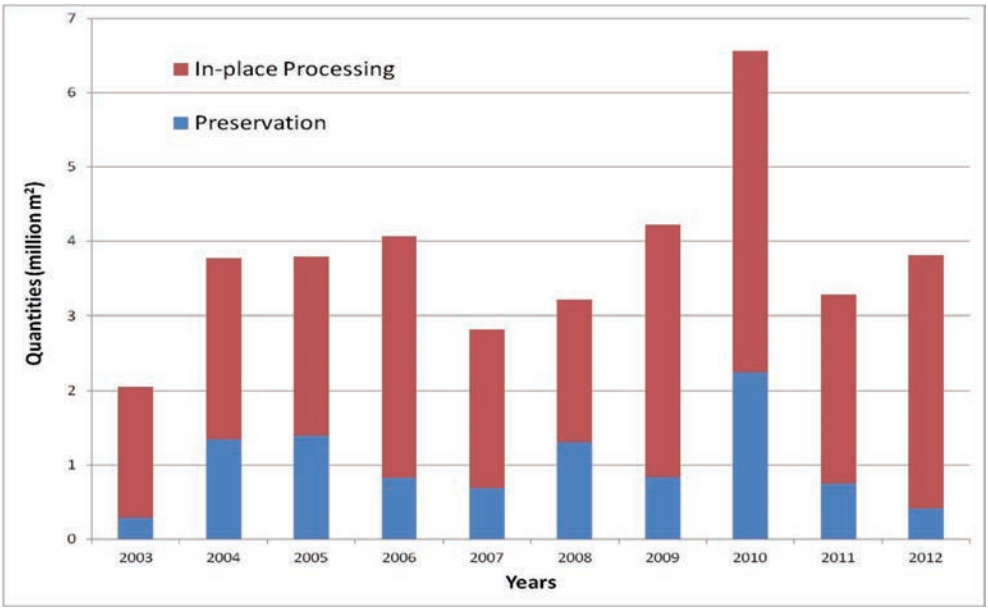

Figure 1. Historical perspective of MTO sustainable pavement quantities.

has demonstrated a relatively long service life, which makes it a cost effective preservation treatment. As an in-place processing strategy, FDR accounts for the vast majority of the Ministry's in-place recycling quantities (59%). However, in recent years the quantities of FDR has been decreasing as a result of the nature and focus of the Ministry's capital construction program and the use of other in-place recycling methods.

Figure 1 presented the 10 years (from 2003 to 2012) historical perspective of the Ministry's preservation and in-place recycling program.

As noted in Figure 1, the preservation treatment and in-place recycling rehabilitation quantities fluctuate year-to-year based on the focus and nature of the capital construction and preservation programs. It is important to note that MTO achieves its sustainable pavement goals by incorporating pavement preservation and in-place recycling strategies in its day-to-day program decision making process.

3 PAVEMENT SUSTAINABILITY METRICS

Recently, MTO has been using the PaLATE software to calculate GHG emissions produced by various road construction activities to assist decision-makers in evaluating the use of recycled materials in highway construction. PaLATE, which stands for Pavement Life-cycle Assessment for Environmental and Economic Effect, was developed at the University of California at Berkley [8]. Material quantities and haul distances are entered for specific treatments and the model calculates the emissions and energy consumption according to production, transportation and processing. Based on a typical 2-lane km highway pavement section, Table 2 below illustrates the environmental effects for the various pavement preservation and in-place recycling treatments estimated using PaLATE.

Table 2 is subdivided into preservation and in-place processing subsections. For the preservation treatment subsection, micro-surfacing appears to be the most environmentally friendly option with the least energy consumption and lowest CO_2 emissions. For the in-place processing subsection, CIR and CIREAM exhibit similar environmental benefits, and they appear to be the most sustainable of the in-place recycling options.

Table 2. Environmental metrics for various construction activities.

Treatment	Energy (MJ)	CO_2 (tonne)	Aggregate (t)
Preservation			
Micro-surfacing	105,993	6	140
50 mm hot in-place recycling	627,646	28	0
Mill 50 mm + pave 50 mm (WMA)	700,015	35	831
Mill 50 mm + pave 50 mm (HMA)	749,586	36	831
In-place processing			
180 mm FDR + 90 mm HMA	1,219,783	63	1,496
100 mm CIR + 50 mm HMA	851,409	45	831
150 mm EAS (180 mm FDR) + 50 mm HMA	1,264,264	68	831
100 mm CIREAM + 50 mm HMA	844,974	44	831
Mill 100 mm + 130 mm HMA	1,481,675	74	2,161

Table 3. Energy consumption and GHG emissions of various preservation treatments.

Treatment	Energy (MJ)	CO_2 (tonne)	NO_x (tonne)	SO_x (tonne)
Mill 50 pave 50 (HMA)	749,586	36	264	159
Mill 50 pave 50 (WMA)	700,015	35	236	148
50 mm HIR	627,646	28	202	127
Microsurfacing	105,993	6	37	25

3.1 *Case study: Preservation treatment*

This case study compares the environmental benefits in terms of energy and GHG emission reductions for selected pavement preservation techniques versus traditional mill and overlay (shave and pave) techniques.

3.1.1 *Quantifying environmental effects using PaLATE*

The following are the pavement preservation treatments selected in this case study for comparison with traditional mill 50 mm and overlay 50 mm HMA:

- Mill 50 mm and overlay 50 mm with Warm Mix Asphalt (WMA)
- 50 mm Hot In-place Recycling (HIR)
- Micro-surfacing

Based on a typical 2-lane km highway pavement section, Table 3 below illustrates the energy consumption and GHG emissions of the selected treatments generated by PaLATE and further verified with other references [9].

According to Table 3, the traditional mill and overlay treatment with conventional HMA generated the greatest energy consumption and GHG emissions compared to the other selected preservation treatments. Since the treatments have different expected service lives, the expected service life should be factored into the energy consumption and GHG emissions to normalize the data to allow for an appropriate comparison [9]. Therefore, all the above treatments were further broken down into the energy and emissions generated per year of service (Table 4). The annualized energy and GHG emissions were calculated by dividing the information from Table 3 by the expected service life of each treatment.

According to Table 4, micro-surfacing is the most sustainable pavement preservation technique among the four treatments. It emits the least GHG and consumes the least amount of energy. It is important to note that the other preservation treatment options are also more sustainable when compared to the traditional mill and overlay techniques.

With the data presented in Table 3 and 4, if MTO were to perform a traditional mill and overlay instead of micro-surfacing over the past 10 years, the figures below show the

Table 4. Annualized energy consumption and GHG emissions generated.

Treatments	Service life	Energy (MJ)	CO_2 (tonne)	NO_x (kg)	SO_x (kg)
Mill 50 pave 50 (HMA)	10	74,959	3.6	26.4	15.9
Mill 50 pave 50 (WMA)	10	70,002	3.5	23.6	14.8
50 mm HIR	9	69,738	3.1	22.4	14.1
Micro-surfacing	7	15,142	0.9	5.3	3.6

Table 5. Additional GHG emissions with mill and overlay only strategy.

	CO_2 (tonne)	NO_x (tonne)	SO_x (tonne)
Mill & overlay (A)	37,593	276	166
Micro-surfacing (B)	6,265	39	26
Additional emissions (A)-(B)	**31,327**	**237**	**140**

Table 6. Additional life cycle GHG emissions if using mill and overlay.

	CO_2 (tonne)	NO_x (tonne)	SO_x (tonne)
Mill & overlay (A)	37,593	276	166
Micro-surfacing (B)	8,951	55	37
Additional emissions (A)-(B)	**28,642**	**220**	**129**

Table 7. Annualized costs savings for micro-surfacing vs. mill and overlay.

Treatments	Unit cost (m^2)	Expected service life (yrs)	Annualized unit cost (m^2/year) (Unit cost/service life)
Mill and overlay	\$15.09	10	\$1.51
Micro-surfacing	\$7.00	7	\$1.00

associated additional GHG emissions (Table 5). This is calculated based on the 10 year micro-surfacing quantity (from Table 1: 7,309,677 m^2, which is equal to 1,044 2-lane km), and the GHG emissions from Table 4.

For a more appropriate comparison, the data should be annualized by factoring in the expected service life. Using the information from Table 4, the associated additional GHG emissions from Table 6 below are calculated to reflect the life cycle emissions. This is calculated based on the 10 year micro-surfacing quantity (from Table 1: 7,309,677 m^2, which is equal to 1,044 2-lane km), multiplied by the annualized GHG emissions from Table 5, and then by the life cycle of 10 years.

3.1.2 *Economic assessment*

As part of the definition of sustainability, it is also important to look at the economics of the various preservation treatments. Table 7 illustrates the approximate cost associated with the preferred preservation technique (micro-surfacing) versus the traditional mill and overlay technique.

According to Table 7, micro-surfacing has an initial 53% construction cost savings when compared to mill and overlay on a m^2 basis. After factoring in the expected service life of the treatment, the annualized unit cost for micro-surfacing has a 34% cost reduction compared to mill and overlay on a m^2 basis. Based on the information from Table 1 and 7, the initial and life cycle cost savings are presented in Table 8 below. This is calculated by multiplying the micro-surfacing

quantity (from Table 1: 7,309,677 m^2) to the associated costs presented in Table 7. Please note the dollar figures have been rounded off, which may cause some discrepancy.

3.1.3 *Aggregate conservation assessment*

As part of the definition of sustainability, it is also important to assess the savings of natural resources in preservation treatments. Table 9 below illustrates the approximate aggregate tonnages associated with the preferred preservation technique (micro-surfacing) versus the traditional mill and overlay technique for a 2-lane-km highway.

Based on the information from Table 1 and 9, the initial and life cycle aggregate consumption quantities are presented in Table 10 below. This is calculated by multiplying the micro-surfacing quantity (from Table 1: 7,309,677 m^2, which is equal to 1,044 2-lane km) to the associated aggregate consumption presented in Table 9. Please note the quantities have been rounded off, which may cause some discrepancy.

3.1.4 *Summary of the quantified sustainability of micro-surfacing*

This is to summarize the environmental and economic benefits of applying micro-surfacing verse mill and overlay as discussed previously. Table 11 below shows the life cycle savings of using micro-surfacing for the past 10 years (2003 to 2012).

Therefore, from a life cycle perspective, if MTO were to have performed a traditional mill and overlay instead of micro-surfacing over the past 10 years, there would have been 28,642 tonnes additional CO_2 emissions released, more than $37.2 million additional cost, and 658,915 tonnes of additional aggregate consumed.

Table 8. Cost savings for using micro-surfacing vs. mill and overlay.

	Initial construction cost ($)	10 years life cycle cost ($)
	(Unit cost × quantity)	(Annualized unit cost × quantity × 10 years)
Mill & overlay (A)	110,303,026	110,303,026
Micro-surfacing (B)	51,167,739	73,096,770
Cost savings (A)-(B)	**59,135,287**	**37,206,200**

Table 9. Annualized aggregate consumption for micro-surfacing vs. mill and overlay.

Treatments	Weight (t)	Expected service life (yrs)	Annualized weight (t/year) (Weight/service life)
Mill and overlay	831	10	83.1
Micro-surfacing	140	7	20

Table 10. Aggregate savings for using micro-surfacing vs. mill and overlay.

	Initial aggregate consumption (t)	10 years life cycle aggregate consumption (t)
	(Weight × quantity)	(Annualized weight × quantity × 10 years)
Mill & overlay (A)	867,763	867,763
Micro-surfacing (B)	146,194	208,848
Aggregate savings (A)-(B)	**721,570**	**658,915**

Table 11. Life cycle savings for micro-surfacing vs. mill and overlay.

	CO_2 (t)	Cost ($)	Aggregate (t)
Mill & overlay (A)	37,593	110,303,026	867,763
Micro-surfacing (B)	8,951	73,096,770	208,848
Savings (A)-(B)	**28,642**	**37,206,256**	**658,915**

For comparison purposes, this savings in CO_2 emissions is equivalent to making a town with a population of 6,952 households carbon-neutral for one year.

4 CONCLUSION

There is an increased focus on sustainable asset preservation, both at the federal, provincial and municipal levels. Pavement preservation and in-place recycling rehabilitation treatments applied at the right time can significantly extend the pavement life and result in improved network performance over time.

Pavement preservation and in-place recycling processes are less disruptive to the travelling public, produce less GHG emissions, consume less energy and conserve materials. With a coordinated pavement preservation/in-place recycling program, the value of our road network investments will increase. Implementation of sustainable asset management principles and performance measures are critical to addressing our infrastructure investment requirements and environmental stewardship obligations over the long-term.

REFERENCES

[1] Alkins, A., Lane, B., and Kazmierowski, T., "Sustainable Pavements—Environmental, Economic and Social Benefits of In-situ Pavement Recycling", Transportation Research Board 87th Annual Conference Proceedings, Washington D.C. (2008).

[2] Chan, S., Lane, B. and Kazmierowski, T., Pavement Preservation—A Solution for Sustainability. Transportation Research Board 90th Annual Conference Proceedings, Washington D.C. (2011).

[3] Kazmierowski T. and Chan, S., Evolution of In-situ Pavement Recycling in Ontario—An Agency's Perspective. 8th International Conference on Concrete Pavements (ISCP) Proceedings, Quebec City, Quebec (2006).

[4] Asphalt Recycling and Reclaiming Association (ARRA), Basic Asphalt Recycling Manual, U.S. Department of Transportation, Federal Highway Administration (2001).

[5] Lane, B., Kazmierowski, T., Chan, S. and Buelow, M., Evaluation of Cold In-Place Recycling with Expanded Asphalt on Highway 7, Perth Ontario, Proceedings of the 49th Annual Conference of Canadian Technical Asphalt Association, Montreal, Quebec, Canada, (2004).

[6] Kazmierowski, T., Marks, P. and Lee, S., Ten Year Performance Review of In-situ Hot Mix Recycling in Ontario, Proceedings of the 78th Annual Conference of Transportation Research Board 1999, Washington D.C., USA. (1999).

[7] Lane, B. and Kazmierowski, T., Expanded Asphalt Stabilization on the Trans-Canada Highway, Proceedings of the 82nd Annual Conference of Transportation Research Board, Washington D.C., USA. (2003).

[8] Horvath, A., "A Life-Cycle Analysis Model and Decision-Support Tool for Selecting Recycled Versus Virgin Materials for Highway Applications", Final report for RMRC Research Project No. 23. University of California at Berkeley, (2004).

[9] Chehovits, J. and Galehouse, L., "Energy Usage and Greenhouse Gas Emissions of Pavement Preservation Processes for Asphalt Concrete Pavements", Transportation Research Board 89th Annual Conference Proceedings, Washington D.C., (2010).

This page intentionally left blank

Asphalt Pavements – Kim (Ed)
© 2014 Taylor & Francis Group, London, ISBN 978-1-138-02693-3

Quantifying the pavement preservation value of chip seals

Alireza Zeinali
University of Kentucky, Lexington, KY, USA

Phillip B. Blankenship
Asphalt Institute, Lexington, KY, USA

Kamyar C. Mahboub
University of Kentucky, Lexington, KY, USA

ABSTRACT: Aging induced embrittlement of the asphalt mixtures makes them more susceptible to cracking. The oxidation and embrittlement rates are the most rapid at the surface of the pavement where the asphalt is exposed to the traffic and various environmental factors. It is envisioned that applying a surface treatment may isolate the asphalt from the environment to some extent, and thereby delay the oxidative aging processes. Asphalt Institute and Minnesota DOT launched a research study to quantify the effect of chip seal on preserving the asphalt pavements. Field cores were taken from a test track which was initially constructed in 1999 in Minnesota. A chip seal layer was applied on different sections of the test track at 1, 2, 3, and 4-year time intervals after the construction. The field core specimens were subjected to IDT creep/strength, and DC(t) tests to evaluate the effect of chip seal and its optimum application time on the low-temperature cracking of the pavement. The overall results revealed that the application of the chip seal significantly decreased the rate of embrittlement of the asphalt layer. Furthermore, the optimum time of sealing was found to be immediately after construction of the pavement, and the advantageous effect of chip sealing diminished as the time of application was postponed to 3 years or longer after construction.

Keywords: asphalt pavement preservation; chip seal; performance testing; thermal cracking

1 INTRODUCTION

Development of an effective pavement management program requires a broad understanding of the maintenance and rehabilitation techniques. In the current practice, the type and timing of maintenance operations are typically determined by projecting the current conditions of the pavement to a common period and into the future [1]. In this approach, the current pavement conditions are assessed in terms of the surface distresses, structural capacity, ride quality, and surface friction. The results of such assessments are then projected over a period of time in terms of Present Serviceability Index (PSI), Pavement Condition Index (PCI), International Roughness Index (IRI), or some specific pavement distresses. As conceptually illustrated in Figure 1, the projection of the pavement conditions without a treatment serves as a baseline to identify the critical points for intervention.

Several surface treatment methods are used in pavement management programs. The goals of such treatments are to arrest light deterioration as well as delay or prevent progressive failures due to either load-related or environmentally-induced damages [2]. The concept of such preventative maintenance methods implies that the treatments should be applied before any visible distress can be observed. Therefore, the optimal timing of such treatments cannot be predicted based on the exiting distresses in the pavement. Furthermore, the benefits of

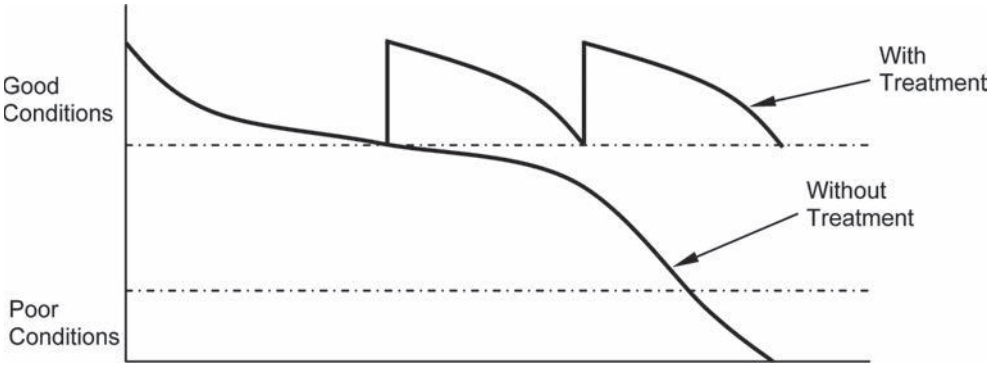

Figure 1. Conceptual approach for identifying proper timing of maintenance operations.

these surface treatments in preserving the performance properties of the pavements are not fully understood.

In cold climates, low-temperature cracking constitutes a major type of distress in asphalt pavements. These pavements become more susceptible to cracking as they age. Oxidation of the asphalt molecules, which gradually takes place over years, makes the asphalt material more brittle, and thus, more susceptible to cracking. At the pavement surface, where the asphalt is exposed to the traffic and environmental factors, the rate of aging is faster than in deeper layers. As a preventative maintenance practice, the surface of the asphalt pavement is coated with a thin layer of asphalt that can be mixed with some fine or coarse aggregate. It is believed that such a coating can reduce the rate of aging by restricting the supply of oxygen to the asphalt pavement, and reducing the permeability.

Chip seal is one of the most commonly used surface treatment techniques which is performed by spraying an asphalt coat on the pavement and covering the coat with aggregate (chips) followed by rolling and brooming [3]. The early uses of chip seal in 1920s predominantly involved making wearing courses on low-volume roads. Since then, chip seals have evolved into popular maintenance treatments due to their low initial costs when compared to thin asphalt overlays [4]. Most of the research studies on chip seals have focused on the durability of the seal coat, and its bond strength to the underneath layer [5–7]. However, the effect of chip seal coating on preserving the pavement performance is not fully known.

Asphalt Institute in cooperation with Minnesota Department of Transportation conducted a research study to gain a better insight into the benefits of chip seal coats on preserving the pavements in cold climates. The primary objective of the study was to optimize the application time of chip seal coating to maximize its preservative effects on the pavement. Furthermore, the effect of chip sealing on the thermal cracking performance of the studied pavement was quantified through laboratory testing. The results of this study could help highway agencies improve their pavement management systems. It is noteworthy to mention that in addition to reducing the aging rate, chip seal provides crack sealing as well as improves the surface friction of the asphalt pavement. This paper, however, only focuses on the performance of the asphalt layer beneath the seal coat.

2 MATERIALS AND EXPERIMENTAL PLAN

Highway 56 near Austin, Minnesota in the United States was used for the study. This is a 24-mile long rural highway with two lanes and an ADT of 2000. According to the LTPPBind database [8], the average high pavement temperature in the area is 52.1°C, and the average low pavement temperature is –23.2°C. The road was originally paved in 1999. Given the environmental and traffic conditions of the road, a PG 58-28 had been used in the mix design. To examine the effect of treatment time on the pavement performance, different sections of the

Table 1. Properties of the field cores.

Specimen group ID	Control	T1	T2	T3	T4
Original construction	1999	1999	1999	1999	1999
Chip sealing year	N/A	2000	2001	2002	2003
Age at treatment time, yr	N/A	1	2	3	4
Emulsion type	N/A	CRS-2P	CRS-2P	CRS-2P	CRS-2P
Aggregate type	N/A	New ulm quartzite	Dresser trap rock	Dresser trap rock	Dresser trap rock
Binder application rate, gal/yd^2	N/A	0.32	0.34	0.38–0.42	0.40
Chip application rate, lb/yd^2	N/A	16	17–18	18–22	19

N/A = not applicable.

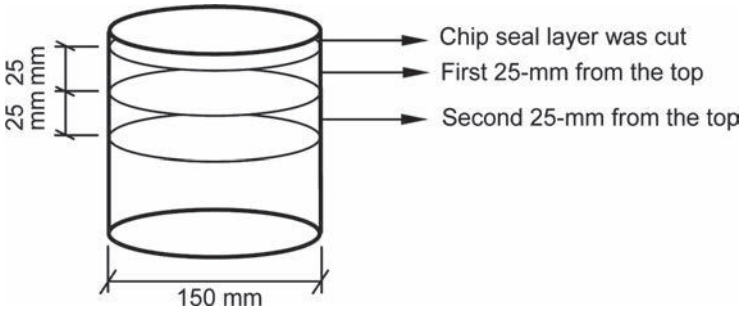

Figure 2. Fabrication of the test specimens from the field cores.

pavement were treated with a chip seal layer at 1, 2, 3, and 4-year intervals after the original construction. After applying the chip seal coat, a fog seal was applied to the pavement surface with CSS-1H emulsion which was diluted at 50:50 ratio with water, and spread at an application rate of 0.11 gal/yd^2. Furthermore, a section of the road was left without any treatment to be used as the control and comparison point for the other sections with chip seal treatment. In year 2011, several field cores were taken from the sections of the highway with various chip sealing time, and transported to the Asphalt Institute laboratory for testing. Table 1 presents the information about the cores used in the study as well as their treatment properties. As seen in this table, the notation used for each specimen group indicates the age of the pavement at which the chip seal treatment was applied. For instance, the T3 cores were taken from the section of the highway that was treated when the original pavement was three years old.

As a part of the study, some of the field cores were subjected to performance testing in order to assess the effect of chip sealing on the mechanical properties of the asphalt layer. To prepare the test specimens, the chip seal layer was cut from the top of the cores. The chip seal layer was distinguished from the main asphalt layer by visual examination of the side of the cores. The difference between the asphalt mixture and chip seal material creates a separation line between the two layers on the circumference of the core. After separating the chip seal layer, a disk shaped specimen was cut from the top of each core to be used for mechanical testing. This specimen was identified as the first 25-mm from the top as depicted in Figure 2. Next, another 25-mm thick specimen was cut from the top of the remaining part of the asphalt mixture cores. This specimen was labeled as second 25-mm from the top and represents the asphalt mixture materials below the surface layer (Fig. 2).

By cutting the cores into layers, the effect of aging could be studied as a function of depth as well as the treatment time. To examine the effect of chip sealing time on preventing the thermal cracking in the pavement, a laboratory test plan was developed which included three performance tests as follows: Disk-shaped Compact tension [DC(t)] fracture test, Indirect Tensile (IDT) creep compliance test, and Indirect Tensile (IDT) strength test. Moreover,

the three aforementioned tests were repeated for first 25-mm from the top specimens as well as the second 25-mm specimens to investigate the effect of aging at various depths of the asphalt layer. Before performance testing, the specimens were individually tested for bulk specific gravity to ensure that all of them have similar air void contents.

3 LABORATORY TESTING

3.1 *Disk-shaped compact tension fracture test*

Presence of cracks and flaws in an engineering material can substantially change its strength as well as cracking susceptibility. Disk-shaped Compact tension [DC(t)] test quantifies the resistance of an asphalt mixture to growing the existing cracks [9]. To make a DC(t) specimen, a notch is cut along a radius of a disk-shaped specimen. Additionally, two loading holes are cored at the two sides of the initial notch. The prepared specimen is then tested by applying a tensile load on the initial notch through the loading holes. The load is applied at a constant displacement rate, and the Crack Mouth Opening Displacement (CMOD) is recorded during the test. As the result of the tensile load, the initial notch grows into the specimen until the specimen fails. The fracture energy of the tested specimen is then determined by calculating the area under the load-CMOD displacement curve, and dividing it by the fractured area of the broken specimen. The DC(t) test method is standardized for asphalt mixtures under the ASTM D7313 [10].

In general, the mixtures with higher fracture energy would provide more cohesion and would have a better resistance to crack growth. Asphalt Institute utilized the DC(t) fracture test in a research study to evaluate the effect of environmentally-induced loads and aging on cracking of various asphalt pavements [11]. This research concluded that to prevent severe thermal cracking, a minimum fracture energy value of 350 J/m^2 is required for the mixture at 10°C warmer than its anticipated cracking temperature. This 350 J/m^2 value was employed as the minimum threshold requirement in this study to investigate the effect of chip seal on preserving the ductility of the pavement.

The DC(t) test was conducted on first and second 25-mm specimens from the top of the cores as depicted in Figure 2. After preparation, the specimens were conditioned at –24°C, which was 10°C higher than the lower temperature grade of the binder in this project, for at least three hours. The temperature of the specimens during the conditioning time was monitored using a dummy specimen with two thermocouples installed at its surface and its center. Figure 3 displays the fracture energy data for the field cores with various treatment times. Moreover, the fracture energy of the cores from the control section is depicted in Figure 3 with horizontal dashed lines.

Typically, the DC(t) test is conducted on 50-mm thick samples. In this study, however, the specimens were made at a thickness of 25 mm to account for the aging of asphalt at various depths. Testing 25-mm DC(t) specimens requires higher accuracy. That is, because the thickness of the specimen does not provide a plane-strain conditions, and the specimen fails at a much lower tensile load. Furthermore, reducing the specimen's thickness influences the obtained fracture energy. Wagoner and Buttlar [12] conducted a research to evaluate the effect of various specimen size parameters on the DC(t) fracture energy of asphalt concrete. The outcome showed that on average, the normalized fracture energy obtained with a 25-mm thick specimen is 41.3% lower as compared to a standard 50-mm specimen. Consequently, the 350 J/m^2 threshold for the fracture energy of 50-mm thick specimens may be reduced to 205 J/m^2 for 25-mm specimens. This adjusted threshold is shown by a solid black horizontal line in Figure 3.

For all sets of field cores, the average fracture energy of the first 25-mm from the top specimens was found to be lower than the second 25-mm specimens (Fig. 2). In other words, the field cores were more brittle at their surface. This finding agrees with the fact that the top part of the cores was more exposed to the environmental factors, which could accelerate the aging of asphalt. Figure 3 demonstrates a clear diminishing trend as the application of the chip seal was deferred to a much later time after the pavement construction. It should be noted that all the field cores were collected when the pavement was about 12 years old. At this age, the first 25-mm from the top specimens from the control section cores exhibited an average fracture

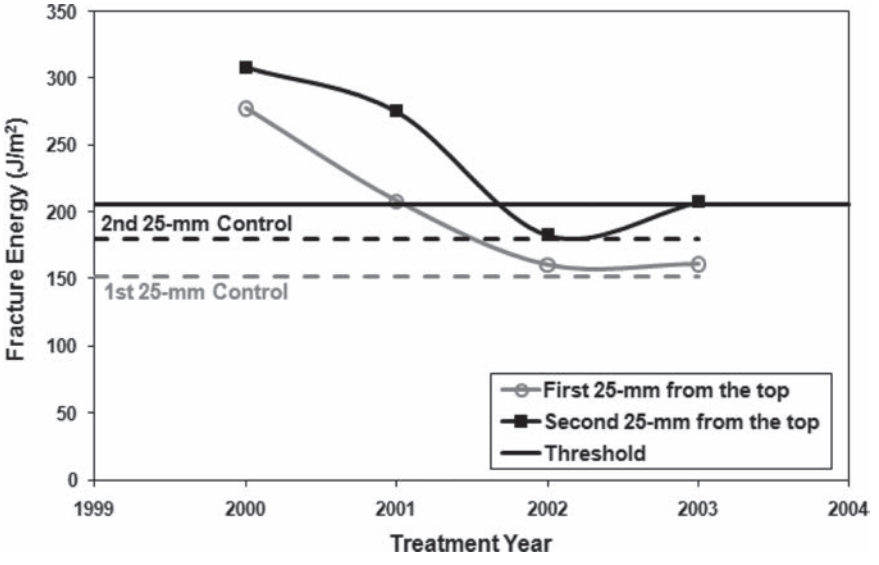

Figure 3. Average DC(t) Data at –24°C and comparison to the control section.

energy of 151 J/m^2. However, the samples from the sections that were covered by a chip seal layer one year after the pavement construction (T1 group in Table 1) had an average fracture energy of 277 J/m^2. As the chip sealing time was postponed to three years after pavement construction (T3 cores), the fracture energy of the field cores reduced to the same amount as the control section without any preventative protection (Fig. 3). In fact, in the first three years of pavement life, the oxidative aging and weathering had already embrittled the pavement to a degree that further protection would not help maintain its ductility.

Comparing the various fracture energy data in Figure 3 to the threshold line sheds more light on the effect of chip seal treatment on preserving the ductility of the pavement. The T1 and T2 cores, which were taken from the sections that were treated by a chip seal layer within 2 years of the original construction, proved to show higher facture energies than the minimum threshold (horizontal solid line in Fig. 3). Nonetheless, when the chip seal layer was applied three years or later after the construction time, the specimen's fracture energy was lower than the minimum threshold of 205 J/m^2. Thus, the chip seal application could have a protective benefit, which was large enough to prevent the excessive aging of the pavement.

A comparison of the DC(t) test load-vs-deformation data plots can better describe the difference between the responses of the samples with various treatment times. Figure 4 presents the fracture DC(t) data plot of one top 25-mm specimen from each treatment year. The DC(t) data plot for the specimen that was sealed in year 2000, one year after construction, exhibited a much higher peak load as compared to the control specimen with no sealing. This implies that the specimen had a much higher resistance to crack initiation. Furthermore, the horizontal stretch of the data plot indicates that the specimen had undergone a significantly lower embrittlement, and it provides a better cohesion as compared to the control specimen. The specimen which was sealed two years after construction (2001) still shows a high peak load; however, the horizontal stretch of its DC(t) data plot shows that it is more brittle than the specimen which was sealed one year earlier. Finally, the specimens that were treated in years 2002 and 2003 demonstrated very similar DC(t) data plots which were both close to the plot of the control specimen with no chip seal treatment.

3.2 *Indirect tensile creep and strength tests*

Asphalt is a viscoelastic material whose response to loading is a function of its temperature and the loading duration. At high temperatures, asphalt behaves similar to a viscous material

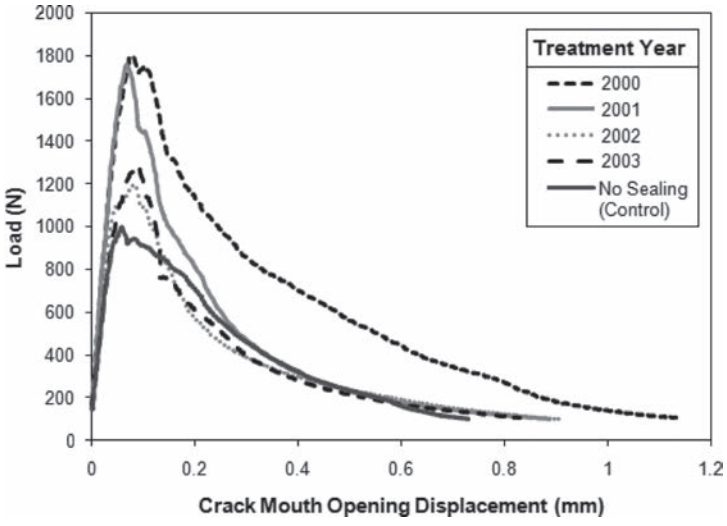

Figure 4. DC(t) data plots for the first 25-mm from the top specimens.

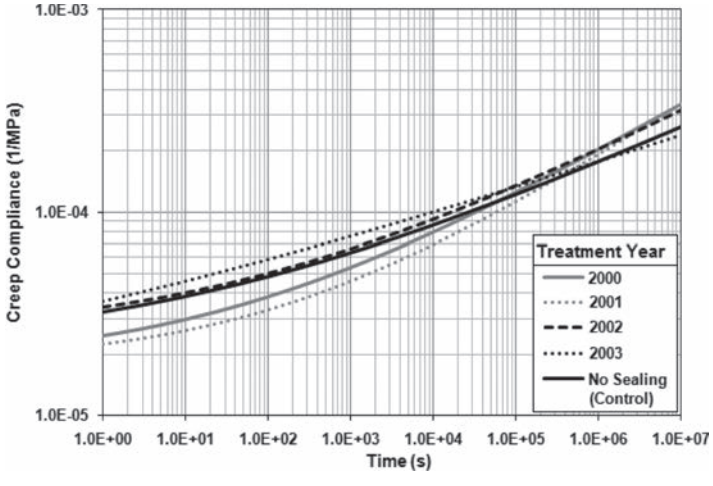

Figure 5. Creep compliance master curves of the first 25-mm from the top at –30°C.

with high stress relaxation properties. By lowering the temperature, asphalt becomes more brittle and its stress relaxation capability diminishes. It is vital for an asphalt pavement in a cold region to maintain its flexibility and stress relaxation property.

To examine whether or not the application of chip seal helped the asphalt pavement in this study preserve its flexibility, a set of IDT creep compliance test was conducted. In this type of test, a disk-shaped specimen in loaded compressively along a diameter. During the test, the deformation of the specimen is recorded using four extensometers, which are installed on the surface of the specimen in vertical and horizontal directions. Based upon the load and deformation data, the creep compliance of the specimen is then calculated along the test duration.

In this study, the creep compliance test was performed in accordance with the AASHTO T 322 standard method [13], and at three temperatures: –20°C, –30°C, and –40°C. At each temperature, triplicate specimens were tested for each sampling group. The creep compliance master curves were then developed by shifting the isotherm creep compliance curves and using the time-temperature superposition principle. Figures 5 and 6 present the final

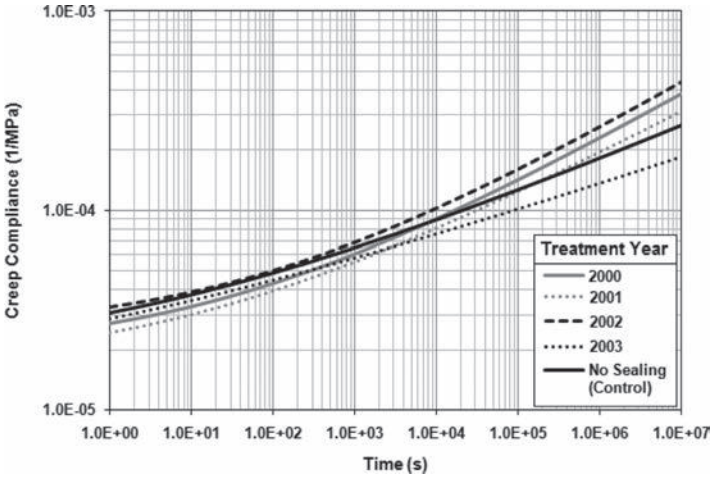

Figure 6. Creep compliance master curves of the second 25-mm from the top at –30°C.

Table 2. Slope of the stiffness curves at –24°C.

Specimen	Treatment year	Age at treatment time (years)	60-second loading		3600-second loading	
			Slope	Stiffness (MPa)	Slope	Stiffness (MPa)
First 25-mm from the top	2000	1	0.14	22247	0.18	11385
	2001	2	0.14	26710	0.19	13572
	2002	3	0.12	17277	0.15	9792
	2003	4	0.13	15817	0.15	8894
	No sealing (control)	N/A	0.11	18756	0.14	11118
Second 25-mm from the top	2000	1	0.15	18821	0.19	9449
	2001	2	0.15	20381	0.18	10414
	2002	3	0.15	16032	0.18	8074
	2003	4	0.11	19249	0.12	11940
	No sealing (control)	N/A	0.13	17684	0.14	10149

N/A = not applicable.

creep compliance master curves for the first 25-mm from the top and second 25-mm from the top specimens, respectively. In general, the stiffness of the mixture is inversely related to its compliance, and a higher creep compliance implies a more compliant mixture with lower stiffness. It was found that, the second 25-mm from top specimens showed a slightly higher compliance (lower stiffness) as compared to the first 25-mm specimens. This could be due to the faster oxidative aging of asphalt at the surface of the pavement.

The capability of a mixture in relaxing the rapid thermally induced stresses can be quantified by measuring the slope of its stiffness (or creep compliance) curve. Table 2 contains the slope of the creep compliance curves of different core groups at –24°C, which is 4°C above the lower temperature grade of the PG 58-28 asphalt binder. These slopes were calculated by fitting a polynomial function to the stiffness-time data at –24°C. All the fits had coefficient of determinations (R^2) higher than 0.9998. The stiffness curve slopes of the top specimens from the pavement sections that were sealed one or two years after construction, as seen in Table 2, were higher than the control section of the pavement. Thus, these sections are expected to have a better stress relaxation capability. However, by postponing the chip seal application to the third or fourth year after construction, the slope of the stiffness curve decreased very

slightly. In other words, delaying the chip seal application resulted in faster loss of relaxation capability of the pavement.

In addition to the creep compliance, the tensile strength of the field cores was measured by the indirect tensile strength test. As presented in Figure 7, deferring the application time of the chip seal had a deteriorating effect on the tensile strength of the field cores. On average, the tensile strength of the first and second 25-mm specimens from the top samples decreased by 0.25 and 0.21 MPa, respectively, with every one year delay in chip seal treatment of the pavement.

The tensile strength data can be used to estimate the critical cracking temperature of the pavement. Since the magnitude of the thermally-induced stresses depends on the rate of temperature drop, a similar cooling scenario was assumed for all the analyses. In this scenario, the cooling starts at 5°C and the pavement temperature continues to decrease at 2°C/hr. Additionally, a coefficient of linear expansion of 0.0002/°C was assumed for the calculation of the imposed stress in the pavement. In a stepwise process, the stress relaxation modulus for each core group was determined at each temperature and using the creep compliance data. The stress relaxation modulus was then utilized to calculate the accumulated tensile strain and the resulted tensile stress at each temperature step. Finally, the critical cracking temperature for each section of the pavement was calculated by comparing the thermally-induced stresses to the tensile strength of the pavement.

Figure 8 displays the effect of application time of chip seal on the critical cracking temperature of the pavement. The horizontal dashed lines represent the critical cracking temperature of the control section without the preventative chip seal layer. Except for the section that was sealed in 2003, the second 25-mm from top specimens from all the sections had lower critical cracking temperatures. This agrees with the data obtained from the fracture energy test and it implies that the deeper layers of the asphalt mixture experienced lower embrittlement and maintained a better flexibility. Furthermore, this analysis revealed that chip sealing had a positive effect on preserving the resistance of the mixtures to thermal cracking. As seen in Figure 8, a critical cracking temperature –27.2°C was obtained for the surface 25-mm layer that was covered with a chip sealed layer in 2000. Comparing this to the critical cracking temperature of the non-sealed control section (–19.9°C) indicates that the chip sealed layer helped preserve the performance of the pavement with respect to low-temperature cracking. In general, an increasing trend was observed in the critical cracking temperature as the sealing time was delayed after the original construction. In conclusion, if the purpose of chip

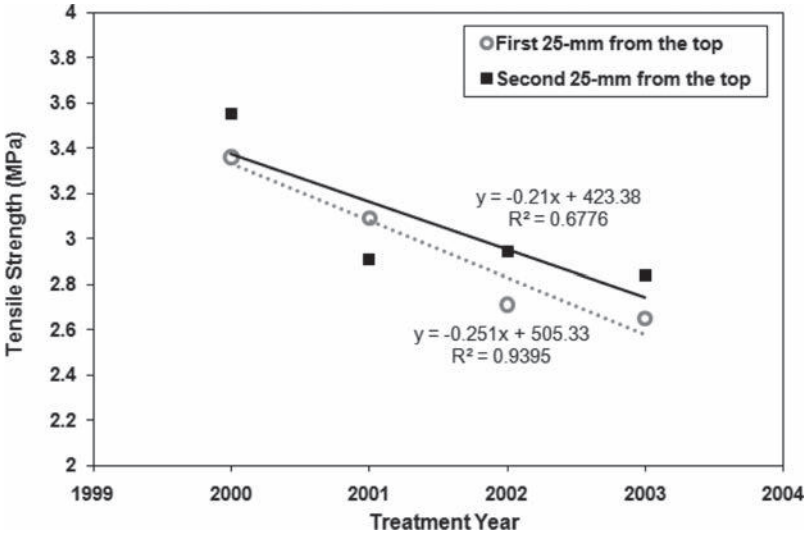

Figure 7. Average tensile strength of the cores with various chip sealing time.

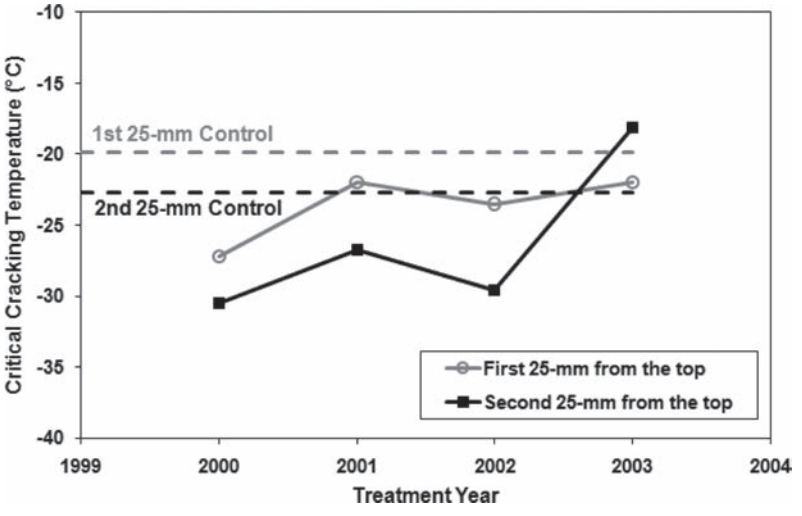

Figure 8. Critical cracking temperatures from IDT creep and strength tests.

sealing is to preserve the cracking performance of the pavement, it is better to be applied during the first year after the pavement construction.

4 SUMMARY AND CONCLUSIONS

An experimental study was conducted to evaluate the effect of chip sealing on preserving the low-temperature cracking performance of asphalt pavements. A pavement in the state of Minnesota, USA was used for the study, which was originally constructed in 1999. A chip seal layer was applied on 1-mile sections of the pavement at 1, 2, 3, and 4-year time intervals after the construction. In 2011, field cores were collected from all the sections with chip seal as well as the control section, which had no treatment. At the Asphalt Institute laboratory, the chip seal layer was separated from the top of the cores and two 25-mm thick disk-shaped specimens were cut from the top of each core. To investigate the low-temperature cracking performance of the pavement with various sealing times and at various depths, the fabricated specimens were subjected to DC(t) fracture energy test, IDT creep compliance test, and IDT tensile strength test.

The fracture energy test results indicated that application of the chip seal layer helped the pavement maintain its ductility and cohesion. The fracture energy data obtained from the first 25-mm from the top of the cores were consistently lower than the values obtained from the second 25-mm layer beneath the surface. Furthermore, the sections which were seal coated one year after the construction exhibited the highest fracture energy. As the chip seal treatment time was postponed, the fracture energy diminished, and after 3 years, it declined to the same level as the control section without any seal coats.

The IDT creep test was conducted at –20°C, –30°C, and –40°C, and the master creep compliance curves were developed for various sections of the pavement. The analysis on the slope of the creep compliance curves showed that the sections with earlier treatment had a better ability to relax the stresses imposed by sudden temperature drops. The field cores were also tested for tensile strength using the IDT test. The results showed that on average, the tensile strength of the first 25-mm specimens from the top of the pavement decreases by 0.25 MPa for every year of delay in applying the chip seal layer. Moreover, the critical cracking temperature of the various pavement sections was estimated by assuming a temperature cooling scenario. The general trend of the critical cracking temperature data agreed with the results from the DC(t) fracture energy test. Again, tensile strength findings indicate that

deferring the application of chip seal to three years or longer after pavement construction, would diminish the beneficial effects of chip seal. Based upon the findings of this research it could be concluded that if the goal of chip seal treatment is to preserve the low-temperature cracking performance of the pavement, its optimal time of application is during the first year after the construction.

ACKNOWLEDGEMENTS AND DISCLAIMER

The authors wish to thank Zack McKay at Asphalt Institute for his work in preparing samples for this study. No project can be started without the preparation of samples. This material is based upon work supported by Minnesota DOT as a part of the project TPF-5(153), "Optimal Timing of Preventive Maintenance for Addressing Environmental Aging in Hot-Mix Asphalt Pavements". Thanks to Tom Wood, Minnesota DOT, as Research Project Manager, and Mike Anderson, Director of Research and Laboratory Services at Asphalt Institute. Any opinions, findings, and conclusions or recommendations expressed in this publication are those of the Author(s) and do not necessarily reflect the view of the Minnesota Department of Transportation, or Asphalt Institute members. Finally, the support of the Member Companies of the Asphalt Institute is gratefully acknowledged. Without their active interest in and support of the Asphalt Institute, none of the work presented could have been accomplished.

REFERENCES

[1] Hunag, Y.H., Pavement Analysis and Design, 2nd Edition, Pearson Prentice Hall, Upper Saddle River, NJ, USA. 2004.
[2] O'Brien, L.G., Evolution and Benefits of Preventative Maintenance Strategies, NCHRP Synthesis of Highway Practice 153, Transportation Research Board, Washington, D.C. 1989.
[3] Walker, D., The Importance of Preserving Pavements, Asphalt, the Magazine of Asphalt Institute, 28(1). 2013.
[4] Gransberg, D., and James, D.M.B., Chip Seal Best Practices, NCHRP Synthesis of Highway Practice 342, Transportation Research Board, Washington, D.C. 2005.
[5] Gransberg, D.D., and Zaman, M., Analysis of Emulsion and Hot Asphalt Cement Chip Seal Performance, Journal of Transportation Engineering, 131(3), pp. 229–238. 2005.
[6] Shuler, S., and Lord, A., A New Laboratory Test for Predicting Very Early Chip Seal Performance, Journal of the Association of the Asphalt Paving Technologists (AAPT), 78, pp. 137–168. 2009.
[7] Lawson, W.D., and Senadheera, S., Chip Seal Maintenance: Solutions for Bleeding and Flushed Pavement Surfaces, Transportation Research Record, 2108, pp. 61–68. 2009.
[8] LTPPBind, Version 3.1 Beta, Federal Highway Administration. 2012.
[9] Wagoner, M.P., Buttlar, W.G., Glaucio, H.P., and Blankenship, P., Investigation of the Fracture Resistance of Hot-Mix Asphalt Concrete Using a Disk-Shaped Compact Tension Test, Transportation Research Record, 1929, pp. 183–192. 2005.
[10] ASTM D7313-07, Standard Test Method for Determining Fracture Energy of Asphalt-Aggregate Mixtures Using the Disk-Shaped Compact Tension Geometry, American Society for Testing and Standards, West Conshohocken, PA. 2007.
[11] Blankenship, P., Anderson R.M., King, G.N., and Hanson, D.I., A Laboratory and Field Investigation to Develop Test Procedures for Predicting Non-Load Associated Cracking of Airfield HMA Pavements, AAPTP Project 06-01 Report, Airfied Asphalt Pavement Technology Program. 2010.
[12] Wagoner, M.P., and Buttlar, W.G., Influence of Specimen Size on Fracture Energy of Asphalt Concrete, Journal of the Association of Asphalt Paving Technologists (AAPT), 76, pp. 391–426. 2007.
[13] AASHTO T 322-07, Standard Method of Test for Determining the Creep Compliance and Strength of Hot-Mix Asphalt (HMA) Using the Indirect Tensile Test Device, American Association of State Highway and Transportation Officials. 2007.

Asphalt Pavements – Kim (Ed)

Final evaluation of LTPP SPS-3 flexible maintenance performance

Dennis Morian & Guangming Wang
Quality Engineering Solutions Inc., Conneaut Lake, PA, USA

Doug Frith
Quality Engineering Solutions Inc., Reno, NV, USA

ABSTRACT: The paper addresses the final performance of LTPP SPS-3 maintenance treatment test sections. The evaluation of SPS-3 monitoring data, with some sections having over 13 years of performance information, was undertaken to assess performance predictions made by the primary author in "Maintaining Flexible Pavements—The Long Term Pavement Performance Experiment SPS-3 5-Year Data Analysis," published in March 1998. A similar distressed based evaluation of the treatments, thin overlay, chip seal, slurry seal, and crack seal, and untreated control section has been used. However, since sections have continued to fall out of service over time, a survivor analysis approach has been used here. Results of the survivor analysis confirm the reasonableness of the original performance estimates.

The authors were able to successfully evaluate deflection data after many years of data collection to assess the effect of the treatments on preserving the stiffness of the pavement sections, as compared with the control sections. This could not be accomplished in the original 5 year analysis. Results indicate that the stiffness response associated with the treatments provided improvement when compared with the stiffness of the associated control section. This relative deflection reduction is believed to impact the overall performance of the test sections.

Keywords: chip seal, slurry seal, thin overlay, crack seal, survivor analysis, pavement performance

1 BACKGROUND

The importance of pavement preservation as a tool for maintaining pavements economically has been well recognized. A synthesis by Geoffroy [1] postulated that each dollar invested in preventive maintenance at the right time in the life of a pavement may save $3-$4 in future rehabilitation or reconstruction costs. However, the actual benefit of these treatments is not well documented. Further, when and what kind of surface maintenance treatments should be applied to the existing pavements presents challenges for highway agencies, which historically have relied heavily on past experience and engineering judgment. To advance the state of knowledge, the Strategic Highway Research Program (SHRP) initiated two projects with focus on flexible pavement maintenance. Project H-101, Pavement Maintenance Effectiveness, and an experiment constructed under the Specific Pavement Studies-3 (SPS-3) were designed under the SHRP program. The SPS-3 experiment was specifically intended to address performance of surface maintenance activities used on flexible pavements. A total of 81 test sites were constructed across the United States and Canada in 1990 to capture the effects of different climate zones, subgrade types, traffic levels, and pavement conditions. Four common surface treatments, thin overlay, slurry seal, crack seal, and chip seal, were applied at each test site, and their performance has been monitored along with that of the adjacent control section which remained untreated. Numerous assessments of portions of the SPS-3 test sites have been made.

Smith *et al*. [2] implemented a sigmoidal (S-shaped) model to perform pavement damage analysis. In general, each type of pavement distress can be expressed as a damage index between zero and one, where zero indicates no damage and one indicates full damage. This model set the base for remaining life analysis used in developing the AASHTO 1993 design guide.

Morian *et al.* [3] conducted a 5-year expert task group evaluation of SPS-3 performance and concluded that the thin overlay performed best after five years relative to other treatments. The chip seal treatment performed best in the wet-no freeze environment in the Southern region. The crack seal treatment appeared to be very cost effective, as compared with the chip seal, and performed well in wet-freeze environments. A year later in 1998, Morian *et al.* [4] used multiple regression analysis to develop performance prediction models for distress (cracking and rutting) using a distress index called Pavement Rating Score (PRS).

Eltahan *et al.* [5] performed survival analysis on the 8-year SPS-3 sites in the LTPP Southern region to determine the life expectancy of each treatment. The results showed that the probability of failure was two to four times higher for sections that were in poor condition at the time the treatment was applied than those sections that were in a better condition. Chen *et al.* [6] evaluated the effectiveness of preventative maintenance treatments using 14 SPS-3 sites in Texas. Their study revealed that the thin overlay is the most effective treatment to resist rutting, and that the chip seal performed well on a wide range of existing pavement conditions. They also found that crack seal provides the best alternative for low volume routes with a sound underlying pavement structure, when initial cost was considered. Shirazi *et al.* [7] conducted a statistical analysis to compare the effectiveness of each treatment in relation to the others and the control section. These researchers concluded that the thin overlay and chip seal treatments are effective options with respect to fatigue cracking for most design conditions. The difference in the performance of crack seal, slurry seal, and control section was not found to be statistically significant with respect to any distress type, or design factor.

Although numerous studies have been conducted to study the performance of the treatments in SPS-3 experiment, most of them have been limited geographically or by the length of monitoring period, such as five years. This paper considers the complete set of SPS-3 monitoring data, i.e., includes all regions and monitoring data since 1990. In addition, the effect of the preservation maintenance treatments through the life of the treatments was evaluated.

2 OBJECTIVE

The primary objective of this study is to evaluate the life expectancy and benefit to maintaining structural stiffness of the SPS-3 treatments. The following tasks were conducted:

- Conduct pavement condition analysis based on Pavement Rating Score (PRS).
- Perform Kaplan–Meier Survival Analysis to assess life expectancy of the treatments in the SPS-3 experiment.
- Evaluate FWD deflection data in the SPS-3 experiment.
- Perform Friedman Test to evaluate the structural contribution of the treatments in the SPS-3 experiment.

3 SCOPE

The research conducted in this study focused on evaluating treatment performance life in terms of the PRS distress index and structural benefit in terms of FWD deflection under the load. All data were obtained from the on-line LTPP database (http://www.ltpp-products.com/index.asp).

4 PERFORMANCE LIFE OF THE SPS-3 TREATMENTS

4.1 *Pavement condition analysis*

To determine the performance life of the SPS-3 treatments it was necessary to determine the condition of each test section. Pavement condition data dating back to 1990 was obtained from the LTPP database. All distress data such as cracking and patching were collected in a table and converted to the single distress index, Pavement Rating Score (PRS), as used in the original SPS-3 5-year Evaluation. The PRS approach was developed for the analysis of LTPP SPS-3 sections by Morian's team [4]. This method is based on a scale of 0 to 100 with deduct values assigned to individual distresses and severity levels. A pavement with no distresses present would have a PRS score of 100; the value decreases with increasing distress.

4.2 *SPS-3 treatment performance life tracking*

To determine the performance life of the SPS-3 treatments, a failure threshold PRS value of 50 was defined in the 1998 study and used in this work as well. However, one of the biggest problems with SPS-3 experimental data is that many of the test sections were not monitored until failure. These sections were removed from the experiment before they reached the failure condition for a variety of reason, making determination of the performance life of the treatments difficult. Therefore, the research team decided to identify the sections that were removed from the experiment, failed, or survived after some number of years. Incremental performance tracking was arbitrarily set at years 3, 5, 8, and 11. To better illustrate this concept, the thin overlay treatment is provided as an example, as shown in Figure 1. For instance, after three years in service, 50 of 81 sections survived (designated as SV), 5 sections failed (designated as FA), and 26 sections were out of the monitoring program (designated OM). After 11 years, only 2 sections survived, 18 sections failed and 61 sections were out of the monitoring program.

4.3 *Kaplan–Meier survival analysis*

As stated early, one of the biggest problems with the SPS-3 experiment is that not all sections were monitored until they reached failure. Obviously, for those sections not monitored until failure, their exact survival time cannot be determined. Such sections are treated as censored data from the perspective of survival analysis. Fortunately, the Kaplan-Meier sur-

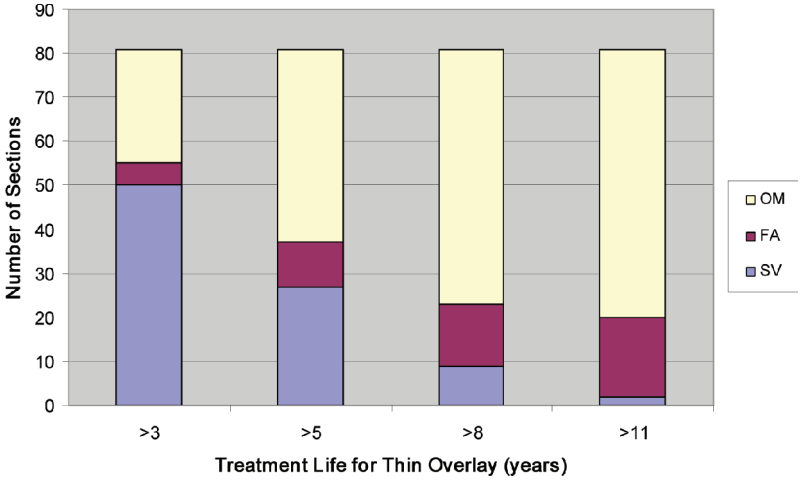

Figure 1. Performance life tracking for thin overlay.

vival analysis can take this kind of censored data into account, particularly right-censoring, which occurs if a section is withdrawn from a study, i.e., is lost from the sample before the final outcome is observed. This approach makes the life determination of the treatments possible. A brief introduction to Kaplan-Meier method is presented below, with details in the literature [8,9].

Let T be the random variable that measures the time of failure and let $F(t)$ be its cumulative distribution function. The survival function $S(t)$ can be expressed as:

$$S(t) = P[T > T] = 1 - P[T \leq t] = 1 - F(t) \tag{1}$$

where, $S(t)$ can be estimated through the Kaplan-Meier estimator:

$$\hat{S}(t) = \prod_{t_i \leq t} \frac{n_i - d_i}{n_i} \tag{2}$$

where, d_i is the number of death events. n_i is the number of survivors just prior to time t_i when there is no censoring. With censoring, n_i is the number of survivors less the number of losses (censored cases). It is only those surviving cases that are still being observed (have not yet been censored) that are "at risk" of an (observed) death.

Based on the above method, the estimated survival probabilities were plotted against the corresponding survival times. The survival curves developed from the SPS-3 experiment data are presented in Figures 2 through 5, with each figure representing a specific maintenance treatment. In each figure, a survival curve was developed based on each original pavement condition. As observed from the figures, the sections in good condition at the time of treatment placement always perform better than either fair or poor conditions for all treatments. However, it is not clear whether sections with a fair initial condition outperform the sections with poor initial condition due to lack of observed "death" events in either the fair or poor conditions. This affects modeling of fair pavement condition performance. Therefore, an average curve that combined all three original pavement conditions was developed for each treatment and is also shown in Figures 2 through 5.

To compare the life expectancy of different treatments, a polynomial curve fitting for each treatment based on the average survival curve was developed using the following format:

$$y = ax^2 + bx + 1 \tag{3}$$

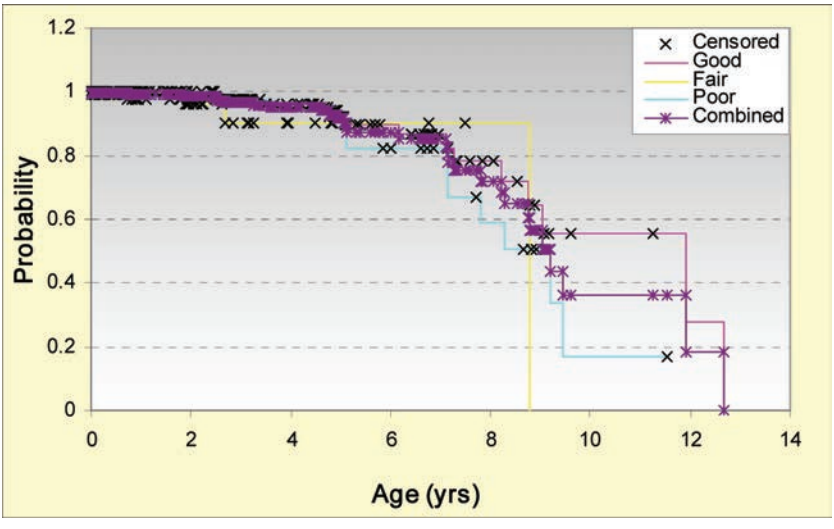

Figure 2. Survival curve for thin overlay.

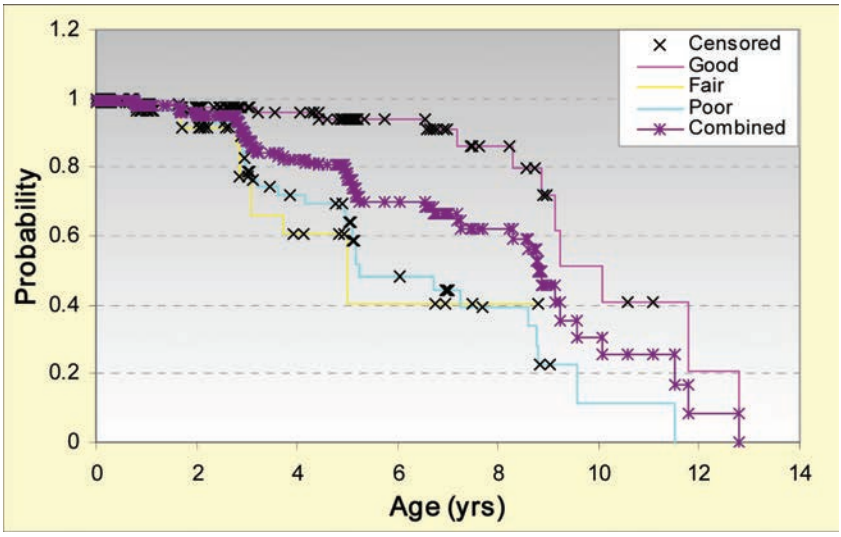

Figure 3. Survival curve for slurry seal.

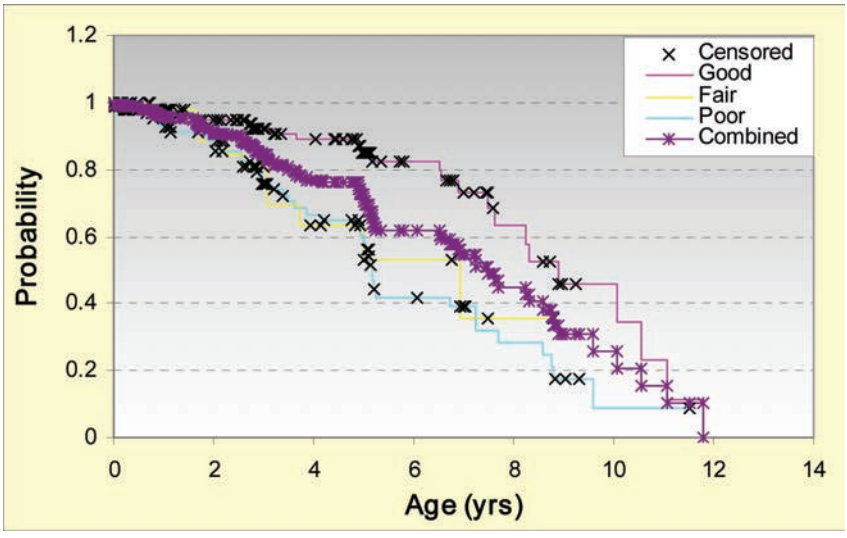

Figure 4. Survival curve for crack seal.

The coefficients, *a* and *b*, for each treatment, as well as their corresponding R squares are summarized in Table 1. Based on the curve developed for each treatment, the life expectancy at three levels of survival probability, namely 0.8, 0.6, and 0.5, was calculated and also summarized in Table 1.

From Figures 2 through 5 and Table 1, the following observations can be made:

- At a high probability of survival (>0.7), the thin overlay performs best, followed in order by chip seal, slurry seal, crack seal, and control section.
- At a low probability of survival (≤0.7), the chip seal performs best, followed in order by thin overlay, slurry seal, control section, and crack sealing.

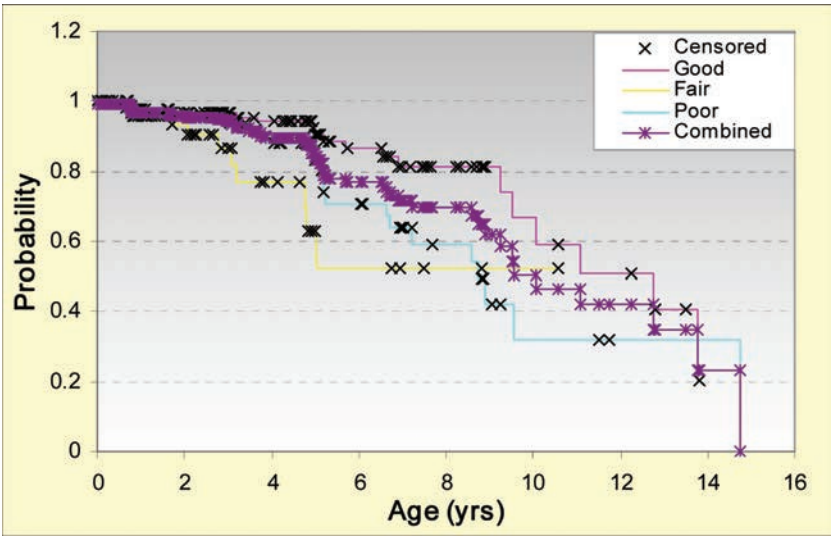

Figure 5. Survival curve for chip seal.

Table 1. Statistical results for survival analysis.

Treatment type	Treatment code	a	b	R^2	Survival probability	Estimated life (yrs)
Thin overlay	310	–0.0072	0.0216	0.9646	0.8	7.0
					0.6	9.1
					0.5	10.0
Slurry seal	320	–0.004	–0.0239	0.9803	0.8	4.7
					0.6	7.4
					0.5	8.6
Crack sealing	330	–0.0034	–0.0426	0.9927	0.8	3.6
					0.6	6.3
					0.5	7.4
Control section	340	–0.0009	–0.0601	0.9846	0.8	3.2
					0.6	6.1
					0.5	7.5
Chip seal	350	–0.0027	–0.0179	0.9795	0.8	5.9
					0.6	9.3
					0.5	10.7

- At 0.5 survival probability, the life expectancy for the thin overlay, slurry seal, crack sealing, control section, and chip seal were 10.0, 8.6, 7.4, 7.5, and 10.7 years, respectively, which agrees well with the ETG estimates from the SPS-3 5-year report [4].
- Compared with the control section, the life benefit for crack sealing is not significant, based on the PRS distress analysis. This is expected, since the distresses are quite similar for the two sections, by definition.

From a practical perspective, the above observations indicate that performance of the treatments can be related to the owner's level of risk associated with the roadway classification. For high profile roads where the objective is to minimize the risk of underachieving the expected performance, the high probability ranking is appropriate. For lower road classifications where higher risk of performance is acceptable, the lower probability ranking of performance is better suited.

5 STRUCTURAL CONTRIBUTION OF TREATMENTS

It has generally been believed that preservative maintenance treatments do not contribute significantly to the structural capacity of a pavement. Although this may be true for some treatments such as crack sealing, it might not be the case for other treatments like the thin overlay. The structural contribution of the treatments in SPS-3 experiment was evaluated on the basis of the complete set of monitoring data. A comparison of the change in deflection under load over time was used to assess the structural contribution of the treatments in SPS-3 experiment. The D_0 deflection values were adjusted for temperature at the time of testing, and the change in deflections over time compared for the several treatments.

5.1 *FWD data processing and temperature adjustment*

Since a large amount of FWD test data exists in the SPS-3 experiment database, the following steps were adopted to process the data:

- Normalize all FWD deflection data to a 40 kN load
- Average the deflection data across the 152 meter test section.

Deflections were normalized to a 40 kN load using the following equation:

$$\bar{D}_0 = \frac{40}{F} D_0 \tag{4}$$

where, F is the actual FWD testing load in kN.

Since the FWD data collection time varied throughout the year, deflection results were adjusted to account for the seasonal and temperature effects. Over the years, a number of methods have been developed to measure the asphalt temperature and to adjust the deflection results for the effects of temperature. Lukanen *et al.* [10] developed a method to calculate Temperature Adjustment Factors (TAF) for FWD tests based on data from the LTTP Seasonal Monitoring Program (SMP), which was adopted in this study. This method of calculating temperature adjustment factors accounts for the strength of the subgrade and for the different asphalt behavior that has been correlated with the site latitude. All the average deflection data were adjusted to a 20° C reference temperature using this method, and the following equations [10]:

$$\bar{D}_{0-ref.Temp.} = TAF \times \bar{D}_{0-Meas.Temp.} \tag{5}$$

$$TAF = \frac{D_{36} + \Delta_{36-ref.Temp.}}{D_{36} + \Delta_{36-Meas.Temp.}} \tag{6}$$

$$\begin{aligned} \log(\Delta_{36}) = {} & 3.05 - 1.13\log(H_{AC}) + 0.502\log(\theta)\log(D_{36}) \\ & - 0.00487T\log(\theta)\log(D_{36}) + 0.00677T\log(H_{AC})\log(\theta) \end{aligned} \tag{7}$$

where,
H_{AC} = Total thickness of the HMA, mm;
θ = Latitude of the pavement section;
Δ_{36} = Deflection (normalized to 9,000 lb or 40 kN) at 915 mm from the load center, μm;
T = Temperature at the mid-depth of the HMA, °C.

Figures 6 and 7 show a typical comparison of FWD deflections before and after the temperature adjustment. As observed, the deflection curves become smoother after this seasonal adjustment.

5.2 *Contribution to preservation of pavement structure*

To test whether the treatments in the SPS-3 experiment have any structural effect on the pavement, the Friedman Test [11,12] was utilized. The Friedman Test was adopted because

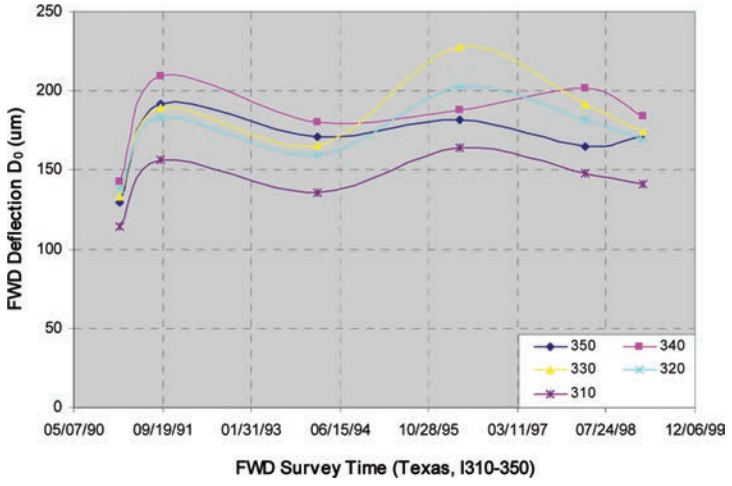

Figure 6. FWD deflections before temperature adjustment.

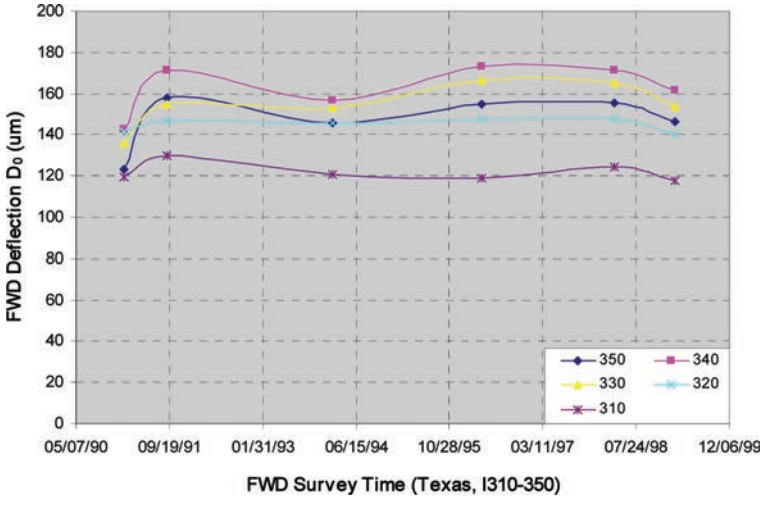

Figure 7. FWD deflections after temperature adjustment.

it is a non-parametric test and can be used for multiple comparisons. Unlike the parametric repeated measures ANOVA or paired t-test, the Friedman Test requires no assumptions about the distribution of the data. In addition, it not only detects the differences in treatments across multiple test sections, but also ranks the performance of the treatments, making it well suited for use in this study. The test statistic for the Friedman Test is a Chi-square (χ^2) with n-1 degrees of freedom, where n is the number of repeated measures.

The effect of the preventive maintenance treatments on the structural capacity of the pavement sections was compared with that of the control sections, as well as among the different treatment types. A total of nine test sites from different climate zones, each with five treatment sections, were randomly selected for the Friedman Test. This resulted in 45 different FWD measures, as reported in Table 2. As shown in Figures 6 and 7, the change in deflection magnitude is small. Therefore, this comparison is relative, and does not imply that the treatments provide significant structural enhancement to the pavement structure.

As shown, there is a statistically significant difference among treatments at the 95% confidence level. The thin overlay had the lowest sum of ranks, followed by slurry seal,

Table 2. Friedman test results of deflection D_0.

Compare pairs	n	Rank sum	Mean rank	Friedman's statistic	DF	p	Significant at 95% level?
Thin overlay	45	56	1.24	80.3	4	<0.0001	Y
Slurry seal	45	133	2.96				
Crack sealing	45	158	3.51				
Control section	45	181	4.02				
Chip seal	45	147	3.27				

Head to head Friedman test	Difference	Friedman's statistic	DF	p	Significant at 95% level?
Crack sealing vs. control section	7	1.09	1	0.2967	N
Chip seal vs. control section	19	8.02	1	0.0046	Y
Slurry seal vs. control section	23	11.76	1	0.0006	Y
Thin overlay vs. control section	43	41.09	1	<0.0001	Y

chip seal, crack sealing, and control section. Here, a lower sum of ranks indicates better contribution in preserving structural capacity, which means the thin overlay has the highest contribution and crack sealing has the lowest contribution when compared with the control section.

A direct comparison between each treatment section and the control was made using the Friedman Test, using deflection as the basis of comparison. The results indicate that all treatments, except for crack sealing, provide statistically significant benefit in the form of preserving pavement structural capacity as measured by the deflection magnitude. The difference between each treatment and the control section was expressed in terms of a rank sum difference. A comparison of the rank sum difference values provides a means of further quantifying the individual treatment benefit to maintaining pavement structural capacity. As shown in Table 2, thin overlay provides about six times the benefit to the pavement structural capacity of crack sealing, and about two times more than both slurry seal and chip seal. Compared to crack sealing, both slurry seal and chip seal could provide approximately three times more benefit to pavement structural capacity as expressed in terms of rank sum difference. Although there is no significant difference between crack sealing and the control section, crack sealing still provides benefit to pavement structural capacity as expressed by the lower rank sum. This can be explained by the mechanism by which crack sealing helps prevent water from entering the pavement, resulting in reduced loss of subgrade support.

From a practical perspective, the relative reduction in deflection as compared with the control section for the treatments are 9% for crack seal, 11% for chip seal, 17% for slurry seal, and 29% for thin overlay.

6 CONCLUSIONS

Based on a statistical analysis of performance life and structural benefit of the treatments in the SPS-3 experiment, the following can be concluded:

- Performance life tracking indicated that chip seal and thin overlay have similar performance life and outperform both crack seal and slurry seal as shown by more survival sections and fewer failure sections within each tracking period.
- Kaplan–Meier survival analysis indicated that test sections with good initial condition always perform better than either fair or poor conditions for all treatments. However, there is no clear distinction indicating whether fair condition sections outperform poor condition sections as a result of insufficient observed "death" events in these categories.

- At a high probability of treatment survival (>0.7), the thin overlay performs best, followed respectively by chip seal, slurry seal, crack sealing, and the control section. This is appropriate for higher roadway classifications. At a lower probability of treatment survival (≤0.7), the chip seal performs best, followed by thin overlay, slurry seal, control section, and crack sealing. This performance expectation is suitable for use on lower classification roadways.
- At 0.5 survival probability, the life expectancy for thin overlay, slurry seal, crack sealing, control section, and chip seal were found to be 10.0, 8.6, 7.4, 7.5 and 10.7 years, respectively. These results agree well with the ETG estimates from SPS-3 5-year report conducted by Morian's team [4].
- Compared with the control section, the life benefit of crack sealing is not significant as determined from the PRS distress data analysis.
- The analysis indicated statistically significant benefit in preserving pavement structural response from all the treatments except crack sealing. This differs from the perspective that the pavement preservation treatments do not enhance pavement structure, but rather demonstrates the effect of maintaining the structural response of the pavement section over time. From a practical perspective, the relative reduction in deflection as compared with the control section for the treatments are 9% for crack seal, 11% for chip seal, 17% for slurry seal, and 29% for thin overlay.

ACKNOWLEDGEMENT

The authors would like to express our thanks to Mr. William Bellinger for his assistance in providing us with a complete set of the monitoring data for the sections included in the SPS-3 Experiment.

REFERENCES

1. Geoffroy, D.N. *NCHRP Synthesis of Highway Practice 223: Cost-Effective Preventive Pavement Maintenance*, Transportation Research Board, National Research Council, Washington, D.C., 1996.
2. Smith, R.E., T.J. Freeman, and O. Pendleton, *Pavement Maintenance Effectiveness*. Strategic Highway Research Program, Report SHRP-H-358, 1993.
3. Morian, D.A., J.A. Epps, and S.D. Gibson, Pavement Treatment Effectiveness, *1995 SPS-3 and SPS-4 Site Evaluations*, Federal Highway Administration, Tech Brief, Report No. FHWA-RD-96-208, 1996.
4. Morian, D.A., S.D. Gibson, and J.A. Epps, *Maintaining Flexible Pavements—The Long-Term Pavement Performance Experiment SPS-3 5-Year Data Analysis*, Federal Highway Administration, Office of Infrastructure Research and Development, Washington, D.C., Report No. FHWA-RD-97-102, 1998.
5. Eltahan, A.A., J.F. Daleiden, and A.L. Simpson, Effectiveness of Maintenance Treatments of Flexible Pavements, In *Transportation Research Record: Journal of the Transportation Research Board*, No. 1680, Transportation Research Board of the National Academies, Washington, D.C., 1999, pp. 18–25.
6. Chen, Dar-Hao, Deng-Fong Lin, and Huan-Lin Luo, Effectiveness of Preventative Maintenance Treatments Using Fourteen SPS-3 Sites in Texas, In *Journal of Performance of Constructed Facilities*, Vol. 17, No. 3, 2003, pp. 136–143.
7. Shirazi, H., R.L. Carvalho, M. Ayres, Jr., and O. Selezneva, Statistical Analysis of LTPP SPS-3 Experiment on Preventive Maintenance of Flexible Pavements, In *First International Conference on Pavement Preservation*, Newport Beach, CA, 2010.
8. Lee, E., *Statistical Methods for Survival Data Analysis*, Wiley, New York, 1992.
9. Kaplan, E.L. and P. Meier, Nonparametric estimation from incomplete observations, *J. Amer. Statist. Assn.* 53, 1958, pp. 457–481.
10. Lukanen, E.O., R. Stubstad, and R. Briggs, *Predictions and Adjustment Factors for Asphalt Pavement*, Federal Highway Administration Report FHWA-RD-98-085, 2000.
11. Conover, W.J., *Practical nonparametric statistics*, Wiley, New York, 1980.
12. Friedman, M., The use of ranks to avoid the assumption of normality implicit in the analysis of variance, In *Journal of the American Statistical Association,* 32 (200), 1937, pp. 675–701.

Recycling—III

This page intentionally left blank

Asphalt Pavements – Kim (Ed)
© 2014 Taylor & Francis Group, London, ISBN 978-1-138-02693-3

Rehabilitation of Ardebil-Khalkhal main road in Iran applying cold recycling with foam bitumen and cement

Leila Hashemian
RAVAN Construction Company, Tehran, Iran

Amir Kavussi
Tarbiat Modares University, Tehran, Iran

Homayoun Abolmali
RAVAN Construction Company, Tehran, Iran

ABSTRACT: Major distresses on the pavement of Ardebil-Khalkhal main road in North-East of Iran caused an immediate pavement rehabilitation process to be planned. Among the different rehabilitation methods, cold in-place recycling technique, using foam-bitumen and cement slurry, was selected to be applied on a 5 Km length of this route.

Using a cold in-place recycling machinery chain, the top layers of the pavement, including Hot Mix Asphalt (HMA) and part of unbound existing sub base layer, were milled and were mixed together applying foam-bitumen and cement slurry and hydrated lime powder. Finally, an HMA layer was laid over to form the final pavement surfacing.

A mix design analysis was carried out using Indirect Tensile Strength (ITS) and Marshall testing. ITS was performed on both dry and conditioned samples and tensile strength ratio parameter was determined. The results indicated that increased mechanical properties were achieved in foam-bitumen and cement recycled layer.

Quality control testing results shows that the applied mix design and cold recycling method was appropriate to rehabilitate this road.

Keywords: Cold in place recycling, stabilization, foam bitumen, Indirect Tensile Testing

1 INTRODUCTION

Ardebil province is located in a mountainous area in North-East of Iran (Fig. 1). The climate conditions are variable in this area. For example, Ardebil city has cold and wet winters and mild summers while Bilesavar and Parsabad cities have warm summers and mild winters.

Ardebil-Khalkhal road is the main route connecting two major cities of Ardebil Province. Sever climatic conditions of the region, poor pavement conditions; including insufficient bearing capacity, improper cross falls, existence of high portion of fine materials in the sub-base layer and shoulders and inadequate drainage system; resulted in sever distresses in the existing pavement. There for rehabilitation of this main road with length of 30 km and width of 7 m was planned. Different methods were proposed for rehabilitation of this route that are summarized as below:

A—Existing HMA patching and overlaying with new HMA layers,

B—Pavement renovation applying a new granular base course and new HMA layers,

C—Cold recycling of existing HMA layer using foam bitumen and cement slurry.

Among the above mentioned rehabilitation methods, cold in-place recycling technique, was chosen and applied along 5 Km length of this main road.

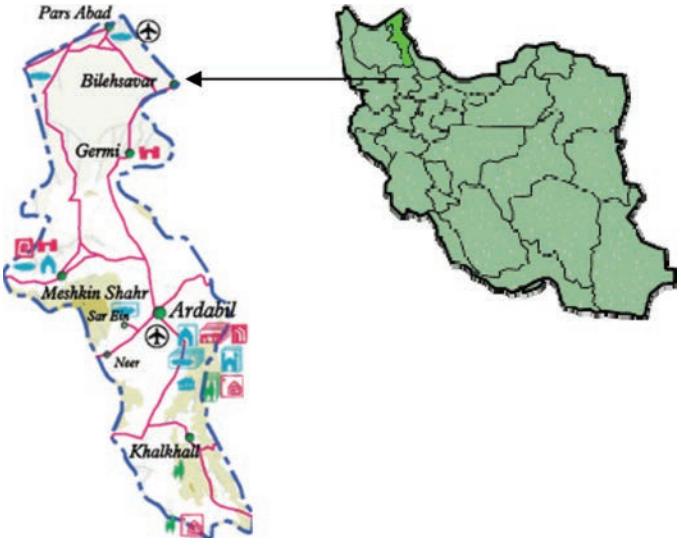

Figure 1. Road project location.

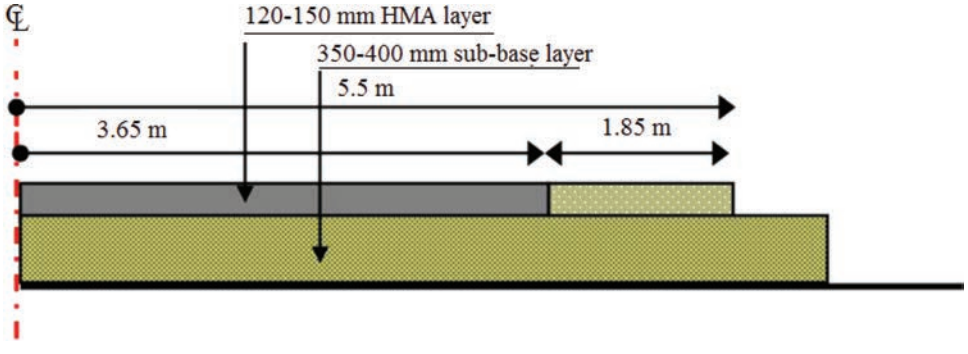

Figure 2. Existing pavement cross section.

2 EXISTING CONDITION

Typical cross section of Ardebil-Khalkhal main road before rehabilitation is shown in Figure 2. The major pavement distresses in this road could be summarized as it follows:

- Alligator cracking due to insufficient bearing capacity of the pavement,
- Non uniform longitudinal profile and rutting,
- Longitudinal and transverse cracking,
- Thermal and fatigue cracking developed due to low winter temperatures,
- Shoulder settlement in some sections and shoulder blow up in other areas.

3 REHABILITATION METHODS

3.1 *Method A: Asphalt patching and overlaying*

According to design requirements, rehabilitation method A included patching of the existing HMA layer and then, overlaying 160 mm of new HMA layer (in three layers) as shown in Figure 3. Due to unsuitable conditions of the sub-base layer such as existence of fine materi-

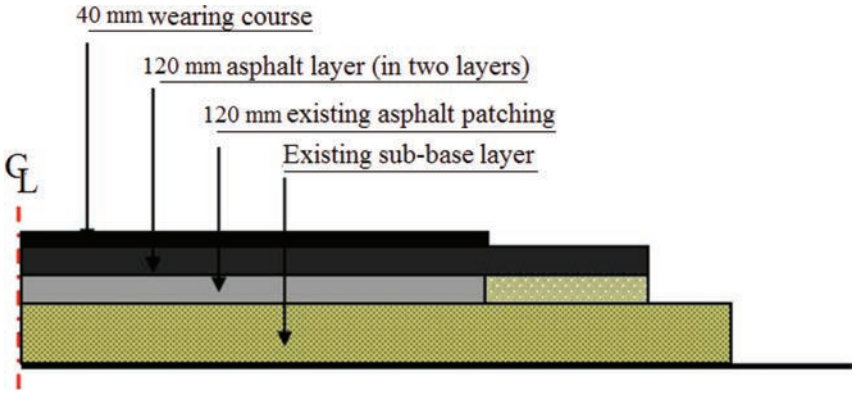

Figure 3. Repaired road cross section using method A.

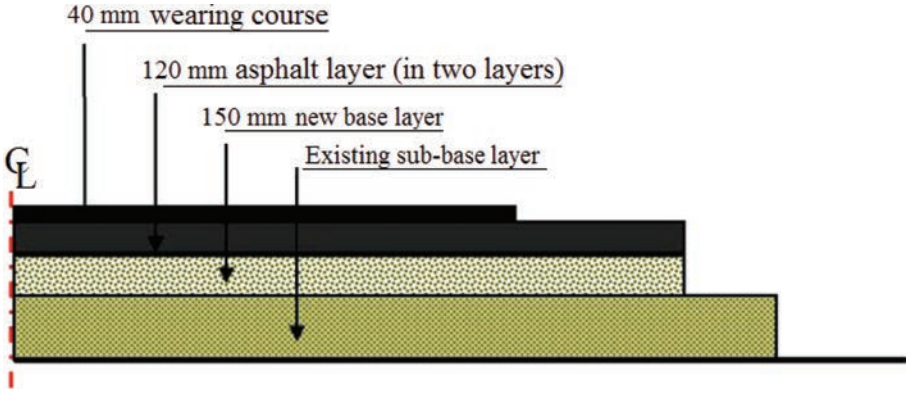

Figure 4. Repaired road cross section using method B.

als in the layer and insufficient layer compaction, and also large required patch working area (about 40% of the total area), the new pavement could not have sufficient strength.

The required HMA (for 30 km of the road) was calculated to be 160000 tons and the required time to construct this layer was estimated to be 18 working months. With regards to the region cold climate, this method needed 3 years to be completed.

3.2 *Method B: Pavement renovation*

Rehabilitation method B included milling 150 mm of the existing asphalt layer, levelling and compacting of the existing sub-base layer, performing 150 mm new base layer and overlaying 160 mm of HMA layer (in 3 layers). Compared with the previous method, the strength of this new pavement would be greater (Fig. 4).

The required time to accomplish this method was estimated to be almost 3 years with regards to limited seasonal working time.

3.3 *Method C: Cold recycling method*

With this method, using an in-situ cold recycling machine (WR 2500), the existing 150 mm HMA layer and 100 mm of existing sub base layer were milled and mixed with foam-bitumen and cement slurry in the machine rotational chamber. The stabilized layer was then protected, applying an HMA layer 60 mm thick (Fig. 5). This method required only 4 months to be completed.

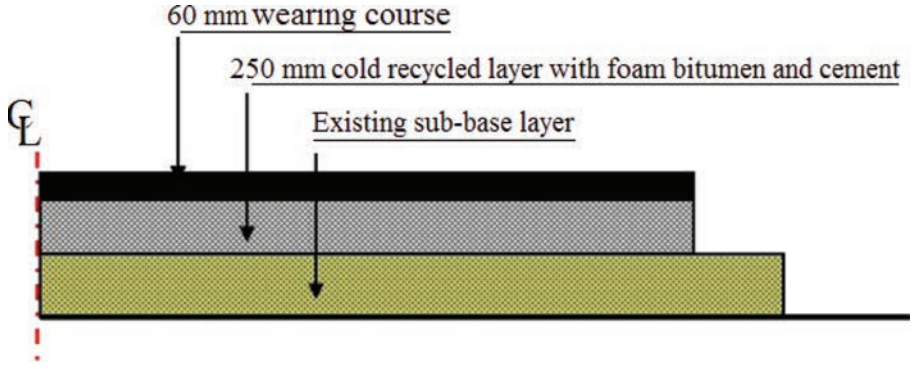

Figure 5. Repaired road cross section using method C.

This alternative design method was selected as the most appropriate method and resulted in the following advantages compared with the previous explained methods:

– 100 mm savings in total pavement thickness,
– No need to transport good quality materials from long distances,
– Greater pavement bearing capacities and structural strength,
– Minimized traffic disruption,
– Decreased total construction period; and,
– Reduced total project cost by using locally available materials.

With regards to client financial limitations, the first stage of the road rehabilitation with 5 km length was approved to be performed applying cold recycling method with foam bitumen and cement.

4 MIXTURE DESIGN

Two mixture designs were selected for foam bitumen stabilized base layers. For the main road pavement, 100 mm of the existing asphalt material and 150 mm of the existing sub-base material were mixed together. For the shoulder area, the existing sub-base was used only. The final aggregate gradations of these mixtures are shown in Figure 6. It can be seen that both gradations were suitable for producing foam bitumen stabilized bases according to South African's Technical Guide [1].

Foam bitumen mixes containing different amounts of cement and lime (at low level cement and lime contents) were tested under Marshall and ITS (Indirect Tensile Test) tests. Because of the poor coating of the aggregate particles with foam bitumen process (in contrast with the case of conventional HMA mixes), all the principal five Marshall parameters could not be determined [2]. Hence, stability and flow values were determined only.

ITS testing was performed on both dry samples and the samples were kept in water for 24 hours at 25°C. From these, Tensile Strength Ratio (TSR), defined as the ratio of tensile strength of the dry samples to the tensile strength of the saturated samples, was determined.

As for the project requirements, the key ITS parameters, Marshall Stability and Marshall Quotient (Q) were set to meet the following minimum limits:

– Dry ITS: 300 kPa,
– Soaked ITS: 200 kPa,
– TSR: 50%;
– Marshal Stability: 700 Kg
– Maximum Marshal Quotient (Marshall Stability/Flow): 150–600 kg/mm

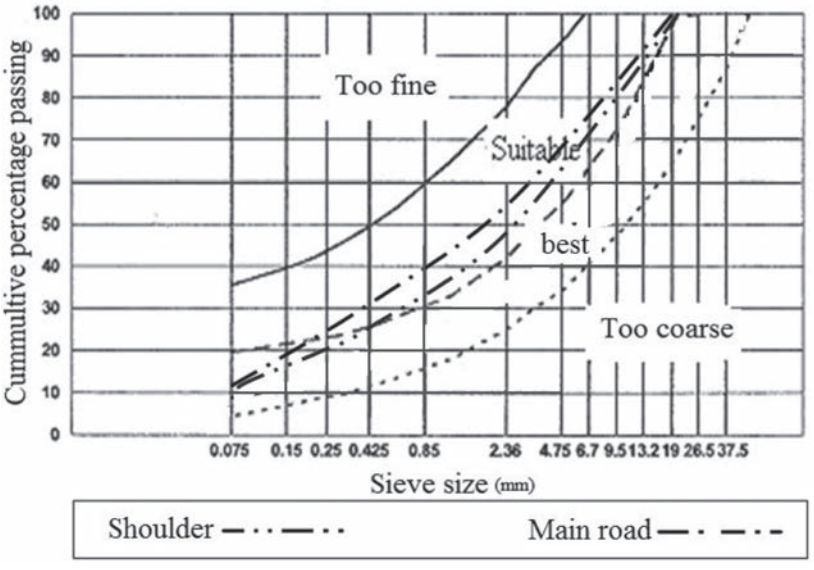

Figure 6. Aggregate gradations of foam bitumen stabilized base layer.

4.1 *Foam bitumen characteristics*

With regards to the cold location of the project, a 85/100 penetration grade bitumen was chosen for making foam bitumen. A laboratory foam making unit, a WLB10 Wirtgen type was used to make foam bitumen samples [3]. Two main characteristics of the foam mixes were determined (Expansion ratio: maximum volume of foam relative to original volume and half life: time taken in seconds for the foam to collapse to half of its maximum volume). The characteristics of the designed foam bitumen were as it follows:

- Bitumen temperature (as it is recommended [1 and 4]): 170° C
- Added water: 3%,
- Expansion ratio: 12; and,
- Half life time: 8 seconds.

4.2 *Mechanical testing*

In order to perform the mix design and determine the optimum bitumen content value, prepared samples (compacted at 75 blows of Marshall Hammer) were tested under dry and soaked ITS conditions.

The results indicate that a value corresponding to 3.1% and 3.8% bitumen content could be considered as the optimum bitumen content value for the main road and shoulder stabilization respectively. However, with mixes having both ITS and Marshall Stability values, these should not be expected to perform properly. In order to strength these conventional foam bitumen mixes, cement and hydrated lime powder were added as the bonding and strengthening agents [5 and 6]. The reasons of adding hydrated lime powder could be summarized as the bellow:

- Sub base material plasticity modification (Sub-base PI = 12),
- Increased frost resistance of the sub-base material,
- Decreased the swelling effect of the existing clay material in the sub base layer,
- Decreased foam bitumen and cement recycled base rigidity.

While the bitumen amounts was kept fixed at above mentioned levels, samples containing different amounts of cement and lime powder were prepared. For the main road, the optimum cement and lime contents were 1.2% and 1.0% respectively. For the shoulders, the

optimum cement and lime contents were 1.0% and 1.5% respectively. At these percentage of cement and lime, both ITS and Marshall testing results were above the specification limits.

5 CONSTRUCTION

For constructing foam bitumen layers, a train of cold recycling machineries were used, as shown in Figure 7. Hydrated lime powder was spread on top of the existing HMA layer and cement was applied in slurry form from a mixing unit and it was injected into the chamber of the main recycler machine while being mixed with aggregates. The stabilized layer was then compacted using a heavy roller to achieve the specified densities. After performing the compaction process, the prepared pavement was overlaid with a 60 mm hot mix asphalt layer.

One of the main advantageous of using this method was minimizing traffic disruption. As it can be seen in Figure 8, the road was open to traffic while the cold recycling train was operating.

Figure 7. Train of cold-in-place recycling machineries.

Figure 8. Base layer recycling and compaction.

Table 1. Quality control testing results of the stabilized base layers.

Testing location	Density (g/cm^3)	Dry ITS (kPa)	Soaked ITS (kPa)	TSR (%)	Stability (kg)	Q (Kg/mm)
Main road						
Km 25+600	2.04	592	469	79	795	300
Km 27+200	2.05	512	370	72	1105	340
Km 28+835	2.03	425	300	71	980	332
Km 30+650	2.03	425	320	75	1020	310
Shoulders						
Km 26+040	2.01	505	330	65	910	331
Km 27+210	2.03	582	390	67	895	308
Km 28+900	2.01	490	335	68	900	300
Km 30+125	2.03	425	300	71	980	332
Specification limits	–	300	200	50	700	150–600

6 QUALITY CONTROL TESTING

For quality control testing of the constructed layers, several tests were performed at different locations. ITS and Marshall testing were performed on cold recycled materials and field densities were performed after compaction of the recycled layer. These testing results showed that the properties of the stabilized base were satisfactory. Table 1 summarizes the testing results.

7 CONCLUDING REMARKS

Using cold recycling with foam bitumen and cement in Ardebil-Khalkhal main road resulted in several achievements as listed below:

- The construction time was reduced and appreciable time saving was achieved. These resulted in the project to be completed in one single working season (i.e. before the start of winter conditions).
- Several other savings were resulted from the reduction in total pavement thickness. In addition, locally available materials were used, limiting the use of high quality virgin aggregates.
- Environment protection was resulted from minimizing the raw materials mining and their transportation to the site.
- Using cold-in place recycling machinery chain minimized the traffic disruption.
- The addition of lime and cement to foam stabilized base resulted in increased strength properties and reduced moisture susceptibility and swelling effect of clay material.
- Quality control tests, carried out after construction showed great improvements in pavement properties. This approves suitability of the laboratory mix design used in constructing the new runway (i.e. the recycling train adopted).

REFERENCES

[1] Asphalt Academy. The Design and Use of Foamed Bitumen Treated Materials. Interim Technical Guideline TG2, Pretoria, South Africa, 2002.

[2] Hashemian, L. and Kavussi, A. Physical Properties and Mix Design Approach on Foam Bitumen Mixes. Modares technical and engineering scientific research journal, No.33, pp. 1–12, 2008.

[3] Wirtgen GmbH, Wirtgen Cold Recycling Technology. Windhagen, Germany, 2012.

[4] Jones A, Review of foamed bitumen stabilization mix design method. Austroads Project No. TT1358, Austroads, Australia, 2011.
[5] Design procedures for soil modification or stabilization, Division of Engineering and Asset Management, Office of Geotechnial Services, Indiana, USA, February 2013.
[6] Halles, F.A. and Thenoux, G.Z. Degree of Influence of Active Fillers on Properties of Recycled Mixes with Foamed Asphalt. In Transportation Research Record: Journal of the Transportation Research Board, Transportation Research Board of the National Academies, Washington, D.C., No. 2095, pp. 127–135, 2009.

Asphalt Pavements – Kim (Ed)
© 2014 Taylor & Francis Group, London, ISBN 978-1-138-02693-3

Temperature and confinement effects on the stiffness of a Cold Central-Plant Recycled mixture

Brian K. Diefenderfer
Virginia Center for Transportation Innovation and Research, Virginia Department of Transportation, Charlottesville, VA, USA

Sara D. Link
University of Virginia, Charlottesville, VA, USA

ABSTRACT: Pavement recycling is a technology that has been shown to be a cost-effective and environmentally sensitive means for pavement rehabilitation. One recycling technique, Cold Central-Plant Recycling (CCPR), produces a paving mixture from reclaimed asphalt pavement without heating the recycled pavement materials. Although there is a significant amount of information in the literature on the fundamental engineering properties of asphalt concrete, there is comparatively little published related to 100% recycled mixtures. This information is essential for the pavement design practitioner when using mechanistic or mechanistic-empirical design procedures for 100% recycled mixtures.

This study describes the effects of temperature and confinement pressure on the results of dynamic modulus testing of a CCPR mixture having foamed asphalt as the recycling agent and hydraulic cement as an active filler. This mixture was produced in the field at a mobile plant, and test specimens were compacted in the laboratory using a gyratory compactor. The results of this study showed that the effects of temperature were statistically significant for nearly all comparisons. The results also showed that the effects of confinement were more pronounced at higher temperatures and slower loading rates. The practical significance of these results can be determined after further study of the long-term performance of recycled materials.

Keywords: pavement recycling, cold central-plant recycling, dynamic modulus, confinement

1 INTRODUCTION

Pavement recycling has been shown to be an effective technology to rehabilitate deteriorated flexible pavements. In general, pavement recycling remixes the existing pavement material (either in-situ or within a mobile plant) and reuses it in the final pavement as a stabilized base layer. Pavement recycling techniques include the processes of hot in-place recycling, cold recycling, and full-depth reclamation. Cold recycling includes the processes of cold in-place recycling and Cold Central-Plant Recycling (CCPR). The most common recycling agents include foamed asphalt, emulsified asphalt, hydraulic cement, fly ash, and lime [1]. These techniques have been shown to produce less greenhouse gas emissions, are often times less costly, and can sometimes be used to rehabilitate a pavement more rapidly than traditional pavement rehabilitation practices [2–4]. Unfortunately, there is relatively little information about the fundamental engineering properties (in particular the dynamic modulus) of recycled materials when compared to the wealth of information that exists for Asphalt Concrete (AC). As dynamic modulus is the primary material input [5] used in current Mechanistic-Empirical (M-E) pavement design procedures (e.g., AASHTO's Pavement M-E), more information about the response of recycled materials in this test is needed if pavement design

practitioners are to use the various pavement recycling techniques within the framework of an M-E design procedure.

The pavement recycling technique explored in this study is CCPR. CCPR can be used as an alternative to newly produced AC base mixtures when stockpiles of quality Reclaimed Asphalt Pavement (RAP) are available. A CCPR plant may consist of a screening and crushing unit to control the maximum particle size, a feed hopper and a conveyor belt with weight scale, computerized controls for recycling agent(s) and water addition, and a pug mill for mixing [1]. An example of a CCPR plant is shown in Figure 1. After the

Figure 1. CCPR plant.

Figure 2. CCPR mixture paving.

CCPR mixture is produced, it may be stored in silos or stockpiles or immediately placed using traditional AC paving techniques. During placement, the CCPR mixture can be deposited directly into a conventional AC paver or in a windrow for pickup and deposit into an AC paver. The CCPR material is then compacted, much like an AC mixture, typically with a series of pneumatic-tire and steel-drum rollers using a control strip to establish a density target. A photograph of a CCPR mixture paving operation is shown in Figure 2.

2 OBJECTIVE AND SCOPE

This objective of this study was to determine the influence of temperature and confinement on the stiffness of a CCPR mixture as measured by the dynamic modulus. Test specimens of a CCPR mixture produced in the field using a mobile plant were compacted in the laboratory using a gyratory compactor. The CCPR mixture was produced from RAP originally obtained during a 2011 pavement recycling project on Interstate 81 in Virginia and was a combination of surface, intermediate, and base AC mixtures [6].

3 MATERIALS

The CCPR materials used for this study were placed on three sections at the pavement test track of the National Center for Asphalt Technology in Auburn, Alabama, as part of a structural study during the 2012 research cycle. The RAP used to produce the CCPR was stockpiled in Virginia for nearly two years and then hauled to the project site in Alabama for construction. The RAP was crushed prior to production in the CCPR mobile plant as large chunks had formed within the RAP stockpile. Prior to construction, a mixture design was developed using procedures described by Wirtgen [7]. The design procedure establishes a recycling agent content offering the desired laboratory properties. In this case, foamed asphalt was used as the primary recycling agent, with hydraulic cement as an active filler. Active fillers may often be combined with recycling agents to improve resistance to the detrimental effects of moisture and improve the early strength [8].

The results of the mixture design procedure found the optimal properties to occur with 2.0% foamed asphalt with 1.0% hydraulic cement. The Indirect Tensile Strength (ITS) is the most often used laboratory test to guide the assessment of CCPR using foamed asphalt during mixture design. A dry ITS value of greater than 310 kPa (45 psi) and a tensile strength ratio (determined as the tensile strength after soaking divided by the dry strength) of greater than 70% are often cited as providing sufficient strength for high-traffic pavements [7]. These tests were conducted to establish the mixture design and then repeated during construction to verify the properties of the CCPR material; the results of these tests conducted during construction are shown in Table 1. The gradation of the CCPR material was in accordance with the requirements of AASHTO T 27 [9] and is shown in Figure 3. Figure 3 also shows the gradation envelope recommended by Wirtgen [7] as a shaded area bordered by two dashed lines. From this figure it can be seen that the CCPR material placed was of a finer gradation than that recommended by Wirtgen [7].

Table 1. CCPR indirect tensile strength results.

Condition	Dry			Soaked		
Specimen	1A	2A	3A	1B	2B	3B
Tensile strength, kPa	658.5	650.3	649.6	527.6	496.1	496.1
Mean tensile strength, kPa	652.8			506.6		
Tensile strength ratio, %	77.6					

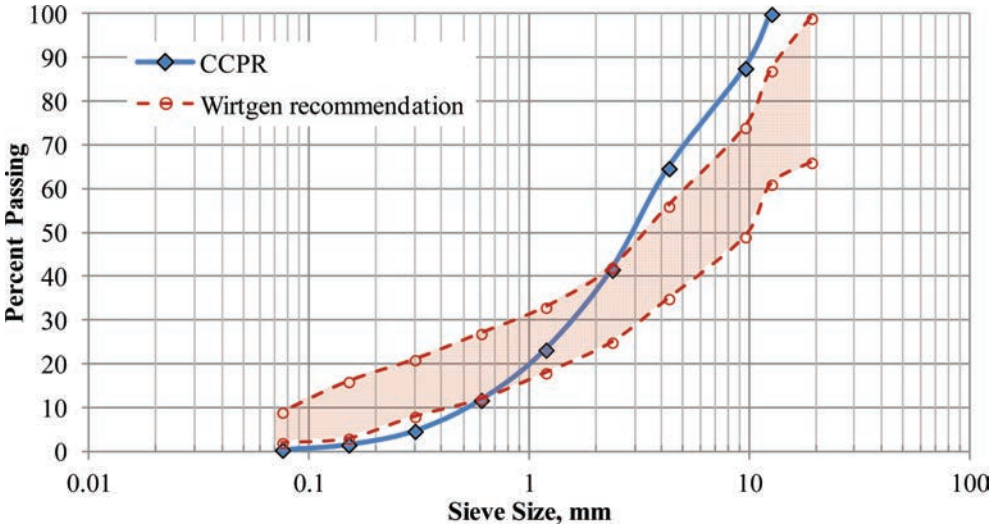

Figure 3. CCPR gradation results.

4 METHODS

4.1 *Dynamic modulus specimen fabrication*

Dynamic modulus specimens were fabricated from loose materials collected at the mobile plant during construction of the test track sections. As the moisture content at production is an important parameter for compaction, the sampled materials were placed in buckets and then sealed for transport to the on-site laboratory. The loose materials were then combined to create one approximately 25-kg batch. About 16 specimens were fabricated per batch. When additional materials were needed, additional buckets were unsealed and combined to create another approximately 25-kg batch.

Dynamic modulus test specimens were fabricated using a gyratory compactor such that they had about the same bulk density as the mixture design ITS specimens; approximately 2202 kg/m^3. For each dynamic modulus specimen, a calculated mass of material was added to a 152.4-mm-diameter gyratory compactor mold and compacted to a desired height of about 170 mm. The mass of material for each dynamic modulus specimen was calculated by multiplying the mixture design ITS specimen mass by the proportional change in volume between the mixture design ITS specimen and the dynamic modulus specimen. The number of gyrations was not recorded but typically ranged from 30 to 50 gyrations. All fabricated specimens were cured in a forced draft oven for 72 hours at 40°C after compaction.

4.2 *Dynamic modulus testing*

The fabricated specimens were stored at approximately 21°C and 70% relative humidity for approximately 6 months prior to testing. The long time between fabrication and testing was due to a backlog of other testing in the laboratory rather than to any specific curing or waiting period. Prior to testing, the fabricated specimens were cored and trimmed to produce test specimens having a 101.4-mm diameter and a 152.4-mm height. The dynamic modulus testing was conducted using an Asphalt Mixture Performance Tester (AMPT) in accordance with AASHTO TP 79 [10] with slight modifications; a reduced set of temperatures was used. Testing was conducted in the axial mode at temperatures of 4.4, 21.1, 37.8, and 54.4°C. At each temperature, testing was conducted at loading frequencies of 25, 10, 5, 1, 0.5, and 0.1 Hz. The test specimens were also tested at different levels of confinement pressure. Four levels of confinement were used: 0, 34.5, 68.9, and 137.9 kPa. For each condition, five replicates were tested.

5 RESULTS AND ANALYSIS

5.1 *Results*

The dynamic modulus of a CCPR mixture was tested in the axial mode at four temperatures, six frequencies, and four confining pressures as stated previously. Each specimen was re-used throughout the testing regime and tested in an increasing order of temperature and a decreasing order of frequency at each temperature to minimize the potential for damage. In general, the between-specimen repeatability values were not within the ranges recommended in AASHTO TP 79 [10] at the higher temperatures and longer loading times. However, this was expected based on the authors' past history with testing recycled mixtures and is important to consider when comparing the results from other recycled mixtures.

Figure 4 shows the results of the dynamic modulus testing at the four test temperatures and four confining pressures and at frequencies of 25, 10, 1, and 0.1 Hz (the results at 5 and 0.5 Hz are not shown for brevity but followed the same trend). The error bars indicate plus/minus one standard deviation. These results show the average unconfined dynamic modulus at 10 Hz to be approximately 7500, 4200, 2300, and 1000 MPa at test temperatures of 4.4, 21.1, 37.8, and 54.4°C, respectively.

5.2 *Analysis*

By visual inspection of the data shown in Figure 4, several trends can be noted: (1) the dynamic modulus of the CCPR materials decreases with increasing temperature at each test frequency; (2) the dynamic modulus of the CCPR materials increases with increasing test frequency at each temperature; and (3) the influence of confinement on the dynamic modulus appears to increase with increasing temperature. These results show trends that are similar for AC materials. Similar observations on the influence of temperature for recycled materials

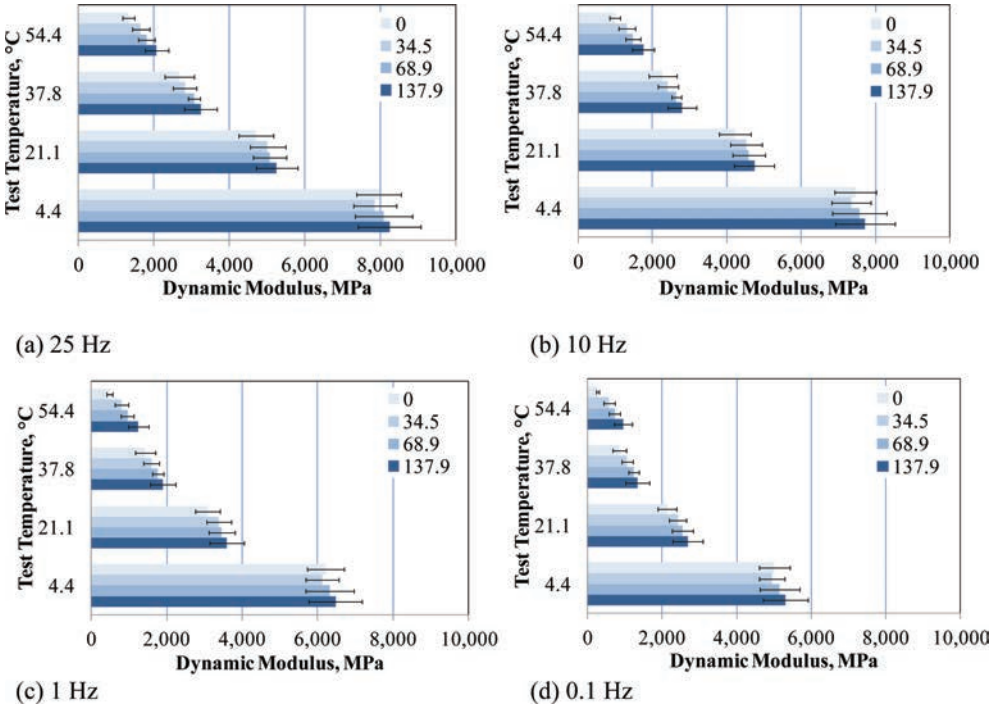

Figure 4. Results of dynamic modulus testing t four confinement pressures: (a) 25 Hz, (b) 10 Hz, (c) 1 Hz, and (d) 0.1 Hz. Error bars represent plus/minus one standard deviation.

have been reported by others [11–13]. These studies also documented stiffness values for recycled materials similar to those shown herein.

5.2.1 *Specimen variability analysis*

The dynamic modulus Coefficient Of Variation (COV) calculated from the five replicates for all tests ranged from approximately 5% to 25% with generally larger COVs at the higher test temperatures and lower test frequencies. The dynamic modulus COV at 4.4, 21.1, 37.8, and 54.4°C tests ranged from approximately 7% to 11%, 9% to 15%, 5% to 24%, and 12% to 25%, respectively, across all confining pressures. The COV values were highest for the 137.9 kPa confinement pressure, but there was no consistent trend across the other three confinement pressures. Bonaquist [5] conducted a study to investigate the precision of the dynamic modulus test for AC using an AMPT. Bonaquist reported that the repeatability COV increased with decreasing stiffness. The study included tests at 4, 20, and 40°C and reported precision statistics with respect to the measured dynamic modulus value, as shown in Table 2. The CCPR materials tested were most similar to the 9.5 mm Nominal Maximum Aggregate Size (NMAS) shown in Table 2 (the other NMASs are shown to illustrate how the variability was found to increase with increasing particle size as could be found for some recycled mixtures containing AC base courses). When compared to those in Table 2, the CCPR dynamic modulus COV values were nearly all outside the range recommended by Bonaquist [5]. However, the information from Table 2 is based on AC materials and extends only to a test temperature of 40°C. The between-specimen variability in this study is higher than that typically found for most AC materials but is consistent with that in other recycled materials studies [11,12].

5.2.2 *Statistical significance analysis for temperature and confinement*

As stated previously, the purpose of this study was to investigate the influence of temperature and confinement on the stiffness of a CCPR mixture as measured by the dynamic modulus. To consider the effects of temperature, a two-tailed Student's *t*-test was applied to determine if differences in the mean dynamic modulus with respect to temperature were statistically significant. The *t*-test was conducted to compare the mean dynamic modulus results of two neighboring test temperatures. That is, the results at 4.4°C were compared to the results at 21.1°C; next, the results at 21.1°C were compared to the results at 37.8°C and so on. If the results at these smaller temperature differences were significant, then differences across larger temperature ranges would also be significant. The *t*-test was performed separately at each test frequency and confinement level. The results showed that the mean differences in dynamic modulus with respect to temperature were all significant (considering a significance level [α] of 0.05) except for the comparison of 37.8°C vs. 54.4°C at 0.1 Hz at 137.8 kPa confinement. The p-value for this condition was found to be 0.10. The reason the difference in dynamic modulus across this temperature difference was found to be not statistically significant stems from the high COV values at 37.8°C and 54.4°C for this condition, approximately 24% and 25%, respectively.

Table 2. Dynamic modulus (|E*|) precision statistics [5].

	Within-laboratory repeatability, |E*|, s_r%			
Average |E*|, MPa	9.5 mm[a]	12.5 mm	19 mm	25 mm
≥137 to <200	15	17	20	24
≥200 to <500	13	14	16	19
≥500 to <1000	11	12	14	16
≥1000 to <2000	9	10	12	13
≥2000 to <5000	8	8	9	11
≥5000 to <10000	7	7	8	9
≥10000 to <16400	6	6	7	7

[a]Nominal maximum aggregate size.

To consider the effects of confinement, an analysis of variance (ANOVA) was conducted. The ANOVA was conducted to determine if differences in the mean value of the dynamic modulus at the four levels of confinement were statistically significant at the six frequencies and four test temperatures. A significance level (α) of 0.05 was used. Although the ANOVA was used to determine if differences between the means were statistically significant, a Tukey's HSD test was used to group like means together. Normally the Tukey's HSD test is not conducted if the ANOVA shows that the differences are not significant, but the results are easy to interpret visually in both cases and so are presented here. Table 3 shows the results of the Tukey's HSD test using grouping letters for the test frequencies of 25, 10, 1, and 0.1 Hz (the results at 5 and 0.5 Hz are not shown for brevity but followed the same trend). The confinement pressures shown in Table 3 having the same grouping letter indicate that the differences in mean dynamic modulus values were not statistically significant. Table 3 shows that the difference in the dynamic modulus resulting from changes in confinement was not statistically significant for the 4.4°C temperature at all test frequencies. Table 3 shows that the difference in the dynamic modulus resulting from changes in confinement was statistically significant for the 54.4°C temperature at all test frequencies. Table 3 also shows that as the test frequency increased, confinement was found to be not statistically significant at the 21.1 and 37.8°C test temperatures.

Previous studies of AC materials also found that confinement is more influential at higher temperatures and slower loading rates [14–16]. Schwartz and Khosravifar [12] found similar results for laboratory- and field-produced CCPR materials and stated that temperature and loading rate had a greater influence on the dynamic modulus than confining stress.

5.2.3 *Practical significance analysis for confinement*

Another way to consider the results is in terms of a practically significant difference. Figure 5 shows select data from the confined dynamic modulus master curve at three confinement pressures plotted with respect to select data from the unconfined dynamic modulus master curve at four temperatures. The solid diagonal line in Figure 5 is the line of equality; the bold dashed lines represent plus/minus 20% of unity; and the thin dashed lines represent

Table 3. Tukey's HSD results[a].

	Confinement pressure, kPa	Test temperature, °C								
		4.4	21.1		37.8		54.4			
25 Hz	0	A	A		A		B			
	34.5	A	A		A		B	A		
	68.9	A	A		A			A		
	137.9	A	A		A			A		
10 Hz	0	A	A		A		C			
	34.5	A	A		A		C	B		
	68.9	A	A		A			B	A	
	137.9	A	A		A				A	
1 Hz	0	A	A		B		C			
	34.5	A	A		B	A	C	B		
	68.9	A	A		B	A		B	A	
	137.9	A	A			A			A	
0.1 Hz	0	A	B		B		C			
	34.5	A	B	A	B	A		B		
	68.9	A	B	A		A		B	A	
	137.9	A		A		A			A	

[a]Confinement pressures having the same grouping letter indicate that the differences in mean dynamic modulus values are not statistically significant.

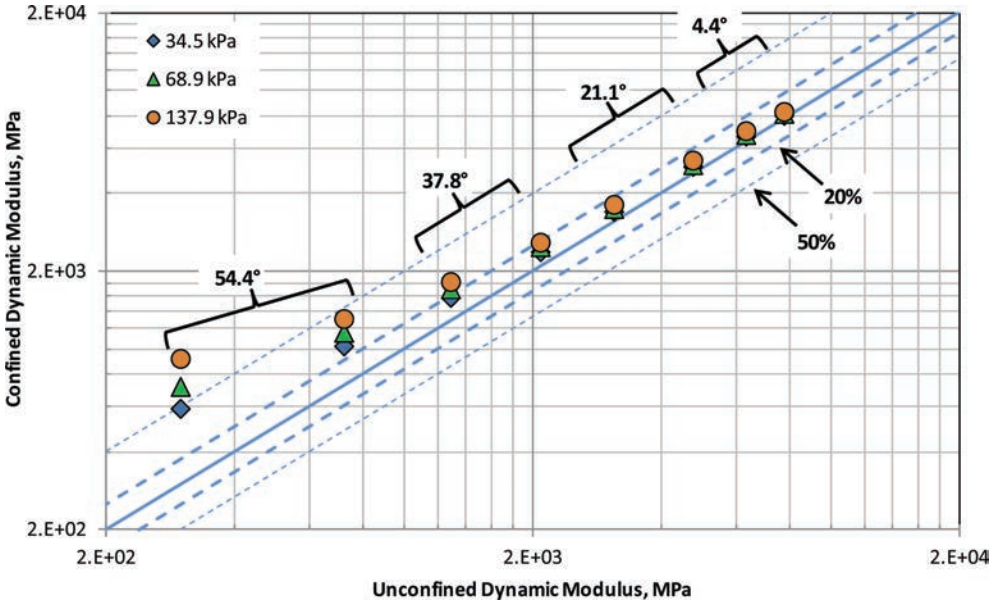

Figure 5. Unconfined dynamic modulus master curve data versus confined dynamic modulus master curve data.

plus/minus 50% of unity. The data points shown in Figure 5 were calculated by using the fitting parameters (α, β, δ, γ) to calculate the dynamic modulus master curve data at select reduced frequency values that were representative of the data at each temperature. The eight sets of data points shown in Figure 5 include two values at each test temperature to illustrate the trend from the complete master curve.

From Figure 5 it can be seen that the data representing the 4.4 and 21.1°C test temperatures are close to the line of equality and are within the +20% dashed line. That is, the confined dynamic modulus is less than 20% stiffer than the unconfined dynamic modulus at these two temperatures. Figure 5 shows that the data representing the 37.8°C test temperature begin to depart more from the line of equality and approach the +20% dashed line. That is, the confined dynamic modulus is approximately 20% stiffer than the unconfined dynamic modulus at 37.8°C. Figure 5 also shows that the data representing the 54.4°C test temperature begin to depart significantly from the line of equality and approach and exceed the +50% dashed line. That is, the confined dynamic modulus is approximately 50% stiffer than the unconfined dynamic modulus at 54.4°C.

The difference between confined and unconfined dynamic modulus is likely not practically significant at the 4.4 and 21.1°C test temperatures. The difference between confined and unconfined dynamic modulus is likely practically significant at the 54.4°C test temperature. It is yet unclear if the differences at the 37.8°C test temperatures are practically significant. This can be determined once a study involving multiple mixtures, operators, and laboratories is completed to determine typical material variability and more in-depth study of the long-term performance of pavements with recycled materials is completed.

6 SUMMARY

This paper presents the results of dynamic modulus testing of a CCPR mixture having foamed asphalt as the recycling agent and hydraulic cement as an active filler. Testing was performed at four temperatures, six loading frequencies, and four levels of confinement to evaluate the effects of temperature and confinement. The study found the differences in mean dynamic modulus

with respect to temperature were all statistically significant except for the comparison of 37.8°C versus 54.4°C at 0.1 Hz at 137.8 kPa confinement. The study found that the differences in mean dynamic modulus with respect to the level of confinement were not statistically significant for the 4°C temperature at all test frequencies. Further, the study found that the differences in mean dynamic modulus with respect to the level of confinement were statistically significant for the 54.4°C temperature at all test frequencies. For the 21.1 and 37.8°C tests, the study showed that as the test frequency increases, confinement was found to be not statistically significant.

In addition to statistical significance testing, the study considered the differences in dynamic modulus with respect to confinement in terms of a practical difference. The study found that the confined dynamic modulus is less than 20% stiffer than the unconfined dynamic modulus at 4.4 and 21.1°C. The confined dynamic modulus was found to be approximately 20% stiffer than the unconfined dynamic modulus at 37.8°C. The differences at the lower two temperatures are not expected to be practically significant. At 54.4°C the confined dynamic modulus was found to be approximately 50% stiffer than the unconfined dynamic modulus. The differences at 54.4°C are expected to be practically significant. It is difficult to determine the implications of these findings as a full-fledged laboratory study involving multiple mixtures, operators, and laboratories has not yet been conducted for recycled materials. In addition, studies of the long-term performance of pavements containing recycled materials and comparisons of the distresses predicted by M-E design methodologies versus those found in-situ have also not been completed.

ACKNOWLEDGMENTS

The authors gratefully acknowledge the assistance of Ken Lanford, Lanford Brothers Co.; Marlin Hewett, B&S Contractors; Richard Schreck and Trenton Clark, Virginia Asphalt Association; Mike Marshall, Wirtgen GmbH; David Timm, Auburn University; Buzz Powell and Jennifer Still, National Center for Asphalt Technology; and Michael Brown, Troy Deeds, Stacey Diefenderfer, Donnie Dodds, and Benjamin Earl, Virginia Center for Transportation Innovation and Research. The authors also acknowledge the assistance of Richard Ferron, Al Soltis, and Shane Moomaw.

REFERENCES

[1] Asphalt Recycling and Reclaiming Association. Basic Asphalt Recycling Manual. Annapolis, MD, 2001.
[2] Nataatmadja, A. Some Characteristics of Foamed Bitumen Mixes. Transportation Research Record, No. 1767. Transportation Research Board, Washington, DC, pp. 120–125, 2001.
[3] Thenoux, G., A. Gonzalez, and R. Dowling. Energy Consumption Comparison for Different Asphalt Pavements Rehabilitation Techniques Used in Chile. Resources, Conservation and Recycling, Vol. 49, pp. 325–339, 2007.
[4] Stroup-Gardiner, M. Recycling and Reclamation of Asphalt Pavements Using In-Place Methods. NCHRP Synthesis 421. Transportation Research Board, Washington, DC, 2011.
[5] Bonaquist, R. Precision of the Dynamic Modulus and Flow Number Tests Conducted with the Asphalt Mixture Performance Tester. NCHRP Report 702. Transportation Research Board, Washington, DC, 2011.
[6] Diefenderfer, B.K., A.K. Apeagyei, A.A. Gallo, L.E. Dougald, and C.B. Weaver. In-Place Pavement Recycling on I-81 in Virginia. Transportation Research Record, No. 2306. Transportation Research Board, Washington, DC, pp. 21–27, 2011.
[7] Wirtgen. Wirtgen Cold Recycling Technology. Wirtgen GmbH, Windhagen, Germany, 2010.
[8] Asphalt Academy. Technical Guideline: Bitumen Stabilised Materials, 2nd Edition. Pretoria, South Africa, 2009.
[9] American Association of State Highway and Transportation Officials. AASHTO T 21-11: Standard Method of Test for Sieve Analysis of Fine and Coarse Aggregates. Washington, DC, 2011.
[10] American Association of State Highway and Transportation Officials. AASHTO TP 79-09: Standard Method of Test for Determining the Dynamic Modulus and Flow Number for Hot Mix Asphalt (HMA) Using the Asphalt Mixture Performance Tester (AMPT). Washington, DC, 2009.

[11] Cross, S.A., and Y. Jakatimath. Evaluation of Cold In-Place Recycling for Rehabilitation of Transverse Cracking on US 412. Report No. AA-5-11816. Oklahoma State University, Stillwater, 2007.
[12] Schwartz, C.W., and S. Khosravifar. Design and Evaluation of Foamed Asphalt Base Materials. Report No. MD-13-SP909B4E. University of Maryland, College Park, 2013.
[13] Lee, H.D., and Y.T. Kim. Validation of the New Mix Design Process for Cold In-Place Rehabilitation Using Foamed Asphalt. Report No. IHRB TR-474. University of Iowa, Iowa City, 2007.
[14] Zeiada, W.A., K.E. Kaloush, K.P. Biligiri, J.X. Reed, and J.J. Stempihar. Significance of Confined Dynamic Modulus Laboratory Testing for Asphalt Concrete: Conventional, Gap-Graded, and Open-Graded Mixtures. Transportation Research Record, No. 2210. Transportation Research Board, Washington, DC, pp. 9–19, 2011.
[15] Lacroix, A., B.S. Underwood, and Y.R. Kim. Reduced Testing Protocol for Measuring the Confined Dynamic Modulus of Asphalt Mixtures. Transportation Research Record, No. 2210. Transportation Research Board, Washington, DC, pp. 20–29, 2011.
[16] Pellinen, T.K., and M.W. Witczak. Stress Dependent Master Curve Construction for Dynamic (Complex) Modulus. Asphalt Paving Technology: Association of Asphalt Paving Technologists, Vol. 71, pp. 281–309, 2002.

Asphalt Pavements – Kim (Ed)
© 2014 Taylor & Francis Group, London, ISBN 978-1-138-02693-3

Laboratory performance evaluation of RAP/RAS mixtures designed with virgin and blended binders

Alireza Zeinali
University of Kentucky, Lexington, KY, USA

Phillip B. Blankenship
Asphalt Institute, Lexington, KY, USA

Kamyar C. Mahboub
University of Kentucky, Lexington, KY, USA

ABSTRACT: When developing blending charts for RAP/RAS mixtures, it is presumed that laboratory testing of blended and virgin binders match the performance characterization of the plant-produced mixtures with the recycled materials. However, the thoroughgoing blend of the virgin binder into the RAP/RAS material is not guaranteed in an asphalt mix plant. In some cases, blending charts results in a virgin binder which is two performance grades softer than the target binder. Kentucky Transportation Cabinet was interested in determining if using a two-grades-softer binder would have a deleterious effect on pavement performance. In this study, four RAP/RAS field mixtures were collected from highway projects in Kentucky. The mixtures were subjected to beam fatigue, IDT creep/strength, and DC(t) fracture tests at the Asphalt Institute laboratory. Furthermore, a laboratory standard mixture was utilized as a control for the expected performance from the mixtures in central Kentucky. The results showed that using virgin binders, which were two grades softer than the target performance grade, resulted in drastically softer mixtures, as compared to the control mixture. This finding suggests the rutting potential of the pavement could escalate by using such a soft virgin binder. Nonetheless, the fracture energy of the mixtures did not improve by using a two-grades-softer binder. In summary, the mixture with one-grade-softer virgin binder exhibited a closer performance to the control mixture.

Keywords: performance testing; reclaimed asphalt pavement; shingles; recycled materials

1 BACKGROUND

Utilizing recycled materials in pavement construction can significantly reduce the environmental impact of highway construction projects. Reclaimed Asphalt Pavement (RAP) and Reclaimed Asphalt Shingles (RAS) are valuable recyclable materials that contain significant amounts of reusable asphalt binder and aggregate. The energy and cost analysis has shown that using 15 percent of RAP materials in a new asphalt pavement results in 5.5 to 6.8 percent savings in the overall cost when compared to a conventional Hot-Mix Asphalt (HMA) pavement. Additionally, this typical 15 percent use of RAP results in a reduction in energy consumption as well as the production emissions by 6 to 7 percent [1].

Despite all these benefits, RAP and RAS may lack some critical mechanical properties, which are essential to a new flexible pavement. RAP is produced by milling off an old asphalt pavement and grinding the material to appropriate size proportions. Post-consumer asphalt shingles are removed from roofs and are separated from construction debris. In both cases the

recycled materials have been extracted from an environment in which they have been exposed to weathering and aging for a long time. This in-service aging and weathering of RAP and RAS normally result in embrittlement of their asphalt binders, and has a deteriorating effect on the mechanical properties of the RAP and mixtures. It has been a challenge to modify the material properties of RAP/RAS to obtain the desired performance characteristics for their inclusion in a new asphalt pavement.

Under the current practice, the RAP/RAS materials are mixed with a softer binder in order to compensate for the brittleness of the aged binder. A set of blending charts is constructed to find the grade of the softer asphalt, which would bring the total blend to the desirable stiffness for use in a new asphalt pavement. Blending charts help determine the critical high, intermediate, and low temperatures for the blended binders with different amounts of RAP/RAS. For a known RAP/RAS content (percentage of the mixture), the blending charts yield the type of the softer virgin binder. In case the design is restricted to a specific virgin binder, the blending charts help determine the amount of RAP/RAS materials [2]. In either case, the aged asphalt binder is extracted and recovered from the RAP/RAS material and subjected to binder testing.

The validation of using blending charts was evaluated in a research by National Cooperative Highway Research Program [3]. Designing the RAP/RAS mixtures by testing the virgin and blended binder testing is essentially based on the assumption that the aged binder from the recycled materials would completely blend into the softer virgin binder during the mixing process. Based upon this assumption, the recovered RAP/RAS binder is completely blended with the virgin binder in the laboratory and subjected to binder testing. However, the thoroughgoing blend of the virgin binder into the RAP/RAS material is not guaranteed in an asphalt mix plant.

Another method is also suggested by Ma et al. to conduct the binder tests without extracting the binder from the recycled materials. In this method, fine RAP materials are used to fabricate the binder test specimens in conjunction with the virgin binder [4]. Although this method avoids chemical extraction and recovery of recycled binders, it does not seem to simulate the incorporation of RAP/RAS into the new material in a mixing plant.

Performance of RAP/RAS mixtures depend on various properties of both recycled and virgin materials. Generally the mixtures with RAS are stiffer at high temperatures [5] and the fibers present in the waste shingles improve the cracking resistance of the mixture [2]. However, RAS mixtures are more susceptible to low temperature cracking due to the high stiffness of their recycled binder. RAP mixtures on the other hand are stiffer at the intermediate temperatures and more susceptible to fatigue cracking [5]. Krishna et al. evaluated the impact of RAP content on volumetric properties and stiffness of HMA. The results showed that the volumetric properties of the mixtures were affected by the amount of RAP and mixtures became stiffer as the amount of RAP increased [6].

In the recent years the processing technology of the post-consumer shingles has improved considerably and an increasing number of agencies are allowing the use of RAS. This necessitates a thorough analysis of the RAS and its combination with RAP material to determine the optimal method of using RAP/RAS in asphalt mixtures.

2 RESEARCH OBJECTIVES

Economic and environmental benefits of using RAP and RAS have been a driving force in using higher percentage of these recycled materials by the construction community. The highway agencies, on the other hand, are concerned that incorporating too much RAP/RAS may lead to premature distress. If such early failure occurs, using RAP/RAS not only yields no benefits, but also imposes additional costs in terms of repairing, resurfacing, and even reconstruction operations. In short, the goal of the asphalt industry is to recycle as much as possible, and yet, take all the precautionary measures to prevent costly failures.

Kentucky Transportation Cabinet (KYTC) has been using the combination of 10 percent RAP and 3 percent RAS in pavement projects for the past few years. Furthermore, KYTC

requires the development of blending charts to determine the grade of virgin binder, which should be added to the RAP/RAS mixture. Considering the environmental conditions of Kentucky, the target performance grade of the blended binder is PG 64-22. In some cases, the stiffness of the RAS combined with its relatively high asphalt content has resulted in the use of a PG 52-34 asphalt binder. The Cabinet has expressed concerns about using a virgin binder grade that is two grades softer (PG XX-34) than their general purpose PG 64-22 grade of binder. Additionally, it has been observed that the final m-value of the recovered asphalt from the mixtures is sometimes lower than the required amount of m = 0.30. This may increase the potential for cracking of pavements containing RAP and RAS.

The main objective of this project was to evaluate the effect of using RAP and RAS under the current practice in Kentucky on the cracking performance and durability of asphalt pavements. The resistance of the mixtures containing RAP and RAS against fatigue and low-temperature cracking was compared to a conventional mixture typically used in Kentucky highways without any recycled materials. Furthermore, the research answers if the expected performance derived from the binder testing and blending charts matches the cracking performance of the mixtures containing RAP/RAS obtained from mixture performance testing.

3 EXPERIMENTAL PLAN

3.1 *Materials*

Hot mix asphalt specimens were collected from four different highway projects in Kentucky. According to the contractors, the specimens were mixed at 149°C (300°F), and the specimens were collected from the hauling trucks before placing in the paver. The mixtures from Bullitt, Flaming, and Robertson Counties contained 10 percent RAP and 3 percent RAS. The mixture from Grant County contained only RAS and it was blended with PG 52–34 asphalt binder. The Bullitt County mixture was designed and utilized as a binder course between the base and surface course of the highway, whereas other mixtures were surface courses. Table 1 contains the design properties for the mixtures used in this study. In addition to the field mixtures, a laboratory standard mixture with design and aggregate properties similar to the typical design of Kentucky surface layers was used as the control. This mixture has been used in several highway projects and has proved to perform satisfactorily in the climatic conditions of the central Kentucky. Since the field performance of this mixture was already known, it could be used as a reference performance point for the RAP/RAS mixtures.

3.2 *Specimen preparation*

The field samples were kept in five gallon metal buckets in a controlled temperature room. Prior to testing, the buckets were heated in an oven at 135°C (275°F) and were divided into

Table 1. Mixture properties.

Property	Bullitt	Fleming	Grant	Robertson	Lab standard
NMAS, mm	25.0	9.5	9.5	9.5	9.5
VMA, %	12.6	15.8	16.9	15.6	15.2
VFA, %	65.9	74.0	76.0	74.0	73.0
G_{mm}	2.555	2.464	2.457	2.452	2.521
RAP, %	10.0	10.0	0.0	10.0	0.0
RAS, %	3.0	3.0	3.0	3.0	0.0
Asphalt content (AC), %	4.1	5.4	5.7	5.4	5.4
Effective AC, %	3.5	5.1	5.6	5.0	4.8
Virgin AC, %	3.0	4.2	5.0	4.2	5.4
Virgin asphalt grade	PG 58-28	PG 58-28	PG 52-34	PG 52-34	PG 64-22

smaller portions using a Quartermaster Asphalt Sample Divider in order to avoid segregation. As per the requirements of the AASHTO R 30 standard, the field-collected mixtures were not subjected to additional laboratory short-term conditioning, since they had already undergone the mixing and hauling processes in the field. The compaction temperature for all the samples was 135°C. To reach this compaction temperature, the mix samples were heated in covered pans. Since this was a comparative study between the mixtures, a similar sampling and conditioning method was applied on all the mixtures to avoid any bias in the test results.

3.3 *Test matrix*

A laboratory test matrix was developed according to the primary focus of the research, which was early cracking in RAP/RAS mixtures. Flexural beam fatigue test, low temperature creep compliance test, indirect tensile strength test (IDT), and disk-shaped compact tension [DC(t)] test were conducted on the mixtures to evaluate their performance with respect to fatigue and low-temperature cracking. All the tests were performed on triplicate specimens, and using annually calibrated equipment in the Asphalt Institute laboratory.

4 MIXTURE PERFORMANCE AND CHARACTERIZATION

4.1 *Fatigue cracking*

A series of flexural constant-strain four-point beam fatigue tests were conducted at 1000 με and 10-Hz loading to evaluate the effect of using reclaimed asphalt pavement and shingles materials on fatigue cracking of the HMA mixtures. This test is performed on a beam shaped specimen which is supported at four points. A repetitive force is applied at the center-point of the specimen to gain the designated strain level of the test. The number of load cycles to initiation of a fatigue crack in the specimen is an indication of the pavement performance under fatigue loading.

Three beam specimens were compacted at 8.0 ± 1.0% air void and tested at the moderate temperature of 20°C for each mixture shown in Table 1. The fatigue failure of each sample was determined in accordance with the ASTM D7460 standard method [7], and based upon the variations of the normalized complex modulus of the specimen during the test. The beam fatigue test results are presented in Figure 1. The dashed lines in this figure represent the average number of cycles to failure for each mixture. It should be noted that the 1000 με corresponds to the condition of extremely heavy loads, or mimicking reflective cracking from underlying pavements. Comprehensive examination of a mixture's fatigue performance requires running the fatigue test at a spectrum of various strains and temperatures. In this study, however, the beam fatigue test was utilized to investigate the brittleness and possibility of early cracking at moderate temperatures. It should also be noted that the frequency of load repetition in an actual asphalt pavement is much lower than in the beam fatigue test. Therefore, the rest period between the loads along with the self-healing property of asphalt material [8] delay the growth of fatigue cracks in asphalt pavements. Consequently, the laboratory cycles to fatigue failure is considerably lower than the real fatigue life of the pavement. The fatigue criterion for asphalt pavements developed by the Asphalt Institute is based upon the suggestion that the pavement fatigue life is 18.4 times greater than the laboratory cycles to failure [9].

As Figure 1 illustrates, except for the Bullitt County mixture, all the RAP/RAS mixtures exhibited a considerably higher fatigue life as compared to the laboratory standard mix. Considering the fact that the control laboratory mixture did not contain any recycled materials, a satisfactory fatigue performance would be expected from the RAP/RAS mixtures under this test conditions.

Statistical Analysis Of Variance (ANOVA) was conducted at 95 percent confidence level ($\alpha = 0.05$) to evaluate the effect of binder type on the fatigue life cycles of the mixtures. The results from the analysis of variance showed that the effect of performance grade of virgin

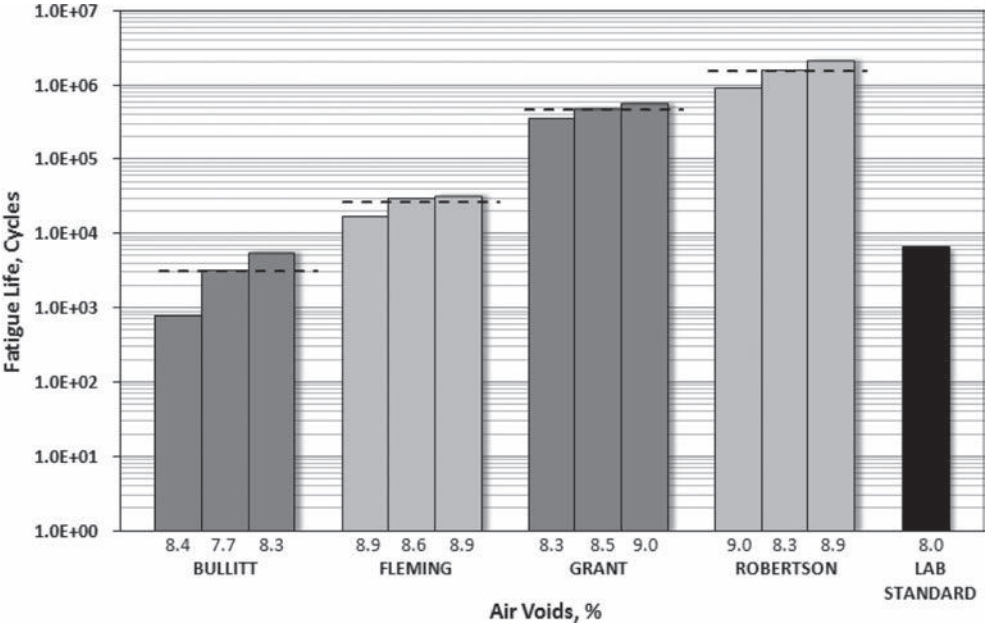

Figure 1. Flexural beam fatigue test data.

binders was highly significant on fatigue life of the samples. Changing the binder type from PG 58-28 to PG 52-34 increased the average fatigue life cycles from 26,000 cycles for Fleming mix to 1,530,000 and 460,000 cycles for Robertson and Grant mixtures, respectively. As can be seen in Figure 1, the Fleming County mixture with PG 58–28 virgin binder still showed better fatigue performance compared to the control mixture.

The Grant County mixture with 3 percent RAS and no RAP showed a significantly higher fatigue life in comparison with the other mixtures. Considering the high strain level of the fatigue test, coupled with PG 52-34 virgin binder, and 5.6 percent effective binder content of this mixture, one might conclude that the mixture was perhaps overdesigned for fatigue cracking. It is noteworthy to mention that the slight differences between the volumetric properties of the mixtures could also contribute to the differences between the fatigue performances. However, these volumetric differences are minimal between the Fleming, Grant, Robertson, and lab standard mixtures. According to the studies on the influence of volumetric parameters on HMA fatigue life [10], the drastically higher fatigue life of the Grant and Robertson mixtures could not only be resulted from slight volumetric variations.

4.2 *Creep compliance and tensile strength*

Creep compliance and tensile strength of the mixtures with RAP/RAS were determined at low temperatures using the indirect tensile test (IDT) configuration, and in accordance with the AASHTO T 322 standard method. In the IDT creep test, a disk shaped specimen is subjected to a static load along its vertical diametric axis, and the deformation of the sample at its center point is measured along the test duration. The creep compliance of the asphalt specimen is then determined based upon the load magnitude and the deformations in vertical and horizontal directions.

For each mixture in this study, samples were tested at three different temperatures and three replicates were fabricated for each test temperature. The time-temperature superposition was then employed along with a power function to determine the master creep compliance curve of the mixtures. The creep compliance tests were conducted at –20°C, –30°C, and –40°C on the Fleming, Grant and Robertson County mixtures. The test temperatures for Bullitt

County mixture were –10°C, –20°C, and –30°C due to its low binder content and high brittleness. Figure 2 displays the final creep compliance master curves at –30°C.

It is expected that HMA mixtures with higher creep compliance would have better ability to relax the stresses caused by rapid thermally induced tensile stresses. In other words, higher compliance means a more compliant mix. The Bullitt mixture, as depicted in Figure 2, did not show considerable change in creep compliance for the first 1000 seconds of reduced loading time. The mixtures with PG 52-34 asphalt binder showed considerably higher creep compliance than the lab standard and Fleming County mixtures with PG 58-22 binder. However, the creep compliance curve for the Fleming mixture appeared to be closer to the one for the control mixture.

The stiffness of the HMA mixtures is inversely related to their creep compliance. In fact, the stiffness decreases by increasing the temperature and/or the loading time. The slope of the stiffness-loading time curve is also an indication of how a mixture relaxes the applied stress. In general, the slope of the stiffness curve varies between zero and 0.5. A horizontal stiffness line (zero slope) represents a fully elastic material and does not relax the stress; whereas, a slope of 0.5 indicates a completely viscous material. Mixtures with higher stiffness curve slope are able to relax the thermally induced stresses much more rapidly. Table 2 shows

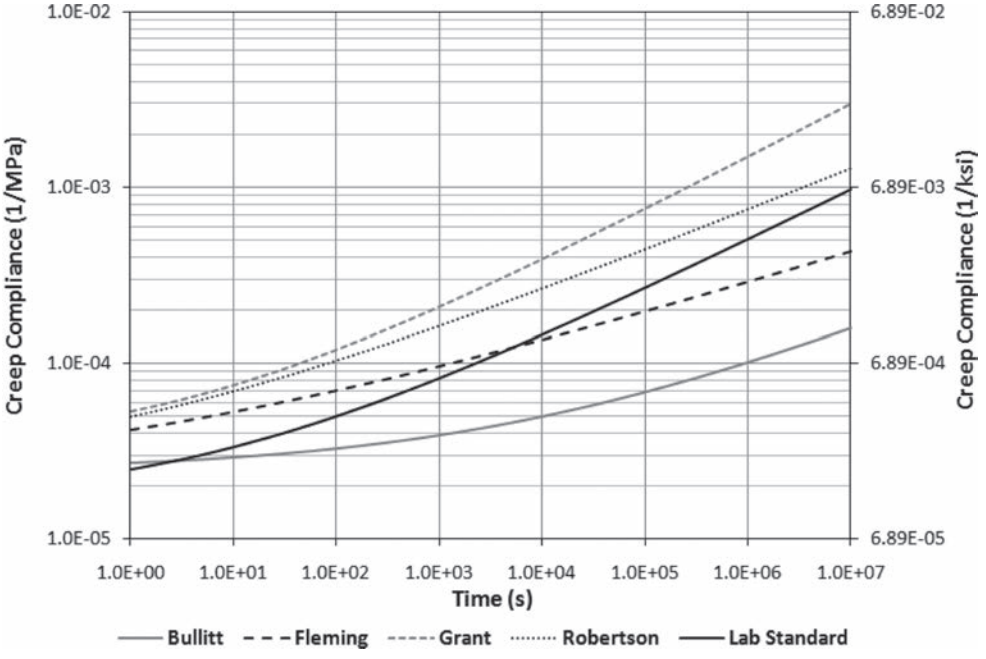

Figure 2. Creep compliance master curves at –30°C.

Table 2. Slope of the stiffness curves at –22°C.

		60 seconds		3600 second	
Mixture	Virgin binder	Stiffness (MPa)	Slope	Stiffness (MPa)	Slope
Bullitt	PG 58-28	23148	0.11	13297	0.16
Fleming	PG 58-28	10549	0.14	5632	0.16
Grant	PG 52-34	5737	0.25	1891	0.27
Robertson	PG 52-34	6640	0.20	2751	0.22
Lab Standard	N/A	12048	0.24	4237	0.26

Note: N/A = not applicable.

the stiffness values as well as the slope of the stiffness curves at –22°C (low temperature of the target binder grade). As seen in this table, the Grant and Robertson mixtures with PG 52-34 binder exhibited a much lower stiffness than the lab standard. Furthermore, their slopes indicate high stress relaxation capability. The Bullitt mixture, as expected from its low binder content, showed a high stiffness with a poor stress relaxation potential.

In overall, the Grant County mixture showed a substantially higher softness than the other mixtures, particularly for higher loading times. Although Grant mixture was mixed with 3% RAS and contained no RAP, mixing it with PG 52-34 resulted in a relatively soft mixture. The increased compliant behavior indicates a softer mixture in the field. This softness may increase the durability of the mixture in terms of low-temperature cracking; however, the potential of rutting distress could increase significantly by using a two grade softer binder.

Indirect tensile strength test was also conducted for each mixture with three replicates at the same temperatures as those employed for the creep compliance tests. The results of the tensile strength tests are presented in Table 3. In order to estimate the critical cracking temperature for different mixtures, a temperature cooling scenario was assumed based on the climatic conditions of central Kentucky. The linear thermal expansion coefficient of the HMA was assumed to be 0.00002/°C. The temperature drop was assumed to start at 5°C and continue to decrease at 2°C/hr rate. Based upon the creep compliance data, the stress relaxation function for each mixture was determined using a numerical method and the data was utilized to calculate the accumulated tensile stress in the pavement surface layer. Comparing the tensile strength data and the viscoelastic stress result, the critical cracking temperature for each mixture was estimated as presented in Table 3.

The critical cracking temperature analysis implied that the mixtures with PG 52-34 virgin binder were highly resistant to low-temperature cracking; however, their critical cracking temperature was much lower than the minimum low temperature expected in the climatic region of the central Kentucky. On the other hand, the critical cracking temperature of the Fleming mixture with PG 58-28 binder was fairly lower than the control mixture and it could be a better representative for the typical surface mixtures used in this area. Considering the difference between the unit cost of two binders, using the PG 58-28 instead of the PG 53-34 binder could result in $2.75/ton of savings in the total price of the asphalt mixture, which could translate into 4.5 to 5 percent of the total price of HMA.

Since the Bullitt mixture was employed as a binder course between the surface and base layers, it would have lower exposure to the sudden drops in air temperature. However, the analysis showed that this mixture was susceptible to low-temperature cracking. Although the cracks in the binder course could not be observed on the pavement surface at their early stages of field performance, they could increase the potential of bottom-up cracking in the surface layer. The low-temperature cracks in this layer in combination with the tensile strain at the bottom of the surface layer could accelerate the initiation of fatigue cracks in the surface layer and reduce the overall service life of the pavement significantly.

Table 3. Tensile strengths and critical cracking temperatures.

Mixture	Tensile strength, MPa				Critical cracking temperature (°C)
	–10°C	–20°C	–30°C	–40°C	
Bullitt	3.45	3.35	2.02	N/A	–21.0
Fleming	N/A	2.77	3.18	3.08	–33.2
Grant	N/A	1.94	2.81	3.42	–46.5
Robertson	N/A	1.91	2.86	3.53	–42.0
Control	N/A	4.08	3.81	N/A	–29.0

Note: N/A = not available.

4.3 *Fracture energy*

In order to evaluate the effect of using RAP/RAS on low temperature cracking, a series of disk-shaped compact tension tests [DC(t)] were conducted to determine the fracture energy of the mixtures. The analysis on the IDT creep and strength data indicated how thermally induced stresses can initiate a crack in the mixtures. Once the crack is initiated, however, the mixtures can exhibit different resistance to growth and propagation of the cracks. This resistance is a function of how the mix can maintain its cohesion and ductility at low temperatures. The DC(t) fracture test manifests how an asphalt mixture would resist against crack growth. In a DC(t) test, a pre-notched sample is subjected to tensile loading, and Crack Mouth Opening Displacement (CMOD) is recorded during the test. The fracture energy is then determined by measuring the area under the load-CMOD curve. Higher fracture energy implies higher resistance to crack growth.

The DC(t) test in this study was conducted according to ASTM D7313-07 standard test method and at –12°C, ten degrees higher than the low temperature grade of the target blended binder.. The dashed line plotted on each dataset in Figure 3 represents the average fracture energy for that particular mixture. Considering the climatic conditions of the central Kentucky, the DC(t) were conducted at –12°C in order to simulate low temperature induced cracking conditions.

The coefficient of variation for the fracture energy data varied between 1 and 11 percent. A minimum threshold of 400 J/m^2 is recommended for the fracture energy of HMA mixtures in order to prevent thermal and reflective cracking [11,12]. As depicted in Figure 3, Bullitt, Fleming and Robertson mixtures demonstrated adequate fracture energy compared to the suggested minimum threshold, while the Grant County mixture had an average fracture energy of 386 J/m^2, which is slightly lower than the suggested minimum.

Fisher's Least Significant Difference (LSD) method was employed to make a statistical pairwise comparison on the fracture energy data. The last column in Table 4 shows the results of the comparisons, and the grouping of the mixtures based on their fracture energy values. The mixtures with similar group letter do not have significantly different fracture energy. For example, the average fracture energy of the Grant mix was not significantly different from Bullitt and Robertson mixtures.

Although Grant and Robertson mixtures were made with PG 52–34 virgin binder (two grades softer than the target blend), they had significantly lower fracture energies than the

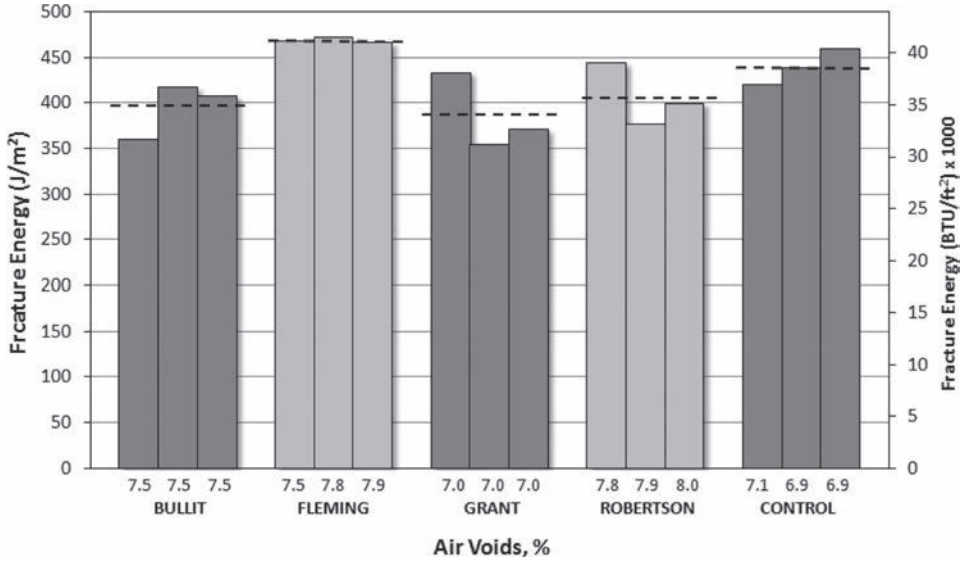

Figure 3. Dc(t) fracture energy data.

Table 4. Pairwise comparison of the mixtures fracture energy.

Mixture	Number of samples	Average fracture energy (J/m^2)	Fisher's grouping	
Fleming	3	467.77	A	
Lab standard	3	438.93	A	B
Robertson	3	406.33		B
Bullitt	3	394.60		B
Grant	3	385.83		B

mixture for Fleming County with PG 58-28 virgin binder. In fact using a virgin binder with two performance grades softer than the target binder resulted in lower fracture energy for the combined mixture. This may indicate that there is an optimum point beyond which adding softer virgin asphalt may not necessarily translate into better resistance to cracking.

As shown in Table 4, there was no significant difference between the Robertson, Bullitt, and Grant mixtures. It should be noted that the Bullitt mixture was a binder course with only 4.1% binder content, 1.3 to 1.6 percent lower than the other mixtures. Again Robertson and Grant mixtures with PG 52-34 binders did not exhibit higher fracture energies than the Bullitt mix with PG 58-28 and much lower binder content.

5 SUMMARY AND CONCLUSIONS

The primary objective of the research was to evaluate the impact of using the current practice of designing RAP/RAS mixture in the states of Kentucky on their cracking performance. This design, which involves the development of the blending charts, sometimes results in a virgin binder which is two grades softer (PG XX-34) than the target blended binder grade in Kentucky (PG 64-22). Four plant-produced hot-mix asphalt mixtures were collected, and subjected to laboratory performance testing. Beam fatigue test, creep compliance test, indirect tensile strength test, and DC(T) fracture energy test were conducted on the specimens containing various amounts of RAP/RAS and different virgin binders. The results of the performance tests were compared to the performance of a laboratory standard mixture with no recycled materials, which has proved to perform satisfactorily on several pavements. The following conclusions were made based upon the laboratory performance test results:

- The performance of mixtures with the PG 58-28 virgin binder and RAP/RAS material in this study was comparable to the lab standard mixture with no recycled material. The mixture with PG 52-34 virgin binder had a higher fatigue life, however more susceptiblity to rutting and low temperature crack growth.
- Using PG 52-34 virgin binder instead of PG 58-28 increased the total cost of the asphalt mixture by about 5%.
- Using PG 52-34 binder instead of PG 58-28 drastically increased the fatigue life of the HMA samples. However, the mixture with PG 58-28 virgin binder could provide adequate resistance against fatigue cracking.
- Creep compliance master curve of the mixture with PG 58-28 virgin binder and 9.5 mm NMAS was the most similar to the master curve of the lab standard mix.
- Mixtures with RAS/RAS and PG 52-34 virgin binder had significantly higher compliance, which could increase the potential risk of rutting.
- Mixture with RAP/RAS and low binder content (4.1%) was susceptible to low-temperature cracking.
- Mixtures with PG 52-34 virgin binder did not have a higher fracture energy level than those with PG 58-28 binder. In other words, PG 52-34 did not provide additional resistance against crack growth compared to the PG 58-28 binder when mixed with the RAP/RAS.

ACKNOWLEDGEMENT AND DISCLAIMER

This material is based upon work supported by Federal Highway Administration through a cooperative agreement with the Asphalt Institute, DTFH61-08-H-00030. Testing materials were collected and provided by Kentucky Transportation Cabinet. The authors wish to thank John Bukowski (FHWA), Allen Myers (KYTC), and Michael Anderson (Asphalt Institute) for their support of the testing program and analysis. Finally, the support of the Member Companies of Asphalt Institute is gratefully acknowledged. Without their active interest in and support of Asphalt Institute, none of the work presented could have been accomplished. Any opinions, findings, and conclusions or recommendations expressed in this publication are those of the Author(s) and do not necessarily reflect the view of the U.S. Department of Transportation.

REFERENCES

[1] Robinette, C., and Epps, J. Energy Emissions Material Conservation and Prices Associated with Construction Rehabilitation and Material Alternatives for Flexible Pavement, Transportation Research Record, 2179, pp. 10–22. 2010.

[2] Asphalt Institute. Mix Design Methods for Asphalt Concrete, MS-2. Lexington, KY. To be published in 2014.

[3] McDaniel, R., and Anderson, R.M. Recommended Use of Reclaimed Asphalt Pavement in the Superpave Mix Design Method: Technician's Manual, Publication NCHRP Report 452, Transportation Research Board of the National Academies, Washington, D.C. 2001.

[4] Ma, T., Mahmoud, E., and Bahia, H.U. Estimation of Reclaimed Asphalt Pavement Binder Low-Temperature Properties without Extraction: Development of Testing Procedure. Transportation Research Record, 2179, pp. 58–65. 2010.

[5] Foxlow, J.J., Daniel, J.S., and Swamy, A.K. RAP or RAS? The Differences in Performance of HMA Containing Reclaimed Asphalt Pavement and Reclaimed Asphalt Shingles, Journal of the Association of Asphalt Paving Technologists, 80, pp. 347–373. 2011.

[6] Krishna Swamy, A., Mitchell, L.F., Hall, S.J., and Sias, D.J. Impact of RAP on the Volumetric, Stiffness, Strength, and Low-Temperature Properties of HMA, Journal of Materials in Civil Engineering, 23(2), pp. 1490–1497. 2011.

[7] ASTM D7460-10. Standard Test Method for Determining Fatigue Failure of Compacted Asphalt Concrete Subjected to Repeated Flexural Bending, ASTM Annual Book of Standards, American Society for Testing and Materials, Vol. 04.03. 2010.

[8] Kim, Y., Little, D.N., Lytton, R.L., D'Angelo, J., Davis, R., Rowe, G., Reinke, G., Marasteanu, M., Masad, E., Roque, R., and Tashman, L. Use of Dynamic Mechanical Analysis (DMA) to Evaluate the Fatigue and Healing Potential of Asphalt Binders in Sand Asphalt Mixtures, Journal of Association of Asphalt Paving Technologists (AAPT), 71. 2002.

[9] Asphalt Institute. Research and Development of the Asphalt Institute's Thickness Design Manual, MS-1, Research Report 82-2, Lexington, KY. 1981.

[10] Christensen, D.W., and Bonaquist, R.F. (2006). Volumetric requirements for Superpave mix design, NCHRP Report 567, Transportation Research Board of the National Academies, Washington D.C. 2006.

[11] Blankenship, P., Anderson, R.M., King, G.N., and Hanson, D.I. A Laboratory and Field Investigation to Develop Test Procedures for Predicting Non-Load Associated Cracking of Airfield HMA Pavements, AAPTP Project 06-01Report, Airfied Asphalt Pavement Technology Program. 2010.

[12] Cascione, A.A., Christopher, R.W.R., Buttlar, W., Sarfraz, A., Hill, B., Haugen, D.S., and Gillen, S. Laboratory Evaluation of Field Produced Hot Mix Asphalt Containing Post-Consumer Recycled Asphalt Shingles and Fractionated Recycled Asphalt Pavement, Journal of the Association of Asphalt Paving Technologists, 80, pp. 377–414. 2011.

Asphalt Pavements – Kim (Ed)
© 2014 Taylor & Francis Group, London, ISBN 978-1-138-02693-3

Effect of rejuvenator on performance properties of HMA mixtures with high RAP contents

Nam Tran, Adam Taylor & Richard Willis
National Center for Asphalt Technology, Auburn, AL, USA

ABSTRACT: Rejuvenators have been used as recycling agents to restore some performance properties of oxidized Reclaimed Asphalt Pavement (RAP) binders for cold in-place recycling and as surface treatments to preserve weathered asphalt pavements. However, they have not been widely used in Hot Mix Asphalt (HMA) containing high recycled asphalt contents because of the uncertain effect of rejuvenators, concern about the lack of adequate mixing of the old binder and the rejuvenator, and the required reaction time on performance properties of the recycled binders and asphalt mixtures. The objective of the study presented in this paper is to evaluate the effect of using a rejuvenator pre-blended with a virgin asphalt binder on performance properties of HMA with a high RAP content. The study consisted of the determination of optimum content for rejuvenator, mix design, and conducting binder and mixture tests to assess the performance characteristics (moisture susceptibility, mixture stiffness, top-down cracking, low-temperature cracking, and rutting) of two recycled asphalt mixtures—50% RAP mix and 50% RAP mix with rejuvenator—relative to those of a virgin mixture. The use of rejuvenator in the recycled mixture improved its cracking resistance without adversely affecting its resistance to moisture damage and permanent deformation.

Keywords: Rejuvenator, performance properties, reclaimed asphalt pavement

1 INTRODUCTION

The cost of materials and energy has significantly increased during the last few years. As a result, Reclaimed Asphalt Pavements (RAP) have been increasingly used in asphalt mixtures to replace virgin asphalt and aggregate materials to reduce production costs. Each year, it is estimated that about 100 million tons of asphalt pavement materials are milled off roads [1]. Using RAP in Hot Mix Asphalt (HMA) reduces not only costs for contractors and agencies but also the negative environmental impacts associated with the extraction, transportation and processing of virgin materials.

Currently, most highway agencies allow asphalt mixtures containing low percentages of RAP (i.e., less than 25% by weight of aggregate). The reason is that the recycled binder in the RAP is aged and stiffer than the binder in a virgin mixture selected from the same location. The recycled binder is less strain-tolerant, consequently more susceptible to various modes of cracking (i.e., fatigue, thermal, and reflection cracking). As the percentage of recycled binder increases, the proportion of the aged binder in the total binder blend increases, likely resulting in higher mixture stiffness and lower resistance to cracking.

To offset the higher binder stiffness and to improve the mixture resistance to cracking when high RAP contents are used, one approach is to use a recycling agent (i.e., a rejuvenator) to restore the performance properties of recycled binder. Rejuvenators have been used as recycling agents to restore some performance properties of oxidized RAP binders for cold in-place recycling and as surface treatments to preserve weathered asphalt pavements. However, they have not been widely used in HMA containing high recycled binder contents because of the uncertain effect of rejuvenators, concern about the lack of adequate mixing of the old

binder and the rejuvenator, and the required reaction time on performance properties of the recycled binders and asphalt mixtures. If an appropriate amount of rejuvenator is added and properly mixed and required reaction time is allowed, the recycled RAP binder may meet the target performance grade, resulting in improved cracking resistance of the asphalt mixture without adversely affecting its resistance to rutting and moisture damage.

The objective of this study is to evaluate the effect of using a rejuvenator pre-blended with a virgin asphalt binder on performance properties of recycled binders and HMA mixtures with high RAP contents.

2 BACKGROUND

The structure of petroleum asphalt is regarded as a colloid in which asphaltenes are the dispersed phase and maltenes are the dispersion medium. Most paving asphalt binders have micelles of asphaltenes diluted in a fairly well-structured dispersion medium. In the dispersion medium, the asphaltenes form aggregates but are unable to create a continuous network [2]. Physical changes in asphalt binder over time are dependent on changes in its chemical composition. As asphalt binder ages, some of the maltene medium is transformed into the asphaltene phase, resulting in higher asphaltene and lower maltene contents. When there are fewer maltenes available to disperse the asphaltenes, the asphaltenes will flocculate. This leads to higher viscosity and lower ductility, which influences the ability of asphalt binder to stretch without breaking [3]. In other words, when the asphaltene micelles are not sufficiently mobile to flow past one another under the applied stress, the resistance of asphalt binder to cracking or fracture is decreased [4].

The aging of asphalt binder occurs in two stages: short-term and long-term. Short-term aging is mainly due to volatilization and/or absorption of oily components in the maltenes during mixing and construction. Long-term aging happens in the field and is due to changes in composition through reaction between asphalt constituents and atmospheric oxygen, chemical reaction between molecular components (polymerization), and formation of a structure within the asphalt binder (thixotropy) [5].

To restore its rheological properties, an aged asphalt binder may be mixed with a recycling agent, which can be a softening agent or a rejuvenator. While softening agents, such as asphalt flux oil, lube stock, and slurry oil, can lower the viscosity of the aged binder, rejuvenators help restore the physical and chemical properties [5]. Rejuvenators often consist of lubricating oil extracts and extender oils, which contain a high proportion of maltene constituents—napthenic or polar aromatic fractions—that help re-balance the composition of the aged binder that lost its maltenes during construction and service [6]. While rejuvenators should have a high proportion of aromatics, which are necessary to keep the asphaltenes dispersed, they should contain a low content of saturates, which are highly incompatible with the asphaltenes [7, 8].

The effectiveness of a rejuvenator depends on the uniform dispersion of the rejuvenator within the recycled mixture and the diffusion of the rejuvenator into the aged binder coated outside of the aggregate. The dispersion of rejuvenators within recycled mixtures at different plants was investigated by Lee et al. [9]. The researchers visually detected the dyes that had been mixed with the rejuvenators. The authors concluded that uniform distribution of the rejuvenators could be accomplished through mechanical mixing at the plants.

Past studies reported that the diffusion process may not be completed after the construction [10, 11]; thus, higher rutting rates were initially observed on roadways and on test sections subjected to accelerated pavement testing [12]. Rejuvenated asphalt mixtures also showed higher susceptibility to low-temperature cracking compared to virgin mixtures when they had not been sufficiently rejuvenated [13]. According to Terrel and Fritchen [14] and DeKold and Amirkhanian [15], the moisture susceptibility of recycled mixtures was similar to or improved over that of virgin mixtures. However, if stripping-susceptible mixtures were recycled, the moisture susceptibility may increase, and anti-stripping additives should be used appropriately [15]. The type of rejuvenator used had little effect on moisture susceptibility [16].

Rejuvenated RAP can be mixed with a virgin binder and aggregate to achieve a desired Performance Grade (PG) and design gradation for an asphalt mixture. The performance of the blended binder, which is affected by the diffusion and/or mixing of the recycled and virgin binders in the blend, significantly affects the performance of the resulting asphalt mixture. The diffusion and mixing of binders in a blend depends upon a number of factors, including compatibility of binders, temperature of mixing, performance grade of virgin and recycled binder, and the percentage of recycled binder in the blended binder [17].

3 EXPERIMENTAL PLAN

A laboratory testing plan was set up to evaluate the effect of a rejuvenator on the performance of HMA mixtures with high RAP contents. Virgin aggregates and RAP used in this study were sampled from the East Alabama Paving (EAP), Inc. plant in Opelika, Alabama. The RAP material had been crushed to pass a ½-in. sieve at EAP. Two 9.5-mm mix designs, including a virgin (control) mix design and a 50% RAP mix design, were used in this study. The virgin binder used in the mix designs was a PG 67-22. For each mix, 0.5% liquid anti-strip AD-here® LOF 65 (by weight of the virgin asphalt binder) manufactured by ArrMaz Custom Chemicals was added to the virgin binder before mixing.

The rejuvenator selected for this study is Cyclogen® L, which does not contain asphalt binder, provided by Tricor Refining, LLC in California. While the diffusion of rejuvenator into the recycled binder would be better if the rejuvenator was mixed with RAP before the RAP materials were added to the mix, this process would be difficult to implement in the field. Hence, in this study, the rejuvenator was added to the virgin binder, and then the blend was added to the mix of virgin aggregate and RAP materials. A total of three mixtures, including a control mix, a 50% RAP mix, and a 50% RAP mix with rejuvenator (hereafter also referred to as rejuvenated 50% RAP mixture), were evaluated in this study.

3.1 *Plan for binder testing*

Testing of virgin and recycled asphalt binders was conducted in two experiments. The first experiment, as shown in Table 1, was to determine: (1) the effect of the rejuvenator on the performance properties of the recycled binders extracted from RAP; and (2) the amount of rejuvenator required to restore the performance properties of the recycled binders to meet the requirements for a PG 67-22, which is the performance grade of the virgin binder used in

Table 1. Binder testing experiments.

Attribute	Level	Description
First experiment—determining rejuvenator content		
Materials		
RAP binder	1	Binder extracted from RAP
Rejuvenator (Cyclogen L)		
Blending rate for RAP	3	0, 12, 20% by weight of RAP binder
No. of blends	3	$1 \times 3 = 3$
Response variable		True grade
Second experiment—determining performance grades of blended binders		
Materials		
Control	1	Virgin binder (PG 67-22)
50% RAP	1	Virgin binder + extracted RAP binder
50% RAP with rejuvenator	1	Virgin binder + extracted RAP binder + rejuvenator
No. of blends	3	1 + 1 + 1 = 3
Response variables		Performance Grade (PG)

the mixtures. The second experiment, as shown in Table 1, was to determine the properties of the blends of recycled binders, virgin binder, and rejuvenator. The rejuvenator was mixed with the virgin binder at the optimum content determined in the first experiment. Then, the blend was mixed with the binders extracted from RAP based on the amount of each binder determined in the 50% RAP mix design. The purpose of this testing was to verify the true grade of each blend and to rule out any compatibility issues.

3.2 *Plan for mixture testing*

Three mixtures, including a control mix, a 50% RAP mix, and a 50% RAP mix with rejuvenator were tested in both Short-Term Aging (STA) and Long-Term Aging (LTA) conditions. The STA and LTA properties were used to evaluate the mixture resistance to permanent deformation and cracking, respectively.

To prepare an asphalt mixture for this study, the virgin binder, virgin aggregates and RAP were heated in an oven to the target mixing temperature of 300°F. The liquid anti-strip was pre-blended with the virgin binder. The rejuvenator was also pre-blended with the virgin binder at its optimum content determined in the first experiment of binder testing. The mixing process was done in several steps. The virgin aggregates were first poured into a mixing bowl. If used, the RAP was then added into the bowl and mixed with the virgin aggregates. After that, the virgin binder, which had been pre-blended with the liquid anti-strip and rejuvenator (if used), was added and thoroughly mixed in the mixture. The mix was then short-term aged in an oven according to AASHTO R 30 for determining the volumetric properties and for mechanical testing. The asphalt sample was then compacted, and the specimen was prepared for further testing.

The Tensile Strength Ratio (TSR) test was conducted to determine the mix resistance to moisture damage. Two tests, including the dynamic modulus (E*) and the Asphalt Pavement Analyzer (APA), were conducted on the short-term aged specimens to determine the short-term aged stiffness and to evaluate the mix resistance to permanent deformation.

To determine the long-term properties, the test specimens cored/cut from the gyratory specimens were long-term aged in an oven at 85°C for 120 hours according to AASHTO R 30. Three tests were performed on the long-term aged specimens: the E* test to determine stiffness of the long-term aged mixture, the Indirect Tensile (IDT) test to determine the critical low-temperature cracking properties, and the Energy Ratio (ER) test procedure to determine the mix resistance to cracking at intermediate temperatures.

4 RESULTS AND ANALYSIS

In this section, the determination of optimum rejuvenator content is first discussed, followed by the analysis of results of binder and mixture tests. In the interest of length, other information on aggregate materials and volumetric properties of asphalt mixtures is not presented in this section but is available elsewhere [18].

4.1 *Rejuvenator content*

As shown in the plan for testing binder, the rejuvenator was blended at three contents with the binders extracted from the RAP. Then, the performance grades of the blends were determined in accordance with AASHTO M 320. Figure 1 shows the effect of the rejuvenator contents on the performance properties of the RAP binder. The correlations between the rejuvenator contents and the critical high and low temperatures of the RAP binder are almost linear, as the R^2 values are greater than 0.95. Based on the correlations, a content of 12% by the total weight of recycled binder was selected based on the critical low-temperature criteria. At this content, the critical high-temperature criteria were also satisfied, and the performance properties of the recycled binders would be restored to meet

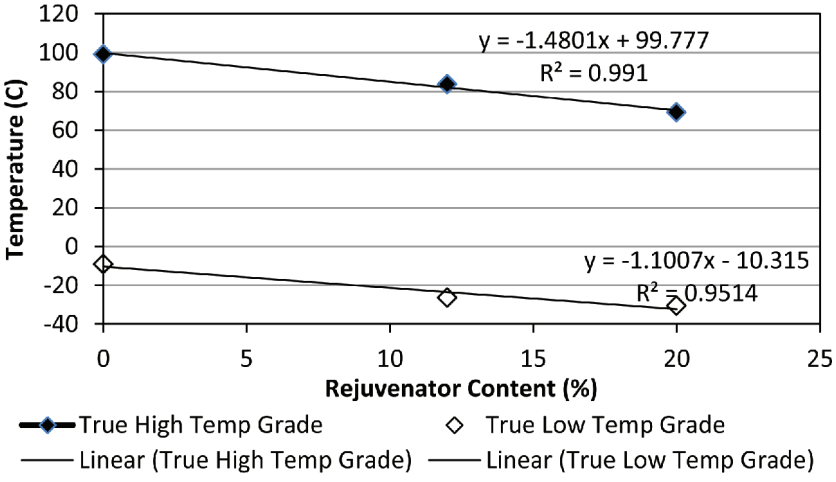

Figure 1. Effect of rejuvenator contents on RAP binder.

Table 2. Performance grades of binders.

Properties	Virgin	50% RAP	50% RAP + RA
Virgin AC*	67.0–23.2	67.0–23.2	67.0–23.2
RAP*		99.1–9.2	99.1–9.2
RA used	No	No	Yes
Total blend	67.0–23.2	85.2–18.2	79.9–21.2

*Performance grade of binder before blending with the rejuvenator.

the requirements for a PG 67-22, which is the performance grade of the virgin binder used in the mixtures.

4.2 *Performance grading of binder blends*

Table 2 summarizes the performance grades determined for the virgin binder, the two binder blends, and each component of the blends. The rejuvenator was able to restore the low-temperature performance grades of the 50% RAP blend from PG 85.2-18.2 to PG 79.9-21.2. Since the rejuvenated blend barely failed the low critical temperature requirements for a PG 67-22, it was decided that the rejuvenator content was kept at 12% by the total weight of recycled binder for further testing in this study.

4.3 *Performance properties of asphalt mixtures*

All mixtures tested in this study were conducted using laboratory-prepared mixes. To prepare a sample in the laboratory, the aggregate was first carefully batched based on the design gradation. The aggregate, base binder, and RAP were heated to the mixing temperature (300°F) in ovens. The liquid anti-strip agent was pre-blended in the base binder at its recommended dosage prior to mixing. If the rejuvenator was used in the mixture, it was also pre-blended in the base binder at the selected content of 12% by weight of recycled binder. After the aggregate, base binder, and RAP (if needed) had reached the mixing temperature, they were mixed in a mixing device. The mixture was then short-term aged in an oven in

accordance with the short-term aging procedure listed in AASHTO R 30-02 and then compacted in a gyratory compactor. The compacted HMA specimens were then tested or long-term aged further in accordance with AASHTO R 30-02 for testing. In this section, results of the following mixture tests are discussed:

- TSR test to evaluate moisture susceptibility
- E* test to evaluate stiffness of short-term and long-term aged mixtures
- ER test on long-term aged specimens to evaluate fracture resistance
- IDT test on long-term aged specimens to evaluate low-temperature cracking resistance
- APA test on short-term aged specimens to determine rutting resistance.

4.3.1 *Mixture resistance to moisture damage*

Moisture susceptibility testing was conducted in accordance with AASHTO T 283-07. Both the saturation and air void requirements specified in AASHTO T 283 were met for each specimen tested. The TSR values for the control mix, 50% RAP mix, and 50% RAP mix with rejuvenator were 0.92, 0.80 and 0.87, respectively, which are equal or greater than the commonly accepted failure threshold of 0.8. The use of rejuvenator at the percentage used in the RAP mixture did not negatively affect the TSR but help increase it slightly.

4.3.2 *Mixture stiffness*

Dynamic modulus (E*) testing was conducted in accordance with AASHTO TP 79-09 on specimens that were prepared in accordance with AASHTO PP 60-09 to 7 ± 0.5% air voids. For each mix, two sets of three specimens were long-term and short-term aged and then tested to assess the effect of aging on the mixtures. The specimens were tested with the temperatures and frequencies recommended in AASHTO PP 61-09 using an IPC Global Asphalt Mixture Performance Tester (AMPT). Based on E* test results, master curves were generated in accordance with the procedure outlined in AASHTO PP 61-09 using the MasterSolver® program in EXCEL®. A reference temperature of 20°C was used for this study.

Figure 2(a) and 2(b) compare the E* master curves at the reference temperature of 20°C for the short-term and long-term aged specimens, respectively. For the short-term aged specimens, compared with the E* master curve of the 50% RAP mixture without rejuvenator, the E* master curve for the rejuvenated 50% RAP mixture is closer to that of the virgin mixture. However, for the long-term aged specimens, the rejuvenated RAP mixture appears to age faster than the other RAP mixture; the E* master curve of the rejuvenated mixture is shifting closer to that of the 50% RAP mixture without rejuvenator. The use of rejuvenator at the determined content in the RAP mixture softened the stiffness of this mixture; however, this mixture was still stiffer than the virgin mix.

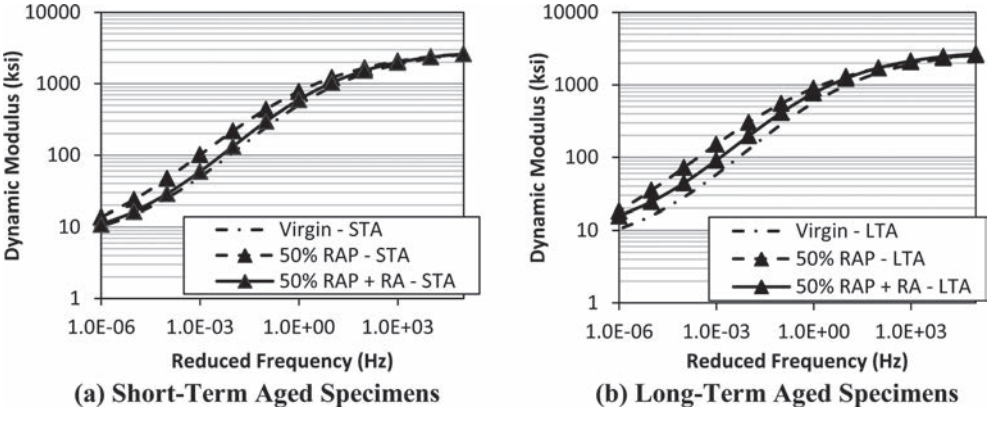

Figure 2. Comparison of E* master curves.

4.3.3 *Mixture resistance to top-down cracking*

The resistance of the three asphalt mixtures to top-down cracking was evaluated using the Energy Ratio (ER) test procedure developed at the University of Florida [19]. The ER test procedure includes three individual tests—resilient modulus, creep compliance, and indirect tensile strength. These tests are performed at 10°C using a universal testing device. Four specimens 150 mm in diameter by approximately 38 mm thick, cut from gyratory compacted samples, are used in the three tests. The target air voids for these samples are 7 ± 0.5%. Based on the data obtained from the three mixture tests, the ER and Dissipated Creep Strain Energy at failure ($DCSE_f$) are determined. An asphalt mixture with higher values of $DCSE_f$ and ER would have better resistance to top-down cracking. Based on an extensive study [19] performed on 22 field test sections gathered from cracked and uncracked sections throughout the state of Florida to evaluate top-down cracking performance, the following criteria were recommended for evaluating the top-down cracking performance of asphalt mixtures:

- The minimum dissipated creep strain energy is 0.75 KJ/m^3.
- The minimum ER is 1.95.

Figure 3(a) and 3(b) compare the fracture properties—dissipated creep strain energy at failure, and energy ratio—for the three mixtures evaluated in this study. Based on the $DCSE_f$ and ER plots, the virgin mix has the best resistance to top-down cracking, followed by the rejuvenated 50% RAP mix, and then the 50% RAP mix without rejuvenator. All the mixes, except the 50% RAP mix without rejuvenator, meet the proposed minimum $DCSE_f$ and ER requirements.

4.3.4 *Mixture resistance to low-temperature cracking*

The resistance of the three mixtures to low-temperature cracking was evaluated using the IDT test procedure in accordance with AASHTO T 322-07. The test procedure includes two individual tests to measure creep compliance of each mixture at three temperatures –0, –10, and –20°C—and tensile strength at –10°C. Four specimens were prepared for each mix. The first specimen was used to find a suitable creep load for that particular mix at each testing temperature. The remaining three specimens were tested at this load for data analysis. Specimens used for the creep and strength tests were 38 to 50 mm thick and 150 mm in diameter. Specimens were prepared to 7 ± 0.5% air voids.

The results were used to determine the critical cracking temperature for each mix tested in this study. A complete description of the thermal stress analysis can be found elsewhere [20, 21]. Figure 4(a) shows the critical temperatures determined at the points where thermal stresses exceed the tensile strengths. The control mixture exhibited the lowest critical failure temperature (–27.7°C), followed by the rejuvenated 50% RAP mixture, and then the 50% RAP mix without rejuvenator. A mix with a lower critical failure temperature would have better resistance to low-temperature cracking.

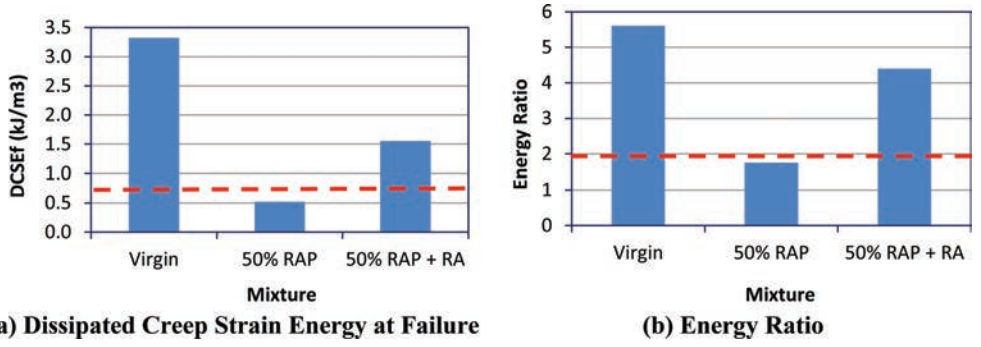

Figure 3. Energy ratio test results.

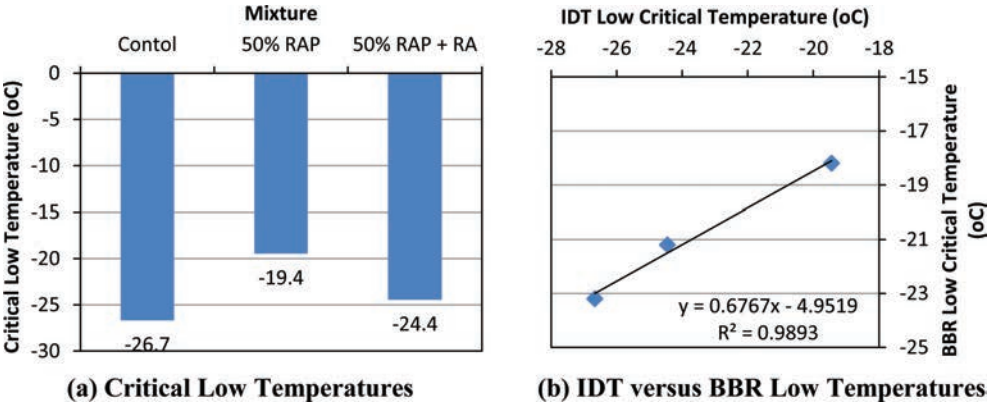

Figure 4. Low temperature cracking testing results.

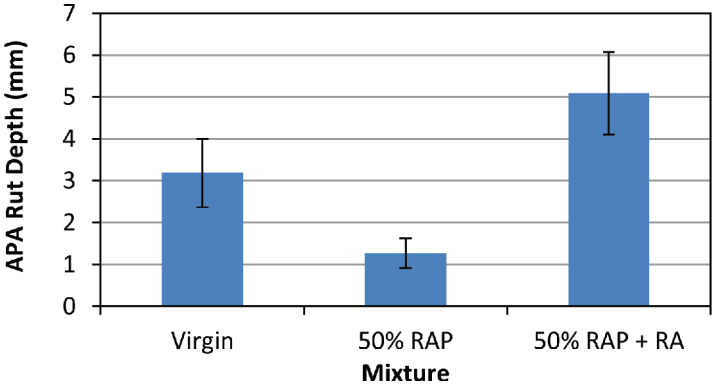

Figure 5. APA testing results.

Figure 4(b) demonstrates a good correlation between the critical low temperatures determined using the IDT and BBR tests for mixture and binder testing. While the critical low temperatures from the IDT test are lower than those of the BBR test, the ranking of the mixtures is similar to that of the binders in terms of their resistance to low-temperature cracking.

4.3.5 *Mixture resistance to permanent deformation*

The rutting resistance of the three mixtures was evaluated using an Asphalt Pavement Analyzer (APA) in accordance with AASHTO T 340-10. The specimens used for this testing were prepared to a height of 75 mm and an air void level of 7 ± 0.5%. Six replicates were tested for each mix. The samples were tested at a temperature of 64°C (the 98 percent reliability temperature for the high PG grade of the binder in Opelika, Alabama). The samples were loaded by a steel wheel (loaded to 100 lbs) resting on a pneumatic hose pressurized to 100 psi for 8,000 cycles. Manual depth readings were taken at two locations on each specimen before and after the loading was applied to determine the specimen rut depth.

Figure 5 compares the average values and variability of the manually measured rut depths for the three mixtures. It can be seen that the rejuvenated mixture has higher manually measured APA rut depths than the control mix, and the 50% RAP mix without rejuvenator has the lowest APA rut depth. A past study at the National Center for Asphalt Technology (NCAT)

Pavement Test Track has shown that if a mixture has an average APA manual rut depth less than 5.5 mm, it should be able to withstand at least 10 million Equivalent Single Axle Loads (ESALs) of traffic at the test track without accumulating more than 12.5 mm of field rutting [22]. Considering this threshold, all three mixtures are expected to pass in terms of rutting.

5 CONCLUSIONS AND RECOMMENDATIONS

This study evaluated the effect of using a rejuvenator on the mechanistic and performance properties of recycled binders and mixtures with high RAP contents in the laboratory. The testing plan for this study consisted of the determination of optimum content for rejuvenator, mix design, and conducting binder and mixture tests to assess the performance characteristics (moisture susceptibility, mixture stiffness, top-down cracking, low-temperature cracking, and rutting) of the two recycled asphalt mixtures—50% RAP mix and rejuvenated 50% RAP—relative to those of the control mixture. The following conclusions and recommendations are offered based on the results of this study.

- The desired amount of rejuvenator can be determined based on a linear relationship between the rejuvenator content and critical low temperature of the blend of recycled binder and rejuvenator. In this study, a rejuvenator content of 12% by the total weight of recycled binder was selected to restore the performance properties of the recycled binder to meet the requirements for a PG 67-22, which is the performance grade of the virgin binder.
- The moisture resistance of the mixtures was evaluated using the Tensile Strength Ration (TSR) test. The TSR values for all the mixtures tested in this study were equal or greater than the commonly accepted failure threshold of 0.8. The use of rejuvenator at the determined content in the 50% RAP mixture did not negatively affect the TSR but help improve it slightly.
- Dynamic modulus testing was conducted to evaluate the mixture stiffness after being short-term and long-term aged. The rejuvenated mixture appeared to age faster than the other mixtures. The use of rejuvenator at the determined content in the recycled mixture softened the stiffness of the mix; however, this mixture was still stiffer than the virgin mix in both long- and short-term aging conditions.
- The resistance of the three asphalt mixtures to top-down cracking was evaluated using the Energy Ratio (ER) test procedure. The use of rejuvenator improved both the fracture properties—$DCSE_f$ and ER—for the 50% RAP mix. All the mixes, except the 50% RAP mix without rejuvenator, meet the proposed minimum $DCSE_f$ and ER requirements.
- The resistance of the three mixtures to low-temperature cracking was evaluated using the Indirect Tensile (IDT) test procedure. The control mixture exhibited the lowest critical failure temperature, followed by the rejuvenated 50% RAP mixture, and then the 50% RAP mix without rejuvenator. The critical low temperatures determined using the IDT correlated well with those determined using the BBR test. The ranking of the mixtures is similar to that of the binders in terms of their resistance to low-temperature cracking.
- The rutting resistance of the three mixtures was evaluated using the APA test. All the mixtures exhibited APA manual rut depths less than 5.5 mm, which was determined based on the past research at the NCAT Pavement Test Track. Thus, all three mixtures were not suspected to fail in terms of rutting.

In summary, the use of rejuvenator in the recycled mixture improved its cracking resistance without adversely affecting its resistance to moisture damage and permanent deformation. The rejuvenator, which is pre-blended with the virgin binder, should be considered to improve the cracking resistance of asphalt mixtures with high RAP contents. However, since the virgin binder pre-blended with the rejuvenator may be much softer than the normal grade of asphalt being used, good mixing of the binder pre-blended with the rejuvenator, aggregate, and recycled material is important to produce a good asphalt mixture that can avoid premature rutting failures. Further research should be conducted to evaluate other rejuvenators

and the use of rejuvenators in asphalt mixtures with higher recycled contents and with recycled asphalt shingles.

REFERENCES

[1] Boomquist, D., G. Diamond, M. Oden, B. Ruth, and M. Tia. *Engineering and Environmental Aspects of Recycled Materials for Highway Construction.* Report No. FHWA-RD-088, FHWA, Washington, DC, 1993.

[2] Thyrion, F. "Asphalt Oxidation," *Asphaltenes and Asphalts: Development in Petroleum Science*, Vol. 40B, Elsevier, NY, 2000, pp. 445–474.

[3] Corbett, L. "Reaction Variables in the Air Blowing of Asphalt." *Industrial and Engineering Chemistry Process Design and Development,* Vol. 14, 1975, pp. 181–187.

[4] Petersen, J. "Chemical Composition of Asphalt as Related to Asphalt Durability: State of the Art," *Transportation Research Record 999*, TRB, Washington, DC, 1984, pp. 13–30.

[5] Roberts, F., P. Kandhal, E.R. Brown, D.Y. Lee, and T. Kennedy. *Hot Mix Asphalt Materials, Mixture Design and Construction,* 2nd Ed. NAPA, Lanham, MD, 1996.

[6] Terrel, R., and J. Epps. "Using Additives and Modifiers in Hot-Mix Asphalt," *Quality Improvement Series (QIP 114 A)*, NAPA, Lanham, MD, 1989.

[7] Bullin, J., R. Davison, C. Glover, J. Chaffin, M. Liu, and R. Madrid. *Development of Superior Asphalt Recycling Agents, Phase 1: Technical Feasibility.* Final Technical Progress Report DE97006951, Department of Energy, 1997.

[8] Dunning, R., and R. Mendenhall. "Design of Recycled Asphalt Pavements and Selection of Modifiers," *Recycling of Bituminous Pavements,* ASTM STP 662, Ed. L. Wood, PA, 1978.

[9] Lee, C., R. Terrel, and J. Mahoney. "Test for Efficiency of Mixing of Recycled Asphalt Paving Mixtures," *Transportation Research Record 911*, TRB, Washington, DC, 1983, pp. 51–60.

[10] Carpenter, S., and J. Wolosick. "Modifier Influence in the Characterization of Hot-Mix Recycled Material," *Transportation Research Record 777*, TRB, Washington, DC, 1980, pp. 15–22.

[11] Kadar, P. "Field and Laboratory Properties of Recycled Asphalt Pavement," *Asphalt Review*, Australia, 1996, pp. 9–12.

[12] Potter, J., and J. Mercer. "Full-Scale Performance Trials and Accelerated Testing of Hot-Mix Recycling in the UK." *Proceedings of the 8th International Conference on Asphalt Pavements*, International Society for Asphalt Pavements, Seattle, 1997, 593–607.

[13] Tam, K., P. Joseph, and D. Lynch. "Five-year experience of low-temperature performance of recycled hot mix," *Transportation Research Record 1362*, TRB, Washington, DC, 1992, pp. 56–65.

[14] Terrel, R., and D. Fritchen. "Laboratory Performance of Recycled Asphalt Concrete," *ASTM STP 662*, L.E. Wood, ed., ASTM, Philadelphia, 1977, pp. 104–122.

[15] DeKold, S., and S. Amirkhanian. "Reuse of Moisture Damaged Asphaltic Concrete Pavements." *Transportation Research Record 1337*, TRB, Washington, DC, 1992, pp. 79–88.

[16] Epps, J., D. Little, and R. Holmgreen. "Guidelines for recycling pavement materials." *NCHRP Report No. 224*, TRB, Washington, DC, 1980.

[17] Karlsson, R., and U. Isacsson. "Application of FTIR-ATR to Characterization of Bitumen Rejuvenator Diffusion," *Journal of Materials in Civil Engineering*, Vol. 15, No. 2, ASCE, 2003.

[18] Tran, N., A. Taylor, J.R. Willis. *Effect of Rejuvenator on Performance Properties of HMA Mixtures with High RAP and RAS Contents*. NCAT Report 12-05, Auburn Univeristy, Alabama, 2012.

[19] Roque, R., B. Birgisson, C. Drakos, and B. Dietrich. "Development and Field Evaluation of Energy-Based Criteria for Top-down Cracking Performance of Hot Mix Asphalt." *Journal of the Association of Asphalt Paving Technologists, Vol. 73*, 2004, pp. 229–260.

[20] Hiltunen, D.R. and R. Roque. "A Mechanics-Based Prediction Model for Thermal Cracking of Asphaltic Concrete Pavements." *Journal of the Association of Asphalt Paving Technologists,* 63, 1994, pp. 81–117.

[21] Kim, J., R. Roque, and B. Birgisson. "Integration of Thermal Fracture in the HMA Fracture Model." *Journal of the Association of Asphalt Paving Technologists*, 77, 2008, pp. 631–662.

[22] Tran, N., R. West, B. Powell, and A. Kvasnak, "Evaluation of AASHTO Rut Test Procedure Using the Asphalt Pavement Analyzer." *Journal of the Association of Asphalt Paving Technologists*, Minneapolis, MN, Vol. 78, 2009, pp. 1–24.

Experimental characterization of asphaltic materials—VIII

This page intentionally left blank

Asphalt Pavements – Kim (Ed)
© 2014 Taylor & Francis Group, London, ISBN 978-1-138-02693-3

Testing asphalt concrete in diametral tension-compression

Eyal Levenberg
Technion—Israel Institute of Technology, Technion City, Haifa, Israel

ABSTRACT: Testing of asphalt concrete in diametral tension-compression is suggested. Given that asphaltic layers experience stress reversals in the field, the underlying motivation is reducing systematic characterization errors. The required experimental setup is shown to be composed of usual testing gear with slight modifications. It is described in detail, validated on an aluminum disk, and then demonstrated for an asphalt concrete specimen. The application of force history that includes several load-unload-rest cycles is advocated. So doing allows separation of the measured response into recoverable and irrecoverable components with only the former being consistent with viscoelastic solid behavior. Reversing the direction of applied force is also beneficial; it effectively confines the accumulation of irrecoverable deformations to a narrow 'band', thereby protecting the mechanical integrity of the specimen. The resulting directional differences in mechanical behavior are demonstrated.

Keywords: Asphalt concrete, linear viscoelasticity, diametral tension, diametral compression, material characterization

1 INTRODUCTION

The response to load of Asphalt Concrete (AC) is best captured with a thermo-sensitive anisotropic nonlinear viscoelastic-viscoplastic constitutive theory [1–6]. For pavement design purposes, AC modeling is currently limited to small-strains and taken as a thermorheologically-simple linear isotropic viscoelastic solid [7–9]. Such parsimonious description, which is inconsistent with observed behavior, is driven by practicality: (i) it involves a relatively small set of material parameters and hence easy to comprehend; (ii) it is simple to calibrate and therefore allows substantial reduction in laboratory workload for characterization; and (iii) it greatly accelerates subsequent pavement modeling computations, mainly due to the legitimacy of applying superposition. When such a limited-complexity model is imposed on calibration test data, systematic errors are included in the inferred material parameters. Unlike random errors, systematic errors cannot be reduced by repeated measurements; they can only be minimized by: (i) constraining the calibration space to the domain of interest; and (ii) using experimental data that cover a broad information range within the domain.

The most basic method for linear viscoelastic characterization of AC [10, 11] partially addresses these requirements; it entails measuring the relaxation modulus in the frequency domain under different isothermal conditions to enable master curve construction. Tests involve the application of haversine stresses in uniaxial compression mode to a cylindrical specimen, 50 mm in radius and 150 mm in height. Axial deformations are measured on-specimen along the mid-height of the cylinder with Linear Variable Displacement Transducers (LVDTs). The 'calibration space' is constrained to small deformations by placing limits on the allowable transient strain amplitude (75 με) and on the irrecoverable strains accumulating throughout the test (1500 με). Broad information range is obtained by combining several temperature levels (from −10C to +54C) and test frequencies (from 0.1 Hz to 25 Hz). Switching between tension and compression is not routinely done despite the fact that AC materials exhibit directional sensitivity [12–14]. This aspect is of practical importance because stress

and strain reversals are produced within AC layers by passing vehicles [15–18]. This means that common calibration results are biased towards compressive properties. Complex modulus in tension-compression is mentioned in [19–23].

Cylindrical AC specimens with the abovementioned dimensions are not standard in size, difficult to fabricate, and impossible to core from as-constructed layers. For these reasons the indirect tensile test has been suggested as a practical alternative to the uniaxial mode [24–29]. The tested specimen is disk-shaped, typically 50 to 75 mm in radius; it is compressed diametrically from opposite sides by two metallic loading strips. Resulting deformations are often measured with on-specimen LVDTs, mounted close to the center of the disk. A similar instrumentation arrangement is used on each side, consisting of one LVDT placed along the loading direction and another placed transversely; a relatively small gauge length of 38 mm is specified. Analysis of AC in diametral tests is traditionally based on two-dimensional elastic theory [30, 31] and on the elastic-viscoelastic analogy. The modeling assumes an isotropic and homogenous disk with forces applied to the outer circumference in the radial direction (i.e., no shear); the theoretical solution is essentially indifferent between tension and compression. With these assumptions the stress intensity at any point in the disk is linearly related to the applied loading and independent of the material properties. Biaxial stress conditions are generated in the disk, with principal stresses that are opposite in sign (except close to the loaded arcs). However, it should be acknowledged that the first stress invariant, at any point, never changes sign; this means that all disk elements are spherically compressed or tensioned depending on the direction of applied force. Consequently, only compressive constitutive behavior is exposed in a typical diametral test [32].

Herein, an idea is explored to test AC in diametral tension-compression. Based on the aforementioned discussion, the underlying motivation is to broaden the information extracted from the test (still constrained to small-deformations) and therefore remove part of the systematic error integrated in the results. Moreover, to further improve consistency with viscoelastic theory, a pulse-rest type of loading history is employed. So doing facilitates the separation between recoverable and irrecoverable deformations in order that the former can used for calibration; this has been demonstrated in a recent study dealing with compressive conditions only [33]. In this connection, reversing the load direction restricts the accumulation of permanent deformations and therefore safeguards the integrity of the specimen, especially under elevated characterization temperatures. The purpose of this paper is to expose and demonstrate the experimental aspects involved in performing a diametral tension-compression test for AC. In-depth analysis for inference of viscoelastic properties is not included due to space restrictions.

2 DIAMETRAL TENSION-COMPRESSION

2.1 *Instrumentation for deformation*

Whenever material characterization is done under small deformations, on-specimen measurement devices must be used to offset compliance issues. This requirement is followed herein, employing LVDTs, with a non-traditional mounting sequence and arrangement. Short thin screws, each 3 mm in diameter and 25 mm in length, are anchored into the tested specimen; these should be fixed to a depth of about 10 mm by a combination of drilling and gluing. A stainless-steel drilling mold can be used to semi-automate this process and ensure repeatability in positioning. These screws serve as 'gauge-points' for mounting four LVDTs, each essentially reading the change in distance between a pair of screws. Anchoring of the gauge-points in the material ensures stability at elevated temperatures, when the material is very soft.

Two optional gauge-point arrangements are shown in Figure 1, superposed over a disk specimen that is 150 mm in diameter. This arrangement is essentially mirrored on the other side of the disk. A Cartesian coordinate system is positioned at the center point, such that the y-axis is parallel to the loading direction. Five gauge-points are shown, denoted as P1 .. P5 with coordinates indicated in brackets (values are in millimeters). The vertical LVDTs

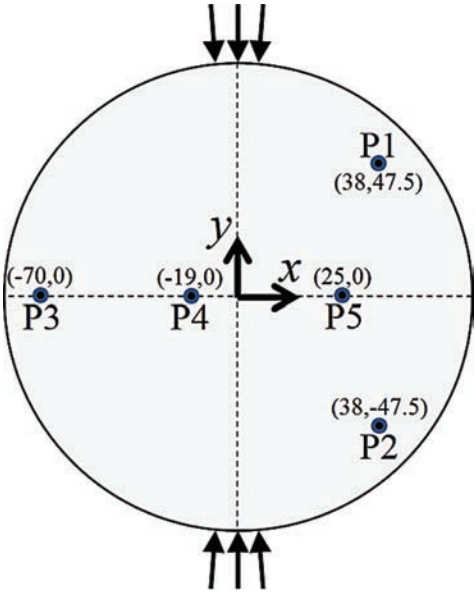

Figure 1. Proposed arrangement of LVDT gauge-points.

span P1-P2 with a gauge length of 95 mm; horizontal LVDTs span either points P3-P4, with a gauge length of 51 mm (Arrangement I) or points P3-P5 with a gauge length of 95 mm (Arrangement II). Two main advantages are provided by these arrangements: (i) better compliance with representative volume element requirements compared with the usual (rather short) gauge lengths [34]; and (ii) retention of some post-peak measurement ability as the off axis instrumentation can potentially function even after the specimen splits in half (not an issue in the current study).

2.2 *Loading setup*

Any standard diametral loading apparatus and single-axis load frame can be used for performing a diametral tension-compression test. The main difference is that the tested disk must be glued to the top and bottom loading strips and the apparatus must be secured to the load frame to permit tension. An off-the-shelve diametral apparatus was employed herein (purchased from Wille Geotechnik). It consists of an aluminum beam sliding vertically over two stainless steel rods, serving as guides. Linear bushings on each side of the beam ensure near-frictionless motion. The bottom loading strip is stationary, attached to the foot of the apparatus; the top strip is attached to the underside of the aluminum beam. Both strips are fixed with hex cap screws and are therefore easy to disconnect; consequently, a glued specimen can be quickly removed from the apparatus if needed (with strips though).

An Instron ElectroPuls (model EP10000) was used as the single-axis load frame. The diametral apparatus was carefully centered and fastened to the EP10000 on top of a 10 kN precision load-cell. The loading piston was attached to the upper side of the beam via a special load-transfer device [20]. This device is composed of two rectangular stainless-steel frames, one attached to the beam and the other fastened to the piston. The frames are interlinked so that there is a certain motion range for which they are not touching; beyond this range they must move together. In their 'neutral' position the EP10000 and diametral apparatus are completely disengaged; tension or compression can only be produced after the frames are brought into contact. The application of pulse-rest loading cycles is greatly simplified with this device. The linked frames help produce fast unloading to true zero stress conditions without any overshooting; they also help produce long true rest intervals without the negative

effects of electromechanical drifts. The only limitation is that the testing must be operated in deformation control mode because of the existence of a neutral range that breaks the feedback loop between load-cell readings and piston movements.

A picture of a glued AC specimen in the diametral apparatus is shown in Figure 2. Callout arrows are included to identify the different setup elements. The LVDTs in this figure are of loose-core type (manufactured by Singer—Instruments and Control), mounted according to Arrangement II. Their precision level, as determined by the driving electronics, was about ±0.1 micron for a measurement range of ±5 mm. As indicated, rubber pads were inserted between the disk and the metallic loading strips; this was done to better comply with the zero friction assumption in theoretical model. A consumer-grade fast setting Epoxy was used for the gluing.

2.3 *Calibration check*

In order to experimentally evaluate the concept and functionality of the setup, a thin aluminum disk, 20 mm thick and 150 mm in diameter, was instrumented and tested. Four LVDTs were positioned according to Arrangement I; readings in the horizontal and vertical directions were separately averaged for subsequent analysis. Positive sign is used to indicate compressive load and also to indicate that gauge points moved closer to each other. LVDTs were pre-calibrated against an optical encoder with submicron accuracy; their effective precision level was considerably improved by oversampling and subsequent smoothing with a quartic kernel smoother. Loading was applied in increasing intensity steps, first in compression mode and then in tension. Deformation response vs. load-cell readings are plotted in Figure 3 by dotted and dashed lines.

As can be seen, applied compressive forces were as high as 6 kN while tensile forces did not exceed 0.7 kN. The latter were essentially limited by the tensile capacity of the glue and rubber

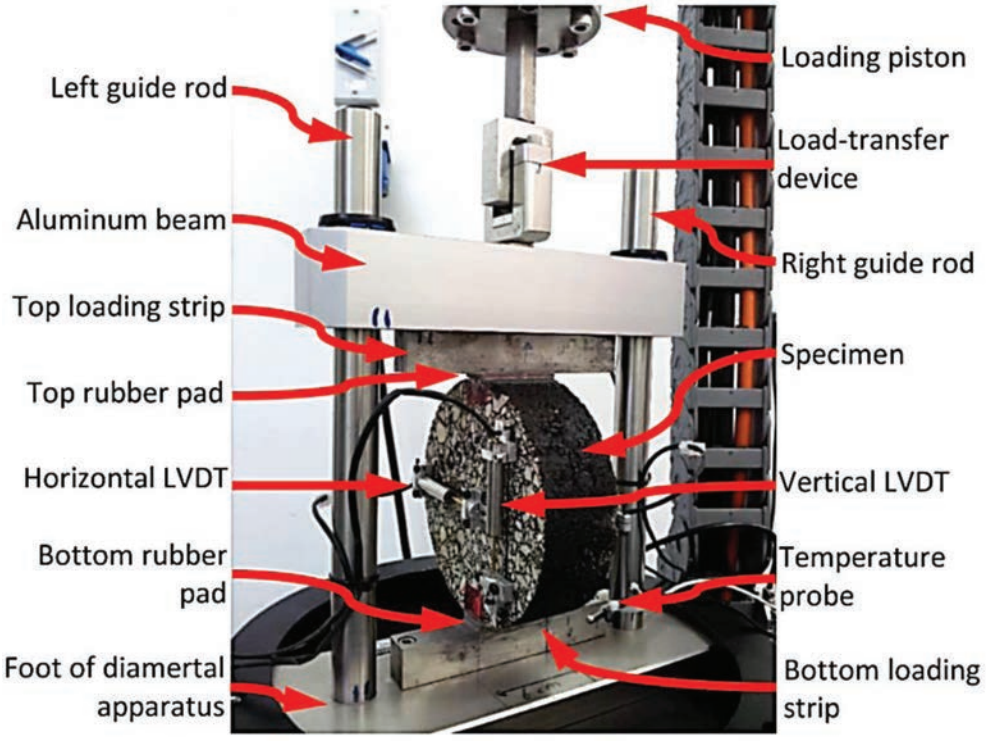

Figure 2. Diametral tension-compression setup.

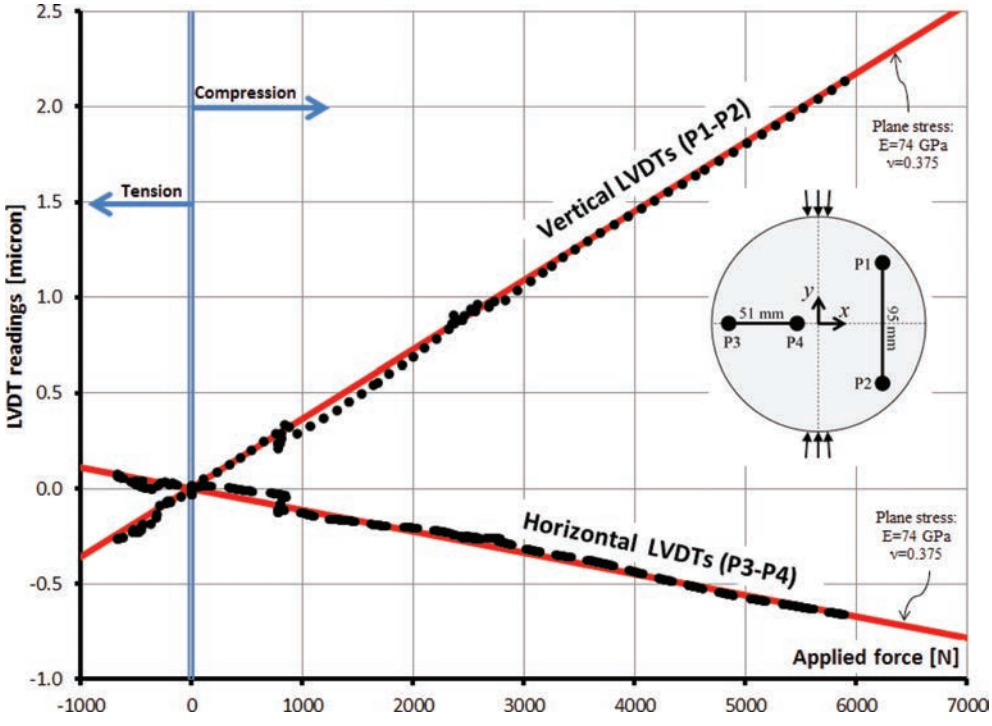

Figure 3. Diametral tension-compression for a thin aluminum disk.

pads. Considering the small contact area, a tensile force of 0.7 kN is equivalent to an average tensile stress intensity of 1.84 MPa. It may also be noticed that the deformation levels are very small; the ordinate in the figure spans a mere 3.5 microns (from +2.5 to −1.0). Visible imperfections in the response are partially related to time-dependent effects; forces where applied in position controlled steps and the aluminum exhibited some stress relaxation. Nonetheless, the overall behavior is graphically consistent with linear elastic theory for both tension and compression directions. Under compression, the vertical LVDTs (P1-P2) were compressed while the horizontal LVDTs (P3-P4) measured tensile deformation. When the loading direction was switched to tension, LVDT readings were reversed along the same trend.

In a two-dimensional linear elastic model the ratio of vertical to horizontal LVDT readings is only a function of the materials' Poisson's ratio. Experimentally, this ratio was measured to equal −3.291. In a plane stress model of Arrangement I, this value corresponds to a Poisson's ratio of $\nu = 0.375$. The slope of the LVDT readings in the figure is controlled by both Young's modulus (E) and ν. As indicated by the two oblique solid lines in the figure, a value of $E = 74$ GPa was obtained from matching the test data. Both inferred E and ν are correct, indicating that the system is accurate and performs well under small deformations.

3 APPLICATION TO ASPHALT CONCRETE

3.1 *Loading*

The proposed setup is hereafter demonstrated for an AC specimen composed of limestone aggregates and unmodified PG 70–10 binder. The aggregate blend was coarse-graded with a nominal maximum aggregate size of 19 mm. Aggregates and binder (4.7%) were mixed at 170°C, allowed to age for two hours at 155°C, and subsequently densified in a gyratory compactor (75 gyrations). The resulting 150 mm diameter pill was trimmed from both sides to arrive at a disk thickness of 58 mm having an air void content of 4.5%. After instrumentation

and gluing to the diametral apparatus, but before any force application, isothermal conditions were imposed until all LVDT readings stabilized. This was done by controlling the laboratory room temperature with an air-conditioning system. In addition, to lessen fluctuations in the vicinity of the apparatus, a controller connected to a temperature probe (see Fig. 2) was used for switching on and off an industrial space heater that faced the specimen. Consequently, a stable temperature level was maintained throughout the test with an average of 25.3°C and standard deviation of 0.23°C.

History of applied forces is shown in Figure 4; consisting of four load-unload-rest cycles with an overall duration of almost 10000 seconds (2 hours and 45 minutes). During the first and third cycles (C1 and C3) tensile forces were applied while the second and fourth cycles (C2 and C4) were compressive. The rest periods, numbered $m = 1 \,..\, 4$ were increasing in duration; the last being 5400 seconds (1.5 hours) long. Such loading history can be used to calibrate the viscoelastic time function over almost six decades in logarithmic scale, between 10^{-2} to 10^{4} seconds [33]. If a similar loading sequence is repeated under additional temperatures, a master curve can be constructed. The advantage here is that two or three temperature levels should suffice to cover any practical range of interest.

Forces were applied in position controlled mode by instructing the piston to move at a constant rate. At the same time, load-cell readings were monitored until a predefined threshold was reached. This was done mainly for the tensile cycles, to protect against gluing failure. Once the preset load level was attained, the piston was instructed to hold its position for two seconds and then retract quickly to produce fast unloading (and subsequent rest interval). The outcome of this sequence is shown in Figure 5, where a magnified view of Cycle 3 is provided. Loading commenced at about $t = 2549$ seconds, after rest period $m = 2$ ended. Tension was induced for a duration of about 4 seconds to a level of approximately −1400 N, at which point the piston movement was stopped for about 2 seconds. During this time the stress level relaxed, mainly due to the specimen

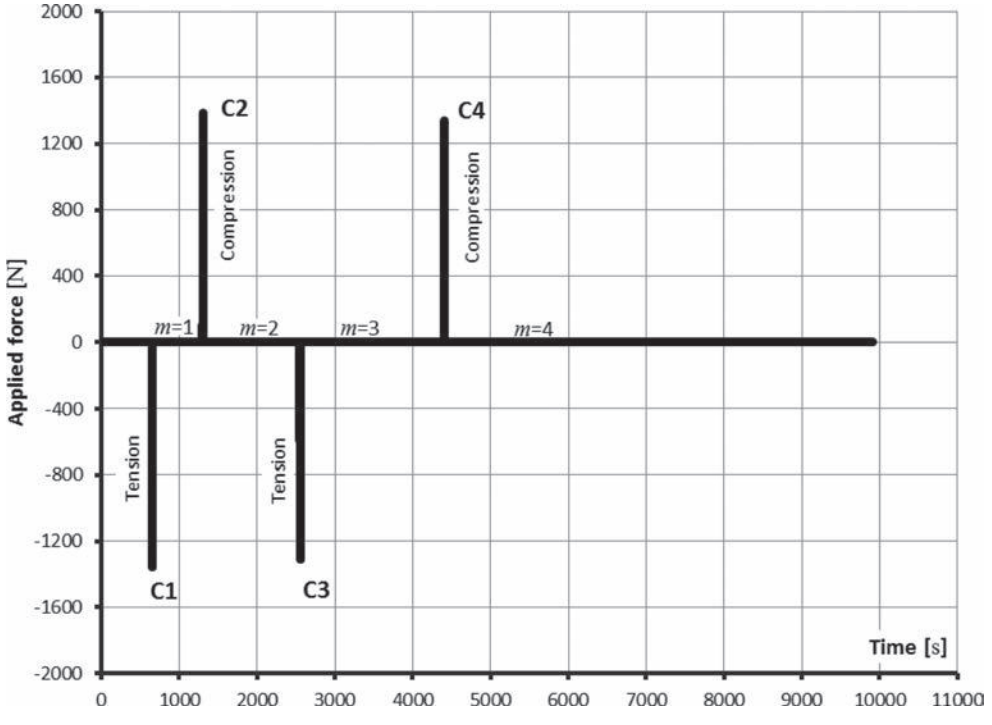

Figure 4. History of applied diametral forces—asphalt concrete disk.

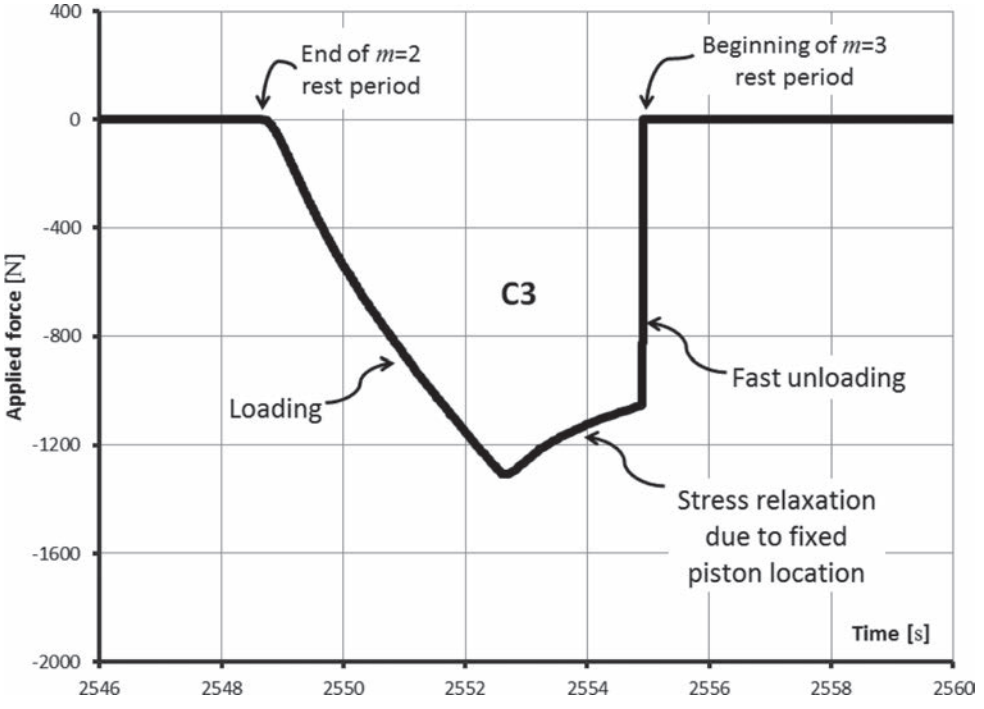

Figure 5. Applied diametral force—magnified view of cycle 3.

deforming; this is clearly seen in the load-cell measurements (and indicated in the figure). From $t = 2555$ seconds the specimen was rapidly unloaded. With the help of the special load-transfer device the force was removed completely within 0.02 seconds, launching another rest period ($m = 3$). It is important to note that the actual (applied) shape of the load-unload pulse is used for interpretation and therefore the above described irregular behavior is not problematic. The most important loading attributes for characterization are: (i) generation of small deformations, (ii) ultra-fast unloading, and (iii) long uninterrupted rest intervals.

3.2 *Deformation response*

Deformations recorded by the vertical and horizontal LVDTs are shown in Figure 6. The individual responses to the four loading cycles are indicated by R1 .. R4. The overall deformation level in the test was very small, as readings varied within a narrow range of ±10 micron. With reference to Figure 1, every micron change in the vertical LVDTs is approximately equivalent to a strain change (in absolute terms) of 15 and 25 microstrains at the disk center in the x and y directions (respectively). The center is the most strained point in the diametral configuration. Even for such small deformation levels irrecoverable response of the order of 25% of the total readings was present in every cycle. This is graphically indicated by the flat asymptotic behavior during the end of the rest intervals. It should also be noticed how the transition between tension and compression confined the permanent deformation component to a narrow band.

A close view of the response in the different cycles is offered by Figure 7. Four charts are included, each displaying 500 seconds of data, from about 100 seconds before the load-unload sequence until approximately 400 seconds afterwards (i.e., the early part of the subsequent rest period). The viscoelastic recovery shape can clearly be noticed, as well as the existence of permanent deformations.

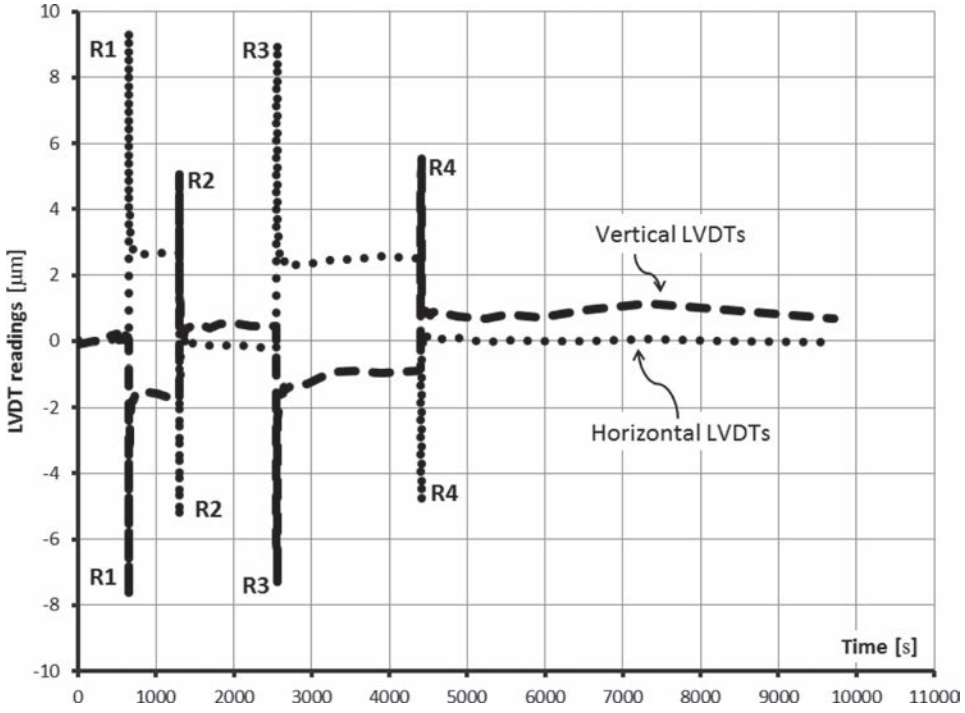

Figure 6. History of deformation response—asphalt concrete disk (refer to Fig. 4).

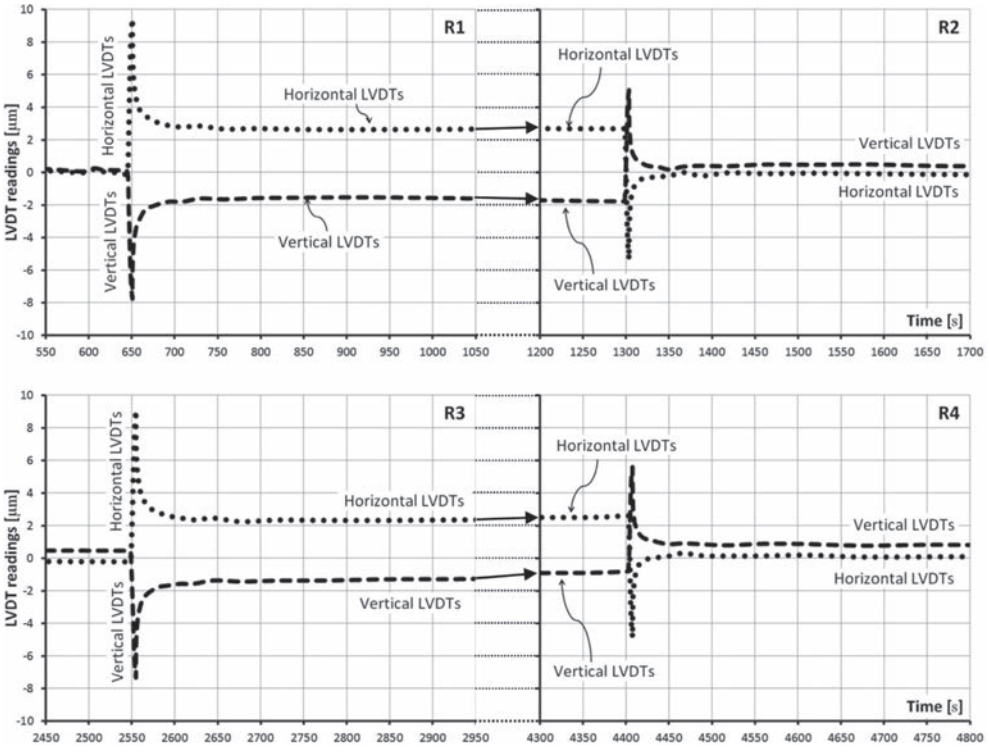

Figure 7. Magnified view of deformation response (refer to Fig. 6).

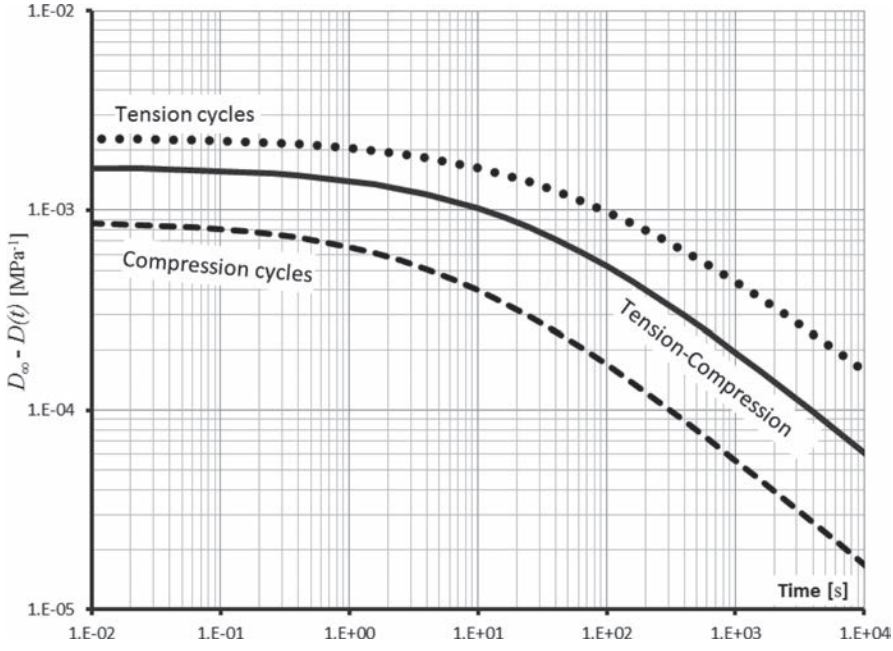

Figure 8. Influence of diametral testing direction on inferred viscoelastic properties.

4 SUMMARY AND COMMENTS

The possibility of performing diametral tension-compression was investigated, and shown to be experimentally feasible with usual testing gear. The underlying motivation is to broaden the calibration range of AC materials for engineering design and analysis of pavements. A pulse-rest type of loading history was offered for characterization as it allows reliable separation between recoverable and irrecoverable deformations. Under the usual application of sinusoidal loads such separation is not possible. A demonstrative test involving one AC specimen under room temperature showed that permanent deformations can be significant, in either loading direction, even in the domain of very small deformations. Reversing the load direction in the test effectively restricted the accumulation of these deformations to remain within a narrow band.

Figure 8 presents the outcome of a preliminary investigation on the influence of loading direction on the inferred viscoelastic properties (for the tested AC specimen). In general terms, the analysis involved simulating the applied force history in a linear viscoelastic model, and matching the LVDT readings (in both directions) during the recovery intervals—when the material was completely unloaded and irrecoverable response assumed inactive. The ordinate represents the viscoelastic creep compliance $D(t)$ subtracted from the long-term (equilibrium) compliance D_∞; the abscissa represents time. There are three curves in this figure: the solid line is associated with matching the entire available dataset from the diametral tension-compression experiment; the dotted line represents the viscoelastic properties when only tensile data is considered in the calibration; and the dashed line is associated only with compressive conditions. Directional differences can be clearly noticed; also the bias involved in calibrating properties for a single direction can be quantified. Utilizing the middle curve for pavement design and analysis should minimize systematic errors.

ACKNOWLEDGEMENTS

The author wishes to thank Mr. Nir Michaeli and Mr. Meir Ovadia for providing experimental assistance. This work was financially supported by the Israeli National Roads Company

(INRC); it is part of a larger research project carried out by the Transportation Infrastructure Laboratory in the Technion, aimed at introducing warm mix technologies into the country in a controlled and systematic manner.

REFERENCES

[1] Lai, J.S. and Anderson, D. Irrecoverable and Recoverable Nonlinear Viscoelastic Properties of Asphalt Concrete, Highway Research Record, 468, pp. 73–88. 1973.

[2] Sidess, A. Mechanism of Fatigue Crack Growth in Bituminous Mixtures, Ph.D. Dissertation, Technion—Israel Institute of Technology (In Hebrew). 1985.

[3] Uzan, J. Asphalt Concrete Characterization for Pavement Performance Prediction, Journal of the Association of Asphalt Paving Technologists, 65, pp. 573–607. 1996.

[4] Levenberg, E. Constitutive modeling of Asphalt-Aggregate Mixes with Damage and Healing, Ph.D. Dissertation, Technion—Israel Institute of Technology. 2006.

[5] Kim, Y.R., Guddati, M.N., Underwood, B.S, Yun, T.Y., Subramanian, V. and Savadatti, S. Development of a Multiaxial Viscoelastoplastic Continuum Damage Model for Asphalt Mixtures, Federal Highways Report, FHWA-HRT-08-073. 2009.

[6] Darabi, M., Abu Al-Rub, R., Masad, E., Huang, C., and Little, D. A thermo-Viscoelastic-Viscoplastic-Viscodamage Constitutive Model for Asphaltic Materials, International Journal of Solids and Structures, 48(1), pp. 191–207. 2011.

[7] ARA Inc. Guide for the Mechanistic-Empirical Design of New and Rehabilitated Pavement Structures, National Cooperative Highway Research Program Report, Project 1-37A. 2004.

[8] Zhou, F. Fernando, E. and Scullion, T. Development, Calibration, and Validation of Performance Prediction Models for the Texas M-E Flexible Pavement Design System, Report FHWA/TX-10/0-5798-2. 2010.

[9] Ullidtz, P., Harvey, J., Basheer, I., Jones, D., Wu, R., Lea, J., and Lu, Q. CalME: Mechanistic-Empirical Design Program for Flexible Pavement Rehabilitation, Transportation Research Record, 2153, pp. 143–152. 2010.

[10] AASHTO TP 62. Standard Method of Test for Determining Dynamic Modulus of Hot-Mix Asphalt Concrete Mixtures, American Association of State and Highway Transportation Officials. 2007.

[11] AASHTO TP 79. Standard Method of Test for Determining the Dynamic Modulus and Flow Number for Hot Mix Asphalt (HMA) Using the Asphalt Mixture Performance Tester (AMPT). American Association of State and Highway Transportation Officials. 2009.

[12] Partl, M., and Rösli, A. An Approximation of Uniaxial Creep During Alternating Tension-Compression Step Loading at Constant Temperature, International Journal of Solids and Structures, 21(3), pp. 235–244. 1985.

[13] Levenberg, E. Viscoplastic Response and Modeling of Asphalt-Aggregate Mixes, Materials and Structures, 42(8), pp. 1139–1151. 2009.

[14] Levenberg, E. and Uzan, J. Exposing the Nonlinear Viscoelastic Behavior of Asphalt-Aggregate Mixes, Mechanics of Time-Dependent Materials, 16(2), pp. 129–143. 2012.

[15] Crockford, W. Role of Principal-Plane Rotation in Flexible Pavement Deformation, Journal of Transportation Engineering, 119(1), pp. 124–141. 1993.

[16] Kim, T. and Tutumluer, E. Unbound Aggregate Rutting Models for Stress Rotations and Effects of Moving Wheel Loads, Transportation Research Record, 1913, pp. 41–49. 2005.

[17] Levenberg E., McDaniel, R.S., and Olek, J. Validation of NCAT Structural Test Track Experiment using INDOT APT Facility: Final Report, Joint Transportation Research Program Report, FHWA/IN/JTRP-2008/26. 2009.

[18] Carvalho, R. and Schwartz, C. The Importance of Simulating Moving Wheel Loads in the Mechanistic Analysis of Permanent Deformations in Flexible Pavements, Airfield and Highway Pavement Conference Proceedings: Sustainable and Efficient Pavements, pp. 1156–1166. 2013.

[19] Kallas, BF. Dynamic Modulus of Asphalt Concrete in Tension and Tension-Compression, Journal of Association of Asphalt Paving Technologists, 39, pp. 1–23. 1970.

[20] Uzan, J. and Levenberg, E. Advanced Testing and Characterization of Asphalt Concrete Materials in Tension, International Journal of Geomechanics, 7, pp. 158–165. 2007.

[21] Doucet, F. and Auger, B. Complex Modulus Determination of Asphalt Mixes at the Ministère des Transports du Québec, Transports Québec Report, RTQ-10-01. 2010.

[22] Underwood, B.S. and Kim, Y.R. Comprehensive Evaluation of Small Strain Viscoelastic Behavior of Asphalt Concrete, Journal of Testing and Evaluation, 40(4), pp. 1–11. 2012.
[23] EN 12697-26. Bituminous Mixtures—Test Methods for Hot Mix Asphalt—Part 26: Stiffness, European Committee for Standardization. 2012.
[24] Buttlar, W.G., and Roque, R. Development and Evaluation of the Strategic Highway Research Program Measurement and Analysis System for Indirect Tensile Testing at Low Temperatures, Transportation Research Record, 1454, pp. 163–171. 1994.
[25] Zhang, W., Drescher, A., and Newcomb, D.E. Viscoelastic Behavior of Asphalt Concrete in Diametral Compression, Journal of Transportation Engineering, 123(6), pp. 495–502. 1997.
[26] Zhang, W., Drescher, A., and Newcomb, D.E. Viscoelastic Analysis of Diametral Compression of Asphalt Concrete, Journal of Engineering Mechanics, 123(6), pp. 596–603. 1997.
[27] Kim, YR., Seo, Y., King, M., and Momen, M. Dynamic Modulus Testing of Asphalt Concrete in Indirect Tension Mode, Transportation Research Record, 1891, pp. 163–173. 2004.
[28] Olard, F. Noël, F., and Loup, F. Modulus Testing in Indirect Tension Mode, Journal of Road Materials and Pavement Design, 7(4), pp. 543–554. 2006.
[29] AASHTO T 322. Determining the Creep Compliance and Strength of Hot-Mix Asphalt (HMA) Using the Indirect Tensile Test Device, American Association of State and Highway Transportation Officials. 2007.
[30] Hondros, G. The Evaluation of Poisson's Ratio and the Modulus of Materials of a Low Tensile Resistance by the Brazilian Test (Indirect Tensile) with Particular Reference to Concrete, Australian Journal Applied Science, 10, pp. 243–264. 1959.
[31] Ma, C.C. and Hung, K.M. Exact Full-field Analysis of Strain and Displacement for Circular Disks Subjected to Partially Distributed Compression, International Journal of Mechanical Sciences, 50, pp. 275–292. 2008.
[32] Katicha, S.W. Analysis of Hot-Mix Asphalt (HMA) Linear Viscoelastic and Bimodular Properties Using Uniaxial Compression and Indirect Tension (IDT) Tests, Ph.D. Dissertation, Virginia Polytechnic Institute and State University. 2007.
[33] Levenberg, E. and Michaeli, N. Viscoelastic Characterization of Asphalt-Aggregate Mixes in Diametral Compression, Road Materials and Pavement Design, 14(S1), pp. 105–119. 2013.
[34] Levenberg, E. and Uzan, J. Quantifying the Confidence Levels of Deformation Measurements in Asphalt Concrete, Journal of Testing and Evaluation, 32(5), pp. 358–365. 2004.

This page intentionally left blank

Asphalt Pavements – Kim (Ed)
© 2014 Taylor & Francis Group, London, ISBN 978-1-138-02693-3

The Reflective Cracking Tester: A third-scale accelerated pavement tester for reflective cracking

Andrew D. Wargo, Shuvo Islam & Y. Richard Kim
North Carolina State University, Raleigh, NC, USA

ABSTRACT: A third-scale accelerated pavement test setup, known as the *Reflective Cracking Tester* (RCT), was developed for this research project to study reflective cracking. Together with Digital Image Correlation (DIC) technology, the RCT was used to investigate the differences in reflective crack propagation seen in layered Asphalt Concrete (AC) pavements, with and without chip seal interlayers. This investigation found that interfacial sliding and separation occurred in both types of pavement, although the samples with chip seal interlayers saw more interfacial movement than those without chip seal interlayers due to the weaker bond between the layers in the chip seal samples. This increased movement meant that the pavement with the chip seal interlayer had a lower number of cycles to failure than the pavement without a chip seal interlayer. Also, this research confirmed that double cracking and triple cracking are possible in pavements with high differential deflections. Further investigation is needed with this test method to determine its ability to capture the benefits of other reflective crack mitigating systems.

Keywords: Reflective cracking, Digital Image Correlation, chip seal interlayer

1 INTRODUCTION

Throughout the world, many kilometers of roadway are surfaced with Asphalt Concrete (AC). Therefore, the maintenance and rehabilitation of these roadways are primary concerns for many highway agencies. One common form of rehabilitation for these roadways is the use of thin AC overlays. These overlays usually consist of one or two courses placed on an existing pavement that may or may not have been cold-milled prior to the placement of the overlay. These treatments are widely used because of their ability to provide a new wearing surface while still taking advantage of the remaining fatigue life and load-carrying capacity of the existing pavement. However, in many cases, stress concentrations due to cracks in the existing pavement cause the formation and rapid propagation of cracks in the overlay. Because these cracks exhibit the same pattern as those in the underlying pavement, this phenomenon is known as *reflective cracking*. The major problem with reflective cracks is that they allow water to enter the pavement structure. Thus, their prevalence in the overlay can be a significant contributing factor to the further deterioration of the overall pavement structure.

Because of this fact, many types of interlayer treatments have been used in an attempt to mitigate reflective cracking over the last fifty years. These treatments include crack sealing, fabrics, grids, Stress-Absorbing Membrane Interlayers (SAMIs), chip seals, fine-graded asphalt layers, and fiber-reinforced asphalt mixtures, just to name a few [1]. Of these, chip seals (which consist of a heavy application of emulsified asphalt binder and the placement of a cover aggregate) are of particular interest to highway agencies due to the fact that they are already used extensively as a wearing surface on low- to medium-volume pavements. As such, equipment for their placement is widely available and construction personnel are familiar with their construction. It is believed that these treatments, as interlayers, can help to absorb the stress that propagates reflective cracking and provide a barrier to water infiltration into

the pavement layers if cracks in the overlay occur. Past research has shown that chip seals used as reflective crack mitigating interlayers are generally effective at delaying reflective cracking, but as with most interlayer types, are unable to prevent it altogether [1, 2].

In order to better understand the performance of these systems, it is desirable to have a means to investigate their behavior in the laboratory. Because of the complicated loading history that is created when a moving wheel passes over a pavement, the realistic simulation of reflective cracking due to traffic loading has been difficult to achieve in the lab, with many researchers opting to use simplified loading conditions to evaluate interlayer behavior. In order to provide a better simulation of field behavior, several researchers have utilized small-scale accelerated pavement tests on layered asphalt samples in an attempt to characterize interface behavior. Most often these tests use a moving wheel, although actuators have been used in some cases [3, 4, 5, 6]. In general, these types of tests have shown that interlayer behavior can be studied in the lab under more controlled conditions than in the field, but care must be taken when interpreting the results, as the conditions of the test protocol may be somewhat different than those typically experienced in the field.

2 RESEARCH OBJECTIVES

- Develop a small-scale accelerated pavement tester to evaluate reflective cracking.
- Employ DIC technology to better understand the mechanisms involved with reflective cracking.
- Test various reflective crack mitigating interlayer systems, such as chip seals, using the RCT and DIC technology.

3 MATERIALS & METHODS

The asphalt concrete mixture used for specimen fabrication in this study was a typical surface mix (S-9.5B) used in North Carolina. This 9.5-mm mixture was collected in metal buckets at the asphalt plant and stored in a climate-controlled room until use. A CRS-2 emulsion was used as both a tack coat for the asphalt layers and as bitumen for the chip seal interlayer. The cover aggregate used for the chip seal interlayer was typical #78M stone used in North Carolina.

In this study, DIC technology was used to study the deformations and displacements of the tested samples. The DIC method works by taking a reference image of the sample before loading and subsequently taking multiple images (known as *test images*) throughout the testing. Next, software (specifically, Vic-2D in this research) is used to compare all of the test images to the reference image, and any differences between the reference image and the test images are explained as deformations or motions of the sample that occurred at the time the test image was taken. In this way, full-field displacements and strains of the sample can be monitored throughout the test procedure. The DIC system has two important advantages for studying reflective cracking. First, it allows for easy tracking of the differential movements seen across the interlayers of a layered AC sample, which otherwise might be difficult to track using traditional gauges. Second, strain contour plots allow for easy visualization of the crack location within the sample, because cracks in the surface show up as areas of extremely high strain. Detailed explanations of DIC methods can be found in the literature and are outside the scope of this paper [7, 8].

4 REFLECTIVE CRACKING TESTER (RCT)

The North Carolina State University pavement laboratory has been using a one-third scale wheel load device known as the MMLS3 for various pavement research projects since the late 1990s. This device typically is used to apply 2.7 kN wheel loads at a rate of 6,000 cycles per

hour. As such, the development of a test device to allow small-scale accelerated simulations of reflective cracking in layered asphalt pavements in the laboratory was seen as a reasonable methodology to study the phenomenon of reflective cracking further. The basic concept of this test method is to construct layered asphalt systems on top of steel plates and subject this pavement system to wheel loads by the MMLS3 (Fig. 1). A compaction frame and vibratory roller are used to compact the pavement layers (Fig. 2).

The reflective cracking test setup is as follows: First, steel tubing and I-beams are attached to the base plate of the testing area. Next, two 914 mm × 610 mm × 12.7 mm grooved A514 steel plates are placed on top of the tubing and the I-beams. The steel plates are then bolted to the tubing. Next, the I-beams are bolted to the plates using clamps (Fig. 3a). This effectively creates two cantilevered plates with a 15.86-mm gap between them. By loosening the clamps and adjusting the position of the I-beams, the length of the cantilever on each side of the joint can be controlled, thus controlling the deflection amplitude of the system under loading.

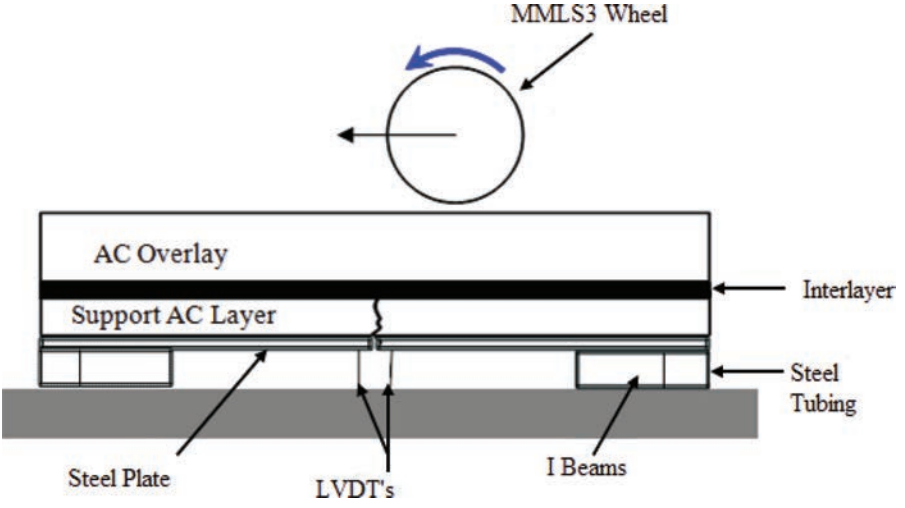

Figure 1. Schematic of the final configuration of the RCT.

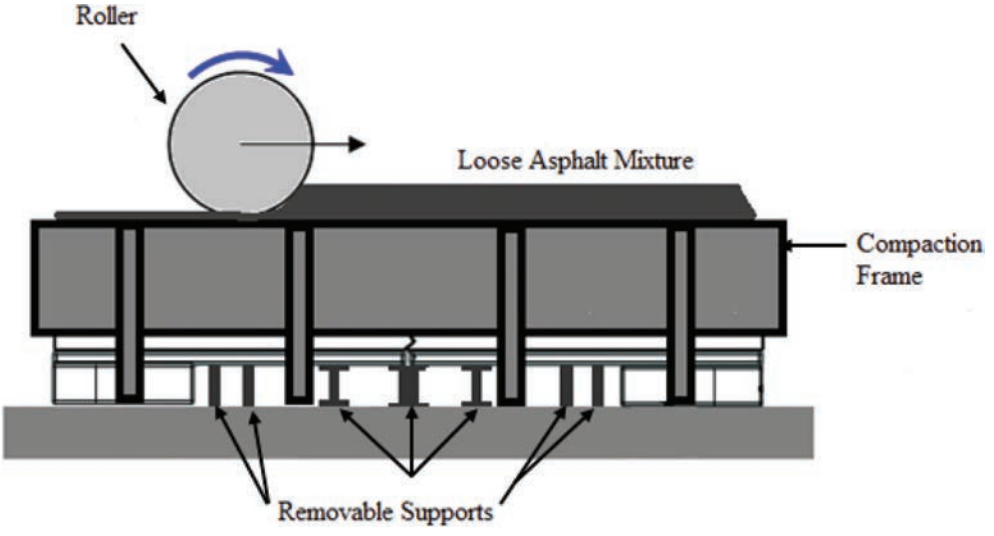

Figure 2. Schematic of the RCT during compaction.

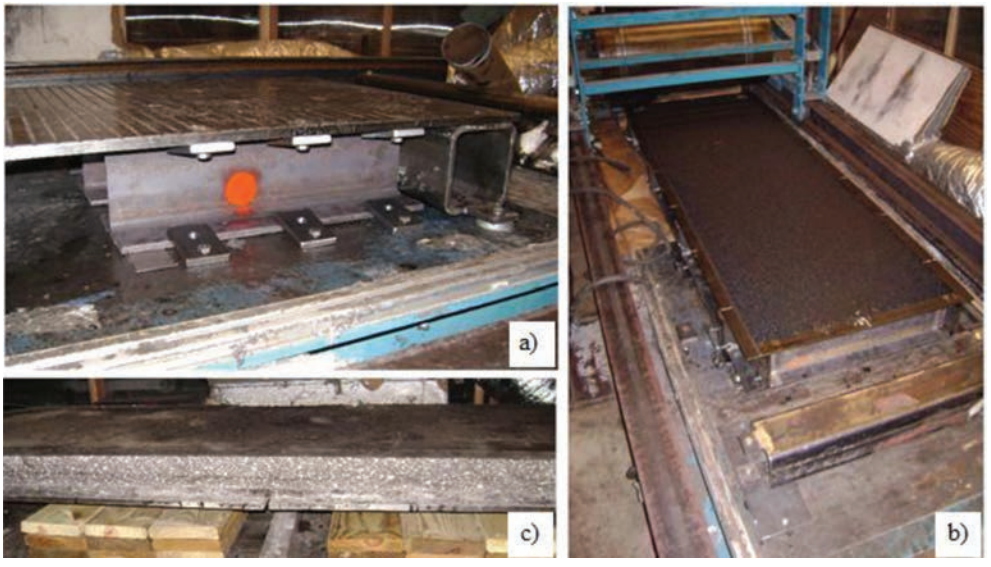

Figure 3. a) Close-up of steel plates bolted to supports, b) RCT and compaction frame during compaction, and c) Final layered system with smoothed surface.

Next, additional supports are provided beneath the steel plates, and a compaction frame is placed around the RCT. The compaction frame is adjusted to the correct height, and a 21-mm layer of AC is compacted using a vibratory steel wheel roller (Fig. 3b). Once the first layer has cooled, a full-depth saw cut is made at the center of the slab at the gap between the two steel plates to simulate a transverse crack in the existing pavement. The RCT is loosened, the two slabs are pushed together slightly to reduce the width of the crack to 3.18 mm in order to match typical crack widths seen in the field, and the RCT is retightened. Next, the desired interlayer is constructed, and the compaction frame is used to construct a second AC layer, bringing the total height of the compacted pavement layers to 59 mm. Once the second layer adequately cools, the vertical edge of the sample is smoothed to provide a flat surface perpendicular to the DIC camera (Fig. 3c). This surface is painted white and then speckled with black spray paint in order to be viewed by the DIC camera. The end result of this procedure is a layered slab specimen of approximately 1845 mm × 584.2 mm with a transverse joint at the middle of the bottom AC layer, supported by two cantilevered steel plates. Typical air void values of the AC layers are approximately 10 percent. This high air void level is due solely to the physical limitations of the laboratory compaction equipment available.

Prior to testing, the removable compaction supports are taken out from beneath the RCT and four spring Linear Variable Differential Transducers (LVDTs) are placed near the joint between the steel plates (two LVDTs at the center of the steel plates and two near the edge). These LVDTs allow the monitoring of deflections of the steel plate during loading to provide independent validation of the DIC measurements and to ensure that the deflections in the center of the slab are similar to those measured at the edge. Next, an environmental chamber is placed around the testing area in order to maintain the temperature of the slab at 20°C ± 1°C. This chamber has a window to allow the placement of the DIC camera and lights outside of the chamber.

Once all the instrumentation is in place, the MMLS3 is placed inside the environmental chamber on top of the RCT slab and wheel loads are run over the pavement at a rate of 1,500 applications per hour until the crack is seen to propagate all the way to the surface. These loads produce deflection amplitudes on the order of that seen in the field (0.76 mm).

5 REFLECTIVE CRACKING TEST RESULTS

In addition to the many trial slabs tested during the design and development of the test method, two reflective cracking tests were performed using the final configuration of the RCT. The first test that was performed in the final configuration utilized a chip seal interlayer and was constructed as follows. The first AC layer was constructed as previously described and saw cut. Next, 1.81 L/m^2 of CRS-2 emulsion was placed on the surface, and 8.14 kg/m^2 of #78M aggregate was placed on the surface and rolled, followed by an application of CRS-2 emulsion of 0.36 L/m^2 as a tack coat. This interlayer was allowed to cure completely before the placement of the second AC layer. The vertical edge was cut and speckled, the compaction supports were removed, and the pavement was subjected to MMLS3 wheel loads until failure.

After failure, the RCT was dismantled and cleaned, and a tack coat only pavement was constructed and tested to provide a basis of comparison for the chip seal test. This control test consisted of a 21-mm S9.5B support layer, 0.32 L/m^2 CRS-2 tack coat, and a 38-mm S9.5B overlay.

5.1 *Crack propagation*

As mentioned previously, cracks in AC samples show up as areas of high strain in the DIC analysis. Contour plots of von Mises strains (Eq. (1)) were used to identify areas of cracking. Figure 5a shows that high strains at the interface of the chip seal sample occurred very rapidly. Interface separations were seen within 700 cycles, and full debonding was observed before 10,000 cycles. As the test progressed, the size of the opening at the interface increased. At around 16,060 cycles, a crack began to propagate vertically approximately 60 mm to the left of the joint and an area of damage began to appear 32 mm to the right of the joint. The crack on the left side of the joint continued to grow until around 44,000 cycles; then, a second crack began to propagate vertically around the interface 124 mm to the left of the joint. It was this second crack that eventually reached the surface of the overlay, just outside of the viewing area of the DIC camera. It is believed that this type of cracking was caused by the rebounding of the right slab while the left slab was still under wheel loading (Fig. 4). It should be noted that at the time of this failure, cracks were also present to the right of the joint and directly above the joint. The total life of this system was around 55,000 cycles.

$$\varepsilon_{von\_Mises} = \frac{\sqrt{2}}{3}\left[\left(\varepsilon_1 - \varepsilon_2\right)^2 + \left(\varepsilon_2 - \varepsilon_3\right)^2 + \left(\varepsilon_3 - \varepsilon_1\right)^2\right]^{1/2} \quad (1)$$

where
ε_1, ε_2, ε_3 = principal strains in x, y, z directions respectively.

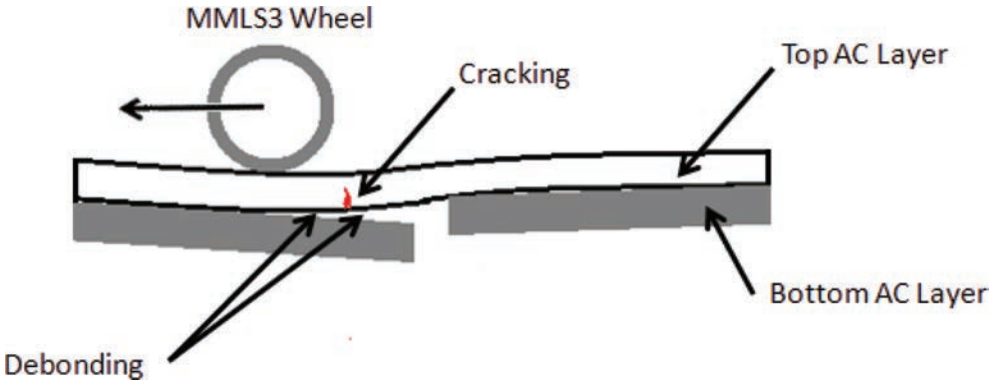

Figure 4. Mechanism of debonding in RCT.

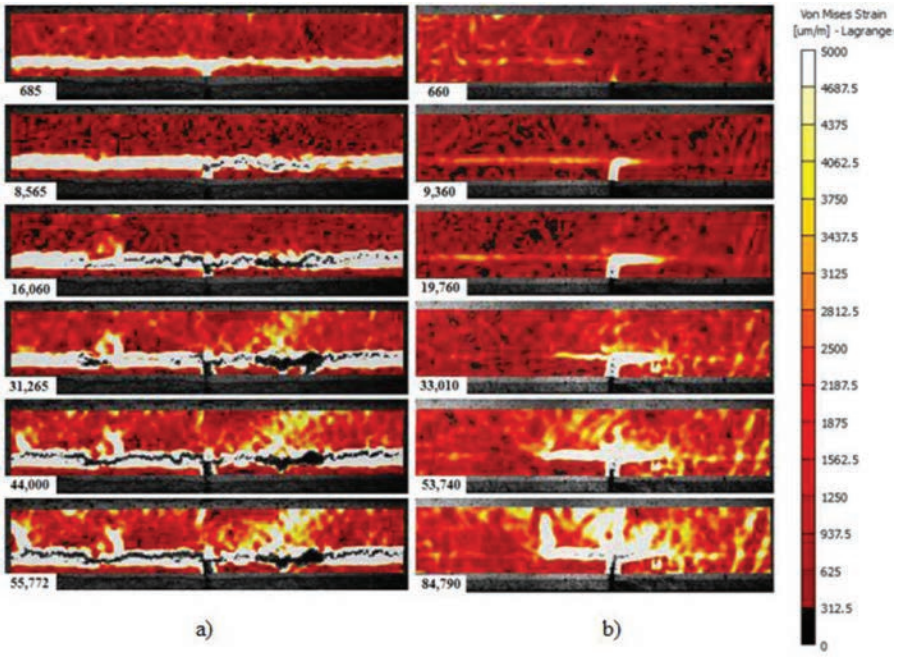

Figure 5. Von mises strain levels for RCT tests: a) Chip seal and b) Tack coat only.

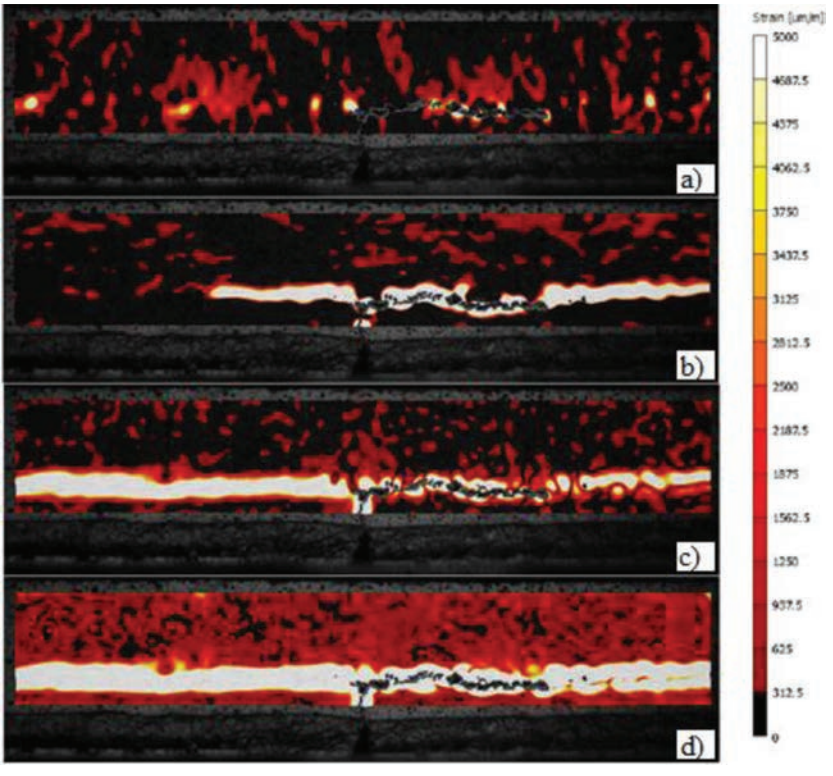

Figure 6. Chip seal strain contour plots: a) Horizontal strain (ε_{xx}), b) Vertical strain (ε_{yy}), c) Absolute value of shear strain ($|\varepsilon_{xy}|$), and d) Von mises strain ($\varepsilon_{Von\text{-}Mises}$).

Figure 5b shows the results from the tack coat only test. These plots indicate that the initial strain along the interface, particularly for the left slab, was significant, but did not result in the large-scale debonding that was evident in the chip seal tests. Next, a crack grew horizontally along the interface on the right slab beginning around 9,000 cycles. After growing for approximately 30.5 mm, the crack stopped at around 33,000 cycles, and a second crack formed on the left slab and propagated about 43.2 mm. At 55,000 cycles both cracks on the right and the left began to propagate upwards, and a third crack began to propagate directly above the joint. Over time, it was this center crack that was the first to reach the surface of the sample. The total number of cycles to failure was approximately 84,000 cycles.

5.2 *Interfacial movements*

Although the von Mises strain contour plots shown in Figure 5 are useful for tracking crack propagation, contour plots of the component strains can give a better understanding of deformations occurring in the system. In order to exemplify this phenomenon, four different plots were made from the same DIC image from the chip seal test showing the four different components of strain at cycle number 11,000 (Fig. 6). These plots indicate that the high von Mises

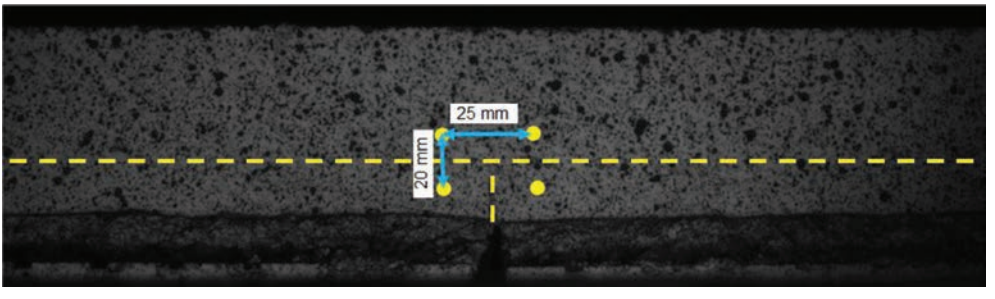

Figure 7. Virtual gauge locations for differential deflections.

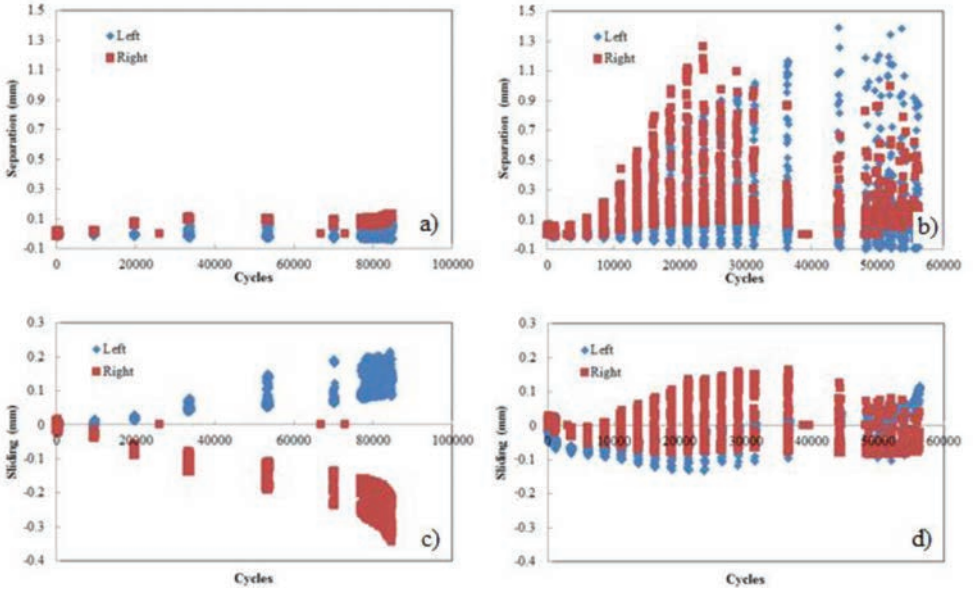

Figure 8. Differential deflection plots: a) Tack coat only separation, b) Chip seal separation, c) Tack coat only sliding, and d) Chip seal sliding.

strain levels seen at the interface are composed of both layer separation and sliding. However, because these strain contour plots can be hard to interpret quantitatively, virtual gauge points were placed on the DIC image, as shown in Figure 7 (the horizontal and vertical dashed lines represent the interface and the joint location, respectively). Because the displacements of each of these points can be tracked independently using the DIC algorithm, the calculation of the differential movements of these points can be used to track both sliding and separation at the interface. Plotting these results can provide a history of these deformations throughout the test. Figure 8 shows that both types of samples experienced sliding movement along the interface between the pavement layers, with the chip seal sample experiencing 2.5 times the sliding amplitude of the control sample (0.23 mm vs. 0.09 mm). Also, both types of samples saw separation at the interface, with the magnitude of the separation in the chip seal sample being over ten times that of the separation seen in the control sample (1.54 mm vs. 0.13 mm).

6 DISCUSSION

The results from the reflective cracking tests indicate that interfacial movement occurred in both types of pavement (with and without chip seal interlayers) and has an effect on the pavement life. The weaker interfacial bonding of the chip seal layer indicates that this pavement experienced more sliding and separation of the layers than the control pavement. This increased movement led to more rapid failure of the overlay. This behavior fits with previous research that suggests that excessive debonding causes high stress concentrations in the pavement and accelerates failure [9, 10]. As such, the common assumption used in the pavement design of complete bonding between pavement layers may lead to inaccurate predictions of the pavement life. Also, these two sets of reflective cracking test results confirm previous research efforts that discuss the possibility of double or even triple cracking in pavements where large relative deflections across the joint in the existing pavement are seen [11, 12, 13, 14, 15, 16, 17]. It is believed that the tendency for both pavement systems to exhibit this type of cracking in the RCT was due to high differential deflections across the joint, and that the reflective cracking test conditions correspond to an extreme case compared to most field uses of chip seal interlayers. These findings help to explain that the chip seal sample performed worse in the RCT than the tack coat only sample, but that chip seal samples have been reported to be generally more effective in the field. Further research is needed using this test method to determine the suitability of the RCT to investigate reflective cracking in pavement systems that utilize different types of interlayer treatments.

7 CONCLUSIONS

- DIC technology is an effective tool for studying layered pavement systems because it allows the calculation of full-field displacements, strains, and the tracking of crack propagation.
- Both types of samples (with a chip seal layer and without a chip seal layer) saw significant separation and sliding of the interface between the pavement layers. This finding suggests that the assumption of complete interfacial bonding commonly used in pavement design may not be realistic.
- Weak interfacial bonds between pavement layers can cause accelerated failure under certain loading conditions.
- Double cracking and triple cracking are possible in cases where differential deflections across the transverse joint are high.

ACKNOWLEDGEMENT

The North Carolina State research team would like to thank the North Carolina Department of Transportation for providing the financial support for this research and providing guidance and technical assistance when needed.

REFERENCES

[1] Barksdale, R.D. *Fabrics in Asphalt Overlays and Pavement Maintenance*. NCHRP Synthesis 171, National Cooperative Highway Research Program, National Research Council, Washington, D.C., 1991.

[2] Elseifi, M. and R. Bandaru. *Cost Effective Prevention of Reflective Cracking of Composite Pavement*. Final Report, Louisiana Department of Transportation, 2011.

[3] Smith, R.D. *Laboratory Testing of Fabric Interlayers for Asphalt Concrete Paving*. Final Report No. FHWA/CA/TL-84/06, 1984.

[4] Abe, N., M. Kamiura, and T. Maruyama. Design and Performance of Overlay Combined with SAMI for Concrete Pavement. Reflective Cracking in Pavement Design and Performance of Overlay Systems. *Proceedings of the 3rd International RILEM Conference*, 1996, pp. 278–287.

[5] Montestruque, G. et al. Stress Relief Asphalt layer and Reinforcing Polyester Grid as Anti-reflective Cracking Composite Interlayer System in Pavement Rehabilitation. *Proceedings of the 7th RILEM International Conference on Cracking in Pavements*, Vol. 2, 2012, pp. 1189–1197.

[6] Solaimanian, M. *Evaluating Resistance of Hot Mix Asphalt to Reflective Cracking Using Geocomposites*. PSU-2008-04, The Mid-Atlantic Universities Transportation Center, 2013.

[7] Chu, T.C., W.F. Ranson, M.A. Sutton, and W.H. Peters. Application of Digital-Image-Correlation Techniques to Experimental Mechanics. *Experimental Mechanics*, Vol. 25, No. 3, 1985, pp. 232–244.

[8] Yates, J.R, M. Zanganeh, and Y.H. Tai. Quantifying Crack Tip Displacement Fields with DIC. *Engineering Fracture Mechanics*, Vol. 75, 2010, pp. 2063–2076.

[9] Zhou, F. and L. Sun. Optimal Thickness of Asphalt Overlay for Composite Pavements. *Proceedings of the 4th International RILEM Conference*, 2000, pp. 69–79.

[10] Dondi, G., A. Bonini, and A. Simone. Reinforced Pavements: Laboratory and Field Experiences. *Proceedings of the 4th International RILEM Conference*, Ottawa, Ontario, Canada, 2000, pp. 441–454.

[11] McCullagh, F.R. *A Five Year Evaluation of Arizona's Three Layer System on the Durango Curve in Phoenix*. Arizona Transportation Research Center, Arizona Department of Transportation, Phoenix, Arizona, 1985.

[12] Judycki, J. and J. Alenowicz. Investigation on Reflective Cracking in Semi-Rigid Pavements in Northern Poland. Reflective Cracking in Pavement Design and Performance of Overlay Systems. *Proceedings of the 3rd International RILEM Conference*, 1996, pp. 512–521.

[13] Scarpas, A., A.H. De Bondt, A.A.A. Molenar and G. Gaarkeuken. Finite Element Modelling of Cracking in Pavements. Reflective Cracking in Pavement Design and Performance of Overlay Systems. *Proceedings of the 3rd International RILEM Conference*, Maastricht, The Netherlands, 1996, pp. 82–91.

[14] Vanelstraete, A. and L. Franken. On Site Behavior of Interface Systems. *Proceedings of the 4th International RILEM Conference*, Ottawa, Ontario, Canada, 2000, pp. 517–526.

[15] Zhou, F. and L. Sun. Mechanistic Analysis of Reflective Cracking and Validation of Field Test. *Proceedings of the 4th International RILEM Conference*, 2000, pp. 81–91.

[16] Zhou, F. and T. Scullion. *Overlay Tester: A Rapid Performance Related Crack Resistance Test*. FHWA/TX-05/0-4467-2, Texas Department of Transportation, 2005.

[17] Zheng, C.C. and A. Najd. Effects of Glass Fiber/Grid Reinforcement on the Crack Growth Rate of an Asphalt Mix. *Proceedings of the 7th RILEM International Conference on Cracking in Pavements*, Vol. 2, 2012, pp. 1145–1155.

This page intentionally left blank

Asphalt Pavements – Kim (Ed)
© 2014 Taylor & Francis Group, London, ISBN 978-1-138-02693-3

Contact characterization of asphalt mixture using image process

Liya Jiao, Na Zuo & Jun Yang
Southeast University, Nanjing, Jiangsu Province, China

ABSTRACT: The internal skeleton structure of asphalt mixtures has great effects on the rutting resistance. However, currently, rutting performance of asphalt mixtures is mainly evaluated through macroscopic tests at high temperature, which is lack of link with the internal structure. Based on image processing technology and X-ray CT detection, the contact properties of asphalt mixtures were studied at microscopic level. Four image analysis indices were developed in this research, namely: number of aggregate contact points, contact length, contact area and contact plane orientation. The results demonstrated a good correlation between the internal contact indices and the mixture rutting performance, which successfully proved the rationality of contact indices.

Keywords: Asphalt mixture, rutting, image processing, contact of aggregate, flow number

1 INTRODUCTION

Asphalt mixture is a kind of typical visco-elastic material. When asphalt pavement is exposed to heat and heavy traffic repetition effect, deformation under wheels will gradually form, which results in rutting in the end. Rutting has a negative impact on the driving comfort and safety. In order to control the severity of rutting and expand the service life of pavement, a full and detailed understanding of rutting and proposal of representative evaluation indices are very necessary. Currently, macroscopic tests are common methods to evaluate the high temperature stability of asphalt mixtures, including Marshall test, triaxial shear test and wheel-track test.

Microstructural study of asphalt mixtures is an important way to characterize macroscopic performance. Digital image processing is a relatively new research tool. The initial studies focused on morphological analysis of coarse aggregate, such as circumference, diameter, flat and elongated particle content, the long axis orientation and so on. With further research, more and more studies focus on the composition features of asphalt mixtures such as porosity and segregation. Yue Z.Q.[1,2] used CCD (Charge-coupled Device) camera to capture the asphalt mixture internal structure and identified particles that were larger than 2.36 mm, which pioneered the use of digital image processing to study the orientation, shape and distribution of coarse aggregates in asphalt mixture quantitatively. With the development of no dilapidation technology, X-ray CT has also been gradually applied to the study of internal structure. Eyad Masad[3] studied the differences in internal structure of specimens compacted with the Superpave Gyratory Compactor and the linear kneading compactor. Specimens compacted with the SGC were found to have aggregates with more preferred orientation and fewer contacts than specimens compacted with the LKC.

Asphalt mixture is a heterogeneous multiphase material that consists of aggregates, asphalt binder, and air voids. These components constitute a complex microstructure. Based on the contact mechanism analysis, Zhu and Nodes[4] demonstrated that the transmission of load in the asphalt mixture is mainly determined by the interaction of aggregates and binder at the contacts of adjacent aggregates. According to Zhu and Nodes[4], changes in mechanical and geometrical parameters in aggregates and binder will affect the overall stress-strain distribu-

tion in an asphalt mixture. The contact based stress-strain equations and models for asphalt mixtures show that the geometrical properties of the contact such as contact area, number of contact zones and contact orientation affect the stress distribution in the mixture as a whole. The features that have been captured and quantified using 2-D imaging processing in most published research have been limited to simplistic analysis of aggregate structure. Features of contacts among coarse aggregates in internal structure captured by X-ray CT are studied in this paper. Additionally, indices including number of contacts, contact area, contact area and contact plane orientation are proposed to relate to and explain rutting resistance of asphalt mixture.

2 LABORATORY TEST

To verify the capability of new indices to regular mixes used in practice, a comparison was done among mixes of the same gradation but different binder additive types, and also mixes of the same binder type but with different gradation. Mixes with significantly different mechanical performances in terms of rutting resistance, as measured by the Flow Number (FN), were chosen for the verification. The following comparisons of image analysis shown in Table 1 were conducted.

2.1 *Binder*

The asphalt binder has significant effect on the behavior of mixture. 50# basic, SBS modified and high-viscosity asphalt binders were selected in this paper. Basic properties of three kinds asphalt binder are shown in following Tables 2 to 4.

2.2 *Aggregate*

Previous researches[5] indicate that the greater density of sample is, the greater value of CT will be and as a result, brightness in the image will be higher. So, samples composed of higher density aggregates should be adopted for X-ray CT scanning. Samples of AC-13 and PA-13

Table 1. Design of asphalt mixtures.

No.	Type of gradation	Type of binder
1#	AC-13	SBS modified asphalt binder, 50# basic binder, high-viscosity asphalt binder
2#	AC-20	SBS modified asphalt binder
3#	PA-13	high-viscosity asphalt binder

Table 2. Properties of 50# basic binder.

Properties	Unit	Requirement	Result test	Test method
Penetration (15°C, 100 g, 5 s)	0.1 mm	–	27	T0604
Penetration (25°C, 100 g, 5 s)	0.1 mm	40~60	53	T0604
Penetration (30°C, 100 g, 5 s)	0.1 mm	–	104	T0604
Ductility (10°C, 5 cm/min)	cm	≥15	32	T0605
Softening point	°C	≥49	66	T0606
Density	g/cm^3	–	1.03	T0661
Mass loss after RTFOT	%	≤±0.8	–0.4	T0610
Residual penetration ratio after RTFOT	%	≥63	73	T0604
Ductility after RTFOT (10°C)	cm	≥4	5.0	T0605

Table 3. Properties of SBS modified asphalt binder.

Properties	Unit	Requirement	Result test	Test method
Penetration (15°C, 100 g, 5 s)	0.1 mm	–	36	T0604
Penetration (25°C, 100 g, 5 s)	0.1 mm	40~60	54	T0604
Penetration (30°C, 100 g, 5 s)	0.1 mm	–	101	T0604
Ductility (5°C, 5 cm/min)	cm	≥20	39	T0605
Softening point	°C	≥45	77	T0606
Density	g/cm^3	–	1.03	T0661
Mass loss after RTFOT	%	≤±1	–0.3	T0610
Residual penetration ratio after RTFOT	%	≥50	92	T0604
Ductility after RTFOT (5°C)	cm	≥10	10.3	T0605

Table 4. Properties of high-viscosity asphalt binder.

Properties	Unit	Requirement	Result test	Test method
Penetration (15°C,100 g, 5 s)	0.1 mm	–	27	T0604
Penetration (25°C,100 g, 5 s)	0.1 mm	40~60	53	T0604
Penetration (30°C, 100 g, 5 s)	0.1 mm	–	103	T0604
Ductility (10°C, 5 cm/min)	cm	≥30	46	T0605
Softening point	°C	≥80	120	T0606
Density	g/cm^3	–	1.04	T0661
Mass loss after RTFOT	%	≤±1	–0.6	T0610
Residual penetration ratio after RTFOT	%	≥50	182	T0604
Ductility after RTFOT (10°C)	cm	≥10	10.6	T0605

Table 5. Properties of aggregates.

Type	No.	Apparent density (g/cm^3)	Bulk density (g/cm^3)
Basalt	1#	2.970	2.888
	2#	2.930	2.849
	3#	2.787	2.722
	4#	2.901	2.829
Limestone	1#	2.708	2.692
	2#	2.689	2.669
	3#	2.715	2.657
	4#	2.686	2.629
Filler	Mineral powder	2.670	–

were made of basalt while those of AC-20 were made of limestone. Properties of basalt and limestone are shown in Table 5.

2.3 *Design of mixture parameters*

Three types of gradation commonly used in practice were chosen for analysis, as shown in the following Table 6.

The asphalt content for AC-13 with SBS, AC-13 with 50#, AC-13 with high-viscosity asphalt, AC-20 with SBS and PA-13 with high-viscosity asphalt is 5.4%, 5.2%, 5.5%, 4.9% and 3.8% respectively, which was decided based on Superpave mixture design method.

Samples were all compacted with a Superpave Gyratory Compactor. Porosity of AC-13, AC-20 and PA-13 respectively reached to 4%~5%, 4%~5% and 18%~19% with 100,83,70

Table 6. Gradation types of mixtures.

Type	Percentage passing through the sieve size (%)										
	19	16	13.2	9.5	4.75	2.36	1.18	0.6	0.3	0.15	0.075
AC-13	–	–	100	98.1	76.7	52.8	36.7	26.7	17.9	12.6	9.9	8.4
AC-20	100	91.8	87.3	74.9	54.5	43.2	27.8	17.5	11.5	8.4	7.4	6.5
PA-13	–	–	100	97.7	70.2	21.2	16.4	12.6	9.1	6.9	5.8	5.1

Table 7. Flow number values of mixtures.

Asphalt mixture		FN
AC-13	SBS modified asphalt binder	619
	High-viscosity asphalt	20000
	50# basic binder	141
PA-13	High-viscosity asphalt	854
AC-20	SBS modified asphalt binder	260

gyrations correspondingly. Cylinder specimen with size of Φ50 mm × 150 mm were obtained through coring and cutting, which can ensure the clarity of image.

After adjusting the position of the specimen and parameters of X-ray CT, scanning will start. In order to reduce the density differences between the upper and lower parts of samples due to rotation compaction, the midpoint of height will become the benchmark for symmetry. Two vertical orthogonal planes with size of Φ50 mm × 54 mm were captured of each sample. The X-ray CT image of an asphalt mixture sample consists of aggregate particles, asphalt mastic, air voids and background.

2.4 *Simple performance test*

Flow Number is chosen to quantify the rutting resistance of asphalt mixture, which has a good relationship with high temperature performance. The greater of flow number is, the stronger the resistance to permanent deformation will be.

Five structures which consist of two parallel specimen with the size of Φ100 mm × 150 mm were compacted with a Superpave Gyratory Compactor. Simple performance test was operated under the condition that temperature was 60°C and the stress level was 700 kPa. The results of test are shown in Table 7.

3 IMAGE PROCESSING AND ANALYSIS

3.1 *Contact parameters*

Aggregates provide the skeleton of the asphalt mixture and carry most of the load. The number of aggregate contacts in the asphalt mixture represents the connectivity of the internal aggregate structure. Increasing the number of contact points leads to a better stress distribution with less stress concentrations. The effectiveness of contact between adjacent aggregates is dependent on the contact area (contact length in 2-D images) and contact plane orientation (measured from horizontal axis). The increase in contact length raises the friction and interlocking between aggregates. Additionally, the closer the normal to contact plane orientation is to the loading direction, the more effective it is in resisting deformation under loading. The following list represents the internal contact indices that are believed to dictate the rutting resistance of the mixture:

- Number of aggregate contacts
- Contact length

- Contact area
- Contact plane orientation

In this study, contact is defined when two aggregates's perimeter pixels are within a distance. Former studies[6] have shown that if two adjacent particles contact completely, the edges of two particles should be less than 2 pixels apart.

3.2 *Image processing*

Laith Tashman[7] proposed an feasible method in his paper which can capture contacts between aggregates using image processing. Figure 1 shows an automated algorithm developed to measure the aggregate contact length, contact area, contact orientation as well as the number of contacts. The image is first thresholded to convert it to a binary image. The second step is applying the Watershed Filter, which erodes the aggregates until they disappear then dilates them again, up to the point prior to coming in contact as shown in Figure 1b. This image is combined with the binary image(a) using MINUS operator. This operation requires that pixels at the same location in both images have the opposite color in order to be retained in the resultant image(c). The resultant image consists of segments of lines representing the regions of aggregate contacts as shown in Figure 1c.

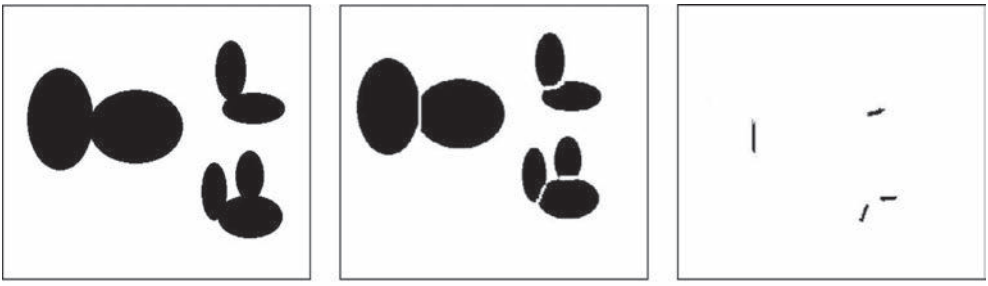

Figure 1. Imaging algorithm to capture aggregate contacts.

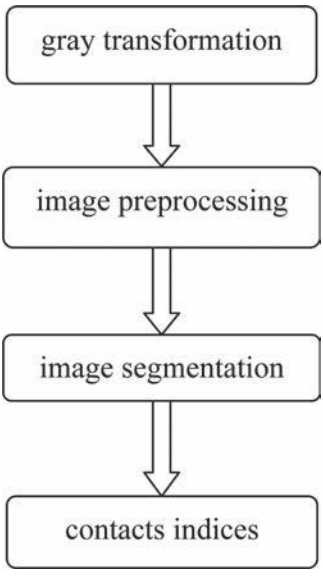

Figure 2. Image processing.

The image processing consists of the following modules.

To reduce the effect of geometric distortion and noise, image preprocessing includes smoothing filter and enhancement process. Segmentation of image is to highlight the shape of aggregates, while asphalt and background are ignored. The ideal segmentation will completely separate aggregates from the asphalt mastic with closed edges, no internal isolated pixels and clear boundary between the particles. However, current segmentation methods cannot meet these requirements, so it is necessary to make a comparison of different processing algorithms to select one which both has fast process speed and ideal segmentation results. Bernsen algorithm which can dynamically changes threshold according to the position of pixel is discovered to satisfy the requirements above.

As smaller aggregates have poor precision in image analysis and permanent deformation is mainly resisted by coarse aggregates, particles smaller than 2.36 mm will be filtered in the image processing (Fig. 3c). Figure 4 shows how to get contact parts among aggregates of PA-13.

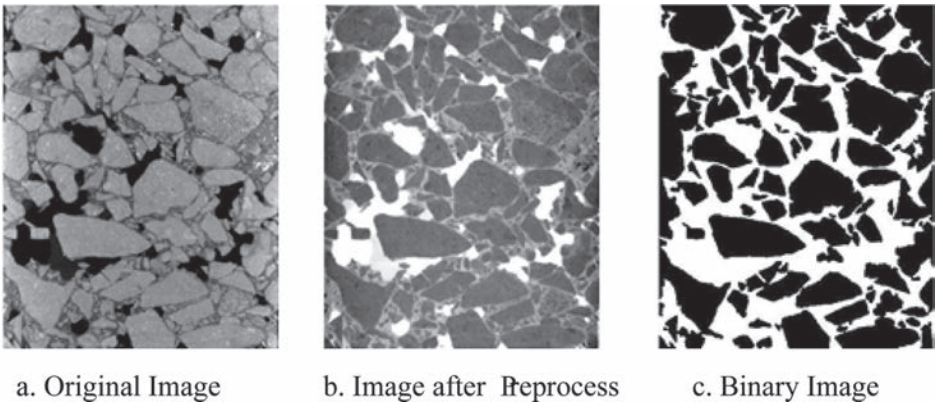

Figure 3. Image processing of PA-13.

Figure 4. Contact parts of PA-13.

Table 8. Analysis results of samples.

Mixture		Number of contact	Contact area/pixel^2	Contact plane orientation/degree	Contact length/pixel
AC-13	High-viscosity asphalt	59	1989	49.3	917
	50# basic asphalt binder	22	745	47.9	301
	SBS modified asphalt binder	26	944	49	371
PA-13	High-viscosity asphalt binder	26	789	43.7	321
AC-20	SBS modified asphalt binder	22	787.5	38.6	282

3.3 *Analysis of contact parameters*

Contact parameters were measured after images had been processed. The number of contact, summary of contact area/length and the average of contact orientation of each sample were calculated as shown in Table 8.

The FN values are plotted in Figure 5 versus contact parameters calculated for AC-13 mixtures with different kinds of binder. As shown in Figure 5, a strong correlation between contact parameters and flow number exists, which supports the aforementioned hypothesis.

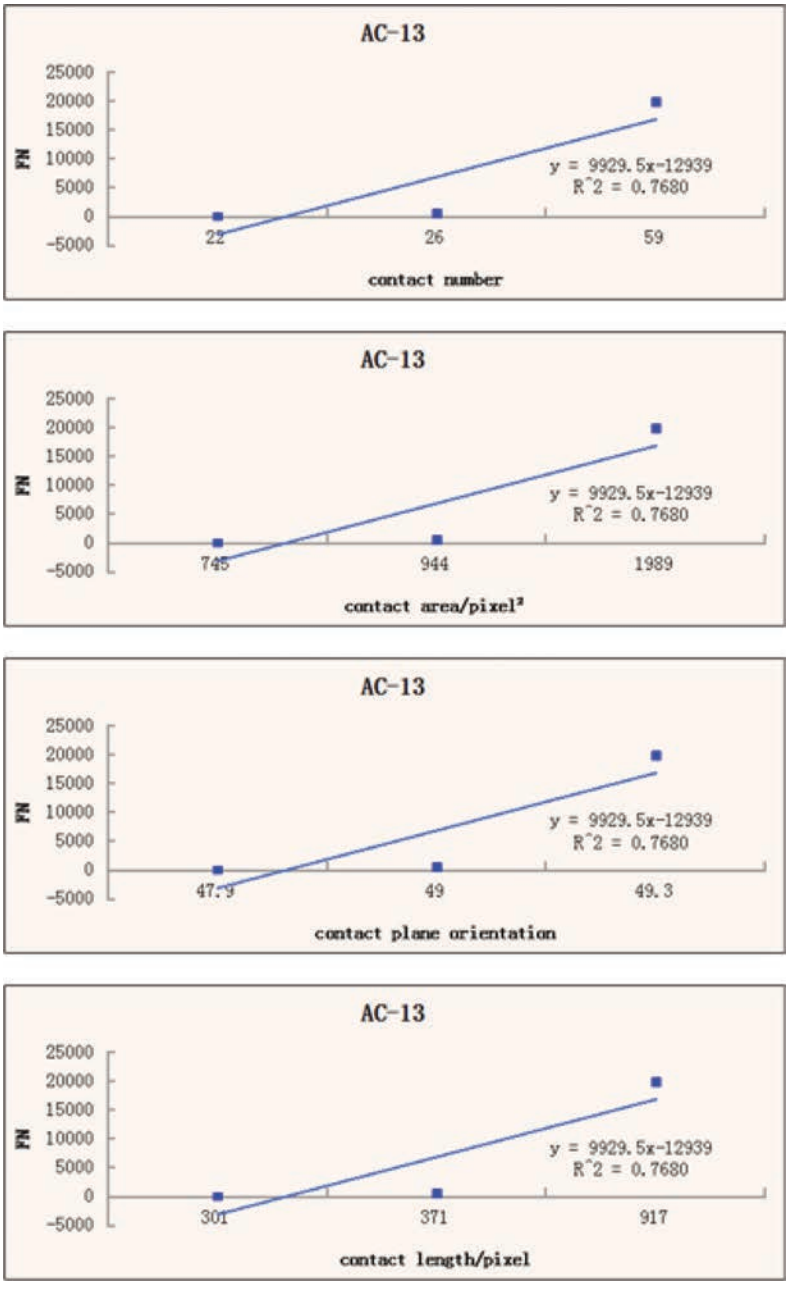

Figure 5. Correlation of different indices with flow number of AC-13.

In addition, as shown in Tables 7 and 8, there is a strong exponential trend between contact indices and flow number of mixtures with the same binder and different gradation.

4 CONCLUSION

In this research, new indices derived from imaging processing are proposed to characterize the internal structure of asphalt mixtures. According to these aggregate contact indices, mixtures with different internal structures could be ranked similar to their mechanical responses to repeated loading as quantified by the Flow Number.

Compared to traditional test, images captured by X-ray CT can effectively can be used to study microscopic internal structure of asphalt mixtures. Besides, after the scanning, samples can also be used for other mechanical test, which improves the utilization efficiency of the material.

The new contact indices, namely: number of contact, contact area, contact length and contact orientation, were measured and compared for a set of mixtures with different rutting performance. The results show that there is a strong correlation between the contact indices and the rutting performance of mixtures.

ACKNOWLEDGEMENT

This research was sponsored by the National Science Foundation of China (51078089). This support is gratefully acknowledged. The results and opinions presented are those of the authors and do not reflect those of the sponsoring agencies.

REFERENCES

[1] Yue Z., Bekking W., Morin I. Application of digital image processing to quantitative study of[J]. Transportation Research Record, 1995, 1492: 53–60.
[2] Yue Z.Q., Morin I. Digital image processing for aggregate orientation in asphalt mixtures mixtures[J]. Canadian Journal of Civil Engineering, 1996, 23(2): 480–489.
[3] Masad E., Muhunthan B., Shashidhar N., et al. Quantifying laboratory compaction effects on the internal structure of asphalt mixtures[J]. Transportation Research Record: Journal of the Transportation Research Board, 1999, 1681(1): 179–185.
[4] Zhu H., Nodes J.E. Contact based analysis of asphalt pavement with the effect of aggregate angularity[J]. Mechanics of Materials. 2000, 32(3), 193–202.
[5] Wang Hainian, Hao Peiwen. Advances in microstructure study on asphalt mixture[J]. 2005.
[6] Duan Yuehua, Zhang Xiaoning. Meso-scale Research on Contact Characteristics of Coarse Aggregates Using CT Image[J]. Journal of Building Materials, 2011, 14(6): 808–813.
[7] Tashman L., Wang L., Thyagarajan S. Microstructure characterization for modeling HMA behaviour using imaging technology[J]. Road materials and pavement design, 2007, 8(2): 207–238.
[8] Masad E., Muhunthan B., Shashidhar N., et al. Internal structure characterization of asphalt mixtures using image analysis[J]. Journal of computing in civil engineering, 1999, 13(2): 88–95.
[9] Tashman L., Masad E., Peterson B., et al. Internal structure analysis of asphalt mixes to improve the simulation of superpave gyratory compaction to field conditions (with discussion)[J]. Journal of the Association of Asphalt Paving Technologists, 2001, 70.
[10] Wang L.B., Frost J.D., Lai J.S. Three-dimensional digital representation of granular material microstructure from X-ray tomography imaging[J]. Journal of Computing in Civil Engineering, 2003, 18(1): 28–35.
[11] Mora C.F., Kwan A.K.H., Chan H.C. Particle size distribution analysis of coarse aggregate using digital image processing[J]. Cement and Mixtures Research, 1998, 28(6): 921–932.
[12] Kwan A.K.H., Mora C.F., Chan H.C. Particle shape analysis of coarse aggregate using digital image processing[J]. Cement and Mixtures Research, 1999, 29(9): 1403–1410.
[13] Wang L.B., Frost J.D., Shashidhar N. Microstructure study of WesTrack mixes from X-ray tomography images[J]. Transportation Research Record: Journal of the Transportation Research Board, 2001, 1767(1): 85–94.

[14] Wang L.B., Frost J.D., Lai J.S. Three-dimensional digital representation of granular material microstructure from X-ray tomography imaging[J]. Journal of Computing in Civil Engineering, 2003, 18(1): 28–35.
[15] Masad E., Button J. Implications of experimental measurements and analyses of the internal structure of hot-mix asphalt[J]. Transportation Research Record: Journal of the Transportation Research Board, 2004, 1891(1): 212–220.
[16] Shu X., Huang B., Chen X., et al. Effect of coarse aggregate angularity on rutting performance of HMA[J]. Geotechnical Special Publication, 2006, 154: 126.
[17] Tashman L., Wang L., Thyagarajan S. Microstructure characterization for modeling HMA behaviour using imaging technology[J]. Road materials and pavement design, 2007, 8(2): 207–238.
[18] Sefidmazgi N.R., Tashman L., Bahia H. Internal structure characterization of asphalt mixtures for rutting performance using imaging analysis[J]. Road Materials and Pavement Design, 2012, 13(sup1): 21–37.
[19] Masad E., Muhunthan B., Shashidhar N., et al. Internal structure characterization of asphalt mixtures using image analysis[J]. Journal of computing in civil engineering, 1999, 13(2): 88–95.
[20] Masad E., Jandhyala V.K., Dasgupta N., et al. Characterization of air void distribution in asphalt mixes using X-ray computed tomography[J]. Journal of Materials in Civil Engineering, 2002, 14(2): 122–129.
[21] Torres A.C. Probabilistic analysis of air void structure and its relationship to permeability and moisture damage of hot mix asphalt[D]. Texas A&M University, 2004.

This page intentionally left blank

Additives and modifiers for asphalt concrete—VI

This page intentionally left blank

Asphalt Pavements – Kim (Ed)
© 2014 Taylor & Francis Group, London, ISBN 978-1-138-02693-3

Reduction of low temperature asphalt binder stiffness using a Renewable Additive

Gerald Reinke & Stacy Glidden
MTE, Onalaska, WI, USA

Susan Listberger & Suzanne Stauduhar
Cargill, Plymouth, MN, USA

ABSTRACT: As crude sources for asphalts have changed it has become more difficult to obtain quality asphalt with adequate low temperature properties to satisfy consumer demand. Many different products have been tested to determine if they can be added to asphalt and provide a lower temperature PG without having a significant negative affect on the high temperature properties of the asphalt. The other concern when using additives to reduce the stiffness of asphalt is that it will have a detrimental effect on the mix properties. Cargill and MTE have investigated a Renewable Additive (RA) that appears to be able to maintain the original mix properties, while also reducing the low temperature stiffness of the asphalt binder. Neat asphalt as well as Polymer Modified Asphalt (PMA) were tested in lab and field trials. The results have shown that the RA can be used to reduce the PG low temperature by 6°C or more and still maintain binder and mixture properties comparable to those obtained from conventional binders of the same PG grade. Furthermore lab and field trials have shown that the RA can be used in the field while still maintaining the quality of the finished product.

Keywords: proprietary renewable additive, reduced low temperature stiffness, modified asphalt, recycled asphalt pavement, recycled asphalt shingles

1 INTRODUCTION

Asphalt binders with low temperature stiffness have always been in high demand. This trend continues as more RAP and RAS are being used in asphalt mix designs. Many RAP designs require a low temperature PG one grade lower than would typically be used to balance out the RAP asphalt that has low temperature stiffness properties higher than the virgin asphalt that would be used. RAS drives the low temperature stiffness of the asphalt binder in the mix even higher. Lee et al. recommended using binder with reduced low temperature and found it to be more effective than lowering design air voids [1]. Mogawer evaluated using rejuvenators to mitigate potential problems with mixes containing RAP and RAS [2]. There is continued demand for higher and higher contents of RAP in asphalt mixes which compounds the problem even further.

In an effort to provide a better asphalt product while still maintaining the high standards that have been set by the asphalt industry. Cargill and MTE entered a partnership to determine if a RA could be used to lower asphalt stiffness while maintaining all the original properties of the asphalt binder. Virgin asphalt was blended with the RA to produce a material that was a PG below the original virgin asphalt (Ex. 64-22 blended to a 58-28). This blend was then compared to virgin asphalt with the same PG as the blend with RA. The RA was also blended with PMA to produce a blend one PG lower and compared to a similar PMA without RA. SHRP PG was done on all the asphalts and the asphalts with the RA performed as well as the asphalts without. Further testing was done in the lab to compare the asphalt

in mix designs using rut testing, AMPT and torsion bars. The blended asphalt performed as well on all of these tests as the asphalt without the RA. Finally two field trials were completed using the RA in polymer modified asphalt with a control section in 2011 and 2013. To date the test and control sections have performed similarly.

The RA has the ability to provide asphalt binders with lower temperature stiffness without compromising asphalt binder or mix properties. It is a useful alternative that can be used immediately to alleviate the continued and growing demand for asphalt binder with lower temperature stiffness that cannot be obtained through many refineries at this time. It blends in easily and can be incorporated into almost any type of asphalt terminal or hot mix plant without a significant capital expense.

2 MATERIALS AND METHODS

2.1 *Asphalt blending and SHRP testing*

The asphalt binders chosen for evaluation were a PG 58-28, 64-22, 64-34P and 70-28P. All materials were characterized using standard SHRP PG. Blending with the RA was done on a hotplate at 165°C for about an hour. The RA is a liquid and easily homogenizes into the asphalt. Blends were left in an oven overnight at 165°C before SHRP testing was commenced. Binders used for mix design testing and field trials were also characterized using standard SHRP PG.

2.2 *Mix designs and testing*

The lab trial mix designs used an E-3, 12.5 mm mix, limestone aggregate and 20% RAP. Pills were compacted to complete rut testing per AASHTO T324-11 and torsion bar testing per ASTM D7552-09. A set of the torsion bar pills was aged in an oven at 85°C for five days prior to cutting torsion bars.

2.3 *Field trials and testing*

The asphalt for both field trials was blended in a tank at an asphalt terminal using a 70-28P with 4% RA to make a 64-34P. The tank used for blending is equipped with a central mixer. All SHRP PG testing was completed to confirm that the AC met the required specifications prior to it being shipped to the plant site. The control asphalt was a 64-34P made with 52-34 base asphalt. The 2011 field trial mix design was an E-3, 19 mm mix; containing trap rock and 20% RAP with 6.2% AC. The percentage of virgin AC added to the mix was 3.8% with a total of 5.2% AC. The 2013 field trial mix design was an E-10, 12.5 mm mix; gravel aggregate and 11% RAP with 5.2% AC. The percentage of virgin AC added to the mix was 5.2% with a total of 5.5% AC.

Field mix was obtained from truck samples for the control and the asphalt binder with RA. Lab compacted specimens were prepared for the 2011 field trial. Half of the pills with each AC type were aged in an oven at 85°C for five days prior to testing. Pills were compacted for torsion bar testing per ASTM D7552-09 and AMPT per AASHTO T342-11. All four pill types also had and extraction and recovery per ASTM D2172. The AC was characterized using standard SHRP PG, WRI 4 mm low temperature testing [3–4] and asphaltene analysis per ASTM D3279-12.

3 RESULTS

3.1 *SHRP testing of asphalt binder*

PG 58-28 binder was modified with 5% RA to make a 52-34 which was compared to a typical 52-34. The RA modified binder had similar high and low temperature properties as the

52-34 without the RA added. A 64-22 was modified with 5% RA to produce a 58-28 which also had similar properties to a 58-28 without RA. For the 2011 field trial a sample of 70-28P was taken from a terminal and modified with 4% RA. The same blend was also done at a terminal. The temperature spread as can be seen in Table 1 for the control 64-34P was 100.9°C, control 70-28P was 102.8°C and for the 64-34P with RA was 101.6°C.

Asphalt cement was recovered from lab compacted pills for the 2011 field trial. One set of the pills had been aged for five days in a forced convection oven at 85°C. Grading was determined based on a DSR of 2.2 which is comparable to RTFO PG material. Low temperature grading was done using the 4 mm DSR procedure developed by WRI [3–4]. The RAP that was used in the field trial was also recovered and tested. All the recovered binder data can be found in Table 2.

3.2 *Mix testing on lab samples*

A set of pills was compacted using the control and the RA containing asphalt from the lab mix. Pills from each aging condition were cut into torsion bars and tested. This data was used to generate the complex modulus curves in Figure 1 [5].

Rut pills were also compacted using the field mix. A set of unaged pills from the control and the RA set were tested and the data plotted in Figure 2.

3.3 *Field trials*

A set of the pills that were made from the mix for the 2011 field trial were used for torsion bar testing. This data was used to generate the complex modulus curves in Figure 3 [5].

Table 1. SHRP data for virgin binders.

SHRP PG	% RA	ODSR	RDSR	PDSR	BBR slope	BBR stiffness	RTFO mass Δ	HT precise	LT precise
58-28	0	1.41	3.98	3630	0.328	245	0.562	60.7	–29.7
52-34	5	1.31	3.25	3838	0.327	209	0.428	54.2	
52-34	0	1.33	3.21	3300	0.324	266	0.758	54.3	–34.6
64-22	0	1.53	3.21	3316	0.322	215	0.214	66.8	–24.4
58-28	5	1.17	2.76	2384	0.365	119	0.157	59.1	
64-34P	4	1.30	3.10	1572	0.344	236	0.881	67.0	–35.9
70-28P[a]	0	1.31	3.25	1389	0.355	201	0.642	73.1	–29.7
64-34P[a]	4	1.15	2.96	1460	0.343	226	0.691	65.6	–36.0
64-34P[a]	0	1.17	2.86	2333	0.334	283	0.772	65.7	–35.2
70-28P[b]	0	1.46	2.97	1390	0.340	214	0.622	73.7	
64-34P[b]	4	1.20	4.98	1586	0.324	249	0.991	66.0	
64-34P[b]	0	1.13	2.73	1530	0.331	269	0.682	65.4	

[a]AC from 2011 field trial.
[b]AC from 2013 field trial.

Table 2. SHRP data for recovered asphalt binders from 2011 field trial.

Days aged	AC grade	% RA	RDSR	Grade based on DSR 2.2	4 mm slope	4 mm stiffness	Asphaltenes
0	64-34P	4	8.86	78.1	–33.9	–34.5	25.8
5	64-34P	4	18.6	85.4	–31.1	–34.5	27.5
0	64-34P	0	7.93	70.8	–37.1	–35.1	23.1
5	64-34P	0	11.2	73.7	–36.1	–37.1	23.4
	RAP	0	4.07	68.8	–27.0	–31.5	20.2

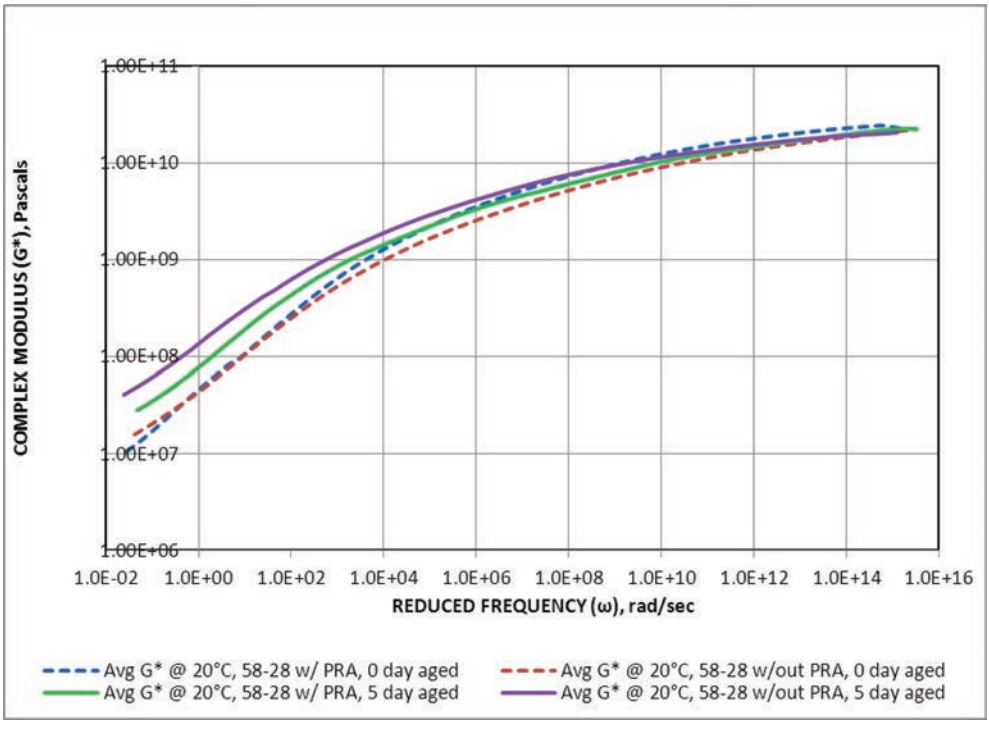

Figure 1. Mastercurve from torsion bars made from lab mix.

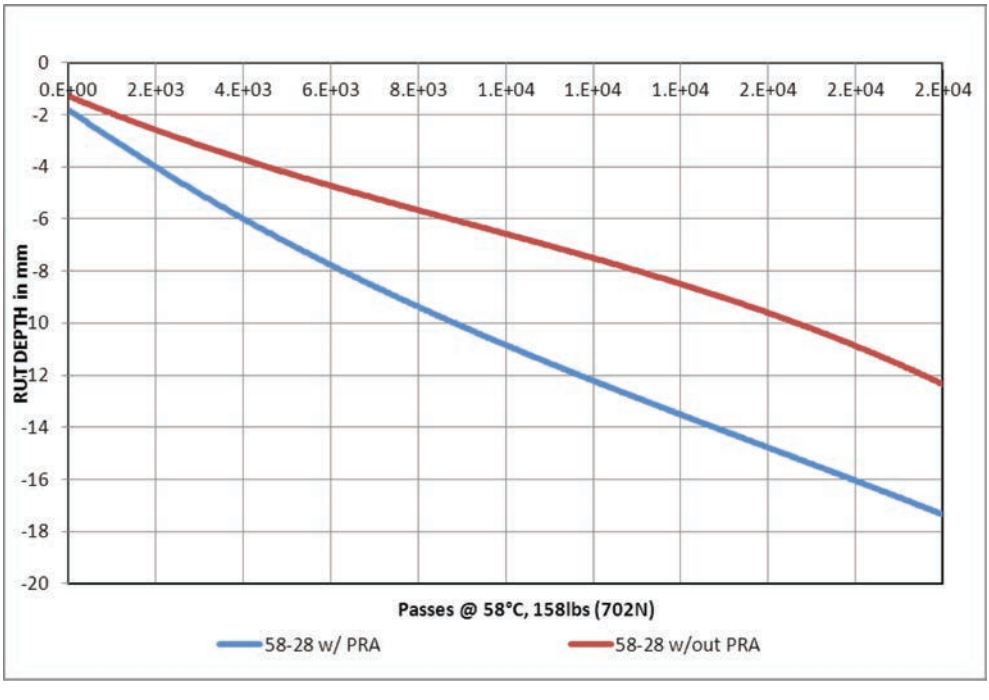

Figure 2. Rut data from lab produced mix.

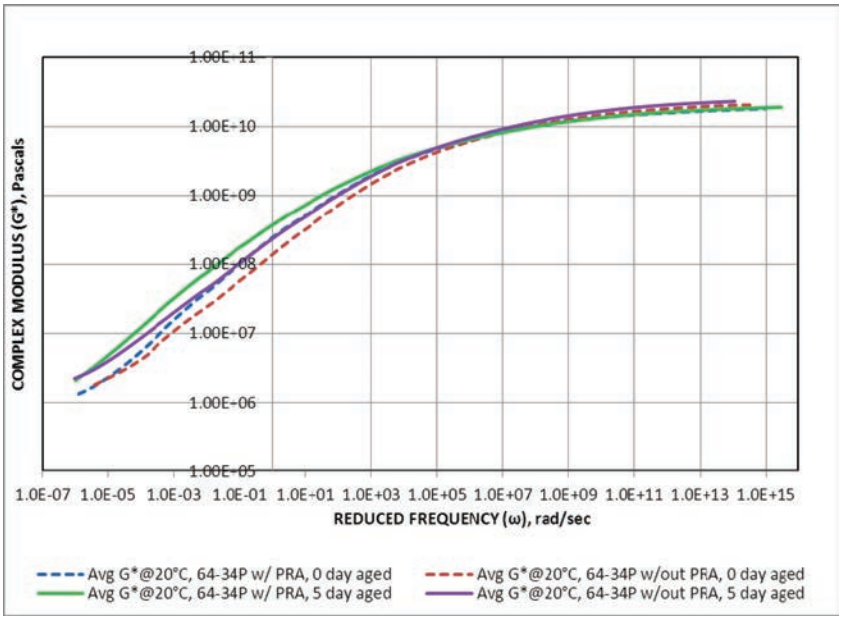

Figure 3. Complex modulus for 2011 field trial from torsion bars.

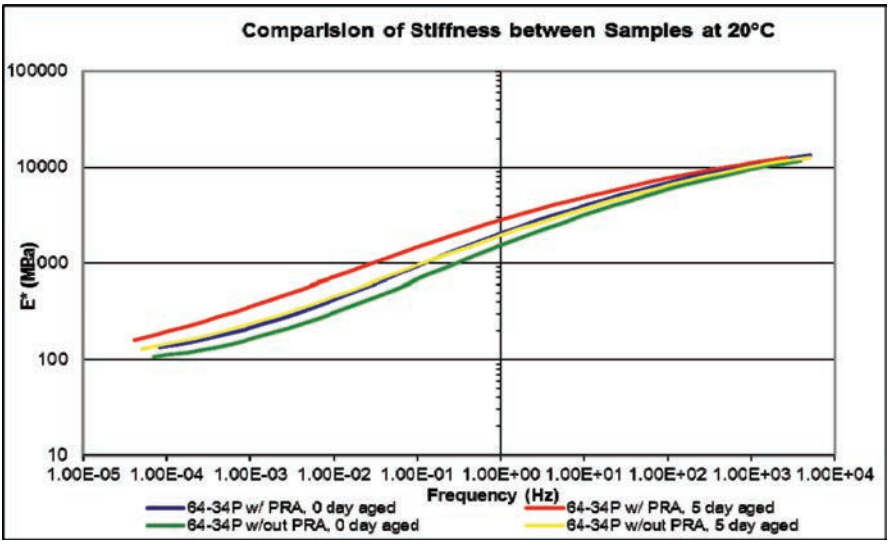

Figure 4. Complex modulus for 2011 field trial from AMPT.

A set of AMPT pills were made from the mix used on the 2011 field trial. Testing was conducted on those and used to generate the complex modulus curves in Figure 4 [5].

4 DISCUSSION

Lab testing of asphalt binder with and without the RA showed the binder to have similar qualities for materials with comparable SHRP PG. Through all of the aging processes

the RA binder performed as well as the material without the RA. Further study using lab prepared mixes and unmodified base binders with and without RA showed similar results. In Figure 1 the complex modulus showed that the RA modified binder reduced the aging of the mix and led to lower long-term stiffness. The rut data in Figure 2 shows the RA modified binder rutting more quickly than the material without the RA. Comparing this to the data in Table 1 shows that the RA binder was less stiff initially and thus it would rut more quickly. This can be alleviated if necessary by using less RA in the binder as was done for the field trials.

The terminal blending of the polymer modified asphalt with the RA and paving of the field trial showed that the material with the RA performed similar to the control asphalt binder mix during all stages of mixing and compaction. The mix that was brought to the lab and compacted and aged showed some variation from the information that was obtained with the lab prepared mix. The recovered binder with the RA showed characteristics of stiffening more than the binder without the RA at both high and low temperatures as can be seen in Table 2. The torsion bar data in Figure 3 and the AMPT data in Figure 4 test show that the material with the RA had a slightly higher stiffness at high temperature in the unaged mix pills which also resulted in a higher stiffness in the aged pills. At low temperature the materials appears to be very similar. The higher stiffness of the asphalt with the RA in the recovered asphalt correlates with the amount of asphaltenes that were found in the recovered binders. It is possible that variation in the RAP asphalt properties is responsible for this difference. This will be monitored in the field to determine if that correlation pertains to actual field aged samples. Further testing of field cores from the field trials will be conducted at two years and five years. The test sections will be monitored and compared to the control sections for a minimum of five years to determine if there are any long-term differences between the two sections.

The RA is an effective alternative to provide asphalt binder with reduced low temperature stiffness to meet the growing demand. It is a readily available material that is economically competitive in current markets. It provides a way to modify asphalts while meeting the current SHRP PG specifications. It also allows for asphalt to be modified that would be able to meet MP19 specifications if the need arose. This additive may be an effective way to lower virgin asphalt cement stiffness and allow for higher RAP contents to be used in mix designs. The RA is very compatible with all current regulatory and field processes and provides a much needed alternative to reducing low temperature stiffness of asphalt cement as demand continues to rise.

REFERENCES

[1] Lee, R., et al. (2013). Evaluation of Use of Recycled Asphalt Shingles in HMA. AAPT 2013.

[2] Mogawer, W.S. (2013). Evaluating the Effect of Rejuvenators on the Degree of Blending and Performance of High RAP, RAS, RAP/RAS Mixtures. AAPT 2013.

[3] Sui, C.F. (2011). New Low Temperature Performance Grading Method Using 4 mm Parallel Plates on a Dynamic Shear Rheometer. *TRB 2011*.

[4] Sui, C.M. (2010). A New Technique for Measuring low-temperature Properties of Asphalt Binders with Small Amounts of Material. *Transportation Research Record: No. 1681, TRB 2010*.

[5] Abatech. (n.d.). RHEA™ Software. PO Pox 356, Blooming Glen, PA 18911, (215) 258 3640.

Asphalt Pavements – Kim (Ed)
© 2014 Taylor & Francis Group, London, ISBN 978-1-138-02693-3

Developing test methods for the determination of the performance and safety of bio-sourced Asphalt Release Agents (ARAs)

Peter Mikhailenko
Laboratoire Matériaux et Durabilité des Constructions (LMDC), Université Paul Sabatier, Toulouse, France

Erick Ringot
Laboratoire Matériaux et Durabilité des Constructions (LMDC), Université Paul Sabatier, Toulouse, France
LR Vision, Castanet-Tolosan, France

Alexandra Bertron & Gilles Escadeillas
Laboratoire Matériaux et Durabilité des Constructions (LMDC), Université Paul Sabatier, Toulouse, France

ABSTRACT: The objective of this study is to develop the testing methods of Asphalt Release Agent (ARA) performance and the degree to which they may damage the asphalt. The testing of ARA performance observed their ability to reduce the adhesion between the asphalt and the surface of steel (asphalt tools, truck beds…) by the asphalt slide test. The testing of the safety of the ARAs consisted of the measurement of the degree to which the compacted asphalt is damaged by the ARA including CBR resistance, indirect-tensile strength and bitumen degradation testing. It was found that the indirect tensile strength test provided more consistent results than CBR resistance. Also included is the study of bio-sourced chemicals and their ability to function as ARAs.

Keywords: asphalt release agents, asphalt testing, ARA, bio-sourced

1 INTRODUCTION

The most important component of an asphalt mixture is bitumen, which through adhesion keeps the aggregates together and the asphalt cohesive. These same adhesion properties can make it very difficult to clean surface of equipment that has been used to work or transport bitumen. For the truck beds used for transporting asphalt for example, the adhesion prevents the asphalt from smoothly sliding out of the bed as the truck attempts to discharge its load. In such cases, workers must manually coax the residual asphalt out of the truck bed, exposing workers to hazardous chemicals [1].

Asphalt Release Agents (ARAs) are used for spraying surfaces that come into contact with asphalt during the asphalt construction process, such as truck beds, pavers, finishers, tools and various other (usually metal) items. The bitumen non-adherence is based on the interaction of the agent, the bitumen and the metal surface. There are three main types of asphalt release agents: petroleum based, fatty-oil based and non-oil based [2,3]. As opposed to bitumen removers, asphalt release agents are not intended to break down the bitumen, but to protect the equipment used to produce and place asphalt from bitumen residue. Therefore, it is important that asphalt release agents do not cause damage to the asphalt when coming into contact with it.

Petroleum-based ARAs function by softening the bitumen on the surface, that is, reducing its viscosity and thereby the adherence. Petroleum products such as diesel fuel however, are

skin irritants and emit volatile compounds harmful to human health [3,4]. For this reason, the U.S. Department of Transportation as well as many state departments have restricted the use of diesel fuel as an asphalt release agent [1]. Petroleum ARAs that will come into contact with the new asphalt on the asphalt truck bed or an accidental spill will cause damage to the bitumen leading to soft spots which are exacerbated by factors such as heat and light. The deterioration effect is also increased with increasing time of contact with the bitumen [2,5,6].

Alternative ARAs include bio-sourced fatty-oil based agents. They consist of purified or partially purified fats and oils including synthetic or naturally occurring glycerides or triglycerides of fatty acids that are sometime etherified or emulsified in water. They work as a surfactant to reduce the interfacial tension between bitumen and the contact surface as well as the friction, forming a separating layer [2,6]. There has also been damage to asphalt observed from the use of bio-sourced ARAs. The agents may have less power to damage the bitumen than petroleum-based ARAs, but will stay in contact with the asphalt for a longer time due to their higher evaporation temperatures [1,7].

Escadeillas et al. [8] mixed gasoil and a vegetable-based ARA with bitumen and observed the changes in penetration (ASTM D5-EN 1426) and softening point (ASTM D36-EN 1427). It was found that the penetration increases significantly with gasoil and ARA addition while the softening point decreases. These were strong indications of the gasoil and the vegetable-based agents deteriorating the bitumen.

The American Association of State Highway and Transportation Officials (AASHTO) National Transportation Product Evaluation Program (NTPEP) for asphalt release agents [9] has two tests for evaluating ARA performance and one for safety. However, their results are pass/fail and subjective the in their implementation.

Asphalt release agents are widely used to protect tools and truck beds from the residue of asphalt; however, the study of their performance or of the damage that they can cause to asphalt has been minimal. The purpose of this paper is to present the testing methods of Asphalt Release Agent (ARA) performance and the degree to which they may damage the asphalt. The objectives of the test development are to provide testing that (i) reflects as much as possible the on-site conditions, (ii) can differentiate between various ARAs, (iii) can provide new insight into the interaction of ARAs and asphalt and (iv) that are relatively simple and cost effective to implement. The testing of ARA performance was done by the asphalt slide test. The testing of the safety of the ARAs consisted of CBR resistance, indirect-tensile strength and bitumen degradation testing. The products tested included gasoil, 3 bio-sourced ARAs and 2 bio-sourced BRs used for reference.

2 MATERIALS AND METHODS

2.1 *Materials*

2.1.1 *Bitumen*

The bitumen used for testing was Total 35/50 as classified by EN 12591, indicating a penetration (ASTM D5-EN 1426) value of between 35 and 50 mm. The bitumen had to be heated before being used and it was taken care not to heat the bitumen more than once due to the volatiles that are lost by the bitumen during the heating process.

2.1.2 *Asphalt*

The asphalt mixes were manufactured in accordance with EN 12697-35+A1 with Total 35/50 bitumen and limestone/silica aggregates. The aggregates, as shown in Table 1, consisted of coarse aggregates, fine aggregates and limestone filler that were graded in accordance with EN 13108-2. The asphalt was separated into 1 kg samples and stored in aluminium containers. As with the bitumen, it was taken care to only reheat the asphalt once before the compaction of the samples.

Table 1. Typical composition of asphalt mixture.

Material	(% by mass)
Sand 0/2 mm	23.69
Aggregates 2/6.3 mm	23.31
Aggregates 6.3/10 mm	44.97
Limestone filler (<80 µm)	2.55
Bitumen total 35/50	5.60
Total mass	100

Table 2. Technical information for commercially available ARAs and BRs.

Product	Origin	Density @ 20°C (kg/L)	Evaporation point (°C)	Kinematic viscosity @ 40°C (mm^2/s)
Gasoil	Petroleum	0.82–0.86	60	9.5 (@20°C)
ARA 1	100%	0.88	250	11
ARA 2	Vegetal-	0.89 (@25°C)	250	14
ARA 3	based	0.86–0,90	350	12.5
BR 1		0.88	170	10–11
BR 2		0.86 (@25°C)	250	5.7

2.1.3 *Commercial asphalt release agents*

The asphalt release agents tested consisted of 3 bio-based ARAs available on the French market. Additionally, gasoil, a petroleum product historically used as an ARA and bitumen remover in the past was also used. Although this product is currently not permitted for use as an ARA on construction sites, it was nevertheless tested as a reference. Additionally, 2 vegetal-based Bitumen Removers (BRs) were used as products that are known to cause damage to asphalt in order to test ARA safety. Technical information for these products is shown in Table 2.

2.2 *ARA performance*

The objective of ARA performance testing is to measure the ability of the ARA to reduce the adherence of bitumen to tools and machinery for asphalt construction (generally metal surfaces). The challenge in this testing is to develop a qualitative analysis that best represents the conditions in the field and is as cost and time effective as possible to implement.

2.2.1 *ARA performance evaluation apparatus*

The ARA Performance Evaluation Apparatus (ARA-PEA) is a device developed by LR Vision of Castanet-Tolosan and LMDC of Toulouse for evaluating the performance of ARAs in reducing the adhesion between bitumen and construction materials (Fig. 1). The device consists of an interchangeable plate (usually steel) that can be adjusted to an incline from 0–70°. The principle of the device is that when an ARA is applied to the plate, sliding asphalt or bitumen from the top of the plate can allow us to observe the performance of the ARA as the asphalt slides or bitumen flows on the incline. In order to facilitate this, a heating mechanism is installed beneath the plate that is capable of heating it to over 200°C.

In order to allow for the quantification of the asphalt release agent performance, there are several measurement devices installed on the apparatus, all though not all of these may be useful for our study as of yet:

– Gage for setting the angle of inclination;
– Temperature gage for adjusting the heating underneath the plate;
– Laser temperature gage over the plate to measure the temperature of the asphalt/bitumen;

Figure 1. ARA Performance Evaluation Apparatus (ARA-PEA).

Figure 2. Asphalt Slide Test: applying ARA (left), asphalt spread on the plate (centre), load of 2,5 kPa distributed on top of the asphalt (right).

– Camera in order to film the flow of the bitumen, allowing for the measure of its speed and the observation of the shape of the bitumen flow;
– Depth gage in order to measure the depth of the bitumen flow on the plate.

2.2.2 *Asphalt slide test*

The mixture slide test is found in the AASHTO program for asphalt release agents [9]. The test developed in this article follows the same principle as the AASHTO one, while adding the ability to quantify ARA performance. The principal of the test is performance of an ARA on a scaled version of an asphalt truck bed using the ARA-PEA.

The test (Fig. 2) involves spraying an ARA over an area of 21.5 × 40 cm on a steel plate resting horizontally. This is followed by placing 1000 ± 10 g of hot asphalt (150 ± 10°C) on the surface of the plate, so that is spread out as evenly as possible. The plate is maintained horizontal and a sheet of wax paper is placed on top of the asphalt to prevent sticking, followed by a wooden board (21 × 40 cm, 883 g). On top of the board, a load of 20 kg is placed creating a distributed pressure on the asphalt of 2,5 kPa. This simulates the transportation of the asphalt where there is a pressure on the asphalt in contact with the truck bed form the asphalt resting on top. The plate rests horizontally for a certain period of time (0,5–1 h), after which it is placed on the ARA-PEA and immediately inclined at a certain angle (0–70°), simulating the discharge of the asphalt from the truck. It is also possible to heat the plate when it is on the device. With the application of an ARA, the asphalt falls off the plate, and from this action, the following data can be taken for judging the performance of the ARA:

– The mass of asphalt residue left on the plate;
– The area of asphalt residue left on the plate (by image analysis);
– The time that it takes the asphalt to slide down after the plate is inclines.

2.3 *ARA effects on asphalt*

The propensity of the ARA to degrade the asphalt needs to be evaluated before it can be determined to be suitable for road construction.

2.3.1 *Asphalt compaction*

Two types of asphalt compaction methods were considered in this study: by proctor and by compression.

2.3.1.1 Compaction by proctor

The first method was similar to the French NF P 18 127 standard for compacting asphalt. The asphalt was heated to around 160°C and placed in a Ø100 mm mould (EN 13297-30). The asphalt is then proctor compacted by 2 series of 25 drops, cleaning the proctor head of bitumen and turning the mould 45° between the series. The mould is removed and placed to cool to around 40°C. The samples produced are Ø100 mm with a height of 60 ± 2 mm.

2.3.1.2 Compaction by compression

The second method of compaction is by compression and is based on the compaction method from the French NF P 98-251-1. This method was adapted in this study for use with Ø100 mm moulds (EN 13297-30). The asphalt was heated so that it was at 160°C before compaction and placed in the mould. The asphalt was compacted by a piston pressed (preheated to 50°C) on the asphalt through a compressor and maintained for a certain period of time at a constant pressure. While the standard provides a pressure of 11.94 MPa for 5 min as the compaction, it was found that these specifications were not necessary or practical for this test. A pressure of 2.55 MPa for 2 min was found to be adequate in keeping the samples under 10% voids (9.2% as determined by NF EN 12697-6). The samples produced were Ø100 mm with a height of 60 ± 2 mm.

2.3.2 *Measuring the resistance to loading of asphalt in contact with ARAs*

2.3.2.1 ARA application

The ARA is applied to the centre of the sample by a graduated burette. This is done either just before compaction or after compaction of the asphalt. The ARA is applied at the centre of the sample via a graduated burette in one pour. It was determined from preliminary testing that a dosage of 5 mL was adequate for the first series of testing (CBR loading).

2.3.2.2 Resistance of asphalt by vertical CBR loading

To test the degradation of the sample by the ARA, the samples were subjected to loading by California Bearing Ration (CBR) piston as in [10] at 1.27 mm/sec. The samples were allowed to rest for 7 days before they are subject to testing in order for the ARA to demonstrate its effects with time. The temperature was checked at each point after the asphalt was heated, before compaction, after compaction and before demoulding.

2.3.2.3 Resistance of asphalt by indirect tensile loading

An alternative to CBR loading was also investigated: resistance by Indirect Tensile (IT) loading, which places the sample on its tangential side and proceeds to load it from the top creating tension forces in the middle of the sample. A test such as this on asphalt can be found in NF EN 12697-34 "Marshall Tests Stability and Flow". The samples are tested 7 days after the application of the ARA and the loading rate is 1.27 kN/mm. The temperature was checked at each point after the asphalt was heated, before compaction, after compaction and before demoulding.

2.3.3 *Bitumen degradation testing*

The degradation of bitumen directly by the ARA is determined by the Bitumen Degradation Test (BDT) as shown in Figure 3. The samples are prepared by pouring 10 ± 1 g of hot

Figure 3. BDT silicon sample moulds (left), sample submerged in product (center) and beakers after test (right).

bitumen (150 ± 10°C), heated at 160°C for 2 h, into circular silicon moulds. This produces "cone with flat top" shaped samples with the dimensions: Ø37 mm top, Ø31 mm bottom, h = 10 mm. The samples are left to cool for 8 ± 4 h after which they are demoulded, and weighed to the nearest 0.01 g. The samples are placed into 150 mL graduated glass beakers of known mass, and the product is poured over it so that the bitumen sample is submerged in it completely. The sample is left for another 24 h, after which, the product is drained out, with the bitumen sample now sticking to the bottom of the beaker. The sides of the beaker above the bitumen sample are wiped with a cloth and the remains of the samples are weighed to the nearest 0.01 g. The Bitumen Degradation (BD%) is taken as the difference between the mass of the bitumen sample before (BB) and after (BA) the test as shown in. Eq. (1).

$$BD\% = 100\% \times (BB - BA)/BB \quad (1)$$

3 RESULTS

3.1 *ARA performance*

3.1.1 *Asphalt slide test*

A number of parameters were used in developing the test in order to find the ones that can lead to the most indicative results; they are shown in Table 3.

For test No. 1, the ARA was applied at around 20 mL/m^2 and the plate was not heated during the test. The asphalt did not move from the plate when inclined, requiring the top of the asphalt to be pushed lightly before the start of the sliding, even at the maximum possible inclination of 70°. The light pushing did not appear to move the control sample.

For test No. 2, the ARA was applied at around 20 mL/m^2 and the plate was heated to around 70°C before ARA application and was heated during the inclination part of the test at 70°C. This time, the asphalt slid after inclination, indicating the necessity of heating the plate before the asphalt slides. A cooling time of 30 min was found to be adequate for the asphalt to develop some adherence to the plate as there was a certain delay between when the plate was inclined and when the asphalt slid as shown in Table 4, allowing for the measuring of time to the beginning of the slide after the inclination as a performance characteristic for the ARAs. An angle of inclination of 45° was found adequate for the sliding as well.

For test No. 3, the cooling time was set at 30 min and the angle of inclination at 45°. The plate was not heated before the asphalt was applied; however, the ARA-PEA was heated at varied temperatures. It was found that for a temperature of 60°C at inclination, the samples with ARAs slide, but the control samples do not. A temperature of 60°C was therefore set for the plate at inclination.

With the optimum parameters for the test determined, the test was conducted with Gasoil, ARA 1 and ARA 2. The photos of the plates after the test are shown in Table 5 and the results of the test in terms of residual mass and time to beginning of slide are shown in Table 6.

Table 3. Parameters for asphalt slide test.

Test no	Quantity of ARA (mL/m²)	Heating of plate before ARA application (°C)	Cooling time	Plate at inclination (°C)	Inclination angle (°)
1	20	–	1 h	–	45–70
2	20	70	30 min	70	45
3	25	–	30 min	Variable	45
Final	25	–	30 min	60	45

Table 4. Results for asphalt slide test for test no. 2.

Product	Asphalt (°C)	Quantity ARA (mL/m²)	Time to beginning of slide
Control	160	–	–
ARA 1	160	20.90	13 s
ARA 2	160	21.41	1 s

Table 5. Images of plates after asphalt slide test.

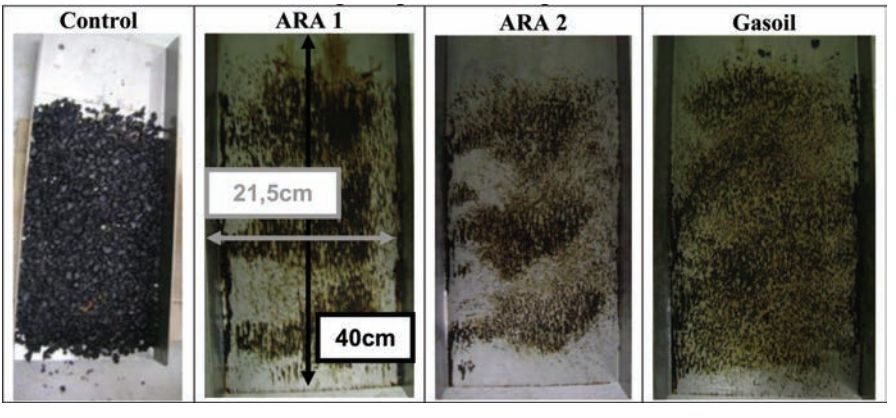

Table 6. Results for asphalt slide test results.

Product	Quantity ARA (mL/m²)	Residual mass %	Time to beginning of slide
Control	–	100%	–
Gasoil	28.65	0.22%	1.00 s
ARA 1	27.00	0.12%	92.67 s
ARA 2	27.57	0.27%	100.00 s

ARA 2 was found to have the least residual mass, which is confirmed by the images of the plate. Gasoil excelled in terms of time to beginning of slide, with the asphalt sliding in under 1 second after inclination.

3.2 *ARA effects on asphalt*

3.2.1 *Asphalt degradation by ARAs*

In evaluating the tests for the degradation of asphalt by ARAs, there were several aspects observed. They included the state of the moulds, the resistance of the ARA to CBR/Indirect Tensile loading and the partition of the ARA inside the sample itself.

3.2.1.1 Resistance of asphalt by vertical CBR loading

All of the samples for CBR loading were made with proctor compaction and had a 5 mL dosage of ARA. The resistance to CBR loading of the control samples manufactured 10 days apart, shows a significant difference in both the shape of the resistance (kN) vs. displacement (mm) curve and the maximum resistance with a Coefficient of Variability (CVAR) of 0.220 for the 6 samples. As this was not acceptable, another set of tests was completed to see if the source of the error was the asphalt, taking extra precautions to keep the asphalt homogenous. The second set of control samples also has a high variability coefficient of 0.133. In addition to this, some ARAs appear to actually increase the resistance of the asphalt relative to the control samples. The images in Figure 4 show the leaching of the bitumen onto the moulds as was observed in [10] as well as the tendency of the ARAs to move to the sides of the samples due to the centre of the samples having a higher density through proctor compaction process.

3.2.1.2 Resistance of asphalt by indirect tensile loading

For IT Trial No. 1, samples were manufactured by compression and the ARA quantity was 5 mL applied immediately after compaction at an asphalt temperature of around 120ºC. The coefficient of variability for the IT control samples (all made on different days) was 0.051, lower than for the CBR samples. The reduction of IT resistance (RR%) represents the difference between the maximum resistance of the ARA and the control samples. It is shown that all of the RR% values are above 50%, indicating that the quantity of ARA should be reduced. This is confirmed by Figure 5 (left) where there is significant leaching on the moulds, which would reduce the repeatability of the test.

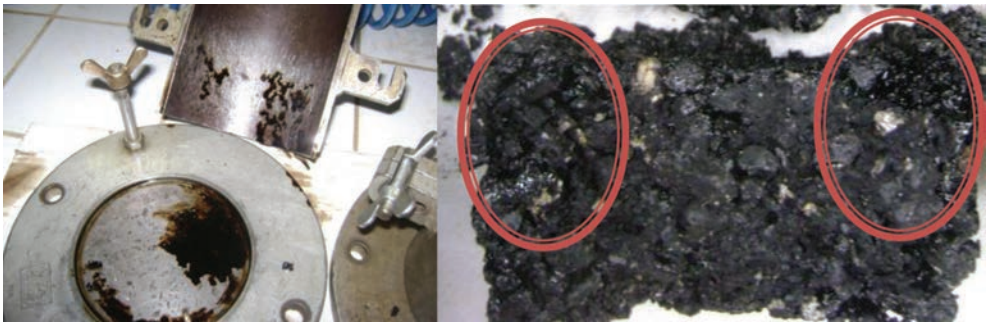

Figure 4. Proctor-CBR loading samples showing leaching of bitumen onto moulds as was observed in [10] and flow of ARA towards the side of the sample.

Figure 5. Compressor compacted IT loading samples showing leaching of bitumen with 5 mL ARA applied after compaction (left) and 2 mL ARA applied before compaction (right).

Table 7. Resistance reduction for IT Trial No. 1 IT (5 mL ARA applied after compaction), IT Trial No. 2 (2 mL ARA applied before compaction) and % BD from bitumen degradation test.

Product	Evaporation on surface	% Resistance reduction		% Bitumen degradation
		5 mL after compaction	2 mL before compaction	
Gasoil	Some	71.4	–	–
ARA 1	Negligible	65.8	55.2	36.22%
ARA 2	Negligible	58.3	54.7	33.79%
BR 1	Negligible	–	66.9	52.90%
BR 2	Negligible	68.9	–	–

For IT Trial No. 2, samples were manufactured by compression and the ARA quantity was 2 mL applied immediately before compaction at around 160ºC. Table 7 shows that all of the RR% values are above 50%, indicating that the ARA quantity is still too high. However there is a clear difference between the ARA resistance values and that for the BR. Additionally, the leaching of bitumen on the moulds (Fig. 5, right) is almost negligible, indicating that nearly the entire quantity of the ARA stays in the sample.

3.2.2 *Bitumen degradation by ARAs*

The results for the bitumen degradation test are shown in Table 7. The mass of all of the bitumen samples are reduced in this test, including the BR, which at 52.9% has a higher reduction than the two ARAs.

4 DISCUSSION

4.1 *Validity and limits of the test methods*

4.1.1 *ARA performance*

The Asphalt Slide Test was tested with ARAs using three different sets of parameters. The ARA-PEA (ARA Performance Evaluation Apparatus) provides a good platform for this test. While the pre-heating of the plate is not necessary, the heating of the plate during inclination is for the asphalt to slide down by itself. A cooling time of 30 min appears to be adequate to allow for the asphalt to adhere to the plate. There were three types of results observed during the testing:

1. Mass of asphalt residue retained on the plate after inclination;
2. Time the asphalt stayed on the plate after inclination.

The parameters are qualitative results that can be used to compare the performance of various ARAs.

4.1.2 *ARA effects on asphalt*

The evaluation of asphalt degradation by ARAs involved testing two different methods of loading with two different methods of compaction. The samples tested with CBR loading and proctor compaction did not provide results that were repeatable. Even though samples manufactured at the same time had similar resistance values, both control samples and samples with ARA addition did not correlate if they were made on different days. Additionally, many of the samples where ARAs were used, showed similar or higher resistance to CBR loading than the control samples.

It was clear that the ARAs had caused the leaching of bitumen of the samples from the observation of moulds after the samples were demoulded as was observed by [10]. However, this effect was not easy to understand from the results of CBR loading. It was interesting to note that from the photos of the insides of the asphalt samples after testing; the ARAs

appeared to move towards the sides the samples. Conversely, the CBR loading tested the middle 50 mm diameter of the sample.

IT (Indirect Tensile) loading was attempted as an alternative to the CBR. As opposed to only loading the middle part, IT loading tests an entire mid-section of the sample. Additionally, the resistance to IT of the samples depends more on the properties of the bitumen (the part of the asphalt affected by ARA degradation). By comparison, CBR loading depends more on the position of the aggregates than with IT.

Compaction with a compressor was used as opposed to proctor compaction in order to have a more evenly distributed density in the sample. The voids content was determined to be 9.2% in accordance with NF EN 12697-6 for a compression pressure of 2.55 MPa for 2 min. With this method, the CVAR for resistance to loading for the control samples was much smaller than with the CBR-proctor samples.

For an ARA quantity of 5 mL applied after compaction, the results in loss of resistance for Gasoil the ARAs and the BRs were all over 50% for the samples. In addition, there was significant leaching of the asphalt by the ARA onto the moulds, indicating that the dosage had to be lowered. There was however, a significant difference in loss of resistance for the IT test between the ARA 2 and BR 2, indicating that the test is able to distinguish between products that are meant to degrade bitumen and those that are not.

For the second IT test, the ARA was applied at 2 mL before compaction of the sample, allowing it to be applied at around 160ºC, which is the peak temperature in asphalt fabrication. After the fabrication, the moulds did not show much presence of bitumen leaching by the ARA, indicating that almost all of the ARA stayed in the sample. This is important because too much bitumen leaching could vary the quantities of ARA that act on the asphalt sample to sample. The loss of resistance was still over 50% for all of the applied products. However, there was a clear difference between the values for the two ARAs and BR 4, indicating a test that can differentiate good and bad ARA products. The difference of adding the ARA before and after compaction should be considered as two relevant tests with this method.

The bitumen degradation test is able to differentiate the degradation from ARAs and BRs on bitumen and is a repeatable test that is relatively simple to implement.

4.2 *Evaluation of ARAs*

4.2.1 *ARA performance*

For the Asphalt Slide Test; ARA 1, ARA 2 and Gasoil (all commercial bio-sourced ARAs, available on the French market) were evaluated. It was found that ARA 2 left the least residual bitumen while with Gasoil, the asphalt slid down almost instantly upon inclination. Although the residual masses were not that far apart, the gasoil performed much better in retention time after inclination than the vegetable based agents. This indicates that there is a performance benefit in using gasoil despite in being banned on most construction sites due to worker health and environmental issues.

4.2.2 *ARA effects on asphalt*

In testing ARA for their effects on asphalt gasoil was tested along with ARA 1, ARA 2 and ARA 3. The gasoil was found to have the most destructive effect (in terms of reducing the resistance of asphalt to IT loading), one similar to a BR, even when applied to the asphalt at high temperatures (130 ± 5ºC). Despite the fact that gasoil is much more volatile (evaporation at around 60ºC) compared to the bio-sourced ARAs (evaporation at 250ºC+), there is always a significant part of gasoil that stays in the sample and degrades the asphalt. The deterioration of asphalt by gasoil has also been described in [2,5,6], added to the fact that it is banned for use as an ARA and BR on construction sites in many countries [3,4]. It should also be added, that under laboratory conditions, many effects that would increase evaporation (and decrease the degradation of apshalt by gasoil) such as wind and UV-rays are not possible to replicate.

In terms of the bio-sourced ARAs, ARA 2 and ARA 3 were found to be less destructive that BRs by asphalt and bitumen degradation testing. More testing still has to be performed on ARA 1 to draw conclusions.

5 CONCLUSIONS

The conclusions in developing test methods for the determination of the performance and safety of bio-sourced ARAs are as follows:

- The asphalt slide test provides three indicators of ARA performance including area of asphalt residue, mass of asphalt residue and time for asphalt to begin sliding after inclination;
- Heating under the plate is needed for the asphalt to begin sliding in the asphalt slide test, making the ARA-PEA ideal for this test;
- Gasoil performs better than the vegetable-based agents in the asphalt slide test in terms of retention time after inclination;
- The testing of asphalt degradation by ARAs with the CBR-loading does not produce reproducible or coherent results;
- The testing of asphalt degradation by ARAs with IT loading produces reproducible results and is able to differentiate the damage from ARAs and BRs;
- Compaction of the asphalt by compression as opposed to proctor produces a more consistent sample in terms of density distribution;
- The bitumen degradation test is able to differentiate the damage from ARAs and BRs on bitumen and be repeatable, making it possible to test bitumen degradation from ARAs.

ACKNOWLEDGMENTS

The authors would like to thank FUI (French Designated Inter-Ministry Fund), AGRIBTP research project (www.agribtp.fr) and USIRF for their financial support as well as Malet (France) and Kemerid (France, www.kemerid.com) for their technical support.

REFERENCES

[1] N. Zaki and R. Troxler. Asphalt Release Agent, U.S. Patent 07140107. July 2006.
[2] M.A. Dituro, F.E. Lockwood, D.J. Dotson and J. Fang. Asphalt release agent, U.S. Patent 648624926. 2002.
[3] B. Tang. Applications of Solid-Phase Microextraction to Chemical Characterization of Materials Used in Road Construction, Division of Highway Engineering, Royal Institute of Technology. 2008.
[4] B. Tang and U. Isacsson. Chemical characterization of oil-based asphalt release agents and their emissions, Fuel, 85(9), p. 1232–1241. June 2006.
[5] E.R. Martin and M.L. Coffey. Asphalt release agents and use thereof, U.S. Patent 614381207. 2000.
[6] P. Lavin. Asphalt Pavements: A Practical Guide to Design, Production and Maintenance for Engineers and Architects, p. 283, CRC Press, London, 2003.
[7] G. Mahr, T. Okabe and K. Ito. Release agents for bituminous substances, U.S. Patent 650644414. 2003.
[8] G. Escadeillas and E. Ringot. Qualification des anti-adhérents pour enrobés, Report for USIRF. 2011.
[9] AASHTO-NTPEP. Asphalt Release Agents. 2013.
[10] G. Escadeillas, M. Jackubowski, E. Ringot, A. Lelarge, S. Limon, M. Mazars, P.H. Navarre and H. Tiraby. Recherche d'un produit anti-adhérent pour les bitumes à chaud, Report for USIRF. 2011.

This page intentionally left blank

Asphalt Pavements – Kim (Ed)
© 2014 Taylor & Francis Group, London, ISBN 978-1-138-02693-3

Laboratory evaluation of Sulphur Extended Asphalt Modifier

Umakant Meena
Government Polytechnic, New Delhi, India

Satish Chandra
Transportation Engineering Group, Civil Engineering Department, IIT Roorkee, Uttarakhand, India

Ankit Gupta
Civil Engineering Department, NIT Hamirpur, Himachal Pradesh, India

ABSTRACT: Flexible pavements with bituminous surfacing are widely used in India. The high traffic intensity in terms of commercial vehicles, overloading of trucks and variations in daily and seasonal temperature of the pavement have been responsible for the early development of distresses like ravelling, undulations, rutting, cracking, bleeding and shoving of bituminous surfacing. So it is essential to build a durable and long lasting road pavement. Designing a road with a strong bituminous base course like Dense Bituminous Macadam (DBM) can provide the load-bearing capacity needed to handle heavy axle loads. Strong base course also provides the load-spreading ability to relieve stresses and strains coming on to the subbase course and subgrade layers. Quality and quantity of binder have greater influence upon performance and durability of flexible pavements. Quality of binder may be modified by using certain modifiers such as polymer, crumb rubber, sulphur and use of these modifiers is dependent upon the type of construction, availability of material, equipment, and climatic conditions. The objective of this study is to evaluate the efficacy of Sulphur Extended Asphalt Modifier (SEAM) to improve the durability and rutting potential of a bituminous base course mix like DBM. Various laboratory tests like Marshall Stability, Tensile Strength Ratio, Retained Stability and Unconfined Creep were conducted on specimens prepared by two different types of binders namely asphalt of penetration grade 60/70 and another with 60% Asphalt + 40% SEAM. The results indicate that with the use of SEAM, reduction in asphalt usage can be significant.

1 INTRODUCTION

In early 1970s, due to concern over asphalt cement supply issues and an anticipated overabundance of elemental sulphur, many organizations such as, Société Nationale des Pétroles d'Aquitaine (SNPA), Gulf Oil of Canada, Sulphur Development Institute of Canada (SUDIC), Texas Chemical Company, U.S. Bureau of Mines, and the Texas Transportation Institute began to evaluate the potential for sulphur to substitute for asphalt as a binder extender; this became known as Sulphur Extended Asphalt (SEA). At the time, it was projected that there would be an abundant amount of sulphur from many sources: pyrite processing into sulphuric acid, natural gas recovery, crude oil refining, coal usage, other chemical processes, and desulphurization from smoke stack emissions. 68 test sections were constructed between 1975 and 1984; 18 of these were monitored under FHWA Demonstration Project No. 54 (DP54). This was initiated in 1979 and provided design, construction, and evaluation assistance. The Demonstration Projects Division organized a task force, with the Sulphur Institute to conduct a comparative performance review of the SEA pavements with that of conventional Asphalt Concrete (AC) pavement control sections. Twenty-six projects in 18 states were evaluated. The results of this review indicated that sulphur could potentially

be used as an asphalt extender with no significant deleterious effect on performance and durability (FHWA, 1990).

SEAM, is a patented additive developed by M/S Shell Global solution for use in asphalt paving mixtures. It is both a binder extender and an asphalt mixture modifier. It improves road strength and reduces pavement cracking and rutting, which results in safer roads and longer road life. It is in the form of pallets as shown in Figure 1.

Important key features of SEAM include:

- An odourless pellet containing sulphur, plasticizer and additives to control fume and odour during asphalt mixing.
- Melts easily on contact with hot asphalt mix; disperses quickly during mixing.
- Meets related health and safety emissions standards.
- No risk of environmental leaching.

It is added into the hot mixture of aggregates and asphalt during the mixing process. It is not pre-blended with asphalt. A portion of the SEAM is chemically combined with the asphalt and acts as an extender. One part of SEAM is dissolved in the asphalt and modifying the asphalt properties, viscosity is lowered and its ductility is increased and another part of SEAM, as free sulphur, when the blend cools, crystallises. Depending on the amount of SEAM added, the crystallisation gives different levels of strengthening. Sulphur crystallisation acts as a structuring agent in the asphalt mixture. This is shown in Figure 2.

Figure 1. SEAM pellets.

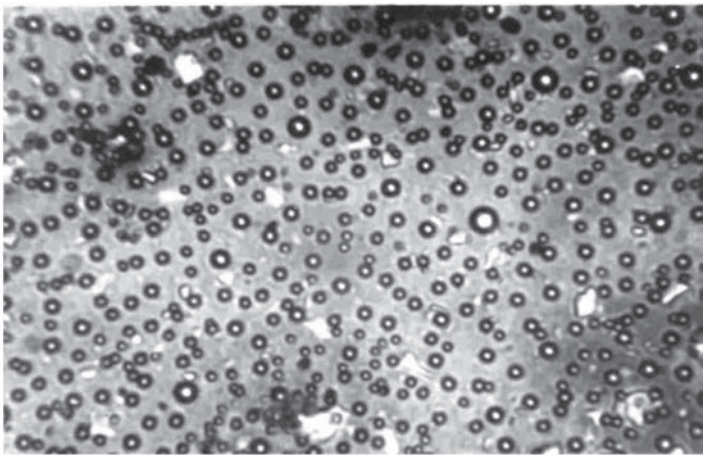

Figure 2. SEAM in the asphalt mixture.

2 EXPERIMENTAL PROGRAMME

In this study, design of DBM was analysed in terms of durability and performance with the help of various laboratory tests like stability, tensile strength ratio, retained stability and unconfined creep. The tests specimens were prepared by two different types of binders namely asphalt of penetration grade 60/70 and with 60% Asphalt + 40% SEAM.

2.1 *Design of DBM*

Bituminous mix design is a delicate balancing act among the proportions of various aggregate sizes and asphalt content. For a given aggregate gradation, the Optimum Bitumen Content (OBC) is estimated by satisfying a number of mix design parameters. Following steps were considered in the case of DBM mix design.

- Selection of materials for DBM:
  Asphalt: 60/70 penetration grade asphalt was used for preparation of DBM mix.
  Additive: Sulphur Extended Asphalt Modifier (SEAM) is used as an additive by replacing 40% asphalt.
  Aggregate: Mix consisted of three types of aggregate; coarse aggregate, fine aggregate, and filler as available in the laboratory. Aggregates were tested for their physical properties and were found suitable for use in DBM Mix. 2% lime and 3% stone dust was used as filler in the mix.

Aggregate were proportioned suitably to get the designed grading for 80–100 mm thick DBM as shown in Table 1.

2.2 *Modified Marshall Method of bituminous mix design*

Modified Marshall Method was developed for mixes composed of aggregates with maximum size up to 38 mm. The procedure is basically the same as the original method, except some differences as given in Table 2.

Table 1. Grading of DBM mix for 80–100 mm thickness.

IS sieve (mm)	Used grading (% passing)	Recommended by MORTH (% passing)
45	100	100
37.5	97–100	95–100
26.5	78	63–93
13.2	65	55–75
4.75	46	38–54
2.36	35	28–42
0.3	14	7–21
0.075	5	2–8

Table 2. Parameters of Marshall method.

Parameter	Marshall method	Modified Marshall Method
Max. size of aggregate	25 mm	38 mm
Height of sample	63.5 mm	95.2 mm
Diameter of sample	102 mm	152.4 mm
Weight of hammer	4.5 kg	10.2 kg
Weight of sample	1200 gm	4000 gm
Compaction level (Number of blows)	75	112

(Source: Asphalt Institute Manual Series No. 2 (MS–2)).

Figure 3. Mixing and compaction of DBM sample.

For making the DBM samples, aggregates were taken as per the grading and heated to a temperature of 180ºC. Hot asphalt (135ºC) was added and mixed by mixture for 2 minutes. The Marshall mould is heated separately in the oven at 160ºC and hot mixture is poured in to the mould kept in the mould assembly. The specimen was prepared by giving 112 blows on each face by 10.2 kg hammer (Fig. 3). The compaction temperature of the mix was kept at 125ºC. Samples with SEAM were prepared in the similar manner. The SEAM was added to hot mixture of aggregate and asphalt at a temperature not less than 125 ºC.

2.3 *Determination of Optimum Binder Content with 60/70 asphalt*

According to Asphalt Institute Manual Series No. 2 (MS–2), the Optimum Binder Content (OBC) is the percentage of asphalt corresponding to four percent air voids.

3 TESTS ON ASPHALT MIXES

The following laboratory tests were carried out to evaluate the performance and durability of IntregraBase modifier in Dense Bituminous Macadam (DBM) course. IntegraBase is an asphaltic modifier which when added to bitumen reacts chemically when mixed with the aggregate. The result is an asphalt with increased workability, a 50%–200% increase in pavement strength, higher fatigue resistance (and therefore, longer life), and increased resistance to rutting and stripping.

3.1 *Stability test*

Marshall Stability of a test specimen is the maximum load required to produce failure when the specimen is preheated to a prescribed temperature is placed in a special test head and the load is applied at a constant strain. While the stability test is in progress, dial gauge is used to measure the vertical deformation of the specimen. The deformation at the failure point expressed in mm is called the Marshall flow value of the specimen (as shown in Fig. 4).

3.2 *Moisture susceptibility*

Presence of moisture in a bituminous mix is a critical factor, which may lead to premature failure of the flexible pavement. The loss of adhesion of aggregates with asphalt was studied

Figure 4. Measurement of stability and flow value.

by utilising Tensile Strength Ratio test (TSR) and Retained Stability test to examine the effect of modifier on resistance to moisture damage.

- Tensile strength ratio test
  The tensile strength ratio of asphalt mixes is an indicator of their resistance to moisture susceptibility. The test was carried out according to AASHTO T283-89 specifications. The specimen was placed and submerged in vacuum container filled with water at room temperature. A vacuum of 13–67 kPa absolute pressure (10–26 inches Hg partial pressure) is applied for 30 minutes. Remove the vacuum and leave the specimen submerged in water for 5 to 10 minutes. There after place the specimen in water bath at 60ºC +/– 1ºC for 24 hours and the remove the specimen from hot bath and place in water bath maintained at 25ºC +/– 0.5ºC for 2 hours. Tests for indirect tensile strength for conditioned and un-conditioned specimens were done at 25°C temperature. The ratio of the tensile strength of the water-conditioned specimens to that of dry specimens is the tensile strength ratio.
- Retained stability test
  This test measures the stripping resistance of a bituminous mixture. The standard modified Marshall specimens of 152.4 mm diameter and 95.2 mm height were prepared. The specimens were kept in water bath maintained at 60°C for 24 hours, and thereafter tested for stability value. The results are reported as the percentage of marshall stability determined in normal condition of the test.

3.3 *Static creep test*

It was developed as a better means of designing and assessing mixtures for resistance to permanent deformation. Laboratory specimen is subjected to unconfined, uniaxial loading with a constant force and the resulting axial deformation is measured with time. The reversible part of the total deformation also determined by removing the load and measuring the deformation after a recovery time that is usually equal to the loading time. Specimen was preloaded at the test temperature (30ºC) for 10 minutes with conditional load to provide a stress equivalent to 10% of the normal applied stress of 100 kPa and any axial deformation is recorded. The load is then quickly increased to the test load and the axial deformation is measured with time. The time intervals for the readings are 10, 40, 100, 400, 1000, 2000, 3000 and 3600 seconds. Loading and unloading conditions are shown in Figure 5.

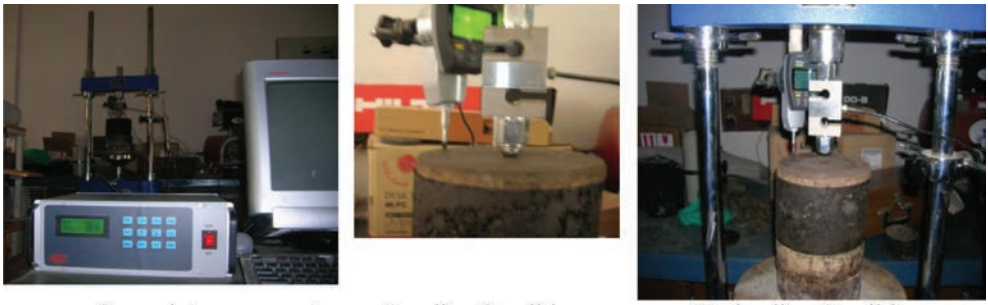

Figure 5. Static creep test for different conditions.

Table 3. Specific gravity of ingredients.

Material	Specific gravity
Coarse aggregate	2.695
Fine aggregate	2.699
Filler	
Rock dust	2.569
Lime	1.242
Asphalt (60/70)	1.020
SEAM	1.230

4 TEST RESULTS AND ANALYSIS

4.1 *Specific gravity of ingredients*

Specific gravity of ingredient was measured according to the guidelines given in Indian Standard Code IS-2386. Values are shown in Table 3.

4.2 *Determination of optimum binder content*

Volumetric and mechanical parameters obtained for DBM with 60/70 asphalt such as Bulk Density, Marshall Stability, Flow, and other volumetric properties are given in Table 4. The test values obtained are plotted graphically and shown in Figures 6 to 9. Using the above parameters, optimum binder content was found to be 4.4% by weight of mix. The Optimum Binder Content (OBC) was determined corresponding to 4% air voids and values of other parameters were checked at this binder content. Durability and performance tests on two types of mixes were conducted at this OBC.

4.3 *Design parameters at OBC with 60/70 asphalt*

The values obtained at the optimum binder content are indicated in Table 5.

4.4 *Mechanical and water susceptibility properties of DBM mixes*

SEAM effect on mechanical and water susceptibility properties of DBM mixes such as bulk density, stability, flow, retained stability, tensile strength ratio was studied. The results are discussed below.

- Unconfined creep test
  The result of Creep test on DBM mixes are shown in Table 6.

Table 4. Volumetric and mechanical parameters obtained for DBM with 60/70 asphalt.

Sample no.	Asphalt content (%)	Sp. gravity of mix (G_t)	Bulk density (G_b) (g/cc)	Stability value (S) (kg)	Flow value (mm)	% Voids in asphalt (V_b)	% Voids in Mineral Aggregate (VMA)	% Voids Filled with Asphalt (VFB)
1	4.0	2.55	2.39	2205.85	5.0	9.39	15.61	60.15
2	4.5	2.50	2.41	2833.33	5.2	10.66	14.25	74.80
3	5.0	2.48	2.39	2820.60	5.9	11.71	14.58	80.34
4	5.5	2.46	2.38	1913.43	7.0	12.83	15.46	83.02

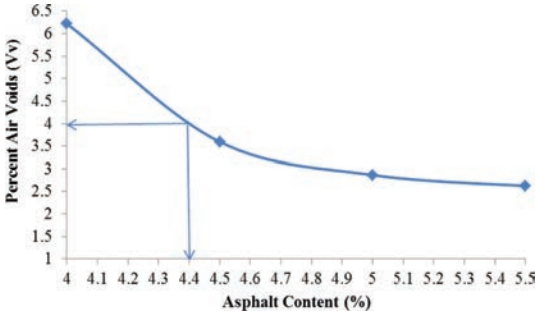

Figure 6. Plot of percent air voids vs asphalt content.

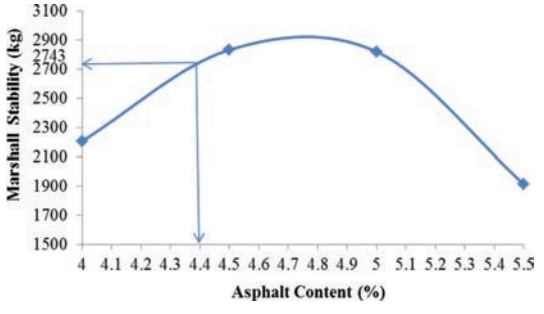

Figure 7. Plot of Marshall stability vs asphalt content.

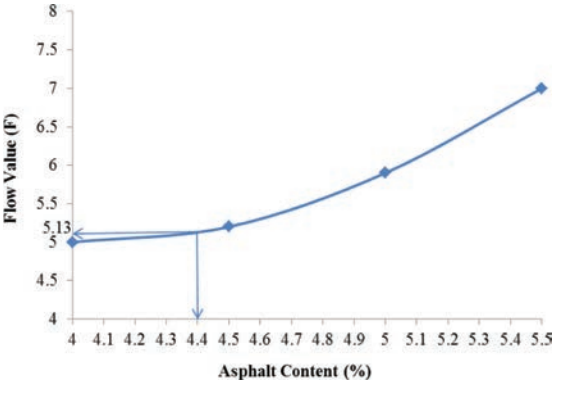

Figure 8. Plot of flow value vs asphalt content.

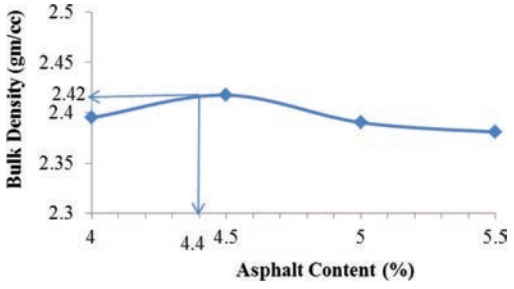

Figure 9. Plot of bulk density vs asphalt content.

Table 5. Marshall parameters at optimum binder content.

Parameters	Values obtained at OBC	Specified values
Stability, kg	2743	2025 kg (minimum)
Air Voids, %	4.0	3–6
Flow, mm	5.13	3 (minimum)
% Voids filled with asphalt	72.28	65–75

Table 6. Strain and creep compliance (J_t) for unconfined creep test.

	DBM with Asphalt 60/70			DBM with 60% Asphalt + 40% SEAM		
Time	Deformation	Strain	Creep compliance (J_t) MPa	Deformation	Strain	Creep compliance (J_t) MPa
Loading condition						
0	0	0	–	0	0	–
10	0.455	0.004815	2.037	0.301	0.003168	3.096
40	0.460	0.004868	2.015	0.312	0.003284	2.987
100	0.468	0.004952	1.980	0.320	0.003368	2.912
400	0.490	0.005185	1.891	0.333	0.003505	2.798
1000	0.504	0.005333	1.839	0.342	0.003600	2.725
2000	0.515	0.005450	1.800	0.351	0.003695	2.655
3000	0.553	0.005852	1.676	0.352	0.003705	2.647
3600	0.555	0.005873	1.670	0.353	0.003716	2.640
Unloading condition						
3610	0.479	0.005069	1.935	0.314	0.003305	2.967
3640	0.439	0.004646	2.111	0.306	0.003221	3.045
3700	0.437	0.004624	2.121	0.305	0.003211	3.055
4000	0.415	0.004392	2.233	0.302	0.003179	3.085
4600	0.409	0.004328	2.266	0.297	0.003126	3.137
5600	0.405	0.004286	2.289	0.296	0.003116	3.148
6600	0.403	0.004265	2.300	0.295	0.003105	3.159
7200	0.403	0.004265	2.300	0.295	0.003105	3.159

Table 7. Retained stability of DBM mixes.

Type of mix	Retained stability (%)
Asphalt	143.4
60% Asphalt + 40% SEAM	75.71

- Retained stability
  Effect of SEAM on retained stability for DBM mixes are shown in Table 7.
- Tensile strength ratio
  Effect of SEAM on Tensile Strength Ratio for DBM mixes is shown in Table 8.

5 SUMMARY OF TEST RESULTS FOR SEAM MIX

SEAM effect on mechanical and water susceptibility properties of DBM mixes such as bulk density, stability, flow, retained stability, and tensile strength ratio are shown below in Table 9.

Table 8. Tensile strength ratio of DBM mixes.

Type of mix	Condition of sample	Maximum load (N)	Indirect tensile strength (N/mm^2)	Tensile strength ratio
Asphalt	Wet	31215.42	14020.64	0.824
	Dry	37967.60	17015.43	
60% Asphalt + 40% SEAM	Wet	32932.30	14758.83	0.7729
	Dry	42034.81	19095.39	

Table 9. Mechanical and water susceptibility properties of DBM mixes.

Types of mix	Dry stability (kg)	Flow (mm)	Retained stability (%)	Tensile strength ratio	Creep stiffness modulus
Asphalt	2743	5.13	143.4	0.824	23.001
60% Asphalt + 40% SEAM	4389.14	3.45	75.71	0.779	31.59

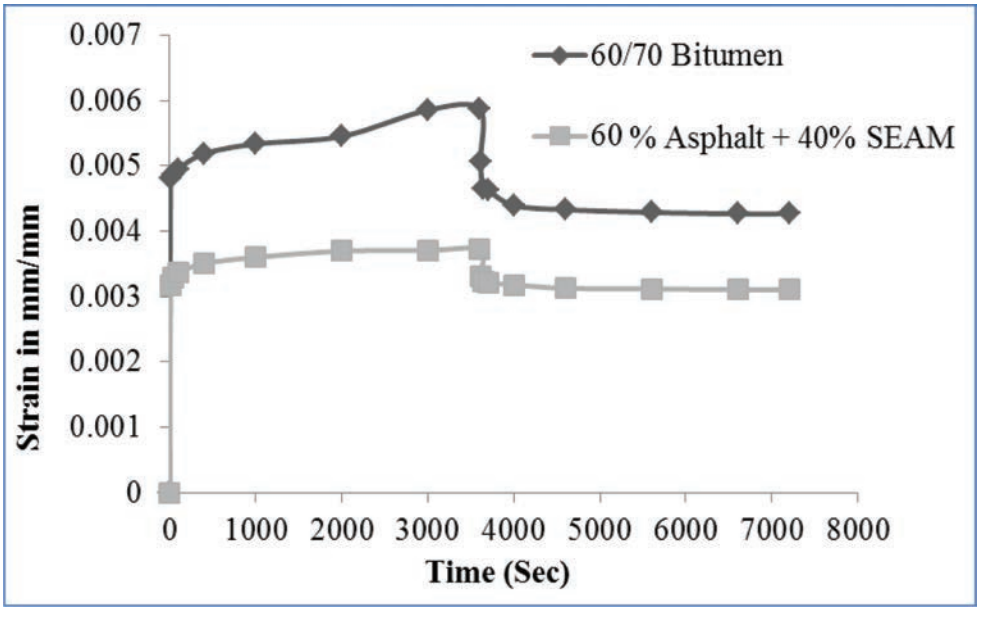

Figure 10. Plot of strain vs time for DBM mixes.

6 CONCLUSION AND RECOMMENDATIONS

Two types of DBM are evaluated in this study, one with 60/70 Asphalt and another with 60% Asphalt + 40% SEAM. The optimum binder content for both mixes was kept 4.4% by weight of total mix. Marshall stability, retained stability, tensile strength ratio and unconfined creep test were conducted there after results were compared and following conclusions are drawn:

- The Marshall stability of DBM with 60/70 binder is 2734 kg. It increases to 4389 kg when 40% of asphalt is replace by SEAM.
- Retained stability of modified mix is 75.7% only which is less than minimum requirement of 80%. It indicated that some stripping of material might have occurred during immersion of sample in hot water.
- Tensile strength ratio which is also moisture susceptibility property of the mix is satisfactory in both the cases.
- Results of static creep test shown in Figure 10 indicate that modified mix has low rutting potential as compare to mix with 60/70 binder.
- The creep modulus of mix with SEAM is around 37% higher than that of mix with 60/70 binder.
- Use of SEAM is likely to reduced consumption of asphalt by weight of 40% which is remarkable considering depleting resources of cured oil.
- This product can be used without harming environment, provided the mixing and compaction temperature are strictly controlled in filed.

REFERENCES

1. Filippis, P.D, Giavarini, C., and Santarelli, M.L. (1998), "Sulphur-Extended Asphalt: Reaction Kinetics of H_2S Evolution" Fuel Vol. 77, No. 5, pp. 459–463.
2. Govt. of India, Ministry of Shipping, Road Transport & Highways Specifications for Road and Bridge Works, Fourth Revision, pp. 170–178.
3. Hunter, R.J. (2000), "Asphalts in Road Construction", First Edition, Thomas Telford, London.
4. Khanna, S.K. and Justo, C.E.G., (2001), "Highway Material Testing", Eight Edition Nem Chand & Bros, Roorkee.
5. "Mix Design Methods for Asphalt Concrete and Other Hot-Mix Types", The Asphalt Institute, Manual Series, No. 2 (MS–2), Sixth Edition, pp. 77–78.
6. Roberts, F.L., Kandhal, P.S., Brown, E.R., Lee, D.Y. and Kennedy, T.W. (1996), "Hot Mix Asphalt Materials, Mixture Design and Construction", Second Edition, NAPA Eduction Foundation Lanham, Maryland.
7. Strickland, D., Colange, J. and Deme, I. "Performance Properties of Sulphur Extended Asphalt Mixtures with SEAM.
8. http://www.shell.com/static/bitumen-en/downloads/wrc/papers/seam_english.pdf (Date of Access: 03–09–2011 now removed from website).

Asphalt Pavements – Kim (Ed)
© 2014 Taylor & Francis Group, London, ISBN 978-1-138-02693-3

Moisture susceptibility of Nano-sized Hydrated Lime-modified foamed Warm Mix Asphalt mixes

Aboelkasim Diab & Zhanping You
Department of Civil and Environmental Engineering, Michigan Technological University, Houghton, MI, USA

ABSTRACT: Despite the obvious benefits of Warm Mix Asphalt (WMA) technologies are stealing the spotlight from classic Hot Mix Asphalt (HMA), there are concerns regarding moisture susceptibility of the mixes especially when it comes to the technologies that mainly depend on applying water (i.e., foaming). The primary objective of the research was to investigate the moisture susceptibility of foamed WMA mixes modified with Nano-sized Hydrated Lime (NHL). Hydrated lime materials in this study included, NHL with particle sizes of 50-nm and 100-nm along with Regular-sized Hydrated Lime (RHL). The Tensile Strength Ratio (TSR) and dynamic modulus (|E*|) tests were employed to accomplish this objective. A secondary objective of this research was to assess the validity of the two utilized TSR and |E*| tests. The |E*| samples passed one and five freeze-thaw cycling processes before each testing. The TSR and |E*| results revealed that foamed WMA mixes are more susceptible to moisture damage in comparison to the control mix. Also, the NHL-modified mixes performed much better than the RHL for both unconditioned and after multiple conditioning. The |E*| test seems more reasonable than the TSR test for moisture susceptibility testing.

Keywords: Foamed warm mix asphalt, nano-sized hydrated lime, tensile strength ratio, dynamic modulus, moisture susceptibility

1 INTRODUCTION

The use of WMA helps drastic reduction of the temperature of an asphalt mix during production, transportation, and compaction. The benefits of WMA technologies are not limited to the heart of potentially mitigating emissions and fuel-use concerns, it also offers the prospect of greater flexibility when transporting, placing and compacting the mix. Different benefits documented by applying the WMA concept have increased the attention to this technology [1–4]. Lower production temperatures are achieved by means of various WMA technologies broadly classified as organic and chemical additives and foaming technologies (either by using water-bearing additives or water-based processes). Organic additives are used to decrease the asphalt binder's viscosity above the melting point of the binder, whereas below the melting point, they tend to increase the stiffness of the binder [5, 6]. Additionally, the organic additives provide not only reduced binder viscosity at mixing and placement temperatures but also increased viscosity at service temperatures, which is an added benefit specific to this type of process [7]. Chemical additives are used to improve the ability of asphalt to coat the aggregate particles at lower temperatures rather than reduce the binder's viscosity. The mechanism of chemical compounds is based on its surfactant activity, which adds lubricity to individual microscopic asphalt particles and that develop slip planes which let the asphalt particles move more easily, requiring lower levels of energy [8, 9].

The foaming concept is based on the cool water expanding when it comes in contact with hot asphalt binder, and increasing the binder's volume and surface area, consequently

decreasing the overall viscosity of the asphalt binder [10–13]. A number of current WMA water-bearing additives use hydrophilic materials such as Aspha-min® and Advera® to produce foamed asphalt. Hydrophilic materials are framework silicates that have large vacant spaces in their structure that allow space for large cations such as sodium, potassium, barium and calcium, and even relatively large molecules and cation groups such as water. The water-based foaming process is another technology to produce the foamed WMA which add benefits by eliminating the need for expensive additives and special asphalt cement by mixing a small amount of water (usually with a mass ratio of 1% to 5% to the asphalt binder) into the hot asphalt to create microscopic bubbles [14]. These small bubbles act to reduce the overall mix viscosity and increase aggregate coating on the rock allowing the mix to be workable at lower temperatures.

However, as the WMA use increases, more research is needed to ensure its performance since questions remain to be answered especially when it comes to susceptibility to moisture damage and rutting in comparison to HMA [15–20]. The rutting susceptibility of WMA mixes is beyond the scope of this investigation. Preliminary laboratory testing has shown that when producing WMA, the combined effect of the initial aggregate moisture content and reduced mixing temperature can have a dramatic impact on the performance of the produced mixes, especially with respect to the resistance to moisture susceptibility. Unfortunately, it is often difficult to control these parameters outside the laboratory testing [9]. The foaming in general transfers water molecules in hot asphalt to lower the overall viscosity of the asphalt binder. The released water molecules may be entrapped in the asphalt pavements during compaction which cause moisture damage and lead to the failure of asphalt pavements. Inadequately dried aggregates due to lower production temperatures, and even the possible introduction of additional moisture to the WMA from the various foaming technologies, may affect the binder-to-aggregate adhesion which likely increases the moisture susceptibility of the mixes. Therefore, more attention is being paid to WMA susceptibility to moisture especially for mixes produced using the foaming methods. As a result, water may be left in close contact with the aggregate surface, which impairs the bond between aggregate and asphalt and increases the susceptibility to moisture damage. Besides, lower mixing temperatures can cause less hardening of the asphalt, thus reducing adhesion to aggregates. Previous researches have shown that WMA may be more susceptible to moisture damage compared to HMA when tested in the laboratory [15, 21, 22].

The hydrated lime with its regular size (which is referred to herein as RHL) has been used as an additive for asphalt mixes from their very beginning. However, the usage of NHL (particle sizes ≤ 100-nm) in asphalt binder materials has only been investigated by the authors. In studies by Diab et al. [13, 23], the effectiveness of hydrated lime to the foamed WMA was investigated and it was concluded that the performance is particle size dependent. This paper extends the authors pioneer work to study the effect of NHL modification on moisture susceptibility of the foamed WMA mixes. The foamed mixes were produced by using the water-bearing additive, Advera®, and a water-based laboratory foaming method. The |E*| test was performed along with the TSR test since the latter shows variability and less connectivity to the moisture susceptibility in the field [24, 25]. The |E*| test was performed on dry samples and one and five cycles-conditioned samples. This will help address the short- and long-term performance of the mixes' moisture susceptibility.

2 MATERIALS, MIX DESIGN, AND SAMPLES PREPARATION

Aggregates used in this study were obtained from Hancock, Michigan. The nominal maximum aggregate size for the asphalt mix gradation was ½″ (12.5-mm) sieve. The E3 mix design traffic level for this gradation is used which is designed to withstand traffic levels greater than 1 million ESALS (Equivalent Single Axle Load) and lower than 3 million according to Michigan Department of Transportation specifications [26]. One original asphalt binder (PG 58-28) from Gladstone, Michigan was used throughout the entire study. The optimal asphalt binder content for the control asphalt mixes using this gradation is 5.7% (by the weight of

the mix). Adjustments were made to the number of gyrations during compaction to achieve desired air voids about 7 ± 1% which simulates the air void content in early stages after pavement construction [27, 28]. All samples were compacted using a Superpave™ gyratory compactor to 51 gyrations to obtain samples that are 100-mm in diameter and approximately 150-mm in height.

Hydrated lime materials used in this study included RHL and NHL (50-nm and 100-nm). The Scanning Electron Microscopy (SEM) images of RHL and NHL materials are shown in Figure 1a, and b, respectively. The RHL was added to the asphalt binder with the ratio of 20% (normal dose in the field), while the NHL was added with the ratios of 5, 10, and 20%, all by the weight of the binder. To ensure the dispersion of the NHL particles into asphalt binder after mixing, the deagglomeration within the NHL-modified asphalt admixture is discussed in the following section. Advera® is a mineral foaming additive used to produce WMA. The SEM image of the crystalized structure of Advera® material is shown in Figure 1c. Advera® WMA is a synthetic mineral of a standard size contains 18–20% moisture, is released at temperatures above 100°C. The release of moisture out of the sub-micron pore causes micro bubbles which decrease the overall viscosity and enhance the workability of the asphalt mix. The Advera® foaming effect lasts for about 6 to 7 hours which gives long lasting workability [29, 30]. The foaming effect is minimized to a certain time due to loss of water in the bag-house at the asphalt plant [31]. The foamed mixes were produced by adding Advera® to the binder with the ratios of 3, 4.5, and 6% (all by the weight). The corresponding ratios were selected to represent 0.15, 0.25 (normal dose in the field), and 0.35%, all by the weight of the mix, respectively. A laboratory water foaming setup also was used to produce the foamed WMA. The water was injected in the asphalt binder by the ratio of 1.5% (by the weight). A detailed procedure to produce the foamed asphalt using the laboratory setup is reported

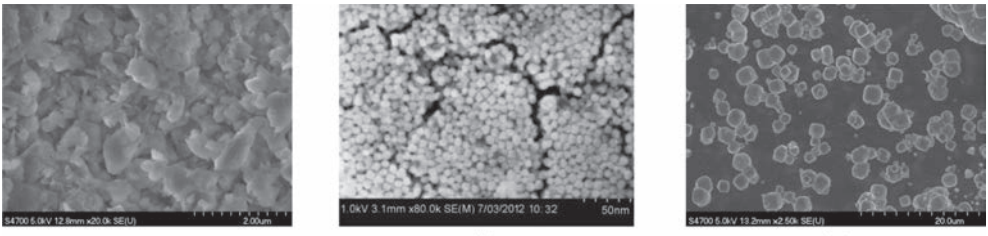

Figure 1. SEM images: (a) RHL, (b) NHL (50-nm) [13, 23], and (c) Advera®.

Table 1. Description of binders used to prepare different mixes.

Mix descriptor	Description of binder used to prepare the mix
Control	Original binder
50-nm (20%)	20% NHL (50-nm)-modified binder
AD (4.5%)	Original binder foamed with 4.5% Advera®
AD (4.5%)_50-nm (20%)	20% NHL (50-nm)-modified binder foamed with 4.5% Advera®
AD (3%)_50-nm (10%)	10% NHL (50-nm)-modified binder foamed with 3% Advera®
AD (4.5%)_50-nm (10%)	10% NHL (50-nm)-modified binder foamed with 4.5% Advera®
AD (6%)_50-nm (10%)	10% NHL (50-nm)-modified binder foamed with 6% Advera®
AD (4.5%)_50-nm (5%)	5% NHL (50-nm)-modified binder foamed with 4.5% Advera®
AD (4.5%)_RHL (20%)	20% RHL-modified binder foamed with 4.5% Advera®
AD (4.5%)_100-nm (20%)	20% NHL (100-nm)-modified binder foamed with 4.5% Advera®
W (1.5%)	Original binder foamed with 1.5% water
W (1.5%)_50-nm (10%)	10% NHL (50-nm)-modified binder foamed with 1.5% water
W (3%)_50-nm (10%)	10% NHL (50-nm)-modified binder foamed with 3% water

Table 2. Range of mixing and compaction temperatures of HMA mixes.

Binder descriptor	Range of mixing temp. (°C)	Range of compaction temp. (°C)
Control	152–156	137–142
50-nm (20%)	167–171	152–158

in details elsewhere [32]. More information about different materials and preparation can be found in related studies [13, 23]. The detailed description of binders used to prepare different WMA and HMA mixes is presented in Table 1. Hydrated Lime (RHL and NHL) and Advera® materials were added with no additional mix design. To avoid the deviation of mix gradation, the percent hydrated lime added was substituted for a portion of the baghouse fines and the asphalt content remained constant for all mixes. The volumetric properties of the all mixes were evaluated again to make sure the target air voids ratio is within limits. Three samples were prepared for each mix type. The TSR samples were prepared by sawing the |E*| samples to a final size of 100-mm diameter and approximately 63.5-mm height. All WMA mixes prepared using Advera® and laboratory water foaming method were mixed and compacted at a temperature of 130°C. Using the rotational viscosity test, the mixing and compaction temperatures for the HMA mixes were determined by using the viscosity against temperature relationship from which the viscosity was 0.17 ± 0.02 Pa-s and 0.28 ± 0.03 Pa-s for the mixing and compaction temperature, respectively. The HMA mixes were prepared according to the mixing and compaction temperatures range shown in Table 2.

3 STUDYING THE DISPERSION AND DEAGGLOMERATION OF NHL INTO THE ADMIXTURE

Concerns have arisen of the excessive agglomeration of NHL particles after mixing with asphalt binder especially if the NHL is added with higher percentages (20%). The agglomeration problem is one challenging issue for pavement scientists and unfortunately there is no unified and accurate method to quantify the dispersion and deagglomeration of the modifier into the admixture. This study employed the so-called Energy Dispersive X-ray Spectroscopy (EDX or EDS) technique to study the dispersion and deagglomeration potential within the admixture. EDX is a relatively simple yet powerful technique used to qualitatively and quantitatively identify the elemental composition of as little as a cubic micron of material. The theory behind EDX technique is that each element into the material has a unique atomic structure allowing unique set of peaks on its X-ray spectrum [33]. The equipment is attached to the SEM machine to allow for elemental information to be gathered about the specimen under investigation. EDX works by detecting X-rays that are produced by a sample placed in an electron beam. The electron beam excites the atoms in the sample that subsequently produce X-rays to discharge the excess energy. As the electron beam can be precisely controlled, EDX spectra can be collected from a specific point/particle on the sample, maps can be acquired which depict a localized chemical analysis across the specimen. In this study, the technique was used to depict a qualitative analysis by mapping the concentrations of Calcium (Ca) element present in the NHL ($Ca(OH)_2$)-modified asphalt binder. A 50-nm NHL (20%)-modified binder sample was cryo sectioned and placed uncoated onto a copper grid and then mounted on an Al mount and imaged using the SEM. The EDX was run using Aztec, Oxford system at Clemson University. From the acquired image shown in Figure 2, there is a small concentration of the NHL particles in some parts of the sample, and almost no concentration in most parts of the sample. The small concentrations can be attributed to the less capability of the high shear mixer to completely disperse and deagglomerate the nanoparticles in the asphalt binder. However, the majority of the image shows satisfactorily dispersed and deagglomerated NHL particles within the asphalt binder.

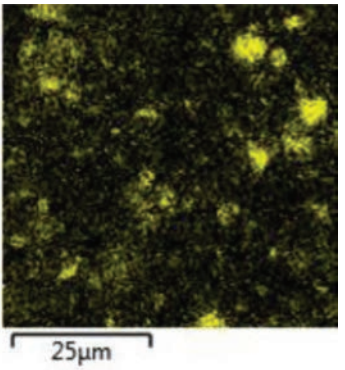

Figure 2. Ca element mapping of 50-nm NHL (20%)-modified binder admixture.

4 MOISTURE CONDITIONING

For the TSR testing, the samples were split into two sets: one of the sets was used unconditioned and the second set was conditioned with one freeze-thaw cycle. |E*| and the second set of TSR samples were vacuum saturated for 5 to 10 minutes at 13–67 kPa. It is worth noting that the |E*| test first was performed on the dry samples according to the AASHTO TP62-03 procedure [34] before passing any conditioning (one and five freeze-thaw cycles). After vacuum saturating, the samples (TSR or |E*| samples) were left submerged in a water bath for 5 to 10 minutes. The degree of saturation was calculated for the samples. If the degree of saturation was between 70% and 80%, the next step proceeded. The vacuum saturation is repeated if the degree of saturation is less than 70%, and the sample is considered damaged and discarded if saturation is greater than 80%. The next step is to bring each valid vacuum saturated sample tightly covered with a plastic wrap and placed into a plastic bag with approximately 10 ± 0.5-ml of water, and sealed. The one freeze-thaw cycle includes: placing the plastic bags in a freezer at –18°C for 16 hours and then placing the samples in a water bath at 60°C for 24 hours with a minimum 25-mm of water above the samples. After the cycle is done, the TSR samples were then placed in a water bath at 25°C for 2 hours with approximately 25-mm of water above the samples before the Indirect Tensile Strength (ITS) testing. The |E*| samples were dried and kept in the Universal Testing Machine (UTM-100) environmental chamber that was set to the designated testing temperature. After |E*| testing, the same samples were brought to four more freeze-thaw cycles prior to another testing.

5 EVALUATION OF MOISTURE SUSCEPTIBILITY

5.1 *Tensile Strength Ratio (TSR)*

The testing procedure of TSR followed the AASHTO T283 procedure [35]. The testing was run after one freeze-thaw cycle conditioning of the samples as described before. The UTM-100 machine was used to determine peak ITS. The TSR value is calculated as the ratio, $[ITS]_{cond.}/[ITS]_{dry}$ of conditioned ITS ($[ITS]_{cond.}$) and dry ITS ($[ITS]_{dry}$). In Superpave™ design, if the average retained strength of the conditioned sample strength is less than 80% of the dry sample strength, the mix is considered to be moisture susceptible. Although the AASHTO T283 is predominately used in the Superpave™ system to evaluate moisture susceptibility of asphalt mixes, many studies have shown the AASHTO T283 to be highly variable. In a study by Zhu and Liang [24], it was found that the AASHTO T283 is highly variable due to specified allowable saturation levels. It was stated that more research work is needed to develop an alternative to the AASHTO T283. In a study conducted by National Cooperative Highway Research Program [25], the laboratory moisture susceptibility tests of the mixes did not satisfactorily match the observed behavior of the field for a number of data groups.

Therefore, adequate moisture susceptibility tests need to be developed for proper evaluation. Diab and You [36] presented a conditioning procedure and evaluation parameter of the mixes' moisture susceptibility based on the |E*| testing.

5.2 *Dynamic modulus (|E*|)*

The |E*| is a fundamental test that captures the viscoelastic behavior of the asphalt mixes, has been used by researchers for moisture susceptibility evaluation on samples conditioned using the environmental conditioning system [37]. Following the AASHTO TP62-03 [34], the test was performed at the temperatures of 4.4°C (40°F), 21.1°C (70°F) and 37.8°C (100°F), and frequencies at each temperature of 0.1, 0.5, 1, 5, 10 and 25 Hz. The samples used in this testing were 100-mm in diameter and approximately 150-mm in height. Load levels were determined by trial and error so that the resulting recoverable axial micro-strain was between 75 and 125 to ensure that the material is in the viscoelastic range [38]. The applied stress and the resulting recoverable axial strain response of the specimen are measured and used to calculate the |E*|. Because the material is being tested in its linear viscoelastic range, no damage is induced and the accumulating strain is due to viscoelasticity only [39]. Therefore, the test can be performed many times on the same samples (dry samples, one and five cycles-conditioned samples). For better explanation of the asphalt mix's performance, |E*| values measured over a range of temperatures and frequencies of loading can be shifted into a master curve for analysing. In general, the master curve can be mathematically represented by a sigmoidal function [40].

6 RESULTS AND DISCUSSION

6.1 *Tensile Strength Ratio (TSR)*

The TSR is used to characterize the moisture susceptibility of asphalt mixes. The minimum TSR necessary to ensure good pavement performance has not yet been identified positively; however, a TSR of 0.8 after one freeze-thaw cycle is generally considered to be a reasonable minimum value under the current Superpave™ mix design system. Figure 3 shows the TSR values calculated from the average dry and conditioned ITS values. The Advera® foamed mix experienced a TSR lower than 0.8 after one freeze-thaw cycle. This proves that the Advera® foamed mixes are more susceptible to moisture damage than the control counterpart. The decrease of the TSR can be attributed to the loss of adhesion between aggregates and

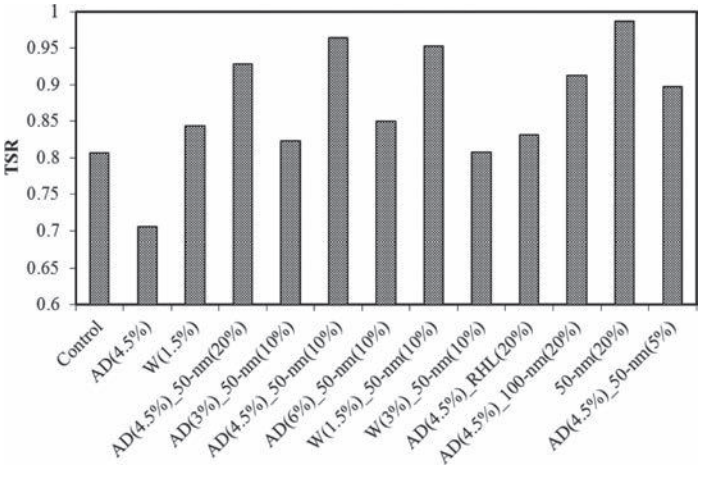

Figure 3. TSR results for different mixes.

asphalt due to the released water. Additionally, the lower compaction temperature used when producing WMA mixes may increase the potential for moisture susceptibility due to inadequate drying of aggregates. The increase of TSR for the control mix can also be attributed to the over aging of the binder compared to the foamed mix. On the other hand, all hydrated lime (RHL and NHL)-modified mixes passed the TSR criteria (>80%). However, the NHL is more competitive in comparison to the RHL. The 50-nm (20%) mix showed a higher TSR value among all the studied mixes. The shown results prove that the hydrated lime particle sizes play an important role in the mitigation of the moisture susceptibility of the asphalt mixes. Generally, the effect of hydrated lime in reducing the moisture susceptibility of mixes has several mechanisms which have been proposed to account for its beneficial effect [41]. The unfoamed NHL-modified mix (50-nm (20%) showed a higher TSR value in comparison to the foamed mix (AD (4.5%)_50-nm (20%)). The increase of water foaming ratio from 1.5% to 3% sharply decreases the TSR values of the NHL-modified mix. However, there is no definite trend of the TSR values for the mixes foamed with different Advera® ratios (3%, 4.5% and 6%). Due to the variability and less connectivity between TSR results and field performance [24, 25], the |E*| also was performed to evaluate the moisture susceptibility since it has been recognized as a fundamental test for asphalt mixtures. Performing the |E*| test would manage the inconsistency encountered from the TSR test results.

6.2 *Dynamic modulus (|E*|)*

The |E*| is suggested to be the best indicator for asphalt pavement distresses [42]. A higher value of the |E*| at a high temperature or low frequency indicates that the asphalt mix has higher rutting resistance and a lower |E*| value at a low temperature or high frequency indicates that the asphalt mix has lower fatigue cracking potential [43]. The test was utilized in this study to evaluate the moisture susceptibility of different asphalt mixes. In order to have a better comparison between different mixes throughout all the temperatures and frequencies, sigmoidal master curves were constructed at a reference temperature of 21.1°C (70°F). The master curves were constructed for dry mixes and one cycle-conditioned mixes as shown in Figures 4 and 5, respectively. Based on the test results shown in Figure 4, it was seen that the addition of NHL increases the |E*| value when compared to the unmodified mixes (control and foamed). It can also be seen that the |E*| of the dry control mix is much lower than the modified mixes and is a little higher than the Advera® and water foamed mix. The increase

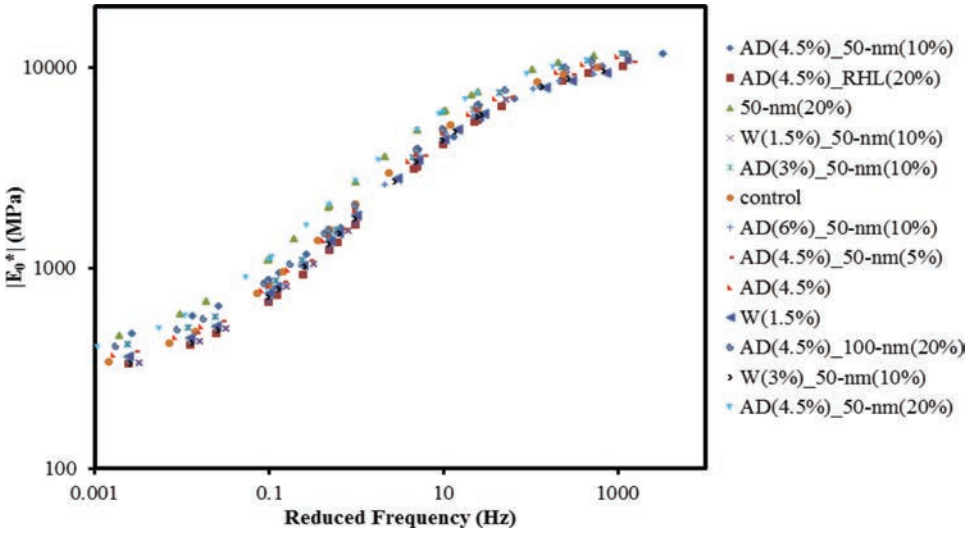

Figure 4. Master curves for dry mixes.

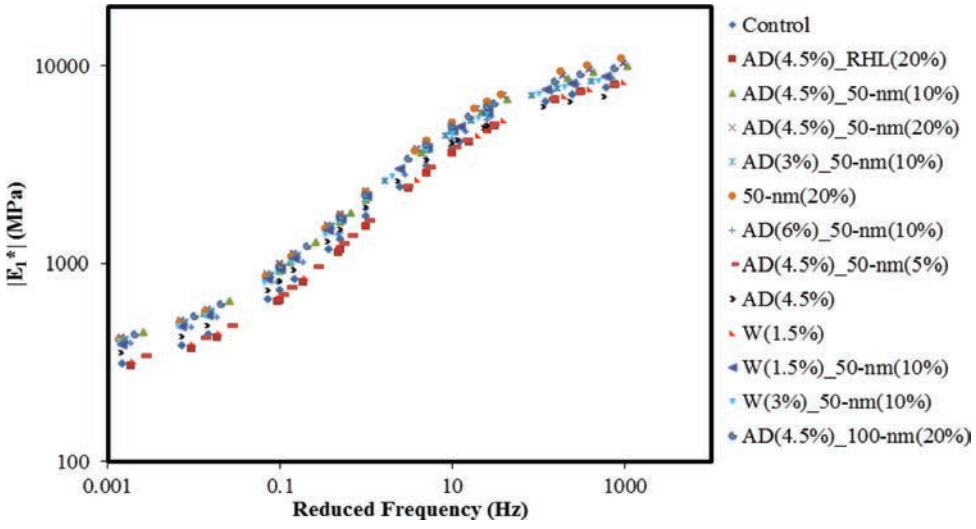

Figure 5. Master curves for one cycle conditioned mixes.

of |E*| of control mix can be attributed to the over aging of the control mix compared to unmodified WMA mixes. However, the water foamed mix shows much lower decrease of the |E*|. The 50-nm (20%) showed a higher |E*| compared to the foamed mix (AD (4.5%)_50-nm (20%)), but this probably can be due to the 50-nm (20%) being over aged since it was prepared as HMA mix (Table 2). The |E*| results of the 100-nm mix are slightly lower than that of the 50-nm. The NHL-modified mixes are more competitive than RHL.

This proves the importance of hydrated lime particle size on the mechanical properties of the mix. The RHL results are very close to the 5% NHL (50-nm)-modified mix results. Comparing the 50-nm (10%) mixes foamed with two percentages of water (1.5% and 3%), it is quite clear that the increase of water significantly decreases the |E*| of the mix. The water foaming adversely affects pavement moisture susceptibility. The existence of water in the asphalt-aggregate matrix is often one of the major factors affecting the durability of mixes. Figure 5 shows that the hydrated lime-modified mixes show higher |E*| values compared to the unmodified mix. The unfoamed NHL-modified mix (50-nm (20%)) slightly increases the |E*| compared to the AD (4.5%)_50-nm (20%) after conditioning. The NHL-modified mixes show higher |E*| values compared to the RHL.

Two ratios were suggested, $R_{0-1} = (|E_0^*| - |E_1^*|)/|E_0^*|$ and $R_{0-5} = (|E_0^*| - |E_5^*|)/|E_0^*|$ to imply how much the dry modulus, $|E_0^*|$, decreased after one and five cycles conditioning ($|E_1^*|$ and $|E_5^*|$, respectively). These ratios would give more information about the effect of short- and long-term conditioning on |E*| for these mixes. The average ratio for all testing temperatures and frequencies was calculated for the control and unmodified foamed mixes and plotted in Figure 6. It should be noted that the two ratios were calculated from mater curves results. It is quite clear from this figure that the foamed mixes exhibited more moisture deterioration after conditioning compared to the control mixes. The control mix deteriorated more slowly compared to the foamed mixes after five cycles conditioning. The Advera® foamed mix deteriorated much more than that foamed with water.

This study suggests that one cycle conditioning is not enough to measure the moisture susceptibility of different mixes. The long-term susceptibility is also essential to completely understand the moisture susceptibility.

6.3 *Comparison between TSR and |E*| results*

Several laboratory test methods have been developed to assess the moisture susceptibility of HMA mixes. Although providing useful information, these tests still do not entirely simulate

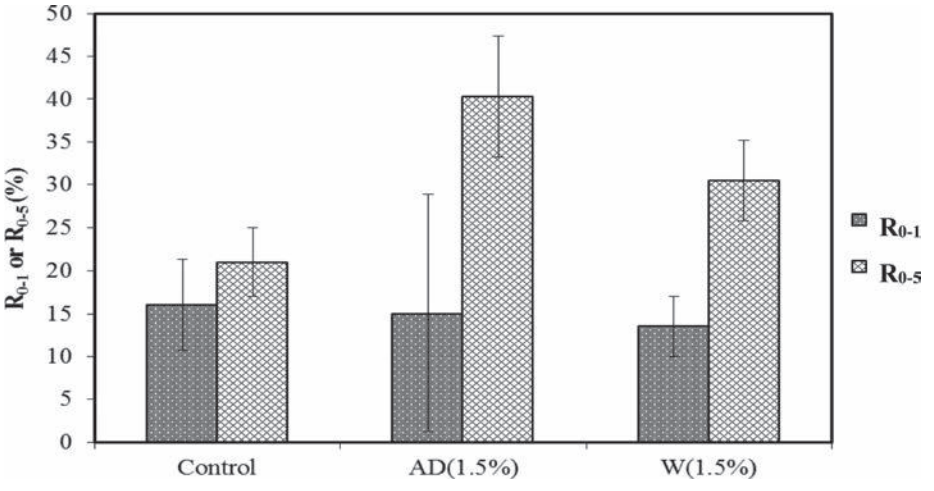

Figure 6. Effect of different conditioning cycles on |E*| ratios (R_{0-1} and R_{0-5}).

field conditions. Most state highway agencies use the AASHTO T 283 test, although they still have concerns about the variability of the test results. Since the current AASHTO T 283 is highly variable [24], Hicks et al. [44] pointed out the need of updating the moisture susceptibility test method that can accurately determine moisture damage resistance of Superpave™ mixes.

By comparing the |E*| and TSR tests results presented above, although the |E*| does not provide a criterion of moisture susceptibility, it seems more representative and comparative than TSR since the test has been run on the same sample after conditioning. The |E*| values of the water foamed mixes are lower than the Advera® foamed, contradicting the TSR results. In another study [36], the authors developed test and parameter to evaluate a moisture influence on asphalt durability based on the |E*| test. Future work will be implemented to validate that methodology and present evaluation criterion based on the |E*| test.

7 CONCLUSIONS AND RECOMMENDATIONS

The primary objective of this research was to investigate the effectiveness of the moisture susceptibility of NHL-modified foamed WMA using the TSR and |E*| tests. A secondary objective of this research was to assess the validity of the two utilized TSR and |E*| tests. RHL was used along with the NHL in this investigation. The NHL was used with two particle sizes of 50-nm and 100-nm. The foamed asphalt was produced by adding Advera® and by using the water-based laboratory foaming method. From the study results, the Advera® foamed mixes did not pass the TSR requirement which means that it is more susceptible to moisture damage compared to the control mixes. The NHL-modified mixes showed less susceptibility to moisture damage compared to the RHL mixes. The Advera® and water foamed mixes are more sensitive to long-term conditioning compared to the control mixes. This study suggests investigating the long-term performance of the moisture susceptibility by using multiple conditioning cycles. The |E*| test has been run on the same sample after conditioning, therefore, it is more representative to the moisture susceptibility of the asphalt mixes than the TSR.

ACKNOWLEDGEMENTS

The authors would like to express their gratitude to Joan Hudson, senior scientist and director of Clemson University Electron Microscopy Facility for assisting in Energy Dispersive X-Ray Spectroscopy images.

REFERENCES

[1] De Groot, P., Bowen, C., Koenders, B., Stoker, D., Larsen, O., and Johansen, J., A comparison of emissions from hot mixture and warm asphalt mixture production. Proc., 14th IRF World Road Congress, International Road Federation (IRF), Geneva, 2001.

[2] Larsen, O., Moen, Ø., Robertus, C., and Koenders, B., WAMFoam asphalt production at lower operating temperatures as an environmental friendly alternative to HMA. Proc., 3rd Eurasphalt and Eurobitume Conference, Book 1, Foundation Eurasphalt, Breukelen, Netherlands, pp. 641–650, 2004.

[3] Cervarich, M., Cooling Down the Mix—New "Warm Mix Asphalt." Technologies Developed in Europe, Hot Mix Asphalt Technology. National Asphalt Pavement Association, Lanham, MD, pp. 13–16, 2003.

[4] Prowell, B.D., Hurley, G.C., and Crews, E., Field performance of warm-mix asphalt at National Center for Asphalt Technology Test Track. In Transportation Research Record: Journal of the Transportation Research Board, No.1998, Transportation Research Board of the National Academies, Washington, D.C., pp. 96–102, 2007.

[5] D'Angelo, J., Harm, E., Bartoszek, J., and et al., Warm-mix asphalt: European practice. Tech. Rep. FHWA PL-08-007, FHWA, AASHTO, NCHRP, Alexandria, Va, USA, 2008.

[6] Croteau, J-M and Tessier, B., Warm mix asphalt paving technologies: a roadbuilder's perspective. In Proceedings of 2008 Annual Conference of the Transportation Association of Canada. Polyscience Publications Inc., Laval, Quebec, Canada, 2008.

[7] Perkins, S.W., Synthesis of Warm-mix Asphalt Paving Strategies for use in Montana Highway Construction. Final Project Report. Western Transportation Institute, Montana State University, Bozeman, MT, USA, 2009.

[8] Anderson, R.M., Baumgardner, G., May, R., and Reinke, G., NCHRP 9-47: engineering properties, emissions, and field performance of warm mix asphalt technologies. Interim Report, National Cooperation Highway Research Program, Washington, DC, USA, 2008.

[9] Kuennen, T., RoadScience. http://www.expresswaysonline.com/pdf/BR%20RS%20AUG%20 2012%20 LOW%20ENERGY%20MIXES.pdf, 2012.

[10] Masson, J.F., Pelletier, L., and Collins, P., Rapid FTIR method for quantification of styrene–butadiene type copolymers in bitumen. J Appl Polym Sci; 79:1034–41, 2001.

[11] Miura, K., Mae, K., Li, W., and Kusakaw, T., Energy & Fuels 15:599, 2001.

[12] Larsen, J.W., Green, T.K., and Kovacn, J., J. Org. Chem. 50:4729, 1985.

[13] Diab, A., You, Z., and Wang, H., Using Modified Creep and Recovery Tests to Evaluate the Foam-based Warm Mix Asphalt Contained Nano Hydrated Lime. Advanced Materials Research Vol. 646 (2013) pp 90–96 © (2013) Trans Tech Publications, Switzerland doi:10.4028/www.scientific.net/AMR.646.90, 2013.

[14] http://foam101.info/Basics/FoamedAsphalt.html.

[15] Kvasnak, A., Taylor, A., Signore, J., and Bukhari, S., Evaluation of Gencor Green Machine Ultrafoam. GX. NCAT Report 10-03. National Center for Asphalt Technology, 2010.

[16] Kvasnak, A., Moore, J., Taylor, A., and Prowell, B., Preliminary Evaluation of Warm Mix Asphalt Field Demonstration: Franklin, Tennessee. NCAT Report 10-01, National Center for Asphalt Technology, Auburn, AL, 2010.

[17] Wielinski, J., Hand, A., and Rausch, D.M., Laboratory and Field Evaluations of Foamed Warm-Mix Asphalt Projects. In Transportation Research Record: Journal of the Transportation Research Board, No. 2126, Transportation Research Board of the National Academies, Washington, D.C., pp. 125–131, 2009.

[18] Abbas, A.R. and Ali, A., Mechanical Properties of Warm Mix Asphalt Prepared Using Foamed Asphalt Binders. Final Report FHWA/OH-2011/6, Federal Highway Administration, Springfield, Virginia, 2011.

[19] Kvasnak, A. and West, R., Case study of warm mix asphalt moisture susceptibility in Birmingham. Transportation Researh Record, 88th Transportation Research Board Annual Meeting, 2009.

[20] Hearon, A. and Diefenderfer, S., Laboratory evaluation of warm asphalt properties and performance. Proc., Airfield and Highway Pavements Conf., ASCE, Reston, VA, 182–194, 2008.

[21] Kanitpong, K., Nam, K., Martono, W., and Bahia, H.U., Evaluation of a warm-mix asphalt additive. Proceedings of the Institution of Civil Engineers, Construction Materials, No. 161, pp. 1–8., 2008.

[22] Su, K., Maekawa, R., and Hachiya, Y., Laboratory Evaluation of WMA Mixture for use in Airport Pavement Rehabilitation. Construction and Building Materials, Vol. 23, pp. 2709–2714, 2009.

[23] Diab, A., You, Z., and Wang, H., Rheology of Aged Foamed Warm Mix Asphalt Modified with Nano-sized Hydrated Lime. 13th COTA International Conference of Transportation Professionals (CICTP 2013), 2013.
[24] Zhu, F. and Liang, R., Developing Simple Lab Test to Evaluate HMA Resistance to Moisture, Rutting, Thermal Cracking Distress. University of Akron, 2008.
[25] Epps, J.A., Sebaaly, P.E., Penaranda, J., Maher, M.R., McCann, M.B., and Hand, A.J., Compatibility of A Test for Moisture-Induced Damage with Superpave Volumetric Mix Design. National Cooperative Highway Research Program Report 444, 2000.
[26] Michigan Department of Transportation (MDOT), Special Provision for Superpave HMA Mixtures. Lansing, MI. p. 6, 2003.
[27] Kandhal, P.S., Moisture susceptibility of HMA mixes, identification of problem and recommended solutions. NCAT No. 92-1, Auburn Univ., Auburn, Ala., 1992.
[28] Kim, S. and Coree, B.J., Evaluation of hot mix asphalt moisture sensitivity using the Nottingham asphalt test equipment. Rep. No. IHRB Project TR-483, Dept. of Civil, Construction, and Environmental Engineering, Iowa State Univ., Ames, Iowa., 2005.
[29] Harnischfeger, S., Aspha-min Retrospectives and Prospects. BASt, Germany, Presentation to WMA Scan Team, 2007.
[30] Hirsch, V., Warm Mix Asphalt Technologies. BASt, Germany, Presentation to WMA Scan Team, 2007.
[31] PQ CORPORATION, Advera® WMA: Production, Testing and Compaction Details. 2012.
[32] Goh, S.W. and You, Z., Moisture Damage and Fatigue Cracking of Foamed Warm Mix Asphalt Using a Simple Laboratory Setup. ASCE T&DI Congress 2011: Integrated Transportation and Development for a Better Tomorrow, Proceedings of the First T&DI Congress 2011, 2011.
[33] Goldstein, J., Scanning Electron Microscopy and X-Ray Microanalysis. Springer. ISBN 978-0-306-47292-3. Retrieved 26 May 2012, 2003.
[34] AASHTO TP 62-03 AASHTO, Standard Method of Test For Determining Dynamic Modulus of Hot-Mix Asphalt Concrete Mixtures. American Association of State Highway and Transportation Officials, 2004.
[35] AASHTO:T283-03, Standard Method of Test for Resistance of Compacted Asphalt Mixture to Moisture Induced Damage. American Association of State Highway and Transportation Officials, 2003.
[36] Diab, A. and You, Z., Development of a Realistic Conditioning and Evaluation System to Study Moisture Damage of Asphalt Materials. Airfield & Highway Pavement Conference, Los Angeles, California, June 9–12, 2013.
[37] Solaimanian, M., Fedor, D., Bonaquist, R., Soltani, A., and Tandon, V., Simple Performance Test for Moisture Damage Prediction in Asphalt Concrete. Journal of the Association of Asphalt Pavement Technologists, 75, 345–380, 2006.
[38] Witczak, M.W., Specification Criteria for Simple Performance Tests for Rutting. Arizona State University; Report nr NCHRP Report 580, 2007.
[39] Kim, Y.R, Daniel, J.S., and Wen, H., Fatigue Performance Evaluation of West Track Asphalt Mixtures Using ViscoelasticContinuum Damage Approach Final Report (Report No. FHWA/NC/2002-004) To North Carolina Department of Transportation,(Research Project No. HWY-0678), 2002.
[40] Applied Research Associates (ARA), Guide for Mechanistic-Empirical Design of New and Rehabilitated Pavement Structures. Report I-37A, National Cooperative Highway Research Program, Champaign, Illinois, 2004.
[41] Huang, S.C., Robertson, R.E., and Branthaver, J.F., Physico-Chemical Characterization of Asphalt-Aggregate Interactions under the Influence of Freeze-Thaw Cycles. TRB Annual Meeting., 2003.
[42] Pellinen, T.K., Investigation of the use of dynamic modulus as an indicator of hot-mix asphalt performance. PhD Dissertation, Department of Civil and Environmental Engineering, Arizona State University, 2001.
[43] Witczak, M.W., Simple Performance Tests: Summary of Recommended Methods and Database. Transportation Research Board. 23p, 2005.
[44] Hicks, R., Leahy, R., Cook, M., Moulthrop, J., and Button, J., Road Map for Mitigating National Moisture Sensitivity Concerns in Hot Mix Pavement. 83rd Transportation Research Board Annual Meeting, Washington, D.C., 2004.

This page intentionally left blank

Microstructural characterization and micromechanics of asphaltic materials—III

This page intentionally left blank

Asphalt Pavements – Kim (Ed)
© 2014 Taylor & Francis Group, London, ISBN 978-1-138-02693-3

Microstructure-property relationships of Sasobit modified Warm Mix Asphalts

Qian Qin
GAF Materials, Ennis, TX, USA

Adam T. Pauli & Michael J. Farrar
Western Research Institute, Laramie, WY, USA

ABSTRACT: Driven by the economic and environmental concerns over the burning fuel emission from asphalt industry, the Warm Mix Asphalt (WMA) technology has been drawing substantial attention in the past decade by achieving a mixing temperature reduction of about 18–54 °C. This paper focuses on effect of one of WAM additives (Sasobit) on asphalt properties and explores the microstructure-property relationships of Sasobit modified asphalts. A 3-D network or pseudo-solid like structure of 3% Sasobit modified WMA is demonstrated both rheologically and morphologically. The network microstructure not only contributes to the blend stiffening resulting in the limiting high temperature being expanded by 5–16 °C, but also accounts for the breakdown of time-temperature superposition at temperature above 30 °C. At Sasobit loading concentration of 1%, dendrites rather than typical "bee structure" are observed. The pseudo-solid or dendritic microstructure only depends on the Sasobit concentration, regardless of asphalt types and grades investigated. Additionally, by using 4 mm parallel plates DSR at low temperatures after proper machine compliance corrections, we were able to obtain the limiting low temperatures, suggesting Sasobit doesn't influence low temperature performance of asphalts in an undue adverse manner.

Keywords: warm mix asphalt, rheology, Sasobit, microstructure, wax

1 INTRODUCTION

As an alternative for Hot Mix Asphalt (HMA), Warm Mix Asphalt (WMA) technology has been drawing substantial attention in the past decade [1–5]. By achieving significant mixing temperature reduction, WMA technology is highly desirable economically and environmentally with the immediate benefit of reducing energy consumption and reducing emission from burning fuels and fumes at asphalt plants and paving sites [1–2].

The focus of this paper is on one of the WMA organic additives called Sasobit®. It is a crystalline, long-chain aliphatic hydrocarbon compound with the melting temperature between 70 °C and 120 °C [3–5]. The melting temperature is high enough to make Sasobit maintain its crystalline structure at pavement service temperatures, imparting a stiffening effect. At temperatures above its melting point, Sasobit acts as a flow improver by lowering the viscosity of the asphalt enabling mixing and compaction temperatures to be reduced by 18 to 54 °C [4, 6].

There have been numerous studies on Sasobit modified binders [7–14], however, only limited systematic work on the correlation between structure and viscoelasticity has been performed. Recently, Polacco and coworkers conducted a comprehensive study regarding the effect of different types of waxes on asphalt morphology, residual crystallinity and mechanical properties [15]. A gel structure of asphalt blends with Fischer-Tropsch (FT) type waxes was suggested by observed high penetration index and low values of phase angle (55 °–65 °) [15].

In this paper, we present direct rheological and morphological evidence for a gel-like or pseudo-solid structure of Sasobit modified WMA. Further, we suggest the sol-gel transition not only on the surface of those blends as depicted by Atomic Force Microscopy (AFM), but also extends to the bulk. The effects from binder types and grades are also investigated in terms of how they impact microstructures and viscoelasticity of Sasobit blends. The objective of this work is to explore the microstructure-property relationship of Sasobit modified binders so as to have a better understanding of their linear viscoelasticity and applications.

2 EXPERIMENTAL

2.1 *Materials*

Four asphalt binders with different types and grades were used as control binders in this study and they are listed in Table 1.

1% and 3% Sasobit loading concentrations (by weight) were selected for this study because 3% is typically the maximum loading concentration above which the low temperature performance of Sasobit modified WMA would be negatively affected [4, 16].

Sasobit modified binders were prepared by heating asphalt to 150 °C, followed by addition of pre-weighted Sasobit and subsequent gentle stirring. The modified asphalt blend was maintained at 150 °C for approximately one hour with occasional stirring to achieve a homogeneous blend. With this type of treatment asphalt should only undergo mild oxidation.

2.2 *Experimental methods*

2.2.1 *Characterization of thermal properties*

Thermal properties were measured using a TA instruments Q2000 Differential Scanning Calorimeter (DSC). Melting temperature (T_m) and heat of fusion (ΔH_f) of Sasobit component were determined from the heating scan made at 10 °C/min, after cooling from 165 °C to –90 °C at 5 °C/min and subsequently isothermal holding at –90 °C for 5 minutes.

The glass transition temperatures of the asphalt component were measured using Temperature Modulated DSC (TMDSC) technique. TMDSC can clearly separate glass transition from other complex overlapped effects, such as cold-crystallization and enthalpy recovery by dividing the total heat flow into reversing and non-reversing parts [17]. The sample was first heated and equilibrated at 165 °C before cooling down to –90 °C. At –90 °C, the sample was held isothermally for 5 minutes, which was followed by a heating scan to 165 °C. Both the cooling and subsequent heating scans were run at the average rate of 2 °C/min with modulation amplitude of 0.5 °C every 80 seconds. The limiting fictive temperature T_f' was determined from the reversing heat flow curve during the second heating scan. T_f' was used as the glass transition temperature T_g due to the widely accepted concept that T_f' is approximately equal to T_g obtained from the cooling scan at the same scan [18, 19].

Table 1. Description of control binders.

Asphalt binder	PG grade	Description
MB	PG 58-28	Unmodified binder from Manitoba, Canada, 150/200 pen, Canadian blend
MN1-3	PG 58-28	Unmodified binder from Rochester Minnesota, Canadian blend
MN1-4	PG 58-28	Unmodified binder from Rochester Minnesota, Blend: Arab heavy, Arab medium, and Kirkuk
YNP	PG 58-34	SBS modified binder from Yellow Stone National Park

2.2.2 *Rheological measurements*

The rheological experiments of the control binders and Sasobit modified binders were conducted with 4 mm diameter parallel plate geometry and a 1.75 mm gap over a temperature range from –30 °C to 30 °C. At 50 °C and 70 °C, the 25 mm diameter parallel plate and a 1 mm gap were used. The dynamic data presented are corrected for machine compliance. The detailed procedure for rheometer compliance correction and equations for obtaining true sample moduli are listed in the literature [20].

2.2.3 *Morphological characterization by AFM imaging*

A Quesant Q-Scope™ 250 Atomic Force Microscopy (AFM) was used to image thin films of asphalt binders and Sasobit modified binders in dynamic wave mode. The thin films were prepared by spin casting of toluene solution of asphalt onto a borosilicate glass microscope slide at 400 rpm. Resultant films were annealed at 64 °C for 2 hours, then rapidly cooled to room temperature prior to imaging. Samples were imaged in the intermittent contact mode (BB Wavemode® per Ambios terminology) under dry nitrogen at room temperature (~24 °C). Topography, phase contrast, and error (derivative) images were collected simultaneously for each sample. All of the images shown are 80 × 80-μm, and all were collected using a scan rate of 1 Hz.

2.2.4 *Fourier Transform Infrared Spectroscopy (FTIR)*

The infrared spectroscopy was performed with a Perkin Elmer 100 FTIR spectrometer equipped with a Universal Attenuated Total Reflectance (ATR) accessory. The Sasobit was molded into a small disk with a flat surface and then smeared onto the ATR diamond. All IR spectra were obtained over a wave number range of 4000–600 cm^{-1} at a resolution of 4 cm^{-1} and 32 scans.

3 RESULTS

3.1 *Thermal analysis and structural characterization*

The limiting fictive temperatures or equivalent glass transition temperatures are listed in Table 2. No significant shifts in glass transition temperatures of the Sasobit blend were observed. Although the heat flow curves and temperature derivative of heat capacity (dC_P/dT) are not shown, it was found that no broadening of glass transition occurs upon the addition of Sasobit into asphalt binders. Those facts imply an absence of strong interactions between Sasobit and asphalt moieties.

The DSC endotherm of Sasobit wax exhibits two characteristic peaks with the onset melting temperature of 77 °C and peak melting temperatures of about 95 °C and 110 °C shown in Figure 1. Given the apparent linear molecular arrangement of Sasobit suggested by FTIR spectrum in Figure 2, two endo-peaks of Sasobit are ascribed to the mixture of linear long chain aliphatic hydrocarbons with melting temperatures of 95 °C and 110 °C.

Table 2. Limiting fictive temperature (T_f') of sasobit modified asphalts.

	T_f' (°C)		
Samples	0% Sasobit	1% Sasobit	3% Sasobit
MB	–18.6	–18.9	–19.0
MN1-3	–18.3	–18.7	–19.0
MN1-4	–23.0	–22.5	–23.3
YNP	–21.4	–21.2	–20.1

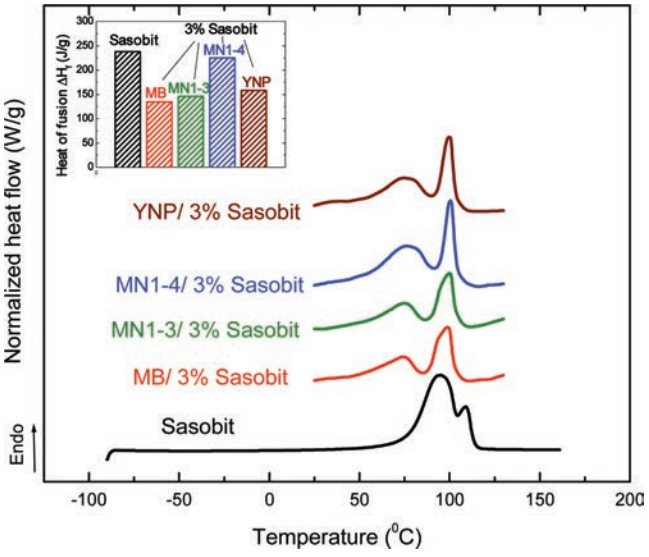

Figure 1. DSC endotherms and heat of fusion (inset plot) of sasobit and 3% sasobit modified binders. (The heat flow was normalized by the sasobit weight).

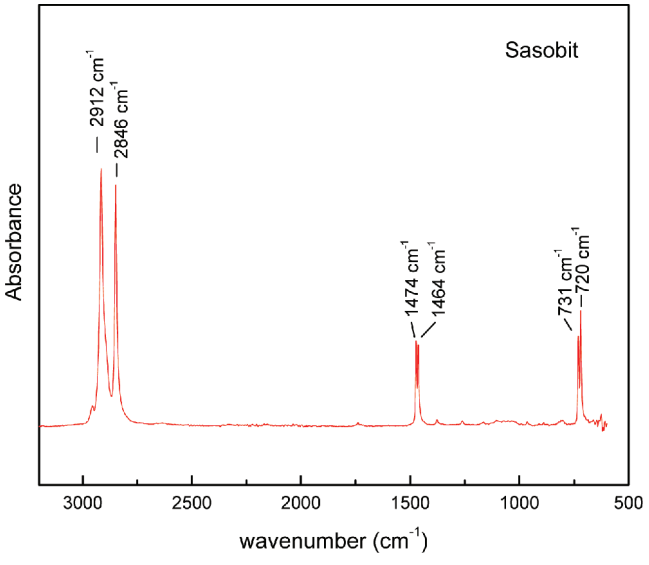

Figure 2. FTIR spectrum of sasobit illustrating the dominance of the linear chains in sasobit. (Strong absorptions at 2912 cm^{-1} and 2846 cm^{-1}: C-H stretching; 1474 cm^{-1}: C-H scissoring; 1464 cm^{-1}: C-H bending; weak absorption at around 720 cm^{-1}: C-H long chain (rocking). No significant absorbance at ~1375 cm^{-1} indicates little branching).

Upon blending the binders with 3% Sasobit, both the melting point and heat of fusion of Sasobit are depressed as seen in Figure 1. Based on the Gibbs-Thomson effect [21, 22], the depressed melting point suggests a smaller crystal size is favourable for Sasobit modified asphalt binders. The observed decrease in the heat of fusion is attributed to the finite size effect or reduced Sasobit crystal size, which is consistent with literature results for small molecules confined in controlled porous media [22–24] and melting of metallic nanocrystals [25].

3.2 *Rheological properties*

Figure 3 is the rheological results for the MN1-4 asphalt binder and its Sasobit blends. The van Gurp-Palmen plots [26] were used to test the applicability of time-Temperature Superposition (tTS) principle. tTS holds for the control binder. Upon the additon of 3% Sasobit, the van Gurp-Palmen plots lose their single curve characteristics above 30 °C, suggesting the break-down of tTS. Although not shown, 3% modified MB, MN1-3 and YNP binders also exhibit deviation from tTS. The DSC results on these samples indicated the onset melting temperature of Sasobit component is higher than 30 °C, therefore, the melting of Sasobit crystals cannot totally account for the failure of tTS for 3% Sasobit modified binders. That fialure is thought to be due to microstructural changes in the blends, leading to different relaxation functions within the binder. This concept will be discussed in more detial later in the paper.

3.2.1 *Low temperature rheology*

Creep stiffness S(t) and creep rate (m-value) have been widely accepted as two important parameters to characterize the low temperataure properties of asphalt binders. The results are listed in Table 3. Instead of using Bending Beam Rheometer (BBR), an estimate of creep stiffness and m-value was obtained from low temperature 4-mm DSR data after machine compliance correction by converting the dynamic modulus to the relaxation data [27].

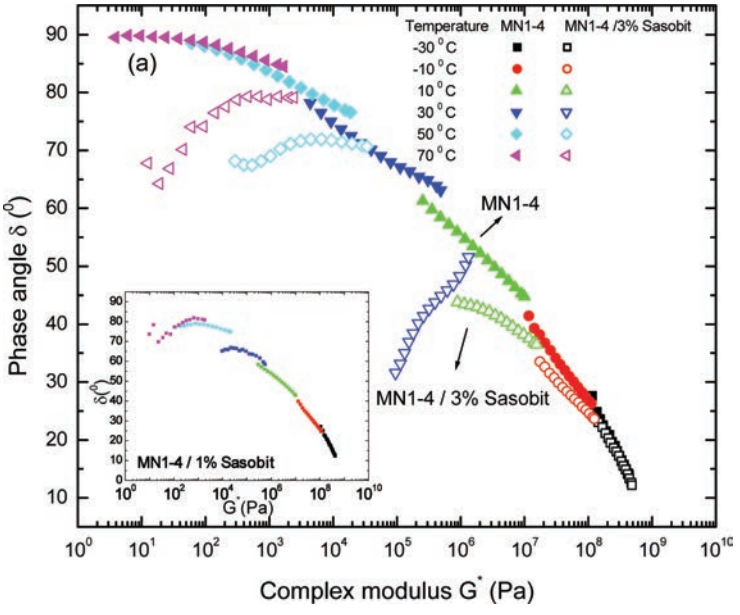

Figure 3. Van Gurp-Palmen plots for MN1-4 binder and sasobit blends.

Table 3. The "limiting low tempertatures" at which S(t) ≤ 300 MP and creep rate m-value ≤ –0.3.

	Calculated "limiting low temperature" (°C) based on S(t) and m-value		
Samples	0% sasobit	1% sasobit	3% sasobit
MB	–42.9	–42.1	–41.2
MN1-3	–40.5	–41.7	–38.2
MN1-4	–45.0	–45.0	–41.5
YNP	–45.2	–45.3	–43

The results suggest an increase in the "limiting low temperature" by about 2 ˚C for 3% Sasobit modified MB, MN1-3 and YNP binders. The increase in the "limiting low temperature" of the YNP Sasobit blends is found to be associated with its slower relaxation of accumulated stress even though its creep stiffness and modulus are lower than the base binder. A slightly larger upshift in "limiting low temperature" (3.5 °C) is found for the 3% MN1-4 Sasobit blend, which is attributed to the unusually large presence of natually occuring wax.

Overall, it does not appear that Sasobit at concentration levels of 3% or less exerts undue adverse effect on binders' low temperature properites.

3.2.2 *High temperature rheology*

The limiting high temperatures are expanded by 5 °C, 9 °C, 13 °C and 16 °C for Sasobit modified MN1-4, MB, MN1-3 and YNP binders respectively as shown in Figure 4, which is highly desirable for high temperature rutting resistance improvement.

At 50 °C, which is far above the glass transition temperature of asphalt binders, the base asphalt binder MB displays typical liquid behavior, i.e., the storage modulus (G′) is proportional to the frequency squared (ω^2) and the loss modulus (G″) is proportional to the frequency (ω) at low frequencies shown in Figure 5. Upon the addition of Sasobit, especially 3% Sasobit by weight, a dramataic change in rheological properties occurs. Instead of keeping the classic liquid response, 3% Sasobit modified MB exhibits the pseudo-solid or semi-solid behavior with the G′—ω slope of less than 0.5. Although loss modulus is generally believed to be insensitive to structure change, its sluggish variation as a function of frequency can be clearly observed for 3% Sasobi modified MB at low frequencies. Those results strongly suggest the formation of pseudo-solid like structures in 3% Sasobit modified binders at 50 °C. Considering the previously observed unchanged glass transition temperatures upon incorporation of Sasobit, the semi-solid structure for 3% systems are more likely to be due to the interactions among Sasobit crystals, where Sasobit might act as physical crosslink joints inside asphalt matrix.

Such pseudo-solid like or gel-like rheological behavior can be seen in Figure 6 where complex viscosity is plotted against complex modulus. Without Sasobit modifications, all binders except YNP demonstrate nearly Newtonian viscosity, which represents typical liquid response. With 3% Sasobit modifications, the viscosity tends to diverge at a finite value of complex modulus, which has been considered as a measure of the yield stress [28]. The presence of nearly diverging viscosity or yield stress is consistent with semi-solid characteristics. Based on the above linear viscoelasticity at 50 °C, the previously observed deviation from time-temperature superposition at temperatures above 30 °C for 3% Sasobit modified binders is attributed to microstructure change, where a gel-like or semi-solid structure is formed as opposed to isolated Sasobit crystals dispersed among binder liquids. The network or semi-solid structure formation alters the temperature dependence of stress relaxation and

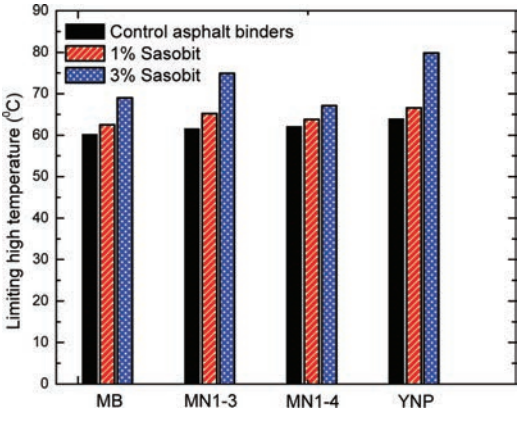

Figure 4. The limiting high temperatures corresponding to $G^*/\sin\delta = 1.0$ kPa ($\omega = 10$ rad/s).

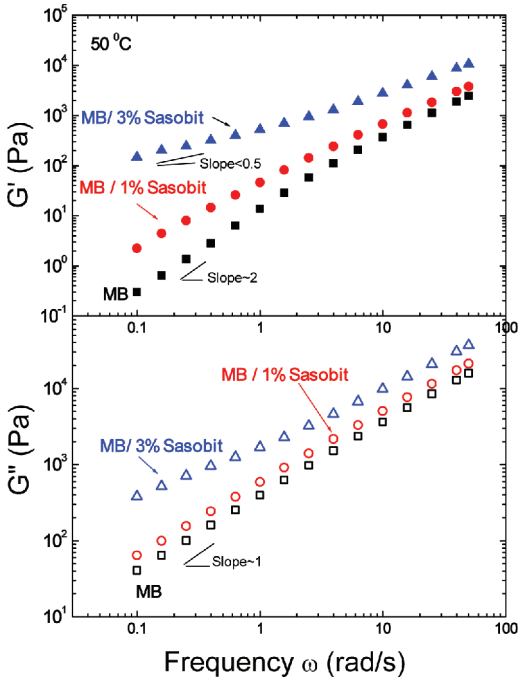

Figure 5. Storage and loss moduli of sasobit modified MB binders at 50 °C.

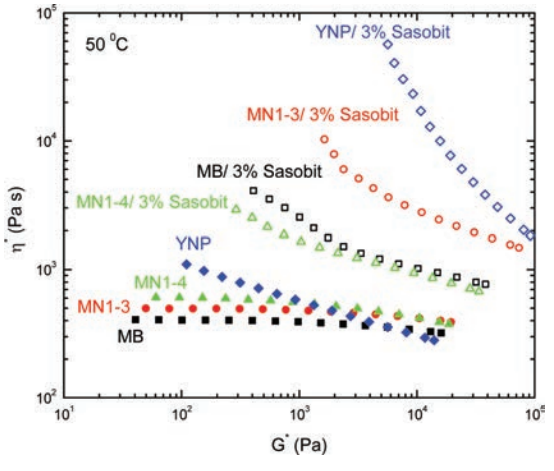

Figure 6. Plots of complex viscosity vs complex modulus for MB, MN1-3, MN1-4, YNP binders and their blends with 3% sasobit at 50 °C.

consequently results in the inapplicability of time-temperature superposition principle. In addition to the rheological analysis, a morphological study was conducted to provide direct visualization for the microstructure change within Sasobit modified WMA.

3.3 *Morphology of asphalt binders and sasobit modified WMA*

In the past decades the concept of a surface microstructure present in asphalt binders has attracted much attention regarding the so-called "bee structures". Bee structures, characterized

as small (~10 μm) oblong shaped structures with rippled interiors, have been observed in a host of neat and aged asphalts [29–32]. By AFM examination on asphalt fractionations extracted through SARA (saturates, aromatics, resins and asphaltenes) chromatography and ion-exchange chromatography, followed by wax separation, Pauli and coworkers investigated the morphology of asphalt fractions before and after wax removal as well as fractions with and without asphaltenes. Their work strongly suggests that the "bee structure" is attributed to wax rather than asphaltene micelles [33].

AFM topography images of MB binder exhibit relative homogenous morphology without apparent structural features as seen in Figure 7 (a). Upon incorporation of 1% and 3% Sasobit, micro-phases develop as seen in Figure 7 (b) and (c), which is attributed to the introduction of Sasobit. But instead of forming "bee structures", the presence of Sasobit gives rise to crystal dendrites in 1% systems [34]. By comparison, the images in Figure 7 (c) illustrate the development of a network gel structure resulting from a 3% Sasobit/MB binder.

Dendritic and network surface microstructures are also observed for 1% and 3% Sasobit modified YNP binders, respectively. Compared with the unmodified MB binder, the YNP binder initially exhibits a micro-phase structure as shown in Figure 8 (a). One possible interpretation for this structure is SBS reported to be present in the YNP binder. The other possibly may be the presence of natural wax in the neat binder. By comparison to 1% Sasobit/MB binder, 1% Sasobit/YNP binder also exhibits dendrite structuring, and by comparison to 3% Sasobit/MB binder, 3% Sasobit/YNP also exhibits a network structure. These findings strongly illustrate Sasobit concentration dependence with the observed surface structuring independent of the binder source. The images depicted in Figure 7(b) and 8(b) may also suggest that Sasobit dendrites preferentially develop at the surface due to interfacial thermodynamic effects [34, 35].

It is presently unknown why dendrite crystals rather than bee structures form in these particular materials with this type of high molecular weight wax (Sasobit), but Pauli *et al*. [33] observed that higher molecular weight waxes, specifically hexacontane doped into SHRP asphalts AAA-1 and AAG-1, exhibited both bee structuring as well as dendrite branching lending to speculation that wax molecular weight may partially contribute to the structuring reported here. Dendritic crystallization is normally characterized as a rapid unstable solidification process driven by steep thermal and concentration gradients. The samples reported in the present studies were, for all practice purposes, prepared at moderate to high wax concentrations (compared to naturally occurring wax concentrations) and quench cooled. Lower Sasobit concentrations and slower cooling processes may produce the familiar bee structures from this type of wax.

Regarding morphology and rheological results of 3% Sasobit modified WMA, we remark that the network structure develops not only on the sample surface, but also in the bulk region of the blends. On the one hand, our AFM images in Figure 7 & 8 suggest the surface microstructure belongs to much larger amount of Sasobit component than 3%, implying the Sasobit structuring preferentially forms at the asphalt surface by molecules diffusing and transporting to the film surface. On the other hand, our rheological results indicate that the network structure does happen in the bulk, providing additional insight on Sasobit microstructures.

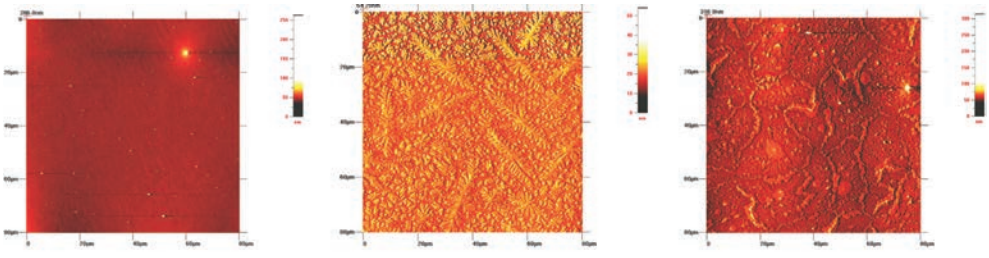

Figure 7. AFM topography image of sasobit modified MB binders.

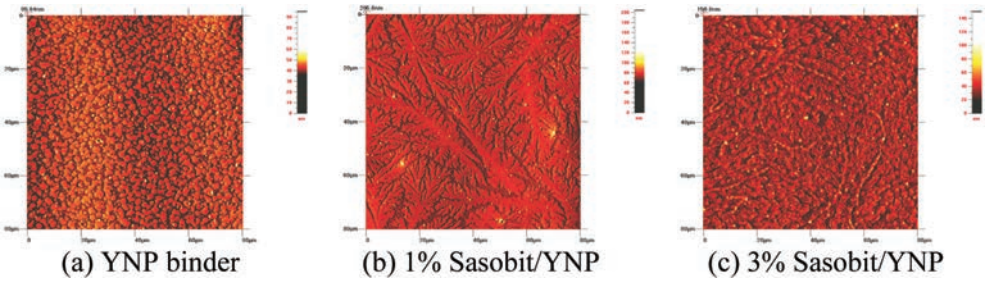

Figure 8. AFM topography image of YNP binder and its sasobit blends.

4 CONCLUSIONS

We examined the thermal, morphological and linear viscoelastic properties of Sasobit modified Warm Mix Asphalts (WMA) with Sasobit weight concentration of no greater than 3%. Four asphalt binders with different types and grades were investigated. Those Sasobit/binder blends exhibit both depressed melting temperatures and reduced heat of fusion, suggesting a smaller crystal size of Sasobit is favourable in the blends.

The time-Temperature Superposition (tTS) fails for 3% Sasobit blends at temperatures above 30 °C, which is below their onset melting points. The results suggest it is the formation of network or semi-solid like structure that is responsible for the breakdown of time-temperature superposition.

Sasobit at concentration levels of 3% or less doesn't exert undue adverse effect on binder low temperature properties. Sasobit reinforces asphalt binders with the limiting high temperature expanded by 5 °C, 9 °C, 13 °C and 16 °C for 3% Sasobit modified MN1-4, MB, MN1-3 and YNP binders respectively. More importantly, the stiffening or reinforcing effect is closely correlated with the microstructure of Sasobit blends. Linear viscoelasticity analysis at 50 °C demonstrates the gel-like or pseudo-solid behavior of 3% Sasobit modified WMA.

Consistent with the rheological results, the AFM images depict an inter-connected network structure for 3% Sasobit modified WMA, which proves to be dependent on the Sasobit concentration rather than asphalt sources. For 1% Sasobit blends, instead of forming the familiar isolated "bee structure" of wax, a dendritic microstructure is observed, which is thought to be partially due to the high molecular weight of Sasobit as well as its relatively larger concentration compared with natural wax in asphalts. Morphology and rheological results suggest that a network structure exists not only on the surface of the sample, but also inside the bulk.

ACKNOWLEDGEMENTS

The authors would like to thank Alec O. Cookman, Pamela J. Coles, Bruce E. Thomas, Gerald E. Forney for performing the tests and generating raw data. The authors also gratefully acknowledge the Federal Highway Administration, U.S. Department of Transportation, for financial support of this project under contract no. DTFH61-07-D-00005.

REFERENCES

[1] Rubio M.C., Martínez G, Baena L, Moreno F. Warm mix asphalt: an overview, J Cleaner Production, 24: 76–84. 2012.

[2] WarmMix Asphalt—A State of the Art Review. Advisory Note 17. AAPA, June 2001. www.aapa.asn.au/content/aapa/download/advisorynote17.

[3] Damm K.W., Abraham J., Butz T., Hildebrand G., Riebeschl G. Asphalt flow improvers as 'intelligent fillers' for hot asphalts—a new chapter in asphalt technology, J App Asphalt Binder Technol, 2(1): 36–39. 2002.

[4] Hurley G.C., Prowell B.D. Evaluation of Sasobit® for use in warm mix asphalt, National center for asphalt technology NCAT Report 05-06. Auburn, AL 2005.
[5] Edwards Y., Isacsson U. Wax in bitumen Part II—Characterization and effects, Road Materials and Pavement Design, 6(4): 439–68. 2005.
[6] Hurley G.C., Prowell B.D. Evaluation of potential process for use in warm mix asphalt, J Assoc Asphalt Paving Technol, 75: 42–90. 2006.
[7] Wu C., Zeng M. Effects of additives for warm mix asphalt on performance grades of asphalt binders, J Test Evaluation, 40 (2): 265–72. 2011.
[8] Lee S.J., Amirkhanian SN, Park NW, Kim KW. Characterization of warm mix asphalt binder containing artificially long-term aged binders, Construc Build Mater, 23: 2371–9. 2009.
[9] Jamshidi A., Hamzah M.O., Aman M.Y. Effects of Sasobit content on the rheological characteristics of unaged and aged asphalt binders at high and intermediate temperature, Mater Res, 15(4): 628–38. 2012.
[10] Banerjee A., Smit A.D.F., Prozzi J.A. The effect of long-term aging on the rheology of warm mix asphalt binders, Fuel, 97: 603–11. 2012.
[11] Lui J., Saboundjian S., Li P., Connor B., Brunette B. Laboratory evaluation of sasobit-modified warm-mix asphalt for Alaskan conditions, J Mater Civil Eng, 23: 1498–1505. 2011.
[12] Merusi F., Giuliani F. Rheological characterization of wax-modified asphalt binders at high service temperatures, Materials and Structures, 44: 1809–20. 2011.
[13] Edwards Y., Tasdemir Y., Isacsson U. Rheological effects of commercial waxes and polyphosphoric acid in bitumen 160/220—low temperature performance, Fuel, 85: 989–97. 2006.
[14] Xiao F., Punith V.S., Amirkhanian S.N. Effect of non-foaming WMA additives on asphalt binders at high performance temperature, Fuel, 94: 144–55. 2012.
[15] Polacco G., Filippi S., Paci M., Giuliani F., Merusi F. Structural and rheological characterization of wax modified bitumens, Fuel, 95: 407–16. 2012.
[16] Butz T., Rahimian I., Hildebrand G. Modification of road bitumens with the fischer-tropsch paraffin sasobit, J Appl Asphalt Binder Technol, 1(2): 70–86. 2001.
[17] Gill P.S., Sauerbrunn S.R., Reading M. Modulated differential scanning calorimetry, J. Therm. Ana., 40: 931–9. 1993.
[18] McKenna G.B., Simon S.L. Handbook of Thermal Analysis and Calorimetry. Cheng SZD Ed. 2002; Chapter 2 Elsevier: New York.
[19] Badrinarayanan P., Zheng W., Li Q., Simon S.L. The glass transition temperature versus the fictive temperature, J Non-Cryst Solids, 353: 2603–12. 2007.
[20] Qin Q., Farrar M.J., Pauli A.T., Adams J.J. Morphology, thermal analysis and rheology of Sasobit modified warm mix asphalt binders, Fuel, 115: 416–25. 2014.
[21] Defay R., Prigogine I., Bellemans A., Everett D.H. Surface Tensions and Adsorption. Wiley: New York 1996.
[22] Qin Q., McKenna G.B. Melting of solvents nanoconfined by polymers and networks, J Poly Sci Part B: Polym Phys, 44: 3475–86. 2006.
[23] Jackson C.L., McKenna G.B. Vitrification and crystallization of organic liquids confined to nanoscale pores, Chem. Mater, 8: 2128–37. 1996.
[24] Zhang Z., Lu X., Jiang Q. Finite size effect on melting enthalpy and melting entropy of nanocrystals, Physica B, 270: 249–54. 1999.
[25] Sun J. Thermodynamics and kinetics at the nanoscale: thermal behavior of aluminum nanoparticles and development of nanoporous low-k dielectrics. PhD Thesis. Texas Tech University: Lubbock, TX 2004.
[26] Van Gurp M., Palmen J. Time-temperature superposition for polymeric blends, J Rheol Bull, 67: 5–8. 1998.
[27] Sui C., Farrar M.J, Harnsberger M.P., Tuminello W.H. A new low-temperature performance grading method using 4 mm parallel-plates on a DSR. In proceedings of Transportation Research Board of the National Academies, Washington DC, Page 11–1827. 2011.
[28] Goel V., Pietrasik J., Matyjaszewski K., Krishnamoorti R. Linear viscoelasticity of spherical SiO_2 nanoparticle-tethered poly(butyl acrylate) hybrids, Ind. Eng. Chem. Res., 49:11985–90. 2010.
[29] Loeber L., Sutton O., Morel J., Valleton J., Muller G. New direct observation of asphalts and asphalt binders by scanning electron microscopy and atomic force microscopy, J Micros, 182 (1): 32–39. 1996.
[30] Loeber L., Muller C., Morel J., Sutton O. Bitumen in colloid science: a chemical, structural and rheological approach, Fuel, 77 (13): 1443–50. 1996.
[31] Wu S.P., Pang L., Mo L.T., Chen Y.C, Z G.J. Influence of aging on the evolution of structure, morphology and rheology of base and SBS modified bitumen, Constru Build Mater., 23: 1005–10. 2009.

[32] Pauli A.T., Grimes W. Atomic force microscopy investigation of SHRP asphalts, ACS Division of Fuel Chemistry Preprints, 46 (2): 104–10. 2001.
[33] Pauli A.T., Grimes R.W., Beemer A.G., Turner T.F., Branthaver J.F. Morphology of asphalts, asphalt fractions and model wax-doped asphalt studies by atomic force microscopy, International Journal of Pavement Engineering, 12 (4): 291–309. 2011.
[34] Hollander, F.F.A., O. Stasse, J. van Suchtelen, and W.J.P. van Enckevort. Recrystallization phenomena of solution grown paraffin dentrites, Journal of Crystal Growth, 233: 868–80. 2001.
[35] Ocko, B.M., X.Z. Wu, E.B. Sirota, S.K. Sinha, O. Gang, and M. Deutsch. Surface freezing in chain molecules: normal alkanes, Physical Review E, 55(3): 3164–82. 1997.

This page intentionally left blank

Asphalt Pavements – Kim (Ed)
© 2014 Taylor & Francis Group, London, ISBN 978-1-138-02693-3

Micromechanical and microstructure analysis of asphalt concrete under triaxial load condition based on Discrete Element Method

Jun Yang
School of Transportation, Southeast University, Nanjing, China

Keli Wang
Zibo Urban Planning Design Institute, School of Transportation, Southeast University, Nanjing, China

Qing Lu
Intelligent Transport System Research Centre, Southeast University, Nanjing, China

Jiantong Zhang & Haopeng Wang
School of Transportation, Southeast University, Nanjing, China

ABSTRACT: There has been a growing interest in the pavement community to study the structures and properties of asphalt concrete from a microscopic view. In this paper, a microstructure and micromechanical model of asphalt concrete is developed based on Discrete Element Method (DEM), calibrated, and applied in virtual triaxial tests of asphalt concrete. In the asphalt concrete microstructure modelling, a new generation algorithm of creating coarse aggregate phase, and a new approach of introducing air void phase, is proposed. The constructed microstructure model is further calibrated based on the aggregate gradation of asphalt concrete. Parameters of the micromechanical model are determined through calibrating virtual mastic test results with laboratory test data. In the virtual triaxial tests based on DEM, the influence of asphalt concrete compositions on the virtual test results and the micromechanical responses of the microstructure of asphalt concrete in the loading process are tracked and analyzed. The simulation results are in good agreement with observations from real laboratory tests, which verifies the feasibility of the algorithms and methodologies developed in this study.

Keywords: Triaxial shear test, microstructure and micromechanical analysis, Discrete Element Method, asphalt mixture, virtual test

1 INTRODUCTION

In the design of asphalt concrete mixtures used in pavement construction, mixture constituents are rationally selected and mixed with the aim to improve properties of asphalt mixture such as resistance of rutting, fracture, and fatigue. However, most of the mix design procedures used presently are strictly empirical such as Marshall Design method. This empirical result can be attributed to vague definition of design method for one specific asphalt mixture. Actually, asphalt mixture is composed of two main parts, composition of constitutes and their distribution in the specimen. However, the specification of asphalt mixture only provide instruction of constitute composition for the designers. As for the other aspect, the different distribution fashions of constitutes mean different structural types of the material. Moreover, it can have different distributional fashions of constitutes for the same type of asphalt mixture specified by the specification. As a result, one specific type of asphalt mixture can not be precisely determined according to the design specification. Therefore, the constitute composition is rather a necessary than a sufficient condition. Herein, one

sufficient and necessary condition can be obtained for a specific property of asphalt mixture if a definition for microstructure of asphalt mixture could be provided besides the composition of each constitute phase.

As it is well known that mechanical characteristics of asphalt mixture significantly depends on load condition. Therefore, it has much point in setting the boundary condition or initial stress environment as real as possible. In reality, the bituminous materials in a pavement structure are under a complex three dimensional stress which has a significant effect on its deformation properties. The triaxial test method is well established, especially in the field of soil mechanics. It has been shown to be suitable for evaluating the strength of asphalt concrete mixtures [1]. The triaxial test has been used to evaluate many mechanical characteristics of soils under various conditions of axial loadings and confining pressures such as shearing resistance, stress-strain, and other properties. However, the usage of the triaxial test for testing bituminous paving materials is slow in acceptance by pavement engineers and the main cause should be attributed to the complexity of the test and high expenses of such an exercise [2].

Therefore, the difficulties of launching the micromechanical analysis of asphalt mixture under the laboratory condition can be easily seen. The microstructure study of asphalt mixture has been kept focused for last two decades, especially in terms of the microstructure reconstruction. As so many successful applications of discrete element method in rock mechanics occur, the method draws attention of researchers in pavement fields. And many meaningful studies have been done. For example, the micro-fabric discrete element method for the microstructure of asphalt mixture in two-dimensional was proposed by Buttlar and You [3]. Then the idealized model in three-dimensional was established to simulate the dilation behavior of asphalt concrete [4]. Afterwards many researchers have adopted the image-based models for reconstruction of asphalt concrete [5–8]. The randomly created model was built for asphalt concrete [9–10]. In the randomly created model, gradation, shape, angularity, orientation, and distribution can be created to represent microstructure of asphalt concrete. However, the distribution of the air voids phase has not been focused in the studies mentioned above. In this paper, one randomly created model is established and utilized to finish the microscopic analysis of asphalt concrete and the distribution of the air voids phase is considered.

To avoid the difficulties of a study under the laboratory condition, the increased usage of numerical techniques can be taken as one available option for the researchers. Virtual test can be utilized to simulate the laboratory test and make microstructure analysis of asphalt concrete under a specific load condition such as displacement, stress and strain status, and coordinate number of coarse aggregate [11–14]. And these microstructure response analyses can be used to explain the fundamental material properties of asphalt concrete and provide a rational mechanical approach for the design and testing of asphalt pavements.

2 OBJECTIVES AND TASKS

Based on discrete element method, a microstructure model for Asphalt Concrete (AC) is established based on its three component phases. It should involve aspects including volume content, distribution, particle shape and orientation and other necessary factors. All of above are for the preparation of the virtual triaxial shear test of asphalt concrete. Finally, the microstructure analysis of asphalt concrete under the triaxial load condition can be made. The following tasks have to be performed in order to achieve that objective:

- A new algorithm used to generate aggregate elements is developed, which could be easily utilized to create a particle with an irregular shape and a designated size. The assembling for all coarse aggregate elements is also a key step in establishing the microstructure of asphalt mixture when single particle could be simulated. Both the distribution characteristics of orientation and location of coarse aggregate phase determine the microstructure or the configuration of material.

- For air voids phase for DE model of AC, this paper introduced statistic regression method into its establishment based on a statistical regression method in DE model. A program will be developed to establish the phase according to analysis result from relevant studies by means of X-ray.
- The virtual test is launched to analyze the microstructure response of AC under triaxial and uniaxial load condition. Some variables, which are used to represent microstructure characteristics of AC, are created and tracked in the simulation process in order to obtain microscopic response of coarse aggregate element. Meanwhile, algorithms are compiled to finish analyzing the influence of the components on the simulation result, including orientation of coarse aggregate phase and distribution of air voids phase.

In this paper, a commercial discrete-element code called Particle Flow Code in 3-Dimensions (PFC3D) is used. The microstructure construction of AC is presented using the PFC3D based on discrete element method.

3 ESTABLISHMENT OF MICROSTRUCTURE MODEL FOR ASPHALT CONCRETE

The Asphalt Concrete (AC) material is a bonded mixture of aggregates, asphalt binders and air voids. The anisotropy of AC was ascribed mainly to the nonrandom distribution of preferential orientation of aggregate particle, air void shape and aggregate particle constitutes.

3.1 *Algorithm for coarse aggregate*

In this section, a new algorithm for coarse aggregates (aggregates that are retained on the 2.36-mm sieve) is developed and implemented to establish a Discrete Element (DE) model of asphalt concrete. A precise control of aggregate particle size, irregular shape, and arbitrary orientation can be easily achieved with the algorithm.

Based on the mechanism of sieving, the size of an aggregate is determined by the minimum cross section area of the aggregate. A plane that is parallel to such cross section is defined as the critical projection plane. For example, for the cuboid shown in Figure 1[a], projection on the XOY plane gives the minimum projection size (Fig. 1[c]), which is 80 by 80 in terms of square opening sieve size. Therefore, XOY plane is the critical projection plane.

Therefore, based on the mechanism of sieving mentioned above the establishment of coarse aggregate can be finished by virtue of three steps as follows:

1. A model with spheres can be created to initiate the physical information of coarse aggregates based on the gradation of asphalt mixture, including radii and coordinates shown in Figure 3[a]. And a regular polyhedron with 14 vertexes could be established shown in Figure 2. By obtaining and altering the coordinates of each vertex of this polyhedron in

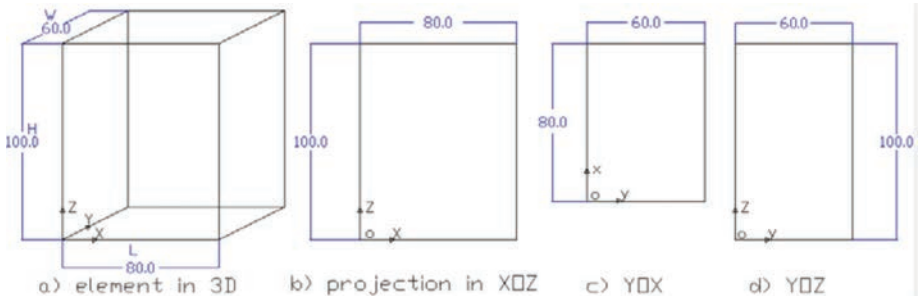

Figure 1. Projections of a particle on three planes.

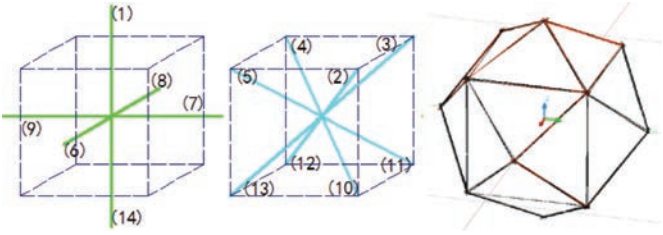

Figure 2. Preliminary polyhedron space for coarse aggregate element.

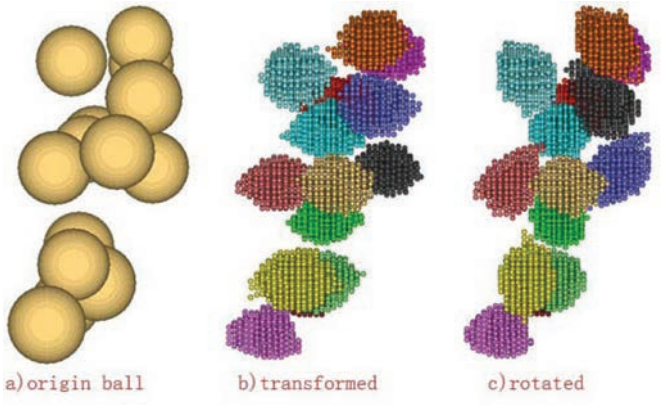

Figure 3. The transformation from the initial sphere model to target model.

the local coordinate system, the main frame the aggregate element is transformed, subjecting to the constraint that the aggregate size remains constant.

2. According to the relative location relationship between endpoints and the projection plane, there are 10 endpoints (vertexes) whose z components can be changed shown in Figure 2. By adjusting the values of the 10 projection components, a variety of shapes can be achieved for one aggregate element, while the aggregate size remains unchanged, no matter whether the final aggregate element becomes thinner (flatted) or thicker (elongated) after the transformations. As might be expected, a particle with more irregular shapes can be easily obtained when various component changes are assigned to different line segments of the main frame shown in Figure 3[b]. However, it can be seen that the orientation of each particle is parallel to the projection plane.
3. To randomize the particles orientations, a method similar to Euler angle rotation is used. If the vertices of the aggregate polyhedron are rotated by the same angle around one, two, or three axes of the local coordinate system, the aggregate's orientation is changed. For the aggregate model in this study, the rotation will give 14 new coordinates of the end points. The shape of the aggregate element essentially remains the same while the orientation changes shown in Figure 3[c].

A Fish program is compiled to eliminate the floaters (contact coordinate number is less than 2 for each unit spheres) on the surface of each coarse aggregate.

3.2 *The establishment of air void phase and asphalt sand mastic phase*

Research has shown that the stiffness of the mixture is highly dependent on the air voids content of the mixture, which is recognized in all stiffness predictive models such as the Shell model, the Witczak et al. model [15–16].

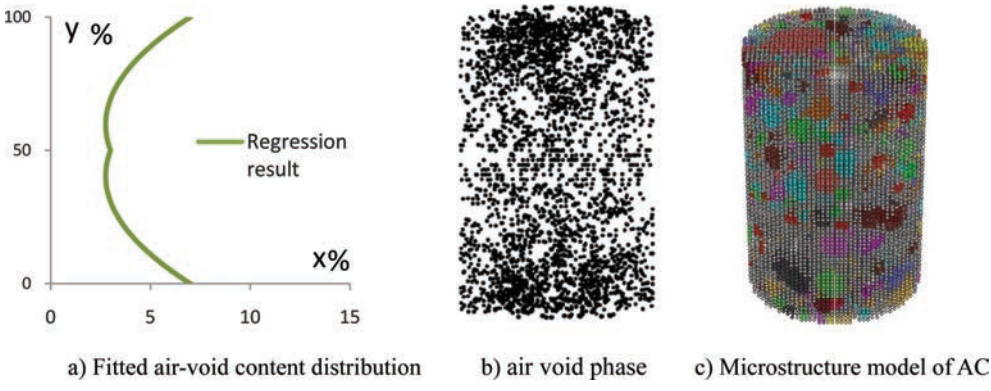

Figure 4. An example of air void distribution introduced in the DE model (air voids are represented by black spheres).

According to the study of air void distribution inside the specimen fabricated by Superpave gyrated compactor using X-ray, a statistical model is proposed to establish the air void phase instead of a model with random distribution shown in Figure 4 [17–18]. The air void phase of microstructure for the virtual specimen is established shown in Figure 4[b].

Finally, the physical components information of the virtual specimen can be calibrated by the basic gradation of asphalt concrete. The left unit spheres in the model compose the asphalt sand mastic phase. So far, the microstructure of asphalt concrete has been established based on DEM. To improve computational efficiency of the three dimensional model, the size of virtual cylinder specimen is reduced to 60:40 mm (height: diameter) and the radius of the unit sphere is 0.5 mm. The virtual specimen of asphalt mixture (Sup-13) is shown in Figure 4[c].

4 MICROMECHANICAL MODEL FOR MICROSTRUCTURE OF ASPHALT CONCRETE

4.1 *Burger model*

The Burger model is utilized to represent the viscoelastic characteristics of asphalt sand mastic. In order to obtain the parameters of burger model, static creep test is carried out in the laboratory. The experimental conditions are as follows: the asphalt mixture is Sup-13, test temperature is 40°C, uniform loading stress is 40 Kpa. The aggregate is granite, the binder is the asphalt modified by SBS. And the aggregate gradation of the tested asphalt mixture is shown in Table 1.

The macroscopic parameters of burger model are shown in Table 2, which are obtained through the regression analysis for laboratory static creep test.

On the basis of the conversion relationship between microscopic parameters and the macroscopic parameters, the microscopic parameters can be obtained [19]. Then the virtual creep test can be utilized to verify the feasibility of the contact model adopted for the microstructure. Finally, the laboratory test result, regression result and the simulation result are shown in Figure 5 respectively.

4.2 *Contact bond model*

According to the conversion relationship between microscopic parameter (bond strength) and the macroscopic parameter (material strength), the indirect tensile test of asphalt sand mastic is carried out to obtain the indirect tensile strength of asphalt mixture. Meanwhile, the virtual indirect tensile test is carried out to calibrate the microscopic parameter obtained from above [20].

Table 1. Gradations of aggregate blends.

		Square opening screen									
Mix type	Sieve size (mm)	16	12	9.5	4.75	2.36	1.18	0.6	0.3	0.15	0.075
Sup-13	Pass rate (%)	100	97.1	78.8	53.0	32.5	19.9	15.3	9.4	7.2	5.5

Table 2. Fitting result for parameters of Burger model.

E_1 (pa)	η_1 (pa·s)	E_2 (pa)	η_2 (pa·s)
8.88178E+06	2.04270E+09	2.01180E+06	1.00472E+08

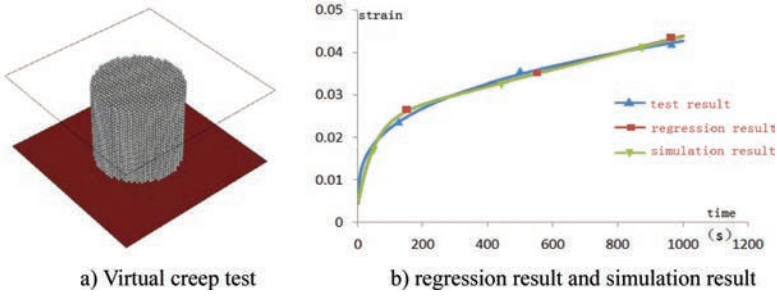

a) Virtual creep test b) regression result and simulation result

Figure 5. Virtual test result of asphalt sand mastic.

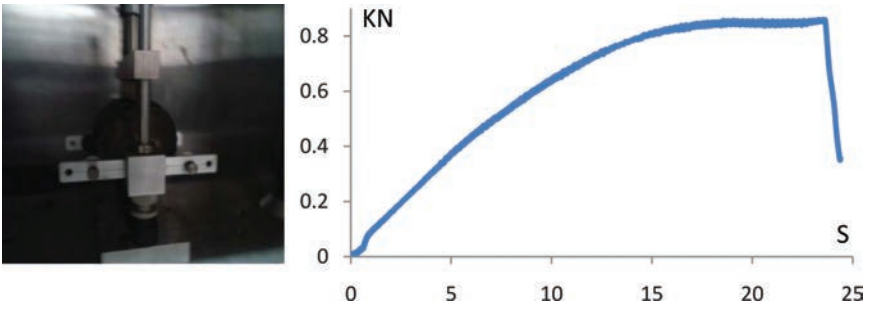

Figure 6. Indirect tension test and test result of asphalt sand mastic.

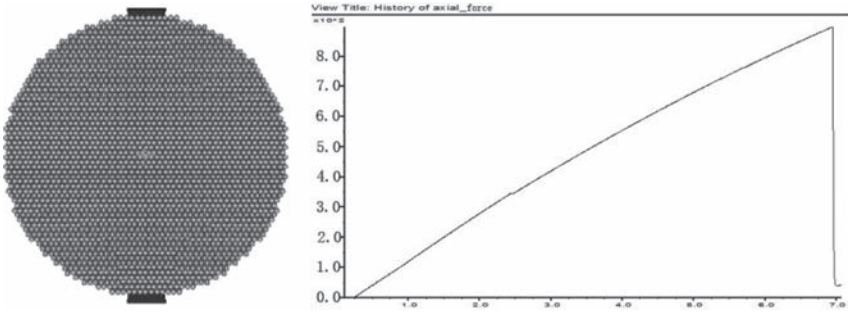

Figure 7. Virtual indirect tensile test and simulation result.

4.2.1 *Laboratory test and result*

Test temperature is 40°C, Loading velocity is 50 mm/min, Specimen size is 101.6 by 63.5 mm (diameter by height).

Three specimens are utilized to obtain the average peak force of the asphalt sand mastic under the same laboratory test condition. Finally, the average result of the three parallel specimens is 859 N.

4.2.2 *Virtual test and result*

The virtual test is launched to calibrate the microscopic parameters, which are obtained according to the abovementioned conversion method. The main experimental condition is same to the laboratory test, including the specimen size, load velocity and so forth. The parameters of the microstructure are as follows: the radius of the unit ball is 1 mm and the ball of the model is in a diamond arrangement. The contact model adopted in the numerical model is the burger model and the parameters have been obtained in last section.

The peak axial force of the virtual specimen acquired in the simulation is 876 N. And the microscopic bond strength value is 0.5 N when the conversion and assumption is made: the value in the normal direction equals the value in the shear direction. However, the value need to be modified according to the virtual triaxial test result of asphalt mixture, and the following assumption should be made: the property of the contact between asphalt sand mastic and coarse aggregate phase is the same to the contact inside the asphalt sand mastic phase.

5 VIRTUAL TRIAXIAL TEST SIMULATION AND MICROSCOPIC ANALYSIS

5.1 *Laboratory triaxial test and calibration of the discrete element model*

To calibrate the micromechanical models adopted in the discrete element model, the triaxial test is launched. Three confine pressure levels are set including 0, 138 Kpa, 276 Kpa [21]. The load equipment is Universe Test Machine (UTM-25). The discrete element model of asphalt mixture (Sup-13) is calibrated on the basis of the laboratory triaxial test results. Finally, simulation result of the calibrated model is reasonable compared with the experimental result shown in Table 3.

The specimen before and after virtual test is shown Figure 8, and the shape change of the specimen can be observed. Meanwhile, a shear band can be differed from the contact failure distribution zone (the red dots represent the tension failure while the black dots represent the compression failure). Apparently, the changes or responses inside the specimen can be easily measured in the virtual test. This advantage of the virtual test should be taken sufficiently in the future.

5.2 *Micro-structural and micromechanical analysis of asphalt mixture*

In this section, the influences of components on the simulation result are analyzed, including the orientation of the coarse aggregate phase, the distribution characteristics of air void phase.

Table 3. Triaxial test result of Sup-13.

	σ_1 (KPa)		
	Laboratory test result		
σ_3 (KPa)	Peak stress	Average	Virtual test result
0	921	964	871
	1007		
138	1499	1583	1513
	1667		
276	2095	2176	2113
	2257		

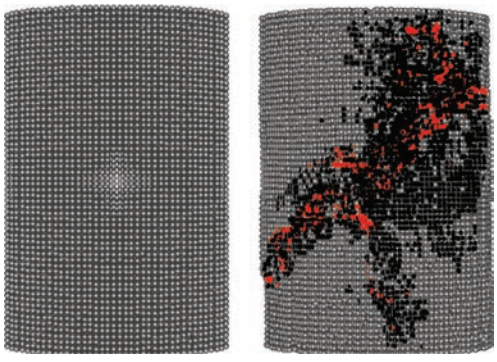

Figure 8. Virtual specimen before and after virtual triaxial test.

Meanwhile, some variables are defined and used to track the micromechanical responses of the microstructure in the loading process, such as coordination number of coarse aggregate, stress distribution of coarse aggregate phase and its evolution characteristics.

5.2.1 *Influence of component characteristics on the simulation result*

As is mentioned above, the algorithm of creation for coarse aggregate can be used to analyze the effect of the orientation of coarse aggregate particle on the simulation result. Therefore, the two special scenarios are established to make the analysis, including vertical orientation distribution and horizontal orientation distribution. These two special scenarios are used to explain the effects of the orientation on the simulation result. Through modifying the algorithm of coarse aggregate developed in this paper, those two special scenarios can be easily established. To differ them clearly, the particles with sieve size between 10 mm and 12 mm are separated from the discrete element model of asphalt concrete shown in Figure 9.

They are particles with horizontal orientation, vertical orientation and arbitrary orientation shown in Figure 9, respectively. The virtual triaxial test result can be seen in Figure 10, including confess pressure equals 0 KPa, and 138 KPa, respectively.

It can be seen that the model of coarse aggregate phase with horizontal orientation shows a poorer property of resistance to vertical loading, and the model of coarse aggregate phase with vertical orientation shows the best property resistance to vertical loading of all three scenarios shown in Figure 9.

Compared with the conventional discrete element model of asphalt mixture, the difference is that the air void phase is established based on the real distributional characteristics instead of a random distribution. To learn the effect of the distribution of air void phase on the simulation result, virtual triaxial shear test for two microstructure models with two air voids distribution are carried out. However, the two microstructure models can have the same coarse aggregate phase. The results of the virtual tests could be found in the following figure.

It can be seen that the model with the real distributional characteristics shows a better test result than the model with a random distribution. Therefore, the proposed establishment method of air void phase in the paper is of more momentous significance than the conventional method. Meanwhile, the result explains that the distribution of the air void phase plays an important part in the property of resistance to deformation.

5.2.2 *Micromechanical responses of the microstructure*

In this section, some key parameters representing microstructure of the model are tracked in the simulation process, including the skeleton particles (defining coarse aggregate with coordinate number > 3), the stress statuses of the coarse aggregates in the loading process. To learn the stress evolution law of the coarse aggregate phase in the loading process, three typical stages are selected: the stable stage, ultimate stage and collapse stage. At the same time, it includes multiple confess pressure level scenarios, namely equal 0, 138 KPa, or 276 KPa.

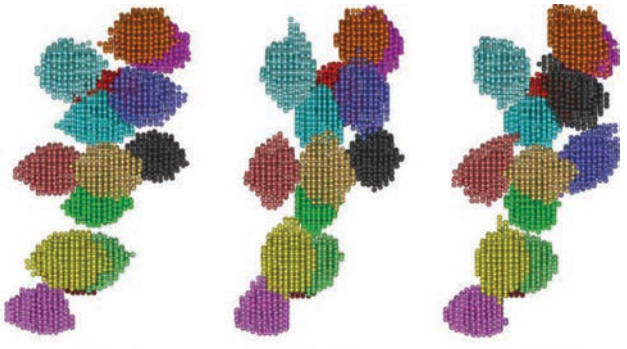

Figure 9. Orientation alignment of coarse aggregate phase.

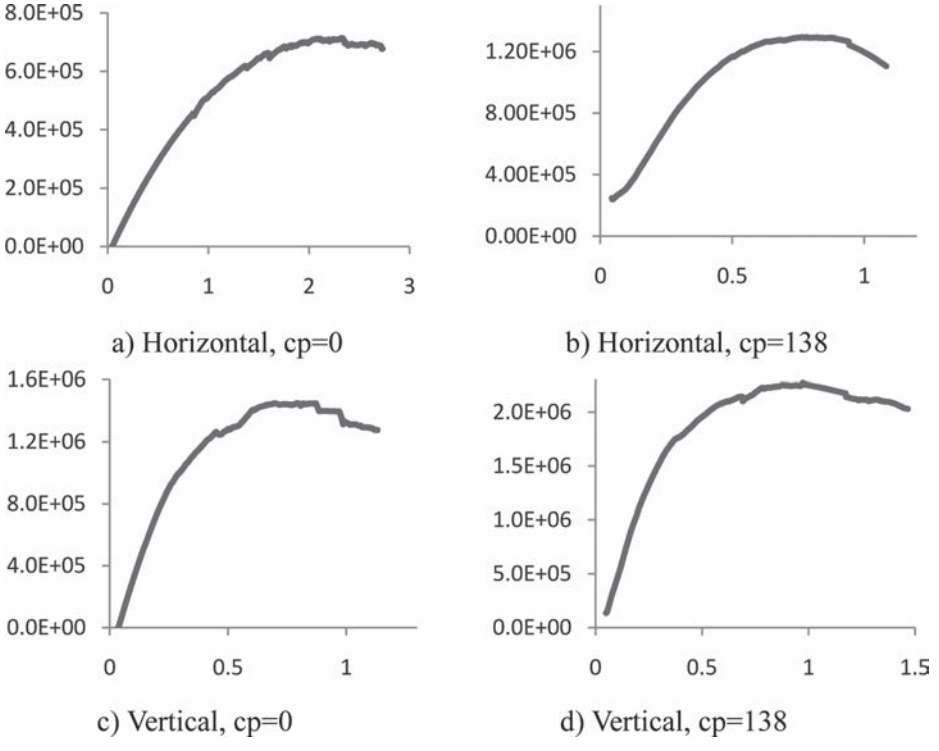

Figure 10. Virtual triaxial test results for coarse aggregate phase.

5.2.2.1 Evolution law of total number of skeleton particles

In three dimensional space a particle with coordinate number larger than three could be taken as a skeleton particle.

At the ultimate state of the specimen in the loading process, the axial stress show different levels at different confess pressure levels. As the confess pressure level increases, the peak load stress of the specimen becomes larger. Meanwhile, the number of the skeleton particles in microstructure at the ultimate load state shows different values at uniaxial load state and triaxial load state. However, that value remains the same when the confess pressure level is elevated to a higher value (276 Kpa). Apparently, the elevated range of the cp can not change the old response mechanism, which is established under cp = 138 KPa or lower, of the virtual

specimen. Accordingly, a higher value would be needed if the number of the skeleton particles was altered for the same specimen.

5.2.2.2 Evolution law of stress statuses of coarse aggregate phase

The internal structure stress distribution of AC in the load condition can not be easily obtained in the laboratory condition. However, the internal structure mechanical response and its evolution law must be very helpful for researchers to understand the relationship between microstructure characteristics and macro properties of AC. Nevertheless, they can be easily obtained through the virtual test simulation. In order to obtain the typical micromechanical response law of coarse aggregate phase in the loading process, three stages are selected to represent the stress statuses of coarse aggregate to explain the evolution law,

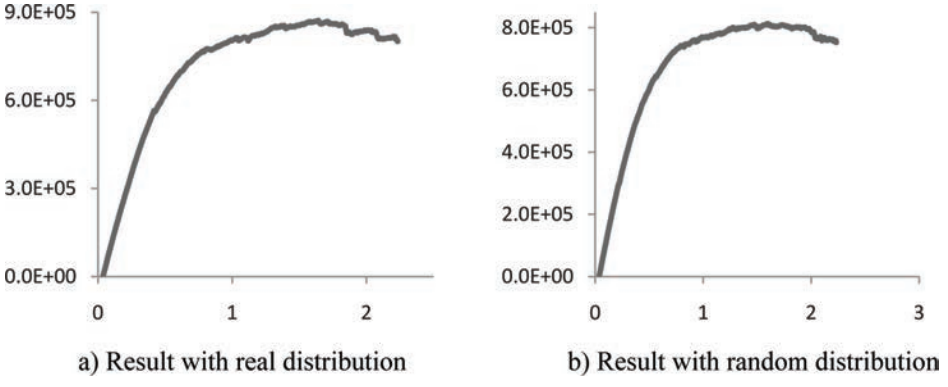

Figure 11. Virtual triaxial test result for air voids phase.

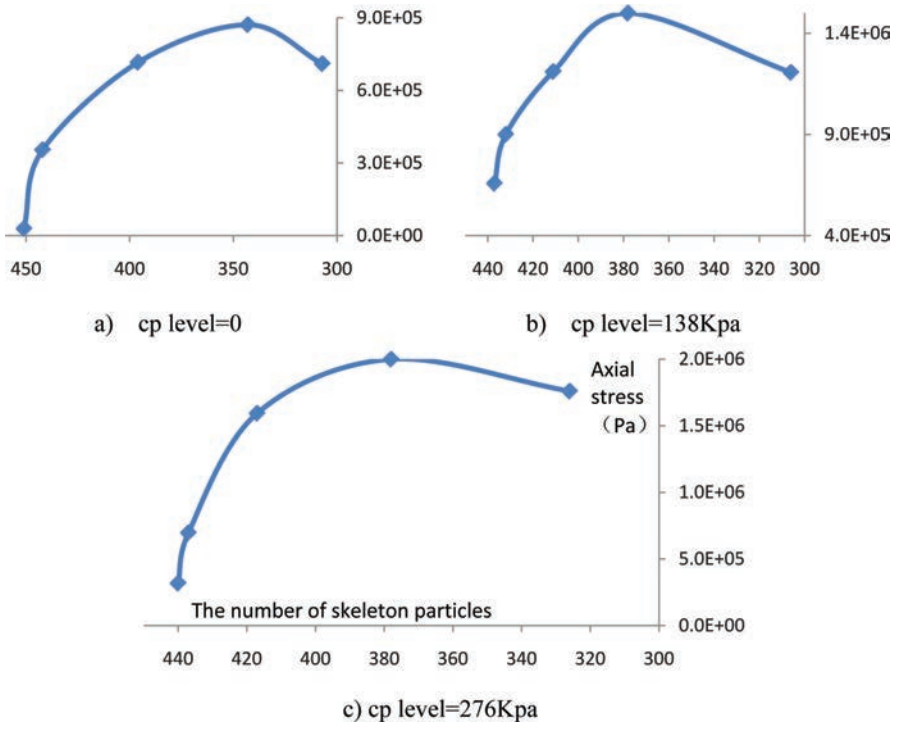

Figure 12. The number of skeleton particles at different confess pressure levels.

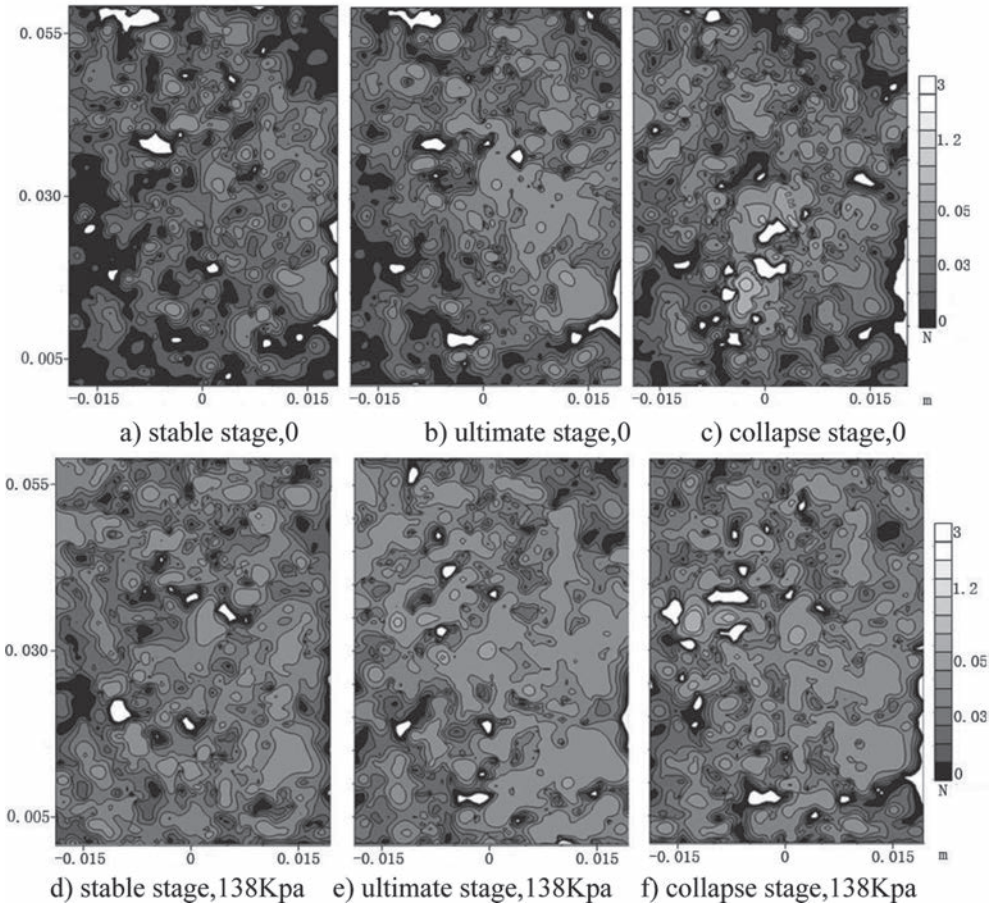

Figure 13. Stress statuses evolution law of coarse aggregate phase.

including the stable stage, ultimate stage, and collapse stage of AC. Meanwhile, the load condition involves two confine pressure level scenarios, namely 0 (shown in Fig. 13[a, b, c]), and 138 KPa (shown in Fig. 13[d, e, f]).

As it is shown in Figure 13, the stress concentration band can be easily differed in the stable stage under the uniaxial load condition. And the dispersed concentration blocks get coalesced, which means the adjacent coarse particles forms a very stable skeleton in the ultimate stage of loading. Typically, this phenomenon becomes more obvious in the triaxial load condition shown in Figure 13[e]. However, the skeleton effect is broken when the microstructure collapses with the accumulating load. For example, the concentration band is broken into many relatively dispersed blocks shown in Figure 13[c]. The stress concentration band of the microstructure is less clear than the one in the uniaxial load condition when the confine pressure is considered in the stable stage. And this result is in good agreement with the result of total number of skeleton particles shown in Figure 12.

6 CONCLUSIONS

A microstructure model of asphalt concrete is established on the basis its components, including the establishment of individual Coarse Aggregate (CA) element, the assembly of CA and air void phases in AC, the acquisition of contact model parameters. Finally, the virtual test is

launched to analyze the microstructure response mechanism under uniaxial and triaxial load condition. The work of this paper and the results of this study are summarized as follows:

- Based on the sieving mechanism, an algorithm for the CA element was developed. This algorithm is proved to be very efficient in creating the CA element with irregular shapes. By adjusting the orientations and lengths of the line segments, an aggregate with more variable irregular shapes and arbitrary orientations can be obtained without changing its size.
- Statistical regression models were developed to introduce varying air void distributions along pavement depth. Uniform distribution was assumed for air voids in the horizontal direction of pavements.
- The simulation of laboratory triaxial shear test was done and the virtual test result was in good agreement with the laboratory test result verifying the feasibility of the numerical model of AC established in this paper.
- On the basis of the numerical model established in this paper, the microstructure analysis of AC in the loading process was done to analyze the factors influencing the virtual test result such as the orientation of the coarse aggregate phase, and the distribution characteristics of air voids phase. The results said the orientation has a large influence on the virtual test result and the distribution of the air voids phase has an influence on the virtual test result too.
- Some variables were defined and used to track the microstructure response to the accumulating load in the test, such as number of skeleton particles, and stress statuses of CAs. And the statistical results are feasible and persuasive that the virtual test had great potential in helping the researchers understand the internal structure responses mechanism in the load condition.

ACKNOWLEDGMENT

This paper is based in part upon the work funded by the National Natural Science Foundation of China (NNSFC) (51078089). Any opinions, findings, and conclusions or recommendations expressed in this paper are those of the authors and do not necessarily reflect the views of NNSFC.

REFERENCES

[1] Smith, V.R. Application of the Triaxial Test to Bituminous Mixtures California Research Corporation Method. Triaxial Testing Soils and Bituminous Mixes, ASTM STP 106, pp 55–78, 1951.
[2] Tan. S.A., Low, B.-H. and Fwa, T-R. Behavior of Asphalt Concrete Mixtures in Triaxial Compression. Journal of Testing and Evaluation, JTEVA, 22(3), pp:195–203, 1994.
[3] Buttlar, W.G., and You, Z. Discrete element modeling of asphalt concrete: A micro-fabric approach. Transportation Research Record. 1757, Transportation Research Board, Washington, D.C, 2001.
[4] Collop, A.C., McDowell, G.R., and Lee, Y.W. Modeling dilation in an idealized asphalt mixture using discrete element modeling. Granular Matter, 8(3–4), pp. 175–184, 2006.
[5] L.B. Wang; J.D. Frost; and J.S. Lai. Three-Dimensional Digital Representation of Granular Material Microstructure from X-ray Tomography Imaging. Journal of Computing in Civil Engineering. 18 (1), pp 28–35, 2004.
[6] Abbas, A., Masad, E., Papagiannakis, T., and Harman, T. Micromechanical modeling of the viscoelastic behavior of asphalt mixtures using the discrete-element method. Int. J. Geomech., 7 (2), pp. 131–139, 2007.
[7] You, Z., and Adhikari, S. Models for Asphalt Mixtures Using X-Ray Computed Tomography Images. International Journal of Pavement Research and Technology, 1(3), pp: 94–99, 2008.
[8] Fu, Y., Wang, L., and Tumay, M.T. Experimental quantification and DEM simulation of irregular particle kinematics and local strains. Journal of Mechanics and Materials, 134(2), 143–154, 2008.
[9] Tian, L., Liu, Y., Hu, X., and Wang, B. Random Generation Algorithm for Simulation of Polyhedral Particles in Asphalt Mixture Aggregate and Its Program (in Chinese). China Journal of Highway and Transport, 20(3), 2007, pp. 5–10.

[10] Y. Liu, Q. Dai, Z. You. Viscoelastic Model for Discrete Element Simulation of Asphalt Mixtures. Journal of Engineering Mechanics, Vol. 135, No. 4, April 1, 2009.
[11] Y. Fu, L. Wang, Ch. Zhou. 3D clustering DEM simulation and non-invasive experimental verification of shear localization in irregular particle assemblies. International Journal of Pavement Engineering. 11(5), pp. 355–365, 2010.
[12] Habtamu Z., Tom P. Simulation of Asphalt Concrete Uniaxial Creep using Discrete Element Method (DEM). ASCE Geotechnical Special Publication Pavement Mechanics and Paving Materials, PP. 99–110, 2010.
[13] Chen Jun, Pan Tongyan, Huang Xiaoming. Micromechanical Modeling of Asphalt Concrete Fracture Using a Three-Dimensional Discrete Element Method. Journal of Wuhan University of Technology-Mater. Sci. Ed., pp. 1215–1221, 2011.
[14] You, Z, Liu, Y., and Qingli, D. Three-dimensional Micro structural-based Discrete Element Viscoelastic Modeling of Creep Compliance Tests for Asphalt Mixtures. J. of Materials in Civil Eng. 23(1), pp. 79–87, 2011.
[15] Bonnaure F., Guest G., Gravois A., Uge P. A New Method of Predicting the Stiffness of Asphalt Paving Mixtures. Journal of the Association of Asphalt Paving Technologist, 46, 1997.
[16] Andrei D., Witczak, M.W., & Mirza, M.W. Development of Revised Predictive Model for the Dynamic (Complex) Modulus of Asphalt Mixtures. Development of the 2002 Guide for the Design of New and Rehabilitated Pavement Structures, NCHRP 1-37A. Interim Team Technical Report. Department of Civil Engineering, University of Maryland of College Park, MD, 1999.
[17] Hu Chichun, Wang Duanyi, Zhang Xiaoning. Characterization of Asphalt Mixture Homogeneity Based on X-ray Computed Tomography. Journal of Testing and Evaluation, 40(7), PP: 1103–1111, 2012.
[18] Masad E, Effects of air void size distribution, pore pressure, and bond energy on moisture damage. Journal of Testing and Evaluation. 34(1), pp. 1–9, 2006.
[19] Liu, Y., Dai, Q., and You, Z. A viscoelastic model for discrete element simulation of asphalt mixture. J. Eng. Mech., 135(4), 324–333, 2009.
[20] Chen Jun. Virtual Fatigue Tests of Asphalt Mixture Based on Discrete Element Method[D]. PHD dissertation. School of Transportation, Southeast University, Nanjing, China, 2010.
[21] T.K. Pellinen, J. Song and S. Xiao. Characterization Of Hot Mix Asphalt With Varying Air Voids Content Using Triaxial Shear Strength Test. Proceedings of the 8th Conference on Asphalt Pavements for Southern Africa, 2004.

This page intentionally left blank

Asphalt Pavements – Kim (Ed)
© 2014 Taylor & Francis Group, London, ISBN 978-1-138-02693-3

Effect of micro-scale morphological parameters on meso-scale response of Asphalt Concrete

Ibrahim Onifade, Denis Jelagin, Alvaro Guarin, Björn Birgisson & Nicole Kringos
KTH—Royal Institute of Technology, Stockholm, Sweden

ABSTRACT: With recent advancement in the use of X-Ray Computed Tomography to capture the internal structure of Asphalt Concrete (AC), results have shown several possibilities to account for the distribution of the different phases in the mix and quantify them in a reliable way. The morphology of asphalt mixtures which includes the aggregate size gradation and the distribution of the air-voids and bitumen phase are captured in a single morphological parameter called the Primary Structure (PS) coating thickness—(T_{ps}). In this study, the effect of variations in the morphological micro-structural property on the meso-scale response of three (3) AC samples is examined using the 3D Finite Element Method (FEM). The AC internal geometry is acquired using X-Ray Computed Tomography (CT); the distribution of the aggregates, mastic and air-voids phase is considered and obtained using Digital Imaging Processing (DIP) techniques. Using a surface-based cohesive behavior and assuming a predominant adhesive failure at the interface between the mastic and aggregate, a maximum traction criterion is used to obtain the damage propensity of the different mixtures. The result of the analysis shows that the microstructural morphological parameter T_{ps} adequately captures the meso-scale response of the mixtures; there exist an inverse relationship between mixture strength characterization and the morphological parameter T_{ps}.

Keywords: X-Ray Computed Tomography, asphalt concrete morphology, Digital Image Processing, damage, micromechanical modeling

1 INTRODUCTION

The morphology of asphalt mixtures (i.e. everything related to the shape and size, and ratio of the different phases that makes up the asphalt mixture) plays an important role in the resulting performance. The morphology of asphalt mixtures is such that the different constituents are very inter-dependent; as a result changes in one of the constituents effect a change in the other mixture constituents. For instance: the distribution of bitumen inside the mixture depends on the aggregate gradations and the required air voids. It should therefore be possible to express the morphology of the mixture with meaningful morphology parameters to be utilized in homogenized meso- and macro scale AC models.

Recently, a new morphology framework was developed [1] which allows for the determination of a morphological parameter called 'Primary Structure' (PS) coating thickness (T_{ps}). The T_{ps} considers the size gradation and distribution of the stones, the distribution of the bitumen and the distribution of the air-voids in the asphalt mixture matrix and hence it is a parameter which can be used to characterize the morphology of asphalt mixtures. Asphalt mixtures with different gradation and volumetric properties have distinct T_{ps} values.

Several researchers have studied the influence of the aggregate morphology on asphalt mixture performance. In [2] the effects of aggregate angularity and binder content on bituminous mixture was related to Fracture Performance. It was concluded that the fracture energy is increased as the aggregate angularity is decreased and the binder content increased. In [3] the influence of coarse aggregate shape on the AC mixture was examined. The different

particle shapes considered in the study were cubical, rod, disk, and blade. A measure of the combined effect of the particle shape, angularity, and surface texture referred to as Particle Index (PI) was used in the study to define the stability of an aggregate in the mix. From the study it was found that since the cubical particles have the highest PI value, they gave a desirable increased aggregate internal friction and improved rutting resistance.

The air-void and bitumen distribution are also important morphological parameters that, together with the aggregates contributes to the resulting response of asphalt mixtures. The Voids in Mineral Aggregates (VMA) which is the volume of the mixture occupied with the effective bitumen content together with the air-voids has been related to the durability of mixtures and its ability to resist changes in the HMA properties. Inadequate VMA can result to rapid oxidization of the asphalt which could make the pavement too brittle [4]. Inadequate air-void content can have an adverse effect on the mixture performance and is mainly manifested in asphalt pavements as bleeding and rutting of the asphalt pavement [5].

The essence of the study presented in this paper is to investigate the influence of T_{ps} value for asphalt mixtures on the overall mixture behavior. X-Ray CT and image processing techniques have been used in the study and characterization of asphalt concrete mixtures by various researchers [6] [7] [8] [9]. In this study, an X-Ray CT system is used to acquire the internal structure of three different asphalt samples. Digital image processing and analysis technique is used to obtain the distribution and quantify the different phases in 3D space. The morphology of the three different asphalt field core samples is defined by their PS coating thickness (T_{ps}) and numerical simulation is performed to characterize the mixtures so as to obtain the effect of changing mixture morphology on mixture performance.

The methodology presented and discussed in this paper can be used to further understand the contribution of mixture morphology to mixture performance. The technique can be used to identify key material parameters and can be used to characterize field mixtures after construction thereby giving a good indication of field performance of different asphalt mixtures and thus reducing the bias between laboratory prepared and field compacted mixtures.

2 OBJECTIVES AND SCOPE

The main objectives of this study are to:

1. Characterize the AC morphology to obtain the PS coating thickness T_{ps} using X-Ray CT and imaging processing techniques to capture the asphalt morphology
2. Characterize the AC mixtures using micromechanical simulations to obtain effect of varying mixture morphology on mixture performance.
3. Evaluate the possibility of the use the morphological parameter T_{ps} in homogenized meso- and macro scale AC models.

3 X-RAY COMPUTED TOMOGRAPHY AND IMAGE PROCESSING

Three different AC field core samples are used in this study. The asphalt cores are scanned using the KTH X5000 X-Ray Computed Tomography (CT) scanner at the Highway and Railway Engineering Laboratory. The scanning resolution is 105 μm without beam filtration. Each scanned samples reveals three distinct lift of AC layers. The scanned samples are labeled Sample A, Sample B and Sample C as shown in Figure 1.

Image processing techniques is used to carefully process and analyze the samples to obtain quantities needed to calculate the T_{ps} value for each sample. The procedure for the digital image processing and analysis developed by Onifade et al. [9] is used. In this study, the median filter not used but instead, an edge-preserving filter together with an anisotropic diffusion filter is used to improve the quality of the segmented image and thus obtain reliable microstructural information needed for the particle size distribution. In this procedure, Avizo

Figure 1. Images of samples A, B and C used in this study.

Fire© is used for the image processing and analysis while Simpleware ScanIP© is used for volume reconstruction and mesh generation.

One lift from each AC sample which results in a cylindrical geometry of approximately 100 mm diameter and 57 m height is quantified and used for the calculation of the T_{ps} values of each sample. The geometry from each sample with known T_{ps} value is used in the micromechanical simulation for material characterization. The same geometry size is used to eliminate errors due to size variation in T_{ps} characterization and numerical simulation.

4 CALCULATION OF PS COATING THICKNESS

The quantities needed to calculate the T_{ps} values are as follows:

a. Size gradation of the aggregates
b. Max specific gravity of the mixture (G_{mm})
c. Binder specific gravity (G_b)
d. Percent binder (P_b)
e. Aggregates bulk specific gravity (G_{sb})
f. Percent absorbed binder (P_{ba})
g. Percent of air voids (V_a)
h. Voids Filled with Bitumen (VFA)

Gradation of the stones is obtained from the image processing and analysis quantification results. The equivalent sphere diameter of the aggregates is used for the particle size distribution of the stones. The minimum Feret diameter is not used as it doesn't adequately represent the aggregate size since the aggregate size in the third direction have to be considered for 3-Dimensional (3D) aggregate quantification. Another advantage of using the equivalent sphere diameter is that the shape is then in conformity with the theory on which the development of T_{ps} is based upon i.e. packing theory. The sieve sizes that have been considered are 19 mm, 12.5 mm, 9.5 mm, 4.65 mm, 2.36 mm and 1.18 mm. Sieve sizes smaller than 1.18 mm have not been considered because aggregate sizes smaller than 2.36 mm are considered as part of the mastic for the micromechanical modeling. The results from the calculation of the T_{ps} show that the interacting aggregate size range is between 12.5 mm and 4.65 mm. This is the rationale for the consideration of aggregate sizes less than 2.36 mm as part of the mastic in the Finite Element simulations. The particle size distribution is shown in Table 1.

The volumes of the mastic and air-voids are obtained directly from the quantification results. The volume of the mastic together with the specific gravity of the mastic is used to

Table 1. Aggregate particle size distribution.

Sieve size (mm)	Sample A	Sample B	Sample C
19	100	100	100
12.5	92.4	81.88	92.8
9.5	77.6	67.32	76.9
4.75	53.3	60.57	47.5
2.36	51	56.13	43.5
1.18	32	30.02	18.2

Table 2. Volume relationship (% volume) for the three different samples.

	Sample A	Sample B	Sample C
Air-voids	3.68	8.80	2.75
Mastic	47.51	38.27	52.05
Aggregates	48.81	52.92	45.21

Table 3. Mixture volumetric properties.

Volumetric properties		Sample A	Sample B	Sample C
Max specific gravity of the mixture	G_{mm}	1.88	2.00	1.81
Binder specific gravity	G_b	2.70	2.70	2.70
Percent binder	P_b	27.08	21.62	30.50
Aggregates bulk specific gravity	G_{sb}	1.66	1.83	1.56
Percentage absorbed binder	P_{ba}	2.13	2.61	1.71
Percentage volume of air voids	V_a	3.70	8.81	2.80
Voids filled with bitumen	VFA	82.19	60.01	87.19

obtain the mass of the binder in the mixture. The specific gravity of the mastic and aggregates are assumed to be 1.035 and 2.7 respectively for all three samples. Table 2 shows the volume relationship for the different phases in the AC samples.

The mixture volumetric properties are obtained using the volume of the three different phases obtained from the quantification and the specific gravity of the mastic and aggregates. The bulk specific gravity of the mixture needed for calculation of the Void in Mineral Aggregate (VMA) and the Percentage Binder Absorbed (P_{ba}) is obtained from the effective specific gravity as shown in Eq. (1).

$$G_{sb} = (0.9397 * G_{se}) + 0.0795 \tag{1}$$

Table 4 is used for classification of the aggregate structure into the 4 different groups. The relationship between the mixture volumetric properties and the porosity of the primary structure is shown in Eq. (2) where $V_a^{SS}$and V_a^{PS} are the volume of secondary structure and primary structure respectively, V_b^{eff} and V_v^{eff} are the effective volume of the binder and voids in the mixture, $V_b^{abs(PS)}$ and $V_b^{abs(SS)}$ are the volume of binder absorbed by the primary and secondary structures respectively.

$$\eta_{ps} = \frac{V_a^{SS} + V_b^{eff} + V_b^{abs(SS)} + V_v^{eff}}{V_a^{PS} + V_a^{SS} + V_b^{eff} + V_b^{abs(PS)} + V_b^{abs(SS)} + V_v^{eff}} \tag{2}$$

There exist several relationships between PS coating thickness index I_{ct} and the porosity of the primary structure η_{ps} for ideal packing arrangements i.e. simple cubic, orthorhombic,

Table 4. Identification of different groups based on aggregate gradation.

	Condition	Four different groups
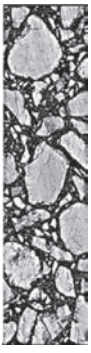	$D_{avg} \geq 0.703\overline{D_n} + 0.297\overline{D_{n+1}}$	*Oversized Structure (OS)*: Larger particles than the PS
	$0.703\overline{D_n} + 0.297\overline{D_{n+1}} \geq D_{avg} \geq 0.311\overline{D_n} + 0.689\overline{D_{n+1}}$	*Primary Structure (PS)*: Interactive grains form the load caring network
	$where,\ D_{avg} = \frac{\varphi_n \cdot \overline{D_n} + \varphi_{n+1} \cdot \overline{D_{n+1}}}{\varphi_n + \varphi_{n+1}}$	
	$D_{avg} \leq 0.311\overline{D_n} + 0.689\overline{D_{n+1}}$	*Secondary Structure (SS)*: Fills the gaps between the PS and provides stability
	Particles passing 0.0075 sieve	*Filler Particles*: Fills the gaps between the SS and improves stability

Note: D_{avg} is the weighted average size of two consecutive sieves n and n + 1. Whereas, φ_n and φ_{n+1} are the concentrations for two contiguous sieves with mean particle size $\overline{D_n}$ and $\overline{D_{n+1}}$ respectively (with $\overline{D_n} > \overline{D_{n+1}}$).

Table 5. PS coating thickness for the three different samples.

	Sample A	Sample B	Sample C
PS coating thickness (T_{ps})	1.99	2.80	1.76
PS range (mm)	4.65–12.5	2.36–12.5	4.65–12.5

tetragonal, rhombohedral packing. However, the packing of the aggregates in the AC mix is in a non-ideal manner and hence prompted the establishment of a relationship between the PS coating thickness index and porosity of the primary structure for non-ideal packing arrangements [10]. Eq. (3) shows the established relationship for the non-ideal packing arrangements.

$$I_{ct} = 0.95(\eta_{ps})^{1.28} \tag{3}$$

Eq. (4) shows the relationship between the PS coating thickness (T_{ps}), the PS coating thickness index (I_{ct}) and the weighted average diameter (d_p) of the PS particles. The PS coating thickness is obtained from equation 3.

$$T_{ps} = I_{ct} * d_p/2 \tag{4}$$

5 NUMERICAL SIMULATION

Micromechanical analysis is carried out to investigate the influence of T_{ps} on asphalt mixture performance i.e. how T_{ps} correlates with mixture behavior. To achieve this purpose, three different samples with the same geometry, material properties, boundary conditions, but different morphology is analyzed to characterize their performance. The morphology is captured and characterized by the PS coating thickness T_{ps}.

The aggregates are considered as linear elastic materials with Young's Modulus of 25 GPa [6] and a Poisson's ratio of 0.3. The mastic is made up of the secondary structure, filler material and the bitumen. The mastic is considered as a viscoelastic material and modeled as a generalized Maxwell's model with springs and dashpots connected in series. The mastic master curve used in this study is generated using the Christensen Anderson Marasteanu (CAM) model. The CAM model can be used to model the rheological behavior of the pure bitumen and mastic and it relates the glassy modulus, the rheological index and the cross-over frequency to the complex modulus of the mastic. The master curve shown in Figure 2 is used to model the viscoelastic response of the mastic.

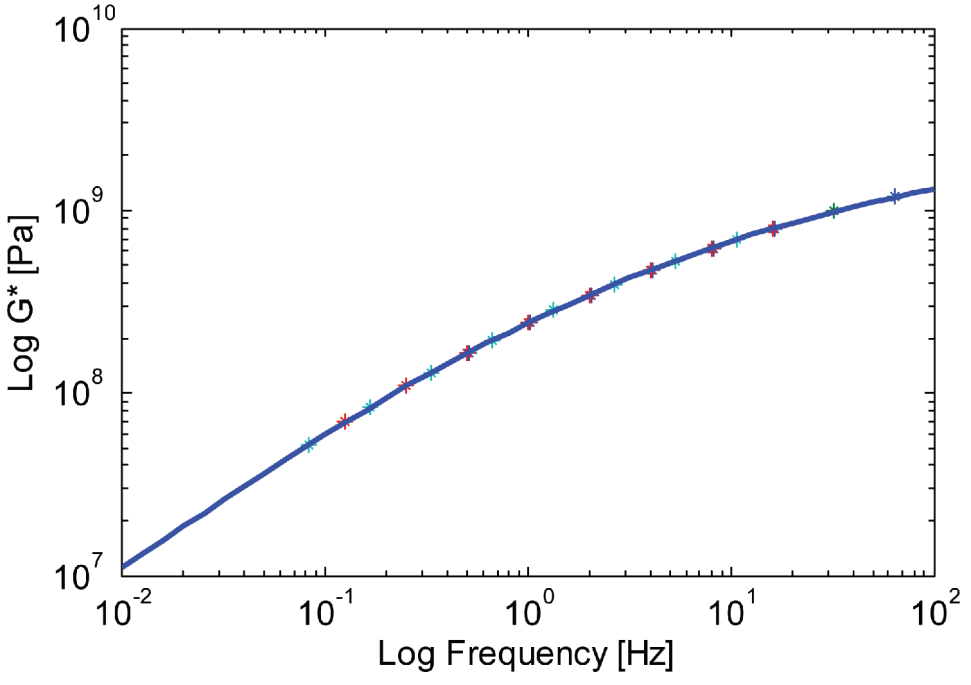

Figure 2. Master curve used to model mastic viscoelastic response.

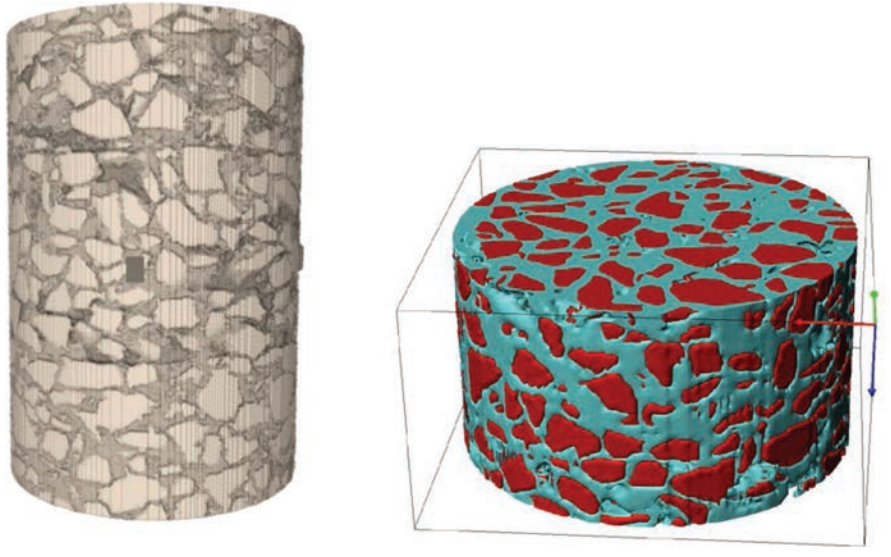

Figure 3. 3D-reconstructed image and geometry of sample A used in numerical simulation.

A uniaxial displacement controlled test is performed to characterize the three different mixture using numerical simulations. The bottom of the samples constrained in the axial direction and the top is subjected to a constant displacement rate of 1e-2 mm/s for 100 s resulting in a final displacement of 1 mm. The final geometry used for the numerical simulation consists of approximately 1.5 Million tetrahedral elements. Figure 3 shows the 3D-reconstructed image and geometry for sample A used in the analysis.

To evaluate the effect of changing microstructural morphological parameter on mixture response, two sets of analysis is considered. In the first set of analysis, it was assumed that there is perfect bonding between the aggregates and mastic phase and in essence there are stress continuities at the interface. Figure 4 shows the plot of the stress and strain in the mastic for the three samples considered in this analysis. The effect of changing morphology is reflected in the amount of stresses developed in the mixture with the mixture with the highest t_{ps} value having the lowest stresses in the mixture vice-versa.

The second sets of analysis consider the inclusion of the interface interaction between the mastic and the aggregate. Surface-based cohesive behavior is used to model the interface behavior in Abaqus. The surface-based cohesive behavior used assumes a linear elastic traction-separation law and is used to obtain the traction at the interfaces. The formulation for the interface behavior is shown in eq. (5).

$$t = K\delta \tag{5}$$

where t is the traction at the interface, K is the elasticity matrix and δ is the separation at the interface.

The components of the elasticity matrix in the normal and shear directions can be varied to check different interface conditions. The components of the elasticity matrix are uncoupled and the value of the normal stiffness and shear stiffness used is shown in Table 6.

A maximum stress-based damage criterion is used to model the initiation of damage. The maximum stress criterion is shown in eq. (6).

$$D = \max\left\{\frac{\langle t_n \rangle}{t_n^0}, \frac{t_s}{t_s^0}, \frac{t_t}{t_t^0}\right\} = 1 \tag{6}$$

where t_n^o, t_s^o, t_t^o represents the peak stress values purely in the normal direction and purely in both shear directions respectively. The peak stress value is chosen arbitrarily as 3 MPa in this study. Compressive normal stresses doesn't not contribute to damage when assuming

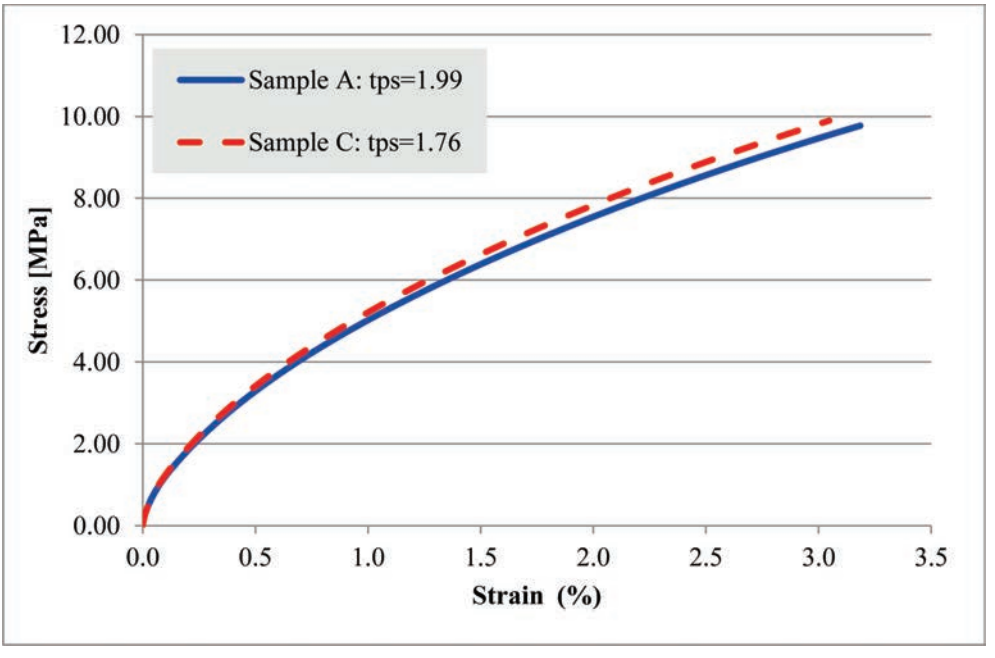

Figure 4. Stress-strain diagram without interface interaction.

Table 6. Interface properties.

	Stiffness (MPa/mm)
Normal stiffness	1500
Shear stiffness	1000

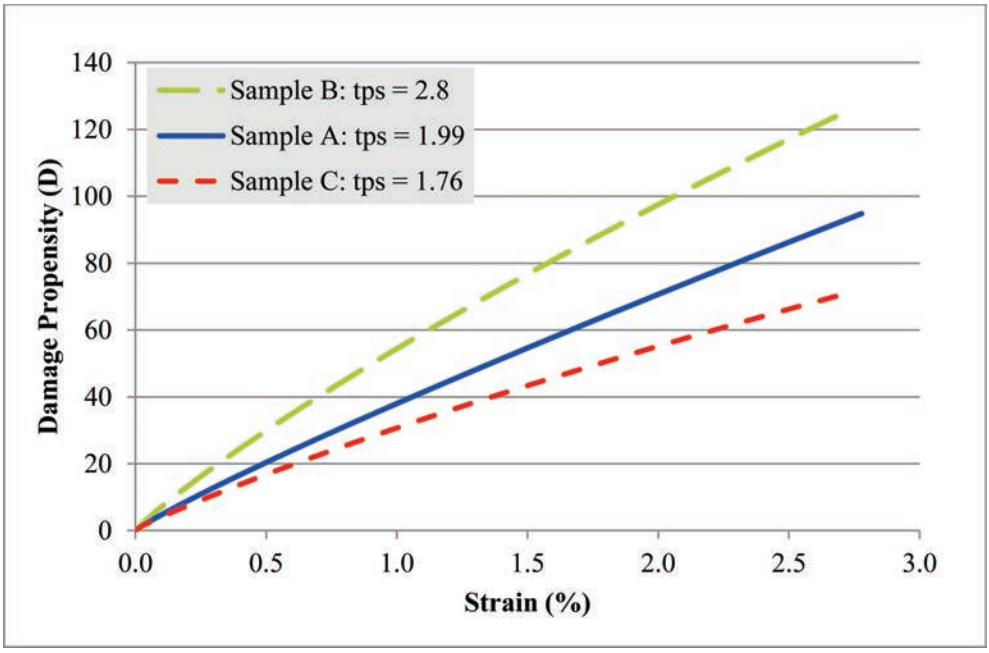

Figure 5. Damage propensity for the three different mixtures.

cohesive behavior at the interface, hence the use of Macaulay brackets in eq. (6). The damage criterion in eq. (6) is used to quantify the damage and obtain the damage propensity of the different mixtures.

Figure 5 shows the plot of damage criterion (D) against strain for the three different mixtures. The material with the highest value of t_{ps} has the highest damage propensity and vice-versa.

Considering adhesive failure, asphalt-based materials tend to lose its integrity due to degradation of the bond at the interface between the mastic and the aggregate. This loss of material integrity leads to damage in the material and which eventually results in failure. With the mastic and aggregate material properties the same for the three mixtures and assuming that the damage is adhesive in nature, we can draw the conclusion that the damage and eventual failure is mainly dependent on the conditions at the interface. For all three mixtures, there will be a nominal traction value for which there will be a complete separation at the interface for the three samples which will result in failure of the material. From Figure 5, it follows that as the value of the nominal traction increases, the strength at the interface increases and the associated failure strain increases. The failure changes from an adhesive failure at the interface to a cohesive failure in the different phases when the value of this nominal traction is more than the cohesive strength of the constituent materials. This means, the nominal traction will not be reached before failure occurs in the material, if the failure is cohesive in nature.

For comparison purpose, a failure criteria which is dependent on the condition at the interface is assumed to be the value of the ratio of the nominal traction to the peak stress value and chosen to be 40 i.e. $D_{crit} = 20$, we can then obtain the failure strain associated with

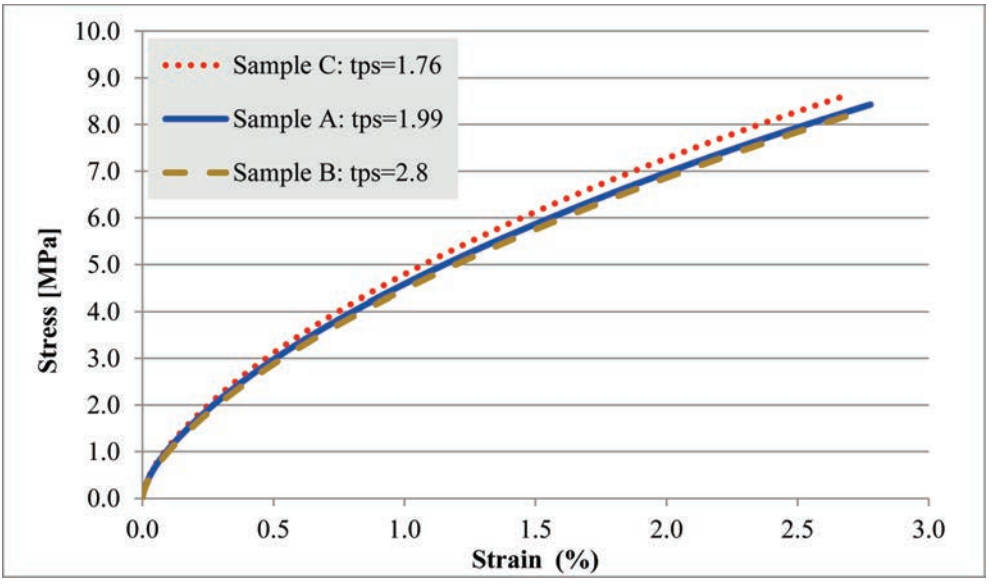

Figure 6. Stress-strain curve considering interface interaction.

Table 7. Summary of results.

Sample	T_{ps}	Failure strain (%)	Failure strength [Mpa]	Fracture energy [kJ/m^3]
A	1.99	0.49	2.96	8.9
B	2.80	0.32	2.14	4.1
C	1.76	0.62	3.55	13.3

the failure criteria for the three mixtures. Failure in materials is characterized with failure strain and failure strength. With the failure strain of each material known, we can obtain the failure strength and then the fracture energy of the different mixtures from the stress-strain diagram in Figure 6.

From Table 7, as the value of T_{ps} increases, the failure strain, failure strength and the fracture energy decreases. There is a good trend and an inverse relationship between the T_{ps} values of the different mixtures and their corresponding mixture strength characteristics. The microstructural morphological parameter T_{ps} can be used as an internal parameter in homogenized meso- and macro scale AC models and can also be used as input in design procedures to predict bulk material properties. Changes in the microstructure due to damage accumulation have not been considered in this approach. Consideration of the damage in the material as a function of loading will further improve the practicality and applicability of the approach. There is also a need for further studies of interfaces in asphalt materials combining experimental techniques and micromechanical modeling approach.

REFERENCES

[1] B. Lira, D. Jelagin and B. Birgisson, "Gradation-based framework for asphalt mixture," Materials and Structures, vol. 46, no. 8, pp. 1401–1414, 2012.

[2] L. Souza, Y. Kim, F. Souza and L. Castro, "Experimental Testing and Finite-Element Modeling to Evaluate the Effects of Aggregate Angularity on Bituminous Mixture Performance," *Journal of Materials in Civil Engineering,* vol. 24, no. 3, pp. 249–258, 2012.

[3] J.-S. Chen, M. Chang and K. Lin, "Influence of Coarse Aggregate Shape on The Strength of Asphalt Concrete Mixtures," *Journal of the Eastern Asia Society for Transportation Studies,* vol. 6, pp. 1062–1075, 2005.
[4] Chadbourn B.A. et al, "The Effect of Voids in Mineral Aggregate (VMA) on Hot—Mix Asphalt Pavements," Minnesota Department of Transportation, St. Paul, Minnesota, 1999.
[5] S. Kandhal and S. Chakraborty, "Evaluation Of Voids In The Mineral Aggregate For Hma Paving Mixtures," National Center for Asphalt Technology, Auburn University, Alabama, 1996.
[6] T. You, R.K.A. Al-Rub, M.K. Darabi, E.A. Masad and D.N. Little, "Three-dimensional microstructural modeling of asphalt concrete using a unified viscoelastic–viscoplastic–viscodamage model.," in *Construction and Building Materials*, 2012.
[7] H.M. Zelelew and A.T. Papagiannakis, "A volumetrics thresholding algorithm for processing asphalt concrete x-ray ct images.," in *International Journal of Pavement Engineering*, 2011.
[8] E. Masad, L. Tashman, D. Little and H. and Zbib, "Viscoplastic modeling of asphalt mixes with the effects of anisotropy, damage and aggregate characteristics," in *Mechanics of Materials*, 2005.
[9] I. Onifade, D. Jelagin, A. Guarin, B. Birgisson and N. Kringos, "Asphalt Internal Structure Characterization with X-Ray Computed Tomography and Digital Image Processing," in *Multi-Scale Modeling and Characterization of Infrastructure Materials*, 2013.
[10] P.K. Das, B. Birgisson, D. Jelagin and N. Kringos, "Investigation of the asphalt mixture morphology influence on its ageing susceptibility," *Submitted: Under Review,* 2013.
[11] Avizo, "Avizo User's Guide," in *Visualization Sciences Group.*, Vordeaux, Frace, 2009.
[12] Simpleware, "ScanIP—Simpleware Reference Guide," Exeter, United Kingdom, 2012.
[13] Dassault Systèmes, "Abaqus 6.12 Analysis User's Manual," 2012.

Asphalt Pavements – Kim (Ed)
© 2014 Taylor & Francis Group, London, ISBN 978-1-138-02693-3

Combined effects of oxidative aging and moisture inclusion on asphalt binder using Molecular Dynamic simulation

Jielin Pan
Department of Civil Engineering, The University of New Mexico, Albuquerque, NM, USA

Mohammad Hossain
Department of Civil Engineering and Construction, Bradley University, Peoria, IL, USA

Rafiqul Tarefder
Department of Civil Engineering, The University of New Mexico, Albuquerque, NM, USA

ABSTRACT: Asphalt Concrete (AC) pavements are exposed to both atmospheric oxygen and moisture-induced conditions. In this paper, the combined effects of oxidation and moisture inclusion on asphalt binder, in the form of energy and density changes, are studied by Molecular Dynamic (MD) simulation. Two hypothetical models of asphalt binder, before and after oxidative aging, are developed and simulated with different moisture contents. The simulation results demonstrate that before moisture inclusion, the oxidized asphalt binder shows hardening phenomenon in the form of energy and density increases, compared to the unoxidized asphalt binder. After moisture inclusion, energies and densities of both unoxidized and oxidized binders decrease with an increase of moisture content. In addition, with the same moisture content, energies and density of the moisture-induced oxidized asphalt binder decrease faster than the moisture-induced unoxidized asphalt binder. From study, the decrease of density is caused by the increase of volume of asphalt binder, which is due to stretching of asphalt binder molecular chains with presence of water molecules. The stretching of molecular chains might cause damage in asphalt binder. Furthermore, Energy losses and density decreases are key indicators of damage in AC. Therefore, Moisture-induced oxidized asphalt binder is most susceptible to be damaged.

Keywords: Asphalt binder, oxidative aging, moisture, molecular dynamic simulation

1 INTRODUCTION

Asphalt binder durability is affected by the resistance of the molecules' chemical composition to change when reacting with atmospheric oxygen, which is called oxidative aging. Oxidative aging is the major factor leading to the hardening and embrittlement of asphalt [1]. Meanwhile, moisture-induced damage can be defined as the loss of strength and durability in Asphalt Concrete (AC) due to the effects of moisture [2]. The sources of moisture into AC are from rainfall and melting ice from the top of the AC pavement and seepage and capillary actions of high water table from the bottom of the AC pavements [3]. Moisture diffuses through asphalt binder and aggregate. Both chemical and mechanical actions take place while moisture diffuses through AC. These chemical and mechanical actions of moisture reduce stiffness of asphalt binder.

Oxidative aging and moisture-induced damage mechanisms are very complex phenomena and many attempts have been made to simplify them [4]. This study is focused on determining aging and damage by measuring energy losses and density changes from a microscopic view using Molecular Dynamic (MD) simulation. The objective of this study is to understand the

oxidation and moisture damage mechanism, and the properties of asphalt binder changes before and after oxidative aging with moisture inclusion. An understanding of these will be substantially helpful in improving the durability of asphalt binder in the future.

2 MOLECULAR STRUCTURES OF ASPHALT BINDER BEFORE AND AFTER OXIDATIVE AGING

Asphalt molecules are composed mainly of carbon and hydrogen atoms; however, most molecules contain one or more heteroatoms such as sulfur, nitrogen and oxygen. Asphalt can be separated into two broad groups: maltenes and asphaltenes. Maltenes can be further divided into a series of fractions with increasing polarity: saturates, aromatics, and resins [1, 5].

2.1 *Molecular structures of asphalt before oxidative aging*

2.1.1 *Maltenes—saturates*

Saturates are composed of alkanes [6]. Saturate fractions lack polar chemical functional groups. They are liquid at ambient temperatures and seldom change with time. Saturates show the least change under oxidation [1]. Figure 1 shows the hypothetical molecular structure of saturates used for this study drawing by Culgi 7.0.2. The black is carbon, and the white ball is hydrogen.

2.1.2 *Maltenes—aromatics*

The molecular structure of aromatics is comprised of condensed non-aromatic rings and at least one aromatic ring structure similar to benzene. They may contain the heteroatoms oxygen, nitrogen and sulfur and are liquid at ambient temperatures. Aromatics are the softening component in asphalt (good solvents for paraffin waxes) and are more polar than saturates [6–7]. The structure of Aromatics is illustrated in Figure 2.

2.1.3 *Matenes—resins*

Resins consist of a much higher polar end group than the other maltene fractions and contain heteroatoms such as oxygen, sulfur and nitrogen, as well as long, nonpolar paraffinic groups. The resins are attracted to the asphaltene micelles through their end group. The resin fraction is solid or semi-solid at ambient temperatures and is also one of the aging fractions in asphalt. Resins can be converted to asphaltenes by oxidation [6–7]. The hypothetical structure of resins is represented by Figure 3. The red ball represents oxygen, and the yellow ball represents sulfur.

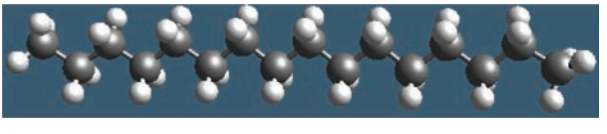

Figure 1. Hypothetical structure of saturates $C_{16}H_{34}$.

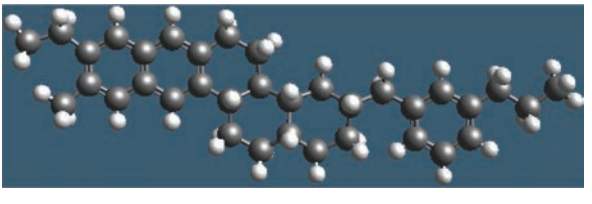

Figure 2. Hypothetical structure of an aromatic molecule $C_{35}H_{44}$ [6].

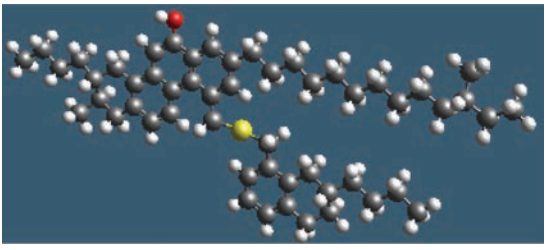

Figure 3. Hypothetical structure of a resin molecule $C_{53}H_{76}OS$ [6].

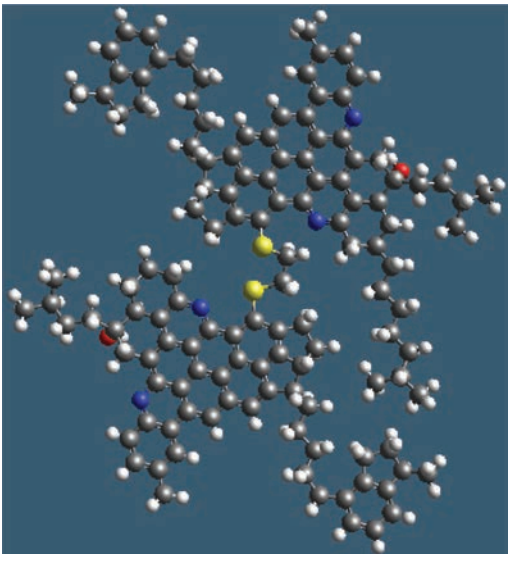

Figure 4. Hypothetical structure of an asphaltene molecule $(C_{67}H_{76}N_2OS)_2$ [6].

2.1.4 *Asphaltenes*

Asphaltenes are the most polar of asphalt's component fractions and act as the viscosity-building ("bodying") agents in asphalt. Therefore, they have a very high tendency to interact and associate. They are not only composed of condensed aromatic and naphthenic molecules, but they also contain a large amount of heteroatoms (O, S, and N) and metal (V and Ni) content from heavy oils incorporated in their polar molecules. Asphaltenes are solid or semi-solid at ambient temperatures [6–7]. Figure 4 illustrates the molecular structure of the fraction of asphaltenes. The blue ball represents nitrogen.

2.2 *Oxidation mechanism*

Many asphalt molecules of different composition have similar chemical functionalities that in turn cause similar effects on the physical properties of asphalt. If the different chemical functionalities, which compose and dominate the properties of the various asphalt molecules are considered, the analysis of asphalt oxidative aging is narrowed to a manageable number of types of functionalities [8].

Asphalt exposed to atmospheric oxygen in pavements rapidly oxidizes with the formation of polar, strongly interacting, oxygen-containing chemical functional groups that greatly increase viscosity and alter complex flow properties [1]. Figure 5 shows the important chemical functionalities before and after aging which are an integral part of large asphalt molecules.

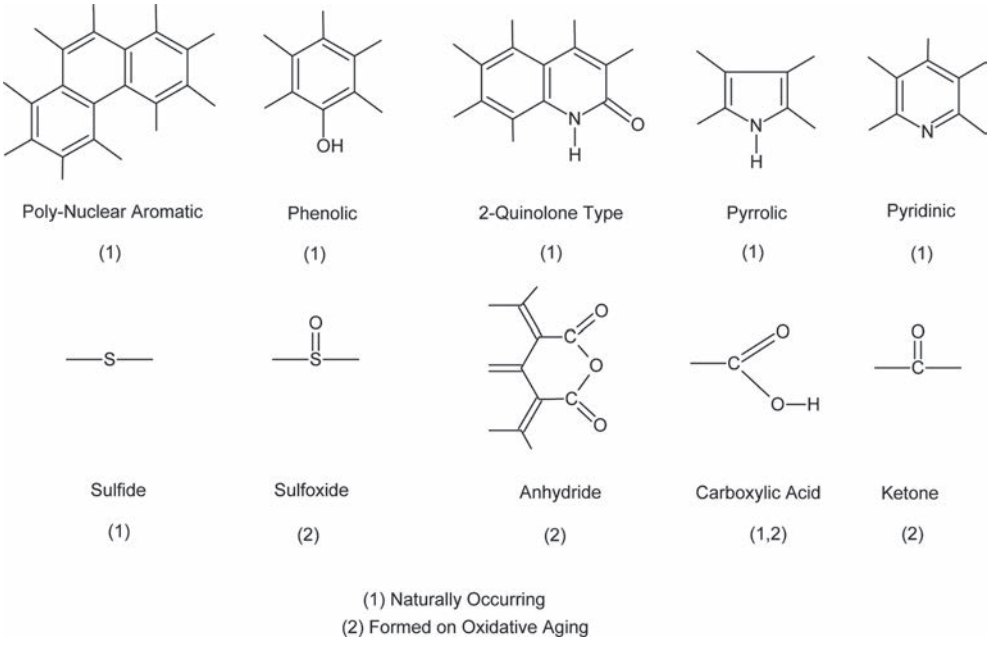

Figure 5. Functional groups present in asphalt molecules [11].

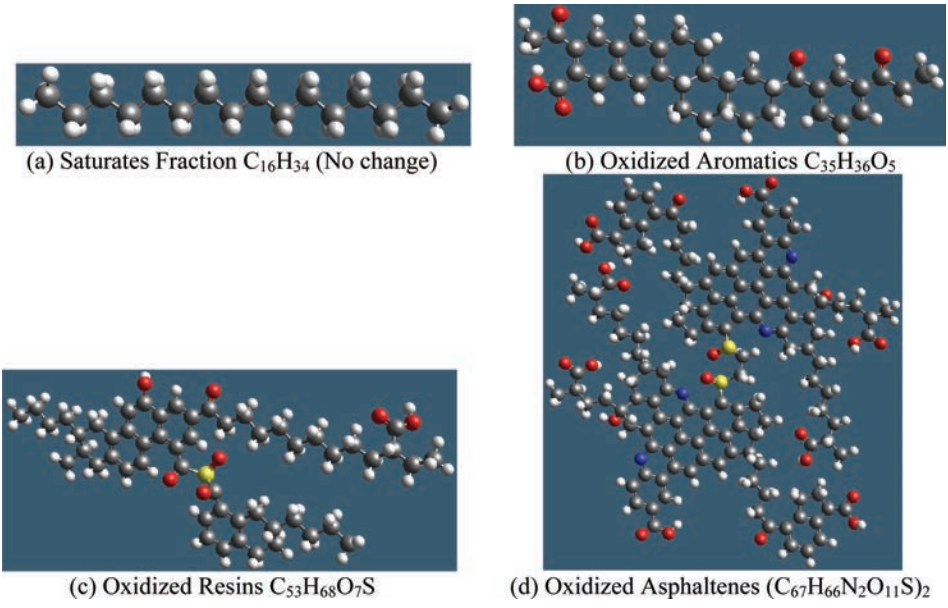

Figure 6. Chemical composition of asphalt after oxidative aging.

Petersen indicated the oxidation products formed are consistent and in good agreement with the hydrocarbon types in asphalts and the general chemistry of hydrocarbon oxidation [1]. The formation of carbonyl compounds through the hydroperoxide intermediate is the major reaction pathway of hydrocarbon air oxidation [9–10]. The most sensitive hydrocarbon moiety present in asphalt is the carbon atom adjacent to an aromatic ring system—a benzylic carbon. The hydrogen atom attached to the carbon atom is relatively easy to displace,

forming a free radical on it. Branching in the attached hydrocarbon chains also increases the sensitivity of the asphalt to oxidation. Generally, ketones and sulfoxides are the major oxidation products.

2.3 *Hypothetical structures of asphalt components after oxidative aging*

Figure 6 shows the hypothetical molecular structures of the four fractions in asphalt after oxidative aging. The amount of fractional components changes from the more nonpolar to the more polar fractions. Saturates show the least change in oxidation in Corbett's analysis [12], while there was a significant increase in the fraction of asphaltenes along with the decrease of aromatics and resins.

3 MD SIMULATION

3.1 *Asphalt composition models*

According to Corbett's studied on composition of asphalt, some unoxidized asphalt is comprised of 5–15% saturates, 30–45% aromatics, 30–45% resins, and 5–20% asphaltenes [13]. Storm and co-workers's studied on asphalt fractions suggests C_{16} to C_{36} average chain lengths of saturate structure [14]. Based on the above references, 10% satures, 30% aromatics, 40% resins, and 20% asphaltenes by weight, respectively, are selected for the unoxidized asphalt in this study. In addition, the chain length of 16 for the saturate fraction is chosen. The four asphalt fractions are put into a simulation box to represent unoxidized asphalt, with the size of 24.8*24.8*24.8 $Å^3$. The size of simulation box is selected considering the smallest box size for containing all the asphalt fractions. The oxidative aged asphalt for simulation is used the same size of simulation box and contains the same number of molecules of each fraction as the unoxidized asphalt.

3.2 *Simulation methods and conditions*

The MD simulation is conducted by Culgi 7.0.2 software and an all-atom model is used to explicitly represent each atom in a molecule [15]. In addition DREIDING force field is selected to define the interaction between the atoms, and atom based method is used to handle long-range interactions. Initial temperature and pressure for all the simulations are set as 298 K (25 ºC) and 101.325 kPa (1 atm), respectively. This study first minimizes the energies of both unoxidized and oxidized asphalt simulation boxes to a reasonable level by the Monte Carlo minimization algorithm implemented in Culgi, and then sets the statistical mechanical ensemble NPT for the MD simulations. The simulation time step is 0.5 fs and the running steps is first set as 1,000,000 to guarantee the system that can reach equilibration.

To analyze how the properties of asphalt change under the combined effects of oxidative aging and moisture inclusion, MD simulations are conducted for both unoxidized and oxidized asphalts with water molecule inclusion at 0% 1%, 2%, 4%, 6%, 8%, 10%, 12%, 14%, 16%, 18%, and 20%, by the weight of simulation box, respectively. The reason to select the moisture content range is based on multiple attempts of the MD simulations. This range can truly show the trend of energy and density changes (from rapid to steady) of both unoxidized and oxidized asphalt binders, and explicitly compare the differences between unoxidized and oxidized asphalt binders, after different moisture content inclusion. There are total 24 simulations conducted by this study. Figure 7 (a) and (b) show two examples of the simulation box with 20% water in unoxidized and oxidized asphalt system, respectively.

3.3 *Results and discussions*

3.3.1 *Density changes*

Figure 8 indicates that densities of both unoxidized and oxidized asphalts decrease with an increase in water content, except the density changes during initial moisture inclusion. It can

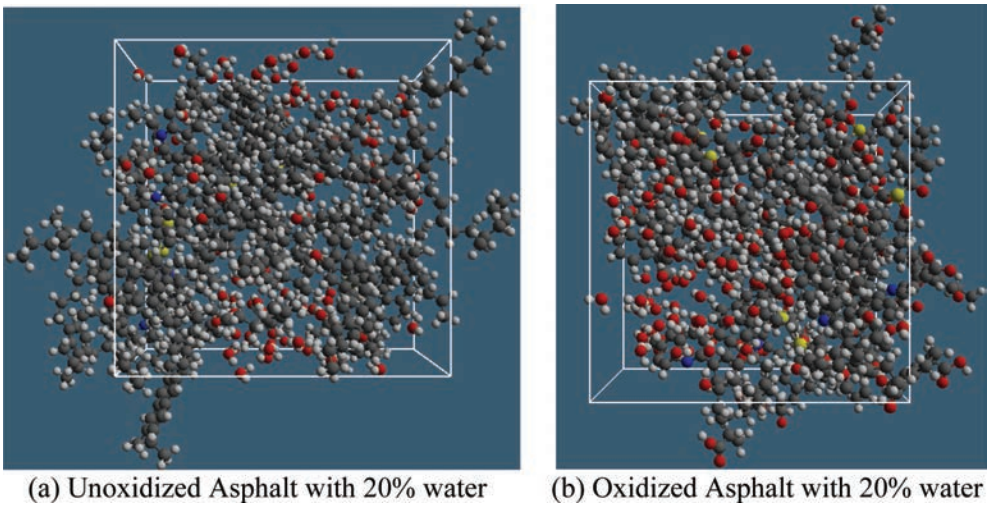

Figure 7. Simulation boxes for both unoxidized and oxidized asphalt with 20% water.

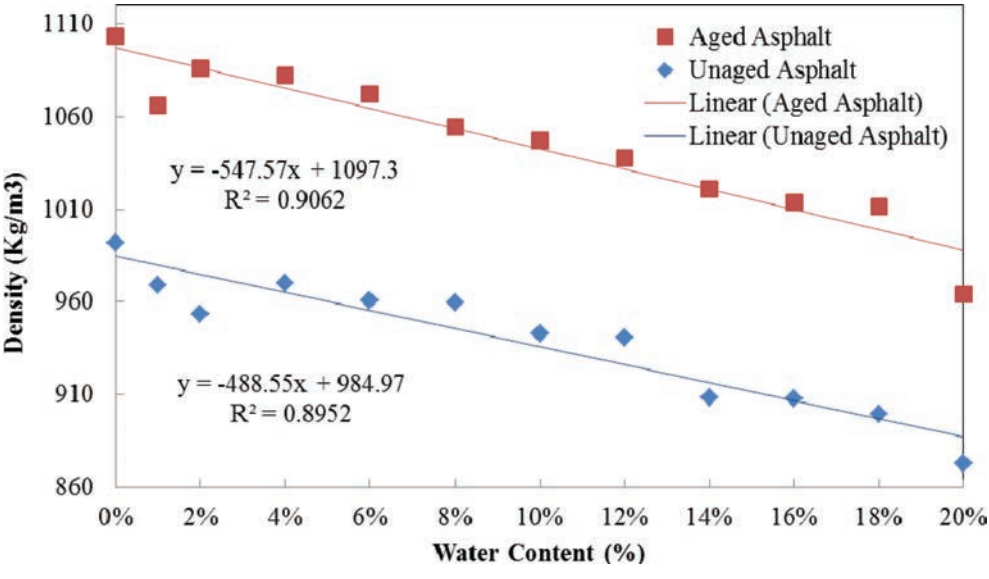

Figure 8. Water content-density relationships for asphalt before and after oxidative aging.

be seen that the densities of both unoxidized and oxidized asphalts decreases significantly during the initial water inclusion and reach a relative low point, as 2% water content for unoxidized asphalt and 1% water content for oxidized asphalt. After the first decrease, the densities show a slight rise and start to decrease with an increase in water content. The reason behind this is that initial moisture inclusion might increase more volume of the system with less weight rise. In addition, density decrease caused by volume increase of the asphalt binder is due to stretching of asphalt binder molecular chains with presence of water molecules. The stretching of the molecular chains might cause damage (stiffness reduction) in asphalt binder. Figure 9 illustrates that bond stretch energies of both oxidized and unoxidized asphalt decrease with the increase of water content. This proves that the addition of water molecules stretches the molecular chains of asphalt to make them lose bonding strength, and

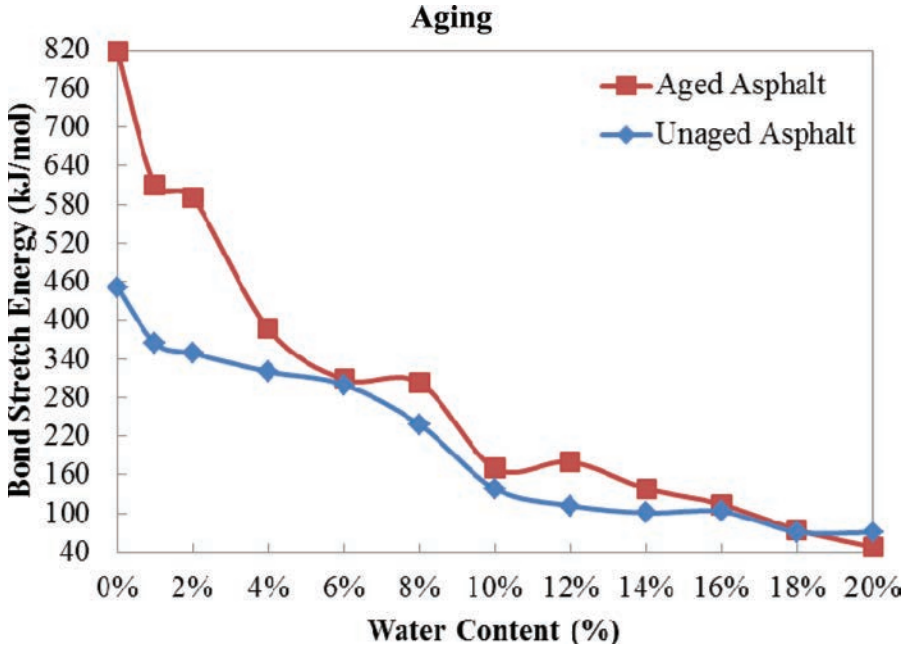

Figure 9. Bond stretch energies of oxidized and unoxidized asphalt vs. water content.

reduces the stiffness of asphalt. Also the bond stretch energy of oxidized asphalt is higher and decreases faster than the unoxidized asphalt, while after 20% water inclusion, the energy of oxidized asphalt is lower than the unoxidized asphalt.

Figure 8 also shows that the density of asphalt after oxidative aging is higher than the one before oxidation at the same water content. This result suggests hardening of asphalt occurs after oxidative aging. Moreover, the oxidative aged asphalt shows a better linear relationship for density vs. water content than the unoxidized asphalt, and the slope of oxidized asphalt linear line is higher than the unoxidized asphalt, which means that the density of oxidized asphalt decreases faster than the unoxidized asphalt with an increase in moisture inclusion. This indicates that oxidative aged asphalt is easily damaged than unoxidized asphalt by moisture inclusion.

3.3.2 *Energy changes*

Energy changes in asphalt before and after oxidative aging combined with moisture inclusion can also reveal the physical property changes. Energies can be grouped into kinetic energies (which are due to particle movement) and potential energies (which are stored energies—energy that a piece of matter has because of its position or because of the arrangement of its parts) [16].

Andersen developed a constant pressure MD based on the, so called, extended system method [17]. This approach is used in the simulation by Culgi 7.0.2 [15]. The simulation system is coupled to an external variable, the volume of the system, which mimics the action of a piston on a real system. The piston is a 3-dimensional virtual piston. If the system has a volume V and the piston has a mass M, the kinetic energy K_V within time t associated with the external variable is,

$$K_V = \frac{1}{2} M \left(\frac{\partial V}{\partial t} \right)^2 \tag{1}$$

The potential energy (E_P) for an arbitrary geometry of a molecule in MD simulation under the Dreiding force field is expressed as a superposition of valence (or bonded) interactions

(E_{val}) that depend on the specific connections (bonds) of the structure and non-bonded interactions (E_{nb}) that depend only on the distance between the atoms [18]:

$$E_P = E_{val} + E_{nb} \tag{2}$$

The valence interactions include bond stretch (E_B), bond-angle bend (E_A), dihedral angle torsion (E_T), and inversion terms (E_I):

$$E_{val} = E_B + E_A + E_T + E_I \tag{3}$$

While the non-bonded interactions are composed of van der Waals or dispersion (E_{vdw}), electrostatic (E_Q), and explicit hydrogen bonds (E_{hb}) terms:

$$E_{nb} = E_{vdw} + E_Q + E_{hb} \tag{4}$$

Table 1 shows the energy changes of both oxidized and unoxidized asphalts with different water content. It can be seen that the differences of kinetic energies between oxidative aged and non-oxidative aged asphalts are almost the same at different water contents. However the

Table 1. Energy changes of unoxidized and oxidized asphalt at different levels of moisture inclusion.

	Unoxidized asphalt			Oxidized asphalt		
Water content (%)	Potential energy (kJ/mol)	Kinetic energy (kJ/mol)	Total energy (kJ/mol)	Potential energy (kJ/mol)	Kinetic energy (kJ/mol)	Total energy (kJ/mol)
0	1159	371	1530	1898	370	2268
1	919	285	1204	1458	285	1742
2	853	232	1085	1380	231	1611
4	758	171	929	885	171	1056
6	688	136	824	729	136	865
8	551	114	665	680	114	794
10	333	98	431	425	98	523
12	287	86	373	415	86	501
14	244	77	321	331	77	408
16	228	71	299	269	71	340
18	182	65	247	186	65	251
20	175	60	235	129	60	189

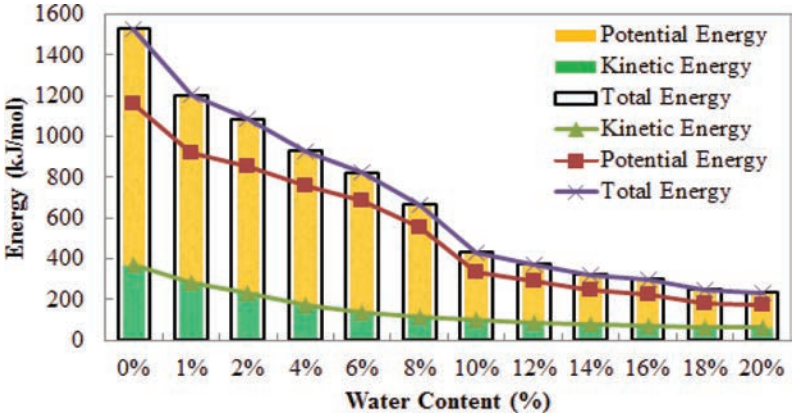

Figure 10. Energy changes of unoxidized asphalt at different water content.

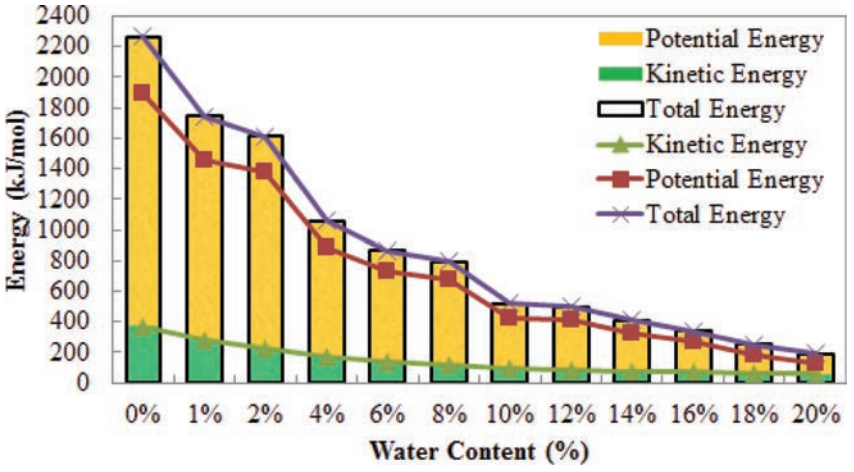

Figure 11. Energy changes of oxidized asphalt at different water content.

potential energies of asphalt after oxidative aging are much higher than the asphalt before oxidative aging at low water content. This suggests the formation of strongly interacting components in oxidative oxidized asphalt, which are responsible for increasing viscosity and altering complex flow properties.

With higher water content, the differences of potential energies between oxidized and unoxidized asphalts tend to be smaller. When water content reaches 20%, the potential energy of oxidized asphalt is lower than the unoxidized asphalt. In addition, total energies of both oxidized and unoxidized asphalt (the sum of kinetic energy and potential energy) show the same trend as potential energies. Figure 10 and Figure 11 illustrate the energy changes vs. water content for unoxidized asphalt and oxidized asphalt, respectively. It can be seen that the potential and total energy of oxidized asphalt decrease faster than the unoxidized asphalt with the increase of water content. This indicates that moisture-induced oxidized asphalt binder is more susceptible to be damaged.

4 CONCLUSIONS

The following conclusions can be made from this study:

Oxidative aging is the main factor that causes the hardening changes of asphalt over time. However, moisture inclusion destroys the bonding strength of asphalt molecules. The simulation results show that for density changes, the decreased densities of both oxidized and unoxidized asphalts with the increase of water content are caused by the expansion of the volume of asphalt system with presence of water molecules. In addition, the densities of oxidized asphalt are higher and show better linear relationship than the densities of unoxidized asphalt at different water content. This indicates that the hardening happens to asphalt after oxidative aging and oxidized asphalt is much more easily affected by moisture inclusion.

The energy changes of asphalt with combined effects of oxidative aging and moisture inclusion show that oxidative aging is responsible for the formation of strongly interacting components in asphalt by increasing energies, while moisture inclusion is accountable for decreasing the potential energies in asphalt system or the strength of asphalt. MD simulation results show that moisture inclusion plays a more significant role in asphalt damage than oxidative aging. The energies (potential energy, kinetic energy) of both oxidized and unoxidized asphalts decrease with the increase of water content. Moreover, potential energy of oxidized asphalt decreases faster than the unoxidized asphalt with the increase of water content. This indicates that moisture-induced oxidized asphalt binder is more susceptible to be damaged than moisture-induced unoxidized asphalt.

From this study, it can be seen that suppressing oxidation of asphalt binder and choosing a stiffer binder (strong bonding strength) are very important for the AC pavement exposed in more humid climates.

The MD simulation used by this study shows its advantages comparing with traditional laboratory test. First, MD simulation realizes the study of internal changes of asphalt in microscopic perspective, since the external property changes of asphalt under different conditions are determined by its internal structure and energy changes. Moreover, it is difficult to determine the property (especially mechanical property) of unoxidized (virgin) asphalt under room temperature in laboratory test, while MD simulation can simulate both unoxidized (virgin) and oxidized asphalt under any temperature and pressure. However, further laboratory tests need to be done to validate MD simulation results of this study.

REFERENCES

[1] J. Claine Petersen. Chemical Composition of Asphalt as Related to Asphalt Durability: State of the Art, Transportation Research Record, 999, pp. 13–30. 1984.

[2] Dallas N. Little. and David R. Jones IV. Chemical and Mechanical Processes of Moisture Damage in Hot-Mix Asphalt Pavements, National Seminar on Moisture Sensitivity of Asphalt Pavements, California: San Diego, USA, pp. 37–70. 2003.

[3] Mohammad I. Hossain. and Rafiqul A. Tarefder. Quantifying moisture damage at mastic–aggregate interface. International Journal of Pavement Engineering ahead-of-print, pp. 1–16. 2013.

[4] Yong-Rak Kim. D.N. Little. and Robert L. Lytton. Effect of Moisture Damage on Material Properties and Fatigue Resistance of Asphalt Mixtures, Transportation Research Record: Journal of the Transportation Research Board, 1891(1), pp. 48–54. 2004.

[5] Yang Lu. and Linbing Wang. Nanoscale Modelling of Mechanical Properties of Asphalt–Aggregate Interface under Tensile Loading, International Journal of Pavement Engineering, 11(5), pp. 393–401. 2010.

[6] C. Lira-Galeana. and A. Hammami. Wax Precipitation from Petroleum Fluids: A Review, Developments in Petroleum Science, 40 pp. 557–608. 2000.

[7] Freddy L.Roberts. Prithvi S. Kandhal. E. Ray Brown. Dah-Yinn Lee. and Thomas W. Kennedy. Hot Mix Asphalt Materials, Mixture Design and Construction, 2nd Edition, pp. 102–114, NAPA Research and Education Foundation, Lanham, Maryland. 1996.

[8] J. Claine Petersen. Quantitative Functional Group Analysis of Asphalts Using Differential Infrared Spectrometry and Selective Chemical Reactions—Theory and Application, Transportation Research Record, 1096, pp. 1–11. 1986.

[9] S.M. Dorrence. F.A. Barbour. and J.C.Petersen. Direct Evidence of Ketones in Oxidized Asphalts, Analytical Chemistry, 46(14), pp. 2242–2244. 1974.

[10] J.C. Petersen. F.A. Barbour. and S.M. Dorrence. Identification of Dicarboxylic Anhydrides in Oxidized Asphalts, Analytical Chemistry, 47(1), pp. 107–111. 1975.

[11] J.F. Branthaver. J.C. Petersen. R.E. Robertson. J.J. Duvall. S.S. Kim. P.M. Harnsberger. T. Mill. E.K. Ensley. F.A. Barbour. J.F. Schabron. Binder Characterization and Evaluation, Volume 2: Chemistry. No. SHRP-A-368. 1993.

[12] L.W.Corbett. and R.E. Merz. Asphalt Binder Hardening in the Michigan Test Road after 18 Years of Service, Transportation Research Record, 544, pp. 27–34. 1975.

[13] Luke W. Corbett. Composition of Asphalt Based on Generic Fractionation, using Solvent Deasphaltening, Elution-Adsorption Chromatography, and Densimetric Characterization, Analytical Chemistry, 41(4), pp. 576–579. 1969.

[14] D.A. Storm. J.C. Edwards. S.J. DeCanio. and E.Y. Sheu. Molecular Representations of Ratawi and Alaska North Slope Asphaltenes Based on Liquid- and Solid-State NMR, Energy & Fuels, 8(3), pp. 561–566. 1994.

[15] Culgi 7.0.2. Software Manual, Culgi B.V., The Netherlands. 2011.

[16] P. Kelly. Energy in Deforming Materials, Solid Mechanics Part I, Section 8.1, pp. 229–239. 2008. <http://homepages.engineering.auckland.ac.nz/~pkel015/SolidMechanicsBooks/Part_I/BookSM_Part_I/08_Energy/08_Energy_01_Energy_in_Deforming_Materials.pdf>, Accessed Sep. 11, 2013.

[17] Hans C. Andersen. Molecular Dynamics Simulations at Constant Pressure and/or Temperature, The Journal of chemical physics, 72(4), pp. 2384–2393. 1980.

[18] Stephen L. Mayo. D. Olafson Barry. and William A. Goddard. DREIDING: A Generic Force Field for Molecular Simulations, Journal of Physical Chemistry, 94(26), pp. 8897–8909. 1990.

Asphalt pavement and environment

This page intentionally left blank

Asphalt Pavements – Kim (Ed)
© 2014 Taylor & Francis Group, London, ISBN 978-1-138-02693-3

Use of Life Cycle Assessment for asphalt pavement at the network and project levels

John Harvey
University of California Pavement Research Center, University of California, Davis, CA, USA

Alissa Kendall
Department of Civil and Environmental Engineering, University of California, Davis, CA, USA

Nick Santero
PE International, San Francisco, CA, USA

Ting Wang
University of California Pavement Research Center, University of California, Davis, CA, USA

ABSTRACT: Life Cycle Assessment (LCA) models and approaches for comparing the environmental impacts of different pavement decisions continue to be developed and improved. These improvements include methods for making data more regionally applicable, more agreement on methodology, more comprehensive consideration of the life cycle, and application of LCA to a broader range of important decisions. This paper summarizes advances over the past several years in the science and practice of LCA and its application to find ways to reduce the environmental impact of asphalt pavements. The paper summarizes recent studies using LCA methodology to evaluate the effects of smoothness at the network level, as well as mix design, pavement structure, recycling and tire technology at the project level, on green-house gas emissions and energy use. Finally the paper discusses possible next steps in the implementation of LCA for pavement in North America and the role of industry.

1 INTRODUCTION

1.1 *Increasing competition based on sustainability*

The US economy relies on its pavement networks at the interstate, state and local levels to move people and goods safely and cost-efficiently. The Maintenance and Rehabilitation (M&R) of existing pavement and construction of new pavement for the US highway system are estimated to annually consume about $160 billion and 320 million metric tons of raw materials (1,2). Operating this national pavement network incurs the use of enormous amounts of energy, more than 120 million gallons of gasoline and 35 million gallons of diesel and other fuels per year on U.S. highways alone (3), and results in the emission of significant quantities of *Greenhouse Gases* (GHG) and regulated air and water pollutants. In addition, the energy consumed by the vehicles operating on the national road system and its economic value are much greater than the energy consumed by pavement operations, and pavement characteristics influence vehicle fuel economy as well.

Traditionally, there has been competition between different pavement products and industries based primarily on cost, but also based on frequency of maintenance, construction speed and other factors. Experience and familiarity with a given pavement type or M&R approach on the part of designers, maintenance engineers and construction

engineers has often also had an influence, particularly in a design-bid-build environment where much of the design is done by state agencies or at the local level by consultants, and high risk-averseness is a part of the culture. However, the recent and rapidly increasing public and policy attention given to environmental concerns, particularly driven by concern about human-influenced climate change caused by GHG, has increased the likelihood that the environmental impacts of different pavement engineering decisions may also play a role in owner decision-making, and may begin to play a role in the procurement process.

Already, legislators in some states have passed laws with the intent of reducing the impact of pavement on the environment. For example, in California the most important legislation is Assembly Bill 32 (AB32, 2008) which commits the state to meeting Kyoto Protocol reductions in GHG emissions: a return to 1990 levels by 2020 and to 20 percent of 1990 levels by 2050, targets based on modeling of reductions needed to avoid certain global warming levels thought to be critical for planetary life systems. An attempt to reverse AB 32 through the initiative process was stopped by a 61:39 margin several years after signing in 2008. All parts of the state economy have been engaged investigating how to reach these targets. In addition, there are laws setting targets for use of rubberized asphalt (AB 338, 2005) to help reduce the stockpiles of tires in landfills, mandates the state to develop specifications for use of at least 40 percent Reclaimed Asphalt Pavement (RAP) in mix designs (AB 812, 2012), and mandating development of guidelines and specifications for use of "cooler" pavement based on urban heat island considerations (AB 296, 2012). Similar legislation has been introduced in some other states.

For building projects and pavements, various pavement features have been incorporated into the "points" calculated to obtain different levels of certification for "greenness" or "sustainability". The well-known LEED system used for buildings has a number of alternatives for gaining points with pavement design, and there are a number of pavement ratings systems that have been established by government and private foundations across North America specific for pavement projects.

In addition to legislation, marketing around various environmental aspects of pavement engineering and policy has also been increasing.

1.2 *Avoiding unintended consequences*

Determining the environmental impact of any civil infrastructure such as pavement can be complex, and it is often difficult to develop simplified policies and categorizations that can capture impacts across widely different situations or sensitivity to conflicting variables. It can also be difficult to determine what the best decision is when the goals of the decision-making have not been clarified. There is the possibility that policies and ratings systems intended to reduce environmental impacts from pavement can cause unintended negative consequences that can actually increase environmental harm. The risk of unintended negative consequences is greatest when changes are made that affect one part of a system or life-cycle phase, but the effects of the changes on the rest of the system and the other life-cycle phases are not evaluated. These gaps in assessing unintended consequences elsewhere within the system can be serious enough that supposedly "green" solutions may actually produce net negative impacts on the environment, thus violating the concept taken from medical practice of "first, do no harm" when prescribing remedies in the face of uncertainty. *Life Cycle Assessment* (LCA) is an approach for investigating the consequences of changes that, when properly applied, considers *system-wide effects* and the entire life cycle.

LCA provides a comprehensive approach to evaluating the total environmental burden of a product, examining all the inputs and outputs, from raw material production to the end-of-life. For pavement, this cycle includes the material production, construction, use, maintenance and rehabilitation (M&R), and End-Of-Life (EOL) phases. These phases and some typical inputs and outputs are shown in Figure 1.

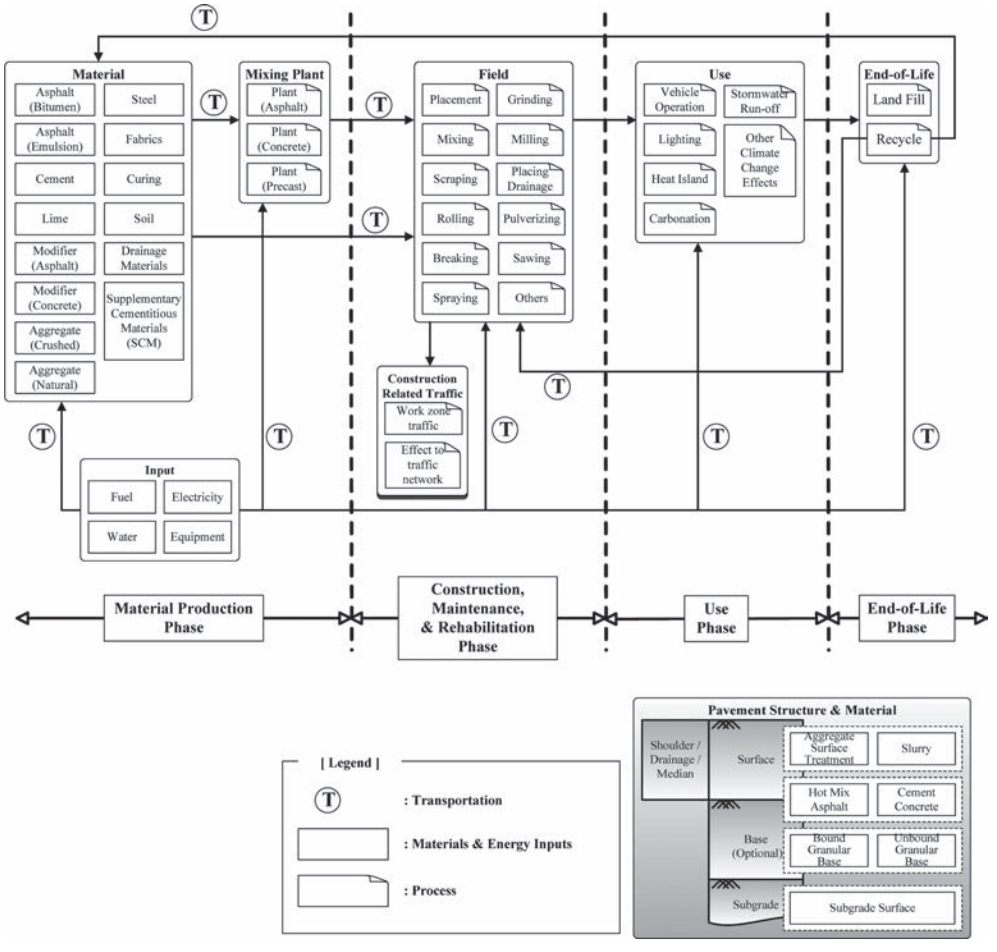

Figure 1. UCPRC pavement LCA framework (adapted from [4]).

2 LIFE CYCLE ASSESSMENT

2.1 *Overview of life cycle assessment*

LCA is an accounting and analysis of the inputs, outputs, and potential environmental impacts of a *product system* throughout its life cycle (International Organization for Standardization [ISO]). The standard ISO 14040:2006 (5) describes the principles and framework for Life Cycle Assessment (LCA) including: definition of the goal and scope of the LCA, the Life Cycle Inventory analysis (LCI) phase, the Life Cycle Impact Assessment (LCIA) phase, the interpretation phase (which occurs throughout the assessment), and reporting and critical review of the LCA, which should include limitations of the LCA, the relationship between the LCA phases, and conditions for use of value choices and optional elements. The standard covers LCA studies and LCI studies, but it neither describes the LCA technique in detail nor specifies methodologies for individual phases of an LCA. Because the standard is meant to apply broadly to any product or system evaluated using LCA, it does not provide recommendations or guidance tailored to pavements, or any other product or system.

A life cycle inventory is the stage of *life cycle assessment* involving the compilation and quantification of inputs and outputs for a product throughout its life cycle (5). An LCI can also be conducted separately, without being part of an LCA study.

Based on *ISO 14040:2006,* the following stages should be followed for conducting an LCA, as shown in Figure 2:

1. *Goal and Scope.* In this first stage, the LCA practitioner should identify the purpose of the LCA and the LCA's intended audience. The scope of the study must also be defined which includes defining the system boundaries and the function, and *functional unit*.
2. *Life Cycle Inventory.* This stage compiles and quantifies the inputs and outputs from the analyzed product at each stage of its life cycle. It requires data collection and modeling of the product. Examples of inventory items include inputs of *primary energy, materials, water and other resources that are consumed, and outputs of solid and hazardous waste flows, air emissions,* and *water pollutants* caused by the product over its life cycle.
3. *Impact Assessment.* The Impact Assessment stage translates the environmental flows compiled during the LCI into indicators of impacts to humans and the environment. The first step in this stage is to assign the appropriate inventory results to the selected Impact Categories. For example, in Europe pavement materials are generally required to have an Environmental Product Declaration (EPD, ISO 14025:2006 [6]) that considers the impact in the following five categories: climate change, photochemical ozone creation, eutrophication, stratospheric ozone depletion and acidification. Additional impact categories can include: fossil fuel depletion, waste disposal, ecotoxicity to land, higher level nuclear waste, ecotoxicity to freshwater, human toxicity, mineral extraction and water extraction (BRE). EPDs are developed following Product Category Rules (PCR, ISO 14025:2006 [6]),which are sets of specific rules, requirements, and guidelines for developing Type III environmental product declarations for one or more Product Categories (PCRs and EPDs are discussed more later in this paper). Once environmental flows are assigned to categories of impact they will be characterized, meaning the extent of their impacts will be quantified. For example, GHGs assigned to the category of climate change will typically be characterized by applying a global warming potential to yield CO_2e emissions, the indicator of choice for climate change. (Note: CO_2e means equivalent CO_2 emissions, accounting for the global warming potential of different types of gases in terms of equivalent mass of CO_2). The final step is *valuation,* which integrates across impact categories using weights or other approaches, thus enabling decision-makers to assimilate and consider the full range of relevant outcomes. This step is optional in the ISO framework.
4. *Interpretation.* The Interpretation stage is an analysis from which conclusions are drawn and recommendations are made, or that is used to otherwise inform the decision-making

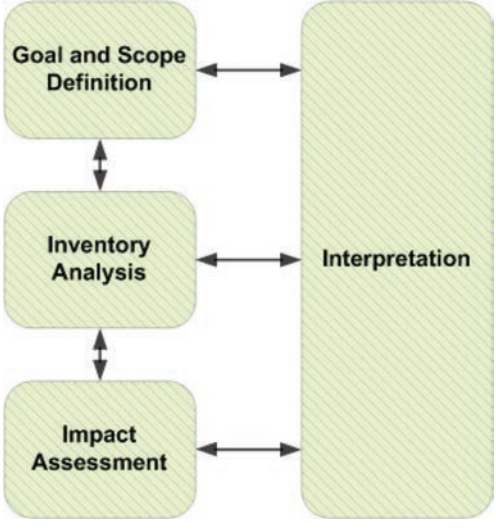

Figure 2. Stages for life cycle assessment (5).

process. Usually, a *sensitivity analysis* and an *uncertainty analysis* are included to confirm any conclusions. Although most studies do not include this review process, as required in ISO 14040:2006, an independent critical review is required by ISO at this stage, especially for comparisons that will be available in the public domain.

2.2 *Developments in the application of LCA to pavement*

An incomplete summary of developments of the application of LCA to pavement is presented in this section. It is intended to illustrate the arc and rapidity of development of LCA for pavements, and not a comprehensive summary of reports, papers and software.

The earliest application of LCA in a software tool in North America is Palate (7) developed by Horvath and his colleagues at UC Berkeley beginning around 2002.

A number of early applications of LCA to pavement and particular studies that had been published up to about 2010 were summarized in several papers by Santero and his colleagues (8). Their results included a critical review of pavement LCA studies to date, which identified problems with:

- Definitions of functional unit
- System boundaries: studies were found to use widely varying system boundaries, and often did not consider the use phase (see Fig. 1), often did not have realistic understanding of M&R schedules, and did not follow consistent practice for consideration of feedstock energy.
- Data quality and uncertainty: studies were found to often not include assessments of data quality or checks on regional and temporal applicability, and often did not use sensitivity analyses or other methods to consider uncertainty in the data.
- Life Cycle Inventories and Life Cycle Impact Assessment: studies generally did not include impact assessment after development of the LCI, and therefore not necessarily providing information useful for decision-making.
- Other problems: studies often did not include adjustment of energy production and other regional differences in development of inventories.

Santero et al. also provided recommendations for filling the gaps in LCA with respect to traffic delay, rolling resistance, albedo, concrete carbonation, roadway lighting, leachate, and end of life considerations (9).

The application of LCA to pavement and more generally to civil construction materials and products has been underway in Europe for a number of years. Early databases were developed in the 1980s in Switzerland, many of which are still referred to today. A European Platform on LCA was established in 2005 (10). Beginning in the same decade, the Netherlands national public works agency sponsored development of an LCA based design software tool called *DuBoCalc* (11), which is used for both design assessment and calculation of an Environmental Cost Indicator (MKI in Dutch) that is used in the preparation of bids, where environmental impact is a part of selecting contractors for Design-Build and Design-Build-Maintain public work projects along with life cycle cost (12).

OFRIR (a French acronym for "Monitoring of Road Infrastructure Recycling") is a project in France, begun in 2002 and coordinated by the French national Central Laboratory for Bridges and Roads (LCPC, now called IFSTTAR) in association with the public research organizations Ademe (environment), Inéris (industrial risks), BRGM (geology), Setra (road engineering) and a significant number of regional LCPC laboratories. The project has generated an original collection of data for the entire country in the field of road-based recycling. The information provided by the project's public partner institutions, in addition to that from members of the data exchange group formed over the course of this project, has gradually been made available to the road community via a website (http://ofrir.lcpc.fr), and more recently to the general public. The project developed underlying principles, structures and systems for the Internet database and the protocol for exchange between participants. OFRIR's primary purpose was to offer the French road community a source of information that had been

sorted, synthesized and, to a certain extent, validated so as to promote protocols for recycling and using local alternative materials (i.e. wastes and byproducts) while indicating the various obstacles, especially those in the geotechnical and environmental fields. The project was intended to assemble the requisite range of skills as well as to provide a forum for exchanges between project drivers and targets, for the purpose of: 1) creating a data exchange platform between participating laboratories and specialists; and 2) offering a research support system in the field of sustainable development (13).

Members of the French road-building community developed and introduced in 2010 another software tool for environmental evaluation of alternatives called *Seve* (14). In the past year, France has begun considering environmental impact using LCA based tools for selection of winning bids for road construction projects.

Following up on the identification of gaps in the application of LCA to pavement by Santero et al. and others, a workshop was held in Davis, California in May 2010 with invited participants from the international community of pavement engineers, LCA experts, contractors, materials producers, and international, federal, state and local government pavement policy-makers (15). The goal of the workshop was to discuss and reach consensus, where possible, regarding many of the issues identified by Santero et al. (8, 9) and others (4). After discussion, recommendations were made by expert teams on particular aspects of pavement LCA. These recommendations were incorporated into a document including guidelines for application of LCA to pavement, and a "transparency document" that is a checklist for documenting assumptions and approaches used in a pavement LCA (4). The move towards standardization of LCA practice for pavements and other building materials was continued at a recent conference in Nantes, France (16).

Several more recent LCA tools have been developed in North America to address different goals, and with different assumptions and definitions of the system boundaries (17, 18). The studies have used life cycle inventories that are available, some developed with more regionally applicable data and some consideration of the use phase.

Addressing other gaps in pavement LCA that were identified in 2010, the Miriam project was created to develop new methods for measuring rolling resistance of pavements (primarily texture), and consideration of rolling resistance due to roughness and texture in pavement management systems (19). Zaabar and Chatti calibrated mechanistic-empirical fuel economy models using field measurements as a function of vehicle type (from cars through heavy tractor-trailer combinations) based on pavement roughness and texture (20).

Wang et al. used Chatti's models and used them and materials and construction inventories for M&R treatments to evaluate the net effects of maintaining smooth pavement considering the materials and construction to keep them smooth and the improved fuel economy of vehicles using smoother pavement for several case studies (21). Wang et al. have more recently extended their models to identify optimal International Roughness Index (IRI) values for triggering several typical M&R treatments as a function of traffic volumes on all segments of the California state highway network (22). The results showed that roughness trigger levels for M&R on the order of 1.6 m/km (100 inches/mile) minimize GHG emissions for the highest traffic volume routes, balancing the improvements in fuel economy from smoother pavement with the increased emissions from more frequent treatment. For the lowest traffic volume routes, benefits from fuel economy never exceed the emissions caused by materials production and construction.

The concrete industry recently sponsored an extensive and rigorous LCA based study looking at methods for reducing the environmental impacts of the materials production and use phases of concrete pavement (23). Eurobitume, the European asphalt producers association produced an Environmental Product Declaration (EPD) following European LCA protocols using typical data from producers for its most widely used products: conventional asphalt, polymer modified asphalt and asphalt emulsion (24).

Another area of increased research is the influence of energy dissipation caused by pavement deflection and increased GHG emissions from vehicles as a result of the decreased fuel economy. Zaabar and Chatti found some influence of pavement structure on fuel economy, developing some data regarding stiffer and more elastic structures (concrete) versus softer

and more viscoelastic structures (asphalt surfaced). Their results indicated that there was a statistically significant difference of several percentage points in fuel economy for the case of heavy trucks operating at slower speeds (about 55 km/hr [35 mph]) when the asphalt pavement was hot, while for other vehicle/speed/temperature conditions the differences were not significant (15). These and other less comprehensive experimental results indicate that this may be a topic requiring additional consideration for designers, and additional research looking at more pavement types, such as composite, semi-rigid, stiff and thick long-life asphalt, as well as a range of vehicles, speeds and climates.

Modeling of energy dissipation due to deflection is the second half of the concrete industry sponsored MIT study (25) and models indicate substantial savings in energy based on their assumptions and extrapolation to the national highway network and several state subnetworks.

2.3 *Current projects*

The Federal Highway Administration (FHWA) is currently developing guidelines for improving the sustainability of pavements. The pavement life cycle (Fig. 1) and LCA concepts form the organizational framework for that document which is expected to be published by early 2014.

Another study is currently underway for the FHWA under the leadership of the University of Illinois to investigate the effects of introducing new generation wide base tires on lower volume asphalt pavement structures. The study includes a preliminary LCA evaluating the net benefits of this change in tire technology considering potential fuel economy improvements and changes in M&R treatment frequency.

The Chicago Tollway Authority is sponsoring work by several organizations to develop an LCA tool in 2014, and to use LCA concepts to evaluate various pavement design and recycling strategies. Part of this work is the development of current, regional databases for materials, construction and other inventory variables.

Studies underway at the University of California Pavement Research Center sponsored by Caltrans and/or the California Air Resources Board include:

- Use of LCA, including climate modeling, to evaluate the impacts of pavement albedo and other properties on urban area temperatures and the impacts on GHG emissions and energy use in buildings and temperature influenced air pollution, with results expected in 2015.
- Modeling of energy dissipation from pavement deflections using models developed by Pouget et al. (26).
- A two phase study of deflection energy dissipation models, with the first phase consisting of evaluation of existing models and comparison of results for a set of different types of pavement structures/vehicles/temperatures/speeds; and the second phase consisting of field validation of fuel economy changes on the same set of variables.
- Evaluation of the net effects on GHG emissions and energy use of various in-place and plant mix recycling strategies for a range of scenarios.
- Extension of previous California studies to consider category air and water pollutants.
- Development of regional inventory data for materials production and construction where possible through the studies described above.

3 DISCUSSION

It is hoped that the summary of LCA and previous and current work provides an indication of the many uses of LCA to answer important pavement questions, as well as some of the problems facing its use. From the review of the development and implementation of LCA in Europe and North America to date, it appears that:

- Knowledge about LCA is growing in the pavement community.
- Practice is becoming more standardized, although further discussion and consensus is needed (compare with list of gaps prepared by Santero et al).

- There is a lack of good, new inventory data for many important products and processes.
- There is some new software becoming available, but good software needs good data to be truly useful.
- How to move forward in North America to obtain better data and more standardization of practice is not clear.
- There are still some fundamental gaps in the life cycle phase models that need further research.
- What is the future range of uses for LCA is not clear beyond research and information dissemination and some policy analyses. It is not clear to what extent, if any, it will be used for project-level design, consideration in tendering, or network-level pavement management decision making.
- Industry must be involved in the development of better data, and in the discussion regarding the use of LCA for pavement.

One major incremental issue is the development of current, regionally applicable inventory data. The technical approach laid out by ISO, and being moved forward in Europe as well as North America, albeit with various difficulties, is the development of Product Category Rules (PCR) for conducting LCA studies on materials (becoming common in Europe and beginning to occur in North America), and potentially on pavement systems consisting of those materials as well as construction (not common). These are used to then create Environmental Product Declarations (EPD), such as the EPD produced by Eurobitume for its typical products (24). According to ISO, Type III environmental declarations as described in this International Standard (14025) are primarily intended for use in business-to-business communication, but their use in business-to-consumer communication under certain conditions is not precluded. Clearer definition of the future roles of LCA in the world of pavement will help define their use. It appears likely that until there is more definition, a large use of pavement LCA will be for business-to-consumer communication, where the consumer is the pavement designer, the policy-maker, and potentially pavement system (as opposed to materials) providers and procurers.

The process of creating PCRs includes a PCR proposal, development of a draft, open consultation, a panel review, and approval and publication. PCRs are developed and regulated by "program operators" who host the PCR, verify the EPDs and register the EPDs. To date the following organizations have established PCR programs in the North America that are known to the authors, not limited to pavements:

- Underwriter's Laboratories
- National Science Foundation
- ASTM (formerly American Society for Testing and Materials)
- Institute for Environmental Research and Education
- National Ready Mix Concrete Association
- Scientific Certification Systems
- Building and Industrial Furniture Manufacturer's Association
- Canadian Standards Association
- FP Innovations

(27, 28)

A PCR for pavement preservation products was produced by IERE in 2011 (28). A review of the status of PCRs and EPDs in North America was recently prepared for the National Institute of Standards and Technology (29). It is not clear what governmental or other organizing may occur in North America with respect to pavement PCRs. The role of academia in helping to sort out both organizational and methodology issues is also unclear. This process has followed the enactment of legislation at the national level in Europe, and industry and government have generally had their roles defined by that legislation, albeit with a great deal of discussion. Whether the process will be similar in North America is unclear at this time, as most governmental organizations dealing with pavement are just moving up the learning curve with regard to LCA in general.

While this uncertainty regarding organization and regulation is vexing and confusing, it is a sign that the use of LCA in pavements is maturing.

4 RECOMMENDATIONS

Industry should be involved in the establishment of the organizations, processes and data development for LCA for pavement. Good data can only come from industry. All industry participants, including the refining industry and asphalt pavement materials producers and constructors, need to be involved in the set-up and operation of these organizations and processes to ensure that there is full transparency, and that all aspects of the complexity of pavement systems are considered. The asphalt industry also needs to be involved in all aspects of the use of LCA for pavement so that their innovations to reduce the environmental impact of pavements can be correctly and fairly measured.

REFERENCES

1. U.S. Department of Transportation, Federal Highway Administration and Federal Transit Administration. 2008 Status of the Nation's Highways, Bridges, and Transit: Conditions and Performance, U.S. Department of Transportation, Washington, D.C. 2008.
2. Holtz, K. and T. Eighmy (2000). "Scanning European Advances in the Use of Recycled Materials in Highway Construction". *Public Roads*, Vol. 64, No. 1, pp. 34–40.
3. FHWA (Unknown) *Motor Fuel* in Highway Statistics 2010. U.S. Department of Transportation. http://www.fhwa.dot.gov/policyinformation/statistics/2010/index.cfm. (Accessed Sept 17, 2012).
4. Harvey, J., A. Kendall, I.-S. Lee, N. Santero, T. Van Dam, T. Wang (2010). "Pavement Life Cycle Assessment Workshop: Discussion Summary and Guidelines." UCPRC-TM-2010-03. University of California Pavement Research Center, Davis and Berkeley. http://www.ucprc.ucdavis.edu/PDF/UCPRC-TM-2010-03.pdf (accessed 15 Sept, 2013).
5. International Organization for Standardization. (2006). *ISO 14040 Environmental management—Life cycle assessment—Principles and framework*. ISO 14040:2006(E). International Organization for Standardization, Geneva. http://www.iso.org/iso/catalogue_detail?csnumber=37456 (accessed 2 December, 2012).
6. International Organization for Standardization. (2006). *ISO 14025 Environmental management—Life cycle assessment—Principles and framework*. ISO 14040:2006(E). International Organization for Standardization, Geneva. http://www.iso.org/iso/catalogue_detail?csnumber=37456 (accessed 2 December, 2012).
7. Palate. http://www.ce.berkeley.edu/~horvath/palate.html.
8. Santero, N., E. Masanet, and A. Horvath. 2011. "Life-Cycle Assessment of Pavements Part I: Critical Review." Resources, Conservation, and Recycling. 55(9–10):801–809.
9. Santero, N., E. Masanet, and A. Horvath. 2011. "Life-Cycle Assessment of Pavements Part II: Filling the Research Gaps." Resources, Conservation, and Recycling. 55(9–10):810–818.
10. Guinee, J. Life cycle assessment: past, present and future, International Symposium on Life Cycle Assessment and Construction—Civil engineering and buildings, Nantes, France, RILEM. July, 2012.
11. TheRightenvironment Inc. DuboCalc software. http://www.rijkswaterstaat.nl/rws/bwd/home/www/cgi-bin/index.cgi?site=1&doc=1785, last accessed Sept 15, 2013, in Dutch).
12. Rijkswaterstaat. Dubocalc web page. http://www.rijkswaterstaat.nl/zakelijk/duurzaam/duurzaam_inkopen/duurzaamheid_bij_contracten_en_aanbestedingen/dubocalc/ (Accessed 15 Sept, 2013, in Dutch).
13. Jullien, A., F. de Larrardi, M. Bercovici, L. Lumiere, P. Piantone, J. Domas, P. du Pont, L. Chateau, F. Leray. The OFRIR project: A multi-actor approach to recycling in road infrastructure, paper in preparation.
14. SCREG Ile de France Normandie. Seve software. http://www.colas.com/FRONT/COLAS/upload/bandeaux/pdf/SEVE-une-variante-pointue-pour-l-environnement-VA.pdf (accessed 15 Sept, 2013).
15. Pavement Life Cycle Assessment Workshop web page. www.ucprc.ucdavis.edu/p-lca (Accessed 15 Sept, 2013).

16. Ventura, A., C. de la Roche (editors). Proceedings, International Symposium on Life Cycle Assessment and Construction. Nantes, France, July 2012. http://lca-construction2012.ifsttar.fr/ (Accessed 15 Sept, 2013).
17. Athena Institute. http://www.athenasmi.org/resources/research-projects/impact-estimator-for-highways/.
18. Mukherjee, A. http://www.construction.mtu.edu:8000/cass_reports/webpage/.
19. Miriam (Models for rolling resistance In Road Infrastructure Asset Management Systems). www.miriam-co2.net/ (Accessed 15 Sept, 2013).
20. Zaabar, I., Chatti, K. Calibration of HDM-4 Models for Estimating the Effect of Pavement Roughness on Fuel Consumption for US Conditions, Transportation Research Record, pp. 105–116. 2010.
21. Wang, T., Lee, I.-S., Kendall, A., Harvey, J., Lee, E.B., Kim, C. (2012). "Life cycle energy consumption and GHG emission from pavement rehabilitation with different rolling resistance." J. Cleaner Production, Volume 33, September, Pages 86–96.
22. Wang, T., J. Harvey, A. Kendall. Reducing greenhouse gas emissions through strategic pavement management, submitted to Engineering Research Letters. 2013.
23. Santero, N., A. Loijos, M. Akbarian, J. Ochsendorf. Methods, Impacts, and Opportunities in the Concrete Pavement Life Cycle, Report, Massachusetts Institute of Technology. 2011.
24. Bernard, F., T. Blomberg, M. Southern. Life Cycle Inventory: bitumen, International Symposium on Life Cycle Assessment and Construction—Civil engineering and buildings, Nantes, France, RILEM, pp. 283–290. July 2012.
25. Akbarian, M., F. Ulm. Model Based Pavement-Vehicle Interaction Simulation for Life Cycle Assessment of Pavements, Report, Massachusetts Institute of Technology. April 2012.
26. Pouget, S., Sauzéat, C., Benedetto, H., Olard, F. Viscous Energy Dissipation in Asphalt Pavement Structures and Implication for Vehicle Fuel Consumption. Journal Materials in Civil Engineering, 24(5), pp. 568–576. 2012.
27. Santero, N., J. Harvey, J. Meijer, T. VanDam. Product Category Rules and Their Relevance to the Pavement Community, presentation at the FHWA Sustainable Pavement Task Group Meeting, Madison Wisconsin. June, 2013.
28. Institute for Environmental Research and Education. 2011. Pavement Preservation Products Product Category Rule. Number 2011–01. http://iere.org/wp-content/uploads/2013/07/pavementpreservationproductspcr_v1.pdf (Accessed 26 February 2014).
29. Schenck, R. 2013. Status and Opportunities to Support Product Category Rules in the U.S. National Institutes of Standards and Technology Solicitation Number SB1341-12-RQ-0770. http://iere.org/wp-content/uploads/Status-and-Opportunities-to-Support-Product-Category-Rules-and-Environmental-Product-Declarations-in-the-United-States.pdf (Accessed 26 February 2014).

Asphalt Pavements – Kim (Ed)
© 2014 Taylor & Francis Group, London, ISBN 978-1-138-02693-3

Photocatalytic Warm Mix Asphalt laboratory performance testing

Marwa M. Hassan
Department of Construction Management, Louisiana State University, Baton Rouge, LA, USA

Louay N. Mohammad
Louisiana Transportation Research Center, Director Engineering Materials Characterization Research Facility, Department of Civil and Environmental Engineering, Baton Rouge, LA, USA

Heather Dylla
Department of Construction Management, Louisiana State University, Baton Rouge, LA, USA

Somayeh Asadi
Department of Civil and Architectural Engineering, Texas A&M University-Kingsville, Kingsville, TX, USA

Samuel Cooper
Department of Civil and Environmental Engineering, Louisiana State University, Baton Rouge, LA, USA

ABSTRACT: The use of titanium dioxide (TiO_2) coating for pavements has received considerable attention in recent years to improve air quality near large metropolitan areas. However, the proper method of applying titanium dioxide to asphalt pavements is still unclear. This study evaluated the benefits of incorporating titanium dioxide in the preparation of Warm-Mix Asphalt (WMA). Two application methods to integrate TiO_2 were evaluated, a water-based titanium dioxide solution applied as a thin coating and using TiO_2 as a modifier to asphalt binder in the preparation of WMA. Based on the results of the experimental program, it was determined that the photocatalytic compound was not effective in degrading NOx in the air stream when used as a modifier to the binder in the preparation of WMA. This could be attributed to the fact that only a small amount of TiO_2 is present at the surface. When used as part of a surface spray coating, TiO_2 was effective in removing NOx pollutants from the air stream with an efficiency ranging from 31 to 55%. The maximum NOx removal efficiency was achieved at a coverage rate of 0.05 l/m^2. However, durability of the surface spray coating requires further evaluation. In addition, the increase in flow rate and relative humidity negatively impacted the effectiveness of NOx reduction efficiency. In contrast, the increase in UV light intensity improved the NOx removal efficiency of the surface coating.

Keywords: Titanium dioxide, sustainable asphalt pavement construction, photocatalyst, nitrogen oxides

1 INTRODUCTION

The US faces a significant challenge in controlling air pollution resulting from transportation activities. Although attempts are made to lower vehicle emission standards, a method is needed to remove these pollutants once they are emitted to the atmosphere. The potential of titanium dioxide (TiO_2) as an air purifier in urban and metropolitan areas, which suffer from high concentration of air pollutants, has been widely recognized in literature [1, 2]. Evaluation of concrete pavement treated with TiO_2 provided promising results as recent research by the authors and others show that a thin surface coating

is able to remove a significant portion of Nitrogen Oxides (NO_x) and Volatile Organic Compounds (VOC) pollutants from the atmosphere when placed as close as possible to the source of pollution [3–6]. However, with 94% of the US road network covered with asphalt, it appears that widespread use of titanium dioxide in air purification applications can only be achieved by the development of a novel asphalt mixture that does not affect the mechanical properties of the mix while incorporating a photocatalytic compound into current highway construction practices [7]. In addition, the use of Warm Mix Asphalt (WMA) will have the added benefits of reduced energy and the associated pollution emissions during production.

The objective of this study is to test the hypothesis that TiO_2 can function as a photocatalytic compound when used in the preparation of WMA. To achieve this objective, a crystallized anatase-based titanium dioxide powder was blended with two grades of asphalt binder classified as PG 64-22 and PG 70-22 at three percentages by binder weight (3, 5, and 7%). In addition, a second application method was also evaluated, specifically useful for coating existing pavements, by spraying a water-based solution of TiO_2 on the pavement surface at three coverage levels (0.026, 0.05, and 0.074 l/m^2). Prepared blends were characterized using fundamental rheological tests (i.e., dynamic shear rheometer, rotational viscosity, and bending beam rheometer), the Semi-Circular Bend (SCB) test for fracture resistance, and by measuring the environmental efficiency of the mixture in removing NO_x pollutants from the air stream before and after durability tests.

2 BACKGROUND

Initial interest in environmental photocatalysis began in the 1970s, initiated by Fujishima and Honda's research in photo-electrochemical solar energy conversion [8]. Through biomimicry of plant photosynthesis, the researchers attempted to replicate the photo-induced redox reactions, by oxidizing water and reducing carbon dioxide, using a semiconductor irradiated by UV light. To accomplish this, the semiconductor is used as an electrode, which is connected to a counter electrode to generate electrical work while driving the redox chemical reactions [1]. TiO_2 was the semiconductor chosen, due to a positive valence band edge that theoretically can oxidize water to oxygen [2]. Fujishima and Honda found that when the surface was irradiated, a current was created such that oxidation occurred at the TiO_2 electrode and reduction at the counter electrode [1]. This proved that water could be decomposed into oxygen and hydrogen from solar irradiation, preferred since solar energy equates to roughly 5 x 1024 J per year [9].

The photo-electrochemistry concepts described were extended to research in heterogeneous photocatalysis applications by removing the external circuit [2]. In 1977, Frank and Bard were one of the first to demonstrate this, by illustrating the decomposition of cyanide in water. Since then, increased interest in environmental photocatalysis was realized, which caused TiO_2 to be applied to glass, tile, paper, and pavements for self-cleaning materials, water purification, air purification, sterilization, and oil spill remediation. From these studies, it has been shown that organic and inorganic compounds can be completely decomposed and that the TiO_2 surface has the ability to self-regenerate [2]. Therefore, rather than an absorption of pollutants that is common to traditional air purification methods, heterogeneous photocatalysis can decompose pollutants to nonhazardous waste products with little energy requirements [10]. In the presence of UV light, TiO_2 produces hydroxyl radicals and superoxides, which are respectively responsible for oxidizing and reducing environmental contaminants including VOC and NO_x [1]. A proposed mode of oxidation of NO_x via hydroxyl radical intermediates in the presence of the photocatalyst is described by the following equations:

$$NO + \dot{O}H \xrightarrow{Ti_2O} NO_2 + H\cdot \quad (1)$$

$$NO_2 + \dot{O}H \xrightarrow{Ti_2O} NO_3 + H\cdot \quad (2)$$

Based on this heterogeneous photocatalytic oxidation process, NO_x are oxidized into water-soluble nitrates; these substances can be washed away by rainfall. Available titanium dioxide technologies have been mostly directed towards concrete applications in which a fine mixture consisting of cement, sand, TiO_2, and water is applied as a thin surface layer or slurry to the surface. While few studies are available for asphalt pavements, TiO_2 has been incorporated into asphalt pavements by integrating it into the binder and as a thin surface layer that is sprayed on existing pavements [11, 12]. For the spray application, various TiO_2 nanoparticles were dispersed in a water-based emulsion [11]. The water-based emulsion was then applied by two different methods, referred to as hot and cold method; distinguished by the spraying of the emulsion during asphalt paving laying operations when the pavement temperature is over 100°C or on existing pavements at ambient temperatures. The study results showed that the reduction efficiencies were highly dependent on the TiO_2 nanoparticles used in which efficiencies ranged from 20% to 57% of NO_x reductions. Meanwhile, researchers in China also mixed TiO_2 with an asphalt binder at a 2.5% content of the binder weight to an emulsified asphalt pavement [12]. Evaluation presented in this study showed that a maximum efficiency in removing nitrogen oxide near 40% was achieved.

3 EXPERIMENTAL PROGRAM

Asphalt cement binder blends were prepared by mixing a conventional WMA binder (WMA additive Evotherm was used at 1% by weight of the binder) classified as PG 64-22 and PG 70-22 with a commercial crystallized anatase-based TiO_2 powder at three percentages 3, 5, and 7% by weight of the binder. The blends were prepared at a mixing temperature of 163°C. While short-term aging was simulated using the Rolling-Thin Film Oven (RTFO), long-term aging was simulated using the Pressure Aging Vessel (PAV). The RTFO test simulated construction hardening and asphalt binder aging by subjecting the material to circulating hot air for 85 min. The PAV test simulated long-term oxidative aging for a period ranging from 5–10 years by subjecting the binder to pressurized air for 20 hrs and a temperature maintained at 100°C.

Prepared blends were characterized using fundamental rheological tests (i.e., dynamic shear rheometry, rotational viscosity, and bending beam rheometer) and by comparing the Superpave Performance Grade (PG) of the modified blend to the unmodified WMA binder. To assess the influence of the photocatalytic compound on the binder aging mechanisms and to ensure that TiO_2 does not oxidize the binder, both the control and modified blends were prepared in thin films and were subjected to UV light for a period of seven days. Binders were characterized using the entire suite of PG grading system as per AASHTO M 320-09 (Standard Specification for Performance-Graded Asphalt Binder). Using the same experimental mix design parameters, two replicas of asphalt concrete samples were prepared for both the fracture and environmental tests and were compacted by a gyratory compactor according to AASHTO TP4.

Fracture resistance was assessed by the Semi-Circular Bending (SCB) test using the procedure suggested by Wu et al. [11]. This test characterizes the fracture resistance of HMA mixtures based on fracture mechanics principals, the critical strain energy release rate, also called the critical value of J-integral, or J_c. To determine the critical value of J-integral (J_c), three notch depths of 25.4, 31.8, and 38 mm were selected based on an a/rd ratio (the notch depth to the radius of the specimen) between 0.5 and 0.75. Test temperature was selected to be 25°C. The semi-circular specimen is loaded monotonically till fracture failure under a constant cross-head deformation rate of 0.5 mm/min in a three-point bending load configuration. The load and deformation are continuously recorded and the critical value of J-integral (J_c) is determined using the following equation [11]:

$$J_c = \left(\frac{U_1}{b_1} - \frac{U_2}{b_2} \right) \frac{1}{a_2 - a_1} \tag{3}$$

where,

b = sample thickness;

a = the notch depth; and

U = the strain energy to failure.

A second application method consisting of applying a thin surface coating was also evaluated at three coverage rates (0.11, 0.21, and 0.31 kg/m^2). The spray coat used was a mixture of TiO_2 anatase nanoparticles suspended in an aqueous liquid at 2% by volume. A thin film was spray coated on each asphalt sample in layers using in a cross hatch formation at each of the three defined coverage rates.

3.1 *Photocatalyst material characterizations*

The photocatalytic nanoparticles used were characterized by X-Ray Diffraction (XRD), Brunauer Emmett Teller (BET), and Transmission Electron Microscopy (TEM). Since surface area is an important characteristic for photocatalytic activity, the surface area was obtained using the BET isotherm by nitrogen physisorption. The XRD patterns obtained by a Rigaku, D/Max 2500 PC instrument using CuKα radiation were used to determine the crystal structure and phase composition ratio. The diffraction peaks were analyzed and indexed by match peak using Search Match software.

The resulting nanoparticles were characterized also by TEM using the Tecnai G2 field emission gun (200 kV). The TiO_2 powders were deposited on a 3-mm copper grid for TEM imaging. The copper grid was cleaned with acetone and chloroform before the powders were deposited. The TEM imaging illustrated the morphology of the nanoparticles used.

3.2 *Environmental test setup*

The environmental benefit of the fabricated asphalt blends in trapping and degrading NO_x pollutants from the air stream through a photocatalysis mechanism was investigated. A laboratory test setup that is capable of quantifying the photocatalytic efficiency of asphalt and concrete specimens was used, Figure 1. The test setup was adapted from the Japanese standard JIS TR Z 0018 "Photocatalytic materials—air purification test procedure." The developed experimental setup consists of a pollutant source, zero air source, calibrator, humidifier, photoreactor, and a chemiluminescent NO_x analyzer as shown in Figure 1. The setup simulates different environmental conditions by allowing for control of light intensity and air humidity. The pollutants are introduced through an inlet jet stream to the photoreactor, a photocatalytic testing device. A zero air generator is used to supply the air stream, which is passed through a humidifier to simulate the desired humidity level.

The photoreactor creates an enclosed controlled environment where the light and the atmosphere can be simulated. Fluorescent lamps, attached to the photocatalytic device, are

Figure 1. Experimental laboratory setup.

used to imitate natural sunlight radiation required for photocatalytic activity. The pollutants measured from the recovered air before and after the photoreactor allowed for determination of the absorbed level of pollutants. In this study, NOx and removal efficiency was measured using the Thermo 42i chemiluminescent NOx analyzer. Nitrogen oxides were blown over the surface of the asphalt specimens at a concentration of 450 ppb. All tests were conducted at room temperature while the relative humidity was kept constant at 20%.

4 RESULTS AND ANALYSIS

Results of XRD patterns for the two synthesis methods are shown in Figure 2. Both the nanoparticle powder and the aqueous suspended nanoparticles were indexed as pure anatase using Search Match software anatase.

In spite of the agglomerate formation, Figure 3 reveals two different types of particle morphologies, nanoparticles from the powder (a) and nanorods from the aqueous spray coat (b). The nanorods are clearly larger in size compared to the nanoparticles from the powder. The average diameter of the nanoparticles used was 15 nm. The average diameter of the nanorods was 12 nm and average length was 75 nm. The surface area characterized by BET was 73.3 m^2/g for the nanopowder and 84.8 m^2/g for the aqueous spray coat nanorods.

The samples with TiO_2 in the binder were tested at 1 l/min flow rate and 2 mW/cm^2. Results presented in Table 1 show low NO_x reduction suggesting that the method of incorporation of

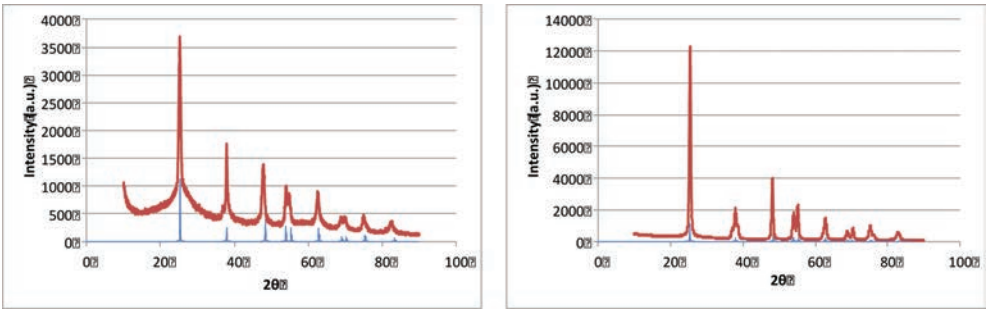

Figure 2. (a) XRD of TiO_2 nanoparticles powder. (b) XRD TiO_2 nanoparticles suspended in aqueous spray coat.

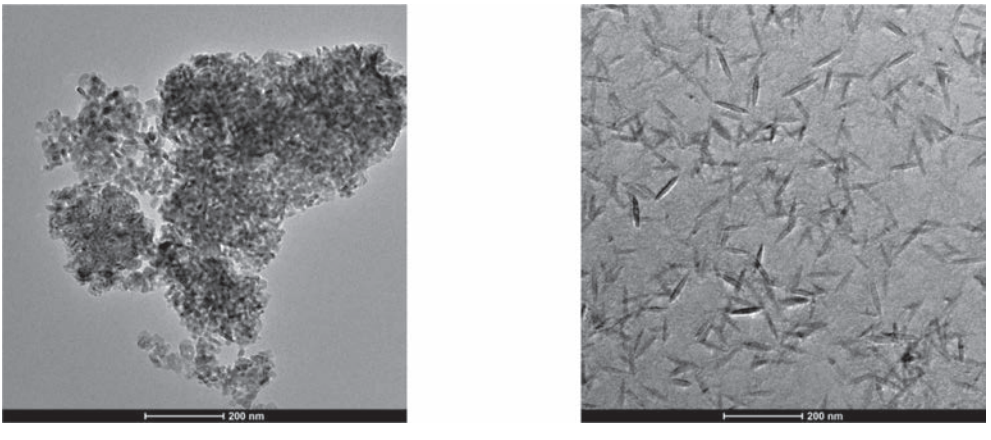

Figure 3. (a) TEM of TiO_2 nanoparticles powder. (b) TEM TiO_2 nanoparticles suspended in aqueous spray coat.

Table 1. Average NO_x reduction and NO reduction for TiO_2 incorporated into binder mixes.

Sample	NO_x reduction %	NO reduction %
Control PG 64-22	2.6%	5.0%
Control PG 70-22	8.5%	9.6%
3% TiO_2 64-22	3.9%	5.6%
5% TiO_2 64-22	4.7%	5.8%
7% TiO_2 64-22	3.3%	5.0%
3% TiO_2 70-22	3.8%	5.4%
5% TiO_2 70-22	4.9%	5.5%
7% TiO_2 70-22	2.9%	4.5%

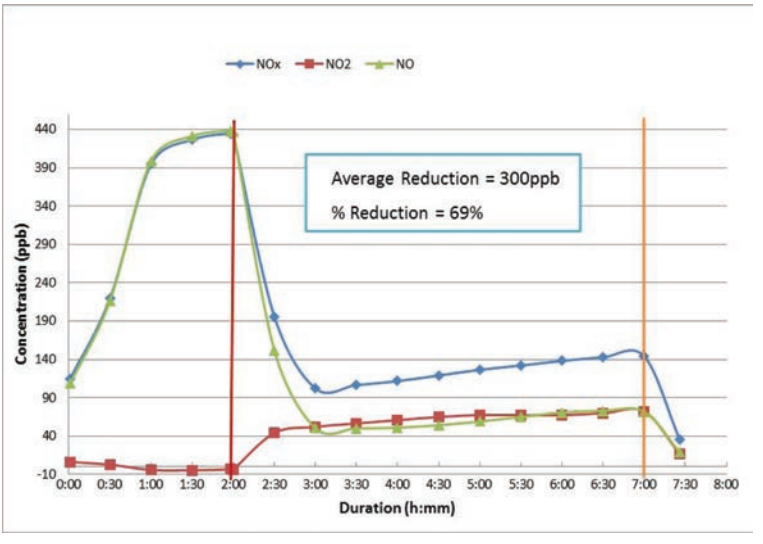

Figure 4. Variation of NO_x concentration during the environmental experiment (TiO_2 applied at a 0.21 kg/m^2 coverage).

TiO_2 into the asphalt binder may not be environmentally-effective. It is noted that the low NO_x reduction measured may be due to a small amount of TiO_2 nanoparticles lost in the photoreactor during handling and testing of the samples. The low efficiencies could be attributed to the fact that only a small amount of TiO_2 is actually present at the surface. Other possible explanations could be that the asphalt binder inhibits the photocatalytic reaction at the surface. While surface weathering due to traffic may expose part of the TiO_2 to UV light, this has not been validated. Therefore, further research is needed to evaluate photocatalytic efficiency over time.

For the second application method consisting of applying a surface spray coating, samples were tested using a flow of 1.5 l/min and a luminosity of 2 mW/cm^2. Figure 4 illustrates the variation of NO_x concentration during the course of the environmental experiment for the asphalt sample treated with a TiO_2 surface spray coat with a coverage rate of 0.21 kg/m^2. The UV light is turned on 2 hours after the start of the experiment in order to ensure equilibrium condition. The inlet concentration reached equilibrium at 430 ppb before the light was turned on. After the light is turned on, a fast drop of NO concentration in the outlet air stream is exhibited and NO_2 is created from the NO oxidation. During the photocatalytic experiment, the NO_x concentration slightly increased. After 5 hours of testing, the light and gas supply was turned off allowing for any desorption to occur. For the test condition shown in Figure 4, the use of TiO_2 photocatalyst coating had an NO removal efficiency of 83% and the overall NO_x reduction was 69%.

The rest of the results for all of the samples are shown in Table 2. As shown in this table, the efficiency of the sample without TiO_2 was negligible validating the efficiency of the photocatalytic compound in removing part of the NO pollutants in the air stream when used as a spray coating. By comparing the effect of the TiO_2 coverage rate, it appears that the improvement of NO_x reduction is not linear. In fact, the maximum environmental performance was achieved at the 0.21 kg/m^2 coverage rate. The increase in TiO_2 application rate beyond an optimum coverage rate may block nanoparticles' access to light and contaminants, and therefore, decrease NO_x removal efficiency.

4.1 *Effects of TiO_2 on rheological properties*

Table 3 presents the measured rheological properties of the TiO_2 modified and unmodified WMA binders based on laboratory testing conducted using rotational viscometer, dynamic shear rheometer, and bending beam rheometer. Results are presented for four types of specimen: PG 70-22 conventional WMA binder, PG 70-22 + 7% TiO_2, and PG 70-22 conventional and + 7% TiO_2 subjected to UV light for seven days. Since UV light will only influence the long-term behavior of the binder, rheological testing of specimens subjected to UV light was only performed on the aged samples (RTFO + PAV). Ultra-violet light initiates the photocatalytic process for the sample with TiO_2. Results presented in Table 3 indicate that

Table 2. Average NO_x reduction and NO reduction for TiO_2 used in a thin surface coating.

Coverage (kg/m^2)	NO_x reduction %	NO reduction %
Control PG (64-22)	2.6%	5.0%
Control PG (70-22)	8.5%	9.6%
PG (64-22) 0.11 kg/m^2	38.9%	51.2%
PG (64-22) 0.21 kg/m^2	53.2%	70.3%
PG (64-22) 0.32 kg/m^2	40%	52.6%
PG (70-22) 0.11 kg/m^2	51%	73%
PG (70-22) 0.21 kg/m^2	66.2%	76.6%
PG (70-22) 0.32 kg/m^2	54.3%	56%

Table 3. Rheological test results of TiO_2-modified asphalt binder.

TiO_2 binder testing	Spec standards	Test temp	PG70 W70CO	PG70 W70CO + UV	PG70 + 7% TiO_2	PG 70 + 7% TiO_2 + UV
Test on original binder						
Dynamic shear, G*/Sin(δ), (kPa), AASHTO T315	1.30$^+$	70°C	1.25	NA	1.44	NA
	1.00$^+$	70°C	0.63	NA	0.73	NA
Rotational viscosity (Pa · s), AASHTO T316	3.0$^-$	135°C	0.7	NA	0.9	NA
Tests on RTFO						
Mass loss, %	1.00$^-$	–	0.1	NA	0.7	NA
Dynamic shear, G*/Sin(δ), (kPa), AASHTO T315	2.20$^+$	70°C	2.69	NA	2.88	NA
Tests on (RTFO + PAV)						
Dynamic shear, G*Sin(δ), (kPa), AASHTO T315	5000$^-$	25°C	3845	3935	4610	4460
BBR creep stiffness, (MPa), AASHTO T313	300$^-$	–12°C	163	142	189	152
Bending beam m-value AASHTO T313	0.300$^+$	–12°C	0.304	0.310	0.305	0.301
Actual PG grading			**70-22**	**70-22**	**70-22**	**70-22**

Table 4. SCB test results for TiO_2 incorporated into binder mixes.

TiO_2 content	J_c (kJ/m^2)
Control	0.29
3.0%	0.45
5.0%	0.46
7.0%	0.28

the addition of TiO_2 only marginally affected the rheological properties of the conventional binder.

Results presented in Table 3 also show that exposing the binder to UV light did not accelerate the aging mechanisms in the material as compared to the sample that was not subjected to UV light. In addition, the use of TiO_2 as an air purification agent did not accelerate the aging mechanisms in the binder. This trend was desirable to ensure that UV light, which is necessary to initiate the photocatalytic process, did not negatively affect the binder rheological properties.

4.2 *Effects of TiO_2 on the mix fracture resistance*

Table 4 presents a comparison of the critical strain energy (J_c) data for the mixtures evaluated in this study. High J_c values are desirable as indicative of fracture-resistant mixtures. As shown by these results, the use of TiO_2 as a binder modifier improved the mix fracture resistance at 3, and 5% while it did not have a noticeable effect when used at a content of 7.0%.

5 SUMMARY AND CONCLUSIONS

This study evaluated the benefits of incorporating titanium dioxide (TiO_2) as an additive to asphalt binder in the preparation of WMA. Two commercial crystallized anatase-based titanium dioxide powder were blended with a conventional WMA asphalt binder classified as PG 64-22 and PG 70-22 at three modification rates (3, 5, and 7%). Prepared blends were characterized using fundamental rheological tests and the SCB test. Two application methods to integrate TiO_2 were evaluated, a water-based titanium dioxide solution applied as a thin coating and using TiO_2 as a modifier to asphalt binder in the preparation of WMA. Based on the results of the experimental program, the following conclusions may be drawn:

- When used as a modifier to asphalt binder in the preparation of WMA, the photocatalytic compound was not effective in degrading NO_x in the air stream. This could be attributed to the fact that only a small amount of TiO_2 is present at the surface.
- When used as part of a surface spray coating, TiO_2 was effective in removing NO_x pollutants from the air stream with an efficiency ranging from 38 to 77%.
- Rheological test results indicated that the addition of TiO_2 did not affect the physical properties of the conventional binder. In addition, exposing the binder to UV light did not appear to accelerate the aging mechanisms in the binder.
- The use of TiO_2 as a binder modifier improved the mix fracture resistance at 3, and 5% while it did not have a noticeable effect when used at a content of 7.0%.

This study represents a step towards evaluation and implementation of photocatalytic asphalt pavements as a feasible solution to mitigate near roadway air pollution problems. Based on the results presented in this study, further research is needed to evaluate the long-term effectiveness and durability of the photocatalytic coating in the field.

ACKNOWLEDGMENTS

This work was funded under NSF award number 1032288. The authors would like to acknowledge the assistance of Cristal Millennium and PURETI for providing this research with nano and ultrafine titanium dioxide, for testing and the Louisiana Transportation Research Center (LTRC) for granting access to their laboratory.

REFERENCES

[1] Fujishima, A., T.N. Rao, and D.A. Tryk, *Titanium Dioxide Photocatalysis. Journal of Photochemistry and Photobiology.* Photochemistry Reviews, 2000. **1**: p. 1–21.

[2] Fujishima, A., and Zhang, Xintong, *Titanium dioxide photocatalysis: present situation and future approaches.* C.R. Chimie, 2006. **9**: p. 750–760.

[3] C.S. Poon, a.E.C., *NO Removal Efficiency of Photocatalytic Paving Blocks Prepared with Recycled Materials.* Construction and Building Materials, 2007. **21**: p. 1746–1753.

[4] Beeldens, A. *An Environmentally Friendly Solution for Air Purification and Self Cleaning Effect: the Application of TiO_2 as Photocatalyst in Concrete.*. In *Proceedings of Transport Research Arena Europe—TRA*. 2006. Göteborg, Sweden.

[5] Dylla, H., Hassan, M.M., Mohammad, L., Rupnow, T., *Evaluation of the Environmental Effectiveness of Titanium Dioxide Photocatalyst Coating for Concrete Pavements.* Journal of the Transportation Research Record, 2010. **2164**: p. 46–51.

[6] Hassan, M.M., Dylla, H., Mohammad, L., and Rupnow, T., *Evaluation of the Durability of Titanium Dioxide Photocatalyst Coating for Concrete Pavement.* Journal of Construction and Building Materials, 2010. **24**(8): p. 1456–1461.

[7] Administration, F.H., *Our Nation's Highways—Selected Facts and Figures*, FHWA-PL-01-1012, Editor 2000, Office of Highway Information Management.

[8] Fujishima, A., and K. Honda, *Electrochemical Photolysis of Water at a Semiconductor Electrode.* Nature, 1972. **238**: p. 37–38.

[9] Cassar, L.P., C.; Tognon, G.; Guerrini, G.L.; Amadelli, R., *White cement for architectural concrete, possessing photocatalytic properties*, in *11th Congress on the Chemistry of Cement* 2003: Durban.

[10] Zhao, J.a.Y., Xudong, *Photocatalytic oxidation of indoor air purification: a literature review.* Building and Environment, 2003. **38**: p. 645–654.

[11] Venturini, L, and Bacchi, M. Research, Design, and Development of a Photocatalytic Asphalt Pavement. Proceedings of 2nd International Conference on Environmentally Friendly Roads: ENVIROAD 2009, Warsaw, Poland, 2009.

[12] Li, L., and Qian, C. A Lab Study of Photo-Catalytic Oxidation and Removal of Nitrogen Oxides in Vehicular Emissions and Its Fieldwork on Nanjing No. 3 Bridge of Yangtze River. Technical Note, International Journal of Pavement Research and Technology, Vol. 2, No. 5, 2009, pp. 218–222.

[13] Wu, Z., Mohammad, L.N., Wang, L.B., Mull, M.A. (2005). "." Vol. 2, No. 3., *Fracture Resistance Characterization of Superpave Mixtures Using the Semi-Circular Bending Test.* Journal of ASTM International, 2005. **2**(3).

This page intentionally left blank

Asphalt Pavements – Kim (Ed)
© 2014 Taylor & Francis Group, London, ISBN 978-1-138-02693-3

Clear asphalt concrete for energy saving in road tunnels

Edoardo Bocci & Maurizio Bocci
Polytechnic University of Marche, Ancona, Italy

ABSTRACT: Nowadays the interest in clear pavements for road tunnel applications is rapidly increasing, as their high photometric properties assure an important reduction of power consumption for electric lighting and an improvement of safety conditions. One of the solutions for manufacturing clear pavements consists in mixing light-colored mineral aggregates with particular transparent asphalt binders. This production technique was used in 2012 to manufacture the clear asphalt concrete for wearing courses of two road tunnels in the north of Italy. The present paper deals with the mix design and the evaluation of mechanical and photometric properties of the clear asphalt concrete used for paving these tunnels. In particular, tests were carried out on the raw materials and on both lab-manufactured and plant-manufactured mixes.

At the end of the tests clear mixtures showed good mechanical properties, similar to a traditional "black" asphalt concrete in terms of indirect tensile strength and indirect tensile stiffness modulus. In addition clear mixtures showed very high photometric properties after five months from the opening to traffic.

Keywords: Clear pavement, clear asphalt concrete, transparent binder, tunnel lighting, photometric properties

1 INTRODUCTION

Application of clear pavements in tunnels, with the aim to reduce the power consumption for electric lighting and improve safety conditions, represents a very interesting topic in the field of road engineering.

According to European Asphalt Pavement Association (EAPA) clear pavements are better than traditional "black" asphalt concretes both in terms of luminance (capability of reflecting light waves) and of contrast with road markings [1]. In addition, recent studies estimated that light-colored surfaces allow an energy saving in tunnel lighting up to 30–40% [2].

It is known that road surface is polished by vehicle tires. After the laying of the wearing course aggregates are still covered with binder but, after some months, the upper faces of the aggregates are polished and the binder is visible only in form of mastic (binder and filler) between coarse particles. So the pavement clear color depends mainly on aggregate and binder colors.

The choice of clear aggregate is related to its availability in a certain area and the incidence of hauling costs.

About the binder, one solution is represented by rigid pavements in Portland cement concrete. Besides the white/grey color, these pavements present the advantages to have a longer fatigue life in general and to be fireproof, which is very important for tunnels in case of fire. On the other hand, cement concrete pavements are very expensive and difficult to be constructed. Moreover, frequent maintenance interventions are necessary in order to assure adequate adhesion levels for drivers' safety.

An alternative solution consists in manufacturing flexible pavements with synthetic resins [3–4] or bitumens with low asphaltene content [5]. These asphalts, characterized by a very clear amber color and a marked transparence, are mainly used with aesthetic purposes in

order to integrate road pavements with the surrounding landscape in important natural and historical places [6]. Moreover, clear binders can serve the purpose of improving urban climate by working on the mitigation of the urban heat island effect and other local warming phenomena [7–8].

Clear asphalts can be manufactured through three different techniques [8–9]:

- extraction of asphaltenes from traditional bitumen;
- production of synthetic binders containing transparent polymeric materials;
- blending resins with particular bio-oils in order to obtain clear materials with rheological properties similar to those of bitumen.

In some cases clear asphalts are used with pigment addicted [10]. These additives, generally metallic oxides in form of powder, have the effect to make the pavement clearer or give it a particular color (red, yellow …).

2 PHOTOMETRIC PROPERTIES

The capability of clear pavements to reflect luminous radiations can be quantified through a property called luminance. Luminance (L) is a photometric measure of the luminous intensity that is emitted or reflected from a surface, per unit area. The luminance indicates how much luminous power will be detected by a driver's eye looking at the surface from a specific angle of view. The luminance is expressed in candela per square meter (cd/m^2) and can be measured through a proper machine called luminance meter.

The luminous intensity reflected by a pavement is strictly dependent on the amount of light that reaches the pavement itself. So, in order to make a comparison between luminance measurements performed in different lighting conditions (between the lab and the road tunnels), two further photometric quantities has to be defined:

- illuminance (E), that is the total luminous flux incident on a surface, per unit area. It is expressed in lux (lx = cd · sr · m^{-2}) and can be measured through an illuminance meter;
- reflectance or reflection coefficient (ρ), that represents the capability of a material to reflect a luminous radiation and it is dimensionless.

As the reflectance depends only from the type of material, the comparison between the clear pavement laid on the tunnel and the mixtures manufactured in the lab was made in terms of ρ.

Known luminance L and illuminance E, reflectance ρ can be determined through Eq. (1):

$$\rho = \frac{L}{E} \cdot \pi \tag{1}$$

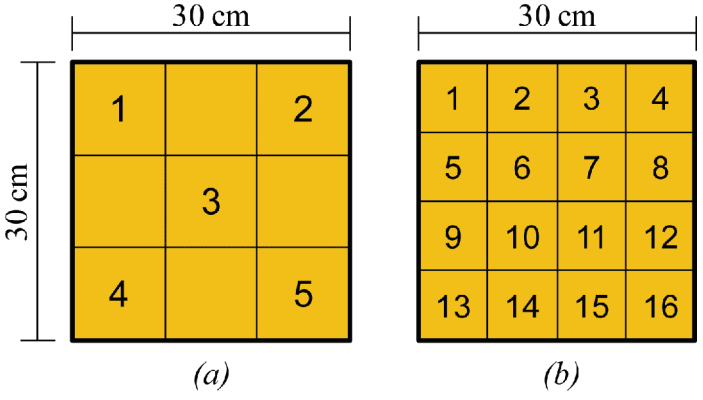

Figure 1. Measurement area for illuminance (a) and luminance (b).

Photometric properties were measured on surface samples with dimensions 30 × 30 cm. Illuminance and luminance were respectively calculated as mean of 5 and 16 values determined in the middle of defined sub-areas, as shown in Figure 1.

3 EXPERIMENTAL PROGRAM

In July 2012 a clear asphalt concrete was used to build the wearing course of two road tunnels in the north of Italy. In the present paper, mix design and mechanical and photometric characterization of this clear mixture are discussed.

The mix design was carried out according to SHRP specifications in order to evaluate the compactability of the mixture and define the binder percentage. Once the job mix formula was found, tests were performed on two mixtures: the first was manufactured in the laboratory, the second was manufactured in a batch plant and was taken from the tunnel construction site.

The experimental program includes:

- Indirect Tensile Strength (ITS) and Indirect Tensile Stiffness Modulus (ITSM) tests on specimens compacted with Shear Gyratory Compactor (SGC);
- determination of skid resistance and photometric properties in situ, directly on the tunnel pavements in 4 locations, and in the laboratory, on slabs compacted with Roller Compactor (RC).

Table 1 shows the detailed scheme of the experimental program.

The aim of the study is to verify that the mechanical behavior of clear mixtures is similar to an ordinary asphalt concrete and quantify the benefits, in term of photometric properties, related to the use of clear mixtures.

Table 1. Experimental program.

Tests on lab-manufactured mix

Test name	Standard	Repetitions	Compaction method and energy	Test temperature
ITS test	EN 12697-23	5	SGC-100 revolutions	25°C
ITSM test	EN 12697-26	5	SGC-100 revolutions	20°C and 40°C
Skid resistance test	EN 13036-4	3	RC-20 passes @ 3 bar	25°C
Luminance test	–	16	RC-20 passes @ 3 bar	25°C
Illuminance test	–	5	RC-20 passes @ 3 bar	25°C

Lab tests on plant-manufactured mix

Test name	Standard	Repetitions	Compaction method and energy	Test temperature
ITS test	EN 12697-23	5	SGC-100 revolutions	25°C
ITSM test	EN 12697-26	5	SGC-100 revolutions	20°C and 40°C
Skid resistance test	EN 13036-4	3	RC-20 passes @ 3 bar	25°C
Luminance test	–	16	RC-20 passes @ 3 bar	25°C
Illuminance test	–	5	RC-20 passes @ 3 bar	25°C

In situ tests

Test name	Standard	Repetitions	Testing points	Test temperature
Skid resistance test	EN 13036-4	3	4	25°C
Luminance test	–	16	4	25°C
Illuminance test	–	5	4	25°C

4 MATERIALS

4.1 *Aggregate*

The granular mixture was composed using grey porphyry coarse aggregate (in two fractions), white-colored limestone sand and filler containing Calcium Carbonate ($CaCO_3$) naturally micronized in powder. Besides, 0.5% by aggregate weight of powdered titanium dioxide (TiO_2) was added as a pigment (Fig. 2). Mechanical properties of coarse aggregate are shown in Table 2.

The different fractions were proportioned in order to build a gradation curve inside the reference envelope [11]. Then the original curve was modified by increasing the percentage of filler (Fig. 3), in order to obtain a more consistent mastic when mixed with the clear binder.

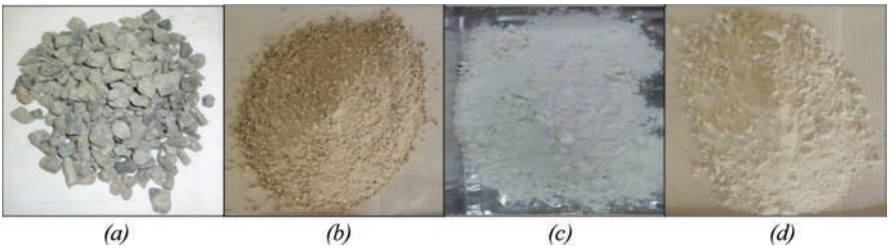

Figure 2. Granular materials: grey porphyry (a), limestone sand (b), $CaCO_3$-based filler (c), titanium dioxide (d).

Table 2. Grey porphyry aggregate properties.

Property	Method	Value
Flakiness index [%]	EN 933-3	12
Shape index [%]	EN 933-4	10
Apparent particle density [Mg/m^3]	EN 1097-6	2.67
Water absorption [%]	EN 1097-6	1.42
Resistance to fragmentation (Los Angeles) [%]	EN 1097-2	17
Polished stone value [%]	EN 1097-8	50

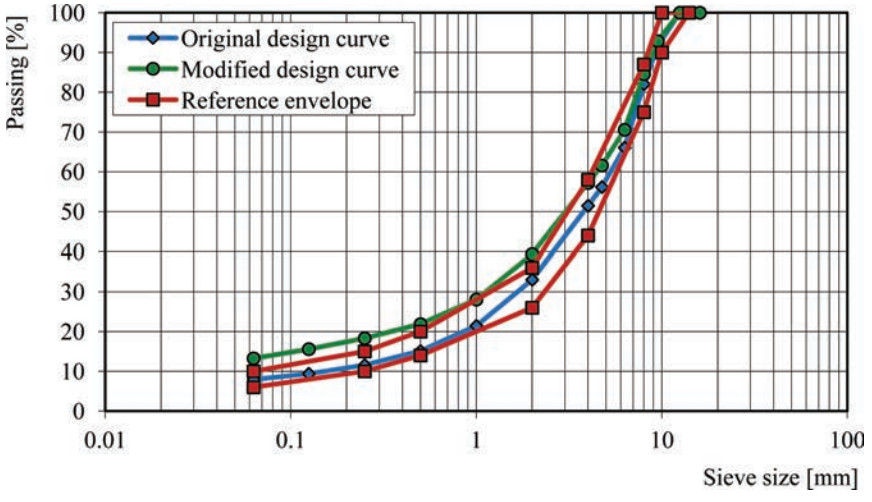

Figure 3. Aggregate gradation in comparison with grading envelope.

Table 3. Clear binder properties.

Property	Method	Value
Penetration at 25°C [dmm]	EN 1426	42
Softening point [°C]	EN 1427	53.8
Dynamic viscosity at 100°C [Pa·s]	EN 13702	16500
Dynamic viscosity at 135°C [Pa·s]	EN 13702	1100
Dynamic viscosity at 160°C [Pa·s]	EN 13702	365
Elastic recovery at 25°C [%]	EN 13398	83
Characteristics after RTFOT—EN 12607-1	Method	Value
Change of mass [%]	EN 12607-1	–0.65
Retained penetration at 25°C [%]	EN 1426	63
Softening point increasing [%]	EN 1427	2

4.2 *Binder*

The clear binder used in this research was a bitumen subjected to asphaltene extraction, so that finally it only included lighter fractions (aromatics, saturates and resins). In order to restore adequate consistence and stability, the binder was than modified by adding a high percentage of elastomeric polymers. Binder mechanical properties are shown in Table 3.

5 MIX DESIGN

Mix design was carried out on 4 series of 3 samples, each series containing respectively 5.0%, 5.5%, 6.0% and 6.5% of clear binder by mix weight. Samples were compacted with 180 revolutions of shear gyratory compactor. For each series Air Void Content (AVC), Voids in the Mineral Aggregate (VMA) and Voids Filled with Bitumen (VFB) were determined at revolution No. 100 (N_{design}). According to SHRP, the following target values were fixed:

- AVC = 4%
- VMA ≥ 13%
- 65% ≤ VFB ≤ 78%

Mix design results are shown in Table 4 and Figure 4.

The volumetric analysis on the compacted specimens showed that all the different mixtures ensured adequate compactability and a good sensitivity to compaction energy, similarly to traditional asphalt concrete. In the light of the results obtained from the mix design procedure, a binder content of 5.66% by mixture weight (6.00% by aggregate weight) was fixed.

6 ANALYSIS OF RESULTS

6.1 *ITS and ITSM tests*

As shown in Table 5, for both lab and plant manufactured clear mixes ITS values were considerably higher (about 50%) than ordinary "black" asphalt concrete for wearing courses. An explanation for this result is that the clear binder was evidently more crack-resistant than traditional bitumen, thus the aggregate-binder adhesion was stronger. In addition it has to be considered that the mastic composed by clear binder and filler is noticeably stiff, as the filler content is very high (about 13%).

From Table 5 it can be observed that ITSM values at 20°C were comparable with that of a traditional asphalt concrete for wearing courses, denoting suitable performance at intermediate temperatures. On the contrary, when the temperature increased to 40°C, ITSM values resulted quite low. This indicates that clear mixtures has a higher thermal sensitivity than ordinary asphalt

Table 4. Mix design results.

Parameter	Series			
	B = 5.00%	B = 5.50%	B = 6.00%	B = 6.50%
AVC [%]	5.6	4.7	3.7	3.4
VMA [%]	14.9	15.3	15.4	16.2
VFB [%]	62.6	69.1	76.3	79.3
G_{mm} [Mg/m³]	2.50	2.48	2.46	2.44
G_{mb} [Mg/m³]	2.36	2.36	2.37	2.36
C_{in} [%]	84.4	85.2	86.1	86.4
C_{des} [%]	94.4	95.3	96.3	96.6
C_{max} [%]	95.8	96.7	97.8	98.1

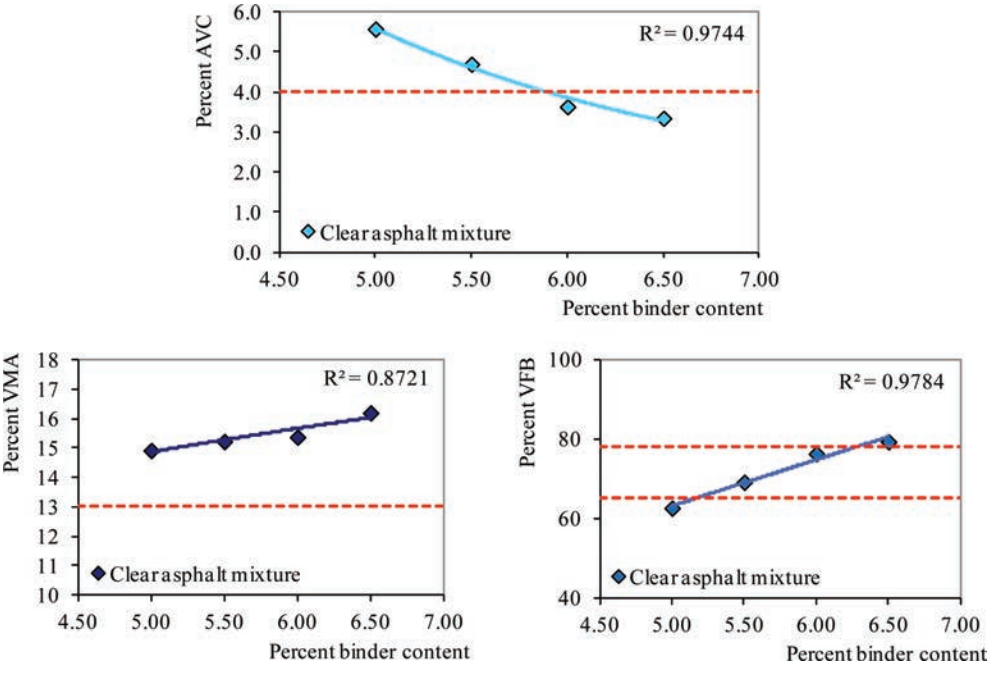

Figure 4. AVC, VMA and VFB as functions of binder percentage.

Table 5. Results from ITS and ITSM tests.

	Lab-manufactured mix			Plant-manufactured mix		
	ITS @ 25°C [MPa]	ITSM @ 20°C [MPa]	ITSM @ 40°C [MPa]	ITS @ 25°C [MPa]	ITSM @ 20°C [MPa]	ITSM @ 40°C [MPa]
	1.769	3261	229.0	2.180	4477	233.5
	1.704	3332	226.0	2.071	4025	266.6
	1.667	3500	402.0	2.144	4222	251.4
	1.673	3285	278.9	2.186	4377	285.9
	1.755	3441	295.6	2.222	4407	262.5
Mean	1.713	3364	286.3	2.161	4302	260.0
St. dev.	0.047	103	71.5	0.057	181	19.4

concretes and consequently they could be subject to early rutting when used in hot areas. However, this risk should be averted in the present applications as in this area climate is generally cool even during summer and pavements are not directly exposed to solar light inside tunnels as well.

6.2 *Skid resistance tests*

Table 6 shows results from skid resistance tests, express in BPN (British Pendulum Number). From the results it can be noticed that BPN values have been similar for all the clear mixtures

Table 6. Results from skid resistance tests.

	Lab-manufactured mix	Plant-manufactured mix	Plant-manufactured mix				"Black" reference mixture
	Lab measurement	Lab measurement	In situ measurement				
	62	63	65	60	60	57	70
	62	65	66	61	58	56	68
	60	65	65	60	60	57	67
Mean	61	64	65	60	59	57	68
St. dev.	1.155	1.155	0.577	0.577	1.155	0.577	1.528

Table 7. Results from photometric tests.

	Lab-manufactured mix	Plant-manufactured mix	Plant-manufactured mix				"Black" reference mixture
	Lab measurement	Lab measurement	In situ measurement				
L [cd/m^2]	22.08	24.36	33.09	2.242	1.751	22.39	2.613
	19.95	21.76	28.59	2.926	2.152	18.33	2.799
	19.48	19.88	24.22	2.442	2.409	16.97	3.859
	19.83	17.73	23.81	1.502	2.334	14.23	3.372
	19.97	22.35	33.85	3.949	1.949	18.03	3.332
	20.36	19.17	31.04	3.995	3.073	19.77	3.446
	21.38	18.67	26.00	2.979	4.179	17.94	3.222
	20.48	17.97	24.01	1.950	2.604	14.82	3.249
	23.85	24.37	33.78	3.333	2.052	18.60	3.817
	19.33	19.20	27.94	3.682	3.059	19.39	3.632
	21.47	18.15	24.07	3.196	3.351	16.12	2.432
	19.42	16.30	25.93	2.213	2.736	14.73	2.436
	22.36	16.80	36.47	2.101	1.509	23.59	3.239
	20.19	21.17	30.45	3.004	2.045	18.04	3.279
	16.73	19.68	27.62	2.632	2.320	15.94	2.678
	18.93	22.99	29.04	1.539	1.825	13.68	2.310
Mean	20.36	20.03	28.74	2.730	2.459	17.66	3.107
St. dev.	1.633	2.541	4.039	0.786	0.689	2.790	0.498
E [lx]	180.6	180.6	604	69.5	92.9	286	180.6
	182.0	182.0	635	87.5	66.7	371	182.0
	202.4	202.4	563	68.6	48.7	306	202.4
	171.9	171.9	594	52.1	57.1	256	171.9
	207.1	207.1	471	55.7	65.2	248	207.1
Mean	188.8	188.8	573	66.7	66.1	293	188.8
St. dev.	15.2	15.2	62.7	13.9	16.6	49.2	15.2
ρ [-]	**0.339**	**0.333**	**0.157**	**0.129**	**0.117**	**0.189**	**0.052**

Figure 5. Clear asphalt concrete compaction in the road tunnel.

tested (lab and plant manufactured, lab and in situ measurements). Compared with the reference mixture, consisting in a wearing course "black" mixture with porphyry aggregates, clear asphalt concretes showed a lower skid resistance (about 10% of reduction). However BPN values were around 60, which represent the limit defined by Italian specifications [11]. In addition it has to be considered that this result is probably related to the clear mastic that creates a smoother film around aggregates. Once this film is removed by traffic, skid properties should be uniform to the reference mixture.

6.3 *Photometric properties*

Table 7 shows the results from photometric tests. From Table 7 it can be noticed that the reflectance calculated for clear pavements is considerably higher than the one found for the reference mixture. In particular the lab-manufactured mix and the plant-manufactured mix tested in the lab denoted photometric properties at least 6 times higher than the black concrete.

However, the same plant-manufactured mix, when laid in situ, showed a halved reflectance in all the 4 locations inside the tunnels. As in situ measurements were carried out five months after the opening to traffic, this result is probably related to the binder natural darkening process that led the pavement to assume a darker yellow color. Nevertheless, reflectance ρ was still 3 times higher than the reference mixture determining a noticeable improvement of lighting distribution in the tunnels (Fig. 5). Besides, photometric properties are supposed to increase once the mastic film that covers the aggregate is removed by traffic and the light-grey color of the aggregate comes out. It has to be taken into account that also surface texture, in both micro and macro scale, influences pavement photometric properties and may have contributed to the different results between lab and field compacted mixture.

7 CONCLUSIONS

The present paper deals with mix design and mechanical and photometric characterization of a clear asphalt concrete for the application in road tunnels. The dense graded mixture was composed by grey porphyry coarse aggregate, limestone sand, calcium carbonate-based filler, titanium dioxide and transparent bitumen with low asphaltene content. The experimental program consisted of traditional and performance-based tests, carried out on the lab-manufactured mix and on the plant-manufactured mix laid on two tunnels in the north of Italy.

According to the results from the mix design, a binder content of 5.66% by mixture weight (6.00% by aggregate weight) was determined. A particular detail of the job mix formula was represented by the high filler-to-binder ratio adopted, in order to have a more consistent mastic.

Clear mixtures showed about 50% higher ITS values than ordinary "black" asphalt concrete for wearing courses, probably due to the sticky binder and the high filler content. ITSM tests pointed out a high thermal sensitivity for this mixture. Thus, particular attention should be paid to avoid early rutting for the application in hot areas.

Skid properties proved to be adequate for all the clear mixtures tested. In addition, skid resistance is supposed to increase once the smooth mastic film the covers the aggregates is removed by traffic.

Finally, as calculated reflectance ρ was at least 3 times higher than ordinary asphalt mixture, clear asphalt concretes demonstrated to be an effective solution in terms of photometric properties, determining a noticeable improvement of lighting distribution in the tunnels and of road marking visibility.

REFERENCES

[1] European Asphalt Pavement Association. Asphalt Pavements in Tunnels, Position paper. 2008.

[2] M. St-Jacques. and Y. Brosseaud. Coloured Bituminous Wearing Courses in France, Overview of Uses, 10th International Conference on Asphalt Pavements, vol. 3, pp. 233–242. Quebec, 2006.

[3] F.J. Navarro. P Partal. F. Martìnez-Boza. and C. Gallegos. Effect of Composition and Processing on the Linear Viscoelasticity of Synthetic Binders, European Polymer Journal, 41, pp. 1429–1438. 2005.

[4] G.D. Airey. M.H. Mohammed. and C. Fichter. Rheological Characteristics of Synthetic Road Binders, Fuel, 87, 1763–1775. 2008.

[5] D. Lesueur. The Colloidal Structure of Bitumen: Consequences on Rheology and on the Mechanism of Bitumen Modification, Advances in Colloid and Interface Science, 145, pp. 42–82. 2009.

[6] J.D. Pineda. Recommendations for the Improvement of the Integration of Roads in Environmentally Sensitive Areas, Proceedings of the 1st European Road Congress. Lisbon, 2004.

[7] A. Synnefa. T. Karlessi. N. Gaitani. M. Santamouris. D.N. Assimakopoulos. and C. Papakatsikas. Experimental Testing of Cool Colored Thin Layer Asphalt and Estimation of its Potential to Improve the Urban Microclimate, Building and Environment, 46, pp. 38–44. 2011.

[8] F. Merusi. and F. Giuliani. Chromatic and Rheological Characteristics of Clear Road Binders, Transportation Research Record: Journal of the Transportation Research Board, 2293, pp. 114–122. 2012.

[9] M. Bocci. A. Grilli. F. Cardone. and A. Virgili. Clear Asphalt Mixture for Wearing Course in Tunnels: Experimental Application in the Province of Bolzano, Procedia—Social and Behavioral Sciences, 53, pp. 115–124. 2012.

[10] D.F. Lin. and H.L. Luo. Fading and Color Changes in Colored Asphalt Quantified by the Image Analysis Method, Construction and Building Materials, 18, pp. 255–261. 2004.

[11] Autonomous Province of Bolzano. Capitolato Speciale d'Appalto per Lavori Stradali. Italy. 2010.

This page intentionally left blank

Asphalt Pavements – Kim (Ed)
© 2014 Taylor & Francis Group, London, ISBN 978-1-138-02693-3

Optimization of thermoelectric system for pavement energy harvesting

Philip Park, Gwan S. Choi, Ehsan Rohani & Ikkyun Song
Texas A&M University, College Station, TX, USA

ABSTRACT: With the increasing emphasis on renewable resources and green technologies, energy harvesting from asphalt pavement has gained momentous attention in the recent years. Thermoelectric energy harvesting is one of the promising methods for collecting and transmitting solar energy into electrical power using temperature gradient along the pavement depth. However, the low energy conversion efficiency must be mitigated in order for this method to be viable for various practical applications. Henceforth, the objectives of this study are to investigate the key factors affecting the energy conversion efficiency and to derive optimal mechanical and circuit configurations. The goal is to compose a thermoelectric energy harvesting system tailored for the pavement application. The design under study is typical and it consists of a thermoelectric generator and thermally conductive rods for transferring heat. The effects of the generator type, circuit design, the shape of the conductive rod, and its insulation are investigated. The results indicate that the controlling of the heat transfer from the pavement to the thermoelectric generator is central to effective thermoelectric energy harvesting. Among the tested thermoelectric systems, the best device configuration yielded 42 mW; about 26 times higher power than the default case in this study.

Keywords: Energy harvesting, pavement, thermoelectric generator, optimization

1 INTRODUCTION

Transportation system is one of the largest and most important infrastructures in modern society. According to Federal Highway Administration (FHWA), a total lane mile of the public roads in the US is 8.6 Million miles in 2012 [1]. In the US, 28% of total produced energy was consumed by transportation sector in 2012. While the moving of vehicle is the major energy consumption of the transportation sector, the transportation facilities uses 25×10^{12} BTU of electrical energy for the roadway lighting, signal, and various sensing and monitoring systems [2]. Additionally about 51×10^{12} BTU, which is about twice that actually consumed, is lost from transmission during power delivery. This is caused by the widespread nature of roadways.

Energy harvesting reclaims otherwise dissipated or wasted energy, and is highly sustainable power generation approach. While energy harvesting technology has successfully been explored in numerous electronics and mechanical systems applications, its application to roadway pavements is currently at its infancy. Since asphalt pavement is a huge storage of solar energy, the pavement energy harvesting technology promises a significant breakthrough in attaining renewable energy at a massive scale. The specific attributes of harnessing energy from pavements are: 1) the size of roadways is massive, and hence, relatively large amount of energy can be collected, 2) there exist various types of available energy sources, e.g. geothermal, solar, mechanical, etc., and 3) a long-distance power transmission is not necessary because the collected electrical energy can be consumed in place by traffic facilities. In situ generation of electrical power can decidedly offset the aforementioned transmission loss of electrical energy. In addition, it can eliminate the installation and maintenance cost of power delivery infrastructures.

The pavement energy harvesting technology has gained attention from various researchers and transportation agencies in the recent years [3]. Mallick et al. suggested collecting energy from pavements by installing water pipes under pavement surfaces [4–5]. Lee and his colleagues tried the water pipe installation [6] and solar panels [7–8] to harvest energy. The method of converting the mechanical energy from traffic loads into electrical energy was suggested by Abramovich et al. [9–11], and investigated by various investigators [12–17]. Bhattacharjee and his colleagues compared the pyroelectric effects of various energy converting materials for the pavement application [18–19].

Another promising energy harvesting method from pavement is using the temperature gradient along the depth of pavements. Thermoelectric Generator (TEG) is a device converting temperature difference into electric potential and vice versa. The efficiency of the thermoelectric energy harvesting is known to be relatively low. However, this method is still promising because the most abundant form of energy on pavements is heat. Wu and Yu [20–21] suggested a thermoelectric energy harvesting system for the pavement application. This system was composed of a commercial TEG connected to aluminium rods at both ends to transfer heat between the surface and the subgrade of an asphalt pavement. A circuit was designed in order to manage generated electric energy, and the energy used to blink a light-emitting diode. In the Wu and Yu's experiment, the applied temperature difference to the system including the heat exchanging rods was 50°K, and the temperature difference across the TEG was 20°K. At this condition, the power generated from the system was 0.05 mW, which was the power to blink the LED with 90 sec interval [21]. Using the commercially available TEG, Wu and Yu suggested a practically feasible thermoelectric system. On the other hand, the low efficiency in energy conversion and the corresponding micro-level low power remain to be the next avenue of the research.

Aiming to optimize the thermoelectric energy harvesting system for the pavement application, the effects of various factors on the efficiency of the system are investigated through the presented study. The electrical impedance matching, selection of TEG and corresponding thermodynamic effect, and the effect of the heat exchangers/insulation are discussed herein. Section 2 states the background knowledge in thermoelectric power generation, Section 3 describes the design and experimental setup, Section 4 discusses the results, and Section 5 draws several observations and concluding remarks.

2 BACKGROUND

2.1 *Principle of thermoelectric generator*

TEG device consists of the circuit connecting a number of p-type and n-type semiconductor devices in series and a pair of dielectric plates, typically made of a ceramic material that contains these junction devices in between them. A TEG device creates voltage when there is a different temperature on each side of the plates. At the junctions, an applied temperature gradient causes charge carriers in the material to diffuse from the hot side to the cold side. This physical phenomenon is referred to as Peltier effect. The result is, when the temperatures at each end of the semiconductors are different, the semiconductors generate electric current flowing in certain direction. As shown in Figure 1, the generated electric current at each semiconductor can be controlled by arranging those semiconductors and covering those with thermally conductive but electrically insulating ceramic plate [22].

2.2 *Temperature gradient in pavement*

An example temperature gradient obtained from an actual pavement in Montana, USA is illustrated in Figure 2. The data is obtained at four different times of a day (4-23-1993). The temperature at the surface widely varies with time while the temperature below 80 cm from

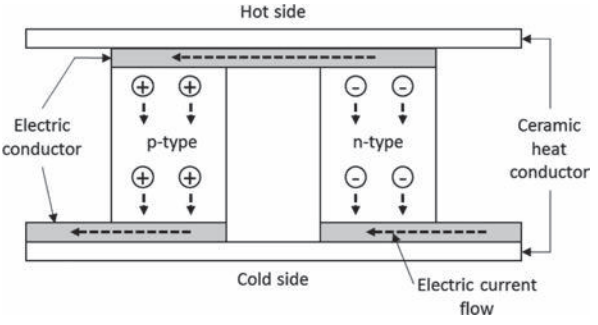

Figure 1. Schematic diagram of TEG.

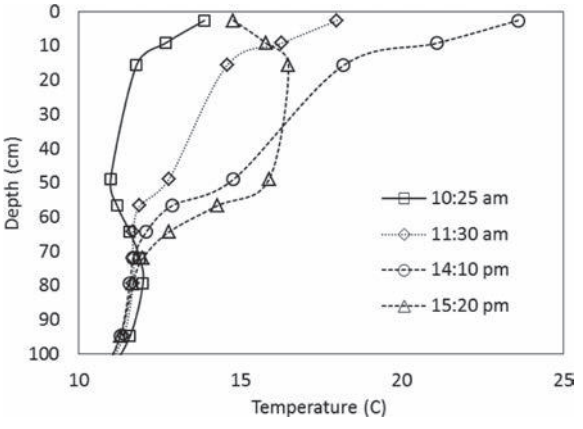

Figure 2. Variation of temperature gradient along the pavement depth: LTPP data from Montana, 4-23-1993 [23].

the surface is almost constant. The maximum temperature difference of this specific example was 13 °C.

3 THERMOELECTRIC SYSTEM DESIGN AND EXPERIMENTAL SET-UP

A thermoelectric system is manufactured for the experiment. Figure 3 illustrates the thermoelectric system used in this study. The design is similar to that proposed by Wu and Yu [21]. The system is composed of a TEG contacted to a pair of heat exchangers. The heat exchangers and TEG are stacked in horizontal direction not to transfer the mechanical force from traffic loads. The amount and loss of heat flow is one of the important factors for the efficiency of the system. To provide high thermal conduction, aluminium bars with 200 (W/m · °K) of thermal conductivity are selected for the heat exchangers. As shown in Figure 3, an extra space around TEG is needed to fasten bolts between the two heat exchangers. To minimize the heat loss, the extra space is filled with the insulation tape with 0.06 (W/m · °K) of thermal conductivity and plastic bolts and nuts were used as the fastener. In most of the tests, the heat exchangers were wrapped up with six layers of the same insulation tape to minimize the heat loss between the heat exchanger and the ambient environment.

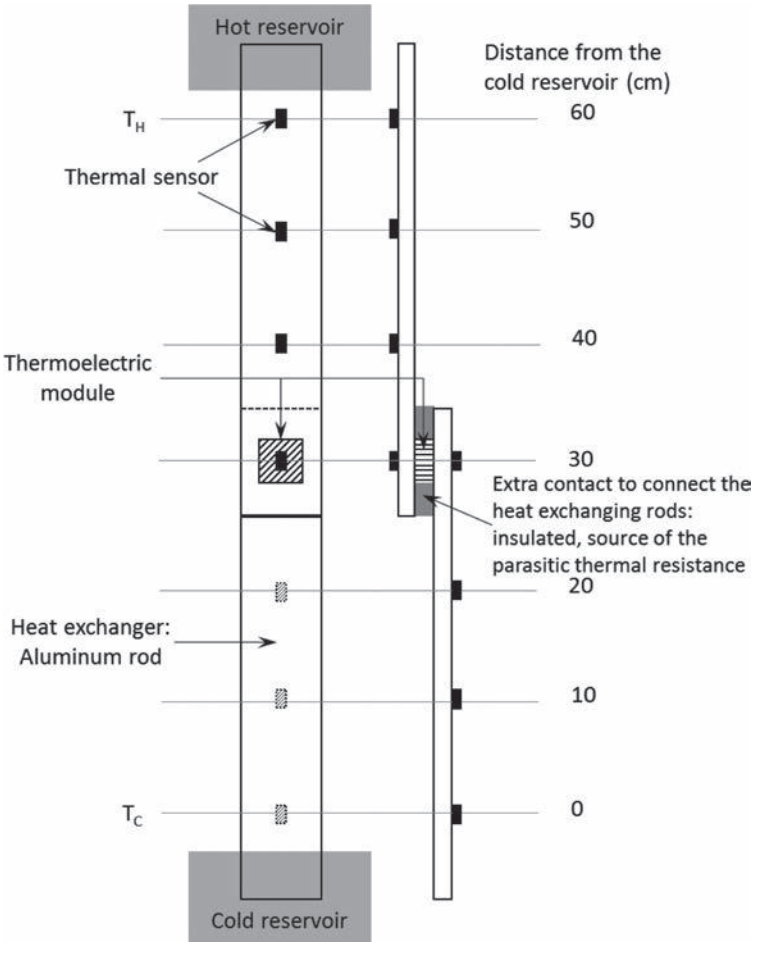

Figure 3. Experimental set-up of the thermoelectric energy harvesting system.

As displayed in Figure 4, three types of cross-sectional shape are tested. The selection of the TEG is another important factor for the effective energy generation. The characteristics of the four different TEGs used in this study are summarized in Table 1. With the assumption of a small temperature difference (up to 40°K) between the top and bottom surface of the TEG, the electric potential generated from TEG can be approximated to be linearly proportional to the temperature difference [22], as shown in Eq. (1).

$$V = \alpha \Delta T_{TEG} \tag{1}$$

where, V is the electric potential (voltage, V), ΔT_{TEG} is the temperature difference (°K) at the TEG, and α is the coefficient (V/°K). Two values of α are given in Table 1. The first column of α values shows the calculated values from the specification, and the second column of α values lists the measured α in the lab. For the latter discussion of this paper, the measured values will be used. As shown in Table 1 and Figure 5, the voltage generated at the same ΔT_{TEG} is approximately proportional to the number of p-n junctions rather than the size of the TEGs. The order of the generated voltage by each TEG is A > B > D > C.

In addition to the electrical considerations, thermodynamic heat flow between the heat exchangers and TEG will affect the efficiency of power generation. To evaluate the heat flow through the system, eight thermal sensors are attached as shown in Figure 3.

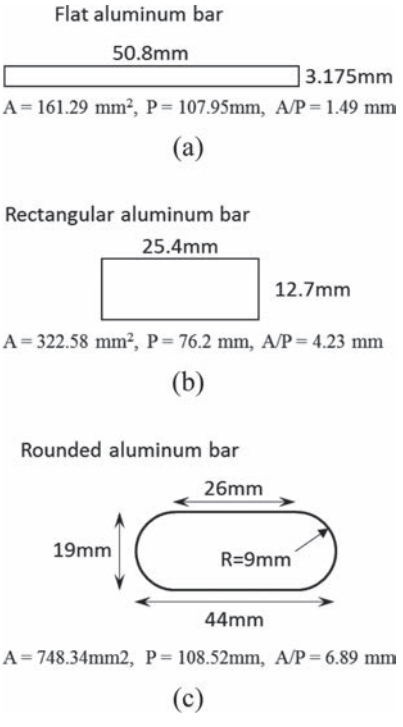

Figure 4. Cross-sectional shape and dimension of the heat exchanger.

Table 1. Properties of the TEG.

TEG ID	Dimension (mm)			Number of p – n junctions	Thermal resistance (K/W)	Electric resistance (Ω)	α (V – ΔT coefficient)	
	W	L	Th				Calculated	Measured
A	40	40	4.12	127	3.45	3.57	0.0514	0.0600
B	15	15	5.1	31	27.50	1.60	0.0125	0.0142
C	9.5	9.5	4.7	7	61.84	0.25	0.0028	0.0031
D	4.9	6.5	2.44	18	115.74	2.40	0.0073	0.0074

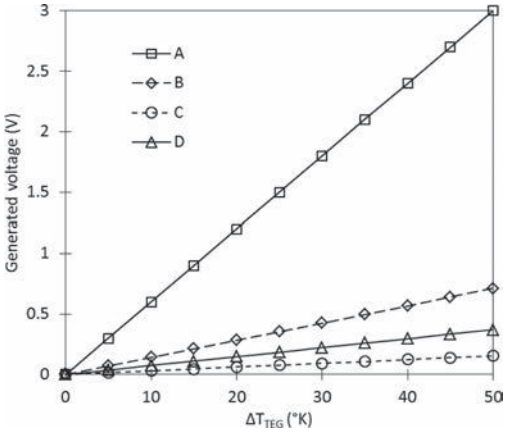

Figure 5. The relationship between electric potential and temperature difference of TEG.

4 RESULTS AND DISCUSSION

4.1 *Electrical impedance matching*

Figure 6 shows a simple circuit model composed of a battery and a load, which consumes electric energy. In the thermoelectric energy harvesting system, the TEG will take the role of the battery. According to Ohm's law, a voltage is linearly proportional to the resistance and current. As shown in Figure 5, the voltage generated by TEG solely depends on ΔT_{TEG}. When the switch in the circuit is open, the voltage output can be obtained by Eq. (1). The work can be done by connecting an electrical load with a resistance, R_L—the situation of closing the switch in Figure 6. Since the TEG has its own internal resistance, R_{TEG}, the total voltage generated by the TEG, V_{TEG}, will be shared by R_{TEG} and R_L. From Ohm's law, the voltage of the electric load, V_L, can be calculated by Eq. (2).

$$V_L = \frac{R_L}{R_L + R_{TEG}} V_{TEG} \tag{2}$$

Since the useful work will be done at R_L, the useful power, P, of this circu it can be calculated by Eq. (3) with the combination of Eq. (2).

$$P = \frac{V_L^{\,2}}{R_L} = \frac{R_L}{R_L + R_{TEG}^{\,2}} V_{TEG}^{\,2} \tag{3}$$

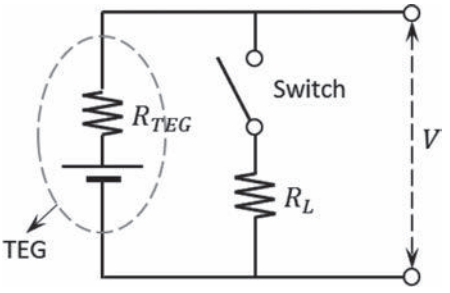

Figure 6. Electric circuit for maximum power output.

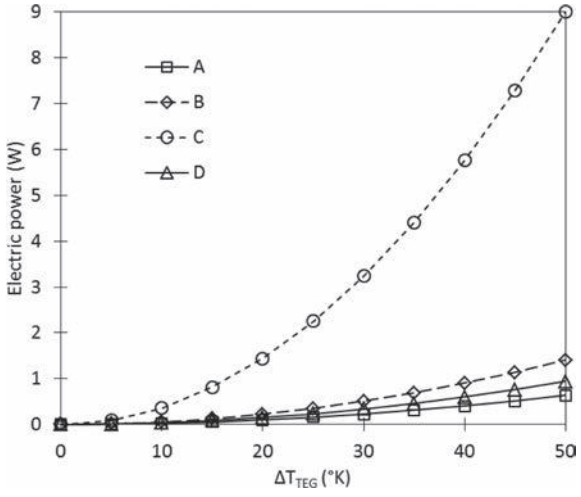

Figure 7. The relationship between electric power and temperature difference of TEG.

In theory, the maximum useful power can be obtained when is $\partial P/\partial R_L = 0$, in other words, $R_L = R_{TEG}$. This implies that the TEG of the pavement energy harvesting system has to be selected in order to match with the impedance of the application. Figure 7 compares the theoretically maximum power of the TEGs used in this study. Because of the low electric resistance, the highest power is obtained from the TEG type C and followed by B, D, and A. In terms of the useful power, the efficiency of the TEGs shows a completely different order from the case of the voltage in Figure 5. For the TEGs used in this study, V_L of each TEG is measured with the resistors with, $R_L = R_{TEG}$ as listed in Table 2. By matching the impedance of the electric load, V_L of each TEG is approximately a half of V_{TEG} as expected.

4.2 *Thermal impedance matching*

The control of the heat flow through the heat exchangers and TEG is another critical factor for improving the energy efficiency. Figure 8 shows the thermal impedance model of the pavement energy harvesting system. T_H and T_C are the temperatures at the hot and cold reservoirs, respectively. $\Delta T_{HC} = T_H - T_C$ is the total temperature difference of the system, which will be the temperature difference between the pavement surface and the subgrade (see Fig. 2) in the actual application. The model has two separated resistors representing the heat exchangers and two thermal resistors at the TEG connection. θ_{HE}, θ_{TEG}, and θ_{par} are thermal resistances of the heat exchanger, TEG, and the extra space around the TEG for fastening (parasitic area), respectively. The combined thermal resistance of the TEG contact, θ_{con}, can be calculated from θ_{TEG} and θ_{par} as shown in Figure 8. The resistors placed horizontally in Figure 8 represent the heat loss between the heat exchanger and the environment, which would be asphalt and soil layers in pavements, but the ambient air in our lab. T_{amb} is the ambient temperature.

Stevens [24] suggested a similar model composed of 3 resistors (equivalent to two $\theta_{HE}/2$ and θ_{con} in Fig. 8), and investigated the thermodynamic optimization. Since the heat exchangers and the TEG are connected in series, the heat flow, Q, is constant throughout the system. Eq. (4) shows the relationship between Q and the thermal resistances.

$$Q = \frac{\Delta T_{TEG}}{\theta_{con}} = \frac{\Delta T_{HC}}{\theta_{con} + \theta_{HE}} \tag{4}$$

Considering that the output voltage of a TEG is proportional to ΔT_{TEG} (Eq. (1)), Eq. (4) implies that the ΔT_{TEG} and corresponding output voltage are functions of θ_{HE}, θ_{TEG}, and θ_{par}. Assuming that the energy conversion efficiency is η, the power generated from the TEG can be calculated using Eq. (5), which is modified version of Stevens' equation [24] tailored for the model in Figure 8.

$$P = \Delta T_{HC}{}^2 \frac{\theta_{con}}{\theta_{con} + \theta_{HE}{}^2} \frac{2\eta}{T_H + T_C} \tag{5}$$

For the given ΔT_{HC} and η, two different scenarios are available for the maximum power output: 1) a specific heat exchangers are pre-selected (θ_{HE} is fixed), and selecting a TEG for the maximum power output, and 2) θ_{con} (calculated from θ_{TEG} and θ_{par}) is given, and designing a heat exchanger. For the first scenario, one extreme case is $\theta_{TEG} \approx \theta_{con} \approx 0$, then the heat flows through the TEG easily, and the TEG will not generate power because $\Delta T_{TEG} \approx 0$. Another extreme case is when $\theta_{TEG} >> \theta_{HE}$, then $\Delta T_{TEG} \approx \Delta T_{HC}$, but the heat flow will be very small (Eq. (4)). Therefore, the maximum P can be obtained when $\partial P/\partial \theta_{con} = 0$, i.e. $\theta_{con} = \theta_{HE}$. The second scenario is the case when a specific TEG is pre-selected. In this scenario, Eq. (5) and Eq. (4) suggest that the maximum power can be obtained when $\theta_{HE} \approx 0$ (the heat exchanger allows infinite heat flow) and hence, $\Delta T_{TEG} \approx \Delta T_{HC}$.

The experimental results shown in Table 2 and Figure 9 and 10 are obtained by using the flat aluminium bar ($\theta_{HE} = 18.6$ °K/W) as the heat exchanger (fixed θ_{HE}), and verify the argument on the first scenario. Compared to θ_{HE} (18.6 °K/W), the thermal resistance of type A

Table 2. Effect of TEG types and arrangement.

TEG ID	Surface area of TEG, $A_{TEG}(mm^2)$	Parasitic area, $A_{par}(mm^2)$	TEG thickness, l(mm)	Parasitic thermal resistance, θ_{par}(k/W)	Thermal resistance at TEG contact, θ_{con}(k/W)	Total temperature difference ΔT_{HC} (°k)	Temperature difference at TEG, ΔT_{TEG} (°k)	TEG voltage V_{TEG} (V)	Voltage at the electrical load, V_L (V)	Produced useful power, P_{out} (mW)
A	1600	3562.28	4.1	22.09	2.98	32.4	2.4	0.1530	0.0750	1.576
B	225	1065.32	5.1	102.32	21.67	46.9	16.7	0.2374	0.1050	6.891
C	90	1200.07	4.7	80.51	34.98	38.3	14.2	0.0436	0.0218	1.901
D	32	1258.47	2.44	24.83	20.45	45.1	16.5	0.1230	0.0597	1.485
A	1600	3562.28	4.1	22.09	2.98	32.4	2.4	0.1530	0.0750	1.576
AA*	1600	3562.28	8.2	59.71	6.19	31.7	6.0	0.2380	0.1175	1.934
AAAA*	1600	3562.28	16.4	144.88	12.60	32.0	9.1	0.3090	0.1548	1.678

* Stacking of TEG. For AA, two A type TEG were stacked, and for AAAA, four TEG were stacked in series.

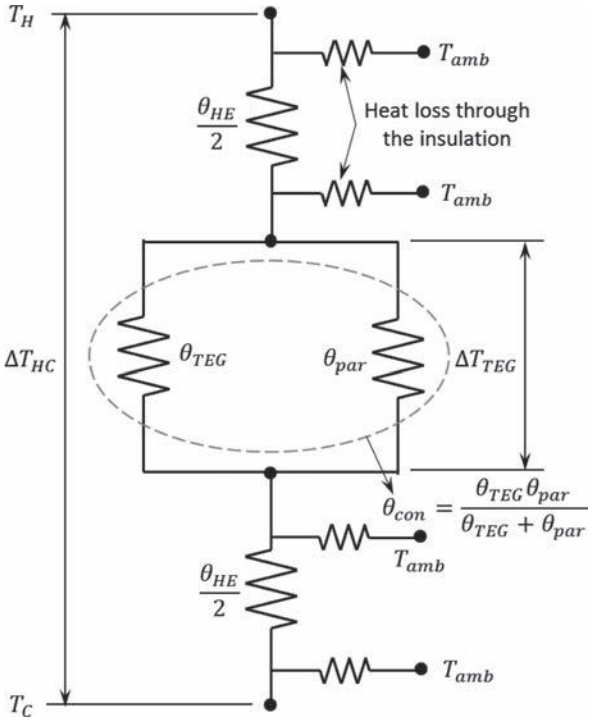

Figure 8. Thermal circuit model of the thermoelectric energy harvesting system.

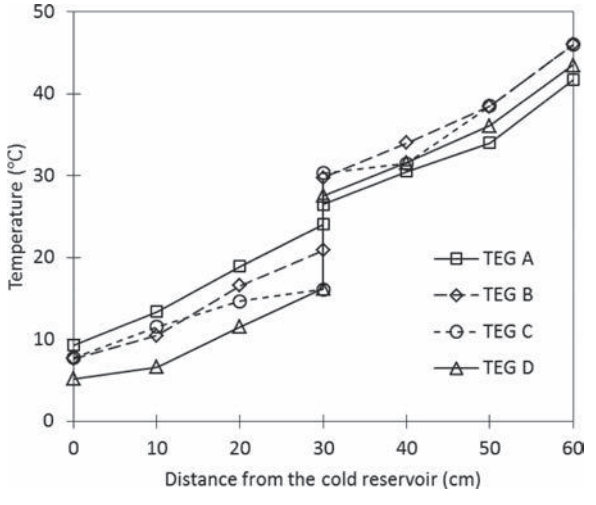

Figure 9. Effect of the TEG types: tested with the flat rod.

TEG is relatively small (θ_{con} = 2.98 °K/W), and the temperature difference used for generating energy, $\Delta T_{TEG} = 2.4 << \Delta T_{HC} = 32.4$ (°K). As a result, although the coefficient α of the type A TEG is larger than other TEGs (Table 1), the generated voltage and power output are smaller than those of type B. θ_{con} of type B, C, and D TEGs are relatively close to θ_{HE}, and resulting in fairly higher ΔT_{TEG}. However, the measured ΔT_{TEG} were smaller than the calculated values from Eq. (4): the measured ΔT_{TEG} are 54–70% of the calculated values. It is inferred that this

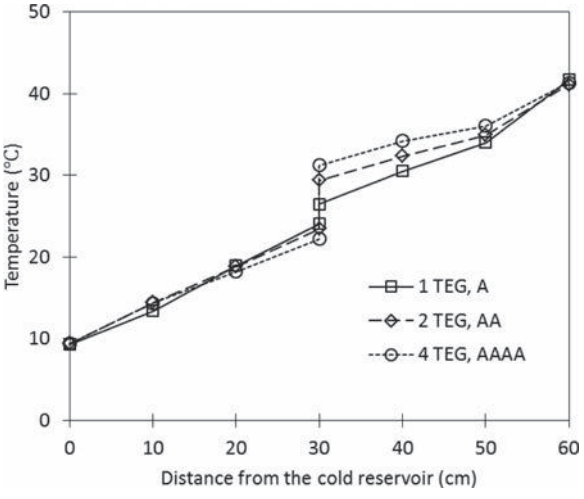

Figure 10. Effect of the TEG stacking: tested with the flat rod and TEG A.

error caused from the heat loss through the insulation between the heat exchanger and the ambient air (T_{amb} in Fig. 8).

The effect of stacking multiple TEGs is investigated by using the type A TEG. It is expected that the stacking TEGs will increase θ_{TEG} and corresponding θ_{con}. Figure 10 compares the temperature gradient along the heat exchangers. As shown in Figure 10 and Table 2, the thermal resistance (θ_{con}) and useful temperature difference (ΔT_{TEG}) proportionally increase by stacking two and four type A TEGs (denoted by AA and AAAA), but the increases in voltage outputs (V_{TEG} and V_L) are smaller than the increase in ΔT_{TEG}. On the other hand, the produced power from the four TEGs is smaller than the two TEGs because of the higher electric resistance. This shows that the stacking of multiple TEGs is not an effective way of improving power generation. From the given condition, $\theta_{HE} = 18.6$ °K/W and $\Delta T_{HC} \approx 50$ °K, the type B TEG generates highest power ($P = 6.9$ mW).

4.3 *Effect of rods and insulation*

The second scenario described in the previous section is investigated by changing the heat exchanger. The type B TEG, which showed the best performance in generating power, was used for examining the effect of θ_{HE}. The dimensions of the flat, rectangular, and rounded heat exchangers are shown in Figure 4, and their θ_{HE} values are 18.6, 9.3, and 4.0 (°K/W), respectively. It is expected that the smaller thermal resistance allows the more heat flow at the heat exchanger, and leads the higher ΔT_{TEG}. Figure 11 compares the temperature gradients along the heat exchangers. As expected, a substantial increase in ΔT_{TEG} is observed at the rounded heat exchanger. The ratio of ΔT_{TEG} to ΔT_{HC} for the rounded bar is 77%, which means that the heat loss of the heat exchanger is 23%. $\Delta T_{TEG} = 36.5$ °K obtained using the rounded heat exchanger and type B TEG under $\Delta T_{HC} = 47.8$ °K is the maximum ΔT_{TEG} among the all tested cases, and the corresponding power output is 42 mW. This is 800 times higher power than the previously reported pavement energy harvesting devices using a TEG.

Another factor that should be included in the thermal flow analysis is the loss of heat between the heat exchanger and environment. The thermal circuit model in Figure 8 shows this factor. But a quantitative analysis is not made in this study because the lab environment (ambient air) is different from pavements. However, the comparative tests with different insulation indicate how significant the insulation is. The temperature gradations with the different number of insulation layers are compared in Figure 12. Compared to the case without the insulation, 1, 2, and 4 insulation layers bring 20, 27, and 31% increase in ΔT_{TEG}, respectively.

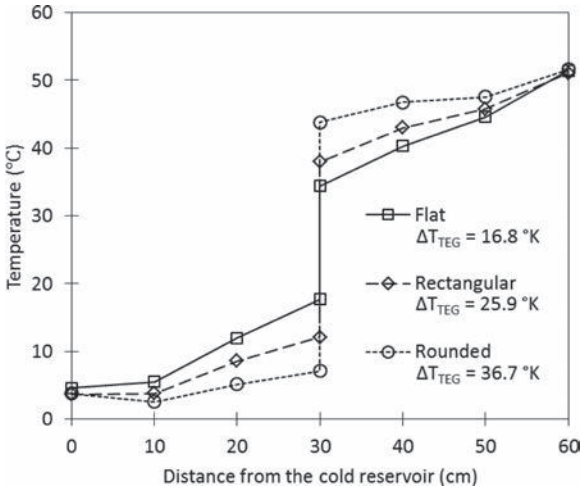

Figure 11. Effect of the heat exchanger: tested with TEG B.

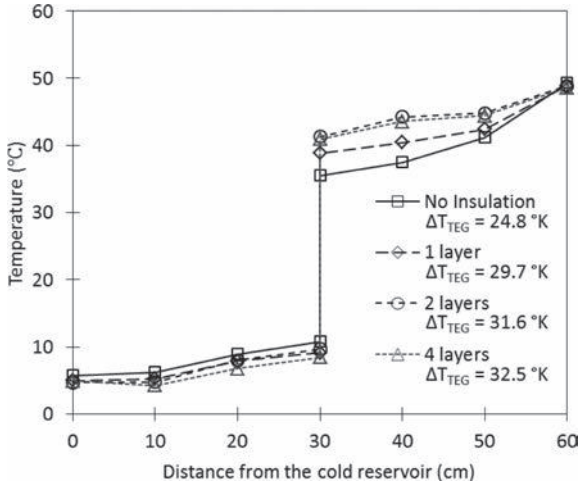

Figure 12. Effect of the insulation: tested with the rounded rod and TEG B.

This shows that the effect of the first insulation layer is remarkable, and the improvements due to the additional layers are less significant.

5 CONCLUSION

With the goal of optimizing the thermoelectric energy harvesting system for the pavement application, various factors affecting the efficiency of the energy harvesting system were investigated. A series of experiments are conducted using a prototype thermoelectric energy harvesting system composed of the heat exchanger and TEG. The results obtained from the theoretical and experimental investigations indicate that the controlling of the heat flow within the system has significant effect on the useful power output. The methods of electrical and thermal impedance matching in selecting an efficient TEG are proposed and experimentally verified. The effects of the thermal impedance and insulation of the heat exchanger are also evaluated. Among the various combinations of the TEGs and the heat exchanger geometries, the best

combination of the device configuration and setup yielded over 40 mW at the load. Design optimization process has produced a system that achieves power output greater than 25 times that of the default design in this study. Given the stated temperature differential, and the device capacities, the power results obtained is about 800 times higher than the power output of the one of the most recently reported study on the pavement energy harvesting using TEG.

REFERENCES

[1] http://www.fhwa.dot.gov/policyinformation/statistics/2012/.

[2] US Energy Information Administration, *Monthly Energy Review*, DOE/EIA-0035 (2013/12), 2013.

[3] Bobes-Jesus, V., Pascual-Muñoz, P., Castro-Fresno, D., and Rodriguez-Hernandez, J. Asphalt solar collectors: A literature review, *Applied Energy*, 102, pp. 962–970, 2013.

[4] Mallick, R.B., Chen, B.L., and Bhowmick, S. Harvesting energy from asphalt pavements and reducing the heat island effect, *International Journal of Sustainable Engineering*, 2(3), pp. 214–228, 2009.

[5] Mallick, R.B., Chen, B.L., and Bhowmick, S. Harvesting heat energy from asphalt pavements-development of and comparison between numerical models and experiment, *International Journal of Sustainable Engineering*, 5(2), 159–169, 2012.

[6] Lee, K.W., and Correia, A.J. *A Pilot Study for Investigation of Novel Methods to Harvest Solar Energy from Asphalt Pavements*, A Final Report for Korea Institute of Construction Technology, Goyang-Si, Gyeonggi-Do, South Korea, 2010.

[7] Lee, K.W., Correia, A.J., Neilian, B.D.J., and Dahn, B. Comparative study of solar panels for roadway operations, *Advanced Materials Research*, 723, pp. 594–600, 2013.

[8] Lee, K.W., Correia, A.J., Lee, K.H., Neilan, B.D.J., and Gregor, S. Solar Energy Harvesting from Roadways, *Proceedings of TRB 2014 Annual Meeting*, Washington D.C., USA, 2014.

[9] Abramovich, H., Harash, E., Milgrom, C., and Amit, U. *Energy Harvesting from Airport Runway*, Patent No. US 2009/0195124A1, 2009.

[10] Abramovich, H., Milgrom, C., Harash, E., Azulay, L.E., and Amit, U. *Multi-Layer Modular Energy Harvesting Apparatus*, System, and Method, Patent No. US 2010/0045111A1, 2010.

[11] Abramovich, H., Harash, E., Milgrom, C., Amit, U., and Azulay, L.E. *Power Harvesting Apparatus System and Method*, Patent No. US 7,830,071 B2, 2010.

[12] Ashebo, D.B., Tan, C.A., Wang, J., and Li, G. Feasibility of energy harvesting for powering wireless sensors in transportation infrastructure applications, *Proceedings of SPIE*, 6934, 2008.

[13] Xiong, H., Wang, L., Wang, D., Druta, C., and Guo, D. Piezoelectric energy harvesting from traffic induced deformation of pavements, *Int. J. Pavement Res. Technol.*, 5(5), pp. 333–337, 2012.

[14] Sun, C., Shang, G., Zhang, Y., and Du, J. Designing Piezoelectric Harvesting Unit from Road Vibration, *Advanced Materials Research*, 712–712, pp. 1368–1371, 2013.

[15] Xiang, H.J., Wang, J.J., Shi, Z.F., and Zhang, Z.W. Theoretical analysis of piezoelectric energy harvesting from traffic induced deformation of pavements, *Smart Materials and Structures*, 22(9), 095024, 2013.

[16] Xiong, H., Wang, L., Wang, D., Druta, C., Guo, D., and Sun, Z. Piezoelectric energy harvesting from traffic induced deformation of pavements, *Proceedings of TRB 2013 Annual Meeting*, Washington D.C., USA, 2013.

[17] Duarte, F., Casimiro, F., Correia, D., Mendes, R., and Ferreira, A. A New Pavement Energy Harvest System, *Renewable and Sustainable Energy Conference (IRSEC), 2013 International*, pp. 408–413, 2013.

[18] Batra, A., Bhattacharjee, S., Chilvery, A., Aggrawal, M., Edwards, M., and Bhalla, A. Simulation of energy harvesting from roads vis pyroelectricity." *Journal of Photonics for Energy*, 1, pp. 014001-1-12, 2011.

[19] Bhattacharjee, S., Batra, A., Meseret, S., and Cain, J. High performance single and polycrystal-based pyroelectric smart materials for energy harvesting from pavements, *Transportation Research Record*, 2252, pp. 75–82, 2011.

[20] Wu, G., and Yu, X. Computer-Aided Design of Thermal Energy Harvesting across Pavement Structure, *International Journal of Pavement Research and Technology*, 6(2), pp. 73–79, 2013.

[21] Wu, G., and Yu, X. Thermoelectric Energy Harvesting System Design across Pavement Structure, *Proceedings of TRB 2013 Annual Meeting*, Washington D.C., USA, 2013.

[22] Priya, S., and Inman, D.J. *Energy Harvesting Technologies*, Springer, New York, USA, 2009.

[23] http://www.infopave.com/.

[24] Stevens, J.M. Optimal design of small ΔT thermoelectric generation systems, *Energy Conversion and Management*, 42, pp. 709–720, 2001.

Performance-related specifications

This page intentionally left blank

Asphalt Pavements – Kim (Ed)
© 2014 Taylor & Francis Group, London, ISBN 978-1-138-02693-3

Investigation of limiting criteria for asphalt mixture low temperature cracking

Augusto Cannone Falchetto
Technical University of Braunschweig, Braunschweig, Germany

Ki Hoon Moon
Samsung C&T, Seoul, South Korea

Mihai Marasteanu
University of Minnesota, Minneapolis, MN, USA

ABSTRACT: This paper proposes a new low temperature limit criteria for asphalt mixtures, similar to what is currently available in the standard specification for asphalt binder. The investigation is based on extensive experimental work that includes Bending Beam Rheometer (BBR) creep tests on asphalt binders and asphalt mixtures at low temperature, on the rheological Christensen, Anderson and Marasteanu (CAM) model and on the semi-empirical Hirsch model. Limiting asphalt mixture creep stiffness values are predicted from creep stiffness data obtained on long term aged binder, and then compared with results available in literature. The BBR creep results determined on short term aged asphalt binder are then used to predict creep stiffness of the corresponding short term aged asphalt mixtures. Based on these results, a range of limiting stiffness values is obtained. A limiting value for the relaxation parameter *m*-value could not be recommended due to large variations in the calculated slopes of the mixture creep stiffness curves.

Keywords: Creep stiffness, CAM model, Hirsch model, low temperature cracking, limiting criteria

1 INTRODUCTION

One of the most significant achievements in the area of asphalt paving materials characterization was the development of the Strategic Highway Research Program (SHRP) Performance Grade (PG) specifications [1] at the beginning of the 1990's. The PG tests and analyses, detailed in a number of AASHTO specifications [2–4], are used to specify the asphalt binders used in pavement applications and also serve as the primary tool to investigate the behavior of asphalt binders in many research studies. The success of the PG system can be attributed on one hand to the innovative application of fundamental concepts to asphalt binder material characterization and on the other hand to the reasonable level of complexity of the tests and analyses required as part of these specifications. However, this level of complexity is the result of a number of simplifying assumptions that, in the past years, have been investigated by a number of researchers who proposed additional tests and analyses to improve the material selection process for the specific use.

The development of the asphalt binder criterion for low temperature cracking was based on previous work performed by Readshaw [5] who analyzed the low temperature cracking resistance of pavements in British Columbia. By using binder penetration index, the corrected Ring & Ball softening point, and assuming a loading time of 2 hours in the Van der Poel's nomograph, he concluded, that cracking could be minimized by using an asphalt binder that

does not exceed 2×10^8 N/m^2 (200 MPa) stiffness values at the lowest temperature experienced. The SHRP research team based on additional information changed the value to 300 MPa, and used the time-temperature superposition principle to reduce testing time by demonstrating that, in general, the binder stiffness at 60 seconds at T_1°C is approximately equal to the stiffness at 2 hours at T_1–10°C [1]. In addition, the slope at 60 seconds of the stiffness vs. time curve on a double logarithmic scale, the *m*-value, was introduced as an additional parameter to control the rheological type of asphalt binders and to eliminate heavily blown asphalts, which in fact were associated with poor fatigue performance. This criterion was based on the idea that a low *m*-value corresponded to slower relaxation of the thermal stresses that build up at low temperatures, which is very detrimental for material performance.

It is important to note that in the pioneering research performed in Canada in the 1960's there is very limited information about mixture low temperature properties. The only reference is found in the paper by Burgess et al. [6] and the discussion provided by N. W. McLeod. Based on McLeod's analysis of data from St. Anne Test Road and other pavements in Canada, he concluded that the critical low temperature pavement modulus of stiffness at which transverse pavement cracking is likely to occur is 1,000,000 psi or 7 GPa, a value twice as high as that previously proposed. These values were obtained for a paving mixture compacted to 3% air voids, Voids in the Mineral Aggregate (VMA) of 14.5%, and a loading time of 20,000 s (5.5 hours).

2 PROBLEM STATEMENT

In the past years, a number of models were developed that allow predicting asphalt mixture properties from binder properties and volumetric information [7–9]. One interesting application is to determine the mixture creep stiffness that corresponds to a binder creep stiffness value of 300 MPa, which is the current PG specification limit. This can provide insight into the possibility of developing a similar criterion for asphalt mixture creep stiffness that can be used, for example, in quality control testing.

3 RESEARCH APPROACH

The main challenge in performing such an investigation is to reasonably match the aging condition of the binder and of the mixture. Since it is generally accepted that binder after Rolling Thin-Film Oven Test (RTFOT) [10] matches the aging condition of the mixture after short term aging or as loose mix, the analysis performed in this paper is based on RTFOT binder data and short term aged mixture data. Calculations were also performed using Pressure Aging Vessel (PAV) [11] binder data to compare the predicted mixture stiffness to the values proposed by McLeod (equal to 7GPa) [6]. The research approach, therefore, consists of the following steps:

1. Bending Beam Rheometer (BBR) binder creep tests [3] are performed on a set of binders for both RTFOT and PAV aging conditions.
2. BBR mixture creep tests are performed on short term aged mixtures prepared with the set of binders in step 1 using the procedure described elsewhere [12].
3. Binder creep stiffness and *m*-value at 60 seconds, at the critical temperatures are calculated from the PAV binder creep testing.
4. Hirsch model [7] is used with the PAV binder data to predict long term aged mixture creep stiffness and compare it to the value proposed by McLeod (= 7GPa) [6].
5. Creep stiffness and *m*-value at 60 seconds, at the critical temperatures (obtained in step 3 for PAV binders), are calculated for the binders in RTFOT condition.
6. Hirsch model is used with the RTFOT binder data from step 5 to predict short term aged mixture creep stiffness and *m*-value at the critical temperatures obtained in step 3.
7. The mixture values predicted in step 6 are compared to the experimental mixture data obtained from BBR mixture testing [12].

4 MATERIALS AND TESTING

In this study, eight different asphalt binders and sixteen corresponding asphalt mixtures were prepared with two different types of aggregate: granite and limestone. Detailed information on the materials used in this study can be found elsewhere [12,13]. Table 1 describes the asphalt binders and corresponding mixtures used in this study.

All asphalt binders were short and long term aged according to RTFOT [10] and PAV [11] procedures and BBR creep tests [3] were performed for both aging conditions at three different temperatures: PG + 10ºC, (PG + 10) – 6ºC and (PG + 10) – 12ºC. All mixtures were short term aged by conditioning the gyratory compacted samples for 2 hours at 135ºC. Then BBR creep stiffness tests for asphalt mixture [12] were performed at three different temperatures, PG + 10ºC, (PG + 10) + 12ºC and (PG + 10) – 12ºC. Two and ten replicates were used per each testing condition for asphalt binder and asphalt mixture respectively.

For BBR binder testing, the standard constant load of 100 g (= 980 ± 50 mN) was applied to the asphalt binder beams (102.0~125.0 mm × 12.7 ± 0.5 mm × 6.25 ± 0.5 mm) and maintained for 240 s. In case of asphalt mixture, BBR creep tests were performed with the same BBR device used for asphalt binder testing. Mixture specimens consisted of thin asphalt mixture beams (102.0~125.0 mm × 12.7 ± 0.5 mm × 6.25 ± 0.5 mm); due to the higher material stiffness, a higher constant load of 4,000 mN, was applied to the specimen, and extended test duration of 1000s, were used [12]. In both test methods, BBR binder and BBR mixture creep tests, mid span deflection, $\delta(t)$, was recorded for the entire duration of the test to compute creep stiffness, $S(t)$, and m-value, $m(t)$. Figure 1 presents the testing setup.

The creep stiffness of asphalt binder and asphalt mixture was calculated as:

$$S(t) = \frac{\sigma}{\varepsilon(t)} = \frac{P \cdot l^3}{4 \cdot b \cdot h^3 \cdot \delta(t)} \tag{1}$$

Table 1. Tested binders and corresponding mixtures.

	Binder		Mixture	
ID	Details	Code	Granite (GR)	Limestone (LM)
B	PG58-34, modifier 1, Elvaloy	58-34 M1	58-34 M1:GR	58-34 M1:LM
C	PG58-34, modifier 2, SBS	58-34 M2	58-34 M2:GR	58-34 M2:LM
D	PG58-28, plain 1	58-28 U1	58-28 U1:GR	58-28 U1:LM
E	PG58-28, plain 2	58-28 U2	58-28 U2:GR	58-28 U2:LM
F	PG64-34, modifier 1, Elvaloy	64-34 M1	64-34 M1:GR	64-34 M1:LM
G	PG64-34, modifier 2, Black Max	64-34 M2	64-34 M2:GR	64-34 M2:LM
H	PG64-28, plain 1	64-28 U1	64-28 U1:GR	64-28 U1:LM
I	PG64-28, modifier 1, Elvaloy	64-28 M1	64-28 M1:GR	64-28 M1:LM

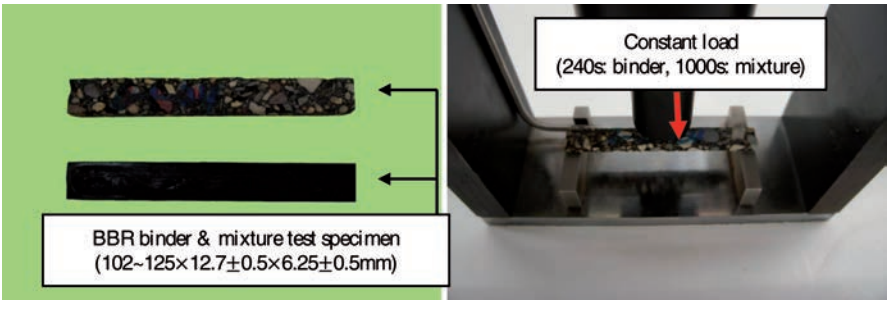

Figure 1. BBR binder and mixture creep testing set up.

where $S(t)$ is the time dependent flexural creep stiffness (MPa), σ is maximum bending stress in the beam (MPa), $\varepsilon(t)$ is the time dependent bending strain in the beam (mm/mm), P is the constant load used (mN), l is length of specimen, (102.0~125.0 ± 1 mm), b is the width of specimen, (12.7 ± 0.5 mm), h is the height of specimen (6.25 ± 0.5 mm), $\delta(t)$ is deflection at the mid span of the beam (mm) and t is the time (s).

The m-value, which is the slope of log stiffness versus log time curve, is computed according to:

$$m(t) = \left| d\log S(t) / d\log t \right| \tag{2}$$

The m-value can be also calculated by fitting a second order polynomial expression to the $\log S(t)$ versus $\log(t)$ curve as: $\log S(t) = a \cdot \log^2(t) + b \cdot \log(t) + c$; m-value can then be obtained as the derivative: $m(t) = |2a\ \mathrm{a} \cdot \log(t) + b|$. According to AASHTO specifications [3,4], critical cracking temperature of asphalt binder is obtained as the lowest temperature at which the following two conditions are met for long term aged binder [11]: $S(t_{60\ \mathrm{sec}}) \leq 300$ MPa and $m(t_{60\ \mathrm{sec}}) \geq 0.300$.

5 MODELING

In this study, the semi-empirical Hirsch model [7] was used to predict asphalt mixture creep stiffness, $S(t)_{\mathrm{mix}}$, from asphalt binder creep stiffness, $S(t)_{\mathrm{binder}}$, data at the critical cracking temperature, T_{CR}. In Hirsch model, the effective modulus is generated by combining aggregate, asphalt binder and air void phases in parallel and series. Figure 2 shows the schematic of Hirsch model.

The Hirsch model formulation for creep stiffness can be expressed as:

$$S_{mixture} = P_c \cdot \left[E_{agg} V_{agg} + S_{binder} V_{binder} \right] + \left(1 - P_c\right) \cdot \left[\frac{V_{agg}}{E_{agg}} + \frac{\left(1 - V_{agg}\right)^2}{S_{binder} V_{binder}} \right]^{-1} \tag{3}$$

where $S_{mixture}$ is the creep stiffness of the mixture (GPa), E_{agg}, V_{agg} are modulus (GPa) and volume fraction (%) of the aggregate, S_{binder}, V_{binder} are stiffness (GPa) and volume fraction (%) of the asphalt binder. P_c is the contact volume (empirical factor) defined as:

$$P_c = \left[\left(P_0 + \frac{VFA \cdot S_{binder}}{VMA} \right)^{P_1} \right] \Big/ \left[P_2 + \left(\frac{VFA \cdot S_{binder}}{VMA} \right)^{P_1} \right] \tag{4}$$

where VFA are the voids filled with asphalt binder (%), VMA are the voids in the mineral aggregates (%) and P_0, P_1, P_2 are fitting parameters.

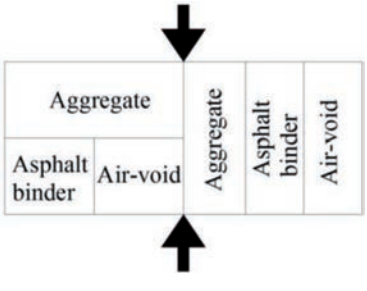

Figure 2. Hirsch model [7].

Zofka et al. [14] investigated the effectiveness of the Hirsch model [7] to predict the BBR mixture stiffness from the properties of the binder and proposed a simplified expression for P_c:

$$P_c = 0.1 \cdot \ln\left(E_{binder} / a\right) + 0.609 \tag{5}$$

where E_{binder} is the relaxation modulus of binder (GPa) and a is a constant equal to 1 GPa.

Input to Equations 3 and 5, which were used to predict mixture creep stiffness from binder creep stiffness, came from laboratory measurements [9], [13]. For granite mixtures E_{agg}, VMA and VFA were set as 4,200,000 psi (= 30 GPa), 16.3% and 75.9%, and for limestone mixture E_{agg}, VMA and VFA were set as 3,600,000 psi (= 25 GPa), 16.2% and 75.0%, respectively. In order to obtain creep stiffness data at 20,000 s and to compare the predicted asphalt mixture creep stiffness to the experimental mixture creep stiffness, stiffness master curves were generated using a form of CAM model [15] expressed in terms of stiffness:

$$S(t) = S_g \cdot \left[1 + \left(t_c / t\right)^v\right]^{-w/v} \tag{6}$$

where S_g is the glassy creep stiffness asymptote (3 GPa for binder and 30 GPa for mixture), t_c is the crossover time (s) and, v and w are fitting parameters. The shift factor, a_T, was expressed as $a_T = 10^{C_1 + C_2 \cdot T}$ where C_1 and C_2 are fitting parameters and T is the reference temperature (ºC).

6 LONG TERM AGED MIXTURE STIFFNESS FROM PAV BINDER STIFFNESS

The first step in the analysis consisted in using the binder PAV data and predicting the corresponding mixture creep stiffness using Hirsch model [7] previously described. The results of predicted mixture S(60 s) are shown in Table 2.

Then, the prediction of asphalt mixture creep stiffness at 20,000 s, $S(20{,}000\text{ s})_{mixture}$, obtained with the Hirsch model and the stiffness value of PAV asphalt binder at 20,000 s, $S(20{,}000\text{ s})_{binder}$, at critical temperature, T_{CR}, were compared to the 7GPa limit proposed by McLeod [6]. To obtain the creep stiffness values at 20,000 s, CAM model [15] was used. First, based on PAV binder creep stiffness, master curve was generated. Then, based on the calculated critical temperature, T_{CR}, (Table 3), the value of shift factor, a_T, at T_{CR} was obtained. Hence, by setting t = 20,000 s in Equation (6), $S(20{,}000\text{ s})_{binder}$ of PAV aged binder at T_{CR} was determined. Finally, the S(20,000 s) for long term aged mixture was calculated from binder

Table 2. Mixture creep stiffness for PAV asphalt binder at S(60 s) and S(20,000 s).

			S(60 s), [MPa]			S(20,000 s), [MPa]		
ID	Binder code	T_{CR} (ºC)	Binder (PAV)	Mixture (granite)	Mixture (limestone)	Binder (PAV)	Mixture (granite)	Mixture (limestone)
B	58-34 M1	–24.4	300	12,271	10,624	43	6517	5613
C	58-34 M2	–26.4				46	6682	5755
D	58-28 U1	–22.7				46	6681	5754
E	58-28 U2	–20.6				41	6363	5480
F	64-34 M1	–25.6				41	6411	5521
G	64-34 M2	–27.0				47	6752	5816
H	64-28 U1	–20.0				47	6755	5819
I	64-28 M1	–23.7				55	7216	6217
Average						46	6,672	5,747
CoV						9.9%	4.0%	4.0%

*CoV: Coefficient of Variation = Standard deviation/average.

Table 3. Binder PAV TCR and corresponding RTFOT binder S(60 s).

ID	Binder ID	PAV binder		RTFOT binder			
		T_{CR} [°C]	R^2 [%]	S(60 s) at T_{CR} [MPa]	R^2 [%]	S(60 s)$_{CAM}$ [MPa]	Diff. [%]
B	PG 58-34 M1	–24.4	99.84	211.0	98.33	210.0	0.5
C	PG 58-34 M2	–26.4	99.47	255.0	99.29	263.5	3.2
D	PG 58-28 U1	–22.7	99.57	206.0	98.22	199.6	3.2
E	PG 58-28 U2	–20.6	99.72	183.0	99.97	184.9	1.0
F	PG 64-34 M1	–25.6	98.71	229.0	99.98	233.3	1.8
G	PG 64-34 M2	–27.0	99.24	238.0	98.37	248.8	4.3
H	PG 64-28 U1	–20.0	99.98	259.0	99.97	262.3	1.3
I	PG 64-28 M1	–23.7	99.99	259.0	99.96	261.9	1.1

(*Diff. = differences).

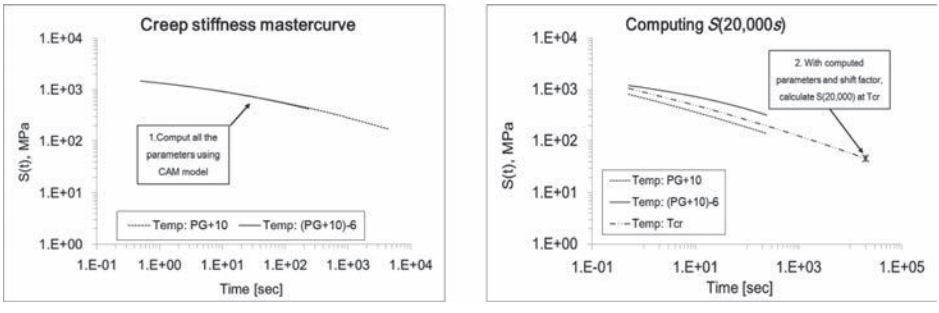

Figure 3. Computation process of PAV binder S(20,000 s) using CAM model.

S(20,000 s) using Hirsch model and finally compared to 7GPa limit [6]. The schematic computation process is shown in Figure 3 while the results of $S(20{,}000\text{ s})_{\text{binder}}$ and $S(20{,}000\text{ s})_{\text{mixture}}$ are presented on the right two columns in Table 2. Note that since master curves were generated for this purpose, the values are slightly different for the eight mixtures.

From the results in Table 2, slightly different T_{CR} values were observed for binder having same PG; this is most likely due to the different types of the modifiers. Using Hirsh model, the mixture creep stiffness, $S(60\text{ s})_{\text{mixture}}$, corresponding to the PAV binder low temperature limit criteria of 300 MPa was calculated: a value of 12.2 GPa and 10.6 GPa were obtained for granite and limestone mixtures, respectively. For asphalt binder an average value of $S(20{,}000\text{ s})_{\text{binder}}$ equal to 46 MPa was determined with a small coefficient of variation, CoV = 9.9%. Finally, $S(20{,}000\text{ s})_{\text{mixture}}$ was calculated from the corresponding $S(20{,}000\text{ s})_{\text{binder}}$. The average values of $S(20{,}000\text{ s})_{\text{mixture}}$ were 6.7 GPa and 5.7 GPa for granite and limestone mixtures, respectively (CoV = 4%). This indicates that the average limiting stiffness values for the two types of mixtures were relatively close to the 7 GPa limit proposed by McLeod [6].

7 SHORT TERM AGED MIXTURE STIFFNESS FROM PAV AND RTFOT BINDER STIFFNESS

In order to determine the creep stiffness of short term aged asphalt mixture, the creep stiffness of the RTFOT asphalt binder at the PAV binder critical temperature, T_{CR}, has to be first determined. Assuming a linear relation between log$S$(60 s) and the test temperature for both PAV and RTFOT creep stiffness data, a corresponding RTFOT binder stiffness value at T_{CR} is easily obtained, as shown in Figure 4.

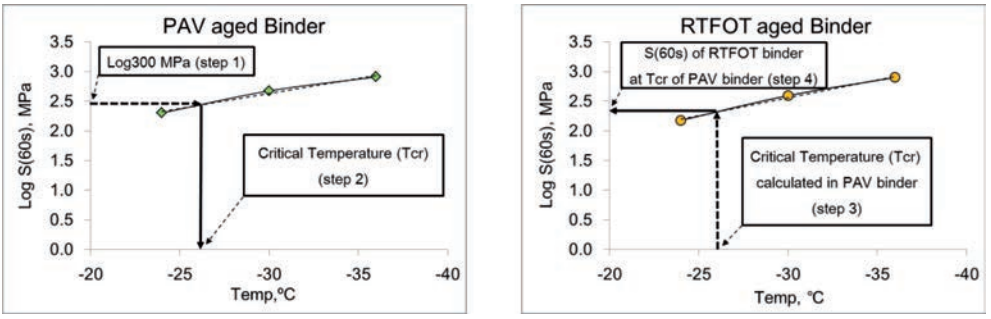

Figure 4. Predicting RTFOT binder S(60 s) at PAV binder critical temperature, T_{CR}.

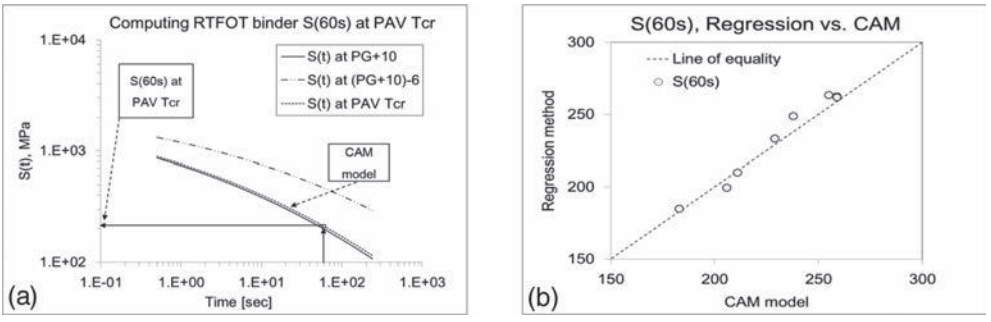

Figure 5. (a) Computing process of RTFOT Binder S(60 s) using CAM Model and (b) Comparison of RTFOT binder S(60 s) at T_{CR} of PAV binder based on regression and CAM model extrapolation.

The schematic computation process of RTFOT binder S(60 s) at the PAV binder critical temperature, T_{CR}, can be explained as follow:

1. Critical temperature, T_{CR}, is determined from the experimental results of PAV binder Log S(60 s) using current low temperature limit specification of asphalt binder (steps 1–2 in Fig. 4).
2. Based on T_{CR} the value of RTFOT binder S(60 s) is easily obtained (step 3–4 in Fig. 4).

Even though high values of coefficient of determination, R^2, were observed for most binders ($R^2 > 0.95$), CAM model [15] was also used to validate the results since small deviations from the linear relation were observed for some binders. A computation procedure similar to section 6 was used for obtaining RTFOT S(60 s) values at the PAV binder T_{CR}. First, based on RTFOT binder creep stiffness experimental results, master curve was generated and the shift factor, a_T, at T_{CR} determined. Then, the RTFOT binder S(60 s) at PAV binder T_{CR} was calculated using CAM model and compared to the results of RTFOT S(60 s) obtained using the simple regression method shown in Figure 4. The schematic procedure for obtaining RTFOT binder S(60 s) at PAV binder T_{CR} using CAM model [15] is shown in Figure 5a while the graphical comparison between regression and CAM model extrapolation of RTFOT S(60 s) $_{\text{binder}}$ are presented in Figure 5b (correlation coefficient, $\rho = 0.989$). The computed results including the values of the coefficient of determination, R^2, are presented in Table 3.

Then simple regression RTFOT binder stiffness values, S(60 s), were used in Hirsch [7] model to predict the mixture creep stiffens S(60 s) at the critical temperature, T_{CR}, obtained from the PAV binder creep stiffness experimental data. The results are shown in Table 4 and Figures 6. In addition, BBR mixture creep data were used with CAM model to obtain mixture S(60 s) at the same critical temperature, T_{CR}. The same calculation process previously

Table 4. Short term aged mixture S(60 s) at PAV binder critical temperature, T_{CR}.

Granite mixtures	S(60 s) at T_{CR}, [MPa] Binder (Hirsch)	Mixture (CAM)	Diff. %	Limestone mixtures	S(60 s) at T_{CR}, [MPa] Binder (Hirsch)	Mixture (CAM)	Diff. %
B: G	11150	11850	5.9	B: L	9640	9340	3.2
C: G	11860	13430	11.7	C: L	10260	11280	9.0
D: G	10990	11790	6.8	D: L	9500	11650	18.5
E: G	10760	12190	11.7	E: L	9300	11230	17.2
F: G	11470	10960	4.7	F: L	9920	10560	6.1
G: G	11680	11910	1.9	G: L	10100	10800	6.5
H: G	11840	13980	15.3	H: L	10250	12530	18.2
I: G	11840	12720	6.9	I: L	10240	11640	12.0
Average	11,449	12,354	7.3	Average	9,901	11,129	11.8
C.V., %	3.8%	7.9%		C.V.,%	3.8%	8.4%	

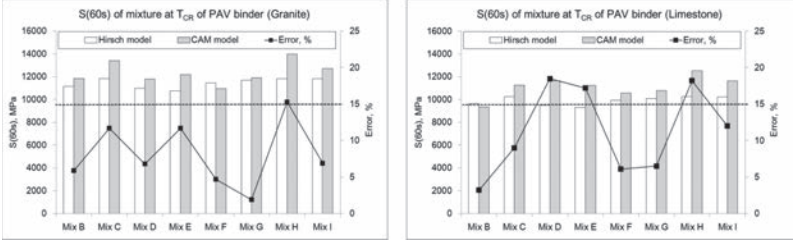

Figure 6. Short term aged mixture S(60 s) at PAV binder critical temperature.

used for RTFOT binder S(60 s) at PAV binder T_{CR} based on the CAM model [15] was followed. These results are also included in Table 4 and Figure 6 to compare the S(60 s) values predicted through Hirsch model with the experimentally obtained S(60 s).

No significant differences were observed, except for three limestone mixtures: D, E and H, with differences little above 15%. The average values of S(60 s) from Hirsch model prediction were 11.4GPa and 9.9GPa for granite and limestone mixtures, respectively, with small variations (C.V. = 3.8% for two mixture groups). Limited differences of S(60 s) were observed between the average Hirsch model prediction and the average extrapolations obtained by the CAM model. This suggests that the creep stiffness of mixtures has similar values, both when predicted from the binder data using Hirsh model and when obtained by the CAM model on mixture experimental measurements. The results indicate that for short term aged asphalt mixtures, the 300 MPa limit imposed on PAV binders result in limiting value S(60 s) for mixture in the range of 9 to 12GPa.

8 SHORT TERM AGED MIXTURE M(60 S) AT PAV BINDER T_{CR} FOR M(60 S) = 0.300

The m(60 s) of short term aged asphalt mixture at the corresponding T_{CR} for PAV binder were also calculated using Hirsch and CAM model, similarly to the creep stiffness calculations. The results are shown in Table 5 and Figure 7.

Based on the results in Table 5 and Figure 7, large differences were observed between the values of m(60 s) predicted with Hirsch model and those extrapolated through CAM model. This is most likely due to fitting difficulties experienced when the log stiffness slopes are close to zero and therefore, it makes the use of mixture m-value as a limiting parameter questionable.

Table 5. Mixture m(60 s) values at PAV binder T_{CR}.

Granite mixtures	m(60 s) at T_{CR} Binder (Hirsch)	Mixture (CAM)	Diff. %	Limestone mixtures	m(60 s) at T_{CR} Binder (Hirsch)	Mixture (CAM)	Diff. %
B: G	0.117	0.141	17.0	B: L	0.118	0.154	23.4
C: G	0.096	0.137	29.9	C: L	0.098	0.143	31.5
D: G	0.098	0.134	26.9	D: L	0.099	0.139	28.8
E: G	0.106	0.157	32.5	E: L	0.107	0.175	38.9
F: G	0.111	0.158	29.7	F: L	0.112	0.147	23.8
G: G	0.100	0.165	39.4	G: L	0.102	0.148	31.1
H: G	0.086	0.143	39.9	H: L	0.087	0.135	35.6
I: G	0.086	0.143	39.9	I: L	0.087	0.132	34.1
Average	0.100	0.147	31.9	Average	0.101	0.147	31.2
C.V., %	11.1%	7.6%		C.V.,%	10.9%	9.2%	

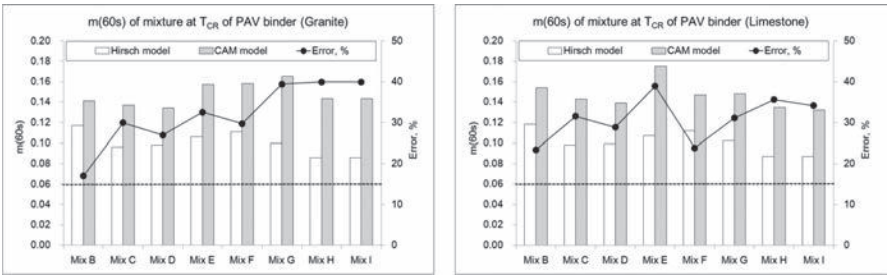

Figure 7. Short term aged mixture m(60 s) at PAV binder critical temperature.

9 SUMMARY AND CONCLUSIONS

The possibility of developing low temperature limit criteria for asphalt mixture, analogous to that used for asphalt binder, was investigated in this paper. Experimental data were obtained from BBR creep tests on eight asphalt binders and sixteen short term aged asphalt mixtures prepared with two different types of aggregate. The critical temperature of PAV aged binder was calculated and the limiting stiffness value for PAV binder data was used to predict long term aged mixture stiffness using Hirsch model. Then, the creep stiffness of PAV and RTFOT binders was used in combination with Hirsch model to predict the corresponding creep stiffness and m-value limits for short term aged asphalt mixtures at the binder critical temperature. It was then shown that similar results were obtained from mixture BBR creep stiffness experimental data.

Based on the analysis performed, three main conclusions can be drawn:

1. The predicted creep stiffness of long term aged asphalt mixtures at 20,000 s is in the range of 5.7 ~ 6.7 GPa. These values are in reasonable agreement with the 7.0 GPa limit previously proposed by McLeod.
2. The limiting creep stiffness, S(60 s), for short term aged mixtures, predicted from RTFOT binders creep stiffness data is comparable to that obtained through extrapolation from experimental BBR mixture creep stiffness. The values range between 9 GPa and 12 GPa for all mixtures investigated. These results support the idea of using BBR creep mixture testing as a routine test to discriminate mixtures that are too stiff and more prone to cracking. More research is needed to further validate and refine these findings.
3. Due to large variations in the mixture m(60 s) values, a limiting value for this relaxation parameter cannot be proposed at this time.

ACKNOWLEDGMENTS

This research was sponsored by Federal Highway Administration National Pooled Fund Study TPF 5(132). This support is gratefully acknowledged. The results and opinions presented are those of the authors and do not necessarily reflect those of the sponsoring agencies.

REFERENCES

[1] Anderson D.A. and Kennedy, T., Development of SHRP Binder Specification, Journal the Association of Asphalt Paving Technologists (AAPT), 62, pp. 481–507, 1993.
[2] AASHTO T313-12-UL, Standard Method of Test for Determining the Rheological Properties of Asphalt Binder Using a Dynamic Shear Rheometer (DSR) (DSR), 2012.
[3] AASHTO T313-12-UL, Standard Method of Test for Determining the Flexural Creep Stiffness of Asphalt Binder Using the Bending Beam Rheometer (BBR), 2012.
[4] AASHTO M320-10-UL, Standard Specification for Performance-Graded Asphalt Binder, 2010.
[5] Readshaw, E.E., Asphalt Specifications in British Columbia for Low Temperature Performance, Journal the Association of Asphalt Paving Technologists (AAPT), 41, pp. 562–581, 1972.
[6] Burgess R.A., O. Kopvillem, and F.D. Young., Ste. Anne Test Road—Relationship between Predicted Fracture Temperatures and Low Temperature Field Performance, Journal the Association of Asphalt Paving Technologists (AAPT), 40, pp. 148–193, 1971.
[7] Christensen D., Pellinen T., Bonaquist R.F., Hirsch Model for Estimating the Modulus of Asphalt Concrete, Journal the Association of Asphalt Paving Technologists (AAPT), 72, pp. 97–121, 2003.
[8] Di Benedetto H., Olard F., Sauzéat C. and Delaporte B., Linear Viscoelastic Behavior of Bituminous Materials: from Binders to Mixtures, Road Material and Pavement Design (RMPD), 5, Supplement 1, pp. 163–202, 2004.
[9] Cannone Falchetto A., Marasteanu M.O., and Di Benedetto H., Analogical Based Approach to Forward and Inverse Problems for Asphalt Materials Characterization at Low Temperatures, Journal the Association of Asphalt Paving Technologists (AAPT), 80, pp. 549–581, 2011.
[10] AASHTO T240–13-UL, Standard Method of Test for Effect of Heat and Air on a Moving Film of Asphalt Binder (Rolling Thin-Film Oven Test), 2013.
[11] AASHTO R028–12-UL, Standard Practice for Accelerated Aging of Asphalt Binder Using a Pressurized Aging Vessel (PAV), 2012.
[12] Marasteanu M., Velasquez R., Cannone Falchetto A., Zofka A., Development of a Simple Test to Determine the Low Temperature Creep Compliance of Asphalt Mixture, IDEA Program Final Report NCHRP 133, Transportation Research Board of the National Academies, 2009.
[13] Marasteanu O.M. Zofka A., Turos M., Li X., Velasquez R. and Li X., National Pooled Fund Study 776: Investigations of Low-Temperature Cracking in Asphalt Pavements, Research report 2007–43, Minnesota Department of Transportation (MN/DOT), Saint Paul, 2007.
[14] Zofka A. Marasteanu M., Li X., Clyne T. and McGraw J., Simple Method to Obtain Asphalt Binders Low Temperature Properties from Asphalt Mixtures Properties, Journal of the Association of Asphalt Paving Technologists (AAPT), 74, pp.255–282, 2007.
[15] Marasteanu M., and Anderson D.A., Improved Model for Bitumen Rheological Characterization, Presented at European Workshop on Performance-Related Properties for Bituminous Binders, Luxembourg, Belgium, 1999.

Asphalt Pavements – Kim (Ed)
© 2014 Taylor & Francis Group, London, ISBN 978-1-138-02693-3

A simplified flexible pavement guide with analytical reliability analysis

Jacob Uzan
Faculty of Civil and Environmental Engineering, Technion, Haifa, Israel

Shimon Nesichi & Noam Weinstein
Netivei Israel—National Transport Infrastructure Company, Or Yehuda, Israel

ABSTRACT: A PRS—Performance Related Specifications QA/QC program is under development in Israel. The literature review revealed that in the last decade, two systems for performance based QA/QC—NCHRP 9-22 and in California, were developed. They are similar in their approaches. They both address QA/QC of asphalt layers. They use regressions and/or data bases derived from runs of the AASHTO Guide or WesTrack results and Monte Carlo simulations to compute reliability. It was found that both systems have several limitations. It was decided to develop a new program that will (a) reproduce reliably AASHTO Guide results; (b) include a calibration of the transfer functions to local climatic and materials conditions (c) include all pavement layers and subgrade, and (d) be used in LCCA (Life Cycle Cost Analyses).

The new program uses the models from the Guide and (a) Hourly temperature distribution in the AC layers; (b) One design ESAL (Equivalent Single Axle Load); (c) No traffic wander (The effect of wander is taken into account via calibration functions); (d) Distress variability is computed analytically from the variability of the pavement properties using Rosenblueth-Harr approach. After preliminary calibration, the results of fatigue cracking, rutting and IRI (International Roughness Index) obtained from the new program fit very well with those of the Guide. A comprehensive calibration and verification steps are scheduled in the next few years. The short running time of the program, less than one minute, justifies its use in both QA/QC and LCCA analyses.

Keywords: Flexible pavement distresses, performance related QA/QC, AASHTO Guide, variability

1 INTRODUCTION

A Performance Related Specifications (PRS) QA/QC (Quality Assurance / Quality Control) program is under development in Israel. The objectives of the program are to (a) Provide a system with models to predict flexible pavement performance from both as designed and as constructed structure; (b) Include all pavement layers, both unbound and asphalt layers (c) Develop correlations between material properties defined in the models (such as moduli, transfer functions) and properties from construction (such as air void, moisture, asphalt content, back-calculated moduli), from literature survey and testing of local materials and (d) Calibrate the models for local conditions. The predicted pavement performance will be used in LCCA (Life Cycle Cost Analyses). The paper will describe the first step of developing a reliable prediction system that will be used in both QA/QC and LCCA.

The literature review revealed that in the last decade, two systems dealing with performance based QA/QC—NCHRP 9–22 [1–2] and in California [3–6], were developed. The systems are similar in their approach and deal only with the construction of the asphalt layers.

They use regressions and/or data bases and Monte Carlo simulations to compute reliability. They could not be adopted in Israel because: (a) Only asphalt layers are considered; (b) The reliability of their prediction was judged inadequate for both QA/QC and LCCA; (c) Calibration of the models requires new development of the regression equations or data bases. Therefore the literature review was directed toward flexible pavement design systems that predict performance.

Two programs for flexible pavement design were developed in the last decade—NCHRP 1–37 A (known as MEPDG—Mechanistic Empirical Pavement Design Guide, AASHTO—American Association of State Highway and Transportation Officials Guide or DARWin-ME—[7]) and CalME in California [8–11]. The programs are in essence similar and represent the state of the art in pavement distress predictions, mainly rut depth and fatigue cracking. A slightly different scheme for computing permanent deformation during the design period was proposed by Uzan [12]. These three sources were reviewed with the aim to adopt models and computation scheme that will serve for the prediction of performance, with the highest reliability and shortest running time possible.

The paper presents: (a) A critical literature review of the three sources for predicting performance; (b) A description of Rosenblueth and Harr approaches to deal with the effect of variability of pavement properties on the variability of the performance; (c) A description of the proposed models and analysis scheme and finally (d) A comparison of the verification results using MEPDG and the proposed program.

2 REVIEW OF THE FLEXIBLE PAVEMENT DESIGN PROGRAMS

The flexible pavement part of MEPDG was developed by Witczak and his group. CalME was developed under the guidance of Monismith. (Another program is being developed at Texas A&M [13]). Both programs are mechanistic—empirical in the sense that they compute the pavement response (stresses, strains and displacement) using elastic multilayer systems (JULEA—Jacob Uzan Linear Elastic Analysis and LEAP—Linear Elastic Analysis Program), they implement transfer functions to predict distress and they calibrate their predicted results with field or accelerated testing results. The strategy is to analyse the entire history of the distress development under varying climatic conditions and load distribution.

There is a basic difference between these programs in the way the evolution of damage is evaluated. In CalME, the approach is incremental and recursive, i.e. the material properties vary after every load pass and with temperature change. In the MEPDG, the approach is incremental and global, i.e. the material properties remain unchanged by damage (fatigue cracking and permanent deformation) but vary with temperature and moisture. The damage effect is indirectly included in the transfer functions which are calibrated during the entire pavement life.

As a consequence of the above, the approach of generating seasons which represent the pavement condition during the design period is different. In CalME, every month is represented by the hourly (24) temperature distributions during one day of the month. In the MEPDG and for every month of the design period, the temperature distributions are grouped into five bundles. The average monthly moisture content is used, unless frost depth indicates the need for subdividing the month into two sub seasons. The five temperature bundles do not cross each other, thus they may represent only part of the temperature distributions. Uzan [12] proposed to use all the hourly distributions for the entire design period and to group them into a finite number of temperature bundles (or season bands), 5 to 10C wide. The seasons may cross each other. Every hourly temperature distribution of the analysis period is then identified with one season. The number of seasons depends on the local conditions, the asphalt layer thickness and the width of the band, and may vary between 20 to about 50. This approach produces temperature distributions similar to the ones in CalME. The total number of seasons, for which either JULEA or LEAP is called, is 5*12*N for MEPDG, 24*12*N for CalME, where N is the analysis period in years, and 20–50 for Uzan approach.

The incremental recursive approach used in CalME is claimed to be more rational, however it is not flexible and is running time consuming. Therefore its use is not practical for QA/QC and LCCA analyses. The approach proposed by Uzan [12] seems more realistic and attractive than the approach in MEPDG if only temperature effects are considered, i.e. the moisture content at equilibrium in the unbound layers and aging of the asphalt layers are set at the beginning of the analysis period and kept unchanged during the design period. This moisture assumption holds for Israeli conditions, where the moisture condition reaches equilibrium in a relatively short period after construction, a few months or years. This may not be the case for sites where freeze-thaw and/or varying water table conditions exist. Similarly, aging in the upper AC layer occurs in the first 30 months. Fluctuations after reaching equilibrium are considered a second order effect. Since in this case, the total number of seasons is 20 to 50, the computation effort and running time are reduced drastically. It is worth to mention that temperature and moisture variations and aging effects are considered in the design programs, but not in the QA/QC programs. Therefore inclusion of seasons in the new program is a sensible improvement compared to existing QA/QC programs.

The above approach of generating season bands together with the MEPDG models and transfer functions are implemented in the new QA/QC program. The reliability system included in the MEPDG [7] does not consider directly the variability of the properties such as layer thickness, moduli and, as such, is not adequate for QA/QC programs. Even for a reduced number of seasons, Monte Carlo simulations used in QA/QC programs, of the order of thousands, can be very time consuming and thus, may not be considered. The theory of component analysis developed by Harr [14] seems to provide a solution to the problem. It is described in the next paragraph.

3 RELIABILITY

The point estimate method in probabilistic analyses was developed by Rosenblueth [15]. The statistical moments of a random function (Y) of several n variables $X(x_1, x_2, \ldots, x_n)$ are computed at a finite number of concentration points of X. The two points estimate, together with the assumption that the distribution of X is normal (symmetric) is widely used and will be presented hereafter. It states that the first, second and third moments (mean, standard deviation and coefficient of skewness) of Y can be computed from 2^n realisations of Y. Different weighting functions of the correlation coefficients between $x_1, x_2, \ldots, x_n$ are assigned to each concentration point. Rosenblueth approach is used in QRSS (Quality Related Specifications Software [2]) in the thermal cracking evaluation where the number of independent variables is small ($n = 4$). The thermal cracking program, without any approximation is run 16 ($=2^4$) times, and the mean and the standard deviation are evaluated. When the number of variables X is large, the approach becomes less attractive and unpractical.

In 1989, Harr [14] extended Rosenblueth [15] two point estimate method and reduced the number of realisations from 2^n to 2n. In this case only the first two moments can be evaluated. Harr's approach is based on the principal component analysis (similar to the principal stresses analysis, Harr [16]). The correlation matrix representing the statistical relationship (or dependence or correlation) among the variables X is rotated to the principal axes. The resulting correlation matrix is diagonal. The concentration points are now located on the principal axes. The rotation of the correlation matrix leads to $i = 1$ to n eigenvalues (similar to principal stresses) and to the corresponding normalized matrix of eigenvectors $E(i,j)$, with $j = 1$ to n (similar to the direction cosine vectors of the principal stresses). For each eigenvalue λ_i, two sets of concentration points— $x_{ij}^{(1)}, x_{ij}^{(2)}$ $j = 1, n$ at which the function Y is computed— $Y_i^{(1)}$ *and* $Y_i^{(2)}$, are given by:

$$x_{ij}^{(1)} = \bar{x}_j + sign(E(i,j)) \cdot s_j \cdot E(i,j) \cdot \sqrt{n} \tag{1}$$

$$x_{ij}^{(2)} = \bar{x}_j + sign(E(i,j)) \cdot s_j \cdot E(i,j) \cdot \sqrt{n} \tag{2}$$

where: $\bar{x}_j$ —mean value of x_j and s_j—standard deviation of x_j with $j = 1$ to n. Each of the $i = 1$ to n realisations uses two concentration points for each variable. Therefore the total number of realisations is $2n$.

The mean and the variance of Y are computed using the following:

$$E[Y] = \frac{1}{n}\sum_{i=1}^{n}\{Y_i^{(1)} + Y_i^{(2)}\}/2 \tag{3}$$

$$E[Y_i^2] = (Y_i^{(1)})^2 + (Y_i^{(2)})^2/2 \tag{4}$$

$$Var[Y] = \left\{ \sum_{i=1}^{n} \{E[Y_i^2] - (E[Y])^2\} \cdot \lambda_i / n \right\} \tag{5}$$

where: $E[a]$—expected value of a, $Y_i^{(1)}, Y_i^{(2)}$ are the computed values of Y at the two sets of concentration points.

Hong [17] presented a procedure to compute higher moments of the variable Y by $m \times n$ point estimates, where m is the number of concentration points per variable X. He developed a $2n + 1$ point estimates that can consider skewness and kurtosis of the probability distribution of Y.

The program developed for QA/QC and LCCA uses Harr's approach. Every realisation of Y requires one call to JULEA multilayer system. Therefore the number of X variables—n should be kept to minimum and include only variables with a sensible effect on Y. It is limited to $n = 30$ in the program. In the adopted computation scheme, the number of JULEA calls is of the order of 500 to 1500 (20–50 seasons bands times 2*n).

4 DESCRIPTION OF THE QA/QC PROGRAM

4.1 *Input data*

The input data includes:

1. Project information.
2. Traffic: Number of ESAL (Equivalent Single Axle Load) in first year, growth, design period and truck speed. In Israel the ESAL is a 13 tons dual wheel.
3. Two climatic files generated using EICM (Enhanced Integrated Climatic Model) program, *.icm and thermal.tmp files [7].
4. Structure description: Up to four AC (Asphalt concrete) layers, one base, one subbase, one fill and one subgrade layers. The modulus of the AC layers can be computed using Witczak equation [7] or be entered as a 6 parameters describing the time-temperature shift and the relaxation modulus functions. Table 1 summarizes the variables required for each layer. In the table, the number of X-variables is $4 \times$ nAC + 4, where nAC is the number of AC sub layers.
5. Correlation matrix of all variables X: In most cases, we have two independent correlation matrices, one for the AC layers and the other for the unbound layers. It is important to input the dependence between variables. Assuming independence between variables may lead to unrealistic results. It is also very important to input a clean standard deviation of the variables, without the added variability due to testing, results interpretation and other [3].
6. Transfer functions for asphalt cracking at the bottom AC layer and permanent deformation for all layers. For the AC layers, the transfer function shapes correspond to those in MEPDG. The user may change the coefficients. For unbound layers, a permanent deformation transfer function shape similar to that of the AC layer was chosen, with moisture content replacing temperature (Wang et al. [18]). It is worth mentioning that each layer has its own transfer function, a sensible improvement compared to MEPDG.

Table 1. Summary of input for structure description.

Variable	Mean	Coefficient of variation
AC layers		
Thickness	√	√
Modulus	√	√
Air void	√	√
Effective asphalt content	√	√
Poisson's ratio	√	–
Gradation	√	–
Unbound layers		
Thickness	√	√
Modulus	√	√
Poisson's ratio	√	–
Density	√	√
Moisture content	√	√
AASHTO classification	√	–

4.2 *Generation of season bands*

The thermal.tmp file includes hourly temperatures at the surface, half inch and every two inches below the surface for several years. From these temperature distributions, the program computes the minimum and maximum temperatures at the surface and at the bottom of the AC layer. The temperature variation range is divided into m_1 (at the surface) and m_2 (at the bottom AC layer) intervals 7 C or less wide. Then $M = m_1 \times m_2$ season bands are generated, and every hourly temperature distribution is identified with one season. A finer and more elaborate subdivision can be found in Uzan [12]. The value of M is limited to 30 in the program. When the number of seasons is larger than 30, the width of the bands is increased until this limit is reached.

For each season band an average temperature distribution at all depths is computed. It is based on averaging all hourly temperatures that enter the band. Then, the temperature at mid depth of each AC layer is interpolated and stored to represent the temperature distribution for the season band.

Each season is assigned an identification number between 1 and M. The program then generates one long vector ($iseq(1,k)$, k = 1 to 8760 N) where every hour in the design period (N years) is identified by the corresponding season number. The damage/distress computation follows the season sequence in vector *iseq*.

4.3 *Pavement response computation*

Eigenvalues λ_i and eigenvectors $E(i,j)$ of the correlation matrix, and then the means of all variables ($\overline{x}_j$ in equations 1 and 2) for all M seasons are computed first. The AC moduli are computed at the prevailing temperature and loading time at mid depth of each sub layer. Using equations 1 and 2, the concentration points are generated, leading to 2n × M different structures. Input data for JULEA is generated and the pavement response is computed for all $2n \times$ M structures. The response from JULEA includes: (a) Tensile strain at the bottom of the AC layers and (b) Deflections at the pavement surface and at all interfaces between layers. The elastic deformation of each AC sub layer and unbound layers is computed by subtracting the deflection at the bottom interface from the deflection at the upper interface.

It is worth mentioning that JULEA can easily be replaced by a 2D-FE (Finite Element) program and reproduce level 1 of MEPDG. The reliability of the response and of the entire system may be improved by introducing nonlinear, more realistic characterization of the materials. The running time is expected to increase to about fifteen to thirty minutes.

4.4 *Analysis scheme*

The analysis scheme begins with hour $k = 1$ at:

a. Reading season number m from vector *iseq*(1,k).
b. Computing the hourly traffic.
c. Reading the pavement response at $x^{(1)}$ and season m.
d. Computing the corresponding distresses $Y^{(1)}$ (fatigue cracking, permanent deformation of all AC and unbound layers, AC and total rut depth and IRI).
e. Reading the pavement response at $x^{(2)}$ and season m.
f. Computing the corresponding distresses $Y^{(2)}$ (fatigue cracking, permanent deformation of all AC and unbound layers, AC and total rut depth and IRI).
g. Computing the mean and standard deviation of each distress at hour k.
h. Paragraphs 1 to 7 are repeated with $k = k+1$ until k reaches the end, i.e. $k = 8760$ N hours in the analysis period.
i. The output summarizing month number, accumulated number of ESAL, fatigue cracking, rut depth in the AC layers, IRI and their standard deviations is printed out in tabular form (see Fig. 1) and EXCEL diagrams.

4.5 *Preliminary calibration and verification of the system*

The system was developed to reproduce reliably AASHTO Guide results with the smallest running time. Previous studies showed that a significant part of the running time of MEPDG was consumed by the computation of the distresses, at different lateral distances for a non-zero traffic wander. Therefore the present system uses a zero traffic wander and all response computations were made under the centre of one wheel. The calibration for correcting the lack of traffic wander was made using 8 pavement structures with different AC layer

	A	B	C	D	E	F	G	H	I	J	K	L
1		-----	13tons	Fatigue	Stand_dev	AC_rut	Stand_dev	Total_Rut	Stand_dev	PSI	IRI	
2		month	axles	cracking,%	Fatigue	mm.	AC_rut	mm.	Total_Rut	(1-5)	m/km	
3		1	12508.6	0.0218	0.0049	0.5763	0.0397	2.4506	0.1599	4.4089	1.1495	
4		2	25034.2	0.0406	0.009	0.6976	0.0476	2.8499	0.1838	4.3992	1.1586	
5		3	37525.7	0.0523	0.0114	0.721	0.0534	2.9956	0.1961	4.3942	1.1631	
6		4	50000	0.0629	0.0136	0.7332	0.0561	3.1006	0.2046	4.3904	1.1669	
7		5	62577	0.076	0.0163	0.7634	0.0594	3.2324	0.2137	4.386	1.1712	
8		6	75017.1	0.0964	0.0207	0.8613	0.0633	3.4751	0.2251	4.3796	1.1775	
9		7	87611.2	0.1245	0.027	1.026	0.0752	3.8145	0.2431	4.3706	1.1857	
10		8	100000	0.1585	0.0348	1.2826	0.1059	4.2563	0.273	4.3578	1.1957	
11		9	112594.1	0.2028	0.0456	1.8041	0.2164	4.9986	0.3605	4.3268	1.2111	
12		10	125000	0.2464	0.0563	2.172	0.2872	5.5409	0.4241	4.2996	1.223	
13		11	137525.7	0.2869	0.066	2.3513	0.3007	5.8495	0.4425	4.2872	1.2307	
14		12	150034.2	0.3232	0.0743	2.4438	0.3033	6.0385	0.4503	4.2796	1.2363	
15		13	162508.6	0.3545	0.0814	2.5035	0.3039	6.1722	0.455	4.274	1.2408	
16		14	175102.7	0.378	0.0864	2.5327	0.3036	6.2512	0.4577	4.2704	1.2443	
231		229	2862509	7.7613	1.6454	10.0385	1.2462	17.7716	1.4697	3.2343	1.9197	
232		230	2875017	7.7875	1.6501	10.0446	1.2461	17.7837	1.4699	3.2331	1.922	
233		231	2887594	7.8039	1.6528	10.046	1.2464	17.7888	1.4703	3.2323	1.9241	
234		232	2900051	7.8182	1.6551	10.0466	1.2465	17.7928	1.4706	3.2317	1.9262	
235		233	2912594	7.8366	1.6582	10.0491	1.2466	17.7995	1.4709	3.2309	1.9284	
236		234	2925017	7.8634	1.663	10.0563	1.2463	17.8128	1.4709	3.2297	1.9307	
237		235	2937611	7.8998	1.6699	10.0693	1.2465	17.8346	1.4714	3.2277	1.9333	
238		236	2950017	7.9428	1.6784	10.0951	1.249	17.8713	1.4741	3.2236	1.9362	
239		237	2962543	7.997	1.6897	10.1636	1.2629	17.9554	1.4874	3.2112	1.9401	
240		238	2975034	8.049	1.7005	10.2239	1.2744	18.0301	1.4985	3.2005	1.9438	
241		239	2987526	8.096	1.71	10.2565	1.2766	18.0749	1.501	3.196	1.9469	
242		240	3000051	8.1381	1.7181	10.2754	1.2772	18.1039	1.5019	3.1933	1.9497	
243												

Sheet1 / Fat_Cracking / AC_Rut / Total_rut / IRI / thermal-Harr

Figure 1. Output table.

thicknesses. Since the transfer functions for permanent deformation in the unbound layer is different from the one in MEPDG, the calibration involves only fatigue and rut depths in the AC layers.

It was found that the effect of traffic wander on damage D (the ratio of actual to failure number of load repetitions) for the fatigue cracking and on the rut depth RD of the AC layers is a power law of the AC layer thickness, i.e.:

$$\frac{D_{new}}{D_{MEPDG}} = 0.92815 \cdot h_{AC}^{\ 0.18253} \tag{6}$$

$$\frac{RD_{new}}{RD_{MEPDG}} = 0.1704 \cdot h_{AC}^{\ 0.3310} \tag{7}$$

where: h_{AC}—AC layer thickness, in mm. It should be noted that the damage ratio in Equation 6 (between 2 and 2.6) is very close to the ratio between pass to coverage for highways.

After the above calibration, the IRI coefficients were evaluated using nonlinear regression between IRI predicted by MEPDG and the distresses computed by the new program (without the longitudinal cracking which is not computed in new program). The corrected equation for the IRI is:

$$IRI = 69.96885 + 28.38803 * RD + 0.658362 * FC + 5.24977 * SF \tag{8}$$

$$SF = age * (0.000577 * (PI + 1) + 0.007947 * (Rain + 1) + 0.000636) \tag{9}$$

where: IRI—inch/mile, RD—mean rut depth, inch, FC—mean fatigue cracking, percentage of total area, SF—Site Factor, age—years, PI—subgrade Plastic Index, percentage and Rain—annual average rainfall, inch.

Six additional structures were used to verify the new program against MEPDG. The results are presented in Figures 2 to 5. The numbers in the legend correspond to the structure number. It is seen that the fitting is very good, except for the total rut depth. This is due to the fact that the transfer functions for permanent deformation in the unbound layers are different.

It should be noted that the number of structures for calibration and verification is small. However, this is a preliminary calibration intended to take care of the few simplifications introduced in the program, compared to MEPDG. A comprehensive calibration to local conditions is planned in the next few years.

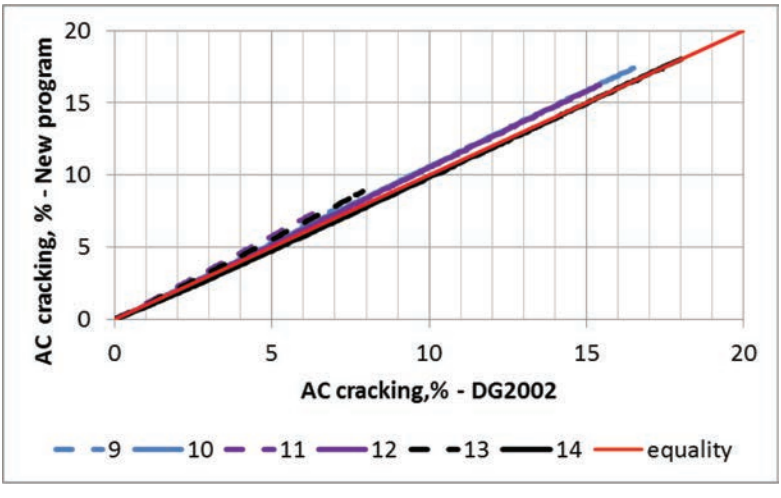

Figure 2. Verification of the AC layer cracking.

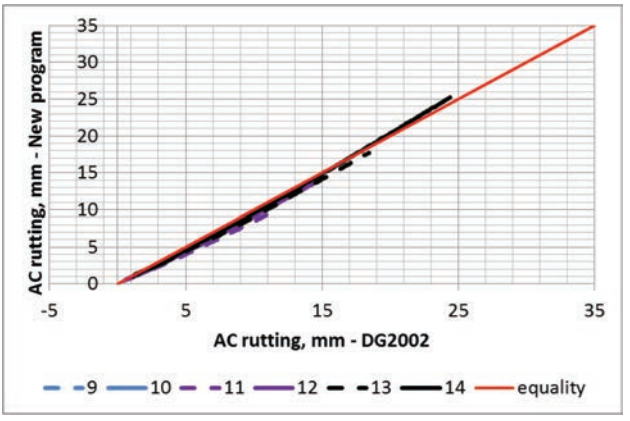

Figure 3. Verification of the AC layer rutting.

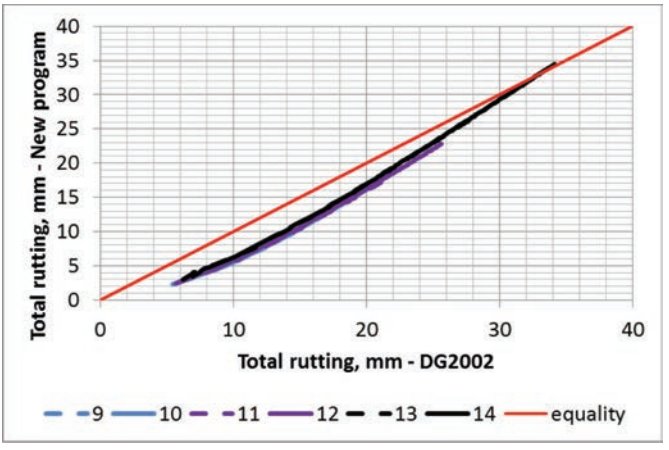

Figure 4. Verification of the total rutting.

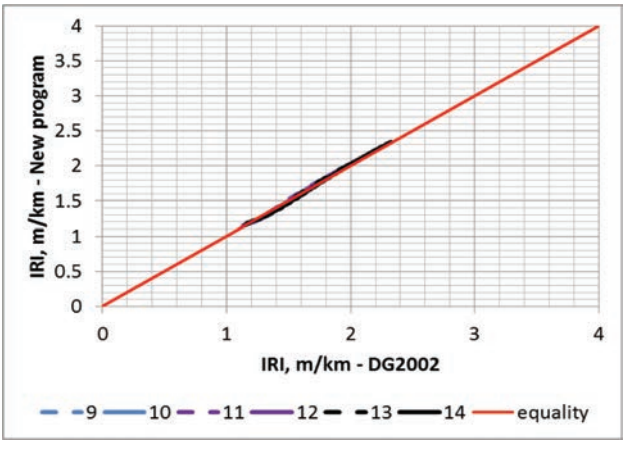

Figure 5. Verification of the IRI.

4.6 *Remarks*

Countries outside North America (like Israel) may encounter some difficulties in implementing MEPDG, by not having the climatic input, *.hcd files or by not collecting all climatic variables included in *.hcd files. For example, cloud cover is not measured in Israel. Fortunately, the global radiation, affected by cloud cover and other factors is measured. The cloud cover during daylight is computed using the relation in the EICM between global radiation, computed direct radiation and cloud cover. The cloud cover during night hours is assumed to be equal to the computed cloud cover at sunset. The effect of this assumption on temperature distribution is relatively small.

5 CONCLUSIONS

A new program for performance related QA/QC and LCCA is described. It uses the models and transfer functions of MEPDG and is calibrated against MEPDG. The program includes the following simplifications and improvements, compared to MEPDG:

a. The traffic distribution is replaced by its ESAL.
b. The effect of wander is included via calibration.
c. Initial moisture changes of the unbound materials and aging of upper asphalt layers are assumed to take place instantaneously. Only temperature effects on the AC layers are considered. This assumption holds for Israeli conditions but this may not be the case for sites where freeze-thaw and/or varying water table conditions exist.
d. The generation of season bands proposed by Uzan [12] is adopted. It represents the temperature distributions in the AC layers better than MEPDG.
e. The running time of the program, less than one minute, is suitable for QA/QC and LCCA purposes.
f. The reliability of the distresses is computed analytically using Harr [14] approach.

ACKNOWLEDGEMENTS

This work was sponsored by Netivei Israel, National Company for Transport Infrastructures, Ltd. The help and support from Adrian Cotrus is greatly appreciated.

REFERENCES

[1] Jeong, M.G. and El-Basyouny, M. "Statistical Applications and Stochastic Analysis for Performance Related Specification of Asphalt Pavement Quality Assurance", presented at the 89th Annual Meeting of the Transportation Research Board, 2010.
[2] NCHRP Report 704, "A Performance Related Specification for Hot-Mixed Asphalt", NCHRP, Transportation Research Board, p 133, 2011.
[3] Deacon, J.A., Monismith, C.L., Harvey, J.T. and Popescu, L., "Pay Factors for Asphalt-Concrete Construction: Effect of Construction Quality on Agency Costs", Technical Memorandum TM-UCB-PRC-2001-1, Pavement Research Centre, Institute of Transportation Studies, University of California, Berkeley, February 2001.
[4] NCHRP Report 455, "Recommended Performance-Related Specification for Hot-Mix Asphalt Construction: Results of the WesTrack Project", NCHRP, Transportation Research Board, 2002.
[5] Monismith, C.L. and Popescu, L., Harvey, J.T. and Hoover, T.P., "Performance-Based Pay Factors for Asphalt-Concrete Construction", Proc. 8th Conf. on Asphalt Pavements for Southern Africa, CAPSA, Sun City, South Africa, paper 097, 2004.
[6] Monismith, C.L. and Popescu, L., "Performance-Based Pay Factors for Asphalt-Concrete Construction: Comparison with a Currently Used Experience-Based Approach", Research Report: UCPRC-RR-2006-16, University of California, Pavement Research Centre, UC Davis and Berkeley, November 2006.

[7] NCHRP 1-37 A, "Guide for Mechanistic-Empirical Design of New and Rehabilitated Pavement Structures, Part III, Chapter 3", NCHRP, Transportation Research Board, March 2004.
[8] Ullidtz, P., Harvey, J., Tsai, B.-W and Monismith, C.L., "Calibration of CalME models using WesTrack Performance Data", Report No. UCPRC-RR-2006-14, University of California Pavement Research Centre, Davis and Berkeley, November 2006.
[9] Ullidtz, P., Harvey, J., Tsai, B.-W and Monismith, C.L., "Calibration of Incremental-Recursive Flexible Damage Models in CalME using HVS Experiments, Report No. UCPRC-RR-2005-06, University of California Pavement Research Centre, Davis and Berkeley, May 2007.
[10] Ullidtz, P., Harvey, J., Basheer, I., Wu, Q. and Lea, J., "Process of Developing a Mechanistic-Empirical Asphalt Pavement Design System for California", 11th Int. Conf. on Asphalt Pavements, ISAP, Nagoya, Japan, 2010.
[11] Harvey, J. Lu, Q. Lea, J.D., Ullidtz, P., Wu, R., Basheer, I., "Features of Mechanistic Empirical Asphalt Pavements Models for New Design and Rehabilitation in California", 11th Int. Conf. on Asphalt Pavements, ISAP, Nagoya, Japan, 2010.
[12] Uzan, J., "Permanent deformation in flexible pavements", ASCE, Journal of Transportation Engineering, Vol.130, Issue 1, pp. 6–13, Jan–Feb. 2004.
[13] Hu, S., Zhou, F. and Scullion, T, "Texas M-E Flexible Pavement Design System: Literature Review and Proposed Framework", Report FHWA/TX-12/0-6622-1, Texas A&M University System, p. 130, 2012.
[14] Harr, M.E., "Probabilistic estimates for multivariate analyses", Appl. Math. Modelling, Vol.13, pp. 313–318, 1989.
[15] Rosenblueth, E., "Two-point estimates in probabilities", Appl. Math. Modelling, Vol. 5, pp. 329–335, 1981.
[16] Harr, M.E., *Reliability-Based Design in Civil Engineering*, Dover Publications Inc., Mineola, New York, 1987.
[17] Hong, H.P., "An efficient point estimate method for probabilistic analysis", Reliability Engineering and System Safety, 59, pp. 261–267, 1998.
[18] Wang R., Zhou, F., Chen, D-H., Zheng, G., Scullion, T. and Walubita, L.F., "Characterization of Rutting (Permanent Strain) Development of A-2–4 and A-4 Subgrade Soils under the HVS Loading", Journal of Performance of Constructed Facilities, Vol. 24, No. 4, pp. 382–389, 2010.

Asphalt Pavements – Kim (Ed)
© 2014 Taylor & Francis Group, London, ISBN 978-1-138-02693-3

Integration of Mechanistic-Empirical design and performance based specifications: California experience to date

John Harvey
University of California Pavement Research Center, University of California, Davis, CA, USA

James Signore
University of California Pavement Research Center, University of California, Berkeley, CA, USA

Rongzong Wu
University of California Pavement Research Center, University of California, Davis, CA, USA

Imad Basheer, Sri Holikatti, Peter Vacura & T. Joe Holland
California Department of Transportation, Sacramento, CA, USA

ABSTRACT: Mechanistic-Empirical (ME) pavement design is being implemented for pavement rehabilitation and reconstruction in California. ME design lends itself to the development of Performance Based Specifications (PBS) for Hot Mix Asphalt (HMA) incorporating both locally available materials and properties needed to achieve desired service lives. This integration of ME design and PBS presents challenges for quality control and quality assurance, particularly for design-bid-build project delivery, more so when both ME and PBS are being introduced for the first time. This paper summarizes recent experience with integration of ME and PBS in California and ideas for addressing challenges that were identified from that experience.

Keywords: mechanistic-empirical, performance based specifications, design, construction, quality assurance

1 INTRODUCTION

Mechanistic-Empirical (ME) design tools allow the designer much greater flexibility to consider alternative materials, pavement structures, and construction quality specifications (particularly compaction) than do empirical design methods. ME design is able to consider specific materials properties in its response and performance models for both conventional and alternative materials, such as stiffness, fatigue resistance, low-temperature cracking properties, permanent deformation resistance and thermal expansion. ME design can also consider placement of different materials and compaction requirements in the structure to make best use of their unique properties, while taking into consideration constructability. ME design permits the development of reasonable designs even for materials and structures that have not been used before.

ME design also provides calculation of damage and development of each type of distress (cracking, rutting) and roughness (based on correlation with distresses, or more directly through calculation of longitudinal distribution of rutting in the wheelpaths), which allows the designer to consider alternative trigger levels for maintenance and rehabilitation and therefore their required frequency. This permits the designer to mechanistically consider pavement preservation through the life cycle based on either damage, distress or time.

Performance Based Specifications (PBS) have been defined as: "Quality Assurance Specifications that describe the desired levels of fundamental engineering properties (e.g. resilient

modulus, creep properties, and fatigue) that are predictors of performance and appear in primary prediction relationships (i.e. models that can be used to predict stress, distress, or performance from combinations of predictors that represent traffic, environment, supporting materials, and structural conditions) (1).

The advantages of integrating PBS and ME design are clear. PBS permit the designer to assume that materials constructed on the grade will have similar properties to those that are being used in the ME design structural analyses. They also permit the tailoring of specific materials requirements, such as stiffness, rutting and cracking properties, to unique features of a given project. These unique features include the particular traffic, climate, subgrade and existing pavement layers, and to locally available materials including local Reclaimed Asphalt Pavement (RAP). PBS also allow the designer to "raise the bar" with regard to specific expectations for performance related mix properties compared to what is possible with specifications that rely on aggregate and binder specifications, volumetric mix design and empirical mix tests.

The development of PBS for pavement and asphalt has been a subject of a great deal of research, including the first Strategic Highway Research Program which included the development of two approaches to mechanistic-empirical performance models and testing methods for performance-based specifications for asphalt binders and mixtures to control three distress modes: rutting, fatigue cracking and thermal cracking (2, 3). There was significant early work in this area in The Netherlands (4), particularly with regard to development and use of four-point bending for stiffness and fatigue. There has been ongoing work in Europe, mostly through RILEM, towards development of performance based testing methods and specifications going back to the 1960s (References 5, 6, 7 provide snapshots as of 1997, 2003, 2009) towards the development of international standards for characterizing and specifying mix performance properties. Several European countries are regularly using PBS for asphalt, primarily for Design-Build (DB) and Design-Build-Maintain (DBM) projects where the designer has access to precise understanding of the materials to be used and some control over their properties as part of the design process. There has been extensive work in Australia and New Zealand towards developing tests and PBS for granular bases (8, 9, 10). In addition to go/no-go specifications, performance-based incentive/disincentive pay factors for asphalt have been developed based on mechanistic-empirical performance estimates (11).

While the benefits of implementation of PBS are clear, there are a number of issues that have been identified throughout the literature, and in discussions with early implementers. One example was identified in Reference (1): "Because most fundamental engineering properties associated with pavements are currently not amenable to timely acceptance testing, performance-based specifications have not found application in highway construction".

The purpose of this paper is to provide a summary of California experience regarding development and implementation of PBS, integration of ME design and PBS, challenges that have been identified, and ideas for overcoming those challenges from an owner's headquarters perspective.

2 SUMMARY OF CALIFORNIA PRACTICE AND EXPERIENCE

California's initial implementation of PBS based on ME design began in the late 1990s when the asphalt industry was faced with the challenge of building Long-Life Asphalt Pavements (LLAP). Together, industry, the California Department of Transportation (Caltrans) and the University of California Pavement Research Center (UCPRC) determined that existing mix and pavement design methods and specification frameworks were not adequate to achieve desired goals.

The initial project was for the long-life rehabilitation of I-710 in Long Beach in southern California, designed to handle more than 200 million 80 kN (18 kip) equivalent axles, including overlays of existing concrete pavement and full-depth asphalt pavement beneath overpasses. The concepts of 1) increased compaction, 2) use of stiffer binders in thick sections and polymer modified binders in the surface layer, 3) Rich Bottom layers (better compaction,

4) slightly more binder) for bottom-up fatigue cracking and moisture sensitivity, and 5) flexural beam and repeated simple shear (RSST) laboratory testing, were implemented in the pavement designs and specifications from previous UCPRC and SHRP research (12). The designs and specifications were based on 50 percent loss of stiffness in the flexural fatigue test, repetitions to five percent permanent shear strain in the RSST, and flexural stiffness at 20 C, 10 Hz (13). The baseline materials were high quality well crushed alluvial aggregate, standard AR-8000 and special polymer modified asphalt that were locally available, but selected to provide improved performance. Use of these concepts permitted a reduction in thickness of the asphalt layers in the full-depth section of more than 35 percent, which was essential for meeting the required construction schedule with 55 hour weekend traffic closures. Phase 1 construction was completed in 2002, followed by two more phases resulting in about 100 lane-km total rehabilitated. Surveys of change in back-calculated stiffness after more than five years showed little damage, and no distresses other than some localized raveling in the sacrificial open-graded wearing course (14).

Beginning in 2000, UCPRC, Dynatest Consulting Inc and Caltrans developed the *CalME* design software which is based on incremental-recursive damage models and materials parameters from repeated load tests for fatigue and rutting (currently flexural and RSST), and frequency sweeps for testing (currently flexural). *CalME* was calibrated using accelerated pavement testing from different studies and some field sections, and evaluates reliability using Monte Carlo analysis and variability of existing layers using back-calculated stiffness measurements (15).

Ten years after the initial project, Caltrans decided to implement ME design using CalME and PBS on three northern California interstate highway rehabilitation projects, with heavy long-haul truck traffic, although fewer E80 s per year than on I-710. Design goals were at least 40 year fatigue (bottom-up or reflective) and rutting (asphalt and unbound layers) lives. Each project involved a new contractor/materials producer, and two districts also went through the process for the first time. These projects were also the first to use 25 percent RAP in the asphalt layers below the surface layer as opposed to the previous maximum 15 percent, and ME design was intended to help with consideration of the unfamiliar materials properties in the design.

All of the projects were delivered using the Design-Bid-Build (DBB) low bid approach, with the designs and specifications prepared by the owner and construction bid on by the contractor/supplier. This presents additional challenges compared to practice in Europe, where PBS have mostly been used for DB or DBM. There, the contractor prepares the design for their own materials, or can compare designs and costs for alternative materials that they can consider using. In DBM contractor develops the life cycle cost, and can consider cash flow, balancing initial construction and future preservation or maintenance activities, as well as total net present value of cost. In California, the designer must prepare specifications which are biddable, and the contractor must bid, with neither knowing beforehand exactly what the contractor can or will deliver.

2.1 *Materials and structures*

Pavement cross-sections for the three projects designed using *CalME* are shown in Table 1. Each project included milling off of thick layers of existing cracked, and at times moisture damaged asphalt to provide RAP. The thickness of the middle layer with 25 percent was the main variable changed in the structural design.

2.2 *Specifications*

The RSST (based on AASHTO T-320 [ASTM D7312]) was used to select the design binder content for each of the mixes, except the Rich Bottom materials, where 0.5% was added to the binder content found with the RSST to facilitate better compaction. To determine mix fatigue response at the selected design binder content, the flexural fatigue test (AASHTO T-321, ASTM D7460) was utilized. The moisture sensitivity response of each of the mixes was evalu-

Table 1. Pavement rehabilitation structural sections.

Red Bluff (I-5, Tehama county)	Weed (I-5, Siskiyou county)	Dixon (I-80, Solano county)
30 mm (0.1 ft.) RHMA-G-HB[a]	30 mm (0.1 ft.) RHMA-G-HB	30 mm (0.1 ft.) RHMA-G-HB
90 mm (0.3 ft.)	60 mm (0.2 ft.)	60 mm (0.2 ft.)
PG 64-28PM 15% RAP[b]	PG 64-28PM 15% RAP	PG 64-28PM 15% RAP
60–200 mm (0.2–0.65 ft.)	110–180 mm (0.35–0.6 ft.)	75–180 mm (0.25–0.6 ft.)
PG 64-10 25% RAP[c]	PG 64-16 25% RAP	PG 64-16 25% RAP
60 mm (0.2 ft.) PG 64-10	60 mm (0.2 ft.) PG 64-16	30 mm (0.1 ft.)
Rich Bottom 15% RAP[d]	Rich Bottom 15% RAP	PG 64-16 25% RAP with asphalt impregnated fabric on top
110 mm (0.35 ft.) existing CTB[e]	150–230 mm (0.5–0.75 ft.) varying CTB, AB[f], CSJPC[g]	0.7 ft. CSJPC

[a]Rubberized Hot Mix Asphalt Gap-Graded High-Binder content.
[b]Dense-Graded polymer modified hot mix asphalt, 6% air-voids.
[c]Dense-Graded conventional hot mix asphalt, 6% air-voids.
[d]Dense-Graded conventional hot mix asphalt, Rich Bottom (+0.5% binder), 0 to 3% air-voids.
[e]Cement treated base; [f]Aggregate base; [g]Cracked and seated jointed plain portland cement concrete.

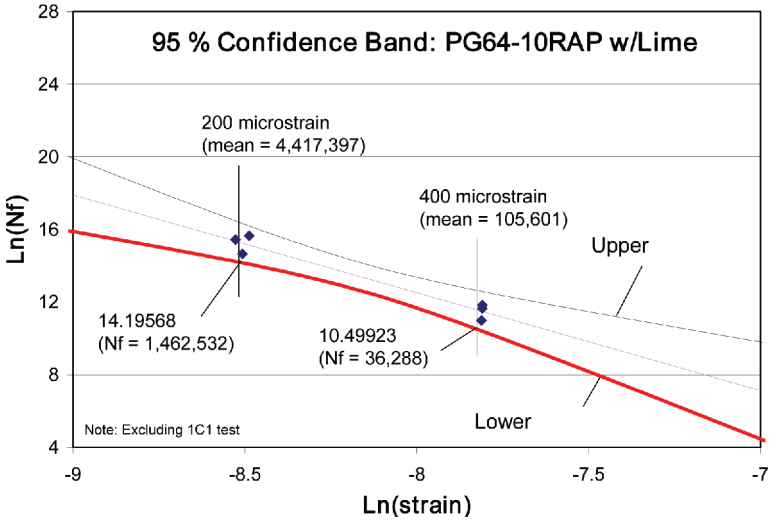

Figure 1. Fatigue 95% confidence band, PG 64-10 25% RAP with lime (AC = 5.38% [by weight of virgin aggregate], AV = 6.0%.

ated using the Hamburg WTT (AASHTO T-324). All of the specimens for the performance tests were prepared using Rolling Wheel Compaction (RWC) because the aggregate structure prepared by this method is similar to that obtained in mixes during pavement construction. RWC was developed during SHRP (AASHTO PP3-94.4). In developing the test data used to define the performance requirements, the AASHTO procedures were subsequently modified published in the Caltrans Flexible Pavement Test Method LLP-AC1 (16),(17).

Specification limits were selected based on the 95 percent confidence interval for the given property based on replicate tests as shown in Figure 1. Caltrans accepts 95 percent of the risk of laboratory test variability. The procedure for developing the specification limits was developed by Tsai et al. (18). An example of the PBS is shown in Table 2. The specification requires that the PBS be applied to plant produced mix. Two contractors used plant mix and one contractor used laboratory mix to develop preliminary mix designs. All three contractors used plant mix for mix design acceptance testing as per the specification.

Table 2. Asphalt mix performance-based specification for red bluff project.

Design parameters	Test method	Requirement
Permanent deformation (min.)	AASHTO T 320	360,000 stress repetitions[3,4]
PG 64-28PM (with lime)[2a]	Modified[1]	360,000 stress repetitions[3,4]
PG 64-10 (with RAP and lime)[2b]		
Fatigue (min.)	AASHTO T 321	23,000,000[4,8]
PG 64-28PM (with lime)[5a,6]	Modified[1]	345,000,000[4,9]
PG 64-10 (with RAP and lime)[5b,7a]		25,000 repetitions[4,8]
PG 64-10 RB[11] (with lime)[5c,7b]		950,000 repetitions[4,9]
		182,000 repetitions[4,8]
		2,700,000 repetitions[4,9]
PG 64-10 (with RAP and lime)	AASHTO T 324 Modified[1]	20,000 repetitions[10]

Notes:

1. Included in the testing procedure, LLP-AC1 (rolling wheel compaction), "Sample Preparation and Testing for I-710–Long-Life HMA,"

2a. At proposed asphalt binder content (mix containing 1.2% lime) and with mix compacted to 3%+/–0.3% air voids.

2b. At proposed asphalt binder content (mix containing RAP and 1.2% lime) and with mix compacted to 3%+/–0.3% air voids.

3. In repeated simple shear test at constant height (RSST-CH) at a temperature of 55°C at 100 kPa.

4. Minimum test value measured from tests on three specimens.

5a. At proposed asphalt binder content (mix containing 1.2% lime) and with mix compacted to 6%+/-0.3% air voids (determined using AASHTO 209 [Method A]).

5b. At proposed asphalt binder content (mix containing RAP and 1.2% lime) and with mix compacted to 6%+/–0.3% air voids (determined using AASHTO 209 [Method A]).

5c. At proposed asphalt binder content (mix containing 1.2% lime) and with mix compacted to 3%+/-0.3% air voids (determined using AASHTO 209 [Method A]).

6. At proposed asphalt binder content, the average mix stiffness at 20°C and a 10 Hz load frequency must be in the range 2859 to 3349 MPa (415,000 to 486,000 psi). At proposed asphalt binder content, the minimum stiffness at 30°C and a 10 Hz load frequency must be equal to or greater than 1516 MPa (220,000 psi).

7a. At proposed asphalt binder content (mix containing RAP and 1.2% lime), average stiffness at 20°C and a 10 Hz load frequency must be in the range 5589 to 6890 MPa (870,000 to 1,000,000 psi).

7b. At proposed asphalt binder content (with 1.2% lime), average stiffness at 20°C and a 10 Hz load frequency must be in the range 5443 to 6890 MPa (790,000 to 1,000,000 psi.).

8. At 400×10^{-6} strain, results shall be reported for this strain level but may be obtained by extrapolation. Minimum number of repetitions required prior to extrapolation defined within test procedure.

9. At 200×10^{-6} strain, results shall be reported for this strain level but may be obtained by extrapolation. Minimum number of repetitions required prior to extrapolation defined within test procedure.

10. Minimum number of repetitions for rut depth of 12.5 mm (0.5 in.) at 50°C (average of two specimens).[1]

11. The Rich Bottom (RB) mix contains the same binder as the mix with RAP, i.e., the PG 64-10; the binder content of this mix is increased 0.5% (mix basis) above the binder content used for the mix containing RAP.

Conventional Hveem mix design requirements are also included in the specification, including air void content under Hveem kneading compaction (for bleeding), aggregate specifications, voids in the mineral aggregate, voids filled with asphalt, dust proportion and tensile strength ratio (untreated and lime treated). The district where the Red Bluff and Weed projects were built generally requires lime treatment because of historical moisture sensitivity problems. Quality control and quality assurance testing during construction was based on conventional tests listed above because of the time requirements for performance related repeated load tests. The contractor had to provide new specimens for testing if the aggregate or binder source or the job mix formula changed.

The Red Bluff and Weed projects have been successfully completed in 2012. The Dixon project is paving in 2013 and 2014.

2.3 *Challenges*

A number of challenges were encountered on these three projects, including:

1. Selection of baseline material to develop specifications that are locally achievable but get the best performance possible at the lowest cost.
2. Communication of what specifications mean to potential bidders.
3. Procurement of representative local materials for design properties, especially RAP.
4. Writing of PBS, description of reliability and statement of quality requirements for different layers, and relationship to expected distress modes.
5. Communication of specification language to district materials engineers for writing of final specifications and bid package, and district construction engineers for administration of the process, including:
   a. Mix properties with respect to distress modes,
   b. Reliability, and
   c. Reasons for selection of air-void contents for each material and test.
6. Procurement of lab testing services.
7. Comparison of laboratories for performance-related tests not included in AMRL (auditable reference testing system). A similar challenge has just been experienced with tests using the AMPT testing device.
8. Assistance in advising contractor during mix design with regard to:
   a. Producing specimens,
   b. What tests mean and dealing with variability,
   c. Performance based mix design considering sensitivity of rutting, fatigue and stiffness to changes in mix, and
   d. Meeting values for conventional specifications at same time.
9. Performance-related testing values for laboratory versus plant produced mix.
10. Schedule pressures and time to perform performance-related tests.
11. Consideration of interaction of stiffness and fatigue test values from actual material on predicted structural life if materials exceeded one property by a wide margin but missed other property.

4 APPROACHES AND PROPOSED ALTERNATIVES TO DEAL WITH CHALLENGES

The approach used to meet the challenges listed in the previous section, or in some cases ideas for how to improve the PBS/ME design process are briefly discussed in this section, with number from the previous section.

Challenge 1. To obtain a better idea of what is available in the region, Caltrans/UCPRC will likely continue testing of more materials to establish regional databases. There is discussion internally and with the state industry association (CalAPA) regarding how high to set the bar within locally available materials. Experience to date shows that explicitly setting mechanistic properties will result in mix design changes to improve those properties, while under the old system those properties were unknown for the materials purchased by the state.

Challenge 2. Considering the many alternatives for aggregate in a geologically diverse state and multiple (although diminishing) sources of binder, Caltrans and industry are working to provide more explicit direction to contractors prior to bidding, particularly to address major gaps in common knowledge in a low-bid system. For example, a statement similar to this may be included on a slide in the pre-bid meeting: "Binder source for a given PG grade can possibly have a large influence on the ability of HMA to meet stiffness and fatigue specification requirements. PG grade specification only controls binder properties at the high and low temperatures, not the temperatures in between, and does not address fatigue."

Similarly, information regarding the improvement in chances of meeting stiffness and rutting requirements when using 100% crushed (>2 faces) coarse and fine aggregates will likely

also be provided. Getting the message out through industry/Caltrans meetings is also underway based on lessons learned from these three projects.

This is not a trivial matter. Bidders/contractors generally didn't seem to understand the "seriousness or severity" of the PBS requirements, and had no idea when preparing paving schedules whether mixes previously accepted by the state based on Hveem mix design would meet PBS by the date assumed. This became critical in project management after award of the contract more due to time constraints of changing plant operations and then testing time from iterations on the mix design rather than the cost of testing.

Challenge 3. Obtaining regionally representative materials in a DBB environment for laboratory testing to establish mechanistic properties for design presented some challenges, but designers relied primarily on the experience of district materials engineers. Use of properties for design from other regions is much more problematical. It was much easier to identify the effects of RAP on mix properties when the RAP samples could be milled from the existing project by district forces. On projects where the RAP was not coming from the existing pavement, obtaining representative RAP samples is more difficult, and there is risk for both the contractor and the state if RAP used is particularly different.

Overall, it is expected that as the effort to expand regional databases of properties continues there will be less need to do as much pre-testing for design (19). It is desired that contractors will become more aware of the properties of their mixes, and if there is sufficient opportunity to bid on and win PBS/ME projects this will incentivize innovation, the "if" condition being critical.

Challenge 4. Attention needs to be given to the testing and specification of properties for the polymer modified layer for top-down cracking. A bigger issues is the current approach to specifying huge numbers of required repetitions based on extrapolation of results from reasonable testing times and load repetitions for fatigue and rutting repeated load tests to specified limits initially caused consternation on the part of both contractors and district engineers. The approach used for the Caltrans specifications is described in Reference (16). It is also known that 50 percent loss of stiffness is a conservative criteria for many polymer and rubber modified binder mixes, and estimation of cracking initiation or some other "failure" criteria, as well as extrapolation is an area of additional investigation on the part of various researchers, as is discussed in References (20,21) which compare methods developed by Rowe, Franken, Hopman, Ghuzlan and Carpenter, and Pronk as well as a more recent comparison by Rowe et al. (22). *CalME* uses a damage function fit to the entire damage curve from the test in incremental-recursive analysis, and 50 percent loss of stiffness is only used for specification. A better parameter for specification of fatigue and to a lesser extent rutting, based on the damage curves, needs to be developed.

Based on discussions of The Netherlands approach and other ideas at the recent 4 Point Bending Conference, a new simpler approach for classifying materials based on the three performance tests is also being considered. The approach would require a critical mass of projects (dollars and numbers of projects) each year over a five year or longer period, for contractors to justify the cost of testing, and for commercial laboratories to consider developing equipment and human resources. In this system there would be categories of performance for rutting (Repeated Load Triaxial [RLT] or RSST), fatigue (flexural fatigue) and stiffness (flexural or compressive). Results for repeated load tests would be based on the log of the repetitions to failure to produce a linear scale of loss of stiffness for fatigue and permanent strain for RLT or RSST. How to handle two strains for fatigue needs to be determined, or a single point might be used, such as the strain that results in one million load cycles used in The Netherlands. On the order of five to ten categories might be considered. A mix may then have an A through J category for fatigue, 1 through 10 for rutting, and a through j for stiffness.

Contractors could then test their current most used mixes in advance, and know whether their mix will meet the specifications, or be close enough that they can reasonably adjust the mix design to meet them. Designers would use regional materials in the ME analysis for several mix types that should be available in the region, such as an E2f or an F3e, and determine the mixes that will provide at least the minimum required performance in the specific

structural design. While considering allowable differences in grade elevations for rehabilitation projects, alternative designs with different materials might be prepared for design by the state.

Challenge 5. Interaction headquarters and the district for each project has been found to be the best way to communicate the intent and requirements of the PBS. Some prior training may be useful for basic background, but the experience of working through a first project with assistance is invaluable. Having sufficient headquarters resources to answer questions and address problems as they arise is critical.

Challenge 6. As mentioned previously, for the laboratory testing to be moved from research laboratories to commercial or even contractor laboratories will require a multi-year commitment of enough projects to amortize the equipment and recoup the investment in human resources with a profit. Concern about whether equipment manufacturers will/can produce equipment and provide long-term service at affordable prices is also an issue. For this reason, the recent wave of investment in AMPT equipment is leading to consideration of moving to RLT testing for rutting with that device, not because the RSST is not an excellent test (and can test field cores), but because it does not have a critical mass of numbers of deployed devices. There is a concern on the part of California that initial enthusiasm for the AMPT may wane, as it did for the RSST.

Challenge 7. Certification of any repeated load testing equipment will be an issue. Quality control procedures are available, such as standard materials with known properties (developed after SHRP for SST and flexural devices), as is round robin testing of the same materials. These again need a critical mass of projects and laboratories to be worthwhile. Based on experience comparing RSST results with the University of Nevada, Reno for the Red Bluff project, and recently completing a round robin comparison of flow number and dynamic modulus results (AMPT) with three laboratories for NCHRP 9–52 shows that there will need to be clarification of steps and procedures in test methods as a part of this process.

Challenge 8. Production of rolling wheel core and beam specimens using the Caltrans method (16) was not found to be a problem using contractor built molds at the plants. Contractor training of their staff to strictly follow the specimen preparation process eliminated most problems. Similar experience has been found with Superpave gyratory specimens for RLT.

Although contractors have extensive experience with Hveem, and are learning Superpave volumetric mix design, there is not much experience balancing sometimes opposing specific performance related properties, namely fatigue and rutting. Applying in practice the "theoretical" ideas that most contractors are familiar with for balancing mix design to achieve these requirements requires additional experience. Working with contractor staff on the three recent projects showed that in a relatively short time that this experience was obtained. Having an experienced consultant (mix design and plant operations) for guidance and assistance communicating with the state also seemed to be helpful to the contractors.

Challenge 9. The time and materials required to produce plant mixed materials are considerable. However, for several mixes there was a notable difference between the properties from the plant and laboratory produced mixes. Although an exact cause was not determined, indications were that interactions of the lime treatment and mixing may have played a role, as well as binder aging. This challenge will require more investigation, however, the state wants to reduce its risk by requiring that final acceptance be based on plant mixed material which can add a significant amount of time to the testing process.

Challenge 10. It is apparent that Caltrans/UCPRC working with industry needs to improve the specifications and acceptance process, while maintaining the shared commitment to achieving the benefits of PBS combined with ME design, or else there will not be future bidders. Going up the learning curve noted in this process, while faced with the schedule delays and cost of adjusting a mix to meet PBS for the first time is a stressful experience that few contractors would want to repeat. The requirement that plant produced mix is used to pass the specification, and the length of time for low strain fatigue testing, were found to be the largest contributors to the schedule. Making adjustments to balance shear, fatigue and laboratory compaction (three variable decision-making instead of just adjusting binder content) was the biggest mix design issue. The proposed specification scheme (Challenge 4), where

contractors would test their mixes prior to bidding, is intended to help address this. However, few contractors at this time would be willing to go through that relatively expensive testing process without having already won the contract. The taking on of some additional risk by the owner by some reductions in the amount of fatigue testing, or increasing the strain levels, is one alternative that is being considered.

Because of schedule constraints for the flexural and shear tests used for acceptance of the mix design, quality control and assurance during construction relies on standard tests including checking of the job-mix formula proportions and standard aggregate and mix tests. Rapid tests that can be performed in the field and that are reasonably well calibrated with the repeated load tests used for design and mix acceptance are currently being investigated for Caltrans by the UCPRC and corresponding researchers (23).

Challenge 11. Different combinations of stiffness and fatigue behavior will produce a structure that meets the design fatigue requirements for a given project. In addition to providing a more transparent specification framework for contractors, the proposal described for Challenge 4 is intended to provide more flexibility for designers to consider alternative combinations of these properties.

5 CONCLUSIONS AND RECOMMENDATIONS

Performance based specifications and mechanistic-empirical designs provide a means to produce materials and designs that decrease life cycle cost for the state, and a framework for competitive innovation to "raise the bar" for contractors and materials producers. Challenges have been identified, many particular to the design-bid-build project delivery method, and lessons learned from the three projects described in this paper. These should result in changes to the current process to reduce risk for contractors and the state, and particularly to improve transparency and understanding of what they need to do to be successful for contractors.

It is recommended that Caltrans, industry and academia work together, as they have in the past in California, to meet these challenges.

REFERENCES

1. Transportation Research Board Committee on Management of Quality Assurance (A2F03). Glossary of Highway Quality Assurance Terms, Transportation Research Circular Number E-C037. 2002. http://onlinepubs.trb.org/onlinepubs/circulars/ec037.pdf (accessed Sept 13, 2013).
2. Lytton, R., J. Uzan, E. Fernando, R. Roque, D. Hultinen, S. Stoffels. Development and Validation of Performance Prediction Models and Specifications, Strategic Highway Research Program, National Research Council, Report A-357. 1993.
3. Leahy, R., R. Hicks, C. Monismith, F. Finn. Framework for Performance-Based Approach to Mix Design and Analysis, Journal of the Association of Asphalt Paving Technologists, Vol. 64, pp. 431–473. 1995.
4. Molenaar, A., T. Medani. Rational Testing Methods for Performance Based Specifications, 1st World of Asphalt Pavements International Conference, Sydney, Australia, pp. 2–18. 2000.
5. Di Benedetto, H., L. Franken (editors). 5th International RILEM Symposium on Mechanical Tests for Bituminous Materials, Lyon, France. 1997.
6. Partl, M. (editor). 6th International RILEM Symposium on Performance Testing and Evaluation of Bituminous Materials, Zurich, Switzerland. 2003.
7. Loizos, A., T. Scarpas, M. Partl, I. Al-Qadi (editors). 7th International RILEM Symposium on Advanced Testing and Characterization of Bituminous Materials, Rhodes, Greece. 2009.
8. Vuong, B. Development of performance-based specifications for unbound granular materials, Part A: issues and recommendations, Austroads Report Number AP-T29/03. 2003.
9. Arnold, G. Reducing the risk of pavement failure and utilisation of local materials in New Zealand through repeated load triaxial and beam fatigue tests, Thirteenth International Flexible Pavements Conference, Surfers Paradise, Queensland, Australia. 11–13th October 2009.
10. Transit New Zealand. 2007. TNZ T15 Specification For Repeated Load Triaxial (RLT) Testing Of Unbound And Modified Road Base Aggregates. 2007.

11. Deacon, J., C. Monismith, J. Harvey, L. Popescu. Performance-Based Pay Factors for Asphalt Concrete Construction Reflecting Fatigue and Rutting Effects, 9th International Conference on Asphalt Pavements, Copenhagen, Denmark, Vol. II, pp. 17–22. August, 2002.
12. Harvey, J., J. Deacon, A. Tayebali, R. Leahy, C. Monismith. A Reliability-Based Mix Design and Analysis System for Mitigating Fatigue Distress, 8th International Conference on Asphalt Pavements, Seattle, pp. 301–324. 10–14 August, 1997.
13. Monismith, C., F. Long, J. Harvey. California's Interstate-710 Rehabilitation: Mix and Structural Section Designs, Construction Specifications, Journal of the Association of Asphalt Paving Technologists, Volume 70, pp. 762–799. 2001.
14. Monismith, C., J. Harvey, B.W. Tsai, F. Long, J. Signore. The Phase 1 I-710 Freeway Rehabilitation Project: Initial Design (1999) to Performance after Five Years of Traffic (2008), Summary Report UCPRC-SR-2008-04, UC Pavement Research Center, Davis and Berkeley, CA. 2009.
15. Ullidtz, P., J. Harvey, I. Basheer, D. Jones, R. Wu, J.D. Lea, Q. Lu. CalME: A new mechanistic-empirical design program for flexible pavement rehabilitation, Transportation Research Record 2153, pp. 143–152. 2010.
16. California Department of Transportation. Sample preparation and testing for long life asphalt concrete pavements. Lab procedure, May 20, 2011. http://www.dot.ca.gov/hq/esc/Translab/ofpm/pdf/AC1-LLP_Dist-02.pdf. (Accessed on Sept 14, 2013).
17. Mandapaka, V., I. Basheer, K. Sahasi, P. Vacura, B.W. Tsai, C. Monismith, J. Harvey, P. Ullidtz. Application of four-point bending beam fatigue test for the design and construction of a long-life asphalt concrete rehabilitation project in Northern California, 4 Point Bending, CRC/Balkema, Leiden, The Netherlands, pp. 49. 2012.
18. Tsai, B.W., R. Wu, J. Harvey, C. Monismith. Development of fatigue performance specification and its relation to mechanistic-empirical pavement design using four-point bending beam test results, 4 Point Bending, CRC/Balkema, Leiden, The Netherlands, pp. 59. 2012.
19. Popescu, L., J. Signore, J. Harvey, R. Wu, I. Basheer, J.T. Holland. Development of a standard materials library for mechanistic-empirical fatigue and stiffness evaluation, 4 Point Bending, CRC/Balkema, Leiden, The Netherlands, pp. 71. 2012.
20. Anderson, R.M., S. Carpenter; J. Daniel; B. Prowell; S. Shen; S. Bhattacharjee; A. Swamy; E.R. Brown; H. Von Quintus; S. Maghsoodloo. Validating the Fatigue Endurance Limit for Hot Mix Asphalt NCHRP Report 646, Transportation Research Board. 2010.
21. M. Souliman, W. Zeiada, K. Kaloush, M. Mamlouk. Assessment of different flexure fatigue failure analysis methods to estimate the number of cycles to failure of asphalt mixtures, 4 Point Bending, CRC/Balkema, Leiden, The Netherlands, pp. 27. 2012.
22. Rowe, G., P. Blankenship, T. Bennert. Fatigue assessment of conventional and highly modified asphalt materials with ASTM and AASHTO standard specifications, 4 Point Bending, CRC/Balkema, Leiden, The Netherlands, pp. 101. 2012.
23. Saadeh, S., O. Eljairi, B. Kramer, E. Hajj. Development of quality control test procedure for characterizing fracture properties of asphalt mixtures, CRC/Balkema, Leiden, The Netherlands, pp. 221. 2012.
24. Tsai, B.W., J. Signore, C. Monismith. Development of Hot Mix Asphalt Pavement Performance Properties for Long-life Pavement Designs: Caltrans District 2, Interstate-5 Red Bluff and Weed, CA, Summary Report UCPRC-SR-2012-01, UC Pavement Research Center, Davis and Berkeley, CA. 2013.

Asphalt Pavements – Kim (Ed)
© 2014 Taylor & Francis Group, London, ISBN 978-1-138-02693-3

The use of performance specifications to improve pavement design and sustainability in the UK

Bachar Hakim & Richard Elliott
URS Infrastructure & Environment, Nottingham, UK

ABSTRACT: Recent developments in UK pavement design using performance specification and end-product testing, have helped designers to optimise the materials and improved construction quality, future performance and sustainability. Assessment of unbound and hydraulically bound materials performance using the Springbox and the Light Weight Deflectometer (LWD), permit the use of a wide range of binders including cement, lime, slag and fly ash with marginal, recycled and secondary local aggregates. The Springbox characterises stiffness and deformation resistance of unbound and weakly bound materials to ensure durability. The LWD is a hand held device that measures the in-situ foundation surface stiffness during construction. Asphaltic materials are also specified in terms of performance rather than recipe to ensure the design parameters are met during construction. This paper describes the recently introduced UK pavement design, testing and specification requirements. Case studies are presented which demonstrate the implementation of the procedures in order to improve pavement performance and sustainability.

Keywords: Pavement design, performance specification, materials optimisation, sustainability

1 INTRODUCTION

Traditionally, the UK pavement specifications were based on a recipe approach, where selected materials are laid and compacted with specified plant in a specified manner to achieve a minimum level of performance. However, performance specifications and end-product testing have gradually been introduced to the UK standards in order to optimise the range of materials used (including recycled, locally won, and industrial by-products), to improve both quality and sustainability. Therefore, the impact of improved material properties on the pavement design thickness and expected life can be considered. This paper presents the design development and testing requirements together with practical case studies to demonstrate the advantages achieved.

2 UK PAVEMENT DESIGN DEVELOPMENT

2.1 *Foundation design*

UK pavement foundation design was based primarily on the use of the California Bearing Ratio (CBR) to characterise the subgrade, capping and sub-base materials [1]. The thicknesses of sub-base and capping materials are determined from the subgrade CBR to achieve a "standard pavement foundation" (see Fig. 1). The foundation design was independent of traffic levels and had no impact on upper pavement bound layer thicknesses. The benefit of using a stiffer foundation, such as a cement bound sub-base below the asphalt, did not reduce the upper pavement layer thickness in this design method; even though it would improve pavement support and overall bearing capacity.

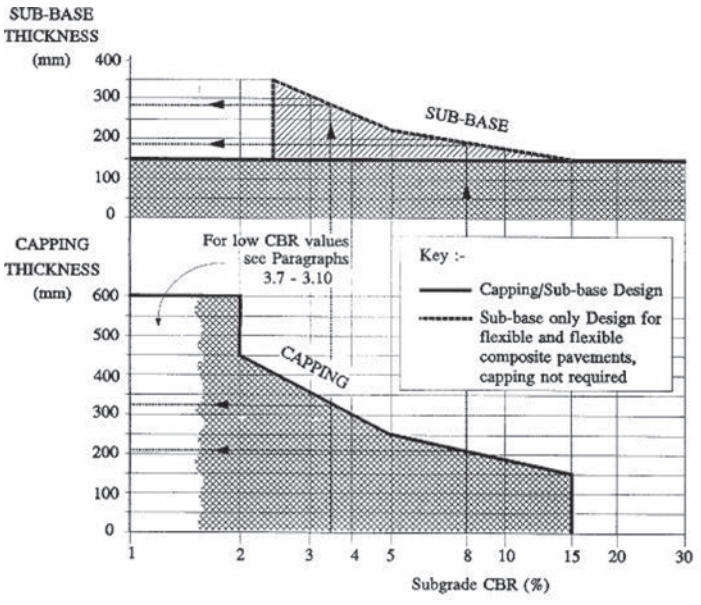

Figure 1. UK standard pavement foundation design [1].

Although CBR has been correlated with pavement performance in many countries over many years and provides a trusted empirical indicator of material behaviour, the use of CBR as a performance parameter is widely acknowledged as being not wholly satisfactory [2]. Furthermore, the need for a fundamental engineering property (such as stiffness) to describe the unbound and weakly bound materials has become important for use in analytical/mechanistic design methods. The stiffness modulus of a pavement foundation is a measure of the quality of support which is provided to the overlaying asphalt or concrete layers. Advances in the in-situ testing of pavement foundation materials now allow the performance parameter of stiffness (and, more indirectly, strength and resistance to permanent deformation) to be measured on a routine basis during construction. This in turn enabled a performance based specification for road foundation layers to be introduced in the UK, hence facilitating the use of secondary aggregates, marginal materials and stabilised ground.

The Falling Weight Deflectometer (FWD) and Light Weight Deflectometer (LWD) measure the composite foundation stiffness under a transient load pulse, which is applied to the ground by dropping a weight onto a bearing plate via a rubber buffer (see Fig. 2). The deflection of the ground is measured and combined with the applied load to calculate the stiffness using conventional Boussinesq analysis. However, the LWD is a hand held device and hence more practical for compliance monitoring during foundation construction.

The Springbox was developed by URS/Scott Wilson as part of a UK Highways Agency sponsored project [3], in response to the fact that over the last 10 years, pavement designers have been moving towards the use and measurement of stiffness modulus for pavement foundations and away from traditional empirical index tests such as CBR. One of the objectives of this recent approach is to allow a wider range of materials to be used for capping and subbase construction, based on their mechanical properties, within the general move towards end-product based specifications. The Springbox (see Fig. 3) is used to assess the stiffness and deformation properties of unbound and weakly bound materials in the laboratory. The equipment enables a realistic material compaction level to be applied during preparation, followed by repeated vertical loading with various magnitudes to represent trafficking during construction with appropriate pavement confinement. The device can be used to characterise the fundamental material properties, considering various mixtures with different moisture

Figure 2. Falling Weight Deflectometer (FWD) and Light Weight Deflectometer (LWD) tests on a trial foundation.

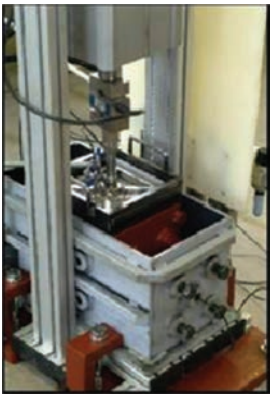

Figure 3. The springbox test.

contents and binder types, as well as ageing, temperature and saturation levels, for use in the analytical/mechanistic pavement design approach.

The recent UK pavement design method [4] considers four foundation classes defined by a long term in service "Foundation Surface Modulus":

- Foundation Class 1 ≥ 50 MPa (typically capping layer over subgrade).
- Foundation Class 2 ≥ 100 MPa (typically unbound sub-base over subgrade).
- Foundation Class 3 ≥ 200 MPa (weakly bound sub-base over subgrade).
- Foundation Class 4 ≥ 400 MPa (strongly bound sub-base over subgrade).

The "Foundation Surface Modulus" is based on application of a known load at top of the foundation (e.g. by LWD) and represents a composite value with contribution from all underlying layers. A "Layer Stiffness Modulus" is assigned to a given foundation layer to represent the in-situ condition and account for long term degradation and cracking. An "Element Stiffness Modulus" is assigned to a discrete sample of material and usually characterised

by laboratory testing (e.g. Springbox) of an intact sample with no account of degradation and cracking. Therefore, the foundation layers are characterised in the laboratory and then assigned a "Layer Stiffness Modulus" to account for future deterioration. The design charts (or a multi-layered elastic model) are then used to calculate the layer thickness over a given subgrade stiffness to meet the specified Foundation Class. A demonstration area is constructed and tested to assess the actual expected foundation performance for the site under consideration; and finally end-product testing is carried out to ensure that the foundation design requirements are met during construction. The details of laboratory and in-situ testing, demonstration area and compliance testing during construction are presented in the foundation design guidance [4].

Figure 4 shows a typical design chart for Foundation Class 2 with a "Foundation Surface Modulus" of 100 MPa. However, using a multi-layered elastic model provides the flexibility to consider multiple foundation layers and/or different layer stiffnesses to meet the "Foundation Surface Modulus" requirements.

Figure 4 shows that 225 mm of unbound subbase (typically with a layer stiffness of 150 MPa) over a subgrade with 5% CBR (stiffness modulus of 50 MPa) is needed to meet the Foundation Class 2 requirements. However, a sub-base thickness of 160 mm with a layer stiffness of 350 MPa (typically stabilised) can also meet the above foundation class. Therefore, using marginal, recycled and secondary aggregates with the appropriate binder content to achieve the subbase layer stiffness can justify foundation thickness reduction, leading to cost and sustainability benefits, provided end-product performance testing (e.g. LWD) is carried out. This option was not permitted in the previous design standard as shown in Figure 1. An additional advantage of introducing the four foundation classes is the possible reduction of upper pavement layers to account for the contribution of stronger/stiffer foundations as detailed in next section.

The design standard still permits the use of recipe foundation design, but with thicker construction compared with the performance design to account for materials variability. This option would be used on the smaller projects where the cost of additional materials testing is not justified.

2.2 *Hydraulically bound mixture*

The recent UK pavement design standard allows the use of a wide range of Hydraulically Bound Mixtures (HBM) with cement, lime, slag and fly ash binders with marginal, recy-

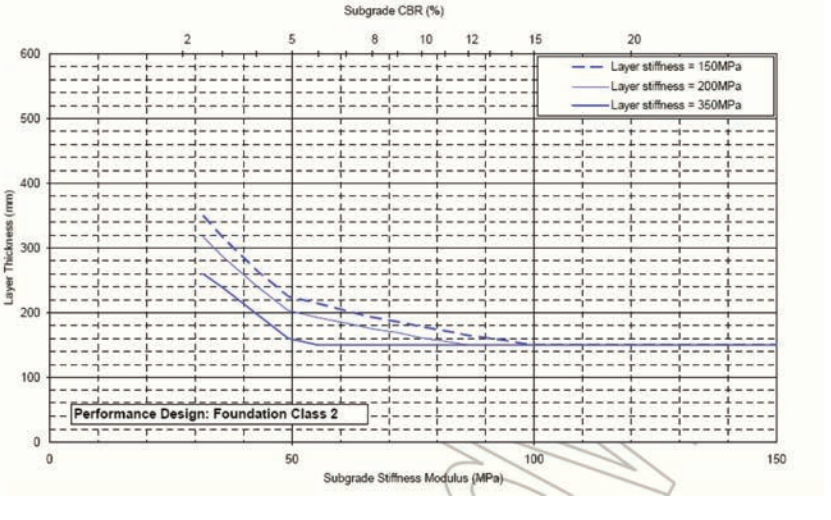

Figure 4. Foundation performance based design—foundation class 2 [4].

cled and secondary local aggregates, provided their fundamental properties are assessed during the design and monitored during construction. HBM can be used in the foundation to meet the above foundation classes or as a lower base in flexible composite constructions, where HBM base thickness and category are specified during the design stage and monitored for compliance during the construction stage. Examples of HBM categories and strength requirements for various binder and aggregate types are shown in Table 1. Cement Bound Granular Mixtures (CBGM), Slag Bound Mixtures (SBM) and Fly Ash Bound Mixtures (FABM) with various compressive/tensile strengths are presented in Table 1 to comply with HBM categories and design requirements.

2.3 *Asphaltic material*

The UK asphaltic material includes various types such as Hot Rolled Asphalt (HRA), Dense Bituminous Macadam (DBM) and High Modulus Base (e.g. EME2) materials with different mix design, stiffness and binder properties. The design allows the use of thinner constructions if stiffer asphaltic materials are used (see Fig. 5). The asphaltic mixtures are specified in terms of laboratory stiffness during the design stage and monitored for compliance during construction by testing samples extracted from the pavement. Additional testing to assess the deformation resistance, water sensitivity and durability of the asphaltic mixtures are also recommended during the mix design stage. Other mixtures such as those containing percentages of reclaimed asphalt and cold/hot in-situ/ex-situ recycled materials are permitted, provided their properties are assessed and tested. The use of recipe mixtures is also permitted in the current standard if required.

Figure 5 shows an asphalt thickness of 265 mm incorporating EME2 binder/base compared with 320 mm incorporating DBM50 binder/base over foundation class 3, to carry a traffic loading of 80 millions of equivalent standard axle load (msa). Another advantage of the design method is the reduction in asphalt thickness when stiffer (e.g. stabilised) foundation is specified. Figure 5 indicates an asphalt thickness incorporating DBM50 binder/base of 280 mm over Foundation Class 4, compared with 360 mm over Foundation Class 2 to carry future traffic of 80 msa.

2.4 *Pavement quality concrete*

The use of jointed reinforced/un-reinforced concrete pavements for new construction is restricted due to high maintenance cost, construction delay, noise and poor ride quality. However, Continuous Reinforced Concrete Pavement (CRCP) and Continuous Reinforced

Table 1. Examples of UK design HBM categories [5].

HBM category	A	B	C	D
Crushed rock coarse aggregate: (with coefficient of thermal expansion $<10 \times 10^{-6}$ per °C)	–	CBGMB—C8/10 (or T3) SBMB1—C9/12 (or T3) FABMl—C9/12 (or T3)	CBGMB—C12/15 (or T4) SBMB1—C12/16 (or T4) FABMl—C12/16 (or T4)	CBGMB—C16/20 (or T5) SBMBl—C15/20 (or T5) FABMl—C15/20 (or T5)
Gravel coarse aggregate: (with coefficient of thermal expansion $\geq 10 \times 10^{-6}$ per °C)	CBGMB—C8/10 (or T3) SBMB1—C9/12 (or T3) FABMl—C9/12 (or T3)	CBGMB—C12/15 (or T4) SBMB1—C12/16 (or T4) FABMl—C12/16 (or T4)	CBGMB—C16/20 (or T5) SBMB1—C15/20 (or T5) FABMl—C15/20 (or T5)	

Note: C8/10, T3 indicate compressive and tensile strengths respectively.

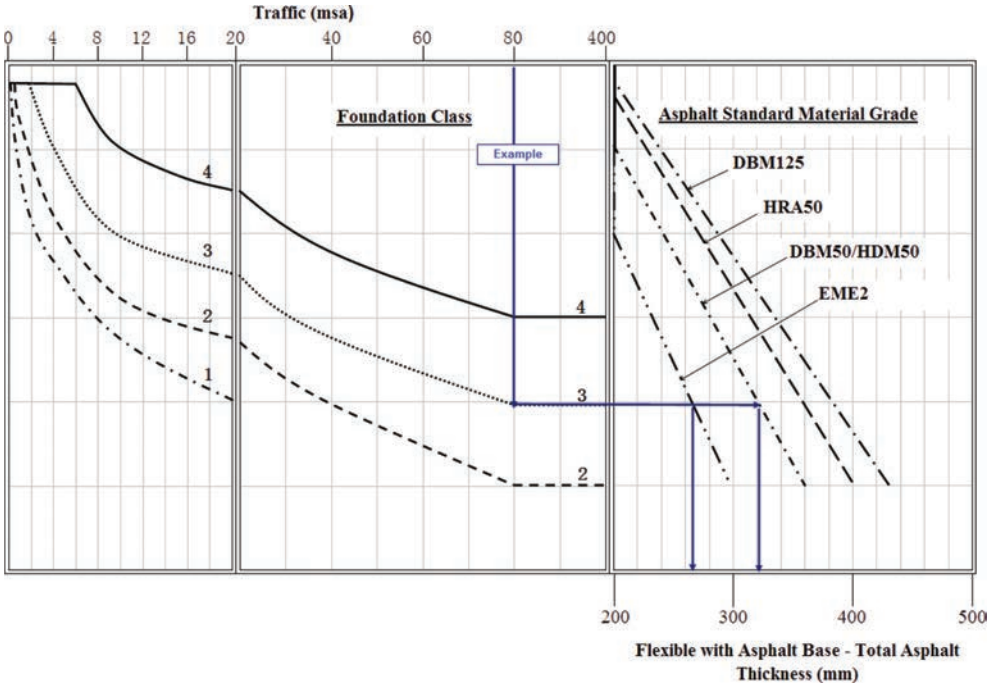

Figure 5. Extract from the UK flexible pavement design guide [5].

Concrete Base (CRCB) with asphalt surfacing are recommended for heavy traffic and poor subgrade, if initial construction and life cycle cost is appropriate. The recent design standard [5] has introduced various concrete grades with flexural strength of 4.5, 5.0, 5.5 and 6.0 MPa to allow the use of wider design options. The previous design was based on a single concrete compressive strength, and limited to 40 MPa.

3 ENVIRONMENTAL BENEFITS

Potential benefits to the environment from using the recent standard can be expected as a result of a number of factors such as; using marginal, secondary, local and recycled aggregates with a wider range of binders including slag and fly ash in foundation design, reducing foundation thickness when stabilised, and using thinner upper bound layers with a stiffer foundation. Advantages of using thinner but stiffer pavements include; reducing aggregates and binder use; reducing aggregate production (crushing, processing and transportation); reducing the effort of mixing, transporting, laying and compacting the asphalt/concrete mixes and associated vehicle movements during construction; reducing fuel cost and CO_2 emissions; and reducing project time, resources requirements, noise and disruption to the public.

The performance testing improves construction quality and provides a better material durability with longer service life and/or less maintenance work. This helps reduce the requirement for premium aggregates for maintenance or resurfacing works.

4 CASE STUDIES

Case studies carried out before and during the introduction and implementation of the performance specification are presented. Foundation material design optimisation, ex-situ recy-

cling using "Foamix" base, stabilised surfacing for a cycle track, and asphalt mixture design for an airport taxiway are detailed in the following section.

4.1 *Use of secondary and marginal materials in pavement foundation*

The use of local secondary and marginal materials in pavement construction has environmental and economic advantages, such as reducing the importation of virgin graded granular materials. However, these materials do not usually comply with the current standards in terms of grading and mechanical properties. Therefore, performance specifications rather than those based on recipes need to be implemented in order to ensure that the design assumptions are met during construction. Examples of UK projects where secondary and marginal materials have been used in pavement foundations are:

- A2—M2 (Kent): Various subgrade improvement materials including cement stabilised chalk, Ragstone (local sandstone) and recycled crushed concrete.
- A27 Polegate (Sussex): Lime/cement stabilised Weald clay.
- A43 Towcester to M40 (Northampton): Oolitic limestone and planings.
- Doncaster North Bridge: Urban widening of road incorporating marginal materials.
- A63 Selby Bypass: Sand subgrade improvement and sand/PFA/cemented sub-base.
- Tilbury Docks: Berths 41–43: Crushed concrete capping and sub-base.

The test results were used to support and validate the recent design standard [4]. Various performance tests were carried out during field trials and actual constructions to ensure quality control. These tests are summarised by Brown [6]. The test results of a section of the A63 Selby Bypass project are shown in Figure 6, where an in-situ initial foundation surface stiffness of 500 MPa was specified for all but two from ten consecutive tests, with an absolute minimum stiffness of 250 MPa.

4.2 *Pavement foundation design optimisation, Romania*

The Transylvanian motorway, sponsored and owned by the Government of Romania, is one of the largest highway projects in Europe. The construction of the new 26 m wide dual two-lane motorway, stretching 415 km northwest from Brasov in central Romania to Oradea on the country's border with Hungary is particularly important for Romania's integration into the European economy. The indicative pavement design raised a number of sustainability issues and recommended optimising the foundation design using local aggregates for the production of a cost effective sustainable solution. The design team visited the country in order to gather useful local knowledge and to identify the most economic and sustainable pavement design.

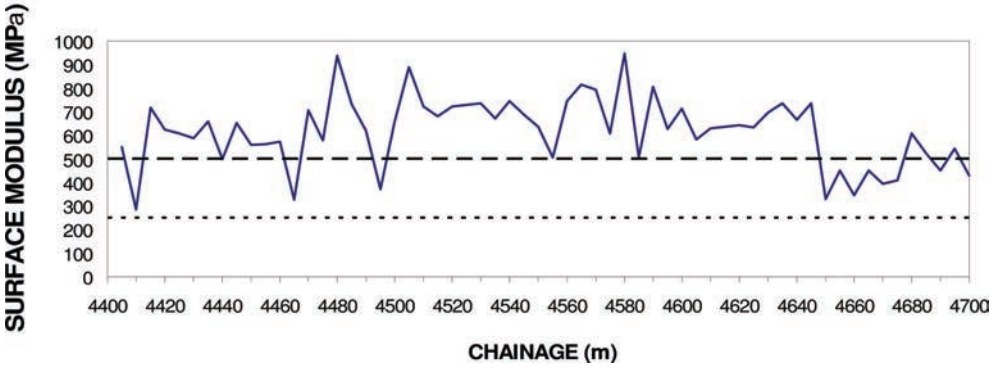

Figure 6. A63 Selby Bypass FWD foundation stiffness at 28 days.

The Springbox equipment was used to assess the mechanical properties of unbound and weakly bound materials. Various mixes with different binder contents were tested to measure stiffness. For subgrade improvement, silty-clay subgrade, local sand and gravel, and crushed rock subbase, as well as cement treated base materials were tested. The effect of high moisture content on stiffness was also investigated.

The design presented a number of benefits for the client including:

- Minimum performance requirements specified for locally sourced cement bound base, which otherwise shown to have a high impact on the life of the overall pavement.
- In situ foundation performance specification introduced, and technology transfer.
- Designs mitigated against early wheelpath rutting failure.

4.3 *Using ex-situ cold mix base materials*

Ex-situ cold mix base using recycled aggregates offers an alternative, environmentally friendly pavement solution. However, the mixture properties in terms of stiffness and durability need to be established in order to design pavements incorporating such materials. Experiments with seven variants of cold recycled mixes were conducted at a Quarry. These included natural aggregates, processed demolition waste, blast furnace slag, crushed concrete and reclaimed asphalt planings. Cement was added to all but one section, which incorporated granulated blast furnace slag and PFA activated by steel slag fines as a hydraulic binder (see Fig. 7). The recycled base was laid to a thickness of 150 mm, in 15 m long and 3 m wide test sections. The test pavements were monitored for a period of one year, with all sections instrumented with stress and strain gauges in an attempt to evaluate the response of the pavement to traffic loading. FWD data showed strength steadily increasing over the first six months, at which point curing appeared to be substantially complete as shown in Figure 8. Design stiffnesses of 2500 MPa were achieved after 1 year, comparable to conventional hot-mix asphalt.

4.4 *A9 Millennium Route cycleway, Scotland*

Site investigation along selected sections of the A9 Millennium Route cycleway in Scotland showed that the natural ground generally consisted of topsoil and soft material (with CBR of less than 5%) ranging from 50 mm to over 1000 mm in depth, on a non-cohesive subgrade capable of achieving over 15% CBR.

The investigation and optimisation work included tests carried out on virgin land along the proposed cycle track route; advice on construction that made best use of local resources; in-situ and laboratory based testing carried out over selected lengths during construction; and finally, in-situ and laboratory based testing carried out over the length of the completed cycle track. The design used a geotextile to 'float' the track across

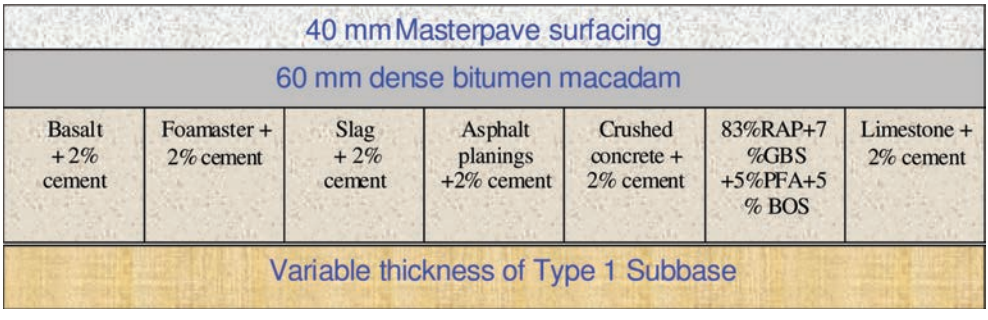

Figure 7. Ex-situ cold mixes with recycled aggregate trials.

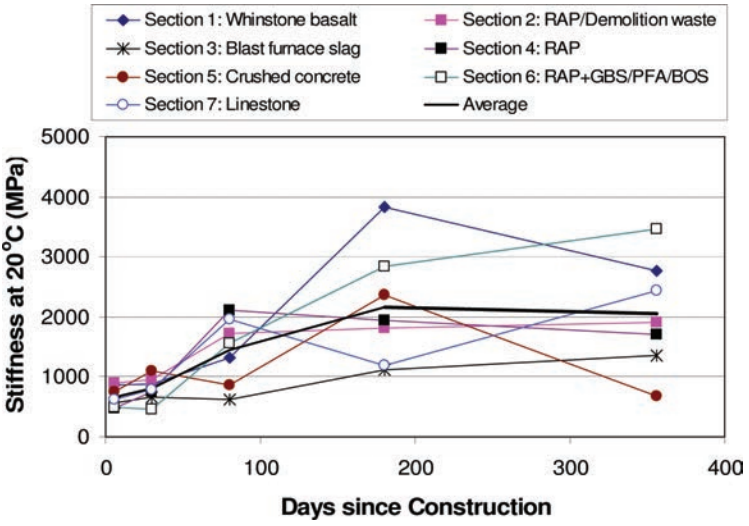

Figure 8. Ex-situ cold recycled mix trials and FWD stiffness development over one year.

lengths of deep peat subgrade, and a slag-bound subbase (comprising 5% GGBS with 2% cement and 93% granular material—i.e. making good use of locally available raw and secondary materials), surfaced with Fibredec, to provide a cheaper and more environmentally friendly alternative to conventional bituminous materials. Fibredec is a unique combination of bitumen emulsion, chopped glass fibres and aggregate. Final testing, around 18 months after construction began, revealed good structural performance characteristics, with only one localised crack defect, coinciding with a length of peat subgrade being visible. It was recommended that laying of hydraulically bound materials incorporating slow setting binders should be restricted to the summer months, when there is no risk of the minimum air temperatures falling below 10°C, if the potential strength and stiffness properties of such materials are to be achieved in-situ. Furthermore, due to the slow strength of HBM, particular attention should be given to protecting the surface of the material with a surface seal (e.g. surface dressing, slurry surfacing or a proprietary product) applied to ensure water is shed, and the long term durability of the pavement structure is improved.

4.5 *Airport pavement design, Isle of Man Airport, UK*

A detailed pavement investigation indicated that the airport taxiways were in poor condition and required reconstruction to carry future traffic loading. An alternative pavement option (to the conventional asphalt reconstruction) using cold in-situ recycling to meet the technical and financial requirements was considered for the taxiway strengthening. The design process included materials testing and performance specification to ensure the appropriate HBM category (incorporating existing aggregates) would be met during construction. The pavement rehabilitation consisted of in-situ cold recycling of 250–265 mm of existing pavement with 100 mm new asphalt surfacing to carry future traffic loading.

The design considered the Waste and Resources Action Programme (WRAP) Halving Waste to Landfill Initiative and negated the need to dispose hazardous tar bound materials found during the pavement investigation. The recycling option delivered a sustainable solution with substantial reductions in cost (40%), energy consumption (44%) and carbon dioxide emissions (32%), when compared against the conventional reconstruction design. Full details of the project are given by Hakim and Ferguson [7].

5 CONCLUSIONS

The advantages of pavement design using performance specifications include; wider construction options; using local, marginal, secondary and recycled materials; better quality control and durability; and improvements to pavement sustainability and whole life cost.

The use of improved foundations with stiffer/stabilised materials to reduce the pavement layer thicknesses is permitted in the recent design approach. These advantages, together with the flexibility of using a wider range of Hydraulically Bound Mixtures (HBMs), plus asphaltic and concrete materials, have helped designers to optimise the pavement construction and materials compared with the previous design requirements. However, there is the need for associated laboratory and end-product performance testing to assess the fundamental material engineering properties as part of the design and construction process.

Case studies have demonstrated the successful introduction of the design approach where material development, laboratory testing and performance requirements were carried out, and design solutions with sustainability and cost benefits were developed.

REFERENCES

[1] Highways Agency, Foundations, Design Manual for Roads and Bridges, Volume 7, Pavement design and maintenance, HD25/94, 1994.

[2] Brown S.F., Soil mechanics in pavement engineering, 36th Rankine Lecture of the British Geotechnical Society, Geotechnique, Vol. 46 No. 3, pp 383–426, 1996.

[3] Edwards J.P., Thom N.H., Fleming P.R., and Williams J., Accelerated laboratory based mechanistic testing of unbound materials within the newly developed NAT Springbox, Journal of Transportation Research Board, Record 1913, 2005.

[4] Highways Agency, Design guidance for road pavement foundations, Design Manual for Roads and Bridges, Volume 7, Pavement Design and Maintenance, Interim Advice Note IAN73/09, 2009.

[5] Highways Agency, Pavement design, Design Manual for Roads and Bridges, Volume 7, Pavement Design and Maintenance, HD26/06, 2006.

[6] Brown S.F., Application of soil mechanics principles to design and testing of pavement foundations, Proc. 8th Conf. on Asphalt Pavements for Southern Africa, pp 668–680, 2004.

[7] Hakim B., and Fergusson C., Sustainable pavement construction at the Isle of Man airport, Asphalt Professional Journal, No. 46, 2010.

Experimental characterization of asphaltic materials—IX

This page intentionally left blank

Asphalt Pavements – Kim (Ed)
© 2014 Taylor & Francis Group, London, ISBN 978-1-138-02693-3

Impact on the use of Reclaimed Asphalt Shingles on mixture and recovered binder properties

Gerald Reinke, Stacy Glidden, Steve Engber, Mary Ryan & Doug Herlitzka
MTE Services Inc., Onalaska, WI, USA

ABSTRACT: The use of reclaimed asphalt shingles in bituminous mixtures has increased significantly in recent years. The information reported is part of a series of on-going investigations into the impact of RAS (Reclaimed Asphalt Shingles) and RAP (Reclaimed Asphalt Pavement) at 20% or higher levels of binder replacement. Laboratory mixtures using recovered shingle binder blended with virgin PG 58-28 and PG 52-34 were compared to mixtures produced with 20% binder replacement using reclaimed shingles. Rutting tests on unaged and Overlay Tester evaluation of mixes before and after aging at 85°C were conducted. Results indicate that initial properties of RAS mixtures appear acceptable, however mixture properties after aging show severe degradation, especially with regard to fatigue for all mixtures. In 2012 a field study was initiated to evaluate mixes produced with 20% RAS and 10% RAP binder replacements. Both PG 58-28 and PG 52-34 virgin binders were used. Control sections of 20% and 31% RAP only were constructed using PG 58-28. Initial evaluation of field cores followed by laboratory aging indicate that the RAS containing mixtures' stiffness and recovered binder properties deteriorated at a faster rate than RAP only mixtures. Increases in asphaltenes with aging are highly correlated to a significant increase in the m-value failure temperature of the RAS mix recovered binders. Cores procured approximately one year after construction show substantial aging, especially of recovered binders. Also reported are data from cores removed after 2 and 3 years in service wherein the binder lifts were constructed using 20% RAS binder replacement.

Keywords: shingles, RAS, RAP, binder replacement, mixture fatigue, 4 mm DSR (Dynamic Shear Rheometer) test

1 INTRODUCTION

In the past several years the rising cost of crude oil has pushed the price of paving grade asphalt binders to historically high values. There is little reason to believe that this situation will revert. As a consequence pressure has increased to use higher levels of binder replacement from Reclaimed Asphalt Pavements (RAP) and more recently from Reclaimed Asphalt Shingles (RAS). While historically the amount of binder replacement in bituminous mixtures averaged in the 15–20% range in states that embraced the use of RAP, recent economic pressures have resulted in efforts to allow upwards of 50% binder replacement and higher in some locations. The burgeoning growth and sophistication of the post-consumer waste shingle grinding industry has added another dimension to the issue of binder replacement. Ready access to reliably available ground shingles coupled with the knowledge that shingles typically contain 20% or more bituminous material has further increased pressure on agencies to allow 20% or more binder replacement from RAS plus 10% or more binder replacement from RAP in bituminous mixtures. Some states were early adopters as they saw the use of shingles as a means to reduce the need to use more expensive polymer modified binders to reduce pavement rutting. Some agencies had reservations about the wisdom of using high levels of binder replacement derived from the very stiff and brittle binder present in shingles.

Regardless of the position taken on the use of RAS in bituminous mixtures there does not appear to have been an evaluation of the long term impact of binder replacement obtained from RAS on pavement performance, especially with respect to fatigue and thermal cracking performance. The information provided in this report is an effort to introduce data on the aging characteristics of RAS containing mixtures and initiate discussion and evaluation of these mixtures within the asphalt research community with a view towards the long range benefit to user agencies and the paving industry of using RAS materials in bituminous pavements.

2 INVESTIGATIONS

2.1 *Initial laboratory research*

An initial experiment was designed to investigate the impact of aging on a Wisconsin 3 million ESAL limestone aggregate mix produced with 22% RAS binder replacement in PG 58-28 and PG 52-34 binders. Most of the blends were produced with the addition of 5.4% RAS into the mix, but two sets of mixes were produced with PG 58-28 and PG 52-34 blended with 22% RAS binder which had been extracted and recovered (using ASTM D5404) from the shingle source used in the study. The complete list of samples tested is shown below:

1. PG 58-28 virgin binder mix control
2. PG 58-28 + 22% recovered shingle binder
3. PG 58-28 + 5% RAS (=22% binder replacement)
4. PG 58-28 + 5% RAS + 0.5% warm mix additive
5. PG 58-28 + 5% RAS treated with 5% of a Proprietary Renewable Additive (PRA) bio oil added by wt. of binder in the RAS
6. PG 52-34 + 22% recovered shingle binder
7. PG 58-28 + 5% RAS (=22% binder replacement)
8. PG 52-34 + 5% RAS treated with 5% a PRA bio oil added by wt. of binder in the RAS

All mixes were produced at 135°C, conditioned for 2 hours at 135°C and compacted at 135°C. One set of specimens was tested without further aging and another set was aged for 5 days at 85°C prior to testing. Hamburg testing under water at 50°C and dry at 58°C was performed on the unaged mix. That data will not be presented, but is available. Overlay tests [1] were performed at 20°C on both the unaged and aged mix samples. The results are shown in Figure 1. The PG 58-28 unaged virgin mix shows very good results, but there is substantial reduction in cycles to failure after 5 days of aging. Several of unaged RAS mixes performed at an acceptable level; most notably the PG 52-34 + 22% recovered shingle binder, the PG 52-34 with 5.4% RAS and the PG 52-34 with 5.4% RAS to which the PRA oil had been added. After 5 days of aging at 85°C the overlay results of those mixes, as well as all the other mixes containing either preblended shingle binder or RAS shingle additive, collapsed to 8-18 cycles to failure. The results for the unaged mixes produced with PG 58-28 preblended with shingle binder, PG 58-28 with 0.5% M-1 warm mix additive plus 5.4% RAS, and PG 58-28 plus 5.4% RAS were nearly identical. The results of mix produced with PG 52-34 preblended with shingle binder and mix produced with PG 52-34 where the RAS was added to the aggregate showed similar overlay results. These data indicate that for short term aged mixes (2 hours prior to compaction) there is little or no difference between whether the shingle binder is intimately blended with the virgin binder or the virgin binder and RAS binder are combined at the time of mixing.

As a further investigation of the impact of shingle binder on mix behaviour mixture stiffness modulus was determined using a DSR torsion bar test (ASTM D7552). Mixture stiffness was measured in 10°C increments from –40°C to +40°C over a frequency range of 100 to 0.02 radians/sec. Using RHEA™ software published by Abatech [2] the measured complex modulus mastercurves was interconverted to relaxation modulus mastercurves. Figure 2 is plot of selected relaxation modulus mastercurves at a reference temperature of 20°C. Not all data has been plotted so that what has been shown is readable. As the mixes are aged the

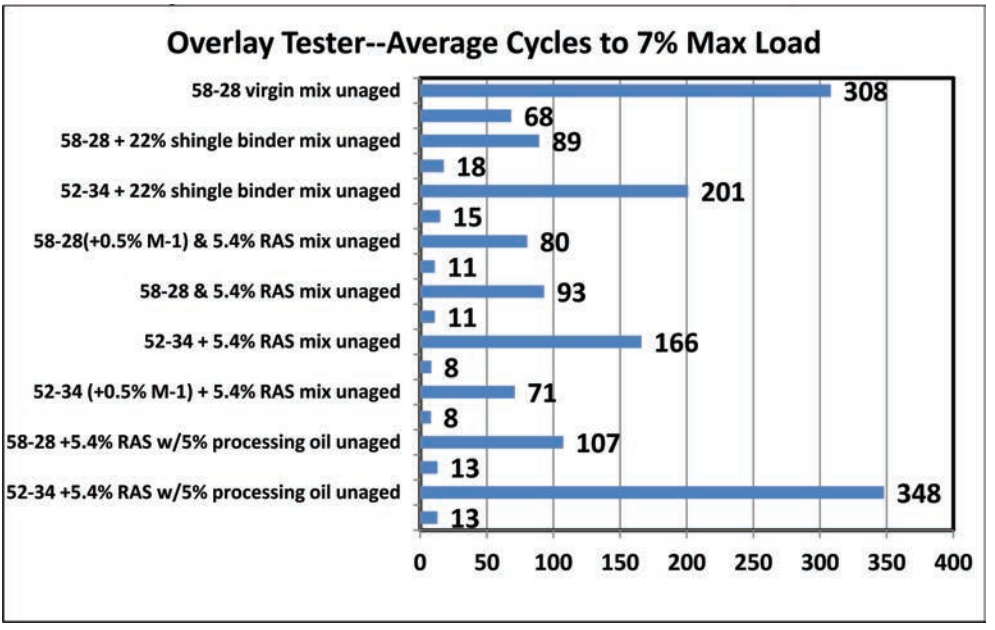

Figure 1. Overlay test results for unaged and aged mix specimens.

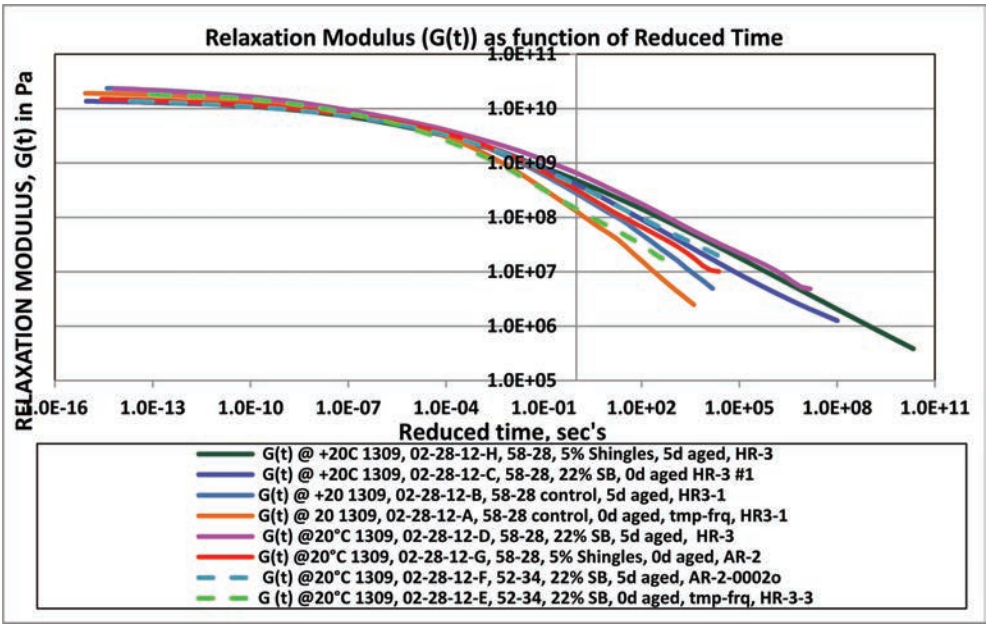

Figure 2. Relaxation modulus of unaged and 5 day aged mixes.

slopes of the relaxation modulus mastercurves begin to flatten as relaxation time increases. The PG 58-28 virgin control mix has been plotted to provide a reference for comparison. It is important to note that the relaxation modulus for the PG 58-28 + 22% added shingle binder and the PG 58-28 + 5.4% RAS are nearly identical for both the unaged and the 5 day aged condition. The moduli of these mixes is a more fundamental property than the overlay test,

but the modulus data also demonstrates that whether there is 100% preblending of the shingle binder with virgin binder or the shingle binder is introduced into the mix via the ground shingles the relaxation properties of the unaged and 5 day aged mixes are the same. The relaxation moduli of the unaged and 5 day aged PG 52-34 + 22% shingle binder mixes has also been plotted. Unlike the overlay test result where the 5 day aged mix exhibited the same cycles to failure as the aged PG 58-28 shingle mixes, the PG 52-34 + 22% shingle binder 5 day aged mix has a relaxation modulus plot comparable to the unaged PG 58-28 shingle binder and RAS containing mixes. However this result does mean that the PG 52-34 shingle binder mix suffered substantial stiffening and is now comparable to the unaged PG 58-28 shingle containing mixes whereas the unaged PG 52-34 + 22% shingle binder mix was comparable to the PG 58-28 virgin control.

2.2 *RAS and RAP shoulder paving research study*

In September of 2012 Mathy Construction Company placed four test sections using varying levels of RAS and RAP on the shoulder of a project on USH 14 east of St. Charles, Minnesota. The project consisted of the following test sections produced with a 3 million ESAL mix:

1. PG 52-34 binder, 6% RAS (22% binder replacement), 11% RAP (12% binder replacement)
2. PG 58-28 binder, 6% RAS (22% binder replacement), 11% RAP (12% binder replacement)
3. PG 58-28 binder, 31% RAP (32% binder replacement)
4. PG 58-28 binder, 20% RAP (21% binder replacement), the control mix for the project

2.2.1 *Initial testing of mixes*

In November of 2012 three cores were cut from each test section and tested. One unaged core, one core aged 5 days at 85°C and one core aged 10 days at 85°C from each test section was cut into torsion bars for mixture modulus testing at –40°C to +60°C. Following these mix tests binder from the torsion bars of each section and aging condition were extracted and recovered and the binder tested using a 4 mm DSR test procedure [3] at –40°C to +60°C following procedures developed by Western Research Institute (WRI). The 4 mm DSR test enables determination of full mastercurves of the binders, which were generated at +20°C. In addition using procedures developed by WRI the low temperature PG properties of the binders were determined [4]. Lastly Iatroscan [5] testing was performed on the recovered binders to obtain asphaltene, cyclic (aromatic), resin and saturate fractions of each recovered binder.

2.2.2 *Follow-up testing of mixes*

In August of 2013 four cores were obtained from each test section. These cores for each section were taken within approximately a 3 meter length of pavement. The top 12 mm and second 12 mm layers were cut from one core and the binder from each layer was extracted and recovered. The top 12 mm and second 12 mm layers were cut from another core and each layer was cut into torsion bars for mixture modulus testing. Testing of both layers was performed to ascertain the extent of mix and binder aging with depth. The other two cores were set aside if additional follow-up testing was needed. The binder and mixture testing performed was similar to that described for the initial cores.

2.2.3 *Findings from initial and follow-up testing*

The low temperature recovered binder properties based on 4 mm DSR testing is shown in Table 1; the asphaltene content is also shown.

Asphaltenes were determined as the n-heptane insoluble fraction. Based on the recovered binder testing of the initial cores, the m-critical temperature is highly correlated to the per cent asphaltenes in the recovered binder. This is shown in Figure 3.

Table 1. Asphaltene and low temperature critical data for 2012 & 2013 cores USH14 shoulders.

Mix type	Days of 85°C core aging (or as noted in table)	Asphaltenes	m-critical temp, °C (mcT)	S-critical temp, °C (ScT)	ΔTc (S-critical-m-critical)
Sec 1					
52-34	0	18.4	–34.2	–35.9	–1.8
6% RAS	5	20.1	–32.3	–34.9	–2.6
11% RAP	10	21.2	–29.9	–35.6	–5.7
Top 12 mm	11 months field	19.3	–32.9	–35.7	–2.8
2nd 12 mm	11 months field	18.6	–34.3	–35.9	–1.6
Sec 2					
58-28	0	23.5	–31.0	–33.2	–2.3
6% RAS	5	26	–28.0	–30.7	–2.7
11% RAP	10	27.2	–24.1	–30.9	–6.8
Top 12 mm	11 months field	25.8	–28.2	–30.8	–2.6
2nd 12 mm	11 months field	25.1	–29.4	–31.3	–1.9
Sec 3					
58-28	0	20.5	–32.2	–31.9	0.4
0% RAS	5	23.6	–29.1	–29.8	–0.7
31% RAP	10	24.8	–26.7	–29.6	–2.9
Top 12 mm	11 months field	23.2	–30.2	–31.3	–1.1
2nd 12 mm	11 months field	21.9	–31.6	–31.4	+0.2
Sec 4					
58-28	0	19.7	–33.4	–33.4	0.0
0% RAS	5	21.9	–31.3	–31.9	–0.6
21% RAP	10	23.4	–30.3	–32.3	–2.0
Top 12 mm	11 months field	22.7	–32.0	–32.2	–0.2
2nd 12 mm	11 months field	22.1	–32.3	–31.9	+0.4

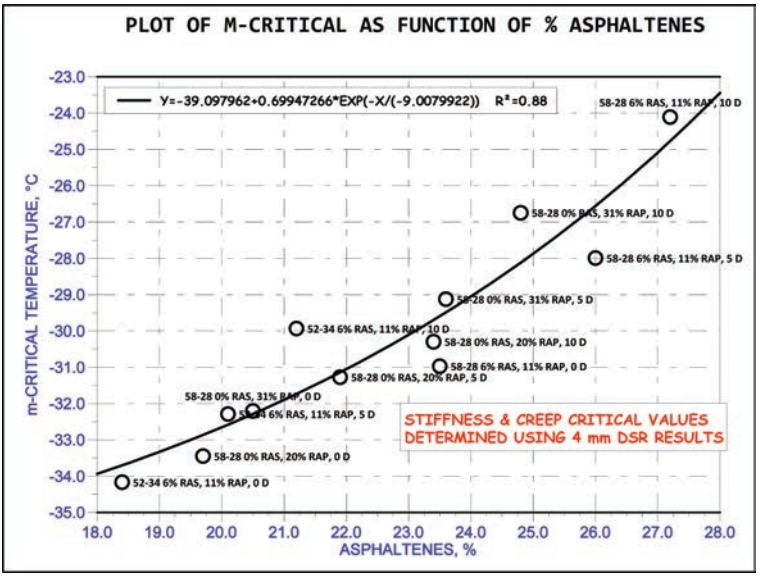

Figure 3. m-critical temperature as a function of per cent asphaltenes for 2012 cores.

When the asphaltene data for the top and second 12 mm mix layers of the 2013 cores is plotted on this same data set (Fig. 4) it is apparent that the binder from the top 12 mm layers have moved substantially towards that of the 5 day aged 85°C aged mixes. The PG 58-28 RAS/RAP recovered binders from the both layers plot much closer to the 5 day aged data than the unaged. The data for the PG 58-28 with 20% RAP has not been plotted on this chart so the other data is easier to visualize. For the 20% RAP mix Table 1 shows about a 1°C increase in m-critical for the recovered binder, but the asphaltene content for both layers has increased from 19.7% to 22.7%, which is comparable to the increases for the other mixes. At the same time the ΔTc for the 20% RAP only mix and to a lesser extent the 31% RAP only has not increased by the same amount as the ΔTc increase for the RAS containing mixes when compared to the ΔTc increases for the binders recovered from original unaged cores taken in 2012. This increase in the rate at which ΔTc increases for the binder in RAS containing mixes may well be a causative factor in the poorer fatigue performance and loss of relaxation properties in these mixes. What is not known however is a mechanism by which this process occurs and a means of altering or stopping it.

Mixture stiffness modulus was obtained on the top two 12 mm layers using the DSR torsion bar test procedure. Mastercurves were determined at a reference temperature of 20°C. Results for Test Section 2, the PG 58-28 mix containing 6% RAS and 11% RAP is plotted in Figure 5. There was a moderate increase in mixture stiffness between the unaged and 5 day aged mixture samples; however, there was a more substantial increase in stiffness for the 10 day aged core specimens. For the 11 month field cores taken in 2013 the stiffness modulus of the top 12 mm of mix is greater than the stiffness of the 5 day aged core from 2012, while the second 12 mm layer has stiffness equal to or slightly less than the original unaged core. Figure 6 is a similar plot for the Section 1 cores. Only the top 12 mm mixture modulus results are shown and again the mixture stiffness after 11 months in the field shows that the mix is as stiff as the 5 day aged core in 2012. The second 12 mm layer stiffness for the 2013 core was similar to the unaged 2012 core.

The top layer of the 11 month field core for the 31% RAP mix had stiffness comparable to the 5 day aged core taken in 2012; however the 5 day aged mix from 2012 was only moderately

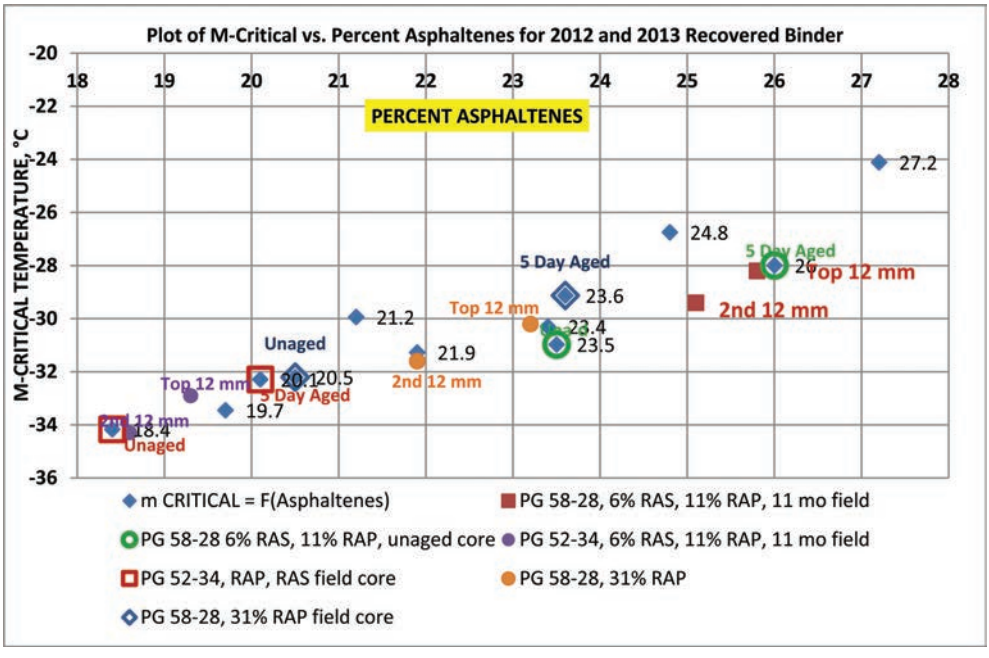

Figure 4. m-critical versus asphaltenes for 2013 top and 2nd layer recovered binder.

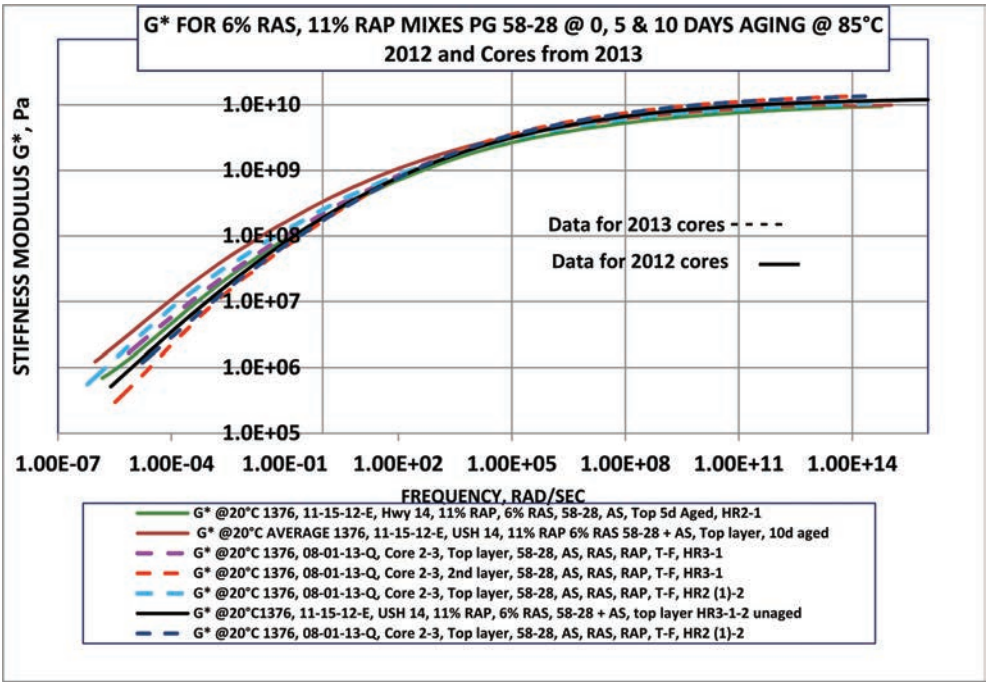

Figure 5. Compare torsion bar complex modulus for section 2, PG 58-28, 6% RAS, 11% RAP, 2012 and 2013 cores.

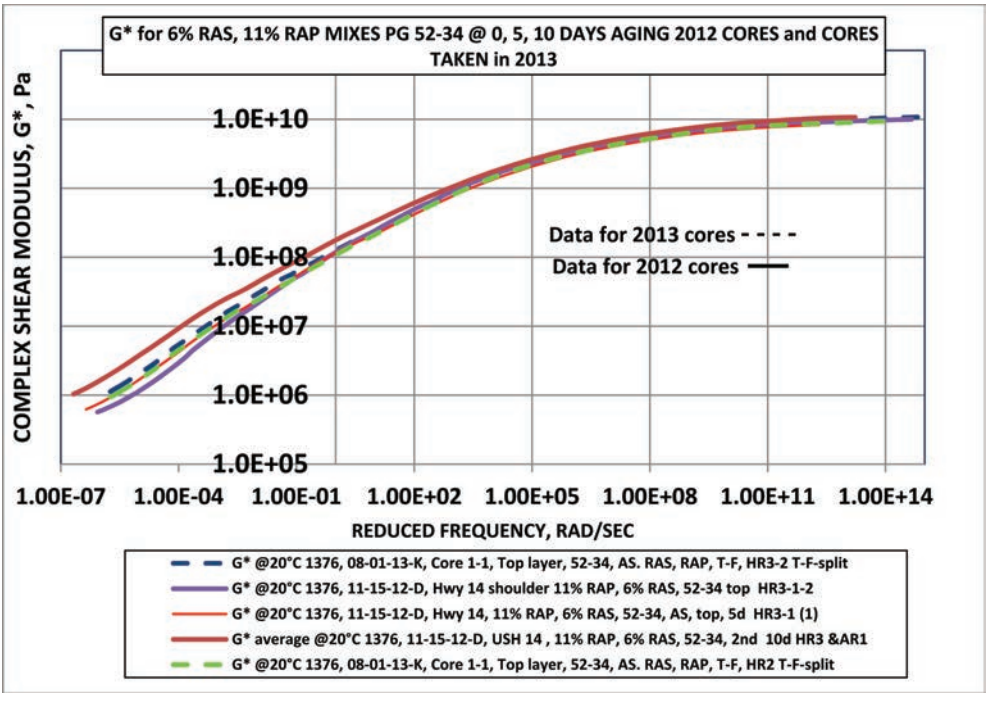

Figure 6. Compare torsion bar complex modulus for section 2, PG 52-34, 6% RAS, 11% RAP, 2012 and 2013 Cores.

stiffer than the unaged core taken in 2012. The top layer of the 11 month field core for the 20% RAP mix was stiffer than the unaged mix from 2012 but not as stiff as the 5 day aged mix. Those data are not shown in this report.

2.3 *Testing of binder lift mixes using RAS placed in 2010 and 2011*

In 2010 and 2011 Mathy Construction Co. placed RAS & RAP containing mixes using PG 64-22 on the two lower lifts of Interstate paving projects conducted in those years. The design was a 19 mm 30 million ESAL mix. Cores were taken in 2012 and again in 2013 to ascertain whether the same apparent accelerated rate of aging was occurring in those mixes as was being observed in laboratory studies and in the USH 14 initial core aging investigation. After coring the upper lift (PG 70–28, 20% RAP, 12.5 mm) was removed and two 12 mm layers were cut from top of the binder lift. These two layers were cut into torsion bars for DSR stiffness testing and were extracted and recovered for asphaltene determination and binder rheological characterization using the 4 mm DSR test procedure. Table 2 summarizes the asphaltene and low temperature properties of the recovered binder from the cores. In 2012 only one layer of binder was recovered and based on the similarity of the data for the two layers in 2013 there would have been little information to glean from the second layer data in 2012. Although the original mix design called for the use of RAS and RAP it is apparent from these data that the specific west bound cores obtained in 2012 contained no RAS and the cores from 2013 may have contained a low amount of RAS. The projects were approximately 14 miles long and cores were purposely not taken in the same location in 2012 and 2013 primarily because of the west bound core data from 2012. Evaluation of the quality control data from 2010 showed a span of approximately 4.5 miles when, due to RAS feeding problems, only 15% RAP binder replacement was used. There were also several days when 3% RAS (16.7% binder replacement) and 11% RAP (15.3% binder replacement) was used. The majority of the 2010 paving used 4% RAS (18.6% binder replacement) and 12% RAP (14% binder replacement). While there was some variability during the project the 2011 paving was much more consistent with an average of 24.5% RAS binder replacement and 8.4% RAP binder replacement. The asphaltene and low temperature data shows that no apparent aging is taking place over the course of the one year time period between the 2012 and 2013 cores for either project. The variations in results between cores taken in 2012 versus 2013 are most likely due to variations in the RAS and RAP content of the mixes. Only additional data can answer the extent to which RAS containing mix placed 75 or more mm below the surface is impacted by aging time. What does appear clear from the 2010 versus the 2011 I-94 data is the substantial impact that the presence of shingles in the 2011 mix has on the low temperature properties of that mix compared to the specific 2010 mix samples tested, which appear to have contained little or no shingle additive.

Table 2. Asphaltene and low temperature critical data for 2012 & 2013 cores of I-94 pavements.

Sample location (WB-West Bound) (EB-East Bound)	Core year	Asphaltene, %	m-critical temp (mcT)	S-critical temp (ScT)	ΔTc (ScT-mcT)	High temp PG grade $1/\sin(\delta) = 2.2$
WB 2010	2012	22.4	–28.96	–29.82	–0.86	70.3
WB 2010 top 12 mm	2013	23.3	–26.86	–28.2	–1.34	75.9
WB 2010 2nd 12 mm	2013	23.5	–28.23	–28.75	–0.52	74.6
WB 2010 base top 12 mm	2013	21.8	–27.99	–28.36	–0.38	72.8
WB 2010 base 2nd 12 mm	2013	22.3	–27.80	–28.0	–0.20	71.7
EB 2011	2012	27.7	–22.97	–27.55	–4.58	85.2
EB 2011 top 12 mm	2013	26.7	–21.71	–25.89	–4.18	87.6
EB 2011 2nd 12 mm	2013	26.9	–21.87	–25.63	–3.76	86.0
EB 2011 base top 12 mm	2013	26.1	–24.16	–25.97	–1.81	80.7
EB 2011 base 2nd 12 mm	2013	25.6	–26.07	–27.86	–1.78	79.1

Mastercurves for the recovered binders from 2012 and 2013 are shown in Figure 7. The mastercurve data supports the asphaltene and low temperature data showing the west bound sections had recovered binder properties that were much less stiff than the east bound recovered binders.

Figure 8 shows plots of the torsion bars complex modulus at a 20°C reference temperature. Data from both 2012 and 2013 cores are plotted showing minor variation within the east and west bound mix stiffness between the two years, but also showing a substantial difference in mixture stiffness for the east bound mix compared to the west bound mixes over those two years.

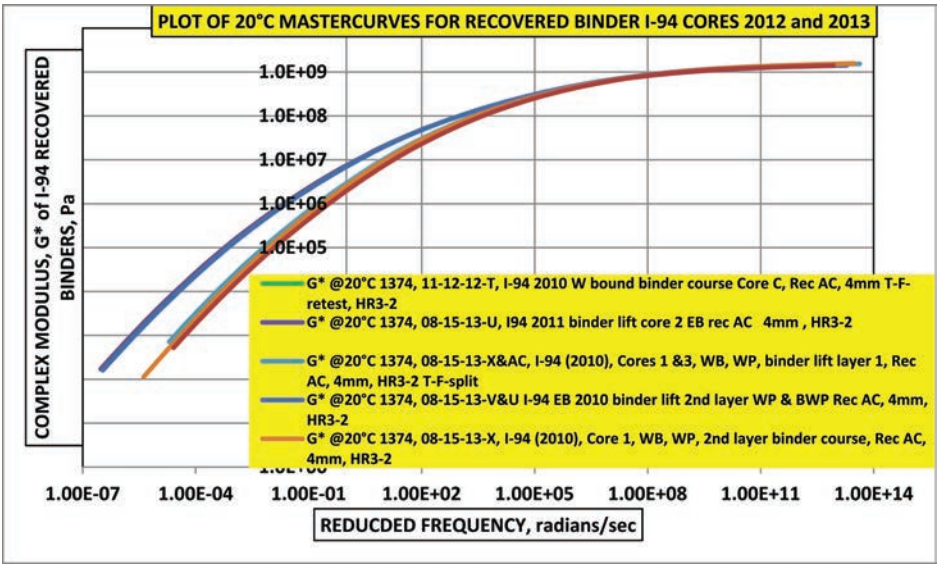

Figure 7. Mastercurves @ 20°C of recovered binder for 2012 & 2013 cores.

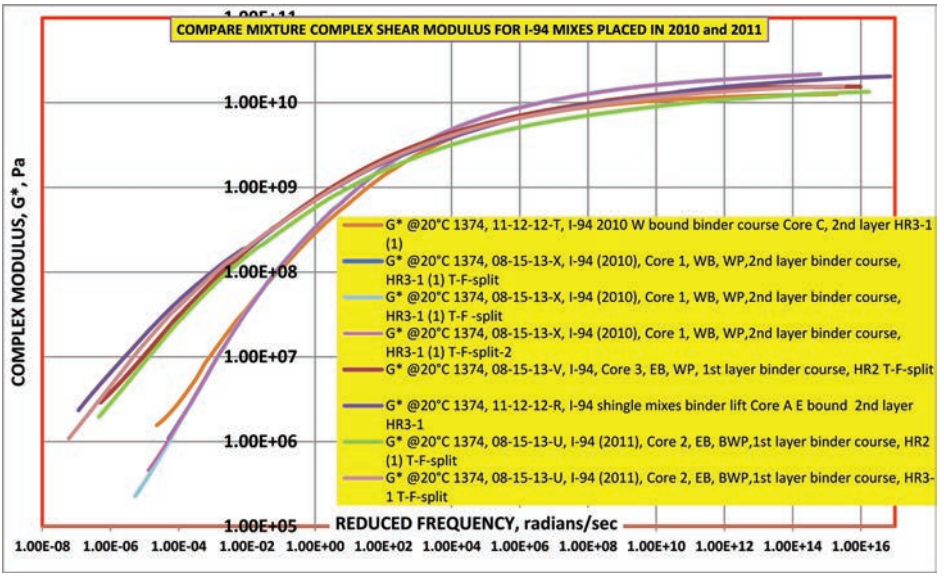

Figure 8. Mixture mastercurves @ 20°C for 2012 & 2013 cores.

3 DISCUSSION

Much of the discussion regarding the impact of RAS on mix and binder aging has been included within each section in the body of the paper. The field data presented supports the initial laboratory investigation findings of rapid mixture aging when shingle binder is present in the mix and exposed to oxidation. The laboratory investigation supports, in the authors' opinion, that regardless of whether intimate blending of shingle binder with virgin binder occurs prior to mix production or the shingle binder is introduced via ground shingles (RAS) there is no appreciable difference in mixture performance and more importantly the impact that shingle binder exerts on the aging rate of mixtures. Until a different or better mechanism can be developed it appears as though the presence of shingle binder in bituminous paving mixtures is the causative factor in the rapid aging of the binders in the mixtures and therefore deterioration of the low temperature and relaxation properties of the binders and consequently the mixtures produced with those binders. Based on the I-94 core data it does appear that sequestering the RAS containing mix in a lower lift can reduce and perhaps retard the aging impact of shingle binder on mix properties. Further testing must be performed to substantiate this observation. It is prudent however to keep in mind that today's binder lift could well become tomorrow's binder replacement material for a new wearing course. The shoulder mix placed on US Highway 14 is only one year old and already the upper 12 mm of the RAS containing mixes are showing characteristics comparable to a 5 day 85°C aged mix especially with respect to the divergence of low temperature limiting stiffness temperature and the limiting temperature value based on the binder relaxation characteristic. This is concerning and the aging rate of the RAS containing mixes compared to the high RAP only mix will be tracked over time to determine if there is in fact a mixture performance difference between similar levels of binder replacement but binder replacement that is composed of RAP and RAS compared to RAP only.

REFERENCES

[1] Overlay Tester procedure based on methodology following TxDOT procedure Tex-248-F.

[2] Abatech. *RHEA*™ software, PO Box 356, Blooming Glen, PA 18911, 215–258–3640.

[3] Sui, C., Farrar, M., Tuminello, W., Turner, T.A., New Technique for Measuring low-temperature Properties of Asphalt Binders with Small Amounts of Material, Transportation Research Record: No 1681, TRB 2010.

[4] Sui, C., Farrar, M.J., Harnsberger, P.M., Tuminello, W.H., Turner, T.F., New Low Temperature Performance Grading Method Using 4 mm Parallel Plates on a Dynamic Shear Rheometer. TRB Preprint CD, 2011.

[5] Shantha, N.C., Thin-Layer Chromatography-flame ionization detection Iatroscan system, Journal of Chromatography A, Vol. 624, Issues 1–2, pp. 21–35, 1992.

Asphalt Pavements – Kim (Ed)
© 2014 Taylor & Francis Group, London, ISBN 978-1-138-02693-3

Mode II fatigue and reflective cracking performance of GlasGrid-reinforced asphalt concrete under repeated loading

Amirshayan Safavizadeh & Y. Richard Kim
NC State University, Raleigh, NC, USA

ABSTRACT: The main purpose of this research is twofold: to study the shear fatigue and fracture characteristics of GlasGrid-reinforced asphalt concrete and to examine the effects of different interfacial conditions on the performance of GlasGrid-reinforced asphalt concrete beams using four-point bending beam fatigue testing. In order to fulfill the first objective, a double shear test device and a method for determining crack lengths, referred to as the *bisectional approach*, were developed and used to track the length of cracks along the interface under Mode II fracture. The asphalt concrete interface was reinforced with GlasGrid 8501 with and without a tack coat. The four-point bending beam fatigue test plan included an additional interface condition, which was a tack coat without GlasGrid. The shear tests and beam fatigue tests were conducted at temperatures of 20°C and 23.2 ± 0.5°C, respectively. The results indicate that the presence of a tack coat improves shear fatigue resistance and extends the four-point bending beam fatigue life of GlasGrid-reinforced specimens. The four-point bending beam fatigue test results show that GlasGrid-reinforced specimens outperform non-reinforced specimens.

Keywords: Asphalt concrete interface, GlasGrid reinforcement, Mode II fracture, reflective cracking, Digital Image Correlation (DIC)

1 INTRODUCTION

Given the increase in demand for roads and attention to safety concerns, pavement maintenance and rehabilitation costs continue to rise. These demands and rising costs are all happening in an economic environment where budgets are decreasing and the market is becoming more competitive. Therefore, it is becoming more and more important to construct long-lasting asphalt pavements and find better ways to rehabilitate old pavements.

Reflective cracking is one of the most common distresses in asphalt pavements and is a major problem for the pavement industry. Reflective cracking is a mechanism found in new overlays and is caused by the inability of the overlay to withstand movement of the underlying pavement. Such movement may be due to traffic loading and/or thermal loading. Reflective cracking destroys the continuity of the pavement surface, decreases the structural strength of the pavement, and allows water to penetrate the pavement system, which subsequently leads to further deterioration [1].

Several remedial techniques have been used to control reflective cracking, including placing a thin layer between the old and new layers, rubberizing the existing concrete pavement, cracking and sealing the existing pavement, and increasing the thickness of the Hot Mix Asphalt (HMA) overlay. Among these techniques, interlayer systems have been the most effective in controlling reflective cracking. The effectiveness of the interlayers depends on the selection of the type of interlayer system, the interlayer conditions, installation procedures, and the conditions and characteristics of the existing pavement and HMA overlay [2].

One of the interlayer systems that have been proven effective is geotextile. Three uses of geotextiles in asphaltic concrete overlays are strain relief, reinforcement, and under sealing.

Strain relief occurs in cases where geotextile has a lower elastic stiffness value than the surrounding asphalt concrete. Geotextiles with higher elastic stiffness values than the asphalt concrete are able to reinforce the pavement system. Polypropylene grids and glass fabrics and grids are classified as reinforcing geotextiles and, if constructed properly, can redirect reflection cracks and retard the cracking process. Under sealing geotextiles prevent or reduce penetration of water into the pavement once the crack occurs, and so prevent further deterioration [1].

Laboratory performance evaluation of different geotextiles requires careful consideration of different contributing causes of reflective cracking. These factors include traffic loads and volume, crack spacing, temperature changes, temperature gradient, subgrade stiffness, presence or absence of voids beneath the pavement surface, degree of aggregate interlock across the crack in the old and new pavements, overlay thickness, geotextile position, and tack coat type and application rate [1]. Also, the interlayer bond plays an important role in making the pavement system structurally stiff and also has an important role in stress-strain distribution. So, the long-term performance of pavements and also the cracking pattern depend on interlayer bonding and conditions [3–5].

A large part of the pavement life cycle includes crack propagation prior to failure. Therefore, a primary reason for using geogrids in asphalt pavements is to retard the reflective crack propagation process. As such, it is critical to understand how different interlayer conditions affect crack propagation in both Mode I (opening mode) and Mode II (shearing mode) fracture. In order to study and understand the mechanical behavior of GlasGrid-reinforced asphalt concrete pavements, fracture mechanics concepts and test methods must be applied. So far, Mode I fracture has been the main focus of most of the previous research efforts, and even though some of them have targeted Mode II cracking of asphalt concrete interfaces, more investigation on this Mode seems to be needed in order to fully understand all the mechanisms. The number of studies that address Mode II fracture of grid-reinforced asphalt concrete under repeated loading is even fewer. Since reflective cracking of GlasGrid-reinforced asphalt pavements usually includes cracks that turn and move along the interface, understanding the characteristics of Mode II fatigue and fracture of the interface is vital for an accurate prediction of pavement performance and pavement life. This study seeks to provide a better understanding of the Mode II fatigue performance and fracture characteristics of GlasGrid-reinforced asphalt concrete.

2 EQUIPMENT, TESTS, AND MEASUREMENT METHODS

2.1 *Equipment*

2.1.1 *Development of Double Shear Tester (DST)*

After reviewing different types of shear tests, including direct and simple shear tests and single and double interlayer shear tests, the double shear test concept appeared to offer the best options for this study. In this type of shear test, the side parts of the sample are fixed and its middle part is free to move and is subjected to loading (Fig. 1(a)). The advantage of double shear test over single interlayer shear test methods is that the two interfaces symmetrically undergo a relatively pure shear stress, whereas in single interlayer tests normal forces are applied to the interface at areas that are close to the ends of the specimen in addition to the shearing load. In other words, bending problems usually are associated with single interlayer shear tests [6].

For this study, a specific Double Shear Tester (DST) was designed and fabricated based on the optimum required size of the specimen and GlasGrid opening size (Fig. 1(b) and (c)). The dimensions of the interface were chosen to be 152.4 mm in the direction of compaction and loading by 101.6 mm in the transverse direction to allow for acceptable shear stress distribution and also to provide enough ribs in each specimen interface.

The device was modified at different stages to attain desired characteristics, such as stiffness, test repeatability, and interface area visibility. Figure 1(d) shows the modified DST in

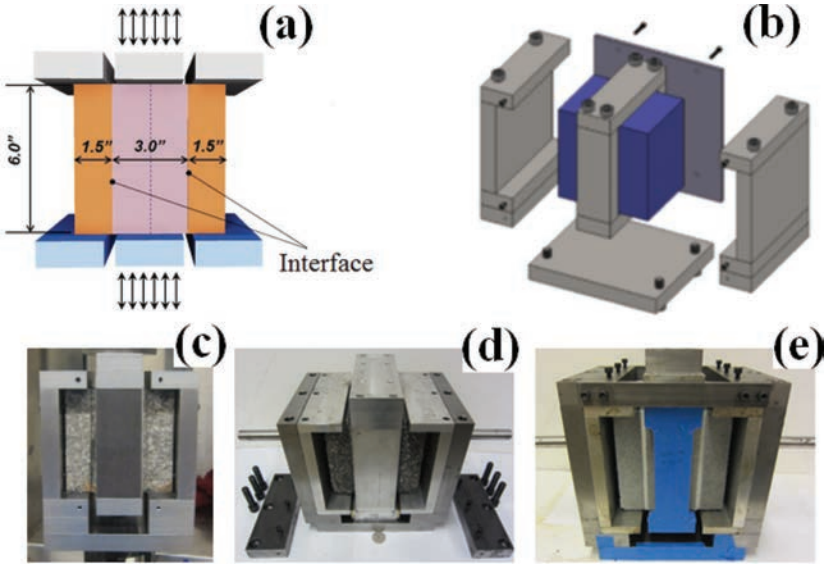

Figure 1. (a) DST concept, (b) DST schematic, (c) Original DST, (d) Modified DST parts, and (e) Final version of DST.

which aluminum parts were added to make the device capable of running more tests per day. Figure 1(e) shows the final version of the DST after a few more minor modifications.

2.1.2 *Four-point beam fatigue test apparatus*

A Cox and Sons four-point beam test apparatus was accommodated for use in the MTS 811 universal testing machine. In this apparatus the spacing between the clamps is 119 mm and the length of the beam between the outside clamps is 357 mm.

2.2 *Tests and test conditions*

2.2.1 *Double shear test*

In order to gain a better understanding of the interface shear fatigue performance of specimens reinforced with GlasGrid, double shear tests were conducted on DST specimens. Different interface conditions, i.e., GlasGrid with an asphalt binder tack coat with an application rate of 500 g/m² (GGTC), and GlasGrid without a tack coat (GGP), were tested. The test temperature was 20°C and the number of replicates for each condition was three. All the specimens were kept at 20°C inside the testing climate chamber for three hours before testing. The tests were carried out under load control mode. A sinusoidal alternating load with a frequency of 5 Hz and a zero mean was applied to the middle part of the shear specimens using an MTS 810 servo-hydraulic material testing system. Different load levels were used for different conditions because of the considerable difference in shear strength under the different interlayer conditions. Table 1 presents the load levels for each condition.

2.2.2 *Four-point bending beam fatigue TEST*

In order to investigate crack propagation patterns and fatigue performance of GlasGrid-reinforced asphalt concrete, four-point beam fatigue tests were carried out on beam specimens. Beam specimens with four different interlayer conditions were tested. The conditions were the same as Double Shear Test conditions (GGTC, and GGP) plus an asphalt binder tack coat with an application rate of 300 g/m² without GlasGrid (TC). The tests were performed according to ASTM D7460. The interlayer was located at one-third depth from the bottom

Table 1. DST load levels (Kgf).

Specimen	GGTC	GGTF	GGP
1	612	227	204
2	567	204	147
3	567	204	147

of the beam. All the specimens were kept in the testing room and at the temperature of 23.2°C ± 0.5°C for at least six hours before testing. The tests were carried out in displacement control mode. A sinusoidal displacement with zero and maximum negative bending deflection peaks was applied to the specimen at a frequency of 5 Hz. That is, the beams were pushed down to reach the maximum strain level of 1400 micro strain and then pulled back to the zero position. The number of test replicates for each condition was two. Some extra tests with only one replicate were performed at different maximum strain levels ranging from 1200 to 1600 micro strain to obtain more crack propagation data for specimens with different interlayer conditions.

2.3 *Digital Image Correlation (DIC)*

Digital Image Correlation (DIC) was used to track and measure the deformations, displacements, and strains on the surface of the specimens and especially at areas around the interlayer. Using spray paint, the specimens were speckled with a white background and black dots in a certain pattern to allow for image analysis and a 5 MP camera was used for capturing images. The distance of the camera from the surface of the specimen was kept the same and in the range of 76 cm to 89 cm for each type of test. VIC-2D software was used for analyzing the images and calculating the displacements and strains on the surface of the specimens.

3 MATERIALS AND SPECIMEN PREPARATION

3.1 *Materials*

A RS9.5B mixture with PG 64-22 binder was used for this study. A PG 64-22 asphalt binder was used as the tack coat. One type of geogrid, GlasGrid 8501, was used for the reinforcement of the HMA interlayer. This geogrid was supplied by Saint-Gobain ADFORS America. GlasGrid 8501 is a self-adhesive glass fiber grid with 12.5-mm wide openings and impregnated with acrylic polymer resin. This polymer resin makes the grid compatible with the asphalt binder [7].

3.2 *Specimen preparation*

Double-layer slabs were compacted using a roller compactor. GlasGrid was installed on top of the first layer and immediately before compaction of the second layer. The double shear test specimens consisted of two double-layer specimens from the same slab bonded together. The first step in fabricating the shear specimens was to make a rough cut using a hand-held saw. Then, using an automatic saw, the top and bottom layers were trimmed to a 38.1-mm thickness and the sides were trimmed to provide a 152.4-mm long, 114.3-mm wide, and 76.2-mm thick specimen. The final step was gluing the top surface of the two specimens together using a two-part metal-filled epoxy glue. Figure 2 shows these steps schematically. By following this method of sample preparation, both interfaces have the same characteristics in terms of compaction, roughness, interlayer systems, tack coat application rate, etc.

The beam specimens were cut out of the slab using a hand-held saw. Then, the bottom and top layers of each beam were trimmed to thicknesses of 18 mm and 36 mm, respectively.

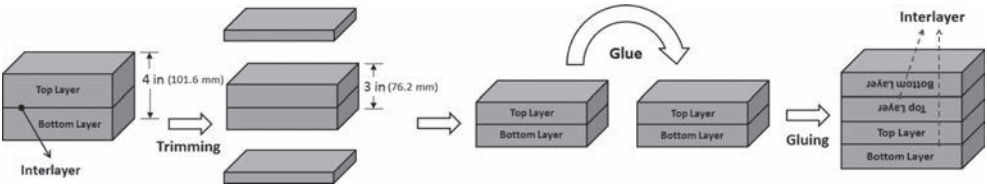

Figure 2. DST specimen preparation procedure.

Finally, the sides were trimmed to provide a 380-mm long and 63-mm wide beam specimen. The length of each beam was in the same direction as grid rolling and slab compaction.

4 CRACK LENGTH DETERMINATION

The main challenge in the analysis of the double shear test data was determining the crack tip during the tests. Three different approaches were evaluated for determining the crack tip: using strain contours, visual detection, and a bisectional approach. Shear and von Mises strain contours of the surface of the shear specimens were obtained during the tests utilizing DIC analysis. Von Mises strain is an equivalent strain and is used as a yielding criterion. This strain provides the equivalent uniaxial strain of the existing strain state from the yielding point of view. The von Mises strain can be calculated using Equation (1).

$$\varepsilon^e = \frac{\sqrt{2}}{3}\left[\left(\varepsilon_1 - \varepsilon_2\right)^2 + \left(\varepsilon_2 - \varepsilon_3\right)^2 + \left(\varepsilon_3 - \varepsilon_1\right)^2\right]^{1/2} \tag{1}$$

where ε_1, ε_2, and ε_3 are the principal strains at an element, and ε^e is the von Mises strain.

Figure 3 presents the evolution of the von Mises strain contour of the specimen GGP_2. The observed increase in the von Mises strain at high numbers of cycles is more obvious around the interlayer and represents the failure process of the interface. Two main problems are associated with using this approach as the failure criterion. The first problem is the error or noise of the strain results, which is a considerable portion of the calculated strain at areas with high strain levels and is inevitable with current DIC analysis. The other problem is determining the threshold of cracking or failure for the different samples and test conditions.

The second approach, i.e., visual observation, was investigated using a speckled sample that was painted white along both interfaces (Fig. 4(a)). The images were examined after the test to determine the crack length. This approach failed because the crack was especially fine around the crack tip and difficult to detect. Also, another problem was that the paint and interface conditions were not compatible, and thus, a crack in the paint might not necessarily be indicative of an interface crack.

The third approach is the bisectional approach. As shown in Figure 4(b), virtual gauges were used at certain positions to track the displacement of two sides of the interlayer during the test. Each of these virtual gauges is composed of 101 points, which is the default number of points in VIC-2D software and more than enough for a precise measurement. The displacement of each gauge is assumed to be equal to the average displacement of these points. After calculating the displacements using image analysis and drawing the relative displacement of two sides versus the number of cycles, it was observed that relative displacement increases linearly with an increase in the number of load cycles until the interface crack reaches the evaluation point. After this point the curve starts to deviate from the virtual line (Fig. 5). Romanoschi et al. [8] reported the same interface behavior under shear fatigue testing.

This deviation point is the failure point. By looking at the relative displacements versus the number of cycles at different positions along the interface, the crack tip can be tracked,

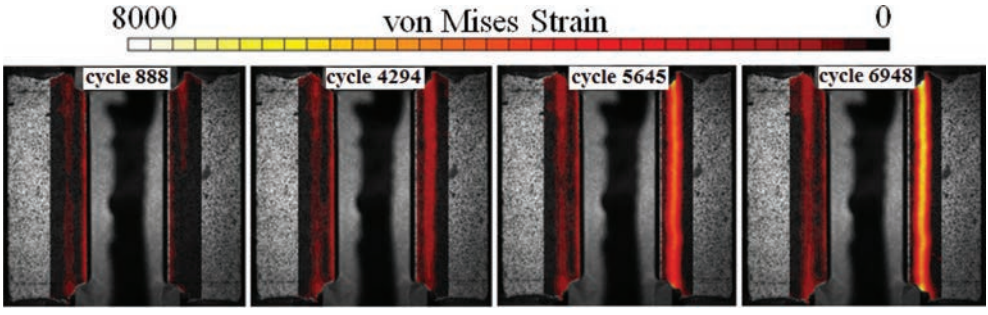

Figure 3. GGP2 shear specimen's von mises strain contour evolution.

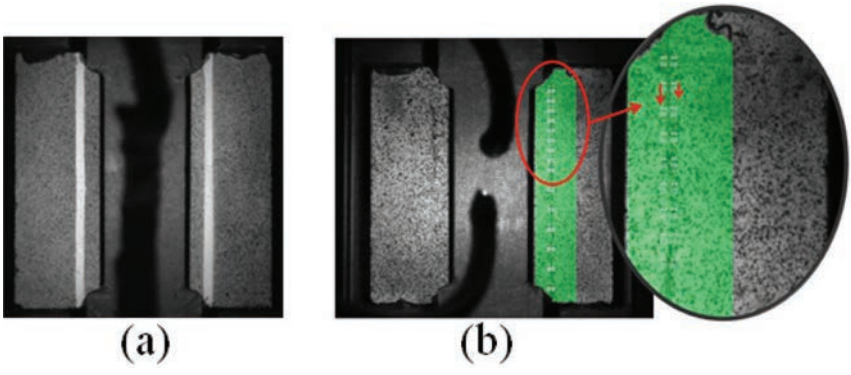

Figure 4. (a) White paint along the interlayers (the second approach) and (b) Virtual gauges defined at certain positions (third approach).

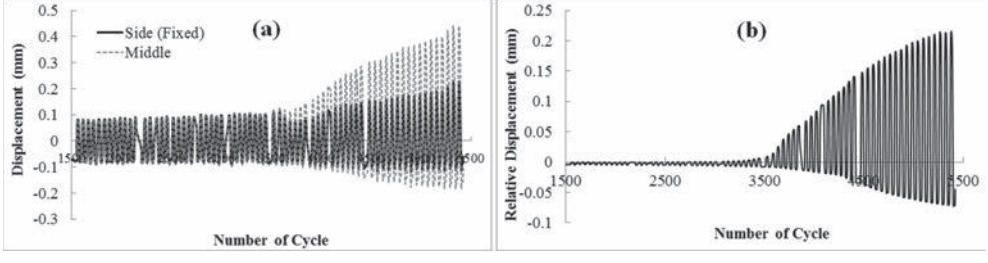

Figure 5. (a) Displacement and (b) Relative displacement of gauges located on opposite sides of the interface and at the same level.

and the crack growth rate and Paris law parameters can be found for each sample. Figure 6 displays an example of how this bisectional approach works.

5 RESULTS AND DISCUSSION

5.1 *Double shear test*

The bisectional approach was used to find the length of the cracks at different numbers of cycles for all the shear tests. Figure 7(a), and (b) shows the crack growth rate ($\Delta a/\Delta N$) versus

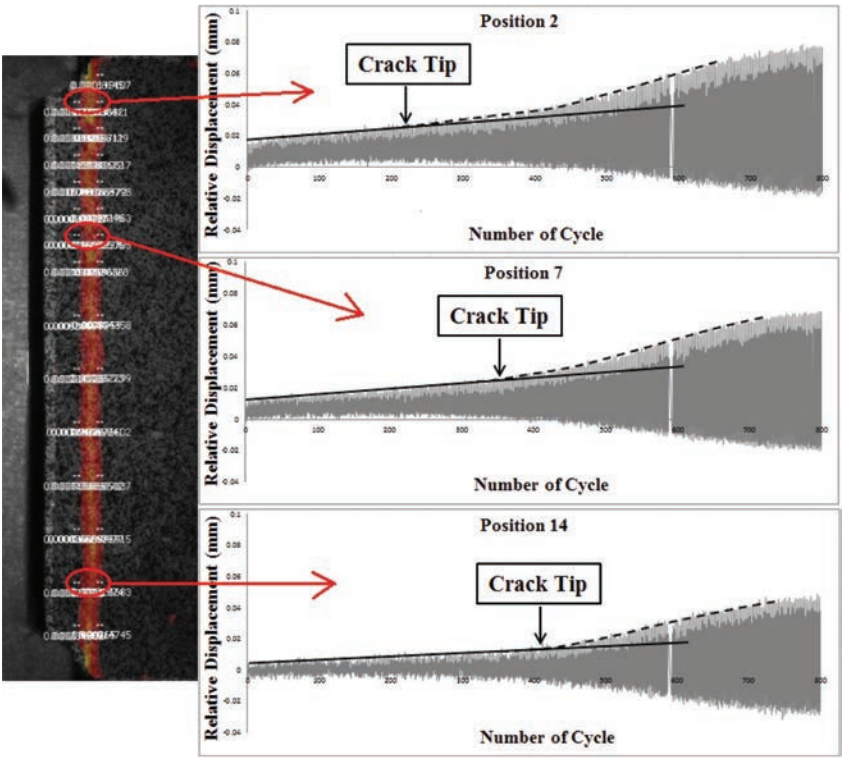

Figure 6. Bisectional approach for finding the crack tip.

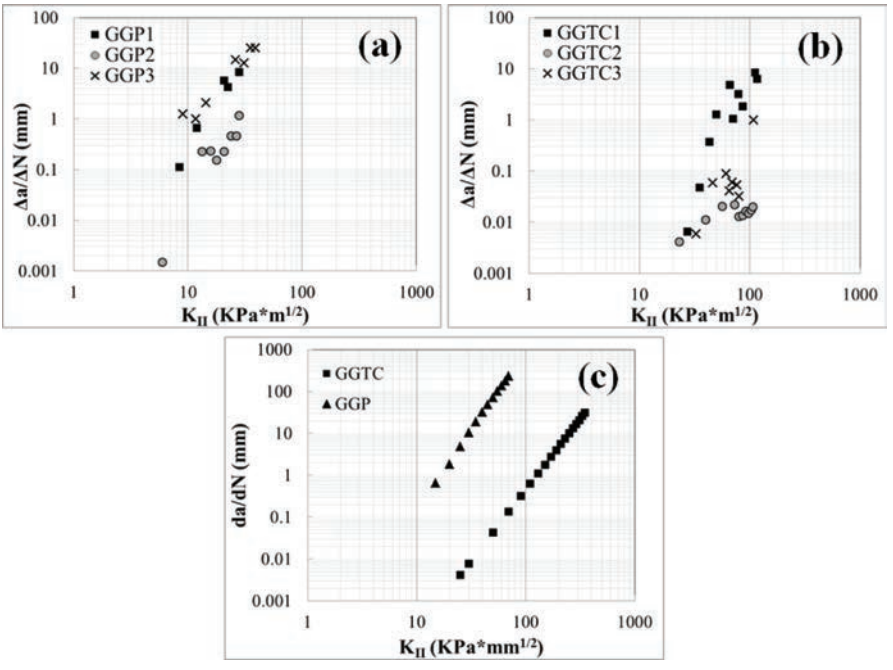

Figure 7. Measured crack growth rate for: (a) GGTC, (b) GGTF, and (c) GGP specimens, and (d) Fitted average crack growth rate for each interlayer condition.

the Mode II stress intensity factor (K_{II}) for all the replicates of the GGTC, and GGP specimen tests. All the results were fitted into the Paris law equation, Equation (2), using regression analysis. The fitting was performed separately for each specimen, and the average of the fitted data for each interlayer condition was calculated.

$$\frac{da}{dN} = A \cdot K_{II}{}^{n} \tag{2}$$

where a is the length of the crack, N is the number of cycles, K_{II} is the Mode II stress intensity factor, and A and n are the Paris law constants.

Figure 7(c) presents the fitted average crack growth length for each interlayer condition. This figure shows that the specimens with a tack coat (GGTC) have a much lower rate of crack growth comparing to the specimens without tack coat (GGP). This observation shows that existence and quality of tack coat can make a big difference in performance of reinforced interlayer.

5.2 *Four-point beam fatigue test*

In order to find the number of cycles to failure (N_f) for each beam fatigue test, the stiffness value times the number of cycles was plotted versus the number of cycles. The maximum or peak of the plotted curve was considered as the failure point. In some cases where no obvious peak was evident, the phase angle drop was used as the failure criterion. Figure 8 presents all the results for the number of cycles to failure versus the strain levels. By comparing the number of cycles to failure at different maximum strain levels, it was found that the GGTC specimens exhibit the best performance, and the numbers of cycles to failure for the GGP specimens are a little bit higher than those for the TC specimens. At the strain level of 1400 μstrain, it was observed that the use of GlasGrid with a tack coat (GGTC), and only GlasGrid (GGP) improved the fatigue life of the reference beam specimens (TC) by 82%, and 24%, respectively.

The DIC results were used for a deeper investigation of fatigue performance and reflective cracking in GlasGrid-reinforced asphalt concretes beams. The von Mises strain was calculated on the surface of the middle span of the beam specimens using VIC-2D software. A good understanding of the effects of the GlasGrid and interlayer conditions on crack propagation and reflective cracking mechanisms can be attained by looking at the strain contours during the tests.

The changes in the strain contours of beam specimens were monitored during the tests to see how the crack propagates across the beam. The GGP specimens showed very high strain levels around the interlayer area even before any cracks initiated at the bottom of the beams.

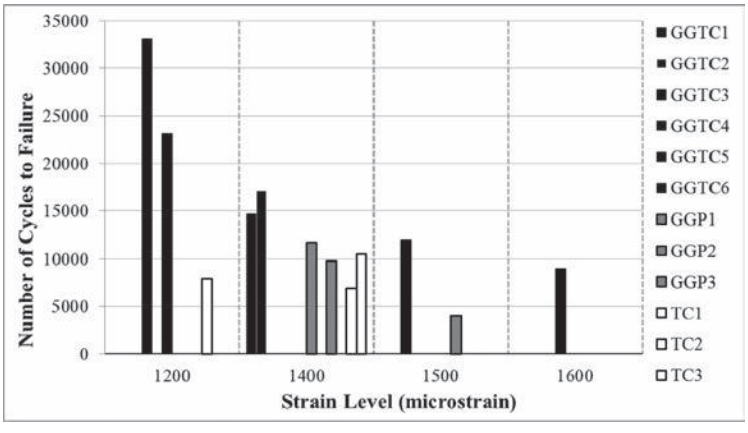

Figure 8. Number of cycle to failure vs. strain level for four-point beam fatigue tests.

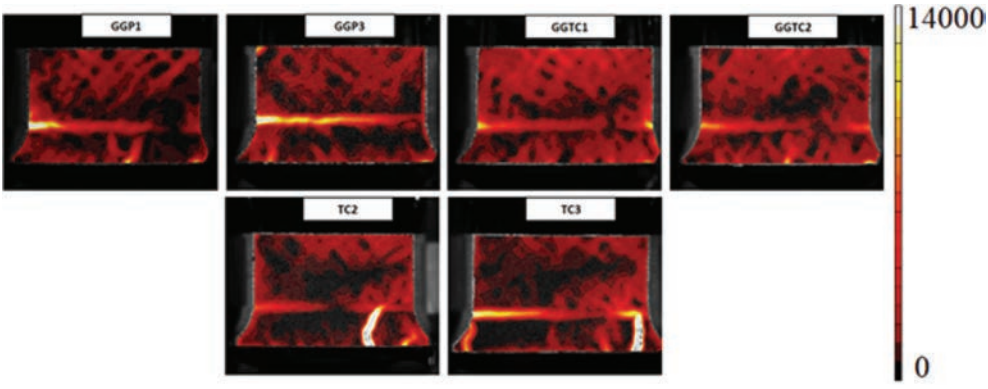

Figure 9. Von mises strain contours at cycle number 9000 (1400 μstrain).

For the GGTC specimens, in most cases the formation of high strain levels around the interface occurred simultaneously with the formation of bottom-up cracks, or in some cases, the interface strain levels started rising quickly after the bottom-up crack reached the interface. In all the GlasGrid-reinforced beam specimens, once the bottom-up crack reached the interface, it turned horizontally or joined the interface horizontal crack. So, it seems that GlasGrid is able to stop or delay the cracking and not allow it to penetrate the interlayer. However, in these cases a top-down crack formed and propagated downward toward the interlayer. Depending on the interlayer condition and maximum strain level, the formation of interface and top-down cracks took place either simultaneously with the formation of a bottom-up crack or after the bottom-up crack intersected with the interface. Similar types of crack propagation have been reported in previous studies [1, 9-11]. In all the non-reinforced beam specimens, it was observed that the bottom-up crack passed the interface and moved toward the top surface of the beam specimen.

In order to make it easier to compare the fatigue performance of beam specimens with different interlayer conditions, the von Mises strain contours of all the beam specimens subjected to a maximum strain level of 1400 μstrain at cycle of loading number 900 are shown in Figure 9. This figure shows an evenly distributed strain across the GGTC, high strains at the interface of the GGP, and bottom-up cracks penetrating the interface of TC specimens.

6 CONCLUSIONS

Based on the materials and methods used in this research, the following conclusions can be drawn:

- A DST and a bisectional crack tip determination approach were developed and used in this research for measuring the length of interface cracks under Mode II loading.
- The relative displacement of the opposite sides of the interface under Mode II repeated loading increases linearly until the interface cracks. At this point the relative displacement deviates from the line and starts growing faster.
- Under the same shear fatigue loading conditions, DST specimens that have GlasGrid and a tack coat have a much lower crack growth rate compared to specimens without a tack coat. This observation emphasizes the role that bond quality plays in interface fatigue shear resistance.
- Specimens with GlasGrid and a tack coat show the best performance in four-point bending beam fatigue tests. GlasGrid without a tack coat, and non-reinforced interface with a tack coat hold the next positions in the ranking, respectively.

- The strain contours determined from the four-point bending beam fatigue tests show that the bond quality between the layers is important in the development of interlayer cracks and slippage.
- Beam fatigue test strain contours show that specimens with GlasGrid and a tack coat have a more even distribution of strain and stress across the beam compared to the other interlayer conditions discussed in this paper. Also, the GlasGrid and no tack coat specimens show more even strain distributions comparing to the TC specimens.
- The results suggest that GlasGrid prevents reflective cracking by providing some constraints at the crack tip and turning the crack direction horizontally. Also, the results indicate that GlasGrid reduces the stress concentrations by means of transferring the load along the interface that becomes possible through the bonding provided by tack coat and interlocking between the GlasGrid and the aggregate.

REFERENCES

[1] Lytton, R.L. Use of Geotextiles for Reinforcement and Strain Relief in Asphalt Concrete. *Journal of Geotexiles and Geomembranes*, Vol. 8, 1989, pp. 217–237.

[2] Baek, J. *Modeling Reflective Cracking Development in Hot-Mix Asphalt Overlays and Quantification of Control Techniques*. Ph.D. dissertation, University of Illinois at Urbana-Champaign, Urbana, IL, 2010.

[3] Raab, C. and M.N. Partl. Effect of Tack Coat on Interlayer Shear Bond of Pavements. *Proceedings of the 8th Conference of Asphalt Pavements for Southern Africa* (CAPSA'04), Sun City, South Africa, 2004, pp. 847–855.

[4] Romanoschi, S. *Characterization of Pavement Layer Interfaces*. Ph.D. dissertation, Louisiana State University, Baton Rouge, LA. 1999.

[5] Canestrari, F., G. Ferrotti, M.N. Partl, and F. Santagata. Advanced Testing and Characterization of Interlayer Shear Resistance. *Transportation Research Record: Journal of the Transportation Research Board*, No. 1929, Transportation Research Board of the National Academies, Washington, D.C., 2005, pp. 69–78.

[6] Diakhate, M., A. Phelipot, A. Millien, and C. Petit. Shear Fatigue Behaviour of Tack Coats in Pavement. *Journal of Road Materials and Pavement Design*, Vol. 7, No. 2, 2006, pp. 201–222.

[7] Lee, J.S. Mechanical Performance and Crack Retardation Study of a Fiberglass-Grid-Reinforced Asphalt Concrete System. *Canadian Journal of Civil Engineering*, Vol. 35, Issue 10, 2008, pp. 1042–1049.

[8] Romanoschi S.A., and J.B. Metcalf. The Characterization of Asphalt Concrete Layer Interfaces. *Transportation Research Record: Journal of the Transportation Research Board*, No. 01-2080, Transportation Research Board of the National Academies, Washington, D.C., 2001.

[9] Kuo, C.M. and T.R. Hsu. *Traffic Induced Reflective Cracking on Pavements with Geogrid-Reinforced Asphalt Concrete Overlay*. Presented at the 82nd Transportation Research Board Annual Meeting, CD-ROM, Transportation Research Board of the National Academies, Washington, D.C., 2003, pp. 1–23.

[10] Khodaii, A., S. Fallah, and F. Moghadas Nejad. Effects of Geosynthetics on Reduction of Reflection Cracking in Asphalt Overlays. *Journal of Geotextiles and Geomembranes*, Vol. 27, 2009, pp. 1–8.

[11] Jayawickrama, P.W. and R.L. Lytton. Methodology for Predicting Asphalt Concrete Overlay Life Against Reflection Cracking. *Proceedings of the 6th International Conference on Structural Design of Asphalt Pavements*, Ann Arbor, Michigan, Volume I, 1987, pp. 912–924.

Asphalt Pavements – Kim (Ed)
© 2014 Taylor & Francis Group, London, ISBN 978-1-138-02693-3

Evaluating the effects of volumetric properties on the electrical resistivity characteristics of asphalt mixes

Seyed Arash Forough & Fereidoon Moghadas Nejad
Highway Division, Department of Civil and Environmental Engineering, Amirkabir University of Technology, Tehran, Iran

ABSTRACT: The relationships between the electrical resistivity characteristics, E_r, and the volumetric properties of asphalt mixtures, i.e., bulk specific gravity, G_{mb}, air voids in mixture, V_{bm}, and voids in mineral aggregates, V_{ma}, were investigated through a novel approach. To this end, 455 Marshall specimens containing calcareous crushed type stone aggregate with 60/70 penetration asphalt binder were fabricated and tested at five different aggregate gradations and seven bitumen contents with thirteen replicate specimens for each experimental combination. Statistical analysis of variance and significance tests were conducted on the test data and the effects of volumetric properties on the electrical resistivity of the specimens were evaluated. Finally, regression analysis method was used to develop some simple correlations between the two data sets.

Keywords: asphalt mixture, volumetric properties, electrical resistivity, simple correlation

1 INTRODUCTION

It is well known that the volumetric properties of asphalt mixes including bulk specific gravity, G_{mb}, air voids in mixture, V_{bm}, and voids in mineral aggregates, V_{ma}, are frequently used in the mix design process and/or as quality control measures during the construction operations. So far, many different methods have been proposed to measure the G_{mb} of compacted asphalt mixes among which the dimensional analysis method, as defined by AASHTO T269, water displacement or saturated surface dry method, as defined by ASTM D2726 or AASHTO T166, and paraffin coating method, as described by AASHTO T275, may be the most important ones. Then, V_{ma} may be calculated using the G_{mb} together with the bulk specific gravity of solids (G_{sb}) and binder content (P_b). In addition, to calculate the V_{bm} of an asphalt mixture, the maximum theoretical gravity, G_{mm}, of the mix must first be determined using the Rice method.

The present study was undertaken with the aim of proposing a novel testing method to determine the electrical resistivity of both the laboratory-fabricated or field-drilled asphalt mixture specimens [1], and to correlate the electrical resistivity, as a physical property, to all the mentioned volumetric properties of asphalt mixtures. Generally, electrical current may be conducted through a material in two ways: (1) the material, e.g. iron or copper, is a natural electrical conductor, in which the electrical current is conducted via numerous free electrons, (2) the material, e.g. cement paste, cement concrete or soil, is a natural electrical insulator (dielectric), but it may be changed to an electrical conductor using a chemical combination or an artificial method; thus, the electrical current is conducted electrolytically via the ionic conduction.

Asphalt mixture is a composite material, which comprises of the following constituents: (a) coarse and fine aggregates, (b) filler, (c) bitumen, (d) air, and (e) other additives such as anti-stripping agents [2]. Asphalt mixture, as a blend of aggregates and bitumen, is an electrical insulator (dielectric) with a high electrical resistivity of around 10^{13} Ohms. Thus, no free electrons exist in the mix to directly conduct the electrical current. However, if an asphalt mixture specimen becomes an electrical conductor by an artificial method, it is possible to

obtain its electrical resistivity within a reasonable range and to relate this electrical resistivity to the volumetric properties of the specimen [1].

Comparatively little work has been undertaken on the electrical properties of asphalt mixture, especially on the relation of electrical resistivity to its volumetric properties. Almost all the earlier work in this field has been undertaken on the electrical conductivity of asphalt mixtures containing electrically conductive materials such as basalt aggregate, limestone powder, carbon black, graphite particles and steel wool for generating heat by passage of an electrical current through the asphalt mixture to prevent the accumulation of frozen precipitation thereon [3]. It is theoretically feasible to improve the electrical conductivity of asphalt mixtures by the addition of electrically conductive additives to melt and remove snow and ice on asphalt pavement thermo-electrically [4, 5]. Furthermore, adding electrically conductive materials into an asphalt mixture has been previously used to monitor fatigue damage mechanism [6], softening temperature, storage modulus, damping capacity and electrical resistivity of modified asphalt mixture [7]. According to the previous studies [8, 9, 10], the electrical conductivity of the asphalt mixture is proportional to the concentration of electrically conductive additives.

Unlike the asphalt mixtures, various works have been undertaken on the electrical properties of cement mortars, cement pastes and even more on cement concretes, especially on the variation of electrical resistivity during the stages of initial setting and subsequent hardening [11, 12, 13, 14]. The conduction of electricity by moist concrete could be expected to be essentially electrolytic. The electrolytic conduction of moist concrete is linked to the circulation of fluid through the pore network [15]. Thus the electrical resistivity of concrete is sensitive to the volume of porosity and to the porous interconnectivity degree [16]. Moist concrete behaves essentially as an electrolyte with a resistivity of around 10^4 ohm-cm, a value in the range of semiconductors. Oven-dried concrete has a resistivity in the order of 10^{11} ohm-cm, a reasonably good insulator [17].

During this research, the conduction of electricity through the asphalt mixture specimens was performed similar to the electrolytically conduction of cement concrete. This aim was possible by saturating the interconnected air voids of the specimens using an electrolyte solution. Asphalt mixture, saturated by an electrolyte solution is electrically conductive by virtue of its interconnected pore network partially or fully filled with the electrolyte solution containing mobile ions. Thus, the electrical conductivity of such an asphalt mixture is related to the volume fraction of pores, the conductivity of pore solution and the interconnectivity of the porosity. In fact, the electrical resistivity is a measure of this interconnectivity.

2 EXPERIMENTAL PROGRAM

2.1 *Material properties*

Continuous aggregate gradation was used to comply with the gradation limits given by the Iran Highway Asphalt Paving Code [18] for wearing course. The gradations used in this study and the gradation limits are plotted in Figure 1.

The aggregates were calcareous type crushed stone obtained from the local resources. The filler was Portland cement (type II) with apparent specific gravity of 3.13 g/cm^3. The 60/70 penetration bitumen, corresponding to PG 64-16, obtained from a local oil refinery was used as binder for the specimen fabrication.

2.2 *Specimen fabrication*

The variables of bitumen content and aggregate gradation were selected to study in the experimental design. Seven bitumen contents of 3.5% to 6.5% in 0.5% increments and five different gradations form the coarsest, gradation 1, to the finest, gradation 5, as shown in Figure 1, were used to make 455 asphalt mixture specimens.

Thirteen replicate specimens (one replicate as the 1st group for the G_{mb} additional tests, five replicates as the 2nd group for the volumetric (G_{mb}, V_{bm}, and V_{ma}) tests, two replicates

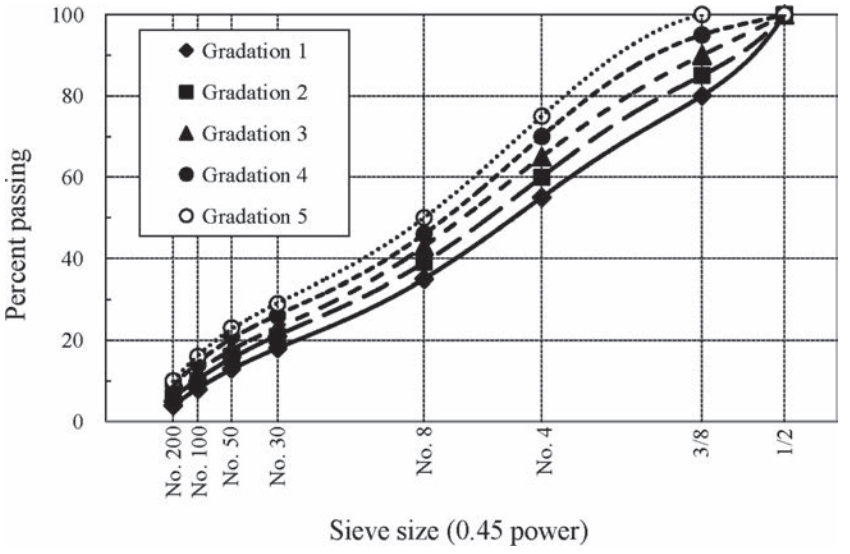

Figure 1. Aggregate gradations used in this study.

Table 1. Experimental design used in this study for testing.

Experimental variables	No. of levels	Variable levels
Bitumen content	7	3.5%, 4%, 4.5%, 5%, 5.5%, 6%, 6.5%
Aggregate gradation	5	The coarsest to the finest
Replication 1 (1st group)	1	G_{mb} additional tests
Replication 2 (2nd group)	5	Volumetric tests
Replication 3 (3rd group)	2	Saturating tests
Replication 4 (4th group)	5	Electrical resistivity tests

as the 3rd group for the saturating tests and five replicates as the 4th group for the electrical resistivity tests) were fabricated for each experimental combination. The experimental design used in this study is shown in Table 1.

Laboratory asphalt mixture specimens were fabricated in accordance with the Marshall mix design method in a laboratory environment, utilizing 75 blows representing heavy traffic conditions as specified in ASTM D1559-76 [19]. All the specimens were compacted using the same load by the standard Marshall hammer.

2.3 *Conducted tests*

2.3.1 *First group: G_{mb} additional tests*

To capture advantages of both the saturated surface dry and paraffin coating methods, all the specimens of the 1st group were tested for the G_{mb} using both methods. Afterwards, an adjusting factor was calculated for each experimental combination to convert the inaccurate result of saturated surface dry method to the accurate result of paraffin coating method.

2.3.2 *Second group: Volumetric tests*

The volumetric tests were carried out on the specimens of the 2nd group. To this end, all the specimens of the 2nd group were tested for the G_{mb} using the saturated surface dry method and the results were converted to the accurate G_{mb} of the paraffin coating method using

the adjusting factors of the previous section. Finally, all the specimens of the 2nd group were tested for the G_{mm} using the Rice method and both the properties of V_{bm} and V_{ma} were calculated.

2.3.3 *Third group: Saturating tests*

2.3.3.1 Electrical conduction through the specimens

Asphalt mixture, saturated in an electrolyte solution, becomes electrical conductor. The electrolyte solution, used in this study, was NaCl (sodium chloride in pure water). In addition, it was necessary to find the best concentration of the solution. For this purpose, different amounts of sodium chloride in 1 litter of pure water were examined, and it was found that 100 grams of sodium chloride in 1 litter of pure water (corresponding to the concentration of 9.1%) would be the minimum concentration for the solution by which the electrical resistance was readable for all the specimens.

2.3.3.2 Saturating the specimens

To saturate the interconnected V_{bm} of the specimens, they were immersed in the electrolyte solution under a high pressure. For this purpose, an apparatus was constructed. It consists of a pressure vessel equipped with a pressure gauge, an air-solution container, an air pump, two high pressure connective hoses, and a pressure control valve. Figure 2 shows configuration of the apparatus. The pressure vessel was capable to sustain a pressure less than or equal to 15 psi. Thus, the specimens of the 3rd group were placed in the pressure vessel filled by the NaCl solution under the pressure of 15 psi and the weight variations were monitored versus time. On the basis of weight variation as the controlling criterion, each specimen was expected to be saturated, when there was no more increase in its weight. It was found that all the specimens were saturated within 24 hours under this condition. If the pressure vessel was capable to sustain a pressure more than 15 psi, the required testing time would be decreased significantly.

2.3.4 *Fourth group: Electrical resistivity tests*

Electrical resistance tests were conducted on all the specimens of the 4th group at the saturated surface dry condition. Therefore, no electricity was allowed to conduct on the wet surface of the specimens. The tests were carried out using another apparatus constructed for this purpose. The apparatus consists of a mast frame, a main shaft, a rotational handle, a ring and

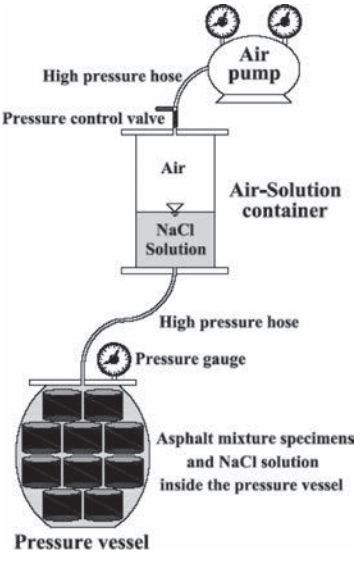

Figure 2. Configuration of the apparatus used for saturating the specimens under pressure of 15 psi.

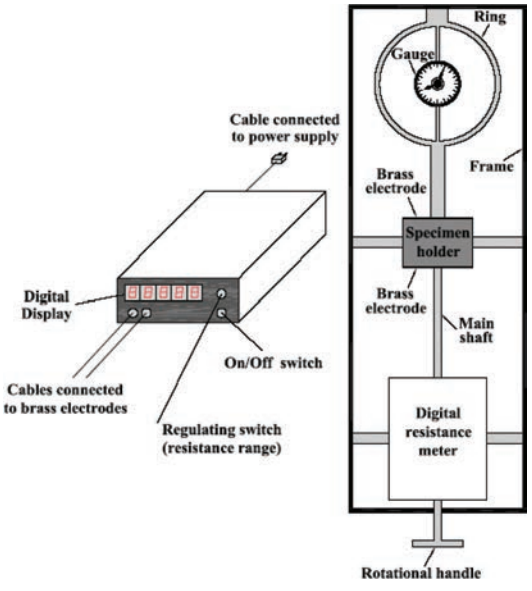

Figure 3. Configuration of the apparatus used for the electrical resistance measurements.

gauge set, a specimen holder, two electrodes, and a digital resistance-meter. Figure 3 shows configuration of the apparatus used in this study for the electrical resistance measurements.

The specimen holder can be used for either laboratory-fabricated or field-drilled specimens. The electrodes were made by brass with a diameter of 101.6 mm, equal to the diameter of the specimens. The main shaft was used to apply uniform axial compression on each side of the specimens through the brass electrodes by clockwise rotation of the handle. In addition, since the electrical resistance measurements should be carried out under the same conditions on all the specimens of the 4th group, the ring and gauge set was used to verify the equality of axial compression applied to the specimens. The measurement test set-up was done at room temperature of 25°C. To ensure a perfect contact between the electrodes and the specimens and to minimize the measurement error due to the jagged and rough texture of the asphalt mixture specimens, cement grout in a liquid-plastic form was used to fill the gaps between the electrodes and the specimens. It must be noted that the total contact resistance between the brass electrodes and the cement grout was less than 1 ohm, which was negligible with respect to the high resistance values, more than 1000 ohms, of the specimens. After the electrical resistance measurements, the electrical resistivity, E_r, of each specimen was obtained using the electrical resistance and dimensions, both the length in the current direction and the cross sectional area perpendicular to the current direction, of the specimen.

3 TESTS RESULTS AND DISCUSSION

3.1 *Volumetric test results*

Volumetric properties (G_{mb}, V_{bm}, and V_{ma}) of the specimens versus bitumen content, P_b, are shown in Figures 4 to 6 for the five selected gradations. These figures show the average results of the five replicate specimens for each experimental combination. Therefore, each figure represents the results of 175 specimens.

The test results on Figures 4 to 6 indicate that all the volumetric properties are sensitive to both the variables of aggregate gradation and bitumen content and they have very strong nonlinear quadratic relationships with these variables. All these observations are in agreement with the previous studies which are well established in the existing literature.

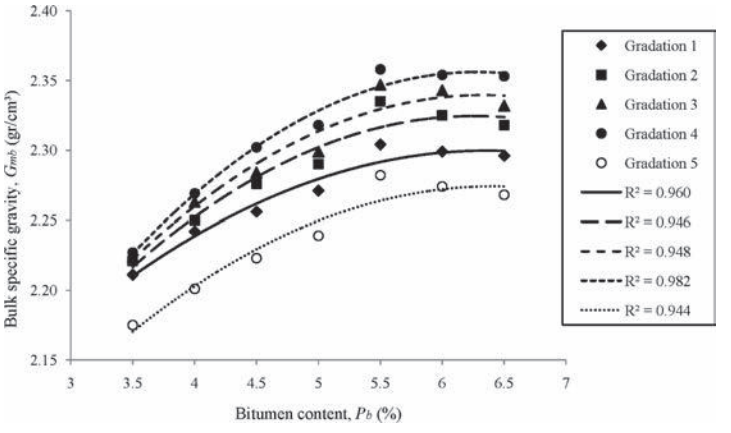

Figure 4. G_{mb} versus P_b for the five gradations.

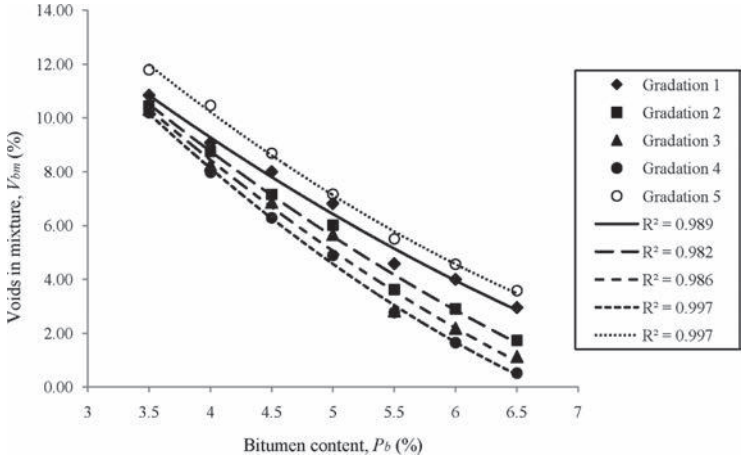

Figure 5. V_{bm} versus P_b for the five gradations.

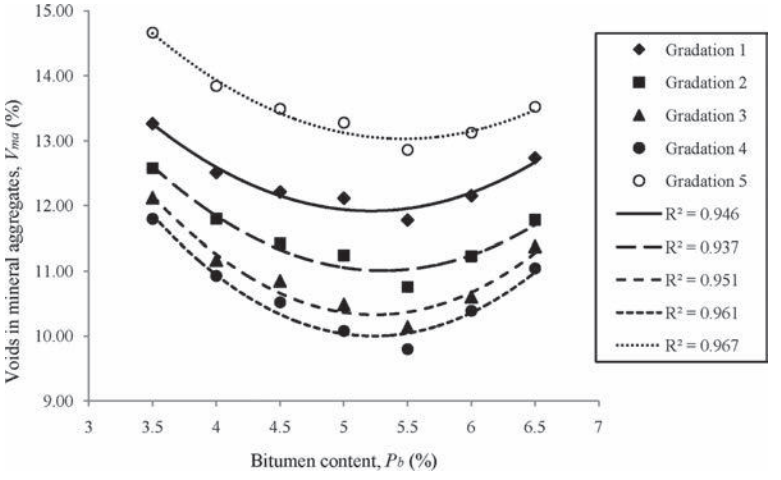

Figure 6. V_{ma} versus P_b for the five gradations.

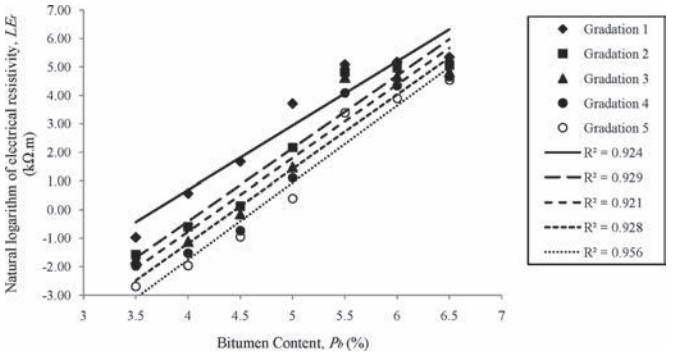

Figure 7. LE_r versus P_b for the five gradations.

3.2 *Electrical resistivity test results*

The electrical resistivity test results versus bitumen content, P_b, for the five gradations are shown in Figure 7. This Figure shows the average results of the five replicate specimens for each experimental combination. Therefore, it represents the results of 175 specimens. Because variation of the electrical resistivity values versus both the variables of aggregate gradation and bitumen content strongly follows an exponential pattern, it was decided to use natural logarithm of electrical resistivity, LE_r, instead of E_r in Figure 7. It is seen on Figure 7 that LE_r increases linearly as bitumen content increases under a constant gradation. This is because the interconnected V_{bm} and weight of the penetrating solution decrease as bitumen content increases under a constant gradation. In addition, it is clearly evident on Figure 7 that LE_r decreases linearly as gradation becomes finer from gradation 1 towards gradation 5 under constant bitumen content. As aggregate gradation becomes finer, the interconnected V_{bm} and weight of the penetrating solution decrease continuously; thus, LE_r is expected to increase. However, Figure 7 shows the results aren't in agreement with this expectation due to the following reason. The filler used in this study was cement which becomes an electrical conductor by the addition of water. Moreover, weight percent of the cement in the mixtures increases as aggregate gradation becomes finer. When the NaCl solution penetrates the asphalt mixture and combines with the cement, the electrical conductivity of the mixture increases and its electrical resistivity decreases. Therefore, as gradation becomes finer and weight percent of the filler increases, it seems the effect of high electrical conductivity of the combination of cement and water, in the initial setting phase before any hardening, is more significant on the electrical conductivity/resistivity of the asphalt mixture specimens. To examine this hypothesis, lime stone was used as a new filler to fabricate five extra specimens with the different gradations under a constant, 5.5%, bitumen content. The electrical resistance of these specimens were measured after saturating process. Unlike the previous trend for the specimens with the cement filler, the specimens having the lime stone filler showed more LE_r for the finer gradations than those for the coarser ones. In other words, based on the results of a limited laboratory experiment on the specimens with lime stone filler, it was realized that the effect of cement paste, in the initial setting phase before any hardening, prevails on the electrical conductivity/resistivity of the asphalt mixture specimens. However, more specimens with different aggregate gradations and bitumen contents are needed to investigate the real effects of lime stone filler on the electrical resistivity characteristics of asphalt mixtures and to reliably support the above hypothesis.

4 STATISTICAL ANALYSES

4.1 *Relationships between LE_r and the volumetric properties*

The volumetric test results versus LE_r for the five gradations are shown in Figures 8 to 10. It is seen on these figures that under a constant gradation, G_{mb} increases and V_{ma} decreases

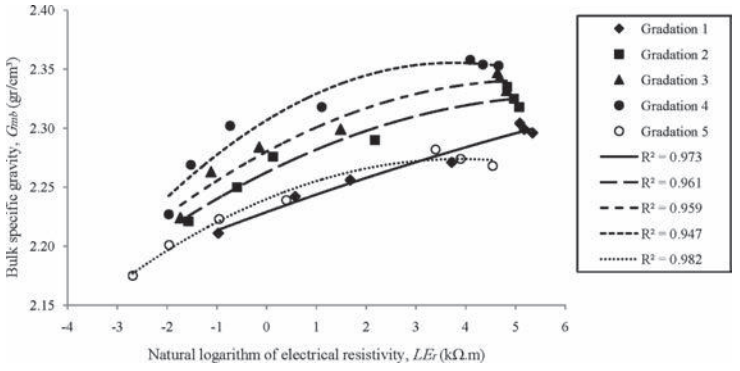

Figure 8. G_{mb} versus LE_r for the five gradations.

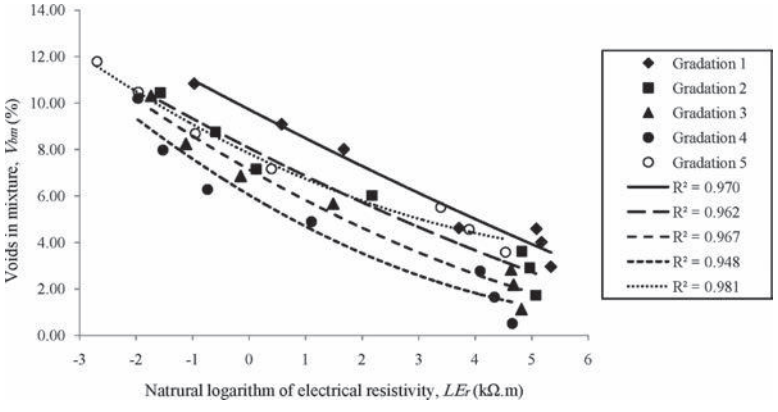

Figure 9. V_{bm} versus LE_r for the five gradations.

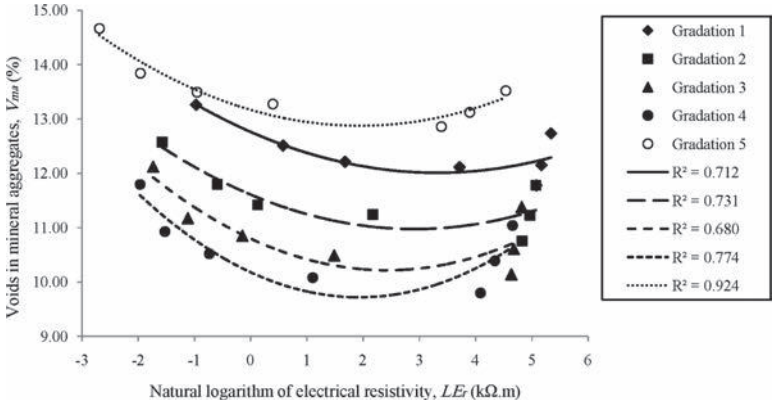

Figure 10. V_{ma} versus LE_r for the five gradations.

as LE_r increases up to a peak point and then as LE_r increases again, G_{mb} decreases and V_{ma} increases. However, under a constant gradation, V_{bm} decreases continuously as LE_r increases. These results show again that there is a significant direct linear relationship between bitumen content, P_b, and LE_r. On the other hand, as gradation becomes finer from gradation 1 towards gradation 4 under constant LE_r, G_{mb} increases and both the properties of V_{ma}

and V_{bm} decrease. Afterwards, as gradation becomes finer again from gradation 4 towards gradation 5, G_{mb} decreases and both the properties of V_{ma} and V_{bm} increase suddenly.

The test results on Figures 8 to 10 indicate that all the volumetric properties are sensitive to LE_r and they have very strong nonlinear quadratic relationships with this physical property of the asphalt mixtures.

Because of very strong nonlinear quadratic relationships between LE_r and the volumetric properties, Pearson linear correlation method cannot be used to determine the nonlinear correlation coefficients. Thus, the relationships between LE_r and all the volumetric properties are evaluated using the statistical analysis of variance (ANOVA) and significance tests. To this end, one-way ANOVA was conducted at 95% confidence level on G_{mb}, V_{bm}, and V_{ma} using the SPSS statistical package. The Fisher numbers and the probability of significance for LE_r at the given confidence level were calculated for each volumetric property and presented in Table 2.

It is understood from Table 2 that all the relationships between LE_r and the volumetric properties are significant at 95% confidence level. The significance levels can be compared for the volumetric properties using the calculated Fisher numbers. It is seen that V_{bm} is the most affected property by LE_r followed by the G_{mb} and the V_{ma}, respectively. In other words, the V_{bm} is strongly dependent on the LE_r having the largest Fisher number, 30.264, among the other volumetric properties. Similarly, the G_{mb} also proves a strong dependence on the LE_r and LE_r shows also a significant influence on the V_{ma} at 95% confidence level.

4.2 *Correlations between LE_r and the volumetric properties*

Regression analyses were carried out on the test data to develop simple correlations between LE_r and all the volumetric properties. Because variations of all the volumetric properties

Table 2. ANOVA for the volumetric properties at 95% confidence level.

	LE_r	
Property	F	Prob > F
G_{mb}	30.264	0.000
V_{bm}	76.225	0.000
V_{ma}	3.464	0.043

Table 3. Regression analysis for each correlation.

Property	Grad.	a	b	c	R^2
	1	–0.0004	0.015	2.229	0.973
	2	–0.0017	0.021	2.263	0.961
G_{mb}	3	–0.0021	0.023	2.280	0.959
	4	–0.0034	0.026	2.307	0.947
	5	–0.0022	0.017	2.240	0.982
	1	0.020	–1.258	9.718	0.970
	2	0.034	–1.236	8.060	0.962
V_{bm}	3	0.064	–1.381	7.136	0.967
	4	0.099	–1.452	6.038	0.948
	5	0.080	–1.178	7.826	0.981
	1	0.068	–0.454	12.761	0.712
	2	0.075	–0.434	11.608	0.731
V_{ma}	3	0.099	–0.478	10.796	0.680
	4	0.124	–0.476	10.177	0.774
	5	0.078	–0.302	13.166	0.924

versus LE_r strongly follow nonlinear quadratic patterns and due to the fact that LE_r has significant effects on all the volumetric properties, it was decided to develop simple correlations between LE_r and the volumetric properties for each gradation based on the general quadratic formulation of $a(LE_r)^2 + b(LE_r) + c$. Table 3 shows regression coefficients and coefficients of determination for correlation.

5 CONCLUSION

This study was to evaluate the relationships between electrical resistivity and volumetric properties of asphalt mixtures, i.e. G_{mb}, V_{bm}, and V_{ma}. To this end, all the volumetric properties were determined at various aggregate gradations and bitumen contents, and the electrical resistivity of each specimen was measured using a novel testing method. Correlation analysis, statistical analysis of variance and significance tests were performed on the test data, and simple correlations were formed between the natural logarithm of electrical resistivity, LE_r, and the volumetric properties for each gradation.

While the correlations developed for the tested specimens were characterized by high coefficients of determination, general application of these correlations to asphalt mixes having aggregate types, gradations, and absorptions, filler types, and bitumen types different than those tested would not likely yield accurate results. More research is needed to account for the effects of these important variables.

REFERENCES

[1] Forough, S.A. Predicting the Results of Marshall Test Using the Electrical Resistivity of Asphalt Mixtures, M.Sc. Thesis, Amirkabir University of Technology (Polytechnic of Tehran), Iran. 2002.

[2] Walubita, L.F. Comparison of Fatigue Analysis Approaches for Predicting Fatigue Lives of Hot-Mix Asphalt Concrete (HMAC) Mixtures, PhD Dissertation, Texas A&M University, College Station, Texas, USA. 2006.

[3] Zaleski, P.L. Derwin, D.J. Flood J.R. and Walter. H. Electrically conductive paving mixture, United States Patents, N. 20040062606. 2004.

[4] Shaopeng, W. Liantong, M. Zhonghe, S. and Zheng, C. Investigation of the conductivity of asphalt concrete containing conductive fillers, Carbon, 43(7), pp. 1358–1363. 2005.

[5] García, Á. Schlangen, E. van de Ven, M. and Liu, Q. Electrical conductivity of asphalt mortar containing conductive fibers and fillers, Construction and Building Materials, 23(10), pp. 3175–3181. 2009.

[6] Shaopeng, W. Xiaoming, L. Liantong, M. and Qunshan, Y. Research of self-monitoring mechanism of electrically conductive asphalt-based composite, Key Engineering Materials, 236–328(2), pp. 1499–1502. 2006.

[7] Sihai, W. and Chung, D.D.L. Effects of carbon black on the thermal, mechanical and electrical properties of pitch-matrix composites, Carbon, 42(12–13), pp. 2393–2397. 2004.

[8] Wu, S.P. Mo, L.T. and Shui, Z.H. Improvement of electrical properties of asphalt concrete, Journal of Wuhan. University of Technology, M.Sc. Thesis, 17(4), pp. 69–72. 2002a.

[9] Wu, S.P. Mo, L.T. and Shui, Z.H. Preparation of electrically conductive asphalt concrete, Journal of Wuhan. University of Technology, Transportation and Engineering. 26(5), pp. 566–569. 2002b.

[10] Wu, S.P. Mo, L.T. and Shui, Z.H. Piezoresistivity of graphite modified asphalt-based composites, Key Engineering Materials, 249, pp. 391–5. 2003.

[11] Li, Z. Xiao, L. Xiaosheng, W. Determination of concrete setting time using electrical resistivity measurement, Journal of Materials in Civil Engineering, 19(5), pp. 423–427. 2007.

[12] Sengul, O. and Gjrv, O.E. Electrical resistivity measurements for quality control during concrete construction, ACI Materials Journal, 105(6), pp. 541–547. 2008.

[13] Xiao, L. and Li, Z. Early-age hydration of fresh concrete monitored by non-contact electrical resistivity measurement, Cement and Concrete Research, 38(3), pp. 312–19. 2008.

[14] Koleva, D.A. Copuroglu, O. van Breugel, K. Ye, G. and de Wit, J.H.W. Electrical resistivity and microstructural properties of concrete materials in conditions of current flow, Cement and Concrete Composites, 30(8), pp. 731–744. 2008.

[15] Lataste, J.F. Sirieix, C. Breysse, D. and Frappa, M. Electrical resistivity measurement applied to cracking assessment on reinforced concrete structures in civil engineering, NDT & E International, 36(6), pp. 383–394. 2003.
[16] Andrade, C. Alonso, C. Arteaga, A. and Tanner, P. Methodology based on the electrical resistivity for calculation of reinforcement service life, Fifth CANMET/ACI International Conference, USA, pp. 899–915. 2000.
[17] Malhotra, N. and Carino, J. Handbook on nondestructive testing of concrete, Chapter 10 (Magnetic/Electrical Methods), Taylor & Francis Ltd CRC Press LLC. 2004.
[18] Iran Highway Asphalt Paving Code, Ministry of Road and Transportation Research and Education Center, Pub. No. 234, Iran. 2011.

This page intentionally left blank

Asphalt Pavements contains the proceedings of the International Conference on Asphalt Pavements (Raleigh, North Carolina, USA, 1-5 June 2014), and discusses recent advances in theory and practice in asphalt materials and pavements. The contributions cover a wide range of topics:

- Environmental protection and socio-economic impacts
- Additives and modifiers for asphalt concrete
- Maintenance and rehabilitation
- Experimental characterization of asphaltic materials
- Life cycle cost analysis/modeling of compaction in the laboratory and in the field
- Perpetual pavements
- Pavement management systems
- Sustainable asphalt technologies
- Nondestructive testing of asphalt pavement
- Pavement condition survey/pavement smoothness/quality control/quality assurance
- Microstructural characterization and micromechanics of asphaltic materials
- Long-term pavement performance prediction
- Mineral aggregate in asphalt concrete/mix design methodology/novel methods to aid mix design
- Warm mix asphalt technologies
- Innovative pavement analysis and design
- Pavement response analysis under static and moving wheel loads
- Recycling
- Modeling of asphaltic materials and pavements
- Microstructural characterization and micromechanics of asphalt materials
- Asphalt pavement and environment
- Performance-related specifications

Asphalt Pavements will be of interest to academics and professional involved in asphalt engineering.

CRC Press
Taylor & Francis Group
an informa business
www.crcpress.com

6000 Broken Sound Parkway, NW
Suite 300, Boca Raton, FL 33487
Schipholweg 107C
2316 XC Leiden, NL
2 Park Square, Milton Park
Abingdon, Oxon OX14 4RN, UK

ISBN 978-1-138-02693-3

an informa business